

THE
JOURNAL OF
PHYSICS
AND
CHEMISTRY
OF SOLIDS

AN
INTERNATIONAL
JOURNAL

PERGAMON PRESS

NEW YORK • OXFORD • LONDON • PARIS

VOLUME 32

NUMBER 5

MAY 1971

Editor-in-Chief
HARVEY BROOKS
Cambridge, Mass.

Associate Editors

H. B. G. CASIMIR
Eindhoven

B. CHALMERS FRAZER
and
DAVID E. COK
Brookhaven

JACQUES FRIEDEL
Paris

I. M. LIFSHITZ
Khar'kov

THE JOURNAL OF PHYSICS AND CHEMISTRY OF SOLIDS

Editors

- PROF. HARVEY BROOKS (*Editor-in-Chief*), 217 Pierce Hall, Harvard University, Cambridge 38, Mass., U.S.A.
 PROF. DR. H. B. G. CASIMIR, *N.V. Philips' Gloeilampenfabrieken, Eindhoven, The Netherlands*
 DR. B. CHALMERS FRAZER and DR. DAVID E. COX (*Assistant Editor*), Brookhaven National Laboratory, Upton, Long Island, New York, U.S.A.
 PROF. JACQUES FRIEDEL, *Laboratoire de Physique des Solides, Bâtiment 210, Faculté des Sciences, 91-Orsay, France*
 PROF. I. M. LIFSHITZ, *Chief, Theoretical Department, Institute of Physical Problems, Moscow V-334, Vorobevskoe Shosse 2, U.S.S.R.*

Editorial Advisory Board

U.S.A.

E. N. ADAMS, White Plains, N.Y.
 D. ALPERT, Urbana, Ill.
 L. APKER, Schenectady, N.Y.
 J. BARDEEN, Urbana, Ill.
 D. S. BILLINGTON, Oak Ridge, Tenn.
 R. G. BRECKENRIDGE, Canoga Pk., Calif.
 LEO BREWER, Berkeley, Calif.
 E. BURSTEIN, Philadelphia, Penn.
 J. A. BURTON, Murray Hill, N.J.
 N. CABRERA, Charlottesville, Va.
 G. C. DANIELSON, Ames, Iowa
 G. J. DIENES, Long Island, N.Y.
 J. C. FISCHER, Schenectady, N.Y.
 H. K. HENISCH, University Park, Penn.
 F. HERMAN, San Jose, Calif.
 C. HERRING, Murray Hill, N.J.
 A. R. VON HIPPEL, Cambridge, Mass.
 J. H. HOLLOMON, Norman, Okla.
 W. V. HOUSTON, Houston, Texas
 H. B. HUNTINGTON, Troy, N.Y.
 H. M. JAMES, Lafayette, Ind.
 C. KITTEL, Berkeley, Calif.
 W. KOHN, La Jolla, Calif.
 J. A. KRUMHANS, Ithaca, N.Y.
 A. W. LAWSON, Riverside, Calif.
 H. W. LEVERENZ, Princeton, N.J.
 O. T. MARZKE, Pittsburgh, Penn.
 B. T. MATTHIAS, La Jolla, Calif.
 L. R. MAXWELL, Silver Spring, Md.
 J. E. MAYER, La Jolla, Calif.
 J. W. MITCHELL, Charlottesville, Va.
 E. W. MONTROLL, Rochester, N.Y.
 D. PINES, Urbana, Ill.
 M. H. L. PRYCE, Los Angeles, Calif.
 G. T. RADO, Washington, D.C.

H. REISS, Thousand Oaks, Calif.
 J. R. REITZ, Dearborn, Mich.
 A. ROSE, Princeton, N.J.
 R. A. SMITH, Cambridge, Mass.
 R. SMOLUCHOWSKI, Princeton, N.J.
 F. H. SPEDDING, Ames, Iowa
 J. TAUC, Providence, R.I.
 D. TURNBULL, Cambridge, Mass.
 J. H. VAN VLECK, Cambridge, Mass.
 B. E. WARREN, Cambridge, Mass.
 E. P. WIGNER, Princeton, N.J.
 B. H. ZIMM, La Jolla, Calif.

A. HERPIN, Gif-sur-Yvette
 B. JACROT, Grenoble
 LOUIS NÉEL, Grenoble

Germany

ULRICH DEHLINGER, Stuttgart
 R. HILSCH, Göttingen
 G. LEIBFRIED, Aachen
 E. MOLLWO, Erlangen
 H. PICK, Stuttgart
 W. WELKER, Erlangen

Israel

I. ESTERMANN, Haifa

Italy

F. G. FUMI, Genova

Japan

TOSHINOSUKE MUTO, Tokyo

The Netherlands

G. W. RATHENAU, Eindhoven

Sweden

J. O. LINDE, Stockholm
 PER-OLOF LÖWDIN, Uppsala

Switzerland

G. BUSCH, Zurich

U.S.S.R.

G. S. ZHDANOV, Moscow

Canada

R. E. BURGESS, Vancouver
 W. B. PEARSON, Ottawa

United Kingdom

A. CHARLESBY, Shrivensham, Berks.
 W. J. DUNNING, Bristol
 F. C. FRANK, Bristol
 H. JONES, London
 A. B. PIPPA, Cambridge
 O. C. SIMPSON, Baldock, Herts.
 K. W. H. STEVENS, Nottingham
 F. C. TOMPKINS, London

Czechoslovakia

B. VELICKY, Prague

France

E. F. BERTAUT, Grenoble
 J. BOK, Paris
 B. DREYFUS, Grenoble
 A. GUINIER, Orsay

Publishing and Advertising Offices

American Continent: Pergamon Press Inc., Maxwell House, Fairview Park, Elmsford, N.Y. 10523.

Rest of the World: Pergamon Press Ltd., Headington Hill Hall, Oxford OX3 0BW, England.

Published monthly. Annual subscription for libraries, research establishments and all other multiple-reader institutions, £60 (\$150.00); private individuals, whose departmental libraries subscribe, may obtain this Journal for their personal use at a reduced price of £10 (\$25.00) per annum, including postage. All subscription enquiries are to be addressed to The Manager, Subscriptions Department, Pergamon Press, Headington Hill Hall, Oxford OX3 0BW, England. Back issues are available, write for Back Issues Price Lists.

Copyright © 1971 Pergamon Press Ltd.

PERGAMON PRESS

MAXWELL HOUSE, FAIRVIEW PARK, ELMSFORD, N.Y. 10523

HEADINGTON HILL HALL, OXFORD OX3 0BW

INTERNATIONAL JOURNAL OF
SOLIDS &
STRUCTURES

Editor-in-Chief
George Herrmann
Stanford University

contents of a recent issue

F. R. NORWOOD: Interior motion of an elastic half-space due to a normal finite moving line load on its surface

NORMAN JONES, T. O. URAN and S. A. TEKIN: The dynamic plastic behavior of fully clamped rectangular plates

O. W. DILLON, JR. and J. KRATOCHVIL: A strain gradient theory of plasticity

G. P. SENDECKYJ: Elastic inclusion problems in plane elastostatics

L. M. KERR and C. SVE: On the bending of cracked plates

**Published Monthly—
£30.00 (\$75.00)**

**Order your subscription
now from:**

**Robin Dean,
Dept. ED.
Pergamon Press,
Oxford.**

THE INSTITUTE OF PHYSICS
LONDON & BRISTOL

GaAs

Conference Series No. 9
A comprehensive report of the proceedings of the Third Gallium Arsenide Symposium held in Aachen last October

SBN 85498014 8 Price £6.25 SPRING 1971

Orders should be sent to: Dawsons of Pall Mall, Cannon House, Park Farm Road, Folkestone, Kent

Remember also Journal of Physics C (Solid State Physics) Journal of Physics F (Metal Physics). Further details from The Institute of Physics, 1 Lowther Gardens, Prince Consort Road, London SW7

.... ARE THESE
JOURNALS IN
YOUR LIBRARY?

ELECTROCHIMICA ACTA
INFRARED PHYSICS
MATERIALS RESEARCH BULLETIN
PHYSICS OF METAL &
METALLOGRAPHY

WRITE FOR DETAILS TO:
DEPT. E. D.,
PERGAMON PRESS
OXFORD.....

journal of the mechanics and physics of solids

Editor-in-chief: PROFESSOR H. G. HOPKINS, Institute of Science and Technology,
University of Manchester, England.

An international journal of the theoretical and applied mechanics and the physics of solids. It provides a forum of research for those mathematicians, engineers, metallurgists and physicists who are working on establishing the properties of constructional materials. This journal gives equal coverage to both theory and experiment, but it is particularly concerned with the development and application of fundamental ideas bearing on the connections between continuum and microstructural properties of materials and on the solution of practically significant problems.

The Journal of the Mechanics and Physics of Solids is therefore of particular interest to applied mathematicians, physical metallurgists, metal physicists and engineers, to research institutes, and to those in the engineering and metallurgical industries.

Papers appearing in a recent issue of the journal:

The upper bound theorem for rigid/plastic solids generalized to include Coulomb friction
I.F. COLLINS

On mathematical forms for the material functions in non-linear viscoelasticity
R.O. STAFFORD

Some constitutive equations applicable to problems of large dynamic plastic deformation
J.R. WILLIS

Stress-intensity factors at the tips of a star-shaped contour in an infinite tensile sheet
H. ANDERSSON

Spherical wave propagation in elastic-plastic work-hardening materials
L.W. MORLAND

Thermal stresses in fibre reinforced composites
A.R.T. de SILVA and G.A. CHADWICK

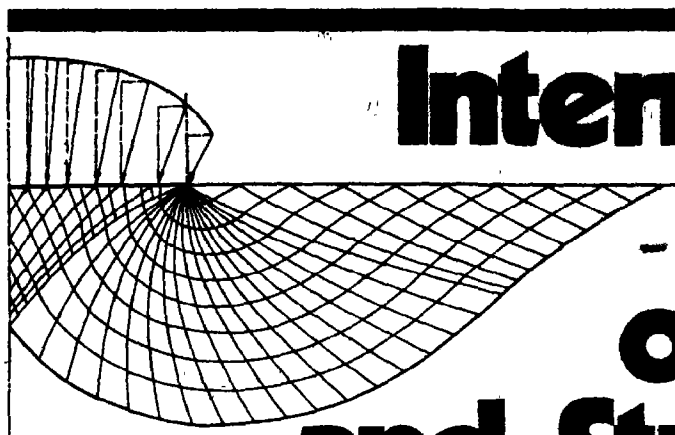
Published Bi-monthly

Please write now for subscription rates, a free inspection copy of the journal, and details of related journals.



Pergamon Press

OXFORD : LONDON : NEW YORK
PARIS : SYDNEY : TORONTO



International Journal of Solids and Structures

Editor-In-Chief

George Herrmann

School of Engineering Stanford University

Stanford California USA

This journal has as its objective the publication and dissemination of original research in Mechanics of Solids and Structures as a field of Applied Science and Engineering.

Standing as it does at the cross-roads of Materials Science, Mathematics, Physics and Engineering Design, the Mechanics of Solids and Structures is experiencing considerable growth as a result of recent technological advances. The Journal, by providing an international medium of communication, is encouraging this growth and is encompassing all aspects of the field from the more classical problems of structural analysis to mechanics of solids continua interacting with other media, and including fracture, flow, wave propagation, heat transfer, thermal effects in solids, optimum design methods, model analysis, structural topology and numerical techniques.

The emphasis is placed on contributions, both analytical and experimental, which appear to be of permanent interest to research workers and engineers in the field.

Papers from a recent issue include:

T.A. Cruse: Numerical solutions in three dimensional elastostatics

J. Lubliner and M. Valathur: Some wave-propagation problems in plastic-viscoplastic materials

H. Neuber: Anisotropic nonlinear stress-strain laws and yield conditions

Y.R. Rashid: Three-dimensional analysis of elastic solids—I. Analysis procedure

A.P. Sinitsyn: Vibrations and stability of shells due to loads and temperature

Published monthly

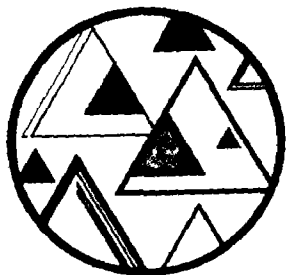
Please write now for subscription rates, a free inspection copy of this journal and details of related publications.



Pergamon Press

OXFORD · NEW YORK · TORONTO · SYDNEY · BRAUNSCHWEIG

1/70



are these important journals in your library?

Acta Metallurgica and Scripta Metallurgica

Editor:
PROFESSOR BRUCE CHALMERS
Harvard University
Cambridge Massachusetts 02138
USA

Sponsored by: The American Society for Metals
The American Institute of Mining, Metallurgical and
Petroleum Engineers
The American Society for Testing and Materials

ACTA METALLURGICA is an international journal for the science of metallic and non-metallic solids
It provides a medium for the publication of papers describing theoretical and experimental investigations that contribute to the understanding of the properties and behaviour of metals in terms of fundamental particles, forces and energies. Emphasis is placed on those aspects of the science of materials that are concerned with the relationship between the structure of solids and their properties

SCRIPTA METALLURGICA, the companion volume, is concerned with the same subject matter but provides a medium for shorter papers and letters which demand a more rapid publication process. Abstracts of both journals are in the original language of publication as well as English, French and German.
Both published monthly

Journal of Physics and Chemistry of Solids

Editor-in-Chief:
PROFESSOR HARVEY BROOKS
Harvard University
Cambridge Massachusetts 02138
USA

The purpose of this journal is to provide an international medium of publication in the field of solid state: the fields of interest are the statistical mechanics of condensed systems. As an international medium, the journal accepts manuscripts in French and German, as well as English. Short communications may be published as Technical Notes. While the Journal publishes both experimental and theoretical papers it is generally interested in experimental papers only to the extent that they can throw light on fundamental processes and theories. *Preference is given in publication to work on well-characterised materials, such as single crystals*
Published monthly

Solid State Communications

Editor-in-Chief:
PROFESSOR ELIAS BURSTEIN
University of Pennsylvania
Philadelphia Pennsylvania USA

A Supplement to the Journal of Physics and Chemistry of Solids
SOLID STATE COMMUNICATIONS is the international medium for the rapid publication of short communications on important developments in the solid sciences. The primary aim of the Journal is to give scientists working in this field immediate access to important work just completed. In keeping with this aim the Journal also publishes short versions of important papers being submitted to national journals

Inspection Copies

Inspection copies of all Pergamon Learned Journals are available on request from Dept. ED (t), Pergamon Press, Oxford.



Pergamon Press

Headington Hill Hall Oxford OX3 0BW
Maxwell House Fairview Park Elmsford New York 10523 USA
Pergamon House 19a Boundary Street Rushcutters Bay NSW 2011 Australia

THE JOURNAL OF PHYSICS AND CHEMISTRY OF SOLIDS

VOLUME 32 NUMBER 5

1971

MAY

CONTENTS

J. P. DISMUKES, R. T. SMITH and J. G. WHITE: Physical properties and crystal structure of a new semiconducting I-III-VI ₂ compound, CuScS ₂	913
J. S. ANDERSON and R. BURCH: Lattice energies and heats of formation of the Ti ₂ O _{2n-1} shear phases	923
W. F. SCHLOSSER, G. M. GRAHAM and P. P. M. MEINCKE: The temperature and magnetic field dependence of the forced magnetostriction and thermal expansion of Invar	927
W. F. SCHLOSSER: A model for the Invar alloys and the Fe-Ni system	939
S. N. VAIDYA and G. C. KENNEDY: Compressibility of 27 halides to 45 kbar	951
F. P. LARKINS: Electronic structure of the isolated vacancy in silicon	965
L. M. LEVINSON and S. SHTRIKMAN: Theory of elastic stiffness <i>c</i> ₃₃ of gadolinium in the spin rotation region	981
S. K. GUPTA and M. L. NARCHAL: Dynamic orientation by saturation of forbidden transitions	993
V. G. BHIDE and M. K. BAHL: X-ray <i>K</i> -absorption studies of niobium selenides and tellurides	1001
T. TAKAHASHI, K. MINEMATSU and K. MIYATANI: Single crystal growth and some properties of HgCr _{2-<i>x</i>} In _{<i>x</i>} Se ₄ solid solutions	1007
R. BENEDEK and A. BARATOFF: The influence of lattice strain on the electrical resistivity of vacancies in simple metals	1015
P. BRÜESCH and C. SCHÜLER: Raman and infrared spectra of crystals with α-NaFeO ₂ structure	1025
J. E. GREEDAN: Electrical resistivity and optical absorption in EuLiH ₃ and SrLiH ₃	1039
A. J. HENDERSON, JR., H. MEYER and H. J. GUGGENHEIM: The specific heat of RbMnF ₃ and MnF ₂ between 0.5 and 4.2°K	1047
B. WINDOW: Electric field gradients at ⁵⁷ Fe nuclei in gold alloys	1059
C. OVIEDO DE GONZÁLEZ and N. E. WALSÖE DE RECA: Isotope effect in iron diffusion in Fe/3% Si alloy	1067
L. R. SARAVIA and L. CASAMAYOU: Calculation of the photoelectric effect in silicon	1075
V. A. LODATO: Line broadening of uranyl salts at low temperature	1087
Technical Notes:	
D. CHAKRAVORTY: Energy of migration of anion vacancy and interstitial in calcium fluoride	1091
L. G. CONTI and R. D'ALESSANDRO: ⁸¹ Br magnetic resonance in fresh silver bromide	1092
N. REZLESCU and E. CUCIUREANU: Cation distribution and Curie temperature in the copper-manganese-zinc ferrites	1096

NOTES FOR CONTRIBUTORS

I. GENERAL

1. Submission of a paper to *The Journal of Physics and Chemistry of Solids* will be taken to imply that it represents original research not previously published (except in the form of an abstract or preliminary report), that it is not being considered for publication elsewhere, and that if accepted it will not be published elsewhere in the same form, in any language, without the consent of the Editor-in-Chief. It should deal with original research work in the field of the physics and chemistry of solids.

2. Papers should be submitted to the appropriate regional editor (all English-language papers to be sent to the U.S. editor).

3. Short communications may be published as "Technical Notes" and will receive somewhat more rapid handling than full length articles. Short communications requiring the maximum speed of publication should be submitted to one of the editors of "Solid State Communications."

II. SCRIPT REQUIREMENTS

1. **Papers** submitted should be concise and written in a readily understandable style. Scripts should be typed and double spaced with good margins on one side of the paper only and submitted in duplicate to facilitate refereeing.

It will be appreciated if authors clearly indicate any special characters used. An abstract not exceeding 200 words, should be provided in the language of the paper. French and German papers should be submitted with English abstract and titles, but if this is not possible the abstract will be translated by the publishers. To conserve space, **authors are requested to mark less important parts of the paper**, such as details of experimental technique, methods, mathematical derivations, etc. **for printing in small type**. The technical description of methods should be given in detail only when such methods are new. Authors will receive proofs for correction when their papers are first set, and **alterations must be restricted to printer's errors**. Other than these, any substantial changes may be charged to the authors.

2. **Illustrations** should not be included in the typescript of the paper, and legends should be typed on a separate sheet. Line drawings which require redrawing should include all relevant details and clear instructions for the draughtsman. If figures are already well drawn it may be possible to reproduce them direct from the originals, or from good photo-prints if these can be provided. It is not possible to reproduce from prints with weak lines. Illustrations for reproduction should normally be about twice the final size required. The lettering should be sufficiently large and bold to permit this reduction. Photographs should only be included where they are essential.

3. **Tables and figures** should be so constructed as to be intelligible without reference to the text. Every table and column should be provided with an explanatory heading. Units of measure must always be clearly indicated. The same data should not be published in both tables and figures. The following standard symbols should be used on line drawings since they are easily available to the printers: ○, ●, +, ×, □, ■, △, ▲, ◇, ◆, ▽, ▼.

4. **References** are indicated in the text by numbers on the line in brackets, and the full reference should be given in a list at the end of the paper in the following form:

1. BARNES R. G., BORSA F. and PETERSON D., *J. appl. Phys.* 36, 940 (1965).
2. KNIGHT W. D., In *Solid State Physics* (Edited by F. Seitz and D. Turnbull), Vol. 2, p. 93. Academic Press, New York (1957).

Abbreviations of journal titles should follow those given in *World List of Scientific Periodicals* (4th Edn.). It is particularly requested that authors' initials, and appropriate volume and page numbers, should be given in every case.

Footnotes, as distinct from literature references, should be indicated by the following symbols—*, †, ‡, §, commencing anew on each page; they should *not* be included in the numbered reference system.

5. Due to the international character of the journal no rigid rules concerning notation and spelling will be observed, but each paper should be consistent within itself as to symbols and units.

CONTENTS

R. S. ITOGA and C. R. KANNEWURF: Electrical resistivity, Hall effect and optical absorption in TiS_2 , $\text{TiS}_{0.9}\text{Se}_{0.1}$ and TiSe	1099
SAI-KIT CHAN: f electrons in a strong crystal field. The relationship between paramagnetic and saturation moments	1111
C. F. LAVINE and A. W. EWALD: Two-band galvanomagnetic effects in gray tin	1121
A. B. KUNZ and N. O. LIPARI: Hartree-Fock determination of the energy bands and the optical properties of lithium bromide	1141
C. N. R. RAO, M. NATARAJAN, G. V. SUBBA RAO and R. E. LOEHMAN: Phase transitions and conductivity anomalies in solid solutions of VO_2 with TiO_2 , NbO_2 and MoO_2	1147
W. ZAWADZKI and W. SZYMAŃSKA: Electron scattering and transport phenomena in n -InSb	1151
P. RIGNY, A. J. DIANOUX et P. PLURIEN: Résonance paramagnétique et déformation locale dans les complexes de type UF_6M	1173
P. MACKO: Thermoelectrical parameters of fast-neutron-irradiated Te-Se-Bi, Te-Sb-Bi and GeSi	1181
G. OLLIVIER and G. BUISSON: Influence de la préparation chimique sur les structures magnétiques de Ca_2MnO_4	1189
J. E. GRAAG, JR.: The determination of atomic force constants in cubic solid solutions—I. Theory	1193
C. L. FOILES: Transport anomalies in dilute silver-rare earth alloys	1205
A. R. BEAN and R. C. NEWMAN: The solubility of carbon in pulled silicon crystals	1211
P. J. WEBSTER: Magnetic and chemical order in Heusler alloys containing cobalt and manganese	1221
N. KURODA and A. KAWAMORI: Effects of phase transition on ESR and optical spectra in $\text{NH}_4\text{Cl}:\text{Cu}^{2+}$	1233
A. J. BENNETT and L. M. ROTH: Electronic structure of defect centers in SiO_2	1251
J. G. BROERMAN: A conjecture on the anomalous mobility of α -Sn	1263
P. JOYES: Alternations in the secondary emission of molecular ions from noble metals	1269
S. P. MURARKA and R. A. SWALIN: Cation self-diffusion in strontium oxide (SrO)	1277
S. V. PAPPU and K. A. MCCARTHY: On the colloidal centers in irradiated sodium chloride crystals	1287
E. CATALANO and H. R. LEIDER: Calorimetric evidence of molecular hydrogen in irradiated lithium hydride	1297
D. L. FANCHER and G. R. BARSCH: Lattice theory of alkali halide solid solutions—III. Pressure dependence of solid solubility and spinodal decomposition	1303
J. M. MOREAU, C. MICHEL, R. GERSON and W. J. JAMES: Ferroelectric BiFeO_3 , X-ray and neutron diffraction study	1315
B. E. COOK and P. G. LE COMBER: The optical properties of anthracene crystals in the vacuum ultra-violet	1321
C. M. OSBURN and R. W. VEST: Defect structure and electrical properties of NiO —I. High temperature	1331
C. M. OSBURN and R. W. VEST: Defect structure and electrical properties of NiO —II. Temperatures below equilibrium	1343
C. M. OSBURN and R. W. VEST: Electrical properties of NiO grain boundaries	1355
S. SAKODA and Y. ONODERA: Theory of the effects of uniaxial stress on the exciton states in CuCl	1365
R. H. BAUGHMAN and D. TURNBULL: Vacancy formation parameters in organic crystals	1375
Technical Notes:	
M. AVINOR and M. PASTERNAK: Hyperfine interaction on ^{57}Fe impurity in ferromagnetic MnSb	1395
B. L. SHARMA, R. K. PUROHIT and S. N. MUKERJEE: Diffusion of mercury in indium arsenide	1397
Erratum	1401

NOTES FOR CONTRIBUTORS

I. GENERAL

1. Submission of a paper to *The Journal of Physics and Chemistry of Solids* will be taken to imply that it represents original research not previously published (except in the form of an abstract or preliminary report), that it is not being considered for publication elsewhere, and that if accepted it will not be published elsewhere in the same form, in any language, without the consent of the Editor-in-Chief. It should deal with original research work in the field of the physics and chemistry of solids.

2. Papers should be submitted to the appropriate regional editor (all English-language papers to be sent to the U.S. editor).

3. Short communications may be published as "Technical Notes" and will receive somewhat more rapid handling than full length articles. Short communications requiring the maximum speed of publication should be submitted to one of the editors of *Solid State Communications*.

II. SCRIPT REQUIREMENTS

1. Papers submitted should be concise and written in a readily understandable style. Scripts should be typed and double spaced with good margins on one side of the paper only and submitted in duplicate to facilitate refereeing.

It will be appreciated if authors clearly indicate any special characters used. An abstract not exceeding 200 words, should be provided in the language of the paper. French and German papers should be submitted with English abstract and titles, but if this is not possible the abstract will be translated by the publishers. To conserve space, authors are requested to mark less important parts of the paper, such as details of experimental technique, methods, mathematical derivations, etc. for printing in small type. The technical description of methods should be given in detail only when such methods are new. Authors will receive proofs for correction when their papers are first set, and alterations must be restricted to printer's errors. Other than these, any substantial changes may be charged to the authors.

2. Illustrations should not be included in the typescript of the paper, and legends should be typed on a separate sheet. Line drawings which require redrawing should include all relevant details and clear instructions for the draughtsman. If figures are already well drawn it may be possible to reproduce them direct from the originals, or from good photo-prints if these can be provided. It is not possible to reproduce from prints with weak lines. Illustrations for reproduction should normally be about twice the final size required. The lettering should be sufficiently large and bold to permit this reduction. Photographs should only be included where they are essential.

3. Tables and figures should be so constructed as to be intelligible without reference to the text. Every table and column should be provided with an explanatory heading. Units of measure must always be clearly indicated. The same data should not be published in both tables and figures. The following standard symbols should be used on line drawings since they are easily available to the printers: \circ , \bullet , $+$, \times , \square , \blacksquare , \triangle , \blacktriangle , \diamond , \blacklozenge , ∇ , \blacktriangledown .

4. References are indicated in the text by numbers on the line in brackets, and the full reference should be given in a list at the end of the paper in the following form:

1. BARNES R. G., BORSA F. and PETERSON D., *J. appl. Phys.* **36**, 940 (1965).
2. KNIGHT W. D., In *Solid State Physics* (Edited by F. Seitz and D. Turnbull), Vol. 2, p. 93. Academic Press, New York (1957).

Abbreviations of journal titles should follow those given in *World List of Scientific Periodicals* (4th Edn.). It is particularly requested that authors' initials, and appropriate volume and page numbers, should be given in every case.

Footnotes, as distinct from literature references, should be indicated by the following symbols—*, †, ‡, §, commencing anew on each page; they should not be included in the numbered reference system.

5. Due to the international character of the journal no rigid rules concerning notation and spelling will be observed, but each paper should be consistent within itself as to symbols and units.

CONTENTS

H. OSTERREICHER: Magnetic characteristics of $TbCo_{1-x}Al_x$	1405
R. CHANG: Pseudo-potential calculations of relaxation and formation energy of a vacancy in sodium	1409
R. HALES: The origin of the near-surface effect of diffusion in oxidizing metals	1417
A. C. SARMA and W. G. BOS: The L_{III} X-ray emission edge in lanthanum hydrides	1423
K. MIYATANI, K. MINEMATSU, Y. WADA, F. OKAMOTO, K. KATO and P. K. BALTZER: Magnetic and electrical properties of $CuCr_2Se_4$, Br_2 and $CuCr_2Se_4$, Cl_2	1429
V. LEUTE and A. JAMOUR: Double conversion between PbS-single crystals and polycrystalline CdTe in solid state	1433
T. TSANG, A. N. THORPE, G. DONNAY and F. E. SENFTLE: Magnetic susceptibility and trigonal exchange coupling in the tourmaline mineral group	1441
B. ČELUSTEKA and Z. OGORELEC: Evaluation of some physical quantities in the two phase region in cuprous selenide	1449
F. J. ARLINGHAUS and W. A. ALBERS, JR.: Electronic energy bands and optical transitions in tetragonal germanium dioxide	1453
G. SUSILA and G. SURYAN: Electron-hole recombination in cobalt-doped <i>p</i> -type germanium	1461
B. BOUCHER, R. BUHL et M. PERRIN: Structure et propriétés magnétiques du manganite de chrome	1471
J. A. CORNET: Le volume d'activation pour l'autodiffusion du plutonium en phase α	1489
SONIA GRADSZTAJN, D. VIVIER et J. CONARD: Etude de la surface de solides par résonance magnétique nucléaire haute résolution de liquides adsorbés—II. Molécules à protons mobiles	1507
YU. A. OSIPIYAN and I. S. SMIRNOVA: Partial dislocations in the wurtzite lattice	1521
M. S. LUBELL and R. H. KERNOHAN: Comparison of calculated and measured lower critical field for some Nb-Ti alloys	1531
L. R. SARAVIA and L. CASAMAYOU: Calculation of the photoelectric effect in germanium	1541
D. CALECKI: Phénomènes galvanomagnétiques non linéaires—A. Mesures sur l'antimoniure d'indium	1553
V. G. BHIDE, B. A. PATKI and A. S. NIGAVEKAR: X-ray spectroscopic investigation of bismuth selenide, bismuth telluride and their alloy	1565
L. A. FELDkamp, D. K. STEINMAN, N. VAGELATOS, J. S. KING and G. VENKATARAMAN: Lattice dynamics of cubic zinc sulfide by neutron scattering	1571
N. G. PACE and G. A. SAUNDERS: Elastic wave propagation in the group VB semimetals	1583
M. C. BHARDWAJ and R. ROY: Effect of high pressure on crystalline solubility in the system NaCl-KCl	1601
D. J. CHAKRABARTI and P. A. BECK: Transport properties of Cr-Al solid solutions	1609
KOJI KAJIMURA and AKIRA IKUSHIMA: Frequency dependence of the ultrasonic attenuation in superconducting niobium in the mixed state	1617
E. I. AKSEL'ROD, B. G. ALAPIN, I. I. VISHNEVSKY and B. YA. SUKHAREVSKY: Structural and phase relations in nonstoichiometric ferrites with oxygen deficiencies	1627
P. FISCHER, G. ROULT and D. SCHWARZENBACH: Crystal and magnetic structure of silver difluoride—II. Weak 4 <i>d</i> -ferromagnetism of AgF_2	1641
G. WOLF and B. BARANOWSKI: Specific heat of nickel hydride from 10° to 200°K	1649
D. LANGBEIN: Non-retarded dispersion energy between macroscopic spheres	1657
A. P. MALOZEMOFF: The optical spectrum and magnetic properties of $TmFeO_3$ in the single-ion model	1669
Technical Notes:	
P. GAUNT and P. D. LOLY: Magnetic susceptibility and lattice distortion in an antiferromagnet, $AuMn$	1687
J. P. DISMUKES: Semiconducting properties and doping of Sc_2S_3 and Sc_2Se_3	1689
P. DE V. DU PLESSIS: On the magnetization dependence of the magnetocrystalline anisotropy of iron	1691
C. M. HURD and J. E. A. ALDERSON: Hall resistivity and electron scattering in monocrystals of Cu containing Zn, Mn, Ni or Fe	1696
M. N. SHARMA and S. P. SRIVASTAVA: Temperature variation of dielectric constants in rock-salt crystals	1699
RICHARD DALVEN: <i>f</i> -sum rule calculation of the light hole effective mass in InP	1700
P. B. FABRITCHNYI, A. M. BARSCHKEIN and A. N. NEMERMANOV: Etude par effet Mössbauer de structure hyperfine nucléaire de ^{119}Sn dans $\alpha-Fe_2O_3$	1701
Erratum	1705

NOTES FOR CONTRIBUTORS

I. GENERAL

1. Submission of a paper to *The Journal of Physics and Chemistry of Solids* will be taken to imply that it represents original research not previously published (except in the form of an abstract or preliminary report), that it is not being considered for publication elsewhere, and that if accepted it will not be published elsewhere in the same form, in any language, without the consent of the Editor-in-Chief. It should deal with original research work in the field of the physics and chemistry of solids.

2. Papers should be submitted to the appropriate regional editor (all English-language papers to be sent to the U.S. editor).

3. Short communications may be published as "Technical Notes" and will receive somewhat more rapid handling than full length articles. Short communications requiring the maximum speed of publication should be submitted to one of the editors of *Solid State Communications*.

II. SCRIPT REQUIREMENTS

1. Papers submitted should be concise and written in a readily understandable style. Scripts should be typed and double spaced with good margins on one side of the paper only and submitted in duplicate to facilitate refereeing.

It will be appreciated if authors clearly indicate any special characters used. An abstract not exceeding 200 words, should be provided in the language of the paper. French and German papers should be submitted with English abstract and titles, but if this is not possible the abstract will be translated by the publishers. To conserve space, authors are requested to mark less important parts of the paper, such as details of experimental technique, methods, mathematical derivations, etc. for printing in small type. The technical description of methods should be given in detail only when such methods are new. Authors will receive proofs for correction when their papers are first set, and alterations must be restricted to printer's errors. Other than these, any substantial changes may be charged to the authors.

2. Illustrations should not be included in the typescript of the paper, and legends should be typed on a separate sheet. Line drawings which require redrawing should include all relevant details and clear instructions for the draughtsman. If figures are already well drawn it may be possible to reproduce them direct from the originals, or from good photo-prints if these can be provided. It is not possible to reproduce from prints with weak lines. Illustrations for reproduction should normally be about twice the final size required. The lettering should be sufficiently large and bold to permit this reduction. Photographs should only be included where they are essential.

3. Tables and figures should be so constructed as to be intelligible without reference to the text. Every table and column should be provided with an explanatory heading. Units of measure must always be clearly indicated. The same data should not be published in both tables and figures. The following standard symbols should be used on line drawings since they are easily available to the printers: \circ , \bullet , $+$, \times , \square , \blacksquare , \triangle , \blacktriangle , \diamond , \blacklozenge , ∇ , \blacktriangledown .

4. References are indicated in the text by numbers on the line in brackets, and the full reference should be given in a list at the end of the paper in the following form:

1. BARNES R. G., BORSA F. and PETERSON D., *J. appl. Phys.* 36, 940 (1965).
2. KNIGHT W. D., In *Solid State Physics* (Edited by F. Seitz and D. Turnbull), Vol. 2, p. 93. Academic Press, New York (1957).

Abbreviations of journal titles should follow those given in *World List of Scientific Periodicals* (4th Edn.). It is particularly requested that authors' initials, and appropriate volume and page numbers, should be given in every case.

Footnotes, as distinct from literature references, should be indicated by the following symbols—*, †, ‡, §, commencing anew on each page; they should not be included in the numbered reference system.

5. Due to the international character of the journal no rigid rules concerning notation and spelling will be observed, but each paper should be consistent within itself as to symbols and units.

CONTENTS

C. CANALI, G. OTTAVIANI and A. ALESSANDRI QUARANTA: Drift velocity of electrons and holes and associated anisotropic effects in silicon	1707
P. J. TORIN, D. J. SELLMYER and B. L. AVERBACH: Effect of indium impurities on the De Haas-Van Alphen effect in lead	1723
L. B. ZLATKIN and A. M. KANOV: Character of disorder at transition from crystal to vitreous phase in semiconductors	1733
R. M. LOGAN and D. T. J. HURLE: Calculations of point defect concentrations and nonstoichiometry in GaAs	1739
R. M. LOGAN: Analysis of heat treatment and formation of gallium-vacancy-tellurium complexes in GaAs	1761
A. W. SOLBRIG, JR.: Valence force potentials for calculating crystal vibrations in silicon	1761
R. SRINIVASAN and R. RAMJI RAO: Anharmonic properties of the hexagonal metals, magnesium, zinc and beryllium—I. Lattice dynamics and third order elastic constants	1769
M. ROBBINS, R. D. PIERCE and R. WOLFE: Magnetic properties of fluoride substituted orthoferrites	1789
D. M. GASS, B. J. ALDER and T. E. WAINWRIGHT: The thermal conductivity of a hard sphere solid	1797
K. SUZUKI and O. UEMURA: Knight shift, magnetic susceptibility and electrical resistivity of pure gallium and gallium-indium eutectic alloy in the normal and the supercooled liquid state	1801
A. BASTIN, C. LEWINER, O. BETBEDER-MATIBET et P. NOZIERES: Quantum oscillations of the Hall effect of a fermion gas with random impurity scattering	1811
J. E. HOLLIDAY: The electronic properties of titanium interstitial and intermetallic compounds from soft X-ray spectroscopy	1825
D. CALECKI: Phénomènes galvanomagnétiques non linéaires B—Théorie quantique	1835
C. DEENADAS, A. W. THOMPSON, R. S. CRAIG and W. E. WALLACE: Low temperature heat capacities of laves phase lanthanide-aluminum compounds	1853
A. M. VAN DIEPEN, R. S. CRAIG and W. E. WALLACE: Crystal field and magnetic heat capacity in PrIn_3 and CeIn_3	1867
I. PETRESCU-PRAOVA and N. N. WINOGRADOFF: Photoluminescence in compensated <i>n</i> -type, Si-doped gallium arsenide	1873
P. E. GREGER-HANSEN: Measurements at 4.2 K of galvanomagnetic effects in bismuth in weak magnetic fields	1881
C. Y. SHE, JON D. MASSO and D. F. EDWARDS: Raman scattering by polarization waves in uniaxial crystals	1887
P. RIGNY, A. J. DIANOUX et P. PLURIEN: Susceptibilité magnétique d'un électron <i>s</i> en coordination de huit	1901
O. MEYER and W. SCHERBER: Analysis of silicon nitride layers deposited from SiH_4 and N_2 on silicon	1909
M. STESLICKA, S. G. DAVISON and U. SRINIVASAN: Electronic states of heavy diatomic crystals	1917
E. M. AMRHEIN and H. HEIL: Dielectric absorption of polymers from the millimeter to the far infrared region	1925
H. R. PHILIPP: Optical properties of non-crystalline Si, SiO , SiO_2 and SiO_3	1935
A. LICHANOT et S. GROMB: Domaine d'existence du sulfure d'étain et phénomène d'associations des lacunes d'étain	1947
K. AIZU: Phenomenological lattice-dynamical theory of ferroelasticity	1959
G. MÜLLER and R. HELBIG: Über den Einbau von Kupfer in ZnO-einkristallen	1971
S. MISHRA, P. A. BECK and S. FONER: Paramagnetism in dilute alloys of Fe in $\text{Cu}_{1-x}\text{Ni}_x$	1979
J. G. SIMMONS: Theory of metallic contacts on high resistivity solids—I. Shallow traps	1987
G. E. STEDMAN and D. J. NEWMAN: Crystal field in rare-earth fluorides—III. Analysis of experimental data for the alkaline earth fluorides	2001
Technical Notes:	
R. K. KERR and C. F. SCHWERTFEGER: Temperature dependence of the EPR spectrum of $\text{CdIn}_2\text{S}_4: \text{Mn}^{2+}$	2007
F. AGULLÓ-LÓPEZ and F. JAQUE: Role of interstitial aggregation on the <i>F</i> -coloring curve of alkali halides	2009

NOTES FOR CONTRIBUTORS

I. GENERAL

1. Submission of a paper to *The Journal of Physics and Chemistry of Solids* will be taken to imply that it represents original research not previously published (except in the form of an abstract or preliminary report), that it is not being considered for publication elsewhere, and that if accepted it will not be published elsewhere in the same form, in any language, without the consent of the Editor-in-Chief. It should deal with original research work in the field of the physics and chemistry of solids.

2. Papers should be submitted to the appropriate regional editor (all English-language papers to be sent to the U.S. editor).

3. Short communications may be published as "Technical Notes" and will receive somewhat more rapid handling than full length articles. Short communications requiring the maximum speed of publication should be submitted to one of the editors of *Solid State Communications*.

II. SCRIPT REQUIREMENTS

1. Papers submitted should be concise and written in a readily understandable style. Scripts should be typed and double spaced with good margins on one side of the paper only and submitted in duplicate to facilitate refereeing.

It will be appreciated if authors clearly indicate any special characters used. An abstract not exceeding 200 words, should be provided in the language of the paper. French and German papers should be submitted with English abstract and titles, but if this is not possible the abstract will be translated by the publishers. To conserve space, authors are requested to mark less important parts of the paper, such as details of experimental technique, methods, mathematical derivations, etc. for printing in small type. The technical description of methods should be given in detail only when such methods are new. Authors will receive proofs for correction when their papers are first set, and alterations must be restricted to printer's errors. Other than these, any substantial changes may be charged to the authors.

2. Illustrations should not be included in the typescript of the paper, and legends should be typed on a separate sheet. Line drawings which require redrawing should include all relevant details and clear instructions for the draughtsman. If figures are already well drawn it may be possible to reproduce them direct from the originals, or from good photo-prints if these can be provided. It is not possible to reproduce from prints with weak lines. Illustrations for reproduction should normally be about twice the final size required. The lettering should be sufficiently large and bold to permit this reduction. Photographs should only be included where they are essential.

3. Tables and figures should be so constructed as to be intelligible without reference to the text. Every table and column should be provided with an explanatory heading. Units of measure must always be clearly indicated. The same data should not be published in both tables and figures. The following standard symbols should be used on line drawings since they are easily available to the printers: ○, ●, +, ×, □, ■, △, ▲, ◇, ◆, ▽, ▼.

4. References are indicated in the text by numbers on the line in brackets, and the full reference should be given in a list at the end of the paper in the following form:

1. BARNES R. G., BORSA F. and PETERSON D., *J. appl. Phys.* 36, 940 (1965).
2. KNIGHT W. D., In *Solid State Physics* (Edited by F. Seitz and D. Turnbull), Vol. 2, p. 93. Academic Press, New York (1957).

Abbreviations of journal titles should follow those given in *World List of Scientific Periodicals* (4th Edn.). It is particularly requested that authors' initials, and appropriate volume and page numbers, should be given in every case.

Footnotes, as distinct from literature references, should be indicated by the following symbols—*, †, ‡, §, commencing anew on each page; they should not be included in the numbered reference system.

5. Due to the international character of the journal no rigid rules concerning notation and spelling will be observed, but each paper should be consistent within itself as to symbols and units.

PHYSICAL PROPERTIES AND CRYSTAL STRUCTURE OF A NEW SEMICONDUCTING I-III-VI₂ COMPOUND, CuScS₂

J. P. DISMUKES* and R. T. SMITH

RCA Laboratories, Princeton, N. J. 08540, U.S.A.

and

J. G. WHITE

Department of Chemistry, Fordham University, New York, N. Y. 10458 U.S.A.

(Received 13 July 1970; in revised form 31 August 1970)

Abstract—The compound CuScS₂ has been prepared for the first time, and single crystals have been grown by chemical transport reaction with I₂. The crystals are trigonal with $a = 3.7333 \pm 0.0005$ Å, $c = 6.098 \pm 0.001$ Å, and are non-centrosymmetric with space group $P3m1$. The crystal structure has been determined by single crystal X-ray methods and is based on a hexagonally close packed arrangement of sulfur atoms, with one formula unit per cell. The scandium atoms occupy octahedral sites and the copper atoms tetrahedral sites giving a new structure type intermediate between the structures of NiAs and hexagonal ZnS. The compound is a semiconductor and optical absorption measurements show two band gaps, one at 2.30 eV representing a direct transition and the other at 1.8 ± 1 eV representing an indirect transition. Doping experiments with Zn produced low resistivity *n*-type material, but attempts to prepare *p*-type material were unsuccessful.

1. INTRODUCTION

TERNARY semiconducting compounds of the general type I-III-VI₂ having the chalcopyrite structure[1] have been known for many years, where I = Cu, III = Al, Ga, In and VI = S, Se, or Te. The energy gaps for these materials have been summarized in a recent paper[2]. A series of monoclinic I-III-VI₂ compounds[3, 4] have been reported, where I = Cu, III = a rare earth element and VI = S, Se. However, only limited data are available on their crystallography and physical properties.

In this paper we report the synthesis and crystal growth of the new semiconducting I-III-VI₂ compound, CuScS₂, the X-ray determination of its crystal structure, optical measurement of the energy gap, and investigation of doping behavior.

2. EXPERIMENTAL

(a) Preparation, crystal growth and doping

Copper scandium sulfide, CuScS₂, was prepared by heating a stoichiometric mixture of Cu and Sc₂S₃ powders at 1050°C in an evacuated quartz ampule for 16 hr in the presence of the required stoichiometric amount of sulfur. The scandium sulfide, Sc₂S₃, was prepared by reacting Sc₂O₃, contained in a carbon boat, with a helium stream saturated with CS₂ for 24 hr at 1050°C. X-ray diffraction powder photographs of CuScS₂ showed no evidence of the starting materials or of sulfides of copper. Copper and scandium were determined by complexometric titration with EDTA[5, 6] and sulfur was determined using the idometric method for hydrogen sulfide[7]. Anal. Calcd. for CuScS₂: Cu, 36.8%; Sc, 26.1%; S, 37.1%. Found: Cu, $37.0 \pm 0.3\%$; Sc, $25.9 \pm 0.2\%$; S, $37.3 \pm 0.3\%$. Copper scandium sulfide is stable at room temperature in air and water, and reacts slowly with strong acids.

Single crystals of CuScS₂ for X-ray crystal

*Laboratories RCA Ltd, 569 Badenerstrasse, 8048 Zurich, Switzerland.

structure determination, for optical measurements, and for investigation of doping behavior were prepared by chemical transport reaction [8], using I_2 in a sealed, evacuated quartz ampule. Single crystal platelets up to 1 cm^2 in area, and with the c axis perpendicular to the platelet, were transported from hot to cold using an I_2 concentration of about 2 mg/cm^3 in a temperature gradient of $1050\text{--}950^\circ\text{C}$.

A series of experiments was conducted to determine whether CuScS_2 could be readily doped n - and p -type by simple chemical substitution for Cu, Sc, or S. N -type doping was attempted both by annealing chemically transported crystals in $\frac{1}{2}$ atmosphere Zn vapor at 900°C for 16 hr, and by chemically transporting CuScS_2 with additions of Zn. P -type doping was attempted both by annealing chemically transported crystals in $\frac{1}{2}$ atmosphere of P_4 vapor at 900°C , and by chemically transporting CuScS_2 with additions of P or Ca.

(b) Physical measurements

The density of single crystal CuScS_2 platelets was determined by the method of hydrostatic weighing [9], employing Archimedes' principle and using water as the immersion fluid.

Electrical resistivity of CuScS_2 crystal platelets was measured by the four-point probe technique [10]. The CuScS_2 crystals were also tested for conductivity type using a simple thermal probe technique capable of detecting conductivity type of silicon with resistivity less than 100 ohm-cm .

Optical absorption measurements at 300°K in the spectral range $2.0\text{--}0.48\mu$ were taken with a Cary Model 14 Spectrometer on chemically transported CuScS_2 platelets with a grown thickness in the range $100\text{--}230\mu$, and on mechanically thinned specimens in the range $10\text{--}20\mu$. The thickness t was determined by interferometry, and the optical absorption coefficient α was calculated from the simple relation [11], $\alpha = (1/t) \ln(I_0/I_T)$, where I_0 and I_T are the initial and transmitted intensi-

ties, respectively. This procedure neglects reflection, but still gives sufficiently accurate values of α in the spectral region near the band edge where α is large.

(c) X-ray measurements

The crystal system was found to be trigonal from Laue and Weissenberg photographs. Accurate cell dimensions, $a = 3.7333 \pm 0.0005\text{ \AA}$, $c = 6.098 \pm 0.001\text{ \AA}$, were obtained from the powder diffraction pattern given in Table 1. Ni-filtered $\text{CuK}\alpha$ radiation was used and the pattern was taken at 23°C with a 114.6 mm dia. camera. The cell volume gives a calculated density of 3.90 g-cm^{-3} for one formula weight per unit cell. The measured density value, $3.79 \pm 0.15\text{ g-cm}^{-3}$, obtained on a 13 mg crystal agrees with the calculated value to within experimental uncertainty.

The crystals originally prepared were very thin, and distorted on cutting. For the collection of single crystal intensity data a naturally occurring flake elongated along the b axis and with an approximately constant cross section of $0.26 \times 0.05\text{ mm}$ was used. The integrated intensities of the $h0l$, $h1l$, and $h2l$ levels were measured on a Buerger single crystal diffractometer using Zr-filtered $\text{MoK}\alpha$ radiation. Because of the high absorption ($\mu = 107.1\text{ cm}^{-1}$) and the rather unsuitable crystal shape, absorption corrections were made by the method of Albrecht [12]. The residual absorption errors are mainly due to departure of the actual crystal shape from the idealized shape assumed. A set of F values was obtained for each level after application of Lorentz and polarization factors and the three sets were brought to a single scale by means of the common reflections.

From the three dimensional Patterson function it was immediately clear that the atoms were located in the following special positions of the space group $P3ml$: Sc in (a) $0,0,z$ with $z = 0$; Cu in (b) $\frac{1}{3}, \frac{2}{3}, z$ with $z \sim \frac{3}{4}$; S(1) in (b) $\frac{1}{3}, \frac{2}{3}, z$ with $z \sim \frac{3}{4}$; S(2) in (c) $\frac{2}{3}, \frac{1}{3}, z$ with $z \sim \frac{1}{4}$. Refinement was carried out first by difference Fourier synthesis and

Table 1. Calculated and observed lattice spacings and intensities for CuScS_2 ($\text{CuK}\alpha$ radiation)

<i>hkl</i>	d_{CALC}	d_{OBS}	I_{OBS}
001	6.10	6.10	m^+
100	3.23	3.23	s^-
002	3.049	3.046	m^+
101	2.857	2.856	vs
102	2.218	2.218	s
003	2.033	2.032	w
110	1.867	1.864	s
111	1.785	1.783	w
103	1.721	1.720	s
200	1.617	1.615	w
112	1.592	1.592	m
201	1.563	1.563	m
004	1.525	1.523	vvw
202	1.428	1.427	m
113	1.375	1.376	m
203	1.265	1.265	m
005	1.219	1.220	w
211	1.1982	1.1986	m
114	1.1808	1.1803	m^-
105	1.1412	1.1404	w
212	1.1343	1.1339	m
300	1.0777	1.0774	m^-
213	1.0473	1.0471	m
115	1.0210	1.0209	m^-
205	0.9736	0.9733	vvw
106	0.9696	0.9693	w
214	0.9535	0.9531	vvw
220	0.9333	0.9336	w
116	0.8926	0.8927	vvw
311	0.8872	0.8873	w
304	0.8800	0.8805	vw
215	0.8633	0.8632	w
312	0.8603	0.8604	m^-
313	0.8204	0.8204	m^-
305	0.8076	0.8076	w
401	0.8017	0.8016	vvw
324	0.7960	0.7962	vvw
117	0.7895	0.7894	vvw
216	0.7814	0.7814	m^-

vs = very strong, s = strong, m = medium, w = weak, vw = very weak, vvw = very, very weak.

then by full matrix least squares methods [13]. Attempts to refine using anisotropic thermal parameters led to physically unreasonable results, presumably because of incomplete correction for absorption. Since the isotropic temperature factors refined independently for each atom did not differ signifi-

cantly from each other, the number of variables was further reduced by refining only a single isotropic temperature factor, the scale factor, and the z parameters for Cu, S(1), and S(2). The weighting scheme used set $w = 1/\sigma^2$ where σ was based on the counting statistics for each reflection. Convergence was obtained to a conventional R of 0.087 for 91 independent reflections. The final calculated and observed values of F are given in Table 2. The scattering factors used are those given in the International Tables [14] corrected for anomalous dispersion [15]. The choice between hkl and $\bar{h}\bar{k}\bar{l}$ was made on the basis of the set giving better agreement with the calculated values. Since the anomalous dispersion effect is quite small the result is not absolutely clear cut. The direction of intensity change from I_{hkl} to $I_{\bar{h}\bar{k}\bar{l}}$ is in agreement with that calculated for 27 pairs and is in the opposite direction for 16 pairs.

3. RESULTS AND DISCUSSION

(a) Crystal structure

The crystal structure found for CuScS_2 is shown in Fig. 1. The structure is essentially a hexagonally close packed array of sulfur atoms in which the copper atoms occupy tetrahedral and the scandium atoms octahedral interstices. Consequently, the two sulfur atoms in the unit cell are differentiated physically as well as crystallographically. The atom S(1) is tetrahedrally coordinated to one copper and three scandium atoms while S(2) is octahedrally coordinated to three copper atoms and three scandium atoms. The structure thus belongs to a new basic structure type intermediate between the structures of NiAs and ZnS (wurtzite). This relationship is illustrated in Fig. 2 where all the structures shown are based on hexagonal close packing of the anions with two anions per unit cell.

The bond distances found in CuScS_2 are given in Table 4 and the bond angles in Table 5. The Sc-S bonds average 2.60 Å almost identical with the value of 2.59 Å found in Sc_2S_3 .

Table 2. Observed and calculated structure factors for CuScS_2 ($\text{MoK}\alpha$ radiation). F_c for one formula unit, F_0 scaled to F_c

h	k	l	$ F_0 $	$ F_c $	h	k	l	$ F_0 $	$ F_c $	h	k	l	$ F_0 $	$ F_c $
1	0	0	31.8	27.8	1	0	6	38.7	45.9	2	0	0	66.6	59.2
1	0	1	36.8	32.1	1	0	-6	36.6	41.8	-2	0	0	61.7	63.7
1	0	2	55.7	53.5	1	0	-1	43.7	38.4	-2	0	0	73.9	70.4
1	0	3	65.6	55.2	1	0	1	39.7	38.6	-2	0	0	65.8	67.9
1	0	4	44.9	46.0	1	0	-3	86.0	90.2	-2	0	0	36.6	36.6
1	0	5	49.4	48.4	1	0	3	79.3	92.7	-2	0	0	32.8	37.3
1	0	6	35.6	38.7	1	0	-4	30.2	29.6	-2	0	0	27.3	30.0
1	0	7	39.7	33.3	1	0	4	23.5	27.5	-2	0	0	22.7	28.6
1	0	8	51.6	58.6	1	0	-5	43.7	43.5	-2	0	0	22.9	27.8
1	0	9	59.9	59.2	1	0	5	38.9	42.9	-2	0	0	99.0	105.9
1	0	10	33.0	32.4	1	0	-6	41.3	40.6	-2	0	0	23.9	20.8
1	0	11	55.1	46.7	1	0	6	47.8	38.9	-2	0	0	24.7	24.4
1	0	12	54.9	47.6	1	0	0	63.8	72.8	-2	0	0	39.7	40.3
1	0	13	79.5	86.3	2	0	0	36.0	36.2	-2	0	0	45.1	41.9
1	0	14	76.7	81.6	2	0	0	35.6	35.3	-2	0	0	34.4	35.9
1	0	15	86.4	81.6	2	0	1	27.1	30.3	-2	0	0	39.7	38.1
1	0	16	76.7	88.2	2	0	-1	28.3	30.1	-2	0	0	33.2	33.1
1	0	17	91.3	90.8	2	0	3	67.4	75.8	-2	0	0	37.9	27.9
1	0	18	40.1	44.7	2	0	-3	76.9	73.4	-2	0	0	49.4	50.4
1	0	19	45.5	43.9	2	0	4	21.5	22.5	-2	0	0	58.9	51.0
1	0	20	30.0	35.8	2	0	-4	24.1	24.5	-2	0	0	25.7	28.8
1	0	21	34.4	37.0	2	0	5	39.3	37.4	-2	0	0	27.1	26.5
1	0	22	23.3	26.0	2	0	-5	38.3	38.1	-2	0	0	26.7	29.0
1	0	23	26.1	31.1	2	0	5	38.3	38.1	-2	0	0	26.7	29.0
1	0	24	26.1	31.1	2	0	-5	38.3	38.1	-2	0	0	26.7	29.0
1	0	25	26.1	31.1	2	0	5	38.3	38.1	-2	0	0	26.7	29.0
1	0	26	26.1	31.1	2	0	-5	38.3	38.1	-2	0	0	26.7	29.0
1	0	27	26.1	31.1	2	0	5	38.3	38.1	-2	0	0	26.7	29.0
1	0	28	26.1	31.1	2	0	-5	38.3	38.1	-2	0	0	26.7	29.0
1	0	29	26.1	31.1	2	0	5	38.3	38.1	-2	0	0	26.7	29.0
1	0	30	26.1	31.1	2	0	-5	38.3	38.1	-2	0	0	26.7	29.0
1	0	31	26.1	31.1	2	0	5	38.3	38.1	-2	0	0	26.7	29.0
1	0	32	26.1	31.1	2	0	-5	38.3	38.1	-2	0	0	26.7	29.0
1	0	33	26.1	31.1	2	0	5	38.3	38.1	-2	0	0	26.7	29.0
1	0	34	26.1	31.1	2	0	-5	38.3	38.1	-2	0	0	26.7	29.0
1	0	35	26.1	31.1	2	0	5	38.3	38.1	-2	0	0	26.7	29.0
1	0	36	26.1	31.1	2	0	-5	38.3	38.1	-2	0	0	26.7	29.0
1	0	37	26.1	31.1	2	0	5	38.3	38.1	-2	0	0	26.7	29.0
1	0	38	26.1	31.1	2	0	-5	38.3	38.1	-2	0	0	26.7	29.0
1	0	39	26.1	31.1	2	0	5	38.3	38.1	-2	0	0	26.7	29.0
1	0	40	26.1	31.1	2	0	-5	38.3	38.1	-2	0	0	26.7	29.0
1	0	41	26.1	31.1	2	0	5	38.3	38.1	-2	0	0	26.7	29.0
1	0	42	26.1	31.1	2	0	-5	38.3	38.1	-2	0	0	26.7	29.0
1	0	43	26.1	31.1	2	0	5	38.3	38.1	-2	0	0	26.7	29.0
1	0	44	26.1	31.1	2	0	-5	38.3	38.1	-2	0	0	26.7	29.0
1	0	45	26.1	31.1	2	0	5	38.3	38.1	-2	0	0	26.7	29.0
1	0	46	26.1	31.1	2	0	-5	38.3	38.1	-2	0	0	26.7	29.0
1	0	47	26.1	31.1	2	0	5	38.3	38.1	-2	0	0	26.7	29.0
1	0	48	26.1	31.1	2	0	-5	38.3	38.1	-2	0	0	26.7	29.0
1	0	49	26.1	31.1	2	0	5	38.3	38.1	-2	0	0	26.7	29.0
1	0	50	26.1	31.1	2	0	-5	38.3	38.1	-2	0	0	26.7	29.0
1	0	51	26.1	31.1	2	0	5	38.3	38.1	-2	0	0	26.7	29.0
1	0	52	26.1	31.1	2	0	-5	38.3	38.1	-2	0	0	26.7	29.0
1	0	53	26.1	31.1	2	0	5	38.3	38.1	-2	0	0	26.7	29.0
1	0	54	26.1	31.1	2	0	-5	38.3	38.1	-2	0	0	26.7	29.0
1	0	55	26.1	31.1	2	0	5	38.3	38.1	-2	0	0	26.7	29.0
1	0	56	26.1	31.1	2	0	-5	38.3	38.1	-2	0	0	26.7	29.0
1	0	57	26.1	31.1	2	0	5	38.3	38.1	-2	0	0	26.7	29.0
1	0	58	26.1	31.1	2	0	-5	38.3	38.1	-2	0	0	26.7	29.0
1	0	59	26.1	31.1	2	0	5	38.3	38.1	-2	0	0	26.7	29.0
1	0	60	26.1	31.1	2	0	-5	38.3	38.1	-2	0	0	26.7	29.0
1	0	61	26.1	31.1	2	0	5	38.3	38.1	-2	0	0	26.7	29.0
1	0	62	26.1	31.1	2	0	-5	38.3	38.1	-2	0	0	26.7	29.0
1	0	63	26.1	31.1	2	0	5	38.3	38.1	-2	0	0	26.7	29.0
1	0	64	26.1	31.1	2	0	-5	38.3	38.1	-2	0	0	26.7	29.0
1	0	65	26.1	31.1	2	0	5	38.3	38.1	-2	0	0	26.7	29.0
1	0	66	26.1	31.1	2	0	-5	38.3	38.1	-2	0	0	26.7	29.0
1	0	67	26.1	31.1	2	0	5	38.3	38.1	-2	0	0	26.7	29.0
1	0	68	26.1	31.1	2	0	-5	38.3	38.1	-2	0	0	26.7	29.0
1	0	69	26.1	31.1	2	0	5	38.3	38.1	-2	0	0	26.7	29.0
1	0	70	26.1	31.1	2	0	-5	38.3	38.1	-2	0	0	26.7	29.0
1	0	71	26.1	31.1	2	0	5	38.3	38.1	-2	0	0	26.7	29.0
1	0	72	26.1	31.1	2	0	-5	38.3	38.1	-2	0	0	26.7	29.0
1	0	73	26.1	31.1	2	0	5	38.3	38.1	-2	0	0	26.7	29.0
1	0	74	26.1	31.1	2	0	-5	38.3	38.1	-2	0	0	26.7	29.0
1	0	75	26.1	31.1	2	0	5	38.3	38.1	-2	0	0	26.7	29.0
1	0	76	26.1	31.1	2	0	-5	38.3	38.1	-2	0	0	26.7	29.0
1	0	77	26.1	31.1	2	0	5	38.3	38.1	-2	0	0	26.7	29.0
1	0	78	26.1	31.1	2	0	-5	38.3	38.1	-2	0	0	26.7	29.0
1	0	79	26.1	31.1	2	0	5	38.3	38.1	-2	0	0	26.7	29.0
1	0	80	26.1	31.1	2	0	-5	38.3	38.1	-2	0	0	26.7	29.0
1	0	81	26.1	31.1	2	0	5	38.3	38.1	-2	0	0	26.7	29.0
1	0	82	26.1	31.1	2	0	-5	38.3	38.1	-2	0	0	26.7	29.0
1	0	83	26.1	31.1	2	0	5	38.3	38.1	-2	0	0	26.7	29.0
1	0	84	26.1	31.1	2	0	-5	38.3	38.1	-2	0	0	26.7	29.0
1	0	85	26.1	31.1	2	0	5	38.3	38.1	-2	0	0	26.7	29.0
1	0	86	26.1	31.1	2	0	-5	38.3	38.1	-2	0	0	26.7	29.0
1	0	87	26.1	31.1	2	0	5	38.3	38.1	-2	0	0	26.7	29.0
1	0	88	26.1	31.1	2	0	-5	38.3	38.1	-2	0	0	26.7	29.0
1	0	89	26.1	31.1	2	0	5	38.3	38.1	-2	0	0	26.7	29.0
1	0	90	26.1	31.1	2	0	-5	38.3	38.1	-2	0	0	26.7	29.0
1	0	91	26.1	31.1	2	0	5	38.3	38.1	-2	0	0	26.7	29.0
1	0	92	26.1	31.1	2	0	-5	38.3	38.1	-2	0	0	26.7	29.0
1	0	93	26.1	31.1	2	0	5	38.3	38.1	-2	0	0	26.7	29.0
1	0	94	26.1	31.1	2	0	-5	38.3	38.1	-2	0	0	26.7	29.0
1	0	95	26.1	31.1	2	0	5	38.3	38.1	-2	0	0	26.7	29.0
1	0	96	26.1	31.1	2	0	-5	38.3	38.1	-2	0	0	26.7	29.0
1	0	97	26.1	31.1	2	0	5	38.3	38.1	-2	0	0	26.7	29.0
1	0	98	26.1	31.1	2	0	-5	38.3	38.1	-2	0	0	26.7	29.0
1	0	99	26.1	31.1	2	0	5	38.3	38.1	-2	0	0	26.7	29.0
1	0	100	26.1	31.1	2	0	-5	38.3	38.1	-2	0	0	26.7	29.0

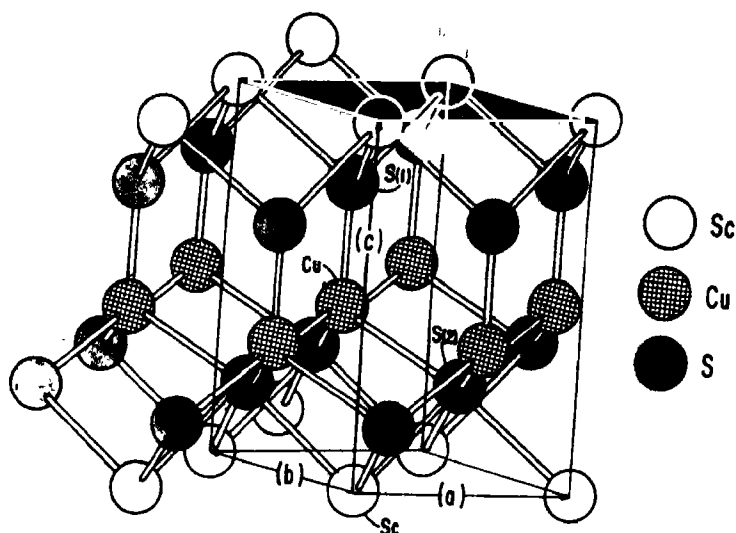


Fig. 1. The crystal structure of CuScS_2 , showing one unit cell outlined by axes (a), (b), and (c). The one Cu atom, one Sc atom, and two crystallographically independent sulfur atoms, S(1) and S(2) in the unit cell are indicated.

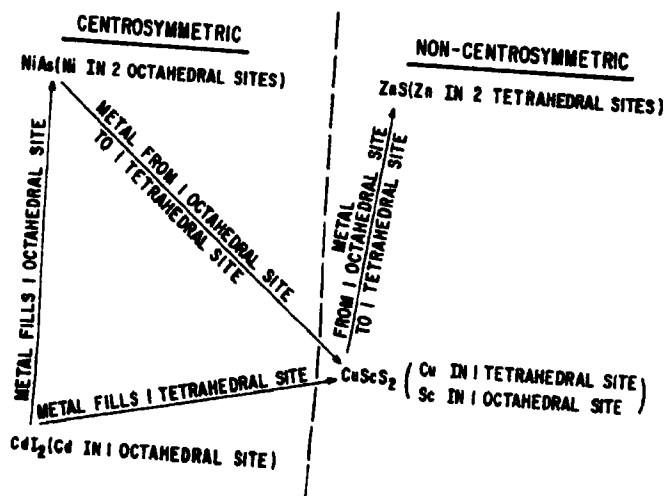


Fig. 2. The relationship between the CuScS_2 structure and the other basic structure types based on hexagonal close packing of anions. All the structures shown contain two anions per unit cell. The distribution of the cations per cell between octahedral and tetrahedral sites is also indicated.

[16]. The Cu-S bonds as measured differ considerably among themselves. However, it should be noted that the length of the Cu-S bond parallel to the c axis has a much higher standard deviation than the others since the free parameters for both atoms are in the bond

direction. The average Cu-S distance is 2.32 Å, which is much smaller than the sum of the ionic radii, 2.80 Å [17], and indicates considerable covalent character. The bond angles are fairly regular for the coordination groups of sulfur atoms surrounding the central metal

Table 3. Structural parameters for CuScS_2

Atom	<i>x</i>	<i>y</i>	<i>z</i>	<i>B</i>
Sc	0.0	0.0	0.0	0.31(14)
Cu	0.3333	0.6667	0.4126(28)	0.31
S(1)	0.3333	0.6667	0.7760(41)	0.31
S(2)	0.6667	0.3333	0.2542(36)	0.31

Table 4. Bond distances in CuScS_2

Number of bonds	Atoms	Distance (Å)
1	Cu-S(1)	2.216(30)
3	Cu-S(2)	2.361(13)
3	Sc-S(1)	2.552(13)
3	Sc-S(2)	2.655(13)

shortest Cu-Sc distance is 3.31 Å, compared with the sum of the metallic radii, 2.92 Å. Metal-metal bonding between Cu and Sc is unlikely to occur because Cu^{1+} has a completely filled *d*-shell and Sc^{3+} has a completely empty *d*-shell. In a very recent paper published after the completion of this work, Gorter[19]

Table 5. Bond angles in CuScS_2

Coordination group	Number of angles	Atoms	Angle (°)
Cu-centered tetrahedron	3	S(1)-Cu-S(2)	114.1
	3	S(2)-Cu-S(2)	104.5
S(1)-centered tetrahedron	3	Sc-S(1)-Sc	94.0
	3	Cu-S(1)-Sc	122.4
Sc-centered octahedron	3	S(1)-Sc-S(1)	94.0
	3	S(2)-Sc-S(2)	89.4
	6	S(1)-Sc-S(2)	88.3
S(2)-centered octahedron	3	Cu-S(2)-Cu	104.5
	3	Sc-S(2)-Sc	89.4
	6	Cu-S(2)-Sc	82.4

atoms. However, for the coordination of the sulfur atoms by the metal atoms there is considerable distortion in order to accommodate the rather different Cu-S and Sc-S bond distances.

The occurrence of the CuScS_2 structure type is probably restricted to pairs of metal atoms one of which has a very strong tetrahedral site preference and the other a very strong octahedral site preference as is the case with Cu^{1+} and Sc^{3+} . The structure of CuCrS_2 [18] has Cu^{1+} in tetrahedral sites and Cr^{3+} in octahedral sites. However, the sulfur atoms are cubic close packed, and the structure is believed to be stabilized by *d*-electron interactions between Cu and Cr, resulting in short (2.77 Å) Cu-Cr distances. In CuScS_2 the

discussed three possible structures for the then unknown compound CuScS_2 . These are: (I) the structure of CuCrS_2 , (II) the structure of CuScS_2 which we have determined and (III) a more complex structure in which regions of cubic and hexagonal close packing are interleaved, resulting in a twelve layer sulfur stacking sequence. Of these, Gorter prefers structure (III) since it minimizes repulsive forces between second nearest neighbors. The fact that CuScS_2 has structure (II) based on simple hexagonal packing of sulfur atoms, is apparently the consequence of its largely covalent character.

Since the chemistry of the rare earth elements is similar to that of Sc, one might expect compounds of the general formula CuRS_2 ,

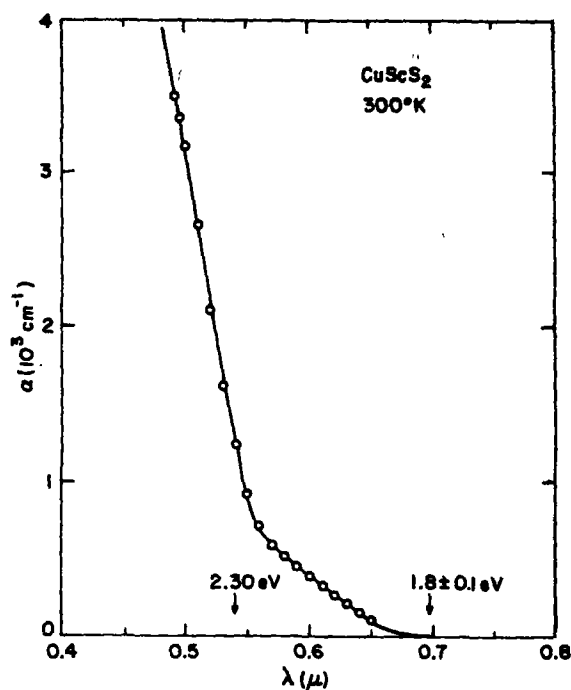


Fig. 3. The dependence of the optical absorption coefficient (α) of CuScS_2 upon wavelength (λ) at 300°K measured on a 15μ -thick crystal. Values of direct bandgap (2.30 eV) and of indirect bandgap ($1.8 \pm 0.1 \text{ eV}$) are indicated.

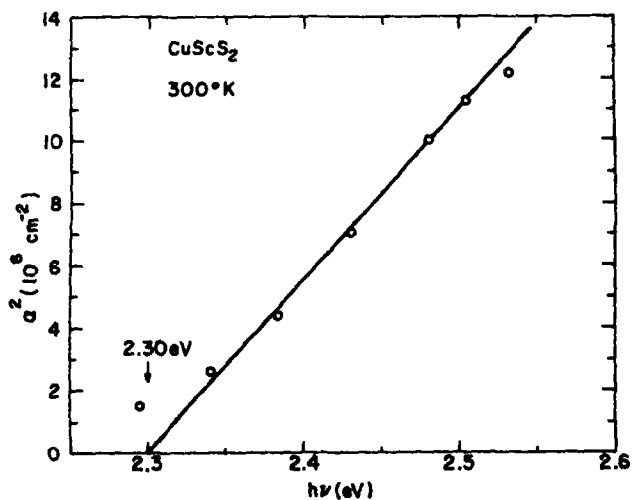


Fig. 4. The dependence of the square of the optical absorption coefficient (α^2) of CuScS_2 at 300°K upon photon energy ($h\nu$) in the range 2.25 – 2.55 eV . Data are taken from Fig. 3.

where R = a rare earth element, to form with the CuScS_2 structure. Compounds of the type CuRS_2 have been reported[3], but only for the elements from La through Tb. However, the compounds do not have the CuScS_2 structure, but rather form monoclinic crystals of an unknown structure. Probably these rare earth elements have too large atomic radii to permit close packing of sulfur atoms required for the existence of the CuScS_2 structure.

A series of nonstoichiometric copper rare earth sulfides ($n\text{Cu}_2\text{S.R}_2\text{S}_3$, with $n > 1$ and $R = \text{Tb to Lu}$) have been reported by Ballesstracci and Bertaut[20]. These compounds have a structure in which rare earth and sulfur atoms occupy approximately the same relative positions as do Sc and S in CuScS_2 . However, the copper atoms are distributed at random between the two tetrahedral sites, $\pm\frac{1}{4}$, $\frac{3}{4}$, z , with $z \sim \frac{3}{8}$, giving a centrosymmetric

structure. As n increases and the occupancy of tetrahedral sites by Cu also increases, the rare earth occupancy of the octahedral sites must decrease to maintain charge balance. It appears that the stability of this nonstoichiometric phase is favored by the incomplete site occupancy which relieves some of the strain which would occur in a stoichiometric CuRS_2 phase due to the disparate size of the metal atoms.

(b) Optical energy gap

Figure 3 shows a representative plot of optical absorption coefficient α of CuScS_2 as a function of wavelength λ at 300°K. There is a sharp absorption edge at 2.30 eV and a shallow absorption edge at 1.8 ± 0.1 eV. The absorption coefficient in a semiconductor is known to vary with photon energy as $(h\nu - E_g)^n$ [11, 21], where E_g is the energy gap,

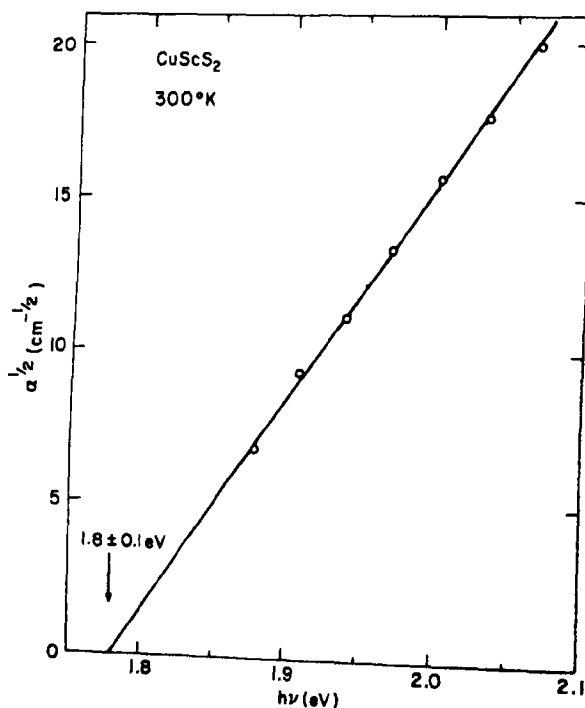


Fig. 5. The dependence of the square root of the optical absorption coefficient ($\alpha^{1/2}$) of CuScS_2 at 300°K upon photon energy ($h\nu$) in the range 1.75–2.1 eV. Data were taken on a 230 μ -thick crystal.

$n = \frac{1}{2}$ for a direct, symmetry allowed transition, and $n = 2$ for an indirect transition. Therefore, plots of α^n vs. $h\nu$ were constructed from the data in Fig. 3. The linear relation between α^2 and $h\nu$ in Fig. 4 indicates that the energy gap at 2.30 eV is direct. We believe the shallow edge at 1.8 ± 0.1 eV represents an intrinsic, indirect energy gap in CuScS_2 rather than an extrinsic effect such as impurity band tailing, since measurements on a 230 μ -thick crystal, for which the shallow edge covered the full range of the spectrometer, indicated the linear relation between $\alpha^{1/2}$ and $h\nu$ shown in Fig. 5. The quoted uncertainty is typical for a room temperature measurement of an indirect energy gap.

The direct bandgap of CuScS_2 (2.30 eV) lies in the range expected for CuGaS_2 by interpolation between CuAlS_2 (3.35 eV)² and CuInS_2 (1.2 eV)[22]. However, more detailed and quantitative comparisons of the optical energy gaps of I-III-VI₂ compounds are not possible at this time, since data on their band structure are almost entirely lacking.

(c) Doping experiments

The electrical resistivity of undoped CuScS_2 crystals was about 2×10^3 ohm-cm as measured by the four-point probe technique, but their conductivity type could not easily be determined since the thermal probe showed no deflection. No further measurements were attempted on these very high resistivity crystals, since the principal objective in this work was to achieve heavily doped ($\leq 10^{-2}$ ohm-cm) material, both n - and p -type.

The tetrahedral coordination of Cu and the octahedral coordination of Sc in CuScS_2 suggested that p - and n -type doping of this compound could be achieved by taking advantage of the tetrahedral site preference of Zn, for n -type doping, and of the octahedral site preference of Ca, for p -type doping. P -type doping was also attempted by substituting P for S . Crystals of CuScS_2 annealed in Zn vapor at 900°C became highly conducting n -type, with resistivity about 10^{-3} ohm-cm.

Small crystallites of CuScS_2 , chemically transported in the presence of Zn were also highly n -type. The n -type doping appears to be due to substitution of Zn for Cu, as anticipated, since emission spectrographic analysis indicated the presence of Zn in concentrations of 100 ppm for chemically transported specimens and of 1000 ppm for specimens annealed in Zn vapor.

Crystals of CuScS_2 annealed in P_4 vapor, or in vapors of P_4 plus S_2 remained high resistivity. Likewise, chemical transport of CuScS_2 in the presence of Ca or P failed to give p -type crystals. Emission spectrographic analysis indicated the incorporation of these impurities in concentrations of several hundred ppm. Thus, neither calcium nor phosphorus, the most obvious impurities which would be expected to give p -type doping, readily give CuScS_2 with p -type conductivity.

Acknowledgements—The authors thank R. J. Ulmer for chemical syntheses and optical measurements, B. J. Goydich for chemical analyses, and R. J. Paff for X-ray powder photographs.

REFERENCES

- HAHN H., FRANK G., KLINGLER W., MEYER A. and STORGER G., *Z. anorg. allg. Chem.* **271**, 153 (1953).
- HONEYMAN W. N., *J. Phys. Chem. Solids* **30**, 1935 (1969).
- BALLESTRACCI R. and BERTAUT F., *Bull. Soc. franc. Min.-Crist.* **88**, 575 (1965).
- JULIEN-POUZOL M., GUITTARD M. and ADOLPHE M. C., *Compt. rend.* **267**, 823 (1968).
- CHENG K. L., *Anal. Chem.* **33**, 761 (1961).
- CHENG K. L., *Anal. Chem.* **34**, 1392 (1962).
- KOLTHOFF I. M. and ELVING P. J., *Treatise on Analytical Chemistry*, Part II, Vol. 7, p. 75, John Wiley, New York (1961).
- SCHÄFER H., *Chemical Transport Reactions*, p. 5, Academic Press, New York (1964).
- SMAKULA A. and SILS V., *Phys. Rev.* **99**, 1744 (1955).
- VALDES L., *Proc. I.R.E.* **42**, 420 (1954).
- MCLEAN T. P., in *Progress in Semiconductors*, Vol. 5, p. 73, John Wiley, New York (1960).
- ALBRECHT G., *Res. scient Instrum* **10**, 221 (1939).
- BUSING W. R., MARTIN K. O. and LEVY H. A., *A Fortran Crystallographic Least Squares Program*, Oak Ridge National Laboratory, Oak Ridge, Tennessee, Report TM-305 (1964).

14. International Tables for X-Ray Crystallography, Kynoch Press, Birmingham, Vol. III (1962).
15. DAUBEN C. H. and TEMPLETON D. H., *Acta crystallogr.* **8**, 841 (1955).
16. DISMUKES J. P. and WHITE J. G., *Inorg. Chem.* **3**, 1220 (1964).
17. PAULING L., *The Nature of the Chemical Bond*, 3rd Edition, Cornell University Press, Ithaca, N. Y. (1960).
18. BONGERS P. F., VAN BRUGGEN C. F., KOOPSTRA J., OMLOO W. P. F. A. M., WIEGERS G. A. and JELLINEK F., *J. Phys. Chem. Solids* **29**, 977 (1968).
19. GORTER E. W., *J. Solid State Chem.* **1**, 279 (1970).
20. BALLESTRACCI R. and BERTAUT E. F., *Proceedings of the International Conference on the Thermodynamic, Physical, and Structural Properties of Semimetals*, p. 41, Centre National de la Recherche Scientifique, Paris (1967).
21. DRESSELHAUS G., *Phys. Rev.* **105**, 135 (1957).
22. AUSTIN I. G., GOODMAN C. H. L. and PENGELLY A. E., *J. electrochem. Soc.* **103**, 609 (1956).

LATTICE ENERGIES AND HEATS OF FORMATION OF THE $\text{Ti}_n\text{O}_{2n-1}$ SHEAR PHASES

J. S. ANDERSON and R. BURCH

Inorganic Chemistry Laboratory, Oxford University, England

(Received 10 June 1970; in revised form 24 August 1970)

Abstract—Electrostatic lattice energy calculations have been carried out by Bertaut's method for the oxides $\text{Ti}_n\text{O}_{2n-1}$ ($n = 4$ to 9), for a random oxygen vacancy model and for the observed shear structures. The electrostatic energy is lowered by 10–15 per cent for the shear structures, but ordering alone, without crystallographic shear, would give a similar stabilization. Heats of formation of the oxides have been derived; experimental values for the titanium oxides are lacking, but the results compare well with observed ΔH° values for the cognate vanadium oxides.

SLIGHTLY reduced rutile forms a series of ordered shear phases of general formula $\text{Ti}_n\text{O}_{2n-1}$ ($n = 4$ to 9) in which the non-stoichiometry is accommodated by the elimination at regular intervals of complete planes of oxygen atoms parallel to the $\bar{1}21$ plane of rutile (1). Very little thermodynamic data are available for these phases (2) so that it is of some interest to calculate the lattice energies (U) and heats of formation (ΔH°) of these compounds.

In the simplest Born–Meyer ionic model the lattice energy is given by an expression of the form

$$U = U_0 \left(1 - \frac{1}{n} \right) \quad (1)$$

where U_0 is the electrostatic energy and n is the repulsion coefficient. For the present work, where accuracies of the order of ± 0.1 per cent were considered sufficient, electrostatic energies were calculated using the Bertaut [3] method by incorporating the modifications suggested by Templeton *et al.* [4]. For present purposes the Bertaut method was preferred to the more commonly used Ewald method [5] firstly because fewer computations are required to produce this degree of accuracy and secondly because the terms in the Bertaut equation are more easily computed.

The electrostatic energy is given [4] by the equation

$$U_e = -\frac{g-Q}{RM} \sum_j (Z_j)^2 + \frac{\pi R^2}{MV} \sum_h |F|^2 \phi \quad (2)$$

where $g = \frac{26}{35}$

$Q = 0.0003013$

R = half the nearest neighbour distance

M = number of molecules per unit cell

Z_j = charge on atom j

V = volume of unit cell

h = magnitude of the vector hkl in reciprocal space

x_j, y_j, z_j = coordinates of atom j

$F = \sum_j Z_j \exp(2\pi i(hx_j + ky_j + lz_j))$

$\phi = 288(\alpha \sin \alpha + 2 \cos \alpha - 2)^2 / \alpha^{10}$

and $\alpha = 2\pi hR$.

The experimentally observed crystallographic data necessary for the utilisation of equation (2) is available only for the Ti_5O_9 phase. However Andersson *et al.* [1] have derived lattice parameters and atomic coordinates for idealized structures for each member of the series and these idealized values have been used in our calculations. The distribution of ionic charges among the titanium ions was based on the structural data of Andersson *et al.* [1] which indicates that the shear plane region has the corundum

structure so that titanium ions in this region can be designated a +3.0 charge while all the remaining titanium ions are +4.0.

Using this model the results shown in Table 1 were obtained. These results show that, as the oxygen content is increased, the electrostatic energy of these phases decreases (more negative) to a minimum energy for the terminal composition TiO_2 . The variation of electrostatic energy with composition for the shear phases is almost linear and extrapolates to close to the value for TiO_2 . This is to be expected since TiO_2 corresponds to a shear phase with an infinitely large separation of the shear planes.

Table 1. Electrostatic energies of $\text{Ti}_n\text{O}_{2n-1}$ phases

Composition	Structure	Electrostatic energy U_r (kJ g at Ti^{-1})
Ti_4O_7	Shear	-10.840
	Random vacancy	-9.131
Ti_5O_9	Shear (ideal)	-11.400
	Shear (observed)	-11.480
Ti_6O_{11}	Random vacancy	-9.931
	Shear	-11.760
Ti_7O_{13}	Random vacancy	-10.500
	Shear	-12.030
Ti_8O_{15}	Random vacancy	-10.910
	Shear	-12.250
Ti_9O_{17}	Random vacancy	-11.220
	Shear	-12.490
TiO_2	Random vacancy	-13.620

In the particular case of Ti_5O_9 , where data are available, the energy of the observed structure has also been calculated and as can be seen (Table 1) the observed structure has a slightly lower energy than the ideal structure. This is quite reasonable since the transition from the ideal to the real structure corresponds to a relaxation of the ions in the shear plane region which results in a decrease in the repulsive interactions between like ions. The smallness of the energy difference between the real and ideal structures as compared to the energy difference between ad-

jacent structures means that changes in energy between different idealized structures are probably a good reflection of differences between the corresponding real structures.

An estimate of the comparative stability of each shear structure has been obtained by calculating the energies of structures corresponding to the random distribution of oxygen vacancies on a basic rutile lattice. In these latter calculations the correct $\text{Ti}_n\text{O}_{2n-1}$ stoichiometry has been obtained by designating to each oxygen ion a charge of $1 - 2n/n$ and to each titanium ion a corresponding charge of $4n - 2/n$. The results (Table 1) show that in each case the electrostatic energy of the shear structure is more negative by about 10–15 per cent than the energy of the corresponding random vacancy structure. This energy difference is of the same order of magnitude (≈ 1000 kJ g. at Ti^{-1}) as is observed [6] in defect TiO where the more stable state contains ordered vacancies rather than shear planes.

This similarity between the stabilisation of shear and ordered vacancy structures relative to the respective disordered structures makes it interesting to compare the stability of different *ordered* structures for the same composition. A hypothetical ordered vacancy structure corresponding to a composition Ti_4O_7 has therefore been examined. The structure chosen was a double rutile unit cell ($c' = 2c_r$) with vacancies at (0.3056, 0.3056, 0) forming an ordered superlattice. While this choice of unit cell is purely arbitrary it is probably reasonable to expect the energy of this structure to represent fairly well the energy of any ordered vacancy structure of this type. The electrostatic energy obtained was -10,840 kJ g. at Ti^{-1} which, within experimental error, is identical to the energy of the corresponding shear structure. This result is somewhat surprising as one might have expected the experimentally observed shear structure to have a substantially lower energy than any other postulated structure. These results indicate that while there is a

large difference in energy between an ordered and a disordered structure the energy difference between different ordered structures is rather small and it is doubtful whether electrostatic energy calculations can give much information concerning the most favourable structure when several ordered structures are possible. Accepting this limitation, however, some useful information on the relative stabilities of different members of the same family of phases can still be obtained.

The evaluation of lattice energies from equation (1) requires a knowledge of the repulsion coefficient n . Usually [7] n is derived from compressibility data for the compound in question. However no such data are available for the Ti_nO_{2n-1} series. Nevertheless, since there is a close structural similarity between the shear phases and rutile, a sufficiently accurate estimate of n can be obtained by using the value which applies to TiO_2 itself. Ladd [8] has estimated n as ≈ 10.5 . In contrast, however, from the data of Wackmann *et al.* [9] we find $n \approx 6.24$ when polarization energy terms are neglected. Since there seems little to choose between these two evaluations we have calculated the lattice energies using both values of n . Using these lattice energies the heat of formation of Ti_nO_{2n-1} can then be obtained from the equation.

$$\Delta H^0 = U + \Delta H_{\text{sub1}}^0 + \frac{2n-1}{2n} D(O_2) + \frac{2}{n} \sum_3 I + \frac{n-2}{n} \sum_4 I - \frac{2n-1}{n} E_A \quad (3)$$

where H_{sub1}^0 is the heat of sublimation of 1 g of Ti

$D(O_2)$ is the dissociation energy of 1 mole oxygen

$\sum_3 I$ is the sum of the first three ionization potentials of Ti

$\sum_4 I$ is the sum of the first four ionization potentials of Ti

and E_A is the electron affinity of oxygen.

Minor corrections such as polarisation energies and zero point energies have been neglected since it is likely that these will not contribute more than about 2 per cent to the lattice energy term. Wackmann *et al.* [9] have used the following values for the constants in equation (3): $\Delta H_{\text{sub1}}^0 = 423$ kJ/mole, $D(O_2) = -491$ kJ/mole, $\sum_4 I = 8792$ kJ/mole, $E_A = -703$ kJ/mole. From Moore [10] $\sum_3 I = 4622$ kJ/mole.

Using these values the results in Table 2 were obtained. The final column in Table 2 gives the heats of formation obtained using an average value for n of 8.37. These heats of formation may be compared with the only available experimental data, which are the

Table 2. Repulsive energies (kJ g at Ti^{-1}) and heats of formation of Ti_nO_{2n-1} phases

Composition	U_1^*	$\Delta H_1^{\dagger*}$	U_2^{\ddagger}	$\Delta H_2^{\ddagger\dagger}$	U_3^{\ddagger}	$\Delta H_3^{\ddagger\ddagger}$
Ti_4O_7	-9.102	-302	-9.810	-1.010	-9.545	-745
Ti_5O_9	-9.573	-307	-10.317	-1.051	-10.038	-772
Ti_6O_{11}	-9.875	-300	-10.643	-1.068	-10.355	-780
Ti_7O_{13}	-10.102	-301	-10.887	-1.086	-10.593	-792
Ti_8O_{15}	-10.286	-322	-11.086	-1.122	-10.786	-822
Ti_9O_{17}	-10.488	-396	-11.303	-1.211	-10.998	-906

* $n = 6.24$ in equation (1).

$\dagger n = 10.50$ in equation (1).

$\ddagger n = 8.37$ in equation (1).

heats of formation of V_nO_{2n-1} compounds as measured by Anderson *et al.* [11] given in Table 3. The agreement between the two sets of results is quite reasonable. However, since the theoretical evaluation of the heats of formation is clearly very dependent on the value of n it is not possible to obtain much information from these results other than the conclusion that the stability of the oxide increases as the oxygen content is increased.

In conclusion, these calculations have again illustrated the principle first noted by Bertaut [3] that defects in ionic crystals will have a strong tendency to order. In addition, however, it has been found that electrostatic

energy calculations may not be sufficient to distinguish between alternative ordered structures for compounds of the same chemical composition. Nevertheless within the obvious limitations of a purely ionic model the agreement between the calculated and observed heats of formation of these shear planes has been found to be satisfactory.

REFERENCES

1. ANDERSON S. and JAHNBERG L., *Arkiv Kemi* **21**, 413 (1963).
2. KAHN A. S., *D. Phil. Thesis*, Oxford (1967).
3. BERTAUT E. F., *J. Phys. Radium* **13**, 499 (1952).
4. TEMPLETON D. H. and JOHNSON Q. C., In *Computing Methods and the Phase Problem in X-ray Crystal Analysis*, p. 150. Pergamon, Oxford (1961).
5. TOSI M. P., *Solid State Phys.* **16**, 1 (1964).
6. O'KEEFFE M. and VALIGI M., *J. Chem. Phys.* **50**, 1490 (1969).
7. LADD M. F. C. and LEE W. H., In *Progress in Solid State Chemistry*, Vol. 1. Pergamon Press, Oxford (1964).
8. LADD M. F. C., *Acta crystallogr.* **A25**, 486 (1969).
9. WACKMANN P. H., HIRTHE W. M. and FROUNFELKER R. E., *J. Phys. Chem. Solids* **28**, 1525 (1967).
10. MOORE W. J., *Physical Chemistry*. Prentice-Hall Englewood Cliffs, New York (1962).
11. ANDERSON J. S. and KAHN A. S., *J. less Common Met.* **22**, 209 (1970).

Table 3. Heats of formation of V_nO_{2n-1} phases from data of Ref. [11]

Composition	Heat of formation kJ g. at V^{-1}
V_4O_7	-673.6
V_5O_9	-682.3
V_6O_{11}	-664.4

THE TEMPERATURE AND MAGNETIC FIELD DEPENDENCE OF THE FORCED MAGNETOSTRICTION AND THERMAL EXPANSION OF INVAR

W. F. SCHLOSSER, G. M. GRAHAM and P. P. M. MEINCKE

Department of Physics, University of Toronto, Toronto 5, Ontario, Canada

(Received 11 June 1970; in revised form 14 August 1970)

Abstract—The forced linear magnetostriction coefficient, h , of Invar (Carpenter Free Cut) has been measured parallel and perpendicular to the applied magnetic field using a capacitor dilatometer in the temperature range from 1 to 120 K and for fields from about 5 to 55 kOe. Both heat treated and cold worked specimens have been used. Measurements of the thermal expansion coefficient, α have also been made.

The temperature variation of h is roughly as $\log T$, exhibiting a sharp drop below 20 K and a small anomaly (≈ 6 per cent) near 90 K which is accentuated by the heat treatment. h is isotropic. The field dependence of h is reasonably fitted at most temperatures by a linear field dependence of the form $h = A - BH$ where A and B are positive.

In the temperature range below about 10 K, the length change exhibits a reversible creep after a change of the field which is also accentuated by the heat treatment and is of maximum effect near 4 K. The creep is logarithmic in time and it amounts to a change in length after one hour of as much as 8 per cent of the immediate change.

At low temperatures the absolute magnitude of h is only about 50 per cent of that to be expected from the pressure dependence of the magnetic moment. Also, $\partial\alpha/\partial H \ll \partial h/\partial T$. These results indicate that thermodynamics fails for this alloy at low temperatures.

1. INTRODUCTION

THERE has recently been renewed interest in the properties of the iron-nickel alloys in the vicinity of the Invar concentration (approximately 35 at.% Ni), particularly among several groups of Japanese workers.

The work on this alloy in this laboratory has been briefly reviewed by Graham and Cochran[1]. Among the unusual features of Invar, the magnetostriction ranks importantly because of its large magnitude in the 'forced' or paraprocess regime, i.e. in the range of applied fields beyond those necessary to produce technical saturation due to domain effects. This is a natural consequence of the anomalous magnetoelastic coupling in these alloys, for which magnetostriction measurements are an ideal probe. However, until recently, there has been little magnetostriction data available for the low temperature region, which represents a serious gap in our knowledge of the equilibrium properties of Invar.

We have undertaken an ambitious program of investigation of these rather complicated effects, of which this paper reports on a preliminary study of changes in specimen length, using the commercial polycrystalline material on which most of the earlier work here has been done. A brief notice on the first results of this series of measurements has been reported[2]. In the course of this work, a study of the magnetostriction of Invar alloys at low temperatures by Matsumoto, Kaneko, and Fujimori[3] has appeared. The agreement with our work is not as good as we would wish; the strain gauges used by them suffer from lack of accuracy and sensitivity. Our own work makes use of the capacitance dilatometer techniques pioneered by White[4], which do not suffer from these defects.

2. EXPERIMENT

The samples were cylinders from the same rod of commercial Free Cut Invar, (previously

called N-37 in our publications), made by the Carpenter Steel Co., Reading, Pa. The length and diameter were about 2.7 and 0.5 cm. The analysed composition of this alloy in atomic percent is shown in Table 1. The unannealed

top of the cylinder were polished flat. A spacer of brass shim stock lying on the top edge of the copper cylinder set the capacitance gap. This method avoids the parallelism requirements due to separate polishing of the sample

Table 1. *Analysed composition of Invar samples (at.%)*

Element Content	Fe 64.1	Ni 33.7	Mn 0.92	Si 0.72	C 0.42	Cr 0.09	Co 0.05	Se 0.01
--------------------	------------	------------	------------	------------	-----------	------------	------------	------------

sample had been drawn to size by the manufacturer and was in a worked state. The annealed sample was heat treated at 1373 K for one hour in a helium atmosphere, and water quenched. It was then held at 580 K for eight hours in air, air cooled to 368 K, and held at this temperature for two days. This heat treatment is close to that recommended for stabilizing the dimensions of the alloy at room temperature.

Etching the unannealed sample revealed that the grains were considerably elongated in the direction of the cylinder axis. Long, thin grains were apparent on the sides of the cylinder. The ends of the cylinder had a peculiar velvet appearance due to preferential etching between the thin ends of the crystallites. The heat treatment considerably increased the crystallite size and reduced the velvet appearance of the ends of the cylinder. Unusual round pits were apparent in the crystallites before and after the heat treatment.

Measurements of the magnetostriction and thermal expansion parallel to the axis of the cylindrical specimen were made using a three terminal capacitance dilatometer. The dilatometer cell, designed by Slavin[5], is a modification of the one used by White[4] for thermal expansion measurements. Copper plates are soldered to the top and bottom of the Invar cylinder. The bottom plate, larger than the top, and with an insulated central section to which the specimen was attached, was screwed to the bottom of a copper cylinder which surrounded the specimen. The assembly was clamped, and the top copper plate and the

and holder in the procedure used by White.

OFHC copper was used in the cell construction. Tests have shown its magnetostriction to be negligible.

Capacitance measurements were made using a General Radio Type 1632-A Three Terminal Capacitance Bridge. The sensitivity of the apparatus to relative changes in length $\Delta l/l$ was 1.5×10^{-8} . The absolute temperature was known to ± 0.3 deg using a copper constantan thermocouple above 4.2 K, and to better than ± 10 mdeg at and below 4.2 K using the helium bath vapour pressure. A temperature controller with a noise of $0.2 \mu V$ regulated the temperature of the specimen above 4.2 K. Below 4.2 K manual pressure regulation sufficed.

The magnetic field, parallel to the cylinder axis, was supplied by a superconducting solenoid. Magnetic field changes were measured with a precision of 1 per cent by monitoring the magnet current. The transverse experiments used a field perpendicular to the cylinder axis, which was supplied by a 20 kOe conventional electro-magnet regulated to better than 10^{-5} .

The parallel forced magnetostriction of the sample was measured using two procedures. In order to cover a large temperature range the change in length of the specimen was determined only for changes of the magnetic field from 21.6 to 24.7 kOe and back. Adequate time was allowed after each field change to ensure that equilibrium had been reached. The fields used were well into the paraprocess region for the specimens. At several tempera-

tures, measurements over the entire range of field, from zero to a maximum of 52.5 kOe, were made to determine the field dependence of the forced magnetostriction. Transverse magnetostriction measurements were made at several temperatures to check the isotropy of the forced magnetostriction and the field dependence of the forced magnetostriction in a transverse field.

Thermal expansion measurements were made in a magnetic field of 21.6 kOe for both the annealed and unannealed samples by heating the specimen and the cell. These are values relative to the thermal expansion of OFHC copper and were reduced to absolute thermal expansion coefficients using the data for copper of Bunton and Weintraub[6]. Some measurements of thermal expansion were also made in zero field, and between 9 K and 20 K for $H = 20.0$ and 16 kOe.

Temperature dependence of the forced magnetostriction

The temperature dependence of the forced magnetostriction $(\partial l / \partial H)_{PT} = h$, evaluated for the field change from 21.6 to 24.7 kOe is shown in Fig. 1, for both the annealed and unannealed specimens. Preliminary results on the annealed specimen[2] indicated that the forced magnetostriction varied as the logarithm of the absolute temperature between 4.2 and 120 K. The more detailed results reported here can be fairly well fitted to the logarithm of the absolute temperature. However, in this paper we have presented the results on a linear temperature scale. The transverse measurements tend to lie below the longitudinal, probably due in part to the unfavourable specimen geometry for this type of measurement (see next section). The results of Matsumoto, Kaneko and

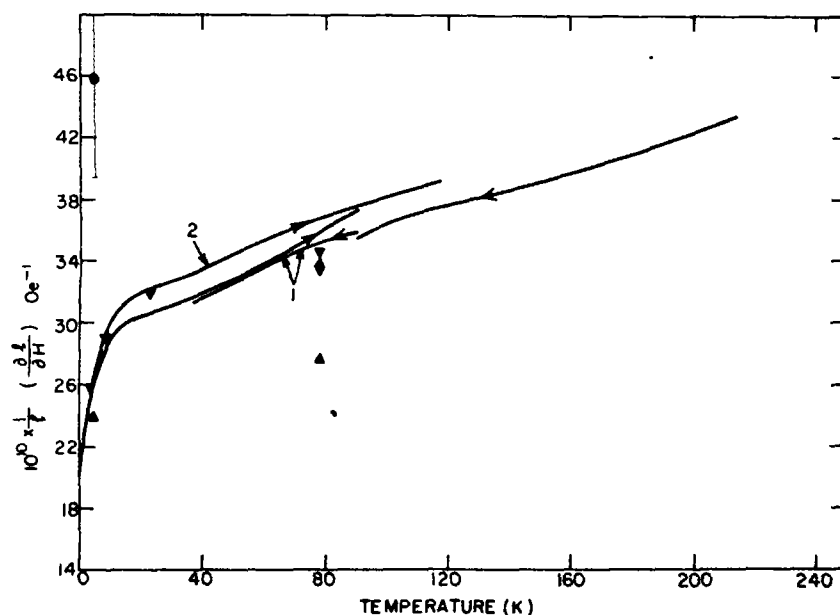


Fig. 1. Temperature dependence of the longitudinal and transverse forced linear magnetostriction coefficient, h , of Invar (33.7 at.% Ni). Curve 1 refers to the annealed sample, and curve 2 to the cold worked sample. The arrows indicate the direction of temperature change. ∇ , \diamond , the transverse forced magnetostriction for the unannealed and annealed samples respectively; \triangle the results of Matsumoto, Kaneko and Fujimori[3] for a 34.1 at.% Ni alloy. \circ the equivalent h expected through the Maxwell relation from the $\partial \sigma / \partial p$ results of Kondorskii and Sedov[11] for a 33.3 at.% Ni alloy.

Fujimori[3] for the forced magnetostriction of a 34.1 at.% Ni Invar at 4.2 and 77 K are also plotted in Fig. 1. The 77 K value is considerably less than we have observed, although the 4.2 K value is in reasonable agreement with our results.

The forced magnetostriction decreases by ~ 27 per cent in the interval 20 to 1.1 K and is still falling rapidly at 1.1 K, the lowest temperature reached, for both samples. As the temperature decreases, the difference between the forced magnetostriction of the samples diminishes.

Small anomalies were observed in the forced magnetostriction of both samples between

40 and 130 K, as shown in expanded scale in Fig. 2. A discontinuity at 90 K and temperature hysteresis were observed for the annealed sample. For this sample, the temperature region of interest was covered twice, once with temperature increasing, and again with temperature decreasing. The two curves almost superimpose at higher temperatures, but show a hysteresis below 90 K. These effects were observed in a single experiment, and have not yet been investigated in detail.

Magnetic field dependence of the forced magnetostriction

The dependence of the forced magneto-

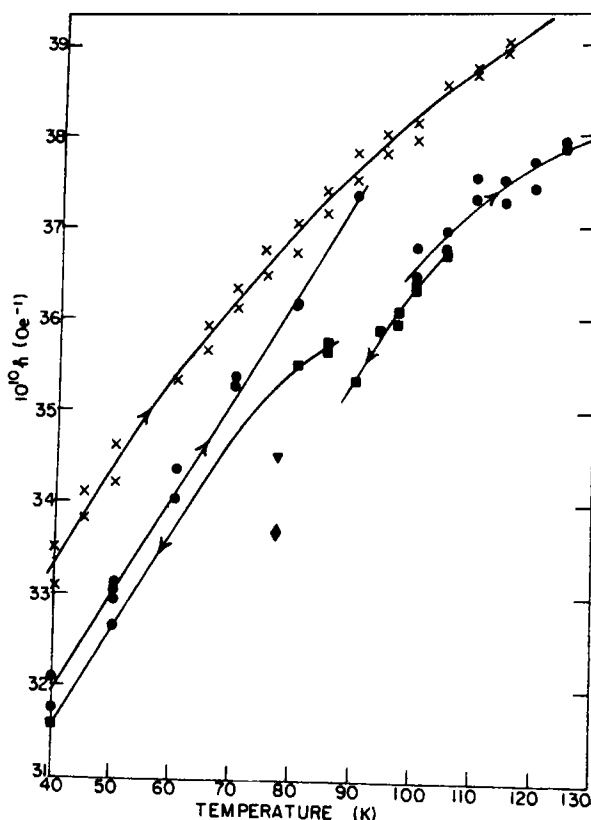


Fig. 2. The anomaly in the longitudinal forced linear magnetostriction at 90 K for the cold-worked sample (x) and the annealed sample (●, ■). The arrows indicate the direction of temperature change. (▼, ◆) values of the transverse forced linear magnetostriction for the unannealed and annealed samples for the equivalent field range (see text).

striction on magnetic field strength was measured at several temperatures. A typical plot of change in the length of the specimen vs. applied field parallel to the measurement direction is given in Fig. 3. This plot illustrates the extremely strong paraprocess in the Invar alloys which, for the fields used, changes the length of the specimen more than the saturation magnetostriction does. In the paraprocess region the forced magnetostriction coefficient parallel to the applied field has a field dependence expressible as $h = A - BH$ where A and B are positive. The parameters of the fits are given in Fig. 4 as plots of A and B vs. T . The unannealed sample has a larger forced

magnetostriction and a larger field dependence than the annealed sample.

The field dependence of h for the unannealed sample exhibits a maximum at 105 K. The data for the unannealed sample exhibited some curvature which was not included in the analysis. The fit parameters A and B for the annealed sample at 10.9 K have larger error limits. The larger scatter in the points taken at this temperature coincided with the onset of a relaxation phenomenon involving the response of the length of the specimen to a change in the magnetic field. This phenomenon is dealt with in detail in the next section.

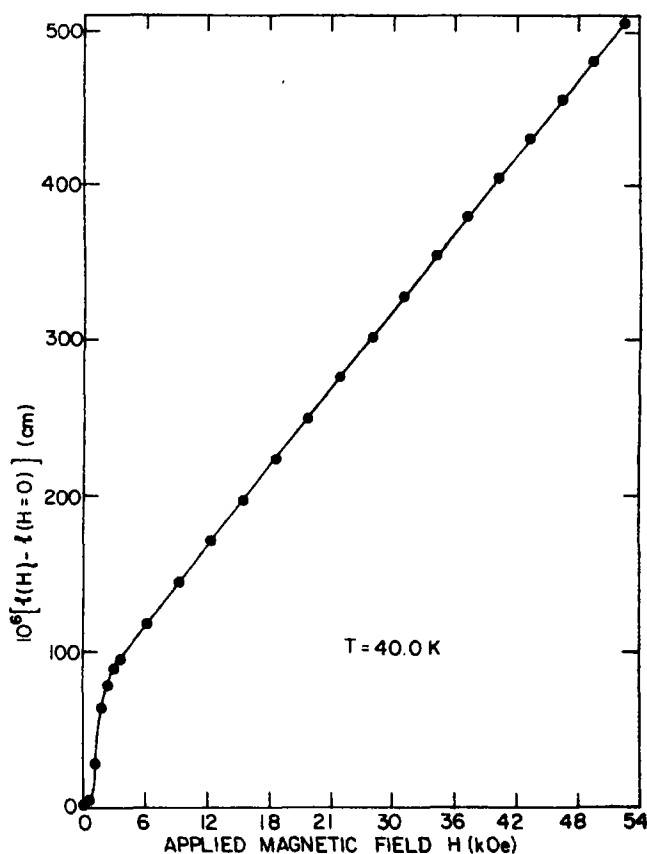


Fig. 3. The change in length $l(H) - l(H=0)$ for the annealed sample at 40.0 K with the magnetic field applied parallel to the cylinder axis. Note the large magnitude of the paraprocess magnetostriction relative to the saturation magnetostriction.

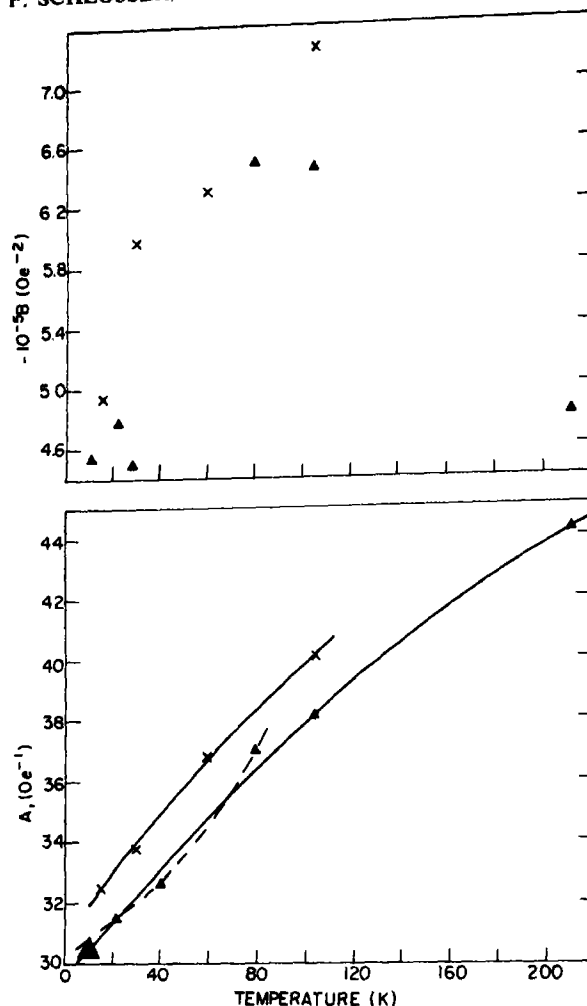


Fig. 4. Temperature dependence of the coefficients A and B in the relation $10^{10}h = A - BH$ for the annealed (Δ) and the cold worked (\times) samples. The solid curve for A is an overall fit, the dashed curve is thought to be the significant fit to the low temperature points. The point size represents the error.

The data of Fig. 4 appears to show some anomalous behaviour in the region between 80 and 105 K, in agreement with the detail of Fig. 2. The error limits on the values of A below 90 K are sufficiently small to warrant giving a positive curvature to the curve through these points (dashed line in Fig. 4) in contrast to the negative curvature of a general fit to all points (solid line), indicating two regions of differing behaviour.

The magnetostriction of the annealed sample perpendicular to the applied field was negative in the low field region. Figure 5 shows the change in length of the sample as a function of applied field at 77.4 K for both the annealed and unannealed samples, showing similar paraprocess magnetostriction but very different saturation magnetostriction. The very large negative transverse magnetostriction at low fields is very remarkable. It implies a

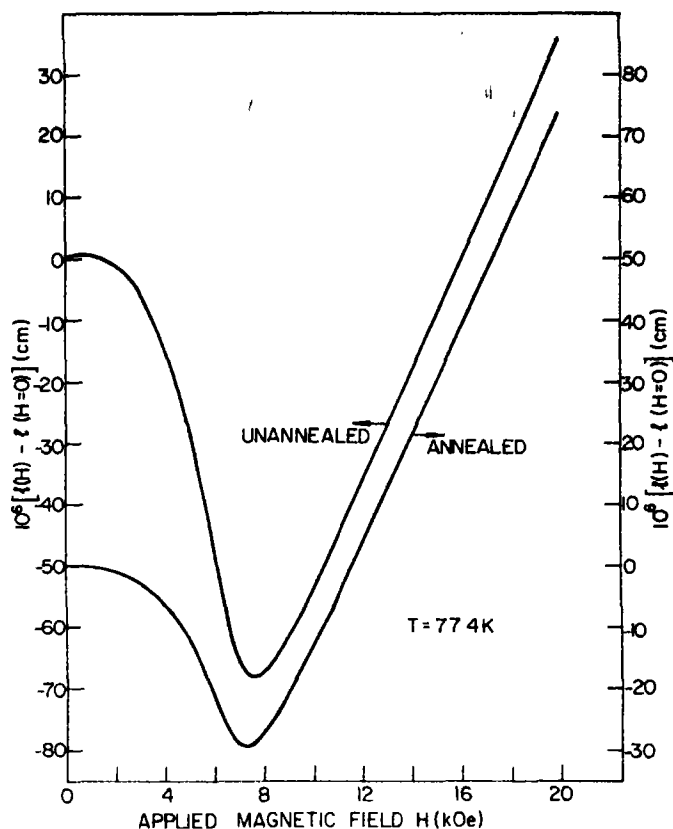


Fig. 5. The change in length $l(H) - l(H = 0)$ for the unannealed and annealed samples at 77.4 K with the magnetic field applied perpendicular to the cylinder axis. The paraprocess magnetostriction is large relative to the (negative) saturation magnetostriction.

large volume reduction during the saturation process. The field dependence of h is not linear but has a positive slope decreasing with increasing h , indicating an approach to a uniform paraprocess variation, and was considered in extrapolating to a 23.1 kOe field for comparison with longitudinal values in Figs. 1 and 2. Our values of the transverse forced magnetostriction agree with the values of the longitudinal forced magnetostriction at the corresponding temperatures and magnetic fields, showing that, to within the errors of these preliminary measurements, the forced linear magnetostriction is isotropic and $\Delta V/V = 3\Delta l/l$.

Matsumoto, Kaneko and Fujimori[3] reported that no field dependence was observed in their results. The sensitivity of their apparatus and the limited field range used made it unlikely that a field dependence of the magnitude noted here would be apparent, as the small curvature in Fig. 3 illustrates.

3. THE LOW TEMPERATURE LENGTH RELAXATION

For temperatures below 11 K the length of the specimens was observed to relax after a change in the magnetic field for both longitudinal and transverse fields, but only for fields in the paraprocess region. An increase in the

magnetic field produced a large immediate change in the length of the specimen. If the magnetic field was then held constant, the length of the specimen continued to increase with time. This process was reversible in that a decrease in the magnetic field was followed by a decrease in sample length. No creep in sample length was observed after a change of temperature in a magnetic field. The creep of the specimen in constant field was found to be approximately proportional to the logarithm of the time elapsed since the field change began. It generally took about 30 sec to change the magnetic field. At 4.2 K, for the annealed sample, the change in the length of the specimen was still varying as the logarithm of the time after 80 min. This relaxation prevented the gathering of extensive data below 11 K.

The extent and rate of the relaxation process was determined for temperatures between 1.1 and 11 K. The longitudinal magnetic field was changed between the two values 21.6 and 24.7 kOe, and the slope of the curve of

capacitance against the logarithm of the time since the field change began was determined. Figure 6 shows these slopes plotted against temperature.

At 2.5 K, for instance, for the annealed sample, 7.5 per cent of the total change in capacitance occurred in 80 min after the field has stopped changing, and the time dependence was still logarithmic after this time. In general, the time during which a logarithmic time dependence was observed was directly related to the slope of the creep vs. $\log t$ curve, or to the rate at which the creep occurred.

The creep phenomenon, like the anomaly between 40 and 130 K, was present for both the cold worked and annealed samples. At low (1–2 K) and high (7–11 K) temperatures, the samples show similar behaviour. However, the annealed sample had a strong peak in creep rate at about 4 K. A much smaller peak occurred for the cold worked sample for which there was only slight temperature dependence of the creep rate. This difference in creep rates

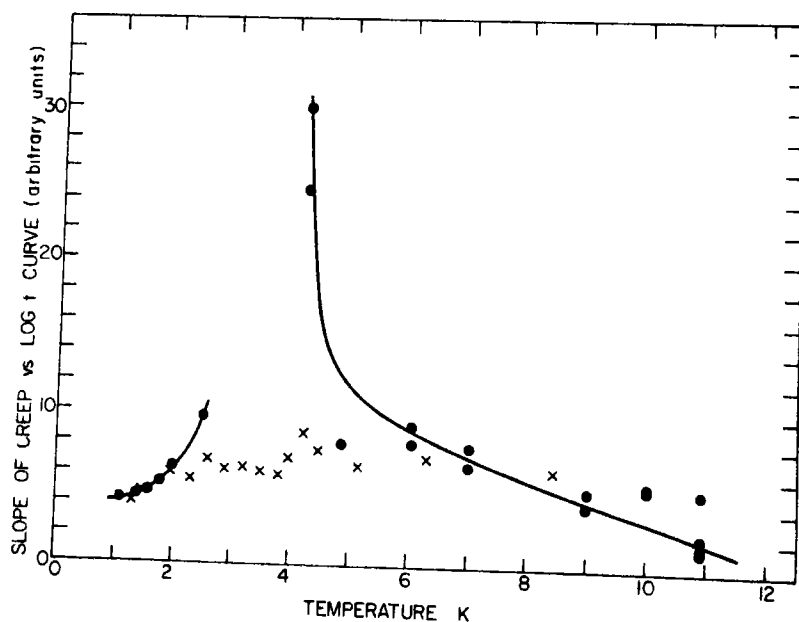


Fig. 6. Temperature dependence of the slope of the creep in the sample length vs. the logarithm of the time elapsed since a field change was initiated for the annealed (●) and (×) the cold worked samples.

can be correlated with the sharpness of the anomaly in the temperature dependence of h at about 90 K, and this is done in the following paper.

4. THERMAL EXPANSION

Results of the measurements of the thermal expansion of the Invar samples are shown in Fig. 7 as plots of α vs. T . The thermal expansion of the un-

annealed specimen was less than that of the annealed, or stabilized sample, although both are certainly less than the values obtained by Meincke on an annealed sample. In agreement with the empirical finding that cold work accentuates the invar anomalies at high temperatures, the thermal expansion of the un-

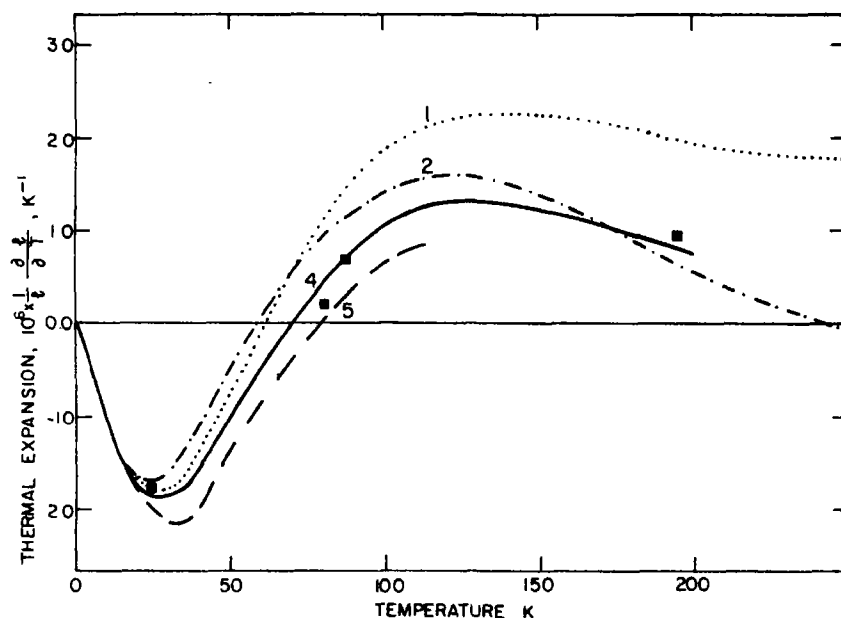


Fig. 7. Temperature variation of the linear thermal expansion coefficient of Invar alloys and the effect of a longitudinal magnetic field (1) $H = 0$; Annealed Invar, Meincke [7]; (2) $H = 0$, Annealed Invar, Zakharov and Fedotov [9]; (4) $H = 21.6$ kOe, Annealed Invar, present results; (■) $H = 0$, Annealed Invar, present results; (5) $H = 21.6$ kOe cold-worked Invar, present results.

sion of the annealed Invar at 293 K was $(0.07 \pm 0.1) \times 10^{-6} \text{ K}^{-1}$, the large uncertainty being due to possible error in the thermal expansion of the copper cell.

The few results in zero magnetic field are not appreciably different from the results taken in a field of 21.6 kOe for the annealed sample. Thermal expansion measurements between 9 and 23 K in transverse fields of 16 and 20 kOe for the unannealed sample did not differ from the results for this sample in a field of 21.6 kOe. The results in general follow those of

annealed specimen was less than that of the annealed, or stabilized sample, although both are certainly less than the values obtained by Meincke on an annealed sample.

The low temperature region is shown on an expanded plot in Fig. 8. Despite the large differences above 30 K which are believed to reflect differences in composition and heat treatment of the specimens, the reported results show remarkable similarity below 20 K. As noted, the forced magnetostriction also exhibited a similar insensitivity to heat treat-

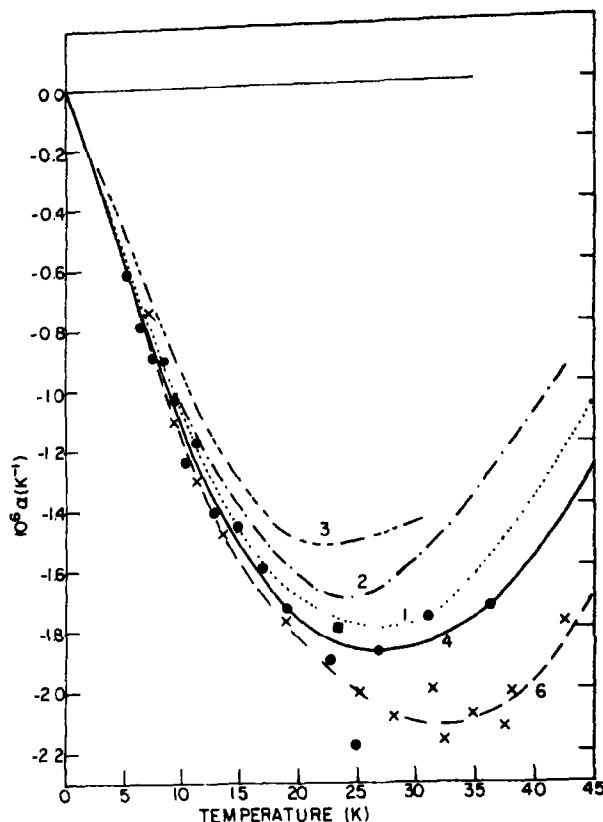


Fig. 8. Low temperature linear thermal expansion coefficient of Invar alloys. (1) $H = 0$, Annealed Invar, Meincke[7]; (2) $H = 0$, Annealed Invar, Zakharov and Fedotov[9]; (3) $H = 0$, Annealed Invar, White[8]; (4) \bullet , $H = 21.6$ kOe, Annealed Invar, present results. \blacksquare , $H = 0$, Annealed Invar, present results. (6) \times , $H = 21.6$ kOe, Coldworked Invar, present results.

ment at low temperatures except for the relaxation process.

5. DISCUSSION

At present, the theories of metallic ferromagnets are inadequate to account for the temperature and field dependence of magnetostriction of ferromagnets. It is possible to correlate many of the present observations and other properties of the Invar alloys in a qualitative model, which takes particular account of the steep drop of h below 20 K, and the creep phenomena observed below 11 K. This is done in the following paper. Here, we

wish only to point out that the results indicate an irreversibility of the sample volume with respect to the variables P , T , and H , below about 20 K, which is consistent with the creep and demonstrated by the failure of two of the derivative relations, i.e. both $\partial(\partial V/V\partial H)/\partial T = (\partial V/V\partial T)/\partial H$ and the Maxwell relation $-\partial M/V\partial P = \partial V/V\partial H$ are violated where M is the magnetic moment of the sample, V its volume, T the temperature, P the pressure and H the applied magnetic field.

The failure of the first relation is the most striking as the measurements were done on the same sample, in the same apparatus, and

during the same run. We have found that the forced linear magnetostriction is isotropic within the error of the present results, despite the specimen geometry and the existence of a macroscopic texture. The forced volume magnetostriction $\partial V/V\partial H$ is thus given as $3h$. The first derivative relation states that $\partial\alpha/\partial H = \partial h/\partial T$. For $T < 10$ K, where $\partial h/\partial T$ is large, a change in α of approximately $2 \times 10^{-6} \text{deg}^{-1}$ would be expected on this basis for $\Delta H \approx 20$ kOe. This is much larger than the small changes in α which are observed, larger in fact than α itself. Moreover, it is not necessary to appeal to the zero field value of

α to demonstrate the failure of this relation, since our measurements of α at 16 and 21.6 kOe both lie well within the paraprocess region and do not differ within the experimental error at 10 K, where the expected difference is about $2.2 \times 10^{-7} \text{K}^{-1}$, or 20 per cent. At higher temperatures, the predicted changes are too small, compared to the experimental error, to make any discrepancy detectable.

We have compared our data on $\partial V/V\partial H$ with the magnetization vs. pressure data of Kondorskii and Sedov[10, 11] on iron-nickel alloys of various compositions. At 4.2 K, 8.6 kOe, the ratio of $-\partial I/\partial P$ ($I = M/V$) for

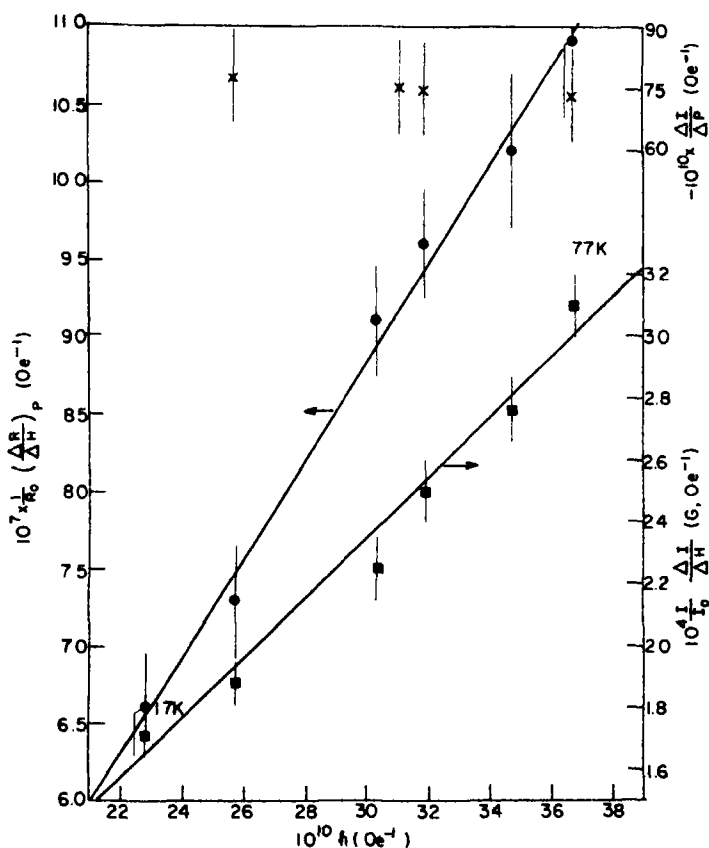


Fig. 9. Plots of the pressure dependence of the magnetization $\Delta I/\Delta p$, the forced magnetoresistance coefficient $\Delta R/R_0\Delta H$ and (I/I_0) ($\Delta I/\Delta H$) for the 36.8 at.% Ni alloy of Kondorskii and Sedov[10] all vs. h for the present cold worked sample, showing the good correlation of the temperature variations of the two latter quantities with the temperature variations of h , and the lack of any correlation with the former.

the 33.5 at.% Ni (34.9 wt.% Ni) sample of Kondorskii and Sedov[11] to $\partial V/V\partial H = 3h$ for our 33.3 at.% Ni alloy is given by $-(\partial I/\partial P)/3h = 1.75$. At 77.3 K, 8.6 kOe, the ratio $-(\partial I/\partial P)/3h$ is still approximately 1.2.

More extensive measurements of the temperature dependence of $\partial I/\partial P$ have been made[10] on a 36.8 at.% Ni sample, which show that $\partial I/\partial P$ is effectively independent of temperature below 77 K, quite unlike the temperature dependence of h (see Fig. 9). By itself, the discrepancy might well be attributed to the differences between our specimens and those of Kondorskii and Sedov. However, values of the pressure dependence of the magnetization have been deduced for these specimens by an independent method [12] and show good agreement with the former work. This fact, together with the existence of the completely internal discrepancy discussed above leads us to suppose it is real and we are thus led to conclude that the specimen volume is not a function of state, and the thermodynamic arguments of Graham and Cochrane[1] are not applicable to this alloy below ~ 20 K. The results indicate the freezing in of a high temperature state of lower volume which is not equilibrated by changes in H . (The following paper indicates a plausible mechanism.) In this regard it is interesting to note the good correlation of the temperature dependence of h with that of two other field derivatives, those of the electrical resistance and the magnetization. These are shown in Fig. 9 as plots of the magnetoresistance coefficient $\partial R/R_0\partial H$ and the reduced constant pressure susceptibility $(I/I_0)(\partial I/\partial H)_p$ vs. h . This data is also for the 36.8 at.% Ni specimen of Kondorskii and Sedov[10]. The correlation of h with the magnetoresistance is reminiscent of the similar correlation found by Hayashi[13] over a considerable range of

both temperatures, above 77 K, and compositions from 32 to 100 per cent Ni. The correlation with the susceptibility was suggested by the relation $\omega \propto I^2$ where ω is the relative volume change occurring when all exchange interactions are switched off, which has been derived by Belov[14] from an expansion of the free energy about the Curie point, but is known to hold more generally[15]. The factor I/I_0 which would be expected from the quadratic dependence, is from separate data[12]. Some part of these correlations would be due to geometrical factors which enter in reducing resistance to resistivity, or the susceptibility to constant-volume susceptibility, but these could not account for all of the correlation.

Acknowledgements—We are indebted to Mr. R. H. Munnings for technical assistance. This work was supported by the National Research Council.

REFERENCES

1. GRAHAM G. M. and COCHRANE R. W., *Phys. Rev.* **184**, 543 (1969).
2. SCHLOSSER W. F., MEINCKE P. P. M., VITTORATOS E. and GRAHAM G. M., *J. phys. Soc. Japan* **27**, 1696 (1969).
3. MATSUMOTO M., KANEKO T. and FUJIMORI H., *J. phys. Soc. Japan* **26**, 1083 (1969).
4. WHITE G. K., *Cryogenics* **1**, 151 (1961).
5. SLAVIN A., M. Sc. Thesis, University of Toronto (1968).
6. BUNTON G. V. and WEINTROUB S., *Cryogenics* **8**, 354 (1968).
7. MEINCKE P. P. M., Ph.D. Thesis, University of Toronto (1963).
8. WHITE G. K., *Proc. Phys. Soc.* **86**, 159 (1965).
9. ZAKHAROV A. I. and FEDOTOV L. I., *Fiz. Metall. Metallov.* **23**, 759 (1967).
10. KONDORSKII E. I. and SEDOV V. L., *Soviet Phys. JETP* **8**, 586 (1959).
11. KONDORSKII E. I. and SEDOV V. L., *Soviet Phys. JETP* **11**, 561 (1960).
12. COCHRANE R. W. and GRAHAM G. M., *Can. J. Phys.* **48**, 264 (1970).
13. HAYASHI, J. F., *Mem. Coll. Sci., U. of Kyoto, Ser. A.* **30**, 39 (1962).
14. BELOV K. P., In *Magnetic Transitions*, p. 89. Consultants Bureau, New York (1961).
15. MEINCKE P. P. M., *Can. J. Phys.* **48**, 859 (1970).

A MODEL FOR THE INVAR ALLOYS AND THE Fe-Ni SYSTEM

W. F. SCHLOSSER

Department of Physics, University of Toronto, Toronto 5, Ontario, Canada

(Received 11 June 1970; in revised form 14 August 1970)

Abstract—A model is proposed to account for the metallurgical and physical properties of f.c.c. Fe-Ni alloys, including the Invar anomalies around 34 at.% Ni. Microscopic inhomogeneity due to short range atomic ordering on the basis of the FeNi_3 compound is assumed to be a dominant feature of the alloy system. Regions of both f.c.c. Fe and FeNi_3 are present in alloys in the invar region. The electronic state of only the Fe atoms, and hence their volume, magnetic moment, and sensitivity to external variables, is further assumed to be a function of the number of Ni nearest neighbours, which in turn depends on such variables as cold work. With these assumptions, the properties of the annealed alloys above the Curie point are developed, the phase diagram and metastability of the alloys is explained and the Invar anomalies below the Curie point are accounted for. Furthermore, the model explains the unusual low temperature properties of these alloys as due to exchange coupling between ferromagnetic FeNi_3 regions and antiferromagnetic Fe regions. An extension of the model is made to other binary alloy systems that exhibit Invar-type anomalies.

1. INTRODUCTION

THE F.C.C. iron-nickel alloys in the Invar concentration range, ~ 35 at.% Ni, are anomalous in many respects; in particular, the fall of the $T = 0$ magnetization with increased concentration of Fe[1,2], the departure from Vegard's Law[3] and the associated large spontaneous volume magnetostriction[4] and low thermal expansion[5] below the Curie temperature, may be cited. The preceding paper[6] has described measurements of the large forced magnetostriction below room temperature in invar. There is also an anomalously large paramagnetic susceptibility[7,8] and large temperature variation of the magnetization[1,7,8].

A feature of these anomalies is their persistence to quite high Ni concentrations in somewhat attenuated form. Deviations in the concentration dependence of the lattice parameter are evident at ~ 57 at.% Ni[3], and in the magnetic moment at ~ 58 at.% Ni[1]. The positive volume anomaly[5] that occurs below the Curie temperature of the invar alloys, although largest at ~ 34 at.% Ni, is still quite prominent at 60% Ni and becomes

small and negative only above 70% Ni. Similarly, a negative term proportional to the temperature is still present[9] in the experimental fit to the thermal expansion near $T = 0$ for a 50 at.% Ni alloy.

Attempts to explain these anomalous properties have often involved the assumption of a random distribution of Fe and Ni atoms [10-17], with some further assumptions about differences in the interatomic interactions for the different possible pairings[16,17]. These models do not seem able to account for the persistence of the anomalies to very high Ni concentrations.

In this paper we propose a new model applicable not only to the invar alloys, but to the whole Fe-Ni system. The invar anomalies then are seen to be a consequence of the factors that determine the behaviour of this system.

The existence of microscopic inhomogeneity in the alloy is regarded as a premise. Given this, the model rests on two main assumptions: first (a) that the atomic ordering of Fe-Ni alloys is not random, but is characterized by extremely marked short range atomic order

on the basis of the FeNi_3 compound with the f.c.c. $L1_2(\text{CuAu}_3)$ structure[18], and secondly (b) that the number of Ni nearest neighbours determines the electronic state of a Fe atom while the Ni atoms are not sensitive to the local atomic environment.

These assumptions are expanded on and justified in Section 2. The model is developed from them in Section 3, and applied to distinguish between the behaviour of well annealed and cold worked alloys.

The model is applied to the explanation of the invar properties in Section 4, with particular emphasis on the results of the preceding paper. Section 5 generalizes the model to other invar-type alloy systems.

2. ASSUMPTIONS

In the models of several authors[10-15] inhomogeneity has been arbitrarily assumed to avoid a singularity in the alloy properties at ~ 30 at.% Ni. While the introduction of a fine scale inhomogeneity certainly has important consequences for such models, it has been given no experimental or theoretical justification. The model of Shiga and Nakamura [19,20] also assumes a random distribution of Fe and Ni atoms[21], but with a variable electronic state for the Fe atoms. This random distribution is insufficient to explain the properties of Fe-Ni alloys over a wide range of compositions and temperatures.

Neutron scattering data[22-24] and electrical resistance studies[25,26] on the Fe-Ni system indicate that extensive short range atomic order is present over wide composition and temperature ranges in supposedly disordered alloys. This ordering is based on the FeNi_3 compound. This compound is ferromagnetic[18] with a Curie temperature between 863 and 980 K, probably closer to 863 K. There is considerable uncertainty in this temperature as the compound disorders at a lower temperature, 780 K. The Curie temperature of the disordered alloy with 75 at.% Ni is ~ 873 K. The importance of the short range atomic ordering based on the FeNi_3

compound is stressed in this paper. To illustrate this, in Fig. 1 we have plotted the liquidus for the Fe-Ni alloy system, the heat of formation of these alloys, the coefficient of the linear term in the low temperature specific heat, and the Debye θ . Again we wish to point out that it is not the peculiar behaviour of these alloys around 35 at.% Ni that is significant, but the observation that this peculiar behaviour begins near 75 at.% Ni. This first assumption will allow us to make semi-quantitative statements about the local environments of particular atoms.

Collins *et al.*[22] proposed a structure in which the cube corner sites of the f.c.c. cells are occupied mainly by Fe atoms and the face-centre sites are randomly occupied by the remaining Fe atoms and the Ni atoms. The structure maximizes the number of Fe-Ni nearest neighbour *pairs*. The present assumption differs from theirs in stressing the importance of the contribution to the stability of the system of the FeNi_3 structure as a whole. It is probably not possible to decide between these models on grounds of their relative stability by a fundamental calculation; the analogy with the f.c.c. Cu-Mn alloys, which are known to evolve by segregation of Mn atoms[27], would seem to offer some support for the present model. In any case, the main practical difference between these models lies in the existence of a more well defined interface between Fe-rich and Ni-rich regions under our assumption. The properties of the system are then conveniently discussed in terms of the positions of atoms with respect to the interface, or transition region, without reference to the details of the background statistical inhomogeneity which is the important feature of the alternative assumption[22].

Our second assumption relates the atomic behaviour to particular environments. It follows more nearly the idea of Shiga than the 'two states of iron' idea of Weiss[33], in that we suppose that the electronic configuration of a particular Fe atom, which determines its interaction with nearby atoms and hence the

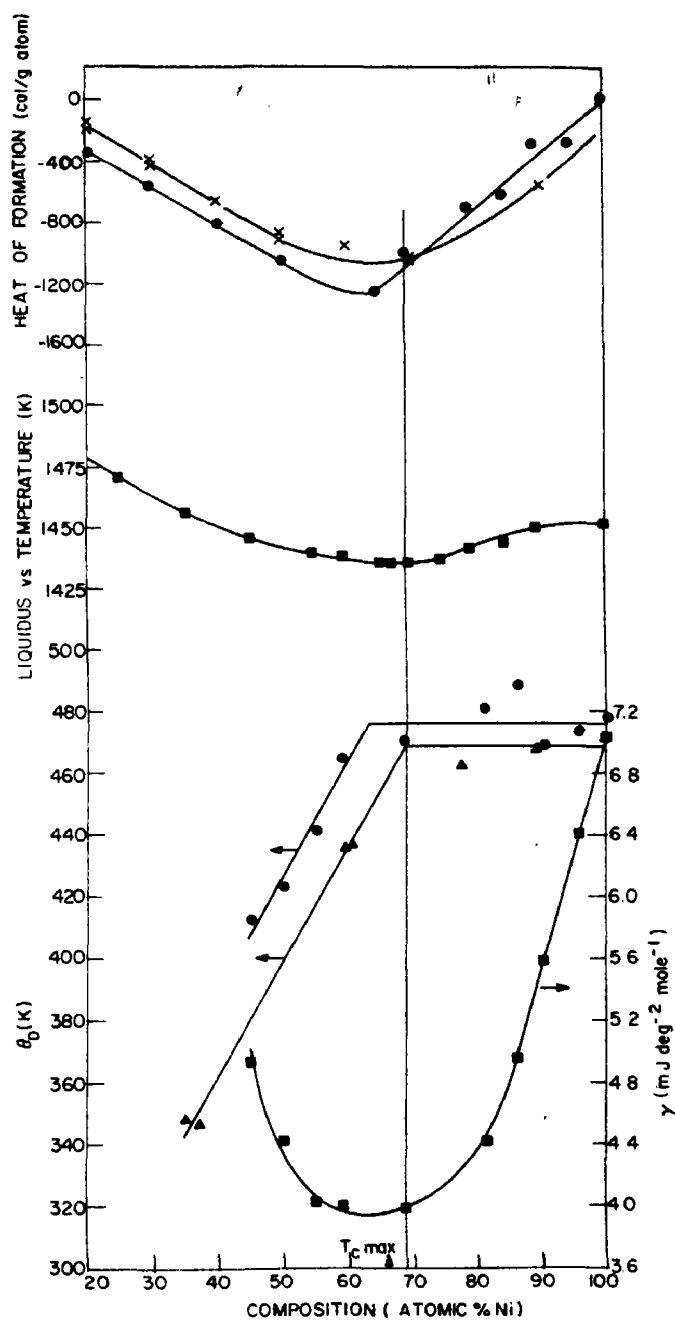


Fig. 1. The liquidus[28], the heat of formation[29, 30] and the low temperature specific heat γ [31] and θ [31, 32] for the Fe-Ni alloy system.

nearest neighbour distances and the ordered state magnetic moment on the atom, can vary between two limits depending primarily on local atomic environment, and on external variables such as temperature and magnetic field. This assumption has theoretical support in the work of Goodenough[34] and Bailyn [35]. The main experimental justification for this assumption is the observation that the lattice parameter of γ Fe in its region of stability (1183 to 1662 K) linearly extrapolates to a 300 K lattice parameter of ~ 3.574 Å [36,37]. The 300 K lattice parameters[18] of Fe-C, Fe-N, and Fe-Mn alloys against concentration extrapolate also to ~ 3.57 Å for pure Fe. However, Fe atoms enter into solution in Fe-Ni, Fe-Pd and Fe-Pt alloys, for not too large Fe concentrations, causing a change in lattice parameter[38] which extrapolates to a 300 K lattice parameter of ~ 3.64 Å in each case. The small parameter state of Fe appears to be antiferromagnetic at low temperatures with a magnetic moment of $\sim 1 \mu_B$ or less[39-42]. The large parameter state of Fe contributes a large moment ($\sim 2.8 \mu_B$) per atom when alloyed with Ni[1], Pd [43-46] or Pt[47] at sufficiently high concentrations (7-10 at.%). An Fe atom with all Fe nearest neighbours will then have a low 'volume', (the volume of an atom being defined in terms of the nearest neighbour distances), and have a small magnetic moment oppositely oriented to the moment on the atoms around it at low temperatures. Above some minimum effective number of Ni neighbours, an Fe atom has essentially its maximum moment and volume. Between these extremes the moment and volume of the Fe atom in question are strongly dependent on the number of Ni nearest neighbours, as well as on external variables. The increase in volume with magnetic moment is a result of a change of bonding electrons with no moment, into non-bonding electrons with magnetic moment[19,48]. This lower number of bonding electrons results in a reduction of the cohesive force, an increase in nearest neigh-

bour distances, and an expansion of the whole alloy relative to a linear interpolation (Vegard's Law) of the lattice parameters of the two components of the alloy, f.c.c. Ni and f.c.c. Fe. Thus, this assumption alone explains why the presence of Ni nearest neighbours produces an increase in volume and a large positive departure from Vegard's Law above T_c . Another related effect appears for those Fe atoms with insufficient Ni neighbours to have the maximum atomic volume at T_c . As the alloy is cooled below its Curie temperature these atoms will increase their moment due to a net increase in the magnetization with decreasing temperature. The conversion of non-magnetic, bonding, 3d electrons to magnetic, non-bonding electrons in the polarization process reduces the bonding of this atom to its neighbours, resulting in a large positive spontaneous magnetostriction below the Curie temperature and a corresponding large decrease in the thermal expansion coefficient. Furthermore, an applied magnetic field, by increasing the magnetization also converts Fe atoms to high moment states, producing a large high field susceptibility and forced volume magnetostriction. The essential feature of this paper is the application of these ideas to the particular constraints imposed on a model in which most of the Ni atoms are in the FeNi_3 compound.

3. THE MODEL

1. *Inhomogeneity and the alloy structure*

We consider first a well annealed alloy. By this we mean an alloy annealed at low temperatures sufficiently to allow the diameters of the ordered regions to exceed several lattice parameters. These regions are single phase ordered domains and are generally of irregular size and shape. An alloy contains three regions of interest due to the existence of ordering. These are illustrated in Fig. 2. Type 1 regions consist of FeNi_3 of assumed perfect order. In this core, each Fe atom has ideally 12 Ni nearest neighbours and exhibits its maximum moment and nearest neighbour

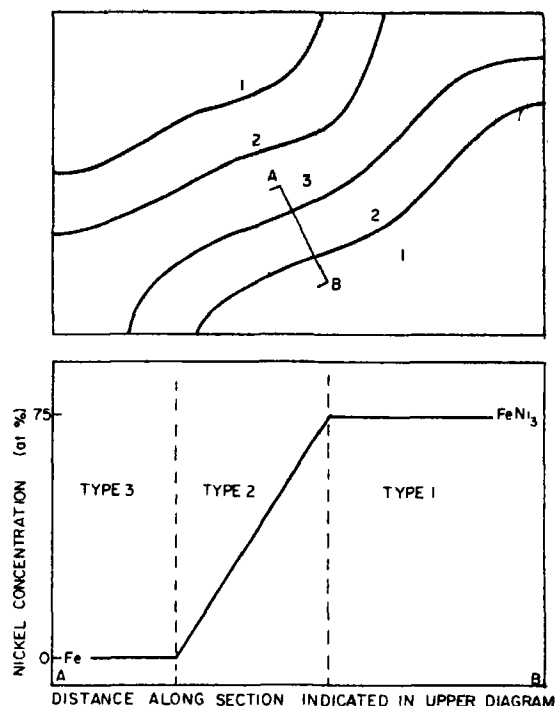


Fig. 2. The three types of regions defined in our model of the Fe-Ni alloys. The upper diagram illustrates the regions for a low nickel concentration alloy. The lower diagram illustrates the variation of the nickel concentration in the various regions.

distance. Type 2 regions form shells around the regions of perfect order and are the regions of decreasing Ni concentration and decreasing order that separate the perfectly ordered type 1 regions from regions designated type 3 which are the f.c.c. iron excluded from regions 1 and 2 due to the existence of FeNi_3 order in Fe rich alloys. Type 3 regions contain no nickel, but consist of the segregated f.c.c. Fe atoms with small nearest neighbour distance ($\sim 1.26 \text{ \AA}$) and with low moment ($\sim 1 \mu_B$ or less).

The boundary of a type 1 region is drawn along iron atoms with sufficient Ni nearest neighbours that they exhibit practically their full volume and moment at high temperatures (above $\sim 900 \text{ K}$). The material in type 2 regions is that which can exhibit large changes in volume or moment in response to changes in external variables. Thus an important para-

meter is the volume of the type 2 regions in an alloy. For well annealed alloys, it may be assumed that the thickness of type 2 regions is approximately constant and independent of the size of type 1 regions.

The general effects of decreasing the nickel concentration in an alloy from the 75 at.% Ni ordered compound are then as follows. Down to 65–70 at.% Ni no change in the alloy properties are apparent. The minimum number of Ni nearest neighbours has not fallen below the defining value for type 1 regions. At concentrations below 65 at.% Ni, added Fe atoms can no longer be accommodated in ordered FeNi_3 regions, and begin to appear as isolated type 2 regions, still containing some nickel which will influence the state of the Fe atoms. As additional iron is added to the alloy, the total alloy volume in type 2 regions increases. The presence of ordering in the alloy, obtained through atomic diffusion, dictates that the type 2 regions take the form of thin layers tending to surround and isolate the ordered type 1 regions. A maximum volume of type 2 material occurs when the ordered regions are just separated from each other by type 2 material. The composition at which this occurs may be estimated by considering the type 1 material to be in spheres. The maximum surface area of the spheres (and therefore maximum type 2 volume for a well annealed alloy) will occur when the spheres come into contact. If the spheres are in a cubic array, this will be when half the total volume is inside the spheres.

If the material outside the spheres is pure Fe and that inside is FeNi_3 , the maximum occurs at $\sim 37.5 \text{ at.\% Ni}$. This figure is in good agreement with the Ni concentration of the alloy exhibiting the largest invar anomalies ($\sim 35 \text{ at.\% Ni}$) and with the Ni concentration of the alloy exhibiting the maximum deviation from Vegard's Law ($\sim 43 \text{ at.\% Ni}$). The difference in these concentrations can be understood when the finite thickness of the type 2 regions is considered. The maximum high temperature deviation from Vegard's

Law is expected to occur at a higher Ni concentration than that corresponding to the maximum in the invar anomalies, because the former is determined by the amount of type 1 material only (by the expansion mechanism outlined in the previous section), while the anomalies are due to the type 2 material. The maximum amounts of type 1 and type 2 will not occur at the same Ni concentration if there is a finite thickness of type 2 material.

2. Effect of cold working

For well annealed alloys the thickness of the type 2 regions is approximately independent of further annealing, yet the size of the ordered type 1 regions increases with further annealing by growth of the more favourable regions at the expense of others. Therefore the type 3 regions will increase in size with further annealing, while the volume of the type 2 regions decreases.

In general, since both quenching and cold working result in a reduction of the degree of order in an alloy, both processes increase the amount of type 2 material at the expense of material of both types 1 and 3. Remembering that the amount of type 2 material is a measure of the magnitude of the anomalies, the model's prediction of an increase of this with increase in the disordering of the alloy is in agreement with experiment [4, 49]. These assumptions as to the presence of FeNi_3 ordering are sufficient to explain the effects of rolling on the properties of invar single crystals observed by Chikazumi *et al.* [49], which they could not interpret on the basis of Fe_3Ni ordering.

3. Stability and the phase diagram

f.c.c. γ iron is unstable below 1183 K, and transforms to the b.c.c. α form. In finely divided form, f.c.c. Fe can be maintained below this temperature through coherency with a suitable lattice [50, 51] although the lattice match is rarely perfect, and there is in general a coherency strain at the interface. In the f.c.c. Fe-Ni alloys, the f.c.c. Fe regions are stabilized by coherency with nearby

ordered type 1 regions. The stability of the alloy can be maintained only if a large interface area is present. As we have just seen, annealing reduces this. The Fe regions grow until they become unstable, and then transform to the b.c.c. phase. The alloys are metastable up to 65–70 at.% Ni. The time required for equilibrium is, however, extremely long below 400°C as the necessary migration of nickel atoms must occur by diffusion, a very slow process at low temperatures.

From our model the low temperature equilibrium is between b.c.c. Fe and the ordered FeNi_3 compound with some excess of Fe. This is in good agreement with the experimental phase diagram of Hansen [52] (Fig. 3) and with the more recent delineation of the phase boundaries of the ordered regions of the Fe-Ni system by Kneller [53]. The phase diagram of Ananthanarayanan and Peavler [54], obtained with very fine particles, extends the region of stable ordered f.c.c. alloy to ~57 at.% Ni. At concentrations below 65 at.% Ni, this model is in accord with the work of Kneller in assuming the lack of strong Fe_1Ni_1 ordering in the Fe-Ni system.

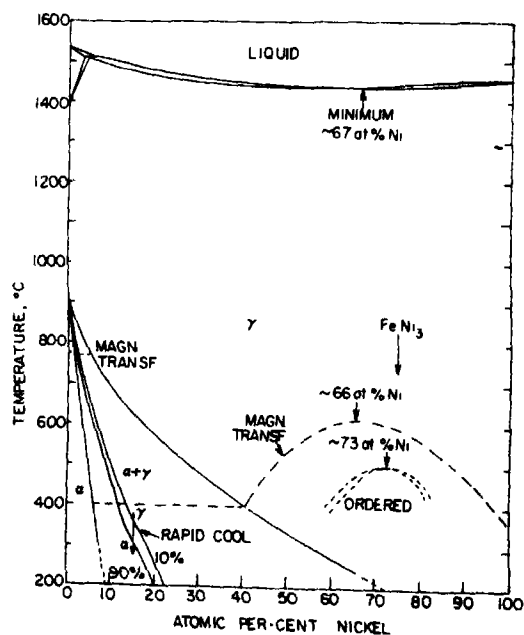


Fig. 3. The phase diagram of the Fe-Ni system [52].

4. EXPLANATION OF INVAR PROPERTIES

1. General

Turning to application of these ideas to the observed properties of the invar alloys, sufficient mention has already been made of those properties which depend on the inhomogeneity per se, such as the departure from Vegard's Law.

A large class of anomalous properties depend particularly on the amount of type 2 material present, since this is the fraction whose behaviour is sensitive to external influences. It may be stressed again that this model explains in a natural way the persistence of anomalies in properties like the paraprocess susceptibility or thermal expansion to high Ni alloys. The general nature of the magnetic ordering with decreasing temperature according to this model is as follows — individual regions of the alloy interact more strongly through common type 2 regions or type 1 overlaps to form larger regions of magnetic order, and eventually a macroscopic Curie transition. The Curie transition is thus quite broad, with a high temperature tail, reflecting the inhomogeneity of the alloy [4,55,56]. The continual increase of the magnetic moment of the alloy due to both the coupling of isolated regions and increased induced magnetization in type 2 regions results in a curve of magnetization vs. temperature that falls considerably below a Brillouin curve fitted at $T = 0$ and at T_c . This flattened curve is a well known feature of the invar alloys [1]. The large spontaneous magnetostriction and hence the thermal expansion anomaly below the Curie point are a consequence of the increased induction of Fe in type 2 regions due to increased ferromagnetism in the alloy.

2. Exchange coupling in the 35% Ni invar

In order to fully explain the results presented in the preceding paper [6], and other data for invar alloys in the vicinity of 35 at.% Ni, where all three types of regions are pre-

sent: pure f.c.c. Fe, ordered FeNi₃, and the type 2 transition region, one additional assumption is necessary: as mentioned, it is supposed that the type 3 regions are antiferromagnetic at low temperatures, for investigations [57] have shown that f.c.c. Fe is antiferromagnetic at low temperatures with a Neel point below 100 K. Mossbauer results for low Ni concentration alloys [2,58–61] show that a paramagnetic line, which we attribute to the type 3 regions, is prominent. It broadens below 90 K [2,58,59], indicating an antiferromagnetic transition in type 3 regions to a magnetic state with low internal field. Extrapolation of the Néel temperature of antiferromagnetic Fe–Mn alloys [62–65] to pure Fe also indicate that f.c.c. Fe should become antiferromagnetic below ~ 80 K.

According to this model, the invar alloys have a very unusual structure below this transition. Type 1 and type 2 regions are ferromagnetic, type 3 regions are antiferromagnetic, and the two types of magnetic regions interact at the boundary between the type 2 and type 3 regions. In this temperature range both regions vie for control of the type 2 material and there is a very large area of interface between the ferromagnetic and antiferromagnetic regions. Kouvel [66] proposed a mechanism of very strong coupling between ferro- and antiferromagnetic regions in f.c.c. Mn alloys to explain their magnetic properties. These alloys are believed to have a similar microstructure to that proposed here for the Fe–Ni alloys. This type of strong coupling between ferro- and antiferromagnetic regions has been observed in other materials [67] and is attributed to exchange of magnetic electrons between atoms on opposite sides of the boundaries of the regions. In an ideal ferromagnet and an ideal antiferromagnet the direction of the magnetization at zero field relative to the crystal axes is determined by the magnetic anisotropy of the material. For the antiferromagnet this refers to the sublattice magnetization. Rotation of antiferromagnetic moments is comparatively difficult

and requires large magnetic fields to achieve small rotations. Thus, if there exists an exchange coupling between ferromagnetic and antiferromagnetic atoms at the boundary separating them, the antiferromagnetic atoms can seriously affect the behaviour of the ferromagnetic region.

We assume that this coupling energy has a temperature dependence and magnitude relative to the anisotropy energy of the antiferromagnet as given in Fig. 4. Just below the

T_E , at which the coupling energy is equal to the antiferromagnetic anisotropy energy, is approached, ferromagnetic and antiferromagnetic regions become more tightly coupled. The antiferromagnetism of the type 3 regions increasingly restricts the induction of ferromagnetism in adjoining type 2 regions. The forced magnetostriction thus decreases in this region, and the rigidity of the lattice increases as less material can transform between the low volume and the high volume states.

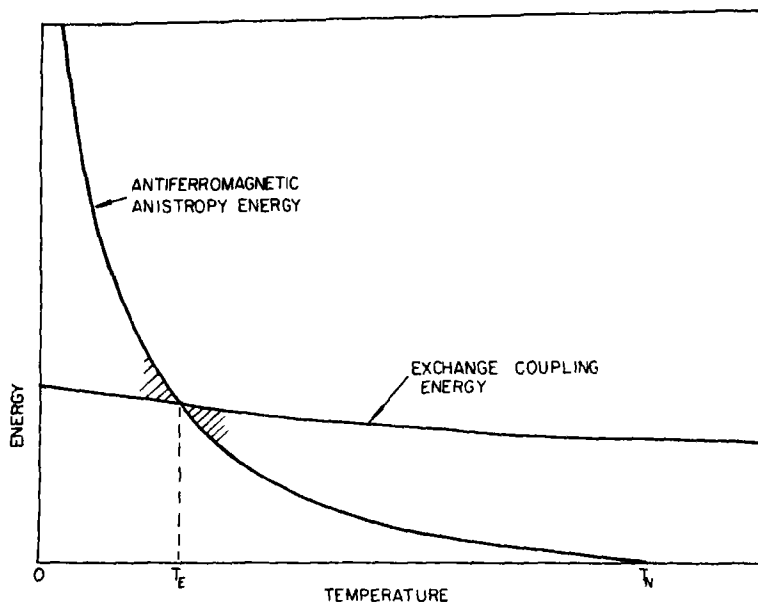


Fig. 4. The relation assumed between the anisotropy energy of the antiferromagnetic regions and the exchange energy coupling these regions to neighbouring ferromagnetic regions.

Néel temperature, the anisotropy energy of the antiferromagnet is small and the ability of the ferromagnetic regions to respond to a magnetic field is only slightly reduced by the constraint of the exchange coupling to the antiferromagnetic regions. However, losses can be expected in this region as the antiferromagnetic moments are rotated against their anisotropy energy. A peak in the ultrasonic attenuation has been reported for invar alloys below 100 K by both Meincke and Litva [68] and by Fletcher [69]. As the temperature

Experimentally an increased rigidity of the material—a decrease in the magnetoelastic coupling—is observed below ~ 20 K. The forced magnetostriction decreases by ~ 30 per cent below this temperature [6], the magnetic susceptibility exhibits a corresponding decrease [70], the velocity of sound rises [68], and the compressibility correspondingly falls below ~ 40 K.

According to our model, cold worked and annealed alloys are distinguished by the amount of type 2 material present. As we have

seen, increased coupling of the antiferromagnetic regions to the lattice reduces the ability of type 2 regions to respond to changes in temperature or magnetic field. For very strong coupling, i.e. below T_E , cold worked and annealed alloys can be expected to behave identically, as has been observed experimentally[6]. Despite large differences in the thermal expansion coefficient above 20 K for entirely different samples from different manufacturers and of different purity, there is remarkably little difference between the values for these samples below 20 K. Similarly the forced magnetostriction of annealed and cold worked samples, from the same rod, begin to converge to a common value at 20 K.

The response of such exchange coupled magnetic systems to a rapid change in external conditions is generally logarithmic in time. For example, experiments on exchange coupled Co-CoO and Ni-NiO films by Schlenker[71] have shown this time dependence of the response of the magnetization to a change in magnetic field. A logarithmic time dependence of the rotational torque at high magnetic fields was found in $\text{Fe}_{65}(\text{Ni}_{1-x}\text{Mn}_x)_{35}$ alloys exhibiting exchange coupling by Nakamura and Miyata[21]. It is expected in view of the observation of rotational torque hysteresis in 29–32 at.% Ni invar alloys by Nakamura, Takeda and Shiga[59], which correlated with the widening of the paramagnetic Mossbauer line in these alloys at low temperatures, that exchange coupling time effects would be found in the higher Ni invar alloys. The observation of a logarithmic time dependence of the *volume* of a 33 at.% invar alloy following a change in the magnetic field (above saturation only) seems to confirm its presence. The temperature dependence of this length relaxation is similar to the temperature dependence of the torque relaxation reported for the $\text{Fe}_{65}(\text{Ni}_{1-x}\text{Mn}_x)_{35}$ alloys[21]. This temperature dependence follows from Fig. 3, where relaxation can only occur by thermal excitation for temperatures within kT of T_E (the hatched regions) but with some broadening in

a real alloy due to the variable conditions affecting different regions in the alloy. For a change in magnetic field, the response of the alloy, principally occurring at the boundary between type 2 and type 3 regions and involving a change in the state of Fe atoms, relaxes through a *volume* creep because of the strong magnetoelastic coupling. The slope of the logarithmic creep curve and the extent of the relaxation depend on the existence of a well defined boundary between type 2 and type 3 regions, which is favoured by annealing. The temperature dependence of the rate of the logarithmic creep thus reflects the shape of the anomaly at 90 K[6].

The decrease in magnetoelastic coupling observed below 20 K is a common feature of a wide range of alloys, (up to 45% Ni). In the alloy $\text{Fe}_{65}(\text{Ni}_{10.7}\text{Mn}_{0.3})_{35}$ there is a sharp drop in the magnetic moment of the alloy below 20 K[19]. The magnetization results of Cochrane and Graham[18] also show an unexpected fall of the moment from the high temperature extrapolated values below 20 K ($1 \text{ in } 10^4$). This similarity of the temperature dependence of the magnetoelastic coupling, despite a wide range of magnitude and alloy compositions can be accounted for quite readily by our model where the temperature dependence of the coupling exhibits different behaviour above and below a temperature determined only by the antiferromagnetic anisotropy energy of the pure Fe type 3 regions, which we assume occur in all of these alloys, and the exchange coupling between type 3 and type 2 regions, which does not vary greatly with alloy composition.

CONCLUSIONS

In summary, we have proposed a model for the Fe-Ni alloy system, which stresses the atomic inhomogeneity. By assuming that this inhomogeneity is due to short range atomic order based on the FeNi_3 compound, and that the state of an Fe atom depends on the number of Ni nearest neighbours, the model is made sufficiently simple that it can be used to make

predictions of a wide variety of physical properties that turn out to be reasonably in accord with experiment.

It is possible to generalize this model to other systems under the following conditions for the appearance of invar properties.

(1) The alloy system must exhibit considerable short range atomic ordering based on a magnetic compound in a paramagnetic or diamagnetic matrix. The compound involved in the invar properties will be the most stable compound in an alloy system.

(2) The magnetic compound and matrix must have the same or a similar crystal structure, similar, though not equal, lattice parameters and some degree of coherence across the compound-matrix interfaces.

The invar anomalies will be most intense at a composition approximately half-way between the composition of the matrix and the stoichiometric composition of the compound responsible for the short range order.

There are two other binary alloy systems that exhibit invar anomalies: Fe-Pd and Fe-Pt. They differ from the Fe-Ni system in easily forming stable ordered 1:1 ferromagnetic compounds FePd[72] and FePt[73]. The invar anomalies are found in the iron-rich disordered alloys of these systems, are most intense in the region 25-27 at.% Pd or Pt [74-78] and are destroyed by the Fe₃Pt ordering in the Fe-Pt system[79,80]. Also, the concentration dependence of the invar anomalies is sharper for the Fe-Pd and Fe-Pt systems, and the anomalies are stronger [5,74-80].

Partial satisfaction of the above conditions in other alloy systems may result in the appearance of weak invar-like anomalies. We have tried to show that the effects of inhomogeneous structure of the alloy must be considered as an essential part of the analysis of data on such systems. These effects may even dominate the behaviour of the material. Although present knowledge of the consequences of these structural features is limited, a re-examination of existing data on

invar and related alloys should provide further correlation of the physical and metallurgical properties of these alloy systems.

Acknowledgements—The author wishes to thank Dr. G. M. Graham, Dr. P. P. M. Meincke, and Dr. E. Fawcett for their assistance in the preparation of this paper. This work was supported by the National Research Council of Canada.

REFERENCES

1. CRANGLE J. and HALLAM G. C., *Proc. R. Soc.* **272**, 119 (1963).
2. ASANO H., *J. phys. Soc. Japan* **27**, 542 (1969).
3. OWEN E. A., YATES E. L. and SULLY A. H., *Proc. Phys. Soc.* **49**, 315 (1937).
4. TINO Y. and MAEDA T., *J. phys. Soc. Japan* **24**, 729 (1968).
5. CHEVENARD P., *Rev. Metall. Paris*, **25**, 14 (1928).
6. SCHLOSSER W. F., GRAHAM G. M. and MEINCKE P. P. M., (Preceding paper).
7. TINO Y. and MAEDA T., *J. phys. Soc. Japan* **18**, 955 (1963).
8. COCHRANE R. W. and GRAHAM G. M., *Can. J. Phys.* **48**, 264 (1970).
9. WHITE G. K., *Proc. Phys. Soc. London* **86**, 159 (1965).
10. SHIMIZU M. and HIROOKA S., *Phys. Lett.* **27A**, 530 (1968).
11. SHIMIZU M. and HIROOKA S., *Phys. Lett.* **30A**, 133 (1968).
12. KATSUKI A. and TERAOKA K., *J. phys. Soc. Japan* **26**, 1109 (1969).
13. TERAOKA K. and KATSUKI A., *J. phys. Soc. Japan* **27**, 321 (1969).
14. TERAOKA K. and KATSUKI A., *J. phys. Soc. Japan* **27**, 826 (1969).
15. KACHI S. and ASANO H., *J. phys. Soc. Japan* **27**, 536 (1969).
16. KONDORSKII E. I., *Soviet Phys. JETP* **10**, 4284 (1960).
17. SIDOROV S. K. and DOROSHENKO A. V., *Phys. Status Solidi* **16**, 737 (1966).
18. KOUVEL J. S., In *Intermetallic Compounds* (Edited by J. H. Westbrook), p. 540. J. Wiley, New York (1967).
19. SHIGA M., *J. phys. Soc. Japan* **22**, 539 (1967).
20. SHIGA M. and NAKAMURA Y., *J. phys. Soc. Japan* **26**, 24 (1969).
21. NAKAMURA Y., and MIYATA M., *J. phys. Soc. Japan* **23**, 223 (1967).
22. COLLINS M. F., JONES R. V. and LOWDE R. D., *J. phys. Soc. Japan* **17**, Suppl. B-III, 19 (1962).
23. GOMAN'KOV V. I., PUZEI I. M. and RUKOSUEV M. N., *Soviet Phys. crystallogr.* **13**, 449 (1968).
24. GOMAN'KOV V. I., PUZEI I. M. and MALTSEV E. I., *Ukr. Fiz. Zh.* **14**, 1716 (1969).
25. MARCHAND A., BROSSON P. and DAUTREPPE D., *C.R. Acad. Sci. Paris* **262C**, 1770 (1966).

26. CHAMBEROD A. and PAULEVE J., *J. Phys. Chem. Solids* **29**, 1683 (1968).
27. SMITH J. H. and VANCE E. R., *J. appl. Phys.* **40**, 4853 (1969).
28. HANSON D. and FREEMAN J. R., *J. Iron Steel Inst.* **107**, 1, 307 (1923).
29. STEINER W. and KRISEMENT O., *Arch. Eisenhüttenw.* **32**, 701 (1961).
30. DENCH W. A., *Trans. Faraday Soc.* **59**, 1279 (1963).
31. DIXON M., HOARE E. E. and HOLDEN T. M., *Proc. R. Soc. A* **303**, 339 (1968).
32. BOWER D. I., CLARIDGE E. and TSONG I. S. T., *Phys. Status Solidi* **29**, 617 (1968).
33. WEISS R. J., *Proc. Phys. Soc.* **82**, 281 (1963).
34. GOODENOUGH J. B., *J. appl. Phys.* **39**, 403 (1968).
35. BAILYN M., *Phys. Rev.* **139**, 1905 (1965).
36. BASINSKI Z. S., HUME-ROTHERY W. and SUTTON A. L., *Proc. R. Soc. A* **229**, 459 (1955).
37. KOHLHAAS R., DUNNER P. H. and SCHMITZ-PRANGHE N., *Z. angew. Phys.* **23**, 245 (1967).
38. PEARSON W. B., In *A Handbook of Lattice Spacings and Structures of Metals and Alloys*, V.1 (1958), V.2 (1967). Pergamon Press, Oxford.
39. ABRAHAMS S. C., GUTTMAN L. and KASPER J. S., *Phys. Rev.* **127**, 2052 (1962).
40. NATHANS R. and PICKART S. J., *J. Phys. Chem. Solids* **25**, 183 (1964).
41. KOUVEL J. S. and KASPER J. S., *J. Phys. Chem. Solids* **24**, 529 (1963).
42. ISHIKAWA Y. and ENDOH Y., *J. phys. Soc. Japan* **23**, 205 (1967).
43. FUJIMORI H. and SAITO H., *J. phys. Soc. Japan* **20**, 293 (1965).
44. FALLOT M., *Ann. Phys. Paris* **10**, 291 (1938).
45. CRANGLE J., *Phil. Mag.* **5**, 335 (1960).
46. CABLE J. W., WOLLAN E. O. and KOEHLER W. C., *Phys. Rev.* **138**, A755 (1965).
47. KUSSMAN A. and GRAFIN v. RITTBERG G., *Ann. Phys. (Leipzig)* **7**, 173 (1950).
48. GOODENOUGH J. B., In *Magnetism and the Chemical Bond*, Ch. III, Section III, Interscience and John Wiley, New York (1963).
49. CHIKAZUMI S., MIZOGUCHI T., YAMAGUCHI N. and BECKWITH P., *J. appl. Phys.* **39**, 939 (1968).
50. NEWKIRK J. B., *Trans. AIME* **209**, 1214 (1957).
51. GONSER U., MEECHAN C. J., MUIR A. H. and WIEDERSICH H., *J. appl. Phys.* **34**, 2373 (1963).
52. HANSEN M., In *Constitution of Binary Alloys* 2nd Ed. p. 677, McGraw-Hill, New York (1958).
53. KNELLER E., In *Magnetism and Metallurgy* (Edited by A. E. Berkowitz and E. Kneller), Vol. 2, p. 549. Academic Press, New York (1969).
54. ANANTHANARAYANAN N. I. and PEAVLER R. J., In *Advances in X-Ray Analysis* (Edited by J. B. Newkirk and G. R. Mallet), Vol. 10, p. 240. Plenum Press, New York (1967).
55. TINO Y. and MAEDA T., *J. phys. Soc. Japan* **18**, 955 (1963).
56. BELOV K. P., In *Magnetic Transitions*, p. 74. Consultants Bureau, New York (1961).
57. KOHLHAAS R. and LANGE H., *Z. angew. Phys.* **18**, 453 (1965).
58. ASANO H., *J. phys. Soc. Japan* **25**, 286 (1968).
59. NAKAMURA Y., TAKEDA Y. and SHIGA M., *J. phys. Soc. Japan* **25**, 287 (1968).
60. NAKAMURA Y., SHIGA M. and SHIKAZONO N., *J. phys. Soc. Japan* **19**, 1177 (1964).
61. LIN A., Ph.D. Thesis, U. of Toronto, Toronto, Ontario, Canada (1967).
62. SEDOV V. L., *Soviet Phys. JETP* **15**, 88 (1962).
63. UMEBAYASHI H. and ISHIKAWA Y., *J. phys. Soc. Japan* **21**, 1281 (1966).
64. ISHIKAWA Y. and ENDOH Y., *J. phys. Soc. Japan* **23**, 205 (1967).
65. HASHIMOTO T. and ISHIKAWA Y., *J. phys. Soc. Japan* **23**, 213 (1967).
66. KOUVEL J. S., *J. Phys. Chem. Solids* **24**, 795 (1963).
67. JACOBS I. S. and BEAN C. P., In *Magnetism* (Edited by G. T. Rado and H. Suhl), Vol. 3. Academic Press, New York (1963).
68. MEINCKE P. P. M. and LITVA J., *Phys. Lett.* **29A**, 390 (1969).
69. FLETCHER R., *J. Phys. C*, Ser. 2, 2, 2107 (1969).
70. KONDORSKII E. I. and SEDOV V. L., *Soviet Phys. JETP* **35**, 586 (1959).
71. SCHLENKER C., *Phys. Status Solidi* **28**, 507 (1968).
72. HANSEN M., In *Constitution of Binary Alloys*, 2nd Ed. p. 696, McGraw-Hill, New York (1958).
73. HANSEN M., In *Constitution of Binary Alloys*, 2nd Ed. p. 698, McGraw-Hill, New York (1958).
74. KUSSMANN A., AUWARTER M. and GRAFIN v. RITTBERG G., *Ann. Phys. Leipzig* **6**, 174 (1948).
75. MATSUMOTO H. and KOBAYASHI T., *Sci. Repts. RITU* **2**, 856 (1950).
76. MATSUMOTO H. and KOBAYASHI T., *Trans. JIM* **6**, 113 (1965).
77. MATSUMOTO H., SAITO H. and KOBAYASHI T., *Trans. JIM* **4**, 114 (1963).
78. KUSSMANN A. and JESSEN K., *J. phys. Soc. Japan* **17**, Suppl. B-1, 136 (1962).
79. BELOV K. P. and SIROTA Z. D., *Soviet Phys. JETP* **36**, 752 (1959).
80. TAKAKI H., NAKAMURA Y. and NAKAJIMA T., *J. phys. Soc. Japan* **17**, Suppl. B-1, 349 (1962).

COMPRESSIBILITY OF 27 HALIDES TO 45 KBAR

S. N. VAIDYA and G. C. KENNEDY

Institute of Geophysics and Planetary Physics, University of California, Los Angeles, Calif. 90024, U.S.A.

(Received 10 August 1970)

Abstract—New compressibility data on 27 halides are reported. Compressibilities were determined by observations of piston displacement in the static high pressure apparatus to 45 kbar. We report measurements on a number of halides for the first time. Our results are in fair agreement with prior measurements by Bridgman on some of the halides where our data overlap. Our agreement with reductions of shock data is in many cases extremely poor because the reductions of the shock data did not take into account the phase transitions found in the halides.

1. INTRODUCTION

VARIOUS static and dynamic methods have been used in the past for measurement of the compressibility of metal halides. These experimental investigations have been principally motivated by the theories of cohesion of solids in which the alkali halides have served as typical examples of ionic crystals. Theoretical interest in the transition of the B1, NaCl, structure to the B2, CsCl, structure in the alkali halides has also given impetus to several detailed high pressure investigations.

Compressibility measurements of various metal halides using a piston displacement method were first made by Slater[1] to 12 kbar. Bridgman extended the measurements to 45 kbar[2] and later to 100 kbar using a double staging piezometer[3]. Kennedy and La Mori[4] reported transition pressures in KCl, KBr, and KI from measurements in a rotating piston apparatus. Pistorius and Snyman[5] and Pistorius[6, 7] have determined the polymorphic transition pressures in the halides of Li, Na, K and Rb to 200°C using an externally heated piston-cylinder apparatus. The temperature dependence of the transition pressure and the volume change of the transition in potassium and rubidium halides have also been reported by Darnell and McCollum[8] using an internally heated piston-cylinder apparatus. Their experiments

ranged from 25°C to temperatures near the melting point of the halides.

Opposed X-ray anvils have also been used in the study of the compressibility and the crystal structures of the low and high pressure polymorphs of the metal halides. Drickamer *et al.*[9] measured the compressibility of NaCl, KCl, CsCl, NaI, LiF and NaF to about 300 kbar using supported tungsten carbide anvils. Schock and Jamieson[10] have reported structures of the pressure induced phase transformations in the silver halides by X-ray studies of samples between opposed anvils. Jamieson[11] also reported studies on the B1 to B2 transition in 60% NaCl–40% KCl mixed crystals. Opposed diamond anvils with X-rays have been used in the study of the high pressure polymorphs of AgI[12] and in the measurement of the volume change associated with the transitions in potassium and rubidium halides[13, 14]. Bassett *et al.* [15] have also studied the B1–B2 transitions in NaCl in the neighborhood of 300 kbar by similar methods.

In the last decade a number of measurements of the second order elastic constants, C_{ij} , their pressure derivatives, $\partial C_{ij}/\partial p$, and, in some cases, the third order elastic constants, C_{ijk} , of metal halide crystals have been determined using ultrasonic measuring techniques. Ultrasonic measurements have yielded valu-

able information on the elastic properties of both low and high pressure polymorphs and on elastic properties in the vicinity of phase transitions. Methods of estimating isothermal bulk modulus, B_T , and its pressure derivative B'_T from the measured values of C_{ij} , $\partial C_{ij}/\partial P$ and C_{ijk} are well known [16-18].

The second order elastic constants and their pressure derivatives have been determined from ultrasonic techniques on single crystals of lithium fluoride and sodium fluoride [19], sodium chloride and potassium chloride [20, 21], sodium bromide and potassium fluoride [22], potassium iodide [23], cesium chloride, cesium bromide and cesium iodide [24, 25]. The isothermal bulk modulus and its pressure derivatives have been estimated from ultrasonic work on polycrystalline samples of silver chloride [26], rubidium iodide and rubidium chloride [27, 28].

Useful measurements on the elastic properties of ammonium chloride and ammonium bromide which have elucidated the nature of phase transitions in these halides have been reported by Garland and coworkers [29-31]. Anderson [17] and Barsch and Chang [32] have evaluated B_T and B'_T for some halides from the measured ultrasonic values. Third order elastic constants of sodium chloride, potassium chloride and lithium fluoride have been measured by Chang [33], Stanford and Zener [34] and Drabble [35] respectively. Chang and Barsch [36] observed a non-linear pressure dependence of the elastic constants of cesium halides and have estimated the values of higher order elastic constants from these measurements.

Unfortunately, measurements of compression at very high pressures by X-ray lack precision whereas the ultrasonic measurements to date have been limited to the low pressure range. For several metals, V/V_0 from Bridgman's static measurements, the shock dynamic studies, and the ultrasonic elastic constant determinations are not in a satisfactory agreement. A piston displacement method for V/V_0 measurements to 45

kbar has been developed and data reported on several metals [37]. In this paper we give V/V_0 values for some metal halides and intercompare our results with data from shock and ultrasonic measurements.

2. EXPERIMENTAL METHOD

The details of our apparatus and the methods used in the V/V_0 measurements have been previously described [37]. Cylindrical samples of metal halides were pressed out in a pill press from powdered material. Cylinders of 0.485" dia. and 0.50" long were wrapped in an indium sheath of approximately 0.007" thickness. The indium sheath aided in obtaining a hydrostatic pressure distribution around the sample and, in addition, reduced friction between the sample and the wall of the carbide vessel. All measurements were made differentially with respect to gold. The V/V_0 values of gold were calculated from ultrasonic measurements [38]. The density of the metal halides was taken from the published X-ray lattice parameters [39]. The double value of friction encountered in these measurements was generally small and was substantially less than that previously encountered in measurement of several of the more incompressible metals. In general, the double value of friction ranged from a low value of 2.6 kbar encountered for AgI up to 7.2 kbar encountered in the work on RbF.

Measurements were made on at least two samples of each of the halides. Raw experimental values were averaged by a polynomial regression fit of the type

$$\frac{V_0 - V}{V_0} = aP + bP^2 + cP^3 + \dots \quad (1)$$

A simple quadratic fit adequately represented most of the data (Table 3), however, a Murnaghan equation of the form

$$P = \frac{B_T}{B'_T} \cdot \left\{ \left(\frac{V_0}{V} \right)^{B'_T} - 1 \right\} \quad (2)$$

and the modified Murnaghan equation [40] of

the form

$$\frac{2B_T + (\sqrt{B_T'^2 - 2B_TB_T''} + B_0')P}{2B_T - (\sqrt{B_T'^2 - 2B_TB_T''} - B_0')P} = \left(\frac{V_0}{V}\right) \sqrt{B_T'^2 - 2B_TB_T''} \quad (3)$$

were employed in the estimation of the isothermal bulk modulus, B_T , and its pressure derivatives B_T' and B_T'' .

A number of polymorphic transitions were encountered in these studies. Unfortunately many of these proceeded slowly and the value of the transition was taken as a mean of the transition pressure on both compression and decompression strokes.

Most of the halides used in the present work were obtained from Research Inorganic and Organic Chemical Co., Sun Valley, California. State, purity, form of materials, our values of compressibility along with those of other determinations are given in Table 1. The values for the transitions encountered are summarized in Table 2.

In Table 2 we also show the 'region of indifference' over which the transition runs. The 'region of indifference' was determined by observation of the apparent pressure over which a transition ran on a compression cycle and on a decompression cycle. Appropriate corrections were made for friction in determining this region of indifference and the region indicates the sluggishness of the transition under the conditions of our experiment. Obviously our values in this Table are somewhat rough and are somewhat approximate. The region of indifference is both rate sensitive and temperature sensitive. No special effort was made to keep these numbers constant from run to run. We note that for some substances the region of indifference was zero. We suggest that these substances be candidates for high pressure calibration points.

3. RESULTS

Lithium halides

The compressibility of LiCl, LiBr, and

LiI are reported here for the first time. Bridgman's measurements on LiF to 30 kbar[43] are shown and have been extended to 45 kbar. In general our results and the results obtained by reduction of the shock wave data are in good agreement. The only outstanding deviation is that between our results for LiI and the shock wave results where we obtained compressions about 30 per cent greater than indicated by the shock results. Our value of V/V_0 at 45 kbar for LiI is 0.8373 whereas the value from reduction of the shock data is 0.888.

No polymorphic transitions were observed in any of the four lithium halides for the pressure interval investigated. This is in agreement with the results of Pistorius and Snyman[5] and Pistorius[6, 7].

Sodium halides

Pistorius and Snyman[5] have examined the behavior of NaF at high pressure. They report an anomalous compressibility curve in which the compressibility apparently increases with increasing pressure and also suggest the presence of a transition that extends from approximately 16.8 kbar at room temperature to 18.3 kbar at 157.5°. We did not find any evidence of the anomalous compressibility reported by Pistorius and Snyman but do detect a change in curvature of the compressibility curve at approximately 20 kbar which lends support to their observation. Unfortunately, our results on four experimental setups showed substantial scatter and the values we present are extremely tentative. Our value at 45 kbar, $V/V_0 = 0.9174$, is in fair agreement with the value reported from shock studies. The accordance between our static work and the shock results suggest that the volume change of any transition which might be present is small.

NaCl is one of the most widely studied of the alkali halides. Our results are in remarkably close agreement with both Bridgman's and with the reduced shock wave measurements. Relative volumes at 45 kbar from

Table 1. Comparison of V/V_0 values from the present work with those of Bridgman and Keeler

p (kbar)	LiF $\rho = 2.638 \text{ g/cc}$			LiCl $\rho = 2.074 \text{ g/cc}$			LiBr $\rho = 3.464 \text{ g/cc}$		
	This work	Bridgman	Shock	This work	Bridgman	Shock	This work	Bridgman	Shock
5	0.9924	0.992		0.9852			0.9811		
10	0.9852	0.985		0.9710		0.972	0.9632		0.960
15	0.9782	0.979	0.978	0.9576		0.959	0.9463		0.942
20	0.9716	0.972	0.971	0.9448		0.947	0.9306		0.926
25	0.9654	0.966	0.964	0.9327		0.935	0.9159		0.912
30	0.9594	0.961	0.958	0.9213		0.925	0.9023		0.898
35	0.9538		0.952	0.9106		0.914	0.8897		0.886
40	0.9485		0.946	0.9006		0.905	0.8782		0.874
45	0.9435		0.940	0.8912		0.896	0.8677		0.863
	RIOC, 99.99%, an. polycryst. powder*			RIOC, 99.7%, an. polycryst. powder			RIOC, 99.7%, an. polycryst. powder		
p	LiI $\rho = 4.115 \text{ g/cc}$			NaF $\rho = 2.802 \text{ g/cc}$			NaCl $\rho = 2.164 \text{ g/cc}$		
	This work	Bridgman	Shock	This work	Bridgman	Shock	This work	Bridgman	Shock
5	0.9728		0.985	0.9899			0.9798	0.980	
10	0.9487		0.971	0.9803		0.980	0.9616	0.962	0.963
15	0.9273		0.958	0.9711		0.970	0.9452	0.947	0.946
20	0.9083		0.945	0.9623		0.961	0.9306	0.932	0.932
25	0.8913		0.933	0.9540		0.953	0.9172	0.919	0.918
30	0.8760		0.921	0.9462		0.944	0.9050	0.907	0.905
35	0.8620		0.910	0.9388		0.936	0.8930	0.895	0.894
40	0.8492		0.899	0.9319		0.929	0.8828	0.884	0.883
45	0.8371		0.888	0.9254		0.921	0.8724	0.874	0.873
	RIOC, 99.5% an. fused solid.			RIOC, 99.999% single crystals.			RIOC 99.999% single crystals.		
p	NaBr $\rho = 3.200 \text{ g/cc}$			NaI $\rho = 3.670 \text{ g/cc}$			KF $\rho = 2.524 \text{ g/cc}$		
	This work	Bridgman	Shock	This work	Bridgman	Shock	This work	Bridgman	Shock
5	0.9768	0.978		0.9690	0.970	0.976	0.9710		
10	0.9561	0.953	0.958	0.9422	0.944	0.955	0.9460		0.936
15	0.9374	0.937	0.939	0.9191	0.922	0.936	0.9249		0.910
20	0.9206	0.919	0.923	0.8990	0.902	0.918	0.8374 ^(a)		0.888 ^(b)
25	0.9053	0.904	0.907	0.8812	0.883	0.902	0.8229		0.869
30	0.8913	0.890	0.893	0.8652	0.866	0.887	0.8105		0.852
35	0.8784	0.877	0.880	0.8506	0.851	0.873	0.7995		0.837
40	0.8663	0.866	0.868	0.8364	0.837	0.860	0.7893		0.823
45	0.8547	0.855	0.856	0.8222	0.825	0.848	0.7794		0.811
	RIOC, 99.999% an. polycryst. powder			RIOC, 99.999% single crystals			RIOC, 99.99% single crystals		
p	KCl $\rho = 1.9865 \text{ g/cc}$			KBr $\rho = 2.7533 \text{ g/cc}$			KI $\rho = 3.1257 \text{ g/cc}$		
	This work	Bridgman	Shock	This work	Bridgman	Shock	This work	Bridgman	Shock
5	0.9740	0.974		0.9712	0.970		0.9634	0.965	0.954
10	0.9509	0.951		0.9450	0.944		0.9324	0.935	0.916
15	0.9307	0.932		0.9215	0.923		0.9071	0.907	0.886
20	0.8014 ^(c)	0.801 ^(d)		0.8023 ^(e)	0.800 ^(f)		0.8000 ^(a)	0.802 ^(h)	0.859 ^(b)
25	0.7887	0.787		0.7867	0.785		0.7836	0.785	0.837
30	0.7770	0.775		0.7727	0.770		0.7686	0.770	0.816
35	0.7664	0.764		0.7602	0.757		0.7551	0.756	0.798
40	0.7568	0.754		0.7493	0.745		0.7431	0.743	0.782
45	0.7482	0.745		0.7399	0.734		0.7325	0.730	0.767
	RIOC, 99.999% an. polycrystalline.			RIOC, 99.999% an. polycrystalline.			RIOC, 99.99% polycryst. powder.		

Table 1. (cont.)

p (kbar)	RbF $\rho = 3.8665 \text{ g/cc}$			RbCl $\rho = 2.818 \text{ g/cc}$			RbBr $\rho = 3.359 \text{ g/cc}$		
	This work	Bridgman	Shock	This work	Bridgman	Shock	This work	Bridgman	Shock
5	0.976			0.9709	0.830 ⁽¹⁾	0.886 ^(b)	0.8267 ^(m)	0.830 ⁽ⁿ⁾	0.946 ^(b)
10	0.9393 ⁽¹⁾		0.944 ^(b)	0.8066 ^(k)	0.811	0.849	0.8067	0.811	0.903
15	0.9196		0.921	0.7900	0.795	0.820	0.7883	0.794	0.870
20	0.9016		0.901	0.7755	0.780	0.796	0.7714	0.777	0.842
25	0.8851		0.883	0.7628	0.765	0.775	0.7561	0.762	0.818
30	0.8702		0.867	0.7515	0.752	0.757	0.7424	0.748	0.797
35	0.835 ^(d)		0.852	0.7411	0.740	0.741	0.7303	0.735	0.779
40	0.820		0.838	0.7312	0.728	0.727	0.7198	0.722	0.762
45	0.8095		0.826	0.7215	0.717	0.713	0.7108	0.711	0.748
RIOC, 99.99% polycryst.			RIOC, 99.99% an. white powder			RIOC, 99.9% an. white powder			
RbI $\rho = 3.564 \text{ g/cc}$			CsCl $\rho = 3.988 \text{ g/cc}$			CsBr $\rho = 4.456 \text{ g/cc}$			
5	0.8332 ^(a)	0.832 ⁽ⁿ⁾	0.954 ^(b)	0.9736	0.975		0.9695	0.972	0.979
10	0.8081	0.807	0.917	0.9504	0.952	0.952	0.9432	0.947	0.959
15	0.7866	0.783	0.886	0.9302	0.930	0.932	0.9207	0.924	0.941
20	0.7682	0.762	0.860	0.9124	0.913	0.914	0.9012	0.904	0.925
25	0.7523	0.743	0.838	0.8967	0.895	0.898	0.8844	0.885	0.910
30	0.7385	0.725	0.817	0.8826	0.880	0.884	0.8696	0.868	0.896
35	0.7261	0.710	0.799	0.8698	0.867	0.870	0.8563	0.851	0.883
40	0.7147	0.695	0.783	0.8579	0.855	0.858	0.8440	0.837	0.871
45	0.7036	0.683	0.768	0.8463	0.844	0.846	0.8319	0.823	0.859
RIOC, 99.9% an. white powder			RIOC, 99.5% an. polycryst.			RIOC, 99.9% an. polycryst. powder			
CsI $\rho = 4.525 \text{ g/cc}$			AgF $\rho = 7.0743 \text{ g/cc}$			AgCl $\rho = 5.57 \text{ g/cc}$			
5	0.9639	0.964	0.966	0.9886			0.9888	0.990	
10	0.9334	0.934	0.937	0.9792			0.9782	0.979	
15	0.9078	0.907	0.913	0.9718			0.9682	0.970	
20	0.8860	0.884	0.892	0.9497 ^(u)			0.9588	0.961	
25	0.8674	0.865	0.873	0.8812 ^(r)			0.9500	0.953	
30	0.8509	0.848	0.855	0.8686			0.9417	0.945	
35	0.8357	0.832	0.840	0.8583			0.9341	0.937	
40	0.8210	0.816	0.826	0.8501			0.9271	0.930	
45	0.8059	0.802	0.813	0.8441			0.9206	0.923	
RIOC, 99.9% an. polycryst. powder			RIOC, 98%, an. yellowish-green material			RIOC, 99.9% Baker 99.2%			
AgBr $\rho = 6.48 \text{ g/cc}$			AgI $\rho = 5.683 \text{ g/cc}$			CuBr $\rho = 5.170 \text{ g/cc}$			
5	0.9879	0.989		0.8222 ⁽ⁿ⁾	0.820 ^(u)		0.9860	0.986	
10	0.9764	0.978		0.8103	0.810		0.9730	0.975	
15	0.9656	0.968		0.7998	0.800		0.9609		
20	0.9554	0.959		0.7903	0.790		0.9496		
25	0.9460	0.950		0.7818	0.779		0.9389		
30	0.9372	0.941		0.7739	0.770		0.9286		
35	0.9290	0.932		0.7666	0.761		0.9186		
40	0.9216	0.923		0.7596	0.752		0.9086		
45	0.9148	0.915		0.7526	0.743		0.8985		
RIOC, 99.9% powder			RIOC, 99.9% an. powder			RIOC, 99.8% an. powder			

Table 1. (cont.)

Ammonium chloride			Ammonium bromide		Ammonium iodide		
p	$\rho = 1.527 \text{ g/cc}$		p	$\rho = 2.431 \text{ g/cc}$	p	$\rho = 2.514 \text{ g/cc}$	
(kbar)	This work	Bridgman	(kbar)	This work	(kbar)	This work	Bridgman
5	0.9728	0.973	5	0.9714	0.973	5	0.8275 ^[u]
10	0.9501	0.952	10	0.9471	0.950	10	0.8046
15	0.9311	0.933	15	0.9265	0.929	15	0.7848
20	0.9152	0.917	20	0.9089	0.910	20	0.7677
25	0.9018	0.901	25	0.8934	0.893	25	0.7527
30	0.8898	0.888	30	0.8793	0.878	30	0.7395
35	0.8788	0.875	35	0.8660	0.863	35	0.7276
40	0.8679	0.864	40	0.8526	0.850	40	0.7165
45	0.8564	0.853	45	0.8384	0.838	45	0.7058
Aldrich, ultrapure analyzed impurities 25 ppm. polycryst. Baker reagent grade. polycryst. powder.			Baker reagent grade. polycryst. powder.		Aldrich ultrapure Analyzed impurities 25 ppm, polycryst. Baker reagent, grade polycryst. powder.		

*Supplier, stated purity and physical form of the material used in the present experiments.

Abbreviations: an: anhydrous, cryst.: crystalline, polycryst.: polycrystalline.

^[a] P_{tr} from the two measurements 17.3 ± 1.5 and 17.4 ± 3.5 kbar with V/V_0 values 0.9164 and 0.8468.

^[b]Shock calculation does not take into account the volume change of transition.

^[c] P_{tr} from the two measurements 19.3 ± 4.0 and 19.3 ± 3.75 kbar with V/V_0 values 0.9156 and 0.8034.

^[d] P_{tr} 19.65 kbar with V/V_0 values 0.915 and 0.803.

^[e] P_{tr} from the two measurements 17.0 ± 3.0 and 17.2 ± 3.3 kbar with V/V_0 values 0.911 and 0.808.

^[f] P_{tr} 18.05 kbar with (V/V_0) values 0.912 and 0.807.

^[g] P_{tr} 18.0 kbar with (V/V_0) values 0.896 and 0.8115.

^[h] P_{tr} 17.85 kbar with (V/V_0) values 0.895 and 0.810.

^[i]A sluggish transition at P_{tr} 9.4 kbar (V/V_0) values in one experiment were 0.955 and 0.942 and in the other experiment 0.960 and 0.952.

^[j] P_{tr} 31.3 kbar with (V/V_0) values 0.875 and 0.847.

^[k] P_{tr} 5.2 kbar with (V/V_0) values 0.9695 and 0.8240.

^[l] P_{tr} 4.9 kbar with (V/V_0) values 0.970 and 0.830.

^[m] P_{tr} 4.5 kbar with (V/V_0) values 0.968 and 0.832.

^[n] P_{tr} 4.5 kbar with (V/V_0) values 0.967 and 0.834.

^[o] P_{tr} 3.35 kbar with (V/V_0) values 0.970 and 0.842.

^[p] P_{tr} 4.0 kbar with (V/V_0) values 0.965 and 0.839.

^[q] P_{tr} 17.85 kbar with (V/V_0) values 0.967 and 0.953.

^[r] P_{tr} 24.85 kbar with (V/V_0) values 0.943 and 0.882.

^[s] P_{tr} 3.15 kbar with (V/V_0) values 0.988 and 0.826.

^[t] P_{tr} 2.9 kbar with (V/V_0) values 0.989 and 0.826.

^[u] P_{tr} 0.5 kbar with (V/V_0) values 0.995 and 0.856.

^[v] P_{tr} 0.5 kbar with (V/V_0) values 0.997 and 0.856.

these three determinations are 0.8724, 0.874 and 0.873. In addition we do not find the phase transition in NaCl reported by Pistorius[6]; we confirm the results of later investigations [45, 46].

Our results, Bridgman's results and the shock results on NaBr are in markedly close agreement. Our results on NaI are in agreement with those of Bridgman but, as in the case of LiI, we are in substantial disagree-

ment with the shock wave results, which report a much greater stiffness than we find for this material. We found no phase changes up to 45 kbar in any of the sodium halides.

Potassium halides

Wier and Piermarini[13] report from X-ray studies a NaCl structure to CsCl structure transition in KF at about 35 kbar. Pistorius

Table 2. Transition pressure (P_{tr}), region of indifference, (R.I.), single value friction at 40 Kbar for the high pressure polymorph (S.F.) and volume change at the transition ($\Delta V/V_0$) of halides

Halide	Present work			Bridgman P_{tr} (Kbar)	Darnell and McCollum[8]		Wier and Piermarini[13]	Bassett, Takahashi and Campbell[14] ($\Delta V/V_0$)
	P_{tr} (Kbar)	R.I. (Kbar)	S.F. (Kbar)		P_{tr} (Kbar)	$\Delta V/V_0$		
KF	17.3	0.29	1.30			0.0696	~ 35	0.108
	17.4	3.31	2.16			0.073		
KCl	19.3	4.89	1.68		19.65	0.1126	~ 22	0.183
	19.3	3.45	2.30			0.1118		
KBr	17.7	1.01	2.30		18.05	0.1031	~ 22	0.193
	17.2	3.16	2.08			0.1023		
KI	18.0	1.29	1.65		17.85	0.0835	~ 19	0.222
	17.5	1.59	1.80			0.0866		
RbF I-II	9.4	0.0	3.10			0.0127	~ 12	0.173
	9.4	0.0	3.60			0.0084		
RbF II-III	31.2	7.34	2.59		34.47	0.0212		
	31.3	7.19	2.66			0.0286		
RbCl	5.2	0.0	0.86			0.1455		
	4.3	0.0	1.94		4.9	0.140	~ 5	0.134
RbBr	4.7	0.0	1.58		4.5	0.133	~ 5	0.134
	3.3	0.0	1.58		4.0	0.126	~ 4.5	0.139
AgF I-II	17.8	16.12	1.51			0.0144		
	17.9	16.29	1.65			0.0160		
AgF II-III	24.9	16.72	1.51			0.0176		
	24.7	0.44	3.10			0.0607		
AgI	24.8	1.58	2.45			0.0628		
	3.1	0.0	1.30		2.9	0.1623	0.163	
	3.1	0.0	2.38			0.1605		

and Snyman[5] place the transition in KF at 14.6 ± 1.3 kbar, but Darnell and McCollum[8] failed to observe this transition. We made two measurements on KF and found transitions at 17.3 kbar with $\Delta V/V_0$ of 0.069 on one measurement and a transition at 17.4 kbar with a $\Delta V/V_0$ of 0.073 on the other measurement. Calculations from shock data are reported in Table 1, but they cannot be directly compared with our static measurements as they do not take into consideration phase transitions.

We find a transition in KCl at 19.3 kbar. This value is close to previously reported values. Bridgman reports 19.65 kbar, Pistorius reports 19.22[6], Darnell and McCollum report 19.55 and Kennedy and La Mori have previously reported 19.28 ± 0.21 . $\Delta V/V_0$ values of the transitions from the present work and from Bridgman's, Darnell and McCollum, Bassett *et al.*, measurements are in good agreement. Wier and Piermarini[13] report values that appear to be too large. Our compressibility measurements are in close agreement with Bridgman's.

Two different measurements on KBr yield transitions at 17.7 and 17.2 kbar respectively. These compare well with Bridgman's value of 18.05, Pistorius' values of 17.61, Darnell and McCollum value of 17.99 and with Kennedy and La Mori's value of 17.88 ± 0.06 . The $\Delta V/V_0$ of the transition; 0.103 and 0.1023, agree with results from Bridgman and from Bassett *et al.*, whereas Wier and Piermarini's value, 0.193, appears too high. Bridgman's compressibility values for KBr are very slightly greater than ours.

Our results on KI are concordant with those of other investigators in that they show a transition circa 17.75 kbar. Reported values of $\Delta V/V_0$ for this transition are all in good agreement with the exception of the results by Wier and Piermarini who report $\Delta V/V_0$ of the transition approximately two and a half times greater than found by other investigators. Bridgman's and our measurements of the compressibility of KI are essentially identical,

whereas here again as in the case of the other iodides the shock wave data is in marked disagreement and shows a much lower compressibility.

Rubidium halides

A number of phase transitions have been reported by different investigators in rubidium fluoride. However, there has been no agreement as to the pressure or ΔV of these transitions. For instance, Wier and Piermarini report a transition at approximately 12 kbar, Darnell and McCollum report one at 34.47 kbar, Knof and Maish[4] reported transitions at 33 kbar and Pistorius and Snyman[5] find a transition at 6.2 kbar. Our two experiments with RbF show the presence of two transitions, one at 9.4 kbar and the other at 31.25 kbar. The transitions are somewhat sluggish and the $\Delta V/V_0$ of the transition could not be measured with precision. The shock calculations of $\Delta V/V_0$ for RbF do not take into account these transitions and thus are not to be relied upon.

Low pressure transitions occur in RbCl, RbBr and RbI. Our results as well as those from the work by Bridgman, Darnell and McCollum and Wier and Piermarini agree to almost within the limits of experimental error. Compressibilities we report are essentially the same as those reported by Bridgman. Again the results from reduction shock data cannot be relied upon as they do not take into account the presence of transitions.

Cesium halides

Our results on the compressibility of cesium chloride are in close harmony with the results from Bridgman and from reduction of the shock data. At 45 kbar these numbers for V/V_0 are respectively 0.8464, 0.844 and 0.846. We do not find such good agreement in the of CsBr. Our results and Bridgman's are in fair agreement but the shock data report much smaller compressions. Bridgman and

Table 3. Coefficients in the equation $\Delta V/V_0 = a_0 + aP + bP^2 + cP^3$, with P in units of kbar. $a_0 = 0$ unless otherwise indicated

Halide	Source	a_0	$-a \times 10^4$	$b \times 10^6$	$-c \times 10^8$	Range (kbar)	$\sigma \times 10^3$
LiF	This work		15.491	6.5364		0-45	0.40
	Bridgman		15.577	8.571		0-30	0.38
	Keeler		15.460	4.811		0-45	0.22
LiCl	This work		30.342	13.705		0-45	0.31
	Keeler		29.310	13.832		0-45	0.30
LiBr	This work		38.951	21.239		0-45	0.40
	Keeler		44.331	42.242	2.5356	0-45	0.29
LiI	This work		57.466	66.674	4.3154	0-45	0.75
	Keeler		30.528	17.762	1.1500	0-45	0.17
NaF	This work		20.648	9.0621		0-45	0.88
	Keeler		20.847	7.486		0-45	0.36
NaCl	This work		42.730	46.578	3.2499	0-45	0.53
	Bridgman		41.430	44.289	3.2168	0-45	0.38
	Keeler		40.595	35.451	1.7691	0-45	0.36
NaBr	This work		48.734	51.871	3.4037	0-45	0.71
	Bridgman		50.507	56.177	3.4965	0-45	1.16
	Keeler		46.368	43.249	2.5054	0-45	0.32
NaI	This work		66.622	96.809	8.1299	0-45	0.42
	Bridgman		61.165	68.368	4.1803	0-45	0.64
	Keeler		49.053	46.503	2.7817	0-45	0.25
KF (I)	This work		61.814	78.118		0-15	1.93
KCl (I)	This work		54.906	57.969		0-15	0.69
	Bridgman		55.900	70.000		0-15	0.22
KCl (II)	This work	0.13753	34.664	20.600		20-45	0.81
	Bridgman	0.13800	35.000	20.000		20-45	0.00
KBr (I)	This work		60.351	53.606		0-15	1.01
	Bridgman		64.900	90.000		0-15	0.22
KBr (II)	This work	0.12006	45.007	30.882		20-45	1.10
	Bridgman	0.12637	41.314	22.857		20-45	0.27
KI (I)	This work		78.860	112.85		0-15	0.81
	Bridgman		72.300	70.000		0-15	0.67
KI (II)	This work	0.11957	46.086	29.361		20-45	0.74
	Bridgman	0.12314	41.571	20.000		20-45	0.44
RbF (II)	This work	0.01672	47.177	31.636		10-30	0.83
RbCl (II)	This work	0.15178	47.902	68.724	5.5232	10-45	0.20
	Bridgman	0.15030	41.649	37.302	2.2896	5-45	0.40
RbBr (II)	This work	0.15165	44.797	31.635		5-45	1.54
	Bridgman	0.14988	41.696	28.442	1.0101	5-45	0.32
RbI (II)	This work	0.13756	63.083	94.145	7.1946	5-45	0.71
	CsCl		56.401	73.842	5.4194	0-45	0.72
CsBr	This work		53.302	50.559	2.0357	0-45	0.57
	Keeler		53.937	63.810	4.4444	0-45	0.24
	This work		65.652	96.190	7.3963	0-45	0.59
CsI	Bridgman		58.198	57.319	3.4188	0-45	0.40
	Keeler		45.081	42.751	2.7195	0-45	0.21
	This work		78.488	130.42	11.548	0-45	0.61
AgF (I)	Bridgman		77.288	116.99	9.5882	0-45	0.50
	Keeler		70.855	98.252	7.3504	0-45	0.67
	This work		24.665	38.967		0-15	1.42
AgF (III)	This work	0.23130	49.231	43.843		25-45	1.18
AgCl	This work		22.951	11.800		0-45	0.90
	Bridgman		22.590	12.354	0.93240	0-45	0.44
AgBr	This work		24.981	13.451		0-45	0.44
	Bridgman		21.547	6.2121		0-45	0.48

Table 3. (cont.)

Halide	Source	a_0	$-a \times 10^4$	$b \times 10^6$	$-c \times 10^5$	Range (kbar)	$\sigma \times 10^3$
AgI (II)	This work	0.16437	28.491	34.613	2.7313	5-45	0.63
	Bridgman	0.16976	20.118	2.8139	1.0101	5-45	0.44
CuBr	This work		29.325	25.314	2.2872	0-45	0.33
	NH ₄ Cl		59.396	104.55	9.6573	0-45	0.89
NH ₄ Br	This work		54.019	73.24	5.6876	0-45	0.71
	Bridgman		62.162	102.73	9.8655	0-45	1.07
NH ₄ I	This work		55.501	60.98	3.9161	0-45	0.36
	Bridgman	0.14607	56.688	79.921	6.0249	5-45	0.65
	Bridgman	0.13496	72.747	145.64	14.074	5-45	1.80

our results on cesium iodide are in good agreement whereas in the case of the other iodides the shock data seems to show too low a compressibility.

Silver halides

Among the most puzzling substances investigated was silver fluoride. No phase transitions were encountered on a compression cycle until a pressure of approximately 27.5 kbar was reached. However, on a decompression cycle two transitions were observed. One which we have interpreted as occurring at an equilibrium position of approximately 17.85 kbar and the other at an equilibrium position of approximately 24.8 kbar. $\Delta V/V_0$ values associated with them are approximately 0.165 and 0.061 respectively. Because of the anomalous behavior of silver fluoride these are extremely tentative results. A thorough investigation of AgF will probably modify these preliminary results in a major way.

AgCl and AgBr appeared to have very deleterious effects on our tungsten carbide pressure vessels and the results of a number of experiments had to be discarded. Apparently this effect is because of the high ductility of AgCl and AgBr which tends to wedge into minute cracks in the tungsten carbide and act as a stress raiser. We find a slightly higher compressibility of AgCl than did Bridgman, whereas our results on AgBr are identical to those of Bridgman at 45 kbar.

Our results on the low pressure transition in AgI are almost identical with those of Bridgman. However, we report a somewhat lower compressibility than that indicated by Bridgman.

Copper bromide

We report data to 45 kbar on copper bromide. No phase transitions were observed. There is little other data with which our new measurements can be compared.

Ammonium halides

Compressibility measurements were made on Baker reagent grade material and also on Aldrich ultrapure NH₄Cl and NH₄I. The ammonium halides from the both sources yielded closely agreeing compression values. For all the three halides the V/V_0 values from the present measurements are in excellent agreement with Bridgman's values.

4. DISCUSSION

The present study corroborates and supplements Bridgman's extensive work on metal halides. Bridgman examined only one fluoride and our work on NaF, KF, RbF and AgF serves to fill in this gap. In addition we have examined LiCl, LiBr and LiI which have not previously been studied by static methods.

In general, where the data overlap, our results are in fair agreement with Bridgman's.

The outstanding exceptions are RbI, CsBr and AgI where Bridgman reports greater compressibilities than we find. We note large discrepancies between our results on LiI, NaF, NaI, CsBr and CsI and the results from reduction of the shock data. In every case we show a greater compressibility than indicated by the shock measurements. Intercomparison between our static data and the shock data for the potassium and rubidium halides does not seem to be meaningful as the volume change associated with various transitions was neglected in the reduction of the shock data. It seems likely that a new reduction of the shock data which takes into account these known transitions will be useful in providing much better agreement between the two sets of data. This, of course, brings up the possibility, if not the probability, that transitions lying at pressures above 45 kbar may be present in these substances where the shock data and our static measurements do not agree. For the most part, the shock data represents extrapolation of high pressure results into the lower pressure regime we reported. Disagreement between reduced and extrapolated shock data and static measurements may be one of the surest indicators of a high pressure transition.

Our measurements of the $\Delta V/V_0$ of various transitions encountered is almost identical to those reported by Bridgman. In no case have we made any significant improvement over his measurements. Agreement with the results of Darnell and McCollum is not as good. At least four of their seven reported measurements seem to be significantly too high. Finally, the measurements by Bassett, Takahashi and Campbell on the volume change of a transition by use of a microfocus X-ray tube through diamond anvils seem to be excellent and they agree much more closely with our results and Bridgman's results than do the measurements through diamond anvils by Wier and Piermarini.

The bulk modulus and its pressure derivatives have been evaluated by application of

equations (2) and (3) to the compression data. These, with the values determined from ultrasonic measurements, are summarized in Table 4. The Gruneisen parameter, estimated from B'_T , in accordance with the well known Slater relation $\gamma_{SL} = 0.5 (B'_T - 0.33)$ together with the thermodynamic value $\gamma_{th} = (v \cdot \alpha \cdot B_T / C_p)$ where V is molar volume, α the coefficient of volume thermal expansion, and C_p the specific heat per mole are also given in this table. In general there seems to be a fair agreement among γ_{th} and γ_{SL} values though in some cases the discrepancies are fairly large. It also appears that γ_{th} values are systematically lower than γ_{SL} values calculated from B'_T determined from shock measurements.

There is a good overall agreement between the static and sonic values of B_T and B'_T for NaCl, NaF, NaI, CsCl, CsBr and CsI, though for LiF and NaBr, B'_T values differ widely. Since B'_T values generally range from 4 to 6 [52], static value of B'_T in the case of LiF and the sonic value in case of NaBr are probably incorrect. Our values of B_T and B'_T of AgCl are in excellent agreement with the values estimated from the ultrasonic measurements on polycrystalline samples [26]. Using well known thermodynamic relations [16, 17], B_T and B'_T of NH_4Cl , NH_4Br and cesium halides were evaluated from the elastic constants and their pressure derivatives (Table 4). Values of elastic constants for NH_4Cl and NH_4Br as functions of pressure and temperature were determined by Garland and co-workers [29, 30]. These yield B_T and B'_T values in a fair agreement with results from the static measurements. This is contrary to conclusions, however, of Garland and co-workers who report disagreement with Bridgman's static work. The B_T and B'_T values for cesium halides from which we calculate elastic constant data of Chang and Barsch [36] are in agreement with the results from the static measurements.

From the observed nonlinear pressure dependence of C_p 's one also obtains $B''_T = -0.0347, -0.0410$ and $-0.0507 \text{ kbar}^{-1}$ for

Table 4. Compressibility parameters and Gruneisen constants of the metal halides. Murnaghan equation (ME) and modified Murnaghan equation (MME) were fitted to all the experimental data

Halide	B_T (kbar)	B_T	B_T (kbar ⁻¹)	σ of (V/V_0) $\times 10^3$	γ_{th}^*	γ_{SL}	Reference
LiF	627.85	6.818		0.39	1.75	3.25	ME This work
	621.43	9.146		0.44		4.41	ME Bridgman
	621.51	8.827	0.0372	0.54		4.25	NME Bridgman
	637.6	4.23		0.24		1.95	ME Keeler[42]
	665.7	5.24				2.45	Anderson[17]
	664.0	5.23				2.45	Barsch and Chang[32]
LiCl	318.5	3.36		0.36	1.78	1.51	ME This work
	328.8	3.82		0.41		1.74	ME Keeler
LiBr	242.7	3.50		0.55	2.02	1.58	ME This work
	222.5	4.10		0.35		1.88	ME Keeler
	222.4	4.11	-0.0007	0.37		1.89	NME Keeler
LiI	168.35	4.32		0.80	2.22	1.99	ME This work
	135.7	4.94	-0.0709	0.71		2.31	NME This work
	333.1	2.17		0.29		0.92	ME Keeler
	324.3	3.49	-0.0648	0.18		1.58	NME Keeler
NaF	467.4	5.18		0.91	1.72	2.42	ME This work
	470.0	3.64		0.38		1.66	ME Keeler
	461.6	5.09				2.38	Anderson[17]
	461	5.28				2.47	Barsch and Chang[32]
NaCl	232.3	4.92		0.56	1.74	2.29	ME This work
	241.4	4.61		0.47		2.14	ME Bridgman[41]
	239.2	4.54		0.42		2.10	ME Keeler[42]
	234.2	5.39				2.53	Barsch and Chang[32]
NaBr	234.2	5.35				2.51	Anderson[17]
	203.1	4.19		0.76	1.81	1.93	ME This work
	192.3	4.81		1.23		2.24	ME Bridgman
	212.2	3.82		0.36		1.74	ME Keeler
NaI	192.0	9.17				4.42	Barsch and Chang[32]
	151.0	4.15		0.90	1.90	1.91	ME This work
	155.6	3.94		0.51		1.81	ME Bridgman
	200.1	3.58		0.19		1.63	ME Keeler
CsCl	171.2	5.09		0.71	2.74	2.38	ME This work
	168.59	5.54	-0.0237	0.73		2.60	NME This work
	174.9	4.55		1.12		2.11	ME Bridgman
	181.6	4.45		0.31		2.06	ME Keeler
	178.8	4.91	-0.0233	0.34		2.29	NME Keeler
	168.0	5.89				2.78	Chang <i>et al.</i> [25]
CsBr	168.0	5.85				2.76	Barsch and Chang[32]
	167.6	5.97	$B_s'' = -0.0347$				Chang and Barsch[36]
	143.97	5.32		0.46	1.93	2.49	ME This work
	168.4	3.09		0.36		1.38	ME Bridgman
	221.8	3.66		0.28		1.67	ME Keeler
	145.0	5.71				2.69	Barsch and Chang[32]
CsI	143.5	5.98	$B_s'' = -0.0410$				Chang and Barsch[36]
	124.7	4.50		0.93	2.00	2.08	ME This work
	116.0	6.12	-0.0884	0.53		2.89	NME This work
	126.7	4.05		0.87		1.86	ME Bridgman
	120.8	5.10	-0.0545	0.93		2.38	NME Bridgman
	134.8	4.30		0.41		1.98	ME Keeler
	133.8	4.47	-0.0089	0.42		2.06	NME Keeler
	119.0	5.79				2.73	Chang <i>et al.</i> [25]
	119.0	5.67				2.67	Barsch and Chang[32]
	118.9	5.87	$B_s'' = -0.0507$				Chang and Barsch[36]

Table 4. (cont.)

Halide	B_T (kbar)	B_T	B_T (kbar ⁻¹)	σ of (V/V_0) $\times 10^3$	γ_{th}^*	γ_{SL}	Reference
AgCl	414.57	5.98		0.92	1.92	2.82	ME This work
	462.6	2.14		0.49		0.90	ME Bridgman
	461.5	2.32	-0.0110	0.54		1.00	MME Bridgman
	440.3						Hidshaw <i>et al.</i> [48]
AgBr	406.0	5.20				2.43	Voronov <i>et al.</i> [26]
	381.7	5.85		0.54	2.27	2.76	ME This work
	451.2	2.59		0.50		1.13	ME Bridgman
	426.4	6.34	-0.1833	0.35		3.00	MME Bridgman
CuBr	412.4						Tannhauser <i>et al.</i> [49]
	362.2	2.87		0.62		1.27	ME This work
NH ₄ Cl	338.0	6.56	-0.1807	0.43		3.11	MME This work
	167.2	6.70		1.27	1.17	3.18	ME This work
NH ₄ Br	179.1	5.40		0.68		2.53	ME Bridgman
	173.0	6.48	-0.0568	0.55		3.07	MME Bridgman
	176.7	8.21				3.94	Garland and Renard[29]
NH ₄ Br	163.83	4.84		1.74	1.10	2.25	ME This work
	174.8	4.01		0.28		1.84	ME Bridgman
	158.6	7.66				3.66	Garland and Yarnell[30]

* Values of γ_{th} for Li, Na, and Cs halides taken from Ref. [50], for AgCl and AgBr from Ref. [51].

CsCl, CsBr and CsI respectively[36]. Conversion of B_T'' into B_T' using thermodynamic relations is not possible because of lack of experimental data on $(\partial^2 B_T / \partial T^2)_p$ and $(\partial^2 B_T / \partial P \partial T)$. This difficulty is circumvented by applying Cook's method[53] to the raw elastic constants data as was done by Ho and Ruoff in the case of sodium[54]. Values of B_T'' obtained by application of modified Murnaghan equation to our static data are -0.0237 for CsCl, 0.0 for CsBr and -0.0884 for CsI. An accurate estimate of B_T' can be made from the static measurements only in the case of highly compressible substances such as potassium and rubidium for which V/V_0 values at 45 kbar are about 0.584 and 0.561 respectively[40]. Even in the case of sodium for which (V/V_0) value at 45 kbar is about 0.693, B_T'' could not be estimated with certainty, and it is therefore not surprising to find a similar difficulty in the case of the metal halides which are less compressible than sodium. In the ultrasonic work, elastic constants, and hence the bulk modulus as a function of pressure, may be measured to a high

degree of precision so that B_T'' can be estimated in the 10-20 kbar range.

Acknowledgements—Our thanks are due to Mr. Geza Budai for assistance with the experiments and to Miss Sharon Bailey for data processing and several numerical calculations. The upkeep of the apparatus is due to J. Yamane and L. Faus. This work is supported by our AEC Contract.

REFERENCES

1. SLATER J. C., *Phys. Rev.* **23**, 488 (1924); *Proc. Am. Acad. Arts Sci.* **61**, 135 (1926).
2. BRIDGMAN P. W., *Proc. Am. Acad. Arts Sci.* **74**, 21 (1940).
3. BRIDGMAN P. W., *Proc. Am. Acad. Arts Sci.* **76**, 1 (1945).
4. KENNEDY G. C. and LA MORI P. N., *J. Geophys. Res.* **67**, 851 (1962).
5. PISTORIUS C. W. F. T. and SNYMAN H. C., *Z. Phys. Chem. Neue Folge* **43**, 1 (1964).
6. PISTORIUS C. W. F. T., *J. Phys. Chem. Solids* **25**, 1477 (1964).
7. PISTORIUS C. W. F. T., *J. Phys. Chem. Solids* **26**, 1003 (1965).
8. DARNELL A. J. and MCCOLLUM W. A., *J. Phys. Chem. Solids* **31**, 805 (1970).
9. DRICKAMER H. G., LYNCH R. W., CLENDENEN R. L. and PEREZ-ALBUERNE E. A., *Solid State Phys.* **19**, 135 (1966).
10. SCHOCK R. N. and JAMIESON J. C., *J. Phys. Chem. Solids* **30**, 1527 (1969).
11. JAMIESON J. C., *Physics of Solids at High Pressure*

- (Edited by C. T. Tomizuka and R. M. Emerick), Academic Press, New York (1965).
12. BASSETT W. A. and TAKAHASHI T., *Am. Miner.* **50**, 1576 (1965).
 13. WIER C. E. and PIERMARINI G. I., *J. Res. NBS.* **68A**, 105 (1964).
 14. BASSETT W. A., TAKAHASHI T. and CAMPBELL J. K., *Trans. Amer. Cryst. Assoc.*, Proceedings of symposium on crystal structures at high pressure (Edited by W. B. McWahn), v. 5, 93 (1969).
 15. BASSETT W. A., TAKAHASHI T., MAO H. and WEAVER J. S., *J. appl. Phys.* **39**, 319 (1968).
 16. OVERTON W. C. JR., *J. Chem. Phys.* **37**, 116 (1962).
 17. ANDERSON O. L., *J. Phys. Chem. Solids* **27**, 547 (1966).
 18. BARSCH G. R., *Phys. Status Solidi* **19**, 129 (1967).
 19. MILLER R. A. and SMITH C. S., *J. Phys. Chem. Solids* **25**, 1279 (1964).
 20. BARTELS R. A. and SCHEULE D. E., *J. Phys. Chem. Solids* **26**, 537 (1965).
 21. BOGARDUSE H., *J. appl. Phys.* **36**, 5344 (1965).
 22. KOLIWAD K. M., GHATE P. B. and RUOFF A. L., *Phys. Status Solidi* **21**, 507 (1967).
 23. REDDY P. J. and RUOFF A. L., *Bull. Am. Phys. Soc.* **9**, 534 (1964).
 24. KOLIWAD K. M. and RUOFF A. L., *Bull. Am. Phys. Soc.* **10**, 1113 (1965).
 25. CHANG Z. P., BARSCH G. R. and MILLER D. L., *Phys. Status Solidi* **23**, 577 (1967).
 26. VORONOV F. F., CHERNYSHEVA E. V., GONCHAROVA V. A. and STAT'GOROVA O. V., *Soviet Phys., solid State* **8**, 1870 (1967).
 27. VORONOV F. F. and GONCHAROVA V. A., *Soviet Phys., JETP* **23**, 777 (1966).
 28. VORONOV F. F., GONCHAROVA V. A. and AGAPOVA T. A., *Soviet Phys., solid State* **8**, 2726 (1967).
 29. GARLAND C. W. and RENARD R., *J. Chem. Phys.* **44**, 1130 (1966).
 30. GARLAND C. W. and YARNELL C. F., *J. Chem. Phys.* **44**, 1112 (1966).
 31. GARLAND C. W. and YOUNG R. A., *J. Chem. Phys.* **49**, 5282 (1968).
 32. BARSCH G. R. and CHANG Z. P., *Phys. Status Solidi* **19**, 139 (1967).
 33. CHANG Z. P., *Phys. Rev.* **140**, A 1788 (1967).
 34. STANFORD A. L. and ZEHNER S. P., *Phys. Rev.* **153**, 1025 (1967).
 35. DRABBLE J. R. and STRATHEN R. E. B., *Proc. Phys. Soc.* **92**, 1090 (1967).
 36. CHANG Z. P. and BARSCH G. R., *Phys. Rev. Lett.* **19**, 1381 (1967).
 37. VAIDYA S. N. and KENNEDY G. C., *J. Phys. Chem. Solids* **31**, 2329 (1970).
 38. Refer to Table in Ref. [37].
 39. Powder diffraction file 1969, American Society for Testing and Materials, Philadelphia, Pa.
 40. VAIDYA S. N., GETTING I. C. and KENNEDY G. C., *J. Phys. Chem. Solids* (in press).
 41. KENNEDY G. C., in *American Institute of Physics Handbook* (to be published).
 42. KEELER R. N., in *American Institute of Physics Handbook* (to be published).
 43. BRIDGMAN P. W., *Proc. Am. acad. Arts Sci.* **77**, 189 (1949).
 44. BRIDGMAN P. W., *Proc. Am. acad. Arts Sci.* **72**, 45 (1937).
 45. References on this subject are given in AKELLA, J., VAIDYA S. N. and KENNEDY G. C., *Phys. Rev.* **185**, 1135 (1969).
 46. CORILL J. A. and SAMARA G.-A., *Solid State Commun.* **4**, 283 (1966).
 47. KNOF H. and MAISH W. G., *J. Phys. Chem. Solids* **24**, 1625 (1963).
 48. HIDSHAW W., LEWIS J. T. and BRISCOE C. V., *Phys. Rev.* **163**, 876 (1967).
 49. TANNHASER D. S., BRUNER L. J. and LAWSON A. W., *Phys. Rev.* **102**, 1276 (1956).
 50. KACHHAVA C. M. and SAXENA S. C., *J. Chem. Phys.* **44**, 986 (1966).
 51. AKELLA J., VAIDYA S. N. and KENNEDY G. C., *J. appl. Phys.* **40**, 2800 (1969).
 52. ANDERSON O. L., *J. Geophys. Res.* **72**, 3661 (1967).
 53. COOK R. K., *J. Acoust. Soc. Am.* **29**, 445 (1957).
 54. HO P. J. and RUOFF A. L., *J. Phys. Chem. Solids* **29**, 210 (1968).

ELECTRONIC STRUCTURE OF THE ISOLATED VACANCY IN SILICON

F. P. LARKINS*†

Mathematical Institute, Oxford, England

(Received 4 August 1970)

Abstract—The electronic structure of the isolated vacancy in its various charge states in the silicon lattice has been calculated using the molecular approach outlined by Coulson and Kearsley. Atomic Hartree-Fock functions determined by Clementi are used to approximate the $3s$ and $3p$ orbitals on the silicon atom in the crystal. The energies of the lowest electronic states from an undistorted model calculation are corrected using a modified first order treatment for the symmetric relaxation and Jahn-Teller distortions of the vacancy system. Two cases are considered using the analytical value and a semi-empirical value for Q , the one-centre Coulomb integral. The symmetric energy corrections are in general at least an order of magnitude larger than the Jahn-Teller splittings of the degenerate levels. The spin multiplicities of the ground state for the various charged centres using the modified value for Q agree with the experimental results obtained by Watkins, even though the present many-electron treatment differs significantly from his one electron model.

1. INTRODUCTION

THE EXPERIMENTAL work of Watkins[1,2] has established, with reasonable certainty, that the isolated vacancy in silicon exists in at least three charged states: single positive (V^+), neutral (V^0), and single negative (V^-), and possibly also in the double negative charged state (V^{2-}) under suitable conditions. Watkins has had considerable success in explaining his electron spin resonance results in terms of a one-electron model. However, this is a very oversimplified approach and is inadequate for quantitative work, as has been demonstrated by Stoneham and Lannoo [3]. From the alternative viewpoint, within the framework of the pseudo-potential band theory method Callaway and Hughes[4,5] have had only limited success with their Green's function calculation for the neutral single vacancy and divacancy in silicon. Besides the computational difficulties their band theory approach, which is also a one-

electron theory, is not easily adaptable to charged centres or to incorporating the relaxation effects which may be large for defects in silicon.

In this paper we extend the many-electron molecular approach developed by Coulson and Kearsley[6] to the isolated vacancy in silicon. The limitations of this method will be at least as serious for the silicon problem as for the calculations in the diamond crystal. Nevertheless, it is valuable to investigate the quantitative predictions of this model, because it is possible to obtain information about the symmetric relaxation and Jahn-Teller distortion effects associated with the lowest electronic states of the various charged centres. The results may also be used when calculating the formation energy and volume change associated with the vacancy[7]. In the next section the molecular approach is outlined and then the results obtained for the undistorted vacancy centre using two alternative values for the one-centre coulomb integral are presented. The corrections to the various electronic levels which result from electron-lattice coupling are then calculated, in first order, using the rigid atom approximation[8] and modified values

*Work undertaken at: Theoretical Physics Division, Atomic Energy Research Establishment, Harwell, United Kingdom.

†Now at Chemistry Department, Monash University, Australia 3168.

for the linear response frequencies. The corrected results are then compared with the known experimental findings and the characteristics of the one-electron model.

2. THE MOLECULAR APPROACH

The method adopted for the determination of the electronic properties of the isolated vacancy in silicon closely resembles the approach used for the study of point defects in the diamond crystal [6, 9, 10]. We assume that the electronic behaviour of the system in the immediate neighbourhood of the vacancy is determined primarily by the n vacancy electrons which are localized within the defect. Electron spin resonance studies suggest that some delocalisation of the electrons from the vacancy does occur; however, for limited delocalisation a preliminary study of the vacancy system in diamond [10] suggests that the localized model will predict the same relative ordering of the lowest electronic states as one incorporating delocalisation. Although there will be some relaxation and distortion of the atoms surrounding the vacancy, the consequences of this effect are considered as a first order correction to the electronic energy states obtained from the undistorted vacancy investigation. The problem now to be solved is the distribution of the vacancy electrons in the tetrahedral field of the neighbouring atoms and the much weaker field of the rest of the crystal.

The atoms of the perfect silicon crystal are considered to be in a tetrahedral sp^3 state. On removal of an atom the four valence electrons associated with the atoms nearest the vacancy which were covalently bonded to this atom are initially taken to be in sp^3 hybrid orbitals $a-d$ directed towards the centre of the defect, as shown in Fig. 1. Polarisation effects by other electron clouds are neglected, but the exchange term in the Hamiltonian between the vacancy electrons and the other valence electrons on the atoms nearest the defect is included. It is now

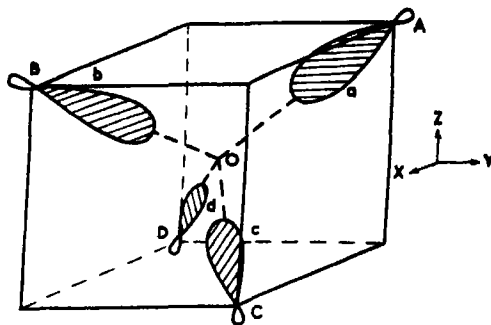


Fig. 1. Defect molecule for the undistorted vacancy: T_d symmetry.

possible to use the well-established techniques of molecular orbital theory to simplify the problem. A suitable set of mutually orthogonal single-electron molecular orbitals of correct symmetry are as follows

$$\begin{aligned} v &= N_1(a+b+c+d) & \subset a_1 \\ t_x &= N_2(-a+b+c-d) \\ t_y &= N_2(a-b+c-d) \\ t_z &= N_2(a+b-c-d) \end{aligned} \quad \left. \vphantom{\begin{aligned} t_x \\ t_y \\ t_z \end{aligned}} \right\} \subset t_2 \quad (1)$$

where $N_1 = \frac{1}{2}(1 + 3S_{ab})^{-1/2}$, $N_2 = \frac{1}{2}(1 - S_{ab})^{-1/2}$ and S_{ab} is the overlap integral between two hybrids on neighbouring atoms to the vacancy. The symmetry states belonging to the various configurations $a_1^n t_2^{n-p}$, where $p = 0, 1$ or 2 and n is the number of vacancy electrons, may now be determined and the corresponding determinantal wave-functions $\psi(R)$ expressed in terms of the single-electron molecular orbitals. In the present problem we have $n = 3, 4, 5$ or 6 depending upon whether we are considering the V^+ , V^0 , V^- or V^{2-} centre.

The spin-independent Hamiltonian may be expressed as follows

$$H = \sum_{i=1}^n \left(T_i + \sum_N V_{Ni} \right) + \sum_{i>j}^n \frac{1}{r_{ij}} \quad (2)$$

where N denotes the nearest neighbours to the vacancy, A, B, C or D . T_i is the kinetic energy operator for the i th electron; V_{Ni} is the potential energy of interaction of the

i th electron with the nucleus of atom N , with the K and L shell electrons surrounding the nucleus and with the bonded valence electrons of this atom. All the contributions to V_{Ni} have not been evaluated explicitly because of the computational time required. However, we may write,

$$V_{Ni} = -\frac{Z_{\text{eff}}}{r_{Ni}}$$

+ repulsion from the tetrahedral hybrids around N - exchange interaction between the vacancy electron i and bonded valence electrons on N .

(3)

where Z_{eff} is the effective nuclear charge as seen by the valence electrons due to inner shell screening. If the nucleus was totally screened by its K and L shell electrons then Z_{eff} would be 4.0. For the interatomic potential terms such as $\langle b|V_A|b \rangle$ and $\langle a|V_A|b \rangle$ it is reasonable to use this value. For the intra-atomic potential term, $\langle a|V_A|a \rangle$ this is a rather extreme approximation. From Slater's rules the effective nuclear charge experienced by an electron in the valence shell due to inner shell screening is calculated to be 5.2; however, these rules are less accurate for predicting screening constants for the higher shells. Therefore, we have preferred to use the estimate of $Z_{\text{eff}} = 4.88$ obtained from the work of Clementi and Raimondi[11] on atomic Hartree-Fock functions. We have evaluated equation (3) explicitly and not used the Goeppert-Mayer and Sklar approximation[12]. The orthonormal set of atomic Hartree-Fock functions determined by Clementi[13] for the 3P ground state of the silicon atom are chosen as a suitable approximation to the $3s$ and $3p$ orbitals on the atoms nearest the defect.

The energy of the various states, R , belonging to each configuration before configuration interaction was determined using the relation

$$E(R) = \frac{\langle \psi(R) | H | \psi(R) \rangle}{\langle \psi(R) | \psi(R) \rangle}. \quad (4)$$

Formal expressions for the V^0 , V^- and V^{2-} systems are given by Yamaguchi[14] in terms of a series of molecular integrals which we have denoted $A-K$ as in Ref. [6]. (These integrals are defined in Table 1.) All one-

Table 1. Molecular integrals required for the silicon vacancy calculations using atomic Hartree-Fock functions

Integral	Unmodified case $Q = 11.45 \text{ eV}$	Modified case $Q = 8.10 \text{ eV}$
$A = \langle v H^0 v \rangle$	-31.2772*	-31.2772
$B = \langle t_x H^0 t_x \rangle$	-29.2541	-29.2541
$C = \langle vv H^1 vv \rangle$	6.8430	6.4416
$D = \langle t_x t_x H^1 t_x t_x \rangle$	6.8653	5.6528
$E = \langle vt H^1 vt \rangle$	6.7682	6.1704
$F = \langle t_x t_y H^1 t_x t_y \rangle$	6.6601	5.2262
$G = \langle vt_x H^1 t_x v \rangle$	1.8168	1.1645
$J = \langle t_x t_y H^1 t_y t_x \rangle$	1.5573	0.2341
$K = \langle vt_x H^1 t_y t_x \rangle$	-1.6236	-0.6945

$$H^0 = T_1 + \sum_N V_{Ni}$$

$$H^1 = 1/r_{12}$$

*All energies are in eV.

and two-centre integrals are evaluated explicitly while values for three- and four-centre integrals are determined using the Mulliken approximation[15]. Configurational mixing between states of the same symmetry from different configurations is used to obtain the lowest electronic levels for each undistorted centre.

3. RESULTS FOR THE UNDISTORTED VACANCY SYSTEM

The value for the one-centre Coulomb integral, Q ($Q \equiv \langle a(1)a(2) | 1/r_{12} | a(1)a(2) \rangle$) calculated from the analytic wave functions was 11.45 eV compared with a semi-empirical estimate of 8.10 eV obtained using the procedure outlined in Appendix 3 of Ref. [6] and the values of C , $G_1(\text{sp})$ and $F_2(\text{pp})$ given by Skinner and Pritchard[16]. The difference in these estimates suggests that it may be valuable to consider both cases in any calcula-

tions. The semi-empirical estimate of Q is subject to reasonable uncertainty because of the lack of reliable data for the term values; nevertheless, some information about the sensitivity of the ordering of the lowest levels to variations in Q can be obtained. Table 1 contains the values of the one- and two-electron molecular integrals, $A-K$, which form the basis of this work. As for the diamond calculations there are considerable changes in the values of the two-electron integrals as Q decreases. These differences effect the energy level scheme which results.

The one-electron integrals A and B differ by 2.02 eV compared with a difference of nearly 12 eV in the diamond calculation [10]. Configuration interaction is even more important in determining the ordering of the lowest levels than in the diamond system. The energy difference, $A-B$, is the separation between the levels of a_1 and t_2 symmetry in the one-electron model used in the qualitative discussion by Watkins [1] to describe his results. The delocalisation investigation on the diamond vacancy suggests that this separation will decrease further with increasing delocalisation of the electronic wave-function from the vacancy.

The predicted energy level schemes for the undistorted V^+ , V^0 , V^- and V^{2-} centres before and after configuration interaction are shown

in Figs. 2 to 5 respectively. In the calculations with $Q = 8.10$ eV the energy levels are much more compact than when the alternative value of Q is used. There are cases for $Q = 8.10$ eV where symmetry states from 'higher' configurations are almost degenerate with like symmetry states from 'lower' configurations before mixing. For example, in the neutral vacancy calculations the 3T_1 level from the $a_1^2t_2^2$ configuration is only 0.06 eV below the 3T_1 level from the $a_1t_2^3$ configuration. Also in the V^- calculation only 0.30 eV separates the 2T_2 symmetry states from the $a_1^2t_2^3$, $a_1t_2^4$ and t_2^5 configurations. If we were to use the simple one-electron model neglecting all electron-electron interaction terms symmetry states from different configurations should be separated from one another by 2.02 eV. From the one-electron model, all the symmetry states belonging to a particular configuration are degenerate. This is not the case in the present calculation. For example, the 1A_1 , 1E , 1T_2 , and 3T_1 symmetry states from the $a_1^2t_2^2$ configuration span 4.9 eV with $Q = 11.45$ and 1.2 eV with $Q = 8.10$ eV. We now look in more detail at the calculation for each centre.

For the positively charged vacancy the results shown in Fig. 2 predict the same relative order of the energy levels for both estimates of the one-centre Coulomb integral. The 2T_2 level is lowest in energy only after

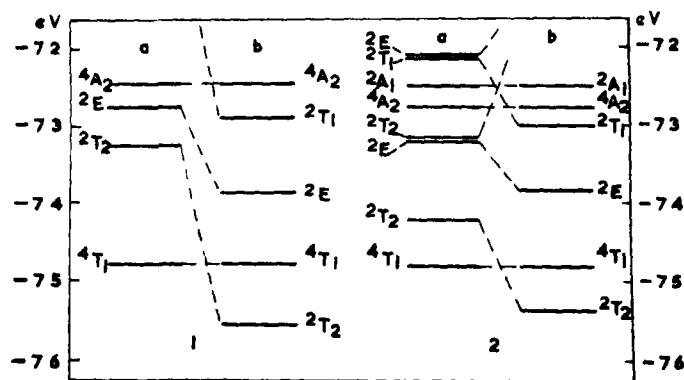


Fig. 2. Electronic structure of the positively charged undistorted vacancy in silicon. (a) before configuration interaction, (b) after configuration interaction. (1) $Q = 11.45$ eV, (2) $Q = 8.10$ eV.

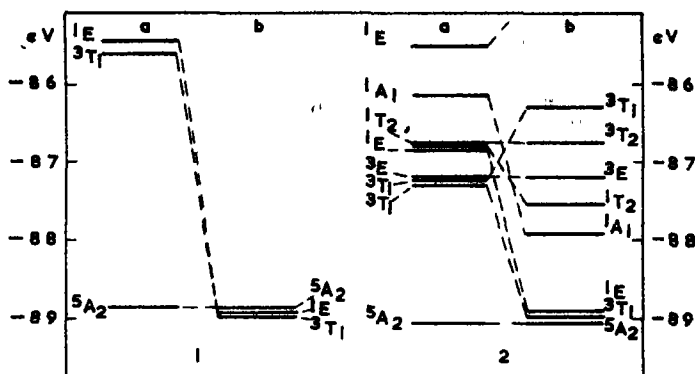


Fig. 3. Electronic structure of the neutral undistorted vacancy in silicon. (a) before configuration interaction, (b) after configuration interaction. (1) $Q = 11.45$ eV, (2) $Q = 8.10$ eV.

configuration interaction. This differs from the diamond vacancy calculation where the 2T_2 level is always lowest in energy[10]. Electronic transitions from the 2T_2 to the 2T_1 and 2E levels are allowed, but since they are estimated to be above the ground state by more than the band gap they are unlikely to be observed.

The 5A_2 , 3T_1 and 1E electronic states of the V^0 centre are predicted to be very close together after configuration interaction in both calculations shown in Fig. 3. The position of the 1E and 3T_1 levels is strongly dependent on the extent of configurational mixing. For

$Q = 11.45$ eV the 3T_1 level is lowest, but is only 0.02 eV below the 1E level and 0.05 eV below the 5A_2 level. For $Q = 8.10$ eV the 5A_2 level is lowest, 0.06 eV below the 3T_1 level and 0.15 eV below the 1E level. These levels are so close together that such factors as the Jahn-Teller instability, symmetric relaxation terms and possibly interlevel coupling effects will be important in determining the ground state for this centre. The position of the 1A_1 and 1T_2 levels is very sensitive to the value chosen for Q .

The unmodified study for the negatively charged vacancy, Fig. 4, predicts that the 4A_2

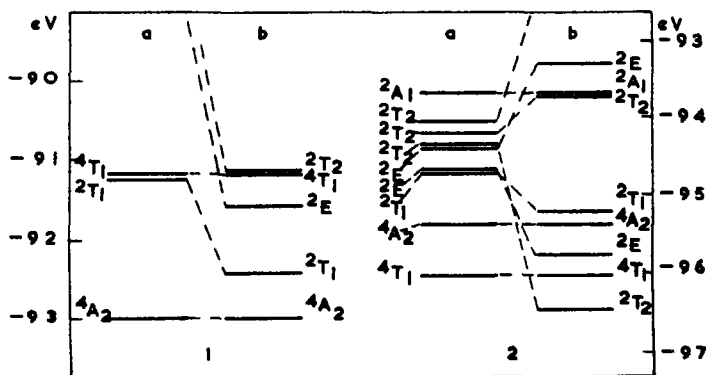


Fig. 4. Electronic structure of the single negatively charged undistorted vacancy in silicon. (a) before configuration interaction, (b) after configuration interaction. (1) $Q = 11.45$ eV, (2) $Q = 8.10$ eV.

the silicon atom and ω_α the effective or linear response frequency of the lattice for the α mode. The static equilibrium distortion is

$$Q_\alpha = F_\alpha / (M\omega_\alpha^2) \quad (6)$$

and the corresponding distortion energy

$$\Delta E(Q_\alpha) = -F_\alpha^2 / (2M\omega_\alpha^2). \quad (7)$$

Within the limitations of this approach the total energy change of the system undergoing several distortions is simply,

$$\Delta E = \sum_\alpha \Delta E(Q_\alpha). \quad (8)$$

The adiabatic linear response frequencies required in these calculations have recently been determined by Larkins and Stoneham [7] and have the following values:

$$\omega_\alpha = 0.18 \times 10^{14} \text{ rad./sec}$$

$$\omega_E = 0.21 \times 10^{14} \text{ rad./sec}$$

$$\omega_T = 0.18 \times 10^{14} \text{ rad./sec.}$$

However, as they have shown use of these values leads to extremely large relaxation terms and an unsatisfactory value for the formation energy of the vacancy in silicon. The failure of their calculations is interpreted as demonstrating the importance of nonlinear terms in the calculations of the distortion energy. The evaluation of these higher order terms is difficult as well as unreliable without better wavefunctions for the defect system than are available at present. Therefore, we have chosen an alternative approach and used values for the effective frequencies, ω'_α , which give reasonable values for the distortions. This procedure may be considered to at least partially include the effect of nonlinear terms and also the neglect of any hybridisation change for the nearest-neighbours to the vacancy (see Section 5). This

approach is adequate since we are primarily interested in the sensitivity of the ordering of the lowest electronic levels. For convenience, we use values for ω'_E and ω'_T obtained by using a restricted relaxation model which corresponds to using the sudden approximation [7, 8, 21]. Since the results to be presented show that the symmetric relaxation terms are most important, we use two values for ω'_α corresponding to $\omega'_\alpha = \omega'_E$ and $\omega'_\alpha = \omega'_T$ to investigate the dependence of the ordering of the lowest levels on the value chosen for ω'_α . The required values are $\omega'_E = \sqrt{2} \omega'_T = 0.825 \cdot 10^{14} \text{ rad/sec}$.

With these frequencies and known values of the forces, F_α , for the various electronic states it is possible to calculate the equilibrium distortion and corresponding energy lowering using equations (6) and (7). The magnitude of Q_α and $\Delta E(Q_\alpha)$ for the various levels if the adiabatic frequencies were used may be readily obtained from the values in Tables 3 to 8 by multiplying the tetragonal terms by 15.4, the trigonal terms by 10.5, and the symmetric terms by 21.0.

4.2 Symmetric relaxation effect

Since to first order there is no coupling between the various normal modes we may consider the interaction between all electronic states and the symmetric mode independently of the Jahn-Teller problem. For an electronic level with configuration interaction wave function ψ_k , the total symmetric force F_a on the atoms nearest the defect is defined, using the rigid atom approximation, as

$$F_a = - \left(\frac{\partial}{\partial Q_a} \langle \psi_k | H | \psi_k \rangle \right)_0. \quad (9)$$

This expression reduces to a sum of terms involving the derivatives of the molecular integrals, $A-K$, and terms involving the derivatives of the coefficients of the configuration interaction wave function. These latter first order terms were included, but make only a small contribution to the symmetric

force in most cases. Further reduction yields terms in the derivatives of the atomic hybrid integrals which were evaluated by calculating the particular integral $f(r)$ at the internuclear distances $r_0 + h$ and $r_0 - h$ where $r_0 = 3.84 \text{ \AA}$ and $h = 0.1 \text{ \AA}$ and using the numerical form

$$f'(r)/r_{\approx r_0} = \frac{f(r_0 + h) - f(r_0 - h)}{2h}. \quad (10)$$

Values for these derivatives are given in Table 2. When evaluating the derivatives of the molecular integrals it is very important to include terms involving the derivative of the overlap integral. The results for the lowest electronic levels of the various charged centres are shown in Tables 3 to 6 using the

Table 2. Values of the derivatives of the atomic integrals for the silicon vacancy calculation

$\frac{d}{dR_{AB}}(\text{Integral})$	Clementi functions	$\frac{d}{dR_{AB}}(\text{Integral})$	Clementi functions
$\langle a b \rangle$	-0.1845*	$\langle ab \frac{1}{r_{12}} ab \rangle$	-2.1329
$\langle a T b \rangle$	-0.5307	$\langle ab \frac{1}{r_{12}} ba \rangle$	-0.8105
$\langle a V_A b \rangle$	2.7116	$\langle aa \frac{1}{r_{12}} ab \rangle$	-1.8829
$\langle a V_B a \rangle$	2.6797		

* All derivatives in eV/Å°.

value for ω'_a given previously. These results demonstrate that the symmetric force term, F_a , is not constant for all the electronic levels of a given centre. Therefore, it is important to consider the symmetric relaxation energy corrections when determining the relative ordering of the lowest electronic levels. In most cases the force terms are not too sensitive to the value chosen for the one-centre Coulomb integral and are of the same order of magnitude for all the charged centres considered.

For the case where $\omega'_a = \omega'_r = 0.583 \cdot 10^{11} \text{ rad/sec}$ the energy lowering and distortion terms may be readily obtained from the results in Tables 3 to 6 by multiplying the appropriate terms by a factor of 2.0. With either value for ω'_a very reasonable distortions for the atoms neighbouring the vacancy are predicted. When the electronic levels from the undistorted calculations shown in Figs. 2 to 5 are corrected for symmetric relaxation effects the relative order of the lowest electronic levels for the various charge states is the same irrespective of which value is chosen for ω'_a .

The 3T_2 level of the V^+ centre is predicted to be lowest in energy in all cases even further below the 4T_1 level than in the undistorted study. The corrected results for the V^0 centre with $\omega'_a = 0.825 \cdot 10^{14} \text{ rad/sec}$ are given in Fig. 6. Conflicting results are now obtained for different values of Q . With $Q = 11.45 \text{ eV}$ the electronic symmetric corrections, i.e. $2\Delta E(Q_a)$, result in small changes in the relative energies of the lowest three levels. The 5A_2 level is predicted to be lowest just below the 1E and 3T_1 levels. The electron-lattice coupling term is larger for the 1T_2 level than for the other levels shown in Table 4; however, in the unmodified study this level is several electron volts above the lowest levels. For the calculation with $Q = 8.10 \text{ eV}$ the electron-lattice coupling terms for the 1A_1 and 1T_2 levels are larger than for the other levels such that the corrected 1A_1 level is lowest 0.23 eV below the 1T_2 level and 0.35 eV below the 5A_2 level for $\omega'_a = 0.825 \cdot 10^{14} \text{ rad/sec}$. With the alternative value for ω'_a the 1A_1 level is lowest 0.11 and 1.83 eV below the 1T_2 and 5A_2 levels respectively.

Figure 7 and Table 5 give the corrected results for the V^- centre with $\omega'_a = 0.825 \cdot 10^{14} \text{ rad/sec}$. The order of the lowest level is as calculated for the undistorted model, with a strong dependence on the value chosen for Q . No change in the order of the lowest levels for the V^{2-} centre result when the corrections given in Table 6 are made to the

Table 3. Values of the symmetric terms for the lowest 2T_2 and 4T_1 levels of the positive vacancy in silicon

Value of Q eV	$-F_a$ eV/Å	$\Delta E(Q_a)$ eV	Q_a Å	Value of Q eV	$+F_a$ eV/Å	$\Delta E(Q_a)$ eV	Q_a Å
1. 2T_2 Level				2. 4T_1 Level			
11.45	7.49	-1.42	-0.38	11.45	7.12	-1.25	-0.36
8.10	7.45	-1.40	-0.38	8.10	7.14	-1.28	-0.36

Effective frequency $\omega'_a = 0.825 \cdot 10^{14}$ rad/sec.

results from the undistorted model calculation.

4.3 Jahn-Teller effect

The degeneracy of an electronic level may be lifted by coupling to a distortion mode which lowers the symmetry of the system. A detailed account of the theory of this effect has been given by Öpik and Pryce [20] and applied to the vacancy in diamond by Friedel *et al.* [19]. This study is based upon the theory outlined in these papers and interlevel coupling effects are not considered. The only asymmetric distortion for a two-fold degenerate E level with states $|\theta\rangle$ and $|\epsilon\rangle$ results from a coupling to E modes giving a tetragonal distortion of the centre. There are three possible tetragonal distortions of the vacancy system with symmetry axes along the $\langle 100 \rangle$, $\langle 010 \rangle$ and $\langle 001 \rangle$ directions which represent equivalent energy minima for the

system. We will consider just the potential energy surface of the $\langle 100 \rangle$ configuration for which Q_x is zero and the magnitude of Q_θ is given by equation 6. The sign of Q_θ cannot be determined without evaluating higher order terms. The force term associated with this distortion is defined as,

$$F_{EE} = - \left(\frac{\partial}{\partial Q_\theta} \langle \theta | H | \theta \rangle \right)_0^* \quad (11)$$

and the total energy lowering ΔE_{EE} which equals $\Delta E(Q_\theta)$ is evaluated from equation (7).

A three-fold degenerate electronic level of T_1 or T_2 symmetry with states $|\xi\rangle$, $|\eta\rangle$ and $|\zeta\rangle$ may couple with the E or T_2 distortion modes causing a tetragonal or trigonal dis-

* In terms of the definitions used in Ref. [10]

$$F_{EE} = -I_{EE}, F_{TE} = -\frac{1}{3}I_{TE}, F_{TT} = -\frac{1}{3}I_{TT}.$$

Table 4. Values of the symmetric terms for the lowest 3T_1 , 1T_2 , 1E , 1A_1 and 5A_2 levels of the neutral vacancy in silicon

Value of Q eV	$-F_a$ eV/Å	$\Delta E(Q_a)$ eV	Q_a Å	Value of Q eV	$-F_a$ eV/Å	$\Delta E(Q_a)$ eV	Q_a Å
1. 3T_1 Level				2. 1E Level			
11.45	7.57	-1.45	-0.38	11.45	7.61	-1.46	-0.38
8.10	7.39	-1.38	-0.37	8.10	7.57	-1.45	-0.38
3. 1T_2 Level				4. 5A_2 Level			
11.45	8.89	-2.00	-0.45	11.45	7.68	-1.49	-0.39
8.10	9.70	-2.38	-0.49	8.10	7.87	-1.56	-0.40
5. 1A_1 Level							
8.10	9.55	-2.31	-0.48				

Effective frequency $\omega'_a = 0.825 \cdot 10^{14}$ rad/sec.

Table 5. Values of the symmetric term for the lowest 2T_2 , 2T_1 , 2E , 4T_1 and 4A_2 levels of the negatively charged vacancy in silicon

Value of Q eV	$-F_a$ eV/Å	$\Delta E(Q_a)$ eV	Q_a Å	Value of Q eV	$-F_a$ eV/Å	$\Delta E(Q_a)$ eV	Q_a Å
1. 2T_2 Level				2. 2T_1 Level			
11.45	8.18	-1.69	-0.41	11.45	8.35	-1.76	-0.42
8.10	9.33	-2.20	-0.47	8.10	8.36	-1.76	-0.42
3. 2E Level				4. 4T_1 Level			
11.45	7.95	-1.60	-0.40	11.45	8.08	-1.64	-0.41
8.10	8.99	-2.04	-0.45	8.10	9.06	-2.06	-0.46
5. 4A_2 Level							
11.45	8.64	-1.89	-0.44				
8.10	8.58	-1.86	-0.43				

Effective frequency $\omega_a = 0.825 \cdot 10^{14}$ rad/sec.

tortion of the vacancy system. Mixed tetragonal and trigonal distortions occur only for cases of accidental degeneracy[3]. There are four equivalent trigonal distortions with symmetry axes along the $\langle \bar{1}, \bar{1}, \bar{1} \rangle$, $\langle 1, 1, \bar{1} \rangle$, $\langle 1, \bar{1}, 1 \rangle$ and $\langle \bar{1}, 1, 1 \rangle$ directions and three of tetragonal symmetry as previously. We consider just the potential energy surfaces for the tetragonal distortion with $\langle 100 \rangle$ symmetry axis and for the trigonal distortion for which $Q_t = Q_\eta = Q_\zeta$. For these cases the corresponding force terms are defined as follows

$$F_{TE} = -2 / \sqrt{3} \left(\frac{\partial}{\partial Q_t} \langle \eta | H | \eta \rangle \right)_0^* \quad (12)$$

and

$$F_{TT} = -2/3 \left(\frac{\partial}{\partial Q_t} \langle \eta | H | \zeta \rangle \right)_0^* \quad (13)$$

The values for the Q_a and $\Delta E(Q_a)$ terms may be determined from equations (6) and (7). The total energy change for the tetragonal distortion ΔE_{TE} is equal to $\Delta E(Q_t)$, whereas, for the trigonal distortion considered the total energy change ΔE_{TT} is $\Delta E(Q_t) + \Delta E(Q_n) +$

Table 6. Values of the symmetric term for the lowest 3T_1 , 1E , 1T_2 , 3T_2 and 1A_1 levels of the doubly negatively charged vacancy in silicon

Value of Q eV	$-F_a$ eV/Å	$\Delta E(Q_a)$ eV	Q_a Å	Value of Q eV	$-F_a$ eV/Å	$\Delta E(Q_a)$ eV	Q_a Å
1. 3T_1 Level				2. 1T_2 Level			
11.45	8.33	-1.75	-0.42	11.45	8.05	-1.64	-0.41
8.10	9.01	-2.05	-0.46	8.10	9.11	-2.10	-0.46
3. 1E Level				4. 3T_2 Level			
11.45	8.11	-1.66	-0.41	11.45	7.72	-1.50	-0.39
8.10	8.59	-1.86	-0.43	8.10	9.59	-2.32	-0.48
5. 1A_1 Level							
11.45	7.97	-1.60	-0.40				
8.10	10.18	-2.62	-0.51				

Effective frequency $\omega_a = 0.825 \cdot 10^{14}$ rad/sec.

$\Delta E(Q_e)$ which is equal to $3\Delta E(Q_t)$. The force terms given by equations (11), (12) and (13) were evaluated by the same procedure as outlined for the symmetric terms using the derivatives given in Table 2. Terms involving the derivative of the overlap integral were included. The Jahn-Teller results for the degenerate electronic levels

chosen for the one-centre Coulomb integral, although, in general the splittings are predicted to be slightly larger for the case with $Q = 11.45$ eV. We have been unable to account for the unsatisfactory value obtained for the trigonal distortion of the lowest levels of the positive vacancy. The wave-function and formulae leading to the expressions for

Table 7. Values of the Jahn-Teller terms for the lowest 2T_2 and 4T_1 levels of the positive vacancy in silicon

Value of Q eV	F_{TE} eV/Å	ΔE_{TE} eV	Q_0 Å	F_{TT} eV/Å	ΔE_{TT} eV	Q_t Å
1. 2T_2 Level						
11.45	0.58	-0.01	0.029	3.75	-2.14	0.38
8.10	0.60	-0.01	0.031	3.57	-1.94	0.36
2. 4T_1 Level						
11.45	1.26	-0.04	0.07	-3.15	-1.51	-0.32
8.10	1.33	-0.04	0.07	-3.10	-1.46	-0.31

of the V^+ , V^0 and V^- centres are given in Tables 7, 8 and 9 respectively. In Figs. 6 and 7 the lowest electronic levels have been corrected for their equilibrium Jahn-Teller splittings.

With the exception of the 2T_2 and 4T_1 levels of the V^+ centre the splittings of the degenerate levels are predicted to be very small. They are not very dependent upon the value

F_{TT} appear to be correct; therefore, it would seem that higher-order terms may be very important for this system. Table 8 shows that both calculations predict that the lowest 3T_1 and 1T_2 levels of the V^0 system will undergo a trigonal distortion. However, for the 1T_2 level the energy difference between the trigonal and tetragonal equilibrium configuration is only about 0.01 eV in both cases. The pre-

Table 8. Values of the Jahn-Teller terms for the lowest 1E , 3T_1 and 1T_2 levels of the neutral vacancy in silicon

Values of Q eV	F_{TE} eV/Å	ΔE_{TE} eV	Q_0 Å	F_{TT} eV/Å	ΔE_{TT} eV	Q_t Å
1. 3T_1 Level						
11.45	-0.28	-0.002	-0.015	-1.04	-0.17	-0.10
8.10	-0.27	-0.002	-0.014	-0.63	-0.06	-0.06
2. 1T_2 Level						
11.45	-0.98	-0.024	-0.05	0.49	-0.045	0.05
8.10	-0.42	-0.004	-0.02	0.29	-0.01	0.03
3. 1E Level	F_{EE} eV/Å	ΔE_{EE} eV	$ Q_0 $ Å			
11.45	-0.36	-0.003	0.02			
8.10	-0.30	-0.002	0.02			

Table 9. Values of the Jahn-Teller terms for the lowest 2E , 2T_1 , 2T_2 and 4T_1 levels of the negatively charged vacancy in silicon

Value of Q eV	F_{T_2} eV/Å	ΔE_{TE} eV	Q_0 Å	F_{T_1} eV/Å	ΔE_{T_1} eV	Q_1 Å
1. 2T_2 Level						
11.45	-0.08	$-2 \cdot 10^{-4}$	-0.005	0.09	$-1 \cdot 10^{-3}$	0.009
8.10	0.22	$-1 \cdot 10^{-3}$	0.012	-0.21	$-6 \cdot 10^{-3}$	0.021
2. 2T_1 Level						
11.45	0.26	$-2 \cdot 10^{-3}$	0.014	0.84	-0.11	0.09
8.10	0.01	$-3 \cdot 10^{-6}$	$4 \cdot 10^{-4}$	0.95	-0.14	0.10
3. 4T_1 Level						
11.45	1.61	-0.06	0.086	0.39	-0.002	0.004
8.10	0.36	-0.003	0.002	0.37	-0.002	0.003
	F_{EE} eV/Å	ΔE_{EE} eV	$ Q_0 $ Å			
4. 2E Level						
11.45	-1.21	-0.04	0.06			
8.10	-0.46	-0.004	0.02			

dicted splitting for the 1E level is extremely small. Figure 6 shows how small the Jahn-Teller corrections to the energy levels are compared with the symmetric corrections. In the study with $Q = 11.45$ eV the correction to

the 3T_1 level is sufficient for it to again become lowest in energy 0.31 eV below the 5A_2 . Figure 7 shows that no change in the relative ordering of the energy levels for the V^- centre results from including the equilibrium Jahn-Teller

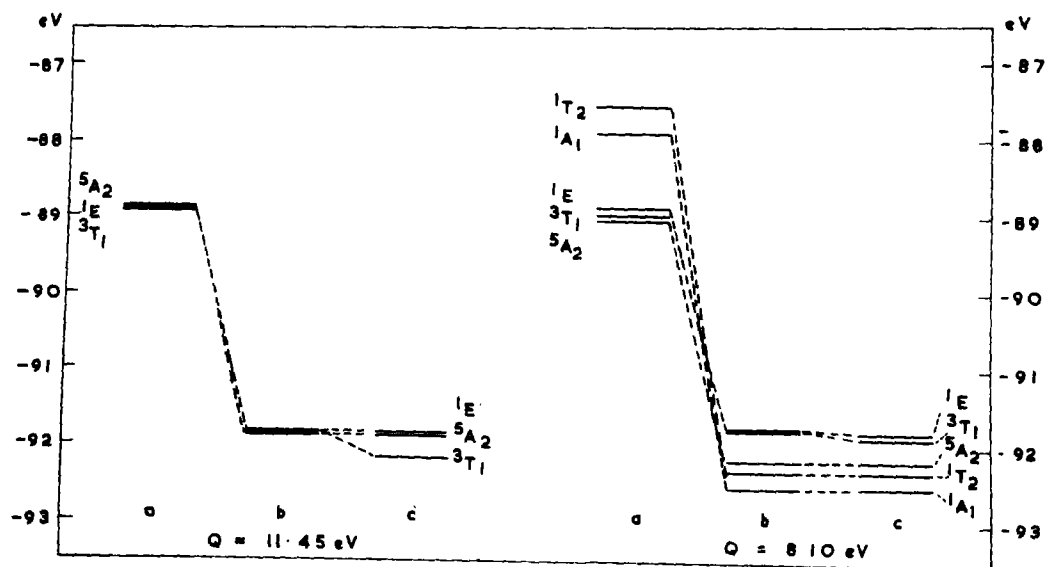


Fig. 6. Electronic structure of the neutral vacancy in silicon for $\omega_a = 0.825 \times 10^{14}$ rad./sec. (a) undistorted system (b) first-order electronic symmetric distortion corrections, (c) first order electronic Jahn-Teller corrections.

correction terms. The 2T_2 favours a trigonal distortion, but there is less than 0.005 eV between the energies ΔE_{TT} and ΔE_{TE} . The 2T_1 level also favours a trigonal distortion while the 4T_1 level is predicted to have a tetragonal equilibrium distortion. For the V^{2-} centre a very small tetragonal equilibrium distortion is predicted for the 3T_1 , 3T_2 and 1T_2 levels. No change in the ordering of the energy levels result from these corrections.

5. DISCUSSION OF RESULTS

Our calculations show that using the defect molecule approach electron-electron inter-

using a rigid-atom model and only linear coupling terms for the symmetric relaxation and Jahn-Teller effects suggest that the former effect is more important in determining the ordering of the lowest levels. The calculated Jahn-Teller splitting of a given level, to first order, is in general smaller for the silicon vacancy than for the same level of the diamond vacancy [10]. These results suggest that in a more sophisticated treatment at least the symmetric relaxation should be included as an integral part of the calculation.

The molecular model predicts that the

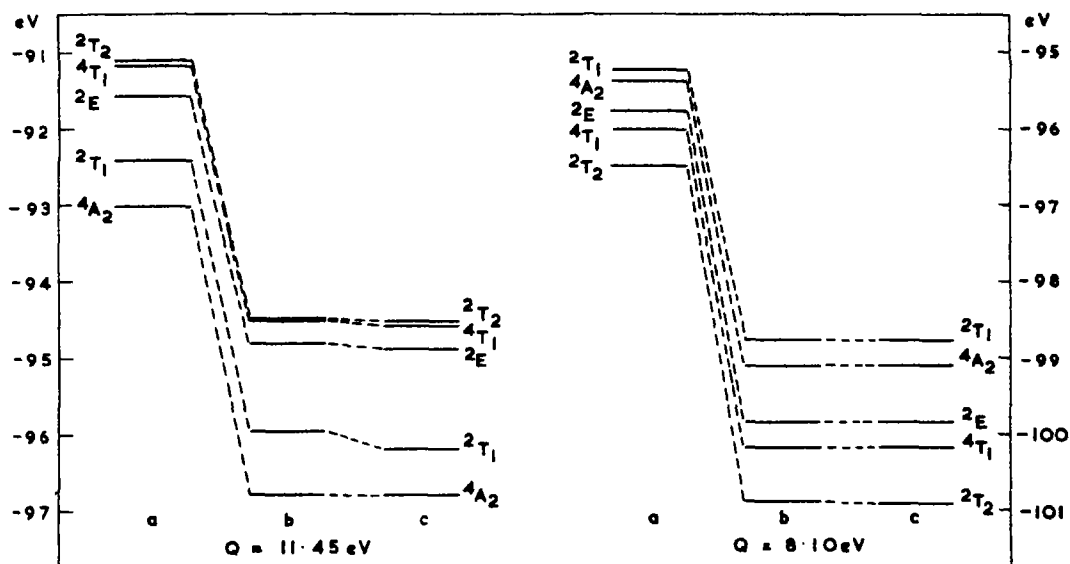


Fig. 7. Electronic structure of the negative vacancy in silicon for $\omega_a = 0.825 \times 10^{14}$ rad./sec. (a) undistorted system, (b) first-order electronic symmetric distortion corrections, (c) first-order electronic Jahn-Teller corrections.

action terms and configuration interaction effects are very important in determining the relative ordering of the lowest levels. The order of these levels does depend upon the value chosen for the one-centre Coulomb integral for all systems except the positive vacancy. While there is uncertainty as to the true value for Q it is expected to have a value in the range 8.10–11.45 eV. The calculations

nearest neighbour atoms to the vacancy relax inwards towards its centre on rebonding, but since the model used constrains the system by requiring these atoms to remain sp^3 hybridized such a result was inevitable. In the crystal, it is probable that some electronic re-organisation of the valence electrons on each silicon atom will occur (by analogy with the isolated radicals) resulting in a change

towards greater sp^2 character for the bonded valence hybrids and greater p character for the vacancy hybrid orbital. The symmetric electronic force which is associated with this re-organisation opposes the symmetric re-bonding force. Hence the calculated energy lowering would be reduced. It has not been possible to satisfactorily calculate the forces arising from the reorganisation. The 'tension' in the Si-Si bonds in crystalline silicon is considered to be small, because the nearest neighbour bond length is 2.35 \AA compared with $2.32 \pm 0.02 \text{ \AA}$ in such compounds as Si_2H_6 and Si_2Cl_6 [18]. We have considered only the equilibrium configuration for the various levels, whereas for the vacancy system energy changes for the higher levels are determined by the extent of distortion of the ground state. From the results given in Tables 3 to 6 and equation (5) this information may easily be obtained. It is interesting that, with the one exception of the V^0 centre with $Q = 8.10 \text{ eV}$, the Jahn-Teller and symmetric corrections do not alter the ground state of the system predicted using an undistorted model. The next section shows that the predicted ground states from the modified study largely agree with the experimental results. In view of the size of the symmetric distortion non-linear coupling terms of the kind $KQ_\alpha Q_\alpha$ where $\alpha = \epsilon, \theta, \xi, \eta, \zeta$ may be very important in determining the magnitude of the Jahn-Teller splittings. Delocalisation of the electronic wave-function from the vacancy is unlikely to effect the relative ordering of the lowest levels, but the magnitude of the Jahn-Teller coupling and the separation between the levels may be sensitive to this effect.

For the positive vacancy the 2T_2 level is predicted as the ground state of the system and a trigonal distortion is favoured due to Jahn-Teller effects. The accuracy of the calculation for the neutral vacancy with $Q = 11.45 \text{ eV}$ is not reliable enough for us to decide which of the three levels 1E , 3T_1 or 5A_2 is the predicted ground state. With the

alternative value for Q the 1A_1 and 1T_2 levels are close together therefore interlevel coupling may result. The general theory of this effect has been discussed by Stoneham and Lannoo [3]. This coupling may cause a trigonal distortion of the system or a mixed tetragonal and trigonal distortion. For the negative vacancy, the 4A_2 level is always lowest in the study when $Q = 11.45 \text{ eV}$; however, several levels depend strongly on the value of Q and with $Q = 8.10 \text{ eV}$ the 2T_2 level is lowest for reasons discussed previously. With only intralevel coupling terms this level favours a small trigonal distortion. However, ignoring spin-orbit coupling, the 2T_2 level may couple with either the 2E or 2T_1 levels to give various possible distortions, including a mixed trigonal and tetragonal distortion. From the present results the interlevel coupling, $^2T_2 + ^2E$ is more probable. The calculation suggests that the separation between these two levels is too large for this effect to be significant; however, this simple model does neglect delocalisation and polarisation contributions which it is hoped will not significantly effect the relative ordering of the lowest levels, but will certainly influence the separations.

6. COMPARISON WITH EXPERIMENT

The electronic properties of point defects in silicon have been investigated experimentally principally by Watkins and Corbett using elegant electron spin resonance methods incorporating uniaxial stress techniques. Watkins [1, 2] has identified the positively ionized vacancy, V^+ , and the negatively ionized vacancy, V^- , in p -type silicon irradiated with 1.5 MeV electrons at 4 and 20°K . The ground states of these centres are doublets with $S = \frac{1}{2}$. The V^+ centre is believed to be tetragonally distorted and the V^- centre to have a mixed tetragonal and trigonal distortion as a result of the Jahn-Teller coupling of a degenerate ground state. The magnitudes of the Jahn-Teller splittings are estimated experimentally to be very large for point defects in silicon and to vary from $\sim 0.4 \text{ eV}$

for V^+ to 1 eV for the group V -vacancy pairs to 1–2 eV for the divacancy [21, 22]. It has been argued [2] that the neutral vacancy does exist but has not been observed because it has a diamagnetic ground state ($S = 0$). Since neither the spectrum for V^+ or V^- has been observed in low resistivity n -type silicon, Watkins suggests that an additional charge state, the doubly-negatively charged vacancy, V^{2-} , may exist with a diamagnetic ground state ($S = 0$). Watkins has had considerable success in explaining his results on the basis of a one-electron model. Within the framework of this model configuration interaction and electron-electron repulsion terms are considered to be much smaller than Jahn-Teller terms and may therefore be ignored.

Using the modified case ($Q = 8.10$ eV) of the many-electron defect molecule method the predicted spin-multiplicities of the ground states for the various charge states of the isolated vacancy, V^+ , V^0 , V^- and V^{2-} , are in agreement with the experimental observation. However, the quantitative aspects of the calculation are very different from those implied by a one electron treatment. Configuration interaction and electron-electron repulsion terms are essential features of the model. Further, with the exception of the V^+ centre calculations, the linear Jahn-Teller coupling terms are predicted to be small and at least an order of magnitude less than the symmetric force terms. The analysis of the experimental stress splitting results to determine the magnitude of the Jahn-Teller coupling assumes that the atoms neighbouring the vacancy move under the applied stress exactly as do the perfect lattice atoms. A detailed study of this problem [7] demonstrates that this is not the case. The important ratio $(\omega_a^0/\omega_a^v)^2$, where ω_a^0 is the effective frequency of the α mode for the perfect crystal and ω_a^v is the effective frequency of the corresponding mode of a crystal with a vacancy, is equal to 10.6 for the A_1 mode, 1.4 for the E mode and 1.8 for the T mode compared with the assumed value of 1.0

by Watkins in all cases. It seems probable therefore that the Jahn-Teller splittings deduced from the experimental observations are overestimates. The importance of the symmetric mode in determining the relative ordering of the energy levels has not been studied experimentally. The calculations also suggest that non-linear terms in the Jahn-Teller energy may be important, but these have not been included in the experimental analysis.

The tetragonal distortion of the ground state of the V^+ centre is not predicted by the first-order Jahn-Teller calculation, but inclusion of higher order terms may account for the difference. The mixed tetragonal and trigonal distortion for the V^- centre may be explained in the many-electron model by interlevel coupling between the lowest 2T_2 and 2E levels. It seems probable therefore that the results obtained from the detailed study of the many-electron problem are not incompatible with the experimental findings and may give a better description of the isolated vacancy than the one-electron model.

7. CONCLUSION

The many-electron defect molecule method has been used to predict the correct spin multiplicities for the ground states of the various charged vacancy centres in silicon. A modified first-order response theory predicts that the symmetric relaxation energies are much larger than the Jahn-Teller energies. The quantitative features of the model are very different to those implied by the one-electron model, but the results suggest they may not be incompatible with the experimental findings.

Acknowledgements—I would like to thank Professor C. A. Coulson and Drs. A. M. Stoneham and A. B. Lidiard for helpful discussions. I also gratefully acknowledge the award of the Victorian Rhodes Scholarship by the Rhodes Trust and a Senior Scholarship from Wadham College, Oxford.

REFERENCES

1. WATKINS G. D., *Int. Conf. Crystal Lattice Defects 1962*, *J. phys. Soc. Japan* **18**, Suppl. 11, 22 (1963).
2. WATKINS G. D., *Proc. Symp. On Radiation Damage in Semiconductors* p. 97 Dunod, Paris (1965).
3. STONEHAM A. M. and LANNON M., *J. Phys. Chem. Solids* **30**, 1769 (1969).
4. CALLAWAY J. and HUGHES A. J., *Phys. Rev.* **156**, 860 (1967).
5. CALLAWAY J. and HUGHES A. J., *Phys. Rev.* **164**, 1043 (1967).
6. COULSON C. A. and KEARSLEY M. J., *Proc. R. Soc. A* **241**, 433 (1957).
7. LARKINS F. P. and STONEHAM A. M., *J. Phys. C*, in press.
8. LIDIARD A. B. and STONEHAM A. M., *Science and Technology of Industrial Diamonds* 1, 1, Industrial Diamond Information Research, London (1967).
9. COULSON C. A. and LARKINS F. P., *J. Phys. Chem. Solids* **30**, 1963 (1969).
10. COULSON C. A. and LARKINS F. P., *J. Phys. Chem. Solids*, to be published.
11. CLEMENTI E. and RAIMONDI D. L., *J. Chem. Phys.* **38**, 2686 (1963).
12. GOEPPERT-MAYER M. and SKLAR A. L., *J. Chem. Phys.* **6**, 645 (1938).
13. CLEMENTI E., *Supplement to I.B.M. J. Res. Dev.* **9**, 2 (1965).
14. YAMAGUCHI T., *J. phys. Soc. Japan* **17**, 1359 (1962).
15. MULLIKEN R. S., *J. Chim. Phys.* **46**, 500 (1949).
16. SKINNER H. A. and PRITCHARD H. D., *Trans. Faraday Soc.* **49**, 1255 (1963).
17. JAHN H. A. and TELLER E., *Proc. R. Soc. A* **161**, 220 (1937).
18. SUTTON L. E., *Interatomic Distances*, Suppl. Chem. Soc. Special Publication No. 18 (1965).
19. FRIEDEL J., LANNON M. and LEMAN G., *Phys. Rev.* **164**, 1056 (1967).
20. ÖPIK U. and PRYCE M. H. L., *Proc. R. Soc. A* **238**, 425 (1957).
21. ELKIN E. L. and WATKINS G. D., *Phys. Rev.* **174**, 881 (1968).
22. WATKINS G. D., private communication.

THEORY OF ELASTIC STIFFNESS c_{33} OF GADOLINIUM IN THE SPIN ROTATION REGION*

L. M. LEVINSON

Department of Electronics, The Weizmann Institute of Science, Rehovot, Israel and General Electric
Research and Development Center, Schenectady N.Y. 12301, U.S.A.†

and

S. SHTRIKMAN

Department of Electronics, The Weizmann Institute of Science, Rehovot, Israel

(Received 27 July 1970)

Abstract—We have constructed a simple, model free-energy function to interpret the anomalous decrease in the elastic stiffness c_{33} of Gd in the spin rotation region. Our model qualitatively exhibits the observed drop in c_{33} , and an order of magnitude estimate of the decrease is in agreement with measured values. In the presence of sufficiently large magnetic fields, spin rotation causes large changes in the shape-dependent magnetostatic self-energy, which 'freezes out' strain-induced spin rotation, thereby eliminating the drop in c_{33} . As is borne out experimentally, we predict that the anomalous decrease in c_{33} should disappear for fields of the order of 5 kG. We also evaluate the magnetic field dependence of c_{33} and obtain fair qualitative agreement with the measurements.

1. INTRODUCTION

THE ELASTIC properties of materials undergoing magnetic phase transitions have been the subject of considerable study [1, 2]. More recently [3-7], changes have been observed in the elastic properties of magnetic materials following the application of magnetic fields large enough to cause a reorientation of the magnetic spin direction. Spin reorientation may, however, also be induced in some magnetic materials by changes in the sample temperature [8], and this is what occurs in gadolinium [9-12]. We may expect to find unusual behavior of the elastic constants in the spin reorientation region in this case also.

The easy direction of magnetization in the rare earth element gadolinium ($T_c \approx 290^\circ\text{K}$) is known [9-12] to lie along the hexagonal

z-axis in the temperature region immediately below T_c . On cooling to below 240°K the spin direction rotates away from the z-axis, and lies on a cone of directions about the z-axis. The temperature dependence of the cone half-angle θ has been evaluated using torque magnetometer [9] neutron diffraction [10, 11] and a.c. permeability [12] measurements, and the qualitative features of its behavior are well established. Below 240°K the cone half-angle increases quite rapidly from zero, reaching a rather flat maximum of about $\theta = 70^\circ$ near 180°K . On further cooling, a slow decrease in θ takes place. Qualitatively, the various determinations are in agreement. There are, however, substantial differences between quantitative details of the behavior of θ as determined by the various investigators [9-12].

The temperature and field dependence of the elastic stiffness c_{33} of Gd has been closely studied by Long *et al.* [13]. They observed a minimum in c_{33} at about 220°K , which they identified as arising from the spin rotation in this temperature region. The application of a sufficiently strong magnetic field serves to

*Research at the Weizmann Institute sponsored in part by the Materials Physics Division (MAYT), Air Force Materials Laboratory (AFML) Wright-Patterson AFB, Ohio 45433, through the European Office of Aerospace Research, OAR United States Air Force, under contract AF EOAR 61052-67C-0040.

†Present Address.

suppress this minimum. For the reader's convenience we reproduce their results in Figs. 1 and 2. We have also added to the figures approximate [9-12] values of θ at a few appropriate temperatures.

In their discussion of the anomaly observed in c_{33} , Long *et al.* [13] note the probable relevance of volume-dependent magneto-elastic interactions coupling the strain ϵ_{zz} and the spin S_z^2 . In Section 2(a) below, we shall present a simple model to demonstrate how terms of the form $\epsilon_{zz}S_z^2$, treated as a first-order perturbation of the isotropic exchange Hamiltonian, do give rise to a drop of

the correct order of magnitude in c_{33} in the spin rotation region. We limit the treatment of Section 2(a) to the case of zero applied magnetic field. In Section 2(b), we demonstrate that if the effect of an external magnetic field H is regarded as simply contributing a term $-\mathbf{M} \cdot \mathbf{H}$ to the energy, results in sharp disagreement with experiment are predicted. A proper treatment requires explicit consideration of the role of the shape-dependent magnetostatic self-energy in determining the behavior of the system. The qualitative predictions of our model, upon incorporating magnetostatic effects, are sufficiently similar

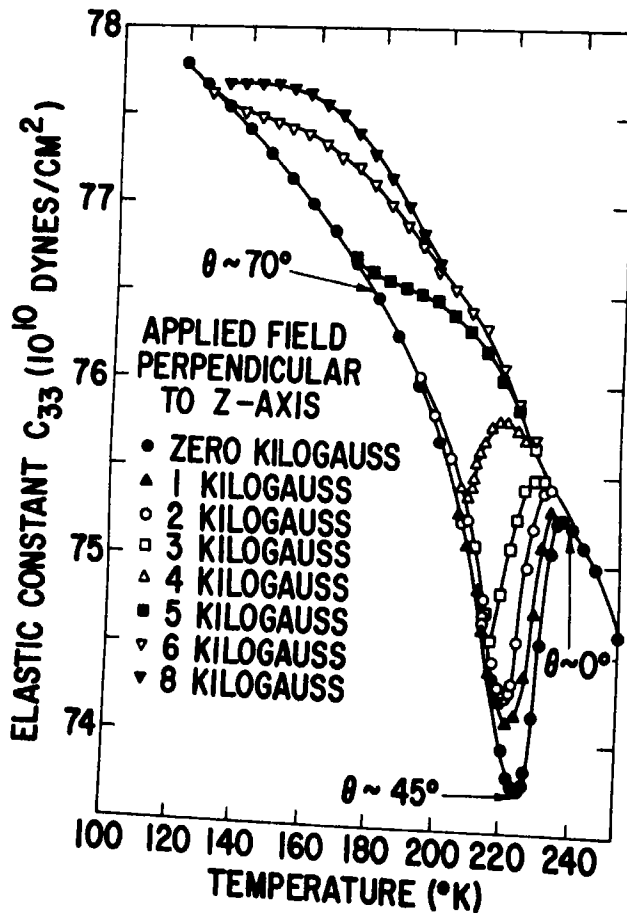


Fig. 1. Elastic constant c_{33} vs. temperature for various values of the magnetic field applied perpendicular to the hexagonal z -axis, as measured by Long *et al.* [13]. We have inserted values [9-12] of the rotation angle θ in zero field at a few temperatures.

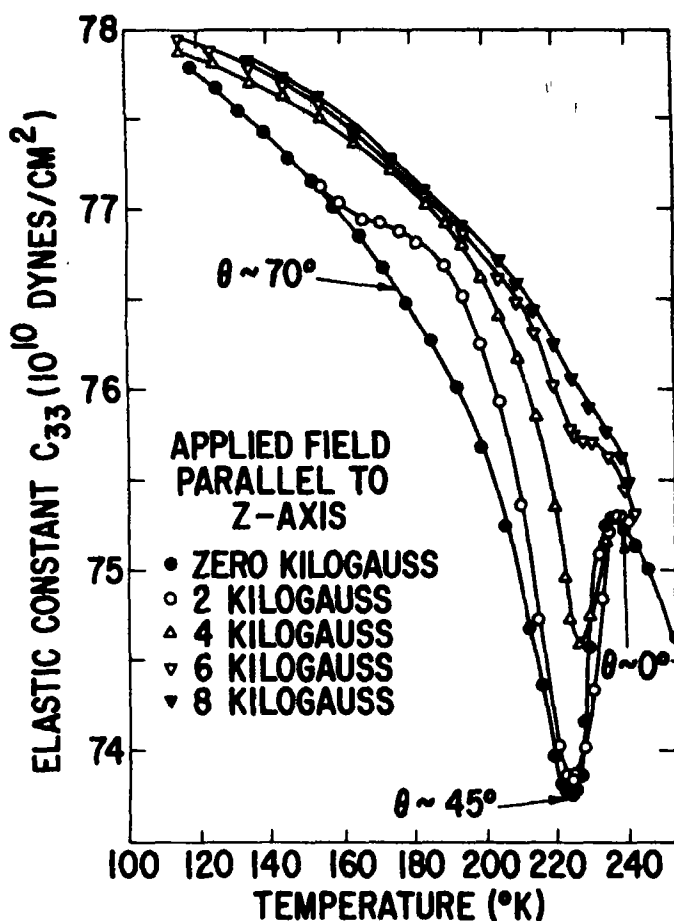


Fig. 2. Elastic constant c_{33} vs. temperature for various values of the magnetic field applied along the hexagonal z-axis of the crystal, as measured by Long *et al.*[13]. We have inserted values [9-12] of the rotation angle in zero field θ at a few temperatures.

to the measured [13] properties of c_{33} , to lead us to believe, that by our approach, we have succeeded in incorporating the essential features relevant to a proper interpretation of the experimental results of Long *et al.*[13]. Our results indicate that the influence of a magnetic field upon c_{33} in the spin rotation region does not reflect an intrinsic property of Gd, but should rather be associated with shape dependent effects connected with the particular sample [13] studied. As is borne out experimentally, we predict that the anomalous decrease in c_{33} should tend to disappear

for fields of the order of 5 kG. We also obtain fair qualitative agreement between the measured and predicted magnetic field dependence of c_{33} .

2. DESCRIPTION OF THE MODEL

(a) Zero applied field

Before we present the rather simple, model free-energy function which we will utilize to calculate the longitudinal elastic stiffness constant c_{33} of Gd in the spin rotation region, it is probably relevant to present to the reader the reasons which decided us to opt for a

rather crude model calculation of c_{33} , in lieu of attempting an exact quantitative calculation.

We shall assume that the anomalous decrease observed in c_{33} in the spin rotation region arises from magnetoelastic coupling between the magnetization and strain variables in the system Hamiltonian. As will become clear below, the detailed temperature dependence of the decrease in c_{33} is determined both by rotation of the easy direction of magnetization, and by the temperature dependence of the appropriate magnetoelastic coupling coefficients. The former is in turn controlled by the temperature dependence of the 3 magnetocrystalline anisotropy constants[9] pertinent to Gd. Values of θ , the half-cone angle of the magnetization in the spin rotation region, have been computed [9] from measured values of these magnetocrystalline anisotropy constants, and are in poor quantitative agreement with values of θ obtained by other methods[10-12]. Moreover, the size and temperature dependence of the 4 magnetoelastic coupling coefficients* appropriate to a quantitative computation of c_{33} are not available in the literature. An exact calculation would thus involve 7 untrustworthy or unknown parameters, and, in our opinion, attempting a quantitative 'fit' between experiment and theory with such a multiplicity of adjustable parameters should be regarded with some suspicion. On generalizing our calculation to include the effect of an applied magnetic field (Section 2(b)), the prospects of an exact calculation become even worse. In this case, details of the inhomogeneous internal field distribution and the domain rearrangement process, on spin rotation in the cylindrical specimen studied by Long *et al.*[13], should play a crucial role in a quantitative comparison between theory and experiment.

*These are the two single-ion, and the two two-ion terms in the magnetoelastic Hamiltonian which contain ϵ_{zz} , the strain in the z direction. Their explicit form is given by Callen and Callen[14].

In view of the above, we have chosen to avoid the complexity and obscurity inherent in attempting a detailed fit to the measured results. Instead we will make some rough approximations to obtain a tractable model, whose qualitative properties (as will be seen in the following) reflect the behavior of the elastic constants of Gd in the spin rotation region.

To obtain our model free-energy, we shall be guided by the exact spin Hamiltonian for Gd, including magnetoelastic terms, which has been given by Callen and Callen[14]. Following their notation, we write the spin Hamiltonian as

$$\mathcal{H} = \mathcal{H}_m + \mathcal{H}_e + \mathcal{H}_{me} + \mathcal{H}_a. \quad (1)$$

\mathcal{H}_m is the Hamiltonian of the spin system, consisting of isotropic exchange terms arising from the Ruderman-Kittel[15] interaction.

\mathcal{H}_e is an essentially classical, additive, elastic energy associated with homogeneous strain.

\mathcal{H}_{me} is the magnetoelastic interaction coupling the spin system to the strain.

\mathcal{H}_a is the magnetocrystalline energy, representing the interaction of the unstrained lattice with the magnetic spin system.

We may regard \mathcal{H}_{me} and \mathcal{H}_a as perturbations upon the 'unperturbed' Hamiltonian \mathcal{H}_m , and to first order in the perturbation, the free energy is given as

$$F = F_m + \mathcal{H}_e + \langle \mathcal{H}_{me} \rangle + \langle \mathcal{H}_a \rangle, \quad (2)$$

where the angular brackets denote thermal averaging using the unperturbed density operator of the spin system. F_m is the free energy corresponding to \mathcal{H}_m , and, as will be evident from the treatment below, contributes nothing to the elastic constant c_{33} since \mathcal{H}_m is both unaltered by spin rotation, and is independent of strain.

We shall take $\langle \mathcal{H}_a \rangle$ to be of the form

$$\langle \mathcal{H}_a \rangle = K_1(T) \sin^2 \theta + K_2(T) \sin^4 \theta, \quad (3)$$

where K_1 and K_2 depend on the temperature T , and θ is the angle between the mean spin direction and the hexagonal z -axis of Gd. The equilibrium angle at any given temperature follows [8] upon minimization of the free energy with respect to θ .

The above choice of $\langle \mathcal{H}_a \rangle$ is a somewhat crude approximation to the general form of the crystal-field anisotropy energy permitted by the lattice symmetry [9, 13]. In fact, $\langle \mathcal{H}_a \rangle$ of the form given in (3) would predict [8] that θ increases continuously from $\theta = 0$ to $\theta = \pi/2$, whereas the results of Corner *et al.* [9] explicitly indicate that a term of the type $K_3 \sin^6 \theta$ is necessary to take account of the slow decrease of θ from its maximum value of 70° (at about 180°K), to $\theta \approx 30^\circ$ below 80°K . Figures 1 and 2 indicate, however, that the anomaly in c_{33} is practically over for $T < 180^\circ\text{K}$, and following the spirit of our model calculation, we have adopted the simple form for $\langle \mathcal{H}_a \rangle$ given in (3).

The general form for \mathcal{H}_c allowed by the crystal symmetry of Gd is listed by Callen and Callen [14]. Since we will evaluate c_{33} by the result $c_{33} = d^2F/d\epsilon_{zz}^2$, we shall restrict ourselves to the term in \mathcal{H}_c quadratic in ϵ_{zz} , which we write

$$\mathcal{H}_c = \frac{1}{2} c'_{33} \epsilon_{zz}^2 \quad (4)$$

In (4), c'_{33} is the elastic stiffness in the absence of magnetoelastic effects.

Callen and Callen [14] have given in full the lengthy expressions for the one-ion and two-ion magnetoelastic Hamiltonian \mathcal{H}_{me} of Gd. \mathcal{H}_{me} is a sum of terms linear in strain, and zero or second order in the spin components. We will not repeat the expression here. We obtain magnetoelastic contributions to c_{33} from those terms in \mathcal{H}_{me} which contain products of ϵ_{zz} and S_z^2 . The contribution of such terms to c_{33} arises from the angular dependence of $\langle S_z^2 \rangle$ in the spin rotation region.

Let \mathbf{n} be a unit vector in the direction of the net magnetization, and let \mathbf{k} be a unit vector perpendicular to \mathbf{n} . We then have

$$\begin{aligned} \langle S_z^2 \rangle &= \langle (S_n \cos \theta + S_k \sin \theta)^2 \rangle, \\ &\approx \sin^2 \theta [S(S+1) - 2\langle S_n^2 \rangle] + \langle S_n^2 \rangle, \end{aligned}$$

using the molecular-field approximations $\langle S_n S_k \rangle = 0$ and $S_k^2 + S_n^2 = S(S+1)$. Thus terms of the form

$$\langle S_z^2 \rangle \epsilon_{zz} = [S(S+1) - 2\langle S_n^2 \rangle] \epsilon_{zz} \sin^2 \theta + \langle S_n^2 \rangle \times \epsilon_{zz} \quad (5)$$

appear in $\langle \mathcal{H}_{me} \rangle$. The second term on the right of (5) vanishes upon evaluating $d^2F/d\epsilon_{zz}^2$, but since the equilibrium value of θ depends on ϵ_{zz} , the first term on the right of (5) will produce a magnetoelastic contribution to c_{33} . We thus write

$$\langle \mathcal{H}_{me} \rangle = Q(T) \epsilon_{zz} \sin^2 \theta, \quad (6)$$

which is the lowest order magnetoelastic contribution to the free energy compatible with the symmetry, and which contributes to c_{33} . To a first approximation we neglect the temperature dependence of $Q(T)$ in the spin rotation region.

Substituting (3), (4), and (6) in (2), we have

$$F = F_m + \frac{1}{2} c'_{33} \epsilon_{zz}^2 + Q \epsilon_{zz} \sin^2 \theta + K_1 \sin^2 \theta + K_2 \sin^4 \theta. \quad (7)$$

Equation (7) represents the model free-energy function of our system, and we shall utilize it to evaluate the elastic stiffness c_{33} in the presence of magnetoelastic coupling.

The equilibrium value of θ at any given strain is determined by

$$\begin{aligned} \frac{\partial F}{\partial \theta} \Big|_{\epsilon_{zz}} &= 0 \\ &= 2(K_1 + Q \epsilon_{zz}) \sin \theta \cos \theta + 4 K_2 \sin^3 \theta \times \cos \theta. \end{aligned} \quad (8)$$

This has solution $\theta = 0$, $\theta = \pi/2$, or

$$\sin^2 \theta = -(K_1 + Q \epsilon_{zz}) / (2K_2). \quad (10)$$

In this simple case we could substitute (10) in (7) and evaluate $c_{33} = d^2F/d\epsilon_{zz}^2$ directly. We shall, however, proceed using the rules for partial differentiation, since this technique will prove more convenient in Section 2(b).

Using

$$\begin{aligned} \frac{dF}{d\epsilon_{zz}} &= \left. \frac{\partial F}{\partial \epsilon_{zz}} \right|_{\theta} + \left. \frac{\partial F}{\partial \theta} \right|_{\epsilon_{zz}} \frac{d\theta}{d\epsilon_{zz}} \\ &= \left. \frac{\partial F}{\partial \epsilon_{zz}} \right|_{\theta} \text{ by (8),} \\ &= Q \sin^2 \theta + c'_{33} \epsilon_{zz}, \end{aligned}$$

we have

$$c_{33} = d^2F/d\epsilon_{zz}^2 = c'_{33} + 2Q \sin \theta \cos \theta (d\theta/d\epsilon_{zz}). \quad (11)$$

Evaluating $d\theta/d\epsilon_{zz}$ from (10), we obtain

$$c_{33}/c'_{33} = 1 - Q^2/(2K_2 c'_{33}) \quad (12)$$

for $0 < \theta < \pi/2$ (i.e. in the spin rotation region), and

$$c_{33} = c'_{33} \quad (13)$$

when $\theta = 0$, or $\theta = \pi/2$.

We wish to emphasize once again that experiment[9-12] indicates that in Gd. θ does not simply increase from $\theta = 0$ to $\theta = \pi/2$, as would follow[8] from the simple form (3) for the magnetocrystalline energy, assuming K_1 and K_2 to be monotonic functions of the temperature. The measured temperature dependence of θ has been described in Section 1, and is in fact controlled by an anisotropy energy having the form[9] $K_1 \sin^2 \theta + K_2 \sin^4 \theta + K_3 \sin^6 \theta$. By incorporating the additional term $K_3 \sin^6 \theta$ in the free energy (7), we would obtain, by a calculation analogous to that above,

$$c_{33}/c'_{33} = 1 - Q^2/[2c'_{33}(K_2 + 3K_3 \sin^2 \theta)] \quad (14)$$

in the spin rotation region, where the value of θ in (14) is determined by the relation

$$K_1 + (2K_2 - Q^2/c'_{33}) \sin^2 \theta + 3K_3 \sin^4 \theta = 0. \quad (15)$$

Clearly (14) reduces to (12) on putting $K_3 = 0$. Since the measured[9] temperature dependence of K_1 , K_2 and K_3 is perhaps unreliable for evaluation of $\theta(T)$, we shall, however, adopt the simpler expression (12) for our model.

If we neglect the temperature dependence of $Q^2/(2K_2 c'_{33})$, equation (12) predicts a drop* in c_{33} in the spin rotation region, reflecting the induced softening of the crystal via magnetoelastic coupling, when the net magnetization is 'free' to rotate. The zero field curves of Figs. 1 or 2 confirm the existence of a drop in c_{33} in the spin rotation region of Gd. Experimentally, the magnitude of the drop is not a constant. This discrepancy of detail is to be expected, however, in view of the approximations made in setting up our model.

We may estimate the magnetoelastic anomaly predicted by (12) using measured values[9] of the anisotropy coefficients of Gd. Corner *et al.*[9] find $K_2 \approx 10^5 \text{ erg/cm}^3$ in the spin rotation region ($T \approx 220^\circ \text{K}$). Callen and Callen[14] quote data of Coleman[17] which indicates that 10^{-4} is a perhaps typical value of a magnetostriction constant λ in Gd. Since, roughly,

$$Q \approx c'_{33} \lambda \approx 5 \times 10^{11} \times 10^{-4} \text{ dynes/cm}^2$$

we estimate $Q^2/(2K_2) \approx 10^{10} \text{ dynes/cm}^2$. This is the right order of magnitude for the observed $c_{33} - c'_{33}$ (Figs. 1 and 2).

(b) Effect of magnetic field

We consider first the case of a magnetic field H_{\perp} applied in the basal plane. The most straightforward (but as we shall show, inadequate) way of including the effect of H_{\perp} would be to add a term $-H_{\perp} M \sin \theta$ to the

*Exactly this type of behavior has recently been observed in the spin rotation region of ErFeO_3 by Gorodetsky and Lüthi[16].

free energy, (7), to obtain

$$F(\theta, H_{\perp}) = F_m + \frac{1}{2}c'_{33}\epsilon_{zz}^2 + Q\epsilon_{zz}\sin^2\theta + K_1\sin^2\theta + K_2\sin^4\theta - H_{\perp}M\sin\theta. \quad (16)$$

We proceed to evaluate $c_{33} = d^2F/d\epsilon_{zz}^2$ as in Section 2(a). At equilibrium,

$$\begin{aligned} \left(\frac{\partial F}{\partial \theta}\right)_{\epsilon_{zz}} &= 0 \\ &= 2(Q\epsilon_{zz} + K_1)\sin\theta\cos\theta + 4K_2\sin^3\theta \\ &\quad \times \cos\theta - H_{\perp}M\cos\theta. \end{aligned} \quad (17)$$

This has solution $\cos\theta = 0$, or

$$2(Q\epsilon_{zz} + K_1)\sin\theta + 4K_2\sin^3\theta - H_{\perp}M = 0. \quad (18)$$

Using

$$\left(\frac{dF}{d\epsilon_{zz}} = \frac{\partial F}{\partial \epsilon_{zz}}\right)_{\theta},$$

we have

$$c_{33} = \frac{d^2F}{d\epsilon_{zz}^2} = c'_{33} + 2Q\sin\theta\cos\theta \frac{d\theta}{d\epsilon_{zz}}. \quad (19)$$

Evaluating $d\theta/d\epsilon_{zz}$ from (18), we obtain

$$c_{33}(H_{\perp})/c'_{33} = 1 - f(\theta, H_{\perp})Q^2/(2K_2c'_{33}) \quad \text{if } 0 < \theta < \pi/2, \quad (20)$$

where

$$f(\theta, H_{\perp}) = \sin^3\theta/[MH_{\perp}/(8K_2) + \sin^3\theta],$$

and θ is determined by

$$2K_1\sin\theta + (4K_2 - 2Q^2/c'_{33})\sin^3\theta = MH_{\perp}. \quad (21)$$

(Equation (21) follows from (18), upon noting that $\partial F/\partial \epsilon_{zz}|_{\theta} = 0$, at equilibrium, and using this relation to determine ϵ_{zz} .) When $\cos\theta = 0$, i.e. $\theta = \pi/2$, our model gives

$$c_{33}(H_{\perp}) = c'_{33}, \quad (22)$$

since then $d\theta/d\epsilon_{zz} = 0$.

Equation (22) implies that when H_{\perp} is sufficiently strong to constrain the spins to the basal plane, we observe no anomaly in c_{33} . This result is of course physically reasonable, as in such a case no spin rotation can take place to reduce the energy upon the application of strain.

It is of interest to obtain an estimate of the field $H_{\pi/2}$ at which $\theta = \pi/2$, and the anomaly in c_{33} should vanish. From (21), when $\theta = \pi/2$

$$MH_{\pi/2} = 2K_1 + (4K_2 - 2Q^2/c'_{33}) \approx 10^5 \text{ erg/cm}^3.$$

At 220°K, the magnetic moment [18] of Gd is 1.3×10^3 e.m.u./cm², and it follows that $H_{\pi/2} \approx 100$ G.

Thus the free-energy function (16) predicts that the application of a few hundred gauss is sufficient to completely suppress the anomaly in c_{33} in the spin rotation region. This result is in complete disagreement with the measurements of Long *et al.* [13] and we explain the source of the discrepancy below.

Thus far we have neglected possible self-magnetostatic energy terms in the free-energy, assuming tacitly that our sample is demagnetized, and that spin rotation will not alter the magnetostatic energy. Upon application of a sufficiently strong magnetic field, however, it is clear that surface poles will form in the sample in such a way that spin rotation will necessarily alter the magnetostatic energy, and we must explicitly include such considerations in our free energy function.

Before the magnetic field is switched on, the Gd sample will, at least to a good approximation, be demagnetized, with the spins lying in domains oriented along the easy directions of magnetization (e.g. making angles θ , $\pi - \theta$ with the z-axis). We depict the position schematically in Fig. 3. Application of a small external field will cause growth of those domains whose magnetization lies closest to the applied field direction ('plus' domains) at the expense of the domains with magnetization largely opposed to the applied field

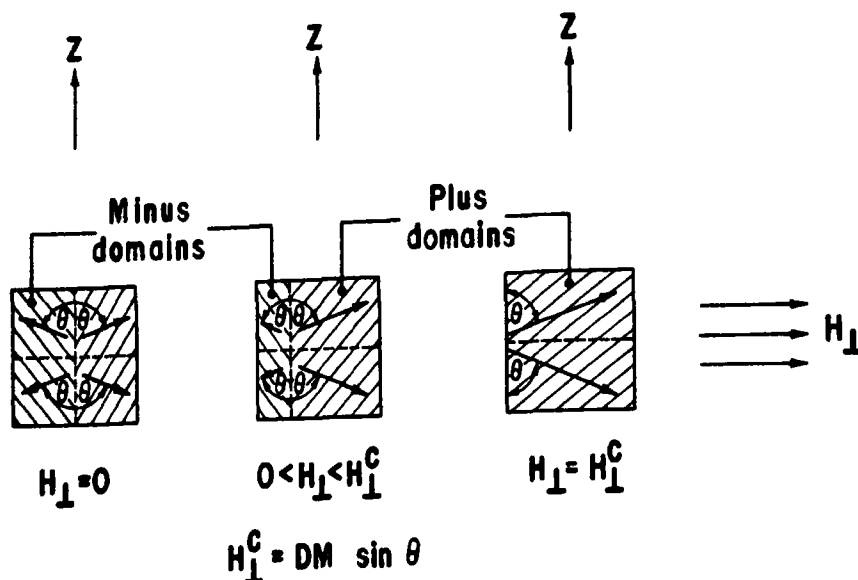


Fig. 3. Schematic outline of the domain rearrangement process upon the application of an external field H_{\perp} in the basal plane. For $0 < H_{\perp} < H_{\perp}^C = MD \sin \theta$, the internal field in the sample remains zero, as the 'plus' domains (oriented largely along the positive field direction) grow at the expense of the 'minus' domains (oriented largely against the field) so as to cancel the effect of increasing H_{\perp} .

('minus' domains). The net result of this process is the creation of a demagnetizing field in the sample of the correct size and direction to cancel the applied field.

In general, the details of the domain rearrangement process are rather complicated, and depend on the sample symmetry, on its shape, and on the orientation of the applied field with respect to the crystal axes of the sample. (Typical domain rearrangement processes in a crystal of iron have been treated using the 'phase model' of Néel [19–21]. Pauthenet and his co-workers [22, 23] have extended this model to uniaxial materials.) In our case, a quantitative treatment of the effect of a magnetic field is complicated by the cylindrical shape of the sample used by Long *et al.* [13], which gives rise to a non-uniform demagnetizing field in the sample upon approach to saturation. However, on the basis of treating a tractable, simple model, as discussed at length at the beginning of Section 2(a), we shall take account of magneto-

static effects using the 'phase model' and by assuming the sample to be characterized by a demagnetizing factor D . Since the cylindrical specimen studied by Long *et al.* [13] had a diameter of the same order as the height, we shall take D to be roughly $4\pi/3 \approx 4$.

From Fig. 3 it is clear that domain rearrangement can no longer preserve zero internal field when the applied H_{\perp} reaches the critical value

$$H_{\perp}^C = MD \sin \theta, \quad (23)$$

where D is the demagnetizing factor, and $M \sin \theta$ is the component of the magnetization in the direction of the applied field when the minus domains have just vanished. For $0 < H_{\perp} < H_{\perp}^C$ the applied field has no effect upon strain-induced spin rotation, since in the 'phase model' the internal field acting upon the spins is zero. For fields greater than H_{\perp}^C the magnetization will start to rotate towards the field.

An alternative, perhaps more physical description of the effect of strain for $0 < H_{\perp} < H_{\perp}^c$ is as follows: Let us assume that the application of strain induces the spins to rotate towards the hexagonal z -axis via magnetoelastic coupling. This rotation will not alter the magnetic energy, since a simultaneous growth of minus domains at the expense of plus domains will cause the magnetization component in the direction of the applied field to remain unchanged. (Note that we neglect possible energy changes associated with domain wall motion. A similar assumption was made by Néel[19].) As soon as $H_{\perp} > H_{\perp}^c$, however, the bulk of the sample consists of one type of domains (plus domains), and strain-induced spin rotation will then alter the magnetostatic energy.

Including therefore the magnetostatic self-energy in our free energy (16), we have

$$F(\theta, H_{\perp}) = F_m + \frac{1}{2}c'_{33}\epsilon_{zz}^2 + Q\epsilon_{zz}\sin^2\theta + K_1 \times \sin^2\theta + K_2\sin^4\theta - H_{\perp}M\sin\theta + \frac{1}{2}DM^2\sin^2\theta, \text{ for } H_{\perp} > H_{\perp}^c, \quad (24)$$

and

$$F(\theta, H_{\perp}) = F_m + \frac{1}{2}c'_{33}\epsilon_{zz}^2 + Q\epsilon_{zz}\sin^2\theta + K_1\sin^2\theta + K_2\sin^4\theta, \text{ for } H_{\perp} < H_{\perp}^c. \quad (25)$$

For $H_{\perp} < H_{\perp}^c$, the free energy is independent of the applied field H_{\perp} and (25) has exactly the same form as (7).

Equation (24) has the same functional dependence on θ and ϵ_{zz} as does (16). We therefore obtain immediately

$$c_{33}(H_{\perp})/c'_{33} = 1 - f(\theta, H_{\perp})Q^2/(2K_2c'_{33}), \quad \text{for } H_{\perp} > H_{\perp}^c, \quad (26)$$

where

$$f(\theta, H_{\perp}) = \sin^3\theta/[MH_{\perp}/(8K_2) + \sin^3\theta],$$

and θ is determined by

$$MH_{\perp} = 2(K_1 + \frac{1}{2}DM^2)\sin\theta + 2(2K_2 - Q^2/c'_{33}) \times \sin^3\theta. \quad (27)$$

Equations (26) and (27) follow from (20) and (21), respectively, upon replacing K_1 by $K_1 + \frac{1}{2}DM^2$. Since (7) is identical to (25), we once again obtain the 'field-free' result,

$$c_{33}/c'_{33} = 1 - Q^2/(2K_2c'_{33}), \text{ for } H_{\perp} < H_{\perp}^c. \quad (28)$$

Clearly, for $H_{\perp} > H_{\perp}^c$, the equilibrium value of θ is a function of H_{\perp} , and $f(\theta, H_{\perp})$ has a somewhat complicated dependence on H_{\perp} . The exact behavior of $f(\theta, H_{\perp})$ is particular to our model, and of little interest; an order of magnitude estimate is enlightening, however. Noting that at temperatures of interest to us ($\approx 220^\circ\text{K}$) the magnetic moment of Gd[18] is 1.3×10^3 e.m.u./cm³, it follows from (23) that for $H_{\perp} > H_{\perp}^c$, $MH_{\perp}/(8K_2) \geq DM^2 \sin\theta/(8K_2) \geq \sin^3\theta$, since [9] $K_2 \approx 10^6$ erg/cm³ in this temperature region. We may thus obtain an upper bound to $f(\theta, H_{\perp})$ as

$$\begin{aligned} f(\theta, H_{\perp}) &= \sin^3\theta/[MH_{\perp}/(8K_2) + \sin^3\theta] \\ &\leq \sin^3\theta/[DM^2 \sin\theta/(8K_2)] \\ &< 8K_2/(DM^2) \\ &\approx 5 \times 10^{-2}, \end{aligned}$$

taking $D \approx 4\pi/3$ as discussed above. Referring back to our results (26) and (28), we note that the drop in $c_{33}(H_{\perp})$ induced by magnetoelastic effects in the field-free case should practically vanish for $H_{\perp} > DM \sin\theta = H_{\perp}^c$, since the factor $f(\theta, H_{\perp})$ multiplying the field-free anomaly $Q^2/(2K_2c'_{33})$ is so small. For the remainder of our discussion we shall put $f(\theta, H_{\perp}) \approx 0$.

The physical basis for the disappearance of the drop in c_{33} lies in the high energy cost of spin rotation due to magnetostatic effects, when the sample consists of only 'plus' domains having their magnetization largely along the positive magnetic field direction. Since in this case, spin rotation is no longer

easily induced by the application of strain (as is the case for $H_{\perp} < H_{\perp}^c$, when domain wall motion compensates changes in magneto-static energy induced by spin rotation), the 'softening' observed in zero or low external fields is effectively eliminated.*

From (23), (26) and (28), for a given equilibrium value of θ , the applied H_{\perp} which serves to reduce the zero field drop in c_{33} , is given by

$$H_{\perp} = H_{\perp}^c = DM \sin \theta \approx 5 \sin \theta \text{ kG}. \quad (29)$$

This value is in reasonable agreement with the results of Long *et al.*[13] (Fig. 1). Of course, in comparing the predictions of our model with measurements of $c_{33}(H_{\perp})$, we cannot expect to observe the sharp drop in $c_{33}(H_{\perp})$ which we have obtained from our treatment. As in the zero field case, discontinuities in c_{33} arise from the approximations we have made in setting up our model free-energy, and especially in the assumption of spheroidal instead of cylindrical geometry. Qualitatively, however, as we shall presently show, our model exhibits field-dependent features in good agreement with the observed effects.

An analogous treatment can be undertaken when the magnetic field H_z lies parallel to the hexagonal z-axis. In this case for $H_z < H_z^c$, the appropriate free energy is

$$F = F_m + \frac{1}{2}c_{33}'\epsilon_{zz}^2 + Q\epsilon_{zz}\sin^2\theta + K_1\sin^2\theta + K_2\sin^4\theta - MH_z\cos\theta + \frac{1}{2}DM^2\cos^2\theta. \quad (30)$$

*A more exact description of the effect of an applied field upon the magnetoelastic anomaly in c_{33} in terms of our model is as follows:

For $H_{\perp} < H_{\perp}^c$ the internal field H_{int} is zero, and the equilibrium angle for the magnetization is independent of H_{\perp} . As H_{\perp} reaches H_{\perp}^c , the anomaly is reduced from $Q^2/(2K_2c_{33})$ to $f(\theta, H_{\perp})Q^2/(2K_2c_{33}') < 5 \times 10^{-2}Q^2/(2K_2c_{33}')$.

Upon further increase of H_{\perp} , H_{int} is no longer zero and the spins rotate towards the field. When the spins lie along the field in the basal plane, the magnetoelastic anomaly disappears altogether. As noted at the beginning of this section, the latter process requires an extra applied field of only a few hundred gauss. It would generally be swamped by the grosser effects of the magnetic domain rearrangement processes occurring in the neighborhood of H_{\perp}^c in Long's[13] cylindrical sample.

Evaluating $c_{33}(H_z)$ as before, we find in the spin rotation region,

$$c_{33}(H_z)/c_{33}' = 1 - g(\theta, H_z)Q^2/(2K_2c_{33}') \quad (31)$$

$$\text{for } H_z > H_z^c = DM \cos \theta,$$

where $g(\theta, H_z) = \cos^3\theta/[MH_z/(8K_2) + \cos^3\theta]$, and θ is determined by the equation

$$MH_z = 2(\frac{1}{2}DM^2 - K_1)\cos\theta + 2(Q^2/c_{33}' - 2K_2) \times \cos\theta \sin^2\theta. \quad (32)$$

As when the field is applied in the basal plane, we obtain the zero field result for $H_z < H_z^c$, namely

$$c_{33}(H_z)/c_{33}' = 1 - Q^2/(2K_2c_{33}'), \text{ for } H_z < H_z^c. \quad (33)$$

By an argument analogous to that used for $f(\theta, H_{\perp})$ we can show that $g(\theta, H_z) \leq 5 \times 10^{-2} \approx 0$, for our purposes.

In Fig. 4, we present schematic plots of equations (26), (28), (31), and (33). Consider first the case when H_{\perp} is applied in the basal plane. Our model predicts that low applied fields affect c_{33} for small values of θ ; when θ is large the anomalous drop in c_{33} remains unchanged. This prediction is born out by the data of Fig. 1, where we observe that the low field curves are coincident with the zero field curve for large values of θ . Similarly, and once more in agreement with the experimental data, the larger H_{\perp} the larger the range over which c_{33} shows no anomalous drop.

Turning now to the experimental results when the applied field lies along the z-axis, we notice that small fields cause large variations in c_{33} when θ is large ($\approx 70^\circ$). On the other hand, at small angles, the 2 kG and 4 kG curves coincide with the zero field measurements. Our model does in fact predict that for the field along the z-axis, no effect should be observed at low angles upon the application of moderate fields. At high values of the angle, however, according to our model even

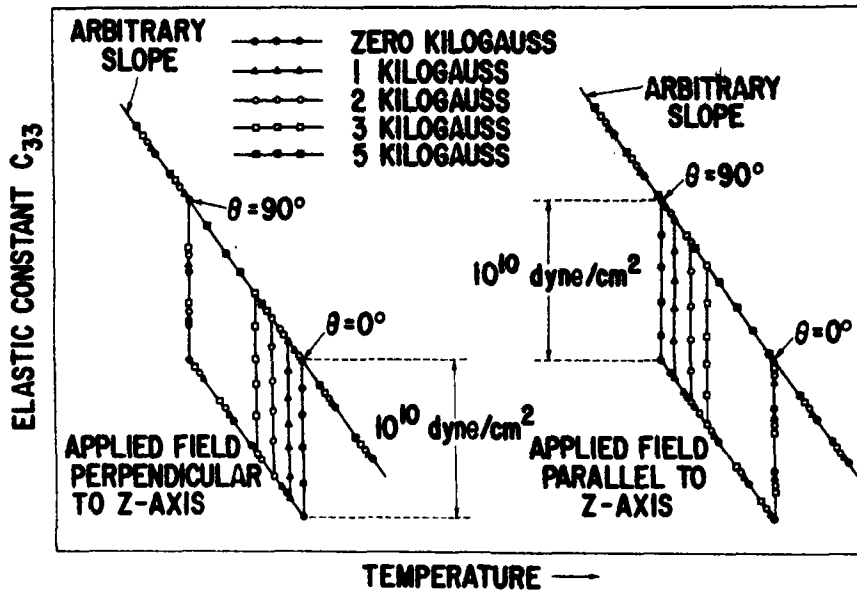


Fig. 4. Behavior of c_{33} for zero and non-zero applied fields, as predicted by our model free-energy. The qualitative agreement with the experimental data of Figs. 1 and 2 is discussed in the text. We have taken $f(\theta, H_{\perp}) \approx 0$ for $H_{\perp} > DM \sin \theta = H_{\perp}^c$ [equation (26)] and $g(\theta, H_z) \approx 0$ for $H_z > DM \cos \theta = H_z^c$ [equation (31)]. The slope assumed for c'_{33} is arbitrary, and $Q^2/(2K_z c'_{33})$ has been taken to be temperature-independent.

small applied fields serve to eliminate the anomaly in c_{33} , and in fact a substantial decrease of the anomaly is observed experimentally.

Finally, we note that a comparison of the critical fields for $c_{33}(H_{\perp})$ and $c_{33}(H_z)$ also shows that the two results transform into one another upon replacing θ by $\pi/2 - \theta$. This prediction is in qualitative agreement with the data in Figs. 1 and 2, where the anomalies in c_{33} measured with the magnetic field perpendicular to, and parallel to the hexagonal z -axis are roughly related by a mirror symmetry about $\theta = 45^\circ$.

3. SUMMARY

We have motivated and constructed a simple, model free-energy function to interpret the anomalous decrease in the elastic stiffness c_{33} , measured [13] in Gd in the spin rotation region. Our model qualitatively exhibits the observed drop in c_{33} , and an order

of magnitude estimate of the decrease is in agreement with measured values. A magneto-elastic term in the free energy having the form $Q\epsilon_{zz}\sin^2\theta$ couples the mean spin direction and the strain ϵ_{zz} , and the spin rotation induced upon application of strain in the z -direction is the physical origin of the crystal 'softening' observed. In the presence of a sufficiently large applied magnetic field, spin rotation associated with the strain causes large changes in the self-magnetostatic energy, and the freedom of the spins to rotate upon application of strain (and thereby to lower c_{33}) is effectively frozen out. In agreement with experiment, we predict that the drop in c_{33} should vanish for applied fields of the order of 5 kG.

In qualitative agreement with experiment our model further predicts: (a) for fields applied in the basal plane, the larger the angle of rotation from the hexagonal z -axis, the larger the field required to eliminate the

anomaly in c_{33} . (b) for fields applied along the hexagonal z -axis, the smaller the rotation angle, the larger the field required to eliminate the anomaly in c_{33} . (c) the effect of a magnetic field applied in the basal plane when the spins are characterized by a given spin rotation angle θ , is roughly equivalent to the effect of the same field applied along the z -axis when the spins are characterized by the angle $\pi/2 - \theta$.

Acknowledgement—Helpful discussions with Dr. B. R. Cooper, Dr. G. Gorodetsky and Dr. I. S. Jacobs are gratefully acknowledged.

REFERENCES

1. LECRAW R. C. and COMSTOCK R. L., in *Physical Acoustics*, Vol. III B, p. 127, Academic Press, New York (1965).
2. TRUELL R. and ELBAUM C., in *Handbuch der Physik*, Vol. 11, p. 153, Springer, Berlin, (1962).
3. SHAPIRA Y. and ZAK J., *Phys. Rev.* **170**, 503 (1968).
4. SHAPIRA Y., *Phys. Lett.* **24A**, 361 (1967).
5. SHAPIRA Y., *Phys. Rev.* **184**, 589 (1969).
6. MELCHER R. L. and BOLEF D. I., *Phys. Rev.* **178**, 864 (1969).
7. MELCHER R. L. and BOLEF D. I., *Phys. Rev.* **186**, 491 (1969).
8. LEVINSON L. M., LUBAN M. and SHTRIKMAN S., *Phys. Rev.* **187**, 715 (1969).
9. CORNER W. D., ROE W. C. and TAYLOR K. N. R., *Proc. Phys. Soc. Lond.* **80**, 927 (1962).
10. WILL G., NATHANS R. and ALPERIN H. A., *J. appl. Phys.* **35**, 1045 (1964).
11. CABLE J. W. and WOLLAN E. O., *Phys. Rev.* **165**, 733 (1968).
12. MILSTEIN F. and ROBINSON L. B., *Phys. Rev.* **177**, 904 (1969).
13. LONG M., WAZZAN A. R. and STERN R., *Phys. Rev.* **178**, 775 (1969).
14. CALLEN E. and CALLEN H. B., *Phys. Rev.* **139**, A455 (1965).
15. RUDERMAN M. A. and KITTEL C., *Phys. Rev.* **96**, 99 (1954).
16. GORODETSKY G. and LÜTHI B., *Phys. Rev.* (in press).
17. COLEMAN W. E., Thesis, West Virginia University, Morgantown, West Virginia, 1964, (unpublished).
18. ELLIOTT J. F., LEGVOLD S. and SPEDDING F. H., *Phys. Rev.* **91**, 28 (1953).
19. NÉEL L., *J. Phys. Radium* **5**, 241 (1944).
20. LAWTON H. and STEWART K. H., *Proc. R. Soc.* **193A**, 72 (1948).
21. STEWART K. H., "Ferromagnetic Domains", Cambridge Univ. Press (1954).
22. PAUTHENET R. and RIMET G., *Compt. Rend.* **249**, 656 (1959).
23. BARNIER Y., PAUTHENET R. and RIMET G., *Compt. Rend.* **252**, 3024 (1961).

DYNAMIC ORIENTATION BY SATURATION OF FORBIDDEN TRANSITIONS

S. K. GUPTA and M. L. NARCHAL

Physics Department, Punjabi University, Patiala, India

(Received 9 March 1970; in revised form 23 July 1970)

Abstract—The dynamic nuclear orientation by saturation of first order EPR forbidden transitions for nuclei with spin greater than 1 is theoretically studied in samples having well resolved h.f.s. with a paramagnetic ion of spin = $\frac{1}{2}$ and a comparison is made with corresponding results obtained by saturation of allowed transitions. It has been found that Jeffries–Abragam effect shows better results from the stand point of EPR power requirements and relaxation insensitivity in dynamic nuclear orientation experiments. It has also been found that the Jeffries–Abragam effect when the static magnetic field is applied parallel to the crystal symmetry axis presents the most reliable method of producing a high degree of nuclear orientation.

INTRODUCTION

THE THEORETICAL [1–8] and experimental [9–26] studies of dynamic nuclear orientation by Overhauser [27] and Jeffries [28]–Abragam [29] effects which involve the saturation, complete or partial, of an allowed ($\Delta M = \pm 1$, $\Delta m = 0$) or first order forbidden ($\Delta M = \pm 1$, $|\Delta m| = 1$) EPR transition respectively in an electron nuclear coupled spin system subjected to a static magnetic field, have already been made in very simple systems of spin $\frac{1}{2}$ or 1 nuclei. These studies in general, and those of Jeffries [30] in particular with $S = \frac{1}{2}$, $I = \frac{1}{2}$ systems have established that better results may be expected from the stand point of EPR power requirements and relaxation insensitivity in dynamic nuclear orientation experiments in which first order forbidden transitions are saturated. The present paper represents an attempt at investigating the relative superiority or otherwise of Jeffries–Abragam effect in systems [31–36] where the nuclear spin may have arbitrary values greater than 1 and are in resolved hyperfine interaction with a paramagnetic ion of spin = $\frac{1}{2}$.

Competing and non-competing pumps

The electron nuclear spin system under investigation having a strong hyperfine inter-

action and subjected to a static magnetic field H , can be characterised by the spin Hamiltonian

$$\mathcal{H} = g_{\parallel}\beta H_z S_z + \frac{\beta g_{\perp}}{2} (H_- S_+ + H_+ S_-) + A I_z S_z + \frac{B}{2} (S_- I_+ + I_- S_+)$$

where g_{\parallel} and g_{\perp} are the electronic g values in directions \parallel and \perp to the crystal symmetry axis., A, B are the hyperfine constants, and

$$H_{\pm} = H_x \pm iH_y, S_{\pm} = S_x \pm iS_y, I_{\pm} = I_x \pm iI_y$$

The first order perturbation energy eigen values for such a system for any inclination θ of H with crystal symmetry axis is

$$E(M, m) = g\beta HM + \{(A - B)g^2 \cos^2 \theta / g^2\} \times Mm$$

where M, m are the magnetic quantum numbers of electron and nucleus respectively and $g^2 = g_{\parallel}^2 \cos^2 \theta + g_{\perp}^2 \sin^2 \theta$. The energy level diagram of the system is depicted in Fig. 1 for $A > 0$.

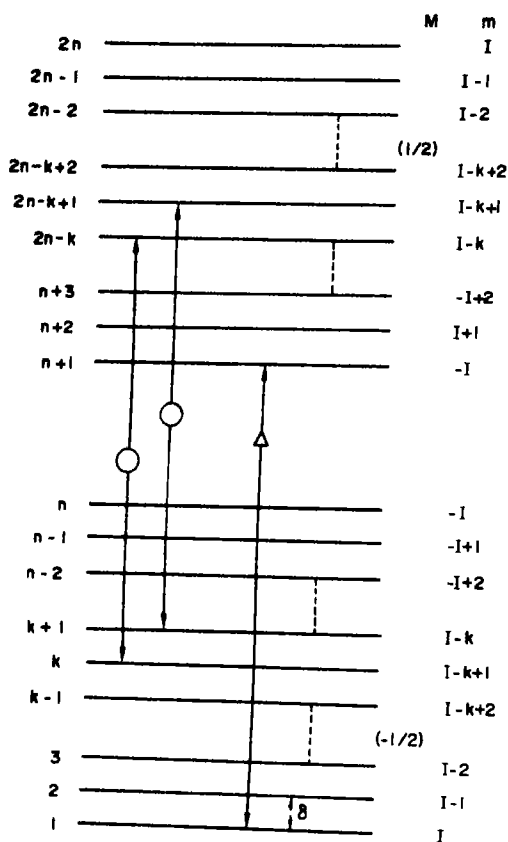


Fig. 1. Energy level diagram of an electron-nuclear coupled spin system when the hyperfine interaction dominates over the nuclear Zeeman interaction and the hyperfine interaction constant $A > 0$. Two simultaneous pumps of the same frequency are applied between levels k and $2n-k$ and between levels $k+1$ and $2n-k+1$.

The EPR transition probabilities[30] for such a system for arbitrary relative orientations of the crystal symmetry axis, the static and the time varying magnetic fields have been computed and reported elsewhere[37] by the authors. The significant features from the point of view of the present paper are (a) When the h.f.s. is isotropic or $\theta = 0$, the flip-flip transition ($\Delta M = \pm 1$, $\Delta m = \pm 1$) is completely forbidden and the only transition which can be induced is flip-flop ($\Delta M = \pm 1$, $\Delta m = \mp 1$). (b) When the h.f.s. is anisotropic along with $\theta = \pi/2$, both the cross transitions have finite probabilities and it may be possible to induce simultaneously the two transitions with

almost equal probability ($B = 0$).

We refer to the former situations as non-competing pumps and to the latter as competing pumps.

Taking into consideration the effect of competing pumps i.e. by assuming the simultaneous saturation of the transitions between the levels $(-\frac{1}{2}, I-k+1 \rightarrow \frac{1}{2}, I-k)$ and $(-\frac{1}{2}, I-k \rightarrow \frac{1}{2}, I-k+1)$ (Fig. 1) $k = 1, 2, \dots, 2I = (n-1)$ by the same EPR pump frequency and competitive relaxations, we have calculated, using well established techniques [38, 39] suitably modified[40], the theoretically expected dynamic nuclear polarization [6], alignment [6] and NMR enhancement [7]. The general expressions for these parameters can be obtained for $4 \leq k \leq n-2$ ($n \geq 6$). Other values of k and n require special individual treatment. We omit the details of calculations in view of their being cumbersome and space consuming, and give below only the typical expressions for the general case ($k = k; k = 4, 5, \dots, n-2$) and for one special case ($k = 1$) assuming complete EPR saturation.

$$\text{Pol}_k = \left\{ \left\{ \frac{(n+1)}{2} T_1(1, k-1) - T_2(1, k-1) \right\} 2(1+\eta)B_4 + (n-2k)B_3B_4 \right. \\ \left. + \left\{ \frac{(n+1)}{2} T_1(k+1, n) - T_2(k+1, n) \right\} \cdot 2B_4B_5 / \left(\frac{(n+1)}{2} \right) \cdot D_k \frac{1}{2} \{ (A \ln_k \right. \\ \left. (n-1)(n-2)/2 + (n-1)(n+1)/4 \} \right. \\ \left. = \left\{ \left\{ \frac{(n+1)}{2} T_1(1, k-1) - (n+1) \right\} \right. \right. \\ \left. T_2(1, k-1) + T_3(1, k-1) \right\} 2(1+\eta)B_4 \\ \left. + ((n^2 - 4nk + 4k^2 + 1)/2)B_3B_4 \right. \\ \left. + \left\{ \frac{(n+1)}{2} T_1(k+1, n) - (n+1)T_2 \right. \right. \\ \left. (k+1, n) + T_3(k+1, n) \right\} \cdot 2B_4B_5 / D_k \right\}$$

$$\text{Enh}_k = \left\{ \left\{ -nT'_2(1, k-2) + T'_3(1, k-2) \right\} \right. \\ \left. \cdot 2(1+\eta)B_4(1 - e^{-\delta}) + (k-1)(n-k+1) \{ \exp(-\Delta - (n-k+2)\delta) - \exp \right. \right. \\ \left. \left. (-k-1)\delta \} \times 2(1+\eta)B_4 + 2\{\eta \exp \right. \right. \\ \left. \left. (\Delta - (3k-n+1)\delta) + (2+\eta) \times \exp \right. \right. \\ \left. \left. (-\Delta - (n-k+1)\delta) - (2\eta+1) \exp \right. \right. \\ \left. \left. (-k\delta) - \exp(-2\Delta - (2n-3k)\delta) \} B_4 \right. \right. \\ \left. \left. + (k+1)(n-k-1) \{ \eta \exp(\Delta - (3k \right. \right. \\ \left. \left. - n+2)\delta) + \exp(-\Delta - (n-k+2)\delta) \right. \right. \\ \left. \left. - \eta \exp(-k-1)\delta) - \exp(-2\Delta - (2n \right. \right. \\ \left. \left. - 3k-1)\delta) \} \cdot 2B_4 + \{ -nT'_2(k+1, \right. \right. \\ \left. \left. n-1) + T'_3(k+1, n-1) \} \cdot 2B_5B_4 \right. \right. \\ \left. \left. (1 - e^{-\delta}) / D_k \cdot SSP \right\}$$

and

$$\begin{aligned} \text{Pol}_1 &= ((n-2)B \cdot B_1 + (((n+1)/2) T_1(3, n) \\ &\quad - T_2(3, n)) B_2) / ((n-1)/2) D_1 \frac{1}{2} (A \ln n_1 \\ &\quad (n-1)(n-2)/2 + (n-1)(n+1)/4) \\ &= (((n^2 - 4n + 5)/2) B \cdot B_1 + (((n+1)^2/4) \\ &\quad T_1(3, n) - (n+1) T_2(3, n) + T_3(3, n) B_2) / D_1 \end{aligned}$$

$$\begin{aligned} \text{Enh}_1 &= (2(n-2)(\exp(-3\delta) - \exp(-\Delta - (n-2)\delta)) B_2 + 2(\exp(-\Delta - (n-1)\delta) \\ &\quad - \exp(-\Delta - (n-3)\delta)) \cdot B_1 + (-n \times T'(3, n-1) + T'_3(3, n-1)) B_2 (1 - e^{-\delta})) / \\ &\quad D_1 \cdot \text{SSP} \end{aligned}$$

where

$$D_k = \{2(1+\eta)T_1(1, k-1) + 2B_3 + 2B_5 \\ T_1(k+1, n)\} B_4$$

$$D_1 = 2B \cdot B_1 + B_2 T_1(3, n)$$

$$B = 2 + \exp(-\Delta - (n-3)\delta) + \exp(-\Delta - (n-1)\delta)$$

$$B_1 = 1 + \eta \exp(-\Delta - (n-4)\delta)$$

$$B_2 = \eta \exp(3\delta) + \exp(-\Delta - (n-3)\delta) \\ + \exp(-\Delta - (n-6)\delta) + \exp(2\delta)$$

$$B_3 = (2\eta + 1) \exp(-k\delta) + \exp(-2\Delta - (2n-3k)\delta) + \eta \exp(\Delta - (3k-n+1)\delta) \\ + (2+\eta) \exp(-\Delta - (n-k+1)\delta)$$

$$B_4 = (1+\eta) \exp(-\Delta - (n-3)\delta) + (1/\eta) \exp(-\Delta - (n-4)\delta) + \exp(-2\Delta - (2n-8)\delta)$$

$$B_5 = \eta \exp(\Delta - (2k-n)\delta) + \exp(-\Delta - (n-2k)\delta)$$

$$T_l(l', k') = S_{l+3}(l', k') + S_l(l', k') \exp(-\Delta - (n+1)\delta)$$

$$T'_l(l', k') = S_{l+3}(l', k') + S_l(l', k') \exp(-\Delta - n\delta) \\ (l = 1, 2, 3; l' \text{ and } k' = 1, 2, \dots, n)$$

$$\text{SSP} = [-nT'_2(1, n-1) + T'_3(1, n-1)] (1 - e^{-\delta}) / S_4(1, n) (1 + e^{-\Delta})$$

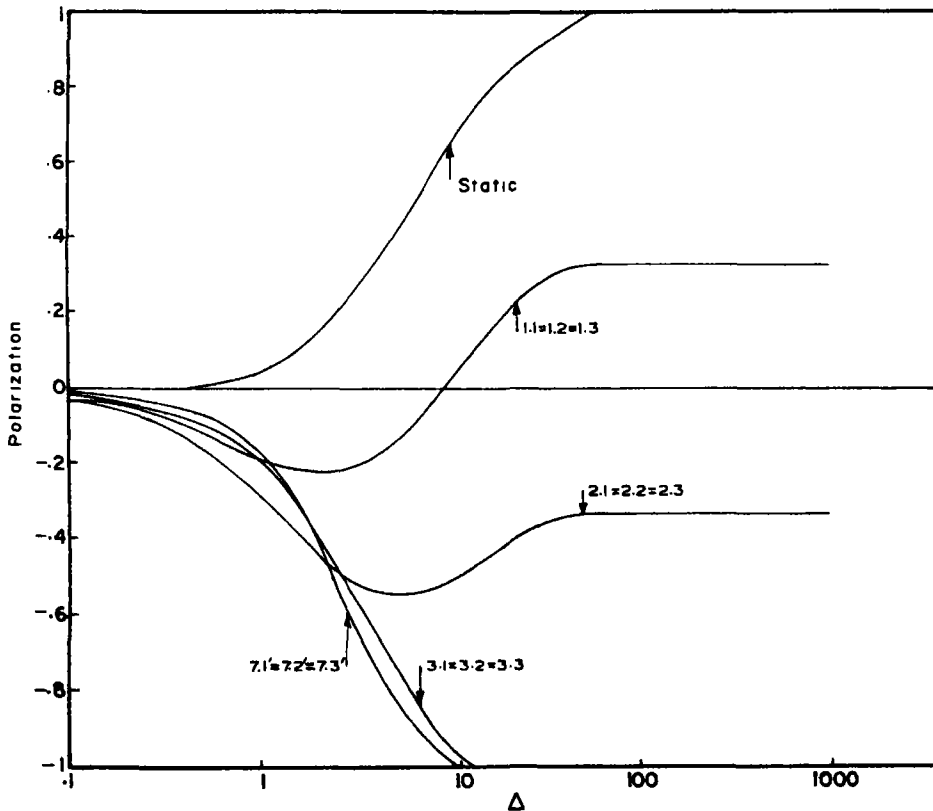


Fig. 2. Curves showing the relation between polarization and Δ for complete saturation for non-competing pumps. Primed curves are for Nd^{3+} and unprimed are for Pa^{4+} . The curves are numbered as a, b where a stands for any value of k and $b = 1, 2, 3$ stands for $\eta = 0.01, 1, 100$.

$\eta = w_1/w_2$ where w_1 and w_2 are the downward thermal transition probabilities associated with flip-flip and flip-flop transitions respectively.

$$\Delta = (E_{n+j} - E_j)/kT \quad j = 1, 2, \dots, n$$

$$\delta = (E_j - E_{j-1})/kT \quad j = 2, 3, \dots, n, n+2, \dots, 2n$$

Where E 's are the energy eigen values of the system. k is the Boltzmann constant and T the temperature of the system.

Values of S 's used above can be obtained from the following expressions by putting appropriate values of k and n in them.

$$S_1(k+1, n) = \exp(n\delta) (1 - \exp(-(n-k)\delta)) / (1 - \exp(-\delta))$$

$$S_2(k+1, n) = \left\{ n e^{n\delta} - e^{(n-1)\delta} \frac{(1 - e^{-(n-k-1)\delta})}{(1 - e^{-\delta})} - (k+1) e^{k\delta} \right\} / (1 - e^{-\delta})$$

$$S_3(k+1, n) = \left\{ n^2 e^{n\delta} - (n^2 + 2n - 1) e^{(n-1)\delta} + 2 e^{(n-2)\delta} \frac{(1 - e^{-(n-k-1)\delta})}{(1 - e^{-\delta})} - k^2 e^{k\delta} + (k+1)^2 e^{(k+1)\delta} \right\} / (1 - e^{-\delta})^2$$

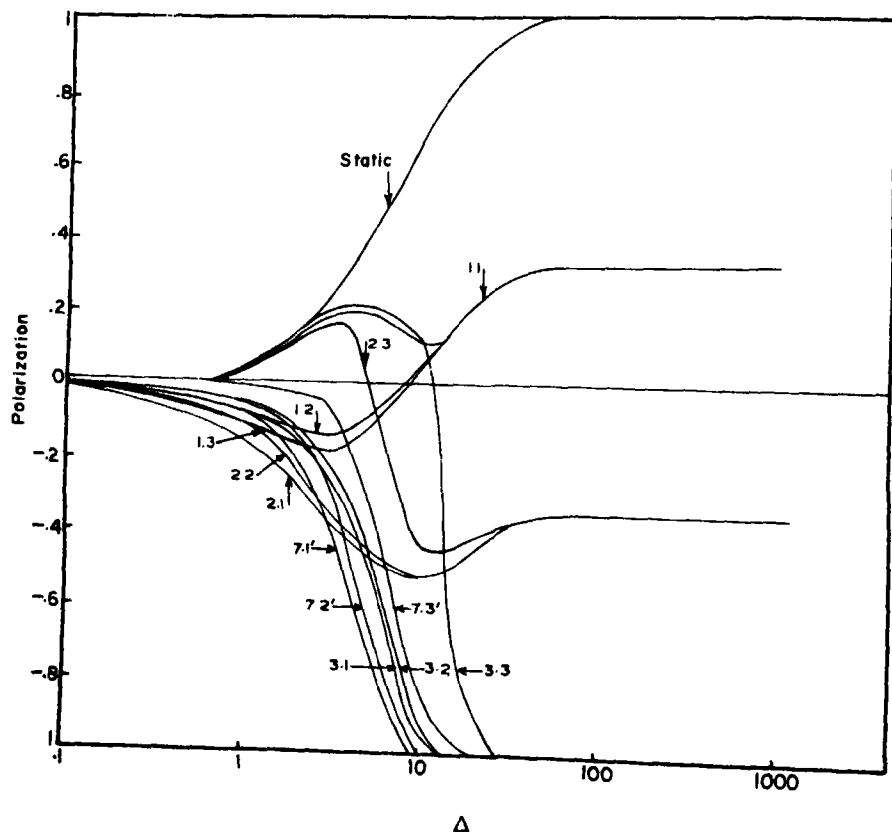


Fig. 3. Curves showing the relation between polarization and Δ for 50 per cent saturation for non-competing pumps. Primed curves are for Nd^{3+} and unprimed are for Pa^{4+} . a, b has the same meaning as in Fig. 2.

$$S_4(k+1, n) = e^{-(k+1)\delta} (1 - e^{-(n-k)\delta}) / (1 - e^{-\delta})$$

$$S_5(k+1, n) = \left\{ (k+1) e^{-(k+1)\delta} + e^{-(k+2)\delta} \right. \\ \left. \times \frac{(1 - e^{-(n-k-1)\delta})}{(1 - e^{-\delta})} - n e^{-(n+1)\delta} \right\} / (1 - e^{-\delta})$$

$$S_6(k+1, n) = \left\{ (k+1)^2 e^{-(k+1)\delta} - k^2 e^{(k+2)\delta} \right. \\ + 2 e^{-(k+2)\delta} \frac{(1 - e^{-(n-k-1)\delta})}{(1 - e^{-\delta})} \\ - (n^2 + 2n - 1) e^{-(n+1)\delta} + n^2 \\ \left. \times e^{-(n+2)\delta} \right\} / (1 - e^{-\delta})^2.$$

DISCUSSION OF RESULTS

We plot in Figs. 2-5 the low temperature dynamic nuclear polarization against Δ for two actual samples namely Pa^{4+} in Cs_2ZrCl_6 [32] and Nd^{3+} in $(\text{La}, \text{Mg})_3(\text{NO}_3)_{12} \cdot 24\text{H}_2\text{O}$ [31] for which $I = 3/2$, $\Delta/\delta = 10$, and $I = 7/2$, $\Delta/\delta = 100$ respectively*. It is reasonable to assume that the conclusions derived there from, as presented below, have wider applicability.

In Jeffries-Abragam method, as in Overhauser's [40], the dynamic methods are best utilized in the temperature range $1 \leq \Delta \leq 10$, in which the magnitude of the dynamic orientation parameters is greater than their corres-

*Similar curves for other parameters are omitted.

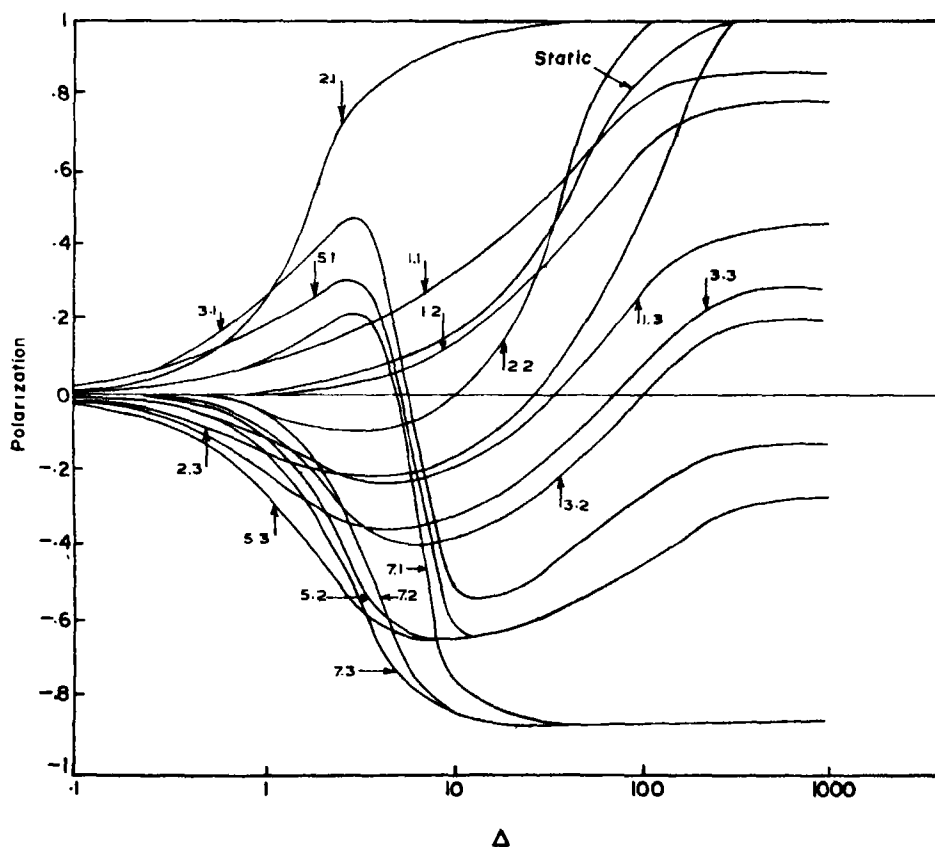


Fig. 4. Curves showing the relation between polarization and Δ for complete saturation for completing pumps for Nd^{3+} . a, b has the same meaning as in Fig. 2.

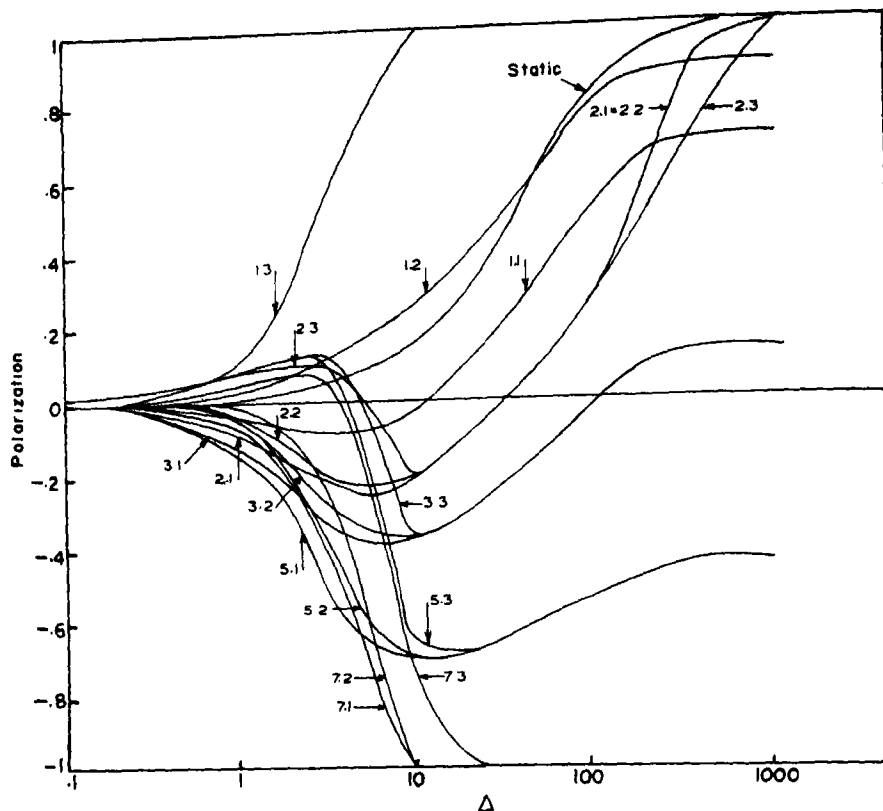


Fig. 5. Curves showing the relation between polarization and Δ for 50 per cent saturation for competing pumps for Nd^{3+} . a, b has the same meaning as in Fig. 2.

ponding Overhauser's values. The magnitude of parameters decrease when the saturation is lowered but the effect is less than proportional. Systems with high electronic to nuclear splitting ratios seem to be less sensitive to saturation and hence more useful from the experimental view point. The Jeffries-Abragam technique is on the average much less relaxation sensitive than the Overhauser's. The relaxation sensitivity seems to increase at lower saturations.

The magnitude of the effect and its relaxation sensitivity also depends on the pumping scheme employed. Pumping in the middle seems to give the best polarization which is least effected by thermal processes. Similarly one may choose the best pumping schemes for alignment and NMR enhancement.

The orientation of the crystal axis with respect to the static magnetic field, which determines the degree of competition between the pumps, has a very significant bearing on the experimental results. The parallel orientation in which the pumps do not compete at all seem to be the most suitable for obtaining polarization and alignment and the \perp orientation the most suitable for NMR enhancement.

On the whole the Jeffries-Abragam method seems to be more powerful than the Overhauser's and may have an additional advantage in terms of microwave power requirement for reasonably good saturation.

Acknowledgement—One of us (S.K.G.) wishes to thank C.S.I.R. for financial assistance. The hospitality of Punjabi University, Patiala is also gratefully acknowledged.

REFERENCES

1. BARKER W. A., *Rev. Mod. Phys.* **34**, 173 (1962).
2. NARCHAL M. L. and BARKER W. A., *Bull. Am. phys. Soc.* **6**, 298 (1961).
3. NARCHAL M. L. and BARKER W. A., *Appl. Opt.* **2**, 787 (1963).
4. BARKER W. A., NARCHAL M. L., MISRA S., BEVOLO ALBERT J., HAAS FRANCIS X., BIRKBECK CLAIRE M., BARBARA M. KUCHNE and WITTE J. C., *Rev. mod. Phys.* **36**, No. 3, 872 (1964).
5. BREITBART M. D. S. and BARKER W. A., *Nucl. Phys.* **52**, 641 (1964).
6. BHATIA K. L. and NARCHAL M. L., *Appl. Opt.* **4**, 175 (1965).
7. BHATIA K. L. and NARCHAL M. L., *Appl. Opt.* **5**, 1075 (1966).
8. MIDHA J. M., GUPTA S. K. and NARCHAL M. L., *Appl. Opt.* **8**, 1732 (1969).
9. PARKER D. J., McCLAREN G. and CONRADI J. J., *J. chem. Phys.* **33**, 629 (1960).
10. ALLIAS E., *Compt. Rend.* **246**, 2123 (1958).
11. SOLOMON I. J., *Phys. Rend.* **19**, 837 (1958).
12. CARVER T. R. and SLICHTER C. P., *Phys. Rev.* **92**, 212, (1953). 102, 975 (1956).
13. BENNETT L. H. and TORREY H. C., *Phys. Rev.* **108**, 499 (1957).
14. BELJERS H. G., VANDER KIN L. and VAN WIERINGEN J. S., *Phys. Rev.* **95**, 1683 (1954).
15. ABRAGAM A., COMBRISSE J. and SOLOMON I., *Compt. Rend.* **245**, 157 (1957). **246**, 1035 (1958). **247**, 2337 (1958).
16. POINDEXTER E. H., *Nature, Lond.* **182**, 1087 (1958).
17. POINDEXTER E. H., *J. chem. Phys.* **31**, 1477 (1959).
18. KREPS J., *J. chem. Phys.* **34**, 326 (1961).
19. ABRAGAM A., LANDESMAN A. and WINTER J. M., *Compt. Rend.* **247**, 1852 (1958).
20. ABRAGAM A., MECAUSLAND M. A. H. and ROBINSON F. N. H., *Phys. Rev. Lett.* **2**, 449 (1959).
21. LEIFSON O. and JEFFRIES C. D., *Phys. Rev.* **122**, 1781 (1961).
22. BORGINI M., *Proc. VII Int. Conf. Low Temp. Physics Toronto* p. 152. (1960).
23. SCHMUGGE T. J. and JEFFRIES C. D., *Phys. Rev. Lett.* **9**, 268 (1962).
24. LUSEHIKOV V. I., MANEKOV A. A. and TARAN Y. V., *Soviet Phys. solid State* **5**, 1191 (1963).
25. SCHMUGGE T. J. and JEFFRIES C. D., *Phys. Rev.* **138**, No. 6A, 1785 A (1965).
26. HANPT J. and MULLER-WARMTH W. Z., *Nature forach* **214**, No. 12, 158 (1966).
27. OVERHAUSER A. W., *Phys. Rev.* **89**, 689 (1953). **92**, 411, (1953).
28. JEFFRIES C. D., *Phys. Rev.* **106**, 164 (1957).
29. ABRAGAM A. and PROCTOR W. G., *Compt. Rend.* **246**, 2253 (1958).
30. JEFFRIES C. D., *Dynamic Nuclear Orientation* Interscience Publishers, New York (1963).
31. BOWERS K. D. and OWE J., *Rep. Prog. Phys.* **18**, 304 (1955).
32. AXE J. D. and STARLETAN H. J. and JEFFRIES C. D., *Phys. Rev.* **121**, 1630 (1961).
33. PIPKIN F. M., *Phys. Rev.* **112**, 935 (1958).
34. PIPKIN F. M. and CULVHOUSE J. W., *Phys. Rev.* **109**, 1423 (1953).
35. KYI R., *Phys. Rev.* **128**, 151 (1962).
36. LYONS R. H. and KEDZIC R. W., *Phys. Rev.* **145**, 148 (1966).
37. GUPTA S. K. and NARCHAL M. L., *Phys. Rev.* **B2** No. 5, 1405 (1970).
38. KEATING J. D. and BARKER W. A., *J. Franklin Institute* **274**, 253 (1962).
39. HOBBS E. W., *J. Franklin Institute* **274**, 270 (1962).
40. GUPTA S. K. and NARCHAL M. L., *Appl. Opt.* **8**, 1677 (1969).

X-RAY K-ABSORPTION STUDIES OF NIOBIUM SELENIDES AND TELLURIDES

V. G. BHIDE and M. K. BAHL

National Physical Laboratory, New Delhi-12, India

(Received 30 April 1970; in revised form 23 July 1970)

Abstract—X-ray *K*-absorption studies of niobium selenides and tellurides have been carried out using 400-mm bent crystal (mica, 100 planes) transmission spectrograph. In Nb_3Se_4 , *K*-absorption edge of niobium as well as of selenium lies on the higher energy side with respect to the corresponding metals while in NbSe_2 , it lies on the lower energy side.

1. INTRODUCTION

X-RAY spectroscopy is an important experimental tool for studying chemical bonding in various intermetallic compounds. Although several workers[1-3] have studied the *K*-absorption edge of the transition metal and selenium atoms in the respective selenides and obtained therefrom useful information regarding chemical bonding, very little seems to have been done on the selenides and tellurides of second transition series. In recent years Nb-Se and Nb-Te binary systems have received considerable attention because of their interesting electrical and magnetic properties. These systems have been investigated from the structural[4] point of view. The magnetic[5] and electric[6] properties have also been investigated in some detail. However, these studies have thrown little light on the nature of chemical bonding. It was therefore thought worthwhile to investigate the position and fine structure of the *K*-absorption edge of niobium in its selenides, Nb_3Se_4 , NbSe_2 and tellurides, Nb_3Te_4 and NbTe_4 . These measurements have led us to infer the nature of chemical bonding in these selenides and tellurides.

2. EXPERIMENTAL

A 400-mm bent crystal transmission spectrograph using a mica crystal oriented to reflect from the (100) planes was used to

record the absorption spectra as described in our earlier communication[7]. The niobium *K*-absorption edge was photographed in the second order where it could be bracketed between the first order $\text{CuK}\beta_1$ and $\text{WL}\beta_1$ lines. The tungsten lines appeared in the spectrum due to the deposition of tungsten from the hot tungsten filament on the copper anticathode. Suitable absorbers of compounds, kindly provided by Dr's. Kadijk and Brown, were prepared by spreading fine powders of the substance to the required thickness on cellophane tape. The exposure time of each of the spectrograms was about 10 h. The spectra were microphotometered with a Hilger watts microphotometer coupled to a honeywell chart recorder at magnification of about 50. The microphotometer trace of niobium metal is shown in Fig. 1. At least five spectra were recorded for each substance and each spectrum was microphotometered at five heights. Thus the values reported here are the average of at least 25 measurements.

The position of the absorption edge was taken at half the maximum of the absorption curve. Alternatively, the X-ray *K*-absorption position was determined by arc tangent curve fitted to the observed absorption spectra[8]. Both these methods gave almost identical position of the *K*-absorption edge. The position of the absorption edge depends in a

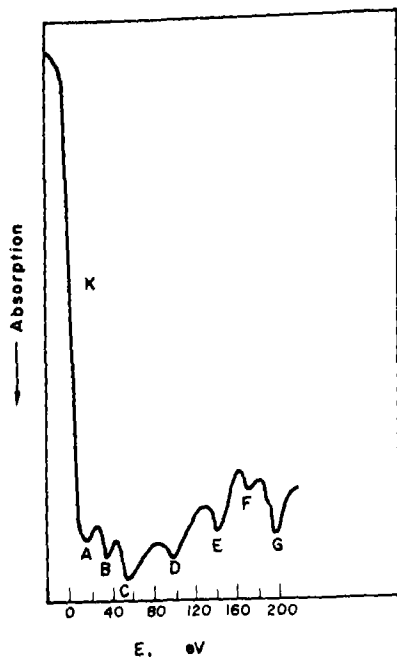


Fig. 1. A microphotometer trace of the spectrum obtained on the record paper for the niobium metal.

complicated way on a number of factors, such as the net resolving power of the spectrograph, the shape of the spectral window and the true absorption curve. The position of the absorption edge, in addition, depends sensitively on the densitometer curve and its reliable position can be obtained only when the density is a linear function of the absorption coefficient. In a few cases, the *K*-absorption edge discontinuity for niobium in Nb_3Se_4 and NbSe_2 were recorded on the same film, giving the same exposure time and under identical tube conditions. The shift in the *K*-absorption edge of niobium in Nb_3Se_4 and NbSe_2 as determined from these cases agreed within experimental error with that determined from individual *K*-absorption spectra of Nb_3Se_4 and NbSe_2 , taken on different films. The error mentioned along with the values of the position of the *K*-absorption edge denote the spread in values obtained over a large number of microphotometer records.

3. RESULTS AND DISCUSSION

Figures 2 and 3 show the absorption edge of niobium in the selenides Nb_3Se_4 and NbSe_2 and the tellurides Nb_3Te_4 and NbTe_4 respectively. The zero of the energy scale is taken

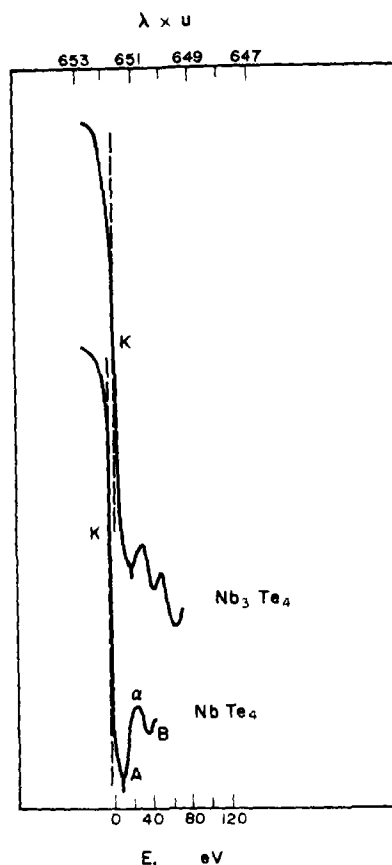


Fig. 2. Fine structure of X-ray *K*-absorption edge of niobium in its tellurides.

as the *K*-absorption edge of niobium in niobium metal. It is to be seen (Table 1) that as in the case of oxides[7], the position of the *K*-absorption edge of niobium in Nb_3Se_4 and Nb_3Te_4 shifts towards the higher energy side; the shift in Nb_3Te_4 being smaller than that in Nb_3Se_4 . In contrast, the *K*-absorption edge of niobium in higher selenides and tellurides NbSe_2 and NbTe_4 shifts towards low energy side (Table 1). In addition to the

Table 1. Position of the *K*-absorption edge and fine structure of *K*-absorption of niobium in its selenides and tellurides

Name of the material	Position of the absorption edge in X.U.	<i>K</i>	Position of the fine structure <i>E</i> in eV*				
			<i>A</i>	α	<i>B</i>	β	<i>C</i>
Nb metal [1]	651.69 \pm 0.02	0	16.21	27.25	34.42	46.74	55.75
Nb ₃ Te ₄	651.61 \pm 0.04	+2.3	20.5	31.0	41.4	48.9	65.0
NbTe ₄	651.81 \pm 0.04	-3.5	7.3	23.9	33.7	—	—
Nb ₃ Se ₄	651.56 \pm 0.04	+3.8	14.7	21.1	33.1	—	—
NbSe ₂	651.76 \pm 0.03	-2.0	15.6	32.3	41.6	57.4	77.6

*Zero of the energy scale is chosen at the position of absorption edge of niobium metal. *K* denotes the position of the absorption edge. Capitals *A*, *B*, *C* show absorption maxima and Greek letters α , β , γ show absorption minima.

[1] Taken from Ref. [7] and checked in the present investigation.

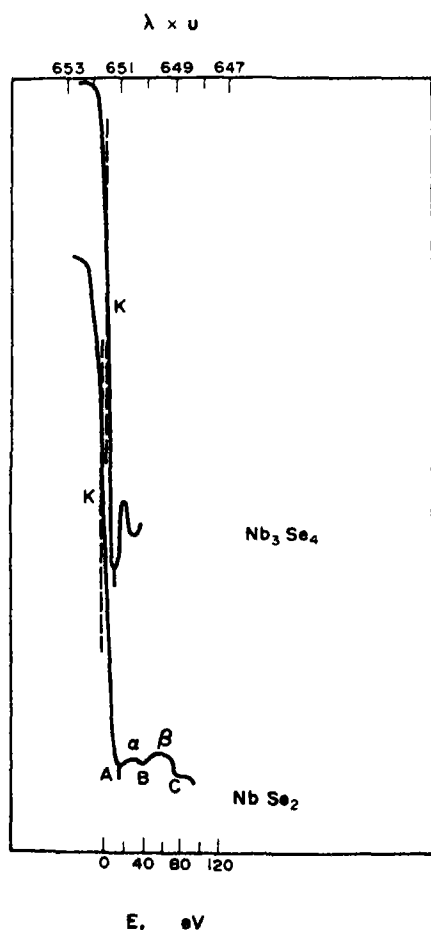


Fig. 3. Fine structure of X-ray *K*-absorption edge of niobium in its selenides.

shift of the absorption edge, the first absorption maxima *A* (Table 1) in these compounds also shifts towards the low energy side. The shift of the *K*-absorption edge in the selenides and tellurides on the opposite side of the *K*-absorption edge in the metal has a parallel in the studies of the *K*-absorption edge of copper in its oxides [9] and of lanthanum in its sulphides [10].

In order to understand the mechanism of the shifts of the *K*-absorption edge of niobium in these selenides, it was thought necessary to study of the *K*-absorption edge of selenium in these selenides. It is interesting to mention that the X-ray *K*-absorption edge of selenium in these selenides (Table 2) shifts with respect to the *K*-absorption edge of selenium in the selenium metal in the same way as the shift of the *K*-absorption edge of niobium.

The shift of the *K*-absorption edge of both niobium and selenium towards higher energy side in Nb₃Se₄ and towards lower energy side

Table 2. The position of the selenium *K*-absorption edge for selenium metal and niobium selenides investigated

S. No.	Substance	Wavelength (in X.U.)
1.	Selenium metal	977.78 \pm 0.04
2.	Nb ₃ Se ₄	977.46 \pm 0.06
3.	NbSe ₂	978.01 \pm 0.05

in NbSe_2 seems to indicate that the observed shifts cannot be explained on the simple consideration of the transfer of valence electrons from one element to the other. Although the shift of the K -absorption edge in these selenides with reference to the K -absorption edge in the respective metals cannot be explained on simple considerations, the above results show few consistencies. Thus for example, the shift in the selenide is greater than the shift in the corresponding telluride. Secondly, in both Nb_3Se_4 and NbSe_2 , niobium ion is coordinated by six selenium ions with an average Nb-Se distance of 2.67 and 2.53 Å respectively [11, 12]. Reduction in interatomic distance in NbSe_2 as compared to Nb_3Se_4 suggests that the atomic volume reduces and hence valence electron density increases in going from Nb_3Se_4 to NbSe_2 . Indeed it has been shown by Kjekshus *et al.* [12] that Nb-Se distance as well as unit cell volume decreases when selenium content increases from 60 to 67 atomic per cent. The shift of the K -absorption edge of niobium as well as that of selenium in NbSe_2 with respect to that in Nb_3Se_4 is expected because an increase in the electron density causes a decrease in the effective charge of both ions in NbSe_2 as compared to that in Nb_3Se_4 . It is interesting to point out that both Nb_3Se_4 and NbSe_2 are known to be superconductors; the critical temperature being 1.61 and 7.0 K respectively [13]. According to the empirical formula suggested by Robert [14], the higher value of the transition temperature of NbSe_2 with respect to that of Nb_3Se_4 suggests that valence electron density in NbSe_2 is larger than that in Nb_3Se_4 . This is consistent with the X-ray data.

What is of considerable importance is the shift of both niobium and selenium K -edges in these selenides towards the same side with respect to the corresponding metals. A similar situation has been reported in the case of iron selenide [15]. These observations do not find any unique explanation. However, several possibilities may be suggested.

The observed shift in the K -absorption edge of niobium as well as that of selenium in niobium selenides with reference to their positions in the respective metals may either be due to changes in the outermost levels of the respective atoms or may be due to the possible shift in the K -level. Although theoretically as well as experimentally [16], it has been shown that in some cases, the shift in core levels is quite large when a change in chemical bonding occurs, but in most cases and especially in heavy elements because of the fact that K level is lying deep, either the K level remains unaltered or there is a negligible shift in its position [17]. It may therefore be reasonable to assume that the observed shifts in the absorption edge positions of both Nb and Se as one goes from the elements to the selenides may be entirely due to changes in the outermost levels.

The electronic structure of niobium is $(\text{Kr}) 4d^4 5s^1$. We have noted earlier [7] that the initial part of the absorption edge corresponds to the transition of the $1s$ electron to the $4d$ - $5s$ band which has some admixture of p states, while the higher energy part near the first absorption maxima A corresponds to the transition to the $5p$ band itself. It is likely that the observed low energy shift of the niobium in NbSe_2 may be due to increase in the overlap of $4d$ - $5s$ band with the p band. In fact such an increase in hybridization is expected from simple considerations of crystal structure of NbSe_2 [18]. NbSe_2 structure is made up of alternate layers of niobium and selenium atoms in such a way that the structure can be looked upon as a stacking of trigonal bipyramids, wherein each niobium atom is surrounded by six selenium atoms. This implies that d orbitals ($d^2 sp^3$ or $d^4 sp$) of niobium are involved in chemical bonding. The interbond angles ($80^\circ 10'$ and $82^\circ 50'$) as reported by Brown *et al.* [18] from their structural analysis of NbSe_2 suggests the existence of $d^4 sp$ hybridization on niobium ion in NbSe_2 . Niobium metal crystallize in body centered cubic structure [19] with

d^4sp^3 hybridization on niobium. Thus crystal structure consideration also suggest an increase in the overlap of $4d-5s$ bands with $5p$ band in $NbSe_2$ as compared to that in niobium metal, in agreement with the shift of the K -absorption edge.

It is to be noted that the kink K' as observed in various oxides of niobium[7] is absent in $NbSe_2$. The disappearance of the kink K' further suggests considerable overlap of the $4d-5s$ band with the p type of band. Since in $NbSe_2$, the distance between two nearest niobium ion is considerably larger than that observed in the corresponding oxide NbO_2 [20], the selenium p electrons should be playing a dominant role in the band formation in $NbSe_2$. This further suggests an increase in the hybridization for selenium ions also, shifting the selenium edge also, towards low energy side as observed.

The increase in hybridization in $NbSe_2$ is also reflected in the energy separation (ΔKA) between the inflection point K and the maxima A as one moves from niobium metal to $NbSe_2$. ΔKA is 16.21 eV for niobium metal and 17.6 eV for $NbSe_2$ (Table 1). Since ΔKA is a rough measure of the width of the unoccupied $5p$ band, an increase in its magnitude by 1.4 eV suggests that in going from niobium metal to $NbSe_2$, the $5p$ band has broadened out, increasing the overlap. On the above consideration, the reduction in the value of ΔKA (10.9 eV) for the Nb_3Se_4 as compared to that in the niobium metal suggests the narrowing of the band and hence reduction in the hybridization in Nb_3Se_4 . This is expected to reflect in the shift of niobium as well as of selenium edge towards higher energy side with respect to that in the respective metals. The decrease in hybridization in Nb_3Se_4 as compared to niobium metal can't however be substantiated by the crystal structure of Nb_3Se_4 nor by any change in the structure of the K -absorption edge as observed in oxides of niobium[7].

Another possible explanation for the shift of K -absorption edge can be given in terms of valence band model, assuming the transfer

of electrons from niobium to selenium as suggested by electronegativity data. This situation is shown schematically in Fig. 4. The forbidden energy gap in the crystalline form of selenium is 1.6 eV, while $NbSe_2$ shows metallic character[13]. In this figure

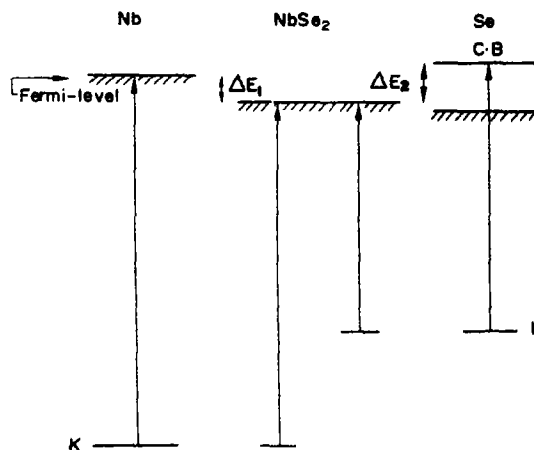


Fig. 4. A schematic energy level diagram of $NbSe_2$ and its components. (Energy levels not to scale) ΔE_1 : Shift in Nb K -absorption edge, ΔE_2 : Shift in Se K -absorption edge.

we have followed the approach suggested by Nemnonov[21] viz., the inflection point in the X-ray absorption edge in the case of semiconductor represents the bottom of the conduction band. The K -levels of niobium and selenium are chosen as reference levels and mutual positions are determined to give a common conduction band in the compound. On the above consideration, it is possible to explain the shift of both niobium and selenium towards low energy side in $NbSe_2$. However, the shift of the K -absorption edge of niobium and selenium towards the higher energy side in Nb_3Se_4 cannot be explained on valence band model.

Thus we see that out of various parameters (effective charge, hybridization and shift in the fermi level) responsible for the shift of the K -absorption edge, hybridization seems to be playing a major role in determining the shift of the K -absorption edges in niobium-

selenium system. On the basis of hybridization, one can explain the shift of niobium and selenium in these selenides towards the same side with respect to the corresponding metals and also the shift towards low energy in NbSe_2 with respect to Nb_3Se_4 .

Acknowledgements—We wish to express our grateful thanks to Dr. F. Kadijk of University of Groningen, The Netherlands and Dr. Bruce E. Brown of University of Wisconsin, USA for supplying the compounds. One of us (M.K.B.) wishes to express his sincere thanks to the Council of Scientific and Industrial Research for the award of research fellowship held during the course of this study. Thanks are also due to Dr. Arun Nigavekar and B. A. Patki for taking interest in this work.

REFERENCES

1. BALLY D. and MÜLLER L., *Studii Cercetari Fiz.* **13**, 437 (1962).
2. MANDE C. and NIGAVEKAR A. S., *Proc. Ind. Acad. Sci.* **65A**, 376 (1967).
3. BHIDE V. G., BHAT N. V. and RAMBHAD K. R., *J. appl. Phys.* **39**, 4744 (1968).
4. SELTE K., BJERKELUND E. and KJEKSHUS A., *J. less-common Metals* **11**, 14 (1966).
5. SELTE K. and KJEKSHUS A., *Acta Chem. Scand.* **19**, 258 (1965).
6. BRIXNER L. H., *J. inorg. nucl. Chem.* **24**, 257 (1962).
7. BHIDE V. G. and BAHL M. K., *J. Chem. Phys.* **52**, 4093 (1970).
8. RICHTMEYER F. K., BARNES S. W. and RAMBERG R., *Phys. Rev.* **46**, 843 (1934).
9. VERMA L. P. and AGARWAL B. K., *J. Phys. C. (Proc. Phys. Soc.)* **1**, 1658 (1968).
10. OVSYANNIKOV I. A., VAYNSHTEYN E. Ye. and SAMSONOV G. V., *Fiz. Metal Metalloved* **18**, No. 4, 637 (1964).
11. SELTE K. and KJEKSHUS A., *Acta crystallogr.* **17**, 1568 (1964).
12. SELTE K. and KJEKSHUS A., *Acta. Chem. Scand.* **18**, 697 (1964).
13. KADIJK F., Ph.D. Thesis, University of Groningen (1969).
14. ROBERTS B. W., G.E. Report No. 64-R1-3540 M, Jan. (1964).
15. VISHNOI A. N. and AGARWAL B. K., *Ind. J. Pure appl. Phys.* **7**, 819 (1969).
16. FAHLMAN A., HAMRIN K., HEDMAN J., NORDBERG R., NORDLING C. and SEIGH-BAHN K., *Nature, Lond.* **210**, 4 (1966).
17. SANDSTROM ELD, ARNE., *Handbuch Der Physik*. Volume 30, p. 159, Springer-Verlag (1957).
18. BROWN B. E. and BEERNTSEN D. J., *Acta crystallogr.* **18**, 31 (1965).
19. RUNDLE R. E., *Acta crystallogr.* **1**, 180 (1948).
20. MARINDER B. O., *Acta. Chem. Scand.* **15**, 707 (1961).
21. NEMONOV S. A. and GUSATINSKII A. N., *Fiz. Metal. Metalloved* **17**, No. 3, 42 (1964).

SINGLE CRYSTAL GROWTH AND SOME PROPERTIES OF $\text{HgCr}_{2-x}\text{In}_x\text{Se}_4$ SOLID SOLUTIONS

T. TAKAHASHI, K. MINEMATSU and K. MIYATANI

RCA Research Laboratories, P. O. Box 5151, Tokyo International 100-31, Japan

(Received 20 July 1970)

Abstract—Indium was found to substitute for Cr ions to a limited extent in the ferromagnetic spinel HgCr_2Se_4 . For the solid solution $\text{HgCr}_{2-x}\text{In}_x\text{Se}_4$, the maximum value of x was determined to be 0.45. The lattice parameter increases with increasing x from $a_0 = 10.743 \text{ \AA}$ for $x = 0$, to $a_0 = 10.836 \text{ \AA}$ for $x = 0.45$. The u -parameter is 0.390 for all compositions. The single crystals of $\text{HgCr}_{2-x}\text{In}_x\text{Se}_4$ studied were all grown by chemical transport either from an $\text{HgCr}_{2-x}\text{In}_x\text{Se}_4\text{--CrCl}_3$ system or from an $\text{HgCr}_2\text{Se}_4\text{--CrCl}_3\text{--InCl}_3$ system. In the former system, the fractionation of In during crystal growth was quite marked in that the In content in the large single crystals was always significantly lower than in the polycrystalline powder. Attempts to grow single crystals with an In concentration near the solubility limit were not successful. The maximum lattice parameter obtained for single crystals grown by chemical transport was 10.777 \AA , which corresponds to $x = 0.17$. The Curie temperature of the $\text{HgCr}_{2-x}\text{In}_x\text{Se}_4$ single crystals grown was found to be a monotonically decreasing function of the In content. The electrical resistivity of the single crystals grown had a maximum near the Curie temperature just as did the 'In-doped' HgCr_2Se_4 which had been previously grown by chemical transport from $\text{Hg}_{1-y}\text{In}_y\text{Cr}_2\text{Se}_4$ powders ($y \leq 0.02$) using CrCl_3 as a transport agent. The magnetoresistance of the single crystals was negative and had a maximum near T_c , as was also the case for the 'In-doped' HgCr_2Se_4 . However, the increase in resistivity from room temperature to T_c for the present crystals was found to be markedly lower than for the 'In-doped' HgCr_2Se_4 , indicating that for the system $\text{HgCr}_{2-x}\text{In}_x\text{Se}_4$ the conduction is nearly metallic in the temperature range studied.

1. INTRODUCTION

RECENTLY, the electrical, magnetic, and optical properties of HgCr_2Se_4 single crystals, both In-doped and undoped, have been reported [1, 2]. In general, the physical properties of these single crystals were found to be very similar to those of CdCr_2Se_4 , another well-investigated ferromagnetic spinel [3-5]. However, the 'In-doped' HgCr_2Se_4 crystals, which were grown by chemical transport from $\text{Hg}_{1-y}\text{In}_y\text{Cr}_2\text{Se}_4$ ($y \leq 0.02$) using CrCl_3 as a transport agent [6], were different from n -type CdCr_2Se_4 in the following respects. (1) The 'In-doped' HgCr_2Se_4 crystals had a small positive Seebeck coefficient at room temperature in contrast to a large negative coefficient for n -type CdCr_2Se_4 , (2) the sign of the Seebeck coefficient of 'In-doped' HgCr_2Se_4 became negative at low temperatures ($T \leq T_c$), and (3) the room temperature resistivity of 'In-doped' HgCr_2Se_4 was much higher than that of the undoped crystals,

whereas n -type CdCr_2Se_4 had a lower room temperature resistivity than undoped CdCr_2Se_4 .

In order to explain this peculiar behavior of 'In-doped' HgCr_2Se_4 crystals, we had postulated that In^{3+} ions substitute for Cr^{3+} ions (B -site substitution)* in HgCr_2Se_4 [2]. In CdCr_2X_4 ($X = \text{S}$ or Se) however, there seems to be some uncertainty as to whether In^{3+} ions replace Cd^{2+} or Cr^{3+} ions. Pinch and Berger [7] observed a decrease in the magnetic moment per Cr atom with increasing In content for the $\text{Cd}_{1-y}\text{In}_y\text{Cr}_2X_4$ alloys. To explain this phenomenon, they postulated that some of the chromium ions in these alloys were in the divalent state and that the alloy could be represented by the formula $\text{Cd}_{1-y}\text{In}_y[\text{Cr}_y^{2+}\text{Cr}_{2-y}^{3+}]X_4$ with $y > 0$.

*In a normal spinel AB_2X_4 , A site cations are in tetrahedral interstices of X anions whereas B site cations are in octahedral interstices of X anions.

Recently however, Lotgering and van der Steen[8] prepared single phase $\text{CdCr}_{2-x}\text{In}_x\text{S}_4$ ($x=0.1$ and 0.2) which contains only Cr^{3+} ions and observed an identical decrease in the magnetic moment per Cr atom with increasing In content. These authors maintain that the decrease in magnetic moment per Cr atom is not sufficient evidence for the existence of Cr^{2+} ions. They attribute the observed decrease in magnetic moment per Cr atom to a dilution of magnetic Cr^{3+} by either non-magnetic In^{3+} substitution into Cr^{3+} sites (*B*-sites) or by vacancies.

A direct and straight-forward way to determine if In^{3+} ions go into *A*-sites or into *B*-sites is to investigate the solid solubility of indium in HgCr_2Se_4 . This report presents the results of such a study and is divided into three parts. We first describe the solid solubility study of $\text{HgCr}_{2-x}\text{In}_x\text{Se}_4$ polycrystalline powder. The single crystal growth of $\text{HgCr}_{2-x}\text{In}_x\text{Se}_4$ solid solutions is then described. And finally, some of the electrical and magnetic properties of the $\text{HgCr}_{2-x}\text{In}_x\text{Se}_4$ single crystals grown are described.

2. SOLID SOLUBILITY OF INDIUM IN HgCr_2Se_4

To investigate whether In^{3+} ions tend to go into *A* or *B* sites of the ferromagnetic spinel HgCr_2Se_4 , and also to determine the solubility limit of In^{3+} in HgCr_2Se_4 , two series of alloys, $\text{Hg}_{1-y}\text{In}_y\text{Cr}_2\text{Se}_4$, $0.1 \leq y \leq 0.5$, and $\text{HgCr}_{2-x}\text{In}_x\text{Se}_4$, $0.05 \leq x \leq 1.0$, were prepared from a stoichiometric mixture of HgSe , Cr , Se , and In_2Se_3 . All of the chemicals used had a purity of 99.9 per cent or better.

A stoichiometric mixture of ingredients was pressed into pellets and heated in an evacuated quartz ampoule at 700°C for 24 hr. After annealing at 600°C for 48 hr, the fired product was taken out. The X-ray powder pattern of the product was taken using a Debye-Scherrer camera. Whenever impurity lines were detected, the product was reground, heated, annealed, and analyzed again.

For the $\text{Hg}_{1-y}\text{In}_y\text{Cr}_2\text{Se}_4$ alloys with $0.1 \leq y$

≤ 0.5 , no single phase samples were obtained even after repeated firings*. The weak impurity lines observed in our material indicate the presence of $\gamma\text{-CrSe}$. The lattice parameter of the spinel phase found in the synthesized material increased with increasing Indium addition. These observations are consistent with our hypothesis that In^{3+} ions substitute for Cr^{3+} ions, which are on *B*-sites, and that the excess Cr combines with the Se present to form $\gamma\text{-CrSe}$.

For the $\text{HgCr}_{2-x}\text{In}_x\text{Se}_4$ alloys with $0.05 \leq x \leq 1.0$, single phase spinels were obtained up to $x=0.30$. For $x>0.30$, a second phase appeared which was later identified to be a tetragonal HgIn_2Se_4 phase[9]. The lattice parameters of the spinel phase were determined from the back reflections of Debye-Scherrer photographs using Nelson-Riley's extrapolation. They increased sharply with increasing x up to about $x=0.40$ and then reached a saturation value at about $x=0.45$ as shown in Fig. 1. Since the ionic radius of In^{3+} (0.81\AA) is larger than that of Cr^{3+} (0.64\AA) but smaller than that of Hg^{2+} (1.10\AA), the increase in lattice parameter with x is consistent with a straight-forward substitution of In^{3+} for Cr^{3+} ions, which are on the *B*-sites. A more positive confirmation for the *B*-site substitution was obtained from the measurements of the intensity of the X-ray lines. With the intensity of the (440) peak taken as an internal standard, the relative intensity of the (222) line of the $\text{HgCr}_{2-x}\text{In}_x\text{Se}_4$ alloys is very sensitive to changes in x , since the structure factor for the (222) line is given by,

$$F(222) = -2f_B + f_X(\sin 2\pi u - 3 \sin \pi u)$$

where f_B and f_X are the atomic scattering factors for cations on the *B*-sites and anions *X*, respectively. The intensity measurements

*This result was also obtained for the similar alloys, $\text{Cd}_{1-y}\text{In}_y\text{Cr}_2\text{S}_4$, by Lotgering and van der Steen[8] who found that impurities were present in the alloys they had synthesized.

were made using JEOL* diffractometer with a scanning speed of $\frac{1}{4}^\circ/\text{min}$. The intensity of a given X-ray line was taken as the area under the corresponding diffraction peak. In Table 1 the relative intensities of the (222) line of the $\text{HgCr}_{2-x}\text{In}_x\text{Se}_4$ alloys with respect to that for

deduced from magnetic measurements [8].

Using the intensities of the first ten reflections, the structural u -parameters for the $\text{HgCr}_{2-x}\text{In}_x\text{Se}_4$ alloys were also determined. In Fig. 2, the residual, $R = \sum |I_{\text{obs}} - I_{\text{cal}}| / \sum I_{\text{obs}}$, where I_{obs} and I_{cal} are the observed and calculated relative intensities for the HgCr_{2-x} -

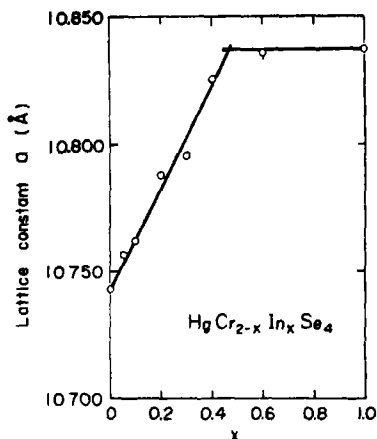


Fig. 1. Lattice parameter of $\text{HgCr}_{2-x}\text{In}_x\text{Se}_4$ alloys.

pure HgCr_2Se_4 , are given along with the calculated ratios for these alloys. As can be seen, the observed intensity ratios are in good agreement with the calculated ones. Therefore, we can conclude that in the spinel HgCr_2Se_4 , In^{3+} ions preferentially substitute

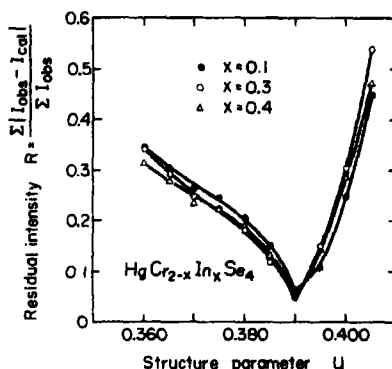


Fig. 2. Residual intensity, $R = \sum |I_{\text{obs}} - I_{\text{cal}}| / \sum I_{\text{obs}}$, vs. structure parameter, u .

In_xSe_4 alloys, is plotted against u . The u -parameter which is given by the value of u at the minimum value of R , was found to be 0.390 for all values of x , which is the same value as was found for HgCr_2Se_4 [10].

Table 1. Observed and calculated intensity ratios for the (222) peak of the spinel $\text{HgCr}_{2-x}\text{In}_x\text{Se}_4$

		x or y			
		0.1	0.2	0.3	0.4
Calculated intensity ratio $I(222)_i / I(222)_0$ for $u = 0.390$ $i = x$ or y	A-site substitution ($\text{Hg}_{1-y}\text{In}_y\text{Cr}_2\text{Se}_4$)	1.025	1.090	1.121	1.151
	B-site substitution ($\text{HgCr}_{2-x}\text{In}_x\text{Se}_4$)	0.920	0.834	0.754	0.691
Observed intensity ratio		0.852	0.813	0.756	0.710

for Cr^{3+} ions up to a solubility limit of about 31 at.% of Cr^{3+} ions. Our present results are consistent with Lotgering and van der Steen's conclusions for In-substituted CdCr_2S_4 that

3. SINGLE CRYSTAL GROWTH

In order to investigate the physical properties of $\text{HgCr}_{2-x}\text{In}_x\text{Se}_4$ alloys, single crystals were grown by chemical vapor transport [11] from $\text{HgCr}_{2-x}\text{In}_x\text{Se}_4$ powder using CrCl_3 as the transport agent, and from the HgCr_2Se_4 -

*Japan Electron Optics Laboratory

CrCl_3 - InCl_3 system. In both cases, the $\text{HgCr}_{2-x}\text{In}_x\text{Se}_4$ used was synthesized from HgSe , Cr , Se , and In_2Se_3 , using the procedure described in the preceding section. For growth from the $\text{HgCr}_{2-x}\text{In}_x\text{Se}_4$ - CrCl_3 system, about 1 m-mole of $\text{HgCr}_{2-x}\text{In}_x\text{Se}_4$ and 0.4–0.5 m-mole of CrCl_3 were used as the starting mixture, while for the HgCr_2Se_4 - CrCl_3 - InCl_3 system 1 m-mole of HgCr_2Se_4 , 0.4 m-mole of CrCl_3 , and 0.05–1.0 m-moles of InCl_3 were used. For each system the starting mixture was sealed in an evacuated quartz ampoule and heated in a two zone furnace. The hot end of the ampoule was maintained at $T_{\text{high}} = 650^\circ\text{--}680^\circ\text{C}$ and the cold end was kept at $T_{\text{low}} = 610\text{--}650^\circ\text{C}$. In the $\text{HgCr}_{2-x}\text{In}_x\text{Se}_4$ - CrCl_3 system, the single crystals obtained always had a smaller lattice parameter than the $\text{HgCr}_{2-x}\text{In}_x\text{Se}_4$ polycrystalline powder which was used as the starting material. Furthermore, it was found that crystal growth became progressively more difficult as the indium content of the starting alloy was increased. The maximum lattice parameter of the single crystals grown from this system was 10.777\AA which corresponds to a value of $x = 0.17$ for the $\text{HgCr}_{2-x}\text{In}_x\text{Se}_4$ alloys. The growth conditions used and the size of crystals obtained are summarized in Table 2.

InCl_3 (or InCl_2) during growth. Therefore, in the series of experiments using this system, the amount of InCl_3 was varied while the amounts of HgCr_2Se_4 and CrCl_3 were held constant. The single crystals thus grown always had a larger lattice parameter than that of the undoped HgCr_2Se_4 starting material which indicated that indium had been incorporated as expected. However, no correlation was found between the amount of InCl_3 added and the measured lattice parameter. Moreover, when more than 1.5 m-mole of InCl_3 was used in the starting mixture no single crystals were obtained. The results obtained for this system are summarized in Table 3.

The absence of any correlation between the initial InCl_3 concentration and the observed lattice parameter might be due to the occurrence of some chemical reactions involving InCl_3 which would result in an InCl_3 (or InCl_2) partial pressure which is not proportional to the amount of InCl_3 added to the system.

4. ELECTRIC AND MAGNETIC PROPERTIES OF $\text{HgCr}_{2-x}\text{In}_x\text{Se}_4$ SINGLE CRYSTALS

The Seebeck coefficients were measured by the hot-point method using a copper-constantan thermocouple whose measuring junction was 0.1 mm in dia. Magnetic measurements

Table 2. Growth conditions and some physical properties of $\text{HgCr}_{2-x}\text{In}_x\text{Se}_4$ single crystals grown from the $\text{HgCr}_{2-x}\text{In}_x\text{Se}_4$ - CrCl_3 system

Sample no.	x^* in starting material	T_H ($^\circ\text{C}$)	T_L ($^\circ\text{C}$)	a_0 (\AA)	x^* in single crystal	α ($\mu\text{V}/^\circ\text{C}$)
1	0.1	670	650	10.750	0.035	+21.2
2	0.2	685	650	10.753	0.050	+20.5
3	0.2	640	605	10.756	0.065	+21.2
4	0.4†	680	650	10.763	0.100	-21.2
5	0.6†	640	605	10.777	0.170	-68.6

* x = In concentration in $\text{HgCr}_{2-x}\text{In}_x\text{Se}_4$.

†Starting material contains HgIn_2Se_4 as an impurity.

Growth from the HgCr_2Se_4 - CrCl_3 - InCl_3 system was used primarily in an attempt to control the indium concentration in $\text{HgCr}_{2-x}\text{In}_x\text{Se}_4$ by controlling the partial pressure of

were obtained using a vibrating sample magnetometer. The Curie temperature was determined from the kink of the magnetization curve in zero applied field. The electrical

Table 3. Lattice parameters for single crystals grown from the $\text{HgCr}_2\text{Se}_4\text{-CrCl}_3\text{-InCl}_3$ system

InCl_3 (m-mole/cm ³)*	Lattice parameter (Å)
0.01	10.747 ± 0.002
0.02	10.755
0.04	10.746
0.06	10.751
0.08	10.765
0.10	10.753
0.12	10.754
0.14	10.758

*Each ampoule had an inner volume of $\sim 10 \text{ cm}^3$ and contained 1.0 m-mole of HgCr_2Se_4 and 0.4 m-mole of CrCl_3 .

transport properties were measured by the four probe method using ohmic contacts. These contacts were fabricated by plating thin gold lead wires (1 mil thick) onto a thin film of indium which had been locally evaporated onto the polished surface of the sample crystal.

The Curie temperature, T_c , of the $\text{HgCr}_{2-x}\text{In}_x\text{Se}_4$ alloys, both for single crystals and for polycrystalline powder, was found to decrease monotonically with increasing indium concentration as shown in Fig. 3, indicating a drastic decrease in the ferromagnetic interaction when In^{3+} is substituted for Cr^{3+} ions.

As shown in Fig. 4 the electrical resistivity of single crystals of $\text{HgCr}_{2-x}\text{In}_x\text{Se}_4$ showed an interesting temperature dependence that

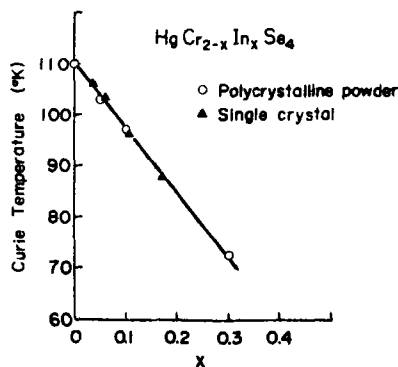


Fig. 3. Curie temperature of $\text{HgCr}_{2-x}\text{In}_x\text{Se}_4$ alloys.

changed little with indium concentration. As is seen, the resistivity decreased slightly as the temperature went down in spite of a rather large room temperature resistivity ($10\text{--}10^2 \Omega\text{-cm}$). As the sample temperature approached T_c , its resistivity increased and reached a maximum value near T_c . As the sample temperature decreased below T_c , the resistiv-

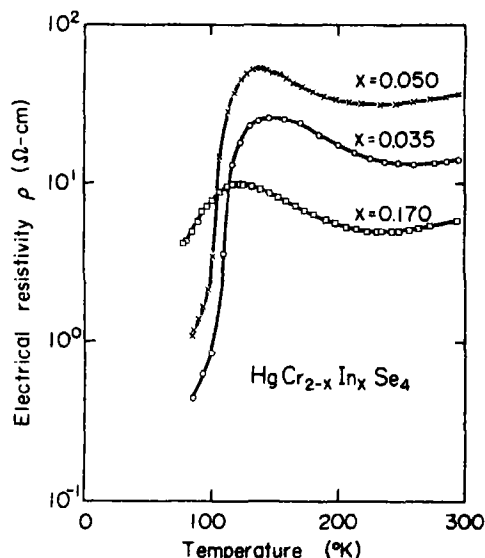


Fig. 4. Electrical resistivity of $\text{HgCr}_{2-x}\text{In}_x\text{Se}_4$ single crystals at $H = 7 \text{ KOe}$ and $I = 1 \text{ mA}$.

ity began to decrease again. The observed decrease at low temperatures ($T < T_c$) is unexpectedly sharp. Since our measurements were performed only down to 78°K , we do not know how low the resistivity would become if the temperature is further reduced. However, the magnitude of the resistivity at any given temperature of the $\text{HgCr}_{2-x}\text{In}_x\text{Se}_4$ single crystals had no systematic dependence on the indium concentration in the crystals. This indicates that the indium concentration has little to do with the carrier density in the crystals. It seems that the observed resistivities fluctuate because of complicated compensation mechanisms for the various impurities and vacancies which are included in the individual crystals during growth.

As shown in Fig. 5 the Hall voltage at a

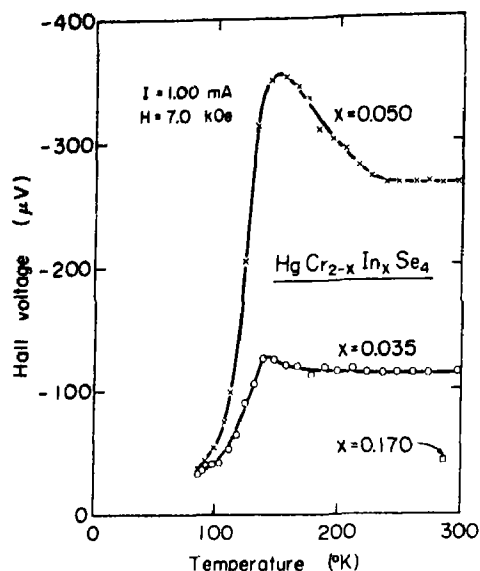


Fig. 5. Hall voltage of $\text{HgCr}_{2-x}\text{In}_x\text{Se}_4$ single crystals at $H = 7 \text{ kOe}$ and $I = 1 \text{ Ma}$.

constant magnetic field of 7 kOe, normalized with respect to I/t , where I is the current and t is the sample thickness, changed with temperature in a manner quite similar to the resistivity. The fact has been well established [3] that the normalized Hall voltage is proportional to $(R_0H + R_1M)$, where R_0 is the normal Hall coefficient, R_1 is the extraordinary Hall coefficient, H is the effective magnetic field in the sample, and M is the sample magnetization.

The interesting temperature dependence obtained for the resistivity and the Hall

voltage is quite similar to that observed in n -type CdCr_2Se_4 [3] and in 'In-doped' HgCr_2Se_4 [2].

The temperature dependence of the magneto-resistance of the present crystals, which has a large negative maximum near T_c as shown in Fig. 6, is also very similar to that obtained for n -type CdCr_2Se_4 [2]. However, the tail of the magnetoresistance peak in the present alloys extends well into the paramagnetic region, unlike the situation obtained for n -type CdCr_2Se_4 and for 'In-doped' HgCr_2Se_4 . The general origin of these phenomena has been discussed by Lehmann [3] and by Haas *et al.* [4, 5]. Lehmann attributed the decrease in resistivity at $T < T_c$ to an increase in the carrier density, whereas Haas *et al.* proposed that the major cause for the decrease was an increase in mobility due to a decreased interaction between the magnetic spins and the conduction electrons. The measured temperature dependence of the optical absorption edge shift [1, 12], seems to support Lehmann's hypothesis. However, the photoconductivity data for the europium chalcogenides [13], which have considerably different characteristics than the ferromagnetic spinels, seems to support the mobility theory advanced by Haas and his coworkers.

For a single-carrier semiconductor, the normal Hall coefficient can be directly related to the carrier density. However, for the ferromagnetic spinels, the magnetic field dependence of the Hall voltage is generally non-linear

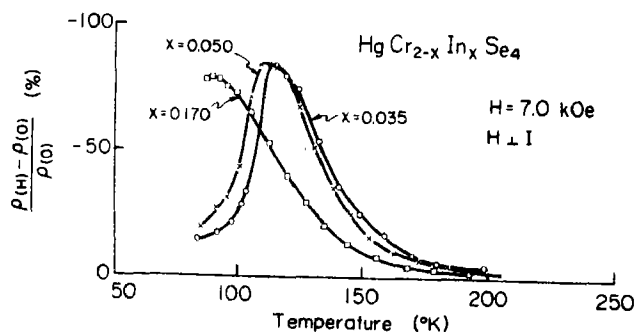


Fig. 6. Magnetoresistance of $\text{HgCr}_{2-x}\text{In}_x\text{Se}_4$ single crystals at $H = 7 \text{ kOe}$.

below T_c . This makes the separation of the normal Hall coefficient from the total measured Hall voltage difficult.

The room temperature Seebeck coefficient, α , of $\text{HgCr}_{2-x}\text{In}_x\text{Se}_4$ single crystals changes from positive to negative with increasing indium content (see Table 2). In addition, the sign of α for low indium content crystals becomes negative at low temperatures as in the case of 'In-doped' HgCr_2Se_4 [2]. This suggests that electrical transport in $\text{HgCr}_{2-x}\text{In}_x\text{Se}_4$ crystals is the result of two-carrier conduction. Therefore, the determination of the carrier densities becomes virtually impossible from just Hall effect measurements. Independent measurements of carrier densities and mobilities are required in order to settle this issue.

Let us now return to our original question of whether In^{3+} ions in the 'In-doped' HgCr_2Se_4 crystals are on the tetrahedral A sites or on the octahedral B sites. Since it has now been well established that In^{3+} ions do in fact substitute for Cr^{3+} ions at large In^{3+} concentrations, one may extrapolate the results for high In^{3+} concentrations to the much lower Indium concentrations which are present in the 'In-doped' HgCr_2Se_4 crystals. Moreover, the striking similarity of the transport properties of $\text{HgCr}_{2-x}\text{In}_x\text{Se}_4$ crystals to those of the 'In-doped' HgCr_2Se_4 crystals suggests that the occurrence of such phenomena is not sensitive to specific site location of In^{3+} ions in the HgCr_2Se_4 lattice. We, therefore, conclude

that even in the 'In-doped' HgCr_2Se_4 crystals, the In^{3+} ions are probably in B -sites, i.e. in octahedral interstices, rather than in A -sites.*

Acknowledgements—We wish to thank Mr. T. Oka for his help in the crystal growth experiments, and Messrs. Yoshida and Yoshikawa for their help in making the electrical and magnetic measurements. We are also grateful to Dr. P. K. Baltzer for his helpful discussions during the preparation of this manuscript.

REFERENCES

1. LEHMANN H. W. and EMMENEGGER F. P., *Solid State Commun.* **1**, 965 (1969).
2. MINEMATSU K., MIYATANI K., and TAKAHASHI T., *J. phys. Soc. Japan* (to be published).
3. LEHMANN H. W., *Phys. Rev.* **163**, 488 (1967).
4. HAAS C., van RUN A. M. J. G., BONGERS P. F. and ALFERS W., *Solid State Commun.* **5**, 657 (1967).
5. BONGERS P. F., HAAS C., van RUN A. M. J. G. and ZANMARCHI G., *J. appl. Phys.* **40**, 958 (1967).
6. TAKAHASHI T., *J. Cryst. Growth* **6**, 319 (1970).
7. PINCH H. L. and BERGER S. B., *J. Phys. Chem. Solids* **29**, 2091 (1968).
8. LOTGERING F. K. and van der STEEN G. H. A. M., *Solid State Commun.* **7**, 1827 (1969).
9. HAHN H., FRANK G., KLINGLER W., STORGER A. D. and STORGER G., *Z. anorg. Chem.* **279**, 16 (1955).
10. BALTZER P. K., WOJCIOWICZ P. J., ROBBINS M. and LOPATIN E., *Phys. Rev.* **151**, 367 (1966).
11. SCHÄFER H., *Chemical Transport Reactions*, Academic Press, New York (1964).
12. HARBEKE G. and PINCH H. L., *Phys. Rev. Lett.* **17**, 1090 (1966).
13. BACHMANN R. and WACHTER P., *Solid State Commun.* **6**, 711 (1968).
14. PINCH H. L., Private communication

*A similar line of reasoning may not apply to In-doped CdCr_2Se_4 , because attempts to prepare $\text{CdCr}_{2-x}\text{In}_x\text{Se}_4$ always led to two-phase material even for low x [14].

THE INFLUENCE OF LATTICE STRAIN ON THE ELECTRICAL RESISTIVITY OF VACANCIES IN SIMPLE METALS*

R. BENEDEK† and A. BARATOFF

Brown University, Providence, R. I. 02912, U.S.A.

(Received 9 July 1970)

Abstract—The effect of lattice distortion on the resistivity of vacancies in the simple metals Na, K and Al has been calculated within the framework of the weak pseudopotential approximation. The required structure factor $S(\mathbf{q})$ of the strained lattice has been calculated to first order in the displacements from undistorted equilibrium positions by means of a method due to Kanzaki which avoids continuum or semi-discrete approximations made in previous work. Effective interatomic force constants fitted to phonon spectra derived from neutron scattering data were used as input in calculating $S(\mathbf{q})$, while Ashcroft's pseudopotential was used in evaluating the resistivity. Additional approximations were made in the case of Al, but the important effect of plane wave mixing near zone boundaries was included in the matrix elements for Umklapp scattering. The change in potential due to strain lowers the resistivity by about 30 per cent in all three cases. Our calculated value is in fair agreement with the most reliable experimental estimate for Al. The method illustrated here should be especially useful for realistic calculations of the resistivity of isoelectronic impurities in simple metals.

1. INTRODUCTION

IN SPITE of extensive work over the past forty years, the electrical resistivity of point defects in metals continues to attract the attention of solid state physicists. In recent calculations [1, 2], the effective potential of a point defect has been described either by phase shifts or by a pseudopotential form factor. Many such calculations have neglected the effect of the static strain around the defect. Since this strain disturbs the periodicity of the lattice, it also contributes to the scattering of electrons. In the rigid ion (or pseudoatom) approximation, the total potential acting on an electron is a superposition of spherically symmetric contributions from each ion. This picture appears to be valid in simple metals where the pseudopotential is weak and can be treated by perturbation theory [3]. The effect of lattice strain on the electrical resistivity of vacancies

is then completely determined by the static structure factor of the distorted lattice [3]‡:

$$S(\mathbf{q}) = \sum_l \exp(-i\mathbf{q} \cdot \mathbf{r}_l) \\ = \sum_l \exp(-i\mathbf{q} \cdot [\mathbf{r}_l^{(0)} + \mathbf{u}_l]) \quad (1.1)$$

where \mathbf{u}_l is the displacement of l -th ion from its position $\mathbf{r}_l^{(0)}$ in the perfect lattice. In evaluating $S(\mathbf{q})$, it has been common to assume that the displacements $\mathbf{u}_l = \mathbf{r}_l - \mathbf{r}_l^{(0)}$ can be determined from continuum elasticity theory. Using this approach, Dexter [4] argued that the effect of strain on the resistivity of vacancies and substitutional impurities amounts to only a few per cent. This result cannot be considered conclusive, however, since the applicability of the continuum approximation to the problem at hand is open to doubt.

*Work supported in part by the advanced Research Projects Agency under contract SD-86.

†National Science Foundation Predoctoral Fellow, 1969-70.

‡We assume a lattice with one atom per primitive unit cell. Following common practice, we define $S(\mathbf{q})$ such that the defect site at $\mathbf{r}_0 = 0$ is included in the sum over l .

A realistic calculation of the structure factor, based on a normal coordinate expansion first introduced by Kanzaki[5], is in fact possible. This is the approach taken in the present work.

As we have mentioned, previous estimates of $S(\mathbf{q})$ have been based on the strain field appropriate to a point defect in an isotropic continuum. Thus, a number of authors [4, 6, 7] have assumed a strain field

$$\mathbf{u}(\mathbf{r}) = A \frac{\mathbf{r}}{r^3} \quad (1.2)$$

corresponding to a solution to the equations of elasticity in such a medium [8].

The structure factor associated with (1.2) is, to first order

$$S_i(\mathbf{q}) = -i \sum_l \mathbf{q} \cdot \mathbf{u}_l e^{-i\mathbf{q} \cdot \mathbf{r}_l^{(0)}} \quad (1.3)$$

$$= -iA \sum_{l \neq 0} \frac{\mathbf{q} \cdot \mathbf{r}_l^{(0)}}{r_l^{(0)3}} e^{-i\mathbf{q} \cdot \mathbf{r}_l^{(0)}}. \quad (1.4)$$

Beal-Monod and Kohn [7] have pointed out that the sum in (1.4) may be conveniently evaluated by a procedure similar to that of Ewald for electrostatic lattice sums.

Unfortunately (1.2) does not provide a realistic description of the lattice displacements. Recently, Kanzaki's method of 'lattice statics' has been extensively applied by Flocken and Hardy to vacancies and interstitials in simple metals [9]. Their results show that the asymptotic r^{-2} dependence of the strain field is only reached at very large distances from the defect. In addition, the lattice distortion shows considerable anisotropy, especially in the alkali metals [9, 10].

An even simpler though cruder attempt to incorporate lattice strain in the theory of electron scattering by point defects is the 'effective charge' correction extensively used by Blatt [11] which assumes a continuum strain field given by (1.2). According to that concept, the charge difference entering the Friedel sum rule should be modified by an amount equal to

the electronic charge displaced by the strain (a clear discussion of this is given by Ziman [12]). This treatment is in a sense equivalent to approximating the sum (1.4) by an integral, a procedure which introduces significant errors for $q \geq k_F$ (the free-electron Fermi wave vector) as discussed in reference [7]. Similar objections apply to the so-called semi-discrete method in which the sum over all but the first few shells of neighbors is replaced by an integral [6].

The purpose of this work is to present a realistic calculation of the d.c. resistivity of the simplest point defect, the vacancy, in the simple metals sodium, potassium, and aluminum. It is found that the lattice distortion lowers the resistivity by about 30 per cent in each of the metals considered. Thus it is a significant correction which should be included before one can make meaningful comparisons with experiment.

In Section 2, we explain how lattice statics may be applied to calculation of the structure factor, particular attention being given to vacancies. The resistivity calculation is described in Section 3 while in Section 4, we discuss our results and compare them with experimental data. A short derivation of the equations of lattice statics, emphasizing connections with the basic concept of structure factor, is presented in the Appendix.

2. THE STRUCTURE FACTOR

Atomic displacements around a defect are determined by the equations of static equilibrium. If the effective interionic forces are central and the displacements are small, the equilibrium condition for the distorted lattice is expressed by the fundamental equation of lattice statics (see Ref. [9] and Appendix),

$$\mathbf{Q}^q = [\mathbf{V}^q]^{-1} \mathbf{F}^q. \quad (2.1)$$

In (2.1)

$$\mathbf{Q}^q = \sum_l \mathbf{u}_l e^{-i\mathbf{q} \cdot \mathbf{r}_l^{(0)}} \quad (2.2)$$

is the normal coordinate with wavevector \mathbf{q}

corresponding to the displacements u_i and

$$V_{\alpha\alpha'}^q = \sum_l \Phi_{\alpha\alpha'}^l e^{-iq \cdot r_l^{(0)}} \quad (2.3)$$

in the standard dynamical matrix of the host lattice. Equation (2.1) relates the normal coordinates Q^q associated with the strain to the atomic forces operating in the crystal. The Fourier transform of the force F^q depends on the type of defect one is considering; in the case of a vacancy

$$F^q = \sum_l \nabla \psi|_{r_l} e^{-iq \cdot r_l^{(0)}} \quad (2.4a)^*$$

while for an impurity at $r = 0$

$$F^q = \sum_l \nabla (\psi - \psi_l)|_{r_l} e^{-iq \cdot r_l^{(0)}} \quad (2.4b)^*$$

where $\psi_l(r)$ is the effective pair potential acting between the impurity and a host ion, and $\psi(r)$ is that between host ions. The utility of Equation (2.1) for our present purpose derives from the simple relation between Q^q and the structure factor,

$$S_1(q) = -iq \cdot Q^q. \quad (2.5)$$

A method of solving Equation (2.1) for Q^q has been given by Flocken and Hardy[9]. The simplest calculations pertain to a vacancy. Indeed, for this type of defect, explicit knowledge of $\psi(r)$ is not required since F^q may itself be expressed in terms of the atomic force constants $\Phi_{\alpha\alpha'}^l$ [9]. For vacancies, therefore, the set of force constants $\Phi_{\alpha\alpha'}^l$ allows a complete determination of the displacement pattern. The force constants can be determined by *i*. Born-Von Karman fits to inelastic neutron scattering data[13] or *ii*. from calculated pair potentials based on pseudopotential theory[14]. In the present article, we deliberately restrict our attention to vacancies and use fitted force constants since they are

more reliable. However, as better pseudo-potential methods are developed for calculating $\psi_l(r)$, lattice statics should also become useful in obtaining realistic results for impurities and more complex defects.

The structure factor, calculated along three symmetry directions for a vacancy in sodium, is shown in Fig. 1.† $S_1(q)$ is positive for small q , reflecting the tendency of atoms to move inward towards the void left by the missing atom. The structure factor evidently is quite anisotropic‡ as illustrated, particularly in Fig. 2.

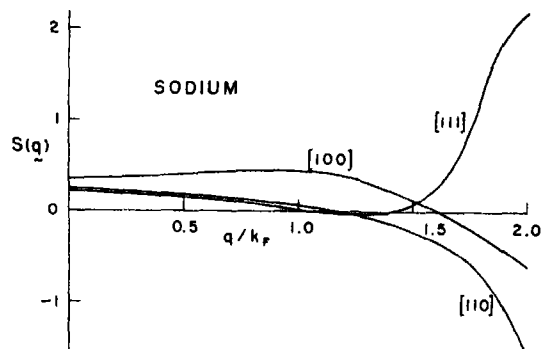


Fig. 1. The structure factor $S(q)$ along [100], [110] and [111] directions for a vacancy in sodium (first order approximation).

As a check on the first order approximation ($S(q) = S_1(q)$), the second order term $S_2(q)$ has also been calculated. In terms of the normal coordinates introduced earlier one has

$$S_2(q) = -\frac{V_a}{2} \int_{BZ} \frac{-d^3 q'}{(2\pi)^3} (q \cdot Q^{q'}) (q \cdot Q^{q-q'}),$$

where V_a is the atomic unit cell volume, and the integration extends over the volume of the first Brillouin zone. Both $S_1(q)$ and $S_2(q)$ for a vacancy in sodium, with $q \parallel [100]$ are shown

*In equations (2.4a, b), $\psi(r_l)$ should actually be represented by $\psi(r_l^{(0)} + u_l \cdot \nabla \psi(r_l^{(0)}))$ to be consistent with the harmonic approximation (see appendix).

†The procedure outlined in Ref. [9] was followed in this calculation. Force constants for Na and K, extending up to fifth nearest neighbors, were taken from Table 2, columns 2 and 4, of that reference.

‡Note that $S(q)$ remains anisotropic even as $q \rightarrow 0$; this is a reflection of the elastic anisotropy of the crystal.

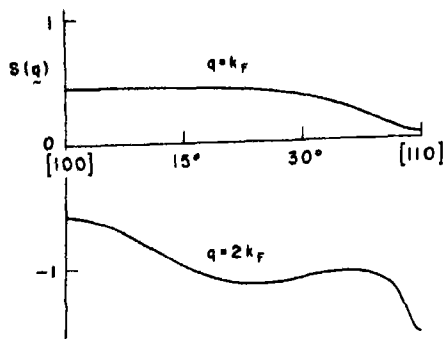


Fig. 2. Variation of the structure factor $S(q)$ with q in the (001) plane ($q = k_F$ and $2k_F$) for a vacancy in sodium (first order approximation).

in Fig. 3. S_2 becomes more important as q increases. However, the electrical resistivity involves an integration for $q < 2k_F$ and in calculating this property it seems quite reasonable to approximate $S(q)$ by $S_1(q)$.*

The structure factor becomes infinite as q approaches a reciprocal lattice vector. One finds from (2.3, 4) that $V \sim |\mathbf{q} - \mathbf{G}|^2$ and $F \sim |\mathbf{q} - \mathbf{G}|$ in the neighborhood of any reciprocal lattice vector \mathbf{G} ; accordingly

$$S_1(q) \propto \mathbf{q} \cdot [\mathbf{V}^q]^{-1} \mathbf{F}^q \sim |\mathbf{q} - \mathbf{G}|^{-1} \text{ for } \mathbf{q} \approx \mathbf{G} \neq 0 \quad (2.6)$$

(The higher order terms $S_2(q)$, etc. are non-singular.) The same singularity appears in the structure factor for electron-phonon scattering [15]. Certain results concerning matrix elements for the scattering of electrons by phonons therefore apply equally well to point defect scattering. The singularity in (2.6) leads to an (unphysical) infinite scattering rate between *single* plane wave electron states \mathbf{k}' and \mathbf{k} as $\mathbf{q} (= \mathbf{k}' - \mathbf{k})$ approaches \mathbf{G} . This becomes an important consideration in treating polyvalent metals, in which the free electron Fermi sphere intersects one or more zone boundaries. Electron states with wavevector \mathbf{k} near a zone boundary must actually be described by a mixture of at least two plane waves (i.e. a Bloch wave). The matrix elements for scattering between Bloch waves are finite in the limit $\mathbf{q} \rightarrow \mathbf{G}$ even though $S_1(q)$ diverges in that limit [15].

Although our present interest is restricted to the electrical resistivity, the same structure factor can be used in calculations of electric field gradients at the nuclei of displaced atoms [7, 16] and energies of vacancy formation [3].

3. CALCULATIONS OF RESISTIVITY

In the framework of the weak pseudopotential

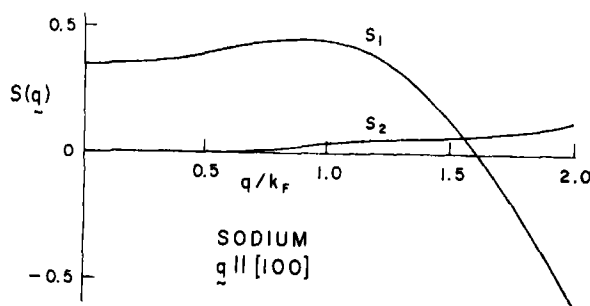


Fig. 3. First and second order contributions, $S_1(q)$ and $S_2(q)$, to the structure factor for a vacancy in sodium along the [100] direction.

*Similar structure factor calculations were performed for potassium, rubidium and cesium as well as for sodium, using force constants tabulated in Ref. [9]. $S_2(q)$ was found to be quite large for rubidium and cesium, so that the first order approximation is a poor one for these metals.

tial approximation, the structure factor appears directly in the matrix elements which govern the scattering processes responsible for electrical resistivity. The calculations are

relatively simple for sodium and potassium. There are two reasons for this: *i.* the Fermi surface of these metals is spherical to better than 1 per cent [17] and *ii.* the strain around vacancies in sodium and potassium is adequately described by $S_1(\mathbf{q})$. Experimentally, the resistivity of vacancies is difficult to determine for the alkalis. Careful experimental studies have been made on aluminum and therefore we also consider this metal here. The difficulties encountered in the calculations for aluminum are typical of polyvalent metals.

The variational principle corresponding to the Boltzmann equation yields the following upper bound on the resistivity of a metal [18]:

$$\rho < \frac{P}{\mathbf{J} \cdot \mathbf{J}}, \quad (3.1)$$

where

$$P = \frac{V\pi}{\hbar^3} \frac{1}{32\pi^6} \int_{FS} \int_{FS'} \frac{dS_{\mathbf{k}}}{v_{\mathbf{k}}} \frac{dS_{\mathbf{k}'}}{v_{\mathbf{k}'}} (g_{\mathbf{k}} - g_{\mathbf{k}'})^2 |M(\mathbf{k}', \mathbf{k})|^2 \quad (3.2)$$

$$\mathbf{J} = \frac{e}{4\pi^3\hbar} \int \frac{dS_{\mathbf{k}}}{v_{\mathbf{k}}} \mathbf{v}_{\mathbf{k}} g_{\mathbf{k}}. \quad (3.3)$$

Here $g_{\mathbf{k}}$ is the variational trial function for the deviation of the electron distribution from its equilibrium form, $M(\mathbf{k}', \mathbf{k})$ is the matrix element for an individual electron scattering event, $dS_{\mathbf{k}}$ is an element of Fermi surface area, $v_{\mathbf{k}}$ is the electronic group velocity at the Fermi surface, and V is the volume of the sample.

(a) Alkali metals

The Fermi surface of alkali metals is nearly spherical, and the behavior of an electron is well described by a single orthogonalized plane wave (OPW). The matrix element for scattering by vacancies between such states is given in first order Born approximation by

$$M_1(\mathbf{k}', \mathbf{k}) = \frac{1}{N} (S(\mathbf{q}) - 1)w(\mathbf{q}), \quad (3.4)$$

where $\mathbf{k}' - \mathbf{k} = \mathbf{q}$ is the momentum transfer and $w(\mathbf{q})$ is the form factor of the screened host ion pseudopotential which we take to be local i.e. dependent on the difference $\mathbf{k}' - \mathbf{k}$ alone [3]. Since $M_1(\mathbf{k}', \mathbf{k})$ is not isotropic (cf. Fig. 1) the exact form of $g_{\mathbf{k}}$ which minimizes (3.1) is not easily determined. According to Greene and Kohn [19] the standard ansatz

$$g_{\mathbf{k}} \propto k_z \quad (3.5)$$

(for a uniform electric field applied along z -axis) which is exact in the case of an isotropic scattering potential is still a good approximation even for moderately anisotropic scattering. These authors considered the intrinsic resistivity of sodium (due to electron-phonon scattering) and found that corrections to (3.5) affected their results only slightly.

Inserting (3.5) into (3.2) and (3.3) we obtain an upper bound which should be close to the actual value of the resistivity from the variational expression (3.1).

$$\rho \approx \frac{3m^*V}{\hbar^3 e^2 k_F^2} \int_{\zeta < 1} |M_1(\zeta)|^2 \zeta d^3\zeta, \quad (3.6)$$

where $\zeta = (\mathbf{k}' - \mathbf{k})/2k_F$.

The effective mass m^* should include an average band structure correction to the free electron mass. For sodium and potassium this correction is negligible [20]. The results of numerical integrations of (3.6) appear in Table 1. The simple local pseudopotential of Ashcroft [21] was employed in these calculations.

(b) Aluminum

Aluminum presents more problems than the alkali metals because of intersection of the Fermi sphere with zone boundaries. One possible difficulty is associated with the distortion (i.e. deviation from a free electron sphere) of the Fermi surface itself. To integrate (3.2) over the distorted Fermi surface would be quite difficult. However $dS_{\mathbf{k}}/v_{\mathbf{k}}$ and \mathbf{J} may be shown to be unaffected to first order

Table 1. Resistivity of vacancies
(in $\mu\Omega\text{-cm/at.}\%$)

	Theory		Experiment	
	Including strain	Without strain	High temperature	Quenching
Sodium	0.69	0.95	1.9-2.1	
Potassium	1.00	1.36		
Aluminum	1.02	1.44	3.0-3.3	1.0-1.2

in the pseudopotential by the presence of a zone boundary intersecting the Fermi sphere. We therefore proceed as if the Fermi surface were spherical, and make the substitution $dS_k/v_k \approx m^*k_F d\Omega/\hbar$ in (3.2).

Individual scattering events may formally be divided into normal and Umklapp processes. The normal scattering is adequately described by the single-OPW matrix element $M_1(\mathbf{k}', \mathbf{k})$. On the other hand Umklapp processes include those for which $\mathbf{k}' - \mathbf{k} \approx \mathbf{G}$ so that at least a 2-OPW description is necessary to avoid unphysical infinite scattering rates.*

In the 2-OPW approximation the pseudo-wave functions with wave vector \mathbf{k} and \mathbf{k}' are written in terms of the relevant plane waves as

$$\psi_{\mathbf{k}} = C_{\mathbf{k}}|\mathbf{k}\rangle + C_{\mathbf{k}+\mathbf{G}}|\mathbf{k}+\mathbf{G}\rangle, \quad \mathbf{k} \cdot \mathbf{G} \approx -\frac{G^2}{2}$$

$$\psi_{\mathbf{k}'} = C_{\mathbf{k}'}|\mathbf{k}'\rangle + C_{\mathbf{k}'-\mathbf{G}}|\mathbf{k}'-\mathbf{G}\rangle,$$

$$\mathbf{k}' \cdot \mathbf{G} \approx \frac{G^2}{2}$$

where

$$\frac{C_{\mathbf{k}}}{C_{\mathbf{k}+\mathbf{G}}} = \frac{\frac{\hbar^2}{2m}(k^2 - |\mathbf{k}+\mathbf{G}|^2)}{2w(\mathbf{G})} \pm \left(\left(\frac{\frac{\hbar^2}{2m}(k^2 - |\mathbf{k}+\mathbf{G}|^2)}{2w(\mathbf{G})} \right)^2 + 1 \right)^{1/2},$$

*It is important to properly include the plane wave mixing in calculating the Umklapp contribution. Thus Fukai [2] found the residual resistivity of a series of dilute aluminum based alloys to be approximately doubled and closer to measured values when calculated in a 2-OPW rather than in the 1-OPW approximation on which previous work was based.

the sign being chosen so that $|C_{\mathbf{k}}/C_{\mathbf{k}+\mathbf{G}}| \geq 1$.

The scattering matrix element between ψ and ψ' is then

$$M_2(\mathbf{k}', \mathbf{k}) = \frac{1}{N} \{ (C_{\mathbf{k}+\mathbf{G}} C_{\mathbf{k}'} + C_{\mathbf{k}} C_{\mathbf{k}-\mathbf{G}}) \\ \times (S(\mathbf{q}) - 1)w(\mathbf{q}) + C_{\mathbf{k}} C_{\mathbf{k}'} \\ \times (S(\mathbf{G} + \mathbf{q}) - 1)w(|\mathbf{G} + \mathbf{q}|) + C_{\mathbf{k}+\mathbf{G}} \\ \times C_{\mathbf{k}'-\mathbf{G}} (S(\mathbf{G} - \mathbf{q}) - 1)w(|\mathbf{G} - \mathbf{q}|) \} \quad (3.7)$$

where $\mathbf{k}' - \mathbf{k} = \mathbf{G} + \mathbf{q}$.

Using (3.7) and (2.6) one may verify that M_2 remains finite as \mathbf{q} goes to zero.

By means of a judicious choice of variables due to Collins and Ziman [22] the regions of normal and Umklapp scattering can be separated in an approximate way. In terms of the variables defined in Fig. 4, the solid angle differential $d\Omega d\Omega'$ may be written

$$d\Omega d\Omega' = d \cos \theta d \cos \theta' d\phi d\phi' = \frac{1}{k_F^2 G} q dq dp d\phi d\phi', \quad (3.8)$$

where ϕ and ϕ' are azimuthal angles with respect to the polar axes along \mathbf{G} and $\mathbf{p} = \mathbf{k} + \mathbf{G}$, respectively. With the help of (3.8), one obtains the following approximate decomposition of the integral of a function $f(\mathbf{k}', \mathbf{k})$ over the Fermi surface:

$$\frac{1}{(4\pi)^2} \int_{FS} \int_{FS} d\Omega d\Omega' f(\mathbf{k}', \mathbf{k}) \approx \frac{1}{2k_F^2} \left\{ \int_0^{q_0} q dq \frac{d\Omega_q}{4\pi} f(\mathbf{k}', \mathbf{k}) + \sum_{\mathbf{G}}' \frac{1}{2G} \right. \\ \times \int_0^{2k_F - G} dq q \int_{k_F - q}^{k_F + q} dp \int_0^{2\pi} \frac{d\phi'}{2\pi} \int_0^{2\pi} \frac{d\phi}{2\pi} f(\mathbf{k}', \mathbf{k}) \\ \left. + \sum_{\mathbf{G}}'' \frac{1}{2G} \int_{|2k_F - G|}^{q_0} dq q \int_{G - k_F}^{k_F + q} dp \int_0^{2\pi} \frac{d\phi'}{2\pi} \int_0^{2\pi} \frac{d\phi}{2\pi} \right. \\ \left. \times f(\mathbf{k}', \mathbf{k}) \right\} \quad (3.9)$$

In the first term on the right side of (3.9) $f(\mathbf{k}', \mathbf{k})$ is assumed to be well-represented by a function of $\mathbf{q} (= \mathbf{k}' - \mathbf{k})$. The limits of integration have been determined by replacing Brillouin zones by spheres of radius q_0 , with $q_0 = 1.50 \text{ \AA}^{-1}$ chosen so that (3.9) is an equality for $f(\mathbf{k}', \mathbf{k}) \equiv 1$ (q_0 differs slightly from the conventional Debye radius $(6\pi^2/V_a)^{1/3}$). The first sum includes all reciprocal lattice vectors such that $2k_F - q_0 < G < 2k_F$, i.e. $\langle 111 \rangle$ and $\langle 200 \rangle$ in Al, while the second one runs over those for which $2k_F - q_0 < G < 2k_F + q_0$, i.e. $\langle 111 \rangle$, $\langle 200 \rangle$ and $\langle 220 \rangle$ in Al. Applying (3.9) to the function

$$f(\mathbf{k}', \mathbf{k}) = \frac{3\pi m^* V}{e^2 h^3 k_F^2} (1 - \hat{\mathbf{k}}' \cdot \hat{\mathbf{k}}) |M(\mathbf{k}', \mathbf{k})|^2,$$

which is obtained by substituting (3.5) into (3.1-3), one can write the resistivity as a sum of three contributions which must be evaluated separately:

$$\rho = \rho_N + \rho'_V + \rho''_V. \quad (3.10)$$

The term ρ_N corresponds to normal processes ($M \approx M_1$) and is identical in form to (3.6). The other two terms account for Umklapp processes ($M \approx M_2$). For vacancies in aluminum, the contribution from ρ_N is only ~ 20 per cent. To simplify the integrations in ρ'_V and ρ''_V we further approximate the integrand $f(\mathbf{k}', \mathbf{k})$ by one which is independent of ϕ . This is accomplished with the help of the following relations:

$$S(\mathbf{q}) = \int S_1(\mathbf{q}) \frac{d\Omega_q}{4\pi} \equiv \bar{S}(q) \quad (3.11)$$

$$S(\mathbf{G} + \mathbf{q}) \approx \bar{S}(q) \frac{(1 + \mathbf{q} \cdot \mathbf{G})}{q^2} \quad (3.12a)^*$$

$$S(\mathbf{G} - \mathbf{q}) \approx \bar{S}(q) \frac{(1 - \mathbf{q} \cdot \mathbf{G})}{q^2}. \quad (3.12b)^*$$

*This follows from (3.11) and the approximate relation $\mathbf{Q}^{\mathbf{q}+\mathbf{G}} \approx \mathbf{Q}^{\mathbf{q}} \approx \mathbf{q} \cdot \mathbf{Q}^{\mathbf{q}} \mathbf{q} / q^2$ which is exact whenever \mathbf{q} is along a symmetry direction.

When (3.12a, b) are substituted into (3.7), the resulting expression becomes independent of ϕ and ρ'_V and ρ''_V reduce to integrals with respect to q , p and ϕ' .

The results of numerical integrations for aluminum are given in Table 1. Ashcroft's pseudopotential [21] was used with a core radius of $.61 \text{ \AA}$ [2]. We have taken $m^* = 1.04 m$ [20]. The averaged structure factor $\bar{S}(q)$ was evaluated with force constants determined from an eight nearest neighbors Born-Von Karmann fit to neutron scattering data at 80°K [13].

4. RESULTS AND DISCUSSION

For each of the metals considered, the resistivity of a vacancy has been calculated both with and without strain included. The results appear in the first two columns of the table. *The effect of strain is seen to be fairly large* (~ 30 per cent). In all three metals the inclusion of lattice strain has the effect of lowering the resistivity. This trend is a consequence of the positive sign of the structure factor over most of the volume of reciprocal space which contributes appreciably to the integrations in (3.6) and (3.10); thus the negative contribution to the scattering amplitude from the missing atom is partially cancelled (cf. (3.4) and (3.7)).

Unfortunately the residual resistivity corresponding to a known concentration of single vacancies cannot be measured directly. The number of vacancies present in equilibrium at a given temperature is appreciable near the melting point only. The total number of defects formed via thermal activation can be determined from the small difference between changes in the length and lattice parameter of a long sample in that range [23, 24]. A significant fraction of divacancies may well exist in aluminum at these high temperatures, however [23, 25]. The residual resistivity associated with monovacancies must be extracted from *i*. The total resistivity observed in the above-mentioned range [26, 27] or *ii*. Low-temperature measurements on quenched

specimens[28]. In the first case systematic errors may arise due to our insufficient knowledge of the temperature dependence of the intrinsic resistivity (which must be subtracted) and of the scattering properties of divacancies [26]. Deviations from Matthiessen's rule are also possible. In the second case one presumably measures the resistivity of monovacancies if the pre-quenching temperature is not too high, but their concentration must be inferred from the above-mentioned high temperature equilibrium data. In addition the resistivity must be extrapolated to infinite quenching speed[28].

Both methods have been applied to aluminum, but the second one is inapplicable to sodium where vacancies cannot apparently be frozen in, due to their very low activation energy for migration[24]. Estimates derived from the best available experimental data are given in the last two columns of Table 1. For sodium we used Feder and Charbneau's determination of equilibrium concentration[24] and Bradshaw and Pearson's resistivity measurements between 300 and 370°K[27]. The intrinsic background, fitted to a quadratic polynomial between 160 and 260°K, was subtracted out to obtain the vacancy contribution.* In the case of aluminum we used the monovacancy concentrations derived by Simmons and Balluffi[23], extrapolated to the range (600–800°K) where their fits allowing for a divacancy binding energy of 0 or 0.25 eV essentially coincide. The resistivity was extrapolated from (i) Simmons and Balluffi's high temperature fit, which assumed the inverse relaxation time for divacancies to be twice that for monovacancies[26], or (ii) Bass's comprehensive analysis of quenching experiments[28]. Satisfactory agreement between

our calculated values and the above-mentioned experimental estimates is only found for quenched aluminum. Unfortunately the uncertainty introduced by extrapolations is almost as large as the decrease in residual resistivity associated with strain, although the calculated value including strain appears to be favored.

Estimates derived from high temperature resistivity measurements are three times larger than calculated values for both sodium and aluminum. It seems unlikely that such big discrepancies could be ascribed to deviations from Matthiessen's rule, as suggested by Fukai[29]. We have no alternative explanation at present.

It is interesting that in his latest communication Fukai[29] reported a calculated resistivity of $1.06 \mu\Omega\text{-cm/at.}\%$ vacancies in aluminum. OPW mixing was included, albeit in a somewhat simpler fashion, but the structure factor $S(q)$ was approximated by the angular average of (1.4), with A adjusted to fit the volume of formation V_F of a monovacancy derived from high temperature thermopower measurements under pressure[25]. The close agreement between that value and ours is not surprising in retrospect. First $V_F/V_a (= 0.52)$ turns out to be close to $1 + \delta$, $\delta (= -0.51)$ being the lattice dilation determined from our lattice statics calculation according to the relation derived by Hardy[30]. Second, as pointed out above, the resistivity of aluminum is dominated by the Umklapp contribution which is weighted towards small values of q where the pseudo-potential form factor $w(q)$ is large, as implied

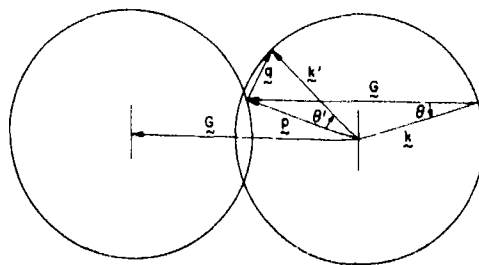


Fig. 4. Geometry for Umklapp scattering integration. For clarity, k , k' and G are drawn as coplanar.

*Fits over different ranges were tried. Our final choice is such that all significant differences between measured and extrapolated background resistivities lie close to a straight line on a semilog plot. The slope of that line corresponds to a vacancy formation energy of 0.37 eV, in fair agreement with that determined in a similar way from concentration measurements (0.42 eV)[24].

by (3.7). In that range $S(q)$ is determined by the displacement pattern at large distances from the defect, which is well-represented by (1.2), providing the pattern is not too anisotropic, as seems to be the case in aluminum [10].

The major source of error in the present calculations is not altogether clear. There may be an accumulation of errors, i.e. in the pseudopotential form factor itself* and our neglect of nonlocal corrections, in the approximation (3.11, 3.12), in the crude variational ansatz (3.5). More disturbing is the possibility that the pseudoatom approach underlying the whole formulation is not adequate in dealing with such a large perturbation as a vacancy, especially in aluminum. In deriving the scattering amplitudes (3.4) and (3.7), as well as the screening of the pseudopotential form factor $w(q)$ itself† one relies on the first Born approximation. More precisely, in the spirit of 'Babinet's principle' of diffraction theory [12], a vacancy is represented by the removal of an ion and its screening charge (the 'pseudoatom').

Of course, the screening of ions in the neighborhood of the vacancy is modified by its presence and this is not taken into account in the present treatment. To remedy this one would have to calculate self-consistently the screening potential at least in the neighborhood of the defect, a difficult nonlinear problem which has not been tackled to date. If such a calculation revealed Babinet's principle to be seriously in error, then the pseudoatom approach would have to be modified or abandoned in treating vacancies.

*In his short note [2] Fukai reported calculations performed with Harrison's OPW pseudopotential [3], as well as with the Ashcroft [2] and the Heine-Abarenkov model potentials. The corresponding values of the resistivity did not differ by more than 12 per cent. The value obtained with Ashcroft's model potential (without strain), viz. $1.58 \mu\Omega\text{-cm/at } \%$, compares favorably with ours, viz. 1.44 (Cf. table). The difference could be accounted for by Fukai's cruder treatment of plane wave mixing.

†The effective potential between ions in the vicinity of the vacancy would also be modified as a result of nonlinear screening effects.

Even if this were the case, the method would still be useful for isoelectronic impurities. The latter represent a much smaller perturbation than do vacancies. On the other hand the relative contribution to the resistivity from lattice strain is expected to be more important for this type of defect. Finally the residual resistivity can be measured directly and should provide a more stringent test of the accuracy of similar calculations. Further work along these lines is now in progress.

Acknowledgements — We wish to thank Dr. Yuh Fukai for calling our attention to his recent communication [29].

APPENDIX

In this appendix we present a derivation of (2.1). Consider a Bravais lattice of atoms interacting via two-body central forces. If a single vacancy is introduced at $r_0 = 0$ the atoms relax to new equilibrium positions. The energy of the strained crystal can be written as

$$U = \frac{1}{2} \sum_{l,l' \neq 0} \psi(|r_l - r_{l'}|) = \frac{1}{2} \sum_{l,l'} \psi(|r_l - r_{l'}|) - \sum_m \psi(|r_m|) \\ + \text{const.} = \int d^3q \left(\frac{1}{2} F(q) S(q) S(q) - F(q) S(q) \right) + \text{const.}, \quad (\text{A.1})$$

where $\psi(r) = \int d^3q F(q) e^{iq \cdot r}$ is the net effective potential acting between a pair of ions. We expand the structure factor, keeping terms to second order in the displacements from the equilibrium positions in the undisturbed lattice:

$$S(q) = \sum_l e^{-iq \cdot r_l^{(0)}} (1 - iq \cdot u_l - \frac{1}{2} (q \cdot u_l)^2) = S_0(q) + S_1(q) \\ + S_2(q). \quad (\text{A.2})$$

Also, to second order,

$$S(q)S(q) = S_0(q)S_0(q) + 2S_0(q)S_1(q) + S_1(q)S_1(q) \\ + 2S_0(q)S_2(q).$$

The terms in the expansion (A.2) may conveniently be written

$$S_0(q) = \frac{(2\pi)^3}{V_a} \sum_G \delta(q - G) \quad (\text{A.3})$$

$$S_1(q) = -iq \cdot Q^q \quad (\text{A.4})$$

$$S_2(q) = -\frac{V_a}{2} \int \frac{d^3q'}{(2\pi)^3} (q \cdot Q^{q'}) (q \cdot Q^{q-q'}). \quad (\text{A.5})$$

The normal coordinate $Q^q = \sum_l u_l e^{-iq \cdot r_l^{(0)}}$ is periodic in reciprocal space: $Q^q = Q^{q+G}$. In particular, $Q^G = 0$ by symmetry. Hence, in view of (A.3) and (A.4), $S_0(q)S_1(q) = 0$. Ignoring terms which are independent of the internal

strain (viz. $S_0(\mathbf{q})S_0(\mathbf{q})$), one obtains

$$U = U_H - U_D,$$

where

$$U_H = \int d^3q \frac{1}{2} F(q) (S_1(\mathbf{q})S_1(\mathbf{q}) + 2S_0(\mathbf{q})S_2(\mathbf{q})),$$

and

$$U_D = \int d^3q q F(q) (S_1(\mathbf{q}) + S_2(\mathbf{q})).$$

Using (A.3-5), one may rewrite U_H in the form

$$U_H = -\frac{V_0}{2} \int \frac{d^3q}{(2\pi)^3} \mathbf{Q}^q \mathbf{V}^q \mathbf{Q}^q,$$

where

$$\mathbf{V}^q = \frac{(2\pi)^3}{V_0} \sum_{\mathbf{G}} [\mathbf{F}(\mathbf{q} + \mathbf{G})(\mathbf{q} + \mathbf{G})(\mathbf{q} + \mathbf{G}) - \mathbf{F}(\mathbf{G})\mathbf{G}\mathbf{G}] \quad (\text{A.6})$$

is the dynamical matrix of the host lattice whose eigenvalues $M\omega^2(\mathbf{q})$ yield the phonon spectrum of the host crystal. For atoms interacting via two-body central forces, (A.6) is easily shown to be equivalent to the more familiar definition of the dynamical matrix given by (2.3). The equation of lattice statics obtains if one sets $\partial U / \partial \mathbf{Q}^q = 0$, i.e. $\mathbf{V}^q \mathbf{Q}^q = \mathbf{F}^q$ or

$$\mathbf{Q}^q = (\mathbf{V}^q)^{-1} \mathbf{F}^q \quad (2.1)$$

where

$$\mathbf{F}^q = \sum_i \nabla(\psi(r) + \mathbf{u}_i \cdot \nabla\psi(r))|_{\mathbf{r}_i^{(0)}} e^{-i\mathbf{q} \cdot \mathbf{r}_i^{(0)}} \quad (\text{A.7})$$

For other types of point defects in a Bravais lattice, only the form of \mathbf{F}^q must be changed (e.g. (2.4b)). Equations (2.1) can easily be generalized to lattices with a basis.

To determine the normal coordinates of the distortion around a vacancy one must evaluate the factors on the right side of (2.1). The dynamical matrix is directly related to the force constants $\Phi_{\alpha\alpha'}$ by (2.3). The derivatives appearing in (A.7) can also be determined from the force constants through the relation*

$$\Phi_{\alpha\alpha'}^l = \left[\frac{\psi'(r_l^{(0)})}{r_l^{(0)}} - \psi''(r_l^{(0)}) \right] \hat{r}_{l\alpha}^{(0)} \hat{r}_{l\alpha'}^{(0)} - \frac{\psi'(r_l^{(0)})}{r_l^{(0)}} \delta_{\alpha\alpha'}$$

where $\hat{r}_{l\alpha}^{(0)}$ is the α -th component of a unit vector pointing towards the l -th site of the undistorted lattice. In evaluating \mathbf{F}^q the displacement \mathbf{u}_i must also be known. In practice the displacements decrease rapidly enough so that the second term in (A.7) may often be neglected for all but the first few neighbors around the defect. The corresponding displacements may be calculated self-consistently by a method described by Flocken and Hardy[9]. In calculating \mathbf{F}^q for the alkalis the displacements of the first three sets of neighbors were accounted for, while for aluminum those of the first two sets of neighbors were included.

* $\psi'(r_l^{(0)})/r_l^{(0)}$ and $\psi''(r_l^{(0)})$ are the familiar tangential and radial force constants of lattice dynamics[13].

REFERENCES

1. DICKEY J. M., MEYER A. and YOUNG W. H., *Phys. Rev.* **160**, 490 (1967); GUPTA O. P., *Phys. Rev.* **174**, 668 (1968).
2. FUKAI Y., *Phys. Lett.* **27A**, 416 (1968); vacancies; *Phys. Rev.* **186**, 697 (1969); dilute alloys.
3. HARRISON W. A., *Pseudopotentials in the Theory of Metals*, p. 31, W. A. Benjamin, New York (1966).
4. DEXTER D. L., *Phys. Rev.* **87**, 768 (1952).
5. KANZAKI H., *J. Phys. Chem. Solids* **2**, 24 (1957).
6. OVERHAUSER A. W. and GORMAN R. L., *Phys. Rev.* **102**, 676 (1956); Ref. [3], p. 145.
7. BEAL-MONOD M. and KOHN W., *J. Phys. Chem. Solids* **29**, 1877 (1968).
8. ESHELBY J. A., in *Solid State Physics* (Edited by F. Seitz and D. Turnbull) Vol. 3, p. 79. Academic Press, New York (1956).
9. FLOCKEN J. W. and HARDY J. R., *Phys. Rev.* **177**, 1054 (1969).
10. FLOCKEN J. W. and HARDY J. R., *Phys. Rev.* **181**, 2447 (1970).
11. BLATT F. J., *Phys. Rev.* **108**, 285 (1957); **108**, 1204 (1957).
12. ZIMAN J. M., in *Physics of Metals*, (Edited by J. M. Ziman) p. 261. Cambridge University Press, London (1969).
13. e.g. GILAT G. and NICKLOW R. M., *Phys. Rev.* **143**, 487 (1966) for aluminum.
14. SHYU W. M. and GASPARI A. D., *Phys. Rev.* **163**, 667 (1967).
15. SHAM L. J. and ZIMAN J. M. in *Solid State Physics* (F. Seitz and D. Turnbull, eds.) Vol. 15, p. 221. Academic Press, New York (1963).
16. SAGALYN P. J., PASKIN A. and HARRISON R. J., *Phys. Rev.* **124**, 428 (1961).
17. SCHOENBERG D. and STILES P. J., *Proc. R. Soc. Lond.* **A281**, 62 (1964).
18. ZIMAN J. M., *Electrons and Phonons*, Chap. 7, Oxford University Press, Oxford (1960).
19. GREENE M. P. and KOHN W., *Phys. Rev.* **137**, A513 (1965).
20. WEAIRE D., *Proc. Phys. Soc. Lond.* **92**, 956 (1967).
21. ASHCROFT N. W., *J. Phys.* **C1**, 232 (1968).
22. COLLINS J. G. and ZIMAN J. M., *Proc. R. Soc. Lond.* **264A**, 60 (1961).
23. SIMMONS R. O. and BALLUFFI R. W., *Phys. Rev.* **117**, 52 (1960).
24. FEDER R. A. and CHARBNAU P., *Phys. Rev.* **149**, 464 (1966).
25. BOURASSA R. R., LAZARUS D. and BLACKBURN D. A., *Phys. Rev.* **165**, 853 (1968).
26. SIMMONS R. O. and BALLUFFI R. W., *Phys. Rev.* **117**, 60 (1960).
27. BRADSHAW F. J. and PEARSON S., *Proc. Phys. Soc. Lond.* **B69**, 441 (1956).
28. BASS J., *Phil. Mag.* **15**, 717 (1967).
29. FUKAI YUH, *Phil. Mag.* **20**, 1277 (1969).
30. HARDY J. R., *J. Phys. Chem. Solids* **29**, 2009 (1968).

RAMAN AND INFRARED SPECTRA OF CRYSTALS WITH α -NaFeO₂ STRUCTURE

P. BRÜESCH and C. SCHÜLER

Brown Boveri Research Center, Baden, Switzerland

(Received 7 July 1970)

Abstract—We have studied the Raman spectra of twelve NaBX₂ compounds, which crystallize in the common α -NaFeO₂ structure, namely $B = \text{Cr, In, Er, Ho, Y, Yb}$, and $X = \text{O, S}$. Adopting a simple force model for the Raman active normal modes, the repulsive forces between the vibrating anion layers are calculated and correlated with the structural parameters of the crystals.

For NaCrS₂ we present a detailed analysis of the Raman and i.r. spectra which is based on the rigid-ion approximation. The potential energy is given by $V = V_s + V_c$, where V_s is the contribution of the short range overlap forces and V_c represents the long range Coulomb interactions. V_s is expressed in terms of a simple force model which contains three important short range force constants. In order to account for the observed TO-LO splitting of the i.r. active modes, a rigid-ion model is used for V_c which contains two independent effective charges. The comparatively small effective charges obtained from this analysis suggest that the valence electrons in NaCrS₂ are delocalized to a large extent.

1. INTRODUCTION

THERE is a large number of compounds of the general formula ABX_2 , which crystallize in the common, α -NaFeO₂ layer type structure. Here, A represents an alkali-metal ion, B a trivalent ion like Cr, In or Y and X one of the chalcogenes O, S or Se. These compounds are of interest, because they provide a chance to study correlations between physical properties and chemical constitution in a given crystal structure similar to other well known cases, as for example the spinels or perovskites.

Two aspects are particularly important. First of all, compounds with identical A and B ions but different X ions exist which are insulators for $X = \text{O}$ but semiconductors for $X = \text{S}$ or Se. In addition the B -site can be occupied by ions with a full d -shell like In, an unfilled d -shell like Cr or an unfilled f -shell like the rare earth ions. The unpaired spins give rise to magnetic moments which are in many cases strongly coupled so that magnetic ordering is observed. Recently, a number of papers reported on magnetic [1-4] and optical [5, 6] properties as well as NMR studies of a number of such compounds.

No information is so far available about lattice vibrations and force constants. This paper deals with results of systematic Raman and i.r. investigations we have undertaken in order to contribute to a further understanding of this class of ternaries.

We have studied the Raman spectra of twelve NaBX₂ compounds, namely $B = \text{Cr, In, Er, Ho, Y, Yb}$ and $X = \text{S, O}$. Based on the observed Raman frequencies and adopting a simple force model for the Raman active modes, the force constants of the repulsive forces between the vibrating anion layers are calculated and correlated with the structural properties of the crystals.

For NaCrS₂ where in addition to the Raman frequencies also the i.r. data are available, a central force model is used. Firstly neglecting long range dipole forces, the short range overlap forces and normal coordinates are calculated. Finally the effect of the long range dipole forces, which are responsible for the TO-LO splitting of the polar i.r. active modes, is discussed.

2. CRYSTAL STRUCTURE AND $k = 0$ PHONONS

Compounds of the NaCrS₂ type crystallize

in the space group D_{3d}^5 ($R\bar{3}m$)[7]. In the hexagonal system the atoms of the NaBX_2 units are on sites with symmetries and coordinates given below:

$$\begin{aligned} B: & (3a, D_{3d}) \quad 0, 0, 0 \\ \text{Na}: & (3b, D_{3d}) \quad 0, 0, \frac{1}{2} \\ X: & (6c, C_{3v}) \quad 0, 0, u, \quad 0, 0, \bar{u}. \end{aligned}$$

Figure 1 shows the primitive rhombohedral unit cell which contains one NaBX_2 unit. The ions are arranged in layers perpendicular to the optic axis. The anions form a cubic close-packed structure, while the cations occupy the octahedral interstices in this packing in alternate layers. The ions in the primitive unit cell are numbered as follows (see Fig. 8):

$$B = 1, \quad \text{Na} = 2, \quad X = 3, 4.$$

In Fig. 2 the i.r. and Raman active symmetry modes are shown. There are 4 ions in the primitive unit cell, implying a total of 12 vibrational modes. The reduction of the reducible representation Γ into the irreducible representations of the unit cell group D_{3d} is:

$$\Gamma = 1A_{1g} + 3A_{2u} + 1E_g + 3E_u.$$

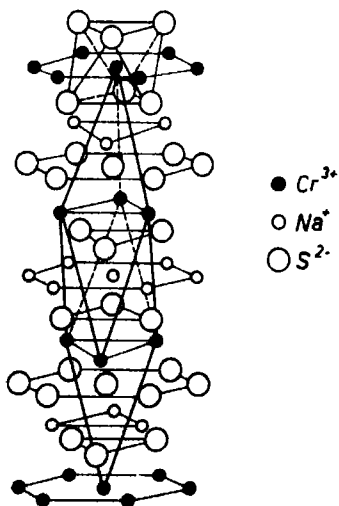


Fig. 1. Crystal structure of NaCrS_2 .

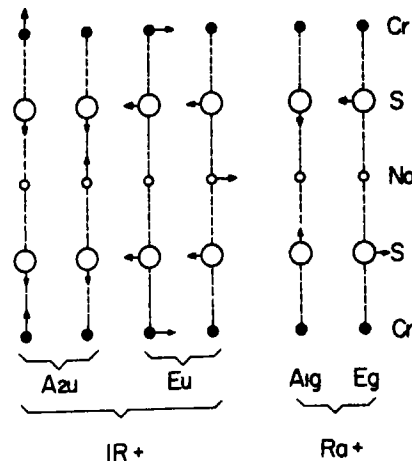


Fig. 2. $k = 0$ phonons of NaCrS_2 .

There are 4 i.r. active polar modes, two of species A_{2u} and two of species E_u , in which the lattices of the cations move against the lattices of the anions. The two Raman active modes, one of the species A_{1g} , the other of species E_g , are especially simple. In the A_{1g} mode two adjacent anion layers move rigidly against each other and parallel to the optic axis and in the E_g mode perpendicular to the optic axis.

The scattering tensors corresponding to the Raman active modes A_{1g} and E_g of point group D_{3d} , referred to the hexagonal system x, y, z have the form[8]:

$$\alpha(A_{1g}) = \begin{pmatrix} a & 0 & 0 \\ 0 & a & 0 \\ 0 & 0 & b \end{pmatrix}$$

$$\alpha(E_g) = \begin{pmatrix} c & 0 & 0 \\ 0 & -c & d \\ 0 & d & 0 \end{pmatrix}, \begin{pmatrix} 0 & -c & -d \\ -c & 0 & 0 \\ -d & 0 & 0 \end{pmatrix}$$

Based on the form of the scattering tensors the A_{1g} and E_g modes can be assigned unambiguously: if α_{zz} is observed, only the A_{1g} modes should appear, but in the α_{xy} , α_{xz} or α_{yz} -geometry only the E_g mode should appear. In our experiments the z axis is always perpendicular to the thin crystal

plates, but no attempt has been made to determine the x - y orientation. Improper sample orientation in the x - y plane does not result in incorrect assignment of the A_{1g} and E_g phonons as can easily be seen by transforming the above scattering tensors from the crystal fixed system x, y, z into the laboratory fixed system x', y', z .

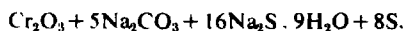
3. EXPERIMENTAL TECHNIQUES AND RESULTS

(a) Materials

Most of the compounds investigated in this work have been described before. We have, however, tried to prepare them in single crystalline form. In the following compilation we give details of the most successful procedure as found by experiments. Only flux methods were used.

NaInO₂[9]: One part of In₂O₃ was dissolved in 10–15 parts (by weight) of a mixture of NaOH (10 Mol %) and Na₂CO₃ (90 Mol %) by heating these substances in a recrystallized Al₂O₃ crucible taking 7 hr to reach a temperature of 1350°C. After cooling the melt subsequently at about 70°/hr. most of the flux had evaporated and the rest could be dissolved away in cold water. The remaining NaInO₂ crystals were in the form of thin platelets up to 50 μ thickness and about 5 \times 5 mm maximum size, with the hexagonal basal planes forming their large faces. Optically they were either completely transparent or had a somewhat milky appearance.

NaCrO₂[10]: For this compound, it was found necessary to employ a flux containing an appreciable amount of sulfur in order to increase the solubility at temperatures around 1300°C. The following mixture (in mols) was most successful:



A recrystallized Al₂O₃ crucible was again used. The temperature was raised to 1320°C during 2 hr and the oven shut off immediately afterwards. After cooling to room temperature the remaining flux was dissolved in cold water. Small crystal platelets of 3 \times 3 mm maximum size and 5–20 μ thickness remained. Both NaCrO₂ and NaCrS₂ were found simultaneously. NaCrO₂ is dark green in transmission, thicker crystals are almost opaque.

NaYO₂, NaErO₂, NaHoO₂, and NaYbO₂[11, 12]: These compounds could be obtained in powder form only. A mixture of 1 part (RE)₂O₃ and 1 part of Na₂O₂ (by weight) was held in a Pt crucible at 550°C for 24 hr. After cooling, the sintered cake was ground again and heated to 550°C for another 48 hr. The excess of Na₂O₂ was dissolved away and white or slightly coloured powders of the respective compound NaREO₂ remained.

NaCrS₂: Crystals were grown by a method described by Rüdorff *et al.*[13, 14], slightly modified to obtain larger specimens of uniform thickness and with shiny, flat surfaces. A mixture of 9.9 parts K₂Cr₂S₇, 36.5 parts Na₂CO₃, 45.4 parts S, and 8.2 parts B₂O₃ (all by weight) was heated in a tightly covered crucible of recrystallized

Al₂O₃ to 1100°C and slowly cooled at about 100°C/hr. The remaining flux was dissolved in H₂O and the crystals washed very briefly in dilute HCl. Single hexagonal platelets of 7 mm dia. and 10–20 μ thickness could be grown in this way. Omitting B₂O₃ resulted in intergrown crystals up to 20 mm dia. and 0.5 mm thickness.

NaInS₂[15]: A mixture of 2g In metal, 4g S, and 12g Na₂S \cdot 9H₂O was heated in a recrystallized Al₂O₃ crucible to 800°C and cooled at about 100°C/hr. After dissolving the flux in water, the remaining crystals had a more or less intensive orange to yellow colour. This was thought to be due to some contamination with polysulfides. After washing in saturated Na₂S solution, only a slightly yellow colour remained.

NaYS₂, NaErS₂, NaHoS₂, and NaYbS₂[16]: Single crystal platelets of 1 to 4 mm dia. and about 10–20 μ thickness were grown by the following method: A mixture of 1 part RECl₃ and 15 parts Na₂CO₃ (by weight) was heated in an Al₂O₃ boat in streaming H₂S to 1300°C, brought to 1250°C for 30–60 min and then cooled. During the heating period, Na₂CO₃ reacts with H₂S to form a Na₂S flux. While the temperature is kept at 1250°C, most of the flux evaporates. Residual flux was washed off with cold water. All crystals were transparent, with a light tint of brown (NaHoS₂), pink (NaErS₂), and yellow (NaYbS₂). Table 1 contains the relevant structural parameters.

(b) Raman spectra

All Raman spectra were excited with a HeNe Laser (6328 Å). The output of the linearly polarized Laser beam was about 70 mW. Light scattered through 90° is passed through a double monochromator and detected photoelectrically using a cooled ITT FW 130 photomultiplier. In most of the spectra the instrumental width is about 4 cm⁻¹. The spectrometer was calibrated with the spectrum of the HeNe Laser. All wave numbers are corrected for vacuum and the error in frequency is estimated to be ± 3 cm⁻¹.

The Raman spectra are shown in Figs. 3 and 4. In these figures the spectra of the transparent crystals were observed in the $z(x'x')y'$ – or in the $z(x'x' + x'z)y'$ geometry in which both modes appear. NaCrS₂ and NaCrO₂ were observed in the back scattering geometry with an angle of incidence of 68°, whereas powder discs have been used for the Raman spectra of NaYO₂, NaHoO₂, NaErO₂, and NaYbO₂. In the Raman spectrum of NaCrO₂ only the high frequency line could be observed: the weak line near 450 cm⁻¹ is

Table 1. Structural parameters of α -NaFeO₂ type crystals

Compound	a_h (Å)	c_h (Å)	u	r_B (Å)	d (Å)	Element in origin
NaCrS ₂	3.534	19.49	0.264[X]	0.69	2.69[X]	Cr
NaInS ₂	3.803	19.89	0.26[X]	0.90	2.90[X]	In
NaYS ₂	3.968	19.89	0.26[*]	0.92	2.98[*]	Y
NaHoS ₂	3.949	19.86	0.26[*]	0.92	3.02[*]	Ho
NaErS ₂	3.939	19.98	0.258[*]	0.90	3.00[*]	Er
NaYbS ₂	3.91	20.0	0.26[*]	0.88	2.96[*]	Yb
NaCrO ₂	2.96	15.9	0.220[X]	0.69	1.68[X]	Na
NaInO ₂	3.235	16.35	0.257[X]	0.90	2.49[X]	In
NaYO ₂	3.386	16.43	0.26[*]	0.92	2.32[*]	Y
NaHoO ₂	3.394	16.61	0.26[*]	0.92	2.29[*]	Ho
NaErO ₂	3.377	16.57	0.26[*]	0.90	2.28[*]	Er
NaYbO ₂	3.350	16.53	0.26[*]	0.88	2.28[*]	Yb

[X] values from X-ray studies.

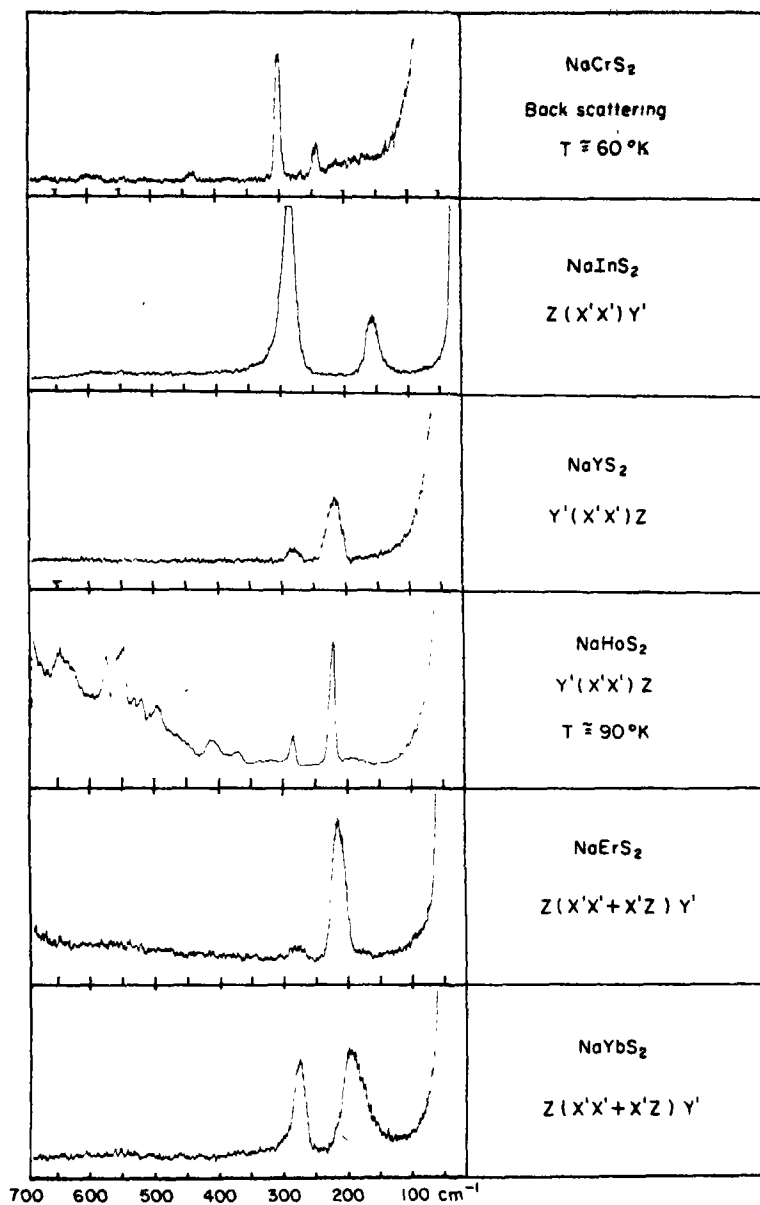
[*] values estimated based on ionic radii r_B of the trivalent metal B given in Ref.[16]; in the rare earth sulfides $r_s = 1.82$ Å and in the rare earth oxides $r_o = 1.36$ Å is used. d is the distance between nearest anion layers.

a grating ghost line. NaCrS₂ was studied at room temperature and at liquid Helium temperature, but in the latter case the crystal temperature was as high as 60°K due to absorption of the Laser beam. This temperature was determined by observing the ratio of the Stokes and Anti-Stokes Raman intensities of the A_{1g} mode.

Strong fluorescence in the Stokes part of the Raman spectra is observed in the rare earth compounds NaErO₂, NaErS₂, NaHoO₂ and NaHoS₂. This is especially disturbing in NaHoS₂, NaHoO₂ and NaErO₂, where the fluorescence spectra of the rare earth ions overlap partly with the Raman spectra. The Raman spectra of these compounds could be observed either by cooling with liquid N₂ in the case of NaHoO₂ or by observing the Anti-Stokes Raman lines in the case of

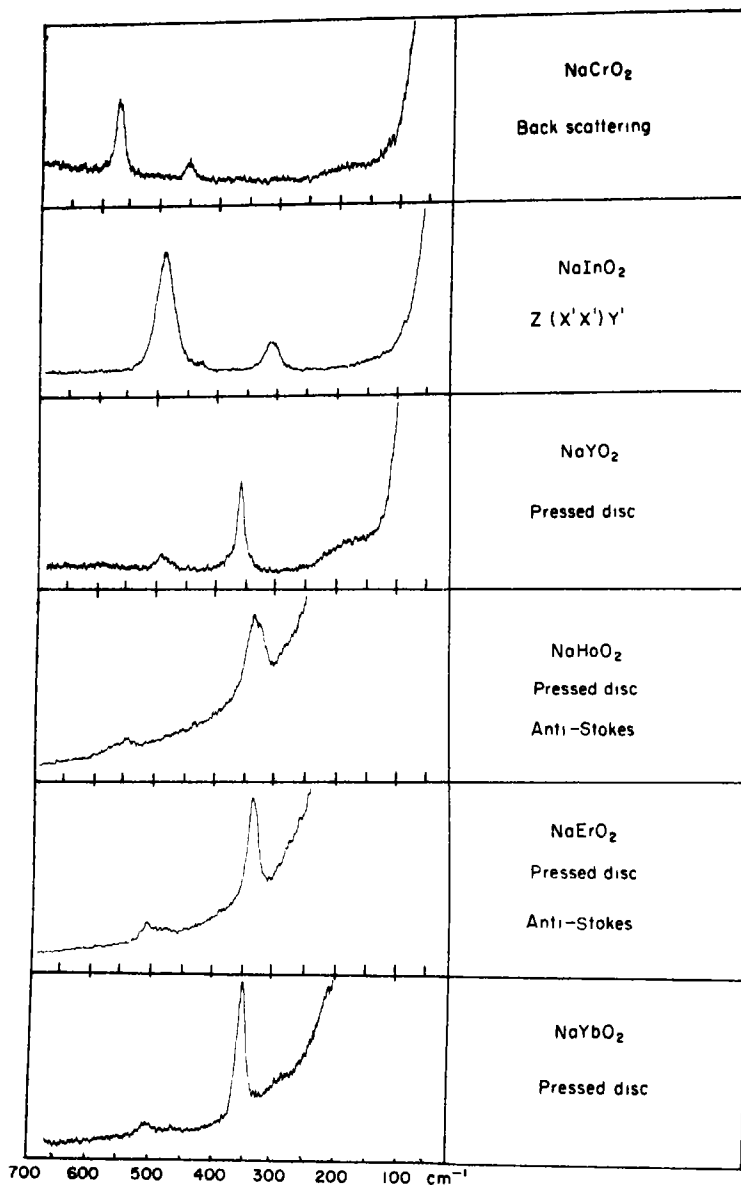
NaHoO₂ and NaErO₂. In Table 2 the observed Raman frequencies are listed.

The intensities of the Raman lines do not strictly obey the selection rules as discussed in the last section. According to selection rules the α_{zz} spectra should show only the A_{1g} mode and the $\alpha_{x'y'}$ and $\alpha_{x'z}$ spectra only the E_g mode but most of these spectra show two lines, a strong one and a weak one. The observations can be summarized as follows: In the α_{zz} spectra the high frequency line is always considerably stronger than the low frequency line and in the $\alpha_{x'y'}$ and $\alpha_{x'z}$ spectra the low frequency line is stronger than the high frequency line. Figure 5 illustrates this situation for the Raman lines of NaYS₂. As mentioned in the last section, incomplete orientation in the crystal xy plane does not explain these observations. Reduction of the

Fig. 3. Raman spectra of the NaBS_2 compounds.

internal cone angles of the incident and scattered beams did not significantly change the intensity ratio of the two Raman lines. The smallest half-angular divergence of incident and collected scattered light within the crystal was 0.5° and 4° , respectively. Furthermore, depolarization due to bire-

fringence, as observed and discussed by Porto *et al.*[17] is ruled out here because the crystals are too thin. The most probable reason for this anomalous behavior in intensities is depolarization due to surface effects of the thin crystals which have thicknesses comparable to the phonon wavelengths. We

Fig. 4. Raman spectra of the NaBO_2 compounds.

therefore assign the high frequency line to the A_{1g} mode and the low frequency line to the E_g mode. As will be seen in the next section this assignment is also supported by the normal coordinate calculations of the Raman and i.r. active modes of NaCrS_2 .

(c) *Far i.r. spectra of NaCrS_2*

Far i.r. spectra of NaCrS_2 were studied using absorption and reflection techniques. The absorption spectrum was obtained with the material in the form of a mull of nujol. The mull was placed between CsI windows

Table 2. Observed Raman frequencies and calculated force constants for crystals with α -NaFeO₂ structure

Compound	$\omega(E_g)$ (cm ⁻¹)	$\omega(A_{1g})$ (cm ⁻¹)	C_x (m dyn/Å)	C_z (m dyn/Å)
NaCrS ₂	240	308	0.54	0.89
NaInS ₂	158	289	0.24	0.82
NaYS ₂	216	279	0.44	0.73
NaHoS ₂	221	284	0.46	0.76
NaErS ₂	221	284	0.46	0.76
NaYbS ₂	204	282	0.39	0.75
NaCrO ₂	?	580	?	1.60
NaInO ₂	320	493	0.47	1.15
NaYO ₂	363	493	0.62	1.15
NaHoO ₂	346	547	0.57	1.41
NaErO ₂	346	514	0.57	1.24
NaYbO ₂	353	512	0.59	1.23

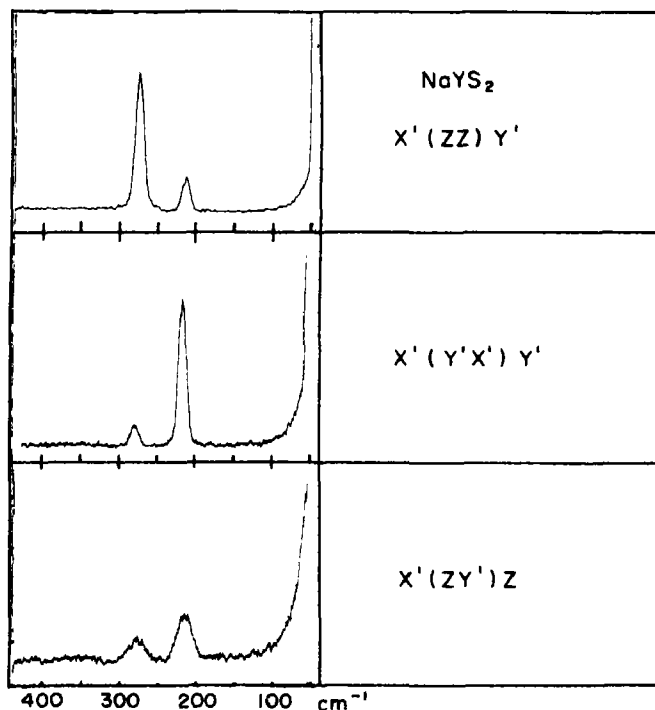


Fig. 5. Intensity behavior of the Raman lines of NaYS₂.

or between high density polyethylene wedges. Polyethylene wedges were used to avoid disturbing interferences. Figure 6 shows the powder spectrum which has been corrected for background absorption.

The reflection spectrum of a large single crystal of NaCrS_2 with its hexagonal basal plane perpendicular to the optic axis was measured with an RHC interferometer.*

The angle of incidence was 12° and the beam was polarized perpendicular to the plane of incidence, thus only the E_u modes should appear. Making use of the Kramers-Kronig transformations, the complex dielec-

tric constant $\epsilon_x = \epsilon'_x + i\epsilon''_x$ was evaluated. Figure 7 shows $\epsilon''_x(\omega)$. This spectrum clearly identifies the two transverse E_u modes at 146 and 309 cm^{-1} . The corresponding longitudinal E_u -frequencies are obtained from $\epsilon'_x(\omega) = 0$ and are 150 and 368 cm^{-1} , respectively. The absorption band at about 235 cm^{-1} , in Fig. 6 is assigned to the low frequency A_{2u} mode. The high frequency A_{2u} mode overlaps partly with the high frequency E_u mode giving rise to the strong absorption band centered at about 325 cm^{-1} . Support for this view is given by the normal coordinate analysis which locates these two frequencies close together (see Table 3). Further support for this assignment is also given by the powder spectrum of NaInO_2 , in which these two

*These measurements were kindly performed by Dr. G. R. Wilkinson of King's College, London University.

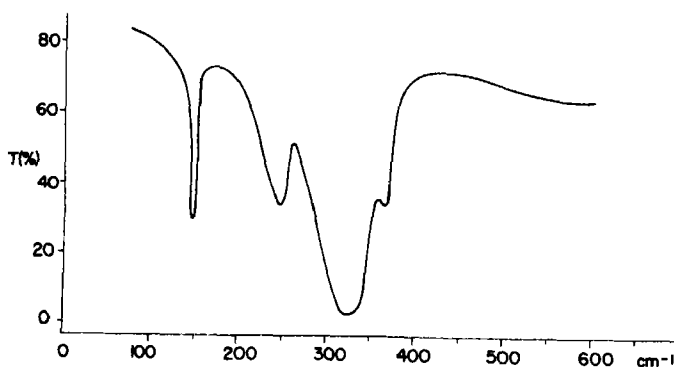


Fig. 6. Infrared spectrum of powdered NaCrS_2 at 300°K .

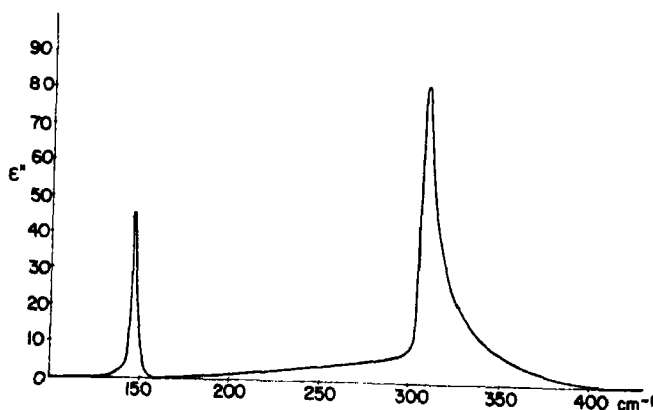


Fig. 7. Imaginary part of the complex dielectric function of NaCrS_2 vs. wave number.

absorption bands can be clearly resolved. The additional peak at about 370 cm^{-1} on the high frequency side of the strong absorption maximum is probably due to a second order absorption process as observed in many polar crystals[18].

The accuracy of the E_u frequencies derived from the reflection measurements is about $\pm 1\text{ cm}^{-1}$. The frequencies of the powder spectra are less accurate, partly due to the overlap of absorption bands and partly as a consequence of the transverse longitudinal splitting which is large for the intense modes. The absorption maximum will therefore be located at some ill-defined position between the transverse and longitudinal frequencies and will depend on particle size and distributions. The inaccuracy of the high frequency A_{2u} absorption maximum at about 330 cm^{-1} is at least $\pm 10\text{ cm}^{-1}$.

4. ANALYSIS

(a) Analysis of the Raman spectra

The form of the two Raman active A_{1g} and E_g modes, as discussed in Section 2, makes it possible to work with a very simple force model. In the A_{1g} mode the even numbered anion planes $2s$, $2s+2$, etc. move in the positive z direction, and the odd numbered anion planes in the opposite direction (see Fig. 8). Let u_{2s} , u_{2s+1} , etc. be the displacements of the anions in the planes $2s$, $2s+1$, etc. Then we have the following equations of motion:

$$m_X \ddot{u}_{2s+1} = C_1(u_{2s} - u_{2s+1}) + C_2(u_{2s+2} - u_{2s+1})$$

$$m_X \ddot{u}_{2s} = C_1(u_{2s+1} - u_{2s}) + C_2(u_{2s-1} - u_{2s}).$$

In these equations m_X is the mass of anion X and C_{1z} and C_{2z} are the force constants shown in Fig. 8. C_{1z} and C_{2z} contain contributions from nearest cation-anion and anion-anion repulsions. The frequency of the optical A_{1g} mode is given by

$$\omega(A_{1g}) = (2C_z/m_X)^{1/2}, \text{ where } C_z = C_{1z} + C_{2z}.$$

Table 3. Observed and calculated normal frequencies and calculated normal coordinates Q_k in terms of cartesian coordinates x_i

Obs. (cm^{-1})	Assign.	Calc.[*] V_s	Calc.[\square] $V_s + V_c$	$Q_k = \sum_i L_{ik}x_i$; L_{ik} in (amu) $^{1/2}$
368	(E_u, L)	331	367	$Q_1^L(E_u) = -4.82x_1 - 0.92x_2 + 2.87x_3 + 2.87x_4$
309	(E_u, T)		303	$Q_1^0(E_u) = -5.10x_1 - 0.49x_2 + 2.80x_3 + 2.80x_4$ $Q_1^T(E_u) = -5.10x_1 - 0.49x_2 + 2.80x_3 + 2.80x_4$
150	(E_u, L)	157	152	$Q_2^L(E_u) = -3.05x_1 + 4.28x_2 - 0.62x_3 - 0.62x_4$
146	(E_u, T)		146	$Q_2^0(E_u) = -2.55x_1 + 4.35x_2 - 0.90x_3 - 0.90x_4$ $Q_2^T(E_u) = -2.55x_1 + 4.35x_2 - 0.90x_3 - 0.90x_4$
~ 330	A_{2u}	320	372	$Q_1^L(A_{2u}) = -4.81z_1 - 0.95z_2 + 2.88z_3 + 2.88z_4$
			308	$Q_1^0(A_{2u}) = -4.63z_1 - 1.18z_2 + 2.90z_3 + 2.90z_4$ $Q_1^T(A_{2u}) = -5.17z_1 - 0.37z_2 + 2.77z_3 + 2.77z_4$
~ 235	A_{2u}	200	220	$Q_2^L(A_{2u}) = -3.08z_1 + 4.27z_2 - 0.60z_3 - 0.60z_4$
			212	$Q_2^0(A_{2u}) = -3.33z_1 + 4.22z_2 - 0.44z_3 - 0.44z_4$ $Q_2^T(A_{2u}) = -2.41z_1 + 4.36z_2 - 0.98z_3 - 0.98z_4$
240	E_g	253	236	$Q(E_g) = -4.00x_3 + 4.00x_4$
308	A_{1g}	294	320	$Q(A_{1g}) = -4.00z_3 + 4.00z_4$

[*] The short range force constants used in V_s are: $F_1 = 0.85$, $F_2 = 0.18$, $F_3 = 0.08\text{ mdyne/\AA}$.

[\square] The effective charges used in V_c are: $e_{\text{Cl}}^* = 1.1e$, $e_{\text{Na}}^* = 0.4e$.

A similar treatment for the E_g mode yields:

$$\omega(E_g) = (2C_x/m_x)^{1/2}, \text{ where } C_x = C_{1x} + C_{2x}.$$

The force constants C_z and C_x are listed in Table 2 along with the frequencies $\omega(A_{1g})$ and $\omega(E_g)$. It is interesting to note that the force constants for the oxides are always considerably larger than the force constants for the corresponding sulfides. This is not surprising because the distances between the nearest anion planes, d , are considerably shorter for the oxides than for the sulfides (see Table 1). According to Loh[19] the force constants of optical phonons increase with decreasing inter-nuclear distance and with increasing amount of covalent bonding.

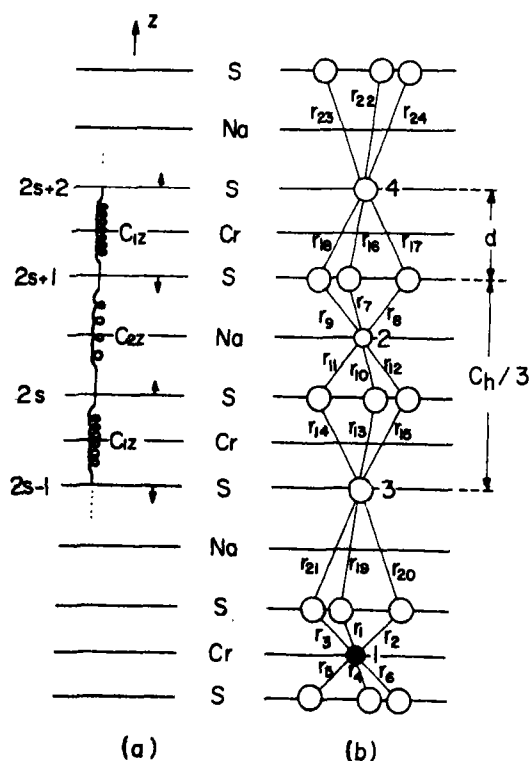


Fig. 8. (a) Force model for the A_{1g} mode used in Section 4a. (b) Local internal coordinates r_i belonging to a primitive unit cell containing the atoms Cr = 1, Na = 2, S = 3, 4; (see Section 4B).

In the present series these two effects are competing with each other because the oxides are less covalent than the sulfides but the effect of distance dominates the effect of covalency. This correlation between the force constants and the distance d is shown in Fig. 9.

(b) Normal coordinate analysis for NaCrS_2

For the potential energy of the $\mathbf{k} = 0$ modes we write

$$V = V_s + V_C$$

where V_s is the short range part due to the overlap forces between nearest ions and V_C is the long range Coulomb interaction. In terms of translationally symmetrized, mass-weighted coordinates q [20], V_s and V_C are given by

$$V_s = \frac{1}{2} q^T f q, \quad V_C = \frac{1}{2} q^T \Delta f q$$

and diagonalization of $F = f + \Delta f$ yields the

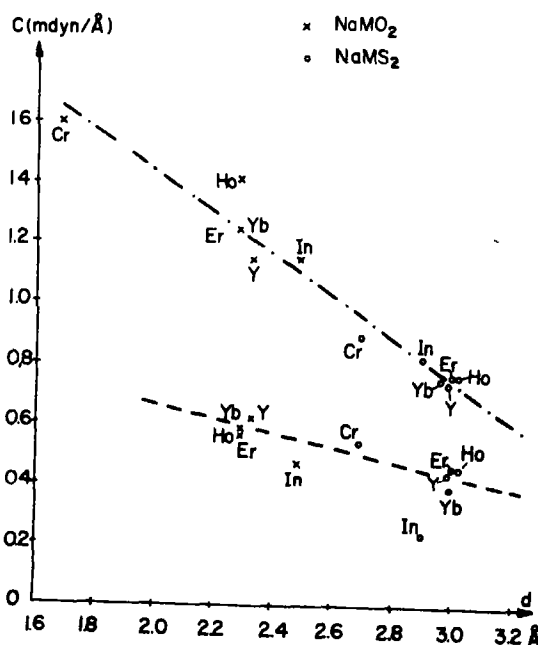


Fig. 9. Force constants C_2 (---) and C_x (-.-) for the A_{1g} and E_g modes respectively, vs. the shortest distance d between anion layers.

eigenvalues λ_k and the normal coordinates Q_k . We first neglect V_C and restrict ourselves to the short range problem.

In order to introduce only a few but physically meaningful force constants in V_s we express V_s in terms of translationally symmetrized internal coordinates $R = Aq$:

$$V_s = \frac{1}{2} R^T \phi R.$$

The matrix f is then given by:

$$f = A^T \phi A = f_x + f_y + f_z.$$

The unit cell group D_{3d} allows the decomposition into a x , y , and z problem. Diagonalization of the two 4 dimensional symmetric matrices $f_x = f_y$ and f_z yields the eigenvalues λ_k^0 and normal coordinates Q_k^0 of the short range problem.

The coordinates R_l are given by $R_l = N^{-1/2} \sum_i r_i^l$ where N is the number of unit cells in the crystal and r_i^l is the l th local internal coordinate belonging to the unit cell i . In order to obtain a reasonable approximation with a diagonal ϕ matrix a good choice of the coordinates r_i^l is essential. In the NaCrS_2 structure we introduce in each unit cell 24 stretching coordinates, namely 6 Cr-S coordinates ($l=1 \dots 6$) with force constants F_1 , 6 Na-S coordinates ($l=7 \dots 12$) with force constants F_2 , 6 S-S coordinates ($l=13 \dots 18$) with force constants f_3 , and 6 S-S coordinates ($l=19 \dots 24$) with force constants F_4 . These coordinates are defined and numbered in Fig. 8b.

The four infrared frequencies depend only on the force constants F_1 and F_2 but not on the S-S force constants F_3 and F_4 because in these modes all sulfur ions move in phase. Putting $F_1 = 0.85$ and $F_2 = 0.18$ m dyn/Å we obtain fair agreement between observed and calculated frequencies (see Table 3). On the basis of the short range approximation it is, of course, not possible to account for the observed LO-TO splitting. The Raman frequencies depend on all four force con-

stants. For NaCrS_2 , however, the S-S distances corresponding to F_4 are considerably larger than the S-S distances corresponding to F_3 (4.33 Å compared with 3.48 Å), so that F_4 will be much smaller than F_3 . Good agreement between observed and calculated Raman frequencies is obtained using the values F_1 and F_2 determined from the i.r. frequencies and putting $F_3 = 0.08$ m dyn/Å, $F_4 = 0$.

Table 3 includes also the normal coordinates $Q_k^0 = \sum_i l_{ik} \sqrt{m_i} x_i$ in terms of cartesian displacement coordinates. From the form of the normal coordinates it can be seen that in the high frequency E_u and A_{2u} modes the lattices of both cations move against the lattices of the anions producing large induced dipole moments. However, in the low frequency E_u and A_{2u} modes the Cr lattice moves against the Na lattice while the amplitudes of the anions are comparatively small. In these modes the induced dipole moments are therefore small and the intensities are expected to be weak compared with the intensities of the high frequency modes. These predictions are in agreement with the observed intensities (see Figs. 6 and 7).

In order to account for the TO-LO splitting we must include the long range part, V_C . We shall calculate Δf on the basis of the rigid ion model using effective point charges. By straightforward calculation of the Coulomb forces acting on the displaced ions we obtain

$$\Delta f_{\sigma ij} = \frac{e_i^* e_j^*}{\sqrt{m_i m_j}} S_{\sigma ij} - \delta_{ij} \frac{e_i^*}{m_i} A_{\sigma i}$$

where

$$A_{\sigma i} = \sum_k e_k^* S_{\sigma ik}, \sigma = x, y, z.$$

In these expressions e_i^* and m_i are the effective charges and masses, respectively, of ion i . $S_{\sigma ij}$ is the dipole field at site i produced by all unit dipoles at sites j oriented in the σ direction [21]. Due to the site symmetries D_{3d} and C_{3v} the elements $S_{\sigma\sigma'ij}$ with $\sigma' \neq \sigma$ vanish. The explicit expression is given by

$$S_{\sigma ij} = \sum_{l'} \frac{r_{ij}^{(l'')^2} - 3r_{\sigma}^2(i_{ij}^{(l'')})}{r_{ij}^{(l'')^5}}$$

where $r_{ij}^{(l'')}$ is the distance between the site i in unit cell l and site j in unit cell l' and $r_{\sigma}(i_{ij}^{(l'')})$ is the σ -component of this distance. Neglecting surface effects these sums are independent of the location of the unit cell l . The method we have applied for the evaluation of these sums is described elsewhere [22]. Due to the symmetry of the NaCrS₂ structure and the definition of the $S_{\sigma ij}$ -sums we have $S_{xij} = S_{yij}$ and a given matrix S_{σ} will have a number of repeated elements, namely

$$S_{\sigma} = \begin{pmatrix} S_{11} & S_{12} & S_{13} & S_{13} \\ S_{12} & S_{11} & S_{23} & S_{23} \\ S_{13} & S_{23} & S_{11} & S_{34} \\ S_{13} & S_{23} & S_{34} & S_{11} \end{pmatrix}.$$

We have used the numbering 1 = Cr, 2 = Na, 3 = S, 4 = S. The values calculated are:

$$\begin{aligned} S_{x11} &= -0.125004 \text{ \AA}^{-3} & S_{x12} &= -0.00444 \text{ \AA}^{-3} \\ S_{x13} &= -0.078283 \text{ \AA}^{-3} & S_{x23} &= -0.030299 \text{ \AA}^{-3} \\ S_{x34} &= -0.007362 \text{ \AA}^{-3} \end{aligned}$$

In order to distinguish between *TO* and *LO* phonons in NaCrS₂ we may suppose the exterior boundaries to consist of infinite parallel planes. In an uniaxial crystal with its optic axis parallel to the z axis there are two important geometries: (a) The exterior boundaries are perpendicular to the z axis; in this case we have two z polarized longitudinal A_{2u} modes and two degenerate transverse modes, corresponding to $\mathbf{k} \parallel z$ as $\mathbf{k} \rightarrow 0$. (b) The exterior boundaries are perpendicular to the x axis; in this case there are two transverse z polarized A_{2u} modes, two transverse y polarized E_u modes and two x polarized longitudinal E_u modes, corresponding to $\mathbf{k} \parallel x$ as $\mathbf{k} \rightarrow 0$. In case (b) the two fold degeneracy of the E_u modes is lifted [23].

The shape dependence of the Coulomb summation leads to the distinction between

transverse and longitudinal sums, $S_{\sigma ij}^T$ and $S_{\sigma ij}^L$, depending on whether the displacements of the ions are parallel or perpendicular to the exterior boundaries. The sums defined above are the transverse dipole sums. The sums relevant to case (a) are $S_{xij}^T = S_{yij}^T$, and S_{zij}^L , those relevant to case (b) are S_{xij}^L , S_{yij}^T , and S_{zij}^T . Using the relations $\sum_{\sigma} S_{\sigma ij}^T = -(4\pi/v)$ [24] and $S_{\sigma ij}^L = S_{\sigma ij}^T + (4\pi/v)$ [21], where v is the volume of the primitive unit cell we obtain

$$S_{zij}^L = -2S_{xij}^T = S_{zij}^T + 4\pi/v$$

$$S_{xij}^L = -S_{xij}^T - S_{zij}^T = S_{xij}^T + 4\pi/v.$$

The matrices $\Delta f_{\sigma ij}^T$ and $\Delta f_{\sigma ij}^L$ are obtained by substitution of the appropriate sums $S_{\sigma ij}^T$ and $S_{\sigma ij}^L$ in the general expression for $\Delta f_{\sigma ij}$. Diagonalization of $F_{\sigma}^T = f_{\sigma} + \Delta f_{\sigma}^T$ and $F_{\sigma}^L = f_{\sigma} + \Delta f_{\sigma}^L$ yields the eigenvalues and normal coordinates of the transverse and longitudinal modes, respectively. Table 3 contains the results of these calculations. We have found reasonable agreement between observed and calculated frequencies with the following five parameters:

$$\begin{aligned} F_1 &= 0.85, \quad F_2 = 0.18, \quad F_3 = 0.08 \text{ m dyn/\AA} \\ e_{\text{Cr}}^* &= 1.1e, \quad e_{\text{Na}}^* = 0.4e. \end{aligned}$$

The effective charge e_s^* is then given by $e_s^* = -\frac{1}{2}(e_{\text{Cr}}^* + e_{\text{Na}}^*) = -0.75e$. With these effective charges large LO-TO splittings are predicted for $\omega_1(E_u)$ and $\omega_1(A_{2u})$ but comparatively small splittings for $\omega_2(E_u)$ and $\omega_2(A_{2u})$ in agreement with the observations. No LO-TO splitting is predicted for the Raman active modes. This can be seen directly if $\lambda_k^L - \lambda_k^T$ is calculated using first order perturbation theory. One obtains

$$\lambda_k^L - \lambda_k^T = \frac{4\pi}{v} \left(\frac{\partial \mu}{\partial Q_k} \right)_0^2,$$

where the dipole derivative is given by

$$\left(\frac{\partial \mu}{\partial Q_k} \right)_0 = \sum_i l_{ik} \frac{e_i^*}{\sqrt{m_i}}.$$

For the Raman active modes $(\partial\mu/\partial Q_k)_0 = 0$ and therefore $\lambda_{R_k}^L = \lambda^T$

(c) *Discussion of the results from the normal coordinate analysis*

The effective charges $e_{Cr}^* = 1.1e$, $e_{Na}^* = 0.4e$, and $e_S^* = -0.75e$ obtained from the preceding analysis are only about one third of the formal charges of the ions. That the effective charges might be considerably smaller than the full formal charges is to be expected if one keeps in mind that the ionicity of the Cr-S bond as deduced from the difference in electronegativity is only about 20 per cent.

In order to estimate the accuracy of our effective charges we must discuss two points: (a) Our calculated effective charges depend on the short range force constants F_1 , F_2 , F_3 . Admittedly, we have used a very simple model for the short range problem, but the calculations show that the effective charges are not very sensitive to small changes in these parameters. (b) We have completely neglected the polarizabilities of the ions. However, we have shown* that the effective charges calculated on the basis of polarizable ions would be even smaller than the effective charges obtained from the rigid-ion model. In fact, the comparatively small effective charges suggest, that the valence electrons in $NaCrS_2$ are delocalized to a large extent. In such cases the electronic polarization can not be expressed in terms of point-dipole interactions; the electronic and vibrational polarizations are decoupled and it can be shown[25, 26] that the resulting relation between the static and high frequency dielectric constants is identical with that derived for a rigid-ion model. On this basis and in view of the scarcity of the experimental data a rigid-ion model seems to be appropriate for $NaCrS_2$.

It would be interesting to compare the effective charges of $NaCrS_2$ with those of

$NaCrO_2$. Unfortunately, no i.r. reflection data are available for $NaCrO_2$, but from the i.r. powder spectrum it is apparent that the TO-LO splittings of the E_g modes are at least twice as large as those for $NaCrS_2$. One would therefore expect larger effective charges for $NaCrO_2$ than for $NaCrS_2$ in accordance with the fact that the ionicity of the Cr-O bond is higher than the ionicity of the Cr-S bond.

Recently, the effective charges of a series of crystals with α - $NaFeO_2$ structure were determined from Nuclear Quadrupole Coupling Constants[27]. In this study the electric field gradients at the sodium site was calculated using a point charge model and assuming that the charge on the sodium is $+1e$; comparison with the experimental field gradients yields the effective charge on the trivalent metal ions, which is $2.08e$ for the Cr ion in $NaCrS_2$. This value is nearly twice as large as our value $e_{Cr}^* = 1.1e$. In order to explain this discrepancy we have calculated the effective charges by the *NQR*-method using our sums S_z^T . We have found complete agreement with the charges given in Ref.[27], if it is assumed that the charge on the sodium is $+1e$. But if the charge on the sodium is less than $+1e$, the *NQR*-method yields smaller charges for the trivalent metal ions. This might also explain why the charges of the trivalent metal ions in $NaCrO_2$, $NaTiO_2$, and $NaScO_2$ exceed three in Ref.[27]. In fact, if we assume that the charge on the sodium ion is only $0.8e$ in $NaCrO_2$, we obtain for the charge on the Cr ion a value of $2.0e$ instead of $3.62e$ as was obtained in Ref.[27].

Finally we should like to emphasize that we have adopted a very simple model for the analysis of the lattice modes of $NaCrS_2$. Consequently, the effective charges will not be very accurate. On the other hand, this approach leads to reasonable results for $NaCrS_2$, and it would be interesting to apply this method to other crystals for which extended experimental data are available.

*The appropriate expressions of the Δf -matrix for polarizable ions will be published later.

Acknowledgements—We wish to express our appreciation to Mrs R. Loitzl for preparing the crystals, to A.

Beck for the construction of the liquid He-cell, and to V. Fronz for technical assistance during the Raman experiments. We also thank Dr. G. R. Wilkinson from King's College, London University, who has kindly performed the far i.r. reflection measurements of NaCrS_2 and F. D'Ambrogio for developing the computer programs.

REFERENCES

1. BONGERS P. F., VAN BRAGGEN C. F., KOOPSTRA J., OMLOO W. P. F. A. M. and JELLINEK F., *J. Phys. Chem. Solids* **29**, 977 (1968).
2. ENGELSMAN F. M. R., VAN LAAR B., WIEGERS G. A. and JELLINEK F. (Preprint).
3. CARR S. L., ERDÖS P., MOULTON W. G. and ROBINSON J., *Solid State Commun.* **7**, 1673 (1969).
4. MÜLLER K. A. and BERLINGER W., *Phys. Rev.* **A5**, 503 (1968).
5. BLAZEY K. W. and ROHRER H., *Phys. Rev.* **185**, 712 (1969).
6. CAMPANION A. L. and MADIN M., *J. Chem. Phys.* **42**, 4219 (1964).
7. WYCKOFF W. G., *Crystal Structure* Second Edn, **2**, 292 (1964).
8. LOUDON R., *Proc. Phys. Soc. Lond.* **82**, 393 (1963).
9. HOPPE R. and SCHEPERS B., *Z. Anorg. Allg. Chem.* **295**, 233 (1958).
10. RÜDORFF W., and BECKER H., *Z. Naturf.* **98**, 614 (1954).
11. HOPPE R., *Bulletin de la Société Chimique de France* **4**, 1115 (1965).
12. MURAV'eva J. A., KOVBA L. M. and SPIGYN V. I., *Dokl. Akad. Nauk. SSSR* **172**, 1380 (1967).
13. RÜDORFF W. and STEGEMANN K., *Z. Anorg. Allg. Chem.* **251**, 376 (1943).
14. BOON J. W. and MacGILLAVRY C. H., *Rec. Trav. Chim.* **61**, 910 (1942).
15. HOPPE R., LIDECKE W., and FRORATH F. C., *Z. Anorg. Allg. Chem.* **309**, 49 (1961).
16. BALLESTRACCI R. and BERTAUT E. F., *Bull. Soc. franç. Minér. Crist.* **87**, 512 (1964) *Bull. Soc. franç. Minér. Crist.* **88**, 136 (1965).
17. PORTO S. P. S., GIORDMAINE J. A. and DAMEN T. C., *Phys. Rev.* **147**, 608 (1966).
18. BAK T. A., *Phonons and Phonon Interactions*, Aarhus Summer School Lectures, **281**, (1963).
19. LOH E., *Phys. Rev.* **169**, 750 (1968).
20. WILSON E. B., DECIUS J. C. and CROSS P. C., *Molecular Vibrations*, McGraw-Hill, New York **14**, (1955).
21. DECIUS J. C., *J. Chem. Phys.* **49**, 1387 (1968).
22. BRÜESCH P. and LIETZ M., *J. Phys. Chem. Solids* **31**, 1137 (1970).
23. DAMEN T. C., PORTO S. P. S., and TELL B., *Phys. Rev.* **142**, 570 (1966).
24. MÜLLER H., *Phys. Rev.* **47**, 950 (1935).
25. BRODSKY M. H. and BURSTEIN E., *Bull. Am. Phys. Soc.* **7**, (11), 214 (1962).
26. BAK T. A., *Phonons and Phonon Interactions*, Aarhus Summer School Lectures, 295-298 (1963).
27. PETERSON G. E. and BRIDENBAUGH P. M., *J. Chem. Phys.* **51**, 2610 (1969).

ELECTRICAL RESISTIVITY AND OPTICAL ABSORPTION IN EuLiH_3 AND SrLiH_3 *

J. E. GREEDAN†

Department of Chemistry, Tufts University, Medford, Mass. 02155, U.S.A.

(Received 23 April 1970; in revised form 22 June 1970)

Abstract—The electrical and optical properties of single crystals of SrLiH_3 and EuLiH_3 were investigated. Electrical resistivity measurements were carried out in the temperature range from 0 to 400°C using the van der Pauw technique. The room temperature resistivity values were 10^7 ohm-cm for both materials. The thermal activation energies observed were attributed to impurity effects. Optical transmission and diffuse reflectance measurements were made over the spectral range from 0.6 to 5.5 eV. Evidence was found for both impurity and intrinsic absorptions. For SrLiH_3 , a single intrinsic absorption was found at about 4.0 eV. Three intrinsic absorptions were found for EuLiH_3 at 2.0, 4.0 and 5.2 eV. The common absorption at 4.0 eV is attributed to the valence band, which is largely H^- in character, to conduction band transition. The two additional absorptions for EuLiH_3 are assigned to transitions between localized 4f levels located within the band gap and 5d bands in analogy with results for other divalent europium compounds.

1. INTRODUCTION

RECENT studies provide strong evidence that the newly synthesized divalent europium compound, EuLiH_3 , belongs to a growing class of materials which are ferromagnetic insulators [1]. EuLiH_3 as well as the strontium analog, SrLiH_3 , have also been obtained as reasonably pure, stoichiometric single crystals [2]. With the availability of single crystals studies of the electronic structure of both EuLiH_3 and SrLiH_3 can be initiated. This paper describes the results of electrical resistivity and optical absorption experiments using single crystals of both SrLiH_3 and EuLiH_3 .

2. EXPERIMENTAL SECTION

Electrical resistivity measurements

Electrical resistivity measurements were carried out using the van der Pauw method [3]. Flat discs suitable for use in this method were prepared by hand grinding in an argon-filled glove box the atmosphere of which was continuously gettered using Na-K liquid alloy adsorbed on CaSO_4 pellets. Unless otherwise

noted all operations and handling of the very air-sensitive crystals were carried out in such a glove box. The details of the grinding operation are essentially the same as those described later in the section on optical measurements. The discs prepared were of irregular circumference and varied in thickness from 2.4 to 0.6 mm.

Ohmic contacts to crystals of both materials could be obtained with regularity by vapor deposition of indium metal under high (10^{-6} torr) vacuum. Ohmic contacts could not be made by simply painting with some standard electronic silver paint or paste. Contacts made by vapor deposition of zinc metal were usually not ohmic at room temperature but sometimes became ohmic above 300°C under a hydrogen atmosphere.

The crystal under measurement was placed on the mica platform of an all aluminum sample holder. Electrical contact from the four crystal electrodes to the four firmly held, well insulated electrode wires was made by a strip of silver paste. Sample temperatures were monitored using a thermocouple placed in a well about 1 mm below the sample.

For reasons mentioned earlier it was necessary to contain the sample and sample holder

*This work was supported by the U.S.A.E.C.

†Present address: Department of Chemistry, University of Pittsburgh, Pittsburgh, Pennsylvania 15213, U.S.A.

in an anaerobic enclosure in order to carry out the resistivity measurements. Such an enclosure was constructed from a borosilicate glass tube fitted with a high vacuum electrical feed-through and a stopcock suitable for evacuation or filling with hydrogen. Access to the tube was gained by means of a standard glass-to-glass joint sealed with a rubber o-ring. Measurements were always carried out under ultra pure hydrogen at slightly greater than one atmosphere of pressure.

A 67 1/2 V battery and a variable resistor were used as the power supply. Currents were measured with an RCA WV-84C microammeter and voltages with a model 610B Keithley electrometer. The electrical measurements were carried out over the temperature range from 0 to 400°C. A commercial tube furnace was used as the constant temperature bath. Thermal control to about $\pm 1^\circ\text{C}$ was obtained using an on-off type thermal controller and a constant voltage regulator. A total of eight measurements were made at each temperature. The voltage drop was recorded for two different current levels at each of the two positions required in the van der Pauw method and for both current polarities. Measurements could not be carried out above 400°C because of apparent deterioration of either the silver paste connections or the evaporated contacts.

Optical transmission measurements

Reasonably flat samples suitable for optical transmission measurements could be prepared using the manual grinding and polishing techniques described below. To provide the working surface for the grinding operation a hard silk cloth (Beuhler) was bonded to a section of flat plate glass using rubber cement. The abrasive compound was 600 or 800 mesh alumina suspended in paraffin oil. During the grinding and polishing operations the crystal was firmly fastened to the flat end of cylindrical rod of aluminum which in turn fit snugly into a larger cylindrical block also of aluminum which provided easy manipulation of the

sample over the working surface. A thermoplastic resin, picoline wax, generously supplied by Dr. Ronald Goldner, was used to fix the crystal to the holder described above. This wax was soluble in various hydrocarbon solvents such as trichloroethylene, benzene, and xylene. Because of its low volatility, xylene presented fewer problems for use in the glove box.

Some comment concerning the preparation of the xylene and paraffin oil for use on these highly reactive crystals is in order. First the liquids were shaken in a closed flask with molecular sieves to remove any traces of water. Then they were contained in glass vessels equipped with two sidearms, one attached to a high vacuum system and the other equipped with a breakseal. Liquid nitrogen was used to freeze the liquids, the vessel was evacuated to about 10^{-5} torr, and the liquid was permitted to thaw under high vacuum. This cycle was repeated five to ten times in order to remove traces of dissolved air. The final step involved freezing the solvent and sealing the vessel under high vacuum. Once transfer to the glove box was completed, the liquid could be dispensed through the breakseal.

When an appropriate thickness had been reached by grinding the polishing operation was commenced. Beuhler's Sylvet cloth bonded to plate glass was used as the working surface. The polishing materials were 0.3 micron and 0.06 micron alumina suspended, again, in paraffin oil. Each crystal surface was given approximately 500 laps with each polishing solution using a figure-eight motion. Every effort was made to give each surface a consistent polish.

Using the above methods four crystals each of SrLiH_3 and EuLiH_3 ranging in thickness from about 400 to 40 microns and of 2 to 4 mm^2 in surface area were prepared. It was very difficult to obtain crystals thinner than about 100 microns due to the brittleness of these materials. Samples thicker than 100 microns could be measured using a micrometer; how-

ever, for the very thin samples an extrapolation technique was used. Assuming that at a given wavelength $T = (1 - R)^2 e^{-\alpha d}$ where T is the transmittance, R is the reflectance, α is the absorption coefficient, and d is the sample thickness, plots of $\log T$ vs. d for a series of selected frequencies could be constructed using data accumulated for thicker samples. The thickness of the unknown crystal could then be estimated by measuring T at some convenient wavelength and extrapolating using the above mentioned curves to find d .

The actual transmittance measurements were carried out using a Perkin-Elmer 450 spectrophotometer and an evacuable sample cell.* The sample cell consisted of a glass cylinder of a size convenient to fit into the cylindrical cell holder of the spectrophotometer with a high vacuum stopcock and two quartz windows. One window is permanently sealed with high vacuum cement and the other with a low softening-point wax to permit easy access to the sample which is attached to the inside wall of the detachable window by a dab of wax. This cell could be evacuated to about 10^{-6} torr and all measurements were carried out at this level of vacuum.

Diffuse reflectance measurements

To supplement and extend the transmittance data diffuse reflectance measurements were carried out on powdered samples of SrLiH_3 and EuLiH_3 . Powdered EuLiH_3 is brick-red in color while SrLiH_3 powders tend to be a very pale beige, almost colorless. The powders were protected from the atmosphere during measurement by means of a simple but effective device. The samples were bound to a strip of masking tape which had an adhesive surface on both sides. One side of the tape strip (7 mm \times 20 mm) was bound to a flat

piece of microscope slide. A rectangular quartz plate (10 mm \times 25 mm) was placed directly over the sample and the space between the quartz plate and the backing glass was sealed using a quick hardening black wax with a low softening point. In such a cell the powdered samples which are extremely reactive could be handled outside of the glove box atmosphere for days at a time without noticeable deterioration.

The reflectance spectra were obtained using a commercial reflectance accessory manufactured by Perkin-Elmer for use with the model 450 spectrophotometer. Strictly speaking this attachment is best used for specular reflectance studies; however, satisfactory diffuse reflectance spectra could also be obtained. A Bausch and Lomb Spectronic 20 diffuse reflectance attachment was also available but the range and resolution of this instrument is inferior to that of the Perkin-Elmer instrument. Spectra in the visible range (1.8–3.0 eV) obtained on both instruments differed quantitatively in the magnitude of the reflectance effect but were in very good agreement regarding the position and shape of absorption peaks. The reflectance standard used in all cases was MgO of high purity contained in a cell identical to those used in containing the hydrides.

3. RESULTS AND DISCUSSION

Resistivity measurements

The results of the resistivity measurements, plotted as $\log \rho$ vs. $1/T$, for EuLiH_3 and SrLiH_3 crystals are shown in Figs. 1 and 2 respectively. First note that the room temperature resistivities are fairly high and very similar for both materials, 4×10^7 ohm-cm for SrLiH_3 and 1.5×10^7 ohm-cm for EuLiH_3 . Secondly note that the data as plotted form three distinct straight-line regions for both materials. Both of these points merit further discussion.

The occurrence of such a relatively high value for the resistivity of crystals which are known to be rather impure by ordinary elec-

*According to specifications quoted by the manufacturer the spectral band pass of the Perkin-Elmer 450 under the conditions of operation in this work was less than 10^{-3} eV or 8 cm^{-1} .

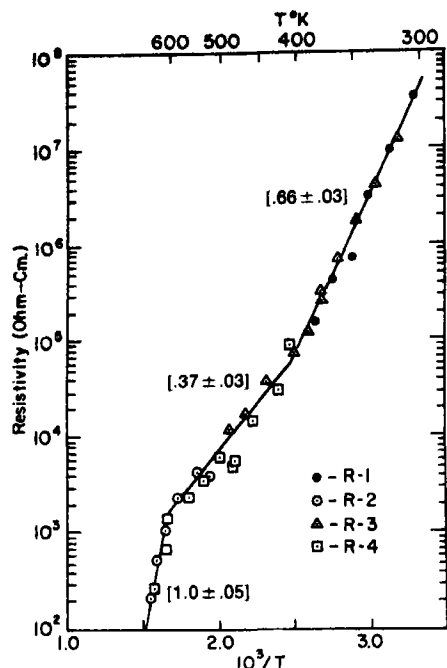


Fig. 1. Temperature dependence of the resistivity for SrLiH_3 . The numbers in brackets are activation energies in eV.

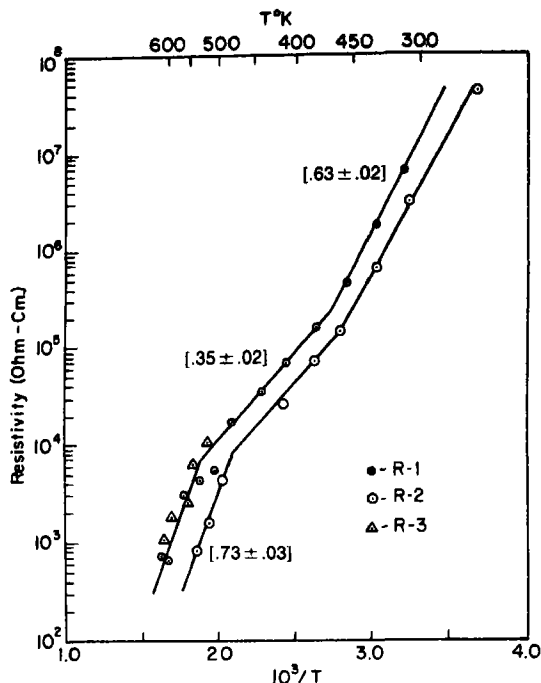


Fig. 2. Temperature dependence of the resistivity for EuLiH_3 . The numbers in brackets are activation energies in eV.

tronic standards is mildly surprising. Some estimate of the concentration of free carriers, n , present at room temperature in these crystals can be obtained by assuming reasonable values for carrier mobility. If the mobility, μ , in these hydrides is not too different from those found in other divalent europium magnetic semiconductors, then a value of $10 \text{ cm}^2 \text{ V}^{-1} \text{ sec}^{-1}$ at around room temperature is not unreasonable. Assuming, perhaps naively, that $\rho \sim (ne\mu)^{-1}$ a free carrier concentration at room temperature of $n \approx 6 \times 10^{10} \text{ cm}^{-3}$ can be estimated. The explanation for this rather low value of n can probably be found in an interplay of two factors; the predominance of deep-lying impurity levels over shallow levels, i.e. over levels so shallow as to be completely ionized at room temperature, and the presence of considerable donor-acceptor compensation evidence for which is presented in the following paragraph.

Figures 1 and 2 also show the activation

energies calculated by least squares from the slope of the $\log \rho$ vs. $1/T$ plots for each of the three distinct thermal regions. Ignoring the highest temperature range for a moment, notice that the activation energies in the lower two ranges are approximately the same in both hydrides. This suggests that the particular impurity or defect active in this region is common to both. Furthermore, the activation energy in the lowest range is approximately double that in the middle range. This behavior is characteristic of a compensated semiconductor[4]. It is tempting to assume that the data obtained in the highest temperature range studied represent intrinsic conductivity in both materials. Such an assumption can be dangerous, particularly since the thermal range covered in the measurements is narrow, the known impurity levels in these materials are fairly high, and also nothing is known regarding the tendency of these hydrides to change chemical composition at elevated tempera-

tures. Granting the above we can cautiously calculate band gaps from the thermal data assuming $E_{\text{act}} = E_{\text{gap}}/2$. These gaps are 2.1 ± 0.1 eV for SrLiH_3 and 1.46 ± 0.06 eV for EuLiH_3 .

There is one further point worthy of discussion before leaving the electrical results. One sample of EuLiH_3 , sample R-2 (Fig. 2), was annealed for about 100 hr, at 700°C in 3 atm. hydrogen before taking resistivity measurements. The absolute values for this sample were somewhat lower by about a factor of two or three than the values obtained for the other two unannealed samples cut from the same parent crystal but the activation energies in all three ranges were apparently not changed. This increase in conductivity upon annealing might be related to an improvement in crystalline perfection during the annealing process or to a slight change in chemical composition.

Diffuse reflectance and optical absorption measurements

Due to difficulties in preparing very thin single crystal samples of both materials it was not possible to scan the available spectral range using optical transmittance measurements. Diffuse reflectance measurements on powdered samples of SrLiH_3 and EuLiH_3 were carried out in order to fix the position of strong absorption effects which can then be investigated in more detail using single crystals. The results of the diffuse reflectance measurements are shown in Fig. 3. The data are plotted in terms of the Kubelka-Munk function[5], $f(r) = (1-r)^2/2r = \alpha/s$, where r is the ratio of the sample reflectance to the MgO reflectance, α is the usual absorption coefficient, and s is a scattering coefficient. The scattering coefficient varies smoothly with energy, so $f(r)$ provides a qualitative picture of the energy dependence of the absorption coefficient. Note that SrLiH_3 shows only a single strong absorption peak in the vicinity of 4.0 eV. EuLiH_3 on the other hand shows three peaks, a very strong, broad

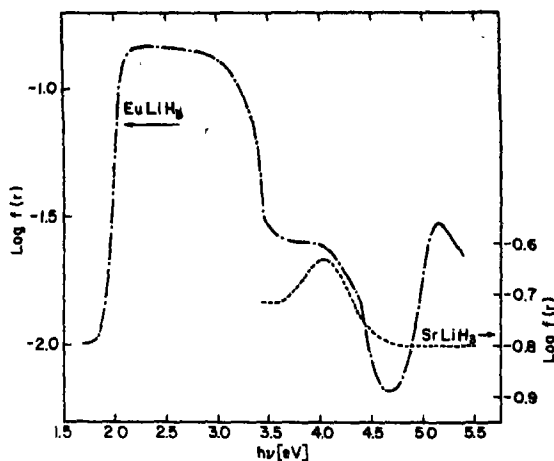


Fig. 3. Diffuse reflectance spectra of EuLiH_3 and SrLiH_3 .

absorption beginning sharply at about 2.0 eV and extending through the visible, a shoulder on the visible peak centered at about 4.0 eV, and a relatively sharp peak at 5.15 eV.

More quantitative information regarding the magnitude and energy dependence of these absorption edges as well as information on absorption occurring at energies lower than the edges can be obtained from the single crystal transmittance data. Values of the absorption coefficient were derived from transmittance data using the approximation, $T = (1-R)^2 e^{-\alpha d}$, where T is the transmittance, R the perpendicular reflectance, α the absorption coefficient (in cm^{-1}), and d the crystal thickness. The procedure used in the calculation of α was to feed the measured transmittance data for each of the six possible pairs of crystals (data were collected using four crystals of each material) into the following relationship: $\alpha = 1/(d_1 - d_2) \ln T_2/T_1$ from which an average value of α for each energy was determined. The uncertainty in the values for the absorption coefficient obtained in this manner is estimated to be from 10 to 20 per cent.

The absorption spectra of SrLiH_3 and EuLiH_3 are shown in Fig. 4. Note first of all that α rises sharply to the largest value measurable in these experiments, about 1000

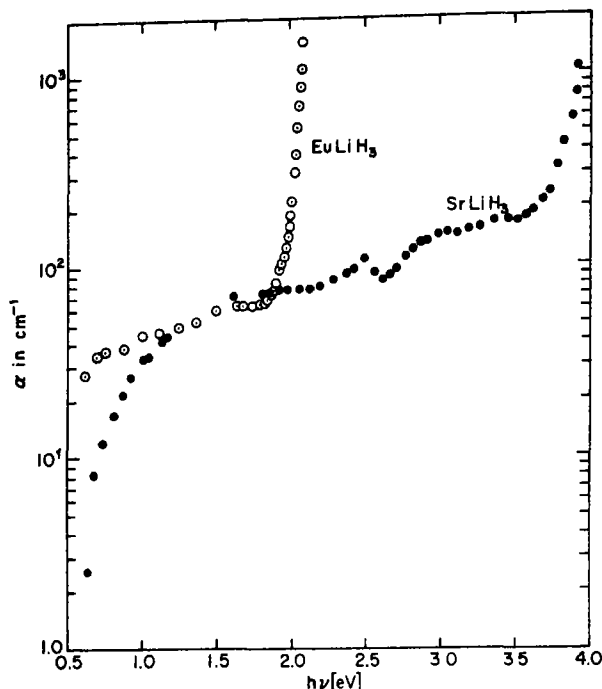


Fig. 4. Absorption spectra of EuLiH_3 and SrLiH_3 .

cm^{-1} , in the vicinity of 4.0 eV for SrLiH_3 and 2.0 eV for EuLiH_3 in excellent agreement with the reflectance data. This behavior suggests the occurrence of an absorption edge in each material at these respective energies. These findings are not in agreement with the band gaps derived from electrical resistivity data mentioned earlier (2.1 eV for SrLiH_3 , 1.5 eV for EuLiH_3) and it appears that the activation energies measured in the high temperature regions for both materials are probably due to impurities. Note also evidence for structure in the absorption coefficient at low energies in both compounds. This is most marked in the spectrum of SrLiH_3 where the absorption coefficient rises sharply at about 0.6 eV from a value of 3 cm^{-1} and attains a level value of 70 cm^{-1} until 2.5 eV where there is a distinct peak ($\alpha = 100 \text{ cm}^{-1}$) followed by a somewhat broader peak centered at about 3.0 eV. Similar behavior is seen in the low energy spectrum of EuLiH_3 . This structure can be attributed to the presence of deep-lying impurity centers

which, lacking more extensive experimental study, must remain unidentified.

A more detailed picture of the absorption edge in EuLiH_3 is afforded by examination of Fig. 5. Here the absorption coefficient in the region of the absorption edge, corrected for the flat background absorption in the region just below the edge, is plotted against an expanded energy scale. Note the apparent existence of two distinct regions, that extending from 1.82 to about 2.02 eV in which α rises slowly to about 100 cm^{-1} and that beginning at 2.02 eV in which α increases from 100 cm^{-1} to greater than 1000 cm^{-1} through about 0.05 eV. This behavior is in contrast to the behavior of the absorption edge in the europous monochalcogenides, which, according to Methfessel *et al.*[6], follows an exponential law even for low values of the absorption coefficient. Actually, there is some confusion on this point as in an earlier publication[7] the same authors claim that the absorption edge for EuSe follows the usual

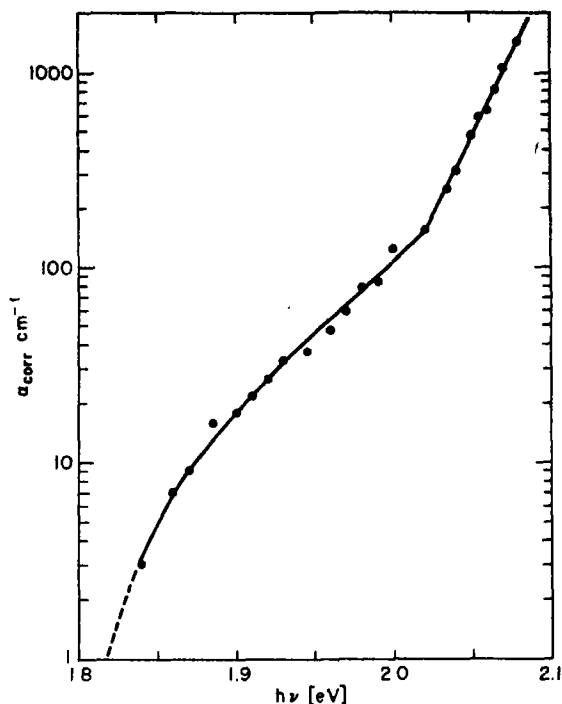


Fig. 5. Absorption spectrum of EuLiH_3 corrected for background in the region of the absorption edge.

$(h\nu)^{1/2}$ dependence predicted for direct transitions. Note from Fig. 5 that the absorption coefficient for EuLiH_3 appears to follow an exponential law from about 100 cm^{-1} to the limit of these measurements which was slightly greater than 1000 cm^{-1} . However, as indicated in Fig. 6, the energy dependence of the edge can also be fit to an $(h\nu)^{1/2}$ law with an extrapolated direct gap of 2.06 eV using essentially the same data. Additional data involving absorption coefficients in the region greater than 10^3 cm^{-1} are needed to aid in settling this matter of the energy dependence of the high energy region of the absorption edge in EuLiH_3 . The low energy portion of the EuLiH_3 absorption edge could be due to impurity absorption or to the presence of phonon-assisted indirect transitions or even parity-forbidden direct transitions. The preparation of new crystals of EuLiH_3 , perhaps using a different growth technique, would be useful in order to determine whether or not

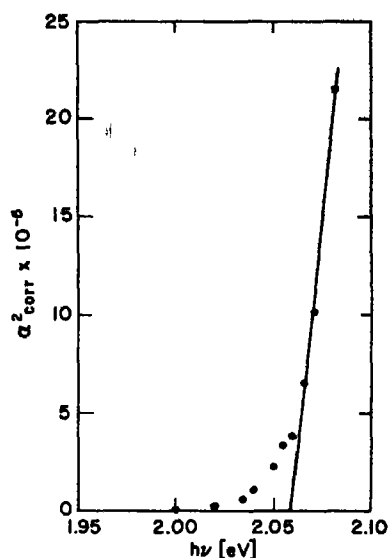


Fig. 6. Evidence for an $(h\nu)^{1/2}$ dependence of the absorption edge in EuLiH_3 .

the low energy portion of the edge in EuLiH_3 is due to impurities or is an intrinsic property of this material.

A detailed analysis of the edge region of SrLiH_3 was precluded by the extensive impurity absorption in this material. The absorption data of SrLiH_3 as obtained in this work are, however, suggestive of an energy gap at energies greater than about 3.9 eV .

The gross features of the electronic structures of SrLiH_3 and EuLiH_3 can be represented by the simple band scheme presented in Fig. 7. The valence band for both hydrides is undoubtedly of $1s$ character as there are of course no p electrons in H^- . The common absorption at 4.0 eV is probably due to a transition from the valence band to a conduction band which is probably $\text{Li-}2s$ -like in character, at least for SrLiH_3 . The absorption edge for LiH , an electronically similar material, occurs at slightly below 5 eV [8]. The constitution of the conduction band in EuLiH_3 is likely to be more complicated than in SrLiH_3 or in other binary europous compounds due to the importance of $5d$ and $6s$ europium orbitals as well as lithium $2s$ orbitals.

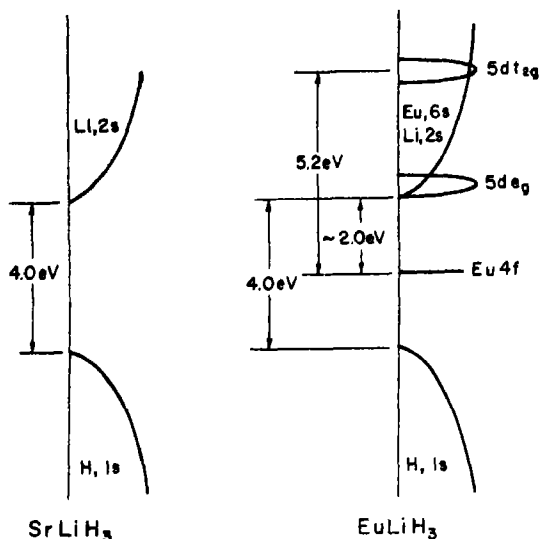


Fig. 7. Proposed band schemes for EuLiH_3 and SrLiH_3 .

The studies described here shed no light on the nature of the conduction band in EuLiH_3 .

Tentative assignment of the additional absorptions found in EuLiH_3 which are not found in SrLiH_3 can be made with reference to the extensive body of experimental and theoretical results which exist for the europous monochalcogenides and other divalent europium compounds[9]. The common feature of the absorption spectrum of cubic compounds containing Eu^{+2} whether concentrated or dilute is the presence of two strong peaks occurring somewhere between 1 to 6 eV[6, 9]. There is general agreement that these two peaks have their origin in transitions from localized 4f orbitals which are situated in the gap between the valence and conduction bands to a narrow 5d band which is split by the cubic crystal

field into sub-bands of e_g and t_{2g} symmetry [10]. In perovskite symmetry the e_g band will be lower in energy than the t_{2g} band. It is reasonable then, to conclude that the edge at about 2.0 eV and the peak centered at 5.15 eV are due to 4f to 5d (e_g) and 4f to 5d (t_{2g}) transitions respectively. The unusually broad absorption following the 2 eV edge suggests that other effects may also be important in this region.

Acknowledgments—The author acknowledges useful discussions with Drs. T. R. P. Gibb, Jr. and R. Goldner. The author is also indebted to Dr. Goldner for the use of laboratory facilities.

REFERENCES

1. GREEDAN J. E., **32**, 819 (1971).
2. GREEDAN J. E., *J. Cryst. Growth*, **6**, 119 (1970).
3. VAN DER PAUW L. J., *Philips Res. Rep.* **13**, 1-9 (1958).
4. See for example, KITTEL C., *Introduction to Solid State Physics*, 3rd edition, pp. 312, John Wiley, New York (1967), or HANNAY N. B., *Solid State Chemistry*, p. 84, Prentice Hall (1966).
5. See WENDLANDT W. W. and HECHT H. G., *Reflectance Spectroscopy*, Chapter 3, for a complete discussion of the Kubelka-Munk function, Interscience, New York (1966).
6. FREISER M. J., HOLTZBERG F., METHFESSEL S., PETTIT G. D., SHAFER M. W. and SUITS J. C., *Helv. Phys. Acta* **41**, 832 (1968).
7. HOLTZBERG F., MCGUIRE T. R., METHFESSEL S. and SUITS J. C., *Phys. Rev. Lett.* **13**, 18 (1964).
8. PRETZEL F. E., RUPERT G. N., MADER C. L., STROMS E. K., GRITTEN G. V. and RUSHING C. C., *J. Chem. Phys. Solids* **16**, 10 (1960).
9. METHFESSEL S., and MATTIS D. C., in *Handbuch der Physik* (Edited by S. Flügge) Vol. 18, Pt. 1, p. 389, Springer-Verlag, Berlin, Germany (1968). This reference and Ref. [6] provide a detailed summary of the available optical data on europous compounds.
10. FEINLEIB J., SCOULDERS W. J., DIMMOCK J. O., HAUNS J., REED T. B. and PIDGEON C. R., *Phys. Rev. Lett.* **22**, 1385 (1969).

THE SPECIFIC HEAT OF RbMnF_3 AND MnF_2 BETWEEN 0.5 AND 4.2°K

A. J. HENDERSON, Jr.* and H. MEYER†

Department of Physics, Duke University, Durham, N.C. 27706, U.S.A.

and

H. J. GUGGENHEIM

Bell Telephone Laboratories, Murray Hill, N.J. 07971, U.S.A.

(Received 8 June 1970)

Abstract—Measurements have been made of the specific heats of RbMnF_3 and MnF_2 both for single crystals (5–20 g) and for sintered material with particle sizes of the order of $10\ \mu$. No conclusive effect of particle size on the specific heat was observed, which is consistent with theoretical predictions. A difference in the specific heats of two single crystals of RbMnF_3 are attributed to differences in preparation. An analysis of the specific heat has been made in terms of the sum of contributions from the lattice vibrations (C_L), the magnetic spin-waves (C_M) and the nuclear hyperfine splittings (C_N). For RbMnF_3 , the contribution ($C_L + C_M$), which is proportional to T^3 , is 14 per cent larger than that predicted using data from other experiments. The term C_N , proportional to T^{-2} , is about 5 per cent larger than predicted from the 'unpulled' NMR frequency of ^{55}Mn nuclei. For MnF_2 , analysis gives very good agreement with the predictions for C_M and C_N using parameters obtained from AFMR, NMR and neutron scattering experiments. The Debye theta is $463 \pm 5^\circ\text{K}$, compared with $475 \pm 10^\circ\text{K}$ calculated from the elastic constants by Melcher.

1. INTRODUCTION

MEASUREMENTS have been made of the low temperature specific heats of the antiferromagnets RbMnF_3 and MnF_2 . The results are analyzed in terms of the contributions from the lattice and spin-wave modes, and the nuclear hyperfine field. The reasons for this study have been twofold. First, it was hoped to detect surface effects by a comparative study of large single crystals and very fine powders. The incentive for this research came from the theoretical predictions for surface effects [1–12] and also from an anomalously large, and as yet unexplained, excess in the measured specific heat of sintered samples of several iron garnets between 0.5 and 4.5°K [13].

The second reason was to improve upon, and extend to lower temperatures, previous measurements on these two antiferromagnets [14, 15]. The reanalysis includes the results of recent measurements of the elastic constants [16, 17] to estimate the lattice specific heat.

Sintered samples of powder were prepared from the same material as the single crystals. Within the sample, particle sizes ranged from about 5 to $30\ \mu$. No evidence is observed above 2°K of enhanced specific heats due to surface effects. Below 2°K the contribution to the total specific heat from the hyperfine field the ^{55}Mn nuclei becomes so large that it masks any possible surface effects. Without this h.f.s. contribution, the magnetic surface contribution should be detectable at temperatures below about 1.2°K for MnF_2 [9].

For MnF_2 the analysis of the bulk specific heat gives excellent agreement with the predictions from theory and with parameters

*Now at General Electric Co., Hendersonville, N.C. 28739 U.S.A.

†The part of the research carried out at Duke University was supported by a Grant from the Army Research Office, Durham, N.C. and by a Contract from the Office of Naval Research.

determined from other experiments. For RbMnF_3 , however, serious discrepancies between the analysis of the experiment and the predicted behavior exist that cannot be explained at this time.

2. REVIEW OF THEORY FOR THE BULK SPECIFIC HEAT

It is assumed that the specific heat is the sum of the three terms

$$C = C_L + C_M + C_N$$

which are respectively the contribution from the lattice vibrations, from the magnetic interactions and from the hyperfine field at the nuclei.

(a) The bulk lattice contribution

For temperatures $T < \Theta_D/50$ where Θ_D is the Debye temperature, the molar lattice specific heat is given by

$$C_L = 234 r R (T/\Theta_D)^3 \quad (1)$$

where r is the number of atoms per unit cell and

$$k_B \Theta_D = h |q_{\max}| \bar{v}.$$

Here $|q_{\max}|$ is the radius of the Debye sphere

$$|q_{\max}| = \left(\frac{3r N}{4\pi V} \right)^{1/3}.$$

The average sound velocity \bar{v} is obtained from the expression

$$(\bar{v})^{-3} = \frac{1}{3} \sum_{i=1}^3 \int v_i^{-3} \frac{d\Omega}{4\pi}. \quad (2)$$

The velocities v_i are respectively a longitudinal and two transverse ones, and the integration is over all propagation directions.

The three low temperature elastic constants of RbMnF_3 have been measured by Melcher and Bolef[16]. The Debye temperature and corresponding molar lattice contribution C_L for these values are shown in Table 1.

The elastic constants of MnF_2 were recently

Table 1. Parameters for comparison to the specific heat results for RbMnF_3

Quantity	Value	Source	Ref.
r	5		
Θ_D	386.4 ± 1.5 (°K)	Sound velocity at 4.2°K from Θ_D above	[16]
C_L/RT^3	20.3×10^{-6}		
Structure	Perovskite		
z	6		
S	$\frac{1}{2}$		
A_1	$3^{3/2}$	Spin-wave theory	[21]
J_1/k_B	-4.0 ± 0.1 (°K)		
	-3.3 ± 0.04	from AFMR	[22]
J_1/k_B	-3.4 ± 0.3 (°K)	High Temperature Susceptibility	[23]
J_2/k_B	0.0 ± 0.2	neutron diffraction	[24]
J_3/k_B	0.0 ± 0.4		
(1) H_r	890 ± 20 (kOe)	AFMR	[22]
(2) H_e	760 ± 60 (kOe)	from neutron diffraction	[24]
H_a	4.47 ± 0.04 (Oe)	AFMR	[22]
T_D	0.11 (°K)	from H_r and H_a above	[24], [22]
$^{55}\text{Mn} \left\{ \begin{array}{l} I \\ \Delta/k_B \end{array} \right.$	$5/2$ 0.0330 (°K)	NMR, NDR from NMR, NDR results	[33], [34]
$C_N T^2/R$	3.18×10^{-3}		

determined by Melcher[17] at various temperatures and these values were extrapolated to 0°K giving $\Theta_D = 475 \pm 10^\circ\text{K}$ [18]. This value is used to obtain that of C_L given in Table 2. Another recent measurement of the elastic constants has been carried out by Ikushima[19] at 77.4°K, and his results are consistent within a few per cent with those of Melcher.

(b) *The bulk magnetic contribution*

For a review of the spin-wave theory of magnetism, the reader is referred to the detailed article by Keffer[20].

In zero applied field, the gap for an anti-ferromagnet between the ground state and

the acoustic spin-wave mode at $\mathbf{k}=0$ is given by

$$k_B T_u = g\mu_B (H_a^2 + 2H_a H_e)^{1/2} \quad (3)$$

where H_a is the anisotropy field and $H_e = (2zJS)/g\mu_B$ is the exchange field. The symbols g and μ_B denote the gyromagnetic ratio and the Bohr magneton, z is the number of neighbors, J is the exchange parameter, and S is the spin. In the limit of low temperatures, the specific heat is given by

$$C_M/N_s k_B = A_l \frac{4\pi^2}{15} \left(\frac{T}{T_e}\right)^3 \mathcal{C}(x, H) \quad (4)$$

where N_s is the total number of spins, A_l is a geometrical factor, $T_e = g\mu_B H_e/k_B$ and $\mathcal{C}(x, H)$

Table 2. Parameters for comparison to specific heat results for MnF_2

Quantity	Value	Source	Ref.
r	6		
Θ_D	$\begin{cases} 458^\circ\text{K}^{(a)} \\ 475 \pm 10^{(a)}^\circ\text{K} \end{cases}$	Specific Heat near 1.7°K Elastic constants at 77°K	[15] [17], [18]
C_L/RT^3	13.0×10^{-6}	from $\Theta_D = 475^\circ\text{K}$	
Structure	Rutile	X-Rays and Neutrons	[19], [25]
z	8		
S	$\frac{1}{2}$		
A_l	4	Spin-wave theory	[21]
J_2/k_B	-1.76°K	at 1°K	[27]
J_1/k_B	$+0.32 \pm 0.01^\circ\text{K}$	Neutron scattering	[28], [29]
J_2/k_B	$-1.76 \pm 0.01^\circ\text{K}$		
J_3/k_B	$-0.05 \pm 0.01^\circ\text{K}$		
T_c	70.5°K	Calculated for $J_2/k_B = -1.76^\circ\text{K}$	
T_a	1.06°K	χ_1 at 1°K	[27]
T_u	$12.54 \pm 0.07^\circ\text{K}$	AFMR	[32]
	$12.8 \pm 0.6^\circ\text{K}$	AFMR	[30]
	$12.3 \pm 0.6^\circ\text{K}$		
	$12.5 \pm 0.3^\circ\text{K}$	High Field Magnetization	[31]
$^{55}\text{Mn} \left\{ \begin{matrix} I \\ \Delta/k_B \end{matrix} \right.$	$\begin{matrix} \frac{5}{2} \\ 0.0322^\circ\text{K} \end{matrix}$	NMR	[37], [38]
$^{19}\text{F} \left\{ \begin{matrix} I \\ \Delta/k_B \end{matrix} \right.$	$\begin{matrix} \frac{1}{2} \\ 0.0077^\circ\text{K} \end{matrix}$	NMR	[36]
$C_N T^2/R$	3.06×10^{-3}	Calculated from NMR results	

^(a)The definition of Θ_D used in this paper differs by $(6^{1/3})$ that of Ref. [15].

is a function of the energy gap $x = T_g/T$, and of H , the field. When $H = 0$ one obtains

$$\mathcal{C}(x, H) = \frac{15}{8\pi^4} x^4 \sum_{p=1}^{\infty} [K_2(px) + K_4(px)]. \quad (5)$$

The functions $K(px)$ are modified Bessel functions. In the limit where $x \ll 1$ the function $\mathcal{C}(x) = 1$. In the other extreme when $x \rightarrow \infty$ the specific heat expression becomes

$$C_M/k_B N_s = A_l \left(\frac{H_a}{H_e} \right)^{7/4} \left(\frac{T_g}{T} \right)^{1/2} \exp(-x). \quad (6)$$

The structure of RbMnF_3 is Perovskite. The manganese ions are located on the corners of a simple cubic lattice. The magnetic unit cell is like NaCl for which Kubo[21] finds $A_l = 3^{3/2}$. The measurements of Teaney, Freiser and Stevenson[22] give $H_a = 4.47$ Oe and $H_e = 890$ kOe. From this, one calculates $T_g = 0.12^\circ\text{K}$. Using the more recent value $H_e = 760$ kOe from susceptibility[23] and neutron scattering work[24] one obtains $T_g = 0.11^\circ\text{K}$ as shown in Table 1. Hence the quantity $\mathcal{C}(x)$ equals unity over the entire range of the specific heat measurements. As a result, no departures from a T^3 behavior should be observable for C_M . The relative sizes of the T^3 lattice and spin-wave contributions to the specific heat can be compared for RbMnF_3 using equations (1) and (4):

$$\frac{C_M}{C_L} = \frac{13.7}{234} \frac{r'}{r} \left(\frac{\Theta_D}{T_g} \right)^3 = 0.68. \quad (7)$$

Here (r'/r) is the ratio of magnetic to non-magnetic ions per molecule. From Table 1, $\Theta_D = 386^\circ\text{K}$ and $H_e = 760$ kOe (or $T_g = 100^\circ\text{K}$) so the ratio is 0.68, as shown.

The unit cell of MnF_2 has a rutile structure [19, 25] with the magnetic ions in a body centered tetragonal configuration in which $c/a = 0.68$. This structure can be reduced mathematically to a body-centered cubic structure (like CsCl) in k -space by an appropriate substitution[26]. The geometrical factor

of equation (4) is [21] $A_l = 4$. The nearest neighbor spins along the c -axis ($z_1 = 2$) are weakly coupled ferromagnetically. The dominant interaction is that between the next nearest neighbor spins ($z_2 = 8$) and is antiferromagnetic[27-29] (Table 2). Among several determinations of the energy gap [30-32] in the low temperature limit, the most accurate one is that obtained by Johnson and Nethercot[32], $T_g = 12.54^\circ\text{K}$. For measurements in the liquid helium temperature range, the argument x of equation (5) varies between about 3 and 12. The function $\mathcal{C}(x)$ no longer be approximated by a simple expression. Instead, it has been evaluated numerically.

(c) The nuclear specific heat

In systems with strongly ordered electron spins, it is quite common to find steady effective fields H_N at the sites of the nuclei. Such fields need not be the same at every atom in the crystal, but will be identical at equivalent sites α . For an isotope j at the site with nuclear spin I_j and magnetic moment μ_j , there will be $(2I_j + 1)$ nuclear levels with a separation between them of

$$\Delta_{j,\alpha} = 2\mu_j H_{N,\alpha} / 2I_j.$$

For the case where $\Delta_{j,\alpha} \ll k_B T$, the specific heat is given by

$$C_N T^2 / R = \sum_{\alpha} \sum_j a_{\alpha} a_j \frac{I_j(I_j + 1)}{3} \left(\frac{\Delta_{j,\alpha}}{k_B} \right)^2 \quad (8)$$

where a_{α} and a_j represent the concentrations respectively of sites with field $H_{N,\alpha}$ and those with isotopic species j .

Let us first consider the case for RbMnF_3 . One can calculate C_N from low temperature NMR frequencies. The nuclei that have a spin are F^{19} for which $I = \frac{1}{2}$ and ^{55}Mn for which $I = \frac{5}{2}$. Both isotopes occur with 100 per cent abundance. The effective h.f.s. field at the F^{19} nuclei is averaged out for zero applied field because of the symmetry of the two manganese sublattices. Interpretation of the

^{55}Mn NMR measurements is complicated because of pulling effects between the nuclear and electron spin systems that act like coupled oscillators. The 'unpulled' nuclear hyperfine frequency $\omega_N/2\pi$ was found to be 686.2 MHz by Heeger and Teaney[33]. This is consistent with double resonance measurements by Ince[34] who obtained value of 687.8 MHz. A detailed theoretical and experimental study of coupled AFMR and NMR has been done by Ince[35]. It is the unpulled frequency that should be relevant in specific heat measurements[36], at least in the high temperature limit ($k_B T \gg \hbar\omega_N$), and it corresponds to $\Delta/k_B = 0.0330^\circ\text{K}$. Based on the NMR results, then, the specific heat per mole RbMnF_3 is

$$\frac{C_N T^2}{R} = 3.18 \times 10^{-3}.$$

For MnF_2 , there is an effective field acting on both the F^{19} and ^{55}Mn nuclei. The fluorine NMR frequency[37] at 0°K is 160.0 MHz giving a splitting $\Delta/k_B = 7.7 \times 10^{-30}^\circ\text{K}$. The manganese frequency[38, 39] is 671.4 MHz which corresponds to $\Delta/k_B = 32.2 \times 10^{-30}^\circ\text{K}$. No pulling effects occur, since the antiferromagnetic resonance frequency[32] (2.61×10^5 MHz) is very much larger than the NMR one. The predicted h.f.s. specific heat per mole MnF_2 is

$$\frac{C_N T^2}{R} = 3.06 \times 10^{-3}$$

of which only 1 per cent is contributed by the F^{19} nuclei.

3. REVIEW OF THEORIES ON THE SURFACE CONTRIBUTION TO THE SPECIFIC HEAT

(a) Lattice vibrations

The existence of a surface elastic wave was predicted as early as 1887 by Lord Rayleigh[1]. The low temperature surface specific heat for a solid with first and second neighbor interactions was examined by Stratton[2] and by Dupuis *et al.*[3]. The contribution is expressed in terms of the longitudinal and transverse sound velocities. In

the case of an isotropic crystal $v_t^2 = 3v_l^2$, and the expression reduces to

$$\delta C_L = \frac{3\pi k_B^3}{\hbar^2} \zeta(3) \left(\frac{10}{v_l^2}\right) A T^2 \quad (9)$$

where $\zeta(3)$ is a Riemann zeta function and A is the surface area. A review of much of the theoretical and experimental work was published by Maradudin[4]. Shortly afterwards, the low temperature specific heat contribution was calculated using the free surface as a crystal defect by Green's function methods[5]. The result of that work by Maradudin and Wallis is identical to equation (9). This method may be applied to non-isotropic crystals. A recent calculation considers the problem in which the force constants near the surface depart from those in the bulk[6].

In the case of MnF_2 , for example, assuming $v_l = 6000$ m/sec, and $\Theta_D = 475^\circ\text{K}$ one has approximately

$$\delta C_L/C_L = 0.07 \frac{aA}{V} \cdot \frac{\Theta_D}{T}. \quad (10)$$

Furthermore taking $a \approx 4.34 \text{ \AA}$, one obtains for a grain 10μ in diameter $aA/V \approx 10^{-4}$; so at 1°K the ratio is at most 0.3 per cent.

(b) Spin-waves for finite volume in antiferromagnets

Surface effects similar to those which occur for the lattice modes can occur in the treatment of the spin-wave modes. The effects on the specific heat of an antiferromagnet have been calculated by Mills and Saslow[9]. The system considered is a cubic antiferromagnet of the CsCl structure with a free (100) surface. The assumption was made that $H_a \ll H_e$. It is found that the surface mode excitation energies lie in the gap below the bulk excitation spectrum. In zero applied field, the surface modes at $k=0$ have a gap T_{as} which is a factor of $\sqrt{2}$ lower in energy than the gap for bulk modes T_a (see equation (3)). For the case where $T_{as} \leq T \leq T_N$ ($T_N = \text{Néel Temperature}$)

Mills and Saslow obtain the expression

$$\delta C_M(T) = \frac{32\pi^2}{15} \frac{V k_B}{a^3} \left(\frac{T}{T_e} \right)^3 \left[\frac{\zeta(3)}{\zeta(4)} \frac{g\mu_B H_e}{k_B T} + \left(\frac{10}{\pi} - 3 \right) \right] \frac{\pi a A}{8 V}. \quad (11)$$

This case corresponds to the situation in RbMnF_3 where $\mathcal{C}(x) = 1$. In the situation of the CsCl structure, we recall that $z = 8$ and one has $A_l = 4$. The first term in equation (11) is due to the surface modes. The second one is due to the redistribution of the bulk modes. For a grain of 0.2μ dia., the quantity aA/V equals about 0.02. For RbMnF_3 at 1°K , the second term is then about unity while the third is about 10^{-3} .

In the limit in which the surface magnon gap is large compared to the thermal energy, the specific heat retains its exponential character displayed in equation (6). Because the gap in the surface modes is less by about $\sqrt{2}$ than that for the bulk modes, the surface effects should be easily distinguished from the bulk behavior. However, since the exponential damps out the specific heat rapidly, such effects can be detected only when the magnon specific heat is comparable to or greater than $(C_L + C_N)$. In MnF_2 below 2°K , where $T_{us} \gg T$ the ratio of the surface contributions to those of the bulk is of the form

$$\delta C_M/C_M \approx 0.37 \frac{aA}{V} \left(\frac{T_e}{T_n} \right)^{1/4} \left(\frac{T_e}{T} \right)^{1/2} \times \exp. [(-T_{us} + T_u)/T] + \frac{1}{2} \frac{aA}{V} \left(\frac{T}{T_u} \right). \quad (12)$$

For MnF_2 , taking $(g\mu_B H_e/k_B) = 80^\circ\text{K}$, $(g\mu_B H_n/k_B) = 1^\circ\text{K}$ and for particles of 4μ dia. one finds that the surface contribution at $T = 1^\circ\text{K}$ is about 10 per cent of that of the bulk. This ratio drops by a factor of nearly 10 for $T = 2^\circ\text{K}$. This particle diameter is an order of magnitude larger than that required to observe surface effects in RbMnF_3 , and also in ferromagnets (e.g. see Ref. [8]).

In a recent paper by de Wames and Wolfram

[11], the surface mode spectra have been calculated for a cubic antiferromagnet in which both the surface exchange and anisotropy parameters are allowed to depart from their bulk values. They use the (100) surface of a simple cubic lattice. Their results are somewhat different from those of the free surface calculation of Mills and Saslow since in their theory spins of both sublattices lie in the surface. Whereas in the Mills and Saslow theory the surface modes lie a factor $\sqrt{2}$ below the bulk modes those found by Wolfram and de Wames have about the same energy as those in the bulk. For the simple cubic antiferromagnet RbMnF_3 they estimate that the range of the surface modes is about 200μ .

4. EXPERIMENTAL

(a) Cryostat

The cryostat used in the experiments was essentially that used in earlier work in this laboratory [13], and no detailed discussion of it will be given. The range of temperatures from 0.3 to 4.5°K was accessible by regulating the vapor pressure over a refrigerant, either boiling He^3 or He^4 . The sample was hung from a support within a vacuum jacket. This support was part of a mechanical heat switch with which the sample could be put in thermal contact with the refrigerant. For experiments made in the presence of an external magnetic field, the sample was further tied to fastenings along the side of the vacuum jacket by means of cotton threads. The sample support consisted of a quartz disk and thin copper foils which contacted the heater wire and the carbon thermometer. A small amount of Apiezon N grease was used for better thermal contact. For the techniques of calibrating the thermometers and for the experimental procedure we refer to our previous work [13].

(b) The samples

The samples were prepared by one of us (H.J.G.) at Bell Telephone Laboratories. A summary of the samples used in the experiments can be seen in Table 3. The single

Table 3. Summary of sample details

The quantity $p(T)$ is the ratio of the addenda heat capacity to that of the sample expressed as a percentage at $T^\circ\text{K}$

Sample	Composition	Mass (g)	$p(1)$	$p(4)$
R1	RbMnF ₃ single crystal	5.04	10	120
R2	RbMnF ₃ two crystals	23.94	2	28
PR1	RbMnF ₃ sintered powder	15.16	3	42
M1	MnF ₂ single crystal	19.24	1	20
PM1	MnF ₂ sintered powder	20.72	1	18

crystal (R1) of RbMnF₃ was a clear pink-orange sphere of 1.31 cm dia. Six small flats were ground on this sphere to indicate the [100] directions. The sample was mounted in the cryostat in such a way that the field (max. 13 kOe) of an electromagnet could be applied parallel to a [100] direction. The sample of powder (PR1) was prepared by grinding some of the same crystal material as R1. The grains were then sifted through a #400 mesh screen. The resulting powder contained grains between about 5 and 30 μ in dia. This estimate was made from a direct comparison of the hole widths in a #400 grid with the sample surface and with material scraped from it. The sample was made by sintering these grains to form a block. As a result of an unexpected difference in the specific heat of PR1 and R1, additional measurements were made on a sample consisting of two large crystals (R2) produced from a different melt.

The single crystal of MnF₂ (M1) was a large clear orange rectangular prism. The sintered powder (PM1) was prepared as described above from material from the same melt as M1. The rod of material had a diameter of about 1.5 cm and a length of 3.7 cm.

(c) Errors

A reasonable estimate of all sources of error indicates there is an absolute uncertainty between ± 1 and 2 per cent. The major sources of systematic error in the specific heats obtained in these experiments arise from (1) the uncertainty in the slope of the cali-

bration curve which was about 1 per cent, and (2) from the heat capacity of the support, which was known to about 2 per cent accuracy.

For all of the samples but R1 the addenda heat capacity was less than 40 per cent of that of the sample over the whole temperature range (see Table 3). Hence the uncertainty in the R1 sample heat capacity resulting from that of the support is about 1 per cent.

As mentioned in a previous publication [13], the present calorimeter was tested by measurement of the specific heat of a cylinder of ASARCO grade 58 copper (99.999+ per cent) lent by Dr. D. W. Osborne of Argonne National Labs. Comparison with the best available measurements on similar samples [40] show our results to be systematically high by 2 per cent at 1°K, the difference decreasing to less than 0.5 per cent at 3°K and above. At the same time we find that for a sample of EuO at temperatures below 0.7°K, the specific heat [41] (associated with the Eu h.f.s.) to be in agreement within about 1 per cent with the predictions from NMR measurements of the field at the Eu nuclei, and the same is true for the specific heat of europium iron garnet [13] below 0.8°K.

5. RESULTS AND DISCUSSION

(a) RbMnF₃

Measurements were first made on the samples R1 and PR1. It was expected (see Section 3) that since the powder grain sizes were about 10 μ in PR1 that there should be no detectable surface effects. The two specific heats should be identical, or if not, the powder

should show the larger one. The reverse, however, was found. The specific heat of PR1 was systematically lower by the order of 4 per cent above 2°K, the difference diminishing to zero as the temperature decreases to the region where the nuclear term C_N dominates. The measurement of the new sample R2 then gave a specific heat above 2°K which was lower by roughly 3 per cent than that of PR1. Below 1.3°K, the specific heats were identical, indicating the same hyperfine contribution. For measurements with sample R1 made in the presence of external fields up to 13 kOe, no change from the $H = 0$ specific heats were observed within the experimental scatter. This is different from the findings of Montgomery [14], who reported a maximum increase by about 5 per cent of the total specific heat around 2.3°K for an applied field of 14 kOe, this increase disappearing as the temperature changes in both directions from 2.3°K. As Montgomery discussed in his paper, only a negligible change in the specific heat is to be expected from spin-wave theory in a field around 14 kOe, and he speculated about the possibility of effects from magnetic impurities in his sample.

A portion of the data from these three samples in zero field is shown in Fig. 1. A tabulation of smoothed data at regular temperature intervals appears in Table 4.

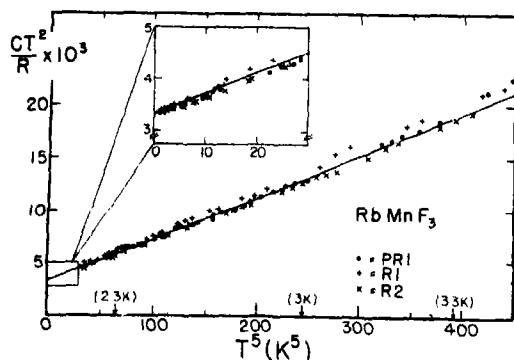


Fig. 1. Specific Heats of three RbMnF_3 samples. The solid line is for $1000 \times C/R = 3.34 T^{-2} + 0.039 T^3$. The insert shows a magnification of the data below 1.8°K.

Table 4. Smoothed specific heats of RbMnF_3 and MnF_2 expressed as $(C/R) \times 1000$ (The labeling of the samples is explained in the text)

$T(K)$	RbMnF_3			MnF_2	
	R1	R2	PR1	M1	PM1
0.6	9.28	9.28	—	—	—
0.7	6.83	6.83	—	—	—
0.8	5.24	5.24	—	—	—
0.9	4.15	4.15	—	—	—
1.0	3.38	3.38	—	3.11	3.05
1.1	2.80	2.80	—	2.58	2.53
1.2	2.37	2.37	—	2.16	2.13
1.3	2.04	2.03	—	1.85	1.85
1.4	1.80	1.78	—	1.610	—
1.5	1.60	1.58	—	1.415	—
1.6	1.45	1.42	1.44	1.265	—
1.7	1.35	1.30	1.32	1.140	—
1.8	1.27	1.22	1.23	1.040	—
1.9	1.21	1.15	1.17	0.959	0.959
2.0	1.17	1.11	1.12	0.900	0.900
2.1	1.14	1.08	1.10	0.860	0.860
2.2	1.12	1.07	1.09	0.832	0.832
2.4	1.14	1.08	1.10	0.810	0.810
2.6	1.22	1.15	1.17	0.836	0.840
2.8	1.34	1.24	1.28	0.897	0.913
3.0	1.51	1.39	1.44	1.007	1.028
3.2	1.71	1.57	1.63	1.161	1.187
3.4	1.94	1.79	1.86	1.351	1.383
3.6	2.19	2.05	2.11	1.582	1.619
3.8	2.46	2.31	2.38	1.85	1.89
4.0	2.75	2.59	2.66	2.13	2.19
4.2	—	2.91	2.98	2.48	2.55

The theoretical predictions of Section 2 indicate that the total specific heat is of the form

$$\frac{C}{R} = b_1 T^{-2} + b_2 T^3. \quad (13)$$

Least squares fits to the data obtained on the three samples produced identical values of b_1 . With errors including an estimate of confidence, one obtains

$$b_1 = (3.34 \pm 0.05) \times 10^{-3}$$

which is identical with the value from calorimetric data of Montgomery [14] between 1.2 and 4.2°K. Both values are significantly

higher than that calculated from NMR data, $b_1 = 3.18 \times 10^{-3}$. The difference of 5 per cent in the specific heat, which corresponds to 2.5 per cent in the nuclear frequency ω_N remains to be explained but could perhaps be accounted for by the pulling effects mentioned before, hence contradicting the arguments by de Gennes *et al.*[36].

For the constant b_2 , least squares fits produced the values

$$b_2 = (40.7 \pm 1) \times 10^{-6} \quad (\text{R1})$$

$$= (38.5 \pm 1) \times 10^{-6} \quad (\text{PR1})$$

$$= (37.3 \pm 1) \times 10^{-6} \quad (\text{R2}).$$

On the basis of these results, it is concluded that for all RbMnF_3 samples one would have $b_2 = (39 \pm 2) \times 10^{-6}$. The variation in b_2 is presumed to be primarily due to sample preparation, which is not quite unexpected since this compound is a 'mixed fluoride' more difficult to reproduce exactly than a 'simple fluoride' like MnF_2 . The agreement with Montgomery's[14] term ($b_2 = 40.2$) is satisfying.

The total predicted term in T^3 (equation (7)) assuming $\Theta_D = 386^\circ\text{K}$ and $J/k_B = -3.4^\circ\text{K}$ is

$$(C_L + C_M)/RT^3 = 34.0 \times 10^{-6}.$$

The disagreement with the experiment is well outside the experimental uncertainties. Conversely, assuming that C_L is correct as given in Table 1, one can determine a value of C_M from the experimental data. From this the exchange is found to be $J/k_B = -2.94 \pm 0.1^\circ\text{K}$ which is well below the values[23, 24] given in Table 1.

The disagreement of both the nuclear hyperfine and bulk spin-wave terms with their

expected values suggests an incomplete understanding of the specific heat of RbMnF_3 . Along with this problem it should be pointed out that the temperature dependence of the magnetization is found experimentally[42, 43] to be proportional to T^3 rather than the expected T^2 .

(b) MnF_2

The specific heats of the two samples were found to be identical within the scatter of the data points at temperatures below 2.6°K . In that region the nuclear contribution is the dominant one. Above 2.6°K , the specific heat of the powdered sample becomes about 3 per cent larger than that of the single crystal, but the difference is not considered significant to claim the existence of surface effects. Smoothed data at regular temperature intervals are presented for both samples in Table 4. The experimental points, about 96 for M1 and 76 for PM1, with a few exceptions scatter less than about 0.5 per cent around the curves drawn through the smoothed values. Our values are uniformly higher than those of Catalano and Phillips[15] by amounts ranging from about 0.5 per cent near 1°K to 4 per cent near 2°K and this difference is not understood.

After some experimentation with graphical techniques of analyzing the data, the following least squares method was used. The data were fitted to an equation of the form

$$\frac{C}{R} = a_1 T^3 + a_2 \left(\frac{12.54}{T} \right) T^3 + a_3 T^{-2} \quad (14)$$

corresponding to the lattice, magnetic and nuclear terms respectively. The results of the fit to the single crystal data above 1.1°K are shown in Table 5. The errors indicated there

Table 5. Results of least-squares analysis of MnF_2 single crystal data

Term	Fit coefficient	Related parameter
Lattice	$a_1 = (14.1 \pm 0.5) \times 10^{-6}$	$\Theta_D = 463 \pm 5^\circ\text{K}$
Magnetic	$a_2 = (29.1 \pm 0.5) \times 10^{-6}$	$T_c = 71.2 \pm 0.6^\circ\text{K}$
Nuclear	$a_3 = (3.08 \pm 0.04) \times 10^{-3}$	$J/k_B = -1.78 \pm 0.03^\circ\text{K}$

take into account the possibility of systematic effects. The fit is relatively insensitive to the use of the fixed parameter $T_0 = 12.54^\circ\text{K}$. For example, a change of ± 1 per cent in T_0 produces changes: of $\pm 0.1 \times 10^{-6}$ in a_1 and in a_4 , and of less than $\pm 0.01 \times 10^{-3}$ in a_3 . These quantities are all small compared to the estimated errors.

Below about 1.7°K the magnetic contribution is less than 1 per cent of the total specific heat; and it is less than 6 per cent of the lattice contribution. Below 1.7°K , then, the specific heat can be represented as the sum of only two terms: $C = a_1RT^3 + a_3RT^{-2}$. In Fig. 2 the data taken for the single crystal below 1.9°K are presented in a manner which reflects this fact. The small magnetic contribution has been subtracted off. It can be seen that the points below 1.2°K depart upward by up to 2 per cent from the fitted curve. Because such departures have not been observed in other materials, such as RbMnF_3 and EuIG , measured in the cryostat, the rise is not due simply to an error in thermometer calibration. Instead, it may possibly be a systematic error in the determination of the thermal drift rates resulting from the increasing nuclear spin-lattice relaxation time. It is for this reason that only the points above 1.1°K were used in the least-squares fit analysis. The data obtained with the sintered sample showed somewhat more scatter, but did not reflect the systematic departure from the straight line in Fig. 2.

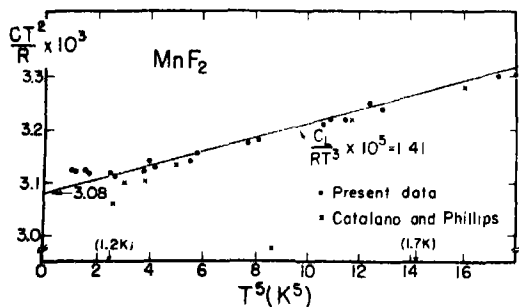


Fig. 2. The specific heat of MnF_2 sample M1 below 1.8°K showing the nuclear and lattice contributions. The solid line is for $1000 \times C/R = 3.08 T^{-2} + 0.0141 T^3$.

The value of a_3 found by the least-squares method is relatively insensitive to the systematic error in the lowest temperature points. However, the 2 per cent error quoted for a_3 in Table 5 allows for this problem. This value is somewhat lower than that obtained by Cooke and Edmonds[42] from their data in the range 0.5 to 2.0°K , namely $a_3 = 3.2 \times 10^{-3}$, but is in good agreement with the value $a_3 = (3.06 \pm 0.05) \times 10^{-3}$ obtained from a graphical analysis of the data by Catalano and Phillips over the range 1.5 to 2.0°K . There is also good agreement with the value a_3 calculated from the NMR frequencies (Table 2).

The fit coefficient of the lattice term, a_1 , corresponds to a Debye temperature of $463 \pm 5^\circ\text{K}$. This is in good agreement with the value obtained by Catalano and Phillips from their specific heat data, $\Theta_D = 458^\circ\text{K}$. The elastic constants of MnF_2 measured by Melcher[17], give $475 \pm 10^\circ\text{K}$. Because of the nearly exponential temperature dependence of the magnetic term the T^3 lattice term is well resolved and hence the fit is quite sensitive to the choice of Θ_D . For example, one can choose $\Theta_D = 475^\circ\text{K}$ to characterize the lattice term and perform a least squares fit to select the corresponding C_N and C_M . The result is to increase the mean deviation of the fit by about 10 per cent.

The fit coefficient a_2 of the magnetic term yields an exchange temperature $T_e = 71.2 \pm 0.6^\circ\text{K}$. Ignoring the weak nearest neighbor exchange interaction, this corresponds to an exchange integral $J_2/k_B = -1.78 \pm 0.03^\circ\text{K}$ which is in excellent agreement with the results of neutron diffraction studies[28,29] (see Table 1). To further demonstrate the agreement of the fit with the spin-wave theory, the following plot has been prepared. For each data point $[T, C(T)]$, the corresponding quantity $\mathcal{E}(12.54/T)$ was formed from the relation:

$$\mathcal{E}(x) = \frac{1}{a_2 T^3} \left[\frac{C(T)}{R} - a_1 T^3 - a_3 T^{-2} \right] \quad (15)$$

using the values in Table 5 for both the single crystal and the powder. This is plotted in Fig. 3 along with the theoretical curve for $\mathcal{G}(x)$ given by equation (5). The systematic deviation shown towards low temperatures is drastically reduced by choosing slightly smaller values of a_1 and a_2 which are within our limit of uncertainty, but this will be at the expense of the fit at the higher temperatures.

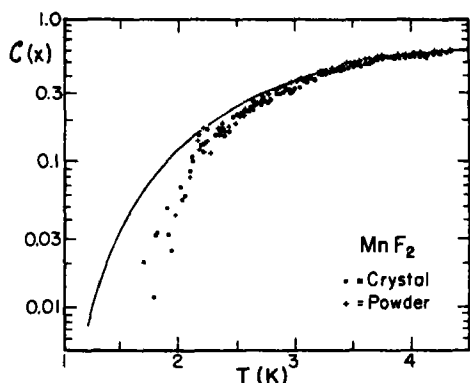


Fig. 3. Presentation of the gap function $\mathcal{G}(x)$. The solid line represents the calculated $\mathcal{G}(x)$ with $x = 12.54/T$ as given by equation (5). The points have been constructed from the measured specific heat as described in the text.

7. CONCLUSIONS

As a result of the specific heat measurements described and analyzed above, it is concluded that no surface contributions to the specific heat have been observed, a result to be expected for the particles of material with dimensions 5 to 30 μ . As was discussed in Section 3, MnF_2 was the material most likely to exhibit observable surface effects in its specific heat. Unfortunately, the large nuclear contribution that dominates below about 2°K prevented their observation. Also, sample preparation introduces some uncertainty into the lattice and magnetic specific heat as was clearly seen for RbMnF_3 . The nuclear contribution however is not affected. Hence a search for surface effects must be made on particles with diameter at least an order of magnitude smaller than what was available in this experiment. For such powders, the expected effect

is comparable to the bulk specific heat. In conclusion, since no surface effects could be detected on these antiferromagnets the origin of the anomalous contribution to the specific heat of sintered samples of iron garnets[13], which was tentatively attributed to surface effects, remains unexplained.

For RbMnF_3 , there is disagreement well outside the uncertainties for both the contributions C_N and $(C_L + C_M)$ which are respectively 5 per cent and ~14 per cent higher than expected from theory using parameters from other experiments.

For MnF_2 , the bulk specific heat, which could be analyzed as a sum of contributions from the lattice, the nuclear hyperfine splittings and the spin-waves, is in very good agreement with the predictions that used parameters determined by other experiments.

Acknowledgements—The authors are very indebted to Dr. D. L. Mills for a most stimulating correspondence on the subject of MnF_2 . They acknowledge receiving from Professor J. W. Stout tabulated results of specific heat above 4°K and the mention of several references. They also are grateful to Dr. N. E. Phillips for sending a tabulation of his data, and to Dr. A. Ikushima and R. Melcher for a tabulation and preprints of their respective unpublished elastic moduli for MnF_2 . They thank Dr. L. Lessin at the Duke Medical Center for putting at their disposal the photomicrography equipment for the particle size estimation.

REFERENCES

1. LORD RAYLEIGH, *London Math. Soc. Proc.* 17, 4 (1887).
2. STRATTON R., *Phil. Mag.* 44, 519 (1953); *J. Chem. Phys.* 37, 2972 (1962).
3. DUPUIS M., MAZO R. and ONSAGER L., *J. Chem. Phys.* 33, 1452 (1960).
4. MARADUDIN A. A., *Solid State Physics*, (Edited by F. Seitz and D. Turnbull) 19, p. 117, Academic Press, New York (1966).
5. MARADUDIN A. A. and WALLIS R. F., *Phys. Rev.* 148, 945 (1966).
6. WALLIS R. F., CLARK B. C. and HERMAN R., *Phys. Rev.* 180, 716 (1969).
7. PATTERSON D., MORRISON J. A. and THOMPSON F. W., *Can. J. Chem.* 33, 240 (1955); MORRISON J. A. and PATTERSON D., *Trans. Faraday Soc.* 52, 764 (1956).
8. MILLS D. L. and MARADUDIN A. A., *J. Phys. Chem. Solids* 30, 784 (1969).
9. MILLS D. L. and SASLOW W., *Phys. Rev.* 171, 488 (1968).

10. PALMBERG P. W., DE WAMES R. E., VRE-DEVOE L. A. and WOLFRAM T., *J. appl. Phys.* **40**, 1158 (1969).
11. DE WAMES R. E. and WOLFRAM T., *Phys. Rev. Lett.* **22**, 137 (1969).
12. WOLFRAM T. and DE WAMES R. E. (To be published).
13. HENDERSON A. J., ONN D. G., MEYER H. and REMEIK A. J. P., *Phys. Rev.* **185**, 1218 (1969).
14. MONTGOMERY H., *Ann. Acad. Sci. Fennicae* **214** (1966).
15. CATALANO E. and PHILLIPS N. E., *J. phys. Soc. Japan* **17**, 527 (1962). PHILLIPS N. E., private communication.
16. MELCHER R. L. and BOLEF D. I., *Phys. Rev.* **178**, 864 (1969). There also exist unpublished elastic constants data at 4.2°K by B. Golding that are systematically lower by 1-2 per cent than those of Melcher and Bolef (B. Golding, private communication).
17. MELCHER R. L., (to be published).
18. We point out the difference in the definition of Θ_D used in this work and in that of Melcher[17], who apparently took $C_L = 234 R(T/\Theta_D)^3$. Hence his quoted result, 261°K, is to be multiplied by $(r)^{1/3} = 1.81_6$ to give the value we list in this paper.
19. IKUSHIMA A., (private communication).
20. KEFFER F., *Handbuch der Physik* (Edited by S. Flugge) **18/2**, p. 1. Springer-Verlag, Berlin (1966).
21. KUBO R., *Phys. Rev.* **87**, 568 (1952).
22. TEANEY D. T., FREISER M. J. and STEVENSON R. W. H., *Phys. Rev. Lett.* **9**, 212 (1962).
23. WALKER M. B., *Proc. Phys. Soc.* **87**, 45 (1966).
24. WINDSOR C. G. and STEVENSON R. W. H., *Proc. Phys. Soc.* **87**, 501 (1966).
25. ERICKSON R. A., *Phys. Rev.* **90**, 779 (1953).
26. JOENK R. J., *Phys. Rev.* **128**, 1632 (1962).
27. TRAPP C. and STOUT J. W., *Phys. Rev. Lett.* **10**, 157 (1963).
28. NIKOTIN O., LINDGARD P. A., DIETRICH O. W., *J. Phys. C. (Solid State Phys.)* **2**, 1168 (1969).
29. OKAZAKI A., TURBERFIELD K. C. and STEVENSON R. W. H., *Phys. Lett.* **8**, 9 (1964); *Proc. Phys. Soc.* **85**, 743 (1965).
30. FONER S., *Phys. Rev.* **107**, 683 (1957); *J. Phys. Radium* **20**, 336 (1959).
31. JACOBS I. S., *J. appl. Phys. Suppl.* **32**, 61 S (1961).
32. JOHNSON F. M. and NETHERCOT A. H., *Phys. Rev.* **114**, 705 (1959).
33. HEEGER A. J. and TEANEY D. T., *J. appl. Phys.* **35**, 846 (1964).
34. INCE W. J., *Phys. Rev.* **177**, 1005 (1969).
35. INCE W. J., *Phys. Rev.* **184**, 574 (1969).
36. DE GENNES P. G., PINCUS P. A., HARTMANN-BOUTRON F. and WINTER J. M., *Phys. Rev.* **129**, 1105 (1963).
37. JACCARINO V. and SHULMAN R. G., *Phys. Rev.* **107**, 1196 (1957); JACCARINO V. and WALKER L. R., *J. Phys. Radium* **20**, 341 (1959).
38. JONES E. P. and JEFFERTS K. B., *Phys. Rev.* **135**, A1277 (1964).
39. YASUOKA H., NGWE T., JACCARINO V. and GUGGENHEIM H. J., *Phys. Rev.* **177**, 667 (1969).
40. OSBORNE D. W., FLOTOW H. E. and SCHREINER F., *Rev. scient. Instrum.* **38**, 159 (1967); AHLERS G., *Rev. scient. Instrum.* **37**, 477 (1966); MARTIN D. L., *Phys. Rev.* **170**, 650 (1968).
41. HENDERSON A. J., BROWN G. R., REED T. B. and MEYER H., *J. appl. Phys.* **41**, 946 (March, 1970).
42. SEIDEN P. E., *Phys. Lett.* **28A**, 239 (1968).
43. TEANEY D. T., *Bull. Am. phys. Soc.* **13**, 164 (1968).
44. COOKE A. H. and EDMONDS T. D., *Proc. Phys. Soc.* **71**, 517 (1958).
45. The same remark made before (Ref. [18]) applies to the analysis of the specific heat data by Catalano and Phillips.

ELECTRIC FIELD GRADIENTS AT ^{57}Fe NUCLEI IN GOLD ALLOYS

B. WINDOW

Materials Physics Division, A.E.R.E., Harwell, Didcot, Berks., England

(Received 24 March 1970; in revised form 26 May 1970)

Abstract—The 300°K spectra of 1 at. % ^{57}Fe in AuX alloys (3–12 at. % X) where X = Ti, V, Cr, Mn, Fe, Co, Ni, Pd, Pt and Sn, have been analysed to give the quadrupole splitting and isomer shift change for an iron nucleus with one X neighbour, and the behaviour of these parameters correlated with that of the residual resistivity per atomic per cent solute. This correlation suggests that the electric field gradients arise from the distortion of the iron screening electrons due to the increased density of states on an impurity in the nearest neighbour shell. The low temperature spectra also appear to support this explanation.

1. INTRODUCTION

THE OBSERVATION of electric field gradients (efg) at iron impurities in cubic alloys using the Mössbauer effect has been limited to a few systems[1–6], and little attention has been paid to investigating their origin more thoroughly. Quadrupole splittings were observed initially in Fe X alloys[1], but here the assignment was difficult because of comparable magnetic and isomer shift effects in these ferromagnetic alloys. Preston *et al.*[2] observed quadrupole effects in V Fe alloys, and they showed how, if one assigned a point charge to each constituent of an alloy, then for a sufficiently large difference of charge, the Mössbauer spectrum in concentrated alloys would be a doublet. Although V_{zz} , the largest in magnitude principal value of the efg tensor, can be positive or negative, and the asymmetry parameter, $\eta = |(V_{xx} - V_{yy})/V_{zz}|$, will range from 0 to 1, the splitting $Q \propto |V_{zz}(1 + \eta^2/3)^{1/2}|$ covers a small range for the probable atomic configurations.

However, the well known example of efgs at ^{57}Fe in alloys is in gold iron alloys[3, 4], and investigations of this system over a range of iron concentrations (up to 20 at. %) do support the conclusions of Preston *et al.*[2], as the spectrum tends towards a well defined doublet. The quadrupole effects observed in

this alloy system are much larger than those found for ^{57}Fe in other systems, and must arise from the method of screening of the iron impurities. Similar effects can be observed for iron in the other noble metal solvent, copper[6] but here one is restricted to low concentrations of iron because of the limited solid solubility. Another interesting result comes from the study by Longworth[5] of the effects of band filling in the Pd Au alloy system on the Mössbauer spectra of dilute ^{57}Fe incorporated as a probe. Besides obtaining a sharp change in the behaviour of the isomer shift as a function of gold concentration near 50 at. % gold, presumably due to filling of the palladium *d* band, there is also a marked increase in the linewidth at this concentration and doublets appear in the spectra. The screening of the iron and/or palladium atoms alters at this point, and the probe ^{57}Fe nucleus is perturbed electrostatically in different ways by the presence of palladium or gold neighbours.

We have studied the Mössbauer spectra at 300 and 4.2°K of alloys of 1 at. % ^{57}Fe in Au X (3–10 at. %) solid solutions, where X = Ti, V, Cr, Mn, Fe, Co, Ni, Pd, Pt and Sn, and have determined from the 300°K spectra the electric field gradients and changes of isomer shift for ^{57}Fe nuclei in Fe–X

nearest neighbour pairs. These effects follow the behaviour of the residual resistivity per atomic per cent of X in gold, and this correlation may be explained in terms of the increased density of states on an X neighbour associated with the formation of a virtual bound state[7]. The low temperature results are also as expected for this model.

2. EXPERIMENTAL

The spectra were recorded using a multi-channel analyser operating in time mode[8] with an electromagnetic drive, the linearity of which was ascertained as 0.1 per cent from curve fitting magnetic iron calibration spectra. The source used was ^{57}Co in Pd, and gave a Lorentzian line with a full width at half maximum of 0.21 mm/sec against a thin absorber.

The absorbers were made by adding 0.5 mgm of ^{57}Fe (> 86% ^{57}Fe) to 200 mgm of the master Au X alloy in an argon arc furnace and cold rolling to a 8 μm foil. The concentration of the masters were calculated from the weights used in the melting.

3. RESULTS

In Fig. 1 are shown the spectra of the alloys of 1% ^{57}Fe in Au X alloys at 300°K; the concentrations of X are shown in the figure. The spectra all show broadening due to efg's and isomer shift effects.

The Au Fe 1 per cent sample shows a doublet due to iron-iron pairs, and a single line due to iron atoms with no iron neighbours in the nearest neighbour sites. The full line shown is fitted on this assumption with a singlet and a doublet with a linewidth of 0.28 mm/sec⁻¹ (FWHM), and the relative areas agree with that expected on a random distribution of iron atoms. The linewidth found (0.28 mm sec⁻¹) is 1.4 times the linewidth expected for such thin absorbers, and the broadening of the single line must come from efg's produced by neighbours further than the nearest neighbour shell.

The fitted curves shown have been obtained

by fitting seven lines of linewidth 0.28 mm sec⁻¹, these lines being constrained as follows.

(a) A doublet for Fe-Fe pairs with their separation and position determined from the AuFe 1 per cent sample.

(b) A singlet for Fe atoms with all Au atoms in the nearest neighbour shell.

(c) A doublet for Fe- X pairs shifted by δ from the isolated iron centroid.

(d) A doublet for Fe-2 X configurations shifted by $2 \times \delta$ from the isolated iron centroid and separated by 1.32 times the separation found for (c). (This splitting is that expected on a point charge model[2] for the most probable (0.7) of the two nearest neighbour configurations.)

For the Au Ti sample, the single line (b) is split by the efg's produced by the Ti neighbours further than the nearest shell, and so, for this sample, a doublet has been fitted instead of the singlet (b). The relative intensities in all cases were determined from the known concentrations of the alloys assuming randomness. A linewidth of 0.28 mm sec⁻¹ (FWHM) has been chosen for the fitting instead of the experimental linewidth of 0.21 mm sec⁻¹ to 'subtract' the effect on the iron resonance of the iron impurities further removed than the nearest neighbour shell. Although in the fitting many less significant configurations have been neglected, the parameters found will be correct to the accuracy necessary for the discussion. A more exact analysis of the data would be extremely difficult. As one can see in Fig. 1, some of the fits are not particularly good, presumably due to uncertainties in the alloy concentrations and deviations from randomness. Where the effects of nearest neighbours are resolved e.g. Ti, V, Fe the reasonable fits obtained suggest that these impurities are randomly distributed with respect to the iron atoms. The parameters most affected by non randomness are those which determine the isomer shifts, the quadrupole splitting being relatively insensitive to clustering.

In Fig. 2 the quadrupole splitting and isomer

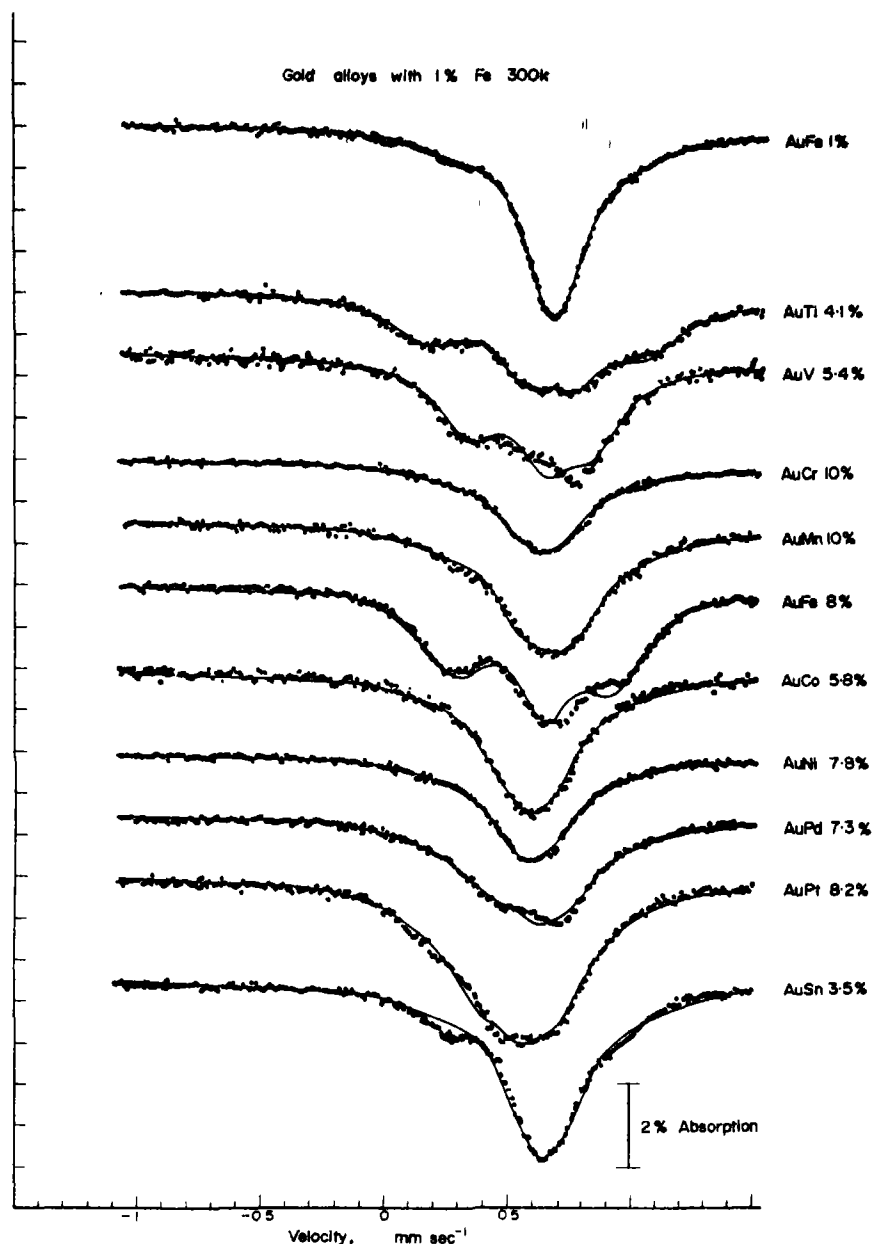


Fig. 1. Mössbauer spectra for 1 at.% ^{57}Fe in gold alloys at 300°K. The zero of velocity is taken as the centre of the α -Fe spectrum. The fitted curves are explained in the text.

shift change per X neighbour are plotted for each solute X . Also shown for comparison is the increase in residual resistivity per atomic per cent solute X [9, 10], and we note

the close correspondence between the behaviour of these three parameters for the $3d$ series solutes.

Another parameter derived from the fitting

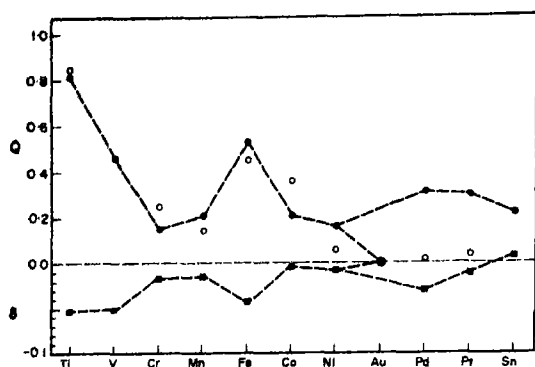


Fig. 2. Quadrupole splitting Q (mm sec $^{-1}$) (●) and isomer shift change δ (mm sec $^{-1}$) (■) for a ^{57}Fe nucleus with an impurity neighbour X . The residual resistivities per atomic per cent of X (○) are shown scaled to fit the Q variation.

is the isomer shift of the isolated iron atom in the gold lattice, and, as this should depend on lattice parameter, we have plotted these parameters for the various solutes X in Fig. 3. There is no obvious linear relation between the isomer shift and the lattice parameter, but there is a general trend—impurities which contract the lattice decrease the isomer shift, while the one impurity which expands the lattice (Sn)[11] also increases the isomer shift. The dotted line drawn in Fig. 3 shows

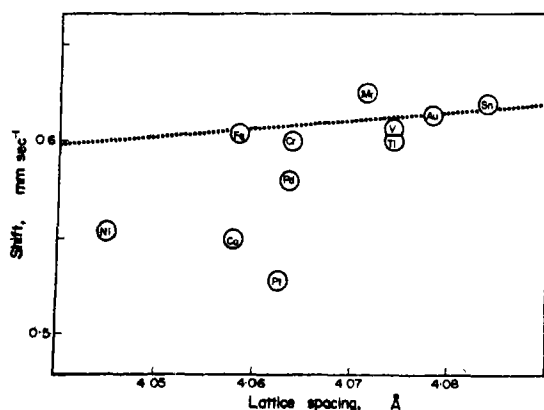


Fig. 3. Dependence of isomer shift of isolated Fe atoms in Au X alloys on lattice parameter. The dotted line is derived from the variation with pressure of the isomer shift of Fe in gold [12].

the variation of isomer shift for ^{57}Fe in gold with lattice parameter, derived from the pressure experiments of Ingalls *et al.* [12].

The 4.2°K data (Fig. 4) show that all the samples are ordered magnetically. The iron concentration in these samples could be different from 1 at.% by as much as 50 per cent, but one can see that certain solutes have decreased the ordering temperatures from that expected for a 1 at.% Fe in gold alloy i.e. 12°K [13] to near 4°K.

4. DISCUSSION

Electric field gradients

The correspondence between residual resistivity per atomic per cent of X and the electric field gradient at ^{57}Fe due to an X neighbour limits the number of possible explanations for the origin of these field gradients; for example, strain and valency effects will not directly provide this correlation. The resistivity trends are adequately explained on the virtual bound state (vbs) model of Friedel and co-workers [7, 9, 14, 15], and it is in the framework of this model that we account for the correspondence between residual resistivity and electric field gradients.

The conduction electrons are scattered by the excess nuclear charge Z on the impurity, and this scattering can be analysed using partial waves to derive the phase shifts η between incoming and outgoing plane waves. The density of states in energy is shifted by an amount $(1/\pi)(d\eta_l/dE)$ for each component, and the total number of new states below energy E is $(1/\pi)\sum (2l+1)\eta_l(E)$. This gives Friedel's sum rule $Z = (2/\pi)\sum (2l+1)\eta_l(E_F)$. For 3d atoms dissolved in noble metals the atomic d -states will lie in the conduction band, and the resonance between the conduction electrons and the d -states will make η_2 large, with $\eta_0 = \eta_1 \approx 0$. This d -resonance has associated with it an excess density of states of Lorentzian shape of width Γ and centred at E_r , the value of E_r being such that the necessary screening electrons are accommodated below the Fermi level. The

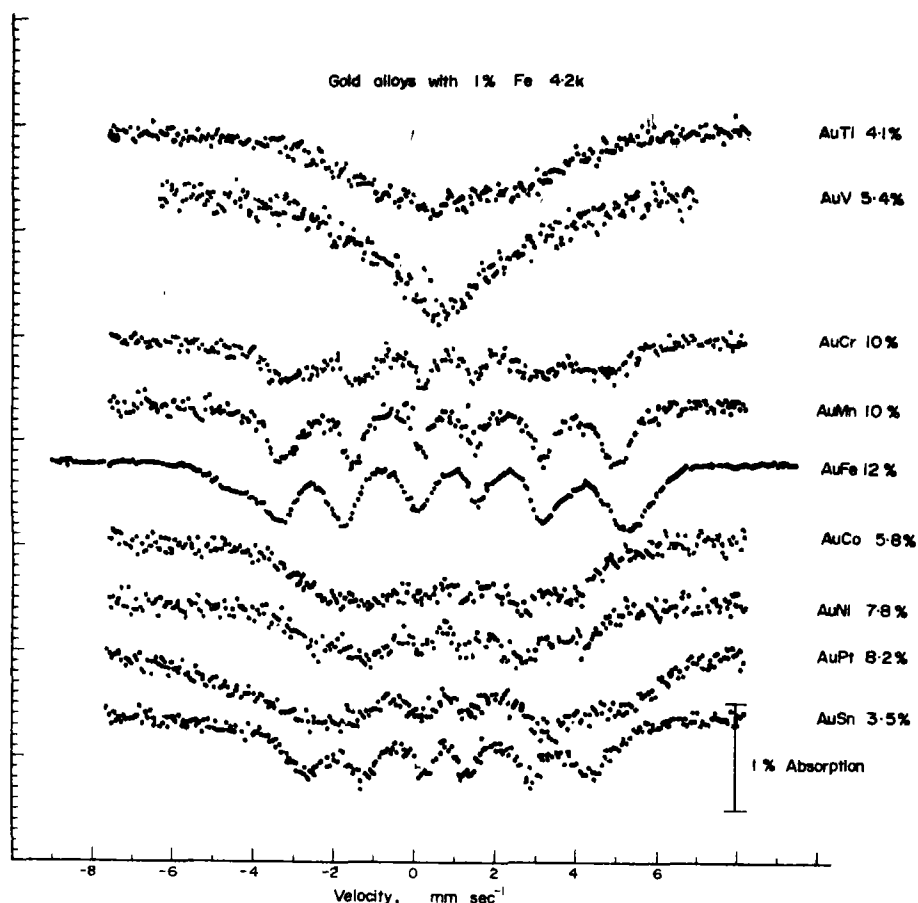


Fig. 4. The Mössbauer spectra of 1 at.% Fe in Au *X* alloys at 4.2°K. The per cent absorption scale for Au Fe 12 per cent has been reduced by a factor of ten.

increase of density of states at the Fermi level E_F is

$$n(E_F) = \frac{10}{\pi} \frac{\Gamma/2}{(E_F - E_r)^2 + (\Gamma/2)^2}$$

and the increase in residual resistivity R per atomic per cent solute due to scattering is

$$R \propto \frac{(\Gamma/2)^2}{(E_F - E_r)^2 + (\Gamma/2)^2} \quad (\text{see [15]}).$$

Similar results have been obtained by Anderson [16] by considering the effect of s - d mixing on the atomic d -states.

The resistivity trends for 3d transition atoms

in Al, Cu and Au, may be explained on this model. For aluminium one obtains a peak in the residual resistivity near the middle of the 3d series as the d -resonance crosses the Fermi surface (i.e. $\eta_2 = \pi/2$). In copper and gold, where for some 3d solutes the exchange energy is sufficient for the vbs to magnetise [14], the residual resistivity should show two peaks as the centres of the up and down spin resonances cross the Fermi level. The fact that some impurities magnetise and some do not, could upset this prediction, but two peaks are observed.

There are two mechanisms whereby one could obtain field gradients proportional to the residual resistivity. The simplest model is

one is which the iron nucleus is treated as an independent probe, and the efg is produced by the charge oscillations around the X neighbour. Kohn and Vosko[17] have explained the nuclear magnetic resonance results for copper nuclei in dilute copper alloys[18] by this oscillating charge polarisation, falling off as the inverse cube of distance. This theoretical derivation is only valid well away from the impurity, and the behaviour of the polarisation near the impurity will not necessarily be of this form. For a free electron gas of Fermi vector k_F and a spherical scattering potential, the asymptotic form of the excess charge density $\rho(r)$ at large r is given by [7, 15, 17]

$$\rho(r) = (\alpha/2\pi^2 r^3) \cos(2k_F r + \phi)$$

where α and ϕ are given by

$$\alpha \sin \phi = \sum_l (-1)^l (2l+1) \sin^2 \eta_l$$

$$\alpha \cos \phi = \sum_l (-1)^l (2l+1) \sin \eta_l \cos \eta_l.$$

The resulting electric field gradient at a probe nucleus is [17]

$$q = (2\alpha/\pi r^3) \mu \cos(2k_F r + \phi)$$

where μ is an enhancement factor due to antishielding effects by the atomic electrons. Using the values of η_2 for 3d impurities in gold[9], the values of α do correspond approximately with the variation of efg shown in Fig. 2. However $(2k_F r)$ for a first nearest neighbour in gold is 2.21π , and the effect of the additive ϕ is to destroy the correspondence. Also in alloys as concentrated as Au Fe 20 at.%, the sharp discontinuity in occupancy at a certain Fermi vector k_F will be smeared out, and the second oscillation at the first nearest neighbours will be reduced in amplitude and broadened. Results for AuFe alloys show that the spectra can be fitted quite well on a point charge model[2], with a charge per iron neighbour which decreases only by 30 per cent

in going from 1 to 20 at.% iron (Window, unpublished).

There are many qualifications concerning the applicability of Friedel oscillations at nearest neighbours in these alloys, and, apart from antishielding of the Friedel oscillations, no account has been taken of the influence of an impurity X neighbour on the probe's own electrons. A simple alternative model which does to some extent include this effect may be derived from a Thomas Fermi model for the screening near the impurity. The magnitude of the efgs observed suggests that the iron screening electrons on the atomic site are responsible.

The virtual bound state on the impurity produces an increased local density of states at the Fermi level, and this enhancement, which varies in the same way as the residual resistivity, distorts the screening charge on the neighbouring iron atom. The iron screening, because of the low density of states at the Fermi level in the gold matrix, extends appreciably into the nearest neighbour cells. On a Thomas Fermi model for the screening of a charge Z ($= 7$ for Fe in Au), the screening charge $\rho(r)$ i.e. the charge in excess of that for the unperturbed matrix, is given as a function of distance r by

$$\rho(r) = -\frac{1}{16\pi^2} Z \lambda^2 e^{-\lambda r/r}$$

where $\lambda^2 = 4\pi n(E_F)$ (see [7]), and $n(E_F)$ is the density of states at the Fermi level. For Ag and Au, λ is 1.8 \AA^{-1} , and thus about 12 per cent of the screening charge resides outside the atomic cell. This large screening length ($1/\lambda$) explains why quadrupole effects at ^{57}Fe nuclei are observed mainly in noble metal rich matrices.

If an impurity atom is in a nearest neighbour site the increased local density of states will cause the screening length in this direction to decrease. It becomes energetically more favourable to remove electrons from this region than from the neighbouring gold atoms, and the screening will change so that more

electrons are localised between the iron atom and the impurity and correspondingly fewer are present in the directions of the gold atoms. The magnitude of the distortion from cubic symmetry will depend upon the increase in density of states on the impurity, and it is only for *d* impurities (with a narrow virtual bound state accommodating ten electrons) that this increase is sufficiently large to produce resolvable quadrupole splittings.

This explanation also accounts for the fall off in the effective point charge on an iron neighbour found by analysing the spectra of Au-Fe (1–20 per cent) alloys on the point charge model. The seven screening electrons will be distributed according to the density of states on the twelve neighbours. If the ratio of densities of states (Fe/Au) is α , and the number of iron atoms present is n , then the charge in the direction of one iron neighbour will be

$$\rho' = \frac{7\alpha}{(12-n) + n\alpha}.$$

Analysis on the point charge model for a 1% Fe sample ($n = 1$), and a 20% Fe sample ($n = 3$) shows that the effective point charge per iron neighbour decreases by $\frac{1}{3}$ for $n = 1$ to $n = 3$ i.e. $\alpha = 5$. The increase in density of states expected is from 0.25/eV for a gold atom to about 2/eV at the maximum in the Lorentzian density of states i.e. a factor of 5, so these order of magnitude calculations agree with experiment. Effects of this sort will act to make the Mössbauer spectra of concentrated alloys resemble doublets even more closely than is expected on the point charge model.

For some impurities, in particular Ti and to a lesser extent Fe, one can observe the effects of neighbours further than the nearest shall. The magnitude of this effect found from fitting the AuTi spectrum was approximately 0.25 of that for first nearest neighbours. As there is a low probability that one of the 6 second nearest neighbour sites is occupied, the bulk of this effect must come from *X* atoms

in the 24 third nearest neighbour position. The magnitude of this effect indicates an inverse cube dependence on distance of the distortion of the screening charge for the neighbours in the first three shells, but it is to be expected that these direct screening effects will fall off much more rapidly for further shells. Friedel oscillations could also be important for these 1–3 per cent alloys.

In explaining this correlation with virtual bound states, the possibility that the magnetised iron atoms will also force neighbouring atoms (Ni, Co) to magnetise [19] has not been considered. The splitting of the vbs for impurities with nearly full *d* states will not affect the density of states much on the scale we are considering here. The correspondence between the efg and the residual resistivity observed for 3*d* impurities does not hold for transition elements of the same column e.g. Ni, Pd, Pt (Fig. 2). On a Thomas Fermi model the efg will be increased by the larger 4*d* and 5*d* impurities, whereas the resistivity which depends mainly on the screening charge via the phase shifts should not change.

5. ISOMER SHIFT EFFECTS

The changes in isomer shift with a neighbour *X* (Fig. 2) follow the quadrupole effects and presumably have the same origin. The distortion of the screening charge will alter the isomer shift i.e. the *s*-electron density at the nucleus.

In Fig. 3 the results for the isomer shift of the isolated iron atom as a function of lattice parameter are plotted. In general the pressure dependence defines the smallest change of isomer shift with various solutes, and deviations from this straight line are produced by discrepancies in the fitting and by valency effects where the impurities donate electrons to the host conduction band.

6. MAGNETIC ORDERING

Impurities which show the biggest electric field gradients and do not have localised

moments e.g. Ti, V, Ni, Pd, Pt decrease the ordering temperature. This is as expected—impurities which increase the resistivity most will strongly scatter the conduction electrons and decrease the indirect exchange interaction between iron localised moments. Those impurities which do have localised moments e.g. Cr, Mn increase the ordering temperature.

The range of hyperfine field values for those spectra where the iron hyperfine field is almost saturated in Fig. 4 (Cr, Mn, Fe) correlates also with the magnitude of the efg and isomer shift change. For example, the Au Fe 12 per cent sample gives a spectrum which is broader than those for the Au Cr 10 and Au Mn 10 samples. The distortion of the screening charge will alter the hyperfine field at the iron nucleus. The change in hyperfine field at the iron nucleus for a nearest neighbour iron atom in gold iron alloys is much smaller than is observed for iron in copper—in copper the acquisition of an iron neighbour increases the magnetic hyperfine field from 80 kOe for the isolated iron atom to approximately 150 kOe [6], but it could be that this change is associated with an increase in stability of the localised moment [19].

7. CONCLUSIONS

The Mössbauer spectra of 1 at.% ^{57}Fe in Au X alloys have been analysed to show that the efg at an iron nucleus with an impurity neighbour comes from the distortion of the atomic shielding electrons due to the enhanced density of states on the neighbour. The electric field gradient produced is proportional to the extra density of states, and a model, where the number of shielding electrons localised in the direction of a neighbour is

proportional to the density of states on the neighbour accounts for the behaviour of concentrated gold iron alloys.

The electric field gradient, the residual resistivity per atomic per cent X , the effect on the ordering temperatures, and the distribution of magnetic hyperfine interactions for the impurity X are shown to be consistent with virtual bound states on the 3d impurities in gold.

Acknowledgements—The assistance and advice of G. Longworth and C. E. Johnson during all stages of this work are gratefully acknowledged.

REFERENCES

1. CRANSHAW T. E., JOHNSON C. E. and RIDOUT M. S., *Prof. Int. Conf. on Magnetism*, Nottingham. Inst. of Physics and Phys. Soc., London, p. 141.
2. PRESTON R. S., LAM D. J., NEVITT M. V., VAN OSTENBURG D. O. and KIMBALL C. W., *Phys. Rev.* **149**, 440 (1966).
3. VIOLET C. E. and BORG R. J., *Phys. Rev.* **162**, 608 (1967).
4. RIDOUT M. S., *J. Phys. C* **2**, 1258 (1969).
5. LONGWORTH G., *Phys. Lett.* **30A**, 180 (1969).
6. WINDOW B., *J. Phys. C* **3**, 922 (1970).
7. FRIEDEL J., *Nuovo Cim. Suppl.* **7**, 287 (1958).
8. CRANSHAW T. E., *Nucl. Instrum. Meth.* **30**, 101 (1964).
9. DANIEL E., *J. Phys. Chem. Solids* **23**, 975 (1962).
10. LINDE J. O., *Annln Phys.* **10**, 52 (1931).
11. PEARSON W. B., *A Handbook of Lattice Spacings and Structures of Metals and Alloys*, vol. 2. Pergamon Press, Oxford (1967).
12. INGALLS R., DRICKAMER H. G. and DePASQUALI G., *Phys. Rev.* **155**, 165 (1967).
13. VIOLET C. E. and BORG R. J., *Phys. Rev.* **149**, 540 (1966).
14. BLANDIN A. and FRIEDEL J., *J. phys. Radium* **20**, 160 (1959).
15. DANIEL E. and FRIEDEL J., *Low Temp. Phys.* **LT9**, 933 (1965).
16. ANDERSON P. W., *Phys. Rev.* **124**, 41 (1961).
17. KOHN W. and VOSKO S. H., *Phys. Rev.* **119**, 912 (1960).
18. ROWLAND T. J., *Phys. Rev.* **119**, 900 (1960).
19. MORIYA T., *Prog. theor. Phys.* **33**, 157 (1965).

ISOTOPE EFFECT IN IRON DIFFUSION IN Fe/3% Si ALLOY

C. QVIEDO DE GONZÁLEZ* and N. E. WALSKÖE DE RECA†

(Received 16 March 1970; in revised form 8 May 1970)

Abstract—Values of ^{55}Fe , ^{59}Fe and a mixture of ^{55}Fe and ^{59}Fe diffusion coefficients in Fe/3% Si single-crystals were measured over a temperature range from 707 to 902°C, by tracer sectioning method. The D dependence with temperature can be expressed in paramagnetic and ferromagnetic ranges as follows:

$$D_{\text{param.}}^{55} = 0,22 \pm 0,06 \exp (52 \cdot 200 \pm 1 \cdot 320/RT)$$

$$D_{\text{ferrom.}}^{55} = 0,58 \pm 0,29 \exp (54 \cdot 322 \pm 1 \cdot 310/RT)$$

$$D_{\text{param.}}^{59} = 0,23 \pm 0,07 \exp (51 \cdot 567 \pm 1 \cdot 300/RT)$$

$$D_{\text{ferrom.}}^{59} = 0,60 \pm 0,30 \exp (53 \cdot 668 \pm 1 \cdot 300/RT)$$

$$D_{\text{param.}}^{55+59} = 0,19 \pm 0,05 \exp (51 \cdot 086 \pm 1 \cdot 240/RT)$$

$$D_{\text{ferrom.}}^{55+59} = 0,47 \pm 0,23 \exp (52 \cdot 695 \pm 1 \cdot 290/RT).$$

Because of the 'magnetic anomaly' the possible diffusion mechanism was studied by measuring the isotope effect in the whole range of temperatures with the isotope pair ^{55}Fe – ^{59}Fe .

The isotope effect data are consistent with a highly relaxed vacancy mechanism or a interstitialcy one and the same process seems to be valid in both paramagnetic and ferromagnetic regions.

1. INTRODUCTION

THE FERROMAGNETIC order produces a deviation of the Arrhenius plot ($\ln D$ vs. $1/T$) in the vicinity of the Curie Temperature (T_c). This 'magnetic effect' was observed by several authors in self-diffusion and ferromagnetic tracer diffusion in α -Fe[1–7]; in nonferromagnetic tracer diffusion in α -Fe[5] and by internal friction measurements in Fe/V[8]. An anomalous behavior was also found in Young's modulus measurements as a function of temperature in Fe/3% Si near T_c [9]. This phenomenon is not confined to b.c.c. elements.

The small decrease of diffusion coefficients (D), below T_c was explained as a change in

elastic properties related to magnetic order [10]. This effect was also associated to a decrease in vacancy concentration related with a long-range magnetic order influence on the formation energy of vacancies[4, 11].

The presence of a 'fast impurity' in α -Fe lattice enabled us to study the possible diffusion mechanism far below T_c (756°C) of Fe/3% Si alloy, although errors on E values are considerable higher than those in paramagnetic range. Previous isotope effect works in pure iron[12, 13] only report a value below T_c [13].

Isotope effect measurements were performed in paramagnetic and ferromagnetic ranges with the isotope pair ^{55}Fe – ^{59}Fe (~7 per cent mass difference). The more advantageous pair ^{52}Fe – ^{59}Fe was not used because of the impossibility for us to acquire the ^{52}Fe isotope of very short half-life ($\lambda = 8,2$ hr).

We assume valid for the isotope pair ^{55}Fe –

*CITEFA (Instituto de Investigaciones Científicas y Técnicas de las Fuerzas Armadas). Ciudad de la Paz 1340, Buenos Aires, Argentina.

†CIFEFA and CNICT (Consejo Nacional de Investigaciones Científicas y Técnicas).

^{59}Fe the well known relation:

$$E = f \cdot \Delta K = \frac{1 - D^{59}/D^{55}}{1 - (m^{55}/m^{59})^{1/2}} \quad 0 < \Delta K \leq 1 \quad (1)$$

where: E : strength of isotope effect. ΔK : is related to elastic relaxation of atoms neighboring a vacancy and to the coupling of the neighboring atoms to the jumping atom. f : correlation factor. D^{55} and D^{59} : diffusion coefficients of ^{55}Fe and ^{59}Fe in the alloy. m^{55} and m^{59} : masses of ^{55}Fe and ^{59}Fe .

If $\Delta K \sim 1$ it is possible to identify the diffusion mechanism because the isotope effect measurements give an unambiguous value of f . The self-diffusion behavior in a dilute alloy is not a simple mechanism because in addition to the jumping atom there is another impurity atom participating in the process. ΔK is then related to one or some magnitudes associated with the lattice elasticity, such as: the formation volume of the defect which includes the relaxation around the defect; the activation volume of motion, which takes in account the displacement of neighboring atoms at the saddle point or the dilation around an impurity. The contribution of these effects yields $\Delta K < 1$.

E values of our work are comparable with those evaluated for Na[14] and $\alpha\text{-Fe}$ [12] and suggest an interstitialcy or a relaxed vacancy mechanism.

2. EXPERIMENTAL PROCEDURE

High purity Fe/3% Si single-crystals were cut by the spark method in pieces of about 10 mm \times 10 mm \times 10 mm. Impurities contents are given in Table 1.

All specimens were previously annealed together at 900°C during 20 days in vacuum (10^{-6} mm Hg).

A mixture of pure ^{55}Fe and ^{59}Fe (as chlo-

rides) in a proportion 10:1 was electroplated on one of the specimen surfaces from an ammonium oxalate bath. Characteristics of both isotopes are given in Table 2. To get D^{55} and D^{59} , other specimens were deposited with pure ^{55}Fe or ^{59}Fe , by the same method.

Table 2.

Isotope	Half-life	Radiation	Absorption in iron
^{55}Fe	4 years	Mn-X (6 KeV)	715 cm $^{-1}$
^{59}Fe	44 days	β (0.46–0.26 MeV) γ (1.1–1.3 MeV)	0.41 cm $^{-1}$

Diffusion annealing temperatures were measured with a controlled chromel–alumel thermocouple, with a precision $\Delta T \leq \pm 1^\circ\text{C}$, during times reported in Table 3, under dynamical vacuum (10^{-6} mm Hg). The deposited surfaces of the samples were placed together to avoid radioisotopes evaporation during annealing.

To avoid surface diffusion effects 0.20/0.30 mm were removed from the specimen sides after diffusion annealings.

(a) Diffusion coefficients measurements

^{59}Fe diffusion coefficients (D^{59}) were measured by Gruzin's method, modified by Seibel[15].

The solution of Fick's second law for a thin layer on the planar surface of the specimen considered as a semi-infinite medium is:

$$\mu I_n - \partial I_n / \partial x_n = \frac{k \cdot M}{\sqrt{\pi D t}} \exp(-x_n^2 / 4Dt) \quad (2)$$

where: μ : linear absorption coefficient. I_n : residual activity of the specimen after removal of a thickness x_n . D : diffusion coefficient. t : diffusion annealing time. For γ -radiation of ^{59}Fe , equation (2) is reduced to equation (3) because:

$$\mu I_n \ll \partial I_n / \partial x_n$$

$$-\partial I_n / \partial x_n = \frac{k \cdot M}{\sqrt{\pi D t}} \exp(-x_n^2 / 4Dt). \quad (3)$$

Table 1. Impurities content

Si = 2.998%	C = 0.0015%	O = 0.008%
Mn = 0.044%	P = 0.012%	Ni = 0.036%

This solution is integrated between $0 \leq x_n \leq \infty$

$$I_n = I_0 [1 + \operatorname{erf}(-x_n/2\sqrt{Dt})] \quad (4)$$

where: I_0 : initial activity at $t = 0$ and $x = 0$.

$$\operatorname{erf}(z) = 2/\sqrt{\pi} \int_0^z e^{-t^2} dt \quad (5)$$

is the error function.

Experimental residual activity after each section is plotted vs. penetration in Gauss-arithmetic graph:

$$I_n/2I_0 = \frac{1}{2} [1 + \operatorname{erf}(-x_n/2\sqrt{Dt})] \quad (6)$$

from the slope $-(1/2\sqrt{Dt})$ of the straight line for volume diffusion D values are obtained. Sections were removed by polishing and thickness was evaluated by weight differences with a precision of 10^{-6} g. Diffusion coefficients measurements with ^{59}Fe (γ -radiation) were performed with a 3×3 NaI(Tl) scintillation counter.

^{55}Fe X-rays were counted with a flow counter filled with a mixture of methane and pure Argon. For soft ^{55}Fe radiation equation (7) is valid:

$$\ln I_n/I_0 = -x_n^2/4Dt. \quad (7)$$

Low temperature D measurements with ^{55}Fe are the mean value of five determinations with a high initial activity. Diffusion coefficients with the mixture $^{55}\text{Fe} + ^{59}\text{Fe}$ were measured by counting ^{55}Fe X-rays and ^{59}Fe β -radiation with the flow counter protected by an Aluminium absorber ($2,5 \mu$).

Counting error was diminished under 0,5 per cent and some corrections, detailed below were taken in account.

3. RESULTS

Table 3 gives values of experimental D^{55} , D^{59} and D^{55+59} diffusion coefficients in Fe/3%Si alloy in the range of temperatures between 707 and 902°C and the corresponding diffusion times. Figures 1 and 2 show typical activity profiles for D^{59} and D^{55} in Fe/3%Si alloy for diffusion annealings at 735 and 803°C respectively. The diffusion coefficients dependence on temperature follows the Arrhenius law in paramagnetic and ferromagnetic ranges and evidences the 'magnetic anomaly', near the Curie point (Fig. 3.). Table 4 shows values of ΔH (activation energy variation from paramagnetic to ferromagnetic range). Values of diffusion coefficients (D), frequency factors (D_0), activation energies (Q) and their errors were calculated with an electronic

Table 3.

T (°C)	D^{55} (cm ² /sec)	D^{59} (cm ² /sec)	D^{55+59} (cm ² /sec)	t (sec)
902	$(6,01 \pm 0,24) \cdot 10^{-11}$	$(5,85 \pm 0,21) \cdot 10^{-11}$	$(5,77 \pm 0,21) \cdot 10^{-11}$	$6,60 \cdot 10^4$
874	$(3,48 \pm 0,14) \cdot 10^{-11}$	$(3,46 \pm 0,12) \cdot 10^{-11}$	$(3,38 \pm 0,12) \cdot 10^{-11}$	$1,20 \cdot 10^5$
855	$(2,50 \pm 0,10) \cdot 10^{-11}$	$(2,39 \pm 0,09) \cdot 10^{-11}$	$(2,42 \pm 0,09) \cdot 10^{-11}$	$1,36 \cdot 10^5$
827	$(1,33 \pm 0,05) \cdot 10^{-11}$	$(1,29 \pm 0,05) \cdot 10^{-11}$	$(1,28 \pm 0,06) \cdot 10^{-11}$	$1,73 \cdot 10^5$
810	$(9,33 \pm 0,37) \cdot 10^{-12}$	$(8,98 \pm 0,32) \cdot 10^{-12}$	$(8,94 \pm 0,32) \cdot 10^{-12}$	$2,31 \cdot 10^5$
803	$(7,92 \pm 0,32) \cdot 10^{-12}$	$(7,71 \pm 0,28) \cdot 10^{-12}$	$(7,70 \pm 0,28) \cdot 10^{-12}$	$4,02 \cdot 10^5$
789	$(6,50 \pm 0,26) \cdot 10^{-12}$	$(6,30 \pm 0,23) \cdot 10^{-12}$	$(6,18 \pm 0,22) \cdot 10^{-12}$	$4,10 \cdot 10^5$
766	$(3,12 \pm 0,19) \cdot 10^{-12}$	$(3,29 \pm 0,16) \cdot 10^{-12}$	$(3,23 \pm 0,16) \cdot 10^{-12}$	$7,60 \cdot 10^5$
750	$(2,96 \pm 0,18) \cdot 10^{-12}$	$(3,18 \pm 0,16) \cdot 10^{-12}$	$(3,06 \pm 0,15) \cdot 10^{-12}$	$8,60 \cdot 10^5$
743	$(1,97 \pm 0,12) \cdot 10^{-12}$	$(2,05 \pm 0,10) \cdot 10^{-12}$	$(1,91 \pm 0,10) \cdot 10^{-12}$	$9,70 \cdot 10^5$
735	$(1,39 \pm 0,08) \cdot 10^{-12}$	$(1,37 \pm 0,07) \cdot 10^{-12}$	$(1,35 \pm 0,07) \cdot 10^{-12}$	$3,76 \cdot 10^6$
723	$(1,07 \pm 0,06) \cdot 10^{-12}$	$(1,04 \pm 0,05) \cdot 10^{-12}$	$(1,04 \pm 0,05) \cdot 10^{-12}$	$3,43 \cdot 10^6$
707	$(6,50 \pm 0,39) \cdot 10^{-13}$	$(6,46 \pm 0,32) \cdot 10^{-13}$	$(6,50 \pm 0,32) \cdot 10^{-13}$	$8,59 \cdot 10^6$

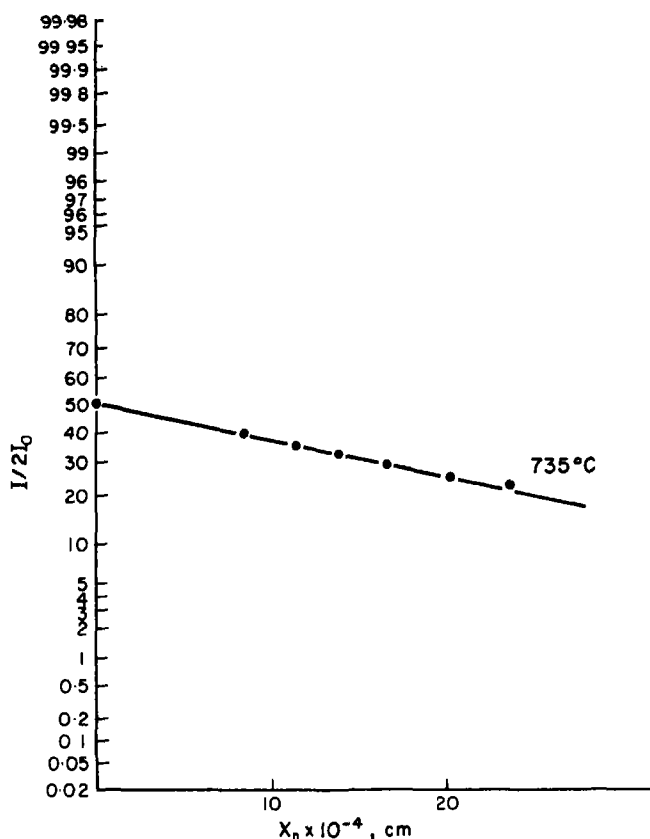


Fig. 1. Typical activity profile for ^{55}Fe diffusion in Fe/3%Si (735°C), $\text{erf } I/2I_0$ vs. x_n .

computer machine. We used least squares method.

4. DISCUSSION

Activation energies values of iron diffusion in Fe/3%Si alloy in the considered range of temperatures are in excellent agreement with previous works on diffusion [16] and creep [17] in b.c.c. phase of the same alloy at high temperatures.

Self-diffusion in α -Fe is enhanced by the presence of a 3 per cent of a substitutional 'fast impurity' in its lattice, due to electronic and steric effects (in which we work at present) besides the correlation factor associated to a change in vacancy jump frequency in the immediate neighborhood of impurity.

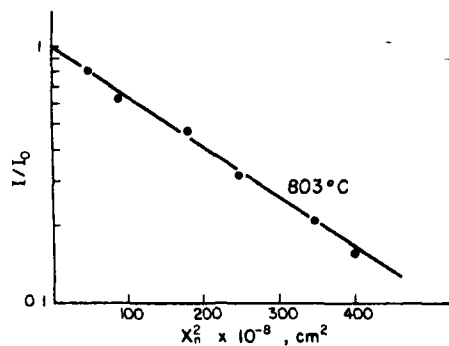


Fig. 2. Typical activity profile for ^{55}Fe diffusion in Fe/3%Si (803°C), $\ln I/I_0$ vs. (x_n^2) .

The 'magnetic anomaly' is observed in Iron diffusion in Fe/3%Si and the magnitude of the difference between activation energies of

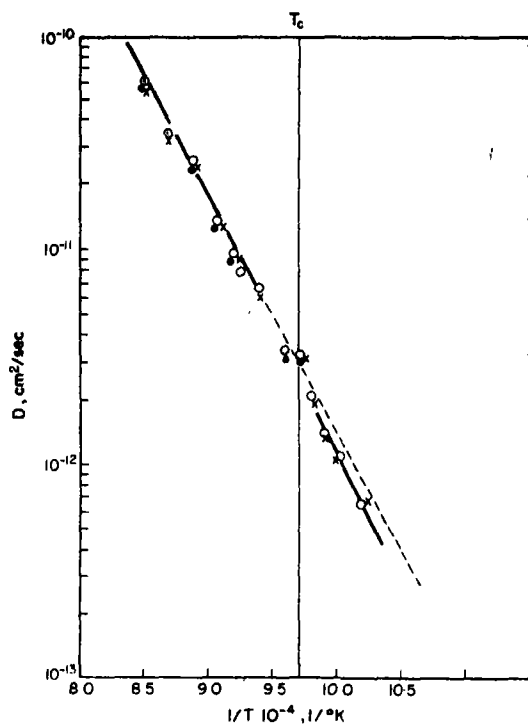


Fig. 3. $\ln D$ vs. $(1/T)$, $\circ = D^{55}$; $\bullet = D^{59}$; $\times = D^{55+59}$.

Table 4.

Isotope	ΔH (cal/mole)
^{55}Fe	2122
^{59}Fe	2101
$^{55+59}\text{Fe}$	1609

ferromagnetic and paramagnetic ranges (ΔH) is comparable to ΔH values reported by previous works[1-7]. In spite Graham's data [13] don't report this anomalous effect.

To avoid grain boundary contribution to bulk diffusion, which is significant at low temperatures[18] we employed single-crystal specimens.

The observed decrease in diffusion rate below Curie temperature seems to be justified by a change in elastic constants and in vacancy concentration accompanying the magnetic ordering process. Both magnitudes, which are not independent, modify the diffusion rate and diffusion jump frequency. Lytton[9]

reports for Fe/3%Si an unusual variation of Young's modulus with temperature at T_c , similar to that observed in pure iron. Besides, it would be interesting to confirm experimentally, the changes in vacancy concentration near T_c in iron, calculated by Schoijet y Girifalco[11] employing a statistical model analogous to that of order-disorder, in which spontaneous magnetization replaces the degree of long-range order.

(a) Isotope effect measurements

Special precautions were necessary in the isotope effect experiments to achieve measurements with the required accuracy.

Isotope effect was measured on specimens deposited with the mixture $^{55}\text{Fe} + ^{59}\text{Fe}$ and separation of both isotopes activity was performed by their different radiation. Specimens were annealed together with those used for D determinations. Sectioning was performed, in this case, with ultramicrotome and cuttings were dissolved in hot HCl, and measured as liquids, which were standardized to constant volume. We treat to maintain concentration of dissolved metal constant to avoid variation of self-absorption. Errors due to non-parallel cuttings with ultramicrotome were negligible.

Measurements were achieved by counting the activity of each section with the mentioned counters (^{55}Fe X-rays with the flow counter and ^{59}Fe γ -radiation with the scintillation counter). The liquid specimen activity was measured simultaneously by the two detectors placed vertically above and under the specimen. This arrangement, detailed by Heumann *et al.*[19] enabled to conserve the same counting geometry. We used a plastic container for each measurement because we had difficulties in decontaminating them. We confirmed that error in changing (identical) containers was negligible by measuring successively the same solid standard specimen in different containers. The absorption of ^{59}Fe γ -radiation by the plastic container bottom wall was considered negligible too.

As the flow counter registered the contribu-

tion of ^{59}Fe β -radiation to ^{55}Fe X-rays we corrected each measurement using a pure ^{59}Fe liquid standard specimen [19]. In addition, we performed several measurements with the flow counter with a Beryllium absorber (0,078 cm thickness) to separate the soft ^{55}Fe X-rays from ^{59}Fe β -radiation but the efficiency of our flow counter (filled with a mixture of Argon and methane) was poor [20].

Temperature effects on counters were considered because at higher temperatures the counter plateau becomes shorter and more sloping and its starting potential becomes higher. Precautions were taken to measure when radiative solution temperature was near 20°C.

Atmospheric pressure dependence on counting rate was taken in account. Gas flux in flow counter was maintained constant. High voltage was constant during measurements. Dead time of counters was taken in account and this correction was significant when counting rate was high. Background data were subtracted from each measurement; this correction was important for specimen with low activity. Corrections for decay of ^{55}Fe and ^{59}Fe during experience time were taken in account too; previously we had measured ^{59}Fe half-life (See Table 2. $\lambda = 44$ days).

As desintegration is a random event Poisson's distribution is valid. The standard deviation (σ) is related to the total counts number (N) by $\sigma = \sqrt{N}$. We considered the standard proportional deviation $\sigma/N = N^{-1/2}$ which gives a good idea of the required accuracy. It can be reduced by counting large N in longer times of measurements. The higher value of $N^{-1/2}$, with which we worked was 0,5 per cent. If isotope concentration after a diffusion annealing during t is given as a function of x_n as:

$$I = I_0 / \sqrt{\pi D t} \cdot \exp(-x_n^2 / 4 D t). \quad (8)$$

Since both isotopes are diffused simultaneously the relative concentration as a

function of position will differ because their D are different, and:

$$\ln I^{55}/I^{59} = cte + (1 - D^{59}/D^{55}) x_n^2 / 4 D^{59} t. \quad (9)$$

According to equation (8) it is possible to rewrite equation (9) as:

$$\ln I^{55}/I^{59} = cte - (1 - D^{59}/D^{55}) \ln I^{59}. \quad (10)$$

The plot $\ln I^{55}/I^{59}$ vs. $\ln I^{59}$ gives a straight line of slope $(1 - D^{59}/D^{55})$. Values of slopes in equation (10) are introduced in equation (1) to get E values. $(1 - D^{59}/D^{55})$ and E values and their errors were calculated with a computer machine with programs specially developed for this work.

5. RESULTS

Figure 4 is the normalized plot $\ln I^{55}/I^{59}$ vs. $\ln I^{59}$ for different temperatures. Note that abscissa scale is a decreasing one from left to right. Table 5 gives E values with their errors in the considered range of temperatures and ΔK values assuming a vacancy mechanism ($f = 0,727$ for b.c.c. elements [21]).

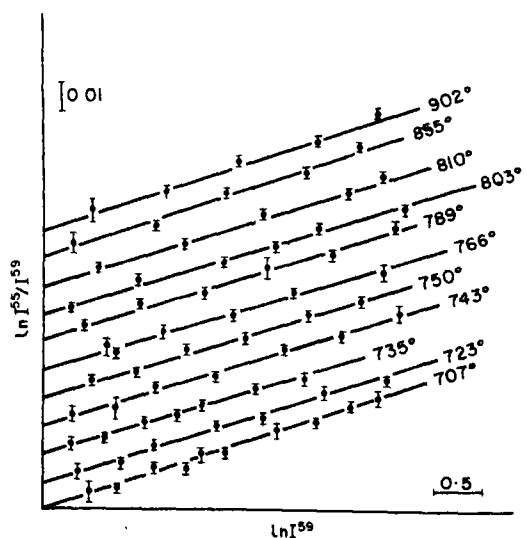


Fig. 4. $\ln I^{55}/I^{59}$ vs. $\ln I^{59}$. Ordinate division: 0,01 and Abscissa division: 0,5 (Abscissa scale decreases from left to right).

Table 5.

$T (^{\circ}\text{C})$	$1 - D^{50}/D^{55}$	E	ΔK
902	$0,0137 \pm 0,0016$	$0,397 \pm 0,040$	$0,546 \pm 0,050$
855	$0,0130 \pm 0,0015$	$0,377 \pm 0,034$	$0,517 \pm 0,047$
810	$0,0119 \pm 0,0014$	$0,346 \pm 0,035$	$0,475 \pm 0,048$
803	$0,0120 \pm 0,0016$	$0,349 \pm 0,036$	$0,480 \pm 0,044$
789	$0,0119 \pm 0,0016$	$0,346 \pm 0,037$	$0,475 \pm 0,051$
766	$0,0118 \pm 0,0016$	$0,343 \pm 0,038$	$0,471 \pm 0,052$
750	$0,0117 \pm 0,0018$	$0,339 \pm 0,041$	$0,466 \pm 0,056$
743	$0,0118 \pm 0,0020$	$0,343 \pm 0,045$	$0,471 \pm 0,061$
735	$0,0116 \pm 0,0020$	$0,336 \pm 0,044$	$0,461 \pm 0,061$
723	$0,0117 \pm 0,0020$	$0,339 \pm 0,045$	$0,466 \pm 0,062$
707	$0,0116 \pm 0,0021$	$0,336 \pm 0,048$	$0,461 \pm 0,066$

6. DISCUSSION

The near equality of isotope effect value reported by this work in paramagnetic and ferromagnetic ranges shows that the details of diffusion are the same in both ranges. Analogous results were found by Peterson *et al.*[22] in isotope effect in Zn diffusion in ordered and disordered Cu/Zn, although validity of equation (1) is questioned in this work.

Low E values (Table 5) can be attributed to a strongly relaxed vacancy mechanism. Experiences of diffusion coefficient variation with pressure in Fe/2%V and Fe/3%V alloys [23] support a vacancy mechanism. Activation volume enables to get information on ΔK ; if there is a lattice relaxation a small $\Delta V/V$ is related to a low ΔK . As $\Delta V/V$ was not still measured for α -Fe or Fe/3% Si, we used the value reported by Hanneman *et al.* [23] ($\Delta V/V = 0,45$) to compare with our values (Table 5) and agreement is good. Results are also compatible with an interstitialcy mechanism.

7. CONCLUSIONS

Diffusion coefficients of ^{55}Fe , ^{50}Fe and $^{55+50}\text{Fe}$ in Fe/3%Si single-crystal specimen were measured in a range of temperatures between 707 and 902°C. Diffusion coefficient variation with temperature follows the Arrhenius law in paramagnetic and ferromagnetic ranges showing the 'magnetic anomaly', near the Curie temperature. Iso-

tope effect measurements show that the same mechanism is valid in both regions. Low E values are associated to a highly relaxed vacancy mechanism or to an interstitialcy one.

Acknowledgements—Thanks are given to Professor K. Hirano for his encouragement in our work, to Dr. R. Borg and Ing. J. Mazza for helpful discussions, and to Dr. J. Walter for the Fe/3%Si single-crystals. We are indebted too with the Metallurgy Department and Centro de Cálculo of the Universidad Tecnológica Nacional, Facultad Regional Buenos Aires, because we used their laboratories and their Computer IBM/360 respectively.

REFERENCES

- BORG R. and BIRCHENALL E., *Trans. AIME* **218**, 980 (1960).
- BUFFINGTON F. S., HIRANO K. and COHEN M., *Acta Metall.* **9**, 434 (1961).
- HIRANO K., AWARGALA R. P., AVERBACH B. L. and COHEN M., *J. appl. Phys.* **33**, 3049 (1962).
- HIRANO K., COHEN M. and AVERBACH B. L., *Acta Metall.* **9**, 440 (1961).
- BORG R. J. and LAI D. F., *Acta Metall.* **11**, 861 (1963).
- BORG R. J. and LAI D. F., *Report Univ. California, Livermore, Calif.* (1962).
- LAI D. F. and BORG R. J., *Trans. AIME* **233**, 1973 (1965).
- STANLEY J. and WERT C., *J. appl. Phys.* **32**, 267 (1961).
- LYTTON J. L., DSM Report No. 62-4, Stanford Univ. Calif. (1962).
- BORG R. J., *J. appl. Phys.* **35**, (1), 567 (1964).
- SCHOIJET M. and GIRIFALCO L. A., *J. Phys. Chem. Solids* **29**, 481 (1968).
- WALTER C. M. and PETERSON N. L., *Phys. Rev.* **178**, 178 (1969).
- GRAHAM D., *J. appl. Phys.* **40**, 2386 (1969).
- BARR L. W. and MUNDY J. N., *Diffusion in b.c.c. Metals*, ASM, Ohio, (1965).
- LEYMONIE C., *Les traceurs radiatifs en Métallurgie physique*, Dunod, Paris (1960).

16. MILLS B., WALKER G. K. and LEAK G. M., *Phil. Mag.* **12**, 939 (1965).
17. HONDROS E. D., *Phys. Status Solidi* **21**, 375 (1967).
18. HAYNES C. W. and SMOLUCHOWSKY R., *Acta Metall.* **3**, 130 (1955).
19. HEUMANN T. and IMM R., *J. Phys. Chem. Solids* **29**, 1613 (1968).
20. BUFFINGTON F. S., BAKALAR I. D. and COHEN M., *The Physics of Powder Metallurgy*, McGraw-Hill, New York (1951).
21. ADDA Y. and PHILIBERT J., *La diffusion dans les Solides*, Presses Univ. de France, Paris (1965).
22. PETERSON N. L. and ROTHMAN S. J., *Phys. Rev.* **154**, 558 (1967).
23. HANNEMAN R. E., OGILVIE R. E. and GATOS H. C., *Trans. AIME* **233**, 691 (1965).

CALCULATION OF THE PHOTOELECTRIC EFFECT IN SILICON

L. R. SARAVIA and L. CASAMAYOU

Instituto de Física, Facultad de Ingeniería y Agrimensura, Universidad de la República, Montevideo,
Uruguay

(Received 9 February 1970; in revised form 4 May 1970)

Abstract—The contribution from direct interband transitions to the photoelectric effect in Silicon is calculated for photon energies up to 10 eV. Refined computational techniques for the calculation of the energy distribution curves allow a detailed comparison of the theoretical and experimental curves. The agreement for the higher electron energies is excellent and the structure is interpreted in terms of the details of the energy bands.

1. INTRODUCTION

THERE has been considerable interest on the photoelectric energy distributions in Si as a means of studying its energy band structure. There exist experimental results[1-4] for photon energies covering the range 3-10 eV and showing very interesting structure. Theoretical analysis has been performed for photon energies below 6 eV on the assumption that the bulk of the optical transitions are direct. Kane[5] has developed a theory for the critical point structure on the energy distributions. Brust[6] has performed a detailed calculation of the distributions using a model of the energy bands of Si based on a pseudopotential approach. Its resolution is not enough to allow a clear identification of the structure in terms of the energy bands.

On the present work we improve the resolution of the photoelectric energy distribution calculations applying the numerical techniques introduced by Gilat and Raubenheimer [7] to study the critical point structure of phonon spectra and recently used in the study of the optical properties of Si in terms of its electron energy bands[8]. Also, the photon energy range for the calculation is extended to 10 eV, allowing the interpretation of structure of importance because of its relation with conduction bands not usually studied through optical experiments. It is expected that the

structure at higher energies will be easier to interpret as several effects, like escape probability factors and transport effects, are not so important for those energies.

The procedure to compute the photoemission energy distributions is described in Section 2. A direct transition model is adopted. The contribution from the different energy band transitions is calculated, but no detailed study of the scattering of electrons in the crystal is performed. The escape probability factor is calculated using the hypothesis adopted by Brust[6]. The model adopted for the energy bands of Si is explained in Section 3. They are calculated using a pseudopotential approach combined with a *k.p* extrapolation procedure. Spin-orbit effects are included. The theoretical results are given in Section 5. The agreement is shown to be excellent for the higher electron energies. The experimental structure shows considerable broadening, making difficult its interpretation in terms of individual critical points. All the same, the contribution from a whole interband transition is in general quite localized, and it is possible to interpret the peaks in terms of them as well as indicate the region in the Brillouin Zone responsible for the structure. For lower electron energies, especially for the higher photon energies, the discrepancies are large, showing that other effects should be

taken into account. Several types of transport processes[9-11] as well as contributions from non-direct transitions[12] have been considered in the past as possible sources for the difference. No attempt has been made to include them in the present calculation.

2. CALCULATION OF THE ENERGY DISTRIBUTIONS

We are dealing with photoelectrons produced in the volume of a semiconductor by direct optical excitation. If ω is the frequency of the incident photon and E the final conduction band energy of the excited electrons, the energy distribution function $N(E, \omega)$ is given by

$$N(E, \omega) = A \sum_{n,s} \int_{BZ} |\mathbf{p}_{ns}(\mathbf{k})|^2 P_{(E,\mathbf{k})} \delta(\omega_{ns}(\mathbf{k}) - \omega) \delta(E_n(\mathbf{k}) - E) d^3k. \quad (1)$$

The sum is over all conduction bands n and valence bands s . The integral is performed over all the Brillouin Zone (BZ). $\mathbf{p}_{ns}(\mathbf{k})$ is the momentum matrix element between bands n and s , A is a normalization constant and $\hbar\omega_{ns}(\mathbf{k})$ is equal to $E_n(\mathbf{k}) - E_s(\mathbf{k})$. $P(E, \mathbf{k})$ is the probability that the electron produced with energy E and wave vector \mathbf{k} will escape.

We are interested in the calculation of $N(E, \omega)$. A method previously used[6] consists on the calculation of the energy bands $E_n(\mathbf{k})$ at a number of points over a cubic mesh in the BZ, and their classification according to energy and photon frequency. Because of the double classification, we need a large number of points in order to reduce the scattering on the histograms to a reasonable value. This was solved by Brust[6] increasing considerably the number of points initially obtained with the energy band calculation through a quadratic interpolation. All the same, the resolution obtained by this method is not enough to study in details the sharp structure produced by the two dimensional critical point structure related to the energy distributions.

We develop here a method based on the

analytical calculation of integral[1]. If we consider ω and E as independent variables, we can perform a change of variables in (1). Because of the delta functions, the integrations in E and ω are immediate and we get

$$N(E, \omega) = A \sum_{n,s} \int_C |\mathbf{p}_{ns}(\mathbf{k})|^2 P(E, \mathbf{k}) \times \frac{1}{|\nabla_{\mathbf{k}} E \times \nabla_{\mathbf{k}} \omega|} d\mathbf{l}. \quad (2)$$

The curve C in the BZ is defined by the surfaces

$$E_n(\mathbf{k}) = E, \omega_{ns}(\mathbf{k}) = \omega \quad (3)$$

$d\mathbf{l}$ is an element of the curve C .

In order to perform the integration in (2) we need an analytic expression for $E_n(\mathbf{k})$ and $\omega_{ns}(\mathbf{k})$. The energy band calculation gives numerical values for the energy bands over a cubic mesh on the BZ. We introduce a linear interpolation as explained elsewhere [8]. Briefly, each cube in the mesh is divided in six tetrahedrons. Inside a tetrahedron we adopt a linear expression for $E_n(\mathbf{k})$:

$$E_n(\mathbf{k}) = \mathbf{a} \cdot \mathbf{k} + b. \quad (4)$$

The four constants in (4), \mathbf{a} and b , are determined by matching the values of $E_n(\mathbf{k})$ at the four corners of the tetrahedron, which are known from the numerical calculation.

Inside each tetrahedron, the surfaces defined by (3) are planes and the curve C is a straight line. Its length and end points can be determined algebraically. If we also fit the other terms in the integrand of (2) by a linear form, the evaluation of the contribution from each tetrahedron is immediate.

For the calculations to be performed in this work, the cubic mesh necessary to obtain a good resolution will have about 1600 points in the asymmetric part of the BZ. The energy distributions will be computed at intervals of energy equal to 0.01 eV. As an example, we show in Fig. 1 the result of a calculation for an

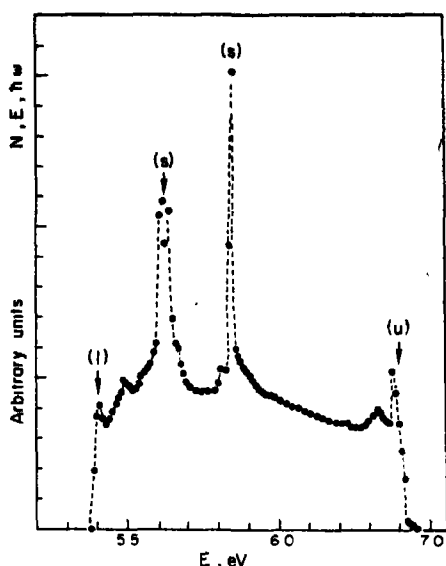


Fig. 1. Contribution of an interband transition in Si to the photoemission energy distribution curve for a value of photon energy equal to 5.39 eV. The calculated values are indicated as obtained from the computation (black dots). The scattering of the points is typical for this type of calculation. Structure produced by the three types of two-dimensional critical points can be seen in the figure.

interband transition in Si where the three types of two dimensional critical points discussed by Kane[5], minimum (l), maximum (u), and saddle point (s), are present. We see that the scattering of the calculated points is small and the critical points are well defined.

In (1) and (2) there appears the escape probability factor $P(E, \mathbf{k})$. To treat this function exactly would require having rather detailed information about the surface potential and scattering mechanisms. We will compute it adopting the hypothesis proposed by Brust[6]. We assume that an electron produced with an energy $E_n(\mathbf{k})$ has a momentum \mathbf{k} which is completely randomized by elastic scattering processes before the electron reaches the surface of the crystal. Electrons whose momentum is directed towards the surface are assumed to leave the crystal with an escape probability

$$\begin{aligned} &\text{Constant, if } E_n(\mathbf{k}) > \frac{\hbar^2 k_T^2}{2m} \\ &0, \text{ if } E_n(\mathbf{k}) < \frac{\hbar^2 k_T^2}{2m} \end{aligned} \quad (5)$$

where k_T is the component of \mathbf{k} parallel to the surface of the crystal and E_{vac} is the vacuum level. This factor is obtained on the supposition that the absolute value of the momentum \mathbf{k} is conserved during the process and k_T is continuous through the escape surface. Next, we average the escape probability over all the available states of energy E in the BZ, obtaining an escape probability factor $P(E)$ independent of \mathbf{k} .

3. CALCULATION OF THE ENERGY BANDS

We need to compute the energy bands and the dipole matrix elements over a cubic mesh in the BZ containing a considerable number of points. We use a pseudopotential method to generate the bands and a $\mathbf{k} \cdot \mathbf{p}$ extrapolation procedure to increase the size of the cubic mesh as explained elsewhere[8]. Briefly, one computes eigenvalues and eigenvectors at a small number of points in a coarse cubic mesh (around 100 points in the asymmetric part of the BZ) by solving the secular equation generated by the semiempirical pseudopotential approach. Then, a refined mesh of points is generated from the previous one (around 1600 points) by a $\mathbf{k} \cdot \mathbf{p}$ extrapolation procedure. The combination has the advantage of greatly expediting the computational work.

The convergence errors have been discussed elsewhere [6], and the same conclusions apply here.

The spin-orbit terms have also been considered. We use the formalism developed for Ge[14], taking the orthogonalization coefficients proper to Si.

The pseudopotential parameters used for Si are: $V(1, 1, 1) = -0.21$ Ryd, $V(2, 2, 0) = 0.058$ Ryd, $V(3, 1, 1) = 0.078$ Ryd. The spin parameter was selected to fit the experimental value of the spin-orbit splitting at the $\Gamma_{25'}$ level[15]. The spin-orbit parameters in Si are rather small and have little importance from the point of view of the interpretation of the photoemission results. The splitting at some of the most important levels are given in Table 1. The present pseudopotential model for the Si energy bands is very similar to one previously discussed by Saravia and Brust[8], and we refer to their work for a comparison with the energy bands calculated by other authors[16, 17].

The resulting energy bands along two principal directions in the BZ are shown in Fig. 2. The double group notation is not used. In the discussion that follows the energy value at a general point in the BZ is denoted by E_i ($i = 1, 2, \dots$), not taking into account Kramer's degeneracy, i.e., each value of i corresponds to two eigenvalues.

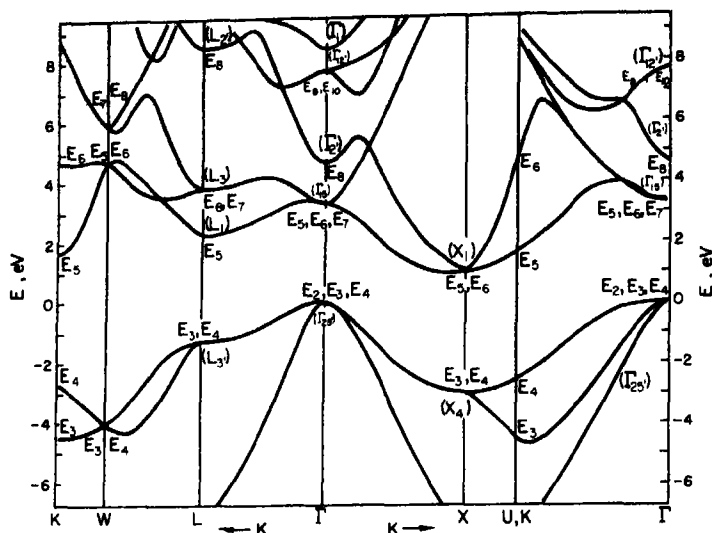


Fig. 2. Energy bands of Si along some principal symmetry lines. They were computed using the pseudopotential method together with a k.p extrapolation procedure. The energy bands are labeled by E_i ($i = 1, 2, \dots$), with i increasing with energy. The single group notation is given for some of the points of the BZ.

Table 1. Si: theoretical spin-orbit splittings in eV

Levels	Splittings
$\Gamma_{25'}$	0.044
$\Gamma_{15'}$	0.031
$L_{3'}$	0.030
L_{21}	0.012

4. RESULTS

(a) Escape probability

Calcott [2] has published energy distribution curves measured on surfaces covered with Cesium films of different thicknesses: one monolayer, 0.3 of a monolayer, and no monolayer. The film thickness affects the escape probability function, since the position of vacuum level is changed. Also, the dynamic processes related to the emitted electron, especially the randomization of the crystal momentum accepted as one of our hypothesis, are altered. We are not going to attempt a study of the last point and the same hypothesis are used throughout all the calculation. We adopt different vacuum levels for the three

cases: 5.15, 3.0 and 2.2 eV over the top of the valence band respectively. The resulting escape probability curves are shown in Fig. 3.

In the discussion that follows all the electron energies are referred to the top of the valence bands.

(b) The photoelectric energy distribution curves

One of the calculated curves, not taking into account the escape probability factor $P(E)$, is shown in Fig. 4. We include interband transitions involving valence bands 2–4 and conduction bands 5–12.

The results are extremely rich in details and the structure is in general quite sharp. This is produced by the fact that the structure due to saddle points is logarithmic, and the discontinuities related to maxima and minima points can take large values, even approaching infinite. A direct interpretation of the experimental peaks is not possible because they are much broader than the calculated ones, as can be seen from Figs. 5–7. This is expected because effects such as electron–

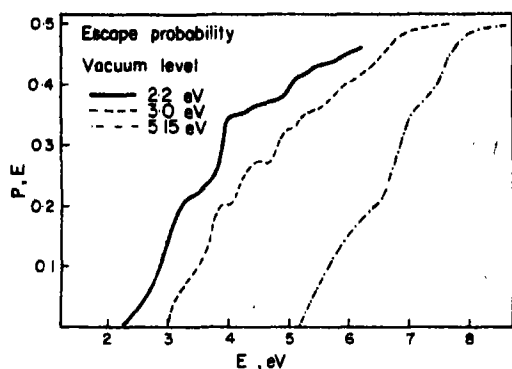


Fig. 3. Shows the three different escape probability functions used in the present calculation. The differences are produced by the position assumed for the vacuum level in each case.

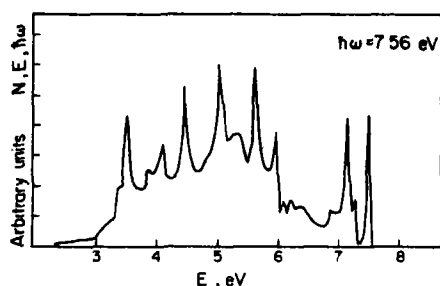


Fig. 4. Photoemission energy distribution curves of Si for a photon energy of 7.56 eV. Escape probability and broadening factors have not been included.

phonon and electron-electron scattering, interaction of the electrons with the Cesium film and band bending have not been considered.

In order to perform a comparison, we introduce a phenomenological broadening of the form

$$N'(E', \omega) = \int_0^\infty N(E', \omega) L(E, E') dE' \quad (6)$$

where

$$L(E, E') = \frac{1}{\pi} \frac{\Gamma}{\Gamma^2 + (E - E')^2} \quad (7)$$

Γ is the broadening constant. We adopt different values of Γ according to the thickness of the Cesium film: 0.15 eV, for the case with no Cesium, 0.20 eV for 30 per cent of a monolayer, and 0.25 eV for a full monolayer.

The energy distribution curves for different

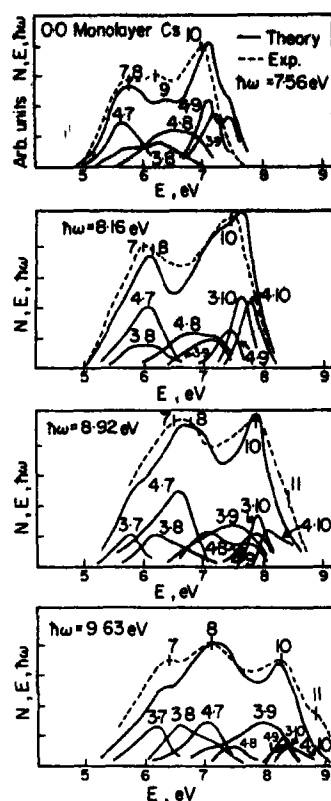


Fig. 5. Shows the calculated (solid lines) and the experimental (broken lines) energy distribution curves in Si for several values of photon energy corresponding to a sample with no Cs on its surface. The experimental curves are those given by Callcott (Ref.[2]). Their peaks are identified by numbers, from 1 to 11, as used by Callcott (Ref.[2]). The calculated curves include an escape probability factor with the vacuum level at 5.15 eV and a broadening factor equal to 0.15 eV. Partial results indicating the contribution from some of the interband transitions are also shown. They are identified by the numbers labeling the bands involved in the transition (e.g. label 4-7 indicates the contribution from transitions between valence band E_4 and conduction band E_7). For the sake of clarity only partial contributions important from the point of view of the interpretation of the peaks were included.

photon energies, including the effects of the escape probability factor and broadening, are given in Figs. 5-7. The experimental curves (2) are included. Relative scales have been selected since the absolute one has not been measured. Partial results from the most important interband transitions are also indicated.

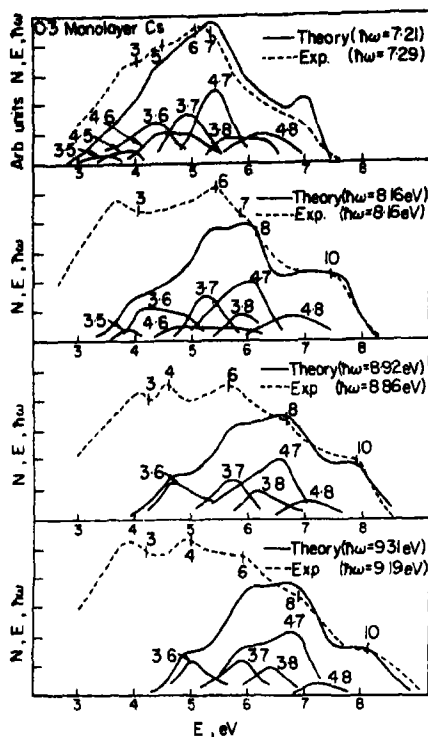


Fig. 6. Shows the calculated (solid lines) and the experimental (broken lines) energy distribution curves in Si for several values of photon energy corresponding to a sample with 0.3 of a monolayer of Cs on its surface. The experimental curves are those given by Callcott (Ref.[2]). Their peaks are identified by numbers, from 1 to 11, as used by Callcott (Ref.[2]). The calculated curves include an escape probability factor with the vacuum level at 2.8 eV and a broadening factor equal to 0.20 eV. Partial results indicating the contribution from some of the interband transitions are also shown. They are identified by the numbers labeling the bands involved in the transition (e.g., label 4-7 indicates the contribution from transitions between valence band E_4 and conduction band E_7). For the sake of clarity only partial contributions important from the point of view of interpretation of the peaks were included. Particularly, partial contributions producing peak No. 10 are not included since they were discussed in connection with the clean surface experiments.

5. DISCUSSION OF THE STRUCTURE

Two general remarks can be made about the results shown in Figs. 5-7. First, the structure at higher electron energies is well reproduced both in position and relative intensity. We will be able to interpret it in terms of the details of the energy bands. Second, the energy distribu-

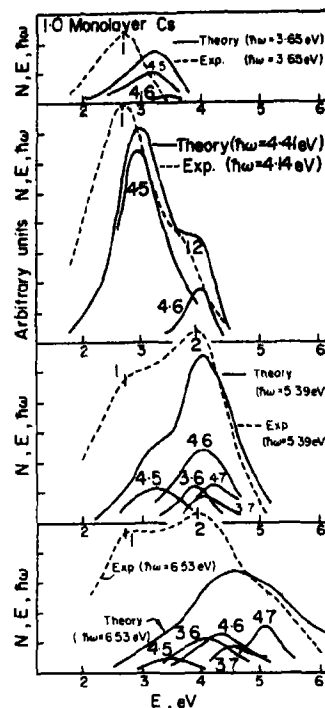


Fig. 7. Shows the calculated (solid lines) and the experimental (broken lines) energy distribution curves in Si for several values of photon energy corresponding to a sample with 1.0 of a monolayer of Cs on its surface. The experimental curves are those given by Callcott (Ref.[2]). Their peaks are identified by numbers, from 1 to 11, as used by Callcott (Ref.[2]). The calculated curves include an escape probability factor with the vacuum level at 2.2 eV and a broadening factor equal to 0.25 eV. Partial results indicating the contribution from some of the interband transitions are also shown. They are indicated by the numbers labeling the bands involved in the transition (e.g., label 4-7 indicates the contribution from transitions between valence band E_4 and conduction band E_7). For the sake of clarity only partial contributions important from the point of view of the interpretation of the peaks were included.

tions at lower energies show a large contribution, increasing as the electron energy decreases, which is not reproduced at all by our calculation. Part of the direct interband structure is superposed on this contribution. The pair production scattering mechanism [9, 13] or contributions from indirect transitions [12] could be possible sources for a secondary distribution of this type, although this is not definitive and the possibility is open

for errors in the experiment, the band calculation or the escape probability factor.

On the following we study the interpretation of the different peaks in terms of the direct interband transition contributions. We use the notation adopted by Callcott [2] for the experimental peaks. We will not perform a detailed study of the critical point structure appearing in the theoretical calculation because it would be too lengthy.

We find that each peak is produced by contributions from a few interband transitions at most. They are indicated in Table 2. In general, the energy distributions for each

transition shows a dominant peak. This is shown for some photon energies in Figs. 8-10. A plot $E-\hbar\omega$ for these peaks is shown in Fig. 11 together with the experimental ones as given by Callcott [2]. The regions of the BZ producing most of the contribution to these peaks are shown in Figs. 12-19, where the electron energy and optical energy contours in the principal symmetry planes of the BZ are given. Regions where both types of contours are parallel give the large contributions to $N(E, \hbar\omega)$. This data establishes the connection between the experimental structure and energy bands and it has been summarized in Table 2.

Peak No. 10 is well reproduced by the present calculation. For the higher photon energies most of the contribution comes from interbands E_{3-10} and E_{4-10} . The main contribution comes from a region near the Γ point. Since the bands E_3 and E_4 have very similar

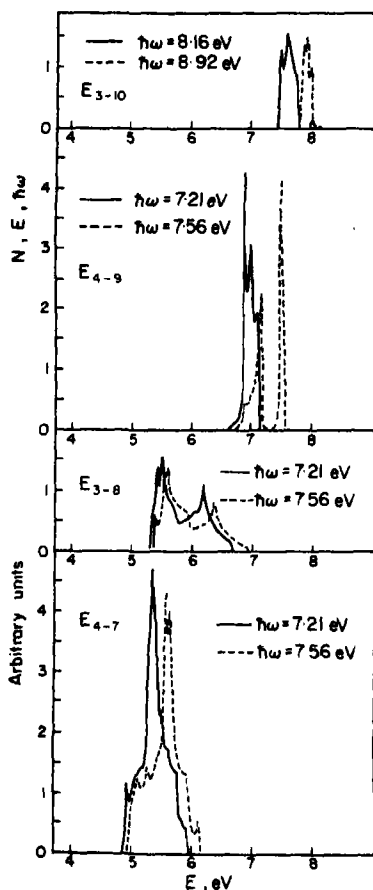


Fig. 8. Shows the contributions from different interband transitions in Si to the energy distribution curves corresponding to several values of photon energy. Escape probability and broadening factors are not included.

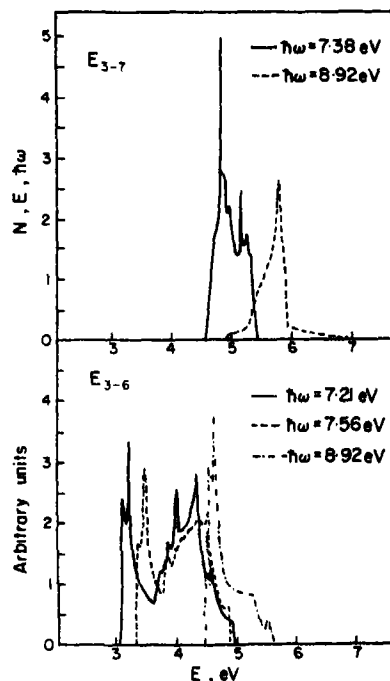


Fig. 9. Shows the contributions from different interband transitions in Si to the energy distribution curves corresponding to several values of photon energy. Escape probability and broadening factors are not included.

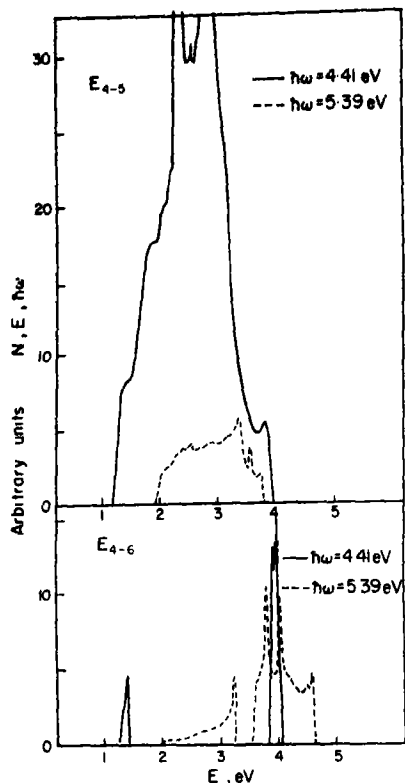


Fig. 10. Shows the contributions from different interband transitions in Si to the energy distribution curves corresponding to several values of photon energy. Escape probability and broadening factors are not included.

values at Γ , it is reasonable to expect them to contribute to the same peak. The photon energy corresponding to the $\Gamma_{25'} - \Gamma_{12'}$ transition, about 7.7 eV, indicates the limit below which these bands will give no contribution to the peak. Below 7.7 eV interbands E_{3-9} and E_{4-9} are mainly responsible for peak No. 10. The analysis of their energy distribution curves is complicated somewhat by the fact that level E_9 is really composed of different crossing bands. For example, for $\hbar\omega = 7.56$ eV there are two different surfaces in the BZ contributing to the energy distribution curves.

Peak No. 9 appears in a small range of values of photon energy. Interband E_{3-8} is mainly responsible for it. The energy distribution function shows two peaks. The upper

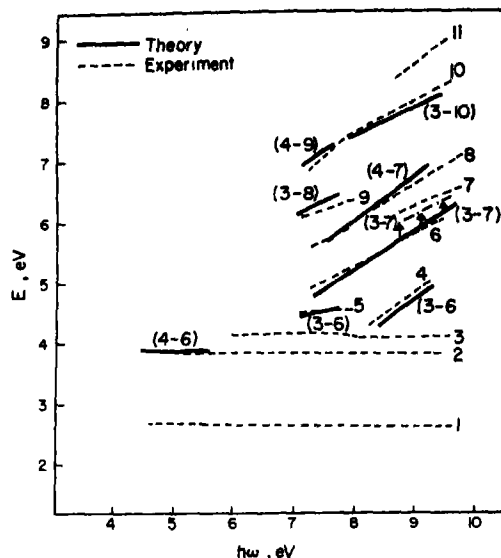


Fig. 11. E - $\hbar\omega$ curves for the most prominent calculated peaks (solid lines) and for the experimental peaks as given by Callcott (Ref.[2]), (broken lines). The curve corresponding to transition 3-7 is shown twice. The second one corresponds to the peak shifted by the inclusion of the escape probability factor.

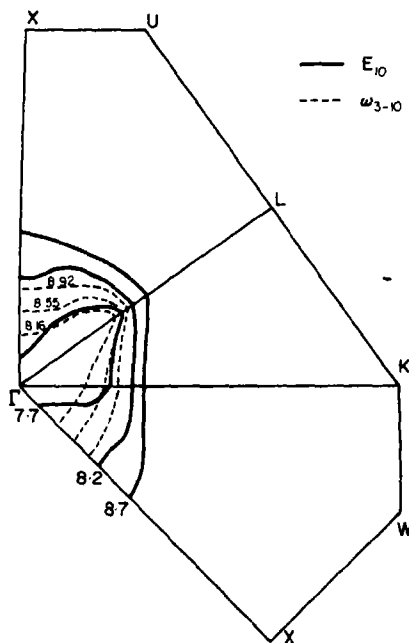


Fig. 12. Contours of constant electron energy (solid lines) for band E_{10} and constant photon energy (broken lines) for interband transition E_{3-10} for some of the principal planes of the BZ (in eV).

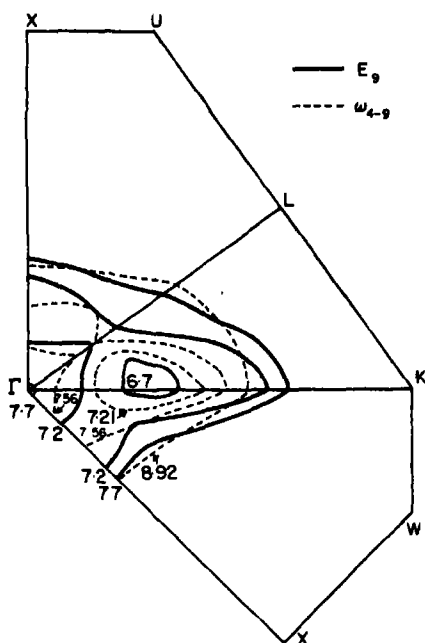


Fig. 13. Contours of constant electron energy (solid lines) for band E_9 and constant photon energy (broken lines) for interband transition E_{4-9} in some of the principal planes of the BZ (in eV).

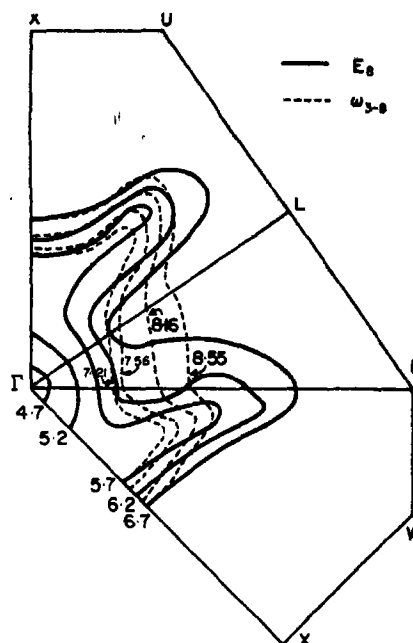


Fig. 14. Contours of constant electron energy (solid lines) for band E_8 and constant photon energy (broken lines) for interband transition E_{3-8} in some of the principal planes of the BZ (in eV).

Table 2. Interpretation of experimental structure in terms of interband transition contributions. The region of the Brillouin Zone responsible for the peak is indicated. Photon ($\hbar\omega$) and electron (E) energies in eV for the most prominent theoretical peaks are given for each interband transition

Peak No.	Interband transition	Location in* Brillouin Zone	Data for prominent peak $\hbar\omega$ — upper value (eV) E — lower value (eV)
10			
$\hbar\omega > 7.7$	3-10	Region along Λ line near Γ point	8.16 8.55 8.92 9.31
	4-10	Similar	7.50 7.70 7.86 8.06
$\hbar\omega < 7.7$	4-9	Near Σ line	7.21 7.38 7.56
	3-9	Similar	6.90 7.00 7.12
9	3-8	Along Σ line	7.21 7.38 7.56
			6.20 6.28 6.40
8	4-7	Plane LKWU	7.56 8.16 8.92
			5.65 6.10 6.60
7	3-7	Plane LKWU	7.21 7.56 8.16 8.92
6			4.76 4.98 5.32 5.80
5	3-6	Plane Γ LK	7.21 7.38 7.56
			4.40 4.46 6.56
4	3-6	Plane XWU near WU line	8.55 8.92 9.31
			4.36 4.62 4.98

*For details of location see Figs. 12-19.

the energy distribution curves could be increased considerably. At lower energies the agreement is worse but we expect to improve it by the consideration of other physical effects.

Acknowledgements—One of the authors (L.R.S.) is grateful to Dr. David Brust for many discussions on the subject. We thank G. Lesino for her help on the preparation of some of the computer programs used in this work. The calculations were performed at the 'Centro de Computación de la Universidad de la República, Montevideo, Uruguay'. We acknowledge its staff for technical assistance. This research was supported by the 'Fondo de Investigación Científica de la Universidad de la República, Montevideo, Uruguay'.

REFERENCES

1. ALLEN F. G. and GOBELLI G. W., *Phys. Rev.* **144**, 558 (1966), and previous works by the same authors, cited in the mentioned reference.
2. CALLCOTT T. A., *Phys. Rev.* **161**, 146 (1967).
3. SPICER W. E. and SIMON R. E., *Phys. Rev. Lett.* **9**, 385 (1962).
4. SPICER W. E. and EDEN R. C., *Proc. Internl. Conf. Phys. Semiconductors*, Vol. 1, p. 65 Moscow, (1968).
5. KANE E. O., *Phys. Rev.* **175**, 1039 (1968).
6. BRUST D., *Phys. Rev.* **139**, A489 (1965).
7. GILAT G. and RAUBENHEIMER L. J., *Phys. Rev.* **144**, 390 (1966).
8. SARA VIA L. R. and BRUST D., *Phys. Rev.* **171**, 916 (1968).
9. KANE E. O., *J. phys. Soc. Japan Suppl.* **21**, 37 (1966).
10. KANE E. O., *Phys. Rev.* **147**, 335 (1966).
11. KANE E. O., *Phys. Rev.* **159**, 624 (1967).
12. SPICER W. E. and EDEN R. C., *Bull. Am. phys. Soc.* **10**, 1198 (1965).
13. SPICER W. E., *J. phys. Soc. Japan Suppl.* **21**, 42 (1966).
14. SARA VIA L. R. and BRUST D., *Phys. Rev.* **176**, 915 (1968).
15. DRESSELHAUS G. G., KIP A. F. and KITTEL C., *Phys. Rev.* **98**, 368 (1955).
16. HERMAN F., KORTUM R. L., KUGLIN C. D. and SHORT R. A., *Quantum Theory of Atoms, Molecules, and the Solid State* p. 381. Academic Press, New York (1966).
17. BRUST D., *Phys. Rev.* **134**, A1337 (1964).

LINE BROADENING OF URANYL SALTS AT LOW TEMPERATURE

V. A. LODATO

Gulf General Atomic Inc. P.O. Box 608, San Diego, Calif. 92115, U.S.A.

(Received 9 April 1970)

Abstract—A model is developed for the energy transfer between uranyl ions for the resonant and non-resonant cases. The periods of excitation transfer are estimated and the spectral broadening of the resonant line is examined in terms of the excitation transfer between ions. The question of whether the initial excitation is due to dipole or quadrupole radiation is resolved.

1. INTRODUCTION

ONE OF the main features [1, 2] of the fluorescence spectra of the uranyl salts is the loss of high resolution at low temperatures. The width of the spectral lines can be attributed to five basic processes: (1) the emission of light energy which is accompanied by the transition of the uranyl ion into the non-excited electron state; (2) the conversion of the electron energy of the uranyl ion to the energy of the oscillations of the lattice; (3) the conversion of the energy of the intramolecular oscillations to the energy of oscillations of the lattice; (4) the energy transfer of intermolecular oscillations initially located around the absorbing or the emitting uranyl ion along the whole lattice; (5) the transfer of the energy of the electron excitation from one uranyl ion onto other uranyl ions.

Stepanov [3] has obtained an order of magnitude for the line widths for the first four processes from the Heisenberg uncertainty principle arguments, but he was not able to draw any conclusive evidence for the period of excitation transfer for the fifth process. According to Rabinowitch and Belford [4], the width of the fluorescent bands is due primarily to the excitation transfer between uranyl ions, but there has been no quantitative analysis for the frequency of exchange. In this paper, an order of magnitude calculation is presented to estimate the line widths due to

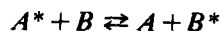
resonance and non-resonant broadening that may occur due to excitation transfer between neighboring UO_2^{+2} ions in the lattice.

In the non resonance case the excitation transfer is considered between different isotopic species of uranyl ions. (The isotopic splitting is of the order of 0.5 cm^{-1} .) We conclude that the excitation transfer accounts for the line broadening in the fluorescent spectra at low temperature.

2. MODEL

Consider the system of two molecules *A* and *B* that are fixed at some distance. The interaction with lattice vibrations of the surrounding medium is considered to be negligible since the total system is at a very low temperature. We assume that each molecule has a single electronic state in the energy region of interest.

Given an initial excitation on *A*, designated as A^* , the question is what is the characteristic time for excitation transfer between two states.



(State 1) (State 2). (1)

If the period of molecular vibration is much less than the period of excitation transfer between *A* and *B*, then for any probable nuclear configuration in the neighborhood of

the minimum of the potential surface of A^*B a number of vibrations will be complete within a single period of excitation transfer: the potential field felt by the two ions is that obtained by applying the adiabatic approximation to the coupled system of A and B .

The total Hamiltonian for the system is

$$\mathcal{H} = H_A^{e1}(\mathbf{q}_1) + H_A^{vib}(\mathbf{Q}_1) + H_B^{e1}(\mathbf{q}_2) + H_B^{vib}(\mathbf{Q}_2) + v(|\mathbf{q}_2 - \mathbf{q}_1 + \mathbf{R}|) \quad (2)$$

where the coordinates \mathbf{q}_1 , \mathbf{Q}_1 and \mathbf{q}_2 , \mathbf{Q}_2 are the collective electronic and nuclear coordinates of A and B respectively and $|\mathbf{R}|$ is the distance between the two. In the present two state case the total wavefunction for the system may be written as

$$\begin{aligned} \psi(\mathbf{q}_1, \mathbf{q}_2, \mathbf{Q}_1, \mathbf{Q}_2, t) = & C_{A^*B}(t) \phi_{A^*}(\mathbf{q}_1) \phi_B(\mathbf{q}_2) \\ & \times \chi_{A^*}(\mathbf{Q}_1) \chi_B(\mathbf{Q}_2) e^{i\epsilon_1 t} \\ & + C_{AB^*}(t) \phi_A(\mathbf{q}_1) \phi_{B^*}(\mathbf{q}_2) \\ & \times \chi_A(\mathbf{Q}_1) \chi_{B^*}(\mathbf{Q}_2) e^{i\epsilon_2 t} \quad (3) \end{aligned}$$

where the ϕ 's and χ 's correspond to the electronic and vibrational wavefunctions and ϵ_1 and ϵ_2 are the sums of the electronic and vibrational frequencies in states 1 and 2 respectively.

The squares of the moduli of the two coefficients, $|C_{A^*B}(t)|^2$ and $|C_{AB^*}(t)|^2$, correspond to the probability of finding the system in State 1 or State 2. Using time dependent perturbation theory, the Schrodinger equation reduces to two coupled linear first order differential equations with explicit time dependent factors

$$\begin{aligned} i\hbar \dot{C}_{A^*B}(t) e^{-i\epsilon_1 t} = & \langle \phi_{A^*} \phi_B | v | \phi_A \phi_B \rangle e^{-i\epsilon_1 t} \\ & \times C_{A^*B}(t) + \langle \phi_A \phi_{B^*} | v | \phi_{A^*} \phi_B \rangle \\ & \times \langle \chi_A | \chi_{A^*} \rangle \langle \chi_B | \chi_B \rangle \\ & \times e^{-i\epsilon_2 t} C_{AB^*}(t) \quad (4a) \end{aligned}$$

$$\begin{aligned} i\hbar \dot{C}_{AB^*}(t) e^{-i\epsilon_2 t} = & \langle \phi_A \phi_{B^*} | v | \phi_{A^*} \phi_B \rangle \\ & \times \langle \chi_A | \chi_{A^*} \rangle \langle \chi_B | \chi_{B^*} \rangle \\ & \times e^{-i\epsilon_1 t} C_{A^*B}(t) + \langle \phi_A \phi_{B^*} | v | \\ & \times \phi_A \phi_B \rangle C_{AB^*}(t) e^{-i\epsilon_2 t}. \quad (4b) \end{aligned}$$

Defining the variables $y_{A^*B}(t) = C_{A^*B}(t) e^{-i\epsilon_1 t}$ and $y_{AB^*}(t) = C_{AB^*}(t) e^{-i\epsilon_2 t}$, the equations become

$$\begin{aligned} i\hbar \dot{y}_{A^*B}(t) = & [\langle \phi_{A^*} \phi_B | v | \phi_A \phi_B \rangle \\ & - \hbar \epsilon_1] y_{A^*B}(t) + \langle \phi_{A^*} \phi_B | v | \phi_A \phi_{B^*} \rangle \\ & \times \langle \chi_A | \chi_{A^*} \rangle \langle \chi_B | \chi_{B^*} \rangle y_{AB^*}(t) \quad (5a) \end{aligned}$$

$$\begin{aligned} i\hbar \dot{y}_{AB^*}(t) = & \langle \chi_A | \chi_{A^*} \rangle \langle \chi_B | \chi_{B^*} \rangle \langle \phi_{A^*} \phi_B | v | \phi_A \phi_{B^*} \rangle \\ & \times y_{A^*B}(t) + [\langle \phi_A \phi_{B^*} | v | \phi_A \phi_B \rangle \\ & - \hbar \epsilon_2] y_{AB^*}(t). \quad (5b) \end{aligned}$$

Solving these two differential equations subject to the boundary conditions

$$C_{A^*B}(0) = A_1 \text{ and } C_{AB^*}(0) = A_2,$$

the probability of excitation transfer is

$$\begin{aligned} |C_{AB^*}(t)|^2 = & A_2^2 \cos^2 \left\{ \frac{1}{2} [4\beta^2 + \gamma^2]^{1/2} \frac{t}{\hbar} \right\} \\ & + \frac{(A_2 \gamma - 2A_1 \beta)^2}{4\beta^2 + \gamma^2} \\ & \times \sin^2 \left\{ \frac{1}{2} [4\beta^2 + \gamma^2]^{1/2} \frac{t}{\hbar} \right\} \quad (6) \end{aligned}$$

where β is the product of the electronic exchange energy $\langle \phi_{A^*} \phi_B | v | \phi_A \phi_{B^*} \rangle$ and the Franck-Condon factors $\langle \chi_A | \chi_{A^*} \rangle \langle \chi_B | \chi_{B^*} \rangle$, and $\gamma = \langle \phi_A \phi_{B^*} | v | \phi_{A^*} \phi_B \rangle - \langle \phi_A \phi_{B^*} | v | \phi_A \phi_B \rangle + \Delta E$, where $\Delta E = \hbar(\epsilon_2 - \epsilon_1)$.

In the case of exact resonance $\gamma = 0$, and equation (6) reduces to the well known formula (5,6) for the probability of excitation transfer $|C_{AB^*}(t)|^2 = A_2^2 \cos^2 \{ \beta(t/\hbar) \} + A_1^2 \sin^2 \{ \beta(t/\hbar) \}$ with the period of excitation transfer being $t = (\hbar/4\beta)$.

The second case of interest is that in which the excited electronic state of A is the same as B , and the energy difference ΔE is due to the vibrational isotope shift in the resonant state.

The probability of excitation transfer for the case, (7,8) with the initial conditions $A_1 = 1$ and $A_2 = 0$ is

$$|C_{AB^*}(t)|^2 = \frac{4\beta^2}{4\beta^2 + \Delta E^2} \times \sin^2 \left\{ \frac{1}{4} [4\beta^2 + \Delta E^2]^{1/2} \frac{t}{\hbar} \right\}. \quad (7)$$

The period of transfer is $\tau = (h/2)\{4\beta^2 + \Delta E^2\}^{-1/2}$. The effect of ΔE will clearly be greatest if $\Delta E \gg \beta$. As will be seen below, this is the relevant case.

Under these conditions the period of excitation transfer becomes small, however the amplitude of the transition probability is also small, being given by

$$\max\{|C_{AB^*}(t)|^2\} = |C_{AB^*}(\tau)|^2 = \frac{4\beta^2}{4\beta^2 + \Delta E^2}. \quad (8)$$

Representing the decay of initially excited A^* as a first order process

$$n_{A^*}(t) = n_{A^*}(0) e^{-kt} \quad (9)$$

k can be evaluated as follows. The amount of A^* at the end of successive periods, τ , is given by the series:

$$\begin{aligned} n_{A^*}(\tau) &= [1 - |C_{AB^*}(\tau)|^2] n_{A^*}(0) \\ n_{A^*}(2\tau) &= [1 - |C_{AB^*}(\tau)|^2]^2 n_{A^*}(0) \\ n_{A^*}(t) &= [1 - |C_{AB^*}(\tau)|^2]^{t/\tau} n_{A^*}(0). \end{aligned} \quad (10)$$

Then

$$[1 - |C_{AB^*}(\tau)|^2]^{t/\tau} = e^{-kt} \quad (11)$$

substituting from (8) and taking the logarithms

$$\frac{1}{\tau} \log \left[1 - \frac{4\beta^2}{4\beta^2 + \Delta E^2} \right] = -k. \quad (12)$$

Since $\Delta E^2 \gg \beta^2$

$$\frac{1}{\tau} \frac{4\beta^2}{4\beta^2 + \Delta E^2} = k \quad (13)$$

approximating τ on the same $\Delta E \gg \beta$ basis

$$k = \frac{2\Delta E}{h} \frac{4\beta^2}{4\beta^2 + \Delta E^2} \approx \frac{8\beta^2}{\hbar \Delta E} \quad (14)$$

To carry out the evaluation of β the electronic exchange matrix element, the interaction Hamiltonian, which is the coulombic energy between electrons of A and B , can be expanded in a multipole series which is

$$\begin{aligned} v &= \{e^2/\epsilon R^3\} \{M_A \cdot M_B - 3(M_A \cdot \hat{R})(M_B \cdot \hat{R})\} \\ &+ \{e^2/\epsilon R^4\} \left\{ \frac{1}{2}(R \cdot Q_A \cdot \hat{R})(M_B \cdot \hat{R}) \right. \\ &\quad \left. - (M_B \cdot Q_A \cdot \hat{R}) \right\} \\ &+ \{e^2/\epsilon R^4\} \left\{ \frac{1}{2}(\hat{R} \cdot Q_B \cdot R)(M_A \cdot \hat{R}) \right. \\ &\quad \left. - (M_A \cdot Q_B \cdot \hat{R}) \right\} \\ &+ \{e^2/\epsilon R^5\} \left\{ (\hat{R} \cdot Q \cdot Q_B \cdot \hat{R}) + \frac{1}{4}(\hat{R} \cdot Q_A \cdot \hat{R}) \right. \\ &\quad \left. \times (\hat{R} \cdot Q_B \cdot \hat{R}) + \frac{1}{6}(Q_A : Q_B) \right\} + \dots \end{aligned} \quad (15)$$

Here M_A , M_B and Q_A , Q_B are the dipole and quadrupole transition moment operators

$$M_B = \sum_i r_{Bi}, \quad Q_B = 3M_B M_B - M_B \cdot M_B 1 \quad (16)$$

The vector $R = |R| \hat{R}$ is the internuclear separation, e is the electronic charge, and ϵ is the static dielectric constant of the medium. In the case where the transitions $A \rightarrow A^*$ and $B \rightarrow B^*$ are optically allowed, the major interaction is dipole-dipole. However, if the transitions are strictly forbidden due to odd parity in the product of the wavefunctions of the initial and final states the major interaction arises from the quadrupole term in the interaction potential. Hence the matrix element may be approximated by

$$\langle \phi_A \phi_B | v | \phi_A \phi_B \rangle =$$

$$\begin{aligned} \frac{e^2}{\epsilon R^3} u_A u_B & \quad \text{Dipole-Dipole} \\ \frac{e^2}{\epsilon R^5} Q_A Q_B & \quad \text{Quadrupole-Quadrupole.} \end{aligned} \quad (17)$$

Here the u 's and Q 's correspond respectively to the dipole and quadrupole transition elements.

With regard to the evaluation of the vibra-

tional overlap integrals, it is sufficient to consider the transition $O \rightarrow O$ in the vibrational spectrum. Hence the Franck-Condon factors become

$$\langle X_A | X_{A'} \rangle = \frac{2\delta \delta_A}{\delta_A^2 + \delta^2} \exp \left\{ -\frac{1}{2} \delta^2 \Delta Q^2 \times \frac{\delta^2}{\delta_A^2 + \delta^2} \right\} \quad (18)$$

where $\delta_A = \{R_A M / \hbar^2\}^{1/2}$ and R_A is the force constant for A and M its mass. We have another corresponding expression for B .

Evaluation of the force constant factors from the spectral data of Dieke and Duncan [9] gives a value of ~ 0.997 ; these terms can be assumed to be unity and β is given by electronic interaction matrix elements.

The following is a table for the relaxation times where τ is the energy transfer period in the resonant case and the inverse of the decay constant in the non resonant case, and ϵ is the static dielectric constant $\text{CsUO}_2(\text{NO}_3)_3$ which is approximately equal to two.

3. CONCLUSION

Using the numerical values from Hall and Dieke [10] for $\text{CsUO}_2(\text{NO}_3)_3$ at 4.5°K one may calculate the dipole and quadrupole transition elements which are 3.66×10^{-38} esu²cm² and 3.6×10^{-46} esu²cm⁴ respectively.

Since the uranyl ions are separated by approximately 10 \AA one calculates from Table 1 that for dipole-dipole ($D-D$) interaction the relaxation time is 8.9×10^{-11} sec, while for quadrupole-quadrupole ($Q-Q$) interaction it is 1.06×10^{-21} sec. Since the resonant line width (3.9) is less than 0.3 cm^{-1} and much larger than the natural line width, one con-

cludes that the excitation transfer can not be due to $Q-Q$ interaction but agrees with the $D-D$ case.

In the non resonant case the two isotopic species of uranyl ion of the natural salt is separated by 50 \AA and the energy splitting is 0.5 cm^{-1} at 20°K [3]. Using Table 1, one calculated a relaxation time of 3.9×10^{-11} sec for the $D-D$ case while for $Q-Q$ interaction one has 5.2×10^{-21} . Hence from the relaxation time the interaction must be dipole-dipole, if it were not, one would not observe the isotopic splitting.

Since UO_2^{2+} is linear in character a dipole-dipole transition would be zero. However the electron cloud around the uranylion is distorted, due to the crystal field interaction with other ligands. A relaxation of the selection rules occurs and one has a forced dipole transition occurring. This is based on the fact that the oscillator strength for most uranyl salts is 10^{-8} [4].

Thus from the above discussion we conclude that the excitation transfer between uranyl ions must be dipole-dipole and the line width can be explained in terms of the energy transfer.

Acknowledgement—I would like to thank Dr. John P. Porter for several helpful conversations.

REFERENCES

1. UMREIKO D. C. and LARKIN G. N., *Z. Prikl. Spek.* **3**, 567 (1968).
2. STEPANOV B. I., *Z. Eksp. teor. Fiz.* **10**, 1153 (1951).
3. STEPANOV B. I., *Z. Eksp. teor. Fiz.* **10**, 1158 (1951).
4. RABINOWITCH E. and BEDFORD R., *Spectroscopy and Photochemistry of Uranyl Compounds*, p. 53, MacMillan, New York (1964).
5. LANDAU L. D. and LIFSHITZ E. M., *Quantum Mechanics Nonrelativistic Theory*, Chap. VI, Pergamon Press, London (1958).
6. Th. Forster, *Disc. Faraday Soc.* **27**, 7 (1959).
7. ROBINSON G. and FROSCHE R. P., *J. Chem. Phys.* **37**, 1962 (1961).
8. KATSUURA K., *J. Chem. Phys.* **43**, 4149 (1965).
9. DIEKE G. H. and DUNCAN A. B. F., *Spectroscopic Properties of Uranium Compounds*, p. 60, McGraw-Hill, New York (1949).
10. HALL L. A. and DIEKE G. H., *J. Opt. Soc. Am.*, **47**, 1092 (1957).

Table 1.

$\tau(\text{sec})$	Dipole-Dipole	Quadrupole-Quadrupole
Resonance	$\frac{h\epsilon R^3}{4e^2\mu_A\mu_B}$	$\frac{h\epsilon R^5}{4e^2Q_AQ_B}$
Non-resonance	$\frac{h\Delta E\epsilon^2R^6}{8e^4\mu_A^2\mu_B^2}$	$\frac{h\Delta E\epsilon^2R^{10}}{8e^4Q_A^2Q_B^2}$

TECHNICAL NOTES

Energy of migration of anion vacancy and interstitial in calcium fluoride

(Received 14 May 1970; in revised form 16 July 1970)

A CALCULATION based on Born model has been made of activation energies of migration for F^- vacancies as well as F^- interstitials in CaF_2 lattice. The method used was that described by Franklin[1].

For vacancy migration the path considered was along the $\langle 100 \rangle$ direction. The saddle point configuration was assumed to consist of two neighbouring vacant anion sites and a F^- ion at the mid-point of the anion cube edge. Region I ions (interactions treated explicitly) included both the nearest as well as the next nearest neighbours. Each of these ions was assumed to relax radially with respect to the nearest defect site. The displacements and dipole moments of Region II ions were found by the Mott-Littleton[2] dielectric continuum theory assuming each defect to distort Region II independently of the others present. The Brauer effect[3] however has been neglected in the present case. The displacements and dipole moments of Region I ions were determined by minimizing the energy to create the defects making up the saddle point configuration. The minimisation was done by using Rosenbrock's method[4]. Table 1 gives the breakdown of the Coulomb, Repulsive and Polarization terms for the activation energy values obtained using repulsive parameters suggested by different authors[1,5].

It is evident from this table that Franklin parameters used with Born-Mayer-Verwey modification[6] as well as Axe potential give activation energies which are in satisfactory agreement with experimental value 0.56 eV[7].

For interstitial migration the saddle point for the anion was first assumed to be at $(\frac{1}{4}, \frac{1}{4}, \frac{1}{4})$ of the cubic cell of the f.c.c. cation lattice. By

Table 1. Breakdown of terms in activation energy values for anion vacancy migration (eV)

Repulsive parameters	$\Delta E^{\text{Coul.}}$	$\Delta E^{\text{Rep.}}$	$\Delta E^{\text{Pol.}}$	ΔE^{Total}
Franklin	-0.95	+1.04	+0.22	+0.31
Axe	-0.95	+1.19	+0.22	+0.46
Franklin (Born-Mayer-Verwey modification)	-0.71	+1.15	+0.20	+0.64

treating Regions I and II in identical manner as above an activation energy of 2.08 eV was obtained, the breakdown of terms being shown in Table 2. This is rather large compared to the experimental value of 1.55 eV[7].

Table 2. Breakdown of terms in activation energy value for anion interstitial migration (eV)

Repulsive parameter	$\Delta E^{\text{Coul.}}$	$\Delta E^{\text{Rep.}}$	$\Delta E^{\text{Pol.}}$	ΔE^{Total}
Franklin	-1.85	+4.73	-0.80	+2.08
Axe	-1.19	+4.65	-0.94	+2.52

Finally, migration of F^- ions by interstitialcy replacement in a $\langle 111 \rangle$ direction was investigated. Figure 1 shows schematically the configuration of the two anions B and C participating in the mechanism and the corresponding vacant site A . Denoting the distances of the interstitial ions B and C from the lattice site A by $\xi_1 a$ and $\xi_2 a$ respectively, a being the inter-anionic spacing, energies were calculated for different values of ξ_1 and ξ_2 . From these results, the saddle point configuration was found to be $\xi_2 = 0.577$, $\xi_1 = 0.485$

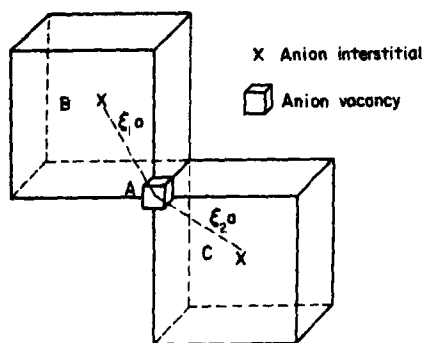


Fig. 1. Schematic diagram of anion interstitialcy configuration in CaF_2 .

and the breakdown of different energy terms is as shown in Table 3.

It is evident that Franklin parameters used with Born-Mayer-Verwey modification give an activation energy which is in agreement with experimental value.

Table 3. Breakdown of terms in activation energy value for anion interstitialcy migration (eV). Saddle point configuration: $\xi_2 = 0.577$, $\xi_1 = 0.485$

Repulsive parameters	ΔE^{Coul}	ΔE^{rep}	ΔE^{Pol}	ΔE^{Total}
Franklin	+0.63	+0.87	-0.21	+1.29
Franklin (Born-Mayer-Verwey modification)	+1.10	+0.70	-0.24	+1.56

However, in these calculations the ground state of the interstitial has been assumed to be at the anion cube body center. Also, other possible reaction paths have to be explored before a true comparison with experimental value could be made. Such work is now in progress.

Acknowledgements—I would like to acknowledge very helpful correspondence with Drs. A. B. Lidiard and A. D. Franklin, the benefit of discussions with Dr. E. C. Subbarao and the help of Dr. B. Sarkar with some of the computations. Part of this work was supported by U.S. National Bureau of Standards.

D. CHAKRAVORTY

Department of Metallurgical Engineering,
Indian Institute of Technology,
Kanpur, India

REFERENCES

1. FRANKLIN A. D., *J. Phys. Chem. Solids* **29**, 823 (1968).
2. MOTT N. F. and LITTLETON M. J., *Trans. Faraday Soc.* **34**, 485 (1938).
3. BRAUER P., *Z. Naturf.* **6A**, 255 (1951).
4. ROSENBROCK H. H., *The Computer Journal* **3**, 175 (1960).
5. AXE J. D., *Phys. Rev.* **139**, A1215 (1965).
6. VERWEY E. J. W., *Rec. Trav. Chim. Pays-Bas* **65**, 521 (1946).
7. ROSSING B., Ph.D. Thesis, M.I.T. (1966).

J. Phys. Chem. Solids Vol. 32, pp. 1092-1096.

^{81}Br magnetic resonance in fresh silver bromide*

(Received 16 April 1970)

AGING of fresh silver bromide has been studied by recording the intensity of the magnetic resonance absorption derivative line of ^{81}Br . Other potentialities of the method are discussed.

Silver bromide is an interesting material for starting nuclear magnetic resonance absorption studies of aging phenomena in fresh insoluble salts. Its aging has been investigated in the past by means of the technique of isotopic exchange (Kolthoff and O'Brien (1939); Langer (1943); Kolthoff and Bowers (1954)) and very detailed bromine magnetic resonance work has been performed by Reif (1955) on the pure annealed salt and samples with controlled concentration of point defects.

One still open question is whether the isotopic exchange in fresh precipitates takes place by recrystallization of the individual

*Based on part of the Dr. Chem. thesis presented by Rodolfo d'Alessandro at the University of Rome, March 1969.

microcrystals (by motion of crystal surfaces in contact with the solution) or by some other mechanism. The most direct evidence for recrystallization offered by Kolthoff and his co-workers in their important investigations was the isotopic exchange behavior of fresh lead chromate (Kolthoff and Eggertsen (1941)). However, it has been shown (Collotti, Conti and Zocchi (1959)) that in this case a phase transition occurs in the fresh precipitate. Therefore its exchange behavior must be carefully interpreted (Conti, d'Alessandro and di Napoli (1970)). We believe that some diffusion mechanism in the solid can explain the exchange experiments when there is no phase transition. (Precipitates obtained by flocculation from the colloidal state should perhaps be considered a special case.) Aging is detected as a decrease of the rate of exchange with time.

By the nuclear magnetic resonance technique one can attempt to detect this diffusion in very fresh microcrystals by motional narrowing of the absorption line and to follow, if the resonant nucleus has an electric quadrupole moment, the decrease of lattice imperfection densities with aging. Silver bromide is a simple ionic solid, it has a face-centered cubic lattice, two bromine isotopes, ^{79}Br and ^{81}Br , of nearly equal abundance, both with spin number $I = \frac{3}{2}$ (hence both with an electric quadrupole moment), and undergoes no phase transition after precipitation from aqueous solutions.

In order to get information on the order of magnitude of the possible Br^- diffusion coefficient in fresh AgBr we have analyzed the data of Kolthoff and O'Brien on the ^{80}MBr isotopic exchange in fresh precipitates obtained at room temperature ($\sim 25^\circ\text{C}$) from approximately 0.1 *M* solutions of KBr and AgNO_3 . (We discovered a mistake made by them in calculating the exchange values given in Table 7 and curve 1 of Fig. 3 of their second paper. Starting from their radioactivity data, it can be seen that the maximum exchange, asymptotically approached, is not higher than

the thermodynamic value, 100 per cent exchange, but is equal to it. Hence the diffusion hypothesis is justified and recrystallization appears to be unlikely.) Knowing from the work of Kolthoff and O'Brien that the number of Br^- ions in the surface of the microcrystals so prepared is 2.0 per cent of the total number of Br^- ions in the solid and utilizing the curves given by Crank (1956) for the ideal case of diffusion of matter in spherical particles from a well stirred solution of limited volume, an apparent average Br^- diffusion coefficient of the order of $10^{-15} \text{ cm}^2/\text{sec}$ has been calculated for a fresh AgBr precipitate and for an isotopic exchange time of the order of 1 hr. (The microcrystals were initially supposed to be of cubic shape with $\{100\}$ faces and of uniform size. Since the Br^- ions in the surface can be imagined to be contained in a depth of half lattice constant, it is simple to calculate the edge of the cubic-shaped microcrystals. From this value the radius of spherical microcrystals has been obtained with the assumption of equal volumes.) The above Br^- diffusion coefficient can be compared with the equilibrium value of $10^{-26} \text{ cm}^2/\text{sec}$ obtained by a rather uncertain extrapolation from the high temperature data of Tannhauser (1958).

In order to see if the apparent Br^- diffusion coefficient in fresh AgBr is so high as to have the possibility to cause motional narrowing of the ^{81}Br magnetic resonance line we have used the equation valid for a face-centered cubic lattice (Spokas and Slichter (1959))

$$\Delta\nu\tau = \frac{\Delta\nu a^2}{12D_N} \approx 1$$

where $\Delta\nu$ is the rigid-lattice width of the resonance line, τ the average time between two consecutive diffusion jumps of a bromine ion, a the lattice constant and D_N the limit diffusion coefficient which causes motional narrowing. This formula is valid for a vacancy diffusion mechanism. Applying this formula to our case, with $\Delta\nu = 1.02 \text{ kc/sec}$, the theoretic-

cal ^{81}Br magnetic width of the observed magnetic resonance absorption line, corresponding to the $\frac{1}{2} \leftrightarrow -\frac{1}{2}$ transition (Reif (1955)), and $a = 5.77 \cdot 10^{-8} \text{ cm}$, a value $D_N = 2.8 \cdot 10^{-13} \text{ cm}^2/\text{sec}$ is obtained. As can be seen, at least in the limit of the crude approximations introduced above, in no case can one expect a narrowing of the ^{81}Br resonance line in moderately fresh precipitates prepared from 0.1 M KBr and AgNO_3 solutions. As an attempt to introduce in the solid a higher concentration of defects, we have precipitated AgBr, at a temperature of $\sim 18^\circ\text{C}$, from equimolar solutions approximately 0.5 and 2 M of KBr and AgNO_3 . Besides, we have precipitated AgBr also from solutions approximately 0.5 M of HBr and AgNO_3 . All chemicals used were of C.P. quality.

The ^{81}Br magnetic resonance was examined with a Pound-Knight-Watkins radiofrequency spectrometer (Pound and Knight (1950); Watkins and Pound (1951); Pound (1952) equipped with a permanent magnet (manufactured for this laboratory by Soc. Imicam Nucleare, Milano, Italy) which provides a field strength of 5880 G in a 3.8-cm gap. The field was varied linearly with time by a current regulator and field-modulation was used at 280 c/sec. The lock-in amplifier was a commercial instrument of the Princeton Applied Research Corporation, Model HR-8. Absorption line derivatives were recorded from which peak-to-peak intensities \hat{S} relative to a standard of commercial polycrystalline AgBr were obtained. Peak-to-peak line widths $\Delta\nu$ can be found from the relative intensities by the relation $(\Delta\nu)^2 = K/\hat{S}$, where K was determined to be $4.0 \text{ kc}^2/\text{sec}^2$.

No line narrowing was found in all the cases considered, even in samples examined about 10 min after precipitation. This negative result can be explained in several ways. First, it is of course quite possible that even in the very fresh precipitates obtained from the given supersaturations the Br^- diffusion coefficient does not reach the value of about $3 \cdot 10^{-13} \text{ cm}^2/\text{sec}$. Second, a high initial concen-

tration of Ag point defects (which are very mobile) might preclude the possibility to observe the ^{81}Br line narrowing effect by causing, by quadrupole interaction, a shortening of the spin-lattice relaxation time of the ^{81}Br nuclei, so leading to lifetime broadening of the ^{81}Br line. (As Reif has shown, this mechanism, for Ag vacancies, is particularly effective near room temperature.) Third, diffusion short circuits, i.e., stationary or moving dislocation channels, could justify both high Br^- diffusion coefficients and the absence of motional narrowing of the resonance line. Returning to our experiments, aging was apparent by an increase of the relative intensity \hat{S} with time elapsed after precipitation. Line widths were larger than the magnetic width thus showing presence of point defects and/or dislocations (Reif (1955); Bloembergen (1955)); in the microcrystals. The best results obtained are shown in Figs. 1 and 2. The aging at room temperature of AgBr microcrystals precipitated from solutions of HBr and AgNO_3 and dried at 120°C for 1.5 hr is shown in Fig. 1. Figure 2 shows the aging at room temperature of microcrystals precipitated from the same solutions and stirred in the mother solution. Very probably the aging of fresh dry AgBr is due to the low Tammann temperature of this salt. These results suggest that a diffusion study of aging of AgBr by the isotopic exchange technique should not be interpreted only in terms of a decrease of exchange rates of Br^- and Ag^+ ions ascribed to Ostwald ripening of the precipitate (Langer (1943)). A decrease of crystalline imperfection densities and therefore of diffusion coefficients should not be overlooked in similar experiments. Unfortunately these densities cannot be estimated by nuclear magnetic resonance absorption unless one has an idea of the nature of the imperfections. Further experiments, both by nuclear resonance and isotopic exchange, on the same microcrystals should help to clarify some of the above discussed points.

One of us (L.G.C.) thanks George Murray

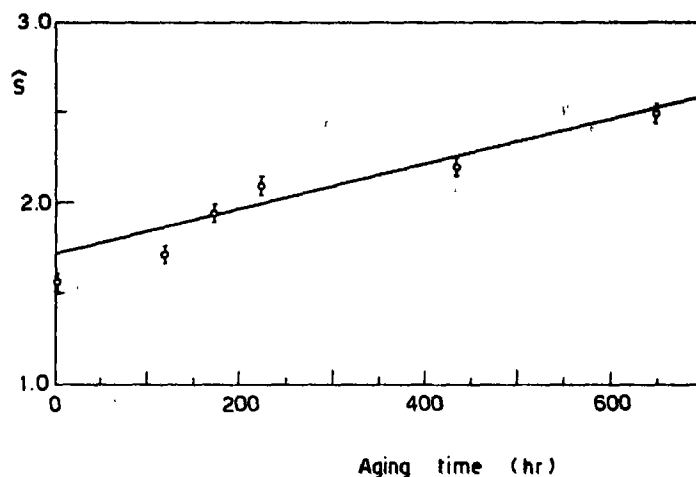


Fig. 1. Aging of fresh dry silver bromide (^{81}Br resonance).

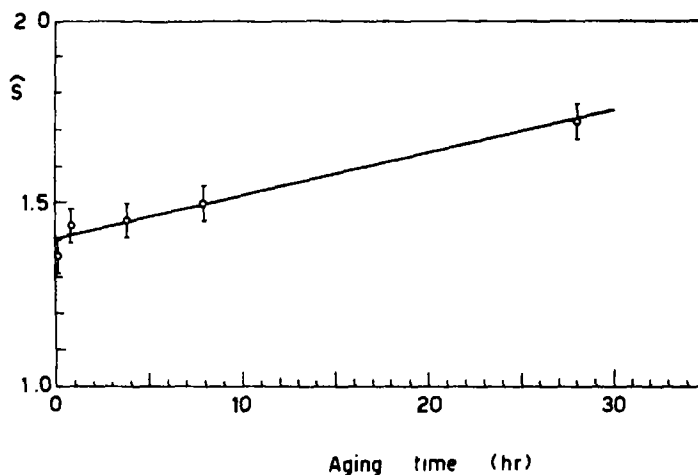


Fig. 2. Aging of fresh silver bromide stirred with mother solution (^{81}Br resonance).

for information obtained some years ago at the Pennsylvania State University about his version of the Pound-Knight-Watkins spectrometer. We are also indebted to Antonio Bolle for much help with electronics. This work was supported in part by the National Research Council, Italy.

L. G. CONTI
R. D'ALESSANDRO

*Laboratorio di Chimica delle Radiazioni
e Chimica Nucleare del C.N.E.N.,
Istituto di Chimica Generale e Inorganica,
Università di Roma,
00185 Roma,
Italy.*

REFERENCES

1. BLOEMBERGEN N. *Report of the Conference on Defects in Crystalline Solids*. Bristol 1954, p. 1. London: The Physical Society (1955).
2. COLLOTTI G., CONTI L. G. and ZOCCHI M., *Acta crystallogr.* **12**, 416 (1959).
3. CONTI L. G., D'ALESSANDRO R. and DI NAPOLIV., *J. Phys. Chem. Solids*, To be published (1971).
4. CRANK J., *The Mathematics of Diffusion*, pp. 88-91, Oxford University Press, London (1956).
5. KOLTHOFF I. M. and BOWERS R. C., *J. Am. chem. Soc.* **76**, 1503, 1510 (1954).
6. KOLTHOFF I. M. and EGGERTSEN F. T., *J. Am. chem. Soc.* **63**, 1412 (1941).
7. KOLTHOFF I. M. and O'BRIEN A. S., *J. Am. chem. Soc.* **61**, 3409, 3414 (1939).
8. LANGER A., *J. chem. Phys.* **11**, 11 (1943).
9. POUND R. V., *Prog. nucl. Phys.* **2**, 21 (1952).
10. POUND R. V. and KNIGHT W. D., *Rev. scient. Instrum.* **21**, 219 (1950).
11. REIF F., *Phys. Rev.* **100**, 1597 (1955).
12. SPOKAS J. J. and SLICHTER C. P., *Phys. Rev.* **113**, 1462 (1959).
13. TANNHAUSER D. S., *J. Phys. Chem. Solids* **5**, 224 (1958).
14. WATKINS G. D. and POUND R. V., *Phys. Rev.* **82**, 343 (1951).

J. Phys. Chem. Solids Vol. 32, pp. 1096-1097

Cation distribution and Curie temperature in the copper-manganese-zinc ferrites

(Received 10 July 1970)

WE have previously investigated the influence of cation distribution on the Curie point of the copper-zinc ferrites[1]. In the present note, some preliminary results concerning this problem for copper-manganese-zinc ferrites are discussed.

The samples, of toroidal shape, were prepared from oxides by usual ceramic techniques. Sintering in air at 1200°C for 4 hr was followed by quick cooling. X-ray and chemical analyses, carried out after sintering, showed only the presence of a spinel phase with a small deviation from the initial chemical composition. The Curie temperature was determined from the temperature dependence of the saturation magnetization, with a precision of 1-2°C. The cation distribution was

modified by thermal treatment in an oxygen atmosphere. Results obtained for two samples of three compositions are shown in the Table.

Because the sintering temperature is higher than 950°C, where the reduction of Cu^{2+} to Cu^{1+} ions begins[2], the number of Cu^{1+} ions at the end of the sintering process is large. Assuming that Cu^{1+} ions have a certain preference for the tetrahedral sites, this fact accounts for a lowering of the Curie temperature[1]. The oxidation of $\text{Cu}^{1+} \rightarrow \text{Cu}^{2+}$ ions involves movement of the copper ions from the tetrahedral to the octahedral sites since Cu^{2+} ions prefer octahedral sites[3]. This will result in an increase in the Curie temperatures. At the same time with the migration of copper ions from tetrahedral to octahedral sites, an inverse migration of Fe^{3+} ions takes place.

Oxidation of Cu^{1+} ions in the sintered samples was accomplished by an oxygen treatment followed by rapid cooling. As can be seen in the Table the Curie point does in fact shift to higher temperatures after this treatment. After an analogous nitrogen treatment however, the Curie point does not change since in an inert atmosphere oxidation cannot take place.

The change in Curie point after oxygen treatment, for copper-manganese-zinc ferrites, is less pronounced in comparison with the copper-zinc ferrites[1]. We explain this fact in the following way. In the copper-manganese-zinc ferrites, on the tetrahedral sites there are Cu^{1+} , Mn^{2+} , Zn^{2+} and Fe^{3+} ions, and on the octahedral sites there are Cu^{2+} , Mn^{3+} , Fe^{2+} and Fe^{3+} ions (Mn^{3+} ions on the octahedral sites are present due to the existence of Fe^{2+} ions on these sites[4]; the Fe^{2+} ions result from the reduction $\text{Fe}^{3+} \rightarrow \text{Fe}^{2+}$ in the sintering process due to the evaporation of zinc at the ferrite surface[5]). In the oxidation process, as a result of the oxidation $\text{Fe}^{2+} \rightarrow \text{Fe}^{3+}$, migration of manganese ions from octahedral to tetrahedral sites takes place; this causes a small decrease in the Curie temperatures.

The passage of copper ions from the tetrahedral to the octahedral sites in the oxidation process, accompanied by an inverse passage of the Fe^{3+} ions (or of Mn^{2+} ions), has been proved by saturation magnetization measurements.

zation of this lattice. This fact is responsible for the decrease in magnetization of the ferrites. The substitution of Fe^{3+} ions by Cu^{2+} ions on the octahedral lattice, decreases the magnetization of this lattice, having a similar effect upon the magnetization of the ferrite.

Table 1. Initial chemical composition, Curie temperature (T_c) and saturation magnetization (J_s) for the ferrites studied

Initial chemical composition	sintering in air (1200°C for 4 hr)		treatment in O_2 (1000°C for 2 hr)		treatment in N (1000°C for 2 hr)	
	T_c (°C)	J_s (Gs/g)	T_c (°C)	J_s (Gs/g)	T_c (°C)	J_s (Gs/g)
$\text{Cu}_{0.2}\text{Mn}_{0.2}\text{Zn}_{0.6}\text{Fe}_2\text{O}_4$	45	398	66	369	—	—
	43	389	—	—	43	387
$\text{Cu}_{0.3}\text{Mn}_{0.3}\text{Zn}_{0.4}\text{Fe}_2\text{O}_4$	158	276	193	234	—	—
	162	273	—	—	165	269
$\text{Cu}_{0.55}\text{Mn}_{0.25}\text{Zn}_{0.2}\text{Fe}_2\text{O}_4$	268	183	310	112	—	—
	273	179	—	—	271	181

In the Table, the saturation magnetizations, measured at 77°K, for three of the samples studied are shown. We observe that the saturation magnetization decreases in the oxidation process but does not change in the nitrogen treatment. Because the magnetization of ferrites is determined by the difference between the magnetizations of octahedral and tetrahedral lattices, the substitution of Cu^{1+} ions (which have no magnetic moment) by the Fe^{3+} ions (which have a magnetic moment) on the tetrahedral lattice, increases the magneti-

Research Center of Physics,
Iassy, Romania

N. REZLESCU
E. CUCIUREANU

REFERENCES

1. REZLESCU N. and CUCIUREANU E., *C. R. Acad. Sci. Paris* **269**, 952 (1969).
2. STIERSTADT K., BENZ H. and RECHENBERG H., *Proc. Int. Conf. Magnetism*, Nottingham, p. 609 (1964).
3. OHNISHI H. and TERANISHI T., *J. phys. Soc. Japan* **16**, 33 (1961).
4. MILLER A., *Phys. Rev.* **116**, 1481 (1959).
5. SMIT J. and WIJN H. P. J., *Les Ferrites*, *Bibl. Tech. Philips*, Dunod, Paris (1961).

ELECTRICAL RESISTIVITY, HALL EFFECT AND OPTICAL ABSORPTION IN TlS, $\text{TlS}_{0.5}\text{Se}_{0.5}$ AND TlSe*

R. S. ITOGA† and C. R. KANNEWURF

Department of Electrical Engineering, Northwestern University, Evanston, Ill. 60201, U.S.A.

(Received 11 June 1970; in revised form 2 October 1970)

Abstract— Various ternary compositions in the TlS–TlSe system were prepared and found to have the same tetragonal structure as TlS and TlSe. Resistivity and Hall measurements on the compositions TlS, TlSe and $\text{TlS}_{0.5}\text{Se}_{0.5}$ were performed over the temperature range of 78 to 400°K. Activation energies obtained from these data are compared to direct and indirect band transition energies obtained from optical absorption measurements for radiation polarized both parallel and perpendicular to the direction of the principal crystallographic symmetry axis. Some results are identified with previously proposed band structure details. In the case of TlSe a comparison is made with band gap energies reported by several other investigators.

1. INTRODUCTION

IN THE thallium chalcogenide systems with sulfur and selenium several binary compounds have been identified[1]. Probably the most studied and best known are Tl_2S from the Tl–S system and TlSe from the Tl–Se system. Recent interest in TlSe has been concerned primarily with electrical transport and related properties. Similar studies have not been reported for TlS. The preparation and study of crystalline ternary systems based on binary thallium chalcogenide compositions have also not been considered for the most part in the literature. The present investigation of the binaries, TlS and TlSe, has two objectives: to develop ternary compositions of the form $\text{TlS}_x\text{Se}_{(1-x)}$, $0 \leq x \leq 1$, which provides the simplest chalcogenide interchange and to extend the study of the binary compositions by electrical and optical measurements on TlS.

The crystal structure of TlSe is body-centered tetragonal[2]; the crystal structure of TlS is isotypic to that of TlSe[3]. The general bonding arrangement consists of chains in which thallium atoms are surrounded tetrahedrally by four chalcogenide atoms; the remaining thallium atoms are located between the chains[4]. The identification of semiconductor behavior in TlSe was first reported by Mooser and Pearson[5]. Subsequently, in over thirty papers various properties of TlSe have been discussed. Conductivity and Hall measurements indicate an intrinsic activation energy of 0.57 to 0.60 eV at 300°K. Optical measurements place this energy in the range of 0.7 to 0.8 eV. Reference to specific papers will be given in later sections. In the measurements reported here electrical data obtained for TlSe are also presented for comparison, and optical absorption measurements extend the previously reported work.

*This research was supported in part by the Advanced Research Projects Agency of the Department of Defense through the Northwestern University Materials Research Center. This paper is based on a thesis submitted by R. S. Itoga in partial fulfillment of the requirements for the Ph.D. degree.

†Present Address: General Dynamics, Pomona Division, Pomona, California, U.S.A.

2. EXPERIMENTAL

(a) Sample preparation

To obtain single crystal material of the specific compositions TlS, $\text{TlS}_{0.5}\text{Se}_{0.5}$ and TlSe, stoichiometric quantities of the constituent elements were first sealed in tapered

quartz ampoules at a pressure of 10^{-5} Torr.* The usual precautions were taken throughout this investigation to prevent oxide formation on all ingot material containing thallium; nearly all operations were performed in an argon atmosphere. In the case of $\text{TlS}_{0.5}\text{Se}_{0.5}$ and TlSe the ampoules were placed in a furnace and the temperature increased to 375°C , maintained for several hours, and then slowly cooled to room temperature. The ampoules were then placed in a vertical zone melting furnace and lowered at rates varying from 3 to 9 mm/h through three separate heating stages: the top region is 100°C below the ingot melting point, the center 15 to 20°C above the melting point and the bottom at 150°C for TlSe and 130°C for $\text{TlS}_{0.5}\text{Se}_{0.5}$. Large single crystal sections were found to have developed in the ingots. Preparation of TlSe by various methods has been described in the literature [6, 7].

In the case of TlS polycrystalline material decomposes upon heating by way of a peritectic transformation and satisfactory single crystal development was not possible by vertical zone melting. A modification of a horizontal zone levelling technique for crystal growth as discussed by Pfann [8] was employed. In this method the polycrystalline ingots are sulfur enriched; the range of 52 to 56 at. % sulfur was found to give the most satisfactory results. The zone heating furnace moved at the rate of 5 mm/h. The minimum temperature along the ingot was maintained at 130°C . The furnace travels four or five times in each direction. The ingot is then annealed at 150°C for a period of 24 hr and slowly cooled to room temperature. Single crystal sections of TlS ingots were generally of smaller volume than those of TlSe .

(b) Ternary compositions

Since TlS and TlSe are isotypic in crystal

structure, nearly all combinations of TlS and TlSe may be part of a continuous solid solution. It was found that the TlS - TlSe ternary system may be represented as a quasibinary system except at compositions near TlS . A thermal analysis for the ternary $\text{TlS}_x\text{Se}_{(1-x)}$ was performed over the temperature range of 180 to 400°C . For some samples the cooling curves were monitored until the temperature returned to 23°C . Although super-cooling effects were observed, the thermal breaks in the cooling curves were reproducible to $\pm 5^\circ\text{C}$. The solidus and liquidus temperatures, T_M and T_F respectively, obtained from the thermal breaks are given in Table 1 for various ternary compositions.

From a least squares analysis of X-ray powder film patterns the tetragonal lattice parameters were determined for each composition to $\pm 0.01 \text{ \AA}$ and are also listed in Table 1. A linear variation in a and c between the two binary compositions was observed. The phase diagram for the Tl-S binary system indicated an incongruent melting point of TlS [1]; consequently, as x approaches 1.0 another phase will precipitate along with the $\text{TlS}_x\text{Se}_{(1-x)}$ ternary from the liquid state. The X-ray analysis indicated that a continuous tetragonal solid solution exists for ternaries containing more than 3 at. % selenium. From these results and additional metallographic studies samples in this range of composition were found to be homogeneous. For lower selenium percentages an unidentified amorphous material is also present with the crystalline ternary and melt compositions appear to deviate from the quasi-binary system.

(c) Crystal orientation

As shown in Table 1 the lattice parameters determined in the present work for the two binary compositions are in good agreement with those reported in the literature. The body-centered tetragonal space group is $14/m\bar{c}m - D_{4h}^{18}$; there are eight formula units of the compound per unit cell; the structural

*Thallium, sulfur and selenium were obtained from the American Smelting and Refining Co., purity of each element: 5 - nines +.

Table 1. Solidus and liquidus temperatures, and lattice parameters for ternary compositions $\text{TlS}_x\text{Se}_{(1-x)}$

x	$T_M(^{\circ}\text{C})$	$T_L(^{\circ}\text{C})$	$a(\text{\AA})$	$c(\text{\AA})$
0.0	345	345 330 ^(a)	8.03 8.031 ^(b)	6.98 6.989 ^(b)
0.1	332	336	8.00	6.97
0.2	316	330	7.99	6.95
0.3	304	325	7.97	6.93
0.4	291	317	7.92	6.91
0.5	279	305	7.90	6.90
0.6	270	295	7.88	6.86
0.7	263	285	7.87	6.85
0.8	256	277	7.83	6.84
0.9	249	264	7.81	6.82
1.0	235 245 ^(a)	251 257 ^(a)	7.79 7.787 ^(c)	6.80 6.807 ^(c)

^(a) Estimated from [1].

^(b) From [10].

^(c) From [11].

arrangement is labeled the B37 type. The natural cleavage planes were confirmed to be (110) type planes[9]. Freshly cleaved surfaces, which have a reflective luster, are metallic gray for most samples; those of TlS appear more gray-black. All ingots prepared to obtain single crystal material were found to have the [001] direction along the length of the ingot. All single crystal material was prepared for stoichiometric composition. The following is a typical chemical analysis of the binary compositions: (1) TlS experimental 85.49 ± 0.1 per cent Tl, 14.42 ± 0.1 per cent S; calculated 86.44 per cent Tl, 13.56 per cent S and (2) TlSe experimental 72.78 ± 0.05 per cent Tl, 27.19 ± 0.05 per cent Se; calculated 72.13 per cent Tl, 27.87 per cent Se. Samples containing sulfur as a constituent generally showed greater deviations from stoichiometric composition. In view of the general behavior of the various ternary phases as summarized in Table 1, the intermediate composition $\text{TlS}_{0.5}\text{Se}_{0.5}$ was selected for optical and electrical measurements as representative of these compositions.

(d) Resistivity and Hall measurements

Single crystal samples for all electrical measurements were cleaved from selected

ingot material. Typical dimensions for the rectangular samples were: length 5 to 10 mm, width 1 to 3 mm and thickness 1 to 3 mm. Some samples had nearly a square cross-sectional area. Electrodes for simultaneous Hall and resistivity measurements at the same temperature were attached to samples in the usual five-probe configuration at either freshly cleaved surfaces or regions that were treated with a disodium EDTA solution. A gold film was first deposited using vacuum evaporation at the contact areas and 3.5 mil copper wires attached to the gold film with indium alloy solders. This technique gave ohmic contacts for nearly all TlSe samples. As the concentration of sulfur increased in the $\text{TlS}_x\text{Se}_{(1-x)}$ compositions to TlS, many samples showed some degree of nonohmic behavior and were discarded.

Resistivity and Hall voltages were obtained with a conventional d.c. type measurement system; the principal electronic units were Keithley types: 610B electrometer and 147 nanovolt detector. In all measurements the applied current direction was parallel to the crystallographic c axis of the samples. The crystals and electrode connectors with temperature sensors were attached to a bakelite support, suspended in a dewar which was

then evacuated and later filled with helium gas. This procedure provided a controlled temperature range from 78 to 400°K by keeping liquid nitrogen in the outer jacket of the dewar to obtain the temperatures below 300°K and by supplying current to a small resistance heater attached to the sample mounting support to obtain temperatures above 300°K. In Fig. 1 the behavior of the resistivity over this temperature range is shown for single crystal samples of TlS, $\text{TlS}_{0.5}\text{Se}_{0.5}$ and TlSe. The data shown in Fig. 1 is representative of the behavior of all samples studied in this investigation. Few samples were found to have resistivities either significantly greater or less than those selected for Fig. 1.

For Hall measurements the magnetic field was perpendicular to the crystallographic *c* direction and along the [110] direction. Thermal probe tests in addition to the Hall measurements on single crystal material indicated all samples to be *p*-type. In previous Hall measurements on TlSe it has been demonstrated that at high temperatures lattice scattering predominates [6, 12]. Therefore all Hall data was analyzed using the following expression: $R_H = 3\pi/8pe$. Above a magnetic field strength of 10 kG Hall voltages were found to vary linearly with field strength. In Fig. 2 the variation of the Hall coefficient with temperature is shown for $\text{TlS}_{0.5}\text{Se}_{0.5}$ and TlSe; the field strength is 13 kG. The samples selected for Fig. 2 are representative of the range in R_H encountered for all crystals prepared for Hall measurements. Electrode problems prevented Hall data from being obtained for TlS. Preliminary data indicated lower carrier concentrations than those found for $\text{TlS}_{0.5}\text{Se}_{0.5}$ samples over the temperature range of Fig. 2. The variation of the Hall mobility for all samples examined was 15 to 150 $\text{cm}^2/\text{V}\cdot\text{sec}$ for TlSe and 3 to 30 $\text{cm}^2/\text{V}\cdot\text{sec}$ for $\text{TlS}_{0.5}\text{Se}_{0.5}$.

(e) Optical measurements

The optical measurements system was

developed around a Zeiss MM12 monochromator; the general features of this system have already been described elsewhere [13]. A discussion of the technique for obtaining specular reflectance measurements using polarized radiation with this system has also been given previously [14]. All reflection and transmission measurements were taken at 300°K with the incident radiation along the [110] direction polarized both parallel and perpendicular to the principal symmetry axis, the *c* direction.

Reflectivity data at approximately normal incidence was obtained to provide reflection coefficients in order to analyze transmission data at the onset of the fundamental absorption edge. Although not reproduced here the peaks in the reflection spectrum between 0.5 and 5.5 eV for TlSe compare favorably with those reported in the literature [9, 15]. The reflection spectrum for $\text{TlS}_{0.5}\text{Se}_{0.5}$ has peaks which show a general correspondence to those in the TlSe spectrum; fewer peaks were observed in the corresponding data for TlS [16].

Samples selected for absorption measurements were prepared with freshly cleaved surfaces normal to the incident radiation. Sample thickness varied from 10 to 100 μ . In Fig. 3 the absorption coefficient (α) as a function photon energy ($h\nu$) is shown for all three materials with both $E \parallel c$ and $E \perp c$. These curves are the result of processing data obtained from many samples. Absorption coefficients were obtained from transmission and reflection data by computer methods [17]. The shapes of the three curves just above the onset of the absorption edge are quite similar for both polarizations. However at $\alpha \approx 10^3 \text{ cm}^{-1}$ the TlSe curves show a more pronounced change in slope. On the long wavelength side of the absorption edge a considerable variation in the magnitude of the background absorption was observed; typical behavior is shown by the curves of Fig. 3. Hall measurements show different samples contain different extrinsic conditions; for

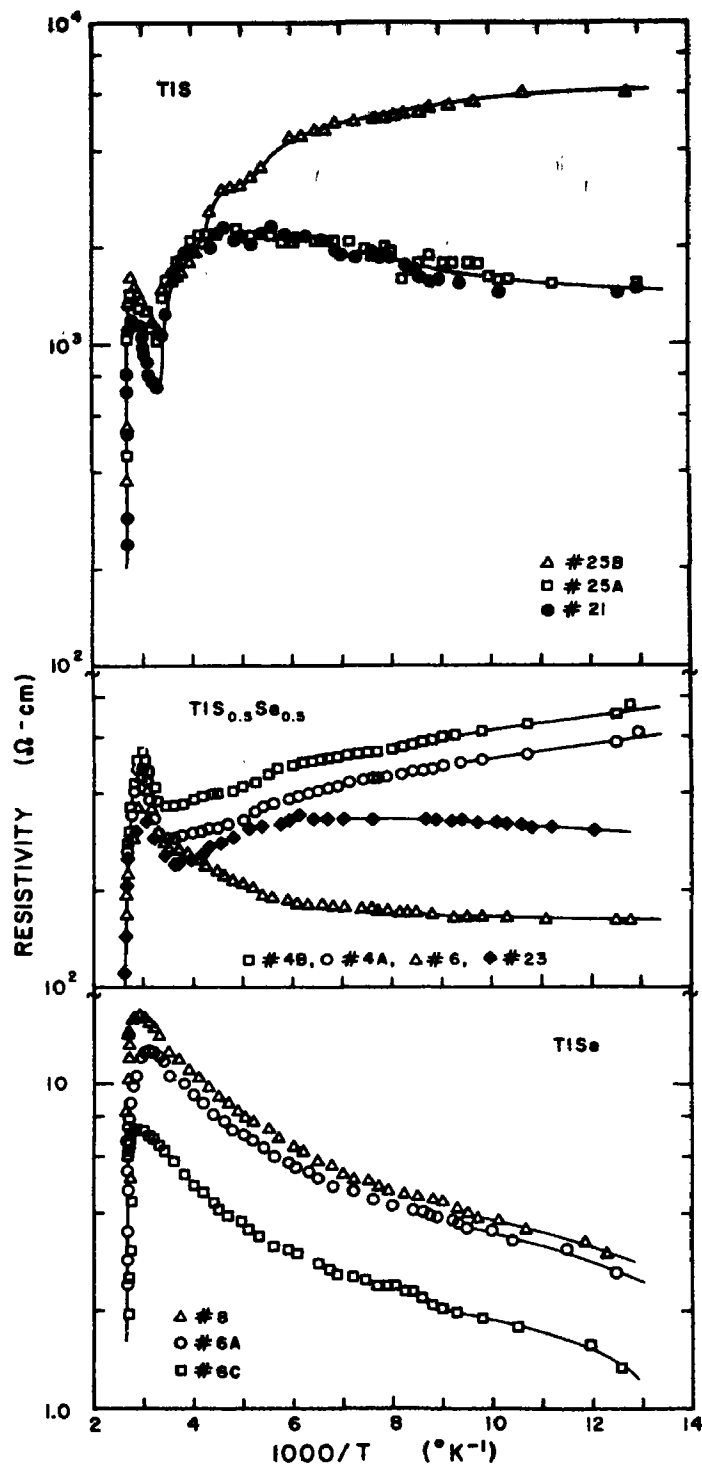


Fig. 1. Resistivity vs. temperature for various samples of TIS, $\text{TIS}_{0.5}\text{Se}_{0.5}$ and TISe.

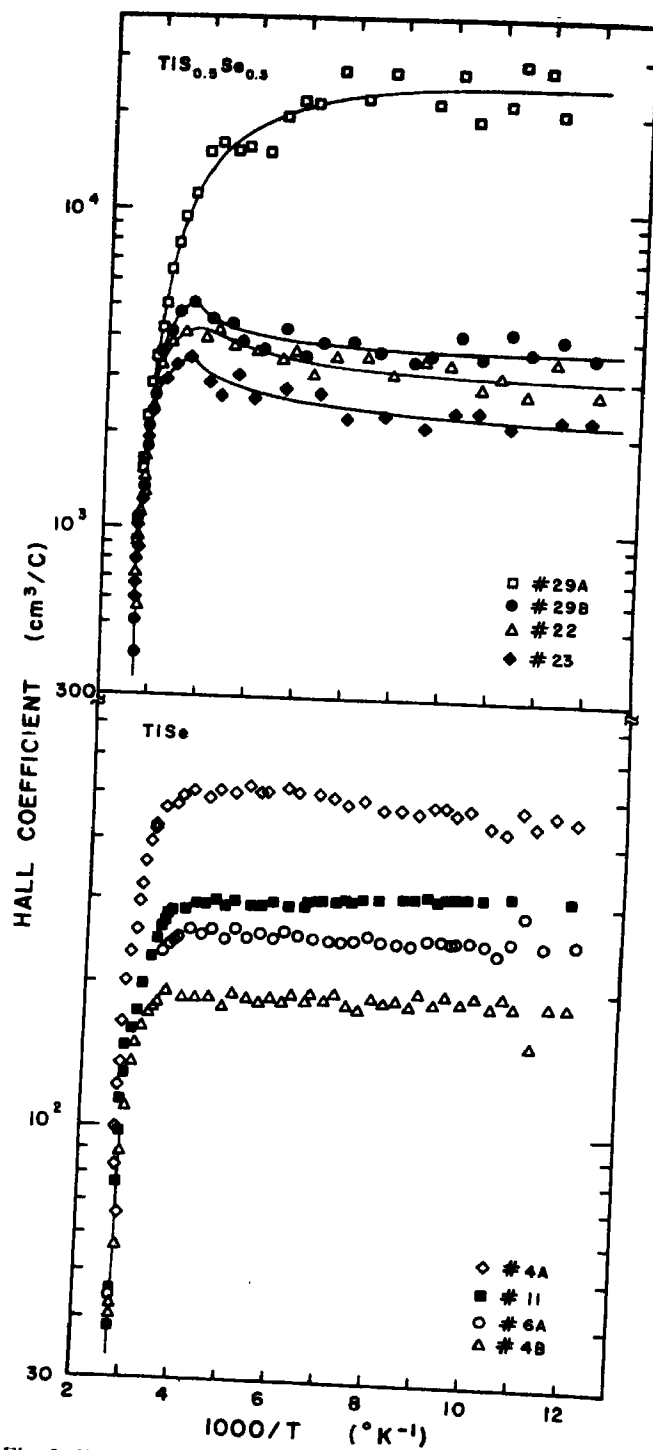


Fig. 2. Hall coefficient vs. temperature for various samples of $\text{TIS}_{0.5}\text{Se}_{0.5}$ and TISe at a field strength of 13 kG.

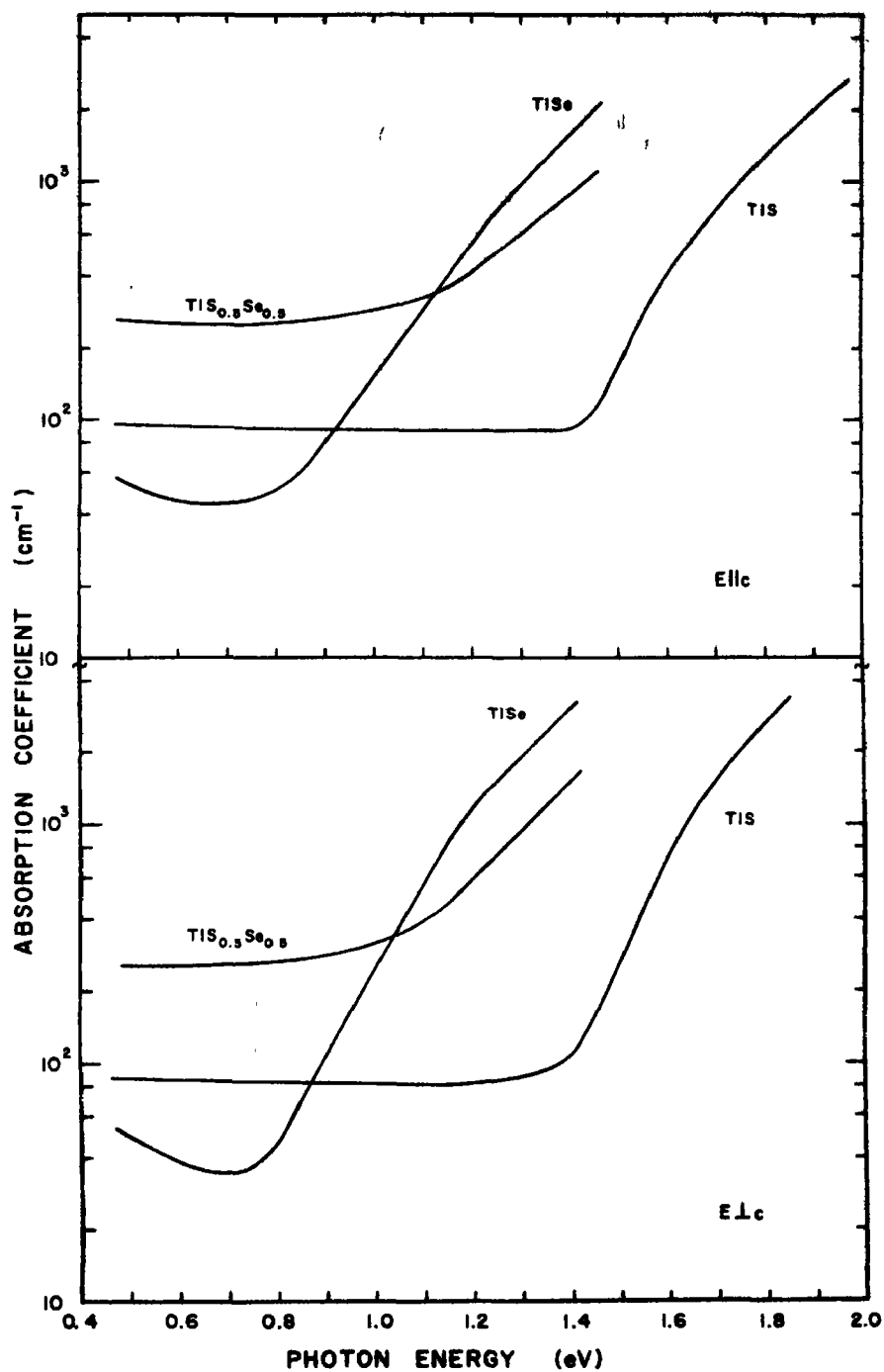


Fig. 3. Absorption coefficient vs. photon energy for TiS , $\text{TiS}_{0.5}\text{Se}_{0.5}$ and TiSe with the incident radiation polarized both parallel and perpendicular to the direction of the c axis.

TlSe the thicker optical samples had carrier concentrations in the order of 10^{16} cm^{-3} ; those of $\text{TlS}_{0.5}\text{Se}_{0.5}$, 10^{15} cm^{-3} .

3. RESULTS AND DISCUSSION

A general discussion of the symmetry features of the energy bands for the body-centered tetragonal D_{4h}^{18} space group and its application to TlSe type crystals has been given by Gashimzade[18,19]. Of major interest has been the determination of the intrinsic activation energy for TlSe itself. From the electrical resistivity and Hall data, such as shown in Figs. 1 and 2, the intrinsic activation energies were obtained for TlS, $\text{TlS}_{0.5}\text{Se}_{0.5}$ and TlSe and are listed in Table 2. The top part of the table is a summary of the various activation energies determined in the present investigation; the bottom part is a condensed summary of the corresponding values previously reported for TlSe.

The resistivity curves for TlS in Fig. 1 show a definite minimum before entering the intrinsic region. The presence of this minimum is interpreted as evidence of some defect or impurity energy levels in the forbidden gap region. Some samples of $\text{TlS}_{0.5}\text{Se}_{0.5}$ also show a shallow minimum in the resistivity data; samples of TlSe do not show similar behavior. As the percent of sulfur increases toward TlS, the deviation from crystal stoichiometry becomes greater and maybe partly responsible for this behavior. In studies on *p*-type TlSe it has been noted that the usual presence in sufficient concentration of acceptor levels associated with intrinsic lattice defects tends to mask the effect of chemical impurities[26].

The combined behavior of the resistivity and Hall coefficient for TlSe indicates that, as the temperature increases above liquid nitrogen temperatures, the increase in the resistivity is due primarily to the decrease in mobility since carrier concentrations remain effectively constant until the intrinsic region is reached (e.g. sample # 6A in Figs. 1 and 2). This same observation was also made for

similar measurements on TlSe[21,6]. Some samples of $\text{TlS}_{0.5}\text{Se}_{0.5}$ exhibit this same general behavior in the change of resistivity and Hall coefficient with temperature.

The absorption curves of Fig. 3 were analyzed for evidence of direct and indirect band transitions[27]. At the onset of the absorption edge the absorption coefficient for both polarizations was found to be proportional to the energy dependence for an allowed indirect transition: $(h\nu - E_g^i \pm E_p)^2/h\nu$, where E_g^i is the indirect band gap energy and E_p is the energy of the phonon absorbed (+) or emitted (−) during the process. In Fig. 4 the extrapolated threshold values for E_g^i are shown for TlS and TlSe. Background absorption prevented any information from being obtained concerning the phonon interaction in the transition. The indirect band gaps are listed in Table 2. The relatively high background absorption in $\text{TlS}_{0.5}\text{Se}_{0.5}$ crystals prevented a similar analysis for the ternary being performed with meaningful results. The energy values entered in Table 2 were obtained from a consideration of the rate of change in α where the absorption becomes appreciable.

The curves of Fig. 3 were also examined for evidence of direct band transitions. As shown in Fig. 5, a good fit for both polarizations was obtained with the absorption coefficient having the following dependence on photon energy for a forbidden type direct transition: $(h\nu - E_g^d)^{3/2}/h\nu$, where E_g^d is the direct band gap energy. The values of E_g^d for TlS and TlSe are also listed in Table 2. No fit for either polarization to the energy dependence for a direct allowed type transition could be found in the high absorption region over any appreciable energy interval. The absorption data for $\text{TlS}_{0.5}\text{Se}_{0.5}$ did not extend far enough into the high absorption region to identify the threshold for direct band transitions.

The papers referenced in Table 2 are representative of the various groups that have considered TlSe; the energy values listed

Table 2. Activation energies for TlS, $\text{TlS}_{0.5}\text{Se}_{0.5}$ and TlSe

Sample	Activation energy (eV)	Technique and sample orientation ^(a,b)	Ref.
TlS	~ 2.7	ρ $I \parallel c$	
	≤ 1.36 (indirect)	α $E \perp c$	
	≤ 1.37 (indirect)	α $E \parallel c$	
	1.50 (direct)	α $E \perp c$	
	1.57 (direct)	α $E \parallel c$	
$\text{TlS}_{0.5}\text{Se}_{0.5}$	0.73	ρ $I \parallel c$	
	0.75	R $I \parallel c, H \parallel [110]$	
	~ 0.92	α $E \perp c$	
	~ 0.96	α $E \parallel c$	
TlSe	0.71	ρ $I \parallel c$	
	0.67	R $I \parallel c, H \parallel [110]$	
	≤ 0.74 (indirect)	α $E \perp c$	
	≤ 0.77 (indirect)	α $E \parallel c$	
	0.97 (direct)	α $E \perp c$	
	1.03 (direct)	α $E \parallel c$	
TlSe	0.57	ρ	[20]
	0.56	ρ $I \parallel c$	[21]
	0.6 and 1.3	ρ, R	[22]
	0.567	ρ $I \parallel c$	[6]
	0.57	R $I \parallel c$	[6]
	0.65	PC	[23]
	0.8	α	[24]
	0.574	ρ $I \parallel [110]$	[12]
	0.73 (indirect)	α $E \perp c$	[25]
	0.72	PC $E \perp c$	[25]
	1.03	OR $E \parallel c, E \perp c$	[15]

^(a)The symbols refer to the following measurement techniques: ρ , electrical resistivity; R , Hall coefficient; α , optical absorption; PC, photoconductive response; OR, optical reflectivity.

^(b)Orientation of current, I ; electrical field, E ; and magnetic field, H ; with respect to crystallographic directions.

denote measurements on p -type material, and in the case of the optical data the values quoted are for a temperature of 300°K. As observed in previous papers, the energy values for the minimum band gap obtained by electrical measurements are less than the threshold values for indirect optical transitions. In the present work the band gaps obtained from resistivity and Hall data are larger than the 0.56 eV values obtained by most other investigations but are in much closer agreement with the optical values. However, a comparison of electrical data

shows that several workers report data farther into the intrinsic region at higher temperatures for samples with a wider variation in resistivity-carrier concentration than those shown in Figs. 1 and 2. Therefore, possibly the previously reported lower energy values represent a more accurate determination from the intrinsic region. The rather short intrinsic range in the TlS data of Fig. 1 is believed to be responsible for the band gap energy being considerably larger than the more accurately determined values from the optical analysis. In both the resistivity and Hall measurements

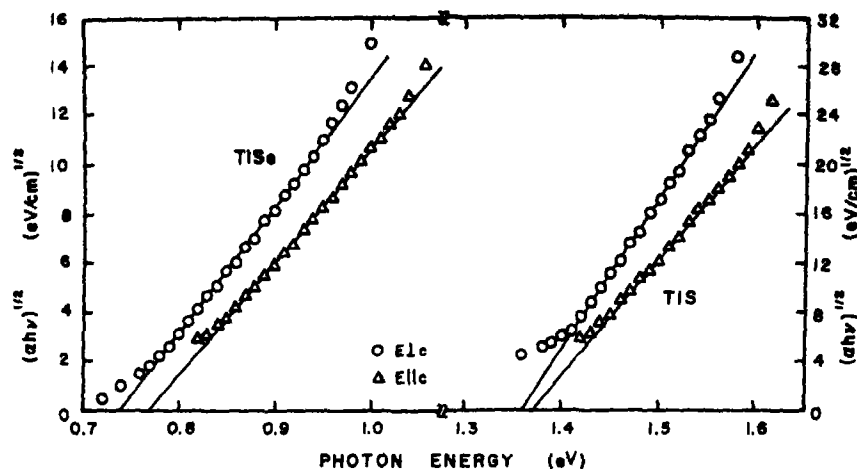


Fig. 4. $(\alpha h\nu)^{1/2}$ vs. photon energy extrapolated to the threshold energy for indirect transitions in TlS and TlSe.

on all materials the maximum temperature was kept considerably below the melting point in order to insure that there would be no crystal decomposition and loss of the chalcogenide constituents.

The optical band gap of TlSe, $E \perp c$ is in very good agreement with the previously reported energy value[25]. The separation of both the indirect and direct band gaps for $E \parallel c$ and $E \perp c$ for all three materials is quite small, being only a few hundredths of an electron volt. The activation energies for $\text{Tl}_{0.5}\text{Se}_{0.5}$ obtained by electrical and optical measurements differ by about 0.2 eV. As also noted for TlSe, the values obtained by optical measurements give the larger band gap energies.

Optical absorption measurements beyond the onset of the fundamental edge are not available for comparison with direct transition energies reported here. In the reflection spectrum for TlSe a reflection peak has been identified at 1.03 eV for both $E \parallel c$ and $E \perp c$, which are the peaks with the lowest energy of all those observed[15]. These reflectivity peaks agree quite well with the TlSe direct transition energies. These transitions for both polarizations are forbidden according to selec-

tion rules for dipole transitions, but allowed for both polarizations if spin is accounted for [9]; in Fig. 5 the direct transitions for both polarizations have been identified as the direct-forbidden type.

The various irreducible representations and group characters for the possible electronic transitions in the TlSe type materials have been developed in the literature[18, 9]. Some of these tables were confirmed during the present work[16]. It has been proposed that the valence band maximum is located at the M point (termination of the Σ axis on the zone boundary) and belongs to the representation M_8 [9]. From the optical absorption analysis all band gap energies for $E \perp c$ are slightly less than those for $E \parallel c$. Depending upon the location of the conduction-band minimum, which in view of the identification of indirect optical transitions is presumed to lie at a different point in the Brillouin zone, the optical absorption analysis tentatively substantiates the location of the valence band maximum in the Σ direction.

This work has shown that TlS, TlSe, and TlS-TlSe ternary compositions are not only isotypic in the B37 structure type but also exhibit similar behavior in several electrical

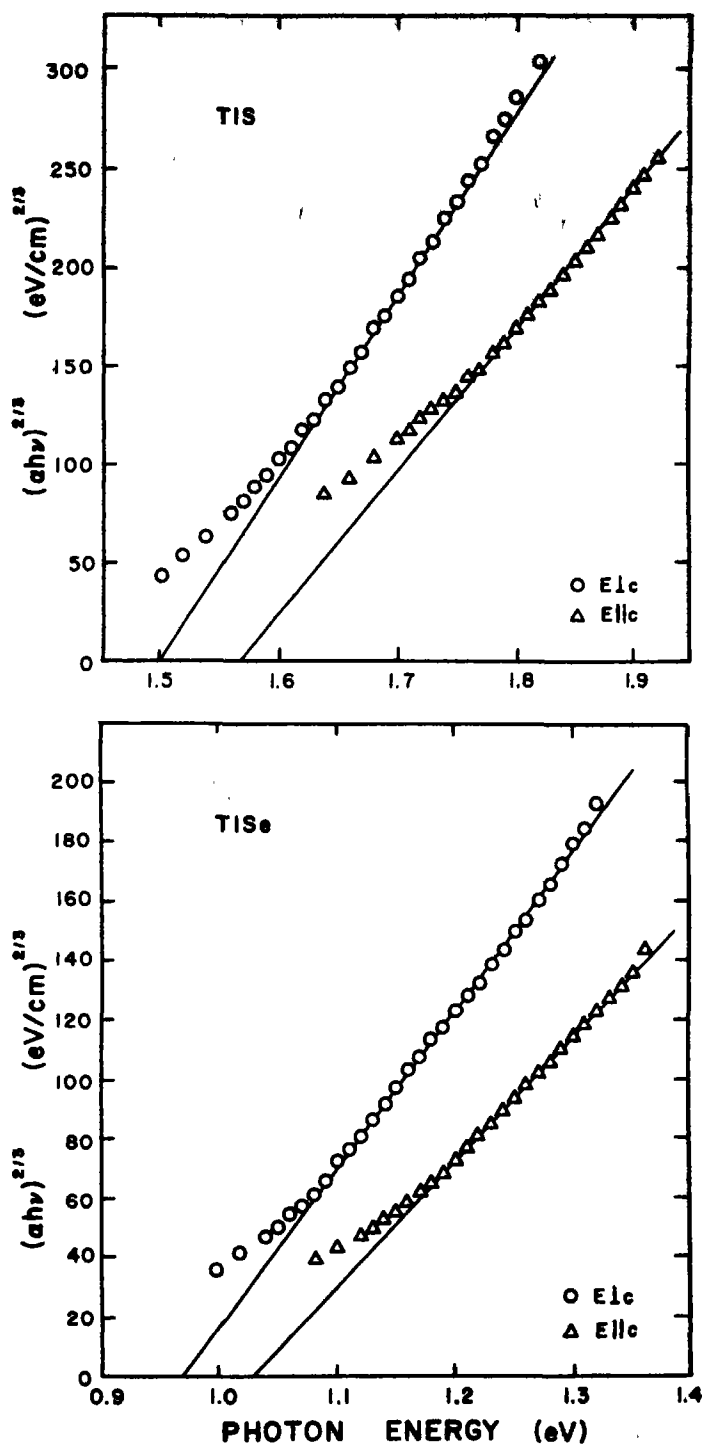


Fig. 5. $(\alpha h\nu)^{2/3}$ vs. photon energy extrapolated to the direct band gap energy value for TIS and TlSe.

and optical properties. Measurements on TlSe have been extensively compared to previously reported work and a more comprehensive optical absorption analysis presented. Similar measurements on TlS and $\text{TlS}_{0.5}\text{Se}_{0.5}$ have not been previously reported. A satisfactory explanation has not been given for the difference in the intrinsic activation energies determined by electrical and optical methods for these materials. The identification of some results with proposed band structure details is of interest.

REFERENCES

1. HANSEN M., *Constitution of Binary Alloys*, McGraw-Hill, New York (1958).
2. KETELAAR J. A. A., t'HART W. H., MOEREL M. and POLDER, D., *Z. Kristallogr.* **101**, 396 (1939).
3. HAHN H. and KLINGER W., *Z. anorg. Chem.* **260**, 110 (1949).
4. MOOSER E. and PEARSON W. B., *J. Electron.* **1**, 629 (1956).
5. MOOSER E. and PEARSON W. B., *Phys. Rev.* **101**, 492 (1956).
6. GUSEINOV G. D., AKHUNDOV G. A. and ABDULLAEV G. B., *Soviet Phys.—solid State* **4**, 885 (1962).
7. RZAEV K. I. and KHALILOV Kh. M., *Soviet Phys.—Acoust.* **13**, 360 (1968).
8. PFANN W. G., *Zone Melting*, Ch. 7. John Wiley, New York (1966).
9. GASHIMZADE F. M. and NIZAMETDINOVA M. A., *Soviet Phys.—solid State* **10**, 2097 (1969).
10. MAMEDOV K. K., KERIMOV I. G., KOSTRYUKOV V. N. and MEKHTIEV M. I., *Soviet Phys.—Semicond.* **1**, 363 (1967).
11. SCATTURIN V. and FRASSON E., *Ricerca Scient.* **26**, 3382 (1956).
12. NAYAR P. S., VERMA J. K. D. and NAG B. D., *J. phys. Soc. Japan* **23**, 144 (1967).
13. RAU J. W. and KANNEWURF C. R., *Z. Mitt.* **5**, 199 (1970).
14. RECHTIEN J. J., Ph.D. Thesis, Northwestern University (1966).
15. ALI-ZADE Z. I. and NIZAMETDINOVA M. A., *Soviet Phys.—Semicond.* **2**, 499 (1968).
16. ITOGA R. S., Ph.D. Thesis, Northwestern University (1970).
17. KAHAN A., *Appl. Optics* **3**, 314 (1964).
18. GASHIMZADE F. M., *Soviet Phys.—solid State* **2**, 2700 (1961).
19. GASHIMZADE F. M., *Izv. akad. nauk Azerb. S.S.R., Ser. Fiz.—Mat. i Tekhn. Nauk* **1962**, 83 (1962).
20. FIELDING P., FISCHER G. and MOOSER E., *J. Phys. Chem. Solids* **8**, 434 (1959).
21. AKHUNDOV G. A., ABDULLAEV G. B. and GUSEINOV G. D., *Soviet Phys.—solid State* **2**, 1378 (1961).
22. MORI R. and HASHIMOTO K., *J. phys. Soc. Japan* **16**, 1797 (1961).
23. AKHUNDOV G. A., ALIEVA M. Kh. and PASHAEV A. M., *Dokl. akad. nauk. Azerbaidzhan. S.S.R.* **16**, 1053 (1960).
24. AKHUNDOV G. A. and KERIMOVA T. G., *Phys. Status Solidi* **16**, K15 (1966).
25. PICKAR P. B. and TILLER H. D., *Phys. Status Solidi* **29**, 153 (1968).
26. GUSEINOV G. D., AKHUNDOV G. A., ALIEVA M. Kh., and ABDULLAEV G. B., *Bulletin of the Academy of Sciences, USSR, Physical Series* **28**, 1226 (1964).
27. BARDEEN J., BLATT F. J. and HALL L. H., *Photoconductivity Conference* (Edited by R. G. Brechenridge, B. R. Russell and E. E. Hahn) p. 146, John Wiley, New York (1956).

f* ELECTRONS IN A STRONG CRYSTAL FIELD. THE RELATIONSHIP BETWEEN PARAMAGNETIC AND SATURATION MOMENTS

SAL-KIT CHAN†

Argonne National Laboratory, Ill. 60439, U.S.A.

(Received 22 June 1970; in revised form 17 September 1970)

Abstract—The relationship between paramagnetic and saturation moments of localized *f* electrons in a strong crystal field is examined. It is found that while the simple atomic-like results $\mu_s = g_J J$ and $\mu_p = g_J \times \sqrt{J(J+1)}$ no longer hold, there exist definite bounds for the ratio μ_s/μ_p according to the symmetry of the crystal field. Experimental data on the heavy rare earth and actinide compounds are examined in the light of these results.

1. INTRODUCTION

THE QUESTION of whether a particular magnetic solid fits closer into the localized or itinerant models of magnetism is often controversial. Various types of experimental data are often invoked as criteria[1]. Among the most common types are the paramagnetic moments (measured by high-temperature susceptibility experiments) and the saturation moments (measured by magnetization and/or neutron experiments). According to the localized model of a moment sitting in the mean molecule field of all others[2], when the total angular momentum *J* is a good quantum number, the saturation moment is given by $\mu_s = g_J J$ and the high-temperature susceptibility should follow Curie-Weiss law corresponding to an effective moment of $\mu_p = g_J \sqrt{J(J+1)}$, where g_J is the Landé factor and the units are in Bohr magnetons. (These expressions for μ_s and μ_p are often referred to as atomic-like results.) In such a situation, we have a definite ratio between μ_s and μ_p so that one quantity determines the other. On the itinerant model, there is in general no

such simple relation between these two quantities.

This kind of criterion is believed to be borne out in most compounds of the rare earths in which the *f* electrons are well localized and the total angular momentum *J* is a conserved quantity because of weak crystal field. The paramagnetic moments are found to follow the Hund's rule values closely while the saturation moments are only slightly below [17]. Recently, it has been suggested that compounds of the actinides should fit also into the localized picture. Studies[3] on the magnetic properties of intermetallic compounds of uranium with group VA and VIA elements using the Russel-Saunders coupling scheme however reveals a difficulty. While it is possible, by invoking crystal field and molecular field effects, to bring the saturation moments in line with the experimental values, it is not always possible to obtain simultaneously reasonable agreement for the susceptibility data. This raises the interesting question of what the implication of this pitfall is. Since according to the atomic representation in Hubbard's theory of electron correlation in narrow bands[4], the concept of crystal and molecular fields remains valid even in solids which are not ionic, this difficulty may indicate either

*Work carried out under the auspices of the U.S. Atomic Energy Commission.

†Now at Cavendish Laboratory, Free School Lane, Cambridge, England.

a breakdown of Russel-Saunders coupling scheme or that the localized model is not appropriate for these uranium compounds. The original motivation of this work was to clarify this matter. The objectives of this paper are therefore limited to (1) establishing a relation between the paramagnetic and saturation moments in situations in which the crystal field is strong enough to cause a significant mixing of J -multiplets resulting in a breakdown of the simple atomic-like results and (2) applying the modified form of atomic-like results to uranium and other actinide compounds as a criterion to test whether the experimental data on paramagnetic and saturation moments favour the localized model.

The plan of this paper is as follows. In Section 2, μ_s and μ_p are expressed in terms of the eigenvalues of the Hamiltonian rather than in terms of J . In Section 3, the relation between μ_s and μ_p are examined according to the symmetry of the crystal field. It is found that while we no longer have the simple atomic-like results, the ratio $r = \mu_s/\mu_p$ should lie within definite bounds. The results in the weak crystal field limit when J becomes a good quantum number are also examined. In Section 4, the significance of the results are summarized. Experimental data on both the actinide and heavy rare earth compounds are discussed in the light of these results.

2. THE PARAMAGNETIC SUSCEPTIBILITY AND THE MAGNETIZATION

Van Vleck[5] has shown that when the temperature range is such that the crystal field energy levels may be separated into low and high frequency groups, the one-ion paramagnetic susceptibility is to a good approximation given by

$$\chi_0(T) = \frac{\beta^2}{Z} \left\{ \frac{1}{kT} \sum_{\Gamma}^1 \sum_{\Gamma'}^1 |\langle \Gamma | \mu_z | \Gamma' \rangle|^2 + 2 \sum_{\Gamma}^1 \sum_{\Gamma'}^2 |\langle \Gamma | \mu_z | \Gamma' \rangle|^2 / (E_{\Gamma'} - E_{\Gamma}) \right\}.$$

Here \sum^1 and \sum^2 sum over the low and high frequency groups respectively. $|\Gamma\rangle$ is the crystal field eigenstate. The partition function is $Z = \sum \exp(-E_{\Gamma}/kT) \cong \sum^1 \exp(-E_{\Gamma}/kT) \cong N$, where N is the total multiplicity of the low frequency group. The paramagnetic moment is therefore given by

$$\mu_p^2 = \frac{3}{N} \sum_{\Gamma}^1 \sum_{\Gamma'}^1 |\langle \Gamma | \mu_z | \Gamma' \rangle|^2.$$

The magnetic dipole moment operator $\mu = \sum l_i + g_s \sum S_i$ is in general a Hermitian operator. In Ref.[6], it is shown how the matrix elements between crystal field states may be calculated. For the present purpose, all we need is the Hermitian property. From a mathematical theorem (Appendix 1) which states that the sum of the squares of the moduli of elements of a Hermitian matrix is equal to the sum of the squares of its eigenvalues, we have

$$\mu_p^2 = \frac{3}{N} \sum_i \epsilon_i^2 \quad (1)$$

where ϵ_i represent the eigenvalues of the matrix whose elements are $\langle \Gamma | \mu_z | \Gamma' \rangle$.

In the presence of an exchange field, the Hamiltonian of the magnetic ion is $H = H_0 + H_1$, where $H_1 = -\beta \mathcal{H} \sigma \mu_z$. Here we restrict the discussion to the cases when the exchange field is parallel to one of the symmetry axes of the crystal. H_0 includes the Coulomb, spin-orbit and crystal field interactions. The eigenvalues and eigenstates of H_0 are E_{Γ} and $|\Gamma\rangle$ respectively. $\sigma = \pm 1$ indicates that the magnetization may be either parallel or antiparallel to the exchange field. The eigenstates $|\Psi_m\rangle$ of H are given by the unitary transformation R that diagonalizes H , i.e., by

$$|\Psi_m\rangle = \sum_{\Gamma}^1 R_{\Gamma m} |\Gamma\rangle.$$

The eigenvalues \mathcal{E}_m are given by the roots of the secular determinant

$$\|(E_{\Gamma} - \mathcal{E}_m) \delta_{\Gamma\Gamma'} - \beta \mathcal{H} \sigma \langle \Gamma' | \mu_z | \Gamma \rangle\| = 0. \quad (2)$$

The magnetization is

$$\text{Tr}[\mu_z \exp(-H/kT)] = \frac{1}{Z} \sum_m \langle \Psi_m | \mu_z | \Psi_m \rangle \times \exp(-\mathcal{E}_m/kT).$$

The saturation moment may be obtained by letting T tend to zero. We have

$$\mu_s = \langle \Psi_0 | \mu_z | \Psi_0 \rangle, \quad (3)$$

where $|\Psi_0\rangle$ is the lowest eigenstate of $H = H_0 + H_1$.

The matrix elements $\langle \Psi_m | \mu_z | \Psi_m \rangle$ may be expressed in terms of the eigenvalues \mathcal{E}_m in equation (2) in the following manner. Since R is the unitary transformation that diagonalizes H , we have

$$(R^{-1}HR)_{mm'} = \mathcal{E}_m \delta_{mm'}.$$

But

$$\begin{aligned} (R^{-1}HR)_{mm'} &= \sum_{\Gamma\Gamma'}^1 (R^{-1})_{m\Gamma} (H_0 - \beta \mathcal{H} \sigma \mu_z)_{\Gamma\Gamma'} \\ &\quad \times R_{\Gamma'm'} \\ &= \sum_{\Gamma\Gamma'}^1 R_{\Gamma'm}^* (E_{\Gamma} \delta_{\Gamma\Gamma'} - \beta \mathcal{H} \sigma \\ &\quad \times \langle \Gamma | \mu_z | \Gamma' \rangle) R_{\Gamma'm'}. \end{aligned}$$

It follows therefore that

$$\begin{aligned} \langle \Psi_m | \mu_z | \Psi_m \rangle &= \sum_{\Gamma\Gamma'}^1 R_{\Gamma'm}^* \langle \Gamma | \mu_z | \Gamma' \rangle R_{\Gamma'm} \\ &= \left(\sum_{\Gamma\Gamma'}^1 R_{\Gamma'm}^* R_{\Gamma'm} E_{\Gamma} \delta_{\Gamma\Gamma'} - \mathcal{E}_m \right) / (\beta \mathcal{H} \sigma) \\ &= \left(\sum_{\Gamma}^1 E_{\Gamma} |R_{\Gamma'm}|^2 - \mathcal{E}_m \right) / (\beta \mathcal{H} \sigma). \end{aligned} \quad (4)$$

3. THE CONNECTION BETWEEN PARAMAGNETIC AND SATURATION MOMENTS

Equations (1), (2), (3) and (4) contain all the information on how the paramagnetic and saturation moments are related. For

convenience, we set the energy scale in such a manner that the original ground crystal field eigenvalue is zero. We shall analyze the following three separate cases.

A. When the low-frequency group is made up of a single crystal field state, the secular determinant (2) becomes

$$\|\mathcal{E}_m \delta_{\Gamma\Gamma'} + \beta \mathcal{H} \sigma \langle \Gamma' | \mu_z | \Gamma \rangle\| = 0. \quad (5)$$

We obtain from equations (3) and (4) the result

$$\mu_s = \langle \Psi_0 | \mu_z | \Psi_0 \rangle = -\mathcal{E}_0 / (\beta \mathcal{H} \sigma), \quad (6)$$

where \mathcal{E}_0 is the lowest eigenvalue of H . In equation (5), the matrix of the secular determinant is just a constant $(\beta \mathcal{H} \sigma)$ times the matrix of the magnetic dipole moment operator between crystal field eigenstates. We obviously have $\mathcal{E}_m = \beta \mathcal{H} \sigma \epsilon_m$, where ϵ_m is as defined in equation (1). The saturation moment is from equation (6)

$$\mu_s = -\epsilon_0. \quad (7)$$

Equations (1) and (7) determine the relationship between the paramagnetic and saturation moments.

For all point-group symmetries, the Zeeman splittings are symmetrical with respect to the original level and may be classified into doublets, triplets and quadruplets as shown in Fig. 1. We shall use the short-hand notations $(\pm a)$, $(\pm a, 0)$ and $(\pm a, \pm b)$ to represent the eigenvalues of matrix $\|\langle \Gamma | \mu_z | \Gamma' \rangle\|$ in the doublet, triplet and quadruplet situations respectively. We have from equations (1) and (7) the following results:—

1. Doublet (Γ_6, Γ_7):

We have $\mu_p^2 = 3a^2$ and $\mu_s = a$ so that

$$\mu_s = \frac{1}{\sqrt{3}} \mu_p.$$

2. Triplet (Γ_4, Γ_5):

We have $\mu_p^2 = 2a^2$ and $\mu_s = a$ so that

$$\mu_s = \frac{1}{\sqrt{2}} \mu_p.$$

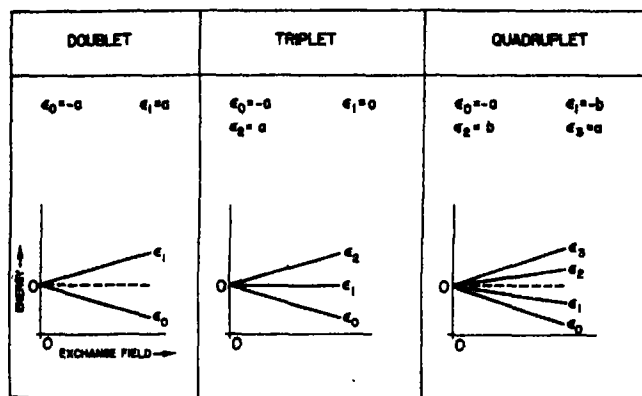


Fig. 1. Splittings of a single crystal field level by an exchange field. The splittings in all three cases increase linearly with the magnitude of the exchange field. They are also symmetrical with respect to the unperturbed level.

3. *Quadruplet* (Γ_8):

We have $\mu_p^2 = \frac{2}{3}(a^2 + b^2)$ and $\mu_s = a$. But b must lie in the range $0 < b < a$. We obtain

$$\sqrt{\frac{2}{3}} \mu_p > \mu_s > \frac{1}{\sqrt{3}} \mu_p.$$

Therefore, when the ground state is a quadruplet, we can only narrow down the ratio $r = \mu_s/\mu_p$ to a range of values without doing a detailed calculation. The precise value of the ratio depends on the nature of the admixture of different J components in the Γ_8 wave function and on the ratios of the 2nd, 4th and 6th order terms of the crystal field potential.

The above results 1–3 are independent of the magnitude of the exchange field and hold for both ferromagnetic and antiferromagnetic substances.

B. When the low-frequency group includes one or more other crystal field states that have matrix elements connecting the ground state, the saturation moment is obtained by first solving equation (2) and then using equations (3) and (4). We have

$$\mu_s = \left(\sum_i^1 E_i |R_{i0}|^2 - \mathcal{E}_0 \right) / (\beta \mathcal{H} \sigma),$$

where \sum_i^1 sums over all the higher states that

are coupled to the ground state. Since $E_i > 0$ and \mathcal{E}_0 is more depressed with the exchange coupling than without (Appendix 2), the magnitude of the saturation moment is invariably increased as a result of the coupling with the higher states. This is illustrated schematically in Fig. 2. We may interpret this as 'transfer of moment' from the higher states to the ground state via the coupling effect of the exchange field. This increase is independent of the direction of the exchange field and is therefore the same for both ferromagnetic and antiferromagnetic materials. The result however varies with the magnitude of the exchange field and we can only establish a lower bound to the saturation moment. We have the following results:

4. *Doublet* (Γ_6, Γ_7) or *quadruplet* (Γ_8) lowest:

$$\mu_s > \frac{1}{\sqrt{3}} \mu_p.$$

5. *Triplet* (Γ_4, Γ_5) lowest:

$$\mu_s > \frac{1}{\sqrt{2}} \mu_p.$$

6. *Non-magnetic singlet* (Γ_1, Γ_2) or *doublet* (Γ_3) lowest:

$$\mu_s > 0.$$

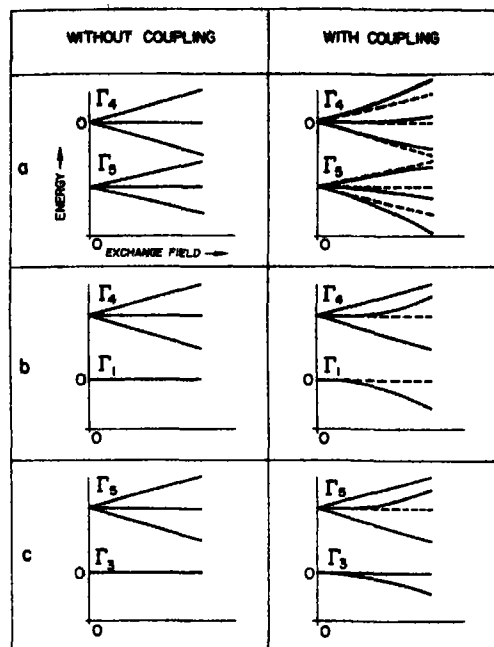


Fig. 2. Schematic illustration of the difference between the splittings of coupled and uncoupled crystal field levels in the cases of (a) two triplets, (b) a singlet and a triplet and (c) a doublet and a triplet. Without exchange coupling, the splittings increase linearly with the magnitude of the exchange field and are symmetrical with respect to the respective unperturbed levels. With exchange coupling, the splittings become nonlinear and asymmetrical. The effect of the upper state on the lower is to bend down the splittings of the latter. This leads to an increase in the saturation moment.

The precise value of μ_s depends on the magnitude of the exchange field and the spacing between the crystal field states.

The results obtained so far hold even when Russel-Saunders coupling scheme breaks down and when there is J -mixing. They are summarized in Table 1. For convenience, the selection rules governing the matrix elements of the magnetic dipole moment operator between crystal field states are summarized in Tables 2 and 3.

C. In the special case when J is a good quantum number, we can speak of at least an intermediate coupling Landé factor g_J . The crystal field eigenstates are in general constructed from linear combination of $|M\rangle$, M being the magnetic quantum number. We can therefore write

$$|\Gamma\rangle = \sum_M Q_{M\Gamma} |M\rangle,$$

where $Q_{M\Gamma}$ represents the matrix of the unitary transformation Q that diagonalizes H_0 , the sum of the Coulomb, spin-orbit and crystal field Hamiltonians. From this we have

$$\langle \Gamma | \mu_z | \Gamma' \rangle = \sum_{MM'} Q_{M\Gamma}^* \langle M | \mu_z | M' \rangle Q_{M'\Gamma'}.$$

It can be shown easily that $\langle M | \mu_z | M' \rangle = g_J M \delta_{MM'}$ when J is a good quantum number.

Table 1.

Number of localized f electrons	Symmetry of ground state	Number of excited states coupled to the ground state by exchange field	$r = \mu_s/\mu_p$	Remark
even	Γ_4, Γ_5	0	$r = 0.71$	A, C
even	Γ_4, Γ_5	≥ 1	$r > 0.71$	B, C
even	$\Gamma_1, \Gamma_2, \Gamma_3$ (non-magnetic)	≥ 1	$r > 0$	B, C
odd	Γ_6, Γ_7	0	$r = 0.58$	A, C
odd	Γ_6, Γ_7	≥ 1	$r > 0.58$	B, C
odd	Γ_8	0	$0.82 > r > 0.58$	A, C
odd	Γ_8	≥ 1	$r > 0.58$	B, C

A: r independent of magnitude of exchange field.

B: r increases with magnitude of exchange field.

C: Result hold for both ferromagnetic and antiferromagnetic materials.

Table 2.

$\Gamma_b \backslash \Gamma_a$	Γ_1	Γ_2	Γ_3	Γ_4	Γ_5
Γ_1	0	0	0	\times	0
Γ_2	0	0	0	0	\times
Γ_3	0	0	0	\times	\times
Γ_4	\times	0	\times	\times	\times
Γ_5	0	\times	\times	\times	\times

Table 3.

$\Gamma_b \backslash \Gamma_a$	Γ_6	Γ_7	Γ_8
Γ_6	\times	0	\times
Γ_7	0	\times	\times
Γ_8	\times	\times	\times

Substituting this in, we get

$$\langle \Gamma | \mu_z | \Gamma' \rangle = g_J \sum_M M Q_{M\Gamma} Q_{M\Gamma'}^*.$$

This leads to the equation

$$\begin{aligned} \sum_{\Gamma\Gamma'} |\langle \Gamma | \mu_z | \Gamma' \rangle|^2 &= g_J^2 \sum_M M^2 \left(\sum_{\Gamma'} |Q_{M\Gamma'}|^2 \right) \\ &\quad \times \left(\sum_{\Gamma} |Q_{M\Gamma}|^2 \right) + g_J^2 \sum_M \\ &\quad \times M \left\{ \sum_{M' \neq M} M' \left(\sum_{\Gamma'} Q_{M\Gamma'} Q_{M'\Gamma'}^* \right) \right. \\ &\quad \left. \times \left(\sum_{\Gamma} Q_{M'\Gamma}^* Q_{M\Gamma} \right) \right\}. \end{aligned}$$

From the orthonormal condition $\sum_{\Gamma} Q_{M\Gamma} Q_{M'\Gamma}^* = \delta_{MM'}$, we find that the second term vanishes while the first term is $g_J^2 \sum_M M^2$. The paramagnetic moment is therefore given by

$$\mu_p^2 = \frac{3g_J^2}{N} \sum_M M^2,$$

where M runs from $-J$ to J . Making use of the

formula

$$\sum_{n=1}^J n^2 = \frac{1}{6} J(J+1)(2J+1),$$

we finally get

$$\mu_p^2 = g_J^2 J(J+1).$$

We therefore have the following result.

7. When J is a good quantum number, the paramagnetic moment has its free-ion value, i.e. $g_J \sqrt{J(J+1)}$ regardless of the symmetry and the strength of the crystal field, provided that all the crystal field splittings of the ground state of total angular momentum J may be included in the low-frequency group. The ratio $r = \mu_s/\mu_p$ however still obeys results 1-6 so that the saturation moment μ_s may differ quite considerably from the value $g_J J$.

4. DISCUSSIONS

The analysis of the preceding sections demonstrates clearly the intimate relationship between the paramagnetic moment, saturation moment and the nature of the low-lying multiplets of the localized f electrons. The most significant result is that for an odd number of localized f electrons, the ratio of the saturation to paramagnetic moment is always greater than 0.58 while for an even number, this ratio should be normally greater than 0.71. In the latter case, a smaller ratio is nevertheless possible if a nonmagnetic ground state acquires a moment via the exchange coupling with a higher magnetic state. These ratios hold only in the simple ferromagnetic and antiferromagnetic alignments. They break down when effects such as anisotropy and magnetostriction become important. The results summarized in Table 1 represent an extension of the simple atomic-like results in the presence of a strong crystal field. When the localized model is appropriate, they provide a 'theoretical link' between the high temperature (susceptibility and paramagnetic scattering of neutrons) and low

temperature (magnetization and coherent magnetic scattering of neutrons) experiments. An experimentalist, with both types of measurements on hand, may benefit from these results in several ways. If the situation is such that the ionicity of the magnetic ion and hence the symmetry of the wave function are known, he may use these results to cross-check his high and low temperature measurements. On the other hand, if the nature of the localized electrons is largely unknown but there is reason to believe that both types of measurements are highly reliable, he may use the results to select a model for the interpretation of the experiments. The usefulness of these results may be further extended if magnetic entropy measurements above the transition temperature are also available. Such measurements can provide the valuable information of the total multiplicity of the low-frequency group.

To conclude this paper, we shall examine some of the available experimental results. Although it was the actinide compounds that

stimulated this work, we shall also examine the heavy rare earth compounds because we have results for the weak crystal field limit. We choose to leave out the light rare earth compounds due to lack of neutron data. The experimental results on the actinide and the heavy rare earth compounds are summarized in Tables 4 and 5 respectively. Before we discuss them, we should bear in mind the difficulties associated with these experiments. In general, the results do not seem to have a better than 10 per cent accuracy as is evident in most cases when more than one measurement have been carried out.

Table 4 shows values of the measured moments for some of the actinide compounds. All the intermetallic ones are of the NaCl type structure. The ionic UO_2 and Np_2O_7 have CaF_2 type structure. The crystal field splittings are 500 cm^{-1} upward[6]. There is of course the possibility of crossing of levels of different symmetry. The relative strength of the exchange field may be estimated from the transition temperature. Except with UN and

Table 4.

Compound	Structure	Ordering	Transition temperature (°K)	μ_s	μ_p	$r = \mu_s/\mu_p$
UN[8]	NaCl	A	53 ± 2	0.75	3.11	0.24
UP[8]	NaCl	A	123	1.90	3.56	0.53
				1.72	3.31	0.52
UAs[8]	NaCl	A	128	1.89	3.54	0.53
				2.13		0.60
USb[8, 9]	NaCl	A	213	2.85	3.85	0.74
UBi[8, 9]	NaCl	A	290	3.0	4.06	0.74
UO_2 [10, 11]	CaF_2	A	31	1.8	3.12	0.58
					3.2	0.56
US[12]	NaCl	F	178 ± 2	1.55	2.12	0.73
				1.8		0.85
USe[8]	NaCl	F	160.5	1.31	2.51	0.52
UTe[8]	NaCl	F	103	1.10	2.84	0.39
					2.36	0.47
NpC[13, 14]	NaCl	F/A	310 (A)	1.4	3.0	0.47
			220 (F)	2.1		0.70
NpO_2 [13, 15]	CaF_2	A	25	<0.5	2.95	<0.17
PuP[16]	NaCl	F	126	0.42	1.06	0.40

A: Antiferromagnetic ordering.

F: Ferromagnetic ordering.

Table 5.

Compound	Structure	Ordering	Transition temperature (°K)	μ_L [17]	Neutron [17]	Observed μ_p Susceptibility [18]	$r = \mu_L/\mu_p$	R-S Coupling	Calculated μ_p Intermediate [19]
TbN	NaCl	F	42	6.7 7.0	9.7		0.69 0.72	9.7	9.0
TbP	NaCl	A	9	6.2		9.56	0.65	9.7	9.0
TbAs	NaCl	A	12	7.7		9.65	0.80	9.7	9.0
Tb6b	NaCl	A	14	8.2	9.9	9.57	0.83 0.86	9.7	9.0
DyN	NaCl	F	26	4.8 7.4			0.6	9.7 10.6	9.0 9.95
HoN	NaCl	F	18	6.0 8.9	10.8		0.55 0.82	10.6	9.95
HoP	NaCl	F	5.5	8.8		10.34	0.85	10.6	9.95
HoSb	NaCl	A	9	9.3		10.35	0.90	10.6	9.95
ErN	NaCl	F	5	3.0 6.0	9.4		0.32 0.64	9.6	8.97
ErP	NaCl	A	3.1	5.7		9.32	0.61	9.6	8.97
ErSb	NaCl	A	3.7	7.0	9.8	9.36	0.72 0.75	9.6	8.97
TmN	NaCl					7.32		7.0	7.0

NpO_2 , the results show that the ratio μ_s/μ_p lies either within the range predicted for magnetic ground state or slightly on the lower side of it. At this stage, it is too optimistic to contemplate a classification of the symmetry of the ground state and the number of localized electrons using only the results in Table 1. We can nevertheless apply the results to conclude that something is anomalous about NpO_2 because the ratio is too small to be accountable. Unless the $6d$ electron plays a role, the ratio of saturation to paramagnetic moments should be greater than 0.58. If both the susceptibility and neutron experiments are reliable and if the $5f$ electrons are solely responsible for the magnetic properties, it would probably mean that some kind of structural changes takes place below the ordering temperature. X-ray experiments should help to sort this out even though neutron experiments do not have the required sensitivity. The intermetallic UN is out of step with other members of the group VA compounds of uranium. The apparently small ratio is only accountable if the number of localized $5f$ electrons is even and if the ground state is non-magnetic but coupled to a nearby magnetic state.

Table 5 shows results for intermetallic compounds of the heavy rare earths. They all have NaCl type structure. The crystal field splittings are of the order 100 cm^{-1} with the possibility of crossing of levels of different symmetry. The ratio $r = \mu_s/\mu_p$ lies well within the range predicted for magnetic ground state. Comparison of the measured paramagnetic moments with the calculated values for the free ions indicate that the agreement is better on the Russel-Saunders coupling scheme than on the intermediate coupling scheme. This need not mean that the Russel-Saunders coupling scheme is closer to reality. It probably means that conduction electrons play some role in the susceptibility of the intermetallic compounds. It is significant to point out that the paramagnetic moment of trivalent Er in ionic

Er_2O_3 is 9.2 Bohr magnetons [7] which is very close to the values for the intermetallic compounds of Er in spite of the difference in symmetries. This is precisely the conclusion reached in result 7 that the paramagnetic moment does not depend on symmetry in the weak crystal field limit.

To sum up, when the crystal field is strong enough to cause a significant breakdown of the Russel-Saunders coupling scheme, the simple atomic-like results $\mu_s = g_s J$ and $\mu_p = g_J \sqrt{J(J+1)}$ no longer hold. Instead we have definite bounds for the ratio μ_s/μ_p as summarized in Table 1. Allowing for such a possibility, then the available susceptibility and neutron data on the actinide compounds are not inconsistent with the picture of localized f electrons.

Acknowledgement—The author wishes to thank Drs. D. J. Lam and F. Y. Fradin for helpful discussions.

REFERENCES

1. HERRING C., in *Magnetism* (Edited by G. T. Rado and H. Suhl) Vol. 4, Ch. 6, Academic Press, New York (1966).
2. MARTIN D. H., *Magnetism in Solids*, The M.I.T. Press, Cambridge, Massachusetts (1967).
3. GRUNZWEIG-GENOSSAR J., KUZNIETZ M. and FRIEDMAN F., *Phys. Rev.* **173**, 562 (1968).
4. HUBBARD J., *Proc. R. Soc. A* **285**, 542 (1965).
5. VAN VLECK J. H., *The Theory of Electric and Magnetic Susceptibilities*, Oxford University Press, London (1965).
6. CHAN S. and LAM D. J., *Bull. Am. phys. Soc.* **11**, 14, 351 (1969).
7. KOEHLER W. C. and WOLLAN E. O., *Phys. Rev.* **92**, 1380 (1953).
8. References may be found in Table 1 of Ref. [3].
9. KUZNIETZ M., LANDER G. H. and CAMPOS F. P., *J. Phys. Chem. Solids* **30**, 1642 (1969).
10. FRAZER B. C., SHIRANE G., COX D. E. and OLSEN C. E., *Phys. Rev.* **140**, A1448 (1965).
11. COSTA P., LALLEMENT R., ANSELIN F. and ROSSIGNAL D., *Symposium on Compounds of Interest in Nuclear Technology* (Edited by Waber, Chiotti and Miner) AIME (1964).
12. GARDNER W., private communication.
13. ROSS J. W. and LAM D. J., *J. appl. Phys.* **38**, 1451 (1967).
14. DUNLOP B. D., KALVIUS G. M., LAM D. J. and BRODSKY M. B., *J. Phys. Chem. Solids* **29**, 1365 (1968).
15. LANDER G. H., HEATON L., MUELLER M. H. and ANDERSON K. D., *J. Phys. Chem. Solids* **30**, 733 (1969).

15. HEATON L., MUELLER M. H. and WILLIAMS J. M., *J. Phys. Chem. Solids* **28**, 1651 (1967).
COX D. E. and FRAZER B. C., *J. Phys. Chem. Solids* **28**, 1649 (1967).
16. LAM D. J., FRADIN F. Y. and KRUGER O. L., *Phys. Rev.* **187**, 606 (1969).
17. CHILD H. R., WILKINSON M. K., CABLE J. W., KOEHLER W. C. and WOLLAN E. O., *Phys. Rev.* **131**, 922 (1963).
18. IANDELLI A., *Rare Earth Research* (Edited by E. V. Kleber), MacMillan, New York (1961).
19. CARNALL W. T., private communication (*g-factors obtained from spectroscopic measurements of tripositive actinide ions in solutions*).

APPENDICES

1. Let ϵ_i be the eigenvalues of Hermitian matrix A and let P be the orthogonal transformation that diagonalizes it. Then

$$(PAP^{-1})_{ij} = \epsilon_i \delta_{ij} \text{ so that } A_{ij} = \sum_k P_{ik}^{-1} \epsilon_k P_{kj}.$$

We therefore have

$$\begin{aligned} \sum_{ij} |A_{ij}|^2 &= \sum_{ij} A_{ij} A_{ji} \\ &= \sum_{kl} \sum_{ij} P_{ik}^{-1} \epsilon_k P_{kj} P_{ji}^{-1} \epsilon_l P_{il} = \sum_k \epsilon_k^2. \end{aligned}$$

2. To show that the ground state is more depressed as a result of coupling with a higher state through the exchange field, we note that such coupling involves only one component from each of the original crystal field states. The problem therefore involves only solving a 2×2 determinant. In short-hand notations, with 0 representing the original ground crystal field state, 1 the coupled higher state and $V_0 = -\beta \mathcal{H} \sigma \times \langle \Gamma_i | \mu_z | \Gamma_i \rangle$, the secular determinant of equation (2) reduces to

$$\begin{vmatrix} V_{11} + E_1 - \mathcal{E} & V_{10} \\ V_{01} & V_{00} - \mathcal{E} \end{vmatrix} = 0.$$

Solving this, we find that the ground state energy is

$$\mathcal{E}_0 = \frac{1}{2} \{ V_{11} + V_{00} + E_1 - \sqrt{(V_{11} - V_{00} + E_1)^2 + 4|V_{10}|^2} \}.$$

Without the exchange coupling, the ground state energy is V_{00} . The difference is therefore

$$\mathcal{E}_0 - V_{00} = \frac{V_{11} + E_1 - V_{00}}{2} - \sqrt{\left(\frac{V_{11} + E_1 - V_{00}}{2} \right)^2 + |V_{10}|^2}.$$

The ground state is always more depressed as a result of coupling.

TWO-BAND GALVANOMAGNETIC EFFECTS IN GRAY TIN*

CHARLES F. LAVINE† and A. W. EWALD
Northwestern University, Evanston, Ill. 60201, U.S.A.

(Received 7 May 1970; revised 4 August 1970)

Abstract—A study of the temperature, magnetic field, and doping dependence of the conductivity, Hall coefficient, and magnetoresistance of gray tin has been interpreted within the framework of the Groves-Paul band structure model allowing the determination of several of its parameters as well as an investigation of the charge carrier scattering mechanisms. Suitable choice of temperature and doping limited conduction to at most two bands so that the single-band characteristics could be obtained using standard two-band theory. In a series of filaments having donor concentrations, N_d , between 5×10^{16} and $2.5 \times 10^{19} \text{ cm}^{-3}$ the 4-2°K values of Hall number, number from oscillatory magnetoresistance period, low field magnetoresistance, and Γ_8^+ electron mobility all exhibit discontinuous behavior as functions of N_d at a critical concentration, $N_c \approx 5 \times 10^{17} \text{ cm}^{-3}$, at which the (111) minima begin to be populated. The observed mobility enhancement is in good qualitative agreement with screened-ionized-impurity scattering theory. The energy separation of the two conduction bands is evaluated ($E_g = 0.092 \text{ eV}$), and an upper limit is placed on the (111) density of states effective mass ($m_{1d} \leq 0.21 m_e$). For $N_d < N_c$ the mobility agrees well with the above theory if a doping dependent dielectric constant is employed. Between 4-2 and 100°K samples having $2 \times 10^{17} \leq N_d \leq 2.5 \times 10^{18} \text{ cm}^{-3}$ exhibit an increasing Hall coefficient with temperature due to thermal transfer of electrons from the (000) to the (111) minima. This is consistent with the above energy separation and mass values. We also show that $dE_g/dT \leq -4 \times 10^{-5} \text{ eV/°K}$. For intrinsic single crystal samples the hole mobility follows a $T^{-3/2}$ dependence down to 20°K and has an absolute value compatible with acoustic phonon scattering.

1. INTRODUCTION

IN THIS paper measurements of the electrical conductivity, magnetoresistance, and Hall coefficient of gray tin as functions of magnetic field strength, temperature and doping are analyzed within the framework of the Groves-Paul band structure model[1] shown in Fig. 1. Several previous galvanomagnetic studies contributed to the development and acceptance of this model. In particular, the change in symmetry type of the magnetoresistance between 77 and 273°K was the first definitive evidence of a complicated conduction band

structure[2]. Early oscillatory magnetoresistance measurements[3] yielded an electron effective mass that was too large to be consistent with a 'mass energy gap' of about 0.1 eV [4], the measured thermal gap[5]. Thirdly, the $T^{-3/2}$ dependence of the intrinsic Hall coefficient at low temperatures which did not change with hydrostatic pressure confirmed the postulated zero band gap at the zone center[1]. While they proved to be particularly significant, these results constituted only a fraction of the experimental data that had been accumulated[6] when the model was proposed. Much of it, including extensive data on doped samples, could not be analyzed because it had unwittingly been taken under conditions in which three bands contributed. In the present experiments conduction was limited to two, or in some cases a single band through suitable choice of temperature and doping. The results are in good agreement

*Research supported by the Advanced Research Projects Agency of the Department of Defense through the Northwestern Materials Research Center and by the National Science Foundation. The work is part of a dissertation submitted by one of the authors (C.F.L.) to the Graduate School of Northwestern University in partial fulfillment of the requirements for the Ph.D. degree.

†Present Address: Honeywell Corporate Research Center, Hopkins, Minn. 55343, U.S.A.

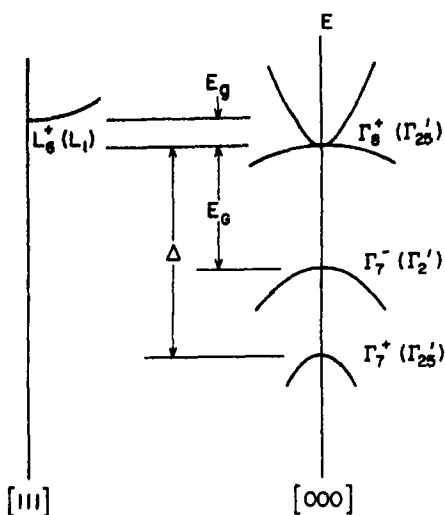


Fig. 1. The Groves-Paul band structure model of gray tin. The band edges are labeled in both the double group, and in parentheses, single group representation. The energy gap between the Γ_8^+ conduction and valence bands is zero. The subsidiary conduction band minima, L_6^+ , are separated from Γ_8^+ degeneracy by the energy E_g .

with the model giving firm support to its validity and permitting us to determine some of its parameters.

Having established that our measurements are consistent with this energy band scheme we are able to devote considerable attention to the other aspect of transport properties, the relaxation mechanisms. These are studied under a variety of experimental conditions. For extrinsic samples at low temperatures the mobility of both electrons and holes is shown to be limited by ionized impurity scattering and the dependence of the mobility on impurity concentration is explained by the Dingle [7] and Brooks-Herring [8] treatments of screened, ionized-impurity scattering. At low donor concentrations this involves the introduction of a doping-dependent dielectric constant. When both electron bands are populated, a screening enhanced mobility is observed at 4.2°K. This is analogous to the enhanced lifetime observed in oscillatory magnetoresistance experiments under similar doping conditions [9].

For pure and lightly doped *n* and *p* type samples the $T^{-3/2}$ dependence of the Hall coefficient, characteristic of a zero band gap semiconductor, is observed. Using this result and the temperature dependence of the conductivity and magnetoresistance we are able to determine the behavior of the light electron and hole mobilities as a function of temperature. The $T^{-3/2}$ dependence of the hole mobility strongly suggests that it is limited by acoustic phonon scattering, at least down to 30°K.

2. EXPERIMENTAL DETAILS

(a) Sample preparation and mounting

Most of the samples were prepared by transforming cast, single crystal white tin wires to the gray phase [10]. For the present work this method offered several advantages over that of growing single crystals from mercury solution [11]. Besides growing faster and being easier to prepare, the samples could be made with a pre-determined, easily controllable, and homogeneous impurity concentration. The starting material from which the alloys were prepared was Cominco six-nine pure tin. Low temperature Hall measurements on this material indicate 8×10^{15} donors/cm³. These presumably are residual Sb atoms which are not removed by zone refining due to the small segregation coefficient of antimony in tin. A master alloy containing 3×10^{20} Sb atoms/cm³ and a submaster alloy of 2×10^{18} cm⁻³ were used to prepare other alloys covering the high and low concentration ranges. In this way the impurity could be controlled to within a few per cent of nominal without making excessively large quantities of alloy.

After seeding and starting the transformation at -35°C, the wires were maintained at a temperature of either -10 or -2°C. The rate of transformation depends upon the temperature, impurity type and concentration, and upon the orientation of the white tin *c* axis relative to the filament axis. The above temperatures were chosen to give a transformation rate of about 0.5 cm per week. This represents a com-

promise since better crystal quality is achieved by raising the temperature but this results in a decreased rate [12a]. Samples were selected by finding straight segments about 0.5 cm long, free of cracks and other macroscopic imperfections. While single crystal segments can be found in the transformed wires, this requires heavy etching which distorts the cylindrical shape thereby introducing greater uncertainty in the conductivity and Hall coefficient values. Therefore, except for a few high purity samples [12b] grown from mercury solution, the samples were somewhat polycrystalline. To ensure proper determination of the Hall voltage a 4-to-1 or greater length-to-diameter ratio was always used.

After selection the sample was mounted on the copper sample probe using eutectic alloy solder of 23 per cent indium and 77 per cent gallium having a melting point of 16°C. The copper thermally coupled the sample to the heater and thermometers all of which were isolated from the bath by a vacuum space. To make electrical connections to the sample, four spring-loaded pressure contacts were used. These provided low resistance, small area contacts and allowed measurements of the resistance and Hall effect at two different places on the sample. These measurements were averaged to give a value more representative of the sample and were also used as an indication of sample inhomogeneity [13a]. The probe was designed to fit into a conventional liquid helium dewar having a tail section that extended between the magnet pole pieces.

(b) Measurement techniques

The oscillatory magnetoresistance of each Sb-doped filament was measured at 4.2°K. To do this, the magnetic field was swept continuously and its value displayed on the x -axis of an x - y recorder, using a Hall probe to sense the field. A constant current source supplied the sample current so that voltage across the potential probes was proportional to the sample resistance. This voltage was amplified and impressed upon the y -axis of the recorder. The

magnetic field was oriented to give the smallest non-oscillatory magnetoresistance. This was generally near the longitudinal direction. No attempt was made to crystallographically orient the samples, even though it is quite possible that only one crystallite was being measured because of the close spacing of the potential probes. This uncertainty in orientation introduces an error no greater than 5 per cent in the determination of the number of carriers in the central minimum due to the asphericity of the Fermi surface [13b].

The same apparatus was used for fixed temperature measurements of $R(H)$ and $\sigma(H)$, the field dependent Hall coefficient and conductivity. Here the absolute values of the voltages were read directly from the recorder tracing after calibrating the entire system by replacing the sample voltage with a known voltage of comparable magnitude. These measurements were generally taken at bath temperatures of 4.2, 47, 63 and 77°K. The temperature could also be stabilized above that of the bath using a feedback heater circuit.

To measure $R(0)$, $1/\sigma(0)$ and $\Delta\rho(0)$ (the low field limits of Hall coefficient, reciprocal conductivity, and magnetoresistance) an a.c. double modulation technique was used [14]. Consider the low field expression for E :

$$E = (1/\sigma)J + R(J \times H) + \Delta\rho H^2 J. \quad (1)$$

If J and H vary sinusoidally, E is given by

$$\begin{aligned} E = & (1/\sigma) J_0 \exp(i\omega_J t) + R(J_0 \times H_0) \\ & \times \exp[i(\omega_J \pm \omega_H)t] + \Delta\rho H_0^2 J_0 \\ & \times \exp[i(\omega_J \pm 2\omega_H)t]. \end{aligned} \quad (2)$$

The sample mixes the two frequencies generating a system of side band frequencies about the carrier frequency, ω_J . If the amplitudes J_0 and H_0 are kept constant and the d.c. magnetic field is zero, then $R(0)$ is proportional to the voltage component of frequency $\omega_J \pm \omega_H$ and $\Delta\rho$ is proportional to the voltage component of

frequency $\omega_j \pm 2\omega_H$. There is also a component of frequency ω_H due to the inductive coupling between the magnet and sample wires. In these experiments $\omega_j \approx 400$ hz and $\omega_H \approx 25$ hz. The composite signal was amplified. The desired frequency component was selected, and its magnitude obtained from the d.c. output of a wave analyzer and impressed upon the y axis of the recorder. The thermometer signal was supplied to the x axis and the temperature swept to obtain a trace of $1/\sigma(0)$, $R(0)$ or $\Delta\rho(0)$ vs. $f(T)$. Here $f(T)$ relates the temperature to the thermometer output voltage. No a.c. calibration was made; the d.c. measurements provide the absolute values. The a.c. measurements are shown as solid curves in the figures.

3. EXPERIMENTAL DATA AND RESULTS AT 4.2 K

In this and the following sections the experimental data are presented and analyzed to determine some of the physical properties of electrons and holes in gray tin. We show how certain of the band structure parameters are evaluated and examine the scattering mechanisms present under a number of different conditions. We start with the data that is simplest to interpret and then proceed to more complex situations [15].

(a) Populations of the conduction bands

The magnetic field dependence of the Hall coefficient of the series of Sb-doped samples at 4.2°K is shown in Fig. 2. Defining the Hall number for degenerate statistics as

$$n_H \equiv -1/[R(0)ec] \quad (3)$$

we may compare n_H with the donor concentration, N_d . This is done in Table 1. We note that for $N_d < 5 \times 10^{17} \text{ cm}^{-3}$ n_H and N_d are equal within the experimental uncertainty. (The approximately 10 per cent uncertainty exists mainly because of the difficulty in measuring the sample dimensions). For samples having $N_d > 5 \times 10^{17} \text{ cm}^{-3}$ a discrepancy exists be-

tween n_H and N_d which increases with increasing N_d . Also, in this concentration range the Hall coefficient is magnetic field dependent. Both effects are manifestations of two-band conduction which begins at the critical donor concentration $N_c = 5 \times 10^{17} \text{ cm}^{-3}$. At this concentration the Fermi level at low temperatures just touches the subsidiary conduction band minima at the L points in reciprocal space. Independent evidence of this is the sudden increase in the amplitude of Shubnikov-de Haas oscillations as N_d reaches N_c [9].

In the two-band region the Hall coefficient in the high field limit, $R(\infty)$, allows an evaluation of $n_T = n_0 + n_1$, the total electron concentration in both the central (subscript 0) and $\langle 111 \rangle$ (subscript 1) valleys. The total concentration is obtained from the expression,

$$n_T = -1/[R(\infty)ec]. \quad (4)$$

To reach the high field limit, however, H must be much larger than 10 kOe. An alternative approach, requiring much smaller magnetic fields, is to obtain $R(\infty)$ from $R(H)$. This is possible at low temperatures where both bands have degenerate statistics through the following equations.

$$R(H) = -(1/ec)(\alpha + \beta H^2)/(\gamma + \delta H^2) \quad (5)$$

where

$$\begin{aligned} \alpha &\equiv n_0\mu_0^2 + n_1\mu_1^2 & \beta &\equiv (n_0 + n_1)\mu_0^2\mu_1^2 \\ \gamma &\equiv (n_0\mu_0 + n_1\mu_1)^2 & \delta &\equiv (n_0 + n_1)^2\mu_0^2\mu_1^2. \end{aligned} \quad (6)$$

Then

$$R(0) = -(1/ec)(\alpha/\gamma), \quad R(\infty) = -(1/ec)(\beta/\delta) \quad (7)$$

and

$$\begin{aligned} \left[\frac{\Delta R}{R(0)H^2} \right]^{-1} &= \left[\frac{R(H) - R(0)}{R(0)H^2} \right]^{-1} \\ &= \frac{\alpha\gamma + \alpha\delta H^2}{\beta\gamma - \alpha\delta} \end{aligned} \quad (8)$$

Table 1. Summary of experimental parameter of Sb-doped samples at 4.2° K

N_d (cm^{-3})	n_H (cm^{-3})	n_0 (cm^{-3})	n_T (cm^{-3})	$R(0)$ (cm^2/coul)	$\sigma(0)$ ($\Omega\text{-cm}^{-1}$)	$\mu_H = R_0$ ($\text{cm}^2/\text{V-sec}$)	n_i (cm^{-3})
1.0×10^{17}	1.0×10^{17}	1.0×10^{17}	—	62.5	1,145	7.16×10^4	—
2.0×10^{17}	2.1×10^{17}	1.9×10^{17}	—	29.3	2,270	6.65×10^4	—
2.5×10^{17}	2.0×10^{17}	2.4×10^{17}	—	30.8	1,800	5.54×10^4	—
3.0×10^{17}	2.7×10^{17}	2.7×10^{17}	—	23.2	—	—	—
4.0×10^{17}	3.7×10^{17}	4.0×10^{17}	—	17.0	2,860	4.85×10^4	—
5.0×10^{17}	4.4×10^{17}	4.8×10^{17}	—	14.3	4,520	6.45×10^4	2×10^{18}
7.0×10^{17}	5.6×10^{17}	—	—	11.2	5,020	5.62×10^4	1.4×10^{17}
1.0×10^{18}	6.1×10^{17}	6.1×10^{17}	—	10.3	7,880	8.08×10^4	3.9×10^{17}
2.5×10^{18}	7.3×10^{17}	6.8×10^{17}	2.3×10^{18}	8.6	8,420	7.20×10^4	1.8×10^{18}
5.0×10^{18}	9.2×10^{17}	7.9×10^{17}	4.6×10^{18}	6.8	9,040	6.17×10^4	4.2×10^{18}
1.0×10^{19}	1.5×10^{18}	9.6×10^{17}	9.4×10^{18}	4.3	10,300	4.43×10^4	9.0×10^{18}
2.5×10^{19}	3.5×10^{18}	1.3×10^{18}	2.8×10^{19}	1.8	12,200	2.20×10^4	2.4×10^{19}

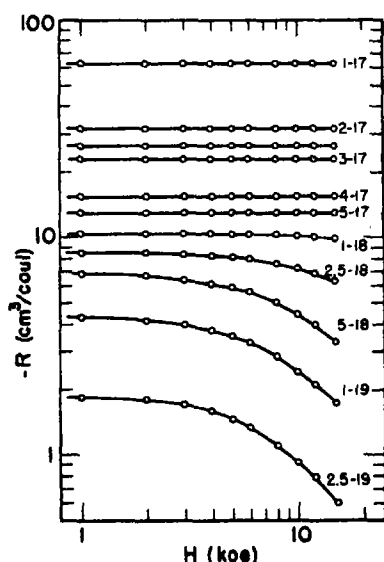


Fig. 2. The field dependence of the Hall coefficient at 4.2°K is shown for the series of Sb-doped samples. The curves are denoted by their donor concentrations, 1-17 = 1×10^{17} donors/cm³. For samples having 5×10^{17} donors/cm³ or less, conduction is confined to the Γ_8^+ conduction band and R is field independent. As the donor concentration exceeds 5×10^{17} cm⁻³ a field dependence is observed which increases with concentration and indicates that two bands contribute to the conductivity.

or, using equation (7)

$$\left[\frac{\Delta R}{R(0)H^2} \right]^{-1} = \frac{\gamma}{\delta} \left[\frac{R(\infty)}{R(0)} - 1 \right]^{-1} + H^2 \left[\frac{R(\infty)}{R(0)} - 1 \right]. \quad (9)$$

A plot of $[\Delta R/R(0)H^2]^{-1}$ vs. H^2 should then be a straight line of slope $B \equiv [R(\infty)/R(0) - 1]^{-1}$ and intercept $A \equiv (\gamma/\delta)B$. Such curves are shown in Fig. 3 for the four most heavily doped samples. Using the measured values of $R(0)$ and B we obtain n_T from equation (4) and the definition of B with the results shown in Table 1. The excellent agreement between n_T and N_d (within the same experimental uncertainty as for the lower concentration

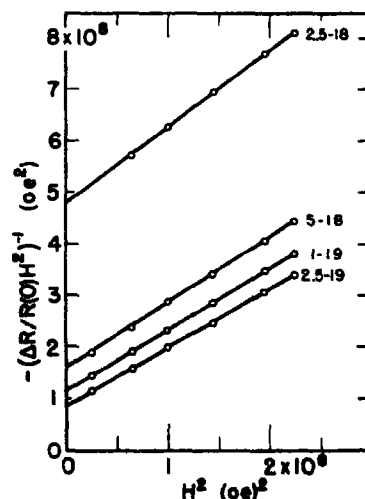


Fig. 3. The data of Fig. 2 for the four most heavily doped samples has been used to obtain $\Delta R/R(0)H^2$ as a function of field. The notation 1-18 = 1×10^{18} donors/cm³ is again used. The data has been plotted against H^2 to show, through equation (9), the excellent fit to simple two band theory that is possible when both bands are degenerate.

samples) gives firm support to our hypothesis that two-band conduction causes the discrepancy between n_H and N_d and introduces the field dependence. We also conclude that all of the Sb atoms put into the white tin alloys have become ionized donors in the gray tin. The curves of Fig. 3 give a good example of the excellent fit to the simple two-band theory that is obtainable when the conditions of extreme degeneracy are valid for both bands. Information deduced from the intercepts in Fig. 3 will be discussed later in conjunction with the mobility.

We consider now the determination of n_0 throughout the donor concentration range. For $N_d < N_c$ it is equal to n_H obtained from the low field Hall coefficient. This is no longer true in the two band region. From equations (6) and (7) the low field Hall coefficient may be rewritten as

$$R(0) = -(1/ecn_0)(1 + \xi b^2)/(1 + \xi b)^2 \quad (10)$$

where $\xi = n_1/n_0$ and $b = \mu_1/\mu_0$. Only for $\xi b \ll 1$ is n_H approximately equal to n_0 and this is not satisfied in most of the two-band region.

A more straightforward way of measuring n_0 is from the period of the oscillatory magnetoresistance. It may be shown that for an electron band having spherical energy surfaces the electron density is related to the period of oscillation by

$$n = (3 \cdot 17 \times 10^6/P)^{3/2} \text{ cm}^{-3}, \quad (11)$$

where P is in (oersteds) $^{-1}$. Ignoring the ~ 6 per cent anisotropy in the period of the oscillations we obtain values of n_0 from data such as that shown in Fig. 4, using equation (11). These values should be accurate to better than 9 per cent. The L_6^+ electrons do not enter here because their heavier mass requires a much larger field to obtain conditions for quantization of their energy. The values of n_0 for the series of Sb-doped filaments are listed in Table 1.

These results of the 4.2°K Hall coefficient

measurements leading to n_H and n_T and of the oscillatory magnetoresistance measurements leading to n_0 are summarized in Fig. 5 where n_0 , n_H , and n_T are shown as functions of N_d . There are several points worth reemphasizing: first, the n_T data are very close to the line represented by $n_T = N_d$; second, both n_0 and n_H break sharply from this line at $N_d = N_c$, when the subsidiary minima begin to be populated; third, for $N_d > N_c$, n_H increases more rapidly than does n_0 because of the contributions to $R(0)$ of the L_6^+ electrons shown in equation (10).

(b) *Determination of the density-of-states effective mass and the energy separation of the subsidiary minima at 4.2°K*

It is a simple matter to find n_1 , the carrier density in the L_6^+ states, by subtracting n_0 from either n_T or N_d . We prefer to use the latter because of the smaller experimental uncertainty. Thus $n_1 = N_d - n_0$, and the values may be found in Table 1.

We use these values of n_1 , and the corresponding Fermi levels, to obtain an estimate of m_{1d}^* , the density-of-states effective mass, and E_g , the 4.2°K energy separation of the two conduction bands. This may be done by using the standard expression for the carrier population in the limit of extreme degeneracy,

$$n_1 = (\frac{1}{3}\pi^2) (2m^*kT/\hbar^2)^{3/2} [(E_F - E_g)/kT]^{3/2} \quad (12)$$

or

$$E_F = E_g + 3 \cdot 64 \times 10^{-15} (4^{2/3} m_{1d}^*)^{-1} n_1^{2/3}. \quad (13)$$

Here the $4^{2/3}$ enters because there are four ellipsoids in the subsidiary conduction band.

Values of E_F may be obtained from the work of Booth and Ewald [16] who from detailed measurements of the effective mass of the central valley, have obtained a semi-empirical expression relating E_F with n_0 . Thus knowing n_0 and n_1 , and hence E_F , we may obtain a straight line fit to equation (13) with a plot of E_F vs. $n_1^{2/3}$. The intercept and slope then

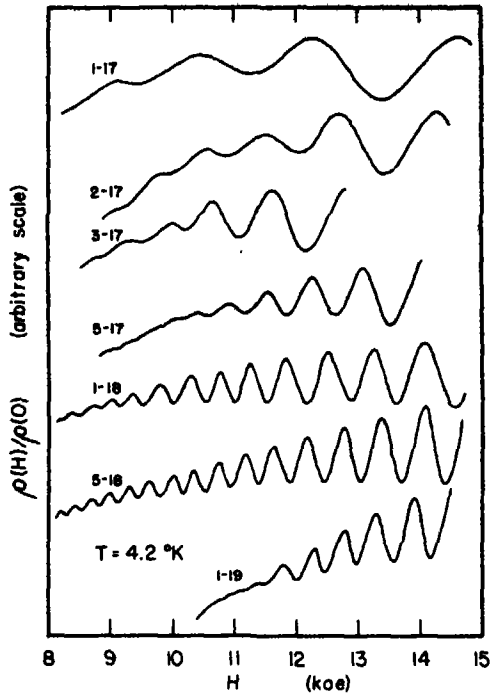


Fig. 4. The oscillatory magnetoresistance is shown for the series of Sb-doped samples. The period of oscillation is used to obtain the number of carriers in the central minimum through equation (11). Notice in particular that oscillatory behavior begins at lower field strengths for the samples having 1 and 5×10^{18} donors/cm³ because the screening is enhanced by electrons in the subsidiary minima.

yield values for E_g and m_{1d}^* . This approach involves several assumptions. First, equation (12) is valid only for parabolic bands and it is questionable whether the L_6^+ band edge is parabolic for doped material. In fact, it will be shown later that the band edge appears to be distorted due to the presence of quasi-bound impurity states that have merged with the band minimum. This distortion must also be a function of N_d . We have also assumed that E_g is a constant independent of N_d . This is rather unlikely because the L_6^+ electrons, those that screen the impurity sites most effectively, must have their energy lowered because of this additional attractive impurity potential. A recent theory by Wolff[17] estimates the magnitude of the band edge shift, δE_g , as ~ 2.5

$R_y^* a_0^* N_d^{1/3}$, where R_y^* and a_0^* are the effective Rydberg and Bohr radius, respectively, in the crystal. This amounts to many meV in our case; certainly not a negligible amount. A compensating factor is that the central minimum will also be lowered, presumably by a smaller amount.

In spite of these complications we fit the data to equation (13) in curve (a) of Fig. 6. In curve (b) an attempt has been made to correct for the presumed impurity-induced energy shift, δE_g . This quantity has been added to the experimental values of E_F to allow plotting both curves together. We may see this from equation (13) by introducing δE_g so that

$$E_F - [E_g(0) - \delta E_g(N_d)] = \text{const. } n_1^{2/3}$$

or

$$E_F + \delta E_g(N_d) = E_g(0) + \text{const. } n_1^{2/3}.$$

The correction has little effect on the energy separation, E_g ; however, it must be realized that the corrected curve gives an estimate of $E_g(0)$ while the uncorrected curve assumes a rigid band structure. It is also clear that changes in the magnitude or doping dependence of δE_g will have little effect on E_g . We may thus assign a value

$$E_g = 0.092 \pm 0.005 \text{ eV}$$

for this band structure parameter in pure gray tin at 4.2°K.

Evaluation of the effective mass from the slope is not so clear-cut. From curve (a) of Fig. 6 a value of $m_{1d}^* = 0.21 m_e$ is obtained for the density-of-states effective mass. This must be considered an upper limit, for any correction δE_g will increase the slope and thus decrease the experimental value for m_{1d}^* . We speculate that a value as low as $0.17 m_e$, [obtained from (b) of Fig. 6] is not unreasonable. The value of this parameter in Ge is $0.22 m_e$.

Finally we note the band edge distortion

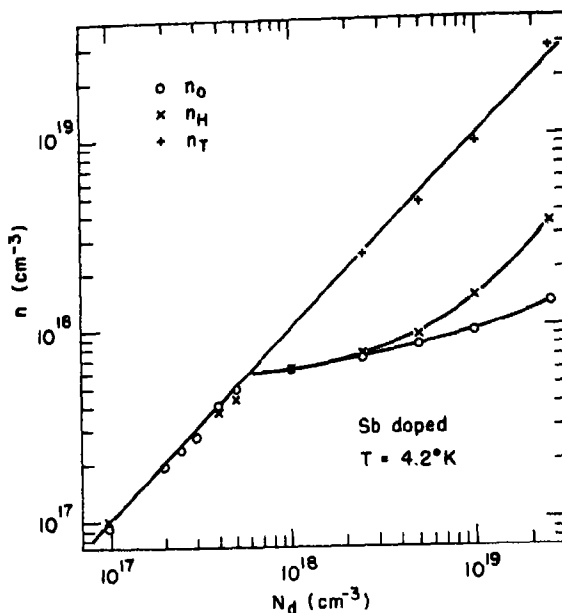


Fig. 5. Electron concentrations are shown as a function of donor concentration. The Γ_8^+ concentration n_0 was obtained from the oscillatory magnetoresistance period; the total concentration n_T from the field dependence of the Hall coefficient. The concentration $n_H \equiv 1/ecR(0)$ was obtained from the low field Hall coefficient. The critical concentration at 5×10^{17} donors/cm³ is clearly indicated.

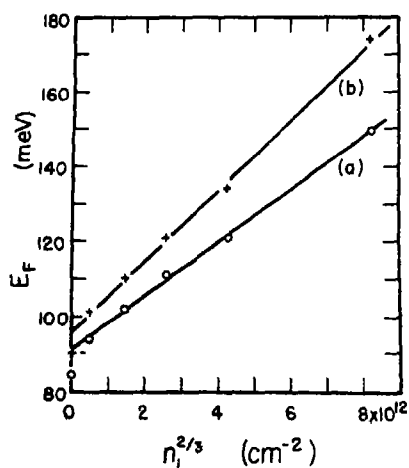


Fig. 6. The Fermi energy at 4.2°K is shown as a function of the L_8^+ electron concentration to the $\frac{2}{3}$ power. The intercepts and slopes give determinations of E_v and m_{1d}^* for the two models studied.

mentioned above. For small values of n_1 the data points fall below the curve representing a parabolic band and we take this as an indication of a small density of states lying below the band edge proper due to a stronger interaction of a small number of electrons with the array of impurity potentials. If the band edge under consideration were not a subsidiary minimum, we would consider these states to be formed from the coalescence of discrete impurity levels into an impurity band wide enough to have merged with the conduction band. Such a band edge 'tail' has been discussed theoretically by Parmenter[18] and Kane[19]. A good experimental discussion of the problem is the work of Shepherd[20]. In the case of gray tin the central minimum causes further complications for there are now quasi-continuous band states degenerate with the im-

purity levels. A similar system, GaSb, has been studied by Kosicki and Paul[21], although at lower donor concentrations. We will not attempt to fit our limited data to any theory, but merely note the presence of a band edge 'tail'.

(c) *Mobilities at 4.2°K limited by ionized impurity scattering*

In doped gray tin at 4.2°K ionized impurity scattering should dominate. In this section we will obtain experimental values for the mobilities of both electrons and holes as functions of impurity concentration and compare these results with the screened ionized impurity scattering theories of Brooks and Herring[8] and of Dingle[7].

In the limit of extreme degeneracy the mobility when one carrier type is present is given by

$$\mu = R(0) \sigma(0). \quad (14)$$

In the region of two electron-band conduction the contributions of the two carrier types must be separated. The data obtained from the Sb-doped filaments may be used in different ways to obtain μ_0 and μ_1 . From the measurements at 4.2° on the four most heavily doped samples we know: $R(0)$ and $\sigma(0)$ from $R(H)$ and $\sigma(H)$; A and B , the intercept and slope of $(\Delta R/R(0)H^2)^{-1}$ vs. H^2 ; $\Delta\rho/\rho(0)$; n_0 from oscillatory period; and N_d , the alloy donor concentration. In all there are seven known quantities that may be used to obtain the four unknowns (n_0 , n_1 , μ_0 , μ_1). Clearly the problem is over determined. We will again use the measured n_0 and N_d to obtain the two unknowns n_1 and μ_1 . We choose not to use $\Delta\rho/\rho(0)$ for there appears to be a spurious contribution to it due to inhomogeneities. There remain four measured quantities to determine μ_0 and μ_1 so that there should be at least two independent ways of doing so, providing a check of the internal consistency of the data.

In the two band region μ_0 may be found

from

$$\mu_0 = R(0) \sigma(0) (1 + b\xi)/(1 + b^2\xi) \quad (15)$$

where, as before, b and ξ are the mobility and number ratios, μ_1/μ_0 and n_1/n_0 . This expression is the most direct way of obtaining μ_0 because the factors involving b and ξ are not very different from unity. In fact, for the samples studied, $1 + b^2\xi$ is never more than 3 per cent larger than unity. This procedure does have the disadvantage, however, that R and σ depend upon the sample dimensions and therefore have large uncertainties.

The most direct way of obtaining μ_1 is from

$$\mu_1 = (B/A)^{1/2} (1 + b\xi)/(1 + \xi) \quad (16)$$

obtained from equations (6) and (9). This should be very accurate since A , B , and ξ are known to a few per cent and b enters weakly. Then the ratio of equations (15) and (16)

$$b = (\mu_1/\mu_0) = (B/A)^{1/2} (1 + b^2\xi)/(1 + \xi) \times R(0)\sigma(0) = C(1 + b^2\xi) \quad (17)$$

gives the best estimate of b . Explicitly,

$$b = [-1 + (1 - 4C^2\xi)^{1/2}]/2C\xi. \quad (18)$$

Values of A , B , $R(0)$, and $\sigma(0)$ are given in Table 2 and μ_0 , μ_1 , and b computed from equations (15), (16), and (18) are given in Table 3. To check the consistency of the data we have computed $R(0)$, $\sigma(0)$, A , and B from n_0 , n_1 , μ_0 , and μ_1 using equation (10) and the following.

$$\sigma(0) = en_0\mu_0 (1 + b\xi) \quad (19)$$

$$-B = (1 + b^2\xi) (1 + \xi)/(1 - b)^2\xi \quad (20)$$

$$A = B(1 + b\xi)^2/\mu_1^2(1 + \xi)^2. \quad (21)$$

These results are compared with the experimental values in Table 2. As can be seen the agreement is excellent, especially for A and B .

Table 2. Comparison of experimental and calculated parameters of heavily doped samples at 4.2° K. Values of the parameters A and B (defined in text) are the intercepts and slopes, respectively, of the curves of Fig. 3.

$N_d(\text{cm}^{-3})$	$A(\text{oe})^2$		B		$R(0)(\text{cm}^3/\text{coul})$		$\sigma(\Omega - \text{cm})^{-1}$	
	expt	calc	expt	calc	expt	calc	expt	calc
2.5×10^{18}	4.82	4.72	1.46	1.43	8.59	8.25	8.4×10^8	8.7×10^8
5.0×10^{18}	1.63	1.64	1.25	1.25	6.83	6.39	9.0×10^8	1.01×10^4
1.0×10^{19}	1.11	1.14	1.19	1.16	4.32	4.56	1.03×10^4	1.00×10^4
2.5×10^{19}	0.85	0.84	1.14	1.13	1.77	2.12	1.22×10^4	1.02×10^4

Table 3. Electron concentration ratios and electron mobilities of heavily doped samples at 4.2° K

$N_d(\text{cm}^{-3})$	$\xi = n_1/n_0$	$b = \mu_1/\mu_0$	$\mu_0(\text{cm}^2/\text{V-sec})$	$\mu_1(\text{cm}^2/\text{V-sec})$
2.5×10^{18}	2.7	0.021	7.6×10^4	1.6×10^3
5.0×10^{18}	5.3	0.022	7.2×10^4	1.5×10^3
1.0×10^{19}	9.4	0.022	5.4×10^4	1.2×10^3
2.5×10^{19}	18.2	0.028	3.2×10^4	0.9×10^3

The mobility, μ_0 , determined above together with the values given in Table 1 for $N_d < N_c$ are exhibited in Fig. 7 as a function of donor concentration. Also included are the measured values of other investigators. We notice in the curve a gradual drop-off in μ_0 as N_d is increased until the critical concentration, $N_c = 5 \times 10^{17} \text{ cm}^{-3}$, is reached. At this point μ_0 rises to a maximum and then falls at a somewhat faster rate. This rise in μ_0 at N_c is similar to the effect seen by Becker, Ramdas and Fan in GaSb [22]. We shall return to it after considering the theory.

In the limit of extreme degeneracy the mobility limited by ionized impurity scattering is given by

$$\mu_1 = \left(\frac{3}{\pi}\right) \pi (\hbar/e)^3 (\kappa/m^*)^2 n/N_d g(\bar{z}) \quad (22)$$

where

$$g(\bar{z}) = \ln(1 + \bar{z}) - \bar{z}/(1 + \bar{z}) \quad (23)$$

and

$$\bar{z} = (3/\pi)^{1/3} \pi^2 (\hbar/e)^3 \kappa_n^{1/3}/m^* = (2k_F a)^2. \quad (24)$$

Here k_F is the wave vector at the Fermi level

and a is the screening length. When there are two types of carriers equation (22) is still valid but \bar{z} becomes

$$\bar{z} = \left(\frac{3}{\pi}\right)^{1/3} \pi^2 \left(\frac{\hbar}{e}\right)^2 \frac{\kappa n_0^{1/3}}{m_0^*} \left\{1 + 4^{2/3} \frac{\pi n_1^{1/3}}{\pi n_0^{1/3}} \left(\frac{n_1}{n_0}\right)^{1/3}\right\}^{-1} \quad (25)$$

to include the screening by both carrier types.

The calculated values of \bar{z} and $g(\bar{z})$ have been used to obtain a theoretical curve for μ_0 which is shown in Fig. 7 along with the experimental values. The agreement between theory and experiment shows that the general notion of a screening enhanced mobility for $N_d > N_c$ is correct. Satisfactory agreement is obtained for the decade $4 \times 10^{16} < N_d < 4 \times 10^{17} \text{ cm}^{-3}$, where \bar{z} is the largest. As N_d is made smaller the theoretical curve increases too slowly, until at $1 \times 10^{15} \text{ cm}^{-3}$ it is a factor of 2.5 below the experimental values. At large concentrations the slopes of the two curves agree rather well although the absolute values differ by a factor of two. Just above the critical concentration a sharp rise in mobility is predicted; a much more gentle maximum is observed. We

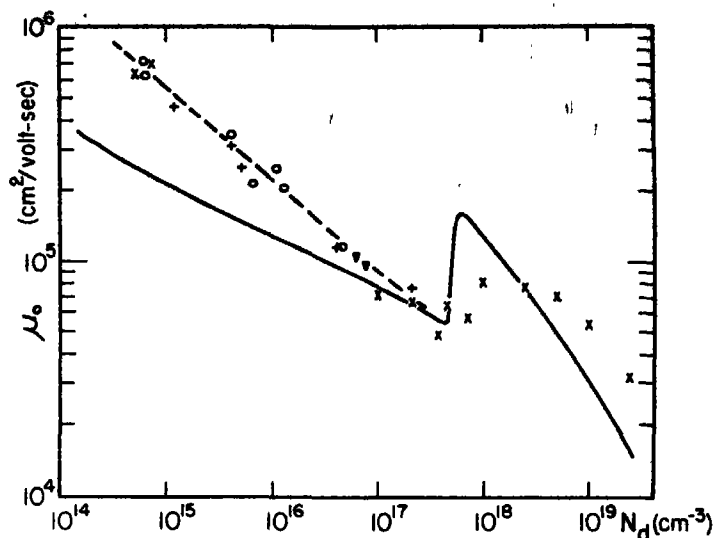


Fig. 7. Light electron mobility at 4.2°K is plotted as a function of donor concentration. The solid line represents calculated values using the screened-ionized-impurity scattering theory. The dashed line results from a similar calculation using the dielectric constant values shown in Fig. 8. The mobility increase due to screening enhancement may be seen for concentrations greater than $5 \times 10^{17} \text{ cm}^{-3}$. Experimental points are from Refs. [1] (plus signs), [2] (triangles), [3] (open circles) and the present work (crosses).

now discuss these deviations in greater detail.

The above discussion is based upon the Born approximation, used in obtaining the expressions for the mobility. For the screened coulomb potential used here, it is possible to show[23] that the Born approximation is valid if the scattered wave amplitude at $r=0$ is much less than unity. This may be over-restrictive. This inequality holds by a factor of more than ten for all concentrations above 10^{16} cm^{-3} , and by a factor of three at 10^{14} cm^{-3} . In view of this we judge the Born approximation and the mobility expressions to be valid over most of the range of concentrations studied.

The concentration range just above N_c is that dominated by the impurity band tail noted above. Because of this tail the density of states could be much lower than that predicted by the parabolic band model used to obtain \bar{z} . Since the screening length squared is inversely proportional to the density of states

at the Fermi level the presence of the tail states should make the screening less effective for $5 \times 10^{17} < N_d < 1 \times 10^{18} \text{ cm}^{-3}$. It is just this region, at the onset of the screening enhancement, where the parabolic model predicts a much more dramatic rise than is observed. A corresponding discrepancy exists between the predicted sharp drop and the observed more gradual decrease in the Dingle temperature[9]. For still higher concentrations it must be remembered that we have ignored the anisotropy of the subsidiary conduction band, concerning ourselves only with the total number of states. This approximation, as well as the fact that for such large impurity concentrations the overlap of the impurity potentials must become important, leads us to consider the agreement for $N_d > N_c$ quite good.

Considerably more may be done for the concentration region $N_d < N_c$ where these problems do not exist. Of principal concern

here is the dielectric constant. We have assumed that κ is doping-independent and equal to 24. That this might not be the case for lightly doped samples may be seen from the following argument. Direct interband transitions between the Γ_8^+ bands are allowed away from $k = 0$, and have been observed optically for the light and heavy hole bands in Ge. These transitions can contribute to the dielectric constant only if the valence band state is occupied and the conduction band state empty. Furthermore the strength with which they contribute depends inversely upon the energy. Thus as the Fermi level approaches zero energy more transitions of smaller energy are possible and the dielectric constant can be expected to increase dramatically. The contribution of these transitions to the dielectric constant has been computed by Wagner[24] who obtains an expression of the form

$$\kappa_{12} = 1 + \frac{e^2}{m_e^2} \frac{m_{12}^3}{\hbar^2} \left| A_{12} \right|^2 \frac{64}{\pi} \frac{1}{k_F} \quad (26)$$

where $1/m_{12} = (1/m_0^*) + (1/m_p^*)$, kA_{12} is the optical (momentum) matrix element between the two bands and $\hbar k_F$ is the Fermi momentum. By relating k_F to $n_0^{1/3}$ and adding the two contributions, we obtain the total dielectric constant

$$\kappa = \kappa_\infty + C n_0^{-1/3} + 1 \quad (27)$$

where C is a constant and $\kappa_\infty = 24$. We have used our mobility data to obtain κ indirectly by forcing the computed mobility (through adjustment of κ) to agree with the experimental values in the range $N_d < N_c$. The adjusted theoretical curve for the mobility is shown in Fig. 7. The values of κ needed to obtain agreement are plotted against $n_0^{-1/3}$ in Fig. 8. The fit to equation (27) is excellent.

Although the experimental evidence is indirect, it appears that the dielectric constant is enhanced by a contribution from the zero-band-gap aspect of the band structure. Theoretically it has been shown[25, 26] that

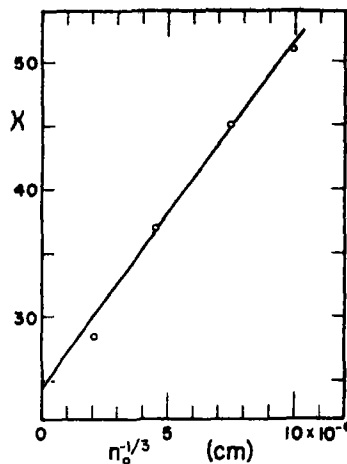


Fig. 8. The variation of the dielectric constant with light electron concentration. The values of κ were obtained from the adjustment of the computed values of μ_0 to give agreement with experiment.

in the random phase approximation the static dielectric constant $\epsilon(q)$ of pure α -Sn diverges as q^{-1} as $q \rightarrow 0$. The presence of impurity carriers removes the divergence leaving a finite interband part which is strongly dependent on concentration. Liu and Tosatti[27] have calculated $\epsilon(q)$ under these conditions and find an enhanced ionized-impurity-limited mobility in agreement with the experimental values of Fig. 7. This explanation of the enhanced mobility has recently been questioned by Broerman[28] who fits the data without resort to a concentration dependent $\epsilon(q)$ by taking account of the nonparabolicity of the conduction band and the p -like character of the conduction electrons. Clearly the interesting phenomenon of mobility enhancement merits further study. In particular, measurements on higher purity samples would be desirable because the above calculations predict quite different mobility values at $n_0 = 10^{14} \text{ cm}^{-3}$.

4. TEMPERATURE DEPENDENT EFFECTS IN THE Γ_8^+ AND L_6^+ CONDUCTION BANDS

(a) Determination of $E_d(T)$ and m_{1d}^*

The temperature dependence of the low field Hall coefficient for the series of Sb-doped

filaments is shown in Fig. 9. Of particular interest is the rising Hall coefficient with increasing temperature observed between 4.2 and 110°K for samples having $2.0 \times 10^{17} < N_d < 2.5 \times 10^{18} \text{ cm}^{-3}$. Outside this concentration range $R(T)$ more typically decreases with increasing temperature. Similar effects have been seen in some compound semiconductors having subsidiary conduction band minima[29], and have been attributed to thermal transfer of carriers from the central to the subsidiary valleys. If the number of low mobility carriers (electrons in the subsidiary valleys) is small, the low field Hall coefficient is approximately proportional to $1/n_0$, so that an increase in R signifies a decrease in n_0 with increasing temperature. The decrease in n_0 is caused by two effects: the change in E_g with temperature and an increase in the kT spread of the Fermi distribution function. A further

contribution to the increase in R is the temperature variation of $r(\eta, \beta)$, the ratio of the low field Hall and conductivity mobilities (in which $\eta = E_F/kT$ and $\beta = kT/E_g$). In fact, this is the dominant effect for the 1 and $2 \times 10^{17} \text{ cm}^{-3}$ doped samples.

By generalizing equation (10) for arbitrary statistics we may write

$$R(0) = -(1/ecn_0)(r_0 + r_1 b^2 \xi)/(1 + b\xi)^2 \quad (28)$$

for the low field Hall coefficient. In the concentration range under study both b and ξ are small, this allows the approximate form

$$n_0 \cong n_H r_0(\eta, \beta) \quad (29)$$

to be used, where $n_H = -1/ecR(0)$ and $r_0(\eta, \beta) = \langle \tau^2 \rangle / \langle \tau \rangle^2$; τ is the relaxation time for the light electrons. This approximation introduces an error that is at most 5 per cent for the $1 \times 10^{18} \text{ cm}^{-3}$ sample and considerably less for those having lower donor concentrations. Using the values of $r(\eta, \beta)$ tabulated by Kolodziejczak[30] it is possible to solve equation (29) by an iterative procedure to obtain n_0 and η from n_H . The values of β are based on a value of $E_g = 0.41 \text{ eV}$ [31] and n_0 is related to E_F and thus to η via the empirical relation of Booth and Ewald[16] discussed in Section 3(b). This relation is exact only for large values of η and gives too large a value of E_F for a given n_0 ; as η is always larger than 6, however, the error involved is less than 3 per cent. This error, of course, decreases as the doping level is increased, but the approximation of equation (29) becomes worse. We now may use values of $n_0(T)$ and $E_F(T)$ to obtain information about the subsidiary minima. Since these samples are extrinsic below about 100°K the total number of electrons is constant. This fact allows n_1 to be given by $n_1(T) = N_d - n_0(T)$. For those samples having $N_d < N_c$ we will use $n_1(T) = n_0(4.2^\circ\text{K}) - n_0(T)$ for this gives greater accuracy. Neglecting any distortion of the subsidiary band edge, n_1 is given as a function of E_g

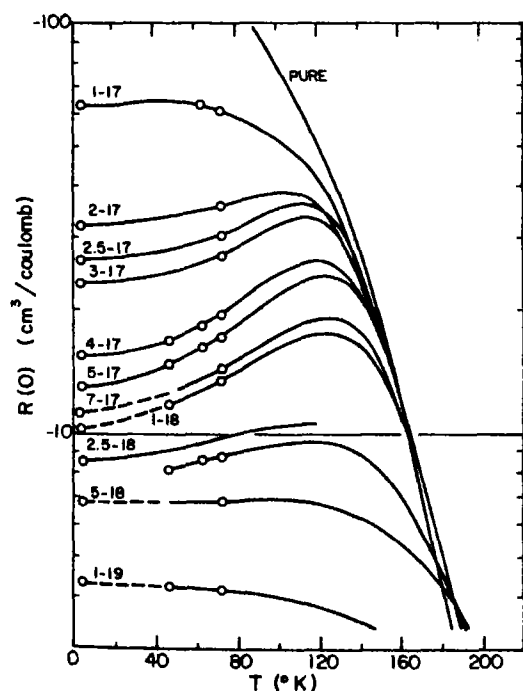


Fig. 9. The temperature dependence of the low field Hall coefficient for the Sb-doped series of samples. The circles represent d.c. measurements at fixed temperature, used to calibrate the a.c. temperature-sweep measurements represented by the continuous curves.

and E_F by

$$n_1(T)/T^{3/2} = 4.831 \times 10^{15} \times 4(m_{1d}^*/m_e)^{3/2} \mathcal{F}_{1/2}[\eta - E_v(T)/(kT)] \quad (30)$$

where $\mathcal{F}_{1/2}$ is a Fermi integral and the 4 arises because there are four ellipsoids, each having a density-of-states effective mass of m_{1d}^* . If the temperature is high enough, $\mathcal{F}_{1/2}$ may be replaced by the non-degenerate approximation, $\exp(\eta - E_v/kT)$. Using this in equation (30) and taking logarithms gives

$$\ln(n_1/T^{3/2}) - \eta = \left(\frac{3}{2}\right) \ln(m_{1d}^*/m_e) - E_v(T)/(kT) + \text{const.} \quad (31)$$

If we now express $E_g(T)$ as

$$E_g(T) = E_g(0) + (dE_g/dT)T \quad (32)$$

equation (31) becomes

$$\begin{aligned} \ln(n_1/T^{3/2}) - \eta &= \left[\left(\frac{3}{2}\right) \ln(m_{1d}^*/m_e) - (1/k) \right. \\ &\quad \left. (dE_g/dT) - E_g(0)/(kT) \right] \\ &\quad + \text{const.} \end{aligned} \quad (33)$$

so that a plot of the left-hand side vs. $1/T$ gives a slope of $E_g(0)/k$ and an intercept, I , related to the effective mass and dE_g/dT . We expect dE_g/dT to be small but not constant in this temperature range so the value must be considered an average. Also, the mass and dE_g/dT values can not be separated from one another but the upper limit established earlier for the mass allows a similar limit for dE_g/dT . Curves of $[\ln(n_1/T^{3/2}) - \eta]$ vs. $1/T$ are shown in Fig. 10 for three of the samples studied. The experimental slopes and intercepts (minus the constant) are tabulated in Table 4 for all samples exhibiting a substantial effect. The variation of these values with doping probably reflects the experimental uncertainties, approximations made, and over-simplification of the model rather than a physical effect. The more heavily doped samples have a smaller

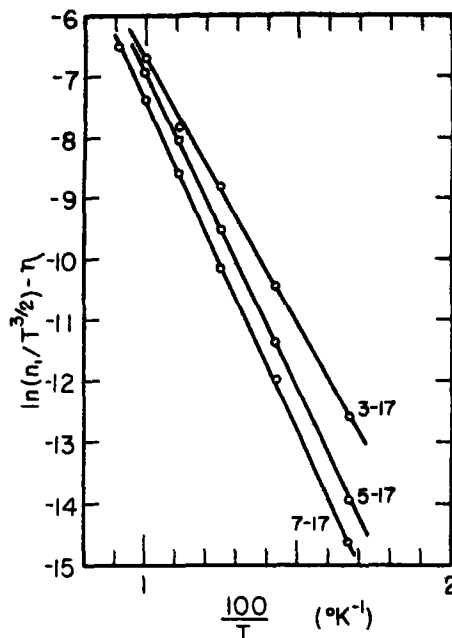


Fig. 10. A fit to the two-band model of data obtained from the temperature dependence of the Hall coefficient for samples having donor concentrations near the critical concentration, 5×10^{17} donors/cm³ = 5-17. The slopes of these curves give a measure of the subsidiary minima energy separation at 0°K through equation (33).

Table 4. Parameters evaluated from the slopes and intercepts of curves such as those of Fig. 10. The intercept I is equal to $\left(\frac{3}{2}\right) \ln(m_{1d}^*/m_e) - (1/k)dE_g/dT$

$N_d(\text{cm}^{-3})$	$E_g(0)(\text{meV})$	I
2.5×10^{17}	83	3.16
3.0×10^{17}	76	2.05
4.0×10^{17}	84	3.23
5.0×10^{17}	90	3.49
7.0×10^{17}	93	3.14
1.0×10^{18}	92	3.42

uncertainty in n_1 and thus provide more reliable results. The values of E_g for these agree well with the 0.092 eV value obtained above. By taking the average value of the intercept and using the fact that $m_{1d}^* \leq 0.2 m_e$ we see

that $dE_g/dT \leq -4 \times 10^{-5}$ eV/°K. The limiting absolute value is small, about an order of magnitude smaller than the estimated high temperature value ($\sim -5 \times 10^{-4}$ eV/°K). This is as it should be for dE_g/dT must approach zero at absolute zero. The inseparability of m_{1d}^* and dE_g/dT is similar to the inseparability of m_{1d}^* and dE_g/dN_d discussed in Section 3(b). In fact, the argument presented here parallels that of the earlier section with T replacing N_d as the parameter which increases the population of the subsidiary minima.

(b) *The temperature dependence of μ_0 for samples having $N_d \approx N_c$*

The screening enhancement and resultant increase in μ_0 with doping discussed in Section 3(c) leads one to an interest in the temperature dependence of μ_0 for samples having $N_d \approx N_c$. For these samples n_1 increases with temperature so that perhaps a similar screening enhancement can occur. Experimentally $\mu_0(T)$ may be obtained from $\sigma(T)$ since, under the approximations of b and $\xi \ll 1$, $\mu_0(T) \approx \sigma(T)/en_0(T)$. Measurement of $\sigma(T)$ for $4.2 < T < 273^\circ\text{K}$ have been made for the entire series of Sb-doped filaments and values of $\mu_0(T)$ were obtained for the $4, 5$ and $10 \times 10^{17} \text{ cm}^{-3}$ samples for $T < 100^\circ\text{K}$. The mobility is little enhanced (not at all for the $1 \times 10^{18} \text{ cm}^{-3}$ sample); this requires some explanation. In the earlier section the screening was analyzed using expressions valid for extremely degenerate statistics. Here these no longer apply and the expression which includes the Fermi integrals and temperature dependence exactly, must be used. If the L_0^+ electrons dominate the screening then

$$a^2 = \frac{\kappa}{2\pi e^2} \frac{kT}{n_1} \frac{\mathcal{F}_{1/2}(\eta - E_g/kT)}{\mathcal{F}_{-1/2}(\eta - E_g/kT)} \quad (34)$$

In order for a^2 to decrease (better screening) with increasing temperature n_1 must increase faster than kT , the cause of the increase of n_1 in the first place. This happens for the 4 and $5 \times 10^{17} \text{ cm}^{-3}$ samples but not for the 1×10^{18}

cm^{-3} sample where n_1 is already large at 4.2°K . The ratio of the Fermi integrals also decreases slowly with increasing T . We thus expect, at best, a weak decrease in screening length with temperature for samples having $N_d < N_c$ and an increase in a^2 , due to kT , for samples in the $N_d > N_c$ concentration range. From the expression for the mobility of the degenerate ($\eta > 5$) central electrons [equation (22)] we see that μ_0 will also decrease as n_0 decreases with kT . This may easily overwhelm a much stronger screening enhancement because the screening enters only logarithmically through $g(\bar{z})$. Thus it is clear that no pronounced mobility enhancement should occur and our results are in good qualitative agreement with the screened ionized impurity scattering theory.

(c) *The temperature dependence of the magnetoresistance for Sb-doped filaments*

Measurements of the temperature dependence of the magnetoresistance for the Sb-doped series of filaments have been made and qualitatively analyzed. The data for pure samples represents an upper limit for the magnetoresistance at any temperature, a limit that is approached by all the samples as the temperature is raised. Deviations from this intrinsic curve occur at the higher temperatures for samples having the larger N_d values. Below 100°K two different types of behavior may be distinguished. For samples having $N_d < N_c$ the magnetoresistance, tending toward the small one-band value, decreases with decreasing temperature. For more heavily doped samples an increase with decreasing T is observed. This is clearly a manifestation of the two-band conduction. Analysis of this data is complicated by the contribution of the one-band magnetoresistance to the multi-band effects.

5. TEMPERATURE DEPENDENT TWO-BAND CONDUCTION IN THE Γ_0^+ ELECTRON AND HOLE BANDS

In this section data from samples having very few impurities will be presented and dis-

cussed. Under these conditions intrinsic behavior extends to temperatures at least as low as 30°K and properties of the hole and light electron bands may be studied at temperatures below about 100°K.

(a) *The temperature dependence of μ_0 for intrinsic samples*

Hall coefficient vs. temperature data for two lightly doped *p*-type samples and two *n*-type samples, one of purified material and one of material as supplied by Cominco, are shown in Fig. 11. The log-log plot is used to emphasize the $T^{-3/2}$ behavior of the Hall coefficient in this intrinsic region; behavior characteristic of a zero-band-gap semiconductor. No sign of carrier freeze-out is evident for either *n* or *p*-type samples.

In the two-band portion of the intrinsic range

$$R(0) = -(1/n_0 ec) (r_0 - r_p b^2)/(1+b)^2 \quad (35)$$

and

$$\sigma = ec n_0 \mu_0 (1+b) \quad (36)$$

where b is now μ_p/μ_0 . The product $R\sigma$ equals μ_H ; solving for μ_0 we find

$$\mu_0 = -(\mu_H/r_0)(1-b)/[1 - (r_p/r_0) b^2]. \quad (37)$$

The temperature dependence of μ_0 shown in Fig. 13 was determined using equation (37) with $r_0 = 1.4$, $r_p = 1.2$, and values of b obtained in the following section. We may easily compare $\mu_0(T)$ with $\mu_0(N_d)$ obtained earlier if

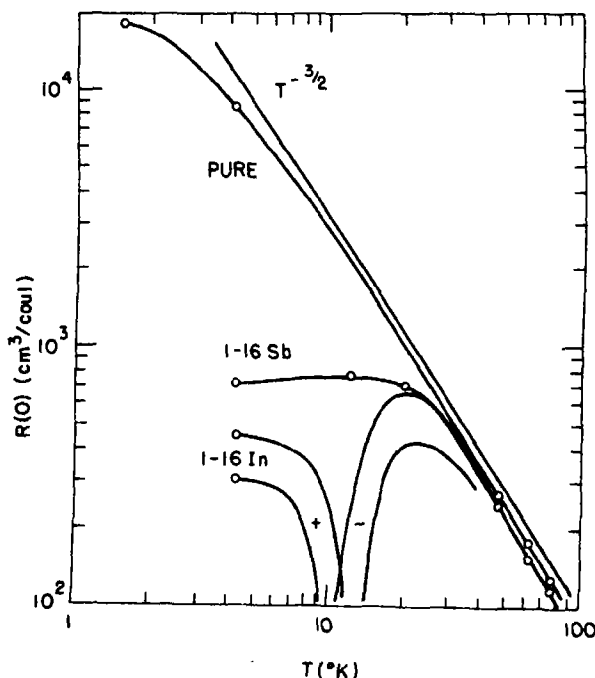


Fig. 11. Temperature dependence of the low field Hall coefficient for pure and lightly doped *n* and *p*-type samples. The log-log plot emphasizes the $T^{-3/2}$ dependence of $R(T)$. The notation 1-16 = 1×10^{16} indium acceptors/cm³. The circles represent d.c. measurements used to calibrate the a.c. temperature sweep measurements denoted by the continuous curves.

we now assume electron-hole scattering dominates for the light electrons. If more than one band is populated the inverse squared screening length is

$$a^{-2} = \frac{2\pi e^2}{\kappa kT} \sum_i n_i \frac{\mathcal{F}_{-1/2}(\eta - \theta_i)}{\mathcal{F}_{1/2}(\eta - \theta_i)} \quad (38)$$

where i is the band index and θ_i the band-edge energy divided by kT . For the pure sample $n_0 = p$ and evaluating the two terms in the sum for $\eta = 2.35$ we obtain

$$a^{-2} = (2\pi e^2 n_0 / \kappa kT) (0.98 + 1.94) \\ = (n_0 / E_F) 6.85. \quad (39)$$

For the degenerate sample the second term of equation (38) is zero and using approximate forms for $\mathcal{F}_{1/2}$ and $\mathcal{F}_{-1/2}$, valid when $\eta \gg 0$, gives

$$a^{-2} = (2\pi e^2 n_0 / \kappa kT) (3/\eta) = (n_0 / E_F) 3. \quad (40)$$

Comparison of equations (39) and (40) shows that for a given n_0 the screening length for a pure sample is less than half that of the degenerate sample and, all else being the same, we may relate the two mobilities by merely changing a . This similarity between $\mu_0(N_d)$ and $\mu_0(T)$ is present because electron-hole scattering in the pure sample is similar to ionized impurity scattering in the doped samples.

(c) *The temperature dependence of the magnetoresistance; evaluation of μ_p*

Curves of $\Delta\rho/\rho_0 H^2$ vs. T for the pure and $\sim 1 \times 10^{16} \text{ cm}^{-3}$ doped n and p -type samples are shown in Fig. 12. Clearly the addition of small amounts of impurities can have pronounced effects on the measured magnetoresistance. Comparing the doped and pure samples we see that the values are nearly the same for temperatures above about 80°K. Below this temperature the effects of the impurities begin to dominate. With decreasing

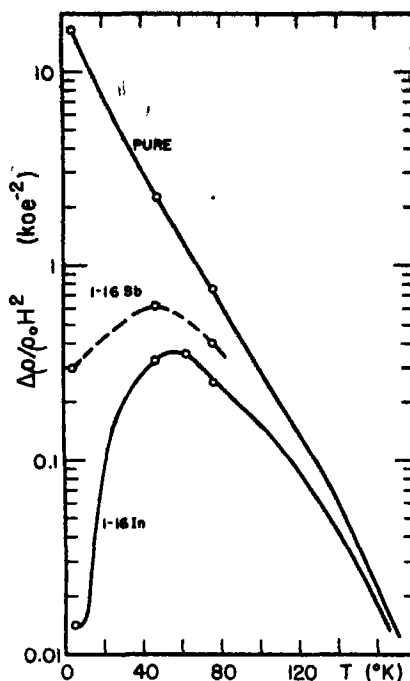


Fig. 12. Temperature dependence of the low field magnetoresistance coefficient for pure and lightly doped n and p -type samples.

temperature the pure sample magnetoresistance continues to rise while the doped samples, as they become closer to a one-band, degenerate system, show a sharp drop in $\Delta\rho/\rho_0 H^2$. This results in a difference of three orders of magnitude between the pure and p -type sample values at 4.2°K. The n -type sample has a higher value at 4.2°K because of the inhomogeneity contribution to the magnetoresistance. This is much smaller for the p -type sample because the hole mobility is much smaller than the electron mobility under these conditions and the inhomogeneity contribution is proportional to μ^2 .

In the intrinsic region the two-band magnetoresistance is given approximately by

$$\Delta\rho/\rho_0 H^2 = 10^{-10} \mu_0 \mu_p r_0^2 [1 + (r_p/r_0)b]^2 / (1+b)^2. \quad (41)$$

Solving this for μ_p and using equation (37) for

μ_0 gives

$$\mu_p = 10^{10}(\Delta\rho/\rho_0 H^2)[(1+b)/r_0\mu_H] \\ [1 - (r_p/r_0)b^2]/[1 + (r_p/r_0)b]^2. \quad (42)$$

Letting $\mu_p' = 10^{10}(\Delta\rho/\rho_0 H^2)(1/r_0\mu_H)$ and $\mu_0' = \mu_H/r_0$ be first approximations to μ_p and μ_0 , respectively, we obtain from the pure sample data an estimate of b as μ_p'/μ_0' . This is used in the complete expressions [equations (37) and (42)] to obtain $\mu_0(T)$ and $\mu_p(T)$ shown in Fig. 13. The electron mobility is seen to agree with theory including the $\kappa(n)$ dependence, both in absolute value and slope. The hole mobility temperature dependence is a more interesting result. Because of the small value of b the holes enter only weakly into the conductivity coefficients. This makes the hole mobility a rather elusive quantity, generally approach-

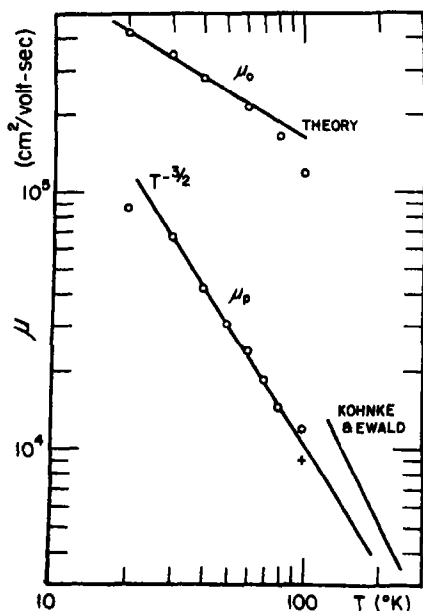


Fig. 13. Temperature dependence of the Γ_8^+ electron and hole mobilities. The electron mobility μ_0 agrees well with theory if the carrier concentration dependent dielectric constant is introduced. The hole mobility μ_p obeys a $T^{-3/2}$ power law that strongly suggests acoustic phonon scattering as the dominant mechanism. Estimates of $\mu_p(T)$ by Kohnke and Ewald (see Ref. [33]) obtained from data at higher temperatures, are shown for comparison.

able only through a field dependent effect such as $\Delta R/R_0$ or $\Delta\rho/\rho_0$. For intrinsic samples, however, $\Delta R/R_0 \approx 0$. This leaves the present method as possibly the only way μ_p may be determined in pure gray tin, although $\Delta R/R_0$ might be used for nearly intrinsic samples. Over most of the intrinsic range $\mu_p(T)$ exhibits a $T^{-3/2}$ temperature dependence that strongly suggests scattering by acoustic lattice vibrations. Theoretically, for non-degenerate statistics (because $\eta = -2.3$), we have

$$\mu_L = \left(\frac{4}{3}\right) \sqrt{\pi e \tau_0 / m^*} \text{ and } \tau_0 \\ = (2\pi\rho v_s^2 \hbar^4) / [U^2 (2m^*)^{3/2} T^{3/2}]. \quad (43)$$

Here ρ is the density and v_s the sound velocity. We have obtained an estimate of μ_L at 100°K using equation (43) and the known physical constants for gray tin. The value for the deformation potential, $U = -(1.9 \pm 0.5) \text{ eV}$, was obtained from the work of Roman[32]. The calculated value of μ_L is shown slightly below the experimental curve in Fig. 13, reinforcing our thesis that in intrinsic samples the holes are scattered predominantly by acoustic phonons.

We also notice from equation (43) a strong dependence upon the effective mass, $m^{*-5/2}$. It is this behavior that makes phonon scattering insignificant for electrons. If only lattice scattering were present μ_0 would be $3 \times 10^6 \text{ cm}^2/\text{V-sec}$ at 100°K. This is 20 times larger than the observed value.

One might ask why electron-hole scattering does not enter into the hole scattering appreciably. It may be argued that the reduced mass is the same for electrons scattering from holes and holes scattering from electrons, thus the apparent mass dependence of equation (22) is misleading. The only difference in calculated mobility arises from the Fermi integrals. This difference in statistics would cause only a factor of 2 reduction of μ_p below μ_0 . The measured hole mobility is much lower than this except below about 30°K so electron-hole

scattering clearly does not limit the mobility above 30°K. Below 30°K there is some evidence that another scattering mechanism is present. This may be electron-hole scattering as b has risen to about 0.25.

Also shown in Fig. 13 are data of Kohnke and Ewald[33] for $\mu_p(T)$ obtained by analyzing the conductivity and Hall coefficient for relatively pure filaments at high temperatures. Their analysis was based on the then conventional two-band semiconductor model. We might expect their results to agree more closely with our extrapolated $T^{-3/2}$ behavior at high temperatures where the two band model is more appropriate. This does occur, the two determinations giving the same result when extrapolated to somewhat above room temperature. From all of these considerations we conclude that phonon scattering dominates the hole mobility at all temperatures above about 30°K. Contributions from two valence bands, which in Ge give a stronger temperature dependence, are not present here so that at least at low temperatures the theoretical $T^{-3/2}$ behavior is observed.

6. CONCLUSIONS

The results of this study fall into three distinct categories: Those obtained at 4.2°K from Sb-doped samples, making use of the oscillatory magnetoresistance. The temperature dependence of these same samples for temperatures below 100°K, and results obtained from 'pure' and lightly doped samples in this same temperature range. The first two provide information about the Γ and L conduction bands. The third involves the, Γ_8^+ , light electron and hole bands. All results are consistent with the Groves-Paul band structure model.

At 4.2°K the existence of a critical donor concentration, above which two bands participate in the conduction processes, was observed. The contributions of the two bands were separated and a consistent picture of all the galvanomagnetic effects formulated. From the population of the two bands, a value of

their energy separation, E_g , and an upper limit for the density-of-states effective mass of the ellipsoids were determined. The presence of an impurity band-tail, consisting of states below the ellipsoidal band edge proper, was also noted.

The mobility of the central electrons at 4.2°K was shown to be screening enhanced for donor concentrations above the critical concentration, in complete analogy with the reduction in Dingle temperature reported by Booth and Ewald. Our results are in good qualitative agreement with screened, ionized impurity scattering theory. At considerably lower donor concentrations serious discrepancies exist between this theory and the measured values. A doping dependent dielectric constant was assumed to account for this difference.

The temperature dependences of the galvanomagnetic properties were also shown to be consistent with the Groves-Paul band structure model. The rising Hall coefficient with temperature, observed for samples having donor concentrations near the critical concentration, was attributed to a thermal transfer of electrons from the central minimum to the ellipsoids. Values of the energy separation, E_g , and dE_g/dT were determined from these data. Using the conductivity and Hall coefficient data we were able to obtain the central electron mobility as a function of temperature. This is not strongly screening-enhanced because of the temperature dependence of the screening length. We have treated the magnetoresistance in a qualitative manner because of spurious contributions to it due to impurity density fluctuations. We still are able to distinguish one or two-band behavior as the temperature is lowered depending upon the relation of the donor concentration to the critical concentration.

Pure and lightly doped n and p -type samples were shown to exhibit a $T^{-3/2}$ temperature dependence of the Hall coefficient, thus extending Groves' result to lightly doped samples. The magnetoresistance of the pure

sample is very large. This indicates that two-band effects extend into the liquid He temperature range. Lightly doped samples (especially *p*-type) show a sharp drop in magnetoresistance as the temperature is lowered, making the material extrinsic. By using measurements of conductivity, Hall coefficient and magnetoresistance and the intrinsic nature of the material the electron and hole mobilities were obtained as functions of temperature. The light electron mobility was then related to the 4.2°K value having the same Fermi level. The two are equivalent if the additional screening of the holes is taken into account. The hole mobility follows a $T^{-3/2}$ dependence in this intrinsic temperature range. This, combined with a theoretical estimate of the magnitude of the mobility, strongly support the contention that phonon scattering dominates the hole mobility in pure material at least down to 30°K.

REFERENCES

1. GROVES S. H. and PAUL W., *Phys. Rev. Lett.* **11**, 194 (1963), and in *Proceedings of the Seventh International Conference on the Physics of Semiconductors*, p. 41 Paris (Dunod Cie. Paris) (1964). See also GROVES S. H., Ph.D. Thesis, Harvard University (1963).
2. TUFTE O. N. and EWALD A. W., *Phys. Rev.* **122**, 1431 (1961) and *J. Phys. Chem. Solids* **8**, 523 (1959).
3. HINKLEY E. D. and EWALD A. W., *Phys. Rev.* **134**, A1261 (1964) and HINKLEY E. D., Ph.D. Thesis, Northwestern University (1963).
4. BASSANI F. and LIU L., *Phys. Rev.* **132**, 2047 (1963).
5. KENDALL J. T., *Proc. Phys. Soc.* **B63**, 821 (1950); BUSCH G., WIELAND J., and ZOLLER H., *Helv. Phys. Acta* **24**, 49 (1951).
6. BUSCH G. A. and KERN R., In *Solid State Physics*, (Edited by F. Seitz and D. Turnbull), Vol. **11**, p. 1. Academic Press, New York, (1960).
7. DINGLE R. B., *Phil. Mag.* **46**, 831 (1955).
8. BROOKS H., *Phys. Rev.* **83**, 879 (1951).
9. BOOTH B. I. and EWALD A. W., *Phys. Rev. Lett.* **18**, 491 (1967).
10. EWALD A. W., *Phys. Rev.* **91**, 244 (1953).
11. EWALD A. W. and TUFTE O. N., *J. appl. Phys.* **29**, 1007 (1958).
- 12a. BECKER J. H., *J. appl. Phys.* **29**, 1110 (1958).
- 12b. The higher purity was achieved through the following solvent extraction technique. The $\beta \rightarrow \alpha$ transition at -35°C of a 3 weight per cent Hg alloy with Sn yields massive chunks of α -Sn. This material, placed in contact with liquid Hg, absorbs additional Hg (approximately 25 per cent by volume) as the temperature is raised to 4°C . The Hg, saturated with Sn, is extracted by lowering the temperature to -15°C . Finally, the purified Sn is reclaimed from solution by cooling to -35°C . This procedure reduces the *n*-type impurity content (determined by Hall measurements) from $\sim 8 \times 10^{13} \text{ cm}^{-3}$ to $\sim 5 \times 10^{14} \text{ cm}^{-3}$.
- 13a. The maximum allowable difference between the two Hall voltages was arbitrarily set at 10 per cent. Samples showing greater inhomogeneity were rejected.
- 13b. BOOTH B. I. and EWALD A. W., *Phys. Rev.* **168**, 805 (1968).
14. RUSSELL R. B. and WAHLIG C., *Rev. scient. Instrum.* **21**, 1028 (1950).
15. The book, *Galvanomagnetic Effects in Semiconductors* (Academic Press, New York, 1963) by A. C. Beer, has served as a general reference for much of following discussion.
16. BOOTH B. I. and EWALD A. W., *Phys. Rev.* **168**, 796 (1968).
17. WOLFF P. A., *Phys. Rev.* **126**, 405 (1962).
18. PARMENTER R. H., *Phys. Rev.* **104**, 22 (1956).
19. KANE E. O., *Phys. Rev.* **131**, 79 (1963).
20. SHEPHERD F. D., *Office of Aerospace Research, Physical Sciences Research Papers* #150 (1965).
21. KOSICKI B. B. and PAUL W., *Phys. Rev. Lett.* **17**, 246 (1966).
22. BECKER W. M., RAMDAS A. K. and FAN H. Y., *J. appl. Phys.* **32**, 2094 (1961).
23. SCHIFF L. I., *Quantum Mechanics* Ch. 7, p. 171 (McGraw-Hill, New York, 2nd Edition).
24. WAGNER R. J., Ph.D. Thesis (unpublished), Northwestern University (1967).
25. LIU L. and BRUST D., *Phys. Rev. Lett.* **20**, 651 (1968) and *Phys. Rev.* **173**, 777 (1968).
26. SHERRINGTON D. and KOHN W., *Rev. mod. Phys.* **40**, 767 (1968).
27. LIU L. and TOSATTI E., *Phys. Rev. Lett.* **23**, 772, (1969).
28. BROERMAN J. G., *Phys. Rev. Lett.* **24**, 450 (1970).
29. SAGAR A., *Phys. Rev.* **117**, 93 (1960); AUCKERMAN L. and WILLARDSON R., *J. appl. Phys.* **31**, 939 (1960); FILIPCHENKO A. S., *Phys. Status Solidi* **14**, K195 (1966).
30. KOLODZIEJCZAK J., *Acta Phys. Polonica* **XX**, 289 (1960).
31. GROVES S. H., PIDGEON C. R., EWALD A. W. and WAGNER R. J., *Proceedings of the Ninth International Conference on the Physics of Semiconductors*, Moscow, 1968, (Nauka Publishing House, Leningrad, 1968), p. 43.
32. ROMAN B. J., Ph.D. Thesis (unpublished), Northwestern University (1969).
33. KOHNKE E. E. and EWALD A. W., *Phys. Rev.* **102**, 1481 (1956).

HARTREE-FOCK DETERMINATION OF THE ENERGY BANDS AND THE OPTICAL PROPERTIES OF LITHIUM BROMIDE*

A. BARRY KUNZ and NUNZIO O. LIPARI

Department of Physics and Materials Research Laboratory, University of Illinois, Urbana, Ill. 61801, U.S.A.

(Received 1 July 1970)

Abstract—Using the nonrelativistic mixed basis (M.B.) method and self-consistent local orbitals for the LiBr crystal, energy bands in the Hartree-Fock approximation have been obtained. These results are similar in quantitative features to those recently obtained by one of us (A.B.K.) for the LiCl crystal. Using the polarization corrections of Fowler these bands have been modified to incorporate many body effects. The final band structure has been fitted with pseudopotential and a density of states computed for the upper valence bands and the lower conduction bands. A joint valence-conduction band density is also obtained. These results are compared to several recent experiments. In general, the experimental comparison is excellent. Suggestions for further investigations are made.

1. INTRODUCTION

OF ALL the alkali halides, the lithium halides are the least understood and studied. The lack of experimental investigations are understandable since, excepting LiF, these crystals are hygroscopic and hence very difficult to experiment with. In regard to optical properties the substances LiCl, LiBr, and LiI seem to be quite similar. This has been seen in the region of the fundamental absorption edge and in the soft X-ray absorption[1-5]. Using potentials structured on modifications of the Slater exchange, energy band calculations have been reported for the Lithium halides[6]. These calculations were incomplete in the sense that insufficient points in the brillouin zone were computed to allow complete experimental analysis. In addition, the use of an effective exchange approximation is questionable[7, 8].

In this paper we present a calculation for LiBr which avoids the difficulties associated with the previous work. That is, the correct Fock exchange is used and, via a pseudo-

potential interpolation, densities of states are obtained for the valence bands, the lower conduction bands and a joint valence conduction density of states is computed. It has been seen in previous work that the inclusion of the correct Fock exchange yields results which differ greatly from those obtained using a Slater type potential. This difference is chiefly associated with the width of the valence bands[8, 9]. In this calculation, many body corrections are included via the method of Fowler[10]. It will be seen that these corrections are substantial and necessary.

In the next section the techniques used in this calculation are briefly reviewed. In Section 3, the results are presented and these are compared to experiment. Finally, in Section 4 conclusions are made and suggestions for further work are made.

2. THE METHOD OF CALCULATION

The various techniques used in this calculation have been given previously and hence only a sketch of them will be given at this time. Firstly, a self consistent charge density is obtained for the LiBr crystal. To do

*This research was supported in part by the Advanced Research Projects Agency under Contract SD-131.

this one solves the local orbital equations for the LiBr lattice correct to first order in interatomic overlap[11]. These are obtained by solving the equations

$$[F_A + U_A - \epsilon_{A_l}] \phi_{A_l} = \sum_k' \phi_{A_k} \langle A_k | U_A | A_l \rangle, \quad (1)$$

for the Li^+ and the Br^- ions. Here the ϕ_{A_j} 's are local orbitals about the lattice site A . The quantum number j refers to the usual set of orbital, angular and spin quantum numbers. The quantities U_A and F_A are given as

$$F_A \phi_{A_l} = \left[-\nabla_l^2 - \frac{2Z_A}{r_{A_l}} + 4 \sum_j' \int \phi_{A_j}^2(r_2) \frac{1}{|r_{12}|} dr_2 \right] \phi_{A_l} - 2 \sum_j \phi_{A_j}(r_1) \int \phi_{A_j}(r_2) \phi_{A_l}(r_2) \times \frac{1}{|r_{12}|} dr_2, \quad (2)$$

$$U_A = - \sum_B' \frac{2Z_B}{|r_{Bl}|} + 4 \sum_{B,j}' \int \phi_{B_j}^2(r_2) \frac{1}{|r_{12}|} dr_2. \quad (3)$$

Here we include only one member of a spin up, spin down pair of orbitals in a sum. The prime in U_A means that we exclude site A in the sum. The exact expression for the local orbitals for LiBr are being reported elsewhere[11] and are not included in this manuscript.

Once one obtains the local orbitals one must evaluate the energy bands. This is done using the mixed basis (M.B.) method[6]. As this method has been discussed in great detail elsewhere as have the techniques of evaluating elements of the Fock operator in this method [8, 9] it needs no discussion at this time. In this calculation the technique used for evaluating matrix elements of the Fock operator and plane waves is that of Ref.[9] rather than that of Ref.[8] which was used previously for LiCl. As will be seen from the results the bands for LiBr are very similar to those for LiCl and it is suggested that both techniques are equally accurate.

Polarization corrections are included using the static limit as demonstrated by Fowler[10].

Polarization corrections occur for several reasons: (1) all electron correlation is neglected except for that which arises from a totally antisymmetric wavefunction; (2) we assume an invariant core (Koopmans's theorem); (3) we assume the ionic positions remain undisturbed during an excitation. Of these assumptions only (3) is justified. The technique of Fowler allows for inclusion of types (1) and (2) effects.

Fowler's method is an extension of the theories of Haken and Schottky and of Toyozawa[12]. Fowler demonstrates for the insulator these theories tend to a static limit, and this is evaluated by a Mott and Littleton approach[13]. This result which we apply in an appropriate manner lowers the conduction bands with respect to the valence bands by about 3.82 eV. As we apply this theory it is essentially k independent.

The method of application is quite simple. One evaluates the amount of wavefunction contained within the ionic radius of Li^+ ion and assume the rest to be associated with the Br^- ion. Then the polarization correction to an energy is given by

$$E_{\text{pol}} = \pm [d(+) E_{\text{elect}} + d(-) E_{\text{hole}}]. \quad (4)$$

Here E_{pol} is the correction, $d(+)$ is the wavefunction density about the $(+)$ ion and $d(-) = 1 - d(+)$. E_{elect} is the correction due to an extra electron on the alkali ion and E_{hole} is the correction due to a hole on the halogen ion. The $+$ sign is used for a hole and the $-$ sign for an electron.

3. THE RESULTS AND COMPARISON TO EXPERIMENT

The M.B. calculation was performed using 181 planewaves at the Γ point and also 137 plane waves at the point. The changes were negligible and 181 planewaves were used for subsequent calculations. The points Γ , X , L were actually computed. The core states included in the calculation were the Li^+ 1s and the Br^- 1s, 2p, 3s, 3p, 3d. In Table 1 the values of the core states and the valence

Table 2. The conduction levels of LiBr and LiCl are given. In column 1 the state is given, in column 2 the H-F result for LiBr is shown and in column 3 this is corrected for polarization and is with respect to the $4p\Gamma_{15}$ level. In column 4 the H-F LiCl result is shown.

1	2	3	4
Li ⁺ 1s	-67.39	-56.52	-66.74
Br ⁻ 1s	-13335.00	-13325.00	-2854.00
2s	-1773.00	-1763.00	-287.7
2p	-1594.00	-1584.00	-218.5
3s	-268.1	-258.5	
3p	-200.8	-191.2	
3d	-87.13	-77.53	
4s(3s)Γ ₁	-29.59	-19.99	-31.56
X ₁	-26.86	-17.26	-28.79
L ₁	-27.52	-17.92	-29.45
4p(3p)Γ ₁₈	-9.60	0.00	-8.00
X ₁ '	-16.47	-7.14	-15.25
X ₈ '	-12.00	-2.40	-10.44
L ₂ '	-17.17	-7.57	-15.96
L ₂ '	-10.31	-0.71	-8.69

1	2	3	4
Γ_1	2.62	8.40	3.47
Γ_{15}	8.87	14.65	11.22
Γ_{12}	11.44	17.22	14.07
Γ_{15}	10.75	16.53	13.98
X_1	3.59	9.37	5.37
X_3	3.82	9.60	5.31
X_5	11.18	16.96	14.04
X_4	10.35	16.13	12.60
X_2	14.71	20.49	17.41
L_1	2.81	8.59	3.84
L_3	4.75	10.53	7.55
L_2	10.77	16.55	13.61
L_4	12.23	18.01	16.42
L_3	11.68	17.46	17.28
L_1	15.64	21.42	18.51

The principal results may be summarized as follows. The 4s valence band is 2.73 eV wide and the 4p valence band is 7.57 eV wide, results in good agreement with those found for LiCl. In the Hartree-Fock approximation, the photo emission threshold is found to be 9.6 eV, the electron affinity is found to be -2.62 eV and the optical band gap is 12.22 eV. If one includes polarization corrections, the band gap reduces to 8.40 eV.

Fig. 1. The probable energy bands for LiBr are shown. Only the points Γ , X , and L were actually computed.

by a pseudopotential scaled from that used for LiCl[8]. Using 505 nonequivalent points in $1/48$ of the Brillouin zone a density of states was evaluated for the valence bands and the lower conduction bands. These results are shown in Figs. 2-4. Also a joint valence-conduction density was computed and is given in Fig. 5. In Fig. 4, the optical absorption from the Li^+K shell after Brown [5] is given.

possible to directly compare the joint density calculation with experiment due to the neglect of spin orbit effects in the calculation. These effects are of some size since the spin-orbit splitting of the $4p$ band at the Γ point is about 0.5 eV. We note, however, there seems to be a fair degree of correlation between the joint density curve and the experiment of Teegarden and Baldini commencing about 2 eV above the band edge. We attribute the

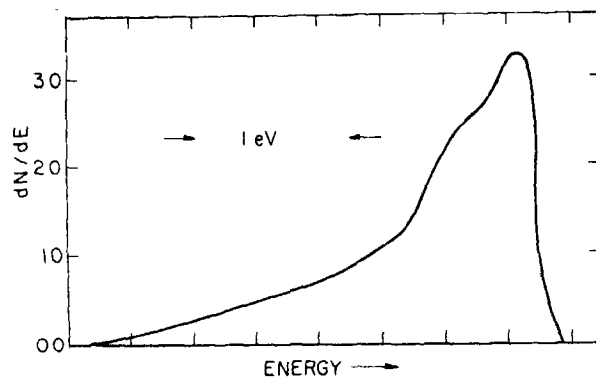


Fig. 2. The density of states for the $4s$ valence band is shown.

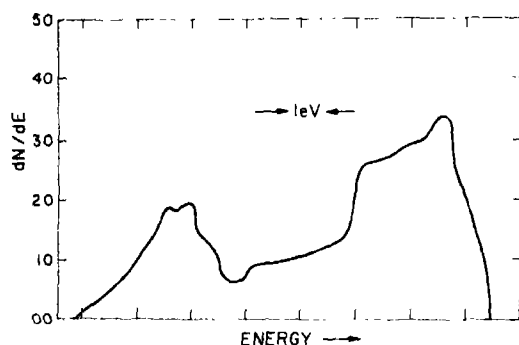


Fig. 3. The density of states for the 4 valence band is shown.

One expects that the density of states calculation for the $4s$ and $4p$ levels in LiBr should be useful in interpreting X-ray emission data or electron emission data for these substances as they become available, just as this calculation for LiCl has been useful. It is not

poor agreement in the lower energy region to the omission of exciton levels in the calculation. It is expected that exciton activity could be present at the L and X points as well as at Γ . This is felt to be consistent with the above discussion.

In the case of the soft X-ray region, LiBr presents a system which is ideal. In the region from about 60 to 300 eV there are the $\text{Li}^+ 1s$, $\text{Br}^- 3d$, $\text{Br}^- 3p$ and $\text{Br}^- 3s$ core levels. These levels are well separated and of good diversity of symmetry type. In Fig. 4 the computed conduction density of states and the Lithium K shell absorption is shown. It is seen that if we assume a constant transition matrix element there is an excellent degree of correlation between the theory and experiment. It is seen that the presence of excitons are not necessary to enable us to understand the X-ray structure. This is in keeping with previous results for KI and LiCl[15, 8].

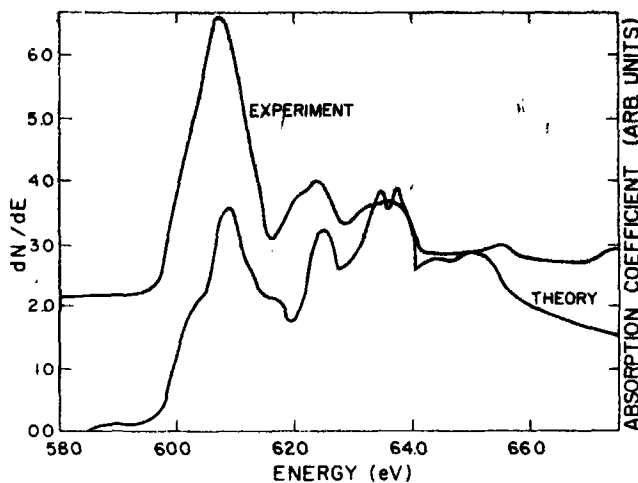


Fig. 4. The density of states for the conduction band of LiBr is given and the soft X-ray Li^+ K shell absorption data after Brown is given. The zero of energy is arbitrary.

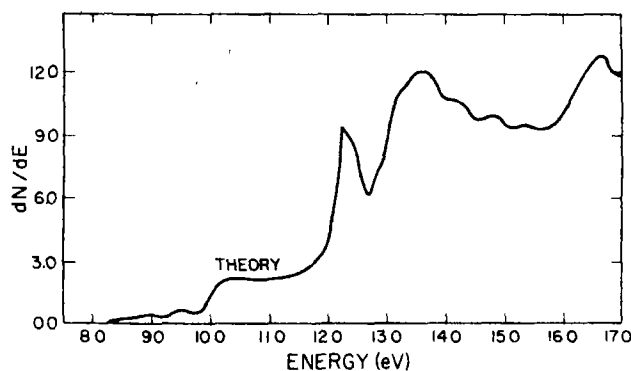


Fig. 5. The joint density of states for the valence and conduction bands of LiBr is shown.

4. CONCLUSIONS

It has been possible to compute self consistent Hartree-Fock energy bands for LiBr crystal. These results feature a valence band which is wide (ca. 8 eV for the $4p$ band) and which exhibits a band gap about 4.5 eV greater than experiment. If one includes polarization corrections the band gap decreases to the point where it is about 0.7 eV or less greater than experiment. Thus in LiBr as in LiCl, Ar, Kr the polarization corrections are very great. It is suggested that including

polarization corrections by other than a static limit approximation should be tried.

Experimentally, the emission spectra from the $4s$ and $4p$ levels should be measured as should the soft X-ray absorption spectrum in the range 60–300 eV.

Acknowledgement—The authors wish to thank Professor F. C. Brown for permission to use his unpublished data for LiBr.

REFERENCES

1. EBY J. E., TEEGARDEN K. J. and DUTTON D. B., *Phys. Rev.* **116**, 1099 (1959).

2. TEEGARDEN K. J. and BALDINI G., *Phys. Rev.* **155**, 896 (1967).
3. BALDINI G. and BOSACCHI B., to be published.
4. HAENSEL R., KUNZ C. and SONNTAG B., *Phys. Rev. Lett.* **20**, 262 (1968).
5. BROWN F. C. and GAHWILLER Ch., to be published.
6. KUNZ A. B., *Phys. Rev.* **175**, 1147 (1968); **180**, 934 (1969); *Phys. Status Solidi* **29**, 115 (1968).
7. LINDGREN I., *Ark. Fys.* **31**, 59 (1965); KUNZ A. B., FOWLER W. B. and SCHNEIDER P. M., *Phys. Lett. (Netherlands)* **28A**, 553 (1969).
8. KUNZ A. B., *J. Phys. C. (Great Britain)* **3**, 1542 (1970) and others to be published.
9. LIPARI N. O., *Thesis* (Lehigh University, unpublished) (1970); and others to be published.
10. FOWLER W. B., *Phys. Rev.* **151**, 657 (1966).
11. KUNZ A. B., *Phys. Status Solidi* **36**, 301 (1969); and others to be published.
12. HAKEN H. and SCHOTTKY W., *Z. Phys. Chem.* **16**, 218 (1958); TOYOZAWA Y., *Prog. theor. Phys. (Kyoto)* **12**, 421 (1954).
13. MOTT N. F. and LITTLETON M. J., *Trans. Faraday Soc.* **34**, 485 (1938).
14. BOUCHAERT L. P., SMOLUCHOWSKI R. and WIGNER E., *Phys. Rev.* **50**, 58 (1936).
15. BROWN F. C., GAHWILLER CH., FUJITA H., KUNZ A. B., SCHEIFFLEY W. and CARRERA N., *Phys. Rev.*, to be published.

PHASE TRANSITIONS AND CONDUCTIVITY ANOMALIES IN SOLID SOLUTIONS OF VO_2 WITH TiO_2 , NbO_2 AND MoO_2^*

C. N. R. RAO, M. NATARAJAN, G. V. SUBBA RAO and R. E. LOEHMAN†

Department of Chemistry, Indian Institute of Technology Kanpur, Kanpur-16, India

(Received 16 June 1970)

Abstract—The solid solutions $\text{V}_{1-x}\text{Ti}_x\text{O}_2$ ($0.02 \leq x \leq 0.4$) which are monoclinic at room temperature (with the monoclinicity decreasing with increasing x) transform to rutile structures at T_i . The T_i , ΔH as well as the conductivity jump (at T_i) decrease with increase in x . Incorporation of 2 at.% of Nb (or Mo) lowers the T_i of VO_2 considerably, while 10% Nb stabilizes the high-temperature rutile structure. The high temperature rutile phases of all the solid solutions show semiconducting behavior indicating that the conductivity anomalies correspond to semiconductor-semiconductor transitions.

1. INTRODUCTION

SINCE the discovery of the semiconductor-metal transition in VO_2 by Morin[1], there have been several reports on the phase equilibria in the vanadium-oxygen system[2] and on the mechanism of the phase transition in VO_2 [3-5] and related oxides[5, 6]. The crystallography, magnetic susceptibility (χ) and electrical conductivity (σ) of the pseudo-binary system VO_2 - TiO_2 have been examined by a few workers[7-9]. Some of these studies are limited to narrow ranges of composition; further, the variation of χ with T of this binary system reported by two groups of workers [7, 8] differ significantly. We now wish to report the preliminary results of our investigations of $\text{V}_{1-x}\text{Ti}_x\text{O}_2$ employing X-ray crystallography, differential thermal analysis (DTA) and electrical conductivity measurements; these studies are of value in understanding the mechanism of the conductivity anomalies in these solid solutions. Rüdorff and Marklin[10] have reported the crystallography and χ of the binary system, $\text{V}_{1-x}\text{Nb}_x\text{O}_2$, along with some conductivity data; the conductivities have, however, not been measured as functions of

temperatures. We have presently examined the effect of addition of Nb and Mo on the transition of VO_2 .

2. EXPERIMENTAL

The solid solutions were prepared by taking the metals and their stable oxides (all of better than 99.99 per cent purity) in stoichiometric proportions and melting the mixture in a d.c. arc furnace in an atmosphere of gettered argon [11]. X-ray powder diffraction patterns were recorded with a GE diffractometer. DTA curves were recorded (in an atmosphere of N_2 or Ar) by employing an Aminco thermo-analyzer[12]. Conductivity measurements were made on polycrystalline pellets by the four-probe technique (in an argon atmosphere) after cycling[13] each sample 3-4 times through T_i .

3. RESULTS AND DISCUSSION

Crystal structure data on $\text{V}_{1-x}\text{Ti}_x\text{O}_2$ in the low (monoclinic) and high (rutile) temperature phases are shown in Table 1. We see that the monoclinic structure persists up to $x = 0.4$, the monoclinicity decreasing with increasing x . These results differ from those of Ariya and Grossman[8] who report a rutile structure at room temperature for $x = 0.4$. It seems possible that the solid solution with $x \geq 0.6$ may possess the rutile structure[14]. DTA results

*Supported by the U.S. National Bureau of Standards through the grant G-51 under the Special International Program.

†Department of Materials Science, University of Florida.

Table 1. Crystal structure, DTA and conductivity (in $\text{ohm}^{-1} \text{cm}^{-1}$) data on the $V_{1-x}Z_xO_2$ systems ($Z = \text{Ti, Nb or Mo}$)

Composition	Distorted rutile (25°C)				Rutile (80°C)		DTA		Electrical Conductivity			
	x	a, Å	b, Å	c, Å	β°	a, Å	c, Å	$T_i, ^\circ\text{C}^{[a]}$	ΔH , cal/mole	$\sigma(40^\circ\text{C}) \times 10^2$	$T_i, ^\circ\text{C}$	E_a , eV $T < T_i$ $T > T_i$
0.00		5.744	4.520	5.376	122.6	4.559	2.801	69	750	0.8	69	0.15 ^[b] (0.28)
$V_{1-x}\text{Ti}_x\text{O}_2$ ^[c]												
0.02		5.729	4.530	5.364	122.3	—	—	65	630	1.2	65	0.18
0.05		5.727	4.560	5.390	122.5	4.545	2.844	63	600	—	—	—
0.10		5.716	4.499	5.424	122.0	4.537	2.868	60	400	5.8	63	0.15 0.25
0.20		5.704	4.490	5.448	121.3	4.539	2.891	58	190	4.7	59	0.23 0.43
0.40		4.833	4.380	5.530	97.9	4.546	2.894	48	100	0.3	45	0.16 0.31
$V_{1-x}\text{Nb}_x\text{O}_2$												
0.02 ^[d]		4.510	—	2.890	—	—	—	42	250	4.5	35	0.13 0.41
0.05 ^[e]		4.540	—	2.880	—	—	—	38	200	5.9	34	0.12 0.33
0.10 ^[f]		4.569	—	2.880	—	—	—	—	—	2.8	—	0.06
$V_{1-x}\text{Mo}_x\text{O}_2$												
0.02 ^[d]		4.560	—	2.868	—	—	—	45	350	4.6	40	0.12 0.41

[a] Peak temperatures; thermal hysteresis of $\sim 15^\circ$ is seen with all samples.

[b] Value in parenthesis is E_a just before transformation

[c] Monoclinic at 25°C .

[d] This has monoclinic distortion, but we have indexed it as rutile.

[e] Shows another transformation at $\sim 7^\circ\text{C}$ (possibly monoclinic \rightarrow distorted rutile) with $\Delta H \approx 50$ cal. mole $^{-1}$ (Fig. 1); the 40° transition may be from distorted rutile to rutile (like in NbO_2).

[f] Rutile structure at room temperature.

(Fig. 1 and Table 1) clearly show that both the T_i and ΔH decrease with increase in x . The transition is first order in VO_2 [3, 4], but seem to show higher order components in solid solutions with high x .

The room-temperature σ of $V_{1-x}\text{Ti}_x\text{O}_2$ with $x = 0.02$ – 0.20 is higher than that of VO_2 , σ being maximum when $x \approx 0.10$; when $x = 0.40$, however, the room temperature σ is lower than in VO_2 . The T_i values determined from the σ – T data agree well with the DTA results (Table 1). The jump in conductivity, $\Delta\sigma$, at T_i is always smaller in the solid solutions than in pure VO_2 ; $\Delta\sigma$ is largest when $x = 0.02$ and lowest when $x = 0.40$. The values above T_i are of the same magnitude for $0.02 \leq x \leq 0.20$ even though the σ values at $T < T_i$ are appreciably different (Fig. 2a). In this regard, the σ – T curves of the present study are similar to the χ – T curves of Rüdorff and co-workers [7] rather than those of Ariya and Grossman [8]. Rüdorff and co-workers find that χ values of the solid solutions are similar

above T_i , but considerably different below T_i .

All the solid solutions presently studied, $0.02 \leq x \leq 0.40$ (as well as the composition with $x = 0.01$ studied by MacChesney and Guggenheim [2]), seem to show semiconductor behavior above T_i with activation energies (E_a) in the range 0.25 – 0.43 eV (Table 1); we realize, however, that it is difficult to distinguish between semiconducting and metallic behavior on the basis of such conductivity data alone. Our results support the observation of MacChesney and Guggenheim [2] that the incorporation of Ti^{4+} in VO_2 reduces T_i . Futaki and Aoki [15] report that T_i in such solid solutions increases with c -axis of the rutile phase. The present results on the series of $V_{1-x}\text{Ti}_x\text{O}_2$ solid solutions, however, show the opposite trend.

In the monoclinic structure of VO_2 , addition of Ti^{4+} creates holes in the valence band* and

*Seebeck coefficient and Hall data on these solid solutions would be necessary to be able to obtain a complete understanding of this aspect.

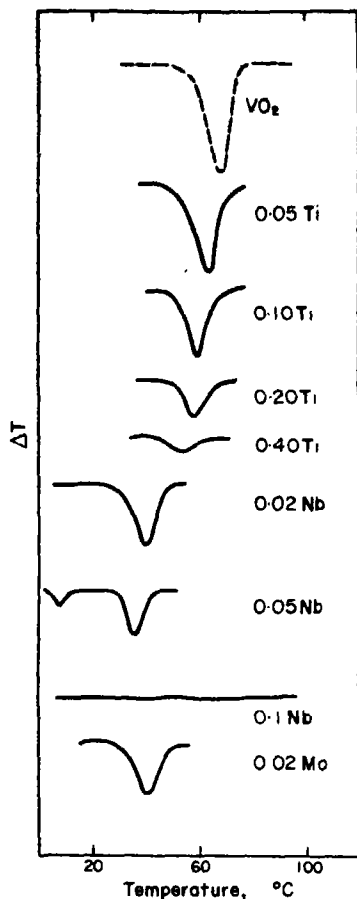


Fig. 1. DTA curves (heating rate $16^\circ \text{ min}^{-1}$) of VO_2 and $\text{V}_{1-x}\text{Z}_x\text{O}_2$ ($\text{Z} = \text{Ti, Nb or Mo}$); x values are shown next to the curves.

decreases the energy gap thereby causing higher σ at $T < T_i$ and lower $\Delta\sigma$ at T_i . In VO_2 , the homopolar $\text{V}^{4+} - \text{V}^{4+}$ bonds can trap conduction electrons in the low-temperature phase [16]. Apparently, the heteropolar bonds in the solid solutions are not as effective in the trapping of charge carriers. The $\Delta\sigma$ (just as the ΔH) in the solid solutions decreases with the monoclinicity of the low temperature phase (Table 1 and Fig. 2a). This is reasonable since the magnitude of crystal distortion should in principle determine these changes; this observation may be taken as indirect evidence for the Adler-Brooks model [17] of semiconductor-semimetal transitions. The c/a ratio of the high-temperature rutile phase approaches the value in pure TiO_2 at high x . This would cause a decrease in σ above T_i with increase in x as observed experimentally. Above T_i it is possible that the cation-cation and cation-anion-cation overlaps are much lower than the critical overlap [18] necessary to make them metallic.

NbO_2 has a distorted rutile structure at room temperature and transforms to a rutile phase [19] at $\sim 800^\circ\text{C}$ ($\Delta H = 250 \text{ cal/mole}$) with a hysteresis of 10° . The solid solutions $\text{V}_{1-x}\text{Nb}_x\text{O}_2$ have rutile structure (Table 1) when $x \geq 0.1$ in agreement with the results of Rüdorff and Marklin [10]. When $x \leq 0.05$, the solid solution seems to possess a distorted

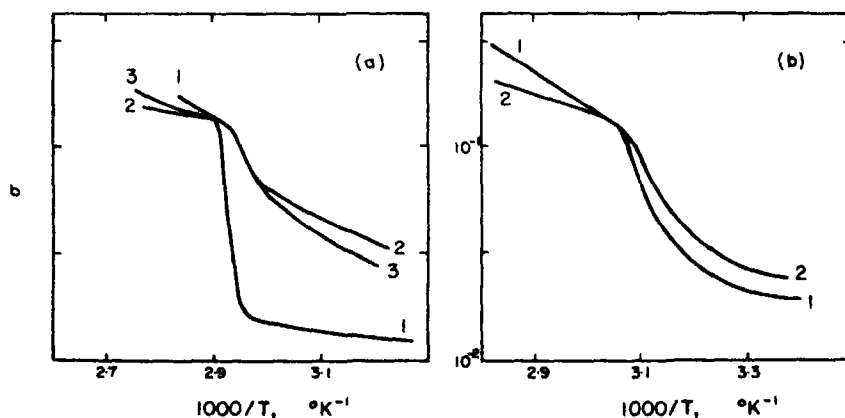


Fig. 2. Plot of electrical conductivity ($\text{ohm}^{-1} \text{ cm}^{-1}$) against reciprocal of absolute temperature (heating curves): (a) $\text{V}_{1-x}\text{Ti}_x\text{O}_2$; 1, $x = 0.02$; 2, $x = 0.10$; 3, $x = 0.20$ (b) $\text{V}_{1-x}\text{Nb}_x\text{O}_2$; 1, $x = 0.02$; 2, $x = 0.05$.

rutile structure as evidenced by the DTA phase transition data (Fig. 1); when $x \geq 0.1$, there is no transition in the range $15^\circ\text{--}800^\circ\text{C}$. $\text{V}_{0.98}\text{Mo}_{0.02}\text{O}_2$ seems to possess a distorted rutile structure which transforms to the rutile structure at 40°C (Table 1 and Fig. 1).

In $\text{V}_{1-x}\text{Nb}_x\text{O}_2$, the T_i and $\Delta\sigma$ are both lower when $x = 0.02$ and 0.05 (Table 1 and Fig. 2b) relative to VO_2 ; the conductivities of the low-temperature phases are higher. It is interesting that T_i is about the same when $x = 0.02$ and 0.05 . The high-temperature rutile phases are semiconducting with E_a in the range of $0.3\text{--}0.4$ eV. When $x = 0.05$, we have noticed a change of slope in the $\sigma\text{--}T$ curve at $\sim 7^\circ\text{C}$ in addition to the transition at 34°C . This is in accord with the DTA curve (Fig. 1), which shows two phase transitions, the one at $\sim 7^\circ\text{C}$ being associated with much lower ΔH . When $x = 0.10$, the rutile structure is stabilized and we do not see any conductivity anomaly corresponding to that of VO_2 or NbO_2 consistent with the DTA results (Fig. 1); instead, it appears to be semiconducting with a low E_a of 0.06 eV in $20^\circ\text{--}90^\circ\text{C}$ range.

The solid solution with 2% MoO_2 shows a higher σ of the low-temperature phase compared to VO_2 , lower T_i and $\Delta\sigma$. Here again, the high-temperature phase seems to show semiconducting behavior with an E_a of 0.4 eV. The 5% MoO_2 sample appears to be metallic just as expected [20].

REFERENCES

1. MORIN F. J., *Phys. Rev. Lett.* **3**, 34 (1959).
2. MacCHESNEY J. B. and GUGGENHEIM H. J., *J. Phys. Chem. Solids* **30**, 225 (1969) and the references cited therein.
3. KOSUGE K., *J. phys. Soc. Japan* **22**, 551 (1967).
4. ADLER D., *Rev. mod. Phys.*, **40**, 714 (1968).
5. BERGLUND C. N. and GUGGENHEIM H. J., *Phys. Rev.* **185**, 1022 (1969).
6. RAO C. N. R., and SUBBA RAO G. V., *Phys. Status Solidi (a)* **1**, 597 (1970).
7. RÜDORFF W., WALTER G. and STADLER J., *Z. anorg. allgem. Chem.* **297**, 1 (1958).
8. ARIYA S. M. and GROSSMAN G., *Soviet Phys. solid State*, **2**, 1166 (1960).
9. KRISTENSEN I. K., *J. appl. Phys.* **39**, 5341 (1968).
10. RÜDORFF W. and MARKLIN J., *Z. anorg. allgem. Chem.* **334**, 142 (1964).
11. LOEHMAN R. E., RAO C. N. R., SMITH C. E. and HONIG J. M., *J. Sci. Industr. Res. (India)* **28**, 13 (1969).
12. RAO K. J. and RAO C. N. R., *J. Mat. Sci.* **1**, 238 (1966).
13. OHASHI T. and WATANABE A., *J. Am. ceram. Soc.* **49**, 519 (1966).
14. SAKATA K. and SAKATA T., *Japan J. appl. Phys.* **6**, 112 (1967).
15. FUTAKI H. and AOKI M., *Japan J. appl. Phys.* **8**, 1008 (1969).
16. GOODENOUGH J. B., *Phys. Rev.* **117**, 1442 (1960).
17. ADLER D. and BROOKS H., *Phys. Rev.*, **155**, 826 (1967).
18. GOODENOUGH J. B., *Czech. J. Phys.* **17B**, 304 (1967).
19. SAKATA T., SAKATA K. and NISHIDA I., *Phys. Status Solidi*, **20**, K155 (1967); SAKATA K., *J. phys. Soc. Japan* **26**, 582 (1969).
20. GOODENOUGH J. B., in *Transition Metal Compounds*, Gordon and Breach, New York (1964).

ELECTRON SCATTERING AND TRANSPORT PHENOMENA IN *n*-InSb

W. ZAWADZKI

Institute of Electron Technology, Polish Academy of Sciences, Warsaw, Poland

and

W. SZYMAŃSKA

Institute of Physics, Polish Academy of Sciences, Warsaw, Poland

(Received 15 June 1970)

Abstract—Theory of electron transport phenomena in the relaxation time approximation, treating consistently the nonparabolic band structure of InSb, has been compared with available experimental data for various effects. Mixing of *p*-like components into the conduction band wave function in the nonparabolic region of energies has been incorporated into the theory of electron scattering by charged centers, polar optical phonons and acoustic phonons. In the limit of high degeneracy the analytical formulas for the mixed scattering mode have been obtained. Numerical values for the Hall mobility at 77, 300, 500 and 773°K, the thermoelectric power, and the longitudinal and transverse Nernst-Ettingshausen effects at room temperature for electron concentrations up to $1 \times 10^{19} \text{ cm}^{-3}$ have been computed for mixed scattering and compared with experimental data of various authors to obtain the best over-all fit, treating a controversial value of the deformation potential as an adjustable parameter. It has been found that all the effects, together with the free-carrier optical absorption, can be satisfactorily described with the deformation potential constant of 14.6 eV. Using this value it has been demonstrated that at room temperature the electron scattering at high electron concentrations is dominated by charged impurity and acoustic phonon modes, whereas at lower concentrations all three scattering mechanisms should be taken into account. The presented procedure can be readily applied to other III-V compounds.

1. INTRODUCTION AND HISTORICAL SURVEY

SINCE the nonparabolic shape of the conduction band in InSb had been derived by Kane [1], it was recognized that the band nonparabolicity must be taken into account when interpreting the electron transport phenomena in this material. Kane showed that, due to the narrow energy gap between the conduction and the valence bands, the energy-wave vector dependences in the conduction and light-hole bands differ appreciably from the simplest parabolic relation $\epsilon = \hbar^2 k^2 / 2m^*$. The second consequence of the strong coupling between the bands is the mixing of *p*-like components into the total wave function of a conduction electron in the region of band's non-parabolicity. Kane's $\epsilon(k)$ relation for electrons in InSb has been confirmed by many experimental data in wide range of energies, the earliest

being those of Spitzer and Fan[2] and Smith *et al.*[3]. On the other hand the predominant scattering modes at various temperatures and impurity concentrations have been until recently a matter of controversy. It seems of interest to review briefly the previous work devoted to this problem.

Scattering processes

In the range of validity of the relaxation time approximation, i.e. for elastic collisions, the theory of scattering has to take into account the influence of band structure on the relaxation time behavior. As is well known, the relaxation time for electrons in a spherical energy band can be expressed in the form

$$1/\tau(\epsilon) \sim \rho(\epsilon)W(\epsilon) \quad (1.1)$$

where $\rho(\epsilon)$ is the density of states in k space for the surface $\epsilon = \text{const.}$, and $W(\epsilon)$ is the scattering probability for a given energy surface integrated over the angles. It is easy to show that for a spherical band the density of states per unit energy is

$$\rho(\epsilon) = (1/\pi^2)k^2(dk/d\epsilon). \quad (1.2)$$

For a parabolic band this becomes $\rho(\epsilon) = (1/2\pi^2)(2m^*/\hbar^2)^{3/2}\epsilon^{1/2}$. Since in this case also the scattering probability can be shown to be a power function of energy, the resulting relaxation time is of the form $\tau_p = \tau_{p0}\epsilon^p$, with $p = \frac{3}{2}$ for scattering by charged centers (i.e. ionized impurities and heavy holes),* $p = \frac{1}{2}$ for polar optical phonons and $p = -\frac{1}{2}$ for acoustic phonons.

For a non-parabolic band neither k nor $d\epsilon/dk$ are power functions of energy, so that the relaxation time also can not be expressed in this simple form. A number of authors calculating relaxation times for various modes took into account the non-parabolic density of states, computing, however, the scattering probability $W(\epsilon)$ like in the case of a parabolic band. In other words they used the proper $\epsilon(k)$ dependence but took the electron wave functions which apply only to the parabolic region of the band. Thus, for polar optical phonons (OP) it was done by Howarth and Sondheimer[4], for acoustic scattering (AC) by Radcliffe[5], for charged impurity (CC) and non-polar optical modes by Barrie[6]. The screening length for electron-hole collisions in a non-parabolic band was calculated by Ehrenreich[7] and for ionized impurity scattering by Kolodziejczak[8]. These results were summarized by Kolodziejczak and Sosnowski[9] (hereafter referred to as KS) who observed that, taking into account the energy dependence of the effective mass, the mobilities for the main modes can be expressed by

the general formula,

$$u_r = u_{r0}(d\epsilon/dk)^2 k^r \quad (1.3)$$

where the values of u_{r0} and r are to be specified for a given mode: $r = +1$ for scattering by charged centers, $r = -1$ for polar optical phonons, and $r = -3$ for acoustic phonons. The above expression for the mobilities has been widely used in many interpretations of experimental results. It proved very convenient, since on its basis one could express all integrals occurring in the transport theory by the generalized Fermi-Dirac integrals ${}^nL_k^m$ [10, 11].

However, a complete and consistent theory of electron scattering for non-parabolic bands should take into account not only the actual $\epsilon(k)$ relation in the band, but also the wave functions appropriate for the band region with pronounced non-parabolicity. In other words, the non-standard structure of energy band influences not only $\rho(\epsilon)$ but also $W(\epsilon)$. This was first observed by Ehrenreich[7, 12], who used the complete wave functions when solving the Boltzmann equation by the variational procedure[12]. Also Haga and Kimura[13] used the correct wave functions calculating the scattering processes for the free-carrier optical absorption in InSb. Recently Korenbliit and Sherstobitov[14] calculated relaxation times for the main scattering modes taking into account the non-parabolic structure of energy bands in InSb-like crystals. Unfortunately this work contains numerous mistakes and the problem has been redone by the present authors[15]. In the next section we present the main assumptions and results of this theory.

Formula (1.3) contains one more oversimplification which has been widely applied until recently. Namely, for scattering by charged centers the complete energy dependence of mobility contains, due to screening effects, an additional function of energy, which is usually considered constant and as such incorporated into u_{r0} . However, as

*Assuming, as it has been usually done, that an additional energy dependence due to screening $F_{cc} = \text{const.}$, see equation (3.7).

shown recently by Szymanska and Ginter[16], this additional energy dependence gives important corrections, particularly to the thermoelectric effects, and it must be considered explicitly in the theory.

Hall mobility

All authors agree that in heavily doped samples at low temperatures the electrons are scattered mainly by ionized impurity atoms. A theoretical analysis of mobility in this range has been carried out by Kolodziejczak[8] who, using essentially formula (1.3) and taking into account compensation effects, found a good agreement between the theory for CC scattering and experimental data. Ehrenreich [7, 12] in the first detailed analysis of mobility in intrinsic samples concluded that at room temperature polar optical phonons constitute the most effective scattering mode. Using the values $\kappa(\infty) = 16$ for the dielectric constant in electron-hole scattering, $0.13 < e^*/e < 0.20$ for the effective ionic charge and $\theta = 290^\circ\text{K}$ for the Einstein temperature in optical phonon mode, Ehrenreich was able to give a fairly good theoretical account of the temperature variation of mobility in intrinsic samples, as measured by Hrostowski *et al.*[17]. For the deduced value of the deformation potential $\epsilon_d = 7.2\text{ eV}$ Ehrenreich concluded that scattering by acoustic phonons gives negligible contribution to the observed mobility. This was confirmed by Hilsum and Barrie[18]. Further support of this conclusion came from Galavanov and coworkers[19] who were able to describe their experimental mobility data for various temperatures and impurity concentrations using KS treatment with the above values of material constants and assuming combined CC and OP scattering. They observed, however, that at higher temperatures and impurity concentrations AC scattering should also come into play. This was further developed by Filipchenko and Nasledov[20] who combined all three scattering modes to account for the temperature dependence of mobility in an impure sample.

On the other hand Haga and Kimura[13], interpreting free-carrier absorption data of Kessler and Sutter[21], concluded that electrons are scattered mainly by acoustic phonons and deduced the deformation potential value of 30 eV. This conclusion was supported by another optical work of Kessler and Sutter [22]. Other methods also gave quite different values of the deformation potential. Puri[23] from the phonon-drag thermoelectric power in a magnetic field obtained $\epsilon_d = 8.25\text{ eV}$, Nill and McWhorter[24] from magneto-acoustic experiments -4.5 eV . In newer estimations Whalen and Westgate[25] from a direct measurement of the electron relaxation time obtained $\epsilon_d = 16.2\text{ eV}$, Tanaka *et al.*[26] from acousto-conductive effect $\epsilon_d = 16\text{ eV}$, and Szymanska and Maneval[27] from hot electron experiments $\epsilon_d = 13\text{ eV}$.

Thermoelectric power

Early measurements[28–30] were interpreted with the use of relations for a parabolic band and employed to determine the effective mass in the material. Values obtained this way showed an increase with growing electron concentration indicating a non-parabolic shape of the band. In such a procedure, however, the non-parabolicity is introduced *ex post*, and only via the effective mass. Ehrenreich[12], using Kane's band model in the variational procedure, described flawlessly the temperature dependence of the thermoelectric power, as measured by Weiss[31] in intrinsic material. As we have mentioned before, Ehrenreich's treatment taking into account only the polar optical and electron-hole scattering is valid only for pure samples. KS[9] working in the relaxation time approximation developed a procedure which was subsequently used in many investigations. Using equation (1.3) for the mobilities they computed numerically the thermoelectric power curves α_r for single scattering modes at $T = 300^\circ\text{K}$ as functions of electron concentration and compared them with experimental data of various authors. It turned out that the

experimental points lie between the theoretical lines for CC and OP scattering modes, the AC line being far away. This was interpreted as an extension of Ehrenreich's conclusion about the predominant role of OP + CC scattering at room temperature to higher impurity concentrations. (For pure samples it was once again confirmed by Wagini[32], who used KS procedure for temperature dependence). There was, however, one feature that did not fit into this picture. Namely, at the highest impurity concentrations, due to the predominant role of impurity scattering as compared to the optical mode, the experimental points should fit almost exactly to the theoretical CC curve. Instead, they lie rather close to the OP curve. In terms of the index r appearing in formula (1.3) this means that for high impurity concentrations the experimental points should correspond to the theoretical values for $r = +1$, whereas they correspond to the values of $-1 < r < 0$. The experimental results were subsequently confirmed by Byszewski *et al.* [33], and also by Filipchenko and Nasledov [20] who emphasized the role of AC scattering at higher electron concentrations. However, combining all three scattering modes according to KS theory and using material constants according to Ehrenreich, they showed that at high concentrations the mixed mode curve runs very close to the CC curve. In other words the effective scattering index $R = r_{cc} = +1$, whereas the experimental points lie clearly lower, corresponding almost to $R \approx -1$. A similar thing is observed in HgSe[34], HgTe[35] and CdSnAs₂[36].

It was this discrepancy between the theory and experiment which made us undertake the present investigation.

Longitudinal and transverse Nernst-Ettingshausen effects

The transverse Nernst-Ettingshausen effect in weak magnetic fields has been always an important criterion in the controversy on scattering processes in InSb as it is considered to be very sensitive to the nature of electron

collisions. This is due to the fact that for a parabolic band, both in the non-degenerate and strongly degenerate limits, the effect for a single scattering mode is proportional to the scattering index p . Thus the *sign* of the effect can, in principle, distinguish between various kinds of scattering; for AC mode, $p = \frac{1}{2}$, the effect should be positive, for OP mode, $p = +\frac{1}{2}$, it should be negative, and for CC scattering, $p = +\frac{3}{2}$, the effect should have large negative values. The same may be said about the longitudinal Nernst-Ettingshausen effect, by which we understand the difference between the thermoelectric powers in a very strong and a vanishing transverse magnetic field.

An early measurement of Zhuze and Tsidilkovskii[37], who found in a pure sample ($n = 7.3 \times 10^{16} \text{ cm}^{-3}$) the sign of the transverse effect changing from negative to positive with increasing temperature, was interpreted as an indication that at low temperatures the electrons are scattered predominantly by CC and at higher ones by AC. This was followed by a similar interpretation of Emeljanenko *et al.* [38]. Rodot[39], who first clearly recognized that one can obtain similar information employing the transverse effect at low magnetic fields and the longitudinal effect at high fields, investigated the range of low electron concentrations (up to $n = 2.4 \times 10^{17} \text{ cm}^{-3}$) and found at room temperature the negative sign of both effects. According to formulas for a parabolic band his measurements correspond to small positive values of the scattering index p , and they were taken as a confirmation of Ehrenreich's conclusion that in pure samples at room temperature the electrons are scattered mainly by OP mode. Subsequently, however, KS showed theoretically for the limit of high degeneracy that at higher electron concentrations the effect for the single OP mode ($r = -1$ in equation (1.3)) can change sign and become positive due to the pronounced non-parabolicity of the band. They concluded that the observed change of sign from negative to positive with growing

impurity concentration at room temperature, as observed in [38], is consistent with the theory for OP scattering in the entire concentration range. On the other hand Guseva and Tsidilkovskii [40] carried out numerical integration for arbitrary degeneracy and showed that the N - E effect for OP mode of scattering is positive in the entire concentration range, due to band's non-parabolicity. A substantial progress in this matter was made by Nasledov and Filipchenko [41] who, using KS theory and carrying numerical integrations for the mixed mode of all three scattering processes, were able to give a fairly good theoretical account of their experimental data. They used the values of material constants according to Ehrenreich and observed that, even upon using his value of $\epsilon_d = 7.2$ eV for the deformation potential constant, the AC scattering is mainly responsible for the positive sign of the effect at high electron concentrations (or temperatures), since the combined CC + OP mode gives the negative sign of the effect. One should, however, bear in mind that their procedure used equation (1.3) for the mobilities, which, as we shall show later, leads to considerable overestimation of the role of CC scattering in thermoelectric effects.

2. GENERAL FORMALISM

Now we shall summarize general expressions for the galvanomagnetic, thermoelectric and thermomagnetic effects of interest, as derived for a spherical energy band with arbitrary $\epsilon(k)$ dependence by Kolodziejczak [42]. Expressions for other thermomagnetic, diffusive and optical effects in the same formalism can be found in Ref. [43-45], respectively.

The effective mass which enters into the transport properties of carriers in a spherical energy band of arbitrary shape is given by

$$1/m^* = (1/\hbar^2 k) (d\epsilon/dk). \quad (2.1)$$

It can be seen that in general this mass depends on energy. The electron concentra-

tion in the band is,

$$n = (1/3\pi^2) \langle 1 \rangle \quad (2.2)$$

where, in general we define

$$\langle A \rangle = \int_0^\infty (-\partial f_0 / \partial \epsilon) A k^3(\epsilon) d\epsilon. \quad (2.3)$$

Here

$$f_0 = 1 / [\exp(z - \eta) + 1] \quad (2.4)$$

is the Fermi-Dirac distribution function, with

$$z = \epsilon/k_0 T \quad \eta = \zeta/k_0 T \quad (2.5)$$

denoting the reduced energy and reduced Fermi level, respectively. k_0 is the Boltzmann constant and T the absolute temperature.

The average values are defined in general as,

$$\bar{A} = \langle A \rangle / \langle 1 \rangle. \quad (2.6)$$

The mobility of a carrier is,

$$u = q\tau/m^* \quad (2.7)$$

where τ is the relaxation time, and q the electric charge: $q = -e$ for electrons and $+e$ for holes, with $e = |q|$ denoting the absolute value of the electron charge.

The electric conductivity in a single band,

$$\sigma = qn\bar{u} \quad (2.8)$$

where \bar{u} denotes the average mobility according to equation (2.6).

The Hall constant at low magnetic fields,

$$R_H = a_r/qnc \quad (2.9)$$

where

$$a_r = \langle u^2 \rangle \langle 1 \rangle / \langle u \rangle^2 = \bar{u}^2 / \bar{u}^2 \quad (2.10)$$

is the Hall scattering factor. We have

$$R_H \sigma = a_r \bar{u} / c. \quad (2.11)$$

The thermoelectric power in a vanishing magnetic field,

$$\alpha(0) = \frac{k_0}{q} \left(\frac{\langle zu \rangle}{\langle u \rangle} - \eta \right). \quad (2.12)$$

The thermoelectric power in a strong transverse magnetic field,

$$\alpha(\infty) = \frac{k_0}{q} \left(\frac{\langle z \rangle}{\langle 1 \rangle} - \eta \right). \quad (2.13)$$

The longitudinal Nernst-Ettingshausen effect in a strong magnetic field,

$$\Delta\alpha = \alpha(\infty) - \alpha(0) = \frac{k_0}{q} \left(\frac{\langle z \rangle}{\langle 1 \rangle} - \frac{\langle zu \rangle}{\langle u \rangle} \right). \quad (2.14)$$

The transverse Nernst-Ettingshausen coefficient, defined for weak magnetic fields as $\mathbf{E} = P_{N-E} \cdot \mathbf{H} \times \text{grad } T$, is*

$$P_{N-E} = -\frac{k_0}{q} a_r \frac{\bar{u}}{c} \left(\frac{\langle zu^2 \rangle}{\langle u^2 \rangle} - \frac{\langle zu \rangle}{\langle u \rangle} \right). \quad (2.15)$$

In order to calculate all the above quantities one has to know explicitly $\epsilon(k)$ dependence in the band (or the inverse function $k(\epsilon)$), and the energy dependence of mobility.

In the present paper we shall use a simplified version of Kane's band model, in which the energy of the spin-orbit interaction Δ is assumed to be much larger than the energy gap ϵ_g . (The validity of this approximation for InSb is discussed in Section 5). In this case the dependence between the energy and the absolute value of the wave vector in the conduction band is given by the following relation (we set the zero of energy at the bottom of the band, i.e. at $k = 0$),

$$\hbar^2 k^2 / 2m_0^* = \epsilon(1 + \epsilon/\epsilon_g) \quad (2.16)$$

where m_0^* is the effective mass at the bottom

of the band. Hence, using equation (2.1), the effective mass for energy ϵ above the bottom of the band is

$$m^* = m_0^* (1 + 2\epsilon/\epsilon_g). \quad (2.17)$$

The concentration of free carriers in the band, given by equation (2.2), becomes

$$n = \frac{1}{3\pi^2} \left(\frac{2m_0^* k_0 T}{\hbar^2} \right)^{3/2} \int_0^\infty \left(-\frac{\partial f_0}{\partial \epsilon} \right) (z + \beta z^2)^{3/2} dz \quad (2.18)$$

where

$$\beta = k_0 T / \epsilon_g. \quad (2.19)$$

3. SCATTERING PROCESSES

We shall now summarize the results of the present authors[15] concerning the relaxation times for scattering of electrons by charged centers, polar optical phonons and acoustic phonons. The theory has been carried out for the real energy band structure of InSb-like crystals taking into account mixing of valence p -like components into the total wave functions of conduction electrons. Consistently with our approach to InSb we shall use simplified formulas putting $\Delta \gg \epsilon_g$.

Scattering by charged centers (CC) -

It has been calculated for the screened Coulomb potential of Brooks and Herring[46] following essentially the procedure presented in Ref. [14]. Since in InSb holes are much heavier than electrons, it has been the common practice to treat the scattering of electrons by heavy holes in analogy to that by immobile ionized impurities. In principle the Coulomb interaction in the first case is described by the high frequency dielectric constant $\kappa(\infty)$ and in the second by the low frequency constant $\kappa(0)$, but in InSb both values differ only slightly. Thus we shall apply the usual procedure noticing that the number of scattering charged centers, i.e. ionized impurities and holes, is equal to the number of

*The sign of the effect is defined according to tradition to agree with experimental results, see Fig. 7.

free electrons in the conduction band,

$$N_i + p = n.$$

Final result for the relaxation time is

$$\tau_{cc} = \frac{\kappa^2 \hbar}{2\pi e^4 n} \frac{1}{F_{cc}} \frac{d\epsilon}{dk} k^2. \quad (3.1)$$

Function F_{cc} is to a good approximation given by

$$F_{cc}(\xi_0, \xi_1) = \left[1 + \frac{4\xi_1}{\xi_0} \left(1 - \frac{\xi_1}{8} \right) \right] \ln(\xi_0 + 1) - \frac{\xi_0}{\xi_0 + 1} - 2\xi_1 \left(1 - \frac{5}{16} \xi_1 \right) \quad (3.2)$$

with

$$\xi_0 = \left(\frac{2k}{\lambda} \right)^2 \quad \text{and} \quad \xi_1 = \frac{2\epsilon/\epsilon_g}{1 + 2\epsilon/\epsilon_g} \quad (3.3)$$

where $1/\lambda$ is the screening length. According to Kolodziejczak [8]

$$\xi_0 = \frac{2\pi\kappa\hbar}{e^2(2m_0^*k_0T)^{1/2}} \frac{\epsilon(1 + \epsilon/\epsilon_g)}{{}_0L_1^{1/2}(\eta, \beta)} \quad (3.4)$$

with

$${}_0L_1^{1/2}(\eta, \beta) = \int_0^\infty (-\partial f_0/\partial z) (z + \beta z^2)^{1/2} \times (1 + 2\beta z) dz. \quad (3.5)$$

The reduced Fermi level η is to be determined from the carrier concentration according to equation (2.8). Using equations (2.1) and (2.7) we can write the mobility for the scattering by charged centers in the form

$$\mu_{cc} = \frac{\kappa^2}{2\pi e^3 \hbar n} \frac{1}{F_{cc}} \left(\frac{d\epsilon}{dk} \right)^2 k^1. \quad (3.6)$$

In order to reduce the above formula to the case of a parabolic band one has to put $\epsilon \ll \epsilon_g$. This gives $\xi_1 \rightarrow 0$, and

$$F_{cc}^{par}(\xi_0) = \ln(\xi_0 + 1) - \xi_0/(\xi_0 + 1) \quad (3.7)$$

in agreement with the well known expression.

As we have mentioned before, it has been the general practice to regard the function F_{cc} as a constant, taking it out of the integral sign when calculating various average values of mobility in galvanomagnetic and thermomagnetic effects. We want to emphasize here once again that this procedure can lead to serious errors, as we shall show later.

Scattering by polar optical phonons (OP)

The relaxation time is calculated assuming all optical longitudinal phonons to have the same energy $\hbar\omega_L$. For temperatures at which the scattering may be regarded as elastic, i.e. for $k_0T > \hbar\omega_L$ the relaxation time is obtained in the form,*

$$\tau_{op} = \frac{1}{8\pi} \frac{Mv_a\hbar\omega_L^2}{(e^*)^2k_0T} \frac{1}{F_{op}} \frac{d\epsilon}{dk} \quad (3.8)$$

where M — the reduced mass of the ions, v_a — the volume of the elementary cell, ω_L — the optical frequency of longitudinal oscillations and e^* — the effective ionic charge. The function F_{op} is

$$F_{op} = 1 - \frac{2\epsilon/\epsilon_g}{1 + 2\epsilon/\epsilon_g} + \frac{3}{8} \left(\frac{2\epsilon/\epsilon_g}{1 + 2\epsilon/\epsilon_g} \right)^2. \quad (3.9)$$

Hence, the mobility for optical polar scattering can be written as

$$\mu_{op} = \frac{1}{8\pi} \frac{Mv_a(k_0\theta_L)^2}{\hbar^3e(e^*)^2k_0T} \frac{1}{F_{op}} \left(\frac{d\epsilon}{dk} \right)^2 k^{-1} \quad (3.10)$$

where θ_L is the Einstein temperature, defined as $k_0\theta_L = \hbar\omega_L$. The transition to the case of a parabolic band can again be made by putting $\epsilon < \epsilon_g$, which gives $F_{op} \equiv 1$.

Scattering by acoustic phonons (AC)

The deformation potential scattering in the narrow sense, i.e. scattering due to short range

*This result agrees with that of Korenblit and Sherstobitov.

component of the potential has been considered in the deformed ion model. It turns out that, due to the p -like components of the total electronic wave functions, also transverse phonons give rise to scattering, particularly at higher electron energies. Taking into account both spin conserving and spin-flip transitions the final result for the longitudinal acoustic mode is obtained in the form

$$\tau_{ac}^L = \frac{\pi \hbar \rho u_L^2}{\epsilon_d^2 k_0 T} \frac{1}{F_{ac}^L} \frac{d\epsilon}{dk} \frac{1}{k^2} \quad (3.11)$$

where ρ —the density of the crystal, u_L —the longitudinal sound velocity in the crystal and ϵ_d —the deformation potential constant. The function F_{ac}^L is to a good approximation

$$F_{ac}^L = \left(1 - \frac{1.3\epsilon}{\epsilon_g + 2\epsilon}\right)^2. \quad (3.12)$$

It should be noted that F_{ac}^L determines the energy dependence of the matrix element which is a constant for a parabolic band. The relaxation time for the transverse phonons can be expressed in a similar form

$$\tau_{ac}^t = \frac{\pi \hbar \rho u_t^2}{\epsilon_d^2 k_0 T} \frac{1}{F_{ac}^t} \frac{d\epsilon}{dk} \frac{1}{k^2} \quad (3.13)$$

where

$$F_{ac}^t = 0.53 \frac{17}{72} \left(\frac{\epsilon}{\epsilon_g + 2\epsilon}\right)^2. \quad (3.14)$$

One can write the mobility associated with both kinds of acoustic phonons

$$u_{ac} = \frac{\pi e \rho u_L^2}{\epsilon_d^2 \hbar k_0 T} \frac{1}{F_{ac}^L} \left(\frac{d\epsilon}{dk}\right)^2 k^{-3} \quad (3.15)$$

where

$$F_{ac} = \left(1 - \frac{1.3\epsilon}{\epsilon_g + 2\epsilon}\right)^2 + \frac{u_L^2}{u_t^2} 0.53 \frac{17}{72} \left(\frac{\epsilon}{\epsilon_g + 2\epsilon}\right)^2. \quad (3.16)$$

The calculation of scattering by acoustic phonons involves integrals which could not be

calculated directly for InSb. In the final expressions (3.12) and (3.14) the approximate values of these integrals were used taken as averages between the values for atomic and empty lattice limiting approximations.

The transition to the parabolic band formula can be made putting $\epsilon \ll \epsilon_g$, which gives $F_{ac} = 1$.

General expression

We note that the above expressions for mobilities can be written in the following general form,

$$u_r = u_{r0} \frac{1}{F_r} \left(\frac{d\epsilon}{dk}\right)^2 k^r \quad (3.17)$$

where $r = +1$ for CC scattering, $r = -1$ for OP scattering and $r = -3$ for AC mode. F_r and u_{r0} for the three modes can be easily deduced from the above equations.

Thus, as compared to KS formula (1.3), we deal with the additional energy dependences introduced by F_r . It should be emphasized that for all three modes F_r increase the mobility values as compared to those given by formula (1.3), i.e. $F_{op} < 1$, $F_{ac} < 1$, and $F_{cc}^{npur} < F_{cc}^{par}$ as given by equations (3.2) and (3.7). Since F_r functions can not be expressed by power series of k or $d\epsilon/dk$, the statistical integrals involving mobility *can not be* in general represented by ${}^nL_k^m(\eta, \beta)$ functions, although they still remain the integrals with two parameters η and β .

If, which is usually the case, one has to consider simultaneously more than one mode of scattering, the total relaxation time is as usual, $1/\tau = 1/\tau_{cc} + 1/\tau_{op} + 1/\tau_{ac}$. Hence

$$u = (1/u_{cc} + 1/u_{op} + 1/u_{ac})^{-1}. \quad (3.18)$$

4. TRANSPORT PHENOMENA IN HIGHLY DEGENERATE ELECTRON GAS

Now we are going to discuss the transport phenomena in conditions of high degeneracy, i.e. for large positive values of the reduced Fermi level η . As we shall demonstrate later

the validity of expressions obtained for this case is rather limited (e.g. in InSb at room temperature they can be used only for $n > 10^{18} \text{ cm}^{-3}$). On the other hand the possibility of avoiding the numerical integrations is very attractive, since the analytical expressions, which can be obtained in this case, give a much better physical insight and are often instructive. Also the influence of band's non-parabolicity is strongest for high electron concentrations since the Fermi level probes high energies in the band. In the derivations we shall be essentially following Refs. [8] and [9] paying, however, due attention to the modified expression (3.17) for the mobilities. Moreover, we shall consider the case of the mixed scattering mode.

For large positive values of η it is possible to approximate the statistical integrals $\langle A \rangle$ of equation (2.3) using the following expansion [47]

$$\langle A \rangle = 2 \sum_{L=0}^{\infty} \left| \frac{d^{2L}C}{dz^{2L}} \right|_{z=\eta} \frac{\pi^{2L} (2^{2L-1} - 1) B_{2L}}{(2L)!} \quad (4.1)$$

where $C = Ak^3(\epsilon)$, and B_{2L} are the Bernoulli numbers. In general this expansion omits a contribution of the order of $\exp(-\eta)$. For large η values the series is quickly converging and the first two terms give a good approximation, i.e.

$$\langle A \rangle = \left[C + \frac{\pi^2}{6} \frac{d^2C}{dz^2} \right]_{z=\eta}. \quad (4.2)$$

Actually, we shall limit ourselves to the first non-vanishing approximations. For the galvanomagnetic phenomena this amounts to retaining only the first term in equation (4.2). This is equivalent to putting in equation (2.3): $\partial f_0 / \partial \epsilon = \delta(\epsilon - \zeta)$, the Dirac delta function. In physical terms this means the complete degeneracy of the electron gas.

In this approximation we obtain from equation (2.18)

$$n = \frac{1}{3\pi^2} \left(\frac{2m_0^* k_0 T}{\hbar^2} \right)^{3/2} (\eta + \beta\eta^2)^{3/2} \quad (4.3)$$

which can be solved for the Fermi energy, to give

$$\zeta \approx (\frac{1}{2}\epsilon_0) (\sqrt{\Delta} - 1) \quad (4.4)$$

where

$$\Delta = 1 + 2\pi^2 (3/\pi)^{2/3} (\hbar^2/m_0^* \epsilon_0) n^{2/3}. \quad (4.5)$$

Using equation (2.17) the effective mass at the Fermi energy is obtained in the form

$$m^*(\zeta) = m_0^* \sqrt{\Delta}. \quad (4.6)$$

From equations (2.1) and (2.2) we obtain

$$de/dk = \hbar^2 k / m^* \text{ and } k = (3\pi^2 n)^{1/3}. \quad (4.7)$$

This way all the quantities at the Fermi level can be expressed by the electron concentration n . It can also be seen from definition (2.6) that in this case we have for the average values $\bar{A} = A(\zeta)$.

Thus the Hall scattering factor $a_r \equiv 1$ in this approximation. Using equation (3.6) we obtain for the mobility in case of CC scattering

$$\bar{\mu}_{cc} = \frac{3\pi}{2} \frac{\kappa^2 \hbar^3}{e^3} \frac{1}{F_{cc}(m^*)^2} \quad (4.8)$$

where in the parameters ξ_0 and ξ_1 , necessary to calculate the value of F_{cc} , we are to put $\epsilon = \zeta$ in equations (3.3) and (3.4). These quantities can be also expressed directly by n and m^* ,

$$\xi_0 = \pi^2 \left(\frac{3}{\pi} \right)^{1/3} \frac{\kappa \hbar^3}{e^2} \frac{n^{1/3}}{m^*} \quad \xi_1 = 1 - \frac{m_0^*}{m^*}. \quad (4.9)$$

Similarly, for the mobility in case of OP scattering,

$$\bar{\mu}_{op} = \frac{1}{8} \left(\frac{3}{\pi} \right)^{1/3} \frac{v_a M \hbar (k_0 \theta_L)^2}{e (e^*)^2 k_0 T} \frac{n^{1/3}}{F_{op}(m^*)^2} \quad (4.10)$$

and for AC scattering

$$\bar{\mu}_{ac} = \left(\frac{\pi}{3} \right)^{1/3} \frac{e \rho \mu_L \hbar^3}{\epsilon_d^2 k_0 T} \frac{1}{F_{ac}(m^*)^2 n^{1/3}} \quad (4.11)$$

where in F_{op} and F_{ac} , given by equation (3.9) and (3.16), we are to put $\epsilon = \zeta$.

On the basis of equation (3.18) the mobility for the mixed scattering mode in case of complete degeneracy becomes

$$\bar{u} = (1/\bar{u}_{cc} + 1/\bar{u}_{op} + 1/\bar{u}_{ac})^{-1}. \quad (4.12)$$

In order to calculate the thermoelectric effects in the region of high degeneracy we have to use two terms in expansion (4.2), since in conditions of absolute degeneracy, as described by the first term alone, all thermoelectric effects vanish identically. Thus the full formula (4.2) gives in this case the first non-vanishing approximation.

First we shall calculate the thermoelectric power $\alpha(0)$. Since, in general

$$\frac{d^2(zC)}{dz^2} = z \frac{d^2C}{dz^2} + 2 \frac{dC}{dz} \quad (4.13)$$

we obtain from equation (2.12) for electrons

$$\alpha(0) = -\frac{k_0 \pi^2}{e} \frac{1}{3} k_0 T \left(\frac{1}{C} \frac{dC}{d\epsilon} \right)_{\epsilon=\zeta} \quad (4.14)$$

where, in our case, $C = uk^3$. This yields

$$\alpha(0) = -\frac{k_0 \pi^2}{e} \frac{1}{3} k_0 T \left(\frac{1}{u} \frac{du}{d\epsilon} + \frac{3}{k} \frac{dk}{d\epsilon} \right)_{\epsilon=\zeta}. \quad (4.15)$$

In order to proceed further we have to specify the mobility as a function of energy. First, we shall consider a single scattering mode. Using the general expression (3.17), we have for any single mode

$$\frac{du_r}{d\epsilon} = u_{r0} \frac{1}{F_r} \frac{d\epsilon}{dk} k^{r-1} \left[r - \frac{k}{F_r} \frac{dF_r}{dk} + 2k \left(\frac{d\epsilon}{dk} \right)^{-1} \frac{d^2\epsilon}{dk^2} \right]. \quad (4.16)$$

We introduce a parameter γ by means of relation

$$\begin{aligned} \gamma &= \frac{k^3}{(1/k)(d\epsilon/dk)} \frac{d[(1/k)(d\epsilon/dk)]}{d[k^3]} \\ &= \frac{1}{3} \left[1 - k \left(\frac{d\epsilon}{dk} \right)^{-1} \frac{d^2\epsilon}{dk^2} \right] \end{aligned} \quad (4.17)$$

and observe that, upon using equation (4.7),

$$\gamma = (n/m^*) (dm^*/dn). \quad (4.18)$$

With the use of equations (3.17), (4.16) and (4.17), we have

$$\frac{1}{u_r} \frac{du_r}{d\epsilon} = \frac{dk}{d\epsilon} \frac{1}{k} \left[r - \frac{k}{F_r} \frac{dF_r}{dk} + 2 - 6\gamma \right]. \quad (4.19)$$

Taking into account equation (4.7) we obtain finally the thermoelectric power for a single scattering mode in highly degenerate conditions

$$\alpha_r(0) = -\frac{1}{3} \left(\frac{\pi}{3} \right)^{2/3} \frac{k_0^2 T}{e \hbar^2} \frac{m^*}{n^{2/3}} (r' + 5 - 6\gamma) \quad (4.20)$$

where

$$r' = r - (k/F_r) (dF_r/dk) \quad (4.21)$$

denotes the effective scattering index for the scattering mode in question.

Formula (4.20) is similar to that obtained by KS, with the important difference that, due to the additional energy dependence F_r in equation (3.17) as compared to equation (1.3), we deal with the effective scattering factor r' instead of r .

Now we shall consider the combined mode of scattering. Suppose we deal with two different modes represented by u_1 and u_2 , whose energy dependences can be expressed by equation (3.17). The total mobility is given by equation (3.18). Hence

$$u = (1/u_1 + 1/u_2)^{-1}. \quad (4.22)$$

We are to substitute this mobility into general formula (4.15). Since, using equation (4.19)

we obtain

$$\frac{1}{u} \frac{du}{d\epsilon} = u \left(\frac{1}{u_1^2} \frac{du_1}{d\epsilon} + \frac{1}{u_2^2} \frac{du_2}{d\epsilon} \right) = u \frac{dk}{d\epsilon} \frac{1}{k} \left[\frac{1}{u_1} (r'_1 + 2 - 6\gamma) + \frac{1}{u_2} (r'_2 + 2 - 6\gamma) \right] \quad (4.23)$$

the general formula for the thermoelectric power of highly degenerate electron gas is

$$\alpha(0) = -\frac{1}{3} \left(\frac{\pi}{3} \right)^{2/3} \frac{k_0^2 T m^*}{e \hbar^2 n^{2/3}} (R + 5 - 6\gamma) \quad (4.24)$$

where

$$R = \frac{r'_{cc}/\bar{u}_{cc} + r'_{op}/\bar{u}_{op} + r'_{ac}/\bar{u}_{ac}}{1/\bar{u}_{cc} + 1/\bar{u}_{op} + 1/\bar{u}_{ac}} \quad (4.25)$$

is the effective scattering index for the combined mode. Here we have generalized the procedure outlined in equations (4.22) and (4.23) to take into account three scattering modes. Also the denominator and numerator of equation (4.25) has been divided by (1) in order to express R in terms of the phenomenological average mobilities. It can be easily seen that if a mobility for one scattering mode is much lower than the other two, the effective index R reduces to r' for this mode.

As follows from the derivation, all quantities in the above relations, i.e. m^* , γ , r'_i and \bar{u}_i , are to be taken at the Fermi energy or expressed directly by the electron concentration corresponding to its value. Thus the parameter γ on the basis of equations (4.18), (4.5) and (4.6) becomes

$$\gamma = (\Delta - 1)/3\Delta. \quad (4.26)$$

It changes from $\gamma = 0$ at low electron concentrations n to $\gamma = \frac{1}{3}$ at high n .

Applying expansion (4.2) and equation (4.13) to the thermoelectric power in a strong magnetic field $\alpha(\infty)$, as given by equation (2.13), we obtain for electrons

$$\alpha(\infty) = \pi^2 \frac{k_0 T}{q} \left(\frac{1}{k} \frac{d\epsilon}{dk} \right)_t = - \left(\frac{\pi}{3} \right)^{2/3} \frac{k_0^2 T m^*}{e \hbar^2 n^{2/3}} \quad (4.27)$$

This is a very simple result, depending neither on r nor γ . The non-parabolicity of the band enters here only through $m^*(n)$. This fact has been commonly employed to determine the $\epsilon(k)$ dependence in many energy bands.

Using equations (4.24) and (4.27) we can calculate directly the longitudinal Nernst-Ettingshausen effect,

$$\Delta\alpha = \alpha(\infty) - \alpha(0) = \frac{1}{3} \left(\frac{\pi}{3} \right)^{2/3} \frac{k_0^2 T m^*}{e \hbar^2 n^{2/3}} (R + 2 - 6\gamma). \quad (4.28)$$

Finally, we can use expansion (4.2) to calculate the transverse Nernst-Ettingshausen effect, as given in equation (2.15). We have

$$P_{N-E} = - \frac{\pi^2 k_0^2 T \bar{u}}{3 q c} \left(\frac{1}{u} \frac{du}{d\epsilon} \right)_t \quad (4.29)$$

and now the procedure used in the derivation of the thermoelectric power can be applied again, to give for electrons

$$P_{N-E} = - \frac{1}{3} \left(\frac{\pi}{3} \right)^{2/3} \frac{|\bar{u}|}{c} \frac{k_0^2 T m^*}{e \hbar^2 n^{2/3}} (R + 2 - 6\gamma). \quad (4.30)$$

Comparing expressions $\Delta\alpha$ and P it is easy to see that the following relation occurs

$$P_{N-E} = - |\bar{u}/c| \Delta\alpha \quad (4.31)$$

or, putting it in more phenomenological terms

$$\begin{aligned} - \frac{P_{N-E}}{|R_H \cdot \sigma|} + \alpha(0) &= \alpha(\infty) \\ &= - \left(\frac{\pi}{3} \right)^{2/3} \frac{k_0^2 T m^*}{e \hbar^2 n^{2/3}}. \end{aligned} \quad (4.32)$$

Thus, as observed by Zhitinskaja *et al.* [48], the above combination of quantities measured experimentally at low magnetic fields provides another way to determine the effective mass value avoiding the considerations of carriers' scattering.

5. ASSUMPTIONS AND PROCEDURE

As far as the band structure is concerned we have assumed, both in equation (2.16) and the expressions for mobilities, the validity of the so called two-band model for the conduction band of InSb. This amounts to taking in Kane's model the $k \cdot p$ interaction between the s -like conduction band and the p -like valence bands and then putting $\Delta \gg \epsilon_g$, since $\Delta = 0.9$ eV. This model neglects also the small free electron term $\hbar^2 k^2 / 2m_0$ in the energy. When interpreting results of precise optical experiments the complete Kane's model is necessary[49], however in transport phenomena the simplified relation (2.16) seems to be adequate up to energies corresponding to electron concentrations of $n = 10^{19} \text{ cm}^{-3}$.

Thus, there remain two parameters describing the band: ϵ_g and m_0^* . At $T = 0^\circ\text{K}$ we have taken the commonly used value of $\epsilon_g = 0.23$ eV. As to the temperature dependence of the forbidden gap, it has been often assumed after Ehrenreich[7] that it is only the dilatation part of the temperature dependence of the gap that determines the effective mass value. This dilatation change has been deduced by Ehrenreich to be

$$(d\epsilon_g/dT)_p = -9.6 \times 10^{-5} \text{ eV/deg.} \quad (5.1)$$

On the other hand, according to theoretical analysis of Ravitch[50] the total change of the gap, due both to the dilatation and lattice vibrations, should be used in calculating the effective mass value at the bottom of the band. It should be noted that, according to low temperature optical measurements of Roberts and Quarrington[51], the total temperature change of the gap is $(d\epsilon_g/dT)_{p, \text{tot.}} = 2.9 \times 10^{-4} \text{ eV/deg.}$ Thus the shift of ϵ_g due to dilatation is only about $\frac{1}{3}$ of the total shift in InSb. There have been some experimental indications (Smith *et al.*[52]) that it is equation (5.1) which should be used to calculate the effective mass at higher temperatures. We have assumed the validity of equation (5.1) for all temperatures. Moreover, assuming that the

interband matrix element of momentum does not depend on temperature we calculate the effective mass $m_0^*(T)$ according to the relation

$$m_0^*(T) = m_0^*(0) \cdot \epsilon_g(T)/\epsilon_g(0). \quad (5.2)$$

For the low temperature value of the effective mass we took $m_0^*(0) = 0.0145 m_0$ according to the newest optical data[49]. Table 1 gives the values of $\epsilon_g(T)$, $m_0^*(T)$ and $\beta = k_0 T / \epsilon_g(T)$ used in the calculations.

Table 1. Energy gap, effective mass, $\beta = k_0 T / \epsilon_g$ and intrinsic electron concentration in InSb at various temperatures, as used in the theory

$T(^{\circ}\text{K})$	$\epsilon_g(\text{eV})$	m_0^*/m_0	β	$n_{\text{intr}}(\text{cm}^{-3})$
77	0.22	0.0139	0.03	
300	0.20	0.0126	0.13	1.8×10^{18}
500	0.18	0.0113	0.24	3.4×10^{17}
773	0.15	0.00946	0.44	1.3×10^{18}

It is clear from the above considerations that there is significant uncertainty about the values of these band parameters, especially at the higher temperatures.

All throughout the present investigation we assume validity of the relaxation time approximation in the description of transport phenomena. As is well known, this approximation holds only for elastic or nearly elastic collisions. In case of scattering by optical phonons this amounts to restriction $T > \theta_L$, where θ_L is the Einstein temperature for the longitudinal optical phonons in question. Since $\theta_L = 283^\circ\text{K}$ we use the relaxation time for OP mode in calculations for 300, 500 and 773°K, and assume no OP scattering at 77°K. In our treatment we also neglect the electron-electron collisions. Bate *et al.*[53] showed that e-e scattering can affect the mobility at liquid nitrogen temperature in pure samples, i.e. outside the region of our main interest.

In order to calculate the mobility due to CC scattering according to equation (3.6) it is

necessary to know the low frequency dielectric constant $\kappa(0)$. The value of $\kappa(0) = 17.5$ was taken, in agreement with optical measurements of Spitzer and Fan[2] and Sanderson[54]. It should be mentioned (see [16]) that at the highest impurity concentrations the formal criteria for the validity of Dingle's model of CC scattering[55], on which the calculation is based, are not fully satisfied.

Computing the mobility due to OP scattering we took the reduced mass of ions $M = 0.99 \times 10^{-22}$ g, the volume of the unit cell $v_a = a^3/4$, where the lattice constant $a = 6.48 \times 10^{-8}$ cm. In his calculations Ehrenreich[7] used the value of $\theta_L = 290^\circ\text{K}$ corresponding to $\nu_L = 6.0 \times 10^{12} \text{ sec}^{-1}$, determined from the measurements of Yoshinaga and Oetjen[56]. Value of effective ionic charge e^* (defined according to Callen[57]) was used by Ehrenreich as an adjustable parameter in fitting experimental data for mobility, thermoelectric power and optical reflectivity in pure InSb samples, and estimated $0.13 < e^*/e < 0.20$. Taking the value of $\theta_L = 283^\circ\text{K}$, corresponding to $\nu_L = 5.91 \times 10^{12} \text{ sec}^{-1}$ as determined by Hass and Hennis[58], we used the value of e^* as one of the two adjustable parameters according to the procedure described below, and found $e^* = 0.13e$, in close agreement with Ehrenreich's values. Hass and Hennis from optical experiments obtained $e^* = 0.16e$. Thus, for scattering by charged centers and polar optical phonons we employ the values of material constants very similar to those used by Ehrenreich in his analysis of pure InSb samples.

In calculations for AC (deformation potential) scattering we used sound velocities $u_L = 3.4 \times 10^5$ cm/sec. and $u_t = 2.3 \times 10^5$ cm/sec. according to McSkimin *et al.*[59], and Slutsky and Garland[60] (Ehrenreich in his estimations used $u_L = 3.7 \times 10^5$ cm/sec.), and the crystal density $\rho = 5.77 \text{ g/cm}^3$ according to Potter[61]. As to the controversial value of the deformation potential, it was used in our procedure as the second adjustable parameter. The best overall agreement was achieved

for $\epsilon_d = 14.6 \text{ eV}$ and this value was subsequently used in all detailed calculations.

In experimental mobility data of Galavanov *et al.*[19] the authors do not quote electron concentrations in the conduction band at a given temperature but the number of impurities N_i , measured at low temperatures. Since all our plots are made as functions of the actual electron concentration in the conduction band, we have replotted the mobility data assuming that to a good approximation: $n(T) = n_{\text{intr.}}(T) + N_i$. The intrinsic concentrations $n_{\text{intr.}}(T)$, as calculated from the Hall effect measurements of Madelung and Weiss[62], are quoted in Table 1 ($n_{\text{intr.}}$ at 773°K was found by extrapolation). When determining $n_{\text{intr.}}$ from R_H it was assumed that the Hall scattering factor $a_r = 1$ at all temperatures. As we show in the next section, this is certainly a good approximation, at least at room temperature.

In actual calculations we have related the reduced Fermi level η to the electron concentration n in the band at a given temperature employing equation (2.18) and using the values of m_0^* and β according to Table 1. Then all the other integrals appearing in the theory were computed for the same values of η and this way related to the same electron concentration. In the formulas for high degeneracy it was more natural to use the electron concentration as the initial parameter.

The adjusting procedure carried out in order to determine the values of e^* and ϵ_d was performed in the following way. First, the separate integrals involved in \bar{u}_{cc} , \bar{u}_{op} and \bar{u}_{ac} at room temperature were computed according to the formulas given in Sections 2 and 3. Then the value of the total mobility was calculated using the approximate formula

$$1/\bar{u} \approx 1/\bar{u}_{cc} + 1/x\bar{u}_{op} + 1/y\bar{u}_{ac} \quad (5.3)$$

with two adjustable parameters x and y . The values of x and y were determined from the set of two equations obtained by requiring that \bar{u} at room temperature for $\eta = -1$ ($n = 1.83 \times$

10^{16} cm^{-3}) and $\eta = 15$ ($n = 8.12 \times 10^{18}$) were equal to the experimental values of mobility, as shown in Fig. 1. Then the total mobility was computed according to the exact formula

$$\bar{\mu} = \langle (1/\mu_{cc} + 1/x\mu_{op} + 1/y\mu_{ac})^{-1} \rangle / \langle 1 \rangle \quad (5.4)$$

with the same values of x and y . Moreover, the values of mobility at 500° and 773°K were computed employing the same parameters according to both formulas (5.3) and (5.4). It turned out that the exact values of mobilities were lower from the approximate ones by the following amounts;* at 300°K: for $\eta = -1$ –13 per cent and for $\eta = 17$ –2 per cent; at 500°K: for $\eta = 3$ –13 per cent and for $\eta = 11$ –5 per cent; at 773°K: for $\eta = 5$ –15 per cent and for $\eta = 7$ –10 per cent. Now one could determine better values of x and y from the approximate equation (5.3), taking in advance the values of $\bar{\mu}$ larger by the proper amount in order to arrive at the assumed exact values of mobility. It was possible to find the values of parameters giving good results at all temperatures. It turned out, however, that appreciable changes of the deformation potential value do not influence strongly the theoretical value of mobility at room temperature for $\eta = 15$. In other words, to the slightly different values of the assumed total mobility at 300°K for high electron concentrations there correspond fairly large differences in the values of ϵ_d . Also the comparison between the theoretical and experimental mobilities at higher temperatures was not discriminating enough. For this reason we have used also the reliable experimental data for the thermoelectric power and longitudinal Nernst–Ettingshausen effect at room temperature for high electron concentrations, as shown in Figs. 4 and 5, and tried to obtain an agreement between the theory and experiment for the same values of parameters. This means that the effective scattering index at high electron concentra-

tions, as given by equation (4.25), calculated for the parameters fitting the mobility data, should have the value of $R \approx -0.5$. This proved to be possible and has led us to the values of e^* and ϵ_d given above. Then all the computations of other effects were performed for these values of material constants.

Table 2 presents the values of F_r and r'_i which, together with expressions for mobilities, can be used in calculating the effective scattering index R in the high degeneracy region.

Table 2. Values of F_r and effective scattering indices, as defined by equation (4.21), for various electron concentrations at room temperature (in the high degeneracy region)

$n(\text{cm}^{-3})$	F_{cc}	r'_{cc}	F_{op}	r'_{op}	F_{ac}	r'_{ac}
1×10^{18}	1.66	0.38	0.526	-0.67	0.386	-2.41
2×10^{18}	1.63	0.35	0.490	-0.72	0.340	-2.48
5×10^{18}	1.59	0.30	0.455	-0.79	0.294	-2.58
1×10^{19}	1.57	0.26	0.436	-0.84	0.270	-2.66

6. RESULTS AND DISCUSSION

The comparison between the theory and experimental Hall mobility at room temperature is presented in Fig. 1. The experimental points of Barrie and Edmond[28] and Galavanov *et al.*[19] lie somewhat lower than those of Rupprecht *et al.*[64]. Mobility values determined from the free-carrier optical absorption[22] are also included. Accounting for a rather low accuracy of this method and an assumption of complete degeneracy, as made by the authors, which does not occur in this region of concentrations, the agreement with the Hall mobility data seems reasonable. The solid line represents theoretical mobility calculated with the use of final values of parameters ($\kappa(0) = 17.5$, $e^* = 0.13e$, $\theta_L = 283^\circ\text{K}$, $\epsilon_d = 14.6 \text{ eV}$) and the dashed lines denote theoretical values of separate mobilities $\bar{\mu}_{cc}$, $\bar{\mu}_{op}$ and $\bar{\mu}_{ac}$ calculated for the same values of material constants. The presented picture contains essentially all the information about

* It should be mentioned that Galavanov *et al.*[63] combining CC and OP modes obtained theoretically $\bar{\mu}_{\text{exact}} > \bar{\mu}_{\text{approx.}}$.

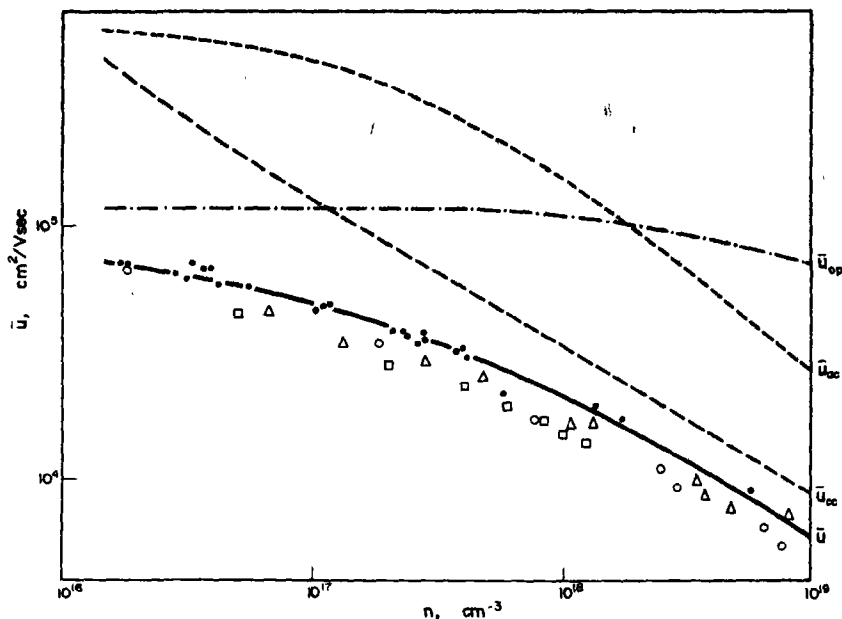


Fig. 1. Electron mobility in n -InSb vs. electron concentration at room temperature. Experimental data: \circ —Galavanov *et al.*[19], \triangle —Barrie and Edmond[28], \bullet —Rupprecht *et al.*[64], \square —Kessler and Sutter[22]. Dashed lines denote the theoretical mobilities for various single scattering modes, solid line shows the theoretical mobility for the mixed mode calculated with the same values of material constants.

the role of various electron scattering modes in InSb at room temperature. In the intrinsic material the polar OP mode, giving the lowest mobility, is the dominant scattering mechanism, with the electron-hole collisions also contributing to the total mobility. This agrees with Ehrenreich's conclusions about the predominant modes in pure samples. However, it can be noticed that, using our value of the deformation potential, the AC mobility in the intrinsic region is only 50 per cent higher than that due to CC scattering. Its contribution to the total mobility is negligible, but, as we demonstrate later, the contribution of AC phonons in this region is already felt in thermomagnetic effects. With growing electron concentration the role of CC scattering grows rapidly. However the mobility due to AC mode also decreases strongly with n , and for the electron concentrations above $2 \times 10^{18} \text{ cm}^{-3}$ this mode becomes more important than OP scattering. Thus, at the highest

electron concentrations it is the CC and AC modes which determine the scattering processes. The relative shift of importance of various modes with growing electron concentration can be qualitatively realized by comparing expressions (4.8), (4.10) and (4.11) for the mobilities in highly degenerate conditions.

It should be noted that Galavanov *et al.*[19] were able to obtain agreement between theory and experiment employing the value of $\epsilon_d = 7.2 \text{ eV}$. However, the authors were using equation (1.3) for the mobilities, whereas according to the new theory all mobility values are higher than those given by equation (1.3) due to the appearance of F_r functions. This is illustrated in Table 2 where the values of F_r are given for a few electron concentrations in the region of high degeneracy. Thus, according to the older theory ($F_{cc} = 2.42$, $F_{op} = F_{ac} = 1$) the mobility due to mixed CC and OP mode at $n = 1.1 \times 10^{19} \text{ cm}^{-3}$ is $\bar{u} = 4.4 \times 10^3 \text{ cm}^2/\text{V sec.}$, which is in agreement

with the experimental data and corresponds to the interpretation of Galavanov *et al.* However, using the new theory with the same parameters $\bar{\mu} = 7.1 \times 10^3 \text{ cm}^2/\text{V sec}$ which is clearly too high a value. Using $\epsilon_d = 7.2 \text{ eV}$ and taking into account all three modes according to the new theory one obtains $\bar{\mu} = 6.6 \times 10^3 \text{ cm}^2/\text{V sec}$ which is still too high. However, as we have said before, the theoretical value of the total mobility is not sensitive enough to the deformation potential constant to serve as the only basis for its determination. It can be seen from Fig. 1 that the mobility values obtained from optical data[22] are not reliable enough to serve for determination of the deformation potential constant $\epsilon_d = 30 \text{ eV}$ [13].

Figure 2 presents the numerical values of the Hall scattering factor a_r , defined in equation (2.10), calculated for separate CC and AC modes and for the combined CC + OP + AC mode at room temperature. We have also calculated a_{op} for OP scattering and it is to a good approximation equal to unity in the entire concentration range. It can be seen that the scattering index for the mixed mode, calculated with the use of final parameters, is equal to 1 within 2 per cent deviation in the whole concentration range. Thus at room temperature in InSb the electron Hall mobility

is to a good approximation equal to the drift mobility.

Figure 3 presents the experimental results for electron mobilities in InSb at 77, 500 and 773°K, as determined by various authors, together with the theoretical curves computed according to the above theory for the final set of parameters.

The mobility at liquid nitrogen temperature is almost completely dominated by ionized impurity scattering. The AC mode is entirely negligible in pure samples and it lowers the total values of mobility by about 10 per cent at the highest electron concentrations. As we have mentioned before, the OP mode was omitted in the calculation for 77°K since it would require the variational treatment. Due to relatively high excitation energy of the optical phonons the importance of this mode is diminished at low temperatures but at the temperature in question it is still not negligible. This is probably the main reason for the discrepancy between the theory and experiment at lower electron concentrations. Two other features may also contribute here. First, the compensation of impurities becomes appreciable in this concentration range. In the compensated samples the real number of scattering centers is larger than that indicated by the

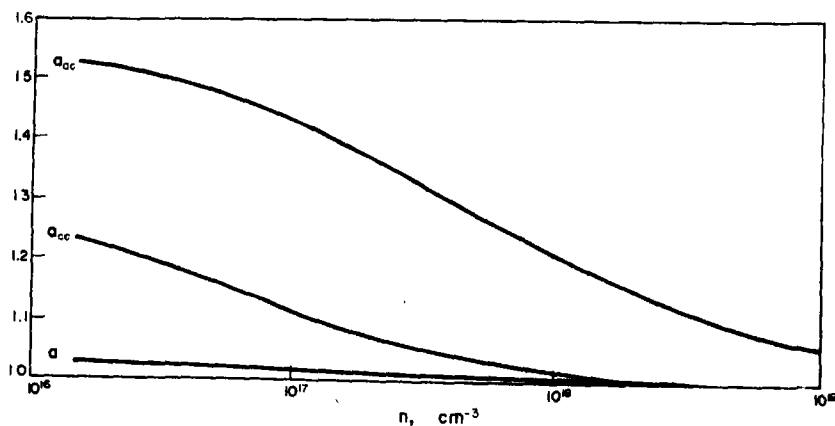


Fig. 2. Theoretical values of the Hall scattering factor in *n*-InSb vs. electron concentration at room temperature for charged center scattering (a_{cc}), acoustic phonon scattering (a_{ac}) mixed mode (a). For the optical phonon mode $a_{op} \approx 1$ in the entire concentration range.

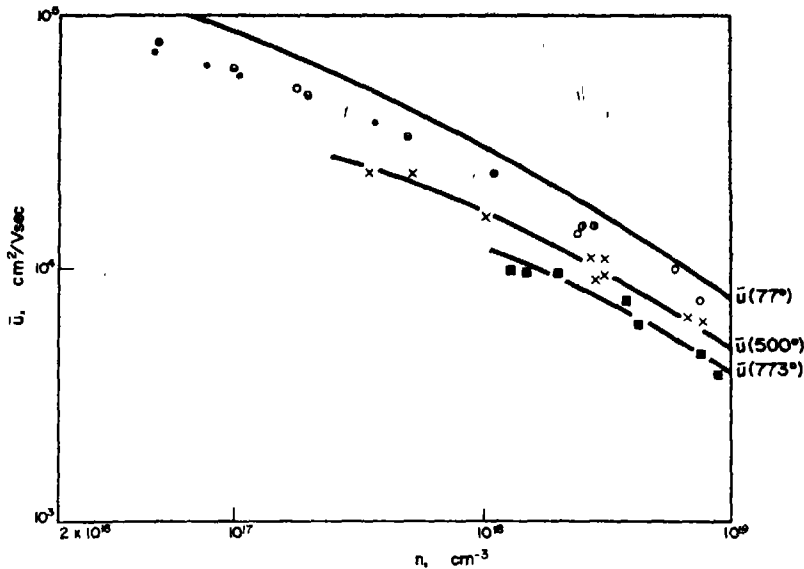


Fig. 3. Electron mobility in *n*-InSb vs. electron concentration at various temperatures. Experimental data; 77°K: ○—Galavanov *et al.*[19], ●—Rupprecht *et al.*[64], ◐—Strauss[65], ◑—Champness[66], ◒—Putley[67], a few lower experimental values are not included; 500°K: ×—Galavanov *et al.*[19]; 773°K: ■—Galavanov *et al.*[19]. Solid lines show the theoretical mobilities calculated for the corresponding temperatures.

free electron concentration, so that the theoretical values of $\bar{\mu}_{cc}$ should be lower. It is easy to take this effect into account in the theory but the degree of compensation in a sample is usually not known. This problem has been considered in detail by Kolodziejczak[8]. Secondly, the theory does not take into account inelastic electron-electron collisions which, as shown by Bate *et al.*[53], may lower the values of mobility in this region.

At 500°K the picture of various modes contributing to the total mobility is essentially similar to the situation at 300°K. In pure samples the role of CC mode becomes comparable to that of OP scattering (at $n = 4.82 \times 10^{17} \text{ cm}^{-3}$, $\bar{\mu}_{cc} = 5.6 \times 10^4$, $\bar{\mu}_{op} = 7.1 \times 10^4$ and $\bar{\mu}_{ac} = 1.34 \times 10^5 \text{ cm}^2/\text{sec}$), whereas at high concentrations the CC and AC mechanisms give comparable contributions (at $n = 8.0 \times 10^{18}$, $\bar{\mu}_{cc} = 9.8 \times 10^3$, $\bar{\mu}_{op} = 4.6 \times 10^4$ and $\bar{\mu}_{ac} = 2.0 \times 10^4 \text{ cm}^2/\text{V sec}$). The experimental data of Galavanov *et al.*[19] are seen to be in agreement with the theory for the mixed mode.

At 773°K all three modes give comparable contribution to mobility in the entire concentration range (at $n = 2.2 \times 10^{18} \text{ cm}^{-3}$, $\bar{\mu}_{cc} = 2.3 \times 10^4$, $\bar{\mu}_{op} = 3.9 \times 10^4$ and $\bar{\mu}_{ac} = 3.6 \times 10^4 \text{ cm}^2/\text{V sec}$, and at $n = 8.9 \times 10^{18} \text{ cm}^{-3}$, $\bar{\mu}_{cc} = 9.4 \times 10^3$, $\bar{\mu}_{op} = 2.9 \times 10^4$ and $\bar{\mu}_{ac} = 1.2 \times 10^4 \text{ cm}^2/\text{V sec}$). Again the measurements of Galavanov *et al.*[19] agree with the theoretical mobility for the mixed scattering mode.

The agreement between theoretical and experimental values of mobility at high temperatures confirms the chosen value of the deformation potential constant, although there still remains some ambiguity due to the dispersion of experimental data and the fact that the electron effective mass at these temperatures is not known with high accuracy.

Figure 4 presents the thermoelectric power of InSb at room temperature, as measured by various authors, together with the theoretical curve computed for the final set of parameters. The experimental points of Barrie and Edmond[28] for lower electron concentrations

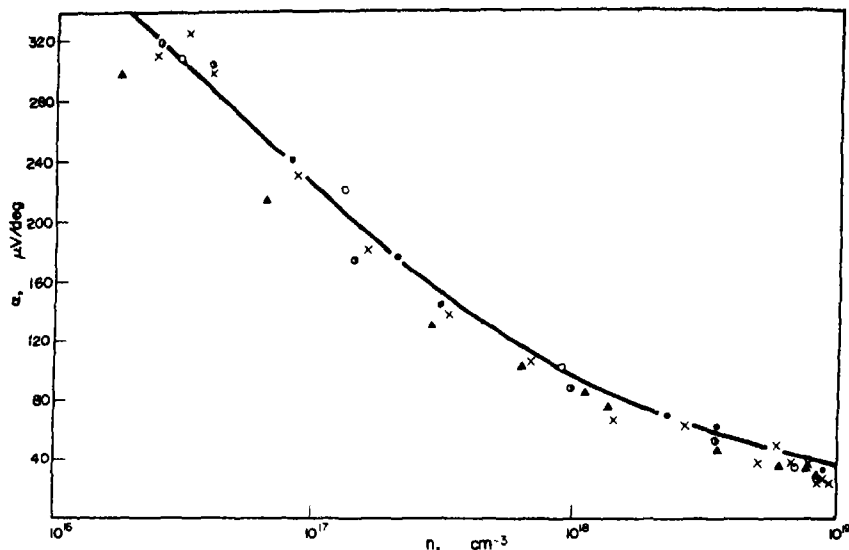


Fig. 4. Thermoelectric power in *n*-InSb vs. electron concentration at room temperature. Experimental data: x—Filipchenko and Nasledov[20], ▲—Barrie and Edmond[28], ○—Emeljanenko *et al.*[30], ●—Byszewski *et al.*[33], ⊙—Ginter and Szymanska[68]. Solid line shows the result of theoretical calculation.

lie systematically lower than the data of other authors. The calculations have been performed numerically with the use of equations (2.12) and (3.18) and the expressions for the mobilities. It can be seen that satisfactory agreement between the theory and the experiment is obtained.

As we have mentioned in the introduction the previous disagreement between the theory and the experimental thermoelectric power at higher electron concentrations induced us to undertake the present investigation. In order to get some insight into this problem we shall consider the thermoelectric power in highly degenerate electron gas using equations (4.24) and (4.25). According to equation (4.24) the scattering modes enter the theoretical formula via the effective scattering index R . We shall calculate R for $n = 1.1 \times 10^{19} \text{ cm}^{-3}$ and quote the arithmetic as it is rather instructive. Using the final set of parameters we have at the above concentration: $\bar{u}_{cc} = 7.90 \times 10^3$, $\bar{u}_{op} = 7.01 \times 10^4$, $\bar{u}_{ac} = 2.43 \times 10^4 \text{ cm}^2/\text{V sec}$, and $r'_{cc} = 0.27$, $r'_{op} = -0.84$ and $r'_{ac} = -2.66$.

Thus

$$R = \frac{r'_{cc}/\bar{u}_{cc} + r'_{op}/\bar{u}_{op} + r'_{ac}/\bar{u}_{ac}}{1/\bar{u}_{cc} + 1/\bar{u}_{op} + 1/\bar{u}_{ac}} = \frac{3.42 - 1.20 - 10.25}{12.65 + 1.43 + 4.11} = -0.48. \quad (6.1)$$

This value of R inserted into formula (4.24) gives the result which is in agreement with the experimental data in this concentration range. As it can be seen, in spite of the fact that the CC scattering gives the largest contribution to the mobility, it is the AC mode which mainly determines the sign of R . This is due to the large value of r'_{ac} or, in more physical terms, to the strong energy dependence of AC scattering. It so happens that the effective value of R comes out fairly close to r_{op} for the single optical mode. That is why the experimental points lie fairly close to the theoretical curve for the single optical mode ($r_{op} = -1$) in the interpretation of Kolodziejczak and Sosnowski[9]. But it can be seen from above that this coincidence is accidental since the OP mode

gives small contribution to both \bar{u} and R in this concentration range. Using the older scattering theory ($r_{cc} = +1$, $r_{op} = -1$, $r_{ac} = -3$, $F_{cc} = 2.42$, $F_{op} = F_{ac} = 1$) and the material constants $\epsilon_d = 7.2$ eV and $u_L = 3.7 \times 10^5$ cm/sec the resulting scattering index is $R \approx 0.27$. This corresponds to the calculation of Filipchenko and Nasledov [20] and gives too high theoretical values of the thermoelectric power. According to the new theory and employing the value of $\epsilon_d = 7.2$ eV we obtain $R = -0.03$ mainly due to the decreased role of the CC scattering ($r'_{cc} = 0.27$ instead of $r_{cc} = 1$). This value of R is still too large indicating that Ehrenreich's value of ϵ_d is too small. This is even better demonstrated in the thermomagnetic effects which we shall discuss presently.

Figure 5 presents the longitudinal Nernst-Ettingshausen effect $-\alpha(\infty) - \alpha(0)$, as measured at room temperature by various authors, together with the theoretical curve computed according to equation (2.14) for the mixed scattering mode using the final set of parameters. We plot $-\Delta\alpha$ according to the tradition, and also in order to have the same sign of the longitudinal and transverse $N-E$ effects. The original values of $\Delta\alpha$ measured by Rodot[39] were retrieved by inverting the procedure mentioned in his paper. His measurement $-\Delta\alpha = 4.4 \mu\text{V/deg}$ at $n = 1.3 \times 10^{16} \text{ cm}^{-3}$ has been omitted since the intrinsic concentration at room temperature is higher.

It can be seen that the theory correctly describes the experimental data predicting the change of sign around $n = 6 \times 10^{17} \text{ cm}^{-3}$. Again, to get some insight into the problem we can consider formula (4.28) for the longitudinal $N-E$ effect in degenerate electron gas. As follows from equation (4.26) $\gamma = \frac{1}{2}$ at high concentrations so that $2 - 6\gamma = 0$ and according to equation (4.28) the sign of R determines the sign of the effect. From equation (6.1) we have $R = -0.48$ at $n = 1.1 \times 10^{19} \text{ cm}^{-3}$ which gives the value of $-\Delta\alpha$ shown in Fig. 5 in this concentration range. As follows from our previous discussion the old scattering theory together with the value of $\epsilon_d = 7.2$ eV give $R = 0.27$, i.e. the wrong sign of $-\Delta\alpha$ at high impurity concentrations. This value of the deformation potential also according to the new theory, giving $R = -0.03$ does not describe properly the experimental data.

Again, quite accidentally, the final theoretical predictions for the mixed mode give very similar results to the theory for the single optical mode of scattering. This is illustrated in Fig. 6, which gives the values of $(\langle z \rangle / \langle 1 \rangle - \langle zu \rangle / \langle u \rangle)$ for different single scattering modes as functions of electron concentration at room temperature.

It should be noted that the dependence of $-\Delta\alpha_{op}$ for OP mode at room temperature is rather intricate. According to the theory for a parabolic band the sign of $-\Delta\alpha_{op}$ is negative

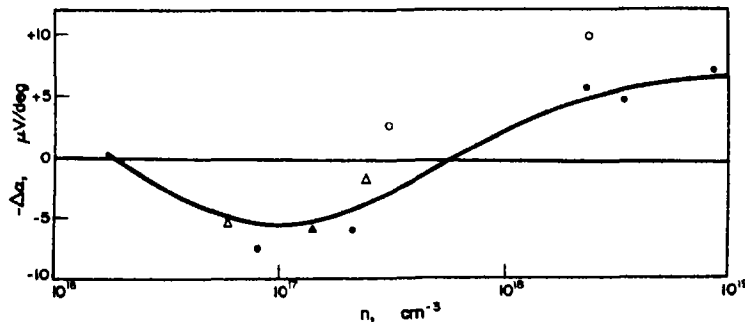


Fig. 5. Longitudinal Nernst-Ettingshausen effect in n -InSb vs. electron concentration at room temperature. Experimental data: Δ —Rodot[39], \bullet —Byszewski[69], \circ —Galavanov *et al.*[70], \blacktriangle —Rodot[71]. Solid line shows the result of theoretical calculation.

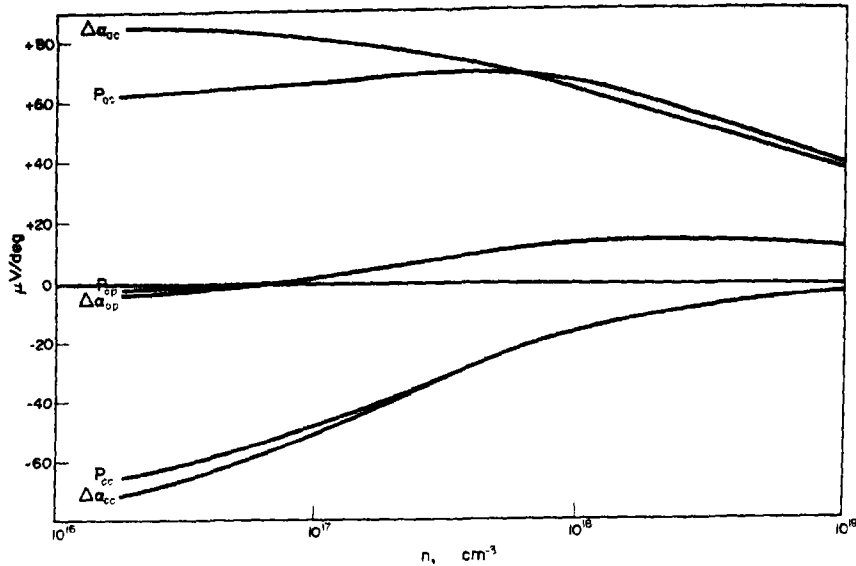


Fig. 6. Theoretical values of $(k_0/q)(\langle z \rangle / \langle 1 \rangle - \langle zu \rangle / \langle u \rangle)$ denoted as $\Delta\alpha$ and $(k_0/q)(\langle zu \rangle / \langle u \rangle - \langle zu^2 \rangle / \langle u^2 \rangle)$ denoted as P for various single scattering modes vs. electron concentration in n -InSb at room temperature.

in the entire concentration range (see e.g. Rodot[39] and Tsodilkovskii[72]). The older scattering theory for a nonparabolic band, summarized in equation (1.3) gives positive values of $-\Delta\alpha_{op}$ for all electron concentrations (Guseva and Tsodilkovskii[40])* . On the other hand the new scattering theory gives the values of $-\Delta\alpha_{op}$ changing sign from negative to positive with increasing electron concentration.

Now, having in mind the relative importance of various scattering modes illustrated by contributions to mobility in Fig. 1, we can say that the positive sign of $-\Delta\alpha$ at high electron concentrations is caused by the influence of AC scattering, whereas the negative sign at low concentrations is due to combined effect of OP and CC modes. Predicted by the theory another increase of $-\Delta\alpha$ for the lowest concentrations is due to the influence

of AC mode in this region, which we mentioned in the discussion of mobility. It should be emphasized, however, that the theoretical values at these concentrations are not very reliable since they depend rather strongly on the assumed value of the deformation potential. Actually, this sensitivity could be used for a precise determination of ϵ_d if dependable experimental values of $-\Delta\alpha$ in this region were available.

Figure 7 presents the transverse Nernst-Ettingshausen effect in InSb at room temperature, as measured by various authors, together with the theoretical curve computed, according to equation (2.15), for the mixed scattering mode and using the final set of parameters. It can be seen that the dispersion of experimental points is larger than for the longitudinal effect. This agrees with the observation of Rodot[39] that it is easier to obtain reliable data from the longitudinal N - E effect. It seems that the main experimental problem is to ensure isothermal conditions of the measurement and a proper extrapolation to $H = 0$, especially for high electron

*The theoretical curve for $-\Delta\alpha_{op}$ presented in Ref. [73] as well as some experimental points have been erroneously extrapolated to low electron concentrations without due regard to the lack of degeneracy in this region.

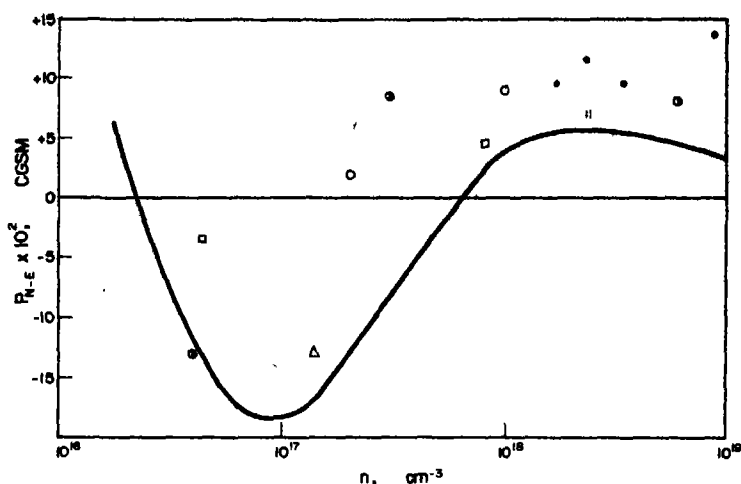


Fig. 7. Transverse Nernst-Ettingshausen effect in n -InSb vs. electron concentration at room temperature. Experimental data: \square —Wagini[32], \odot —Emeljanenko *et al.*[38], \circ —Nasledov and Filipchenko[41], Δ —Rodot[71], \bullet —Holas[74]. Solid line shows the result of theoretical calculation.

mobilities, i.e. in the region of low electron concentrations. One experimental point of Wagini: $P = -25 \cdot 10^{-2}$ [CGSM] at $n = 2 \times 10^{16} \text{ cm}^{-3}$ has not been included in Fig. 7. It can be seen that on the whole there is a reasonable qualitative agreement between the theory and the experimental data.

In Fig. 6 we have also plotted the values of $(\langle zu \rangle / \langle u \rangle - \langle zu^2 \rangle / \langle u^2 \rangle)$ for different single scattering modes as functions of electron concentration at room temperature. They indicate that the relation

$$\langle z \rangle / \langle 1 \rangle - \langle zu \rangle / \langle u \rangle \approx \langle zu \rangle / \langle u \rangle - \langle zu^2 \rangle / \langle u^2 \rangle \quad (6.2)$$

is approximately valid not only in the high degeneracy region, as shown by equation (4.31), but in the entire concentration range at room temperature, with some discrepancy for AC mode at low degeneracy. Also the values for the mixed mode are very much alike (they have not been included in Fig. 6, being small out of scale), so that the theoretical values for the transverse N - E effect plotted in Fig. 7 are to a good approximation simply the values of $-\Delta\alpha$ multiplied by the values of

mobility for corresponding electron concentrations, as plotted in Fig. 1. Thus all the above discussion for the longitudinal effect applies also here. We want to emphasize once again that the comparison of the theory with experiment at low electron concentrations is not very meaningful due to the considerable dispersion of experimental data and high sensitivity of the theoretical results to the assumed value of the deformation potential.

It can be seen from Figs. 4 and 7 that at high electron concentrations the experimental data for thermoelectric power lie slightly lower and for the transverse N - E effect somewhat higher than the theoretical curves. In terms of the formulas for high degeneracy, equations (4.24) and (4.30), this suggests lower values of R or higher values of γ . Lower values of R would require a slightly higher deformation potential constant ϵ_d , but this would lead to disagreement between the theory and experiment at lower electron concentrations, especially for $\Delta\alpha$. It has been suggested recently by Nasledov *et al.*[75] that the conduction band of InSb exhibits at high energies stronger non-parabolicity than that given by the Kane model, which has been employed

throughout this paper. Such a stronger non-parabolicity would lead to higher values of γ at high electron concentrations, which in turn would bring the theory closer to the experimental points. A final solution of this problem calls for more experimental investigations of the transverse and longitudinal Nernst-Ettingshausen effects.

On the basis of comparison between the theory and the experimental data for all the above effects we estimate the value of the deformation potential constant $\epsilon_d = 14.6 \pm 2$ eV, which agrees well with the newest independent estimations [25–27].

7. CONCLUSIONS

We have attempted to give a unified description of existing experimental results on transport phenomena in *n*-InSb, taking consistently into account the nonparabolic structure of the conduction band in this material. It turned out to be possible to describe satisfactorily the experimental data on mobility at different temperatures as well as thermoelectric power, the longitudinal and transverse Nernst-Ettingshausen effects and the free-carrier optical absorption at room temperature in the range of electron concentrations from 2×10^{16} to 1×10^{19} cm⁻³ with the following values of the material constants: $\kappa(0) = 17.5$, $\theta_L = 283^\circ\text{K}$, $e^* = 0.13e$ and $\epsilon_d = 14.6 \pm 2$ eV. On the basis of the performed analysis one can draw the following conclusions concerning the material properties:

1. All three scattering modes, i.e. the charged center scattering, the polar optical scattering and the acoustic (deformation potential) scattering must be taken into account when interpreting the electron transport phenomena in InSb. At room temperature in pure samples OP and CC modes dominate the scattering processes, whereas for high impurity concentrations CC and AC modes are of main importance.

2. At room temperature the negative values of the longitudinal and transverse Nernst-Ettingshausen effects at low electron concen-

trations are due to combined influence of OP and CC modes and the positive values at high concentrations are caused mainly by AC scattering mechanism.

As far as the interpretation of transport phenomena in narrow-gap materials is concerned, the above analysis allows to conclude the following:

1. In the theory of scattering the nonparabolic structure of the conduction band must be taken into account not only through the $\epsilon(k)$ dependence entering the density of states, but also through the use of complete wave functions necessary to compute the matrix elements of transitions.

2. Complete energy dependences of mobilities for various scattering modes must be considered explicitly. The usual procedure of neglecting the energy dependence due to screening in CC scattering leads to considerable overestimation of this mode in thermomagnetic effects.

3. Comparison of experimental data for thermoelectric and thermomagnetic effects with theoretical results for separate single scattering modes can lead to incorrect conclusions since the latter do not depend on material constants which determine real contribution of a given mode to the total scattering.

4. Extension of formulas applicable to highly degenerate electron gas to the non-degenerate region can lead in case of thermomagnetic effects to completely misleading results.

It seems that the presented procedure can find applications in the theoretical description of transport phenomena in a number of narrow-gap semiconducting materials. Recently Ravitch and Morgovskii [76] carried out a theoretical analysis of acoustic and polar optical scattering in PbTe-type semiconductors taking into account the real band structure of these compounds,

Acknowledgements—The authors are greatly indebted to Dr. J. Ginter for help in some aspects of this work and to Dr. J. Blocki for performing the numerical calculations.

It is a pleasure to thank Drs Ju. I. Ravitch and L. L. Korenblit of The Institute of Semiconductors in Leningrad for informative discussions.

REFERENCES

1. KANE E. O., *J. Phys. Chem. Solids* **1**, 249 (1957).
2. SPITZER W. G. and FAN H. Y., *Phys. Rev.* **106**, 882 (1957).
3. SMITH S. D., MOSS T. S. and TAYLOR K. W., *J. Phys. Chem. Solids* **11**, 131 (1959).
4. HOWARTH D. J. and SONDEHEIMER E. H., *Proc. Phys. Soc. A219*, 53 (1953).
5. RADCLIFFE J. M., *Proc. Phys. Soc. A68*, 675 (1955).
6. BARRIE R., *Proc. Phys. Soc. B69*, 553 (1956).
7. EHRENREICH H., *J. Phys. Chem. Solids* **2**, 131 (1957).
8. KOŁODZIEJCZAK J., *Acta Phys. Polon.* **20**, 289 (1961).
9. KOŁODZIEJCZAK J. and SOSNOWSKI L., *Acta Phys. Polon.* **21**, 399 (1962).
10. ZAWADZKI W., KOWALCZYK R. and KOŁODZIEJCZAK J., *Phys. Status Solidi* **10**, 513 (1965).
11. KOWALCZYK R., KOŁODZIEJCZAK J. and ZAWADZKI W., *The Generalized Fermi-Dirac Integrals Tables*, Institute of Physics, Polish Academy of Sciences, Warsaw (1965).
12. EHRENREICH H., *J. Phys. Chem. Solids* **9**, 129 (1959).
13. HAGA E. and KIMURA H., *J. phys. Soc. Japan.* **18**, 777 (1963).
14. KORENBLIT L. L. and SHERSTOBITOV V. E., *Fiz. Tekhn. Poluprov.* **2**, 675 (1968).
15. ZAWADZKI W. and SZYMANSKA W., *Phys. Status Solidi*. In press.
16. SZYMANSKA W. and GINTER J., *Phys. Status Solidi*, **27**, K103 (1968).
17. HROSTOWSKI H. J., MORIN F. J., GEBALLE T. H. and WHEATLEY J. H., *Phys. Rev.* **100**, 1672 (1965).
18. HILSUM C. and BARRIE R., *Proc. Phys. Soc. B71*, 676 (1958).
19. GALAVANOV V. V., NASLEDON D. N. and FILIPCHENKO A. S., *Phys. Status Solidi* **8**, 671 (1965).
20. FILIPCHENKO A. S. and NASLEDON D. N., *Phys. Status Solidi* **19**, 435 (1967).
21. KESSLER F. R. and SUTTER E., *Z. Naturf.* **16a**, 1173 (1961).
22. KESSLER F. R. and SUTTER E., *Proc. Intern. Conf. Phys. Semicond.* p. 175, Paris (1964).
23. PURI S. M., *Phys. Rev.* **139**, A995 (1965).
24. NILL K. W. and McWHORTER A. L., *Proc. Int. Conf. Phys. Semicond.*, p. 755 Kyoto (1966).
25. WHALEN J. J. and WESTGATE C. R., *Appl. Phys. Lett.*, **15**, 292 (1966).
26. TANAKA S., ASAI S. and KOGAMI M., *Proc. Int. Conf. Phys. Semicond.* p. 799, Moscow (1968).
27. SZYMANSKA W. and MANEVAL J. P., *Solid State Commun.* **8**, 879 (1970).
28. BARRIE R. and EDMOND J. T., *J. Electron.* **1**, 161 (1955).
29. TAUC J. and MATYAS M., *Czech. J. Phys.* **5**, 369 (1955). CHASMAR R. P. and STRATTON R., *Phys. Rev.* **102**, 1686 (1956).
30. EMELJANENKO O. V., KESAMANLY F. P. and NASLEDON D. N., *Fiz. tverd. Tela* **3**, 1161 (1961).
31. WEISS H., *Z. Naturf.* **11a**, 430 (1956).
32. WAGINI H., *Z. Naturf.* **19a**, 1527 (1964).
33. BYSZEWSKI P., KOŁODZIEJCZAK J. and ZUKOTYNSKI S., *Phys. Status Solidi* **3**, 1880 (1963).
34. SHALYT S. S. and ALIEV S. A., *Fiz. tverd. Tela* **6**, 1979 (1964).
35. SZYMANSKA W., *Phys. Status Solidi* **23**, 69 (1967).
36. KASAMANLY F. P. and KORSHAK., *Izv. Akad. Nauk.* **3**, 490 (1967).
37. ZHUSE V. P. and TSIDILKOVSKII I. M., *Z. Tek. Fiz.* **28**, 2373 (1958).
38. EMELJANENKO O. V., KESAMANLY F. P. and NASLEDON D. N., *Fiz. tverd. Tela* **4**, 546 (1962).
39. RODOT M., *Ann. Phys. Paris* **5**, 1085 (1960).
40. GUSEVA G. I. and TSIDILKOVSKI I. M., *Fiz. tverd. Tela* **4**, 2490 (1962).
41. NASLEDON D. N. and FILIPCHENKO A. S., *Fiz. Tekhn. Poluprov.* **1**, 221 (1967).
42. KOŁODZIEJCZAK J., *Acta Phys. Polon.* **20**, 379 (1961).
43. ZAWADZKI W., *Phys. Status Solidi* **2**, 385 (1962).
44. ZAWADZKI W., *Phys. Status Solidi* **3**, 1006 (1963).
45. KOŁODZIEJCZAK J., *Acta Phys. Polon.*, **21**, 637 (1962).
46. BROOKS H., *Phys. Rev.* **83**, 879 (1951). HERRING C., unpublished.
47. SOMMERFELD A., *Z. Phys.* **47**, 1 (1928). BLANKENBECKER R., *Amer. J. Phys.* **25**, 279 (1957).
48. ZHITINSKAJA M. K., KAIDANOV V. I. and CHERNIK I. A., *Fiz. tverd. Tela* **8**, 295 (1966).
49. PIDGEON C. R. and BROWN R. N., *Phys. Rev.* **146**, 575 (1966).
50. RAVITCH Ju. I., *Fiz. tverd. Tela* **7**, 1821 (1965).
51. ROBERTS V. and QUARRINGTON J. E., *J. Electron.* **1**, 152 (1956).
52. SMITH S. D., PIDGEON C. R. and PROSSER V., *Proc. Int. Conf. Phys. Semicond.* p. 301, Exeter (1962).
53. BATE R. T., BAXTER R. D., REID F. J. and BEER A. C., *J. Phys. Chem. Solids* **26**, 1205 (1965).
54. SANDERSON R. B., *J. Phys. Chem. Solids* **26**, 803 (1965).
55. DINGLE R. B., *Phil. Mag.* **46**, 831 (1955).
56. YOSHINAGA H. and OETJEN R. A., *Phys. Rev.* **101**, 526 (1956).
57. CALLEN H. B., *Phys. Rev.* **76**, 1394 (1949).
58. HASS M. and HENVIS B. W., *J. Phys. Chem. Solids* **23**, 1099 (1962).
59. MCKIMIN H. J., BOND W. L., PEARSON G. L. and HROSTOWSKI H. J., *Bull. Am. phys. Soc.* **1**, 111 (1956).
60. SLUTSKY L. J. and GARLAND C. W., *Phys. Rev.* **113**, 167 (1959).
61. POTTER R. F., *Phys. Rev.* **103**, 47 (1956).

62. MADELUNG O. and WEISS H., *Z. Naturf.* **9a**, 527 (1954).
63. GALAVANOV V. V., NASLEDON D. N. and FILIPCHENKO A. S., *Fiz. tverd. Tela* **6**, 3471 (1964).
64. RUPPRECHT H., WEBER R. and WEISS H., *Z. Naturf.* **15a**, 783 (1960).
65. STRAUSS A. J., *J. appl. Phys.* **30**, 559 (1959).
66. CHAMPNESS C. H., *J. Electron.* **4**, 201 (1958).
67. PUTLEY E. H., *Proc. Phys. Soc.* **73**, 280 (1959).
68. GINTER J. and SZYMAŃSKA W., *Bull. Acad. Polon. Sci.* **9**, 419 (1961).
69. BYSZEWSKI P., Masters Thesis, Physics Department, Warsaw University (1963), unpublished.
70. GALAVANOV V. V., EMELJANENKO O. W. and KESAMANLY F. P., *Fiz. tverd. Tela* **5**, 616 (1963).
71. RODOT M., *Comp. Rend.* **245**, 1051 (1957).
72. TSIDILKOVSKII I. M., *Thermomagnetic Phenomena in Semiconductors*, p. 208 Fizmatgiz, Moscow (1960).
73. SOSNOWSKI L., *Proc. Int. Conf. Phys. Semicond.* p. 341, Paris (1964).
74. HOLAS J., Masters Thesis, Physics Department, Warsaw University (1963) unpublished.
75. NASLEDON D. N., RADAJKINA L. N. and FILIPCHENKO A. S., *Fiz. tekhn. Poluprov.* **4**, 621 (1970).
76. RAVITCH Ju. I. and MORGOVSKII L. Ja., *Fiz. tekhn. Poluprov.* **3**, 1528 (1969).

Note added in proof. After completion of this work we have calculated explicitly the influence of free-carrier screening on polar optical scattering [15]. It turns out that to a good approximation the effect of screening is represented by replacing unity in equation (3.9) by $1 - (2/\xi_0) \ln(\xi_0 + 1)$, where ξ_0 is defined in equation (3.3). For low carrier concentrations, where the optical mode is of importance, this increases theoretical values of mobility $\bar{\mu}_{op}$ by a factor of 1.25. Adjusting the value of the effective ionic charge (in order to bring $\bar{\mu}_{op}$ to the level indicated in Fig. 1 for low electron concentrations), the value of $e^* = 0.145e$ is obtained, which is closer to the results of other investigations [58]. The modified energy dependence of $\bar{\mu}_{op}$ does not practically affect the theoretical results for the mobilities and the thermoelectric power calculated for mixed scattering mode, as presented above. On the other hand it may somewhat influence the theoretical results for $\Delta\alpha$ and P_{N-E} at lower concentrations. However, it does not seem meaningful to try for a better agreement between the theory and experiment until more precise data concerning these effects are available.

RESONANCE PARAMAGNETIQUE ET DEFORMATION LOCALE DANS LES COMPLEXES DE TYPE UF_6M

P. RIGNY, A. J. DIANOUX* et P. PLURIEN

Département de Physico-Chimie, Centre d'Etudes Nucléaires de Saclay, B.P. n°2, 91,
Gif-sur-Yvette, France

(Received 3 June 1970)

Résumé—Les complexes de formule UF_6M où $M = Na, Li, Cs, NO$ contiennent un électron $5f$ célibataire environné d'un octaèdre d'atomes de fluors. Les spectres de résonance paramagnétique montrent que les octaèdres UF_6^- ont une légère déformation axiale. On présente ici un calcul des paramètres de déformation à partir des facteurs g expérimentaux, effectué par la théorie du champ cristallin. Au préalable, il a fallu déterminer les fonctions d'onde d'un électron $5f$, en symétrie cubique, quantifiées suivant l'axe 111 de l'octaèdre. La validité des résultats peut être vérifiée sur le cas d' UF_6Cs , bien connu cristallographiquement; des valeurs des paramètres de déformation sont proposées pour les autres complexes étudiés, pour lesquels la RPE est beaucoup plus sensible que la radio-cristallographie.

Abstract—In the complexes of formula UF_6M , with $M = Na, Li, Cs, NO$, the unpaired $5f$ electron is surrounded by an octahedron of fluorine atoms. Paramagnetic resonance studies show that the UF_6^- ions are slightly axially distorted. A calculation is presented, where crystal field theory is used to calculate the strength of the distortion from the experimental g factors. The wave functions of a $5f$ electron in a cubic environment, quantized along a 111 axis of the octahedron are first determined. The validity of the results can be checked with UF_6Cs on which accurate cristallographic studies have been made; values of the angles of distortion are proposed for the other complexes studied, for which paramagnetic resonance studies, are much more sensitive than radiocrystallography.

1. INTRODUCTION

LES SPECTRES d'absorption de résonance paramagnétique électronique des complexes de type UF_6M ($M = Na, Cs, Li, NO$) sont caractérisés par des valeurs très élevées des champs de résonance. Ceci a été développé dans des travaux antérieurs[1,2] où les facteurs g ont été interprétés comme caractéristiques de la présence d'un électron célibataire de type $5f$ situé dans un environnement de symétrie cubique ou presque cubique.

La forme des raies d'absorption des échantillons pulvérulents révèle que la symétrie locale n'est pas strictement cubique, mais présente une faible déformation axiale. Le facteur g a une valeur $g_{||}$ ou g_{\perp} selon que le champ magnétique est parallèle ou perpendiculaire à l'axe de la déformation. L'étude de monocristaux[2] nous a permis de montrer qu'aussi bien dans les cristaux rhomboédri-

ques ($M = Li, Cs, NO, Na$) que dans la forme cubique de $NaUF_6$, la déformation des ions UF_6^- est de symétrie trigonale (D_{3d}).

Dans ces conditions, on peut espérer qu'une interprétation quantitative des valeurs de $g_{||}$ et g_{\perp} fournisse les valeurs des paramètres de la déformation des ions UF_6^- . C'est cet aspect quantitatif que nous voulons expliciter ici.

Les fonctions d'onde des électrons des atomes lourds, et en particulier leur répartition radiale sont trop mal connues pour qu'on puisse songer à présenter un traitement exact. Nous prendrons comme point de départ le modèle des charges ponctuelles et considérerons l'électron comme soumis au potentiel électrostatique de six charges $-e$ situées à l'emplacement des ions fluor. Cette approximation serait très bonne si l'électron célibataire occupait une orbitale $5f$ pure de l'uranium, ce qui serait le cas si la liaison $U-F$ était purement ionique. En fait on sait que cet électron a une probabilité non nulle d'occupation des orbitales des fluors[1]. Cependant comme elle est assez faible, nous nous con-

*Adresse Actuelle: Department of Chemistry and Chemical Engineering University of Illinois. Urbana. Ill. USA.

tenterons d'en tenir compte à l'aide de certains paramètres ajustables qui seront discutés par la suite.

La déformation de l'octaèdre UF_6^- que nous considérons étant de symétrie trigonale, dans tout ce qui suit, nous prendrons l'axe 111 de l'octaèdre comme axe de quantification.

2. POTENTIEL CRISTALLIN

Le potentiel électrostatique qui couple un électron à son environnement assimilé à un ensemble de charges $-e$ s'exprime commodément par son développement en harmoniques sphériques[3]:

$$v_c = \sum_{n,m} B_n^m r_l^n y_n^m(\theta_l, \varphi_l) \quad (1)$$

r_l , θ_l et φ_l sont les coordonnées polaires de l'électron, et les coefficients B_n^m s'expriment en fonction des coordonnées l_j , α_j , β_j des charges électriques de l'environnement par la formule

$$B_n^m = -\frac{4\pi}{2n+1} \sum_j \frac{e^2}{l_j^{n+1}} y_n^{m*}(\alpha_j, \beta_j). \quad (2)$$

On a coutume d'exprimer ce potentiel cristallin à l'aide des opérateurs équivalents O_n^m dont les expressions en fonction des harmoniques sphériques sont données par exemple dans la revue de Hutchings[4], où figurent également des tables d'éléments de matrice. Pour le calcul des éléments de matrice dans des fonctions f , l'expression du potentiel n'est utile que jusqu'aux termes de degré au plus égal à 6.

Le potentiel de symétrie D_{3d} le plus général dépend de six paramètres. Cependant un octaèdre de symétrie D_{3d} peut se déduire d'un octaèdre régulier par la donnée d'un seul angle: par exemple l'angle θ de l'axe ternaire et d'un des axes de l'octaèdre. La paramètre que nous prendrons est l'angle $\epsilon = \theta - 54^\circ 42'$, ϵ étant nul pour l'octaèdre régulier et positif si la déformation de l'octaèdre correspond à une compression. Si ϵ est faible, on calcule par les formules (1) et (2) l'expression du terme non-cubique du potentiel cristallin:

$$\begin{aligned} \frac{v_c - v_{\text{cubique}}}{\epsilon e} = & -3\sqrt{2} \frac{\langle r^2 \rangle}{l^3} \alpha_j 0_2^0 \\ & + \frac{5\sqrt{2}}{12} \frac{\langle r^4 \rangle}{l^5} \beta_j (0_4^0 - 7\sqrt{2} 0_4^{30}) \\ & + \frac{7\sqrt{2}}{2} \frac{\langle r^6 \rangle}{l^7} \gamma_j \left(0_6^0 + \frac{35\sqrt{2}}{2} 0_6^{30} \right. \\ & \left. - \frac{11}{2} 0_6^6 \right). \end{aligned} \quad (3)$$

La formule ci-dessus est valable dans le référentiel dont l'axe polaire Oz est un axe de symétrie ternaire du site, l'axe x étant l'axe de symétrie C_2' qui lui est orthogonal (Fig. 1); α_j , β_j et γ_j sont des coefficients dont les valeurs sont données dans la revue de Hutchings. r est la distance de l'électron au centre du site et $\langle r^n \rangle$ est la valeur moyenne de r^n ; l est la valeur de la distance $U-F$. Anticipant sur les calculs numériques, il est intéressant de signaler ici que le terme en 0_2^0 auquel on se limite quelquefois pour des calculs approximatifs, n'est absolument pas prépondérant devant les deux autres termes.

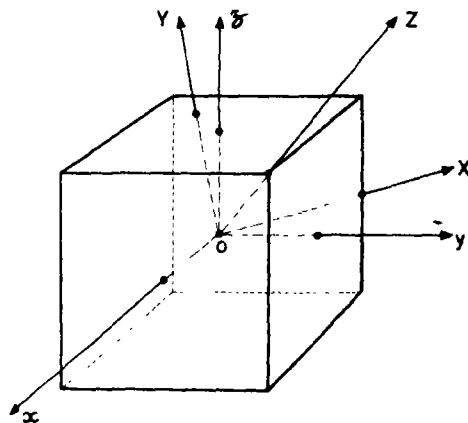


Fig. 1. Systèmes d'axes appropriés à l'étude de déformations quadratiques ($Ox' y' z'$) ou trigonale ($Ox y z$). L'axe Ox est une axe de symétrie C_2' du cube.

3. FONCTIONS D'ONDE EN SITE D_{3d}

Les environnements que nous considérons sont des octaèdres qui présentent des déformations de symétrie D_{3d} et de faible amplitude par rapport aux octaèdres réguliers. Pour obtenir les fonctions d'onde d'un électron $5f$

dans un tel environnement, il faut d'abord déterminer une base de fonctions classées suivant les symétries du cube, et quantifiées suivant l'axe de la déformation, puis déterminer les fonctions d'onde en diagonalisant l'hamiltonien principal, de symétrie cubique, et enfin perturber ces fonctions par le potentiel $v_c - v_{\text{cubique}}$ [5].

Fonctions en symétrie cubique quantifiées suivant l'axe 111

Un potentiel cristallin cubique décompose les sept fonctions f en un triplet symétrie Γ_4 , un triplet de symétrie Γ_5 et un singulet Γ_2 . Les fonctions d'onde de ces niveaux, exprimées comme combinaisons linéaires d'harmoniques sphériques quantifiées suivant un axe ternaire du cube (0z) sont indiquées dans le Tableau 1. Le système d'axes choisi pour ce calcul est indiqué sur la Fig. 1. Ces fonctions peuvent être obtenues par diagonalisation directe d'un potentiel cristallin cubique, dont l'expression peut être déduite simplement de la formule (1).

Pour tenir compte du couplage spin-orbite, il faut en fait connaître les 14 fonctions spin-orbitales. Les fonctions orbitales doivent donc être multipliées par les fonctions de spin, qui sont de symétrie Γ_6 . Les six fonctions $\Gamma_4 \times \Gamma_6$ se décomposent en quatre fonctions Γ_8 et deux fonctions Γ_6 ; de même les six fonctions $\Gamma_5 \times \Gamma_6$ donnent un quadruplet Γ_8 et un doublet Γ_7 et les deux fonctions $\Gamma_2 \times \Gamma_6$ donnent un doublet Γ_7 . On obtient les fonctions de chaque type de symétrie en diagonalisant le couplage spin-orbite par la technique d'Abragam et Pryce où on l'exprime à l'aide d'un moment orbital fictif. Il est importante à ce stade de poursuivre la construction des fonctions d'onde en les classant systématiquement. A cette fin on cherche les combinaisons linéaires des fonctions de chaque symétrie telles que les matrices des rotations du groupe cubique soient les mêmes respectivement dans le quadruplet Γ_8 et dans les quatre fonctions propres de la composante z d'un spin $\frac{3}{2}$ ou respectivement dans un doublet Γ_6 (ou Γ_7) et dans les 2 fonctions propres de la composante z d'un spin $\frac{1}{2}$.

Tableau 1. Fonctions d'onde orbitales et spin-orbitales d'un électron 5f en site cubique. L'axe de quantification est une axe de symétrie d'ordre 3. Une barre au-dessus d'une orbitale indique que le spin est dans l'état $-\frac{1}{2}$

Γ_4 :	Γ_5 :
$\delta_{-1} = -\frac{\sqrt{6}}{6} y_3^1 - i \frac{\sqrt{30}}{6} y_3^{-2}$	$\eta_{3/2} = \delta_1$
$\delta_0 = \frac{2}{3} y_3^0 + i \frac{\sqrt{10}}{6} (y_3^3 + y_3^{-3})$	$\eta_{1/2} = \frac{\sqrt{6}}{3} \delta_0 + \frac{\sqrt{3}}{3} \bar{\delta}_1$
$\delta_{-1} = -\frac{\sqrt{6}}{6} y_3^{-1} - i \frac{\sqrt{30}}{6} y_3^2$	$\eta_{-1/2} = \frac{\sqrt{6}}{3} \delta_0 + \frac{\sqrt{3}}{3} \delta_{-1}$
	$\eta_{-3/2} = \bar{\delta}_{-1}$
	Γ_6 :
	$\zeta_{1/2} = \frac{\sqrt{3}}{3} \delta_0 - \frac{\sqrt{6}}{3} \bar{\delta}_1$
	$\zeta_{-1/2} = -\frac{\sqrt{3}}{3} \delta_0 + \frac{\sqrt{6}}{3} \delta_{-1}$
Γ_5 :	Γ_6 :
$\epsilon_1 = i \frac{\sqrt{30}}{6} y_3^1 + \frac{\sqrt{6}}{6} y_3^{-2}$	$\chi_{3/2} = \frac{i}{3} \epsilon_1 + \frac{2\sqrt{2}}{3} \bar{\epsilon}_{-1}$
$\epsilon_0 = -\frac{1}{\sqrt{2}} (y_3^3 - y_3^{-3})$	$\chi_{1/2} = \frac{-i\sqrt{6}}{3} \epsilon_0 - i \frac{\sqrt{3}}{3} \bar{\epsilon}_1$
$\epsilon_{-1} = -i \frac{\sqrt{30}}{6} y_3^{-1} - \frac{\sqrt{6}}{6} y_3^2$	$\chi_{-1/2} = i \frac{\sqrt{6}}{3} \epsilon_0 + i \frac{\sqrt{3}}{3} \epsilon_{-1}$
	$\chi_{-3/2} = -\frac{2\sqrt{2}}{3} \epsilon_1 - \frac{i}{3} \bar{\epsilon}_{-1}$
	Γ_7 :
	$\varphi'_{1/2} = i \frac{\sqrt{3}}{3} \epsilon_0 - i \frac{\sqrt{6}}{3} \bar{\epsilon}_1$
	$\varphi'_{-1/2} = -i \frac{\sqrt{3}}{3} \epsilon_0 + i \frac{\sqrt{6}}{3} \epsilon_{-1}$
Γ_2 :	Γ_7 :
$\beta = \frac{\sqrt{5}}{3} y_3^0 - i \frac{\sqrt{2}}{3} (y_3^3 + y_3^{-3})$	$\varphi_{1/2} = \beta$
	$\varphi_{-1/2} = \bar{\beta}$

Les fonctions ainsi classées sont indiquées dans le Tableau 1.

Dans le cas des ions UF_6^{3-} , l'ordre des énergies des niveaux orbitaux, peut s'obtenir de façon assez certaine. Contrairement à ce qui se passe [6] pour des ions UF_6^{3+} , l'existence d'un degré de covalence appréciable dans ces ions, qui peuvent exister en solution est ici une hypothèse sûre. On peut voir qu'alors les niveaux doivent se classer comme la Fig. 2

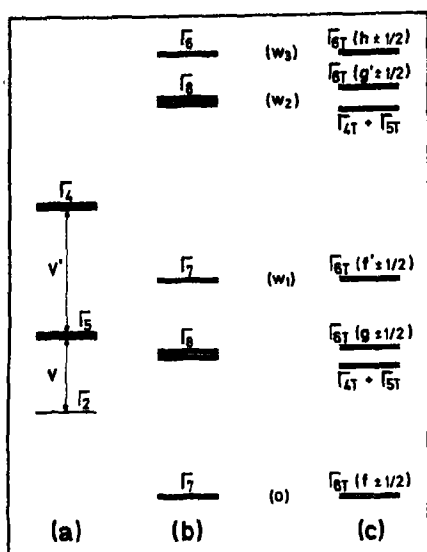


Fig. 2. Niveaux d'énergie d'un électron 5f en champ cubique ou presque cubique. (a) Niveaux orbitaux en champ cubique. (b) Décomposition des niveaux par l'action combinée du potentiel cristallin et du couplage spin-orbite. (c) Décomposition supplémentaire apportée par une déformation trigonale. Les types de symétrie des niveaux et la nomenclature de certaines énergies ou fonctions d'ondes sont indiquées. En (a) et (b) les positions des niveaux sont appropriées au complexe UF_6Cs .

l'indique; si l'énergie du singulet est prise comme référence, l'énergie du triplet Γ_5 est v et celle du triplet Γ_4 est $v + v'$, avec $v, v' > 0$.

Les fonctions d'onde s'obtiennent finalement par diagonalisation simultanée du potentiel cristallin cubique et du couplage spin-orbite, dans la base des fonctions que nous venons de déterminer; puisque celles-ci ont été classées convenablement, les équations séculaires sont au plus du deuxième degré.

Fonctions d'onde perturbées

En présence d'une déformation de symétrie D_{3d} , les niveaux se décomposent comme la Fig. 2 l'indique. L'axe de quantification que nous avons choisi étant l'axe de la déformation trigonal, les fonctions valables à l'ordre zéro sont celles qui ont été déterminées au paragraphe précédent. Il y a cinq doublets de

Kramers de symétrie Γ_{6T} dont les fonctions d'onde sont:

$$\begin{aligned} f_{\pm 1/2} &= \varphi'_{\pm 1/2} \cos \theta - \varphi_{\pm 1/2} \sin \theta \\ f'_{\pm 1/2} &= \varphi'_{\pm 1/2} \sin \theta + \varphi_{\pm 1/2} \cos \theta \\ g_{\pm 1/2} &= \eta_{\pm 1/2} \cos \varphi - \chi_{\pm 1/2} \sin \varphi \\ g'_{\pm 1/2} &= \eta_{\pm 1/2} \sin \varphi + \chi_{\pm 1/2} \cos \varphi \\ h_{\pm 1/2} &= \zeta_{\pm 1/2} \end{aligned}$$

Les angles θ et φ sont déterminés par les équations séculaires, qui ont été données dans la réf. [1]. Si f est l'état fondamental, et si g est d'énergie inférieure à g' elles s'écrivent

$$\tan 2\theta = -\frac{2\sqrt{3}\zeta}{v - \frac{1}{2}\zeta}, \quad \tan \varphi = \frac{3\sqrt{5}\zeta}{2(\zeta - v')}$$

ζ est la constante du couplage spin-orbite. Les énergies des états de fonctions f, g, g' et h sont respectivement 0, ω_1, ω_2 et ω_3 .

Les fonctions d'onde perturbées au premier ordre par le potentiel (3) sont de la forme

$$\psi_{\pm 1/2} = f_{\pm 1/2} + \lambda g_{\pm 1/2} + \mu g'_{\pm 1/2} + \nu h_{\pm 1/2};$$

λ, μ et ν sont des éléments de matrice de $v_c - v_{\text{cubique}}$, fonctions calculables de θ et φ , divisés respectivement par les énergies ω_1, ω_2 et ω_3 .

4. FACTEURS g ET DÉFORMATION LOCALE

Les éléments du tenseur g peuvent être déduits des fonctions d'onde du doublet fondamental par les expressions

$$\begin{aligned} g_{\parallel} &= 2 \langle \psi_{\pm 1/2} | l_z + 2S_z | \psi_{\pm 1/2} \rangle \\ g_{\perp} &= + \langle \psi_{+1/2} | l_+ + 2S_+ | \psi_{-1/2} \rangle \end{aligned}$$

où l et S sont respectivement les moments cinétiques d'orbite et de spin de l'électron célibataire. On obtient ainsi

$$\begin{aligned} g_{\parallel} &= g_0 + 2\gamma \\ g_{\perp} &= g_0 - \gamma \end{aligned}$$

g_0 est le facteur g de l'électron situé en symétrie cubique. Son expression, donnée dans la

Réf. [1], n'est fonction que de l'angle θ , c'est-à-dire du paramètre v/ζ .

Le facteur γ est de la forme

$$\gamma = \frac{\epsilon F_1(\theta, \varphi)}{\omega_1} + \frac{\epsilon F_2(\theta, \varphi)}{\omega_2} \quad (4)$$

où F_1 et F_2 sont des fonctions de θ et φ ; bien entendu, γ est nul en symétrie parfaitement cubique ($\epsilon = 0$). Les valeurs moyennes ainsi que les anisotropies des facteurs g mesurées précédemment [1, 2] dans les complexes $UF_6 Li$, $UF_6 Na$ (cubique) et $UF_6 Cs$, sont indiquées dans le Tableau 2. Les signes négatifs des facteurs g moyens ont été justifiés dans la Réf. [1].

Tableau 2. Paramètres des raies de résonance, et angles de déformation calculés pour plusieurs complexes $UF_6 M$

	g_0	$\gamma \times 10^3$	ϵ
Li UF_6	-0.768	7	8'
Na UF_6 (cubique)	-0.748	36	39'
Na UF_6 (rhomboédr.)	-0.745	36	39'
Cs UF_6	-0.709	70	1° 15'
NO UF_6	-0.748	< 2	< 2'

On a également indiqué les valeurs correspondant à la forme rhomboédrique de $UF_6 Na$, ainsi qu'à $UF_6 NO$. Dans ce dernier complexe, les largeurs des raies (500 G) sont environ dix fois plus importantes que dans les autres complexes. Ceci peut être dû à des phénomènes dynamiques qui doivent intervenir dans ce complexe du fait de la forme non-sphérique du cation; dans ce cas les valeurs des anisotropies que nous donnons ne seraient que des moyennes au cours d'un mouvement. Les valeurs ϵ des angles de déformation peuvent en principe être déduites de $g_{||}$ et g_{\perp} par la formule (4). En fait, celle-ci contient plusieurs paramètres que nous ajusterons pour tenir compte du caractère partiellement covalent des liaisons $U-F$.

Les calculs numériques ont été effectués pour le complexe $UF_6 Cs$ pour lequel on dispose d'une étude cristallographique récente complète [7], qui a donné une distance $U-F$ $l = 2.057 \text{ \AA}$ ainsi qu'un angle de déformation $\epsilon = +1^\circ 54'$. D'un autre côté les positions des niveaux d'énergie excités dans ce complexe sont connues [8]: $\omega_1 = 4587 \text{ cm}^{-1}$, $\omega_2 = 12705 \text{ cm}^{-1}$. Les quantités $\langle r^2 \rangle$, $\langle r^4 \rangle$ et $\langle r^6 \rangle$, qui dépendent de la partie radiale de la fonction d'onde électronique ont été estimées de la façon suivante. Nous avons supposé qu'elles étaient proportionnelles aux grandeurs correspondantes calculées pour l'ion U^{5+} isolé [9], et le coefficient de proportionnalité a été ajusté de façon à rendre compte des valeurs des paramètres du champ cubique qui peuvent être déduits des spectres d'absorption optique.

Pour tenir compte de la covalence on doit également ajuster le paramètre k déjà défini dans la Réf. [1], et qui est déterminé par l'étude du facteur g moyen. Ce paramètre est relié à la réduction que l'hybridation apporte à l'amplitude de probabilité pour que l'électron magnétique se trouve dans une orbitale de l'uranium, et qui a été prise égale à 19 pour cent. La constante de couplage spin-orbite ζ d'un électron de l'uranium V a été prise égale à 1955 cm^{-1} .

Dans ces conditions, on détermine une valeur de l'angle de la déformation de $+1^\circ 15'$ pour $UF_6 Cs$. Ce résultat est inférieur d'environ 30 pour cent à l'angle de $1^\circ 54'$ déterminé cristallographiquement.

Cet accord relativement bon indique que le calcul de champ cristallin est essentiellement valable dans notre cas. Un meilleur accord serait illusoire au vu des approximations grossières que nous avons été amenés à faire, et dont les plus délicates sont probablement l'emploi de fonctions d'ondes f pures, alors que les couches $6d$ et $5f$ ont des énergies *a priori* assez peu différentes et l'emploi d'un modèle de charges ponctuelles pour l'évaluation d'un potentiel cristallin. Pour s'affranchir de ces approximations, il faudrait une bonne

description des liaisons chimiques dans l'ion UF_6^- . Ceci permettrait également le traitement des interactions orbite-phonons, dont nous n'avons pas tenu compte mais qui peuvent, dans certains cas apporter des contributions non-négligeables ([10-11]). Ces termes varient probablement assez peu dans les ions UF_6^- des différents composés $UF_6 M$ dont on peut comparer les structures par les spectres de résonance paramagnétique.

Les anisotropies des autres complexes $UF_6 M$ étudiés fournissent par le même calcul les valeurs des angles de déformation qui sont indiquées dans le Tableau 2. Les paramètres que nous déterminons n'étant que très approximatifs (par exemple 50 pour cent par défaut pour $UF_6 Cs$), nous avons négligé les différences entre les valeurs des énergies d'excitation ainsi que des facteurs g moyens des différents complexes.

Des déformations extrêmement faibles, probablement imperceptibles aux rayons X , sont ainsi mises en évidence par l'étude des spectres de R.P.E.

Remerciements—Ce travail a bénéficié de nombreuses discussions avec Mme P. Charpin et M. M. Drifford. Nous tenons à les en remercier chaleureusement.

RÉFÉRENCES

1. RIGNY P. et PLURIEN P., *J. Phys. Chem. Solids* **28**, 2589 (1967).
2. DRIFFORD M., RIGNY P. et PLURIEN P., *Phys. Lett.* **A27**, 620 (1968).
3. ABRAGAM A. et BLEANEY B., *Electron Paramagnetic Resonance of Transition Ions*, Oxford University Press (1970).
4. HUTCHINGS M. T., Dans *Solid State Physics*, Vol. 16, (Editeurs F. Seitz et D. Turnbull), Academic Press, New York (1964).
5. DIANOUX A. J., *Thèse de doctorat*, Lyon 1969, Rapport CEA. R-3859.
6. RIGNY P., DIANOUX A. J. et PLURIEN P., (article précédent).
7. ROZENZWEIG A. et CROMER D. T., *Acta crystallogr.* **23**, 865 (1967).
8. REISFELD M. J. et CROSBY G. A., *Inorg. Chem.* **4**, 65 (1965).
9. LIBERMAN D., WABER J. T. et CROMER D. T., *Phys. Rev.* **137**, A27 (1965).
10. BIRGENEAU R. J., *Phys. Rev. Lett.* **19**, 160 (1967).
11. BAGGULEY D. M. S. et VALLA G.,—Colloquio—*J. Phys. C. (Proc. Phys. Soc.)* **2**, 2310 (1969).

THERMOELECTRICAL PARAMETERS OF FAST-NEUTRON-IRRADIATED Te-Se-Bi, Te-Sb-Bi AND GeSi

PAVEL MACKO

Department of Physics, Slovak Technical University, Bratislava

(Received 1 June 1970)

Abstract—In this paper a review of measurement of electrical conductivity σ , Seebeck coefficient α , thermal conductivity λ and Z -parameter of semiconductor-thermomaterials of Te-Se-Bi, Te-Sb-Bi, resp. GeSi, irradiated with fast neutrons with doses of $0-1 \times 10^{18} \text{ n' cm}^{-2}$ is given. The experimental values are interpreted by relatively simple expressions. Negative as well as positive changes of investigated parameters were observed, which begin to appear if the concentration of radiation defects N_D is greater than the concentration of intrinsic defects N_{D0} before irradiation.

1. INTRODUCTION

RADIATION damages, which are formed in semiconductors by bombarding with fast neutrons, result in changes of practically all characteristic parameters of the material. The sensitivity of the material to radiation damages is more pronounced for homogeneous, single crystal-like, semiconductors with the lowest possible number of primary imperfections. While there exists a large number of publications concerning the changes of some physical parameters of more commonly used semiconductors after irradiation with fast neutrons, thermoelectrically active semiconductor materials seem to be neglected, although these semiconductors could possibly be utilized for conversion of the secondary thermal energy of nuclear reactors into electrical energy. Therefore in the present paper we tried to investigate the influence of neutron irradiation on the characteristic parameters of some thermoelectrically active semiconductors which are expressed by the so-called Z -parameter, defined as

$$Z = \frac{\alpha^2 \sigma}{\lambda} \quad (1)$$

where α is the Seebeck coefficient, σ the electrical conductivity, and λ the thermal conductivity.

The parameters contained in equation (1)

were measured by a twin-lead modification of the pulse method described in detail in [1] and [2].

By means of this measuring method we were able to determine the ratio of both α/λ and α^2/λ directly, and together with the measured electrical conductivity σ to calculate the sought for parameters.

Each measured sample (with dimensions cca $20 \times 5 \times 5 \text{ mm}$) was fixed in a separate holder. The samples were prepared and measured as described in [3].

The experiments were carried out with samples of

1. Te-Se-Bi and Te-Sb-Bi, respectively.
2. GeSi.

2. THE INFLUENCE OF NEUTRON RADIATION ON THE CHARACTERISTIC PARAMETERS OF Te-Se-Bi (n -TYPE) AND Te-Sb-Bi (p -TYPE)

Samples of these materials which were available for measuring were prepared by powder metallurgic methods. The grain size for sample preparation was 1.5 mm maximum (A -material), and 0.08 mm minimum (B -material). The method of preparation proved to be of utmost importance and led to diametrically different behaviour for A -type and B -type material.

The semiconductor material was irradiated in the nuclear reactor of the Institute of Nuclear Research at Prague-Rez with a

neutron flux of $3 \times 10^{13} \text{ n' (cm}^{-2} \text{ s}^{-1})$ and a total dose of $1 \times 10^{18} \text{ n' cm}^{-2}$. Experiments showed a negative influence on physical parameters of *A*-material (big grain) and positive changes for *B*-material (small grain). Measuring results are given in Tables 1–3.

As *B*-material proved to be more convenient from the aspect of practical application, the following experiment i.e. the measurement of *Z*-parameter and electrical conductivity changes as a function of neutron flux, was carried out with these semiconductor samples.

The measured values are plotted in Fig. 1.

3. INTERPRETATION OF MEASURED VALUES

An investigation of the cause of the changes of the mentioned physical parameters should start contemplating the following types of defects:

(a) Defects of the bulk material, which have the character of vacancy clusters, displacement wedges etc, which have mostly negative influence.

(b) Defects of surface layers and intermediate layers between individual grains, which may be of positive influence.

For an explanation of the different changes

Table 1. Measuring results before and after irradiation for *n*-type of *A*-material (grain size 1.5 mm)

σ [$\mu\text{V deg}^{-1}$]		σ [$\Omega^{-1} \text{ cm}^{-1}$]		$\lambda \times 10^3$ [$\text{W cm}^{-1} \text{ deg}^{-1}$]		$Z \times 10^3$ [deg^{-1}]	
184	175	741	474	13.2	13.3	2.2	1.1
180	175	964	805	13.0	12.9	2.4	1.9
184	176	768	648	12.5	12.6	2.12	1.6
182	176	640	502	13.4	13.5	1.6	1.24

Table 2. Measuring results before and after irradiation for *p*-type of *B*-material (grain size 0.08 mm)

α [$\mu\text{V deg}^{-1}$]		σ [$\Omega^{-1} \text{ cm}^{-1}$]		$\lambda \times 10^3$ [$\text{W cm}^{-1} \text{ deg}^{-1}$]		$Z \times 10^3$ [deg^{-1}]	
189	189	1012	1168	19.2	13.6	1.9	3.13
204	196	835	914	14.6	12.9	1.9	2.6
190	188	506	620	17.5	15.9	0.85	1.37
225	221	507	650	20.1	15.1	1.44	2.1

Table 3. Measuring results before and after irradiation for *n*-type of *B*-material (grain size 0.08 mm)

α [$\mu\text{V deg}^{-1}$]		σ [$\Omega^{-1} \text{ cm}^{-1}$]		$\lambda \times 10^3$ [$\text{W cm}^{-1} \text{ deg}^{-1}$]		$Z \times 10^3$ [deg^{-1}]	
176	176	760	900	12.5	11.1	1.91	2.55
171	175	910	1150	10.5	12.4	2.5	2.9
174	172	820	1005	12.2	12.1	2.0	2.46
176	173	850	950	11.3	11.1	2.3	2.55

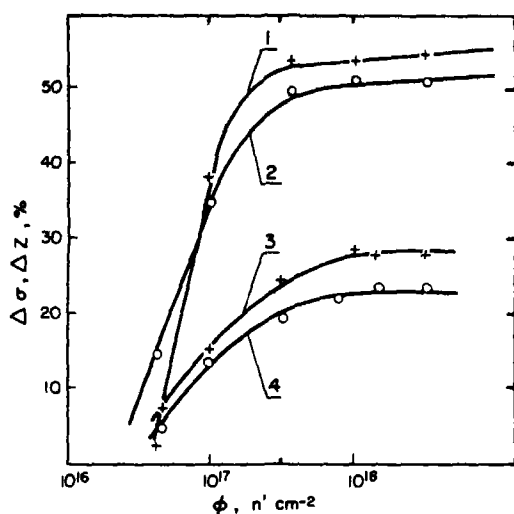


Fig. 1. Dependence of relative changes of electrical conductivity and Z-parameter on fast-neutron flux of Te-Se-Bi, and Te-Sb-Bi, respectively. Curve (1) represents the changes of Z-parameter and curve (2) the changes of electrical conductivity σ for a *p*-type sample, curve (3) changes of Z-parameter and curve (4) changes of electrical conductivity for an *n*-type sample.

of the sample parameters mentioned in Table 1, and samples in Tables 2 and 3. We start from the difference of structure of the materials *A* and *B*. During the technological processing of the powdery material on air the individual grains are covered by oxide layers mainly by SeO_2 , SeO_3 and TeO_3 . In the first case—if the material was hot-pressed from big grains (*A*-material), the influence of negative changes in the bulk material inside the grain dominate, in the second case (*B*-material) the influence of radiation damages of the dominating oxide layers causes positive changes.

The change of electrical conductivity and naturally of the Z-parameter, too, was the most outstanding change in all experiments with practically constant thermal conductivity and Seebeck coefficient.

The electrical conductivity σ is composed of two parts: (1) σ_n the electrical conductivity of the bulk material, and (2) σ_R the electrical conductivity of intermediate oxide layers.

Scattering of free carriers causes a decrease of σ_n with increasing radiation defects.

The component σ_R is being changed by neutron interaction with atoms forming the intermediate layer. The displacement wedges cause the increase of electrical conductivity in the intermediate layer. The total change of electrical conductivity then depends on the respective influence of changes of σ_n and σ_R .

For *A*-material the change of σ_n is dominating, therefore the total electrical conductivity decreases.

For *B*-material, which is composed of small grains, the ratio of the outer oxide layer to the inside volume of the grains is sufficiently great, therefore the positive influence of defects in the oxide layers dominates.

Theoretical interpretation of the measured results is practically impossible with respect to the polycrystalline nature of the material concerned, which also in its microvolume is very inhomogeneous.

4. CHANGES OF THERMOELECTRICAL PARAMETERS IN GeSi

Measuring samples were prepared from phosphorus doped *n*-type GeSi alloy, the content of Si being 71.3 per cent. Five samples of this material were irradiated in a nuclear reactor with fast neutrons of an energy of 2 MeV as follows: sample 1 was not irradiated, samples 2 to 5 were irradiated with an integral flux of 1×10^{16} , 1×10^{17} , 5×10^{17} , 1×10^{18} $n' \text{ cm}^{-2}$ respectively. The temperature during irradiation was 300°K.

The changes of the investigated parameters were measured as a function of neutron radiation dose and temperature.

Non-irradiated GeSi is dealt with in paper [4].

GeSi semiconductor alloy is a homogeneous material of polycrystalline character. The damages, which originate from the interaction of bombarding neutrons with the atoms of the semiconductor, are distributed regularly throughout the whole volume of the

sample. In most cases they are vacancy clusters, interstitials or displacement wedges. The influence of these radiation damages is negative, because they reduce conductivity by compensating free carriers and increasing the scattering probability.

The results of $n = f_n(\phi)$ and $u = f_u(\phi)$ at $T = 300^\circ\text{K}$ are given in graphical form in Fig. 2. It is evident that the determining parameter is the change of carrier concentration, which after irradiation with $\phi = 1 \times 10^{18} \text{ n' cm}^{-2}$ changes by about three orders of magnitude, while their mobility changes only by about one order of magnitude.

The investigated properties were measured in the temperature interval from 100 to 400°K . The measured values are plotted with solid lines Fig. 3 shows the dependence of the Seebeck-coefficient on temperature, $\alpha = f_\alpha(T)$, Fig. 5 shows the temperature dependence of the thermal conductivity, $\lambda = f_\lambda(T)$, and in Fig. 6 there is the temperature dependence of the Z-parameter, $Z = f_Z(T)$, for the irradiated samples as well as for the non-irradiated ones. The measurements showed that radiation damages have a negative influence on all investigated parameters.

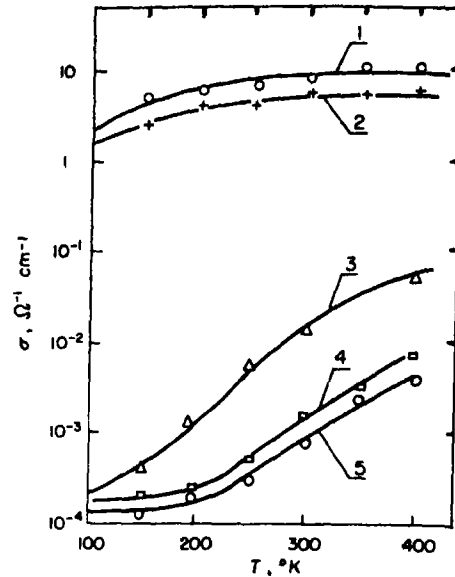


Fig. 3. Temperature dependence of electrical conductivity for samples No. 1, 2, 3, 4 and 5.

5. DISCUSSION AND RESULTS

(a) Electrical conductivity

From the Boltzmann equation follows for the electron conductivity of an ideal n -type semiconductor with spherical energy surfaces,

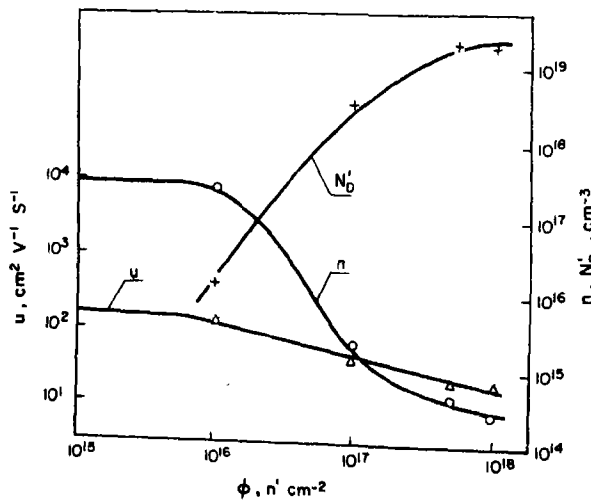


Fig. 2. Flux dependence of free carrier mobility (u), of radiation defects concentration (N'_D), and of free carrier concentration (n).

the following relation:

$$\sigma = \frac{K_{1,2} \exp[-\Delta E_{1,2}/2kT]}{AT^{3/2} + BN_D T^{-3/2}} \quad (2)$$

For the region of extrinsic conductivity (low temperatures), we have

$$K_1 = \frac{e}{\sqrt{2}} (A_n N_d)^{1/2} \quad \text{and} \quad \Delta E_1 = \Delta E_d \quad (3a)$$

and for the region of intrinsic conductivity (high temperatures) there is

$$K_2 = e (A_n A_p)^{1/2} \quad \text{and} \quad \Delta E_2 = \Delta E \quad (3b)$$

where A and B are numerical coefficients, N_D is the total concentration of defects in the semiconductor, A_n and A_p are effective densities of states of donors and holes, respectively.

Supposing that the term $AT^{3/2}$ is negligible, the relation can be approximated at constant temperature, as follows:

$$\sigma = \frac{\text{const.}}{N_D} \quad (4)$$

The total concentration of defects in the semiconductor can be expressed in the form

$$N_D = N_{D0} + N'_D, \quad (5)$$

where N_{D0} is the concentration of the defects in the non-irradiated material and N'_D is the concentration of the defects, formed by neutron irradiation. In case $N'_D \gg N_{D0}$, equation (4) relating to equation (5) can be written as follows

$$\sigma = K \frac{N_{D0}}{N'_D} \quad (6)$$

which is in good agreement with experimental results. For the constant K and N_{D0} the following numerical values were found:

$$K = 5.1 \, \Omega^{-1} \text{cm}^{-1}, \quad N_{D0} = 4 \times 10^{15} \text{cm}^{-3}.$$

Using the results of paper[5] the following expression for the concentration of radiation defects was obtained.

$$N'_D = \frac{5 \times 10^{23} \text{cm}^{-3}}{n}, \quad (7)$$

where n is the concentration of free carriers.

The values of electrical conductivity, calculated from equation (6), are in good agreement with the experimental results. For the sake of comparison in Fig. 7 the experimental as well as the theoretical values of electrical conductivity are plotted as a function of neutron radiation. The influence of the formed defects N'_D will be evident from the change of the investigated parameters only in the case when $N'_D > N_{D0}$.

(b) Seebeck coefficient

To discuss the dependence of $\alpha = f_a[\phi, T]$, we start from the general expression for the Seebeck coefficient:

$$\alpha_0 = -\frac{k}{e} \left[\left(r + \frac{5}{2} \right) - \frac{E_F}{kT} \right], \quad (8)$$

where r is the coefficient of scattering and E_F is the energy of the Fermi level.

In order that the expression for the Seebeck coefficient may express at the same time not only its temperature dependence but also the influence of the neutron irradiation, we can write

$$\alpha = k_n^m G \alpha_0, \quad (9)$$

where the coefficient k_n^m expresses the dependence of the Seebeck coefficient on the neutron dose according to

$$k_n^m = -\frac{\Delta \alpha}{\Delta \phi} \quad (10)$$

where the exponent m has the form

$$m = \log \frac{\phi}{\phi_0} \quad (11)$$

and ϕ_0 expresses numerically the lower limit of neutron irradiation. According to the given conditions the numerical factors have the following values for GeSi: $k_n = 0.337 \text{ V cm}^2 \text{ n}^{-1} \text{ deg}^{-1}$, $G = 2.6 \times 10^{-2} \text{ n}^\circ \text{ deg V}^{-1} \text{ cm}^{-2}$ and $\phi_0 = 1 \times 10^{16} \text{ n}^\circ \text{ cm}^{-2}$.

The values of the Seebeck coefficient calculated from the given relation are plotted in Fig. 4 with dotted lines. The values of the Seebeck coefficient as a function of neutron flux at constant temperature are plotted in Fig. 8.

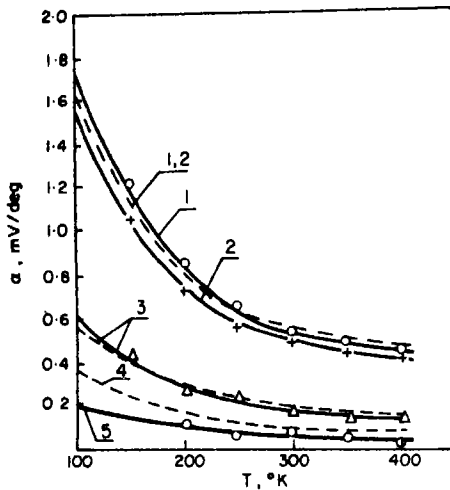


Fig. 4. Temperature dependence of the Seebeck coefficient for 5 samples. Solid lines represent experimental curves, dotted lines are theoretical curves.

(c) Thermal conductivity

Neglecting the electron component of thermal conductivity which usually represents only a small correction of the total thermal conductivity of semiconductors, we get according to Peierls for thermal conductivity the expression:

$$\lambda^{-1} = R_1 T^y \exp \left[-\frac{\theta}{T} \right] + R_2 N_D T^z, \quad (12)$$

where R_1 , R_2 , y and z are numerical constants. We are looking for a dependence of the changes of thermal conductivity on the con-

centration of defects N_D , or N'_D , resp. That is why we express equation (12) in such a way that the influence of the defects caused by neutrons on the changes of total thermal conductivity may be clearly visible. When $N'_D \gg N_{D0}$ we get for the irradiated samples

$$\lambda = \frac{R'_2 T^{-z}}{b N'_D}. \quad (13)$$

In agreement with experimental results the factor b , which expresses the influence of radiation on the change of thermal conductivity, has the form:

$$\frac{1}{b} = 2^{\log \frac{10 N'_D}{N_{D0}}} \quad (14)$$

where the numerical coefficients have the values of $R'_2 = 5.75 \times 10^{18} \text{ W cm}^{-4} \text{ deg}^{0.8}$, $z = 1.8$.

The values of thermal conductivity, $\lambda = f'_\lambda(T)$ calculated from equation (13) are plotted in Fig. 5 with dotted lines and the values of $\lambda = f_\lambda(\phi)$ for $T = 300^\circ \text{K}$ are plotted in Fig. 8.

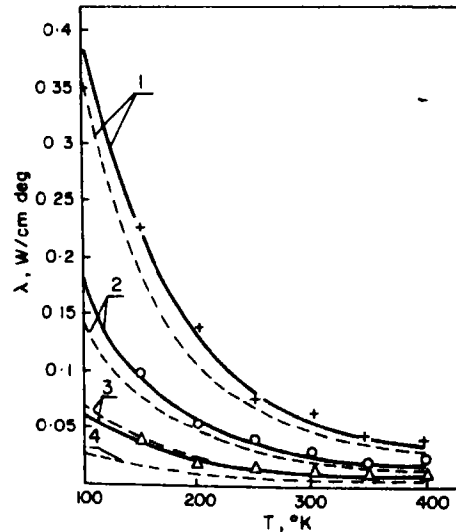


Fig. 5. Temperature dependence of thermal conductivity. Solid lines experimental, dotted lines theoretical.

(d) *Z*-parameter

We get the dependence of the *Z*-parameter on the integral neutron flux, if we substitute the corresponding relations for the electrical conductivity (6), the Seebeck coefficient (9) and the thermal conductivity (13) into the expression for the *Z*-parameter. After rearrangement we get the *Z*-parameter in the form

$$Z = K_z \frac{k_n^{2 \log \phi / \phi_0}}{2^{\log 10 N'_D / N_{D0}}}, \quad (15)$$

where K_z has a numerical value of $K_z = 2.15 \times 10^{-18} \text{ deg}^{-1}$. Equation (15) applicable for $N'_D > N_{D0}$. The values of $Z = f'_z(T)$ and $Z = Z = f'_\phi(\phi)$ are plotted in Fig. 6 and 7 with dotted lines.

6. CONCLUSION

The most important results which were obtained for both investigated semiconductor materials may be summarized as follows:

1. The changes of electrical conductivity and also of the *Z*-parameter are conspicuous

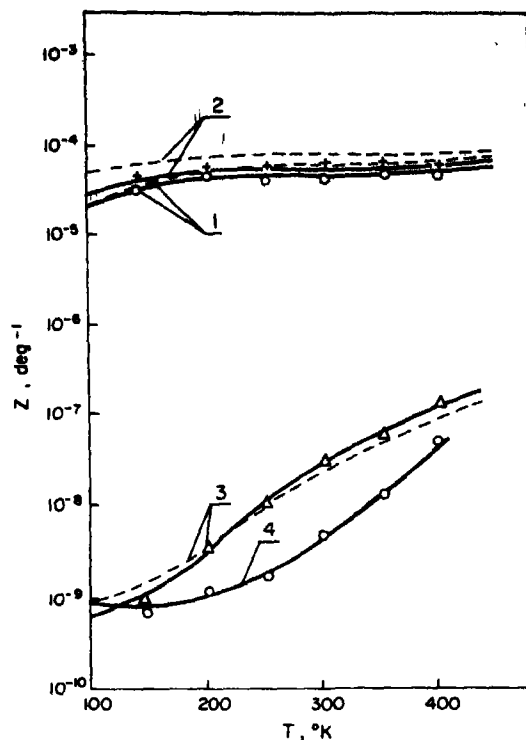


Fig. 6. Temperature dependence of the *Z*-parameter. Solid lines experimental, dotted lines theoretical.

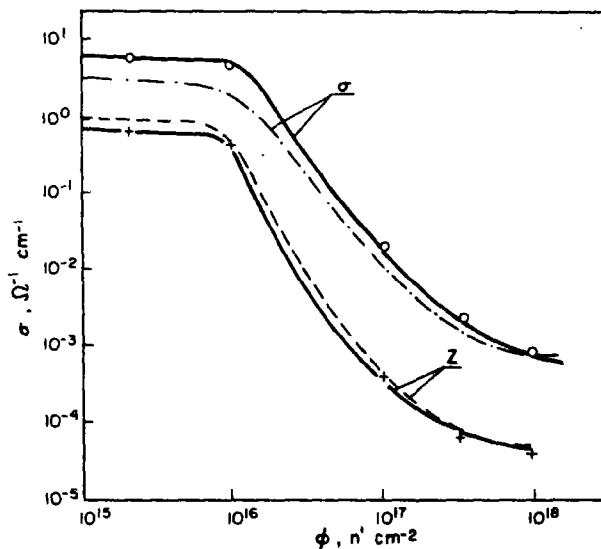


Fig. 7. Flux dependence of electrical conductivity and *Z*-parameter respectively at $T = 300^\circ\text{K}$. 1-experimental and 2-theoretical electrical conductivity. 3-experimental and 4-theoretical values of the *Z*-parameter.

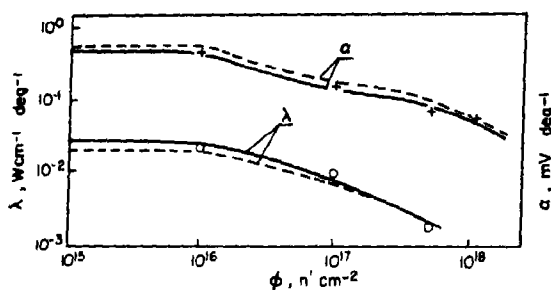


Fig. 8. Experimental and theoretical flux dependence of the Seebeck coefficient and thermal conductivity, respectively.

at relatively small changes of the Seebeck coefficient and the thermal conductivity.

2. The change of the values of measured parameters begins only when $N'_n > N_{D0}$.

3. The investigated parameters are not changed any more if the total neutron dose reaches the value of about $1 \times 10^{18} \text{ n' cm}^{-2}$.

REFERENCES

1. KREMPASKY J., *Czech. J. Phys.* **B14**, 533 (1964).
2. KREMPASKY J., *Cs. Cas. Fys.* **A16**, 136 (1966).
3. MACKO P., *Doctor Thesis Work*. Bratislava (1969).
4. DISMUKES J. P., ELSTROM L., STEIGMEIER E. F., KUDMAN J. and BEERS D. S., *J. appl. Phys.* **35**, 2899 (1964).
5. KINCHIN G. H. and PEASE R. S., *Rep. Prog. Phys.* **18**, 1 (1955).

INFLUENCE DE LA PREPARATION CHIMIQUE SUR LES STRUCTURES MAGNETIQUES DE Ca_2MnO_4

G. OLLIVIER and G. BUISSON

Centre d'Etudes Nucléaires, Cédex 85, 38-Grenoble Gare, France

(Received 5 February 1970; in revised form 26 May 1970)

Resumé—L'étude par diffraction neutronique sur échantillons polycristallins de Ca_2MnO_4 révèle la coexistence de deux structures magnétiques distinctes dont les vecteurs de propagation sont: $\mathbf{K} = [\frac{1}{2}\frac{1}{2}0]$ et $\mathbf{K} = [\frac{1}{2}\frac{1}{2}\frac{1}{2}]$.

Nous montrons que la présence de deux phases magnétiques dépend de la préparation chimique. La présence d'ions Mn^{3+} sur les sites de Mn^{4+} nous permet d'interpréter le comportement magnétique différent d'un monocristal de formule $\text{Ca}_{1.7}\text{Bi}_{0.3}\text{MnO}_4$.

Abstract—A neutron diffraction study on Ca_2MnO_4 polycrystalline samples shows two distinct magnetic phases: $\mathbf{K} = [\frac{1}{2}\frac{1}{2}0]$ and $\mathbf{K} = [\frac{1}{2}\frac{1}{2}\frac{1}{2}]$ = propagation vector.

Depending on the chemical preparation, one or both of these magnetic phases are found. The magnetic behaviour of a single crystal with formula $\text{Ca}_{1.7}\text{Bi}_{0.3}\text{MnO}_4$ is explained by the existence of the Mn^{3+} ions on Mn^{4+} sites.

INTRODUCTION

DEPUIS deux ans le volume des articles publiés sur l'ordre magnétique à deux dimensions a considérablement augmenté. Parmi ces composés, ceux à structure K_2NiF_4 semblent posséder un grand intérêt et parmi eux Ca_2MnO_4 . La préparation chimique de Ca_2MnO_4 et l'étude cristallographique ont été décrites par Ruddlesden et Popper[1] puis par Brisi et Borlera[2] qui signalent la difficulté d'obtenir du Mn^{4+} pur. J. B. Mac Chesney *et al.*[3] ont observé des températures d'ordre magnétique constantes ($\approx 115^\circ\text{K}$) pour les composés CaMnO_3 , $\text{Ca}_4\text{Mn}_3\text{O}_{10}$, $\text{Ca}_3\text{Mn}_2\text{O}_7$ et Ca_2MnO_4 . Goodenough[4] suggère un modèle d'électrons itinérants pour expliquer ce phénomène et Lines[5] dans une étude théorique sur K_2NiF_4 prévoit une diminution de spin due à un ordre bidimensionnel dans ces composés.

Avant la publication définitive de cet article, est publiée une étude par diffraction neutronique sur Ca_2MnO_4 [12] qui concerne une partie de notre travail.

1. PREPARATION

1.1 Echantillon polycristallin

Le composé Ca_2MnO_4 a été préparé selon la méthode préconisée par Ruddlesden et Popper[1] en calcinant à 1100°C dans un creuset en platine, un mélange de CaCO_3 et de Mn_2O_3 en proportion stoechiométrique pendant 48 hs. Après divers broyages nous procédons à un recuit durant quatre jours à 1300°C suivi d'une trempe à l'air. Les paramètres sont: $a = 3,67 \text{ \AA}$, $c = 12,06 \text{ \AA}$.

1.2 Echantillon monocristallin

Nous dissolvons dans un flux de Bi_2O_3 les constituants et nous cristallisons par refroidissement lent après fusion complète du mélange. Pour obtenir Ca_2MnO_4 nous sommes obligés de mettre un fort excès de CaO , car avec Bi_2O_3 les produits qui cristallisent ont des formules comprises entre BiMnO_3 et Ca_2MnO_4 suivant le pourcentage croissant de CaO introduit par rapport à Mn_2O_3 .

Nous avons donc fondu à 1350°C le mélange $4\text{CaO} + 2\text{Bi}_2\text{O}_3 + \frac{1}{2}\text{Mn}_2\text{O}_3$, et

cristallisé par refroidissement de 5° par heure des cristaux possédant la structure K_2NiF_4 de formule $Ca_{1,7}Bi_{0,3}MnO_4$. Les paramètres sont: $a = 3,685 \text{ \AA}$, $c = 12,08 \text{ \AA}$.

2. ETUDE PAR DIFFRACTION NEUTRONIQUE

Le diagramme de diffraction neutronique enregistré à la température ambiante avec une longueur d'onde $\lambda = 1 \text{ \AA}$ nous a permis d'affiner la structure nucléaire et de déterminer les paramètres de position de Ca^{2+} et O^{2-} . Un premier calcul donne un facteur de confiance de 7 pour cent. En admettant l'hypothèse émise par Brisi et Borlera dans le système Ca-Mn-O selon laquelle les ions Mn^{2+} peuvent se substituer aux ions Ca^{2+} nous avons procédé à un nouvel affinement qui conduit à 15 pour cent de Mn^{2+} sur les sites de Ca^{2+} et qui aboutit aux paramètres suivants: $Z_{Ca^{2+}} = 0,350$, $Z_{O^{2-}} = 0,157$. Le facteur de confiance descend alors à 4,5 pour cent.

Cette hypothèse ne nous paraît pas invraisemblable pour trois raisons; primo les poudres sont chauffées à 1300°C ce qui favorise la présence de Mn^{2+} , secundo la coexistence de Mn^{4+} et Mn^{2+} n'est pas impossible comme le prouve la structure de Mn_6O_8 ($Mn_2^{2+}Mn_4^{4+}O_8$) [11], tertio si la décroissance du résidu n'est pas une preuve en elle-même de la présence de Mn^{2+} , on peut remarquer que les longueurs de Fermi ($b(Ca) = 0,49 \cdot 10^{-12} \text{ cm}$, $b(Mn) = -0,36 \cdot 10^{-12} \text{ cm}$) influent fortement sur le facteur de confiance.

2.1 Structure magnétique

Pour indexer les réflexions magnétiques observées à la température de l'hélium liquide sur l'échantillon polycristallin (Fig. 1) il est nécessaire d'introduire deux vecteurs de propagation correspondant à deux types de mailles magnétiques, l'une de paramètres $[a\sqrt{2}, c]$ l'autre de paramètres $[a\sqrt{2}, 2c]$ ce qui correspond dans le groupe d'espace $F(4/m)m$ aux vecteurs: $K = [000]$ et $K = [00\frac{1}{2}]$.

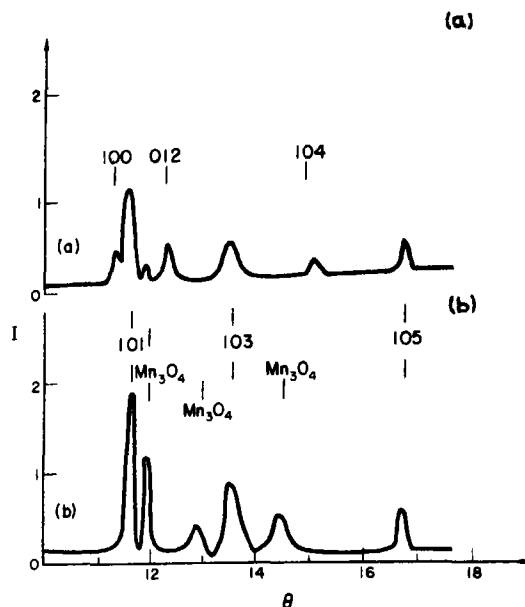


Fig. 1. Diagramme différence $I(293^\circ K) - I(4,2^\circ K)$ de diffraction neutronique de: (a) l'échantillon stoechiométrique, (b) l'échantillon A.

(a) $K = [000]$

Les intensités magnétiques calculées avec ces valeurs rendent compte d'un modèle identique à celui observé dans K_2NiF_4 , les moments étant dirigés selon l'axe c et antiparallèles dans les plans (Tableau 1). On note une imprécision due à la faiblesse des intensités observées notamment (102), (013) et à leur petit nombre.

(b) $K = [00\frac{1}{2}]$

Nous avons procédé de manière identique. Les intensités calculées montrent un arrangement antiferromagnétique dans les plans mais contrairement au cas précédent les plans sont antiparallèles après une translation c (Tableau 1). Le calcul porte sur les réflexions (101, 103, 105). On note un net élargissement de la réflexion (103). En supposant l'égalité des moments magnétiques dans les deux phases obtenues nous déterminons un pourcentage de 75 pour cent pour la phase $K = [00\frac{1}{2}]$ et 25 pour cent pour la phase $K = [000]$. A partir de ces

Tableaux 1. Echantillon stoechiométrique

	<i>hkl</i>	<i>I</i> _{obs/L}	<i>I</i> _{calc}		<i>hkl</i>	<i>I</i> _{obs/L}	<i>I</i> _{calc}
K = [000]	100	109,18	96,65	K = [00½]	101	458,82	508,64
	011	134,27	156,54		103	379,96	356,15
	102	100,0	99,10		105	232,80	207,28
	013	65,10	56,7				

2. Echantillon A

	<i>hkl</i>	<i>I</i> _{obs}	<i>I</i> _{calc}
K = [00½]	101	166,79	161,48
	103	117,03	113,57
	105	56,45	65,80

3. Echantillon D

	hkl	$I_{\text{obs/L}}$	I_{calc}		hkl	$I_{\text{obs/L}}$	I_{calc}
$K = [000]$	100	51,15	55,49	$K = [00\frac{1}{2}]$	101	298,5	307,8
	011	89,45	89,90		103	212,00	214,98
	102	61,68	56,90		105	136,46	125,11
	013	40,1	32,70				

1. Intensités magnétiques de l'échantillon stoechiométrique pour $K = [000]$ et $K = [00\frac{1}{2}]$.

2. Intensités magnétiques des échantillons A pour $K = [00\frac{1}{2}]$.

3. Intensités magnétiques de l'échantillon D pour $K = [000]$ et $K = [00\frac{1}{2}]$, I_{obs} = Intensité observée

L = Facteur de Lorentz, I_{calc} : Intensité calculée pour une direction de moment parallèle à l'axe cristallographique c , K : Vecteur de propagation.

pourcentages on tire la valeur de moment magnétique: $S = 2,1 \pm 0,2 \mu_B$.

Les premiers calculs effectués sur ce composé [7] réalisé avec le facteur de forme de Cr^{3+} montraient un accord des intensités observées et calculées pour une direction de moment faisant un angle avec l'axe quaternaire. Cependant la théorie des groupes montre l'impossibilité d'un tel arrangement si l'on se limite aux interactions d'ordre deux. Ceci nous a conduit à déterminer un facteur de forme de Mn^{4+} en extrapolant les résultats de Watson et Freemann [6].

2.2

Nous avons recherché sur le monocristal, à 4,2°K les réflexions magnétiques 100, 101, 102, 103, et 10 $\frac{1}{2}$, 10 $\frac{3}{2}$, 10 $\frac{5}{2}$, correspondant aux deux

vecteurs de propagation $K = [000]$ et $K = [00\frac{1}{2}]$.

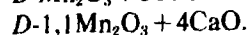
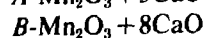
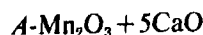
Nous n'avons observé aucune réflexion magnétique. L'étude magnétostatique sur un échantillon de monocristaux agglomérés montre un faible ferromagnétisme (Fig. 2). Une étude par neutrons polarisés confirme un moment ferromagnétique de $0,5 \mu_B$.

La présence de deux phases antiferromagnétiques sur l'échantillon polycristallin, d'une phase ferromagnétique sur le monocristal, nous a conduit à penser que la structure de Ca_2MnO_4 était liée à la préparation chimique et dépendait de la concentration en ions Mn^{4+} , Mn^{3+} , Mn^{2+} . On peut penser en effet qu'avec un excès de CaO, le manganèse n'aura pas tendance à se mettre sur les sites de Ca^{2+} . Inversement avec un excès de Mn_2O_3

nous aurons tendance à substituer Ca^{2+} par Mn.

2.3 Etude par diffraction neutronique d'échantillons A-B-D

Nous avons alors préparé divers composés selon la technique initiale mais de composition non stoechiométrique. Nous avons étudié les échantillons suivants:



L'étude magnétostatique sur l'échantillon A confirme qualitativement les résultats obtenus par Mac Chesney *et al.* [3]

magnétiques sont dirigés selon l'axe c (Table 2) avec un module de $2\mu_B$.

Pour l'échantillon D réalisé avec un excès de Mn nous retrouvons la configuration de l'échantillon stoechiométrique, c'est-à-dire deux vecteurs de propagation \mathbf{K} , les moments étant dirigés selon l'axe c avec un module de $2\mu_B$ dans les deux phases (Tableau 3).

3. REMARQUES

Ces différents résultats amènent plusieurs remarques.

3.1. Influence de la préparation

Nous pensons avoir prouvé que la présence de deux phases magnétiques était liée à la préparation chimique. Dans ce type de struc-

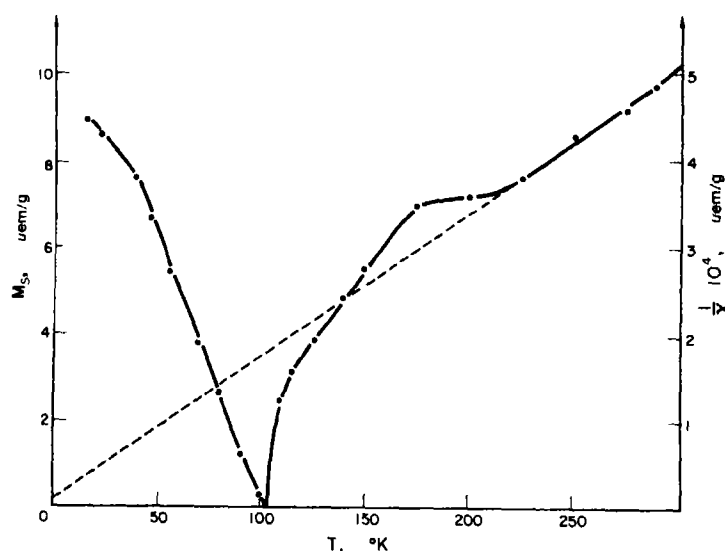


Fig. 2. Variation thermique de l'aimantation spontanée et de l'inverse de la susceptibilité de l'échantillon de monocristaux agglomérés $\text{Ca}_{1.7}\text{Bi}_{0.3}\text{MnO}_4$.

L'étude par diffraction neutronique de ces composés donne lieu aux résultats suivants:

Les échantillons A et B (Fig. 1) contenant un excès de calcium présentent des réflexions magnétiques s'indexant toutes dans la maille magnétique $a\sqrt{2}$, $a\sqrt{2}$, $2c$. Les réflexions correspondant au vecteur $\mathbf{K} = [000]$ ont donc disparu. Dans ces deux composés les moments

l'échange magnétique négatif entre ions Mn^{4+} est prépondérant cependant que les forces d'échange, selon l'axe c , sont faibles. Ces forces peuvent être, soit de nature anisotrope antisymétrique entre plans premiers voisins, soit dues à un mécanisme de superéchange de type Heisenberg entre plans seconds voisins ($\approx 12 \text{ \AA}$). On peut alors

envisager l'hypothèse qu'il coexiste deux types de grain dans lesquels le pourcentage de Mn est différent sur les sites de calcium, pourcentage dépendant de la préparation. Cette hypothèse est difficilement vérifiable par analyse chimique sur des poudres non homogènes qui possèdent toujours un excès de CaO et de Mn_3O_4 . Mais la préparation avec un excès de CaO correspond avec la disparition d'une phase magnétique et inversement la présence de deux phases magnétiques lorsqu'on synthétise le produit avec un excès de Mn_2O_3 nous conduit à penser que Mn intervient sur les sites de Ca^{2+} pour faire lien entre plan de Mn^{4+} . Ces ions Mn créeraient ainsi des ponts magnétiques entre plans seconds voisins et produiraient des échanges positifs ou négatifs selon le pourcentage de Mn. La valence du manganèse sur les sites de calcium n'est pas déterminée mais les raisons que nous avons énoncées précédemment ainsi que l'analogie des rayons ioniques nous conduisent à penser que le manganèse devrait être sous forme Mn^{2+} .

Nous avons observé sur les diagrammes des échantillons polycristallins un élargissement notable de la réflexion (103) appartenant à la phase $K = [00\frac{1}{2}]$. Ce phénomène est à rapprocher de celui décrit par Plumier[8] sur K_2NiF_4 . Toutefois l'observation de la réflexion (105) étant difficile (superposée à la réflexion nucléaire 101) il paraît prématuré de conclure à des défauts d'empilement et ceci d'autant plus qu'il est impossible d'observer le phénomène sur la phase $K = [000]$.

3.2 Cristal

Nous n'avons pas observé de réflexions correspondant à l'antiferromagnétisme mais par contre, un faible moment ferromagnétique par neutrons polarisés ($0,5 \mu_B$). Il faut remarquer que le cristal renferme 30 pour cent de Mn^{3+} sur les sites de Mn^{4+} . Or les interactions $Mn^{4+}-Mn^{3+}$ sont positives de signe opposé aux interactions $Mn^{4+}-Mn^{4+}$. On peut alors admettre qu'en dessous de 115°K les moments magnétiques s'ordonnent mais que

chaque ion Mn^{3+} présente un spin de signe opposé à celui que devrait avoir un ion Mn^{4+} . Il s'ensuit une incohérence des spins, qui, sous champ, donne lieu à un moment résultant non nul.

Par la technique des neutrons polarisés on peut observer le ferromagnétisme car il correspond à un moment moyen sur chaque atome. Par contre l'antiferromagnétisme n'est pas visible; nous pensons que *la taille des domaines cohérents est trop faible pour donner lieu à un phénomène de diffraction visible*. Des expériences sont actuellement en cours sur un monocristal de composition différente.

3.3. Diminution de spin

Un phénomène constant observé sur poudre est la réduction du moment magnétique. La valeur de $2 \mu_B$ ($S_{th} = 3 \mu_B$) peut s'expliquer par un modèle d'électrons délocalisés suggéré par Goodenough. Cependant les études récentes faites par Birgeneau *et al.*[9] sur K_2NiF_4 ont montré la présence réelle d'un ordre à deux dimensions pour lequel Lines[5] prévoit une réduction de spins de 13 pour cent. Ceci est toutefois insuffisant pour interpréter la réduction observée de 30 pour cent.

Il est possible d'expliquer la différence par *l'incohérence d'une partie des spins* en regard des considérations faites sur le monocristal. En effet, sur le monocristal le moment mesuré sur les intensités correspondant aux vecteurs $K = [000]$ et $K = [00\frac{1}{2}]$ est nul. Sur poudre, du fait d'un plus faible pourcentage de Mn^{3+} , le moment est voisin de $2 \mu_B$, mais ne peut atteindre la valeur théorique. Ces considérations sont à rapprocher des résultats de Wollan et Koehler[10] sur $CaMnO_3$ où les auteurs trouvent une diminution du moment correspondant à l'augmentation du pourcentage de Mn^{3+} .

Nous pensons d'autre part que la présence du ferromagnétisme signalé par Mac Chesney *et al.*[3] sur les poudres, et que nous avons observé sur tous les produits étudiés, est de

même nature que celui observé sur monocristal.

Remerciements—Nous remercions Monsieur E. F. Bertaut, Directeur de Recherches au C.N.R.S. pour l'attention qu'il a apporté à ce travail. Des remerciements s'adressent à Monsieur Schweizer du CEN-G pour l'étude de neutrons polarisés. Mademoiselle Veyret qui a mis obligeamment à notre service les appareillages de mesure d'aimantation du laboratoire de Monsieur Pauthenet. Nous remercions le groupe d'analyse du S.P.C.C. qui a réalisé les analyses chimiques.

REFERENCES

1. RUDDLESSEN S. N. et POPPER, P., *Acta crystallogr.*, **10**, 538 (1957).
2. BRISI C. et BORLERA M. L., *Att. Acad. Sci. Torino* **96**, 805 (1961-62).
3. MAC CHESNEY J., WILLIAMS H. J., POTTER J. F. et SHERWOOD R. C., *Phys. Rev.* **164**, 779 (1967).
4. GOODENOUGH J. B., *Phys. Rev.* **164**, 785 (1967).
5. LINES M. E., *Phys. Rev.* **164**, 736 (1967).
6. WATSON R. E. et FREEMAN A. J., *Acta crystallogr.* **14**, 27 (1961).
7. OLLIVIER G., Thèse 3ème Cycle, Grenoble (1968).
8. PLUMIER R., *J. Phys.* **24**, 741 (1963).
9. BIRGENEAU R. J., GUGGENHEIM H. J. et SHIRANE G., *Phys. Rev. Lett.* **22**, 14, 720 (1969).
10. WOLLAN E. O. et KOEHLER W. C., *Phys. Rev.* **100**, 546 (1955).
11. OSWALD H. R., WAMPETICH M., *Helv Chim. Acta* **50**, 2023 (1967).
12. COX D. E., SHIRANE G., BIRGENEAU R. J., MAC CHESNEY J. O., *Phys. Rev.* **188**, 930 (1969).

THE DETERMINATION OF ATOMIC FORCE CONSTANTS IN CUBIC SOLID SOLUTIONS—I. THEORY

J. E. GRAGG, Jr.

Department of Metallurgy and Materials Science, Carnegie-Mellon University, Pittsburgh,
Penn. 15213, U.S.A.

(Received 12 October 1970)

Abstract—A method is described for determining the coupling parameters (force constants) in b.c.c. and f.c.c. solid solutions from measurements of the elastic constants and the diffuse X-ray intensity scattered by *static* atomic displacements in the solid solution. Both measurements can be made on the same single crystal, the diffuse intensity measurements consisting of radial scans (varying 2θ only) along the [100], [110], and [111] reciprocal lattice directions. The analysis of the diffuse intensity allows the scattering due to thermal lattice vibrations to be eliminated from measurements at one temperature. With this method, it is possible to determine all of the coupling parameters of the first three coordination shells in b.c.c. solid solutions, while it is necessary to assume that some of the coupling parameters are dependent variables in order to determine the coupling parameters of the first three coordination shells in f.c.c. solid solutions. If one assumes that the third-nearest neighbor forces in the f.c.c. lattice are central forces, it can be shown that one need know the diffuse intensity along only the [100] and [110] directions in order to determine the remaining independent coupling parameters of the first three coordination shells. The proposed method is applicable to concentrated solid solutions where there are large mass differences in the solute and solvent atoms and where the interaction distances are short-range in nature.

1. INTRODUCTION

IN DISORDERED solid solutions, the atoms are generally observed to be displaced from the average lattice sites as a result of 'size' differences in the solute and solvent atoms. Ekstein[1] and Huang[2] were among the first to recognize the effect of these *static* displacements on the X-ray scattering pattern of solid solutions, Huang[2] having treated the problem in detail assuming that the solute atoms behaved as Coulomb distortion centers in an elastic continuum in order to calculate the displacement field about the solute atom. Matsubara[3] and Kanzaki[4] refined this theory by using the microscopic theory developed by Born and von Kàrmàn[5] for lattice dynamics to calculate the displacement field about an interstitial solute atom and this same theory was applied independently by Krivoglaз[6] to the case of a substitutional solute. Khachatryan[7] first proposed that this theory could be used to

determine the coupling parameters in solid solutions and Cook[8] has recently applied the Matsubara-Kanzaki-Krivoglaз (M.K.K.) theory to calculate the solute-lattice coupling parameters in Cu_3Au and β brass using estimated values of the lattice coupling parameters. A detailed derivation of the M.K.K. theory is given in this latter paper while the microscopic theory of elasticity for solid solutions has been treated in a recent paper by Cook and deFontaine[9].

The present work is an extension of the analysis developed by Cook[8] using the symmetry analysis of the total diffuse intensity of Borie[10] and Sparks and Borie[11] to obtain the individual diffuse intensity components (short-range order, size-effect modulation, etc.) without any assumptions about the magnitudes of the coupling parameters other than that they can be adequately described by the first three coordination shell interactions. The planar coupling parameters

defined by Cook [8] can be determined directly from these diffuse intensity components which, upon inversion of the linear relationship between the planar coupling parameters and the solute-lattice and lattice coupling parameters along the highly symmetric directions [100], [110], and [111], gives both the solute-lattice and lattice coupling parameters.

2. THE DETERMINATION OF THE COUPLING PARAMETERS

In the M.K.K. theory, the diffuse intensity scattered *solely* by static atomic displacements and local order is given by*

$$I_D(h_1, h_2, h_3) = C(h_1, h_2, h_3) \left[1 + \frac{2\pi i(x_A f_A + x_B f_B)}{a_0(f_A - f_B)} \times \sum_j h_j \Theta_j(h_1, h_2, h_3) \right]^2 \quad (1)$$

where

$$\Theta_j(h_1, h_2, h_3) = \sum_k \tilde{\Phi}_{jk}(h_1, h_2, h_3) \Phi_k(h_1, h_2, h_3). \quad (2)$$

The quantity $C(h_1, h_2, h_3)$ is the diffuse intensity due to local order in Laue units at the reciprocal lattice point (h_1, h_2, h_3) , f_A, f_B and x_A, x_B are the atomic scattering factors and composition of the solute and solvent atoms respectively, and a_0 is the lattice parameter of the solid solution unit cell. The function $\tilde{\Phi}_{jk}(h_1, h_2, h_3)$ is the j - k element of the inverse matrix of the Fourier transform of the lattice coupling parameters, $\varphi_{jk}(l, m, n)$, while the function $\Phi_k(h_1, h_2, h_3)$ is the Fourier transform of the solute-lattice coupling parameters, $\varphi_k(l, m, n)$. The lattice coupling parameters are the elements

*The derivation of equation (1) is given in Ref. [8]. Equation (2) follows from the force-balance relation between the solute composition variation and the static displacement field [6].

of the force constant matrix derived in the theory of Born and von Kármán [5] while the solute-lattice coupling parameters are related to the initial force in the undistorted lattice acting in the k -direction on the atom at site \mathbf{p} ,

$$f_k(\mathbf{p}) = \sum_{\mathbf{p}'} \varphi_k(\mathbf{p} - \mathbf{p}') q(\mathbf{p}'), \mathbf{p} - \mathbf{p}' = \mathbf{r}_{lmn} \quad (3)$$

where $q(\mathbf{p}')$ is the solute atom composition variation at the site \mathbf{p}' ,

$$q(\mathbf{p}') = \begin{cases} x_B, & \text{if a solute atom (A) is at site } \mathbf{p}' \\ -x_A, & \text{if not.} \end{cases}$$

The shorthand notation for these coupling parameters is given in Table 1(a).

Although the function $\Theta_j(h_1, h_2, h_3)$ will generally be a complicated, non-linear function of the coupling parameters, in the cubic lattices it reduces to a rather simple function along the principal symmetry axes $[\xi_1, \xi_2, \xi_3]$ equal to [100], [110], and [111],

$$\Theta_j(h\xi_1, h\xi_2, h\xi_3) = \frac{\Phi_j(h\xi_1, h\xi_2, h\xi_3)}{\sum_k \xi_k \Phi_{jk}(h\xi_1, h\xi_2, h\xi_3)} \quad (4)$$

As will be seen, it is this linear relationship between the coupling parameters and the diffuse intensity along these highly symmetric directions which allows us to determine these parameters from the diffuse X-ray scattering pattern.

(a). The b.c.c. coupling parameters

From the relationships given in Table 1(b), it can be seen from equation (4) that for the b.c.c. lattice

$$\Theta_1(h, 0, 0) = \frac{i[\hat{\Psi}_1 \sin \pi h + \hat{\Psi}_2 \sin 2\pi h]}{[\Psi_1(1 - \cos \pi h) + \Psi_2(1 - \cos 2\pi h)]} \quad (5a)$$

$$\Theta_1(h, h, 0) = \frac{i[\hat{\Psi}_3' \sin 2\pi h + \hat{\Psi}_3 \sin 4\pi h]}{[\Psi_3(1 - \cos 2\pi h) + \Psi_4(1 - \cos 4\pi h)]} \quad (5b)$$

Table 1(a). The solute-lattice and lattice coupling parameters*

The b.c.c. lattice		The f.c.c. lattice	
$\varphi_{1f}(1, 1, 1) = \begin{bmatrix} -\alpha_1 & -\gamma_1 & -\gamma_1 \\ -\gamma_1 & -\alpha_1 & -\gamma_1 \\ -\gamma_1 & -\gamma_1 & -\alpha_1 \end{bmatrix}$	$\varphi_f(1, 1, 1) = \begin{bmatrix} \hat{\alpha}_1 \\ \hat{\alpha}_1 \\ \hat{\alpha}_1 \end{bmatrix}$	$\varphi_{1f}(1, 1, 0) = \begin{bmatrix} -\alpha_1 & -\gamma_1 & 0 \\ -\gamma_1 & -\alpha_1 & 0 \\ 0 & 0 & -\beta_1 \end{bmatrix}$	$\varphi_f(1, 1, 0) = \begin{bmatrix} \hat{\alpha}_1 \\ \hat{\alpha}_1 \\ 0 \end{bmatrix}$
$\varphi_{1f}(2, 0, 0) = \begin{bmatrix} -\alpha_2 & 0 & 0 \\ 0 & -\beta_2 & 0 \\ 0 & 0 & -\beta_2 \end{bmatrix}$	$\varphi_f(2, 0, 0) = \begin{bmatrix} \hat{\alpha}_2 \\ 0 \\ 0 \end{bmatrix}$	$\varphi_{1f}(2, 0, 0) = \begin{bmatrix} -\alpha_2 & 0 & 0 \\ 0 & -\beta_2 & 0 \\ 0 & 0 & -\beta_2 \end{bmatrix}$	$\varphi_f(2, 0, 0) = \begin{bmatrix} \hat{\alpha}_2 \\ 0 \\ 0 \end{bmatrix}$
$\varphi_{1f}(2, 2, 0) = \begin{bmatrix} -\alpha_3 & -\gamma_3 & 0 \\ -\gamma_3 & -\alpha_3 & 0 \\ 0 & 0 & -\beta_3 \end{bmatrix}$	$\varphi_f(2, 2, 0) = \begin{bmatrix} \hat{\alpha}_3 \\ \hat{\alpha}_3 \\ 0 \end{bmatrix}$	$\varphi_{1f}(2, 1, 1) = \begin{bmatrix} -\alpha_3 & -\delta_3 & -\delta_3 \\ -\delta_3 & -\beta_3 & -\gamma_3 \\ -\delta_3 & -\gamma_3 & -\beta_3 \end{bmatrix}$	$\varphi_f(2, 1, 1) = \begin{bmatrix} \hat{\alpha}_3 \\ \hat{\beta}_3 \\ \hat{\beta}_3 \end{bmatrix}$

*In integer units of $a_0/2$.

$$\Theta_1(h, h, h) =$$

$$\frac{i[\hat{\Psi}'_4 \sin \pi h + \hat{\Psi}'_5 \sin 2\pi h + \hat{\Psi}'_4 \sin 3\pi h + \hat{\Psi}'_6 \sin 4\pi h]}{[\Psi'_5(1 - \cos \pi h) + \Psi'_6(1 - \cos 2\pi h) + \Psi'_5(1 - \cos 3\pi h) + \Psi'_6(1 - \cos 4\pi h)]}. \quad (5c)$$

The parameters $\hat{\Psi}_j$ and Ψ_j are called the solute-lattice and lattice planar coupling parameters [8]. The unprimed planar coupling parameters comprise a set of linearly independent functions of the solute-lattice and lattice coupling parameters given by the equations

$$\Psi_1 = 8\alpha_1$$

$$\begin{aligned} \Psi_2 &= 2\alpha_2 + 8\alpha_3 \\ \Psi_3 &= 4\alpha_1 + 4\gamma_1 + 2\alpha_2 + 2\beta_2 + 4\alpha_3 + 4\beta_3 \\ \Psi_4 &= 2\alpha_3 + 2\gamma_3 \\ \Psi_5 &= 2\alpha_1 + 4\gamma_1 \\ \Psi_6 &= 4\alpha_3 + 2\beta_3 + 4\gamma_3 \\ \hat{\Psi}_1 &= 8\hat{\alpha}_1 \\ \hat{\Psi}_2 &= 2\hat{\alpha}_2 + 8\hat{\alpha}_3 \\ \hat{\Psi}_3 &= 2\hat{\alpha}_3. \end{aligned}$$

Table 1(b). The Fourier transforms of the solute-lattice and lattice coupling parameters*

The b.c.c. lattice	The f.c.c. lattice
$\Phi_{11}(h_1, h_2, h_3) = 8\alpha_1(1 - \cos \pi h_1 \cos \pi h_2 \cos \pi h_3) + 2\alpha_2(1 - \cos 2\pi h_1) + 2\beta_2(2 - \cos 2\pi h_2 - \cos 2\pi h_3) + 4\alpha_3[2 - \cos 2\pi h_1(\cos 2\pi h_2 + \cos 2\pi h_3)] + 4\beta_3(1 - \cos 2\pi h_2 \cos 2\pi h_3)$	$\Phi_{11}(h_1, h_2, h_3) = 4\alpha_1(2 - \cos \pi h_1 \cos \pi h_2 - \cos \pi h_1 \cos \pi h_3) + 4\beta_1(1 - \cos \pi h_2 \cos \pi h_3) + 2\alpha_2(1 - \cos 2\pi h_1) + 2\beta_2(2 - \cos 2\pi h_2 - \cos 2\pi h_3) + 8\alpha_3(1 - \cos 2\pi h_1 \cos \pi h_2 \cos \pi h_3) + 8\beta_3[2 - \cos \pi h_1(\cos 2\pi h_2 \cos \pi h_3 + \cos \pi h_2 \cos 2\pi h_3)]$
$\Phi_{12}(h_1, h_2, h_3) = 8\gamma_1 \sin \pi h_1 \sin \pi h_2 \cos \pi h_3 + 4\gamma_3 \sin 2\pi h_1 \sin 2\pi h_2$	$\Phi_{12}(h_1, h_2, h_3) = 4\gamma_1 \sin \pi h_1 \sin \pi h_2 + 8\gamma_3 \sin \pi h_1 \sin \pi h_2 \cos 2\pi h_3 + 8\delta_3(\sin 2\pi h_1 \sin \pi h_2 + \sin \pi h_1 \sin 2\pi h_2) \cos \pi h_3$
$\Phi_1(h_1, h_2, h_3) = i[8\hat{\alpha}_1 \sin \pi h_1 \cos \pi h_2 \cos \pi h_3 + 2\hat{\alpha}_2 \sin 2\pi h_1 + 4\hat{\alpha}_3 \sin 2\pi h_1 (\cos 2\pi h_2 + \cos 2\pi h_3)]$	$\Phi_1(h_1, h_2, h_3) = i[4\hat{\alpha}_1 \sin \pi h_1 (\cos \pi h_2 + \cos \pi h_3) + 2\hat{\alpha}_2 \sin 2\pi h_1 + 8\hat{\alpha}_3 \sin 2\pi h_1 \cos \pi h_2 \cos \pi h_3 + 8\hat{\beta}_3 \sin \pi h_1 (\cos \pi h_2 \cos 2\pi h_3 + \cos 2\pi h_2 \cos \pi h_3)]$

*The remaining parameters may be obtained from cyclic permutation of the coordinate subscripts.

The primed planar coupling parameters are not linearly independent, but can be expressed as linear combinations of the unprimed planar coupling parameters,

$$\begin{aligned}\Psi'_3 &= \Psi_1 - \Psi_5 \\ \Psi'_6 &= -\Psi_1/2 - \Psi_2 + 2\Psi_3 + 8\Psi_4 - 2\Psi_5 - 4\Psi_6 \\ \hat{\Psi}'_3 &= \hat{\Psi}_1/2 + \hat{\Psi}_2 - 2\hat{\Psi}_3 \\ \hat{\Psi}'_1 &= \hat{\Psi}_1/4 \\ \hat{\Psi}'_5 &= \hat{\Psi}_2 - 4\hat{\Psi}_3 \\ \hat{\Psi}'_6 &= 2\hat{\Psi}_3.\end{aligned}$$

From these relationships and the results of equations (5a) through (5c), one can see that the planar coupling parameters must satisfy the conditions

$$\begin{aligned}\Psi_1(1 - \cos \pi h) + \Psi_2(1 - \cos 2\pi h) \\ + \hat{\Psi}_2 \sin 2\pi h/i\Theta_1(h, 0, 0) \\ = -\hat{\Psi}_1 \sin \pi h/i\Theta_1(h, 0, 0) \quad (6a)\end{aligned}$$

$$\begin{aligned}\Psi_3(1 - \cos 2\pi h) + \Psi_4(1 - \cos 4\pi h) \\ + \hat{\Psi}_2 \sin 2\pi h/i\Theta_1(h, h, 0) \\ + \hat{\Psi}_3(\sin 4\pi h - 2\sin 2\pi h)/i\Theta_1(h, h, 0) \\ = -\hat{\Psi}_1 \sin 2\pi h/2i\Theta_1(h, h, 0) \quad (6b)\end{aligned}$$

$$\begin{aligned}\Psi_1(1 - 2\cos \pi h + \cos 2\pi h)/2 \\ + (-\Psi_2 + 2\Psi_3 + 8\Psi_4)(1 - \cos 2\pi h) \\ + \Psi_5(-1 + 2\cos 2\pi h - \cos 3\pi h) \\ + \Psi_6(-3 + 4\cos 2\pi h - \cos 4\pi h) \\ + \hat{\Psi}_2 \sin 2\pi h/i\Theta_1(h, h, h) \\ + \hat{\Psi}_3(2\sin 4\pi h - 4\sin 2\pi h)/i\Theta_1(h, h, h) \\ = -\hat{\Psi}_1(\sin \pi h + \sin 3\pi h)/4i\Theta_1(h, h, h). \quad (6c)\end{aligned}$$

If the function $\Theta_1(h_1, h_2, h_3)$ is known along the directions [100], [110], and [111], these equations can be solved for the planar coupling parameters to within an unknown factor of proportionality. Thus, if we choose the parameter $\hat{\Psi}_1$ as the unknown proportionality factor, we can then solve for the ratios $\Psi_j/\hat{\Psi}_1$ and $\hat{\Psi}_j/\hat{\Psi}_1$. As Cook [8] has shown, this

proportionality factor can be determined from the long wave relation for the elastic constant c_{11} , since this relation is a linearly dependent function of the planar coupling parameters,

$$\Psi_1 + 4\Psi_2 = 4a_0c_{11} \quad (7a)$$

and hence

$$\hat{\Psi}_1 = \frac{4a_0c_{11}}{[\Psi_1/\hat{\Psi}_1 + 4\Psi_2/\hat{\Psi}_1]}. \quad (7b)$$

With this proportionality factor thus determined, one can determine the remaining planar coupling parameters $\hat{\Psi}_2$ and $\hat{\Psi}_3$ and Ψ_1 through Ψ_6 . While the three solute-lattice planar coupling parameters are sufficient to determine the three independent components of the solute-lattice coupling parameters ($\hat{\alpha}_1$, $\hat{\alpha}_2$, and $\hat{\alpha}_3$), there are only six independent planar lattice coupling parameters and seven independent components for the lattice coupling parameters. The long wave relation for c_{44} (or c_{12}), however, unlike the long wave relation for c_{11} , is linearly independent of the planar lattice coupling parameters and may be used as an additional equation which thus determines the seven lattice coupling parameter components for the first three coordination shells.

Choosing the long wave relation for c_{44} as the seventh independent equation, the components of the first three lattice coupling parameters are given by

$$\begin{aligned}\alpha_1 &= \Psi_1/8 \\ \gamma_1 &= -\Psi_1/16 + \Psi_5/4 \\ \alpha_2 &= \Psi_3/2 - \Psi_5/2 - a_0c_{44}/2 \\ \beta_2 &= -\Psi_1/8 - \Psi_2/4 + \Psi_3/4 + 2\Psi_4 - \Psi_5/4 \\ &\quad - \Psi_6 + a_0c_{44}/4 \\ \alpha_3 &= \Psi_2/8 - \Psi_3/8 + \Psi_5/8 + a_0c_{44}/8 \\ \beta_3 &= -\Psi_4 + \Psi_6/2 \\ \gamma_3 &= -\Psi_2/8 + \Psi_3/8 + \Psi_4/2 - \Psi_5/8 - a_0c_{44}/8\end{aligned}$$

while the components of the first three solute-lattice coupling parameters are given by

$$\begin{aligned}\alpha_1 &= \hat{\Psi}_1/8 \\ \alpha_2 &= \hat{\Psi}_2/2 - 2\hat{\Psi}_3 \\ \alpha_3 &= \hat{\Psi}_3/2.\end{aligned}$$

These results are predicated only on the assumption that the static displacements in the solid solution are adequately described by first, second, and third nearest neighbor interactions only.

(b) *The f.c.c. coupling parameters*

As in the case of the b.c.c. lattice, it can be shown from the relations given in Table 1(b) and equation (4) that the function $\Theta_1(h_1, h_2, h_3)$ can be described by a set of planar solute-lattice and lattice coupling parameters which must satisfy the conditions

$$\begin{aligned}\Psi_1(1 - \cos \pi h) + \Psi_2(1 - \cos 2\pi h) \\ + \hat{\Psi}_2 \sin 2\pi h / i\Theta_1(h, 0, 0) \\ = -\hat{\Psi}_1 \sin \pi h / i\Theta_1(h, 0, 0)\end{aligned}\quad (8a)$$

$$\begin{aligned}\Psi_3(1 - \cos \pi h) + \Psi_4(1 - \cos 2\pi h) \\ + \Psi_5(1 - \cos 3\pi h) + 2\Psi_2 \sin \pi h / i\Theta_1(h, h, 0) \\ + \hat{\Psi}_3(\sin 2\pi h - 2 \sin \pi h) / i\Theta_1(h, h, 0) \\ + \hat{\Psi}_4(\sin 3\pi h - 3 \sin \pi h) / i\Theta_1(h, h, 0) \\ = -\hat{\Psi}_1 \sin \pi h / i\Theta_1(h, h, 0)\end{aligned}\quad (8b)$$

$$\begin{aligned}(-\Psi_1/4 - \Psi_2 + \Psi_3/2 + 2\Psi_4 + 9\Psi_5/2) \\ (1 - \cos 2\pi h) + \Psi_6(-3 + 4\cos 2\pi h - \cos 4\pi h) \\ + (3\hat{\Psi}_2/2 - \hat{\Psi}_3/2 - 2\hat{\Psi}_4)\sin 2\pi h / i\Theta_1(h, h, h) \\ + (-\hat{\Psi}_2/4 + \hat{\Psi}_3/4 + \hat{\Psi}_4)\sin 4\pi h / i\Theta_1(h, h, h) \\ = -\hat{\Psi}_1(10\sin 2\pi h - \sin 4\pi h) / 16i\Theta_1(h, h, h)\end{aligned}\quad (8c)$$

where

$$\begin{aligned}\Psi_1 &= 8\alpha_1 + 16\beta_3 \\ \Psi_2 &= 2\alpha_2 + 8\alpha_3 \\ \Psi_3 &= 4\alpha_1 + 4\beta_1 + 4\alpha_3 + 4\beta_3 - 8\delta_3 \\ \Psi_4 &= 2\alpha_1 + 2\gamma_1 + 2\alpha_2 + 2\beta_2 + 4\beta_3 + 4\gamma_3 \\ \Psi_5 &= 4\alpha_3 + 4\beta_3 + 8\delta_3 \\ \Psi_6 &= 2\alpha_3 + 4\beta_3 + 4\gamma_3 + 8\delta_3 \\ \hat{\Psi}_1 &= 8\alpha_1 + 16\beta_3 \\ \hat{\Psi}_2 &= 2\alpha_2 + 8\alpha_3\end{aligned}$$

$$\begin{aligned}\hat{\Psi}_3 &= 2\alpha_1 + 2\alpha_2 + 4\beta_3 \\ \hat{\Psi}_4 &= 4\alpha_3 + 4\beta_3\end{aligned}$$

As before, these equations can be solved to within an unknown factor of proportionality if the function $\Theta_1(h_1, h_2, h_3)$ is known along the [100], [110], and [111] directions. If we choose the planar coupling parameter $\hat{\Psi}_1$ as the proportionality factor and solve these equations for the ratios $\Psi_i/\hat{\Psi}_1$ and $\hat{\Psi}_j/\hat{\Psi}_1$, we can determine the proportionality factor from the long wave relation for c_{11} ,

$$\Psi_1 + 4\Psi_2 = 2a_0c_{11}\quad (9a)$$

in which case it can be seen that

$$\hat{\Psi}_1 = \frac{2a_0c_{11}}{[\Psi_1/\hat{\Psi}_1 + 4\Psi_2/\hat{\Psi}_1]}\quad (9b)$$

Unlike the case of the b.c.c. lattice, however, the planar lattice coupling parameters in the f.c.c. lattice are nowhere sufficient to determine all of the nine independent components of the lattice coupling parameters for the first three coordination shells, even when the long wave relations for the elastic constants are used as additional equations (either c_{44} or c_{12} , since only one of these can be taken as a linearly independent function, the other being determined by the planar coupling parameters and the elastic constant chosen as the independent variable).

To reduce the number of independent parameters in the first three coordination shells, it has been assumed that the third neighbor forces are central forces [12], in which case one must have

$$\alpha_3 = 2\delta_3 = 4\beta_3 = 4\gamma_3$$

$$\hat{\alpha}_3 = 2\hat{\beta}_3.$$

For this situation, the planar coupling parameters $\hat{\Psi}_4$ and Ψ_6 are no longer linearly independent functions, but satisfy the relations

$$4\hat{\Psi}_4 = 3\hat{\Psi}_1/4 + 3\hat{\Psi}_2 - 3\hat{\Psi}_3$$

$$9\Psi_6 = 8\Psi_5.$$

As can be seen from equation (8c), this means that the function $\Theta_1(h_1, h_2, h_3)$ along the [111] direction is not independent of the values obtained along the [100] and [110] directions and, hence, one need know the diffuse intensity along only these two directions in order to determine the coupling parameters. Thus, using the long wave relation for c_{44} and the independent planar coupling parameters Ψ_1 through Ψ_5 we can now solve for the six independent components of the coupling parameters for the first three coordination shells in the f.c.c. lattice

$$\begin{aligned}\alpha_1 &= \Psi_1/8 - \Psi_5/18 \\ \beta_1 &= -\Psi_1/8 + \Psi_3/4 + \Psi_5/36 \\ \gamma_1 &= -\Psi_1/8 - \Psi_2/2 + \Psi_3/8 + \Psi_4/2 + 5\Psi_5/8 \\ &\quad - a_0 c_{44}/4 \\ \alpha_2 &= \Psi_2/2 - 4\Psi_5/9 \\ \beta_2 &= -\Psi_3/8 - 17\Psi_5/72 + a_0 c_{44}/4 \\ \alpha_3 &= \Psi_5/9 \\ \alpha_1 &= 3\hat{\Psi}_1/32 - \hat{\Psi}_2/8 + \hat{\Psi}_3/8 \\ \alpha_2 &= -\hat{\Psi}_1/8 + \hat{\Psi}_3/2 \\ \alpha_3 &= \hat{\Psi}_1/32 + \hat{\Psi}_2/8 - \hat{\Psi}_3/8.\end{aligned}$$

There are two assumptions which influence the validity of these results; (1) that the static displacements are adequately described by only the first, second, and third nearest neighbor interactions, and (2) that the third nearest neighbor forces are central forces.

3. THE DETERMINATION OF THE FUNCTION

$$\Theta_1(h_1, h_2, h_3)$$

We have seen in the preceding section that if the function $\Theta_1(h_1, h_2, h_3)$ is known along the principal symmetry axes [100], [110], and [111], one can determine the coupling parameters of the first three coordination shells in the b.c.c. and f.c.c. lattices. In this section we will show that this function can be determined directly from measurements of the total diffuse intensity without any assumptions about the values of these coupling parameters.

Thus, from the symmetry of the b.c.c. and

f.c.c. lattices we can see that along the principal symmetry axes,

$$\Theta_1(h, h, 0) = \Theta_2(h, h, 0)$$

$$\Theta_1(h, h, h) = \Theta_2(h, h, h) = \Theta_3(h, h, h)$$

and, hence, for $[h_1, h_2, h_3]$ equal to $[h, 0, 0]$, $[h, h, 0]$, and $[h, h, h]$ the expression for the diffuse intensity given in equation (1) is of the form

$$I_D(h_1, h_2, h_3) =$$

$$C(h_1, h_2, h_3) + hU_1(h_1, h_2, h_3) + h^2U_2(h_1, h_2, h_3) \quad (10)$$

where

$$U_1(h_1, h_2, h_3) = \frac{+4\pi i(x_A f_A + x_B f_B)}{a_0(f_A - f_B)}$$

$$K_1(h_1, h_2, h_3)\Theta_1(h_1, h_2, h_3)C(h_1, h_2, h_3)$$

$$U_2(h_1, h_2, h_3) = \frac{-4\pi^2(x_A f_A + x_B f_B)^2}{a_0^2(f_A - f_B)^2}$$

$$K_2(h_1, h_2, h_3)\Theta_1^2(h_1, h_2, h_3)C(h_1, h_2, h_3)$$

$$K_1(h, 0, 0) = 1, \quad K_1(h, h, 0) = 2, \quad K_1(h, h, h) = 3$$

$$K_2(h, 0, 0) = 1, \quad K_2(h, h, 0) = 4, \quad K_2(h, h, h) = 9.$$

Borie[10] and Sparks and Borie[11] have considered expressions of this form for the total diffuse intensity and have shown that terms such as $U_1(h_1, h_2, h_3)$ and $U_2(h_1, h_2, h_3)^*$ can be separated by rather simple symmetry considerations of the total diffuse intensity. This approach, which was first suggested by Schwartz[13], is as follows: If we assume that the ratio f_A/f_B is constant throughout the reciprocal space volume (which is generally a valid approximation, the variation in this ratio being on the order of a few percent over

*In the theory of Borie and Sparks, the term $U_1(h_1, h_2, h_3)$ corresponds to linear combinations of their term $Q_x(h_1, h_2, h_3)$ which is due solely to static displacements. The term $U_2(h_1, h_2, h_3)$ corresponds to the static component of the terms $R_x(h_1, h_2, h_3)$ and $S_{xu}(h_1, h_2, h_3)$, which also include thermal (vibrational) displacements in the theory of Borie and Sparks.

a rather large range of $\sin \vartheta/\lambda$, it can be seen that the functions $U_1(h_1, h_2, h_3)$ and $U_2(h_1, h_2, h_3)$ are periodic functions in reciprocal space with the period of the reciprocal lattice unit cell. Following the analysis of Sparks and Borie[11], we define

$$I_D(2+h_j) = \begin{cases} I_D(2+h_1, 2+h_2, 2+h_3), \\ [h_1, h_2, h_3] = [h, h, h] & 2U_1(h_1, h_2, h_3) \\ I_D(2+h_1, 2+h_2, h_3), \\ [h_1, h_2, h_3] = [h, h, 0] & = I_D(2+h_j) - I_D(h_j) - 4(1+h)U_2(h_1, h_2, h_3) \\ I_D(2+h_1, h_2, h_3), \\ [h_1, h_2, h_3] = [h, 0, 0] & \end{cases} \quad (12a)$$

which, from equation (11c), is equivalent to the expression

with a similar definition for $I_D(4+h_j)$. Then it can be seen that

$$8U_2(h_1, h_2, h_3) = I_D(4+h_j) - 2I_D(2+h_j) + I_D(h_j). \quad (11a)$$

However, since $U_2(h_1, h_2, h_3)$ is a periodic function in reciprocal space, equation (11a) is equivalent to the expression

$$8U_2(h_1, h_2, h_3) = I_D(2+h_j) - 2I_D(h_j) + I_D(h_j-2). \quad (11b)$$

Moreover, since the total diffuse intensity must obey the point group symmetry of the

This equation requires that the total diffuse intensity be known over a considerably smaller range of $\sin \vartheta/\lambda$ than does equation (11a) and hence improves our approximation that the ratio f_A/f_B is constant.

Knowing $U_2(h_1, h_2, h_3)$, it can then be shown that

$$4U_1(h_1, h_2, h_3) = (1-h)I_D(2+h_j) + 2hI_D(h_j) - (1+h)I_D(2-h_j). \quad (12b)$$

Therefore, from the results of equations (11c) and (12b) and the expression for the total diffuse intensity given in equation (10), it can be shown that

$$8C(h_1, h_2, h_3) = -h(2-h)I_D(2+h_j) + 2(4-h^2)I_D(h_j) + h(2+h)I_D(2-h_j). \quad (13)$$

Thus, from the definition of the function $U_1(h_1, h_2, h_3)$ it can be seen that the function $\Theta_1(h_1, h_2, h_3)$ is given by the expression

$$\Theta_1(h_1, h_2, h_3) = \frac{-ia_0(f_A - f_B)}{2\pi K_1(h_1, h_2, h_3)(x_A f_A + x_B f_B)} \times \frac{[(1-h)I_D(2+h_j) + 2hI_D(h_j) - (1+h)I_D(2-h_j)]}{[-h(2-h)I_D(2+h_j) + 2(4-h^2)I_D(h_j) + h(2+h)I_D(2-h_j)]}. \quad (14)$$

cubic system, it must be symmetric across the planes $h_j = 0$, in which case equation (11b) is equivalent to the expression

$$8U_2(h_1, h_2, h_3) = I_D(2+h_j) - 2I_D(h_j) + I_D(2-h_j). \quad (11c)$$

From this expression, it can be seen that in order to determine the function $\Theta_1(h_1, h_2, h_3)$ at the points $(h, 0, 0)$, $(h, h, 0)$, or (h, h, h) one need know the total diffuse intensity at the points $(h, 0, 0)$, $(2+h, 0, 0)$, $(2-h, 0, 0)$, $(h, h, 0)$, $(2+h, 2+h, 0)$, $(2-h, 2-h, 0)$, (h, h, h) , $(2+h, 2+h, 2+h)$, and $(2-h,$

$2-h, 2-h$). Moreover, since the total diffuse intensity also contains a contribution from thermal diffuse scattering which is proportional to h^2 , the operation given in equation (11c) for separating the function $U_2(h_1, h_2, h_3)$ will also eliminate this contribution at the same time (first-order thermal diffuse scattering), giving not the function $U_2(h_1, h_2, h_3)$ but this function plus thermal diffuse intensity.

4. DISCUSSION

In the preceding sections, it was shown that both the solute-lattice and lattice coupling parameters could be determined for the first three coordination shells in the b.c.c. and f.c.c. lattices from measurements of the total diffuse intensity along the [100], [110], and [111] reciprocal lattice directions and the elastic constants. In the b.c.c. lattice, this result assumes only that the interaction forces of the first three coordination shells are adequate to describe the static displacement field in the solid solution while for the f.c.c. lattice it is necessary to assume as well that the third nearest neighbor forces are central forces.

The analysis of the diffuse intensity assumes (1) that the scattering contribution of both the static and thermal (vibrational) displacements can be described by a second order expansion of the phase factor due to these displacements (an approximation which is consistent with the harmonic approximation of the microscopic elastic theory) and (2) that the ratio of the scattering factors is constant over the range of $\sin \vartheta/\lambda$ in which the total diffuse intensity is measured. This latter assumption appears to have little effect on the results of the analysis of Sparks and Borie [11], since the application of this analysis to volume measure-

ments of the scattering due to local order have routinely yielded values for α_{000} (which should theoretically be equal to unity) on the order of 1.2 to 1.4 [14, 15, 16].

In practice, the two factors which one would expect to most influence the results of this analysis are (1) the assumption that the coupling parameters are zero beyond the third coordination shell (or the assumption of the central third nearest neighbor force in the f.c.c. lattice) and (2) the failure of the symmetry analysis to eliminate the higher order contributions of thermal diffuse scattering. This latter contribution can be significant in materials with low Debye temperatures and it has been shown that the contribution of second-order thermal diffuse scattering can account for an error of over 20 per cent in α_{000} in dilute Al-Ag alloys [17].

Insofar as the error introduced by assuming that all coupling parameters are zero beyond the third coordination shell is concerned, the proposed analysis has several built in checks against the validity of this assumption. For example, in both the b.c.c. and f.c.c. lattices only one of the two independent elastic constant longwave relations is used to determine the lattice coupling parameters (either c_{44} or c_{12}) and hence the remaining elastic constant value can be used as a check for consistency between the calculated coupling parameters and the measured elastic constant value. Moreover, if the variation of the lattice parameter of the solid solution with solute composition is known (which is not required for the determination of the coupling parameters), the long wave relation for the solute-lattice coupling parameters given in Table 1(c) can be used as a check for consistency in

Table 1(c). The long wave relations for the elastic constants

The b.c.c. lattice	The f.c.c. lattice.
$2\alpha_1 + 2\alpha_2 + 8\alpha_3 = a_0 c_{11}$	$4\alpha_1 + 4\alpha_2 + 16\alpha_3 + 8\beta_3 = a_0 c_{11}$
$2\alpha_1 + 2\beta_1 + 4\alpha_3 + 4\beta_3 = a_0 c_{44}$	$2\alpha_1 + 2\beta_1 + 4\beta_2 + 4\alpha_2 + 20\beta_3 = a_0 c_{44}$
$4\gamma_1 + 8\gamma_3 = a_0 (c_{12} + c_{44})$	$4\gamma_1 + 8\gamma_3 + 32\delta_3 = a_0 (c_{12} + c_{44})$
$4\hat{\alpha}_1 + 2\hat{\alpha}_2 + 8\hat{\alpha}_3 = \frac{a_0}{2} \frac{da_0}{dx_A} (c_{11} + 2c_{12})$	$8\hat{\alpha}_1 + 4\hat{\alpha}_2 + 16(\hat{\alpha}_3 + \hat{\beta}_3) = \frac{a_0}{2} \frac{da_0}{dx_A} (c_{11} + 2c_{12})$

these values. In the case of the f.c.c. lattice, one can also check the validity of the assumed central third nearest neighbor force by measuring the diffuse intensity along the [111] reciprocal lattice direction and comparing the resulting values (which we know are not independent of the values obtained along the [100] and [110] directions in the case of central third nearest neighbor forces) to the predicted values in equation (8c).

The advantage of this method over the determination of the coupling parameters from the dispersion relationship of the phonon spectrum[12] is that it is applicable to concentrated solid solutions where there are large mass difference in the solute and solvent atoms and where the interaction forces are short-range in nature.

Finally, in interpreting the results of this analysis, it should be recognized that the measured coupling parameters are 'averages' over all types of pair-wise interactions in the solid solution and as such are valid only for an 'average' solid solution lattice. This does not mean that the solid solution is assumed to be random, for the solute composition variation is inherent in the analysis, but it does imply that every atom interacts with its neighbors in an identical manner, independent of the local environment. Certainly this is not the actual situation, for it is well known that the displacement of any one atom is a function of a manybody interaction which depends on the local surroundings of the atom[18, 19, 20]. Hence, the results of this analysis will probably be most meaningful in solid solutions which have either a low degree of short-range order or a high degree of long-range order which can be described in terms of small deviations from perfect long-range order[13].

In the second part of this series of papers, we will present some results on the coupling

parameters in Cu_2Au above and below the critical temperature and for several dilute solutions of molybdenum in iron which will be discussed in terms of the properties of these two systems.

Acknowledgements—It is with pleasure that the advice and comments of Professors J. B. Cohen and R. F. Sekerka, both of whom kindly read this manuscript, are acknowledged as are the comments of Professor D. deFontaine on the microscopic elastic theory. The author gratefully acknowledges the support of the Ford Foundation through a grant to Carnegie-Mellon University during the period in which this work was performed.

REFERENCES

1. EKSTEIN H., *Phys. Rev.* **68**, 120 (1945).
2. HUANG K., *Proc. R. Soc. (London)* **190**, 102 (1947).
3. MATSUBARA T. J., *Proc. phys. Soc. Japan* **7**, 270 (1952).
4. KANZAKI H., *J. Phys. Chem. Solids* **2**, 24 (1957).
5. BORN M. and HUANG K., *Dynamical Theory of Crystal Lattices*, Oxford University Press, Oxford (1954).
6. KRIVOGLAZ M. A., *Soviet Phys. JETP* **34**, 139 (1958).
7. KHACHATURYAN A. G., *Soviet Phys. solid State* **4**, 2081 (1963).
8. COOK H. E., *J. Phys. Chem. Solids* **30**, 1097 (1969).
9. COOK H. E. and DE FONTAINE D., *Acta Metall.* **17**, 915 (1969).
10. BORIE B., *Acta crystallogr.* **14**, 472 (1961).
11. SPARKS C. J. and BORIE B., In *Local Atomic Arrangements Studied by X-ray diffraction* (Edited by J. B. Cohen and J. E. Hilliard), pp. 3–50, Gordon and Breach, New York (1966).
12. WALKER C. B., *Phys. Rev.* **103**, 547 (1956).
13. SCHWARTZ L. H. and COHEN J. B., *J. appl. Phys.* **36**, 598 (1965).
14. EPPERSON J. E. and SPRUIELL J. E., *J. Phys. Chem. Solids* **30**, 1733 (1969).
15. ERICSSON T. and COHEN J. B., *Acta crystallogr.* In press.
16. ERICSSON T., MOURIKIS S., and COHEN J. B., *J. Mat. Sci.* **5**, 901 (1970).
17. GRAGG J. E., Jr. and COHEN J. B., *Acta. Metal.* **19**, 507 (1971).
18. BORIE B., *Acta crystallogr.* **10**, 89 (1957); **12**, 280 (1959).
19. COWLEY J. M., *Acta crystallogr.* **A24**, 557 (1968).
20. RUDMAN P. S., *Acta Metall.* **13**, 387 (1965).

TRANSPORT ANOMALIES IN DILUTE SILVER-RARE EARTH ALLOYS

C. L. FOILES

Department of Physics, Michigan State University, East Lansing, Mich. 48823, U.S.A.

(Received 20 July 1970; in revised form 5 October 1970)

Abstract—It is noted that the residual resistivities for Ag alloyed with rare earth impurities from the latter half of the rare earth series are approximately three times the residual resistivity for any other trivalent impurity. Moreover, these residual resistivities are essentially independent of the magnetic character of the impurities. New thermoelectric power data indicate the impurity contributions to the diffusion thermoelectric power are *positive*. These anomalies are shown to be consistent with a very simple model which includes core contributions to the scattering.

THE REALIZATION that local magnetic moments (LMM) at impurity sites were causing anomalies in the properties of dilute alloys has produced a plethora of experiments involving noble metal and noble metal alloy hosts containing transition metal impurities [1]. Interpretation of results for these systems is complicated by the fact that the LMM forms as the result of a resonant interaction with the conduction electrons. Self-consistency is essential and thus 'a priori' knowledge of many relevant parameters is not possible—a striking example being the continuous range of possible magnetic moment values. Very sophisticated theoretical models are required to handle the resonant interaction properly. The possibility of finding similar anomalous behavior produced by well defined magnetic moments has stimulated the study of transport properties for numerous noble metal and noble metal alloy hosts containing dilute rare earth impurities. Despite metallurgical problems, samples have been prepared and most investigations have studied the low temperature behavior of electrical resistivity [2-7], and thermoelectric power (TEP) [8, 9]. These investigations have been disappointing in the sense that only a few 'Kondo-like' anomalies have been found and these anomalies are very weak. This situation has been attributed to a very weak coupling

between the 4-*f* electrons and the conduction electrons.

Concentration upon 'Kondo-like' anomalies seems to have caused a general oversight, or slight, of several other anomalies which are nearly as striking. First, the residual resistivity per atomic per cent, ρ_0 , for each impurity from the latter half of the rare earth series (hereafter all references to rare earth impurities will be limited to those from the second half of the series) lies within the range of 5-7 to 6-8 $\mu\Omega\text{-cm}$ when alloyed with Ag. Ytterbium, the one exception, will be explicitly considered below. These resistivities display no systematic dependence upon either the magnetic moment or the deGennes factor. Susceptibility measurements [8, 10] and EPR measurements [10] clearly indicate the presence of moments and the validity of normal crystalline field considerations. The independence of ρ_0 from the specific impurity seems consistent with two ideas; (1) magnetic coupling between the 4-*f* electrons and the conduction electrons is very weak and thus no pronounced 'Kondo-like' anomalies are to be expected, and (2) impurity resistivity is dominated by charge scattering.

Charge domination of the impurity resistivity does not mean that the rare earth impurities will all produce the same value of ρ_0 . Lattice parameter changes for the various alloy

systems alter the effective charges of the impurities. Blatt[11] has applied this correction to noble metal hosts containing non-transition impurities and his results indicate specific values change but the general pattern does not change. The general order of magnitude for the changes in specific values was about 10 per cent. Thus, for rare earths containing the same number of 5-*d* and 6-*s* electrons and having charge dominated scattering, one would expect ρ_0 to fluctuate about a common value. The susceptibility and the EPR data[8-10] indicate the rare earth impurities are trivalent. However, this explanation leads directly to an anomaly; Table 1 shows the residual resistivities for trivalent impurities in Ag. Clearly the rare earths produce an effect which is approximately 3 times larger than any other trivalent impurity.

The exception Ytterbium reinforces this anomaly. Boes *et al.*[6] have shown that as Ytterbium goes from a trivalent impurity with a magnetic moment in Au to a divalent impurity with no magnetic moment in a Au-Ag host the residual resistivity decreases sharply. ρ_0 for Yb in Au is $6.7 \mu\Omega\text{-cm}$. Edwards and Legvold[12] found that Gd, Tb, and Ho dissolved in Au gave a ρ_0 of $7.4 \mu\Omega\text{-cm}$. These values are similar and are approximately three times as large as those for nontransition, trivalent impurities in Au.

A second anomaly is derived from the TEP curves for the three alloys given in Fig. 1. The AgTm and AgHo samples were rolled from the same melts as those used to provide susceptibility specimens for Hirst *et al.*[10]. Low temperature resistivity measurements [13] and TEP measurements[14] indicated the fabrication produced no significant contamination

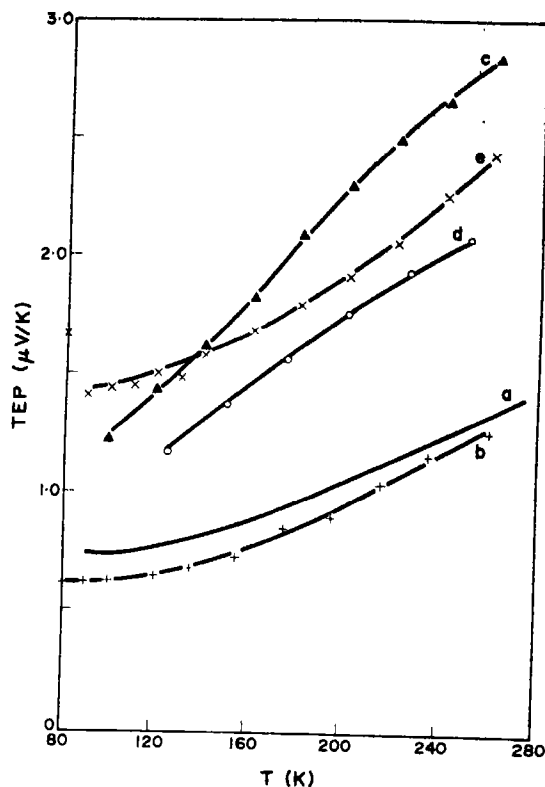


Fig. 1. The thermoelectric powers for pure Ag and various dilute alloys: (a) Pure Ag as reported by Schroeder *et al.*[15]. (b) Silver normal used as reference material. This alloy displays the decreased thermoelectric power typical of most alloys. (c) AgTm (~ 0.55 at. %). (d) AgHo (~ 0.2 at. %). (e) AgGd (~ 0.2 at. %).

from transition impurities. The AgGd sample was prepared by induction melting and handled in a similar manner. The TEP for each alloy was measured using a standard integral technique with silver normal as reference material and a copper thermometer. Standard fixed temperature points were used to calibrate the thermometer and a pure lead sample (59's) was used to calibrate the silver

Table 1. The residual resistivities, in $\mu\Omega\text{-cm/at. \%}$, for trivalent impurities dissolved in Ag

Al	Ga	In	Tl	Gd	Tb	Dy	Ho	Er	Tm	Yb
1.95	2.35	1.8	2.2	6.0	6.0	6.6	6.8	6.1	5.7	2.5

normal. The anomaly in Fig. 1 is that the TEP for each alloy exceeds that of the pure host and monotonically increases with temperature at a rate equal to or greater than the rate of increase for the pure host.

The analysis of the TEP contributions in noble metal alloys is usually accomplished with the aid of the relation

$$S = \frac{\rho_1}{\rho} S_{d_1} + \frac{\rho_2}{\rho} S_{d_2} + S_g \quad (1)$$

where ρ_1 is the resistivity of the pure solvent, ρ_2 is the residual resistivity of the solute, ρ is the total resistivity of the alloy, S_g is the phonon drag contribution, S_{d_1} is the diffusion contribution of the pure solvent, S_{d_2} is the impurity diffusion contribution, and S is the total TEP of the alloy. The first two terms of equation (1) are the Gorter-Nordheim relation. To the same order of approximation used to achieve equation (1)

$$S_{d_2} = \frac{\pi^2 k^2 T}{3|e|} \cdot \frac{\partial \ln \rho_2}{\partial \epsilon} \bigg|_{\epsilon = \epsilon_F} \quad (2)$$

where k is Boltzmann's constant, T is the absolute temperature, e is the charge of an electron, ϵ is the energy of an electron, and ϵ_F is the Fermi energy. At very low temperatures (i.e. ... < 4.2°K) or near room temperature $S_g \sim 0$ and a Gorter-Nordheim plot* allows a separation of S_{d_1} and S_{d_2} . Non-transition impurities in Ag yield $S_{d_2}/T \sim (-2 \text{ to } -5) 10^{-3} \mu V/^{\circ}K^2$ and transition impurities which do not form a magnetic moment yield $S_{d_2}/T \sim (-10 \text{ to } -60) 10^{-3} \mu V/^{\circ}K^2$. Specific values vary but the essential feature is that all values are negative. Therefore, the addition of impurities reduces the

host contribution by reducing ρ_1/ρ , adds a negative impurity contribution and produces an alloy with smaller TEP. Figure 1 shows alloys having increased TEP, and the most logical explanation is a positive S_{d_2} contribution. If one uses the less restrictive plot noted in Schroeder *et al.*[15], the respective S_{d_2}/T results for Gd, Tm, and Ho are ~ 15.2 , 13.6 , $12.1(10^{-3}) \mu V/^{\circ}K^2$. These absolute magnitudes are consistent with the results for Pd and Pt impurities in Ag.

The anomalous behavior in Fig. 1 can now be stated in different terms; the anomaly lies in the positive sign of the impurity diffusion TEP contribution. To the best of the author's knowledge only one other instance of a positive impurity contribution in noble metal alloys has been reported†. CuCd by Blatt *et al.*[16]. Blatt suggested core scattering as the cause of the reversal, but this suggestion has not been explored. The positive signs of S_{d_1} for Cu, Ag, Au have been a traditional source of embarrassment, and Robinson[17] has recently used the idea of core scattering to explain these positive signs.

It is very tempting to combine the concept of core contributions to scattering with the standard phase shift analysis for alloys in an attempt to explain the positive sign of the impurity TEP in these alloys. Before succumbing to this temptation these points should be made explicit:

(a) The occurrence of this positive sign for $J \neq S$ (Tm and Ho) and for $J = S$ (Gd) indicates crystalline field effects are not essentially related to the positive sign.

(b) Although residual resistivities are relatively insensitive to the exact shape of the scattering potential, the TEP is very sensitive to the specific potential used[18]. Therefore, the attainment of a particular value for S_{d_2} for

*The usual procedure is to plot S vs. $1/\rho$ at a fixed temperature for a series of alloys with different concentrations. The temperature is usually chosen so that $S_g \sim 0$. A second alternative, which is less restrictive, is to plot S/T vs. $1/\rho$ for an alloy of fixed concentration. This second alternative requires a more complete knowledge of S_g and the reader is referred to Schroeder *et al.*[15] for a more complete discussion.

†The alloy systems having LMM are not included in this statement. A positive contribution in these systems may well be possible but the complexity of the resistivity weighting factors and the size of the TEP anomaly make a unique separation very difficult. The author knows of no reference which claims a unique separation.

a given model is not significant. Indeed even the attainment of the correct sign for S_{d_1} without an accompanying increase in ρ_0 will be viewed as not significant.

(c) Since the large ρ_0 's occur for all rare earth impurities except Yb and positive S_{d_0}/T occur for three different rare earth impurities (and by inference for all impurities in the last half of the rare earth series), the model should give this result over a range of parameters rather than at a particular critical value.

With the above guidelines as reference, a *very simple* phenomenological model was invoked. The alloying behavior of 3-*d*, 4-*d*, and 5-*d* impurity electrons in Cu, Ag, or Au hosts is often depicted as a donation of these electrons to the conduction band with resultant formation of a very strong positive ion which is then screened. The screening cloud has approximately the same number of electrons as the neutral impurity had *d* electrons and the net result is a resonance which blurs the distinction between impurity electrons and conduction electrons. In contrast, the 4-*f* electrons should remain well-defined. However, the screening which occurs with a normal trivalent impurity will lower the energy of some conduction electrons. This lowering increases the closer one approaches the impurity and it is not unreasonable to expect a modification of screening charge at the core due to the 4-*f* electrons. For computational purposes, this model was represented by a spherical square well of standard size combined with a small, spherically symmetric core. This core varied in diameter from 15 to 25 per cent of the major square well diameter, was allowed to be repulsive or attractive, and ranged in strength up to 15 times that of the major square well. The depth of this major square well was varied until the Friedel sum rule was satisfied and the associated phase shifts were used to calculate ρ_0 . The impurity TEP was calculated from equation (2).

The repulsive cores gave neither increased ρ_0 nor positive impurity TEP. However, the

attractive cores displayed both features and a typical pattern is shown in Fig. 2. The primary cause of this pattern is the relation between the *s*-phase shift, δ_0 , and the *p*-phase shift, δ_1 . Below the resistive peak $\delta_0 - \delta_1 < \pi/2$. As $\delta_0 - \delta_1$ approaches $\pi/2$ the resistivity increases

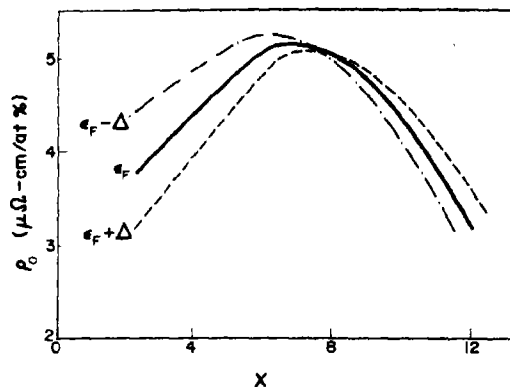


Fig. 2. The variation of residual resistivity as a function of core strength. The core strength is plotted as $X \equiv$ normalized depth of core well below the bottom of major well. The normalizing factor is the Fermi energy, ϵ_F . $\Delta \equiv$ a small, virtual variation in ϵ_F .

and then decreases sharply as $\delta_0 - \delta_1$ exceeds $\pi/2$. It should be noted in Fig. 2 that near the peak the order of resistivity curves relative to the Fermi energy changes. One effect of this change is the impurity TEP becomes positive. The actual values of ρ_0 and impurity TEP obtained are not fully consistent with those obtained experimentally; ρ_0 at the peak is slightly greater than $5 \mu\Omega\text{-cm}$ (~ 2.5 times the result for other trivalent impurities) with the impurity TEP just becoming positive. The magnitude of the latter increases in the region where ρ_0 decreases sharply. A modification of the model potential which preserves the $\delta_0 - \delta_1$ relation and permits the difference of $\pi/2$ to be achieved at lower absolute values should produce results in closer accord with experiment. However, the need for more detailed experimental results and item (b) above would seem to indicate the significance of such a modification is far too obscure to justify the attempt. Instead, we deem it

sufficient to note that this very simple model has produced both general features, increased resistivity and positive impurity TEP.

We conclude with a few comments about our model potential. First, the general pattern shown in Fig. 2 and the phase relations discussed in the preceding paragraph can occur at all the values of small core diameter used. The only criterion is that the strength increases sufficiently to include $\delta_0 - \delta_1 > \pi/2$. At the smaller core diameters this behavior was not actually achieved with the range of strengths employed but the increase of ρ_0 which precedes the maximum was clearly evident. Second, since this model employs charge scattering only, the magnetic moment and/or spin of the 4-*f* electrons are not essential for the results. This feature agrees with the experimental facts that ρ_0 and, to the extent of limited data, impurity TEP show no obvious dependence upon which rare earth impurity is present. Finally, an 'after-the-fact' physical picture of the model potential can be given. A key feature in the model was the assumption that the 4-*f* electrons retained their identity in the alloy and thus do not participate in screening. The radius of the 4-*f* shell should be large in comparison to other core shells and it is not implausible to picture the screening charge penetrating this shell. Such penetration would be seen as an increased scattering potential. Clearly this physical picture is very crude and is intended to do no more than suggest that the

model potential is a not pure mathematical construction.

Acknowledgements—The author wishes to acknowledge gratefully the support of the NSF (initially in the form of a post-doctoral fellowship and later in the form of a research grant) which has made this work possible. In addition, the author, gratefully, and inadequately, acknowledges the help and guidance of the Metal Physics Group under the direction of Professor B. R. Coles at Imperial College.

REFERENCES

1. DAYBELL M. D. and STEYERT W. A., *Rev. mod. Phys.* **40**, 380 (1968), reviews the experimental results and provides an extensive list of references.
2. SUGAWARA T., SOGA R. and YAMASE I., *J. Phys. Soc. Japan* **19**, 780 (1964).
3. BIJVOET J., DEHON B., DEKKER J. A. and VAN BEEK F., *Solid State Commun.* **3**, 289 (1965).
4. ARAJS S. and DUNMYRE G. R., *J. less common Metals* **10**, 220 (1966).
5. BIJVOET J., VAN DAM A. J. and VAN BEEK F., *Solid State Commun.* **4**, 455 (1966).
6. BOES J., VAN DAM A. J. and BIJVOET J., *Phys. Lett.* **28A**, 101 (1968).
7. DE VRIES G. and BIJVOET J., *J. appl. Phys.* **39**, 797 (1968).
8. GAINON D., DONZÉ P. and SIERRO J., *Solid State Commun.* **5**, 151 (1967).
9. ALLALI V., DONZÉ P., GAINON D. and SIERRO J., *J. appl. Phys.* **41**, 1154 (1970).
10. HIRST L. L., WILLIAMS G., GRIFFITHS D. and COLES B. R., *J. appl. Phys.* **39**, 844 (1968).
11. BLATT F. J., *Phys. Rev.* **108**, 285 (1957).
12. EDWARDS L. R. and LEGVOLD S., *J. appl. Phys.* **39**, 1242 (1968).
13. COLES B. R. and LOWDIN R., private communication.
14. FOILES C. L., unpublished.
15. SCHROEDER P. A., WOLD R. and WOOLLAM J. A., *Phys. Rev.* **138**, A 105 (1965).
16. BLATT F. J. and KROPSCHOT R. H., *Phys. Rev.* **118**, 480 (1960).
17. ROBINSON J. E., *Phys. Rev.* **161**, 533 (1967).
18. BLATT F. J., *Phys. Rev.* **99**, 1708 (1955).

THE SOLUBILITY OF CARBON IN PULLED SILICON CRYSTALS

A. R. BEAN and R. C. NEWMAN

J. J. Thomson Physical Laboratory, Whiteknights, Reading RG6 2AF, England

(Received 7 August 1970; in revised form 21 September 1970)

Abstract—Single crystals of silicon grown by the Czochralski technique have been annealed at various temperatures in the range 600–1350°C. I.R. measurements have been made of the strength of the absorption bands due to carbon (16.5 μm) and oxygen (9 μm). From the measurements, heats of solution of the two impurities of 53 ± 6 and 38 ± 4 kcal/mole have been deduced respectively. When carbon precipitates broad absorption is produced in the region of 12 μm which is attributed to silicon carbide particles. The strength of this absorption is found to be consistent with the estimated loss of carbon from solution. Precipitation of silicon carbide was not observed in oxygen free crystals.

1. INTRODUCTION

It is now well established that silicon crystals may contain appreciable amounts of carbon. An i.r. absorption band due to the localized vibrations of ^{12}C at 607 cm^{-1} (77°K) has been ascribed to carbon atoms which occupy isolated substitutional sites [1, 2]. In heat treated crystals other techniques have indicated the presence of silicon carbide particles [3, 4], and it has been suggested that carbon may be present in interstitial sites or in the form of graphitic inclusions in epitaxially grown silicon [5]. Clearly a chemical or radio-activation analysis of a given sample would normally measure only its total carbon content and give little or no information about the form in which it was present. On the other hand, the use of a spectroscopic technique, with particular reference to i.r. absorption measurements, has one clear advantage since in principle it may allow the various possible configurations to be separately identified. This technique does however suffer from two disadvantages; (a) the strength of an absorption band has to be calibrated by examining samples which have a *known* concentration of the impurity in a specific form, and (b) certain configurations of the impurity may not give rise to any detectable absorption features.

The strength of the i.r. absorption band due

to substitutional carbon was first calibrated from measurements made on pulled single crystals containing ^{14}C , the total concentration of which was determined by a standard radiochemical technique; the band from ^{14}C at 573 cm^{-1} is clearly resolved from that of ^{12}C and hence no assumptions had to be made about the relative abundance of the two isotopes in these samples [1, 2]. Apart from some other relatively very weak absorption bands, which were attributed to carbon-oxygen complexes [2], there were no other absorption features which could be related to the presence of carbon. With the assumption that no appreciable amount of carbon was present in any form other than simple isolated substitutional sites, it was then possible to determine a value for the apparent charge associated with the vibrational mode of these atoms as $\eta \approx 2.6e$ [6]. This value is very high compared for example with substitutional B^- ions which have $\eta \approx e$, but is in fact consistent with the corresponding value determined for silicon carbide crystals. The apparent charge η is defined as $\eta^2 = \Lambda(e^*)^2$, where Λ is a local field correction and e^* is the effective charge. In the work on the intrinsic reststrahl absorption in silicon carbide, Λ was assumed to take the value $(\epsilon_\infty + 2)^2/9$, where ϵ_∞ is the high frequency dielectric constant and a value of

$e^* = 0.9e$ was thereby obtained [7]; the apparent charge is thus $\eta = 2.5e$ since $\epsilon_\infty = 6.7$. It follows that if a significant fraction of the carbon impurities had been present in some other form in the silicon crystals examined, the value of η would have had to be correspondingly greater, which does not seem to be plausible on physical grounds. Hence we regard the calibration as established, with only a small degree of possible error; this conclusion has received further support from other recent independent measurements which again showed overall self-consistency [8].

It has already been mentioned that heat treatment of silicon may lead to the precipitation of silicon carbide, which is to be expected as a result of previous measurements that indicated that the solubility of carbon in silicon decreases as the temperature is decreased below the melting point [9]. Consequently, the strength of the i.r. band due to substitutional carbon should decrease if precipitation occurs and the residual strength should give a measure of the solid solubility of the impurity. Results will be presented in this paper which show that this is so. In addition, the precipitated silicon carbide particles might be expected to give rise to i.r. absorption in the spectral region near $12.6 \mu\text{m}$. Again it will be shown that this does occur, although the detailed nature of the absorption is modified somewhat compared with that from a slab of pure silicon carbide. From these measurements, it has been possible to determine the solid solubility of substitutional carbon in pulled silicon single crystals as a function of temperature. These results, together with other apparently anomalous observations made on oxygen-free crystals will then be compared with the available information about the solubility of carbon in silicon as reported elsewhere.

2. EXPERIMENTAL DETAILS

Various crystals of high p -type resistivity (greater than $50 \Omega\text{-cm}$), grown by either the

Czochralski or floating zone techniques, were first characterized by their i.r. absorption spectrum to determine their oxygen and carbon concentrations. Spectra were obtained at 77°K using the differential technique as described previously [2]. The concentration of oxygen present was determined from the calibration given by Pajot [10], while the concentration of substitutional carbon was estimated from our own previous calibration (see Fig. 2 of Ref. [2]).

Most samples were then heated in an open silica tube for various times in the temperature range $600\text{--}1350^\circ\text{C}$; other samples were heated in sealed-off evacuated silica tubes. After each heat treatment the sample was reground and repolished before it was examined optically; this was necessary to remove surface layers of silica and silicon carbide respectively [11].

In addition a few samples were given a prior irradiation by 2 MeV electrons at room temperature to a total dose of about 10^{19} electrons cm^{-2} before they were annealed in the high temperature region; a discussion of the reasons for carrying out these treatments is deferred to Section 3.

3. HIGH TEMPERATURE HEAT TREATMENTS

3.1. Spectroscopic results

Two samples each containing 1.4×10^{18} atom cm^{-3} of oxygen, and carbon concentrations of less than 10^{17} and 2×10^{18} atom cm^{-3} respectively were given successive anneals, each of one hour's duration, at 600 up to 1000°C in 50° intervals. In both samples a large proportion of the dissolved interstitial oxygen precipitated at a temperature of 800°C as deduced from the observation of the formation of a broad absorption band near $9 \mu\text{m}$ due to silica particles, and Rayleigh scattering in the spectral region from $1\text{--}4 \mu\text{m}$. Precipitation of the carbon, as judged from the fall in the strength of the local mode band at 607 cm^{-1} , did not occur until the second sample had been given a further heat treatment for 10 hr at 1040°C . At the same time, an intense asym-

metric band of halfwidth of about 60 cm^{-1} and peak absorption at $12.0\text{ }\mu\text{m}$ was produced, similar to that observed previously by Balkanski *et al.* in polycrystalline silicon[12]. Although both the width and position of the peak varied somewhat with further heat treatments at higher temperatures (see Fig. 1), the integrated absorption remained essentially constant at a value of 230 cm^{-2} ; at the highest temperatures there was an indication that this value was reduced by about 10 per cent, but this is not considered to be particularly significant because of the errors involved in measurement.

When the anneal temperature was increased above 1050°C , the concentrations of both the dissolved oxygen and carbon increased as shown in Figs. 2 and 3. In order to ensure that equilibrium conditions had been reached at each temperature, the samples were heated for successive periods of up to 100 hr at temperatures in the region of 1000°C and for 2 to 3 hr at 1350°C and examined at various stages during each treatment; in no cases were there significant differences in the measurements at a given temperature. Similar measurements were then performed in a second series of anneals in which the temperature was reduced. These results were entirely consistent with the first set which indicates that a genuine equilibrium situation was achieved in the samples examined. Apart from errors of measurement, the determination of the carbon solubility at the lowest temperature may have been in some error because of the uncertainty of the carbon concentration in the untreated float-zone silicon reference sample used in the differential transmission measurements; this may have been as high as $5 \times 10^{15}\text{ atom cm}^{-3}$. From the results shown in Fig. 3, the heat of solution of substitutional carbon is found to be $53 \pm 6\text{ kcal/mole}$ (2.3 eV). An extrapolation of this data to the melting point yields a solubility of $4.5 \times 10^{17}\text{ atom cm}^{-3}$ which is substantially lower than the carbon content of $2 \times 10^{18}\text{ atom cm}^{-3}$ of the sample in its

as-grown state; this point will be discussed in Section 4.

Figure 2 indicates that the heat of solution of oxygen in interstitial sites is $38 \pm 4\text{ kcal/mole}$ ($1.65 \pm 0.15\text{ eV}$), which is significantly greater than the value of 22 kcal/mole obtained by Hrostowski and Kaiser[13]. In this previous work, measurements were made on samples which had been annealed in the limited temperature range from 1000 – 1250°C . These measurements were made with a nominal sample temperature of 4.2°K , although it is clear from Fig. 1 of Ref. [13] that the

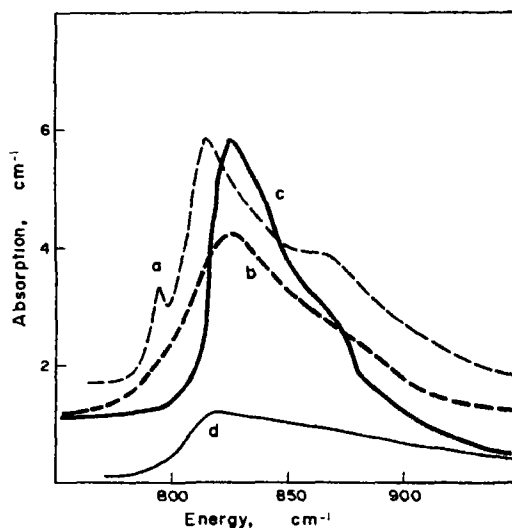


Fig. 1. Differential Absorption Spectra at 80°K of heat-treated silicon.

Curve a sample 2, $^{12}\text{C} + ^{13}\text{C}$, after 4 hr at 1310°C

Curve b sample 1, ^{12}C after 60 hr at 1040°C

Curve c sample 1, ^{12}C after 10 hr at 1240°C

Curve d sample 5, $^{13}\text{C} + ^{12}\text{C}$, after 1 hr at 1350°C

The spectra have been vertically displaced relative to one another for convenience of representation.

actual sample temperature was considerably higher than this value (cf. Fig. 2 of Ref. [10]), and furthermore, the instrumental resolution must have been much lower than the intrinsic linewidth of the oxygen vibrational absorption band. It was pointed out that there was a difficulty in determining the integrated absorption in this band particularly at the lower temperatures because of the underlying in-

trinsic absorption arising from the silicon lattice and also from the very broad band due to the precipitated silica which has a peak at around 1100 cm^{-1} . In fact, further inspection of Fig. 1 of Ref. [13] indicates that the magnitude of this latter absorption becomes smaller, as the fraction of precipitated oxygen increases which is clearly unreasonable and is not consistent with the present observations. It seems possible therefore that the integrated absorption in the oxygen $9\text{ }\mu\text{m}$ band was overestimated for samples annealed at the lower temperatures and that the quoted solubilities were higher than they should have been. This could then explain the difference in the two values of the heats of solution. It should be pointed out that there is not any discrepancy in the value of the solubility at a temperature of 1250°C when allowance is made for the modified calibration of Pajot as used in the present work. At this temperature, the integrated absorption in the $9\text{ }\mu\text{m}$ band is large and hence subtraction of background absorption will make only minor corrections. It is clear therefore that the measurements are difficult to interpret in a completely unambiguous manner. It should be remembered that the part of the background absorption due to the silicon lattice has been eliminated in the present work, because of the technique of measurement used. Since our measurements also extend to higher temperatures of 1350°C , we consider that the present estimate of the heat of solution is likely to be more reliable than that previously reported. Finally our results give some indication that the solubility of oxygen may be decreased slightly when carbon is present, although this is a relatively small effect.

At this stage, it should be emphasized that a *single* heat treatment of other similar samples containing high concentrations of both oxygen and carbon did not lead to significant precipitation of either impurity, although a second heat treatment did produce this effect. It would appear that nucleation sites are produced during the cooling procedure which facilitate

the precipitation process in the second heat treatment. Consequently, an attempt was made to produce such sites by a completely different process. Previously untreated samples were therefore irradiated by 2 MeV electrons at room temperature to total doses of $5 \times 10^{18}\text{ electrons cm}^{-2}$ (or 10^{19} cm^{-2}); the effects of such a treatment have been discussed elsewhere [14]. These samples were then given a *single* anneal in the high temperature region which did lead to precipitation of both carbon and oxygen, and the residual solubility was entirely consistent with the measurements shown in Figs. 2 and 3. It was concluded that

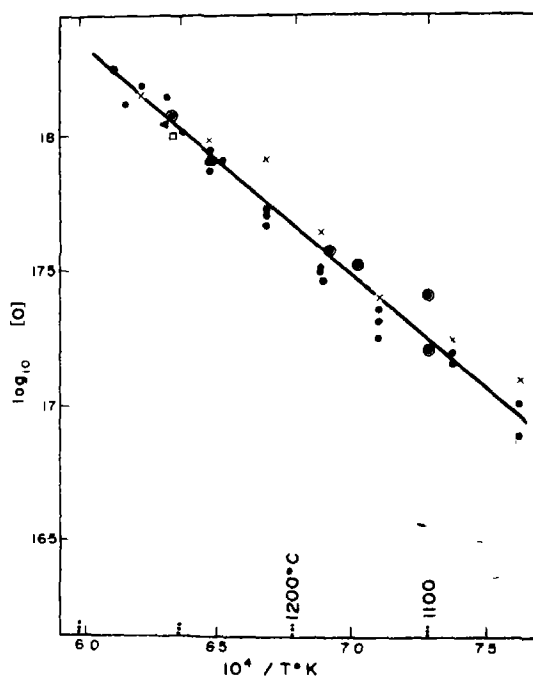


Fig. 2. Dissolved oxygen concentrations after heat treatment

- $[C] = 2 \cdot 10^{18}\text{ atoms cm}^{-3}$, increasing temperatures, sample 1
- ⊙ $[C] = 2 \cdot 10^{18}\text{ atoms cm}^{-3}$, decreasing temperatures, sample 1
- $[C] = 2 \cdot 10^{18}\text{ atoms cm}^{-3}$, sample 2
- △ $[C] = 2 \cdot 10^{18}\text{ atoms cm}^{-3}$, sample 3
- X $[C] < 10^{17}\text{ atoms cm}^{-3}$, sample 4

the irradiation did have the desired effect of producing nucleation sites, which are most likely to be vacancy or interstitial clusters. One of these samples contained approximately equal concentrations of ^{12}C and ^{13}C ,

and it was noted that the broad band in the region of $12\text{ }\mu\text{m}$ was shifted somewhat to lower energies and a small subsidiary and relatively sharp feature was produced at $12.61\text{ }\mu\text{m}$. The halfwidth of this feature was about 7 cm^{-1} while its contribution to the total absorption relative to the broad band was about 4 per cent. It was definitely established by successive grinding and repolishing of the sample that this was not a feature due to surface contamination[11] and its presence is somewhat puzzling since no corresponding feature was observed in another sample containing only ^{12}C .

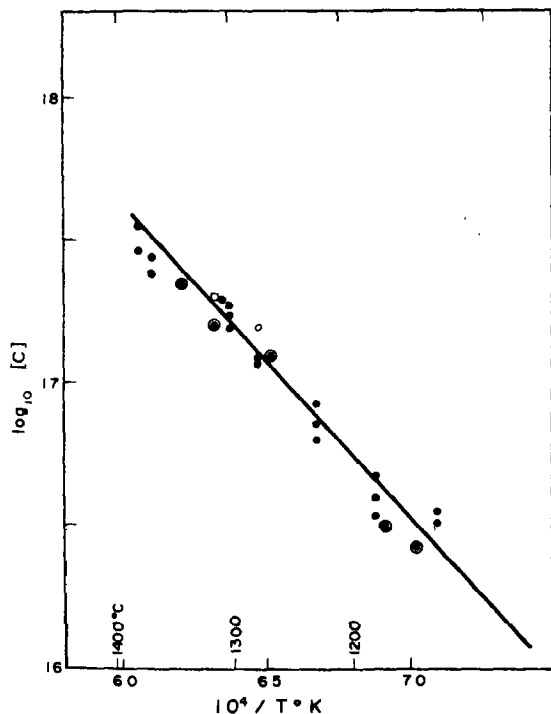


Fig. 3. Dissolved carbon concentrations after heat treatment.

- sample 1, increasing temperatures
- ⊙ sample 1, decreasing temperatures
- sample 2.

The results described above all relate to pulled crystals. In order to compare the behaviour of carbon in oxygen free samples, two samples from a particular crystal grown

by the floating zone technique and with dislocation densities of about 10^4 cm^{-2} were given similar heat treatments in open silica tubes. The first sample showed some very anomalous results. After treatments at 1260°C the concentration of substitutional carbon increased from its initial value of 4×10^{17} to 9×10^{17} atoms cm^{-3} , only to fall again to its original value after subsequent treatments. The second sample was heated for 9 hr at each of a number of temperatures between 550 and 1300°C which led to no significant changes in the carbon concentration. In neither sample was a band produced at $12\text{ }\mu\text{m}$, but very weak absorption was observed at wavelengths around $21\text{ }\mu\text{m}$ which is in the band mode region for silicon[6]. Attempts to induce precipitation by giving a sample a prior electron irradiation treatment also failed.

Since these heat treatments were carried out in air, diffusion of oxygen into the samples occurred at the high temperatures. For one sample an estimate was made of the diffusion coefficient on the assumption of an error function complement distribution and using a surface concentration equal to the solubility at 1260°C shown in Fig. 2. The estimated value of D was found to be $1.8 \times 10^{-9}\text{ cm}^2\text{ sec}^{-1}$ which is considered to be consistent with the value of $9 \times 10^{-10}\text{ cm}^2\text{ sec}^{-1}$ calculated from the accepted variation with temperature of $D = 0.21 \exp(-2.55\text{ eV}/kT)\text{ cm}^2\text{ sec}^{-1}$ [15].

3.2. Interpretation of the band at $12\text{ }\mu\text{m}$

The band in the region of $12\text{ }\mu\text{m}$ was only produced when a large fraction of carbon had been removed from normal substitutional sites. The most simple explanation is that it arises from precipitated particles of silicon carbide. However, the position of the peak absorption is different from that of $12.6\text{ }\mu\text{m}$ found from slabs of silicon carbide[7], and the width of the line is also much greater. These differences can be explained since (a) the precipitates are in the form of small particles and (b) they are embedded in a matrix of high dielectric constant. The theory relevant

to absorption under these conditions has been reviewed recently by Ruppén and Englmán [16] and their results will now be used to analyse the present observations.

Absorption by ionic crystalline particles of a finite size occurs via surface modes at energies above that of the normal frequency of absorption corresponding to the transverse optic mode ω_T at the Γ point in the zone. For a small spherical particle of radius R (where $\nu_T R \ll 1$) embedded in a medium of dielectric constant ϵ_M , absorption will occur at ω_1 given by:-

$$\frac{\omega_1^2}{\omega_T^2} = \frac{\epsilon_0 + 2\epsilon_M(1 + \Delta)}{\epsilon_\infty + 2\epsilon_M(1 + \Delta)} \quad (1) \quad \text{and}$$

where

$$\Delta = \frac{6}{5} \left(\frac{\epsilon_0 + 2\epsilon_M}{\epsilon_\infty + 2\epsilon_M} \right) \epsilon_M \left(\frac{\omega_T}{c} R \right)^2 \quad (2)$$

and ϵ_0 and ϵ_∞ are the low and high frequency dielectric constants of the material of the particle. For silicon carbide $\epsilon_0 = 10.0$, $\epsilon_\infty = 6.7$ and for silicon $\epsilon_M = 11.8$. Hence the position of the peak absorption corresponds to $\lambda = 11.95 \mu\text{m}$ ($R \leq 1 \mu\text{m}$), $12.25 \mu\text{m}$ ($R \approx 3 \mu\text{m}$) and $12.6 \mu\text{m}$ ($R \gg 12 \mu\text{m}$). From other evidence on the precipitation of silicon carbide, it is thought that the particle size in the present samples is of the order of, or smaller than $1 \mu\text{m}$, in which case a simpler expression may be used to determine ω_1 ; that is:-

$$\frac{\omega_1^2}{\omega_T^2} = \frac{\epsilon_0 - \epsilon_M(1 - 4\pi/N_i)}{\epsilon_\infty - \epsilon_M(1 - 4\pi/N_i)} \quad (3)$$

where N_i is an appropriate depolarizing factor that depends on the shape of the particle. For cylinders and planar particles $N = 0$ for at least one principal axis and this should lead to absorption at ω_T ($12.60 \mu\text{m}$). In general this was not observed, there being negligible absorption at wavelengths greater than about $12.3 \mu\text{m}$. It follows that under the present experimental conditions, rod and platelet

precipitation probably did not occur. Particles with other non-spherical shapes will however produce absorption at wavelengths above and below $11.95 \mu\text{m}$ (ω_1).

The magnitude of the absorption now has to be considered. This will be estimated only for small spherical particles, in which case the absorption coefficient is given by:-

$$K = 3k_0 I m a \quad (4)$$

where

$$a = \frac{\epsilon - \epsilon_M}{\epsilon + 2\epsilon_M}$$

$$\epsilon = \epsilon_\infty + \frac{4\pi\rho}{1 - (\omega/\omega_T)^2 - i\gamma\omega/\omega_T}$$

$4\pi\rho = (\epsilon_0 - \epsilon_\infty)$ and k_0 is the wavevector of the incident radiation. These expressions apply to unit volume of the precipitate and so the absorption has to be scaled down according to the number of carbon atoms which have precipitated in unit volume of silicon. If γ is taken as 0.0107 corresponding to the width of the reststrahl band of β -SiC [7] the integrated absorption deduced from the above equations is 220 cm^{-2} , assuming a volume fraction of silicon carbide of 4.1×10^{-5} (corresponding to a loss of 2×10^{18} carbon atoms cm^{-3} from solution). At this stage, it should be made clear that if the particles were all spherical, the predicted band should have a peak absorption coefficient of 25 cm^{-1} and half-width of about 9 cm^{-1} . This may be compared with the observed band which has a maximum absorption coefficient of about $3-4 \text{ cm}^{-1}$ and a much larger half-width of $\sim 60 \text{ cm}^{-1}$. This result suggests that the precipitate particles have a range of ellipsoidal shapes, each particle giving rise to absorption at a slightly different wavelength; this interpretation would not however be expected to greatly modify the estimate of the total integrated absorption in the band. The variations in the shape of the observed band are now

easily explained as modifications of the form and size of the particles as a function of the annealing treatment given to the samples. Moreover, the total calculated absorption from the silicon carbide is entirely consistent with the absolute number of carbon atoms lost from substitutional sites on the basis of our previous calibration. The shift of the main band to lower energies in the sample containing ^{13}C is also explained, although the reason for the relatively weak feature at $12.6\ \mu\text{m}$ is still not clear. This peak which at first sight appears to correspond to ω_T for Si^{12}C would obviously be expected to occur at a lower energy due to the presence of the ^{13}C if this were the correct interpretation. However this discrepancy is considered to be of minor significance in the context of the present work and will not be discussed further.

4. DISCUSSION

It has been shown that substitutional carbon impurities in pulled silicon single crystals precipitate to form silicon carbide particles after suitable heat treatments, and the silicon carbide gives rise to optical absorption which is explicable in terms of the theory discussed by Ruppini and Englman[16]. It has also been demonstrated that the magnitude of the absorption arising from the precipitated phase is consistent, within experimental error, with that to be expected from the measured loss of carbon from solution.

The solubility of carbon as a function of temperature may now be compared with the values determined in earlier diffusion measurements involving ^{14}C . The present results, which are consistent with a heat of solution of $53 \pm 6\ \text{kcal/mole}$, are considered to be more reliable than the former[9] which suggested a lower value of $34\ \text{kcal/mole}$. However, there does appear to be a discrepancy at temperatures close to the melting point of silicon, since the diffusion measurements gave surface concentrations as high as $1-1.5 \times 10^{18}\ \text{cm}^{-3}$, whereas the extrapolated value from the optical measurements was only

$4-5 \times 10^{17}\ \text{atom cm}^{-3}$. The higher value certainly appears to be the more reasonable, since it has been demonstrated that as-grown crystals may contain up to $2-3 \times 10^{18}$ carbon atom cm^{-3} [2, 17]. This would imply that the solubility rises to its maximum value at a temperature which is only slightly lower than the melting point and that the relation

$$[C] = A \exp(-\Delta H/RT)$$

certainly does not hold close to this temperature.

A determination of the solubility close to the melting temperature is of interest because it is related to the solubility in molten silicon via the segregation coefficient k . Evidence obtained from the distribution of ^{14}C along the length of grown silicon crystals has suggested that k is less than unity, although the two values of 0.005[1] and 0.09[18] that have been quoted are not consistent. However it is well known that this method of determining k is not very accurate if $k \leq 0.1$, since the precise value obtained depends upon a detailed examination of the very last part of the crystal to freeze. If it is assumed that $k \approx 0.1$, it is implied that the solubility of carbon in molten silicon at the melting point is about $2-3 \times 10^{19}\ \text{atom cm}^{-3}$, which is an order of magnitude greater than that which has been reported[19]. The liquid solubility was determined by measuring the weight of solid silicon carbide which dissolved in a measured weight of liquid silicon which was itself in contact with solid silicon. This experimental result is however open to the criticism that carbon from other sources, such as the original solid silicon and from the ambient in which the melting was carried out, may have partially saturated the liquid and so limited the amount of silicon carbide which dissolved. It would appear that this problem could only be resolved by repeating the experiment and using ^{14}C as a tracer.

The present results have indicated that precipitation only occurs in pulled crystals

which also contain substantial amounts of oxygen. A possible implication of this result that precipitated silica particles act as nucleation centres for the growth of silicon carbide is supported by other observations of the precipitated phase using the technique of the microbeam analyser[4]. It has also been found that a single heat treatment of an as grown crystal does not in general lead to significant precipitation of either the carbon or oxygen. It is well known that heating silicon under the conditions used in the present work can lead to the introduction of copper and other metallic impurities. It is possible that these elements in precipitated form, or alternatively vacancy clusters produced by such precipitation can act as nuclei for oxygen precipitation in a second treatment of the same sample. The fact that a prior electron irradiation treatment has also been found to induce precipitation in a single anneal suggests that vacancy aggregates could well be important. Hence it may be speculated that oxygen precipitates on vacancy clusters and these particles then act as nuclei for the growth of silicon carbide particles. It has been suggested elsewhere[20] that the detailed behaviour of copper precipitation may also be related to the carbon content of samples but this is difficult to assess as detailed measurements of the carbon content of the samples examined were not reported. In any case, there would not appear to be any discrepancies in these various observations.

The question of the detailed behaviour of carbon in oxygen free crystals is still somewhat open. The present results, taken in conjunction with other observations relating to electron irradiation damage[21] seem to suggest that not all the carbon may be present on substitutional sites. Since there is also no indication that the impurity is present as a precipitated silicon carbide phase, it is implied that it must be present in interstitial sites or as graphitic inclusions. The former possibility seems to be unlikely in view of infra-red measurements made on electron irradiated

material[22]. The second possibility certainly cannot be ruled out and evidence for carbon in this form has been reported in epitaxial layers[5]. Such inclusions may not give rise to any detectable i.r. absorption, although no adequate explanation has yet been found for the weak band mode absorption found in such samples as reported in this work.

Finally, it is necessary to consider the estimates of carbon contents of crystals obtained by chemical and other methods. In some cases very high values of up to and even greater than 10^{19} atom cm^{-3} have been reported[23–25]. Clearly there is no limit to the amount of carbon which may be incorporated as silicon carbide since this is a distinct second phase. This may provide an explanation of some of the results, particularly those relating to polycrystalline material and epitaxial layers[5] where heat treatment of silicon can produce a substantial surface coating of silicon carbide[11]. One of our own previous determinations, based on optical microscopic measurements of the size of precipitate particles[9], is now considered to be too high since the size of the particles was probably overestimated because of the techniques used (for a discussion of this see for example Ref. [26]). Great care must also be exercised in estimating 'blanks' in straightforward chemical methods. In other possible methods including bombardment of samples by high energy heavy ions to produce nuclear reactions with ^{12}C there are again certain problems. Such treatments usually produce a surface coating of cracked organic material on the samples. It may then be possible, under the conditions of the irradiation, to produce interstitial carbon atoms which diffuse into a surface layer since such atoms are almost certainly mobile at room temperature[14, 21]. These interstitials could then recombine with vacancies also produced by the irradiation and so carbon may actually be introduced into material which was originally free of this impurity.

It is concluded finally that great care is

necessary in estimating the total carbon content of a given silicon sample and it appears that further work is necessary to clarify the situation with respect to oxygen free crystals. In pulled material the present results, taken in conjunction with previous work, do appear to be self consistent and indicate that the carbon is probably present only as substitutional impurities or as silicon carbide precipitates.

Acknowledgements—The authors wish to thank Mr. R. L. Rouse of AEI/GEC for making available the crystals used in this investigation. One of us A. R. B. thanks the S.R.C. for a research studentship, and we should also like to thank Professor E. W. J. Mitchell for his interest and providing the laboratory electron irradiation facilities.

REFERENCES

1. NEWMAN R. C. and WILLIS J. B., *J. Phys. Chem. Solids* **26**, 373 (1965).
2. NEWMAN R. C. and SMITH R. S., *J. Phys. Chem. Solids* **30**, 1493 (1969).
3. NEWMAN R. C., *Proc. Phys. Soc.* **76**, 993 (1960).
4. SHUL'PINA I. L., ZASLAVSKII A. I. and DEDEGKAEV T. T., *Soviet Phys.-solid State* **10**, 1070 (1968).
5. RAI-CHOUDHURY P., NOREIKA A. J. and THEODORE M. L., *J. electrochem. Soc.* **116**, 97 (1969).
6. NEWMAN R. C., *Adv. Phys.* **18**, 545 (1969).
7. SPITZER W. G., KLEINMAN D. A. and FROSCHE C. J., *Phys. Rev.* **113**, 133 (1959).
8. BAKER J. A., TUCKER T. N., MOYER N. E. and BUSCHERT R. C., *J. appl. Phys.* **39**, 4365 (1968).
9. NEWMAN R. C. and WAKEFIELD J., *J. Phys. Chem. Solids* **19**, 230 (1961), *Metallurgy of Semiconductor Materials* (Edited by J. B. Schroeder) **15**, 201 (Interscience, 1961).
10. PAJOT B., *Solid State Electron.* **12**, 923 (1969).
11. NEWMAN R. C. and WAKEFIELD J., *Proc. Int. Conf. on Solid State Phys. in Electronics and Telecommunications, Brussels*, p. 318 (Edited by M. Desirant and J. L. Michiels) Academic Press N. Y. (1958).
12. BALKANSKI M., NAZAREWICZ W. and DA SILVA É., *C.R. Acad. Sci. Paris* **251**, 1277 (1960).
13. HROSTOWSKI H. J. and KAISER R. H., *J. Phys. Chem. Solids* **9**, 214 (1959).
14. BEAN A. R., NEWMAN R. C. and SMITH R. S., *J. Phys. Chem. Solids* **31**, 739 (1970).
15. HAAS C., *J. Phys. Chem. Solids* **15**, 108 (1960).
16. RUPPIN R. and ENGLMAN R., *Reports on Progress in Physics* **33**, 149 (1970).
17. VOOK F. L. and STEIN H. J., *Appl. Phys. Lett.* **13**, 343 (1968).
18. HAAS E., BRANDT W. and MARTIN J., *Solid State Electron.* **12**, 915 (1969).
19. SCACE R. J. and SLACK G. A., *J. Chem. Phys.* **30**, 1551 (1959).
20. FIERMANS L. and VENNIK J., *Phys. Status. Solidi* **22**, 463 (1967).
21. NEWMAN R. C. and BEAN A. R., In *Proc. Int. Conf. on Radiation Effects in Semiconductors*, Albany 1970, to be published.
22. BEAN A. R. and NEWMAN R. C., *Solid State Commun.* **8**, 175 (1970).
23. PAPAIZIAN H. A. and WOLSKY S. P., *J. appl. Phys.* **27**, 1561 (1956).
24. SCHINK N., *Solid State Electron.* **8**, 767 (1965).
25. DUCRET L. and CORNET C., In *Ultrapurification of Semiconductor Materials*, p. 461 (Edited by M. S. Brooks and J. K. Kennedy) Macmillan, New York (1962).
26. PHILLIPS V. A., In *Advances in Materials Research* Vol. 1, p. 51 (Edited by H. Herman) Interscience, New York (1967).

MAGNETIC AND CHEMICAL ORDER IN HEUSLER ALLOYS CONTAINING COBALT AND MANGANESE

P. J. WEBSTER

Department of Pure and Applied Physics, University of Salford, Salford 5, England

(Received 13 July 1970; in revised form 14 September 1970)

Abstract—Saturation magnetization, X-ray and neutron diffraction measurements have been made on ferromagnetic alloys at the compositions Co_2MnAl , Co_2MnSi , Co_2MnGa , Co_2MnGe , Co_2MnSn and Co_2MnSb . The alloys have the Heusler, $L2_1$, chemical structure and are highly ordered except for Co_2MnAl which exhibits extensive preferential Mn-Al disorder and Co_2MnSb which contains the 2 approximate phases $\text{Co}_{1.5}\text{MnSb}$ and Co.

This is the first series of Heusler alloys in which magnetic moments have been definitely observed on atoms other than Mn. The alloys containing group IVB elements have nett moments of approximately 5.1 β per molecule with individual moments of 0.75 and 3.6 β on Co and Mn sites respectively. The alloys containing the group IIIB elements Al or Ga have nett moments of approximately 4 β and correspondingly smaller moments on both Co and Mn sites. The non-stoichiometric alloy $\text{Co}_{1.5}\text{MnSb}$ has a nett moment 4.9 β and moments 0.75 and 3.76 β respectively on the Co and Mn sites.

1. INTRODUCTION

THE HEUSLER alloys have been of interest since 1903 when Heusler[1] reported that ferromagnetic alloys could be made from non-ferromagnetic constituents copper-manganese bronze and group B elements such as aluminium and tin. Potter[2] and Persson[3] demonstrated that the ferromagnetic properties were related to the chemical ordering and to the concentration of the Mn atoms.

The Cu-Mn-Al system has been investigated in most detail, in particular alloys near the composition Cu_2MnAl that exhibit an almost complete change in chemical and magnetic structure with heat-treatment. Such alloys are strongly ferromagnetic when quenched from about 800°C but are practically non-magnetic when slow-cooled. Bradley and Rodgers[4] established the structure of quenched Cu_2MnAl from a comparison of X-ray powder diffraction photographs taken using 3 different X-radiation wavelengths and confirmed the existence of a Mn sub lattice. The Heusler structure (Strukturbericht type $L2_1$) is illustrated in Fig. 1.

Felcher *et al.*[5] determined in quantitative detail the magnetic and chemical structures

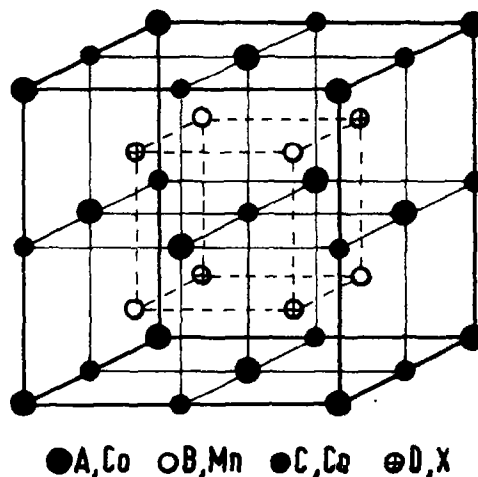


Fig. 1. The Heusler structure.

of Cu_2MnAl from neutron diffraction powder measurements. The magnetic and nuclear contributions to the Bragg peaks were separated using a magnetic field of 12 kOe, and it was concluded that the alloy was chemically highly ordered and that the measured moment of 3.2 β per molecule at 298°K was confined to the Mn sites.

Many more alloys with the Heusler, $L2_1$, structure have since been reported. In parti-

cular, $L2_1$ alloys occur in the series Cu_2MnX [4, 6, 7], Ni_2MnX [8–11], Pd_2MnX [11–13, 8], and Au_2MnX [14, 15], where X is a B sub group element such as Al, Si, Ga, Ge, In, Sn or Sb. In all cases when their magnetic properties have been investigated it has been found that the alloys have an ordered magnetic structure with a moment of approximately 4β confined to the Mn sites. The alloys are usually ferromagnetic but some antiferromagnetic structures have been established [11–13].

In addition to the above series other $L2_1$ alloys have been discovered at the composition Co_2MnX but their magnetic properties have not been examined. The present paper reports an investigation of the chemical and magnetic structures of the alloys Co_2MnAl , Co_2MnSi , Co_2MnGa , Co_2MnGe , Co_2MnSn and Co_2MnSb .

2. STRUCTURE FACTORS AND ORDER IN $L2_1$ ALLOYS

The structure illustrated in Fig. 1 produces Bragg reflections with non-zero structure amplitudes when the Miller indices of the scattering planes are either all odd or all even.

$$S = \frac{\text{No. of } A \text{ atoms on } A \text{ sites} - \text{No. of } A \text{ atoms on } A \text{ sites when randomly ordered}}{\text{No. of } A \text{ atoms on } A \text{ sites when fully ordered} - \text{No. of } A \text{ atoms on } A \text{ sites when randomly ordered}}$$

The reflections are of 3 types with structure amplitudes given by the following

h, k, l , all odd

$$F(111) = 4[(f_A - f_C)^2 + (f_B - f_D)^2]^{1/2}$$

$(h+k+l)/2 = 2n+1$

$$F(200) = 4|f_A - f_B + f_C - f_D|$$

$(h+k+l)/2 = 2n$

$$F(220) = 4|f_A + f_B + f_C + f_D| \quad (1)$$

where f_A, f_B, f_C and f_D are the average scattering factors for the atoms on the A, B, C and D sites respectively.

Alloys at the composition Co_2MnX with the $L2_1$ structure have A and C sites entirely occupied by Co atoms and B and D sites occupied by Mn and X atoms respectively. For such alloys the structure amplitudes reduce to the following

$$F(111) = 4|f_{\text{Mn}} - f_X|$$

$$F(200) = 4|2f_{\text{Co}} - (f_{\text{Mn}} + f_X)|$$

$$F(220) = 4|2f_{\text{Co}} + (f_{\text{Mn}} + f_X)|. \quad (2)$$

The reflections for which $(h+k+l)/2 = 2n$ are the principal reflections and are unaffected by the state of chemical order. The remaining 2 groups of reflections are superlattice reflections.

When disorder occurs in ternary alloys it may do so in a variety of ways. If disorder occurs randomly all the superlattice lines will be reduced in intensity by a factor S^2 where S is the degree of long range order defined as in the binary case, i.e.

If, however, preferential disorder occurs only between certain sites then the 2 groups of superlattice reflections will be affected differently and it is not then generally possible to describe the state of order in terms of a single ordering parameter.

The effects of different types of disorder on the structure amplitudes of ternary alloys of the Heusler type have been discussed in detail by Johnson and Hall [16], and Webster [11], but in this particular series only one type of preferential disorder is observed and discussion will be limited to this case. In these alloys the Co atoms either remain ordered or

contribute only to the random disorder. Any preferential disorder, if it occurs, is only between Mn and X sites, and may be described in terms of a preferential disordering parameter $\alpha(\text{Mn}-X)$ defined as the fraction of Mn atoms preferentially occupying X sites. The total state of order is then completely represented by the two factors S and α . These two factors may be readily derived from the relative intensities of principal and superlattice lines. The even superlattice lines are unaffected by preferential (Mn- X) disorder and are only reduced in intensity by the factor S^2 , whereas the odd lines are reduced by the factor $(1-2\alpha)S^2$. When $\alpha=0.5$, complete disorder exists between Mn and X atoms and the structure reduces to the $B2$, CsCl type.

The coherent neutron diffraction peaks of ferromagnetic alloys contain both nuclear and magnetic contributions. For unpolarized neutrons the magnetic and nuclear scattering intensities are additive and the total structure factor is given by the equation

$$F^2 = F_{\text{nuc}}^2 + q^2 F_{\text{mag}}^2 \quad (3)$$

F_{nuc} is obtained by substituting the appropriate nuclear scattering lengths b [17] in equation (2), and F_{mag} by substituting the appropriate magnetic scattering lengths p . p is related to the atomic moment μ (in Bohr magnetons β) by the equation

$$p = 0.269\mu f_\theta \quad (4)$$

where f_θ is the magnetic form factor correction at the angle of reflection. The form factors used were those derived by Nathans and Paoletti [18], and Corliss *et al.* [19] for Co and Mn respectively. If α is the angle between the magnetic and scattering vectors, then $q^2 = \sin^2\alpha$. For cubic magnetic structures in zero magnetic field q^2 takes the average value $\frac{2}{3}$, but may be reduced to zero by the application of a saturating magnetic field along the scattering vector.

3. EXPERIMENTAL PROCEDURES

(1) Alloy preparation

The alloys were prepared in the form of 20g ingots by melting together the appropriate quantities of spectrographically pure elements in an Argon arc furnace. Specimens were cut from different parts of the ingots for magnetic analysis and the remainders were crushed to provide powder samples for X-ray and neutron diffraction analysis. All the samples were hard and brittle and crushed readily in a hardened steel mortar. The samples were annealed for 24 hr in sealed evacuated quartz ampoules and then quenched. The weight losses recorded on melting, and the annealing temperatures are given in Table 1. The compositions of the alloys that

Table 1. Details of alloy preparation

Alloy	% wt. loss on melting	Annealing Temp. °C
Co ₂ MnAl	2.4	720
Co ₂ MnSi	0.9	720
Co ₂ MnGa	0.4	800
Co ₂ MnGe	0.7	800
Co ₂ MnIn		
Co ₂ MnSn	0.7	720
Co ₂ MnSb	0.6	720

had lost more than 1 per cent by weight on melting, or that showed any evidence of a second phase, were checked by chemical analysis.

(2) Magnetic analysis

All the alloys were strongly ferromagnetic with Curie temperatures between 600 and 1000°K. Bulk magnetization measurements were made, using a Sucksmith ring-balance, on specimens shaped in the form of rough ellipsoids. Magnetic isothermals were obtained in applied fields up to 16 kOe at a series of temperatures between 4.2°K and 1000°K. Effective internal fields were obtained by subtracting calculated demagnetizing fields from the applied fields. At low temperatures the spontaneous magnetization,

σ_{OT} , was obtained by linear extrapolation of the isothermals to zero fields, but near the Curie temperature σ_{OT} was derived from σ^2 vs. H/σ plots [20]. Extrapolation of the resulting spontaneous magnetization curves to 0°K was made using the $T^{3/2}$ law.

(3) Structure analysis

X-ray powder diffraction measurements were used to determine lattice parameters and for preliminary chemical structure analysis. The X-ray diffraction photographs were obtained with a 9 cm Unicam camera in a van Arkel mounting, using iron $K(\alpha)$ radiation. Lattice parameters were determined accurately from Nelson-Riley extrapolations, and line intensities were estimated visually.

Details of the chemical and magnetic structures, including quantitative estimates of degrees of order, were obtained from neutron diffraction powder measurements. The neutron diffraction patterns were obtained at AERE Harwell using the Curran diffractometer and monochromatic neutrons of wavelength 1.056 Å from the Dido high flux reactor. All measurements were made at 4.2°K on powder samples enclosed in Ti-Zr null matrix cans in either a vanadium tailed cryostat or in the SRC/Cambridge cryostat which incorporates a superconducting magnet that was used to apply a horizontal magnetic field of 7 kOe over the sample region.

The states of chemical order were determined from measurements of the intensities of the coherent Bragg peaks observed with the magnetic field aligned along the scattering vector so that $q^2 = 0$, and $F^2 = F_{\text{nucl}}^2$. The (220) principal reflections were used for normalization purposes since their intensities are unaffected by the states of order. In the single phase alloys excellent agreement was obtained between the observed intensities and those calculated for $L2_1$ alloys at the stoichiometric composition. In the alloys containing a small amount of second phase the neutron diffraction peak intensities were used in conjunction with the chemical analysis

to estimate the composition and state of order of the principal phases.

The magnetic moment distributions were determined by subtracting the peak intensities observed with the magnetic field on ($q^2 = 0$), from the corresponding peak intensities observed in zero field ($q^2 = \frac{4}{3}$). The (220) peaks were again used to normalize the data since the intensities of the principal magnetic reflections depend essentially upon the total magnetic moment and not upon the moment distribution, except for any necessary correction for any differences in the magnetic form factors. The magnetic moment distributions were derived from the intensities of the magnetic superlattice peaks. The intensities of the odd peaks depend only upon the magnetic moments on the Mn sites whereas the intensities of the even superlattice peaks depend upon the difference in moment between Mn and Co sites. Fortunately, in these alloys the magnetic moment distributions are such that small changes in relative moment distributions have a marked effect upon the superlattice peak intensities, and consequently the magnetic moments on the Co and Mn sites may be obtained accurately.

4. RESULTS

Co₂MnAl

Tsuboya and Sugihara [21] investigated alloys in the ternary Co-Mn-Al system up to 30 At. % Co and found ferromagnetic and ferrimagnetic κ phase alloys in the region up to 25 At. % Co.

An alloy was prepared at the composition Co₂MnAl, annealed and quenched. The X-ray diffraction photograph that was taken was consistent with that expected for a $B2$ alloy at this composition, or for a Heusler alloy with a large amount of preferential Mn-Al disorder as the odd superlattice lines could not be resolved. Some additional weak lines that were present were indexed as f.c.c. with a lattice parameter 3.628 Å, which is the same as that reported by Schneider and Wunderlich [22] for Co-Mn alloy containing 57 at. % Mn.

Because of the relatively large loss in weight that occurred on melting and the presence of a second phase it was possible for the primary phase to differ substantially from the stoichiometric composition, and so a chemical analysis was performed. The atomic compositions determined by chemical analysis were Co, 49.4%; Mn, 25.1%; Al, 25.5%. It was estimated from the relative intensities of the diffraction lines that the amount of second phase present was only about 1 per cent, consequently the principal phase could not have differed substantially from the stoichiometric composition.

The spontaneous magnetization curve for this strongly ferromagnetic alloy is illustrated in Fig. 4, together with the corresponding curves for the alloys containing Si, Ga, Ge, Sn and Sb. The principal magnetic features of the same alloys are summarized in Table 8.

The neutron diffraction patterns recorded from Co_2MnAl at 4.2°K indicated some disorder. The (111) and (311) peaks, which for an ordered Heusler alloy would be the most intense, were extremely weak indicating a large amount of preferential Mn-Al disorder. The calculated and observed intensities are compared in Table 2. The results indicate a small amount of random disorder, almost complete Mn-Al disorder, and a substantial moment on both Co and Mn sites.

Co_2MnSi

A summary of X-ray diffraction investigations of alloys in the Co-Mn-Si system has

been given by Pearson[23]. Gladyshevskij *et al.*[24] report that the alloy at the composition Co_2MnSi has the $B2$ structure with lattice parameter 2.833 Å, but Kuz'ma *et al.* [25] report that an alloy at the same composition, when quenched from 800°C, has the $L2_1$ structure with a lattice parameter 5.670 Å.

An alloy was made at the composition Co_2MnSi , annealed and quenched. Both odd and even superlattice lines were present on the X-ray photograph as expected for an $L2_1$ alloy. The lattice parameter was 5.654 Å.

The alloy was very strongly ferromagnetic with a saturation moment 5.07 β and a Curie temperature 985°K.

In contrast to Co_2MnAl the neutron diffraction patterns of Co_2MnSi , illustrated in Fig. 2, have very strong (111) and (311) superlattice peaks characteristic of ordered Heusler alloys. It is seen from the comparison of observed and measured intensities in Table 3 that the alloy is fully ordered in the $L2_1$ structure with a moment on both Co and Mn sites.

Co_2MnGa

Hames[8] reported that an alloy at the composition Co_2MnGa was ferromagnetic and probably had the $L2_1$ structure but was unable to positively identify the Co, Mn and Ga sites from X-ray photographs. The same structure was obtained after both quenching and furnace cooling, but with slightly different lattice parameters, 5.77 and 5.78 Å respectively.

Table 2. A comparison of the calculated and observed neutron diffraction intensities from Co_2MnAl at 4.2°K

<i>hkl</i>	Calc.			Measured	
	$L2_1$ Nuclear	Nuclear	Magnetic $S = 0.9, \alpha(\text{Mn-Al}) = 0.4$ $\mu(\text{Co}) = 0.5, \mu(\text{Mn}) = 3.01$	Field on nuclear	Field off-field on magnetic
111	80.8	2.6	1.3	3 ± 1	1 ± 1
200	23.6	17.9	4.7	18 ± 1	5 ± 2
220	22.2	22.2	22.8	(22.2)	(22.8)
311	68.6	2.2	0.3	2 ± 1	1 ± 1
222	10.2	9.4	0.4	9 ± 1	0 < 2
400	5.8	5.8	1.9	5 ± 1	2 ± 2

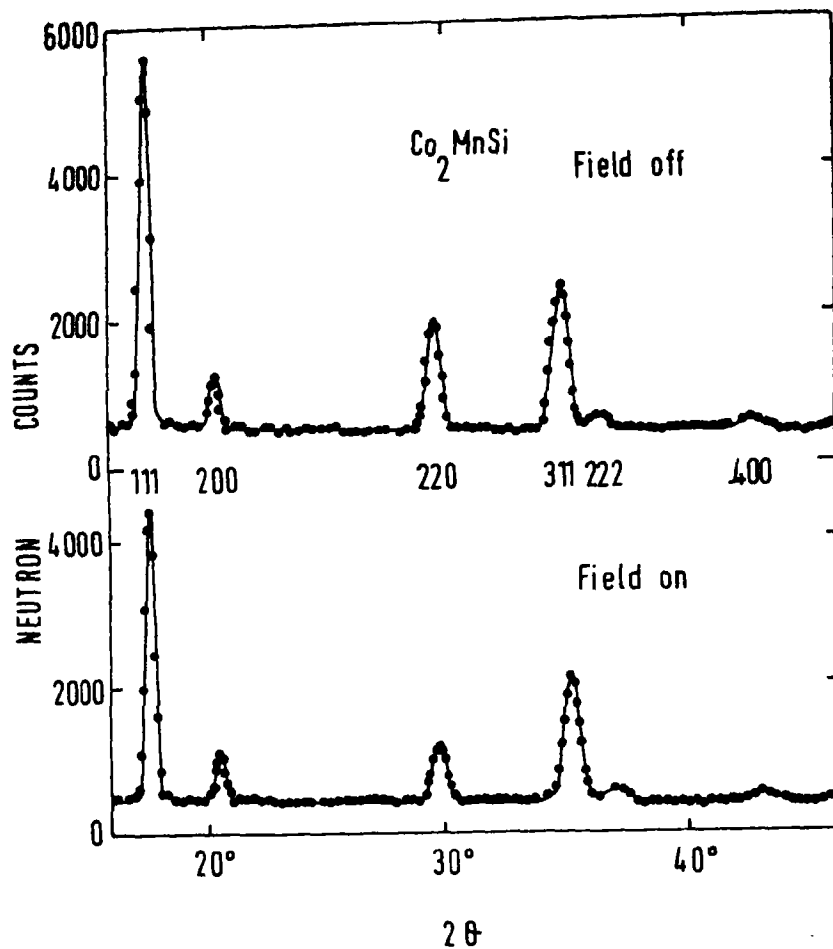


Fig. 2. Neutron diffraction patterns of Co_2MnSi at 4.2°K .

Table 3. A comparison of the calculated and observed neutron diffraction intensities from Co_2MnSi at 4.2°K

<i>hkl</i>	Calc.		Measured	
	Nuclear	Magnetic $\mu(\text{Co}) = 0.75, \mu(\text{Mn}) = 3.57$	Field on nuclear	Field off-field on magnetic
111	94.2	50.6	96 ± 4	50 ± 5
200	16.9	4.7	17 ± 1	4 ± 1
220	28.0	35.6	(28.0)	(35.6)
311	80.1	11.0	80 ± 3	11 ± 4
222	7.8	0.3	8 ± 1	$0 < 1$
400	7.3	3.7	7 ± 1	3 ± 1

An alloy was made at the composition Co_2MnGa , annealed and quenched. The X-ray pattern was consistent with that expected for an $L2_1$ alloy at this composition, with a lattice parameter 5.770 \AA . The odd superlattice lines were just visible but the even ones could not be resolved, but this is to be expected since in the fully ordered $L2_1$ structure the calculated intensities of the even superlattice lines are only $\sim 3 \times 10^{-4}$ the intensity of the principal lines.

The alloy was strongly ferromagnetic with a saturation moment 4.05β and a Curie temperature 694°K .

The observed and calculated neutron diffraction intensities are compared in Table 4. The alloy is highly ordered in the $L2_1$ structure with a small amount of preferential disorder corresponding to $\alpha(\text{Mn-Ga}) = 0.01$, and a magnetic moment on both Co and Mn sites.

Co_2MnGe

Cerkasin *et al.* [26] concluded from X-ray diffraction measurements that Co_2MnGe has an $L2_1$ structure with a lattice parameter 5.73 \AA .

An alloy was prepared at the composition Co_2MnGe , annealed and quenched. The resulting X-ray photograph indicated an $L2_1$ structure with lattice parameter 5.743 \AA .

The alloy was very strongly ferromagnetic with a saturation moment 5.11β and a Curie temperature 905°K .

The observed and calculated neutron diffraction results are compared in Table 5. The alloy is fully ordered with magnetic moments on both Co and Mn sites.

Co_2MnIn

An attempt was made to form an alloy at the composition Co_2MnIn , but the In did not go into solution.

Table 4. A comparison of the calculated and observed neutron diffraction intensities from Co_2MnGa at 4.2°K

<i>hkl</i>	$L2_1$ Nuclear	Calc. $\alpha(\text{Mn-Ga}) = 0.01$		Measured	
		Nuclear	Magnetic $\mu(\text{Co}) = 0.52, \mu(\text{Mn}) = 3.01$	Field on nuclear	Field off-field on magnetic
111	188.0	180.4	37.7	182 ± 6	34 ± 7
200	1.8	1.8	5.6	2 ± 1	6 ± 1
220	68.6	68.6	23.9	(68.6)	(23.9)
311	159.5	153.0	8.7	152 ± 5	11 ± 6
222	0.8	0.8	0.4	1 ± 1	$0 < 1$
400	17.8	17.8	1.9	17 ± 2	4 ± 2

Table 5. A comparison of the calculated and observed neutron diffraction intensities from Co_2MnGe at 4.2°K

<i>hkl</i>	Nuclear	Calc.		Measured	
		Nuclear	Magnetic $\mu(\text{Co}) = 0.75, \mu(\text{Mn}) = 3.61$	Field on nuclear	Field off-field on magnetic
111	231.0		56.3	225 ± 7	55 ± 8
200	0		5.5	$0 < 1$	5 ± 1
220	88.2		38.6	(88.2)	(38.6)
311	195.0		12.7	192 ± 5	18 ± 6
222	0		0.3	$0 < 1$	$0 < 1$
400	22.9		3.0	22 ± 1	3 ± 1

Co₂MnSn

Castelliz [9] investigated alloys in the series CoMnSn-Co₂MnSn and reported that the alloy at the latter composition had the Heusler structure with a lattice parameter 5.977 kX. The structure was verified by Kripjakevic *et al.* [27] but with a slightly different lattice parameter, 5.991 kX.

An alloy was made at the composition Co₂MnSn. It was annealed and quenched and the resulting X-ray photograph was consistent with an L2₁ structure with lattice parameter 6.000 Å.

The alloy was very strongly ferromagnetic with a saturation moment 5.08β and a Curie temperature 829°K.

The neutron diffraction peak intensities compared in Table 6 show that the alloy is fully ordered with a magnetic moment on both Co and Mn sites.

Co₂MnSb

Nowotny and Glatz [28] reported that an

alloy at the composition CoMnSb has a Cl structure, but were unable to distinguish between Co and Mn sites. The alloy at the stoichiometric composition contained 2 phases

An alloy was made at the composition Co₂MnSb, but a small amount of Co remained undissolved, and the X-ray photograph taken after annealing and quenching revealed a 2 phase structure. The principal phase appeared to have an L2₁ structure with a lattice parameter 5.929 Å, and the small amount of secondary phase was indexed as f.c.c. with a lattice parameter 3.552 Å. Cobalt has an f.c.c. structure with lattice parameter 3.542 Å. A chemical analysis was performed to check any departure from stoichiometry. The atomic compositions determined by the analysis were Co, 50.2%; Mn, 25.0%; Sb, 24.8%.

The nuclear peaks of the neutron diffraction pattern from the primary phase Co_xMnSb are very sensitive to order and to

Table 6. A comparison of the calculated and observed neutron diffraction intensities from Co₂MnSn at 4.2°K

hkl	Nuclear	Calc.	Field on nuclear	Measured Field off-field on magnetic
		Magnetic $\mu(\text{Co}) = 0.75, \mu(\text{Mn}) = 3.58$		
111	173.2	66.8	167 ± 5	68 ± 7
200	6.2	6.6	5 ± 1	8 ± 2
220	56.3	45.7	(56.3)	(45.7)
311	138.6	15.9	139 ± 5	16 ± 6
222	2.8	0.4	3 ± 1	0 < 1
400	14.5	3.9	14 ± 1	3 ± 1

Table 7. A comparison of the calculated and observed neutron diffraction intensities from Co_{1.5}MnSb at 4.2°K

hkl	Co ₂ MnSb Nuclear	Calc. Co _{1.5} MnSb	Field on nuclear	Measured Field off-field on magnetic
		Nuclear Magnetic $\mu(\text{Co}) = 0.75, \mu(\text{Mn}) = 3.75$		
111	137.9	140.5	139 ± 10	63 ± 13
200	9.9	3.3	3 ± 1	14 ± 2
220	45.3	30.0	(30.0)	(38.0)
311	116.7	118.9	117 ± 5	20 ± 7
222	4.5	1.5	1 ± 1	1 ± 1
400	11.7	7.8	6 ± 2	3 ± 2

composition. The results, shown in Table 7, obtained with the magnetic field applied indicate that the primary phase must have been very highly ordered in the Heusler structure and that $x = 1.5 \pm 0.15$. A comparison of the line intensities of the two phases suggested that approximately 5 At. % Co was present as the secondary phase, rather than the 12.5 % expected from the composition of the primary phase and the chemical analysis. The apparent discrepancy between these two figures is probably due to an underestimate of the secondary phase that could occur using the diffraction data if the secondary phase is dispersed in small regions.

The spontaneous magnetization curves for the alloy are shown in Fig. 3. The upper curve is the observed composite curve for the entire alloy. The lower is the projected curve for a 5 at. % admixture of Co assuming a magnetic moment of 1.716β per Co atom. The curve for 95 at. % $\text{Co}_{1.5}\text{MnSb}$ is the difference between the two. $\text{Co}_{1.5}\text{MnSb}$ has a saturation moment 4.9β and a Curie temperature 600°C .

The observed and calculated nuclear and

magnetic neutron diffraction peak intensities are compared in Table 7. The agreement between observed and calculated intensities is good, but because the alloy contains a second phase and is not at the stoichiometric composition, there is an increase in error in estimating the moments on Co and Mn sites. However, as in all the other alloys, there is definitely a substantial magnetic moment on both Co and Mn sites.

5. DISCUSSION

All the alloys investigated had the Heusler ($L2_1$) structure, and the ones containing the group IVB elements Si, Ge and Sn were completely ordered. The 2 alloys containing the group IIIB elements Ga or Al each exhibited a small amount of random disorder but in the latter there was also a large amount of preferential (Mn-Al) disorder. This amount of preferential disorder is so large that the structure of Co_2MnAl may be alternatively described as singly ordered $B2$ with small (~ 20 per cent) doubly ordered $L2_1$ regions. It was not possible to dissolve all the Co in

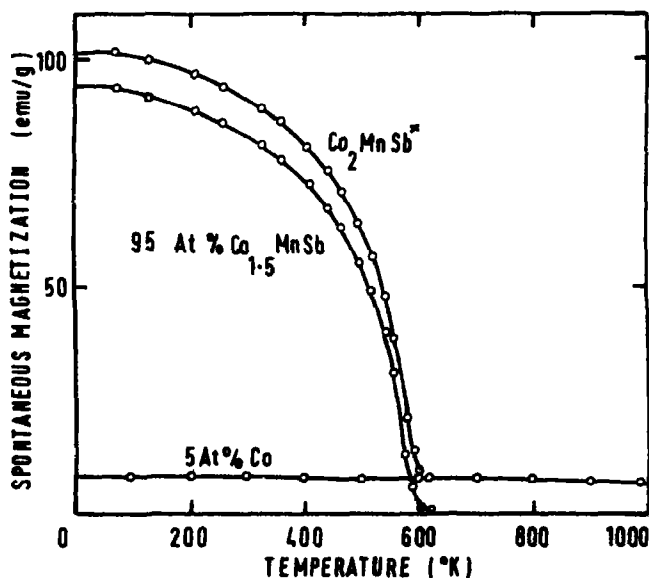


Fig. 3. Spontaneous magnetisation σ_{OT} vs. temperature for Co_2MnSb^* , 95 at. % $\text{Co}_{1.5}\text{MnSb}$ and 5 at. % Co.

Table 8. A summary of the principal magnetic and structural data for the alloys Co_2MnAl , Co_2MnSi , Co_2MnGa , Co_2MnGe , Co_2MnSn and $\text{Co}_{1.5}\text{MnSb}$

Alloy	Lattice parameter (Å)	Curie temp. (°K)	$\mu_{00}/\text{molecule}$ (β)	$\mu_{00}(\text{Co})$ (β)	$\mu_{00}(\text{Mn})$ (β)
Co_2MnAl	5.756	693 ± 3	4.01 ± 0.05	0.5 ± 0.12	3.01 ± 0.24
Co_2MnSi	5.654	985 ± 5	5.07 ± 0.05	0.75 ± 0.08	3.57 ± 0.16
Co_2MnGa	5.770	694 ± 3	4.05 ± 0.05	0.52 ± 0.08	3.01 ± 0.16
Co_2MnGe	5.743	905 ± 3	5.11 ± 0.05	0.75 ± 0.08	3.61 ± 0.16
Co_2MnSn	6.000	829 ± 4	5.08 ± 0.05	0.75 ± 0.08	3.58 ± 0.16
$\text{Co}_{1.5}\text{MnSb}$	5.929	600 ± 10	4.9 ± 0.1	0.75 ± 0.12	3.76 ± 0.24

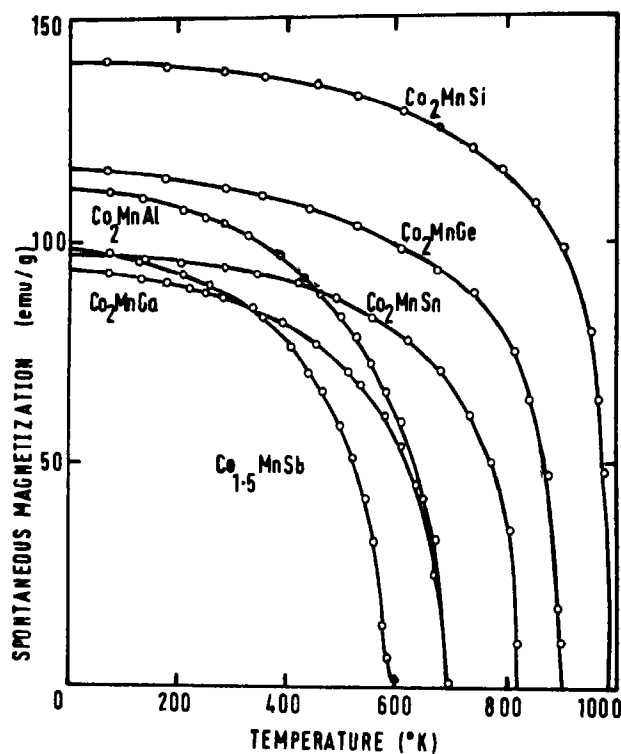


Fig. 4. Spontaneous magnetization σ_{0T} vs. temperature for Co_2MnAl , Co_2MnSi , Co_2MnGa , Co_2MnGe , Co_2MnSn and $\text{Co}_{1.5}\text{MnSb}$.

Co_2MnSb and the resultant alloy contained 2 phases, but the degree of long range order in the primary phase, $\text{Co}_{1.5}\text{MnSb}$, was still high.

The lattice parameters of the alloys vary in a regular manner. Alloys containing group IVB elements have smaller lattice param-

eters than those containing adjacent group IIIB elements, and within each sub-group the lattice parameters increase with atomic number.

It is unprofitable to analyse the magnetic structures of these alloys in terms of any

simple model since too many possible exchange forces must be considered. However, several distinct features are evident from the summary of magnetic and structural data presented in Table 8. The alloys containing group IVB elements have almost identical magnetic properties. They all have a nett moment of $\sim 5.1 \beta$ per molecule and individual moments of ~ 3.6 and 0.75β per Mn and Co site respectively. The Curie temperatures decrease with increasing lattice parameter in the series Si, Ge to Sn. The alloys containing group IIIB elements each have a nett moment of $\sim 4\beta$, correspondingly lower Curie temperatures, and smaller moments on both Co and Mn sites. The alloy $\text{Co}_{1.8}\text{MnSb}$ has moments similar to that of the alloys containing group IVB elements, but it has a relatively low Curie temperature. The low Curie temperature of this non-stoichiometric alloy is probably due to the reduced number of possible exchange interactions resulting from the vacancies on some of the Co sites. In L_{21} alloys nearest neighbour Mn atoms are separated by $a/\sqrt{2}$ and next neighbours by a , but in Co_2MnAl , where there is considerably Mn-Al disorder, Mn atoms may also be at distances $a/2$ and $\sqrt{3} a/2$ from neighbouring Mn atoms. It is to be expected that this difference would be reflected in the Curie temperature, but only to a small extent since the Co-Mn and Co-Co distances are unaffected. As may be seen from Fig. 4, the Curie temperature of Co_2MnAl is lower, relative to the ordered Co_2MnGa , than might have otherwise been expected.

This series of alloys is the first in which it has been established that Heusler alloys exist in which atoms other than Mn may carry a substantial magnetic moment. Consequently the series is characterised by large nett magnetic moments and high Curie temperatures.

Acknowledgements—Much of this work has been carried out at AERE Harwell with the aid of a grant from the

SRC Neutron Beam Research Committee. The author is particularly grateful to the University support section at Harwell for their assistance.

REFERENCES

1. HEUSLER F., *Verh. dt. phys. Ges* 5, 219 (1903).
2. POTTER H. H., *Proc. Phys. Soc.* 41, 135 (1929).
3. PERSSON E., *Z. Phys.* 57, 115 (1929).
4. BRADLEY A. J. and RODGERS J. W., *Proc. R. Soc. A* 144, 340 (1934).
5. FELCHER J. P., CABLE J. W. and WILKINSON M. K., *J. Phys. Chem. Solids* 24, 1663 (1963).
6. COLES B. R., HUME-ROTHERY W. and MYERS H. P., *Proc. R. Soc. A* 196, 125 (1949).
7. OXLEY D. P., TEBBLE R. S. and WILLIAMS K. C., *J. appl. Phys.* 34, 1362 (1963).
8. HAMES F. A., *J. appl. Phys.* 31, 370S (1960).
9. CASTELLIZ L., *M. Chem.* 84, 765 (1953).
10. CASTELLIZ L., *M. Chem.* 82, 1059 (1951).
11. WEBSTER P. J., *The Magnetic and Chemical Structures of the Heusler Alloys*, Thesis, Sheffield University (1968).
12. WEBSTER P. J. and TEBBLE R. S., *Phil. Mag.* 16, 347 (1967).
13. WEBSTER P. J. and TEBBLE R. S., *J. appl. Phys.* 39, 471 (1968).
14. MORRIS D. P., PRESTON R. R. and WILLIAMS I., *Proc. Phys. Soc.* 73, 520 (1959).
15. BACON G. E., *Proc. Phys. Soc.* 79, 938 (1962).
16. JOHNSON G. B. and HALL E. O., *J. Phys. Chem. Solids* 29, 193 (1968).
17. BACON G. E., *Neutron Diffraction*, O.U.P. (1962).
18. NATHANS R. and PAOLETTI A., *Phys. Rev. Lett.* 2, 254 (1959).
19. CORLISS L. M., ELLIOTT N. and HASTINGS J. M., *Phys. Rev.* 104, 924 (1956).
20. KOUVEL J. S., *Gen. Electric Research Report No. 57-RL-1799*, (1957).
21. TSUBOYA L. and SUGIHARA M., *J. phys. Soc. Japan* 17, 410 (1962).
22. SCHNEIDER A. and WUNDERLICH W., *Z. Metallk.* 40, 250 (1949).
23. PEARSON W. B., *A Handbook of Lattice Spacings and Structures of Metals and Alloys*, Vol. 2, Pergamon Press, Oxford, (1967).
24. GLADYSEVSKIJ E. I., KRIPIJAKEVIC P. I. and KUZ'MA Ju. B., *Fiz. Metal. Metalloved.* 2, 454 (1956).
25. KUZ'MA Ju. B. and GLADYSEVSKIJ E. I., *Z. Neorg. Khim.* 9, 674 (1964).
26. CERKASIN E. E., GLADYSEVSKIJ E. I. and KRIPIJAKEVIC P. I., *Dopovidi ta povidomlenija, L'vivsk un-ta* 3, 180 (1957).
27. KRIPIJAKEVIC P. J., GLADYSEVSKIJ E. E. and ZARECHNYNK O. S., *Dokl. Akad. Nauk, SSSR.* 95, 525 (1954).
28. NOWOTNY H. and GLATZL B., *M. Chem.* 83, 237 (1952).

EFFECTS OF PHASE TRANSITION ON ESR AND OPTICAL SPECTRA IN $\text{NH}_4\text{Cl}:\text{Cu}^{2+}$

N. KURODA and A. KAWAMORI

Faculty of Science, Kwansei Gakuin University, Nishinomiya, Japan

(Received 5 August 1970; in revised form 28 September 1970)

Abstract—ESR and optical studies of Cu^{2+} ions in NH_4Cl single crystals were performed in the temperature range from 150 to 300°K. The spectra showed tetragonal symmetry at the site of Cu^{2+} and a pronounced anomaly around 243°K, corresponding to an order-disorder transition related to NH_4^+ ions. The results were analyzed and discussed on the basis of the behavior of NH_3 molecules which coordinated to Cu^{2+} in the cube center of Cl^- lattice.

The order parameter p for the NH_3 molecules was introduced in calculation of g , A and crystalline splitting. Using molecular orbitals for the $\text{Cu}(\text{NH}_3)_2\text{Cl}_4$ system and crystalline field splittings of 0.95×10^4 and $1.37 \times 10^4 \text{ cm}^{-1}$ obtained from optical measurement, 11 per cent mixing of B_{1g} to the ground A_{1g} state as well as 15 per cent of covalency with NH_3 molecules was found through ordering process of NH_3 molecules.

1. INTRODUCTION

AMMONIUM halides have been known as typical substances which undergo an order-disorder type phase transition related to the orientation of NH_4^+ ion. Various phenomena due to this transition have been observed, for example, by NMR[1], neutron diffraction[2] and specific heat studies[3], etc. Among many observations of ESR spectra of doped transition metal ions in these substances, the spectrum of Cu^{2+} has been of interest to many workers, because it was found to be greatly affected by this transition[4-12]. The complete analysis, however, has not yet been done because of two main difficulties. One is that the identification of centers has been difficult and many kinds of models were proposed for identical ESR spectra by different authors. The other is that the mechanism which produces the temperature dependence of the spin Hamiltonian parameters has not yet been understood.

Trappeniers and Hagen[7-9] showed that the kind of centers could be controlled by pH of the aqueous solutions from which crystals were grown. They proposed models for three kinds of centers (centers I, II and III). Center I and center II were found in

crystals which were grown from the HCl acidic and NH_4OH basic aqueous solutions, respectively. In crystals grown from the neutral solutions, center III was found as well as center I and center II. Pilbrow and Speath [10, 11] also proposed different schemes for the same kinds of centers as center I and III. They attempted to explain the temperature dependence of their ESR spectra by taking account of the lattice expansion and the librational motion of a neighboring NH_4^+ ion.

In this paper, ESR and optical studies of Cu^{2+} ions of one kind of center will be reported and our results will be analyzed by a different scheme from that considered by Pilbrow and Speath. Our previous DTA (Differential thermal analysis) study on the shift of the transition temperature T_λ with increase of Cu^{2+} concentration showed[12] a clear correlation between the order parameter p and the shift of T_λ . p was first introduced by Nagamiya[13] and was defined as probability for a NH_4^+ ion to take the favored orientation in the crystal ammonium halide. This result was explained by a statistical treatment over the whole crystal with the defect centers associated with Cu^{2+} ions. Our present problem will be treated based on

the statistical aspect of order-disorder phenomena with the assumption that the crystalline field of Cu^{2+} ions produced by coordinating ions is also correlated with this parameter. Our study is restricted to the center II, because it is believed that center II consists of four planar Cl^- ions with Cu^{2+} ion and of two NH_3 molecules coordinated above and below this plane. The NH_3 molecules will produce more pronounced effect on Cu^{2+} ion than four Cl^- ions in the plane [14]. Accordingly this center is considered to be the best indicator of order-disorder effect among various kinds of centers. In section 2, the crystal structure and the defect site of Cu^{2+} ion are shown. In section 3, our experimental process and results of ESR and optical measurements will be presented. The optical study was initiated to obtain the useful information about crystalline environments through crystalline field splitting. In Section 4, a model based on center II which is related to the ordering process of NH_3 molecules in the crystal will be given, and then g and A tensors will be calculated by the basic wave functions derived from this model. In Section 5, our experimental results will be analyzed through some simplifications of our theoretical calculations.

2. CRYSTAL STRUCTURE [15-17]

Ammonium chloride, NH_4Cl , has CsCl-structure below 457°K . Tetrahedral NH_4^+ ion at the center of a cube formed by eight Cl^- ions has two possible orientations which are antiparallel to each other as shown in Fig. 1(a). An order-disorder transition associ-

ated with the orientations of NH_4^+ ions occurs at 243°K . Above this transition temperature, T_λ , NH_4^+ ions reorientate randomly through the tunnelling rotation between these two antiparallel orientations. Although the translational symmetry is lost, its space symmetry can be expressed by $O_h^1 - P_{4m3m}$. Below T_λ , NH_4^+ ions are parallel to each other with their N-H bonds pointing toward four Cl^- ions at the cube corners as shown in Fig. 1(b).

There are two possible sites for the doped Cu^{2+} ion to occupy in the crystal; one is the substitutional site for NH_4^+ ion, the other an interstitial site in the cube faces accompanied by appropriate defects for charge compensation. Hagen suggested for center II that Cu^{2+} ions were incorporated into the latter sites.

3. EXPERIMENTAL PROCESS AND RESULTS

3.1 Sample preparation

Single crystals were grown by evaporation of water from a saturated aqueous solution of NH_4Cl , about 0.01 mol. % of $\text{CuCl}_2 \cdot 2\text{H}_2\text{O}$, and 30 per cent urea as the growth aid with respect to NH_4Cl at 40°C . A few drops of 28 per cent ammonia water were added to the solution for the purpose of obtaining only the center II in the sample. The initial yellow green color of the solution changed to light blue. Too much addition of the ammonia water produced Prussian blue color of the solution, when no crystal was grown. The solution was kept in the desiccator with KOH as an absorbant of water, to prevent the escape of ammonia from the solution. After about a week, rect-

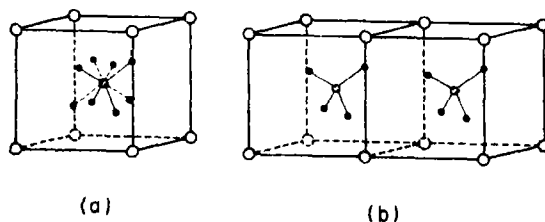


Fig. 1. Crystal structure of NH_4Cl and orientation of NH_4^+ ions in CsCl phase. (a) Antiparallel orientations and (b) parallel orientations.

angular crystals with light blue color were obtained. Their size was about 0.1 cm^3 which was large enough for ESR and optical measurements. The concentrations of Cu^{2+} ion in samples used in our experiments were determined by a chemical analysis and the result is listed in Table 1.

Table 1. Concentration of Cu^{2+} in various samples

Sample	Concentration (mol. %)
N-1	0.77 ± 0.03
N-2	1.75 ± 0.20
N-5	0.088 ± 0.010
N-7	0.054 ± 0.002
N-02-2	0.47 ± 0.02
N-02-5	0.29 ± 0.04

3.2 ESR measurements

Observations of the ESR signals were recorded on a chart using a standard X-band spectrometer with 100 kHz modulation. The sample temperature was measured by a copper-constantan thermocouple and con-

trolled to within $\pm 0.1^\circ\text{K}$ by nitrogen gas flow from a dewar in which the heater current was regulated.

Angular variation in the (100) crystal plane was measured by means of the rotation of the sample tube holder above the cavity of TE_{102} mode at constant temperature. The signals obtained consisted of twelve components, which corresponded to 3 sets of hfs components from the copper nucleus with $I = \frac{3}{2}$. The observed center was confirmed to be of one kind and to occupy the face center of four Cl^- ions from the symmetry of the angular pattern as shown in Fig. 2. In order to analyze the experimental results, the spin Hamiltonian for a Cu^{2+} ion with tetragonal symmetry was assumed as given in following

$$\mathcal{H} = \beta g_{\parallel} S_z H_z + \beta g_{\perp} (S_x H_x + S_y H_y) + A_{\parallel} I_z S_z + A_{\perp} (I_x S_x + I_y S_y). \quad (1)$$

Here β is the Bohr magneton, g 's and A 's are the components of the g and hyperfine tensors, respectively, and S and I are electron and

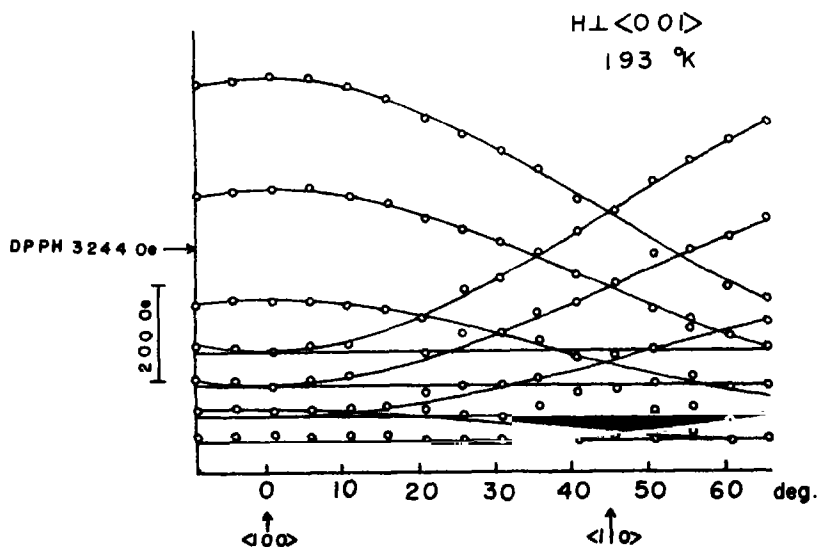


Fig. 2. Angular variation of resonance lines at 193°K . Magnetic field H was rotated in the crystal (001) plane. Angles were measured between H and crystal (100) axis. Solid lines are the calculated curves in accordance with equation (2) using $g_{\parallel} = 1.999$, $g_{\perp} = 2.217$, $A_{\parallel} = 217 \times 10^{-4} \text{ cm}^{-1}$ and $A_{\perp} = 64.5 \times 10^{-4} \text{ cm}^{-1}$.

nuclear spin operators, respectively. The expression for the transition frequency corresponding to $\Delta m_I = 0$ has been derived by Bleaney to second-order approximation in the hyperfine coupling [18], as follows

$$h\nu = g\beta H_0 + Km_I + \frac{A_{\perp}^2}{4g\beta H_0} \frac{A_{\parallel}^2 + K^2}{K^2} \\ \times \{I(I+1) - m_I^2\} + \frac{1}{2g\beta H_0} \\ \times \left(\frac{A_{\parallel}^2 - A_{\perp}^2}{K} \right)^2 \left(\frac{g_{\parallel}g_{\perp}}{g^2} \right)^2 \sin^2\theta \cos^2\theta m_I^2 \quad (2a)$$

$$\text{with } g^2 = g_{\parallel}^2 \cos^2\theta + g_{\perp}^2 \sin^2\theta \quad (2b)$$

$$K^2 g^2 = A_{\parallel}^2 g_{\parallel}^2 \cos^2\theta + A_{\perp}^2 g_{\perp}^2 \sin^2\theta \quad (2c)$$

where θ is the angle between H_0 and z -axis. In the temperature range from 150 to 300°K, g_{\parallel} , g_{\perp} , A_{\parallel} and A_{\perp} were determined so that the experimental angular variation fitted with equation (2a) at each temperature. The temperature variations of these parameters are shown in Fig. 3. A pronounced change around T_{λ} was observed in each of the parameters.

3.3 Optical measurements

Optical absorption was measured on a recorder using a Cary model 14 spectro-

meter in the wavelength region from 0.3 to 1.5 μ at the temperatures from 100 to 300°K. The temperature of the sample was again controlled by nitrogen gas flow and regulated within ± 0.1 degree. The samples were 0.1 to 0.5 mm thick along the $\langle 100 \rangle$ direction. The optical absorption due to doped Cu^{2+} ions can be described by Beer's law as given by

$$T = T_0 e^{-nd\epsilon \ln 10} \quad (3)$$

where T is the transmittance of the doped crystal, and T_0 corresponds to that in a pure crystal. n is the molar concentration of Cu^{2+} ion, d , the thickness of the sample and ϵ , the molar extinction coefficient. The molar extinction coefficient ϵ for sample N-2 at room temperature is shown in Fig. 5. It was found that Cu^{2+} ions give rise to two main absorption bands; one at about 0.4 μ with relatively high intensity and the other at about 0.7 μ with lower intensity accompanying a shoulder at about 1.0 μ . Hereafter 0.4 and 0.7 μ bands denote the above mentioned bands respectively. The oscillator strengths are estimated to be 8×10^{-4} for 0.7 μ band and larger than 10^{-2} for 0.4 μ band, respectively. 0.7 μ band was identified to be due to $d-d$ transition and the other attributed to the charge transfer band from their intensities [19].

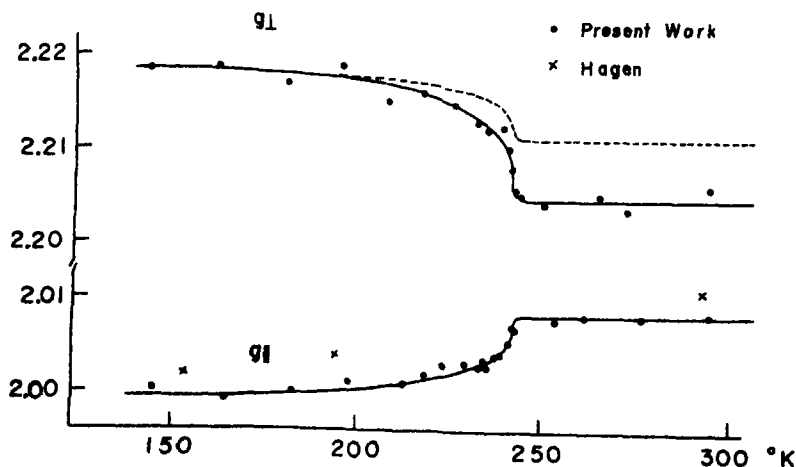
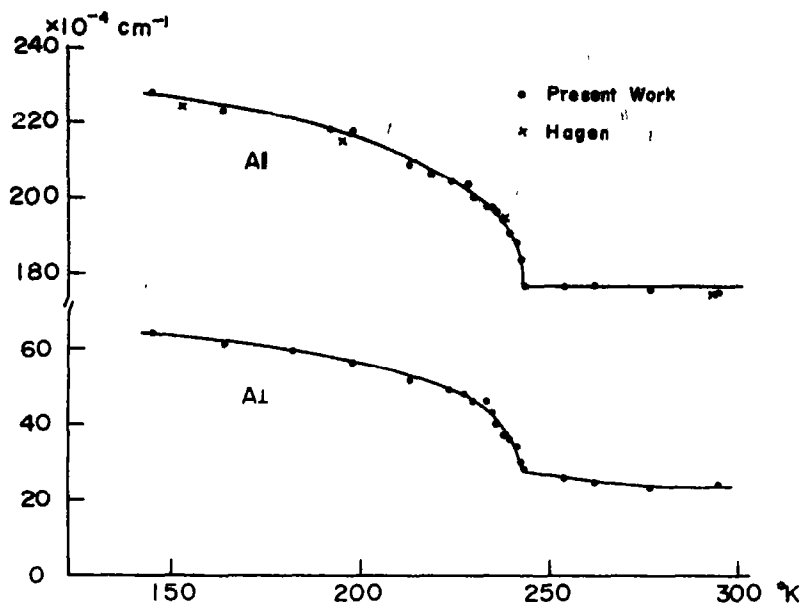
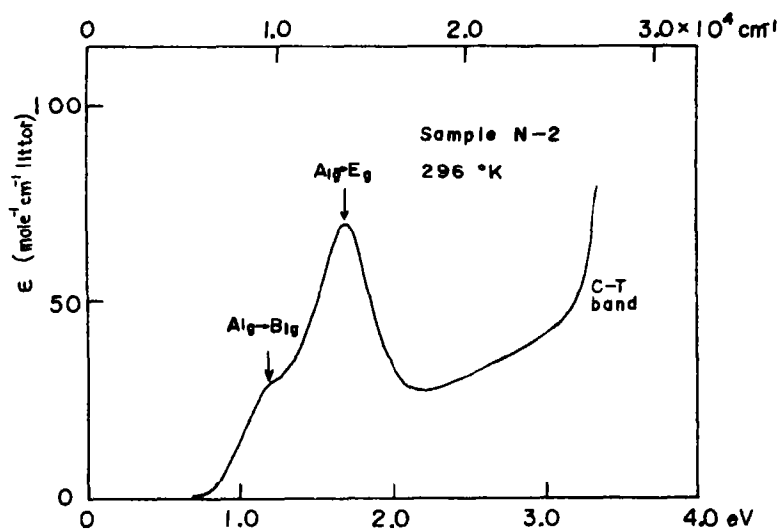


Fig. 3. Temperature variation of g_{\parallel} and g_{\perp} . Solid lines are the smoothed curves of experimental data and the broken line is the calculated one. See text.

Fig. 4. Temperature variation of $A_{||}$ and A_{\perp} .Fig. 5. Molar extinction coefficient, ϵ , due to Cu^{2+} ions in NH_4Cl at 296°K . Details for each assignment are described in Section 5.2.

In the present work the temperature dependence of $0.7\ \mu$ band has been studied in detail, since our interest is in the crystalline field splittings of d -orbitals of the Cu^{2+} ion.

Figure 6 shows the shift in the position of the absorption maximum, ν_{max} , with decreasing temperature. A pronounced anomaly was found around T_λ as expected. Furthermore

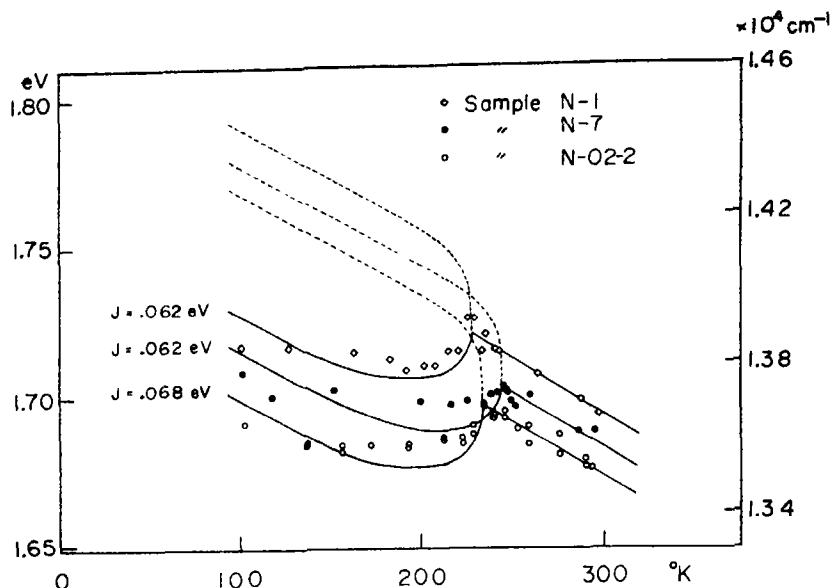


Fig. 6. Temperature variation of the absorption maximum, ν_{\max} , of 0.7 μ band for several specimens. Solid lines are the calculated curves in accordance with equation (14) with the contribution from the lattice thermal expansion shown by the broken lines and the appropriate values of J , where $J = \frac{1}{2} \beta_0^2 \Delta E_{10}$.

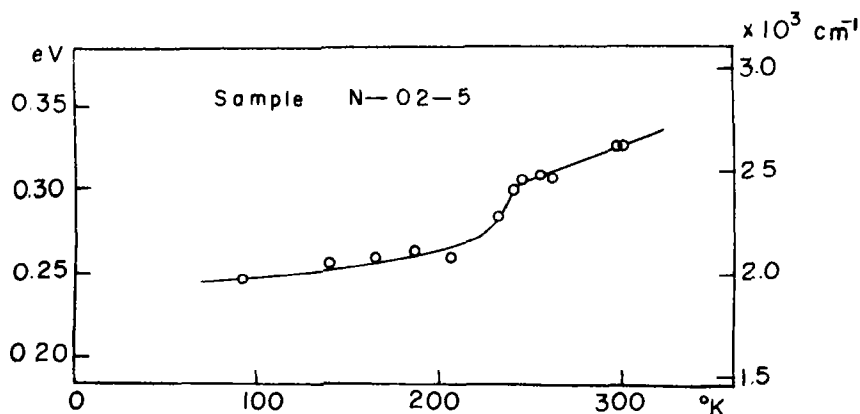


Fig. 7. Temperature variation of the half-width of $A_{1g} \rightarrow E_g$ band.

a decrease in the width of the absorption band was observed just below T_λ , as shown in Fig. 7.

4. THEORY

4.1 Behavior of NH_3 molecules

In order to explain the experimental results, a model based on center II is proposed. In

center II, Cu^{2+} ions are surrounded octahedrally by four coplanar Cl^- ions and two NH_3 molecules above and below this plane. Since the behavior of NH_3 molecules surely plays an essential role in the anomalous effects on ESR and optical absorption spectra, it will be considered in detail in the following treatment. In our model it is assumed that

the nonbonding orbital of each NH_3 molecule lies along one of four N-Cl sides in the octahedron surrounding Cu^{2+} ion and the NH_3 molecules also undergo the order-disorder transition associated with these four equivalent orientations. NH_3 molecules are assumed to have long range cooperative interaction with the surrounding NH_4^+ ions and to take the same favored orientation as that of NH_4^+ ions in the ordered phase (as shown in Fig. 8), while each NH_3 molecule

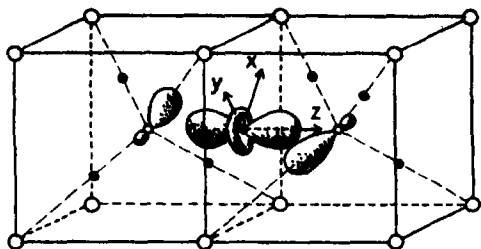


Fig. 8. Favored orientation of coordinated NH_3 molecules in center II in the ordered phase. Lobes represent the nonbonding orbitals of NH_3 molecules and the ground $d_{3z^2-r^2}$ orbital of Cu^{2+} ion. x , y and z denote the principal axes of this center.

reorients randomly over the four orientations in the disordered phase. Then a pair of NH_3 molecules give rise to the manifold configurations in their orientations. The process of the order-disorder transition can

be described phenomenologically in terms of the order parameter p , where p is defined as the probability that a NH_3 molecule takes the favored orientation in the crystal.* The probability of occurrence of each configuration is given by a function of p in Fig. 9. If we neglect the existence of the proton on the bonding orbital directed to the Cl^- ion on the opposite side in the Cu-Cl_4 plane, configurations Ia and Ib can be considered to produce the crystalline field with tetragonal symmetry around Cu^{2+} , while IIa and IIb to do that with orthorhombic symmetry.† in the completely ordered phase corresponding to $p = 1$, only configurations Ia and Ib are present in the crystal. In the region $\frac{1}{2} \leq p < 1$, however, configurations IIa and IIb are also present as well as Ia and Ib.

*The order parameter, s , defined by Nagamiya is not identical with p but related by $s = 2p - 1$.

†Since the bonding orbital is known to be elongated along the N-H direction compared to the nonbonding one, it is expected to have stronger negative charge effect on Cu^{2+} than the nonbonding orbital. This effect compensates partly the positive charge effect due to the proton on the same orbital. In practice, the two sp^3 hybridized orbitals of NH_3 contribute dominantly to the crystalline potential and the positive point charge of the proton is considered as a small perturbation to that. This treatment was justified by a rough estimate which showed the perturbing field has the energy with the order of 0.1 of the orthorhombic crystalline effect shown later.

	Ia	Ib	IIa	IIb
Probability of Occurrence	$\frac{1}{4} p^2$	$\frac{1}{4} (1-p)^2$	$\frac{1}{4} p(1-p)$	$\frac{1}{4} p(1-p)$
Configuration of NH_3 Molecules				
Nondiagonal Matrix Element	—	—	$\langle z^2 \parallel x^2 - y^2 \rangle$	$\langle z^2 \parallel x^2 - y^2 \rangle$

Fig. 9. Classification of possible configurations of NH_3 molecules of center II. Black and open circles represent the center of gravity of the nonbonding orbital of NH_3 above (positive z direction) and below (negative z direction) the xy plane, respectively.

We turn our attention next to the effect of the reorientational motion of NH_3 on ESR and optical absorption spectra in the region $\frac{1}{2} \leq p < 1$. The two kinds of the crystalline field mentioned above would yield two kinds of values for the measurable quantities, g 's, A 's and ν_{max} , unless the correlations between the configurations are small. The correlation frequency for the reorientational motion of NH_3 is given in general form as

$$\nu_c = \nu_0 e^{-U/kT} \quad (4)$$

where U is a potential barrier. ν_0 and U are known for the case of pure NH_4Cl to be $5.9 \times 10^7 \text{ MHz}$ and 4.7 kcal/mol . [20], respectively. The value of U for NH_3 , however, should be considerably smaller than that for NH_4^+ because of the lack of one proton. Thus the correlation frequency of the reorientational motion of NH_3 is considered to be much higher than the difference in Larmor frequency, so that motional narrowing effect on ESR spectrum takes place. In fact no more components than twelve were observed in our ESR experiment. On the other hand, broadening in the optical spectrum was observed around T_λ , which showed existence of splitting in the d_{yz} and d_{zx} levels in Cu^{2+} . Accordingly the correlation frequency may be high enough to cause motional narrowing in the ESR but not in the optical spectrum.

In configurations IIa and IIb, the average crystalline field is of tetragonal symmetry, although it is orthorhombic instantaneously. Therefore the symmetry of the crystalline field becomes effectively tetragonal even in the disordered phase because of motional narrowing. In the transition region around T_λ , however, some effects due to the orthorhombic crystalline configuration are expected to arise through an admixture of $d_{3z^2-r^2}$ and $d_{x^2-y^2}$ orbitals. Then such effects will appear in ESR and optical spectra through statistical average of each observable over all configurations.

On the other hand, d -orbitals of the central Cu^{2+} ion may have covalency with $2s$ and $2p$ orbitals of ligands. It should cause reduction in values of some parameters, e.g. spin orbit coupling constant, from those for pure Cu^{2+} ion. Furthermore, thermal expansion of the lattice should cause variation of the Cu-N distance as well as the Cu-Cl distance, leading to a variation of the crystalline field potential. Thus it will also have an influence on the optical spectrum of the Cu^{2+} ion.

Consequently, the behavior of NH_3 manifests its effect through an admixture between the $d_{3z^2-r^2}$ and $d_{x^2-y^2}$ orbitals, the formation of covalent bond with the nonbonding orbital of NH_3 and the thermal variation of Cu-N distance.

4.2 Wave functions and energies

According to the above mentioned model, the symmetry of the defect center restricts the ground orbital of $3d^9 - {}^2D$ state of Cu^{2+} ion to $d_{3z^2-r^2}$ or $d_{x^2-y^2}$. Then a consideration based on the spectro-chemical series shows that the ground orbital is $d_{3z^2-r^2}$. The experimental fact that $g > g_{\parallel} \approx 2.00$ verifies this consideration.

In the case of configurations IIa and IIb, the wave functions suitable to our model are expressed as follows in descending order of energy, in hole formalism,

$$\Psi_4 = (1 + \beta_1^2 + \beta_2^2)^{-1/2} (|xy\rangle + \beta_1|3z^2 - r^2\rangle + \beta_2|x^2 - y^2\rangle) \quad (5a)$$

$$\Psi_3 = (1 + \beta_3^2)^{-1/2} (|yz\rangle + \beta_3zx) \quad (5b)$$

$$\Psi_2 = (1 + \beta_3^2)^{-1/2} (|zx\rangle - \beta_3|yz\rangle) \quad (5c)$$

$$\Psi_1 = (1 + \beta_4^2 + \beta_5^2)^{-1/2} (|x^2 - y^2\rangle - \beta_4|xy\rangle + \beta_5|3z^2 - r^2\rangle) \quad (5d)$$

$$\Psi_0 = (1 + \beta_6^2 + \beta_7^2)^{-1/2} (|3z^2 - r^2\rangle - \beta_6|x^2 - y^2\rangle - \beta_7|xy\rangle) \quad (5e)$$

where β_i 's are the coefficients of the admixture between the states. In the above expressions, a small monoclinic distortion is also taken

into account for the generalization of the discussion. The effect of the proton charge on the bonding orbital of NH_3 and other crystalline distortion may be included in β_i 's except β_5 and β_6 . Each state without admixture can be expressed by the anti-bonding LCAO-MO in a tetragonal environment;

$$B_{2g} : |xy\rangle = N_4 d_{xy} + \rho \pi_4 \quad (6a)$$

$$E_g : |yz\rangle = N_3 d_{yz} + \rho \pi_3 + \rho' \pi_3' \quad (6b)$$

$$E_g : |zx\rangle = N_2 d_{zx} + \rho \pi_2 + \rho' \pi_2' \quad (6c)$$

$$B_{1g} : |x^2 - y^2\rangle = N_1 d_{x^2-y^2} + \chi \sigma_1 \quad (6d)$$

$$A_{1g} : |3z^2 - r^2\rangle = N_0 d_{3z^2-r^2} + \chi \sigma_0 + \chi' \sigma_0' \quad (6e)$$

In equations (6a)–(6e), B_{2g} , etc. are the irreducible representations of D_{4h} symmetry. π and σ stand for the appropriate linear combinations of π - and σ -type molecular orbitals of ligands, of which those primed belong to the two NH_3 molecules and those unprimed belong to four Cl^- ions. Parameters N , χ and ρ are constrained by the normalization conditions;

$$N_4^2 + 2N_4\rho S + \rho^2 = 1 \quad (7a)$$

$$N_3^2 + 2N_3\rho S + 2N_3\rho' S' + \rho^2 + \rho'^2 = 1 \quad (7b)$$

$$N_2^2 + 2N_2\rho S + 2N_2\rho' S' + \rho^2 + \rho'^2 = 1 \quad (7c)$$

$$N_1^2 + 2N_1\chi S + \chi^2 = 1 \quad (7d)$$

$$N_0^2 + 2N_0\chi S + 2N_0\chi' S' + \chi^2 + \chi'^2 = 1 \quad (7e)$$

where S and S' are the overlap integrals between the central $3d$ and ligand molecular orbitals. The orbital energies E_n 's represent the contribution of the crystalline field arising from the neighboring ions, and may be written as follows, correct to the second order in β_i 's,

$$E_4 = E_4^0 + \beta_1^2 \Delta E_{40}^0 + \beta_2^2 \Delta E_{41}^0 \quad (8a)$$

$$E_3 = E_3^0 + \frac{1}{2}\delta + \beta_3^2 \delta \quad (8b)$$

$$E_2 = E_2^0 - \frac{1}{2}\delta - \beta_3^2 \delta \quad (8c)$$

$$E_1 = E_1^0 - \beta_4^2 \Delta E_{41}^0 + \beta_5^2 \Delta E_{10}^0 \quad (8d)$$

$$E_0 = E_0^0 - \beta_6^2 \Delta E_{10}^0 - \beta_7^2 \Delta E_{40}^0 \quad (8e)$$

with $\Delta E_{mn}^0 = E_m^0 - E_n^0$ and $\delta = \langle yz | V_c | yz \rangle - \langle zx | V_c | zx \rangle$, where V_c is the crystalline field potential.

The orbital energies for configurations Ia and Ib, which have tetragonal symmetry, can be expressed by a modification of equations (8a)–(8e), putting β_5 , β_6 and $\delta = 0$ in them. The remaining terms are identical with those in equations (8a)–(8e) because of the equality of E_n^0 's and β_i 's for all configurations. The temperature dependence of energy levels due to thermal expansion of the lattice is implicitly included in E_n^0 's. Figure 10 shows the energy level diagram of the $3d^9-2D$ state of Cu^{2+} ion based on the above scheme. The energy difference between excited and ground states were measured in the optical absorption spectra and will be analyzed in the next paragraph.

4.2. g and A tensors

The components of g and A tensors can be calculated by means of the perturbation method to second order in $\lambda \mathbf{L} \cdot \mathbf{S}$ following the method developed by Abragam and Pryce [21]. Although Bleaney, Bowers and Pryce [22] have extended the theory of Abragam and Pryce to the case of orthorhombic symmetry including the second order term in λ , their results are not available for the present work since they ignored the covalency effect. Calculations here include the covalency. Detailed derivations for g and A tensors will be given in the Appendix. Taking account that $\langle E_2 \rangle = \langle E_3 \rangle$ and $\langle \beta_i \rangle = \langle \delta \rangle = 0$, where $\langle \rangle$ means configurational average, application of the wave functions in equation (5a)–(5e) to equation (A4a), (A4b) and (A5b) results in, correct to the second order in β_i 's,

$$g_{\parallel} = 2.0023 - 8P_{14}\lambda_{3d}(\beta_6^2/\Delta E_{40}^0 + \beta_7^2/\Delta E_{10}^0) - 3\zeta^2 N_0^2 N_2^2 (1 + \rho^2) \quad (9a)$$

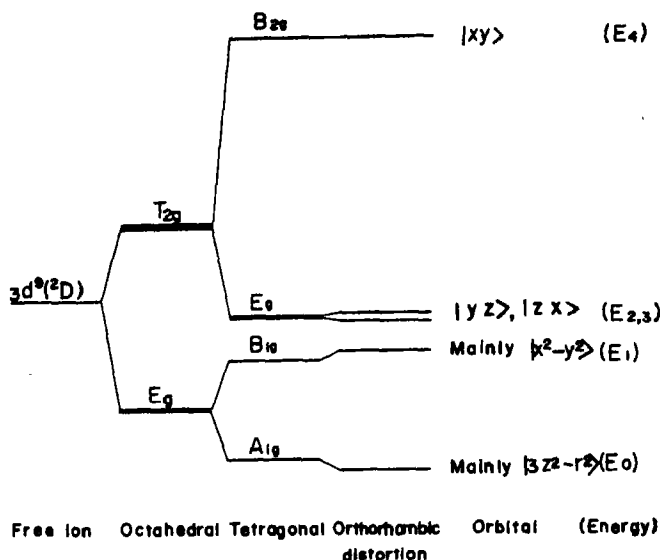


Fig. 10. Crystalline field splittings of 2D state in Cu^{2+} ion as the octahedral symmetry is reduced by successive tetragonal and orthorhombic distortions.

with

$$P_{14} = N_1 N_4 \langle x^2 - y^2 | L_z | xy \rangle /$$

$$\langle d_{xz} \dots y^2 | L_z | d_{xy} \rangle = N_1 N_4 k_{14}$$

$$= N_1 N_4 \{ N_1 N_4 + (N_1 \rho + N_4 \chi) S - \frac{1}{2} \chi \rho T(n) \}$$

$$\zeta = \lambda_{3d} / \Delta E_{20}^0$$

and

$$g_{\perp} = 2.0023 - 6\zeta \{ P_{02} - (3P_{02} - P_{12})\beta_6^2/3 - (3P_{02} - P_{24})\beta_7^2/3 \} - 3\zeta^2 N_2^2 (N_0^2 + P_{02}) \quad (10a)$$

with

$$P_{02} = N_0 N_2 k_{02} = N_0 N_2 \{ N_0 N_2 + (N_0 \rho + N_2 \chi) S + (N_0 \rho' + N_2 \chi') S' - \frac{1}{\sqrt{6}} \chi \rho T(n) - \frac{1}{\sqrt{3}} \chi' \rho' T(n) \} \quad (10b)$$

$$P_{24} = N_2 N_4 k_{24}$$

$$= N_2 N_4 \{ N_2 N_4 + (N_2 + N_4) \rho S + N_4 \rho' S' + \frac{1}{\sqrt{2}} \rho^2 \} \quad (10c)$$

$$P_{12} = N_1 N_2 k_{12}$$

$$= N_1 N_2 \{ N_1 N_2 + (N_1 \rho + N_2 \chi) S + N_1 \rho' S' - \frac{1}{\sqrt{2}} \chi \rho T(n) \} \quad (10d)$$

Here the contribution from the ligand orbitals to the orbital matrix element of the form $\langle m | \lambda L_i | n \rangle$ is neglected, since λ is proportional to $\langle r^{-3} \rangle$ and the contribution from ligand is small compared to that from d -orbitals. k_{mn} 's are the orbital reduction factors [23], $T(n)$ is the contribution from ligand orbitals through the linkage of σ - and π -orbitals by the angular momentum operators, and n is the fraction of p -character in the σ -orbital. Unless $\langle \beta_i \rangle$'s vanished, g -tensor would have orthorhombic symmetry.

Similarly the components of the A -tensor are derived to the second order in λ and β_i 's from equations (A4c), (A4d) and (A5b), and expressed as follows

$$A_{\parallel} = P [-N_0^2(1-3N_2^2\zeta^2)\kappa + \frac{1}{4} \times (1 + \frac{3}{2}N_2^2\zeta) \{N_0^2 - (N_0^2 + N_1^2)\beta_6^2 - (N_0^2 + N_4^2)\beta_7^2\} - 8N_1^2N_4^2\lambda_{3d} \times (\beta_6^2/\Delta E_{40}^0 + \beta_7^2/\Delta E_{10}^0) + (\frac{27}{4}N_2^2 - \frac{1}{4})N_0^2N_2^2\zeta^2] \quad (11a)$$

$$A_{\perp} = P [-N_0^2(1-\frac{3}{2}N_2^2\zeta^2)\kappa - \frac{1}{4} \times (1 + \frac{3}{2}N_2^2\zeta) \{N_0^2 - (N_0^2 + N_1^2)\beta_6^2 - (N_0^2 + N_4^2)\beta_7^2\} - 6N_2^2\zeta \times \{N_0^2 - (3N_0^2 - N_1^2)\beta_6^2/3 - (3N_0^2 - N_4^2)\beta_7^2/3\} - (\frac{27}{4}N_2^2 - \frac{3}{4}N_2N_4 + \frac{3}{4}N_1N_2 - \frac{9}{4}N_0N_2 + \frac{9}{4})N_0^2N_2^2\zeta^2] \quad (11b)$$

where $P = 2\beta_{\text{GN}}\mu_{\text{N}}\langle r^{-3} \rangle_{3d}$ and $P\kappa$ is the Fermi contact term for Cu^{2+} ion.

4.4. Temperature dependence of E , g - and A -tensors

As mentioned in the foregoing sections, the measurable quantities are given by the weighted average over all configurations. The weight in the tetragonal configurations Ia and Ib is $p^2 + (1-p)^2$ and that in the orthorhombic configurations IIa and IIb is $2p(1-p)$ as seen in Fig. 9. Thus from equation (8e) the energy of the ground state is given by

$$\begin{aligned} \langle E_0 \rangle &= \{p^2 + (1-p)^2\} (E_0^0 - \beta_7^2\Delta E_{40}^0) \\ &\quad + 2p(1-p) (E_0^0 - \beta_7^2\Delta E_{40}^0 \\ &\quad - \beta_6^2\Delta E_{10}^0) = (E_0^0 - \beta_7^2\Delta E_{40}^0) \\ &\quad - 2p(1-p)\beta_6^2\Delta E_{10}^0. \end{aligned} \quad (12)$$

The energy of the excited state will be also modified as follows by weighed average,

$$\langle E_4 \rangle = E_4^0 + \beta_1^2\Delta E_{10}^0 + \beta_2^2\Delta E_{11}^0 \quad (13a)$$

$$\langle E_3 \rangle = \langle E_2 \rangle = E_2^0 \quad (13b)$$

$$\begin{aligned} \langle E_1 \rangle &= E_1^0 - \beta_4^2\Delta E_{11}^0 \\ &\quad + 2p(1-p)\beta_5^2\Delta E_{10}^0. \end{aligned} \quad (13c)$$

Therefore the optical absorption frequency will have temperature dependence through $p(1-p)$. At the same time, g - and A -tensors will have similar temperature dependence as given in the following forms,

$$g_i = g_i^0 + 2p(1-p)g_i' \quad (14a)$$

$$A_i = A_i^0 + 2p(1-p)A_i' \quad (14b)$$

where g_i' and A_i' represent the terms proportional to β_6^2 , and g_i^0 and A_i^0 the remaining terms in the expressions of g_i 's and A_i 's in equations (9a) to (11b).

5. ANALYSIS AND DISCUSSION

5.1. Order parameter

In order to confirm the ordering effect in the temperature dependence of the spin Hamiltonian parameters and crystalline field splitting, the order parameter p was determined from the experimental result for g_{\parallel} in Fig. 3 using equation (14a). The obtained p vs. temperature is plotted in Fig. 11. These values for p are for NH_3 molecules and there should be some correlation with those for NH_4^+ ions in the crystal. The latter can be obtained by a numerical integration of the specific heat which has been measured by Simon[3]. The result is also shown in Fig. 11. The order parameter for NH_3 is found to coincide with that for NH_4^+ , which shows the existence of correlation between NH_3 and NH_4^+ in the crystal at low Cu^{2+} concentration. A number of workers have determined the long range order parameter in NH_4Cl : Ueda and Itoh by NMR experiment[25], Garland and Schumaker by i.r. absorption [26], Tokunaga and Koyano by neutron diffraction[27], etc.. The result by Garland

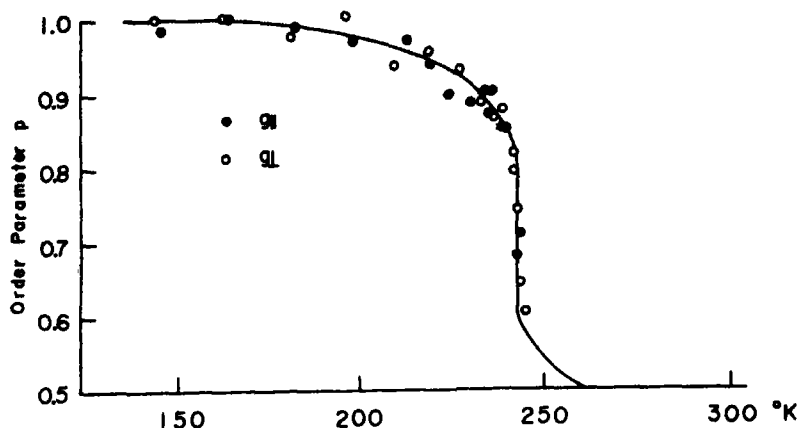


Fig. 11. Order parameter, p , of NH_3 molecules of center II obtained from the experimental data of g_{\parallel} and g_{\perp} . Derivation from g_{\perp} was performed under an assumption described in Section 5.1. Order parameter of NH_4^+ ions in pure NH_4Cl obtained by the numerical integration of the specific heat measured by Simon is also shown by a solid curve for comparison.

and Schumaker, which is in good agreement with ours for NH_3 , showed that the order-disorder transition took place over the wide range of temperature from about 150 to 243°K. On the other hand, the results of NMR and neutron diffraction were coincident with each other and showed that the transition took place over a rather narrow range of temperature from 235 to 243°K. Although the physical origins for such a discrepancy in p are not yet fully understood, the presence of short range order may be thought of as one of the probable origins. Our ESR results can be considered to demonstrate the long range order through the nature of the electronic state of Cu^{2+} in the crystal.

5.2. Optical absorption

The absorption spectrum in Fig. 5 shows that the 0.7μ band consists of two bands whose centers are located at 1.37×10^4 and $0.95 \times 10^4 \text{ cm}^{-1}$, respectively, with their intensity ratio of 2:1. Since the orthorhombic crystalline distortion can be considered to be of small perturbation to the tetragonal crystalline field, the higher frequency band is assigned to the unresolved two lines due to the optical transition $\Psi_0 \rightarrow \Psi_2$, Ψ_3 and the

lower frequency band to $\Psi_0 \rightarrow \Psi_1$. The steep increase in line width of higher frequency band around T_λ indicates the onset of such line splitting.

Next let us consider the temperature dependence of ν_{\max} of the higher frequency band. The energy difference corresponding to the band is given from equations (12) and (13b) by

$$\langle E_{20} \rangle = \Delta E_{20}^0 + \beta_7^2 \Delta E_{40}^0 + 2p(1-p)\beta_6^2 \Delta E_{10}^0 \quad (15)$$

The first and second terms in the right hand side of equation (15) represent the energy difference common to the all crystalline configurations of a pair of NH_3 molecules. The third term represents the contribution from the order-disorder process of NH_3 molecules. The more p increases from $\frac{1}{2}$, the more the third term decreases. The steep change in ν_{\max} just below T_λ , as seen in Fig. 6, shows this effect. However, the steady decrease of ν_{\max} with increase in temperature above T_λ cannot be explained by this effect. The thermal expansion of the interatomic distances must be taken into account. NH_3 molecules are regarded as consisting of

electric multipoles. The temperature dependence of the average distance R between nitrogen and copper atoms is assumed to coincide with the thermal expansion of the lattice. Then the crystalline field splitting due to NH_3 molecules is shown to be proportional approximately to $\langle r^3 \rangle_{3d} R^{-4}$ and/or to $\langle r^5 \rangle_{3d} R^{-6}$ by a simple calculation of Coulomb energy. In our model, the effect from NH_3 was assumed to be much stronger than that from Cl^- . Neglecting the contribution from Cl^- , the frequency of the optical transition can be given by

$$\nu_{\max} = a \langle r^3 \rangle_{3d} R^{-4} + b \langle r^5 \rangle_{3d} R^{-6} \quad (16)$$

where a and b are constants. The small change of R due to the thermal expansion is given by $\Delta R = R \alpha_L \Delta T$, where α_L denotes the thermal expansion coefficient of the lattice. If α_ν is defined as $\Delta \nu_{\max} / \Delta T \nu_{\max}$, the ratio α_ν / α_L is found from equation (16) to be -4 to -6 , provided that $\langle r \rangle_{3d}$ is independent of temperature. This value agrees well with the experimental value -4.2 above T_λ with $\alpha_L = 0.52 \times 10^{-4} \text{ deg}^{-1}$ [28]. Extending the value of $\alpha_\nu / \alpha_L = -4.2$ above T_λ to the whole range of temperature, the contribution from the thermal expansion is shown in Fig. 6. The difference between the experimental value and the contribution from the thermal expansion shows the ordering effect of NH_3 .^{*} The contribution from the term including $2p(1-p)$ shown in equation (15) are also shown in Fig. 6 for three different samples, with the values of $\frac{1}{2} \beta_6^2 \Delta E_{10} = 500 \text{ cm}^{-1}$ (0.062 eV) for N-1 and N-2 and 550 cm^{-1} (0.068 eV) for N-02-2, using the value of $p(1-p)$ obtained from the temperature dependence of g_{\parallel} . Putting $\Delta E_{10} = 0.95 \times 10^4 \text{ cm}^{-1}$ at room temperature, the value 0.11 ± 0.01 was obtained for β_6^2 , the mixing coefficient from $|x^2 - y^2\rangle$ orbital.

^{*} From equation (15), the contribution from the thermal expansion should coincide with the experimental value far below T_λ with $p = 1$, although the curve was drawn in Fig. 6 by fitting the values above T_λ .

5.3. Spin Hamiltonian parameters

As shown in Section 4, the expressions for g - and A -tensors are of fairly complicated form with many unknown parameters. In order to analyze our results some simplifications will be made in the following discussion. As for ligand contribution through covalency with Cu^{2+} , σ - and π -orbitals are assumed to yield the same values for mixing parameters χ 's and ρ 's, namely $\chi = \rho$ for the molecular orbitals arising from 4 Cl^- and $\chi' = \rho'$ for those arising from 2 NH_3 's. Accordingly further simplifications, $N_0 = N_{2,3}$ and $N_1 = N_4$, are deduced. Next, for numerical parameters of the overlap integral and the linkage integral, owing to the lack of a theoretical basis to determine the precise values, empirical values of $S = S' = -0.05$ and $T(n) = T(n)' = 0.5$ are used [24, 29-31]. N 's and χ 's have little sensitivity to the values of these parameters. An additional requirement is that χ' is larger than χ on the basis of our model since NH_3 is known to have more covalent character than Cl^- in metal ion complexes.

Let us pay attention first to the g factors. Solving equations (7b), (10a) and (10b) simultaneously under the condition $\chi' > \chi > 0$, with the values $\Delta g_{\perp} = 0.2162$ and $\Delta E_{20} = 1.37 \times 10^4 \text{ cm}^{-1}$ at 150°K from experiments and with $\lambda_{3d} = -828.7 \text{ cm}^{-1}$ for free Cu^{2+} ion, one finds

$$N_0^2 = 0.850 \pm 0.003, \chi^2 = 0.05 \pm 0.05,$$

$$\chi'^2 = 0.15 \pm 0.04, k_{02} = 0.747 \mp 0.003$$

where the terms including β_6^2 in equation (10a) are omitted since $p = 1$ at 150°K , and also the terms including β_7^2 are neglected since they are very small in comparison with the experimental error. Substituting these values into equations (7d), (9b), (10c) and (10d), the values of other parameters are obtained;

$$N_1^2 = 0.99 \mp 0.01, k_{14} = 0.96 \mp 0.04,$$

$$k_{24} = 0.911 \mp 0.002, k_{12} = 0.84 \mp 0.04$$

Furthermore, using the values $\Delta g_{\parallel} = -0.0015$ at 150°K and $\Delta g_{\parallel} = 0.0060$ at 300°K in addition to the values of known parameters, the values of the remaining two parameters are obtained from equation (9a)

$$\beta_7^2 = 0.008 \pm 0.001,$$

$$\Delta E_{40} = (4.0 \pm 0.2) \times 10^4 \text{ cm}^{-1}$$

of which ΔE_{40} was not observed by our optical measurement. In the above derivation the temperature dependence of the parameter except for p was neglected. With the above obtained values for parameters and for p determined from g_{\parallel} , however, the calculated value of g deviates from the experimental value in the disordered phase as seen in Fig. 3. This discrepancy can be explained by the 3.7 per cent change in the factor $P_{02}\zeta$ in equation (10a) below and above T_{λ} . It may have arisen from the increase in the average overlap of the central $d_{3z^2-r^2}$ and the non-bonding orbital in NH_3 through the reorientational rotation of NH_3 . Assuming that $P_{02}\zeta$ also include a part proportional to $p(1-p)$, p was obtained from the temperature depen-

dence of g and found to agree well with that from g_{\parallel} as shown in Fig. 11.

Next let us turn our attention to the A -tensors. P and κ , which appear in the expressions of equations (11a) and (11b), can be calculated from the experimental values of hyperfine constants. In order to obtain the values of these two parameters from the experimental values, their relative sign must be taken into consideration. Assuming $A_{\parallel}/A_{\perp} < 0$, one finds that $P = 0.07 \text{ cm}^{-1}$ at 120°K and 0.057 cm^{-1} at 300°K, and $\kappa = 0.14$ and 0.10 below and above T_{λ} , respectively, which seems to be quite unreasonable since $P = 0.036 \text{ cm}^{-1}$ [24] and $\kappa \approx 0.4$ [28] are known in the ordinary copper salts. On the other hand assuming $A_{\parallel}/A_{\perp} > 0$, it is found that $P = 0.039$ and 0.042 cm^{-1} below and above T_{λ} , respectively, κ being negative. The temperature dependence of P and κ for $A_{\parallel}/A_{\perp} > 0$ is shown in Fig. 12, where κ is found to vary remarkably with temperature. Since our experimental result for the temperature dependence of ν_{max} has shown that $\langle r \rangle_{3d}$ is almost constant in the whole temperature range, P can be considered to be almost constant. Thus taking account of relatively

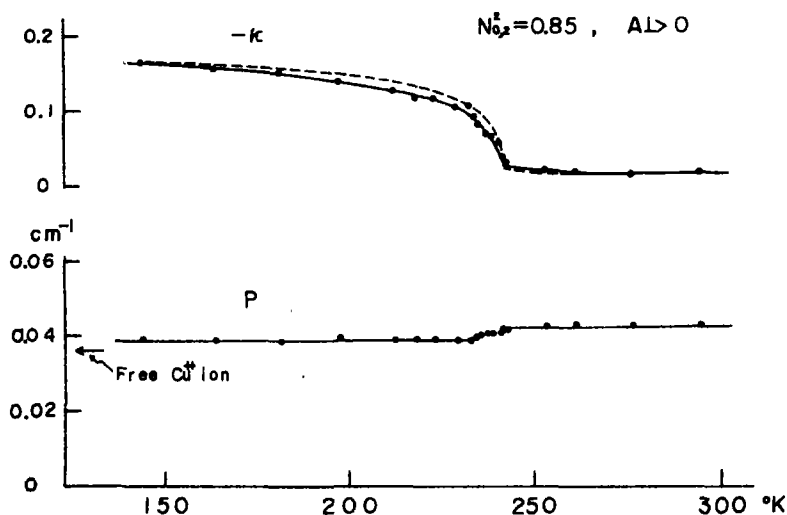


Fig. 12. Temperature variation of P and k . Broken line is the calculated curve. See text.

rough approximation in determining A above T_λ , these values seem to be more likely than those for $A_\parallel/A_\perp < 0$. As for the origin of κ , the mixing of the excited $4s$ to the ground $3d$ orbital would give the additional hyperfine field which had the different sign from the contribution of the core polarization. Therefore the anomalous nature of κ may be interpreted to have arisen from the change of the mixing of a small amount of the excited $4s$ orbital to the ground $3d$ orbital through the change of symmetry around T_λ . Since the s orbital can hybridize with $d_{3z^2-r^2}$ but not with $d_{x^2-y^2}$, the change of symmetry will cause the temperature dependence in κ of the form $\kappa = \kappa_0 + 2p(1-p)\kappa'$. A curve with $\kappa_0 = -0.165$ and $\kappa' = 0.300$ is drawn in Fig. 12. It agrees fairly well with the experimental values, which is evidence for the above interpretation. Details for this problem are left for further investigations.

6. CONCLUSION

ESR of Cu^{2+} in NH_4Cl has shown that the defect coincides with center II found by Trappeniers and Hagen. The anomalous temperature dependence in g - and A -tensors around T_λ were studied in detail. The anomalous shift and line broadening of the optical absorption line due to the $d-d$ transition of Cu^{2+} with temperature were first observed around T_λ . In order to analyze our results a model is proposed, in which two NH_3 molecules coordinating to a Cu^{2+} ion undergo the order-disorder transition of their orientations. The various configurations of possible orientations of two NH_3 molecules can be classified into those producing tetragonal symmetry and others producing orthorhombic symmetry at the site of Cu^{2+} . Introducing the order parameter p for NH_3 to take the favored orientation, all the anomalous temperature dependencies were explained well in terms of the statistical average over those configurations. The obtained value of p for NH_3 molecules coincides with that for NH_4^+ ions obtained from the specific heat

data measured by Simon in pure NH_4Cl . Numerical calculations have shown that the configurations with orthorhombic symmetry give rise to the admixture of about 11 per cent of the excited $|x^2 + y^2\rangle$ orbital into the ground $|3z^2 - r^2\rangle$ orbital, and also shown that $|3z^2 - r^2\rangle$ has the covalency of about 15 per cent with the σ -orbitals of two NH_3 molecules. Optical measurements allowed to determine the crystalline field splitting of the ground 2D state of Cu^{2+} ; $\Delta E_{10} = 0.95 \times 10^4 \text{ cm}^{-1}$ and $\Delta E_{20} = \Delta E_{30} = 1.37 \times 10^4 \text{ cm}^{-1}$ at room temperature. The value of ΔE_{40} was derived to be about $4.0 \times 10^4 \text{ cm}^{-1}$ from the analysis. The Fermi contact term was found to be negative, which suggested a contribution from the $4s$ orbital in addition to the core polarization.

Acknowledgements—We wish to express our sincere thanks to Professor K. Suzuki for many valuable discussions and continual encouragements throughout this work, and to Professor J. Ooshika for useful comments. Thanks are also due to Professors J. Itoh, M. Date and Dr. K. Shiratori of Osaka University for their interests and illuminating discussions. We are indebted to Professor T. Tominaga and Mr. K. Okamoto for their kind help in chemical analysis of Cu^{2+} in NH_4Cl . Grateful acknowledgment is made to K. Takemoto and S. Nakayama for the help in the optical absorption measurements.

REFERENCES

1. ITOH J. and YAMAGATA Y., *J. phys. Soc. Japan* **17**, 481 (1962).
2. For instance, LEUNG P. S., TAYLOR T. I. and HAVENS W. W., Jr., *J. chem. Phys.* **48**, 4912 (1968).
3. SIMON F., *Ann. Phys.* **68**, 4 (1922).
4. ZARIPOV M. M. and CHIRKIN G. K., *Soviet Phys. solid state* **6**, 1290 (1964).
5. ZARIPOV M. M. and CHIRKIN G. K., *Soviet Phys. solid state* **7**, 74 (1965).
6. ZARIPOV M. M. and CHIRKIN G. K., *Soviet Phys. solid state* **7**, 2391 (1966).
7. TRAPPENIERS N. J. and HAGEN S. H., *Physica* **31**, 122 (1965).
8. TRAPPENIERS N. J. and HAGEN S. H., *Physica* **31**, 251 (1965).
9. HAGEN S. H., Ph.D. thesis, Universiteit van Amsterdam, (1966).
10. PILBROW J. R. and SPAETH J. M., *Phys. Status Solidi* **20**, 225 (1967).
11. PILBROW J. R. and SPAETH J. M., *Phys. Status Solidi* **20**, 237 (1967).
12. KURODA N., KAWAMORI A. and MITO E., *J. phys. Soc. Japan* **26**, 868 (1969).

13. NAGAMIYA T., *Kotai-ron (Theory of Solids)*, Kyoritsu, Tokyo, p. 130 [in Japanese] (1951).
14. ORGEL L. E., *J. chem. Phys.* **23**, 1004 (1955).
15. WAGNER E. L. and HORNIG D. F., *J. chem. Phys.* **18**, 296 (1950).
16. LEVY H. A. and PETERSON S. W., *Phys. Rev.* **83**, 1270 (1951).
17. LEVY H. A. and PETERSON S. W., *Phys. Rev.* **86**, 766 (1952).
18. BLEANEY B., *Phil. Mag.* **42**, 441 (1951).
19. DUNN T. M., McCLURE D. S. and PEARSON R. G., *Some Aspects of Crystal Field Theory*, Harper and Row, New York (1965).
20. WOESSNER D. E. and SNOWDON B. S., Jr., *J. Phys. Chem.* **71**, 952 (1967).
21. ABRAGAM A. and PRYCE M. H. L., *Proc. R. Soc.* **205**, 135 (1951).
22. BLEANEY B., BOWERS K. D. and PRYCE M. H. L., *Proc. R. Soc.* **228**, 166 (1955).
23. SUGANO S. and SHULMAN R. G., *Phys. Rev.* **130**, 517 (1963).
24. MAKI A. H. and MCGARVEY B. R., *J. chem. Phys.* **29**, 31 (1958).
25. UEDA S. and ITOH J., *J. phys. Soc. Japan* **22**, 927 (1967).
26. GARLAND C. W. and SCHUMAKER N. E., *J. Phys. Chem. Solids* **28**, 799 (1967).
27. TOKUNAGA M. and KOYANO N., *J. phys. Soc. Japan* **24**, 1407 (1968).
28. GARLAND C. W. and RENARD R., *J. chem. Phys.* **44**, 1130 (1966).
29. KIVELSON D. and NEIMAN R., *J. chem. Phys.* **35**, 149 (1961).
30. SHARNOFF M., *J. chem. Phys.* **42**, 3383 (1965).
31. BULUGGIU E., DALLOLIO A., DASCOLA G. and VARACCA V., *Phys. Rev.* **179**, 289 (1969).

APPENDIX

The detailed derivation of equations (9a)–(11b) in 4.2. is given. The perturbation Hamiltonian can be represented as follows:

$$H' = \lambda L \cdot S + \beta(L + 2.0023S) \cdot H + P[-\kappa S \cdot I + L \cdot I + \xi\{L(L+1)S \cdot I - \frac{1}{2}(S \cdot S)(L \cdot I) - \frac{1}{2}(L \cdot I)(L \cdot S)\}] \quad (A1a)$$

where

$$\xi = \frac{(21+1) - 4S}{S(21-1)(21+3)(2L-1)} \quad (A1b)$$

$$P\kappa = \frac{8\pi}{3} g_N g_M \mu_N \beta \sum_n (|\psi_{n\downarrow}(0)|^2 - |\psi_{n\uparrow}(0)|^2). \quad (A1c)$$

Then the perturbation energy of the ground state is given from the ordinary perturbation theory by

$$E_0' = E^{(1)} + E^{(2)} + E^{(3)} + \dots \quad (A2a)$$

with

$$E^{(1)} = \langle 0|H'|0 \rangle \quad (A2b)$$

$$E^{(2)} = \sum_n \frac{\langle 0|H'|n \rangle \langle n|H'|0 \rangle}{E_0^{(0)} - E_n^{(0)}} \quad (A2c)$$

$$E^{(3)} = \sum_{m,n} \frac{\langle 0|H'|m \rangle \langle m|H'|n \rangle \langle n|H'|0 \rangle}{(E_0^{(0)} - E_m^{(0)})(E_0^{(0)} - E_n^{(0)})} - \sum_m \frac{\langle 0|H'|m \rangle \langle m|H'|0 \rangle}{(E_0^{(0)} - E_m^{(0)})^2} \langle 0|H'|0 \rangle \quad (A2d)$$

g - and A -tensors are derived, reducing the perturbation energy to the spin Hamiltonian:

$$\mathcal{H} = S \cdot g \cdot H + I \cdot A \cdot S + \dots \quad (A3a)$$

with

$$g = g^{(1)} + g^{(2)} + g^{(3)} + \dots \quad (A3b)$$

$$A = A^{(1)} + A^{(2)} + A^{(3)} + \dots \quad (A3c)$$

Following the calculations by Abragam and Pryce,[21]

$$g_{ij}^{(1)} = 2.0023 \quad (A4a)$$

$$g_{ij}^{(2)} = -2\Lambda_{ij} = -2 \sum_n \frac{\langle 0|L_i|n \rangle \langle n|\lambda L_j|0 \rangle}{E_n^{(0)} - E_0^{(0)}} \quad (A4b)$$

$$A_{ij}^{(1)} = -P\kappa\delta_{ij} \quad (A4c)$$

$$A_{ij}^{(2)} = -P(3\xi l_{ij} + 2\Lambda_{ij} - 3\xi u_{ij}) \quad (A4d)$$

where

$$l_{ij} = \frac{1}{2} \langle 0|L_i L_j + L_j L_i - \frac{2}{3} L(L+1)|0 \rangle \quad (A4e)$$

$$u_{ij} = -\frac{i}{2} \epsilon_{ikl} \sum_n \frac{\langle 0|\lambda L_i|n \rangle \langle n|L_j L_k + L_k L_j|0 \rangle}{E_n^{(0)} - E_0^{(0)}} \quad (A4f)$$

As for $g_{ij}^{(3)}$ and $A_{ij}^{(3)}$, application of equation (A1a) into equation (A2d) results in

$$\begin{aligned} g_{ij}^{(3)} = & \sum_{m,n} \frac{i}{(E_0^{(0)} - E_m^{(0)})(E_0^{(0)} - E_n^{(0)})} (\langle 0|L_i|m \rangle \langle m|\lambda L_k|n \rangle \\ & \times \langle n|\lambda L_l|0 \rangle + \langle m|L_l|n \rangle \langle n|\lambda L_i|0 \rangle \langle 0|\lambda L_k|m \rangle \\ & + \langle n|L_i|0 \rangle \langle 0|\lambda L_k|m \rangle \langle m|\lambda L_l|n \rangle) \\ & - \sum_m \frac{1}{(E_0^{(0)} - E_m^{(0)})^2} \{ (\langle 0|\lambda L_k|m \rangle \langle m|\lambda L_k|0 \rangle \\ & + \langle 0|\lambda L_l|m \rangle \langle m|\lambda L_l|0 \rangle) \delta_{ij} - \langle 0|\lambda L_i|m \rangle \\ & \times \langle m|\lambda L_j|0 \rangle p_{ij} \} \end{aligned} \quad (A5a)$$

and especially for $S = \frac{1}{2}$ for simplicity,

$$\begin{aligned}
 A_{ij}^{(3)} = \sum_{m,n} & \frac{iP}{(E_0^{(0)} - E_m^{(0)})(E_0^{(0)} - E_n^{(0)})} \{ (L_i)_{0m} (\lambda L_k)_{mn} \\
 & + (\lambda L_k)_{0m} (\lambda L_i)_{mn} (L_i)_{n0} + \frac{i}{14} \sum_{k \neq i} \\
 & \times \{ (L_i L_j + L_j L_i)_{0m} (\lambda L_k)_{mn} (\lambda L_k)_{n0} \\
 & - (\lambda L_k)_{0m} (L_i L_j + L_j L_i)_{mn} (\lambda L_k)_{n0} + (\lambda L_k)_{0m} \\
 & \times (\lambda L_k)_{mn} (L_i L_j + L_j L_i)_{n0} + \frac{1}{2} (L_j L_k + L_k L_j)_{0m} \\
 & \times (\lambda L_k)_{mn} (\lambda L_i)_{n0} + \frac{1}{2} (\lambda L_k)_{0m} (L_j L_k + L_k L_j)_{mn} \\
 & \times (\lambda L_i)_{n0} - \frac{1}{2} (\lambda L_k)_{0m} (\lambda L_i)_{mn} (L_j L_k + L_k L_j)_{n0} \}
 \end{aligned}$$

$$\begin{aligned}
 & + \frac{1}{28} (L_i L_j + L_j L_i)_{0m} (\lambda L_i)_{mn} (\lambda L_i)_{n0} \\
 & + \frac{1}{28} (\lambda L_i)_{0m} (L_i L_j + L_j L_i)_{mn} (\lambda L_i)_{n0} \\
 & + \frac{1}{28} (\lambda L_i)_{0m} (\lambda L_i)_{mn} (L_i L_j + L_j L_i)_{n0} \\
 & - \sum' \frac{P}{2(E_0^{(0)} - E_m^{(0)})^2} \left[\left(\frac{4}{7} - \kappa \right) (\lambda L_k)_{0m} (\lambda L_k)_{n0} \right. \\
 & \left. + (\lambda L_i)_{0m} (\lambda L_i)_{n0} \delta_{ij} - (\lambda L_i)_{0m} (\lambda L_j)_{n0} P_{ij} \right. \\
 & \left. - \frac{1}{14} (L_j L_i + L_i L_j)_{00} \sum_k (\lambda L_k)_{0m} (\lambda L_k)_{n0} \right] \quad (A5b)
 \end{aligned}$$

where $p_{ij} = 1$ for $i \neq j$, and $p_{ij} = 0$ for $i = j$. (jkl) is a cyclic permutation of (xyz) .

ELECTRONIC STRUCTURE OF DEFECT CENTERS IN SiO_2

A. J. BENNETT and L. M. ROTH

General Electric Research and Development Center, P.O. Box 8, Schenectady, N.Y. 12301, U.S.A.

(Received 31 August 1970)

Abstract—Molecular orbital calculations based on the Extended Huckel Theory have been performed for clusters of two and eight SiO_2 molecules. We report here the results for an ordered structure in which periodic boundary conditions are imposed to saturate the peripheral bonds which otherwise cause extraneous localized states to appear. We find an energy gap of ~ 13 eV as compared to the experimental value of ~ 11 eV. The removal of an oxygen results in several levels in the energy gap which move upon displacement of the two neighboring silicons. The levels appear to account for the observed ultraviolet optical absorption band and are also a possible origin for the positively charged slow surface states present near a SiO_2 -Si interface. The addition of either atomic or molecular hydrogen to a perfect crystal is predicted to yield preferentially a double hydrogen-single oxygen center. If ambient oxygen atoms are present, a two hydroxyl group center is then most favorable.

1. INTRODUCTION

THE PROPERTIES of various defects in SiO_2 are of great technological interest. Vacancies and interstitials have been invoked to explain both 'fast' and 'slow' surface states at the semiconductor-oxide interface of a metal-oxide-semiconductor field effect transistor (Mosfet)[1-3]. The 'fast' states which affect the voltage, frequency, and temperature dependence of the capacitance characteristics can interact rapidly with the Si space charge and are known to be well localized at the interface. These states lie within the Si band gap.

We consider here the 'slow' states which are responsible for translation of the $C(V)$ curves along the V axis, and are thought to be localized at defect centers in the oxide (within 200 Å of the silicon). These defects are induced by the junction fabrication. The growth of the SiO_2 -Si interface may result in oxygen vacancies and accompanying trivalent Si near the interface. This structure is indicated schematically in Fig. 1(b).

If, as is often the case, hydrogen is present during fabrication, a variety of other defects may exist. Hydrogen additions to the perfect crystal are shown in Figs. 1(c) and 1(d); additions to the vacancy structure in Fig. 1(e) and

1(f). A structure which may result if oxygen interstitials and/or water is also present, is shown in Fig. 1(g).

Experiments by Bell, Hetherington and Jack[5] have shown that exposure of vitreous silica to hydrogen or to water vapor at high temperatures leads to the formation of OH groups in the SiO_2 system. These are detected by a strong i.r. absorption at 2.75μ due to the stretching of the O-H bond.

Defect states also result when pure amorphous or crystalline SiO_2 is irradiated with neutrons, electrons or gamma rays[6]. In particular optical absorption[7] and Epr studies [8-10] have indicated the existence of a paramagnetic state associated with an oxygen vacancy.

There have been no even semiquantitative calculations of the electronic properties of the various postulated defects states. We attempt such a treatment in this paper.

The defect states may lie well within the SiO_2 band gap (~ 10 eV)[11] and as a result can not be considered using the effective mass approximation[12]. We apply a simple molecular orbital scheme, the Extended Huckel Theory (EHT) developed by Hoffman and his collaborators[13-15], to a finite array of Si

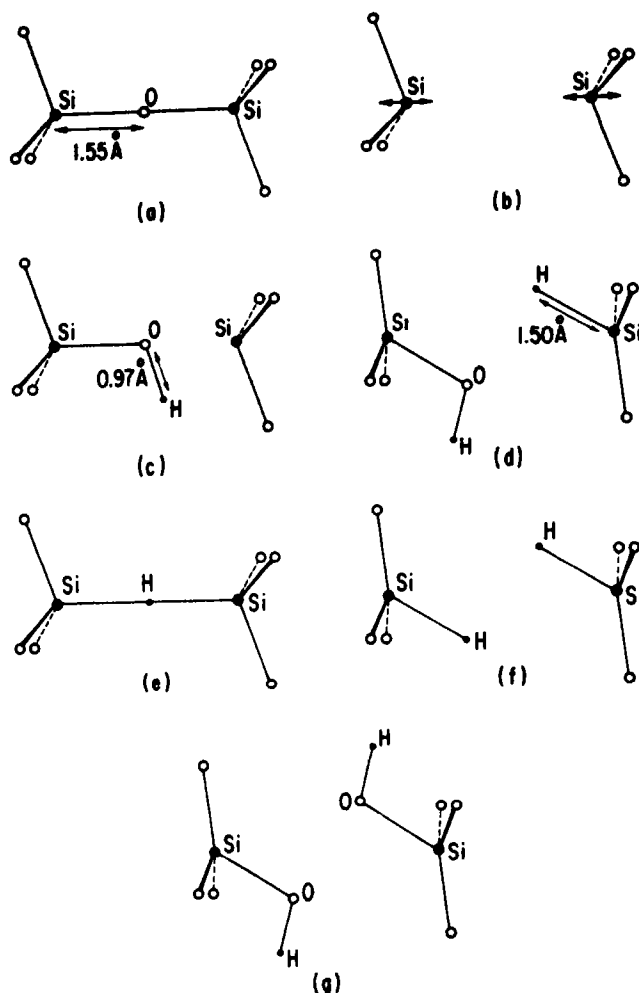


Fig. 1. Atomic configurations in β cristobalite in the vicinity of (a) a normal oxygen site (b) an oxygen vacancy and (c-g) various centers containing hydrogen. The plane of the paper is the $(\bar{1}\bar{1}0)$ plane in which we have assumed the defect atoms to lie. The x and y axes are (111) and $(\bar{1}\bar{1}2)$ respectively. The arrows in (b) show the extent of the Si displacements.

and O atoms chosen to represent the insulator.

As is well known, the EHT yields quite useful semi-quantitative results when applied to small molecules. Interaction effects, not considered in single bond arguments, are naturally included in such calculations. Recently Messmer and Watkins[16] have successfully used the method in a study of the nitrogen defect in diamond. Although probably best

suited to totally covalent systems, the method will be applied here to SiO_2 where the ionicity is not extremely large[17].

The SiO_2 films present in Mosfets are, in general, amorphous. Locally, however, there exists strong short range order. X-ray and neutron scattering data indicate that even in SiO_2 glasses, the basic SiO_4 tetrahedra are maintained[18]. Since the defect states are

probably well localized on an atomic scale, we use a crystalline model of the insulator, in particular a simplified cubic β -cristobalite structure[19]. β cristobalite has a density similar to that of the amorphous phase and hence is a reasonable choice for a crystalline model. The structure can be visualized by noting that the silicons form a diamond lattice with oxygens midway between adjacent silicons. In the actual crystal, the oxygens are somewhat displaced from these positions. One disadvantage of the use of an ordered structure is that we are unable to consider certain network defects such as non-bridging oxygens.

The edge atoms of our finite representation of the SiO_2 system have unsaturated bonds which are responsible for perimeter states, localized at the edge of the representation. In this study periodic boundary conditions will be applied to eliminate these states.

In the next section we briefly describe the EHT, the representations used, and the application of periodic boundary conditions. Section 3 contains our results and comparison with experiment. We summarize in a final section.

2. FORMALISM

The Extended Huckel Theory has been discussed extensively in various publications [13-15]. It is a molecular orbital method in which the wave functions φ_i are taken as linear combinations of all the valence orbitals, $|\lambda\rangle$ (Slater functions) centered on the various atoms of the system.

$$\varphi_i = \sum C_{i\lambda} |\lambda\rangle. \quad (2.1)$$

The Schrödinger equation written in that non-orthogonal representation is given by

$$|H - ES| = 0 \quad (2.2)$$

where

$$H_{\lambda\lambda} = -I_\lambda \quad (2.3)$$

$$H_{\lambda\sigma} = \frac{1}{2}K(I_\lambda + I_\sigma)S_{\lambda\sigma} \quad (2.4)$$

$$S_{\lambda\sigma} = \langle \lambda | \sigma \rangle \quad (2.5)$$

I_λ is the valence state ionization potential, K is a constant equal to 1.75, and $\langle \lambda | \sigma \rangle$ is an overlap integral between atomic orbitals.

Cohesive energies are calculated as the difference between the sum of the molecular one-electron energies and the sum of the one electron energies of the separated constituent atoms. The neglect of explicit electron-electron and core-core interaction is a distinct weakness of the approach. The results are, therefore, only semiquantitative. We find, for example, too much ionicity in the system which is a consequence of the lack of any provision for self consistency in the method.

Two representations of the SiO_2 structure, consisting of six and twenty four atoms respectively, were used in our calculations. The smaller representation is shown in Fig. 2 by the solid circles.

Extraneous perimeter states are eliminated by including Si-Si and Si-O bonds between an atom in the cluster and its nearest and next-nearest neighbors in translated versions of the representation. The cluster thus serves as one unit cell of a periodic system.

The dotted circles in Fig. 2 represent atoms in the translated versions of the small cluster. The silicons 1a, 1b, and 1c, which are not in the cluster, are considered to be equivalent to silicon 1. To the overlap matrix element between silicon 1 and oxygen 2, we add the overlap between silicon 1a and oxygen 2. Similarly, we add overlaps of silicon 1b with oxygen 3 and silicon 1c with oxygen 4, to the silicon 1-oxygen 3 and silicon 1-oxygen 4 overlap integrals respectively. In addition, we add to the overlap matrix element between silicon 1 and silicon 2, three terms corresponding to overlaps between silicons 1a, 1b and 1c with silicon 2.

We are able to use the small cluster due to the short range nature of the overlaps in SiO_2 . For some defects containing two hydrogens, however, it was found necessary to go to a larger cluster of 8 SiO_2 molecules, which

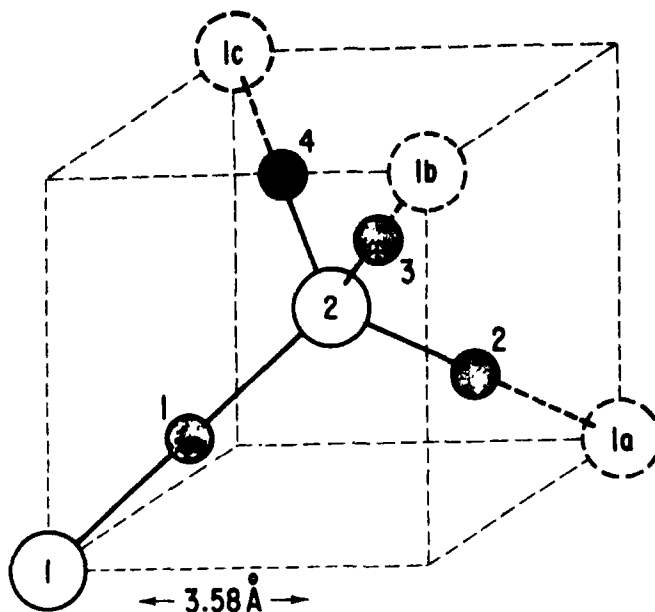


Fig. 2. A portion of our idealized beta cristobalite lattice showing the small cluster which consists of silicons 1 and 2, and oxygens 1, 2, 3, 4. Silicons 1a, 1b, and 1c are outside the cluster and are equivalent to silicon 1. The dashed cube shown is $\frac{1}{4}$ of the cubic unit cell for the diamond lattice upon which the silicons occur and is drawn to show the tetrahedral arrangement of silicons. (It is not a unit cell—the neighboring cube has no Si in the center.)

then serves as the unit cell. Similar periodic boundary conditions were applied to this larger model.

The above procedure for applying periodic boundary conditions is intuitively the obvious one to use. It is interesting to justify it formally by requiring the wave function for the system repeated periodically, to be periodic with unit cell given by our cluster. This is accomplished by adopting as basis functions the $k = 0$ Bloch states.

$$|\lambda\rangle' = \frac{1}{\sqrt{N}} \sum_i |\lambda_i\rangle. \quad (2.6)$$

Here i labels the unit cell in which $|\lambda_i\rangle$ is to be centered, and N is the number of cells. The overlap integral is then

$$\langle \mu | \lambda \rangle' = \sum_i \langle \mu_0 | \lambda_i \rangle. \quad (2.7)$$

The rule is therefore to add to a given overlap $S_{\mu_0 \lambda_0}$ within the cluster, all overlaps $S_{\mu_0 \lambda_i}$ between μ_0 in the cluster and the λ_i outside the cluster which are equivalent to λ_0 .

We have followed this rule in the procedure described above. However, the overlaps beyond a certain distance are quite small (< 10 per cent of those included) and are ignored.

In practice a difficulty could arise which should be noted. The matrix S associated with a finite molecule is readily shown to be positive definite [20]. If arbitrary additional overlaps are added to that matrix this property can be destroyed creating technical difficulties.

The positive definite property holds also for a periodic array of molecules with *all* overlaps included. In practice, therefore, if the S matrix ceases to be positive definite, we must include more overlaps. Our system is quite tightly

bound and we have had relatively little difficulty in this regard.

Our method is equivalent to a tight binding energy band calculation with nonorthogonality taken into account. The wave vector is, however, restricted to $k = 0$ for the Brillouin zone of the unit cell corresponding to the cluster. The energy values correspond to those of a selected set of k values for the Brillouin zone of the conventional primitive unit cell of the crystal.

3. RESULTS

The basis set consists of $2s$ and $2p$ orbitals on the oxygen and $3s$, $3p$, and $3d$ orbitals on the Si. The calculations were performed on a GE 635 computer using a modified version of an EHT Program used in chemisorption calculations[21]. The silicon and oxygen orbital exponents are taken as 1.38 and 2.27 respectively. The ionization potentials are

shown in Fig. 3. Because of computer time limitations we have selected reasonable configurations for various defects rather than extensively varying the configuration to obtain a minimum energy.

(a) Perfect lattice

We begin with the perfect β cristobalite lattice[19]. Figures 3(a) and 3(b) show respectively the electron states associated with the 24 atom representation of the actual Beta cristobalite lattice and the simplified model of that lattice used in the following calculations. The band gap is changed somewhat by the simplification. In these figures, and those that follow, the levels which are due to the oxygen $2s$ state lie at about -32 eV and are not shown. Their position is relatively insensitive to the existence of the various defects. Notice that the present calculation gives a somewhat lower energy to the simplified

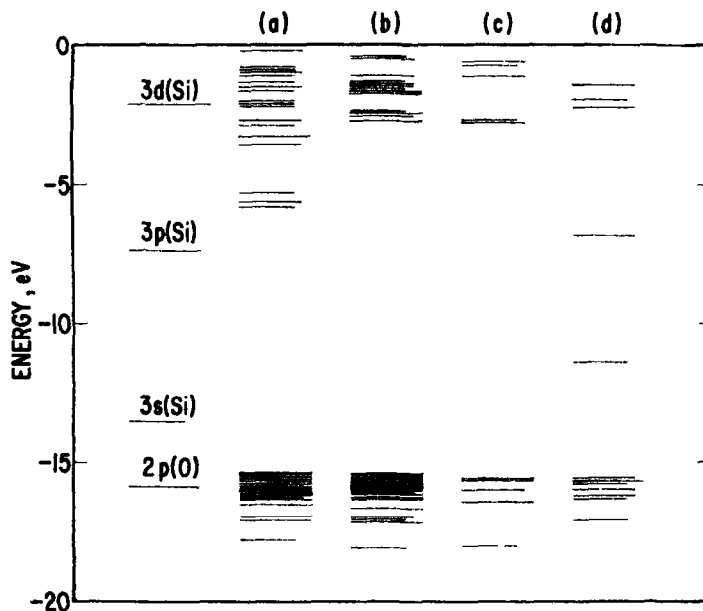


Fig. 3. Energy levels for SiO_2 clusters. The longer lines correspond to two and threefold degenerate or near degenerate levels. The occupation of gap levels for electrical neutrality is shown by the arrows. Unless otherwise noted, the clusters are members of a periodic array (a) eight molecule cluster with actual β cristobalite structure (b) eight molecule cluster with model structure (c) two molecule cluster (d) isolated two molecule cluster.

structure. The total energy of various structures is given in the first column of Table 1; their cohesive energy—in the second column. Figure 3(c) shows the energy levels in the small cluster. The main effect of the decrease in cluster size is the removal of energy levels.

The calculation gives an energy gap of ~ 13 eV as compared with ~ 10 eV obtained by Phillip experimentally[11]. This result was substantially unchanged upon going from the large cluster to the small cluster. Consideration of the cohesive energy as a function of the lattice constant shows that the maximum binding of 26.85 eV/molecule for the small lattice and 27.45 eV/molecule for the large lattice is obtained for the experimentally known Si-O separation of ~ 1.56 Å. This value, as is usually the case for EHT calculations, is larger than the experimental value of ~ 18.8 eV/molecule[22].

The wave functions which characterize the lowest level shown consist of a linear combination of silicon *s* orbitals and oxygen *p* orbitals, the latter directed along the bond. The remaining valence levels correspond primarily to oxygen *p* orbitals. As mentioned above, there is too much ionicity. The calculation gives about 7.5 electrons on each oxygen and 1 on each silicon. The calculation shows very little *d* contribution to the valence band states. In fact, a calculation without *d*-states gave virtually the same results for the valence band

energies. The conduction band is however dominated by the *d* levels, and if they are not included, the lowest conduction band level appears at +6 eV.

Figure 3(d) shows the energy levels of the small cluster which result when periodic boundary conditions are *not* applied. States localized on Si 1 then lie in the gap.

(b) Oxygen vacancy

Calculations on silicon and oxygen vacancies show that approximately three times as much energy (~ 25 eV) is required to remove the tetrahedrally bonded Si. We may, therefore, restrict our attention to the oxygen vacancy. Figures 4(a), 4(b) and 4(c) show the energy levels of the small representation for the case of an oxygen vacancy (oxygen 1 of Fig. 1) with and without distortion of the neighboring silicons. The three spectra correspond to unperturbed, reduced and increased Si-Si separations respectively. Figures 4(d) and 4(e) show the results for the unperturbed and reduced cases as calculated on the larger representation. Comparison of Figs. 4(a) and 4(d), as well as Figs. 4(b) and 4(e), shows that the smaller lattice is an adequate model of the defect. The reduced Si-Si separation was chosen to approximate that of pure silicon.

The removal of one oxygen causes two levels to appear in the gap, the upper level being doubly degenerate. Upon displacing the

Table 1.

Configuration	Total energy (eV)	Cohesive energy (eV)	Total energy relative to perfect crystal (eV)	Total energy relative to vacancy structure (eV)
Si ₆ O ₁₆ (actual crystal)	-2600.73	-215.77		
Si ₆ O ₁₆	-2604.58	-219.62		
Si ₆ O ₄	-649.94	-53.70		
Si ₂ O ₃ ($d_{\text{Si-O}} = 2.40$ Å)	-512.92	-44.84	8.86	
Si ₆ O ₁₅ ($d_{\text{Si-O}} = 2.40$ Å)	-2466.57	-209.77	9.85	
Si ₂ O ₄ H	-658.01	-48.17	5.53 (7.90)	
Si ₆ O ₁₆ H ₂	-2630.78	-218.62	1.00 (5.75)	
Si ₂ O ₃ H	-523.06	-41.38	12.32 (14.69)	3.46 (5.83)
Si ₆ O ₁₆ H ₂	-2495.35	-211.35	8.27 (13.02)	-1.58 (3.17)
Si ₆ O ₁₇ H ₂	-2766.28	-225.96	3.51 (8.26)	-6.34 (-1.59)

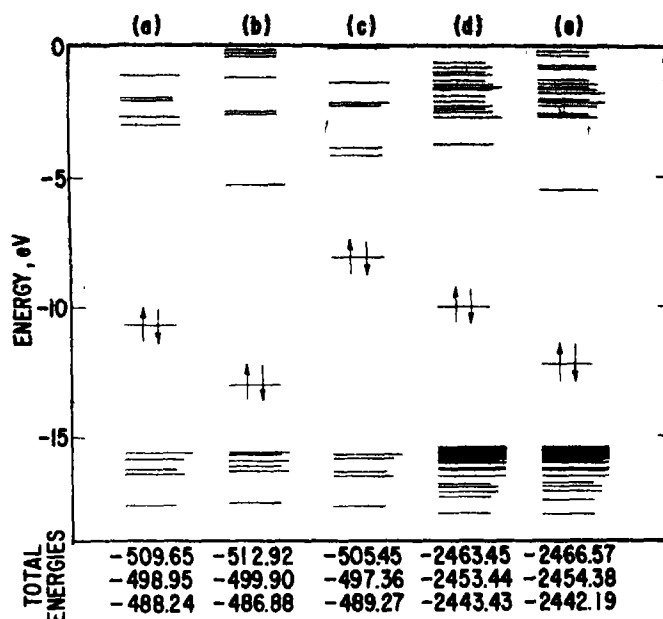


Fig. 4. Energy levels for SiO_2 clusters containing oxygen vacancies. The longer lines correspond to two and threefold degenerate or near degenerate levels. The occupation of gap levels for electrical neutrality is shown by the arrows. The clusters are members of a periodic array. The total energies (eV) listed beneath the figures are for the (neutral) doubly occupied, singly occupied, and unoccupied centers. (a) two molecule cluster containing an oxygen vacancy with silicons undisplaced, $d_{\text{Si-Si}} = 3.10 \text{ \AA}$ (b) two molecule cluster containing an oxygen vacancy with silicons displaced inward, $d_{\text{Si-Si}} = 2.41 \text{ \AA}$ (c) two molecule cluster containing an oxygen vacancy with silicons displaced outward, $d_{\text{Si-Si}} = 3.79 \text{ \AA}$ (d) eight molecule cluster containing an oxygen vacancy with silicons undisplaced, $d_{\text{Si-Si}} = 3.10 \text{ \AA}$ (e) eight molecule cluster containing an oxygen vacancy with silicons displaced inward, $d_{\text{Si-Si}} = 2.41 \text{ \AA}$.

neighboring silicon ions toward each other, the levels move down while if the silicons are pulled apart, the levels move up and the upper one merges with the continuum. At the bottom of each column in Fig. 4 is the total energy of each configuration with the lower gap level doubly occupied (the neutral configuration), singly occupied, and unoccupied. If the lower gap level is doubly or singly occupied, it is energetically favorable for the neighboring silicons to come together; while if it is unoccupied, they tend to move apart.

The neutral oxygen vacancy with neighboring silicons brought together, for both small

and large clusters, is described in Table 1. The energy of formation, defined here as the difference between the total energy of the particular center plus isolated oxygen atoms and the total energy of the comparable unperturbed lattice is given in the third column of the table.

An examination of the eigenfunctions connected with the gap levels shows that the lower one is composed of a bonding combination of s and p orbitals (with z along the bond direction between the two silicons) whereas the upper level corresponds to p_x and p_y orbitals also in a bonding combination. The energy separation between those levels, as

obtained in the calculation on the large cluster, is 6.6 eV, and there is a dipole moment for the optical transition between them.

These results suggest strongly that this pair of levels is to be identified with an u.v. absorption band at ~ 6 eV observed in neutron irradiated quartz and amorphous silica by Nelson and Weeks [7]. This band was denoted as E'_1 , and was assigned by the authors to the singly occupied oxygen vacancy. They also describe a possible precursor, E''_1 , which would be the neutral oxygen vacancy. A similar ultraviolet band is observed in certain synthetic samples before oxidizing.

Weeks and Nelson [8] and Silsbee [9] have observed electron spin resonance signals which are correlated with the E'_1 absorption. In addition Nishi [10] has observed electron spin resonance in amorphous SiO_2 films. Silsbee [9] has examined the anisotropy of the g -factor and hyperfine interaction in detail for the case of quartz, and finds three principle pairs of weak satellites, with maximum hyperfine splitting of 400, 9, and 8 G with intensities of $\sim 2\frac{1}{2}$ per cent of the main line. These splittings are due to interaction with ^{29}Si nuclei, whose abundance is 4.7 per cent. The magnitude of the largest splitting and its intensity lead Silsbee to argue that the electron involved must belong to a single silicon, and interact weakly with two other silicon atoms. Since the g and hyperfine tensors bear no relationship to Si-O or Si-Si directions this model is still far from certain.

Our result indicates that an electron trapped on an oxygen vacancy would be shared between two neighboring silicons which are pulled together. It is possible that this could give a large enough hyperfine interaction since an electron shared between two silicons in irradiated silicon, the A center [23], has a maximum hyperfine splitting of 153 G and, in our case, the silicons are closer. The intensity predicted by the two silicon model is not, however, correct. Clearly further work remains before this center is understood.

At a Si-SiO₂ junction, the 1.2 eV silicon

energy gap is in the middle of the large SiO_2 gap. Levels in the SiO_2 below the middle of the gap would be filled and those above—empty. The oxygen vacancy with silicons moved together would probably be uncharged and not affect the electronic properties of the interface. The doubly charged center, in which the silicons tend to separate, has its emptied level above the Si band gap and would thus remain charged. It could serve, therefore, as a positively charged 'slow' surface state. We should reiterate, however, that there are a number of relevant defects which we cannot consider in the context of our present model—such as the non bridging oxygen and defects on the interface.

(c) Hydrogen centers

We now consider the hydrogen centers shown in Figs. 1(c–g). The cristobalite structure is quite open and calculation indicates that an interstitial hydrogen is relatively uninfluenced by the lattice. It is, in fact, known that atomic and molecular hydrogen freely diffuse through fused silica [24].

In the following cases, some primitive attempts have been made to minimize the configuration energy by varying the atom positions. Again the total and cohesive energies of the various centers are summarized in the first and second columns of the Table. The third column gives the total energy relative to that of suitable reference structures consisting of the appropriate perfect large or small SiO_2 cluster and isolated hydrogen molecules and atoms. These numbers indicate the thermodynamic favorability of the center, but its formation rate depends on potential surfaces not calculated here.

Figure 5(a) shows the energy levels resulting from the addition of a single hydrogen to a normal bond (Fig. 1(c)). The wavefunction of the highest occupied level is concentrated on the OH group. The third column of the Table shows that this configuration has a rather high energy compared to that of the unperturbed lattice plus hydrogen interstitial. Here the

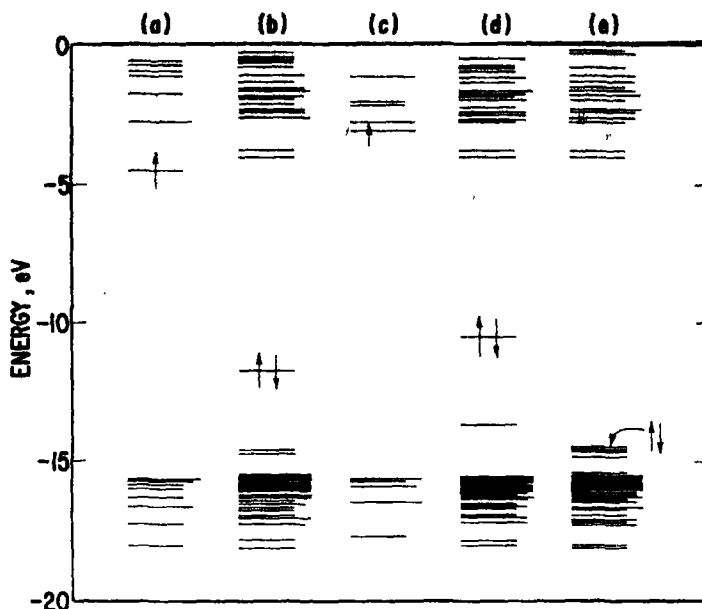


Fig. 5. Energy levels for SiO_2 clusters containing hydrogen. The longer lines correspond to two and threefold degenerate or near degenerate levels. The occupation of gap levels for electrical neutrality is shown by the arrows. The clusters are members of a periodic array (a) two molecule cluster containing one hydrogen at a normal bond (Fig. 1(c)) (b) eight molecule cluster containing two hydrogens at a normal bond (Fig. 1(d)) (c) two molecule cluster containing one hydrogen at an oxygen vacancy (Fig. 1(e)) (d) eight molecule cluster containing two hydrogens at an oxygen vacancy (Fig. 1(f)) (e) eight molecule cluster containing two hydrogens and an oxygen at a normal bond (Fig. 1(g)).

number in parenthesis gives the formation energy/center when two centers are formed from molecular hydrogen (binding energy 4.75 eV). The total energy of the singly ionized version of this center (653.51 eV) is lower than that of the interstitial proton.

The energy levels resulting from the addition of two hydrogen atoms to the normal bond (Fig. 1(d)) are shown in Fig. 5(b). The wave function of the highest occupied gap level is primarily localized on the hydrogen member of the HSi unit, though it spreads onto the three oxygens nearest to the hydrogen. The doubly occupied (neutral) center is comparable in energy to the normal lattice plus two hydrogen interstitials (column 3). The energy for formation from a hydrogen molecule is shown in parenthesis.

As mentioned in the Introduction, Bell,

Hetherington and Jack have heated samples of amorphous silica in hydrogen and found that OH groups are formed. These groups are the origin of a strong 2.75μ i.r. absorption band which is associated with the stretching of their bond. One or the other of the above centers was postulated as the site of the hydroxyl ion. Our calculation indicates the two hydrogen center is more favorable than two one hydrogen centers.

We now consider the addition of one and two hydrogens to the oxygen vacancy. A single hydrogen equidistant from the two silicons (Fig. 1(e)) results in the energy diagram shown as Fig. 5(c). Asymmetric hydrogen positions were energetically less favorable. The highest singly occupied level consists of silicon p orbitals. The level most localized on the hydrogen is more strongly bound. The addi-

tion of the atom apparently splits the vacancy levels further apart (cf. Fig. 4). The total energy of the center plus interstitial oxygen compared to that of the perfect lattice plus interstitial hydrogen is given in the third column of the Table. The formation energy center for two centers formed from a hydrogen molecule is given in parenthesis. Analogous results for the case when an oxygen vacancy is initially present are given in the fourth column. The ionized defect is energetically more advantageous than the ionized interstitial plus vacancy.

The energy spectrum characteristic of two hydrogens bound to the oxygen vacancy (Fig. 1(f)) is shown in Fig. 5(d). As in the case of two hydrogen atoms at the normal site, the configuration is a more favorable one. That is, a comparison of the total energy of the center plus oxygen interstitial with that of the relevant perfect crystal plus hydrogen interstitials shows that the formation of a center containing two hydrogens requires less energy than the formation of two centers containing one hydrogen. The energy for formation from a molecule is again given in parenthesis. Similar results for the case when an oxygen vacancy is initially present are given in the fourth column. The formation is then quite favorable.

The final configuration to be considered is the center containing two hydrogens and two oxygens (Fig. 1(g)) whose energy levels are shown in Fig. 5(e). This could occur if interstitial oxygen due to vacancy formation and hydrogen interstitials are present, or upon the addition of water to the perfect lattice. Experiment indicates that OH stretching modes are also observed with the latter addition[5]. The occupied gap level just above the valence band edge consists mainly of $p\pi$ orbitals on the oxygens. The total energy of this center plus a vacancy center (taken as the source of the oxygen) is compared in the third column with the energy of two perfect lattices plus the energy of two interstitial hydrogens. The comparison with an interstitial hydrogen molecule present is given in parenthesis. Similar

comparisons assuming the presence of ambient O are given in the fourth column. The energy of formation from a water molecule is the underlined number in the third column.

It is interesting to consider the combination of a SiOH-SiOH center and an oxygen vacancy. The Table shows that the total energy of these two configurations is 3.5 eV less favorable than that of two normal bonds and hydrogen interstitials. Hetherington and Jack observed that certain samples exhibiting both OH stretching modes and u.v. modes, associated presumably with optical absorption at oxygen vacancies, when heated lost both spectra. The combination of the two centers appears to be a likely cause of this loss. Glasses which exhibit u.v. but not i.r. absorption require an oxygen atmosphere to remove the u.v. absorption.

4. SUMMARY

We have found that the EHT gives a reasonable semiquantitative description of the electronic states of ordered SiO_2 and of defects in that material involving the oxygen vacancy and the addition of hydrogen. It appears that the oxygen vacancy is responsible for certain ultraviolet absorption bands and electron spin resonance signals, although some evidence suggests that we should examine other possible defects to explain the resonance examined in detail by Silsbee. The doubly ionized oxygen vacancy may account for some of the slow states observed in Mosfet systems.

Our examination of defects involving hydrogen enables us to compare the energy for formation of various configurations as given in Table 1. The results in the third and fourth columns of the Table indicate that the most likely defect formed by the addition of either atomic or molecular hydrogen to the perfect glass is the SiOH-SiH center. If, however, oxygen vacancies with accompanying interstitial oxygen or ambient atomic oxygen are present, the SiOH-SiOH center is then most favorable.

A comparison of our results with single

bond arguments based on standard bond energies[25] shows that the energy cost we find for center production is in general larger than that predicted by single bonds arguments. This is often the case with EHT calculations, which we emphasize are semi-quantitative. Our conclusions as to which centers are lowest in energy are in agreement with single bond arguments. EHT calculations include interaction between various bonds in the system; in the cases studied these interactions are apparently not of great importance. We emphasize that computer time restrictions have limited our efforts to minimize the various configuration energies by considering many possible atomic arrangements.

The EHT also yields information about the electronic states associated with various defects, as we have reported in the text and figures.

In future work we shall examine less ordered structures by distorting the present mode in various ways. We hope to examine defects which are not characteristic of the ordered structure, and to obtain some information on the electronic density of states in an amorphous material.

REFERENCES

1. GRAY P. V., *Proc. IEEE* **57**, 1543 (1969).
2. REVESZ A. G. *IEEE Trans. Electron Dev.* **ED-12**, 97 (1965).
3. KOOI E., *Phillips Res. Rept.* **21**, 477 (1966).
4. DEAL B. Z., SKLAR M., GROVE A. S. and SNOW E. H., *J. electrochem. Soc.* **114**, 266 (1967).
5. BELL T., HETHERINGTON G. and JACK K. H. *Phys. Chem. Glasses* **3**, 141 (1962).
6. LELL E., KREIDL N. J. and HENSLEY J. R. in *Progress in Ceramic Science* (Edited by J. Burke), Vol. 4, Pergamon Press, New York (1966).
7. NELSON C. M. and WEEKS R. A., *J. Am. ceram. Soc.* **43**, 396 (1960).
8. WEEKS R. A. and NELSON C. M., *J. Am. ceram. Soc.* **43**, 399 (1960).
9. SILSBEE R. H., *J. appl. Phys.* **32**, 1459 (1961).
10. NISHI Y., *Japan J. appl. Phys.* **5**, 333 (1966).
11. PHILLIPP H. R., *Solid State Commun.* **4**, 73 (1966).
12. KOHN W., in *Solid State Physics* (Edited by F. Seitz and D. Turnbull) Vol. 5, p. 257, Academic Press, New York (1957).
13. HOFFMAN R. and LIPSCOMB W. N., *J. Chem. Phys.* **36**, 2179 (1962).
14. HOFFMAN R., *J. Chem. Phys.* **39**, 1397 (1963).
15. HOFFMAN R., *J. Chem. Phys.* **40**, 2474 (1964).
16. MESSMER R. P. and WATKINS G. *Phys. Rev. Lett.* **26**, 656 (1970).
17. PAULING L., *J. Phys. Chem.* **56**, 361 (1952).
18. BELL R. J. and DEAN P., *Nature* **212**, 1354 (1966).
19. WYCKOFF R. W. G., *Crystal Structures*, Vol 1, Interscience, New York (1963).
20. This is readily proven by considering the sum, for any vector α ;

$$\sum_{\lambda\sigma} \alpha_{\lambda\sigma} \alpha_{\sigma} = \int \left(\sum_{\lambda} \alpha_{\lambda} |\lambda\rangle \right)^* \left(\sum_{\sigma} \alpha_{\sigma} |\sigma\rangle \right) d\nu \geq 0$$
 (MESSMER R. P., private communication).
21. BENNETT A. J., MCCARROL B., and MESSMER R. *Surface Sci.* to be published.
22. *Handbook of Chemistry and Physics* 49th ed. pp. D-38, F-158, Chem. Rubber Co., Cleveland (1968).
23. WATKINS G. D. and CORBETT J. W., *Phys. Rev.* **121**, 1001 (1961).
24. NORTON F. J., *J. Am. ceram. Soc.* **36**, 90 (1953).
25. PAULING L., *The Nature of the Chemical Bond*, Cornell University Press, Ithaca (1960).

A CONJECTURE ON THE ANOMALOUS MOBILITY OF α -Sn*

J. G. BROERMAN

McDonnell Douglas Research Laboratories, McDonnell Douglas Corporation, St. Louis, Miss.
63166, U.S.A.

(Received 28 August 1970)

Abstract—It is suggested that the anomalously low mobility of α -Sn is due to the presence of neutral native defects. A calculation of the mobility using a superposition of scattering on these objects and on RPA-screened ionized impurities is in excellent quantitative agreement with the observed mobilities over the range of donor concentrations from 6×10^{14} – 2.5×10^{19} cm $^{-3}$, even reproducing the peculiar shape of the mobility enhancement above $N_d = 5 \times 10^{17}$ cm $^{-3}$ due to screening by the L_0^+ electrons. The electron mean free path due to these extra scattering processes is deduced to be $\approx 1.75 \times 10^{-4}$ cm, which would correspond, for example, to a concentration of about 3×10^{18} cm $^{-3}$ of defects with a scattering length of 5×10^{-8} cm. This concentration of native defects is typical of defect concentrations present in similar materials before annealing.

ONE OF the interesting properties of structures with Γ_8 conduction bands is that the random phase approximation[1] (RPA) dielectric function $\epsilon(q)$ diverges at zero momentum transfer in the intrinsic material[2]. The presence of impurity carriers removes this singularity leaving a finite interband part which is strongly dependent on carrier concentration[3]. This strong dependence on carrier concentration should produce a striking anomaly in the concentration dependence of the low temperature mobility[3–6].

Three materials are known to have this band structure: α -Sn[7], HgSe[8–10] and HgTe[11]. A calculation[4] of the mobility of α -Sn using the RPA dielectric function yields values about three times higher than experiment[12–14] at low impurity concentrations and higher than experiment at all concentrations. On the other hand, mobilities calculated[5] with the observed[15] concentration-independent background dielectric constant are in good agreement with experiment. It was concluded[4] that either the RPA considerably overestimates the inter-

band polarization or the donors are not singly ionized. It has since been shown[6] that the RPA calculation is in very good agreement with experiment for HgSe[8, 10] and HgTe [15], and thus the first alternative seems quite unappealing since one would be pressed to provide some exotic reason for the RPA to work in ionic but not in covalent materials. The second alternative has been shown to be false in a recent experiment[14] by Lavine and Ewald. However, the results of this experiment are highly suggestive of a third alternative which has heretofore been overlooked.

Lavine and Ewald carefully controlled the concentration of Sb impurities in the range 10^{17} – 2.5×10^{19} cm $^{-3}$. Their results indicate that all the antimony enters the lattice as singly ionized donors and that there are no appreciable numbers of other charged impurities in their samples. In this range of electron concentration, the Fermi Energy crosses the band edge of a high mass band believed to be L_0^+ . They were able to measure the density of states of this band as well as the energy gap. They also obtained the mobility of the Γ_8^+ electrons alone in this region of overlapping bands and observed a mobility

*Research supported under the McDonnell Douglas Independent Research and Development Program.

enhancement, due to the extra screening by the L_6^+ electrons, analogous to the enhancement of Shubnikov-de Haas oscillations[16] seen in this range of electron concentration. These data are the open circles on Fig. 1. The dotted curve is the result[14] of a Brooks-Herring type calculation of the mobility. It rises rapidly at the threshold of the enhancement to a peak more than twice as high as the data and then decreases to a value of less than half the experimental value at $2.5 \times 10^{19} \text{ cm}^{-3}$. A calculation using the methods of Ref. [17] indicates that the L_6^+ effective mass should be constant to within a few per cent in this range of donor concentration so that the large width of the enhancement cannot be ascribed to nonparabolic effects in the L_6^+ density of states.

At this point we make a short theoretical digression to include screening by the L_6^+ electrons in the RPA calculation of Ref.

[4][18]. This can be accomplished by changing n_e in equation (22) to $n_e/(1 + n_1/n_e)$ and

$$\left(\lambda^{1/2} + \eta \frac{d\lambda}{d\xi_F}\right)^2$$

in equation (19) (for $E_F > E_{g1}$) to

$$\left(\lambda^{1/2} + \eta \frac{d\lambda}{d\xi_F}\right)^2 + 4 \left(\frac{\mu_1}{\mu}\right)^{3/2} \left(\frac{E_F - E_{g1}}{E_g}\right)^{1/2}, \quad (1)$$

where n_e is the electron density in the central minimum, n_1 is the total electron density in the four inequivalent L_6^+ minima, μ_1 is the effective mass ratio of the L_6^+ minima and $E_{g1} = E_{L_6^+} - E_{\Gamma_8^+}$. n_1 is given by

$$n_1 = \frac{4}{3\pi^2} \left(\frac{2\mu_1 m_0}{\hbar^2}\right)^{3/2} (E_F - E_{g1})^{3/2}. \quad (2)$$

The result of this calculation for $E_{g1} = 0.092$

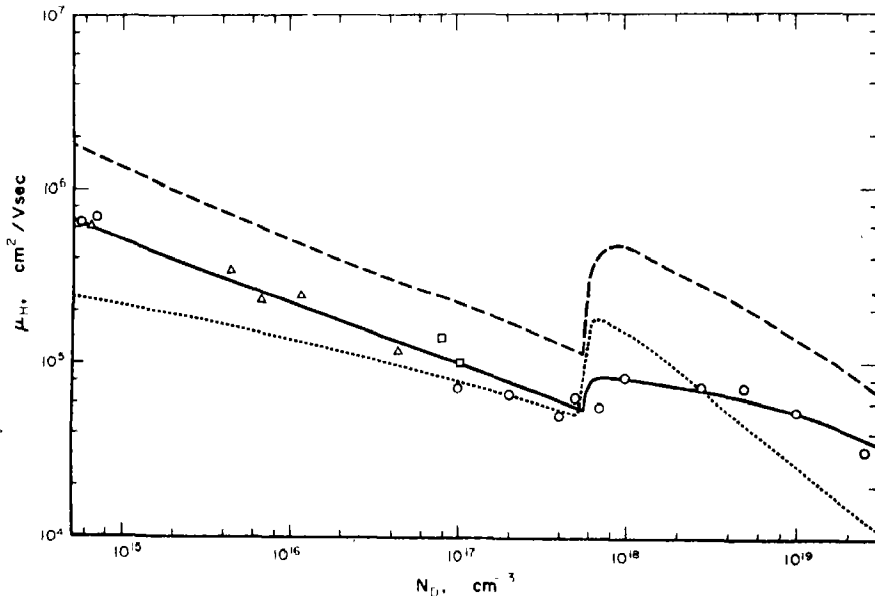


Fig. 1. Low temperature Hall mobility of α -Sn. The experimental points are from Ref. [12] (squares), Ref. [13] (triangles), and Ref. [14] (circles). The dashed curve is the RPA-screened ionized-impurity-limited calculation of Ref. [4], modified to include the screening by the L_6^+ electrons. The dotted curve is the Brooks-Herring calculation of Ref. [14]. The solid curve is a calculation using RPA-screened ionized impurity scattering superimposed on a scattering mechanism with an electron-concentration-independent mean free path of $1.75 \times 10^{-4} \text{ cm}$.

eV and $\mu_1 = 0.17$ [14] is the dashed curve on Fig. 1. This curve is not only much higher, but also the enhancement is much broader than the Brooks-Herring calculation, due to the variation of effective mass and wave function which is included here. The ratio of peak mobility to mobility at enhancement threshold is about the same for both calculations and is much larger than that seen experimentally.

It is instructive to forget detailed theory for the moment and compare α -Sn to HgSe in the 10^{17} cm $^{-3}$ range of concentration. Both have Γ_8 conduction bands and their background dielectric constants and effective masses are the same to within 10 per cent. Thus, up to 5×10^{17} cm $^{-3}$, they should be almost indistinguishable from the point of view of ionized-impurity-limited mobility. Yet samples of HgSe have been found [8] at 2×10^{17} cm $^{-3}$ with mobilities of more than 150,000 cm 2 /Vsec—more than twice that of α -Sn at the same concentration. Since these samples of α -Sn are known to have singly ionized donors, one is led to believe that there are scattering mechanisms operative in α -Sn, other than ionized impurity scattering, that are not operative in HgSe.

It is fairly obvious from an inspection of Fig. 1 that the data in the range $N_D = 10^{17} - 2.5 \times 10^{19}$ cm $^{-3}$ can be fitted by a superposition of some concentration-independent scattering mechanism and RPA-screened ionized impurity scattering (dashed curve). As a matter of fact, the data in this range is well fitted by a superposition of either a constant mean free path or constant mean free time process on either the RPA calculation or the constant-dielectric constant calculation of Ref. [5]. (These calculations are fairly close in this range of N_D .) What is not so obvious is that all the data, from $6 \times 10^{14} - 2.5 \times 10^{19}$, can be fitted by RPA-screened ionized-impurity scattering superimposed on scattering processes with a concentration-independent mean free path.

We write the mobility one would see if only

these extra processes were present as

$$\mu_0 = \frac{e\tau_0}{m^*}, \quad (3)$$

where τ_0 is the mean free time for these processes. We assume one can add the frequency of these events to that of ionized impurity scattering to obtain the total scattering frequency:

$$\frac{1}{\tau} = \frac{1}{\tau_0} + \frac{1}{\tau_I}, \quad (4)$$

or

$$\frac{1}{\mu_H} = \frac{1}{\mu_0} + \frac{1}{\mu_I}, \quad (5)$$

where τ_I and μ_I are the mean free time and mobility for ionized impurity scattering and μ_H is the observed Hall mobility. We write τ_0 in terms of a mean free path, Λ_0 , as

$$\tau_0 = \frac{\Lambda_0}{v_F}, \quad (6)$$

where v_F is the Fermi velocity,

$$v_F = \frac{\hbar k_F}{m^*}. \quad (7)$$

Finally, we write Λ_0 in terms of the number of scattering centers N_0 and their scattering length d_0 :

$$\Lambda_0 = \frac{1}{N_0 d_0^2}. \quad (8)$$

The postulated defect must be neutral, and thus one would expect d_0 to be independent of electron concentration, unless it is a hydrogen like chemical impurity, which does not seem likely [19]. Let us further assume that N_0 has only small statistical variations from sample to sample. Then if we assume that the dashed curve correctly describes μ_I , we can calculate Λ_0 for all concentrations

from the observed mobility of a 'typical' sample. If we choose the sample at $6.4 \times 10^{14} \text{ cm}^{-3}$ with a mobility of $6.2 \times 10^5 \text{ cm}^2/\text{Vsec}$ as 'typical,' we obtain $\Lambda_0 \approx 1.75 \times 10^{-4} \text{ cm}$. This would correspond, for example, to $N_0 \approx 3 \times 10^{18} \text{ cm}^{-3}$ for scatterers with $d_0 = 5 \times 10^{-8} \text{ cm}$. The mobilities one would expect to observe are then given by the solid curve on Fig. 1. It is in excellent agreement with experiment over the whole concentration range, even quantitatively reproducing the peculiarly flat shape of the mobility enhancement above $N_D = 5 \times 10^{17} \text{ cm}^{-3}$. The samples above 10^{17} cm^{-3} are, on the whole, slightly below the curve, probably reflecting the fact that they were grown by a transformation from the white tin phase. Although it is not worthwhile showing, a slightly better fit can be obtained in this restricted range by changing μ_1 to 0.19 and calculating Λ_0 from the $2 \times 10^{17} \text{ cm}^{-3}$ sample. It is worthwhile to point out that simply using the RPA dielectric function in the Brooks-Herring calculation cannot produce the required shape for the enhancement. This raises the curve slightly but it then descends even more rapidly on the high concentration side of the peak, having almost the same value as that of the dotted curve of Fig. 1 at $2.5 \times 10^{19} \text{ cm}^{-3}$. Although one can do without the RPA in explaining this portion of the data, it is very difficult to see how one can do without either the additional neutral scattering mechanism (to provide the proper threshold to peak ratio for the enhancement) or the varying wave function and density of states (to provide the proper width for the enhancement). However, since this data merges smoothly into that at lower concentrations, the RPA calculation is preferred.

A parallel with HgSe is again instructive in examining the reasonableness of this explanation. These samples of α -Sn are not annealed because of the low transition temperature to the white tin phase[19]. HgSe grows[20] with a native charged defect, probably a mercury interstitial, fairly uniformly and in about the same concentration

as we have postulated for the neutral defect in α -Sn. Although the concentration of the charged defect can be lowered by annealing, there is evidence[21] through the resonant scattering of acoustic phonons for a neutral native defect which is extremely stable and whose concentration is almost independent of the history of the sample.

Thus we feel that scattering by neutral native defects is a reasonable explanation of both the anomalously low mobility of α -Sn at low donor concentrations and the anomalous shape of the mobility enhancement at high concentrations. The existence of these defects could perhaps be verified in a study of the lattice thermal conductivity of the material.

Acknowledgement—I would like to thank Dr. A. W. Ewald and Dr. C. F. Lavine for use of their results prior to publication and Dr. Lavine for a very informative discussion of his sample preparation. I would like to thank Dr. C. R. Whittett and Dr. S. L. Lehoczky for useful discussions of this problem and Dr. D. P. Ames for support of this work.

REFERENCES

1. NOZIERES P. and PINES D., *Nuovo Cim.* **9**, 470 (1958).
2. LIU L. and BRUST D., *Phys. Rev. Lett.* **20**, 651 (1968).
3. LIU L. and TOSATTI E., *Phys. Rev. Lett.* **23**, 772 (1969).
4. BROERMAN J. G., *Phys. Rev.* **B1**, 4568 (1970).
5. BROERMAN J. G., *Phys. Rev. Lett.* **24**, 450 (1970).
6. BROERMAN J. G., *Phys. Rev.* **B2**, 1818 (1970).
7. GROVES S. and PAUL W., *Phys. Rev. Lett.* **11**, 194 (1963).
8. WHITSETT C. R., *Phys. Rev.* **138**, A829 (1965).
9. BROERMAN J. G., *Phys. Rev.* **183**, 754 (1969).
10. GALAZKA R. R., SEILER D. G. and BECKER W. M., *Phys. Rev.*, to be published.
11. PIDGEON C. R. and GROVES S. H., *II-VI Semiconducting Compounds, 1967 International Conference* (Edited by D. G. Thomas) p. 1080, W. A. Benjamin, New York (1967).
12. TUFTE O. N. and EWALD A. W., *Phys. Rev.* **122**, 1431 (1961).
13. HINCKLEY E. D. and EWALD A. W., *Phys. Rev.* **134**, A1260 (1964).
14. LAVINE C. F. and EWALD A. W., *J. Phys. Chem. Solids*, **32**, 1121 (1971).
15. IVANOV-OMSKII V. I., KOLOMIETZ B. T., OGORODNIKOV V. K. and SMEKALOVA K. P., *Fiz. Tekh. Poluprov.* **4**, 264 (1970).

16. BOOTH B. L. and EWALD A. W., *Phys. Rev. Lett.* **18**, 491 (1967).
17. BROERMAN J. G., *J. Phys. Chem. Solids* **29**, 1147 (1968).
18. I would like to take this opportunity to correct an error in the representation nomenclature of Refs. [4] and [5]: Γ_6^- should everywhere be replaced by Γ_7^- .
19. LAVINE C. F., private communication.
20. WHITSETT C. R., private communication.
21. NELSON D. A., BROERMAN J. G., PAXHIA E. C. and WHITSETT C. R., *Phys. Rev. Lett.* **22**, 884 (1969).

ALTERNATIONS IN THE SECONDARY EMISSION OF MOLECULAR IONS FROM NOBLE METALS

P. JOYES

Laboratoire de Physique des Solides*, Bâtiment 510, Faculté des Sciences, Orsay, Essonne, France

(Received 2 April 1970; in revised form 10 August 1970)

Abstract—The secondary emission of molecular ions Cu_n^+ or Ag_n^- shows a steady alternation according to the parity of n . We give an interpretation of this phenomenon by studying the stability, the ionization potential and the electron affinity of these clusters. These characteristics are directly related to the energy spectrum of the molecular levels. We calculate these spectra for the external s electrons by a tight binding method. Our results agree with the experimental effect. We extend the model to secondary ions of the X_n^+ type where X is any atom having two s external electrons.

A METALLIC crystal submitted to a ionic bombardment of a few keV in energy emits, among others, molecular ions of different charges. As far as copper is concerned, $I(\text{Cu}_n^+)$ intensities in Cu_n^+ ions, as measured with the Slodzian's ionic analyzer [1] are given in [2], up to $n = 4$ (these values are normalized by dividing all the currents by $I(\text{Cu}^+)$). The research of the value of $I(\text{Cu}_5^+)$ current made with the same apparatus allows, taking due consideration of the previous results, to set up an interesting characteristic. As a matter of fact one can note that the secondary emission of Cu_5^+ ions ($I(\text{Cu}_5^+)/I(\text{Cu}^+) = 1.25 \cdot 10^{-1}$) is more important than the emission of Cu_4^+ ions ($I(\text{Cu}_4^+)/I(\text{Cu}^+) = 4.5 \cdot 10^{-2}$). This confirms the fact that, contrary to most of the transition metals (Ti, V, Mn, Fe, Co, Ni [2]), intensities $I(\text{Cu}_n^+)$ show a steady alternation according to the parity of n : ($I(\text{Cu}_{2n}^+) < I(\text{Cu}_{2n-1}^+)$, $I(\text{Cu}_{2n}^+) < I(\text{Cu}_{2n+1}^+)$).

Results recorded by Krohn [3] and those recorded by Hortig *et al.* [4] cover negative molecular ions emitted by another noble metal i.e. silver (bombardment: Cs^+). The authors have noticed that Ag_n^- type ions show, up to $n \approx 30$, same alternation ($R(\text{Ag}_{2n}^-) < R(\text{Ag}_{2n-1}^-)$, $R(\text{Ag}_{2n}^-) < R(\text{Ag}_{2n+1}^-)$; where $R(\text{Ag}_n^-) = I(\text{Ag}_n^-)n^3$).

This paper is intended to show that several properties of the particles considered allow us to understand this phenomenon. We discuss more particularly the stability of Cu_n^+ and Ag_n^- ions, the first ionization potential of Cu_n and the electronic affinity of Ag_n .

Both experimentally and theoretically, information about such metallic groupings is rather scarce. Nevertheless, one can note that the study of the rotation spectrum of Cu_2 molecule enabled Aslund *et al.* [5] to suggest the following fundamental state: $3d^{10}3d^{10}\sigma_g^2$, this evidences the essential part taken by the $4s$ electrons in the bond. Thus, though d electrons take a part in the molecule stability, more particularly with high n values, we shall limit us in this paper to the tight binding study of external s electrons. It appears therefore that our work cannot aim at a well defined determination, for each value of n , of the geometrical characteristics of the most stable forms of Cu_n^+ or Ag_n^- . In such a calculation one could not neglect the part taken by d electrons.

In order to evidence the effect anticipated we first describe our calculation which uses the Hückel approximation and we show that our results are in agreement with the experimental effect. Then we discuss the adjustment of these results to secondary ionic emission models and finally extend our model to second-

* Associated laboratory to the C.N.R.S.

dary ions of the X_n^+ type where X is any atom having two s external electrons instead of a single one.

1. DESCRIPTION OF THE MODEL

The study of the stability of polyatomic clusters can be done in the same way as for diatomic molecules. According to several authors for instance in the case of H_2 [6,7], the dissociation energy is the difference between two terms: on the one hand, the electronic energy gained on approaching the atoms from infinity to the internuclear distance, on the other hand, the Coulomb repulsion energy of the nuclei. We notice that in this model the zero point vibration term is neglected.

For the clusters Cu_n^+ and Ag_n^- we can also define the dissociation energy as the difference between an electronic term and a repulsion term. We shall study these two quantities for the various geometric shapes that we now introduce. We consider all the geometric shapes which appear when one disposes n atoms ($n \leq 5$) in such a manner that each of them—is separated by a given distance d from one or various near neighbours—is separated by a distance larger than d from all other atoms.

For a given value of n , one finds various values l_n for the number of pairs of atoms separated by the distance d ($l_n \geq n-1$). The numbers $N(n, l_n)$ of shapes with the same n and the same l_n are given in Fig. 1.

To obtain, for each of these shapes, the electronic energy ϵ_e^+ gained in the formation of an ion Cu_n^+ (every time that it will be necessary, we shall put a '+' or '-' index to some of the quantities which characterise positive or negative ions), we proceed in two steps. We must first eject a $4s$ electron from one of the atoms (the transmitted energy is E_J) and next approach the n nuclei. If ϵ is the energy of the atomic level and E_q the energy of the q^{th} molecular level, we have

$$\epsilon_e^+ = -E_J + \sum_{q \text{ occupied}} (E_q - \epsilon).$$

In the preceding formula the molecular levels E_q are calculated by using the simple Hückel approximation [8,9].

In the case of negative ions we similarly have

$$\epsilon_e^- = E_J + \sum_{q \text{ occupied}} (E_q - \epsilon).$$

ω^+ and β^+ or ω^- and β^- being the usual overlap integrals, the results can be written:

$$\begin{aligned} \epsilon_e^+ &= -E_J + (n-1)\omega^+ + k^+\beta^+ \\ \epsilon_e^- &= E_J + (n+1)\omega^- + k^-\beta^- \end{aligned} \quad (1)$$

where k^+ or k^- are parameters which depend on the shape considered.

The study of ϵ_e is more difficult. We shall simply make the assumption that the repulsion energy is negligible for two nuclei separated by a distance larger than d and is proportional to the number l_n of bonds in the cluster.

Starting from the results of the previous paragraphs we can eliminate a part of the initial clusters. Among the $N(n, l_n)$ clusters of same n and same l_n , the most stable is the one which has the largest ϵ_e energy. If, as we shall suppose in this paper ω^+ and β^+ for Cu_n^+ and ω^- and β^- for Ag_n^- are independent of n and of the shape studied, this condition leads us to keep only the shape which has the largest k . In some cases another selection operation is possible. Thus, when we consider two clusters with the same n but with different l_n , the cluster which has the largest l_n is less stable than the other if it has a lower k . Taking these two points into consideration we can eliminate a great number of situations*. We shall study all the remaining clusters. We shall call x_n any one of the clusters of n atoms and $\mathcal{N}(n)$ the total number of these clusters. In Table 1 we give, as an example, the values of k^+ for the most stable shapes of Cu_n^+ .

*Owing to the approximate character of the hypothesis on the repulsion energy, we have eliminated only the cases where the last effect was sufficiently strong ($> 10\%$).

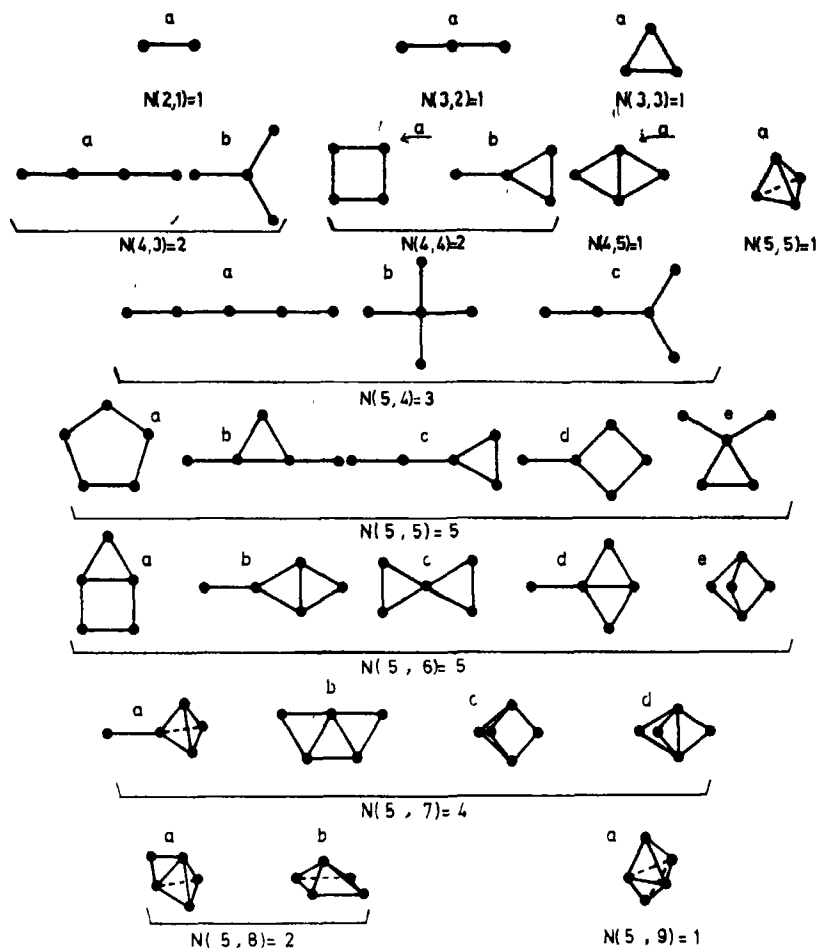


Fig. 1. Arrangements studied. We index the different shapes having the same n and l_n by a different letter.

Table 1. Values of k^+ for Cu_n^+ . The symbols α are indicated on Fig. 1

n	2	3	4	5	6	7	8	9
l_n	1	2	3	3	4	5	6	6
α	a	a	a	a	b	a	a	a
k	1.00	2.82	4.00	3.86	4.41	5.12	5.00	5.00
n								
l_n	4	5	6	7	8	9	9	9
α	a	c	c	b	a	a	a	a
k	5.46	6.42	7.12	7.10	7.36	7.30	7.30	7.30

As we mentioned before, in this model it is not possible to determine the most stable of the geometric shapes. However, we do notice that our results agree with those of Poshusta *et al.*[10] since the most stable shapes obtained by these authors for H_3^+ , H_4^+ and H_5^+ are among the shapes that we have selected.*

2. ALTERNATIONS IN THE PROPERTIES OF Cu_n^+ AND Ag_n^-

2.1 Stability

(a) *Statement of the problem.* We now want to verify the dissociation energy $D = \epsilon_c - \epsilon_r$ has alternations which depend on the parity of n .

Let us consider two arrangements x_{n+1} (of $n+1$ particles and l_{n+1} bonds) and x_{n-1} (of $n-1$ particles and l_{n-1} bonds), the quantities

$$\epsilon_c(n+1, l_{n+1}) - \epsilon_c(A)$$

$$\epsilon_c(A) - \epsilon_c(n-1, l_{n-1})$$

(in the energies D , ϵ_r , ϵ_c and in the parameter k we shall now explicit the dependence on the shape studied) where A is any one of the shapes of n particles, can be supposed equal if

$$l_{n+1} - l_A = l_A - l_{n-1}. \quad (2)$$

*The distances between nearer neighbours obtained by these authors are nearly equal: the lowest ratio between two values of d is 0.75.

In this case the comparison of the two differences

$$\Delta_{n+1}(x_{n+1}, A) = D(x_{n+1}) - D(A) \quad (3)$$

and

$$\Delta_n(A, x_{n-1}) = D(A) - D(x_{n-1}) \quad (4)$$

reduces to the comparison of the electronic terms and more precisely to the comparison of

$$k(n+1, l_{n+1}) - k(A) \text{ and } k(A) - k(n-1, l_{n-1}).$$

A similar condition can be introduced by grouping two comparisons. A'' and B'' being two x_{n+1} , A and B two x_n and A' and B' two x_{n-1} , the comparison of

$$\Delta_{n+1}(A'', A) + \Delta_{n+1}(B'', B) \quad (5)$$

and

$$\Delta_n(A, A') + \Delta_n(B, B') \quad (6)$$

will reduce to the comparison of the k values if the condition

$$(l_{A''} - l_A) + (l_{B''} - l_B) = (l_A - l_{A'}) + (l_B - l_{B'}) \quad (7)$$

is fulfilled. For a given n , the total number of comparisons that we have to do is $\omega(n-1)\omega(n)\omega(n+1)$. A part of them satisfy (2) (case "a" in the Table 2). By taking into account only one time each of the others and by grouping them so that (7) be fulfilled (case

Table 2. Study of the stability of Cu_n^+ and Ag_n^- . The meaning of the letters a and b is given in the text

Ion	n	$\frac{\omega(n-1)x}{\omega(n)\omega(n+1)}$	case (a)		case (b)		total number of cases studied	total number of cases in agreement
			studied	in agreement	studied	in agreement		
Cu_n^+	2	2	1	1			1	1
	3	8	2	2	6	6	8	8
	4	48	6	4	2×21	2×20	48	44
Ag_n^-	2	1	1	1			1	1
	3	3	2	2			2	2
	4	15	3	2	6×2	5×2	15	12

"b" in Table 2) we can consider almost all the comparisons (see Table 2).

(b) *Results.* For Cu_n^+ as for Ag_n^- the cases in agreement with experiment are those for which (3), or respectively (5), is smaller than (4), or respectively (6), for n odd; the reverse being true for n even. From Table 2 we see that almost all the comparisons agree with experiment.

2.2 Ionization energy and electron affinity

Other results can be deduced from the calculation. The ionization energy \mathcal{I} of Cu_n is given by the distance between the last occupied level and zero energy and the electron affinity \mathcal{A} of Ag_n is given by the distance between the first unoccupied level and zero energy. These results will be in agreement with experiment if $\mathcal{I}(x_n) < \mathcal{I}(x_{n-1})$ and $\mathcal{A}(x_n) > \mathcal{A}(x_{n-1})$ for n odd; the reverse being true for n even. The number of comparisons that we have to do and the number of cases giving the expected alternation are given in Table 3. We note that the agreement with experiment is less good than for stability.

2.3 Order of magnitude of the energy variations

All the previous results concern parameters such as k which always are multiplied by the integral β (see formulas 1). To check the validity of our conclusions we want to verify that the term $k\beta$ has an order of magnitude comparable with ω and the repulsion energy. The evaluation of the overlap integrals for Cu_2^+ (in which the internuclear distance is

2.62 Å [11]) gives $\omega = 3.89$ eV and $\beta = 1.34$ eV. By using the dissociation energy of Cu_2 (2.1 eV [5]), the calculation of the repulsion term of Cu_2 (see for instance [6]) gives 3.2 eV. So, if we suppose that for Cu_n^+ the order of magnitude of ω , β and $\epsilon_c(n, l_n) - \epsilon_c(n-1, l_{n-1} = l_n - 1)$ are given by the previous values (3.89, 1.34, 3.2 eV), we see that, for the linear shapes for instance where $k(n, l_n) = n-1) - k(n-1, l_{n-1} = n-2) = \begin{cases} 1, 65 & n \text{ odd} \\ 1 & n \text{ even} \end{cases}$,

we have $\Delta_n = 2.9$ eV for n odd and 2 eV for n even. The alternation effect seems to appear with a quite strong amplitude (40%) in the dissociation energy.

3. DISCUSSION OF THE RESULTS

3.1 Application to secondary ionic emission

Until now our work has been limited to the study of molecular properties and we noted every time one of the energies D , \mathcal{I} or \mathcal{A} had variations in agreement with experiment. We now want to discuss in what manner these parameters can act in the phenomenon of secondary emission.

Many authors have introduced thermal theories to explain some aspects of secondary emission. The general scheme is the following: one supposes that after irradiation, the incident energy is distributed in various small regions (~ 20 Å³). Thermal equilibrium established at high temperatures (3–5000°C) and sublimation of the metal occurs from these regions [12,13]. Let us note that a thermal model seems to be particularly well suited to study the secondary emission of molecular

Table 3. Study of the ionization energy of Cu_n and of the electronic affinity of Ag_n

Ion	Cu_n^+		Ag_n^-	
	n	$\omega(n)\omega(n-1)$	n	$\omega(n)\omega(n-1)$
	2	1	1	1
	3	2	2	1
	4	8	4	3
	5	24	14	15

ions whose kinetic energies are lower than those of monoatomic ions[14]. It is easy to see that in such a model the dissociation energy (which acts through the formation enthalpy) is an essential parameter and that the emission increases when D increases. We can also notice that a great similarity seems to exist between evaporation[15] and secondary emission of neutral particles[16] since for the two phenomena the abundances of Cu_n decrease regularly when n increases.

Other mechanisms can be responsible for the formation of secondary molecular ions. One knows that the kinetic model gives a good account of secondary emission of variously charged monoatomic ions[17,18]. The extension of this mechanism to polyatomic clusters seems to be possible. The ease with which the cluster may be ejected without being broken depends on its stability and the probability of being ionized depends either on \mathcal{F} for Cu_n^+ or on \mathcal{A} for Ag_n^- . Therefore it appears that our results act directly in the description of the phenomenon and allow to understand the experimental data.

3.2 Clusters made from atoms with 2 external electrons

Finally let us analyse the possible extension of the preceding conclusions to the study of X_n^+ ions in the case where the element X possesses two external electrons instead of one. Here again we make the assumption that the other electrons do not participate in the binding.

The most stable geometric shapes being selected as before, we notice that, among all the possible comparisons, the cases where the dissociation energy presents a continuous decrease are the most numerous.

The results of the study of ionization potentials of X_n show that when n increases the average behaviour is decreasing.

If, as for copper and silver, it is the behaviour of the stability which governs the relative abundance of X_n^+ ions, we shall expect to

observe a continuous lowering of $I(X_n^+)$ when n increases.

To check the validity of this conclusion, we have experimental data concerning the first transition series[2]. It is convenient to note that, for these metals, the hypothesis which supposes that the s electrons, and they alone, act in the binding can be questioned. We know that in the limiting case of the crystal ($n \rightarrow \infty$), the number of $4s$ electrons in the conduction band is clearly less than the number ν of $4s$ electrons in the fundamental state of the isolated atom. If, in spite of this remark, we suppose that in the molecule the number of external s electrons per atom is equal to ν we notice that the behaviour of the metals is in agreement with our results.

— $\nu = 2$: regular decrease of X_n^+ with n observed for Ni ($n \leq 4$), Co ($n \leq 5$), Fe ($n \leq 4$), Mn ($n \leq 5$), V ($n \leq 5$), Ti ($n \leq 4$).

— $\nu = 1$: case of copper studied before, alternation observed for Cr ($n \leq 3$).

4. CONCLUSION

Several other effects seem to confirm the whole of the above study. Let us report the behaviour of silver for which current Ag_3^+ is larger than Ag_2^+ ; measurements made with the ionic analyzer[1] give: $I(Ag_2^+)/I(Ag^+) = 0.3$ and $I(Ag_3^+)/I(Ag^+) = 0.68$. At that stage of the study one must however take care not to have an excessive confidence in such concordances and if, for the elements of the first transition series, the most external electrons do not seem to conceal the effect, may be could it be different for other transition series. All our conclusions should actually need a check with an examination of a true divalent as magnesium for instance. The experimental study of Cu_n^- ions, which should present alternations like Cu_n^+ or Ag_n^- and Ag_n^+ , would be also interesting.

Continuing this study for n values over 5 gives rise to important difficulties due to an increased number of geometrical forms on consideration. The study of linear chains, where analytical formulas exist[19] shows

that, in agreement with experiment, the alternation is continuing until high n values.

Acknowledgements—I would like to express my thanks to Professors R. Castaing and J. Friedel for reading the manuscript and useful comments. I am grateful to Mrs. H. Duval whose efficient technical cooperation allowed me to carry out this work.

REFERENCES

1. SLODZIAN G., Thèse de doctorat, 1964, Paris; *Ann. Phys.* **9**, 591 (1964).
2. BLAISE G. and SLODZIAN G., *C. R. Acad. Sci. Paris série B*, **266**, 1525 (1968).
3. KROHN V. E., *J. appl. Phys.* **33**, 3523 (1962).
4. HORTIG G. and MÜLLER M., *Z. Phys.* **221**, 119 (1969).
5. ÅSLUND N., BARROW R. F., RICHARDS W. G. and TRAVIS D. N., *Ark. fys.* **30**, 171 (1965).
6. MULLIKEN R. S., *J. Chim. Phys.*, **46**, 675 (1949).
7. COULSON C. A., Valence, Oxford (1961).
8. HÜCKEL E., *Z. Phys.*, **70**, 204 (1931), **76**, 628 (1932).
9. SALEM L., Molecular Orbital Theory of Conjugated Systems, Benjamin (1966).
10. POSHUSTA R. D. and MATSEN F. A., *J. chem. Phys.*, **47**, 4795 (1967).
11. ORGEL L. E., *J. chem. Soc.*, 4186 (1958).
12. THOMPSON M. W., *Le Bombardement ionique*, Bellevue, p. 143 (Décembre 1962), THOMPSON M. W. and NELSON R. S., *Phil. Mag.* **7**, 2015 (1962).
13. NELSON R. S., The observation of Atomic Collisions in crystalline solids. Serie defect in crystalline solids. North Holland Publishing Company, 1968, see for instance p. 265.
14. JURELA Z. and PEROVIĆ B., *Can. Phys.* **46**, 773 (1968).
15. SCHISSEL P., *J. chem. Phys.*, **26**, 1276 (1957).
16. WOODYARD J. R. and COOPER C. B., *J. appl. Phys.* **33**, 1107 (1964).
17. JOYES P. and CASTAING R., *C. R. Acad. Sci. Paris série B*, **263**, 384 (1966).
18. JOYES P., Thèse de Doctorat, Orsay, n° CNRS A. O. 2386 (1968). JOYES P. and HENNEQUIN J.-F., *J. Phys.* **29**, 483 (1968). JOYES P., *J. Phys.* **29**, 774 (1968), **30**, 224 (1969), **30**, 365 (1969).
19. LENNARD-JONES J. E. and TURKEVITCH J., *Proc. R. Soc., Lond.* **A158**, 280 (1937), and **A158**, 297 (1937).

CATION SELF-DIFFUSION IN STRONTIUM OXIDE (SrO)*

S. P. MURARKA and R. A. SWALIN

Metallurgy and Materials Sciences, University of Minnesota, Minneapolis, Minn. 55455, U.S.A.

(Received 23 April 1970; in revised form 10 August 1970)

Abstract—Cation self-diffusion studies were carried out in SrO in the temperature range $1200^{\circ}\text{C} \leq T \leq 1600^{\circ}\text{C}$ and in the oxygen partial pressure range $2 \times 10^{-5} \text{ atm} \leq p_{\text{O}_2} \leq 1 \text{ atm}$. The isotope ^{88}Sr was used and Gruzin's residual activity method was employed. The bulk diffusion coefficients obtained from these data for specimens annealed in argon ($p_{\text{O}_2} = 2 \times 10^{-5} \text{ atm}$) could be represented by the following equations

$$D_{\text{Sr/SrO}}(1450-1600^{\circ}\text{C}) = (2.52^{+15.16}_{-3.16}) \times 10^2 \exp \{-(4.61 \pm 0.066 \text{ eV})/kT\} \text{ cm}^2/\text{sec.}$$

$$D_{\text{Sr/SrO}}(1200-1400^{\circ}\text{C}) = (4.48^{+11.43}_{-3.22}) \times 10^{-4} \exp \{-(2.76 \pm 0.038 \text{ eV})/kT\} \text{ cm}^2/\text{sec.}$$

No appreciable dependence of D on p_{O_2} was observed below 1400°C . At higher temperatures an influence was observed and at 1500°C

$$D \propto p_{\text{O}_2}^{1/8-2/3}.$$

It is postulated that cation diffusion occurs by a vacancy mechanism. The concentration of vacancies is (i) impurity controlled below 1450°C and (ii) controlled by oxygen partial pressure above 1450°C . From the low temperature data an enthalpy of migration of 2.76 eV was obtained. Combining this value with high temperature data, the formation enthalpy of a doubly ionized cation vacancy was calculated to be 2.96 eV .

1. INTRODUCTION

INTEREST in the crystalline alkaline earth oxides has stemmed from the development of the vacuum tube cathodes coated with mixtures of barium and strontium oxides, which have been used for many years as low temperature sources of electrons in vacuum tubes. Except for MgO , little has been done to elucidate the intrinsic defect structure of these compounds and their relation to the intrinsic disorder in other binary compounds such as alkali halides, which are the monovalent structural analogues of these oxides.

In SrO a limited number of studies have been made, which have tried to identify the defect structure of this compound. A review of these studies appears in the work of Copeland and Swalin[1], who reported the results

of investigation of the phase equilibria, lattice parameter, electrical conductivity, thermoelectric power and thermogravimetric analysis in the temperature range of $600^{\circ}\text{C} \leq T \leq 1400^{\circ}\text{C}$ and oxygen pressure range $10^{-12} \text{ atm} \leq p_{\text{O}_2} \leq 1 \text{ atm}$.

Bessent *et al.*[2] have reported the occurrence of singly ionized oxygen vacancies (F^+ centers) in lightly neutron irradiated crystals of SrO . The presence of cation vacancies associated with the trivalent transitional impurities in SrO was also demonstrated in the ESR study of SrO by Auzins *et al.*[3].

Under the shadow of uncertainties about the defect structure of SrO , it was decided that a study of cation self-diffusion in SrO at high temperatures should be made both as a function of temperature and oxygen partial pressure. The results of this research are discussed in this paper. In a subsequent paper the results of cation self-diffusion

*This work was supported by the National Science Foundation.

studies in BaO will be reported and discussed with other self diffusion studies in other alkaline earth oxides.

2. EXPERIMENTAL PROCEDURES

SrO crystals were obtained from W. & C. Spicer Ltd. England. These crystals were grown by the electric arc fusion technique from the melt. Crystals, as obtained, were colorless and transparent and had dimensions as large as 1 cm × 1 cm × 1 cm. All these crystals were annealed in our laboratory in a large MgO crucible at 1500°C in pure argon for 48 hr. The semi-quantitative spectrographic analysis of these crystals shows 0.12% of BaO, 0.003% of MgO, < 0.025% CaO and < 0.002% of Al₂O₃ as the principal impurities.

The high reactivity of the SrO crystals with water vapor and CO₂ necessitated special care in handling. Preparation of the crystal surface for radioactive deposition and radioactive deposition itself were carried out in a dry box in an atmosphere of dry argon. All annealings were carried out in sintered MgO or single crystal MgO crucibles in the presence of excess dry SrO powder and crystal chips in an atmosphere of dry argon or appropriate argon-oxygen mixture.

Flat surfaces of the crystals were obtained by use of a precision polishing jig. The crystal was fastened on the jig with quartz cement which was later removed by grinding and by use of the solvent 2-butoxyethanol. Polishing was done progressively on 300, 400 and 600 grade SiC papers. Just prior to deposition of the radioactive material final preparation of one of the surfaces was made inside the dry box by polishing on 4/0 emery paper and the sample was cleaned with water free analar acetone. Typical polished surfaces of crystals were examined by use of a scanning electron microscope at different magnifications. Scratches present on the surface due to polishing paper were found to be between one and two micrometers in width and the distribution of scratches on the surfaces was uniform.

Radioactive ⁸⁵Sr isotope was used as the tracer. Strontium oxalate was precipitated from the nitrate solution. Oxide was obtained by drying at 150°C in an oven and igniting the oxalate in a closed crucible at 1000°C in a furnace. The radioactive oxide was then evaporated as a thin film over the prepared crystal surface inside the drybox[4]. Under the conditions of the experiment a film of about 0.1 to 0.5 μm in thickness was deposited on the exposed crystal surface. Microscopic examination of the films showed no obvious discontinuity. After evaporation the other five surfaces of the rectangular specimen were ground to remove any radioactive material which might have been deposited during evaporation.

Diffusion annealing times ranged from a few hours at high temperatures to a few weeks at low temperatures. The temperature range of the studies was 1200–1600°C. All furnaces were controlled to within ± 1°C at temperatures below 1400°C and ± 2°C between 1450–1600°C. Temperatures up to 1450°C were measured with a Pt vs. Pt-10% Rh thermocouple. Higher temperatures were measured with a Pt-20% Rh vs. Pt-40% Th thermo-

couples. Thermocouples were calibrated periodically with reference thermocouples, which had been calibrated by Engelhard Industries by use of a National Bureau of Standards reference thermocouple. Since the temperature was measured above the crucible surface in the isothermal zone and due to the fact that the reference grade thermocouple had 0.15 per cent maximum uncertainty of calibration. The accuracy of the temperature of diffusion could be quoted to be within ± 4°C in the range of 900–1400°C and within ± 5°C in the range 1400–1600°C.

A gas flow (dry argon or argon-oxygen mixture) of 100 cc per min was maintained for a period of 24 hr before the annealings to the end of annealing experiments. The oxygen partial pressure was measured by an oxygen-gauge, which had been calibrated by use of a standard gas.

Gruzin's residual activity method[5] was employed in which counts from the face of the crystal were monitored after each section is removed. The penetration profiles were determined by mounting the specimen (after all sides but one, on which the radioactive layer was deposited, were ground to remove any radioactivity which might have diffused along these surfaces during the diffusion anneal) on a precision lapping device similar to that of DeBruin and Watson[6]. The device is designed so that sections 2.5 μm in thickness could be removed parallel to the originally exposed surface.

The counting of the 0.51 MeV gamma radiation from ⁸⁵Sr was performed with a 2π geometry NaI, Tl activated scintillation crystal assembly. A brass ring was used to ensure that the lapping device sat on the crystal in the same position every time. Since the sectioning device had to be taken out of the drybox after each sectioning for counting, a polyethylene bag made of one mil thick sheet was used to protect the sample from exposure to the atmosphere. When the sectioning was completed background counts were taken with the polyethylene bag on the device but without the SrO crystal inside.

3. RESULTS

The typical results obtained from these experiments are presented in Fig. 1, which shows plots of the surface activity I vs. penetration distance x into the crystal. For the boundary conditions applicable to the experiment, namely diffusion from a thin film into a semi-infinite medium, the solution of the uni-dimensional Fick's second law is given by

$$C(x, t) = \frac{C_0}{\sqrt{\pi Dt}} \exp\left(-\frac{x^2}{4Dt}\right) \quad (1)$$

where C is the concentration, C_0 is the total amount of material initially present on the surface, D is the concentration independent diffusion coefficient and t is the time of anneal.

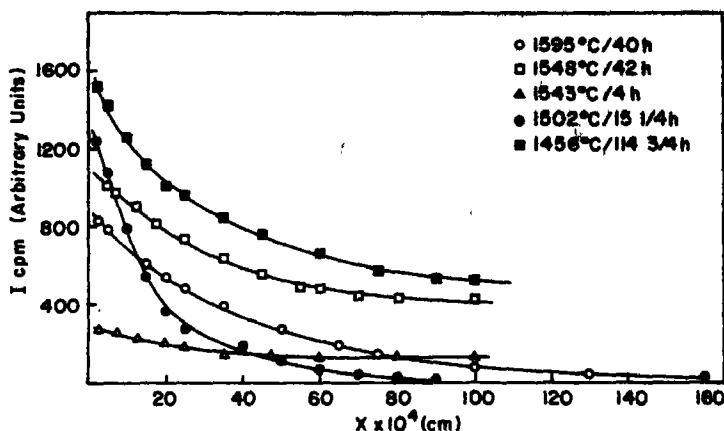


Fig. 1. Penetration profiles for cation self-diffusion in SrO ($p_{O_2} = 2 \times 10^{-5}$ atm).

For the surface counting methods[5], this equation can be employed to obtain a quantity I^* where

$$I^* = \mu I - \frac{dI}{dx} = \text{const.} \exp\left(-\frac{x^2}{4Dt}\right) \quad (2)$$

where I represents the number of counts per unit time after a thickness x has been removed and μ is the linear absorption coefficient in the crystal for the radiation being monitored. For the 0.51 MeV γ radiation of ^{85}Sr μ was calculated to be 0.404 cm^{-1} [7].

To calculate I^* and hence evaluate D from the experimental data, a digital computer was used[4]. The logarithm of I^* was plotted vs. x^2 for each sample. Equation (2) predicts a straight line with a slope equal to $1/4Dt$. Figure 2 shows some typical plots. The experimental data in these graphs did not fit a single line but rather it was observed that the data fit two intersecting lines. The one near the surface has a considerably larger slope than the line at larger distances. While the first region was restricted to a maximum of about $20 \mu\text{m}$ in SrO the 2nd segment extended up to about $200 \mu\text{m}$. This phenomenon was observed in all the samples.

A set of experiments was carried out in order to check if the hydroxide layer formed

on the surface caused the apparently anomalous behavior in the region near the surface of the crystal. A set of SrO crystals, exposed to the atmosphere for different periods of time, were used for diffusion studies. Figure 3 shows the $\log I^*$ vs. x^2 plots for these specimens together with the time of exposure to atmosphere. While there was not much difference in the value of the near surface penetration distance for crystals exposed for 5, 10 min and 1 hr, there was an observable increase in the near surface penetration distance for the specimen exposed for 10 hr. These crystals become rapidly hydrated. It is possible that this leads to the formation of a protective layer of hydroxide on the surface which then slows down further hydroxide formation. This observation would then explain the results presented in Fig. 3. It would then appear that the discontinuity in the slope of $\log I^*$ vs. x^2 curves, in the region close to the surface of the crystal, was due to a chemically different phase on the surface.

Temperature dependence of D

Figure 4 shows a plot of $\log D$ vs. $1/T$. A discontinuity in slope appears to occur at about 1425°C . A least square straight line fit for the two segments yields the following temperature dependence relations for dif-

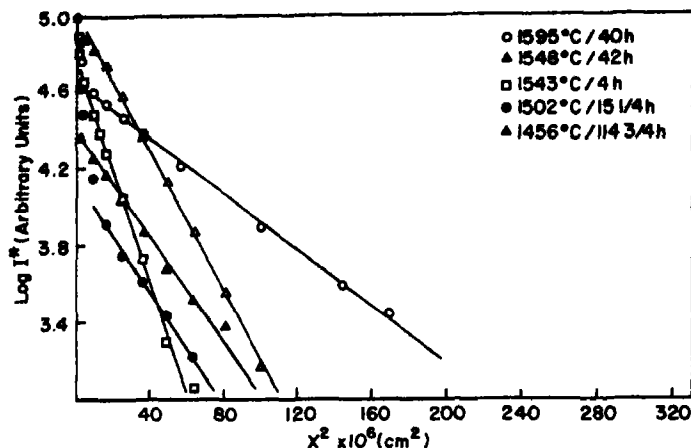


Fig. 2. $\log I^*$ vs. x^2 plots for cation self-diffusion in SrO ($p_{O_2} = 2 \times 10^{-5}$ atm).

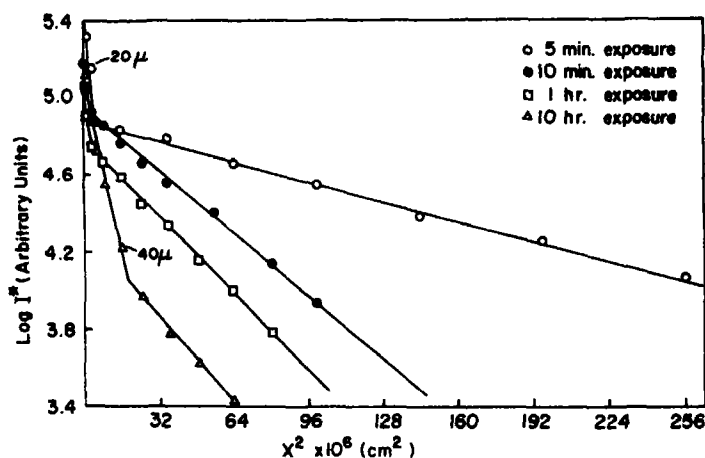


Fig. 3. $\log I^*$ vs. x^2 plots cation self-diffusion in SrO crystals exposed to atmosphere for different periods of time.

fusion coefficients in pure argon ($p_{O_2} = 2 \times 10^{-5}$ atm).

$$D(1450-1600^\circ\text{C}) = (2.52 \pm_{2.18}^{15.18}) \times 10^2 \exp$$

$$[-(4.61 \pm 0.066) \text{ eV}/kT] \text{ cm}^2/\text{sec}$$

$$D(1200-1400^\circ\text{C}) = (4.48 \pm_{3.22}^{1.48}) \times 10^{-4} \exp$$

$$[-(2.76 \pm 0.038) \text{ eV}/kT] \text{ cm}^2/\text{sec}.$$

Accuracy limits on D_0 and Q were calcu-

lated by use of the method described by Guest[8].

Oxygen partial pressure dependence of D

In Fig. 4, the diffusion coefficients obtained in pure oxygen are also plotted. It is observed that, at low temperatures, there is no influence of oxygen partial pressure on D but that as the temperature is increased a change in oxygen partial pressure affects the cation diffusivity. In Fig. 5 is shown a plot of \log

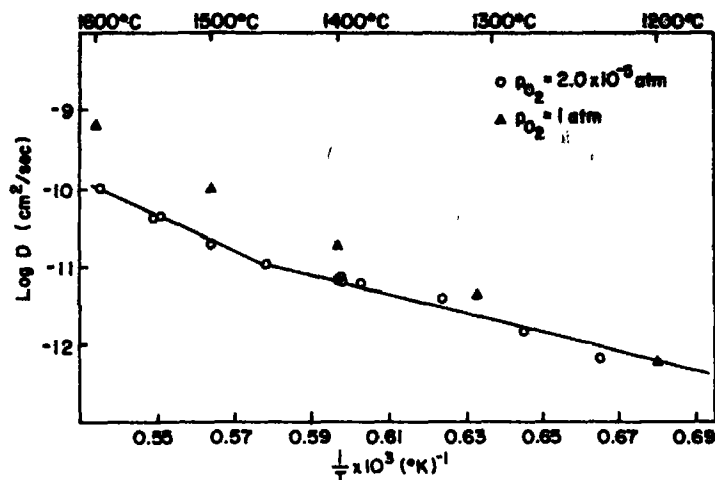


Fig. 4. Diffusion coefficients for cation self-diffusion in SrO as a function of temperature.

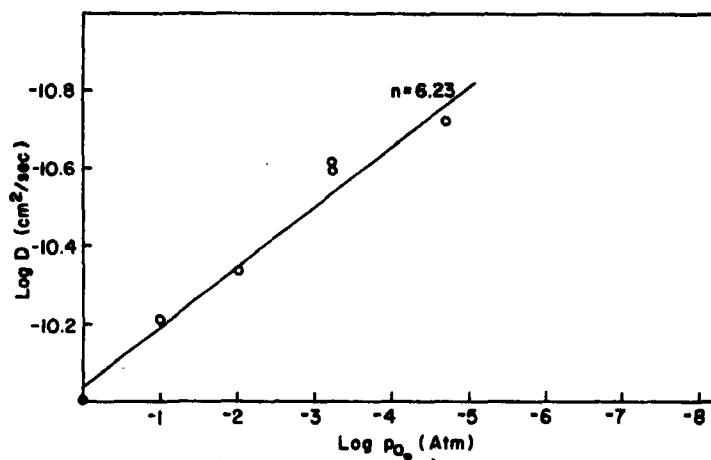


Fig. 5. Diffusion coefficient for cation self-diffusion in SrO as a function of p_{O_2} ($T = 1500^\circ\text{C}$).

D vs. $\log p_{O_2}$ at 1500°C . The data can be described by the relation

$$D \sim p_{O_2}^{1/n}$$

and a least square analysis indicates that $n = 6.23 \pm 0.51$. It appears that D represents the volume diffusion coefficient. Aside from the fact that D was found to be reproducible there are other reasons to believe that D does represent volume diffusion. In all these

studies well annealed single crystals were used which rules out the possibility of contribution from grain-boundary diffusion. Contribution from other short circuiting paths such as dislocations cannot be ruled out completely. The lowest temperature of study, however, was higher than half the absolute melting point and diffusion along these paths would not appear to be dominating mechanism of mass transport at these temperatures. This is supported by the fact that high activation

energies were obtained for diffusion in these oxides.

4. DISCUSSION

The object of performing the present studies was to help elucidate the defect structure of SrO. In spite of the lack of the clear understanding of the observed near surface phenomenon in the present case it appeared that it was caused due to the hydroxide formation on the surface of the oxide crystals. Observation of this type of effect is common and a detailed description of factors, which might be responsible, is presented in Ref.[4]. There was no systematic behavior of the results in this region and hence a detailed examination is not fruitful.

Volume diffusion of ^{88}Sr in SrO could occur by either (a) a mechanism in which strontium interstitials are involved—namely direct interstitial mechanism or interstitialcy mechanism or (b) a mechanism in which cation vacancies exchange with Sr tracer ions. For an ion diffusing by these mechanisms, the random walk method of calculation of diffusion coefficient D leads to the following equations [9]: for interstitial mechanisms

$$D_i = \gamma_i f_i a^2 \omega_i n \quad (3)$$

and for vacancy mechanism

$$D_v = \gamma_v f_v a^2 \omega_v x_v \quad (4)$$

where subscripts i and v stand for respective mechanisms, γ is a geometrical factor, f is the correlation factor which is unity for direct interstitial mechanism of diffusion, a is the lattice parameter, ω is the probability per unit time that ions will jump into a particular vacant lattice or interstitial site, x_v is the mole fraction of the cation vacancies and n is the fraction of time that a given atom exists interstitially. Similarly n is equal to the fraction C_i/C of ions of a certain type which reside on interstitial sites at a given time. C_i is the concentration per unit volume of ions of a

type on interstitial site and C is their total concentration per unit volume. For an interstitial mechanism, therefore [9]

$$D_i = \gamma_i f_i a^2 \omega_i C_i / C.$$

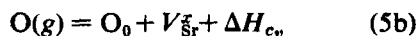
Thus the diffusion coefficient can be dependent on the point defect concentration for both the interstitial and vacancy mechanisms. If one writes down the defect reaction equation for Frenkel defects on the cation and anion sublattices and the equation for formation of Schottky defects and combines them with the appropriate equations for incorporation of oxygen into the lattice from the gas phase it can be shown that the strontium interstitial concentration will decrease as the partial pressure of oxygen increases. This will result in a decrease in D_i as p_{O_2} increases. For a vacancy mechanism on the other hand, the concentration of cation vacancies will increase with p_{O_2} and this will result in an increase of D_v as p_{O_2} increases.

Figures 4 and 5 show that in SrO at temperatures above 1200°C, an increase in partial pressure of oxygen resulted in an increase in experimental values of D . The changes in partial pressure of oxygen will not affect materially the factors f , γ , ω and a . The data therefore are inconsistent with an interstitial mechanism but are consistent with a vacancy mechanism of diffusion.

Following the above argument, and the fact that both anion and cation vacancies have been observed in ESR studies of SrO [2, 3], it is postulated that diffusion in SrO occurs by the vacancy mechanism and that oxygen is incorporated (at temperatures above 1450°C) as the oxygen lattice ions with concurrent formation of vacancies on strontium site. The fact that D is independent of p_{O_2} at low temperatures is consistent with the vacancy mechanism under the condition that the concentration of vacancies is controlled by the impurity concentration of the crystals as observed also in MgO [10] and CaO [11, 12]. At sufficiently high temperatures, the concen-

tration of vacancies will depend on p_{O_2} and will not be influenced by impurities. As a consequence it will be useful to derive a defect-structure model for SrO and obtain a relation between the diffusion coefficient D_v and p_{O_2} and compare this relation with the experimentally observed relation between D and p_{O_2} . The defect model could be described with the help of following reactions and equilibrium conditions (in the following the Kroger-Vink[13] notations are employed to denote the defects and their concentrations in moles per unit volume and it is assumed that defect concentrations are small so that while writing the equilibrium equations in terms of defect concentrations all the activity coefficients will be assumed to be concentration independent).

Incorporation of the oxygen in the lattice



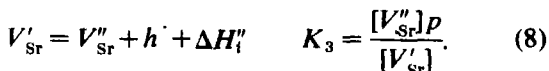
such that a combination of these will give

$$K_1 = \frac{[V_{Sr}^{\times}]}{p_{O_2}^{1/2}} \quad (5c)$$

Schottky defects formation



Ionization of the vacancies



If we assume that doubly charged cation vacancies are predominant, the following relations hold.

$$2[V_{Sr}'] = p \quad (9)$$

and solving for $[V_{Sr}']$ from the above relation we find

$$[V_{Sr}'] = 4^{-1/3}(K_1 K_2 K_3)^{1/3} p_{O_2}^{1/6} \quad (10)$$

This gives the relation between the cation vacancy concentration and p_{O_2} . Since it was assumed that V_{Sr}'' are predominant, $[V_{Sr}']$ can be substituted for x_v in equation (4), such that

$$D_v = f_v \gamma_v a^2 [V_{Sr}'] \omega_v j \quad (11)$$

where the constant j on the right side of the equation takes into account the change in the units of concentration of the vacancies when x_v is replaced by $[V_{Sr}']$. Upon making the usual substitutions in the equation (11), we obtain

$$D_v = D_0 p_{O_2}^{1/6} \exp - [(\Delta H_0 + \Delta H_{cv})/3 + \Delta H_m]/kT \quad (12)$$

where

$$D_0 = f_v \gamma_v a^2 j \nu \exp [(\Delta S_0 + \Delta S_{cv})/3 + \Delta S_m]/k \quad (13)$$

and the ΔH and ΔS terms represent the enthalpy and entropy components of free energy ΔG . ΔH_0 now consists of the following terms:

$$\Delta H_0 = \Delta H_i' + \Delta H_i'' + \Delta H_a. \quad (14)$$

The factors in the right side of the above equations represent respectively the processes described by equations (7) and (8) and by the equation (5a). From equation (12) we see that at constant temperature, the exponential term is a constant and therefore D_v is proportional to $p_{O_2}^{1/6}$. This compares well with the experimentally observed result at 1500°C i.e.

$$D \propto p_{O_2}^{1/n} \text{ with } n = 6.23$$

and supports the assumption of doubly ionized vacancies as the predominant defects responsible for diffusion.

When the experiments are carried out at a constant oxygen pressure but at various temperatures, equation (12) yields an activa-

tion energy of diffusion given by

$$Q = \frac{\Delta H_0 + \Delta H_{cv}}{3} + \Delta H_m. \quad (15)$$

On the other hand if the temperature and impurity concentration are such that the intrinsic vacancy concentration is less than the extrinsic vacancy concentration as controlled by the impurity content, then

$$D_v = \text{const} \exp(-\Delta H_m/kT) \quad (16)$$

and under these circumstances $Q = \Delta H_m$.

Utilizing these equations in conjunction with the experimental data we see that

$$Q_{\text{Low temp.}} = 2.76 \text{ eV} = \Delta H_m \text{ and}$$

$$Q_{\text{High temp.}} = 4.61 \text{ eV} = \frac{\Delta H_0 + \Delta H_{cv}}{3} + \Delta H_m.$$

Hence $\Delta H_0 + \Delta H_{cv} = 5.55 \text{ eV}$, and by use of the equation (14)

$$\Delta H_{cv} = 5.55 \text{ eV} - \Delta H'_i - \Delta H''_i - \Delta H_a. \quad (17)$$

The energy of dissociation $-\Delta H_a$ of a gaseous diatomic oxygen molecule is 2.59 eV [14]; therefore the enthalpy of formation of a doubly ionized cation vacancy $\Delta H''_{cv}$ is 2.96 eV and the enthalpy of formation of a neutral cation vacancy is

$$\Delta H_{cv} = 2.96 - \Delta H'_i - \Delta H''_i.$$

Values of $\Delta H'_i$ and $\Delta H''_i$ are not known. Since doubly ionized cation vacancies were found to be predominant in the working temperature range, these two enthalpies would be small—of the order of kT . As an upper limit the sum $\Delta H'_i + \Delta H''_i$ is assumed to be about 1 eV , so that

$$\Delta H_{cv} \approx 2 \text{ eV}.$$

The Schottky defect formation energy

ΔH_s for formation of neutral defects in SrO cannot be obtained uniquely from the present data. If, however, one arbitrarily approximates that the contributions to ΔH_s by anion and cation vacancy formation energies are equal, then

$$\Delta H_s \approx 2 \Delta H_{cv} \approx 4 \text{ eV}.$$

In previous cation self-diffusion studies in MgO [10], CaO [11, 15] or BaO [16], where the p_{O_2} dependence of D was not investigated, it was assumed that at the experimental temperatures and oxygen partial pressures, stoichiometry of the crystal was maintained. This assumption implies that the diffusion activation energy from the so called intrinsic range is given as

$$Q = \frac{\Delta H_s}{2} + \Delta H_m.$$

On this basis in the present case we would obtain $\Delta H_s = 3.7 \text{ eV}$. It is, however, apparent from the above discussion of present results in SrO that one cannot get the correct value of ΔH_s from the diffusion data alone without establishing first that the experimental conditions are such as to maintain stoichiometry of the crystal.

Copeland and Swalin [1] have postulated the existence of Frenkel disorder on the anion sublattice of SrO in the temperature range $600^\circ\text{C} \leq T \leq 1400^\circ\text{C}$ and p_{O_2} ranges $10^{-12} \text{ atm} \leq p_{O_2} \leq 1 \text{ atm}$. Their electrical conductivity measurements showed two characteristic slopes in log conductivity vs. $1/T$ plots. At lower p_{O_2} values an electrical conductivity region characterized by a 2.1 eV slope was observed. Conductivity in this region was independent of changes in p_{O_2} and the charge carries were not clearly identified, although it was suggested that this region could as well be due to slowly migrating cation vacancies [17]. At higher p_{O_2} values, however, an activation energy of 1.6 eV was obtained, which was attributed to the motion of singly ionized oxygen interstitials.

It is difficult to explain these results and the present results in one framework. An alternative approach would be to assume two competitive mechanisms—with Frenkel disorder on the oxygen sublattice at lower temperatures, i.e. below 1400°C and Schottky disorder at higher temperatures. This type of disorder has been suggested in the past for silver halides [18].

If $\Delta H_S'' > \Delta H_F'$ ($\Delta H_F'$ was calculated to be 3.0 eV by Copeland and Swalin [1]) at lower temperatures and lower p_{O_2} values the conductivity will be due to cationic vacancies whose concentration is impurity controlled. At these p_{O_2} values a 2.1 eV slope corresponding to the migration of extrinsic vacancies was obtained. At higher p_{O_2} values $[O_i']$ predominates over the extrinsic vacancy concentration in controlling the conduction and a 1.6 eV slope was obtained. The impurity controlled $[V_{Sr}'']$ is not significantly changed at these temperatures and low p_{O_2} values due to incorporation of oxygen as O_i' and therefore the 2.1 eV conductivity region was found to be independent of p_{O_2} . The temperature dependence of conductivity and D under these conditions yield activation energies of 2.1 and 2.76 eV, which are quite close in view of the fact that O_i' may have contributed to some extent in the conduction.

At higher temperatures Schottky defects could control the defect structure. Also at these temperatures the vacancy concentration is controlled by oxygen pressure, so that both

higher activation energy of diffusion and oxygen partial pressure dependence of D was detected.

REFERENCES

1. COPELAND W. D. and SWALIN R. A., *J. Phys. Chem. Solids* **29**, 313 (1968).
2. BESSENT R. G., CAVENETT B. C. and HUNTER I. C., *J. Phys. Chem. Solids* **29**, 1523 (1968).
3. AUZINS P., ORTON J. W. and WERTZ J. E., in *Proc. 1st Int. Conf. on Paramagnetic Resonance* Jerusalem 1962, Vol. 1, p. 90, Academic Press, New York (1960).
4. MURARKA S. P., Ph. D. Thesis *Cation diffusion in BaO and SrO Crystals* University of Minnesota, June (1970).
5. GRUZIN P. L., *Dokl. Akad. Nauk SSSR* **86**, 289 (1952).
6. DeBRUIN H. J. and WATSON G. M., *USAEC Repts—ORNL—3526* (1963).
7. BLEULER E. and GOLDSMITH J., in *Experimental Neutronics*, Rinehart, New York (1952).
8. GUEST P. G., in *Numerical methods of Curve fitting*, Cambridge Univ. Press, London (1961).
9. SHEWMON P. G. in *Diffusion in Solids* McGraw-Hill, New York (1963).
10. LINDNER R. and PARFITT G. D., *J. Chem. Phys.* **26**, 182 (1957).
11. KUMAR V., and GUPTA Y. P., *J. Phys. Chem. Solids* **30**, 677 (1969).
12. GUPTA Y. P. and WEIRICK J., *J. Phys. Chem. Solids* **28**, 811 (1967).
13. KRÖGER F. A. and VINK H. J., *Solid State Physics* (Edited by F. Seitz and D. Turnbull), Vol. 3, p. 307 (1956).
14. From *Handbook of Chemistry and Physics*, Chemical Rubber Co. (1968–69).
15. LINDNER R., *Acta. Chem. Scand.* **6**, 468 (1952).
16. REDDINGTON R. W., *Phys. Rev.* **87**, 1066 (1952).
17. COPELAND W. D., Ph.D. Thesis *The Defect Structure of SrO* Univ. of Minnesota (1966).
18. TANNHAUSER D. S., *J. Phys. Chem. Solids* **5**, 224 (1958).

ON THE COLLOIDAL CENTERS IN IRRADIATED SODIUM CHLORIDE CRYSTALS*

S. V. PAPPU and K. A. McCARTHY

Department of Physics, Tufts University, Medford, Mass. 02155, U.S.A.

(Received 4 June 1970; in revised form 7 August 1970)

Abstract—A systematic investigation of the formation and properties of colloidal centers in irradiated sodium chloride crystals is made and the results are compared with our published results on additively colored crystals.

The main results and conclusions of this investigation are: (1) The colloid (designated as C_1 centers) evolution is not observed in a 'lightly' irradiated (i.e. corresponding to the fast stage of the coloration process) and thermally bleached crystal; it is observed when a 'heavily' irradiated (i.e. corresponding to the slow stage of the coloration process) crystal is thermally bleached at any temperature in the range 160–200°C. There is no evidence that the concentration of F centers *per se* has any influence on the C_1 center evolution. (2) The C_1 centers are found to be unstable under prolonged heating at any temperature in the range 160–200°C whereas in additively colored crystals they are stable up to about 250°C. The peak position of C_1 band is the same in both irradiated and additively colored crystals and it is about 560 nm. The half-width of C_1 band in irradiated crystals (about 0.5 eV) is larger than the half-width of C_1 band in additively colored crystals (about 0.18–0.32 eV). (3) The C_1 band in irradiated crystals is not affected by bleaching with either 560 nm light or F, M, R, N band peak light; it is affected, however, by white-light and u.v. light. In contrast, the C_1 band in additively colored crystals is unaffected by any of the aforementioned light. (4) The presence of slow stage F centers and the electron-hole recombination processes appear to play a significant role in the evolution of C_1 centers in irradiated crystals. (5) In view of the genetic relationship between F centers and C_1 centers, it is believed that our earlier proposed tentative mechanism for colloid evolution in additively colored crystals might be applicable in the case of colloid evolution in irradiated crystals.

1. INTRODUCTION

RECENTLY we have published the results of our investigations on the colloid evolution in additively colored NaCl crystals, and there we have proposed a tentative mechanism for the colloid formation in colored alkali halides [1]. The literature on colloidal centers in additively colored alkali halides is quite extensive [2–4], but the literature on colloids in irradiated crystals is rather meagre; in the few papers that have dealt with colloids in irradiated crystals the emphasis has been on the study of the changes in physical properties such as hardness, volume and density, etc. (see Refs. [2–9]). McLennan [10] has observed blue coloration in NaCl crystals colored by 40–50 KeV electron bombard-

ment and he has also observed electron diffraction lines of metallic sodium. Compton [11] has studied the influence of substitutional hydroxyl impurity on the colloid evolution in γ -irradiated NaCl crystals and recently Ikeda and Yoshida have studied the effect of divalent cation impurities on the formation and bleaching of colloids in electron irradiated NaCl crystals [12]. More recently ESR techniques have been used in detecting colloids in neutron irradiated LiF [13] and some azides [14]. However, it appears from the existing literature that there is the need for a systematic investigation of the formation and physical properties of colloidal centers in irradiated alkali halides. Encouraged by our studies on additively colored NaCl that have enabled us to propose a tentative mechanism for the colloid evolution in alkali halides, we continued a

*Supported in part by a grant (GP-15993) from the National Science Foundation.

systematic investigation of colloidal centers in irradiated NaCl crystals. The purpose of the present paper is to discuss our results on colloidal centers in irradiated NaCl crystals.

2. EXPERIMENTAL

Single crystals of 'pure' Optovac NaCl are irradiated with either γ -rays (from a 1.2 MeV, 1.1×10^6 R/hr, ^{60}Co source) or X-rays (40 KV, 32 mA X-rays from a General Electric XRD-5 unit fitted with a Machlett AEG-50S tungsten target). The same techniques [1, 15, 16], for irradiating, thermal annealing, and measuring the optical absorption of the crystals with a recording type Beckman DK-1A spectrophotometer are used in the present study.

A tungsten ribbon filament lamp (6V, 18A General Electric microscope illuminator) is used for bleaching the colored crystals with white light; the same lamp in association with appropriate Baird-Atomic interference filters is used for bleaching with monochromatic light. Filters with their transmission peaks at the following wavelengths have been used in the present study: (a) 460 nm corresponding to the *F* band peak. (b) 550 nm, 590 nm and 620 nm corresponding to the *R* band region. (c) 720 nm corresponding to the *M* band peak. (d) 820 nm corresponding to the *N* band peak. (e) 560 nm corresponding to the colloid band peak.

During the bleaching operation the crystal is located at a suitable distance from the light source to keep it at room temperature. Continuous u.v. light from a Nester type low pressure hydrogen discharge lamp fitted with a fused quartz window is used for u.v. light illumination.

We have made use of crystals colored into the 'first stage' (corresponding to the fast rising portion of the *F* center growth curve and a dose of about 10^6 R) as well as into the 'second stage' (corresponding to the slowly rising portion of the *F* center growth curve and a dose larger than 10^6 R); we designate

these crystals as 'lightly' irradiated and 'heavily' irradiated, respectively. The results obtained with γ -irradiated and x-irradiated crystals are the same.

3. RESULTS AND DISCUSSION

3.1 Thermal bleaching of irradiated crystals

A 'heavily' irradiated crystal (whose absorption showed the *F*, *M*, *R*, *N*, and *V* bands, curve 1 in Fig. 1(a) has turned violet in color (as revealed under transmitted light) upon isothermal bleaching at any temperature in the range 160–200°C, and the absorption of such a crystal at room temperature shows a single band with its peak located at about 560 nm (curve 2 in Fig. 1(a). During thermal bleaching, the *F*-aggregate bands *N*, *R*, *M* [17], are the first to disappear; the *F* band has decreased monotonically while the 560 nm band has evolved. Subsequently, with continued thermal bleaching the 560 nm band has disappeared, and the crystal becomes colorless. The line shape of the 560 nm band is insensitive to the temperature of the crystal (see Fig. 1(b) with measurements at room temperature and at liquid nitrogen temperature); this band is also resistant to bleaching with 560 nm light. In view of these properties, we have identified the centers responsible for the 560 nm band as small colloids [2, 3, 10], and hereafter we shall refer to the 560 nm band as *C*₁ band [1, 15, 16].

The *C*₁ centers in irradiated crystals are unstable under prolonged heating at any temperature in the range 160–200°C, whereas in additively-colored crystals they are stable up to about 250°C. The peak (560 nm) position of *C*₁ band in irradiated crystals is the same as in additively colored crystals. The half-width (about 0.5 eV) of *C*₁ band in irradiated crystals is larger than the half-width (about 0.18–0.32 eV) in additively colored crystals [1].

The evolution of *C*₁ centers is not observed in the following cases: (1) When a 'lightly' irradiated crystal is thermally bleached.

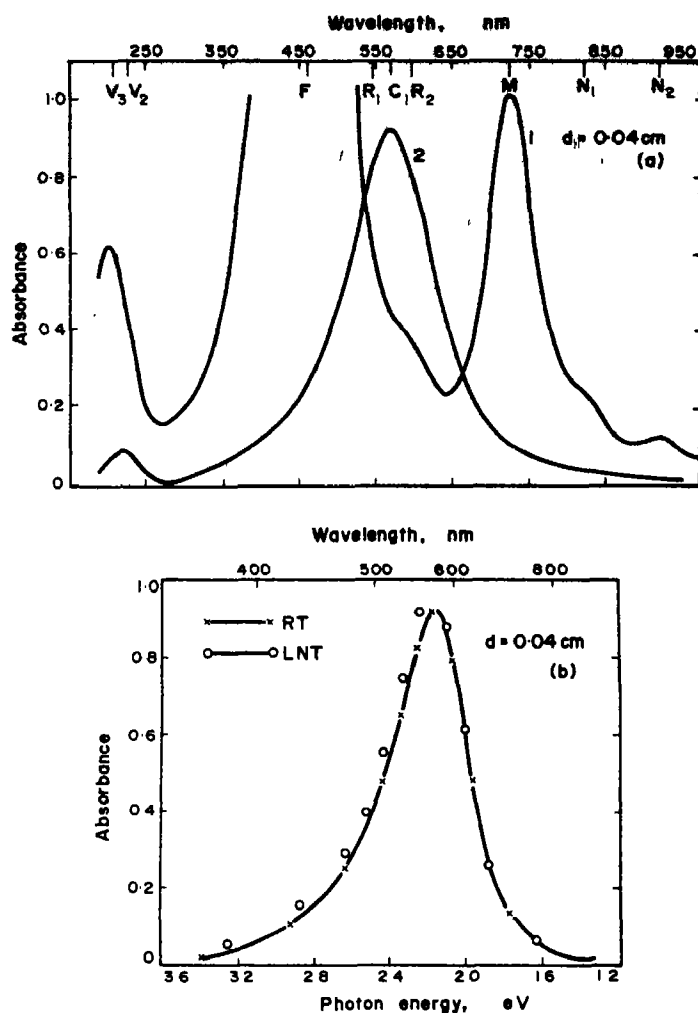


Fig. 1. Absorbance as a function of wavelength and photon energy for irradiated Sodium Chloride Crystals. (a) Curve 1—RT absorption of a 'heavily' γ -irradiated crystal (dose $4 \times 10^6 \text{ R}$). Showing the presence of F, M, R, N and V bands. Curve 2—RT absorption of the same crystal after heating it at 200° for about $2\frac{1}{2}$ hr, showing the presence of C_1 band. (b) (x---x) C_1 band recorded at RT. (\odot --- \odot) C_1 band recorded at LNT.

(2) When a crystal is *only* 'heavily' irradiated. We shall elaborate on these observations in the following section. It might be pointed out here that insofar as the second observation above is concerned, Compton[11] has made similar observation with γ -irradiated Optovac NaCl and also with some natural rock-salt crystals.

3.2 Effect of concentration of F centers and second stage coloration on the evolution of C_1 centers

It is reasonable to assume that in irradiated crystals, as in the case of additively colored crystals, the F centers diffuse and agglomerate upon heat treatment. We believe that our proposed mechanism for colloid evolution,

namely, that the neutral F centers diffuse via the vacancy mechanism and agglomerate to give rise to colloids[1]*, might be valid in the case of irradiated crystals also. Of course, we must recognize that in irradiated crystals there are the additional factors, such as lattice damage done during irradiation and electron-hole recombination, both of which might play a significant role in the formation of C_1 centers.

Almost two decades ago Westervelt[18] commented that in photochemically colored alkali halides, the colloid band can hardly be noticed during annealing unless the initial density of color centers is of the order of 10^{18} cm^{-3} . As mentioned above, we have not observed C_1 center evolution upon thermal bleaching of a 'lightly' irradiated crystal and C_1 center evolution is observed upon thermal bleaching of a 'heavily' irradiated crystal. These observations pose the interesting question: Is the evolution of C_1 centers dependent upon the concentration of F centers or on the existence of second (or slow) stage F centers (implying therefore the presence of lattice damage created by irradiation)? The results of a systematic investigation to answer this question follow.

In what follows, we use for convenience the notation $CV(t)$ to refer to a virgin crystal x -irradiated for a time (t) and $CR(t)$ to refer to a crystal re-irradiated with X-rays (after it has received a specified pre-treatment in its virgin state) for a time (t).

Three identical $CV(40)$ crystals† are

*It must be emphasized here that our proposed mechanism for colloid evolution is phenomenological and tentative[1]. It might be worth mentioning, however, that Dr. A. B. Scott has informed us recently in a private communication that they have found evidence for neutral F center diffusion by vacancy mechanism from their studies on M center formation by thermo-aggregation at moderate temperatures.

†The coloration in these crystals corresponds to the second (or slow) stage and the concentration of F centers in these crystals is estimated to be about 10^{18} cm^{-3} . It may be mentioned that in the heavily irradiated crystals there is appreciable optical absorption in the M , R , etc. band region (see Fig. 1(a) which we have not taken into account in the present discussion.

bleached at 200°C ; the bleaching behaviour of F and C_1 bands in these crystals is shown in Fig. 2 and the crystals are ultimately decolorized by prolonging the heating. They are then re-irradiated with the same intensity

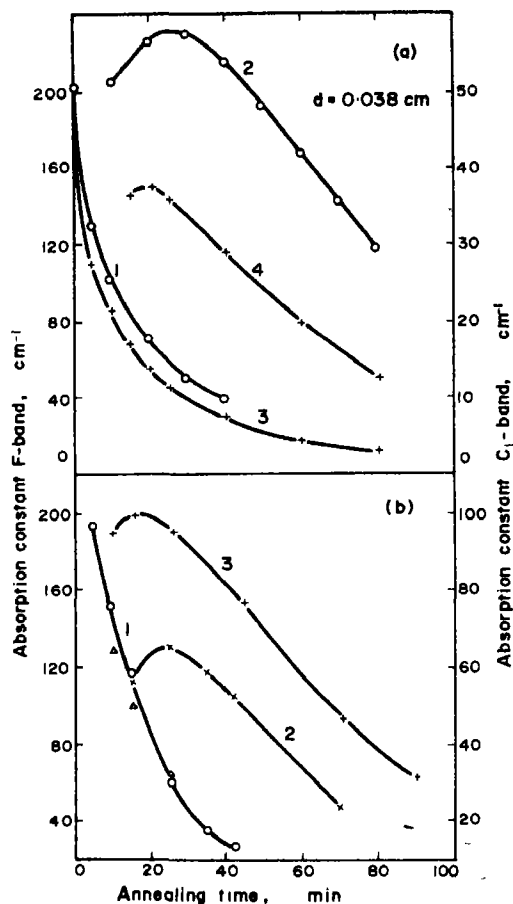


Fig. 2. Thermal bleaching of 'heavily' x -irradiated sodium chloride crystals. (a) Curve 1—Thermal bleaching at 200°C of F band in a virgin crystal irradiated for 40 min. Curve 2—Thermal bleaching at 200°C of C_1 band in the same crystal. Curve 3—Thermal bleaching at 200°C of F band in the above crystal after it has been decolorized and re-irradiated for 40 min with the same intensity X-rays. Curve 4—Thermal bleaching at 200°C of C_1 band in the 40 min re-irradiated crystal. (b) Curve 1 (open circles) Thermal bleaching at 200°C of F band in a virgin crystal irradiated for 40 min. Curve 2—Thermal bleaching at 200°C of C_1 band in the same crystal. Curve 1 (open triangles) Thermal bleaching at 200°C of F band in the above crystal after it has been decolorized and re-irradiated for 80 min with the same intensity X-rays. Curve 3—Thermal bleaching at 200°C of C_1 band in the 80 min re-irradiated crystal.

X-rays for periods of 5, 40 and 80 min, respectively, and following the above-mentioned notation we designate the three re-irradiated crystals as CR(5), CR(40) and CR(80).

It is observed that the *F* center concentration in CR(5) is almost equal to the *F* center concentration in CV(40); one concludes that the vacancies created by irradiation in CV(40) still exist in the crystal and that these vacancies have trapped photoelectrons during re-irradiation to become *F* centers rather easily[15]. Hence, we believe the coloration process in CR(5) could be considered as corresponding to the first (or fast) stage. Upon thermal bleaching at 200°C, we did not observe any *C*₁ center evolution in CR(5); but we did observe *C*₁ center formation in CR(40) and CR(80). In addition, it is found that: (1) The magnitude of *C*₁ band in CR(40) is less (compare curves 2 and 4 in Fig. 2a) and the magnitude of *C*₁ band in CR(80) is more (compare curves 2 and 3 in Fig. 2b) than the magnitude of *C*₁ band in the corresponding CV(40). (2) The bleaching curve for the *F* band in CR(40) is slightly below the bleaching curve for the *F* band in the corresponding CV(40). (2) The bleaching curve for the *F* band in CR(40) is slightly below the bleaching curve for the *F* band in the corresponding CV(40) (see curves 3 and 1 in Fig. 2a) and in the case of CR(80) the bleaching curve for *F* band follows the same path as the bleaching curve for *F* band in the corresponding CV(40) (see curve 1 in Fig. 2b).

At this stage, we believe it is appropriate to elaborate and stress the significance of the terms 'lightly' irradiated and 'heavily' irradiated used above. For this purpose we compare the results on CR(5) with the results on: (a) CV(5). (b) CR(40) and CR(80).

As mentioned above, the *F* center concentration in CR(5) is about 10^{18} cm^{-3} and no *C*₁ center evolution is observed upon thermally bleaching it at 200°C. In CV(5), the *F* center concentration is found to be about 10^{17} cm^{-3} and in it also no *C*₁ center evolution

is observed upon thermal bleaching. Insofar as the coloration process is concerned, both CR(5) and CV(5) have been treated identically, in that they both have been colored into the first (or fast) stage and the term 'lightly' irradiated is used to refer to coloration into the fast stage. In view of the pretreatment given to CR(5) and remembering the fact that vacancies created by irradiation in CV(40) could still exist in it even after thermal bleach, it is not difficult to reconcile with the difference in *F* center concentration between CR(5) and CV(5).

Now comparing the results on CR(5) with the results on CR(40) and CR(80): (a) It is observed that the variation in *F* center concentration from CR(5) to CR(40) and CR(80) is rather slow. (b) The values for *F* center concentration in CR(5), CR(40), CR(80), though different, are of the same order of magnitude (about 10^{18} cm^{-3}). In view of this behaviour, we believe that the coloration process in CR(40) and CR(80) corresponds to the slow stage and the term 'heavily' irradiated is used to refer to coloration into the slow stage. As mentioned above, *C*₁ center evolution is observed in CR(40) and CR(80), but it is not observed in CR(5).

The following conclusions may be drawn from the above discussion: (1) No *C*₁ center evolution is observed upon thermal bleaching of a 'lightly' irradiated crystal and the concentration of *F* centers *per se* is not a significantly important factor in the formation of *C*₁ centers. (2) *C*₁ center evolution could be observed in a 'heavily' irradiated (implying therefore the presence of lattice damage done during irradiation) and thermally bleached crystal. The work of Compton[11] indicated that mere heavy irradiation with no subsequent thermal bleaching is enough to produce *C*₁ centers, provided the crystals contain hydroxyl impurity.

There appears no reason to doubt the fact that in irradiated crystals, as in additively colored crystals, there exists a genetic relationship between *F* centers and *C*₁ centers.

It is apparent from the foregoing discussion, however, that the mere presence of a certain number of F centers is not enough to produce C_1 center evolution in irradiated crystals. We might mention here that this behaviour is not typical of irradiated crystals. For example, in additively colored crystals we have obtained the following results: (a) We have observed C_1 center evolution upon thermal bleaching at moderate temperatures of a crystal with an F center concentration of about 10^{16} cm^{-3} and whose absorption revealed only F type bands and no u.v. bands. (b) In a crystal with U centers, however, no C_1 center evolution could be observed with an F center concentration of about 10^{16} cm^{-3} or even more [1, 19, 20]. These results have been interpreted as an indication that in the presence of efficient competing reactions such as F to U , the reaction F to C_1 could be inhibited [19, 1]. In irradiated crystals, electron-hole recombination is probably the reaction which competes with the F to C_1 reaction. It appears that in 'lightly' irradiated crystals the electron-hole recombination is more efficient than in 'heavily' irradiated crystals and hence the inhibition of C_1 center evolution in 'lightly' irradiated crystals.

3.3 Optical and thermal bleaching of irradiated crystals

One of two identical 'heavily' irradiated crystals is heated at 200°C and the bleaching of F band is represented on curve 1 in Fig. 3(b) (open circles) and that of C_1 band is represented by curve 2 in Fig. 3(b). The second crystal is initially bleached with white light for about 20 hr during which the F, M , etc. bands have diminished and a prominent band at about 670 nm has appeared (curves 1 and 2 in Fig. 3(a)). The 670 nm band (referred to as C_2 band) has been discussed elsewhere [15, 16]. It is found necessary to heat the optically bleached crystal to observe the evolution of C_1 centers and during heating at 200°C , the residual F band and the C_2

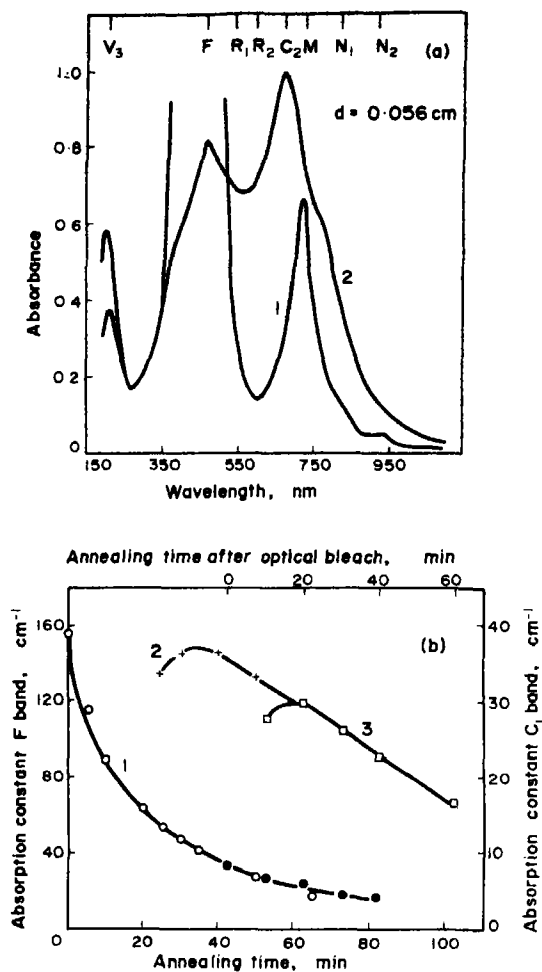


Fig. 3. Absorption as a function of wavelength and annealing time for irradiated sodium chloride crystals. (a) Curve 1—RT absorption of a 'heavily' γ -irradiated crystal. Curve 2—RT absorption of the same crystal after bleaching it with white light for about 20 hr. (b) Curve 1 (open circles) Thermal bleaching at 200°C of F band in the above 'heavily' γ -irradiated crystal. Curve 2—Thermal bleaching at 200°C of C_1 band in the above 'heavily' γ -irradiated crystal. Curve 1 (Full circles) Thermal bleaching at 200°C of F band in the above optically bleached crystal. Curve 2—Thermal bleaching at 200°C of C_1 band in the above optically bleached crystal.

band have decreased while the C_1 band has evolved (Fig. 3(b)). From these observations we conclude that the ultimate products in a 'heavily' irradiated and thermally bleached crystal are always C_1 centers, independent of

whether the electrons in the crystal are trapped to give rise to F, M, R , etc. bands or F, C_2 etc. bands. In the case of additively colored NaCl crystals, Etzel[20] has made a similar observation and there he found that the same C_1 band (he referred to the colloid band as the Δ band) is obtained from the thermal treatment of a crystal containing F, M, R, N centers (which are produced by exposing the crystal containing F centers to light from a tungsten lamp). In our studies, however, we have found that the magnitude of C_1 band developed in an as-irradiated crystal is greater than that developed in an irradiated and optically bleached crystal (compare curves 2 and 3 in Fig. 3(b)). The reason for this may be the fact that in irradiated crystals, unlike in additively colored crystals, the electron loss by electron-hole recombination is possible.

3.4 Some more properties of C_1 centers

It is known that the colloids in silver halides exhibit many of the characteristics attributed to colloids in alkali halides and it is an established fact that the colloid band in silver chloride could be selectively bleached with light of wavelength corresponding to the peak of the colloid band[2, 21]. Also, Gyulai[22] observed that the photoconductivity spectrum of a blue colored rock-salt crystal (obviously containing colloids) did not coincide with the optical absorption spectrum and that the absorption spectrum did not change by illumination of the crystal with light that provoked photo-conduction. We thought it worthwhile to investigate the effect of light of different wavelengths on the C_1 band in both additively colored and irradiated crystals.

The C_1 band, in additively colored crystals as well as in irradiated crystals, is found to be unaffected by light of the following wavelengths: (a) 560 nm light corresponding to the peak of C_1 band. (b) F, M, R etc. band light. Surprisingly, however, we have noticed that

the C_1 band in irradiated crystals is affected by white light. Once we have exposed the violet crystal (obtained by thermal bleaching of a 'heavily' irradiated crystal) inadvertently to room light for a number of hours and as a result the color of the crystal has become blue. Investigating further with white light from a tungsten lamp we have observed that the C_1 band in irradiated crystal is markedly affected, but the C_1 band in additively colored crystal is not affected at all. For example, during the white light illumination the height of C_1 band in irradiated crystal is diminished, its half-width is increased, its peak position is shifted to longer wavelengths and the area under the absorption curve is almost conserved during this change (Fig. 4). The color of the crystal is blue at this stage and when it is heated at 200°C for a few minutes the peak is shifted back to the original value of 560 nm (curve 4 in Fig. 4b) and the color of the crystal at this stage is violet again. Similar observations have been made by Fulda[23] with natural violet rock-salt crystals from Stassfurt-Kleinschierstedt and it is interesting to note that in some respects our synthetic crystals behave the same way as some of the natural crystals.

Further it is observed that the C_1 band in irradiated crystals is influenced by u.v. light in a manner similar to the white light case (Fig. 5), except for the important difference that with u.v. light a prominent F band (curves 2 and 3 in Fig. 5, the only temperature sensitive band) has appeared. The presence of the F band suggests that under u.v. light illumination the C_1 centers might be acting as a source of electrons and/or vacancies, a finding consistent with our earlier finding with x -irradiated violet crystals[15]. Again the u.v. light illumination has no effect at all on the C_1 band in additively colored crystals.

It is believed that more intensive and quantitative (probably considering the light intensity) investigations are needed before we can offer any explanation of the aforementioned phenomena.

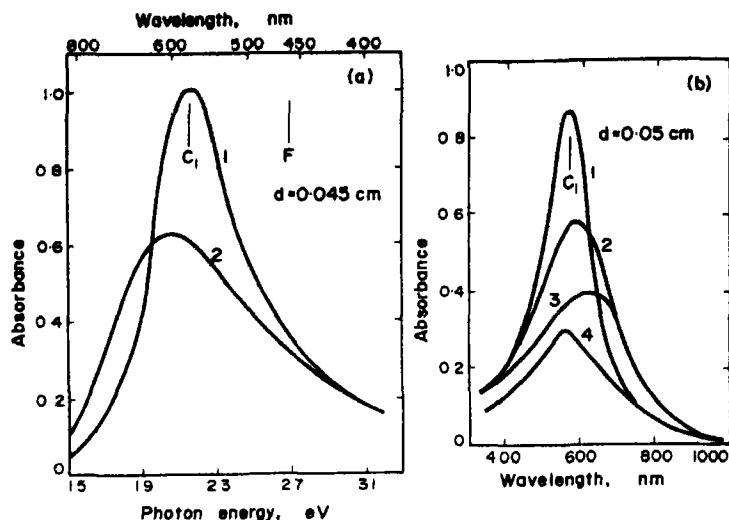


Fig. 4. Effect of white light illumination on a violet crystal (Showing C_1 band) obtained by heating a 'heavily' irradiated crystal at 200°C for a few hr. Curve 1—RT absorption of a violet crystal (showing C_1 band) obtained by heating a 'heavily' x -irradiated crystal. Curve 2—RT absorption of the same crystal after it has been illuminated with white light for about 24 hr. (b) Curve 1—RT absorption of a violet crystal (showing C_1 band) obtained by heating a 'heavily' γ -irradiated crystal. Curves 2 and 3—RT absorption of the above crystal after it has been illuminated with white light for about 24 hr and 94 hr respectively. Curve 4—RT absorption of the above optically bleached crystal after it has been heat-treated at 200°C for a few minutes.

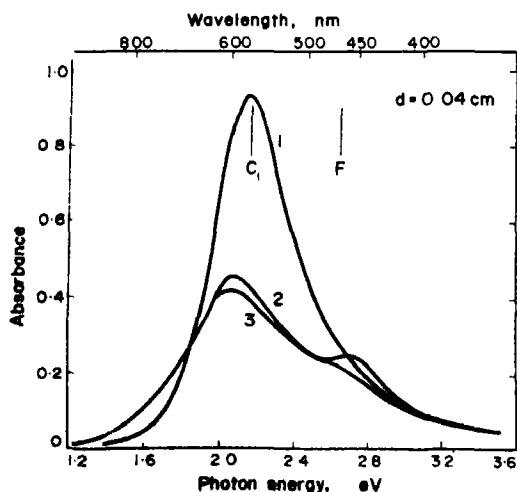


Fig. 5. Effect of u.v. light illumination on a violet crystal (showing C_1 band) obtained by heating a 'heavily' γ -irradiated crystal at 200°C for a few hours. Curve 1—RT absorption of the violet crystal showing C_1 band. Curve 2—LNT absorption of the above crystal after it has been illuminated with u.v. light for about 18 hr. Curve 3—RT absorption of the u.v. light bleached crystal.

4. CONCLUSIONS

1. The evolution of C_1 centers (i.e. colloids) is observed upon thermal bleaching of a 'heavily' irradiated NaCl crystal at any temperature in the range 160–200°C and the C_1 centers are unstable under prolonged heat treatment at any temperature in the range 160–200°C. In contrast, the C_1 centers in additively colored crystals are observed to be stable up to about 250°C [1].

The peak position of C_1 band is the same in both irradiated and additively colored crystals and it is 560 nm. The half-width of C_1 band in irradiated crystals (about 0.5 eV) is larger than the half-width of C_1 band in additively colored crystals (about 0.18–0.32 eV) [1].

2. The C_1 center evolution is not observed upon thermal bleaching of a 'lightly' irradiated crystal (i.e. crystal colored into the fast stage), but it is observed upon thermal bleaching of a

'heavily' irradiated crystal (i.e. crystal colored into the slow stage). The F center concentration *per se* does not appear to be a significantly important factor in the evolution of C_1 centers.

3. The C_1 band in irradiated crystals is not affected by either 560 nm light or light of wavelength corresponding to the peak position of F, R, M , etc. bands. But it is affected by white light as well as u.v. light. In contrast, none of these have any effect on the C_1 band in additively colored crystals.

4. Our proposed tentative mechanism for the colloid evolution in additively colored crystals (1) (namely, that neutral F centers diffuse via the vacancy mechanism to agglomerate and when the agglomerate of F centers attains a critical size the F center electrons enter the valence levels of the alkali ions to form alkali metal atoms) might be valid in the case of irradiated crystals also.

It appears that the presence of second (or slow) stage F centers (implying therefore the presence of lattice damage done by irradiation) and the electron-hole recombination process have significant influence on the C_1 center formation in irradiated crystals.

REFERENCES

1. SASTRY R. V., *J. phys. Soc. Japan*, **26**, 73 (1969).
2. COMPTON W. D. and SCHULMAN J. H., *Color Centers in Solids*, Macmillan, New York (1962).
3. SEITZ F., *Rev. mod. Phys.*, **26**, 7 (1954).
4. PRZIBRAM K., *Irradiation Colours and Luminescence*, Pergamon Press, London (1956).
5. MERRIAM M. F., WIEGAND D. A. and SMOLUCHOWSKI R., *J. Phys. Chem. Solids*, **25**, 273 (1964).
6. KOBAYASHI K., *Phys. Rev.*, **102**, 348 (1956); **107**, 41 (1957).
7. CUYPERS R. and AMELINCKX S., *Acta. Metall.*, **8**, 551 (1960).
8. AERTS E., AMELINCKX S. and DEKEYSER W., *Acta. Metall.*, **7**, 29 (1959).
9. RAO K. V. and SHARMA J., *Physica*, **28**, 653 (1962).
10. McLENNAN D. E., *Can. J. Phys.*, **29**, 122 (1951).
11. COMPTON W. D., *Phys. Rev.*, **107**, 1271 (1957).
12. IKEDA T. and YOSHIDA S., *J. phys. Soc. Japan*, **22**, 138 (1967).
13. KAPLAN R. and BRAY P. J., *Phys. Rev.*, **129**, 1919 (1963).
14. McMILLAN R. C., KING G. J., MILLER B. S. and CARLSON F. F., *J. Phys. Chem. Solids*, **23**, 1379 (1962).
15. SASTRY P. V. and MCCARTHY K. A., *Phys. Status Solidi*, **10**, 585 (1965).
16. SASTRY P. V. and MCCARTHY K. A., *Phys. Rev. Lett.*, **12**, 690 (1964).
17. COMPTON W. D. and RABIN H., *Solid State Physics* (Edited by F. Seitz and D. Turnbull) Vol. **16**, p. 121 (1964).
18. WESTERVELT D. R., Comment made in the discussion part of the paper by Scott *et al.*, *J. Phys. Chem.*, **57**, 757 (1953).
19. SASTRY P. V., *Phys. Status Solidi*, **18**, K127 (1966).
20. ETZEL H. W., *Phys. Rev.*, **118**, 1150 (1960).
21. BROWN F. C. and WAINFAN N., *Phys. Rev.*, **105**, 93 (1957).
22. GYULAI Z., *Z. Phys.*, **35**, 411 (1935b).
23. See Ref. [4], p. 145.

CALORIMETRIC EVIDENCE OF MOLECULAR HYDROGEN IN IRRADIATED LITHIUM HYDRIDE*

E. CATALANO and H. R. LEIDER

c/o Technical Information Department, Lawrence Radiation Laboratory, University of California
Livermore, Calif. 94550, U.S.A.

(Received 23 July 1970)

Abstract—A calorimetric measurement employing the thermal arrest technique has independently confirmed the presence of molecular hydrogen in irradiated LiH previously detected by pulsed nuclear magnetic resonance (NMR). The melting endotherm of the hydrogen indicates adsorption of hydrogen on the surfaces of the bubbles containing the hydrogen.

1. INTRODUCTION

IRRADIATED LiH decomposes considerably into lithium metal and H_2 gas which remains trapped in the lattice. This occurs whether the radiation source is external, such as γ -irradiation of LiH[1-4], or internal, as in LiH containing 3H [1, 2].

The hydrogen that is produced has properties expected of the gaseous molecular form [2, 3]. In particular, an ortho-para transition has been observed[3] which positively indicates diatomic hydrogen. Furthermore, no paramagnetism has been detected in irradiated LiH by electron spin resonance except that attributed to either colloidal lithium metal or F -centers, even when irradiated at liquid nitrogen temperature[1]. If irradiation produced atomic hydrogen, trapped somehow in the lattice, paramagnetism due to the resulting atoms would probably be detectable. This is also indirect evidence that the 'free' hydrogen present is diatomic in nature.

The V -center absorption spectrum in irradiated LiH has been attributed to molecular hydrogen[5]. More direct evidence that hydrogen is present in gaseous form is the recent observation of cubic voids in irradiated

LiH by electron microscopy[6]. These voids are predominantly oriented with their walls parallel to the [100] crystallographic directions. Upon observation of these voids, an NMR experiment was performed on an irradiated single crystal. The object was to observe the angular variation of the spin-echo T_2 -relaxation time of the gaseous hydrogen as a function of crystal orientation relative to the applied magnetic field[7]. The results are entirely consistent with the existence of hydrogen gas trapped in a cubic bubble. The variation of the NMR relaxation time with crystal orientation agrees with a model where loss of phase coherence of the hydrogen magnetic moments is due to interactions with the bubble walls.

The purpose of this work is to provide independent calorimetric evidence of molecular hydrogen gas trapped in irradiated LiH. The experiment measures the thermal arrest caused by fusion of molecular hydrogen trapped in crystals of γ -irradiated LiH for which motionally narrowed NMR measurements are available.

2. EXPERIMENTAL

LiH crystals were prepared by directly combining the elements in a manner similar to that of Pretzel *et al.*[8]. The lithium metal

*Work performed under the auspices of the U.S. Atomic Energy Commission.

used was high purity reactor grade (Foote Mineral Company). The hydrogen was 99.999 per cent pure (Matheson Gas Products). Typical spectroscopic analyses of the resulting LiH showed the following impurities: 60–150 ppm sodium, 3–90 ppm aluminum, calcium and copper, and 3 ppm iron. Oxygen and carbon content were measured by (γ , n) activation analyses and proved to be 1000–5000 ppm and 250 ppm, respectively. LiH was always handled under vacuum or in an atmosphere of carefully purified argon.

The LiH was irradiated with ^{60}Co γ -rays [3] at 160°C to a total dose of 1.44×10^{10} rad. The density of the irradiated material was 0.638 g/cm³ while the unirradiated crystals had a density of 0.776 g/cm³; the material therefore swelled ($\Delta V/V_0$) = 21.6 per cent. The weight of the sample used in these measurements was 2.8713 g. Pulsed NMR measurements of this sample [3] showed that it contained 0.022 mole of hydrogen and 0.036 moles of lithium metal. Determination of the stored energy release on thermal anneal [4] gave 314 cal/g, which agrees with the NMR determination. After irradiation this material was severely fragmented and it was impossible to determine the size of the hydrogen bubbles by electron microscopy. However, from a model relating the temperature of release of the stored energy to bubble size and concentration [4], an average size of 415 Å and a bubble concentration of 2.5×10^{18} cm⁻³ can be inferred.

To make the calorimetric measurement, the irradiated LiH was sealed in a cylindrical can made of platinum-10 per cent rhodium of 0.5 mm thickness. The container was 3.7 cm long and 2.5 cm in dia. The lid, which had a 1-mm hole in the center, was set into place and the container press-fitted into a massive copper heat sink. The argon atmosphere box was then evacuated to 10^{-7} torr and the top electron beam-welded to the can. The sample container was next back-filled with argon and was transferred to a small vacuum chamber, pumped out again, and then back-filled with

purified helium gas which acted as the heat exchange fluid in the calorimeter. At this point, the 1-mm hole in the can was quickly sealed with low melting solder.

The sample cannister was then wound with manganin resistance wire ($\sim 1500 \Omega$). A Honeywell germanium resistance thermometer calibrated between 4.2° and 100°K and optimized for the 4.2°–20°K range was glued into a copper sleeve with glyptal varnish. The sleeve was then attached with varnish to the flat surface of the capsule. To provide a radiation shield, aluminum foil was wrapped around the assembly and varnished.

The calorimeter cryostat used for these measurements is a conventional isothermal calorimeter equipped with a mechanical heat switch for low temperature measurements. The encapsulated sample was set in a copper holder suspended by nylon threads. The total mass of platinum and copper is much greater than the mass of sample. Therefore, while the heat of fusion expected for the amount of hydrogen in the sample was large, a specific heat measurement would have been quite inaccurate. A thermal arrest measurement is adequate for detection and estimation of the amount of molecular hydrogen.

Data were acquired primarily by computer-controlled digital techniques to be described in detail at a later date. The primary measuring instrument is a high precision digital voltmeter. Thermometric data can be-acquired and processed on-line over a large range of sampling rates limited only by the characteristics of the digital voltmeter. The data was treated by the Forsythe method [9] adapted by Catalano *et al.* [10] to small computers. Thermometric data were obtained at 15-sec intervals for a series of different values of constant power input.

The sample was first cooled to 77°K over a period of about 18 hr, and then cooled to 4.2°K in approximately 10 min. Six series of thermal arrest measurements were obtained over an interval of about four days. These were taken with heating rates that varied from

10^{-6} W to 2.6×10^{-3} W. The sample environment was held at 4.2°K . Sample temperature was not allowed to rise above 30°K during the measurements. Temperatures were precise to several tenths of a per cent. Temperature differences were recorded to a millidegree, although the fitting procedure is accurate to only a few millidegrees.

3. RESULTS AND DISCUSSION

Figure 1 presents the results of two thermal arrest runs obtained with a power input of 2.6×10^{-3} W. Data were taken at 15-sec intervals. The points show the temperature rise for power input as a function of temperature. All six thermal arrest runs exhibited

sample. There is also a large spread in temperature for the endothermic heat effect. We attribute this heat effect to the fusion of molecular hydrogen. The triple point of normal bulk hydrogen is 13.96°K ; one would expect the maximum of the heat effect to appear at this or a slightly higher temperature since there are thermal lags associated with any thermal arrest measurement. The maximum in the heat effect is $\sim 13.65^\circ\text{K}$ and is not found to be markedly dependent on the power levels used. Furthermore, the onset of the thermal effect is at an unusually low temperature, 12.65°K . These effects are outside experimental errors and cannot be due to the ortho-para conversion. The triple

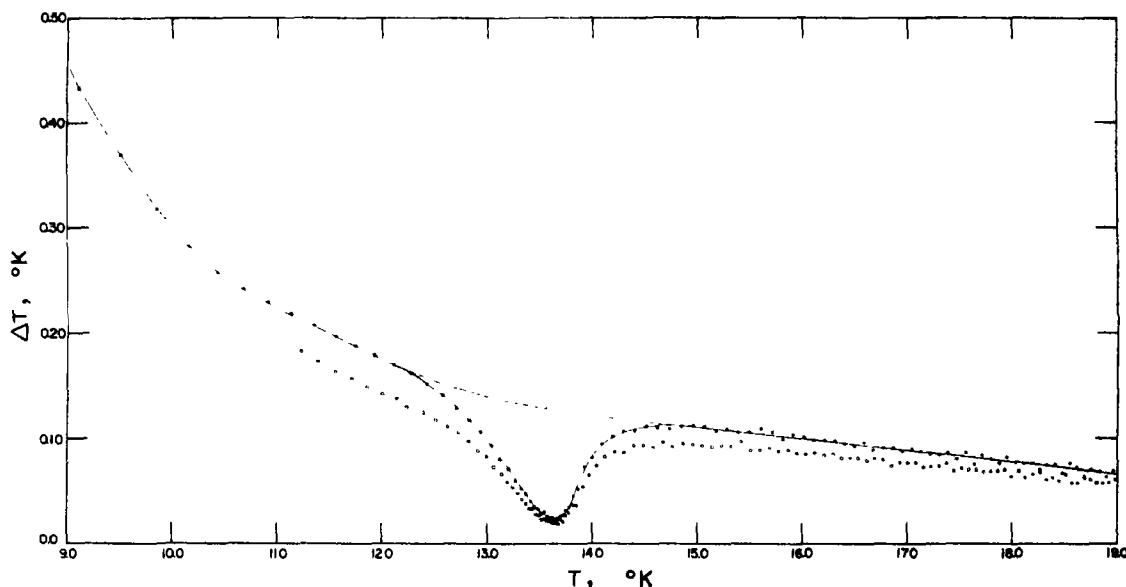


Fig. 1. Thermal arrest of irradiated LiH. Response of sample at constant power input with sampling at 15-sec intervals (see text).

the endothermic effect between 12.15° and 14.75°K . In Fig. 1, the solid circle points describe a run in which the sample had been cold for four days; the open circles represent a run in which the sample had been cold for two days. All other conditions were identical. It is evident that the magnitude of the heat effect depends on the thermal history of the

point for the ortho-para equilibrium mixture characteristic of 20.4°K is at 13.81°K . The rate for the ortho-para hydrogen conversion observed at 77°K in similar irradiated LiH [3] is much too slow for detection in this experiment.

An estimate of the enthalpy due to fusion of the trapped molecular hydrogen was made

from the run illustrated by the solid circles in Fig. 1. The dashed line is the assumed background thermogram. The enthalpy represented by the thermal anomaly in this run is 0.163 cal, indicating 0.006 mole of normal molecular hydrogen for a heat of fusion of 28.0 cal/mole. This heat accounts for only 26 per cent of the hydrogen seen by pulsed NMR measurements at room temperature. The NMR measurements were repeated after these thermal arrest measurements and showed the sample to be unchanged. This precludes the possibility of accidental loss of hydrogen during sample handling. We cannot measure the heat of vaporization as the system comprises an ensemble of constant volume systems (bubbles) for which the temperature of the liquid-vapor transition is not invariant.

A plausible explanation of our observations can be made if the hydrogen is adsorbed on the walls of the bubbles. If all bubbles are 415 Å on edge and the total volume increase resulting from irradiation is entirely due to formation of hydrogen bubbles[2, 3], then the sample will contain 1.13×10^{16} such bubbles with a surface area of $\sim 1.2 \times 10^6 \text{ cm}^2$. Assuming the hydrogen is uniformly distributed throughout the bubbles, adsorption will form about 4–16 monolayers from 0.022 mole of hydrogen, depending on the value taken for the number of molecules per cm^2 [11]. This estimate agrees with observations on similar systems discussed below.

For a few adsorbed monolayers of a gas, it has been found that the temperature at which the heat capacity anomaly occurs due to melting is substantially lower than the normal value[12–15]. Furthermore, the enthalpy is smaller than for the bulk. No heat effect from melting was seen for a single adsorbed monolayer[14]. The specific cases of argon and nitrogen on rutile were studied; the heat capacity and the melting temperature were determined as a function of the thickness of the adsorbed gas layer[12–15]. The heat capacity curves for the melting region in

Ref.[14] suggest by analogy that we are probably observing the melting of a few monolayers of hydrogen adsorbed on the bubble walls.

4. CONCLUSIONS

These thermal arrest measurements have shown that molecular hydrogen is present in irradiated LiH. The unusually low temperature of the thermal anomaly due to melting indicates adsorption of hydrogen on internal surfaces in thicknesses of a few monolayers. The temperature at which the peak of the melting endotherm occurs and its temperature range implies that the effective number of monolayers is less than 5, by analogy to the case of nitrogen on rutile [14]. The high temperature at which this thermal effect disappears is probably due to thermal lag inherent in this type of measurement.

Acknowledgement—We wish to thank E. W. Wrenn and J. C. English for their assistance in making the measurements. We also wish to thank D. Helsper for welding the sample capsule.

REFERENCES

1. PRETZEL F. E., LEWIS W. B., SZKLART E. G. and VIER D. T., *J. Appl. Phys.* **33**, (Suppl.), 510 (1962); The unabridged version is *Radiation Effects on Lithium Hydride*, Los Alamos Scientific Lab., N. M., Report LA-2463 (1961).
2. SOUERS P. C., JOLLY T. A. and CLINE C. F., *J. Phys. Chem. Solids* **28**, 1717 (1967).
3. SOUERS P. C., BLAKE T. S., PENPRAZE R. M. and CLINE C. F., *J. Phys. Chem. Solids* **30**, 2469 (1969); P. C. SOUERS, IMAI T., BLAKE T. S., PENPRAZE R. M. and LEIDER H. R., *J. Phys. Chem. Solids* **31**, 1461 (1970).
4. NEWKIRK H. W. and LEIDER H. R., *J. Phys. Chem. Solids* **31**, 1221 (1970).
5. PRETZEL F. E. and RUSHING C. C., *J. Phys. Chem. Solids* **17**, 232 (1961).
6. IMAI T., *Phil. Mag.* **21**, 281 (1970).
7. SOUERS P. C., BLAKE T. S. and PENPRAZE R. M., *Phil. Mag.* **21**, 287 (1970).
8. PRETZEL F. E., RUPERT G. N., MADER C. L., STORMS E. K., GRITTON G. V. and RUSHING C. C., *J. Phys. Chem. Solids* **16**, 10 (1960).
9. FORSYTH G. E., *J. Soc. Ind. Appl. Math* **5**, 74 (1957).
10. CATALANO E., SHROYER B. L. and ENGLISH J. C., *Rev. Scient. Instrum.* **41**, 1663 (1970).

11. DUSHMAN S., *Vacuum Technique*, 2nd ed., pp. 32-39. John Wiley, New York (1962).
12. YOUNG D. M. and CROWELL A. D., *Physical Adsorption of Gases*, pp. 98-101. Butterworths, Washington (1962).
13. MORRISON J. A. and DRAIN L. E., *J. chem. Phys.* **19**, 1063 (1951).
14. MORRISON J. A., DRAIN L. E. and DUGDALE J. S., *Can. J. Chem.* **30**, 890 (1952).
15. DENNIS K. L., PACE E. L. and BAUGHMAN C. S., *J. Am. Chem. Soc.* **75**, 3269 (1953).

LATTICE THEORY OF ALKALI HALIDE SOLID SOLUTIONS—III. PRESSURE DEPENDENCE OF SOLID SOLUBILITY AND SPINODAL DECOMPOSITION*

D. L. FANCHER†

Materials Research Laboratory, The Pennsylvania State University,
University Park, Penna. 16802, U.S.A.

and

G. R. BARSCH

Materials Research Laboratory and Department of Physics, The Pennsylvania State University,
University Park, Penna. 16802, U.S.A.

(Received 30 April 1970)

Abstract—The solid solubility and the chemical spinodal have been calculated for several pressures from an extended theory of the authors based on the substitutional defect model of Dick and Das. The systems considered are LiBr–LiI, NaBr–NaI, KBr–KI, RbBr–RbI, and NaCl–KCl. The maxima of the exsolution dome, of the chemical spinodal and of the coherent spinodal are found to increase and to become narrowed with increasing pressure. For three systems the temperature difference between the chemical and the coherent spinodal decreases with increasing pressure, for one system it increases, and for the remaining system it increases initially with increasing pressure and decreases after passing through a maximum. The direction in which spinodal decomposition should occur is found to be dependent on pressure for several systems.

1. INTRODUCTION

IN TWO previous papers [1, 2] (referred to as I and II) the authors have investigated the heat of formation, the entropy of mixing and the solid solubility of alkali halide solid solutions on the basis of an extension of the substitutional defect model of Dick and Das [3]. While this earlier work was restricted to zero pressure, it is the objective of the present paper to extend the previous work to investigate theoretically the pressure dependence of solid solubility for several alkali halides and to determine the effect of pressure on spinodal decomposition.

A study of solid solubility at high pressure is relevant for several reasons. First, it is of interest to investigate whether the effect of thermal motion and of external pressure

act, as is usual for many physico-chemical properties in opposite directions. In the absence of any experimental data for alkali halides this question cannot be answered beforehand because the elastic shear constants determine the solid solubility curve and the coherent spinodal via the vibrational contribution to the entropy of mixing, and through the strain term, respectively, and because for some alkali halides the pressure derivative of the shear constant c_{44} is negative (See e.g. the compilation in [4]).

The pressure dependence of solid solubility is also of interest in geophysics. For example, in determining the composition of the core of the earth the solubility of the main constituent of the mantle, olivine $((\text{Mg}, \text{Fe})_2\text{SiO}_4)$ in the iron-rich core must be known in the megabar range [5]. Although the two systems are very different one would hope that the present work on alkali halides may serve as a first step towards the study of more complicated systems.

*This work was supported by the National Science Foundation.

†Present Address: Department of Physics, Kansas Wesleyan University, Salina, Kansas 67401, USA.

Finally, the decomposition of solid solutions, especially through the spinodal mechanism, has recently been utilized for the preparation of multiphase and high-strength materials [6-8], and it is conceivable that the application of pressure as an additional parameter will be useful for materials engineering.

Spinodal decomposition was first predicted from thermodynamic principles by Gibbs[9]. It consists of a mechanism for the decomposition of solid solutions which occurs in that region of the p - T - x phase diagram in which the second derivative of the Gibbs free energy with respect to composition is negative. While for metals[10], glasses[11] and ionic materials [12] the occurrence of spinodal decomposition has been confirmed experimentally, it is still uncertain, however, whether or not observed phase separations in alkali halides are due to the spinodal mechanism[13-15]. This lack of understanding has in part motivated the present study. It is hoped that the theoretical results obtained will stimulate further experimental work in this area. Perhaps a crucial experiment may be designed by introducing pressure as an additional variable, or the interpretation of new experimental data may be facilitated, so that it will be possible to determine whether the spinodal mechanism is active or not.

2. METHOD AND ASSUMPTIONS

The solid solubility curves at non-zero pressure are determined by the free energy function

$$G^* = Q_F - T\Delta S + p(V_{SS} - V_M) \quad (2.1)$$

where Q_F is the heat of formation, ΔS is the total entropy of solution, V_{SS} and V_M are the volumes of the solid solution and mechanical mixture, respectively, and p and T are the pressure and temperature respectively. All extensive quantities will be referred to one mole throughout this paper. The solid solubility curve can be calculated from the free energy function (2.1) by the method of equal tangents[16].

The chemical spinodal is the boundary between the two regions in which the crystal should decompose theoretically either by classical nucleation (metastable region) or by spinodal decomposition, commonly referred to as nonclassical nucleation (unstable region). The chemical spinodal is defined as the locus of points for which

$$\frac{\partial^2 G^*}{\partial x^2} = 0 \quad (2.2)$$

where G^* is the free energy function and x represents the composition in mole fractions of one of the components. Cahn[17, 18] has introduced another spinodal, called the coherent spinodal, which is defined by

$$\frac{\partial^2 G^*}{\partial x^2} + W = 0 \quad (2.3)$$

and which should describe the spinodal observed experimentally. The 'strain term' W takes into account the elastic strain associated with the decomposition. This strain term is positive and causes a lowering of the chemical spinodal, i.e. it enhances the stability of the solid solution by increasing the metastable region and decreasing the unstable region. For cubic crystals the strain term is given by[18]

$$W = 2\eta^2 Y \quad (2.4)$$

where $\eta = (1/r)(\partial r/\partial x)$ is the derivative of the nearest neighbor distance in the solid solution with respect to composition, and Y is an orientation dependent elastic coefficient. Spinodal decomposition occurs in the direction for which the coefficient Y has a minimum, which corresponds to $\langle 100 \rangle$ for $\alpha < 0$ and $\langle 111 \rangle$ for $\alpha > 0$ where

$$\alpha = \frac{c_{11} - c_{12} - 2c_{44}}{2c_{44}} \quad (2.5)$$

is the elastic anisotropy factor. The corre-

sponding minimum values of the coefficient Y are [18]

$$Y = \begin{cases} (C_{11} + 2c_{12})(c_{11} - c_{12})/c_{11} & (\alpha < 0) \\ 6(c_{11} + 2c_{12})c_{44}/(c_{11} + 2c_{12} + 4c_{44}) & (\alpha > 0) \end{cases} \quad (2.6)$$

The temperature difference $\Delta T = T_s - T_{s'}$ between the chemical and coherent spinodals (T_s and $T_{s'}$, respectively) may be according to Hilliard [19] approximately written as

$$\Delta T = T_s - T_{s'} = -2\eta^2 Y / \left(\frac{\partial^2 \Delta S}{\partial x^2} \right) \quad (2.7)$$

If ΔS is assumed to consist of the entropy of ideal mixing only [20, 2] equation (2.7) becomes

$$\Delta T = \frac{2\eta^2 Y}{kN_0} x(1-x) \quad (2.8)$$

where k is Boltzmann's constant and N_0 is the number of molecules per unit volume.

The composition dependence of the heat of formation and of the solid solubility were calculated for several pressures in the same manner as in I and II, but with (2.1) as free energy function, and with Q_F , ΔS , V_{ss} and V_M occurring in (2.1) dependent on pressure. As in I and II, the heat of formation has been assumed to be independent of temperature. The pressure dependence of Q_F results from the pressure dependence of the nearest neighbor distance and of the electronic polarizabilities. The pressure dependence of the nearest neighbor distance was calculated from the isothermal bulk modulus and its isothermal pressure derivative obtained from the data presented in Table 1 by using Murnaghan's equation of state [21]. The pressure dependence of the polarizabilities was calculated from the available experimental data of the pressure dependence of the refractive index [30-32] by assuming that the electronic polarizabilities of cations and anions are additive.

Table 1. Isothermal elastic constants (in 10^{11} dynes/cm²) and their isothermal pressure derivatives for several alkali halides

	c^T	c_{12}^T	c_{44}	$(\partial c_{11}^T / \partial p)_T$	$(\partial c_{12}^T / \partial p)_T$	$(\partial c_{44} / \partial p)_T$
LiBr	3.74[a]	1.67	1.93	8.02[h]	2.20	0.19
LiI	2.64[b]	0.78	1.35	9.60[h]	2.07	0.09
NaBr	3.82[c]	0.958	1.015	11.04[i]	1.80	0.423
NaI	2.93[d]	0.807	0.742	11.85[d]	2.36	0.584
KBr	3.35[e]	0.450	0.508	13.03[j]	1.66	-0.328
KI	2.62[e]	0.344	0.369	13.93[j]	2.36	-0.241
RbBr	3.10[f]	0.404	0.383	13.43[f]	1.38	-0.54
RbI	2.52[f]	0.322	0.279	13.64[f]	1.45	-0.50
NaCl	4.77[g]	1.13	1.27	11.74[g]	2.16	0.37
KCl	3.97[g]	0.615	0.630	12.89[g]	1.67	-0.385

[a] Calculated from adiabatic data of Haussühl [22].

[b] Calculated from adiabatic data of Haussühl [23].

[c] Koliwad *et al.* [24].

[d] Barsch and Shull [25].

[e] Reddy and Ruoff [26].

[f] Chang and Barsch [27].

[g] Bartels and Schuele [28].

[h] Theoretical data by Ghate [29] (Table 4, repulsive parameter $b = 0.333$).

[i] Calculated from the isothermal derivatives of the adiabatic elastic constants of Koliwad *et al.* [24].

[j] Calculated from the isothermal derivatives of the adiabatic elastic constants of Reddy and Ruoff [26].

The volume of the solid solution, V_{ss} , is calculated by assuming Vegard's law for the nearest neighbor distance of the solid solution, i.e. a linear variation with composition. Even though the individual volumes, V_{ss} and V_M , are temperature-dependent, the difference ($V_{ss} - V_M$) is assumed to be independent of temperature*, but dependent on pressure according to Murnaghan's equation of state. Below 100 kbar, the work term, $p(V_{ss} - V_M)$, in (2.1) amounts only to less than about 10 per cent of the heat of formation, so that neglecting the temperature dependence of this term is not critical.

The total entropy of solution consists of two parts, the entropy of ideal mixing, ΔS^{id} , and the vibrational contribution, ΔS^{vib} , as explained in II. The term, ΔS^{vib} , is assumed to be independent of temperature. Calculations were made to test this assumption about ΔS^{vib} and it was found that ΔS^{vib} was essentially independent of temperature. The pressure dependence of the vibrational contribution to the entropy was, however, taken into account through the pressure dependence of the constant A occurring in the formula for the composition dependence of the elastic constant c_{11} II:

$$\Delta c_{11} = Ax(1-x) \quad (2.9)$$

Δc_{11} is the difference between the elastic constant of the solid solution and that of the

solid mixture, and A depends on the molar volumes and the bulk moduli of the two end members of the solid solution series (equations (2.8) and (2.13) of II), which are here considered as pressure-dependent according to Murnaghan's equation of state, and according to the linear pressure dependence of the elastic constants, respectively. For the alkali halide systems contained in Table 1 the constant A and the relative deviation $\Delta c_{11}/c_{11}^{Mtz}$ of the elastic constant c_{11} in the solid solution from the value in the solid mixture are for a composition $x = 0.5$ presented in Table 2 for several pressures.

3. RESULTS AND DISCUSSION

Solid solubility curves and chemical spinodals were calculated for five alkali halide systems for several pressures from

Table 2. The quantity A (in 10^{11} dynes/cm²) defined in equation (2.9) and the predicted relative deviation (in per cent) of the elastic constant c_{11} for the solid solution from the value for the solid mixture at $T = 300^\circ\text{K}$ and at the composition $x = 0.5$ for several pressures p (in kbar)

System	p	A	$\Delta c_{11}(0.5)/c_{11}^{Mtz}(0.5)$
LiBr-LiI	0	-2.514	-19.7
	50	-0.887	-2.9
	100	-0.439	-0.91
NaBr-NaI	0	-0.587	-4.3
	5	-0.476	-3.01
	10	-0.390	-2.16
	50	-0.055	-0.15
KBr-KI	100	+0.139	+0.23
	0	-0.444	-3.7
	10	-0.233	-1.3
RbBr-RbI	20	-0.124	-0.55
	0	-0.314	-2.8
	2	-0.293	-2.4
NaCl-KCl	4	-0.275	-2.1
	0	-1.225	-7.0
	10	-1.048	-4.7
	20	-0.935	-3.4

*As the reviewer has kindly suggested it would have been easy to take into account the temperature dependence of the term $\Delta V = V_{ss} - V_M$ in an approximate manner by assuming, e.g. the ratio $\Delta V/\bar{V}$ to be temperature independent, so that ΔV has the same thermal expansion as $\bar{V} = (V_{ss} + V_M)/2$. This improvement would have increased the work term $p\Delta V$ by about 5 to 10 per cent, and the total Gibbs free energy by about 0.5 to 1 per cent, at the highest pressures considered, and at temperatures corresponding to the maximum of the exsolution dome. At lower pressures and/or temperatures the change would be proportionally smaller. It is therefore safe to assume that the resulting changes would be barely noticeable in Figs. 1-5. It would be desirable, however, to have this effect included in any future calculations.

equation (2.1) in connection with the assumptions stated in Section 2 and the methods used in I for calculating Q_F and ΔS . Figures 1–4 show the solid solubility curves (exsolution domes) and the chemical spinodals for the systems LiBr–LiI, NaBr–NaI, KBr–KI, and RbBr–RbI. In addition, the solid solubility curves were calculated for NaCl–KCl at two pressures and are shown in Fig. 5. The systems chosen were selected in view of the possibility of detecting any effect of increasing cation size on solid solubility and its pressure dependence. The system NaCl–KCl was added since an experimental determination of the pressure dependence of the solid solubility was started in this laboratory while the present theoretical work was in progress [33].

With the exception of the system NaBr–NaI all pressures selected for the solid solubility curves are smaller than the transition pressures for the transition from the NaCl to the CsCl structure. For the Li-halides no transition has been observed so far. Theoretical estimates for LiBr and LiI have been made on the basis of the Born model [34] and give 105 and 68 kbar, respectively. Quantum theoretical calculations [35] give 140 and 67 kbar, respectively. For NaBr and NaI the theoretical values from the Born model [34] are 53 and 39 kbar respectively, and from quantum theory [35] 78 and 44 kbar, respectively. Pistorius, however, observed the transition in NaBr at 11.5 kbar and 200°C, and in NaI at 10.2 kbar and 164°C [36]. At room temperature no transition was observed. These results are, however, subject to doubt because of the large discrepancies between the experimental and the quantum theoretical results, and because the theoretical results show a tendency for the transition pressure to increase in the sequence rubidium, potassium and sodium halides. In fact, for the potassium and rubidium halides the quantum theoretical calculations agree quite well with the available experimental data which indicate transition pressures near 4 kbar for the rubidium halides, and near 18 kbar for the potassium halides [35, 36].

Moreover, a large discrepancy exists among the transition pressures reported for NaCl by various investigators, and the low transition pressure for NaCl of 18 kbar found by Pistorius [37] has been challenged by Basset *et al.* [38], who propose a transition pressure of 300 kbar for NaCl. In view of these arguments it is conceivable that the transition pressures near 10 kbar reported by Pistorius [36] for NaBr and NaI are also much too low, and that the true transition pressures for these materials may well be near or above 100 kbar.

For these reasons the solid solubility curves of the system NaBr–NaI were calculated for two different sets of pressure, one set (5 and 10 kbar) below the

transition pressure reported by Pistorius [36], and one set (50 and 100 kbar) in a pressure range in which this system possibly (i.e. if Pistorius' data should turn out to be due to secondary effects) still occurs in the rocksalt structure.

For KBr and KI the transition occurs at 17.4 and 17.3 kbars respectively [36], so that the highest pressure for the KBr–KI diagram in Fig. 3 lies slightly outside the stability range of the rocksalt structure. For RbBr and RbI the experimental transition pressures are 4.2 and 3.6 kbars, respectively [36], so that the solubility curve at 4 kbar shown in Fig. 4 lies slightly outside the stability range of the rocksalt phase.

The results displayed in Figs. 1–5 show that for all five systems considered the exsolution domes become narrower and their maxima are moved toward higher temperatures with increasing pressure, while for a given temperature the solubility gap increases with increasing pressure. This indicates that the effect of pressure on solid solubility is opposite to the effect of temperature. This is what one would expect intuitively. Upon application of pressure, the ions are moved in their potential wells toward the high repulsive core making them effectively 'harder'. This reduces the possibility for accommodating misfits. Hence, increasing the pressure decreases the solid solubility, while an increase in temperature increases the solid solubility.

For the system LiBr–LiI in Fig. 1 the exsolution domes for pressures of 50 and 100 kbar extend above the approximate melting temperature curve, so that at those pressures, it is not possible to have complete solid solubility over the whole composition range.

The chemical spinodals shown in Figs. 1–4 exhibit the same pressure dependence as their respective solid solubility curves. The area under the chemical spinodal increases with increasing pressure. This means that the range in which the solid solution would decompose by spinodal decomposition in the absence of the strain term is increased both in temperature and in composition.

The temperature difference ΔT between the chemical and coherent spinodals was calculated (from equation (2.8)) at the maximum

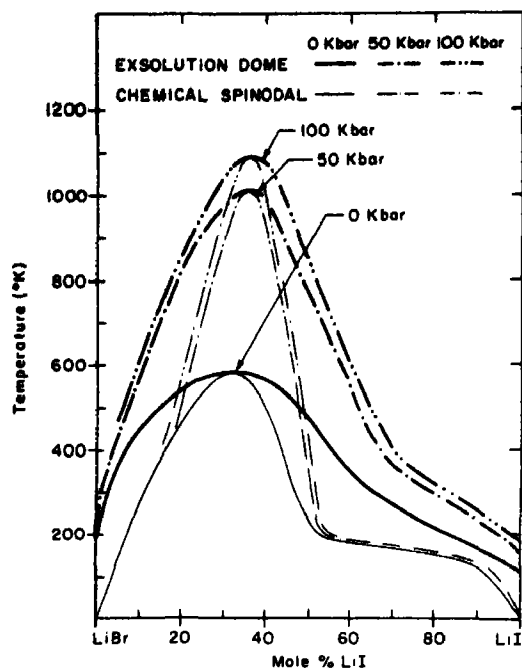


Fig. 1. Exsolution dome and chemical spinodal of LiBr-LiI for three pressures.

of the exsolution dome for the five systems under investigation. In order to calculate Y (in 2.6) the elastic constants were evaluated at the proper temperature, pressure, and composition. The pressure data were those of Table 1, while the values for the temperature dependence of the elastic constants were taken from the compilation of Leibfried and Ludwig[39]. The zero pressure values of the molar volumes were calculated from the lattice constants compiled[40]. The values of the maximum temperature T_m of the exsolution dome, for the maximum temperature $T_{coh} = T - \Delta T$ of the coherent spinodal, and of the temperature difference ΔT are listed in Table 3 for several pressures. Also included in Table 3 are the values of the anisotropy factor (2.5).

The values of T_{coh} listed in Table 3 represent an estimate of the temperature below which one might observe spinodal decomposition for each alkali halide solid solution, assuming the coherent spinodal is properly

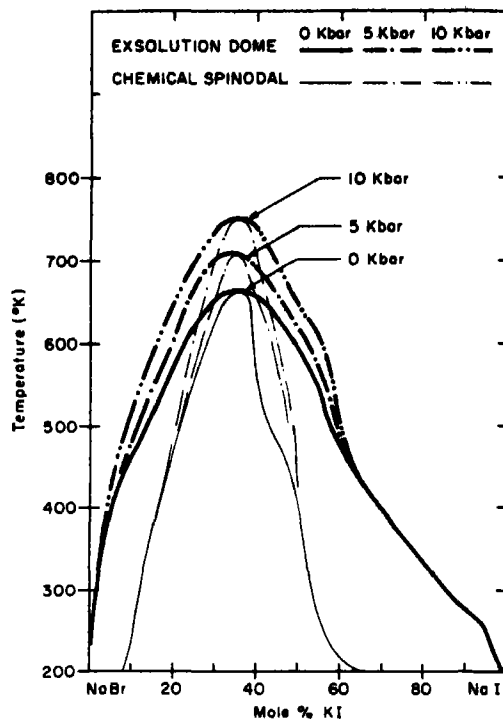


Fig. 2(a). Exsolution dome and chemical spinodal of NaBr-NaI for several pressures.

calculated. However, the strain term, given by equation (2.4) and the method outlined for relating the strain term to the temperature drop given by (2.8) are both approximate enough to make one cautious about drawing quantitative conclusions about the temperature differences between the chemical and coherent spinodals.

With these reservations in mind one may observe from the data of Table 3 that for all systems, except NaBr-NaI, the maximum temperature T_{coh} of the coherent spinodal increases monotonically with pressure. For NaBr-NaI, however, the temperature T_{coh} increases initially and decreases at high pressure after passing through a maximum. This maximum is caused by the fact that for NaBr-NaI the temperature difference ΔT between the chemical and the coherent spinodal increases with pressure, whereas for LiBr-LiI, KBr-KI, and RbBr-RbI, ΔT decreases with increasing pressure. For

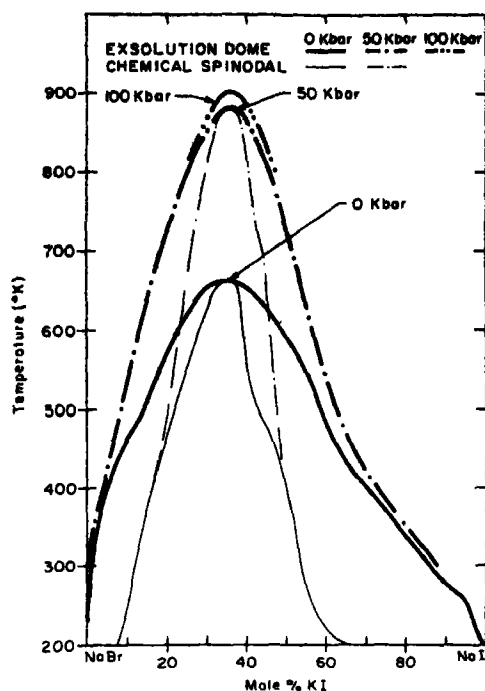


Fig. 2(b). Exsolution dome and chemical spinodal of NaBr-NaI for zero pressure and for two pressures above the transition pressure.

NaCl-KCl the difference ΔT increases initially and decreases after passing through a maximum; however, the initial increase is not large enough to cause a decrease in the maximum temperature T_{coh} .

The different pressure dependence of the temperature difference ΔT arises from the competing effects of the pressure dependence of the different factors (equation (2.8)). The elastic modulus Y usually increases monotonically with pressure, except for KBr-KI and RbBr-RbI, where a maximum occurs near 15 and 2 kbar, respectively. These maxima are caused by the negative pressure coefficient of the shear modulus c_{44} , but since they are very broad they have no effect on the temperature difference ΔT which for these two systems decreases monotonically with pressure. The factor η decreases monotonically with pressure, except for NaBr-NaI, where a minimum occurs, which has, however, no effect on the monotonical increase of the

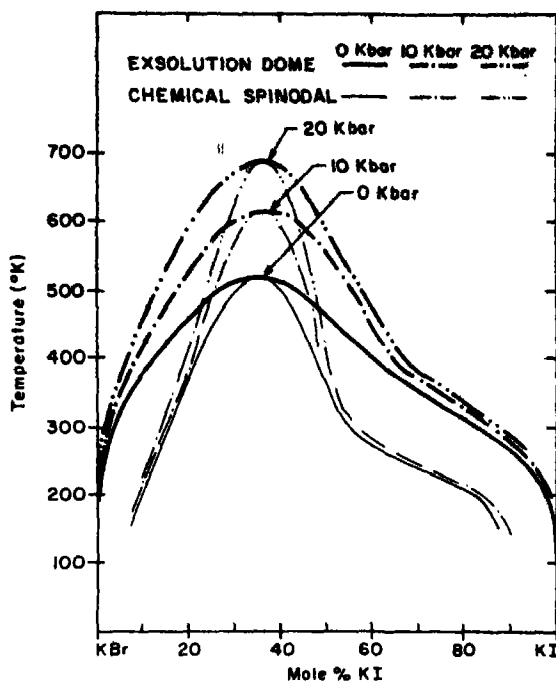


Fig. 3. Exsolution dome and chemical spinodal of KBr-KI for three pressures.

temperature difference with pressure. The third factor $1/N_0$ is the volume per molecule and decreases monotonically with pressure.

The data of Table 3 indicate that for LiBr-LiI and for KBr-KI the maximum of the coherent spinodal should lie very close to 300°K, so that no spinodal decomposition is to be expected at room temperature. For NaBr-NaI, RbBr-RbI and NaCl-KCl, however, the maximum of the coherent spinodal lies from 50° to 100°C above room temperature, and spinodal decomposition should take place. This is contrary to the observations of Wolfson *et al.*[14], who did not observe spinodal decomposition in NaCl-KCl at room temperature. Probably this discrepancy reflects the large uncertainty of the theoretical estimates for the coherent spinodal.

In spite of the uncertainty in the absolute magnitude of T_{coh} one should expect the pressure dependence to be predicted correctly. Thus spinodal decomposition may be ex-

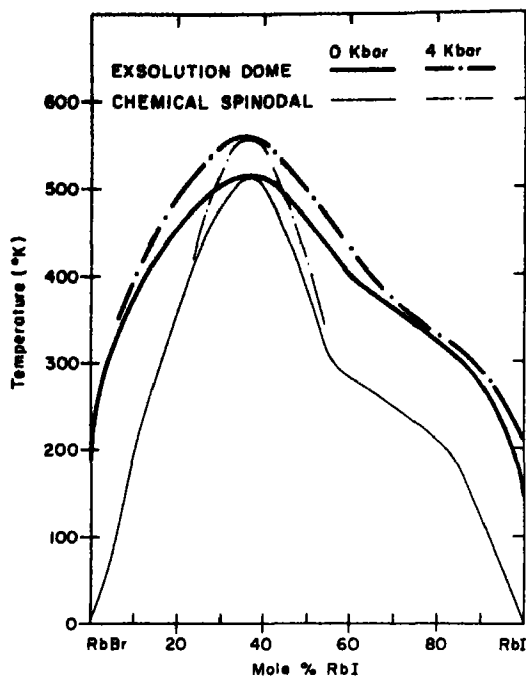


Fig. 4. Exsolution dome and chemical spinodal of RbBr-RbI for two pressures.

pected to occur at high pressure for LiBr-LiI, KBr-KI, and KCl-NaCl, whereas in NaBr-NaI very high pressure (above 50 kbar) should suppress spinodal decomposition if it were ever favored at intermediate pressures. For RbBr-RbI spinodal decomposition may take place at pressures close to the phase transition at 4 kbar, but the rise of T_{coh} is not large enough to predict this effect with certainty.

It is interesting to note that for LiBr-LiI, NaBr-NaI and NaCl-KCl the elastic anisotropy factor α changes sign at pressures of the order of 45, 35 and 8 kbar, respectively. One may therefore conclude that for these systems the direction of spinodal decomposition should change from $\langle 100 \rangle$ at low pressures to $\langle 111 \rangle$ at high pressures, whereas for the remaining systems KBr-KI and RbBr-RbI decomposition should occur in $\langle 111 \rangle$ at all pressures.

For the system NaCl-KCl the spinodal curves have not been included in Fig. 5 since

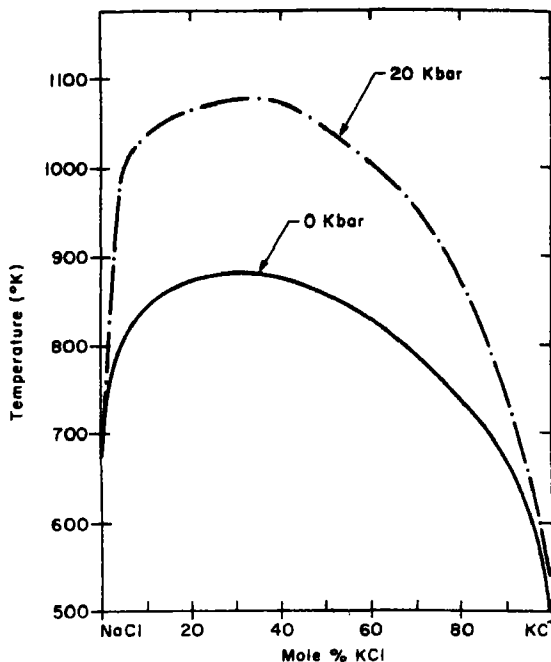


Fig. 5. Solid solubility curves for NaCl-KCl at two different pressures.

for this system the free energy-vs. composition curve shows three minima, instead of the usual two. The exsolution dome shown in Fig. 5 was obtained from the common tangent to the two minima corresponding to the lowest and highest compositions, respectively.

The occurrence of three minima in the free energy curve would be indicative of an ordered phase resulting in two exsolution domes and two spinodal curves. No such effect has been observed, however, in alkali halides. In two papers, which only recently came to our attention, Hovi[41,42] reports theoretical results for KBr-KI and RbBr-RbI solid solutions which show the same effect. These results are based on the theory of Wasastjerna [43, 44] which includes the entropy contribution from local order but does not include the vibrational entropy contribution. Since for the theoretical model used in the present work only one solubility gap is obtained for KBr-KI and RbBr-RbI it is suggested that the occurrence of two solubility gaps arises from the entropy term, and not from the heat of formation. The results obtained for these two systems and, on the basis of the present model, for NaCl-KCl seem to indicate that both the entropy contribution from local order and the vibrational entropy can cause two solubility gaps. Since experimental verification of two solubility gaps would be a rather difficult task the question must remain undecided whether the theoretical entropy contributions due to local order

and due to thermal vibrations are calculated correctly or result erroneously in two solubility gaps.

Table 3. Maximum temperature T_m (in °K) of the exsolution dome, temperature difference ΔT (in °K) between the chemical and the coherent spinodal, maximum temperature T_{coh} of the coherent spinodal, and elastic anisotropy α at the maximum of the chemical spinodal for several pressures (in kbar)

System	p	T_m	ΔT	T_{coh}	α
LiBr-LiI	0	575	269	306	-0.64
	50	1010	241	769	0.19
	100	1080	225	855	1.39
NaBr-NaI	0	665	324	341	-0.18
	5	705	345	360	-0.003
	10	750	369	381	0.156
	50	880	467	413	1.55
KBr-KI	100	900	591	309	2.87
	0	520	215	305	1.36
	10	615	182	433	2.72
RbBr-RbI	20	690	158	532	4.44
	0	515	183	332	1.87
	2	538	172	365	2.26
NaCl-KCl	4	560	162	398	2.69
	0	883	487	396	-0.29
	10	980	552	428	0.10
	20	1077	515	562	0.51

The parameters used in the present calculations that determine the pressure dependence of the solid solubility curve are the compressibilities and the electronic polarizabilities, the first pressure derivatives of these quantities, and the lattice parameters. It is still conceivable, however, that the solid solubility and its pressure dependence can be correlated to a smaller number of parameters. Such a correlation would be useful for more complicated systems where lattice theoretical calculations are too difficult. One such 'empirical' correlation of the theoretical results is plotted in Fig. 6, which shows the ratio of the maximum temperature of the exsolution dome $T_m(p)$ at the pressure p to the maximum temperature $T_m^0 = T_m(0)$ at

zero pressure as a function of $(V_0/V)^{4/3}$, where V and V_0 are the molar volumes (corresponding to the composition of the maximum of the exsolution dome) at pressure p and at zero pressure, respectively. For all four systems a linear correlation is found for values of $(V_0/V)^{4/3}$ close to 1, i.e. for small pressure. For LiBr-LiI and NaBr-NaI deviations from the linear dependence occur at higher values of $(V_0/V)^{4/3}$. For these two systems the cation-anion radius ratio r_+/r_- is smaller or close to the value $(\sqrt{2}-1) = 0.41$ below which the repulsive interaction between second nearest neighbors becomes more pronounced than that between first nearest neighbors. Although because of the occurrence of the B1-B2 phase transition the data for KBr-KI and RbBr-RbI have not been extended to higher pressures to allow a comparison, it is conceivable that the deviation from linearity in Fig. 6 is associated with the small cation anion radius ratio. This behavior warrants further study, especially for other systems. Apart from this observation, no other effect of the radius ratio on solid solubility could be found.

The only experimental data on the pressure dependence of the solid solubility in alkali halides that are available for comparison with the theoretical results are recent and as yet unpublished results of Bhardwaj and Roy for the system NaCl-KCl[33]. The solid solubility curve at zero pressure found by these authors agrees well with the earlier data of Sheil and Stadelmaier[45] and lies therefore about 100°C below our theoretical curve (II, Fig. 3). Possible reasons for this discrepancy have been discussed in II. Good agreement between the theoretical and experimental results is found, however, for the pressure dependence of the solid solubility; the experimental and theoretical curves for the maximum of the exsolution dome vs. pressure have the same shape and differ only by a parallel shift of about 100°C[33]. This pressure dependence corresponds therefore to the linear dependence of the maximum

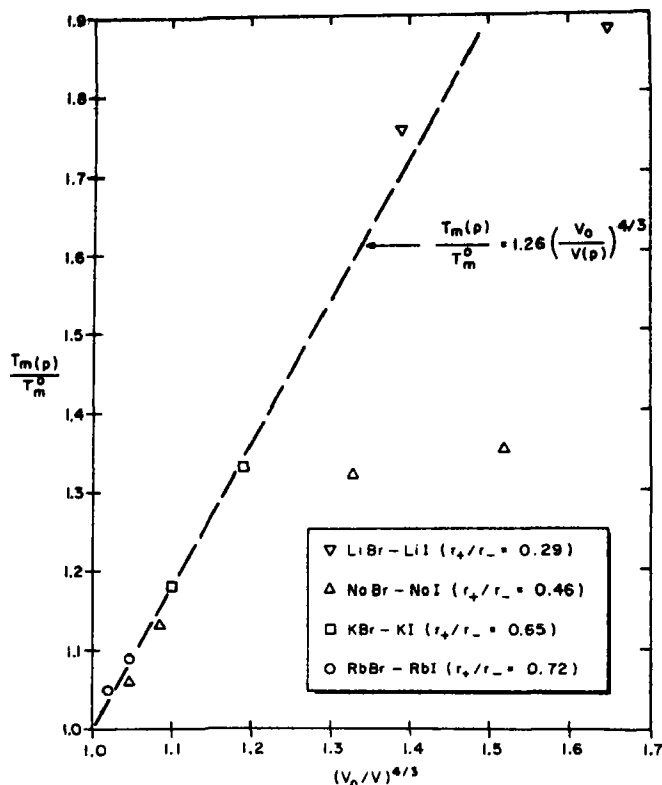


Fig. 6. Dependence of maximum temperature of exsolution dome on volume for several pressures and several systems.

of the exsolution dome on the volume ratio $(V_0/V)^{4/3}$ displayed in Fig. 6.

4. CONCLUSIONS AND SUMMARY

It is found that for all alkali halide systems considered the solid solubility curve becomes narrowed and is shifted toward higher temperatures as the pressure increases. A similar behavior is found for the chemical spinodal. The increase with pressure results primarily from the increase of the heat of formation through the decreasing interionic distance. The temperature difference between the chemical and the coherent spinodal does not follow a general pattern and may either increase monotonously, decrease monotonously, or decrease at high pressure after initially at low pressures passing through a maximum.

For all five systems considered the coherent spinodal at zero pressure does not rise very much above 300°K, but of these systems NaCl-KCl is most likely to show spinodal decomposition at 300°K and zero pressure. In most cases the maximum temperature of the coherent spinodal increases with increasing pressure, so that, for example, for KBr-KI spinodal decomposition is expected to occur at 10 kbar over a certain composition range. For NaCl-KCl a similar behavior is expected, but the increase with pressure occurs more slowly, and pressures of the order of 20 kbar are required to raise the coherent spinodal significantly above the zero pressure value.

For LiBr-LiI, NaBr-NaI and NaCl-KCl the direction in which spinodal decomposition occurs changes with pressure because the elastic anisotropy changes sign

with increasing pressure. It would be interesting, although quite difficult, to verify this effect experimentally.

In order to check the theoretical results it would be desirable to have experimental data on solid solubility as a function of pressure. Such measurements for the system NaCl-KCl have been performed in this laboratory[33] and are in reasonable agreement with the theoretical data. However, no spinodal decomposition has been observed. Another possible experiment would be the investigation of the system KBr-KI in the pressure range 0-20 kbars. By application of a rapid quench technique in order to reach the unstable region under the exsolution dome, unambiguous experimental verification of spinodal decomposition in alkali halides might be obtained.

Acknowledgement—The authors would like to thank Professor R. Roy for his interest in this work, for many stimulating discussions, and for a preprint of his paper prior to publication.

REFERENCES

- FANCHER D. L. and BARSCH G. R., *J. Phys. Chem. Solids* **30**, 2503 (1969).
- FANCHER D. L. and BARSCH G. R., *J. Phys. Chem. Solids* **30**, 2517 (1969).
- DICK B. G. and DAS T. P., *Phys. Rev.* **127**, 1053 (1962); *J. appl. Phys.* **33**, 2815 (1962).
- BARSCH G. R. and CHANG Z. P., *Phys. Status Solidi* **19**, 139 (1967).
- ALDER B. J., *J. Geophys. Res.* **71**, 4973 (1966).
- CARPENTER R. W., AHMADIEH A. and PARKER E. R., *Acta Metall.* **14**, 543 (1966).
- CARPENTER R. W., *Acta Metall.* **15**, 1297 (1967).
- DOUGLASS D. L. and BARBEE T. W., *J. Mat. Sci.* **4**, 121 (1969).
- GIBBS J. W., *Trans. Conn. Acad.* **3**, 343 (1878).
- CAHN J. W., *J. appl. Phys.* **34**, 3581 (1963).
- GOLDSTEIN M., *J. Am. ceram. Soc.* **48**, 126 (1965).
- SCHULTZ A. H. and STUBICAN V. S., *Phil. Mag.* **18**, 929 (1968).
- WIMMER F. T., KOBES W. and FINE M. E., *J. appl. Phys.* **34**, 1775 (1963).
- WOLFSON R. G., KOBES W. and FINE M. E., *J. appl. Phys.* **37**, 704 (1966).
- GRAEFFE G. and NURMIA, M., *Z. Naturf.* **21a**, 165 (1966).
- DARKEN L. S. and GURRY R. W., *Physical Chemistry of Metals*, McGraw Hill, New York (1953).
- CAHN J. W., *Acta Metall.* **9**, 795 (1961).
- CAHN J. W., *Acta Metall.* **10**, 179 (1962).
- HILLIARD J. E., *Ind. Eng. Chem.* **58**, 19 (1966).
- SLATER, J. C., *Introduction to Chemical Physics*, McGraw Hill, New York (1963).
- MURNAGHAN F., *Proc. Natl. Acad. Sci.* **30**, 244 (1944).
- HAUSSÜHL S., *Z. Phys.* **159**, 223 (1960).
- HAUSSÜHL S., *Z. Kristallogr.* **110**, 67 (1958).
- KOLIWAD K. M., GHATE P. B. and RUOFF A. L., *Phys. Status Solidi* **21**, 507 (1967).
- BARSCH G. R. and SHULL H. E., *Phys. Status Solidi* **43** (1971).
- REDDY P. J., *In Physics of Solids at High Pressure* (Edited by C. T. Tomizuka and R. M. Emrick) Academic Press, New York (1965).
- CHANG Z. P. and BARSCH G. R., *J. Phys. Chem. Solids* **31** (1970).
- BARTELS R. A. and SCHUELE D. E., *J. Phys. Chem. Solids* **26**, 537 (1965).
- GHATE P. B., *Phys. Rev.* **139**, A1666 (1965).
- VEDAM K. and SCHMIDT E. D. D., *J. Mat. Sci.* **1**, 310 (1966).
- VEDAM K., SCHMIDT E. D. D., KIRK J. L. and SCHNEIDER W. C., *Mat. Res. Bull.* **4**, 573 (1969).
- VEDAM K., *Phys. Rev.* (to be published).
- BHARDWAJ M., DACHILLE F. and ROY R., *J. Phys. Chem. Solids* **31**, (1970).
- BORN M. and HUANG K., *Dynamical Theory of Crystal Lattices*, Clarendon Press, Oxford (1954).
- LOMBARDI E. and JANSEN L., *Phys. Rev.* **136**, 1011 (1964).
- PISTORIUS C. W. F. T., *J. Phys. Chem. Solids* **26**, 1003 (1965).
- PISTORIUS C. W. F. T., *J. Phys. Chem. Solids* **25**, 1477 (1964).
- BASSET W. A., TAKAHASHI T., MAO H. K. and WEAVER J. S., *J. appl. Phys.* **39**, 319 (1968).
- LEIBFRIED G. and LUDWIG W., in *Solid State Physics* (Edited by F. Seitz and D. Turnbull) Vol. 12, p. 275, Academic Press, New York (1961).
- LANDOLT BÖRNSTEIN, *Zahlenwerte und Tabellen*, Vol. 1, part 4, Springer Verlag, Berlin (1955).
- HOVI M., *Ann. Univ. Turkuensis AI*, No. 89, 1 (1966).
- HOVI M., *Ann. Acad. Sci. Fennicae AVI*, No. 315, 1 (1969).
- WASASTJERNA J. A., *Soc. Sci. Fennicae, Comment. Phys.-Math.* **XV**, No. 3 (1949).
- HOVI M., *Soc. Sci. Fennicae, Comment. Phys.-Math.* **XV**, No. 12 (1950).
- SCHEIL E. and STADELMAIER H., *Z. Metallk.* **43**, 227 (1952).

FERROELECTRIC BiFeO_3 X-RAY AND NEUTRON DIFFRACTION STUDY

J. M. MOREAU, C. MICHEL*, R. GERSON and W. J. JAMES

Departments of Chemistry and Physics and Graduate Center for Materials Research, University of Missouri-Rolla, Rolla, Mo. 65401, U.S.A.

(Received 31 July 1970; in revised form 16 October 1970)

Abstract—Ferroelectric BiFeO_3 is rhombohedral with lattice constants, $a_H = 5.5876$, $c_H = 13.867$ Å at room temperature. The space group is $R3c$ with two formula units in the unit cell. The atomic positions have been determined employing both X-ray single crystal and neutron powder diffraction. The oxygen atomic positions could be determined only by neutron diffraction and are interpreted as a rotation of rigid octahedra around the trigonal axis by an angle $\omega = 11^\circ 40'$ from the ideal perovskite positions.

The X-ray intensities were visually estimated by the multiple film technique using a Weissenberg camera. The cation positions, refined by least-squares, are in good agreement with those determined from neutron powder diffraction analysis. The final results are given with a reliability factor $R = 0.02$ for neutron powder data and $R = 0.09$ for X-ray single crystal data. With respect to the ideal perovskite structure, the cations are shifted along the trigonal axis in accord with the observed dielectric properties.

1. INTRODUCTION

THE STUDY of perovskite-type structures which exhibit long range ordering of electrical moments as well as the ordering of magnetic dipole moments has received considerable attention. The distorted perovskite BiFeO_3 is claimed to exhibit such properties. Although its antiferromagnetic structure was determined without ambiguity as being G -type[1], the electrical nature of BiFeO_3 was, until recently, in question due to contradictory reports in the literature.

Several investigators employing powder diffraction techniques reported[2–4] that BiFeO_3 possessed a rhombohedrally distorted perovskite-like structure with a unit cell parameter of $a = 3.96$ Å, $\alpha = 89^\circ 28'$ at room temperature. For this monomolecular unit cell, Tomasphpolskii *et al.*[5, 6] proposed, from single crystal data, the space group $R3m$ which permits ferroelectricity. These results were in contradiction with those of Kiselev *et al.*[7] who reported the unit cell to be bi-

molecular on the basis of superstructure lines observed on neutron diffraction powder diagrams. No atomic coordinates were reported, but it was concluded that BiFeO_3 could be antiferroelectric.

Furthermore, the space group $R3m$ did not allow for the weak ferromagnetism detected by magnetic susceptibility measurements[8].

The discrepancies in the experimental investigations resulted from the lack of suitable single crystals and/or pure polycrystalline material. Thus in the absence of a completely defined atomic structure, one could not state whether BiFeO_3 was ferroelectric compensated antiferromagnetic, antiferroelectric weak ferromagnetic or ferroelectric weak ferromagnetic.

The determination of the exact atomic structure of BiFeO_3 , therefore, appeared basic to an understanding of its behavior. Accordingly, the purpose of this paper is to present data establishing the atomic structure and electrical nature of BiFeO_3 . Some correlations of the structure of BiFeO_3 with its physical properties and with the structures

*Present Address: Philips Laboratories, 345 Scarborough Road, Briarcliff Manor, N.Y. 10510, U.S.A.

and properties of some related compounds are also discussed.

2. EXPERIMENTAL

Cell determination

Our first attempts to solve the ambiguous question of the cell dimension included neutron powder diffraction on a very pure sample[9]. A diffraction pattern was obtained at 600°C, considerably above the Néel temperature. Two extra peaks at $\theta_1 = 26.3^\circ$ and $\theta_2 = 41.5^\circ$ could not be indexed in a monomolecular cell. These lines did not correspond to any possible impurity peaks such as the major peaks of Fe_2O_3 , Bi_2O_3 or $\text{Bi}_2\text{Fe}_4\text{O}_9$. These peaks could be indexed employing a bimolecular unit cell, in agreement with Platkii's results[10]. Confirmation that these peaks were indeed superstructure peaks was provided by X-ray single crystal diffraction. The crystals used were needles grown by slow cooling of a Bi_2O_3 - Fe_2O_3 mixture containing an excess of Bi_2O_3 . The superstructure reflections, although very weak, appeared after very long exposure times (12 days on rotating crystal, $\text{Cu-K}\alpha$ radiation). The true unit cell was, therefore, bimolecular with the rhombohedral unit vector related to the perovskite-like cell by the matrix:

$$\begin{vmatrix} 0 & 1 & 1 \\ 1 & 0 & 1 \\ 1 & 1 & 0 \end{vmatrix}.$$

To better understand the atomic framework, the corresponding hexagonal cell is used. The hexagonal cell, containing six formula units of BiFeO_3 is related to that of the perovskite by the matrix:

$$\begin{vmatrix} \bar{1} & 1 & 0 \\ 0 & \bar{1} & 1 \\ 2 & 2 & 2 \end{vmatrix}.$$

The room temperature hexagonal parameters were determined from high angle powder diffraction photographs of very pure

ceramic material taken with a Straumanis camera (Co radiation).

$$a = 5.5876 \pm 0.0003 \quad c = 13.867 \pm 0.001.$$

Neutron diffraction study

Examination of the scattering factors strongly suggested that the X-ray data did not reflect the oxygen positions. Consequently, a neutron diffraction study was undertaken. The neutron scattering lengths were 0.86, 0.96 and 0.577 for Bi, Fe and O, respectively. Therefore, the oxygen contribution, relative to Bi and Fe, was increased considerably over that found in X-ray diffraction.

Neutron powder diffraction patterns of BiFeO_3 up to $2\theta = 48^\circ$ were obtained for different temperatures at the Oak Ridge National Laboratory Research Reactor. At room temperature the pattern shows a magnetic structure superimposed upon the nuclear structure. The magnetic and crystallographic cells were found to be identical. The Néel temperature T_N was derived from the thermal variation of the magnetic intensity of (003). The value of $T_N = 640$ K was in good agreement with that reported by Kiselev *et al.*[7].

The magnetic pattern revealed a simple G-type antiferromagnetic structure in which each magnetic Fe ion is surrounded by six antiparallel-aligned Fe ions as previously reported[1]. Analysis of the nuclear structure was carried out, using intensities obtained at 880 K. The *R* factor was calculated for different models using 15 nuclear reflections. In these models, both parallel and antiparallel shifts of the Fe ions were used as well as different types of possible oxygen octahedra distortion. The superstructure peaks could only be generated in the *R3c* space group.

The least-square analysis was carried out using the U.C.I.L.S.I. program[11]. In the final model, calculated and observed intensities agree with a discrepancy factor, $R = 0.023$, Table 1. The resulting atomic positions are given in Table 2 in fractions of the hexagonal edges.

Table 1. High temperature neutron diffraction data for BiFeO₃

<i>hkl</i>	<i>I</i> _{calculated}	<i>I</i> _{observed}	
0 1 2	623	555	
1 0 4	1542	2747	2752
1 1 0	1205		
1 1 3	1112		
0 0 6	185	1282	1306
2 0 2	1097		
0 2 4	6392	4900	6230
2 1 1	722		
1 1 6	3630		
1 2 2	548	7764	8054
0 1 8	1574		
2 1 4	3557		
3 0 0	2633	6910	516
1 2 5	631		
2 0 8	2496		
2 2 0	4414	6846	6846

$$R = \frac{\sum |I_o| - |I_c|}{\sum I_o} = 0.023$$

correction factors for absorption were taken from the International Tables [14].

Structure factors, F_{hkl} , were computed up to a value of $(\sin \theta/\lambda) = 0.73$ using the atomic form factors given in the International Tables for X-ray crystallography. Seventy-eight independent reflections with non-zero observed intensities were taken into account. The superstructure reflections with $l = 2n + 1$ were too faint to be reliably measured. Intensities largely affected by extinctions were also excluded. A least-square refinement using U.C.I.L.S.I. program and assuming isotropic temperature factors, was carried out on all the observed structure factors (Table 4). The Bi-Fe distance converged rapidly and remained, in any case, constant within error limits in agreement with the values calculated from the neutron data. Despite the reasonable R factor, the results appeared extremely

Table 2. Atomic coordinates for BiFeO₃

Atom	Ideal model			Final model		
	<i>x</i>	<i>y</i>	<i>z</i>	<i>x</i>	<i>y</i>	<i>z</i>
Bi	0	0	0	0	0	0
Fe	0	0	0.250	0	0	0.2212 ± 15
O	0.5	0	0	0.443 ± 2	0.012 ± 4	0.9543 ± 20

The pseudosymmetric positions can be described by cation shifts from the ideal cubic positions along the trigonal axis (0001) while the oxygen octahedra were rotated slightly around the (0001) direction as observed in LaCoO₃ [12] and LaAlO₃ [13].

X-ray study

The crystals, selected under a polarizing microscope, were needle-like growing along the (111) and about 30 microns in diameter. A Weissenberg camera was used to collect the reflections using Zr-filtered Mo K α radiation. The intensities were visually estimated by the multiple-film technique with a calibrated intensity scale, and corrected for absorption and Lorentz polarization factors. The crystal shape was similar to that of a cylinder of 30 μ diameter and accordingly the

insensitive to any variation of the oxygen atom positions. As expected, only the Bi-Fe distance could be determined with a standard deviation smaller than that obtained from neutron data. Along the triad axis the Bi-Fe distance is found to be 3.089 ± 0.005 and $3.921 \text{ \AA} \pm 0.005$. The isotropic temperature factors are 0.5 \AA^2 for Bi and 0.8 \AA^2 for Fe. Anisotropic temperature factors could be used to reduce the discrepancy factor, but this would not affect the atomic parameters and furthermore would be of questionable accuracy. The reported parameters in Table 2 were determined with a final R factor of 0.098.

4. DISCUSSION AND CONCLUSIONS

The atomic coordinates can be expressed in terms of small systematic displacements of atoms from the ideal perovskite model by the

following parameters:

$$\begin{aligned}\text{Bi: } & 0, 0, \frac{1}{4} + \epsilon \\ \text{Fe: } & 0, 0, \delta \\ \text{O: } & \frac{1}{2} - u, v, \frac{1}{2}.\end{aligned}$$

In this model, the quantities, ϵ , δ , u , v , represent the respective departure from the ideal perovskite positions:

$$\epsilon = 0.0457; \delta = 0.0169; u = 0.057; v = 0.012.$$

Table 3 gives the interatomic distances and the bond angles. The spread of the 0-0 distances in the octahedra is less than 3 per cent

around their three fold axes. In a previous article[16], we have reported for this type of deformation a theoretical relationship between the angle of rotation and the cell deformation

$$\alpha = \arccos \frac{4 - \cos^2 \omega}{4 + 2 \cos^2 \omega} \quad (1)$$

where ω is the angle of rotation around the trigonal axis of the octahedron from the perovskite positions and α the corresponding rhombohedral angle related to the hexagonal parameter ratio c/a by:

$$\frac{c}{a} = \frac{9}{4 \sin^2 \frac{\alpha}{2}} - 3. \quad (2)$$

Table 3. Interatomic distances and angles in BiFeO_3

Hexagonal cell		$a = 5.5876 \text{ \AA}$	$c = 13.776 \text{ \AA}$
Bi-Bi	3.986 ± 0.001	Bi-Fe	3.089 ± 0.005
Fe-Fe	3.986 ± 0.001		3.324 ± 0.005
			3.592 ± 0.005
Bi-O	2.31 ± 0.01		3.921 ± 0.005
	2.53 ± 0.01	O-O	2.74 ± 0.03
Fe-O	1.95 ± 0.02		2.84 ± 0.03
	2.11 ± 0.02		2.87 ± 0.03
			2.98 ± 0.03
Angles (in degrees)	O-Fe-O	99.3 ± 0.1	
		88.4 ± 0.1	
		89.7 ± 0.1	
		81.0 ± 0.1	

around the average value of 2.8 \AA . Thus, the FeO_6 octahedra, despite a large shift of the Fe from its geometrical center, can be considered as approximately regular. In other words, the magnitude of the parameter v related to the octahedral distortion is of a second order approximation compared to u which is directly related to the octahedron tilt. In a note[15], Megaw had suggested the anion framework of such a rhombohedral pseudo-symmetric structure could be described as derived from the ideal octahedral framework in the perovskite configuration ($v = 0, u = 0$) by rotating the rigid octahedra

The experimental value $\omega = 11^\circ 40'$ is in good agreement with the theoretical angle relationship[1].

One of the characteristic properties of the ferroelectric compounds ABO_3 is the off-center displacement of the octahedrally coordinated B cation. A study of Abrahams *et al.*[17] on many displacive ferroelectrics including LiTaO_3 and LiNbO_3 (isomorphous with BiFeO_3) has shown that a relationship exists between the displacement Δz of the central atom and the Curie temperature:

$$T_c = 2 \cdot 10^4 (\Delta z)^2. \quad (3)$$

Table 4. Observed and calculated structure factors

<i>h</i>	<i>k</i>	<i>l</i>	<i>F</i> _{obs.}	<i>F</i> _{cal.}	<i>h</i>	<i>k</i>	<i>l</i>	<i>F</i> _{obs.}	<i>F</i> _{cal.}
1	1	0	531	489	0	6	6	215	186
3	0	0	470	432	6	0	6	221	174
2	2	0	438	421	5	2	6	131	167
4	1	0	360	322	2	5	6	133	168
3	3	0	331	280	0	1	8	341	371
6	0	0	236	251	2	0	8	332	315
5	2	0	297	257	1	2	8	318	314
4	4	0	255	209	3	1	8	268	288
1	5	2	161	164	0	4	8	254	263
4	2	2	212	180	2	3	8	270	251
5	0	2	232	203	5	0	8	218	220
3	4	2	138	163	4	2	8	236	216
0	1	2	309	304	1	5	8	228	211
2	0	2	352	343	3	4	8	219	189
1	2	2	225	246	1	0	10	325	346
3	1	2	185	219	0	2	10	258	278
0	4	2	197	235	2	1	10	332	302
2	3	2	188	219	1	3	10	254	277
6	1	2	145	148	4	0	10	267	242
5	3	2	118	136	3	2	10	262	233
1	0	4	521	484	0	5	10	258	206
0	2	4	504	489	2	4	10	268	210
2	1	4	417	409	5	1	10	171	209
1	3	4	345	343	4	3	10	161	183
4	0	4	320	337	0	0	12	238	206
3	2	4	337	315	1	1	12	281	247
0	5	4	284	294	3	0	12	248	210
2	4	4	304	271	0	3	12	245	209
5	1	4	289	254	2	2	12	221	189
4	3	4	278	238	4	1	12	168	181
1	6	4	195	210	1	4	12	170	181
0	0	6	335	321	3	3	12	181	173
1	1	6	369	329	0	1	14	351	297
0	3	6	305	281	2	0	14	298	267
3	0	6	312	269	1	2	14	243	271
2	2	6	235	254	3	1	14	252	246
1	4	6	190	221	0	4	14	210	226
4	1	6	188	229	2	3	14	204	217
3	3	6	175	208	5	0	14	223	202

Although no Curie point has been determined directly on pure BiFeO₃ below its decomposition temperature (850°C), an extrapolation of data from high-temperature dielectric measurements[18] and X-ray studies[19,20] on BiFeO₃-PbTiO₃ solid solutions, suggested a Curie temperature of 850°C. According to relation[3], the value of $\Delta z = 0.236 \text{ \AA}$ determined by our structural investigation would give a Curie temperature of $841 \pm 10^\circ\text{C}$ which is in good agreement with the extrapolated

value. Also, an empirical relationship between the cation shifts $\delta_{(A)}$ and $\delta_{(B)}$ has been reported[21] for the isomorphous series Pb(Zr_{0.9}Ti_{0.1})O₃, BiFeO₃, LiTaO₃, LiNbO₃. Moreover, a relationship between atomic parameters and the unit cell dimensions has been developed[22] in a model possessing *R3c* symmetry. Thus a trifluoride series *BF*₃ (*B* = Ru, Co, V, Fe, Ti) and different perovskite-type series *ABO*₃ (*A* = Pb, La, Li and *B* = Sr, Ti, Co, Al, Nb, Ta) were related to BiFeO₃ as being based on the same anion framework.

Finally a minor hysteresis loop has been observed for the first time on a single crystal of BiFeO₃[22]. The reversal of the electrical moments was not complete due to the high coercive field and thus saturation polarization could not be attained. However, it provides evidence as to the ferroelectric nature of BiFeO₃, the only non-pressure synthesized compound possessing both ferroelectric and magnetic ordering with a trivalent ion in the *A* site of the *ABO*₃ perovskite lattice.

Acknowledgement—The authors are indebted to Dr. W. C. Koehler of O.R.N.L. for his assistance in obtaining the neutron diffraction data. The support of the U.S. Atomic Energy Commission and the U.S. Air Force—Project Themis AFOSR-F-44620-69-C-0122 is gratefully acknowledged.

REFERENCES

1. KISELEV S. V., OZEROV R. P. and ZHDANOV G. S., *Soviet Phys. Dokl.* 7, 742 (1963).
2. ZASLAVSKII A. I. TUTOV A. G., *Soviet Phys. Dokl.* 5, 1257 (1960).
3. TOMASHPOL'SHII Yu. Ya., VENEVTSEV Yu. N. and ZHDANOV G. S., *Soviet Phys. crystallogr.* 9, 6, 715 (1965).
4. FILIP'EV V. S., SMOL'YANINOV I. P., FESENKO E. G. and BELYAEV I. I., *Soviet Phys. crystallogr.* 5, 913 (1960).
5. TOMASHPOL'SKII YU. YA., VENEVTSEV YU. N. and ZHDANOV G. S., *Soviet Phys. crystallogr.* 9, 715 (1964).
6. TOMASHPOL'SKII YU. YA., VENEVTSEV YU. N. and ZHDANOV G. S., *Soviet Phys. crystallogr.* 12, 2, 209 (1967).
7. KISILEV, S. V., OZEROV R. P. and ZHDANOV G. S., *Soviet Phys. Dokl.*, 7, 742 (1962).
8. SMOLENSKII G. A. and YUDIN V. M., *Soviet Phys.-solid State* 16, 12, 2936 (1965).

9. MICHEL C., MOREAU J. M., ACHENBACH D., GERSON R. and JAMES W. J., *Solid State Commun.* **7**, 865 (1969).
10. PLAKHTII V. P., MAL'TSEV E. I. and KAMINKER P. M., *Izv. AN SSSR, ser. fiz.*, **28**, 436 (1964).
11. U.C.I.L.S.I. Program—The current version, from the University of Chicago, is an adaptation of the Northwestern modification of the Busing–Martin–Levy program ORFLS.
12. MENYUK N., DWIGHT K. and RACCAH P. M., *J. Phys. Chem. Solids* **28**, 549 (1967).
13. DE RANGO C., TSOUCARIS G. and ZELWER C., *Acta crystallogr.* **20**, 590 (1966).
14. International Tables for X-ray Crystallography, Vol. II, Kynoch Press, Birmingham, England, 1967.
15. MEGAW H., *Acta crystallogr.* **A24**, 583 (1968).
16. MOREAU J. M., MICHEL C., GERSON R. and JAMES W. J., *Acta crystallogr.* **B26**, 1425 (1970).
17. ABRAHAM S. C., KURTZ S. K. and JAMIESON P. B., *Phys. Rev.* **172**, 2, 551 (1968).
18. ROGINSKAYA YU. E., TOMOSHPOL'SKII YU. YA., *et al.*, *J.E.T.P. (USSR)* **50**, 69 (1966).
19. FEDULOV S. A., VENEVTSEV YU. N., *et al.*, *Soviet Phys. crystallogr.* **7**, 62 (1962).
20. KRAINIK N. N., KHUCHNA N. P., *et al.*, *Soviet Phys. solid State*, **8**, 3, 654 (1966).
21. MICHEL C., MOREAU J. M., ACHENBACH D., GERSON R. and JAMES W. J., *Solid State Commun.*, **7**, 701 (1969).
22. MICHEL C., MOREAU J. M. and JAMES W. J., *Acta crystallogr.* **B26** (1970).
23. TEAGUE R., GERSON R. and JAMES W. J., *Solid State Commun.* **8**, 1073 (1970).

THE OPTICAL PROPERTIES OF ANTHRACENE CRYSTALS IN THE VACUUM ULTRAVIOLET

B. E. COOK* and P. G. LE COMBER

Department of Physics, The University, Dundee, Scotland

(Received 31 August 1970)

Abstract—The normal incidence reflectivity spectrum of anthracene crystals has been measured in the range from 2 to 13 eV using unpolarised light. The data were analyzed by means of the Kramers-Kronig relation. The results extend our knowledge of the optical constants well beyond the range of previous measurements. A check on the internal consistency of the analysis is provided by the application of sum rules. A tentative energy level scheme is proposed that is able to account for the majority of the spectral features in the $\epsilon_2(\omega)$ curve. In the interpretation, it is suggested that the initial filled states are the ground state and two lower bands lying 2.9 and 6.6 eV below the ground state. From these, transitions occur to the following final states; (a) surface states, (b) the singlet at 3.1 eV above the ground state, (c) the second conduction band extending from 4.4 to 5.0 eV, and (d) possibly another level beginning at about 5.3 eV.

1. INTRODUCTION

OF ALL the organic materials, anthracene has probably been the most extensively studied in recent years, both from an experimental and a theoretical point of view. Much of this work has been concerned with establishing an energy level scheme for the material. There now seems fairly general agreement on the type of levels expected above the ground state, although the details of some of these are still somewhat uncertain.

Previous work [1, 2] on the optical constants of anthracene has been limited to photon energies of less than 6 eV. The aim of the work described in this paper was to extend the known optical constants to considerably higher energies and, as a consequence, obtain some information about the relatively unknown levels below the ground state.

2. EXPERIMENTAL PROCEDURE AND RESULTS

The vacuum monochromator and the experimental arrangement used in this work have been described in a previous publication [3] and only a brief description will be given here. The monochromator has a 1 m normal inci-

dence concave grating as the dispersive element; the source was a high voltage d.c. hydrogen discharge tube, the light from which was chopped at about 400 Hz. A photomultiplier-sodium salicylate combination was used as the detector system. The signal from the photomultiplier was amplified with a high-gain low-noise preamplifier and then fed into a phase sensitive detector.

All measurements were made within 2° of normal incidence and with a relatively low resolving power ($\sim 30 \text{ \AA}$) for the reasons given in Ref. [3]. The corresponding energy resolution varied from about 0.02 at 3.0 eV to about 0.4 at 13.0 eV as indicated in Fig. 1. All the experimental results were taken on a 'point by point' basis which made it possible to apply a correction for stray light in those regions of the spectrum where this procedure was necessary.

The majority of the measurements were made on platelets grown from solution at the solvent interface. Practically identical results were obtained in a few measurements on samples cleaved from an anthracene boule. The surfaces studied were natural ab planes. Repeated runs on the same specimen gave consistent results as long as the crystal was kept

*Present Address: Kent Instruments, Luton, England.

under vacuum. Prolonged exposure to the atmosphere obscured detail in the measured reflectivity and also gradually diminished its absolute value.

The reflectivity curve shown in Fig. 1, obtained with unpolarised light, is typical of the results for all the samples studied. The experimental range extended from 2 to 13 eV.

3. ANALYSIS OF RESULTS

The Kramers-Krönig relation used in the analysis of these results to give the phase change on reflection, $\theta(\omega_0)$, for radiation of angular frequency ω_0 , is

$$\theta(\omega_0) = \frac{\omega_0}{\pi} \int_0^{\infty} \frac{\ln R(\omega)}{\omega^2 - \omega_0^2} d\omega \quad (1)$$

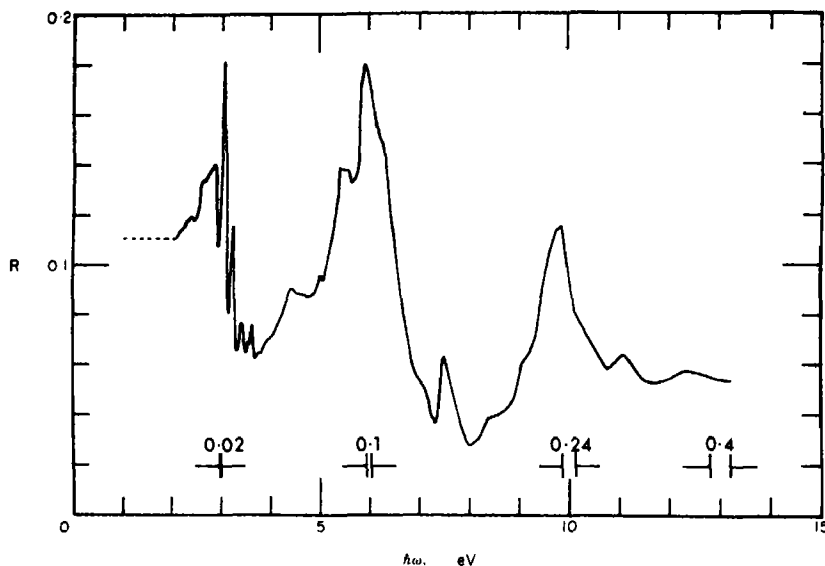


Fig. 1. The spectral dependence of the normal incidence reflectivity from an anthracene crystal, measured with unpolarised light. The experimental energy resolution, in eV, is indicated at four parts of the spectrum.

The reflectivity values shown for energies less than 2 eV were extrapolated from the published refractive index data[14]. These measurements show that between about 4500 and 7000 Å the refractive index is practically constant and ranges from about 1.6 to 2.2 for the three principal directions. In addition, the measured[15] value of $\sqrt{\epsilon_s} = 1.86$, where ϵ_s denotes the static dielectric constant, suggests that there is also no appreciable dispersion at longer wavelengths, so that below 2 eV the reflectivity should be essentially constant. Our extrapolated value of $R = 0.11$ for unpolarised light corresponds to an average refractive index of 2.0.

where $R(\omega)$ is the reflectivity at normal incidence for light of angular frequency ω . The obvious difficulty in applying equation (1) is that the integral is to be taken from 0 to ∞ , whereas the range of experimentally observed $R(\omega)$ is limited. Following the discussion given in Ref.[3] we split the integral in equation (1) into three components:

$$I_1(\omega_0) = \frac{\omega_0}{\pi} \int_0^a \frac{\ln R(\omega)}{\omega^2 - \omega_0^2} d\omega \quad (2)$$

$$I_2(\omega_0) = \frac{\omega_0}{\pi} \int_a^b \frac{\ln R(\omega)}{\omega^2 - \omega_0^2} d\omega$$

$$I_2(\omega_0) = \frac{\omega_0}{\pi} \int_b^a \frac{\ln R(\omega)}{\omega^2 - \omega_0^2} d\omega. \quad (4)$$

The interval (a, b) is defined as that region over which the reflectivity has been measured. I_2 was then calculated directly from the experimental data by means of a computer programme based on the three point Simpson procedure. In order not to lose fine structure the step length was fixed at 0.025 eV; thus, approximately 500 data points were calculated in each run.

As there is no appreciable absorption in the range from $0 < \omega < a$ for anthracene, the reflectivity remains constant. Equation (2) can then be integrated analytically to give:

$$I_1(\omega_0) = -\frac{1}{2\pi} \ln R(a) \ln \left(\frac{\omega_0 + a}{\omega_0 - a} \right). \quad (5)$$

The remaining contribution to $\theta(\omega_0)$ is the high frequency part I_3 and it is this that presents the major difficulty in the analysis. In the calculation the criterion that the phase angle must be zero in regions of negligible absorption was used. Based on calculated values of $I_1 + I_2$ the following suitable form for I_3 was chosen:

$$I_3(\omega_0) = -[A + B \ln(b + \omega_0) - C \ln(b - \omega_0)]. \quad (6)$$

The values of A , B and C were evaluated by solving three simultaneous equations obtained by equating $\theta(\omega)$ to zero at two energies below the region of significant absorption, (i.e. < 2 eV), and at 4.25 eV, where the absorption is also negligible (see for example, Bree and Lyons[1]). From equations (3), (5) and (6) the phase angle θ could then be calculated as a function of energy. $\theta(\omega)$, together with the measured reflectivity, then led to the various optical constants. Figure 2 shows the absorption coefficient $\alpha(\omega)$ and Fig. 3 the energy dependence of the (real) index of refraction n and the index of absorption k , where $k = \alpha\lambda/4\pi$. The imaginary part of the dielectric constant, $\epsilon_2 = 2nk$, is shown in Fig. 4.

It is worth emphasising at this point that the spectral characteristics of the calculated optical constants are almost completely determined by $I_2(\omega)$, the experimentally determined part of $\theta(\omega)$. Any interpretation of the ϵ_2 curve, leading to a suggested energy level diagram should, therefore, be largely inde-

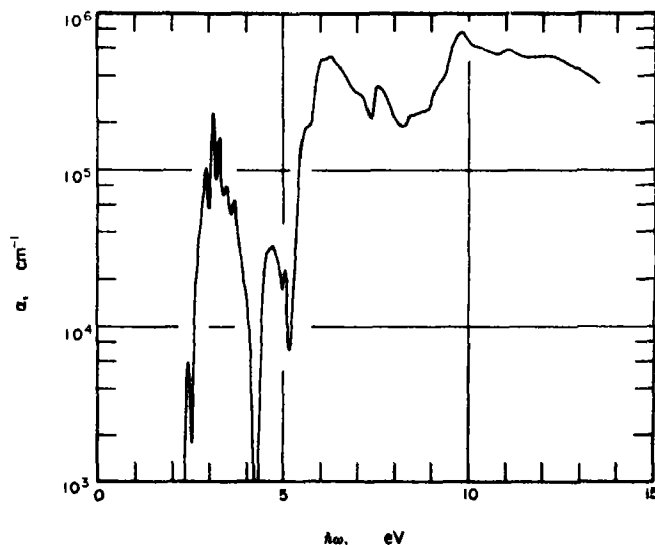


Fig. 2. The spectral dependence of the computed absorption coefficient, α .

pendent of the extrapolation procedure used. The absolute magnitudes of the calculated optical constants do, however, depend on the extrapolation procedure used and should thus be regarded with some caution. On the other hand, the calculated magnitudes were not very sensitive to the values of the constants in equation (6). The results shown in Figs. 2, 3 and 4 were calculated using $A = 0.85$, $B = -325$ and $C = 296$ (in arbitrary units). Yet, a choice of $A = 0.75$, $B = -128 = -C$, in the

4. DISCUSSION

4.1. The absorption coefficient

The calculated absorption coefficient is shown as a function of photon energy in Fig. 2. The spectral features in the range from 3.1 to 5.5 eV are in good agreement with the data of Bree and Lyons[1]. The calculated magnitude of the absorption coefficient is consistent with their data, although a direct comparison is difficult since they used polarised light. One major difference in the two sets of

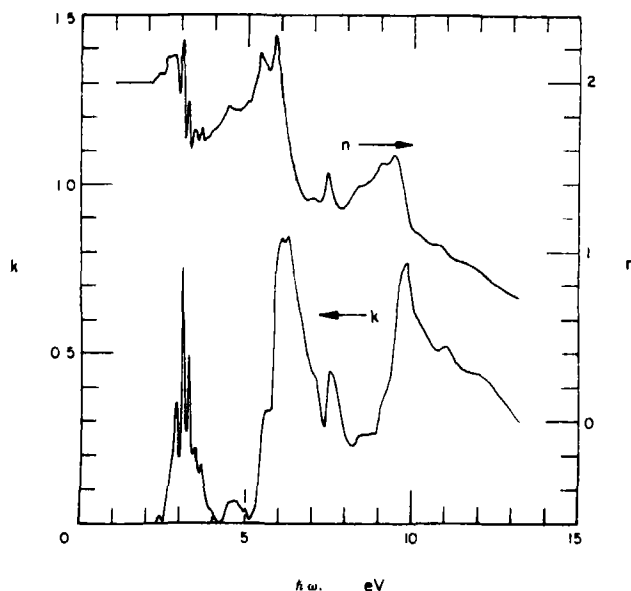


Fig. 3. Plot of the calculated real index of refraction, n , and the index of absorption, k .

same relative units, gave a set of results little different in either shape or absolute magnitude to those shown. For example, the $\epsilon_2(\omega)$ curve calculated with these values only differed significantly for $\omega > 10$ eV where the magnitude was somewhat less than that shown in Fig. 4. In general, this result may be expected from the form of the dispersion relations, but the insensitivity of the fitting procedure as the upper limit of the experimental energy range is approached emphasises the caution with which absolute magnitudes in this region must be regarded.

data occurs below 3.0 eV. Their measured absorption coefficient is essentially zero for energies less than 3.0 eV. The data shown in Fig. 2 indicates the onset of absorption well below this value. It is interesting in this context to note that the reflectivity data of Bree and Lyons[1] also shows structure below 3.0 eV which would confirm our measurements. It is possible that this absorption, beginning at about 2.3 eV, is associated with transitions from the ground state to surface states. Baessler and Vaubel[4] have suggested the existence of surface states, in an energy range

from (2.4 ± 0.2) eV above the ground state to about 3.7 eV, to explain their results on the threshold for photoemission of electrons or holes from various metals into anthracene. The agreement between their figure for the energy at which surface states become significant and the energy at which our absorption coefficient first increases lends support to the interpretation. If this is correct, then the peak in α at 2.9 eV may well arise from transitions from the ground state to a peak in the surface state distribution at this energy.

4.2. Sum rules

It is possible to check the internal consistency of the analysis by the application of the following sum rules: [3]

$$\int_0^\infty n \alpha \, d\lambda = (n_0^2 - 1) \pi^2 \quad (7)$$

where n_0 is the zero frequency value of the refractive index;

$$\int_0^\infty \alpha \, d\lambda = (n_0 - 1) 2\pi^2 \quad (8)$$

and

$$\int_0^{\omega_0} \omega \epsilon_2(\omega) \, d\omega = \frac{2\pi N e^2}{m} n_{eff} \quad (9)$$

where N is the number of molecules per unit volume and n_{eff} is the effective number of electrons per molecule (see, for example, Ref. [5]).

We have evaluated the integrals in equations (7) and (8) between $\lambda = 800 \text{ \AA}$ and ∞ by numerical integration leading to values of 10.1 and 6.9 respectively. These should be compared with $(n_0^2 - 1) \pi^2 = 29.5$ and $(n_0 - 1) 2\pi^2 = 19.7$. The low values obtained from the integrals indicates that the spectral region studied does not contain all the significant optical transitions. It is significant that both integrals, which are over the same interval, yield approximately the same proportion of the predicted value, 34 and 35 per cent respectively. This agreement demon-

strates the internal consistency of the analysis.

As a final check we have evaluated the integral in equation (9) for $\omega_0 = 15.5 \text{ eV}$ and calculated $n_{eff} = 10.1$. This represents 36 per cent of the available 28 electrons that are involved in molecular orbitals. The agreement between this and the other sum rules provides yet another check on the analysis.

5. INTERPRETATION OF THE RESULTS

In interpreting our data, the quantity of most interest is the imaginary part of the dielectric constant. $\epsilon_2(\omega)$ is determined predominantly by the joint density of states function, provided the matrix elements linking initial and final states for a particular transition do not vary greatly over the Brillouin zone. For the purpose of suggesting a possible energy level diagram from our $\epsilon_2(\omega)$ data it has been assumed that the only significance of the matrix elements is to make certain transitions allowed and others forbidden.

The $\epsilon_2(\omega)$ spectrum shown in Fig. 4 has its predominant features numbered. In Fig. 5 we show a suggested energy level scheme for anthracene that could, in principle, account for most of these features. The transitions in Fig. 5 are numbered to correspond to the features in Fig. 4. Before proceeding with a discussion of these, we would like to emphasise the tentative nature of our interpretation. In order to provide more conclusive evidence, or otherwise, for the proposed scheme, we feel it necessary for further experiments to be carried out, particularly with polarised light.

The $\epsilon_2(\omega)$ curve in Fig. 4 and the transitions shown in Fig. 5 have been divided, for the purpose of discussion, into three regions. The first, region I, comprises those transitions from the ground state to a number of higher levels. Region II involves transitions to the same set of levels above the ground state, but from a deeper level, denoted by A , at about -2.9 eV . Similarly, region III describes transitions from an even deeper level at about -6.6 eV , denoted by B , to the same states above the ground state. These transitions, from successively

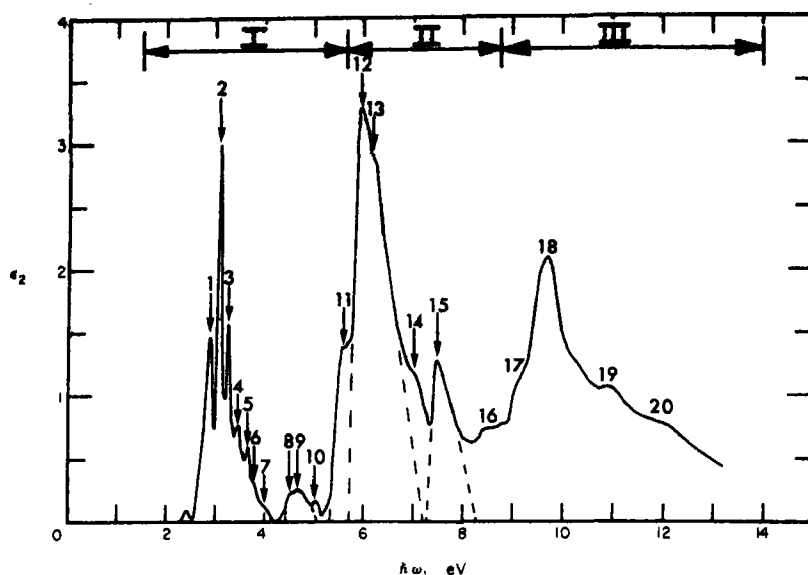


Fig. 4. The spectral dependence of the imaginary part, $\epsilon_2(\omega)$, of the complex dielectric constant. The numbers above certain features are used in the discussion.

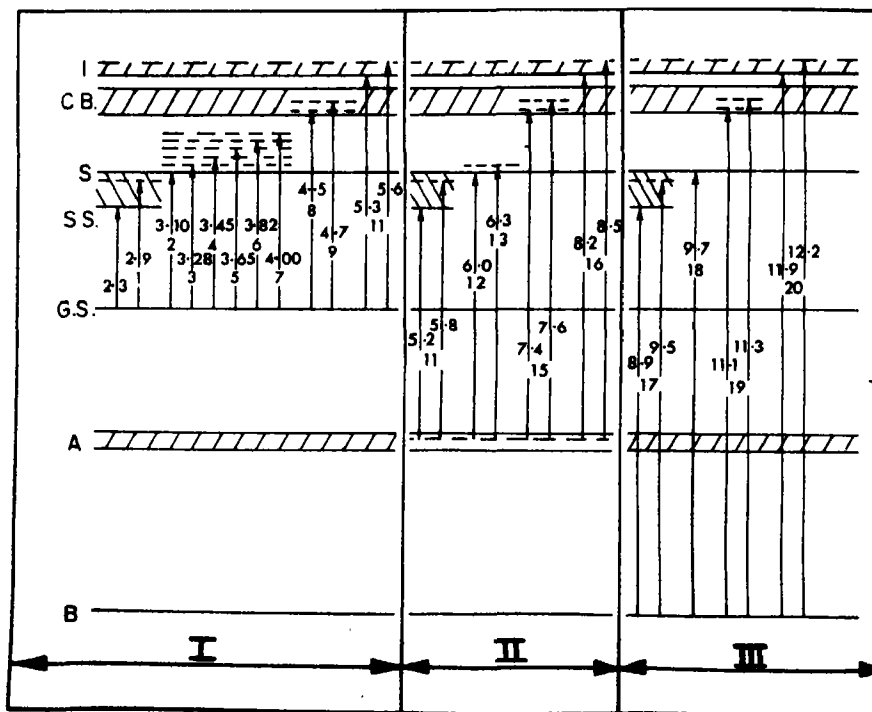


Fig. 5. Suggested interpretation of the main features of the $\epsilon_2(\omega)$ curve. The transitions are numbered to correspond to particular features in Fig. 4. Above these numbers the energies of the transitions are given in eV. I: ionization edge; C.B.: second conduction band; S: singlet state; S.S.: surface states; G.S.: ground state. A and B denote levels below the ground state and are discussed in the text.

deeper levels to the same set of unfilled states, result in an $\epsilon_2(\omega)$ curve that repeats its general spectral features three times, as the data in Fig. 4 suggest. The decrease in the experimental spectral resolution and possibly the increase in the width of the energy levels below the ground state, results in the loss of sharp structure at the higher energies. In the following, this interpretation will be discussed in more detail.

The final states involved in transitions below 3.0 eV, (region I), we have tentatively assigned to surface states as discussed in Section 4.1. There seems little doubt that the peak at 3.1 eV (2) is due to transitions from the ground state to the singlet level [1]. The features (3) to (7) could then be identified with transitions to vibrational levels associated with this singlet. The average energy interval between these transitions is 0.18 eV, in good agreement with the vibrational energy deduced by other measurements [1, 6]. However, in view of the existence of the charge-transfer state at 3.45 [7] and the narrow conduction band somewhere between 3.7 eV [7] and 3.9 eV [8], the identification of all these features with transitions to vibrational singlet states can not be made with complete confidence.

At about 4.4 eV the onset of a smoothly varying $\epsilon_2(\omega)$ signifies the beginning of band transitions. We would thus identify these transitions as those from the ground state to the second, broader conduction band. Since the ground state bandwidth is ≤ 0.1 eV [9] the width of this conduction band can be estimated to be 0.6 ± 0.1 eV. Both the position and width of this band are in good agreement with that deduced from other experiments [8, 10]. Significant density of states maxima seem to occur in this band at 4.5 eV (8) and 4.7 eV (9).

The spectral features observed just beyond 5.3 eV (11) could be explained in three ways: (a) by transitions from the ground state to a higher unfilled band beginning at about 5.3 eV, having a density of states maximum at about 5.6 eV; (b) by transitions from a density of states maximum below the ground state, at

−2.9 eV, to the surface states beginning at about 2.3 eV; (c) by a combination of (a) and (b). As we cannot distinguish between these, both (a) and (b) are represented in Fig. 5. It is possible that the structure in $\epsilon_2(\omega)$ at about 5.6 eV may be associated with the photoemission of electrons from the ground state of anthracene into vacuum. The threshold for this process occurs at 5.65 eV [11]. The relatively low quantum yields obtained by Lyons and Morris in their photoemission experiments [11], could be caused by the competing excitation from the level at −2.9 eV to the surface states.

As suggested above, the transitions in region II are associated with a level, denoted by *A* in Fig. 5, having a density of states maximum at −2.9 eV. Transitions from this level to the surface states (Section 4.1) could also explain the structure commencing at 5.3 eV as proposed in the previous paragraph. More convincing evidence for level *A* comes from the observed peak in $\epsilon_2(\omega)$ at 6.0 eV (12). This we have identified as a transition to the singlet at 3.1 eV. The feature marked (13) would then correspond to transitions to the first vibrational state of the singlet. The loss of sharp structure in this region could be due to the width of the band *A*. From the width of the ϵ_2 peak around 6 eV we would estimate this band to be about 0.4 eV wide.

The peak at 7.5 eV (15) could be connected with transitions from the proposed density of states maximum at −2.9 eV to the density of states maxima in the conduction band at 4.5 and 4.7 eV. From the width of this peak 1.0 eV, and the estimated width of the conduction band of 0.6 ± 0.1 eV, we obtain the band width for the −2.9 level of 0.4 ± 0.1 eV, in agreement with that estimated above. Transitions from *A* to the level beginning at 5.3 eV could explain the feature denoted (16) in the $\epsilon_2(\omega)$ curve.

In order to account for the subsequent high energy data (region III) it is necessary to postulate a second level *B* below the ground state, at about −6.6 eV. Transitions from *B* to the surface states, to the singlet, to the second

conduction band and to the level beginning at 5.3 eV could then give rise to the features denoted (17), (18), (19) and (20) respectively, in Figs. 4 and 5. Due to our limited resolution in this range, it is not possible to estimate the width of the proposed band at -6.6 eV.

If we accept the existence of the surface states suggested in Section 4.1 then the only features that do not seem to fit into the suggested band scheme of Fig. 5 are the small peak in $\epsilon_2(\omega)$ at 5.0 eV (10), and the shoulder around 7.0 eV (14). Apart from the surface states, all the levels used in the interpretation of the calculated $\epsilon_2(\omega)$ data are represented in Fig. 6(a), together with their energetic positions with reference to the ground state energy.

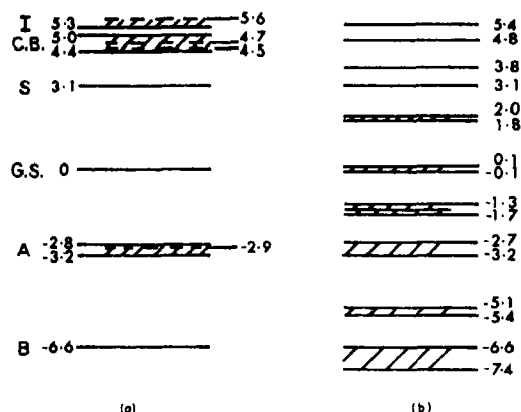


Fig. 6(a). Energetic position of the levels used in the interpretation of the calculated $\epsilon_2(\omega)$ data. The broken lines indicate regions of high density of states in the relevant bands. The levels are identified with the same notation used in Fig. 5. (b) LCAO-HCO calculation of the energy levels of anthracene (after Jäger[12]). All energies are in eV.

Jäger[12] has recently made a LCAO-HCO calculation of the energy bands of anthracene. The resulting energies are obtained in terms of the Hückel parameter β for adjacent C-atoms. Unfortunately, the values of β quoted in the literature vary between wide limits (see, for example, Table 1 of Ref.[13]). In order to make use of Jäger's results we have, therefore, normalized his energy levels so that the ground state to singlet separation agrees with the well established value of 3.1 eV. This

required that one β unit be equivalent to 2.5 eV, a value not inconsistent with other determinations[13]. This value of β also gives an energy level at 1.8 eV that can be identified with the triplet state[6], providing a check on this procedure. With this normalization, Jäger's calculated band scheme is shown in Fig. 6(b). It is of interest to note that filled levels are predicted close to those we have postulated at -2.9 and -6.6 eV, although we do not appear to observe transitions from the levels at about -1.5 and -5.0 eV. Whether the latter are relatively forbidden, or whether the calculations are not sufficiently correct, so that, for example, the -1.5 eV level may have merged with that at -2.9 eV, we are not able to say. In view of the somewhat arbitrary normalization we have made to the calculated levels we feel that it is not possible to draw further conclusions at this stage.

6. CONCLUSIONS

- (1) The normal incidence reflectivity of anthracene has been measured using unpolarised light in the range from 2 to 13 eV.
- (2) The optical constants of anthracene in this energy range have been calculated from the measured reflectivity using the Kramers-Kronig analysis.
- (3) The spectral features of the $\epsilon_2(\omega)$ curve have been tentatively explained by the model shown in Fig. 6(a). This model is based on transitions to (a) the singlet at 3.1 eV, (b) the conduction band at 4.4 eV, and possibly (c) another band at 5.3 eV, from filled levels at (i) the ground state, (ii) a level having a density of states maximum at -2.9 eV and (iii) a level at approximately -6.6 eV.

Acknowledgements—The authors would like to express their gratitude to Professor W. E. Spear for his continuous help and encouragement, to Dr D. J. Gibbons of the E.M.I. Laboratories for kindly supplying the anthracene crystals grown from solution, and to Mr R. Dalrymple for making the measurements on the boule crystals.

REFERENCES

1. BREE A. and LYONS L. E., *J. Chem. Soc.* 3, 2662 (1956).
2. WRIGHT W. H., *J. chem. Phys.* 46, 2951 (1967).

3. COOK B. E. and SPEAR W. E., *J. Phys. Chem. Solids* **30**, 1125 (1969).
4. BAESSLER H. and VAUBEL G., *Phys. Rev. Lett.* **21**, 615 (1968).
5. PHILIPP H. R. and EHRENREICH H., *Phys. Rev.* **A129**, 1550 (1963).
6. See, for example, AVAKIAN P., ABRAMSON E., KEPLER R. G. and CARIS J. C., *J. chem. Phys.* **39**, 1127 (1963).
7. POPE M., BURGOS J. and GIACHINO J., *J. chem. Phys.* **43**, 3367 (1965).
8. VAUBEL G. and BAESSLER H., *Phys. Status Solidi* **26**, 599 (1968).
9. WILLIAMS R. and DRESNER J., *J. chem. Phys.* **46**, 2133 (1967).
10. BAESSLER H., RIEHL N. and VAUBEL G., *Phys. Status Solidi* **26**, 607 (1968).
11. LYONS L. E. and MORRIS G. C., *J. Chem. Soc.* **5192** (1960).
12. JÄGER J., *Phys. Status Solidi* **35**, 731 (1969).
13. SLIFKIN M. A., *Nature Lond.* **200**, 877 (1963).
14. EICHIS A., *Z. eksp. teor. Fiz.* **20**, 471 (1950).
15. KRONBERGER H. and WEISS J., *J. Chem. Soc.* **464** (1944).

DEFECT STRUCTURE AND ELECTRICAL PROPERTIES OF NiO—I. HIGH TEMPERATURE*

C. M. OSBURN† and R. W. VEST

Purdue University, Lafayette, Indiana 47907, U.S.A.

(Received 16 July 1970)

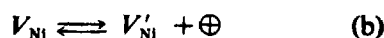
Abstract—Electrical conductivity and weight change measurements were made on single crystal and polycrystalline nickel oxide as a function of temperature from 900 to 1400°C and oxygen partial pressure from 1 atm to 10^{-4} atm. Samples of several different purities were measured. Both conductivity and weight change were proportional to the one-sixth power of the oxygen partial pressure, and had an activation energy of 18.6 ± 1.0 kcal/mole for the highest purity samples. Impurities increased both the activation energy and the pressure dependence for conduction. The integrated carrier density of states, N_v , would fit a $T^{3/2}$ temperature dependence supporting a band model. The hole mobility was $0.53 \text{ cm}^2/\text{V-sec}$ and was almost temperature independent. The magnitude and temperature dependence of the mobility would not easily fit either a band or a hopping transport model.

1. INTRODUCTION

THE MECHANISM responsible for electrical conduction in nickel oxide has been under question for some time. The structure of NiO would at first indicate a metallic $3d$ band, but all experiments have shown a very low conductivity at lower temperatures. This low conductivity was initially explained by Verwey and de Boer[1] with a model of localized $3d$ electrons. Later studies[2-6] as reviewed by Bosman and Crevecoeur[7] found evidence for a thermally activated mobility as would be expected in the hopping polaron regime, but several recent investigations have concluded that conduction occurs via a narrow band mechanism[7-11]. The magnitude and temperature dependence of the Hall[9-17] effect as well as the Seebeck voltage[7, 8] is the primary evidence for conduction in narrow bands. Alternating current conductivity measurements[18-21] have been taken to further resolve the conduction mechanism,

however, the interpretation of the results is not unequivocal.

Whereas the transport mechanism has been the focus of attention at temperatures of 500°K and below, the defect structure has been the important phenomenon to study at temperatures over 1000°K. At high temperatures, the defect structure of NiO is still questionable, although it is generally considered to be a metal deficit, p -type semiconductor. At temperatures high enough for equilibration to occur with the gas phase, the usual reactions which are considered in NiO are:



and



where the notation is that of Kröger and Vink[22]. Considering only these three reactions neglects any contributions from impurities or defect associates in addition to other isolated point defects and electrons.

If K_{O_2} , K_1 , and K_2 are taken to be the equilibrium constants for reactions (a), (b) and (c), then the law of mass action gives:

*This work was supported in part by the National Science Foundation, the Advanced Research Projects Agency of the Department of Defense, Delco Radio Division of General Motors Corporation, and the Basil S. Turner Foundation.

†Present Address: IBM Watson Research Center, Yorktown Heights, New York 10598, U.S.A.

$$[V_{Ni}] = (K_{Ox} \cdot P_{O_2})^{1/2} \quad (1)$$

$$p[V'_{Ni}]/[V_{Ni}] = K_1 \quad (2)$$

$$p[V''_{Ni}]/[V'_{Ni}] = K_2 \quad (3)$$

and electroneutrality requires

$$p = [V'_{Ni}] + 2[V''_{Ni}]. \quad (4)$$

When the singly-ionized nickel vacancy concentration is much greater than the doubly-ionized vacancy concentration, the hole concentration is proportional to the fourth root of the oxygen partial pressure ($P_{O_2}^{1/4}$); when doubly-ionized vacancies predominate, the hole concentration is proportional to the sixth root of the oxygen partial pressure ($P_{O_2}^{1/6}$). If the mobility is independent of the concentration of holes, then the conductivity is proportional to the fourth or the sixth root of the pressure, depending on the vacancy charge.

Many studies have attempted to determine the charge on the nickel vacancies, but the results were contradictory. Conductivity measurements have found singly ionized [23-27] and doubly ionized [28-32] vacancies. One weight change [28] and two coulometric titration [33-34] studies have found doubly-ionized vacancies at high pressures, and one weight change study [35] was unable to resolve the charge of the predominant defect.

The objective of the present study was to determine the high temperature defect structure of pure NiO by means of conductivity and weight change measurements. Measurements were made above 900°C and over oxygen pressure ranges where the samples would equilibrate with the gas phase. The combination of these two measurements can give information on the carrier concentrations and hence shed light on the defect structure and the mobility of the carriers.

2. EXPERIMENTAL

(a) Materials

Samples from several different sources were

used in the course of this investigation. Polycrystalline nickel oxide samples used for weight change and conductivity measurements were made from 5N (99.999%) pure powder supplied by United Mineral and Chemical Corporation. Mass spectrographic analyses of the starting powder as well as of polycrystalline samples taken after both conductivity and weight change measurements are given in Table 1. The polycrystalline samples were fabricated by uniaxially pressing the NiO powder at 11,000 psi with distilled water as a binder to enhance green strength. The pellets were dried at 200°C and sintered in air at 1500°C for 24 hr. Samples prepared in this manner had 82 per cent theoretical density and grain sizes up to 20 μ . Single crystals of three different purity levels were used for conductivity measurements. Before and after analyses on the high purity crystal, and after analyses on the intermediate and low purity crystals are given in Table 2. The high and low purity crystals were grown by the Verneuil technique in an arc image furnace, while the intermediate purity crystal was grown by halide decomposition.

(b) Weight change

Thermogravimetric measurements were made from 900 to 1400°C with an Ainsworth type FV-AU-1 recording microbalance. The details of the balance have been described elsewhere [36] and will not be repeated here. Calibration runs were made with inert sapphire in each different gas mixture as a function of temperature in order to determine the apparent weight changes due to the effects of buoyancy, thermal convection currents, and gas viscosity. A primary source of error in the gravimetric determination of changes in point defect concentrations is the fact that these apparent weight changes are often much greater than the real weight changes desired. This requires extreme accuracy in both the measurements on the sample as well as on the inert sapphire. The required accuracy can be readily obtained for weight change as a function of temperature

Table 1. Analysis of polycrystalline NiO. Values in ppmw

Element	Starting powder United Mineral 99.999%	Sample 7691 after conductivity measurements	Sample 12681 after weight change measurements
Li	<0.01	10	10
F	<0.03	<3	<3
Na	10	50	15
Al	1	20	4
Si	5	100	50
S	1	20	1
Cl	3	30	2
K	0.3	30	2
Ca	2	50	5
Ti	0.2	3	1
V	<0.03	3	2
Cr	<0.04	10	2
Mn	<0.03	1	35
Fe	3	40	400
Co	<0.3	10	4
Cu	1	8	1
Zn	<1	8	<1
Ga	<0.5	1	5
Ba	<0.1	1	4
Pt	<0.4	2	<1
Total Determined	27	397	541

All other impurities < 1 ppmw.

at constant atmosphere (isobars), but it is very difficult to maintain the required accuracy for measurements as a function of atmosphere at a constant temperature (isotherms).

A new analysis technique was developed during this study that required using only isobars of weight change measurements, thereby eliminating the need to make measurements at a constant temperature at different pressures. If the assumption of a single predominant defect is made, the sample weight can be expressed as

$$W = (\alpha/N_0)(M_n + 16) + CP_0^\alpha e^{-E/RT} \quad (5)$$

where M_n = atomic weight of the metal
 α = number of metal atoms in the sample

N_0 = Avogadro's number

E = activation energy for the predominant defect

C = constant containing the entropy

of formation of the predominant defect

x = pressure dependence of the predominant defect.

In general, thermogravimetric measurements are taken as a weight change or the total sample weight (W) minus a reference weight (W_i). Thus

$$\Delta W = W - W_i. \quad (6)$$

Combining equations (5) and (6) and differentiating twice yields

$$\frac{d}{d(1/T)} \left[\ln \frac{d\Delta W}{d(1/T)} \right] = -E/R. \quad (7)$$

Equation (7) can be used with the experimental data to determine the activation energy for the formation of the defects; it might be pointed out that the derivatives can be taken

Table 2. Analysis of NiO single crystals. Values in ppmw

Element	High purity Sample 66910 before measurements	High purity Sample 66910 after measurements	Intermediate purity Sample 106927 after measurements	Low purity Sample 11684 after measurements
Li	0.1	2	0.6	10
F	< 10	< 3	< 3	< 1
Na	3	30	30	20
Mg	< 6	20	20	< 10
Al	6	20	20	40
Si	30	20	20	< 10
S	10	40	10	20
Cl	4	10	25	5
K	1	15	5	2
Ca	4	15	10	10
Ti	< 1	3	< 1	10
Cr	< 0.3	0.3	2	5
Mn	—	2	25	< 10
Fe	10	40	200	500
Co	5	30	25	500
Cu	1	8	6	20
Ga	< 2	2	3	50
Br	—	—	20	—
Pt	—	2	< 3	< 1
Total Determined	74	259	422	1262

All other impurities < 1 ppmw.

either numerically or graphically. Once the value of E has been determined, equations (5) and (6) can be differentiated to give

$$\frac{d\Delta W}{d(e^{-E/RT})} = CP_{O_2}^x \quad (8)$$

Taking logarithms and differentiating again yields

$$\frac{d}{d(\log P_{O_2})} \left[\log \frac{d\Delta W}{d(e^{-E/RT})} \right] = x. \quad (9)$$

Equation (9) can be used to determine the pressure dependence with the required derivatives being taken either numerically or graphically. In both equations (7) and (9) the first derivatives are taken with respect to a function of temperature; hence, only isobars are necessary. Two different isobars are then used to compute the second derivative in equation (9).

(c) Conductivity

The conductivity measurements were made in variable atmosphere furnaces utilizing high purity alumina muffle tubes of a design similar to one previously described [36]. Oxygen partial pressures were established with oxygen and with oxygen/argon mixtures. Since the phase field is limited at high temperatures, oxygen partial pressures below 10^{-4} atm were not routinely used.

Conductivity measurements were made using standard four-point potentiometric techniques. Engelhard 6082 platinum paste was used to paste 0.1 mm platinum wires to the samples for the measurements. While most of the measurements were d.c., a.c. measurements were also taken to check the frequency characteristics; no dispersion of conductivity was found up to 100 kHz. The sample holder was constructed from the highest purity recrystallized alumina available. Thus only the sample, Pt-Rh wires, and 99 per cent

alumina were in the hottest section of the furnace. Even with these precautions, there was a considerable pick-up of impurities as demonstrated by the before and after analyses in Tables 1 and 2.

3. RESULTS AND DISCUSSION

(a) Weight change

Weight change isobars for nickel oxide are shown in Fig. 1. The positions of the isobars relative to one another were determined only after completion of the analysis described in the preceding section. The activation energy for weight change was computed to be 18.6 kcal/mole; to within two standard deviations the error in the activation energy was 1.3 kcal/mole. The pressure dependence was computed to be 0.19 ± 0.03 to one standard deviation. Thus the weight change data will fit a defect model requiring a pressure dependence of $\frac{1}{6}$ or $\frac{1}{3}$, but cannot be fit to a model requiring $\frac{1}{2}$. Figure 2 shows the weight change as a function of the one-sixth power of the oxygen partial pressure. To one standard deviation, straight lines intersecting at zero pressure will fit all of the data which is the required behavior for a single defect model involving fully-ionized nickel vacancies. Thus the deviation from stoichiometry (δ), which

is also plotted on Fig. 2, can be related to the doubly-ionized vacancy concentration and can be expressed analytically as:

$$\delta = \frac{[V_{Ni}^{''}]}{[Ni_{Ni}]} = 0.107 P_{O_2}^{1/6} e^{-(18,400 \pm 1,300)/RT} \quad (10)$$

From coulometric titration Tretyakov and Rapp[33] reported

$$\delta = 0.51 P_{O_2}^{1/6} e^{-(19,000 \pm 8,700)/RT} \quad (11)$$

and Mitoff[28] obtained

$$\delta = 0.11 P_{O_2}^{1/6} e^{-17,800/RT} \quad (12)$$

from weight change measurements. Tripp and Tallan's[35] weight change data can be expressed as either

$$\delta = 0.56 P_{O_2}^{1/4} e^{-(23,000 \pm 3,000)/RT} \quad (13)$$

or

$$\delta = 0.114 P_{O_2}^{1/6} e^{-(18,800 \pm 3,000)/RT} \quad (14)$$

according to the pressure dependence; their data were not sufficient to determine which expression was the correct one. With the exception of equation (13), these expressions are quite similar. The results of Tretyakov

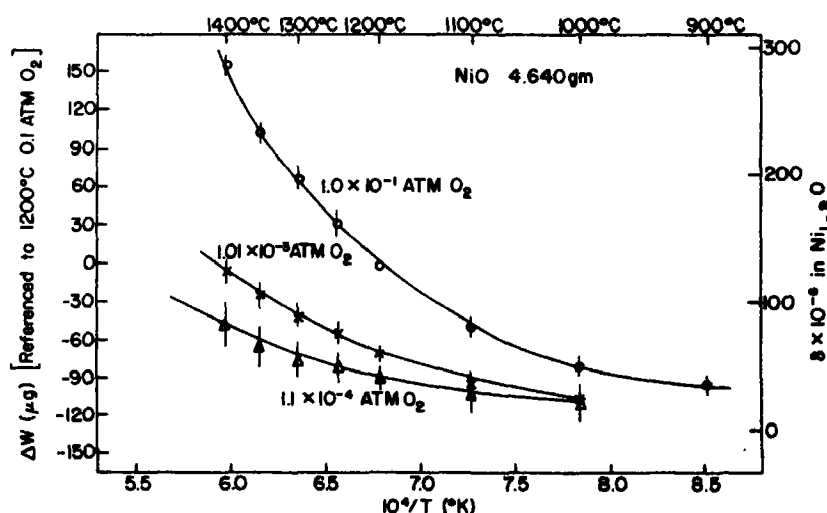


Fig. 1. Temperature dependence of the weight change in nickel oxide.

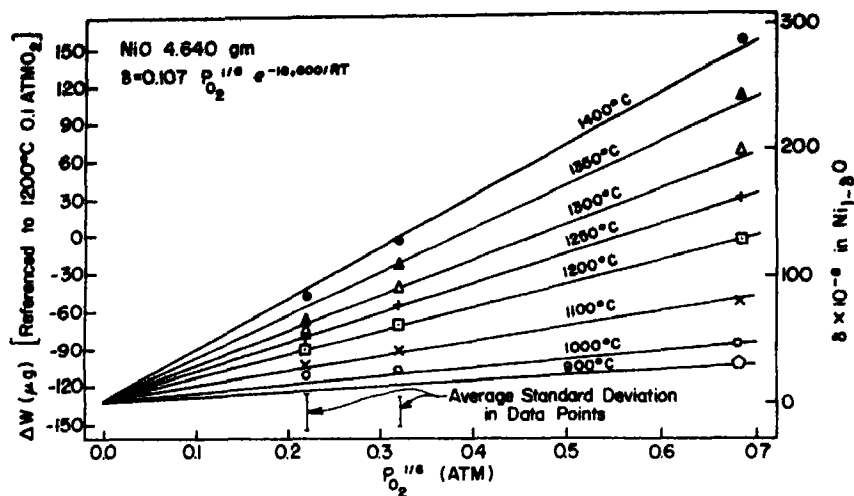


Fig. 2. One-sixth oxygen pressure dependence of the weight change in nickel oxide at 900–1400°C.

and Rapp[33] are, in general, a factor of 3 or 4 higher than the other results, however, their experimental error in the activation energy is the largest. It should be pointed out that the present study was made over the highest temperature range to date.

(b) Conductivity

Conductivity measurements were made on the NiO samples listed in Tables 1 and 2, and the results for the low purity and the intermediate purity crystals are summarized in Table 3. The errors given for ΔH_c represent one standard deviation. The data show a very pronounced temperature variation of the pressure dependence as well as a pronounced pressure variation of the activation energy for conduction. This variation is more pronounced with the lower purity sample. For the low purity sample the average activation energy is about 25 kcal/mole and the average pressure dependence is about one-fourth; several other workers[23–27] have found similar results. For the intermediate purity sample, the activation energy varies from 22 to 26 kcal/mole while the pressure dependence is between one-fourth and one-sixth. As the temperature increases, the pressure

Table 3. Pressure dependence and activation energy for conduction in low and intermediate purity NiO single crystals

$\sigma = AP_{O_2}^{1/4} \exp(-\Delta H_c/RT)$		
	Sample 11684 low purity	Sample 106927 intermediate purity
$T(^{\circ}\text{C})$	x	x
1000	2.79	4.70
1100	3.16	4.99
1200	3.65	5.28
1300	4.22	5.55
1400	4.81	5.83
Log P_{O_2}	$\Delta H_c(\text{Kcal/mole})$	$\Delta H_c(\text{Kcal/mole})$
-0.01	21.1 ± 0.1	22.1 ± 0.2
-1.01	23.6 ± 0.1	21.2 ± 0.2
-2.01	23.6 ± 0.2	22.9 ± 0.2
-3.00	25.3 ± 0.1	23.9 ± 0.4
-3.96	41.7 ± 0.1	25.6 ± 0.4

dependence approaches one-sixth as observed in a recent study [27].

The conductivity isobars and isotherms are given in Figs. 3 and 4 for the highest purity single crystal sample measured. The lines drawn are computer calculated by a least squares fit to the experimental data, and the errors for ΔH_c , given in parentheses, represent one standard deviation.

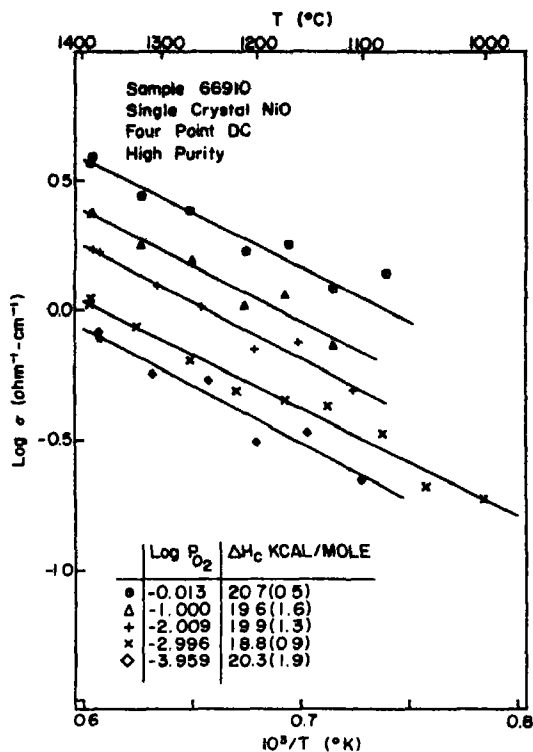


Fig. 3. Conductivity isobars for high purity nickel oxide single crystal.

In this crystal the activation energy is independent of the oxygen partial pressure and is about 20 kcal/mole while the pressure dependence is independent of temperature and is about $1/5.7$.

The highest initial purity sample measured was polycrystalline; the isobars and isotherms are shown in Figs. 5 and 6. These data were not corrected for porosity; to make such a correction the conductivity given should be multiplied by 1.22. As with the high purity single crystal sample, the activation energy and the pressure dependence are only slowly varying functions of the temperature and pressure. The activation energy for conduction in this case is slightly lower than in the less pure single crystal and averages about 18.6 kcal/mole. Furthermore, the pressure dependence is very close to one-sixth.

From the progression of samples having different purity, several conclusions become apparent. As the overall purity increases, the activation energy decreases and the pressure dependence approaches one-sixth. Conversely a high impurity content gives conductivities which have higher temperature and pressure

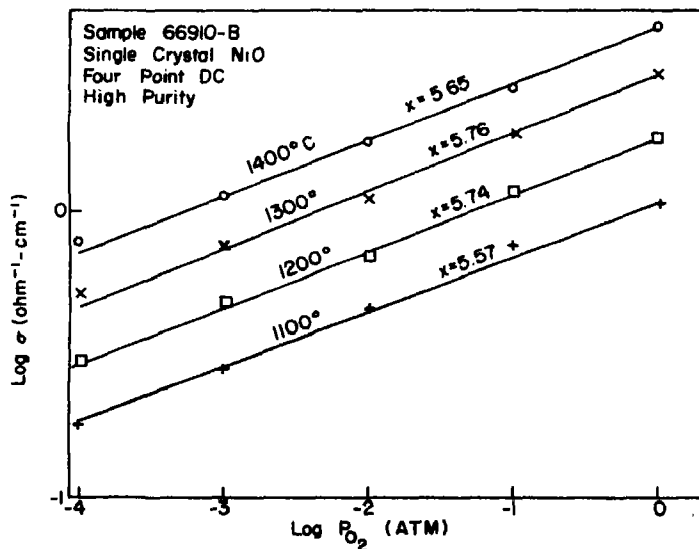


Fig. 4. Conductivity isotherms for high purity nickel oxide single crystal.

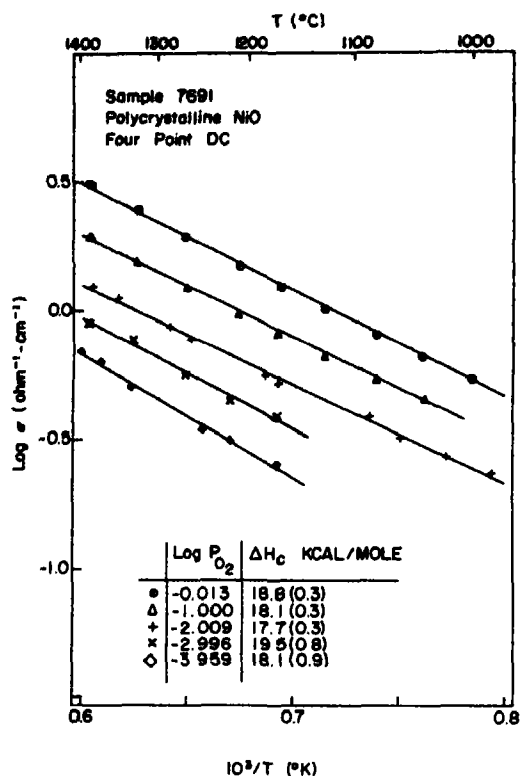


Fig. 5. Conductivity isobars for polycrystalline nickel oxide.

dependencies. Furthermore, impurities yield activation energies that vary with the pressure and pressure dependencies that vary with the temperature. The effect of impurities is dramatically seen in Fig. 7. Conductivity isobars were measured immediately after the sample was electroded and then again after the sample had been in the furnace above 1000°C for more than 100 hr. The relative purities are approximately those given in Table 2 for the before and after high purity crystal. This increase in impurity content brought about a marked change in the conductivity at lower temperatures and lower oxygen partial pressures. Even at 10^{-4} atm the conductivity remained the same at the maximum temperature, whereas at the lower extreme of the equilibration region there was a marked deviation. Activation energies calculated from these high temperature isobars show very little change at high oxygen pressures where the native disorder is the highest, but at $P_{O_2} = 10^{-4}$ atm, which represents the smallest degree of native disorder, the apparent change in activation energy amounts to 25 per cent. Isotherms plotted from the initial data show a $\frac{1}{4}$ power depen-

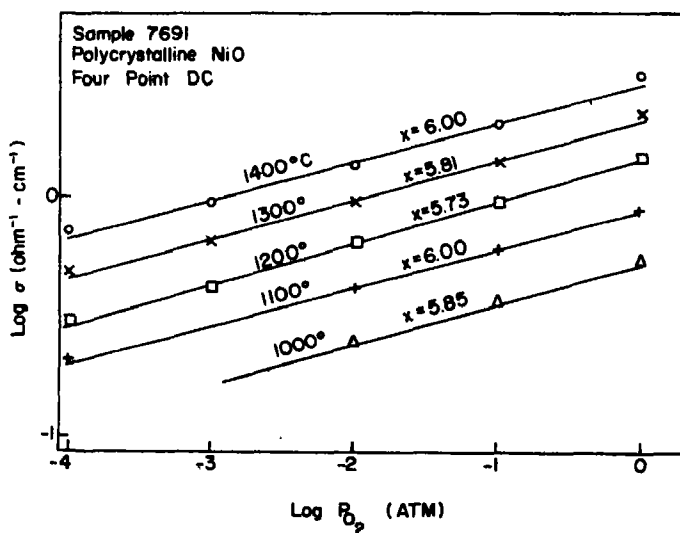


Fig. 6. Conductivity isotherms for polycrystalline nickel oxide.

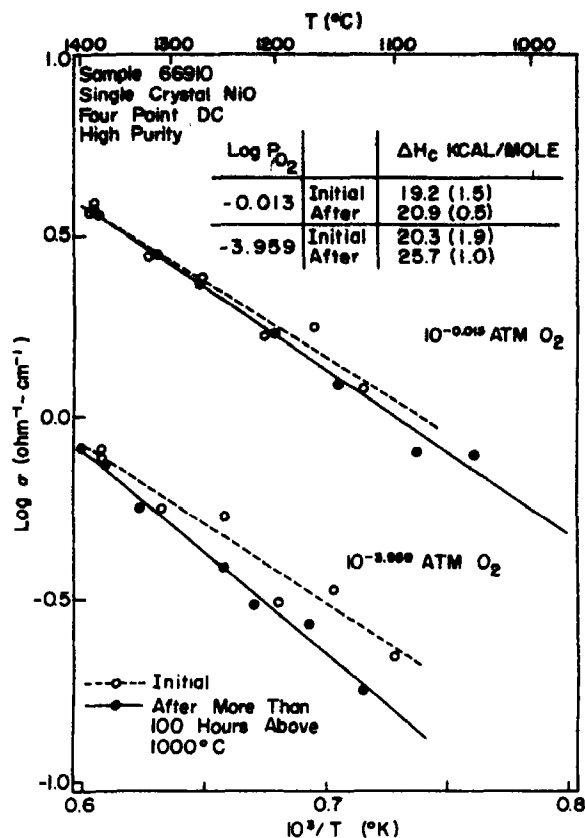


Fig. 7. Conductivity change in nickel oxide after long periods at high temperatures.

dence on oxygen partial pressure as do the highest temperature isotherms after impurity pick-up. However, the low temperature isotherms on the contaminated crystal yield an oxygen partial pressure dependence approaching the $\frac{1}{2}$ power. It is also significant to note that the conductivity decreased with increasing impurity content which indicates that the important impurity must be a donor that partially compensates the hole concentration. From Table 2 it can be seen that the iron content has increased to 40 ppm which is approximately the same as the concentration of nickel vacancies at 1100°C and $P_{O_2} = 10^{-4}$ atm (see Fig. 2).

(c) *Density of states and mobility*

Based on the results and discussion

presented in the proceeding section the conductivity of pure nickel oxide in thermodynamic equilibrium with the vapor is best expressed as

$$\sigma = 9.8 \times 10^2 P_{O_2}^{1/6} \times e^{-(18,800 \pm 1,000)/RT} (\text{ohm}^{-1} - \text{cm}^{-1}). \quad (15)$$

This conductivity equation can be used in conjunction with the thermoelectric power data of Bransky and Talian[26] to compute the temperature dependence of the carrier density of states term, N_v . For a material satisfying the condition $p\mu_h \gg n\mu_e$, the Seebeck coefficient is usually given by [37]:

$$\alpha = k/e (\ln (N_v/p) + A) \quad (16)$$

where p is the hole concentration, N_v is the integrated carrier density of states term, and A is the kinetic energy term. Equation (16) can be differentiated with respect to temperature to yield

$$\frac{d\alpha}{d(1/T)} = k/e \left[\frac{d(\ln N_v)}{d(1/T)} - \frac{d(\ln p)}{d(1/T)} \right]. \quad (17)$$

The $d\alpha/d(1/T)$ term is given by Bransky and Tallan as 0.66 ± 0.03 eV although later work by the same authors suggests a slightly higher value[38]; the last term in equation (17) as determined by this study is 18.6 ± 1.0 kcal/mole or 0.81 ± 0.04 eV. Then clearly

$$k \frac{d(\ln N_v)}{d(1/T)} = -0.15 \pm 0.07 \text{ eV}. \quad (18)$$

This rules out a temperature independent N_v from a hopping model. For a normal wide band conductor N_v is given by

$$N_v = 2(2\pi m^* kT/h^2)^{3/2}. \quad (19)$$

Over the temperature range 850 to 1250°C Kröger[39] has shown that T^3 can be approximated by the following exponential representation:

$$T^3 = 5 \times 10^{10} e^{-0.34 e/kT} \quad (20)$$

Then if N_v is proportional to $T^{3/2}$

$$k \frac{d(\ln N_v)}{d(1/T)} = -0.17 \text{ eV} \quad (21)$$

which agrees with the experimental value of -0.15 eV in equation (18). Thus Seebeck and conductivity data give a density of states, N_v , that varies as $T^{3/2}$ which supports a band conduction model.

Equations (10), (16), and (19) can be used to determine the kinetic energy term, A . Assuming the effective mass is approximately equal to the free electron mass and using Bransky and Tallan's thermoelectric power

data, one finds

$$A \approx 1.5. \quad (22)$$

This value is in good agreement with Bosman and Crevecoeur's[7] approximation of $e^A = 5$ at low temperatures and further supports a band picture. For A to be zero as suggested by others[2, 3, 26] would require an effective mass of 30 times the free electron mass.

The mobility data, however, do not support a band picture. Neglecting singly-ionized vacancies, equation (15) can be combined with equations (4) and (10) to determine the hole mobility which is merely the conductivity divided by the charge-concentration product. The hole mobility calculated in this way is $0.53 \text{ cm}^2/\text{V-sec}$ and is independent of temperature over the range 1000° to 1400°C to within the experimental error on the activation energies for conduction and weight change (2.3 kcal/mole). Room temperature measurements[40] of the drift mobility of holes in NiO gave $0.3 \pm 25\% \text{ cm}^2/\text{V-sec}$. Thus the increase in hole mobility is less than a factor of two over a range of 1400°C.

Lattice scattering in a wide band conductor predicts a mobility which varies as $T^{-3/2}$ [41]; this would correspond to an activation energy of about 4 kcal/mole which is much larger than the limits of error would allow. Likewise, ionized impurity scattering which varies roughly as $T^{3/2}$ [41] would not fit the data. However, a combination of the two mechanisms could yield a mobility that was relatively temperature independent over a wide temperature range.

In the hopping regime, it is possible to have a mobility of the form

$$\mu_n \propto T^{-n} e^{-H_m/RT}. \quad (23)$$

If both n and H_m are positive, the pre-exponential and exponential terms have opposite temperature dependencies and conceivably could have a very small net temperature

variation. The occurrence of the case where the two terms cancel each other exactly would be quite coincidental. The fact that the temperature dependence of the density of states clearly supports a band and not a hopping model raises further doubt as to the validity of the use of a hopping mobility.

The very low temperature dependence of the mobility is thus seen to be very difficult to explain in terms of either band or hopping conduction. The magnitude of the mobility falls between the ranges usually associated with either band conduction or hopping conduction and suggests a narrow energy band or polaron band conduction mechanism.

4. CONCLUSIONS

Both the conductivity and the weight change of pure nickel oxide vary as the one-sixth power of the oxygen partial pressure, indicating that the predominant defect in NiO is a doubly-ionized nickel vacancy. The activation energy for both conduction and weight change is 18.6 kcal/mole, which is one third the enthalpy for the formation and complete ionization of the nickel vacancies.

The total deviation from stoichiometry is quite small in general and is of the order of 10^{-4} . Thus only a hundred parts per million of impurities can be sufficient to control the carrier concentration. The effects of donor impurities, presumably iron, were observed. It is believed that these impurities are responsible for some of the observations of a one-fourth oxygen pressure dependence of the conductivity. Although nickel oxide powder of 5N purity is available, it is very difficult to grow crystals and make measurements at high temperatures without introducing at least 100 ppm of impurities.

Although the temperature dependence of the density of states, N_D , varies as $T^{3/2}$ supporting a band model, the magnitude and temperature dependence of the mobility are inconsistent with either a broad band or a hopping polaron model for conduction.

Acknowledgements—The authors would like to express their appreciation to M. L. Volpe and W. T. Reeves for their assistance in obtaining crystals from the Argonne National Laboratories. Thanks are also due to D. S. Tannhauser of the Technion, Haifa, Israel for supplying additional crystals.

REFERENCES

- (a) VERWEY E. J. W. and DE BOER J. H., *Rec. Trav. Chem.* **55**, 531 (1936).
(b) DE BOER J. H. and VERWEY E. J. W., *Proc. Phys. Soc. London* **49**, 59 (1937).
- (a) MORIN F. J., *Phys. Rev.* **93**, 1199 (1954).
(b) MORIN F. J., *Bell Syst. Tech. J.* **37**, 1047 (1958).
- VAN HOUTEN S., *J. Phys. Chem. Solids* **17**, 7 (1960).
- NACHMAN M., COJOCARU L. N. and RIBCO L. V., *Phys. Status Solidi* **8**, 773 (1965).
- PARRAVANO G., *J. chem. Phys.* **23**, 5 (1955).
- HEIKES R. R. and JOHNSTON W. D., *J. chem. Phys.* **26**, 582 (1957).
- BOSMAN A. J. and CREVECOEUR C., *Phys. Rev.* **144**, 763 (1966).
- (a) AUSTIN I. G., SPRINGTHORPE A. J., SMITH B. A. and TURNER C. E., *Proc. Phys. Soc.* **90**, 157 (1967).
(b) AUSTIN I. G., SPRINGTHORPE A. J. and SMITH B. A., *Phys. Lett.* **21**, 20 (1966).
(c) SPRINGTHORPE A. J., AUSTIN I. G. and SMITH B. A., *Solid State Commun.* **3**, 143 (1965).
- KSENDZOV Y. M., AVDEENKO B. K. and MAKAROV V. V., *Fiz. tverd. Tela* **9**, 1058 (1967).
- VAN DAAL H. J. and BOSMAN A. J., *Phys. Rev.* **158**, 736 (1967).
- BOSMAN A. J., VAN DAAL H. J. and KNIVERS G. F., *Phys. Lett.* **19**, 372 (1965).
- ROILOS M. and NAGELS P., *Solid State Commun.* **2**, 285 (1964).
- NACHMAN M., PAPESCU F. G. and RUTTER J., *Phys. Status Solidi* **10**, 519 (1965).
- KSENDZOV Ya. M., ANSEL'M L. N., VASIL'EVA L. L. and LALYSHEVA V. M., *Fiz. tverd. Tela* **5**, 1537 (1963).
- ZHUZE V. P. and SHEL'YKH A. I., *Fiz. tverd. Tela* **5**, 1756 (1963).
- LUPU'N. Z., TALLAN N. M. and TANNHAUSER D. S., *Rev. scient. Instrum.* **38**, 1658 (1968).
- TALLAN N. M. and TANNHAUSER D. S., *Phys. Lett.* **26A**, 131 (1968).
- (a) SNOWDEN D. P. and SALTSBURG H., *Phys. Rev. Lett.* **14**, 497 (1965).
(b) SNOWDEN D. P., SALTSBURG H. and PEREUE, J. H., JR., *J. Phys. Chem. Solids* **25**, 1099 (1964).
- AUSTIN I. G., CLAY B. C., TURNER C. E. and SPRINGTHORPE A. J., *Solid State Commun.* **6**, 53 (1968).
- KABASHIMA S. and KAWAKUBO T., *J. phys. Soc. Japan* **24**, 493 (1968).
- AIKEN J. G. and JORDAN A. G., *J. Phys. Chem. Solids* **29**, 2153 (1968).

22. KRÖGER F. A. and VINK H. J., In *Solid State Physics*, Vol. 3, p. 307. Academic Press, New York (1956).
23. BAUMBACH H. H. V. and WAGNER C., *Z. Phys. Chem.* **24**, 59 (1934).
24. EROR N. G., JR., Ph.D. Thesis, Northwestern University (1965).
25. ZINTL G., *Z. Phys. Chem.* **54**, 110 (1967).
26. BRANSKY I. and TALLAN N. M., *J. chem. Phys.* **49**, 1243 (1968).
27. (a) VOLPE M. L. and REDDY J., presented at the fall meeting of the Basic Science Division of the American Ceramic Society, Oct. 14-18, St. Paul Minn. (1968).
(b) VOLPE M. L. and REDDY J., *J. chem. Phys.* **53**, 1117 (1970).
28. MITOFF S. P., *J. chem. Phys.* **35**, 882 (1961).
29. PIZZINI S. and MORLOTTI R., *J. electrochem. Soc.* **114**, 1179 (1967).
30. PETTIT F. S., *J. electrochem. Soc.* **113**, 1249 (1966).
31. HERBST R. J., Ph.D. Thesis, University of Illinois (1963).
32. MEIER G. H., Ph.D. Thesis, Ohio State University (1968).
33. TRETYAKOV Y. D. and RAPP R. A., *Trans. AIME* **245**, 1235 (1969).
34. SOCKEL H. G. and SCHMALZRIED H., *Ber. Bunsenges. Phys. Chem.* **72**, 745 (1968).
35. TRIPP W. C. and TALLAN N. M., *J. Am. ceram. Soc.* **53**, 531 (1970).
36. (a) TRIPP W. C., VEST R. W. and GRAHAM H. C., *Vacuum Microbalance Techniques* **6**, 107 (1967).
(b) TRIPP W. C., VEST R. W. and TALLAN N. M., *Vacuum Microbalance Techniques* **4**, 141 (1965).
(c) OSBURN C. M., Ph.D. Thesis, Purdue University, June (1970).
37. IOFFE A. F., *Physics of Semiconductors*, Infosearch London (1960).
38. BRANSKY I. and TALLAN N. M., Presented at *Electronic Phenomena in Ceramics*, University of Florida (November 10, 1969).
39. KRÖGER F. A., *Chemistry of Imperfect Crystals*, p. 693 John Wiley, New York (1964).
40. MAKAROV V. V., KSENDZOV Ya. M. and KRUGLOO V. I., *Fiz. tverd. Tela* **9**, 663 (1967).
41. SMITH R. A., *Semiconductors*, p. 135, Cambridge University Press, Cambridge, England (1961).

DEFECT STRUCTURE AND ELECTRICAL PROPERTIES OF NiO-II. TEMPERATURES BELOW EQUILIBRATION*

C. M. OSBURN† and R. W. VEST

Purdue University, Lafayette, Indiana 47907, U.S.A.

(Received 16 July 1970)

Abstract—The electrical conductivity of pure nickel oxide is almost independent of temperature from 300 to 1000°C. The addition of just a few hundred parts per million of donor impurities increases the activation energy for conduction from a few hundred cal/mole to 40 kcal/mole. These impurities decrease the magnitude of the conductivity at 400°C from 0.1 to 10^{-8} ohm⁻¹.cm⁻¹. Seebeck measurements confirm that the carrier concentration, rather than the mobility, decreases as the temperature decreases. A point defect model incorporating five charged and two neutral species was formulated and solved. The resulting theoretical carrier concentrations agree well in magnitude as well as temperature and oxygen pressure dependence with conductivity measurements on samples of different purities. The hole mobility is found to be almost independent of temperature.

1. INTRODUCTION

AT TEMPERATURES below 1000°C, the kinetics of equilibration between nickel oxide and the ambient vapor phase are slow. For a given cooling rate there will be some temperature T_{equil} below which the sample is not in equilibrium with the gas and the concentration of atomic defects at all lower temperatures should be that concentration quenched in at T_{equil} . Since the electronic carrier concentration is related to the concentration of atomic defects, the temperature dependence of the conductivity at low temperatures is usually associated with the mobility. This reasoning led earlier investigators [1-3] to conclude that the mobility in NiO was activated. Other measurements [4-6] at high temperatures have also pointed to an activated mobility. However, a combination of Seebeck and conductivity measurements [7] at room temperature showed that the carrier concentration and

not the mobility was activated. Furthermore, high temperature measurements on high purity NiO [8] show that the mobility is almost independent of temperature, and that the room temperature [9] and the high temperature mobilities are about the same.

The preceding paper [8] demonstrated that impurities can have a very pronounced effect on the high temperature activation energy and oxygen pressure dependence for conductivity. Since the effect of impurities is important at even the high temperatures where the degree of native disorder is highest, it is imperative that the exact effect of impurities be determined before the low temperature conductivity results can be interpreted in terms of carrier concentration and mobility. Conductivity measurements were extended from the previous work [8] to include the temperature range 300 to 1000°C. Measurements were made in the same atmosphere furnaces as described earlier. Four-point dc measurements were made predominately, although four-point and three-terminal ac measurements were also made. No frequency dispersion from dc to 20 kHz or voltage dependence of the conductivity was observed

*This work was supported in part by the National Science Foundation, the Advanced Research Projects Agency of the Department of Defense, Delco Radio Division of General Motors Corporation, and the Basil S. Turner Foundation.

†Present Address: IBM Watson Research Center, Yorktown Heights, New York 10598, U.S.A.

in either the four-point or three-terminal measurements.

Impurity analyses performed by spark mass spectrometry on the samples before and after measurements are presented in Table 1. Designating these samples as 'low' and 'high' purity is justified because the concentrations of potential aliovalent impurities bracket the concentration range of native defects possible under the experimental conditions employed.

2. RESULTS

Conductance isobars for the low purity single crystal are shown in Fig. 1; the activation energies are computer calculated by the least squares method, and the errors given in parentheses represent one standard deviation. The isobars are labeled according to the oxygen partial pressure at high temperature; although NiO does not equilibrate with the gas at low temperature, the isobars are reproducible on both heating and cooling.

The high temperature slope changes in the isobars are indicative of the cessation of equilibration between the sample and the vapor, and the temperatures at which they occur (T_{equil}) are a function of the cooling rate. Therefore, the concentration of charge carriers at low temperatures is a function of the cooling rate. A special attempt was made to keep the cooling rate constant at about 40°C/hr for all samples; for each data point the temperature was held constant for a time sufficient to insure thermal equilibrium of the sample. At high pressures the activation energy (ΔH_c) decreases as the temperature decreases, while at low pressures the activation energy increases as temperature decreases. At an intermediate pressure there are three activation energy regions. Figure 2 shows the thermoelectric power for a crystal of the same purity at three different oxygen pressures. The data are plotted as the logarithm of the Seebeck coefficient in order to

Table 1.

Element	High purity crystal		Low purity crystal	Polycrystalline	
	Before measurements	After measurements	After measurements	Starting powder	After measurements
Li	0.1	2	10	< 0.01	10
F	< 10	< 3	< 1	< 0.03	< 3
Na	3	30	20	10	50
Mg	< 6	20	< 10	—	—
Al	6	20	40	1	20
Si	30	20	< 10	5	100
S	10	40	20	1	20
Cl	4	10	5	3	30
K	1	15	2	0.3	30
Ca	4	15	10	2	50
Ti	< 1	3	10	0.2	3
V	—	—	—	< 0.03	3
Cr	< 0.3	0.3	5	< 0.04	10
Mn	—	2	< 10	< 0.03	1
Fe	10	40	500	3	40
Co	5	30	500	< 0.3	10
Cu	1	8	20	1	8
Zn	—	—	—	< 1	8
Ga	< 2	2	50	< 0.5	1
Pt	—	2	< 1	< 0.4	2
Total Determined	74	259	1262	27	397

All other impurities < 1 ppmw.

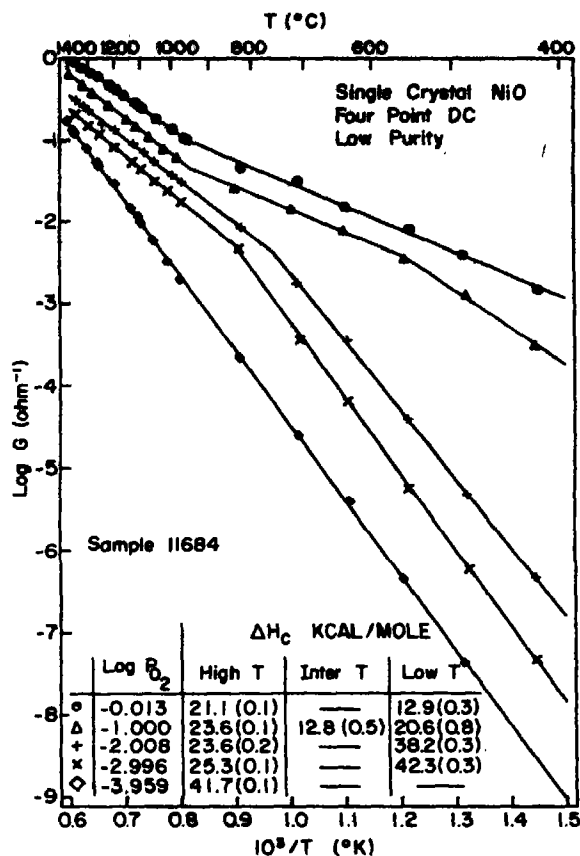


Fig. 1. Conductance isobars for low purity nickel oxide.

display the large variation observed as a function of temperature. At low pressures where the native disorder is expected to be the least, the Seebeck coefficient increases rapidly with decreasing temperature indicating a rapidly decreasing hole concentration. At high pressure where the quenched-in vacancy concentration is the greatest, the Seebeck coefficient is almost independent of temperature from 1400°C to below 400°C.

Conductivity isobars for the high purity single crystal are shown in Fig. 3, and they are seen to be strikingly different compared to the low purity crystal. At low temperatures, the activation energies are about 3 kcal/mole rather than 20 kcal/mole. Furthermore, the low temperature activation energies are relatively independent of pressure. Due to the

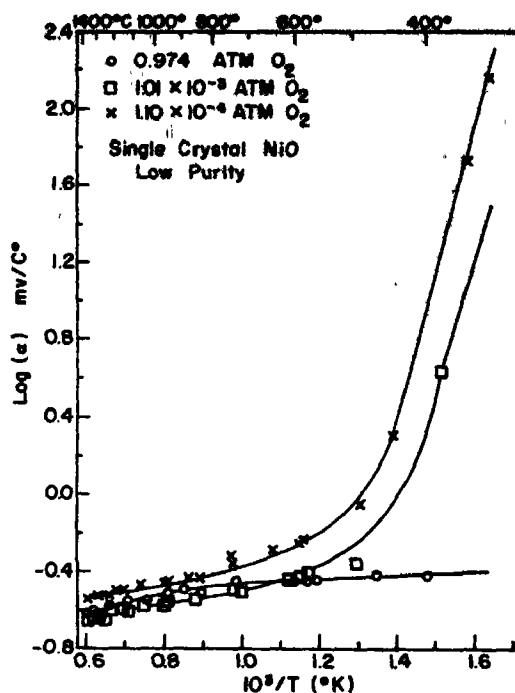


Fig. 2. Seebeck coefficient isobars for low purity nickel oxide.

much lower temperature dependence, the conductivity of the pure crystal is about $0.1 \text{ ohm}^{-1}\text{-cm}^{-1}$ at 400°C as compared to 10^{-3} to $10^{-8} \text{ ohm}^{-1}\text{-cm}^{-1}$ for the low purity crystal at that temperature. At high pressure and intermediate temperature, the high purity crystal reproducibly shows a sharp decrease in the conductivity by a factor of two.

A comparison of three-terminal and four-point conductivity for the high purity single crystal is shown in Fig. 4. The lower three-terminal conductivity at high temperature and high pressure is due to series resistance of the leads, but the five orders of magnitude difference at 400°C and $10^{-4} \text{ atm } O_2$ cannot be due to the leads. For the low purity crystal, three- and four-terminal measurements were the same. Four-point measurements on the high purity crystal could not be made at temperatures much below 400°C because of decreasing galvanometer sensitivity, believed to be due to a series resistance in the potential

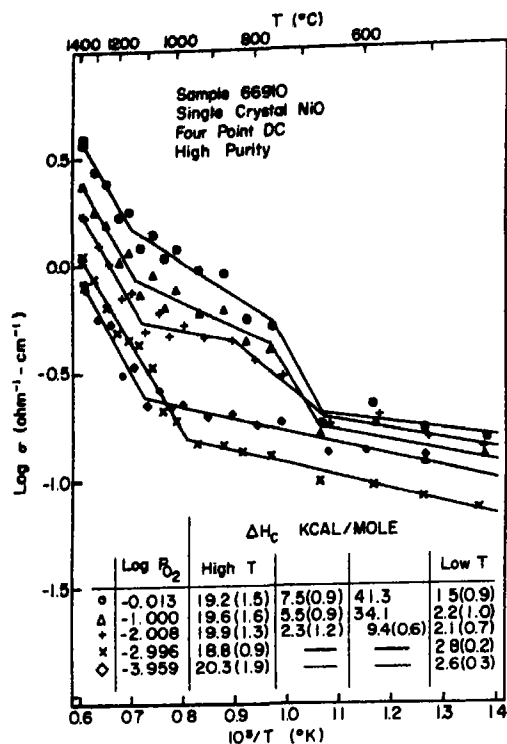


Fig. 3. Conductivity isobars for high purity nickel oxide.

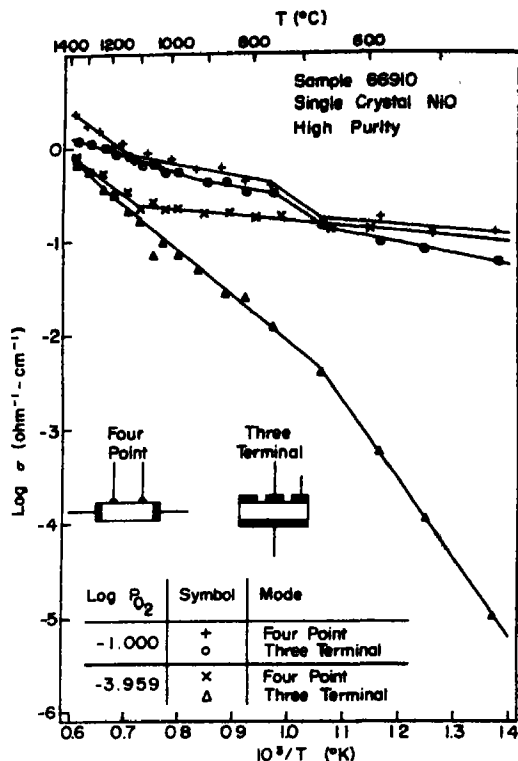


Fig. 4. Three-terminal and four-point conductivity of nickel oxide.

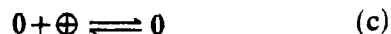
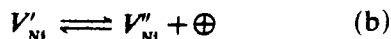
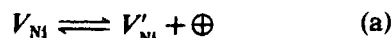
circuit of the sample of the order of 10 megohms. These observations point to a low conductivity surface layer or low conductivity contact on the pure sample. The voltage and frequency independence of the conductance indicate that the surface and not the contact has the low conductance. This phenomenon is most likely responsible for the differences in ac and dc conductivity reported by Bosman and Crevecoeur[7]. Although they attributed the difference to grain boundary effects, the present results indicate that the difference was due to a low conductivity surface layer.

Conductivity isobars were also measured for polycrystalline NiO which was the highest purity sample studied; these results are shown in Fig. 5. These data were not corrected for porosity; to make such a correction the conductivity given should be multiplied by 1.22. The behavior is very much like the

behavior of the high purity (but slightly less pure) single crystal. The low temperature activation energy is a little lower (1 kcal/mole) and the sharp drop at high pressure and intermediate temperature is not observed. Thermoelectric power measurements were also made on this material as shown in Fig. 6. As contrasted to the low purity crystal, the Seebeck coefficient is almost independent of temperature at all oxygen partial pressures.

3. DEFECT MODEL

In order to more precisely describe the effect of impurities in NiO, the following equilibria among point defects were considered:



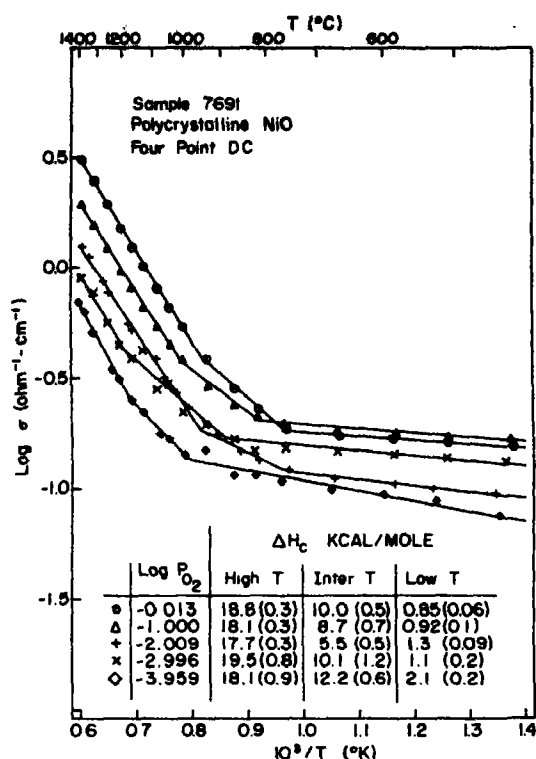


Fig. 5. Conductivity isobars for polycrystalline nickel oxide.

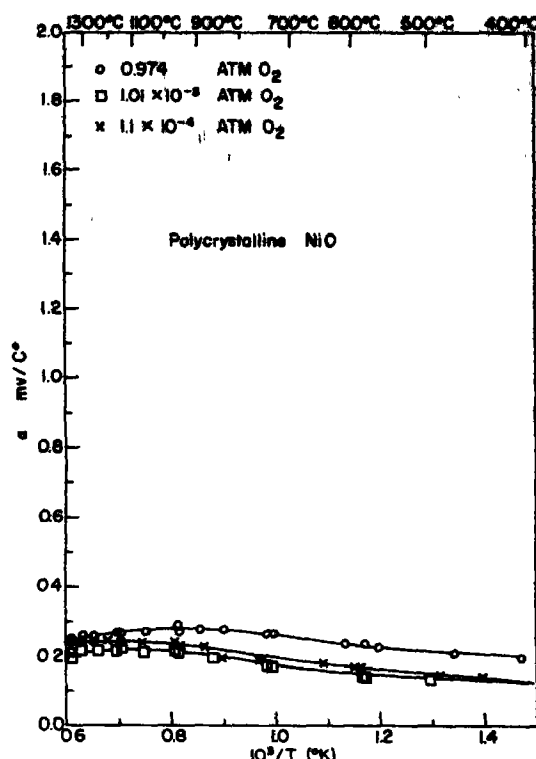
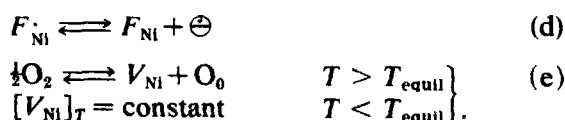


Fig. 6. Seebeck coefficient isobars for polycrystalline nickel oxide.



The notation is that of Kroger and Vink [10] where F_{Ni} indicates a substitutional impurity on a nickel site, and the total vacancy concentration is given by:

$$[V_{Ni}]_T = [V_{Ni}] + [V'_{Ni}] + [V''_{Ni}].$$

Applying the law of mass action to these equilibria gives:

$$p[V'_{Ni}]/[V_{Ni}] = K_1^0 e^{-E_1/RT} \quad (1)$$

$$p[V''_{Ni}]/[V'_{Ni}] = K_2^0 e^{-E_2/RT} \quad (2)$$

$$np = K_i^0 e^{-E_i/RT} \quad (3)$$

$$n[F_{Ni}]/[F_{Ni}] = K_{17}^0 e^{-E_{17}/RT} \quad (4)$$

$$\left. \begin{array}{l} [V_{Ni}] = (K_{OX} \cdot P_{O_2})^{1/2} \quad T > T_{\text{equil}} \\ [V_{Ni}]_T = \text{constant} \quad T < T_{\text{equil}} \end{array} \right\} \quad (5)$$

Conservation of impurities and electrical neutrality considerations yield:

$$[F_{Ni}]_T = [F_{Ni}] + [F'_{Ni}] \quad (6)$$

$$n + [V'_{Ni}] + 2[V''_{Ni}] = p + [F_{Ni}]. \quad (7)$$

In solving this system of seven equations in seven defect concentrations, it is customary to assume that all terms but one on each side of the neutrality condition are negligible, and that the impurities are present in only one charge state. Experimental results show that impurities cannot be ignored and that quite likely singly-ionized vacancies contribute to the charge carriers. In such a case, the neutrality condition cannot be greatly simplified, and the entire set of equations must

be solved without simplifying assumptions. The concentration of each charged defect was expressed as a function of p , the hole concentration, and the neutrality equation was then rewritten to the form $f(p) = 0$. The roots of this equation were then determined utilizing a digital computer.

To perform the computations, it was necessary to have values for all the equilibrium constants in the system of equations. Since very few constants had previously been determined, it was necessary to make certain assumptions to get numbers. The pre-exponential terms were computed after Kröger[11] assuming a band model for conduction; it should be noted that equally good results were obtained using pre-exponential factors that were obtained from a hopping model. The ionization energies of the vacancies (E_1, E_2) were computed using a hydrogen atom-model for ionization and a dielectric constant of 11.9[12]. The optical bandgap[13, 14], corrected to give the thermal bandgap, was used for the hole-electron formation energy E_i . Weight change data from the high temperature study[8] were then used to obtain the remaining equilibrium constant K_{OX} . The temperature dependence of the bandgap as well as the exponential term for impurity ionization were chosen to fit the experimental data. Table 2 summarizes the values and the sources for the equilibrium constants. The energy level diagram associated with these equilibrium constants is shown in Fig. 7.

Computed hole concentration isobars are given in Figs. 8–10 for 0, 100, and 200 ppm donor impurities. The temperature of equilibrium was chosen to be 977°C ($10^3/T = 0.8$) which is approximately equal to T_{equil} observed under the given experimental conditions. For pure material (Fig. 8) the high temperature activation energy (H_F) is 18.7 kcal/mole and the oxygen pressure dependence is one sixth as observed in the previous study[8]. At low temperatures the activation energy is of the order of 1 kcal/mole

Table 2. Equilibrium constants

$K_1 = 2Ae^{-E_i/RT} = 9.68 \times 10^{15} T^{3/2} e^{-5.11/RT}$
$K_2 = A/2e^{-E_2/RT} = 2.42 \times 10^{15} T^{3/2} e^{-8.83/RT}$
$K_i = A^2 e^{-(E_1+RT)/RT} = 1.17 \times 10^{34} T^3 e^{-90/RT}$
$K_{17} = A/2e^{-E_{17}/RT} = 2.42 \times 10^{15} T^{3/2} e^{-88/RT}$
$K_{OX} = 1.065 \times 10^{49} T^{-6} e^{-98.53/RT}$
1. Experimental parameters
E_i from optical bandgap of 3.7 eV
K_{OX} from weight change data plus $K_1 + K_2$
2. Chosen parameters
β, E_{17}
3. Computed parameters
Band approximation
$A = 2 \left(\frac{2\pi mkT}{h^2} \right)^{3/2} = 4.84 \times 10^{15} T^{3/2}$
Hydrogen atom model
$E_0 = 13.527 \left(\frac{Z}{\epsilon} \right)^2 = 2.21 \text{ kcal/mole}$
($Z = 1; \epsilon = 11.9$)

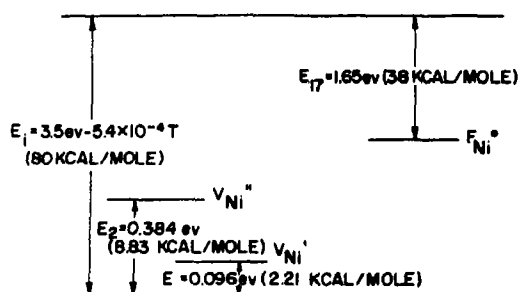


Fig. 7. Proposed energy level diagram for nickel oxide.

and reflects a change from doubly- to singly-ionized vacancies as the temperature is decreased. The effect of even a small number of impurities is very dramatic. For instance at 450°C and 10^{-4} atm O_2 , the hole concentration is about $10^{18}/\text{cm}^3$ and the activation energy is 0.5 kcal/mole for a pure sample (Fig. 8). The addition of 100 ppm impurities (Fig. 9) decreases the hole concentration to $2 \times 10^{12}/\text{cm}^3$ and increases the activation energy to 44.4 kcal/mole. This is a carrier concentration change of six orders of magnitude and an activation energy change of two orders of magnitude. Not only do impurities drastically affect the magnitude and temperature dependence of the hole concentration, but they also change the oxygen pressure

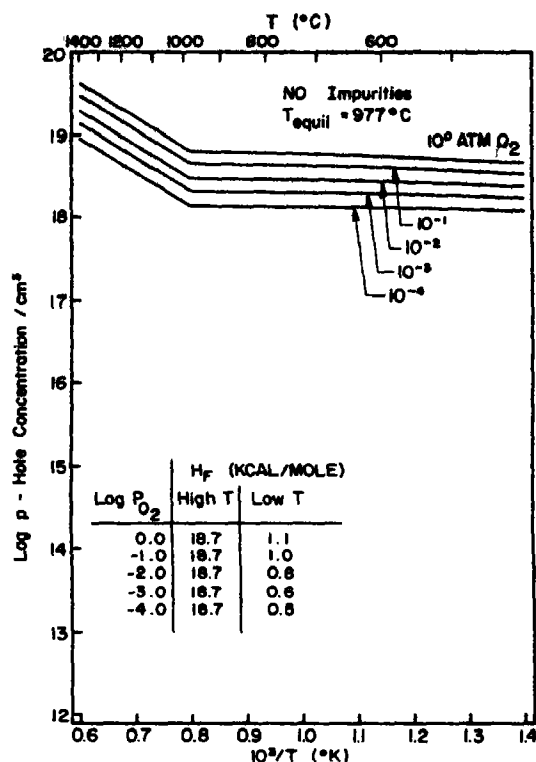


Fig. 8. Calculated hole concentration isobars for nickel oxide. No impurities.

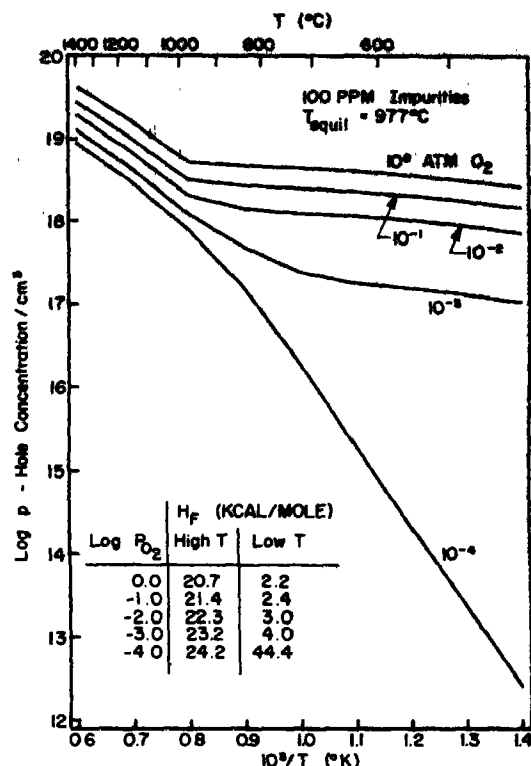


Fig. 9. Calculated hole concentration isobars for nickel oxide. 100 ppm impurities.

dependence. In Fig. 9 the low temperature activation energy is either higher or lower than the high temperature activation energy depending on the oxygen pressure. At high pressure the activation energy is low (2.2 kcal/mole), and at low pressure it is high (44.4 kcal/mole).

The calculated high temperature hole concentrations agree very well with experimental conductivity measurements. For instance compare Fig. 10 of this study with activation energies in Table 3 of the previous study[8]. The analysis (Table 1, Ref.[8]) shows the intermediate purity sample has 200 ppm of iron as the dominant impurity. Over the oxygen pressure range 1 atm to 10^{-4} atm, the measured activation energy varied from 22.1 to 25.6 kcal/mole while the theoretical activation energy varied from 22.2 to 26.4 kcal/mole. This agreement is remark-

able considering the elementary assumptions used in computing equilibrium constants for the model.

The effect of the equilibrium temperature is shown in Figs. 11 and 12 for the 200 ppm case. Decreasing T_{equil} increases both the low and the high temperature activation energy. The most striking result is that with 200 ppm impurities, the low temperature hole concentration is not necessarily higher when the sample is quenched at a higher temperature. High pressure and high T_{equil} as well as low pressure and low T_{equil} favor high hole concentrations. The most pronounced change in low temperature hole concentration as a function of T_{equil} occurs at intermediate and high oxygen partial pressures.

The concentrations of the other charged point defects with 200 ppm impurities present are given in Figs. 13-16. Of particular

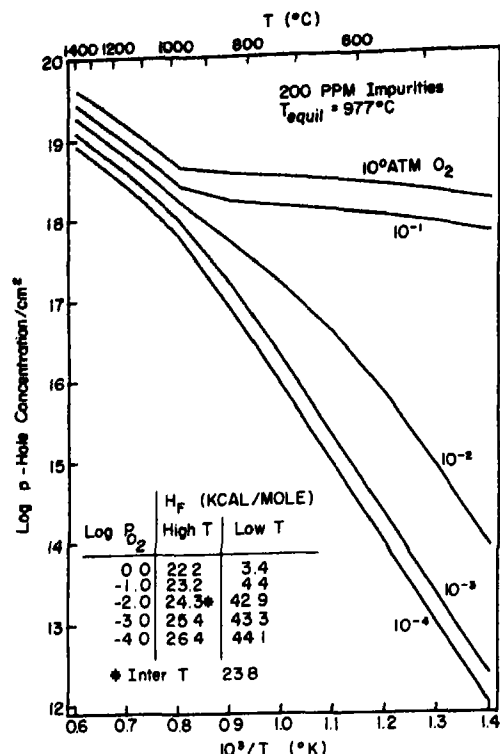


Fig. 10. Calculated hole concentration isobars for nickel oxide, 200 ppm impurities.

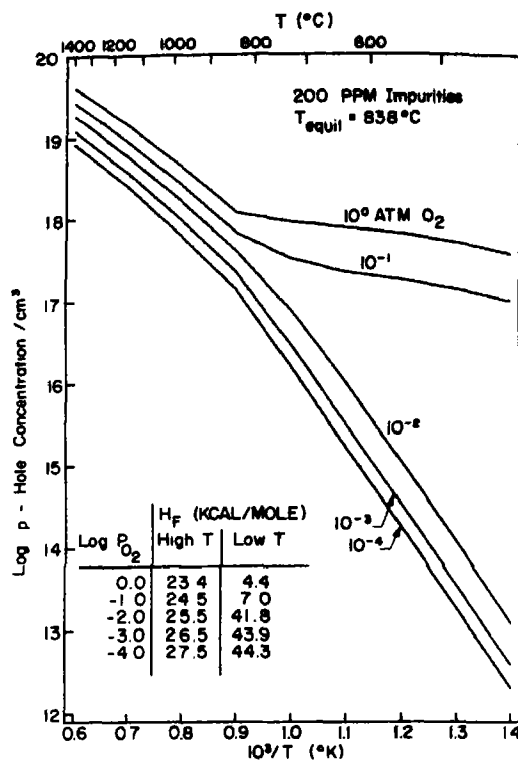


Fig. 11. Calculated hole concentration isobars for nickel oxide $T_{\text{equil}} = 838^\circ\text{C}$.

interest is the sign change of the slope of the singly-ionized vacancy isobars (Fig. 13) at the temperature of equilibrium. At low temperatures the concentration of doubly-ionized vacancies (Fig. 14) is not a monotonic function of oxygen pressures. This behavior is not characteristic of the pure material but rather reflects the complex effect of impurities on the concentrations of various defects.

4. DISCUSSION

At low temperatures for the high purity crystal and polycrystal, both the Seebeck coefficients (Fig. 6) and the electrical conductivities (Figs. 3 and 5) are almost independent of temperature. The activation energy for conduction appears to be 2 kcal/mole or less. Theoretical calculations (Fig. 8) give a 1 kcal/mole activation energy for hole concentration below T_{equil} for pure material. Since the

activation energy for conduction is the sum of the activation energies for carrier concentration and for mobility, it is seen that the activation energy for mobility is very small. The mobility is independent of temperature from 400 to 1000°C to within an activation energy of 2 kcal/mole, further substantiating the earlier observation[8] of a temperature independent mobility from room temperature to 1400°C.

A comparison of the Seebeck coefficients and conductivity isobars of high and low purity nickel oxide samples offers definite evidence that the low temperature conductivity of NiO is controlled by impurities in the low purity sample. The high activation energies (12–43 kcal/mole) observed in the low purity sample (Fig. 1) must be attributed to carriers and not to mobility. Similar results were presented earlier by

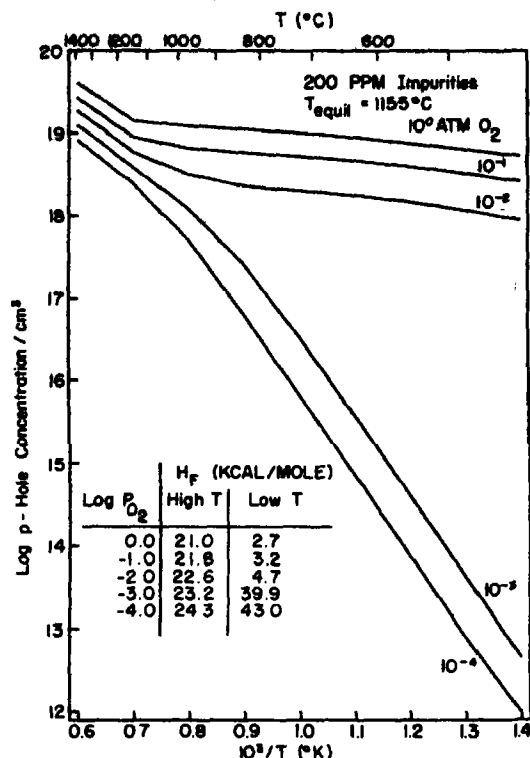


Fig. 12. Calculated hole concentration isobars for nickel oxide $T_{\text{equil}} = 1155^\circ\text{C}$.

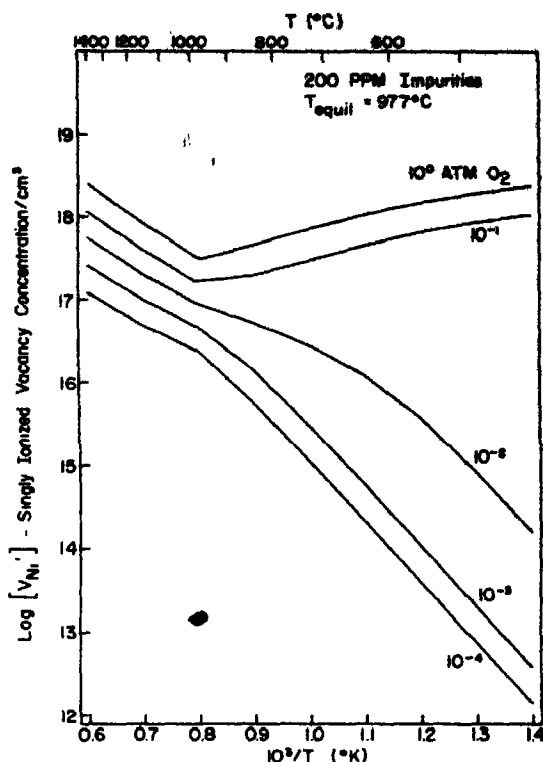


Fig. 13. Calculated singly-ionized vacancy concentration isobars for nickel oxide.

Bosman and Crevecoeur[7] from conductivity and thermoelectric power data around room temperature; they found that the activation energies for conduction and Seebeck coefficient were the same, indicating a temperature independent mobility.

The Seebeck coefficient isobars for the low purity sample (Fig. 2) dramatically illustrate the decrease in hole concentration with decreasing temperature. Only at the highest pressure where the native disorder is greatest is the carrier concentration more temperature independent. The decreasing hole concentration can be explained in terms of compensating impurities. Unfortunately, it is not always fully appreciated that impurities can either raise or lower carrier concentrations; in the present case the important impurities are donors and reduce the hole concentration. For the hole concentration to decrease with

decreasing temperatures, it is necessary to have the impurities ionized at low temperatures and not ionized at high temperatures. Theoretical confirmation of this behavior is shown in Fig. 15.

The difference between three-terminal and four-point measurements (Fig. 4) can also be explained with the proposed defect model. Four-point measurements reflect the bulk conductivity while three-terminal measurements are limited by the surface conductivity when the surface is more insulating than the bulk. In general the surface of a sample would be expected to have a lower T_{equil} than the bulk since the equilibration with the surface does not involve bulk diffusion. The theoretical hole concentration isobars at oxygen partial pressures of 10^{-1} and 10^{-4} atm for a sample with 50 ppm impurities (roughly the iron concentration in sample 66910) are

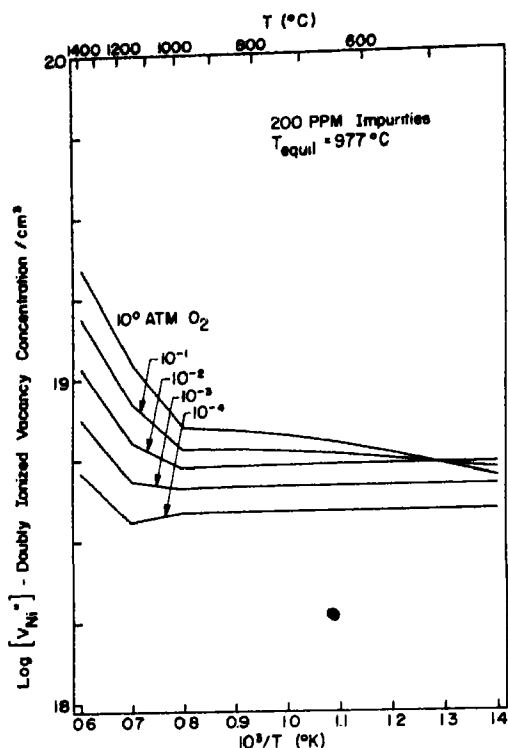


Fig. 14. Calculated doubly-ionized vacancy concentration isobars for nickel oxide.

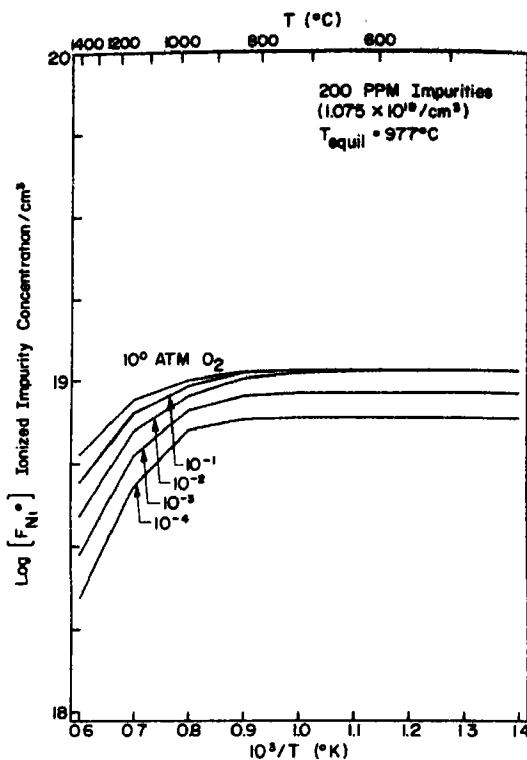


Fig. 15. Calculated ionized impurity concentration isobars for nickel oxide.

compared in Fig. 17 for $T_{\text{equil}} = 977^\circ\text{C}$ and for $T_{\text{equil}} = 838^\circ\text{C}$. An equilibration temperature of 977°C corresponds to the bulk (four-point measurements), and the 838°C temperature corresponds more nearly to the surface (three-terminal measurements). The agreement between the experimental observation (Fig. 4) and the theoretical model (Fig. 17) is good.

Other investigators have observed the same type of phenomena that were observed in this study. Error[4] found a pressure dependence of activation energy. At low temperature he found the low pressure activation energy was higher and the high pressure activation energy was lower than the activation energy at high temperatures. He attributed this to a Meyer-Neldel[15] type of relationship. This study confirms his observation but invalidates his

explanation; the results are merely due to impurities.

The advantage of using the complete neutrality equation is apparent from this study. The concentration of each charged defect (Figs. 10 and 13–16) show that of the five species in the neutrality equation, only the electron concentration was low enough to be neglected. This information is usually never available *a priori*. With the accessibility of digital computers, the solution of the general problem is almost as easy as the solution to the simple problem. The only added difficulty is that numerical equilibrium constants must be used. In the present case, the simplest of constants did a good job of fitting the data; however, a more general treatment would include several impurity reactions with different constants. The consideration of only

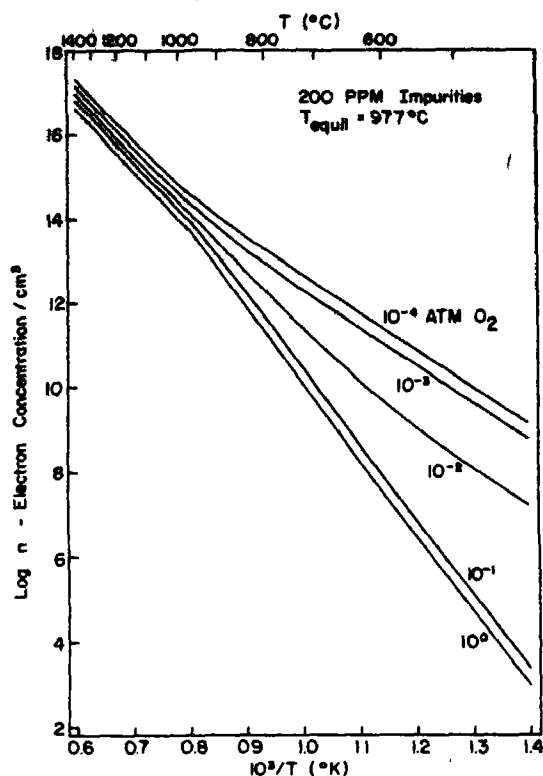


Fig. 16. Calculated electron concentration isobars for nickel oxide.

one impurity, presumably iron, was sufficient to explain the results in this instance.

5. CONCLUSIONS

At low temperatures pure NiO is a much better conductor than has been previously reported. An insulating surface layer is found which can be attributed to an equilibrated surface or adsorbed gasses on the surface, but extrapolations of the present data indicate a room temperature conductivity of 10^{-2} $\text{ohm}^{-1}\text{-cm}^{-1}$.

Conductivity results further show a mobility that is roughly independent of temperature; the maximum possible activation energy for mobility is less than 2 kcal/mole.

At 450°C only 100 ppm impurities can change conductivity by six orders of magnitude and the temperature dependence by two orders of magnitude. The active impurities

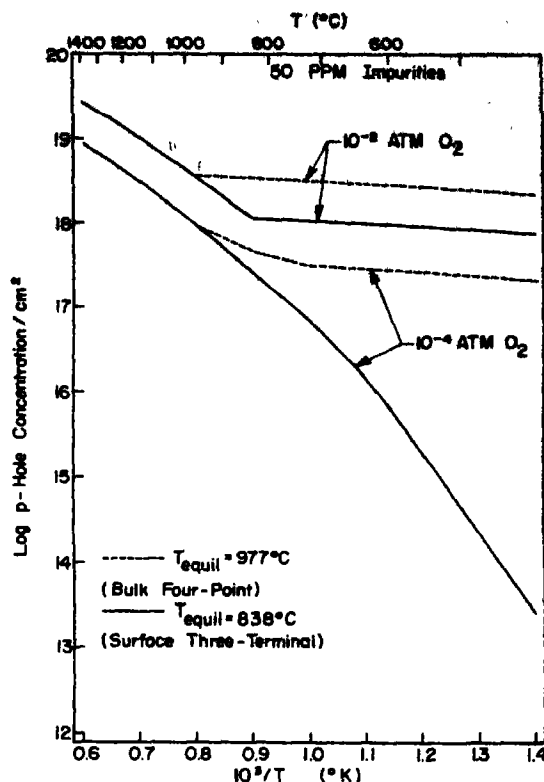


Fig. 17. Calculated effect of T_{equil} on hole concentration for nickel oxide 50 ppm impurities.

are electron donors and most likely are iron since iron often changes from the two plus to the three plus state. The iron concentration determined by mass-spectrometer analysis correlates well with the expected donor impurity concentration from the comparison of the experimental and theoretical results.

Theoretical calculations of the concentrations of seven species with a neutrality condition containing five charged species are entirely feasible. Elementary assumptions about the equilibrium constants gave theoretical carrier concentrations that agree with experimental conductivity measurements as to magnitude, temperature dependence and points of slope changes.

Acknowledgements—The authors would like to express their appreciation to Dr. M. L. Volpe and Mr. W. T. Reeves for their assistance in obtaining crystals from the Argonne National Laboratories.

REFERENCES

1. HEIKES R. R. and JOHNSTON W. D., *J. chem. Phys.* **26**, 582 (1957).
2. (a) MORIN F. J., *Phys. Rev.* **93** 1199 (1954).
(b) MORIN F. J., *Bell Syst. Tech. J.* **37**, 1047 (1958).
3. VAN HOUTEN S., *J. Phys. Chem. Solids* **17**, 7 (1960).
4. EROR, N. G., Jr., Ph.D. Thesis, Northwestern University (1965).
5. BRANSKY I. and TALLAN N. M., *J. chem. Phys.* **49**, 1243 (1968).
6. MITOFF S. P., *J. chem. Phys.* **35**, 882 (1961).
7. BOSMAN A. J. and CREVECOEUR C., *Phys. Rev.* **144** 763 (1966).
8. OSBURN C. M. and VEST R. W., *J. Phys. Chem. Solids* **32**, 1331 (1971).
9. MAKAROV V. V., KSENDZOV YA. M. and KRUGLOO V. I., *Fiz. tverd. Tela* **9**, 633 (1967).
10. KRÖGER F. A. and VINK H. J., In *Solid State Physics*, **3**, 307, Academic Press, New York (1956).
11. KRÖGER F. A., *Chemistry of Imperfect Crystals*, pp. 252-255, John Wiley, New York (1964).
12. RAO K. V. and SMAKULA A., *J. appl. Phys.* **36**, 2031 (1965).
13. NEWMAN R. and CHRENKO, R. M., *Phys. Rev.*, **114**, 1507 (1959).
14. MCNATT, J. L., *Phys. Rev. Lett.* **23**, 915 (1969).
15. NEYER W. and NELDEL H., *Z. Techn. Phys.* **18**, 588 (1937), *Phys. Zeit.* **38**, 1014 (1937).

ELECTRICAL PROPERTIES OF NiO GRAIN BOUNDARIES*

C. M. OSBURN† and R. W. VEST

Purdue University, Lafayette, Indiana 47907, U.S.A.

(Received 16 July 1970; in revised form 17 December 1970)

Abstract—The electrical conductivity of a series of nickel oxide bicrystals was studied as a function of temperature from 400 to 1400°C and as a function of oxygen pressure from 1 atm to 10^{-4} atm. Measurements were made both across and along the grain boundary. The bicrystal conductance was as much as two orders of magnitude different than the crystal conductance; depending on experimental conditions, the boundary region was either more or less conductive than the bulk single crystal. The conductivity was independent of the direction of transport and the effective width of the grain boundary was very large—up to 0.3 mm wide. The results could be explained in terms of increased grain boundary diffusion and segregation of impurities. Incorporation of these two mechanisms into the donor impurity model gave theoretical results which agreed with experiment.

1. INTRODUCTION

IT HAS long been known that defects play an important role in the electrical properties of crystals. These defects can be point defects (vacancies, interstitials), line defects (dislocations), plane defects (grain boundaries), or volume defects (pores). Since point defects are the predominant defects in highly perfect crystals, it is natural that most previous investigations have considered only point defects when studying electrical properties. In materials that are not highly perfect, however, plane defects or grain boundaries can be important. Transport properties of grain boundaries in the elemental and compound semiconductors have been studied [1-8] as a function of grain boundary orientation and direction of transport. The results of these studies show that grain boundaries can greatly influence the electrical properties of a solid.

Electrical property measurements, however, have not been extended to many materials other than the well-known semiconductors. In

oxide materials five important mechanisms have been proposed to describe the electrical properties of grain boundaries: (1) charge trapped at the boundary from broken bonds [1-8]; (2) defect and charge gradients at the boundary from ion motion to the surface [9-11]; (3) impurity segregation changing the composition of the grain boundary region [12-14]; (4) increased grain boundary diffusion [15-18]; and (5) dislocation scattering of the mobile carriers [19, 20].

In his thesis, Thornton [21] specifically considered the effect of grain boundaries on the electrical conductivity in NiO. Using a four-probe technique, he measured conductivity with the applied field both parallel and perpendicular to the grain boundary, and found that the conductivity of the boundary layer was considerably higher than that of the bulk material. The activation energy for grain boundary conduction was less than that for bulk conduction, and the conductivity increased with decreasing grain size in polycrystalline samples. Thornton used a model of free nickel at the grain boundary to explain the results. The experiments were carried out in air, but it is doubtful that the sample equilibrated with the gas phase below 800°C due to the very slow equilibration rates, and observa-

*This work was supported in part by the National Science Foundation, the Advanced Research Projects Agency of the Department of Defense, Delco Radio Division of General Motors Corporation, and the Basil S. Turner Foundation.

†Present Address: IBM Watson Research Center, Yorktown Heights, New York 10598, U.S.A.

tion of the free nickel phase suggests that the samples had never equilibrated with the vapor.

Nickel oxide was chosen for this study because it is probably the most widely-studied semiconducting oxide and because it has the simple rocksalt structure at higher temperatures with isotropic properties. The properties of nickel oxide at high[22] and low temperatures[23] as a function of the concentrations of both native defects and foreign impurities have been the subject of the two preceding papers. The present study extends the work of Thornton[21] by extending the temperature range of the study and by considering the effects of stoichiometry and grain boundary orientation.

2. EXPERIMENTAL

Grain boundary property measurements were made on a series of NiO bicrystals; seven bicrystals were measured having tilt angles from 2° to 45° . The samples were all the same low purity crystals reported on earlier; analyses of one of these samples is given in Table 1 of the preceding paper[23]. The bicrystals were grown by a modified Verneuil technique in an arc-image furnace from two oriented seed crystals, and were previously used in a grain boundary grooving study[24]. The samples were annealed in air at 1500°C for 24 hr. and afterwards had $6 \times 10^3/\text{cm}^2$ thermal etch pits and $5 \times 10^6/\text{cm}^2$ acid etch pits. The interpretation of thermal etch pits is tenuous however since the pit may correspond to a dust particle on the sample rather than to a dislocation.

Conductivity measurements were made using the same apparatus as described earlier [22, 23]. Separate measurements were made with transport across and along the grain boundary. The electroding configuration for the samples is shown in Fig. 1.

3. EXPERIMENTAL RESULTS

Current-voltage measurements were made to check for a blocking layer at the grain boundary. A typical I-V characteristic is

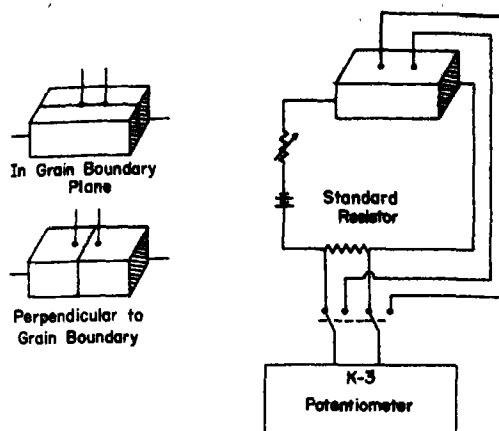


Fig. 1. Electrodes and d.c. conductivity circuit.

shown in Fig. 2; the behavior is ohmic over five orders of magnitude. Conductivity was also measured as a function of frequency up to 100 kHz; no dispersion was observed for any sample.

The most pronounced effects were found by measuring the crystal and the bicrystal conductance on the same sample. The ratio of crystal to bicrystal conductance was sensitive to grain boundary properties and insensitive to heating and cooling rates, errors in temperature and pressure, and variations in impurity con-

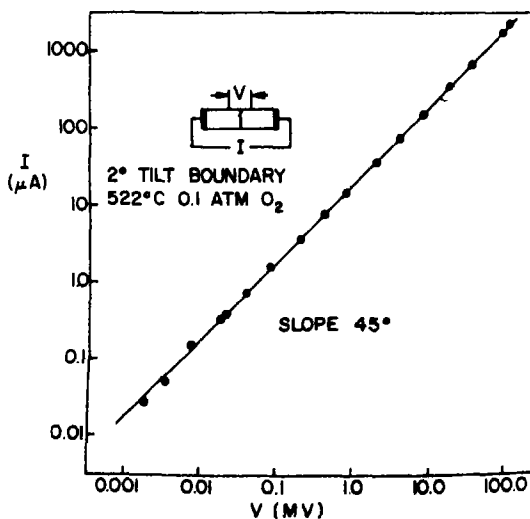


Fig. 2. Typical I-V characteristics perpendicular to tilt boundary in NiO.

centration from one sample to another. These measurements were obtained by modifying the usual four-point technique by adding a fifth contact to the sample. The two end contacts were used for the current contacts as usual, and the bicrystal conductance was obtained from the potential between the contacts on different sides of the grain boundary, while the crystal conductance was obtained from the potential between the two contacts on the same side of the grain boundary. The electrodes were about 0.5 mm in dia. and 0.3–0.5 mm apart, which precluded an accurate determination of absolute conductivities. Although

an attempt was made to obtain the same geometries for both the crystal and bicrystal, it is doubtful that the geometry factors were exactly equal for any of the samples. Hence the ratio of crystal to bicrystal conductance is equal to a geometry factor k times the ratio of the conductivities. Judging from the experimental data (high temperature ratio) the value of k ranged from 0.7 to 1.4.

Isotherms of the ratio of crystal to bicrystal conductance are plotted in Figs. 3–5 for three different tilt angles. Data for other samples are summarized in Table 1. Again it must be remembered that the ratios plotted are some

Table 1. Maximum and minimum in ratio of crystal to bicrystal conductance normalized to the high temperature ratio (440–1000°C)

Tilt angle	Maximum ratio			Minimum ratio		
	Magnitude	P_{\max}	T_{\max}	Magnitude	P_{\min}	T_{\min}
2°	1.4	10^{-1}	440	1/1.1	10^{-2}	800
		10^{-3}	600			
6.5°	1.1	$10^{-3.5}$	650	1/13	$10^{-1.5}$	440
18°	1.2	10^{-3}	440	none		
28°	1.4	10^{-1}	440	1/1.1	10^0	1000
40°	2.5	$10^{-1.5}$	440	none		
44°	1.3	10^0	700	1/300	10^{-2}	440
45°	1.7	10^{-3}	440	1/59	10^{-1}	440

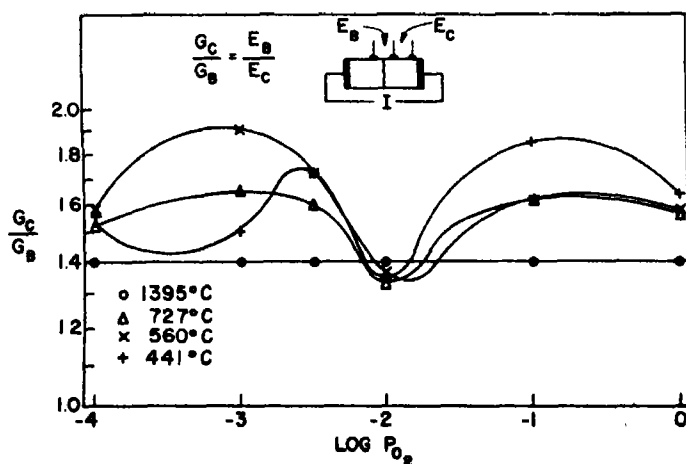


Fig. 3. Crystal to bicrystal conductance isotherms for a 2° NiO tilt boundary.

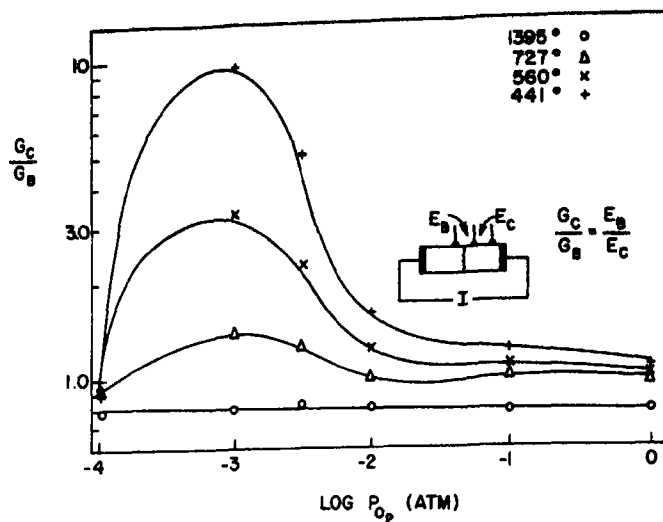


Fig. 4. Crystal to bicrystal conductance isotherms for a 18° NiO tilt boundary.

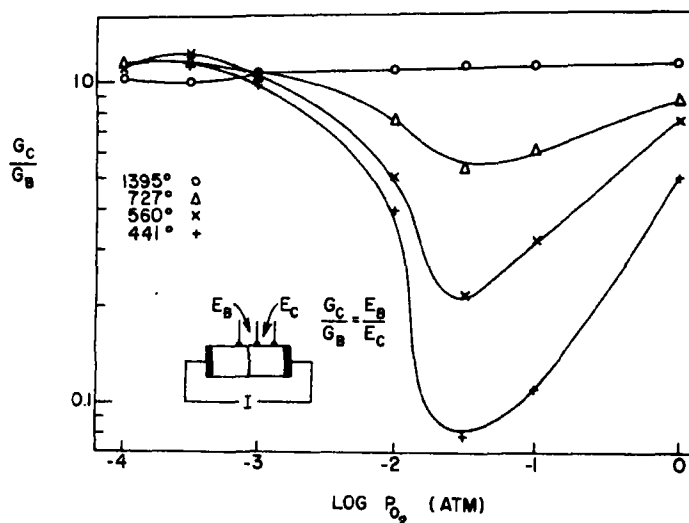


Fig. 5. Crystal to bicrystal conductance isotherms for a 45° NiO tilt boundary.

constant for each bicrystal times the ratio of the conductivities; the maximum and minimum values of the ratio given in Table 1 were normalized to the high temperature value in each case so that comparisons can be made. Many features are of interest in these data. First of all, the grain boundary affected all of the

samples in some fashion. Furthermore, in four of these samples (6.5°, 18°, 44°, and 45°) the change in the ratio is at least an order of magnitude. In all cases the high temperature behavior is constant relative to the lower temperature behavior, and with only minor exceptions, the high (1 atm) and the low

(10^{-4} atm) oxygen partial pressure behavior is relatively constant when compared to intermediate pressures. The greatest changes occur at temperatures at which the sample is not in equilibrium with the surrounding atmosphere. In some of the samples, the grain boundary conductance was considerably higher (Fig. 4) and in others it was considerably lower (Fig. 5) than the crystal conductance at certain oxygen pressures, while in some samples (Fig. 3) both maxima and minima were observed.

Aside from these general trends of behavior, each sample has distinct features. Although the largest changes in the crystal to bicrystal conductance ratio occur at the lower temperatures for most of the samples, the temperatures and pressures of the maximum and the minimum given in Table 1 are seen to be different and unique for each bicrystal. Quite significantly, the angle of tilt does not correlate with the magnitude, pressure, or temperature of the maximum or minimum ratio. Furthermore, the tilt angle does not correlate with the temperature or pressure derivatives of the ratio.

Figure 6 compares conductance isobars measured both along and across the boundary of the 44° bicrystal to the conductance of the crystal. The difference in conductance between the bicrystal and crystal is small at both high and low oxygen partial pressures and is the most pronounced at an intermediate pressure. It is evident that the properties along the boundary are most similar to the properties across the boundary and are different from single crystal properties. At low temperatures and $P_{O_2} = 10^{-1.50}$, the bicrystal conductance (along or across the boundary) is higher than the crystal conductance by several orders of magnitude. The bicrystal conductance rather than the crystal conductance is more like the conductance of the high purity crystal and polycrystal samples presented in the preceding paper[23]; it is striking that even in a low purity sample, the grain boundary and not the bulk crystal has properties characteristic of a more pure sample.

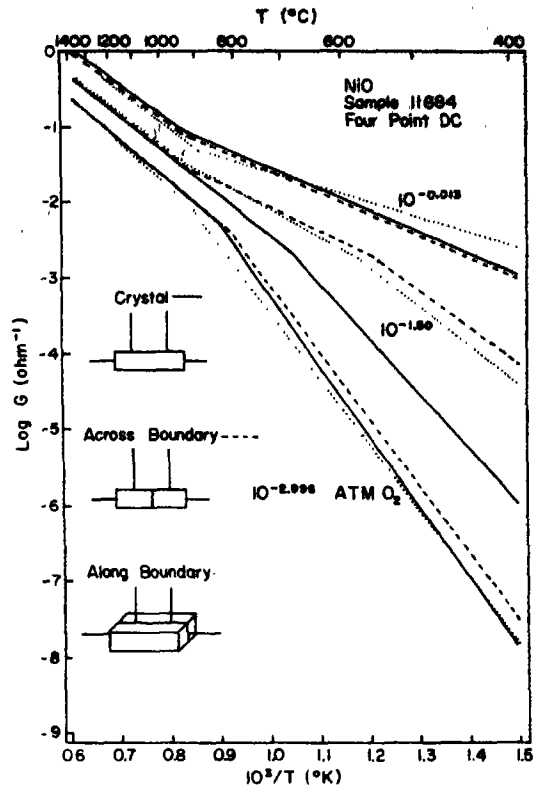


Fig. 6. Conductance along and across boundary and in crystal for nickel oxide.

4. DEFECT MODEL

The donor impurity model as presented in the preceding paper[23] was used to theoretically determine the effect of increased grain boundary diffusion and impurity segregation on grain boundary properties. An increased grain boundary diffusion would be expected to effectively lower the temperature at which the grain boundary region equilibrates with the atmosphere. Hole concentration isotherms were computed for the case where $T_{\text{equil}} = 977^\circ\text{C}$ which corresponds to experimental results on the single crystal region and for $T_{\text{equil}} = 838^\circ\text{C}$ which corresponds to an increased diffusion at the grain boundary. The ratio of the hole concentrations for these cases corresponds to the conductance ratio of a crystal to bicrystal region. Isotherms of the hole concentration ratio are given in Fig. 7.

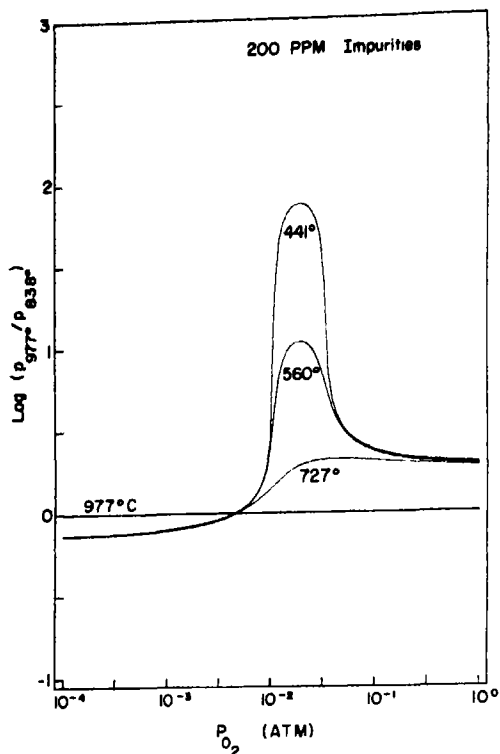


Fig. 7. Ratio of hole concentrations for nickel oxide quenched at different temperatures.

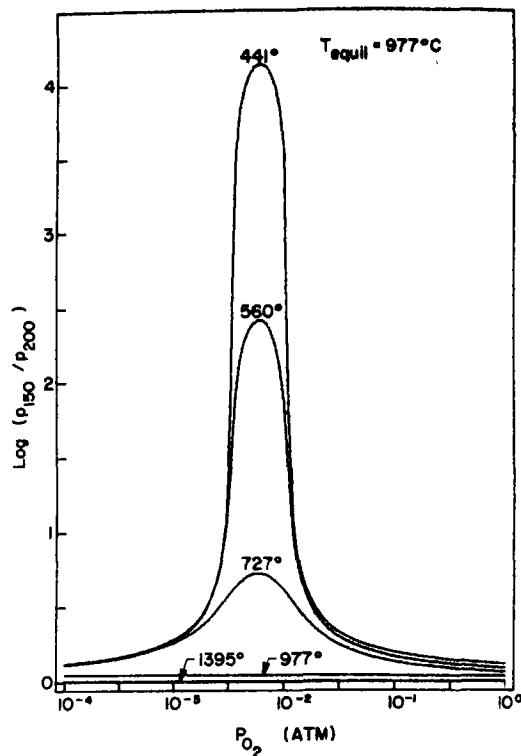


Fig. 8. Ratio of hole concentrations for nickel oxide with different impurity contents.

The high temperature ratio is constant as expected and as observed with conductance ratio measurements on the bicrystal samples (Figs. 3-5). The low temperature ratio increased or decreased depending on the oxygen partial pressure. Peaks are observed in the isotherms in the neighborhood of 10^{-2} atm and the change in ratio is almost two orders of magnitude at low temperatures.

Hole concentration ratios were also computed for the case of 150 and 200 ppm active impurities. Isotherms of this ratio are given in Fig. 8. As before, the high temperature behavior is relatively constant and the deviations occur at low temperatures. The effect of four orders of magnitude is much larger than for the increased diffusion model, and the isotherms are much more symmetric.

It should be noted, however, that with

impurity segregation the theoretical ratio is always greater at low temperatures than it is at high temperatures. This is precisely the opposite of the ratios on the 44° sample (Table 1). In this situation it is necessary to postulate a lower active impurity content in the grain boundary region rather than a higher content. An effective decrease in active grain boundary impurities could arise from: (1) actual segregation of acceptor impurities which would associate with donor impurities and hence reduce the active donor concentration while increasing the total impurity content or (2) a depletion of donor impurities in the grain boundary region; the same energy considerations that favor segregation of certain impurities could favor depletion of others. The effect of a decreased grain boundary impurity content would be to reverse the scale

on Fig. 8, and the maximum in the ratio isotherms would then be a minimum.

The impurity segregation mechanism alone is not sufficient to explain all the experimental results. The theoretical isotherms are too symmetrical, and the effect is too pronounced to explain the results on all samples. Only a combination of increased diffusion and impurity segregation at the grain boundary has the versatility to predict the behavior of the entire collection of bicrystal samples. Figure 9 gives isotherms of the ratio of hole concentrations for different equilibration temperatures and for different impurity contents. The features of this model are: (1) constant high temperature ratio, (2) increasing and decreasing ratio depending on pressure, (3) unsymmetrical isotherms, and (4) large (four orders of magnitude) effect.

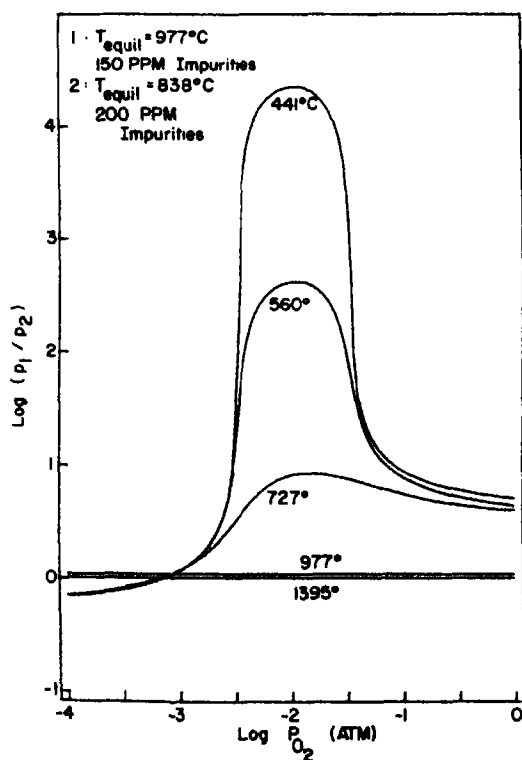


Fig. 9. Ratio of hole concentrations for nickel oxide quenched at different temperatures and with different impurity contents.

5. DISCUSSION

Three experimental observations are crucial in interpreting the grain boundary conduction in nickel oxide: first, with 0.3 mm probe spacings, the grain boundary conductance is roughly independent of the direction of transport, i.e. the same along the across the boundary (see Fig. 6 for example); second, in several cases the bicrystal conductance increases significantly with respect to the crystal conductance; and third, the behavior does not correlate directly with the tilt angle.

The first two observations lead to the conclusion that the region around the grain boundary having properties different than the bulk is very wide (~ 0.3 mm). An increase in conductivity over a narrow grain boundary region would not noticeably affect the overall conductance over a 0.3 mm width; hence, the grain boundary was at least as wide as the probe spacing. The result of a wide grain boundary region is startling. The region of atomic disorder around a grain boundary is only a few lattice constants wide [15a] and the Debye length is such that the electronic disorder should be only a few microns wide. The experimental results cannot be explained by mechanisms such as trapped defects at the boundary because of the localized effect of such mechanisms.

Two mechanisms can, however, be used to explain the results: increased grain boundary diffusion of defects and impurity segregation at the boundary. Normally grain boundary segregation would not be expected to occur over such a wide range, but Westbrook [25] reviews recent work that shows wide grain boundaries due to grain boundary diffusion and segregation. The width is explained in terms of the diffusion of a vacancy or vacancy-impurity complex to a vacancy sink (grain boundary). Thus the width of the boundary becomes the effective diffusion distance under the experimental conditions. To a first approximation, some correlation would be expected between tilt angle and either grain boundary diffusion or impurity segregation at the bound-

ary. However, theoretical models of grain boundaries in oxides, particularly high angle boundaries, are insufficiently developed to allow a confident prediction of tilt angle effects. Consideration of coincidence boundaries [15b, 26] does offer some qualitative help in understanding the results. Small effects were seen in 2°, 28°, and 40° boundaries and larger effects were obtained with 6.5°, 18°, 44°, and 45° bicrystals. The coincidence boundaries for tilt around {100} are [26] at 0°, 22.6°, 28.1°, 36.9°, etc. and one might expect a minimum of the grain boundary effect at these angles. Indeed the 2°, 28° and 40° samples are close to these angles while the other samples were further from the coincidence relationships. Although this consideration does predict which samples would show a smaller or a larger grain boundary effect, it does not explain the relative magnitudes of the effect nor does it predict whether the ratio of crystal to bicrystal conductance should be greater or less than one. Certainly an even larger collection of samples would be necessary to establish a precise correlation between electrical properties and coincidence boundaries in NiO.

6. CONCLUSIONS

The effective grain boundary observed in nickel oxide bicrystals was very wide and of the order of 0.3 mm. This width was attributable to impurity segregation and increased grain boundary diffusion. The effects observed were not a direct function of the tilt angle of the sample, but a correlation with the angle of coincidence is suggested.

The grain boundary can be either more or less conductive than the bulk material. The largest effect observed was with a highly conductive boundary for which the change in the ratio of crystal to grain boundary conductance was several orders of magnitude. Theoretical calculations utilizing a point defect model including a donor impurity show that the segregation of just 50 ppm impurities can

account for a change of four orders of magnitude. The change due to different equilibrium temperatures is not as pronounced, but is nevertheless necessary to account for all of the experimental data.

Acknowledgements—The authors would like to express their appreciation to Dr. M. L. Volpe for supplying crystals and bicrystals from the Argonne National Laboratories.

REFERENCES

1. MATARE H. F., *J. appl. Phys.* **30**, 581 (1959); *Proc. Inst. Elec. Engrs.* (London), **B106** supp. 15, 293 (1960).
2. READ W. T., JR. and SHOCKLEY W., *Imperfections in Nearly Perfect Crystals*, p. 352–376 John Wiley, New York, (1952).
3. TAYLOR W. E., ODELL N. H. and FAN H. Y., *Phys. Rev.* **88**, 867 (1952).
4. MUELLER R. K., *J. appl. Phys.* **32**, 635 (1961).
5. MATUKURA Y., *J. phys. Soc. Japan* **17**, 1405 (1962).
6. HANDLER P., *Ann. N. Y. Acad. Sci.* **101**, 857 (1963).
7. KIMATA M., OZAKE H. and MITAMURA S., *Japan appl. Phys.* **3**, 803 (1964).
8. MUELLER R. K. and JACOBSON R. L., *J. appl. Phys.* **38**, 2244 (1967).
9. LEHOVEC K., *J. Chem. Phys.* **21**, 1123 (1953).
10. ESHELBY J. D., NEWBY C. W., PRATT P. L. and LIDIARD A. B., *Phil. Mag.* **3**, 75 (1958).
11. KOEHLER J. S., LANGRETH D. and VON TURKOVICH B., *Phys. Rev.* **128**, 573 (1962).
12. DAVIDGE, R. W., *Phys. Status Solidi* **3**, 1851 (1963).
13. FORTES M. A. and RALPH B., *Acta. Metall.* **15**, 707 (1967).
14. LEIPOLD M. H., Chapter 12 in *Ceramic Microstructures*, (Edited by R. M. Fulrath, and J. A. Pask), Wiley, New York, (1968).
- 15(a). McLEAN D., *Grain Boundaries in Metals*, Oxford University Press, Great Britain, p. I (1957).
- (b). AUST K. T., *B. Met. Trans.* p. 1, 1095 (1970).
16. LAURENT J. F. and BENARD J., *J. Phys. Chem. Solids* **7**, 218 (1958).
17. HOLT J. B., *J. Nucl. Mater.* **11**, 107 (1964).
18. HOLT J. B. and CONDIT R. H., *Materials Science Research*, Plenum Press, New York **3**, 13 (1966).
19. MATARE H. F., *Solid State Physics in Electronics and Telecommunications*, Academic Press, New York, **1**, 73 (1960).
20. HAMAKAWA Y. and YAMAGUCHI J., *Japan J. appl. Phys.* **1**, 334 (1962).
21. THORNTON H. R., Ph. D. Thesis, University of Illinois (1963).
22. OSBURN C. M. and VEST R. W., *J. Phys. Chem. Solids* **32**, 1331 (1971).

23. OSBURN C. M. and VEST R. W., *J. Phys. Chem. Solids* **32** (1971).
24. READEY D. W. and JECH R. E., *J. Am. ceram. Soc.* **51**, 201 (1968).
25. WESTBROOK H. H., Chapter 8 in *Ceramic Microstructures*, (Edited by R. M. Fulrath and J. A. Pask), Wiley, New York (1968).
26. BISHOP G. H. and CHALMERS B., *Scripta Metall.* **2**, 133 (1968).

THEORY OF THE EFFECTS OF UNIAXIAL STRESS ON THE EXCITON STATES IN CuCl

SHOICHIRO SAKODA and YOSITAKA ONODERA

Department of Physics, University of Kyoto, Kyoto, 606, Japan

(Received 8 September 1970; in revised form 1 November 1970)

Abstract—The reflectivity spectra of the $Z_{1,2}$ and Z_3 exciton bands in CuCl observed under uniaxial stress by Koda and co-workers are analyzed on the effective mass theory of exciton. Strain-induced k -linear terms are introduced into the energy spectrum of the valence band in addition to the usual deformation-potential terms and the spin-orbit interaction. They are incorporated into the effective mass equation with the electron-hole exchange interaction taken into account, and the results of the theory are compared with the experiment. It is shown that a longitudinal exciton can be lower in energy than a transverse exciton in the presence of the external stress, and that the finiteness of the photon wave vector K gives rise to the coupling between the excitons with different symmetry through the strain-induced k -linear term.

1. INTRODUCTION

THE EXCITON band in optical spectra has attracted many investigators, as it lies typically below the fundamental edge and shows up as a prominent peak. Investigations of the structure have been carried on and have given much information on the band structure and the interaction between electron and hole.

The exciton band observed in optical spectra is usually an intricate complex exhibited by exciton states. As a powerful tool for analyzing it, there are reflectivity measurements with polarized light under stress. Application of stress removes the degeneracy of the valence (conduction) band, and as a result that of the exciton states. Over a decade these experiments have been reported. Deformation potential theory was able to interpret them rather well. However, unexpected fine structures in the exciton band have been observed in several experiments.

Koda and Langer[1] detected a strain-induced polarization-dependent splitting of the exciton band in II-VI wurtzite compounds. In these materials the valence and conduction bands have no degeneracy except that due to the time reversal symmetry. Since the simple deformation potential theory takes into

account only the splitting of the valence (conduction) band, it could not account for the observed fine structure. This polarization-dependent splitting has been explained by introducing the two-particle nature of the exciton, namely the electron-hole exchange interaction into the one-electron deformation potential theory[2].

In a reflectivity measurement for CdS[3] an extra shoulder was observed in the 1s B series exciton in spite of its simple valence and conduction band structure. It is the finiteness of the light wave vector that is responsible for this fine structure. In fact, Mahan and Hopfield[4] noted that the valence band Γ_7 from which the B exciton is derived possesses an energy term linear in k and showed that, if the finiteness of the exciton wave vector K which matches the photon wave vector is taken into consideration, the coupling between a pure triplet exciton and a transverse one occurs through the k -linear terms in the valence band. Their theory explained the fine structure successfully.

Very recently Koda *et al.*[5] reported a reflectivity measurement with polarized light on the $Z_{1,2}$ and Z_3 exciton bands in CuCl under uniaxial stress. In this measurement an inter-

esting fine structure was seen in the Z_3 exciton band. In order to understand this structure, it is necessary to introduce the above two points, (1) the electron-hole exchange interaction, and (2) the finiteness of the photon wave vector, into the usual deformation potential theory.

The purpose of this paper is to reveal the behavior of the $Z_{1,2}$ and, in particular, the Z_3 exciton states in CuCl on the above basis. A mechanism which causes the coupling between exciton states through a strain-induced k -linear term is proposed.

In the next section important characteristics of the spectra observed by Koda *et al.* are summarized. Section 3 gives the formalism of the theory and the results of calculation. In Section 4 a qualitative explanation complementary to the results of Section 3 is given. Section 5 is devoted to comparison of the theory with experiment and evaluation of the parameters for CuCl. In the last section, our conclusions are given.

2. THE EXPERIMENT OF KODA *et al.*

CuCl is a zincblende type crystal. Since the valence band Γ_5 consists of the $3d$ orbitals of Cu for the large part [6], it splits into Γ_7 (upper) and Γ_8 (lower) bands by the spin-orbit interaction. The exciton states which originate from Γ_7 and Γ_8 with the common conduction band Γ_6 are denoted by Z_3 and $Z_{1,2}$ respectively by Cardona [7]. Recently Koda *et al.* [5] reported the $Z_{1,2}$ and Z_3 exciton spectra of stressed CuCl using polarized light. A remarkable behavior of the Z_3 band is seen in one configuration as reproduced in Fig. 1. It was inferred [5] that I'_1 was a mixture of longitudinal and transverse waves, and that I''_1 originated from a spin-triplet state. But it was unknown why I'_1 and I''_1 were detected in an optical measurement and why I'_1 became so intense under high stress. Usual deformation potential theory could not answer these questions. This experiment gave a motive to our present investigation.

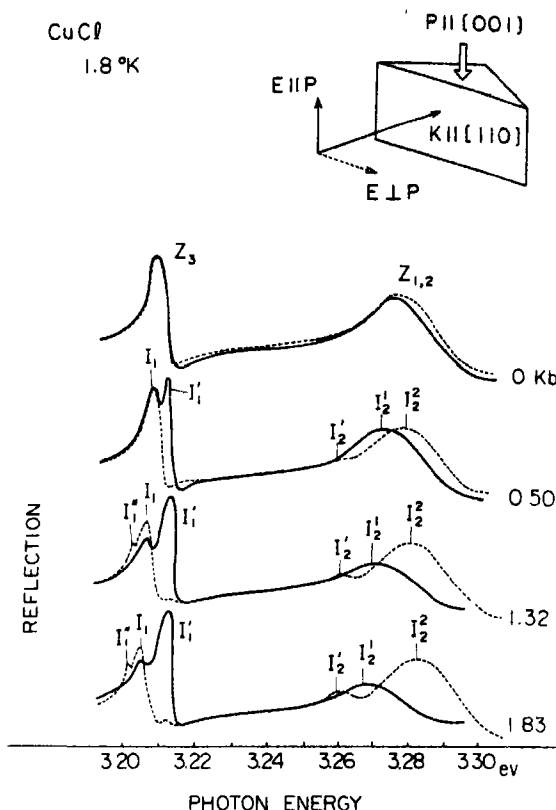


Fig. 1. The reflectivity spectra of the $Z_{1,2}$ and Z_3 exciton bands under the external uniaxial stress measured with polarized light [5].

3. FORMALISM OF THEORY AND THE RESULTS OF CALCULATION

In this section, we investigate the Z_3 and $Z_{1,2}$ exciton states under the external stress. These states are derived from the Γ_5 valence and Γ_1 conduction bands perturbed by the $k \cdot p$ term, spin-orbit interaction and external stress.

The valence-band energy spectrum is expressed as follows:

$$H_{\Gamma_5}(\mathbf{k}) = H_0(\mathbf{k}) + H_d + H_{d-k}(\mathbf{k}), \quad (3.1)$$

$$H_0(\mathbf{k}) = A_0 k^2 E + A_1 [(L_x^2 - \frac{1}{3} L^2) k_x^2 + \text{c.p.}] + A_2 [(L_x L_y + L_y L_x) k_x k_y + \text{c.p.}], \quad (3.2)$$

$$H_d = D_0 (e_{xx} + e_{yy} + e_{zz}) E + D_1 [(L_x^2 - \frac{1}{3} L^2) e_{xx} + \text{c.p.}] + D_2 [(L_x L_y + L_y L_x) e_{xy} + \text{c.p.}], \quad (3.3)$$

$$H_{d-k}(\mathbf{k}) = [B(e_{xy}k_y - e_{xz}k_z) + C(e_{yy} - e_{zz})k_x]L_x + \text{c.p.}, \quad (3.4)$$

where c.p. signifies the cyclic permutation, L is an angular momentum operator with $L = 1$, and E is the unit matrix. Basis functions are the three Bloch functions $\{b_x, b_y, b_z\}$ at Γ_8 . (3.2) represents the second-order terms derived by the $\mathbf{k} \cdot \mathbf{p}$ perturbation. The effect of external stress on Γ_8 is given in (3.3). Here e_{xx}, \dots, e_{yz} are strain tensors, and D_0, D_1 and D_2 are deformation potentials. (3.4) stands for the strain-induced k -linear terms. They can exist only when the crystal lacks the inversion symmetry. The constants $A_0, A_1, A_2, D_0, D_1, D_2, B$ and C are determined by the eigenfunctions and eigenvalues of the bands at the Γ point. Next the spin-orbit interaction is introduced as a perturbation. Basis functions are then taken as $\{b_\mu\} = \{b_x\alpha, \dots, b_z\beta\}$. Eventually the valence band energy spectrum is written as follows:

$$H_{\mu\mu'}(\mathbf{k}) = \{H_0(\mathbf{k})\}_{\mu\mu'} + \{H_d\}_{\mu\mu'} + \{H_{d-k}(\mathbf{k})\}_{\mu\mu'} + \{H_{s-0}\}_{\mu\mu'}, \quad (3.5)$$

where $H_{s-0} = -\frac{1}{2}\lambda\mathbf{L} \cdot \mathbf{s}$, λ is the spin-orbit splitting of the valence band and is taken to be positive.

It will be appropriate here to make a remark on the energy terms linear in k , since they are known to exist in the zincblende structure even in the absence of strain. The strain-induced k -linear terms (3.4) are obtained by second-order perturbation bilinear in $\mathbf{k} \cdot \mathbf{p}$ term and the interband deformation-potential terms. The hitherto known k -linear terms arise from a similar perturbation bilinear in $\mathbf{k} \cdot \mathbf{p}$ and the spin-orbit interaction and exist in the absence of strain. Because of their different origins, the two kinds of k -linear terms possess different properties. The latter will be neglected in this paper for the following two reasons. The first and the more important one is that the latter exists only in the Γ_8 valence band and

vanishes in the Γ_7 band. Since the Z_3 exciton, in which we are most interested, is associated with the Γ_7 band, the intrinsic k -linear terms have little effects on the Z_3 exciton. The other reason comes from the comparison of their magnitude. According to Song's band calculation[6], the coefficient of the intrinsic k -linear term in the Γ_8 band is on the order of 10^{-9} cm-eV. In contrast to this, as will be seen in Section 5, the strain-induced k -linear term can amount to $\sim 10^{-9}$ cm-eV for a pressure of ~ 0.5 kb. It becomes larger for higher pressure. Therefore even in the $Z_{1,2}$ excitons the effects of the strain-induced k -linear terms prevail over those of the intrinsic ones at high pressures. For these two reasons we consider only the k -linear terms induced by strain and neglect the intrinsic ones.

The energy spectrum of the conduction band is expressed in terms of the bases $\{b_\nu\} = \{b_s\alpha, b_s\beta\}$ as

$$H^c(\mathbf{k}) = A_0^c k^2 E + D_0^c (e_{xx} + e_{yy} + e_{zz}) E. \quad (3.6)$$

The Γ excitons with wave vector \mathbf{K} are derived from the energy spectra (3.5) and (3.6) according to the formalism[8] of exciton in degenerate bands,

$$\Psi_{n\mathbf{K}}(\mathbf{r}_e, \mathbf{r}_h) = \sum_{\mu\nu} \exp[i\mathbf{K}(\mathbf{r}_e + \mathbf{r}_h)/2] \times F_{\mu\nu}^{n\mathbf{K}}(\mathbf{r}_e - \mathbf{r}_h) b_\mu^*(\mathbf{r}_h) b_\nu(\mathbf{r}_e). \quad (3.7)$$

The envelope function $F_{\mu\nu}^{n\mathbf{K}}$ satisfies the following effective mass equation,

$$\begin{aligned} \sum_{\mu'\nu'} H_{\mu\nu;\mu'\nu'} F_{\mu'\nu'}(\mathbf{r}) &= E F_{\mu\nu}(\mathbf{r}), \quad (3.8) \\ H_{\mu\nu;\mu'\nu'} &= \delta_{\mu\mu'} H_{\nu\nu}^c(\mathbf{K}/2 - i\nabla) - \delta_{\nu\nu'} \\ &\times H_{\mu'\mu}(-\mathbf{K}/2 - i\nabla) + \delta_{\mu\mu'} \delta_{\nu\nu'} V(\mathbf{r}) \\ &+ \Omega \delta(\mathbf{r}) J_{\mu\nu;\mu'\nu'}(\mathbf{K}). \end{aligned} \quad (3.9)$$

In (3.9) the third term represents the attractive Coulomb interaction and the last term the

exchange interaction,

$$J_{\mu\nu, \mu'\nu'}(\mathbf{K}) = \iint a_\nu^*(\mathbf{r}) a_\mu(\mathbf{r}) \frac{e^2}{|\mathbf{r} - \mathbf{r}'|} \\ \times a_{\mu'}^*(\mathbf{r}') a_{\nu'}(\mathbf{r}') d\mathbf{r} d\mathbf{r}' + \frac{4\pi}{3\Omega} \cdot \\ \times \frac{3(\boldsymbol{\mu}_{\nu\mu} \cdot \mathbf{K})(\boldsymbol{\mu}_{\mu'\nu'} \cdot \mathbf{K}) - (\boldsymbol{\mu}_{\nu\mu} \cdot \boldsymbol{\mu}_{\mu'\nu'}) K^2}{K^2} \\ + 0(K^2),$$

which couples a missing electron-electron pair (μ, ν) with another pair (μ', ν') . a_μ and a_ν are the Wannier functions corresponding to b_μ and b_ν , respectively. $\boldsymbol{\mu}_{\nu\mu} = \int a_\nu^*(\mathbf{r}) \mathbf{r} a_\mu(\mathbf{r}) d\mathbf{r}$ is the transition dipole moment.

Equation (3.8) can be solved by the perturbation method. The exchange term, the spin-orbit term and the terms which contain strain tensors are first neglected. In the resultant equation, we ignore the off-diagonal terms of the hole kinetic energy $H_0(\mathbf{k})$, which is permissible owing to the heavy hole mass[9]. Eventually the unperturbed equation becomes a hydrogenic equation in diagonal form. The neglected terms are then evaluated by the ground state solution $F(\mathbf{r})$, which is independent of the missing electron-electron pair $\{\mu, \nu\}$. Since the binding energies[9] of the $Z_{1,2}$ and Z_3 excitons in CuCl are large compared with the spin-orbit splitting λ , exchange energy, and deformation energy, this procedure is reasonable. The 12×12 matrix thus obtained for the particular configuration of stress ($\| [001]$) and wave vector $K(\| [110])$ is shown in Table 1. The eigen-energies of excitons with wave vector K are given by the eigen-values of this matrix. The definition of the base exciton states in Table 1 is given in the Appendix. There the polarization of the longitudinal exciton state a (and a') is parallel to the exciton wave vector K , and those of the transverse exciton states b and c (or b' and c') are parallel to the $[001]$ and $[1\bar{1}0]$ directions respectively. In Table 1 a dilation term, which causes a uniform shift in the exciton energies, is omitted, and the particular configuration of

the stress retains only one deformation potential D_1 in it.

It is most noticeable in the table that the coupling between a and b (or c and Γ_2) arises through a pure imaginary matrix element $i(4/3)T = (i/3)CK(e_{xx} - e_{zz})$, which originates from the strain-induced k -linear term and the finiteness of the exciton wave vector K . The longitudinal and transverse exchange energies Δ_L, Δ_T are expressed respectively as follows:

$$\Delta_L = 2|F(0)|^2\Omega \left[\iint a_x(\mathbf{r}) a_s(\mathbf{r}) \frac{e^2}{|\mathbf{r} - \mathbf{r}'|} \right. \\ \left. \times a_s(\mathbf{r}') a_x(\mathbf{r}') d\mathbf{r} d\mathbf{r}' + \frac{8\pi}{3} \frac{\mu^2}{\Omega} \right], \\ \Delta_T = 2|F(0)|^2\Omega \left[\iint a_x(\mathbf{r}) a_s(\mathbf{r}) \frac{e^2}{|\mathbf{r} - \mathbf{r}'|} \right. \\ \left. \times a_s(\mathbf{r}') a_x(\mathbf{r}') d\mathbf{r} d\mathbf{r}' - \frac{4\pi}{3} \frac{\mu^2}{\Omega} \right],$$

where $\mu = \int a_s(\mathbf{r}) \mathbf{r} a_x(\mathbf{r}) d\mathbf{r}$ is the transition dipole moment.

Figures 2(a) and 2(b) give the twelve exciton energies vs. strain, together with the oscillator strength normalized to 100 for each polarization, computed by using the values of the parameters indicated in the figure.

The strain-dependent parameter Δ is defined by

$$\Delta = D_1(e_{xx} - e_{zz}) = D_1(S_{11} + |S_{12}|)P,$$

where S_{11} and S_{12} are compliance and P is the strength of pressure.

4. QUALITATIVE EXPLANATION TO THE RESULTS OF SECTION 3

In the preceding section, we have shown that the eigenstates of the exciton can be obtained by diagonalizing the 12×12 matrix. In this section we rephrase the procedure rather schematically following the idea of the Hopfield quasicubic model[10]. Figure 3(b) shows that the spin-orbit interaction splits the valence band Γ_5 into Γ_7 and Γ_8 . The pressure applied in the direction $[001]$

Table 1. The 12×12 matrix derived from the effective mass equation (3.8) for the configuration, pressure $P \parallel [001]$ and exciton wave vector $K \parallel [110]$. The dilation term $(D_0 - D_0) \times (e_{xx} + e_{yy} + e_{zz})$ is omitted. The zero point of energy is taken arbitrarily. The following parameters are used: $\Delta = D_1(e_{xx} - e_{zz})$, $T = CK(e_{xx} - e_{zz})/4$, longitudinal exchange energy Δ_L , transverse exchange energy Δ_T and spin-orbit splitting λ

[illegible]

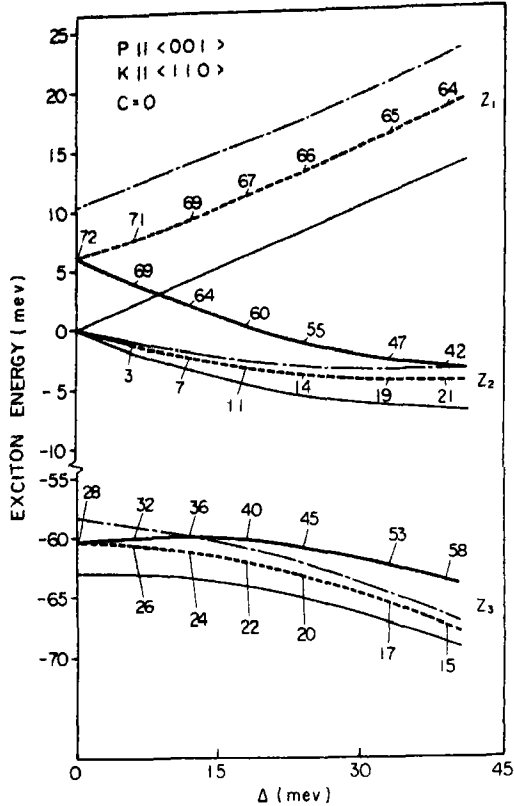


Fig. 2(a). The exciton energies vs. strain-dependent parameter Δ . The strain-induced k -linear term is neglected ($C = 0$). The following values are used in the calculation: $\lambda = 63$ MeV, $\Delta_L = 15$ MeV, $\Delta_T = 8.7$ MeV. The thick solid lines show the transverse exciton b and the thin ones the pure triplet excitons. The dotted lines represent the transverse exciton c , and the dot-dash lines the longitudinal excitons. The figures refer to the oscillator strength normalized to 100 for each polarization.

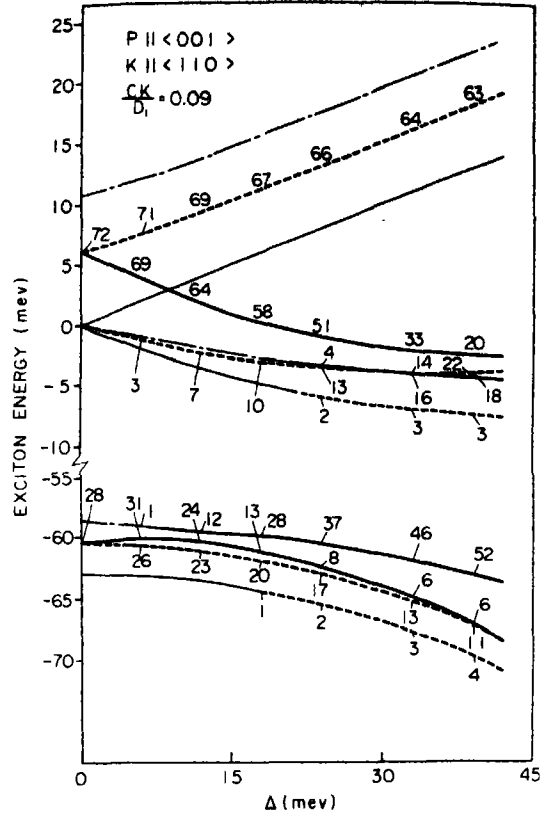


Fig. 2(b). The exciton energies vs. strain-dependent parameter Δ . The strain-induced k -linear term is considered. The coupling parameter C is taken properly. The other parameters and the meaning of the curves are the same as in Fig. 2(a).

lowers the T_d symmetry of the crystal to D_{2d} and splits Γ_8 into Γ_7 and Γ_6 (irreducible representations in D_{2d}), as depicted in Fig. 3(c). Exciton states are derived from each valence band. The excitons are strongly dependent upon stress not only through the valence band shift, but also through the exchange interaction since the wave functions of the valence bands are mixed with themselves by the strain.

In Fig. 4 the behavior of the exciton states under applied stress is shown schematically. For small strain we can calculate the energies

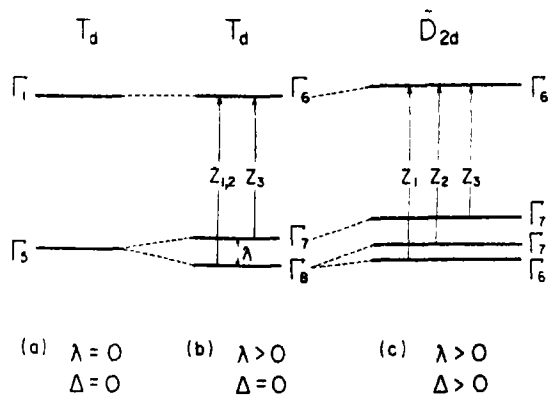


Fig. 3. Schematic explanation for the splitting of the valence band under the spin-orbit interaction and the external stress $P \parallel [001]$.

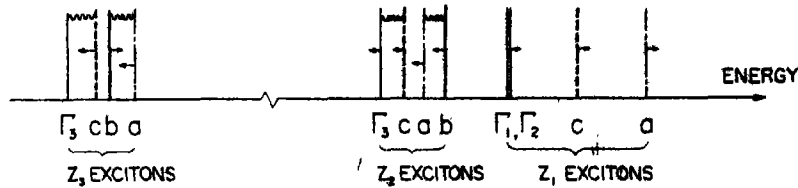


Fig. 4. Schematic explanation for the behavior of the exciton states in the Z_1 , Z_2 and Z_3 exciton bands under the stress. The arrows show the direction of the energy shift by the increased pressure, and the wavy lines the coupling owing to the strain-induced k -linear term.

of the excitons by second-order perturbation, to get the following result. Δ is the strain-dependent parameter defined in Section 3.

Z_3 exciton states $\Gamma_6 \times \Gamma_7 = \Gamma_3 + \Gamma_4 + \Gamma_5$

$$E_{Z_3,a} = -\lambda + \frac{1}{3} \Delta_L - \frac{2\Delta_L^2}{9\lambda} - \frac{2\Delta_L}{9\lambda} \Delta$$

$$E_{Z_3,b} = -\lambda + \frac{1}{3} \Delta_T - \frac{2\Delta_T^2}{9\lambda} + \frac{4\Delta_T}{9\lambda} \Delta$$

$$E_{Z_3,c} = -\lambda + \frac{1}{3} \Delta_T - \frac{2\Delta_T^2}{9\lambda} - \frac{2\Delta_T}{9\lambda} \Delta$$

$$E_{Z_3,\Gamma_3} = -\lambda$$

Z_2 exciton states $\Gamma_6 \times \Gamma_7 = \Gamma_3 + \Gamma_4 + \Gamma_5$

$$E_{Z_2,a} = -\frac{\Delta}{6}$$

$$E_{Z_2,b} = \frac{2}{3} \Delta_T + \frac{2\Delta_T^2}{9\lambda} - \left(\frac{1}{3} + \frac{4\Delta_T}{9\lambda} \right) \Delta$$

$$E_{Z_2,c} = -\frac{\Delta}{6}$$

$$E_{Z_2,\Gamma_3} = -\frac{\Delta}{3}$$

Z_1 exciton states $\Gamma_6 \times \Gamma_6 = \Gamma_1 + \Gamma_2 + \Gamma_5$

$$E_{Z_1,a} = \frac{2}{3} \Delta_L + \frac{2\Delta_L^2}{9\lambda} + \left(\frac{1}{6} + \frac{2\Delta_L}{9\lambda} \right) \Delta$$

$$E_{Z_1,c} = \frac{2}{3} \Delta_T + \frac{2\Delta_T^2}{9\lambda} + \left(\frac{1}{6} + \frac{2\Delta_T}{9\lambda} \right) \Delta$$

$$E_{Z_1,\Gamma_2} = \frac{\Delta}{3}$$

$$E_{Z_1,\Gamma_1} = \frac{\Delta}{3}$$

In obtaining the above result, we have not considered the strain-induced k -linear term. a , b and c are triplet-singlet mixed Γ excitons. a has the polarization parallel to K and it is the longitudinal wave. The polarizations of the transverse waves b and c are parallel to the $[001]$ and $[1\bar{1}0]$ directions respectively. The other states are pure spin-triplet. The above expressions explain our numerical result shown in Fig. 2(a). In the Z_3 band the longitudinal exciton a lowers in energy, as stress increases. On the other hand the transverse exciton b is raised and after the crossing with a , it stands on the high energy side of a . The transverse exciton c comes near to the Γ_3 exciton. Such a behavior of the excitons is a reflection of the stress dependence of the Bloch functions in the uppermost valence band Γ_7 . The stress applied in the $[001]$ direction modifies them in such a way that the z component becomes dominant over the x and y components in them. This modification of the wave functions acts to enhance the exchange energy of the transverse b exciton, which transforms like z , as well as to reduce that of the a (longitudinal) and c (transverse) excitons polarized perpendicular to the z axis.

The exciton levels are shifted by the stress in this way, but there occurs no mixing between them so far as we do not consider the strain-induced k -linear term.

The situation is utterly changed when we take account of the finiteness of the wave vector K . The finiteness of the exciton wave vector which is supposed to match the photon wave vector gives rise to the coupling of the longitudinal wave a with the transverse wave

b , and of the transverse wave c with the triplet Γ_3 . The coupling arises through the strain-induced k -linear terms. Thus in the case of a and b , clamping occurs. Since the b exciton can be excited by the light polarized parallel to the stress and c by the light polarized perpendicular to it, the situation shown in Fig. 2(b) will be understood clearly. Similar fine structure exists also in the Z_2 band.

5. COMPARISON WITH EXPERIMENT AND EVALUATION OF THE PARAMETERS FOR CuCl

In this section we compare Fig. 2(b) with the observed spectra Fig. 1. Since the latter is the reflectivity spectrum, in which the exact resonance energy cannot be known and on the other hand the former is concerned with the intrinsic electronic structure, only semi-quantitative comparison is possible.

(1) Figure 2(b) excellently agrees with the observed spectra; in respects of the energy shift, splitting and intensity of the Z_1 , Z_2 exciton bands under applied stress for both polarizations.

(2) In the Z_3 exciton band the fine structure of the spectra can be reasonably understood by Fig. 2(b). We conclude that I'_1 is a transverse-longitudinal mixed state in which the transverse component becomes dominant at high stress, and I'_2 is a pure triplet-transverse mixed state. Oscillator strength of these states agrees with the observed spectra well for both polarizations.

(3) We have used the following values in the numerical calculation.

$$\lambda = 63 \text{ MeV} [11], \Delta_7 = 8.7 \text{ MeV} [11],$$

$$\Delta_L = 15 \text{ MeV}.$$

The last parameter Δ_L has been determined so that it correctly gives the pressure at which the clamping of the a and b in the Z_3 band occurs. This value is rather small compared with one supposed from a magneto-optical measurement [11].

Comparing the energy separation between the c exciton in the Z_1 band and the b exciton

in the Z_2 band in Fig. 2(b) with experiment, we can determine the deformation potential D_1 to be $D_1 \approx 2 \text{ eV}$ (> 0) by use of the compliance $s_{11}^E = 8.35 \times 10^{-12} \text{ cm}^2/\text{dyne}$, $s_{12}^E = -3.40 \times 10^{-12} \text{ cm}^2/\text{dyne}$ [12]. The remaining parameter C , the coefficient of the strain-induced k -linear term, is a difficult one to estimate. The expression for C can be obtained by second-order perturbation bilinear in $\mathbf{k} \cdot \mathbf{p}$ and strain;

$$C = i \frac{2\hbar}{m} \frac{\langle b_x | V_{x^2-y^2} | b_x^{(1)} \rangle \langle b_x^{(1)} | p_z | b_y \rangle}{\Gamma_5 - \Gamma_5^{(1)}},$$

where $V_{x^2-y^2}$ is the potential conjugate to the strain $(e_{xx} - e_{yy})/\sqrt{2}$, and $b_x^{(1)}$ is the Bloch function at $\Gamma_5^{(1)}$, which lies about 3 eV below the uppermost valence band Γ_5 [6].

$\Gamma_5 - \Gamma_5^{(1)} \approx 3 \text{ eV}$, $|\langle b_x | V_{x^2-y^2} | b_x^{(1)} \rangle| \approx \text{a few eV}$ and

$$\left| \frac{2\hbar}{m} \langle b_x^{(1)} | p_z | b_y \rangle \right| \approx 10^{-7} \text{ cm-eV}$$

give $C \approx 10^{-7} \text{ cm-eV}$.

On the other hand we can infer the value of C from the repulsive width V of the a and b excitons due to the clamping in the Z_3 exciton band,

$$V = \frac{2}{3} C n K (e_{xx} - e_{zz}) \approx \text{a few meV}.$$

where n is the refractive index in the resonant region, K is the wave vector of the incident light. $n \approx 10$, $K \approx 10^5 \text{ cm}^{-1}$ and $D_1(e_{xx} - e_{zz}) = 12 \text{ meV}$ give again $C \approx 10^{-7} \text{ cm-eV}$.

6. CONCLUSION

We have investigated the behavior of the exciton states under external stress. It is interesting to note that a longitudinal exciton can be on the low energy side of a transverse exciton in the presence of the spin-orbit interaction and the external stress. We have proposed a mechanism of the coupling of excitons through the strain-induced k -linear term, which can be present in crystals lacking

inversion symmetry like CuCl. The longitudinal exciton, which is usually inactive in optical measurements, is found to get oscillator strength through such a mechanism (in the particular configuration we have considered). The experimental results have reasonably been explained by the theory.

We can also predict the spectra for another configuration, for example, where the pressure is parallel to [001] and the light is incident in the [100] direction: In this configuration, the two transverse waves are mixed, and the longitudinal wave is mixed with the pure triplet exciton, by the strain-induced k -linear term. Since the energy separation of the two transverse waves increases with pressure, the mixing cannot be observed, and only the shift of each exciton can be detected in the spectra. Furthermore, the longitudinal exciton remains inactive. These predictions have been supported experimentally [13].

Throughout this paper, we have emphasized the strain effects on the Z_3 exciton band. As explicitly seen in Fig. 2(b), some anomalous behavior occurs also in the $Z_{1,2}$ excitons. Similar experiment on CuBr will be very interesting, since in that material the lowest exciton is $Z_{1,2}$.

Acknowledgements—The authors express their cordial gratitude to Professor T. Koda for communicating the experimental data during the present work and for permission to cite them in this paper. They also thank Professor H. Hasegawa for his encouragement.

REFERENCES

1. KODA T. and LANGER D. W., *Phys. Rev. Lett.*, **20**, 50 (1968).
2. AKIMOTO O. and HASEGAWA H., *Phys. Rev. Lett.*, **20**, 916 (1968).
3. HOPFIELD J. J. and THOMAS D. G., *Phys. Rev.*, **132**, 563 (1963).
4. MAHAN G. D. and HOPFIELD J. J., *Phys. Rev.*, **135**, A428 (1964).
5. KODA T., MITANI T. and MURAHASHI T., *Phys. Rev. Lett.*, **25**, 1495 (1970).
6. SONG K. S., *J. Phys.*, **28**, 195 (1967).
7. CARDONA M., *Phys. Rev.*, **129**, 69 (1963).
8. ONODERA Y. and TOYOZAWA Y., *J. phys. Soc. Japan*, **22**, 833 (1967).
9. RINGEISSEN J., CORET A. and NIKITINE S., In *Localized Excitations in Solids* (Edited by R. F. Wallis), p. 297. Plenum Press, New York (1968).
10. HOPFIELD J. J., *J. Phys. Chem. Solids*, **15**, 97 (1960).
11. STAUBE W., *Phys. Lett.*, **29A**, 228 (1969).
12. INOBUCHI T., *Sharp tech. J.*, **8**, 59 (1969).
13. KODA T., MITANI T. and MURAHASHI T., Private communication.

APPENDIX

Exciton states taken as the bases in Table 1.

The valence-band Bloch functions which diagonalize the spin-orbit interaction can be written as

$$\begin{pmatrix} b_0\alpha - \sqrt{2}b_+\beta \\ -b_0\beta + \sqrt{2}b_-\alpha \end{pmatrix} / \sqrt{3} \quad \text{for } \Gamma_7,$$

and

$$\begin{pmatrix} b_+\alpha \\ (\sqrt{2}b_0\alpha + b_+\beta) / \sqrt{3} \\ (\sqrt{2}b_0\beta + b_-\alpha) / \sqrt{3} \\ b_-\beta \end{pmatrix} \quad \text{for } \Gamma_8,$$

where $b_\pm = (-b_x - ib_y)/\sqrt{2}$. $b_0 = b_z$ and $b_\pm = (b_x - ib_y)/\sqrt{2}$ are the eigenstates of the angular momentum operator L_z in Section 3. Excitons can be formed by replacing one of these six states with either of the conduction-band states $\{b_\pm\alpha, b_\pm\beta\}$. In practice, we need symmetry-adapted exciton states, namely the eigenstates $|P_J^M\rangle$ of the total angular momentum $\mathbf{J} = \mathbf{L} + \mathbf{S}$ and its z component M . Their explicit forms are given in the Appendix A of Onodera and Toyozawa's paper [8] in terms of appropriate linear combinations of missing electron-electron pair states.

In the present problem, the light is incident in the [110] direction. It is therefore convenient to use the following transformed states as the bases in our problem:

$$\begin{cases} \Gamma_3^{(1)} = |P_2^0\rangle \\ \Gamma_3^{(2)} = (|P_2^2\rangle + |P_2^{-2}\rangle) / \sqrt{2} \\ \Gamma_4^{(1)} = \frac{-1+i}{2} |P_2^1\rangle + \frac{1+i}{2} |P_2^{-1}\rangle \\ \Gamma_4^{(2)} = \frac{-1-i}{2} |P_2^1\rangle + \frac{1-i}{2} |P_2^{-1}\rangle \\ \Gamma_4^{(3)} = \frac{i}{\sqrt{2}} (-|P_2^2\rangle + |P_2^{-2}\rangle) \\ \Gamma_5 \begin{cases} c, c' = \frac{-1+i}{2} |P_1^1\rangle + \frac{-1-i}{2} |P_1^{-1}\rangle \\ b, b' = -i |P_1^0\rangle \\ a, a' = \frac{1+i}{2} |P_1^1\rangle + \frac{1-i}{2} |P_1^{-1}\rangle \end{cases} \\ \Gamma_2 = |P_0^0\rangle. \end{cases}$$

The unprimed and primed symbols for the Γ_3 exciton refer to the (Γ_7, Γ_8) and (Γ_8, Γ_8) missing electron-electron pairs respectively. a , b , and c transform like $x+y$, z and $x-y$, respectively.

VACANCY FORMATION PARAMETERS IN ORGANIC CRYSTALS*

R. H. BAUGHMAN†‡ and D. TURNBULL

Division of Engineering and Applied Physics, Harvard University, Cambridge, Mass. 02138, U.S.A.

(Received 9 June 1970; in revised form 30 October 1970)

Abstract—Measurements of the temperature dependence of the X-ray and bulk densities of succinonitrile and of cyclooctane single crystals are reported. Actual and upper limiting values of the vacancy concentrations are calculated from these results. In addition, heat capacity data from the literature are analyzed to obtain the vacancy formation enthalpy and entropy of benzene, hexamethylethane, pentaerythritol fluoride, perfluoropiperidine, 2,2,3-trimethylbutane, 1,1-dimethylcyclohexane, cyclooctane, and cis-1,2-dimethylcyclohexane. The vacancy triple point concentrations obtained range from less than 0.1 per cent in succinonitrile and benzene to as high as 0.76 per cent in 2,2,3-trimethylbutane. The corresponding vacancy formation enthalpies range from 0.52 to 1.2 of the triple point sublimation enthalpy, low fractions being found for compounds with low entropy of fusion, $S_m \sim R$. The effect of defect relaxation, zero point energy, and many body forces upon vacancy formation enthalpy is considered. For benzene and hexamethylethane, the ratios of experimental vacancy formation enthalpy to diffusion enthalpy are respectively 0.50 and 0.56, or about the same as is observed in f.c.c. metals. However, the experimental vacancy formation entropies are significantly higher than is observed in metals. The entropic contribution from torsional lattice modes, which contributes to this difference, is calculated. For both vacancy formation and diffusion parameters in these organic crystals, a linear correlation exists between enthalpy, normalized to the melting point, and entropy. Despite the difference in bonding, one empirical equation correlates the available diffusion parameters in both metals and organic crystals.

1. INTRODUCTION

LITTLE is known about vacancy formation parameters in van der Waals bonded crystals. The enthalpy and entropy of vacancy creation has been determined for krypton by Losee and Simmons[1], through simultaneous length and X-ray expansion measurements, and for krypton and argon by Beaumont, Chihara, and Morrison[2], through an analysis of heat capacity data. The vacancy formation enthalpies obtained in these investigations are in disagreement with present two-body central force calculations and suggest that many-body forces must be considered.

Rotationally disordered organic crystals are especially interesting for study because of

their high lattice symmetry and because their self-diffusion coefficients[3,4], as well as their creep behavior[5], had indicated a high point defect concentration. Sherwood *et al.* [6,7], have found in a number of organic rotator crystals that the activation enthalpy for creep is equal to that for self-diffusion. This suggests that low strain rate plastic flow in these crystals is due to the diffusion controlled climb of dislocations.

The most direct way to determine vacancy content is to compare the X-ray lattice parameter derived density, ρ_x , with the macroscopic density, ρ_b . Then the lattice site fraction of vacancies at temperature T , f_v , can be expressed as

$$f_v = \frac{\Delta\rho_b}{\rho_b} - \frac{\Delta\rho_x}{\rho_x}, \quad (1)$$

where the $\Delta\rho_b$ and $\Delta\rho_x$ are measured with respect to the same low temperature at which

*This work was supported by National Science Foundation Grant GP-7022.

†Based on a thesis submitted to Harvard University in partial fulfillment of the requirements for a Ph.D. degree.

‡Present Address: Materials Research Center, Allied Chemical Corporation, Morristown, N.J.

vacancy concentration is negligible. For the case of isotropic operation of vacancy sources and sinks we can rewrite this expression as

$$f_v = 3 \left(\frac{\Delta l}{l} - \frac{\Delta a}{a} \right), \quad (2)$$

where ' l ' is a linear macroscopic dimension and ' a ' is the X-ray lattice parameter. It is advantageous to make the bulk and X-ray measurements simultaneously on the same specimen. This was not done in the present work because the principal uncertainty was not in determining specimen temperature or in maintaining specimen purity between the two types of measurement. Instead, it was in obtaining reliable diffraction data from crystals which, as a result of rotational disorder, yield usable diffraction intensities only at relatively low angles. We report here measurements, using these methods, on crystals of cyclooctane and of succinonitrile. From these results we have calculated the temperature dependence of the vacancy concentration in cyclooctane and the upper limiting vacancy concentration in succinonitrile at its triple point.

Because of the availability in the literature of a number of reliable heat capacity studies on high purity rotator crystals, an analysis of heat capacity data was chosen as a second method of lattice defect determination. The relationship between the enthalpy and entropy of vacancy formation, H_v and S_v , and the corresponding increment to specific heat is easily formulated. The lattice site fraction of vacancies can be expressed as

$$f_v = e^{S_v/R} e^{-H_v/RT}. \quad (3)$$

Then the vacancy formation increment to observed heat capacity at constant pressure is

$$\Delta C = \frac{\partial(f_v H_v)}{\partial T} = \left[\frac{H_v}{R} \frac{\partial S_v}{\partial T} - \frac{H_v}{RT} \frac{\partial H_v}{\partial T} + \frac{H_v^2}{RT^2} + \frac{\partial H_v}{\partial T} \right] e^{S_v/R} e^{-H_v/RT}. \quad (4)$$

In the approximation that $\partial H_v/\partial T$ and $\partial S_v/\partial T$ are zero, the relationship previously derived by Lidiard[8] is obtained,

$$T^2 \Delta C = \left[\frac{H_v^2}{R} \right] e^{S_v/R} e^{-H_v/RT}. \quad (6)$$

If the excess heat capacity due to vacancy formation is known as a function of temperature, equation (6) can be used to calculate H_v and S_v .

2. DETERMINATION OF VACANCY PARAMETERS

2.1 Comparison of dilatometric and X-ray densities of succinonitrile and cyclooctane

(a) Sample preparation and crystal growth.

Commercial succinonitrile with a melting point range from 53 to 56°C was zone refined by forty zone passes at a zone travel rate of one cm per hour. Cyclooctane with a given impurity concentration of 0.01 ± 0.01 mole per cent was used as obtained from the American Petroleum Institute, Carnegie-Mellon University.

Using the Bridgman method and a travel rate of 1 mm per hr. 1.3 cm dia. cylindrical crystals were grown of both purified compounds. These crystals were optically transparent with no visible cracks or voids. Upon X-ray examination they were found to be single crystals. Since the rotator phase crystals of both succinonitrile and cyclooctane were soft and waxy, they were conveniently sectioned using either a razor blade or an electrically heated thin metal strip. These crystals were then annealed for one day at a temperature close to their melting points. As succinonitrile is hygroscopic, care was taken to avoid pickup of atmospheric water during specimen handling and measurement.

(b) Bulk expansion measurements. Since the triple point vapor pressure of cyclooctane [9] is significantly higher than for succinonitrile[10], it was necessary to use different methods for both the bulk and X-ray expansion measurements on these two compounds.

The linear thermal expansion of succinonitrile was determined from 28 to 54°C using a 0.01 in. total travel Lion Research Corporation capacitance micrometer. A nichrome wire wound copper tube, coaxial with the 1.100 in. long succinonitrile specimen, was used to vary temperature. A sheet of $\frac{1}{4}$ in. fused quartz supported the crystal and furnace and provided thermal insulation from the micrometer support platform. The capacitance between a thin copper disk resting upon the crystal and the capacitance micrometer was determined as a function of temperature. Upon calibration of capacitance vs. disk separation, the corresponding crystal expansion as a function of temperature was obtained.

The succinonitrile has a tendency to adhere to both the copper disk and the supporting fused quartz plate. As a result, anomalously high expansion was measured in initial trials. It was possible to remove this effect by applying a thin layer of lubricating graphite to the appropriate crystal faces.

The agreement between data points at the same temperature taken at the beginning and at the end of the experiment, indicates that specimen sublimation and creep were negligible. Whether the temperature was increasing or decreasing in the experiment had no observable effect upon the result.

Specimen temperature was controlled to better than $\pm 0.05^\circ\text{C}$ using a calibrated copper-constantan thermocouple in conjunction with a proportional-output temperature regulator. The uncertainty in determined $\Delta l/l_0$ is less than 3×10^{-5} . The linear expansion data obtained for succinonitrile are given in Fig. 1. Fractional expansion referred to 28°C can be expressed as $\Delta l/l_0 = -3.221 \times 10^{-3} + 9.968 \times 10^{-5} t + 5.649 \times 10^{-7} t^2$, where t is temperature in °C. For this equation the root mean square deviation between calculated and observed data points is 6.3×10^{-6} .

To avoid crystal sublimation, liquid displacement methods were used to measure the thermal expansion of cyclooctane. As the solubility of cyclooctane in distilled water at

room temperature is only 8 ppm by weight [11], water was the first choice for the immersion liquid. The change in buoyancy of a submerged cyclooctane crystal was measured as a function temperature. Knowing the mass of the crystal and the density of water as a function of temperature [12], the corresponding crystal density change with temperature was determined.

Since cyclooctane has a triple point of 14.82°C [9], measurements were performed in a refrigerated cold box. The water was first degassed to eliminate possible bubble formation at the crystal-liquid interface. Attached by a thin wire to the cyclooctane crystal was an invar weight, chosen so that the crystal, wire, and weight combination was slightly more dense than water. This assembly, immersed in a temperature regulated water bath, was connected by a second thin wire to the weighing arm of a Cahn Model G electrobalance. By measuring the weight of the crystal and attached invar in water from 0°C to the melting point of cyclooctane, the fractional density change of cyclooctane over this temperature range was determined. The uncertainty in determined $\Delta\rho_b/\rho_b$ is less than ± 0.0003 . However, due to specimen sublimation after weighing in air and before submersion in water, absolute density determinations by the balance method have an uncertainty of about 0.3 per cent.

The absolute density of cyclooctane was more accurately determined at a number of temperatures by adding 99.9 per cent methanol to distilled water until crystals submerged in the mixture would neither sink nor float. Conversion from null composition at a particular temperature to density was achieved using mixture density tables from the literature [13, 14]. Apparently neither significant amounts of water nor methanol were picked up by the crystals; small crystals melted in the mixture, refrozen, and then remelted did not show any significant change in melting point. Using this method, cyclooctane densities near the melting point were determined to ± 0.05

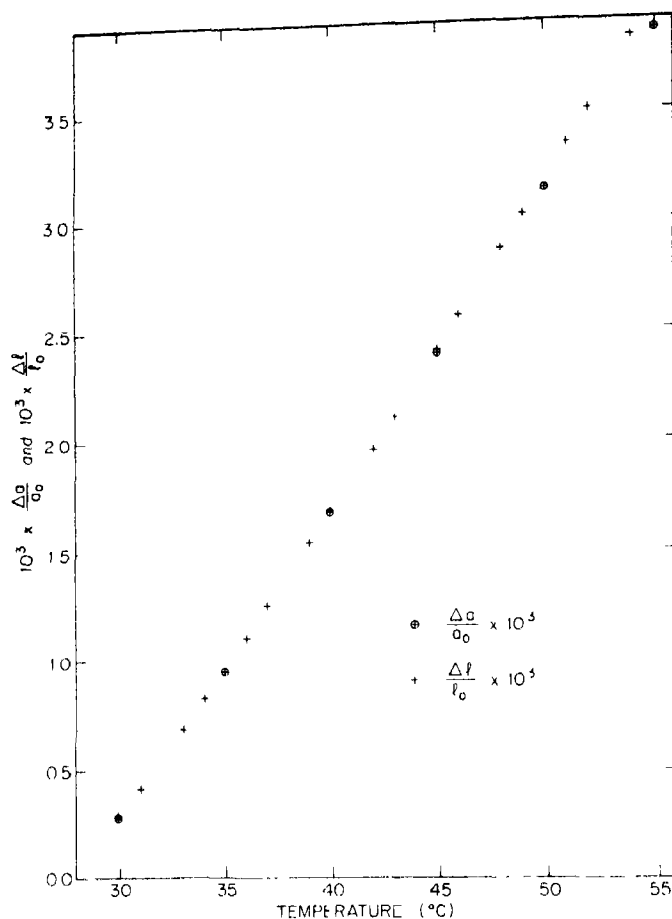


Fig. 1. X-ray and bulk linear thermal expansion of succinonitrile.

per cent, the uncertainty being mainly that of the tabulated densities of methanol-water mixtures. From the results of both measurements, the bulk density of cyclooctane between -4 and 12°C can be expressed as

$$\rho_b = 0.87780 - 0.000547t \text{ (gm/cm}^3\text{)},$$

with standard deviation of intercept and slope respectively 4.4×10^{-4} and 1.1×10^{-5} .

(c) *X-ray expansion measurements.* As a result of the rotational disorder in both succinonitrile and cyclooctane, only relatively low angle X-ray reflections are of sufficient intensity to be used in thermal expansion measurements. Fortunately, succinonitrile

does not have the additional complication of high vapor pressure. The rotator phase of this compound is b.c.c. with two molecules per unit cell [15].

A 1.3 cm dia. cylindrical succinonitrile crystal was sectioned perpendicular to the growth direction to form a specimen of 0.4 cm thickness. This was mounted in an Electronics and Alloys Inc. high temperature camera, placed upon a G.E. XRD-5 diffractometer. After crystal alignment, the change of $\text{CuK}\alpha$ diffraction angle with temperature was determined from room temperature to the melting point. Using a proportional output temperature regulator, temperature was controlled $\pm 0.04^\circ\text{C}$. Fractional change of lattice para-

meter with temperature was determined to within $\pm 1.5 \times 10^{-4}$. No discrepancy was observed between increasing and decreasing temperature data.

The rotator phase of cyclooctane is primitive cubic with eight molecules per unit cell [16]. Its higher vapor pressure, and resulting rapid rate of vapor transport in small temperature gradients, renders the X-ray method used for succinonitrile unsatisfactory for cyclooctane. For the observed low angle peaks, crystal sublimation, corresponding to an effective translation of specimen relative to the X-ray beam, would introduce a dominant source of error.

To avoid sublimation, cyclooctane was sealed in a glass capillary tube. Single crystals were invariably grown when this high purity compound was slowly cooled below its melting point. Because of adhesion of the crystal to the capillary surface and corresponding anomalous behavior of measured diffraction angles with change of temperature, usual single crystal techniques were not readily applicable to this compound.

A mechanical device was constructed which rotated the cyclooctane filled capillary in a random way about three mutually orthogonal axes. As a result, all possible crystal orientations were presented to the X-ray beam and a powder diffraction diagram thus obtained from a single crystal. A stream of nitrogen gas, impinging upon the specimen capillary, provided cooling. A resistance heater, immersed in a liquid nitrogen bath and controlled by a proportional output temperature regulator, provided the chilled gas. Calibration of specimen temperature, relative to the control copper-constantan thermocouple situated nearby, was achieved using crystals with known melting points sealed in capillaries and placed in the same position as the final specimens. Temperature was controlled to $\pm 0.5^\circ\text{C}$ and $\text{CrK}\alpha$ radiation was used. After each change in temperature, the crystal was annealed for one day to allow relaxation of capillary to crystal surface forces. The diffrac-

tion pattern was recorded photographically on a flat film in a casset mounted on the same track as the collimating system and 'crystal randomizer'. By taking two exposures at the same temperature for different measured film translations parallel to the main beam, the crystal to film distance was determined by triangulation. As a result of using film to crystal distances from 20 to 32 cm, high angular resolution was achieved. Due to the uncertainty in camera calibration, the change in lattice parameter with temperature was measured more reliably than was its absolute magnitude. The probable error, in terms of calculated X-ray density, is $\pm 0.0015 \text{ gm/cm}^3$ for ρ_x and ± 0.0005 for $\Delta\rho_x/\rho_x$.

(d) *Comparison of bulk and X-ray expansion measurements.* In Figs. 1 and 2, X-ray and bulk expansion measurements are given as a function of temperature for succinonitrile and cyclooctane. The observed difference between these measurements for succinonitrile is in the direction expected for vacancy formation. However, the magnitude of the difference for the highest temperature data points is less than the estimated uncertainty in X-ray expansion. From these measurements, the vacancy concentration at 54.0°C , 4.0°C below the triple point, is 0.033 ± 0.05 mole per cent. Assuming a vacancy formation enthalpy of about 10 kcal/mole, 0.1 mole per cent is obtained as an upper limit for vacancy triple point concentration in succinonitrile.

As can be seen in Fig. 2, the observed difference between X-ray and bulk density expansion for cyclooctane, in the temperature range from -10 to $+10^\circ\text{C}$, is in agreement with the parameters, $H_v = 6.99 \text{ kcal/mole}$ and $S_v = 13.1 \text{ e.u.}$, derived from heat capacity data by the analysis discussed in part 2.2. From the present measurements, a vacancy fraction change of $(2.0 \pm 0.5) \times 10^{-3}$ is indicated for this temperature interval, compared with 1.8×10^{-3} from the heat capacity study. From the latter work, the vacancy concentration at -10°C is not negligible. A vacancy fraction is indicated of 1.1×10^{-3} at -10°C , compared to

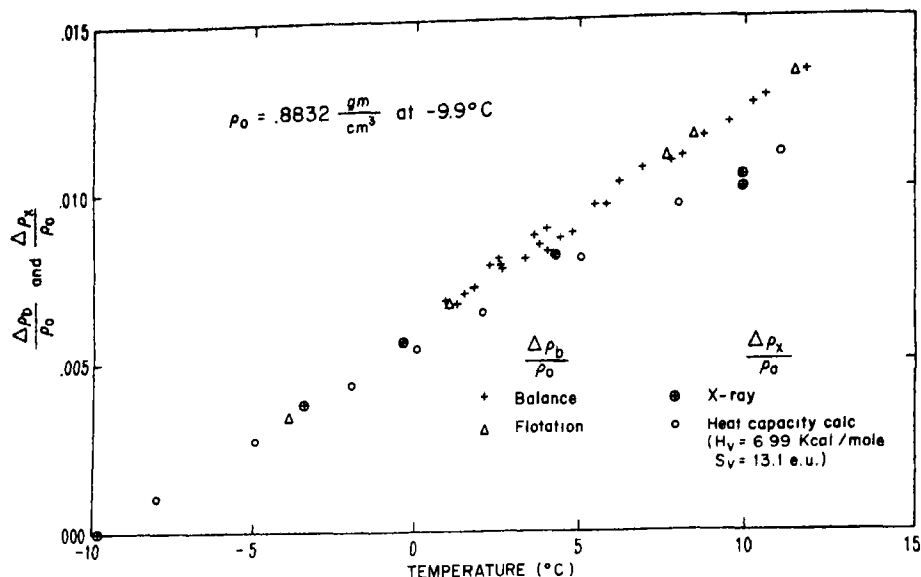


Fig. 2. X-ray and bulk thermal expansion in cyclooctane.

3.6×10^{-3} at the triple point, 14.82°C . Due to the uncertainty in absolute bulk and X-ray density measurements for cyclooctane, only changes in vacancy concentration have been obtained independently by the expansion measurements.

2.2 Analysis of heat capacity data

(a) *Limitation of method and impurity effects.* Knowing the vacancy formation heat capacity (the difference between the observed heat capacity and the heat capacity of a defect-free crystal) vacancy formation enthalpy and entropy can be calculated from equation (6). The determination of vacancy formation parameters from equilibrium heat capacity data is indirect in that assumptions must be made concerning the temperature dependence of the heat capacity of the defect-free crystal.

For all compounds studied here, except benzene, the heat capacity contribution for a perfect crystal was estimated by a linear extrapolation of observed heat capacity from low temperatures, where the vacancy concentration is negligible, to high temperatures.

As will be discussed later, care must be taken in attributing deviations between extrapolated and observed heat capacity to defect formation. Only high purity compounds for which heat capacity was linear with temperature over a wide temperature interval, in the range where defect concentration should be negligible, were considered.

Specification of the impurity level, in so far as it effects high temperature heat capacity, is difficult. A number of studies have been made on solid solution formation in rotator crystals. However, McCullough and Waddington[17] and others[18] have found that heat capacity in the premelting region is sensitive only to the impurity component which is not in solid solution. The solid-insoluble and melt-soluble impurity components of solid solutions is generally overestimated by melting curves, unless the different impurity concentrations and their liquid-to-solid phase distribution coefficients are included in the analysis[17, 19]. The heat capacity increase due to a solid-insoluble and melt-soluble impurity component of low concentration is given by [20]

$$C(\text{impurity}) = \frac{nRT_0^2}{(T_0 - T)^2} \quad (7)$$

where 'n' is the mole fraction of impurity and 'T₀' is the melting point of the solvent.

For all of the compounds studied, except perfluoropiperidine, the impurity mole fraction estimated from melting behavior is in the approximate range 10⁻⁴ to 10⁻³*. These compounds exhibit nonlinear curves of temperatures vs. inverse fraction-melted, which can be attributed to solid solution formation [17]. Consequently, it is not surprising that the solid-insoluble impurity concentrations derived from these curves, neglecting solid solution formation, are too high. Correcting the observed heat capacity data using Equation (7) and these concentrations leads to heat capacity curves of absurd shape. This has previously been observed in a number of other compounds by McCullough and Waddington[17]. For perfluoropiperidine an impurity fraction of 0.0051 is indicated by the slope of temperature vs. inverse fraction-melted curve. However, as is generally true for solid solution forming compounds[17-19], a much smaller impurity correction, corresponding to a solid-insoluble fraction less than 0.00069, is suggested† if a realistic impurity-corrected heat capacity curve is to be obtained.

As a further example, consider the heat capacity of hexamethylethane, due to Scott *et al.* [21]. The highest temperature data points are at 362.97 and 365.79°K, compared with a triple point temperature of 373.97°K for the pure compound. The measured heat capacity at the former temperatures are respectively 1.51 and 1.52 cal/mole above values obtained by a linear extrapolation of measurements from lower temperatures, where point defect formation and impurity effects are negligible.

Assuming that the increase from 1.51 to 1.52 cal/mole is entirely due to a solid-insoluble impurity contribution, equation (7) yields a very small solid-insoluble impurity mole fraction and corresponding impurity contribution at the highest measurement temperature. Consequently, an examination of the temperature dependence of the experimental 'excess' heat capacity, compared with the divergent behavior given by equation (7), justifies neglecting the solid-insoluble impurity heat capacity contribution.

(b) *Vacancy formation parameters from excess heat capacity.* In the present work, vacancy formation parameters have been calculated from heat capacity data for eight rotator crystals. As an example, let us consider the analysis for the rotator phase of hexamethylethane. The experimental heat capacity for this structure[21] is given in Fig. 3. C_{sat.} is the heat capacity of the solid under equilibrium vapor pressure and does not differ significantly from the heat capacity at constant pressure, C_p. Note that the measured heat capacity is linear with temperature from the rotational phase transition, 152.5°K, to about 300°K. This linearity over such a wide temperature interval suggests the validity of a linear extrapolation of normal heat capacity from the low temperature region where vacancy content is negligible to high temperatures. The difference between the extrapolated and observed heat capacity curve is then attributed to vacancy formation. As seen in Fig. 4, log (T²ΔC) for hexamethylethane is linear with inverse temperature and corresponds to a defect formation enthalpy of 10.4 kcal/mole and a formation entropy of 17.4 e.u.

In the same way vacancy formation parameters were obtained for all organic compounds tabulated in Table 1, except benzene. In each case one defect formation enthalpy and entropy was sufficient to describe the data.

Calculating the intramolecular heat capacity contribution using observed vibrational

*See individual references to heat capacity data for each compound (Table 1).

†For each compound considered here, see reference to heat capacity data (Table 1) for a study of impurity concentration.

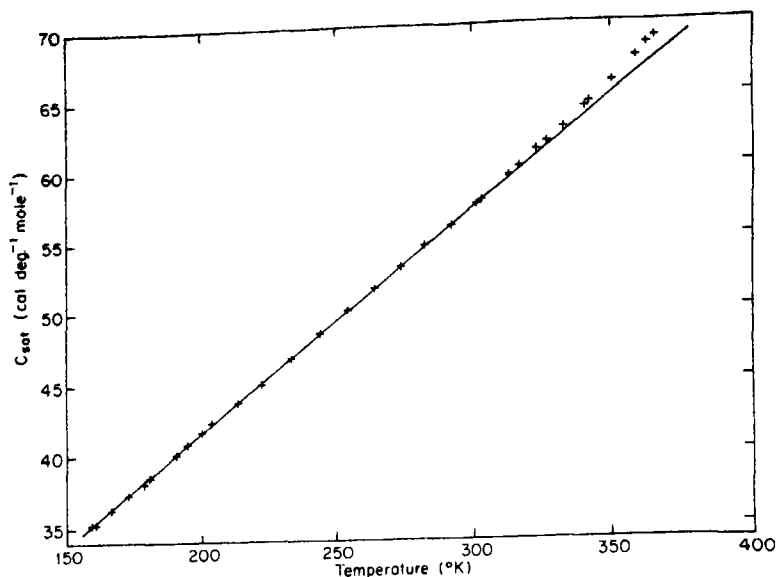


Fig. 3. Experimental heat capacity of hexamethylethane as a function of temperature. (Data from Ref. [21]).

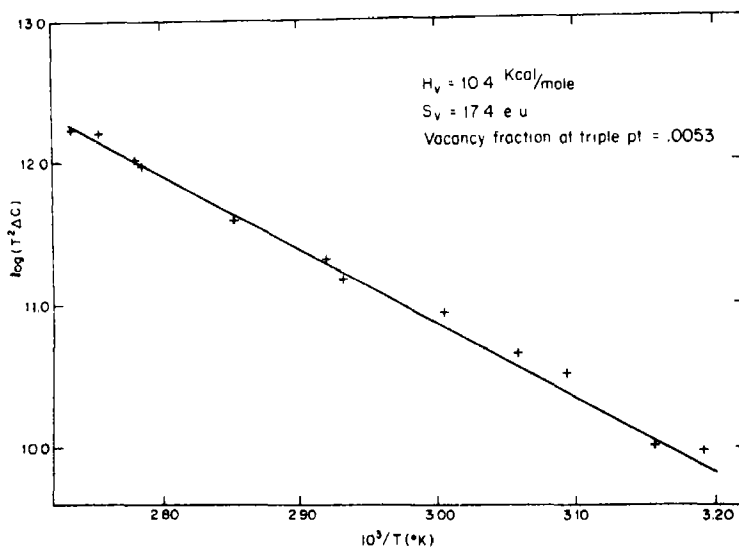


Fig. 4. The function $\log(T^2 \Delta C)$ vs. $1/T$ for hexamethylethane.

frequencies, instead of assuming linear temperature dependence for the total heat capacity of the defect-free crystal, allows one check of the previous treatment for hexamethylethane. The contribution from internal

vibrational and rotational modes was subtracted from the observed heat capacity. Then the defect formation heat capacity was obtained by a low to high temperature linear extrapolation of the difference. The spectro-

Table 1. Vacancy formation and triple point parameters

	$T_m(^{\circ}\text{K})$	$T_i(^{\circ}\text{K})$	$T_{TP}(^{\circ}\text{K})$	$S_f(\text{e.u.})$	$H_f(\text{kcal/mole})$	$S_i(\text{e.u.})$	f_i^{TP}	$H_s^{TP}(\text{kcal/mole})$	Ref.*
cis-1,2-dimethylcyclopentane	141.50	173.1	219.45	1.805	5.12 ± 0.81	12.6 ± 3.4	0.0046 ± 0.0008	9.9†	[a], [j]
cyclooctane	183.8	226.2	287.98	2.000	6.99 ± 1.00	13.1 ± 2.8	0.0036 ± 0.0011	11.06†	[b], [b]
1,1-dimethylcyclohexane	153.15	197.8	239.81	2.016	7.14 ± 0.79	17.6 ± 2.9	0.0022 ± 0.0005	10.3†	[c], [j]
2,2,3-trimethylbutane	121.4	166.6	248.57	2.174	4.64 ± 0.38	9.0 ± 1.2	0.0076 ± 0.0013	8.83	[d], [k]
perfluoropiperidine	171.9	211.9	274.12	2.455	7.14 ± 1.08	14.7 ± 3.5	0.0033 ± 0.0007	8.06†	[e], [e]
pentaerythrityl fluoride	249.40	309.1	367.43	3.35	10.3 ± 2.0	17.8 ± 4.4	0.0060 ± 0.0025	9.4	[f], [f]
hexamethylethane	152.5	292.6	373.97	4.819	10.4 ± 2.2	17.4 ± 5.0	0.0053 ± 0.0020	9.33	[g], [g]
benzene			278.691	8.461	12.5 ± 1.1	31.0 ± 4.1	0.0009 ± 0.0002	10.72	[h], [i]
krypton			115.776	3.386	1.78 ± 0.20	4.0 ± 2.0	0.0030 ± 1.0	2.58	[i], [i]

T_{TP} is the solid state phase transition temperature to the high temperature rotator phase. A linear extrapolation of experimental heat capacities between T_{TP} and T_i provided an estimate of the heat capacity for the defect free crystal between T_i and the triple point temperature (T_{TP}). The parameters H_f , S_f , and f_i^{TP} are respectively the vacancy formation enthalpy, vacancy formation entropy, and triple point vacancy concentration. Vacancy formation parameters for krypton are from Ref. [1]. All other vacancy formation parameters are from the present work.

* First Ref. is for heat capacity data, T_{TP} , T_{TP} , and entropy of fusion (S_f). Second Ref. is for additional data used to calculate triple point sublimation enthalpy to real gas (H_s^{TP}).

† To obtain H_s^{TP} , the difference between vapor and liquid phase heat capacity at constant pressure was approximated to be 12 cal/mole $^{\circ}\text{K}$.

[a] GROSS M. E., OLIVER G. D. and HUFFMAN H. M., *J. Am. Chem. Soc.* **75**, 2801 (1953).

[b] Ref. [9].

[c] HUFFMAN H. M., TODD S. S. and OLIVER G. D., *J. Am. Chem. Soc.* **71**, 584 (1949).

[d] HUFFMAN H. M., GROSS M. E., SCOTT D. W. and McCULLOUGH J. P., *J. Am. Chem. Soc.* **65**, 495 (1961).

[e] GOOD W. D., TODD S. S., MESSERLY J. F., LACINA J. L., DAWSON J. P., SCOTT D. W. and McCULLOUGH J. P., *J. Am. Chem. Soc.* **67**, 1306 (1963).

[f] PAYNE D. H., *Doctoral Dissertation*, University of Michigan, Ann Arbor, Michigan (1953).

[g] Ref. [21].

[h] Ref. [27].

[i] Ref. [2].

[j] DREISBACH, R. R., *Phys. Prop. of Chem. Compounds*, No. 22 of Advances in Chem. Series, *Am. Chem. Soc.* (1959).

[k] SCOTT D. W. and WADDINGTON G., *J. Am. Chem. Soc.* **75**, 2006 (1953).

[l] MILLER G. A., *J. Chem. Eng. Data* **7**, 353 (1962).

scopic assignments and internal rotational frequencies were obtained from Scott *et al.* [21]. The rotational contribution was obtained from the tables of Pitzer *et al.* [22, 23], using the Halford interpolation method [24]. The difference between the observed heat capacity and the calculated internal molecular contribution is given in Fig. 5. The determined vacancy formation parameters are $H_v = 10.7$ kcal/mole and $S_v = 18.2$ e.u., in good agreement with the previous result. The vacancy formation parameters obtained by these two approaches can be compared with experimental values for the enthalpy and entropy of diffusion [25], $H_D = 20.6$ kcal/mole and $S_D = 31$ e.u.

An estimate of vacancy parameters in benzene was obtained by comparing the heat capacity calculated from spectroscopic data by Lord, Ahlberg, and Andrews [26] with that measured by Oliver, Eaton, and Huffman [27]. If the deviation between calculated and observed heat capacity above 240°C is attributed to vacancy formation, a vacancy formation enthalpy of 12.5 kcal/mole, a vacancy

formation entropy of 31 e.u., and a triple point vacancy mole fraction of 9×10^{-4} is obtained. The observed triple point vacancy fraction is the same order of magnitude as determined for krypton [1] and for metals such as Al [28] and Au [29] by simultaneous X-ray vs. bulk expansion measurements. Both vacancy formation enthalpy and entropy seem reasonable when compared with the corresponding self-diffusion parameters calculated from the tracer measurements of Sherwood and associates [30], $H_D = 22.4$ kcal/mole and $S_D = 58$ e.u. However, it must be noted that part of the difference between observed and calculated heat capacity may be due to the approximation made by Lord, Ahlberg, and Andrews that the lattice rotational and translational contribution can be represented by a single Debye function with six degrees of freedom. The discrete rather than continuous nature of torsional energy levels as well as their temperature dependence is neglected. Bondi [31] previously attributed the difference between calculated and observed heat capacity in benzene to vacancy formation. However,

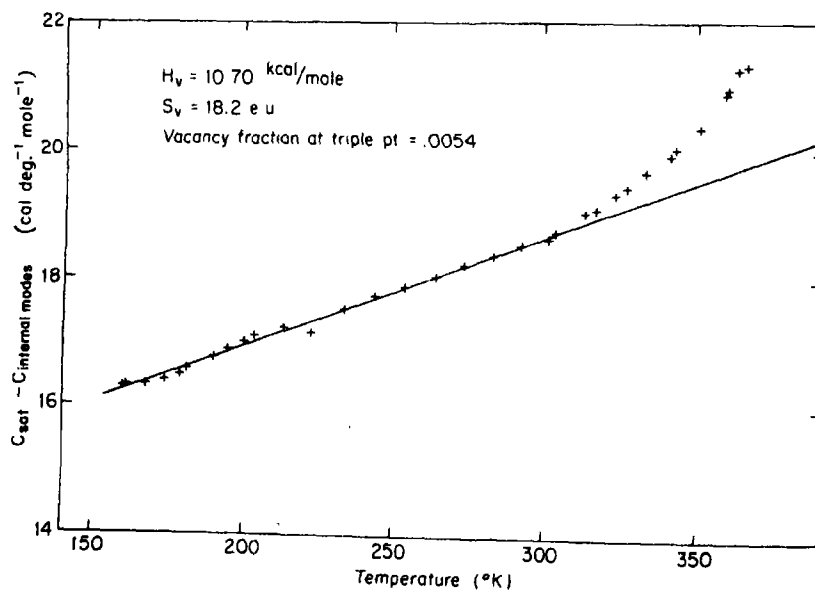


Fig. 5. Difference between the experimental heat capacity of hexamethylethane and the heat capacity contribution calculated for intramolecular modes.

by using expressions valid only for separated ion pair defects, he incorrectly evaluated the vacancy formation parameters.

It is difficult to determine the uncertainty in the vacancy formation parameters obtained by heat capacity analysis. The problem is in evaluating the reliability of the heat capacity determined for the defect-free crystal. The anharmonic contributions to this heat capacity have been included only in so far as they can be represented above the rotational phase transition as a linear function of temperature. The standard deviations tabulated in Table I assume the validity of a low to high temperature linear extrapolation of heat capacity for the defect free crystal.

3. DISCUSSION

3.1 *Relative concentrations of monovacancy, multiple vacancy, and interstitial defects*

Thus far we have been assuming monovacancies to be the main lattice point defect in rotator crystals. The observed positive deviation between bulk and X-ray expansion of cyclooctane indicates that the total monovacancy and multiple vacancy concentration is greater than the interstitial concentration. However, only in the case that $(\Delta l/l - \Delta a/a)$ is known accurately over a wide temperature range might it be possible to separate the contributions from these different defects. Monovacancy, multiple vacancy, and interstitial defects all make a positive contribution to measured heat capacity and it is again only possible to separate these different components by a multiple formation enthalpy analysis of suitable data taken over a wide temperature range. The formation of vacancies, single or in combination, or interstitials has the same effect upon $|\Delta l/l - \Delta a/a|$ at a particular temperature, but a differing one, dependent upon their relative formation enthalpies, upon excess heat capacity. Since the excess heat capacity for all the compounds considered can be interpreted in terms of single formation enthalpy and since the bulk

vs. X-ray determination for cyclooctane is in good agreement with the excess heat capacity result, one dominant point defect type is suggested. However, this experimental data presents only a coarse upper limit on the concentrations of secondary defects of different formation enthalpy from that of the primary defect.

Rotator crystals generally have low packing density, in order to minimize their total free energy by increasing orientational entropy at the expense of lattice enthalpy. Therefore, the interstitial formation enthalpy in a rotationally disordered solid may be less than in a corresponding ordered solid. However, an interstitial molecule would severely hinder the orientational motion of surrounding molecules. Consequently a large negative contribution to formation entropy is expected, corresponding to increases in both local torsional and translational mode frequencies.

The interstitial formation energy can be estimated from elasticity theory by assuming a linear stress-strain relationship is valid down to molecular dimensions, irrespective of the high strains present near the interstitial. Assuming that this severe approximation has the same relative effect upon calculations for all van der Waals bonded crystals of the same structure, a comparison can be made between interstitial formation energy in krypton and in cyclohexane, a typical rotator crystal. The required elastic moduli are not available for any of the rotator crystals for which vacancy concentrations have been determined.

In a simple elastic model due to Brooks, the interstitial formation energy is the work done in expanding a spherical hole of volume V_1 , corresponding to an interstitial site, to the volume V_2 , corresponding to the molecular volume which must be accommodated. Neglecting the compressibility of the interstitial molecule, Brooks obtains for an octahedral site in a f.c.c. lattice an interstitial formation energy of $2.29 G V_2$. Since the nearest neighbors to a molecule in an octahedral site lie in (100) directions, G is approximated

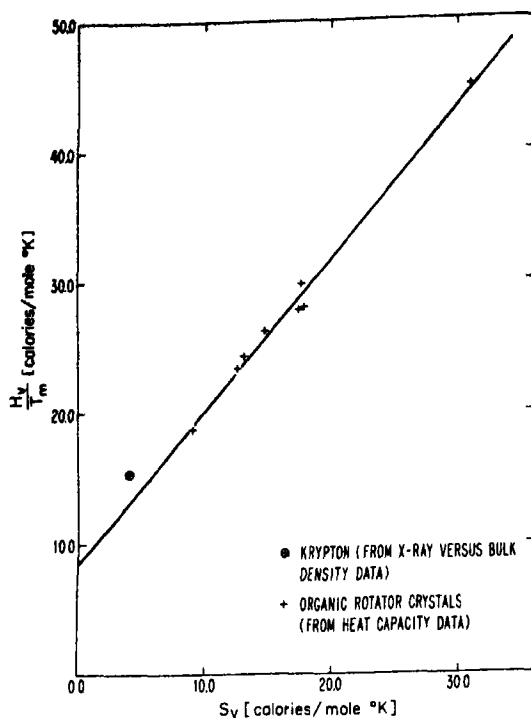


Fig. 6. H_v/T_m vs. S_v for van der Waals bonded crystals. Data points are from Table 1.

by the rigidity modulus for that direction. For the f.c.c. crystals krypton and cyclohexane, V_2 is taken as the van der Waals volume[31, 33]. Using elastic moduli extrapolated to 0°K for the rotator phase of cyclohexane[34] and calculated at 0° for krypton[35], an interstitial formation energy of 34 kcal/mole is obtained for the rotator phase of cyclohexane and 11 kcal/mole for krypton. Using a two-body Morse potential and static lattice approximation, Cotterill and Doyama[36] have calculated 7.40 kcal/mole for the interstitial formation energy in krypton. As mentioned by Simmons and Losee[1], their choice of isothermal compressibility for fitting the parameters of the potential, is not considered correct. No other interstitial energy calculations for van der Waals bonded solids have been found in the literature and no measurements are available. For cyclohexane and

krypton, the respective ratios of above calculated interstitial formation energy to heat of sublimation at the triple point[2, 37] are 4.0 and 4.2. Again normalizing to the respective heats of sublimation, the estimated interstitial formation energies are much higher than the vacancy formation enthalpies determined in the present work.

To estimate divacancy concentrations in van der Waals bonded crystals, gross approximations must be made. Taking a divacancy to be two nearest-neighbor sites and counting the number of distinguishable orientations possible, the ratio of divacancy concentration to single vacancy concentration is

$$\frac{f_{2v}}{f_v} = \frac{Z}{2} f_v e^{g_B^0/RT} \quad (8)$$

where Z is the site coordination number and g_B^0 is the standard free energy of formation difference between two isolated vacancies and a divacancy[1]. The divacancy binding parameter can be written as

$$g_B^0 = h_B - Ts_B^0, \quad (9)$$

where h_B and s_B^0 are respectively the binding enthalpy and entropy.

For van der Waals bonded crystals of the same crystal symmetry, it is reasonable to approximate the ratio of divacancy binding enthalpy to vacancy formation enthalpy as a constant. Neglecting lattice relaxation, many-body forces, and considering only nearest neighbor interactions, a bond count yields $2/Z$ for this ratio. By comparing Burton's calculation[38] of divacancy binding energy in argon with the experimental monovacancy formation enthalpy, a second estimate of this ratio is obtained. Representing two-body interactions with a Lennard-Jones potential, three-body interactions with a triple-dipole potential, and allowing for defect relaxation by an iterative, energy minimization process, Burton obtained a divacancy binding energy of 0.199 kcal/mole. The divacancy binding energy was found to be much less sensitive to the division of total lattice energy into two-body and three-body

components than was the monovacancy energy. From specific heat measurements[2], the experimental vacancy formation enthalpy in argon is 1.27 ± 0.13 kcal/mole, in agreement with the value 1.27 kcal/mole estimated by Simmons and Losee from their measurements on krypton[1]. Using these parameters, the ratio of divacancy binding enthalpy to monovacancy formation enthalpy is about 1/6.4, in agreement with the simple bond count estimate of $2/Z = \frac{1}{2}$ for f.c.c. crystals.

The value of divacancy binding entropy in van der Waals bonded solids is uncertain. Dobrzynski[40] has discussed a recent calculation, due in part to Friedel[41], which gives $s_B^0 = +0.61R$ for f.c.c. crystals. This calculation was made in the harmonic approximation and considers basically only nearest neighbor interactions, neglecting lattice relaxation. Schottky *et al.*[42] have calculated the binding entropy for the f.c.c. metals Cu, Ag, and Au. They treated the region near the defect by lattice dynamics and the region removed from the defect by linear elasticity theory. Neglecting lattice relaxation, they calculate a negative divacancy binding entropy contribution from the first region, in contrast to the previous calculation. Including a correction for lattice relaxation in this region and entropy contributions corresponding to lattice dilation and temperature dependence of the elastic strain field in the region removed from the defect, they obtain $s_B^0 \approx -2.0R$. Consequently, even for the case of a monatomic lattice, the value of divacancy binding entropy is not well established. For the organic molecules of interest here, there is an additional complication. As will be discussed in part 3.3, a contribution to defect formation entropy and consequently to divacancy binding entropy is expected from changes in orientational freedom of molecules surrounding the defect.

The uncertainty in s_B is reflected in estimates of the relative concentrations of divacancies and monovacancies. Simmons and Losee [1], assuming zero divacancy binding entropy,

have used a two- and three-body interactions, nearest-neighbor model to calculate $f_0/f_v \approx 0.088$ in krypton near the triple point. For the organic rotator crystals studied, here, the approximation $h_B \approx 2H_v/Z$ and the assumption $s_B \approx 0$ results in a very high triple point ratio of divacancies to monovacancies. As an example, consider hexamethylethane. For $H_v = 10.4$ kcal/mole, $f_v \approx 3 \times 10^{-3}$, and $s_B^0 = 0$ the calculated ratio of divacancy to monovacancy concentration at the triple point is 0.65. A lower divacancy concentration implies either $s_B^0 > 0$ or h_B is significantly less than its approximated value. In any case, it is not at all clear that the divacancy concentration at high temperatures in van der Waals bonded solids is negligible.

Burton[38] has calculated that divacancies in argon at the melting point move about 10 times faster than do vacancies. If van der Waals bonded solids at high temperatures do have a high relative concentration of divacancies and if these divacancies diffuse more rapidly than do vacancies, a pronounced temperature dependence is expected for the experimental enthalpy of diffusion. From NMR relaxation measurements, Resing[7, 43] has determined the diffusion coefficient for the rotator phase of adamantane over a wide temperature interval. In this interval the diffusion coefficient changed by seven orders of magnitude. Within experimental error, one enthalpy value* described the measurements from low temperatures to the melting point. At least in this particular organic rotator crystal, either the enthalpies for vacancy and divacancy diffusion are nearly equal or the divacancy contribution to self-diffusion is negligible.

3.2 Comparison of vacancy formation and sublimation enthalpies

For a number of the van der Waals bonded

*From high temperature, low strain rate creep measurements, Sherwood and Corke[7] have obtained an enthalpy of diffusion in agreement with Resing's work.

compounds tabulated in Table 1, the experimental vacancy formation enthalpy is significantly less than the sublimation enthalpy. Even neglecting lattice and electronic relaxation, the vacancy formation enthalpy and the sublimation enthalpy should not be equal. As discussed by Burton[38], additive n -body potential energy contributions to the cohesive energy, E_n , reduce the vacancy formation enthalpy by $\sum_{n=3} (n-2)E_n$, as compared to the sublimation enthalpy. Neglecting changes in lattice frequencies upon vacancy formation, the zero-point energy of the lattice, E_0 , contributes to sublimation enthalpy, but not to vacancy formation enthalpy. This zero-point energy correction is relatively larger for molecular crystals than for monatomic crystals, since torsional modes contribute as well as translational ones. Assuming sublimation to the ideal gas state, the difference in $P\Delta V$ for the process of sublimation and of vacancy formation amounts to $(RT - 2P\Omega)$, where P is the pressure and Ω is the molar volume. For temperatures of present interest and atmospheric pressure, the $2P\Omega$ term is negligible. A final contribution arises due to the difference in change of vibrational potential energy terms for the two processes. In the ideal gas state the hindering potentials for both translational and torsional vibration of the molecule as a whole are zero. Consequently, the corresponding potential energy terms disappear in going from the crystalline state to the low-density gas. Again neglecting changes in lattice frequencies upon vacancy formation and making the realistic approximation[44] that the lattice vibrational potential energy contributions can be replaced at high temperature by the equipartition value, a term $3RT$ arises in the difference between vacancy formation and sublimation enthalpies. Combining these contributions, we obtain

$$H_v = H_s - \sum_{n=3} (n-2)E_n + E_0 + 2RT, \quad (10)$$

where H_s is the sublimation enthalpy to the

ideal gas. This relationship neglects any environmental dependence of intramolecular vibrational frequencies.

Simmons and Losee[1], by comparing their experimental vacancy formation enthalpy with the lattice cohesive energy, have estimated a many-body contribution in krypton of $0.375^{+0.30}_{-0.21}$ kcal/mole. The quoted limits of uncertainty reflect both possible errors in their measurements and in their estimate of the effects of electronic and lattice relaxation for the vacancy. An energy of 0.375 kcal/mole represents about 13 per cent of the total cohesive energy. Carrying this percentage over to organic rotator crystals, we might expect an appreciable reduction in vacancy formation energy due to the term $-\sum_{n=3} (n-2)E_n$.

The zero-point energy term in equation (10), while small, is not negligible. For molecular crystals, it is the sum of torsional and the translational lattice zero-point energies, E_0^R and E_0^T . In the Debye approximation, the zero-point energy per degree of freedom is $\frac{1}{2}R\theta_D$, where θ_D is the relevant Debye temperature. The Einstein approximation yields a zero-point energy per degree of freedom of $\frac{1}{2}R\theta_E$, where θ_E is the relevant Einstein temperature. From high temperature X-ray and spectroscopic measurements on benzene[31], E_0^T and E_0^R are expected to be about 0.29 and 0.36 kcal/mole. Using the empirical Lindemann equation, to be discussed later, a translational zero-point energy of 0.16 kcal/mole is calculated for benzene. For other organic crystals in Table 1, this equation yields translational zero-point energies of about 0.1 kcal/mole. Neglecting differences in effective Debye temperatures for torsional and translational modes, by fitting the experimental heat capacity at low temperatures* to a single Debye function with six degrees of freedom, a total low temperature zero-point energy of 0.64 kcal/mole is obtained for benzene and

*For low temperature heat capacity data, see Ref. [27] and references given in Table 1.

energies between 0.34 and 0.58 kcal/mole for other compounds in Table 1.

As has been discussed, equation (10) neglects lattice and electronic relaxation and changes in lattice frequencies resulting from vacancy formation. Doniach and Huggins[45], have estimated that electronic relaxation may reduce the vacancy formation enthalpy in argon by about 10 per cent. However, they noted the strong dependence of this result upon the choice of parameters used in their model. Simmons and Losee[1] have reviewed present calculations of lattice relaxation in argon. Assuming a particular interaction potential, these calculations minimize the vacancy energy for a specific model. The lattice relaxation indicated by several approaches is small, of order 2 per cent of the cohesive energy[46, 49]. Correspondingly, the vacancy formation volume in argon is calculated to be nearly one molar volume. This is in contrast with measured vacancy formation volumes in metals of about 0.5 molar volume[50]. The activation volumes for diffusion measured for the van der Waals bonded crystals cyclohexane, 2,2-dichloropropane, *t*-butyl chloride, *t*-butyl bromide [51], and phosphorous[52] also indicate a significant degree of vacancy volume relaxation. However, there is disagreement between independent studies of diffusion at atmospheric pressure for both these organic crystals[3] and for phosphorous[53].

Note in Table 1 that the four organic compounds with very low entropies of fusion, $S_F \sim R$, have vacancy formation enthalpies considerably lower than the sublimation enthalpy. If these experimental enthalpies are to be explained, a considerable vacancy relaxation and/or many body contribution must be assumed. On the other hand, the four organic compounds with higher entropies of fusion have vacancy formation enthalpies fairly close to the sublimation enthalpy. The vacancy measurements available for krypton [1, 2] suggests that it belongs with the former group.

The structures for most of these compounds are not known. As mentioned earlier, cyclooctane is primitive cubic with eight molecules per unit cell. Hexamethylethane is b.c.c. with two molecules per unit cell[54] and benzene is orthorhombic with four molecules per unit cell[55]. The remainder of the tabulated rotator crystals are likely to have cubic symmetry. A knowledge of their crystal structures and bulk properties, such as elastic constants would facilitate a better understanding of vacancy formation.

3.3 Vacancy formation entropy

As can be seen in Table 1, vacancy formation entropies for rotator crystals are much higher than is found in metals. The entropy of vacancy formation in a monatomic solid is determined by changes in translational lattice frequencies. In the case of polyatomic molecules, an additional contribution is obtained from changes in torsional frequencies. As a result of creating a vacancy, neighboring molecules are less hindered in their rotational motion, corresponding to an increase in rotational entropy.

To estimate the magnitude of this effect, approximate the fractional change in rotational hindering potential of a molecule neighboring a vacancy by the fractional change in its coordination. Let Z be the molecular coordination and V_1 be the hindering potential for rotation in the defect-free lattice. Correspondingly, $Z - 1$ is the molecular coordination and V_2 is the hindering potential for rotation of a molecule neighboring a vacancy. Then $V_2/V_1 \sim (Z - 1)/Z$. The change in rotational thermodynamics of a molecule, when removed from a perfect lattice and placed adjacent to a vacancy, is assumed to be entirely represented by this change in hindering potential. The details of rotational correlation between adjacent molecules and coupling between translational and torsional modes are neglected. Pitzer and Gwinn[22] have calculated the thermodynamic functions corresponding to rotation in a sinusoidal potential

of a symmetrical top attached to a rigid frame. In the present case this rigid frame is the lattice.

Using this approach, a crude numerical calculation can be made for the rotational contribution to vacancy formation entropy. Hexamethylethane is chosen for discussion because this molecule is close to spherical shape with its three principal moments of inertia about equal. As a consequence, the contributions due to changes in rotational freedom about the three molecular axes can be approximated to be equal. Pitzer and Gwinn [22] have tabulated rotational entropy as a function of V/RT , where V is the rotational hindering potential, and the inverse partition function for free rotation, $1/Q_F$. Subtracting the tabulated value of rotational entropy corresponding to V_1/RT from the tabulated value corresponding to V_2/RT at the same $1/Q_F$ and multiplying the product by $3Z$, we obtain the rotational contribution to vacancy formation entropy at temperature T .

From the symmetry number of the molecule, $\sigma = 3$, and the moment of inertia about the C-C central bond, $I = 3.669 \times 10^{-38}$ g. cm² [21], we can calculate $1/Q_F$ at the triple point temperature, $T = 374^\circ\text{K}$.

$$\frac{1}{Q_F} = \frac{\sigma}{2.815} \times (10^{38}/IT)^{-1/2} = 0.0288 \quad (11)$$

Since hexamethylethane is body-centered cubic with one molecule per lattice site [54], $Z = 8$ and $V_2/V_1 \sim (Z-1)/Z = \frac{7}{8}$. From an empirical correlation, due to Bondi [31], between V_1 , sublimation energy, and crystal packing density,

$$V_1 \approx \Delta H_s(3.75\rho^* - 2.0) = 2.23 \text{ kcal/mole.} \quad (12)$$

Using these parameters, the calculated rotational contribution to vacancy formation entropy in hexamethylethane is +3.2 e.u. at the triple point.

In the harmonic oscillator approximation,

$V_2/V_1 \sim (Z-1)/Z$ implies that $\nu_2/\nu_1 \sim ((Z-1)/Z)^{1/2}$, where ν_1 and ν_2 are the torsional frequencies corresponding respectively to V_1 and V_2 . Again approximating the entropic contribution from each degree of intermolecular rotational freedom to be equal, the rotational contribution to vacancy formation entropy is

$$\Delta S_R \sim 3ZR \log \frac{\nu_1}{\nu_2} \sim 3ZR \log \left(\frac{Z}{Z-1} \right)^{1/2}. \quad (13)$$

For both f.c.c. and b.c.c. lattices the harmonic oscillator approximation yields $\Delta S_R \sim 3$ e.u., in good agreement with the previous calculation presented for hexamethylethane. This approach is similar to that taken by Brooks [32] in his calculation of the translational mode entropic contribution to vacancy formation.

In polyatomic molecules an additional contribution to vacancy formation entropy can also arise from changes in intramolecular vibrational frequencies. Even in the extreme case of going from the solid phase to the gaseous phase, there is usually little change in internal mode frequencies, and hence little change in the corresponding entropy. In this situation the internal mode contribution to vacancy formation entropy would certainly be negligible. However, one can consider situations where the hindering potential to molecular rotation of a particular molecular group is mainly of intermolecular origin. A significant contribution to vacancy formation entropy might then be expected from a change in the corresponding torsional mode.

(c) *Relationship between vacancy formation and diffusion parameters.* In Table 2, a comparison is made between vacancy formation and diffusion parameters of van der Waals bonded crystals. For each crystal the entropy of diffusion, S_D , was calculated from the experimental parameter D_0 in the Arrhenius equation

$$D = D_0 \exp(-H_D/RT), \quad (14)$$

Table 2. Comparison of vacancy formation and self-diffusion parameters

	$H_v(\text{kcal/mole})$	$S_v(\text{e.u.})$	Ref.	$H_D(\text{kcal/mole})$	$S_D(\text{e.u.})$	Ref.
Hexamethylethane	10.4 ± 2.2	17 ± 5	[a]	20.6	31	[e]
Benzene	12.5 ± 1.1	31 ± 4	[b]	22.4	56	[f]
Krypton	1.78 ± 0.2	$4.0^{+2.0}_{-1.0}$	[c]	4.8 ± 0.2	14 ± 2	[g]
	1.77 ± 0.2	$6.8^{+1.0}_{-2.2}$	[d]			

[a] and [b] Present work.

[c] Ref. [1].

[d] Ref. [2].

[e] Ref. [25].

[f] Ref. [30].

[g] CHADWICK A. V. and MORRISON J. A., *Phys. Rev. Lett.* 21, 1803 (1968).

where D is the diffusion coefficient and H_D is the enthalpy of diffusion. For vacancy diffusion, S_D can be expressed in terms of D_0 as

$$S_D = R \log \frac{D_0}{\gamma a^2 \nu}, \quad (15)$$

where ν is the jump attempt frequency of the diffusing atom in a jump direction, a is the jump distance, and γ is a numerical factor of order unity. For cubic crystals with one molecule per basis γ is $(Z/6)f$, where f is the correlation factor for diffusion and Z is the molecular nearest-neighbor coordination[56]. Since the effective correlation factor is different for NMR and tracer diffusion measurements[57], γ depends upon the experimental approach, crystal structure, and diffusion mechanism[58]. The frequency ν was approximated by the average vibrational frequency for a Debye solid

$$\nu \sim \frac{3}{4} \nu_D, \quad (16)$$

where ν_D is the Debye frequency. From arguments presented by Omini[59], this should be a fair approximation. An order of magnitude uncertainty in ν would introduce an uncertainty of 4.6 e.u. in the calculated S_D , which is less than 15 per cent of the calculated entropy of diffusion in hexamethylethane and benzene. Moreover, if ν is a constant fraction of ν_D , for a particular class of compounds, the present approximation will not introduce an uncer-

tainty in the difference between S_D for different compounds within that class. Using the empirical Lindemann equation[60], which is very successful in predicting the Debye frequency of rare gas solids[61], ν was evaluated in inverse seconds as

$$\nu = 1.56 \times 10^{10} (T_M/MV^{2/3})^{1/2}, \quad (17)$$

where T_M is the melting temperature in $^\circ\text{K}$ and M and V are molar weight and volume in cgs. units. Using this approach, the diffusion entropies tabulated in Table 2 and those plotted in Fig. 7 were either calculated in this work or in the given references. For crystals with several nearest neighbor distances, an average value was used for the vacancy jump distance.

Both experimental vacancy formation and diffusion parameters are available for only two organic compounds, hexamethylethane and benzene. Note, from Table 2, that the ratios of vacancy formation to diffusion enthalpy are respectively 0.50 and 0.56. For comparison, in f.c.c. metals this ratio is 0.54 ± 0.02 [47]. In contrast, this ratio for krypton is 0.37. Note also that the entropy of diffusion is about twice the vacancy formation entropy for both hexamethylethane and benzene. In other words, both the entropy and enthalpy of motion in these two compounds are about equal to respectively the entropy and enthalpy of vacancy formation.

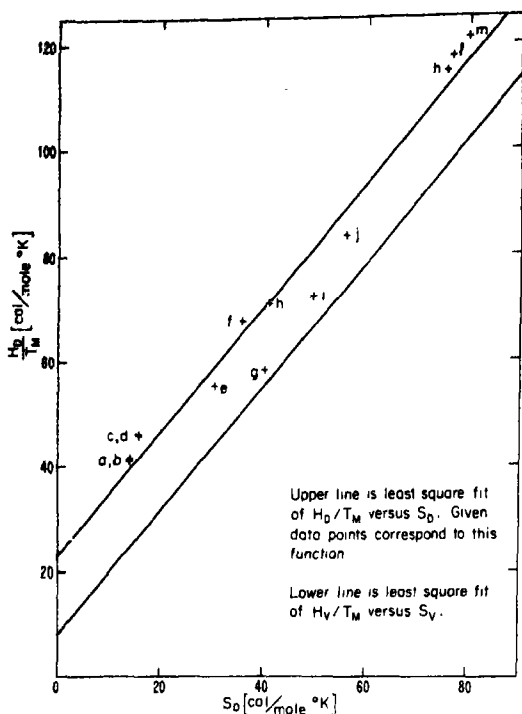


Fig. 7. H_D/T_M vs. S_D for van der Waals bonded crystals. Comparison is made with the corresponding function for vacancy formation parameters.

- a Krypton: CHADWICK A. V. and MORRISON J. A., *Phys. Rev. Lett.* 21, 1803 (1968).
- b Succinonitrile: Ref. [6].
- c Xenon: YEN W. M. and NORBERG R. E., *Phys. Rev.* 131, 269 (1963).
- d Argon: BERNE A., BOATO G. and DEPAZ M., *Nuovo Cim.* 46B, 182 (1966).
- e Hexamethylethane: Ref. [25].
- f Adamantane: Ref. [43].
- g Cyclohexane: Ref. [3].
- h Pivalic Acid: Ref. [6] and Ref. [30].
- i Camphene: Ref. [30].
- j Benzene: Ref. [30].
- k Anthracene: Ref. [30].
- l Biphenyl: CORKE N. T., *Ph.D. Dissertation*, Univ. of Strathclyde, Glasgow. Also Ref. [30].
- m Naphthalene: SHERWOOD J. N. and WHITE D. J., *Phil. Mag.* 15, 745 (1967).

(d) *Relationship between enthalpy and entropy for both vacancy formation and diffusion.* For van der Waals bonded crystals a linear relationship exists between H_v/T_M and S_v , and between H_D/T_M and S_D . See Figs. 6 and 7. The data points for both correlations

correspond to both cubic and lower symmetry lattices. Due to the discrepancy frequently observed between NMR and tracer diffusion results[3, 30], NMR derived parameters for organic crystals were only included when creep data was available to support their validity.

The experimental values of H_v/T_M and S_v for van der Waals bonded crystals were represented by a least squares equation,

$$\frac{H_v}{T_M} - AS_v = B. \quad (18)$$

The data point for krypton is from the work of Simmons and Losee[1] and the remaining data points are from the present work on organic crystals. The parameters H_D/T_M and S_D for van der Waals bonded crystals were represented in the same way. For comparison, the experimental parameters for vacancy formation and diffusion in metals were also represented by an equation of this form. It has been previously noted for metals that H_D/T_M is approximately linear in S_D [62] and that the Gibbs free energy of diffusion normalized to melting point is nearly constant[63]. For metals, the McLellan[64] and the Mukherjee [65] compilation of vacancy formation parameters and the Gibbs compilation of diffusion parameters[63] were used. The parameters calculated with their standard deviations, $\sigma(A)$ and $\sigma(B)$, as well as the standard deviation between calculated and observed H_v/T_M or H_D/T_M , $\sigma(H_v/T_M)$ or $\sigma(H_D/T_M)$, are given in Table 3.

It is interesting to note that, despite the difference in bonding, the experimental H_D/T_M vs. S_D for metals and van der Waals bonded solids can be represented by the same straight line. The slope of enthalpy divided by melting temperature vs. entropy, for both diffusion and vacancy formation in both metals and van der Waals bonded solids, is slightly higher than one. However, in the case of metals the deviation of calculated slope from the value one has little statistical significance.

Table 3. Least squares parameters H_D/T_M vs. S_D

	<i>A</i>	<i>B</i>	$\sigma(A)$	$\sigma(B)$	$\sigma(H_D/T_M)$
van der Waals bonded crystals	1.17	8.38 e.u.	0.046	0.81 e.u.	0.79 e.u.
metals (f.c.c. and b.c.c.)	1.16	14.5 e.u.	0.69	2.45 e.u.	2.0 e.u.
H_D/T_M vs. S_D					
	<i>A</i>	<i>B</i>	$\sigma(A)$	$\sigma(B)$	$\sigma(H_D/T_M)$
van der Waals bonded crystals	1.17	22.8 e.u.	0.073	3.5 e.u.	6.1 e.u.
metals (f.c.c. and b.c.c.)	1.20	23.4 e.u.	0.21	1.8 e.u.	3.4 e.u.
metals (f.c.c. only)	1.28	25.8 e.u.	0.54	4.4 e.u.	2.1 e.u.
metals (b.c.c. only)	1.06	22.3 e.u.	0.15	1.3 e.u.	2.3 e.u.

A and *B* are respectively the slope and intercept of a linear relationship between enthalpy, normalized to melting temp., and entropy. The last three columns give standard deviations.

REFERENCES

- LOSEE D. L. and SIMMONS R. O., *Phys. Rev.* **172**, 934 (1968).
- BEAUMONT R. H., CHIHARA H. and MORRISON J. A., *Proc. Phys. Soc. London* **78**, 1462 (1961).
- HOOD G. M. and SHERWOOD J. N., *Mol. Crystals* **1**, 97 (1966).
- HOOD G. M. and SHERWOOD J. N., *J. Chim. Phys.* **63**, 121 (1966).
- DUNNING W. J., *J. Phys. Chem. Solids* **18**, 1 (1961).
- HAWTHORNE H. M., *Ph.D. Dissertation*, University of Strathclyde, Glasgow.
- RESING H. A., CORKE N. T. and SHERWOOD J. N., *Phys. Rev. Lett.* **20**, 1227 (1968).
- LIDIARD A. B. and FORMAN A. J. E., *Phil. Mag.* **8**, 97 (1963).
- FINKE H. L., SCOTT D. W., GROSS M. E., MESSERLY J. F. and WADDINGTON G., *J. Am. Chem. Soc.* **78**, 5469 (1956).
- WOODMAN A. L., MURBACH W. J. and KAUFMAN M. H., *J. Phys. Soc.* **64**, 658 (1960).
- McAULIFFE C., *J. Phys. Chem.* **70**, 1267 (1966).
- Handbook of Chemistry and Physics*, Vol. 42, p. 2142 (1960).
- CARR C. and RIDDICK J. A., *Ind. and Eng. Chem.* **43**, 692 (1951).
- International Critical Tables **3**, 115 (1928).
- FINBACK C., *Arch. Math. Naturvid.* **B42**, 71 (1938).
- SANDS D. E. and DAY V. W., *Acta crystallogr.* **19**, 278 (1965).
- McCULLOUGH J. P. and WADDINGTON G., *Anal. Chem. Acta* **17**, 80 (1957).
- ASTON J. G., CINES M. R. and FINK H. L., *J. Am. Chem. Soc.*, 1532 (1947).
- MASTRANGELO S. V. R. and DORNTE R. W., *J. Am. Chem. Soc.* **77**, 6200 (1955).
- SKAUE E. L., *J. Am. Chem. Soc.* **57**, 243 (1935).
- SCOTT D. W., DOUSLIN D. R., GROSS M. E., OLIVER G. D. and HUFFMAN H. M., *J. Am. Chem. Soc.* **74**, 883 (1952).
- PITZER K. S. and GWINN W. D., *J. chem. Phys.* **10**, 428 (1942).
- LI J. C. M. and PITZER K. S., *J. Am. Chem. Soc.* **60**, 466 (1956).
- HALFORD J. O., *J. chem. Phys.* **15**, 364 (1947).
- BAUGHMAN R. H. and TURNBULL D., to be published.
- LORD R. C., Jr., AHLBERG J. E. and ANDREWS D. H., *J. chem. Phys.* **5**, 649 (1937).
- OLIVER G. D., EATON M. and HUFFMAN H. M., *J. Am. Chem. Soc.* **70**, 1502 (1948).
- SIMMONS R. O. and BALLUFFI R. W., *Phys. Rev.* **117**, 52 (1960).
- SIMMONS R. O. and BALLUFFI R. W., *Phys. Rev.* **125**, 862 (1962).
- SHERWOOD J. N., *J. Mol. Liq. Cryst.* **9**, 37 (1969).
- BONDI A., *Physical Properties of Molecular Crystals, Liquids, and Glasses*, 35-37, 223, 28-29, and 133, Wiley, New York (1969).
- BROOKS H., *Impurities and Imperfections*, p. 1, American Society for Metals, Cleveland, Ohio (1955).
- SEARS D. R. and KLUG H. R., *J. chem. Phys.* **37**, 3002 (1962).
- GREEN J. R. and SCHEIE C. E., *J. Phys. Chem. Solids* **28**, 383 (1967).
- BARRON T. H. K. and KLEIN M. L., *Proc. Phys. Soc.* **85**, 533 (1965).
- COTTERILL R. M. J. and DOYAMA M., *Phys. Lett.* **25A**, 35 (1967).

37. ASTON J. G., SZASZ G. J. and FINK H. L., *J. Am. Chem. Soc.* **65**, 1135 (1943).
38. BURTON J. J., *Phys. Rev.* **182**, 885 (1969).
39. HUNTINGTON H. B., SHIRN G. A. and WAJDA E. S., *Phys. Rev.* **99**, 1085 (1955).
40. DOBRZYNSKI L., *J. Phys. Chem. Solids* **30**, 2395 (1969).
41. FRIEDEL J., *Jülich Symp. Interlattices and Vacancies* (1968).
42. SCHOTTKY G., SEEGER A. and SCHMID G., *Phys. Status Solidi* **4**, 439 (1964).
43. RESING H. A., *J. Mol. and Liq. Cryst.* **9**, 102 (1969).
44. MARSHALL J. G., HART K. R. and STAVELEY L. A. K., *Nature Lond.* **168**, 519 (1951).
45. DONIACH S. and HUGGINS R., *Phil. Mag.* **12**, 393 (1965).
46. GALLINA V. and OMINI M., *Phys. Status Solidi* **6**, 391 (1964); **6**, 627 (1964).
47. GLYDE H. R. and VENABLES J. A., *J. Phys. Chem. Solids* **29**, 1093 (1968).
48. KANZAKI H., *J. Phys. Chem. Solids* **2**, 24 (1957).
49. HALL G. L., *J. Phys. Chem. Solids* **3**, 210 (1957).
50. GRIMES H. H., *J. Phys. Chem. Solids* **26**, 509 (1965).
51. ANDERSON J. E. and SLICHTER W. P., *J. chem. Phys.* **44**, 3647 (1965).
52. NACHTRIEB N. H. and HANDLER G. S., *J. chem. Phys.* **23**, 1193 (1955).
53. RESING H. A., *J. chem. Phys.* **37**, 2575 (1962).
54. WEST C. D., *Z. Kristallogr.* **88**, 195 (1934).
55. COX E. G., *Rev. mod. Phys.* **30**, 159 (1958).
56. ZENER C., *J. appl. Phys.* **22**, 372 (1951).
57. STOEBE T. G., OGURTANI T. O. and HUGGINS R. A., *Phys. Status Solidi* **12**, 649 (1965).
58. BARR L. W. and LeCLAIRE A. D., *Proc. Brit. Ceram. Soc.* **1**, 109 (1964).
59. OMINI M., *Nuovo Cim.* **54B**, 116 (1958).
60. LINDEMANN L. A., *Phys. Z.* **11**, 609 (1910).
61. CLAUS K., *Z. Phys. Chem. Leipzig* **B31**, 459 (1935).
62. DIENES G. J., *J. appl. Phys.* **21**, 1189 (1950).
63. GIBBS G. B., *Acta Metall.* **12**, 673 (1964).
64. McLELLAN R. B., *Trans. Metall. Soc. of A.I.M.E.* **245**, 379 (1969).
65. MUKHERJEE K., *Trans. Metall. Soc. of A.I.M.E.* **236**, 1324 (1966).

TECHNICAL NOTES

Hyperfine interaction on ^{57}Fe impurity in ferromagnetic MnSb*

(Received 6 August 1970; in revised form 8 September 1970)

1. INTRODUCTION

IN THE course of Mössbauer effect (ME) studies[1] of internal fields systematics in impurities in ferromagnetic MnSb ($T_c = 578^\circ\text{K}$), we wish hereby to report on a measurement performed with ^{57}Fe impurity. Preceding the present studies, Yakimov *et al.* [2] investigated the hyperfine structure of 5 per cent atomic ^{57}Fe embedded in MnSb. These authors observed a ME spectrum consisting of a quadrupole split doublet, attributing the absence of static magnetic interaction to relaxation phenomenon. In the present work, we tried, in vain to reproduce a MnSb(Fe) absorber similar to that of Yakimov *et al.* Both from chemical analysis and ME pattern we concluded that iron does not dissolve in MnSb to any measurable extent. Therefore, we tried another approach, namely, to embed the ^{57}Fe impurity *via* the nuclear decay of MnSb(^{57}Co) used as a source.

2. EXPERIMENTAL

The MnSb(^{57}Co) source was prepared by first diffusing ^{57}Co in Mn. A methanol solution of carrier-free ^{57}Co was mixed with fine manganese powder, thoroughly dried and heated under high vacuum at 700°C for 10 hr. The Mn(^{57}Co) powder was then mixed with a stoichiometric amount of antimony powder, sealed under vacuum in a quartz tube and treated for 24 hr at 800°C to finally form a MnSb(^{57}Co) source.

The ME measurements were done at 300°K ($T/T_c = 0.52$) and at 4.2°K ($T/T_c \approx 0$). The γ -rays resonance was detected with a single line $\text{Na}_4\text{Fe}(\text{CN})_6 \cdot 10\text{H}_2\text{O}$ absorber. In Fig. 1 we display the low temperature spectrum. From the positions of the outer lines, it was found that the overall splitting at 300°K smaller by approximately 20 per cent as compared to that at 4.2°K , following the trend observed in the bulk magnetization[3].

3. SPECTRUM ANALYSIS

Manganese antimonide crystallises in the NiAs structure. Presumably the iron impurity is not in an interstitial site, hence one can assume an axial symmetric electric field gradient (efg) acting on the ^{57}Fe nucleus and with its principal axis along the c -axis. From NMR measurements[4], neutron diffraction [5] and our recent ME studies[1] it has been established that the spins are arranged perpendicular to the c -axis. With these findings in mind one can then assume that the spin-hamiltonian governing the hyperfine interaction of the $I = 3/2$ state in ^{57}Fe is:

$$= -\mu H I_x / I + e^2 q Q / 4I(2I - 1)$$

$$[3I_x^2 - I(I+1)] \dots \quad (1)$$

The quadrupole coupling constant $e^2 q Q$ and the internal magnetic field H were deduced from the lines position by applying the method suggested by Kundig[6]. First, the lines positions were found by the least-squares-fit method and then plotted in a strip of paper so that the outermost lines correspond respectively to those in Fig. 11 in Kundig's paper. A position was then found in the figure which yielded the following parameters

*Work supported by the National Science Foundation under grant No. NSF GP 17135.

$$H = 144 \pm 8 \text{ KOe}$$

$$e^2qQ/2 = +0.75 \pm 0.05 \text{ mm/sec.}$$

The errors were assigned by visually observing the maximum possible deviations.

is known also from neutron diffraction experiments[5] that the form factor could not be fitted by assuming a pure 6S case. The low value of $H(\text{Mn})$ in MnSb can be attributed to two competing mechanisms, namely, (i) the

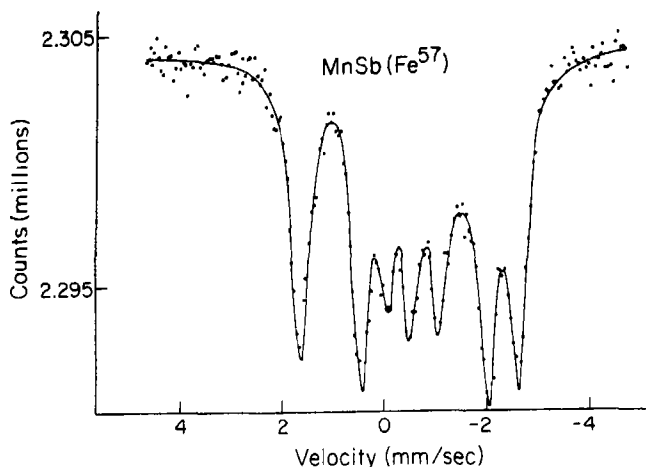


Fig. 1. The Mössbauer effect spectrum of $\text{MnSb}(^{57}\text{Co})$ source against a $\text{Na}_4\text{Fe}(\text{CN})_6 \cdot 10\text{H}_2\text{O}$ absorber at 4.2°K . The solid line through the experimental points is not a theoretical curve and is displayed for the sake of clarity.

4. DISCUSSION AND CONCLUSION

The observation of a static internal field at the iron impurity completely disagrees with the results of Yakimov *et al.*[2]. Very probably the spectrum observed by the Russian authors is due to either Fe alloying with Mn or with other impurities.

It will be instructive to compare the hyperfine constants of the ^{55}Mn , as measured by Tsujimura *et al.* to the present values of the ^{57}Fe impurities. The observed internal field of the Mn nucleus is -270 kOe [7] which is significantly lower than values of $500\text{--}700 \text{ kOe}$ normally obtained for $^6S \text{ Mn}^{2+}$ compounds. As noticed by Van Wieringen[8], $H(\text{Mn}^{2+})$ decreases in magnitude with increase of the ligand covalency, reaching a value of 420 kOe for the case of Te^{2-} ligands. This trend is attributed to the increase in delocalization of the d -orbitals. MnSb is in fact known to have a metallic character. It

contact term H_c where

$$H_c \propto \langle S \rangle \sum_{ns} [|\psi_{ns}(0)|^2 - |\psi_{ns}(0)|_+^2]$$

and (ii) the conduction electrons polarization term H_{ce} . It is well established from both theoretical and experimental evidences that H_c yields negative and large fields, whereas H_{ce} results in positive fields[9], namely, parallel to the local moment. Since $H(\text{Mn})$ is negative, one can assume that the contribution of the contact term is predominant.

The interpretation of the hyperfine interaction is more complicated for the Fe impurity. For simplicity, the following assumptions are made. (i) the contribution of H_{ce} to the resulting field is the same as for Mn, and (ii) the sign of $H(\text{Fe})$ is negative. Thus, the decrease in $H(\text{Fe})$ as compared to that of $H(\text{Mn})$ is attributed to the H_c term and could be either due to a smaller spin density at the

nucleus, a smaller effective spin namely, further delocalization of the d -orbitals, or both. The second possibility is more plausible as inferred from the quadrupole coupling constants in Mn and Fe. The electric field gradient (eq) acting at the Fe nucleus is 3.4×10^{-7} eV/cm². Tsujimura *et al.* measured a value of $e^2qQ(^{55}\text{Mn}) = 22$ Mc/sec from which we deduce $eq(\text{Mn}) = 2.2 \times 10^{-7}$ eV/cm². Assuming that the screening factor $(1 - R)$ for Mn and Fe are identical, one then observes an increase of eq upon substituting the iron impurity. The electric field gradients in both nuclei are too large to be originated from external point charges; it is mainly due to the nonspherical d -shell. Thus, the increase in $eq(\text{Fe})$ may point to a further delocalization of the iron d -orbitals.

Though interpretation of hyperfine interaction in a conductor is a complicated problem[9], and in particular so for a pseudo-metallic compound as MnSb, one still can derive some conclusions namely: (i) the internal fields are originated primarily from the contact term, though the conduction electron polarization as well as contributions from the orbital moment terms are not negligible. (ii) Both the Mn and Fe d -orbitals are significantly delocalized as it is evident from the low values of H and large values of e^2qQ and (iii) the decrease of $H(\text{Fe})$ is presumably due to further delocalization of the Fe impurity d -orbitals. We find evidence for this last conclusion, both from the decrease in $H(\text{Fe})$ and from the increase in the $eq(\text{Fe})$ with respect to Mn.

M. AVINOR*
M. PASTERNAK†

Department of Physics and Materials
Research Laboratory,
University of Illinois,
Urbana,
Ill. 61801, U.S.A.

*On leave of absence from the Scientific Department, Ministry of Defence, Israel.

†Present address: Department of Physics and Astronomy, University of Tel-Aviv, Ramat-Aviv and Soreq Nuclear Research Center, Yavne, Israel.

REFERENCES

1. PASTERNAK M., *Phys. Lett.* **31A**, 215 (1970).
2. YAKIMOV S. S., GAMLITSKII V. Ya., NIKOLAEV V. I. and RODIN S. R., *Soviet Phys.* **12**, 1153 (1968); translated from *Dokl. Akad. Nauk. SSSR* **177**, 1313 (1967).
3. OKITA T. and MAKINO Y., *J. phys. Soc. Japan* **25**, 120 (1968).
4. TSUJIMURA A., HIHARA T. and KOI Y., *J. phys. Soc. Japan* **17**, 1078 (1962).
5. TAJE W. J., COX D. E., and SHIRANE G., *Phys. Rev.* **129**, 2008 (1963).
6. KÜNDIG W., *Nucl. Inst. and Meth.* **48** 219 (1967).
7. The value of $H(\text{Mn})$ at 4.2°K was obtained from that measured at 300°K (see Ref. [3]).
8. VAN WIERENGEN J. S., *Disc. Faraday Soc.* **19**, 118 (1955).
9. WATSON R. E. and FREEMAN A. J., *Hyperfine Interactions*, p. 53, Academic Press, New York, WATSON R. E., *ibid.*, p. 413 (1967).

J. Phys. Chem. Solids Vol. 32, pp. 1397-1399.

Diffusion of mercury in indium arsenide

(Received 27 April 1970; in revised form 24 August 1970)

DIFFUSION of zinc and cadmium, which are acceptor impurities in III-V compounds, has been studied by various workers and the anomalous diffusion behaviour of zinc has been well established. However, the diffusion study of mercury, which also belongs to the zinc subgroup, has so far been limited to InSb[1]. Recent review of Kendall[2] reported the results of Kanz, who has studied the diffusion of mercury in GaAs at 1000°C and obtained a surface concentration of about 5×10^{17} cm⁻³.

The study reported in this paper was undertaken with the view of obtaining the diffusion parameters for mercury in n -type InAs and ascertaining whether the diffusion of this acceptor impurity gives rise to surface concentration several orders of magnitude lower than that of zinc in InAs, as observed in the case of GaAs.

The n -type InAs crystal slices [resistivity $\sim 0.006 \Omega \text{ cm}$ and $n \sim 3.5 \times 10^{16} \text{ cm}^{-3}$ at

300°K; surface orientation (100)], used in this study, were obtained from Texas Instruments, U.S.A. The diffusion specimens were prepared by lapping and cutting the slices into rectangular slabs ($7 \times 10 \times 0.6$ mm) and polishing them by a chemico-mechanical method[3] using bromine-methanol solution.

Radioactive metallic mercury containing ^{203}Hg isotope (specific activity 0.5 c/g), obtained from Bhabha Atomic Research Center, Bombay, was used as a source for diffusion. The specimens together with weighed amounts of mercury source were sealed off in quartz ampoules evacuated to about 10^{-3} Torr and filled with high purity argon at about 1 atmosphere. The diffusion annealings were carried out at various temperatures in the range 650–850°C. The quantity of mercury source for various diffusion temperatures was so adjusted to give vapour pressure of about 1.5 atmosphere. Mercury deposition on specimen was avoided, in all the experiments, by maintaining temperature of the source end of the ampoule 30°C lower than specimen temperature during diffusion annealing and finally quenching this portion in water.

After diffusion annealing the lateral faces of the specimens were trimmed to a depth of about 500 μ . Diffusion profiles were determined by using a successive layer removal method. The layers were removed with the help of micropolishing papers (Geoscience Instruments Corp. N.Y.) and their activity was measured by counting the gamma radiation of ^{203}Hg (0.28 MeV) on a well-type NaI (T1) scintillation counter. The thickness of the removed layers were determined by using an optomechanical indicator. The residual activity after each sectioning was also measured on a flat-type NaI (T1) scintillation counter to provide an alternative method of determining the diffusion profiles. The absolute values of the concentration distribution of mercury in the specimens were determined by comparing the specific activities (counts/sec μ) with the activity of ^{203}Hg standard samples having identical geometry.

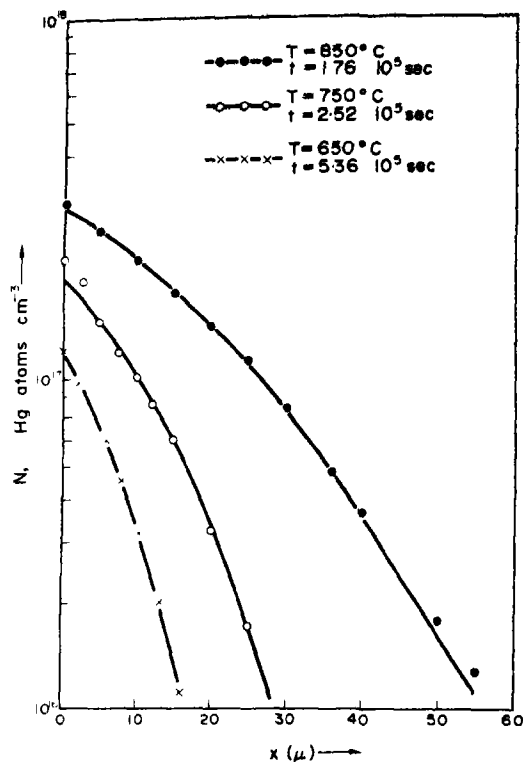


Fig. 1. Typical concentration distribution profiles of mercury in *n*-type InAs at various diffusion temperatures. Solid lines are theoretical complementary error function.

The concentration distribution profiles, obtained by residual activity method and successive layer removal method, were in good agreement. It was observed that all the diffusion profiles could be fitted with a complementary error function distribution of the type $N = N_0 \text{erfc}(x/2\sqrt{Dt})$, where N is the concentration at a penetration depth x , N_0 is the surface concentration, t is the time of diffusion and D is the diffusion coefficient. Typical concentration distribution of mercury in InAs at temperatures 650, 750 and 850°C are shown in Fig. 1. It is clear from these curves that mercury does not behave anomalously during diffusion in InAs at these temperatures.

The diffusion coefficients evaluated from various diffusion profiles in the temperature range 650–850°C varied between 9×10^{-13} –

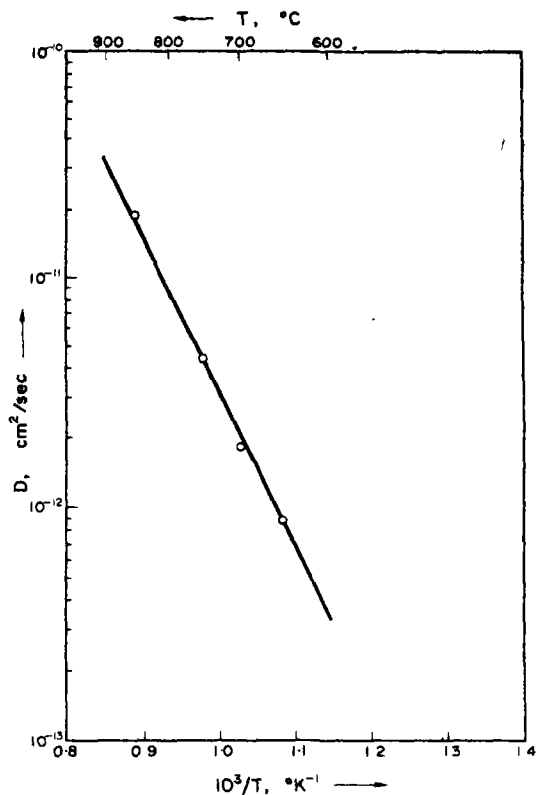


Fig. 2. Temperature dependence for diffusion of mercury in *n*-type InAs.

$1.9 \times 10^{-11} \text{ cm}^2/\text{sec}$. The temperature dependence of the diffusion coefficient of mercury in *n*-type InAs, shown in Fig. 2, can be described

by the expression

$$D = 1.45 \times 10^{-5} \exp - (1.32/kT)$$

where 1.32 eV is the activation energy for diffusion. This activation energy is higher than those reported for zinc[4] and cadmium[5] in *n*-type InAs.

The surface concentrations varied between $1.1 \times 10^{17} \text{ cm}^{-3}$ to $2.9 \times 10^{17} \text{ cm}^{-3}$ in the temperature range 650–850°C.

Acknowledgements—The authors are grateful to Dr. G. R. Cronin of the Texas Instruments Inc. U.S.A. for providing InAs single crystal slices, to Prof. S. C. Jain, Director, Solid State Physics Laboratory for his kind permission to publish this work, to Mr. A. Nagaratnam of the Institute of Nuclear Medicine & Allied Science, Delhi, for providing the facilities for radioactive work and many helpful discussions and to Mr. J. K. Modi for his assistance throughout this work.

Solid State Physics Laboratory,
Lucknow Road,
Delhi, India.

B. L. SHARMA
R. K. PUROHIT
S. N. MUKERJEE

REFERENCES

1. GUSEV I. A. and MURIN A. N., *Soviet Phys. solid State* 6, 1229 (1964).
2. KENDALL D. L., *Semiconductors and Semimetals*, Vol. 4, p. 227 (Edited by R. K. Willardson and A. C. Beer) Academic Press, New York (1968).
3. SHARMA B. L., *Solid-state Electron.* 9, 728 (1966).
4. SHARMA B. L., *J. Inst. Telecom. Engrs.* 12, 209 (1966).
5. ARSENI K. A., BOLTAKS B. I. and REMBEZA S. I., *Soviet Phys. solid State* 8, 2248 (1967).

ERRATUM

B. V. R. CHOWDARI: Electron paramagnetic resonance study of Mn^{2+} in $(NH_4)_2Mg_2(SO_4)_3$ and $(NH_4)_2Zn_2(SO_4)_3$ crystals. *J. Phys. Chem. Solids* 31, 1408 (1970).

FROM the beginning of the last sentence in page 1408 it should be read as: "There are two crystallographically nonequivalent divalent metal ions (Mg^{2+} or Zn^{2+}) and two nonequivalent monovalent metal ions ($(NH_4)^+$). Each divalent ion is surrounded by six oxygens which form slightly distorted octahedron. The distances between oxygen ions and the divalent metal ions (Mg^{2+} or Zn^{2+}) in two octahedra are different which in turn gives rise to the non-equivalency between the two divalent metal ions. The monovalent ion ($(NH_4)^+$) coordination can not be sharply defined; there are four oxygens around one type of monovalent ion and three oxygens around second type of monovalent ion. The difference between the environment of two nonequivalent divalent metal ions is much less as compared to the difference between the environment of the two nonequivalent monovalent metal ions".

Continuation of this should be from the beginning of the first paragraph of page 1409.

MAGNETIC CHARACTERISTICS OF $\text{TbCo}_{0.3}\text{Al}_{1.7}$

H. OESTERREICHER

Oregon Graduate Center, 9340 S. W. Barnes Road, Portland, Oregon 97225, U.S.A.

(Received 2 September 1970; in revised form 27 October 1970)

Abstract— $\text{TbCo}_{0.3}\text{Al}_{1.7}$ crystallizes with the cubic MgCu_2 type structure. The material orders close to ferromagnetically in a field of 30 kOe but exhibits a Néel point of 35 K in a field of 500 Oe. At 1.6 K the magnetization increases in two discontinuous steps to an extrapolated saturation moment of $6.58 \mu_B$. A neutron diffraction experiment at 4.2 K shows a magnetic moment of $6.98 \mu_B$ ordered ferromagnetically only at the Tb sites. The situation seems to be similar to $\text{ErCo}_2\text{-ErAl}_2$ alloys, where disordered antiferromagnetic components stabilize as a function of the free electron concentration.

1. INTRODUCTION

PHASE studies on pseudobinaries of the form $\text{RCO}_2\text{-RAl}_2$ (R = rare earth metal) have revealed changes in crystal structure within the Laves phase type [1-3] depending of the valence electron concentrations (v.e.c.) or Fermi-surface Brillouin-zone interactions. The existence of broad homogeneous regions in crystal type and the fact that Co does not exhibit a magnetic moment, safe at high concentrations [2, 4], make these materials ideally suited for studies of the influence of free electrons on magnetic ordering of rare earth moments. Such an influence should be inherent in materials where an indirect exchange mechanism of the Rudermann-Kittel type [5] is responsible for magnetic exchange, due to an oscillatory polarization of conduction electrons. Mattis [6, 7] e.g. has calculated energies for different magnetic modes depending on the number of free electrons. Ferromagnetism changes to several types of antiferromagnetism as the v.e.c. is increased. Such a sensitivity of the cooperative effect on the band structure has now been observed in several instances [3, 4, 8-15].

Previous investigations on $\text{ErCo}_2\text{-ErAl}_2$ pseudobinaries [2, 4] indicated a more complex situation. Both, results from the magnetic balance and from neutron diffraction show the ordered magnetic moment to oscillate with composition without indications for antiferro-

magnetism. The disorder background scattering at 4.2 K in the neutron diffraction experiment, however, has been observed to increase whenever the ordered moment decreases. We conclude therefore on the absence of crystal field quenching of moment and on the presence of some disordered magnetic components in such 'low moment compounds'. We have expanded our studies to Tb alloys anticipating higher temperatures for possibly interesting effects. Tb is also a suitable candidate for neutron diffraction and Mössbauer spectroscopy.

2. EXPERIMENTAL

Sample preparation and measurement procedures have been previously outlined in more detail [2, 4]. $\text{TbCo}_{0.3}\text{Al}_{1.7}$ has been induction melted in MgO crucibles. X-ray and neutron diffraction showed the presence of pure MgCu_2 type. A commercial magnetometer of the Foner type was employed for the susceptibility measurements.

3. RESULTS

A Debye-Scherrer diagram shows $\text{TbCo}_{0.3}\text{Al}_{1.7}$ to be in the homogeneous region of C15 (MgCu_2) type TbAl_2 . Observed and computed intensities of a room temperature neutron diffraction diagram confirm Tb to occupy 8a sites while Co and Al are statistically distributed on 16d sites. There is little

change in lattice parameters from 7.779 Å at 298 K to 7.755 Å at 4.2 K.

Magnetic moment vs. temperature is shown in Fig. 1. While there is a pronounced peak in magnetization at 37 K in a field of 500 Oe ferromagnetism seems to be predominant in a field of 30,000 Oe, although the 'Néel behavior' is somewhat retained, being shifted to lower temperatures ($T_N = 26$ K). The peaking magnetization with temperature appears to be no straight-forward Néel point, however, since neutron diffraction does not reveal antiferromagnetic order. This point shall be taken up in the discussion. A field dependency at 4.2 K (Fig. 2) would seem to indicate metamagnetism (*S*-type curve) at relatively low fields. The magnetization is still increasing at the highest applied fields,

possibly due to strong anisotropy or the effect of the field on the crystal field splitting of magnetic states. An alternative explanation in terms of partial alignment of disordered antiferromagnetic components at high fields would accord with ideas outlined in the discussion. A saturation moment of $6.68 \pm 0.1 \mu_B$ can be extrapolated from a plot of magnetic moment vs. infinite, reciprocal, effective field. We should mention that Fig. 2 represents an actual field sweep in 7 min without corrections for demagnetization effects. However, we found that such corrections do not alter the essential features of the magnetization behavior. The demagnetization correction according to $D = H_{\text{applied}} - H_{\text{effective}}$ for this material is 725 Oe at $1 \mu_B$ and proportional to the magnetic moment. This also holds for

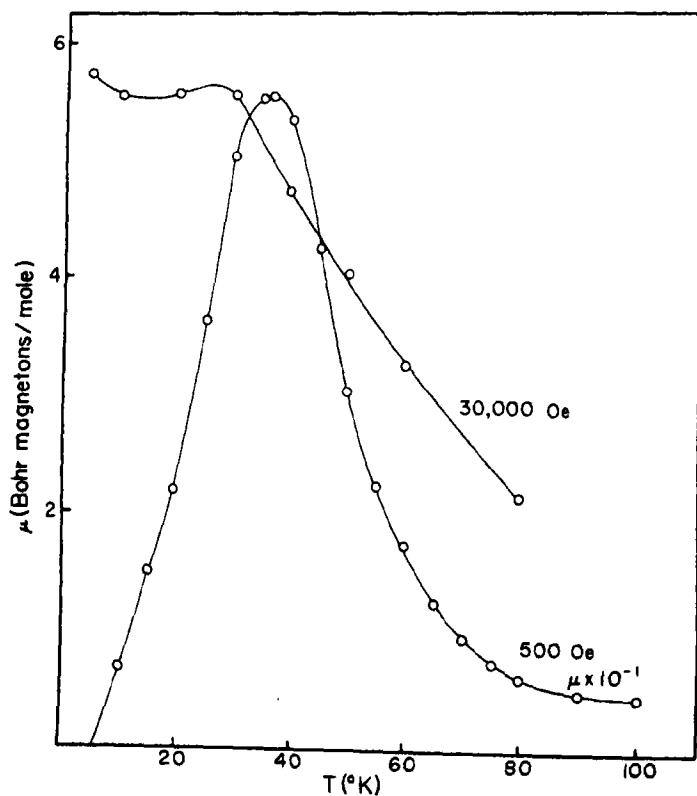


Fig. 1. Magnetic moment (μ) vs. temperature for $\text{TbCo}_{0.9}\text{Al}_{1.7}$ in fields of 500 and 30,000 Oe.

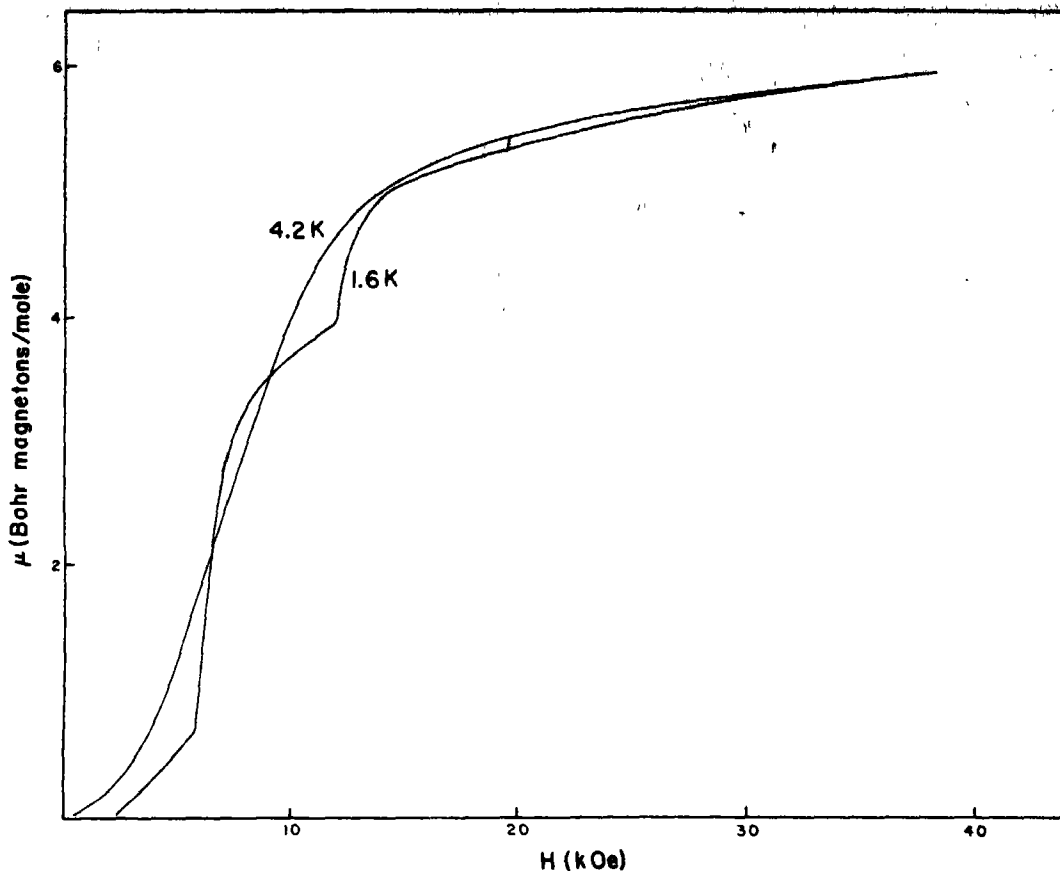


Fig. 2. Field dependency of magnetic moment (μ) per mole $\text{TbCo}_{0.3}\text{Al}_{1.7}$ at 1.6 and 4.2 K.

Fig. 1. A correction for demagnetization actually accentuates the peaks in magnetization vs. temperature.

At 1.6 K two steps occur in the field dependency around 5000 and 12,000 Oe and a saturation moment of $6.58 \mu_B$ can be extrapolated, although saturation is again not yet completely attained. The discontinuous rises in magnetization with field could be connected with a competition of anisotropy forces and the external field or be due to stepwise ordering into the field direction of disordered antiferromagnetic components.

Neutron diffraction diagrams were run at 298 and 4.2 K with a wavelength of 1.0285 \AA . The magnetic intensities were internally calibrated to the nuclear peaks and computed

using the calculated magnetic form factors of Er of Blume, Freeman and Watson[16]. $\text{TbCo}_{0.3}\text{Al}_{1.7}$ is a pure ferromagnet without any extra reflections. The ordered magnetic moment is confined only to the rare earth sites. There is neither magnetic intensity in the (222) peak nor do the intensities of (111) and (220) allow for a Co moment beyond the error limit of $0 \pm 0.2 \mu_B$, assuming a collinear structure. A value of $6.95 \pm 0.2 \mu_B$ per Tb for the ordered magnetic component was derived solely from the (111) and (220) peak because of uncertainties in temperature during the experiment at higher angles. The difference in disorder background scattering between room and liquid He temperature was calibrated to ErAl_2 [4] and yielded $6.91 \pm 0.3 \mu_B$

as the total ordered moment. There is a sizeable magnetic disorder background scattering present at 4.2 K similar to the analogous Er alloys. This can be seen in the pronounced slope of the background due to the magnetic form factor. Since we presently do not have a direct comparison with the background scattering of TbAl_2 , an analysis of the disorder can be made only from a comparison of the slope of the background with that of ErAl_2 . If we subtract a computed and calibrated disorder scattering of $5.6 \pm 0.8 \mu_B$ from the experimental data of $\text{TbCo}_{0.3}\text{Al}_{1.7}$ both slopes coincide. Disordered and ordered magnetic contributions then approximately obey the relation $\mu_d^2 + \mu_o^2 = 9^2$.

Figure 3 shows nuclear and magnetic contributions to the (111) peak. There is a slight 'wing' observed at the base of the 4.2 K peak

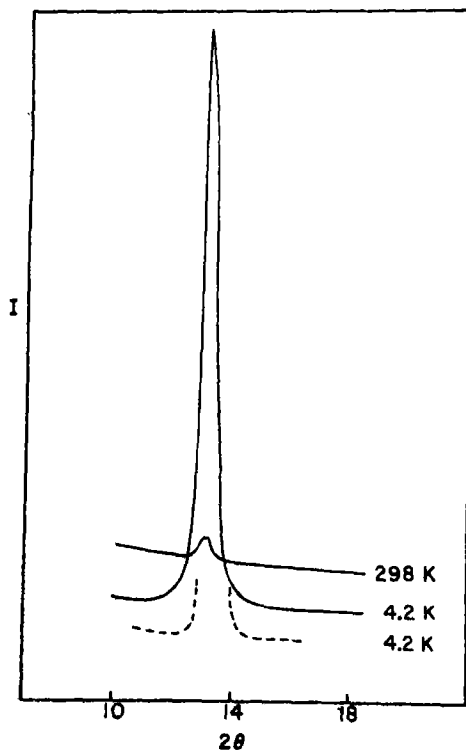


Fig. 3. Intensity (I) in arbitrary units vs. angle (2θ) of the (111) reflection in a neutrodiffraction diagram of $\text{TbCo}_{0.3}\text{Al}_{1.7}$ at 4.2 and 298 K. The dashed curve represents the (111) peak of ErAl_2 at 4.2 K.

compared to ErAl_2 , but there is no broad and wavy background as it would be typical close and beyond the actual ordering temperature. Although the neutron diffraction diagram confirms the absence of ordered antiferromagnetic contributions for $\text{TbCo}_{0.3}\text{Al}_{1.7}$ only at 4.2 K we assume this also to hold for the situation where the magnetization increases stepwise with field since we have found this behavior also in $\text{ErCo}_2\text{-ErAl}_2$ compounds[19] at 4.2 K where neutron diffraction did not reveal ordered antiferromagnetic contributions.

4. DISCUSSION

The situation that pertains magnetically in Tb Laves phases seems to be similar to the Er case. TbAl_2 comparable to ErAl_2 is a ferromagnet[17, 18]. We have, however, recently described a slight peaking of magnetization around 68 K for this material in low fields (500 Oe)[20]. Replacement of Al by Co, which decreases the v.e.c., adds an antiferromagnetic exchange admixture which is evident in the peaking magnetization with temperature and the lower ordered magnetic moments. Neutron diffraction fails to detect ordered antiferromagnetic contributions, but rather reveals the 'lost' magnetic moment or at least the main part of it, as disorder background scattering. The Tb case, however, is more pronounced in its peculiarities. $\text{TbCo}_{0.3}\text{Al}_{1.7}$ has a higher Néel temperature at low fields than the Er materials. Furthermore, the Tb alloy shows more distinct stepwise increases with field at 1.6 K than was recently found on $\text{ErCo}_2\text{-ErAl}_2$ at 1.6 and 4.2 K[19]. Results, however, are quite different for $\text{GdCo}_{0.3}\text{Al}_{1.7}$ [2], where the ferromagnetic saturation moment essentially is unaltered but the Weiss constant and ordering temperature are markedly decreased in comparison to GdAl_2 , suggesting a different effect of the v.e.c. on spin only magnetism.

Several bits of information should be collected for a diagnosis of the remarkable state between order and disorder. Crystal field

effects if active should not play an important part in such 'low moment compounds', since the lost ordered magnetic moment is found again as disorder background scattering. The metamagnetic behavior, the stepwise increases in magnetization with field (which would be typical for the collapse of a helimagnetic arrangement into the field direction) and the peaking magnetization with temperature are not straightforwardly connected with antiferromagnetism.

The failure to observe antiferromagnetism with neutrons in a situation clearly suggestive of it could be explained in a novel but at this point necessarily speculative way. Antiferromagnetic components would be present, but be disordered either statically or dynamically. Some modulated magnetic structure might be altogether in a rapid precession in comparison to the neutron passage time. Neutrons should then only see the projection of magnetization along an axis while disordered components would appear in a manner yet to be specified in the background scattering. Such a fictitious dynamical situation may be related to the magnetic resonances and possibly be accessible to the same techniques. Inelastic neutron diffraction, however, should be the more straightforward proving ground. Mössbauer spectroscopy may be suitable to pin down a lower limit of such a precession since the internal field would result from an average of occurrences during the Larmor frequency of the Mössbauer nucleus. Moments obtained by Mössbauer spectroscopy for DyNi_2 [21] and DyPt_2 [22] e.g. have been distinctly higher than the ones from saturation experiments. This may indicate that these materials have a v.e.c. in the region to stabilize disordered components but that dynamical disorder is slow in comparison to the Larmor frequency.

An alternative explanation for the peaking magnetization vs. temperature and the discontinuous rises in magnetization vs. field could be in terms of anisotropy or domain wall motion. This, however, leaves the low

ordered moments to be explained in a different fashion as for instance originating from magnetic disorder connected with the statistical occupancy of $16d$ sites between Co and Al atoms.

As a final point of interest we should mention that we find C15 ErMnAl and TbMnAl to exhibit a spiral configuration of magnetic moment as well as Néel behavior [19]. According to phase relations both compounds should have a v.e.c. comparable to $\text{TbCo}_{0.3}\text{Al}_{1.7}$. The magnetic intensities of the neutron diffraction diagram well below the Néel temperatures, however, are rather smeared out and rest on considerably wavy backgrounds which again could be due to partly disordered behavior.

Acknowledgement—We should like to cordially thank Drs. L. M. Corliss and J. M. Hastings for the neutron diffraction experiment.

REFERENCES

1. WERNICK J. H., HASKO S. E. and DORSI D., *J. Phys. Chem. Solids*, **23**, 567 (1962).
2. OESTERREICHER H. and WALLACE W. E., *J. less common Metals*, **13**, 91 (1967).
3. OESTERREICHER H. and WALLACE W. E., *J. less common Metals*, **13**, 475 (1967).
4. OESTERREICHER H., CORLISS L. M. and HASTINGS J. M., *J. appl. Phys.*, **41**, 6, 2326 (1970).
5. RUDERMANN M. A. and KITTEL C., *Phys. Rev.*, **96**, 99 (1954).
6. MATTIS D. and DONATH W. E., *Phys. Rev.*, **128**, 4, 1618 (1962).
7. MATTIS D. C., *Theory of Magnetism*, p. 275, Harper and Row, New York (1965).
8. CABLE J. W., KOEHLER W. C. and WOLLAN E. O., *Phys. Rev.*, **136**, A240 (1964).
9. CABLE J. W., KOEHLER W. C., and CHILD H. R., *J. appl. Phys.*, **36**, 3, 1096 (1964).
10. METHFESSEL S., *Z. angew. Phys.*, **18**, 414 (1965).
11. SEKIZAWA K. and YASUKOCHI K., *J. phys. Soc. Jap.*, **21**, 4, 684 (1966).
12. ALFIERI G. T., BANKS E. and KANEMATSU K., *J. appl. Phys.*, **37**, 1254 (1966).
13. MADER K. H. and WALLACE W. E., *J. less common Metals*, **16**, 85 (1968).
14. OESTERREICHER H., MAMMANO N. and SIENKO M. J., *J. Solid State Chem.*, **1**, 38 (1969).
15. PIERRE J., *Proc. Eighth Rare Earth Conf.*, p. 102, Reno, April 19 (1970).
16. BLUME M., FREEMAN A. J. and WATSON R. E., *J. Chem. Phys.*, **37**, 6, 1245 (1962).

17. WILLIAMS H. J., WERNICK J. H., NESBITT E. A. and SHERWOOD R. G., *J. phys. Soc. Japan*, **17**, Suppl. B-1, 91 (1962).
18. BUSCHOW K. H. J., FAST J. F., VAN DIEPEN A. M. and DEWIJN, H. W., *Phys. Status Solidi*, **24**, 715 (1967).
19. OESTERREICHER H., unpublished.
20. OESTERREICHER H., *J. Phys.*, February (1971).
21. OFER S. and SEGAL E., *Phys. Rev.* **141**, 1, 448 (1966).
22. NOWICK I., OFER S. and WERNICK J. H., *Phys. Rev. Lett.*, **20**, 232, (1966).

PSEUDO-POTENTIAL CALCULATIONS OF RELAXATION AND FORMATION ENERGY OF A VACANCY IN SODIUM

R. CHANG

Science Center, North American Rockwell Corporation, Thousand Oaks, Calif. 91360, U.S.A.

(Received 29 April 1970; in revised form 23 October 1970)

Abstract—Pseudo-potential calculations of the relaxation and formation energy of a vacancy in sodium are made using the model potential of Abarenkov and Heine and the optimized model potential of Shaw and Pynn adjusted slightly to fit the experimental Fermi surface data. The calculated vacancy formation energy according to the latter pseudo-potential agrees within a few percent with the experimentally determined values of Feder and Charbneau from thermal expansion measurements.

1. INTRODUCTION

THIS paper presents the results of a study of the relaxation and formation energy of a vacancy in sodium using pseudo-potential (hereafter referred to as PP) methods. A previous study of the PP calculation for a vacancy in aluminum[1] suggests that the application of PP methods to studies of point defects in crystalline solids is very encouraging. There are several objectives to extend the PP calculations to metallic sodium. Sodium has a body-centered cubic lattice; it should be interesting to compare its relaxational parameters with those for a face-centered cubic metal such as aluminum. The experimental vacancy formation energy in sodium has been reported by Feder and Charbneau[2] to be 0.031 ± 0.002 Ry so that a direct comparison can be made between the calculated and the experimental values. Thirdly, studies of the relaxation and formation energy of a vacancy in sodium by means of two-body interatomic potentials[3] as well as force constant methods[4] have appeared in literature; it should be interesting to compare these results with a careful PP calculation presented in this paper. Lastly, but not the least, it has become increasingly clear that atomic calculations of point defects in metals via the PP method can provide an important criterion in regard to the selection

of the best PP form factors for other atomic calculations. This is because the formation energy of a vacancy in metals is usually in the range of 0.01 to 0.1 Ry and is extremely sensitive to the slightest variation of the PP form factors.

2. THE PP FORM FACTORS

Four PP form factors have been chosen for this study:

First is the model potential of Abarenkov and Heine[5], as calculated by Animalu and Heine[6]. This is referred to as PP1.

(b) Weaire[7, 8] has suggested that the energy and k -vector dependence of the PP could be taken into account in first order by multiplying the band structure contribution to the energy by an effective mass correction factor $\mu = \mu^k/\mu^E = 1.233$ for sodium. This is referred to as PP2, where the correction factor $\mu = 1.233$ is applied to PP1 in the band structure energy calculations.

(c) Shaw and Pynn[9] have proposed an optimized model potential to take into account the conduction-electron exchange and correlation corrections. This is referred to as PP3. In this work, the Shaw-Pynn optimized model potential was used between $q/2k_F$ values of zero to 2.2 and joined smoothly to the PP1 form factors between $q/2k_F$ values of 2.2 to 5.0.

(d) The Shaw-Pynn optimized model potential (PP3) is still not too satisfactory in as much as correlation with the experimental Fermi surface data[10] is concerned. Since the Shaw-Pynn optimized model potential given in Ref.[9] is not unique, we have modified the Shaw-Pynn PP form factors slightly (i.e., shifting the W (form factor)- q (wave number) plot along the q axis toward increasing q by 0.04 units) such that the new PP fits exactly the lowest Fourier component of the effective lattice potential V_{110} . This is referred to as PP4. The same exchange and correlation correction of the dielectric function in the manner proposed by Shaw and Pynn is used.

The two lowest Fourier components of the effective potential corresponding to the various PP's are compared with those fitting Lee's Fermi surface data[10] in the following:

where

$$T(\mathbf{q}) = \sum_{\substack{j \neq 0 \\ \text{all atoms}}} [\exp(-i\mathbf{q}\mathbf{R}_j) - \exp(-i\mathbf{q}\mathbf{R}_{0j})]. \quad (3)$$

In equation (3) the atoms can be grouped into crystallographically equivalent shells with respect to the vacancy, hence,

$$\begin{aligned} T(\mathbf{q}) = & T_{\langle 111 \rangle}(\mathbf{q}) + T_{\langle 100 \rangle}(\mathbf{q}) + T_{\langle 110 \rangle}(\mathbf{q}) \\ & + T_{\langle 1\bar{1}\bar{1} \rangle}(\mathbf{q}) + T_{\langle 11\bar{1} \rangle}(\mathbf{q}) + T_{\langle 200 \rangle}(\mathbf{q}) \\ & + T_{\langle 1\bar{1}1 \rangle}(\mathbf{q}) + T_{\langle 210 \rangle}(\mathbf{q}) \\ & + T_{\langle 211 \rangle}(\mathbf{q}) + \dots \end{aligned} \quad (4)$$

In the present calculation all relaxations are assumed to be radial, i.e.,

$$\mathbf{R}_j = (1 + D_j)\mathbf{R}_{0j} \quad (5)$$

	PP1, PP2 Model potential (Heine-Abarenkov)[5, 6]	PP3 Optimized model potential (Shaw-Pynn)[9]	PP4 This paper	Fermi surface data (Lee)[10]
V_{110}	0.266 eV	0.245 eV	0.225 eV	0.225 ± 0.010 eV
V_{200}	0.142 eV	0.204 eV	0.212 eV	0.0 ± 0.3 eV

3. OUTLINE OF THE CALCULATION

A detailed formulation of the PP calculation for a vacancy in aluminum has been presented elsewhere[1]. The formation energy of a vacancy ΔE_v is given by the sum of the electrostatic contribution ΔE_{es} and the band structure contribution ΔE_{bs} ; the free electron contribution ΔE_{fe} is neglected. For the ΔE_{es} and ΔE_{bs} terms it is necessary to calculate the structure factors for both the perfect structure (p) and the vacancy (v). For the perfect crystal, the structure factor is,

$$S_p(\mathbf{q}) = \sum_{\mathbf{G}} \delta_{\mathbf{q}, \mathbf{G}}. \quad (1)$$

For the crystal with the vacancy, the structure factor is,

$$S_v(\mathbf{q}) = \frac{N+1}{N} S_p(\mathbf{q}) + \frac{1}{N} \{T(\mathbf{q}) - 1\} \quad (2)$$

and only the first nine shells are allowed to relax. Although for metallic sodium there is some contribution of the non-central component of the ion-ion forces due to core overlap, the non-central component is still small compared to the central component of the ion-ion forces. This is seen, e.g., in the work of Flocken and Hardy[4] who studied the relaxation problem through the force-constants approach employing "lattice statics; there the ion displacements for the 311, 331, 420, 422, ... shells do not seem to deviate significantly from the radial-displacement approximation. These assumptions reduce the relaxation parameters to nine, namely

$$\left. \begin{aligned} D\left(\frac{1}{2} \quad \frac{1}{2} \quad \frac{1}{2}\right) &= e_1 \\ D(1 \quad 0 \quad 0) &= e_2 \\ D(1 \quad 1 \quad 0) &= e_3 \end{aligned} \right\}$$

$$\begin{aligned}
 D\left(\frac{1}{2} \quad \frac{1}{2} \quad \frac{1}{2}\right) &= e_4 \\
 D(1 \quad 1 \quad 1) &= e_5 \\
 D(2 \quad 0 \quad 0) &= e_6 \\
 D\left(\frac{1}{2} \quad \frac{1}{2} \quad \frac{1}{2}\right) &= e_7 \\
 D(2 \quad 1 \quad 0) &= e_8 \\
 D(2 \quad 1 \quad 1) &= e_9
 \end{aligned} \quad (6)$$

The atomic Rydberg unit ($\hbar = 1$, $m = \frac{1}{2}$, $e^2 = 2$) is used throughout this paper. The parameters for sodium used in this paper are listed in Table 1.

It was shown by Chang and Falicov[1] that for small displacement approximation, keeping terms only up to the second power in the displacements, the electrostatic energy contribution ΔE_{es} consists of four terms:

- Δ_0 (The electrostatic energy difference for a rigid vacancy),
- Δ_1 (The electrostatic energy arising from the displacement of each ion in a perfect lattice),
- Δ_2 (The negative of the interaction between the missing ion and the dipole generated by each displaced ion), and
- Δ_3 (The electrostatic energy due to the mutual interaction between the dipoles generated by the displaced ions).

The pertinent expression for ΔE_{es} are:

$$\Delta E_{es} = \Delta_0 + \Delta_1 + \Delta_2 + \Delta_3 \quad (7)$$

$$\Delta_0 = 1.21308 (Z^{*2} e^2 / a_0) \quad (8)$$

$$\begin{aligned}
 \Delta_1 = (Z^{*2} e^2 / a_0) (8\pi) [e_1^2 + e_2^2 + 4e_3^2 + 11e_4^2 \\
 + 4e_5^2 + 4e_6^2 + 19e_7^2 + 20e_8^2 + 24e_9^2] \quad (9)
 \end{aligned}$$

Table 1. Parameters of sodium metal*

$a_0 = 7.98425$	(cubic lattice constant)
$\Omega_0 = 254.4907$	(volume of primitive cell)
$k_F = 0.48818$	(Fermi wave vector)
$E_F = 0.21794$	(Fermi energy)

*All expressed in atomic Rydberg units (where $\hbar = 1$, $m = 1/2$, $e = \sqrt{2}$ are assumed).

$$\begin{aligned}
 \Delta_2 = (Z^{*2} e^2 / a_0) \left[\frac{16}{\sqrt{3}} (e_1 - e_1^2) + 6(e_2 - e_2^2) \right. \\
 + \frac{12}{\sqrt{2}} (e_3 - e_3^2) + \frac{48}{\sqrt{11}} (e_4 - e_4^2) \\
 + \frac{8}{\sqrt{3}} (e_5 - e_5^2) + 3(e_6 - e_6^2) \\
 + \frac{48}{\sqrt{19}} (e_7 - e_7^2) + \frac{24}{\sqrt{5}} (e_8 - e_8^2) \\
 \left. + \frac{24}{\sqrt{6}} (e_9 - e_9^2) \right] \quad (10)
 \end{aligned}$$

$$\begin{aligned}
 \Delta_3 = (Z^{*2} e^2 / a_0) [18.458 e_1^2 + 7.114 e_2^2 \\
 + 32.489 e_3^2 + 178.083 e_4^2 + 9.229 e_5^2 \\
 + 3.557 e_6^2 + 167.596 e_7^2 + 133.261 e_8^2 \\
 + 125.819 e_9^2 + 45.084 e_1 e_2 + 22.592 e_1 e_3 \\
 + 16.451 e_1 e_4 - 24.116 e_1 e_5 + 4.910 e_1 e_6 \\
 - 4.720 e_1 e_7 + 4.894 e_1 e_8 - 2.977 e_1 e_9 \\
 + 38.819 e_2 e_3 - 2.403 e_2 e_4 + 13.384 e_2 e_5 \\
 - 17.959 e_2 e_6 + 12.659 e_2 e_7 - 3.072 e_2 e_8 \\
 + 4.564 e_2 e_9 + 234.631 e_3 e_4 + 67.604 e_3 e_5 \\
 + 27.449 e_3 e_6 - 79.700 e_3 e_7 - 7.690 e_3 e_8 \\
 + 19.117 e_3 e_9 + 177.866 e_4 e_5 \\
 + 107.390 e_4 e_6 + 226.466 e_4 e_7 \\
 + 90.004 e_4 e_8 - 79.149 e_4 e_9 + 22.542 e_5 e_6 \\
 + 85.645 e_5 e_7 + 83.329 e_5 e_8 - 8.178 e_5 e_9 \\
 + 71.471 e_6 e_7 + 126.793 e_6 e_8 + 64.063 e_6 e_9 \\
 + 560.321 e_7 e_8 + 483.910 e_7 e_9 \\
 + 420.705 e_8 e_9]. \quad (11)
 \end{aligned}$$

In equations (7) to (11), Z^* is the effective valence ($Z^* = 1.075$ according to Harrison [6]) and a_0 is the cubic lattice constant ($a_0 = 7.9842$ Bohr units).

Similarly, the band structure contribution consists of three terms:

Δ_4 (a constant term independent of the

distortions arising from the fact that in equation (2) the structure factor $S_p(q)$ corresponds to $(N+1)$ atoms instead of N),

- Δ_5 (contribution arising from the mixed term in the square of equation (2)), and
 Δ_6 (contribution from the square of the last term of equation (2) averaged over all angles in q space). The pertinent expressions for ΔE_{br} are,

$$\Delta E_{br} = \Delta_4 + \Delta_5 + \Delta_6 \quad (12)$$

$$\Delta_4 = \sum_{G \neq 0} \frac{G}{3} \left[\frac{d}{dq} \left\{ \frac{Q(q)|W(q)|^2}{q^2} \right\} \right]_{q=G} \quad (13)$$

$$\Delta_5 = Y[e_1^2 + e_2^2 + 4e_3^2 + 11e_4^2 + 4e_5^2 + 4e_6^2 + 19e_7^2 + 20e_8^2 + 24e_9^2] \quad (14)$$

$$\begin{aligned} \Delta_6 = & Z_0 + Z_1e_1 + Z_2e_2 + Z_3e_3 + Z_4e_4 + Z_5e_5 \\ & + Z_6e_6 + Z_7e_7 + Z_8e_8 + Z_9e_9 + Z_{11}e_1^2 \\ & + Z_{22}e_2^2 + Z_{33}e_3^2 + Z_{44}e_4^2 + Z_{55}e_5^2 \\ & + Z_{66}e_6^2 + Z_{77}e_7^2 + Z_{88}e_8^2 + Z_{99}e_9^2 \\ & + Z_{12}e_1e_2 + Z_{13}e_1e_3 + Z_{14}e_1e_4 + Z_{15}e_1e_5 \\ & + Z_{16}e_1e_6 + Z_{17}e_1e_7 + Z_{18}e_1e_8 + Z_{19}e_1e_9 \\ & + Z_{23}e_2e_3 + Z_{24}e_2e_4 + Z_{25}e_2e_5 + Z_{26}e_2e_6 \\ & + Z_{27}e_2e_7 + Z_{28}e_2e_8 + Z_{29}e_2e_9 + Z_{34}e_3e_4 \\ & + Z_{35}e_3e_5 + Z_{36}e_3e_6 + Z_{37}e_3e_7 + Z_{38}e_3e_8 \\ & + Z_{39}e_3e_9 + Z_{45}e_4e_5 + Z_{46}e_4e_6 + Z_{47}e_4e_7 \\ & + Z_{48}e_4e_8 + Z_{49}e_4e_9 + Z_{56}e_5e_6 + Z_{57}e_5e_7 \\ & + Z_{58}e_5e_8 + Z_{59}e_5e_9 + Z_{67}e_6e_7 + Z_{68}e_6e_8 \\ & + Z_{69}e_6e_9 + Z_{78}e_7e_8 + Z_{79}e_7e_9 + Z_{89}e_8e_9. \end{aligned} \quad (15)$$

The constant term Δ_4 , equation (13), and the coefficients in equations (14) and (15) are listed in Table 2 for the Heine-Abarenkov-Animalu form factor (PP1, PP2), the Shaw-Pynn optimized form factor (PP3), and the new form factor (PP4). It is seen that all these coefficients are very sensitive to the choice

Table 2. The band structure contribution

	PP1 (PP2)	PP3	PP4
Δ_4	+0.00131	-0.00269	-0.00269
Y	+1.31988	+1.22552	+1.22552
Z_0	-0.23251	-0.27905 (-0.29322)	-0.30487
Z_1	-1.92062	-2.28070 (-2.41809)	-2.50413
Z_2	-1.38312	-1.60675 (-1.67108)	-1.70667
Z_3	-1.82011	-2.12646 (-2.11465)	-2.15018
Z_4	-3.00280	-3.55834 (-3.54589)	-3.61707
Z_5	-0.96042	-1.13818 (-1.13665)	-1.15741
Z_6	-0.62910	-0.74124 (-0.74194)	-0.75049
Z_7	-2.29415	-2.70338 (-2.69964)	-2.74122
Z_8	-2.23225	-2.63301 (-2.62910)	-2.67275
Z_9	-2.03913	-2.41232 (-2.41234)	-2.45115
Z_{11}	-6.90921	-7.71309 (-8.55997)	-8.50648
Z_{22}	-4.31754	-4.76415 (-5.38084)	-5.29391
Z_{33}	-20.03976	-22.86146 (-25.98912)	-26.13069
Z_{23}	-8.59018	-10.03001 (-10.24475)	-10.46629
Z_{24}	-6.41458	-6.08710 (-5.07792)	-4.07346
Z_{25}	-2.81625	-3.29820 (-3.27616)	-3.35295
Z_{26}	+1.61699	+2.05379 (+2.42617)	+2.62219
Z_{27}	-1.35275	-1.59725 (-1.64105)	-1.61925
Z_{28}	+0.93785	+0.90286 (+0.96234)	+0.89229
Z_{29}	-0.53447	-0.60422 (-0.63984)	-0.60015
Z_{34}	-48.86913	-57.82656 (-59.88119)	-61.63618
Z_{35}	-15.22642	-17.68992 (-18.19975)	-18.48646
Z_{36}	-2.89123	-3.38712 (-3.36635)	-3.43422
Z_{37}	-1.34916	+0.47032 (+2.13715)	+3.81786
Z_{38}	-0.47316	+0.06724 (+1.43262)	+2.06243
Z_{39}	-0.83721	-1.36974 (-1.24730)	-1.40961

Table 2 (cont.)

	PP1 (PP2)	PP3	PP4
Z_{45}	-35.46319	-42.25163 (-43.86505)	-45.35089
Z_{46}	-12.62633	-14.63605 (-15.11944)	-15.29260
Z_{44}	-77.10699	-88.46434 (-98.15838)	-99.04312
Z_{35}	-15.99775	-18.11421 (-21.30264)	-21.30241
Z_{66}	-15.07537	-17.02107 (-20.15907)	-20.18863
Z_{77}	-105.38529	-120.31890 (-135.96578)	-136.87940
Z_{88}	-101.25983	-115.3805 (-131.06729)	-131.71510
Z_{99}	-114.82749	-130.68640 (-149.54032)	-150.06550
Z_{12}	-7.99267	-9.75312 (-10.33232)	-10.89905
Z_{13}	-7.46778	-8.22105 (-7.98229)	-7.77182
Z_{14}	-4.51048	-4.81428 (-3.78534)	-3.42730
Z_{15}	+0.87044	+1.93179 (+2.73727)	+3.51802
Z_{16}	-0.50676	-0.60549 (-0.61322)	-0.62668
Z_{17}	+1.80529	+1.94052 (+1.97552)	+1.96257
Z_{18}	-0.53439	-0.63914 (-0.71018)	-0.66131
Z_{19}	+0.30339	+0.33899 (+0.27625)	+0.31458
Z_{47}	-21.94943	-25.47944 (-25.19302)	-25.39620
Z_{48}	-21.78858	-23.13649 (-21.82590)	-20.34200
Z_{49}	-5.57696	-3.63259 (-1.20670)	+1.21710
Z_{56}	-2.30275	-2.73914 (-2.71343)	-2.79877
Z_{57}	-12.64620	-14.24975 (-14.31110)	-14.17662
Z_{58}	-8.80809	-10.31404 (-10.26007)	-10.43592
Z_{59}	-0.70482	-0.15237 (+1.07068)	+1.70209
Z_{67}	-7.39238	-8.73616 (-8.66423)	-8.87332
Z_{68}	-14.31440	-16.65561 (-17.17389)	-17.46803
Z_{69}	-6.75720	-7.92160 (-7.88387)	-8.03054

Table 2 (cont.)

	PP1 (PP2)	PP3	PP4
Z_{78}	-56.96879	-67.73442 (-70.49124)	-72.73890
Z_{79}	-53.17073	-62.38055 (-64.35861)	-65.76700
Z_{89}	-46.46513	-54.30379 (-55.52935)	-56.60746

of PP with considerable variations between PP1 (PP2), PP3 and PP4 for equivalent coefficients. It is noted that in the band structure calculations using PP3 and PP4, the dielectric function proposed by Shaw and Pynn (equation (2.7) of Ref. [9]) including the exchange and correlation corrections was used instead of the Hartree dielectric function.

In order to obtain E_v and the values of the relaxation parameters e_1, e_2, \dots, e_9 , one obtains the sum of equations (7) and (12),

$$\Delta E_v = \Delta E_{es} + \mu \Delta E_{bs} \quad (16)$$

and minimize ΔE_v with respect to all distortion parameters. In equation (16) $\mu = 1.0$ for PP1, PP3 and PP4; $\mu = 1.233$ for PP2. Results obtained in this fashion, allowing increasing number of shells (up to nine) to relax, are listed in Table 3 under the headings PP1, PP2, PP3 and PP4.

4. DISCUSSION

The experimental vacancy energy according to the thermal expansion measurements of Feder and Charbneau [2] is 0.031 ± 0.002 Ry. The calculated ΔE_v values according to the four PP form factors are, respectively, 0.060 (PP1), 0.046 (PP2), 0.049 (PP3) and 0.035 (PP4) Ry. The calculated ΔE_v according to PP4 is within a few per cent of the experimental value. Furthermore, the lattice displacements (see Table 3) decrease continuously in going from PP1 to PP2, PP3 and PP4, the latter yielding lattice displacements much smaller than those reported by Torrens and

Table 3. Energy of vacancy formation and distortions of various shells allowing relaxation of increasing number of shells (up to nine) for PP1, PP2 and PP3

PP1	0	1	2	3	Number of shells relaxed					8	9
					4	5	6	7	8		
e_1	0	-0.0865	-0.0943	-0.1017	-0.0962	-0.1344	-0.1402	-0.1490	-0.1505	-0.1493	
e_2	0	0	+0.0134	+0.0228	+0.0143	+0.0436	+0.0501	+0.0631	+0.0646	+0.0626	
e_3	0	0	0	-0.0186	-0.0153	-0.0174	-0.0186	-0.0258	-0.0264	-0.0249	
e_4	0	0	0	0	-0.0059	-0.0003	-0.0007	+0.0032	+0.0037	+0.0026	
e_5	0	0	0	0	0	-0.0245	-0.0311	+0.0317	+0.0324	+0.0324	
e_6	0	0	0	0	0	0	+0.0079	+0.0109	+0.0105	+0.0108	
e_7	0	0	0	0	0	0	0	-0.0073	-0.0081	-0.0069	
e_8	0	0	0	0	0	0	0	0	+0.0013	+0.0014	
e_9	0	0	0	0	0	0	0	0	0	-0.0019	
ΔE_v , Ry	+0.120	+0.087	+0.086	+0.080	+0.078	+0.066	+0.065	+0.061	+0.061	+0.060	
PP2											
e_1	0					-0.0962	-0.1028	-0.1087	-0.1118	-0.1115	
e_2	0					+0.0379	+0.0435	+0.0514	+0.0542	+0.0537	
e_3	0					-0.0134	-0.0149	-0.0197	-0.0211	-0.0208	
e_4	0					+0.0003	+0.0003	+0.0024	+0.0035	+0.0032	
e_5	0					-0.0211	-0.0231	-0.0235	-0.0247	-0.0247	
e_6	0					0	+0.0082	+0.0103	+0.0096	+0.0097	
e_7	0					0	0	-0.0067	-0.0067	-0.0064	
e_8	0					0	0	0	+0.0023	+0.0023	
e_9	0					0	0	0	0	-0.0004	
ΔE_v , Ry	+0.066					+0.049	+0.048	+0.047	+0.046	+0.046	
PP3											
e_1	0					-0.0803	-0.0831	-0.0860	-0.0864	-0.0859	
e_2	0					(-0.0806)	(-0.0860)	(-0.0944)	(-0.1020)	(-0.1058)	
e_3	0					+0.0176	+0.0205	+0.0255	+0.0259	+0.0246	
e_4	0					(+0.0244)	(+0.0293)	(+0.0405)	(+0.0479)	(+0.0527)	
e_5	0					-0.0119	-0.0126	-0.0163	-0.0165	-0.0153	
e_6	0					(-0.0147)	(-0.0161)	(-0.0233)	(-0.0275)	(-0.0309)	
e_7	0					-0.0023	-0.0028	-0.0008	-0.0005	-0.0017	
e_8	0					(-0.0019)	(-0.0027)	(+0.0015)	(+0.0049)	(+0.0077)	
e_9	0					-0.0166	-0.0174	-0.0171	-0.0173	-0.0175	
e_{10}	0					(-0.0186)	(-0.0203)	(-0.0205)	(-0.0230)	(-0.0234)	
e_{11}	0					0	+0.0051	+0.0066	+0.0064	+0.0067	
e_{12}	0					0	(+0.0078)	(+0.0109)	(+0.0095)	(+0.0089)	
e_{13}	0					0	0	-0.0042	-0.0045	-0.0034	
e_{14}	0					0	0	(-0.0069)	(-0.00114)	(-0.0144)	

ϵ_8	0	0	0	0	+0-0006 (+0-0049)	+0-0006 (+0-0058)
ϵ_9	0	0	0	0	0	-0-0017 (+0-0021)
$\Delta E_v, \text{ Ry}$	+0-069 (+0-055)	+0-050 (+0-041)	+0-050 (+0-040)	+0-049 (+0-038)	+0-049 (+0-037)	+0-049 (+0-037)
PP4						
ϵ_1	0	-0-0437	-0-0454	-0-0480	-0-0485	-0-0475
ϵ_2	0	+0-0083	+0-0100	+0-0146	+0-0151	+0-0133
ϵ_3	0	-0-0111	-0-0117	-0-0155	-0-0159	-0-0141
ϵ_4	0	-0-0041	-0-0046	-0-0023	-0-0019	-0-0036
ϵ_5	0	-0-0106	-0-0113	-0-0106	-0-0108	-0-0110
ϵ_6	0	0	+0-0040	+0-0055	+0-0053	+0-0059
ϵ_7	0	0	0	-0-0043	-0-0049	-0-0030
ϵ_8	0	0	0	0	+0-0006	+0-0003
ϵ_9	0	0	0	0	0	-0-0017
$\Delta E_v, \text{ Ry}$	+0-044	+0-036	+0-036	+0-035	+0-035	+0-035

not calculated

Gerl[3] and Flocken and Hardy[4]. In view of the extreme sensitivity of the vacancy formation energy to slight variations in the PP form factors, the agreement between theory using PP4 and experiment may be considered excellent. It should be noted that the Shaw-Pynn exchange and correlation corrections are not unique and are, as pointed out by the authors in their discussions[9], based on several major assumptions the validity of which is yet to be tested. As an illustration, the numbers (in parentheses) under the heading PP3 in Tables 2 and 3 are the calculated values of the same Z parameters, lattice displacements and vacancy formation energy where the corrected PP form factors (Shaw-Pynn) and the uncorrected Hartree dielectric function were used. The vacancy formation energy (appearing in parentheses in Table 3 under PP3) seems to be closer to the experimental value than that calculated according to PP3 (numbers above parentheses) where the Shaw-Pynn exchange and correlation corrections of both the PP form factors and the dielectric screening function were used. Since PP4 (an improvement over PP3 in respect to fitting with experimental Fermi surface data) yields the lowest lattice displacements and the vacancy formation energy in best agreement with experiment, a choice of the correct PP form factors may be more important than the

exchange and correlation corrections. This is particularly true at low wave numbers ($q \leq 2k_F$), because at large wave numbers ($q \geq 2k_F$) the dielectric screening function (with and without exchange and correlation corrections) is already of the order of unity. As PP4 is also not unique, we can only conclude that PP4 yields the best results among the four PP form factors studied. It is perhaps unlikely that further refinement of the theory will lead to any large alterations in our numerical calculations, and the most convincing way to confirm our choice of the best PP form factors is to investigate how other atomic and electronic properties of sodium are affected by such choice and to extend similar calculations to other elements.

REFERENCES

1. CHANG R. and FALICOV L. M., *J. Phys. Chem. Solids* **32**, 465 (1971).
2. FEDER R. and CHARBNAU H. P., *Phys. Rev.* **149**, 464 (1966).
3. See, e.g., paper by TORRENS I. M. and GERL M., *Phys. Rev.* **187**, 912 (1969).
4. FLOCKEN J. W. and HARDY J. R., *Phys. Rev.* **177**, 1054 (1969).
5. ABARENKOV I. V. and HEINE V., *Phil. Mag.* **12**, 529 (1965).
6. HARRISON W. A., *Pseudopotentials in the Theory of Metals* p. 313. W. A. Benjamin, New York (1966).
7. WEAIRE D., *Proc. Phys. Soc.* **92**, 956 (1967).
8. WEAIRE D., *J. Phys. C* **1**, 210 (1968).
9. SHAW R. W., Jr. and PYNN R., *J. Phys. C* **2**, 2071 (1969).
10. LEE M. J. G., *Proc. R. Soc. A* **295**, 440 (1966).

THE ORIGIN OF THE NEAR-SURFACE EFFECT OF DIFFUSION IN OXIDIZING METALS

R. HALES

Berkeley Nuclear Laboratories, Berkeley, Gloucestershire, England

(Received 8 September 1970; in revised form 15 October 1970)

Abstract—Solutions to the diffusion equation are derived which describe the effect of a surface oxide barrier and of a vacancy flux on the distribution of a tracer element diffusing into a semi-infinite bar. The solutions are compared with the available experimental data on the diffusion of Cu into Pb and Ag into Mg.

1. INTRODUCTION

THE PRODUCTION of vacancies by oxidation when the oxide grows via cation diffusion has been recognised for many years [1]. The effect of these vacancies however has been largely ignored. Recent observations of the dependence of oxidation kinetics on the metal specimen dimensions [2], of the growth of vacancy clusters in thin foils of metals [3] and of the influence of oxidising environments on the creep properties of magnesium [4] have caused the relationship between oxidation processes and point defect production to be re-examined. Two recent papers have considered the effect of a vacancy supersaturation in an oxidising metal on the theoretical oxidation kinetics [5, 6]. Before more progress can be made in assessing the influence of these vacancies it is necessary to be able to measure how many vacancies are produced compared with the number of metal ions incorporated into the growing oxide.

The near surface effect of diffusion (NSE) is the name given to a phenomenon which has been observed in the course of tracer diffusion studies in several binary systems. The diffusion coefficient of a tracer into a solvent is usually determined from the gradient of a plot of log concentration vs. distance². The NSE causes this relationship to deviate from linearity.

The systems in which the NSE has been observed can be divided into two groups:

1. A noble tracer diffusing into a reactive solvent e.g. Cu into Pb [7].

2. A reactive tracer diffusing into a more noble solvent, e.g. U into Au [8].

The latter process has been analysed [8] in terms of the thermally activated dissociation of an oxide. The former process has been attributed to an oxide layer on the solvent acting as a barrier to the tracer [7]. An analytical solution of the diffusion equation is presented which describes this mechanism.

An alternative explanation of the NSE is shown to be a vacancy flux generated by an oxide layer growing on the metal. The vacancy flux in the region of the oxidising surface results in an anomalous diffusion coefficient.

The oxide as a barrier

The thermal conductivity of a composite body is well analysed [9] and provides a useful analogue for this problem. Consider the system shown in Fig. 1, a semi-infinite bar of material 2, in this case the metal, with a thin layer of material 1, the oxide, extending from $x = 0$ to $x = -l$. The tracer is applied to the outer face of the oxide at $x = -l$. The diffusion parameters of the two materials are subscripted 1 and 2 consistently with the schematic diagram of Fig. 1. The initial conditions to be considered are those employed by Dyson *et al.* [7]; namely at $t = 0$, $C = 0$ for all x except at $x = -l$. There is a further restraint imposed on the solution to the diffusion

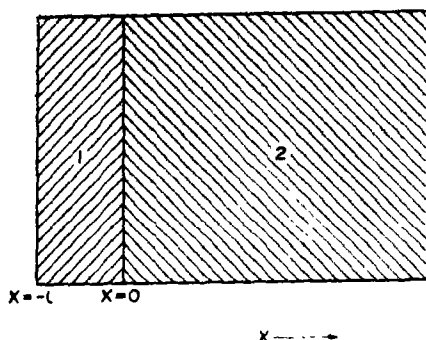


Fig. 1. A cross-section of a semi-infinite metal bar (2) with a surface oxide barrier (1).

equation by the conditions at the oxide/metal interface. In the absence of interfacial resistance to diffusion, the activity of solute at the interface must be equal in both media and the flux of solute across the interface must also be equal. That is at $x = 0$

$$a_1 = a_2 \quad \text{and} \quad D_1 \frac{da_1}{dx} = D_2 \frac{da_2}{dx} \quad (1)$$

where a is the tracer activity and D its diffusion coefficient in the solvent. The solution to the diffusion equation given by Carslaw and Jaeger[9] for an infinite source can be modified to a solution for thin film case of the form

$$a_1(x, t) = \frac{Q}{(1+k)\sqrt{\pi D_1 t}} \times \left\{ (1+k) \exp - \frac{(l+x)^2}{4D_1 t} - (1-k) \exp - \frac{(l-x)^2}{4D_1 t} \right\} \quad (2)$$

and

$$a_2(x, t) = \frac{2kQ}{(1+k)\sqrt{\pi D_1 t}} \exp - \frac{(l+kx)^2}{4D_1 t} \quad (3)$$

where Q is the initial concentration of tracer per unit area and $k = (D_1/D_2)^{1/2}$. These equations satisfy the conditions described by (1) and also the boundary conditions at $x = -l$. Dilute solutions approximately obey Henry's

Law and thus the concentration of tracer element can be considered proportional to its activity and hence obey the distribution given by equations (2) and (3). Thus if $na_2 = C_2$

$$C_2(x, t) = \frac{2kQn}{(1+k)\sqrt{\pi D_1 t}} \exp - \frac{(l+kx)^2}{4D_1 t} \quad (3a)$$

If the oxide barrier exhibits a solubility limit for the tracer the concentration of a tracer at $x = -l$ is constant and the solution to the diffusion equations are those given by Carslaw and Jaeger[9] for an infinite source. A logarithmic plot of the relationship given by equation (3a) is of the form

$$\ln C_2 = \text{const} - \frac{l^2}{4D_1 t} - \frac{2klx}{4D_1 t} - \frac{x^2}{4D_2 t} \quad (4)$$

When the barrier effect is removed equation (4) reduces to the solution of Fick's second law usually employed to determine tracer diffusion coefficients. However it can be seen from equation (4) that a plot of $\ln C$ vs. x^2 will be curved at small values of x and tend to a straight line as x approaches infinity.

The oxide as a vacancy source

A substitutional solute atom migrates by interchanging with vacant lattice sites in a random manner, and therefore it is interesting to consider the effect of a directional flow of vacancies on the migration of substitutional solute.

It is necessary to describe the properties of the vacancy flux. At the metal/oxide interface vacancies are simultaneously created by continued oxidation and removed by diffusion into the metal lattice, hence the concentration of vacancies at the surface, $x = 0$, can be considered constant. Vacancies diffuse through a metal lattice 10^4 to 10^5 times faster than substitutional solute atoms and consequently a large flux of vacancies can be sustained by a small concentration gradient. The sinks to which these vacancies diffuse are grain boundaries and other similar lattice defects. Grain boundaries are known to be efficient sinks for vacancies and are capable of

maintaining the vacancy concentration at the thermal equilibrium concentration. Under these experimental conditions the vacancy flux is quasi-steady state, that is constant with time and distance to some large value of x compared with the diffusion distance of the tracer under consideration.

For a flux of vacancies diffusing into a metal there is an equivalent flux of material diffusing to the surface. This flux comprises of both solute and solvent atoms. The number of solute atoms jumping out of a plane at x into a plane at $x - \Delta x$ depends on the site fraction of solute atoms at x and their jump frequency compared with that of solvent atoms. The site fraction of solute is $C_t/C_t + C_s$, where C_t and C_s are the concentrations of tracer and solute respectively. For dilute solutions $C_t \ll C_s$ and the site fraction reduces to C_t/C_s . The self diffusion coefficient for a metal is the product of the probability of a vacancy being in an adjacent site and the jump frequency. The vacancy concentration at any point in the lattice is the same for both species and therefore the relative jump frequencies of the two types of atoms is given by the ratio of the diffusion coefficients, D_t/D_s . Hence, if solute-vacancy interactions are ignored, the flux of solute returning to the surface, j_t due to the flux of injected vacancies, j_v , is

$$j_t = j_v C_t D_t / C_s D_s \quad (5)$$

Substituting for the solvent concentration in terms of its density, ρ , atomic mass, M , and Avogadro's number, N , a parameter U is defined by

$$U = -j_v D_t M / D_s N \rho \quad (6)$$

and hence

$$-UC_t = j_t \quad (7)$$

where U has the dimensions of velocity.

A combination of this reverse flux with the flux of tracer described by Fick's first law yields the nett solute flux J_t in the positive x direction.

$$J_t = -D_t \frac{dC_t}{dx} + UC_t \quad (8)$$

Fick's second law of diffusion states that

$$\frac{dc}{dt} = -\nabla J \quad (9)$$

and thus for a tracer diffusing in a vacancy flux

$$\frac{dC_t}{dx} = D_t \frac{d^2 C_t}{dx^2} - U \frac{dC_t}{dx} \quad (10)$$

The solution of the diffusion equation describes the concentration of tracer as a function of position and time and must satisfy the boundary conditions

$$C_t = 0 \quad \text{at } x > 0, \quad t = 0$$

and

$$C_t \rightarrow \infty \quad \text{at } x = 0, \quad t = 0.$$

An appropriate solution is

$$C_t(x, t) = \frac{Q}{\sqrt{\pi D_t t}} \exp - \left(\frac{x - Ut}{2\sqrt{D_t t}} \right)^2 \quad (11)$$

It will be noticed that equations (3) and (11) have the same form. A plot of log concentration vs. distance² yields a linear plot with slope $-1/4Dt$ in the absence of a near surface effect. Equations (3) and (11) approach linearity at large x but deviate to show an anomalously high concentration of tracer near the surface.

In addition to the data of Dyson *et al.* [7] the concentration profile of silver in magnesium has been measured. Silver was deposited on a clean magnesium surface and allowed to diffuse into the magnesium under oxidising conditions. A plot of silver concentration vs. distance squared is presented in Fig. 2. The gradient of this function is then plotted against $1/x$ as shown in Figs. 3 and 4. A straight line is obtained with intercept $-1/4Dt$. In both cases the intercept is in good agreement with the published data for diffusion coefficient of the solute/solvent system under consideration.

2. DISCUSSION

If the barrier model is applied to the data presented in Figs. 3 and 4, a value of l/k is obtained. For silver in magnesium $l/k =$

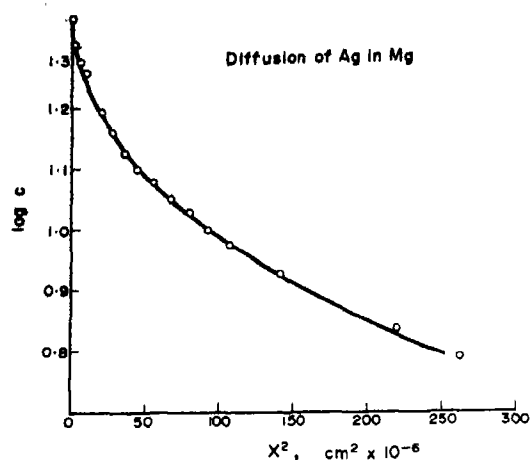


Fig. 2. The logarithm of silver concentration in magnesium as a function of distance squared.

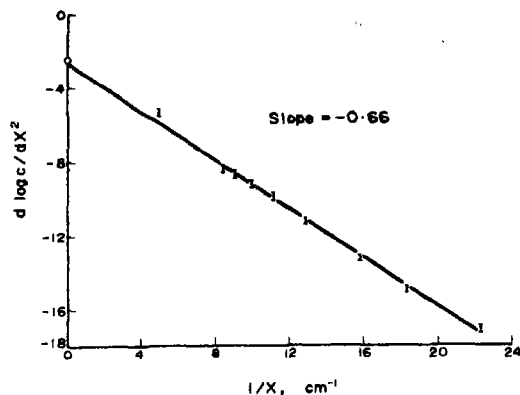


Fig. 4. $d \log C/d(x^2)$ as a function of $1/x$ for copper diffusing into lead from the data of Dyson *et al.* (1966).

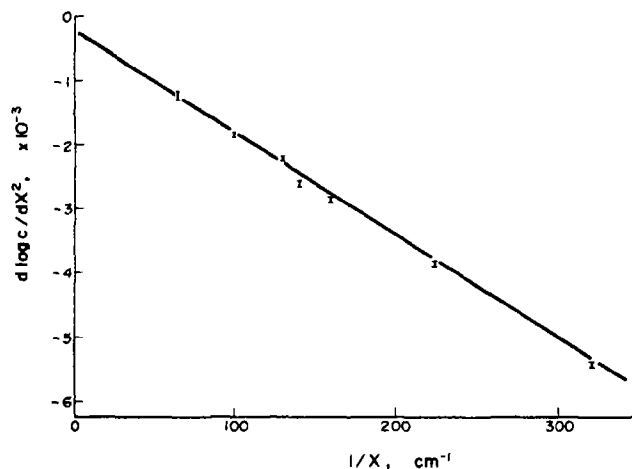


Fig. 3. $d \log C/d(x^2)$ as a function of $1/x$ for silver diffusing into magnesium.

4×10^{-2} mms and for copper in lead $l/k = 1.3 \times 10^{-1}$ mm. The data for cation diffusion in oxides is very limited, but an approximate value for k can be obtained by comparing the metal diffusion coefficient and the cation self-diffusion coefficient for the oxide at the same temperature. The best available diffusion data are listed in Table 1.

It is clear that these data yield values for the thickness of lead oxide and magnesium oxide barriers of 1.3×10^{-9} mms. and 2.6×10^{-8}

mms. respectively. These values are anomalously low as they imply the oxide layers are less than one hundredth of an atomic layer thick. The tracer elements under consideration are aliovalent with respect to the oxides and consequently their diffusivities would differ from that of self-cations by a few orders of magnitude. If the lead oxide barrier is an atomic layer thick ($\sim 10^{-7}$ mm), the diffusion coefficient for Cu in PbO must be 10^4 times greater than that for Pb in PbO and similarly

Table 1. Diffusion data

Solvent	Diffusing species	D_0 (cm ² /sec)	Q Kals/mole	D (cm ² /sec)	Temp. °C	Author	$k(\sqrt{D_1/D_2})$
Pb	Cu	8×10^{-3}	8	2.7×10^{-8}	224	Dyson <i>et al.</i> [7]	10^{-9}
PbO	Pb	10^8	66	2.8×10^{-24}	224	Linder [10]	
Mg	Ag	3.4×10^{-1}	28.5	3.0×10^{-9}	500	Lal [11]	6.5×10^{-9}
MgO	Mg	2.5×10^{-1}	79	1.3×10^{-23}	500	Linder & Parfitt [12]	

the coefficient of Ag diffusing in MgO must be in error by 10^4 . If a reasonable value for the thickness of an air formed film is used, say 5×10^{-6} mm, the tracer atoms must diffuse 10^6 to 10^7 times faster through the cation lattice of the oxides than the host cations can diffuse themselves. There is no evidence available to support this contention.

Further to the arguments employed above, the experimental method of Dyson *et al.* [7] and most other authors precludes the oxide barrier model. A common method employed to precipitate a layer of radio-active tracer onto a metal surface is electrodisplacement, (that is the displacement of a noble ion from solution by a metal placed higher in the electrochemical series). The ionic interchange takes place at the interface between the solution and the metal, oxides are inert to this type of reaction. Therefore a uniform oxide barrier, as envisaged by Dyson *et al.* [7], cannot be applied and the foregoing comments are in direct contradiction to the findings of these workers as reported in the Appendix to their paper.

The model of a vacancy flux causing ano-

malous concentration profiles is more successful in explaining experimental results. An appropriate value of the parameter U (equation (11)) can be obtained from the experimental data and hence the vacancy flux, j_v . The vacancy flux arises from metal ions crossing the metal/oxide interface from the metal into the oxide. These metal ions diffuse through the oxide, via a cation vacancy or interstitial mechanism, to the oxide/oxygen interface where they occupy cation lattice sites and become incorporated into the oxide lattice. In the case of a divalent metal, forming an oxide of the type MeO, each metal ion associates with one oxygen ion, hence the oxygen flux to the oxide is equal to the vacancy flux into the metal. Because of the relationship between the vacancy flux in the metal and the oxygen flux to the surface the vacancy flux can be conveniently compared with experimental weight grain data, as tabulated below, in Table 2.

In Table 2 the oxidation rate quoted is the average linear oxidation rate for a duration similar to that of the diffusion anneal. A further comparison can be made for magnesium

Table 2.

	j_v vacs/ cm ² /sec	Equivalent oxidation rate $\mu\text{g}/\text{cm}^2/\text{hr}$	Observed oxidation rate $\mu\text{g}/\text{cm}^2/\text{hr}$	Author
Magnesium at 500°C	1.9×10^{18}	185	300	Leontis and Rhines [13]
Lead at 256°C	4×10^{12}	0.4	3	Weber and Baldwin [16]

with the vacancy flux generated by oxidation as calculated from creep data [4]. At 450°C the vacancy flux is calculated to be 1.3×10^{13} vacancies/cm²/sec and will clearly increase with temperature. The good agreement between the vacancy fluxes and oxidation rates gives weight to the vacancy flux model as being the source of the NSE. It will be noted that the vacancy flux is less than that predicted by oxidation kinetics indicating that the interface is less than 100 per cent efficient in generating vacancies.

The two systems in this paper and the systems examined by Reimann and Stark [8] exhibit a positive NSE, that is the experimental curve shows an abnormally steep concentration profile near the surface which is associated with slower diffusion than observed under ideal conditions. There is, however, evidence that the opposite effect can be obtained, notably the diffusion of dopants into silicon during the manufacture of semi-conducting devices [15]. *P-N* junctions are produced by diffusing a dopant into silicon wafers in oxidising environments. It is found that the dopant has an anomalously high diffusion coefficient near the surface and can be as great as ten times faster than in the bulk material [15]. This phenomenon cannot be explained in terms of a barrier effect, whereas it is clear from equation (11) that a negative value of U results in reduced diffusivity at small x whilst a positive value of U results in enhanced diffusivity near the surface. The parameter U can be positive or negative according to the direction of vacancy motion; j_v is defined as positive in the positive x direction. The results obtained for silicon, therefore, can be explained in terms of vacancy flux out of the silicon into the growing oxide. Observations on the annealing behaviour of point defect clusters in silicon [16] have shown the growth of a surface layer of silicon oxide absorbs vacancies in contrast to magnesium oxide which generates vacancies.

3. CONCLUSIONS

(1) The uniform oxide barrier to diffusion results in anomalies between the parameters k and l and the magnitude of the observed NSE.

(2) It is not possible to deposit a tracer onto a homogeneous oxide layer by chemical displacement from solution.

(3) A fractured oxide barrier can give rise to a deviation from classical diffusion behaviour and can account in part for the near surface effect.

(4) Analysis of the near surface effect in terms of a vacancy flux in the solvent is successful for cases of both inhibited and enhanced diffusion of a solute and provides a useful method for measuring the magnitude of vacancy fluxes generated by oxidation.

Acknowledgement — This paper is published by permission of the Central Electricity Generating Board.

REFERENCES

1. HAUFFE K., *Oxydation von Metallen und Metallegierungen*. Springer-Verlag OHG Berlin (1956).
2. HANCOCK P. and FLETCHER R., SERAI Proceedings "Journées Internationales d'Etude sur l'oxydation des Metaux", p. 70 (1965).
3. HALES R., DOBSON P. S. and SMALLMAN R. E., *Met. Sci. J.* 2, 224 (1968).
4. HALES R., DOBSON P. S. and SMALLMAN R. E., *Acta Metall.* 17, 1323 (1969).
5. GIBBS G. B., *Phil. Mag.* 18, 1175 (1968).
6. MINDEL M. J. and POLLACK S. R., *J. Phys. Chem. Solids* 30, 993 (1969).
7. DYSON B. F., ANTHONY T. and TURNBULL D., *J. appl. Phys.* 37, 2370 (1966).
8. REIMANN D. K. and STARK J. P., *Acta Metall.* 18, 63 (1970).
9. CARSLAW H. S. and JAEGER J. C., *Conduction of Heat in Solids*, 2nd edition Oxford Univ. Press, p. 319. (1959).
10. LINDER R., *Arkiv Kemi.* 4, 381 (1952).
11. LAL K., *Commis. Energ. At. Rep. No. CEA-R 3136*. (1967).
12. LINDER R. and PARFITT G. D., *J. chem. Phys.* 26, 182 (1957).
13. LEONTIS T. E. and RHINES F. N., *Trans. A.I.M.E.* 166, 265 (1946).
14. WEBER E. and BALDWIN W. M., *J. Metals New York* 4, 854 (1952).
15. SUBASHIEV V. K., LANDSMAN A. P. and KUKHARSKII A. A., *Soviet Phys.-solid State* 2, 2406 (1961).
16. SANDERS I. R. and DOBSON P. S., *Phil. Mag.* 20, 881 (1969).

THE L_{III} X-RAY EMISSION EDGE IN LANTHANUM HYDRIDES

A. C. SARMA and W. G. BOS

Department of Chemistry, University of Louisville, Louisville, Ky. 40208, U.S.A.

(Received 27 May 1970; in revised form 12 October 1970)

Abstract—New evidence supporting the hydridic model of bonding in rare earth hydrides is reported. A weak peak was detected at the L_{III} X-ray emission edge of lanthanum metal and assigned to transitions involving conduction band electrons, $L_{III}O_{IV,V}$ and $L_{III}P_1$. The regular decrease in intensity at the L_{III} emission edge with increasing hydrogen content and the close similarity of the emission edges of $LaH_{2.88}$, La_2O_3 and LaF_3 support the view that hydride ions form at the expense of the population of the lanthanum conduction band.

1. INTRODUCTION

THE NATURE of the hydrogen species in metallic hydrides has been a subject of discussion, and some disagreement, for a number of years. The general arguments for the protonic model, the hydridic model and the interstitial atom model have been reviewed by a number of authors[1-3].

For hydrides of scandium, yttrium and the lanthanides, either the protonic or hydridic model appears to be favored over the interstitial atom model[4]. Schreiber[5] has interpreted the Knight shifts and spin-lattice relaxation times of the metal nuclei and the absence of a hydrogen nmr shift in scandium, yttrium and lanthanum hydrides in terms of the protonic model. Later Bos and Gutowsky[6] showed that the data are also compatible with the hydridic model and discussed the reasons for the ambiguity in the interpretation of these properties. Wallace and Mader[7] have discussed this ambiguity in relation to the magnetic susceptibilities of hydrides of lanthanides with unpaired f electrons. While Kopp and Schreiber[8,9] have interpreted hydrogen NMR shifts in cerium, praseodymium neodymium and gadolinium hydrides in terms of a hydrogen species having a small fraction of an electron associated with it, these results could also be accounted for by a spin polarization mechanism

acting on anions, as is the case in some lanthanide fluorides[10]. Heckman[11] has attributed the positive Hall coefficient observed for cerium hydrides to a protonic structure, but Libowitz and Pack[12] have pointed out that these results are also consistent with a hydridic structure. Isomer shifts in the Mössbauer spectra of dysprosium hydrides favor a hydridic model[13].

We report here the results of a study of the L_{III} X-ray emission edge in La metal, La_2O_3 , LaF_3 and several lanthanum hydrides of compositions between LaH_2 and LaH_3 . Between $LaH_{1.9}$ and LaH_3 , lanthanum hydride is face centered cubic with respect to the metal atoms; the lattice contracts slightly with increasing hydrogen content in this composition range[14]. Previous X-ray spectroscopic studies of lanthanide hydrides have been limited to L_{III} absorption spectra of lanthanum and cerium hydrides and gave some support to the hydridic model[15]. The results of the present study provide additional direct support for this point of view.

2. EXPERIMENTAL

The La metal, 99.9 per cent pure with respect to metal content, was obtained from United Mineral and Chemical Corp. Hydrides were prepared by the reaction of the metal with pure hydrogen from an Elhygen

electrolytic generator. Compositions were determined volumetrically to less than ± 0.05 H/M. La_2O_3 , obtained from American Potash and Chemical Corp., was dried by heating under vacuum. Hydrated LaF_3 from the same supplier was carefully dehydrated by vacuum heating[16]. The polished metal sample was mounted directly in the path of the exciting X-ray beam. Other samples were used as fine powders packed into Leucite holders with cellophane covers under an argon atmosphere.

Recorder traces and count rates for the emission spectra were obtained using Siemens X-ray spectrometry equipment including a high intensity gold anode X-ray tube operated by a Kristalloflex-4 generator at a power level of $50 \text{ kv} \times 30 \text{ mA}$, a vacuum channel goniometer equipped with a lithium fluoride (200) analyzer crystal, $2d = 4.028 \text{ \AA}$, and a beryllium window flow counter. The collimator used had an aperture angle of 0.15° and represented the limiting factor for resolution. The take off angle used was 45° . This equipment was operated with a model 1Z measuring panel.

The choice of a lithium fluoride crystal as an analyzer deserves some comment. Its mosaic structure leads to broadening of the spectral lines but this broadening is unimportant in relation to the resolving power of the collimator which was used. This same mosaic structure is responsible for the excellent intensity characteristics of this analyzer crystal. Since the transitions of interest have a relatively low probability, this was an important consideration. The lithium fluoride crystal also has a compensating feature in that the emission peaks of interest occur at relatively high angles where the energy scale is somewhat expanded. The regularity and reproducibility of the results reported below support the conclusion that the experiments were adequate for their purpose, namely to provide a very direct test of the hydridic vs. the protonic model of bonding.

The spectra of all of the compounds were compared to the spectrum obtained for the

metal under the same instrumental conditions. To compensate for effective concentration differences between the compact metal and the packed powder samples, the intensities of the spectra were corrected for background and adjusted to give the same integrated count for the large peak, having its maximum at 69.8° in 2θ , below the L_{III} emission edge in energy. The measured intensities of this major peak in the various compounds relative to its intensity in the metal were: $\text{LaH}_{2.09}$, 0.30; $\text{LaH}_{2.18}$, 0.40; $\text{LaH}_{2.45}$, 0.40; $\text{LaH}_{2.49}$, 0.36; $\text{LaH}_{2.68}$, 0.34; $\text{LaH}_{2.90}$, 0.31; La_2O_3 , 0.37; and LaF_3 , 0.43. The maximum of this reference peak was constant in energy from compound to compound to within $\pm 0.05^\circ$.

3. RESULTS AND DISCUSSION

The fluorescence spectrum of lanthanum metal between 71° and 67° is shown in Fig. 1. Also shown are the transitions which contribute in this region[17]: $L_{\text{III}}\text{O}_I$ (68.81° , 5450 eV), $L_{\text{I}}\text{M}_V$ (69.05° , 5435 eV), $L_{\text{I}}\text{M}_{\text{IV}}$ (69.29° , 5418 eV) and $L_{\text{III}}\text{N}_{\text{IV,V}}$ (69.81° , 5383 eV), with relative intensities[18] of < 1 , < 1 , < 1 and 60 respectively.

The conduction band of lanthanum metal may be viewed, in simple terms, as two overlapping bands arising from the $5d$ and $6s$ atomic orbitals of lanthanum[19]. $L_{\text{III}}\text{O}_{\text{IV,V}}$ and $L_{\text{III}}\text{P}_I$ transitions would contribute to the structure of the L_{III} emission edge shown in Fig. 2 for six of the materials studied. We take the small peak centered at 68.4° (5478 eV) in the spectrum of lanthanum metal to arise from these transitions. Since this peak has not been previously reported and these transitions have not been previously assigned, our three-fold basis for this assignment deserves some comment. First, the maximum of the peak occurs below the L_{III} absorption edge[17] which arises from transitions from the L_{III} level to the lowest unfilled states of lanthanum. In the metal these are the vacant states just above the Fermi level of the $6s$ - $5d$ conduction band. Second, the $L_{\text{III}}\text{O}_{\text{IV,V}}$ and $L_{\text{III}}\text{P}_I$ transitions

are the only ones allowed and not otherwise accounted for in this region of the spectrum. In Fig. 1, the $L_{III}N_{IV,V}$ peak is shown at 5383 eV and the $L_{III}O_I$ peak at 5450 eV. The $L_{III}O_{II}$ and $L_{III}O_{III}$ transitions are forbidden because $\Delta l = 0$. The O_{II} level is approximately 19 eV above the O_I level [20]. Our assignment places the O_{IV} , O_V and P_I levels about 9 eV above the O_{II} level and about 28 eV above the O_I level. Third, the peak assigned to the conduction band — L_{III}

transition behaves exactly as expected on going from the metal to the oxide and fluoride, i.e. it is present for the metal where there are conduction electrons and nearly disappears for the $La(III)$ compounds.

For the metal, the intensity of the small peak at 68.4° was of the order of one per cent of the intensity of the $L_{III}N_{IV,V}$ reference peak. Curve 1 in Fig. 2 shows the emission edge for the metal as it was recorded on an expanded scale. In the recorder trace from

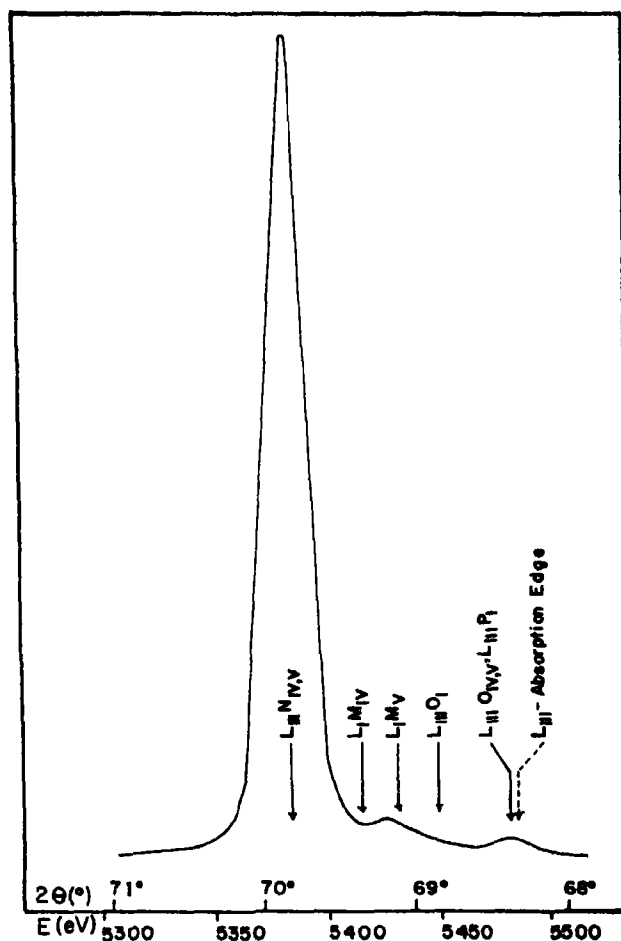


Fig. 1. The L_{III} X-ray emission spectrum of lanthanum metal in the region below the emission edge. 2θ values are for a lithium fluoride (200) analyzer crystal with $2a = 4.028 \text{ \AA}$. Assignments shown here for emission lines and the absorption edge are taken from Ref. [17].

which this curve was obtained, the noise level was less than 0.05 of the maximum of this peak for the metal. Also shown in Fig. 2 are the emission edges of $\text{LaH}_{2.18}$, $\text{LaH}_{2.48}$, $\text{LaH}_{2.88}$, La_2O_3 and LaF_3 . The intensities of these curves have been adjusted to compensate for effective concentration differences by the method described above. Spectra were also obtained for three additional hydride samples: $\text{LaH}_{2.09}$, $\text{LaH}_{2.49}$ and $\text{LaH}_{2.90}$.

Estimates of the relative integrated inten-

of the $\text{L}_{\text{III}}\text{O}_1$ peak lying just below it in energy. The intensities thus obtained are given relative to lanthanum metal in Table 1. This procedure yielded three results for La_2O_3 based on separate measurements which agreed with each other to within five per cent. The data for hydrides of closely similar compositions in Table 1 suggest slightly larger error limits. In any case, these estimates of intensity are somewhat sensitive to the extrapolation procedure and do not take

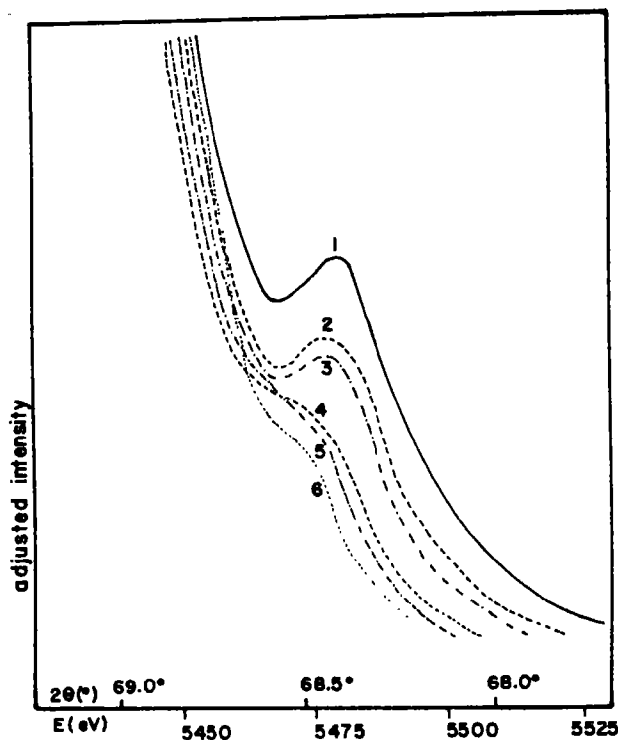


Fig. 2. The L_{III} X-ray emission edge in: 1. La metal; 2. $\text{LaH}_{2.18}$; 3. $\text{LaH}_{2.48}$; 4. $\text{LaH}_{2.88}$; 5. La_2O_3 ; and 6. LaF_3 . 2θ values are for a lithium fluoride (200) analyzer crystal with $2d = 4.028 \text{ \AA}$. The intensities have been normalized with respect to $\text{L}_{\text{III}}\text{N}_{\text{IV,V}}$ reference peak which lies below this emission edge.

sities of the emission edge peak for the various materials were obtained from the intensity adjusted curves. The integrated intensity for each material was taken as the area between the curve for this peak and an extrapolation

self-absorption into account. They are, however, adequate to support the semiquantitative conclusions drawn below.

There might be some question as to whether the peak we have assigned to the $\text{L}_{\text{III}}\text{O}_{\text{IV,V}}$

Table 1. *Relative integrated intensities at the L_{III} X-ray emission edge for lanthanum and lanthanum compounds*

Material	Relative intensity
La	1.00
LaH _{2.00}	0.71
LaH _{2.18}	0.66
LaH _{2.45}	0.52
LaH _{2.49}	0.60
LaH _{2.88}	0.36
LaH _{2.90}	0.39
La ₂ O ₃	0.25
LaF ₃	0.15

and $L_{III}P_1$ transitions is strongly affected by factors other than the conduction band population. For example, changes in the shape of the weak peaks near 69.0° or the very intense peak at 69.8° might affect the smaller peak which we assign to $L_{III}O_{IV,V}$ and $L_{III}P_1$. We believe this is not likely to be a significant effect. Except for the resolution limitations of the collimator, these peaks would probably not appear to overlap so extensively. While this broadening effect might lead to a low intensity tail in the region of 68.4° , it would not give rise to the distinct shape observed here for the metallic materials La metal, LaH_{2.18} and LaH_{2.45}.

Self-absorption might also be thought to play a role in determining the shape of the emission edge. In view of the energy excitation and the 45° take off angle used this must certainly be of some influence here. We do not believe that it occurs in such a way as to produce the peak shown in Fig. 2 or to seriously affect the interpretation of the differences in intensities shown there. The only characteristic feature of the absorption spectrum in this region is the L_{III} absorption edge located about 10 eV above the maximum of the emission peak in question. The effect of self-absorption should decrease from the absorption edge downward in energy. To

produce the minima shown in Fig. 2 would require a rather sharp absorption maximum here more than 10 eV below the absorption edge. There remains the strong possibility that self-absorption has some effect on the intensity of the L_{III} -conduction band peak, particularly toward the high energy side of this peak. To the extent that this is determined by the compactness of the samples, self-absorption would be greatest for the metal and correction for this would accentuate the difference in emission intensity between it and the other materials. As measured by the integrated intensity of the peak shown in Fig. 1, the other samples were of packed densities comparable to each other. Self-absorption should be at least approximately the same in each.

The regular decrease in intensity of the 68.4° peak with increasing hydrogen content and the close similarity of the emission edge of LaH_{2.88} to those of La₂O₃ and LaF₃ lend strong support to the view that hydride ions form at the expense of the conduction band population. Although the hydridic model implies the loss of two conduction electrons per metal atom on going from lanthanum metal to the dihydride and of one additional conduction electron per metal atom on going from the dihydride to the trihydride, the decrease in integrated emission intensity was approximately equal on going from the dihydride to the trihydride and from the metal to the dihydride. This result can be understood in terms of the character of the electrons which are lost. On the basis of an analysis of magnetic data for yttrium hydrides, Parks and Bos[21] have proposed that two s electrons are lost from the conduction band in forming the dihydride from the metal. The electron remaining in the conduction band is of d character. It too is lost upon formation of the trihydride. For the conduction band of lanthanum metal, the $5d$ and $6s$ levels are involved. Transitions from these levels to the $L_{III}(2p_{3/2})$ level involve $\Delta n = 3$ and $\Delta n = 4$, respectively. A higher transition probability

is expected for a $5d$ electron than a $6s$ electron. Thus the results reported here are consistent with the model proposed by Parks and Bos[21]. For La_2O_3 and LaF_3 , there are weak contributions to the shape of the emission edge and these can be attributed to transitions from the valence band. For the highest hydride compositions, there are contributions to the shape of the emission edge from transitions involving the valence band and the small number of conduction electrons which are still present.

In view of the similarity of most of the lanthanide hydrides to those of lanthanum [1, 2, 4] the conclusions reached here may be rather directly extended to other members of the series. Europium and ytterbium hydrides differ somewhat from the other lanthanide hydrides, but close analogies to the alkaline earth hydrides support a hydridic model for these hydrides also[2, 4]. The extension of these conclusions to other transition metal hydrides is less certain; here the choices for bonding models also include the interstitial atom model[3].

Acknowledgements—Support for this research was provided by the National Science Foundation and by the Sustaining University Program of the National Aeronautics and Space Administration.

REFERENCES

1. GIBB T. R. P., Jr., In *Progress in Inorganic Chemistry* (Edited by F. A. Cotton), Vol. 3, p. 315. Interscience, New York (1962).
2. LIBOWITZ G. G., *The Solid State Chemistry of Binary Metal Hydrides*, Benjamin, New York (1965).
3. EBISUZAKI Y. and O'KEEFFE M., In *Progress in Solid State Chemistry* (Edited by H. Reiss), Vol. 4, p. 187. Pergamon Press, Oxford (1967).
4. BOS W. G. and GAYER K. H., *J. nucl. Mater.* **18**, 1 (1966).
5. SCHREIBER D. S., *Phys. Rev.* **137**, A860 (1965).
6. BOS W. G. and GUTOWSKY H. S., *Inorg. Chem.* **6**, 552 (1967).
7. WALLACE W. E. and MADER K. H., *J. chem. Phys.* **48**, 84 (1968).
8. KOPP J. P. and SCHREIBER D. S., *Phys. Lett.* **24A**, 323 (1967).
9. KOPP J. P. and SCHREIBER D. S., *J. appl. Phys.* **38**, 1373 (1967).
10. WATSON R. E. and FREEMAN A. J., *Phys. Rev. Lett.* **6**, 277 (1961).
11. HECKMAN R. C., *J. chem. Phys.* **46**, 2158 (1967).
12. LIBOWITZ G. G. and PACK J. G., *J. chem. Phys.* **50**, 3557 (1969).
13. ABELES T. P., BOS W. G. and OUSEPH P. J., *J. Phys. Chem. Solids* **30**, 2159 (1969).
14. KORST W. L. and WARF J. C., *Inorg. Chem.* **5**, 1719 (1966).
15. VAINSHTEIN E. E., BRIL M. N., STARYI I. B. and KOST M. E., *Dokl. akad. nauk SSSR* **151**, 1360 (1963).
16. CARLSON O. N. and SCHMIDT F. A., In *The Rare Earths* (Edited by F. H. Spedding and A. H. Daane), p. 77. Wiley, New York (1961).
17. BEARDON J. A., *Rev. mod. Phys.* **39**, 78 (1967).
18. JENKINS R. and DE VRIES J. L., *Practical X-ray Spectrometry*, Appendix 2. Springer-Verlag, New York (1967).
19. GSCHNEIDNER K. A., In *Rare Earth Research III* (Edited by L. Eyring), p. 153. Gordon and Breach, New York (1965).
20. SANDSTROM A. E., In *Encyclopedia of Physics* (Edited by S. Flügge), Vol. 30, p. 227. Springer-Verlag, Berlin (1957).
21. PARKS C. D. and BOS W. G., *J. Solid State Chem.* **2**, 61 (1970).

MAGNETIC AND ELECTRICAL PROPERTIES OF $\text{CuCr}_2\text{Se}_{4-x}\text{Br}_x$ AND $\text{CuCr}_2\text{Se}_{4-x}\text{Cl}_x$

K. MIYATANI, K. MINEMATSU, Y. WADA, F. OKAMOTO, K. KATO and P. K. BALTZER
RCA Research Laboratories, Inc., P.O. Box 5151, Tokyo International 100-31, Japan

(Received 31 July 1970; in revised form 9 October 1970)

Abstract—The systems $\text{CuCr}_2\text{Se}_{4-x}\text{Br}_x$ and $\text{CuCr}_2\text{Se}_{4-x}\text{Cl}_x$, both as polycrystal and single crystal, have been synthesized, and their magnetic and electrical properties have been studied. $\text{CuCr}_2\text{Se}_3\text{Br}$ is confirmed to be a *B*-site ferromagnet. A very strong correlation between the magnetic ordering temperature and the electrical properties was found, and is discussed.

1. INTRODUCTION

THE MAGNETIC and electrical properties of copper containing spinels CuCr_2X_4 ($X = \text{S}, \text{Se}$ and Te) are unique and anomalous. The magnetic study[1] of these compounds has shown that the total magnetic moment is very close to $5 \mu_B/\text{mol.}$ and the susceptibility behaves like that of a ferromagnetic material. Neutron diffraction studies[2, 3] have shown that no localized moment exists on the tetrahedral site and support the ionic configuration of the form $\text{Cu}^{2+}\text{Cr}_2^{3+}\text{X}_4$. The nuclear magnetic resonance[4-6] and the interatomic distance studies[7] can also be considered to indirectly support this conclusion. Thus, the spin associated with the copper ion is not localized, but is in fact delocalized, being ordered antiparallel to the localized spins of the chromium ions.

A ' Cu^{2+} ion' effectively appears to form the diamagnetic Cu^{1+} ion and to contribute an itinerant *d*-hole which becomes exchange-coupled and spin polarized antiparallel to the localized spins of the Cr^{3+} ions, like in a ferromagnet[8]. It is, therefore, thought that the existence of this hole-band in the CuCr_2X_4 compounds produces the high Curie temperatures, metallic high conductivity and positive Seebeck effect[1].

The fact[9-13], that the spinel compounds $\text{CuCr}_2\text{X}_3\text{Y}$ ($X = \text{S}, \text{Se}$ or Te ; $\text{Y} = \text{Cl}, \text{Br}$ or I) exist, shows that the concentration of the itinerant *d*-holes, associated with ' Cu^{2+} ions',

can easily be controlled by anion doping. It is for this reason that the present study was undertaken, and new and significant results now have been obtained which manifest a strong correlation between the magnetic and electrical properties in the system $\text{CuCr}_2\text{Se}_{4-x}\text{Y}_x$.

Various and somewhat contradictory studies have been reported in the past for the compounds $\text{CuCr}_2\text{X}_3\text{Y}$. $\text{CuCr}_2\text{Se}_3\text{Br}$ has been shown by neutron diffraction[10] to have a ferromagnetic alignment of the Cr^{3+} spins and to have diamagnetic Cu^{1+} ions on the tetrahedral sites of the spinel lattice. It has been reported[14] that the crystallographic data on $\text{CuCr}_2\text{Se}_3\text{Br}$ is questionable and that the compound is 'too unstable to believe in its existence'. Electrical studies of the system $\text{CuCr}_2\text{Se}_{4-x}\text{Br}_x$ have indicated on one hand [11] that the metallic resistivity behavior at low values of *x* changes to semiconductive behavior at large value of *x*, while on the other hand[12] that the resistivity does not change as a function of *x* and temperature.

In the present study, the systems $\text{CuCr}_2\text{Se}_{4-x}\text{Br}_x$ and $\text{CuCr}_2\text{Se}_{4-x}\text{Cl}_x$, both polycrystals and single crystals, have been readily synthesized. Contrary to the results reported or suggested by other workers[11, 14], the compounds are not only stable at room temperature in air, but also have shown stable, reproducible and consistent magnetic and electrical properties.

2. EXPERIMENTAL RESULTS

(a) Sample preparation

By essentially the same method as that previously described [9, 13], the system $\text{CuCr}_2\text{Se}_{4-x}\text{Y}_x$ ($\text{Y} = \text{Br}$ and Cl) has been prepared both in powder form, by firing mixtures in evacuated sealed quartz tubes, and in single crystal form, by the closed tube vapor-transport method using a halogen carrier gas. Large single crystals (3–4 mm in size) of the bromine system near to the composition ($x = 1$) were also obtained by another vapor-transport method, in which the enclosing quartz ampoule was pulled through a thermal gradient as described separately [15].

The system $\text{CuCr}_2\text{Se}_{4-x}\text{Br}_x$ has been prepared in powder ($x = 0$ to 1) and single crystal ($x = 0.4$ to 1) forms. Wet chemical analysis [16] of the powder samples has shown that the actual compositions are the same as those intended within the experimental error of ± 1 per cent, which originates in the chemical analysis. It has been concluded that no excess-bromine compounds ($x > 1$) can be synthesized. Using the powder samples, the lattice parameter and the Curie temperature have been obtained as functions of composition, as shown in Figs. 1 and 2. Subsequently, the relationships, shown in Figs. 1 and 2, were applied as references to the small single crystals to determine their actual compositions*. Near $x = 1$, the great sensitivity of the physical properties to composition required that the compositions be labeled by Curie temperature.

Similarly, the system $\text{CuCr}_2\text{Se}_{4-x}\text{Cl}_x$ has been prepared in powder ($x = 0$ to 0.8) and single crystal ($x = 0.40$ to 0.55) forms. The main difference from the bromine system is that the synthesis of the compounds for $x = 1$ was not found to be possible. In fact, for the

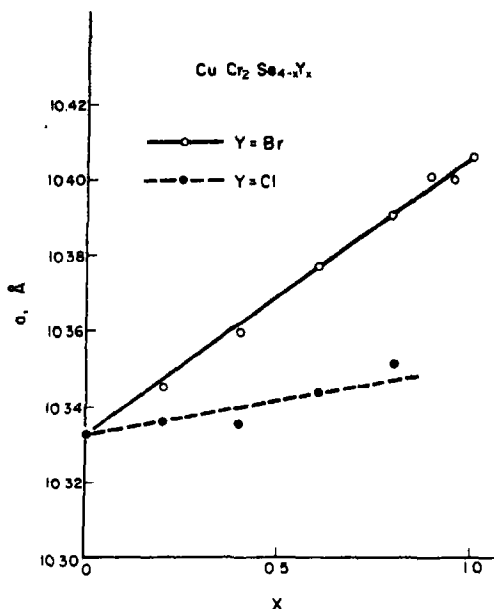


Fig. 1. Lattice constant vs. composition curves, measurement at room temperature.

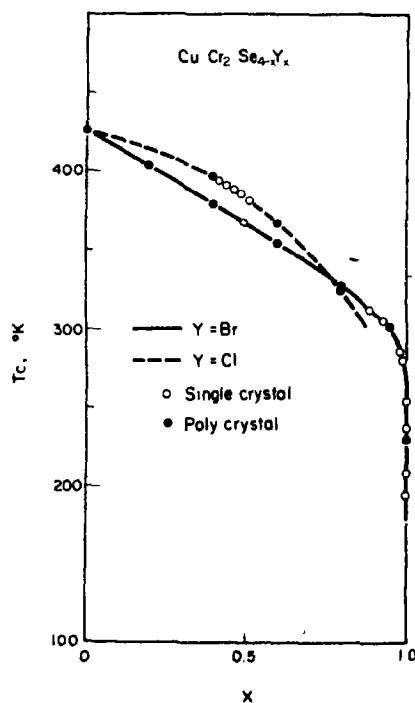


Fig. 2. Curie temperature vs. composition.

*Application of this calibration to the results of magnetic data previously reported [9] for single crystals of ' $\text{CuCr}_2\text{Se}_3\text{Br}$ and $\text{CuCr}_2\text{Se}_3\text{Cl}$ ' indicates that the actual composition of these early crystals are $\text{CuCr}_2\text{Se}_{3.50}\text{Br}_{0.50}$ and $\text{CuCr}_2\text{Se}_{3.22}\text{Cl}_{0.48}$, respectively.

single crystals, it was always found that $0.4 \leq x \leq 0.5$.

(b) Measurements and results

An X-ray analysis was made of all the samples prepared, which were found to be single-phase spinels. The lattice parameters determined for the two systems were found to be the same for polycrystals and single crystals, as given in Fig. 1. Vegard's law is followed indicating no unusual effect due to possible 1:3 ordering of the Br^- and Se^{2-} ions among the anion lattice sites. Although the physical properties were found to change very sharply near the composition $x = 1$, all the compounds near the composition $x = 1$ had essentially the same lattice parameter.

The Curie temperatures, determined from the kink point in extremely low fields, as previously described [17], are shown in Fig. 2. In both systems, the Curie temperature decreases monotonically with increasing values of x , but for the bromine system suddenly drops an equal amount, over 100 deg, in the small range $0.98 \leq x \leq 1.0$. This behavior of the Curie temperature near the value of $x = 1$ is unusual, and is one of the most significant facts discovered in this investigation. The Curie temperature sensitively depends on the method of synthesis, and the lowest observed Curie temperature is about 130°K.

The saturation magnetization is shown versus the compositional parameter in Fig. 3. In the bromine system, the moment increases linearly from $5 \mu_B/\text{mol.}$ to $6 \mu_B/\text{mol.}$ as x increases from 0 to 1 and is explained in terms of an antiparallel spin-polarized hole-band, with a linearly decreasing hole concentration (Cu^{2+}) in the system $\text{Cu}_1^{2+}{}_x\text{Cu}_x^{1+}\text{Cr}_2^{3+}\text{Se}_4^{2-}{}_x\text{Br}_x^{1-}$. However, in the chlorine system, the moment remains constant at $5 \mu_B/\text{mol.}$, independent of x which is not understood.

The ordinary transport properties (electrical resistivity, Hall effect and magnetoresistance) of the single crystals have been studied in order to better understand these compounds, and a strong correlation has been

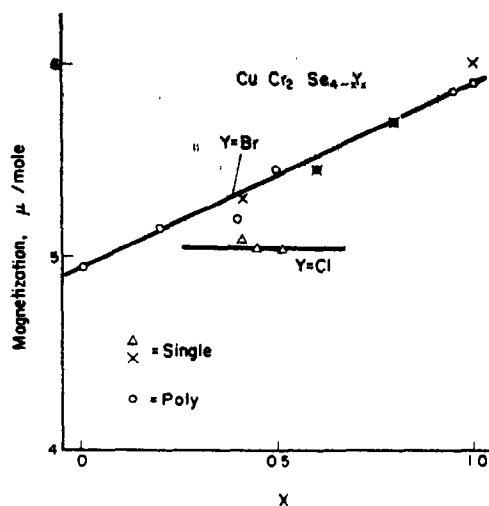


Fig. 3. Saturation magnetization vs. composition.

found between the Curie temperature and the electrical properties. Electrodes of evaporated indium, which gave good ohmic contacts, were used for these measurements. In order to make a good contact, between the sample surface and the evaporated indium thin films, it was always necessary to electron-polish the sample surface in a high vacuum before evaporation. All samples except $x \approx 0$ showed conduction due to surface contamination when they were left in the air, which is believed to have produced the anomalous results reported in the past. To avoid this, a thin film of high-polymer compounds was coated over the sample surface after the electrodes were established. Using the above technique of sample preparation, reliable and reproducible transport data were obtained. The d.c. resistivity was measured by the conventional four-probe method, and the Hall effect was measured using a.c. techniques (1 KHz) to avoid magnetoresistance effects and thermal noise.

The temperature dependence of the resistivity is very flat and shows no anomaly at the Curie temperature. The compositional dependence of the resistivity is shown in Fig. 4 showing clearly the change in magnitude going

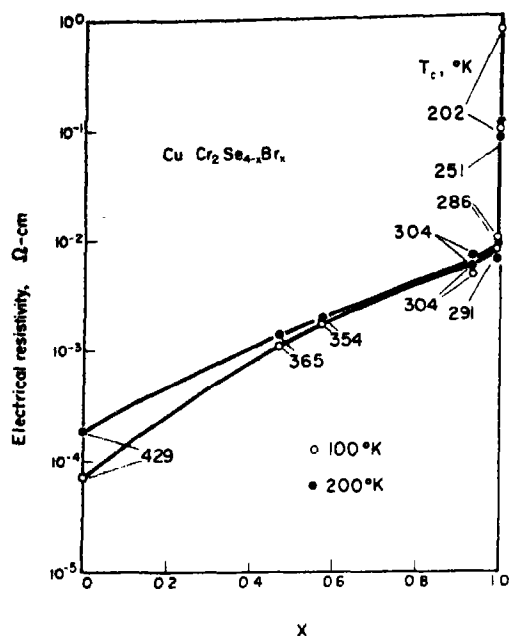


Fig. 4. Electrical resistivity vs. composition.

from metallic to semiconductive-type as x increases from zero to one. The very sharp increase in the resistivity, which occurs near the composition $x = 1$, obviously correlates with the sharp decrease in the Curie temperature over the same compositional range (Fig. 2).

The Hall voltage for the bromine system indicates p -type conductivity, and is, except near $x \approx 0$, proportional to the magnetization as shown for the example given in Fig. 5. The anomalous Hall coefficient, which can be determined at low enough temperatures and from high enough magnetic fields so that both the magnetization and the Hall voltage are nearly saturated, also shows a strong compositional dependence as shown in Fig. 6. The Hall coefficients observed for $x \approx 0$ were complex and anomalous and, therefore, are being reported separately [18]. The magneto-resistance of the stoichiometric $\text{CuCr}_2\text{Se}_3\text{Br}$ ($T_c = 202^\circ\text{K}$) is negative, and is of the order of 1 per cent.

The electrical resistivity of the $\text{CuCr}_2\text{Se}_{4-x}\text{Br}_x$

Cl_x system ($x = 0.40$ and 0.55) is metallic. The Hall effect is found to be very similar to that of the bromine system.

3. DISCUSSION

The most significant results of this study are those obtained for the bromine system, as shown in Figs. 2, 4, and 6, in which the Curie temperature, log electrical resistivity and log. anomalous Hall coefficient are shown vs. composition. If $\log \rho$ and $\log R'$ are plotted against Curie temperature a linear relationship is found which can be described by the following expressions:

$$\begin{aligned}\rho &= 30 \exp[-2.8 \times 10^{-2} \cdot T_c] (\Omega\text{-cm}) \\ R' &= 8 \cdot 10^{-6} \exp[-2.3 \times 10^{-2} \cdot T_c] (\text{V-cm}/ \\ &\quad \text{A-G}),\end{aligned}\quad (1)$$

which indicate that for the whole system $\text{CuCr}_2\text{Se}_{4-x}\text{Br}_x$, $0 \leq x \leq 1$, both the resistivity and Hall effect are dominated by the magnetic exchange interactions.

Although relatively simple relationships between ρ , R' and T_c exist, the almost discontinuous dependence of all these properties on composition near $x = 1$ is a main feature of the above experimental results. The sharp increase of T_c in the semiconducting region can be correlated with the increase in hole-carrier concentration and the slow variation of T_c correlated with metallic conductivity over the large range $0 \leq x \leq 0.98$.

For $0.98 \geq x \geq 1$, the exchange interactions and correlations between the holes would be negligibly small because of the low carrier density, and the spins of the itinerant holes will essentially interact only with the Cr^{3+} spins. The critical value of $x \approx 0.98$ implies that each hole interacts with about one hundred Cr^{3+} ions and does not significantly interact with other holes over a distance of 20 \AA . This indicates the itinerant character of the delocalized copper d -orbitals. On the other hand, for $0 \leq x \leq 0.98$, not only the exchange interactions between the holes and the Cr^{3+} spins, but also the exchange interactions and cor-

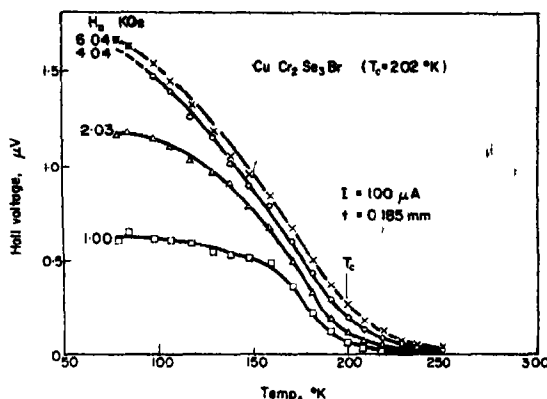


Fig. 5. Hall voltage vs. temperature for $\text{CuCr}_2\text{Se}_3\text{Br}$ ($T_c = 202^\circ\text{K}$).

relations between the holes, influence the magnitude of the antiparallel polarization of the hole-band.

Since a carrier concentration of only 2 per cent, per formula unit, is able to produce an increase of 100 deg in the Curie temperature

the holes must be strongly exchange-coupled to the localized Cr^{3+} spins. This is consistent with the measured low hole mobility ($\mu \approx 10 \text{ cm}^2/\text{Coulomb}$). In the system $\text{CuCr}_2\text{Se}_{4-x}\text{Br}_x$ ($x \approx 1$) all the A-sites are occupied by Cu^{1+} ions. Therefore, virtual transitions are a possibility from $\text{Cu}^+ + h^+$ to a metastable Cu^{2+} state, which would act as an intermediary to exchange-couple the holes to the Cr^{3+} spins. This mechanism is only possible when an itinerant hole can interact with a Cu^+ ion. It is probably more important how many Cu^+ sites are reached by each hole than a direct interaction with the Cr^{3+} sites.

The effect of the hole carrier concentration on the Curie temperature in the above system should be compared to systems in which CdCr_2Se_4 or HgCr_2Se_4 are the host crystals. When such compounds are Ag-doped the hole mobility is quite high, $\mu \approx 40 \text{ cm}^2/\text{Coulomb}$ at room temperature. Although the presence of hole carriers in these host crystals does increase the Curie temperature [19], the influence is an order-of-magnitude less in strength (a 2 per cent doping of Ag produces about a 10 deg increase in Curie temperature). Thus holes in *p*-type Cu-doped CdCr_2Se_4 can not uniformly increase the Curie temperature. Rather, in this case a magnetic two-phase system is produced [20, 21] in a crystallographically single-phase crystal.

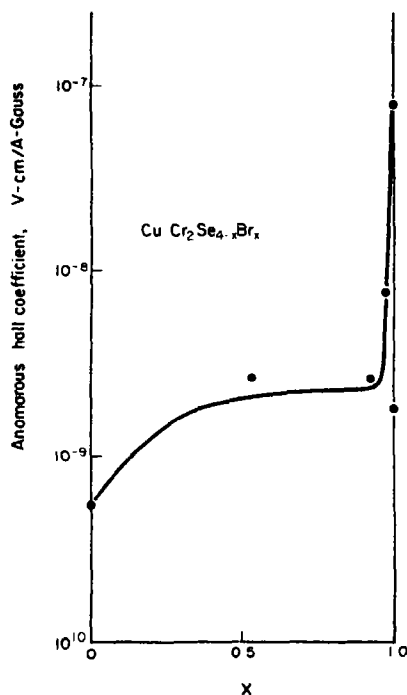


Fig. 6. Anomalous Hall coefficient vs. composition taken in high field.

At the present time no suitable theory has been developed for describing the case of the itinerant hole-band, which is polarized by being exchange-coupled to the localized Cr^{3+} spins. If such a theory can be developed, it should be possible to correlate the electrical and magnetic properties and to obtain a measure of the exchange interaction between the holes and localized spins.

Acknowledgements—The authors are glad to express their sincere thanks to Mr. K. Yoshikawa for assistance in the magnetic measurements and to Mr. K. Yoshida for assistance in the transport measurements. They are also indebted to Mr. S. Harada and Mr. T. Oka for assistance in the material synthesis, and to Mr. K. Ametani for the chemical analysis.

REFERENCES

1. LOTGERING F. K., *Proceedings of the International Conf. on Magnetism*, pp. 533, Nottingham, England (1964).
2. COLOMINAS C., *Phys. Rev.* **153**, 558 (1967).
3. ROBBINS M., LEHMANN H. W. and WHITE J. G., *J. Phys. Chem. Solids* **28**, 897 (1967).
4. YOKOYAMA H., WATANABE R. and CHIBA S., *J. phys. Soc. Japan* **23**, 450 (1967).
5. LOCHER P. R., *Solid State Commun.* **5**, 185 (1967).
6. KHOI L. D., *Solid State Commun.* **6**, 203 (1968).
7. SLEIGHT A. W., *Mat. Res. Bull* **2**, 1107 (1967).
8. GODDENOUGH J. B., *J. Phys. Chem. Solids* **30**, 261 (1969).
9. MIYATANI K., WADA Y. and OKAMOTO F., *J. phys. Soc. Japan* **25**, 369 (1968).
10. WHITE J. G. and ROBBINS M., *J. appl. Phys.* **39**, 664 (1968).
11. ROBBINS M., BALTZER P. K. and LOPATIN E., *J. appl. Phys.* **39**, 662 (1968).
12. SLEIGHT A. W. and JARRETT H. S., *J. Phys. Chem. Solids* **29**, 868 (1968).
13. WADA Y., OKAMOTO F., AMETANI K. and MIYATANI K., to be published.
14. LOTGERING F. K. and VAN STAPLE R. P., *Mat. Res. Bull* **3**, 507 (1968).
15. KATO K. and WADA Y., to be published.
16. AMETANI K., WADA Y. and OKAMOTO F., to be published.
17. MIYATANI K., *J. phys. Soc. Japan* **28**, 259 (1970).
18. MIYATANI K. and MINEMATSU K., to be published.
19. MINEMATSU K., MIYATANI K. and TAKAHASHI T., *International Conference on Ferrite*, Kyoto, 1970.
20. LOTGERING F. K., *J. Phys. Chem. Solids* **29**, 699 (1968).
21. MIYATANI K., to be published.

DOUBLE CONVERSIONS BETWEEN PbS-SINGLE CRYSTALS AND POLYCRYSTALLINE CdTe IN SOLID STATE*

V. LEUTE and A. JAMOUR

Institut of Physical Chemistry, University of Munich, Germany

(Received 21 August 1970; in revised form 5 October 1970)

Abstract—The mechanism of the solid state reaction between a PbS-crystal and polycrystalline CdTe is investigated by use of an electron microprobe. It can be shown that the reaction is composed of an interdiffusion of Pb and Cd and of a diffusion of Cd and Te in the same direction.

The kinetics of this reaction are described by a parabolic time law $P = kt$ with $K = 6.6 \cdot 10^{-3} \exp(-21000/RT)$ [cm²/sec].

IN THIS paper the mechanism of the solid state reaction between PbS and CdTe is investigated by means of optical microscopy and by use of an electron microprobe.†

The PbS-crystals used for the reaction are grown from the melt in a quartz apparatus in a steady flow of H₂S. Polycrystalline CdTe (puriss. Fluka) was used as the other reactant. Small PbS-cubes (about 1 mm³) with microscopically smooth planes (001), produced by cleaving larger crystals, were pressed into the polycrystalline matrix at a pressure of 8 t/cm² [1].

All the reactions were carried out between 400° and 450°C in a nitrogen atmosphere (99.9%, 1 atm).

On the one hand the thickness of product layers was determined by use of optical micrographs (magnification 500x) taken from ground and polished samples. On the other hand, in order to find out the chemical structure of these product layers the line scanning profiles were measured with a microprobe at right angles to the phase boundaries.

An acceleration voltage of 20 KV was used.

In Fig. 1(a, b, c) smoothed line scanning profiles for combinations of two elements

in each diagram are reproduced. The sample was heated 16 min at 450°C.

These profiles show that the reaction layer consists of two different regions i.e. next to the PbS-crystal is a heterogeneous layer containing all four components (Pb, Cd, S, Te) whereas the second layer next to the CdTe-matrix contains essentially only Pb and Te. This latter layer has a thickness of about 6 μm allowing a quantitative analysis using the X-ray intensities measured by microprobe.

In order to insure that this layer (X) really consists of pure PbTe the mass fractions $c_{Pb}^{(X)}$ and $c_{Te}^{(X)}$ were calculated for this layer (X) from the X-ray intensities measured in the pure reactants PbS and CdTe and in the product layer (X). These experimental mass fractions are compared to the theoretical values of pure PbTe.

$$c_{Pb}^{(X)} = f_{Pb} \cdot C_{PbS}^{PbS} \cdot \frac{(J_{Pb}^{(X)} - J_{Pb}^0)}{(J_{Pb}^{PbS} - J_{Pb}^0)}$$

and

$$c_{Te}^{(X)} = f_{Te} \cdot C_{CdTe}^{CdTe} \cdot \frac{(J_{Te}^{(X)} - J_{Te}^0)}{(J_{Te}^{CdTe} - J_{Te}^0)}$$

The correction factors $f_{Pb} = 1.14$ and $f_{Te} = 0.90$ are derived from measurements on pure standards of PbTe, PbS and CdTe [1].

*Part of the thesis of Anton Jamour, University of Munich.

†JXA-3 A JEOL.

J_{Pb}^{PbS} = Pb-intensity in pure PbS; J_{Te}^{CdTe} = Te-intensity in pure CdTe; $J_{Pb}^{(X)}$ = Pb-intensity in layer (X); $J_{Te}^{(X)}$ = Te-intensity in layer (X); J_{Pb}^0 = noise intensity; J_{Te}^0 = noise intensity. In this way the experimental values for the mass fractions in (X) are: $c_{Pb}^{(X)} = 0.61$ and $c_{Te}^{(X)} = 0.36$. The theoretical values for pure PbTe are $c_{Pb}^{PbTe} = 0.62$ and $c_{Te}^{PbTe} = 0.38$.

The satisfactory agreement between experimental and theoretical values show that the layer (X) consists of nearly pure PbTe. In the heterogeneous two phase layer an analysis of this kind is impossible, because the homogeneous regions of the two phases have dimensions of only about $1\text{ }\mu\text{m}$. Because of the finite beamdiameter ($\approx 1\text{ }\mu\text{m}$) in the microprobe this layer always gives intensities which are too low. But from the fact that in

this layer the maxima of Pb always coincides locally with the maxima of Te and with the minima of Cd and S (and vice versa), we must conclude that this heterogeneous product layer is a microcrystalline mixture of the reaction products PbTe and CdS.

Optical microscopy and growth kinetics

Figure 2 also shows clearly the separation of the product layer into two partial layers.

Growth measurements of the layer thickness at 400° , 425° and 450°C show that this reaction is governed by the parabolic time law $l^2 = Kt$.

In Fig. 3 the thickness of the whole product layer i.e. the sum of the thickness of both partial layers is plotted quadratically vs. reaction time. The ratio of thickness of the

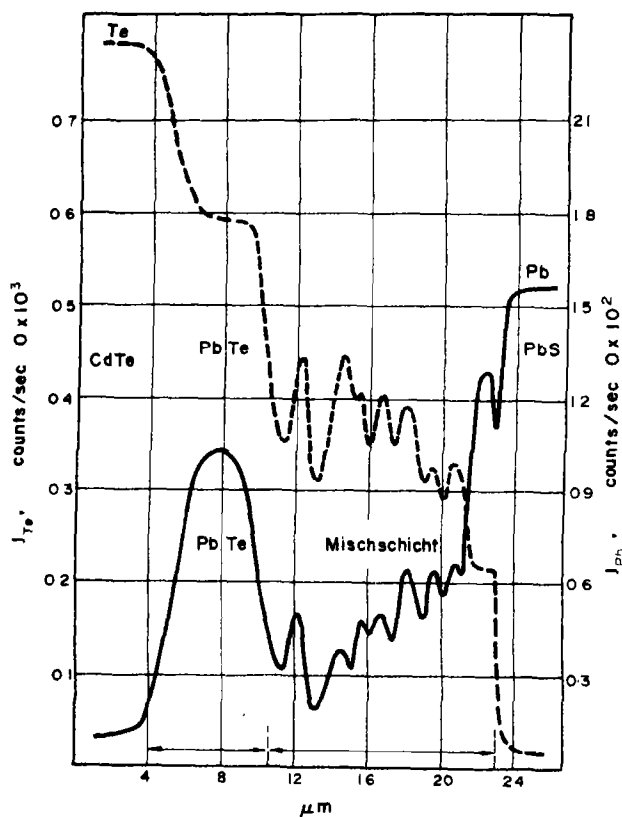


Fig. 1(a).

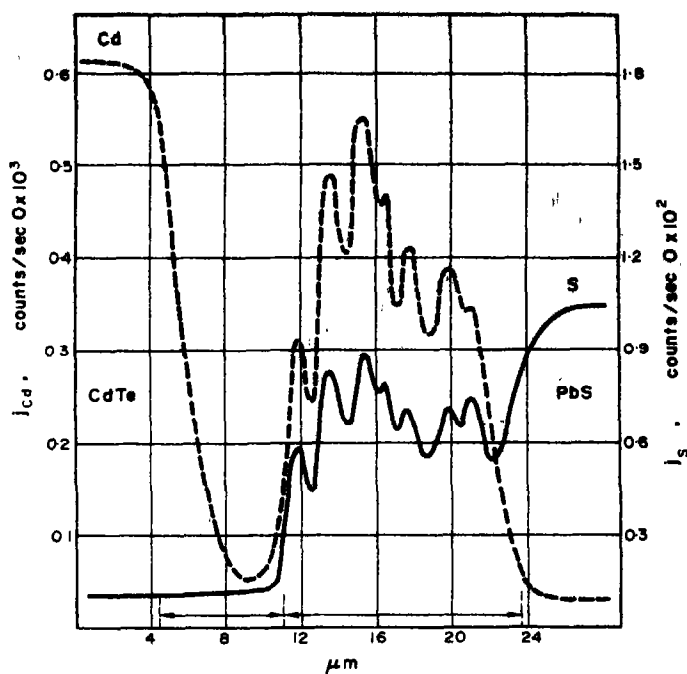


Fig. 1(b).

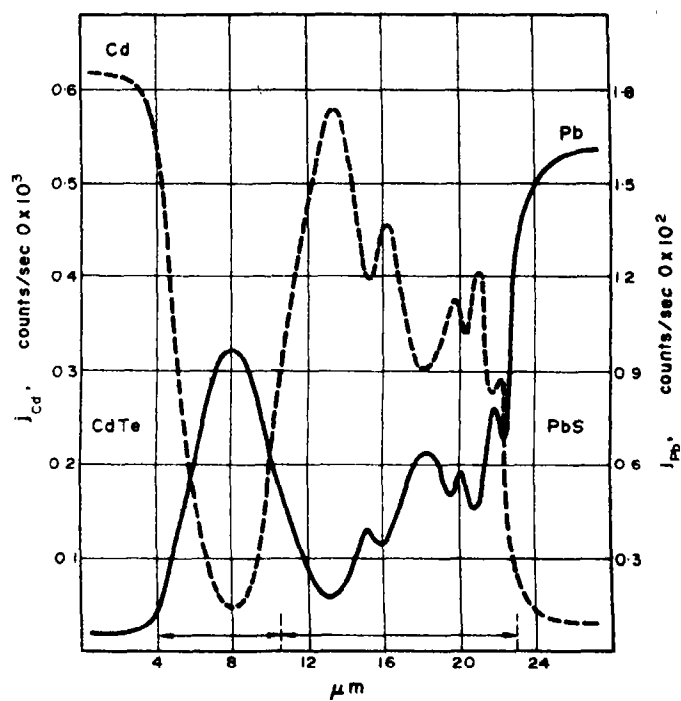


Fig. 1(c).

Fig. 1. Elementspecific X-ray intensities as function of a geometrical coordinate at right angles to the phase boundaries between the reactants (line-scanning-profiles) taken from a sample which was heated 16 min at 450°C. (a) Pb- and Te-profiles, (b) Cd- and S-profiles, (c) Cd- and Pb-profiles.

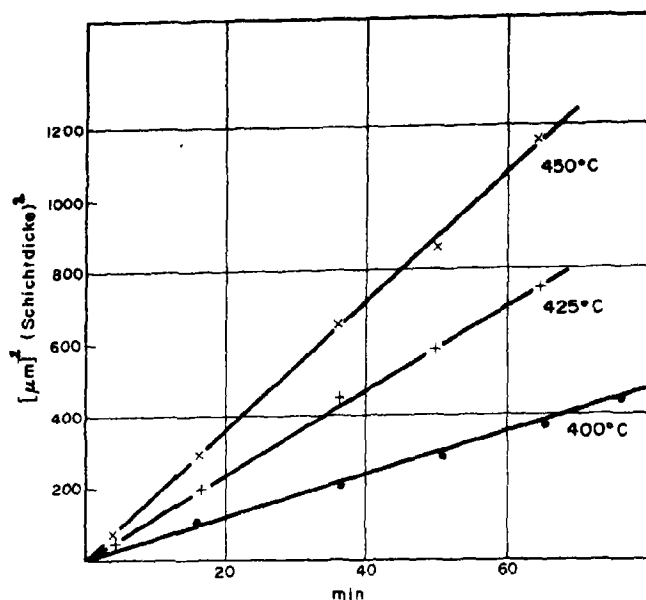


Fig. 3. Square of total layer thickness as function of reaction time for different temperatures.

two partial layers in the whole range of measurements is:

$$d_{\text{PbTe}}/d_{(\text{PbTe}+\text{CdS})} \approx \frac{1}{2}.$$

Within the range of accuracy of measurements, PbS crystals containing 3 per cent of weight CdS yield the same velocity of layer growth as pure PbS-crystals.

For the time law the parable constant is:

$$K = K_0 \exp(-E/RT)$$

$$= 6.6 \cdot 10^{-3} \exp(-21000/RT) \text{ [cm}^2\text{/sec]}.$$

The error in the activation energy is about ± 1500 [cal/Mol].

DISCUSSION

Former measurements[1] on polycrystalline PbS at 335°C showed that there are practically two separated partial layers consisting of PbTe and CdS, as long as the reaction layers are very thin. (see also the reaction between

PbS and CdO[2]). This means that the succession of layers is:



The fact that exactly this order and not



is obtained, means that at the beginning of the reaction the metals exchange faster between PbS and CdTe than the chalcogens do. This is understandable because of the size proportions of the ions or atoms in the lattices.

In the rocksalt lattice of the PbS-crystal a substitution of the large Pb-ions by the smaller Cd-ions occurs considerably easier than a substitution of S-ions by the much larger Te-ions. (Ionic radii[3]: $r_{\text{Pb}^{2+}} = 1.21 \text{ \AA}$; $r_{\text{Cd}^{2+}} = 0.97 \text{ \AA}$; $r_{\text{Te}^{2-}} = 2.21 \text{ \AA}$; $r_{\text{S}^{2-}} = 1.84 \text{ \AA}$).

On the other hand in CdTe crystallizing in the zincblende lattice the effective charges of the ions are considerably smaller than in PbS[4] and, therefore, the tetraedric co-

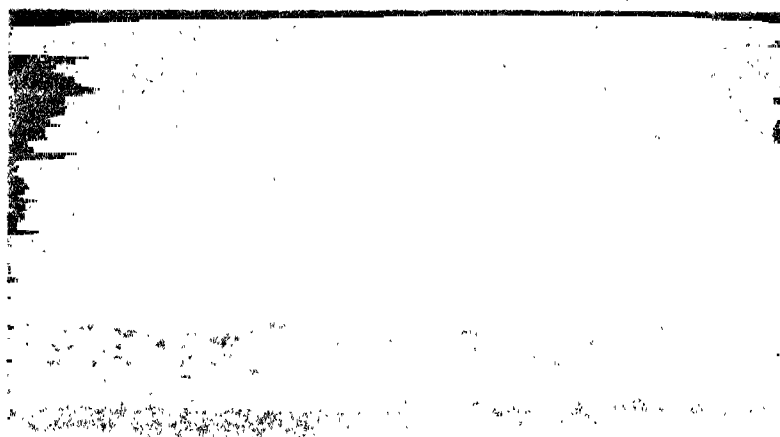


Fig. 2. Product layers formed during the reaction between a PbS-single crystal and polycrystalline CdTe after a heating time of 64 min at 400°C, bright zone = PbTe-layer; dark-spotted zone = heterogeneous layer consisting of (PbTe + CdS); Magnification $\approx 750\times$.



Fig. 4. Product layer formed during the reaction between polycrystalline CdTe and polycrystalline PbS after a heating time of 30 min at 400°C; bright zones = PbTe; dark zone = CdS; Magnification $\approx 750\times$.

valent radii must be used for CdTe instead of ionic radii. This means that in the CdTe lattice Cd and Pb require about the same volume. (Tetrahedric covalent radii[3]: $r_{\text{Pb}} = 1.46 \text{ \AA}$; $r_{\text{Cd}} = 1.48 \text{ \AA}$; $r_{\text{S}} = 1.04 \text{ \AA}$; $r_{\text{Te}} = 1.32 \text{ \AA}$). Therefore in CdTe an exchange of Cd for Pb will cause a much lower distortion of the zincblende lattice than an exchange of Te for S will do.

According to these considerations the following mechanism is supposed for the beginning of the reaction: In both the PbS- and CdTe-lattices interdiffusion of Pb and Cd is favoured. Cadmium diffuses into the PbS-crystal until at its phase boundary to the matrix the crystal is supersaturated with CdS. As a consequence nuclei of the new CdS-phase are formed. These finally grow together forming a continuous product layer of CdS. In the same way a supersaturation of the CdTe boundary layer with PbTe, reached by substitution of Cd by Pb, causes the formation of a PbTe-layer. The fact that for PbS-crystals containing 3% CdS the same velocity of layer growth as for pure PbS-crystals is observed, means that the nucleation of the CdS-product phase cannot be the rate determining step. Therefore most probably the reaction rate is determined by the interdiffusion of cations in one of the reaction layers.

From the described experimental results it is concluded that in the further progress of the reaction with growing layer thickness the pure CdS-layer is replaced by the heterogeneous microcrystalline layer, consisting of a mixture of CdS and PbTe. This process can be interpreted as a consequence of an additional 'rectified' diffusion of Cd and Te in the same direction (Fig. 5).

If the CdS-partial layer contains no Pb, it can dissolve up to 2% CdTe[5] corresponding to the limit of solubility. In this case a further progress of the reaction by diffusion of Te would be possible only by exchange of anions with the neighbouring PbS-phase leading to the formation of a second PbTe-layer situated

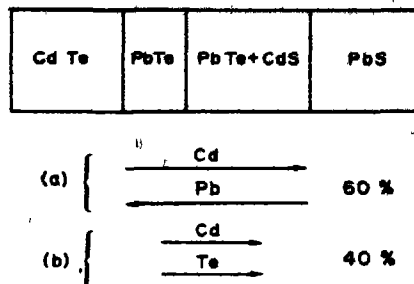


Fig. 5. Succession of layers resulting from the superposition of the two diffusion mechanisms; (a) interdiffusion of Cd and Pb, (b) 'rectified' diffusion of Cd and Te.

between the PbS-crystals and the CdS-product layer. Under certain conditions such a reaction type will be attained (Fig. 4). But in the reactions with PbS-single crystals between 400° and 450°C the CdS-phase contains considerable concentrations of Pb because of the interdiffusion of cations. Therefore the product of solubility of PbTe in this CdS-layer will be reached and exceeded resulting in the formation of PbTe-nuclei inside the CdS-layer.

During the whole reaction time the PbTe-partial layer is preserved as a homogeneous phase. This means that the S-ions do not show any considerable diffusion in the investigated temperature range. This is likely caused by the relatively high lattice energy of the sulfides.

The total diffusion process leading to formation of the observed succession of layers



may be interpreted as a superposition of an interdiffusion of Pb and Cd and a 'rectified' diffusion of Cd and Te. The contribution of these two diffusion processes to the total reaction may be estimated from the ratio of thickness of the two partial layers.

If x and y specify the number of moles of reactants participating in the interdiffusion of Pb and Cd respectively of Cd and Te, and

V_{CdS} and V_{PbTe} are the mole volumina of the product phases concerned, then ratio r of the layer thickness is

$$r = d_{(\text{CdS} + \text{PbTe})} / d_{\text{PbTe}} \\ = \{V_{\text{CdS}}(x + y) + V_{\text{PbTe}}\} / x \cdot V_{\text{PbTe}}$$

$$V_{\text{PbTe}} = 40.2 \text{ [cm}^3\text{/mol];}$$

$$V_{\text{CdS}} = 29.7 \text{ [cm}^3\text{/mol].}$$

With the measured value of $r_{450^\circ\text{C}} \approx 2$ one obtains $x/y \approx 1.38$. This means that the fraction a , contributed by interdiffusion of Cd and Pb to the reaction is

$$a = x/(x + y) \approx 0.58. \quad (1)$$

In the same way for the 'rectified' diffusion of Cd and Te

$$b = y/(x + y) \approx 0.42. \quad (2)$$

That is, the two diffusion mechanisms (1) and (2) participate in the total solid state reaction to about 60 per cent respectively 40 per cent.

The high reaction rate of this double conversion might suggest that a transitory liquid phase would be present during the reaction. Indeed the CdTe used for reaction shows some isolated microscopic precipitates of elementary Te and therefore at the sites where these precipitates touch the PbTe-layer we really must take into consideration small localised melting-zones leading to irregularities in the reaction layer. These localised liquid phases however can not be characterising for the whole reaction process.

At lower temperatures ($< 300^\circ\text{C}$) the chalcogenides do not show any considerable solubility for the elements concerned. Consequently after quenching regularly distributed precipitates of elementary chalcogens or metals must be found in at least one of the two product layers if at reaction temperatures a nonstoichiometric liquid phase would contribute to the normal growth of the reaction layers. Besides the isolated Te-precipitates in the PbTe-partial layer, already mentioned, no elementary precipitates however are determinable by microscope or microprobe.

Consequently the high velocity of layer growth must be attributed to a high mobility of ions in the reaction layer and not to any transitory liquid phase. As in both partial layers the transport of ions can occur mainly by diffusion in a PbTe-phase this high velocity seems to be not unreasonable because of the low activation energy for tracer diffusion of Pb in PbTe of only 13.8 Kcal/Mol. [6].

Acknowledgement—This research was supported by the Deutsche Forschungsgemeinschaft.

REFERENCES

1. LEUTE V., *Doppelte Umsetzungen im festen Zustand*, Abhandlungen der Bayer. Akademie der Wissenschaftern, Neue Folge, Heft 140, München (1969).
2. LEUTE V. and KALB A., *Z. Phys. Chem. N.F.* **69**, 88 (1970).
3. LANDOLT-BÖRNSTEIN, *Zahlenwerte und Funktionen* **14**, 527 (1955).
4. SUCHET J. P. and BAILLY F., *Ann. Chim.* **10**, 517 (1965).
5. VITRIKHOVSKII N. J. and MIZETSKAYA J. B., *Soviet Phys. solid State* **1**, 192 (1959).
6. BOLTAKS B. J. and MOKHOV Y., *J. tech. Phys. USSR* **28**, 1046 (1958); *ibid* **26**, 2448 (1956).

MAGNETIC SUSCEPTIBILITY AND TRIANGULAR EXCHANGE COUPLING IN THE TOURMALINE MINERAL GROUP

T. TSANG and A. N. THORPE

Howard University, Washington, D.C. 20001, U.S.A.

G. DONNAY

Geophysical Laboratory, Carnegie Institution of Washington, Washington, D.C. 20008, U.S.A.

and

F. E. SENFTLE

Building 104, U.S. Geological Survey, Washington, D.C. 20242, U.S.A.

(Received 25 September 1970)

Abstract—Magnetic susceptibilities of three iron-rich tourmaline crystals from Mexquitic (Mexico), Pierpont (New York), and Madagascar with different and known chemical compositions have been studied from 8° to 300°K. The iron atoms in the tourmaline crystal structure, space group $R3m$, $a \sim 15.9$, $c \sim 7.2$ Å, are situated at the three corners of an equilateral triangle and are close enough for magnetic exchange interaction. For buergerite, the Mexquitic sample, the susceptibility data lead to an exchange constant J/k of 7.5°K. Although the amount of aluminum would be sufficient to fill point position 18(c) exactly, the magnetic data are consistent with some substitution of ferric iron for aluminum, as previously determined from X-ray and neutron diffraction studies. Some aluminum thus replaces iron in position 9(b). Exchange constants were also estimated for the other two magnesium-iron specimens, of which the Madagascar sample is aluminum deficient. The results agree with the evidence from optical spectra that there is considerable deviation from octahedral symmetry in the oxygen coordination polyhedra about the 9(b) and 18(c) point positions.

1. INTRODUCTION

THE TOURMALINE group of minerals, well known for its wide range of chemical composition[1], has ferrous and ferric iron end members, both of which are of magnetic interest. The former is the very common variety schorl, of ideal composition $\text{NaFe}_3^{2+}\text{B}_3\text{Al}_6\text{Si}_6\text{O}_{27}(\text{OH},\text{F})_4$, for which a crystal-structure refinement has not yet been reported; the latter is a rarer and only recently discovered variety, buergerite[2], with ideal formula $\text{NaFe}^{3+}_3\text{B}_3\text{Al}_6\text{Si}_6\text{O}_{30}(\text{F},\text{OH})$, for which precise X-ray and neutron structure determinations have been carried out[3, 4].

In the tourmaline-type structure[5], the position occupied by the variable cation, whose chemical nature is used to designate the mineral variety, occupies Wyckoff position 9(b) of point symmetry m in space group $R3m$, where the unit cell is referred to an

R -centered hexagonal lattice. The iron atoms in the case of schorl and buergerite, the magnesium atoms in dravite, the lithium and aluminum atoms in elbaite, thus outline equilateral triangles about the 3-fold axes which lies parallel to the z -direction and have x and y coordinates: $0,0; \frac{1}{3}, \frac{2}{3}; \frac{2}{3}, \frac{1}{3}$. The edges of the metal triangles are $\frac{1}{3}ax$, where for buergerite, a , the cell edge, is $15.869(2)^*\text{Å}$, and x , the atomic x coordinate for the cation, is $0.13320(8)$. This results in an Fe-Fe distance of 3.185Å , a distance small enough to cause exchange interactions (Fig. 1). In actual mineral specimens, some substitution of Al in position 8(c), by Fe also takes place, so that additional Fe-Fe interactions of measurable magnitudes are expected. For

*Throughout the paper, a number in parenthesis following an experimental value represents one standard deviation and refers to the last decimal place quoted.

buergerite the atomic coordinates of this 18(c) position are 0.299, 0.259 and 0.604 [3, 4].

We are here dealing with a mixed magnetic compound, similar to ardennite [6] but containing triangles rather than pairs of magnetic ions. We set out to test a treatment similar to the one used for ardennite, for the mineral group tourmaline. Preliminary results on tourmaline from room temperature to 77°K have been reported [7]. The only other magnetic measurements of tourmaline in the literature are those of Kruglyakova [8] on ten specimens from five different Russian local-

ities. The reported iron contents range from 0.3 to 13.8 weight per cent, and their measured susceptibilities increase from 1×10^{-6} to 31×10^{-6} emu/g. Since experimental details such as temperature of measurements and magnetic field strengths are not specified, the results are difficult to evaluate.

2. EXPERIMENTAL DETAILS

Of nine chemically distinct tourmaline specimens, on which we measured magnetic susceptibilities at room temperature with magnetic fields of differing strengths, only three were completely free from any trace of ferromagnetism. The common magnetic impurity in the tourmaline group is magnetite (Ingamells, pers. comm.). The other six

samples gave susceptibilities ranging from 12×10^{-6} to 21×10^{-6} emu/g at room temperature. These values fall in the median range of the data in the literature [8]. The three samples proved free of ferromagnetic inclusions were selected for detailed study down to 8°K.

A buergerite specimen from the type locality came from the same hand specimen as the crystals used for the chemical analysis (Table 1). The X-ray and neutron diffraction studies agree on the following structural way of writing the cell content (\square denotes vacant sites):

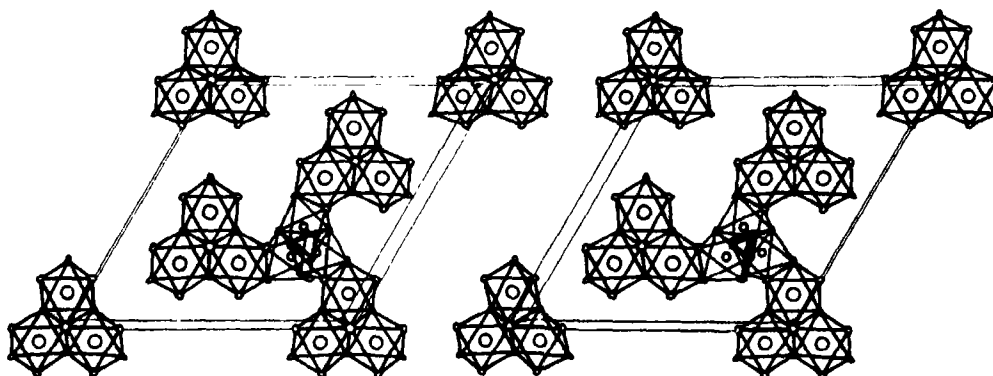
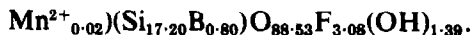
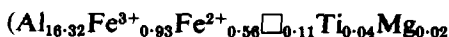


Fig. 1. Stereo view of the magnetic atoms in the tourmaline structure and their oxygen coordination polyhedra. Small circles in the centers of octahedra are Z-sites; large circles are Y-sites.



For the Pierpont sample, we converted the weight percents obtained (Table 1) to a cell content with Si + B ions equal to 27.00 per cell:

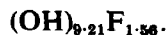
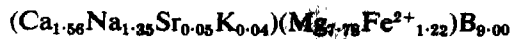
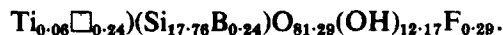
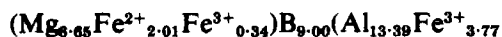


Table 1. Chemical analyses of tourmaline specimens studied

Variety specimen no. locality literature reference analyst.	Buergerite AMNH 35468 Mexquitic, Mexico [2] C. O. Ingamells	Dravite-Schorl USNM 116996 Pierpont, N.Y. [7] C. O. Ingamells	Dravite-Buergerite Harvard Collection Madagascar [19] T. Ito
Wt. % SiO ₂	33.86	35.88	34.57
Al ₂ O ₃	30.79	25.29	22.12
B ₂ O ₃	10.86	10.49	10.42
MgO	0.13	10.43	8.69
Fe ₂ O ₃	17.62	3.16	10.63
FeO	1.27	5.78	4.70
TiO ₂	0.55	0.74	1.56
MnO	0.13	0.02	trace
CaO	0.69	3.07	2.36
Na ₂ O	2.46	1.39	1.41
SrO	trace	0.19	not reported
K ₂ O	0.07	0.06	0.10
BaO	trace	0.01	not reported
H ₂ O ⁺	0.40	2.76	3.55
F	1.86	0.98	0.18
	100.69	100.25	100.29
O ₂ = F ₂	0.78	0.41	0.08
Total	99.91	99.84	100.21

Ionic size considerations suggest that ferrous ions are combined with magnesium on the 9(b) position and that ferric ions as well as the remainder of ferrous, the titanium and the manganous ions be made to substitute for aluminum in the general 18(c) position. For the Madagascar sample, beginning with the chemical data in the literature (Table 1) and calculating the cell content as above, we obtain:



Single-crystal fragments, about 20 mg in weight and oriented on the X-ray precession camera, had their magnetic susceptibilities $\chi_{||}$ and χ_{\perp} measured with their c axis aligned parallel and perpendicular to the applied magnetic field (Figs. 2, 3, and 4). The Faraday method at 5000 oe was used from 300 down to 8°K with a quartz helical spring [9, 10].

Temperature measurements were made with an Au-Co vs. Au-Ag thermocouple above 16°K, and with a calibrated carbon resistor below 16°K.

3. THEORETICAL DISCUSSION

For convenience the general cell content for tourmaline may be written $X_3Y_9Z_{18}B_9Si_{18}O_{83-x}(\text{OH},\text{F})_x$ where $X = \text{Na}, \text{Ca}, \text{K}$ or \square ; $Y = \text{Mg}, \text{Fe}, \text{Li}, \text{Al}$, etc.; and $Z = \text{Al}, \text{Fe}, \text{Ti}$, etc. (The X, Y, Z point positions are sometimes denoted by a, b, c , respectively [11], which refers to the Wyckoff letter of their point positions). The space group $R3m$ provides a ninefold position Y of point symmetry m for the most variable group of cations, which commonly includes the magnetic atoms, primarily Fe^{2+} and Fe^{3+} ions.

The magnetic ions occupy predominantly Y_9 and in smaller amounts Z_{18} sites. The Y sites form magnetically isolated equilateral triangles [5, 11, 12, 13]. Insofar as there is only short range order within the triangles and no significant long range order between triangles,

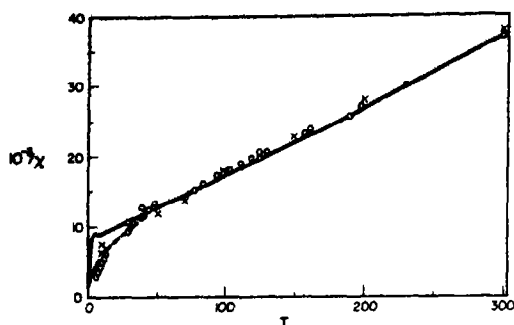


Fig. 2. Reciprocal magnetic susceptibility (emu/g) vs. temperature (°K) for buergerite. Solid curve, calculated, with all Fe-ions on Y-sites; dashed curve, calculated, with 10 per cent of Fe-ions on Z-sites.

no magnetic transitions are expected. For buergerite the lengths of the sides of the triangles are 3.185 Å. In addition to the two nearest neighbor Y-sites in the triangle, each Y-site has two nearest neighbor Z-sites at 3.2 Å. Each Z-site has one nearest neighbor Y-site at 3.2 Å and also four neighboring Z-sites at an average distance of 3.6 Å. We expect exchange coupling to take place between these nearest neighbor pairs. The exchange interaction for YY, ZZ and YZ nearest neighbor pairs will be denoted as J , J' and J'' respectively. Most Fe^{3+} and Fe^{2+} ions are expected to be located on Y-sites, so that we can expect the susceptibility behavior of buergerite to be quite unambiguous, as we are dealing with isolated three,

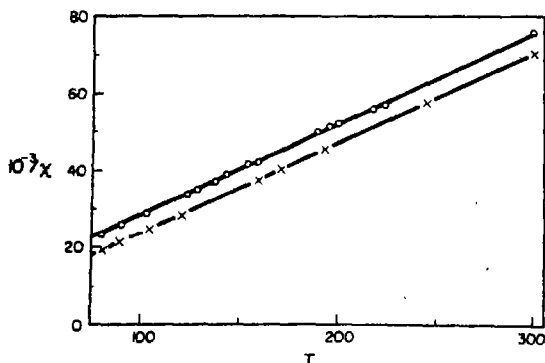


Fig. 3. Reciprocal magnetic susceptibility (emu/g) vs. temperature (°K) for the Pierpont sample (crosses, $H \parallel C$; circles, $H \perp C$).

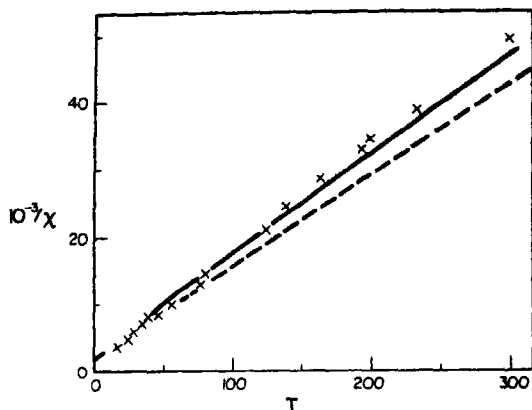


Fig. 4. Reciprocal magnetic susceptibility (emu/g) vs. temperature (°K) for the Madagascar sample. Dashed curve, spin-only behavior; solid curve, calculated from different exchange constant (see text).

two or single magnetic ion systems. Furthermore, because of the high $\text{Fe}^{3+}/\text{Fe}^{2+}$ ratio in buergerite, the susceptibility of buergerite is primarily determined by the Fe^{3+} ion, with a half-filled $3d^5$ shell which is little influenced by crystal fields and surroundings; susceptibility should follow the isotropic spin-only behavior rather closely with $S = \frac{5}{2}$. Optical studies of Fe^{2+} in tourmaline[14] have shown large distortions from octahedral symmetry of the environment about Y- and Z-positions, thus the orbital degeneracy is removed[16]; at room temperature and below, only the ground orbital singlet state is populated, and Fe^{2+} ion may be approximated by the spin-only behavior with $S = 2$. It is reasonable, therefore, to use the Heisenberg exchange interaction between two magnetic ions from the same triangle.

As a first approximation for buergerite, we shall consider the model that all Fe^{3+} and Fe^{2+} ions are randomly distributed on Y-sites. From the chemical analysis, the probabilities of any Y-site being occupied by Fe^{3+} , Fe^{2+} , or nonmagnetic ions are $p_1 = 6.87/9 = 0.76$, $p_2 = 0.55/9 = 0.06$ and $p_3 = 1 - p_1 - p_2 = 0.18$ respectively. For random distribution, the probability of finding r Fe^{3+} ions, s Fe^{2+} ions and t nonmagnetic ions (where r , s , and t

are integers between 0 and 3 such that $r + s + t = 3$) on a given triangle is the coefficient of the term $\alpha^r \beta^s \gamma^t$ in the expansion of $(p_1 \alpha + p_2 \beta + p_3 \gamma)^3$. For example, let us consider three Fe^{3+} ions on the same triangle; the probability is $p_1^3 = 0.44$, and the Hamiltonian H is:

$$H = -g\mu H_z (S_{1z} + S_{2z}) + 2J(S_1 \cdot S_2 + S_2 \cdot S_3 + S_3 \cdot S_1) \quad (1)$$

with spins $S_1 = S_2 = S_3 = \frac{5}{2}$ for Fe^{3+} , $g = 2$, μ and H_z are the Bohr magneton and applied magnetic field respectively. We note that H can also be written in terms of the total angular momentum [15] $S = S_1 + S_2 + S_3$,

$$H = -g\mu H_z S_z + J(S \cdot S - S_1 \cdot S_1 - S_2 \cdot S_2 - S_3 \cdot S_3) = -g\mu H_z S_z + J[S(S+1) - (105/4)] \quad (2)$$

as

$$S_1(S_1+1) = S_2(S_2+1) = S_3(S_3+1) = 35/4.$$

When $H_z = 0$, the vectors S_1 , S_2 and S_3 couple together to form the total angular momentum vector S , with $S = \frac{3}{2}, \frac{5}{2}, \dots, \frac{9}{2}$, the degeneracies g_s are 2, 4, 6, 5, 4, 3, 2, respectively; the relative energy for the state S is $JS(S+1)$. In the presence of an applied field, the susceptibility of each level S is given by the spin-only formula, hence the contributions of all triangles with three Fe^{3+} ions to the susceptibility are given by:

$$\begin{aligned} x_m &= 3.1 \times 10^3 \chi_o \\ &= (3)(p_1^3)(Ng^2\mu^2/3kT) \\ &\quad \times [\sum_s g_s S(S+1)(2S+1) \\ &\quad \times \exp\{-KS(S+1)\}] \\ &\quad \div [\sum_s g_s (2S+1) \exp\{-KS(S+1)\}] \end{aligned} \quad (3)$$

where χ_o and χ_m are the gram and molar sus-

ceptibilities, the formula weight being 3.1×10^3 , $K = J/(kT)$, k and N are the Boltzmann constant and Avagadro's number respectively, and the factor of 3 is included because each mole of solid contains $3NY$ -site triangles.

The calculation is then repeated for all other possible configurations of the triangle ($2\text{Fe}^{3+} + \text{Fe}^{2+}$, $2\text{Fe}^{3+} + \text{nonmagnetic ion}$, etc.). The calculated susceptibility depends on only one parameter, the exchange interaction J , which is to be obtained from the comparison of observed and calculated susceptibility curves.

4. RESULTS AND DISCUSSION

The experimental susceptibilities $\chi_{||}$ (crosses) and χ_{\perp} (circles) of the buergerite, Pierpont, and Madagascar samples at various temperatures have been summarized in Figs. 2, 3, and 4 for crystals aligned with their c -axes parallel and perpendicular to the magnetic field. The only magnetic ions are Fe^{3+} and Fe^{2+} ; susceptibility contributions of small amounts of Mn and Ti will be neglected.

(a) The buergerite sample

The experimental susceptibilities, $\chi_{||}$ and χ_{\perp} , which are shown in Fig. 2, are not very different from each other, therefore justifying the use of the Heisenberg exchange interaction. Using $J/k = 7.5^\circ\text{K}$, the calculated susceptibilities are shown as the solid line in Fig. 2, where $1/\chi_o$ is plotted vs. T . The overall agreement is good except for the low temperature region below 50°K . It turned out to be impossible to fit both low- and high-temperature data with a single exchange parameter J .

Structural refinements on buergerite [3, 4] have shown that approximately 8 per cent of Z -sites are filled by Fe, although the chemical analysis shows sufficient Al to completely fill the Z -position. This indication has also been supported by optical studies [13]. Apparently, the preferences for Y - and Z -positions are determined only approximately and not rigorously by the bond type,

the ionic radius, and charge considerations.

Let us now assume that 90 and 10 per cent of the magnetic ions are distributed on *Y*- and *Z*-sites respectively. Then approximately 75 per cent of the *Y*- and 4 per cent of the *Z*-sites are occupied by magnetic ions. The susceptibility contributions from *Y*-sites can be calculated as before with a slightly different value of the probability. Each *Z*-site has one nearest neighbor *Y*-site at 3.2 Å. Approximately 25 per cent of the magnetic ions on the *Z*-sites are therefore isolated, and the other 75 per cent form a pair of magnetic ions with their *Y*-neighbor. The calculated susceptibilities, using the same $J/k = 7.5^\circ\text{K}$ and assuming J'' to be the same as J , are shown by the dashed line (Fig. 2) and are in better agreement with the experimental data.

It appears that the magnetic susceptibility data of buergerite are compatible with the X-ray and neutron evidence [3, 4] and that about 10 per cent of the iron ions are on *Z*-sites, even though there are enough Al ions present to fill the *Z*-position. From the susceptibility data the exchange interaction, J/k was found to be approximately 7.5°K between nearest neighbor *Y*-sites.

(b) The Pierpont sample

The experimental susceptibilities of the Pierpont sample, which are summarized in Fig. 3, are anisotropic. The spatial average, $\bar{\chi} = (\chi_{\parallel} + 2\chi_{\perp})/3$, agrees well with the Curie-Weiss law,

$$\bar{\chi}_0 = C/(T + \theta). \quad (4)$$

Least-squares fit gives $C = 4.29 \times 10^{-3}$ emu $^\circ\text{K/g}$ and $\theta = 9^\circ\text{K}$. Using the amount of Fe^{3+} and Fe^{2+} given by the chemical analysis, the spin-only behavior ($S = \frac{5}{2}$ and 2 for Fe^{3+} and Fe^{2+}) gives $C = 4.15 \times 10^{-3}$ emu $^\circ\text{K/g}$, in agreement with the experimental data. Optical studies of Fe^{2+} in tourmaline [14] have detected rather large distortions from octahedral symmetry of the iron environments at both *Y*- and *Z*-sites; hence the orbital degeneracies

will be removed, and only the lowest orbital singlet will be populated at room temperature and below. The agreement of our magnetic susceptibilities with the spin-only behavior supports this conclusion.

In the Pierpont sample, for which no structural data are available, we deduce from the assumed formula that 14 at.% of the *Y*-sites and 13 at.% of the *Z*-sites are occupied by iron atoms, ignoring the Ti and Mn contributions. Assuming random distribution, the total exchange interaction 'felt' by magnetic ions at *Y*- and *Z* sites are $0.28J + 0.26J''$ and $0.52J' + 0.14J''$ respectively. About $\frac{1}{3}$ and $\frac{2}{3}$ of the magnetic ions are at *Y*- and *Z*-sites of the Pierpont sample. The weighted average exchange interaction per magnetic ion is $J_{av} = 0.09J + 0.35J' + 0.18J''$. For spin-only behavior, θ is related to J_{av} by:

$$\theta = 2S(S+1)J_{av}/3k \quad (5)$$

where $S = \frac{5}{2}$ and 2 for Fe^{3+} and Fe^{2+} . Using the average $S(S+1) = 7$, $\text{Fe}^{2+}/\text{Fe}^{3+} \approx 2$ and $\theta = 9^\circ\text{K}$, we get $J_{av}/k = 2^\circ\text{K}$. Assuming that the structures of Pierpont and buergerite samples are similar and using $J/k = 7.5^\circ\text{K}$, then we get $(2J' + J'')/k = 8^\circ\text{K}$. Because of the longer distances between nearest neighbor *YZ* and *ZZ* pairs, we expect J'/k and J''/k to be somewhat smaller than $J/k = 7.5^\circ\text{K}$.

We attribute the anisotropy of the magnetic susceptibility to crystal field effects on the ferrous ions. For axial distortions from octahedral environmental symmetry, Tinkham [16] has verified the splitting of the lowest $S = 2$ spin quintuplet by a perturbation of the form S.D.S. Following Tinkham's notation for isolated Fe^{2+} ions, with the ground states described by $S_z = \pm 2$, the susceptibilities are:

$$(\chi_m)_{\parallel} = (2N\beta^2/kT) \{4g^2 + g^2 \exp(-3\xi)\} / \{2 + 2 \exp(-3\xi) + \exp(-4\xi)\} \quad (6)$$

$$(\chi_m)_{\perp} = (2N\beta^2/kT) \{ \frac{3}{2}(g^2/\xi) [1 - \exp(-3\xi)] \}$$

$$+ (3g^2/\xi)[1 - \exp(-\xi)] \exp(-3\xi)] / \\ [2 + 2 \exp(-3\xi) \exp(-4\xi)]. \quad (7)$$

where $g = 2$ and $\xi = 3D_z/2kT$.

The magnitude of the splitting is characterized by the parameter D_z . Usually $\xi \ll 1$, and a power series expansion gives:

$$1/(\chi_m)_\parallel = (kT/2Ng^2\beta^2)(1 - 1.4\xi) \\ = (k/2Ng^2\beta^2)[T - 2.1(D_z/k)]. \quad (8)$$

$$1/(\chi_m)_\perp = (kT/2Ng^2\beta^2)(1 + 0.7\xi) \\ = (k/2Ng^2\beta^2)[T + 1.05(D_z/k)]. \quad (9)$$

For finite concentrations of magnetic ions, it is necessary to replace T by $T + \theta$. We therefore expect the plots of $1/\chi_\parallel$ vs. T and $1/\chi_\perp$ vs. T to be parallel straight lines, with the same slope but different intercepts. Such behavior has been observed in, for example, dilute $\text{Al}_2\text{O}_3\text{-Cr}^{3+}$ systems[17], where the parameter D_z has been measured independently. Also, $(\chi_o)^{-1} = \frac{2}{3}(\chi_\perp)^{-1} + \frac{1}{3}(\chi_\parallel)^{-1}$ is independent of D_z (since $\chi_\perp \approx \chi_\parallel$).

In Fig. 3, the two straight lines are calculated from $10^{-3}/\chi_o = (T + 22.6)/4.286$ for \mathbf{H} parallel to the c -axis and $10^{-3}/\chi_o = (T + 2.8)/4.286$ for \mathbf{H} perpendicular to the c -axis. The agreement with experimental data is acceptable.

(c) The Madagascar sample

Within the accuracy of our measurements, the experimental susceptibilities of the Madagascar sample are isotropic (Fig. 4). The ferrous to ferric atomic ratio for the Madagascar sample (Table 1) is much smaller than that of the Pierpont sample. From ionic radius and charge considerations, we also expect most Fe^{2+} ions to be at Y -sites, where the distortion from octahedral environmental symmetry and hence the value of D_z is smaller than that for the Z -sites. Also, the major distortion of the oxygen octahedron about the

Y -position is along the pseudo 4-fold axis $\text{O}_1\text{-O}_5$ which makes approximately a 65° angle with the c -axis in the tourmaline crystal structure, and thus further reduces the anisotropy. We therefore expect χ_\parallel to be equal to χ_\perp , an expectation born out by the experimental data.

A least-squares fit of the susceptibility data with the Curie-Weiss law, $(1/\chi_o) = (T + \theta)/C$, gives $C = 6.26 \times 10^{-3} \text{ emu}^\circ\text{K/g}$, $\theta = 9.2^\circ\text{K}$, whereas for the spin-only behavior, we expect $C = 7.38 \times 10^{-3} \text{ emu}^\circ\text{K/g}$ from the chemical analysis; as the total Fe concentration of the Madagascar sample is about twice that of the Pierpont sample, we expect $\theta \sim 18^\circ\text{K}$, twice the Pierpont value (9°K). The spin-only behavior is shown as the dashed line in Fig. 4, and does not agree with the experimental data. Susceptibilities calculated from the octahedral symmetry around Fe^{2+} [18] will give a value of C higher than $7.38 \times 10^{-3} \text{ emu}^\circ\text{K/g}$ and hence will give even worse agreement with experimental data.

Some deviation from Curie-Weiss behavior is expected, as we have two types of sites, Y and Z ; If the spins located on Y - and Z -sites are denoted as S_1 and S_2 , then the molecular field approximation, will be:

$$\langle S_i \rangle = [S(S+1)/3](g\mu H/kT) \\ + \sum_j [S(S+1)/3](2J_{ij}/kT)\langle S_j \rangle \quad (10)$$

for $i = 1, 2$ and $j = 1, 2$.

The exchange constants J_{ij} are proportional to J, J', J'' except for a weighting factor (approximately 26 at.% of the Y - and 21 at.% of the Z -sites are occupied by magnetic ions). By solving the two equations (10) ($i = 1, 2$) simultaneously, we calculate the susceptibility, which is a weighted average of $\langle S_1 \rangle/H$ and $\langle S_2 \rangle/H$. Previously, for the preceding two specimens we have estimated $J/k = 7.5^\circ\text{K}$ and $(2J' + J'')/k = 8^\circ\text{K}$. Using $J'/k = 1^\circ\text{K}$ and $J''/k = 6^\circ\text{K}$, the solid curve in Fig. 4 is obtained. It is in somewhat better agreement with the experimental data. For buergerite,

the nearest neighbor distances are 3.18, 3.2, and 3.6 Å, respectively, for YY, YZ, and ZZ pairs; we therefore expect $J > J'' > J'$.

5. CONCLUSION

By studying tourmaline single crystals of various compositions, it is possible to obtain information about the locations of magnetic ions in the crystal structure and the distortion of the oxygen coordination polyhedra about the magnetic ions. The buergerite sample contains very little Mg, and the Fe^{3+} to Fe^{2+} ratio is high. To a first approximation, the system may be represented by magnetically isolated Fe^{3+} triangles and the exchange constant J , between nearest neighbor Y-site pairs, can be evaluated accurately. Our results are consistent with the X-ray and neutron evidence[3] that, despite the presence of sufficient aluminum, a small fraction (about 10 per cent) of Fe-ions replaces Al on Z-sites. The lack of strong anisotropy, the large distances between Y-sites of different triangles, and the applicability of the Heisenberg exchange model suggest that one should not expect a magnetic contribution to the neutron diffraction pattern at low temperature. This is in agreement with recent neutron diffraction measurements[4]. For the Pierpont and Madagascar samples, it is possible to estimate the exchange interactions between YZ and ZZ-pairs. Our results are consistent with the optical spectra evidence[14] that there is considerable deviation from octahedral environmental symmetry at both Y and Z-sites.

Acknowledgements—The authors are grateful to Dr. C. Frondel, Harvard University, for the specimen from

Madagascar, to Dr. Brian Mason, U.S. National Museum, for other specimens and to Dr. Walter Hamilton, Brookhaven National Laboratory for the stereo photograph used in Figure 1. We are also thankful to Sherman White, Howard University, who assisted with the measurements.

REFERENCES

1. BRAGG W. L., *Atomic Structure of Minerals*, p. 40, Cornell University Press, Ithaca, New York (1937).
2. DONNAY G., INGAMALLS C. O. and MASON B., *Am. Mineral.* **51**, 198 (1966).
3. BARTON JR. R., *Acta crystallogr.* **B25**, 1524 (1969).
4. TIPPE A. and HAMILTON W. C., *Amer. Cryst. Assoc. Abstracts*, Ottawa meeting, August 1970.
5. DONNAY G. and BUERGER M. J., *Acta crystallogr.* **3**, 379 (1950).
6. THORPE A. N., SENFTLE F. E. and DONNAY G., *J. Phys. Chem. Solids* **30**, 2235 (1969).
7. DONNAY G., SENFTLE F. E., THORPE A. N. and WHITE S., *Carnegie Institute of Washington Yearbook* **65**, 295 (1967).
8. KRUGLYAKOVA G. I., *Miner. Mag. L'vov Geol. Soc.* **8**, 297 (1954).
9. SENFTLE F. E., LEE M. D., MONKEWICZ A., MAYO J. and PANKEY T., *Rev. scient. Instrum.* **29**, 429 (1958).
10. THORPE A. N. and SENFTLE F. E., *Rev. scient. Instrum.* **30**, 1006 (1959).
11. BUERGER M. J., BURNHAM C. W. and PEACOR D. R., *Acta crystallogr.* **15**, 583 (1962).
12. ITO T. and SADANAGA R., *Acta crystallogr.* **4**, 385 (1951).
13. BELOV N. V. and BELOVA E. N., *Dokl. akad. nauk SSSR* **69**, 185 (1949); **75**, 807 (1950).
14. WILKINS R. W. T., FARRELLE F. and NAIMAN C. S., *J. Phys. Chem. Solids* **30**, 43 (1969).
15. WUCHER J. and GIJSMAN H. M., *Physica* **20**, 361 (1954); SMART J. S., in *Magnetism* (Edited by G. T. Rado and H. Suhl) Vol. 3, p. 73. Academic Press, New York (1963).
16. TINKHAM M., *Proc. R. Soc., London* **A236**, 535, 549 (1956).
17. DAUNT J. G. and BRUGGER K., *Z. physik Chem. (Frankfurt)* **16**, 203 (1968); DAVIS H. L., *Z. Phys. Chem. (Frankfurt)* **16**, 213 (1968).
18. GRIFFITHS J. S., *The Theory of Transition Metal Ions*, Chapter 10, Cambridge Univ. Press (1961).
19. FRONDEL C., BIEDL A. and ITO T., *Amer. Mineral.* **51**, 1501 (1966).

EVALUATION OF SOME PHYSICAL QUANTITIES IN THE TWO PHASE REGION IN CUPROUS SELENIDE

B. ČELUSTKA and Z. OGORELEC

Institute "Rudjer Bošković" and Institute of Physics, Zagreb, Yugoslavia

(Received 13 July 1970; in revised form 14 September 1970)

Abstract—The change of electrical conductivity and thermal dilatation of cuprous selenide at its phase transition was examined. The behaviour of these properties was explained considering a non-stoichiometric Cu_{2-x}Se sample as the binary system (Cu_2Se + copper deficit) and equating the concentration of deficit copper atoms with the concentration of holes. An experimentally attainable equilibrium process of phase transition in which both phases have different concentration of holes is discussed. The equations derived on the basis of this process describe the experimental curves with satisfactory agreement.

1. INTRODUCTION

IT HAS been shown that the range of homogeneity in non-stoichiometric Cu_{2-x}Se varies from $0.14 \geq x \geq 0.0025$ at 400°C [1]. X-ray diffraction studies of Cu_{2-x}Se show a solid-solid α - β phase transition [2, 3] at temperatures which depend on the deviation from stoichiometry [4].

Many physical parameters, such as the electrical conductivity, thermoelectric power and linear coefficient of thermal expansion [5-8] exhibit anomalous changes at temperatures at which the α - β phase transition occurs.

Conductivity variations during the phase change are explained [9] considering non-stoichiometric Cu_{2-x}Se as the binary system (Cu_2Se + Se), in which α and β phases in mutual equilibrium have different compositions. Thus, conductivity measurements give the equilibrium diagram of the (Cu_2Se + Se) system for the α - β transformation. Also, it is possible to calculate the temperature dependence of the conductivity at temperatures at which the two phase region occurs, assuming that part of the sample is in the α -phase and the rest in the β -phase. The result thus obtained is in good qualitative agreement with the experiment.

It has been shown [10] that every deficit

copper atom in Cu_{2-x}Se gives a hole. Conductivity measurements suggest [9] that the mobility and concentration of holes are the same in the α - and β -phases. This may probably be explained considering the similarity in crystallographic structures of both solid phases [2]. Therefore, the phase transition is not complicated from the point of view of semiconductivity measurements.

The aim of this article is to show the possibility of calculating the conductivity and some other physical quantities of cuprous selenide at temperatures at which the two phase region occurs.

2. TWO PHASE REGION

We consider Cu_{2-x}Se to be a solid solution of Cu_2Se and holes ($\text{Cu}_2\text{Se} + p$). Vacancies due to copper deficit in Cu_{2-x}Se serve as acceptor states which are all ionized in both phases. In the temperature range where both phases are in mutual equilibrium, the distribution of copper deficit causes the distribution of holes. Since the diffusion constant of vacancies in Cu_{2-x}Se is high [5, 7], it is easy to achieve thermal equilibrium for temperature measurements if the change of temperature in the sample is sufficiently slow. If the sample is only in the α - or β -phase, the concentration

of holes is the same and equal to p_0 , depending on the deviation from stoichiometry. If, however, part of the sample is in the α -phase and the rest in the β -phase the sum of concentration of holes, denoted by p_α and p_β , respectively can be written in the form $p_\alpha + p_\beta = p_0$, neglecting thermal expansion of the sample. The distribution coefficient of holes between the α - and β -phase will be $k = p_\alpha/p_\beta$.

We shall start our consideration with the case where k is independent of p_0 . Part of the equilibrium diagram of non-stoichiometric cuprous selenide, for $k < 1$, in the T - p representation is shown in Fig. 1. Here

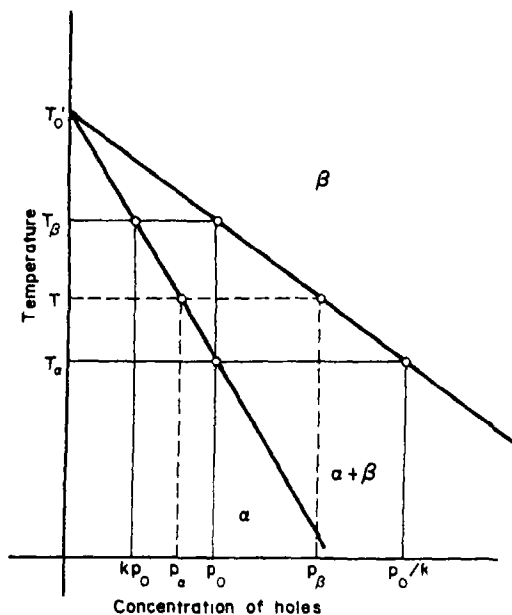


Fig. 1. The diagram of the two phase region for the case where the distribution coefficient is constant.

T'_0 is the temperature of the phase change in stoichiometric Cu_2Se . T_α and T_β are the respective temperatures at which the two phase region starts and ends with increasing temperature. This is valid for a sample whose concentration of holes is equal to p_0 . From Fig. 1 it can be easily shown that the concentrations of holes in the α and β phases of the sample are

$$p_\alpha = p_0 \frac{T'_0 - T}{T'_0 - T_\alpha} \quad p_\beta = p_0 \frac{T'_0 - T}{T'_0 - T_\beta} \quad (1)$$

As we neglected the change of the sample volume with temperature during the phase transition, we can write $V_\alpha + V_\beta = V_0$. Here V_0 is the volume of the sample, V_α and V_β are parts of volumes of the sample in the α and β phases, respectively. From $V_\alpha + V_\beta = V_0$ and $p_\alpha V_\alpha + p_\beta V_\beta = V_0 p_0$ parts of volumes in the α and β phases can be calculated

$$V_\alpha = V_0 \frac{(T_\beta - T)(T'_0 - T_\alpha)}{(T'_0 - T)(T_\beta - T_\alpha)}$$

$$V_\beta = V_0 \frac{(T - T_\alpha)(T'_0 - T_\beta)}{(T'_0 - T)(T_\beta - T_\alpha)} \quad (2)$$

From the definition of the distribution coefficient of holes and equation (1) one can obtain

$$T'_0 = \frac{T_\beta - kT_\alpha}{1 - k} \quad (3)$$

The quantities V_0 and p_0 are generally known (p_0 can be calculated from the deviation from stoichiometry). T_α and T_β can be determined from any physical parameter influenced by the two phase region. T'_0 can also be measured and therefore the distribution coefficient can be calculated. If T'_0 is unknown (exact stoichiometry does not exist) then k and T'_0 must be determined by other properties depending on the physical parameter.

Further consideration of equations (1-3) leads to Raoult's law. In general the phase curves are not linear which was also observed for Cu_{2-x}Se [9]. Thus, to each value of k corresponds a proper hole concentration p_0 . The phase curves can generally be represented by straight lines only over narrow ranges of hole concentration. It means that each sample with a given concentration of holes p_0 has its own distribution coefficient k . Now the problem is to find the mutual orientation of the straight lines of phase curves corresponding to

a given value of p_0 and the real phase curves for different values of p_0 . There is one remark [11] that the straight lines must be tangents to the real phase curves at a point corresponding to the definite value of p_0 .

We shall show another solution of this problem which enables us to calculate the temperature dependence of some physical quantity in the two phase region. It can be shown that formulas (1), (2) and (3) are also valid for the case where k depends on p_0 . The only difference is in the meaning of temperature T_0 . Figure 2 shows that T_0 is now the parameter depending on the variation of $k = f(p_0)$. Knowing k , equation (3) permits the calculation of T_0 . In Fig. 2 T_0 is higher than T'_0 , but it can also be $T_0 < T'_0$, depending on the relation between k and p_0 .

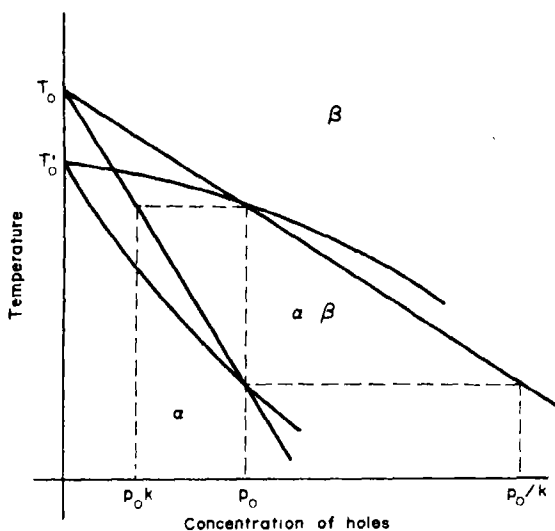


Fig. 2. The diagram of the two phase region for the case where the distribution coefficient depends on p_0 .

3. ELECTRICAL CONDUCTIVITY

The distribution of holes between the two phases at temperatures at which they are in equilibrium causes a change of sample conductivity. The influence of the hole distribution depends on the orientation of the boundary which separates the two phases in the sample. When the discrete phase boundary moves

along the sample remaining perpendicular to the current flow the effect of hole distribution on the conductivity is maximum. If the phase boundary moves parallel to the current flow the distribution of holes has no influence on the conductivity. When the sample has a shape of a long bar with a temperature along it the first case is much more probable than the second. In the conductivity measurements the thermoelectric voltage due to temperature gradient must be eliminated. Now, the sample can be regarded as a serial connection of two resistor, i.e. $R = R_\alpha + R_\beta$, where R_α and R_β are the resistances of the two phases existing in the sample. Using $R = V/\sigma q^2$ and $\sigma = ep\mu_p$ where V is the volume of the sample with the cross section q , we obtain

$$\sigma = \frac{ep_\alpha\mu_\alpha p_\beta\mu_\beta}{V_\alpha p_\beta\mu_\beta + V_\beta p_\alpha\mu_\alpha}. \quad (4)$$

Here σ is the effective conductivity to be measured, μ_α and μ_β are mobilities of holes in the α - and β -phases, respectively. In the case where $\mu_\alpha = \mu_\beta = \mu$, equation (4) can be transformed into

$$F(T) = \frac{\sigma}{\sigma_0} = \frac{(T_0 - T)^2(T_\beta - T_\alpha)}{(T_\beta - T)(T_0 - T_\alpha)^2 + (T - T_\alpha)(T_0 - T_\beta)^2},$$

where $\sigma_0 = ep\mu_0$ denotes the conductivity of the sample outside the two phase region. For temperatures $T_\alpha \leq T \leq T_\beta$ equation (1) gives $F(T) \leq 1$. The minimum of $\sigma(T)$ can be found from $dF/dT = 0$. It occurs at the temperature T_m which is

$$T_m = \frac{T_0(T_\alpha + T_\beta) - 2T_\alpha T_\beta}{2T_0 - (T_\alpha + T_\beta)} = \frac{T_\beta + kT_\alpha}{1 + k}.$$

By measuring $\sigma(T)$, T_α , T_β and T_m it is possible to calculate k ; T_0 can be obtained using equation (3).

4. LINEAR COEFFICIENT OF THERMAL EXPANSION

The thermal expansion in the two phase region varies with temperature in both phases separately. The general equation giving the magnitude of the total length or volume will be influenced by both phases. Knowing $V_\alpha(T)$ and $V_\beta(T)$ we can calculate the thermal expansion of the sample in the two phase region. For this purpose we take into account two facts. Firstly, volumes in different phases (V_α^0 at T_α and V_β^0 at T_β) are not equal. The volume of the sample is $V = V_\alpha^0 V_\alpha + V_\beta^0 V_\beta$, where V_α and V_β have the same meaning as in equation (2). For a sample having a bar shape the above equation can be transformed into $L = L_\alpha^0 V_\alpha + L_\beta^0 V_\beta$, where L_α^0 and L_β^0 are the lengths of the sample at T_α and T_β , respectively. Secondly, the coefficients of thermal expansions (α in the α -phase and β in the β -phase) are not the same. Using equations (2) the relative dilatation of the sample length can be written in the form

$$r = \frac{L - L_\alpha^0}{L_\alpha^0} = V_\alpha [1 + \alpha(T - T_\alpha)] + V_\beta f \frac{1 + \beta(T - T_\beta)}{1 + \beta(T_\alpha - T_\beta)} - 1$$

where $f = L_\beta^0 [1 + \beta(T_\alpha - T_\beta)] / L_\alpha^0$. Figure 3 shows the temperature dependence of r for different values of the parameter f , assuming that α , β , ($\beta > \alpha$), T_α , T_β and T_0 are constants. Figure 3 shows that the shape of $r(T)$ denoted by A , B and C correspond to the values of f given in the figure. Experimental measurements of thermal expansion give T_α , T_β , α , β and f (f can be calculated from $r(T)$ putting in equation (7) $V_\alpha = 0$ and $T = T_\beta$). The distribution coefficient k (or T_0) can be obtained by fitting equation (7) with the experimental results.

5. EXPERIMENTAL RESULTS AND DISCUSSION

Cu_{2-x}Se samples with different values of x were prepared from an initial ingot with

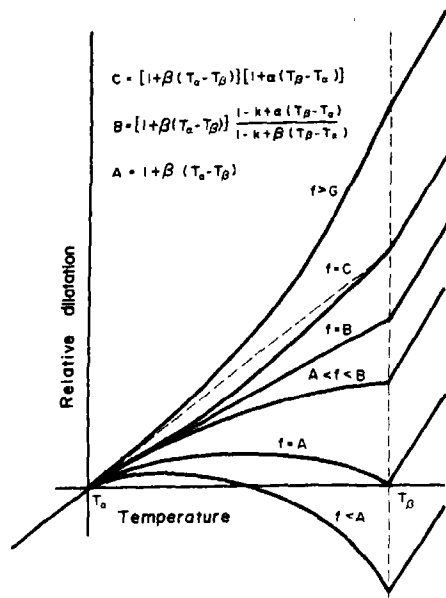


Fig. 3. The temperature dependence of the relative dilatation for various values of parameter f .

large x by successive evaporation of selenium. The samples were prepared from precisely weighed pure components in an evacuated and sealed quartz tube. The initial composition was determined from the masses of copper and selenium used in the synthesis. This initial composition with large x was in the range of homogeneity of cuprous selenide. In all experiments single crystals were used. They were obtained by a simple version of the Bridgman method. The experimental data for the diffusion constant of copper vacancies in Cu_{2-x}Se show very high absolute values [5, 7]. This enabled one to measure the temperature change of conductivity with the thermal equilibrium in the sample. The rate of temperature change of $1^\circ\text{C}/\text{min}$ during the phase transition had been found to be so low that the good reproducibility was obtained in conductivity measurements. Measurements of conductivity were carried out by means of the standard two-probe method. The temperature dependence of conductivity together with the linear coefficient of thermal expansion give characteristic temperatures T_α and T_β .

which denote the beginning and the end of the two phase region. Conductivity measurements allow to determine the temperature T_m between T_α and T_β at which $\sigma(T)$ reaches a minimum.

The data obtained from conductivity measurements are listed in Table 1 together with the distribution coefficient k calculated from (6) and p_0 calculated from the deviation from stoichiometry [12].

Table 1.

Sample	$2-x$	T_α , °C	T_m , °C	T_β , °C	k	$p_0 \cdot 10^{-20} \text{cm}^{-3}$
1	1.802	—	—	62	—	37.7
2	1.874	—	—	103	—	25.8
3	1.893	-80	42	113	0.582	21.8
4	1.910	-50	73	121	0.390	18.2
5	1.918	?	?	125	?	16.5
6	1.929	-35	88	127.5	0.321	14.3
7	1.940	-5	105.5	132	0.240	12.1
8	1.953	10	106.5	133	0.274	9.4
9	1.962	35	108	137	0.397	7.6

Equation (5) can be directly applied to cuprous selenide. The phase transition can be considered to be in equilibrium if the measurements are sufficiently slow. Further, conductivity measurements show that hole mobilities are the same in both phases.

Figure 4 shows the temperature dependence of conductivity for samples 6 and 8 together with the curve calculated from equation (5). It can be seen that the results obtained are in better agreement with experiment than those published in an earlier paper [9]. Table 1 gives the dependence of the distribution coefficient on the index $2-x$ in the samples of Cu_{2-x}Se with a minimum in the middle of the region of homogeneity.

Measurements of the linear coefficient of thermal expansion were performed on samples with conductivities of about 680, 1000 and 7000 $\Omega^{-1} \text{cm}^{-1}$. They were denoted by S0, S1 and S2. The temperature dependence of the relative dilatation measured on sample S0 corresponds to the curve $f < A$ in Fig. 3. The temperatures T_α and T_β are

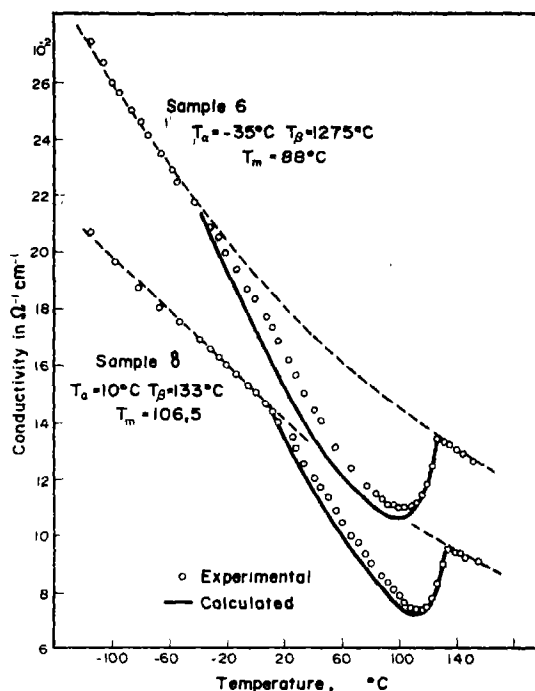


Fig. 4. Temperature dependence of the conductivities of samples 6 and 8.

above room temperature. Sample S1 corresponds to the case $A < f < B$ in Fig. 3. Temperature T_α is below room temperature (it was not possible to measure it with our apparatus). Sample S2 corresponds to the curve $f > C$ in Fig. 3. T_α is far below room temperature. The values of T_α and T_β for S0 and T_β for S1 samples determined by expansion measurements correspond to those obtained by conductivity measurements of samples having the same conductivity.

Table 2 shows the results of thermal expansion measurements for samples S0, S1 and S2.

Only samples S0 and S1 can be used for comparison with equation (7). For sample S0 the value of k (or T_0) must be fitted to experimental results since other values are obtained from thermal expansion measurements. For sample S1 the temperatures T_0 and T_α must be obtained from conductivity measurements performed on the same sample.

Table 2.

Sample	$\alpha \cdot 10^6 (^{\circ}\text{C}^{-1})$	$T_{\alpha} (^{\circ}\text{C})$	$T_{\beta} (^{\circ}\text{C})$	$\beta \cdot 10^6 (^{\circ}\text{C}^{-1})$	f
S0	12	79	146	24	0.99645
S1	?	?	133	24	0.99785
S2	?	?	55	28	?

Experimental points together with the calculated curve from equation (7) for samples S0 and S1 are shown in Fig. 5. The distribution coefficient k obtained by fitting to the experimental results was found to be 0.14. This value is less than expected. This may be due to the difference in temperatures T_{β} determined by electrical conductivity and

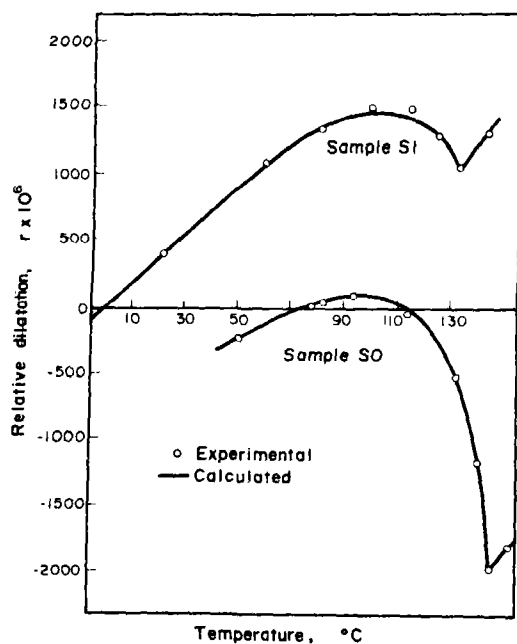


Fig. 5. Temperature dependence of the relative dilatation of samples S0 and S1.

thermal expansion measurements. The difference in T_{β} can arise from the fact that the composition of sample S0 lies at the boundary of the homogeneity range [1] in Cu_{2-x}Se . For sample S1 the result of fitting (with the values $T_{\alpha} = 0^{\circ}\text{C}$ and $T_{\beta} = 175^{\circ}\text{C}$ obtained from conductivity measurements on the same sample) gives $\alpha = 23 \cdot 10^{-6} ^{\circ}\text{C}^{-1}$ and $f = 0.99785$.

6. CONCLUSION

The two phase region is a common feature to a solution whose composition can change at the contact of solid with the melt due to the distribution of the solute. The influence of the two phase region on the electrical conductance in the solid-solid transformation as far as we know, has not yet been reported. The reason for this lies mainly in the fact that the diffusion rate of the solute in a solution is very low causing the distribution effect to be negligible. The α - β solid-solid transformation in cuprous selenide is extraordinarily fast due to the high absolute value of the diffusion constant of copper vacancies. From the experimental point of view this means that temperature changes in the two phase region should be sufficiently slowed down so as to ensure the diffusion rate to produce uniform composition of the copper deficit in both phases separately.

REFERENCES

1. LORENZ G. and WAGNER C., *J. chem. Phys.* **26**, 1607 (1957).
2. RAHLFS P., *Z. Phys. Chem.* **B31**, 157 (1936).
3. BORCHET W., *Z. Kristallogr.* **106**, 5 (1945).
4. HEYDING R. D., *Can. J. Chem.* **44**, 1233 (1966).
5. REINHOLD H. and MÖHRING H., *Z. Phys. Chem.* **B38**, 221 (1938).
6. JUNOD P., *Helv. Phys. Acta* **32**, 567 (1959).
7. OGORELEC Z. and ČELUSTKA B., *J. Phys. Chem. Solids* **27**, 957 (1966).
8. ČELUSTKA B. and OGORELEC Z., *Acta Metall.* **14**, 687 (1966).
9. OGORELEC Z. and ČELUSTKA B., *J. Phys. Chem. Solids* **30**, 149 (1969).
10. ČELUSTKA B., Thesis, University of Zagreb (1969).
11. SCHILDKNECHT H., *Zone Melting*, Academic Press, New York London (1966).
12. ČELUSTKA B. and OGORELEC Z., *Croat. Chem. Acta* **41**, 73 (1969).

ELECTRONIC ENERGY BANDS AND OPTICAL TRANSITIONS IN TETRAGONAL GERMANIUM DIOXIDE

F. J. ARLINGHAUS and W. A. ALBERS, Jr.

Research Laboratories, General Motors Corporation, Warren, Mich.

(Received 19 January 1970; in revised form 3 August 1970)

Abstract—The electronic energy band structure of the tetragonal crystallographic modification of germanium dioxide (GeO_2) has been calculated by the APW method. Application of selection rules indicate only two allowed direct transitions at the center of the Brillouin zone which correlate with observed room temperature optical properties at the fundamental absorption edge in single crystals. The calculated band structure also predicts an indirect transition which, although not inconsistent with the optical data, cannot be completely verified without additional and more refined experimental work.

1. INTRODUCTION

GERMANIUM dioxide is known to exist in at least two different crystallographic forms [1,2]. The commonly occurring form is hexagonal (α -quartz structure) and some small amount of information about the properties of single crystals of this material is available in the literature [3-7]. The form that does not occur naturally is tetragonal (rutile structure) and, until recently, has been prepared only by conversion from the hexagonal material [1,2,6,8,9]. In the last several years methods for the growth of single crystals of tetragonal GeO_2 have been developed in this laboratory [10] and elsewhere [11,12] thus enabling the observation of optical and electrical properties. The purpose of this paper is to report investigations of the room temperature optical absorption edge of such crystals and the correlation of resulting data with a preliminary calculation of the electronic energy bands.

2. THEORETICAL ENERGY BANDS

First considerations

Tetragonal GeO_2 possesses the rutile structure with space group symmetry D_{4h}^{14} [13]. The unit cell is simple tetragonal, with a c/a ratio of 0.65 and contains six atoms, two

germanium and four oxygen. The Brillouin zone is also simple tetragonal and is shown in Fig. 1.

The principal difficulty in performing a first-principle energy band calculation is the choice of a crystal potential. Superposition of atomic potentials for each constituent is usual; the problem in the present case is which atomic potential to choose. The question is basically one of ionicity. Neutral germanium and oxygen, Ge^{+4} ions and O^{2-} ions, or something intermediate? Further, in the APW method, a sphere surrounds each atom—the ionic potential (spherical) is used within that sphere, and a constant potential is chosen between spheres. The question again is what radius sphere to choose, which really gets back to the ionicity problem again (Ge^{+4} ions are much smaller than neutral germanium atoms).

Several tentative, preliminary calculations established the fact that neutral or slightly ionized atoms, with approximately equal germanium and oxygen sphere radii, gave completely unsatisfactory results. Such calculations predicted small band gaps or even metallic properties. The cause may be laid to the unfortunate fact that the rutile structure does not close-pack equal spheres. For equal

sphere radii, only about 35 per cent of space is filled by the spheres. Since the APW method requires the potential to be constant outside the spheres, the method will not work well when this exterior region is a large fraction of the total, as is the case here.

Clearly, Ge^{+4} and O^- ions with germanium spheres small and oxygen spheres large, is more appropriate. As much as 55 per cent of space can be filled with these unequal spheres. A test calculation gives more reasonable results. Another problem arises, however. Free O^- ions are not stable, and the only available potential is Watson's[14], which artificially puts the ion in a stabilizing potential well. This will not give really good results.

The self-consistent calculation

The parameters of the calculation are given in Table 1. Sphere radii were chosen as follows: the oxygen spheres were made to touch, giving as large an oxygen radius as possible; then the germanium spheres were made to touch these. The spheres cannot overlap in the APW scheme. As chosen, the spheres fill 55 per cent of the space in the crystal.

The Ge^{+4} ionic potential was calculated by the Herman-Skillman[15] procedure; the O^- potential is that of Watson[14]. An Ewald problem is solved to obtain the average potential for the region outside the spheres[16]. This was the first trial potential for the iterative calculation. Exchange is included by means of the Slater $\rho^{1/3}$ approximation[17].

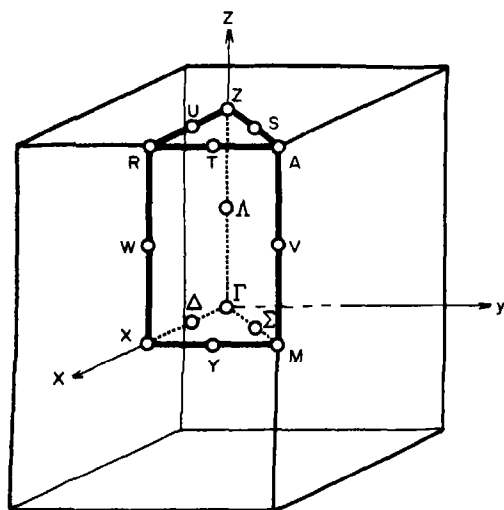


Fig. 1. Brillouin zone for the rutile structure.

We conclude that the potential must be found by a selfconsistent procedure, that the crystal potential cannot be guessed *a priori*. The ionicity question reinforces this belief. To avoid the really impossible task of choosing ionicity at the outset, we must let the charge distribute itself in the course of an iterative calculation. As a starting potential, we use the most reasonable potential found in the preliminary testing, i.e. the Ge^{+4} and O^- ionic potentials, with unequal sphere radii.

Table 1. Parameters for APW band calculation

Tetragonal unit cell dimensions, a	8.3054 a.u. (4.395 Å)
c	5.4028 a.u. (2.859 Å)
u	0.31
Germanium sphere radius	1.2723 a.u.
Oxygen sphere radius	2.2317 a.u.
Type of structure	Rutile
Brillouin zone	simple tetragonal
Space group	$D_{4h}^{14} - P4_2/mnm$

This potential was used to calculate the energy bands; eigenvectors and charge densities were then determined for each eigenstate. The total charge distribution was determined by summing over all occupied states. From the charge distribution a new potential was found by solving Poisson's equation. The average potential outside the spheres is again found by a solution of an Ewald problem. The $\rho^{1/3}$ approximation is used to include exchange. The actual new trial potential is taken to be the average of this potential and the original one (this is to stabilize convergence). Bands are again calculated and the process repeated until the eigenvalues converge.

Ten iterations were needed before the eigenvalues were reasonably stable, conver-

ging to within ~ 0.005 Rydberg. It was necessary to include the higher core states (the oxygen $2s$ and germanium $3d$ bands) to get accurate answers. The bands are depicted in Fig. 2. Because of the complicated crystal structure, with six atoms in the unit cell, there are a large number of bands. The main features are the broad conduction band with a parabolic minimum at Γ , the zone center; the profusion of valence bands, the higher ones quite flat; and a large (~ 5 eV) forbidden energy gap separating the two. Not shown are the germanium $3d$ bands at about -0.5 Ry on this scale and the oxygen $2s$ bands around -0.8 Ry. Each of the latter has appreciable (~ 0.2 Ry) width.

A basic feature of the calculated bands is the presence of an indirect edge. The direct gap from Γ_5^+ to Γ_1^+ at the zone center is 5.52 eV; however the valence band state $R1$ on the top edge of the zone is slightly higher than the Γ_5^+ state, so that the indirect transition $R1^+ \rightarrow \Gamma_5^+$ is only 5.25 eV. This indirect edge is different from that of germanium, in

that the valence band comes up away from the center of the zone; in all other cases of an indirect edge known at present the conduction band comes down.

Table 2 characterizes the charge distribution in the GeO_2 crystal, not counting the oxygen $1s^2$ core or the germanium $1s^2 2s^2 2p^2 3s^2 3p^6$ core. There has not been a great deal of change from the first iteration, except for a slight shifting of charge out of the spheres into the exterior region. Thus the final configuration still corresponds fairly closely to the $\text{Ge}^{+4}\text{O}_2^-$ configuration assumed at the outset. This must not be interpreted to mean that GeO_2 is an ionic compound like, e. g. NaCl ,

Table 2. Charge distribution in GeO_2

Exterior	4.14	
	Ge (2 of them)	Ox (4 of them)
$l = 0$	0.04	1.92
1	0.05	5.14
2	9.47	0.08
	9.56	7.14

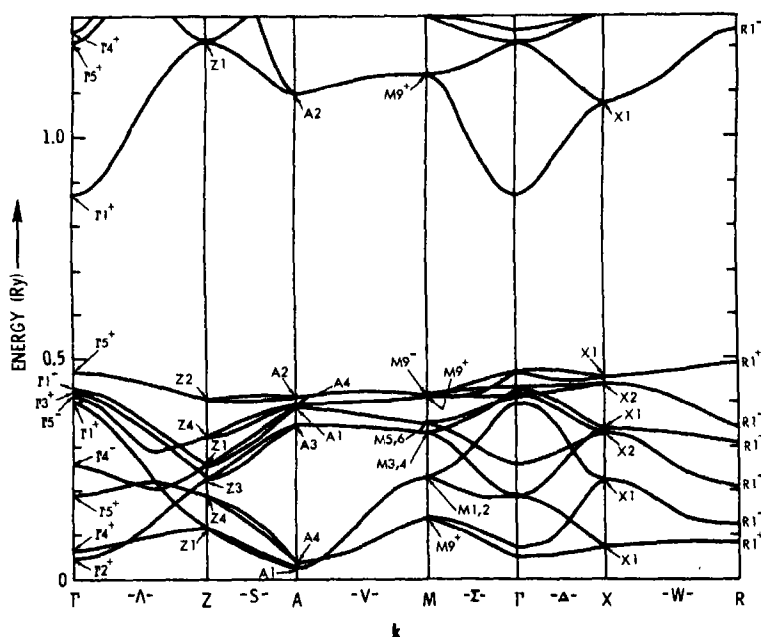


Fig. 2. Tetragonal GeO_2 energy bands.

with an ionicity of four. It does indicate considerable charge transfer, but the bonding must obviously be of a covalent character. There is considerable charge outside the spheres, indicating overlap of the germanium and oxygen wave functions. Figure 3 shows a plot of radial charge density along the nearest neighbor Ge-O direction. The high degree of overlap is apparent in this plot. GeO_2 is clearly covalently bonded with considerable charge transfer. This charge transfer may account for the unusual hardness of the compound.

3. EXPERIMENTAL

Procedure

Single crystals of germanium dioxide available had typical dimensions of $1.0 \times 0.1 \times 0.1 \text{ cm}^3$, with the crystallographic c -axis lying in the direction of the largest dimension. All of the crystals exhibited well-developed flat surfaces which proved to be $[110]$ planes upon examination by X -ray diffraction. This facilitated precise alignment of the optical arrangement relative to the c -axis of the crystals.

Crystals of various thicknesses were prepared by a careful lapping and polishing pro-

cedure as follows. The specimen was cemented to a flat Pyrex glass blank with a $[110]$ face parallel to the glass surface. Several small pieces of glass of approximately the same initial thickness as the specimen were then cemented to the Pyrex flat surrounding the specimen in order to ensure a uniform final thickness after lapping and polishing. The lapping was carried out with successively smaller grit carborundum on a flat plate glass base. The final laps and polish were done using successively smaller particle-size diamond paste with a silk polishing cloth stretched over a flat plate glass base. The finishing diamond particle size was a quarter micron. The resulting surfaces were flat to within 1000 \AA and exhibited optical reflectivity characteristics which were similar to those observed on as-grown surfaces. Sample thicknesses down to 45 microns were obtained this way, but attempts to prepare thinner specimens resulted in breakage.

All of the measurements were made with a Perkin-Elmer model 450 spectrometer. Radiation incident upon the sample was polarized by a 1.5 cm Glan-Thomson calcite prism which was placed at the exit slit of the monochromator, thus facilitating measure-

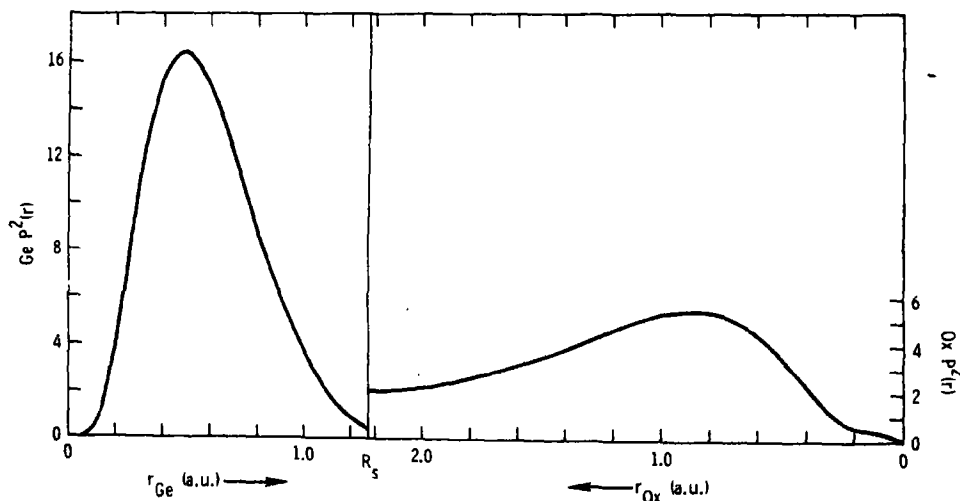


Fig. 3. Radial charge density in GeO_2 (tetragonal) along nearest-neighbor Ge-O directions.

ments with the incident beam of light polarized either perpendicular or parallel to the crystal c -axis. For transmittance measurements, the samples were mounted in a microsampling accessory (Perkin-Elmer No. 350-0160) which was equipped with an aperture that accommodated the sample dimensions. The incident radiation intensity was obtained by removing the sample from the aperture. Reflectance measurements were made in near-normal incidence by deflecting the spectrometer beam onto the sample with one mirror and collecting the reflected beam on a second mirror which in turn focused the radiation on the detector. The reflectance was determined relative to a silver front-surfaced mirror. In order to obtain reliable reflectance values in the near u.v. (4.5–6.0 eV.) it was necessary to etch the crystals in 13 *N* KOH at 100°C for 12 hr. This etch removed only about one micron of material and left the optical quality of the surface high.

The values of the transmittance, T , and the reflectance, R , were used to determine the absorption coefficient, α , through

$$T = (1 - R)^2 / [\exp(\alpha d) - R^2 \exp(-\alpha d)]$$

where d is the sample thickness [18]. Measurements were made on sample thicknesses ranging from 45 to 800 microns, yielding values for the absorption coefficient in the range of 4 cm^{-1} to $1.5 \times 10^3 \text{ cm}^{-1}$. A total of four crystals in all were studied and all four exhibited the same absorption coefficient wavelength dependence within experimental error. The absorption coefficient vs. photon energy curves plotted in this paper represent composites of several hundred data points obtained from these four samples.

Results

The room temperature reflectance, R , and the absorption coefficient, α , for light polarized perpendicular and parallel to the c -axis are presented in Figs. 4 and 5 as functions of

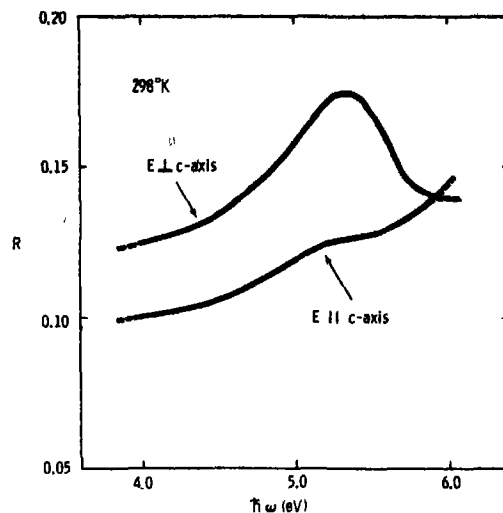


Fig. 4. Reflectance, R , vs. energy, $\hbar\omega$, of tetragonal GeO_2 single crystals at room temperature for light polarized perpendicular and parallel to the crystallographic c -axis.

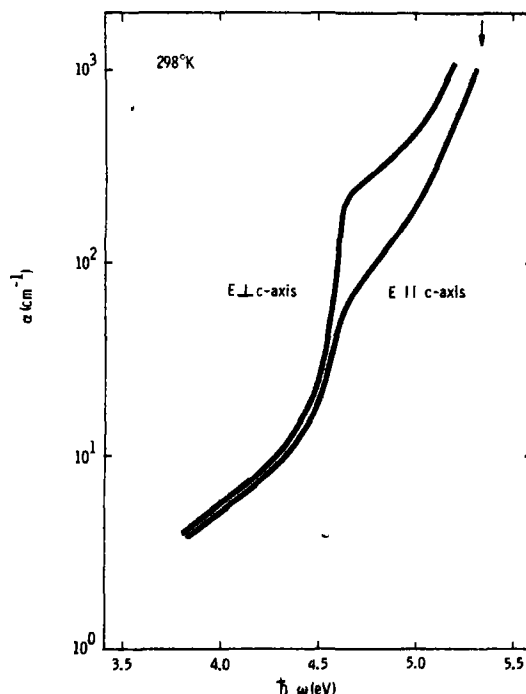


Fig. 5. Absorption coefficient, α , vs. energy, $\hbar\omega$, of tetragonal GeO_2 single crystals at room temperature for light polarized perpendicular and parallel to the crystallographic c -axis. The arrow denotes the location of the peak in the perpendicular polarization reflectance curve of Fig. 4.

incident photon energy, $\hbar\omega$, in the range of 4 to 6 eV. As expected for the optically anisotropic tetragonal crystal structure, dichroism in the fundamental absorption edge is evident. We anticipate, on the basis of the band structure calculations, the existence of an indirect absorption edge which is also suggested by the data of Figs. 4 and 5. That is, the broadness of the absorption edge and the appreciable absorption at intermediate values of absorption coefficient ($\sim 10^2 \text{ cm}^{-1}$) are characteristic of large energy gap materials known to have indirect edges [19, 20]. On the other hand, the peak observed in the reflectance for $E \perp c$ -axis at about 5.35 eV suggests a direct transition in the vicinity of this energy. The $E \parallel c$ -axis reflectance continues to rise as the energy increases to 6 eV, and may possibly peak at higher energies outside the range of our instrumentation. Sample thickness limitations restricted the values of absorption coefficient obtained to less than $2 \times 10^3 \text{ cm}^{-1}$. However, the rapid rise in absorption coefficient at the high energy side of the range seen in Fig. 5 is consistent with the larger values of α expected for a direct gap. The location of the reflectance peak for $E \perp c$ -axis is denoted by the arrow in Fig. 5. On the basis of the data we tentatively conclude that (1) there is a direct gap for the $E \perp c$ -axis mode at about 5.35 eV., (2) the direct gap for the $E \parallel c$ -axis mode lies somewhat above 6 eV, and (3) there is an indirect gap at an as yet undetermined energy well below the direct edges.

The above results can be compared to existing optical data for the hexagonal crystal-line form of GeO_2 . Pajasova [5] has observed the lowest energy peak in the reflectance spectrum of hexagonal GeO_2 at about 6.6 eV. (with unpolarized light). Absorption coefficients obtained from relatively thick crystals by Papazian [4] and one of the authors (WAA, unpublished) are shown in Fig. 6. Just as in the case of tetragonal GeO_2 the absorption edge is broad and there is appreciable absorption at energies well below the peak in reflectance reported by Pajasova. The absorption

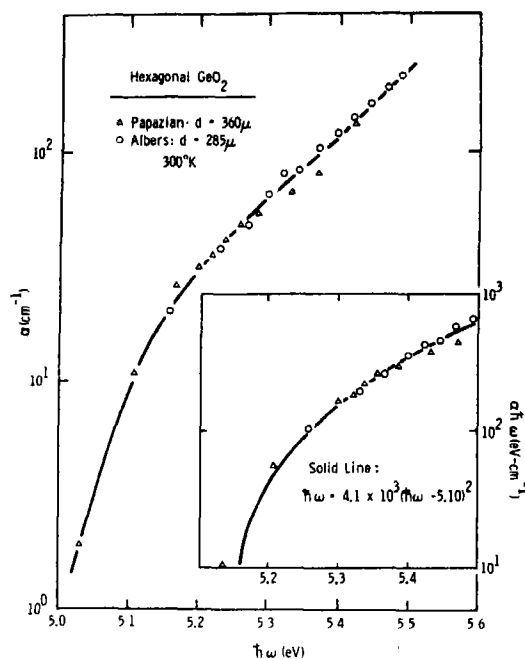


Fig. 6. Absorption coefficient, α , vs. energy, $\hbar\omega$, of a hexagonal GeO_2 single crystal 360 microns thick obtained by Papazian (Ref. [4]) and similar data for a 285 micron thick crystal by Albers (unpublished). In the insert, the data points are fitted with the expression for an indirect absorption edge (see text).

data of Fig. 6 can be examined in terms of the theoretical dependence of absorption coefficient on energy deduced for simple parabolic band indirect transitions [21]

$$\alpha \hbar\omega = B(\hbar\omega - E_g)^2$$

where E_g is the indirect gap energy and B is an energy-independent constant. The hexagonal GeO_2 data is fitted to this expression in the insert of Fig. 6, yielding a value of 5.10 eV. for E_g . We thus tentatively conclude that hexagonal GeO_2 has a direct gap near 6.6 eV. and an indirect gap in the vicinity of 5.1 eV. This is not inconsistent with qualitatively similar conclusions drawn by Reilly using a different approach [22].

A parallel analysis of the indirect transitions in tetragonal GeO_2 has not proven possible. Upon comparison of the data in Figs. 5 and

6 it is readily appreciated that the form of the absorption coefficient dependence on energy for the tetragonal material is apparently somewhat more complex than for the hexagonal form. The determination of the indirect gaps in the tetragonal crystals must await more detailed experimental investigation.

4. DISCUSSION

We now wish to compare the experimental results on tetragonal GeO_2 with the calculated band structure. The application of selection rules for electric dipole transitions at the center of the Brillouin zone [23] reveals only two allowed transitions, $\Gamma_1^- \rightarrow \Gamma_1^+$ for light polarized parallel to the c -axis and $\Gamma_5^+ \rightarrow \Gamma_1^+$ for light polarized perpendicular to the c -axis. All other optical transitions at Γ are forbidden by symmetry.

The energy band calculations indicate that the Γ_1^+ state is the lowest-lying conduction band at Γ while the highest-lying valence band is Γ_5^+ ; the Γ_1^- valence band lies at a somewhat lower energy. We therefore assign the $\Gamma_5^+ \rightarrow \Gamma_1^+$ transition to the direct gap for $E \perp c$ -axis observed at 5.35 eV experimentally. The calculations then predict a direct transition $\Gamma_1^- \rightarrow \Gamma_1^+$ for the parallel light mode at a somewhat higher energy, not inconsistent with the experimental results. The experimentally observed dichroism should then be associated with the separation between the Γ_5^+ and Γ_1^- valence bands. These assignments are consistent with similar ones at the Γ -point of (tetragonal) tin oxide [24].

An important feature of the calculated band structure is the prediction of an indirect gap due to the rise of the valence band at the R-point above the energy of the Γ_5^+ state. The $R_1^+ \rightarrow \Gamma_1^+$ transition is allowed for both polarizations of light on the basis of symmetry considerations [23]. We tentatively conclude that the evidence for indirect transitions observed experimentally supports the theoretical prediction.

The band calculations yield an indirect gap energy of 5.25 eV while the direct gaps are

calculated to be 5.52 and 6.04 eV for the perpendicular and parallel cases, respectively. These numbers are in reasonable agreement with experiment. That is, we observe the \perp gap to be 5.35 eV and the \parallel gap somewhat greater than 6 eV. Although undetermined, the indirect gap could conceivably lie in the vicinity of 5 eV. We conclude that the band calculations correlate quite well with the admittedly preliminary optical data and therefore can be assumed to, at least qualitatively, account for the electronic properties of tetragonal germanium dioxide.

Acknowledgements—The authors are grateful for several useful discussions with J. G. Gay, C. E. Bleil, W. A. Florence, and D. E. Swets who grew some of the crystals used in the investigation. The excellent technical assistance of L. Green is also appreciated.

REFERENCES

- MÜLLER J. H. and BLANK H. R., *J. Am. Chem. Soc.* **46**, 2358 (1924).
- LAUBENGAYER A. W. and MORTON D. S., *J. Am. Chem. Soc.* **54**, 2303 (1932).
- SMITH G. S. and ISAACS P. B., *Acta crystallogr.* **17**, 842 (1964).
- PAPAZIAN H. A., *J. appl. Phys.* **27**, 1253 (1956).
- PAJASOVA L., *Czech. J. Phys.* **B19**, 1265 (1969).
- LIPPINCOTT E. R., VAN VALKENBURG A., WEIR C. E. and BUNTING E. N., *J. Res. Nat. Bureau Stand.* **61**, 61 (1958).
- CHEREMISINOV V. P., *Optical Methods of Investigating Solid Bodies* in Proc. of P. N. Lebedev Physics Institute, Vol. 25.
- KOTERA Y. and YONEMURA M., *Trans. Faraday Soc.* **59**, 147 (1963).
- ALBERS W. A., Jr., VALYOCSEK E. W. and MOHAN P. V., *J. electrochem. Soc.* **113**, 196 (1966).
- SWETS D. E., to be published.
- FAKTOR M. M. and CARRASSO J. I., *J. electrochem. Soc.* **112**, 817 (1965).
- ROY R., private communication.
- GAY J. G., ALBERS W. A., Jr., and ARLINGHAUS F. J., *J. Phys. Chem. Solids* **29**, 1449 (1968).
- WATSON R. E., *Phys. Rev.* **111**, 1108 (1958).
- HERMAN F. and SKILLMAN S., *Atomic Structure Calculations*, Prentice-Hall, Englewood Cliffs, New Jersey (1963).
- SLATER J. C. and DECICCO P. D., M.I.T. *Solid State and Molecular Theory Group Quart. Progress Report* No. 50, p. 46 (October, 1963).
- SLATER J. C., *Phys. Rev.* **81**, 385 (1951).
- MOSS T. S., *Optical Properties of Semiconductors*, Academic Press, New York (1959).
- DEAN P. J. and THOMAS D. G., *Phys. Rev.* **150**, 690 (1966).

20. PATRICK L., HAMILTON D. R. and CHOYKE W. J., *Phys. Rev.* **143**, 526 (1966).
21. JOHNSON E. J., *Semiconductors and Semimetals*, (Edited by R. K. Willardson and A. C. Beer), Academic Press, New York (1967).
22. REILLY M. H., *J. Phys. Chem. Solids* **31**, 1041 (1970).
23. GAY J. G., unpublished work.
24. SUMMITT R., MARLEY J. A. and BORRELLI N. F., *J. Phys. Chem. Solids* **25**, 1465 (1964).

ELECTRON-HOLE RECOMBINATION IN COBALT-DOPED *p*-TYPE GERMANIUM

G. SUSILA and G. SURYAN

Department of Physics, Indian Institute of Science, Bangalore-12, India

(Received 16 July 1970)

Abstract—The recombination properties of cobalt centers in *p*-type germanium containing cobalt in the concentration range 10^{14} to 10^{16} atoms/cm³ have been investigated. The measurement of lifetime has been carried out by steady-state photoconductivity and photo-magneto-electric methods in the temperature range 145 to 300°K. The cross-sections S_n^0 (electron capture cross-section at neutral centers), S_n^- (electron capture cross-section at singly negatively charged centers) and their temperature variations have been estimated by the analysis of the lifetime data on the basis of Sah-Shockley's multi-level formula. The value of S_n^0 is $(15 \pm 5) \cdot 10^{-16}$ cm² and is temperature independent. The value of S_n^- is $\sim 4 \cdot 10^{-16}$ cm² around 225°K and it increases with increase of temperature. The possible mechanisms for capture at neutral and repulsive centers are discussed and a summary of the capture cross-sections for cobalt centers is given. A comparison of the cross-section values of cobalt and their temperature variations with those of the related impurities-manganese, iron and nickel-in germanium has been made.

1. INTRODUCTION

THIS paper describes the investigations of recombination processes in *p*-type germanium doped with cobalt which introduces two acceptor levels in the forbidden gap of germanium[1] (0.25 eV from V.B.: $\text{Co}^0 \rightleftharpoons \text{Co}^-$; 0.30 eV from C.B.: $\text{Co}^- \rightarrow \text{Co}^+$). In *p*-type samples, the Fermi level is below the intrinsic level in the entire temperature range, thereby ensuring that all the cobalt atoms are either singly negatively charged or neutral. Hence a study of carrier lifetimes in *p*-type cobalt-doped samples facilitates the determination of the capture cross-sections S_n^0 and S_n^- associated with the neutral and singly negatively charged centers (the superscript refers to the state of the center before capture and the subscript to the type of the carrier captured). The capture cross-section S_n^0 has been reported to be $10 \cdot 10^{-16}$ cm² by Glinchuk *et al.*[2] but no details on its temperature dependence are known. As far as S_n^- is concerned, some values attributed to Glinchuk are reported in the literature[3]. From the study of steady-state photoconductivity and photomagneto-electric effect in *n*-type samples,

Susila[4] has estimated S_n^- to be about $\sim 0.1 \cdot 10^{-16}$ cm² at 145°K. These measurements have been extended to *p*-type cobalt-doped germanium samples and the results are reported here.

2. MATERIAL PREPARATION AND EXPERIMENTAL DETAILS

P-type germanium crystals doped with spectroscopically pure cobalt (from Johnson Matthey & Co., U.K.) were prepared by adding cobalt-germanium pellets to the *p*-type germanium melt while growing the crystal (by Czochralski pulling technique). The starting material was zone-refined *n*-type germanium to which gallium had been added during crystal growth. Samples from the initial and middle portions of the crystals which exhibit low dislocation densities (maximum limit being one thousand/cm²) were used for measurement purposes.

Measurements of resistivity, Hall effect and lifetime were carried out on a large number of samples in the temperature range 145 to 300°K. Steady-state photoconductivity (*pc*), photo-magneto-electric effect (*pme*) and

compensation methods were employed for lifetime measurement and the experimental arrangement and conditions have already been described in Ref.[4]. The results of a few typical crystals are given below.

3. RESULTS AND DISCUSSION

From the measurements of Hall effect and resistivity in some high-resistivity *p*-type cobalt-doped samples, it was observed that considerable changes in the value of ρ_0 and resistivity (ρ) occurred below 200°K. The semi-log plots of ρ_0 and ρ against $1000/T$ tend to strike into a fairly steep slope at lower temperatures. Unfortunately, the measurements could not be extended below 150°K to get the magnitude of the slope. As in *n*-type [4] the lifetime values were less than 5μ sec

depending upon the cobalt concentration. The values of cross-section were, however, estimated from the data obtained for low- and medium-resistivity samples.

Figure 1 gives the variation of τ_{pc} and τ_{pme} for five samples as a function of temperature and the pertaining data are presented in Table 1. The common features observed in all the samples are (i) unlike *n*-type crystals in which there is a large difference between τ_{pc} and τ_{pme} and in which τ_{pc} increases with decrease temperature, in *p*-type samples both τ_{pc} and τ_{pme} are almost the same, within the limits of the experimental error, in the entire temperature range i.e., no trapping processes occur at low temperatures, (2) all samples show a well-defined plateau in the lifetime curve in the temperature range 145 to approximately

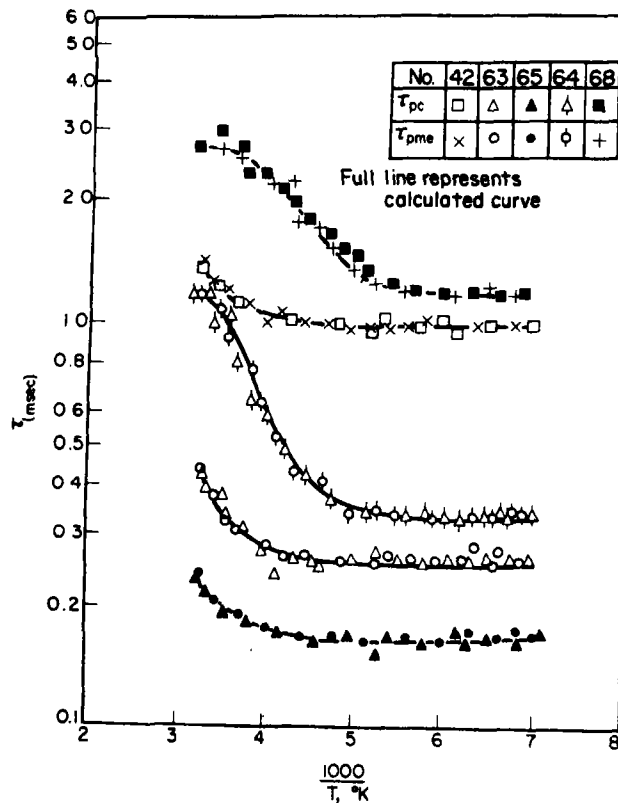


Fig. 1. Temperature variation of τ_{pc} and τ_{pme} for cobalt-doped *p*-type germanium samples.

Table 1.

Sample no.	Hole conc. p_0 (300°K) (No/cm ³)	Cobalt conc. N_f (atoms/cm ³)	Lifetime at 300°K (μ /sec)	Lifetime at 145°K (μ sec)	S_n° (temp. independent) in (10 ⁻¹⁰ cm ²)	S_n^- (T°K) in (10 ⁻¹⁰ cm ²)	$g_1/g_0 = 1/\gamma(\frac{1}{2})$ used in calculations
42	6.20 . 10 ¹³	5.6 . 10 ¹³	1.45	1	18		8
63	2.28 . 10 ¹³	2.4 . 10 ¹⁴	0.44	0.265	16		4
65	9.00 . 10 ¹³	5.00 . 10 ¹⁴	0.224	0.17	12		8
64	3.24 . 10 ¹⁴	1.6 . 10 ¹⁴	1.14	0.33	19	3.9 (225°K)	8
68	1.47 . 10 ¹⁴	8.5 . 10 ¹³	2.7	1.2	10	4.0 (225°K)	8

225°K and (3) at higher temperatures, no well-defined plateau could be seen.

The data were analysed on the basis of Sah-Shockley's [5] multi-level recombination formula:

$$\frac{1}{\tau} = (n_0 + p_0) \left[\frac{(f_0^\circ + f_1^\circ)}{\tau(n, 0)[p_0 + p^*(\frac{1}{2})] + \tau(p, 1)[n_0 + n^*(\frac{1}{2})]} + \frac{(f_1^\circ + f_2^\circ)}{\tau(n, 1)[p_0 + p^*(\frac{3}{2})] + \tau(p, 2)[n_0 + n^*(\frac{3}{2})]} \right] \quad (1)$$

For meaning of symbols see Ref. [4].

Since the Fermi level is below the intrinsic level for *p*-type samples, $f_2^\circ = 0$, i.e., there are no doubly negatively charged cobalt centers. Also for the entire temperature range of investigation $n^*(\frac{1}{2})/p_0 \approx n(\frac{1}{2})/p_0 \ll 1$ and $p^*(\frac{3}{2})/p_0 \approx p(\frac{3}{2})/p_0 \ll 1$ and for all samples $n_0 \ll p_0$.

If the temperature range and hole concentration of the samples are such that the Fermi level is situated well below the 0.25 eV level, then $f_1^\circ \approx 0$ and the second term in the equation (1) can be deleted. Further, the value of S_p^- which represents the capture at an attractive site is generally expected to be large or at least of the same order as S_n° . The values of S_p^- quoted in the literature [6] for various impurities have always been much larger than their corresponding S_n° . Even if $S_p^- \approx S_n^\circ$,

$$\tau(n, 0)[p_0 + p^*(\frac{1}{2})] \gg \tau(p, 1)[n_0 + n^*(\frac{1}{2})].$$

Under such conditions the expression (1) for τ simplifies to the form

$$\tau = \tau(n, 0)(1 + p^*(\frac{1}{2})/p_0). \quad (2)$$

For those cases where $f_1^\circ \neq 0$, the second term in the expression cannot be ignored. The first term can be written in the form $N_f v p_0 S_n^\circ / [p_0 + p^*(\frac{1}{2})]$. The second term can be expressed as follows:

$$\begin{aligned} & \frac{f_1^\circ p_0}{\tau(n, 1)[p_0 + p^*(\frac{3}{2})] + \tau(p, 2)[n_0 + n^*(\frac{3}{2})]} \\ & \approx \frac{p^*(\frac{1}{2}) S_n^- v N_f}{[p_0 + p^*(\frac{1}{2})][1 + (n^*(\frac{3}{2})/p_0)(S_n^-/S_p^-)]} \end{aligned} \quad (3)$$

since

$$f_1^\circ = \frac{p^*(\frac{1}{2})}{[p_0 + p^*(\frac{1}{2})]}.$$

The final expression for τ is then given by

$$\tau = \frac{[p_0 + p^*(\frac{1}{2})]}{N_f v [p_0 S_n^\circ + p^*(\frac{1}{2}) S_n^- (1 + X)^{-1}]} \quad (4)$$

where

$$X = \frac{n^*(\frac{3}{2}) S_n^-}{p_0 S_p^-}$$

when $n^*(\frac{3}{2}) \ll p_0$ and $S_n^- \ll S_p^-$, then τ is given by

$$\tau = \frac{[p_0 + p^*(\frac{1}{2})]}{N_f v [p_0 S_n^\circ + p^*(\frac{1}{2}) S_n^-]}. \quad (5)$$

Whether X is negligible or not depends upon the values of $n^*(\frac{1}{2})$, p_0 , S_n^- and S_p^- and it varies with temperature and from crystal to crystal.

The calculation of Fermi levels for low-resistivity ($p_0 > 10^{18}/\text{cm}^3$) crystals (No. 42, 63 and 65) indicates that the Fermi level is well below 0.25 eV for the entire temperature range (145–300°K), thereby enabling one to use the simple expression (2) for τ . Also in the temperature range 145 to approximately 225°K, $p^*(\frac{1}{2}) \ll p_0$ and τ is given by

$$\tau \approx \tau(n, 0) = \frac{1}{N_f \nu S_n^0} \quad (6)$$

and the temperature dependence of S_n^0 is essentially determined by the temperature dependence of $\tau \approx \tau(n, 0)$. The low temperature plateau region of the lifetime curve gives a value of $(15 \pm 5) \cdot 10^{-16} \text{ cm}^2$ for S_n^0 . The well-defined plateau indicates that S_n^0 is temperature independent from 145 to 225°K and there is no particular reason to expect it to vary above 225°K. The temperature variation of τ observed above 225°K can be attributed to the temperature variation of $p^*(\frac{1}{2})$. Attempts were made to fit the experimental data to equation (2) choosing a suitable value of $g_1/g_0 = 1/\gamma(\frac{1}{2})$ and assuming $E_v - E(\frac{1}{2}) = 0.25 \text{ eV}$. The solid lines in Fig. 1 indicate the calculated lifetime values. For all low-resistivity samples the experimental data could be fitted up successfully to equation (2) for a value of $g_1/g_0 = 8$. However for sample 63, the value 4 for g_1/g_0 gives the best fit.

In the case of medium-resistivity ($p_0 = 10^{14}$ to $10^{15}/\text{cm}^3$) samples also, the lifetime curves exhibit well-defined plateau in the low temperature range (145 to $\sim 170^\circ\text{K}$) where τ is given by the expression (6). The values of S_n^0 calculated are given in Table 1 and they are of the same order of magnitude as that observed in low-resistivity samples. Above 170°K, one has to use the equation (4) to fit up the experimental data. Calculations show that up to 225°K, even if one assumes S_p^- and S_n^-

to be of comparable magnitude, the value of X occurring in the equation (4) is negligible. Hence assuming $g_1/g_0 = 8$, $p^*(\frac{1}{2})$ was calculated and the value of S_n^- was estimated using the equation (5), it is of the order of $4 \cdot 10^{-16} \text{ cm}^2$ at 225°K.

To fit up the experimental data above 225°K, (as a first approximation), the lifetimes were calculated assuming a constant value of $4 \cdot 10^{-16} \text{ cm}^2$ for S_n^- and using the expression (5) for τ . Surprisingly it was found that there is a general agreement between the experimental and calculated values. This apparent fit does not indicate that S_n^- is temperature independent because at higher temperatures the term $X = n^*(\frac{1}{2})S_n^-/p_0S_p^-$ is not negligible and one has to replace S_n^- by $S_n^-/(1+X)$. Hence it is not S_n^- but $S_n^-/(1+X)$ which is approximately constant around $4 \cdot 10^{-16} \text{ cm}^2$. (In addition, since there is appreciable contribution due to $S_n^0p_0$ term even at room temperature, small changes in the value of $S_n^-/(1+X)$ will not be reflected in the lifetime curve). Since X is increasing with temperature, S_n^- should also increase with temperature in the higher temperature range. In view of the uncertainty in the temperature variation of S_p^- at higher temperature [4], the explicit calculation of S_n^- has not been made.

4. γ FOR THE $E(\frac{1}{2})$ (0.25 eV) LEVEL OF COBALT

As in n -type, a knowledge of the degeneracy ratio γ for the $E(\frac{1}{2})$ level of cobalt is necessary for the analysis of lifetime data and no experimental investigation on the value of γ for cobalt $E(\frac{1}{2})$ level in germanium is available in the literature. However, by fitting up the experimental curve to equation (2), $1/\gamma(\frac{1}{2})$ has been estimated. The value 8 for $1/\gamma(\frac{1}{2})$ gave a reasonably good fit over the entire temperature range of investigation for most of the samples.

5. CAPTURE AT NEUTRAL CENTERS

The value of S_n^0 is fairly large and is about $(15 \pm 5) \cdot 10^{-16} \text{ cm}^2$. Its temperature independence is clearly demonstrated by the well-

defined low temperature plateau in the $\log \tau$ vs. $1000/T$ curves of *p*-type samples. According to Lax's [7] theory for neutral centers, the cross-section S_n^0 for electrons is expected to exhibit some weak temperature dependence. The exponent '*n*' in the power law has been estimated [7] to lie between 0 and 1 depending on the relative contributions of optical and acoustical phonons; but the observed S_n^0 is practically independent of temperature. The magnitude of S_n^0 is also large and it is doubtful whether the required number of excited states will be available around a neutral center due to the weak and short-range polarization forces (see Bonch-Bruевич and Glasko [8]). These lead one to suspect whether Lax's cascade theory can completely account for capture at neutral centers. In this connection attention may be drawn to the work of Sheinkman [3] who has proposed a type of Auger recombination process at multiply charged centers in which the energy released on capture at a multi-level center is imparted to another localized carrier of opposite type in that center, which may be ejected to the respective band. He has remarked that for this process, the temperature dependence of S_n^0 is likely to be very small compared to that expected on Lax's theory and that this process may yield large value of cross-section for neutral centers.

6. CAPTURE AT REPULSIVE CENTERS

The value of S_n^- estimated from *p*-type samples around 225°K is about $4 \cdot 10^{-16} \text{ cm}^2$ and it increases with increase of temperature. Hence S_n^- at 300°K will be greater than $4 \cdot 10^{-16} \text{ cm}^2$. On the contrary, the value of S_n^- estimated independently from the steady-state *pc* and *pme* measurements at low temperatures is of the order of $0.1 \cdot 10^{-16} \text{ cm}^2$ and the upper limit estimated roughly at 300°K is $1 \cdot 10^{-16} \text{ cm}^2$. Thus it seems there is a residuary difference between the two S_n^- values obtained in *n*- and *p*-type samples. This difference can be qualitatively under-

stood as follows: it is probable that in *p*-type crystals where the majority carriers are holes there will be a tendency for the holes to cluster around the negatively charged centers. This large concentration of carriers in the immediate vicinity of the negatively charged center reduces the potential barrier around the center and this may result in a larger value of cross-section in the case of *p*-type crystals.

However, the value of S_n^- both in *n*- and *p*-type samples is larger than what is expected for a repulsive center and at present there appears to be no theory to explain the rather large values of cross-sections usually obtained for repulsive centers. The cascade mechanism which accounts for the large values of capture cross-section is not suitable for repulsive centers since no bound orbits for carriers can exist around a repulsive center. One has to look into other mechanisms for the dissipation of recombination energy. Among these the probability for the simultaneous emission of phonons is usually very small. Sheinkman [3] has remarked that the type of Auger process (which he has applied for the case of neutral centers) does not take place at repulsive centers. There seems to be some experimental evidence for radiative recombination to take place at repulsive centers (an example is that of Zn^- centers in germanium at low temperatures [9]). Hence the possibility of radiative recombination cannot be ignored. In general one should look into the various mechanisms particularly radiative and Auger processes in considerable detail to determine their role in recombination at repulsive centers.

From the experimental point of view, the temperature dependence of S_n^- for cobalt (deduced from a study of both *n*- and *p*-type) is as follows: It is practically temperature independent in the lower temperature region (145° to 180°K) but there is a definite tendency for it to increase with increase of temperature at higher temperatures. However data is not sufficient to propose any definite mathematical expression for the same. While classically a

steep temperature dependence is expected for repulsive centers, it has been shown by Bonch-Bruevich[10] that the tunnel effect, if taken into account, will reduce the temperature dependence considerably. This may explain the weak temperature dependence observed in the low temperature region. The possible large increase of S_n^- in the higher temperature region, inferred from the trapping ratio in n -type remains, however, unexplained.

The cross-sections and their temperature dependence determined for the case of cobalt by the authors are summarized in Table 2 which also includes the values of cross-sections for the other related impurities iron, nickel and manganese.

Of the four cross-section S_p^+ , S_p^- , S_n^- and S_n^+ which describe the recombination of carriers at cobalt centers, it has not been possible to estimate the cross-section S_p^- by the experimental methods adopted here because (a) it is difficult to isolate its effect by any choice of temperature range and/or the

position of the Fermi level and (b) its value is generally expected to be large, hence one has to resort to methods like those of Rupprecht [11, 12] and noise method[21] to determine the same.

The cross-sections obtained for cobalt may be compared with those obtained for similar centers like manganese, iron and nickel available in the literature. See Table 2. Some of the cross-sections determined earlier than 1960 are available in Ref. [6].

It is seen that so far as the temperature variation of S_p^- at cobalt centers at low temperatures is concerned, it behaves like iron[16] and manganese[23]; but according to Kalashnikov and Tissen[17], the cross-section S_p^- for nickel is independent of temperature. Some of these investigations have been carried out on diffused samples with rather low concentration of nickel. Wertheim[18] on the other hand, has reported an increase of S_p^- with decrease of temperature for nickel. The values of S_p^- for cobalt [4]

Table 2. Capture cross-sections and their temperature dependence of Fe, Co, Ni and Mn
(Cross-sections given below are in units of 10^{-18} cm²)

Element	Fe	Co	Ni	Mn
Cross-section				
S_n^+	10 (300°K)[2, 13]	10 (300°K)[2] 15 ± 5; temp. indep. (present work)	20[17] 0.96[18] } temp. 0.5[19] } indep.	2 (90°K) weak temp. dep.[22]
S_n^-	< 0.001 (80°K) > 1 (300°K) inc. exp. (0.05 eV)[14]	0.1 ± 0.05 weak temp. dep. below 180°K; inc. with inc. of T[4] above 180°K 4 (225°K) (present work)	3 (300°K) temp. indep.[17] 5.9 (300°K) temp. indep.[18] 3 (300°K) temp. indep. from 280–350°K[19]	0.4 (300°K)[22] 0.1 (300°K)[23] } weak temp. dep.
S_p^-	30 (300°K)[15]		1000 (77°K)[20] (6 to 8) 10 ³ (100°K) varies as $T^{-1/2}$ } [11, 12] 350 (200°K) varies as $T^{-1.5}$ [21]	(2 to 3) 10 ⁴ (100°K) varies as $T^{-1/2}$ [11, 12]
S_p^+	100 (300°K)[15] varies as T^{-3} [16]	22 ± 5 (145°K) varies as T^{-4} ; less steep variation at higher temperature 1 (300°K) lowest estimate[4]	200 (300°K)[17] temp. indep. 100 (300°K) inc. on cooling[18] ≥ 1000 (300°K)[21]	0.6 (300°K) varies as $T^{-4.5}$ [23]

and manganese[23] are small and are around $1 \cdot 10^{-16} \text{ cm}^2$ at 300°K. However the values quoted for nickel[17, 18, 21] are of the order $100 \cdot 10^{-16} \text{ cm}^2$ and more.

The relative magnitudes of S_n^0 and S_n^- for these centers are also interesting. It is found that S_n^0/S_n^- is about 3 to 10 for cobalt, manganese[22] and iron[13, 14], but for nickel Eliseev and Kalashnikov[19] have established a value 0.16 for the ratio S_n^0/S_n^- . This behaviour is similar to those observed in gold and silver[24].

The capture cross-section S_n^0 is practically temperature independent for nickel[17, 18, 19] and cobalt and weakly dependent for manganese[22]. For iron, the temperature dependence of S_n^0 is not available in the literature.

While the temperature variation of S_n^- is weak at low temperatures for cobalt centers similar to what has been observed for manganese and nickel, there seems to be some temperature variation at higher temperatures. For iron also, Belyaev and Mologolovets [14] have observed an increase of S_n^- with the increase of temperature.

It is found that it not possible to put the elements manganese, iron, cobalt and nickel in any particular order from the point of view of their recombination properties. It is clear that more theoretical investigations are called for, particularly on capture at repulsive centers because it has been noticed that the capture cross-section S_n^- is of the same order or sometimes even larger than S_n^0 . At room temperature, both in manganese and cobalt, S_n^- is of the same order as S_p^- . Regarding the capture at attractive centers, one will expect on the basis of Coulombic attraction that $S_p^+ > S_p^0 > S_p^-$ but it has been found experimentally that in some cases S_p^- is very much larger than S_p^+ (see Table 2). The value of S_p^+ is generally small (for example, for copper, S_p^+ at 300°K is $1 \cdot 10^{-16} \text{ cm}^2$ [25]).

On the experimental side it is necessary to determine the values of the degeneracy ratio for the various levels accurately, without

which quantitative calculations cannot be performed. Experiments with impurity level excitation and observation of impurity level recombination radiation may be very valuable since they will serve to isolate many of the relevant cross-sections unambiguously.

Acknowledgements—The authors thank Professor R. S. Krishnan for his constant encouragement and kind interest. Thanks are also due to Mr. M. Venkateswara Rao for growing the crystals.

REFERENCES

1. TYLER W. W., NEWMAN R. and WOODBURY H. H., *Phys. Rev.* **97**, 669 (1955).
2. GLINCHUK K. D., MISELYUK E. G. and FORTUNATOVA N. N., *Ukr. fiz. Zh.* **4**, 207 (1959).
3. SHEINKMAN M. K., *Fiz. tverd. Tela* **7**, 28 *Soviet Phys. solid State* **7**, 18 (1965).
4. SUSILA G., *J. Phys. Chem. Solids* **31**, 963 (1970).
5. SAH C. T. and SHOCKLEY W., *Phys. Rev.* **109**, 1103 (1958).
6. KALASHNIKOV S. G., *Proc. Int. Conf. on Semiconductor Physics, Prague*, p. 241 (1960).
7. LAX M., *Phys. Rev.* **119**, 1502 (1960).
8. BONCH-BRUEVICH V. L. and GLASKO V. B., *Fiz. tverd. Tela* **4**, 510 (1962); *Soviet Phys. solid State* **4**, 371 (1962).
9. POKROVSKII Ya. E. and SVISTUNOVA K. I., *Fiz. tverd. Tela* **6**, 19 (1964); *Soviet Phys. solid State* **6**, 13 (1964).
10. BONCH-BRUEVICH V. L., *Fiz. tverd. Tela, Sbornik (Suppl.)* **II**, 182 (1959).
11. RUPPRECHT G., *Proc. Int. Conf. on Semiconductors Physics, Prague*, 282 (1960).
12. RUPPRECHT G., *J. Phys. Chem. Solids* **22**, 255 (1961).
13. GLINCHUK K. D., MISELYUK E. G. and FORTUNATOVA, *Zh. Tekh. Fiz.* **28**, 1053 (1958); *Soviet Phys. tech. Phys.* **3**, 980 (1958).
14. BELYAEV A. D. and MOLOGOLOVETS V. G., *Fiz. tverd. Tela* **5**, 3043 (1963); *Soviet Phys. solid State* **5**, 2229 (1963).
15. GLINCHUK K. D., MISELYUK E. G. and FORTUNATOVA N. N., *Xh. tekhn. Fiz.* **27**, 2451 (1957); *Soviet Phys. tech. Phys.* **2**, 2283 (1957).
16. BELYAEV A. D. and MOLOGOLOVETS S. S., *Fiz. tverd. Tela* **7**, 1894 (1965); *Soviet Phys. solid State* **7**, 1529 (1965).
17. KALASHNIKOV S. G. and TISSEN K. P., *Fizika tverd. Tela* **1**, 1754 (1959); *Soviet Phys. solid State* **1**, 1603 (1959).
18. WETHEIM G. K., *Phys. Rev.* **115**, 37 (1959).
19. ELISEEV P. G. and KALASHNIKOV S. G., *Fiz. tverd. Tela* **5**, 320 (1963); *Soviet Phys. solid State* **5**, 233 (1963).

20. NEWMAN R. and TYLER W. W., *Solid State Physics* (Edited by F. Seitz and D. Turnbull), Vol. 8. Academic Press, New York, p. 49 (1959).
21. KLAASSEN F. M., BLOK J. and BOOY H. C., *Physica* 27, 48 (1961).
22. LANDSBERG E. G. and KALASHNIKOV S. G., *Fiz. tverd. Tela* 3, 1566 (1961); *Soviet Phys. solid State* 3, 1137 (1961).
23. LANDSBERG E. G. and KALASHNIKOV S. G., *Fiz. tverd. Tela* 5, 1067 (1963); *Soviet Phys. solid State* 5, 777 (1963).
24. MISELYUK E. G. and GLINCHUK K. D., *Proc. Int. Conf. on Semiconductor Physics, Prague*, p. 253 (1960).
25. KALASHNIKOV S. G., *J. Phys. Chem. Solids* 8, 52 (1959).

STRUCTURE ET PROPRIETES MAGNETIQUES DU MANGANITE DE CHROME*

B. BOUCHER, R. BUHL† et M. PERRIN†

Service de Physique du Solide et de Résonance Magnétique, Centre d'Etudes Nucléaires de Saclay, BP n° 2 – 91, Gif-sur-Yvette, France

(Received 5 January 1970; in revised form 1 April 1970)

Abstract—Chromium manganite CrMn_2O_4 is a tetragonally distorted spinel, its formula is $\text{Mn}^{2+}[\text{Cr}^{3+}\text{Mn}^{3+}]\text{O}_4$ (inverse spinel).

The study of the fundamental magnetic properties: paramagnetic susceptibility and magnetization as a function of the field and also the measurements by neutron diffraction leads to the magnetic structure of CrMn_2O_4 at 4.2°K: it is a Yafet-Kittel type structure. The moments of the *A* sites are 4.1 μ_B and those of the *B* sites: 1.68 μ_B . The *B* moments make an angle $\theta = 23^\circ$ with [110] direction in a vertical plane. The relative arrangement of *B* site moments in the magnetic configuration is depending upon the crystallographic direction of the easy axis and this fact suggests the origin of the structure: the anisotropy.

The study at 4.2°K with a polycrystalline sample, by neutron diffraction, of the peak intensities as a function of the magnetic field applied along the *K* diffusion vector allows us to verify the deformation mechanism of the 'anisotropic structures' given in a previous paper. Then, are calculated the anisotropy laws, critical fields of 'flipping' and the volume variations of the different magnetic domains.

The thermal evolution of the parameters of this structure is then worked out from the thermal variation of the intensities of the neutron diffraction peaks. Above the transition temperature (45°K) the structure becomes linear until the Curie point (65°K).

Resumé—Le manganite de chrome: CrMn_2O_4 est un spinelle déformé quadratiquement, il est inverse et sa formule s'écrit: $\text{Mn}^{2+}[\text{Cr}^{3+}\text{Mn}^{3+}]\text{O}_4$.

L'étude des propriétés magnétiques fondamentales: susceptibilité paramagnétique et aimantation en fonction du champ ainsi que les mesures de diffraction de neutrons permettent de définir la structure magnétique de CrMn_2O_4 à 4.2°K: elle est de type Yafet-Kittel. Les moments des sites *A* valent 4.1 μ_B ceux des sites *B*: 1.68 μ_B et le demi angle d'ouverture des moments *B*: $\theta = 23^\circ$. L'arrangement relatif des moments des sites *B* à l'intérieur de la configuration magnétique, dépend de la direction cristallographique de facile aimantation et ceci suggère l'origine de cette structure: l'anisotropie.

L'étude à 4.2°K, sur échantillon polycristallin, par diffraction de neutrons, de l'intensité des raies en fonction du champ magnétique appliqué suivant le vecteur de diffusion *K*, permet de vérifier le mécanisme de déformation des 'structures anisotropes' exposées dans un article précédent, de calculer les lois d'anisotropie, les champs seuils de retournement et les variations de volumes des différents domaines magnétiques.

L'évolution thermique des paramètres de cette structure est ensuite déduite de la variation thermique de l'intensité des raies de diffraction de neutrons. Au-dessus de la température de transition: 45°K, cette structure devient linéaire jusqu'au point de Curie: 65°K.

LA PRÉPARATION du manganite de chrome pur: CrMn_2O_4 a déjà été décrite en détail dans un article précédent[1]. Rappelons simple-

ment qu'il se forme à haute température et que son domaine de stabilité thermique en phase unique s'étend de 1250°C à l'ambiante. Il cristallise dans le système quadratique: groupe d'espace D_{4h}^{19} — c'est un spinelle déformé $c/a = 1.485$ —. La répartition des ions dans les sites cristallographiques n'est pas affectée par les traitements thermiques de refroidissement: c'est un spinelle inverse dont la formule

*Cet article recouvre une partie de la thèse de Doctorat d'Etat de R. Buhl soutenue le 2 Juin 1969 à Paris (N° CNRS AO 3314).

†Laboratoire de Magnétisme, Département de Recherches Physiques Tour 22, Faculté des Sciences—11, Quai St. Bernard, 75—Paris 5ème France.

cristallographique s'écrit: $\text{Mn}[\text{CrMn}]\text{O}_4$, les ions à l'intérieur des crochets sont dans les sites octaédriques B.

L'échantillon étudié ici est celui dont le refroidissement a été lent, lui assurant ainsi une bonne cristallisation et une grande stabilité.

1. PROPRIETES MAGNETIQUES

La température de Curie de CrMn_2O_4 est 65°K . Au-dessus de cette température, la variation thermique de l'inverse de la susceptibilité paramagnétique est celle d'un corps ferrimagnétique (Fig. 1). La température de Curie asymptotique est assez fortement négative: $\theta_p = 300^\circ\text{K}$, elle indique des interactions antiferromagnétiques prépondérantes. La constante de Curie moléculaire déduite de cette courbe: $C_M = 7,16$ est beaucoup plus faible que celle calculée pour une configuration ionique: $\text{Mn}^{2+} \text{ Mn}^{3+} \text{ Cr}^{3+}$ avec des moments de spin seul: $C_M = 9,24$. Comme nous le verrons plus loin, le moment magnétique à basse température de Mn^{2+} dans les

sites A est assez loin de sa valeur théorique: $5 \mu_B$, ceci peut évidemment provenir de fortes fluctuations mais aussi d'une part de covalence dans la liaison avec l'oxygène qui peut effectivement réduire le moment. D'autre part, l'ion Cr^{3+} dans les sites octaédriques peut présenter un certain couplage spin-orbite qui réduit également son moment effectif.

Au-dessous de la température de Curie (65°K), CrMn_2O_4 est ferrimagnétique et la Fig. 2 représente la courbe d'aimantation à $4,2^\circ\text{K}$ obtenue en champs magnétiques intenses pulsés*. Deux points sont intéressants à remarquer: (1) la partie linéaire de la courbe n'est atteinte que vers 80kOe ce qui montre l'importance de l'anisotropie magnétocristalline; (2) la valeur de l'aimantation spontanée — obtenue par extrapolation à champ nul de la partie linéaire de la courbe — est trop faible: $1,08 \mu_B/\text{molécule}$ pour rendre compte d'une

* Les mesures de susceptibilité paramagnétique et en champs magnétiques pulsés ont été effectuées par Mrs. Allain, Krebs et de Gunzbourg — DPh-G/PSRM CEN Saclay.

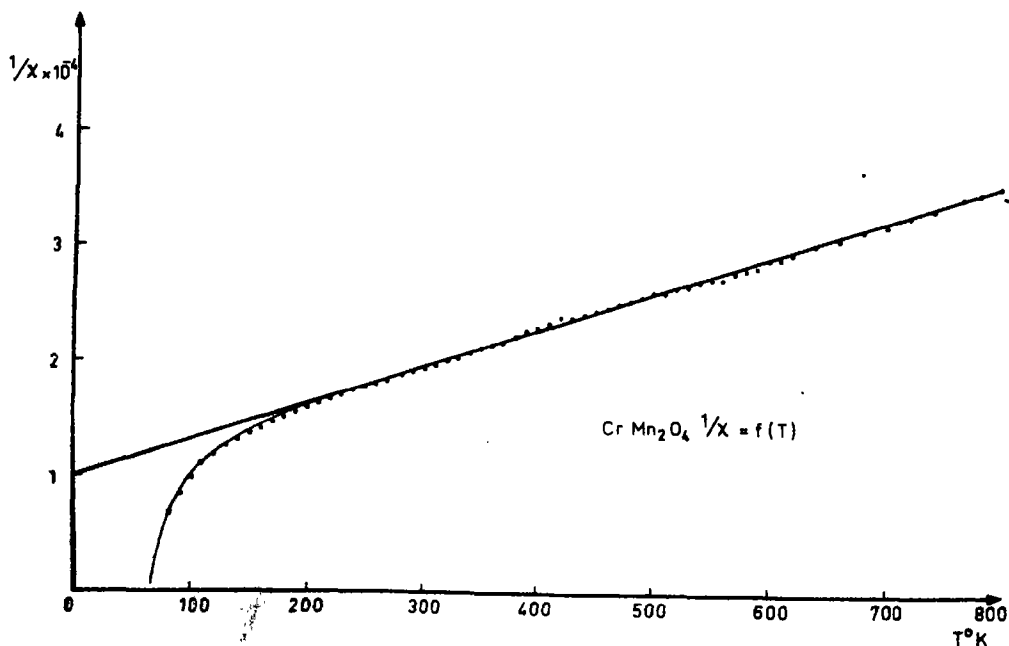


Fig. 1. Variation thermique de l'inverse de la susceptibilité paramagnétique de CrMn_2O_4 .

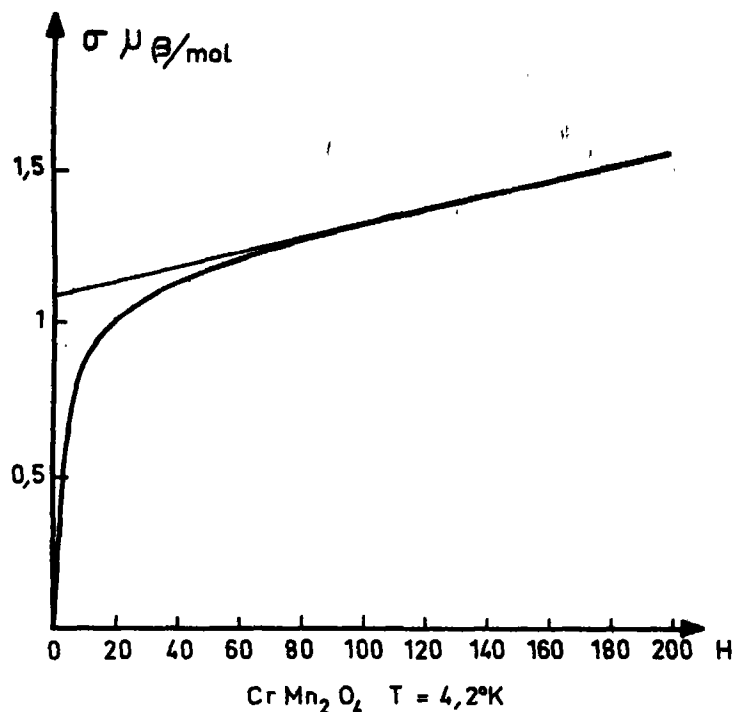


Fig. 2. Aimantation en fonction du champ à 4,2°K.

structure magnétique ferrimagnétique linéaire classique du type étudié par Néel[2]. Ceci est d'ailleurs confirmé par le fait qu'aucune saturation n'est atteinte, le moment magnétique croît linéairement avec le champ au-dessus de 80 kOe.

En transmettant des vibrations mécaniques à une poudre magnétique soumise à l'action d'un champ magnétique extérieur et lorsque le matériau est assez anisotrope, il est possible d'orienter dans la direction du champ un grand nombre de cristallites. La répartition spatiale des grains de la poudre n'est plus statistique et il est facile de détecter par diffraction de neutrons, la direction où se sont orientés les cristallites. En effet, l'intensité de la raie nucléaire correspondant à la direction d'aimantation croît proportionnellement au nombre de cristallites en position de réflexion. C'est ainsi que été déterminée pour CrMn_2O_4 la direction de facile aimantation qui est la direction [110].

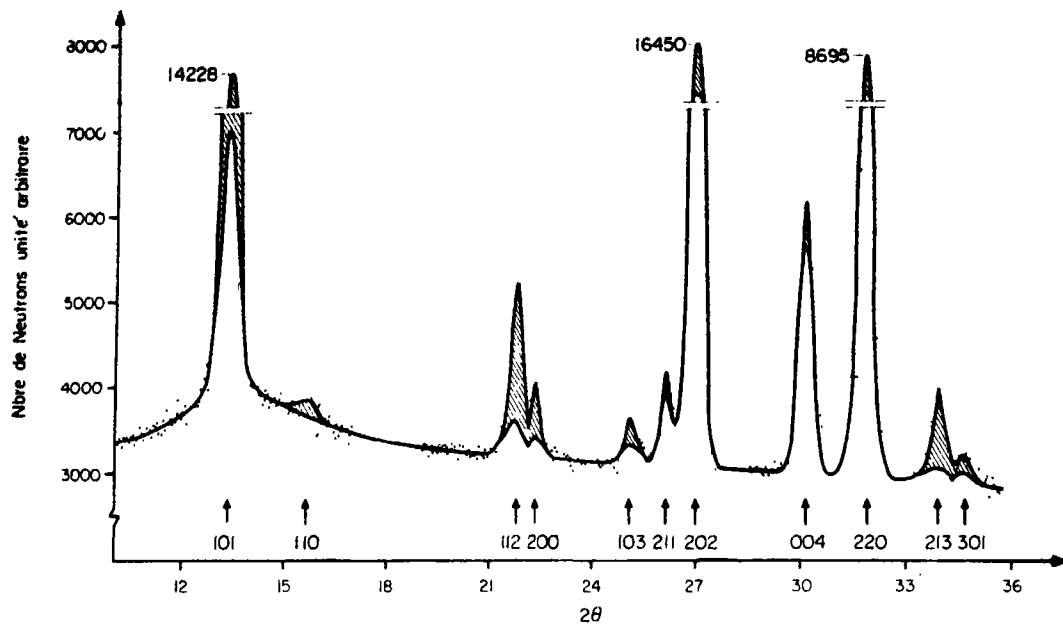
2. STRUCTURE MAGNETIQUE A 4,2°K

Les spectres de diffraction de neutrons ($\lambda = 1,138 \text{ \AA}$) à la température de l'hélium liquide ne révèlent pas de changement dans la symétrie cristalline. La symétrie magnétique reste quadratique centrée à basse température. La maille du spinelle contenant 4 molécules de CrMn_2O_4 , il est possible grâce à la symétrie centrée de ne considérer que la moitié des sous-réseaux magnétiques, les autres s'en déduisent par la translation $\frac{1}{2}, \frac{1}{2}$. Ils seront définis par leur position dans la maille (origine à $\bar{4}m2$):

— 2 sous-réseaux tétraédriques A: $A_1(0, 0, 0)$ et $A_2(0, \frac{1}{2}, \frac{1}{2})$ porteurs des moments M_1 et M_2 .

— 4 sous-réseaux octaédriques B: $B_3(0, \frac{1}{2}, \frac{1}{2})$; $B_4(0, \frac{1}{2}, \frac{1}{2})$; $B_5(\frac{1}{2}, 0, \frac{1}{2})$ et $B_6(\frac{1}{2}, 0, \frac{1}{2})$ porteurs des moments M_3, M_4, M_5 et M_6 respectivement.

Comme le montrent les spectres de diffraction de neutrons, (Fig. 3) il n'existe pas d'ordre nucléaire à longue distance, la répartition des ions sur tous les sites est statistique



CrMn₂O₄ Spectre de diffraction de Neutrons $\lambda = 1,138 \text{ \AA}$, $T = 4,2^\circ\text{K}$, $H = 0$

□ Intensité nucléaire

▨ Intensité magnétique

Fig. 3. Spectre de diffraction de neutrons ($\lambda = 1,138 \text{ \AA}$) à $4,2^\circ\text{K}$ et champ extérieur nul.

et l'on a donc en première approximation:

$$|M_1| = |M_2|$$

et

$$|M_3| = |M_4| = |M_5| = |M_6|.$$

La raie (002) étant nulle avec et sans champ appliqué suivant le vecteur de diffusion, on en déduit:

$$M_1 = M_2 \quad \text{et} \quad M_3 + M_4 = M_5 + M_6.$$

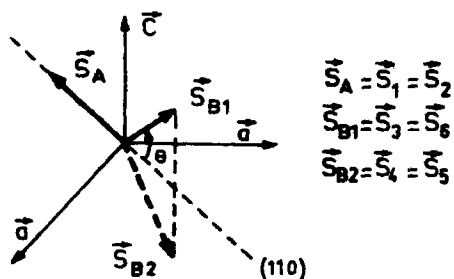
Il serait possible d'admettre l'existence d'un angle entre M_1 et M_2 mais celui-ci devrait rester faible (quelques degrés) pour rendre compte de l'ensemble des résultats expérimentaux, même compte tenu de leur précision relative. Les valeurs de moments magnétiques ainsi déduites en seraient très peu affectées. Les parties cohérentes des vecteurs

M_1 et M_2 seront donc considérées égales par la suite.

L'intensité magnétique de la raie (110) est proportionnelle à la composante transversale des moments des sites B . Cette raie n'étant pas nulle, les moments B ne peuvent pas être colinéaires.

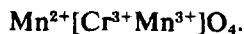
En tenant compte du fait que la direction de facile aimantation est la direction $[110]$ et que l'aimantation spontanée a pour valeur: $1,08 \mu_B/\text{mol.}$, on aboutit finalement à la structure magnétique de CrMn₂O₄. Le modèle le plus simple est celui de Yafet-Kittel[3] ayant pour axe de symétrie la direction $[110]$ (Fig. 4). Les moments des sites tétraédriques M_1 et M_2 ($4,1 \mu_B$) des sites octaédriques B ($1,68 \mu_B$) se trouvent dans le plan $(\bar{1}10)$, ils sont divisés en 2 sous-réseaux:

$$M_{B1} = M_3 = M_6 \quad \text{et} \quad M_{B2} = M_4 = M_5$$

Fig. 4. Structure magnétique de CrMn_2O_4 .

symétriques par rapport à la direction $[110]$ avec laquelle ils font un angle $\theta = 23^\circ$. Cette structure est identique à celle déjà trouvée pour un autre manganite: CoMn_2O_4 [4].

Nous avons déjà vu dans un article précédent [1] que grâce, entre autres, à des considérations d'effet Jahn-Teller, la formule ionique et cristallographique de CrMn_2O_4 devait s'écrire:



On constate donc que la valeur des moments trouvés dans chaque sous-réseau est différente de celle théoriquement prévue. Dans les sites A, Mn^{2+} devrait avoir un moment de spin seul de $5 \mu_B$ et ne peut avoir de contribution orbitale or il n'est que de $4,1 \mu_B$ expérimentalement. Il est possible que la direction de spin de Mn^{2+} fluctue fortement autour de la direction $[110]$ et ceci d'autant plus que son entourage octaédrique est formé d'ions Cr^{3+} et Mn^{3+} en même proportion mais sans aucun ordre à longue distance. Il est également possible que la liaison entre Mn^{2+} et l'oxygène ne soit pas totalement ionique mais soit partiellement covalente comme cela a été souvent proposé dans d'autres cas semblables; la réduction du moment de Mn^{2+} dans ce cas, serait en accord avec la faible valeur de la constante de Curie.

Dans les sites B, la longueur du moment: $1,68 \mu_B$ est très faible par rapport aux valeurs théoriques de Mn^{3+} et Cr^{3+} : 4 et $3 \mu_B$ respectivement. Même si l'on admet un couplage

spin-orbite important pour l'ion Cr^{3+} , cela ne peut suffire à diminuer le moment d'une telle quantité, il faut donc aussi admettre de fortes fluctuations dues au manque d'ordre entre ions chrome et manganèse dans les sites octaédriques. La longueur et la direction détectées ne sont que des valeurs moyennes. Le tableau I donne la comparaison entre intensités magnétiques des raies de diffraction de neutrons, expérimentales et calculées pour le modèle de Yafet-Kittel décrit ci-dessus à $4,2^\circ\text{K}$ et à champ extérieur nul. Les raies correspondant aux 7 premiers hkl sont celles pour lesquelles la précision expérimentale sur l'intensité magnétique est très bonne et l'on peut remarquer l'excellent accord avec les valeurs calculées correspondantes ($R = 2,2$ per cent). Par contre les intensités magnétiques expérimentales des dernières raies sont mesurées avec peu de précision car elles sont: soit superposées à de fortes composantes nucléaires ((202), (004) et (220)), soit situées à des distances angulaires où le facteur de forme f devient très imprécis ((213) et (301)).

Tableau 1.

hkl	Intensités magnétiques ($\mathcal{F} F^2$ en μ_B^2/maille)	
	Expérimentales	Calculées
101	1928	1907
002	0	0
110	56	56
112	1830	1819
200		
103	268	304
211	383	415
202	1082	755
004	1250	1613
220	1955	1613
213	4390	3886
301	1368	1238

La structure magnétique du manganite de chrome n'a été décrit ici que dans une portion de l'espace du cristal caractérisée par la direction $[110]$ comme axe de symétrie des moments des sites B. Il y a évidemment dans un cristal quadratique trois autres directions

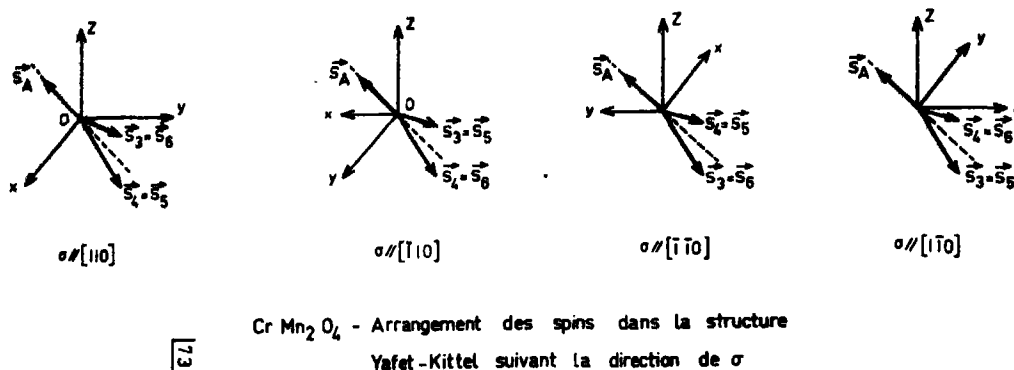


Fig. 5. Configuration des moments B suivant les quatre directions de facile aimantation équivalentes de la forme $[110]$.

équivalentes: $[1\bar{1}0]$, $[\bar{1}10]$ et $[\bar{1}\bar{1}0]$ suivant lesquelles des structures magnétiques d'énergie égale existent. La diffraction de neutrons prouve qu'effectivement existent les mêmes structures de type Yafet-Kittel mais que la disposition relative des quatre moments B dans cette configuration change quand on passe d'une direction de facile aimantation à une autre, comme cela est représenté Fig. 5. Cette propriété a été également trouvée dans le cas des manganites de cobalt [4] et de fer [5].

Il faut remarquer à ce sujet qu'un traitement théorique de champ moléculaire classique (par exemple comme l'on fait Yafet et Kittel [3]) ne permet pas *a priori* d'expliquer cette propriété. En effet, si seule, la minimisation d'une énergie d'interaction isotrope entre moments magnétiques permet de définir une structure stable, celle-ci est indépendante de son orientation dans l'espace. Or le fait frappant est qu'à basses températures tous les manganites quadratiques et en particulier CrMn_2O_4 , sont extrêmement anisotropes, il est donc impossible dans tout essai de traitement théorique de négliger l'anisotropie quelle qu'en puisse être l'origine. Dans un article précédent [6] en partant d'hypothèses simples et en considérant l'anisotropie (d'échange et locale) comme élément fondamental dans le calcul de champ moléculaire, nous avons déterminé les structures magné-

tiques possibles dans les spinelles à 0°K. Un des résultats fondamentaux de cette étude est qu'une configuration magnétique anisotrope dépend essentiellement de sa direction dans l'espace cristallographique. A une structure d'énergie donnée, dans une direction donnée, correspondent dans les directions cristallographiques équivalentes, d'autres structures d'énergie égale mais dont les arrangements internes de moments sont différents. La structure de type Yafet-Kittel d'axe $[110]$ n'est qu'un cas particulier d'une structure anisotrope plus complexe et il est remarquable de constater que les configurations des moments B prévues théoriquement pour les quatre motifs dirigés respectivement suivant les quatre directions équivalentes $[110]$ sont exactement celles qui ont été déterminées expérimentalement pour CrMn_2O_4 (voir Fig. 5). Ce résultat est très important car il montre le rôle que joue l'anisotropie dans CrMn_2O_4 et nous verrons qu'il sera nécessaire d'appliquer les mécanismes théoriques de déformation des structures anisotropes en fonction de leurs changements de direction pour expliquer le comportement de CrMn_2O_4 sous l'action d'un champ magnétique extérieur.

3. COMPORTEMENT DU MOTIF MAGNETIQUE DE CrMn_2O_4 DANS UN CHAMP EXTERIEUR

La Fig. 6 représente le spectre de diffraction de neutrons à 4,2°K lorsqu'un champ

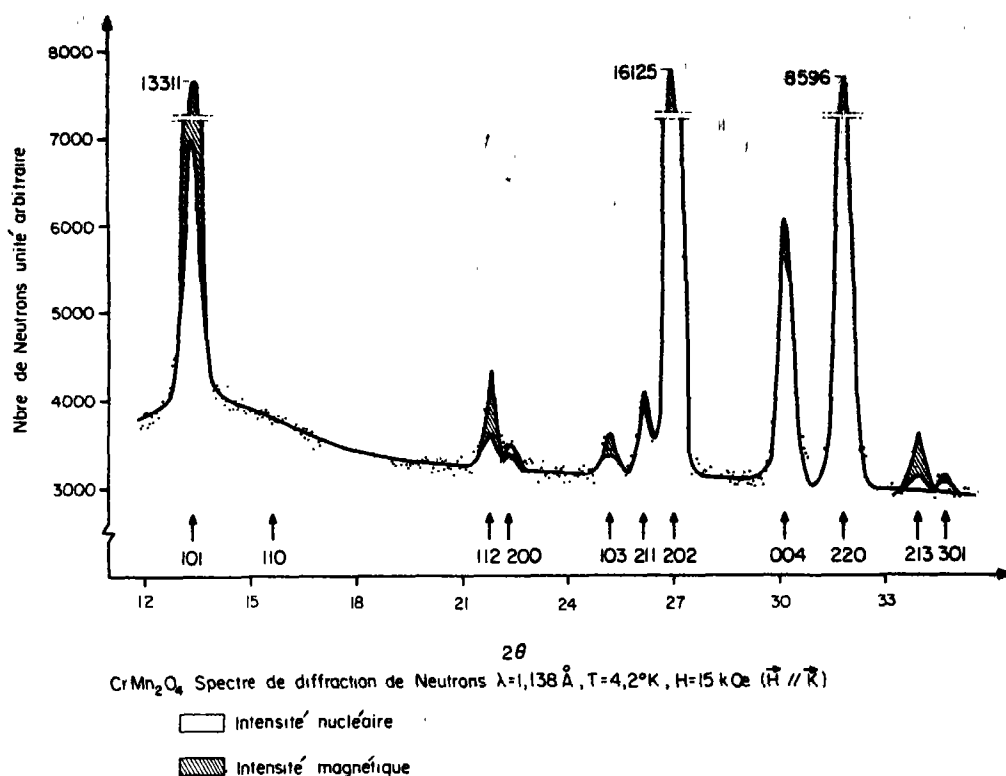


Fig. 6. Spectre de diffraction de neutrons à 4,2°K. Un champ extérieur de 15 kOe est appliqué suivant K.

magnétique de 15 kOe est appliqué suivant le vecteur de diffusion K . Seule l'intensité magnétique de la raie de surstructure $[110]$ devient nulle. Pour expliquer ce fait, revenons tout d'abord à des considérations générales sur les parois séparant des domaines magnétiques dans un monocristal.

3.1 Parois

Considérons un cristallite d'un composé ferrimagnétique quadratique dont la direction de facile aimantation est $[110]$. A champ extérieur nul, il est divisé en quatre sortes de domaines de volume total identique correspondant aux directions de facile aimantation équivalentes: $[110]$, $[\bar{1}10]$, $[1\bar{1}0]$ et $[\bar{1}\bar{1}0]$. Ces domaines sont séparés par des parois.

Lorsque l'on a affaire à une configuration de moments déterminée par des considérations

d'échange magnétique isotrope (par exemple modèles de Néel ou Yafet-Kittel) une paroi séparant deux domaines est la région dans laquelle il y a rotation progressive de l'ensemble du motif magnétique depuis une direction de facile aimantation jusqu'à une autre. La disposition relative des moments n'est pas affectée par le changement de direction.

Dans le cas où la disposition relative des moments B dépend de la direction de facile aimantation comme cela est le cas pour CrMn₂O₄ et pour les structures magnétiques anisotropes, le rôle d'une paroi ne doit pas être seulement de faire passer le motif d'une direction à une autre mais également de modifier la configuration des moments pour que de part et d'autre de cette paroi, les motifs magnétiques soient énergétiquement stables. La notion de paroi est ici beaucoup plus

complexe que celle admise classiquement.

Dans un article précédent [6] nous avons étudié théoriquement l'évolution d'un motif magnétique anisotrope sous l'action d'un champ extérieur et mis en évidence sa déformation en fonction de sa direction dans l'espace. Il y a dans le cas de ce type de structures anisotropes une solution de continuité entre les configurations de deux motifs de directions différents et en l'absence de champ extérieur, une paroi séparant deux domaines de configurations différentes peut être constituée par le même mécanisme. Ceci correspond à la notion élargie de paroi, nous l'appellerons paroi 'avec flipping' pour bien montrer qu'elle sépare deux domaines où l'arrangement des moments est différent.

Admettons maintenant que le composé ferrimagnétique en question soit CrMn_2O_4 , il a donc en première approximation une structure de type Yafet-Kittel et on a vu expérimentalement que l'arrangement des moments B est différent suivant les directions de facile aimantation $[110]$ (Fig. 5). On ne fait pour l'instant aucune hypothèse sur l'origine de cette structure.

Appliquons maintenant le champ magnétique extérieur sur le cristallite suivant la direction $[110]$. Suivant la définition (isotrope ou anisotrope) de la structure, le comportement est différent:

(1) La structure est isotrope: la rotation du motif magnétique dans une paroi classique n'affecte pas sa configuration, le déplacement de cette paroi dans chaque domaine ne fait que changer l'orientation du motif sans en modifier l'arrangement interne. Quand le champ appliqué est devenu suffisamment grand pour qu'il ne subsiste plus qu'une seule direction d'aimantation pour tous les motifs, on se trouverait alors en présence d'un cristal en apparence monodomaine. Ce monodomaine serait effectivement caractérisé par une direction d'aimantation unique mais il comporterait quatre 'sous-domaines' égaux correspondant aux quatre motifs différant par la configuration des moments de leurs sous-réseaux B .

Ces 'sous-domaines' seraient séparés eux-mêmes par exemple par des parois de type interphase.

(2) Les parois sont du type dit 'avec flipping' décrit plus haut, dans ce cas, leurs déplacements correspondent non seulement au changement de l'orientation des motifs mais aussi au réarrangement des moments des sous-réseaux B pour que lorsque le champ est devenu suffisamment grand il ne subsiste plus qu'un véritable monodomaine constitué d'un seul type de configuration magnétique le long d'une direction unique.

Le premier cas correspond à la situation où seul l'échange isotrope définit la structure magnétique, le second à celle où l'anisotropie est un facteur déterminant. Dans le cas de CrMn_2O_4 , le fait que la raie $[110]$ soit nulle quand un champ magnétique est appliqué, va nous permettre de trancher.

A champ nul; pour la réflexion (110) , les facteurs de structure correspondant aux quatre motifs sont: O pour celui dirigé suivant la direction $[110]$ et F pour celui dirigé suivant la direction $[\bar{1}10]$ de même O et F pour ceux dirigés respectivement suivant $[\bar{1}\bar{1}0]$ et $[1\bar{1}0]$.

F est proportionnel à la composante transversale des moments B et, est perpendiculaire au plan (001) ainsi qu'à K . L'intensité de la raie (110) à champ nul est donc $I = 2F^2$.

Si on applique un champ extérieur suffisamment grand (15 kOe) suivant la direction $[110]$ pour qu'il ne subsiste plus qu'un monodomaine dans un cristallite bien orienté, l'intensité de la raie (110) dépend du mécanisme de déplacement de parois:

Si en effet les parois sont de type classique, c'est-à-dire sans 'flipping' de moments, leurs déplacements n'auront pour effet que de changer la direction des motifs sans en modifier l'arrangement interne. On retrouverait dans ce cas un 'monodomaine' comportant quatre sous-domaines égaux dont les facteurs de structure pour la réflexion (110) sont encore O, F, O et F , l'intensité de la raie (110) est $I = 2F^2$ elle n'aurait pas varié par rapport à sa valeur à champ nul.

Si au contraire les parois sont de type 'avec flipping', leurs déplacements, tout en changeant la direction des motifs, en modifient la configuration interne pour finalement aboutir au monodomaine ne contenant plus qu'un seul type de motif. Dans ce cas donc, lorsque le champ appliqué suivant la direction [110] est suffisamment grand pour qu'il ne reste plus dans le cristallite qu'un seul motif magnétique caractérisé par la disposition relative des moments B d'axe [110], le facteur de structure de la réflexion [110] est nul, l'intensité de la raie [110] est donc également nulle.

Il est bien évident que pour des cristallites orientés suivant les trois autres directions cristallographiques équivalentes: $[\bar{1}\bar{1}0]$, $[\bar{1}\bar{1}0]$ et $[1\bar{1}0]$, le raisonnement est identique et il conduit au même résultat.

La raie (110) étant nulle avec champ, seul le type de parois dites 'avec flipping' peut rendre compte de l'expérience. L'origine de la structure et des propriétés magnétiques est donc l'anisotropie. Il va donc être nécessaire de tenir compte des déformations des configurations en fonction de leur direction dans l'espace sous l'action d'un champ extérieur comme cela a été prévu théoriquement [6].

3.2 Action du champ magnétique sur l'intensité des raies de diffraction et étude de l'anisotropie de CrMn_2O_4

La diffraction de neutrons permet de suivre l'évolution de l'intensité des raies en fonction du champ appliqué suivant le vecteur de diffusion K . Ces intensités dépendent de:

- l'orientation dans l'espace des motifs de chacun des domaines (donc de l'anisotropie)
- du volume des différents domaines
- de la déformation des motifs.

Les raies sur lesquelles la précision expérimentale est bonne et qui permettent donc une exploitation quantitative des résultats, sont au nombre de trois: (101), (112) et (200). Les

deux dernières seront étudiées en premier en raison de leurs directions particulières par rapport au motif.

3.2.1 *Raie (200)*. La raie (200) est particulièrement intéressante car son intensité ne dépend que des moments des sites A , d'autre part, sa direction est contenue dans le plan (001) à 45° de la direction de facile aimantation.

Pour pouvoir aller plus avant dans l'interprétation des résultats expérimentaux, il est nécessaire de faire quelques hypothèses sur l'évolution de l'arrangement des moments B en fonction du champ. Nous supposons donc que tous les moments restent contenus dans un plan vertical lorsque l'aimantation du motif se déplace dans le plan de base. Nous supposons de plus que la variation des angles entre les spins, en fonction du déplacement du motif dans le plan de base, est linéaire. Ces hypothèses ne sont que des approximations que permettent la relative précision expérimentale et le manque de renseignements nécessaires, fournis par la diffraction de neutrons sur poudre.

Par rapport à la direction du champ [100], il existe donc dans le cas de la raie (200), quatre sortes de domaines: deux à 45° et deux à 135° — nous continuerons à les appeler ainsi même si les motifs se sont déplacés de leur position d'origine. Sous l'action du champ, tous les motifs commencent à tourner, puis disparaissent les domaines 'à 135° '. Dès lors, seuls subsistent les deux domaines 'à 45° ' de volume égal et qui donnent la même contribution à l'intensité de la raie (200) (Fig. 7). Il est alors possible de déterminer la loi d'anisotropie dans le plan (001).

Si α est l'angle entre la direction de facile aimantation et celle de l'aimantation du motif, en tenant compte de la symétrie quadratique globale, l'énergie d'anisotropie dans le plan de base peut s'écrire:

$$E_{a(001)} = K_1 \sin^2 2\alpha + K_2 \sin^2 4\alpha$$

et l'énergie magnétique totale:

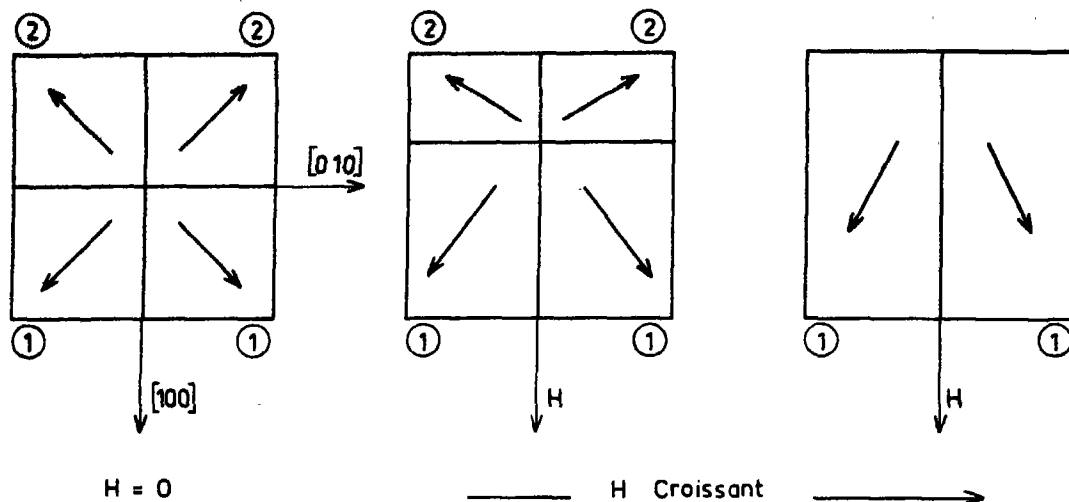


Fig. 7. Représentation schématique de l'évolution des domaines en fonction de l'intensité croissante du champ extérieur dirigé suivant la direction [100]. (1) Domaines 'à 45°' (2) Domaines 'à 135°'.

$$E_{\pi(001)} = K_1 \sin^2 2\alpha + K_2 \sin^2 4\alpha - M.H.$$

La position d'équilibre du motif est donc définie par:

$$\frac{\partial E_T}{\partial \alpha} = 2K_1 \sin 4\alpha + 4K_2 \sin 8\alpha - \frac{\partial}{\partial \alpha} (MH) = 0.$$

Pour la direction [200] et les domaines 'à 45°': $MH = MH \cos((\pi/4) - \alpha)$ et $(\partial/\partial \alpha)(MH) = MH \sin((\pi/4) - \alpha)$.

La variation de l'intensité de la raie (200) en fonction de la valeur du champ appliqué (Fig. 8) (lorsque ce champ est supérieur à 4 kOe pour qu'il ne reste plus que des domaines 'à 45°') permet de déterminer K_1 et K_2 . On trouve:

$$K_1 = 3 \cdot 10^4 \text{ ergs/g}$$

$$\text{et } K_2 = -7,5 \cdot 10^3 \text{ ergs/g}$$

l'énergie d'anisotropie s'écrit donc:

$$E_{a(001)} = 3 \cdot 10^4 \sin^2 2\alpha - 7,5 \cdot 10^3 \sin^2 4\alpha.$$

Il est remarquable de constater que cette expression est identique à:

$$E_{a(001)} = 3 \cdot 10^4 \sin^4 2\alpha.$$

Connaissant la loi d'énergie d'anisotropie, il est possible de calculer le déplacement des motifs 'à 135°' entre 0 et 4 kOe (champ où ils disparaissent) en appliquant l'équation d'équilibre dérivée de

$$E_{\pi(001)} = 3 \cdot 10^4 \sin^4 2\alpha - MH \cos\left(\frac{3\pi}{4} - \alpha\right).$$

Comme cela était prévu, le motif 'à 135°' se déplace progressivement dans le plan (001) pour se rapprocher de la direction du champ, mais quand ce dernier atteint une certaine valeur critique, il n'existe plus de minimum d'énergie stable dans la région considérée. Le motif se déplace alors brusquement pour venir occuper la position stable la plus proche qui est celle du motif 'à 45°'. Ceci est très bien représenté Fig. 9 où sont mis en évidence les déplacements des motifs 'à 45°' et 'à 135°' correspondant aux déplacements des positions des minimums de l'énergie magnétique totale en fonction de l'intensité croissante du champ extérieur appliqué suivant la direction [100]. Le champ correspondant à la disparition d'un minimum de l'énergie sera appelé 'champ seuil de flipping' puisqu'il correspond non seulement au brusque passage d'une direc-

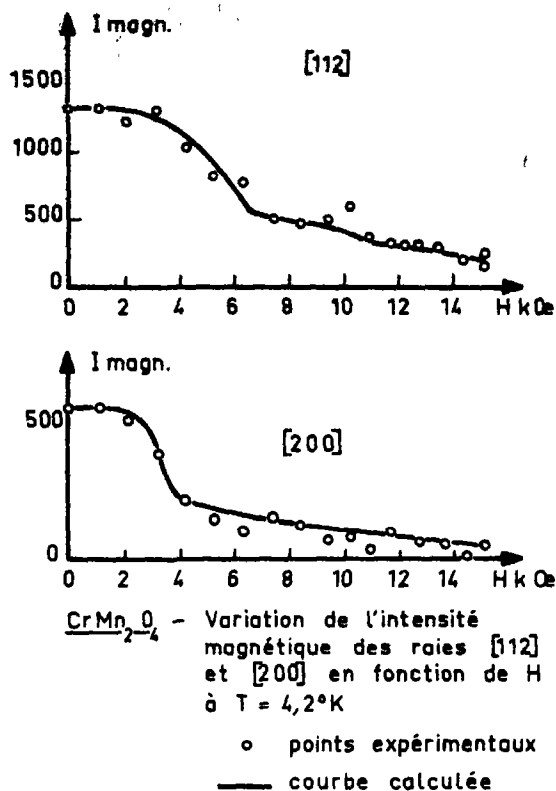


Fig. 8. Variation de l'intensité magnétique (\mathcal{F}^2 en μ_B^2/maille) des raies (200) et (112) en fonction du champ extérieur parallèle à K.

tion à une autre mais également à un réarrangement des moments des sous-réseaux B ('flipping').

Ce champ seuil de flipping correspond évidemment à la disparition du domaine magnétique considéré. Sa valeur est une fonction très pointue des valeurs des constantes d'anisotropie, elle permet ainsi de préciser nettement K_1 et K_2 .

Connaissant l'évolution de la direction des deux motifs en fonction de la valeur du champ appliqué, il est possible de calculer leur contribution à l'intensité globale de la raie [200] et par ajustement à la courbe expérimentale de déduire la variation du volume relatif des domaines 'à 135° ' en fonction du champ appliqué (Fig. 10).

3.2.2 Raie (112). La raie (112) a un facteur

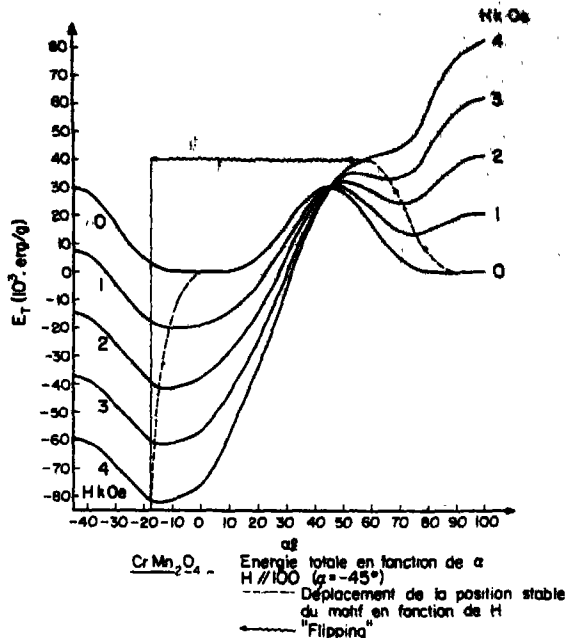


Fig. 9. Variation de l'énergie magnétique totale dans le plan (001) en fonction de α et pour différentes valeurs du champ extérieur. Ce champ H est appliqué suivant la direction [100], c'est-à-dire à $\alpha = -45^\circ$. Les lignes pointillées représentent le déplacement des motifs 'à 45° ' et 'à 135° ' en fonction de H .

de structure plus compliqué que la raie (200), sa direction est cependant intéressante: elle est en effet contenue dans le plan ($\bar{1}10$) où est également située la direction de facile aimantation [110].

Par rapport à la direction [112] existent quatre domaines magnétiques que nous appellerons par extension: 'à 0° ' (1 domaine), 'à 90° ' (2 domaines) et 'à 180° ' (1 domaine), ces angles sont ceux que font les plans des motifs à champ nul avec la projection de H dans le plan de base (Fig. 11).

On voit donc que lorsque les deux sortes de domaines 'à 90° ' et 'à 180° ' auront disparu, il sera possible de calculer l'anisotropie dans un plan vertical. Or comme nous allons le voir un peu plus loin, l'énergie d'anisotropie est beaucoup plus grande dans ce plan que dans le plan de base, le déplacement du motif à 15 kOe n'est pas assez grand (environ 10°)

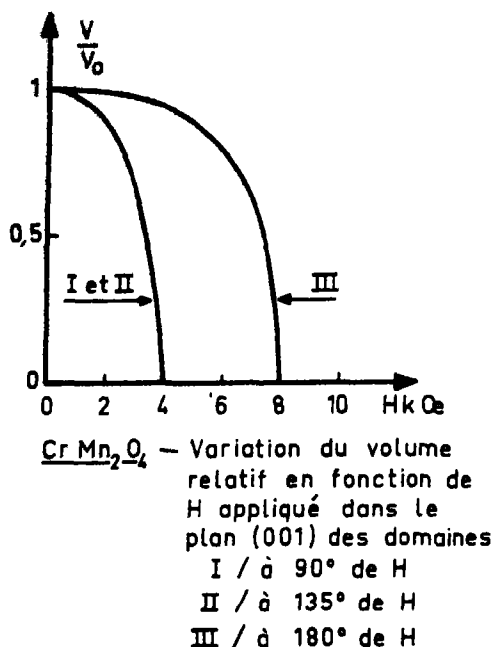


Fig. 10. Variation en fonction du champ appliqué dans le plan (001), du volume relatif des domaines (I) à 90° de H (II) à 135° de H (III) à 180° de H .

l'énergie d'anisotropie a été choisie simplement: $E_{a(z)} = C \sin^2 \varphi$, φ étant l'angle entre l'axe du motif et le plan (001). L'équation d'équilibre en présence d'un champ est:

$$\frac{\partial E_T}{\partial \varphi} = C \sin 2\varphi - \frac{\partial}{\partial \varphi} (MH) = 0.$$

En considérant les champs supérieurs à 11 kOe pour qu'il ne subsiste plus que le domaine 'à 0° ' on aboutit à:

$$C = 1 \cdot 10^6 \text{ ergs/g.}$$

C'est une valeur assez forte qui explique bien le faible déplacement du motif dans le plan vertical (Fig. 12). Comme nous l'avons dit plus haut, l'arrangement relatif des moments des sous-réseaux B doit se modifier en fonction de son déplacement dans le plan vertical, nous avons admis pour ce calcul qu'une si faible désorientation (10° à 15 kOe) ne modifiait pas la structure. Ceci est d'ailleurs largement justifié par la précision expérimentale.

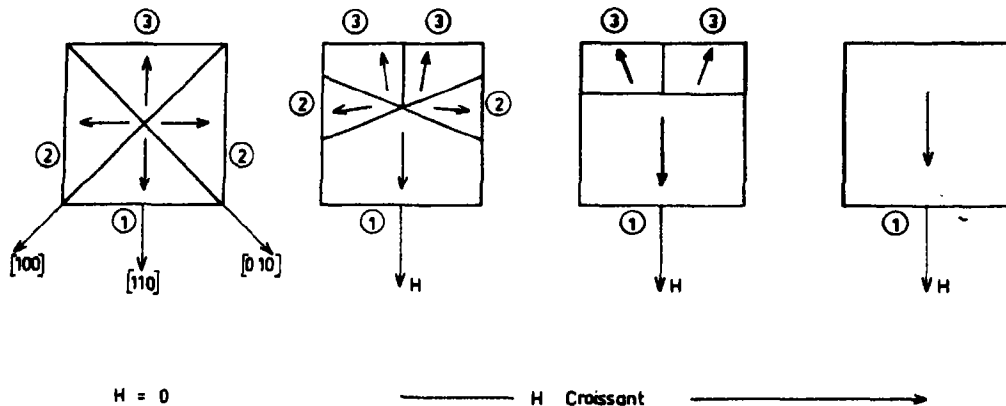


Fig. 11. Représentation schématique de l'évolution des domaines en fonction de l'intensité croissante du champ extérieur dirigé suivant la direction $[110]$ (projection de $H // [112]$ dans le plan (001) (1) Domaines 'à 0° ' (2) Domaines 'à 90° ' (3) Domaines 'à 180° '.

pour que la variation d'intensité de la raie de diffraction soit mesurée avec précision. Dans ces conditions, on ne peut espérer déterminer des constantes d'ordre élevé et la forme de

Connaissant maintenant les deux lois d'anisotropie: dans le plan de base (tirée de la raie $[200]$) et dans le plan vertical (tirée de la raie $[112]$), il est possible de calculer les

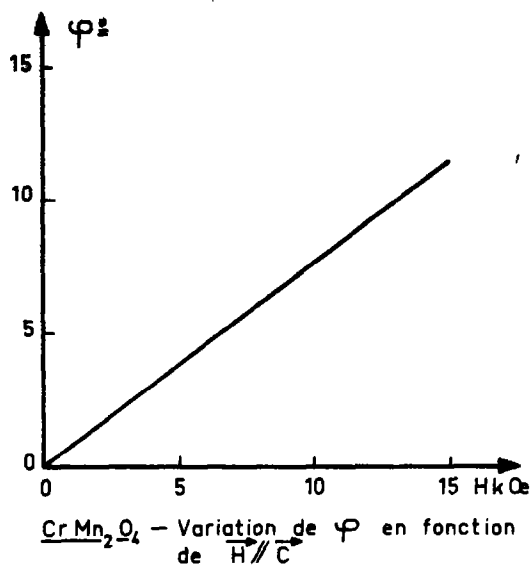


Fig. 12. Variation de φ en fonction de H parallèle à la direction [001].

déplacements des motifs des domaines 'à 90°' et 'à 180°' par rapport à la direction [112]. Les Figs. 13 et 14 représentent les déplacements des motifs 'à 0°', 'à 90°' et 'à 180°' correspondant aux déplacements des minimums de l'énergie magnétique totale en fonction de l'intensité croissante du champ extérieur appliqué suivant la direction [110]. Les champs seuils de flipping des motifs 'à 90°' et 'à 180°' vers le domaine 'à 0°' sont respectivement de 4 et 8 kOe (composantes de H dans le plan (001) suivant la direction [110]).

Les lois de déplacement des différents motifs résumées Figs. 12 et 15 étant connues, il est possible de calculer la contribution de chacun d'eux à l'intensité de la raie (112). Il faut pour cela tenir compte des faits suivants:

(1) Le facteur de structure de la raie (112) dépend des moments B il faut donc tenir compte des déformations des configurations que nous prendrons de la manière définie en 3.2.1.

(2) Les deux motifs des domaines 'à 90°' ne sont pas identiques en effet, au fur et à mesure qu'ils se rapprochent de la direction du champ, dans un cas ce sont les moments

M_3 et M_4 qui se rapprochent du plan de base et dans l'autre cas les moments M_5 et M_6 . La contribution de chacun de ces domaines à l'intensité totale est différente.

(3) Le motif du domaine 'à 180°' à champ nul, peut se rapprocher de la direction du champ en tournant dans un sens ou dans l'autre. La probabilité est égale et, il faudra donc pondérer la contribution à l'intensité magnétique de la raie de chacun des deux cas possibles. En effet, la déformation de la configuration, bien qu'étant globalement la même se différencie par la permutation des moments B qui 'flipent' suivant le sens de rotation du motif.

Ayant pris en considération tous ces phénomènes, un calcul numérique assez long permet de connaître toutes les contributions à l'intensité de la raie (112) et par l'ajustement à la courbe expérimentale de déterminer les variations des volumes relatifs des différents domaines en fonction de l'intensité du champ magnétique extérieur (Fig. 10).

3.2.3 Raie (101). L'intensité de la raie (101) est celle qui est connue expérimentalement avec le plus de précision. Son facteur de structure dépend des moments des sites A et B .

Par rapport au champ magnétique appliqué suivant la direction [101], il existe quatre domaines semblables à ceux qui existaient par rapport à la raie (200). Nous connaissons grâce à l'étude systématique des deux raies (200) et (112) les lois d'anisotropie correspondant au plan de base et au plan vertical, donc les variations de volume relatif de tous les domaines suivant leur orientation, les champs seuils de flipping et la manière dont se passe ce flipping.

Il est donc possible de calculer *a priori* la variation de l'intensité totale de la raie (101) en fonction du champ magnétique appliqué suivant le vecteur de diffusion K (H compris entre 0 et 15 kOe).

La Fig. 16 montre l'excellent accord entre intensités expérimentale et calculée de la raie (101) en fonction du champ.

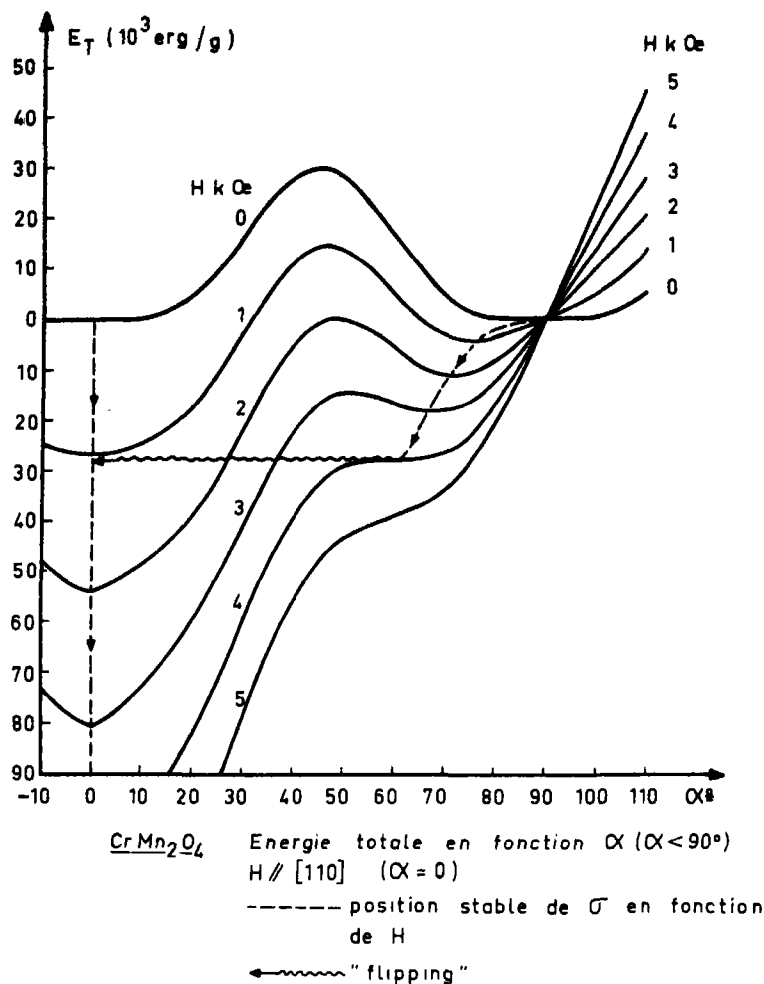


Fig. 13. Variation de l'énergie magnétique totale dans le plan (001) en fonction de α et pour différentes valeurs du champ extérieur. Ce champ H est appliqué suivant la direction $[110]$ ($\alpha = 0$). Les lignes pointillées représentent les déplacements des motifs 'à 0° ' et 'à 90° ' en fonction de H .

Cet accord confirme ainsi l'existence des mécanismes proposés et donc de l'origine anisotrope de la structure magnétique de CrMn_2O_4 car comme cela a déjà été fait remarquer: un modèle Yafet-Kittel défini uniquement par de l'échange isotrope ne peut avoir ces propriétés.

La diffraction de neutrons sur poudre n'apporte pas assez de renseignements — même en ne considérant que des moments moyens dans chaque sous-réseau — pour permettre de

déterminer quantitativement les paramètres théoriques définissant une structure anisotrope [6] mais il est extrêmement intéressant de constater l'excellent accord expérimental découlant de l'application des mécanismes théoriques au cas de CrMn_2O_4 .

4. EVOLUTION THERMIQUE

Le moyen le meilleur pour suivre l'évolution des paramètres définissant la structure

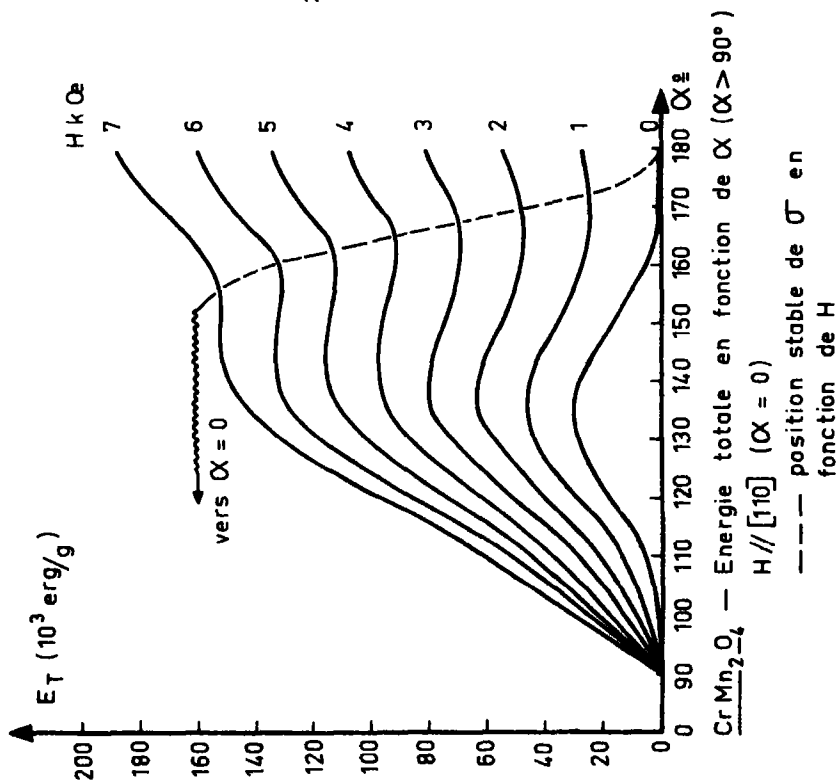


Fig. 14. Suite de la Fig. 13 pour les valeurs de α supérieures à 90° . La ligne pointillée représente le déplacement du motif à 180° .

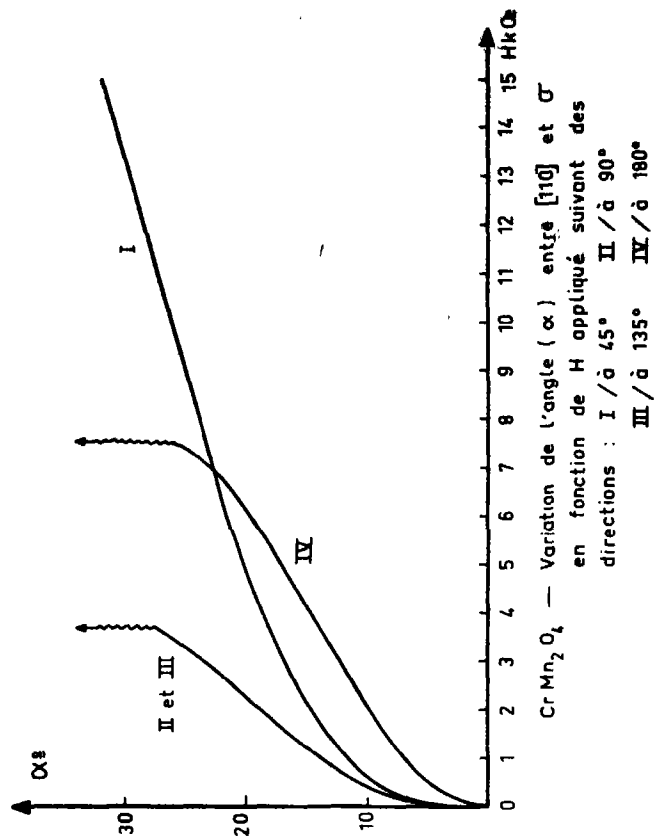


Fig. 15. Variation de l'angle entre un motif magnétique et sa direction à champ nul, en fonction de l'intensité croissante de H appliqué dans le plan (001): (I) à 45° (II) à 90° (III) à 135° (IV) à 180° de la direction de facile aimantation.

**CrMn₂O₄ VARIATION THERMIQUE
DE L'INTENSITE DES RAIES :
[101], [110], [112] et [200]**

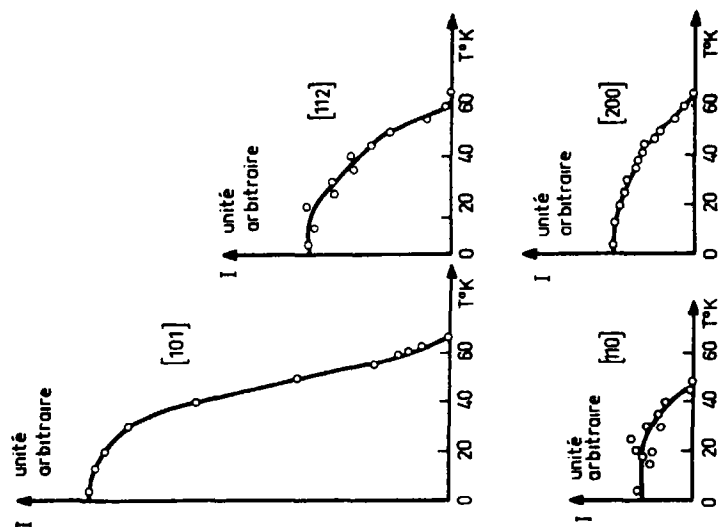


Fig. 17. Variation thermique de l'intensité magnétique des raies de diffraction: (101), (110), (112) et (200).

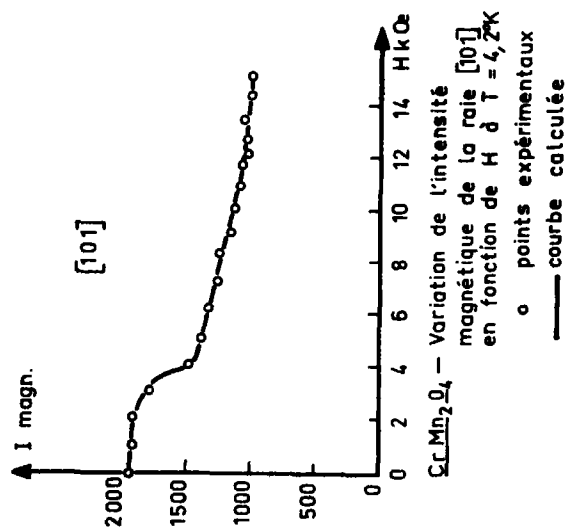


Fig. 16. Comparaison entre valeurs expérimentale et calculée de la variation de l'intensité de la raie (101) (\mathcal{F}^2 en μ_B^2 /maille) en fonction du champ magnétique (H // K).

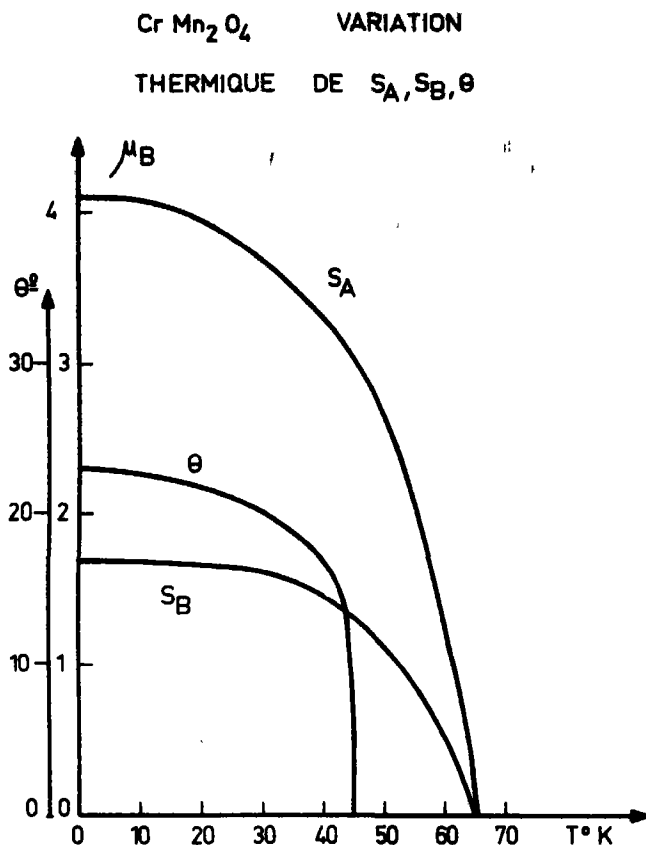


Fig. 18. Variation thermique des longueurs des moments S_A et S_B et du demi angle d'ouverture θ des moments B .

magnétique de CrMn_2O_4 en fonction de la température est de suivre la variation thermique de l'intensité des raies de diffraction de neutrons.

Les résultats expérimentaux concernant quatre raies: (110), (101), (200) et (112) sont représentés Fig. 17.

L'intensité d'la raie (110) s'annule à 45°K donc avant la température de Curie. L'intensité de cette raie étant proportionnelle à la composante transversale des moments B , le fait qu'elle devienne nulle, indique donc la fermeture de l'angle, entre les moments B . Au-dessus de la température de transition, la structure devient donc colinéaire: modèle de Néel.

L'interprétation des variations thermiques de toutes les intensités permet de calculer les longueurs des moments S_A et S_B ainsi que celle de θ en fonction de la température. Ces variations sont représentées Fig. 18.

La variation thermique du moment S_A est très proche de celle calculée théoriquement avec $\mathcal{T} = \frac{1}{2}$, ce qui semble normal puisque Mn^{2+} occupe les sites tétraédriques A et possède un spin de $\frac{1}{2}$. Or, la valeur du moment déterminé expérimentalement n'est que de $4,1 \mu_B$, l'hypothèse de fortes fluctuations dans sa direction est donc renforcée par ce dernier résultat. Il faut pourtant préciser que la concordance entre la variation thermique expérimentale et celle calculée théoriquement, n'est

pas une preuve suffisante car, l'écart entre les courbes calculés avec $\mathcal{T} = \frac{1}{2}$ et $\mathcal{T} = \frac{1}{2}$ n'est pas grand par rapport à la précision expérimentale.

Remerciements—Nous remercions Monsieur le Professeur Herpin qui a suivi de près ce travail et Monsieur Mériel qui nous a constamment aidés par de nombreuses discussions.

REFERENCES

1. BUHL R., *J. Phys. Chem. Solids* **30**, 805 (1969).
2. NÉEL L., *Ann. Phys.* **3**, 137 (1948).
3. YAFET Y. and KITTEL C., *Phys. Rev.* **87**, 290 (1952).
4. BOUCHER B., BUHL R. and PERRIN M., *J. appl. Phys.* **39**, 632 (1968).
5. BOUCHER B., BUHL R. and PERRIN M., *J. appl. Phys.* **40**, 1126 (1969).
6. BOUCHER B., BUHL R. and PERRIN M., *J. Phys. Chem. Solids*, **31**, 2251 (1970).

LE VOLUME D'ACTIVATION POUR L'AUTODIFFUSION DU PLUTONIUM EN PHASE ϵ

J. A. CORNET

D.Tech, SPu, SMPuA-C.E.N. de Fontenay-aux-Roses-92, France

(Received 18 March 1970)

Résumé—On décrit un ensemble expérimental permettant d'obtenir des pressions hydrostatiques variables de 0 à 20 Kbars à des températures allant jusqu'à 1000°C et utilisé pour l'étude de l'autodiffusion sous pression du plutonium en phase ϵ . Les quelques résultats expérimentaux obtenus indiquent que la vitesse d'autodiffusion dans cette phase augmente sous pression: le volume d'activation est négatif ($\Delta V = -4.9 \text{ cm}^3$ soit -33.6 pour cent du volume molaire); les corrélations généralement utilisées n'interdisent pas un tel résultat qui semble cependant peu compatible avec un mécanisme de diffusion lacunaire. On discute de la possibilité d'un mécanisme par interstitiels.

Abstract—An experimental device is described which allows to obtain hydrostatic pressures in the range 0-20 kbars at temperatures up to 1000°C; it was used for the study of self diffusion under pressure in the b.c.c. ϵ phase of plutonium. Only a few experimental results were obtained, but they indicate that the rate of self-diffusion in that phase increases under pressure: activation volume for self-diffusion is negative ($\Delta V = -4.9 \text{ cm}^3$, i.e. -33.6 per cent of the molar volume). The correlations generally used do not preclude such a result, but it does not seem to be consistent with a diffusion vacancy-mechanism. The possibility of an interstitially mechanism is discussed.

1. INTRODUCTION

L'ÉTUDE récente de l'autodiffusion sous pression normale du plutonium en phase ϵ [1] a permis de placer ce métal dans le groupe de plus en plus dense des métaux cubiques centrés dits 'anormaux' du point de vue de la diffusion, pour lesquels aucune théorie satisfaisante du mécanisme mis en jeu n'a pris encore jour: le facteur de fréquence D_0 est très faible et l'enthalpie d'activation ΔH beaucoup plus petite que ne le prévoient les corrélations semi-empiriques de Gibbs [2] ou de Sherby et Simnad [3] (améliorations de la loi de Van Liempt $\Delta H = 34 T_f$, T_f point de fusion) qui donnent pourtant de bons résultats pour les métaux C.F.C. où le mécanisme de diffusion monolacunaire est bien admis.

Sans négliger, dans le cas du plutonium, l'influence possible de paramètres incontrôlables (lacunes extrinsèques liées à l'oxygène en solution ou rôle des dislocations introduites par les changements de phase [1]) on peut se demander si un mécanisme de diffusion avec une aussi faible enthalpie d'activation peut être lacunaire et s'il en est ainsi, quelle peut

être la configuration de la lacune. C'est pour apporter un élément de réponse supplémentaire que nous avons entrepris de mesurer une nouvelle grandeur directement attachée au défaut: son volume d'activation, somme de son volume de formation et de son volume de migration. Parmi toutes les méthodes généralement utilisées pour effectuer cette mesure, l'étude de la variation du coefficient d'autodiffusion en fonction de la pression hydrostatique semble la plus précise et la mieux adaptée bien que dans le cas du plutonium le domaine de pressions utilisables soit réduit [4-6] (Fig. 1).

2. TECHNIQUES EXPÉRIMENTALES

Les recuits de diffusion sous pression et à température constantes ont été réalisés en boîte à gants et sous atmosphère d'argon purifié à l'aide d'une presse hydraulique de 100 tonnes déjà décrite [7]. Par suite du faible domaine de pression exploitable (Fig. 1), nous avons choisi pour cette étude une chambre de compression construite sur le principe classique 'piston cylindre'; un seul étage est néces-

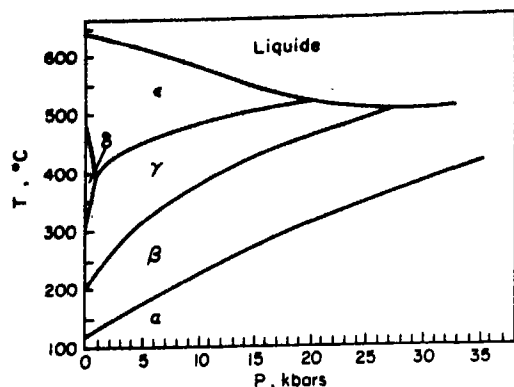


Fig. 1. Le diagramme de phases du plutonium jusqu'à 35 Kbars [4].

saire et les dimensions relativement importantes du coeur (Fig. 2) permettent d'envisager des conditions d'hydrostativité supérieures à celles obtenues dans la chambre à double étage et à fortiori dans l'enclume 'Belt' utilisées primitivement pour faire grossir des grains de plutonium en phase α [7]. Le milieu transmetteur de pression est la pyrophyllite et la chauffage est réalisé à coeur à l'aide d'un résistor en graphite de 1 mm d'épaisseur alimenté sous faible tension (3 à 5 V) (Fig. 3). La puissance nécessaire pour monter à la température de 600°C est voisine de 800 W.

L'inertie thermique du système four-chambre de compression étant extrêmement

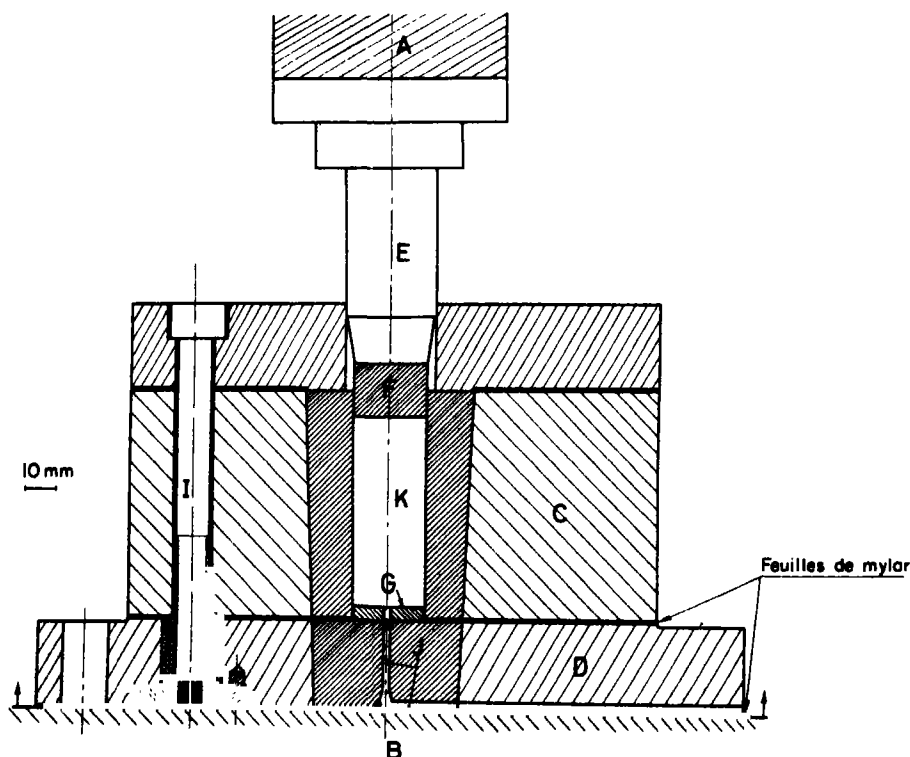


Fig. 2. Schéma de la chambre de compression type 'piston cylindre'. Carbone de tungstène. A — Plateau supérieur fixe. B — Plateau inférieur mobile. C — Chambre de compression proprement dite en acier MTC, 60 Rc (Ugine) et coeur en carbone de tungstène. D — Enclume inférieure (prise de potentiel). E — Piston supérieur. F — Grain poussoir en carbone de tungstène. G — Amenée de puissance avec passage de thermocouple, isolée électriquement par dépôt d'alumine. H — Canon isolant. I — Vis d'assemblage. J — Passage de thermocouples. K — Enceinte de compression (cf. Fig. 3(a)).

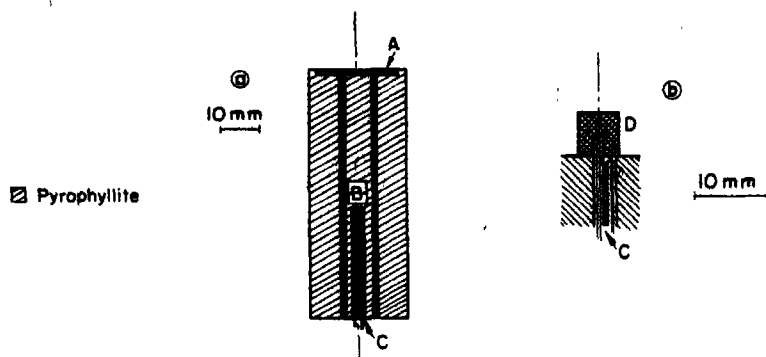


Fig. 3. Microfour pour études aux hautes pressions: diffusion (a) et analyse thermique différentielle (b). Pyrophyllite \square . A—résistor en graphite (épaisseur 1 mm). B—couple de diffusion. C—gaine bifilaire en alumine. D—échantillon pour analyse thermique différentielle.

faible, une régulation par alimentation discontinue s'est révélée impossible. C'est pourquoi nous avons dû, tout d'abord, stabiliser la tension d'alimentation à mieux de 0,3 pour cent puis réaliser un système d'asservissement de la température: l'écart entre la température réelle et la température désirée, modulé par des actions proportionnelle, intégrale et dérivée fait varier, après amplification, la saturation du noyau magnétique, c'est-à-dire l'impédance, d'une self placée en série avec le four. On dispose donc d'une tension d'alimentation variable de façon con-

tinue jusqu'au moment où la température désirée est atteinte. Le réglage des différentes actions est délicat; il dépend, de plus, étroitement de la configuration du four utilisé et des températures de traitement désirées mais il nous a permis de réaliser sur tous nos recuits de diffusion une régulation de température à 1° près. On donne Fig. 4(b) une courbe de traitement typique $T = f(t)$; son allure de fonction créneau rend négligeable l'incertitude sur le temps de recuit et inutile la correction de montée en température.

Afin de s'assurer de l'hydrostaticité de la

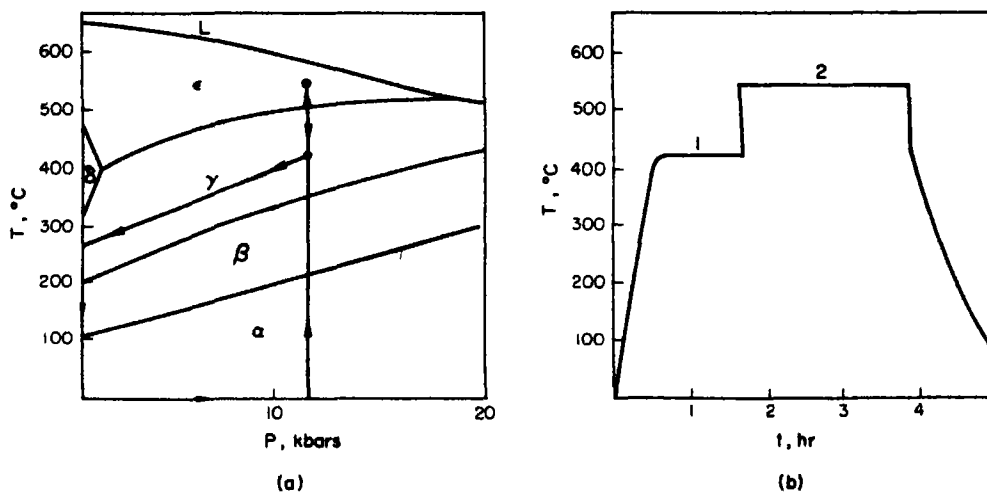


Fig. 4. Cycles pression-température et température-temps lors des recuits de diffusion sous pression. 1—recuit de restauration. 2—recuit de diffusion.

pression à l'intérieur du microfour, nous y avons recuit un échantillon polycristallin de plutonium de haute pureté à 500°C sous 15 Kbars pendant 3 h 30 mn, puis nous l'avons refroidi lentement (vitesse $\approx 2^\circ\text{C}/\text{mn}$) de façon à faire grossir les grains par changement de phase $\beta \rightarrow \alpha$ sous pression [7]. Nous avons constaté que l'échantillon ne révèle aucune déformation macroscopique et les grains aucune direction de croissance préférentielle. On peut donc affirmer que les conditions d'hydrostaticité sont suffisantes, mais, pour éviter que les défauts créés lors de la mise en pression au cours du tassement du matériau transmetteur et lors des premiers changements de phases se produisant au cours de la montée en température n'influencent la cinétique de diffusion en phase ϵ , on effectue un prérecuit de restauration en phase γ pendant quelques heures (le coefficient de diffusion en phase γ , tiré des travaux de Tate [8] est 10^4 fois inférieur au coefficient de diffusion en phase ϵ [1] à la pression normale). A la fin du recuit de diffusion, on trempe l'échantillon jusqu'en phase γ , puis on refroidit lentement tout en relâchant la pression de façon à rester continuellement en phase γ jusqu'à la décompression totale (Fig. 4(a)). Cette façon de procéder permet de réaliser les changements de phase $\gamma \rightarrow \beta$ et $\beta \rightarrow \alpha$ sans pression extérieure, c'est-à-dire de façon forcément hydrostatique. On évite ainsi toute déformation parasite de l'échantillon au passage de ces points de transformation qui se font avec de fortes variations de volume.

La pression disponible à coeur:

$$P = (1 - \gamma) \frac{F}{S}$$

est proportionnelle au rapport force/surface du piston, la constante γ définissant la perte de charge par friction. Cette constante est de l'ordre de 0,26 pour la pyrophyllite à la température ordinaire [9] mais il est certain qu'elle dépend de la température, de la pression et de la géométrie du coeur de la chambre de compression; c'est pourquoi il est nécessaire d'étalonner l'appareil en pression en fonction

de la température. Aussi, plutôt que de passer par la méthode classique qui consiste à repérer les transitions du bismuth ou du thallium en augmentant progressivement la force appliquée à la température ordinaire, nous avons préféré court-circuiter cette étape intermédiaire et étalonner la chambre de compression à l'aide des transitions du plutonium, c'est-à-dire dans les conditions exactes de fonctionnement. Un 'vernier' en série avec le rhéotor principal permet de réaliser, dans une gamme limitée de tension, une montée en température absolument régulière. On donne sur la Fig. 5 deux courbes complètes d'analyse thermique différentielle sans pression et sous pression. Les thermocouples chromel-alumel utilisés, dont les indications n'ont pas à être corrigées sous pression, sont disposés comme l'indique la Fig. 3(b). Les transitions sont facilement décelables surtout $\gamma \rightleftharpoons \epsilon$ où il y a peu ou pas d'hystérésis. Il est alors possible de tracer la courbe d'étalonnage de la chambre de compression dans un domaine de température voisin de 500°C. Elle met en évidence une friction de l'ordre de 30 pour cent sous une pression de 10 Kbars. Notons enfin que le gradient de température axial varie peu en fonction de nos conditions opératoires. Il est de l'ordre de $1^\circ\text{C}/\text{mm}$; il semble que ce soit le gradient minimal que l'on puisse obtenir jusqu'à 600°C dans une installation de ce type.

Le couple de diffusion est constitué de deux pastilles de plutonium polycristallines ($\phi = 5 \text{ mm}$, $e = 3 \text{ mm}$) à teneurs en isotope 240 différentes (Tableau 1) polies mécaniquement puis soudées en phase δ à 420°C pendant 4 hr sous une pression initiale à froid de 3 Kbars dans une petite presse à vis suivant une technique décrite en détail par ailleurs [1]. Insistons sur le fait qu'il est important que les deux lots de plutonium soient de pureté suffisante (Tableau 1) et surtout contiennent les mêmes impuretés en teneurs voisines: $200 \cdot 10^{-6}$ de gallium dans l'un des lots sont suffisants pour abaisser la température de transition $\delta \rightarrow \gamma$ de telle façon que, lors du refroidissement qui suit le recuit de collage, il y a un cisaillement

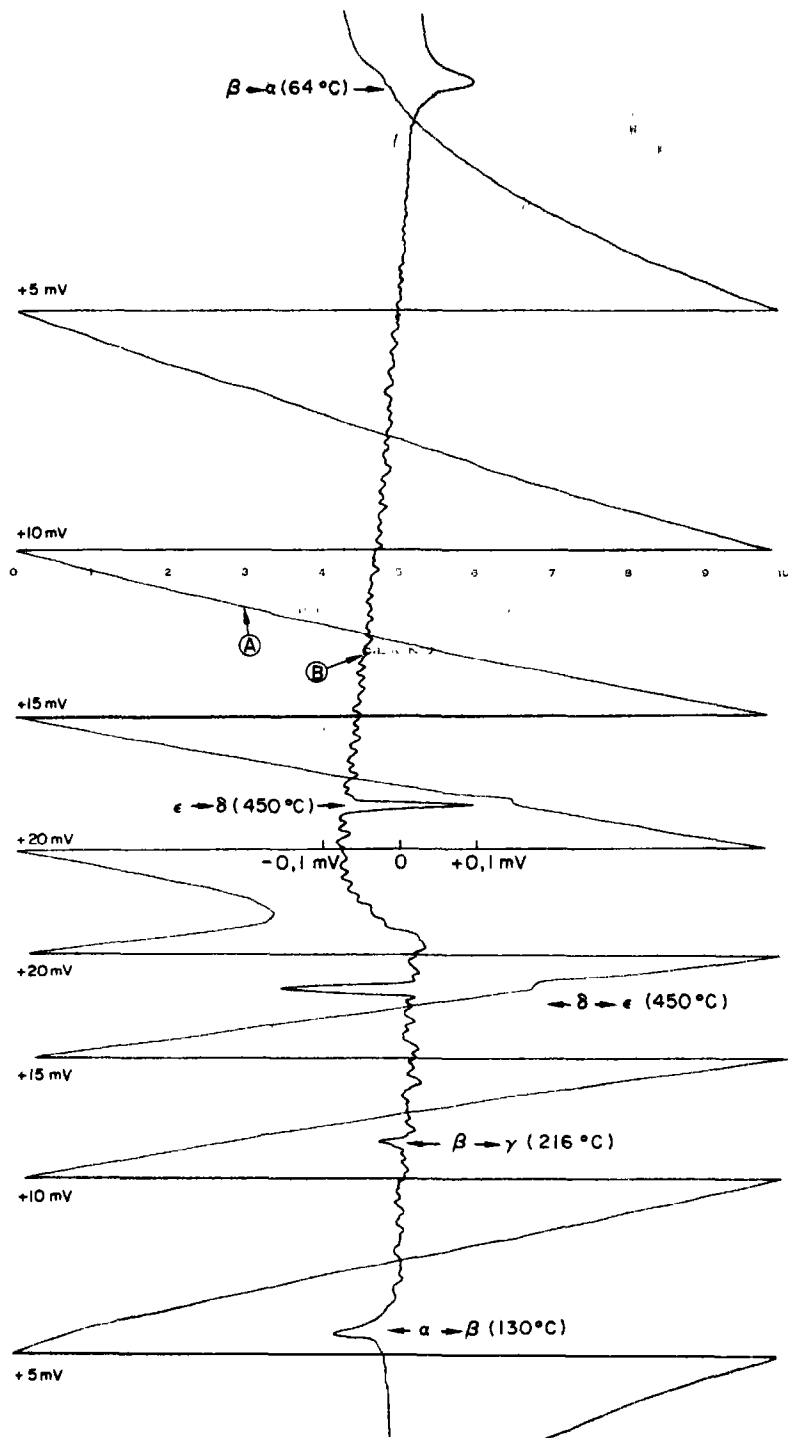


Fig. 5(a).

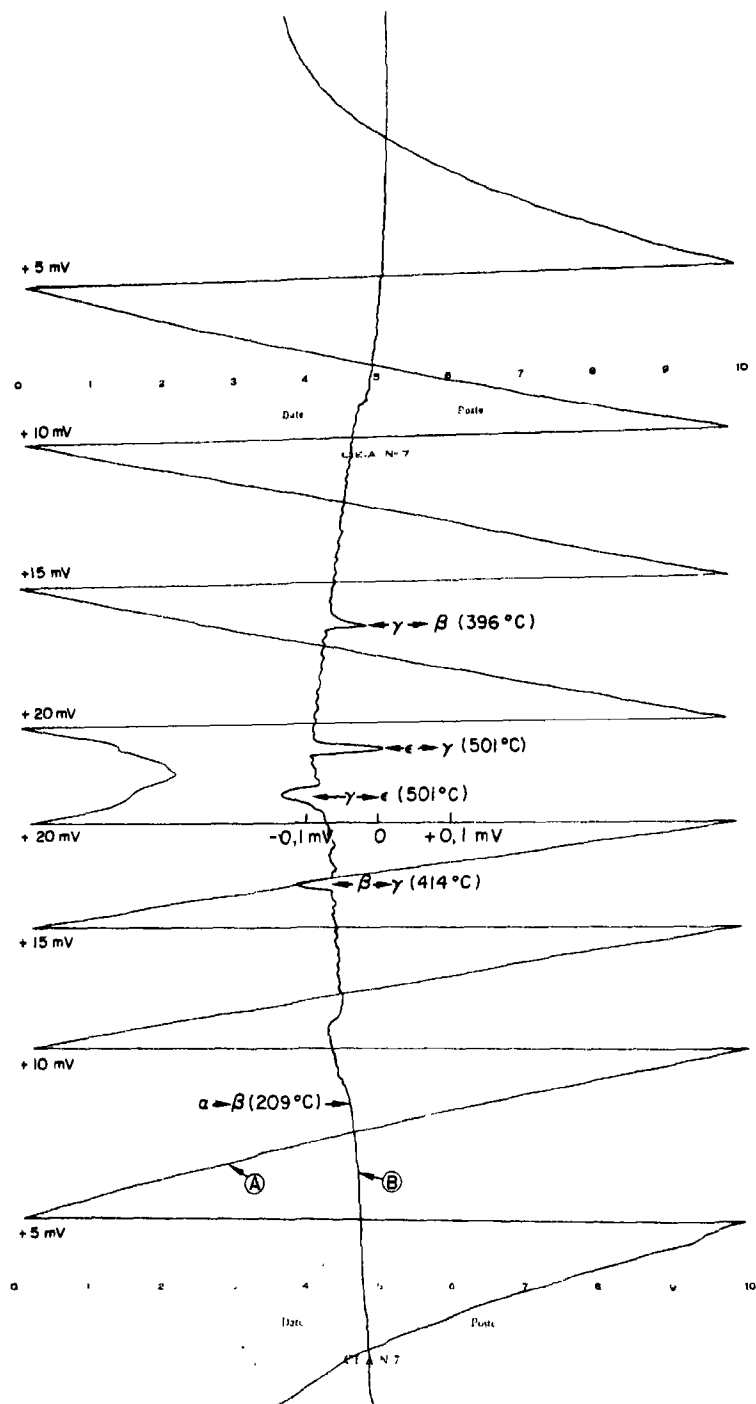


Fig. 5(b).

Fig. 5. Analyse thermique différentielle: Fig. 5(a): sans pression A—Analyse simple (sensibilité 5 mV). B—Analyse différentielle (sensibilité 5 mV). Fig. 5(b): sous 97 tonnes (15 Kbars). A—Analyse simple (sensibilité 5 mV). B—Analyse différentielle (sensibilité 1 mV).

Tableau 1. *Analyse spectrographique et isotopique du plutonium utilisé*

Nature	C	O	Ag	Al	B	Ca	Cr	Cu	Teneur en impuretés ($\times 10^6$)								Analyse isotopique en %					
									Fe	K	Mg	Mn	Na	Ni	Pb	Si	Sn	Ti	Zn	239	240	241
Plutonium peu irradié	127	550	1	20	< 0,5	50	< 10	10	< 10	80	25	15	< 10	15	12	20	≤ 5	50	50	99,04	0,94	0,015
Plutonium très irradié	85	490	1	< 10	< 0,5	< 60	< 7,5	8	< 10	≤ 50	< 20	< 4	< 25	< 10	< 9	10	< 5	< 50	45	89,50	9,39	1,10

important au niveau de l'interface qui décolle les deux pastilles.

Après recuit de diffusion, le couple est enrobé dans de l'araldite de façon à ce que ses faces terminales, parallèles à l'interface de collage soient également parallèles aux faces rectifiées d'une bague d'acier doux: ce dispositif déjà décrit [1] permet de réaliser en boîte à gants des abrasions parallèles à l'interface à l'aide d'une rectifieuse à plateau magnétique. Les épaisseurs abrasées (de l'ordre de 100 μ , la zone de diffusion s'étendant sur 2 à 3 mm) sont mesurées au palmer (précision 1 μ). Après chaque abrasion, on compare suivant une technique proposée par Dupuy [1] les spectres d'émission X des deux faces à l'aide d'un scintillateur plan d'iodure de sodium dopé au thallium ($\phi = 13$ mm, $e = 3$ mm) et d'un analyseur à 400 canaux. On compte l'activité X correspondant à la bande d'énergie des raies de conversion L de l'uranium (17 keV). L'émission X de l'isotope 240 étant 20 fois plus grande que celle de l'isotope 239, l'activité du plutonium très irradié* est dans cette bande d'énergie environ le double de celle du plutonium peu irradié (soit 300.000 coups par heure dans nos conditions expérimentales, en délimitant la surface d'émission par un diaphragme de 3 mm de diamètre).

3. L'AUTODIFFUSION SOUS PRESSION HYDROSTATIQUE DU PLUTONIUM EN PHASE CUBIQUE CENTRÉE

Par suite de la faible activité X de la source et de sa faible variation en fonction de la pénétration, les erreurs statistiques de comptage dans les conditions définies ci-dessus sont les plus importantes et, compte tenu de la largeur des zones de diffusion, bien supérieures aux erreurs de mesure des distances au palmer ($\pm 1 \mu$) ou aux erreurs de géométrie (inclinaison de l'interface de collage de $\pm 5^\circ$ au maximum par rapport aux faces de référence). Il en résulte une incertitude non

négligeable (de 10 à 20 pour cent) sur le coefficient d'autodiffusion D

$$D = \frac{1}{4a^2}$$

où a est la pente de la droite $u = f(x/\sqrt{t})$ avec x = distance à l'interface de collage de la face abrasée à la température de recuit.

t = durée de recuit à cette température

$$u = \text{tel que } \frac{2}{\sqrt{\pi}} \int_0^u e^{-v^2} dv = 2 \left[\frac{I - I_1}{I_0 - I_1} \right] - 1$$

I = activité de la surface abrasée

I_0 = activité de la face riche en Pu 240 (non affectée par la diffusion)

I_1 = activité de la face pauvre en Pu 240 (avant abrasion).

On applique ici la méthode de Gruzin [10], généralisée aux couples soudés par Seibel [11]. Le fort coefficient d'absorption, dans le matériau, des rayons X émis, permet de considérer dans les formules indifféremment les concentrations ou les activités. Il est nécessaire d'effectuer sur les mesures de distance aux température et pressions ordinaire une correction de façon à tenir compte de la dilatation thermique de l'échantillon sous contrainte (cf. Annexe I). On donne à titre d'exemple sur la Fig. 6 les courbes concentration pénétration en coordonnées gaussiennes corrigées, relatives à quatre couples de diffusion recuits à $550^\circ \pm 1^\circ\text{C}$ à des pressions allant de 0 à 11,8 Kbars. L'ensemble des données et des résultats figure au Tableau 2; les courbes $D = f(P)_T$ font apparaître (Fig. 7) une variation, en première approximation exponentiellement croissante, du coefficient de diffusion avec la pression, résultat tout à fait inhabituel, suffisant à lui seul pour caractériser la phase ϵ d'anormale'.

*Le plutonium riche en isotope 240 est obtenu par traitement des combustibles très irradiés.

(a) Volume d'activation

L'évaluation, dans la théorie de l'état activé

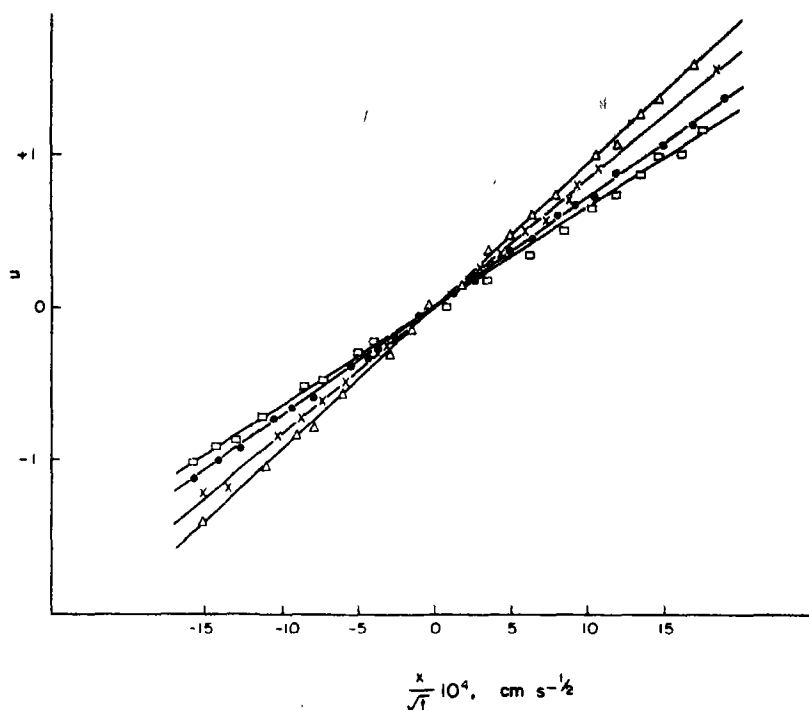


Fig. 6. Courbes concentration-pénétration en coordonnées gaucho-arithmétiques à 550°C. Δ 0 Kbar. \times 2,7 Kbars. \bullet 8,8 Kbars. \square 11,8 Kbars.

Tableau 2. Volume d'activation pour l'autodiffusion du plutonium en phase ϵ

$T^{\circ}\text{K}$	P Kbars	$D \times 10^7$ non corrigé cm^2/s	$D \times 10^7$ corrigé cm^2/s	t_s	$\frac{-RT}{\partial P} \frac{\partial \log D}{\partial P_{\text{cm}^2}}$	$\Delta V_c^* \text{ cm}^3$	$\frac{\Delta V}{V} \%$
788	0	$1,66 \pm 0,37$	$1,87 \pm 0,42$	13305 ± 45	-4,12	-0,62	-32,9
	$8,1 \pm 0,2$	$2,98 \pm 0,44$	$3,22 \pm 0,48$	15720 ± 60			
811	0	$2,15 \pm 0,47$	$2,43 \pm 0,53$	7320 ± 120	-4,44	-0,63	-35
	6,9	$3,55 \pm 0,46$	$3,87 \pm 0,50$	6120 ± 60			
	13,8	$5,53 \pm 0,47$	$5,90 \pm 0,51$	7560 ± 40			
823	0	$2,54 \pm 0,40$	$2,88 \pm 0,45$	10222 ± 70	-4,29	-0,67	-34,7
	2,7	$3,14 \pm 0,44$	$3,50 \pm 0,49$	11972 ± 25			
	8,8	$4,50 \pm 0,50$	$4,87 \pm 0,54$	12540 ± 30			
	11,8	$5,50 \pm 0,47$	$5,90 \pm 0,50$	7520 ± 20			
849	0	$3,40 \pm 0,48$	$3,85 \pm 0,54$	8412 ± 25	-4,04	-0,70	-33
	1,8	$3,85 \pm 0,41$	$4,32 \pm 0,46$	7480 ± 30			
	7	$5,14 \pm 0,35$	$5,62 \pm 0,40$	7324 ± 40			

* $\Delta V_c = -RT\chi_T(\frac{1}{3} - \Gamma_r)$; cf. Fig. 8 pour les valeurs de χ_T .

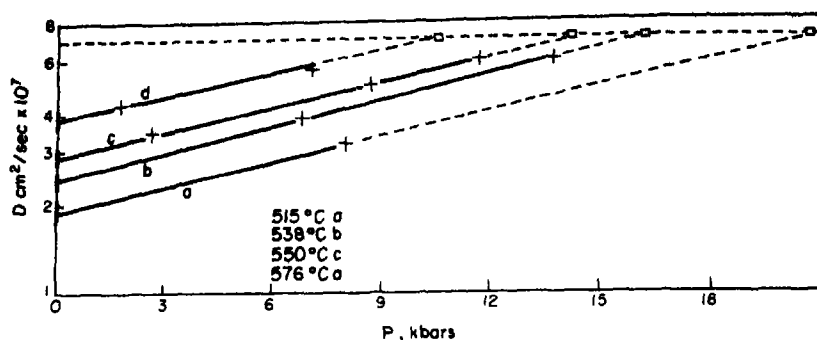


Fig. 7. Autodiffusion sous pression hydrostatique du plutonium ϵ . Isothermes $\text{Log}(D) = f(P)_T$; a: 515°C—b: 538°C—c: 550°C—d: 576°C. Les intersections \square des isothermes avec la droite isodiffusion $D = 7 \cdot 10^{-7} \text{ cm}^2\text{s}^{-1}$ ont lieu aux pressions pour lesquelles s'effectue la fusion aux températures correspondantes.

[12] du volume d'activation ΔV pour l'autodiffusion du plutonium en phase ϵ , à partir de la formule:

$$\Delta V = -RT \left[\left(\frac{\partial \log D}{\partial P} \right)_T + \chi_T \left(\frac{2}{3} - \Gamma_r \right) \right]$$

nécessite pour cette phase la détermination de la compressibilité isotherme χ_T et de la constante Γ_r définie par:

$$\Gamma_r = - \left(\frac{\partial \log \nu}{\partial \log V} \right)_T$$

où ν est une fréquence caractéristique de vibration des atomes. La méthode par résonance ultrasonique appliquée à des échantillons cylindriques nous a donné des valeurs reproductibles jusqu'à 520°C du module d'Young E et du coefficient de Poisson σ [13], c'est à dire aussi de la compressibilité:

$$\chi_T = \frac{3(1-2\sigma)}{E}. \quad (\text{Fig. 8})$$

Quant à Γ_r , la loi de Lindemann

$$\nu \propto \sqrt{\frac{T_f}{MV^{2/3}}}$$

permet d'écrire

$$\Gamma_r = \frac{1}{3} + \frac{1}{2\chi_T} \frac{\partial \log T_f}{\partial P}.$$

La connaissance de la pente du liquidus du diagramme pression-température ($\partial \log T_f / \partial P$) = $7 \cdot 10^{-8} / \text{bar}$ [6] et de la valeur de χ extrapolée à la température de fusion conduit à

$$\Gamma_r = 0,15.$$

On peut alors calculer le terme correctif

$$\Delta V_c = -RT\chi_T \left(\frac{2}{3} - \Gamma_r \right)$$

et on constate (Tableau 2) que ce terme est négatif et de l'ordre de 5 pour cent du volume molaire; on ne peut donc le négliger et on aboutit à la valeur globale du volume d'activation:

$$\Delta V = -4,9 \text{ cm}^3$$

soit -33,6 pour cent du volume molaire au signe près du même ordre de grandeur que pour les alcalins [14-17] et l'uranium γ [18].

(b) Variation de l'enthalpie d'activation avec la pression

Le faible nombre et la dispersion des valeurs

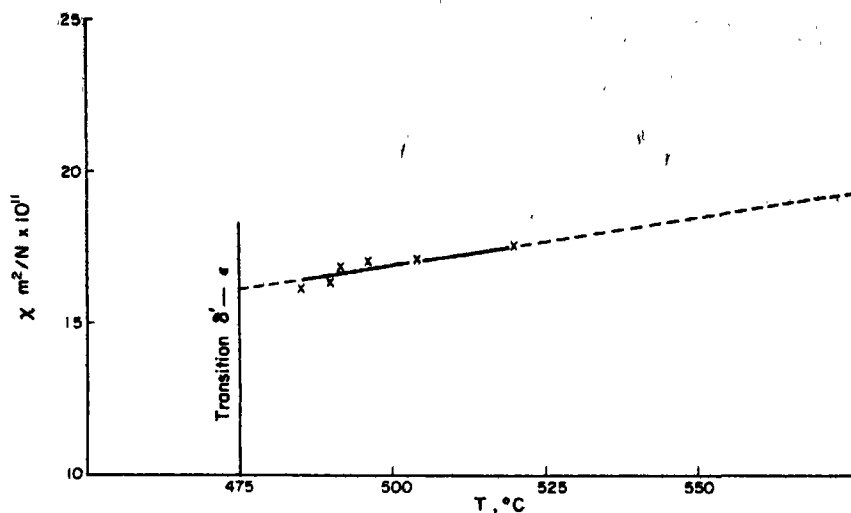


Fig. 8. Compressibilité du plutonium ϵ : xx points expérimentaux[13]; ---- extrapolation linéaire.

expérimentales du volume d'activation (Tableau 2) ne permettent pas une vérification de la formule théorique de Girifalco[19] exprimant la variation avec la température du volume d'activation; mais il est possible, comme nous allons le voir, de vérifier la formule donnant la variation avec la pression de l'enthalpie d'activation[12]

$$\Delta H(P) = \Delta H(0) + \Delta V \cdot P(1 - \alpha T)$$

où les diverses grandeurs ont leur signification habituelle.

Notons tout d'abord que les coefficients de diffusion que nous avons obtenus à pression nulle dans notre dispositif sont légèrement plus élevés dans le domaine des plus basses températures que ceux déterminés par Dupuy [1]. Ils conduisent à des valeurs plus faibles pour le facteur de fréquence et l'enthalpie d'activation (Fig. 9). Nous ne pensons pas que la précision sur nos résultats soit supérieure à celle donnée par Dupuy, mais nous avons conservé nos valeurs pour établir les courbes $\log D = f(P)$ de façon à ce que tous les coefficients de diffusion utilisés soient obtenus dans les mêmes conditions expérimentales.

On compare au Tableau 3 ces différents résultats ainsi que les valeurs des autres fonctions thermodynamiques qu'il est possible de calculer en supposant un mécanisme de diffusion monolacunaire. La corrélation de Van Liempt [20] ou celles plus élaborées de Sherby et Simnad[3] et de Gibbs[2] sont de toute évidence inapplicables.

L'étude expérimentale de la variation de ΔH avec P nécessite généralement le tracé des isobares

$$\log D = f\left(\frac{1}{T}\right)_P.$$

Cependant, nos expériences ayant été effectuées à des températures données reproductibles, mais à des pressions toutes différentes, ces courbes s'appuient sur des points en majeure partie non expérimentaux. Leur analyse s'est révélée incohérente; c'est pourquoi nous avons préféré utiliser la relation empirique

$$\Delta H(P) \approx 17,2 T_f(P)$$

bien représentative de nos résultats (Fig. 10) et que nous analyserons au prochain chapitre.

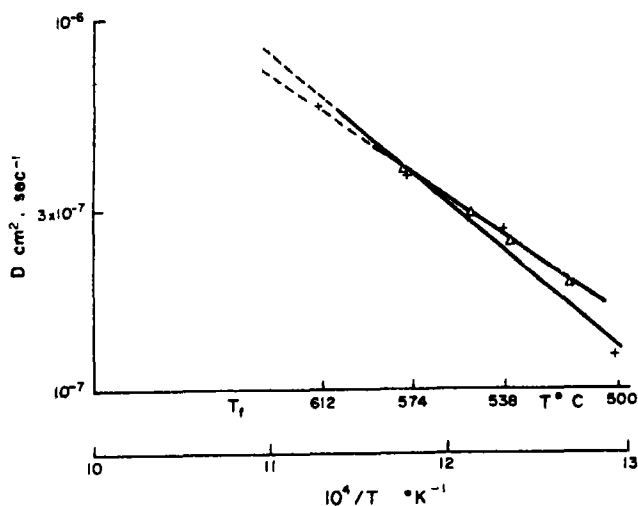


Fig. 9. Autodiffusion du plutonium en phase ϵ sous pression normale: + Dupuy [1], Δ nos résultats.

Tableau 3. Facteur de fréquence et fonctions thermodynamiques pour l'autodiffusion du plutonium ϵ (en supposant un mécanisme lacunaire)

	$\Delta H(0)$ cal/mole	D_0 cm²/s	ΔS cal/mole °C	ΔG cal/mole
Dupuy [1]	18.500 + 2000 - 3000	$2 \cdot 10^{-2}$ $3 \cdot 10^{-3} \leq 9 \cdot 10^{-2}$	5 ± 3	14.500 ± 5000 à $T = 800^\circ\text{K}$
Nos résultats	15.700 ± 1000	$3 \cdot 10^{-3}$ $2 \cdot 10^{-3} \leq 6 \cdot 10^{-3}$	$1,4 \pm 1$	14.500 ± 1000 à $T = 800^\circ\text{K}$

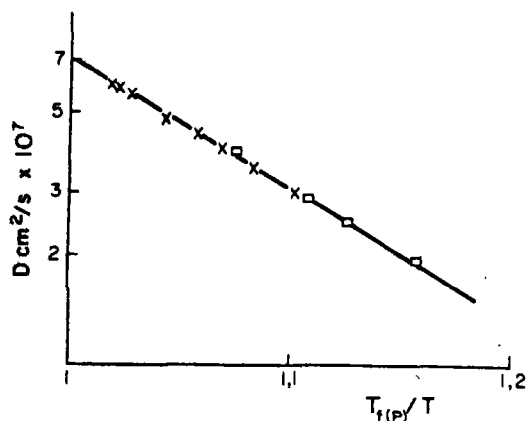


Fig. 10. Corrélation fusion-diffusion pour le plutonium ϵ . La pente de la droite conduit à $\Delta H(P) \approx 17,2 T_f(P)$: x sous pression, □ sans pression.

On constate sur le Tableau 4 que l'accord est satisfaisant entre leur valeurs 'expérimentales' et les valeurs calculées de l'enthalpie d'activation à la pression P .

4. DISCUSSION DES RÉSULTATS-MÉCANISME D'AUTODIFFUSION EN PHASE ϵ

(1) Possibilité d'un effet parasite

Il est nécessaire d'examiner tout d'abord si l'augmentation avec la pression du coefficient d'autodiffusion en phase ϵ ne peut être due à un effet parasite.

(a) *Influence des impuretés.* La teneur en oxygène est de l'ordre de $500 \cdot 10^{-8}$ avant traitement, c'est-à-dire bien supérieure à la limite de solubilité considérée comme nulle.

Tableau 4. Variation avec la pression de l'enthalpie d'activation

P Kbars	$T_f(P)$ °K	$\Delta H_{\text{cal/mole}}$ 'expérimentale'	$\Delta H_{\text{cal/mole}}$ 'calculée'
3	892	15.300	15.400
7	869	14.950	14.950
10	847	14.600	14.600
13	833	14.300	14.300

La pyrophyllite étant un silicate, il faut également considérer la teneur en silicium: elle passe de $15 \cdot 10^{-6}$ avant traitement à $30 \cdot 10^{-6}$ après traitement quelle que soit la pression puisque, par suite de l'état solide du milieu transmetteur, la teneur en impuretés au voisinage de l'échantillon est indépendante de la pression (différence avec un milieu transmetteur gazeux). Dans un mécanisme de diffusion lacunaire et avec une forte interaction lacune-impureté, une augmentation sous pression soit de la limite de solubilité de l'oxygène soit de l'interaction lacune-impureté, permet de rendre compte d'une accélération de la diffusion. Mais une application numérique conduit pour chacun de ces deux schémas à des résultats sans grande signification physique.

(b) *Influence des dislocations.* Une forte densité de dislocations produites au cours des changements de phase lors de la montée en température peut accélérer la diffusion dans les cubiques centrés 'anormaux'* bien que les résultats expérimentaux permettant de vérifier cette hypothèse soient contradictoires[21]. Dans le cas du plutonium ϵ qui subit sous pression trois changements de phase, notre technique opératoire (recuit en phase γ avant traitement de diffusion) nous permet de ne pas considérer les dislocations introduites par les gradients de pression éventuels mais il faut considérer les dislocations et les glissements

intergranulaires dus au changement de phase $\gamma \rightarrow \epsilon$: l'énergie de formation d'une lacune dans les dislocations doit être plus faible qu'ailleurs, par dans le cas d'une dislocation coin par exemple, il y a un demi plan supplémentaire en compression; sous pression cet effet doit s'accroître. Cependant par suite de la diminution sous pression du volume de changement de phase $\gamma \rightarrow \epsilon$ (Fig. 1) ($\Delta V_{\gamma \rightarrow \epsilon}$ passe de 5 pour cent du volume molaire à 2 Kbar à 1 pour cent à 13,5 Kbar), le nombre donc l'influence des dislocations doit diminuer. Elles ne peuvent donc rendre compte du signe de la variation avec la pression du coefficient d'autodiffusion, (signe d'ailleurs indépendant du temps de recuit)† et par voie de conséquence expliquer la faible valeur de $\Delta H(0)$. Un calcul simple montre d'ailleurs qu'une densité très élevée de dislocations ($10^{10}/\text{cm}^2$) serait nécessaire pour interpréter la valeur de $\Delta H(0)$ [1].

D'un autre côté, une recristallisation éventuelle au cours du traitement de diffusion en phase ϵ qui augmenterait le coefficient de diffusion apparent sans que la forme des courbes $c = f(x)$ soit modifiée[22], est moins probable aux hautes pressions qu'aux plus faibles pressions par suite de la diminution de $\Delta V_{\gamma \rightarrow \epsilon}$. Il n'est cependant pas possible de mettre cette recristallisation en évidence.

Enfin une déformation plastique du matériau sous l'influence d'un gradient de pression éventuel au cours des traitements de diffusion, à une vitesse n'entraînant pas, à la fin de l'expérience, de déformation macroscopique ne peut engendrer suffisamment de défauts ponctuels pour interpréter nos résultats.

†On doit souligner que l'effet dû aux dislocations induites par la transformation ne se fait sentir qu'en début de recuit. La comparaison des résultats obtenus à la pression atmosphérique et à la pression $P \approx 8,5$ Kbar pour les deux températures 788 et 823°K, avec les conditions

$$I(P) > I(0)$$

$$\Delta V_{\gamma \rightarrow \epsilon}(P) < \Delta V_{\gamma \rightarrow \epsilon}(0) \quad (\text{cf Tableau 3})$$

*Ces changements de phase existent pour la quasi totalité des métaux cubiques centrés anormaux.

permet donc d'assurer que l'effet de la pression sur la diffusion est supérieur à celui, possible, des dislocations.

(c) *Diffusion intergranulaire et diffusion superficielle.* La première a peu de chances d'être prépondérante car les traitements de diffusion sont effectués dans un domaine de hautes températures; il n'est malheureusement pas possible de s'en assurer par autoradiographie X car le contraste X entre les deux lots de plutonium est trop faible[1]. Notons que pour les polycristaux d'argent qui manifestent, dans une gamme limitée de pression, des coefficients d'autodiffusion supérieurs à ceux des monocristaux[10] la diffusion intergranulaire diminue sous pression[23].

Quant à la diffusion superficielle, nous avons vérifié qu'elle était négligeable:

- l'activité d'une surface abrasée en différents points de celle-ci est la même.
- après abrasion des faces terminales sur 1/10 mm (pour éliminer la couche d'oxyde superficielle), le rapport I_1/I_0 est identique avant et après diffusion et vaut $0,502 \pm 0,003$.

Il est probable que la couche d'oxyde qui se forme très rapidement sur l'échantillon empêche la diffusion superficielle.

(2) Volume d'activation et fusion

Rice et Nachtrieb[24] ont remarqué que le coefficient d'autodiffusion à la pression P et à la température T est, en coordonnées semi-logarithmiques sensiblement proportionnel au rapport $T_f(P)/T$ où $T_f(P)$ est la température de fusion à la pression P , quelle que soit cette pression. Cette loi est bien vérifiée pour les métaux 'normaux' où le mécanisme de diffusion est fort probablement lacunaire. La concentration en lacunes à la fusion est donc constante quelle que soit la pression P , et le volume d'activation est positif et relié à la pente du liquidus par

$$\Delta V = \Delta H \frac{\partial \log T_f}{\partial P} - RT \chi_r \left(\frac{2}{3} - \Gamma_r \right).$$

Cette relation* garde-t-elle un sens dans le cas des métaux dont le volume de fusion est négatif? En ce qui concerne le plutonium ϵ , on peut tout d'abord remarquer (Fig. 7) que les droites $D = f(P)$ coupent la droite isodiffusion $D \approx 7 \cdot 10^{-7} \text{ cm}^2 \text{ s}^{-1}$ aux pressions pour lesquelles s'effectue justement la fusion aux températures considérées: le coefficient de diffusion est donc le même à la température de fusion quelle que soit la pression, ce qui suggère que D ne dépend effectivement que de la variable réduite $T_f(P)/T$. Ceci est confirmé sur la Fig. 10 où nous avons porté nos résultats expérimentaux en fonction de la variable réduite: la pente de la droite permet de calculer l'expression déjà signalée de l'enthalpie d'activation en fonction de la température de fusion.

$$\Delta H(P) \approx 17,2 T_f(P).$$

L'application au plutonium ϵ de la formule de Nachtrieb conduit alors à la valeur moyenne

$$\Delta V \approx -5,2 \text{ cm}^3$$

soit -34,5 pour cent du volume molaire, ce qui est en bon accord avec les résultats expérimentaux.

(3) Les défauts ponctuels en théorie élastique

Compte tenu de la faible probabilité d'un effet parasite et étant donné l'accord ci-dessus, on est amené à considérer que le défaut responsable de la diffusion dans la phase cubique centrée du plutonium doit avoir un volume d'activation négatif. La présence d'effet Kirkendall sans porosité au cours de la dif-

* Il y a lieu de noter que la relation de Nachtrieb conduit, compte tenu de la loi de Lindemann déjà écrite, à

$$\Delta V = -2\Delta H \cdot \chi_r \left[\frac{1}{3} + \frac{\partial \log \nu}{\partial \log V} \right] = 2\Delta H \cdot \chi_r \left[-\frac{1}{3} + \Gamma_r \right].$$

C'est précisément la relation de Keyes[25] issue d'une théorie élastique. La proportionnalité $\Delta H(P) \propto T_f(P)$ pourrait donc recevoir une base théorique dans un modèle élastique.

fusion chimique dans les alliages à base de plutonium en phase cubique centrée ne permet pas de choisir entre le mécanisme par lacunes (mono ou poly-lacunes) ou le mécanisme par interstitiels; elle interdit seulement l'échange simultané de deux atomes et le mécanisme par anneau ("ring mechanism").

(a) *Les lacunes.* Il semble que les expériences d'effet isotopique de Barr et Mundy sur les alcalins [26] ne soient pas suffisantes pour préjuger du mécanisme de diffusion dans ces métaux [27]; cependant les corrélations empiriques y sont bien suivies et il est fort probable que le mécanisme soit en fait lacunaire. Avec un tel mécanisme, on pourrait s'attendre, dans le cas du plutonium dont la compressibilité voisine à celle des alcalins, à une relaxation appréciable de la lacune, conduisant à des volumes d'activation faibles mais positifs. La théorie élastique n'interdit pourtant pas, pour la lacune, un volume d'formation négatif [28]: la formule

$$\frac{\Delta V_f}{V} = 1 - \frac{3(1+Y)}{Y} \frac{\Delta a}{a}$$

avec

$$Y = \frac{1+\sigma}{2(1-2\sigma)}$$

σ = coefficient de Poisson

montre que le volume de formation devient négatif si la relaxation de la lacune $\Delta a/a$ exprimée en % du rayon atomique est supérieure à

$$\frac{Y}{3(1+Y)}$$

c'est-à-dire à 17 pour cent dans le cas du plutonium ϵ pour lequel $\sigma = 0,2$ [13]. En considérant un volume de migration faible mais positif,* il apparaît que pour interpréter nos

résultats expérimentaux, il faudrait que la relaxation de la lacune soit supérieure à 23 pour cent, ce qui est incompatible avec la faible enthalpie d'activation expérimentale.

(b) *Les bilacunes.* Contrairement au cas des métaux C.F.C., l'enthalpie de formation des lacunes doit constituer dans les métaux C.C. de structure assez ouverte, la majeure partie de l'enthalpie d'activation. Il est alors peu probable que l'énergie de liaison d'une bilacune soit égale, si ce n'est supérieure, à l'énergie de formation d'une lacune; c'est-à-dire que la concentration en bilacunes est négligeable à toute température.

(c) *Les interstitiels.* Ce sont des défauts qu'on ne considère généralement pas en autodiffusion par suite de leur énergie de formation trop élevée. A titre d'exemple, l'énergie de formation d'un interstitiel dans la théorie élastique est de 35.400 cal/mole pour le plutonium ϵ dans les sites octaédriques ($\frac{1}{2}, \frac{1}{2}, 0$). De plus le volume de formation ne peut être négatif que si le métal est peu compressible, ce qui n'est pas le cas pour le plutonium ϵ . Nous verrons cependant au chapitre suivant que, compte tenu d'une hypothèse supplémentaire il est possible de rendre compte de nos résultats avec un mécanisme de diffusion par interstitiels.

(4) Mécanisme d'autodiffusion en phase ϵ

Il est peu probable que la contraction du plutonium à la fusion soit liée à une tendance à l'ordre en phase liquide, sous forme d'un réseau aussi dense que le réseau C.F.C. Par analogie avec l'interprétation donnée par Jayaraman [29] pour le cérium (C.C.) dont le diagramme (P, T) se calque très bien sur celui du plutonium, nous pensons au contraire que la contraction à la fusion du plutonium est due à une modification de la structure électronique de l'atome. Cette hypothèse est étayée par plusieurs résultats expérimentaux, en particulier:

— la chaleur spécifique électronique du plutonium liquide est bien plus élevée que pour la phase ϵ [30]

*Ce n'est que dans un modèle de sphères dures que le volume de migration dans une structure cubique centrée est négatif.

— la tension superficielle au point de fusion

$$\gamma_s \approx 550 \text{ dynes/cm}$$

est environ trois fois moindre que pour l'uranium[31]. La relation[32]

$$\gamma_s \propto \frac{1}{\alpha} \left(\frac{\rho^2}{A^2 n} \right)^{1/3}$$

où α est le coefficient de dilatation cubique du liquide

ρ sa densité

A sa masse molaire

n sa valence

permet alors de calculer une valence voisine de 7 en phase liquide. Si on admet avec Zachariasen[33] que la valence du plutonium ϵ est de 5 avec un rayon ionique de 1,59 Å, le rayon ionique en phase liquide serait de 1,4 Å [34].

Rappelons enfin qu'on interprète généralement le coefficient de dilatation négatif de la phase δ (C.F.C.) par une modification électronique du même type[33].

La parenté qui semble exister entre la phase ϵ et la phase liquide (mise en évidence en particulier par les coefficients de diffusion très élevés en phase ϵ , la faible chaleur latente de fusion et la forte viscosité du liquide[35]) nous permet alors d'envisager que le défaut responsable de la diffusion pourrait être un interstitiel dans le même état électronique que les atomes en phase liquide (nous dirons état 'activé'). D'ailleurs, la grande compressibilité du plutonium ϵ et sa variation rapide avec la température mettent en évidence une structure électronique instable pour cette phase, ce qui est un bon argument en faveur d'une promotion d'électrons permettant à certains ions de changer de valence et de réduire leur rayon.

Un calcul classique[28] montre alors que l'énergie élastique nécessaire pour placer un

atome de plutonium de valence 7 dans les sites octaédriques n'est plus que de 16.000 calories par mole. Si la migration de l'interstitiel se fait par un processus indirect, l'enthalpie de migration (comme le volume d'activation pour la migration) peut être très faible, et nos résultats s'interprètent correctement.

En ce qui concerne le volume d'activation ΔV d'un tel processus, on a sensiblement en théorie élastique[28]

$$\frac{\Delta V}{V} \approx \frac{\Delta v}{V} \frac{\beta}{\beta'} - 1$$

où Δv est la différence de volume molaire entre l'interstitiel à l'état "activé" et le site octaédrique.

V le volume molaire.

β le facteur d'Eshelby[36] = $1 + \mu\chi_T/4/3$

μ le module de cisaillement.

χ_T la compressibilité isotherme

$\beta' = 1 + \mu\chi'_T/4/3$ tient compte du fait que la compressibilité χ'_T de l'interstitiel est différente de celle de la matrice.

Les valeurs expérimentales de χ_T , μ et ΔV montrent que ce processus est possible si la compressibilité de l'interstitiel est supérieure au tiers de la compressibilité de la matrice, ce qui est concevable.

5. CONCLUSION

Nous venons de voir qu'il est possible d'interpréter la faible enthalpie d'activation pour l'autodiffusion du plutonium en phase ϵ , et le volume d'activation négatif à l'aide d'un mécanisme par interstitiels indirects à l'état 'activé'. Sous pression la concentration en interstitiels croît et, bien que leur mobilité diminue, le coefficient de diffusion augmente.

Il est possible qu'un mécanisme analogue rende compte de la diffusion dans les autres phases moins denses que leurs liquides ou se superpose à un mécanisme lacunaire pour Ti β , Zr β , Hf β , V où les courbes $\log D = f(1/T)$ ne sont pas linéaires, l'importance relative des deux mécanismes étant reliée à la pente du

liquidus du diagramme (P, T) comme doivent l'être la compressibilité et la constante de Grüneisen.

ANNEXE 1

Dilatation thermique d'un solide sous pression hydrostatique

Désignons par x l'écart d'un atome par rapport à sa position d'équilibre et par

$$V(x) = ax^2 - bx^3$$

le potentiel anharmonique le plus simple responsable de la dilatation thermique. Sous pression P , la position d'équilibre est x_0 telle que

$$-2ax_0 + 3bx_0^2 = Pr_0^2$$

où r_0 est la distance interatomique. Si on désigne par X les déplacements par rapport à x_0 il est facile de voir que le potentiel auquel est soumis l'atome autour de x_0 est:

$$U(X) = (a - 3bx_0)X^2 - bX^3.$$

Par analogie avec un calcul déjà effectué [37], on exprime alors le coefficient de dilatation cubique sous pression P par

$$\alpha_P = \frac{9bk}{4r_0(a - 3bx_0)^2} \approx \frac{\alpha_0}{\left(1 + \frac{2Pr_0^3\alpha_0}{k}\right)^2}$$

où k est la constante de Boltzmann.

L'application de cette formule au plutonium permet de tracer les courbes théoriques $\alpha = f(P)$ pour les phases α , β , γ et ϵ . Compte tenu des volumes de transitions de phases calculés à partir de l'équation de Clapeyron supposée vérifiée même aux fortes pressions avec l'approximation linéaire

$$\Delta H_i(P) = \Delta H_i(0) + \Delta V_i(0)P$$

il est possible de calculer le volume molaire du plutonium en phase ϵ à différentes pressions et températures et de dresser ainsi des abaques que l'on peut utiliser pour calculer, dans nos conditions expérimentales la correction

$$l = \sqrt[3]{\frac{V(T, P)}{V(300^\circ\text{K}, 0 \text{ Kbar})}}$$

à apporter à la mesure des distances à température et pression ordinaires.

ANNEXE 2

Température de Debye de la phase ϵ du plutonium

C'est par définition pour la phase polycristalline supposée isotrope

$$\theta_D = \frac{h}{k} \left\{ \frac{9N}{4\pi V} \frac{1}{\frac{1}{c_l^3} + \frac{2}{c_t^3}} \right\}^{1/3}$$

où N est le nombre d'avogadro

V le volume molaire

c_l et c_t les vitesses longitudinale et transversales du son qui s'expriment sous la forme

$$c_l = \sqrt{\frac{E(1+\sigma)}{(1+\sigma)(1-2\sigma)\rho}} \quad c_t = \sqrt{\frac{E}{2(1+\sigma)\rho}}$$

avec ρ = densité

E = module d'Young déterminé par la méthode de résonance ultrasonique [13].

σ = coefficient de Poisson déterminé graphiquement à partir de la dispersion des harmoniques de la fréquence fondamentale [13].

On obtient:

$$\theta_D \approx 60^\circ\text{K}$$

ce qui est bien plus faible que pour les autres phases du plutonium déjà étudiées [38]; il n'y a pas lieu de s'en étonner étant donnée la très faible rigidité de la phase ϵ (à titre de comparaison $\theta_D \approx 88^\circ\text{K}$ pour le plomb).

Une valeur approchée de θ_D peut aussi être obtenue à l'aide de la loi de Lindemann [39] basée sur la théorie d'Einstein; au voisinage de la température de fusion, tous les modes de vibration sont excités et on peut définir une fréquence moyenne

$$\nu_E = \frac{1}{3}\nu_D$$

par suite de l'allure parabolique du spectre de fréquences de Debye. Si on désigne par d la distance interatomique et $qd/2$ l'amplitude maximale de vibration, c'est à dire l'amplitude à la température de fusion, on a, par suite de l'équipartition de l'énergie entre tous les modes de vibration

$$\frac{1}{2}M\pi^2q^2d^2\nu_E^2 = RT_F$$

c'est-à-dire

$$\nu_E = \frac{1}{\pi qd} \sqrt{\frac{2RT_F}{M}}$$

où M est la masse molaire et R la constante des gaz. Lindemann a montré que q variait très peu d'un métal à l'autre pour une même colonne du tableau périodique des éléments. La température de Debye du thorium (168°K [40]) et de l'uranium (170°K [41]) conduit à prendre pour q la valeur moyenne $q = 0,126$; c'est à dire que, pour le plutonium ϵ ; au voisinage du point de fusion

$$\nu_E \approx 2,12 \cdot 10^{12} \sqrt{\frac{T_F}{MV^{2/3}}}$$

ce qui conduit à

$$\theta_D \approx 109^\circ\text{K}.$$

Cette valeur est bien supérieure à celle obtenue précédemment à partir des propriétés élastiques; le spectre de fréquence est donc certainement plus étendu que la spectre parabolique proposé par Debye et il serait intéressant de vérifier ceci par diffraction neutronique.

BIBLIOGRAPHIE

1. DUPUY M., Thèse Paris (1968); *C.R. Acad. Sci. Paris* **263**, 35 (1966) et *Trans. Met. Soc. AIME* **242**, 1679 (1968).
2. GIBBS G. B., *Acta Metall.* **12**, 673 (1964).
3. SHERBY O. D. et SIMNAD M., *Trans. ASM.* **54**, 227 (1961).
4. STEPHENS D. R., *J. Phys. Chem. Solids* **24**, 1197 (1963).
5. LIPTAI R. G. et FRIDDLE A. J., *J. less common Metals* **10**, 293 (1966).
6. RAPIN M., Thèse Paris (1969).
7. CORNET J. A. et SPRIET B., *Mem. Sci. Rev. Metall.* **64**, 469 (1967).
8. TATE A. E. et EDWARDS G. R., dans *Thermodynamics*, Vol. 2, SM 66/65, p. 105. International Atomic Energy Agency, Vienna (1966).
9. BOYD F. R. et ENGLAND J. L., *J. Geophys. Res.* **65**, 741 (1960).
10. GRUZIN P. L., *Dokl. akad. nauk. U.S.S.R.* **86**, 28 (1952).
11. SEIBEL G., Thèse Paris (1963).
12. PHILIBERT J. et ADDA Y., dans *La diffusion dans les solides*, Vol. 2; p. 811. Presses universitaires de France, Paris. (1966).
13. CORNET J. A. et BOUCHET J. M., *J. Mat. Nucl.* **28**, 303 (1968).
14. NACHTRIEB K. H., WEIL J. A., CATALANO E. et LAWSON A. W., *J. chem. Phys.* **20**, 1189 (1952).
15. ROUFF A. L., dans *Physics of solids at high pressures* (Édité par C. T. Tomizuka et R. M. Emrick), p. 378. Academic Press, New York (1965).
16. KOHLER C. R. et ROUFF A. L., *J. appl. Phys.* **36**, 2444 (1965).
17. HULTSCH R. A. et BARNES R. G., *Phys. Rev.* **125**, 1832 (1962).
18. BEYELER M., Thèse Paris (1968) et Rapport C.E.A.-R-3715.
19. GIRIFALCO L. A., dans *Metallurgy at High Pressures and High Temperatures* (Édité par K. A. Gschneider, M. T. Hepworth et N. A. D. Parlee), p. 260. Gordon and Breach Science, New York (1964).
20. KIDSON G. V. et ROSS R. V., dans *Radioisotopes in Scientific Research* (Édité par R. C. Extermann), Vol. 1, p. 185. Pergamon Press, New York (1958).
21. FEDOROV G. B. et SMIRNOV E. A., *Met. Metalloved Chist Metallov.* **6**, 181 (1967). ROTHMANN S. J. et PETERSON J. L., dans *Diffusion in Body centered Cubic Metals*, p. 183. American Society for Metals, U.S.A. (1965).
22. HART E., *Acta Metall.* **5**, 597 (1957).
23. MARTIN G., BLACKBURN D. A. et ADDA Y., *Phys. Status Solidi.* **23**, 223 (1967).
24. RICE S. A. et NACHTRIEB N. H., *J. Chem. Phys.* **31**, 135 (1959).
25. KEYES A. W., dans *Solids under Pressure* (Édité par W. Paul et D. M. Warschauer), p. 78. McGraw Hill, New York (1963).
26. BARR L. W., MUNDY J. N. et SMITH F. A., *Phil. Mag.* **16**, 1139 (1967).
27. TORRENS J. M. et GERL M., *Phys. Metall.* **29A**, 361 (1969).
28. QUERE Y., dans *Défauts Ponctuels dans les Métaux* (collection de monographies de physique), p. 13-41. Masson et Cie, Paris (1967).
29. JAYARAMAN A., *Phys. Rev.* **137**, A179 (1965).
30. ENGEL T. K., dans *Reactor Fuels and Materials Development MLM 1347*, p. 22, Mound Laboratory (1967).
31. SPRIET B., *Mem. Scient. Rev. Met.* **60**, 531 (1963).
32. FLYNN C. P., *J. appl. Phys.* **35**, 1641 (1964).
33. ZACHARIASEN W. H., dans *The Metal Plutonium*, p. 99. Chicago Press (1961).
34. McWHAN D. B., Thèse Berkeley UCRL 96-95 (1961).
35. JONES L. V., OFTE D., ROHR W. G. et WITTENBERG L. J., *Trans. Am. Soc. Metals* **55**, 819 (1962).
36. ESHELBY J. D., *Acta Metall.* **3**, 487 (1955).
37. KITTEL C., dans *Introduction to Solid State Physics*, p. 153. John Wiley, New York (1956).
38. LALLEMENT R. et PASCARD R., dans *Nouveau Traité de Chimie Générale*, (Édité par P. Pascal), Masson et Cie, Paris. 1970.
39. LINDEMANN F. A., *Phys. Zeit* **14**, 609 (1910).
40. MEISSNER, *Handb. d. exp. Physik* **11**, 50 (1965).
41. POUND G. M., BITTER W. R. et PAXTON W. H., *Phil. Mag.* **6**, 473 (1961).

ETUDE DE LA SURFACE DE SOLIDES PAR RESONANCE MAGNETIQUE NUCLEAIRE HAUTE RESOLUTION DE LIQUIDES ADSORBES—II. MOLECULES A PROTONS MOBILES*

SONIA GRADSTAJN

Institut d'Electronique Fondamentale, Laboratoire associé au CNRS, Faculté des Sciences, 91-Orsay et Faculté des Sciences de Paris, France

D. VIVIEN*

ENSCP, 11, rue Pierre et Marie Curie, Paris Vème et Laboratoire de physicochimie minérale, Faculté des Sciences, 91-Orsay, France

et.

J. CONARD

Institut d'Electronique Fondamentale, Laboratoire associé au CNRS, Faculté des Sciences, 91-Orsay, France

(Received 5 November 1969; in revised form 18 March 1970)

Résumé—Nous avons étudié l'adsorption de l'acide formique et du méthanol sur le noir de carbone Carbolac et l'oxyde de zirconium tétragonal par RMN haute résolution. Le taux de monomère dans ces liquides augmente par adsorption sur ZrO_2 , mais n'est pas modifié par adsorption sur le Carbolac. Pour les deux solides, l'échange chimique entre polymères et monomères reste rapide en phase adsorbée comme dans le liquide libre entre -70° et $35^\circ C$. La largeur de raie du groupe OH est toujours supérieure à celle de l'autre groupe de la même molécule; Ceci peut s'interpréter en admettant que les molécules polaires sont adsorbées sur le solide par leur groupement oxhydre qui est alors moins mobile que l'autre groupe de la molécule. L'élargissement des raies du groupe OH peut être dû à l'interaction dipolaire entre groupes OH des molécules adsorbées et groupes oxhydrides chimisorbés à la surface des adsorbants d'autre part.

Les considérations précédentes sont en bon accord avec les propriétés catalytiques de l'oxyde de zirconium pour la décomposition de l'acide formique.

La résonance magnétique nucléaire, qui permet d'observer le catalyseur en action, peut donner des renseignements sur le processus de catalyse.

Abstract—Adsorption of formic acid and methyl alcohol on the carbon black 'Carbolac' and on tetragonal zirconia has been studied by high resolution N.M.R.

Adsorption on ZrO_2 increases the rate of monomer in these liquids while adsorption on Carbolac has no effect. In both cases, the chemical exchange in the adsorbed phase between monomer and polymer remains fast.

The proton line width is always larger for the OH group than for the other group of the same molecule. This could be understood if the polar molecules were bound to the solid by their OH groups. These would then be less free.

Dipolar interaction between OH groups of adsorbed molecules and chemisorbed OH groups seems to be the predominant cause of the observed increase of the OH line width.

These results agree quite well with catalytic properties of zirconia.

By following the catalytic process with NMR techniques one may obtain informations on catalysis.

*Cet article recouvre en partie le travail de la thèse de doctorat de Mme S. Gradsztajn passée le 13 février 1970 à la Faculté des Sciences d'Orsay (n° d'enregistrement au CNRS: AO 3770). The CNRS, 15 quai A France Paris VII will send a copy of this thesis, which is not printed.

1. INTRODUCTION

DANS le cas des alcools et des acides en phase liquide, la raie de résonance du proton du groupe OH se déplace, par rapport aux autres raies du spectre de la molécule, lorsque la température ou la concentration varie.

Ce phénomène bien connu[1-2] est attribué à la perturbation de la liaison hydrogène (association, dissociation des molécules). La position de la raie du proton de OH caractérise un équilibre chimique entre les états monomères et polymères des molécules d'alcool ou d'acide[3-4] et éventuellement un équilibre plus compliqué où intervient la complexation avec le solvant.

Dans l'état adsorbé de liquides tels que l'acide formique ou l'alcool méthylique nous observons aussi un déplacement de la raie correspondant au groupe OH, variable avec la température et le recouvrement de la surface. Cette raie se distingue en plus par sa largeur beaucoup plus grande que celle des autres raies[5-7].

L'étude préalable des propriétés des raies correspondant aux groupes d'atomes non concernés par la liaison hydrogène (raie du groupe CH de HCOOH) ou raie du groupe CH_3 de CH_3OH) ainsi que l'étude des liquides adsorbés non polaires[8] nous permet de mettre clairement en évidence le comportement particulier des raies correspondant aux groupes OH.

2. ECHANTILLONS

(a) Adsorbants

En plus du noir de carbone 'Carbolac' déjà utilisé pour l'adsorption des liquides non polaires et dont les propriétés sont décrites dans un article précédent[8], nous avons utilisé également l'oxyde de zirconium tétragonal ZrO_2 . Cet adsorbant a été choisi en raison de ses propriétés catalytiques pour la deshydratation de l'acide formique[9].

L'oxyde de zirconium tétragonal est préparé à partir de l'oxyde amorphe par chauffage à 550°C à l'air[10]. Son spectre de rayons

X montre qu'il a la structure tétragonale métastable, avec moins de 10 pour cent de la forme monoclinique. Nous avons préparé deux lots d'oxyde de zirconium dont les surfaces spécifiques (BET/Azote) sont de 20 m²/g pour le lot I et 35 m²/g pour le lot II. Ceci résulte du temps de recuit différent des deux lots. Des clichés de microscopie et de diffraction électronique montrent que la zircone utilisée est constituée de grains polycristallins dont les dimensions sont de l'ordre de 0,1 μ . La densité apparente varie de 1,35 à 1,55 suivant le tassement. La densité théorique de l'oxyde de zirconium est 5,6[11] ce qui donne un coefficient de remplissage de 0,25 bien inférieur à celui d'un empilement compact (0,75) ou même d'un empilement cubique simple (0,52) de grains sphériques.

Ces deux solides (Carbolac et ZrO_2) présentent l'avantage de ne pas trop élargir les raies de liquides adsorbés, ce qui permet de séparer les deux composantes chimiques.

(b) Adsorbats

Les liquides utilisés: acide formique HCOOH et alcool méthylique CH_3OH ont été choisis pour leur spectre RMN simple (deux raies bien séparées). Ils ont déjà été étudiés partiellement en RMN à l'état pur ou en solution (CCl_4 ou H_2O) et en fonction de la température[12-13]. Nous avons aussi utilisé leurs homologues deutérés: CH_3OD , CD_3OH et HCOOD.

(c) Préparation des échantillons

Les échantillons ont généralement été préparés comme pour les études antérieures [8]: avant adsorption du liquide, les solides ont subi un dégazage - à 400°C sous 10^{-4} Torr pendant 48 hr pour le Carbolac; - à 450°C sous 10^{-4} Torr pendant 3 hr pour ZrO_2 .

Les solides ainsi dégazés ont été examinés par RPE à 10 GHz et par R.M.N. à 60 MHz.

En R.P.E, ils présentent des raies: Carbolac 10^{21} spins/g; largeur de raie 2 G

ZrO_2 { une raie symétrique de largeur 6 G
une raie dont la dissymétrie est due
à une anisotropie de g de $1,3 \cdot 10^{-2}$.

En R. M. N. Aucune raie de protons n'est détectable en large bande ou en haute résolution.

N. B. Cas particulier: ZrO_2 (h)

Pour certaines expériences nous avons utilisé un échantillon de ZrO_2 préparé différemment: le dégazage préalable a été fait à température ambiante (au lieu de $400^\circ C$) sous 10^{-4} Torr pendant 4 hr. Dans ces conditions l'examen par R.P.E., après dégazage, ne montre pas la raie de 6 G observée précédemment. Par contre l'examen par R.M.N. révèle l'existence d'une raie large de protons ($\Delta H = 2,2$ G) qui sont vraisemblablement attribuables à des groupes OH liés à la surface comme c'est le cas pour d'autres oxydes [14-16]. Nous noterons l'échantillon ainsi préparé ZrO_2 (h).

Le liquide à adsorber est lui aussi dégazé. Connaissant les surfaces BET des solides, le nombre de couches moléculaires statistiques θ a été déterminé par pesées. On admet que la surface d'une molécule est 17 \AA^2 pour l'acide formique[5], 18 \AA^2 pour le méthanol [17]. Compte tenu des faibles surfaces spécifiques de ZrO_2 , nous n'avons pas pu étudier dans ce cas des recouvrements inférieurs à 4 couches.

(d) Conditions expérimentales et analyse des spectres

L'étude par R.M.N. a été affectuée à 15,1, 60 et 100 MHz sur des spectromètres Varian DP 60 (muni d'une stabilisation externe à proton), Varian HA 100 et Jeol 4H 100.*

Pour l'acide formique et l'alcool méthylique, dans les cas les plus favorables, les

spectres des molécules adsorbées non deutérées présentent deux raies bien séparées (Fig. 1). Dans d'autres cas moins favorables (basse température, faible recouvrement) on n'observe qu'une seule raie très large avec une structure plus ou moins apparente. Nous avons alors effectué une analyse du spectre sur ordinateur, basée sur la seule hypothèse que chacune des raies qui le composent est symétrique.

3. R.M.N. DES PROTONS NON MOBILES DES LIQUIDES ADSORBES (ETUDE DES RAIES DES GROUPES CH ET CH_3)

(a) $HCOOH$ ou CH_3OH adsorbé sur ZrO_2

(1) *Déplacement des raies des groupes CH et CH_3 .* Des expériences faites en utilisant des porte-échantillons sphériques (Fig. 1) montrent que la seule cause importante de déplacement des raies par rapport aux raies du liquide libre est la différence de susceptibilité entre le liquide libre et le mélange adsorbat adsorbant [8, 18]. Les valeurs des susceptibilités que l'on peut déduire des mesures de déplacement des raies de liquides adsorbés (lorsqu'on utilise les porte-échantillons cylindriques) sont différentes:

$$\chi_I = (-0,19 \pm 0,03) 10^{-6} \text{ CGS/g pour } ZrO_2 \text{ (I)}$$

$$\chi_{II} = (-0,07 \pm 0,02) 10^{-6} \text{ CGS/g pour } ZrO_2 \text{ (II)}$$

et montrent le rôle important de la préparation.

La littérature donne

$$\chi = -0,11 \cdot 10^{-6} \text{ CGS/g.}$$

et

$$\chi = -0,19 \cdot 10^{-6} \text{ CGS/g (11).}$$

(2). *Largeur des raies des groupes CH et CH_3 .* Des mesures faites pour des valeurs différentes du champ H_0 (Table 1 et Fig. 2) aux fréquences 15,1, 60 et 100 MHz montrent une contribution importante du champ local

* Nous remercions MM. Duhamel et Dang du Laboratoire de Synthèse Asymétrique du Professeur Kagan, Faculté des Sciences, Orsay et M. E. G. Derouane, Institut de Chimie de l'Université de Liège, Belgique, qui ont contribué aux mesures faites à 100 MHz.

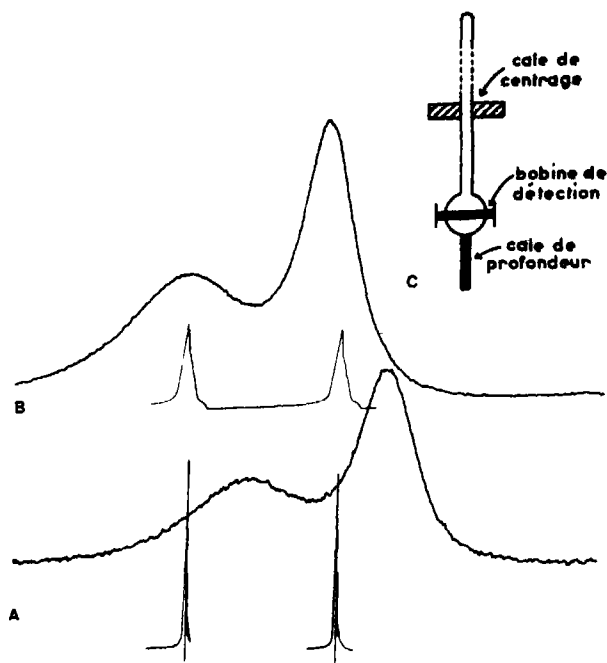


Fig. 1. Spectre de l'acide formique adsorbé sur l'oxyde de zirconium $ZrO_2(II)$. Le champ H_0 croît de gauche à droite. Sous chaque spectre figurent les raies du liquide libre qui servent de référence pour le déplacement des composantes OH (à gauche) et CH (à droite).

A. Echantillon cylindrique

B. Echantillon sphérique

C. Porte échantillon ayant permis de réaliser ces spectres.

Tableau 1. Influence de la rotation (à la fréquence ν) de l'échantillon sur la largeur de raie ΔF à différentes fréquences de mesure F_0

Lot d'adsorbant	Liquide adsorbé	ν (Hz)	ΔF (Hz)		
			$F_0 = 15,1$ MHz	$F_0 = 60$ MHz	$F_0 = 100$ MHz
$ZrO_2(I)$	$CH_3OD(CH_3)$	0	102 ± 5	124 ± 5	172 ± 5
		25		116 ± 5	
		50	94 ± 5	96 ± 5	
		100	88 ± 5		
$ZrO_2(II)$	$HCOOH(CH)$	0	35 ± 5	65 ± 2	87 ± 2
		25		52 ± 2	
		50	28 ± 5	52 ± 2	

d'origine diamagnétique à l'élargissement de la raie. Comme dans le cas des carbones [8] nous avons donc la superposition de deux

distributions: (1) Une distribution du champ dipolaire rétrécie par le mouvement des molécules. Elle est homogène, lorentzienne et sa

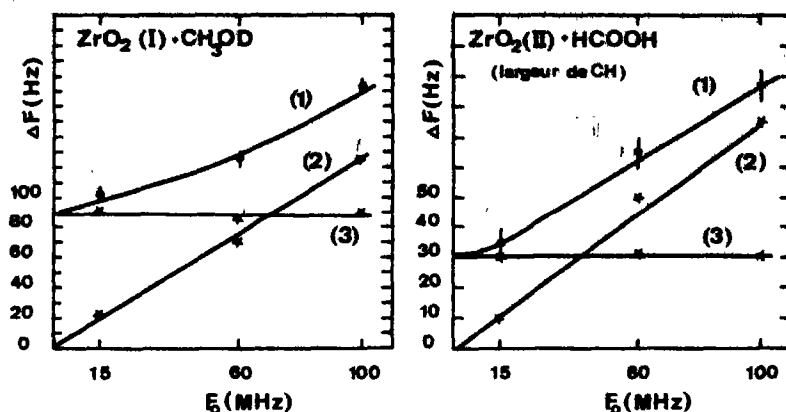


Fig. 2. Variation de la largeur de raie en fonction du champ H_0 (fréquence de mesure correspondante F_0) et décomposition de la largeur expérimentale en largeur dipolaire et largeur inhomogène: (1) Largeur expérimentale, (2) Largeur inhomogène, (3) Largeur homogène.

largeur est indépendante de H_0 . (2) Une distribution du champ local d'origine diamagnétique. Sa forme dépend de la géométrie des grains de la poudre [19, 18, 8] mais sa largeur est inhomogène, proportionnelle à H_0 et à la susceptibilité χ de l'adsorbant [18].

La forme de la raie de résonance résulte donc du produit de convolution de ces deux distributions. Si la distribution du champ local était lorentzienne la raie de résonance serait lorentzienne également (produit de convolution de deux lorentziennes). Les raies que nous obtenons ont une forme intermédiaire entre la gaussienne et la lorentzienne. Nous admettons que la distribution du champ local est gaussienne. Dans ces conditions on peut déterminer les largeurs respectives ΔL et ΔG des deux distributions à partir des largeurs expérimentales $\Delta(G * L)$ obtenues pour plusieurs valeurs du champ H_0 (L est la distribution lorentzienne, G la distribution gaussienne et $L * G$ leur produit de convolution). Cette décomposition (Fig. 2) de la largeur expérimentale en sa partie homogène (d'origine dipolaire) ΔL et sa partie inhomogène (due au champ local diamagnétique) ΔG est obtenue par une construction graphique (Fig. 3) faite à partir de la courbe théorique donnant $\Delta L / \Delta(L * G)$

en fonction de $\Delta G / \Delta$ ($L * G$) calculée par Alquié [20]. On vérifie bien que les pentes des droites ainsi obtenues pour les largeurs inhomogènes, correspondant aux deux lots (I et II) de ZrO_2 , varient comme les susceptibilités obtenues au paragraphe précédent. Cette largeur inhomogène, plus faible que celles prévues par Drain: $\Delta F \sim 3\chi_v F_0$ [19], s'explique bien par le fait que les grains de la poudre sont approximativement sphériques et que leur empilement n'est pas compact. Une rotation rapide de l'échantillon (~ 50 à 100 Hz) module le champ local d'origine diamagnétique et réduit les largeurs des raies mesurées à 60 MHz à la partie homogène (Tableau 1). Ceci montre que la partie inhomogène de la largeur n'avait pas été rétrécie par le mouvement des molécules adsorbées. Il est donc légitime de considérer que toute la molécule voit le même champ local.

(b) HCOOH ou CH_3OH adsorbés sur le noir de carbone 'Carbolac'

Les raies des groupes CH ou CH_3 de l'acide formique ou de l'alcool méthylique adsorbé ont les mêmes propriétés que celles des liquides non polaires, tel que le benzène par exemple, adsorbés sur ce même carbone

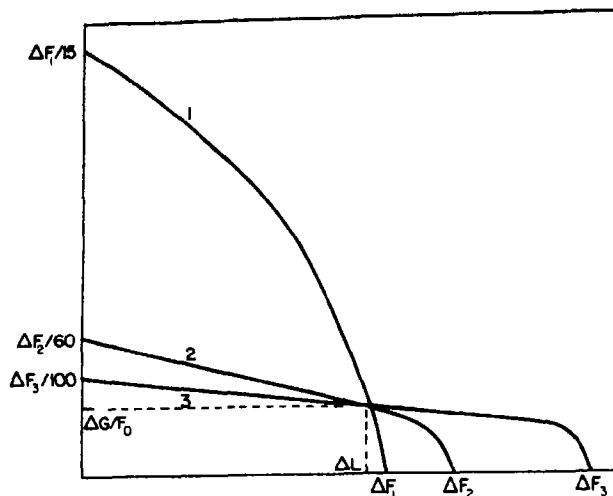


Fig. 3. Décomposition de la largeur de raie en sa partie homogène ΔL (distribution lorentzienne) et sa partie inhomogène ΔG (distribution gaussienne). ΔF_1 , ΔF_2 et ΔF_3 sont les largeurs de raies expérimentales à 15, 60, et 100 MHz. Les courbes 1, 2, 3 sont obtenues à partir de la courbe théorique (20) donnant $y = \Delta G / \Delta(L \cdot G)$ en fonction de $x = \Delta L / \Delta(L \cdot G)$ par la transformation: $X = x \cdot \Delta(L \cdot G)$, $Y = y \cdot \Delta(L \cdot G) / F_0$ pour $F_0 = 15, 60, 100$ MHz, $F_0 = 15$ MHz, $F_0 = 60$ MHz, $F_0 = 100$ MHz et $\Delta(L \cdot G) = \Delta F_1$, $\Delta(L \cdot G) = \Delta F_2$, $\Delta(L \cdot G) = \Delta F_3$. Le point d'intersection des trois courbes donne ΔL et $\Delta G / F_0$.

[8]. Leur déplacement ne peut être réduit par l'utilisation d'un échantillon sphérique. Il est dû à l'anisotropie du champ diamagnétique des grains de carbone. Leur largeur est, comme dans le cas précédent, due à la superposition d'une distribution du champ dipolaire (homogène) et du champ local diamagnétique (inhomogène).

4. R.M.N. DES PROTONS MOBILES: ETUDE DE LA RAIE DU PROTON DU GROUPE OH DE HCOOH OU CH₃OH ADSORBES

(a) Déplacement spécifique de la raie du groupe OH

La raie du groupe OH subit dans certains cas, en plus du déplacement dû au champ local d'origine diamagnétique, un déplacement spécifique que l'on peut mesurer en utilisant la composante CH ou CH₃ du spectre comme référence.

Dans le cas du liquide libre le déplacement

de la raie OH a lieu vers les champs forts, lorsqu'on augmente la température ou lorsqu'on dilue l'alcool ou l'acide (Fig. 4) [12-13].

(1) *Effet de l'adsorption, du recouvrement et de l'état de surface de l'adsorbant.* Pour HCOOH adsorbé sur 'Carbolac' la raie du groupe OH subit le même déplacement vers les champs croissants que celle du groupe CH du spectre, lors de l'adsorption, et ce déplacement varie comme ceux observés pour les liquides non polaires [8], avec le recouvrement θ de la surface (Fig. 5)

Pour HCOOH adsorbé sur Zr O₂ (I ou II) la raie du groupe OH est plus déplacée vers les champs croissants que celle du groupe CH: c'est-à-dire que l'écart des deux raies du liquide adsorbé est plus petit que celui des deux raies du liquide libre (Tableau 2). Ce déplacement augmente encore lorsque le recouvrement θ de la surface diminue (Fig. 6).

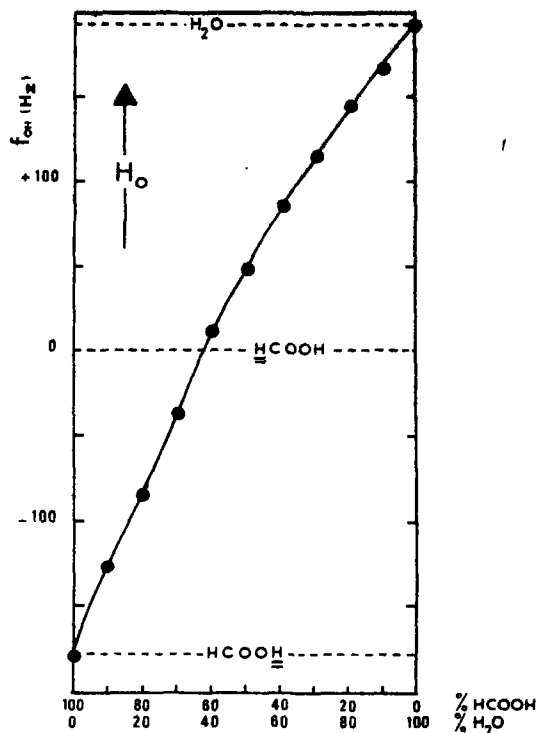


Fig. 4. Déplacement de la raie du groupe OH par rapport à la raie du proton du groupe CH dans un mélange d'acide formique et d'eau en fonction de la concentration (Liquide libre).

Dans le cas particulier de ZrO_2 (h) le déplacement en champ fort de la raie OH est encore plus important que dans le cas précédent (Tableau 2)

Pour CH_3OH adsorbé sur les différents solides on observe les mêmes propriétés mais l'écart des deux raies (CH_3 et OH) étant initialement plus petit, la décomposition du spectre est moins précise.

(2). *Effet de la température et du champ H_0 .* Comme dans le cas du liquide libre un abaissement de la température a pour effet de déplacer la raie du groupe OH des liquides ($HCOOH$ et CH_3OH) adsorbés vers les champs faibles, celle des groupes CH ou CH_3 restant fixe.

A température constante l'écart des raies des liquides adsorbés est proportionnel à H_0 (Tableau 2)

(b) *Largeur et forme de la raie du groupe OH des liquides adsorbés*

(1) *Effet de l'adsorption, du recouvrement et de l'état de la surface.* Dans la phase adsorbée la raie du groupe OH est plus large que l'autre raie du spectre dans tous les cas examinés (Tableau 2, Fig. 1)

Tableau 2. Largeur et écart des raies CH et OH de l'acide formique ($HCOOH$) pour différentes fréquences de mesure F_0 à température ambiante

Adsorbant	F_0 (MHz)	Ecart des raies (Hz)	Largeurs expérimentale des raies ΔF (Hz)		Décomposition de la largeur de raie en largeur homogène ΔL et largeur inhomogène ΔG			
					CH		OH	
			CH	OH	ΔL (Hz)	ΔG (Hz)	ΔL (Hz)	ΔG (Hz)
Carbolac ($\theta \sim 2$)	15	$41 \pm 5^*$	40 ± 10	100 ± 10	35 ± 5	10 ± 2	95 ± 6	15 ± 3
	60	$162 \pm 2^*$	60 ± 10	140 ± 10	35 ± 5	40 ± 8	95 ± 6	60 ± 12
	100	$270 \pm 2^*$	90 ± 5	160 ± 5	35 ± 5	62 ± 13	95 ± 6	100 ± 20
ZrO_2 (II) ($\theta \sim 6$)	15	39 ± 5	35 ± 10	115 ± 10	32 ± 3	$10 \pm 1,5$	113 ± 2	$13 \pm 2,5$
	60	140 ± 2	65 ± 10	145 ± 10	32 ± 3	42 ± 3	113 ± 2	52 ± 10
	100	231 ± 2	87 ± 5	142 ± 5	32 ± 3	61 ± 10	113 ± 2	86 ± 16
ZrO_2 (h) ($\theta \sim 6$)	60	90 ± 2	65 ± 10	180 ± 10				

* Dans ce cas l'écart des raies est égal à celui du liquide libre.

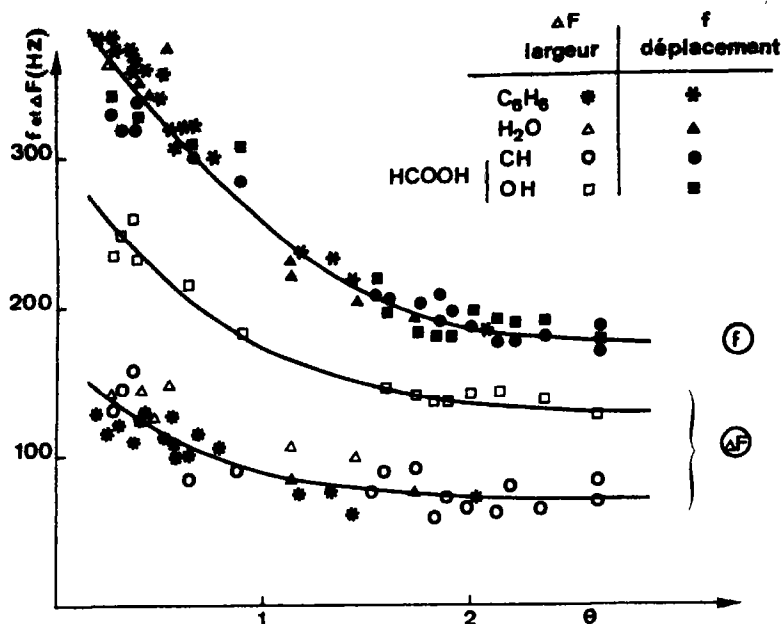


Fig. 5. Variation des largeurs ΔF , et des déplacements f par rapport aux raies correspondantes du liquide libre, des raies de résonance de liquides adsorbés sur le noir de carbone Carbolac en fonction du recouvrement θ de la surface. ($f > 0$ si H_0 croît)

Ce résultat est à rapprocher de ceux obtenus pour l'adsorption de ces mêmes liquides sur gel de silice ou sur alumine (5-7).

Dans tous les cas la raie du groupe OH s'élargit lorsque le recouvrement θ de la surface diminue (Figs 5, 6). A recouvrement égal la raie du groupe OH de HCOOH adsorbé est plus large sur ZrO_2 (h) que sur ZrO_2 (II). La raie du groupe CH, par contre, a sensiblement le même largeur dans les deux cas (Tableau 2, Fig. 7).

(2) *Effet du champ directeur H_0 et de la température.* La raie du groupe OH ne s'élargit pas plus vite avec le champ H_0 que celle du groupe CH (Tableau 2) pour l'acide formique adsorbé sur tous les adsorbants étudiés.

Lorsque la température décroît les deux raies de HCOOH et les deux raies de CH_3OH s'élargissent simultanément (Fig. 8). On remarquera que les variations des lar-

geurs de raies en fonction de la température sont très voisines pour HCOOH et CH_3OH entre $+35^\circ$ et $-50^\circ C$ alors que les températures de congélation de ces deux liquides sont très différentes ($T_c = 8,4^\circ C$ pour HCOOH et $T_c = -97,8^\circ C$ pour CH_3OH).

(c) Saturation des raies

L'amplitude de la raie de résonance OH des liquides adsorbés se sature beaucoup plus difficilement, en fonction du champ RF appliqué, que celle du groupe CH. Par contre dans le liquide libre, nous avons vérifié que les raies OH et CH de l'acide formique se comportaient de la même manière vis à vis de la saturation.

5. RESULTATS DE RESONANCE ELECTRONIQUE ET DE SPECTRAGRAPHIE INFRA-ROUGE

La raie symétrique de R.P.E. de ZrO_2 dégazé (Section 2(c)) disparaît lorsqu'on adsorbe de l'acide formique ou de l'eau. Pour

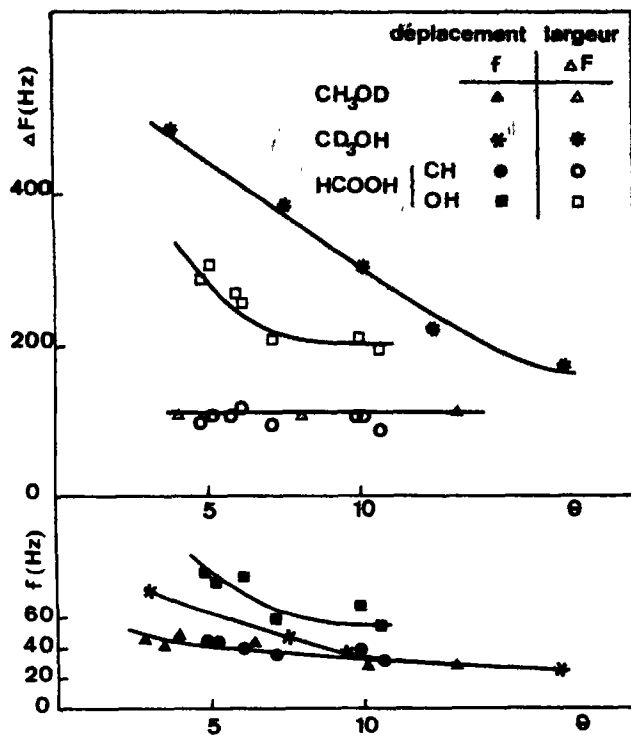


Fig. 6. Variation de la largeur ΔF , et des déplacements f des raies par rapport aux raies correspondantes du liquide libre, des raies de résonance des liquides adsorbés sur l'oxyde de zirconium ZrO_2 (I) en fonction du recouvrement de la surface. ($f > 0$ si H_0 croît).

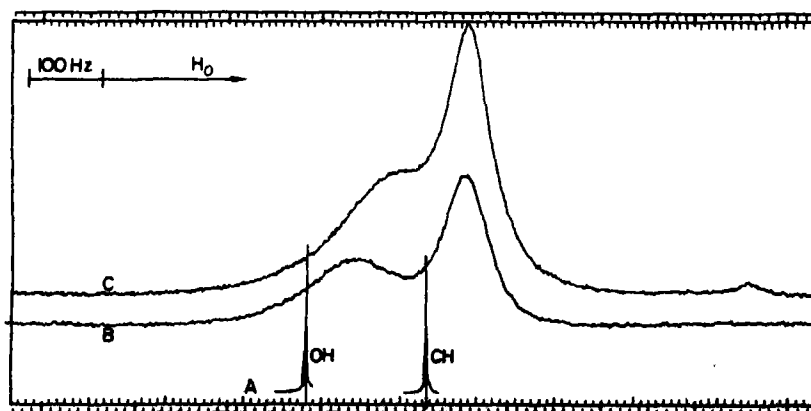


Fig. 7. Spectres de l'acide formique (A) pur, (B) adsorbé sur ZrO_2 (II), (C) adsorbé sur ZrO_2 (h).

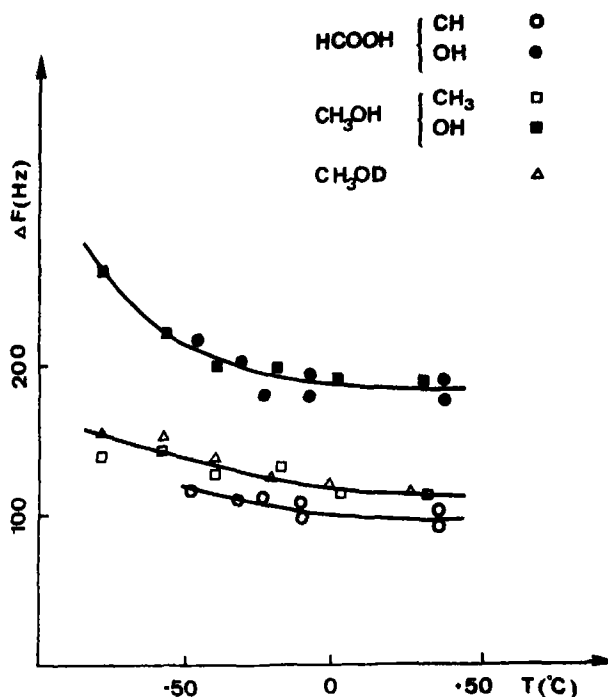


Fig. 8. Influence de la température sur la largeur des raies des différents liquides adsorbés sur ZrO_2 (I). Les recouvrements sont $\theta = 6,5$ pour HCOOH ; $\theta = 10$ pour CH_3OH et $\theta = 6,3$ pour CH_3OD .

ces mêmes liquides la raie de R.P.E. du Carbolac diminue et s'élargit. Ces raies ne sont pas modifiées par l'adsorption d'un liquide non polaire tel que le benzène.

Quand on disperse de l'acide formique pur dans le nujol on observe[9] les bandes d'absorption i.r. CO caractéristiques du dimère (1718 et 1202 cm^{-1})[21]. Par contre quand on examine dans les mêmes conditions ZrO_2 ayant adsorbé HCOOH on observe en plus des bandes précédentes des épaulements caractéristiques de la formation de monomère (1748 et 1103 cm^{-1}).

6. INTERPRETATION

Les raies des groupes OH se distinguent essentiellement des autres raies de liquides adsorbés par leur largeur et leur déplacement plus grands. Nous remarquerons tout d'abord que ces deux effets (élargissement et déplace-

ment) ne sont pas nécessairement corrélés: Dans le cas de l'acide formique adsorbé sur 'Carbolac', on observe en effet un élargissement de la raie OH, bien qu'elle n'ait pas de déplacement spécifique.

(a) Cause du déplacement spécifique de la raie du groupe OH

(1). *Influence des molécules d'eau de surface.* Les déplacements observés pour le groupe OH de l'acide formique ou du méthanol adsorbés sur ZrO_2 pourraient s'expliquer par la présence d'une certaine quantité d'eau sur la surface des adsorbants. Le déplacement de la raie OH serait alors celui obtenu par dilution avec H_2O (Fig. 4). Dans le cas de l'acide formique il faudrait alors que la phase adsorbée ait pour composition, pour $\theta = 6$:

10% H_2O , 90% $HCOOH$ dans le cas de ZrO_2
(II)

20% H_2O , 80% $HCOOH$ dans le cas de ZrO_2
(h).

Cette première hypothèse ne saurait être retenue pour les raisons suivantes;

Nous avons mesuré par thermogravimétrie la quantité de protons qui restent dans l'adsorbant après traitement thermique à $450^\circ C$. Ces protons appartiennent vraisemblablement à des groupes OH de surface (14-15.5) mais même s'ils appartenaient à des molécules d'eau, le mélange $HCOOH + H_2O$ obtenu après adsorption de l'acide formique contiendrait moins de 1,5 pour cent d'eau.

Les quantités d'eau adsorbées sur l'échantillon nécessaires pour obtenir des mélanges acide formique-eau à 10 et 20 pour cent d'eau seraient détectables par RMN large bande avant adsorption de l'acide formique (Section 2c).

La présence de telles quantités d'eau se traduirait par des différences appréciables des surfaces des raies OH et CH. Nous avons vérifié que quand on adsorbe sur ZrO_2 un mélange de 20 pour cent d'eau et 80 pour cent d'acide formique on observe effectivement un rapport $\frac{2}{3}$ entre les intensités des deux raies (c.a.d. leurs surfaces). Précisons que la largeur et le déplacement observés dans cette contre expérience, pour la raie OH, diffèrent de ceux observés pour HCO OH adsorbé sur ZrO_2 (h).

(2) *Equilibre monomère polymères.* Dans le liquide, pur ou en solution, la durée de vie des états associés est courte ($\sim 10^{-10}$ s) de sorte qu'on observe en R.M.N. une seule raie pour OH correspondant à un échange chimique 'rapide' [2] entre les différents états d'association de la molécule. La fréquence de résonance de cette raie est la moyenne, pondérée par le nombre de protons du groupe OH dans chaque état d'association, des fréquences de résonance de chacun de ces états [3-4].

Dans la phase adsorbée le fait que l'on n'observe qu'une seule raie de résonance pour le groupe OH montre que l'échange entre monomères et polymères (CH_3OH) ou entre monomères et dimères ($HCOOH$) reste un échange rapide, même à basse température.

Dans le cas de l'adsorption de $HCOOH$ sur Carbolac, l'équilibre dimère monomère n'est pas modifié par l'adsorption: Il n'y a pas de déplacement spécifique de la composante OH lors de l'adsorption.

Dans le cas de l'adsorption de l'acide formique sur ZrO_2 , l'équilibre dimère-monomère est légèrement modifié en faveur du monomère (déplacement spécifique de la raie du groupe OH vers les champs croissants). Ce déplacement dans l'état adsorbé et à température ambiante est équivalent à celui obtenu pour une dilution dans l'eau de 10 pour cent environ (Fig. 4) ou pour une augmentation de la température de l'ordre de $40^\circ C$ dans le cas du liquide libre.

Cet effet est plus important dans le cas de l'adsorption de $HCOOH$ sur ZrO_2 (h). Le déplacement spécifique est alors équivalent à une dilution de 30 pour cent ou une élévation de température de 150° dans le cas du liquide libre. Il semble donc que la présence de groupes OH à la surface de la zircone favorise la dissociation de l'acide formique.

La formation de monomère par adsorption, déjà mise en évidence dans d'autres cas [5-22], est en bon accord avec les résultats obtenus par spectroscopie i.r. (Section 5).

Contrairement à la surface du Carbolac celle de ZrO_2 favoriserait donc la formation de monomère dans les premières couches d'acide formique ou de méthanol adsorbés. Quand on diminue le recouvrement, le poids statistique du monomère augmente, et la raie de résonance des groupes OH des molécules adsorbées se déplace vers celle du monomère, c'est-à-dire vers les champs forts. Enfin pour l'oxyde de zirconium comme pour le Carbolac, le déplacement de la raie OH des molécules adsorbées vers les champs

faibles quand on diminue la température, traduit comme pour le liquide libre la formation de dimères aux dépens du monomère.

(b) Causes d'élargissement spécifique de la raie du groupe OH

Pour expliquer la différence des largeurs des deux raies (CH et OH de HCOOH ou CH₃ et OH de CH₃OH) on peut envisager les hypothèses suivantes:

(1) *Un ralentissement, lors de l'adsorption, de l'échange chimique entre les différents états d'association des molécules.* Un tel ralentissement aurait pour effet d'élargir la raie de OH (2) sans affecter la largeur de l'autre raie (CH ou CH₃).

Cependant lorsque le champ H_0 croît, l'écart des fréquences de résonance du groupe OH dans le monomère d'une part, et dans le polymère considéré d'autre part, augmente proportionnellement à H_0 . La fréquence d'échange restant la même on devrait observer un élargissement de la raie du groupe OH en fonction de H_0 beaucoup plus rapide que celui de la raie CH (ou CH₃) ce qui n'est pas le cas. (Tableau 2).

La forme de raie OH, est comme pour le groupe CH (ou CH₃), intermédiaire entre une gaussienne et une lorentzienne. Une décomposition de la largeur de raie analogue à celle que nous avons faite pour la raie CH (ou CH₃), en sa partie homogène (invariable avec H_0) et en sa partie inhomogène (proportionnelle à H_0) montre que la partie homogène est beaucoup plus importante pour la raie OH que pour la raie CH (ou CH₃) (Tableau 2). L'élargissement spécifique de la raie OH est donc indépendant de H_0 .

(2) *Une orientation préférentielle des molécules par rapport au solide.* Cette hypothèse [23] a également été proposée par d'autres auteurs qui ont observé un élargissement ou une disparition des raies OH par rapport aux raies CH (5-6-7). Si les groupes OH sont préférentiellement liés au solide (ce qui est vraisemblable puisque leur T_1 est plus court que celui des

autres protons de la molécule Section 4c), leur mobilité sera plus faible que celle des autres groupes qui gardent un degré de liberté supplémentaire. Dans cette hypothèse la distribution des champs locaux aux différents sites d'adsorption est moins bien moyennée par le groupe OH que par l'autre groupe de la molécule.

Pour préciser l'origine de ce champ local nous avons envisagé 3 effets.

Le diamagnétisme de l'adsorbant. Il a pour effet d'élargir la distribution inhomogène proportionnellement à H_0 . Or nous avons vu que la différence des largeurs des composantes OH et CH provient essentiellement d'un élargissement de la distribution homogène indépendante de H_0 (Tableau 2). Il ne peut être retenu.

L'interaction dipolaire entre groupes OH. Ce champ peut être dû soit aux groupes OH de molécules adsorbées voisines, soit aux groupes OH présents à la surface des adsorbants qui n'ont été que partiellement éliminés par le dégazage (cas de ZrO₂ (h)). Ces groupes OH ont pu aussi être recréés par chimisorption en lère couche, avec formation d'ions formiates ou méthylates. Ce phénomène de chimisorption est classique sur les oxydes.

Ce champ a bien pour effet d'élargir la partie homogène de la raie des groupes OH. Cette interprétation permettrait de comprendre les largeurs plus grandes observées pour la raie du groupe OH dans le cas de HCOOH adsorbé sur Zr O₂ (h).

Le champ dipolaire des électrons du solide. Les résultats de RPE montrent qu'il existe une influence des molécules polaires sur les électrons non appariés du solide. Ces expériences peuvent s'interpréter de la façon suivante: la raie de RPE étroite que l'on observe sur les carbones dégazés à température élevée est due à des électrons délocalisés [24]; la raie élargie que l'on observe après adsorption d'acide formique ou d'eau peut être due à une localisation de ces électrons au voisinage du point d'accrochage des

molécules adsorbées. La disparition de la raie symétrique de RPE dans le cas de ZrO_2 ou de ZrO_2 (h) serait même en faveur de l'utilisation de ces électrons dans une liaison entre les molécules adsorbées et le solide. Si son temps de corrélation est assez long, le champ dipolaire des électrons du solide peut donc contribuer à l'élargissement de la raie du groupe OH dans le cas de l'adsorption sur le Carbolac.

(c) *Relation avec les propriétés catalytiques de ZrO_2 pour la décomposition de l'acide formique*

La décomposition de l'acide formique sur l'oxyde de zirconium tétragonal est à 85 pour cent une réaction de déshydratation. Tous les mécanismes proposés pour la déshydratation de $HCOOH$ [25] font intervenir les groupes OH de surface du catalyseur, et une étape intermédiaire où l'acide formique monomère est adsorbé sur le solide par son groupement OH (sur un catalyseur deshydrogénant les 2 hydrogènes de l'acide formique seraient en interaction avec le solide). Nos résultats sont en bon accord avec ces propositions: nous avons mis en évidence la formation de monomère par adsorption de l'acide formique dimère sur la zircone dès la température ambiante. Les molécules d'acide formique sont en interaction avec le solide par leurs groupements oxhydriles. Enfin cette interaction a lieu vraisemblablement, au moins en partie, par l'intermédiaire des groupes OH de surface.

7. CONCLUSIONS

Dans le cas de ZrO_2 , le déplacement des raies de résonance des groupes OH de molécules polaires (après soustraction de l'effet dû au diamagnétisme du solide), et la variation de ce déplacement avec le recouvrement, peuvent s'interpréter si l'on admet qu'une partie des liquides adsorbés se transforme en monomère au contact de la surface du solide. Il n'y a pas modification du taux de monomère par adsorption sur le carbolac

(bien que l'on observe dans ce cas des recouvrements inférieurs à une couche monomoléculaire). Pour les deux adsorbants le déplacement des raies OH quand on abaisse la température, est dû, comme dans le liquide libre, à la formation de dimères ($HCOOH$) ou de polymères (CH_3OH).

La saturation plus difficile, et la largeur plus grande des raies des groupes OH de molécules adsorbées sur ZrO_2 et Carbolac (après déduction de la contribution à la largeur de raie, de la distribution aux sites d'adsorption de champs locaux d'origine diamagnétique) nous conduit à admettre que les molécules étudiées sont en interaction avec le solide par leur groupement OH. La largeur excédentaire de la raie du groupe OH semble alors être due à l'interaction dipolaire entre les groupes OH des molécules adsorbées et les groupes hydroxyles de la surface du solide. Des études par deutération sont en cours pour préciser ce point. Le champ dipolaire des électrons du solide peut également contribuer à cette largeur dans le cas de l'adsorbat Carbolac.

Ces résultats sont en bon accord avec les propriétés catalytiques de ZrO_2 .

BIBLIOGRAPHIE

1. EMSLEY J. W., FEENEY J. and SUTCLIFFE L. H. *High Resolution N.M.R. Spectroscopy*. Pergamon Press, Oxford (1965).
2. POPLER J. A., SCHNEIDER W. G. and BERNSTEIN H. J. *High Resolution N.M.R.* McGraw Hill, New York (1959).
3. MAVEL M. G. *J. Phys.* **21**, 37 (1960).
4. LUSSAN C. J. *Chim. Phys.* **60**, 1100 (1963).
5. HIROTA K., FUERI K., NAKAI Y. and SHINDO K. *Bull. Chem. Soc. Japan* **31**, 780 (1958); *Bull. Chem. Soc. Japan* **32**, 1261 (1959).
6. FRAISSARD J., CAILLAT R., ELSTON J. and IMELIK B. *J. Chim. Phys.* **60**, 1017 (1963).
7. GESCHKE D., MICHEL D., PFEIFER H., WINKLER H. *Tagung Für Hochfrequenzspectroskopie Leipzig* (Sept. 1969).
8. GRADZTAJN S., CONARD J. and BENOIT H. *J. Phys. Chem. Solids* **31**, 1121 (1970).
9. VIVIEN D., Thèse Paris (1970).
10. LIVAGE J., *Bull. Soc. Chim.* **507** (1968). LIVAGE J., DOI K. and MAZIERE C. *J. Am. ceram. Soc.* **51**, 349 (1968).
11. *Handbook of Chemistry and Physics—The Chemical Rubler*, Cleveland, 43rd edition (1961–1962) Cons-

- antes sélectionnées diamagnetisme et paramagnétisme—Vol. 7. Masson 1957 Paris
12. ARNOLD J. T. and PACKARD M. E., *J. chem. Phys.* **19**, 1608 (1951). *J. Chem. Phys.* **21**, 1688 (1953).
 13. DAVIS J.-C. and PITZER K. S. *J. Phys. Chem.* **64**, 886 (1960).
 14. MAYS J. M. and BRADY G. S. *J. Phys. Chem.* **25**, 583 (1956).
 15. MORIMOTO T., NAGAO M. and TOKUDA F. *J. Phys. Chem.* **73**, 343 (1969).
 16. PRIMET M., PICHAT P. and VITAL-MATHIEU M. *C.R. acad. Sci. Paris* **267 B**, 799 (1968).
 17. MIKHAIL R. Sh. and FAHIM K. B. *J. appl. Chem.* **17**, 147 (1967).
 18. GRADSZTAJN S. Thèse Paris 1970 (n° AO 3770).
 19. DRAIN L. E. *Proc phys. Soc.* **80**, 1380 (1962).
 20. ALQUIE G. Thèse 3ème cycle, Paris (1967).
LEGRAND A. P., Thèse, (No. AO 2510) Paris (1968).
 21. NAKAMOTO K. and KISHIDA S. *J. chem. Phys.* **41**, 1554 (1964).
 22. YOUNG R. P. *Can. J. Chem.* **47**, 2237 (1969).
 23. CONARD J., GRADSZTAJN S. and VIVIEN D. *Tagung für Hochfrequenzspektroskopie Leipzig* (Sept. 1969).
 24. CONARD J. and GRADSZTAJN S., *J. de Phys.* **28**, 551 (1967).
 25. DE BOER J. H. *The Mechanism of Heterogeneous Catalysis* Elsevier publishing company (1960).

PARTIAL DISLOCATIONS IN THE WURTZITE LATTICE

YU. A. OSIPYAN and I. S. SMIRNOVA

Solid State Physics Institute of Academy of Sciences of the U.S.S.R., Chernogolovka, U.S.S.R.

(Received 14 July 1970; in revised form 12 September 1970)

Abstract—The analysis has been carried out of the hypothetically possible types of partial dislocations and stacking faults in the wurtzite lattice. The models are made up of the atom arrangements in the cores of the partial dislocations both bordering the stacking fault and being formed in the process of splitting of the perfect dislocations.

The possible types of the dislocation reactions are considered between the partial dislocations, as well as between the partial and perfect dislocations.

INTRODUCTION

THE EXPERIMENTAL discovery of the stacking faults in the crystals having the wurtzite lattice testifies to their comparatively low energy. The investigations of the stacking faults in the wurtzite type crystals were made by different methods: the X-ray diffraction[1-4], the transmission electron microscopy[5-13], the moire fringes[14]. All the workers observed the stacking faults both in basal (0001) and prismatic (11 $\bar{2}$ 0) planes. Drum[9] and Fitzgerald and Mannami[14] carried out a thorough study of the stacking fault displacement vectors and proved that in basal planes the stacking faults have the displacement vector $\frac{1}{3}$ [$\bar{2}$ 023] and those in prismatic planes have the displacement vector $\frac{1}{3}$ [10 $\bar{1}$ 1]. Chikawa[4] observed a Shockley dislocation in plane (0001) in CdS with the Burgers vector $\frac{1}{3}$ [10 $\bar{1}$ 0]. Similar dislocations were also observed by Blank *et al.*[8]. We found it reasonable we have made an analysis of the hypothetically possible dislocations in the wurtzite lattice, constructed models of the atom arrangements in the cores of these dislocations and considered the possible dislocation reactions.

1. THE STACKING FAULTS AND PARTIAL DISLOCATIONS

The Stacking faults in basal planes of the wurtzite are similar to the corresponding

faults in the face centered cubic f.c.c. and the close packed hexagonal structures. The difference is that in the wurtzite (as well as in the sphalerite) a stacking fault of double layers must be considered. Let a , b , c be the atoms of metals and A , B , C —represent the atoms of a non-metal. Hence, the wurtzite structure can be represented by means of the symbol sequence

..... $aAbBaAbBaAbBaAbB$

which are packed normal to the [0001] direction. By the same designation, the sphalerite structure is ... $aAbBcCaAbBcCaA$... The intrinsic stacking fault can be obtained by removing a double layer of atoms and subsequent closing up of the remaining layers. Here, a shear is to be necessarily produced by the value of $\frac{1}{3}$ [02 $\bar{2}$ 3] so that a pair of layers bB will transit into cC , and layers aA into bB , i.e. ... $aAbBaAbBcCbBcCbBcC$... It should be noted that for the wurtzite structure there are two possibilities leading to the same stacking fault, that is, removing of a double layer from distant atoms of the aA type (as it is usually done for the diamond and sphalerite lattices) and removing of a double layer from neighbouring atoms of the Ab or Ba types. Removing of an aA results in breaking of 3 chemical bonds per atom while removing of an Ab — in one bond per atom

only, which means that from this point of view removing of an Ab or Ba is more favourable energetically. This version is being considered now.

In Fig. 1(a) such a fault is shown. The sphalerite layer is given in thick lines. Evidently, such a defect, if it terminates inside the crystal, must be bordered by partial dislocations on both ends. In this case, the Burgers vector of such a dislocation does not lie in the plane of the violation and according to the established terminology this will be a Frank partial dislocation. It is clearly seen in the figure. Its axis lies in the $[2\bar{1}10]$ direction. It is also seen that such dislocations are polar and can be of either α or β configurations.

A similar fault, which is also bordered by a Frank partial dislocation, can be produced by means of introduction of a corresponding double layer Ab or Ba . In Fig. 1(b) such a fault

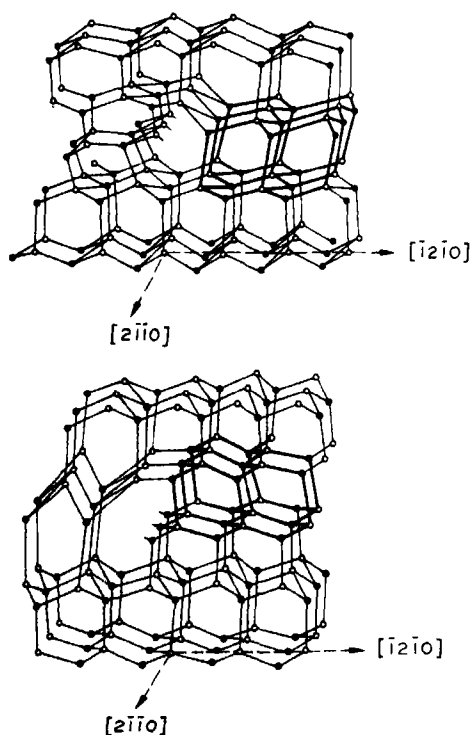


Fig. 1. Frank dislocation with axis $[2\bar{1}10]$ and $b = [\bar{2}02\bar{3}]$
(a) removing of a layer
(b) introducing of a layer.

and a bordering Frank partial dislocation with the Burgers vector $\frac{1}{2}[02\bar{2}3]$ and axis, lying in the $[2\bar{1}10]$ direction, are shown.

If a Frank partial is to be produced with the axis lying in the $[10\bar{1}0]$ direction, its core structure will be quite different, the dislocation is non-polar, as is seen from Fig. 2. The core structure is likely to be the same irrespectively whether the dislocation has been obtained by means of removing or introducing of a double layer.

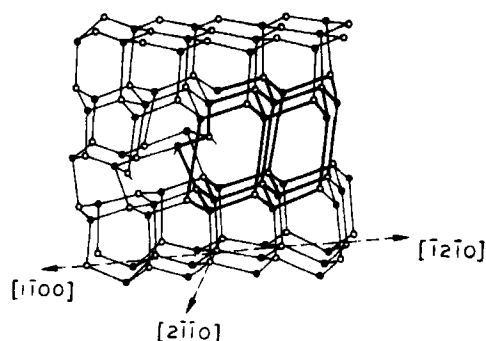


Fig. 2 Frank dislocation with axis $[1\bar{1}00]$ and $b = \frac{1}{2}[2\bar{2}03]$.

A fault of another type can be produced as a result of slip in a basal plane. For convenience, the basal plane between the distant layers will be referred to as B_1 , and the basal planes between the neighbouring layers—as B_2 , the prismatic plane of the kind II is P_2 (Fig. 3). Formerly considered [15] perfect

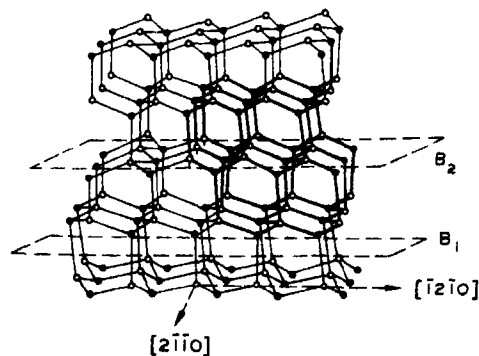


Fig. 3. 30° Shockley dislocation in a basal plane Sh_{1B} .

dislocations in the wurtzite lattice were obtained during slip in the basal planes of the B_1 type. During slip in the basal planes B_2 imperfect dislocations can be produced. The following sequence of layers is obtained during the shear along B_2 into the $\frac{1}{2}[10\bar{1}0]$ vector $\dots AaAbBaAbBcCaAcCaAcC \dots$. If such a fault is limited inside a crystal, it must be bordered by a partial dislocation, that is a Shockley dislocation (Sh.D.). In particular, the Burgers vector of the dislocation shown in Fig. 3 is $\frac{1}{2}[10\bar{1}0]$, its direction is $[2\bar{1}\bar{1}0]$.

Similar to the classification of perfect dislocations, Shockley dislocations can also be distinguished by the angle between the axis and the Burgers vector. In Fig. 3 the 30° Shockley dislocation is given. As is seen, its core is a homoatomic row with broken bonds and, therefore, can have α and β configurations. Its glide plane is B_2 .

In Fig. 4 the Thompson's model is given with designation of the Burgers vectors of the

dislocations. The vectors of the AC, DE, types are the vectors of perfect dislocations. The Shockley partials have the $A\sigma$, $B\sigma$, $C\sigma$ vector types in a basal plane. The vectors of the EA type are the Burgers vectors of Frank dislocations. It can be seen by the figures that formally, the 4 types of Shockley dislocations can be produced, with the angles between the axes and the Burgers vectors of 30° , 90° , 0° and 60° , respectively.

The core structures of the dislocations that border a simple stacking fault are being considered now.

The pattern of a Shockley edge partial dislocation is given in Fig. 5. Its core consists of two parallel homoatomic rows with one broken bond per atom. On the opposite side of a stacking fault (shown in heavy lines) another partial dislocation is lying having the analogous core, consisting of atoms of different type, though.

The Shockley screw dislocation is shown

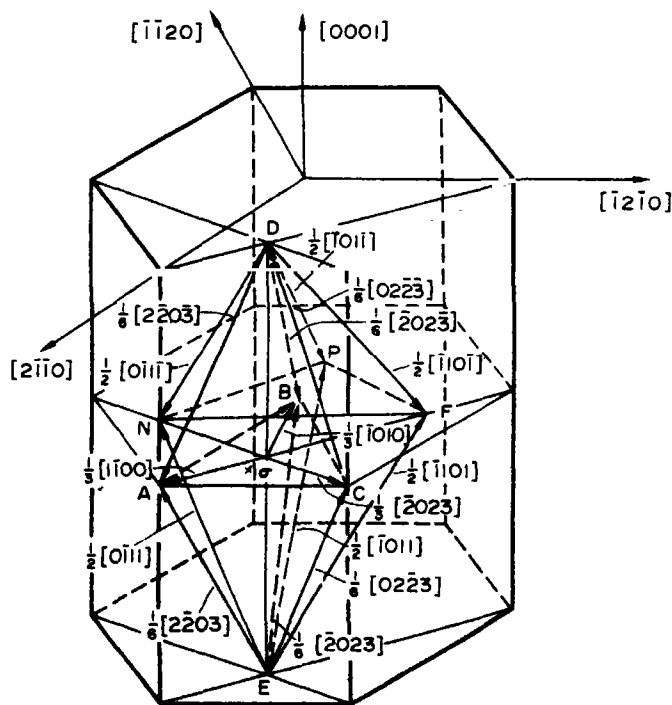


Fig. 4. Thompson's model for the Burgers vectors of partial dislocations in the wurtzite lattice.

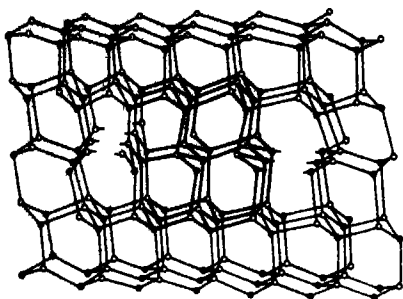


Fig. 5. Two edge Shockley dislocations with opposite signs.

in Fig. 6 (drawn in heavy lines). In the foreground is the sphalerite structure, in the background behind the dislocation, is the wurtzite. The dislocation axis lies in the $[01\bar{1}0]$ direction, the Burgers vector is $\frac{1}{2}[01\bar{1}0]$, respectively.

Naturally, the mobility of this dislocation is limited by the faulting plane, i.e. the basal plane, unlike the perfect dislocations. Figs 7(a) and 7(b) show the cores of the two 60° dislocations of the opposite burgers vectors, that limit the stacking fault on both ends. They are different. One of the dislocations (7-a) is a homoatomic row with three broken bonds. Evidently, the energy of such an atomic configuration can be considerably decreased by means of a break-away of these atoms and removing them by diffusion. At the opposite end of a stacking fault, the 60° dislocation is located of which the core consists

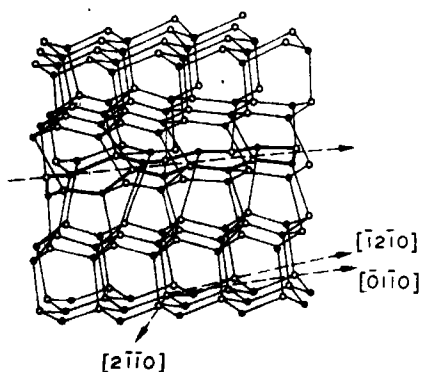


Fig. 6. Screw Shockley dislocation in basal plane Sh_{100} .

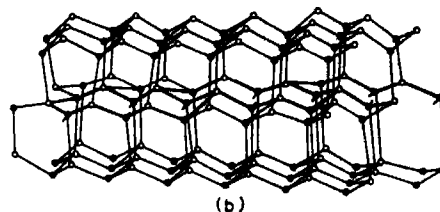
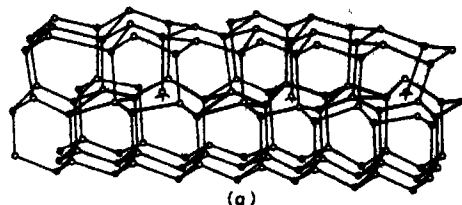


Fig. 7. 60° Shockley dislocation in basal plane of the opposite sign.

of atoms of different type. Here (Fig. 7(b)) single atoms and pairs of atoms with one broken bond alternate along the dislocation line.

Now, let us consider the stacking fault lying in the prismatic plane of the kind II- P_2 ($2\bar{1}\bar{1}0$). The shear with the EF type vector is possible (see Fig. 4). The defect of this type is pictured in Fig. 8. It can be bordered by the Sh.D. with the $\frac{1}{2}[\bar{1}101]$ vector along the C axis. (Fig. 8). The dislocation is non-polar. Along the $[10\bar{1}0]$ direction, the stacking fault in P_2 can be bordered by the Sh.D., pictured in Fig. 9. The dislocation is also non-polar.

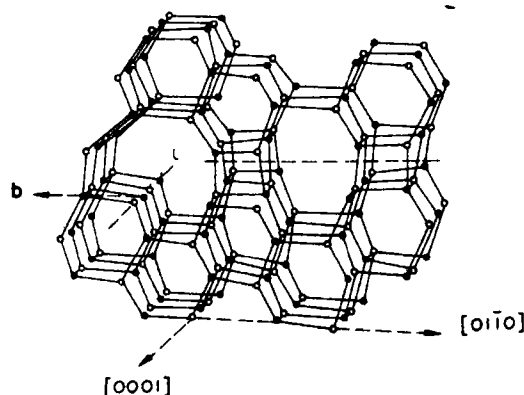


Fig. 8. Stacking fault in prismatic plane of the kind II bordered by Sh.D. with glide plane ($2\bar{1}\bar{1}0$), l -axis, b -Burgers vector Sh_{1P_2} .

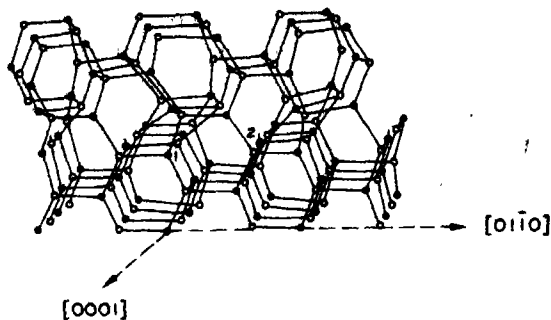


Fig. 9. Shockley dislocation with glide plane $(2\bar{1}10)$, axis $[01\bar{1}0]$ $b = \frac{1}{3}[02\bar{2}3]SH_{2P_1}$.

Unlike the basal Shockley dislocations, these dislocations have the same glide plane as the corresponding perfect dislocations.

2. SPLITTING OF PERFECT DISLOCATIONS IN THE WURTZITE LATTICE

The perfect dislocation in the wurtzite structure, lying in the basal plane (0001) can split into two partial Shockley dislocations, separated by a stacking fault, for instance, according to equation

$$\frac{1}{3}[\bar{1}2\bar{1}0] = \frac{1}{3}[\bar{1}100] + \frac{1}{3}[01\bar{1}0].$$

Here are being considered the splittings of some known types of the perfect basal dislocations (see [15]) and the types of Shockley partial dislocations, originating as a result of this process. The wurtzite and sphalerite structures under consideration, which consist

of the close packed double layers aA , bB , cC have some specific features associated with the fact, that glide can occur in the two types of the parallel basal planes B_1 and B_2 (see Fig. 3). The nucleation and motion of the perfect dislocations occur between distant layers in the planes of the B_1 type, while their splitting and motion of the partial dislocations occur between the neighbouring layers in the basal planes of the B_2 type.

As it turns out to be, the core structure of the partial dislocations, obtained by splitting of the perfect dislocations and the structure of similar to them partial dislocations, which bound the simple stacking fault, can differ sufficiently in spite of the fact, that both their Burgers vectors and dislocation direction are similar. This creates the specific character of the situation, connected with non-coincidence of planes B_1 and B_2 . This will be seen in the figures below.

Another cause of difference in the core structure of dislocations of the same type is that splitting of the perfect dislocation, lying in the B_1 plane, can also occur in the B_2 type plane, that lies either lower, or above the B_1 plane. In such cases different cores can also be nucleated.

2.1 Splitting of the 60° perfect dislocation

Figure 10 pictures splitting of the 60° perfect dislocation into two Shockley partials, one is the edge, another is the 30° dislocation, in accordance with reaction $AB \rightarrow A\sigma + B\sigma$

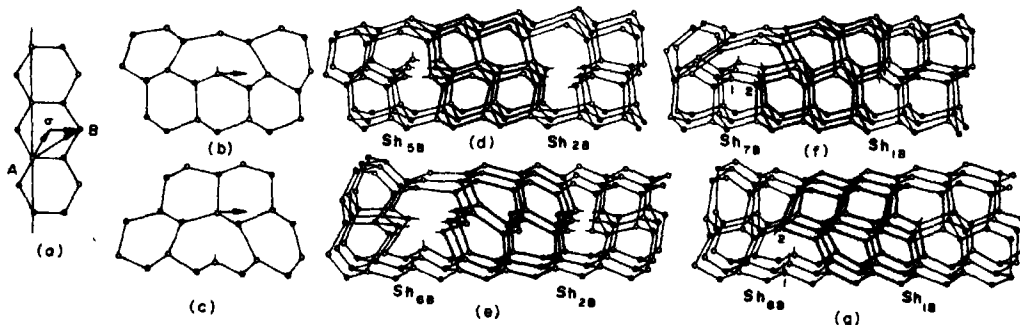


Fig. 10. Possible version of splitting of perfect 60° dislocation into partials.

(Fig. 10(a)). Then, the two types of splitting are shown in schematic drawing, when the plane of splitting lies below (10(b)) and above (10(c)) the plane of the perfect dislocation location. In this connection, four versions of splitting can be realized, which are seen in Fig. 10(d).

Now, the structures of the partial dislocations, nucleated during this process are being considered.

If, in accordance with the drawing 10(b), the edge partial Sh_{2B} is being split, in place of the 60° perfect dislocation, the 30° Sh.D. is formed. The core of this 30° Shockley is different from the core of the above considered corresponding Sh_{1B} (see Fig. 3). This new formed is the Sh_{5B} . Its structure is seen in the left-hand side of Fig. 10(d). The core consists of the parallel homoatomic rows, each atom having one broken bond in one row and two broken bonds per atom in another row. If the row, having two broken bonds per atom is to be removed from the core (by diffusion, for instance) then, the atoms remaining in the core, can realize the configuration without broken bonds.

The corresponding version according to the drawing 10(c) shown in Fig. 10(e). Here, the dislocation Sh_{2B} also splits, the new 30° Shockley dislocation being formed— Sh_{6B} . Its core consists of 3 parallel rows of atoms in two planes with one broken bond per atom. Two homoatomic rows lie in the upper double layer, and row, consisting of atoms of different type, lies in the lower layer. By

means of extra elastic displacement, one of the upper rows can be chemically closed up with the lower one, which sufficiently decreases the number of broken bonds in the core. In case of splitting the 30° dislocation Sh_{1B} type, two new types of Shockley partial edge dislocations Sh_{7B} (Fig. 10(f)) and Sh_{8B} (Fig. 10(g)) are to be formed (compare with Sh_{2B}).

Whether it is possible or not to form covalent bonds between homogeneous atoms and double bonds between heterogeneous atoms, this point is important for energetic stability of the mentioned and subsequent dislocations. If there are such possibilities, sometimes with removal of the atom row off the dislocation core taken into consideration, the interlock of broken bonds can be realized, which sufficiently decreases the chemical energy of the dislocation core. This question is likely to be answered after the detailed quantum-mechanical calculations. In this connection we shall not judge by the number of broken bonds obtained, whether the splitting is advantageous or disadvantageous, but confine ourselves to listing the structures of the dislocations obtained.

2.2. Splitting of a screw dislocation

According to the vector drawing in Fig. 11(a), the two types of splitting of a screw perfect dislocation into two 30° partials can be seen. At first approximation, the cores of both dislocations are similar (see Fig. 11(b) the Sh_{1B} type). They somewhat differ in

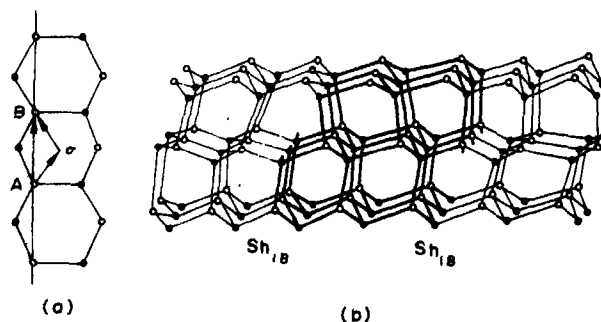


Fig. 11. Splitting of a screw perfect dislocation.

character of their screw component, but this is not seen from the figure. Naturally, their polarity (α, β) is different.

2.3 Splitting of 30° dislocation

The perfect 30° dislocation in a basal plane can split into two Shockley dislocations, of which one is of a screw type, the other is the 60° (Fig. 12(a)). If the shear σ_B is to be produced in plane B_2 , the stacking fault occurs, which is bordered by an ordinary

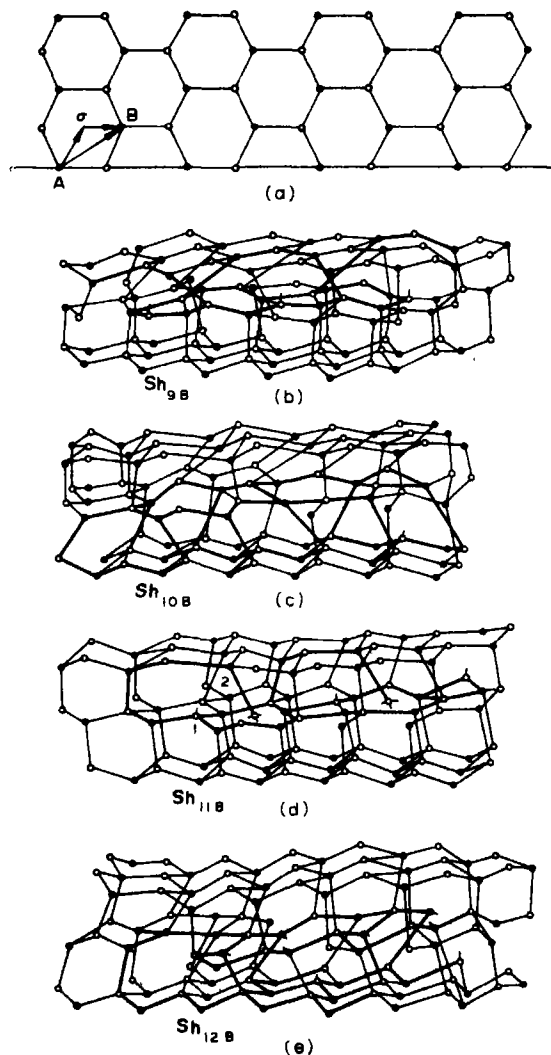


Fig. 12. 4 types of partial dislocation configurations, which occur during splitting of 30° dislocation.

screw partial Shockley dislocation the Sh_{9B} type on one end, and a new 60° Shockley dislocation, the Sh_{10B} type appears on the other end. Its core is shown in Fig. 12(b). Splitting of the 30° perfect dislocation results in formation of four types of new partial Shockley dislocations. This happens due to the fact, that (a) splitting can be produced either above or lower the plane of location of the perfect dislocation and (b) the shear can be of σ_B or $A\sigma$ type. Along with the above mentioned Sh_{9B} , the $60^\circ Sh.D. - Sh_{10B}$ and two types of the screw Sh_{11B} and Sh_{12B} are produced (Fig. 12(c, d, e), respectively). The dislocations Sh_{11B} and Sh_{12B} are no longer the screw ones in the usual sense, because they have broken bonds. It should be pointed out, that during splitting of the 30° dislocation into the screw and 60° ones (Fig. 10(b) and (c)) the number of broken bonds do not increase.

As for Fig. 12(d), here the number of broken bonds can also be decreased by means of removing of the atoms with three broken bonds and further interlock of bonds of atoms 1 and 2.

2.4 Splitting of an edge dislocation

It can be realized with the formation of a stacking fault, bordered by the two 60° Sh.D. As a result of this process the two new types of Shockley dislocations — Sh_{13B} and Sh_{14B} (Fig. 13(b, c)) with a great number of broken bonds are produced. The atomic configurations in the core of both types are rather complex.

To conclude the above said, the considered partial dislocations are given in Table 1.

3. PARTIAL DISLOCATIONS REACTIONS

3.1 Reactions between partial dislocations

Figure 4 represents the totality of the Burgers vectors of the partial dislocations in the wurtzite lattice. The totality is as such:

6 vectors $\pm A\sigma$ type — the Burgers vectors of basal dislocations, the Shockley type.

6 vectors $\pm EC$ type — the Burgers vectors of the Frank dislocations.

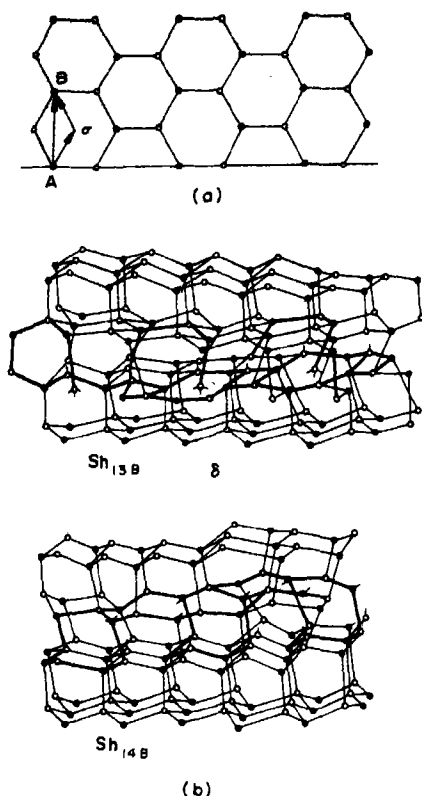


Fig. 13. 2 types of partial dislocation configurations, which arise at splitting of edge perfect dislocation.

12 vectors $\pm EF$ type—the Burgers vectors of the Shockley dislocations, lying in the prismatic planes of the II kind.

At such a set of the burgers vectors, 465 geometrical combinations prove to be possible, which reflect interactions of the dislocations under consideration. In Table 2 are summed up the most interesting reactions, advantageous from the view point of energetic balance. The reaction type (I) means interaction of the two Shockley dislocations, of which, the Burgers vectors form a sharp angle. As a result, a new Sh.D. occurs. The reactions types (2) and (3) describe interactions of Frank and Shockley dislocations. As a result, a new sessile dislocation is formed, with a Frank defect on one end and a Shockley defect on the other end.

Table 1.

N	Dislocation	Axis	Burgers vector	Type	Fig.
1.	Frank	$\langle 2\bar{1}\bar{1}0 \rangle$	$\frac{1}{3}\langle 0\bar{2}23 \rangle$	F_1	1a, b
2.	Frank	$\langle 1\bar{1}00 \rangle$	$\frac{1}{3}\langle 2\bar{2}03 \rangle$	F_2	2
3.	Shockley-30°	$\langle 2\bar{1}\bar{1}0 \rangle$	$\frac{1}{3}\langle 1\bar{1}00 \rangle$	Sh_{1B}	3
4.	Shockley-90°	$\langle 2\bar{1}\bar{1}0 \rangle$	$\frac{1}{3}\langle 01\bar{1}0 \rangle$	Sh_{2B}	5
5.	Shockley-0°	$\langle 10\bar{1}0 \rangle$	$\frac{1}{3}\langle 10\bar{1}0 \rangle$	Sh_{3B}	6
6.	Shockley-60°	$\langle 1\bar{1}00 \rangle$	$\frac{1}{3}\langle 01\bar{1}0 \rangle$	Sh_{4B}	7a
		$\langle 1\bar{1}00 \rangle$	$\frac{1}{3}\langle 0\bar{1}10 \rangle$	Sh_{4B}	7b
7.	Shockley-	$\langle 0001 \rangle$	$\frac{1}{3}\langle 1\bar{0}11 \rangle$	Sh_{1P_1}	8
8.	Shockley	$\langle 01\bar{1}0 \rangle$	$\frac{1}{3}\langle 1\bar{0}11 \rangle$	Sh_{2P_1}	9
9.	Shockley-30°	$\langle 2\bar{1}\bar{1}0 \rangle$	$\frac{1}{3}\langle 1\bar{1}00 \rangle$	Sh_{5B}	10d
10.	Shockley-30°	$\langle 2\bar{1}\bar{1}0 \rangle$	$\frac{1}{3}\langle 1\bar{1}00 \rangle$	Sh_{6B}	10i
11.	Shockley-90°	$\langle 2\bar{1}\bar{1}0 \rangle$	$\frac{1}{3}\langle 01\bar{1}0 \rangle$	Sh_{7B}	10f
12.	Shockley-90°	$\langle 2\bar{1}\bar{1}0 \rangle$	$\frac{1}{3}\langle 01\bar{1}0 \rangle$	Sh_{8B}	10g
13.	Shockley-60°	$\langle 1\bar{1}00 \rangle$	$\frac{1}{3}\langle 01\bar{1}0 \rangle$	Sh_{9B}	12b
14.	Shockley-60°	$\langle 1\bar{1}00 \rangle$	$\frac{1}{3}\langle 01\bar{1}0 \rangle$	Sh_{10B}	12c
15.	Shockley-0°	$\langle 10\bar{1}0 \rangle$	$\frac{1}{3}\langle 10\bar{1}0 \rangle$	Sh_{11B}	12d
16.	Shockley-0°	$\langle 10\bar{1}0 \rangle$	$\frac{1}{3}\langle 10\bar{1}0 \rangle$	Sh_{12B}	12e
17.	Shockley-60°	$\langle 1\bar{1}00 \rangle$	$\frac{1}{3}\langle 01\bar{1}0 \rangle$	Sh_{13B}	13b
18.	Shockley-60°	$\langle 1\bar{1}00 \rangle$	$\frac{1}{3}\langle 01\bar{1}0 \rangle$	Sh_{14B}	13c

The third group of the reactions deal with interaction of Frank defects. These reactions are likely to be interpreted this way: as a result of growth there can occur complex configurations from Frank defects, with different burgers vectors. In between, sessile dislocations will be lying, with the Burgers vectors, pointed out in reactions [4–6].

The fourth group of the reactions describe interactions of the basal Sh.D. and Sh.D., which lie in the prismatic plane of the II kind. The reactions (7), (8) result in formation of a dihedron of stacking faults, between the $\langle 1\bar{2}\bar{1}0 \rangle$ type and $\langle 0001 \rangle$ basal plane. Along the vertex of this angle there forms a stair rod dislocation with the $\langle 01\bar{1}0 \rangle$ type axis and the Burgers vector $\frac{1}{3}[\bar{1}103]$ in case of reaction (7) and $\frac{1}{3}[\bar{1}3\bar{2}3]$ in case of reaction (8).

The group 5 corresponds to interaction of Frank defects, lying in a basal plane and defects, lying in prismatic planes. Exactly such dihedrons have been repeatedly observed in the experiments. In particular, Drum[9] observed a stair rod dislocation, corresponding to reaction (10).

The group 6 deals with interaction of the

Table 2. Reactions between partial dislocations

Group	N	Type reactions	Phys. sense of reactions
I	1	$\frac{1}{2}[01\bar{1}0] + \frac{1}{2}[\bar{1}010] = \frac{1}{2}[\bar{1}100]$	Formation of a new dislocation
II	2	$\frac{1}{2}[0\bar{2}23] + \frac{1}{2}[01\bar{1}0] = \frac{1}{2}[0001]$	Formation of a sessile disloc.
	3	$\frac{1}{2}[0\bar{2}23] + \frac{1}{2}[10\bar{1}0] = \frac{1}{2}[2\bar{2}03]$	Formation of a sessile disloc.
	4	$\frac{1}{2}[0\bar{2}23] + \frac{1}{2}[20\bar{2}3] = \frac{1}{2}[11\bar{2}0]$	Formation of a sessile disloc.
III	5	$\frac{1}{2}[0\bar{2}23] + \frac{1}{2}[02\bar{2}3] = \frac{1}{2}[01\bar{1}0]$	Formation of a sessile disloc.
	6	$\frac{1}{2}[0\bar{2}23] + \frac{1}{2}[\bar{2}023] = \frac{1}{2}[\bar{1}100]$	Formation of a sessile disloc.
IV	7	$\frac{1}{2}[\bar{1}101] + \frac{1}{2}[\bar{1}\bar{1}00] = \frac{1}{2}[\bar{1}103]$	Stair rod disloc.
	8	$\frac{1}{2}[\bar{1}101] + \frac{1}{2}[10\bar{1}0] = \frac{1}{2}[\bar{1}323]$	Stair rod disloc.
	9	$\frac{1}{2}[\bar{1}101] + \frac{1}{2}[0\bar{2}23] = \frac{1}{2}[\bar{3}120]$	Stair rod disloc.
V	10	$\frac{1}{2}[\bar{1}101] + \frac{1}{2}[2203] = \frac{1}{2}[\bar{1}100]$	Stair rod disloc.
	11	$\frac{1}{2}[\bar{1}101] + \frac{1}{2}[20\bar{2}3] = \frac{1}{2}[\bar{5}320]$	Stair rod disloc.
	12	$\frac{1}{2}[\bar{1}101] + \frac{1}{2}[\bar{1}\bar{1}01] = [0001]$	Perfect dislocat.
VI	13	$\frac{1}{2}[\bar{1}101] + \frac{1}{2}[01\bar{1}1] = \frac{1}{2}[\bar{1}2\bar{1}0]$	$\Sigma b_i = 0$
	14	$\frac{1}{2}[\bar{1}101] + \frac{1}{2}[10\bar{1}1] = \frac{1}{2}[01\bar{1}0]$	Stair rod disloc.

Shockley dislocations lying in the prismatic planes of the kind II.

Reaction (12) corresponds to interaction of the two Sh.D., lying in the same plane. As a result of this interaction, a sessile dislocation is being formed, with the Burgers vector $[0001]$ stacking faults with different displacement vectors lying on both ends of this dislocation. It should be noted that as a result of the reaction of the two Sh.D. the Sh_{2P_1} type, an edge dislocation is formed while a screw type dislocation occurs in case of the dislocations the Sh_{1P_2} type.

Reactions (13) and (14) describe the two types of stair rod dislocations as a result of formation of a dehedron of stacking faults. Reaction (13) results in formation of a dislocation with the $[0001]$ axis and the Burgers vector $b = \frac{1}{2}[\bar{1}2\bar{1}0]$ reaction (14)—the $[0001]$ axis and $b = \frac{1}{2}[01\bar{1}0]$, respectively.

3.2 Reactions of partial and perfect dislocations

Below, the following totality of totality

of the Burgers vectors is being considered:

6 vectors $\pm a_i$ type $i = 1, 2, 3$

2 vectors $\pm c$ type

6 vectors $\pm \sigma A$ type

12 vectors $\pm AE$ type

12 vectors $\pm EF$ type.

In Table 3, the 240 physically non-equivalent combinations are given, which are advantageous from the view point of energetic balance.

From the view point of the elastic energy decrease, reaction (1) is energetically advantageous. It can reflect the following process. The perfect dislocation with the Burgers vector the type (Fig. 4) AB splits into two Shockley partials $AB \rightarrow A\sigma + \sigma B$, then, one of the new-formed dislocations annihilate with the other Sh.D. of the opposite Burgers vector, which participates in the initial reaction. As a result, one Shockley partial remains.

$$AB + B\sigma = A\sigma + \sigma B + B\sigma \rightarrow A\sigma.$$

It should be noted that only basal perfect dislocations can participate in such a reaction,

Table 3. Reactions of partial and perfect dislocations

N	Reactions	Phys. sense of reactions
1	$\frac{1}{2}[\bar{2}110] + \frac{1}{2}[10\bar{1}0] = \frac{1}{2}[\bar{1}100]$	Splitting with annihilation of partials of different signs.
2	$\frac{1}{2}[\bar{2}110] + \frac{1}{2}[20\bar{2}3] = \frac{1}{2}[\bar{2}203]$	Formation of a sessile dislocation.
3	$[0001] + \frac{1}{2}[02\bar{2}3] = \frac{1}{2}[02\bar{2}3]$	Splitting with annihilation of partials of different signs.
4	$\frac{1}{2}[\bar{2}110] + \frac{1}{2}[\bar{1}0\bar{1}\bar{1}] = \frac{1}{2}[\bar{1}\bar{1}2\bar{3}]$	Formation of a sessile dislocation.
5	$[0001] + \frac{1}{2}[\bar{1}0\bar{1}\bar{1}] = \frac{1}{2}[\bar{1}0\bar{1}\bar{1}]$	Formation of a sessile dislocation.

because the dislocations, lying in the prismatic plane of the kind I — P_1 , and having the Burgers vector cannot split with violation of a stacking parallel to the basal plane.

Reaction (2) describes the interaction of a perfect dislocation with the Burgers vector a_i and a Frank defect. As a result of this reaction, a new sessile is formed.

Reaction (3) deals with the interaction of a Frank defect and the perfect dislocation, lying in the prismatic plane of the kind I or the kind II, during its interaction with the basal plane. A sessile is formed.

Reaction (4) is of major interest. It describes energetically advantageous formation of a sessile dislocation. In particular, it can occur between the 30° basal perfect dislocation and a Shockley partial the Sh_{1P_2} type.

Another example of this reaction is interaction of a perfect dislocation with the C axis and the Burgers vector a_i , in the prismatic plane of the kind I — P_1 (Fig. 14a) and a partial Sh_{1P_2} type. As a result of this reaction, on one end of the stacking fault a sessile is formed of which, the pattern is given in Fig. 14(b). Its axis lies in the C direction, the Burgers vector is $\frac{1}{2}[\bar{1}\bar{1}2\bar{3}]$. On the other end of the stacking fault, a routine partial Sh_{1P_2} lies. Reaction (5) similarly to reaction (2) results in formation of a sessile dislocation.

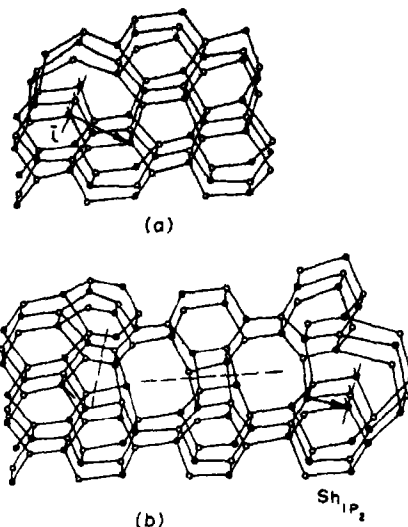


Fig. 14. Sessile, which occurred after splitting of edge dislocation with violation of stacking non-parallel to the glide plane.

Acknowledgement — The authors are grateful to G. Malygyn for help in drawing.

REFERENCES

1. CHIKAWA J., *J. phys. Soc. Japan* **18**, 148 (1963).
2. SKORAKHOD M. J., DATSENKO L. I., *Kristallografiya* **11**, 300 (1966).
3. MÖHLING W., *J. Cryst. Growth* **1**, 115 (1967).
4. CHIKAWA J. and NAKAYAMA T., *J. appl. Phys.* **35**, 2493 (1964).
5. BLANK H., DELAVIGNETTE P. and AMELINCKX S., *Phys. Status Solidi* **2**, 1660 (1962).
6. CHADDERTON L. T., FITZGERALD A. G. and YOFFE A. D., *Phil. Mag.* **8**, 167 (1963).
7. CHIKAWA J., *Japan J. appl. Phys.* **3**, 229 (1964).
8. BLANK H., DELAVIGNETTE P., LEVERS R., AMELINCKX S., *Phys. Status Solidi* **7**, 747 (1964).
9. DRUM C. M., *Phil. Mag.* **11**, 313 (1965).
10. FITZGERALD A. G., MANNAMI M., POGSON E. H. and YOFFE A. D., *Phil. Mag.* **14**, 197 (1966).
11. SECCO D ARAGONA F. and DELAVIGNETTE P., *J. de Phys.* **27**, Suppl. 78 (1967).
12. FITZGERALD A. G., MANNAMI M., POGSON E. H. and YOFFE A. D., *J. appl. Phys.* **38**, 3303 (1967).
13. CAVENEY R. J., *J. Phys. Chem. Solids* **29**, 851 (1968).
14. FITZGERALD A. G. and MANNAMI M., *Proc. R. Soc. A-293*, 469 (1966).
15. OSIPYAN Yu. A. and SMIRNOVA I. S. *Phys. Status Solidi* **30**, 19 (1968).

COMPARISON OF CALCULATED AND MEASURED LOWER CRITICAL FIELD FOR SOME Nb-Ti ALLOYS*

M. S. LUBELL and R. H. KERNOHAN

Oak Ridge National Laboratory† Bldg. 9201-2, P.O. Box Y, Oak Ridge, Tenn. 37830, U.S.A.

(Received 10 August 1970; in revised form 30 October 1970)

Abstract—An expression is obtained from the Maki theory for $H_{c1}(0)$ in terms of three measurable material constants T_c , ρ_n , and $H_{c2}^*(0)$. The calculations are compared to the measured H_{c1} vs. T extrapolated to $T = 0$ K for three vacuum annealed Nb-Ti alloys. Values of $H_{c1}(0)$ are also determined from the computation of Harden and Arp. Both sets of calculated values differ greatly from the measured values showing that the Maki theory is not applicable for $\kappa_{GL} < 30$, and the computation of Harden and Arp is not valid at $T = 0$ K in disagreement with recent results of Echarri *et al.* Analysis of data available in the literature supports our conclusions. Comparison of the magnetization data near T_c with the theory of Neumann and Tewordt shows reasonable agreement.

1. INTRODUCTION

CALCULATIONS of the lower critical field H_{c1} in units of the thermodynamic critical field H_c are not presently available for the complete range of reduced temperature and Ginzburg-Landau parameter κ_{GL} [1]. It would be useful in a.c. applications to be able to calculate H_{c1} from easily obtainable material constants and to avoid the necessity of magnetization measurements.

Harden and Arp[2] have numerically solved an equation derived from the Ginzburg-Landau theory and extended Abrikosov's calculation of H_{c1}/H_c for all $\kappa_{GL} > 1/\sqrt{2}$. However, this result is generally believed to be valid (as was Abrikosov's original solution) only at temperatures close to T_c . Maki[3] was the first to obtain a solution for the temperature dependence of H_{c1} for dirty superconductors ($\xi_0 \gg l$) but only in the limit of large κ_{GL} . The range of validity of Maki's theory (hereafter *M*) has not been adequately tested by experiments partly owing to the difficulty

in measuring H_{c1} in materials with a large κ_{GL} and small electron mean-free-path l . The thermodynamic critical field is also difficult to measure unambiguously in hysteretic superconductors.

Recently Echarri *et al.*[4] (hereafter *E*) have shown for a Mo-34% Re alloy with a $\kappa_{GL} = 5.8$ that the calculations of H_{c1} using Harden and Arp (hereafter *HA*) gave excellent agreement with their measurements of H_{c1} at a reduced temperature of $t = 0.356$. This agreement would seem to indicate that the *HA* computation might be valid over a larger temperature range than originally anticipated. Their measurements of H_{c1} at 4.2 K ($t = 0.356$) are also compared with the *M* prediction for H_{c1} at $T = 0$ K and do not seem to warrant their conclusion that the *M* theory is restricted to $\kappa > 50$. Since there is no well established temperature function for H_{c1} , a zero temperature value could not be obtained from a 4.2 K measurement. If, however, a quadratic temperature variation for $H_{c1}(T)$ is assumed, then calculations based on the *M* theory yield values that on the average are only 7 per cent lower than the extrapolated measured ones. Since as they state, the temperature variation of H_{c1} is slower than parabolic, then the

*Work sponsored by the George C. Marshall Space Flight Center, NASA, Huntsville, and by the U.S. Atomic Energy Commission.

†Operated by Union Carbide Corporation under contract with the U.S. Atomic Energy Commission.

difference between the M theory and the experimental values is even less than this, which is quite surprising.

We have investigated a series of Nb-Ti alloys covering a range of κ_{GL} values from 5 to 24 in which all the material constants necessary for a calculation of $H_{c1}(0)$ have been individually measured. These were compared with experimental values of $H_{c1}(0)$ determined by a smooth extrapolation of H_{c1} vs. T data to $T = 0$ K. In this manner, it was seen whether the M theory would be applicable to lower κ_{GL} than originally anticipated. Also the HA calculation, valid for all κ_{GL} at $T = T_c$, was independently checked for its validity at $T = 0$ K even though agreement could hardly be expected. Magnetization data taken near T_c was in reasonable agreement with theory especially when mean-free-path corrections were considered.

2. DERIVATION OF FORMULA USED IN ANALYSIS

Starting with the M theory as our point of departure and employing well-known type II relationships, a simple formula for $H_{c1}(0)$ is obtained below in terms of easily measurable parameters. Maki[3] gave for $H_{c1}(0)$, in the dirty limit ($\xi_0 \gg l$),

$$\frac{H_{c1}(0)}{H_c(0)} = \frac{\ln \kappa_3(0)}{\sqrt{2} \kappa_3(0)} \quad (1)$$

where $\kappa_3(0) = 1.272 \kappa_1(0) = 1.53 \kappa_{GL}$ is one of the three generalized Ginzburg-Landau parameters which are all equal to κ_{GL} at $T = T_c$. Equation (1) was independently derived by Melik-Barkhudarov[5] who obtained $\kappa_3(0) = 1.54 \kappa_{GL}$ and $\kappa_3(1) = \kappa_{GL}$. The upper critical field at zero temperature is given by [1] $H_{c2}(0) = \sqrt{2} \kappa_1(0) H_c(0)$. Substituting these expressions in equation (1), we find

$$H_{c1}(0) = \frac{H_c^2(0)}{1.272 H_{c2}(0)} \ln \left(\frac{1.272 H_{c2}(0)}{\sqrt{2} H_c(0)} \right) \quad (2)$$

An expression for the calculation of the thermodynamic critical field at zero tempera-

ture in terms of measurable constants is readily obtainable. Combining a BCS equation [1] $H_c(0) = 2.43 \gamma^{1/2} T_c$ and a formula due to Kim *et al.* [6] $H_{c2}^*(0) = 3.11 \times 10^{-5} \gamma \rho_n T_c$, we obtain for $H_c(0)$ in G,

$$H_c(0) = 436 (H_{c2}^*(0) T_c / \rho_n)^{1/2}, \quad (3)$$

where $H_{c2}^*(0)$ is the nonparamagnetically limited GLAG upper critical field at zero temperature in kG, T_c is the transition temperature for zero field in Kelvins, ρ_n is the normal state resistivity in $\mu\Omega\text{-cm}$, and γ is the normal state electronic specific heat coefficient in $\text{ergs/cm}^3\text{-K}^2$. The Kim *et al.* [6] expression for $H_{c2}^*(0)$ assumes $\kappa_{GL} = \kappa_1$ and thus is valid only in the dirty limit [7] which however is a good approximation for this alloy system which has a low intrinsic κ_0 . Substituting equation (3) into equation (2) gives the desired result for $H_{c1}(0)$ in G,

$$H_{c1}(0) = (74.6 T_c / \rho_n) \ln(4.26 H_{c2}^*(0) \rho_n / T_c). \quad (4)$$

3. EXPERIMENTAL

As a test of the range of applicability of equation (4), measurements of T_c , ρ_n , $H_{c2}^*(0)$, and $H_{c1}(T)$ were made on three Nb-Ti alloys of nominal composition Nb-5% Ti, Nb-10% Ti and Nb-25% Ti (at. %).

The samples were made from an ingot which was arc-cast on a copper hearth in an argon atmosphere from starting materials 99.9 per cent pure. After a slight amount of cold working, the ingot underwent a homogenization anneal at 1250°C for 2 hr and was fast-quenched in ice water. The ingot was drawn down to 0.77 mm dia. wire which was measured and then vacuum annealed at 1400°C for 2 hr. Further details on sample preparation have been given [8].

In Table 1 the experimentally determined quantities for the three alloys are tabulated. The normal resistivity ρ_n was measured by a standard four probe d.c. technique at $T = 4.2$ K in a field higher than the upper critical field.

The upper critical field at zero temperature was determined by a flux flow experiment from the Kim *et al.* [6] expression $\rho_f/\rho_n = H/H_{c2}^*(0)$ where the flux flow resistance $\rho_f = dV/dI$ is given by the slope of the linear portion of the voltage vs. current curve taken at constant H and T_B . An example of flux flow data for the annealed Nb-25% Ti sample is shown in Fig. 1. The critical temperature T_c and lower critical field $H_{c1}(T)$ were measured magnetically on a bundle of six 2.6 cm lengths of wire each 0.77 mm in dia. The critical

some scatter in the data shown in Fig. 2, possibly because of the geometry (wire bundle). This method generally yields values less than those obtained by a determination of the first point of the departure from linearity of the Meissner region. The value of H_{c1} at $T = 0$ K was obtained by a smooth extrapolation of the data as shown in Fig. 2.

The critical temperature was about 0.1 K lower in the annealed samples than in the as drawn cold-worked material. Both H_{c2}^* and ρ_n were on the order of 10 per cent lower in the

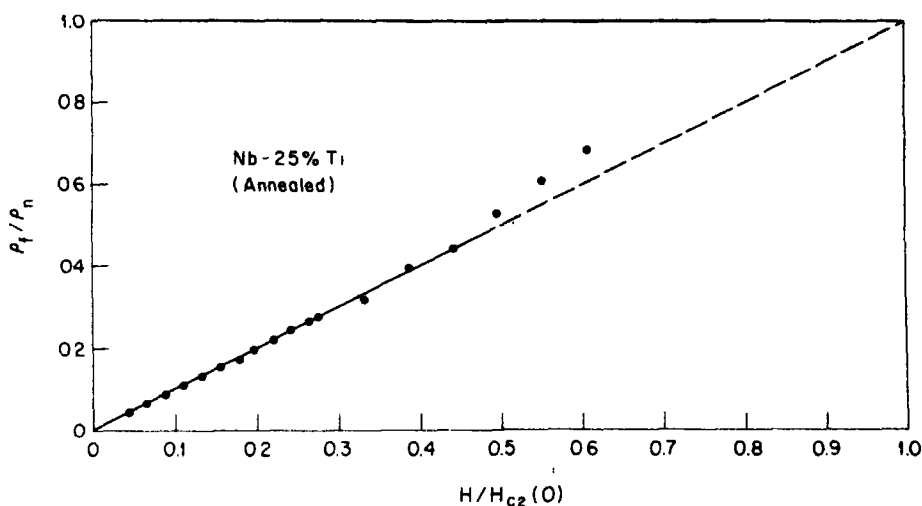


Fig. 1. Normalized flux flow resistivity vs normalized applied transverse field for an annealed Nb-25% Ti wire 0.77 mm dia. at $T_B = 4.18$ K ($t = 0.38$) where $H_{c2}^*(0) = 90.5$ kG.

temperature was taken as the midpoint of a transition having a spread of only 20 mK, however the absolute accuracy was no better than ± 50 mK. The error in the determination of ρ_n and $H_{c2}^*(0)$ is not known exactly, but it is less than 10 per cent. Values of H_{c1} were obtained by measuring small remanent magnetic moments after increasingly higher excursions of the applied field into the Meissner region (perfect diamagnetic state where $B = 0$). Extrapolation of the remanent moment vs. applied field to zero moment then yielded values of H_{c1} . Although the sensitivity of the magnetization equipment [9] is sufficient to detect a flux density of 1 G, there is still

annealed material than in the cold-worked samples. Lower values of H_{c1} than shown in Table 1 could possibly have been obtained by either a higher temperature anneal or a longer anneal, but the accompanying loss of Ti would have had a deleterious effect on the distribution of Ti in each sample.

4. CALCULATIONS

The values calculated from the measurements are shown in Table 2. The thermodynamic critical field $H_c(0)$ was calculated from equation (3). Kappa one at $T = 0$ K $\kappa_1(0)$ was determined from the measured $H_{c2}^*(0)$ and the calculated $H_c(0)$ which is equivalent

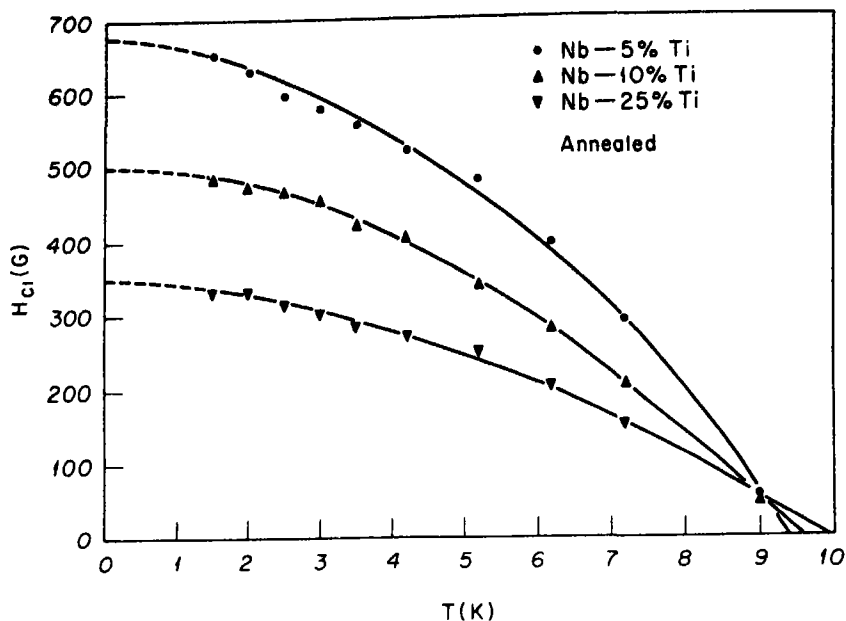


Fig. 2. The lower critical field vs temperature for three Nb-Ti alloys. The measurements were made on a bundle of six 2.6 cm lengths of wire each 0.77 mm in dia. The values at $T = 0$ K determined by a smooth extrapolation of the data are listed in Table 1.

to taking $\kappa_1(0) = 1.203 \kappa_{GL}$, where κ_{GL} is assumed equal to κ_l , the extrinsic value only. Hence $\kappa_1(0)$ is also calculated from the three measured quantities ρ_n , T_c , and $H_{c2}^*(0)$ since by this procedure $\kappa_1(0) = 1.62(H_{c2}^*(0)\rho_n/T_c)^{1/2}$. Kappa three at $T = 0$ K $\kappa_3(0)$ was calculated from $1.272 \kappa_1(0)$.

The first column of $H_{c1}(0)$ values listed in Table 2 was determined from the graph of HA using $\kappa_3(0)$ and $H_c(0)$ calculated from equation (3). As is readily evident, these values are very much below the measured ones. The calculation of $H_{c1}(0)$ using equation (4) derived from the M theory is given in the last column. The disagreement in this case is

even worse. These calculations average between 36 and 57 per cent below the measured values. The disagreement is particularly bad for the sample with higher Ti content, i.e. larger κ_{GL} .

5. DISCUSSION

The discrepancy between the calculated and measured values of $H_{c1}(0)$ is due to either grossly inaccurate measurements, poor assumptions in utilizing the theories of the calculated values, or inapplicability of the theories. Let us examine each of these possibilities in turn.

Of the measured parameters, $H_{c2}^*(0)$ is in

Table 1. Measured values of annealed Nb-Ti alloys

Nominal composition (At. %)	T_c (K)	ρ_n ($\mu\Omega\text{-cm}$)	$H_{c2}^*(0)$ (kG)	$H_{c1}(0)$ (G)
Nb-5% Ti	9.41	6.42	18	675
Nb-10% Ti	9.61	12.1	35	500
Nb-25% Ti	9.93	35.5	90.5	350

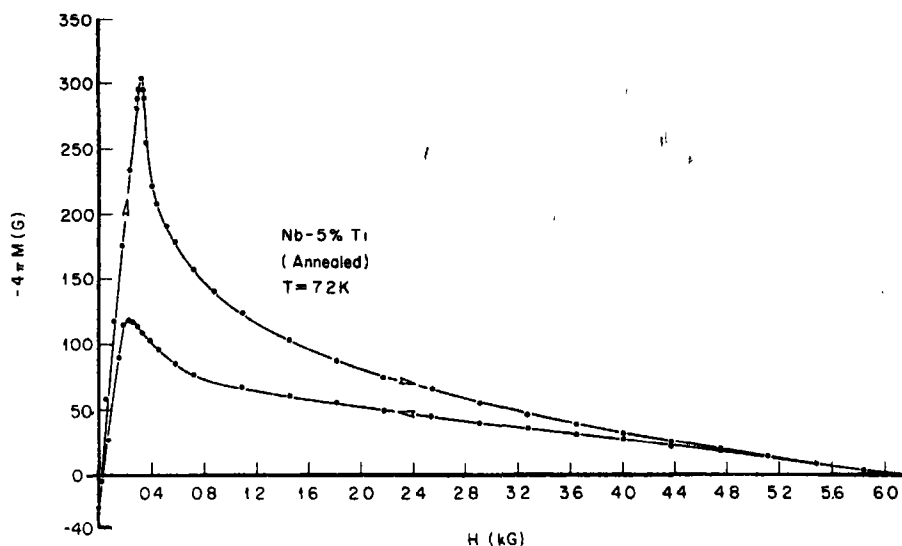


Fig. 3. Magnetization vs. applied axial field for a bundle of six 2.6 cm lengths of annealed Nb-5% Ti wire each 0.77 mm in dia. at $T_B = 7.2$ K ($t = 0.765$).

agreement with values reported in the literature[10,11] for other compositions in the high Nb concentration end of the Nb-Ti system. Our T_c measurements do not agree with Fietz and Webb[10] (hereafter FW) who indicate only 0.1 K change from Nb to Nb-12.5% Ti while our values increase monotonically. We have checked the Vickers hardness for our three compositions, and in qualitative agreement with the T_c data it also shows a monotonic increase with increasing Ti content varying from 78 to 96 to 123

diamond pyramid hardness for the 5, 10, and 25% Ti cold-worked alloys, respectively. The measuring thermometer is unlikely to have a significant systematic error since the T_c of pure Nb measured with it was 9.26 K which is in agreement with many recently reported measurements. The normal resistivity is the easiest and most straightforward parameter to measure, and the only source of difficulty leading to an error is the measurement of the exact length between voltage probes. The measurements of $H_{c1}(T)$ on a

Table 2. Calculated values of the Nb-Ti alloys

Nominal composition (At. %)	$H_c(0)$ (G) equation (3)	$\kappa_1(0)$ [a]	$\kappa_3(0)$ [b]	$H_{c1}(0)$ (G) [c]	$H_{c1}(0)$ (G) equation (4)
Nb-5% Ti	2240	5.7	7.2	556	433
Nb-10% Ti	2300	11	14	364	310
Nb-25% Ti	2200	29	37	174	151

^[a]Determined from the measured value $H_{c2}^*(0)$ and calculated $H_c(0)$ which is equivalent to $\kappa_1(0) = 1.203 \kappa_{GL} = 1.62 (H_{c2}^*(0) \rho_n / T_c)^{1/2}$.

^[b]Calculated from $\kappa_3(0) = 1.272 \kappa_1(0) = 1.53 \kappa_1$.

^[c]Determined from the graph of Harden and Arp[2], using $\kappa_3(0)$ and the calculated $H_c(0)$.

hysteretic material such as Nb-Ti are difficult. As a criterion for determining H_{c1} , we have used the first detectable remanent moment equivalent to detecting a flux of 10^{-1} G-cm². This procedure gives a value that is even less than that obtained by trying to determine the exact deviation from linearity of an M vs. H graph, i.e. the end of the Meissner state. The only value in the literature to compare our results to is a measurement on Nb-3% Ti by DeSorbo[12]. He gives $H_{c1}(4.2\text{ K}) \approx 675$ G which should be and is larger than $H_{c1}(4.2\text{ K}) = 520$ G for our 5% Ti alloy. One would, perhaps, anticipate an anomalously high value of H_{c1} due to surface effects as first proposed by Bean and Livingston[13]. Our specimens did not have smooth surfaces which tend to enhance the formation of an image barrier[14] but instead were left in the roughened state characteristic of the drawing process.

Since there is no simple analytic form for the temperature dependence of H_{c1} , we can only say that the ratio $H_{c1}(T)/H_{c2}(T)$ does increase with decreasing T which is in accordance with the theory of Neumann and Tewordt[15]. This result should be true regardless of the value of κ_{GL} or the ratio ξ_0/l . The temperature dependence of $H_{c1}(T)$ was close but not equal to a quadratic one. A final check on the consistency of our data is given by the calculation of $H_c(0)$ from the three measured quantities $H_{c2}^*(0)$, ρ_n , and T_c utilizing equation (3). The values shown in Table 2 are between the calculated and measured values given by FW on annealed Nb-Ti alloys. The calculation of $H_c(0)$ brings up the first discrepancy between theory and experiment. FW have shown that the calculated BCS $H_c(0)$ using an estimated rather than measured γ is on the average about 18 per cent less than the measured $H_c(0)$ for annealed specimens for compositions covering the range from Nb to Nb-9% Ti. If the same is true for our samples and this is by no means at all certain, then this would account for some of the difference between our calculated and measured $H_{c1}(0)$. Although

H_c could not be measured at low temperatures due to the relatively low applied field available, it was determined at a few high temperature points for the annealed samples, and the extrapolated value at $T = 0$ K using a quadratic temperature dependence yielded values within 5 per cent of the calculated values shown in Table 2.

In applying the theory we used forms containing $H_{c2}^*(0)$ [viz. equations (3) and (4)], the nonparamagnetically limited upper critical field at zero temperature. However this is the value determined from flux flow experiments. In addition the $GLAG$ limit should be dominant for Nb-Ti alloys in this range[16], and paramagnetic limiting probably is absent in all three compositions but most certainly in the 5 and 10 per cent alloys. If the Ginzburg-Landau theory is to be applicable in the dirty limit below T_c , then κ_{GL} must be replaced by $\kappa_3(T)$. The procedure we have followed here in calculating $H_{c1}(0)$ is to replace $\kappa_3(0)$ in the M theory by $1.53 \kappa_{GL}$ where κ_{GL} is given by the extrinsic component κ_l . We have determined κ_l through a calculation involving the normal state resistance. There are other methods[10, 17] for determining κ_{GL} , but these generally yield values within 10 per cent of each other. Since $\kappa_{GL} \geq 5$ for all compositions, a variation of 10 per cent in the magnitude of κ_{GL} would affect the final results by less than 5 per cent. Finally there is one more check that can be made to substantiate the general validity of our calculations. Equation (1) when combined with the definitions preceeding equation (2) in such a way as to eliminate $H_c(0)$ can be put in a form where $H_{c1}(0)$ is a function only of two parameters, i.e., $H_{c2}(0)$ and $\kappa_1(0)$.

$$H_{c1}(0) = (H_{c2}(0)/2.544 \kappa_1^2(0)) \ln 1.272 \kappa_1(0). \quad (5)$$

By extrapolating the $H_{c2}(T)$ and $\kappa_1(T)$ data given by FW to $T = 0$ K, we have obtained values of $H_{c2}(0)$ and $\kappa_1(0)$ for their annealed Nb-4.5% Ti, Nb-9% Ti. The values of $H_{c1}(0)$ computed from equation (5) are 436 and 314 G

for Nb with 4.5 and 9% Ti, respectively. This agreement between our values and those calculated from entirely different measurements (based on measurements of H_{c2} and H_c) lends further support to the conclusion that our measurements and methods of calculation are not seriously in error.

6. MAGNETIZATION MEASUREMENTS NEAR T_c

Although magnetization measurements yielding values of $H_{c2}(T)$ and $H_c(T)$ could only be performed at a couple of temperatures close to T_c , we present an analysis of this data for two reasons. First, we will show that an extrapolation of this data to low temperatures yields results close to our calculations. Second, a comparison of the data near T_c with theory applicable for this region shows reasonable agreement which provides confidence that the samples are not adversely contaminated with impurities.

A calculation of $H_{c1}(0)$ using our high temperature measurements of $H_c(T)$ and $\kappa_1(T) = H_{c2}(T)/\sqrt{2}H_c(T)$ extrapolated to $T = 0$ K using a quadratic approximation for $H_c(T)$ and the M theory for $\kappa_1(T)$ gave results within 5 per cent of those presented in Table 2 for the 5 and 10 per cent samples. Only one high temperature evaluation was obtained for the 25 per cent sample and so an extrapolation was not practical, but a crude estimate gave a 40 per cent higher value for $H_{c1}(0)$ which nevertheless still did not agree well with the measurement. The high temperature values of $\kappa_1(T)$ determined magnetically are compared to the $T = 0$ K calculations based on electrical measurements in Fig. 4.

In Fig. 5 the measured values of $H_{c1}(T)/H_c(T)$ are compared with the theories of M , HA , and Neumann and Tewordt[15]. The M result was obtained from the theoretical value of $\kappa_3(T)/\kappa_1(T)$ in the region near T_c , the measured $\kappa_1(T)$, and equation (1). Note that unlike the zero temperature calculations given previously, here the discrepancy between the M theory and the measurements decreases as κ_{GL} increases (i.e. increasing Ti). Results

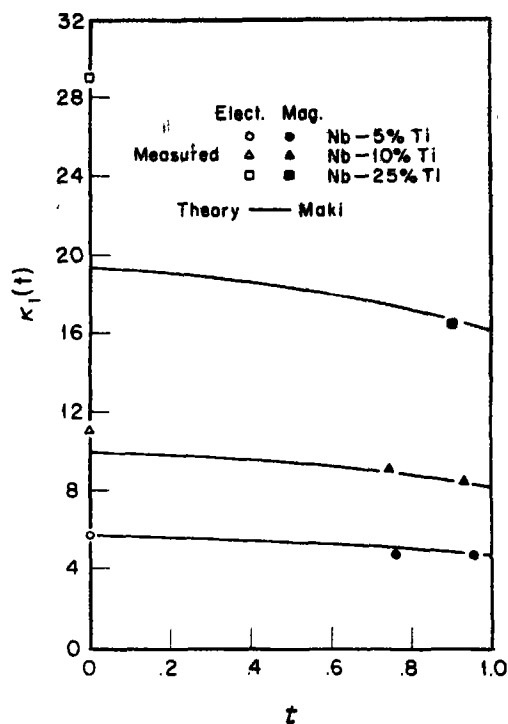


Fig. 4. The measured first generalized Ginzburg-Landau kappa, $\kappa_1(T) = H_{c2}(T)/\sqrt{2}H_c(T)$, vs. reduced temperature ($t = T/T_c$) for three Nb-Ti alloys compared with the values at $T = 0$ K obtained from Table 2.

based on the HA computation using $\kappa_3(T)$ are in closer agreement with experiment than the M theory. The calculations using the Neumann and Tewordt[15] computation includes a correction for mean-free-path dependence. In calculating the mean-free-path parameter, we used a method similar to FW in determining the intrinsic Ginzburg-Landau kappa, κ_0 .

We attempted to use our measured values of $H_{c1}(T)$ and calculated values of $H_c(T)$ (using both a BCS and a quadratic temperature dependence) to obtain 'observed values' of $\kappa_3(T)$ based on the M theory, equation (1) but over a good part of the temperature range, there was no solution.

7. CONCLUSION

The fact that the calculations of $H_{c1}(0)$ differ so greatly from the measurements leads us to conclude that the M theory is not

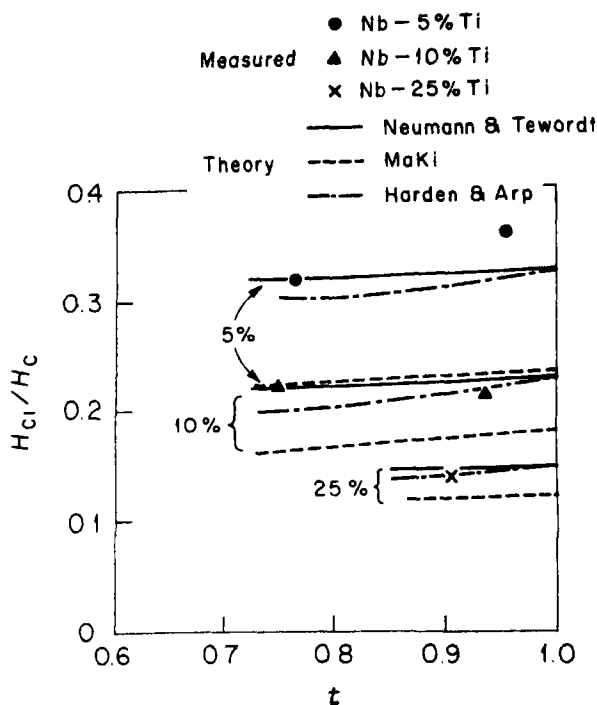


Fig. 5. The measured values of $H_{c1}(T)/H_c(T)$ vs. reduced temperature ($t = T/T_c$) for the three Nb-Ti alloys compared with theory near T_c .

applicable for type II superconductors with Ginzburg-Landau kappa values less than 26. One might anticipate a smaller discrepancy as κ increases toward high values but such was not the case for our samples. We have also concluded that one is not justified in using the computations of HA for zero temperature evaluations. In order to make more comparisons, we have calculated $H_{c1}(0)$ for other low kappa systems, namely the Nb-Ta data of Ogasawara *et al.*[18], the Mo-15% Re and Mo-25% Re data of Joiner and Blaughar[19], the Mo-32.3% Re data of Lerner *et al.*[20], and the Nb-Ta data by Ikushima and Mizusaki[21]. For all of the above cases, $H_c(0)$ was measured and did not have to be calculated. Only a summary of the results are given in Table 3. The widely different values for Mo-32.3% Re are perhaps due to the two-phase nature of the composition

Table 3. Per cent difference between calculated from measured $H_{c1}(0)$ from analysis of published data where H_c was measured

Material	Equation (4)	Equation (1)	HA
Nb-Ta ^(a)	-37	-47	-26
Mo-Re ^(b)	-35	-37	-11
Mo-32.3% Re ^(c)	-50 ^(e)	-11	+20
Nb-Ta ^(d)	-46	-64	-30

^(a)Ref.[18]. The values given are the average for six compositions. We used $\kappa_3(0)$ not $\kappa_1(0)$ as was done by Ogasawara *et al.*[18].

^(b)Ref.[19]. Average of two compositions Mo-15% Re and Mo-25% Re.

^(c)Ref. [20]. This composition is very close to that used by Echarri *et al.*[4].

^(d)Ref.[21]. The values given are the average of six compositions except for the values in the column headed equation (4) where only the three highest Ta compositions could be calculated.

^(e)For this calculation the resistivity values were obtained from an earlier report by the same authors[24].

[22]. Similarly the agreement between theory and experiment by E on a composition close to that used by Lerner *et al.* [20] might be a fortuitous consequence of measurements on a multi-phase material. In all cases, the value of $H_{c1}(0)$ calculated from equation (4) was lower than the measured H_{c1} extrapolated to $T = 0$ K. For low κ_{GL} material, the HA calculation in almost all cases agreed more closely with experiment than the M theory. Nevertheless the agreement is not good enough to warrant the conclusion that the HA results are valid over a wide temperature range. It has also been pointed out recently by Decker and Lacquer [23] that the M theory does not agree with experiment even for a high kappa ($\kappa_{GL} \sim 60$) material. Extension of the GLAG theories covering temperatures far from T_c valid for all κ_{GL} are still needed. Even if obtained, however, agreement with experiment may well require additional refinements such as inclusion of anisotropy of the Fermi-surface, multiple band effects, and as suggested by E normal state spin effects on the lower critical field.

Acknowledgements — We are grateful to R. E. Reed for vacuum annealing the samples and also to S. T. Sekula for helpful discussions.

REFERENCES

1. For an excellent review of basic type II superconductivity, see GOODMAN B. B., *Rep. Prog. Phys.* **29**, Part II, 445 (1966). Superconductivity (Edited by R. D. Parks), Vol. 1 and 2. Marcel Dekker, New York (1969).
2. HARDEN J. L. and ARP V., *Cryogenics* **3**, 105 (1963).
3. MAKI K., *Physics* **1**, 21 (1964); **1**, 127 (1964).
4. ECHARRI A., WITCOMB M. J., DEW-HUGHES D. and NARLIKAR A. V., *Phil. Mag.* **18**, 1089 (1968). These authors employ an unusual nomenclature in their table which we wish to clarify for the unwary reader. The experimental values of H_{c1} (4.2 K) are listed under the heading Harden and Arp (1963) while the calculated values obtained from the Harden and Arp computation are listed under the heading Whitcomb *et al.* (1968). The values of $H_{c1}(0)$ calculated from the Maki theory are listed under that heading.
5. MELIK-BARKHUDAROV T. K., *Soviet Phys. JETP* **20**, 208 (1965).
6. KIM Y. B., HEMPSTEAD C. F. and STRNAD A. R., *Phys. Rev.* **139**, 1163 (1965).
7. The dirty limit $\xi_0 \gg l$ is synonymous with $\kappa_{GL} \gg \kappa_0$ not as is often stated $\kappa_{GL} \gg 1$. For a simple derivation and discussion of this point, see LUBELL M. S., ORNL-TM-2771, p. 15 (1969).
8. LUBELL M. S. and KROEGER D. M., *Adv. Cryog. Eng.* **14**, 123 (1969); ORNL-TM-2075, p. 2 (1967).
9. SEKULA S. T. and KERNOHAN R. H., *J. Phys. Chem. Solids* **27**, 1863 (1966).
10. FIETZ W. A. and WEBB W. W., *Phys. Rev.* **161**, 423 (1967).
11. For a compilation of all recently published values on this system, see LUBELL M. S., ORNL-TM-2771, p. 33 (1969).
12. DESORBO W., *Rev. mod. Phys.* **36**, 90 (1964).
13. BEAN C. P. and LIVINGSTON J. D., *Phys. Rev. Lett.* **12**, 14 (1964).
14. DEBLOIS R. W. and DESORBO W., *Phys. Rev. Lett.* **12**, 499 (1964).
15. NEUMANN L. and TEWORDT L., *Z. Phys.* **189**, 55 (1966).
16. BERLINCOURT T. G. and HAKE R. R., *Phys. Rev.* **131**, 140 (1963).
17. For a recent application of various methods and comparison of the differences, see HECHLER K., HORN G., OTTO G. and SAUR E., *J. Low Temp. Phys.* **1**, 29 (1969).
18. OGASAWARA T., KUBOTA Y. and YASUKŌCHI K., *J. phys. Soc. Japan* **25**, 1307 (1968).
19. JOINER W. C. H. and BLAUGHER R. D., *Rev. mod. Phys.* **36**, 67 (1964).
20. LERNER E., DAUNT J. G. and MAXWELL E., *Phys. Rev.* **153**, 487 (1967).
21. IKUSHIMA A. and MIZUSAKI T., *J. Phys. Chem. Solids* **30**, 873 (1969).
22. DICKINSON J. M. and RICHARDSON L. S., *Trans. Am. Soc. Metals* **51**, 1055 (1959).
23. DECKER D. L. and LACQUER H. L., *J. appl. Phys.* **40**, 2817 (1969).
24. LERNER E. and DAUNT J. G., *Phys. Rev.* **142**, 251 (1966).

CALCULATION OF THE PHOTOELECTRIC EFFECT IN GERMANIUM

L. R. SARAVIA and L. CASAMAYOU

Instituto de Física, Facultad de Ingeniería y Agrimensura, Universidad de la República, Montevideo, Uruguay

(Received 7 August 1970; in revised form 16 October 1970)

Abstract—The contribution from direct interband transitions to the photoelectric effect in Germanium is calculated for photon energies up to 12 eV. Refined computational techniques for the calculation of the energy distribution curves allow a detailed comparison of the theoretical and experimental curves. The agreement is good and the structure is interpreted in terms of the details of the energy bands. A new interpretation is given for some of the peaks.

1. INTRODUCTION

THE POWER of the photoemission experiments for determining important features of the electron energy band structure of semiconductors, especially for the higher electron energies, has been emphasized by Spicer and Eden[1]. From a theoretical point of view, the calculations of the energy distribution curves, necessary for a quantitative analysis of the experimental structure, has been limited to Si. Brust[2] has performed a calculation for Si in the lower photon energy range. Recently, Saravia and Casamayou[3] have extended the calculation in Si up to a photon energy of 10 eV, and used numerical techniques that improved considerably the resolution of the calculation. It was shown that the agreement between the experimental and theoretical distribution curves is excellent for the higher electron energies, allowing a detailed interpretation of the structure in terms of the energy bands.

In the present work a similar calculation is performed in Ge, for which there exist experimental results[4, 5] for photon energies covering the range up to 12 eV that show very interesting structure.

The procedure to compute the photoemission energy distribution curves is described in Section 2. A direct transition model is adopted. The contributions for the different

energy bands are calculated, but no detailed study of the scattering of the electrons by the crystal is performed. The model adopted for the energy bands of Ge is explained in Section 3. They are calculated using a pseudopotential approach combined with a k.p extrapolation procedure. Spin orbit effects are included. The results are given and discussed in Sections 4 and 5. The agreement with the experimental results is good for the higher electron energies, and a detailed analysis is made in terms of the contributions from the different interband transitions. The regions of the Brillouin Zone (BZ) producing the most important structure are indicated. Particularly, the interpretation of the experimental structure corresponding to higher electron energies, previously discussed by Donovan and Spicer[5], is clarified.

2. CALCULATION OF THE ENERGY DISTRIBUTION CURVES

We are dealing with photoelectrons produced in the volume of a semiconductor by direct optical excitation. If ω is the frequency of the incident photon and E the final conduction band energy of the excited electrons, the energy distribution curve $N(E, \hbar\omega)$ is given by

$$N(E, \hbar\omega) = A \sum_{n,s} \int_{BZ} |p_{ns}(\mathbf{k})|^2 P(E, \mathbf{k}) \delta(\omega_{ns}(\mathbf{k}) - \omega) \delta(E_n(\mathbf{k}) - E) d^3k. \quad (1)$$

The sum is over all conduction bands n and valence bands s . The integral is performed over all the BZ, p_{ns}

(\mathbf{k}) is the momentum matrix element between bands n and s , A is a normalization constant, and $\hbar\omega_n(\mathbf{k})$ is equal to $E_n(\mathbf{k}) - E_v(\mathbf{k})$. $P(E, \mathbf{k})$ is the probability that the electron produced with energy E and wave vector \mathbf{k} will escape.

We perform this integration using a method developed elsewhere[3]. Briefly, the integration is reduced to one along a line defined by the surfaces $E_n(\mathbf{k}) = E$ and $\omega_n = \omega$, which is performed analytically using a linear interpolation for the functions $E_n(\mathbf{k})$ and $\omega_n(\mathbf{k})$ inside each cube in the mesh defined by the points of the *BZ* where the bands are calculated numerically.

For the calculations to be performed in this work, the cubic mesh necessary to obtain a good resolution will have about 1600 points in the asymmetric part of the *BZ*. The energy distributions will be computed at intervals of energy equal to 0.01 eV.

In (1) there appears the escape probability factor $P(E, \mathbf{k})$. To treat this function exactly would require having rather detailed information about the surface potential and scattering mechanisms. We will compute it adopting the hypothesis proposed by Brust[2]. We assume that an electron produced with an energy $E_n(\mathbf{k})$ has a momentum \mathbf{k} which is completely randomized by elastic scattering processes before the electron reaches the surface of the crystal. Electrons whose momentum is directed towards the surface are assumed to leave the crystal with an escape probability:

$$P(E, \mathbf{k}) = \begin{cases} \text{Constant, if } E_n(\mathbf{k}) - E_{vac} > \frac{\hbar^2 k_T^2}{2m} \\ 0, \text{ if } E_n(\mathbf{k}) - E_{vac} < \frac{\hbar^2 k_T^2}{2m} \end{cases} \quad (2)$$

where k_T is the component of \mathbf{k} parallel to the surface of the crystal and E_{vac} is the vacuum level. This factor is obtained in the supposition that the absolute value of the momentum \mathbf{k} is conserved during the process and k_T is continuous through the escape surface. Next, we average the escape probability over all the available states of energy E in the *BZ*, obtaining an escape probability factor $P(E)$ independent of \mathbf{k} .

3. CALCULATION OF THE ENERGY BANDS

We need to compute the energy bands and the dipole matrix elements over a cubic mesh in the *BZ* containing a considerable number of points. We use a pseudopotential method to generate the bands, and a $\mathbf{k} \cdot \mathbf{p}$ extrapolation procedure to increase the size of the cubic mesh as explained elsewhere[6]. Briefly, one computes eigenvalues and eigenvectors at a small number of points in a coarse cubic mesh by solving the secular equation generated by the pseudopotential approach. Then, a refined mesh of points is generated from the previous one by a $\mathbf{k} \cdot \mathbf{p}$ extrapolation procedure. The combination has the advantage of greatly expediting the computational work.

The spin-orbit terms have also been considered. We use the formalism developed elsewhere[7].

The pseudopotential parameters used for Ge are the same as those used in a previous work[7]: $V(1, 1, 0) = -0.282$ Ry, $V(2, 2, 0) = 0.058$ Ry, $V(3, 1, 1) = 0.018$ Ry.

The spin-orbit parameter was selected to fit the experimental value of the spin-orbit splitting at the $\Gamma_{25'}$ level[8]. The comparison with other energy bands, calculated by Brust[9], by Cohen and Bergstresser[10], by Herman *et al.*[11], by Cardona and Pollak[12], and by Dresselhaus and Dresselhaus[13] are performed in the mentioned work[7]. The selected pseudopotential formfactors are somewhat different from those used by Brust[9] and by Cohen and Bergstresser[10]. The changes were performed in order to bring down the position of the Γ_{12} level. The spin-orbit splittings in Ge, about 0.3 eV, are of the order of the broadening constants present in the photoemission experiments, what makes them not very important from the point of view of the interpretation of the experimental structure.

The resulting energy bands along several directions in the *BZ* are shown in Fig. 1. The double group notation is not used. In the discussion that follows the energy values at a general point in the *BZ* are denoted by E_i ($i = 1, 2, \dots$), not taking into account Kramer's degeneracy, i.e., each value of i corresponds to two eigenvalues. All the electron energies are referred to the top of the valence band.

4. RESULTS

(a) Escape probability

Donovan and Spicer[5] have measured energy distribution curves obtained from Ge surfaces which have received different treatment in order to change their vacuum level. We have calculated the escape probability curves for two values of the vacuum level: 1.65 and 4.80 eV. They are shown in Fig. 2.

(b) Energy distribution curves

They have been calculated for different values of $\hbar\omega$ up to 12 eV and include inter-band transitions involving valence bands 2, 3, 4 and conduction bands 5 to 12.

The results are extremely rich in details and the structure is in general quite sharp. This is produced by the fact that the structure due to two-dimensional saddle critical points is logarithmic, and the discontinuities related to maxima and minima critical points can take large values, even approaching infinite. It is not possible to make a direct interpretation of the experimental peaks, since they are fewer and look much broader than the calculated ones.

This is expected because effects such as electron-phonon and electron-electron scat-

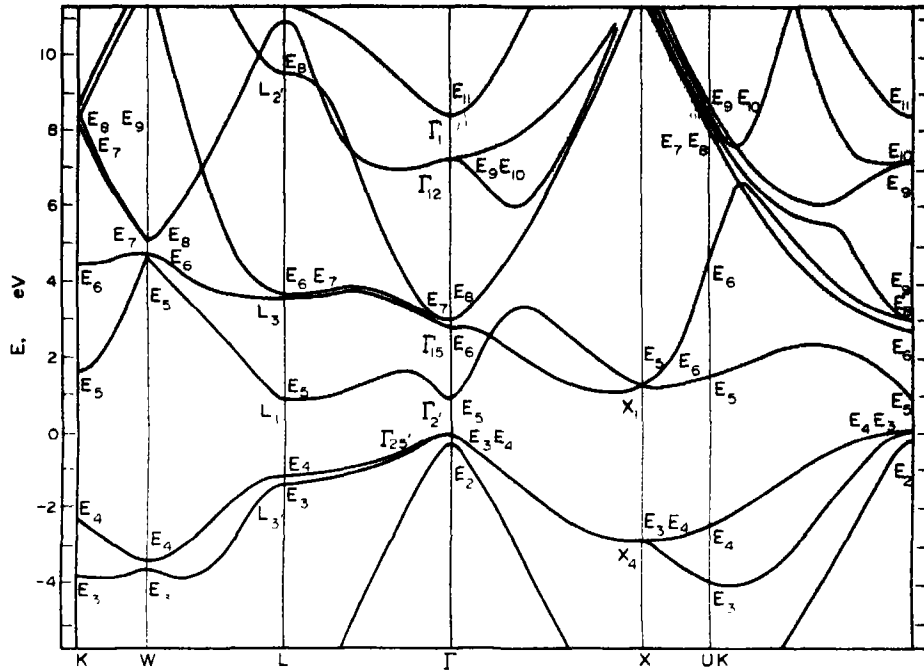


Fig. 1. Energy bands of Ge along some principal symmetry lines. They were computed using the pseudopotential method together with a k.p extrapolation procedure. The energy bands are labeled E_i ($i = 1, 2, \dots$), with i increasing with energy. The single group notation is given for some of the points of the BZ.

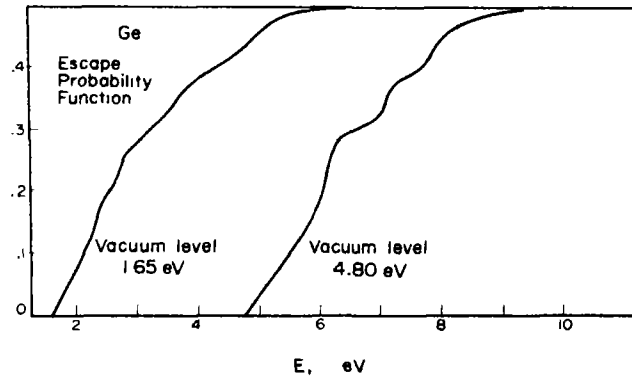


Fig. 2. Shows the two different escape probability functions used in the present calculation. The differences are produced by the position assumed for the vacuum level in each case.

tering, interaction of the electrons with the cesium film and band bending have not been considered.

In order to perform a comparison, we intro-

duce a phenomenological broadening of the form

$$N'(E, \hbar\omega) = \int_0^\infty N(E', \hbar\omega) L(E', E) dE' \quad (2)$$

where

$$L(E', E) = \frac{1}{\pi} \frac{\Gamma}{\Gamma^2 + (E - E')^2} \quad (3)$$

Γ is the broadening constant. We adopt different values of Γ according to the surface treatment: 0.15 and 0.10 eV for the surfaces with vacuum levels at 1.65 eV (cesiated surface) and 4.80 eV (uncesiated surface).

The calculated energy distribution curves for different photon energies, including the effect of the escape probability factor and broadening, are given in Figs. 3 to 6. The experimental ones, as measured by Donovan [5], are shown in Figs. 7 to 10.

5. DISCUSSION

A general remark can be made about the calculated results shown in Figs. 3 to 6. The calculated structure is clearly observed in the experiments, Figs. 7 to 10, but it appears superposed in a contribution not reproduced at all by the present calculation. This contribution is particularly large for the case of cesiated surfaces and low photon energies. It shows a large shoulder and peak which appear for all $\hbar\omega$ at electron energies equal to 2.2 and 3.0 eV. For the uncesiated surface the effect is not so important, but all the same there is a shoulder beginning at 5.0 eV for all $\hbar\omega$ which probably results from the action of the escape probability function on the mentioned contribution. This structure disappears after the surface is cesiated, indicating that it is not related to direct transitions. A similar situation was found in the case of Si[3]. Several authors have mentioned the possibility for this type of structure to be produced by physical effects not mentioned here, such as scattering mechanisms[1, 14, 15, 16] or contributions from indirect transitions[17].

On the following we study the interpretation of the different peaks in terms of the direct interband transition contributions. The position of the structure in the calculated distribution curves is given in Figs. 11 and 12 as

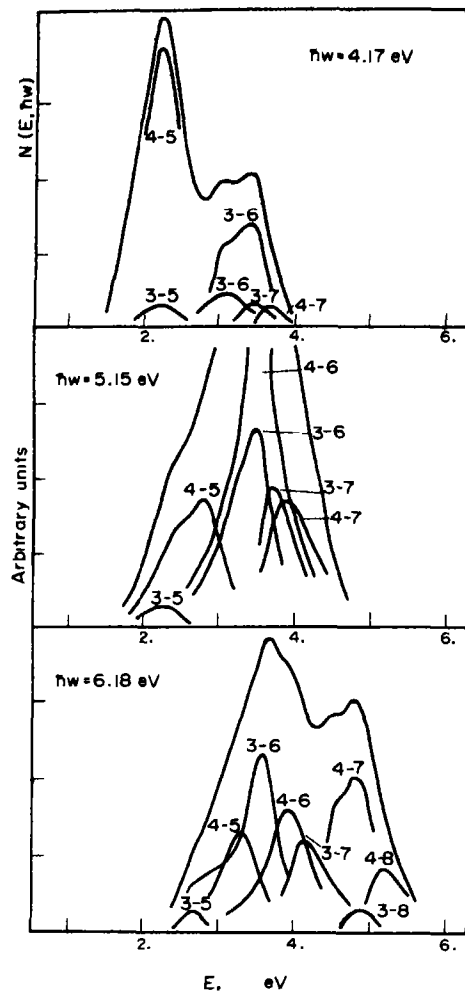


Fig. 3. Shows the calculated energy distribution curves in Ge for several values of photon energy corresponding to a sample with a cesiated surface. The calculation includes an escape probability factor with the vacuum level at 1.65 eV and a broadening factor equal to 0.15 eV. Partial results indicating the contribution from some of the interband transitions are also shown. They are identified by the numbers labeling the bands involved in the transition (e.g., label 4-7 indicates the contribution from transitions between valence band E_4 and conduction band E_7). For the sake of clarity only partial contributions important from the point of view of the interpretation of the peaks were included.

an $E - \hbar\omega$ plot. The experimental results[5] have been superposed in the same diagrams and the structure has been denoted by capital letters, from A to J. We find that each piece of

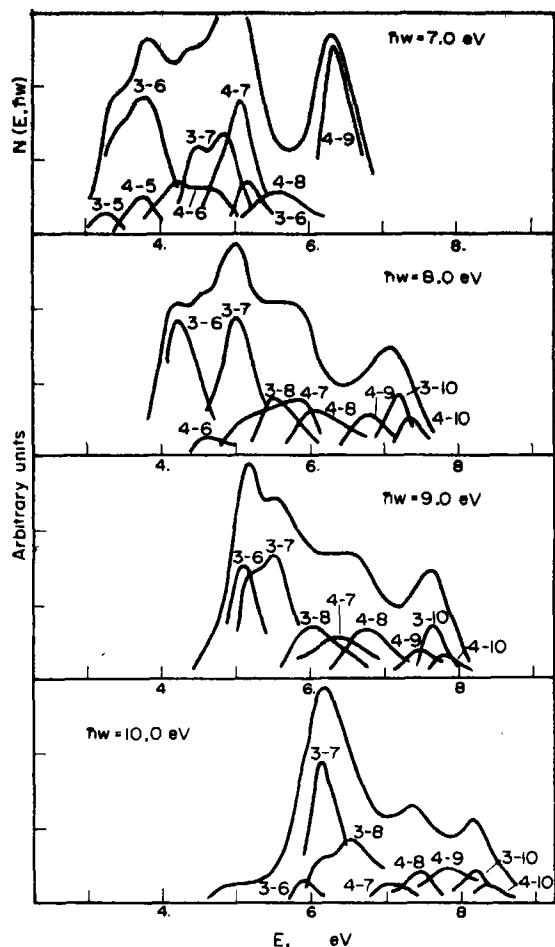


Fig. 4. Shows the calculated energy distribution curves in Ge for several values of photon energy corresponding to a sample with a cesiated surface. The calculation includes an escape probability factor with the vacuum level at 1.65 eV and a broadening factor equal to 0.15 eV. Partial results indicating the contribution from some of the interband transitions are also shown. They are identified by the numbers labeling the bands involved in the transition (e.g., label 4-7 indicates the contribution from transitions between valence band E_4 and conduction band E_7). For the sake of clarity only partial contributions important from the point of view of the interpretation of the peaks were included.

structure is mainly produced by contributions from a few interband transitions. They are indicated in Table 1. The region of the *BZ* producing the structure is also given in Table 1. The region of the *BZ* producing the struc-

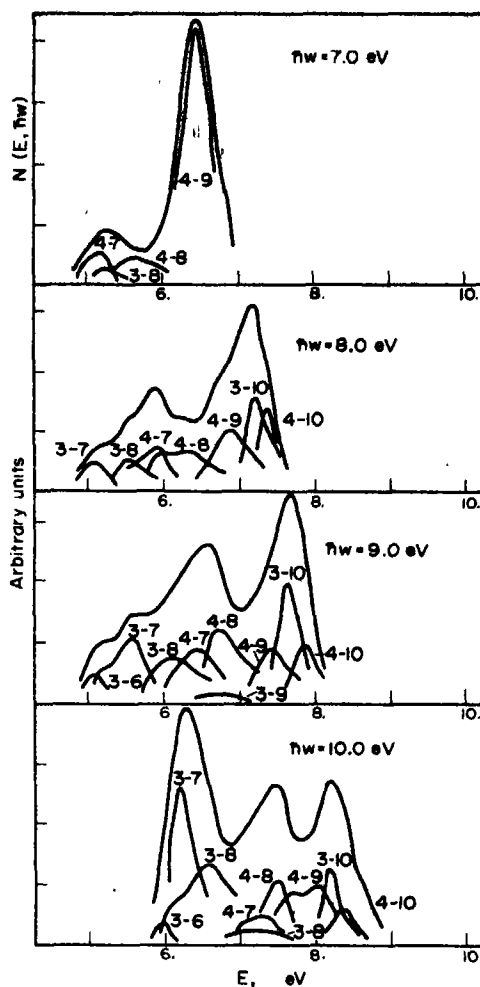


Fig. 5. Shows the calculated distribution curves in Ge for several values of photon energy corresponding to a sample with no cesium on its surface. The calculation includes an escape probability factor with the vacuum level at 4.80 eV and a broadening factor equal to 0.10 eV. Partial results indicating the contribution from some of the interband transitions are also shown. They are identified by the numbers labeling the bands involved in the transition. For the sake of clarity only partial contributions important from the point of view of the interpretation of the peaks were included.

ture is also given in Table 1. Usually, the region of interest in the *BZ* is related to a symmetry line. Plots $E - \hbar\omega$ for the calculated symmetry lines are given in Figs. 13 and 14, together with the position of the calculated

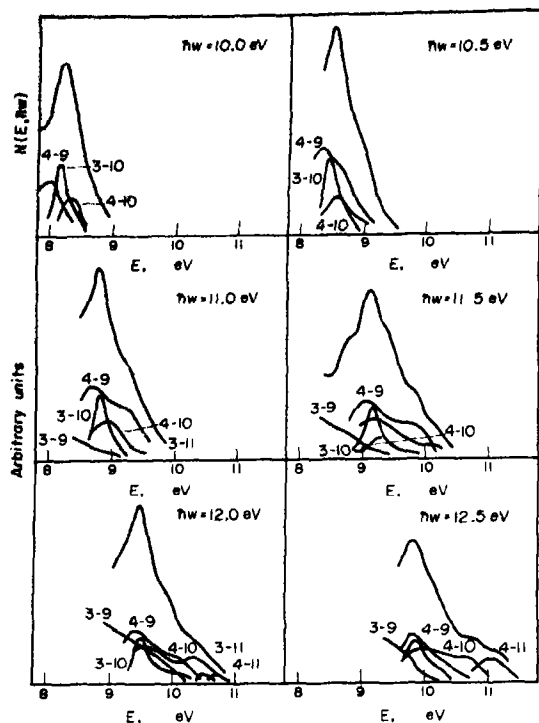


Fig. 6. Shows the calculated distribution curves in Ge for several values of photon energy and high electron energies corresponding to a sample with no cesium on its surface. The calculation includes an escape probability factor with the vacuum level at 4.80 eV and a broadening factor equal to 0.10 eV. Partial results indicating the contribution from some of the interband transitions are also shown. They are indicated by the numbers labeling the bands involved in the transition. For the sake of clarity only partial contributions important from the point of view of the interpretation of the peaks were included.

structure. This data establishes the connection between the experimental structure and the energy bands.

The structure labeled *B* is well reproduced by the present calculation. The main contribution comes from interband transitions E_{3-10} and E_{4-9} . Transition E_{3-10} determines the position of the peaks for the higher photon energies.

There is a region of the *BZ*, in the $\Gamma'KL$ plane, where the surfaces of constant E and constant $\hbar\omega$ are quite parallel. This region begins near the Γ' point and moves mainly along the $\Gamma'K$ line as the photon energy increases.

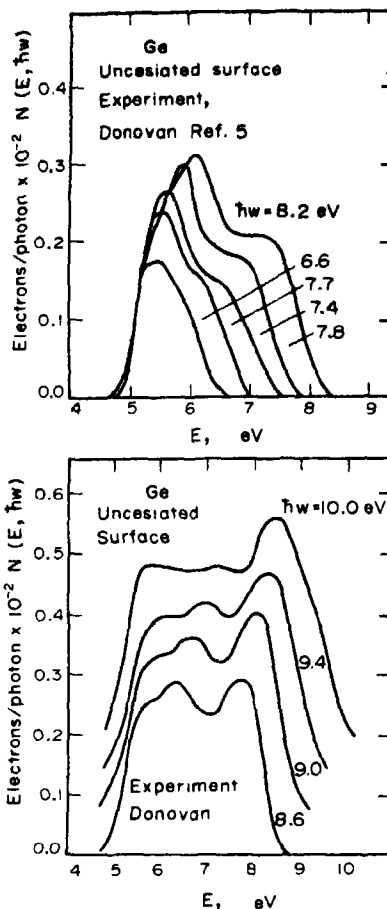


Fig. 7. Shows the experimental normalized energy distribution curves for a *p*-type crystal of Ge with no cesium on its surface, as measured by Donovan [5].

The contribution from transitions E_{4-9} are clearly seen at lower photon energies. An extensive region in the $\Gamma'KX$ plane is responsible for the structure. Band E_9 shows a saddle point which is not at the Γ' point, but somewhat displaced, in the $\Gamma'XK$ plane, as can be seen in Fig. 1. It has an energy value below the one corresponding to Γ_{12} and for this reason interband E_{4-9} produces peaks in the region labeled *F* in Fig. 12, where peaks from E_{3-10} have disappeared. This interpretation clearly indicates that level Γ_{12} , that is the double degenerate level E_9 and E_{10} , is the one related to structure *B*, but its position in the $E -$

Table 1. Interpretation of the structure present in the photoemission experiments in terms of the different interband transitions. Regions of the BZ involved in the transitions as well as energy levels corresponding to the related symmetry points are indicated

Structure	Interband transition	Location in BZ	Related energy level
B	3-10	Plane KL	Γ_{12}
	4-9	Plane KX	
C	$\hbar\omega \leq 8.2$ eV	4-7	X_4
	$\hbar\omega \geq 8.2$ eV	LW line in the hexagonal face	
D	4-8	Plane $\Gamma'KX$, near line ΓX .	X_4
	3-7	Line LW, near the L point.	
E	$\hbar\omega \leq 9.0$ eV	3-6	$W(E_3)$
	$\hbar\omega \geq 9.0$ eV	Hexagonal face, near the W point.	
G	3-7	Hexagonal face, near the W point	$W(E_3)$
G	$\hbar\omega \leq 5.5$ eV	3-6	L_3'
	$\hbar\omega \geq 5.5$ eV	LW line, near the L point	
G	$\hbar\omega \leq 5.5$ eV	4-6	L_3'
	$\hbar\omega \geq 5.5$ eV	LW line, near the L point	

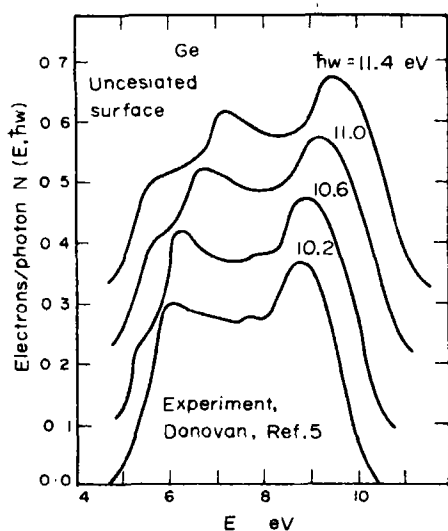


Fig. 8. Shows the experimental normalized energy distribution curves for a *p*-type crystal of Ge with no cesium on its surface, as measured by Donovan [5].

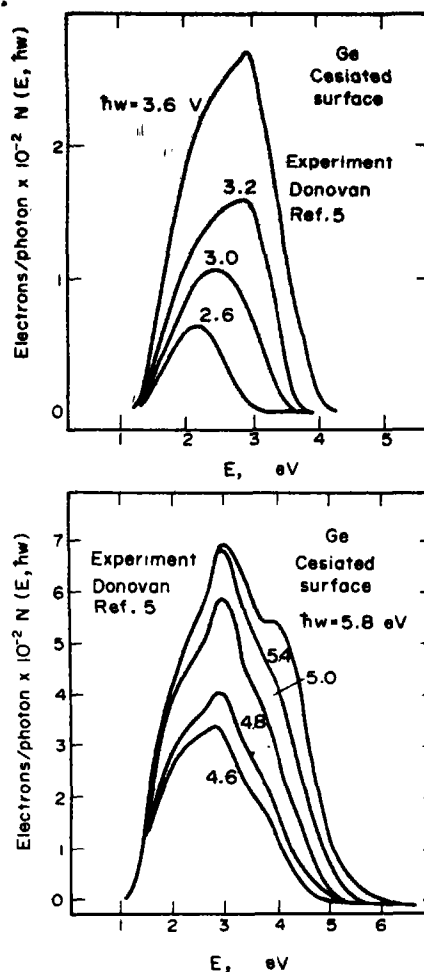


Fig. 9. Shows the experimental normalized energy distribution curves for a *p*-type crystal of Ge with a cesiated surface, as measured by Donovan [5].

$\hbar\omega$ diagram is not directly given by the intersection of the line defined by structure B and the line $E = \hbar\omega$. Its position can be determined taking into account the fact that a shift of the conduction bands E_9 and E_{10} in order to put the Γ_{12} level in the right place, essentially shifts structure B in the diagram $E - \hbar\omega$ along a direction parallel to the line $E - \hbar\omega$. In order to superpose the calculated and experimental structure, the calculated Γ_{12} level has to be shifted in 0.8 eV, what places this level at 8.1 eV approximately. Level Γ_1 has been men-

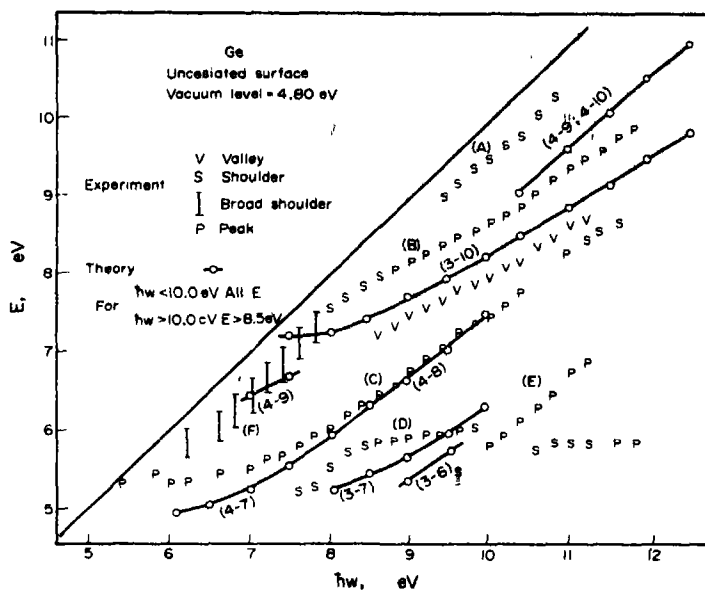


Fig. 12. $E-h\nu$ curves for the most prominent calculated structure and for the experimental structure as given by Donovan[5] for a crystal of Ge with no cesium on its surface. The experimental peaks are labeled by capital letters from A to J. The calculated peaks are indicated by numbers labeling the bands involved in the transitions mainly responsible for the structure.

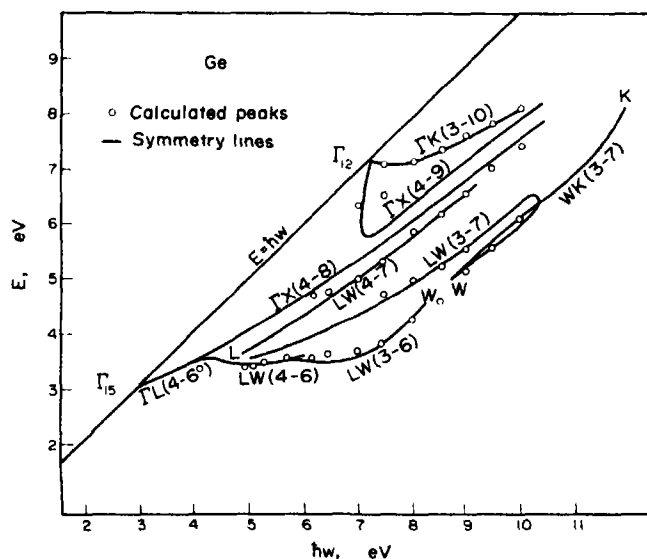


Fig. 13. $E-h\nu$ curves for the most prominent calculated structure (open circles) for a crystal of Ge with a cesiated surface, and for the points along the symmetry lines of the BZ related to the structure (solid lines). The interband transition plotted for a given point are indicated by the numbers labeling the bands involved in the transition. The symmetry lines are identified through the symmetry points in the BZ that determine the line.

gives contribution for the higher photon energies. An extended region in the Γ - K plane, related to the Γ - X symmetry line, is responsible for the contribution. Donovan[5] gives the same interpretation, based on the work of Spicer and Eden for GaAs[1]. It is interesting to notice that the peaks obtained from E_{4-8} define a line in the E - $\hbar\omega$ diagram which becomes parallel to $E=\hbar\omega$ for the higher energies. This means that for the region of the BZ near the X point, the valence band $E_4(X_4)$ is very flat and the energy value corresponding to X_4 can be determined from the experiment. A value between -2.7 and -2.9 eV is obtained [5].

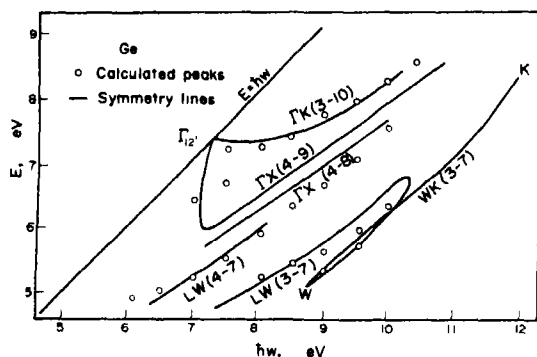


Fig. 14. E - $\hbar\omega$ curves for the most prominent calculated structure (open circles) for a crystal of Ge with no cesium on its surface, and for the interband transitions corresponding to points along the symmetry lines of the BZ related to the structure (solid lines). The interband transitions are indicated by the numbers labeling the bands involved in the transition. The symmetry lines are identified through the symmetry points in the BZ that determine the line.

Structure labeled D is partially produced by contributions from interband transition E_{3-7} , highly distorted by its superposition on the shoulder produced by contributions not due to direct transitions. The main contribution comes from a region in the BZ related to the LW line near the L point. The structure is not very pronounced and it is practically lost between the structure C and E when a cesiated surface is used.

For $\hbar\omega$ larger than 9.0 eV, E_{3-7} intersects

the hexagonal face near the W point, and its contribution becomes significant producing the structure labeled E . As $\hbar\omega$ increases, the region of interest moves from the W to the K point. A similar interpretation has been given by Donovan[5], who noticed that constant values of E_3 near the W point produce a structure moving like E in the E - $\hbar\omega$ diagram. The peaks determine the experimental value of E_3 , -4.2 eV approximately. The calculated value is off by 0.6 eV and for this reason the calculated peaks have to be shifted 0.6 eV in a direction parallel to the $\hbar\omega$ axis in the E - $\hbar\omega$ diagrams, Figs. 11 and 12, to reproduce the position of the experimental structure E . When a cesiated surface is used, the contributions to structure E from interband E_{3-6} become important. They are also produced in a region of the hexagonal face related to the W point.

Structure labeled G is also produced in part by E_{3-6} . For the lower photon energy range the surfaces of constant $\hbar\omega$ find a region in the hexagonal face near the L point where the electron energies are practically constant. We get peaks which are locked at a certain value of E for $\hbar\omega$ up to 7.5 eV. Interband E_{4-6} also contributes to structure G and the structure is also produced in a region near the L point. Structure G determines the position of level $E_6(L'_3)$, giving a value of 4.2 eV approximately [5]. Our calculated bands give a value for L_3 , off by 0.5 eV from the experimental results. This can be clearly seen in the E - $\hbar\omega$ diagram, Fig. 11, where the calculated structure G is about 0.5 eV below the experimental one.

Finally, we have not attempted a study of the structure labeled H , since it is superposed to a large contribution not predicted at all by our calculation not allowing any detailed comparison. Donovan[5] has performed a detailed experimental study and relates the onset of this structure to the Γ_{25}' level. Unfortunately, the spin orbit splittings are not resolved. A value of 3.13 eV is obtained for the center of mass transition energy of the Γ_{25}' - Γ_{15} transition.

6. CONCLUSIONS

The present calculation has allowed a detailed interpretation of the structure present in the photoemission experiments in terms of the energy bands of the semiconductor.

In general, this interpretation is similar to the one given by Donovan[5], based on a direct inspection of the energy bands calculated by Herman[11], and by Brust and Kane [18]. The most important difference is the change in the identification of structure *B*, which is now related to level Γ_{12} , with an assigned energy of 8.1 eV, and not Γ_1 . It is interesting to notice that the same problem in the interpretation of the experimental structure is present in other semiconductors[1]. Actually, we found the same interpretation for Si[3].

These results add a considerable amount of information about the value of the energy levels of some of the symmetry points to that obtained in the past from other types of experiments. The available information has been included in Table 2, where a comparison is performed with some of the energy band calculations. The values indicated in Table 2 for

Γ_2 , L_1 , and L_3 , are obtained from optical experiments[19, 20]. For L_3 , we used a value of the L_3-L_1 transition energy which is 0.1 eV smaller than the one measured for the $\Lambda_3-\Lambda_1$ transition in reflectivity experiments[20]. The position of L_3 is determined since L_1 is known. The L_3-L_3 transition, also measured in reflectivity experiments[20], can be used as a check of the position assigned to L_3 through the photoemission experiment. It is important to remark that most of the values included as results of experiments are really obtained through processes of interpretation which could be eventually revised.

Table 2 shows that the calculation performed by Herman[11] is in excellent agreement with experiment for the valence bands, but the discrepancies become larger for the higher conduction bands. Actually, we see from the pseudopotential calculations shown in Table 2 that the conduction levels Γ_{15} , L_3 , and Γ_{12} are quite sensible to small changes in the parameters. A better overall agreement can be expected if the new data is taken into account in the process of adjustment of the parameters.

Table 2. Shows experimental and theoretical energy level locations in eV. The first experimental value is that obtained from experiment. The second value, between parenthesis, represents the experimental level reduced to the center of mass value without spin-orbit splitting. The theoretical values do not include spin-orbit splittings

Level	Exp.	Herman <i>et al.</i> [c]	Brust [d]	Present calc.	New model
Γ_2	0.8 [b] (0.9)	0.9	0.7	0.9	0.8
Γ_{15}	(3.1) [a]	2.9	3.5	3.0	3.2
Γ_{12}	8.1 [a] (8.2)	9.5	8.5	7.3	7.9
L_3	(-1.4) [b]	-1.3	-1.1	-1.2	-1.2
L_1	0.7 [b] (0.8)	0.8	0.7	0.9	0.8
L_3	4.2 [a] (4.3)	4.1	4.3	3.7	4.0
X_4	-2.8 [a] -3.0 [a]				
	(-2.7, -2.9)	-2.8	-2.5	-2.8	-2.7
$W(E_g)$	-4.2 [a] (-4.1)	-4.1	-3.4	-3.5	-3.5

[a] Obtained from photoemission experiments.

[b] Obtained from optical experiments, Ref. [19-21].

[c] Ref. [11].

[d] Ref. [9].

The pseudopotential model used in the present calculation was obtained in a previous work [7] from a careful adjustment to the experimental energy levels near the band gap, but now it shows large discrepancies for the other levels. We have tried a general adjustment of the pseudopotential parameters a posteriori of the photoemission calculation performed here. The energy levels corresponding to the new model, calculated with the following parameters: $V(1, 1, 1) = -0.251$ Ry, $V(2, 2, 0) = 0.028$ Ry, $V(3, 1, 1) = 0.039$ Ry, are given in the last column of Table 2. They show an average error of 0.2 eV respect to experiment. Although a better general agreement is obtained in the conduction levels, it was not possible to improve the position of the W level. It appears as practically unchanged in all the available pseudopotential calculations and contrasting with the value obtained by Herman [11], which is the same as the experimental one.

Acknowledgements—We are indebted to Dr. T. M. Donovan who made available to us the experimental results of Ge prior to publication, as well as to Dr. D. Brust and Professor W. E. Spicer for bringing some references to our attention. The calculation was performed at the 'Centro de Computación de la Universidad de la República'. We acknowledge its staff for technical assistance. This research was supported in part by the 'Fondo de Investigación Científica de la Universidad de la República, Montevideo, Uruguay'.

REFERENCES

1. SPICER W. E. and EDEN R. C., *Proc. IX Int. Conf. Phys. Semicond.*, Moscow, 65 (1968).
2. BRUST D., *Phys. Rev.* **139**, A 489 (1965).
3. SARAIVIA L. R. and CASAMAYOU L., *J. Phys. Chem. Solids* **32**, 1075 (1971).
4. ALLEN F. G. and GOBELLI G. W., *Phys. Rev.* **144**, 558 (1966).
5. DONOVAN T. M., private communication.
DONOVAN T. M. and SPICER W. E., *Bull. Am. Phys. Soc.*, **113**, 476 (1968).
6. SARAIVIA L. R. and BRUST D., *Phys. Rev.* **171**, 916 (1968).
7. SARAIVIA L. R. and BRUST D., *Phys. Rev.* **176**, 915 (1968).
8. CARDONA, M. and SOMMERS H. S., *Phys. Rev.* **122**, 1382 (1961).
9. BRUST D., *Phys. Rev.* **134**, A 1337 (1964).
10. COHEN M. L. and BERGSTRESSER T. K., *Phys. Rev.* **141**, 789 (1966).
11. HERMAN F., KORTUM R. L., KUGLEMAND, C. D. and SHORT, R. D. *Quantum Theory of Atoms, Molecules, and the Solid State*, Per-Olov Löwdin ed., (Academic Press, N.Y.).
12. CARDONA M. and POLLAK F. H., *Phys. Rev.* **142**, 530 (1966).
13. DRESSELHAUS G. and DRESSELHAUS M. S., *Phys. Rev.* **160**, 649 (1967).
14. KANE E. O., *J. phys. Soc. Japan* **21**, Suppl., 37 (1966).
15. KANE E. O., *Phys. Rev.* **147**, 335 (1966).
16. KANE E. O., *Phys. Rev.* **159**, 624 (1967).
17. SPICER W. E., *Phys. Rev.* **154**, 385 (1967).
18. BRUST D. and KANE E. O., *Phys. Rev.* **176**, 894 (1968).
19. MAC FARLANE G. G., McLEAN J. P., QUARRINGTON J. E. and ROBERTS V., *Proc. Phys. Soc. London* **71**, 863 (1958).
20. GHOSH A. K., *Phys. Rev.* **165**, 888 (1968).

PHENOMENES GALVANOMAGNETIQUES NON LINEAIRES—A MESURES SUR L'ANTIMONIURE D'INDIUM

D. CALECKI

Groupe de Physique des Solides de l'Ecole Normale Supérieure,* Faculté des Sciences, Paris

(Received 9 June 1970; in revised form 24 September 1970)

Résumé— Nous présentons dans ce premier article des mesures de faibles déviations par rapport à la loi d'Ohm dans l'antimoniure d'indium très pur, en fonction de la température ($77^\circ \leq T \leq 210^\circ\text{K}$) et de l'induction magnétique ($0,08 \leq B \leq 1,2 \text{ Wb/m}^2$). A B fixé, nous observons que le coefficient r caractérisant les déviations change de signe à $T = 135^\circ\text{K}$; à T fixé, r varie comme B^p ($0,9 \leq p \leq 2,2$ selon les valeurs de T). Nous utilisons les résultats du second article consacré à la théorie quantique du coefficient r , pour interpréter ces résultats expérimentaux. Nous montrons ainsi que les phonons optiques polaires jouent un rôle essentiel dans les phénomènes d'électrons tièdes. Néanmoins, les variations expérimentales avec la température et l'ordre de grandeur du coefficient r ne sont en bon accord avec la théorie que si l'on tient compte à la fois de l'interaction des électrons avec d'une part les phonons optiques, d'autre part les phonons acoustiques par l'intermédiaire d'un couplage piézoélectrique.

Abstract— In this first paper we present measurements of small deviations from Ohm's law in very pure n -type InSb, as function of temperature ($77^\circ \leq T \leq 210^\circ\text{K}$) and magnetic induction ($0,08 \leq B \leq 1,2 \text{ Wb/m}^2$). At fixed B , we observe that the r coefficient, which characterizes the deviations, change sign at $T = 135^\circ\text{K}$; at fixed T , r varies as B^p ($0,9 \leq p \leq 2,2$, depending on T). We use the results of the second following paper devoted to a quantum theory of the r coefficient to fit our experimental results on InSb. Then we show that polar optical phonons play an essential part in warm electron phenomena. Nevertheless, the experimental variations and the order of magnitude of the coefficient r are in good agreement with our theory only if we take account of both the interaction with optical phonons and piezoelectric acoustical phonons coupling.

1. INTRODUCTION

DANS un article précédent[1] nous avons étudié théoriquement les faibles déviations par rapport à la loi d'Ohm dans des semi-conducteurs soumis à des inductions magnétiques intenses. En particulier, dans le cas où le champ électrique \mathbf{E} et l'induction magnétique \mathbf{B} sont perpendiculaires, nous avons obtenu des expressions du coefficient β caractéristiques des variations avec le champ électrique E du coefficient de conductivité électrique σ_{xx} et tel que:

$$\sigma_{xx} = \sigma_{xx}^{(0)}(B) [1 + \beta(B) E^2] \quad (1)$$

($\sigma_{xx}^{(0)}$ représente la partie de σ_{xx} indépendante de E , mais fonction de B). Nous

avons donné des expressions explicites de β valables dans la limite classique ($\hbar\omega_c \ll kT$, $\omega_c\tau \gg 1$; ω_c : pulsation cyclotron, τ : temps de relaxation de la vitesse moyenne des électrons) et pour 1° une interaction électrons-phonons acoustiques traitée à l'aide du potentiel de déformation; 2° une interaction électrons-phonons optiques. Pour la première interaction notre expression de β était en contradiction avec d'autres résultats théoriques[2]; pour la seconde interaction, elle était inédite. En l'absence de résultats expérimentaux déjà publiés que l'on puisse confronter avec nos formules, nous avons entrepris une série de mesures du coefficient β .

Ce premier article (désigné par *A*) est consacré à l'exposé des résultats de mesure

*Laboratoire associé au C.N.R.S..

et à leur interprétation. Cette dernière a nécessité de modifier la théorie de la Réf.[1]. Ce travail théorique fait l'objet du second article qui suit (désigné par *B*).

Pour l'étude expérimentale, nous avons choisi un semiconducteur où l'on puisse admettre que seuls interviennent des porteurs de même type et de masse effective en première approximation constante—à savoir l'antimoniure d'indium, InSb, de type *n* très pur (densité électronique: $n \approx 10^{14} \text{ cm}^{-3}$ à $T = 77^\circ\text{K}$)—et avec lequel les conditions $\omega_c \tau \gg kT$ soient aisément réalisées ($77 \leq T \leq 300^\circ\text{K}$, $B \leq 1,2 \text{ Wb/m}^2$).

On trouvera dans la Section 2 l'exposé des techniques expérimentales utilisées et les résultats des mesures concernant les variations avec la température et l'induction magnétique non pas du coefficient β , mais d'un coefficient r qui est proportionnel à β .

Nos résultats expérimentaux se sont avérés en désaccord profond avec les expressions du coefficient β de la Réf.[1]. Nous avons dû reprendre son étude théorique; l'article *B*, consacré à la théorie quantique du coefficient β , contient des expressions explicites de β pour trois types d'interaction entre les électrons et les phonons.

La dernière partie (Section 3) est consacrée à la confrontation entre nos résultats expérimentaux et ceux de cette dernière théorie. Les variations de β avec la température et notamment son passage de valeurs négatives à positives, quand la température croît, sont convenablement interprétées quand on suppose que pour les phénomènes d'électrons tièdes, l'interaction électrons-phonons optiques joue un rôle fondamental dans InSb de type *n*. Les variations de β avec l'induction magnétique posent cependant des problèmes non encore résolus.

2. RESULTATS EXPERIMENTAUX

Les mesures ont été faites sur de l'antimoniure d'indium de type *n*, de concentration et de mobilité électroniques respectivement de l'ordre de 10^{20} m^{-3} et $50 \text{ m}^2/\text{V/s}$ à la tem-

pérature de 77°K . Une étude préalable des phénomènes linéaires par rapport au champ électrique nous a permis de retrouver l'ensemble des résultats expérimentaux bien connus dans InSb. Notons simplement ici que le coefficient de magnétorésistance transversale varie linéairement en fonction de l'induction magnétique pour des valeurs de B telles que les conditions $\omega_c \tau \gg 1$, $\hbar\omega_c \ll kT$ sont remplies. Ce résultat est une anomalie bien connue qui se produit dans InSb; il n'est pas expliqué par la théorie qui prévoit une saturation de $\Delta\rho/\rho_0$ en fonction de B .

(a) Schéma de principe du montage de mesure

La mise en évidence des variations de la résistance d'un échantillon en fonction du champ électrique appliqué ne peut se faire qu'en utilisant des champs électriques impulsionnels dont la durée et la fréquence de répétition sont suffisamment faibles pour éviter les effets Joule intempestifs ou destructeurs. Les variations de résistance à mesurer étant très faibles, une méthode de comparaison s'impose. Comme nous désirons distinguer sur l'échantillon entre les contacts d'amenée de courant et les contacts de prise de potentiel le schéma le plus simple que l'on puisse imaginer est celui représenté sur la Fig. 1. Un générateur d'impulsions attaque un échantillon parallélépipédique (*E*) en série avec un potentiomètre (*P*); soient V_1 , V_2 et V_3 les d.d.p. mesurées respectivement entre les points (1), (2) et (3) du circuit et la masse. Admettons que la résistance de l'échantillon

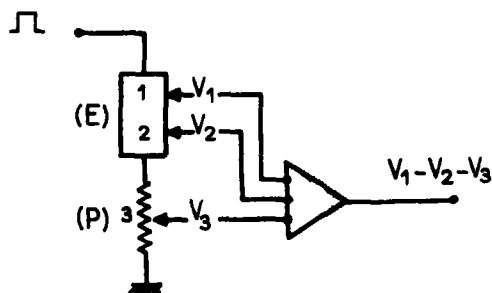


Fig. 1. Schéma de principe du montage.

mesurée entre les points (1) et (2) varie avec la composante longitudinale E_x du champ électrique appliqué suivant la loi:

$$R = R_0(1 + r E_x^2)$$

lorsque E_x est suffisamment faible pour que $r E_x^2 \ll 1$. Supposons que la résistance du potentiomètre (P) soit indépendante de la d.d.p. qui lui est appliquée et que la résistance R_c mesurée entre le curseur et la masse soit exactement égale à R_0 . Dans ces conditions, on trouve immédiatement:

$$\Delta V = V_1 - V_2 - V_3 \approx r \frac{V_3^3}{l^2}$$

où l est la longueur de l'échantillon entre les points (1) et (2). Pour déterminer le paramètre caractéristique r , il suffit de tracer la courbe:

$$(\Delta V)^{1/3} = f(V_3)$$

qui doit apparaître comme une droite dont la pente $(r/l^2)^{1/3}$ fournit le coefficient r cherché.

Notons bien ici que, par cette méthode, nous mesurons un coefficient r , différent du coefficient β intervenant dans (1). Nous réservons

pour le Section 3a d'établir la liaison entre ces deux coefficients (cf. (3.6)).

(b) Montage expérimental et méthode de mesure

Appareillage électronique. Le schéma de l'ensemble des appareils électroniques est représenté sur la Fig. 2. L'organe essentiel est le système de détection de la d.d.p. ΔV , car il conditionne le choix de nombreux appareils qui l'entourent.

En effet, chaque d.d.p. V_1, V_2, V_3 s'élèvera dans les mesures sur InSb à quelques dizaines de volts au maximum; la déviation ΔV sera parfois de l'ordre du millivolt. Il faut donc que la mesure de chacune des 3 d.d.p. s'effectue avec une erreur relative inférieure à 10^{-5} . En particulier il faut que le système de mesure des 3 d.d.p. ne déforme pas les trois impulsions de façon différente, ce qui introduirait dans ΔV un signal qui n'aurait aucun rapport avec un comportement non ohmique de l'échantillon. Pour éliminer cette difficulté nous avons utilisé un appareil unique mesurant directement ΔV : un amplificateur opérationnel (A.O.) différentiel monté en amplificateur de gain unité. Cet A.O. doit (1) posséder une grande bande passante pour

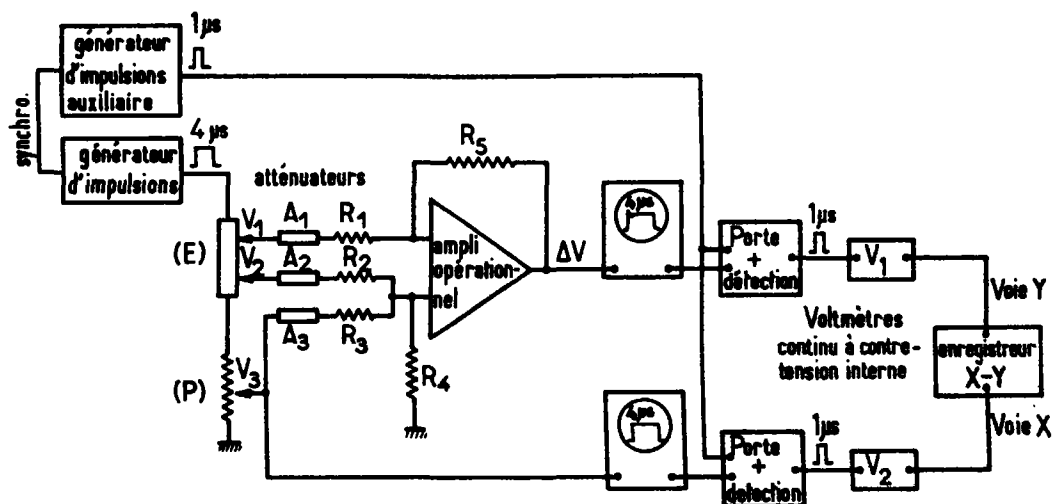


Fig. 2. Appareillage électronique.

opérer avec des impulsions de durée aussi faible que possible; (2) posséder un taux de réjection en mode commun élevé; (3) admettre de fortes d.d.p. à ses entrées. Nous avons utilisé l'A.O. Philbrick P 85 AH et des impulsions de $4 \mu s$ de durée. Cependant on constate que le plateau des impulsions subit une déformation et que seule la dernière microseconde est transmise sans distorsion. Cette remarque est importante car nous transformons ensuite les impulsions en un signal continu proportionnel à l'amplitude de ces dernières et il faut nécessairement ne pas faire intervenir dans cette opération les trois premières microsecondes des impulsions. Cette suppression s'effectue, à la sortie d'un oscillographe utilisé en amplificateur, à l'aide d'une porte qui se débloque et laisse passer l'impulsion uniquement pendant sa dernière microseconde. L'ouverture de la porte est commandée par un générateur d'impulsions synchronisé avec trois microsecondes de retard sur le générateur d'impulsions alimentant l'échantillon. A la sortie de la porte un système de détection à diode transforme les impulsions d'une microseconde en signal continu. Le système de détection fonctionne d'autant mieux que la fréquence f de répétition est élevée et l'on ne peut descendre en-dessous $f = 10 \text{ Hz}$. Cette valeur de la fréquence de récurrence, associée à une durée d'impulsion de $4 \mu s$, n'a jamais entraîné dans nos échantillons des échauffements par effet Joule gênant nos mesures. Nous obtenons finalement une d.d.p. continue proportionnelle à ΔV que nous envoyons sur la voie Y d'un enregistreur dont la voie X doit dévier proportionnellement à l'amplitude de V_3 . Un système oscillographe + porte synchronisée + détecteur — système jumeau de précédant par conséquent — transforme la dernière microseconde de V_3 en signal continu proportionnel. Les deux oscillographes, de la chaîne, outre leur rôle d'amplificateur permettant de faire fonctionner à haut niveau d'entrée les portes et les détecteurs, servent d'étalonnage des voies X et Y de l'enregistreur; c'est sur leur

écran qu'on lit directement la valeur de ΔV associée à une d.d.p. V_3 donnée.

Remarquons que l'enregistreur XY, étant de dimensions relativement grandes ($30 \times 40 \text{ cm}$ par exemple), il est facile de vérifier que la condition d'équilibre initial du montage $R_0 = R_c$ est bien réalisée en s'assurant que la courbe $\Delta V = f(V_3)$ se confond avec l'axe des abscisses quand V_3 est suffisamment faible.

Linéarité de la chaîne. Notre but étant de mesurer des déviations par rapport à une loi linéaire, il est indispensable de s'assurer de la linéarité de la chaîne des appareils électroniques. La détermination expérimentale de cette linéarité s'effectue en branchant à la place de l'échantillon une résistance — un fil de constantan en l'occurrence — indépendante de la d.d.p. appliquée à ses bornes et de valeur sensiblement égale à celle de l'échantillon sur lequel nous allons travailler. Nous traçons alors les courbes $\Delta V = f(V_3)$ pour toutes les valeurs de V_3 que nous utiliserons avec l'échantillon ensuite. Si nous avons préalablement équilibré le montage en ayant réglé égal à l'unité le gain de chacune des trois voies de l'ampli opérationnel et en ayant convenablement placé le curseur du potentiomètre (P) nous devons trouver $\Delta V = 0$. Si au contraire nous avons volontairement déséquilibré le montage en déplaçant le curseur, nous devons trouver $\Delta V = kV_3$ et la courbe enregistrée doit être une droite. Dans le premier cas, pour une d.d.p. de sortie du générateur égale à 60 V , ΔV reste inférieur à 1 mV . Dans le second cas la courbe $\Delta V = f(V_3)$ se confond avec une droite à 5.10^{-3} près, dans les conditions les plus défavorables.

Echantillons — Porte échantillon —

Appareillage environnant. Nous avons étudié une trentaine d'échantillons en forme de barreau parallélépipédique, munis de six oreilles pour les différents contacts (deux pour les amenées de courant et quatre, opposées deux à deux par rapport à l'axe longitudinal du barreau, pour les mesures de d.d.p.). Les

lingots de InSb provenaient de deux fabriques différentes et possédaient sensiblement les mêmes caractéristiques électroniques. Les axes cristallographiques ont eu des orientations diverses par rapport aux arêtes des échantillons parallélépipédiques. Enfin nous avons utilisé comme décuplant tout d'abord du CP4 faible puis un mélange d'acide lactique (10 volumes) et d'acide nitrique (1 à 2 volumes). La plupart de ces échantillons—de sources, d'orientations, de traitements par conséquent différents—ont systématiquement offert les mêmes comportements sous l'action de l'induction magnétique B et du champ électrique E perpendiculaire, à savoir: (1) un changement de signe de la déviation par rapport à la loi d'Ohm quand, à B fixé, la température croît en passant par des valeurs voisines de 135°K; (2) un accroissement de la déviation quand, à température fixée, l'induction magnétique croît. Nous n'avons pas fait une étude systématique des déviations par rapport à la loi d'Ohm en fonction des différents paramètres que nous venons d'évoquer (traitement chimique, distance entre les prises de potentiel, orientation cristallographique...). Nous avons simplement retenu pour des mesures détaillées, les échantillons—au nombre de quelques unités—qui présentaient les caractéristiques suivantes: (1) les quatre courbes de variations de ΔV en fonction de V_3 à T et B fixés (et dans une large gamme de variation de T et de B) tracées pour les quatre orientations relatives où l'induction magnétique B et le vecteur densité de courant $\langle j \rangle$ sont perpendiculaires*, sont des cubiques identiques entre elles. Pour ces échantillons, les deux traitements de surface (CP4 ou acides lactique + nitrique) ont donné les mêmes résultats. De même l'utilisation de l'une ou l'autre des paires d'oreilles, ont fourni des résultats numériques très voisins. (2) La loi

de variation du coefficient de magnétoristance en fonction de l'angle θ entre les directions de B et $\langle j \rangle$ est très voisine d'une loi en $\sin^2\theta$, montrant ainsi (cf. H. Weiss, "Semiconductors and Semimetals" Vol. 1 Academic Press 1966) que ces échantillons étaient assez bien homogènes.

Les échantillons de faible largeur (0,3 mm) et de faible épaisseur (0,2 mm) afin d'adapter leur résistance à l'impédance de sortie du générateur d'impulsions, sont en contact thermique avec une masse de cuivre munie d'une chauffelette à même de faire varier sa température. Le maintien de la température de l'échantillon à une valeur constante pendant tout le tracé d'une courbe $\Delta V = f(V_3)$ est absolument indispensable. En effet, si du fait d'une variation infime de la température du bloc de cuivre (égale à ΔT_0) la résistance de l'échantillon varie pendant le tracé d'une courbe, la condition d'équilibre initiale de notre montage $R_0(T_0) = R_c$ est rompue; la différence ΔV va donc représenter la somme de deux déséquilibres: le premier que l'on cherche à mesurer, dû au phénomène d'électrons tièdes; le second dû au fait que $R_0(T_0 + \Delta T_0) \neq R_c$. Il est bien évident que $R_0(T_0)$ variant très rapidement quand $T_0 > 150^\circ\text{K}$, un déséquilibre produit par ΔT_0 risque d'être très supérieur à celui produit par un champ électrique. Pratiquement un déséquilibre dû à ΔT_0 intervenant en cours de tracé s'observe immédiatement du fait que la courbe $\Delta V = f(V_3)$ obtenue quand V_3 croît ne se confond pas avec elle obtenue quand V_3 décroît. La meilleure vérification que la température est restée constante s'obtient a posteriori quand on s'assure que la courbe $\Delta V = f(V_3)$ est bien une cubique. Remarquons qu'un échauffement par effet Joule produit les mêmes effets qu'un ΔT_0 provoqué par une variation de température du bloc de cuivre, c'est pourquoi la durée des impulsions et leur fréquence de répétition ont été des paramètres importants de notre étude.

Pour maintenir le bloc de cuivre à température constante, nous avons utilisé le système

*L'utilisation dans cet article de la notation $\langle j \rangle$ au lieu de J tout simplement est justifiée dans l'article théorique B qui suit.

suivant. Le bloc de cuivre est placé au fond d'une enceinte tubulaire en acier inox à double paroi. On peut vider ou emplir d'hélium gazeux le milieu où se trouve l'échantillon et le volume contenu entre la double paroi. Le tube en inox est plongé dans un dewar contenant *en permanence* de l'azote liquide. Le maintien du bloc de cuivre à une température constante est dû à l'équilibre qui s'établit entre les calories apportées par la chaufferette (alimentée par un courant stabilisé à 10^{-3} près) et les frigories provenant de l'hélium gazeux se trouvant entre la double paroi du tube en inox. Ce gaz dont la pression est réglable sert d'échangeur entre le milieu gazeux dans lequel baigne l'échantillon et l'azote liquide où le tube en inox est plongé.

Notons enfin que l'échantillon est placé dans l'entrefer d'un électro-aimant de façon que l'induction magnétique soit perpen-

diculaire à son axe longitudinal, comme dans une mesure d'effet Hall ordinaire.

(c) *Résultats des mesures du coefficient r dans InSb*

Les mesures du coefficient r ont été faites dans une gamme de températures comprises entre 77 et 205°K et avec des inductions magnétiques variant entre 0,08 et 1,2 Wb/m². Dans ces conditions, il existe toujours une région où les deux inégalités $\omega_c \tau \gg 1$ et $\hbar \omega_c \ll kT_0$ sont satisfaites.

Nous avons représenté sur la Fig. 3 une courbe expérimentale $\Delta V = f(V_3)$. On reconnaît un tracé par point auquel l'emploi du générateur d'impulsions nous a contraint. A chaque point expérimental nous avons fait correspondre un point calculé, de même abscisse et d'ordonnée égale à $(\Delta V)^{1/3}$. On constate que l'ensemble des points calculés

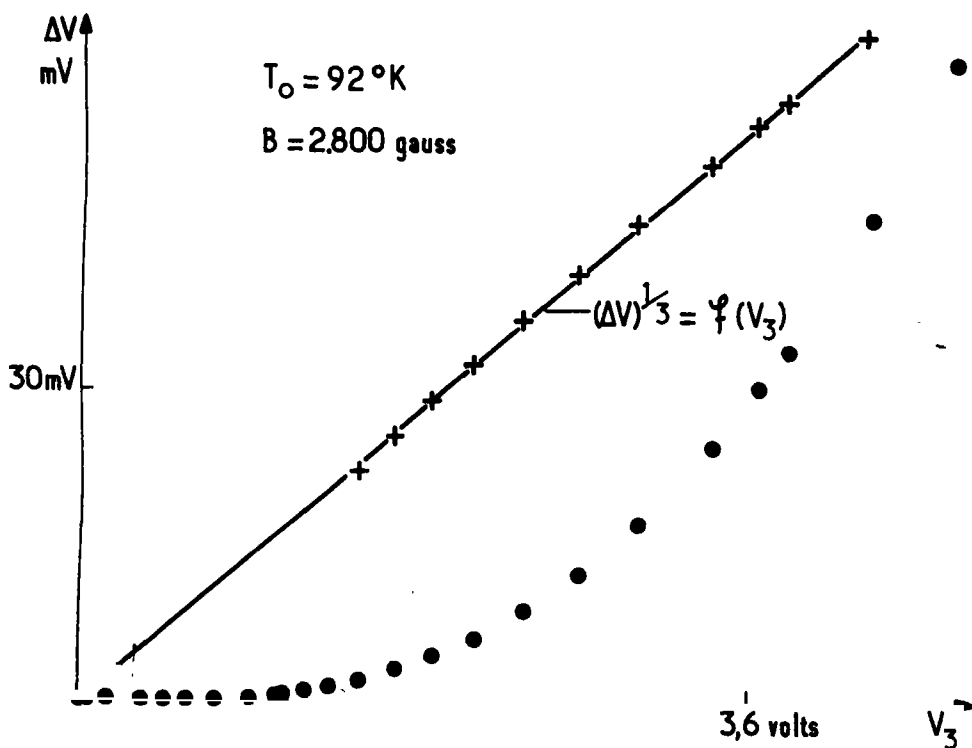


Fig. 3. Enregistrement type d'une courbe $\Delta V = f(V_3)$; vérification de la loi cubique de déviation par rapport à la loi d'Ohms.

s'alignent sur une droite passant par l'origine, ce qui confirme la loi $\Delta V \sim V_3^3$.

Les variations du coefficient r avec l'induction magnétique B , pour différentes valeurs de la température sont représentées sur la Fig. 4. Les remarques essentielles déduites de ce réseau de courbes sont de trois ordres.

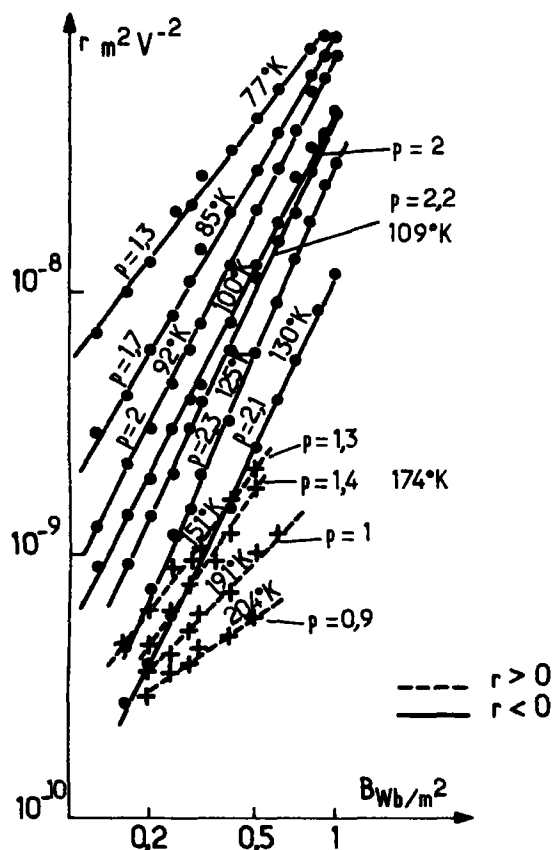


Fig. 4. Réseau des courbes expérimentales $r(B)$ à T fixé.

Primo: A induction magnétique constante, le coefficient r passe de valeurs négatives à positives quand la température évolue entre 77 et 205°K. La Fig. 5 schématise, pour différentes valeurs de B , les variations de r , non pas en fonction de T_0 , mais en fonction du paramètre $\alpha_0 = \hbar\omega_q/2kT_0$ où $\hbar\omega_q$ est l'énergie des phonons optiques dans InSb. Sur la Fig. 5, on constate que la température d'annulation T_a de r est fixée par la condition

$\hbar\omega_q/2kT_a = 0,95$. Comme dans InSb, l'énergie des phonons optiques [3] exprimée en degrés Kelvin vaut 260°K, on en déduit que $T_a = 135^\circ$. Cette température est indépendante de la valeur de B . Notons de plus qu'au-delà de la température d'annulation, quand r est > 0 , sa valeur absolue passe par un maximum et décroît rapidement ensuite en ayant tendance à s'annuler une seconde fois.

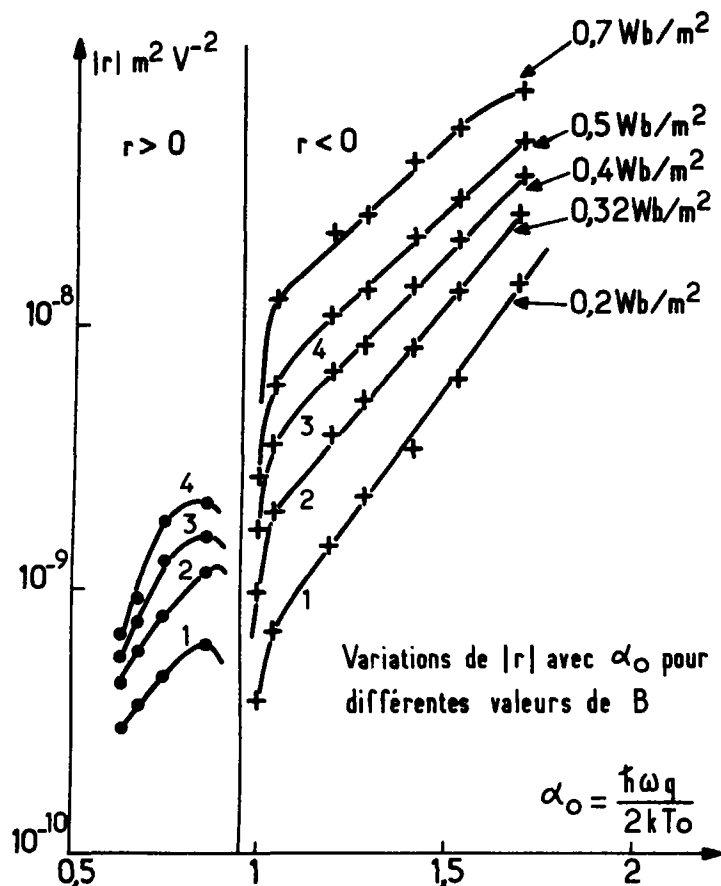
Secundo: A température fixe, le coefficient r est une fonction croissante de l'induction magnétique; les déviations par rapport à la loi d'Ohm sont donc d'autant plus importantes que les valeurs de B sont élevées. Sur la Fig. 4, on constate que les lois de variations de r avec B sont assez bien représentées par des fonctions puissances, $r \sim B^p(T_0)$, où l'exposant p est toujours > 0 et dépend de la température, ses valeurs restant comprises entre 0,9 et 2,2.

Tertio: Les remarques qui suivent ne découlent pas directement des Fig. 4 et 5, mais en expliquent le caractère parfois incomplet. Tout d'abord au voisinage de la température T_a , les mesures de r deviennent impossibles à effectuer pour deux raisons: (1) r devient trop petit; (2) les courbes $\Delta V = f(V_3)$ perdent leur caractère cubique. Par ailleurs, pour les températures supérieures à T_a , nous n'avons pas dépassé des valeurs de B de l'ordre de 0,7 Wb/m² ceci provient du fait que pour les valeurs des champs électriques où la loi d'Ohm n'est plus vérifiée, des instabilités de courants sont produites par des inductions magnétiques supérieures à 0,7 Wb/m² et empêchent la mesure de r .

Nous allons maintenant utiliser les résultats théoriques de l'article B qui vont nous fournir des expressions du coefficient r à confronter avec les lois de variations mesurées et représentées sur les Fig. 4 et 5.

3. CONFRONTATION THEORIE-EXPERIENCE DANS LE CAS DE InSb

A la Section 2, nous avons donné la façon d'effectuer des mesures—et les résultats de ces mesures—sur un certain coefficient r

Fig. 5. Réseau des courbes $r(B)$ à B fixé.

caractérisant les variations de la résistance d'un échantillon d'antimoine d'indium, de forme parallélépipédique allongée, en fonction de la composante longitudinale du champ électrique appliqué. Dans l'article *B*, nous avons exposé la théorie du coefficient β caractérisant les déviations par rapport à la loi d'Ohm. Afin de comparer les résultats théoriques et expérimentaux, il faut préalablement établir la liaison entre les coefficients r et β .

(a) *Relation entre les coefficients r et β*

Quand on fait passer un courant dans un échantillon parallélépipédique allongé et

homogène, on peut imposer au vecteur densité de courant $\langle \mathbf{J} \rangle$ d'être longitudinal. Quand en plus on applique une induction magnétique \mathbf{B} perpendiculaire au courant, le champ électrique \mathbf{E} qui règne dans l'échantillon est perpendiculaire à \mathbf{B} , mais pas parallèle à $\langle \mathbf{J} \rangle$.

Désignons par OX la direction de \mathbf{E} (cf. Fig. 6); d'après les résultats de l'article *B* concernant les phénomènes jusqu'à l'ordre 3 en champ électrique, les composantes du vecteur densité de courant suivant \mathbf{E} et suivant la direction Oy perpendiculaire à \mathbf{E} et à \mathbf{B} , s'écrivent:

$$\langle J_x \rangle = \sigma_{xx}^{(0)} (1 + \beta E^2) E \quad (1)$$

$$\langle J_y \rangle = n e \frac{E}{B} = -\sigma_{xy}^{(0)} E. \quad (2)$$

Le coefficient $\sigma_{xx}^{(0)}$ n'est autre que la conductivité électrique dans la région ohmique. La valeur $-ne/B$ de $\sigma_{xy}^{(0)}$ n'est valable que dans la limite des inductions magnétiques élevées, quand $\omega_c \tau \gg 1$. Les expressions de β que l'on

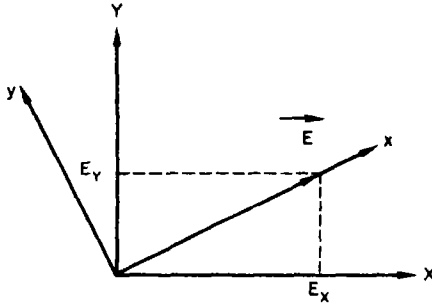


Fig. 6.

trouvera dans l'article B n'ont été établies que dans cette même limite. On déduit de (1) et (2) que, si l'on impose au vecteur densité de courant d'être dirigé suivant la longueur OX de l'échantillon parallélépipédique, alors:

$$\langle J_x \rangle = \sigma_{xx}^{(0)} [1 + \beta (E_x^2 + E_y^2)] E_x + \sigma_{xy}^{(0)} E_y \quad (3)$$

$$\langle J_y \rangle = 0 = -\sigma_{xy}^{(0)} E_x + \sigma_{xx}^{(0)} [1 + \beta (E_x^2 + E_y^2)] E_y. \quad (4)$$

On obtient immédiatement à partir de (3) et (4) une relation entre E_x et $\langle J_x \rangle$, qui définit la résistivité en présence de \mathbf{E} et \mathbf{B} . Quand on tient compte du fait que $\sigma_{xx}^{(0)} \ll \sigma_{xy}^{(0)}$ lorsque $\omega_c \tau \gg 1$, la modification relative de résistivité à l'ordre le plus bas en champ électrique se réduit à:

$$\frac{\Delta \rho}{\rho(E=0)} \approx \beta \left[\frac{\sigma_{xy}^{(0)}}{\sigma_{xx}^{(0)}} \right]^2 E_x^2. \quad (5)$$

Le coefficient r défini à la Section 2a. est donc lié à r par la relation:

$$r = \beta \left[\frac{\sigma_{xy}^{(0)}}{\sigma_{xx}^{(0)}} \right]^2 = \beta \frac{n^2 e^2}{B^2} \frac{1}{(\sigma_{xx}^{(0)})^2}. \quad (6)$$

Du point de vue de la variation de r avec l'induction magnétique, nous avons montré dans l'article B, que pour tous les couplages envisagés dans la limite classique

$$\beta \sim B^{-2} \text{ et } \sigma_{xx}^{(0)} \sim B^{-2}.$$

En conséquence, r doit être indépendant de B en limite classique. Comme r est proportionnel à β , r s'annule et change de signe en même temps que β quand la température varie. Enfin, en ce qui concerne la grandeur de r , comme $\sigma_{xy}^{(0)}/\sigma_{xx}^{(0)} \ll 1$ quand $\omega_c \tau \ll 1$, le coefficient r est toujours supérieur à β .

(b) Interprétation des résultats expérimentaux

Nous revenons sur les résultats expérimentaux de la Section 2c concernant le coefficient r . Examinons tout d'abord les variations de r avec l'induction magnétique B . D'après la remarque qui suit la formule (6), la théorie prévoit que r est indépendant de B en limite classique. Cette conclusion est en contradiction flagrante avec les résultats expérimentaux représentés à la Fig. 4. Cependant, il ne faut pas être trop découragé car, dans l'étude des phénomènes linéaires, la variation de la magnétorésistance avec l'induction magnétique, qui s'avère être une fonction linéaire de B , n'est pas non plus interprétée; la théorie correspondante prévoit en effet une saturation de la magnétorésistance dans la limite $\hbar \omega_c \ll kT$, $\omega_c \tau \gg 1$. Nous abandonnons donc l'idée de faire coïncider la théorie et l'expérience sur ce point particulier.

Passons maintenant à l'analyse des variations de r avec la température, où nous allons rencontrer plus de satisfaction. Nous avons vu que les valeurs expérimentales de r passant de valeurs négatives à positives quand T_0 croît et que r s'annule pour $T_0 \approx 135^\circ \text{K}$. D'après (6), r est proportionnel à β et s'annule donc en même temps que lui. Or, nous pouvons voir à la Section 2c de l'article B que, quand on suppose les électrons interagir avec les phonons optiques, le coefficient β s'annule en passant de valeurs <0 à >0 quand T_0 croît. Plus précisément, pour ce

type de couplage, à partir des formules (3.34), (3.42) de l'article B, le coefficient r a pour expression:

$$r = \frac{3\pi}{160 F_0^2} \frac{1}{K_1^2(\alpha_0) K_0(\alpha_0)} \frac{[5K_2(\alpha_0) - 9K_0(\alpha_0)][K_2(\alpha_0) - 9K_0(\alpha_0)] \sin h^2 \alpha_0}{\alpha_0^2}. \quad (7)$$

Les fonctions $K_i(\alpha_0)$ sont des fonctions de Bessel modifiées de seconde espèce. La quantité F_0 , homogène à un champ électrique est définie par:

$$F_0 = \frac{mD^{(0)}}{2\pi e h^2}$$

qui, dans InSb, vaut 34.10^3 V/m. $D^{(0)}$ est une constante de couplage entre les électrons et les phonons optiques (Cf. (3.27) dans l'article B).

Nous ne présentons pas la courbe déduite de (7) et représentant les variations de r avec $\alpha_0 = \hbar\omega_q/2kT_0$. En effet, bien que cette courbe ait un air de ressemblance avec les courbes expérimentales de la Fig. 5, la température T_a pour laquelle r s'annule en passant de valeurs < 0 à > 0 , déduite de (7) diffère par trop de celle mesurée puisque $(T_a)_{\text{théorique}} = 45^\circ\text{K}$ tandis que $(T_a)_{\text{exp}} = 135^\circ\text{K}$. De plus, les valeurs numériques de r déduites de (7) sont supérieures d'un facteur 10^2 à 10^3 aux valeurs expérimentales.

A ce stade, dans le but d'améliorer l'accord entre théorie et expérience, nous pouvons introduire un élément nouveau. En effet, nous savons d'après l'étude des phénomènes linéaires [4] et [5] que les phonons optiques ne sont pas les seuls à interagir avec les électrons: les phonons acoustiques, par l'intermédiaire du couplage piézoélectrique, jouent aussi un rôle. Nous sommes donc conduit à rechercher une expression de r en présence de deux interactions pour les électrons.

En remontant aux sources de la théorie exposée dans l'article B, nous pouvons aisément démontrer que, dans le cas où les

électrons interagissent avec deux types de phonons, les composantes de $\langle J \rangle$, calculées au second ordre par rapport au coefficient de couplage, s'écrivent:

$$\begin{aligned} \langle J_y \rangle &= n e \frac{E}{B} \text{ et } \langle J_x \rangle \\ &= (\sigma_1 + \sigma_2) \left(1 + \frac{\sigma_1 \beta_1 + \sigma_2 \beta_2}{\sigma_1 + \sigma_2} E^2 \right) E. \end{aligned} \quad (8)$$

Les coefficients σ_1 et σ_2 sont les coefficients de conductivité $\sigma_{xx}^{(0)}$ associés à chacune des deux interactions; de même, β_1 et β_2 sont les coefficients caractérisant les déviations par rapport à la loi d'Ohm associés à chaque interaction.

En partant de (8), à l'aide d'un raisonnement analogue à celui de la Section 3.a on trouve que le coefficient r s'exprime en fonction de $\sigma_1, \sigma_2, \beta_1, \beta_2$ sous la forme:

$$r = \frac{n^2 e^2}{B^2} \frac{\sigma_1 \beta_1 + \sigma_2 \beta_2}{(\sigma_1 + \sigma_2)^3}. \quad (9)$$

Nous admettons que les coefficients β_1 et β_2 qui interviennent dans (9) sont ceux qui ont été déterminés séparément à la Section 2 de l'article B. Appliquons alors (9) au cas où les électrons interagissent avec les phonons optiques et avec les phonons acoustiques par l'intermédiaire du couplage piézoélectrique. A l'aide des formules (20), (26), (34) et (42) de la Section 3 de l'article B, nous obtenons:

$$r = -\frac{3\pi}{160 F_0^2} \frac{1}{\alpha_0} \frac{5 \frac{\hbar\omega_q}{m s^3} \frac{D^{(1)}}{D^{(0)}} + \frac{\alpha_0^3}{\sin h \alpha_0} \frac{K_1(\alpha_0)}{K_0(\alpha_0)} \frac{[5K_2(\alpha_0) - 9K_0(\alpha_0)][K_2(\alpha_0) - 9K_0(\alpha_0)]}{K_2(\alpha_0) - K_0(\alpha_0)}}{\left[\frac{\omega_q}{s} \frac{D^{(1)}}{D^{(0)}} + \frac{\alpha_0^2}{\sinh \alpha_0} K_1(\alpha_0) \right]^3}. \quad (10)$$

La formule (10) fait évidemment intervenir les paramètres $D^{(1)}$, $D^{(0)}$ (ou F_0) qui fixent l'intensité de chacun des couplages et qui ne sont pas tous connus de façon précise dans InSb. Néanmoins, nous pouvons tracer des courbes $r(\alpha_0)$ à partir de (10) pour différentes valeurs du rapport $D^{(1)}/D^{(0)}$. Après quelques tâtonnements, on constate qu'en choisissant pour la quantité sans dimension:

$$A = 5 \frac{\hbar \omega_q}{m s^3} \frac{D^{(1)}}{D^{(0)}} \quad (11)$$

une valeur voisine de 9, la courbe représentative de $r(\alpha_0)$ (cf. Fig. 7) définit par (10) s'insère approximativement dans le réseau des courbes expérimentales de la Fig. 5. Il existe

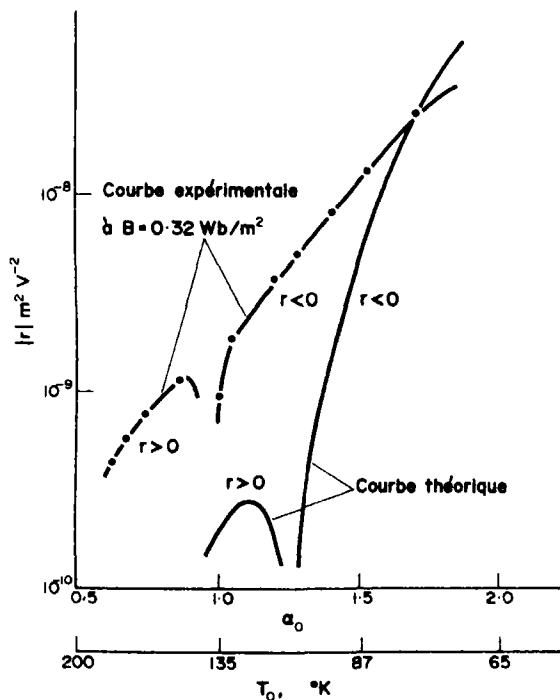


Fig. 7.

toutefois une différence notable entre les deux températures d'annulation de r , théorique et expérimentale, puisque:

$$(T_a)_{\text{exp}} \approx 135^\circ\text{K} \text{ tandis que } (T_a)_{\text{théor}} \approx 105^\circ\text{K}.$$

Donc en choisissant $A = 9$ (c.a.d. $D^{(1)}/D^{(0)} \approx 2 \cdot 10^{-14} m$), nous rendons compte de l'annulation de r à une 'température théorique' qui s'est nettement rapprochée de la 'température expérimentale' T_a par rapport au cas où nous ne considérons que l'interaction électrons-phonons optiques. De plus l'allure des variations expérimentales de r avec α_0 et notamment la tendance, pour r , à s'annuler une seconde fois au-delà de 300°K ($\alpha_0 \sim 0,4$) est bien traduite par la loi (10). Enfin les ordres de grandeur des valeurs de r , théoriques et expérimentales, concordent grossièrement pour certaines températures.

4. CONCLUSIONS

Nous avons mis au point un appareillage relativement sensible, fonctionnant en régime impulsif, mesurant les faibles déviations par rapport à la loi d'Ohm. Nous avons ainsi pu observer dans des échantillons de InSb de type n très pur que les premières déviations par rapport à la loi d'Ohm passent de valeurs > 0 à < 0 quand la température croît à partir de 77°K . Dans la région où r est > 0 , il varie rapidement en passant par un maximum et, au-delà, en ayant tendance à s'annuler une seconde fois pour prendre des valeurs < 0 . La théorie exposée dans l'article B interprète qualitativement l'ensemble de ces résultats; le couplage avec les phonons optiques est le responsable essentiel des annulations de r avec la température. Toutefois l'interaction avec les phonons acoustiques par l'intermédiaire du couplage piézoélectrique joue un rôle secondaire non négligeable. Grâce à ce dernier, les valeurs numériques de r et des températures d'annulation ne sont pas trop éloignées des résultats expérimentaux. Il subsiste cependant des désaccords entre théorie et expérience, notamment en ce qui concerne les variations de r avec l'induction magnétique.

REFERENCES

1. CALECKI D. *J. Phys. Chem. Solids* **28**, 1409 (1967).
2. KAZARINOV R. F. and SKOBV V. G., *Soviet*

- Phys. JETP* **15**, n°4, 726 (1962). BUDD H. F., *Phys. Rev.* **131**, n°4, 1520 (1963).
3. HAAS M. and HENVIS B. W., *J. Phys. Chem. Solids* **23**, 1099 (1962).
4. FIRSOV Yu. A., GUREVICH V. L., PARFENIEV R. V. and SHALYT S. S., *Phys. Rev. Lett.* **12**, 660 (1964).
5. SLADEK R. J., *J. Phys. Chem. Solids* **16**, 1 (1960).

X-RAY SPECTROSCOPIC INVESTIGATION OF BISMUTH SELENIDE, BISMUTH TELLURIDE AND THEIR ALLOY

V. G. BHIDE, B. A. PATKI and A. S. NIGAVEKAR
National Physical Laboratory, New Delhi-12, India

(Received 27 April 1970; in revised form 28 August 1970)

Abstract—The Bi L_{III} and Se K -absorption discontinuities in Bi_2Te_3 , Bi_2Se_3 and Bi_2Te_3Se have been studied using a 40 cm dia. bent crystal X-ray spectrograph. The Bi edge in these compounds is found to shift to higher energies with respect to that of the metal. The Se edge on the other hand moves to lower energy in Bi_2Se_3 and to higher energy in Bi_2Te_3Se . The X-ray absorption data on Bi_2Se_3 and Bi_2Te_3Se brings out clearly the difference in the nature of the chemical bond two types of selenium atoms, Se_I and Se_{II} , have in these compounds. An alternative bonding picture is proposed for Bi_2Se_3 to remove deficiencies in Drabble and Goodman's scheme.

1. INTRODUCTION

COMPOUNDS of the type $A_2^VB_3^{VI}$ and especially those crystallizing in the rhombohedral type structure e.g. Bi_2Se_3 , Bi_2Te_3 have in recent years assumed importance because of their thermo-electric applications [1, 2]. Moreover, bismuth telluride forms unlimited solid solutions with isostructural compounds Bi_2Se_3 and Sb_2Te_3 [3-5]. Many workers [6-9] have tried to explain various properties of Bi_2Se_3 , Bi_2Te_3 and bismuth telluride base solutions from the chemical bond point of view. At present there are two suggestions regarding the nature of bonding in bismuth selenide and bismuth telluride: one by Mooser and Pearson [8] based on the 'semiconducting bond' between neighbouring bismuth and selenium/tellurium atoms and the other by Drabble and Goodman [9] postulating a fully saturated bonding with two electrons per bond due to hybridization of outer orbitals.

The X-ray absorption spectroscopy provides a direct method of studying the empty orbitals in solids. Hence it is possible with the help of absorption data to choose and/or assign a correct bonding picture compatible with the structure as well as electrical properties of compounds. In this paper we present our

results on Bi_2Se_3 , Bi_2Te_3 and the alloy Bi_2Te_3Se .

2. EXPERIMENTAL

A Cauchois type bent crystal spectrograph of 40 cm diameter was used for photographing the spectra. A mica crystal with known optics (100 planes) was used as an analyser. A Philips sealed X-ray tube with Mo target acted as a source of radiations. The tube was run at 25 KV and 15 mA. The absorbers were prepared by spreading a fine powder of the substance under investigation on cellophane tape. The optimum thickness of the absorbing screen for a good contrast in the spectrum was determined by trial. The spectra were recorded on 'Forte' high speed X-ray film, the exposure time varying between 15 to 20 hr.

The Bi L_{III} edge was photographed in the second order where it could be bracketted between Mo $K_{\beta_{1,3}}$ line (third order) and Br K discontinuity (second order). The Mo $K_{\alpha_{1,2}}$ and Mo $K_{\beta_{1,3}}$ lines in the third order were used as reference for the Se K discontinuity in the second order. Each spectrogram was photometred at 5-6 points with a Hilger-Watts microphotometer coupled to a Honeywell chart recorder with a magnification $\times 50$. The

values given in Table 1 are an average of at least 30 microphotometer records.

3. CRYSTAL STRUCTURE AND CHEMICAL BONDING

The *C*-33 structure (rhombohedral unit cell, $R\bar{3}m$ space group) in which Bi_2Te_3 , Bi_2Se_3 and $\text{Bi}_2\text{Te}_2\text{Se}$ crystallize [10–12] is built of multiple layers in the sequence $B_1-B_1-B_1-A-B_{II}-A-B_1-B_1-B_1$. The stacking of these layers is such that each atom inside any of the layers acquires a slightly distorted octahedral neighbourhood. There are two types of *B* atoms. The B_1 atom (Se/Te) at the boundaries of each five layer group have three nearest 'A' neighbours (Bi) in the same multiple layer and three nearest neighbours (B_1) at somewhat greater distance in the adjacent multiple layer group. The central $\text{Se}_{II}/\text{Te}_{II}$ atom has an environment of six Bi atoms in the same multiple layer group.

The nature of chemical bonding in bismuth selenide and bismuth telluride has been discussed by Mooser and Pearson and by Drabble and Goodman.

Mooser and Pearson by considering the bond lengths in Bi_2Se_3 and Bi_2Te_3 suggest that the bonding in these compounds is mainly due to a mixture of two types of valence struc-

tures as shown in Fig. 1. In structure II hybrid p^3d^3 orbitals are formed in Te_I and Bi atoms, the paired *p* electrons of Te_I in the ground state become unpaired with one electron passing into free *d* orbitals. Six hybrid p^3d^3 orbitals thus arise in the Te_I atom. For Bi, six bonds with its neighbours (3Te_I and 3Te_{II}) are formed by resonance of three bonds with respect to six hybrid orbitals. The bonds between the Te_{II} atom and its six Bi neighbours make use of the empty orbitals on Bi to resonate among six positions. The outermost Te_I atom forms a bond with its six neighbours (3Bi and 3Te_I) by resonance of four bonds with respect to six hybrid orbitals. Structure I in Fig. 1 corresponds to no covalent bonding between neighbouring multiple layers and according to the concept of semiconducting bonds leads to semiconducting properties.

Table 1. X-ray absorption data on Bi_2Se_3 , $\text{Bi}_2\text{Te}_2\text{Se}$ and Bi_2Te_3

Substance	$\lambda \text{ X.U.}$	$E \text{ eV.}$	ΔE
<i>L_{III}</i> absorption edge of Bi.			
Bi.	921.704 ±0.06	13423.18	—
Bi_2Se_3 .	921.481 ±0.06	13426.42	+3.24
$\text{Bi}_2\text{Te}_2\text{Se}$.	921.522 ±0.06	13425.83	+2.65
Bi_2Te_3 .	921.590 ±0.06	13424.84	+1.66
<i>K</i> absorption edge of Se			
Se.	977.790 ±0.04	12653.22	—
Bi_2Se_3 .	977.869 ±0.04	12652.20	−1.02
$\text{Bi}_2\text{Te}_2\text{Se}$.	977.683 ±0.04	12654.61	+1.39

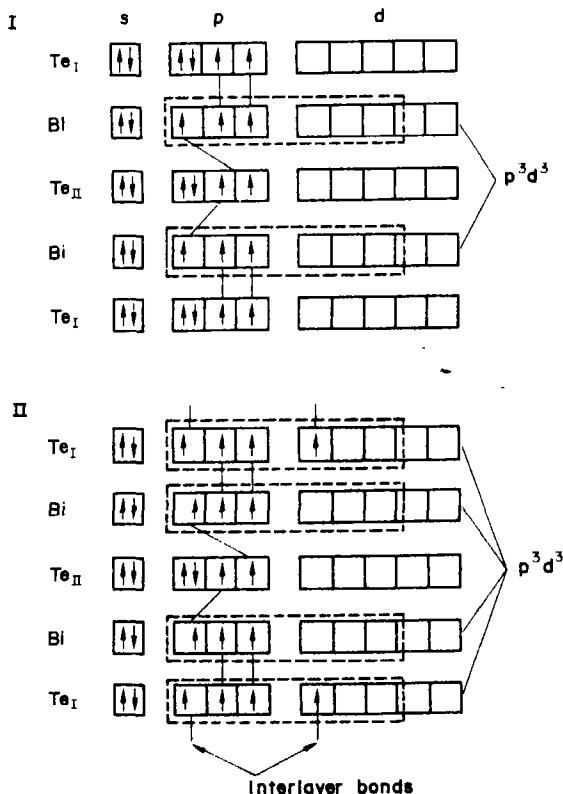


Fig. 1. Two valence structures whose mixture represents the bonding in Bi_2Se_3 and Bi_2Te_3 following Mooser and Pearson.

Drabble and Goodman's bonding (Fig. 2) is based on an application of the method of valence bonds between hybrid orbitals of neighbouring bismuth and tellurium atoms. They assumed that the bond length $\text{Te}_I\text{-Te}_I$ (3.73 Å) is of Van der Waals type being of the same order as the bond length (3.74 Å) between tellurium atoms in the adjacent chains of the tellurium metal structure. This means that the electron density in these bonds is effectively zero and thus the valence electrons in Te_I atom are used only in bonding to the three

4. X-RAY SPECTROSCOPIC DATA AND CHEMICAL BONDING

As described above two hypotheses have been put forward regarding the nature of chemical bonding in Bi_2Se_3 and Bi_2Te_3 . We shall show below how it is possible from X-ray absorption work to choose and/or assign the correct bonding in these compounds.

Following the theoretical and experimental work of Richtmyer *et al.* [13], it is now generally accepted that the inflection point on an absorption edge in the case of a metal repre-

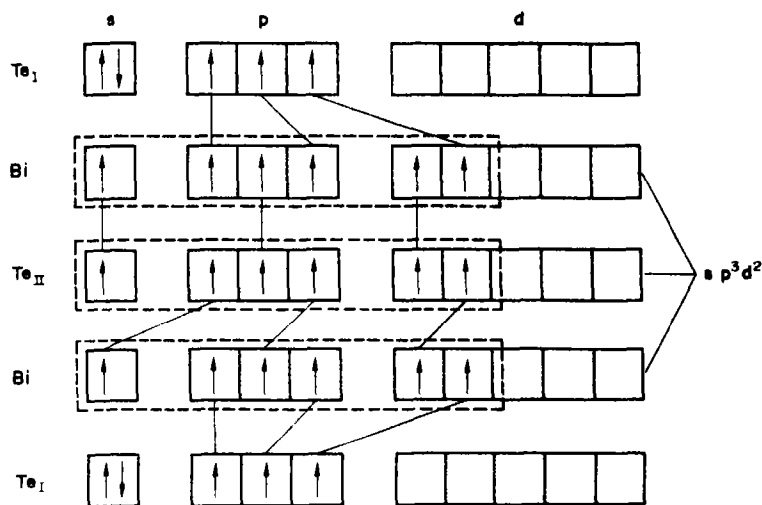


Fig. 2. Drabble and Goodman's bonding picture of Bi_2Se_3 and Bi_2Te_3 .

nearest neighbour bismuth atoms in the same multiple layer group. To satisfy the octahedral co-ordination, Bi and Te_{II} atoms form hybrid sp^3d^2 orbitals. The s electrons of Bi and s and p electrons of Te_{II} become unpaired and occupy their respective d orbitals. Additional electron necessary to form sp^3d^2 hybrid orbitals in case of Bi is drawn from Te_I . The bismuth is thus charged negatively and the Te_I positively. The formal covalent formula of Bi_2Te_3 according to this bond scheme is thus $(\text{Bi}^{-1}\text{Te}^{+1})_2\text{Te}$ emphasizing the difference between the nature of bond formed by two different Te atoms.

sents the position of the Fermi limit. No theoretical calculations on the shape of the absorption discontinuities for semiconductor and insulators have yet been made. The experimental work of Deslattes and DeBen [14] and Mande and Nigavekar [15, 16] on the K absorption and emission spectrum of semiconductor shows that the emission edge coincides with the inflection point of the absorption discontinuity. It may, therefore, be assumed that the inflection point on the absorption discontinuity of a semiconductor represents the top of the outermost filled band. Hence the shift of the absorption discontinuity

in the compound with respect to the discontinuity in the metal could be taken as a measure of the distribution of outer electrons in the valence band. In the present work we have studied the L_{III} absorption edge of Bi and the K absorption edge of Se in metals as well as in compounds. It is known that the absorption transitions like emission ones are governed by the selection rules. Evidently the transition from an L_{III} level never has the same end state as a transition from a K level. However in the present study as we are considering the shift in the same edge in going from the metal to the compound, it (the shift) reflects the change in the electron environment of the atom due to chemical combination. Our choice of these absorption edges was restricted by limitations in our experimental set up. It is also known that the physico-chemical state of the absorbing atom affects the inner levels. However, such a change is comparatively small for the deeply buried inner levels, such as K , than on the outermost levels.

It could be seen from the experimental results (Table 1 see also Fig. 3) that the Bi L_{III} absorption discontinuity in Bi_2Se_3 , Bi_2Te_3 and Bi_2Te_2Se shifts towards the high energy side with respect to the discontinuity in the bismuth metal. This suggests that the outermost empty orbitals in case of bismuth (cations in the compound) get filled either due to promotion of valence electrons or by acceptance of electrons from anions (Se/Te). However, the K absorption edge of Se shifts towards the low energy side in Bi_2Se_3 whereas it shifts towards the high energy side in Bi_2Te_2Se with respect to the K absorption edge in selenium.

Assuming that the Drabble and Goodman's chemical bonding picture for Bi_2Te_3 is applicable to isostructural Bi_2Se_3 the filling of the outer d orbitals of Bi in the compound due to promotion of one $6s$ electron and acceptance of a p electron from Se_1 atom should cause the L absorption discontinuity of the cation to move towards the high energy side as observed by us. But Drabble and Goodman in their bonding picture for Bi_2Te_3 assume the bond

between Te_1 atoms in the adjacent multiple layer groups to be of Van der Waals type which seems to be correct as the distance Te_1-Te_1 is of the same order as the sum of VDW radii. However in Bi_2Se_3 the Se_1-Se_1 bond length (3.31 Å) for neighbouring groups is almost equal to the ionic bond length (2.96 Å). Hence one cannot neglect the bonding of Se_1 atoms with three Se_1 atoms in the adjacent layer. We can thus understand the easy cleavage in Bi_2Te_3 but not so easy a cleavage in Bi_2Se_3 .

Although Mooser and Pearson's picture with resonating p^3d^3 hybrid orbitals provides

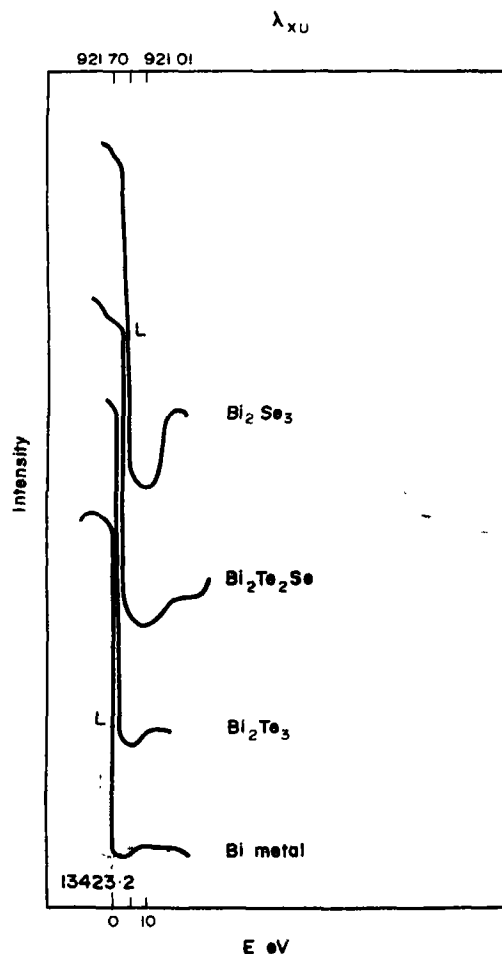


Fig. 3. Bismuth L_{III} absorption edge in Bi_2Se_3 , Bi_2Te_2Se , Bi_2Te_3 and Bi metal.

for such interlayer bonds, it is not compatible with the X-ray absorption data as according to this picture Bi absorption discontinuity should not be affected in the compound which is not the case (see Table 1).

An alternative scheme (Fig. 4) which appears to remove the difficulties discussed above is as follows. The bismuth and both types of selenium atoms have nearly octahedral co-ordination in Bi_2Se_3 . The central Se_{II} atom forms bonds with sp^3d^2 hybrid orbitals, the two s and four p electrons getting redistributed in six orbitals. Bi and Se are linked by resonating bonds. This involves the p - d hybridization since according to Pauling [17] empty orbitals must be available in at least one of the two atoms which are linked by resonating bonds. The donation of one p electron by Se_{I} atom to each Bi atom enables the formation of six two electron covalent Bi- Se_{II} bonds. Thus the bonding between Se_{II} and Bi atom is covalent whereas it is of ionic type between Se_{I} and Bi atoms. The formula for the compound could be written as $(\text{Bi}^{-1}\text{Se}^{+1})_2\text{Se}$ emphasizing the ionic-covalent type of bonding.

Our picture is compatible with the X-ray

absorption data. The Bi L absorption edge as expected shifts towards the high energy side. In our picture the two Se_{I} atoms give two electrons to Bi atoms. This should cause the Se K discontinuity to shift towards the low energy side. On the other hand in Se_{II} atom two s and four p electrons get redistributed to form sp^3d^2 hybrid orbitals and the bonding between Bi and Se_{II} atoms is of covalent type. However because of limited resolution of our spectrograph we observe only an average change and hence the Se K absorption edge is found to shift towards the low energy side.

In the case of Bi_2Te_3 Drabble and Goodman's chemical bonding picture seems to be compatible with the X-ray absorption results. In their picture Bi atom acquires six hybrid sp^3d^2 orbitals in which six electrons (five original and one obtained from Te_{I} atom) are distributed. The high energy side shift of the Bi discontinuity confirms this promotion of one s electron to d orbitals and the acceptance of a p electron from Te_{I} atom. Even though the absorption discontinuity of Te has not been studied it could be anticipated that just like Se K discontinuity in Bi_2Se_3 this would also shift towards the low energy side. The picture

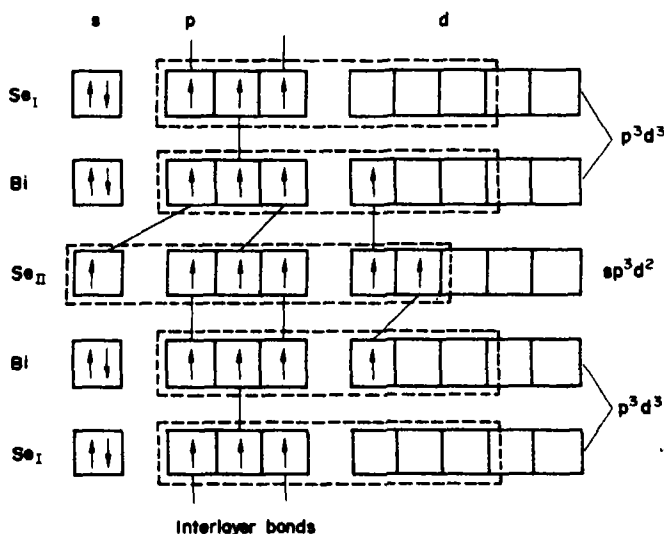


Fig. 4. Suggested bonding in Bi_2Se_3 and Bi_2Te_3 .

of Mooser and Pearson does not fit in the X-ray results since according to this picture neither the cation nor the anion absorption discontinuity should get affected in the compound with respect to the discontinuity in the metal.

Thus in both the compounds viz. Bi_2Se_3 and Bi_2Te_3 the bonding is of iono-covalent type. The bonding between the central atom (Se_{II} or Te_{II}) and the Bi atom is of covalent type. But, in case of $\text{Bi}-\text{Te}_{\text{II}}$ it is predominantly covalent compared to the bonding between $\text{Bi}-\text{Se}_{\text{II}}$. This is also expected since the bond length $\text{Bi}-\text{Te}_{\text{II}}$ (3.24 Å) is longer than $\text{Bi}-\text{Se}_{\text{II}}$ (3.05 Å) bond length. Whereas the $\text{Bi}-\text{Se}_I$ bond (2.99 Å) is more ionic than $\text{Bi}-\text{Te}_I$ bond (3.04 Å). These may be reasons why Bi_2Se_3 has a more metallic behaviour than Bi_2Te_3 .

In $\text{Bi}_2\text{Te}_2\text{Se}$ the situation is a little different. Austin and Sheard [18] have studied the variation of the optical energy gap of alloys of composition $\text{Bi}_2\text{Te}_{3-x}\text{Se}_x$ with increasing selenium content. In these compositions selenium first replaces the Te_{II} atoms in Bi_2Te_3 lattice, being less firmly bound to the bismuth atoms. This substitution leads to greater ionicity, as selenium is more electronegative than tellurium, in the bond with Bi atoms. Thus the bond strength and hence the energy gap will increase with increasing x until x reaches the value of one when $\text{Bi}_2\text{Te}_2\text{Se}$ is formed. X-ray absorption data show that the Bi L_{III} as well as the Se K edge in this compound shifts towards the high energy side. The observed high energy side shift of Se K absorption discontinuity provides a direct evidence for the redistribution of s and p electrons in the central Se atom thereby forming the sp^3d^2 hybrid orbitals. The bond length between Te_I atoms in two adjacent layer groups in case of $\text{Bi}_2\text{Te}_2\text{Se}$ is of the same order (3.65 Å) as the similar bond length for Te_I atoms (3.73 Å) in Bi_2Te_3 . Thus here also the electron density in the Te_I-Te_I bond is effectively zero and the valence electrons in Te_I atoms are only used in bonding the three bismuth atoms in the same multiple layer structure. This and the observed high energy

side shift of the Bi discontinuity suggests the sp^3d^2 hybridization for Bi atoms. Thus the chemical bonding picture in $\text{Bi}_2\text{Te}_2\text{Se}$ is of the same type as Bi_2Te_3 .

Some more tentative conclusions may be drawn for the system $\text{Bi}_2\text{Te}_{3-x}\text{Se}_x$ when x becomes more than one in value. With the increase of x (> 1) the selenium atoms will go into Te_I sites and tend to attract charge along the $\text{Bi}-\text{Te}_I$ bonds, making bismuth atoms more electronegative, which in turn causes charge to move towards the bismuth along the $\text{Bi}-\text{Te}_{\text{II}}$ bonds. This should make the bond length between the Se_I occupying Te_I sites in one multiple layer with Se_I atoms in the other layer group to change from VDW type to more and more ionic with the increase of selenium content until finally Bi_2Se_3 is formed. Thus the bonding picture should also change from that given to Bi_2Te_3 (Fig. 2) to that of Bi_2Se_3 (Fig. 4) in the system $\text{Bi}_2\text{Te}_{3-x}\text{Se}_x$ with increasing selenium content.

Acknowledgements—The authors wish to express their indebtedness to Mr. K. P. Rao of Electronics Corporation of India, Hyderabad for the preparation of Bi_2Te_3 and Bi_2Se_3 and Mr. K. D. Kundra of this Laboratory for $\text{Bi}_2\text{Te}_2\text{Se}$ used in the present investigation. Thanks are also due to Mr. M. K. Bahl for his interest in the work.

REFERENCES

1. GOLDSMID H. J. and DOUGLAS R. W., *Brit. J. appl. Phys.* **5**, 386 (1954).
2. IOFFE A. F., *Semiconducting Thermoelements*. Izd. Akad. Nauk. SSSR (1960).
3. KUZNETSOV V. G., and PALKINA K. K., *Z. neorg. Khim.* **8**, 1204 (1963).
4. McHUGH J. P. and TILLER W. A., *Trans. Am. Inst. Min. Met. Eng.* **215**, 651 (1959).
5. SMITH McJ. KNIGHT R. J. and SPENCER C. W., *J. appl. Phys.* **33**, 218 (1962).
6. MOOSER E. and PEARSON W. B., *Can. J. Phys.* **34**, 1369 (1956).
7. LAGRENAUDIE J., *J. Phys. Radium* **18**, 39A (1957).
8. MOOSER E. and PEARSON W. B., *J. Phys. Chem. Solids* **7**, 65 (1958).
9. DRABBLE J. R. and GOODMAN C. H. L., *J. Phys. Chem. Solids* **5**, 142 (1958).
10. LANGE P. W., *Naturwissenschaften* **27**, 133 (1939).
11. FRANCOMBE M. H., *Brit. J. appl. Phys.* **9**, 419 (1958).
12. BLAND J. A. and BASINSKY S. J., *Can. J. Phys.* **39**, 1040 (1961).

13. RICHTMYER F. W., BARNES S. and RAMBERG R., *Phys. Rev.* **46**, 843 (1934).
14. DESLATTES R. D. and DeBEN, H. S., *Phys. Rev.* **115**, 71 (1959).
15. MANDE C. and NIGAVEKAR A. S., *Proc. Ind. Acad. Sci.* **65A**, 376 (1967).
16. MANDE C. and NIGAVEKAR A. S., *Ibid.* **67A**, 166 (1968).
17. PAULING L., *Nature of the Chemical Bond*. Cornell Univ. Press Ithaca, New York (1960).
18. AUSTIN I. G. and SHEARD A., *J. Electron.* **31**, 236 (1957).

LATTICE DYNAMICS OF CUBIC ZINC SULFIDE BY NEUTRON SCATTERING*

L. A. FELDKAMP,† D. K. STEINMAN, N. VAGELATOS‡ and J. S. KING

Department of Nuclear Engineering, The University of Michigan, Ann Arbor, Mich. 48104, U.S.A.

and

G. VENKATARAMAN

Nuclear Physics Division, Bhabha Atomic Research Centre, Trombay, Bombay, India

(Received 26 August 1970)

Abstract—The dispersion properties of room temperature cubic ZnS were measured in high symmetry directions by the constant- Q method. A valence shell model, following the method of Woods, *et al.*, was least square fitted to the neutron data with only fair success. This model and its comparison with a rigid ion version are discussed. Longitudinal optic branches were not observed.

1. INTRODUCTION

THE LATTICE vibrational properties of semiconductors with the tetravalently bonded diamond and zincblende structures have been extensively studied in recent years by neutron inelastic scattering measurements. Phonon dispersion curves have been measured along the high symmetry directions of the Brillouin zone for Ge[1], diamond[2], Si[3], and for the III-V compounds, GaAs[4] and GaP[5]. Zinc sulfide provides an obvious extension to the II-VI compounds, as well as being an important semiconductor in its own right. Preliminary results for cubic ZnS have been published by us in an earlier paper[6]. The present paper is an extension of that work, both in experimental detail and in modeling.

Both the wurtzite (2H)[7] and zincblende (3C) forms of ZnS have been widely studied by i.r. absorption and reflection[8-10], and by Raman scattering[11-14]; this work includes measurement of first order (zone center phonons) and second order (interpreted as zone boundary phonons), measurement of

successive polytypes for phonons propagating along[111] directions, and mixed crystal sequences. Table 1 lists the most recently reported zone center frequencies and symmetry assignments.

ZnS (3C) has the zincblende crystal structure. The space group is $T_d^2(F\bar{4}3m)$ and there are two atoms per primitive cell. Thus, there are six phonon dispersion branches. ZnS (2H) has the wurtzite structure, with space group $C_{6v}^4(P6_3mc)$ and four atoms per primitive cell. ZnS (2H) has twelve branches. Figure 1 illustrates schematically these branches along representative directions for both forms of ZnS. Also given are the group theoretic labels for the $q = 0$ phonons, both in the notation employed in solid state physics and that used in molecular spectroscopy. In cubic ZnS, both optic modes are Raman and i.r. active. In ZnS (2H), all branches are either Raman or i.r. active except B_1 . Several conclusions can be drawn from Table 1 and its supporting references:

(a) The wurtzite zone center frequencies $E_1(TO)$ and $A_1(LO)$ are well established at 274 cm^{-1} and 352 cm^{-1} , within an accuracy of $\pm 1\text{ cm}^{-1}$. By contrast, the two E_2 modes have been subject to considerable disagreement.

*Work supported by the National Science Foundation under NSF Grant No. GK-12492.

†Present Address: Scientific Research Staff, Ford Motor Company, Dearborn, Michigan, U.S.A.

‡U.S. Atomic Energy Commission Predoctoral Fellow.

Table 1. Long wavelength frequencies of ZnS

Crystal type and branch				Method and reference
2H		3C		
$E_1(TO)$	273 cm^{-1}	$\Gamma_{15}(TO)$	276 cm^{-1}	Raman[13]
$A_1(LO)$	351	$\Gamma_{15}(LO)$	351	Raman[13]
E_2	72			Mixed crystals[13]
E_2	286			Mixed crystals[13]
$E_1(TO)$	274			Raman[12]
$A_1(LO)$	352			Raman[12]
E_2	55			Raman[12]
E_2	274			Raman[12]
E_2	48			i.r. on mixed crystals[10]
E_2	287			i.r. on mixed crystals[10]
TO	274	$\Gamma_{15}(TO)$	282	i.r. reflection[9]
TO	272			i.r. transmission[9]
TO	279	$\Gamma_{15}(TO)$	271	Raman[11]
LO	348	$\Gamma_{15}(LO)$	352	Raman[11]

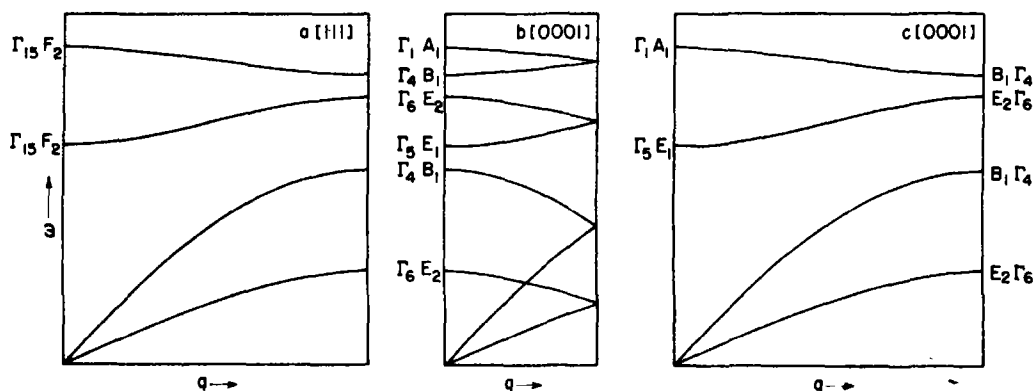


Fig. 1. Comparison of idealized phonon dispersion curves in ZnS (3C) and ZnS (2H) showing two common group theoretic labels: (a) [111] in ZnS (3C), (b) [0001] in ZnS (2H), (c) [0001] in ZnS (2H) in the unfolded scheme. (a) and (c) are nearly identical because the stacking of atoms in the two structures is very similar.

(b) For zincblende, $\Gamma_{15}(LO)$ is identical to the wurtzite frequency of 352 cm^{-1} . Some disagreement exists for $\Gamma_{15}(TO)$, the limits of which appear to be 271 cm^{-1} to 282 cm^{-1} . Because of the close equivalence of force fields, there is little difference expected between the long-wavelength frequencies $\Gamma_{15}(TO, LO)$ for 3C and the A_1 and E_1 frequencies for 2H. However, the small differences are not well established.

(c) First order optical events observed for

hexagonal polytypes have been interpreted as zone boundary and zone interior phonons of the cubic 3C crystal along the [111] (i.e., Λ) direction. Patrick and his associates have successfully applied this technique to SiC[15]. Vetelino *et al.* have similarly used several hexagonal ZnS frequencies to predict the dispersion relations for transverse Λ modes in ZnS (3C)[14]; they assign their observed frequencies of 72 cm^{-1} , 286 cm^{-1} to E_2 modes corresponding to the TA and TO

branches at L in the cubic crystal. It should be noted that only the active modes in the Λ direction can be so treated.

(d) Second order optical events appear to be too ambiguous to provide reliable dispersion points interior to the zone even for the relatively simple zincblende structure.

(e) The mixing of crystal polytypes inherent in vapor phase grown ZnS samples make it difficult to obtain a pure target of either $3C$ or $2H$ unless a very small specimen (~ 0.01 cm along hexagonal C axis) is used [16]. This has introduced ambiguity in some optical experiments. The need for much larger targets in neutron spectroscopy makes it difficult to avoid the presence of a substantial volume fraction of undesired crystal structure.

Lattice dynamical models appropriate to mixed ionic-covalent crystals have been extensively explored [2-5, 17-20] since the initial success of the shell model as applied to ionic crystals. These are equivalent in the sense that they include: (a) short-range interactions between a few nearest neighbors; (b) long-range coulomb forces appropriate to vibrating polarizable atoms with fixed charges; and (c) local vibration-induced displacement of the outer electron distributions relative to the ion cores. Models differ in the treatment of local electron-ion core distortion, but always within the limit of the dipole approximation and always restricted to time invariant core and shell charges. Application of models to neutron data have differed in the number and selection of parameters in eliminating model parameters. GaAs [4] and GaP [5] data were fitted by a standard shell model extending the technique used by Woods *et al.* [17] for NaCl, i.e., ten parameters for short range interactions and five electric parameters. Most recently, Nusimovici and Balkanski [19] have analyzed CdS (wurtzite structure) with a twelve parameter model wherein short range forces are expressed in valence components out to third neighbors, and wherein the electronic polarization includes, in addition to the usual electric field polarizability a local

deformation dipole with an effective deformation charge due to relative mechanical displacements.

The present ZnS data have been analyzed with a 'valence shell model' which combines the short range parameter economy of a valence force description with the electronic and mechanical polarizabilities of the shell model. It is similar to Nusimovici's model. The general validity of the dipole models for the $II-VI$, $III-V$ compounds will be discussed later.

2. EXPERIMENTAL

Phonon peaks were measured at room temperature in three symmetry directions Δ [001], Λ [111], Σ [110], using the constant- Q method [21] on the University of Michigan triple axis crystal spectrometer. The spectrometer monochromator and analyzer crystals are thin (0.13 in.) copper plates reflecting in the (200) planes. In the parallel positions and with no collimation, these crystals have a double crystal rocking width (FWHM) of approximately 30 ± 6 min. Soller collimators precede both crystal positions and have apertures (FWHM) of 26 min. The collimators preceding the target and detector are not limiting. The source plane neutron intensity as determined by foil activation is approximately $1.5 \cdot 10^{13}$ neutron/cm²-sec. The no-target background is about 0.9 ± 0.2 c/min and this rises to a typical level of 2.5 ± 0.5 c/min with a ZnS target in position. Extra source intensity has been achieved by vertical focusing using double monochromator crystals. Because of potential errors from vertical divergence, many of the phonons measured were repeated with a single monochromator crystal. For targets having dense reciprocal lattices or high dispersion surface asymmetry, vertical focusing is probably undesirable; in the case of ZnS, no apparent errors were generated.

Two different ZnS crystals were used. One was a natural crystal from Japan, given to us

by Professor Chihiro Kikuchi of this department. The second was an 18 cm³ synthetic crystal grown by vapor deposition, loaned to us by Eagle-Picher Industries. The natural crystal was used for almost all of the acoustic branch points. The synthetic crystal was used for the optic branches, for the lowest and upper acoustic Σ branches, and for the zone boundary longitudinal acoustic phonons near X and L . The synthetic crystal was also used to check numerous events obtained with the natural crystal; where the latter were strong and well resolved, the agreement was always within the experimental uncertainties.

Both samples were visibly imperfect, and both showed severe twinning as evidenced by neutron diffraction. We infer from the diffraction intensities that the twinning is due to occasional rotations of the lattice, by multiples of 60°, about one unique $[111]$ axis. When viewed in a (110) scattering plane containing the unique $[111]$ axis, this produced a second set of reciprocal lattice points equivalent to a 180° rotation of the normal lattice about the $[111]$ axis. Bragg reflections from these had about half the normal intensity. This alternate lattice was of course avoided in the phonon scanning, but this does not guarantee complete freedom from interference from unwanted events. Such interference may have been responsible for the large limits of uncertainty assigned in Fig. 1 to the acoustic branch data near X and L . Two small pieces (1.44 and 0.5 cm³) were later cut from the natural crystal and found to be relatively free of twinned regions. Several phonons were measured with the larger piece and found to be in agreement with those of the original sample.

A related problem was the presence of polytype structures other than cubic (3C), as has been noted above. The fraction of hexagonal structures (2H, 4H, 6H, 15R, 21R, and higher) depends presumably on growth history. X-ray intensity measurements made by the Eagle-Picher Industries indicated that the synthetic crystal was approxi-

mately 80 per cent cubic and 20 per cent hexagonal [22]. For the same crystal, our neutron diffraction data indicates a content of 60–70 per cent cubic ZnS. The apparent disagreement may be due to the fact that neutrons can probe the bulk of a large crystal, whereas X-rays see only a very limited region because of their greater scattering probability. Our data on the 0.5 cm³ segment of the natural crystal indicates a very small volume of hexagonal structure ZnS (i.e., <1 per cent). The wave vectors of the phonons measured, excluding those in the $[111]$ directions, were in off-symmetry $2H$ directions. We feel it is unlikely, though possible, that the results of our phonon measurements were affected by the presence of the non-cubic ZnS in our target.

The structure factor zone was found, and an initial estimate of the structure factors was made to guide the optimum choice of reciprocal lattice positions for each phonon scan. The resolution ellipsoid was calculated according to the method of Cooper and Nathans [23], and it was used to verify the observed peak widths for most of the data points. Qualitatively, the observed peaks followed the predicted widths as expected, but the absolute agreement fluctuated, disagreeing in a few extreme cases by almost a factor of two. Widths of elastic Bragg events were always calculated to within 20 per cent of observation.

The low net signal-to-background ratio and poor focusing conditions made difficult the positive identification of most of the TO events and LA events near the zone boundary. For these events, advantage was taken of the Q^2 dependence of the coherent cross section by operating with Q in the region of 5 to 7 Å⁻¹ using final energies (in neutron downscattering) up to 55 MeV. The resolution was unavoidably broadened, which is reflected in greater limits of uncertainty shown in Fig. 2 for these events. We found it impossible to reliably identify any LO branch phonons. It should be added that a measure of focusing

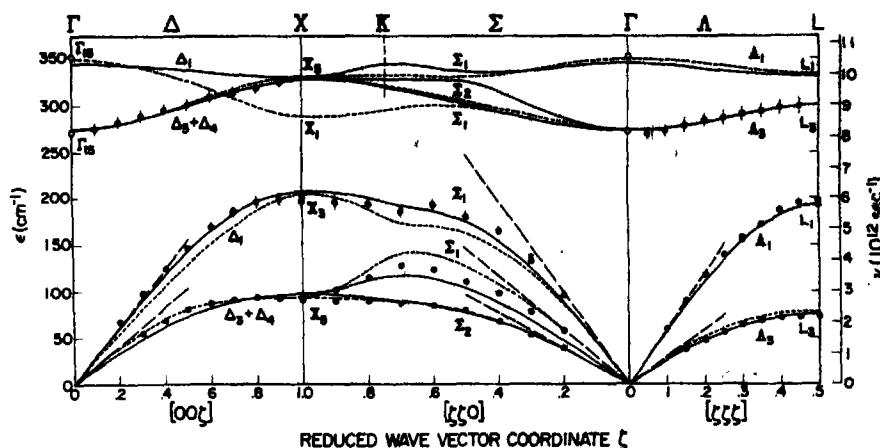


Fig. 2. Dispersion data in the three symmetry directions Δ , Σ , and Λ . The dashed lines are the sound velocities, as determined by the elastic constants of Ref. [30]. The solid curve is the ten parameter VSM. The dashed curve is the six parameter rigid ion model obtained from the VSM code by setting $\alpha_i = d_i = 0$. X_s is the transverse optic frequency.

was regularly achieved for LA events, as noted in our earlier paper, by directing Q slightly off the q direction. The technique was also used for the expected LO events. It is possible that by lowering the target temperature a sufficient background improvement can be achieved to reveal the LO branches.

Experimental results and model fitting

The neutron data are shown in Fig. 2 together with two calculated dispersion curves; group theoretic labels are also shown. The solid circles give the centroid of each neutron peak after background subtraction, the latter being interpolated from the values in the wings. In some cases, the centroid did not coincide exactly with the maximum count rate, but this discrepancy was usually less than the uncertainty in absolute energy calibration. The limits shown for each point include an estimate of uncertainties due to calibration, background structure, and resolution width. The double points for acoustic branches at X and L are the result of two or more scans using different crystal alignments and positions in the reciprocal lattice. The discrepancies are of the order of 3 cm^{-1} and are a reasonable upper limit of the

reproducibility for these difficult points. The acoustic data points in the vicinity of X and L are an extension of our earlier measurements, and for X are significantly lower than the original extrapolation. The present data were obtained with the synthetic crystal, and repeated for several different constant- Q conditions, especially at large Q^2 . These data are considerably more reliable than the earlier work, both because of an improved signal/noise ratio and the more extensive coverage. No adjustment has been made to data points to correct for distortion from resolution overlap out of the scattering plane; this was estimated to be negligible.

The open circles at Γ in Fig. 2 are the zone center frequencies obtained by Nilsen[11] from Raman scattering. Although the neutron data extrapolate fairly well to the TO frequency, a precise comparison is not possible since there is an absolute uncertainty in the neutron optic data of about $\pm 6 \text{ cm}^{-1}$, and, as shown in Table 1, considerable disagreement in the optical data as well. The energy calibration of the spectrometer was checked by measuring several high energy phonons in silicon, and the agreement was within the above accuracy. However, most of the phonon frequencies so

measured were larger than those reported[3] by about 4 cm^{-1} . Table 2 lists the zone boundary neutron-measured frequencies at X and L . The TO branches were measured between $0.1q/q_{\text{max}}$ and $0.9q/q_{\text{max}}$ in both the Δ and Λ directions. The quoted values at the boundaries are extrapolated from those data.

Table 2. Zone boundary frequencies

	X	L
TA	$X_3: 93 \pm 2 \text{ cm}^{-1}$	$L_3: 73 \pm 2 \text{ cm}^{-1}$
LA	$X_3: 199 \pm 8 \text{ cm}^{-1}$	$L_1: 195 \pm 5 \text{ cm}^{-1}$
TO	$X_3: 326 \pm 4 \text{ cm}^{-1}$	$L_3: 300 \pm 6 \text{ cm}^{-1}$

The L_3 frequencies inferred by Brafman and Mitra[13] (Table 1) were 286 cm^{-1} and 72 cm^{-1} ; the latter is in excellent agreement with our 73 cm^{-1} , but the former is somewhat beyond our experimental uncertainties. Aside from these observations, the zone boundary frequencies inferred from various two-phonon Raman data can be compared to the neutron values. Some of these data agree well for one or more points, but there is no set of frequencies from a single experiment which provides a self-consistent set in good agreement with the neutron data.

The dispersion curves of Fig. 2 were obtained from a general 'valence shell model' (VSM) with adjustable parameters fixed by least squares fitting to the neutron data in the Δ and Λ directions.

As in other dipole models[17,19], the dynamical matrix for the VSM includes a short range term and a long range coulomb term:

$$D\left(\frac{q}{kk'}\right) = \sum_{\mu} \phi^{SR}(\rho_{kk'}^{\mu}) e^{iq \cdot x(l',k')} + y_k y_{k'} \sum_{\mu} \phi^c(\rho_{kk'}^{\mu}) e^{iq \cdot x(l',k')} \quad (1)$$

The indices k, k' range over the two cores and two shells of the primitive cell. y_k is the charge assigned to the k^{th} element (core or shell).

The charge on the Zn ion (core plus shell) is Ze . $\phi^{SR}(\rho_{kk'}^{\mu})$ denotes the short range part of the force constant tensor connecting the k^{th} element in the 0^{th} cell with the k'^{th} element in the l'^{th} cell, while $\phi^c(\rho_{kk'}^{\mu})$ is the corresponding coulombic part. $x(l',k')$ represents the equilibrium position of the element concerned (as usual, the equilibrium positions of the shell and core belonging to a given ion are taken to be the same). The coulomb matrices [24] are taken from the tabulation of Kaplan and Sullivan[25] for zincblende structures. In view of the fact that the polarizability tensor is isotropic for the zincblende structure, the shell and core of the same ion are taken to interact isotropically. Interionic forces are assumed to act only through shell-shell coupling. This shell model with tensor forces out to second neighbors requires ten short range parameters and five 'electric' parameters (two shell charges, two core-shell coupling constants, and Z). The short range parameters are reduced to seven by expressing the short range interaction potential (in the harmonic approximation) in valence form:

$$\begin{aligned} \Phi = & \left\{ \phi_0 + \frac{\lambda}{2} \sum_{1-2} (\delta r_{ij})^2 + \frac{\mu}{2} \sum_{1-1} (\delta r_{ik})^2 \right. \\ & + \frac{\nu}{2} \sum_{2-2} (\delta r_{ji})^2 + \frac{k_\theta}{2} r_0^2 \sum_{2-1-2} (\delta \theta_{ij})^2 \\ & + \frac{k'_\theta}{2} r_0^2 \sum_{1-2-1} (\delta \theta_{ijk})^2 + \frac{k_{r\theta}}{2} r_0 \sum_{2-1-2} \delta \theta_{ij} \delta r_{ij} \\ & \left. + \frac{k'_\theta}{2} r_0 \sum_{1-2-1} \delta \theta_{ijk} \delta r_{ij} \right\} \quad (2) \end{aligned}$$

Here $r_0^2 = 3a^2/4$, where a is the lattice constant. The summations are taken over the entire crystal. δr_{ij} represents the change in bond length of the atom pair (ij) . $\delta \theta_{ij}$ is the change in the angle formed by atoms l, i, j with i at the vertex. Further, the valence

coefficients are as follows:

$\lambda = 1-2$	(e.g., $Zn = 1, S = 2$)
$k_\theta = 2-1-2$	bond stretching
$k'_\theta = 1-2-1$	bond angle bending
$k_{r\theta} = 1-2, 2-1-2$	stretch-bend interaction
$k'_{r\theta} = 1-2, 1-2-1$	stretch-bend interaction
$\mu = 1-1$	second neighbor bond stretching
$\nu = 2-2$	second neighbor bond stretching.

The components of the force constant matrices are obtained by the transformation shown in the Appendix. The use of valence parameters is intended to provide relations among the tensor force constants appropriate to covalent bonding. Once the valence parameters have been transformed, our model is a standard shell model. The basic model has twelve disposable parameters: seven valence forces and five electric parameters. We tried several different versions of this model by equating some pairs of parameters and setting others to zero. To further simplify the model, μ and ν were set equal to zero.

As in Ref. [17], the shell charges and the core-shell coupling constants were replaced as parameters by the following:

$$\alpha_i = \frac{y_i^2 e^2}{-4\alpha + k_i} \quad (3a)$$

$$d_i = \frac{-4\alpha y_i}{-4\alpha + k_i} \quad (3b)$$

where k_i is the core-shell coupling constant of the i th ion and α is the diagonal element of the first neighbor force constant matrix (see Appendix). α_i and d_i may be identified as the electronic polarizability and the deformation or mechanical polarizability of the i th ion, respectively.

The dielectric constants ϵ_0 and ϵ_∞ are related to the polarizabilities by the Clausius-Mosotti relations

$$\frac{4\pi\alpha_{\text{pol}}}{3v} = \frac{\epsilon_\infty - 1}{\epsilon_\infty + 2}, \quad \frac{4\pi\alpha(0)}{3v} = \frac{\epsilon_0 - 1}{\epsilon_0 + 2}$$

where v is the volume of a primitive unit cell, $\alpha_{\text{pol}} = \alpha_1 + \alpha_2$, and

$$\alpha(0) = \alpha_{\text{pol}} + \frac{(Z - d_2 + d_1)^2 e^2}{-4\alpha - e^2(d_1^2/\alpha_1 + d_2^2/\alpha_2)}. \quad (4)$$

When all the above quantities and the zone center optic frequencies are computed from the model, the LST relation is obeyed.

The least squares program used the following experimental measurements: neutron determined phonon frequencies in the Δ and Λ directions, Nilsen's [11] zone center optic frequencies, the static dielectric constant and the piezoelectric constant. The latter two were used because the relation [26] between them and the two elastic constants, C_{44}^E and C_{44}^D , which are related to the transverse acoustic (001) branch and the middle acoustic (110) branch, respectively, resulted in a poor fit to that Σ branch:

$$C_{44}^D = C_{44}^E + \frac{4\pi}{\epsilon_0 + 2} e_{14}^2. \quad (5)$$

e_{14} tends to be an order of magnitude too large when computed from shell model parameters unless it is included in the fitting process.

The lack of LO data seriously hindered the fitting process. Often a good fit to the available data in the Δ and Λ directions was a poor fit to the Σ data, and the remaining LO branches were unreasonable. This is because different branches require different combinations of the parameters, and lack of data removes some of the constraints on the parameters. An attempt to overcome this difficulty was made by inventing two sets of LO data. In one, $\omega_{LO(X)}$ was given the value $\sqrt{(M_1/M_2)}$

*It is shown in Ref. [17] that in general the relation $\alpha_{\text{pol}} = \sum_i \alpha_i$ is very closely, but not identically, true unless shell-shell interactions vanish.

$\omega_{LA(X)}$ because this relation holds rather well in GaAs and GaP. $\omega_{LO(L)}$ was located arbitrarily. The second set of LO data was created by drawing relatively flat LO dispersion curves in the Δ and Λ directions.

The first set results in poor fits with the VSM but gave a reasonably good fit with a six parameter rigid ion model derived from the ten parameter VSM by setting the α_i 's and d_i 's equal to zero. The results of this model are shown by dotted lines in Fig. 2. The best general fit was obtained with the ten parameter VSM using the second set of LO frequencies. The dispersion curves for this model are shown as solid lines in Fig. 2.

Table 3 lists the parameters for the two models in Fig. 2 and the physical quantities computed from them. Z^* is identified with the Szigeti effective charge. In the shell model formulation of Ref. [17], this is

$$Z^* = Z - d_2 + d_1 \quad (6a)$$

$$\mu(\omega_{LO}^2 - \omega_{TO}^2)_{q=0} = \frac{4\pi}{v} Z^{*2} e^2 \frac{(\epsilon_\infty + 2)^2}{9\epsilon_\infty} \quad (6b)$$

where μ is the reduced mass and all quantities are computed from the model. ζ^2 is the measure of goodness of fit:

$$\zeta^2 = \frac{1}{4N} \sum_{l=1}^N \frac{(\omega_{cl}^2 - \omega_{ml}^2)^2}{\omega_{ml}^2} \quad (7)$$

where ω_{ml} and ω_{cl} are the l th measured and calculated frequencies, respectively.

4. DISCUSSION

Several other models were calculated in addition to the two shown in Fig. 2, but they were less successful. The rigid ion model had only one minimum of ζ^2 for each set of LO data. When polarizability was introduced, several minima were found. Adding the polarizability and dielectric constants decreased the number of minima for the shell models. Three minima were found with both ions polarizable. One of these had $Z \approx -1.5$. The other two had $Z \approx 0.1$, but differed in the relative magnitudes of α_1 and α_2 . The model chosen had $\alpha_1 > \alpha_2$. While this model

Table 3. Fitted parameters and physical constants

Quantity	10 parameter VSM	6 parameter rigid ion	Measured
λ	12.67×10^4 dynes/cm	10.11×10^4	
k_θ	0.48×10^4	-0.75×10^4	
$k_{\tau\theta}$	0.22×10^4	1.08×10^4	
k'_θ	0.23×10^4	1.11×10^4	
$k'_{\tau\theta}$	-0.13×10^4	-0.05×10^4	
Z	0.08	-0.89	
α_1	4.99×10^{-24} cm ³	0	
α_2	0.68×10^{-24} cm ³	0	
d_1	-1.08	0	
d_2	-0.23	0	
C_{11}	10.42×10^{11} dynes/cm ²	7.78×10^{11}	10.46×10^{11} (30)
C_{12}	6.48×10^{11}	3.29×10^{11}	6.53×10^{11} (30)
C_{44}	3.228×10^{11}	4.93×10^{11}	4.613×10^{11} (30)
C_{44}	3.253×10^{11}	5.34×10^{11}	4.643×10^{11} (30)
e_{14}	4.4×10^4 esu/cm ²	10.50×10^4	4.41×10^4 (30)
Z^*	0.77	0.89	0.88
ϵ_0	8.37	1.61	8.3
$\alpha(0)$	6.7×10^{-24} cm ³	1.6×10^{-24}	6.7×10^{-24}
α_{tot}	5.67×10^{-24} cm ³	0	5.40×10^{-24}
ζ^2	0.784	1.69	

had this one apparently unphysical feature, it was the best in all other respects.

The rigid ion model is a good fit to our ZnS data in spite of the unphysical electric properties associated with the rigid ion scheme. The external constants predicted by the model parameters are reasonable. In particular, the good value of the Szigeti effective charge is well predicted due to a numerical coincidence. Rearranging expression (6b)

$$Z^{*2} = \frac{\mu\nu}{4\pi e^2} (\omega_{LO}^2 - \omega_{TO}^2)_{q=0} \left[\frac{9\epsilon_\infty}{(\epsilon_\infty + 2)^2} \right]. \quad (8)$$

In the rigid ion model, $\epsilon_\infty = 1$ and the factor in brackets is unity. However, it will also be one for $\epsilon_\infty = 4$. In ZnS, $\epsilon_\infty = 5.4$ so that the factor is 0.89. Thus, if the zone center frequencies were perfectly fit, the parameter Z of the rigid ion model would be 6 per cent higher than the value of Z^* as computed from experimental values for ω_{LO} , ω_{TO} , and ϵ_∞ . That the present rigid ion model Z is closer than 6 per cent is due to the inexact fit to the zone center frequencies.

We chose the simplest valence shell model possible to attain a reasonable fit to the available data and external constants. We felt that only second neighbors should be included and chose those valence forces which would seem to be predominant. The worth of the model is demonstrated by the fairly good fit to the upper and middle acoustic branches in the Σ direction. These are governed by the antisymmetric matrix components r_2 and ρ_2 (see Appendix) which do not appear in the Δ and Λ directions. Thus, the model combines economy of parameters with a physical picture of the nature of tetrahedrally bonded materials with the sphalerite structure. Additions to this model could include higher neighbors, nonzero μ and ν and other than shell-shell interactions. The model can be extended to include materials with the wurtzite or diamond structures.

The piezoelectric problem

The piezoelectric constant e_{14} is computed in the shell model for materials with the zincblende structure by the following formula [26]:

$$e_{14} = \frac{\epsilon_0 + 2}{6\nu} eZa \left(-\frac{\beta}{2\alpha} + 5.02884\alpha(0)/\nu \right) \quad (9)$$

where a is the lattice constant and α and β are the diagonal and off-diagonal elements of the nearest neighbors force constant matrix (see Appendix).^{*} For all such materials, e_{14} has a magnitude of the order of 4×10^4 esu/cm². As noted earlier, the computed e_{14} tends to be an order of magnitude too large in the shell model if Z is of order 1. Fitting to e_{14} requires that either Z be small (~ 0.1) or the quantity in the parentheses be small.[†]

All of the shell model calculations for materials with the zincblende structure [4, 5] exhibit small Z 's, as does our chosen ten parameter model. This suggests that: (1) the small Z is indeed significant in materials with the zincblende structure; or (2) there is a fundamental error in the shell model computation of dipole effects and piezoelectricity in such materials. The first of these implies that all such materials have about the same degree of covalent bonding and that covalent bonding is predominant. However, one would expect the degree of covalent bonding to vary considerably from compound to compound [28]. Phillips [28] takes a different approach to piezoelectricity. The sign and magnitude of the piezoelectric constant are determined, in his view, by the competition between ionic polarization and charge redistribution. He explains the apparently opposite signs of e_{14} for II-VI and III-V compounds on this basis.

^{*}Though (9) applies to the present model, it must be modified [26, 27] to apply to more general shell models. In some cases, there is a term which is not proportional to Z . This term is generally small, so that the conclusions here are not invalidated.

[†]For a discussion of this problem, see Ref. [27].

The relative ease with which rigid ion models compute a reasonable ϵ_{14} compared to shell models suggests that the shell model treatment of electronic polarizability is defective in that it overestimates the piezoelectric effect. The rigid ion model cannot make such an overestimate since it ignores electronic polarization. The reason may be found in the observation that the shell model treats electronic and ionic polarization but embodies nothing resembling charge redistribution. The latter could be included in several ways, among them is the implementation of an exchange charge model[29]. Such ideas are being pursued.

REFERENCES

1. BROCKHOUSE B. N. and IYENGAR P. K., *Phys. Rev.* **111**, 747 (1958); BROCKHOUSE B. N., *Phys. Rev. Lett.* **2**, 256 (1959); BROCKHOUSE B. N. and DASANNACHARYA B. A., *Solid State Commun.* **1**, 205 (1963).
2. WARREN J. L., WENZEL R. G. and YARNELL J. L., *Inelastic Scattering of Neutrons*, Vol. I, p. 361. IAEA, Vienna (1965).
3. DOLLING G., *Inelastic Scattering of Neutrons in Solids and Liquids*, Vol. II, p. 37. IAEA, Vienna (1963).
4. WAUGH J. L. T. and DOLLING G., *Phys. Rev.* **132**, 2410 (1963); DOLLING G. and WAUGH J. L. T., *Lattice Dynamics* p. 19, (Edited by R. F. Wallis). Pergamon Press, New York (1965).
5. YARNELL J. L., WARREN J. L., WENZEL R. G. and DEAN P. S., *Neutron Inelastic Scattering*, Vol. I. IAEA, Vienna (1968).
6. FELDKAMP L. A. VENKATARAMAN G. and KING J. S., *Solid State Commun.* **7**, 1571 (1969).
7. We adopt the Ramsdell polytype identification. RAMSDELL L. S., *Am. Mineral.* **32**, 64 (1947). Also VERMA A. R. and KRISHNA P., *Polymerism and Polytypism in Crystals*. John Wiley, New York (1966).
8. DEUTSCH T., *Proc. Int. Conf. Semiconductors*, Exeter, 1962. Institute of Physics and Physical Society, London (1962).
9. MANABE A., MITSUISHI A. and YOSHINAGA H., *Japan J. Appl. Phys.* **6**, 593 (1967).
10. LUCOVSKY G., LIND E. and DAVIS E. A., in *II-VI Semiconducting Compounds*, 1967 International Conference (Edited by D. G. Thomas), W. A. Benjamin, New York (1967).
11. NILSEN W. G., *Phys. Rev.* **182**, 838 (1969).
12. ARGUELLO C. A., ROUSSEAU D. L. and PORTO S. P. S., *Phys. Rev.* **181**, 1351 (1969).
13. BRAFMAN O. and MITRA S. S., *Phys. Rev.* **171**, 931 (1968).
14. VETELINO J. F., MITRA S. S., BRAFMAN O. and DAMEN T. C., *Solid State Commun.* **7**, 1809 (1969).
15. PATRICK L., *Phys. Rev.* **167**, 809 (1968); FELDMAN D. W., *et al.*, *Phys. Rev.* **170**, 698 (1968); FELDMAN D. W., *et al.*, *Phys. Rev.* **173**, 787 (1968).
16. BRAFMAN O. and STEINBERGER I. T., *Phys. Rev.* **143**, 501 (1966).
17. WOODS A. D. B., COCHRAN W. and BROCKHOUSE B. N., *Phys. Rev.* **119**, 980 (1960).
18. NUSIMOVICI M. A. and BIRMAN J. L., *Phys. Rev.* **156**, 925 (1967).
19. NUSIMOVICI M. A. and BALKANSKI M., *Phys. Rev. B-1*, 595 (1970).
20. DOLLING G. and COWLEY R. A., *Proc. Phys. Soc.* **88**, 463 (1966).
21. BROCKHOUSE B. N., in *Inelastic Scattering of Neutrons in Solids and Liquids*, p. 113. IAEA, Vienna (1961).
22. Private communication, Eagle-Picher Industries (Dr. L. Richie); SMITH F. G., *Am. Mineral* **40**, 658 (1955).
23. COOPER M. J. and NATHANS R., *Acta crystallogr.* **23**, 357 (1967).
24. KELLERMAN E. W., *Phil. Trans. R. Soc. London* **238**, 513 (1940).
25. KAPLAN H. and SULLIVAN J. J., *Phys. Rev.* **130**, 120 (1963).
26. COWLEY R. A., *Proc. R. Soc. A-268*, 121 (1962).
27. KAPLAN H., *Lattice Dynamics* (Edited by R. F. Wallis), p. 615. Pergamon Press, New York (1965).
28. PHILLIPS J. C. and VAN VECHTEN J. A., *Phys. Rev. Lett.* **23**, 1115 (1969).
29. DICK B. G., *Lattice Dynamics* (Edited by R. F. Wallis), p. 159. Pergamon Press, New York (1965).
30. BERLINCOURT D., JAFFE H. and SHIAZAWA L. R., *Phys. Rev.* **129**, 1009 (1963).
31. MUSGRAVE M. J. P. and POPLA J. A., *Proc. R. Soc. A-268*, 474 (1962).

APPENDIX

The method of Musgrave and Pople[31] for transforming valence force constants to tensor force constants has been derived for the zincblende structure. The first neighbor force constant matrix for Zn at (0, 0, 0) and S at $a/4(1, 1, 1)$ is:

$$\begin{pmatrix} \alpha & \beta & \beta \\ \beta & \alpha & \beta \\ \beta & \beta & \alpha \end{pmatrix} \quad (\text{A.1})$$

There are three others related by symmetry operations. The second neighbor matrix for Zn at (0, 0, 0) and Zn at $a/2(1, 1, 0)$ is:

$$\begin{pmatrix} \beta_2 & \tau_2 & -\rho_2 \\ \tau_2 & \beta_2 & -\rho_2 \\ \rho_2 & \rho_2 & \gamma_2 \end{pmatrix} \quad (\text{A.2})$$

There are eleven others related by symmetry operations. The second neighbor matrix for S at $a/4(1, 1, 1)$ and S

at $a/4(3, 3, 1)$ is:

$$\begin{pmatrix} b_2 & t_2 & -r_2 \\ t_2 & b_2 & -r_2 \\ r_2 & r_2 & a_2 \end{pmatrix} \quad (\text{A.3})$$

There are eleven others related by symmetry operations.

The transformations are:

$$\alpha = \frac{1}{3} \left\{ -\lambda - 4(k_\theta + k'_\theta) + \frac{4}{\sqrt{2}}(k_{r\theta} + k'_{r\theta}) \right\} \quad (\text{A.4})$$

$$\beta = \frac{1}{3} \left\{ -\lambda + 2(k_\theta + k'_\theta) + \frac{1}{\sqrt{2}}(k_{r\theta} + k'_{r\theta}) \right\} \quad (\text{A.5})$$

$$\gamma_2 = \frac{1}{3}(2k'_\theta - \sqrt{2}k'_{r\theta}) \quad (\text{A.6})$$

$$\rho_2 = \frac{1}{3} \left(k'_\theta + \frac{1}{2\sqrt{2}} k'_{r\theta} \right) \quad (\text{A.7})$$

$$\beta_2 = \frac{1}{3} \left(-4\mu - \frac{k'_\theta}{2} - \frac{k'_{r\theta}}{\sqrt{2}} \right) \quad (\text{A.8})$$

$$\tau_2 = \beta_2 \quad (\text{A.9})$$

$$a_2 = \frac{1}{3}(2k_\theta - \sqrt{2}k_{r\theta}) \quad (\text{A.10})$$

$$r_2 = \frac{1}{3} \left(k_\theta + \frac{1}{2\sqrt{2}} k_{r\theta} \right) \quad (\text{A.11})$$

$$b_2 = \frac{1}{3} \left(-4\nu - \frac{k_\theta}{2} - \frac{k_{r\theta}}{\sqrt{2}} \right) \quad (\text{A.12})$$

$$t_2 = b_2. \quad (\text{A.13})$$



ELASTIC WAVE PROPAGATION IN THE GROUP VB SEMIMETALS

N. G. PACE and G. A. SAUNDERS

Department of Applied Physics and Electronics, The University of Durham,
South Road, Durham, England

(Received 24 August 1970)

Abstract—Elastic wave velocities, particle displacement and energy flux vectors are presented and compared for the three rhombohedral, A7 structure, semimetals arsenic, antimony and bismuth. The wave velocity surfaces are discussed in terms of the crystal symmetry. The pure mode axes in each crystal—knowledge of which is especially useful in experimental pulse echo ultrasonic studies—are given. The elastic wave propagation in antimony and bismuth single crystals is shown to differ not only in degree but also in kind from that in arsenic which exhibits the characteristics expected for a layer-like crystal: high, direction insensitive, ultra-sound velocities in the xy plane and lower velocities along the direction (z) of weakest inter atomic binding. Knowledge of the energy flux and particle displacement vectors has provided a basis for reassessment of the elastic moduli of arsenic at room temperature: $C_{11} = +130.2 \pm 1.0$, $C_{12} = +30.3 \pm 2.1$, $C_{13} = +64.3 \pm 1.1$, $C_{14} = -3.71 \pm 0.52$, $C_{33} = +58.7 \pm 1.0$, $C_{44} = +22.5 \pm 0.5$, $C_{66} = +50.0 \pm 1.6$ in units of 10^{10} dynes cm^{-2} .

1. INTRODUCTION

PLANE elastic waves can be propagated along any direction in an infinitely extended crystal-line medium. In single crystals the phase velocity of sound waves is a function of wave vector; and for any particular direction \mathbf{n} , three waves can propagate. In general these need not be pure longitudinal ($\mathbf{u} \cdot \mathbf{n} = 0$) or pure transverse ($\mathbf{u} \times \mathbf{n} = 0$) waves, although their respective particle displacements \mathbf{u} are orthogonal. Furthermore, only in special crystallographic directions is the energy flow directed along the normal to the planes of constant phase. The mathematical theory of wave propagation in anisotropic media (find a brief review in Ref. [1]) has been used extensively [2-8] to derive the appropriate relationships for phase velocities, particle displacement and energy flux vectors. Emphasis has been placed on cubic and hexagonal crystals, except for a study [8] of the trigonal crystals α -quartz and sapphire. Extension of the problem of plane elastic wave propagation to single crystals of the elements arsenic, antimony and bismuth is the present concern.

Measurement of the attenuation and velocity of ultrasonic waves provides detailed knowledge of the elastic and anelastic properties of solids. A compilation of the orientation dependence of elastic wave propagation in the rhombohedral semimetals will serve as a point of departure for continued ultrasonic studies in these materials. When pulse echo techniques are employed, it is advantageous to choose, whenever possible, crystallographic directions for pure, or failing that, quasi-pure mode propagation: such modes are more readily excited individually, the calculation of the elastic constants from velocity data obtained from such directions is less complex and also the attenuation is more easily analysed. Knowledge of the energy flux vectors is of great value in setting up experiments: then transducers can be sited on samples cut so that the pulses reflected between two parallel crystal faces will not be degraded by wall reflections.

The major aim of this paper is to compile and contrast the orientation dependence of elastic wave propagation in arsenic, antimony and bismuth. By virtue of their unusual

rhombohedral $A7$ crystal structure of space group $D_{3d}^5 (R\bar{3}m)$ —which has been reviewed elsewhere[9]—these elements constitute a unique series. An interesting feature is that while the crystal symmetries are identical, the antimony and bismuth lattices are much less distorted than that of arsenic, which in fact tends towards a layer-like structure. Distinctive differences are found between the characteristics of elastic wave propagation in antimony and bismuth on the one hand and in arsenic on the other.

2. ELASTIC WAVE PROPAGATION IN TRIGONAL CRYSTALS

The generalised form of Hooke's law

$$\sigma_{ij} = C_{ijkl} \epsilon_{kl} \quad (1)$$

relates the components of the stress tensor σ_{ij} to the components of the symmetrical part of the strain tensor ϵ_{kl}

$$\epsilon_{kl} = \frac{1}{2} \left(\frac{\partial u_k}{\partial x_l} + \frac{\partial u_l}{\partial x_k} \right) \quad (2)$$

where u_k and x_k are the k th components of the particle displacement vector and the position vector respectively. Both σ_{ij} and ϵ_{kl} are symmetrical and, as a consequence

$$C_{ijkl} = C_{klij} = C_{iklj} \quad (3)$$

which reduces the number of elastic constants C_{ijkl} in equation (1) from 81 to 36. A further condition is that the strain energy is a function of state and does not depend on the path by which the state is reached; this imposes the symmetry relation

$$C_{ikjl} = C_{jilk} \quad (4)$$

and diminishes the number of independent elastic constants from 36 to 21. Crystal symmetry reduces the number still further; in the case of trigonal crystals belonging to the Laue group $R\bar{1}$, which includes the point

group $\bar{3}m$ of interest here, the C_{ijkl} can be written in matrix notation (replacing 11 by 1, 22 by 2, 33 by 3, 23 and 32 by 4, 13 and 31 by 5 and 12 and 21 by 6) as

$$\begin{vmatrix} C_{11} & C_{12} & C_{13} & C_{14} & 0 & 0 \\ C_{12} & C_{11} & C_{13} & -C_{14} & 0 & 0 \\ C_{13} & C_{13} & C_{33} & 0 & 0 & 0 \\ C_{14} & -C_{14} & 0 & C_{44} & 0 & 0 \\ 0 & 0 & 0 & 0 & C_{44} & C_{14} \\ 0 & 0 & 0 & 0 & C_{14} & C_{66} \end{vmatrix} \quad (5)$$

where C_{66} is equal to $\frac{1}{2}(C_{11} - C_{12})$. The convention used to specify the coordinate system is that used by Cady[10] for quartz, according to which a positive y -axis is chosen to be along the projection of one edge of the primitive rhombohedral cell on the plane perpendicular to the threefold (z) axis (see Fig. 1 of Ref.[9]); the positive x -axis is then chosen along that binary axis which completes the right-handed, orthogonal set. Therefore, suffix 1 refers to the x -axis, 2 to the y -axis and 3 to the z -axis.

In a medium of density ρ and in the absence of body forces, the equations of motion which describe the movement of elastic disturbances are

$$\frac{\partial \sigma_{ij}}{\partial x_i} = \rho \ddot{u}_j \quad (6)$$

Plane waves of the form

$$\mathbf{u} = p \mathbf{u}_0 \exp(i(\omega t - \mathbf{k} \cdot \mathbf{x})) \quad (7)$$

where p is the scalar amplitude of the particle displacement, are a good approximation to those produced in the pulse echo experiments and are taken to be the solutions to the equations (6). Substitution of solutions of this type into the equation of motion (6) yields three equations

$$\begin{aligned} (L_{11} - \rho v^2) u_{01} + L_{12} u_{02} + L_{13} u_{03} &= 0 \\ L_{12} u_{01} + (L_{22} - \rho v^2) u_{02} + L_{23} u_{03} &= 0 \\ L_{13} u_{01} + L_{23} u_{02} + (L_{33} - \rho v^2) u_{03} &= 0 \end{aligned} \quad (8)$$

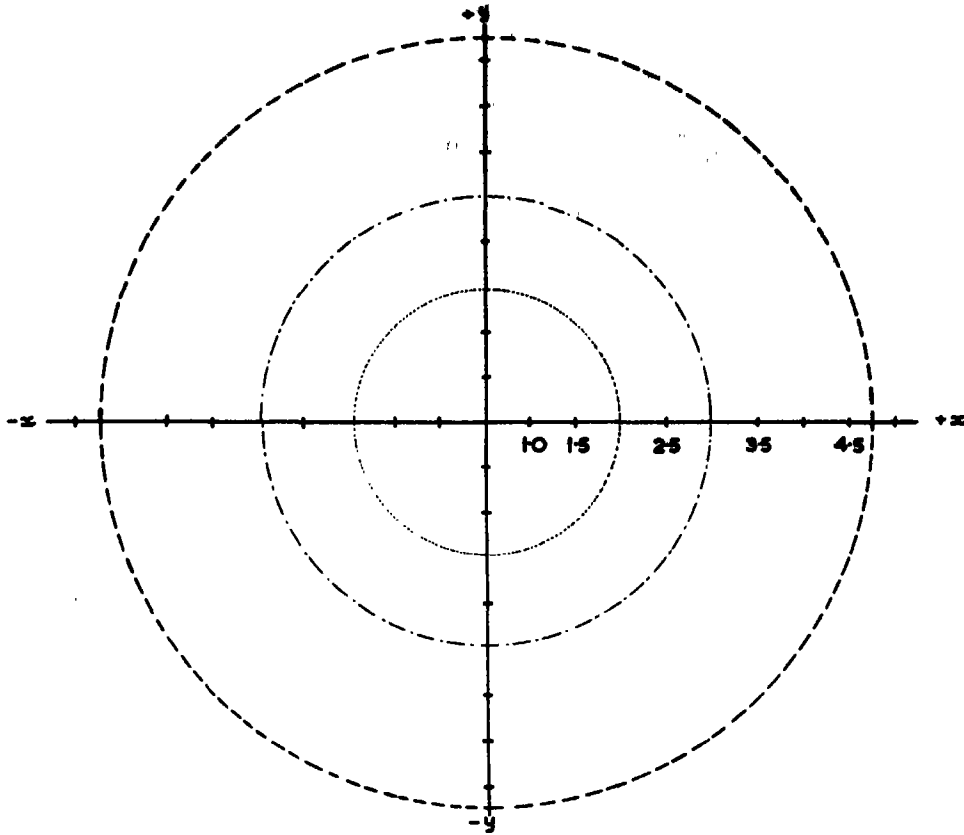


Fig. 1(a).

where for the *RI* Laue group in particular

$$\begin{aligned}
 L_{11} &= n_1^2 C_{11} + n_2^2 C_{66} + n_3^2 C_{44} + 2n_2 n_3 C_{14} \\
 L_{22} &= n_1^2 C_{66} + n_2^2 C_{11} + n_3^2 C_{44} - 2n_2 n_3 C_{14} \\
 L_{33} &= (n_1^2 + n_2^2) C_{44} + n_3^2 C_{33} \\
 L_{12} &= 2n_1 n_3 C_{14} + \frac{1}{2} n_1 n_2 (C_{11} + C_{12}) \\
 L_{13} &= n_1 n_3 (C_{44} + C_{13}) + 2n_1 n_2 C_{14} \\
 L_{23} &= (n_1^2 - n_2^2) C_{14} + n_2 n_3 (C_{13} + C_{44})
 \end{aligned} \quad (9)$$

and (n_1, n_2, n_3) and (u_{01}, u_{02}, u_{03}) are the direction cosines of the propagation and particle displacement directions respectively. The condition that u_{01}, u_{02} and u_{03} are not all zero is

$$\begin{vmatrix} L_{11} - \rho v^2 & L_{12} & L_{13} \\ L_{12} & L_{22} - \rho v^2 & L_{23} \\ L_{13} & L_{23} & L_{33} - \rho v^2 \end{vmatrix} = 0. \quad (10)$$

This is a cubic equation in v^2 . The most straightforward direction for solution is the [001] threefold symmetry (z) direction. Solutions for this direction yield the velocities of a degenerate, pure transverse mode, and a pure longitudinal mode as $(C_{44}/\rho)^{1/2}$ and $(C_{33}/\rho)^{1/2}$ respectively. Any one of the three, indistinguishable x -axes, which are perpendicular to mirror planes, can support three pure modes; but the particle displacement vectors for the two pure transverse modes can only be determined from a priori knowledge of the elastic moduli. This is overcome in practice by rotating the polarisation vector of the driving transducer until two distinguishable transverse wave velocities have been recorded. The angle ϕ , which the particle

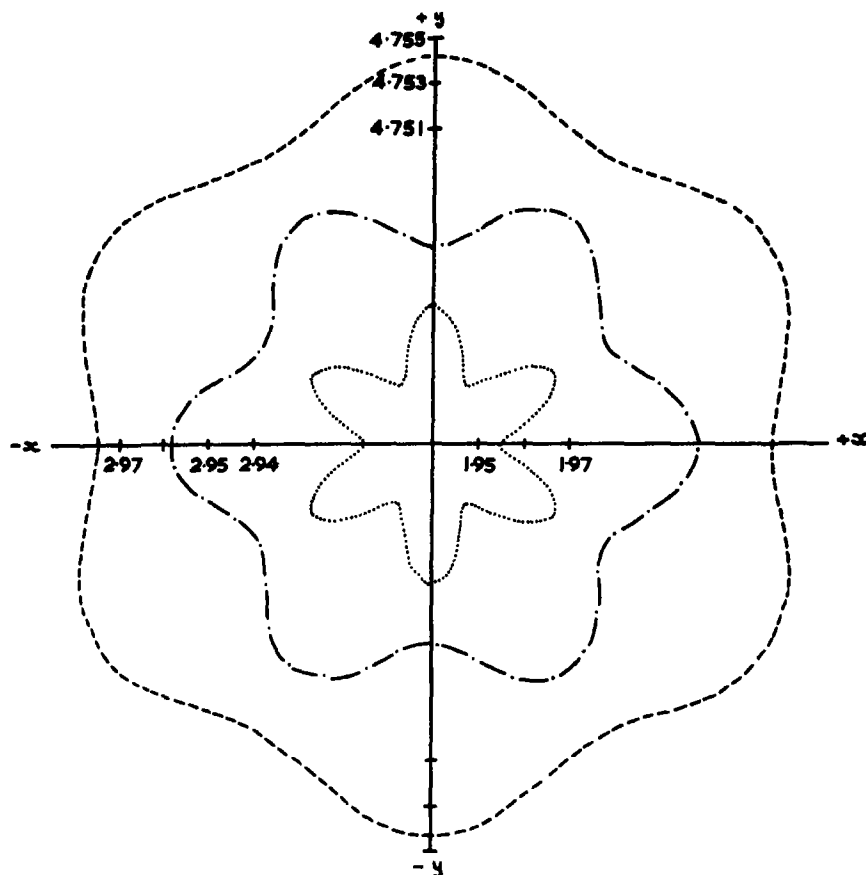


Fig. 1(b).

displacement vector makes with the x - y plane, is given by

$$\tan \phi = \frac{u_{03}}{u_{02}} = \frac{-C_{14}}{C_{44} - \rho v^2}. \quad (11)$$

The two values of ϕ obtained by substituting values of ρv^2 corresponding to the two pure transverse modes, differ by $\pi/2$. The velocities of the three pure modes which can be propagated along an x -axis are related to the elastic moduli by

$$\rho v^2 = C_{11} \quad (12)$$

for the longitudinal mode, and

$$\rho v^2 = \frac{1}{2}[(C_{66} + C_{44}) \pm \{(C_{44} - C_{66})^2 - 4C_{14}^2\}^{1/2}] \quad (13)$$

for the transverse modes.

Therefore, five pure wave velocities—making available all the elastic moduli except C_{13} and the sign of C_{14} —can be obtained from ultrasonic wave propagation along the x and z axes. Inspection of equation (9) shows that C_{13} and the magnitude of C_{14} can be found from knowledge of the velocity in directions for which both n_1 and n_2 are not zero and n_3 is not zero, that is in any direction save for the z -axis and those in the xy plane. The most convenient directions, which embrace these direction cosine requirements, are those which

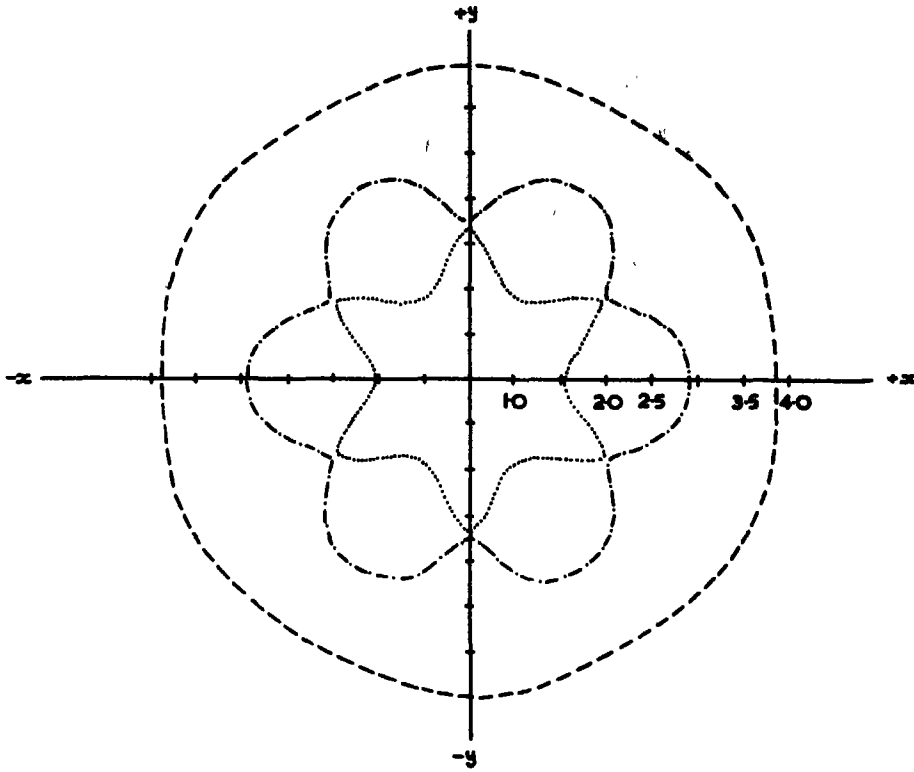


Fig. 1(c).

lie in the yz plane at any angle to the y axis except 0° and integral multiples of $\pi/2$; the sign of C_{14} can be obtained using these propagation directions. Requisite solutions of the secular equation (10) shows that one pure transverse wave can propagate along any direction in the yz plane with a velocity.

$$\rho v^2 = n_2^2(C_{66} - C_{44}) + C_{44} + 2n_2n_3C_{14}. \quad (14)$$

The remaining two orthogonal solutions are quasi-pure modes with velocities

$$\begin{aligned} \rho v^2 = & n_2^2(C_{11} - C_{33}) + C_{44} + C_{33} - 2n_2n_3C_{14} \\ & \pm [(n_2^2(C_{11} - C_{33}) + C_{44} + C_{33} \\ & - 2n_2n_3C_{14})^2 + 4\{(n_2n_3(C_{44} + C_{13}) \\ & - n_2^2C_{14})^2 - (n_2^2C_{11} + n_3^2C_{44} \\ & - 2n_2n_3C_{14})(n_2^2(C_{44} - C_{33}) + C_{33})\}]^{1/2} \end{aligned} \quad (15)$$

where the positive sign corresponds to the

quasi-longitudinal wave and the negative sign to the quasi-transverse wave. For one particular direction in the yz plane in addition to the z -axis, all the modes are pure; this occurs when

$$\frac{n_3}{n_2} = \frac{n_2^2C_{11} + n_3^2C_{44} - 2n_2n_3C_{14} - \rho v^2}{n_2^2C_{14} - n_2n_3(C_{44} + C_{13})} \quad (16)$$

where v is the velocity of the longitudinal mode along this direction.

The solution of equation (10) for a general direction in the xy plane are the solutions of the cubic equation

$$\rho^3 v^6 + A \rho^2 v^4 + B \rho v^2 + C = 0 \quad (17)$$

where $A = -(L_{11} + L_{22} + L_{33})$

$$\begin{aligned} B = & (L_{11}L_{22} + L_{11}L_{33} + L_{22}L_{33} \\ & - L_{23}^2 - L_{12}^2 - L_{13}^2) \end{aligned}$$

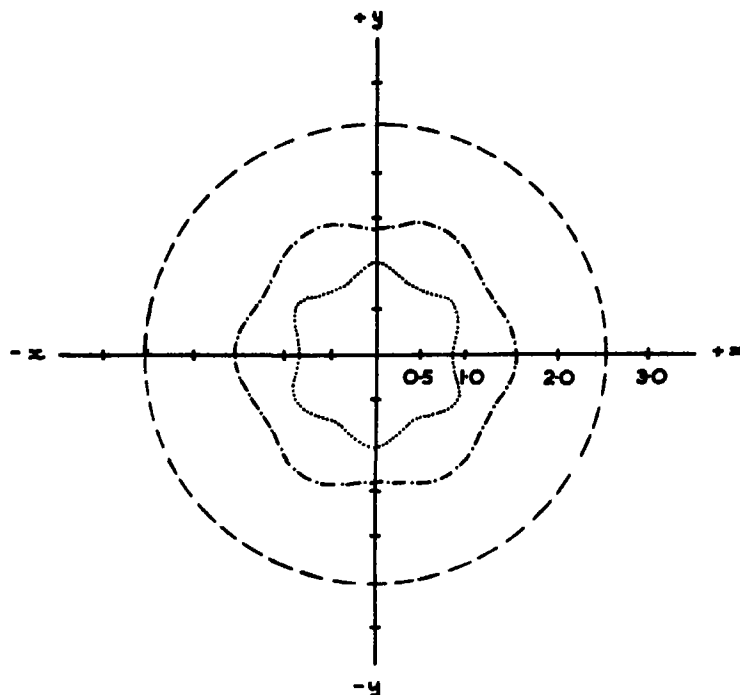


Fig. 1(d).

Fig. 1. The xy cross section of the velocity surfaces of arsenic ((a) and (b)), antimony (c) and bismuth (d) where ---- refers to the quasi-longitudinal wave, - · - · - · - to the fast quasi-transverse wave and · · · · · to the slow quasi-transverse wave. The sections (a), (c) and (d) are drawn to the same scale; the origin of section (d) is zero whereas that for (a) and (c) is 0.5×10^8 cm. sec⁻¹. The Section (b) is (a) drawn on an extended scale. Units are 10^8 cm. sec⁻¹.

$$C = (L_{11}L_{23}^2 + L_{12}^2L_{33} + L_{13}^2L_{22} - L_{11}L_{22}L_{33} - 2L_{12}L_{13}L_{23})$$

with $n_3 = 0$. Similarly, the solutions of equation (10) for the xz plane are solutions of (17) with $n_2 = 0$. Using these solutions to the secular equation, the wave velocities in the xy , yz and zx planes have been computed for all three elements.

3. EXPERIMENTAL DETAILS

To obtain a complete set of elastic constants C_{ijkl} for trigonal crystals, one of the propagation directions required must not be along a major crystallographic axis x , y or z . Without access to such a direction, neither C_{13} nor the sign of C_{14} is available. To this end,

propagation in the yz plane is most convenient. To improve the accuracy of a set of elastic constant measurements, a valuable procedure is to use a predetermined set to estimate first the wave velocity surfaces and the energy flux vectors associated with elastic waves propagating in various directions. This procedure has been followed here. A previously determined [9] elastic constant set was used to establish the overall features of the phase velocities, the directions of the energy flux, and the particle displacement vectors. On this basis, further velocity measurements were founded. In particular to minimise the effects of the quasi-pure mode propagation, the aim was to get close to the pure mode direction in the yz plane (which was found to be 14.5°

from the +y axis in the +y + z quadrant from the data in Ref.[9]).

The measurements were made by the procedure detailed in Ref.[9] on arsenic single crystals grown by the vapour phase method [11] from 99.9995 per cent purity arsenic. The state of perfection of these crystals and their electrical properties have been discussed elsewhere [12]. For the A7 crystal structure, the tensor component signs can depend upon the definition of a right-handed (+x, +y, +z) axial set in the particular specimen; the sign of C_{14} is the only elastic tensor component so affected in this Laue group. The definition of this axial set and its assignment in the arsenic crystals used here can be found in Ref.[9]. The experimental wave velocities obtained for arsenic are given in Table 1.

An extensive survey of the effect of experimental errors in the velocities on the elastic moduli C_{ijkl} has been carried out. In brief, the moduli were calculated by a least-mean-

squares method [12] using combinations of velocity errors. A maximum error of ± 1 per cent in measured wave velocities was taken throughout. The errors obtained are quoted with the moduli in Table 2; moduli most affected by velocity errors are C_{12} and C_{14} . In particular the error in C_{14} , much the smallest modulus, is substantial but by no means large enough to change its sign; this is significant because the sign of C_{14} in arsenic is opposite to that in bismuth and antimony. Another important feature is that C_{13} and C_{33} do not have large errors; because of the layer like nature of the arsenic structure these two moduli dominate the components of the Grüneisen tensor [15].

4. CROSS SECTIONS OF THE VELOCITY SURFACES FOR ARSENIC, ANTIMONY AND BISMUTH

The xy, yz and zx cross sections of the velocity surface of each of these three A7

Table 1. Experimental velocities and their relations with the elastic moduli

Solutions of secular equation (10)	Propagation direction	Polarisation direction	Experimental velocity $\times 10^5$ cm sec ⁻¹
$\rho v_1^2 = C_{11}$	100	100	4.79
$\rho v_2^2 = \frac{1}{2}[(C_{66} + C_{44}) + ((C_{44} - C_{66})^2 + 4C_{14}^2)^{1/2}]$	100	001	2.99
$\rho v_3^2 = \frac{1}{2}[(C_{66} + C_{44}) - ((C_{44} - C_{66})^2 + 4C_{14}^2)^{1/2}]$	100	010	1.89
$\rho v_4^2 = C_{33}$	001	001	3.20
$\rho v_5^2 = C_{44}$	001	in xy plane	2.05
$2\rho v_6^2 = \frac{1}{2}(C_{11} + C_{33}) + C_{44} - C_{14} + ((\frac{1}{2}C_{11} - C_{33} - C_{14})^2 + (C_{13} + C_{44} - C_{14})^2)^{1/2}$	0, 1/√2, 1/√2	0, 1/√2, 1/√2	4.32
$2\rho v_7^2 = \frac{1}{2}(C_{11} + C_{33}) + C_{44} - C_{14} - ((\frac{1}{2}C_{11} - C_{33} - C_{14})^2 + ((C_{13} + C_{44} - C_{14})^2)^{1/2}$	0, 1/√2, 1/√2	0, -1/√2, 1/√2	1.38
$\rho v_8^2 = \frac{1}{2}(C_{66} + C_{44}) + C_{14}$	0, 1/√2, 1/√2	100	2.43
$\rho v_9^2 = \cos^2\theta \cdot C_{66} + \sin^2\theta \cdot C_{44} + 2\sin\theta\cos\theta C_{14}$ ($\theta = 14.5^\circ$)	0, 0.9681, 0.2504	100	2.78

Table 2. Elastic stiffness and compliance constants of arsenic, antimony and bismuth

Elastic stiffness constants $\times 10^{10}$ dynes cm^{-2}	Arsenic*	Antimony ⁽¹³⁾	Bismuth ⁽¹⁴⁾
C_{11}	130.2 ± 1.0	99.4	63.22
C_{12}	30.3 ± 2.1	30.9	24.4
C_{13}	64.3 ± 1.1	26.4	24.7
C_{14}	-3.71 ± 0.52	21.6	7.20
C_{33}	58.7 ± 1.0	44.5	38.11
C_{44}	22.5 ± 0.5	39.5	11.30
C_{66}	50.0 ± 1.6	34.2	19.40
Elastic compliance constants $\times 10^{-13}$ $\text{cm}^2 \text{ dyne}^{-1}$			
S_{11}	30.3	16.2	25.74
S_{12}	20.2	-6.1	-8.01
S_{13}	-55.2	-5.9	-11.35
S_{14}	1.67	-12.2	-21.5
S_{33}	137.8	29.5	40.77
S_{44}	45.0	38.6	115.9
S_{66}	20.2	44.6	67.51

*This work and Ref. [9].

structure crystals are presented in Fig. 1 and 2. Each cross section will now be discussed in turn.

(a) *xy cross section*

In crystals of the $R\bar{3}m$ point group the *xy* plane is the plane normal to the threefold inversion axis and, because sound velocities are independent of the sense of direction, the *xy* velocity sections (Fig. 1) exhibit sixfold rotational symmetry about the *z*-axis. For the purpose of direct comparison, the sections (Fig. 1a, 1c, 1d) of all three elements are drawn to the same scale, although the origins differ. On this scale the three velocities in arsenic appear independent of direction. However, expansion of the scale (Fig. 1b) shows that arsenic also obeys the symmetry requirements. Plausibly the lack of sensitivity of the velocities in the *xy* plane in arsenic, in contrast to those in antimony and bismuth, arises from the relatively small control exercised over the atomic motion in the *xy*

plane by the weak binding forces between the double layers [9].

(b) *zx cross section*

The *zx* plane is normal to the *yz* mirror plane and includes both the binary *x*-axis and the *z*-axis. In consequence, these velocity cross sections show $2m$ symmetry (Fig. 2a, 2b and 2c). The intersection at the *z*-axis of the two quasi-transverse wave sections occurs because two degenerate pure shear waves can be propagated down the *z*-axis. The relative softness of arsenic along the *z*-axis is manifested in the elongation of the sections along the *x*-axis.

(c) *yz cross section*

Cross sections in the *yz* plane reflect the two-fold rotational symmetry about the *x*-axis (Figs 2d, 2e and 2f). The importance of an unambiguous assignment of the right-handed, orthogonal (+*x*, +*y*, +*z*) axial set to the particular sample under investigation is

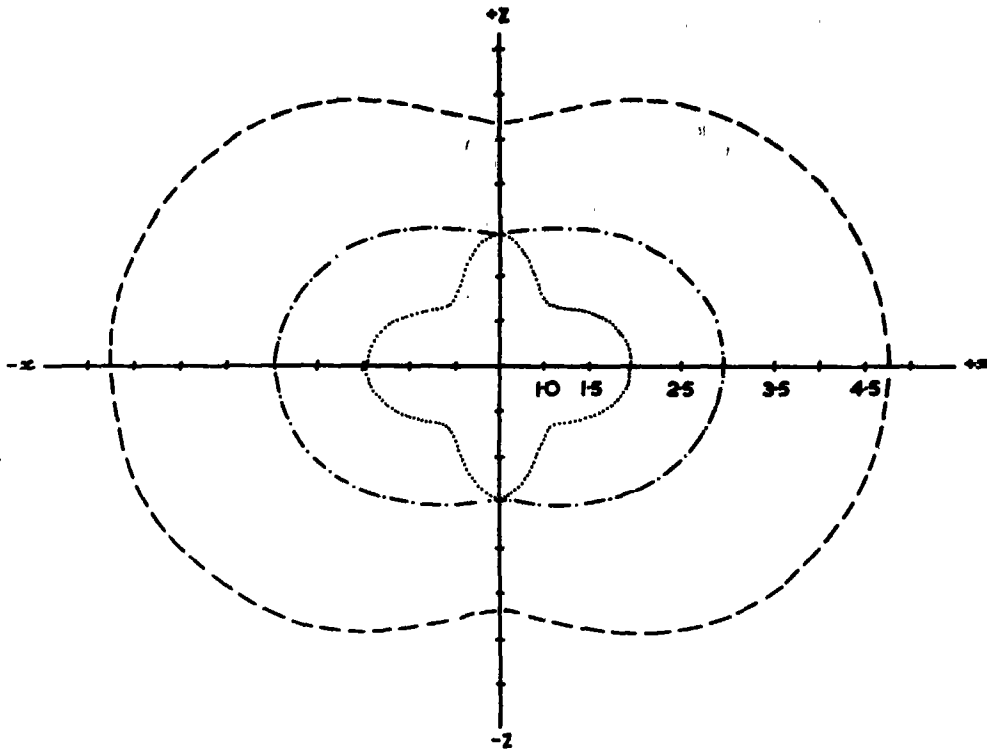


Fig. 2(a).

well demonstrated by these sections: velocities in the $+y+z$ quadrant differ markedly from those in the $-y+z$ quadrant, especially in antimony and bismuth. The arrow labelled A on each section indicates that pure mode direction in the yz plane which occurs in addition to the z -axis itself. For such a direction the particle displacement vectors are either parallel or perpendicular to the propagation direction; in the former case the wave is pure longitudinal and consequently the energy flux vector is also parallel to the propagation direction. We now turn to a detailed discussion of wave propagation in the yz plane.

5. ENERGY FLUX VECTORS FOR DIRECTIONS IN THE yz PLANE

Of considerable interest both experimentally and theoretically are the energy flux vectors associated with elastic wave motion in anisotropic

crystals. For example, in ultrasonic pulse-echo experiments, deviations of energy flow from the propagation direction can result in the wave impinging on the specimen side walls, giving rise to mode conversion and echo train deterioration. Thus, before any detailed studies of anisotropic, anelastic behaviour can be made, the energy flux vectors are required. Love[16] has given the i th Cartesian component of the energy flow P_i as

$$P_i = -\sigma_{ij}\dot{u}_j \quad (18)$$

where \dot{u}_j is the j th component of the particle displacement velocity. The plane wave solution (7) is substituted into equation (18) to give,

$$P_i = \frac{-(p\omega)^2}{2v} C_{ijkl} u_{0j} u_{0k} n_l \quad (19)$$

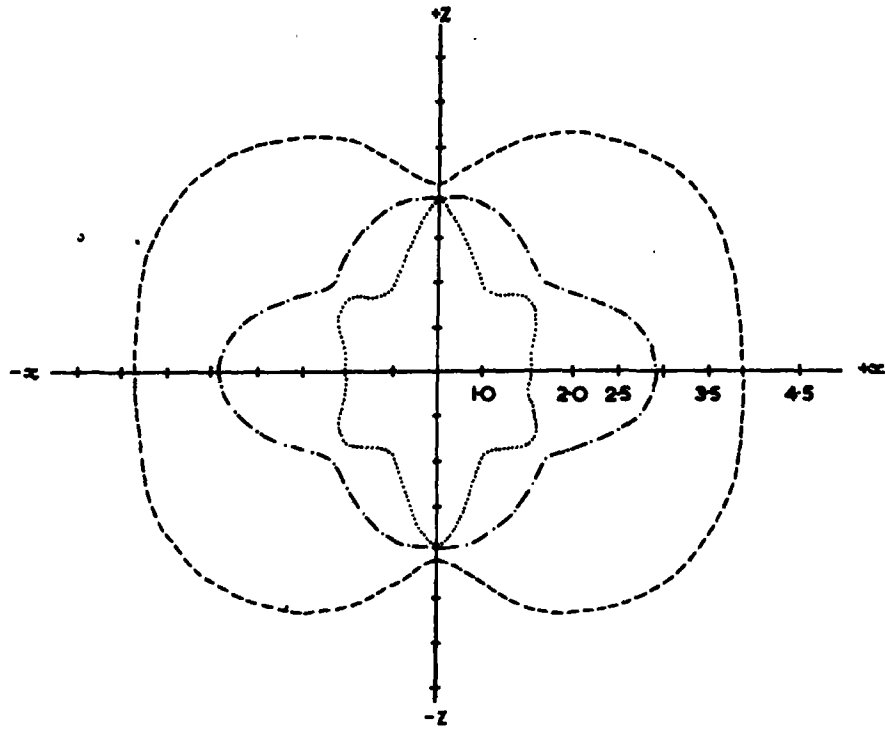


Fig. 2(b).

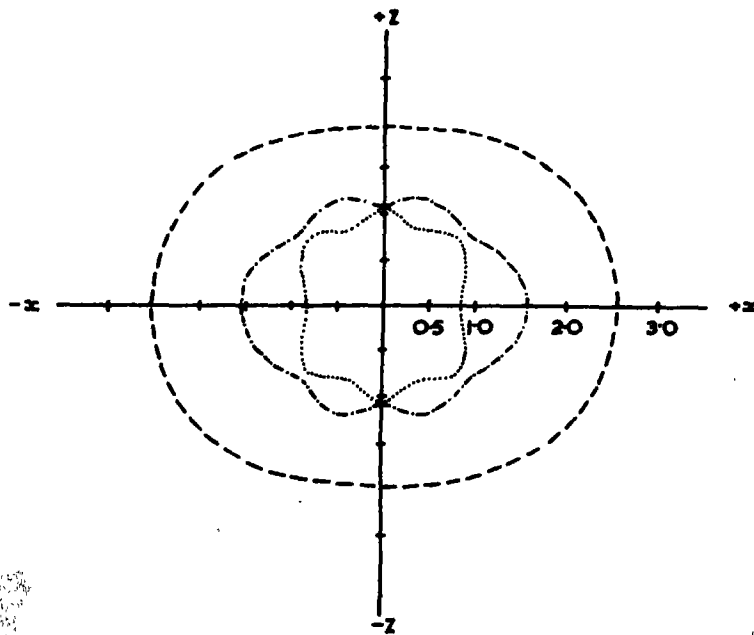


Fig. 2(c).

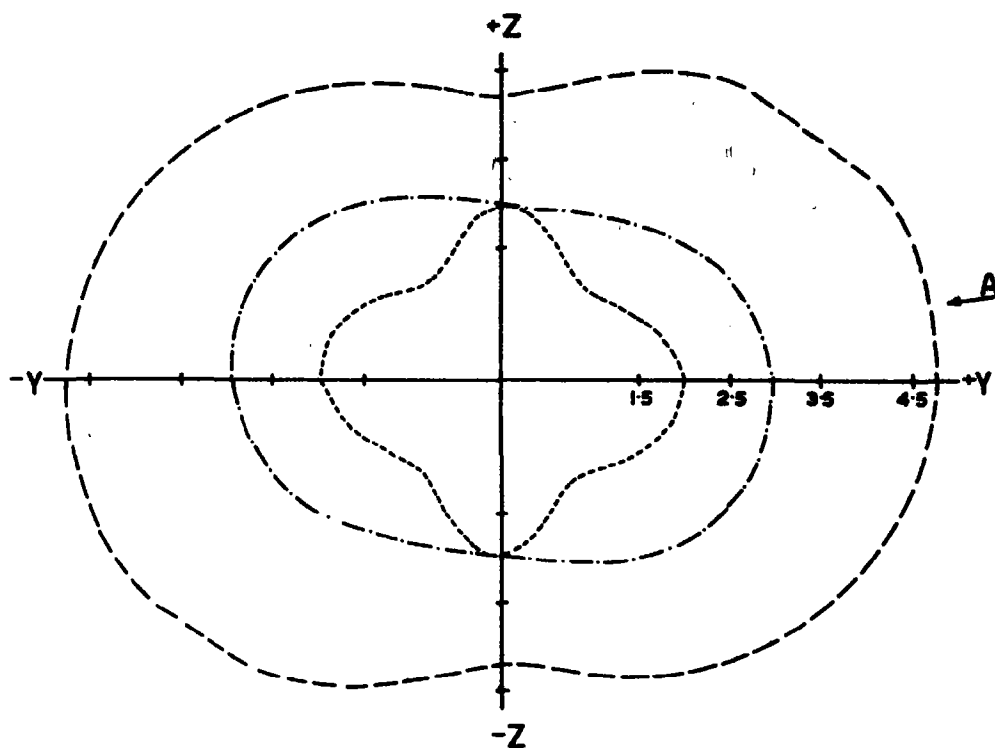


Fig. 2(d).

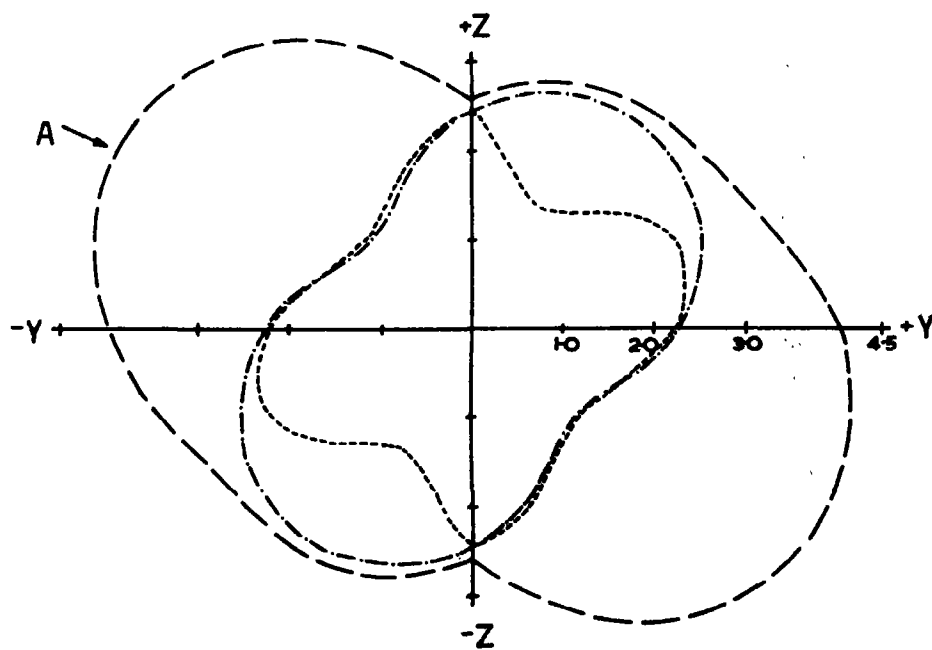


Fig. 2(e).

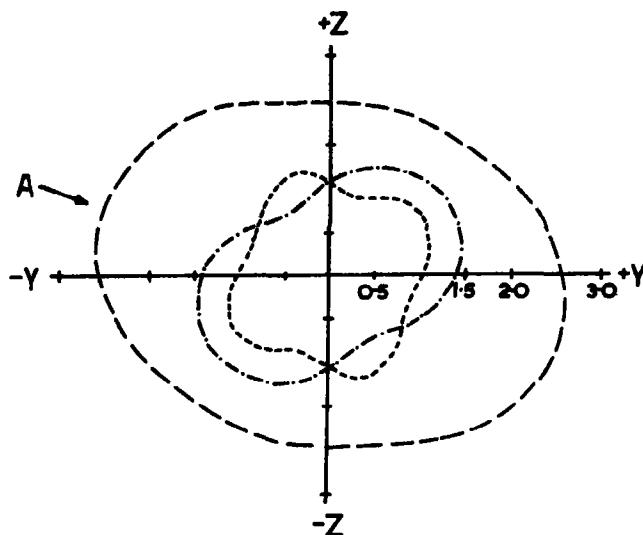


Fig. 2(f).

Fig. 2. The xz and yz cross sections of the velocity surfaces of arsenic ((a) and (d)), antimony ((b) and (e)) and bismuth ((c) and (f)) respectively, where ---- refers to the quasi-longitudinal wave, - · - · - to the fast quasi-transverse wave and · · · · · to the slow quasi-transverse wave. The arrows labelled A on the yz sections indicate a pure mode axis. Units are 10^6 cm. sec $^{-1}$.

where v and n_i are respectively the wave propagation velocity and the propagation direction cosine relative to the i th co-ordinate axis. For propagation in the yz plane in crystals of point group $R\bar{3}m$, it is found that P_1 , that is the energy flux component along the x -axis, is zero for all three modes. Thus, the direction of energy flow is always in the yz plane for any mode propagating along any direction in that plane. Because of this, the direction of energy flow for modes in the yz plane may be described by the angle β the energy flux vector makes with the positive y -axis,

$$\beta = \tan^{-1}(P_3/P_1). \quad (20)$$

For the pure transverse mode which can

propagate along any direction in the yz plane

$$\beta_{T_1} = \tan^{-1} \left(\frac{n_2 C_{14} + n_3 C_{44}}{n_2 C_{66} + n_3 C_{14}} \right). \quad (21)$$

In the case of the quasi-longitudinal and quasi-transverse modes in the yz plane

$$\begin{aligned} P_2 &= (n_2 C_{11} - n_3 C_{14}) u_{02}^2 + (-2n_2 C_{14} \\ &\quad + n_3 \{C_{44} + C_{13}\}) u_{02} u_{03} + n_2 C_{44} u_{03}^2 \\ P_3 &= (-n_2 C_{14} + n_3 C_{44}) u_{02}^2 + n_2 (C_{44} \\ &\quad + C_{13}) u_{02} u_{03} + n_3 C_{33} u_{03}^2. \end{aligned} \quad (22)$$

Thus the angle β_L which the energy flux associated with the quasi-longitudinal mode makes with the positive y axis is

$$\beta_L = \tan^{-1} \left[\frac{-n_2 C_{14} + n_3 C_{44} + n_2 (C_{44} + C_{13}) \tan \phi + n_3 C_{33} \tan^2 \phi}{n_2 C_{11} - n_3 C_{14} + (n_3 (C_{44} + C_{13}) - 2n_2 C_{14}) \tan \phi + n_2 C_{44} \tan^2 \phi} \right]$$

where $\phi (= \tan^{-1}(u_{03}/u_{02}))$ is the direction of particle displacement. The angle β_T , which the energy flux associated with the quasi-transverse mode makes with the positive y -axis is obtained from equation (23) by replacing ϕ by $(\phi + \pi/2)$ since the particle displacement vectors are orthogonal.

For each of the elements arsenic, antimony and bismuth, the particle displacement directions and the energy flux directions associated with the three waves, which can propagate along directions in the yz plane, are plotted in Fig. 3 as angular deviations from the propagation direction vs. the propagation direction. The particle displacement directions for the pure and quasi-pure transverse modes are not shown; the former is always perpendicular to the plane of the diagram and the latter always differs by $\pi/2$ from that for the quasi-longitudinal mode.

In all three elements, the condition for pure longitudinal mode propagation $\mathbf{u} \times \mathbf{n} = 0$

(that is that the propagation direction \mathbf{n} and the particle displacement vector \mathbf{u} are parallel) is obeyed twice in the yz plane. One pure mode axis is the z -axis itself; the other (marked by the arrows A in Figs. 2d, 2e, 2f) is given in Table 3. It is interesting to note that for antimony and bismuth this pure mode direction is much the same but that for arsenic is in a different quadrant. Since one of the transverse waves with propagation vector in the yz plane is always a pure mode, the propagation direction which supports the pure longitudinal mode must by orthogonality carry another pure transverse mode. Whereas the energy flux associated with a pure longitudinal wave is always parallel to the propagation direction, this is not true for pure transverse waves, unless the mode axis has twofold, fourfold or sixfold rotational symmetry or is normal to a plane of reflection symmetry[4]. This is not so here; therefore, the energy flux deviates from this pure mode axis. The angles

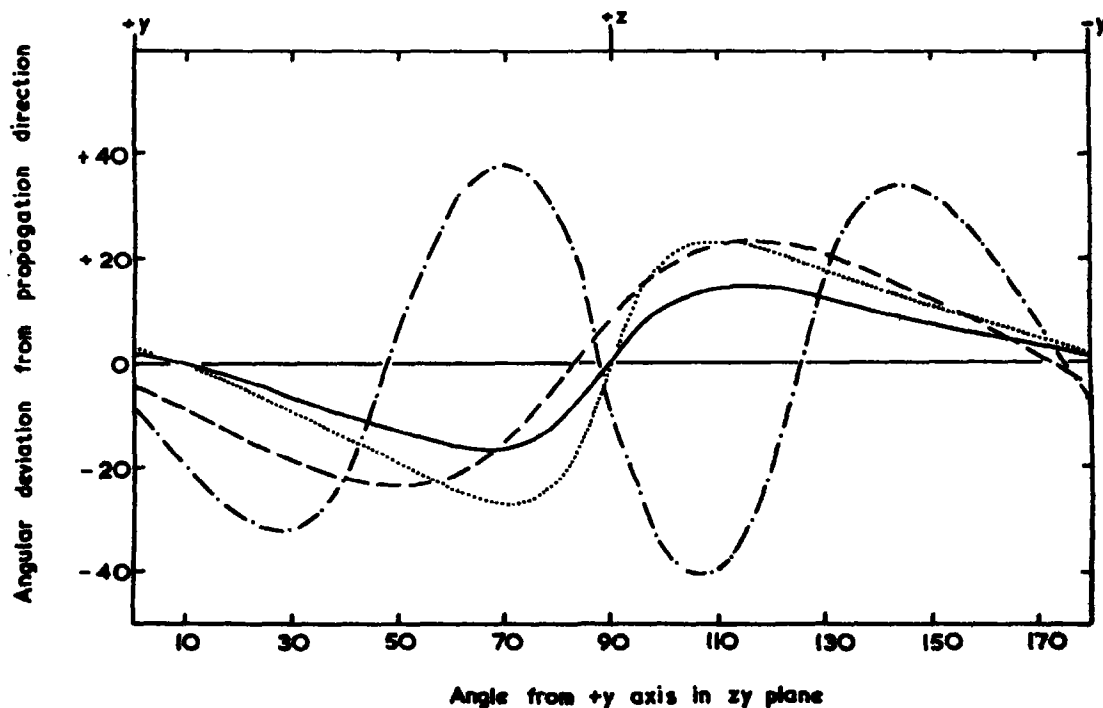


Fig. 3(a).

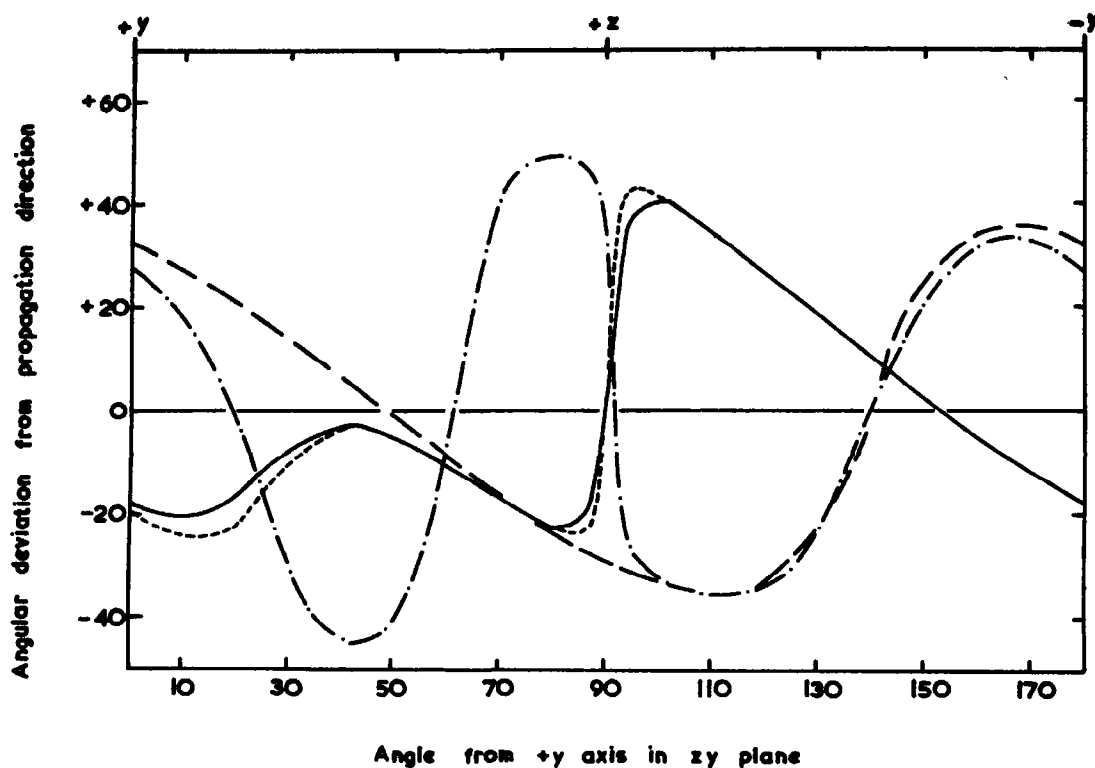


Fig. 3(b).

Table 3. Pure mode direction and energy flux behaviour in the yz plane of arsenic, antimony and bismuth

Pure mode direction Angle from +y axis in yz plane		Arsenic 10°	Antimony 153°	Bismuth 163°
Energy flux deviation from propagation direction				
Pure mode direction	Fast shear	-9.5°	+29°	+30°
	Slow shear	-22°	+25°	+6°
45° to +y axis in yz plane	Fast shear	-23°	+2°	10°
	Slow shear	-17°	-3°	-8.5°
14.5° to +y axis in yz plane	Fast shear	-12°		
	Slow shear	-27°		
	Longitudinal	-2°		
Semi-angle of the cone of internal conical refraction		9°	28.5°	32.5°

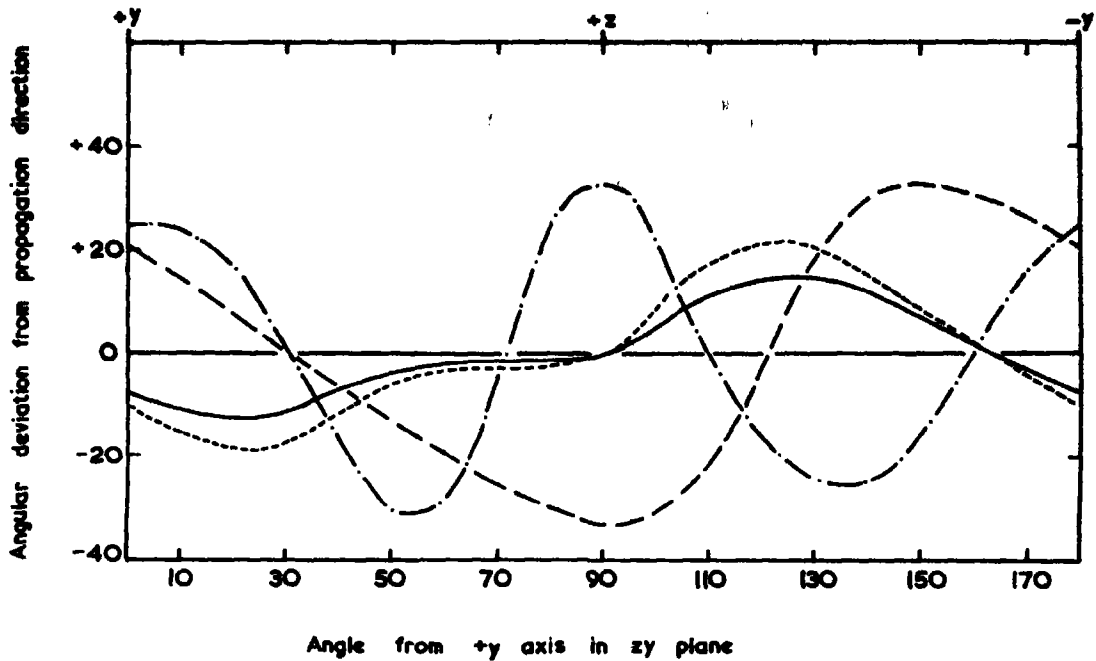


Fig. 3(c).

of deviation for all three elements are collected in Table 3. All previous ultrasonic measurements of the elastic wave velocities of the elements have included either or both the directions at $\pm 45^\circ$ to the z -axis in the yz plane so that a complete set of elastic constants is made available. The deviations of the energy flux from these propagation directions are also given in Table 3; in some cases this deviation is substantial.

An interesting result of the deviation of the energy flux from the propagation direction is the phenomenon of internal conical refraction. Waterman[4] has discussed this in some detail. In the present instance, the degenerate pure transverse waves which can be propagated along the z -axis exhibit internal conical refraction with a cone semiangle given by $\tan^{-1}(|C_{14}|/C_{44})$. This angle is much less in arsenic than in either bismuth or antimony (Table 3). The phenomenon is manifested in Fig. 3 as an equal and opposite deviation at

90° of the energy flux vectors associated with the two transverse waves.

Wave propagation in the xy and zx planes cannot be treated in this straightforward way: examination of equation (19) for these planes shows that, x and z axes excepted, there are three non-zero components of the energy flow.

6. CONCLUSION

The distortion of the crystal lattice of arsenic (rhombohedral angle $\alpha = 54^\circ 10'$) and its resultant layer-like nature in comparison with antimony ($\alpha = 57^\circ 14'$) and bismuth ($\alpha = 57^\circ 19'$) leads to marked differences in its lattice dynamics; mechanical and thermal properties characteristic of layer structures obtain for arsenic but not for bismuth and antimony. Along the trigonal axis arsenic is much the most compressible of the three elements; and the linear compressibility associated with the xy plane is negative in sign: application of

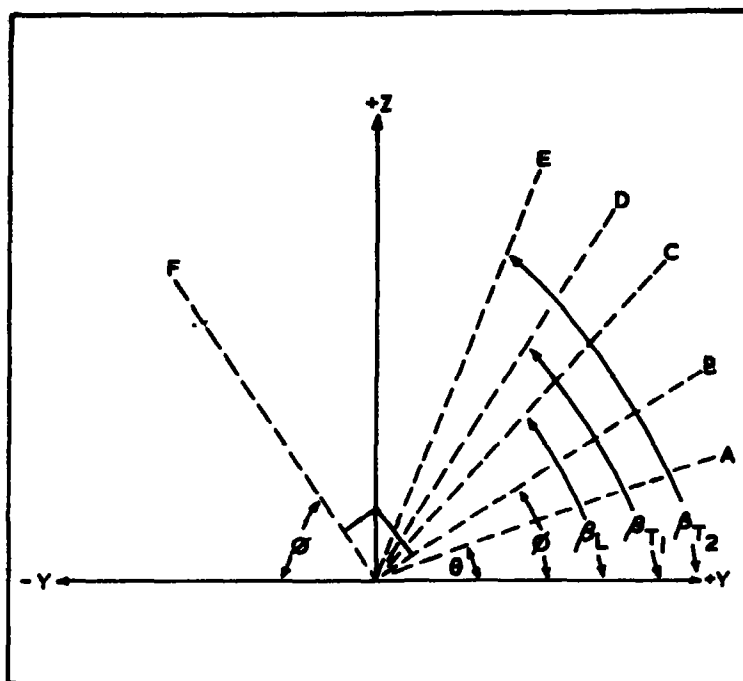


Fig. 3(d).

Fig. 3. The deviations from propagation directions in the yz plane of arsenic (a) antimony (b) and bismuth (c) of the (i) particle displacement associated with the quasi-longitudinal wave ($\phi - \theta$, —), (ii) energy flux associated with the quasi-longitudinal wave ($\beta_L - \theta$,), (iii) energy flux associated with the quasi-transverse wave ($\beta_{T_1} - \theta$, — · — · —) and (iv) energy flux associated with the pure transverse wave ($\beta_{T_2} - \theta$, — — —). The definition of angles is shown in (d).

hydrostatic pressure would result in a large decrease in the separation between double layer planes, while the xy plane would actually enlarge. This has been discussed elsewhere [9] on the basis of a model of weak interlayer binding forces but tight binding within each double layer.

For all three elements the compliance constant S_{13} is negative and S_{33} is positive, but their magnitudes are much larger for arsenic than for antimony and bismuth. If a simple compressional stress σ_{33} is applied (that is on the xy plane in the z -direction), the resultant strains are $\epsilon_{11} = +S_{13}\sigma_{33}$, $\epsilon_{22} = +S_{13}\sigma_{33}$ and $\epsilon_{33} = +S_{33}\sigma_{33}$; thus each material will contract along the z -axis and expand in the xy plane. For arsenic the response to this

applied stress is greater than for antimony and bismuth.

A more striking difference in the behavior of arsenic ensues on a simple compression σ_{11} applied along the x -axis (the y -axis behaviour is similar). Now the resultant strains are $\epsilon_{11} = +S_{11}\sigma_{11}$, $\epsilon_{22} = +S_{12}\sigma_{11}$, $\epsilon_{33} = +S_{13}\sigma_{11}$ and $\epsilon_{23} = \epsilon_{32} = +S_{14}\sigma_{11}$. As S_{11} is positive, each element will contract along the x -axis but S_{12} is positive only for arsenic, so while arsenic contracts also along the y -axis, antimony and bismuth will expand; all three will expand along the z -axis. The sense of the associated shear strain given by the sign of ϵ_{23} is opposite in arsenic to that in antimony and bismuth because the sign of S_{14} differs. The large magnitude of S_{13}

for arsenic is further manifested[15] in the negative sign of the linear compressibility $\beta_{\perp} (=S_{11} + S_{12} + S_{13})$ along directions in the xy plane and in the very small thermal expansion $\alpha_{11} (=0.3 \times 10^{-5} \text{K}^{-1})$ in the xy plane as compared with that $\alpha_{33} (=4.3 \times 10^{-5} \text{K}^{-1})$ along the z -axis.

These differences between relative magnitudes and signs of the elastic constants of arsenic are also reflected in the elastic propagation characteristics which differ from those of antimony and bismuth not only in degree but also in kind.

In general in a layer-type crystal lattice, vibrations will be excited preferentially in the direction of greater linear compressibility on account of the lower vibrational frequencies. Velocities of elastic waves transmitted within the tightly bound layers will be much greater than those of waves transmitted along the direction of weak binding. Thus for arsenic wave propagation velocities are higher in the xy plane than in the z -direction (see Figs. 1 and 2). Strong interatomic binding forces within each double layer control the wave propagation within the xy plane: these waves have velocities which are essentially independent of direction. Hence the close similarity between the xz and yz cross sections (Figs. 2a and 2d) for arsenic.

Acknowledgement—The authors would like to thank Mr. J. M. Farley for many useful discussions.

REFERENCES

1. MUSGRAVE M. J. P., *Rep. Prog. Phys.*, **22**, 74 (1959).
2. GOLD L., *J. appl. Phys.*, **21**, 541 (1950).
3. MUSGRAVE M. J. P., *Proc. R. Soc. A*, **226**, 339 (1954); *Ibid.* **A226**, 356 (1954) *Acta crystallogr. Camb.* **10**, 316 (1957); *Proc. Camb. Phil. Soc.* **53**, 897 (1957).
4. WATERMAN P. C., *Phys. Rev.*, **113**, 1240 (1959).
5. HINTON T. and GREEN R. E., *Trans. AIME* **236**, 439 (1966).
6. HENNEKE E. G. and GREEN R. E., *Trans. AIME* **242**, 1071 (1968).
7. HENNEKE E. G. and GREEN R. E., *J. appl. Phys.*, **40**, 3626 (1969).
8. FARNELL G. W., *Can. J. Phys.*, **39**, 65 (1961).
9. PACE N. G., SAUNDERS G. A. and SUMENGEN Z., *J. Phys. Chem. Solids* **31**, 1467 (1970).
10. CADY W. G., *Piezoelectricity* p. 23 Dover Publications, New York, (1964).
11. JEAVONS A. P., and SAUNDERS G. A. *Brit. J. appl. Phys.*, **2**, 869 (1968).
12. JEAVONS A. P. and SAUNDERS G. A. *Proc. R. Soc. A*, **310**, 415 (1969).
13. EPSTEIN S. and de BRETTEVILLE A. P., *Phys. Rev.*, **138**, A771 (1965).
14. ECKSTEIN Y., LAWSON A. W. and RENAKER D. H., *J. appl. Phys.*, **31**, 1534 (1960).
15. PACE N. G. and SAUNDERS G. A., *J. Phys. C*, **3**, L169 (1970).
16. LOVE A. E. H., *The Mathematical Theory of Elasticity*, p. 177, Dover Publications, New York (1944).

100

EFFECT OF HIGH PRESSURE ON CRYSTALLINE SOLUBILITY IN THE SYSTEM NaCl-KCl

M. C. BHARDWAJ and R. ROY

Materials Research Laboratory, The Pennsylvania State University,
University Park, Penna. 16802, U.S.A.

(Received 28 July 1970)

Abstract—A study of subsolidus phase relations in the system NaCl-KCl has been made up to 20 kbar and 700°C using modified opposed anvil apparatus. It was found that the crystalline solubility in both end members decreased rapidly with pressure and the exsolution 'dome' is raised from 503°C (63 mole % NaCl) at atmospheric pressure to above 710°C (60 mole % NaCl) at 20 kbar. At 503°C and 20 kbar the two equilibrium crystalline solutions contain respectively 9% NaCl and less than 1% KCl. The concentrated crystalline solution phases can be retained metastably by rapid and simultaneous quenching of temperature to dry ice or liquid nitrogen conditions and release of pressure. The experimental results are shown to be in good agreement with the subsolidus phase relations calculated by Fancher and Barsch.

1. INTRODUCTION

THE OBJECTIVE of this study was to explore quantitatively the effect of high pressure on crystalline solubility in a simple binary system. It has been shown that the solubility of solid in liquid decreases as a function of increasing pressure in liquid solutions[1], and in the last decade occasional studies have reported the influence of pressure on various systems with crystalline solutions; none, however, in simple systems which could serve to check simple thermodynamic calculations. It was therefore necessary in such a study to select a system which exhibited extensive crystalline solubility in a simple structure type at atmospheric pressure, and one that would hopefully show substantial change within our experimental conditions. NaCl-KCl was found to be appropriate because it exhibits complete crystalline miscibility above 503°C[2] and almost none at 25°C. The liquidus-solidus minimum in the system lies at 657°C and 50 mole % NaCl[3]. These relations along with the spinodal region are shown in Fig. 1.

Previous studies dealing with some aspects of the pressure dependence of solubility in binary systems include the following:

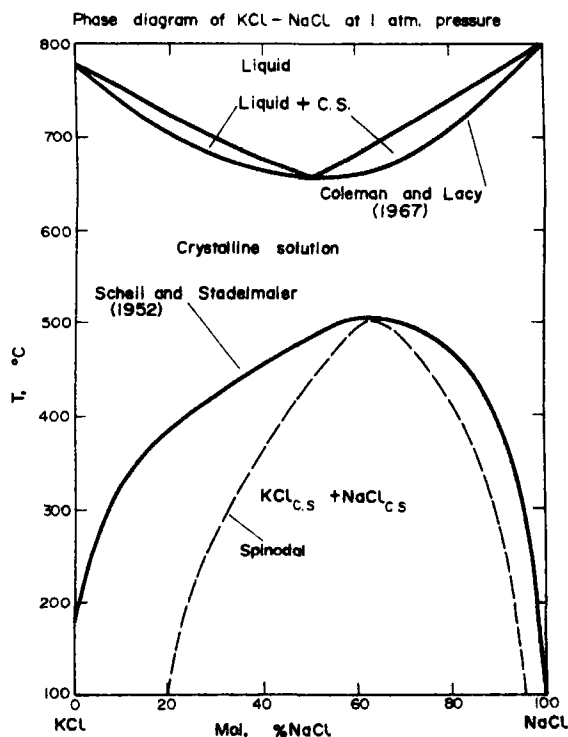


Fig. 1. Phase diagram of system NaCl-KCl.

(a) Bowen and Tuttle[4] showed that the solvus in the system orthoclase-albite rose

by 6°C at 1,000 bars under hydrothermal conditions.

(b) Boyd and England[5] reported the increase of the solubility of Al_2O_3 in $MgSiO_3$ at pressures up to 25 kbars.

(c) Dachille and Roy[6] studied the system Mg_2GeO_4 - Mg_2SiO_4 by hydrothermal and uniaxial high pressure apparatuses and found that substitution of Fe^{2+} for Mg^{2+} markedly increased the maximum silicate content of the spinel solid solution under corresponding pressure and temperature conditions.

(d) Miller, Shafer, Dachille and Roy[7] showed both increase and decrease of solubility in different regions of the system SiO_2 - GeO_2 as a function of increasing pressure.

(e) Jamieson[8] and Darnell[9] studied the system $NaCl$ - KCl (in order to find $CsCl$ type transition in $NaCl$) and the former reported qualitatively the presence of exsolution.

(f) Yagi and Onuma[10] found a decrease in crystalline solubility with increasing pressure in the system $Ca_2MgSi_2O_6$ - $CaTiAl_2O_6$.

(g) Goldsmith and Newton[11] observed the solubility of $MgCO_3$ in calcite at various temperatures as a function of pressure. The measured solubility increase was about 0.12 mole % $MgCO_3$ per kbar in the range of 500–800°C. They further found that their results were conformable to the solubility of $MgCO_3$ in calcite calculated on the basis of regular solution theory.

2. EXPERIMENTAL

The techniques used in this laboratory as developed earlier have been described in considerable detail by Dachille and Roy[12] and by Myers, Dachille and Roy[13].

Premixed mixtures of $NaCl$ and KCl of A.R. quality and fine particle size ($< 44 \mu m$) were pelleted into appropriate nickel rings having diameter to thickness ratios between 18–20. The sample wafers were sandwiched

between Pt-10Rh discs 0.0015 in. thick. All experiments above 500°C were performed by placing a nitrogen jacket around the anvil assembly in order to protect it from corrosion. The mixtures were typically held at desired pressure and temperature conditions for times ranging from 6 to 24 hr before quenching.

2.1 Process of quenching

It was found that the usual quenching processes[12] failed to retain the high pressure phases. After much trial and error, the quenching process was modified by simultaneous release of pressure and lowering of temperature by quickly transferring the entire anvil assembly into a dry ice jacket. A schematic representation of this quenching process showing the variation of temperature and pressure with time appears in Fig. 2. The

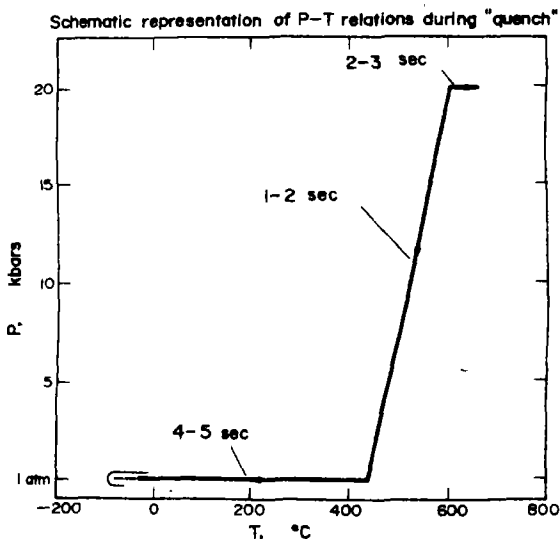


Fig. 2. Schematic representation of P - T relations during quenching process. Times on the diagram indicate the time taken for each step during quenching.

process appears to be crude but was shown to work when checked by using a crystalline solution prepared at atmospheric pressure and processed in this manner. The sample wafers were unaffected by atmospheric water or possible condensation during the quenching

process, as the Pt-10RH discs around the sample ring formed a perfect seal. Subsequently, the samples were always handled in appropriate dry-box conditions.

2.2 X-ray diffraction

Sample preparation for successful phase analysis by X-ray diffraction was also found to be critical for the system investigated. Grinding under ambient conditions immediately caused changes in the metastable phases, especially in the presence of water vapor in the atmosphere. Grinding in the presence of mineral oil did not help. Such observations have also been reported in the studies of Jamieson[8] who used different media for grinding. It was found imperative to avoid grinding altogether to interpret successfully the phase equilibrium in the system NaCl-KCl. The quenched pellet was therefore treated as follows: Holes slightly bigger than the size of the sample pellets were drilled in glass slides. One side of the hole was blocked with bees wax formed into a small cup. The sample pellet with the nickel ring carefully placed in the cup and the latter brought into the plane of the glass slide by gently pushing against another slide and covered with vaseline. This insured an exact location of the surface in the diffractometer.

The undisturbed sample wafers prepared by the process described above were analyzed for phase composition on a Norelco X-ray diffractometer. Sometimes small chips of the samples were also examined by Debye-Scherrer film techniques. The compositions of the crystalline solutions were determined on an ARL electron probe microanalyzer.

When X-ray diffraction showed a single phase (one crystalline solution, (Na, K)Cl) the electron probe showed random distribution of K^+ and Na^+ when two phases (two crystalline solutions, i.e. $NaCl_{c.s.}$ and $KCl_{c.s.}$) were found by X-rays K^+ and Na^+ enrichment in separate domains were detected. X-ray d -spacing shifts were also used to determine the compositions but were found to be less

reliable, probably due to uneven strain and line broadening effects.

On the basis of the reproducibility of the data an estimate of uncertainty would be $\pm 5^\circ C$, ± 3 mole % and ± 5 per cent in pressure, most of which is primarily due to inefficient quenching.

3. RESULTS AND DISCUSSION

The results of the present investigation are shown in Fig. 3. As expected, the crystalline solution limits were found to decrease as a function of pressure and the exsolution dome is raised from $503^\circ C$ at atmospheric pressure to about $710^\circ C$ at 20 kbars with a maximum

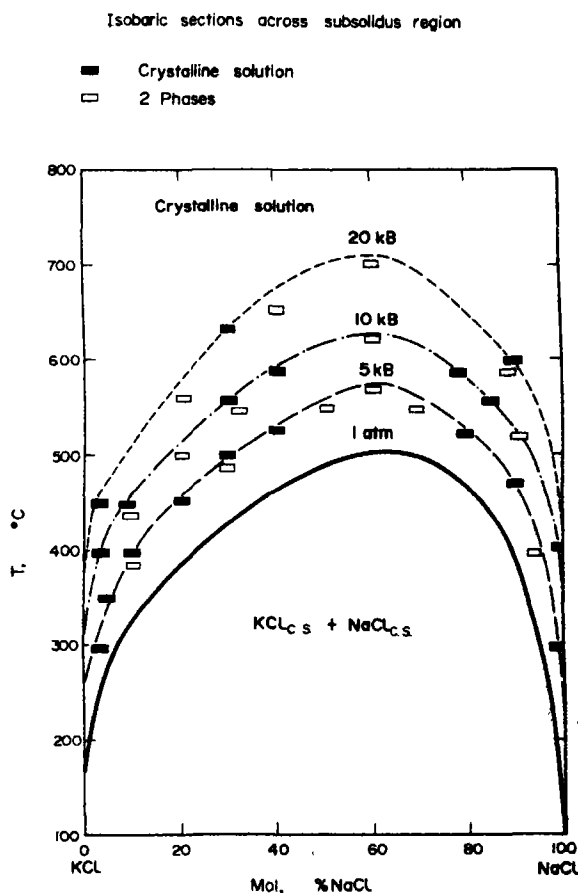


Fig. 3. Isobaric sections across subsolidus region of system NaCl-KCl. ■—one crystalline solution, □—two crystalline solutions.

of approximately 60 mole % NaCl in each case. Thus the solubility of NaCl in KCl at 505°C at atmospheric pressure which is effectively 100 per cent was reduced to about 9 per cent at the same temperature at 20 kbar. A pressure-composition section at 550°C (Fig. 4) shows the solubility at various pressures.

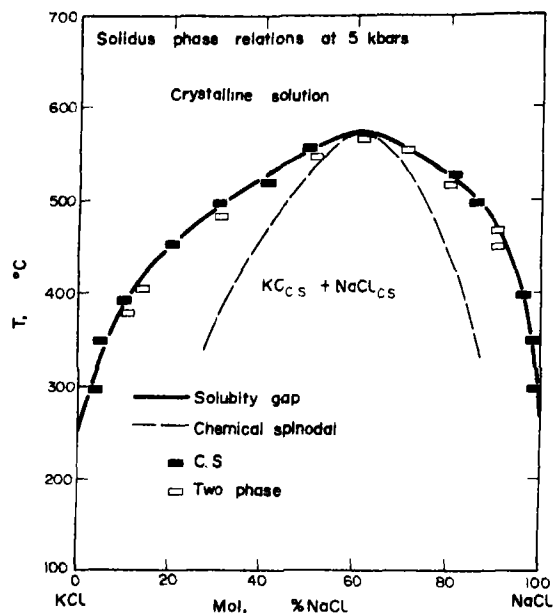


Fig. 4. Solidus phase relations at 5 kbar—solubility gap, ---chemical spinodal (calculated), ■—one crystalline solution, □—two crystalline solutions.

It was noted without any exception that the metastable dilute crystalline solutions were kinetically more favorable for the survival of a single crystalline phase on quenching than the equimolar crystalline solutions at high pressures. This situation is no doubt related to the presence of the chemical spinodal (Fig. 5) calculated after Cook and Hilliard [14]. At higher (equimolar) concentrations during the quenching process the crystalline solution traverses the unstable or spinodal region and thus frequently exsolves. However, more dilute crystalline solutions pass only through the metastable region and can

apparently survive less rigorous quenching. Electron microscopy failed to show any features corresponding to the modulated structures due to spinodal decomposition such as those in the system $\text{SnO}_2\text{-TiO}_2$, as reported by Schultz and Stubican[15].

Recently, Fancher and Barsch[16] have made lattice theoretical calculations of

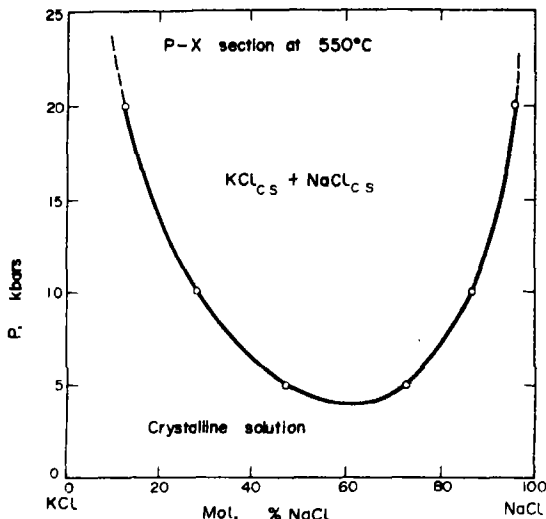


Fig. 5. P-X section at 550°C.

the pressure dependence of the crystalline solubility in certain alkali halide models. On this principle they calculated the pressure dependence for the systems LiBr-LiI and NaBr-NaI up to 100 kbars; NaCl-KCl and KBr-KI up to 20 kbars; and RbBr-RbI up to 4 kbars.

The pressure dependence of solubility in the system NaCl-KCl as calculated by Fancher and Barsch is compared with our experimental work in Fig. 6, which shows the pressure dependence of the temperature of the maxima on the solvus curves. It should be noted that their purely theoretical value for the exsolution dome at atmospheric pressure is approximately 100°C higher than the experimental value at the same pressure; this is regarded as good agreement for such theory. The slopes of the experimental and theoretic-

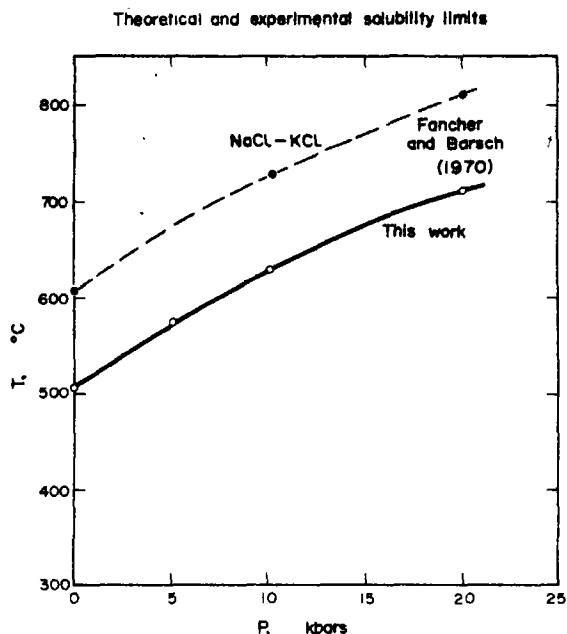


Fig. 6. Comparison of theoretical and experimental solubility limits. — — experimental, ----theoretical.

cal pressure dependence lines are very similar indeed. This agreement between theory and experiment with regard to the slope is considerably better than one might have expected. Indeed, if similar agreement is found for other systems, it would give us considerable confidence in the applicability of Fancher and Barsch's approach in calculating the pressure dependence of crystalline solubility in more complex systems.

Acknowledgements—We are grateful to Dr. F. Dacheille for his help during various stages of the experimental

work and to Dr. G. R. Barsch for critically reviewing the manuscript. This work has been supported by National Science Foundation Grant No. GK-1686X.

REFERENCES

1. ADAMS L. H., *J. Am. Chem. Soc.* **53**, 3769 (1931).
2. SCHEIL E. and STADELMAIER H., *Z. Metallk.* **43**, 227 (1952).
3. COLEMAN D. S. and LACY P. D. A., *Mat. Res. Bull.* **2**, 935 (1967).
4. BOWEN N. L. and TUTTLE O. F., *J. Geol.* **58**, 489 (1950).
5. BOYD F. R. and ENGLAND J. L., *The Fayalite-Spinel Transition and Aluminous Pyroxene*. Annual Report of the Director of the Geophysical Laboratory, Carnegie Institute of Washington, Year-Book (1959-60).
6. DACHILLE F. and ROY R., *Am. J. Sci.* **258**, 225 (1960).
7. MILLER W. S., DACHILLE F., SHAFER E. C. and ROY R., *Am. Miner.* **48**, 1024 (1963).
8. JAMIESON J. C., *Physics of Solids at High Pressures*, pp. 444. Academic Press, New York (1965).
9. DARNELL A. J. and McCOLLUM W. A., *Pressure-Temperature Phase Transition Studies in Solid Solutions of NaCl-KCl*. 153rd Am. Chem. Soc. Meeting, Miami Beach, Florida (1967).
10. YAGI K. and ONUMA K., *J. Fac. Sci. Hokkaido Univ. Series IV, Geol. & Mineral.* **XIII**, 463 (1967).
11. GOLDSMITH J. R. and NEWTON R. C., *Am. J. Sci.* **267A**, 160 (1969).
12. DACHILLE F. and ROY R., *Modern Very High Pressure Techniques*, pp. 163. Butterworths Publication, Washington (1962).
13. MYERS M. B., DACHILLE F. and ROY R., *A.S.M.E. High Pressure Measurement Symposium*, pp. 17-34. Butterworths Scientific Publications Ltd., London (1963).
14. COOK H. E. and HILLIARD J. E., *Trans. Met. Soc. AIME* **233**, 143 (1965).
15. SCHULTZ A. H. and STUBICAN V. S., *Phil. Mag.* **18**, 929 (1968).
16. FANCHER D. L. and BARSCH G. R., *J. Phys. Chem. Solids* **32**, 1303 (1971).

TRANSPORT PROPERTIES OF Cr-Al SOLID SOLUTIONS*

D. J. CHAKRABARTI and P. A. BECK

204 Metallurgy Building, University of Illinois, Urbana, Ill. 61801, U.S.A.

(Received 17 July 1970)

Abstract—The electrical resistivity between 4·2° and 400°K and the Hall coefficient at 78° and 300°K of the b.c.c. Cr-Al solid solutions indicate that below 12% and above 27% Al these alloys are metallic conductors with predominantly hole carriers. The alloys between 15 and 25% Al are narrow gap semiconductors and the carriers are electrons. Low temperature specific heat results are consistent with these conclusions and they suggest that the semiconducting state results from a gap in the d band, which opens at intermediate Al contents and closes again at Al contents of 27 per cent or more.

THE ELECTRONIC specific heat coefficient, γ , of the b.c.c. solid solutions of 3d-transition metals[1] has a sharp minimum at chromium. It was concluded that two 3d- subbands overlap slightly at this point[1,2]. A considerable further decrease in γ occurs in the b.c.c. Cr-Al solid solutions[3], which extend well beyond 30% Al at elevated temperatures [4, 5]. Between 20 and 25% Al γ decreases to a value less than half of that of copper, a surprising condition for alloys consisting largely of a transition metal. The hypothesis was advanced[3, 6, 7] that the decrease in γ for Cr-Al alloys is caused by the separation of the two originally overlapping d subbands, leaving only s states at the Fermi surface. If a gap is formed in the d band at the Fermi surface of Cr-Al alloys, this might be recognizable in the transport properties. The electrical resistivity of b.c.c. Cr-Al alloys was, therefore, measured over a wide temperature range. Hall coefficient measurements were also made at two fixed temperatures over the entire composition range of interest.

The alloys were prepared from electrolytic chromium of approximately 99·95 % purity and from doubly electrolyzed aluminum

of a purity of better than 99·99 %. Eighteen binary alloys from 0·2 to 33·3% Al were prepared by arc melting in a water-cooled copper crucible under argon atmosphere. Each specimen was melted at least six times to improve the homogeneity. Extra aluminum was added to the charge to compensate for vaporization during melting. Chemical analysis of six of the alloys indicated that the aluminum losses were in fact lower than expected, so that the actual aluminum content of all alloys was higher than originally planned. Figure 1 gives the lattice parameter of the alloy specimens vs. Al content. (All compositions in this paper are expressed in atomic per cents.) For

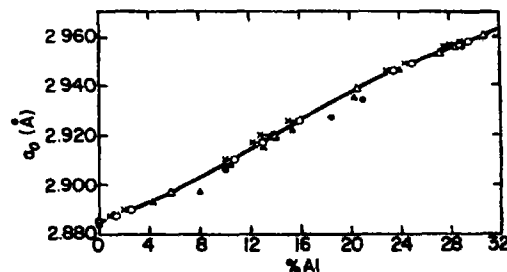


Fig. 1. Lattice parameter (in Å) of Cr-Al b.c.c. solid solutions vs. Al content (in at. pct.). Data from Ref.[8]: Δ ; data from Ref.[9]: \bullet ; present investigation, analyzed Al contents: Δ ; present alloys, intended Al content: \times ; Al content from lattice parameter: \circ .

*This work was supported by a grant from the National Science Foundation.

the alloys not chemically analyzed, the actual aluminium contents were determined from the measured lattice parameter values, Fig. 1. The arc melted elongated alloy bars were annealed at 1170°C for five to seven days in fused silica capsules, which had been evacuated and filled with argon at $\frac{1}{2}$ atmosphere pressure. Following the homogenizing anneal, the specimens were air-cooled to room temperature. Quenching was avoided in order to minimize the formation of cracks due to thermal shock. Most of the alloys were quite brittle, particularly those in the 20–25% Al composition range. Metallographic examination of the homogenized specimens indicated that all of them consisted of a single phase. X-ray diffraction patterns showed the structure to be b.c.c. The monotonic increase in the lattice parameter with the Al content and the absence of any superlattice lines confirms the existence of the b.c.c. solid solution up to 30.7% Al. Both the X-ray patterns (with $\text{CrK}\alpha$ radiation) and metallographic examination indicated that, even at the highest Al concentrations used, no transformation has taken place in the specimens on air-cooling from 1170°C to room temperature. After homogenization at 1170°C, the 33% Al alloy was reannealed for $2\frac{1}{2}$ days at 730°C and air-cooled. In accordance with the published phase diagrams [4, 5], the X-ray diffraction pattern of this specimen showed the MoSi_2 -type structure of Cr_2Al , with the superlattice lines readily visible.

The resistivity specimens were spark cut from the ingots. The length of these specimens varied between 0.25 in. and 1.5 in. The most brittle alloy specimens were particularly difficult to anneal and to shape without the formation of cracks; these specimens, therefore, tended to be short. The resistivity specimens were polished to an approximately square cross section of $\frac{1}{16}$ to $\frac{1}{8}$ in. width. The electrical resistivity was measured by the four-electrode potentiometer method between 4.2° and approximately 400°K. A liquid helium cryostat was used between 4.2° and

300°K. Measurements between 273° and 420°K were made with an electrically heated pyrostat. Both cryostat and pyrostat were constructed so as to minimize temperature gradients. In both instruments the heating elements regulating the temperature were automatically controlled. The temperature was measured by means of a carbon thermometer between 4.2° and 14°K, a platinum resistance thermometer between 10.5° and 300°K and a nickel wire resistance thermometer from 273° to 420°K. It is estimated that the error in the temperature measurements did not exceed 0.05°K at any point in the entire temperature range. Resistivity measurements were made during both the heating and cooling cycles. Except for the 15.9 and 24.9% Al specimens, all the data points fitted to a single smooth curve within the limits of experimental accuracy, indicating the absence of microcracks in the specimens. Because of the uncertainty of the exact position of spot welded potential contacts, the resistance of each specimen was also measured near room temperature across two knife edge EMF contacts, the distance of which was accurately known. The resistivity values obtained with the spot welded electrodes were then normalized to agree with the values obtained using the knife edge electrodes. Because of the possibility of occurrence of internal blowholes, and the uncertainty in the specimen dimensions, we estimate the absolute accuracy of the resistivity measurements to be approximately ± 5 per cent. For two specimens the heating and cooling cycle data did not superimpose accurately, indicating the presence of microcracks; here the absolute resistivity values may have been as much as 30 per cent less than the measured values. However, the relative resistivity values at different temperatures for any one specimen are independent of the dimensional uncertainties mentioned, and the relative accuracies are probably better than ± 1 per cent, within the entire temperature range.

Figure 2 shows the temperature dependence

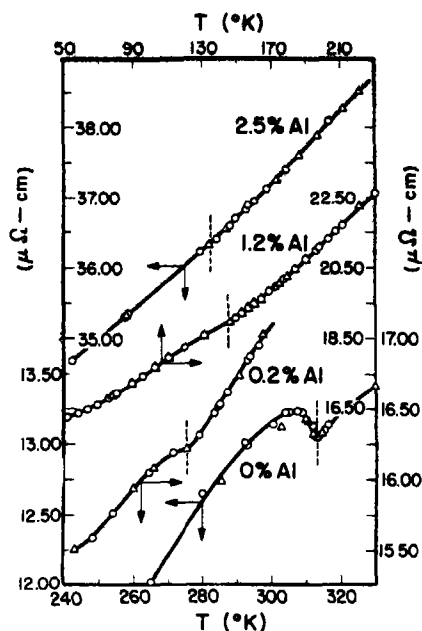


Fig. 2. Resistivity (in $\mu\Omega\text{-cm}$) vs. temperature (in $^{\circ}\text{K}$) for Cr, and for alloys with 0.2, 1.2 and 2.5% Al. Appropriate scales indicated by arrows. Data taken in increasing temperature cycles: \circ . Data from decreasing temperature cycles: \triangle . T_N from resistivity anomaly: vertical dashed lines.

of the resistivity of Cr and of the three alloys with the lowest Al contents. The resistivity anomaly of Cr, corresponding to the Néel temperature, becomes less pronounced when aluminum is added, but it is still discernible in the curves shown in Fig. 2. Figure 3 gives T_N as a function of Al-content, based on the

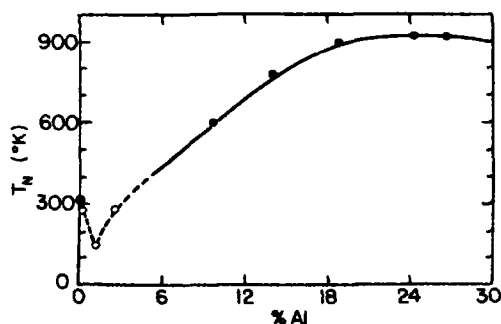


Fig. 3. Néel temperature (in $^{\circ}\text{K}$) vs. Al content (in at. pct.). Solid line, from Ref. [8], filled circles from Ref. [9], empty circles from Fig. 2.

present resistivity data at the lowest Al contents, and on earlier neutron diffraction [8] and susceptibility data [9] for the alloys with higher Al contents. The minimum of T_N at 1.2% Al, found in the present work, probably corresponds to the change from incommensurate to lattice-commensurate antiferromagnetism [8].

The resistivity of the alloys with Al contents not higher than 10.5 per cent is relatively low in the entire temperature range and it increases monotonically with the temperature. Such a typically metallic resistivity curve is shown in Fig. 4. Similar resistivity curves were also found for the alloys with the highest Al contents, namely 30.7 and 33.3 per cent.

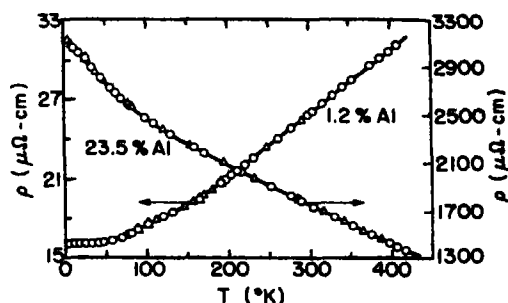


Fig. 4. Resistivity (in $\mu\Omega\text{-cm}$) vs. temperature (in $^{\circ}\text{K}$) for 1.2 and 23.5% Al alloys. Appropriate ordinate scales indicated by arrows.

On the other hand, the alloys with 15.9 to 28.5% Al were found to have very much higher resistivity values and negative temperature coefficients of the resistivity in the entire temperature range studied. A resistivity curve typical of the latter group of alloys, is also shown in Fig. 4. Alloys in the borderline composition range show a more complicated variation of the resistivity with temperature, Fig. 5. As the Al content increases from 13 to 13.9 per cent, the temperatures of the resistivity minimum and maximum come closer together, and at low temperatures the resistivity increases more than at higher temperatures. At still higher Al contents the minimum and the maximum of ρ merge and

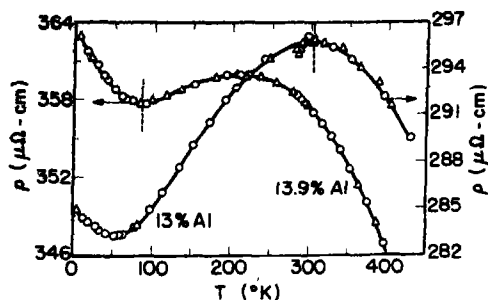


Fig. 5. Resistivity (in $\mu\Omega\text{-cm}$) vs. temperature (in $^{\circ}\text{K}$) for 13 and 13.9% Al alloys. Appropriate ordinate scales indicated by arrows.

disappear, leaving an overall negative temperature coefficient. In the second borderline region, where the temperature coefficient of ρ changes back from negative to positive at high Al contents, the same sequence of changes occurs in reversed order.

Figure 6 shows the resistivity at 4.2 and 400°K as a function of Al content. In the low aluminum region (up to about 10 per cent) the increase of the resistivity with Al content may be considered as typical of the atomic disorder scattering in random alloys in related alloy systems. Figure 6 shows that at around 10% Al this resistivity component is very much larger than that due to phonon scattering. Similar conditions, typical of metallic alloys, also prevail in the 28.8 to 30.7 per cent aluminum composition range. However, in the intermediate composition range between

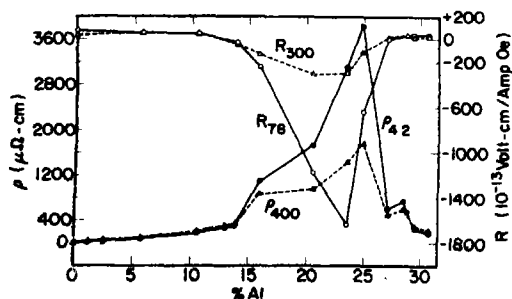


Fig. 6. Electrical resistivity at 4.2° and 400°K (in $\mu\Omega\text{-cm}$) and Hall constant at 78° and 300°K (in $10^{-13}\text{ V. cm Amp}^{-1}\text{ Oe}^{-1}$) vs. Al content (in at. pct.). Hall coefficients for Cr from Ref.[12].

about 15 and 25% Al the resistivity values are much higher than what could be ascribed to atomic disorder scattering. Also the negative temperature coefficient of the resistivity of these alloys is very large as compared with the positive one, below 10 and above 28% Al. The 15 to 25% Al alloys may be considered semiconductor-like. However, the $\log \rho$ vs. $1/T$ line for the present alloys is not straight, as it is for ordinary intrinsic semiconductors. As an example, the 15.9% Al alloy data are shown in Fig. 7. The negative slope of the $\log \rho$ vs. $1/T$ line which defines the semiconductor energy gap, is very small at low temperatures and it increases by three orders of magnitude with increasing temperature from 4.2° to 400°K. The highest energy gap values for the various alloys, measured at 400°K, are shown in Fig. 8 as a function of Al content. Even the largest value found, that for the 23.5% Al alloy, is only 0.06 eV. The conditions shown in Fig. 7, as well as the very low energy gap values, are rather similar to those reported[10] for the narrow gap semiconductor Bi-Sb alloys.

The Hall coefficient was measured at 78° and 300°K for most of the Cr-Al alloys. Because of the great brittleness of these alloys, a specimen thickness of at least 0.4 mm had to be maintained. The copper wire current and potential leads were connected to the alloy specimens with indium solder. The measurements were made in a constant field

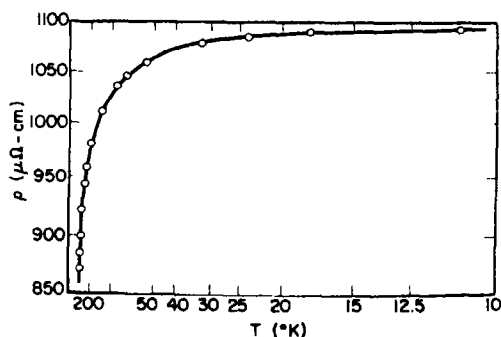


Fig. 7. Electrical resistivity (in $\mu\Omega\text{-cm}$) on logarithmic scale vs. temperature (in $^{\circ}\text{K}$) on reciprocal scale for 15.9% Al alloy.

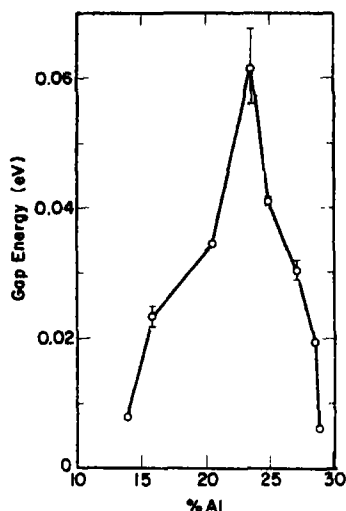


Fig. 8. Gap energy (in eV) at 400°K vs. Al content (in at. pct.).

of 12.6 kOe, using a specimen current of 500 mA. The Hall EMF was measured in all four configurations of current and field directions, in order to eliminate various thermoelectric and magnetocaloric effects. The accuracy of the measurements was limited by the relatively large specimen thickness, which made the magnitude of the Hall EMF relatively low, and by a superimposed drifting EMF pickup in the system. The estimated limits of error ranged from ± 5 per cent for the largest Hall coefficients to about ± 50 per cent for the smallest values.

The results of the Hall coefficient measurements at 78 and 300°K are shown in Fig. 6. It is seen that, for the metallic alloys below 12% Al and above 27% Al, the Hall coefficients are positive, with relatively small temperature variation. On the other hand, the semiconductor-like alloys between 15 and 25% Al have rather large negative Hall coefficients, which vary strongly with the temperature. These findings give further support to the interpretation of the resistivity data in terms of a semiconductor-like behavior. In particular, the large, highly temperature-dependent negative Hall co-

efficients of the 20 to 25% Al alloys show the scarcity of current carriers (electrons) in this composition range. Also, the Hall coefficient data indicate that the metallic alloys with both low and high Al contents are preponderantly hole conductors, as is chromium itself[12]. The fact that, with increasing Al content, the alloys change from hole to electron and back to hole conduction, suggests that the Fermi surface is not passing from one side of a gap to the other. If it did, then electron conduction should persist in the metallic composition range where the Fermi surface, having crossed the band gap, is located near the bottom of the higher energy band.

Since the Cr-Al alloys are antiferromagnetic, one must consider the question whether or not the energy gap indicated by the transport properties may be that associated with the antiferromagnetism. If the antiferromagnetic energy gap were responsible for the narrow gap semiconductor behavior, the collapse of this gap at the Néel temperature may be expected to give rise to a return to normal metallic transport properties when that temperature is reached. Figure 9 shows that the temperature coefficient of the electrical resistivity of the 20.5 and 23.5% Al alloys remains negative at temperatures well above T_N , the latter having been determined by neutron diffraction[8]. Accordingly, the narrow gap semiconductor behavior is evidently not connected with the antiferromagnetic energy gap.

Available low temperature specific heat data for V-Cr and Cr-Fe alloys with 10% Al[3] and with 20% Al[7] allow the calculation of the density of states as a function of energy, by using the method described by Hoare, Mathews and Walling[11]. Additional low temperature specific heat measurements were made in the present investigation with similar ternary alloys containing 30% Al. The results are shown in Table 1. The calculated density of states curves for the 10, 20 and 30% Al alloys in the region around Cr

Table 1. Low temperature specific heat results for ternary Cr alloys with 30% Al

Nominal composition	A (10^{-4} cal. mol $^{-1}$ deg $^{-1}$)	γ (10^{-4} cal. mol $^{-1}$ deg $^{-2}$)	θ_D (deg-K)	RMSD (10^{-4} cal. mol $^{-1}$ deg $^{-1}$)
(Cr $_{0.9}$ V $_{0.1}$) $_{0.7}$ Al $_{0.3}$		4.39	617	0.03853
(Cr $_{0.8}$ V $_{0.2}$) $_{0.7}$ Al $_{0.3}$		7.16	668	0.08798
(Cr $_{0.7}$ V $_{0.3}$) $_{0.7}$ Al $_{0.3}$		8.97	747	0.11032
(Cr $_{0.5}$ V $_{0.7}$) $_{0.7}$ Al $_{0.3}$		8.29	574	0.09394
(Cr $_{0.98}$ Fe $_{0.02}$) $_{0.7}$ Al $_{0.3}$		5.53	946*	0.11060
(Cr $_{0.9}$ Fe $_{0.1}$) $_{0.7}$ Al $_{0.3}$		7.35	664*	0.05738
(Cr $_{0.8}$ Fe $_{0.2}$) $_{0.7}$ Al $_{0.3}$		13.15	(-879)*	0.07910
(Cr $_{0.7}$ Fe $_{0.3}$) $_{0.7}$ Al $_{0.3}$	20.38	22.82	(-260)*	0.31750

*Anomalously high and negative ' θ_D ' values are due to magnetic contributions to the low temperature specific heat.

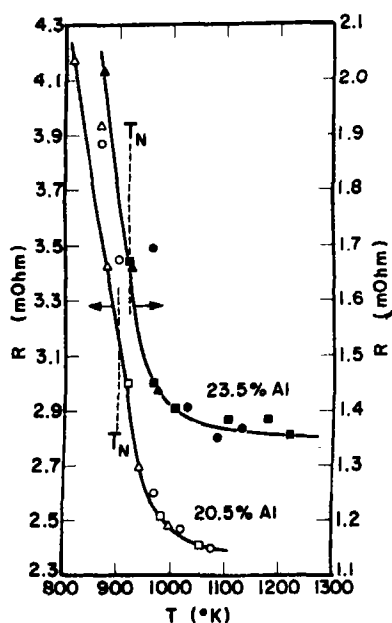


Fig. 9. Resistance (in mOhms) vs. temperature (in °K) for 20.5 and 23.5% Al specimens. Data from decreasing temperature cycle Δ , \blacktriangle ; from increasing temperature cycle \circ , \bullet . Néel temperatures from Ref.[8]. Appropriate ordinate scales indicated by arrows.

are shown in Fig. 10. The calculation was based on the assumption of a rigid band-like behavior for the transition metals, and of no filling of the d-band by the aluminum additions. The electron-phonon enhancement effect for these alloys is not known, and was not considered in the calculation. Figure 10 shows that increasing the Al content beyond

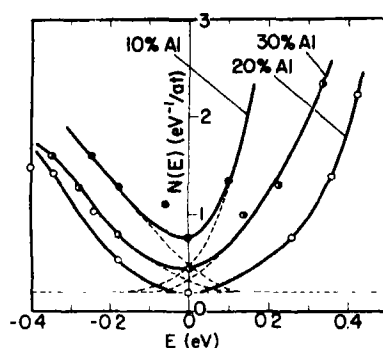


Fig. 10. Electronic density of states (in states per eV, atom) vs. energy (in eV, relative to the Fermi energy of Cr) for 10, 20 and 30% Al alloys.

10 per cent shifts the two slightly overlapping d-subbands away from each other, so that at 20% Al an energy gap of the magnitude shown in Fig. 8 may well be present between the two d-subbands. The electronic specific heat coefficient γ of the Cr $_{0.8}$ Al $_{0.2}$ binary alloy [3] would then indicate only the s-like electron density of states at the Fermi surface, as originally postulated[3, 6, 7]. The minimum of γ is between 20 and 25% Al[3]. As the aluminum content increases to 30 per cent, the two d-subbands are shifted back toward each other, and the overlap between them is re-established (Fig. 10). In this composition range, γ increases with the Al content[3]. The narrow gap semiconductor like transport properties of the alloys with 15 to 25% Al would then result from the separation of the

two 3d-subbands, and the formation of an energy gap between them. This interpretation also accounts for the positive Hall coefficients of the alloys with more than 27% Al: when the energy gap closes upon increasing the Al content above that value, conditions again become similar to those prevailing in chromium itself and hole conductivity predominates. Why the s electrons play here such a minor role in the conduction of electricity is not completely clear.

It should be noted that the maximum of the resistivity, of the absolute value of the Hall coefficient (Fig. 6) and of the gap energy (Fig. 8) occurs at the same composition range where γ is minimum. The maxima of resistivity, Hall coefficient and gap energy were found to coincide also for the Bi-Sb alloys[10]. However, the physical conditions underlying the opening up and the closing of a band gap appear to be quite different in the two systems. Sb and Bi are semi-metals; in their alloys d electrons are not involved in the conduction process.

Acknowledgements—This investigation was supported by a grant from the National Science Foundation. We

benefited from very illuminating discussions with Professor Morrel H. Cohen.

REFERENCES

1. CHENG C. H., WEI C. T. and BECK P. A., *Phys. Rev.* **120**, 426 (1960).
2. GUPTA K. P., CHENG C. H. and BECK P. A., *J. Phys. Radium* **23**, 721 (1962).
3. PESSAL N., GUPTA K. P., CHENG C. H. and BECK P. A., *J. Phys. Chem. Solids* **25**, 993 (1964).
4. HANSEN M., *Constitution of Binary Alloys*, McGraw-Hill, New York (1958).
5. SHUNK F. A., *Constitution of Binary Alloys, Second Supplement*, McGraw-Hill, New York (1969).
6. SRINIVASAN T. M., CLAUS H., VISWANATHAN R., BECK P. A. and BARDOS D. I., *Phase Stability in Metals and Alloys* (Edited by P. S. Rudman, J. Stringer and R. J. Jaffe), McGraw-Hill, New York (1967).
7. SRINIVASAN T. M. and CLAUS H., *J. Phys. Chem. Solids* **28**, 711 (1967).
8. KALLEL A. and DE BERGEVIN F., *Solid State Commun.* **5**, 955 (1967).
9. KÖSTER W., WACHTEL E. and GRUBE K., *Z. Metallk* **54**, 393 (1963).
10. JAIN A. L., *Phys. Rev.* **114**, 1518 (1959).
11. HOARE F. E., MATHEWS J. C. and WALLING J. C., *Proc. R. Soc. A* **216**, 502 (1953).
12. SCHRODER K. and MCCAIN C. E., *Phys. Rev.* **135**, A149 (1964).

FREQUENCY DEPENDENCE OF THE ULTRASONIC ATTENUATION IN SUPERCONDUCTING NIOBIUM IN THE MIXED STATE*

KOJI KAJIMURA

Electrotechnical Laboratory, Mukodai, Tanashi, Tokyo 188, Japan

and

AKIRA IKUSHIMA

The Institute for Solid State Physics, University of Tokyo, Roppongi, Minato-ku, Tokyo 106, Japan

(Received 13 March 1970; in revised form 25 May 1970)

Abstract—Attenuation of longitudinal ultrasonic waves was measured in the frequency range from 25 to 700 MHz in a single crystal of high purity niobium. Ratio of the attenuation coefficients in the superconducting and normal states, α_s/α_n , was measured as a function of magnetic field, H , at various constant temperatures. For the magnetic field near the upper critical field, H_{c2} , the result was found to be composed of two parts: In the immediate vicinity of H_{c2} , the attenuation coefficient obeyed the relation, $1 - (\alpha_s/\alpha_n) = A(H_{c2} - H)$, whereas the result at field rather below H_{c2} was described by $1 - (\alpha_s/\alpha_n) = C(H_{c2} - H)^{1/2}$, a relation of Maki's pure limit theory. The above linear dependence on H hardly seems to obtain a plausible explanation at present. The observed value of C varied rather steeply around the frequency corresponding to $ql \approx 1$, where q is the impressed wave number. The dip of the attenuation just above the lower critical field was also investigated. The depth of the dip was found to depend on the frequency as well as temperature, and the frequency dependence could not be accounted for by the existing proposals.

Besides the above-mentioned results, the superconducting energy gap at 0°K without magnetic field was found to be smaller for higher frequencies.

1. INTRODUCTION

A FEW years ago, one of the present authors (A.I) and his colleagues [1, 2] first measured at various temperatures the attenuation of longitudinal sound waves in the mixed state of the type II superconductor using a single crystal of pure niobium. To measure the ultrasonic attenuation in type II superconductors in the mixed state is very interesting, because the measurement is expected to give useful informations on the elementary excitation in the mixed state where the superconducting order parameter varies spatially due to the penetration of the flux lines into the superconductor. Niobium was chosen since it was the only pure metal recognized an intrinsic type II superconductor at that time. Since that time, several interesting experimental studies have been reported in this field, most of those have

concentrated in niobium [3-7]. Other measurements in vanadium [8, 9], Nb_3Zr [10, 11], MoRe [7], VTa [12] were also reported.

The attenuation coefficient in niobium in the mixed state begins to increase at the lower critical field, H_{c1} , and reaches a value corresponding to the normal state at the upper critical field, H_{c2} . In the previous work [2], the variation of the attenuation in the mixed state was first compared using the 'effective energy gap' concept with the variation of the magnetization of the same specimen. The comparison was made as follows: (1) the 'effective energy gap' in the mixed state was assumed to be proportional to the root mean square of the order parameter. (2) The magnetization near H_{c2} was assumed to be proportional to the square of the averaged order parameter [13, 14]. Consequently, the 'effective energy gap' was proportional to the square root of the measured magnetization. (3) And, by the use of the BCS formula,

*This work was supported in part by The RCA Scientific Grant.

$$\alpha_s/\alpha_n = 2/[1 + \exp(\Delta/kT)], \quad (1) \quad \alpha_s/\alpha_n = 1 - (|\Delta(r)|/2kT) \int_{-\infty}^{\infty} \Phi(\alpha/\epsilon, y) \times \cosh^{-2}(\alpha/2kT) \epsilon^{-1} d\alpha, \quad (2)$$

the magnetization could be converted to the relative attenuation, α_s/α_n , where Δ is a half of the energy gap, and kT the thermal energy.

It was revealed in the above-mentioned treatment[1,2] that the variation of the attenuation coefficient cannot correctly be described by the 'effective energy gap'. There was a discrepancy between the observed attenuation and the calculated result even near the upper critical field and near the superconducting transition temperature where the 'effective energy gap' approximation would probably be valid. Furthermore, the discrepancy was particularly larger at lower temperatures.

Maki[15,16] has proposed a couple of theories of the ultrasonic attenuation in type II superconductor in the mixed state near H_{c2} . The purpose of this paper is to report an experimental result of the attenuation in pure niobium varying the sound frequency from 25 to 700 MHz, and to compare the result with the Maki theory. We will also report here both the frequency effects on the anomalous dip of the attenuation just above H_{c1} [3, 4, 6, 9] and the effect on the attenuation as a function of temperature without magnetic field which was needed to discuss the attenuation in the mixed state.

2. THE MAKI THEORY IN THE PURE LIMIT

The difference of the most importance between the former 'effective energy gap concept' and the Maki theory in the pure limit is that Maki took into account the effect of the shielding supercurrent around the flux lines, assuming that the effect of the supercurrent is similar to that of the usual transport current. The density of states in the superconducting state accordingly varies depending on the electronic mean free path.

In Maki's result for the ultrasonic attenuation, the relative attenuation of the longitudinal waves in a transverse magnetic field is given by the following formula:

where

$$\Phi(x, y) = \pi^{1/2} I_0^{-1} \int_0^1 \exp[-x^2/(1-z^2)] \times (1-3z^2)(1-z^2)^{-1/2} \times \{[(1+3/y^2)(1+y^2(1-z^2))^{-1/2} - 3/y^2](1-y^{-1} \arctan y)^{-1} - 3(3z^2-1)/2y^2\}, \quad (3)$$

$$y = ql, \quad (4)$$

$$I_0 = \arctan y/(y - \arctan y) - 3/y^2, \quad (5)$$

$$\epsilon = (v_F/2)(e\hbar H_{c2}(T)/c)^{1/2}, \quad (6)$$

and

$$\Delta^2 = -(2M/N(0))[H_{c2} - \frac{1}{2}T(\partial H_{c2}/\partial T)]. \quad (7)$$

Here, v_F is the Fermi velocity, e the absolute magnitude of the electronic charge, \hbar the Planck constant divided by 2π , $\Delta(r)$ the superconducting order parameter as a function of the position r , $N(0)$ the density of states in the normal state at the Fermi energy, and M the magnetization.

As the magnetization M of the type II superconductor near H_{c2} depends linearly on $H_{c2} - H$, equation (2) can be written as

$$1 - (\alpha_s/\alpha_n) = C(H_{c2} - H)^{1/2}, \quad (8)$$

where the proportional factor C depends on $y = ql$, temperature and other parameters. It is worthwhile to note that C is inversely proportional to the square root of $N(0)$.

Figures 1 and 2 show the theoretical curves computed from the above formulae, in which values of the parameters are taken as follows: H_{c2} , $\partial H_{c2}/\partial T$ and $M(H_{c2})$ are the measured values for the present specimen, $v_F = 3.5 \times 10^7$ cm/sec as was estimated from the magnetization data of the present specimen [17], and $N(0) = 6.37 \times 10^{24}$ erg $^{-1}$ cm $^{-3}$ ob-

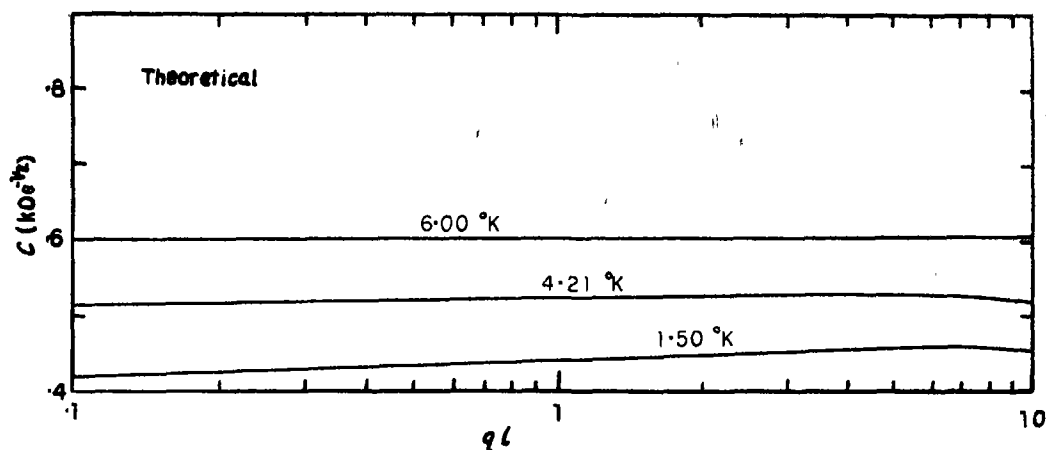


Fig. 1. Variation of theoretical C as a function of reduced temperature, T/T_c . Here, the value $N(0)$ is taken to be $6.37 \times 10^{24} \text{ erg}^{-1} \text{ cm}^{-3}$ as determined from the electronic specific heat.

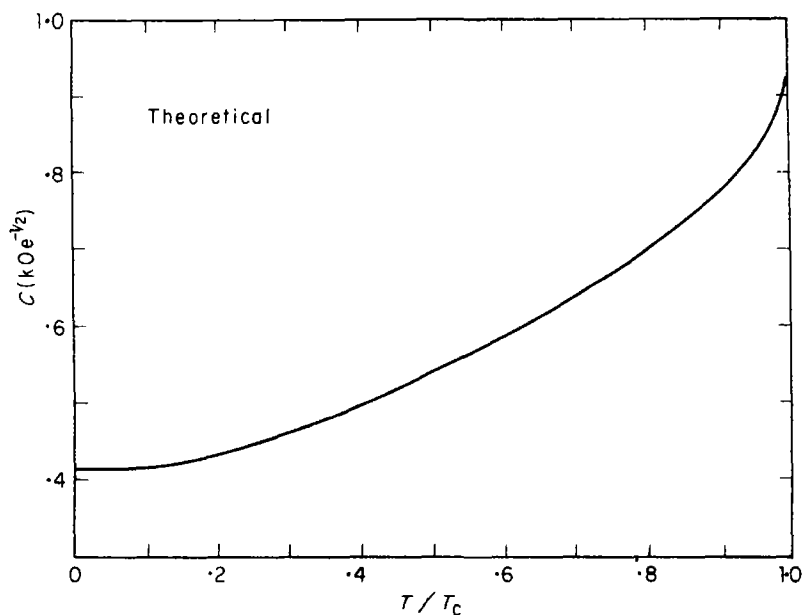


Fig. 2. Variation of theoretical C as a function of T/T_c . Here, $qL = 0.5$ and $N(0) = 6.37 \times 10^{24} \text{ erg}^{-1} \text{ cm}^{-3}$.

tained from the electronic specific heat experiment [18].

3. EXPERIMENTAL PROCEDURE

The single crystal of niobium used in this experiment was the one prepared for the

previous work and the details of the specimen is given in Ref. [2].

Ultrasonic attenuation of longitudinal waves was measured by the pulse-echo method from 25 to 700 MHz. A re-entrant type cavity was used to excite the 700 MHz ultrasonic waves.

Adhesion between the quartz transducer and the specimen was achieved by using 'Nonaq' stopcock grease for all frequencies. The detailed description of the attenuation measurement is also given in Ref. [2].

4. EXPERIMENTAL RESULTS AND DISCUSSION

(a) Attenuation as a function of temperature

First of all, we have to mention the attenuation coefficient measured as a function of temperature. As is shown in Fig. 3, the attenuation varies depending on the sound frequency. Tsuda and Suzuki[5] have also found a similar phenomenon in niobium as an effect of the purity of the specimen.

the curve, α_s/α_n vs. T , where the relation $\alpha_s/\alpha_n = 2 \exp(-\Delta/kT)$ holds well. The present result seems to be in a qualitative agreement with the result of Dobbs and Perz[19, 20] as is shown in Fig. 4.

(b) Attenuation in the mixed state near H_{c2}

Figure 5 is a plot of the attenuation coefficient at 4.2°K for various frequencies as a function of the magnetic field. The result roughly obeys equation (8) as is shown in Fig. 6. However, for magnetic field immediate vicinity of H_{c2} , there seems to be a systematic deviation of data points from the straight line in this figure. Figure 7 is a log-log plot of

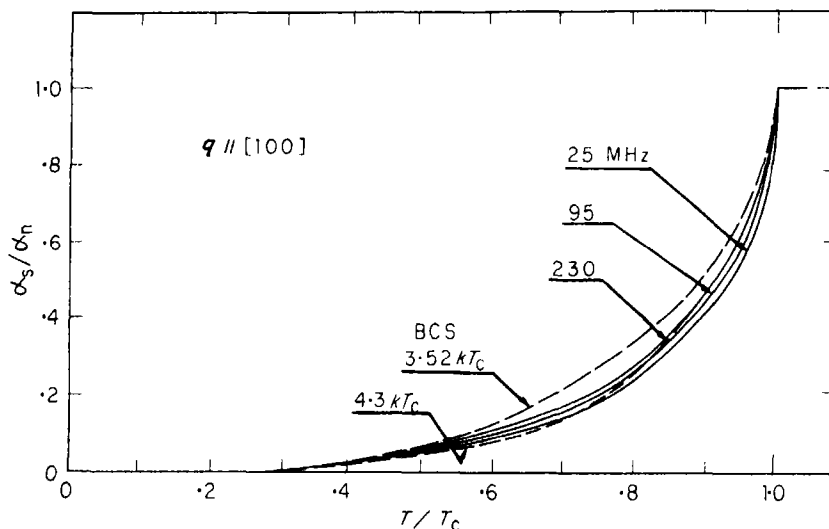


Fig. 3. Variation of the relative attenuation coefficient without magnetic field vs. reduced temperature, T/T_c .

In order to show the present result more clearly, the magnitude of the superconducting energy gap at 0°K, $2\Delta(0)$, was plotted in Fig. 4 as a function of the frequency. Observed variation of the relative attenuation, α_s/α_n , against temperature cannot correctly be described by equation (1) over the temperature range from 0°K to T_c , and the magnitude of $2\Delta(0)$ therefore depends on how we deduce the value. In Fig. 4 is plotted $2\Delta(0)/kT_c$ deduced from the higher temperature part of

$1 - (\alpha_s/\alpha_n)$ vs. $H_{c2} - H$, and the plot indicates that the behavior of the attenuation very close to H_{c2} linearly varies, contradicting equation (8) by the Maki theory. If we crudely deduce the magnitude of C in equation (7) from the plots like those in Fig. 5, C at different temperatures varies against the sound frequency (See Fig. 8)[21]. A theoretical curve due to Maki is also shown in this figure, in which, however, the value of $N(0)$ was tentatively adjusted to fit the theory to the observed C 's

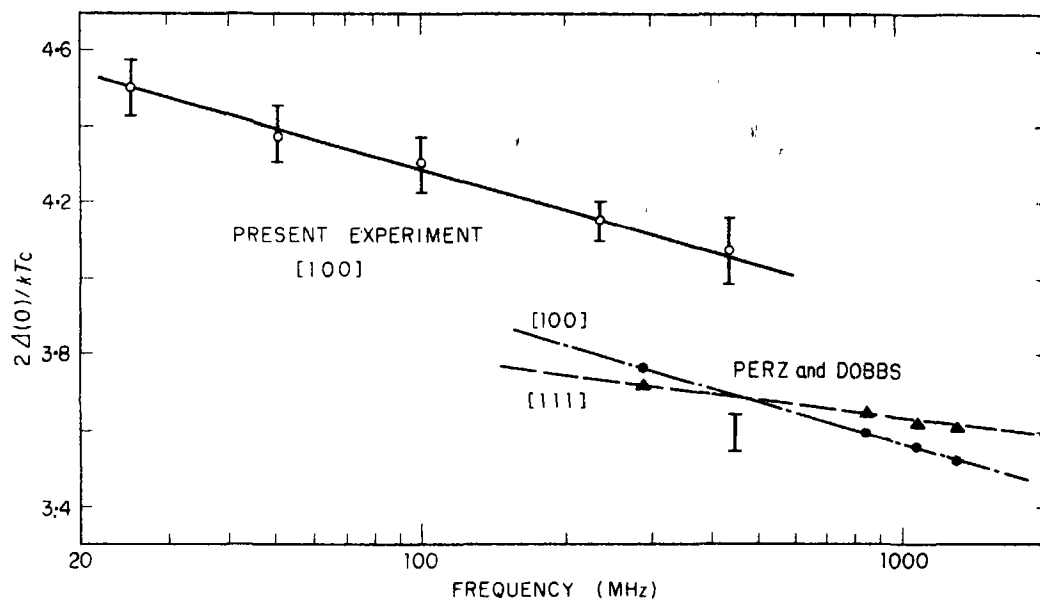


Fig. 4. Apparent value of the superconducting energy gap at 0°K as a function of sound frequency.

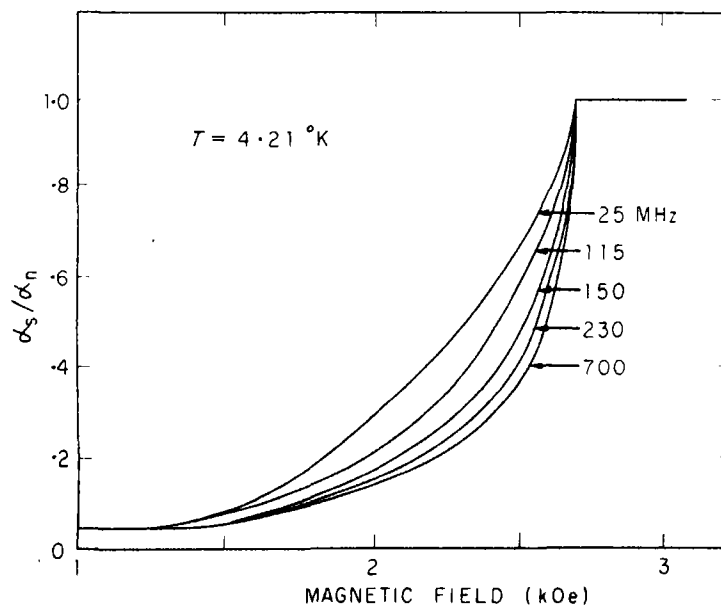
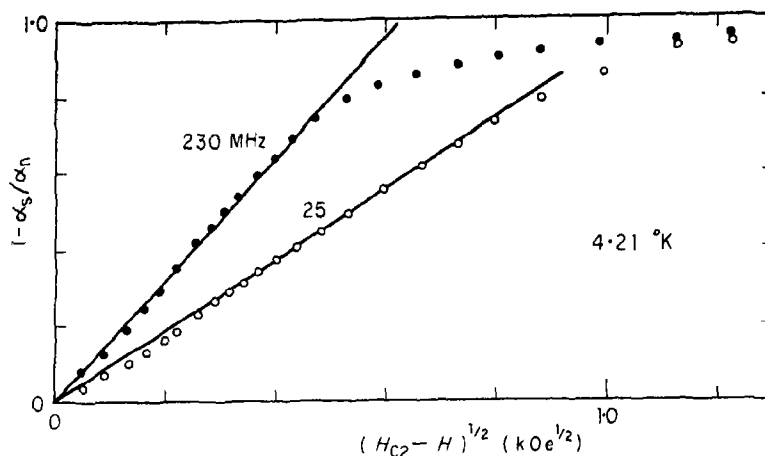
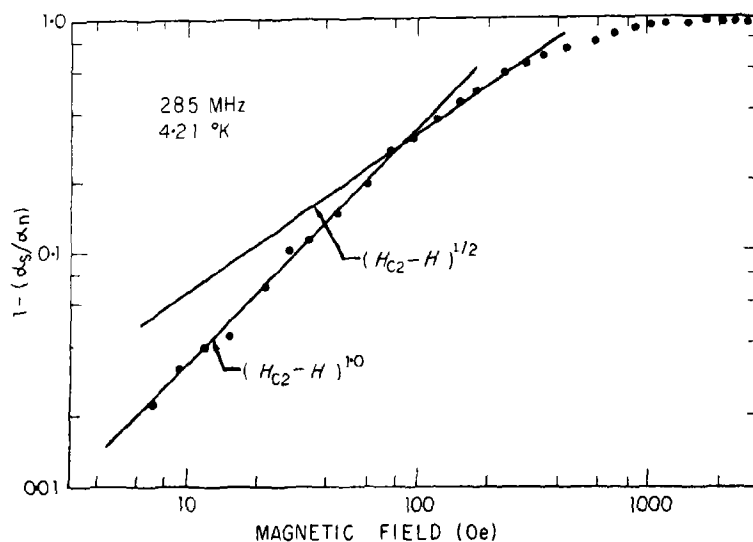


Fig. 5. Variation of the relative attenuation coefficient in the mixed state at 4.21°K for various frequencies.

at lower frequencies. The value of $N(0)$ is $2.34 \times 10^{34} \text{ erg}^{-1} \text{ cm}^{-3}$ at 1.50°K, for instance, which is about 40 per cent of the value estimated from the electronic specific heat [18].

To summarize, the result in Figs. 6 and 7 does not seem to be explained by the Maki theory in three respects. The first point is the behavior of the attenuation coefficient in the

Fig. 6. Plot of $1 - (\alpha_s/\alpha_n)$ vs. $(H_{c2} - H)^{1/2}$.Fig. 7. Log-log plot of $1 - (\alpha_s/\alpha_n)$ vs. $H_{c2} - H$.

immediate vicinity of the upper critical field, where the attenuation coefficient is described by a linear relationship. This fact has really been found in all previous investigations [5-7] if we re-check them carefully, indicating that the present result should not be a spurious effect due to any experimental mistake. We have no plausible explanation for this result.

The second thing to be mentioned is the discrepancy in the value of $N(0)$ between the

specific heat data and the ultrasonic investigation if we would obtain the parameter C in equation (7) excepting the immediate vicinity of the upper critical field. The value of $N(0)$ is much smaller for the present result than for the specific heat data, and we cannot find any reason yet to reduce the value for the present case. This fact was already reported by Kagiwada *et al.* [6], Gottlieb *et al.* [7] for Nb, and Ozaki *et al.* [8] for V. A similar problem

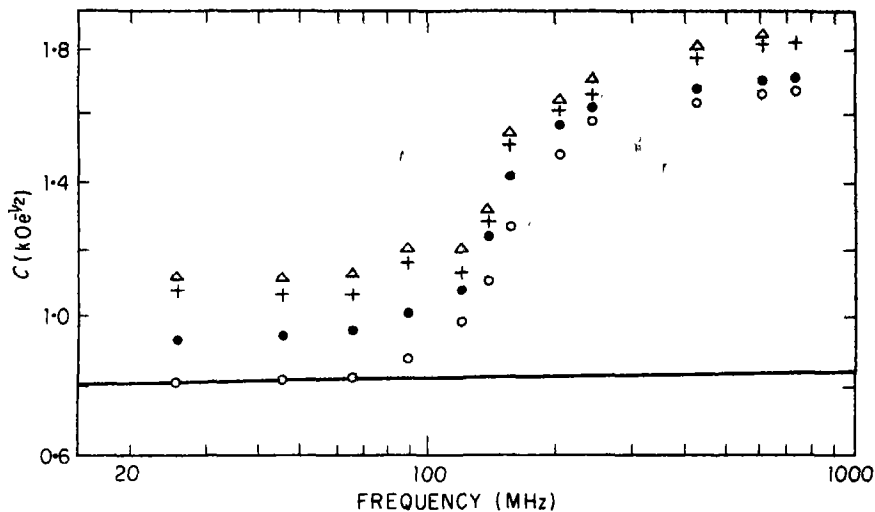


Fig. 8. Variation of C at various temperatures as a function of sound frequency. Δ , 7.00°K; +, 6.30°K; \bullet , 4.21°K; \circ , 1.50°K. Solid line shows theoretical value with $N(0) = 2.34 \times 10^{24} \text{ erg}^{-1} \text{ cm}^{-3}$.

also exists in thermal conductivity measurements in the mixed state[22] that the values of $N(0)$ deduced from these experiments via theory are again much smaller than that from the specific heat.

The final problem is the frequency dependence of the parameter C . C shown in Fig. 8 does not seem to obey the theoretical curve, but varies dispersively around 200 MHz. The larger value of C means the steeper drop of the relative attenuation coefficient below the upper critical field, so the result means that there would be a mechanism in which the dissipation of the energy of sound becomes ineffective in the superconducting state for sound frequency nearly equal to or exceeding 200 MHz.

This frequency roughly corresponds to the frequency where $ql \approx 1$. Therefore, one of the possible mechanisms to account for this problem could be the one related to the electronic one. It is considered in the BCS theory that the energy of sound is dissipated by the direct absorption and the induced emission of the imposed acoustic phonons by thermally excited quasi-particles. Besides this, there could be mechanisms which are related to the

modulation of the superconducting energy gap by the sound waves. One of them is that proposed by Tsuda and Suzuki[5] in which the sound energy is dissipated as an Ohmic loss associated with a flow of the quasi-particles from the wider to the narrower energy gap region. Another mechanism is related to the recombination of the quasi-particles into the Cooper pairs and the re-excitation of the pairs to the quasi-particles. The sound energy could be dissipated due to the delay of the recombination or the re-excitation when the gap is modulated. This is an important mechanism of the internal friction in semiconductors as a number of experimental and theoretical studies have revealed out[23–25]. However, the result we have already seen is that the attenuation in the superconducting state becomes ineffective when the sound frequency is higher. Therefore, the observed result contradicts the above-mentioned recombination mechanism in which the attenuation rather increases when $\omega\tau$ exceeds unity, where ω is the angular frequency of the impressed waves, and τ the recombination time. Moreover, as De Gennes[26] has pointed out, any mechanism related to the modulation of the energy

gap by the sound waves would be unimportant in the ultrasonic attenuation. The direct perturbation is $U\theta(r)$, where U is the 'deformation potential' and $\theta(r)$ is the local dilatation. On the other hand, the shift of the pair potential is about an amount of $K\delta\theta(r)$, where K is a constant of order unity as can be estimated from the pressure dependence of the transition temperature[27]. As U is of the same order of the Fermi energy whereas $K\delta$ is of the order of 10^{-3} eV, the shift of the pair potential is too small in ordinary metals to affect the direct perturbation.

Another possibility would be the mechanism related to the fluxoid motion[28]. There should be a characteristic frequency of the motion of a fluxoid as a string, above which the motion cannot follow the external alternative stress of the sound waves, the motion is overdamped, and the logarithmic decrement becomes less effective. This frequency should correspond to the 'depinning frequency' ω_0 calculated by Gittleman and Rosenblum[29]*. The magnitude of ω_0 is estimated for the external field of 2.5 kOe to be 20 kHz,† a value much lower than the above-mentioned frequency at which varies dispersively.

Therefore, we would like to propose here that the present result is due to the frequency dependent mean free path of electrons in niobium, which would also be the primary cause of that the relative attenuation vs. temperature is affected by the sound frequency, and that the attenuation has a frequency dependent dip just above H_{c1} (see next section). The dissipation mechanism related to the gap modulation could be important when the Fermi energy of the electrons which play

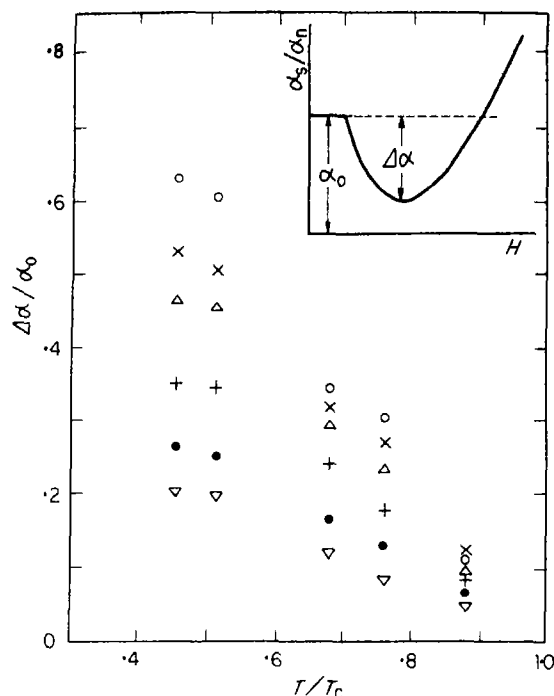


Fig. 9. Variation of the reduced depth of the anomaly in α_n/α_n just above H_{c1} at various frequencies as a function of the reduced temperature. \circ , 700 MHz; \times , 410 MHz; Δ , 230 MHz; $+$, 150 MHz; \bullet , 85 MHz; ∇ , 25 MHz.

the main role in the superconductivity in niobium is very small, say, about $10^{-2} \sim 10^{-3}$ eV. However, such an evidence has not been found so far.

(c) Attenuation in the mixed state near H_{c1}

Recently, Forgan and Gough[3], Tsuda and Suzuki[5], Kagiwada[6], and Sinclair and Leibowitz[9] reported an anomalous dip of the attenuation just above the lower critical field, H_{c1} . Forgan and Gough proposed that this initial decrease is caused by the scattering from the flux lines of the BCS quasi-particles excitations, that is, the thermally excited unbound particles would have a shorter mean free path due to their scattering by the flux lines. They reported, as a support to their proposal, that the decrease is linearly dependent on the purity of the specimen. The estimated scattering diameter of a flux were 4×10^{-7} cm in Nb[3], and 2.4×10^{-6} cm in V[9].

*The present authors do not agree the physical implication Shapira and Neuringer offered for ω_0 . The fluxoid is not thought to unpin from a potential due to obstacles for frequencies above ω_0 , but the motion of the fluxoid for such frequencies is overdamped, making the logarithmic decrement less effective.

†For the estimation of ω_0 we used the values of depinning d.c. current density[30], $J_c = 10^2$ A/cm², d.c. resistivity $\rho_n = 0.1 \mu\Omega\text{-cm}$, and upper critical field at 0°K, $H_{c2}(0) = 4$ kOe.

We have measured the effect of the sound frequency on this dip. Figure 9 is the result of the present investigation, the reduced depth of the dip being dependent on the frequency. This cannot be simply accounted for by the above-mentioned proposal, because the result of which should be frequency independent unless the electronic mean free path is frequency-dependent.

Acknowledgements—The present authors would like to express their thanks to Dr. K. Maki, Dr. T. Tsuneto and also Dr. N. Mikoshiba for their valuable and stimulating discussions and suggestions. One of the present authors (K. K.) thanks Dr. T. Ishiguro, Dr. H. Ozaki, Dr. T. Tsushima, and members of Physics Division of Electro-technical Laboratory for their support. A part of this work was carried out at Osaka University. The help of Mr. S. Maruyama during the experiment is greatly appreciated.

REFERENCES

1. IKUSHIMA A., SUZUKI T., TANAKA N. and NAKAJIMA S., *J. phys. Soc. Japan* **19**, 2235 (1964).
2. IKUSHIMA A., FUJII M. and SUZUKI T., *J. Phys. Chem. Solids* **27**, 327 (1966).
3. FORGAN E. M. and GOUGH C. E., *Phys. Lett.* **21**, 133 (1966).
4. TSUDA N., KOIKE S. and SUZUKI T., *Phys. Lett.* **22**, 414 (1966).
5. TSUDA N. and SUZUKI T., *J. Phys. Chem. Solids* **28**, 2487 (1967).
6. KAGIWADA R., *Theses, UCLA* (1966) (unpublished). KAGIWADA R., LEVY M., RUDNICK I., KAGIWADA H. and MAKI K., *Phys. Rev. Lett.* **18**, 74 (1967).
7. GOTTLIEB M., JONES C. K. and GARBUNY M., *Phys. Lett.* **25A**, 107 (1967); GOTTLIEB M., GARBUNY M. and JONES C. K., *IEEE Trans. Sonics and Ultrasonics* **SU-16**, 159 (1969).
8. OZAKI H., KAJIMURA K., ISHIGURO T. and MIKOSHIBA N., *Phys. Lett.* **28A**, 300 (1968).
9. SINCLAIR A. C. E. and LEIBOWITZ J. R., *Phys. Rev.* **175**, 596 (1968).
10. NEURINGER L. J. and SHAPIRA Y., *Phys. Rev. Lett.* **15**, 724 (1965).
11. NEURINGER L. J. and SHAPIRA Y., *Phys. Rev.* **148**, 231 (1966).
12. TITTMAN B. R. and BÖMMEL H. E., *Phys. Lett.* **28A**, 396 (1968); *J. Phys. Chem. Solids* **31**, 1687 (1970).
13. ABRIKOSOV A. A., *Soviet Phys.-JETP* **5**, 1174 (1957).
14. MAKI K. and TSUZUKI T., *Phys. Rev.* **139**, A868 (1965).
15. MAKI K., *Phys. Rev.* **148**, 370 (1966).
16. MAKI K., *Phys. Rev.* **156**, 437 (1967).
17. IKUSHIMA A. and MIZUSAKI T., *J. Phys. Chem. Solids* **30**, 873 (1969).
18. SHEN L. Y. L., SENOZAN N. M. and PHILLIPS N. E., *Phys. Rev. Lett.* **14**, 1025 (1965).
19. DOBBS E. R. and PERZ J. M., *Rev. mod. Phys.* **36**, 257 (1964).
20. DOBBS E. R. and PERZ J. M., *Proc. R. Soc. (London)* **A296**, 113 (1967).
21. IKUSHIMA A., KAJIMURA K. and AKAO F., *Phys. Lett.* **25A**, 151 (1967).
22. See, for example, NOTO K., *J. phys. Soc. Japan* **26**, 710 (1969).
23. SOUTHGATE P. D., *Phys. Rev.* **110**, 855 (1958).
24. SOUTHGATE P. D., *Proc. Phys. Soc. Lond.* **B76**, 398 (1960).
25. MIKOSHIBA N., *J. phys. Soc. Japan* **16**, 895 (1961).
26. DE GENNES P. G., *Superconductivity of Metals and Alloys*, p. 131, W. A. Benjamin, New York (1966).
27. GARDNER W. E. and SMITH T. F., *Phys. Rev.* **144**, 233 (1966).
28. SHAPIRA Y. and NEURINGER L. J., *Phys. Rev.* **154**, 375 (1967).
29. GITTLEMAN J. I. and ROSENBLUM B., *Phys. Rev. Lett.* **16**, 734 (1966); *J. appl. Phys.* **39**, 2617 (1968).
30. NOTO K. and MUTO Y., Private communication, and to be published.

STRUCTURAL AND PHASE RELATIONS IN NONSTOICHIOMETRIC FERRITES WITH OXYGEN DEFICIENCIES

E. I. AKSEL'ROD, B. G. ALAPIN, I. I. VISHNEVSKY and B. Ya. SUKHAREVSKY
Physio-Technical Institute of Low Temperatures of Academy of Sciences of Ukraine, Lenin's
Prospect 47, Kharkov-86, U.S.S.R.

(Received 1 September 1969; in revised form 3 April 1970)

Abstract—The effect of point defects, specifically anion vacancies which appear after reduction, on the stability of nonstoichiometric ferrites with the spinel structure has been discussed. Exceeding a certain critical vacancy concentration is shown to result in the dissociation of the compounds. The considerations developed here have been confirmed by means of experiments on magnesium ferrite of variable composition, which were carried out under conditions yielding different degrees of imperfection. Above 1600°K the ferrites are observed to dissociate into MgO and solid solutions of Fe_3O_4 in MgFe_2O_4 owing to supersaturation with anion vacancies.

It is pointed out that neglect of the preexponential factor in a description of the cation distribution in terms of Néel's theory leads to an erroneous dependence of inversion energy upon the degree of inversion.

1. INTRODUCTION

DURING the last few years the effect of point defects, in particular vacancies, upon phase transitions in the solid state has been discussed on many occasions. The oxides of the transition metals, since they permit changes of structural vacancy concentrations over large ranges, appear to be suitable compounds for experimental and theoretical studies of this effect. Ferrospinel, in which nonstoichiometric defects can be related to an excess as well as to a deficiency of oxygen, are of special interest. The role of the latter in the case of magnesium ferrite in which oxygen deficiencies appear during heat treatment even in an air atmosphere, is discussed in the present paper. Magnesium ferrite, which is an important material in the radioengineering and refractory industries, is a typical spinel, in which the cation distribution in the crystal lattice sites is essentially temperature-dependent.

A thermodynamic analysis of the hypothetical ferrite with the exactly stoichiometric composition $\text{Me}_x^{2+} \text{Fe}_{1-x}^{3+} [\text{Me}_x^{2+} \text{Fe}_{1-x}^{3+}] \text{O}_4$ carried out by Néel[1] showed a temperature depen-

dence for the degree of inversion λ of the form:

$$\frac{\lambda(1+\lambda)}{(1-\lambda)^2} = \exp\left(-\frac{E}{RT}\right). \quad (1)$$

The energy of inversion E appeared to be close to 3.2 kcal/mole[2] Callen, Harrison and Kriessman[3] have extended the cation distribution theory and concluded that $E = \partial U / \partial \lambda$ (where U is the internal energy) can be dependent on λ .

Magnesium ferrite free from appreciable quantities of Fe^{2+} ions is observed to exist at high temperatures only under oxygen pressure of some tens of atmospheres. Thus heat treatment in atmospheres having oxygen partial pressures lower than the equilibrium value results in dissociation of the ferrite.

The preparation and operation of the devices made from magnesium ferrite, and also many of the experimental studies are carried out in conditions under which deviations from stoichiometry are quite significant.*

*We consider a spinel of nominal composition $\text{Me}'\text{Me}_x^{2+}\text{O}_4$ to be nonstoichiometric if the relation $\text{Me}' + 2\text{Me}''/0 \neq 4$.

Because of this the region of the phase diagram near MgFe_2O_4 has been thoroughly examined as a function of composition, temperature and oxygen pressure.

Blackman[4] has studied the effect of an excess of magnesium oxide in MgFe_2O_4 on the lattice constant, magnetic induction, Curie point and resistance. He interpreted the results obtained in terms of solid solution formation between MgFe_2O_4 and MgO with a limit at MgO concentration of about 8 mole%. Later Paladino[5, 6] and then Tret'yakov[7] in a study of the ternary system $\text{MgO-FeO-Fe}_2\text{O}_3$, concluded that independent of temperature nonstoichiometric magnesium ferrite with the composition 0.092 $\text{MgO} \cdot \text{MgFe}_2\text{O}_4$ is thermodynamically stable, while ' MgFe_2O_4 ' is a mixture of hematite and the above compound.

These findings, however, have not been confirmed by other authors. In papers by Katsura and Kimura[8], Reijnen[9], Speidel[10], and Whilshie and White[11] the single-phase spinel field in the ternary phase diagram is restricted by the ferrites with compositions $\text{MgO} \cdot \text{Fe}_2\text{O}_3$ and $\text{FeO} \cdot \text{Fe}_2\text{O}_3$.

In studies of MgFe_2O_4 a dependence of the

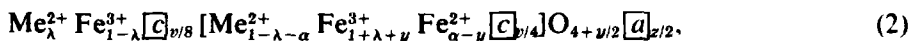
ferrite therefore warrants further study, especially under conditions favoring dissociation, and in particular at high temperatures.

2. POINT DEFECTS IN NONSTOICHIOMETRIC MgFe_2O_4

Because of the fact that ferrite dissociation is accompanied by loss of oxygen, the existence of a single-phase structure, assuming that the electrical neutrality of the crystal is conserved, must be related to point defect formation either of interstitial cation type or anion vacancy type.

The first possibility has been discussed previously[5, 7], and it was suggested that an equilibrium nonstoichiometric ferrite of 0.092 $\text{MgOMgFe}_2\text{O}_4$ composition containing no Fe^{2+} ions would involve excess Mg ions in sites which were not characteristic of the spinel structure; i.e. $\text{Mg}_{1.044} (\text{Mg}_i)_{0.022} \text{Fe}_{1.956} \text{O}_4$ with Mg_i an interstitial cation.

Sukharevsky *et al.*[15, 16] have considered the second possibility and proposed a model for a nonstoichiometric solid solution of ferros spinels MeFe_2O_4 with magnetite Fe_3O_4 involving cation and anion vacancies as follows



lattice parameter and magnetic moment on the quenching temperature up to 1100°C[6] and 1400°C[12] has been observed. Allen[13], in the range up to 1600°C, observed kinks in the curves of lattice parameter and thermal expansion against temperature in the range of 1100°C which he attributed to some phase transition connected with ordering. In an analysis of the diffraction line profiles, Grimes *et al.*[14] did not find, however, any noticeable ordering of Mg and Fe ions in the octahedral ferrite sublattice.

Lack of agreement on the structure and solid solution composition of $\text{MgO-FeO-Fe}_2\text{O}_3$ system in the region near to magnesium

where α is the concentration of magnetite, y is the deviation from stoichiometry, z and $v = y + z$ are quantities proportional to anion $[\text{A}]$ and cation $[\text{C}]$ vacancy concentrations, respectively. This model allowed the derivation of relations connecting point defect concentrations with the thermodynamic parameters of the system, which enabled a description from the theoretical point of view of the experimental dependence of nonstoichiometry upon solution composition.

The idea of the existence of anion structural vacancies is more consistent from the crystallochemical point of view[17]. Firstly, the 3:4 correlation of cation and anion sites

specific for spinel structures is destroyed by the presence of interstitials, a fact which as far as we know has not been observed experimentally. Secondly, since the thermal vacancies exist in cation as well as in anion sublattices, nonstoichiometric structural vacancies can be analogously formed in both sublattices. In this case the thermal vacancies correspond to the extreme case of the stoichiometric solution. And finally, the displacement of a divalent cation from a site, allowed by spinel structure, into an interstitial one can only be due to disappearance of the normal cation site, which is possible only by collective removal of the oxygen atoms surrounding the given site. In the initial stage of reduction when the number of oxygen atoms removed is not great, this condition is hardly possible from the thermodynamical point of view.

One can obtain direct evidence of the applicability of one or the other model by comparing X-ray and bulk density of nonstoichiometric ferrites. Unfortunately, such experiments on single crystals have not been carried out and those on polycrystals were not sufficiently accurate [6].

Thermal conductivity experiments on partially reduced ferrites can be used to provide indirect evidence for the existence of anion vacancies. Point defects of vacancy type in the coordinated crystals are known to cause distortions that scatter phonons strongly. A sharp increase in thermal resistivity with an increase in the degree of reduction for ferrites of Mg, Li and Zn (8-9 times at 100°K) [18] suggests that this phenomenon is connected with the appearance of anion vacancies.

The dependence of extra thermal resistivity due to the substitution by cations of other valencies upon their concentrations ($R = \vartheta(C_{\text{cat}})$) is characterized by a positive second derivative in zero ($\vartheta''(0) > 0$) and by the presence of a kink. Above this point a sharp increase in the thermal resistivity was observed, followed by decomposition of the compounds or solid solutions.

In Ref. [19] it was shown that such behavi-

our of the mentioned dependence was determined by the presence of cation structural vacancies. It is important to note the similarity between the thermal resistivity dependence on cation vacancy concentration in $\text{MgO}-\text{Me}_2\text{O}_3$ ($\text{Me}=\text{Fe}, \text{Cr}$), and $\text{MgAl}_2\text{O}_4-\text{Al}_2\text{O}_3$ solid solutions and the content of ferrous ions in the above ferrites. For example, this is shown for $\text{MgAl}_2\text{O}_4-\text{Al}_2\text{O}_3$ spinel solutions with cation vacancies and for MgFe_2O_4 with different degrees of reduction in Fig. 1. In our opinion this fact indicates that the probable kind of the reduction defects in ferrite is structural anion vacancies.

In Ref. [16] cation vacancies were considered as a factor determining the stability of the ferrospinel solid solutions. Above some critical value of this parameter the solution decomposed as the crystal lattice has the tendency to decrease the free energy by precipitation of a phase which carried away the superstoichiometric atoms. It was proposed that the anion vacancies which are expected to appear on reduction of the ferrite causes instabilities in the crystal lattice as well.

The aim of the present paper is to study the behaviour and properties of magnesium ferrite at high temperatures leading to essential dissociation even in an atmosphere of air.

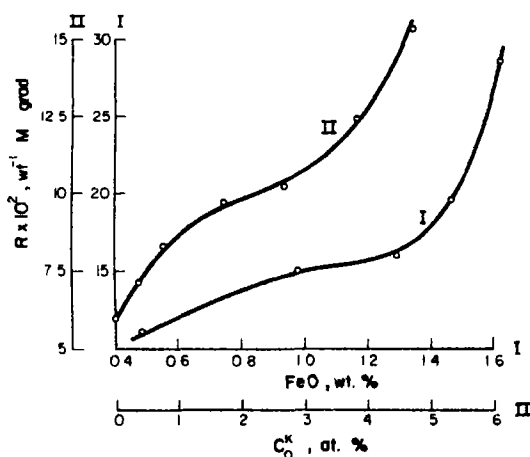


Fig. 1. Thermal resistivity vs. FeO content for MgFe_2O_4 (I) and vs. cation vacancy concentration for $\text{MgAl}_2\text{O}_4-\text{Al}_2\text{O}_3$ solid solution (II). $T = 300^\circ\text{K}$.

3. PREPARATION OF THE SAMPLES

Magnesium ferrite was prepared by ceramic techniques from fine-grained magnesium oxide powder (MgO content > 99.7 wt.%) and ferric oxide powder ($\text{Fe}_2\text{O}_3 = 99.7$ wt.%). The synthesis was carried out by heating a mixture of the oxides at 1620°K for 5 hr. The material was ground and samples pressed in the form of discs of 2–3 mm thickness were subjected to homogenization at 1850°K for 12 hr with subsequent cooling at a rate 30–50°/hr. Heat treatment of the samples was carried out in a platinum-wound furnace in air in the temperature range 600–1900°K, with subsequent quenching in water. The experiments were carried out on two series of samples quenched under various conditions. The results obtained on the second series of samples in the high temperature range seemed to be more reliable. Details of the heat treatment are presented in Table 1.

4. EXPERIMENTAL TECHNIQUES

Magnetic, X-ray and chemical analyses were the main techniques used in the studies. Saturation magnetic moments σ were determined with a Weiss pendulum magnetometer to within ± 2 per cent. To define the absolute saturation moments the measured values were extrapolated to 0°K in accordance with a $\sigma_0 \sim (T^{3/2})$ law in view of previous results[20] where the validity of this law for MgFe_2O_4 was established. The Curie points were determined by means of extrapolation of the σ^2 vs. T plots to zero. The accuracy of the measurements was not more than 2–3°. The error in the measurements of lattice parameters was within limits of ± 0.001 Å. The FeO and free magnesium oxide contents were determined by chemical analyses. To provide a check on the ferrous oxide content obtained by chemical analysis, thermogravimetric measurements at some points have also been carried out.

5. RESULTS

Increasing the quenching temperature up to ~1500°K leads to an increase in saturation

magnetic moment of magnesium ferrite monotonically to $2.8 \mu_B$ (Fig. 2). Previous data from Ref. [6] shown in the plot were obtained between 700 and 1400°K and are in agreement with our results. Further increases in temperature do not affect the magnetic moment value.

The temperature dependence of the Curie point values is also shown and displays a minimum which is close to 1500–1600°K.

The lattice parameters of MgFe_2O_4 are found to change with the quenching temperature along with the magnetic moments (Fig. 3). They increase in a linear fashion up to 1500°K and are constant above this temperature. Allen's data[13] fall satisfactorily on the same

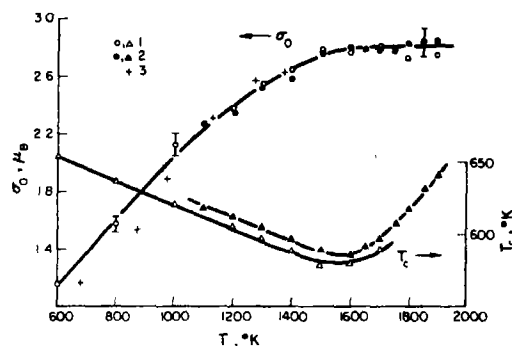


Fig. 2. Absolute saturation σ_0 and Curie temperature T_c of MgFe_2O_4 samples vs. quenching temperature. 1 — the 1st series, 2 — the 2nd series, 3 — [6].

plot, with the exception of the high temperature values, which were subjected to considerable error. Compared with our present results, the previous ones in Ref. [6] appear to be systematically larger by 0.002 – 0.003 Å.

As MgFe_2O_4 is considered to be a 'Néel' type of ferrite the degree of inversion can be calculated from the relation:

$$\lambda = 0.1(\sigma_0 + z), \quad (3)$$

where z is the number of Fe^{2+} ions in the crystal formula $\text{MgFe}_{2-z}^{3+}\text{Fe}_z^{2+}\text{O}_{4-z/2}$. The dependence of λ on the quenching temperature is also plotted in Fig. 3. Because of the smallness of z the shape of this curve, naturally, follows the σ_0 temperature dependence.

Table 1. Heat treatment and properties of MgFe_2O_4 samples

N/N	Samples		Quenching temperature	σ_0 , μ_B		T_c , °K		a , Å		FeO*, wt. %		MgO†, wt. %		z , wt. %		λ	
	1	2		1	2	1	2	1	2	1	2	1	2	1	2	1	2
1	MF6		600-50		1.16		652		8.381		0.49				1.36		0.117
2	MF8		800-30		1.58		637		8.384		0.98				2.72		0.161
3	MF10		1000-20		2.13		620		8.390		1.22				3.39		0.216
4		MF11		1100-13		2.27		619							2.78		
5	MF12		1200-10		2.38	2.37	605	613	8.393	8.394	1.35	0.90		3.75	0.242	0.240	
6	MF13		1300-10		2.54	2.51	596	605	8.394	8.396	1.54	0.77		4.28	0.259	0.255	
7	MF14		1400-8		2.64	2.58	588	597	8.398	8.396	1.76	0.75		4.89	0.270	0.262	
8	MF15		1500-8		2.78	2.75	578	589	8.399	8.400	1.83	0.65		5.09	0.285	0.279	
9	MF16		1600-6		2.77	2.79	580	586	8.399	8.399	1.80	0.90		5.00	0.282	0.283	
10	MF16.5			1650-5		2.78		592									
11	MF17		1700-4		2.80	2.79	590	597	8.398	8.400	2.53	1.60			0.288	0.286	
12		MF17.5		1750-4		2.77		608									
13	MF18		1800-3		2.71	2.82	618	618	8.398	8.399	3.98	2.77			0.284	0.292	
14		MF18.5		1850-1		2.84		632									
15	MF19		1900-0.5		2.74	2.84		641	8.398	8.400	6.52	4.65			0.293	0.301	

Note: Columns 1 and 2 are referred to as number 1 and 2 sample series, respectively.

*FeO values are averaged in the two series.

†MgO values are obtained for the second series.

On the basis of the chemical analysis the temperature dependence of the content of ferrous oxide calculated from Fe^{2+} concentration and of the content of free MgO in the samples exhibited the following behavior. The quantity of FeO slowly increases with increase in quenching temperature up to 1600°K and sharply increases for the higher temperatures.

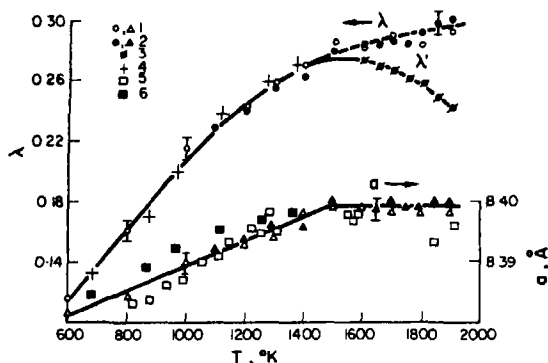


Fig. 3. The degree of inversion λ and lattice parameters α vs. quenching temperature. 1 — the 1st series, 2 — the 2nd series, 3 — values in two-phased range calculated according to equation (22), 4-[6], 5-[13], 6-[6].

The results of the determinations of FeO content by chemical analysis have been compared with those of thermogravimetric experiments. If it is assumed that ferrite dissociation is responsible for weight changes, then the agreement between the results obtained by the two methods can be considered satisfactory (Fig. 4).

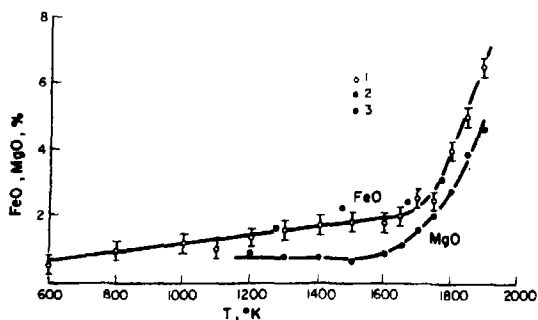


Fig. 4. FeO (1, 2) and free magnesium oxide (3) contents in the samples vs. quenching temperature. 1, 3 — obtained from chemical analysis data. 2 — obtained from gravimetric measurements.

The quantity of free magnesium oxide also increases at high quenching temperatures similar to FeO , while below 1600°K free MgO was observed in all the samples of the second series to the extent of about 0.8 wt. %.

Table 1 presents all the results obtained for the two series of samples.

6. DISCUSSION

(a) Structural characteristics between 600 and 1500°K

For all the properties of MgFe_2O_4 studied, there exists two ranges for the regions below 1500 and above 1600°K , respectively. First we shall consider the interdependence between structure and properties in the low temperature range 600 – 1500°K .

One can conclude that at these temperatures ferrite reduction is not significant enough to lead to structural changes and hence all the observed phenomena occur within a one-phase region. In this case the changes in lattice parameters are determined by variations in the cation distribution and the ferrous ion concentration. In the experiments described above the contributions from these factors are difficult to separate as they act simultaneously and in the same direction. To assess their relative effects on the lattice parameters some experiments were carried out in which both temperature (i.e. the degree of inversion) and partial oxygen pressure were fixed. The results are presented in Table 2, from which it is seen that inversion affects the lattice parameter of magnesium ferrite more strongly than the degree of reduction. This fact permits us to define an approximately linear correlation between a and λ (Fig. 5).

In ferromagnetic spinel solid solutions an inverse dependence between the Curie temperature and the lattice parameter is usually observed. One possible explanation for this is a decrease in strength of the superexchange interaction resulting from an increase in the cation-anion distances. In the present case the increase in lattice parameters with quenching

Table 2. Effect of temperature and oxygen pressure on the composition and structure of MgFe_2O_4

NN	Heat treatment °K	P_{O_2} , atm	C_{FeO} , wt. %	σ_0 , μ_B	a , Å	λ
1	1570.5	0.21	1.2	1.54	8.388	0.15
2	1570.5	60	0.4	1.62	8.389	0.16
3	1170.5	60	0.5	1.19	8.382	0.12

Note: Quenching of the samples was carried out in a gas stream so that the data cited correspond to the low temperature equilibrium state.

temperature leads to a monotonic lowering of the Curie points.

The increase in λ with temperature would presumably be accompanied by a decrease in the number of AB magnetic bonds. The interdependence between a , λ and T_c is shown in the plot of Fig. 6.

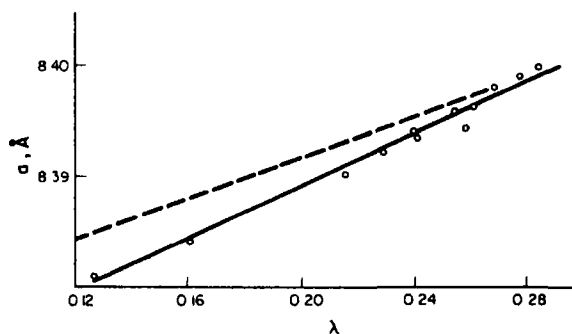
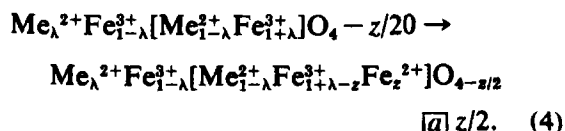


Fig. 5. Variation of lattice parameters with degree of inversion. The dashed line is from [6].

7. THERMODYNAMIC TREATMENT

In accordance with the above considerations on the nature of the defects in non-stoichiometric MgFe_2O_4 , a thermodynamic analysis was carried out using model given in equation (2) which involves anion vacancy formation in ferrite reduction. Schematically this process in the range of the one-phased region can be expressed by the reaction



The degree of reduction z is related to the anion vacancy concentration

$$C_a = \frac{z}{8} = \frac{1}{8} \cdot \frac{C_{\text{FeO}} \cdot \mu_{\text{MgFe}_2\text{O}_4}}{\mu_{\text{FeO}} + \frac{1}{2}C_{\text{FeO}} \cdot \mu_0} \quad (5)$$

(C_i and μ_i are respectively weight concentration and molecular weight of the corresponding oxides).

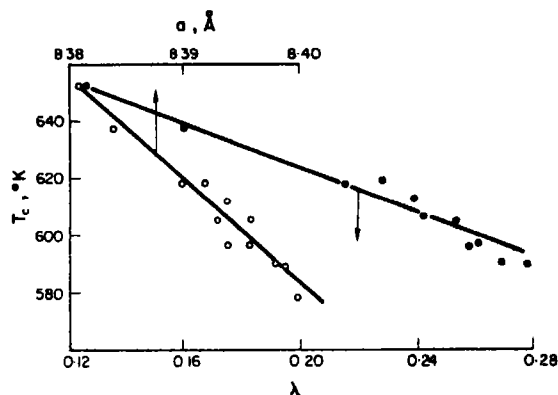


Fig. 6. Curie points vs. degree of inversion and lattice parameters.

It is easy to see that equation (2) reduces to equation (4) when $\alpha = 0$ and $y = z(v = 0)$. The assumption that the transition $\text{Fe}^{3+} \rightarrow \text{Fe}^{2+}$ takes place on the octahedral sites does not affect the number of the anion vacancies which are produced.

Following Refs. [15-17] the free energy change for reduction of a single Fe^{3+} ion can be written in the form:

$$\Delta F = z\beta_z + \lambda E - T\Delta S, \quad (6)$$

where β_z includes the reduction energy, the free energy of an oxygen atom, the work of anion vacancy formation, and the elastic deformation energy, which is related to the size difference between an oxygen ion and a vacancy; E is the energy change on transferring a Me^{2+} from the A to the B sublattice; and ΔS is configurational entropy change.

From the free energy minimum conditions $\partial(\Delta F)/\partial z = \partial(\Delta F)/\partial \lambda = 0$ the following equations relating the degree of nonstoichiometry z to the thermodynamic parameters of the system are obtained

$$\frac{z^{3/2}}{(1+\lambda-z)(8-z)^{1/2}} = \exp\left(-\frac{\beta_z}{RT}\right); \quad (7)$$

$$\frac{\lambda(1+\lambda-z)}{(1-\lambda)^2} = \exp\left(-\frac{E}{RT}\right) = \Lambda. \quad (8)$$

Equation (7) therefore predicts a linear dependence between $\ln[z^3(1+\lambda-z)^{-2}]$ and $1/T$ if $z(\sim 10^{-2})$ in the $(8-z)$ term in the denominator is neglected. This prediction is seen to be correct for MgFe_2O_4 (Fig. 7). There is a relatively weak β_z temperature dependence and the value of β_z calculated from the slope of the line is about 4 ± 0.5 kcal/mole. A theoretical value of β_z cannot be calculated because of a lack of reliable data necessary for the calculation.

Equation (8) is the Néel formula (1) modified by the deviation from stoichiometry given by z . If the inversion energy E is assumed

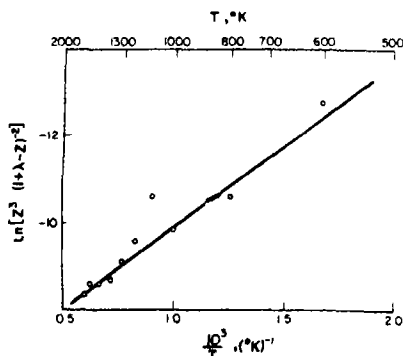


Fig. 7. Graphical treatment of equation (7).

independent of temperature (and consequently of λ) it may be calculated from the slope of a plot of $\ln \Lambda$ against $1/T$. This has been done in Fig. 8 and it is seen that Néel's equation is

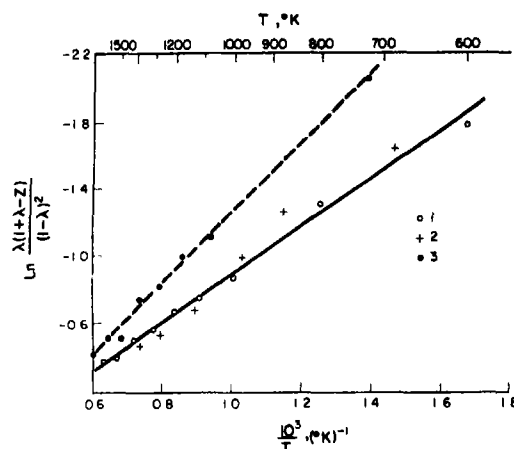


Fig. 8. Graphical treatment of equation (8). 1—our data, 2—[6], 3—[12].

satisfied reliably enough for MgFe_2O_4 in the one-phase region. The value of E is 3 ± 0.3 kcal/mole in good agreement with the previous published value [2].

It has already been mentioned that the thermodynamical theory of cation distribution in ferrites $\text{Me}'_x \text{Me}''_y \text{Fe}_2\text{O}_4$ with two degrees of inversion for the two divalent cations Me' and Me'' had been developed in Ref. [3].

In the particular case of a single ferrite the equilibrium condition according to this theory is

$$\frac{\lambda(1+\lambda)}{(1-\lambda)^2} = \exp\left(-\frac{1}{RT} \frac{\partial U}{\partial \lambda} + 21 \frac{\partial \ln \theta}{\partial \lambda}\right), \quad (9)$$

where U is internal energy, involving the electrostatic energy and the magnetic exchange energy. Equation (9) is obtained using the Debye spectrum; θ being the characteristic temperature.* The difference between (9)

*The fact that the Debye spectrum is used for the description of the high temperature behaviour of ferrites is not quite correct in general.

and Néel's formula (1) is in the possible dependence of $\partial U/\partial \lambda$ on λ , and in the presence of the temperature-independent preexponential factor.

The experimental data for single and mixed ferrites were treated in several papers [6, 12, 21, 22] according to this theory in the following way. $\partial \ln \theta/\partial \lambda$ was assumed to be zero, λ was determined from structure (magnetic or X-ray) measurements, and then $\partial U/\partial \lambda$ was calculated from equation (9). In all the papers mentioned $\partial U/\partial \lambda$ was found to decrease linearly with increasing λ , i.e.

$$U(\lambda) = U_0 + R(\theta_0 \lambda - \theta_1 \lambda^2), \quad (10)$$

where θ_0 and θ_1 are constants expressed in $^\circ\text{K}$.

It is clear that this result disagrees with Fig. 8 in which the data for MgFe_2O_4 † are plotted from Refs. [6] and [12]. These satisfy equation (1) as well, although the authors interpreted them on the basis of equation (9) and attained a linear dependence of $\partial U/\partial \lambda$ on λ . This contradiction is explained by the fact that $\partial U/\partial \lambda$ cannot be calculated from equation (9) if the preexponential factor is neglected.

From these general considerations it follows that this temperature independent preexponential factor must also be present in the Néel equation. Within the framework of the statistical theory its appearance results from the effect of the thermal expansion of the lattice on the inversion energy. This factor is analogous to the entropy term $\exp(S/R)$ which occurs in the calculations of thermal vacancy concentration in metals, and has a value of between 1 and 10 [23].

In general we can write

$$\Lambda = K \exp\left(-\frac{E}{RT}\right), \quad (11)$$

†We note practically an absolute coincidence of the results when the experimental data of Fig. 8 were treated according to (8) and by means of $\Lambda = \lambda(0.94 + 1.06\lambda)/(1 - \lambda)(1 - 0.94\lambda)$ relation, used in [6].

where K is temperature-independent factor. As the theory [3] involves certain assumption, it is difficult to say if K corresponds to $\exp(21(\partial \ln \theta/\partial \lambda))$. At any rate, in view of the small E value, there is no reason to neglect $\partial \ln \theta/\partial \lambda$.

It is evident that the calculation of inversion energy according to the plot of Fig. 8 is insensitive to the existence of the preexponential factor, while the calculation of $\partial U/\partial \lambda$ according to equation (9) with the assumption that $K = 1$ can result in erroneous conclusion. In fact, the expression

$$\frac{\partial U}{\partial \lambda} = -RT \ln \Lambda = E - RT \ln K \quad (12)$$

shows a linear dependence on T . Since the relationship between T and λ is close to linear (Fig. 3), $\partial U/\partial \lambda$ calculated from equation (12) should show a linear dependence on λ as well, while in fact the real inversion energy remains constant with good accuracy. The K value obtained from the plot of Fig. 8 is 1.9, which is within the usual range of values of entropy factors.

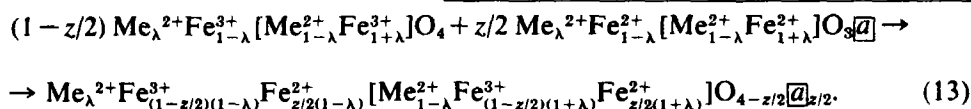
Thus the values of $\partial U/\partial \lambda$, θ_0 and θ_1 determined in the above papers have no real physical meaning, but instead reflect the temperature dependence of λ .

8. PHASE RELATIONS IN MgFe_2O_4 AT HIGH TEMPERATURES

The sharp changes in the properties considered at 1500–1600°K were found to be due to the decomposition of the single-phase system. One can expect that the phase equilibrium conditions are controlled to a greater extent by the increase in the internal energy of the spinel structure due to nonstoichiometric vacancy formation than by the temperature changes. This is supported by the fact that magnesium ferrite decomposes easily in a reducing atmosphere at low temperatures, but remains as a single phase at rather high temperatures under increased oxygen pressure. The anion vacancy concentration $C_a \approx 0.6$

at.% at the knee of the $C_{\text{FeO}} = f(T)$ curve of Fig. 4 is presumably critical for MgFe_2O_4 and any increase leads to the decomposition of the ferrite, and the appearance of the divalent cation excess as a separate MeO phase. The decomposition evidently occurs for various values of the external parameters as soon as the vacancy concentration exceeds this critical value.*

From this point of view the reduction of magnesium ferrite can be formally presented as dissolution of the protoxidic phase of the type $\text{MeFe}_2\text{O}_3\text{[}\bar{\text{a}}\text{]}$ with a spinel structure in MeFe_2O_4 , accompanied by the introduction of anion vacancies in the initial stoichiometric ferrite according to the equation



To simplify the calculation it is assumed that the degree of inversion for the protoxidic phase is the same as that for MgFe_2O_4 and is independent of the solid solution composition. The critical vacancy contents $z^*/2$ are defined by the solubility limit, and when this is exceeded, the ferrite is converted into a two-phase system.

Using the condition of thermodynamic equilibrium for the solid solution of the stoichiometric phase with the protoxidic phase described by equation (13), namely

$$F_1 - F(z^*) = \left(1 - \frac{z^*}{2}\right) \frac{\partial F}{\partial z} \bigg|_{z=z^*/2} \quad (14)$$

one can obtain by analogy with Ref. [16] the temperature dependence of the critical vacancy concentration:

$$\ln \frac{z^*(8-z^*)}{12} = \frac{F_1 - F_2}{3RT} = \frac{q(T - T_0)}{3RTT_0} \quad (15)$$

*It is a characteristic that a rapid increase in the thermal resistivity of magnesium ferrite is observed at a FeO content corresponding to an anion vacancy concentration close to the critical one (i.e., $C_{\text{FeO}} \approx 1.6$ wt.% corresponds to $C_{\bar{\text{a}}} \approx 0.58$ at.%).

F_1 is the free energy of the MeO phase, F_2 is the free energy of the same phase but in a spinel form, q and T_0 are enthalpy and temperature of the fictitious phase transition in which MeO with a rock-salt lattice transits to a spinel structure.

On the other hand the thermodynamic analysis of equation (13) permits one to obtain, as above, the temperature dependence of the degree of nonstoichiometry for magnesium ferrite.†

$$\frac{z^{3/2}}{(2-z)(8-z)^{1/2}} = \exp\left(-\frac{\beta_z}{RT}\right) \quad (16)$$

If we assume $z = z^*$ in equation (16) the com-

bined solution of equations (15) and (16) yields an expression for the critical vacancy concentration which is temperature independent

$$\ln \left\{ \left[\frac{z^*(8-z^*)}{12} \right]^{3\beta_z/q} \frac{(2-z^*)(8-z^*)}{z^{*3/2}} \right\} = \frac{\beta_z}{RT_0} \quad (17)$$

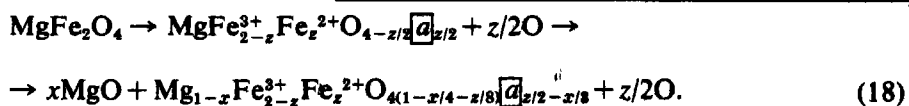
Though the lack of the data for q and T_0 does not permit calculation of z^* , equation (17) still confirms the conclusion that the critical concentration of anion vacancies is a temperature-independent parameter which determines the tendency of a reduced ferrite to decompose.

The chemical analysis data reveal that the MeO phase is magnesium oxide and that its quantity increases as the quenching temperature is raised above 1600°K. On this basis the decomposition of MgFe_2O_4 can be expressed

†The disagreement between equations (16) and (17) is related to an insignificant difference in the degree of inversion for ferrites given by equations (13) and (4).

in the form of the following scheme:

changes of the phase state of magnesium



The remaining spinel phase is a solid solution of magnetite in magnesium ferrite, $(1-\alpha)\text{MgFe}_2\text{O}_4 + \alpha\text{Fe}_3\text{O}_4$, the magnetite concentration being

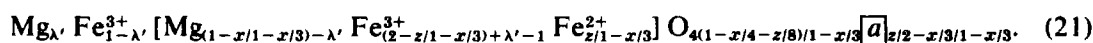
$$\alpha = \frac{2x}{3-x}. \quad (19)$$

From (18) it follows that

$$x = \frac{(\mu_{\text{MgFe}_2\text{O}_4} - z/2\mu_0) \cdot C_{\text{MgO}}}{\mu_{\text{MgO}}}. \quad (20)$$

In connection with the above statements it is necessary to remember that the λ and α values shown in Fig. 3 are characteristics of an own single-phased magnesium ferrite up to 1600°K; at higher temperatures these values are applicable to solid solutions of Fe_3O_4 in MgFe_2O_4 . In this temperature range the degree of inversion obtained according to equation (3) has no specific meaning as it was calculated without taking into account the changes of phase state.

The nonstoichiometric solid solutions formed as a result of the dissociation can be written in the following form:



This formula is normalized in such a way for the number of the tetrahedral, octahedral and oxygen sites to be 1, 2 and 4, respectively. The real degree of inversion of a solid solution, described by equation (21) may be calculated by means of the relation

$$\sigma'_0 = 10\left(\lambda' + \frac{x-0.3z}{3-x}\right). \quad (22)$$

Calculating σ_0 we took into account the

ferrite according to a phase relations, described by equation (18):

$$\sigma_0 = \sigma_m \frac{\mu_{\text{MgFe}_2\text{O}_4} - x\mu_{\text{MgO}} - z/2\mu_0}{\mu_B \cdot N_0 \cdot (1 - C_{\text{MgO}})(1 - x/3)}. \quad (23)$$

σ_m here is in the units of gauss·cm³/g and N_0 is Avogadro number.

Table 3 presents α and λ' values calculated according to equations (19) to (22). The change in the degree of inversion $\lambda' = f(\alpha, T)$ (Fig. 3) is consistent with the decrease in the normality of the solution as the composition approaches magnetite.

The lattice parameters of the solid solutions in the vicinity of MgFe_2O_4 decrease relatively quickly with an increase in the magnetite content; on the other hand, the lattice parameter at constant composition of the solution increases with temperature[16]. The competition between the two factors results in values which are practically constant in the two-phase region.

The increase in the Curie temperatures of samples, which were annealed above 1600°K is convincing evidence of the decomposition of magnesium ferrite and the formation of $\text{Mg}_{1-\alpha}$

$\text{Fe}_{2+\alpha}\text{O}_4$ solid solutions, since the Curie temperature of magnetite ($T_c = 860^\circ\text{K}$) [24] is significantly higher than that of MgFe_2O_4 at the temperature $\sim 1600^\circ\text{K}$ ($T_c \approx 600^\circ\text{K}$).

The concentration dependence of $T_c = f(\alpha)$ was obtained for the samples quenched at 1670°K in the range of values $0.05 \leq \alpha \leq 1$, and is characterized by two linear regions intersecting at $\alpha \approx 0.35$ (Fig. 9). The Curie temperatures for samples MF16-MF19 are presented in the same plot as a function of α

Table 3. Concentration and degree of inversion of $\text{Mg}_{1-\alpha}\text{Fe}_{2+\alpha}\text{O}_4$ solid solutions obtained as a result of high temperature reduction of MgFe_2O_4

Samples	$T_a, ^\circ\text{K}$	X_i , mole %	α , mole %	σ_0, μ_B	λ'
MF 16	1600	4.5	3.0	2.83	0.273
MF16.5	1650	5.7	3.8	2.83	0.269
MF17	1700	7.9	5.4	2.86	0.266
MF17.5	1750	9.9	6.8	2.87	0.260
MF18	1800	13.7	9.5	2.84	0.258
MF18.5	1850	19.0	13.5	3.01	0.248
MF19	1900	22.9	16.5	3.05	0.242

(see Table 3). The lack of coincidence with the $T_c = f(\alpha)$ curve is attributed to the difference in the quenching temperatures. Indeed, after the samples for the $\text{Mg}_{1-\alpha}\text{Fe}_{2+\alpha}\text{O}_4$ system with $\alpha = 0.05$; 0.13 (close in magnetite content to MF17 and MF18.5) had been heat treated at the corresponding temperatures (1700 and 1850°K) agreement between T_c values was significantly better.

It should be noted that the calculated values are slightly low because the FeO content in the MgO phase has been neglected, and because of the presence of a 'background' of free magnesium oxide in the non-dissociated samples.* The use of the true values would lead to still better agreement with the data plotted in Fig. 9.

9. CONCLUSIONS

A number of ideas about the effects of structural defects on the occurrence of phase transitions in spinels have been discussed in this paper. In an earlier paper[16] it was shown that the supersaturation of spinel solid solutions with cation vacancies leads to their dissociation. Anion vacancies are considered to be the most probable type of defect occurring during reduction of ferrosinels. Thermodynamic analysis shows that they can be

considered in terms of a parameter characterizing the stability of the structure in relation to dissociation independently of temperature.

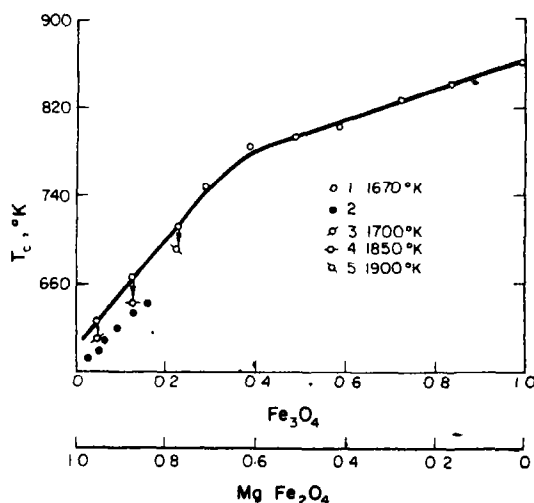


Fig. 9. Curie points of $\text{Mg}_{1-\alpha}\text{Fe}_{2+\alpha}\text{O}_4$ solid solutions vs. concentration. 1—sample, annealed from 1670°K, 2—MF 16, 5—MF 19 samples, 3, 4, 5—samples 1 after quenching from 1700°, 1850° and 1900°K, respectively.

These general considerations have been checked on a sample of reduced magnesium ferrite. The degree of reduction upon heating in an atmosphere of air up to 1600°K increased monotonically within a one-phase structural region up to a value of anion vacancy concentration corresponding to ~ 0.6 at.%. If this value is exceeded (as a result of further heating) the ferrite decomposes into MgO

*The presence of free MgO in the samples annealed at temperatures lower than 1600°K can be due either to a systematic error in the chemical analysis or to ferrite decomposition in the course of the homogenizing annealing treatment (1850°K) followed by slow cooling.

and solid solutions of Fe_3O_4 in MgFe_2O_4 , the concentration of Fe_3O_4 increasing with temperature.

In the one-phase region the energy of inversion E in the Néel equation (1) is found to remain constant within the error of the measurements. The experimental data are evidence of the existence of a preexponential factor K in (1), which has a value close to 1.9. The treatment of the results of measurements yielding a temperature dependence for the degree of inversion λ in the approximation $K = 1$, as used previously [6, 12, 21, 22] is incorrect and leads to an erroneous conclusion concerning the dependence of E upon λ .

Acknowledgement—The authors are indebted to Professors I. M. Lifshitz and Ya. E. Geguzin for their interest in this work, to A. Ya. Chervonenkis for preparing the samples described in Table 2, and to S. T. Baliuk and L. A. Pavlova for carrying out the chemical analyses.

REFERENCES

1. NÉEL L. *Compt. Rend.* **230**, 190 (1950).
2. SMIT J. and WIJN H. P. J., *Ferrites* (Russian translation; *Ferriti, IL., M. str.*) **186** (1962).
3. CALLEN H. B., HARRISON S. E. and KRIESSMAN C. J., *Phys. Rev.* **103**, 851 (1956).
4. BLACKMAN L. C., *Trans. Faraday Soc.* **55**, 391 (1959).
5. PALADINO A. E., *J. Am. ceram. Soc.* **43**, 183 (1960).
6. MOZZI R. L. and PALADINO A. E., *J. chem. Phys.* **39**, 435 (1963).
7. TRET'YAKOV Yu. D., *Termodinamika ferritov, Chimiya, L.* (1967).
8. KATSURA T. and KIMURA S., *Bull. Chem. Soc. Japan* **38**, 1664 (1965).
9. REIYNEN P., *Proc. 5 Intern. Symp. on Reactivity of Solids*, p. 562, Elsevier, Amsterdam (1965).
10. SPEIDEL H., *J. Am. Ceram. Soc.* **50**, 243 (1967).
11. WHILSHEE J. C. and WHITE J., *Trans. Brit. Ceram. Soc.* **66**, 541 (1967).
12. KRIESSMAN C. J. and HARRISON S. E., *Phys. Rev.* **103**, 857 (1956).
13. ALLEN W. C., *J. Am. Ceram. Soc.* **49**, 257 (1966).
14. GRIMES N. W., HILLEARD R. J., WATERS J. and IERKESS J., *J. Phys. (Proc. Phys. Soc.)* **C1**, 663 (1968).
15. SUKHAREVSKY B. Ya., ALAPIN B. G. and AKSEL'ROD E. I., *Dokl. akad. nauk. SSSR* **171**, 359 (1966).
16. SUKHAREVSKY B. Ya. and ALAPIN B. G., AKSEL'ROD E. I., *J. Phys. Chem. Solids* **29**, 1773 (1968).
17. SUKHAREVSKY B. Ya., ALAPIN B. G. and VISHNEVSKY I. I., *Zh. Phys. Chim.* **43**, 3113 (1969).
18. VISHNEVSKY I. I. and SKRIPAK V. N., *Fiz. tverd. tela* **9**, 3633 (1967). *Izv. AN SSSR, Neorg. mater.* **4**, 1989 (1968).
19. VISHNEVSKY I. I. and SUKHAREVSKY B. Ya., *Fiz. tverd. tela* **6**, 2168 (1964). VISHNEVSKY I. I. and SKRIPAK V. N., *Fiz. tverd. tela* **7**, 2925 (1965). *Izv. AN SSSR, Seriya Neorg. mater.* **2**, 1820 (1966).
20. AKSEL'ROD E. I. and VISHNEVSKY I. I., *Fiz. Metal. i Metalloved.* **25**, 753, (1968).
21. EPSTEIN D. J. and FRACKIEWICZ B., *J. appl. Phys.* **29**, 376 (1958).
22. BARTASHEVSKY E. L., KOLOMOITZEV F. I. and SIVTZEV D. C., *Izv. visshikh uchebnikh zavedenii SSSR, Fizika* **1**, 171 (1966).
23. ZENER C., *J. appl. Phys.* **22**, 372 (1951).
24. HAMILTON W. C., *Phys. Rev.* **110**, 1050 (1958).

CRYSTAL AND MAGNETIC STRUCTURE OF SILVER DIFLUORIDE—II.

WEAK $4d$ -FERROMAGNETISM OF AgF_2

P. FISCHER

Delegation AF, Eidgenössisches Institut für Reaktorforschung, 5303 Würenlingen, Switzerland,

G. ROULT

Centre d'Etudes Nucléaires de Grenoble, France

and

D. SCHWARZENBACH

Institut für Kristallographie und Petrographie der Eidgenössischen Technischen Hochschule Zürich,
Switzerland

(Received 27 March 1970)

Abstract—Long-range antiferromagnetic $4d^9$ -ordering was detected in the weak ferromagnet AgF_2 below 163°K by neutron powder diffraction investigations. The symmetry of the magnetic structure is given by the orthorhombic Shubnikov group $Pb'c'a$. The magnitude of the ordered magnetic moments is about $0.7\mu_B$ corresponding approximately to the spin quantum number $S = \frac{1}{2}$ and quenched orbital angular momentum. The spin configuration consists of ferromagnetic planes parallel to (100). The main components of the magnetic moments are parallel to *a* and form an antiferromagnetic structure where silver atoms occupying centers of AgF_4 squares with a common fluorine have opposite spin directions. In addition small ferromagnetic components point along *c*, i.e. perpendicular to the puckered AgF_2 layers formed by AgF_4 squares. The resultant magnetic structure is slightly canted with spins parallel to the pseudohexagonal close-packed nets formed by the fluorines perpendicular to *b*. Presumably the dominant antiferromagnetism is caused by the 130° -cation-anion-cation superexchange coupling within the AgF_2 layers, whereas the spin canting is produced by the Dzialoshinski-Moriya term due to spin-orbit interaction. The magnetic properties of the weak ferromagnets AgF_2 and CuF_2 reflect the similarities of their crystal structures.

1. INTRODUCTION

SILVER difluoride whose crystal structure with space group symmetry $Pbca$ has been derived in the preceding paper[1] is a suitable compound for the investigation by neutron diffraction of $4d$ -magnetic ordering which at present is only little known[2]. The atomic magnetic moments of the divalent silver ions are due to the $4d^9$ electronic state with a spin quantum number $S = \frac{1}{2}$. AgF_2 is the simplest compound known to contain silver in the divalent state. Gruner and Klemm[3] inferred already 1937 from measurements of the magnetic susceptibility of AgF_2 a weak ferromagnetism with a Curie temperature of 163°K. Charpin, Dianoux, Marquet-Ellis

and Nguyen-Nghi[4] in 1967 verified this result and showed the substance to be a ferromagnet with effective magnetic moments $\mu_{\text{exp}} = (2.0 \pm 0.1)\mu_B \cong 2\sqrt{S(S+1)}\mu_B$, since $S = \frac{1}{2}$. Thus although the electronic state of Ag(II) is given by $^2D_{5/2}$ [5] the observed magnetic moment appears to be due predominantly to the electron spin with the orbital angular momentum almost quenched by the electric fields in the crystal, as is usual for $3d$ -compounds. The ferromagnetic component at saturation amounts only to about $0.01\mu_B/\text{Ag}^{2+}$ -ion. Characteristic for the basic antiferromagnetism is the negative paramagnetic Curie-Weiss temperature $\theta_a = (-715 \pm 66)^\circ\text{K}$.

2. NEUTRON DIFFRACTION EXPERIMENTS

The long-range antiferromagnetic ordering in AgF_2 was investigated by neutron powder diffraction below the Curie temperature of 163°K. The measurements were done at Grenoble and at Würenlingen. The sample was filled under a dry helium atmosphere into a cylindrical stainless steel container of 2 cm dia. and 5 cm height and sealed with a teflon ring. The container was then electron welded. Because of the small spin quantum number $S = \frac{1}{2}$, the magnetic neutron intensities are predictably much weaker than the nuclear ones. In addition, the $4d$ form factor decreases rapidly with increasing $(\sin \theta/\lambda)$ -values, as has been shown by neutron diffraction on MoF_3 [2]. Only weak magnetic scattering effects at low scattering angles can therefore be expected. For the calculations, the atom form factor for molybdenum f_{Mo} was used[2] (Table 4).

The Debye-Scherrer neutron diffraction pattern of AgF_2 , taken at 4.2°K using a wavelength $\lambda = 1.146 \text{ \AA}$ is shown in Fig. 1. The most important difference diagram between 4.2°K and room temperature, recorded with longer measuring times, is shown in an insert. The intensities at 4.2°K due to the nuclear scattering are virtually the same as at room temperature, i.e. the structure remained the

same on cooling. The positional parameters of fluorine, an overall temperature factor B and the scale factor C were refined on the low temperature data to $x_F = 0.1808$, $y_F = 0.1944$, $z_F = 0.3714$, $B = 0$ and $C = 5.62$, resulting in a R value of 7 per cent. The crystal structure at low temperature is less accurately determined than the one at room temperature[1], since fewer intensities were measured with a lower resolution. Only the temperature factor changed notably, the positional parameters are approximately the same within the limits of accuracy. The absorption corrections were omitted since they are virtually constant over the scattering angle range 2θ from about 0° to 44° of our measurements ($(\mu R)_{1.146 \text{ \AA}} \approx 0.487$). Table 1 shows the observed and calculated nuclear neutron intensities.

The only important difference between the neutron diagrams at 4.2°K and room temperature lies in the small peak at $2\theta = 8.2^\circ$ which can be indexed as 011 in terms of the original chemical unit cell. The magnetic origin of this reflection could be proved by measuring its temperature dependence which is shown in Fig. 2 (wavelength 1.391 \AA , measurements done at Würenlingen). The 011-intensity decreases with increasing temperature and reaches zero at 163°K, in agreement with the

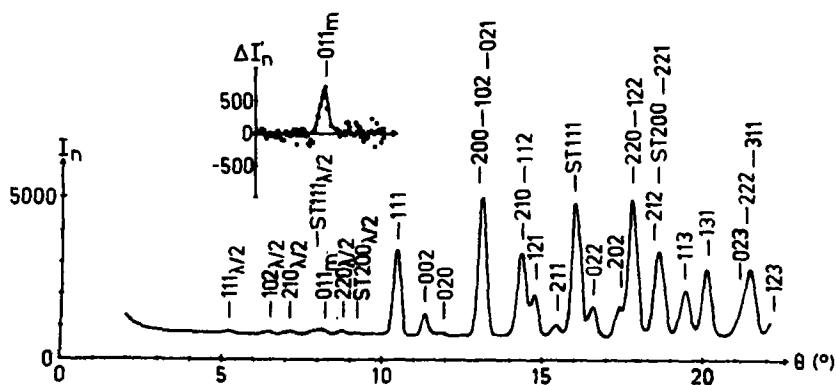


Fig. 1. Debye-Scherrer neutron diffraction pattern of silver difluoride at 4.2°K. The insert shows a part of the difference diagram between 4.2°K and room temperature containing the antiferromagnetic 011-reflection. Reflections from the stainless steel container are marked by ST.

Table 1. Observed and calculated nuclear neutron intensities for polycrystalline silver difluoride at 4.2°K

<i>hkl</i>	$I_0 \pm \Delta$	I_c
111	14143 221	15553
002	3245 164	4177
020	462 117	651
200	26189 238	25313
102		
021		
210	17936 206	16923
112		
121	7481 153	6303
211	2160 139	1273
022	5671 156	5432
202	3779 135	4875
220	30561 235	28200
122		
113	10671 180	10317
131	14991 206	14282
023	19102 235	19372
222		
311		

$R = 0.07$ (defined as in [1]), $RW = 0.08$

Curie temperature determined from the magnetic susceptibility measurements. For comparison a calculated curve of Brillouin type is also shown which is based on molecular field theory and assumes two antiferromagnetically coupled sublattices and the spin quantum number $S = \frac{1}{2}$ [6]. As ferromagnetic reflections are always superimposed on the nuclear reflections, the 011 peak is consequently due to antiferromagnetic long-range ordering. From the absence of additional magnetic reflections the magnetic unit cell may be assumed equal to the chemical one. This means that the wave vector \mathbf{k} is equal to 0 in the Fourier representation of the spin configuration [7].

3. SYMMETRY CONSIDERATIONS

Since the crystal structure of the magnetically ordered silver difluoride is the same as the one of the paramagnetic phase and since cation-anion-cation interactions may be assumed as the main cause of the long-range magnetic ordering, it is reasonable to base the description of the magnetic structure on the space group $Pbca$ or its subgroups. Using Bertaut's representation analysis of magnetic structures [7] it ought to be possible to derive

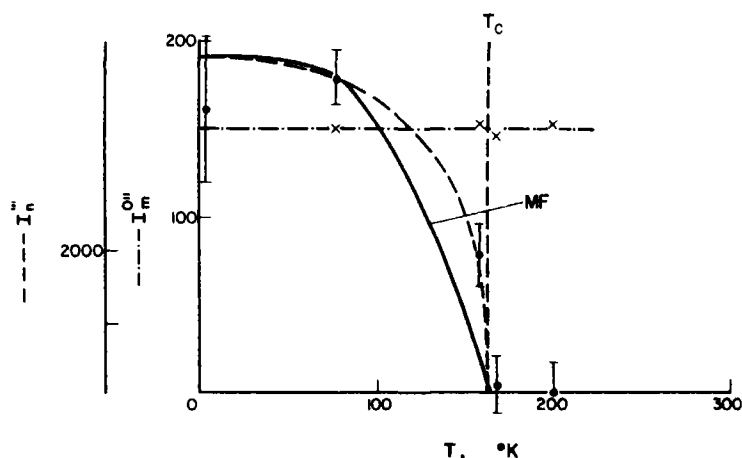


Fig. 2. Temperature dependence of the integrated neutron intensities I of the antiferromagnetic 011- and the nuclear 111-reflection from AgF_2 , in comparison to a molecular field theory calculation (MF). The 4.2°K-values were taken from the Grenoble-measurements.

the magnetic structure of AgF_2 by determining the appropriate Shubnikov group, since there are only real one-dimensional irreducible representations in the case of the space group $Pbca$ and the propagation vector $\mathbf{k} = 0$ (point group mmm [7]). Considering the magnetic moments as axial vectors and start from the space group $Pbca$ with the silver ions at the points of an orthorhombic face-centered lattice there are three Shubnikov groups which allow weak ferromagnetism and fulfill the condition of the magnetic unit cell being equal to the chemical one: $Pb'c'a$, $Pb'ca'$ and $Pbc'a'$. A complete list and description of the Shubnikov groups was published by Koptsik [8]. Conventionally the mark ' denotes the time or spin reversal operator R which is associated with the corresponding crystallographic symmetry operation. The three groups are formally not distinct and correspond to the same abstract group, since they derive from each other through transformations to new coordinate axes by cyclic permutations of the old axes \mathbf{a} , \mathbf{b} and \mathbf{c} . They are, however, distinct with regard to the chemical structure. Table 2 summarizes the symmetry relations between the components M_x , M_y and M_z of the magnetic moments at the equivalent sites. For example in the case of $Pb'c'a$, the resultant of all the M_z -components (M_z) represents the net ferromagnetism, whereas (M_x) and (M_y) yield antiferromagnetic configurations.

Table 2. Symmetry relations between the components M_x , M_y and M_z of the magnetic moments at the special positions $4a$ of the Shubnikov groups derived from the space group $Pbca$. The corresponding irreducible representation τ according to [7], Table 5, is indicated within brackets

Position No.		$Pb'c'a$ (τ_4)	$Pb'ca'$ (τ_3)	$Pbc'a'$ (τ_2)
		$M_x M_y M_z$	$M_x M_y M_z$	$M_x M_y M_z$
0, 0, 0	1	+ + +	+ + +	+ + +
$\frac{1}{2}, \frac{1}{2}, 0$	2	- + +	- + +	+ - -
$\frac{1}{2}, 0, \frac{1}{2}$	3	- - +	+ + -	+ + -
$0, \frac{1}{2}, \frac{1}{2}$	4	+ - +	- + -	+ - +

Ferrimagnetism can be ruled out by the fact that the four silver positions are equivalent. Using these symmetry groups, the occurrence of magnetic domains can be discussed. According to Le Corre [9] two domains may appear in the present case, since the order of the grey point group $mmm1'$ describing the paramagnetic phase is sixteen, whereas the order of the subgroups $m'm'm$ or $m'mm'$ or $mm'm'$, which can in principle be realized in the magnetically ordered state, is eight. As may be deduced from Table 2, the spins are parallel to four different directions. From one spin configuration the second domain may be constructed by changing the directions of all spins by 180° . Since the magnetic neutron intensities are equal for these two configurations, the present problem may consequently be treated as a single domain case.

4. CALCULATED AND OBSERVED MAGNETIC NEUTRON INTENSITIES

After correction for the Lorentz, scale and temperature factors, the magnetic neutron intensity $I_m = |\mathbf{F}|^2$ of a single magnetic domain is determined by the structure factor

$$\mathbf{F} = p \sum_{j=1}^4 \mathbf{q}_j(\mathbf{hkl}) e^{i2\pi(hx_j + ky_j + lz_j)}$$

with the vector $\mathbf{q}_j = \mathbf{e}_{hkl}(\mathbf{e}_{hkl} \cdot \mathbf{e}_j) - \mathbf{e}_j$, where \mathbf{e}_{hkl} is the unit scattering vector and \mathbf{e}_j is the unit vector of the magnetic moment \mathbf{M}_j of the magnetic atom j [10], $p = (0.54 \cdot 10^{-12} \text{ cm}) \cdot S_{\text{eff}} \cdot f$, S_{eff} being the effective spin quantum number or $2S_{\text{eff}}\mu_B$ being the magnetic moment and f the $4d$ -form factor. Application to the Shubnikov groups of Table 2 gives

$$\begin{aligned} I_m/p^2 = & [1 - (dh/a)^2] (\Sigma_x \cos \phi_x)^2 \\ & + [1 - (dk/b)^2] (\Sigma_y \cos \phi_y)^2 \\ & + [1 - (dl/c)^2] (\Sigma_z \cos \phi_z)^2 \\ & - 2d^2 [(hk/ab) \Sigma_x \Sigma_y \cos \phi_x \cos \phi_y \\ & + (hl/ac) \Sigma_x \Sigma_z \cos \phi_x \cos \phi_z \\ & + (kl/bc) \Sigma_y \Sigma_z \cos \phi_y \cos \phi_z], \end{aligned}$$

where $d = 1/[(a/h)^2 + (b/k)^2 + (c/l)^2]^{1/2}$ is the interplanar spacing. ϕ_x , ϕ_y and ϕ_z are the angles of the magnetic moment of Ag at 0, 0, 0 to the basic translations **a**, **b** and **c**. Σ is a geometric structure factor derived from the symmetry relations shown in Table 2.

$$\Sigma = 1 + \text{sign}_{(2)}(-1)^{h+k} + \text{sign}_{(3)}(-1)^{h+l} \\ + \text{sign}_{(4)}(-1)^{k+l},$$

where $\text{sign}_{(j)}$ is the sign of the appropriate component of the magnetic moment **M** at the position *j*. The resulting magnetic neutron intensities I_m for the Shubnikov groups of Table 2 are summarized in Table 3.

neutron intensity I_m is zero for the 011-reflection, in contrast to the measurement. The magnetic neutron intensities for the remaining two cases are compared with the observed values in Table 4. Since the ratio of the ferromagnetic to the total magnetic moment of AgF_2 is approximately 0.01 according to the measurements of the magnetic susceptibility [4], the angles ϕ_z for $Pb'c'a$ and ϕ_x for $Pbc'a'$ should be about 89.5° . In addition the ferromagnetic contribution to the nuclear neutron intensities must be very small. The observed intensity ratio of the magnetic reflections 011 and 100 leads to the Shubnikov group $Pb'c'a$ as the only adequate description of the magnetic structure of AgF_2 . Since the observed

Table 3. Magnetic neutron intensities $I_m = |\mathbf{F}|^2$ for the Shubnikov groups derived from the space group $Pbca$. *g* and *u* denote even and odd integral numbers respectively.

<i>hkl</i>	$Pb'c'a$	$Pb'ca'$	$Pbc'a'$
<i>ggg</i> , <i>uuu</i> , ++++*)	$16p^2 (\cos \phi_z)^2 [1 - (dl/c)^2]$	$16p^2 (\cos \phi_y)^2 [1 - (dk/b)^2]$	$16p^2 (\cos \phi_x)^2 [1 - (dh/a)^2]$
<i>ugg</i> , <i>guu</i> , +---*)	$16p^2 (\cos \phi_x)^2 [1 - (dh/a)^2]$	0	$16p^2 (\cos \phi_z)^2 [1 - (dl/c)^2]$
<i>gug</i> , <i>ugu</i> , +--+*)	0	$16p^2 (\cos \phi_x)^2 [1 - (dh/a)^2]$	$16p^2 (\cos \phi_y)^2 [1 - (dk/b)^2]$
<i>ggu</i> , <i>uug</i> , ++--*)	$16p^2 (\cos \phi_y)^2 [1 - (dk/b)^2]$	$16p^2 (\cos \phi_z)^2 [1 - (dl/c)^2]$	0

*Characterizes the spin configuration.

Since the intensities depend only on the square of $\cos \phi_x$, $\cos \phi_y$ and $\cos \phi_z$, magnetic structures corresponding to different combinations of $\pm M_x$, $\pm M_y$ and $\pm M_z$ at 0, 0, 0 cannot be distinguished. The intensities of the equivalent planes (*hkl*), ($\bar{h}kl$), ($h\bar{k}l$) and ($hk\bar{l}$) coinciding in the same powder reflection are equal and are taken into account by the appropriate powder multiplicity *H*.

The Shubnikov group $Pb'ca'$ can be excluded at once since the magnetic, calculated

intensity of the 001-reflection is zero one obtains $(90 \pm 8)^\circ$ for the angle ϕ_y . ϕ_x is then $(0.5 \pm 8)^\circ$, and the antiferromagnetic components point parallel to the *a*-axis within the limits of experimental accuracy.

By comparing the observed and calculated magnetic intensity of the only observed magnetic reflection 011, an effective spin value $S_{\text{eff}} = gJ/2 = 0.37 \pm 0.05$ is obtained, resulting in an ordered magnetic moment of $2S_{\text{eff}} = 0.7 \pm 0.1$ in units of μ_B . For a quenched orbi-

Table 4. Observed and calculated magnetic neutron intensities $i = I_m/(0.54 f^2)$ for polycrystalline silver difluoride at 4.2°K. The 4d-form factor f was taken to be the same as for Mo^{3+} [2]. H is the multiplicity factor, S_{eff} the effective spin quantum number

hkl	H	f^2	$i_0 \pm \Delta$	$i_c/(S_{\text{eff}})^{1/2} \text{ }_{Pb'c'a}$	$i_c/(S_{\text{eff}})^{1/2} \text{ }_{Pbc'a'}$
001	2	0.587	0.00 0.26	$16 (\cos \phi_y)^2$	0
010	2	0.553	0.00 0.31	0	0
100	2	0.481	0.00 0.44	0	$16 (\cos \phi_x)^2$
011	4	0.307	2.22 0.56	$16 (\cos \phi_x)^2$	$16 (\cos \phi_z)^2$
					$\left(1 - \frac{1/c^2}{1/b^2 + 1/c^2}\right)$
101	4	0.267	0.19 0.34	0	$16 (\cos \phi_y)^2$
110				$16 (\cos \phi_y)^2$	0
				$\left(1 - \frac{1/b^2}{1/a^2 + 1/b^2}\right)$	
111	8			$16 (\cos \phi_z)^2$	$16 (\cos \phi_x)^2$
				$\left(1 - \frac{1/c^2}{1/a^2 + 1/b^2 + 1/c^2}\right)$	$\left(1 - \frac{1/a^2}{1/a^2 + 1/b^2 + 1/c^2}\right)$

tal angular momentum as found through measurements of the magnetic susceptibility [4] ($2S = 1.0$) μ_B is expected. Since in our calculations the magnetic form factor of Mo^{3+} [2] was used for Ag^{2+} , there is an additional uncertainty, and thus the agreement between the results of this neutron diffraction investigation and the measurements of the magnetic susceptibility is reasonable. As the observations could be explained on the basis of Shubnikov groups of the same order as the space group $Pbca$, lower symmetries were not considered.

5. DESCRIPTION OF THE MAGNETIC STRUCTURE

The magnetic moments due to a $4d^9$ electron configuration of Ag^{2+} in the weak ferromagnet AgF_2 are long-range ordered below 163°K. The symmetry of the spin configuration is given by the Shubnikov group $Pb'c'a$. The Ag^{2+} -spins of ordered magnitude $0.7 \mu_B$ are all oriented perpendicular to the b -axis, i.e. parallel to the pseudohexagonal close-packed nets formed by the fluorines within the limits of experimental accuracy. The magnetic structure consists of ferromagnetic planes parallel to (100). The weak ferromagnetism of AgF_2 is due to small components of the spins along

c ($\phi_z \cong 89.5^\circ$), i.e. perpendicular to the puckered layers formed by the AgF_4 squares. The main components, however, are parallel to a

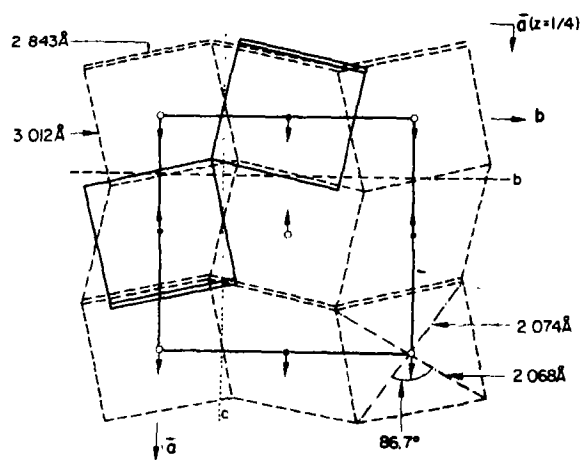


Fig. 3. Projection of the crystal and magnetic structure of AgF_2 on the (001)-plane. \circ and \bullet represent Ag^{2+} -ions at $z = 0$ and $\frac{1}{2}$ respectively. The F^- -ions occupy the corners of approximate AgF_4 squares, which are shown by dashed lines at $z = 0$ and by full lines at $z = \frac{1}{2}$. Double lines mark the highest z -values of the AgF_2 layers. The distances and angles are the ones at room temperature [1]. The anti-ferromagnetic components of the Ag^{2+} -spins are shown by arrows. Together with the small ferromagnetic components along c the resultant magnetic structure is slightly canted.

in an antiferromagnetic arrangement with opposite signs for silver atoms occupying the centers of squares with a common fluorine corner. Thus the resultant magnetic structure, shown in Fig. 3, is slightly canted. Presumably the 129.9° -cation-anion-cation superexchange interaction[1] within the chessboard-like AgF_2 layers parallel to (001) produces the basic antiferromagnetism ($J_{ij}\mathbf{S}_i\mathbf{S}_j$), whereas the weaker Dzialoshinski-Moriya term ($\mathbf{D}_{ij}(\mathbf{S}_i \times \mathbf{S}_j)$, $D_{ij} \approx ((g-2)/g)J_{ij}$) due to spin-orbit coupling causes the spin canting.

CuF_2 , having a Jahn-Teller distorted monoclinic rutile structure[11] with CuF_2 layers formed by CuF_4 squares which are very similar to the AgF_2 layers in AgF_2 [1], shows also the properties of a weak ferromagnet with $S = \frac{1}{2}$, $T_c = 69^\circ\text{K}$, $\bar{g} = 2.3$ [12]. The magnetic structure of CuF_2 may be expected to reflect the structural similarity with AgF_2 and to show an analogous 130.2° Cu-F-Cu superexchange interaction within the CuF_2 layers.

Hälg (ETH) and Professor E. F. Bertaut (Grenoble) for their interest and support of this work.*

REFERENCES

1. FISCHER P., SCHWARZENBACH D. and RIETVELD H. M., *J. Phys. Chem. Solids*.
2. WILKINSON M. K., WOLLAN E. O., CHILD H. R. and CABLE J. W., *Phys. Rev.* **121**, 74 (1961).
3. GRÜNER E. and KLEMM W., *Naturw.* **25**, 59 (1937).
4. CHARPIN P., DIANOUX A. J., MARQUET-ELLIS H. and NGUYEN-NGHI, C. R. *Acad. Sci. Paris C264*, 1108 (1967).
5. KÖNIG E., *Landolt-Börnstein* **2**, 377 (1966), Springer-Verlag.
6. SMART J. S., *Effective Field Theories in Magnetism* **59**, W. B. Saunders Company, London (1966).
7. BERTAUT E. F., *Acta crystallogr.* **A24**, 217 (1968).
8. KOPTSIK V. A., *Shubnikov Groups*, Moscow State University (1966).
9. LE CORRE Y., *J. Phys. Radium* **19**, 750 (1958).
10. SHIRANE G., *Acta crystallogr.* **12**, 282 (1959).
11. GOODENOUGH J. B., *Magnetism and the Chemical Bond* 242, J. Wiley, London (1963).
12. JOENK R. J. and BOZORTH R. M., *J. appl. Phys.* **36**, 3, Pt2, 1167 (1965).
13. FISCHER P. and ROULT G., *Helv. Physica Acta* **41**, 416 (1968).

*Some preliminary results of this investigation have been published in an abstract[13].

Acknowledgements—The authors thank Professor W.

100

SPECIFIC HEAT OF NICKEL HYDRIDE FROM 10° TO 200°K

G. WOLF

Institute of Physical Chemistry, Bergakademie, Freiberg, G.D.R.

and

B. BARANOWSKI

Institute of Physical Chemistry, Polish Academy of Sciences, Warsaw, Poland

(Received 7 February 1969; in revised form 24 February 1970)

Abstract—The heat capacity of NiH_x ($x = 0.68; 0.59; 0.50$) has been measured in the temperature range 10–200°K and extrapolated up to 300°K. The γ -coefficients of the electronic specific heat and Debye temperatures have been evaluated from the results for the 10–20°K region. The values of the standard entropy and the thermal part of the enthalpy have been calculated. The standard entropy of formation of nickel hydride is evaluated and compared with the previous result obtained from the measured free energy and enthalpy of formation. The results for the γ -coefficients do not confirm the rigid band model and seem to follow a simple minimum polarity model.

INTRODUCTION

THE PROPERTIES of non-stoichiometric nickel hydride were the subject of several investigations.

The free energy of formation was calculated from the equilibrium pressure of gaseous hydrogen above the solid hydride phase. This pressure, measured at 25°C, was 3400 ± 70 atm and the standard free energy of formation obtained from this value was $\Delta G^\circ = 5640 \pm 20$ cal/mole H_2 [1]. This pressure is much lower than the minimum necessary for the formation of nickel hydride from gaseous hydrogen and pure nickel[2]. In some systematic investigations nickel hydride formation was observed at about 8000 atm of gaseous hydrogen[3] and in recent experiments, on other nickel samples, a pressure of about 6000 atm was found to be sufficient[4]. Thus we have encountered in nickel hydride a phase which is formed at the highest hydrogen activities so far reported. The enthalpy of formation, determined in a microcalorimeter by a dynamic procedure[5], was found to be -2100 ± 140 cal/mole H_2 .

Nickel hydride has a metallic character,

as indicated by the temperature dependence of the electrical resistance, but, compared with pure nickel, it has an increased residual resistivity and a considerably decreased phonon part[6, 7]. The first effect is obviously due to the creation of new scattering centers by the hydrogen particles introduced. The reduction of the temperature dependent part supports the assumption of the d -band filling of nickel by the hydrogen electrons. As the s - d scattering mechanism is mainly responsible for the electrical resistance of pure nickel, any decrease in the number of d -band holes must effectively cause an increase in the electrical conductivity[6].

The d -band filling concept, formulated previously[8] for Pd-Ag, Pd-H and Ni-Cu systems, seems to be confirmed in the Ni-H system by the continuous decay of ferromagnetism, with increasing hydrogen concentration[9–11]. An alternative explanation of this behavior could be the reduction of the exchange integral as a consequence of the lattice expansion (about 6 per cent) caused by the hydride formation[12].

The subject of this paper is the measurement and discussion of the heat capacity

of nickel hydride as a function of temperature and hydrogen concentration. The results for the low temperature region are used to calculate the electronic heat capacity coefficients and the Debye temperatures. The heat capacity values are also used to calculate the entropy in the available temperature range and the thermal part of the enthalpy.

EXPERIMENTAL

The sample of nickel hydride used in the experiments was prepared by the electrochemical saturation of thin nickel layers, deposited electrochemically on a specially treated aluminium surface. The details of this method have been published[13]. The nickel hydride was pressed into tablets before being placed in the calorimetric vessel. The sample was prepared at temperatures below 200°K because of the known kinetics of desorption [14]. Traces of volatile (water, hydrogen etc.) were removed by prolonged evacuation at a pressure of 10^{-6} mm Hg, and then helium was introduced as a heat conducting medium before the calorimetric vessel was closed. The vessel contains an outer and an inner manganin heater, and the temperature was measured by a Pb resistance thermometer. A quasi-adiabatic procedure was applied which will be described in detail elsewhere. The relaxation time for the thermal equilibrium was about 10 sec in the temperature range below 80°K and did not exceed 20 sec at higher temperatures. The temperature differences were determined with an error less than 0.3 per cent, and the potentials and times were measured with an accuracy better than 0.05 per cent. The initial average atomic ratio H/Ni of the sample investigated was 0.68, and two controlled desorptions from this sample resulted in average atomic ratios of 0.59 and 0.50.

The heat capacity of NiH_x was determined up to 200°K. At higher temperatures the instability of nickel hydride[14] precluded measurements, and all values given here are extrapolated from the lower temperature

region. Table 1 summarizes the numerical results for C_p , entropy and thermal contribution of the enthalpy as functions of temperature. The experimental accuracy of the quantities given is better than ± 1 per cent. For all hydride samples the heat capacities are higher than for pure nickel[15], and the difference increases with temperature and with the atomic ratio H/Ni. The entropy values were calculated from the integral $\int_0^T C_p d\ln T$. The zero point entropy of the NiH_x component was assumed to be zero. For the standard entropies ($T = 298, 16^\circ\text{K}$) the following values result:

$$\begin{aligned} x_1 = 0.68 \quad S_1^0 &= 9.01 \pm 0.03 \text{ cal/deg. mole } \text{NiH}_x \\ x_2 = 0.59 \quad S_2^0 &= 8.92 \pm 0.03 \text{ cal/deg. mole } \text{NiH}_x \\ x_3 = 0.50 \quad S_3^0 &= 8.69 \pm 0.03 \text{ cal/deg. mole } \text{NiH}_x \end{aligned}$$

For the temperature range 0–10°K the T^3 -law was applied for the extrapolation procedure.

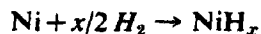
The measured values of the molar heat capacities for the three samples of NiH_x investigated are given in Table 2 for the temperature range 10–20°K. Each sample was measured two or three times, as indicated. Figure 1 represents these results in the C_p/T , T^2 variable set. It can be seen that the numerical values in Table 2 fit the equation

$$C_v = \gamma T + \beta T^3. \quad (1)$$

Thus from Fig. 1 the electronic heat coefficient γ as well as the Debye temperatures (from the β coefficients) could be evaluated. The results are given in Table 3.

DISCUSSION

The entropy of the reaction



was calculated from the evaluated standard

Table 1. Thermodynamic functions of $\text{NiH}_x \cdot C_p$ in cal/mole deg.; $H^0 - H_0^0$ in cal/mole; S^0 in cal/mole deg.

$^{\circ}\text{K}$	C_p	$\text{NiH}_{0.68}$ $H^0 - H_0^0$	S^0	C_p	$\text{NiH}_{0.80}$ $H^0 - H_0^0$	S^0	C_p	$\text{NiH}_{0.80}$ $H^0 - H_0^0$	S^0
10	0,0335	0,125	0,017	0,0331	0,121	0,017	0,0298	0,104	0,015
20	0,118	0,838	0,064	0,120	0,840	0,064	0,113	0,775	0,059
30	0,363	3,01	0,147	0,371	3,06	0,149	0,338	2,85	0,137
40	0,797	8,73	0,311	0,781	8,79	0,314	0,734	8,13	0,290
50	1,35	19,4	0,543	1,32	19,1	0,539	1,27	18,0	0,505
60	1,94	35,8	0,845	1,95	35,6	0,841	1,88	33,7	0,793
70	2,51	58,1	1,18	2,52	58,0	1,18	2,44	55,4	1,12
80	3,02	85,9	1,56	3,02	85,7	1,55	2,88	82,2	1,48
90	3,48	118,3	1,94	3,49	118,3	1,93	3,34	113,1	1,84
100	3,93	155,4	2,33	3,93	155,4	2,33	3,79	149,0	2,22
110	4,38	196,9	2,72	4,37	196,8	2,72	4,24	188,9	2,60
120	4,78	242,8	3,12	4,77	242,7	3,12	4,63	233,6	2,99
130	5,15	292,4	3,52	5,17	292,2	3,51	4,97	281,4	3,37
140	5,47	345,7	3,92	5,43	345,6	3,91	5,26	332,7	3,76
150	5,73	401,7	4,30	5,64	400,7	4,29	5,50	386,4	4,12
160	5,98	460,3	4,68	5,85	458,4	4,67	5,74	442,7	4,49
170	6,20	521,2	5,05	6,06	517,8	5,02	6,00	501,1	4,84
180	6,37	584,1	5,41	6,24	579,5	5,38	6,17	561,9	5,19
190	6,54	648,6	5,75	6,41	642,4	5,71	6,32	624,3	5,52
200	6,69	714,8	6,10	6,55	707,5	6,05	6,46	688,3	5,86
210	6,83	782,3	6,42	6,70	773,4	6,37	6,62	753,4	6,17
220	6,97	851,4	6,75	6,84	841,5	6,69	6,76	820,5	6,49
230	7,11	921,7	7,06	6,98	910,3	6,99	6,90	888,6	6,79
240	7,24	993,5	7,37	7,12	981,1	7,30	7,03	958,4	7,08
250	7,37	106,7	7,66	7,26	1053	7,59	7,16	1029,2	7,37
260	7,50	1141	7,96	7,39	1126	7,88	7,29	1101,6	7,66
270	7,63	1217	8,24	7,52	1200	8,15	7,41	1174,9	7,93
280	7,76	1294	8,52	7,64	1275	8,44	7,54	1249,9	8,21
290	7,88	1372	8,79	7,77	1353	8,70	7,66	1325,7	8,47
300	8,00	1451	9,06	7,89	1432	8,97	7,78	1403,1	8,74

entropy of nickel hydride, with use of the standard entropies of nickel and hydrogen of 7.137 cal/deg., mole [15] and 31.21 cal/deg., mole [19], respectively. The results were as follows:

x	ΔS^0 in cal/deg., mole NiH_x
0,68	-8,72
0,59	-7,41
0,50	-6,24.

For one mole hydrogen the entropy of formation is

$$\Delta S^0 = -25.4 \pm 0.3 \text{ cal/deg., mole } H_2.$$

This value can be compared with the result

obtained from the measured values of the free energy and enthalpy of formation [1, 5]:

$$\Delta S^0 = -26.0 \pm 0.5 \text{ cal/deg., mole } H_2.$$

Both independent determinations are within the error range indicated.

The parabolic rigid band model would require a continuous decrease of the electronic heat coefficient (γ) for nickel hydride from the value characteristic for pure (ferromagnetic) nickel to the value for copper, if a filling up of the d -band vacancy by the hydrogen electrons occurs. Assuming the effective number of electrons in the s -band of nickel to be 0.6, identical to the

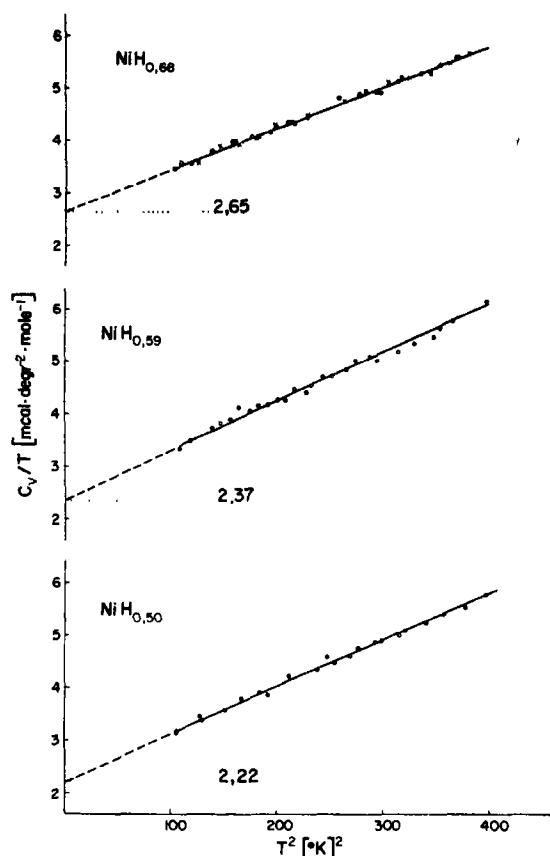


Fig. 1.

Table 3. The electronic specific heat coefficients and Debye temperatures for nickel and nickel hydride samples

x	γ (cal/mole, deg. ²)	θ_0	Refs.
0.00	$1.744 \cdot 10^{-3}$	380	[15-18]
0.50	$(2.22 \pm 0.05) \cdot 10^{-3}$	$376 \pm 4^\circ\text{K}$	this paper
0.59	$(2.37 \pm 0.015) \cdot 10^{-3}$	$372 \pm 1^\circ\text{K}$	
0.68	$(2.65 \pm 0.04) \cdot 10^{-3}$	$388 \pm 3^\circ\text{K}$	

number of d -band holes, one would expect the hydride $\text{NiH}_{0.6}$ to exhibit a γ -coefficient close to the value known for pure copper. This expectation is in complete disagreement with the experimental data (see Table 3), and therefore the rigid parabolic band model

is not applicable here for the interpretation of the electronic heat.

The Ni-H system discussed here should have electronic properties similar to those of the Ni-Cu alloys. Concerning the latter, in recent years a considerable amount of experimental information has been gathered which is clearly in contradiction to the rigid band model[20]. For example, the change in the electronic heat coefficient (γ) as a function of the Ni-Cu alloy composition[21-24] has recently been interpreted as being caused by a separable band of Ni[25]. This model, classified as one of the 'minimum polarity' models[25, 26], assumes no charge exchange between Cu and Ni lattice sites. Consequently the concentration of d -band holes for one atom of the alloy is $1-x$ (where x denotes the atomic ratio of Cu), instead of being zero for $x \geq 0.6$, as assumed by the collective rigid band model.

The simple minimum polarity model can be very useful for the description of the experimental electronic heat capacity results in the Ni-H system. Assuming a negligible contribution of hydrogen to this quantity, there remains in the two-phase region a mixture of ferro- and paramagnetic nickel. The concentration of both modifications can be calculated from the determined intensities of the roentgenographic lines characteristic of nickel and nickel hydride [27]. If both modifications of nickel behave independently with regard to their electronic structure, the effective γ -coefficient will be given, in terms of the minimum polarity model, by the following relation:

$$\gamma_{\text{NiH}_x} = a\gamma_{\text{Ni ferrom.}} + (1-a)\gamma_{\text{Ni param.}} \quad (2)$$

where a denotes the molar ratio of the ferromagnetic nickel and $\gamma_{\text{Ni param.}}$, $\gamma_{\text{Ni ferrom.}}$ are the γ -coefficients for the paramagnetic and ferromagnetic nickel respectively. The second coefficient ($\gamma_{\text{Ni ferrom.}}$) coincides with the measured value for pure nickel. As $\gamma_{\text{Ni param.}}$ cannot be measured directly in the low tem-

perature region, the ratio of density of states for both modifications must be known in order to make use of equation (2). Here a previous estimation of Stoner[28] can be applied, where $\gamma_{\text{Ni param}}/\gamma_{\text{Ni ferrom}} = 1.5$, or a recent calculation of Hodges *et al.*[29], where the ratio of density of states equals about 2.1. The experimental and calculated values of the γ -coefficients are summarized in Table 4.

Table 4. Experimental and calculated values for nickel hydride [e.g. (2)] in $10^3[\text{cal/deg}^2 \text{ mole}]$

x	a	γ_{exp}	$\gamma_{\text{calc (Stoner)}}$	$\gamma_{\text{calc (Hodges)}}$
0.68	0.15	2.65	2.60	3.37
0.59	0.32	2.37	2.43	3.04
0.50	0.49	2.22	2.25	2.72

Stoner's results give better agreement with the experimental data than do those of Hodges *et al.* In both cases the γ -coefficient increases for higher hydrogen concentrations. Especially this aspect is in clear contradiction to the rigid band model, as mentioned earlier. If the minimum polarity model holds in the entire range of hydrogen concentrations, the measured values of the γ -coefficient must vary in a continuous way between the value of 1.744 obtained for the ferromagnetic phase of nickel, and the values of 1.744×1.5 or 1.744×2.1 obtained for paramagnetic nickel according to the estimates of Stoner [28] or Hodges *et al.*[29], respectively. (See Table 4). This conclusion could be checked experimentally by measuring the γ -coefficients for hydrogen concentrations lower and higher than those reported in this paper. In fact the Ni-H system should be more suitable for treatment by the minimum polarity model than the Cu-Ni system because in the former is a two-phase system with a large composition range, whereas the Ni-Cu system can be treated in the low temperature region as a continuous one-phase system.

The possibility of a magnetic contribution into the low temperature specific heat data given here must also be considered, since in the related Ni-Cu system this contribution was found to be significant[23, 24, 30, 31, 32, 20], a similar situation can be expected for the Ni-H system. Unfortunately the available temperature range was insufficient to clear up this question. In addition, systematic measurements of the concentration dependence (with respect to hydrogen) of the γ -coefficient would be required. For these two reasons, and also because the low temperature data satisfy equation (1) satisfactorily, we make no further attempt to answer this question here. It can be said only that our results do not give positive evidence of any magnetic contribution since the experimental results do not require the incorporation of any new terms into equation (1).

Acknowledgement—We thank Professor Mannchen for his interest in this work.

REFERENCES

1. BARANOWSKI B. and BOCHENSKA K., *Z. Phys. Chem. N.F.*, **45**, 140 (1965).
2. BARANOWSKI B. and WISNIEWSKI R., *Bull. Polon. Acad. Sci.*, **14**, 273 (1966).
3. BARANOWSKI B., BOCHENSKA K. and MAJCHRZAK S., *Roczn. Chem.*, **41**, 2071 (1967).
4. BARANOWSKI B. and BOCHENSKA K., in preparation.
5. CZARNOTA I. and BARANOWSKI B., *Bull. Polon. Acad. Sci.*, **14**, 191 (1966).
6. BARANOWSKI B., *Acta Metall.*, **12**, 322 (1964).
7. BAUER H. J., *Z. Phys.*, **177**, 1 (1964).
8. MOTT N. F. and JONES H., *The Theory of the Properties of Metals and Alloys*, University Press, Oxford (1936).
9. BAUER H. J. and SCHMIDBAUER E., *Z. Phys.*, **164**, 367 (1961).
10. ANDRÁJW: *Phys. Status Solidi*, **1**, K135 (1961).
11. KOZŁOWSKI L. and KUBIAK S., *Phys. Status Solidi*, **3**, 117 (1963).
12. JANKO A., *Bull. Polon. Acad. Sci.*, **8**, 131 (1960).
13. BARANOWSKI B., *Roczn. Chem.*, **38**, 1019 (1964).
14. BARANOWSKI B., *Bull. Polon. Acad. Sci.*, **7**, 891 (1959).
15. BUSEY R. H. and GIAUQUE W. F., *J. Am. chem. Soc.*, **74**, 3157 (1952).

16. CLUSIUS K. and GOLDMANN F., *Z. Phys. Chem.*, **31**, 256 (1935).
17. KEESOM W. H. and CLARK C. W., *Physica* **2**, 513 (1935).
18. EUCKEN A. and WERTH H., *Z. Anorg. Allg. Chem.* **188**, 152 (1930).
19. NBS-Technical Note, *Selected Values of Chemical Thermodynamic Properties: Part I* p. 270 (1965).
20. ROBBINS C. G., CLAUS H. and BECK P. A., *Phys. Rev. Lett.* **22**, 1307 (1969).
21. DIXON M., HOARE F. E. and HOLDEN T. M., *Proc. R. Soc. A* **303**, 339 (1968).
22. KEESOM W. H. and KURRELMAYER B., *Physica*, **7**, 1003 (1940).
23. GUTHRIE G. L., FRIEDBERG S. A. and GOLDMAN J. E., *Phys. Rev.* **113** 45 (1950).
24. GUPTA K. P., CHENG C. H. and BECK P. A., *Phys. Rev.*, **133**, A203 (1964).
25. LANG N. D. and EHRENREICH H., *Phys. Rev.* **168**, 605 (1968).
26. KIRKPATRICK S., VELICKY B., LANG N. D. and EHRENREICH H., *J. appl. Phys.* **40**, 1283 (1969).
27. MAJCHRZAK S., *Bull. Polon. Acad. Sci.* **15**, 485 (1967).
28. STONER A. C., *Phil. Mag.* **22**, 81 (1936).
29. HODGES L., EHRENREICH H. and LANG N. D., *Phys. Rev.* **152**, 505 (1966).
30. SCHRÖDER K., *J. appl. Phys.* **32**, 880 (1961).
31. BENNEMANN K. H., *Phys. Rev.* **167**, 564 (1968).
32. ROBBINS C. G., CLAUS H. and BECK P. A., *J. appl. Phys.* **40**, 2269 (1969).

NON-RETARDED DISPERSION ENERGY BETWEEN MACROSCOPIC SPHERES

D. LANGBEIN

Battelle-Institut, Frankfurt(Main), Germany

(Received 17 July 1969; in revised form 2 December 1969)

Abstract—The dispersion energy between two spheres *A* and *B* is calculated by expanding the field fluctuations in these spheres in terms of spherical harmonics. This yields an infinite Taylor series in the reduced radii (= radius/distance of centers). The exact dispersion energy is compared with its upper and lower limits, which correspond to a maximum screening by half-spaces (Lifshitz approach) and to no screening at all (Hamaker approach). The two limits are split into identical frequency and different geometric factors and differ by less than 1 per cent at separations characteristic of adhesion. In a second step we calculate the dispersion energy between spheres whose surface is covered with an adsorbed layer. The effect of such layers on the dispersion energy depends primarily on the cross-sections of the spheres at twice the separation *d* of the interacting partner. An exact treatment of adsorbed layers shows that the dispersion energy is no longer factorized into a frequency and a geometric term and hence depends sensitively on the frequency dependence of the dielectric constants involved. This affects the accuracy of computed results, in particular for separations smaller than and equal to the thickness of the adsorbed layer; for large separations the dielectric properties of the bulk material are predominant.

1. INTRODUCTION

IN SPITE of a keen interest in van der Waals attraction between macroscopic particles in dyeing and washing processes, in pouring and sliding processes and also in problems relating to colloid stability and biological transport, only a few basic experiments have been reported so far. The most direct method is the measurement of the van der Waals attraction between plane parallel plates using a balance. Measurements on quartz and borosilicate plates and on mica show that attraction is due to ordinary van der Waals forces for separations *d* smaller than 100 Å, while for separations above 200 Å retardation effects become important. Somewhat less information is obtained from adhesion experiments involving the adhesion of a sphere to a plate or the adhesion between two plane plates or two crossed cylinders. The adhesive force is measured by application of a centrifugal or electrostatic counter force in the former, and by application of a direct tensile force in the latter case. For an interpretation of such experiments it is important to know exactly the contact area, the minimum separation

and the electrostatic component involved in adhesion. For interacting partners of identical materials and for a minimum separation $d = 4 \text{ Å}$ the correct order of magnitude of the adhesive force is obtained.

Theoretical investigations on the van der Waals attraction between macroscopic particles have been reported by Hamaker[1] who derived the dispersion energy between two spheres from the sum over that between any two molecules without regard to screening, and by Lifshitz[2] who calculated the dispersion energy between two plane parallel half spaces using Maxwell equations modified by adding a term accounting for the spontaneous field fluctuations in dielectric media. The dispersion formula proposed by Lifshitz was derived again by Dzyaloshinskii, Lifshitz and Pitaevskii[3], who used quantum field methods, and by Renne and Nijboer[4] who summed all the interactions between a single molecule and a half space consisting of the same kind of molecules. A review on numerical computations on the van der Waals attraction constant from the dielectric constants of the interacting media was given by Krupp[5].

In an earlier paper I [6] we derived a general dispersion formula for interactions between macroscopic bodies, which represents the non-retarded dispersion energy by an integral over the screened field fluctuations of the bodies under investigation. Here, we apply this model to the dispersion energy between two spheres A and B , in which case the field fluctuations can be expanded in terms of spherical harmonics. We obtain a Taylor series with respect to the reduced radii R_1/z , R_2/z ($R_1, R_2 =$ radii of the spheres, $z =$ distance of their centers), which converges similar to a hypergeometric series. Using suitable approximations for the inherent dielectric quotients we find upper and lower limits, which can be summed explicitly. The correct value of the dispersion energy is close to the upper limit for small separations and close to the lower limit for large separations of the spheres. The upper limit for the dispersion energy between a half space and a sphere coincides with the Lifshitz formula [2] for the dispersion energy between a half space and a cylinder if the cross-section of the cylinder equals the cross-section of the sphere in twice its separation $d = z - R_1 - R_2$ from the half space. This suggests that adsorbed layers on the surface of spheres become

particularly important if their thickness exceeds the separation d . This is confirmed by explicit investigations on the effect of adsorbed layers on the dispersion energy between two spheres in Section 4. We compute the dependence of the dispersion energy on the layer thickness and on the separation and propose an approximate formula for small separations d .

2. DISPERSION FORMULA

According to (I.14), the dispersion energy between two macroscopic bodies A and B is given by

$$\Delta E_{AB} = -\frac{\hbar}{4\pi} \int_{-\infty}^{+\infty} d\omega \left\{ \sum_{i \in A} \sum_{j \in B} \alpha_i T_{ij}^{scr} \alpha_j T_{ji}^{scr} + \frac{1}{2} \sum_{i,k \in A} \sum_{j,l \in B} \alpha_i T_{ij}^{scr} \alpha_j T_{jk}^{scr} \alpha_k T_{kl}^{scr} \alpha_l T_{li}^{scr} + \dots \right\} \quad (1)$$

where T_{ij}^{scr} is the screened field of a dipole i in A at position j outside A , and T_{ji}^{scr} is the screened field of a dipole j in B at position i outside B . In the case of two spheres A and B (Fig. 1) it is convenient to expand the direct fields T_{ij} and T_{ji} and the reaction fields $\sum T_{ik} \alpha_k T_{kj}$, $\sum T_{jl} \alpha_l T_{li}$ in terms of spherical harmonics $Y_m^\mu(\vartheta, \varphi) = P_m^\mu(\cos \vartheta) \exp(i\mu\varphi)$

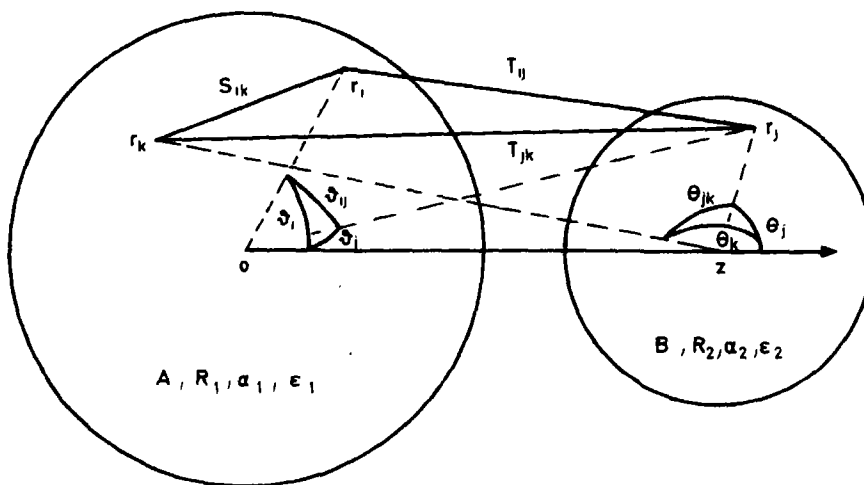


Fig. 1. Reaction field S_{ik} .

with respect to the centers θ and z of A and B . With ρ_1 and α_1 being the density and the polarizability of the molecules in sphere A , we find the first-order polarization field produced by the direct field T_{ij} to be

$$\sum_{k \in A} T_{ik} \alpha_k T_{kj} = \frac{4\pi}{3} \rho_1 \alpha_1 \nabla_i \nabla_j \sum_{m=1}^{\infty} \frac{m-1}{2m+1} \frac{r_i^m}{r_j^{m+1}} Y_m(\vartheta_{ij}). \quad (2)$$

Thus, for the screened field T_{ij}^{scr} we obtain

$$T_{ij}^{scr} = -\nabla_i \nabla_j \sum_{m=1}^{\infty} \frac{1}{1 + \frac{4\pi}{3} \rho_1 \alpha_1 \frac{m-1}{2m+1}} \frac{r_i^m}{r_j^{m+1}} Y_m(\vartheta_{ij}). \quad (3)$$

Compared with expression (1.19) for the screening by a half space A we find a less intensive screening of the contributions with small m , that is a less intensive screening of the long-wave spherical harmonics.

Accordingly, for the screened field of a dipole j inside a dielectric sphere B with center z at an arbitrary position r_k outside B we obtain (Fig. 1)

$$T_{jk}^{scr} = -\nabla_j \nabla_k \sum_{n=1}^{\infty} \frac{1}{1 + \frac{4\pi}{3} \rho_2 \alpha_2 \frac{n-1}{2n+1}} \times \frac{|\mathbf{r}_j - \mathbf{z}|^n}{|\mathbf{r}_k - \mathbf{z}|^{n+1}} Y_n(\theta_{jk}). \quad (4)$$

In order to calculate the macroscopic reaction field S_{ik} of B on A according to (1.15) we transform the polar angles ϑ_{ij} , θ_{jk} in (3), (4) into polar coordinates r , ϑ , φ and $|\mathbf{r} - \mathbf{z}|$, θ , φ with axis z .

From Fig. 1 we have

$$\left. \begin{aligned} \cos \vartheta_{ij} &= \\ \cos \theta_j \cos \theta_k + \sin \theta_j \sin \theta_k \cos (\varphi_j - \varphi_k) \\ \cos \theta_{jk} &= \\ \cos \vartheta_i \cos \vartheta_j + \sin \vartheta_i \sin \vartheta_j \cos (\varphi_i - \varphi_j) \end{aligned} \right\} \quad (5)$$

Then, using the addition theorem for Legendre functions we find the characteristic integral needed for calculating the general reaction field $\sum T_{ij}^{scr} \alpha_j T_{jk}^{scr} \alpha_k T_{ki}^{scr} \dots$ to be

$$\begin{aligned} & \int_B d\mathbf{r}_j \nabla_j \left[\frac{1}{r_j^{m+1}} Y_m^\mu(\vartheta_j, \varphi_j) \right] \\ & \times \nabla_j [|\mathbf{r}_j - \mathbf{z}|^n Y_n^{-\nu}(\theta_j, \varphi_j)] \\ & = 2\pi \delta_{\mu\nu} \frac{2n}{2n+1} \frac{R_2^{2n+1}}{z^{m+n+1}} \frac{(m+n)!}{(m-|\mu|)!(n-|\mu|)!}. \end{aligned} \quad (6)$$

Equation (6) is proved on the basis of some standard generating and orthogonality theorems for Legendre functions. Hence, the macroscopic reaction field of B on A is

$$S_{ik} = \nabla_i \nabla_k \sum_{\mu} \sum_{m,n=1}^{\infty} a_{mn} b_{mn\mu}^{(1)} \times Y_m^\mu(\vartheta_i, \varphi_i) Y_n^{-\mu}(\theta_k, \varphi_k) \quad (7)$$

where

$$a_{mn} = \frac{\eta_2(n)}{1 + \frac{4\pi}{3} \rho_1 \alpha_1} \frac{r_i^m R_2^{2n+1}}{|\mathbf{r}_k - \mathbf{z}|^{n+1} z^{m+n+1}} \quad (8)$$

$$b_{mn\mu}^{(1)} = \frac{(m+n)!}{(m+|\mu|)!(n+|\mu|)!} \quad (9)$$

and

$$\begin{aligned} \eta_i(n) &= \frac{4\pi \rho_i \alpha_i n}{(2n+1) + (4\pi/3) \rho_i \alpha_i (n-1)} \\ &= \frac{n(\epsilon_i - 1)}{n\epsilon_i + (n+1)}; \quad i = 1, 2. \end{aligned} \quad (10)$$

The reaction field S_{ik} of B on A is represented by its multipole expansion with respect to the center z of B . The coefficients a_{mn} of this expansion are proportional to the dielectric quotients $\eta_i(n)$, which can be written as shown by the second equation of (10), where the law of Clausius-Mosotti is assumed to

hold between the polarizabilities α_1, α_2 and the dielectric constants ϵ_1, ϵ_2 of spheres A and B . This dielectric quotient is characteristic of the 2nd-pole contribution to the polarization field of a dielectric sphere in an external electrostatic field.

By using (6) and the equivalent integral relation for A repeatedly, the reaction field caused by ν reflections between A and B results to be

$$\sum_{m,n,\dots \in A} S_{lm} \alpha_m S_{mn} \alpha_n \dots S_{lk} \\ = \nabla_i \nabla_k \sum_{\mu} \sum_{m,n=1}^{\infty} a_{mn} b_{mn\mu}^{(\nu)} Y_m^{\mu}(\vartheta_i, \varphi_i) Y_n^{-\mu}(\vartheta_k, \varphi_k) \quad (11)$$

where

$$b_{mn\mu}^{(\nu+1)} = \sum_{k,l=1}^{\infty} \eta_1(k) \left(\frac{R_1}{z}\right)^{2k+1} \eta_2(l) \left(\frac{R_2}{z}\right)^{2l+1} \\ \times \begin{pmatrix} m+l \\ m+|\mu| \end{pmatrix} \begin{pmatrix} n+k \\ n+|\mu| \end{pmatrix} b_{kl\mu}^{(\nu)} \quad (12)$$

The ν -th order contribution to the dispersion energy ΔE_{AB} according to (1) equals the trace of the ν -th order reaction field (11). Since these reaction fields have no divergence within A , both with respect to \mathbf{r}_i and to \mathbf{r}_k , we transform their traces according to $\text{Tr}[\nabla_i \nabla_k \varphi(\mathbf{r}_i, \mathbf{r}_k)]_{\mathbf{r}_i=\mathbf{r}_k} = \frac{1}{2} \Delta_i \varphi(\mathbf{r}_i, \mathbf{r}_i)$ for arbitrary potentials $\varphi(\mathbf{r}_i, \mathbf{r}_k)$ in A and find

$$\Delta E_{AB} = -\frac{\hbar}{4\pi} \int_{-\infty}^{+\infty} d\omega \sum_{\nu=1}^{\infty} \frac{1}{\nu} \\ \times \sum_{m_1, \dots, m_{\nu}=1}^{\infty} \eta_1(m_1) \left(\frac{R_1}{z}\right)^{2m_1+1} \dots \eta_1(m_{\nu}) \left(\frac{R_1}{z}\right)^{2m_{\nu}+1} \\ \times \sum_{n_1, \dots, n_{\nu}=1}^{\infty} \eta_2(n_1) \left(\frac{R_2}{z}\right)^{2n_1+1} \dots \eta_2(n_{\nu}) \left(\frac{R_2}{z}\right)^{2n_{\nu}+1} \\ \times C(\mathbf{m}, \mathbf{n}) \quad (13)$$

where

$$C(\mathbf{m}, \mathbf{n}) = \sum \begin{pmatrix} m_1+n_1 \\ m_1+\mu \end{pmatrix} \begin{pmatrix} n_1+m_2 \\ n_1+\mu \end{pmatrix} \begin{pmatrix} m_2+n_2 \\ m_2+\mu \end{pmatrix} \\ \dots \begin{pmatrix} n_{\nu}+m_1 \\ n_{\nu}+\mu \end{pmatrix} \quad (14)$$

ΔE_{AB} is a symmetric Taylor series with respect to the reduced radii $R_1/z, R_2/z$. The convergence of this series is guaranteed by the fact that the modulus of the dielectric quotients $\eta_1(m), \eta_2(n)$ is generally smaller than one. The sum over μ in (14) extends over all non-vanishing products. For $\nu=1$ we can sum (14) explicitly. Hence,

$$\Delta E_{AB} = -\frac{\hbar}{4\pi} \int_{-\infty}^{+\infty} d\omega \sum_{m,n=1}^{\infty} \eta_1(m) \left(\frac{R_1}{z}\right)^{2m+1} \\ \times \eta_2(n) \left(\frac{R_2}{z}\right)^{2n+1} \begin{pmatrix} 2m+2n \\ 2n \end{pmatrix} + \dots \quad (15)$$

3. UPPER AND LOWER LIMITS

The coefficients $C(\mathbf{m}, \mathbf{n})$ of the Taylor series (13) are generally composed of binomial coefficients, so that they contain an equal number of integer factors in the numerator and in the denominator. Except for the dielectric quotients $\eta_1(m), \eta_2(n)$ we may understand (13) as a generalized hypergeometric series. This suggests a method permitting the explicit summation of (13) by approximating $\eta_i(n)$ by

$$\frac{2n}{2n+1} \frac{\epsilon_i-1}{\epsilon_i+1} \leq \eta_i(n) \leq \frac{\epsilon_i-1}{\epsilon_i+1} \quad (16)$$

According to (16) both the upper and the lower limit is more exact for large than for small values of n so that the accuracy of the corresponding limits for ΔE_{AB} increases with the number of terms needed for convergence of (13), i.e. with decreasing separation of the spheres. For the dispersion energy arising from the first reflection of the field between

A and B ($\nu = 1$) we obtain the upper limit

$$|\Delta E_{AB}| \leq \frac{\hbar \bar{\omega}}{2\pi} R_1 R_2 \left\{ \frac{1}{2} \left(\frac{1}{z^2 - (R_1 + R_2)^2} + \frac{1}{z^2 - (R_1 - R_2)^2} \right) - \frac{1}{z^2 - R_1^2} - \frac{1}{z^2 - R_2^2} + \frac{1}{z^2} \right\} \quad (17)$$

and the lower limit

$$|\Delta E_{AB}| \geq \frac{\hbar \bar{\omega}}{2\pi} \left\{ \frac{R_1 R_2}{2} \left(\frac{1}{z^2 - (R_1 + R_2)^2} + \frac{1}{z^2 - (R_1 - R_2)^2} \right) + \frac{1}{4} \log \frac{z^2 - (R_1 + R_2)^2}{z^2 - (R_1 - R_2)^2} \right\} \quad (18)$$

where

$$\bar{\omega} = \int_0^\infty d\omega \frac{\epsilon_1(i\omega) - 1}{\epsilon_1(i\omega) + 1} \frac{\epsilon_2(i\omega) - 1}{\epsilon_2(i\omega) + 1} \quad (19)$$

In the case of small separations, $d = z - R_1 - R_2 \ll z$, we are left with

$$|\Delta E_{AB}| \approx \frac{\hbar \bar{\omega}}{8\pi} \frac{R_1 R_2}{d(R_1 + R_2)} \quad (20)$$

in both limits. The dispersion energy becomes inversely proportional to the separation. In the case of large separations, $z \gg R_1, R_2$, both limits become proportional to the volumes of the spheres and to the inverse sixth power of the separation.

The lower limit (18) is essentially the result obtained by Hamaker[1] who disregarded the screening of the fluctuation fields. We find the Hamaker interaction constant to equal $\hbar \bar{\omega}/2\pi$, as Krupp[5] concluded from analogies among the attraction between two half-spaces and between half-space and sphere.

While the lower limit (18) is obtained without any screening, the upper limit (17) corresponds to maximum screening by half spaces. Using the upper limit in (16) we are able to sum analytically all orders ν of the dispersion

energy (13) and find

$$|\Delta E_{AB}| \leq \frac{\hbar}{4\pi} \int_0^\infty d\omega \sum_{\nu=1}^\infty \frac{1}{\nu} \left(\frac{\epsilon_1 - 1}{\epsilon_1 + 1} \frac{\epsilon_2 - 1}{\epsilon_2 + 1} \right)^\nu \times \left\{ \prod_{\mu=1}^\nu \left[z^2 - R_1^2 - R_2^2 - 2R_1 R_2 \cos \frac{2\pi}{\nu} \mu \right]^{-1} + \prod_{\mu=1}^\nu \left[z^2 - R_1^2 - R_2^2 - 2R_1 R_2 \cos \frac{2\pi}{\nu} \mu \right]^{-1} \right\} \quad (21)$$

The proof of (21) is given in the Appendix. The denominators in (21) are positive due to $d = z - R_1 - R_2 > 0$, the smallest one being that arising for $\mu = \nu$ in the first product. Therefore, another upper limit for ΔE_{AB} can be obtained by putting $z = R_1 + R_2$ in all other denominators in (21); this yields

$$|\Delta E_{AB}| \leq \frac{\hbar}{8\pi} \int_0^\infty d\omega \sum_{\nu=1}^\infty \frac{1}{\nu^3} \left(\frac{\epsilon_1 - 1}{\epsilon_1 + 1} \frac{\epsilon_2 - 1}{\epsilon_2 + 1} \right)^\nu \times \frac{R_1 R_2}{d(R_1 + R_2)} \quad (22)$$

The effect of the reaction fields $\nu > 1$ on the upper limit (22) equals that obtained for the dispersion energy between two half spaces in I. The upper limit (22) differs from the Lifshitz formula (I.20) only in the geometrical term, i.e. the dispersion energy between a half-space and a cylinder with the surface area

$$F = 2\pi d \frac{R_1 R_2}{R_1 + R_2} \quad (23)$$

is an upper limit for the dispersion energy between two spheres with radii R_1, R_2 . This result is consistent with our statement made in Section 2 suggesting that the screening of long-wave spherical harmonics by spheres is less intensive than that by half-spaces.

In Fig. 2 we plotted the dispersion energy ΔE_{AB} according to (15), together with its

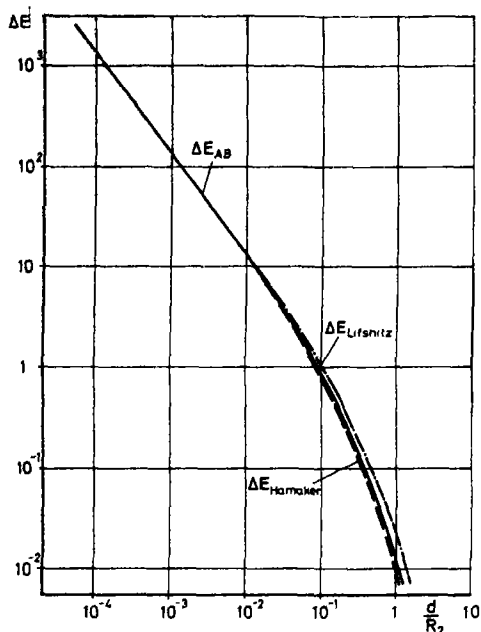
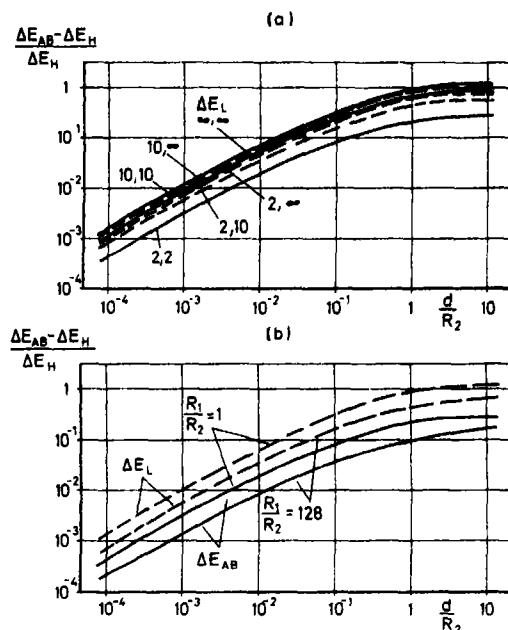


Fig. 2. Dispersion energy vs. separation.

upper and lower limits (17), (18) in first order of reflection $\nu = 1$. We assumed $R_1 = R_2$ and $\epsilon_1(i\omega) = \epsilon_2(i\omega) = 2$ for ω smaller than an appropriate cut-off frequency ω_0 . The unit for the separation d is the relative unit d/R_2 . The unit for the dispersion energy ΔE_{AB} is arbitrary and, in this numerical example, depends primarily on the extension of the ω -region, in which $\epsilon_1(i\omega) = \epsilon_2(i\omega) = 2$ is assumed. Figure 2 shows a close agreement of the dispersion energy and its upper and lower limits for small separations d , so that the modified Lifshitz formula (22) can be used. This region of separations is characteristic of adhesion measurements, that is to say of the adhesion of spheres with a diameter of a few 10^{-4} cm at separations of a few 10^{-8} cm from a plate. In Fig. 2 the values of the exact dispersion energy ΔE_{AB} have been computed by summing the first 120 terms in m and n in (15) exactly and approximating the remaining terms according to (16).

The dependence of ΔE_{AB} on the parameters ϵ_1 , ϵ_2 and R_1 , R_2 is exhibited in Fig. 3. Figure 3(a) shows the relative deviations of ΔE_{AB} and

Fig. 3. Relative position of ΔE_{AB} , ΔE_L , and ΔE_H . (a) depending on ϵ_1 , ϵ_2 ; (b) depending on R_1 , R_2 .

of its upper limit ΔE_L from the lower limit ΔE_H for several values of ϵ_1 , ϵ_2 . For ϵ_i close to one we find the lower limit (16) to equal the correct value of $\eta_i(n)$, whereas for ϵ_i close to infinity the upper limit (16) yields the correct result. We learn from Fig. 3a that this statement is true also for the dispersion energy ΔE_{AB} and that the relation

$$\Delta E_{AB} \approx \frac{1}{\omega} \int_0^\infty d\omega \frac{\epsilon_1 - 1}{\epsilon_1 + 1} \frac{\epsilon_2 - 1}{\epsilon_2 + 1} \left\{ \left(\frac{1}{\epsilon_1 + 1} + \frac{1}{\epsilon_2 + 1} \right) \Delta E_H + \frac{1}{2} \left(\frac{\epsilon_1 - 1}{\epsilon_1 + 1} + \frac{\epsilon_2 - 1}{\epsilon_2 + 1} \right) \Delta E_L \right\} \quad (24)$$

which can be derived when considering first-order correction terms for (16), should be a sufficient approximation for all practical purposes.

The dependence of the relative deviation of ΔE_{AB} and ΔE_L from ΔE_H on the radii R_1 , R_2 is shown in Fig. 3(b). An increase of R_1 with R_2 and d fixed increases the number of terms needed for convergence of the R_1 series and

decreases the number of terms needed for convergence of the R_2 series in (15). The resulting shift of ΔE_{AB} relative to ΔE_L and ΔE_H is negative for $\epsilon_1 = \epsilon_2$ and small separations, the influence of the R_2 series then predominates over that of the R_1 series, and positive for $\epsilon_1 = \epsilon_2$ and large separations $d > R_2$, when only the first terms of the R_2 series are needed. A shift of ΔE_{AB} relative to ΔE_L and ΔE_H in second order of ΔR_1 is found if R_1 and R_2 are changed according to $\Delta R_1/R_1^2 + \Delta R_2/R_2^2 = 0$. This stresses the validity of (22) and enables us to bring the curves of Fig. 3(b) to an approximate coincidence by means of the symmetrized abscissa variable $\frac{1}{2}d(1/R_1 + 1/R_2)$. A slight decrease of ΔE_{AB} with increasing $(\Delta R_1)^2$ is still encountered. The contributions to ΔE_{AB} from higher-order reflections $\nu > 1$, reach at best $\frac{1}{8}$ of the first-order contributions so that for these terms it is sufficient to use the upper limit (22).

4. ADSORBED LAYERS

Equation (23) permits a simple geometrical interpretation: The dispersion energy between a half space and a sphere with radius R equals that between a half space and a cylinder with surface area $2\pi dR$, if the different effectiveness of screening in the two systems is ignored. $2\pi dR$ equals the area of a section of the sphere at twice its separation d from the half-space (Fig. 4), which is the position of the first layer of image charges in the system half space plus cylinder. This coincidence suggests that the dispersion energy between a half space and an inhomogeneous sphere is determined primarily by the composition of the sphere in its cross-section at distance $2d$ from the half space. The dispersion energy between a half space and a sphere which is covered with an adsorbed layer should be determined by the dielectric properties of the adsorbate for separations d smaller than the layer thickness, but by those of the bulk material for separations larger than the layer thickness (Fig. 4).

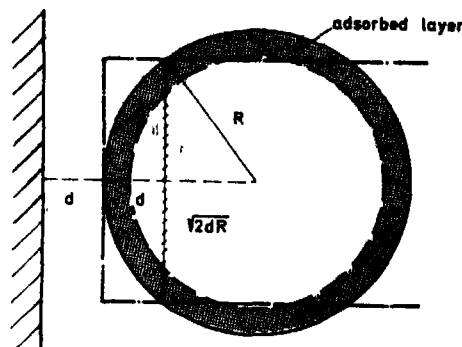


Fig. 4. Half space + sphere covered with an adsorbate.

The method of calculating the dispersion energy from reaction fields also allows an exact treatment of the dispersion energy between spheres whose surface is covered with an adsorbate. While in Section 2 we calculated the reaction field S_{ik} of sphere B on sphere A by means of the microscopic approach, we now adopt for simplicity the macroscopic, purely electrostatic approach.

We start with the screened field T_{ij}^{eff} of a dipole i inside A at an exterior position j , which we represent in terms of spherical harmonics $r_j^{-(m+1)}Y_m^\mu(\vartheta_j, \varphi_j)$. We expand the reaction potential of a sphere B of dielectric constant ϵ_2 , which is covered with an adsorbate layer of dielectric constant ϵ_2' between radii R_2' and R_2 (Fig. 5),

- in spherical harmonics $|\mathbf{r}_j - \mathbf{z}|^n Y_n^\mu(\theta_j, \varphi_j)$ in the exterior $|\mathbf{r}_j - \mathbf{z}| > R_2$,
- in spherical harmonics $|\mathbf{r}_j - \mathbf{z}|^{-(n+1)} Y_n^\mu(\theta_j, \varphi_j)$ in the interior $|\mathbf{r}_j - \mathbf{z}| < R_2'$, and
- in both kinds of spherical harmonics in the adsorbate region $R_2' < |\mathbf{r}_j - \mathbf{z}| < R_2$.

By requiring continuity of the potential and of the normal component of the electric displacement across the surfaces $|\mathbf{r}_j - \mathbf{z}| = R_2', R_2$ we find the reaction potential of B to the exterior perturbation $r_j^{-(m+1)}Y_m^\mu(\vartheta_j, \varphi_j)$ to be

$$\nu = - \sum_{n=\mu}^{\infty} \binom{m+n}{m-|\mu|} \eta_2^{ad}(n) \frac{R_2^{2n+1} Y_n^\mu(\theta_j, \varphi_j)}{z^{m+n+1} |\mathbf{r}_j - \mathbf{z}|^{n+1}} \quad (25)$$

with

$$\eta_i^{ad}(n) = \frac{\frac{n(\epsilon'_i - \epsilon_3)}{n\epsilon'_i + (n+1)\epsilon_3} + \left(\frac{R'_i}{R_i}\right)^{2n+1} \frac{n(\epsilon_i - \epsilon'_i)}{n\epsilon_i + (n+1)\epsilon'_i} \frac{(n+1)\epsilon'_i + n\epsilon_3}{n\epsilon'_i + (n+1)\epsilon_3}}{1 + \left(\frac{R'_i}{R_i}\right)^{2n+1} \frac{n(\epsilon_i - \epsilon'_i)}{n\epsilon_i + (n+1)\epsilon'_i} \frac{(n+1)(\epsilon'_i - \epsilon_3)}{n\epsilon'_i + (n+1)\epsilon_3}} \quad (26)$$

$i = 1, 2$. In deriving (26) we assumed for generality that the dielectric constant of the medium between spheres A and B is ϵ_3 .

If in $T\mathcal{F}^r$ according to (3) we substitute the reaction potential (25) for $r_j^{-(m+1)}Y_m^\mu(\vartheta_j, \varphi_j)$, we again obtain (7) for the reaction field

it depends on the number of terms m, n needed for convergence of (15) whether the bulk material or the adsorbed layer make the main contribution to the dispersion energy ΔE_{AB} . Since this number of terms is roughly determined by R_i/d , we find the dispersion

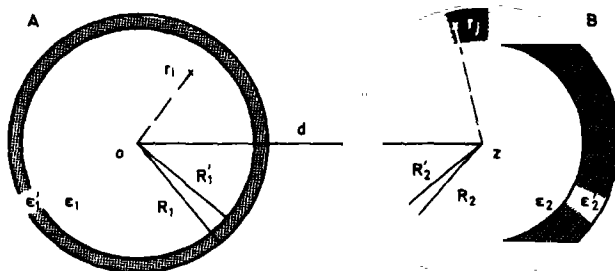


Fig. 5. Spheres covered with adsorbates.

S_{ij} , but with $\eta_2(n)$ replaced by $\eta_2^{ad}(n)$ in (8). Thus, the effect of an adsorbed layer on the dispersion energy ΔE_{AB} is accounted for completely by the substitution of the more elaborate expressions $\eta_i^{ad}(n)$, for the dielectric quotients $\eta_i(n)$, $i = 1, 2$. The limits of $\eta_i^{ad}(n)$ for $R'_i = R_i$ and $R'_i = 0$ are $\eta_i^{ad}(n) = n(\epsilon_i - \epsilon_3)/(n\epsilon_i + (n+1)\epsilon_3)$ and $\eta_i^{ad}(n) = n(\epsilon'_i - \epsilon_3)/(n\epsilon'_i + (n+1)\epsilon_3)$, respectively. The effect of several adsorbed layers or the effect of an arbitrarily r -dependent dielectric constant on the two spheres can likewise be included in our investigations by a further extension of the dielectric quotients $\eta_i(n)$.

If the thickness $R_i - R'_i$ of an adsorbed layer is small compared with the corresponding radius R_i , we find $\eta_i(n)$ to yield an exponential transition from $n(\epsilon_i - \epsilon_3)/(n\epsilon_i + (n+1)\epsilon_3)$ for small values of n to $n(\epsilon'_i - \epsilon_3)/(n\epsilon'_i + (n+1)\epsilon_3)$ for large values of n . Thus,

energy to be determined by the adsorbed layer if $(R'_i/R_i)^{R_i/d} < 1$ and by the bulk material if $(R'_i/R_i)^{R_i/d} \gg 1$.

The effect of adsorbed layers on the dispersion energy between spheres predominates over that of the bulk material for separations d smaller than the layer thickness, and inversely for large d .

This result is in agreement with our preliminary suggestion indicating that the dispersion energy between a half-space and an inhomogeneous sphere is determined primarily by the composition of the sphere in its cross section at distance $2d$ from the half-space.

Figures 6 and 7 show the effect of an adsorbed layer of varying thickness $R_i - R'_i$ on the surface of sphere A . We plotted the dispersion energy $\Delta E_{AB}(ad)$ of a sphere covered with an adsorbate relative to that of a

sphere having a clean surface and identical radius vs. the separation d . The parameter of the different curves is the ratio between the inner radius R'_1 and the outer radius R_1 . In Fig. 6 the dielectric constant $\epsilon'_1(i\omega)$ of the adsorbed layer is assumed larger than that of the bulk material, $\epsilon'_1(i\omega) = 10$, $\epsilon_1(i\omega) = 2$,

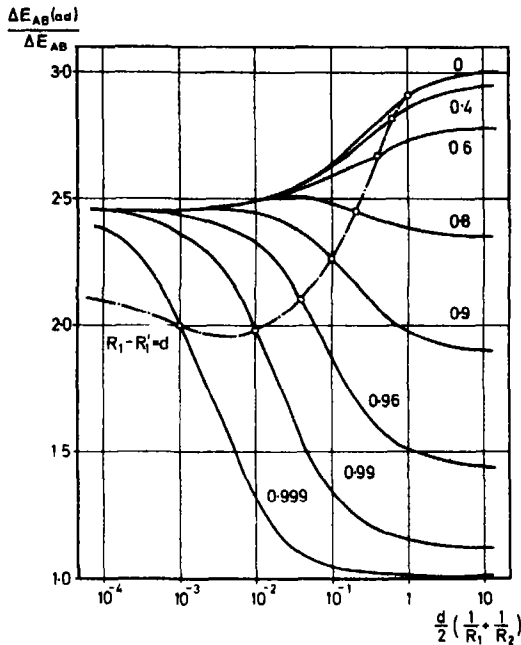


Fig. 6. Effect of adsorbed layers $\epsilon'_1 = 10$, $\epsilon_1 = 2$, $\epsilon_2 = 2$.

whereas Fig. 7 depicts the inverse case. From both figures it is obvious that the adsorbed layer is solely effective if the separation d is smaller than the layer thickness. For separations d larger than the thickness of the adsorbed layer the value of ΔE_{AB} corresponding to $\eta_1(1)\eta_2(1)$ is approached. The weight of adsorbed layers in these leading dielectric quotients is generally larger than their relative volume in the spheres.

In the region of small separations, i.e. where the number of terms n needed for convergence of (15) is so large that in most terms $(R'_1/R_1)^n$ is small compared with one, we can expand $\eta_i^{ad}(n)$ according to

$$\eta_i^{ad}(n) \approx \frac{n(\epsilon'_i - \epsilon_3)}{n\epsilon'_i + (n+1)\epsilon_3} + \left(\frac{R'_1}{R_1}\right)^{2n+1} \times \frac{(2n+1)\epsilon'_i\epsilon_3}{[n\epsilon'_i + (n+1)\epsilon_3]^2} \frac{n(\epsilon_i - \epsilon'_i)}{n\epsilon_i + (n+1)\epsilon'_i} \quad (27)$$

By substituting (27) the dispersion energy (15) splits up into separate contributions of the adsorbed layer and of the bulk material. If only sphere A is covered with an adsorbate, the first-order term of the upper limit (22) reads

$$|\Delta E_{AB}| \lesssim \frac{\hbar}{8\pi} \left\{ \omega' \frac{R_1 R_2}{d(R_1 + R_2)} + \omega'' \frac{R'_1 R_2}{(d + R_1 - R'_1)(R'_1 + R_2)} \right\} \quad (28)$$

where

$$\omega' = \int_0^\infty d\omega \frac{\epsilon'_1 - \epsilon_3}{\epsilon'_1 + \epsilon_3} \frac{\epsilon_2 - \epsilon_3}{\epsilon_2 + \epsilon_3} \quad (29)$$

$$\omega'' = \int_0^\infty d\omega \frac{\epsilon_1 - \epsilon'_1}{\epsilon_1 + \epsilon'_1} \frac{4\epsilon'_1\epsilon_3}{(\epsilon'_1 + \epsilon_3)^2} \frac{\epsilon_2 - \epsilon_3}{\epsilon_2 + \epsilon_3} \quad (30)$$

The first term in (28) is the dispersion energy between spheres with radii R_1 , R_2 and dielectric constants $\epsilon'_1(i\omega)$, $\epsilon_2(i\omega)$. It yields the limit of $\Delta E_{AB}(ad)$ on the left-hand side of Figs. 6 and 7. The second term in (28) is the dispersion energy between spheres with radii R'_1 , R_2 and dielectric constants $\epsilon_1(i\omega)$, $\epsilon_2(i\omega)$, if sphere A is embedded in a medium with dielectric constant $\epsilon'_1(i\omega)$ and sphere B is embedded in a medium with dielectric constant $\epsilon_3(i\omega)$. The adsorbate does not only act as a spacer, but causes an additional screening of the reaction field.

5. CONCLUSIONS

In the numerical computations reported in this paper we assumed that there is essentially one region ω where $\epsilon(i\omega) \neq 1$, i.e. we did not explicitly evaluate the ω -integrals in (13) and

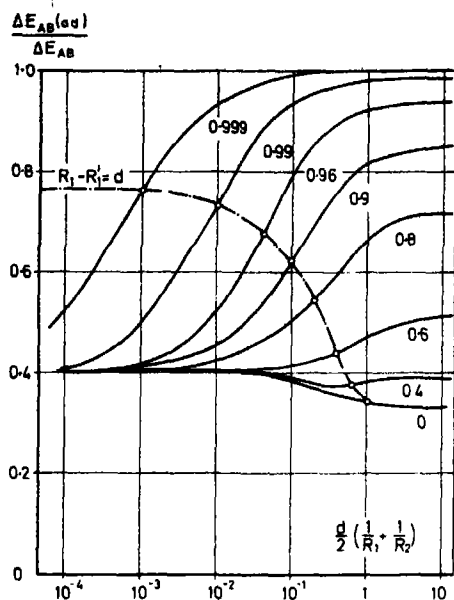


Fig. 7. Effect of adsorbed layers $\epsilon'_1 = 2$, $\epsilon_1 = 10$, $\epsilon_2 = 2$.

(15). A justification for this procedure is the fact that the dependence of the upper and the lower limit (17) and (18) on the dielectric properties of the materials involved is fully contained in the frequency factor $\bar{\omega}$. A more detailed knowledge of $\epsilon_i(i\omega)$ affects both limits in an identical manner so that the exact dispersion energy remains caught in the narrow region enclosed by these limits (Fig. 2). The relative width of this region is smaller than 10^{-2} for separations $d/R < 10^{-3}$ (Fig. 3), which are characteristic of adhesion measurements.

A more critical question is that for $\epsilon'_i(i\omega)$ of adsorbed layers. In our investigations the dielectric constant is essentially a substitute for the local polarizability, i.e. for thin films $\epsilon'_i(i\omega)$ does not generally equal that of bulk material of the same substance, but varies with varying distance from the surface. As we have no exact knowledge of the local dielectric constant or of the effective thickness of adsorbed layers, we have to put up with the fact that ΔE_{AB} may be incorrect by a factor of the order of one (Figs. 6, 7). This applies even more to the dependence of

ΔE_{AB} on the separation d , i.e. to the dispersion force. In the presence of adsorbed layers we no longer find factorized, approximately equal upper and lower limits for ΔE_{AB} . Instead, screening depends sensitively on the separation d .

Though the general dispersion formula (1) is derived on the basis of the Drude model of dispersion, there is some evidence suggesting that those results, which are obtained after substitution of dielectric constants for polarizabilities, are valid also for metals. A first argument in favor of this assumption is the agreement of the results obtained for half spaces with those previously derived by Lifshitz[2]. A general formalism, which instead of using the Drude model is based on the quantum mechanical electron functions of two bodies A and B and describes the dispersion energy ΔE_{AB} by their macroscopic reaction fields, will be reported in a subsequent paper[7].

Acknowledgements—The author wishes to thank the Unilever Research Laboratorium, Vlaardingen, for stimulating discussions and the support in the numerical computations, as well as for the preparation of a preliminary manuscript.

REFERENCES

1. HAMAKER H. C., *Physica* 4, 1058 (1937).
2. LIFSHITZ E. M., *Soviet Phys. JETP* 2, 73 (1956).
3. DZYALOSHINSKII I. E., LIFSHITZ E. M. and PITAEVSKII L. P., *Soviet Phys. JETP* 37 (10), 161 (1960).
4. RENNE M. J. and NIJBOER B. R. A., *Chem. Phys. Lett.* 1, 317 (1967); 2, 35 (1968).
5. KRUPP H., *Advan. Coll. Int. Sci.* 1, 111 (1967).
6. LANGBEIN D., *J. Phys. Chem. Solids*.
7. LANGBEIN D., *Phys. Rev. B*, Oct. 1970.

APPENDIX

The infinite Taylor series

$$G_\nu(x_1, \dots, x_\nu) = \sum_{m_1, \dots, m_\nu=0}^{\infty} x_1^{2m_1+1} \dots x_\nu^{2m_\nu+1} \times \sum_{\mu} \binom{m_1+m_2}{m_1+\mu} \binom{m_2+m_3}{m_2+\mu} \dots \binom{m_\nu+m_1}{m_\nu+\mu} \quad (\text{A1})$$

can be evaluated by using the relation

$$\binom{m_\nu+m_1}{m_\nu+\mu} = \sum_{\lambda} \binom{m_\nu-\mu}{m_\nu-\lambda} \binom{m_1+\mu}{m_1-\lambda} \quad (\text{A2})$$

where the sum over λ extends over all non-vanishing binomial coefficients. Substituting (A2) into (A1) we obtain geometric series in x_1 and x_ν , which we can sum explicitly to give

$$G_\nu(x_1, \dots, x_\nu) = G_{\nu-1}(y_1, \dots, y_{\nu-1}) \quad (\text{A3})$$

where

$$y_1 = \frac{x_\nu}{\sqrt{1-x_\nu^2}} \frac{x_1}{\sqrt{1-x_1^2}}; y_2 = \frac{x_2}{\sqrt{1-x_1^2}}; y_{\nu-1} = \frac{x_{\nu-1}}{\sqrt{1-x_\nu^2}} \quad (\text{A4})$$

$y_\lambda = x_\lambda$ otherwise.

The recurrence formula (A3) enables us to calculate $G_\nu(x_1, \dots, x_\nu)$ by complete induction if we use the initial value

$$G_2(x_1, x_2) = \frac{x_1 x_2}{2} \left(\frac{1}{1 - (x_1 + x_2)^2} + \frac{1}{1 - (x_1 - x_2)^2} \right). \quad (\text{A5})$$

The general result is

$$G_\nu(x_1, \dots, x_\nu) = \frac{x_1 \dots x_\nu}{2} \left(\frac{1}{D_\nu^+(x_1, \dots, x_\nu)} + \frac{1}{D_\nu^-(x_1, \dots, x_\nu)} \right) \quad (\text{A6})$$

where

$$D_\nu^\pm(x_1, \dots, x_\nu) = \begin{vmatrix} 1 & x_1 & & & \pm x_\nu \\ x_1 & 1 & x_2 & & \\ & x_2 & 1 & x_3 & \\ & & & \ddots & \\ +x_\nu & & & x_{\nu-1} & 1 \end{vmatrix}. \quad (\text{A7})$$

In performing the complete induction (A3), (A4) each of the two terms of (A6) results from the other.

In order to prove (21) we need $G_\nu(x_1, \dots, x_\nu)$ for ν even, $x_1 = x_3 = \dots = x_{\nu-1} = R_1/z$, $x_2 = x_4 = \dots = x_\nu = R_2/z$. The zeros of $D_\nu^\pm(x_1, \dots, x_\nu)$ for this periodic case are found on the basis of Floquet's theorem. Hence,

$$D_{2\nu}^\pm\left(\frac{R_1}{z}, \frac{R_2}{z}, \dots\right) = \prod_{\mu=1}^{\nu} \left\{ 1 - \left(\frac{R_1}{z}\right)^2 - \left(\frac{R_2}{z}\right)^2 - 2 \frac{R_1 R_2}{z^2} \cos \frac{2\pi}{\nu} (\mu - \frac{1}{2} \pm \frac{1}{2}) \right\}. \quad (\text{A8})$$

THE OPTICAL SPECTRUM AND MAGNETIC PROPERTIES OF TmFeO_3 IN THE SINGLE-ION MODEL*

A. P. MALOZEMOFF†

Department of Materials Science, Stanford University, Stanford, Calif. 94305, U.S.A.

(Received 9 July 1970)

Abstract—The optical absorption spectrum of trivalent thulium in the orthoferrite is reported as a function of temperature, magnetic field, and photon polarization. Transitions are shown to be electric dipole. Singlet states of the ground multiplet are found at 0, 17.5, 39, and 70 cm^{-1} ; their representation labels, characteristic of the low symmetry C_{1h} site of the thulium ion, are A' , A' , A'' , and A'' respectively. The form of the single-ion Hamiltonian matrices describing the applied and molecular field perturbations on these crystal field states is derived and is used to account for Zeeman splittings. The size of molecular field interactions is estimated from the breakdown of selection rules. Single-ion contributions to the temperature-dependent magnetization and anisotropy are derived on the basis of the optical data and are shown to be compatible with experiment.

1. INTRODUCTION

IN RECENT years there have been several studies of sharp line optical spectra in various rare earth orthoferrites[1], including ErFeO_3 [2, 3], HoFeO_3 [4], and DyFeO_3 [5]. These spectra have been interpreted as single-ion rare earth absorptions. The rare earth energy levels, and their g -factors and molecular field splittings, have been deduced from the data.

In this paper, the spectrum of another one of these compounds, TmFeO_3 , is reported[6]. However, the interpretation of this spectrum is not as straightforward as in the previously studied cases for the following reason. Two of these previous cases, ErFeO_3 and DyFeO_3 , have trivalent rare earth ions with an odd number of electrons, and in the low symmetry C_{1h} site of the ions, the energy level structure is characterized by a series of isolated Kramers doublets, each with its own g -factors and molecular field splittings. Trivalent holmium, by contrast, is an even-electron ion, which in a low symmetry site might be ex-

pected to have a series of isolated singlet states, but which actually has a nearly accidentally degenerate doublet in the ground state[4]. The g -factors and molecular field splittings of this doublet have also been reported[4, 6]. The presence of such doublets in the energy level structure of all these ions provides a simple framework for interpreting their spectra and magnetic properties and obviates the necessity of considering higher order interactions, at least to a first approximation.

Thulium, however, is an even-electron ion with a series of isolated singlet states, as will be shown. It is not possible to assign g -factors or to measure molecular field splittings in the spectrum in any simple way. In spite of its different energy level structure, TmFeO_3 shows many of the interesting magnetic properties that appear in the other rare earth orthoferrites. At high temperatures the iron sublattices show a canted magnetic structure which is known as the $\Gamma_4(F_z)$ magnetic configuration and which has a small net moment in the z direction[7, 8]. Between 94 and 81°K, the moment of TmFeO_3 orients from the z to the x -axis[9], and below 81°K, the iron moments are in the so-called $\Gamma_2(F_x)$ configuration. There is no ordering of the rare

*Work supported by U.S. Army Research Office, Durham, North Carolina, Contract DAHCO4-69-C-0026, and by the Advanced Research Projects Agency through the Center for Materials Research, Stanford University, Contract SD-87.

†Present Address: Clarendon Laboratory, Parks Road, Oxford, England.

earth moments down to at least 1.6°K[10]. A plot of the magnetization of TmFeO_3 , compiled from several sources[11, 12], is given in Fig. 1.

The unusual optical spectrum and interesting magnetic properties of TmFeO_3 pose two important questions. Is it possible to obtain information about the magnetic interactions in TmFeO_3 from the thulium spectrum? If so, can this information be related to the macroscopic magnetic properties of TmFeO_3 ? In this paper, an affirmative resolution is given to both questions. The magnetic effects in a system of isolated singlet states can be accounted for by second order interactions, which have not been considered in the rare earth orthoferrite spectra previously. The form of these interactions is presented in terms of a Hamiltonian matrix for the rare earth ions. It will be shown that an analysis of the selection rules leads to a method for estimating the size of molecular field interactions. Furthermore, macroscopic magnetic properties of TmFeO_3 can be derived on the

basis of the same single-ion theory and will be shown to be compatible with experimental results.

This paper is organized as follows: The experimental results on the optical spectrum of TmFeO_3 are presented in Section 2. In Section 3, the theoretical framework for the single-ion model is developed. The spectrum of TmFeO_3 is analyzed by means of the theory in Section 4. The results are related to the magnetic properties in Section 5. Section 6 summarizes the conclusions.

2. EXPERIMENTAL DETAILS

Single crystals of TmFeO_3 were grown at the Center for Materials Research, Stanford University, by R. Feigelson and H. Swarts, by a slow cooling of a mixture of the thulium and iron oxides in a flux of PbO , PbF_2 , and B_2O_3 . Semiquantitative spectroscopic analysis by American Spectrographic Laboratories indicated 0.1 per cent lead and platinum as the largest impurities. The crystals have orthorhombic symmetry, with axes labeled

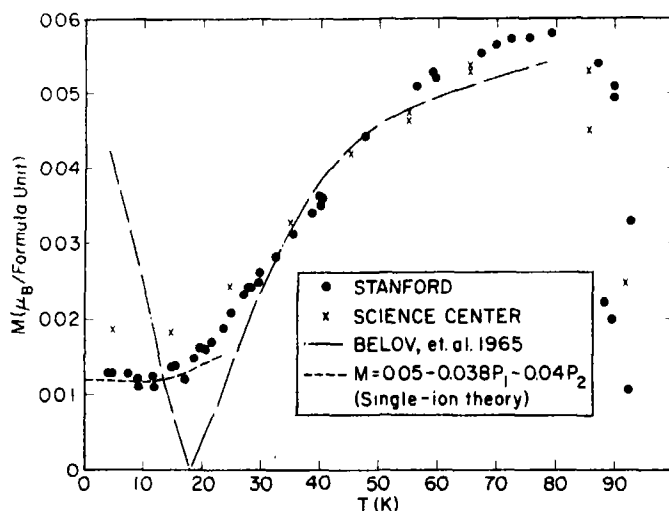


Fig. 1. Spontaneous magnetization M of TmFeO_3 in the x -direction as a function of temperature, from the data of Belov *et al.*[11] and also of Cape and Malozemoff[12] on two different samples, one grown at Stanford and one at the North American Rockwell Science Center. The single-ion theory is fit to the Stanford magnetization data with the formula $M = (0.05 - 0.038p_1 - 0.04p_2) \mu_B/\text{formula unit}$, where p_1 and p_2 are population factors of the lowest two states.

x , y , and z [1], and grew with (001) and (110) faces. They were prepared as platelets along these faces and were polished down to $\sim 100 \mu$ thickness for the optical experiments.

The absorption spectra were taken in two polarizations on each face: $E\parallel x$ or $E\parallel y$ for the (001)-platelets, and $E\parallel z$ or $E\perp z$ (that is, $E\parallel[110]$) for the (110)-platelets. A Bausch and Lomb dual grating spectrometer was used, and absorptions were detected on photographic plates. Line positions were determined relative to an iron arc spectrum, and the accuracy was limited to 0.5 cm^{-1} primarily because of the line widths, the least of which were 3 cm^{-1} at half height.

Spectra were taken from 1.5 up to 100°K . Above 77°K , the lines broadened significantly, and it was not possible to observe any line position or intensity shifts in the region of reorientation. Thus, most of the data was taken in the range from 1.5 to 77°K , where TmFeO_3 is in the $\Gamma_2(F_x)$ magnetic configuration.

The thulium ion has only three groups of transitions which can be observed in the orthoferrite in the visible or near i.r. region of the spectrum—those originating in the 3H_6 and ending in the 3F_2 , 3F_3 , and 3F_4 multiplets. Other transition groups are either masked by the iron absorption edge or lie farther in the i.r. Densitometer traces of the three visible absorption groups at various temperatures and in different polarizations are shown in Figs. 2–4. It must be noted that sensitivities and noise levels in these spectra are not necessarily comparable. Line positions are given in wavenumbers. The notation used to identify the major lines of the spectra will be explained in Section 4. More complete experimental results are available in the author's thesis [13].

3. SINGLE-ION THEORY

(a) *Approximations of the single-ion model*

The rare earth orthoferrites RFeO_3 have the D_{2h}^{16} space group symmetry [1]. There

are four different iron sites and four different rare earth sites per unit cell. The rare earths enter the orthoferrite lattice as trivalent ions. Trivalent thulium has an even number of electrons, and all the subsequent treatment will be limited to even-electron ions, although a similar treatment can also be given for the odd-electron case [13].

As is well-known, a single trivalent rare earth ion may be treated as a system of n electrons, where n is the number of electrons in the $4f$ shell [14]. The various possible electronic configurations— $4f^n$, $4f^{n-1}5d$, and so on—are broken up by electrostatic and spin-orbit coupling into a series of levels characterized by the total angular momentum quantum number J . As is also well-known, the effect of the crystal environment can be treated to a good approximation as a crystal field, which lifts the free ion degeneracy and splits each J -multiplet into a group of crystal field states [14]. In the low symmetry C_{1h} site of the rare earth ions in the orthoferrites, group theory predicts that, barring accidental degeneracies, all degeneracy will be lifted, resulting in $2J+1$ crystal field states in the even-electron case. These states can be characterized by the representation labels A' and A'' of the site group [15]. The electric and magnetic dipole selection rules for transitions between such states are shown in Table 1.

The rare earth crystal field states are in turn influenced by magnetic perturbations, the largest of which are due to the magnetic iron lattices. At the low temperatures in which sharp line spectra have been observed in the rare earth orthoferrites, the iron lattices are almost completely ordered [7]. This net iron magnetization gives rise to what is commonly known as a 'molecular field' at the rare earth site, that is, a hypothetical magnetic field whose components are functions of the averaged magnetization of the iron lattices. In addition, the spin waves associated with these iron moments can affect the linewidths of rare earth absorptions, but such effects

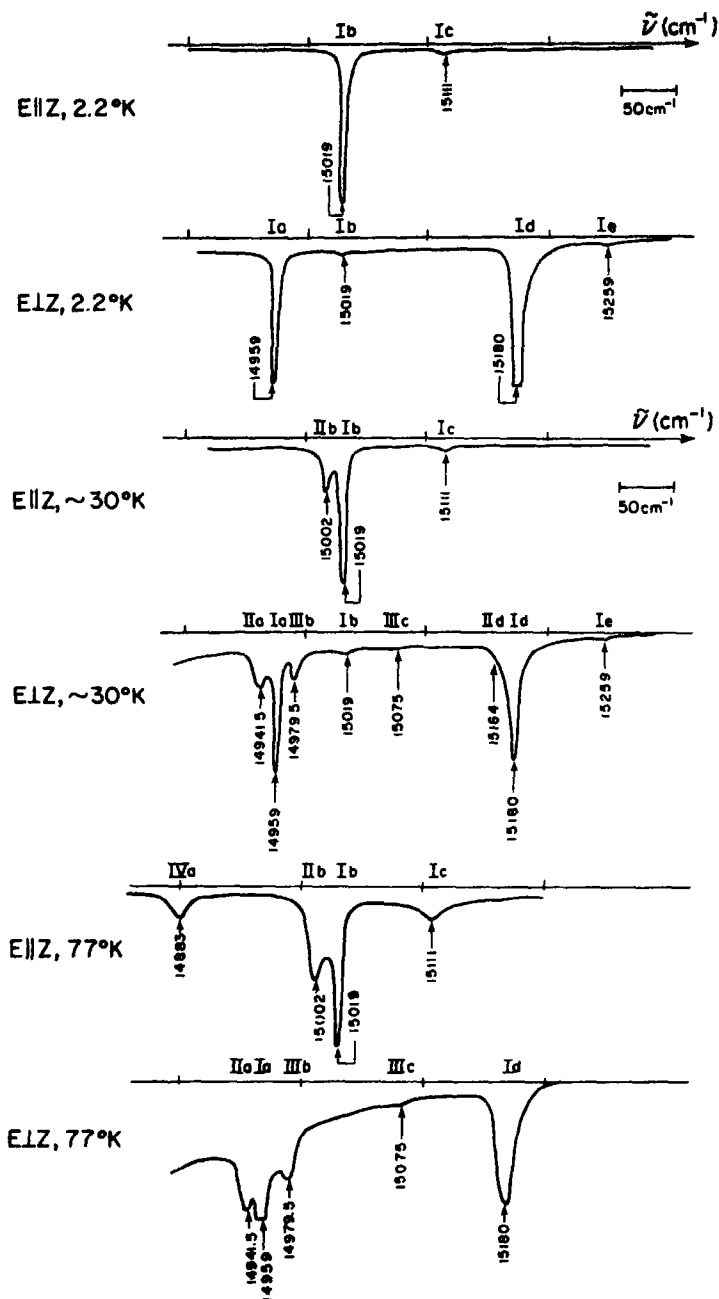


Fig. 2. Densitometer traces of the ${}^3H_6-{}^3F_2$ absorption lines of Tm-FeO₃. Line positions are given in wavenumbers, and prominent electronic transitions are identified as described in Section 4.

will be ignored in this study, which is limited to the analysis of line positions and integrated intensities. The spin waves can also give rise

to optical exciton-magnon absorption in which there is simultaneous excitation of a rare earth exciton and an iron spin wave; such an ab-

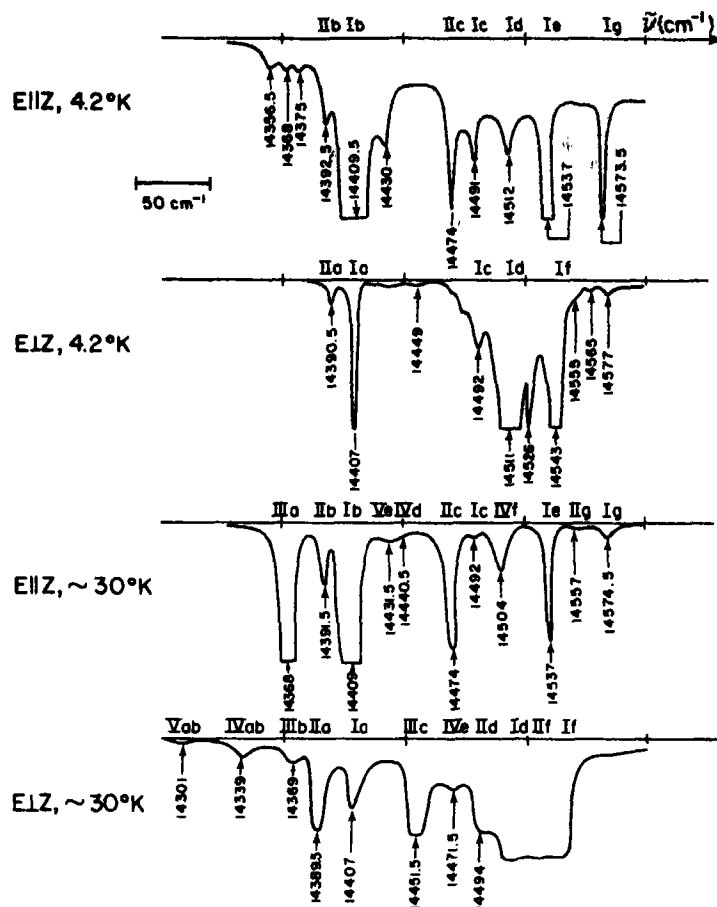


Fig. 3. Densitometer traces of the ${}^3H_6-{}^3F_3$ absorption lines of TmFeO_3 .

Table 1. Selection rules for electric and magnetic dipole transitions in the group C_{1h} . The mirror plane is perpendicular to the z-direction. $E\parallel x$ and $E\parallel y$ specify the polarization of light propagating in the z-direction, $E\parallel z$ and $E\perp z$ of light propagating in the (110)-direction

Transitions	A' to A' or A'' to A''	A' to A'' or A'' to A'
Electric dipole allowed	$E\perp z, E\parallel x, E\parallel y$	$E\parallel z$
Magnetic dipole allowed	$E\perp z$	$E\parallel z, E\parallel x, E\parallel y$

sorption would appear as a sideband of a rare earth single-ion absorption[16]. However, it is possible to show that the integrated intensity of such absorptions should be several orders of magnitude weaker than the intensity

of electric dipole single-ion absorptions, which in this case are not parity-forbidden at the rare earth site[17].

In addition to iron-rare earth interactions, there are also rare earth-rare earth interactions which can affect

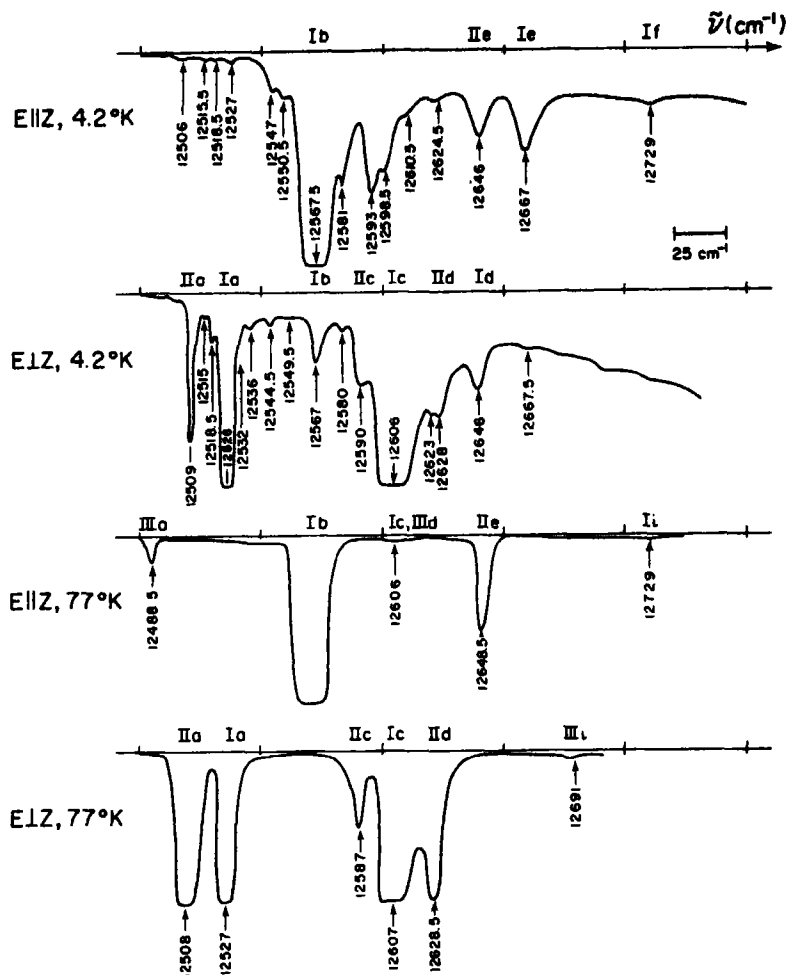


Fig. 4. Densitometer traces of the ${}^3H_6 - {}^3F_4$ absorption lines of $TmFeO_3$. There are other broad higher energy lines to the right of the lines shown here.

the rare earth single-ion energy levels. As in the iron case, surrounding rare earth ions can give rise to a molecular field at the rare earth ion under consideration. Such effects have been measured by Schuchert *et al.*[4], who observed a temperature dependent shift of over 2 cm^{-1} in the exchange splitting of the holmium ground doublet; they attributed this shift to the rare earth molecular field. However, the net rare earth magnetization in $TmFeO_3$ is known to be several orders of magnitude smaller than in $HoFeO_3$, and therefore such effects should be negligible in this case.

Rare earth-rare earth interactions can also give rise to so-called Davydov splittings[18], because there are four different rare earth sites per unit cell. For instance, it is possible to show that every single-ion $A' \rightarrow A'$ transition gives rise to two different $k=0$ exciton transitions which should appear in different polarizations. The

thulium spectra show no such splittings, indicating that in this case an excitonic description is not necessary. This result may not carry over to other rare earth orthoferrites, however, because the two-ion exchange integrals which cause Davydov splitting have the same form as the exchange integrals causing molecular fields; the case of $HoFeO_3$ shows that these integrals can be as large as 2 cm^{-1} .

(b) Hamiltonian matrices

It is the purpose of this section to analyze in greater detail the magnetic perturbations which affect the exact crystal field states of the rare earth ions in the single-ion model. It is impossible to calculate these perturba-

tions directly without the crystal-field state wavefunctions, which are themselves prohibitively difficult to calculate in a site of low symmetry. Instead, a group theoretical approach will be used to analyze the perturbations, and in this way the minimum number of parameters needed to describe the perturbations will be identified.

The zeroth order Hamiltonian may be taken to be the single-ion crystal field Hamiltonian, and therefore, on a basis of exact crystal field states, the zeroth order Hamiltonian matrix will have only on-diagonal entries, each of which represents the energy of a crystal field state.

The magnetic perturbations can be described in terms of the total angular momentum operator J , because by and large the rare earth energy level structure consists of well-separated J -multiplets, each with $2J+1$ different crystal field levels. In this case, the perturbation \mathcal{H}' due to an applied magnetic field \mathbf{H} may be written

$$\mathcal{H}' = -\boldsymbol{\mu} \cdot \mathbf{H} \quad (3.1)$$

where $\boldsymbol{\mu} = -g_J \mu_B \mathbf{J}$ is the moment operator. μ_B is the Bohr magneton (taken to be positive), and g_J is the Lande g -factor.

The perturbation \mathcal{H}'' of the iron lattices on the rare earths may be derived by means of the approximation given in the previous section, namely, that the dominant effect of the iron lattices depends only on the averaged components of iron magnetization. In this case, the most general term in \mathcal{H}'' has the form

$$S_i^n \cdot D_{ij}^{nm} \cdot J_j^m \quad (3.2)$$

where S_i^n represents an irreducible polynomial of n th order in the averaged components of the iron magnetization at iron site i , where J_j^m represents an irreducible tensor operator of m th order in the total angular momentum operator at rare earth site j , and where D_{ij}^{nm} is some coupling constant. The factor $S_i^n \cdot D_{ij}^{nm}$ may be considered as a coefficient

of the J_j^m operator, and such a term may be viewed as part of an expansion of the magnetic energy of the rare earth ion in terms of irreducible tensor operators.

The linear terms in this expansion correspond to the usual molecular field approximation. These terms can be written

$$g_J \mu_B \mathbf{H}^M \cdot \mathbf{J} = -\boldsymbol{\mu} \cdot \mathbf{H}^M \quad (3.3)$$

where \mathbf{H}^M is the molecular field. The directions for the molecular fields in the various magnetic configurations of the orthoferrites may be found by group theory[1]. In the $\Gamma_4(F_x)$ configuration, the molecular fields point in the z -direction at all four rare earth sites. In $\Gamma_2(F_x)$ they point in the xy -plane: for sites 1 and 2 they lie at some angle from the x -axis, and for sites 3 and 4 they lie symmetrically disposed on the other side of the x -axis.

To what extent can group theory simplify the matrix elements of the two perturbations (3.1) and (3.3), which represent the applied and molecular field perturbations respectively? First of all, time reversal symmetry requires that all on-diagonal matrix elements of these perturbations must vanish, because the exact crystal field states are singlet states which are always non-magnetic. Furthermore, time reversal symmetry requires that off-diagonal matrix elements be pure imaginary, provided that the basis states are chosen to be real[19].

The effects of site symmetry on the perturbation matrix elements can be found with reference to the site group character table and the group theoretical matrix element theorem [15]. There are two possibilities depending on the representation labels A' and A'' of the two wavefunctions $|c\rangle$ and $|d\rangle$ of each off-diagonal matrix element[6]: If the two representation labels are the same (both are A' or both are A''),

$$(c|\mu_x|d) = (c|\mu_y|d) = 0, (c|\mu_z|d) \neq 0. \quad (3.4)$$

If the two representation labels are opposite

(one is A' and the other is A''),

$$(c|\mu_x|d) \text{ and } (c|\mu_y|d) \neq 0, (c|\mu_z|d) = 0. \quad (3.5)$$

Finally the symmetry of the unit cell relates the matrix elements of the different sites to each other. In the approximation that the rare earth ions are uncoupled from each other, there is a freedom in the phase of the wavefunctions at each site. By using these phase freedoms and the transformation properties of the axial vector μ from site to site, it is possible to show that the Hamiltonian matrices of sites 1 and 2 are identical, as are those of sites 3 and 4. Furthermore, the relationship between the two different matrices can be described very compactly by introducing a \pm in front of the matrix elements of μ_y , where the upper sign applies to sites 1 and 2, and the lower to 3 and 4. An explicit demonstration of these facts is given in the author's thesis[13].

By taking all these facts into account, it is now possible to write out a Hamiltonian matrix which accounts for the zeroth order crystal field interactions and also for perturbations due to applied and molecular fields. Let $|iA'\rangle$ and $|jA''\rangle$ be crystal field states transforming as A' and A'' respectively, with energies E_i and E_j , where i and j stand for all

other quantum numbers. Let μ_{ij} be the matrix element of a component of the moment operator between the i th and j th states. Let Δ_{ij} be a molecular field matrix element between the i th and j th states; it represents a product of matrix elements μ_{ij} and molecular fields H^M . Then the Hamiltonian matrices for four typical states $|A'\rangle$, $|2A'\rangle$, $|3A''\rangle$, and $|4A''\rangle$ in the two magnetic configurations $\Gamma_2(F_x)$ and $\Gamma_4(F_z)$ are as given in Table 2.

So far, the higher order perturbation terms of the type (3.2) have been ignored in the derivation of the Hamiltonian matrices. To account for these terms, it is necessary to distinguish between those which are of odd or of even order. Terms of even order in J_j^m give rise to magnetostriction, which can be shown to have a negligibly small effect on the thulium energy levels[13]. Therefore, the only important terms are those of odd order in the irreducible tensor operators J_j^m . These operators are odd under time reversal and therefore all the time reversal results which applied to the linear terms apply to these terms also. Furthermore, all these operators can be classified according to the representation labels A' and A'' of the site group. Thus, they all transform either as μ_z or as μ_x or μ_y in this group. Once again, all the results which applied to the linear terms because of site symmetry carry over to these higher order terms. Therefore the parameters which describe the higher order terms can be absorbed directly into the same parameters Δ_{ij} which describe the molecular field terms. This means that the matrices derived heretofore actually take account of terms of arbitrarily high order. The only change introduced by this generalization is that the Δ_{ij} can no longer be interpreted as a product of μ_{ij} , the matrix element of the moment operator, and H^M , a simple molecular field. Instead Δ_{ij} must be interpreted as a matrix element of a

Table 2. Hamiltonian matrices for even-electron rare earth ions in the orthoferrites: in the $\Gamma_2(F_x)$ and the $\Gamma_4(F_z)$ magnetic configurations. The matrices are given for an arbitrary group of four crystal field states of which two transform as A' and two as A'' . E is the energy of a crystal field state, μ a matrix element of the magnetic dipole operator, H the applied magnetic field, and Δ a matrix element of the molecular field energy operator

$\Gamma_2(F_x):$				
$ 1A'\rangle$	$\begin{pmatrix} E_1 & & & \\ & i(\mu_{x12}H_x) & & \\ & & E_2 & \\ & & & E_3 \end{pmatrix}$	$i(\mu_{x13}H_x \pm \mu_{y13}H_y + \Delta_{13})$	$i(\mu_{x14}H_x \pm \mu_{y14}H_y + \Delta_{14})$	$i(\mu_{x23}H_x \pm \mu_{y23}H_y + \Delta_{23})$
$ 2A'\rangle$				
$ 3A''\rangle$				
$ 4A''\rangle$				
			E_4	$i(\mu_{x34}H_x)$
$\Gamma_4(F_z):$				
$ 1A'\rangle$	$\begin{pmatrix} E_1 & & & \\ & i(\mu_{x12}H_x + \Delta_{12}) & & \\ & & E_2 & \\ & & & E_3 \end{pmatrix}$	$i(\mu_{x13}H_x \pm \mu_{y13}H_y)$	$i(\mu_{x14}H_x \pm \mu_{y14}H_y)$	$i(\mu_{x23}H_x \pm \mu_{y23}H_y)$
$ 2A'\rangle$				
$ 3A''\rangle$				
$ 4A''\rangle$				
			E_4	$i(\mu_{x34}H_x + \Delta_{34})$

generalized molecular field H_{ij}^M ; because of the higher order terms, the magnitude of the various components of H_{ij}^M now depends on the particular crystal field states i and j between which the matrix element is evaluated.

The fact that all the zero-field perturbation matrix elements can be described by a generalized molecular field is characteristic of the low symmetry of the rare earth site group in the orthoferrites. In the group C_{1h} , μ_x , μ_y , and μ_z exhaust all the different kinds of transformations, that is, all the different representation labels. By contrast, in larger groups, like C_{3h} , there are more representation labels and hence it is necessary in these cases to consider matrix elements which arise solely from higher order interactions and which can in no sense be attributed to a generalized molecular field.

The matrices in Table 2 provide the framework for interpreting the optical spectra and magnetic properties of TmFeO_3 , as shown in the subsequent sections. Similar matrices can be derived for other magnetic configurations, and for the odd-electron case as well [13].

4. INTERPRETATION OF THE OPTICAL SPECTRUM

Data on the optical spectrum of TmFeO_3 has been presented in Figs. 2–4. A majority of the lines in the spectrum can be identified as single-ion transitions from the states of the ground multiplet, labeled I, II, III, and so on, to the states of an excited multiplet, labeled a , b , c , and so on, in order of increasing energy.

(a) Selection rules

The spectra of Fig. 2, representing transitions from the 3H_6 to the 3F_2 multiplet, give the simplest example of how such identifications can be made. The spectra at 2.2°K show five different lines, appearing in various polarizations. It is apparent that these five lines represent transitions from the ground state to the five electronic levels of the 3F_2 multiplet, and so these transitions may be labeled Ia, Ib, and so on.

The fact that almost every line of Fig. 2 appears primarily in one polarization and not the other indicates that the selection rules of Table 1 are valid to a good approximation and hence that the energy levels may be desig-

nated by representation labels A' or A'' . The data suggests that three of the states of the 3F_2 multiplet belong to one representation and two to the other. Furthermore, comparison with data taken in the $E||x$ and $E||y$ polarizations shows that the same lines which appear in $E\perp z$ also appear in these polarizations. This fact proves that according to the selection rules of Table 1, the transitions are electric rather than magnetic dipole.

At higher temperatures, the data shows new lines which can readily be identified as transitions originating on excited states of the ground multiplet. For example, three lines appear in the 30°K spectra which can be identified as IIa, IIb, and IIc, because they lie $\sim 17.5 \text{ cm}^{-1}$ from the respective I-lines. The fact that IIc and IId are not observable is presumably due to a small transition probability and cannot be considered as significant in terms of the group theory. All the II-lines appear in the same polarization as the corresponding I-lines, which shows that level II must have the same representation label as level I. In the same 30°K spectra of Fig. 2, two other lines appear which are both spaced 39 cm^{-1} from a I-line, and at 77°K another two appear at roughly 70 cm^{-1} from a I-line. The data of this multiplet alone is not extensive enough to confirm these lines as originating from levels III and IV, but comparison with the other multiplets shows similar spacings. Furthermore, the III- and IV-lines always appear in the opposite polarizations from the corresponding I- and II-lines; this shows that levels III and IV must have the opposite representation labels from I and II.

In sum, application of the selection rule principles of Table I has led to an identification of all the lines of the 3F_2 group in terms of a series of ground multiplet levels and a series of 3F_2 levels. These identifications are summarized in Table 3. A similar treatment can be given to the 3F_3 and 3F_4 multiplets. (In these cases the analysis is complicated by the presence of satellite lines such as the series of lines on the low energy tail of the

Table 3. Energy levels of trivalent thulium in TmFeO_3 as determined by optical spectroscopy

Group	Energy ($\pm 1 \text{ cm}^{-1}$ except where noted)	Identifi- cation	Representation label
3H_6	0	I	A'
	17.5	II	A'
	39	III	A''
	70 ± 3	IV	A''
	107 ± 3	V	?
	134 ± 3	VI	A'
	163 ± 3	VII	?
3F_4	12527	<i>a</i>	A'
	12567.5	<i>b</i>	A''
	12605.5 ± 3	<i>c</i>	A'
	12646	<i>d</i>	A'
	12667	<i>e</i>	A''
	12729	<i>f</i>	A''
	12807	<i>g</i>	A'
	12862 ± 2	<i>h</i>	A''
	12886.5 ± 2	<i>i</i>	A'
3F_3	14407 ± 2	<i>a</i>	A'
	14409 ± 2	<i>b</i>	A''
	14492 ± 2	<i>c</i>	A''
	14511.5	<i>d</i>	A'
	14537	<i>e</i>	A''
	14543.5	<i>f</i>	A'
	14574	<i>g</i>	A''
3F_2	14959	<i>a</i>	A'
	15019	<i>b</i>	A''
	15111 ± 2	<i>c</i>	A''
	15180	<i>d</i>	A'
	15259 ± 2	<i>e</i>	A'

14409 cm^{-1} lines in the $E||z$ spectrum of Fig. 3. Most of these satellites can be attributed to defects in the way recently suggested by Faulhaber and Hüfner[20]. Only a few, such as the 12593 cm^{-1} line of Fig. 4 appear to fit neither the satellite nor the electronic category).

It is not possible to determine the absolute representation labels of the energy levels simply from the selection rules because there are always two levels in a transition, and only their relative representation labels govern the selection rules. However, the absolute labels can be derived from the decomposition of D_J , the J th order representation of the full

rotation group, into C_{1h} :

$$\begin{aligned} {}^3F_2 &= 3A' + 2A'' \\ {}^3F_3 &= 3A' + 4A'' \\ {}^3F_4 &= 5A' + 4A''. \end{aligned} \quad (4.1)$$

In the actual data, the following numbers of different types of electric dipole transitions from the ground level are observed:

$$\begin{array}{ccc} & A' \text{ to } A' & A' \text{ to } A'' \\ & \text{or} & \text{or} \\ & A'' \text{ to } A'' & A'' \text{ to } A' \\ {}^3F_2 & 3 & 2 \\ {}^3F_3 & 3 & 4 \\ {}^3F_4 & 5 & 4. \end{array} \quad (4.2)$$

Comparison of (4.1) and (4.2) for each of the three multiplets shows that the ground level must be A' . The complete list of all known energy levels and their absolute representation labels is given in Table 3.

All the above results rely on an application of the selection rules of Table 1. However, in the $\Gamma_2(F_x)$ magnetic configuration, molecular fields can mix states of opposite representations (see Table 2) and can therefore lift these selection rules. Since most of the thulium absorptions obey the selection rules, the molecular field interactions must be small, and their size can be estimated from first order perturbation theory.

For example, the 15019 cm⁻¹ line Ib of the 2·2°K spectra of the 3F_2 multiplet, as shown in Fig. 2, appears to 'leak through' from the $E||z$ polarization into the forbidden $E\perp z$ polarization. One possible cause of this 'leak-through' is molecular field mixing of level I with other levels. Level III is the nearest level with the opposite representation label, and IIIb is one of the strongest high-temperature lines; so admixture of III into I is likely to give the largest forbidden transition intensity for Ib. If Δ_{13} is the molecular field matrix element which connects these levels, and if D is the crystal field separation between the levels, then by first order perturbation theory and the Fermi Golden Rule, the transition probability in the forbidden polarization must be proportional to $(\Delta_{13}/D)^2$. In the 30°K spectrum of Fig. 2, the IIIb line has roughly ten times the intensity of the Ib line, and its true intensity is reduced at 30°K by roughly $\frac{1}{4}$ because of the population factor. Therefore

$$(\Delta_{13}/D)^2 < 1/60, \Delta_{13} \lesssim 5 \text{ cm}^{-1}. \quad (4.3)$$

This estimate should only be considered as an upper limit on Δ_{13} because of the possible other contributions to lifting of the selection rule, such as molecular field mixing in the excited state multiplet or polarizer misalignment. It is difficult to identify these other

contributions because of the strongly polarization-dependent background absorption, which prevents an accurate measurement of the 'leakthrough' intensities in the $E||z$ polarization.

Similar analyses can be carried out on other lines of the TmFeO₃ spectrum, and they all give upper limits on the Δ 's of order 5 cm⁻¹. These results may be compared to those obtained in ErFeO₃, where all the Δ 's were of order 3 cm⁻¹ or less[3]. In the case of a Kramers ion like erbium, Molecular field matrix elements can be measured directly from Kramers doublet splittings. In thulium, the molecular field matrix elements cause only second order line shifts, which are usually too small to measure, and hence, they must be deduced instead from the selection rules and line intensities.

(b) Zeeman effect

The Zeeman effect provides a confirmation of the representation label assignments made in the polarization study. An examination of the matrices of Table 2 shows that applied fields in the z -direction induce splittings between levels with the same representation labels, and applied fields in the xy -plane induce splittings between levels with opposite representation labels.

For example, the Zeeman splittings between the two lowest levels, I and II, are shown in Figs. 5 and 6. The fact that splittings occur for fields in the z -direction but not in the xy -plane implies that the two levels have the same representation labels; this agrees with the polarization results summarized in Table 3. These splittings have been previously described in terms of a spin Hamiltonian formalism[6]. They may be analyzed in more detail with reference to the matrix for $\Gamma_2(F_x)$ in Table 2. If a field is applied in the xy -plane, it is clear that any Zeeman effect must arise from interactions of levels I and II with levels III and IV. These interactions tend to cancel each other out as may be seen from second order perturbation theory, and this explains

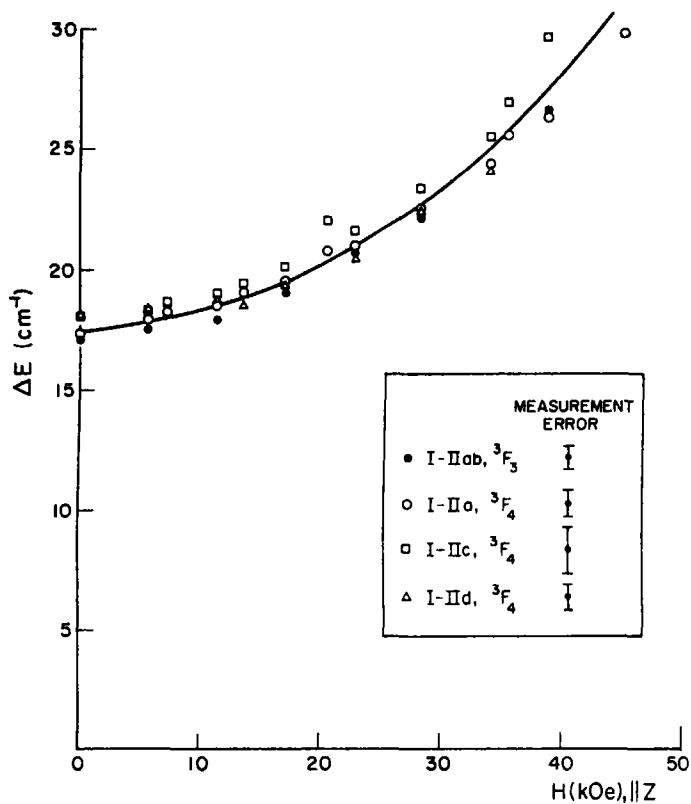


Fig. 5. Zeeman splitting ΔE of the thulium ground doublet in TmFeO_3 at $\sim 10^\circ\text{K}$, for a field H in the z -direction.

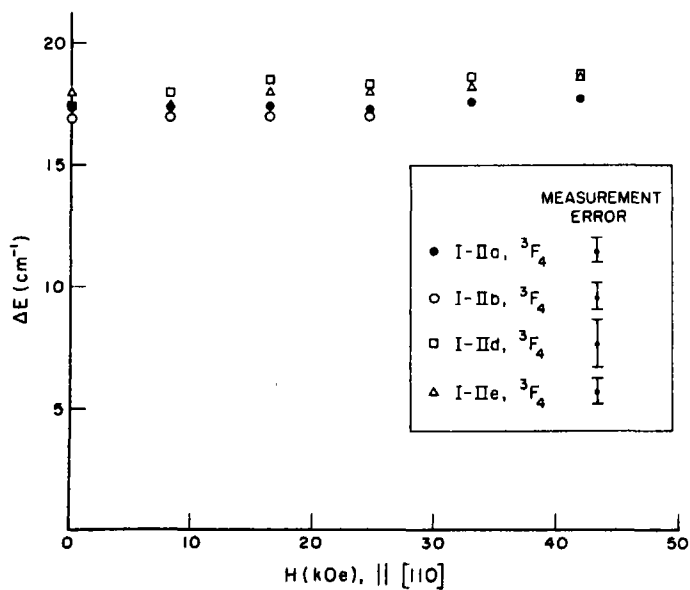


Fig. 6. Zeeman splitting ΔE of the thulium ground doublet in TmFeO_3 at $\sim 10^\circ\text{K}$, for a field H in the $[110]$ -direction.

why the Zeeman splitting in the xy -plane is so small.

However, for fields in the z -direction, the levels I and II are not coupled to III and IV by any Zeeman matrix elements, and therefore couplings to all higher lying states may be ignored to a good approximation. The 2×2 submatrix of states I and II may be solved to give the Zeeman splitting.

$$\Delta E(H) = \sqrt{D^2 + (2\mu_{z12}H_z)^2} \quad (4.4)$$

where D is the zero field splitting of 17.5 cm^{-1} . Magnetostatic effects must be accounted for in fitting equation (4.4) to the data of Fig. 5 [13], with the result that $\mu_{z12} = (4.05 \pm 0.25) \mu_B$.

Another example of the Zeeman effect is the behavior of the Ia-Ib-IIa-IIb lines of the 3F_3 multiplet for a field in the [110]-direction, as shown in Fig. 7. The complicated splitting pattern can be attributed to Zeeman interactions between two levels, a and b , of the excited 3F_3 multiplet, which have opposite representation labels, and which are nearly accidentally degenerate, with a zero field splitting D of $\sim 2 \text{ cm}^{-1}$. It is easily seen from the matrix for $\Gamma_2(F_x)$ in Table 2 that for such a case, the Zeeman splitting is given by

$$\Delta E(H) = \sqrt{D^2 + (2\mu_x H_x \pm 2\mu_y H_y + 2\Delta)^2}. \quad (4.5)$$

Such a splitting is more complex than the splitting observed for levels I and II because the two starting lines fan out into four when the field is applied in the [110]-direction. It is found that $\mu_x = (3.25 \pm 0.5) \mu_B$ and $\mu_y = (1.75 \pm 0.5) \mu_B$, or *vica versa*. It is possible to determine which of these solutions is correct by measuring the Zeeman effect for fields along the x - or y -directions. Such experiments have been done for a similar doublet in holmium by Schuchert *et al.* [4] and have been interpreted in terms of equation (4.5) by Malozemoff and White [6].

Another example of the Zeeman effect occurs in the Ia-Ib group of the 3F_3 multiplet, for a field in the [110]-direction, as shown in Fig. 8. Just as in the previous case, a splitting of the type (4.5) must be assumed, which leads to values of $(2.5 \pm 0.5) \mu_B$ and $(0.5 \pm 0.5) \mu_B$ for μ_x and μ_y . At the same time, the mixing induced by the magnetic field causes the absorptions to become allowed in their respective forbidden polarizations. Their intensity is proportional to the admixture coefficient $(\mu_x H_x \pm \mu_y H_y)/D$, and hence it is possible to estimate μ_x (or μ_y , whichever is larger) from the increase of forbidden intensity with field. The result is $(1.8 \pm 0.3) \mu_B$, which is in reasonable agreement with the previous value $(2.5 \pm 0.5) \mu_B$, considering the rough measures of line positions and intensities which were available using the photographic method.

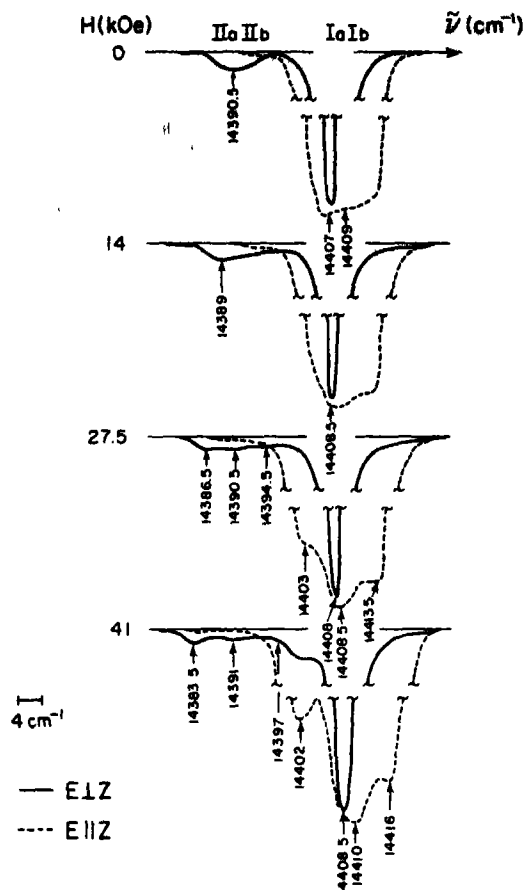


Fig. 7. Zeeman effect of the Ia-IIa-Ib-IIb group of the thulium $^3H_6 - ^3F_3$ absorption lines in TmFeO_3 , for a field H in the [110]-direction. Line positions are given in wavenumbers.

Not all the intensity effects in the Zeeman spectra can be explained so neatly. For example, there is a problem in the spectra of Fig. 7, where the Zeeman mixing of the states a and b might be expected to lift the selection rules in the $E \perp Z$ polarization. Nevertheless the great majority of Zeeman effects in the TmFeO_3 spectrum are in agreement with the theory.

5. MAGNETIC PROPERTIES OF TmFeO_3

It is the purpose of this section to show how the measured magnetic properties of TmFeO_3 can be related to the single-ion theory of Section 3 and the optical results of Section 4.

There are two contributions to the magnetic properties of TmFeO_3 —that of the iron

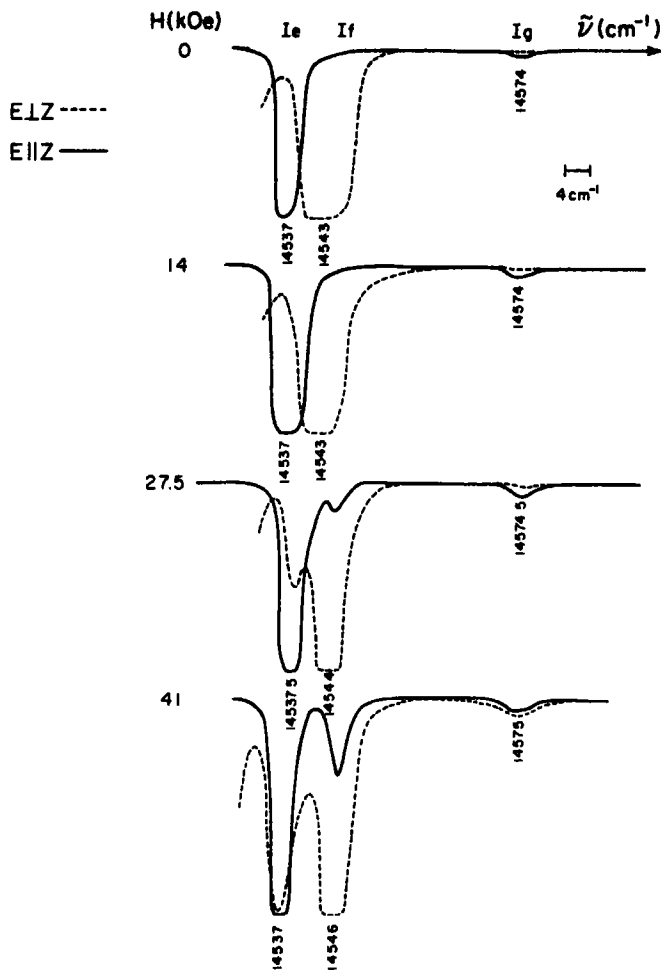


Fig. 8. Zeeman effect of 1e-1f-1g in the thulium ${}^3H_6-{}^3F_3$ absorption lines in TmFeO_3 , for a field H in the $[110]$ -direction. Line positions are given in wavenumbers.

sublattices and that of the rare earths. In general, of course, the iron and rare earth lattices must be considered as a coupled system [21], but because the rare earth magnetization is so small, its back reaction on the iron magnetization may be assumed to be small also. In this approximation, the iron contributions to the magnetic properties of TmFeO_3 can be found from studies of YFeO_3 or LuFeO_3 , which have non-magnetic rare earth ions, and in which the irons alone determine all the magnetic properties. For example, YFeO_3 and

LuFeO_3 show a net magnetization of order $0.05 \mu_B/\text{formula unit}$, which is essentially temperature independent below $\sim 100^\circ\text{K}$. This magnetization may be expected to be of the same size in both the $\Gamma_4(F_2)$ and the $\Gamma_2(F_x)$ configurations, as shown by the case of SmFeO_3 ; SmFeO_3 reorients at a high temperature, where the samarium ions are essentially unpolarized, but shows no discontinuity in the magnitude of the moment below and above the reorientation [7]. YFeO_3 and LuFeO_3 also have susceptibilities of order

$5 \times 10^{-7} \mu_B/\text{Oe/formula unit}$, and magnetic anisotropies favoring $\Gamma_4(F_z)$ over $\Gamma_2(F_x)$ by roughly 0.1 cm^{-1} per formula unit [1, 22].

The magnetization of the rare earth lattices may be deduced from the data of Fig. 1 by subtracting out the iron contribution. At high temperatures, the rare earth magnetization adds to the iron magnetization [8], but at low temperatures it evidently subtracts, decreasing from essentially zero at 70°K to $\sim -0.04 \mu_B/\text{formula unit}$ at 10°K , according to the data of Cape and Malozemoff. The iron susceptibility is negligible compared to the measured low temperature susceptibility of $(2.2 \pm 0.2) \times 10^{-5} \mu_B/\text{Oe/formula unit}$ [12], which is therefore due almost entirely to the rare earths. Furthermore, the reorientation transition at 86°K can be accounted for by a rare earth magnetic anisotropy which favors $\Gamma_2(F_x)$ over $\Gamma_4(F_z)$ and is temperature dependent, increasing to $0.1 \text{ cm}^{-1}/\text{formula unit}$ and overwhelming the constant iron anisotropy as the temperature is lowered below 86°K .

These effects may be interpreted in terms of the single-ion theory in the following way. With every thulium energy level i may be associated a moment m_i and a susceptibility χ_i . Then, for example, the net moment and susceptibility of a single-ion in the x -direction are:

$$m_x = \sum_i m_{xi} p_i \quad (5.1)$$

$$\chi_{xx} = \sum_i \chi_{xix} p_i \quad (5.2)$$

where p_i is the Boltzmann population factor, which may be calculated from the known energy levels of thulium in Table 3. Above 20°K there are too many terms in the expression (5.1) to get a meaningful fit to the data. But below 20°K the two lowest states are over 95 per cent occupied, and therefore only the first two terms give significant contributions. Fig. 1 shows a fit of equation (5.1) to the data of Cape and Malozemoff, with the result that $m_{x1} = (-0.038 \pm 0.01)$ and $m_{x2} = (-0.04 \pm 0.01) \mu_B/\text{formula unit}$. Likewise, the mea-

sured low temperature susceptibility gives $\chi_{xx1} = (2.2 \pm 0.2) \times 10^{-5} \mu_B/\text{Oe/formula unit}$.

The magnetization data of Belov *et al.* [11] does not agree with the data of Cape and Malozemoff and shows an almost linear increase in the magnetization at low temperatures down to 4.2°K . However, the single-ion theory implies that because of the 17.5 cm^{-1} splitting between the ground and excited states, only the ground state is populated below $\sim 10^\circ\text{K}$, and so the magnetization must be essentially independent of temperature in this region. Cape and Malozemoff have measured such a magnetization in several samples, grown independently in two different laboratories, and they have concluded that their data, rather than that of Belov *et al.*, is the best indication of the bulk magnetization of good quality TmFeO₃ [12].

The values of m_{x1} , m_{x2} , and χ_{xx1} , obtained above, may be compared to the predictions of the single-ion theory. For example, the magnetization of a level is the gradient of the energy of that level with respect to the applied field, and it may be calculated by second order perturbation theory directly from the matrices of Table 2. Thus,

$$m_{x1} = 2\mu_{x13}\Delta_{13}/39 + 2\mu_{x14}\Delta_{14}/70 + \dots \quad (5.3)$$

$$m_{x2} = 2\mu_{x23}\Delta_{23}/21.5 + 2\mu_{x24}\Delta_{24}/52.5 + \dots \quad (5.4)$$

Each m_{xi} arises from the molecular field interactions of the i th level with all the other crystal field levels, and therefore the sum for each m_{xi} contains many terms. This sum does not converge rapidly because the energy denominators do not increase rapidly, as can be seen from Table 3. Furthermore, the various terms of (5.3) and (5.4) can be either positive or negative (corresponding to ferro- or antiferromagnetic coupling with the iron magnetization), as may be seen by considering the numerators:

$$\mu_{xij}\Delta_{ij} = \mu_{xu}^2 H_{xu}^M + \mu_{xuj}\mu_{vu} H_{vu}^M. \quad (5.5)$$

The sign of such an expression can depend on

i and j for one of two reasons. Either the sign of the components of H_{ij}^M can vary from term to term because of the higher order exchange couplings described in Section 3, or the relative signs of μ_{xi} and μ_{yj} can vary from term to term. As a result it is extremely difficult to predict the size or the sign of the m_{xi} . It has not been possible to measure explicitly any of the Δ 's or μ 's which appear in (5.3) or (5.4), but the Δ 's are known to be less than 5 cm^{-1} and other μ -parameters which have been deduced in Section 4 are of order 0 to $4 \mu_B$ /formula unit. Therefore the m_{xi} are likely to be of the order of $0.1 \mu_B$ but could range from $1 \mu_B$ down to very small values, depending on the particular Δ 's and μ 's and on the degree of cancellation.

Although this analysis does not provide a very quantitative prediction of m_{x1} and m_{x2} for comparison with the experimental results, it does show that, in the single-ion model, the thulium magnetization is governed not by any one doublet but by the interactions of a number of widely spaced levels. This condition may explain why rare earth magnetizations of the various orthoferrites with even-electron ions are in some cases parallel, in others antiparallel, to the iron moments, and why these magnetizations can vary so much in size.

The susceptibility of the ground level can be derived in a similar way:

$$\chi_{xx1} = 2\mu_{x13}^2/39 + 2\mu_{x14}^2/70 + \dots \quad (5.6)$$

In this case, all the terms are positive; so there is no cancellation, and χ_{xx1} can be predicted to be of order $10^{-5} \mu_B/\text{Oe}/\text{formula unit}$, in agreement with experiment.

A temperature dependent anisotropy can also be derived from the single-ion model: Each energy level i shifts by some amount K_i on passing from the $\Gamma_2(F_x)$ to the $\Gamma_4(F_z)$ configuration, and this shift, multiplied by the population factor, gives a contribution to the rare earth anisotropy K favoring one configuration over the other:

$$K = \sum_i K_i p_i. \quad (5.7)$$

(It is assumed that the energy shifts are small enough that p_i is not appreciably changed between the two configurations). K_i may be calculated directly from second order perturbation theory. For example,

$$K_1 = \Delta_{13}^2/39 + \Delta_{14}^2/70 - \Delta_{12}^2/17.5 + \dots \quad (5.8)$$

Once again there are many terms and it has not been possible to identify enough parameters to achieve a quantitative test of the theory. Nevertheless, if the Δ 's are of order of a few wavenumbers, the parameters K_i can be as large as 0.5 cm^{-1} . Such terms, reduced by their population factors, are large enough to overwhelm the iron anisotropy and to account for the reorientation transition at 86°K . Direct measurements of the temperature dependent anisotropy, of the kind taken by Belov *et al.* on SmFeO_3 [22], would be helpful in pinning down the parameters of this part of the theory more quantitatively.

6. CONCLUSION

This study has made three main contributions. It has developed a single-ion theory for the even-electron rare earth ions in the orthoferrites. It has reported the optical zero-field and Zeeman spectra of TmFeO_3 and has shown that most aspects of the spectra can be understood from the theory. Finally, it has suggested an interpretation of the magnetic properties of TmFeO_3 , based on the single-ion theory; unfortunately, because of the large number of undetermined parameters, this part of the theory cannot be verified conclusively.

These contributions are important in the context of other work on the orthoferrites because they are all based on the existence of molecular field couplings between well-separated crystal field states. The importance of such couplings was recognized in a previous study of ErFeO_3 [3]. This study of TmFeO_3 is the first case of the orthoferrite

series in which such couplings have been analyzed explicitly. The theoretical framework of this analysis is directly applicable to other even-electron rare earth ions in the orthoferrites.

Acknowledgements—I gratefully acknowledge the support and encouragement of Professors R. L. White and R. M. White throughout the course of this work. I also wish to thank Dr. J. A. Cape for his collaboration in the experimental and theoretical work on the magnetic properties of TmFeO_3 , and Dr. R. MacFarlane for his careful reading of the manuscript.

REFERENCES

1. WHITE R. L., *J. appl. Phys.* **40**, 1061 (1969).
2. FAULHABER R., HUFNER S., ORLICH E. and SCHUCHERT H., *Z. Phys.* **204**, 101 (1967).
3. WOOD D. L., HOLMES L. M. and REMEIK A. J. P., *Phys. Rev.* **185**, 689 (1969).
4. SCHUCHERT H., HUFNER S. and FAULHABER R., *Z. Phys.* **220**, 280 (1969).
5. SCHUCHERT H., HUFNER S. and FAULHABER R., *Z. Phys.* **220**, 273 (1969).
6. MALOZEMOFF A. P. and WHITE R. L., *Solid State Commun.* **8**, 665 (1970).
7. TREVES D., *J. appl. Phys.* **36**, 1033 (1965).
8. KURODA C., MIYADAI T., NAEMURA A., NIIZEKI N. and TAKATA H., *Phys. Rev.* **122**, 446 (1961).
9. GYORGY E. M., REMEIK A. J. P. and HAGEDORN F. B., *J. appl. Phys.* **39**, 1369 (1968).
10. LEAKE J. A., SHIRANE G. and REMEIK A. J. P., *Solid State Commun.* **6**, 15 (1968).
11. BELOV K. P., KADOMTSEVA A. M., ORCHINIKOVA T. L. and TIMOFEEVA V. A., *Soviet Phys. — JETP Lett.* **2**, 253 (1965).
12. CAPE J. A. and MALOZEMOFF A. P., *Solid State Commun.* **8**, 24 (1967).
13. MALOZEMOFF A. P., *Technical Report No. 5303-1*, Stanford Electronics Laboratories, Stanford, California, May 1970.
14. WYBOURNE B. G., *Spectroscopic Properties of Rare Earths*, Interscience, New York (1965).
15. TINKHAM M., *Group Theory and Quantum Mechanics*, McGraw-Hill, New York (1964).
16. SELL D. D., GREENE R. L. and WHITE R. M., *Phys. Rev.* **158**, 489 (1967).
17. MALOZEMOFF A. P., *Optical Exciton-Magnon Absorption in Rare Earth Orthoferrites*, Internal Memorandum, Stanford Electronics Laboratories, Stanford, California (1970).
18. McCLURE D. S., in *Solid State Physics* (Edited by F. Seitz and D. Turnbull), Vol. 8, p. 1. Academic Press, New York (1959).
19. GRIFFITH J. S., *Phys. Rev.* **132**, 316 (1963).
20. FAULHABER R. and HUFNER S., *Solid State Commun.* **7**, 389 (1969).
21. BEAULIEU T. J., *Microwave Laboratory Report No. 1530*, Stanford University, Stanford, California (1967).
22. BELOV K. P., KADOMTSEVA A. M., LEVITIN R. Z., TIMOFEEVA V. A., USKOV V. V. and KHOKHLOV V. A., *Soviet Phys. JETP* **28**, 1139 (1969).

TECHNICAL NOTES

Magnetic susceptibility and lattice distortion in an antiferromagnet, AuMn

(Received 6 November 1970; in revised form 22 December 1970)

ABOVE the Néel temperature and near the 50 at. % composition AuMn has a CsCl cubic structure. On cooling this distorts to a tetragonal structure with $c/a < 1$ [1]. This distortion can be well explained if it is assumed that the magnetic exchange energy varies linearly with $(1 - c/a)$. A simple molecular field analysis, modified by the distortion dependent exchange, has been shown to predict the experimentally observed sub-lattice magnetisation, lattice distortion and specific heat within a few per cent [3].

It is now shown that the same model predicts a variation of magnetic susceptibility with temperature which agrees closely with experiment.

The molecular field theory of antiferromagnetism gives the reduced sub-lattice magnetisation, R , in terms of the Brillouin function for spin S as [2]:

$$R = B_S(x) \quad (1)$$

$$x = \frac{3SRT_N}{(S+1)T} \quad (2)$$

where T_N is the Néel temperature.

If the nearest neighbour interaction is antiferromagnetic, (α), and the next nearest ferromagnetic, (γ), then:

$$kT_N = \alpha - \gamma \quad (3)$$

$$k\theta = \alpha + \gamma. \quad (4)$$

The parameter θ is involved in formulas for parallel and perpendicular susceptibilities:

$$\chi_{\parallel} = \frac{3SB'_S(x)}{T(S+1) + 3S\theta B'_S(x)} C \quad (5)$$

$$\chi_{\perp} = \frac{C}{T_N + \theta} \quad (6)$$

where $C = (4\mu_B^2 S(S+1)/3k)$ per magnetic atom. Finbow *et al.* [3] and Rodbell and Bean [4] have shown that if the lattice is distorted, because of a distortion dependent exchange energy then equation (1) is unchanged but equation (2) becomes:

$$x = \frac{3SRT_N}{(S+1)T} (1 + KR^2) = \frac{3SRT'_N}{(S+1)T} \quad (7)$$

where K had to be between 0.25 and 0.33 to correctly predict the sub-lattice magnetisation, distortion and specific heat of AuMn [3].

The magnetic spins in ordered AuMn are arranged in ferromagnetic sheets of alternating sign parallel to the (001) plane of the tetragonal cell [5, 6]. It is assumed that the magnetic spins in the alloy are essentially localised [7] and that exchange coupling probably takes place via conduction electrons. The dominant antiferromagnetic interaction, (α) is supposed to take place along $\langle 111 \rangle$ directions via the gold atom. The lattice distortion is then associated with minimisation of the Mn-Mn exchange energies which are assumed to be positive, (antiparallel spins), along the [001] direction and negative (parallel spins) along [100] and [010] directions. Thus equation (3) becomes:

$$kT'_N = \alpha - \gamma(1 - 2\beta R^2) + 2\gamma(1 + \beta R^2) \quad (8)$$

where α , β and γ are constants. The first term represents the main $\langle 111 \rangle$ antiferromagnetic interaction, the second the [001] axis antiparallel interaction, minimised with respect

to the distortion, and the third the [100] and [010] axes parallel interaction minimised with respect to distortion for a given value of R . The distortion term $2\beta R^2$ along the c axis is twice that along the a axes since $(a_0 - c)$ is twice $(a - a_0)$ where a_0 is the cubic lattice parameter in the absence of exchange.

Thus equation (4) becomes:

$$\begin{aligned} k\theta &= \alpha - \gamma(1 - 2\beta R^2) - 2\gamma(1 + \beta R^2) \\ &= \alpha - 3\gamma \text{ independent of } R \end{aligned} \quad (9)$$

and equation (8)

$$\begin{aligned} kT'_N &= \alpha + \gamma(1 + 4\beta R^2) \\ &= (\alpha + \gamma)(1 + KR^2) \\ &= kT_N(1 + KR^2) \text{ as in equation (7)} \end{aligned}$$

where $kT_N = \alpha + \gamma$ and $K = 4\beta\gamma/(\alpha + \gamma)$. Thus equations (5) and (6) can be used to express the susceptibility if kT_N is replaced by kT'_N :

$$\frac{\chi_{||}}{\chi_N} = \frac{x(1 + \theta/T_N)B'_S(x)}{B_S(x)\{1 + KB_S^2(x)\} + (x\theta/T_N)B'_S(x)} \quad (10)$$

$$\frac{\chi_{\perp}}{\chi_N} = \frac{(1 + \theta/T_N)}{(1 + \theta/T_N) + KB_S^2(x)} \quad (11)$$

These reduce to (5) and (6) in the absence of lattice distortion when $K = 0$. Above the Néel temperature, where $R = 0$, $\chi = C(T + \theta)^{-1}$ as in the undistorted case. In contrast with the undistorted molecular field model χ_{\perp} is not a constant below the Néel temperature but falls slightly. In Fig. 1 $\chi_{||}/\chi_N$ and χ_{\perp}/χ_N are plotted for $\theta/T_N = 0.5$ with $K = 0$ and $K = 0.25$.

Measurements of the susceptibility of polycrystalline AuMn have been made by Giansoldati[8], Meyer[9], and Smith[10]. Alloys containing 50 at.% Au or more are found to have values of $\theta/T_N \sim 0.67$ and the experimental results for the reduced susceptibility χ/χ_N are compared (Fig. 2) with theoretical curves for $\theta/T_N = 0.674$ and

$K = 0, 0.30$ and 0.35 . The experimental results lie remarkably close to these theoretical curves and the choice of K is close to the value of $\frac{1}{2}$ required to explain the specific heat results[3].

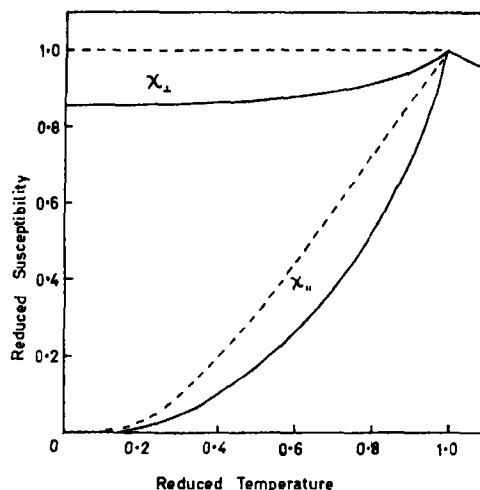


Fig. 1. The reduced susceptibilities $\chi_{||}/\chi_N$ and χ_{\perp}/χ_N below the Néel temperature for $\theta/T_N = 0.5$, with $K = 0$ (dotted lines), and $K = 0.25$ (solid lines).

The absolute values of χ_N have been observed as 1.87×10^{-5} emu/g ($H = 1600$ oe) [8], 1.94×10^{-5} emu/g ($H = 6500$ Oe) [8], 1.73×10^{-5} emu/g [9], 1.67 emu/g [10]. These values compare with a molecular field value for $S = 2$ and $\theta/T_N = 0.674$, of 1.42×10^{-5} emu/g. A lower value of θ/T_N would give agreement with experiment at T_N without significantly altering the shape of the curves below T_N . The value of $\theta/T_N = 0.674$ was, however, chosen to fit a linear extrapolation of observed values of $1/\chi$ against temperature from $T = 2T_N$ and experimental values were normalised to fit the theory at T_N .

Thus although absolute agreement with experiment is not found the model does give a good account of the change in susceptibility through and below the Néel temperature. The success of a molecular field model in this situation implies that the susceptibility

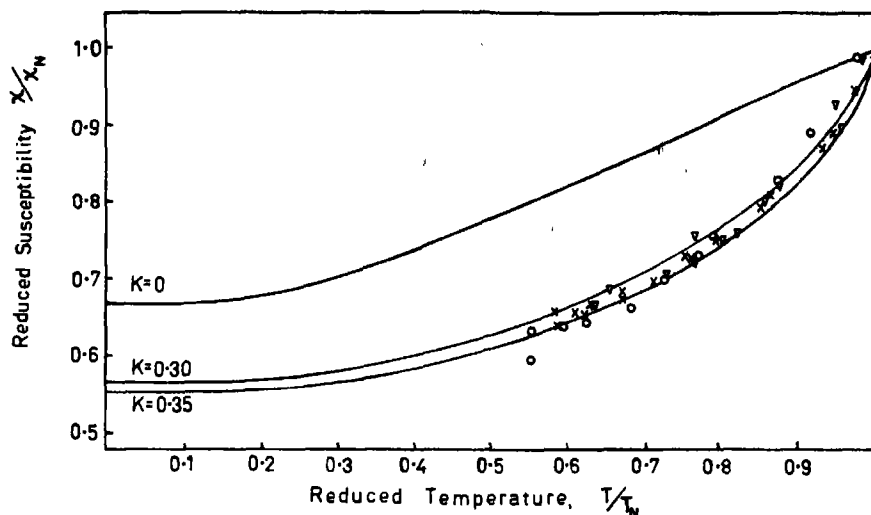


Fig. 2. The polycrystalline reduced susceptibility for $\theta/T_N = 0.674$, $K = 0$, $K = 0.30$, $K = 0.35$. Solid lines are theoretical. Experimental points are for 50 at.% Au^{II} (circles), 51 at.% Au^{II} (triangles), 51.1 at.% Au^{II} (crosses).

change below the Néel temperature is dominated by sub-lattice magnetisation dependent terms.

Acknowledgements—This work was supported by the National Research Council of Canada, Grant Numbers A5030 and A5036.

Department of Physics,
University of Manitoba,
Winnipeg,
Canada

P. GAUNT
P. D. LOLY

REFERENCES

1. SMITH J. H. and GAUNT P., *Acta Metall.* **9**, 819 (1961).
2. SMART J. S., *Effective Field Theories of Magnetism*, W. B. Saunders Co. (1966).
3. FINBOW D. C., MAKHURANE P. and GAUNT P., *J. Phys. Chem. Solids* **31**, 179 (1970).
4. BEAN C. P. and RODBELL D. S., *Phys. Rev.* **126**, 104 (1962).
5. BACON G. E., *Proc. Phys. Soc.* **79**, 938 (1962).
6. BINDLOSS W., *J. Phys. Chem. Solids* **29**, 225 (1968).
7. HO J. C. and BINDLOSS W., *Phys. Lett.* **20**, 459 (1966).
8. GIAN SOLDATI A., *J. Phys. Radium* **16**, 342 (1955).
9. MEYER A. J. P., *J. Phys. Radium* **20**, 430 (1959).
10. SMITH J. H., *Thesis*, University of Sheffield (1960).

J. Phys. Chem. Solids Vol. 32, pp. 1689–1691.

Semiconducting properties and doping of Sc_2S_3 and Sc_2Se_3

(Received 18 December 1970)

SEMICONDUCTORS with energy gaps in the range 2–3 eV are of interest for applications in electronic devices, in particular in visible electroluminescent diodes. In this work the optical and electrical properties of Sc_2S_3 [1] and Sc_2Se_3 [2] were investigated, since their colors indicate they have bandgap values in this range. Standard techniques were used to prepare Sc_2S_3 , namely by reaction of CS_2 with Sc_2O_3 at about 1100°C, and Sc_2Se_3 , namely by reaction of selenium with scandium metal. Single crystals of both compounds were grown by chemical transport reaction with I_2 in quartz ampules at an average temperature of about 950°C, as previously described [1, 2]. Doped crystals were grown by adding impurities to the transport ampule. Particularly large crystals of Sc_2Se_3 with well-

developed (110) facets are shown in Fig. 1. Polycrystalline layers of Sc_2S_3 about $5\ \mu$ thick were also grown on (1102) $\alpha\text{-Al}_2\text{O}_3$, using a vapor deposition apparatus similar to that of Tietjen and Amick[3], but with a single furnace temperature of 900°C . In this apparatus, scandium metal was transported by HCl in H_2 carrier gas as a volatile scandium chloride, which reacted with H_2S diluted in H_2 to give Sc_2S_3 .

Optical absorption measurements were made using a Cary Model No. 14 Spectrophotometer on platelet specimens $15\text{--}200\ \mu$ thick prepared from chemically transported crystals. The optical absorption coefficient α was calculated as $\alpha = (1/t) \ln(I_0/I_T)$, where t is the thickness in cm, and I_0 and I_T are the initial and transmitted intensities, respectively. The dependence of α upon wavelength λ is shown in Fig. 2 both for Sc_2S_3 and for

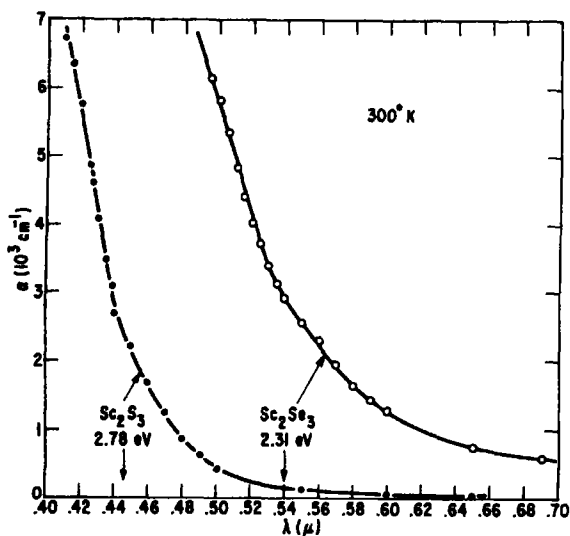


Fig. 2. The dependence of absorption coefficient (α) upon wavelength (λ) for Sc_2S_3 and Sc_2Se_3 .

Sc_2Se_3 . The linear relation between α^2 and $h\nu$ in Fig. 3, where $h\nu$ is the photon energy, indicates that Sc_2S_3 and Sc_2Se_3 have direct energy gaps[4] of 2.78 and 2.31 eV, respectively. Since the energy gaps of these compounds and their solid solution alloys would

be expected to cover the spectral region from green through blue, investigation of doping of Sc_2S_3 was undertaken.

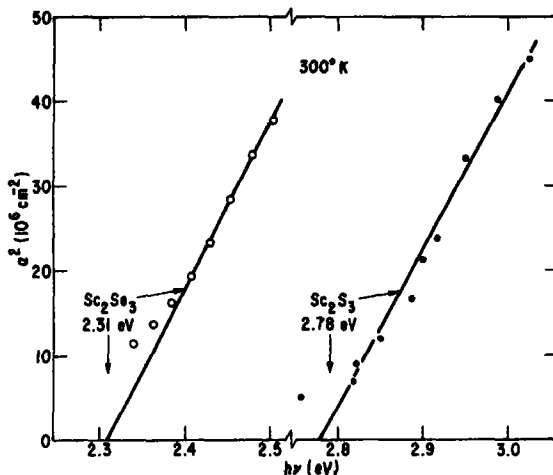


Fig. 3. The dependence of α^2 upon photon energy ($h\nu$) for Sc_2Se_3 and Sc_2S_3 , indicating direct energy gaps with values of 2.31 and 2.78 eV, respectively.

Earlier work had established the feasibility of doping bulk samples of Sc_2S_3 *n*-type[1], and of controlling the conductivity by annealing in sulfur vapor. *N*-type layers of Sc_2S_3 on $\alpha\text{-Al}_2\text{O}_3$ were also readily grown by vapor deposition in this work. The few samples grown were heavily doped, typically with $n = 1.6 \times 10^{21}\ \text{cm}^{-3}$ and $\mu = 38\ \text{cm}^2/\text{volt-sec}$ as determined by Hall measurements, using an a.c. null method which eliminates thermoelectric effects. However, no detailed investigation of *n*-type doping was made. Rather, effort was concentrated on doping Sc_2S_3 with the impurities Mg and Zn, or P, As, and Sb, which would be expected to induce *p*-type conductivity by substitution for Sc or S, respectively. However, none of the doped samples exhibited *p*-type conductivity, although emission spectrographic analysis indicated incorporation of the desired impurities in concentrations between 100 and 1000 ppm. Contrary to expectation, these impurities gave highly conducting *n*-type

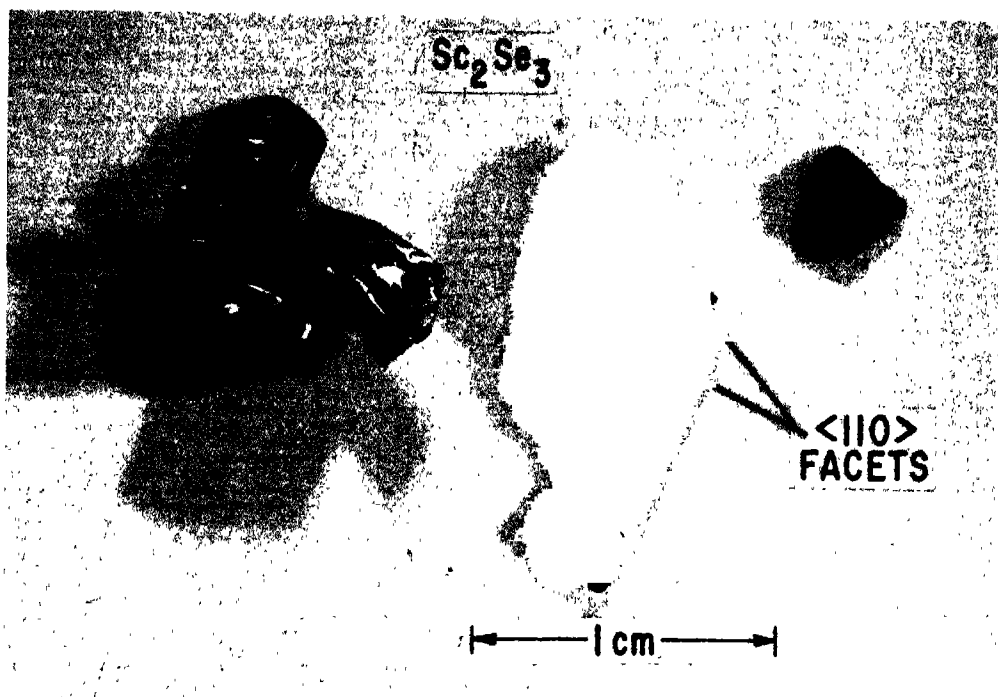


Fig. 1. Chemically transported crystals of Sc_2Se_3 , showing $\langle 110 \rangle$ facets intersecting at an angle of 70° .

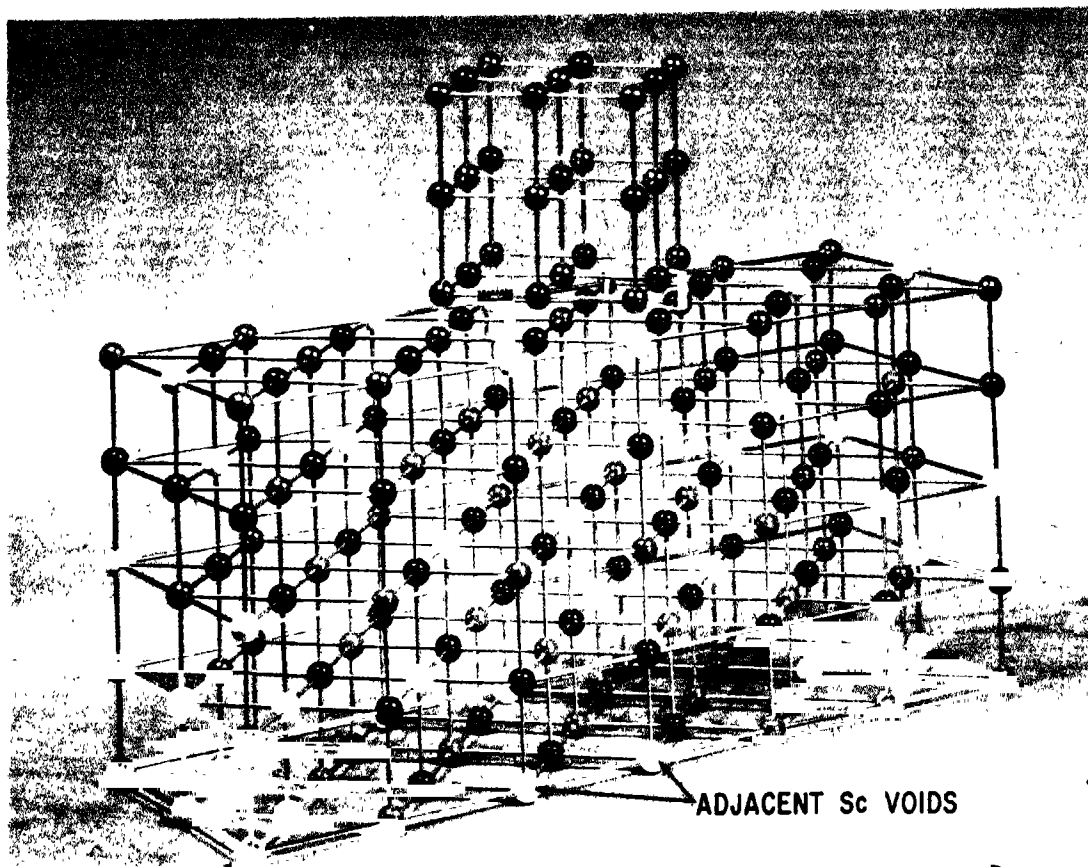


Fig. 4. One unit cell of Sc_2S_3 , with the a axis vertical. The black balls are S atoms, the gray balls are Sc atoms, and the white balls are Sc voids, which occur in adjacent pairs as indicated. One unit cell of 'NaCl' is shown for comparison in the corresponding orientation.

material. Thus, *p*-type doping of Sc_2S_3 does not appear readily possible.

The difficulty of achieving both *p*- and *n*-type doping in high band-gap semiconductors, particularly in the II-VI compounds, is well known. Mandel[5] has attributed this difficulty to the effect of vacancies which can form as the crystal grows, and compensate doping impurities, if the ratio of bandgap energy to energy of vacancy formation approaches or exceeds 1. However, calculations in the manner of Mandel[5] indicate that the value of this ratio for Sc_2S_3 is 0.62, compared to that of GaP (0.61) and that of CdTe (0.63), both of which can be doped *n*- and *p*-type. Thus, self-compensation does not appear to be the cause of the difficulty in doping Sc_2S_3 *p*-type. A more reasonable hypothesis which explains both the inability to achieve *p*-type doping and the fact that the expected *p*-type impurities give *n*-type doping instead, follows from the crystal structure of Sc_2S_3 shown in Fig. 4. The orthorhombic unit cell of Sc_2S_3 [1] is closely related to that of the NaCl structure, by an ordering of Sc voids into adjacent pairs for local neutralization of charge. Each pair of adjacent Sc voids in effect constitutes a large interstitial position, in which the placement of Mg and Zn, or P, As, and Sb is more energetically favorable than their substitution for Sc or S, respectively.

Although *n*- and *p*-type doping was not achieved in Sc_2S_3 , these results provide an insight into the doping behavior of semiconductors. In particular, the role of crystal structure should be considered, in addition to the thermodynamic considerations discussed above.

Acknowledgements—Thanks are due R. Ulmer for most of the experimental work, to H. H. Whitaker for spectrographic analyses, and to R. T. Smith for Laue photographs. The research reported herein was made possible by the support of the Advanced Research Projects Agency under Order No. 1034, through the United States Army Electronics Command, Fort Monmouth, New Jersey, USA 07703, under Contract No. DAAB07-69-C-0145.

RCA Laboratories,
Princeton, New Jersey 08540,
USA

J. P. DISMUKES

REFERENCES

1. DISMUKES J. P. and WHITE J. G., *Inorg. Chem.* **3**, 1220 (1964).
2. DISMUKES J. P. and WHITE J. G., *Inorg. Chem.* **4**, 970 (1965).
3. TIETJEN J. J. and AMICK J. A., *J. electrochem. Soc.* **113**, 724 (1966).
4. DRESSELHAUS G., *Phys. Rev.* **105**, 135 (1957).
5. MANDEL G., *Phys. Rev.* **134**, A1073 (1964).

J. Phys. Chem. Solids Vol. 32, pp. 1691–1696.

On the magnetization dependence of the magnetocrystalline anisotropy of iron

(Received 13 October 1970; in revised form 9 December 1970)

MAGNETIC anisotropy measurements for cubic crystals are usually expressed in terms of anisotropy constants K_1, K_2, \dots of an expansion in the direction cosines α_i of the magnetization with respect to the cubic axes

$$E_A = K_1 s + K_2 p + \quad (1)$$

with $s = \alpha_1^2 \alpha_2^2 + \alpha_2^2 \alpha_3^2 + \alpha_3^2 \alpha_1^2$ and $p = \alpha_1^2 \alpha_2^2 \alpha_3^2$. For a discussion of the magnetization dependence, the direction cosines in (1) should rather be regrouped in terms of spherical harmonics $\mathcal{Y}_l^m(\alpha)$ [1]

$$E_A = \kappa_4 \left(s - \frac{1}{5} \right) + \kappa_6 \left(p - \frac{s}{11} + \frac{2}{231} \right) + \quad (2)$$

where $\kappa_4 = K_1 + (1/11)K_2$. An advantage of this description is that for ferromagnets with localized spins, there are theoretical expressions for the magnetization dependence of the individual κ_l coefficients for both single and two-ion anisotropy. Thus for single-ion terms, for the classical case of infinite spin, $\kappa_l(T) = \kappa_l(0) \hat{I}_{l+1/2}(\mathcal{L}^{-1}(m))$ [2]. $\hat{I}_{l+1/2}$ denotes the ratio of modified spherical Bessel func-

tions of the first kind of order $l + \frac{1}{2}$ and $\frac{1}{2}$, \mathcal{L}^{-1} is the inverse Langevin function and $m = M(T)/M(0)$ is the reduced magnetization. At low temperatures the Bessel function representation reduces to $\kappa_l(T) = \kappa_l(0) m^{l(l+1)/2}$, giving the well-known m^{10} dependence for κ_4 . For two-ion terms an $l(l+1)/2$ -power law also holds, but only at very low temperatures[3]. For an excellent review on the magnetization dependence of single- and two-ion terms the reader is referred to Callen and Callen[3].

Earlier experimental measurements of K_1 for iron were interpreted by Akulov[4] and Zener[1] to be in agreement with a 10th power. Later measurements by Graham[5] yielded a 4th power below room temperature, and this value is increased with temperature to 7.7 at 575°K[6]. It is the purpose of this note to analyze critically the magnetization dependence of the first anisotropy constant of iron using recent results of Klein and Kneller (KK)[7] and Gengnagel and Hofmann (GH)[8]. The results are compared with the above mentioned single- and two-ion theories, with results obtained for localized spins by Green function techniques [9, 10], as well as with a recent band theory calculation[11].

The exponent n to which the reduced magnetization m must be raised in order to yield the experimentally observed $K_1(T)/K_1(0)$ is calculated and depicted against m in Fig. 1. In this analysis the following aspects which are improvements on previous analyses are considered: (1) Previous comparisons were always made using values of K_1 instead of κ_1 . Since GH evaluated K_1 , K_2 and K_3 for iron, κ_4 could be compared with the reduced magnetization m . It must be stressed, however, that the difference in the value of n obtained if κ_4 rather than K_1 is used, is always less than one per cent. Consequently there is little purpose in using κ_4 instead of K_1 . Since K_2 was given at fewer temperature points than K_1 by GH, all values of n reported here are based on the further approximation

$\kappa_4 \approx K_1$. (2) Previous measurements extended only down to 77°K, thus yielding some uncertainty in the value of K_1 at 0°K. The measurements of GH were performed down to 20°K and yield a better extrapolated value, viz. $K_1(0) = 521 \times 10^3$ erg/cm³. (3) Below 123°K where m differs by an extremely small amount from unity, magnetization data of Argyle *et al.*[12] in which changes of less than 1 ppm could be detected were used. Between 123 and 563°K magnetization data given by Graham[6] with a relative accuracy of 0.3 per cent were used. At higher temperatures the magnetization data of Potter[13] were employed. (4) The anisotropy measurements of KK extend up to 921°K and that of GH up to 951°K which are higher than any previous measurements of this accuracy. $K_1(T)/K_1(0)$ takes a value of 0.0148 at 951°K, thus giving the possibility of testing the power law over a range where the anisotropy changes by a factor of nearly seventy.

Error bars are put on a few representative points and are calculated on the basis of the *maximum* change in n which could result from errors in *both* anisotropy and magnetization values. These are probably an overestimate, because absolute errors as given by KK, and errors associated with torque values before a Fourier analysis is performed in the case of GH, were used. The relative accuracy should be better than these values.

The field dependence of the magnetization is not known for the range of magnetization values used in Fig. 1 and consequently magnetization values at finite fields were employed in the calculation, viz. 6670 Oe (Argyle *et al.*), up to 15000 Oe (Graham) and zero field (Potter). At the higher temperatures the anisotropy should increase considerably due to the para-process increase in magnetization. Magnetization-vs.-field values given by Potter[13] at 989°K were used for a linear extrapolation of the high-field magnetization-vs.-inverse field curve to infinite field. A magnetization difference of 4.2 per cent between zero and infinite field

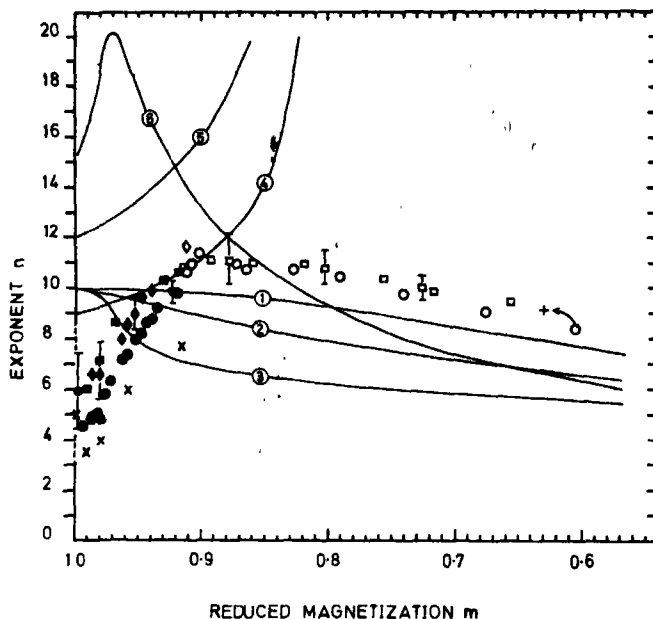


Fig. 1. Experimental values of the exponent n are depicted as a function of the reduced magnetization m . K_1 values from the following authors were used: \diamond Gengnagel and Hofmann (extrapolated to zero field); \circ Gengnagel and Hofmann (extrapolated to infinite field); \square Klein and Kneller (extrapolated to zero field); \times Graham (finite field). Open and closed symbols (circles, diamonds, squares) correspond respectively to magnetization data of Potter or Graham. The magnetization data of Argyle *et al.* was used for the open circle with a dot in the centre. The theoretical curves (1-6) are discussed in the text.

is obtained. This difference will be smaller at the highest temperature where anisotropy measurements are reported (951°K), probably between 2-3 per cent. Using 4.2 per cent as an upper limit, however, gives $n = 9.1_3$ as denoted by a + in Fig. 1 and compared to a value of 8.3_9 found when using the zero field magnetization value. It is clear from the shift of this point as indicated by an arrow, that the difference between GH's values at infinite field and KK's values at zero field may be accounted for by an appropriate correction for the corresponding difference in magnetization.

The theories with which the results are to be compared were derived for constant volume and thus following Brenner[14] and Carr[15] one must correct for the effect of volume ex-

pansion on anisotropy and for the change in magnetization due to volume expansion[16]. The anisotropy constant K'_1 at a finite temperature T , but corresponding to constant volume, viz. that at 0°K is given by

$$K'_1 = K_1 - 3 \int_0^T \beta dT \left(\frac{V}{K_1} \frac{\partial K_1}{\partial V} \right) K_1$$

The thermal expansion coefficient is denoted by β and V is the volume. From torque curves under pressure, $(V/K_1)(\partial K_1/\partial V)$ takes values of 7.8 and 13.5 at room temperature and 77°K respectively[17]. $\int_0^T \beta dT$ was evaluated using Nix and Mc Nair's Grüneisen parameters for iron[18] and Debye internal energy and specific heat functions as tabulated by Gopal[19]. Values of 90×10^{-6} and

2000×10^{-6} at 77 and 293°K respectively are obtained. $(V/K_1)(\partial K_1/\partial V)$ may also be obtained indirectly from the volume change of the cubic crystal due to the anisotropic magnetostriction as is manifested in the magnetostriction constant h_3 . From dilatometric measurements which were made only at room temperature. Becker and Doring[20] deduced that $(V/K_1)(\partial K_1/\partial V) = 9.4$. On the other hand, from strain-gauge measurements of h_3 by Williams and Pavlovic[21] and Lourens and Viljoen[22], one finds negative values for this entity. Gersdorf[23] pointed out that Lourens and Viljoen did not correct for the large effect of the angle between magnetization and field. It is also doubtful whether the least-squares-fit analysis of the rotation measurements by Williams and Pavlovic permits the evaluation of h_3 which takes a value more than an order of magnitude smaller than the other constants which are simultaneously evaluated. One is compelled to take the view that unless more convincing measurements of h_3 are made, the results of Becker and Doring and of Kawai and Sawaoka are to be accepted.

The correction for that part of the magnetization change which is due to the effect of thermal expansion was also employed. The change of magnetization with pressure at room temperature and liquid helium temperature are of the same order[24] and thus the correction at 293 and 77°K is taken to be directly proportional to the thermal volume strain ω . Using the room temperature value $(1/\sigma)(\partial \sigma/\partial \omega) = 0.45$ [16], a decrease of respectively 0.28 and 0.012 per cent in the value of m to be used at room temperature and 77°K is found. The new values of n obtained after the preceding corrections have been employed are given in Table 1. A value of $K_1'(0) = 521 \times 10^3$ erg/cm³ for the calculation of the corrected quantities has been used, i.e. the zero temperature value of K_1 is unchanged by the correction. The validity of this assumption was verified by extrapolating the corrected $K_1'(T)$ values to 0°K.

At low temperatures the difference in n obtained from zero and infinite field anisotropy values is appreciable. Since magnetization values at finite fields are used, values of n between these two limits are expected. It is interesting that KK, using the Holstein-Primakoff prediction for the paraprocess magnetization, found a value of $n = 22$ for the field dependence of K_1 . Assuming K_1 to be a single valued function of $m(T, H)$ it appears that the too large field dependence of K_1 may be due to a lack of technical saturation and not exclusively to the paraprocess. Such a view is supported by the lack of technical saturation found by Foner *et al.* [25] in this field region. Thus the infinite field results in Table 1 are probably an underestimate for n and the zero field data may be a nearer representation. Consequently, if the large uncertainty in n is considered, a 10th power may just fall within the error spread.

For comparison with the experimental results, the predictions of various theoretical models are given in Fig. 1 in terms of the exponent n of an assumed power law $K_1(T) = K_1(0)m^n$, and are indexed with the following numbers: (1) The single-ion $\hat{I}_{5/2}$ -law (for infinite spin); (2) Wolf's[26] single-ion results for spin $S = \frac{5}{2}$; (3) Van Vleck's[27] modified pseudoquadrupolar calculation for the two-ion case; the Green function calculation (4) by Haubenreisser and Jäger[9] and (5) by Brödkorb, Haubenreisser and Jäger[10]; (6) Mori's[11] band theory calculation. For calculating (4) and (5) the spin per iron atom was taken as $S = 1$. For (6), reduced magnetization values given by Graham and by Potter were used.

Agreement with especially the band theory calculation, but also with the localized spin theories is rather poor. Especially at low temperatures more accurate measurements of $K_1(T, H)$ and $m(T, H)$ and their pressure dependences are required before any definite conclusions can be made. In the high temperature region the results, although not coinciding with the $\hat{I}_{5/2}$ -curve, follows its tendency to a

Table 1.

	$\frac{V}{K_1} \frac{\partial K_1}{\partial V}$	293°K			77°K
		GH K_1^∞	GH K_1^0	KK K_1^0	GH K_1^∞
A. Corrected for anisotropy change only	Kawai and Sawaoka	7.2	9.0	9.5	7.8
	Becker and Doring	7.6	9.4	10.0	
B. Corrected for anisotropy and magnetization change	Kawai and Sawaoka	6.3	7.9	8.4	7.4
	Becker and Doring	6.7	8.3	8.8	
C. Uncorrected values		4.8	6.6	7.1	6.0

K_1^∞ and K_1^0 indicate extrapolation to infinite and zero field respectively.

larger extent than that of any of the other existing theoretical predictions. This is surprising, because the 3d electrons of iron are generally considered itinerant and consequently a localized spin model is not expected to apply. Also, it is usually assumed that $S = 1$ for iron and in the single-ion case the term in the Hamiltonian yielding the main contribution to the anisotropy vanishes for $S < 2$ [26]. Keffer [2] proposed that the anisotropy of iron may originate from the two-ion mechanism with the spins of neighbouring atoms highly correlated up to about $0.9 T_c$. A 10th power is then obtained up to this temperature. According to Callen and Callen [3], however, the spin correlations will probably be destroyed by thermal spin waves at quite low temperatures. The recent calculation by Hausmann [28] establishes the validity of the 10th power law within the frame of spin wave theory and without requiring any assumptions on the degree of localization of the magnetic electrons. Spin wave theory is expected to break down at higher temperatures. Thus it will be of interest to investigate the dependence of $K_1(T)$ on $m(T)$ for $m < 0.6$, if possible for values of K_1 a further 2-3 orders of magnitude smaller.

In this region the paraprocess will give an appreciable contribution to the magnetization, thus also giving the possibility to investigate whether K_1 is a single valued function of $m(T, H)$.

Acknowledgement—The author wishes to thank Dr. Nobuo Mori for sending numerical values of the theoretical computed $K_1(T)$.

*Physics Department,
Rand Afrikaans University,
Johannesburg,
South Africa*

P. DE V. DU PLESSIS*

REFERENCES

1. ZENER C., *Phys. Rev.* **96**, 1335 (1954).
2. KEFFER F., *Phys. Rev.* **100**, 1692 (1955).
3. CALLEN H. B. and CALLEN E., *J. Phys. Chem. Solids* **27**, 1271 (1966).
4. AKULOV N., *Z. Phys.* **100**, 197 (1936).
5. GRAHAM C. D. Jr., *Phys. Rev.* **112**, 1117 (1958).
6. GRAHAM C. D. Jr., *J. appl. Phys.* **31**, 150S (1960).
7. KLEIN H.-P. and KNELLER E., *Phys. Rev.* **144**, 372 (1966).
8. GENGNAGEL H. and HOFMANN U., *Phys. Status Solidi* **29**, 91 (1968).
9. HAUBENREISSER W. and JÄGER E., *Phys. Status Solidi* **5**, 33 (1964).
10. BRODKORB W., HAUBENREISSER W. and

*Seconded from the South African Atomic Energy Board.

- JÄGER E., *Phys. Status Solidi* **8**, 551 (1965).
 11. MORI N., *J. phys. Soc. Japan* **27**, 307 (1969).
 12. ARGYLE B. E., CHARAP S. H. and PUGHE W., *Phys. Rev.* **132**, 2051 (1963).
 13. POTTER H. H., *Proc. R. Soc. London A* **146**, 362 (1934).
 14. BRENNER R., *Phys. Rev.* **107**, 1539 (1957).
 15. CARR W. J. Jr., *J. appl. Phys.* **31**, 69 (1960).
 16. KOUVEL J. S. and WILSON R. H., *J. appl. Phys.* **32**, 276S (1961).
 17. KAWAI N. and SAWAOKA A., *J. Phys. Chem. Solids* **29**, 575 (1968).
 18. NIX F. C. and MAC NAIR D., *Phys. Rev.* **60**, 597 (1941).
 19. GOPAL E. S. R., *Specific Heats at Low Temperatures* p. 197 Heywood Books, London (1966).
 20. BECKER R. and DORING W., *Ferromagnetismus* p. 298 Verlag Julius Springer, Berlin (1939).
 21. WILLIAMS G. M. and PAVLOVIC A. S., *J. appl. Phys.* **39**, 571 (1968).
 22. LOURENS J. A. J. and VILJOEN P. E., *Physica* **32**, 1177 (1966).
 23. GERSDORF R., *Physica* **34**, 254 (1967).
 24. VEERMAN J. and RATHENAU G. W., *Proc. Intern. Conf. on Magnetism*, p. 737 Nottingham (Inst. of Physics and Physical Soc.) (1964).
 25. FONER S., FREEMAN A. J., BLUM N. A., FRANKEL R. B., MC NIFF E. J. Jr. and PRADDAUDE H. C., *Phys. Rev.* **181**, 863 (1969).
 26. WOLF W. P., *Phys. Rev.* **108**, 1152 (1957).
 27. VAN VLECK J. H., *Phys. Rev.* **52**, 1178 (1937).
 28. HAUSMANN K., *Phys. Status Solidi* **38**, 809 (1970).

Note added in proof: After acceptance of his own paper, the attention of the author was drawn by Dr. W. P. van Ryneveld to a recently published article by J. J. M. Franse and N. Buis in which values of the pressure dependence of K_1 for iron, $\partial K_1/\partial p$, are reported (Colloques Internationaux: Les Propriétés Physiques des Solides sous Pression, Grenoble, September 1969, p. 371). Their value at room temperature is in agreement with the corresponding value obtained by Kawai and Sawaoka. However, there is not much difference between their $\partial K_1/\partial p$ values at room temperature and 77°K, in contrast to the results of Kawai and Sawaoka who observed a large increase in $\partial K_1/\partial p$ at 77°K. This indicates the need for more measurements.

J. Phys. Chem. Solids Vol. 32, pp. 1696-1699.

Hall resistivity and electron scattering in monocrystals of Cu containing Zn, Mn, Ni or Fe

(Received 7 December 1970)

IN A RECENT paper in this Journal[1] we described the effect of phonon scattering upon

the Hall resistivity (ρ_H) measured in monocrystals of pure Cu and Cu doped with Zn. We showed that with the primary current and the magnetic field (H) along known crystallographic directions, it was possible to obtain from our results qualitative information about the relative effects of phonon scattering upon the electronic lifetime in bands of the different types of cyclotron orbits (viz. electron-like, hole-like and open) which contribute to ρ_H for a given orientation of H . By means of an extension of that work to a study of the isothermal field dependence of ρ_H in monocrystals containing different impurities, we had hoped to observe the effect of these different solutes (particularly the comparison between transition and non-transition examples) upon the electronic motion in the various bands of cyclotron orbits contributing to ρ_H . Our general reasoning was that since these bands traverse regions of the Fermi surface containing states having different predominant symmetries the symmetry of the scattering ion will manifest itself differently among the bands of orbits, and this should be evident from a comparison of the field dependences of ρ_H observed through the high-field/low-field transition. Conceptually the experiment is thus equivalent (neglecting consideration of quantum phase coherence) to the measurement of the field dependence of the de Haas-van Alphen ($dH\nu A$) effect[2], except that in our case we inevitably measure the effect summed over a large number of contributing orbits while the $dH\nu A$ experiment relates to a single extremal orbit.

The results of our experiments do not confirm these expectations. We have studied the field dependence of ρ_H at 4.2°K in monocrystals of Cu containing Zn, Mn, Ni or Fe, and we find no great distinction between the different cases in the intermediate-field condition. However, we think it is worth reporting briefly these findings, partly because of their intrinsic interest (the low-field results lead to an estimate of the anisotropic relaxation time associated with the solute ion) and partly to show

the rather disappointing outcome of such an experiment.

The field dependence of ρ_H measured in the range 0–15.1 kG at 4.2°K for four samples prepared as described previously [1] is shown in Fig. 1. The primary current direction is along [110] in each case, and the solute concentration is given in atomic ppm. The abscissa is the product of H , the field along the indicated crystallographic direction, and $\rho(0)$ the electrical resistivity measured in zero

field at 4.2°K. The product is therefore proportional to $\omega\tau$, where ω is the cyclotron frequency corresponding to H and τ is an average lifetime appropriate to the electrical resistivity.

The results show that as expected in the low-field condition ρ_H is isotropic and a linear function of $H/\rho(0)$. The gradient of this function is, of course, proportional to the low-field value of the Hall coefficient R , and the corresponding values obtained for

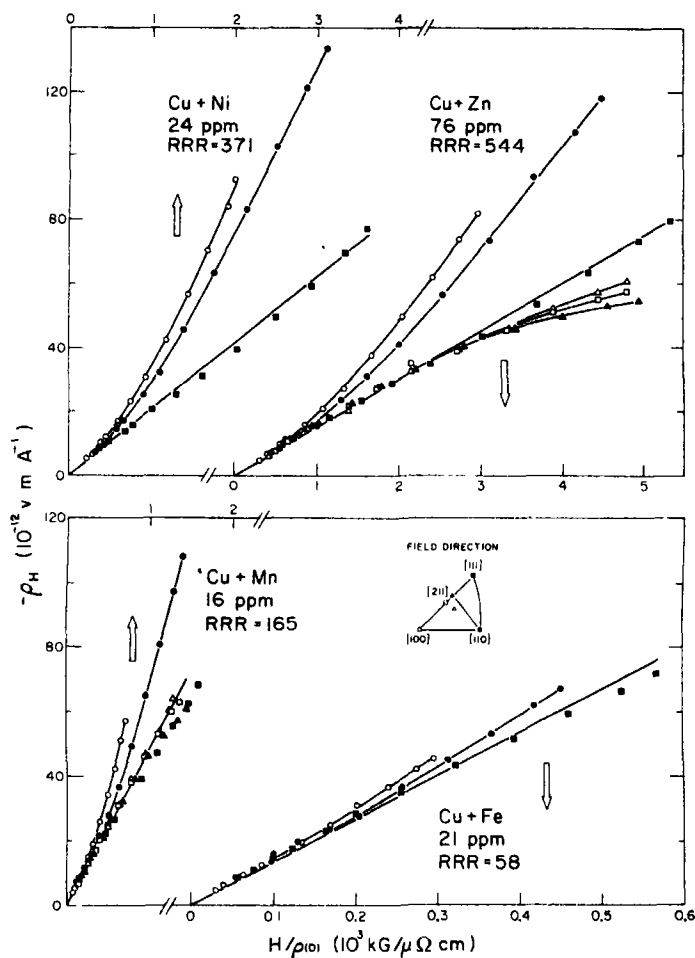


Fig. 1. Field dependence of the Hall resistivity measured in doped monocrystals of Cu at 4.2°K and in fields up to 15.17 kG. H is the field along the direction indicated and $\rho(0)$ is the electrical resistivity at 4.2°K in zero field. $RRR = R_{273K}/R_{4.2K}$ and the concentration is quoted in atomic ppm.

the CuZn, CuMn, CuNi and CuFe systems are respectively -5.28 , -5.06 , -4.97 and $-5.02 (\times 10^{-11} \text{ m}^3/\text{A sec}$ is implied throughout). We estimate the uncertainty in these values to be less than ± 0.08 , including that incurred in establishing the gradient of the function.

In the cases of CuZn, CuMn and CuFe there appear to be no previous comparable results from other sources (some have been obtained in this laboratory from measurements upon polycrystalline samples of CuMn and CuFe[3]). Dugdale and Firth[4] obtained a value of -6.0 for R in CuNi; this is significantly different from our result, and we can presently offer no explanation for this. Substituting our results directly into the two-band model of Dugdale and Firth[4] gives the following values for τ_H/τ_N (in the usual terminology) for the CuZn, CuMn, CuNi and CuFe systems respectively: 1.00 , 0.90 , 0.87 and 0.87 . In each case the estimated uncertainty from the error in R is ± 0.04 , but as an overall estimate this is probably unrealistic since it does not include any error intrinsic to the application of Dugdale and Firth's model. The values of τ_H/τ_N are in qualitative agreement with those obtained from $dHvA$ amplitudes[4] as far as they can be tested, and it is generally accepted that the smaller values observed for the transition metal solutes reflect[4] the reduction in τ_H produced by their additional d -type scattering.

It might be expected that the influence of such d -scattering would become even more obvious in results for monocrystals as the transition to the intermediate field condition is made. For example, those orbits which traverse regions near $\langle 101 \rangle$ which have a high d -symmetry content[2] will be more effectively scattered by a transition metal impurity than by a non-magnetic solute such as Zn. Consequently as H (and hence ω) is increased, such orbits should persist in the low-field condition to larger values of $H/\rho(0)$ when a transition impurity is present than otherwise and a comparison of the field dependences of ρ_H obtained for samples with and without

transition metal solutes should show such differences for those orientations of H which support a significant number of orbits crossing the $\langle 101 \rangle$ regions.

Such an orientation has H along $\langle 100 \rangle$ [1], and yet the results (Fig. 1) show no clear distinction between samples containing transition or non-transition solutes. In fact for any orientation we have studied the onset of the intermediate-field condition (i.e. where anisotropy in ρ_H is first evident) occurs for all samples in the narrow range $H/\rho(0) = 0.2 - 0.6 \times 10^3 \text{ kG}/\mu\Omega\text{cm}$, and the precision of the results is not sufficient to discern any evident distinction between the samples. Note that for a given sample the onset of the intermediate-field condition apparently occurs first for orientations having H along $[100]$ and $[110]$. This presumably reflects the contribution from members of the bands of four-cornered rosette and dog's bone orbits; as we observed in the case of phonon scattering[1], it is relatively easy to render these types of orbit to the high-field condition compared with those characteristic of the other orientations we have studied.

There seems to be no unique explanation for the failure of this experiment, although it is undoubtedly related to the sensitivity of the Hall effect to d -scattering. At least two features presumably adversely affect this sensitivity compared with that of the $dHvA$ effect [2]. First, the fact that ρ_H inevitably measures scattering summed over a large number of different types of contributing orbit will tend to obscure a specific contribution such as d -scattering. Second, there is the consideration of quantum phase coherence; if a small-angle process simply scatters the representative point to another on the same cyclotron orbit, the contribution of this 'high-field' orbit to the Hall effect is not affected, but phase coherence is lost and the $dHvA$ amplitude is directly reduced.

Acknowledgements—It is a pleasure to thank the members of the Analysis Section of NRCC for the work they have done on our behalf, L. Calvert of the X-Ray Section for

his cooperation, and F. Turner of Materials Preparation for his usual careful assistance.

Division of Chemistry,
National Research Council of Canada,
Ottawa 7, Ontario, Canada

C. M. HURD
J. E. A. ALDERSON

REFERENCES

1. HURD C. M. and ALDERSON J. E. A., *J. Phys. Chem. Solids* **32**, 175 (1970).
2. LOWNDES D. H., MILLER K. and SPRINGFORD M., *Phys. Rev. Lett.* **25**, 1111 (1970).
3. ALDERSON J. E. A. FARRELL T. and HURD, C. M., *Phys. Rev.* **B1**, 3904 (1970).
4. DUGDALE J. S. and FIRTH L. D., *J. Phys. C. (Solid State)* **2**, 1272 (1969).

J. Phys. Chem. Solids Vol. 32, pp. 1699-1700.

Temperature variation of dielectric constants in rock-salt crystal*

(Received 6 November 1970)

MOTT and Gü rney[1] have discussed a procedure for evaluating E_{eff} in which the contribution arising from the polarization due to the overlap of the neighbouring ions is also included. If P be the polarization of the medium when placed in a dielectric field of intensity E , the effective field responsible for polarising the molecule is given by

$$E_{\text{eff.}} = E + \frac{4\pi}{3}P. \quad (1)$$

In many crystals there is considerable overlap between the negative and the adjacent positive ions. This causes a reduction in that part of the effective field which is due to the polarization of the medium. This necessitates writing equation (1) in the form

$$E_{\text{eff.}} = E + \frac{4\pi}{3}P(1-\beta) = E + \frac{4\pi}{3}P\gamma. \quad (2)$$

If ϕ_R and ϕ_C be respectively the repulsive and the coulomb parts of the total potential energy function ϕ [2], or γ may be given as

$$\beta = 1 - \gamma = \frac{(d\phi_R/dR)R = r_0}{(d\phi_C/dR)R = r_0}. \quad (3)$$

Here r_0 is the equilibrium interionic distance. For $\gamma = 0$ ($\beta = 1$) there is maximum overlap and for $\gamma = 1$ ($\beta = 0$) there is no overlap between the ions.

According to Mott and Gü rney[1] the high frequency dielectric constant, ϵ_∞ , is given by

$$\begin{aligned} & \frac{\epsilon_\infty - 1}{4\pi} \\ &= \frac{N(\alpha_1 + \alpha_2) - (8\pi/3)N^2\alpha_1\alpha_2(1-\gamma)}{1 - (4\pi/3)N(\alpha_1 + \alpha_2) + (16\pi^2/9)N^2\alpha_1\alpha_2(1-\gamma)} \end{aligned} \quad (4)$$

in which N is the number of ion pairs per unit volume and α_1 and α_2 are the polarizabilities of the two ions.

Again following Mott and Gü rney[1] it can be shown that the low frequency dielectric constant, ϵ_0 , is

$$\begin{aligned} & \frac{(\epsilon_0 - 1)}{3 + (\epsilon_0 - 1)\gamma} = \frac{(\epsilon_\infty - 1)}{3 + (\epsilon_\infty - 1)\gamma} \\ & + \frac{(4\pi/3)\delta}{1 - (4\pi/3)(1-\gamma)\delta} \end{aligned} \quad (5)$$

in which $\delta = Ne^2/p$ where

$$p = 4 \left[\phi_R'' + \frac{2}{r_0} \phi_R' \right]. \quad (6)$$

The equation (5) reduces to equation (25) of Mott and Gü rney[1] for $\gamma = 1$. The relation (6) thus correlates ϵ_0 and ϵ_∞ with the force constant of the crystal[3]. The parameter p becomes independent of the form of ϕ_R and so the dielectric constants if the potential

*Supported by the University Grants Commission, India.

Table 1. Variation of ϵ_0 and ϵ_∞ with temperature of rock-salt crystal

$T^\circ\text{C}$	r_0 (10^{-8} cm)	K (Compressi- bility) (10^{-12} / barye)	γ	δ	$\gamma = 0$	ϵ_0 $\gamma = 1$	γ (variable)	$\gamma = 0$	ϵ_∞ $\gamma = 1$	γ (variable)
80	2.828	4.20	0.734	0.082	3.27	6.24	4.86	1.76	2.30	2.13
180	2.841	4.41	0.744	0.084	3.38	6.54	5.10	1.76	2.27	2.12
280	2.854	4.76	0.753	0.088	3.49	6.85	5.28	1.75	2.25	2.10
380	2.868	5.24	0.758	0.094	3.68	7.44	5.73	1.74	2.22	2.09
480	2.883	5.70	0.764	0.099	3.85	7.95	6.09	1.73	2.20	2.07
580	2.901	6.14	0.772	0.103	3.98	8.32	6.36	1.72	2.17	2.05
680	2.919	6.46	0.781	0.105	3.98	8.34	6.46	1.71	2.14	2.03

parameters are evaluated by using the Born-Mayer temperature dependent equilibrium conditions[2]. This gives an added advantage in discussing the significance of our results. Using the same data of different temperatures, as has been used in our earlier works[5], the variation of ϵ_0 and ϵ_∞ have been studied in case of rock-salt crystal by using the α_1 and α_2 values as reported by Born and Huang[4], the results are given in Table 1.

From the table it is observed that ϵ_∞ decreases with temperature while ϵ_0 increases. This is what other workers[6] have observed in case of KBr and NaI crystals. For NaCl crystal no such experimental data exist.

Physics Department,
Lucknow University,
Lucknow-7,
India.

M. N. SHARMA
S. P. SRIVASTAVA

REFERENCES

1. MOTT N. F. and GURNEY R. W., *Electronic Processes in Ionic Crystals*, Chapter I. Dover Publications, New York (1964).
2. SRIVASTAVA S. P., KUMAR S. and MADAN M. P., *Indian J. Phys.* **41**, 833 (1967).
3. BORN M. and HUANG K., *Dynamical Theory of Crystal Lattices*, p. 108, Clarendon Press, Oxford (1954).
4. BORN M. and HUANG K., *Dynamical Theory of Crystal Lattices*, p. 107, Clarendon Press, Oxford (1954).
5. SRIVASTAVA S. P. and SHARMA M. N., *J. phys. Soc. Japan* **28**, 802 (1970).
6. COWLEY E. R. and COWLEY R. A., *Proc. R. Soc. A* **292**, 209 (1966).

J. Phys. Chem. Solids Vol. 32, pp. 1700-1701.

f-sum rule calculation of the light hole effective mass in InP

(Received 26 October 1970)

FOR A MODEL of a semiconductor in which only the lowest conduction band state $|c\rangle$ and the highest valence band state $|v\rangle$ are considered and for which the effective mass tensor is diagonal, it can be shown[1] that the f -sum rule[2] may be written as

$$[m^*/(m - m^*)] = (m/2|M|^2)E_G. \quad (1)$$

In equation (1), m^* is the carrier effective mass in the band considered, m is the free electron mass, and $E_G \equiv (E_c - E_v)$, where E_c and E_v are the energies of the conduction and valence bands, respectively, at the Brillouin zone point considered. The quantity $M \equiv \langle v|\pi|c\rangle$, where π is the operator defined[2] by $(\pi \cdot \mathbf{k}) = mH'$, where H' is the perturbation used in $(\mathbf{k} \cdot \mathbf{p})$ theory.

Equation (1) shows that a plot of $[m^*/(m - m^*)]$ as a function of the energy gap E_G should be a straight line passing through the origin, i.e., the point $\{[m^*/(m - m^*)] = 0, E_G = 0\}$. This relation has been found[3] to hold, as shown in Fig. 1, for experimental values of E_G and m^* for light holes in InSb

and InAs, and also for electrons[3,4] in InSb, InAs, and InP.

This result has been used to calculate a value of the matrix element $|M|$, which was then used to calculate m^* for light holes in InP. From the slope of the line in Fig. 1, a value of $|M| = 8.22 \times 10^{-14} (\text{gram})^{1/2} - (\text{eV})^{1/2}$ was determined for light holes in InSb and InAs at $\sim 20^\circ\text{K}$. Using the experimentally determined value[5] of $E_G = 1.42 \text{ eV}$ for InP at $\sim 0^\circ\text{K}$, and the value of $|M|$ determined above, a value of $m^* = 0.089m$ was calculated for light holes in InP.

To the author's knowledge, no experimental value of m^* for light holes in InP appears in the literature. An earlier direct $(\mathbf{k} \cdot \mathbf{p})$ calculation[6] gave $m^* = 0.086m$. It should be pointed out that the present calculation makes only the assumption that the value of $|M|$ is the same for light holes in InP as in InSb and InAs. This has been found to be true for electrons in these semiconductors. In addition, their band structures are the same. This calculation also makes use of the matrix element of π , determined directly from experimental data, rather than a momentum matrix element. For these reasons, this calculated value of m^* is believed based on reasonable underlying assumptions. It will be of interest to compare it with an experimentally determined value.

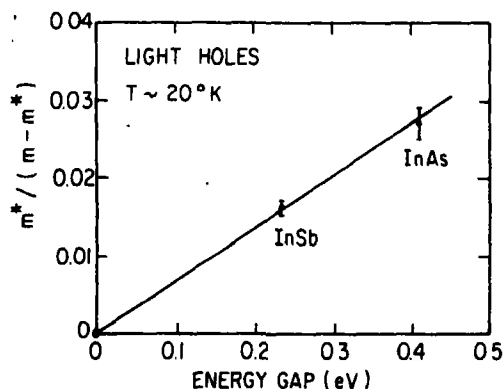


Fig. 1. The quantity $[m^*/(m - m^*)]$, where m^* is the light hole effective mass, and m is the free electron mass, as a function of the energy gap E_G for InSb and InAs. The temperature shown is that at which the experimental data were taken.

Department of Physics,
University of California,
Berkeley,
Calif. 94720,
U.S.A.

RICHARD DALVEN*

REFERENCES

1. DALVEN R., *Phys. Rev. Lett.* **24**, 1015 (1970).
2. See, for example, KITTEL C., *Quantum Theory of Solids*, p. 186, Wiley, New York (1963).
3. DALVEN R., *J. Phys.: Solid State Phys.* **4**, L1 (1971); *Phys. Rev. B*, to be published in May 1971.
4. EHRENREICH H., *J. appl. Phys.* **32**, Suppl., 2155 (1961).
5. TURNER W. J., REESE W. E. and PETTIT G. D., *Phys. Rev.* **136**, A1467 (1964).
6. CARDONA M., *J. Phys. Chem. Solids* **24**, 1543 (1963).

J. Phys. Chem. Solids Vol. 32, pp. 1701-1703.

Etude par effet Mössbauer de structure hyperfine nucléaire de ^{119}Sn dans $\alpha\text{-Fe}_2\text{O}_3$.

(Received 10 April 1970; in revised form 8 September 1970)

IL EST connu que dans la structure antiferromagnétique de l'hématite, $\alpha\text{-Fe}_2\text{O}_3$, à la température -13°C a lieu une transformation appelée souvent transition de Morin. L'application de la méthode de diffraction de neutrons a permis de montrer[1] que cette transformation est due au changement de l'orientation des moments magnétiques des ions Fe^{3+} : aux températures supérieures à celle de la transition de Morin, T_M , les dipôles magnétiques des ions Fe^{3+} s'arrangent dans les plans (111) perpendiculaires à la diagonale spatiale de la maille élémentaire rhomboédrique de $\alpha\text{-Fe}_2\text{O}_3$; aux températures inférieures à T_M les moments magnétiques s'alignent le long de cette diagonale. Les résultats fournis par diffraction de neutrons ont été confirmés plus tard par effet Mössbauer sur les noyaux ^{57}Fe [2,3].

Dans ce travail nous présentons les résul-

*Visiting Research Associate, 1969-1970; present and permanent address, RCA Laboratories, Princeton, N. J. 08540, U.S.A.

tats obtenus par effet Mössbauer sur les noyaux de ^{119}Sn introduits dans le réseau cristallin de l'hématite. Afin d'atteindre la répartition homogène l'impureté de Sn^{4+} (0.52 pour cent, enrichie 88 pour cent en ^{119}Sn) a été introduite au cours de processus de précipitation de l'oxyde hydraté du Fe^{3+} . Le précipité obtenu était chauffé pendant 3h à $T = 750^\circ\text{C}$ et puis soumis à l'analyse par diffraction de rayons X qui nous a montré la formation de $\alpha\text{-Fe}_2\text{O}_3$ avec la dimension des cristallites $\approx 550 \text{ \AA}$. Les spectres Mössbauer ont été enregistrés sur un spectromètre électrodynamique à accélération constante. La source utilisée était $\text{Ba}^{119\text{m}}\text{SnO}_3$ dont la raie d'émission possédait presque la largeur naturelle.

Les spectres Mössbauer obtenus mettent en évidence les structures hyperfines des états fondamental et excité de ^{119}Sn sous l'effet du champ hyperfin $H(O)$ transféré [4,5] par les ions Fe^{3+} voisins dont les moments magnétiques sont orientés par interaction d'échange aux températures considérées. En utilisant la valeur connue de $\mu_{\text{fond}}(^{119}\text{Sn}) = -1.041 \text{ m.n.}$, nous avons calculé à partir des spectres Möss-

bauer $H(O)$ pour deux températures des mesures: $H(O)_{20^\circ\text{C}} = (123 \pm 4)$; $H(O)_{-196^\circ\text{C}} = (132 \pm 4) \text{ KOe}$. La faible différence entre les valeurs de $H(O)$ dans cette région de T est due à la haute température de Néel pour $\alpha\text{-Fe}_2\text{O}_3$ ($T_N = 688^\circ\text{C}$).

La figure montre que le refroidissement de l'échantillon change notablement les positions respectives des raies du spectre hyperfin. Dans un cristal à symétrie axiale en présence simultanée des interactions dipolaire magnétique et quadrupolaire électrique ($\mu H(O) \gg e^2 q Q$) l'énergie E_m des sous-niveaux nucléaires peut être déterminée dans le cas $I = \frac{3}{2}$ par la relation suivante:

$$E_m = -\frac{\mu H(O)m}{I} + (-1)^{|m|+1/2} \frac{e^2 q Q}{4} \times \frac{3\cos^2\theta - 1}{2} \quad (1)$$

où μ et Q sont respectivement les moments magnétique et quadrupolaire d'un noyau dont le spin $= I$; m nombre quantique magnétique et θ l'angle entre la direction de $H(O)$ et l'axe

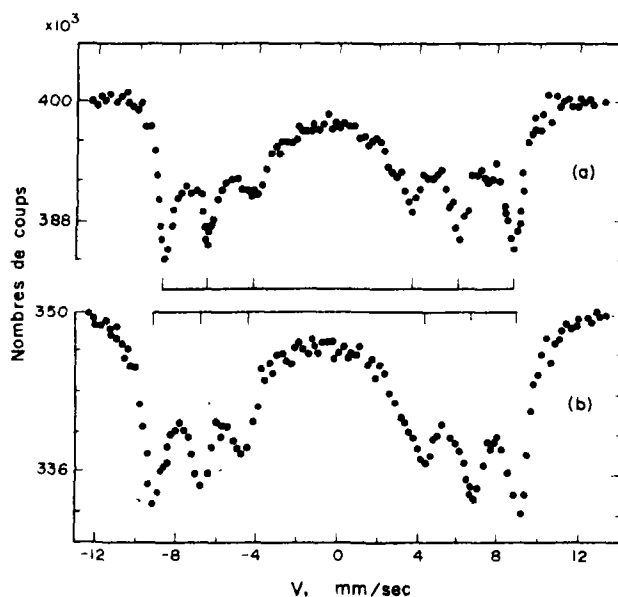


Fig. 1. Spectres Mössbauer de ^{119}Sn dans $\alpha\text{-Fe}_2\text{O}_3$ pour deux températures des mesures: (a) $T = 20^\circ\text{C}$; (b) $T = -196^\circ\text{C}$.

principal du gradient de champ électrique (GCE) q .

Nous avons mentionné plus haut que dans la région des températures $20 \div -196^\circ\text{C}$ la structure magnétique de $\alpha\text{-Fe}_2\text{O}_3$ subit une transition de Morin. A l'aide de l'effet Mössbauer sur ^{57}Fe nous avons vérifié l'existence de cette transformation dans l'absorbant de $\alpha\text{-Fe}_2\text{O}_3$ contenant l'impureté d'étain. Puisque le champ magnétique transféré sur les noyaux ^{119}Sn résulte des interactions d'échange entre les ions Fe^{3+} , il serait naturel de penser que le changement de structure hyperfine de ^{119}Sn observé sur la figure n'est que l'expression indirecte de la réorientation des moments des ions Fe^{3+} .

Si l'on admet que dans le cas de l'impureté Sn^{4+} l'interaction quadrupolaire possède une symétrie approximativement axiale (le paramètre d'asymétrie $\eta \rightarrow 0$), la formule (1) permet de déterminer l'angle θ par comparaison de la valeur e^2qQ avec celle $(e^2qQ)' = e^2qQ[(3\cos^2\theta - 1)/2]$ déduite du spectre Mössbauer à structure hyperfine. Sans avoir fait, en raison de la température trop élevée, des mesures dans le domaine paramagnétique nous avons admis pour e^2qQ la valeur égale à 1.0 mm/sec que nous avons obtenue pour l'impureté de $^{119}\text{Sn}^{4+}$ introduite dans le réseau $\alpha\text{-Al}_2\text{O}_3$ possédant la même structure que $\alpha\text{-Fe}_2\text{O}_3$.

Le calcul nous a donné les valeurs suivantes de θ pour deux températures des mesures:

$$\theta = (31 \pm 8)^\circ \text{ pour } T > T_M;$$

$$\theta = (55 \pm 8)^\circ \text{ pour } T < T_M.$$

La différence entre les valeurs trouvées pour θ de part et d'autre de T_M est certainement corrélée à la réorientation des moments magnétiques des ions Fe^{3+} . Cependant, si l'ion Sn^{4+} est bien substitué à un ion Fe^{3+} et si l'axe du GCE est bien l'axe (111), on attendrait par raison de symétrie $\theta = 0$ pour $T < T_M$ même si le tenseur reliant le champ hyperfin transféré à l'aimantation des ions Fe^{3+} n'était pas isotrope. Or le résultat trouvé ci dessus est en contradiction avec une telle prévision. Il est possible qu'une altération structurale locale (effet de compensation de charge?) perturbe la symétrie du GCE dont l'axe principal pourrait ainsi ne pas coïncider avec la direction (111).

Une étude plus complète avec une application de la spectroscopie Mössbauer d'émission est en cours.

Remerciements—Nous remercions vivement Dr. N. N. Delyagin pour les discussions que nous avons eues ensemble.

Chaire de Chimie nucléaire,
Faculté de Chimie,
Université de Moscou,
U.S.S.R.

P. B. FABRITCHNYI
A. M. BABECHKIN
A. N. NESMEIANOV

RÉFÉRENCES

1. SHULL C. G., STRAUSSER W. A., et WOLLAN E. O., *Phys. Rev.* **83**, 333 (1951).
2. GASTEBOS J. et QUIDORT J., *C. R. Acad. Sci. Paris* **253**, 1257 (1961).
3. KÜNDIG W., BÖMMEL H., CONSTABARIS G. et LINDQUIST R. H., *Phys. Rev.* **142**, 327 (1966).
4. LI HUANG N., ORBACH R., SIMANEK E., OWEN J. et TAYLOR D. R., *Phys. Rev.* **156**, 383 (1967).
5. JECK R. K., KREBS J. J. et FOLEN V. J., *J. appl. Phys.* **41**, 1116 (1970).

ERRATUM

V. C. NELSON and R. J. FRIAUF: Diffusion of vacancies and vacancy pairs in NaCl. *J. Phys. Chem. Solids* 31, 825 (1970).

THE AUTHORS regret that equation (34) and the third line of the second paragraph of the abstract should read:

$$D_v^*(\text{Na}) = 118 \exp(-2.10/kT)$$

and would like to thank Dr. N. L. Peterson for calling the error to their attention.

THE PRINTER regrets that equation (35) should read:

$$D_{pr}^*(\text{Na}) = 1130 \exp(-2.35/kT)$$

and that the third equation below Fig. 2 on p. 828 should read:

$$\lim_{\phi \rightarrow \infty} F(\phi') = b/f_v = 5.6.$$

100

DRIFT VELOCITY OF ELECTRONS AND HOLES AND ASSOCIATED ANISOTROPIC EFFECTS IN SILICON*

C. CANALI, G. OTTAVIANI and A. ALBERIGI QUARANTA

Istituto di Fisica, Università di Modena, Via Vivaldi 70, Modena, Italy

(Received 10 August 1970; in revised form 23 November 1970)

Abstract—The drift velocity of electrons and holes in high purity silicon has been measured, with the time of flight technique, as a function of electric field (0.1–50 KV/cm) at several temperatures between 77 and 300°K. By applying the electric field parallel to the $\langle 111 \rangle$ and $\langle 100 \rangle$ crystallographic directions, an evident longitudinal anisotropy effect has been found for the drift velocity of electrons and also, for the first time, for the drift velocity of holes. At high values of the electric field a saturation drift has been found for the electrons at the temperatures considered in these experiments. On the contrary, no saturation has been attained for holes, even at the highest applied electric fields. The ohmic mobility has been measured between 77 and 300°K for electrons and between 160 and 300°K for holes. When a comparison is possible, our results are in good agreement with other experimental results found in the literature. A qualitative theoretical interpretation of the effects observed is given.

1. INTRODUCTION

SILICON is the most studied and widely employed semiconductor. The problem of the charge transport in low and high fields has been studied since the early 50's [1–25].

However the drift velocity of the charge carriers under non ohmic conditions as a function of the electric field, the crystal axis orientation, and the temperature is little known in the 300–77°K range (almost no data exist for holes) and practically unknown at temperatures below 77°K. In most of the previous papers [5, 9–18] the values of the charge carrier mobility were obtained by indirect measurements (microwaves absorption, conductivity, space charge limited current) based on incompletely verified assumptions and on inexactly known parameters. Therefore we have made a very accurate series of measurements by a technique which, because of its absolute nature (the drift velocity is obtained by simply dividing the distance travelled by the time employed), should ensure the validity of the results obtained within the experimental

errors. A first series of results is presented here, covering the 300–77°K temperature range for fields of 0.1–50 KV/cm and for two crystallographic directions; in a later paper we hope to present data for the temperature range below 77°K.

Our most interesting new results are (a) the finding of a clear anisotropy effect in the hot hole drift along the $\langle 111 \rangle$ and $\langle 100 \rangle$ crystallographic directions, and (b) the determination of the electron saturation drift at different temperatures.

After a short description of the experimental technique, the results obtained are reported and discussed, and when possible, compared with those given in the literature.

2. THE TIME OF FLIGHT TECHNIQUE

Although for many years it was not considered a classical technique by solid state physicists, the time of flight technique has turned out to be one of the most effective in studying carrier transport properties (drift velocity, trapping, etc.) of semiconductors. In order to clarify our experimental results, the principles of the time of flight technique and some of its features are briefly described.

*Partially supported by Consiglio Nazionale delle Ricerche, Italy.

The time of flight technique[19–25] is based on the analysis of the current signal induced by the transport of charge carriers in a region of uniform electric field that extends across a sample of known width W .

If the charge carriers are created by an ionizing radiation with a range R which is shorter than the sample width W (Fig. 1), the carriers of one type are collected after having travelled a negligible fraction of W , while the carriers of the other type have to drift across the whole sample with a velocity v_d and are collected at the opposite electrode after a time $T_R = W/v_d$. In this case the shape of the current signal induced at the ends of the space charge region is determined only by the motion of the carriers which drift across the entire width W [20, 26], and it is given by

$$i(t) = \frac{Nqv_d}{W}u(t - T_R) \quad (1)$$

where N is the number of carriers (electrons or holes) created by the radiation, q is the electron charge, and

$$u(t - T_R) = \begin{cases} 1 & \text{for } 0 \leq t \leq T_R \\ 0 & \text{for } t > T_R \text{ and } t < 0. \end{cases}$$

The time duration of this signal is equal to the transit time T_R and it depends upon the

time necessary for only one kind of charge carriers to travel the distance W . Thus, the time of flight technique permits the investigation, separately, of the transport coefficients of both types of carriers in the same sample.

To measure the drift velocity of electrons and holes in silicon we used surface barrier devices obtained by evaporating a thin gold layer ($< 10^3 \text{ \AA}$) on to the high resistivity silicon wafer. The back contact was a thin evaporated aluminum layer ($< 10^3 \text{ \AA}$).

In our measurements the diodes are inversely biased with a voltage V_A larger than the so-called total depletion voltage V_0 , defined as the voltage necessary for the space charge region to occupy the whole thickness of the sample. The values of V_A were large enough to ensure a practically constant electric field in the samples.

In the first case shown in Fig. 1 an ionizing radiation produces a cloud of electron-hole pairs near the gold contact; the current signal is then due only to the electron flight. On the contrary, if the pairs of charge carriers are created on the opposite side of the space charge region (Al contact), the current signal is due only to the hole motion.

This experimental method has the following advantages over the techniques generally used to investigate transport properties in semiconductors: it provides a direct measurement

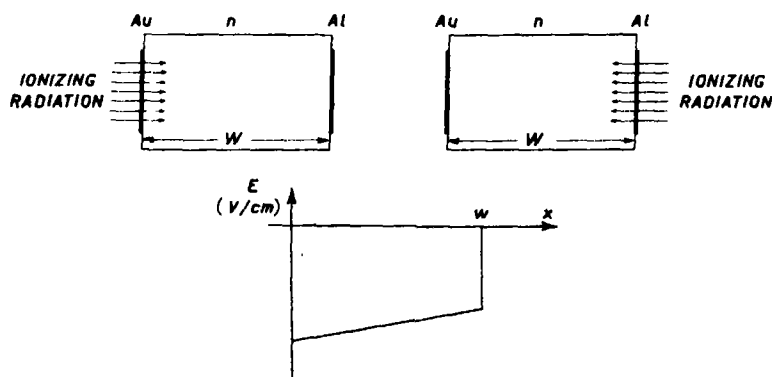


Fig. 1. Schematic view of the ionizing radiation impinging on a surface barrier diode near the Au-Si contact or the Al-Si contact. Also shown is the electric field profile inside the space charge region $V_A > V_0$.

of the drift velocity of the carriers as a function of electric field; it permits investigation of the motion of both electrons and holes in the same sample; it is based entirely on a bulk phenomenon and therefore avoids the difficulties associated with the more traditional techniques, related to surface effects, contact injection, and equivalent circuit of the device; it can be used for drift velocity measurements with high applied electric fields without heating effects, since the current flowing through the device is always very low because of the inverse bias of the junction and the dissipated power is always within a few mW; it is applicable only to samples with very low concentrations of ionized impurities and therefore is the most suitable method for measuring drift velocities as functions of electric field at very low temperatures or in semi-insulating materials; it is not affected by multiplication or secondary ionization phenomena; under suitable experimental conditions it is not affected by the presence of space charge distribution[27, 28], which could vary the field profile inside the sample; under certain conditions, discussed below, it can be used for drift velocity measurements also in the presence of trapping[29].

3. DISCUSSION OF THE TECHNIQUE

(a) *Electric field*

The interpretation of the experimental data is based on the assumption that the electric field is constant inside the region W . In general this is not true in a surface barrier diode, where the electric field is a linear function of x in the space charge region (see Fig. 1). In this case the $v_d(E)$ relation must be obtained from calculation of the time of flight $T_0 = \int_0^W dx/v_d E(x)$. This calculation can be performed by an iterative method. We have avoided this complication by using samples with very high resistivity. In fact the choice of a sample material with a very low impurity concentration diminishes the slope of the electric field inside the space charge region.

Moreover, the choice of a thin junction decreases the effect of electric field variations inside the junction. The error in the transit time measurements due to assumption of a constant electric field rather than use of its real value is given by:

$$\frac{T_0 - T_R}{T_R} = \frac{E_0}{E_1} \ln \frac{1 + \frac{1}{2} \frac{E_1}{E_0}}{1 - \frac{1}{2} \frac{E_1}{E_0}} - 1$$

where T_R and T_0 are the transit times respectively with a constant and a linearly varying electric field*, E_0 is the average value of the electric field, and E_1 is the difference between the values of the electric field at the junction (Au) and at the ohmic contact (Al) ($E_1 = 2 V_0/W$).

In all cases considered in our experiment the error $(T_R - T_0)/T_0$ was less than 2 per cent.

(b) *Space charge effects*

In order to perform drift velocity measurements, particularly in the low field region, the number of carriers created by the ionizing radiation must be large enough to produce a measurable current signal (cf. equation (1)), but not so large as to perturb the electric field inside the device. Such a perturbation would cause an increase in the charge collection time and therefore a fictitious decrease in the mobility. This effect[27, 28] decreases at lower temperatures, higher electric fields, and lower carrier concentrations.

The absence of such a perturbation under our experimental conditions has been both determined theoretically, by solving the charge transport equations in the space charge region, and confirmed experimentally, by varying the density of the $e-h$ pairs without any appreciable effect on the shape and duration of the current signal.

*A quantitative treatment of this problem has been published[20, 21].

(c) *Equivalent circuit effect*

The effect of the equivalent circuit of the device can be easily evaluated under our operation conditions by taking into account that the diode behaves as a pure capacity C [20]. The current signal displayed by a sampling oscilloscope with an input impedance $R_0 = 50 \Omega$ therefore has a risetime approximately equal to $2.2 R_0 C$. We have chosen the effective areas of the diodes, particularly in the thinnest samples, in such a way that this risetime does not introduce an error greater than 2 per cent in the measured duration of the current signal. This duration depends only upon the drift velocity of the carriers and is practically unaffected by their diffusion [30].

(d) *Trapping*

The determination of the transit time by means of the analysis of the current signal induced by the charge carriers at contacts of the sample can be affected by trapping phenomena. A phenomenological theory of this effect [29] shows that practically the true value of the transit time T_R is obtained by measuring if $T_R \approx \tau^+$, where τ^+ is the mean free drift time of the carriers.

In the worst case in our measurements

$T_R \approx 5 \cdot 10^{-8}$ sec, and the value of τ^+ is

$$\tau^+ = \frac{1}{\sigma N_T v_{th}} = 10^{-8} \text{ sec}$$

where $\sigma (< 10^{-13} \text{ cm}^2)$ [31] is the capture cross section of the traps, $N_T (< 10^{12} \text{ cm}^{-3})$ is the trapping center concentration, and $v_{th} (\approx 10^7 \text{ cm/sec})$ is the thermal velocity of the charge carriers.

4. EXPERIMENTAL APPARATUS

Figure 2 is a block diagram of the experimental apparatus. The ionizing radiation consists of bursts of 40 keV electrons. The duration of the bursts is ≈ 70 ps and their repetition rate may be varied. The number of electrons in each burst can be as high as 10^4 . They are produced by an electron gun [32], and their range in silicon is about $7 \mu\text{m}$. This electron accelerator permits control of the number and the density of the pairs created in the sample. Furthermore, it provides a reference time signal related to the arrival of the electron burst on the sample. This signal allows application of pulsed rather than continuous bias voltages to the samples so that higher fields may be applied and heating

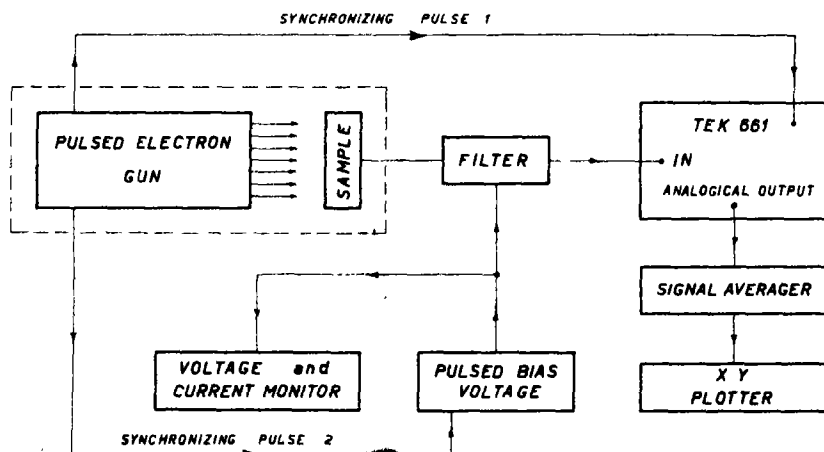


Fig. 2. Block diagram of the experimental setup.

effects, especially at high fields, may be avoided.

The surface barrier diodes are enclosed in a vacuum chamber and can be cooled down to 77°K.

The current signal produced by each burst is sent directly by means of a 50 ohm coaxial cable to a sampling oscilloscope. The geometry and the setup of the sample minimize parasitic capacities and inductances; therefore, the total risetime of the electronic apparatus is less than 100 ps. The current signal recorded by the sampling oscilloscope is sent from the analogic output of the oscilloscope to an XY plotter. When the signal/noise ratio is too low a Signal Averaging Computer (Nuclear Data mod. ND 801) is put between the output and the plotter.

A typical example of a signal recorded by the plotter is shown in Fig. 3. The transit time T_R of the carriers is determined by measuring the full width half maximum of the current signal. A careful examination of the equivalent circuit of the junction (see below) confirmed that, under the bias conditions ($V_A > V_0$) employed in the experiment, the measured values of the transit time depend only upon the drift velocity of the carriers.

The diodes are made of high purity, high

resistivity (30–200 $K\Omega\text{-cm}$ at room temperature) *n*-type silicon monocrystal wafers cut perpendicularly to the $\langle 111 \rangle$ and $\langle 100 \rangle$ crystallographic directions.

All crystals are characterized by high carrier lifetimes ($> 3000 \mu\text{s}$) and a low concentration of dislocations: $\text{EPD} < 15000 \text{ cm}^{-2}$.

The thicknesses of the detectors are between 100 and 600 μm and have been measured with a precision of the order of 1 per cent. Their effective areas are between 4 and 15 mm^2 .

All the devices can be cooled down to 77°K, and bias voltages much higher than the total depletion voltage can be applied.

5. EXPERIMENTAL RESULTS

We have measured the drift velocity of charge carriers (electrons and holes) in high purity silicon, varying the electric field between 0.1 and 50 KV/cm and the temperature between 77 and 300°K.

The measurements were made on 24 samples, 13 oriented in the $\langle 111 \rangle$ crystallographic direction and 11 in the $\langle 100 \rangle$ direction. The final data are the result of the analysis of about 10^4 graphs.

Most of the samples were prepared in our laboratory with high purity, high resistivity *n*-type silicon supplied by Wacker Chemitronic, but a few samples were made with silicon produced by Holder Topsøe and by Hoboken. Some pairs of samples oriented along the $\langle 111 \rangle$ and $\langle 100 \rangle$ directions were obtained from the same ingots.

With the technique used it was possible to measure the drift velocity of both electrons and holes in the same sample. By means of the pulsed electron accelerator we could vary the density of the *e-h* pairs to avoid space charge limited current effects. Finally, the repetition rate of the bias signal in the diode was varied in order to avoid heating effects at high electric fields.

In order to cover the largest possible range of electric fields while maintaining the experimental conditions discussed above, we made

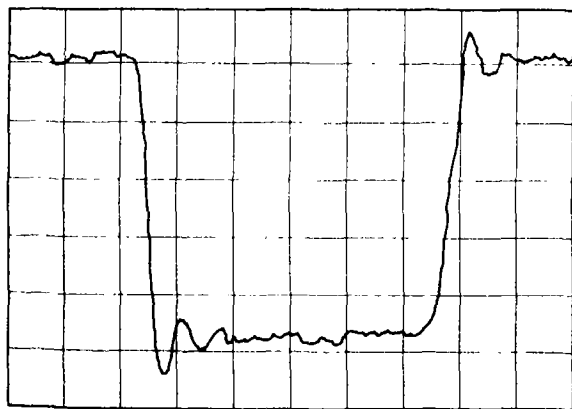


Fig. 3. Typical waveform of the current signal due to electron transport at 300°K. The width of the diode is 500 μm , and the applied voltage is 1250 V. The drift velocity obtained from this signal is $9.23 \times 10^6 \text{ cm/sec}$. Horizontal Sensitivity 1 ns./division.

measurements on samples with different resistivities, thicknesses, and useful surfaces. The experimental results obtained with different samples were always in excellent agreement.

Figure 4 shows a typical set of electron drift velocity data along a $\langle 111 \rangle$ crystallographic direction at 300°K, obtained with 13 different samples not separately identified in the figure. The spread of the experimental data was not more than 5 per cent.

For clarity, only the best fits of the experimental data are shown in the following figures.

(a) Electrons

Figure 5 shows the results obtained for the drift velocity of the electrons as a function of the electric field, applied parallel to the $\langle 111 \rangle$ crystallographic direction, at several temperatures.

Figures 6a, b and c show the longitudinal anisotropy of the electron drift when the electric field is applied along a $\langle 111 \rangle$ or a $\langle 100 \rangle$ direction.

As seen from Figs. 5 and 6, v_d has been

measured from the ohmic region up to the saturation value*. The results obtained for the ohmic mobilities (the same for all crystallographic directions) for several temperatures are shown in Table 1, along with data available in the literature.

Figure 5 shows, as already known[39], that the electron mobility is no longer ohmic for electric fields higher than a certain critical value. It also shows that when the lattice temperature is decreased, the carriers are 'heated up' above the lattice thermal energy at lower applied electric fields because of the higher mobility of the carriers and the lower efficiencies of the scattering mechanisms.

The longitudinal anisotropy of the carrier drift velocity along the $\langle 111 \rangle$ and $\langle 100 \rangle$ directions can be qualitatively understood by taking into account the band structure of silicon and the scattering mechanisms which mix different valleys: when the electric field E is applied parallel to a $\langle 111 \rangle$ direction, all

*Saturation drift velocity is that value of v_d which does not change, within the experimental errors, in a large interval of electric fields (for instance between 14 and 28 KV/cm at 77°K) at a given temperature.

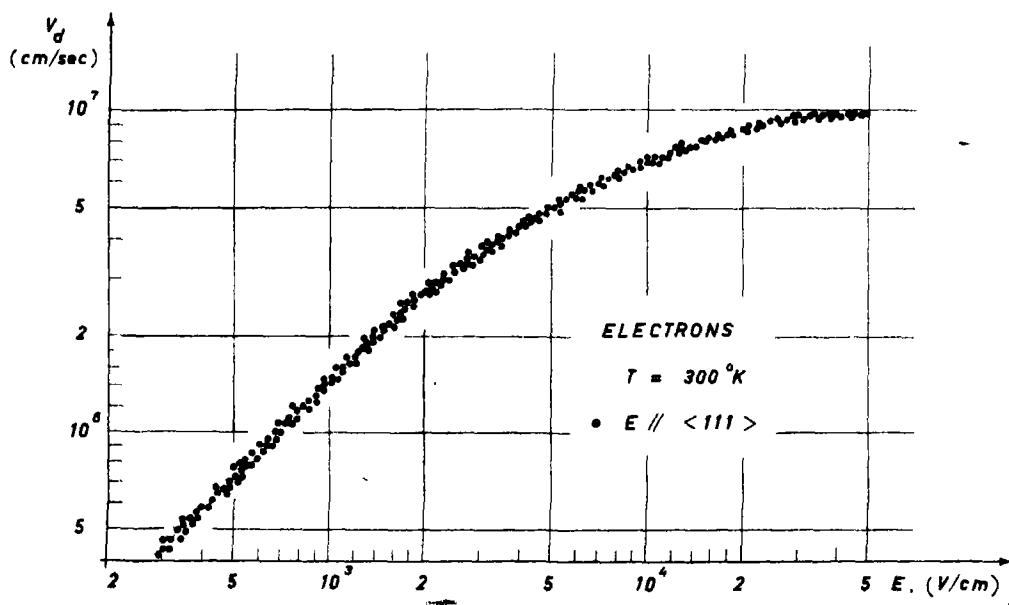


Fig. 4. A typical set of experimental results obtained on 13 different samples.

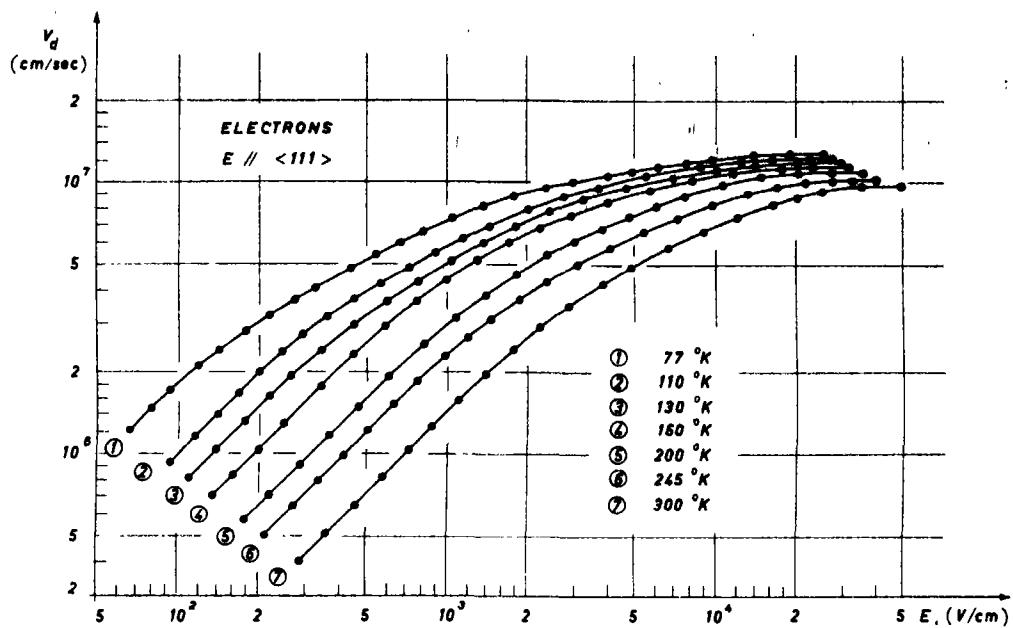


Fig. 5. Electron drift velocity as a function of the electric field parallel to the $\langle 111 \rangle$ crystallographic direction at several temperatures.

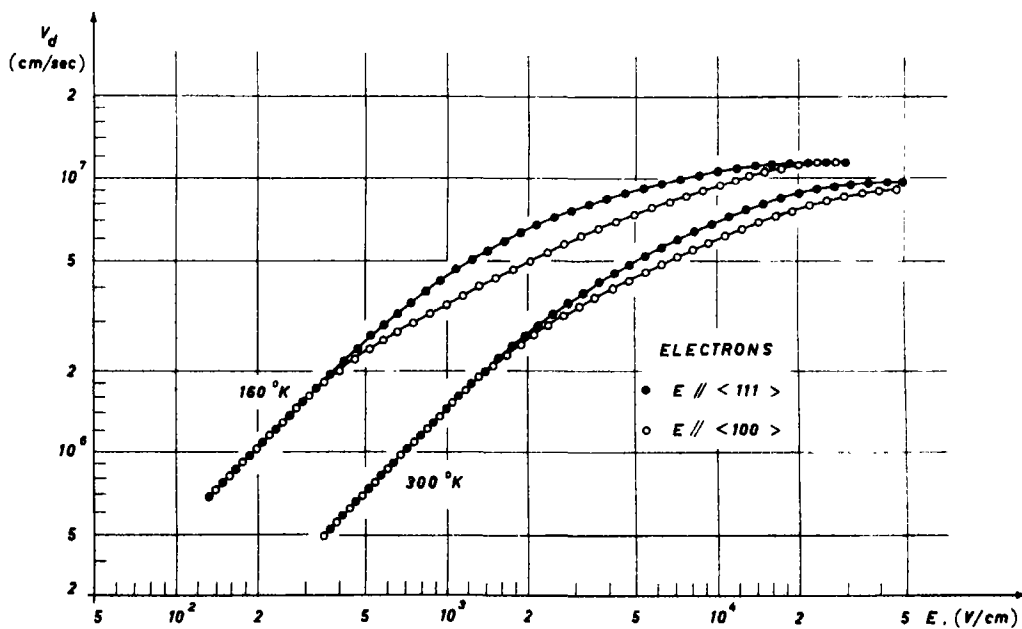


Fig. 6(a)

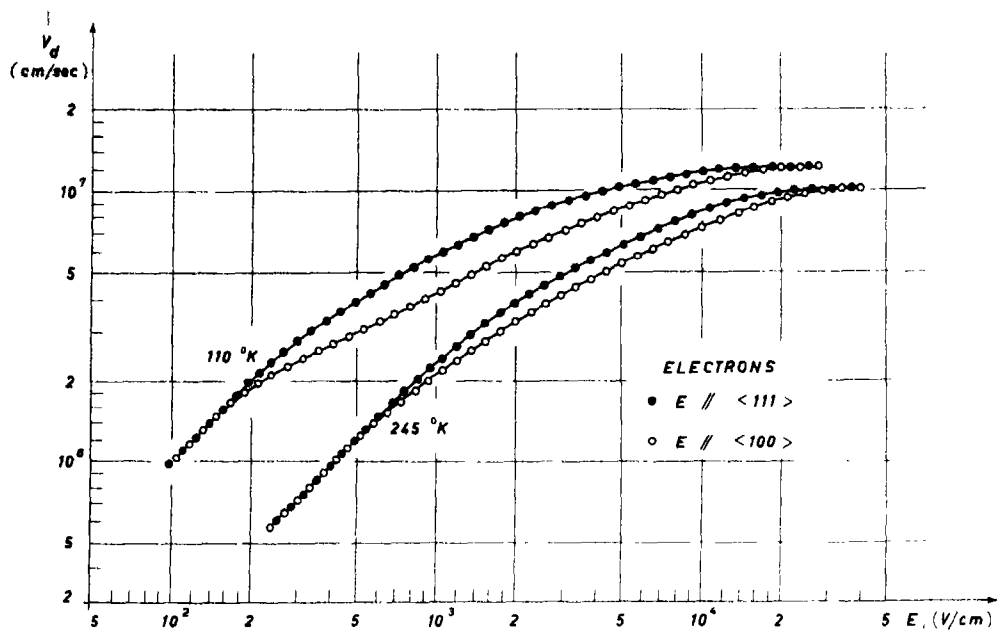


Fig. 6(b)

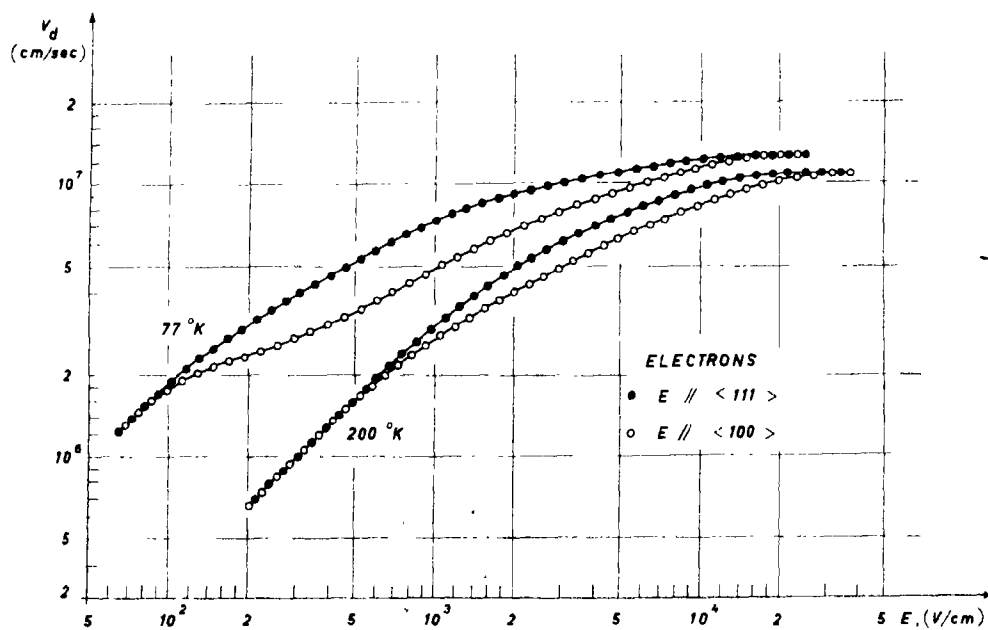


Fig. 6(c)

Figs. 6(a) (b) and (c). Electron drift velocities as functions of the electric field parallel to the $\langle 111 \rangle$ and $\langle 100 \rangle$ directions, at several temperatures.

Table 1. Our values of electron ohmic mobility at various temperatures compared with the results of others. (Reference numbers in brackets)

T °K	Our results	$\mu(\text{cm}^2\text{V}^{-1}\text{sec}^{-1})$				
		1500				
300	1450	1200 ± 100 [33]	1450 [7]	1350 ± 100 [37]	1450 [34]	1318 [38]
245	2400	2350 [36]				1888 [38]
200	3250	3850 [34]	4000 [35]	2600 [9]		2740 [38]
160	5200	6000 [36]				4230 [38]
130	7500	7600 [36]	6500 [9]			6490 [38]
110	10000	10600 [36]				9175 [38]
77	20000	20000 [35, 16]	27000 [34]	11000 [9]		22000 [38]

the six $\langle 100 \rangle$ valleys are oriented alike with respect to E . They all exhibit the same behaviour and therefore give the same contribution to the transport properties of the sample. On the contrary, when E is applied parallel to the $\langle 100 \rangle$ direction, the two valleys $\langle 100 \rangle$ and $\langle \bar{1}00 \rangle$ have their longitudinal axes parallel to the electric field, so that they have states populated predominantly along these axes, characterized by a larger effective mass ($0.9 m_0$, where m_0 is the free electron mass), but the remaining four valleys, whose longitudinal axes are oriented perpendicularly to the field, are characterized by electrons having a lower effective mass ($0.2 m_0$). Lighter electrons are more easily accelerated and thus heated up by the field. Unless the electron concentration is so high that the electron-electron collisions tend to equalize all mean energies of the valleys, the lighter electrons should attain a higher mean energy than the heavier ones. Accordingly the four perpendicular valleys are called 'hot' and the two longitudinal valleys 'cold'. In this case the two parallel valleys (cold) exhibit a lower mobility, and the four perpendicular valleys (hot) a higher mobility.

However, since the presence of intervalley scattering enhances the number of electrons in the cold valleys more than in the hot ones, the overall effect is a final lower drift velocity when the applied electric field is parallel to the $\langle 100 \rangle$ direction than when it is parallel to the $\langle 111 \rangle$.

The anisotropic effect is temperature dependent (Figs. 6) because of the population shift from hotter to colder valleys [39]. With increasing lattice temperature this shift is enhanced, and consequently the anisotropy is less. On the other hand, when the applied electric field is so high that electrons in colder valleys are also energetic enough to emit intervalley phonons, the two processes—from cold to hot and from hot to cold—are nearly equalized, and the drift velocities in the two directions $\langle 111 \rangle$ and $\langle 100 \rangle$ tend to reach the same value and exhibit a saturation velocity. This saturation value (as seen in Figs. 6) is the same for both the $\langle 111 \rangle$ and $\langle 100 \rangle$ crystallographic directions at all temperatures, except at 300°K, where at the highest applied electric field a small anisotropy effect is still present. The drift velocity saturation may be understood by taking into account the non parabolicity of the conduction band [40] and the possible electron-phonon interactions which are forbidden at low fields [41, 42].

In Table 2 our experimental data on the saturation drift velocity are compared with the results of others*. The discrepancies can be justified by the following considerations: Our measurement is an absolute one, in contrast to that obtained with the method used by Rodriguez and Nicolet [43].

*Preliminary measurements of the saturation drift have been made on two samples in the temperature range between 4.2 and 77°K [44].

Table 2. Limiting values of the electron drift velocity at various temperatures. Other values obtained at 300°K are: $9 \cdot 10^6$ cm/sec, Zulliger *et al.*[22]; 10^7 cm/sec, Norris and Gibbons[21]; $9 \cdot 2 \cdot 10^6$ cm/sec, Sigmon and Gibbons[23]; $9 \cdot 10^6$ cm/sec, Ryder[5]

T °K	Drift velocity $\times 10^6$ cm/sec				
	Our results	Duh and Moll [15]	Rodriguez and Nicolet [43]	Costato and Reggiani [41, 42]	Boichenko and Vasetskii [9]
300	9.6	10.5	9.5	10	
245	10.1		10.16 (250°K)	10.9	
200	10.8	11.34	10.73	11.9	
160	11.3		11.6 (150°K)	12.8	
130	11.7			13.5	
110	12		12.45 (115°K)	13.8	
77	12.7	13	13.1	14.2	12.5

The current signal is due to one type of carriers only, namely electrons, and no assumptions need be made on the ratio v_h/v_e of the hole and electron drift velocities and its dependence on the temperature; whereas Duh and Moll[15] had to assume that this ratio was constant and equal to 0.8.

Finally, with our experimental technique

no contact injection can affect the measurements.

(b) Holes

Figure 7 shows the results obtained for the drift velocity of the holes as a function of the electric field, applied parallel to a $\langle 100 \rangle$ crystallographic direction, at several tempera-

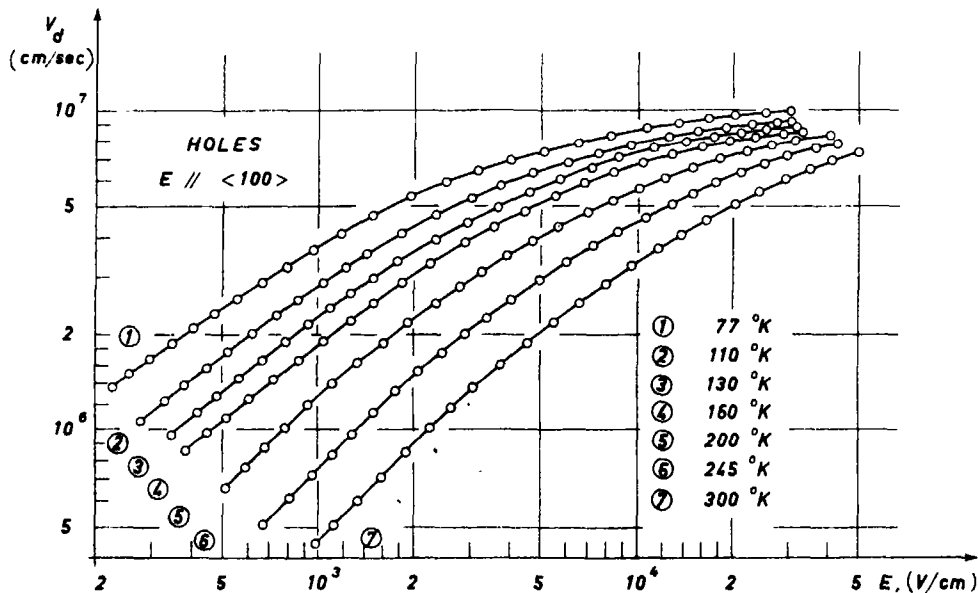


Fig. 7. Hole drift velocity as a function of the electric field parallel to the $\langle 100 \rangle$ direction at several temperatures.

tures. At the highest applied electric fields (up to 50 KV/cm) the drift velocity does not reach a limiting value, at any temperature used. Furthermore, for temperatures below 160°K the smallest applied electric fields were not low enough to give the ohmic value of the mobility.

In Figs. 8a, 8b, and 8c the drift velocity data for the holes are shown as functions of the electric field applied parallel to the $\langle 111 \rangle$ and $\langle 100 \rangle$ directions. To our knowledge, our

results[45] give the first clear experimental evidence of an anisotropy effect of holes in silicon in wide ranges of electric fields and temperatures.

A qualitative physical interpretation of our data[39] may be given on the basis of the hot carriers population effect of the multiple warped valence band of silicon, which exhibits a pronounced anisotropy for the upper heavy hole band. Our experimental results support this picture, exhibiting a higher drift

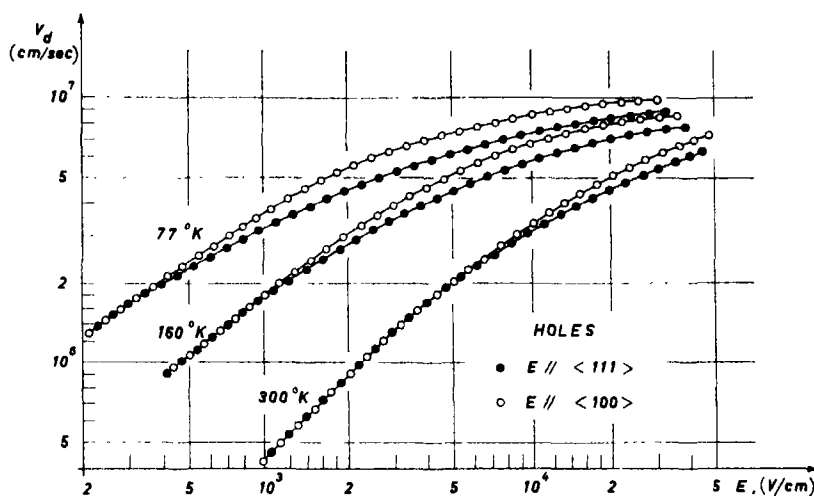


Fig. 8(a)

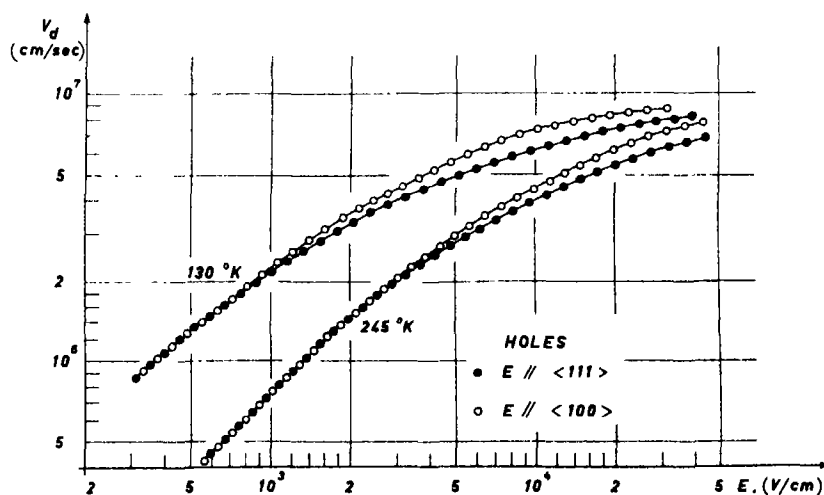


Fig. 8(b)

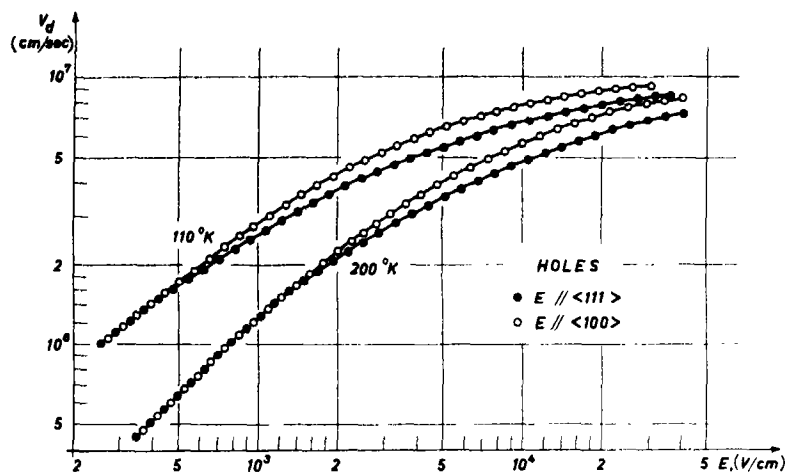


Fig. 8(c)

Figs. 8(a), (b) and (c). Hole drift velocities as functions of the electric field applied parallel to the $\langle 111 \rangle$ and $\langle 100 \rangle$ directions, at several temperatures.

velocity in the direction of lower effective mass $\langle 100 \rangle$ and vice versa $\langle 111 \rangle$, in agreement with the anisotropy of the heavy hole band.

In spite of the difficulty of describing the hole drift velocity quantitatively (due to the complex band structure), two important differences between the transport properties of electrons and of holes must be emphasized, both of which contribute to the lower drift velocity of holes than of electrons for a given electric field: (i) Holes have greater effective masses and therefore are less accelerated by the applied field. (ii) The scattering mechanisms responsible for hole drift seem to be more efficient than in the case of electrons [46, 47].

(c) Comparison of data

Figure 9 shows a comparison of our experimental results for the drift velocity of electrons (77 and 300 K) and holes (300 K) with the results others have obtained by the time of flight technique and by conductivity measurements. Such comparisons are sometimes difficult, since some authors, because of their experimental technique, report only

quantities proportional to the drift velocity [9–11, 14, 15].

The comparison of the electron v_d along the $\langle 111 \rangle$ direction at 300 K shows good agreement between our results and those in the literature.

At 77 K the anisotropy effect found by us is only in qualitative agreement with that reported by Asche *et al.* [17]. The lack of quantitative agreement is due to the low value of the low field mobility measured by them.

Data for the hole drift velocity are at 300 K with the electric field parallel to the $\langle 111 \rangle$ crystallographic direction.

At electric fields between 40 and 110 KV/cm Rodriguez *et al.* [14] found a saturation drift velocity equal to 7.5×10^6 cm/s ± 5 per cent, in disagreement with the results obtained by Seidel and Sharfetter [10], which show that a saturation drift velocity between 0.96 and 1.06×10^7 cm/s may be obtained with electric fields higher than 2×10^5 V/cm.

Our results show that for electric fields as high as 50 KV/cm no appreciable saturation is obtained for the hole drift velocity.

Recently, Asche *et al.* [48] found an anisotropy effect for the holes at 77 K only in low

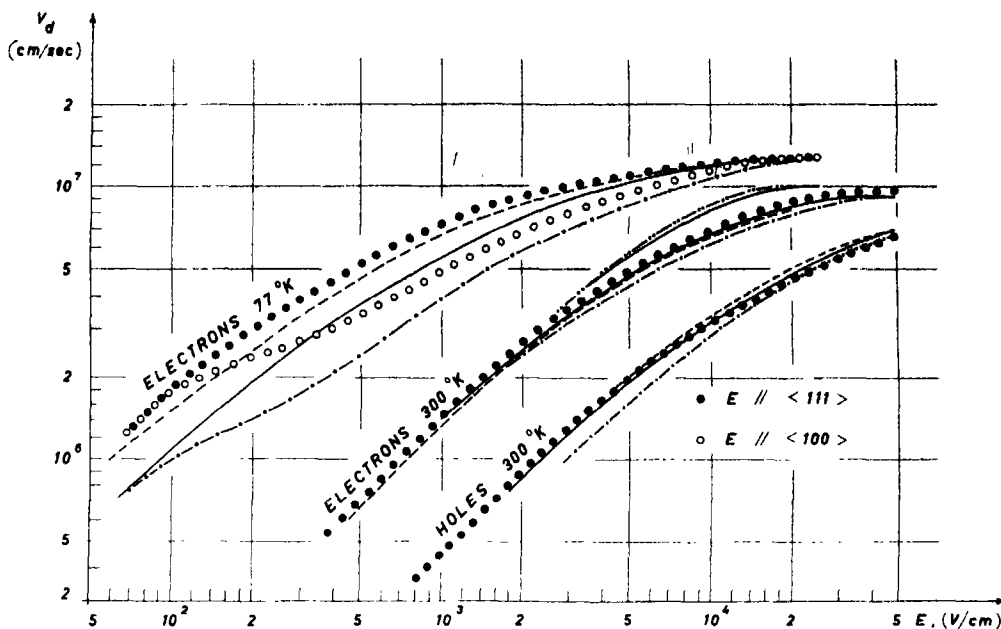


Fig. 9. Comparison between our experimental results on electron and hole drift velocities and the results available in the literature. Electrons $T = 300^\circ\text{K}$ $E \parallel \langle 111 \rangle$, --- Rodriguez and Nicolet[43], — (upper curve) Norris and Gibbons[21], — (lower curve) Sigmon and Gibbons[23], ---- Boichenko and Vasetskii[9], --- Prior[11]. Electrons $T = 77^\circ\text{K}$, ---- Jørgensen *et al.*[16] $E \parallel \langle 111 \rangle$, — Asche *et al.*[17] $E \parallel \langle 111 \rangle$, --- Asche *et al.*[17] $E \parallel \langle 100 \rangle$. Holes $T = 300^\circ\text{K}$ $E \parallel \langle 111 \rangle$, --- Seidel and Scharfetter[10], ---- Norris and Gibbons[21], — Sigmon and Gibbons[23].

resistivity materials, but according to their results this effect seems to disappear completely in purer samples.

6. CONCLUSIONS

Electron and hole drift velocities have been measured in high purity silicon at several temperatures between 77 and 300°K and for electric fields between 10^2 and 5×10^4 V/cm.

The time of flight technique provides a direct determination of the drift velocity of the carriers by means of space and time measurements. Furthermore, with this technique the drift velocity of both electrons and holes is measured in the same samples.

By using this technique the errors on the measurements have been minimized, as confirmed by the small spread (≤ 5 per cent) of the results obtained in several samples.

The samples were prepared in such a way

that the electric field could be applied parallel to both the $\langle 111 \rangle$ and $\langle 100 \rangle$ crystallographic directions. The results obtained showed a clear anisotropy of the electron drift velocity and also, for the first time, of the hole drift velocity.

Furthermore, the electron ohmic mobility (Table 1) and the electron saturation drift velocity (Table 2) have been measured for temperatures between 77 and 300°K . These measurements, performed in high purity samples, are the first made with this technique.

Where possible, our results have been compared with results published by others, and the agreement is generally satisfactory.

The anisotropy effect for the drift velocity of both electrons and holes has been qualitatively interpreted by taking into account the forms of the conduction band and of the valence band of silicon.

Acknowledgements—We are indebted to M. Costato, C. Jacoboni, L. Reggiani, and M. Martini for discussions and suggestions during the course of the work and for constructive criticism of the manuscript. We thank P. Cantoni and M. Bosi for their valuable help in making the measurements.

REFERENCES

1. CONWELL E. M. and WEISSKOPF V. F., *Phys. Rev.* **77**, 388 (1950).
2. SHOCKLEY W., *Bell. Syst. Tech. J.* **30**, 990 (1951).
3. RYDER E. J. and SHOCKLEY W., *Phys. Rev.*, **81**, 139 (1951).
4. CONWELL E. M., *Proc. IRE* **40**, 1331 (1952).
5. RYDER E. J., *Phys. Rev.* **90**, 766 (1953).
6. MORIN F. J., *Phys. Rev.* **93**, 62 (1954).
7. MORIN F. J. and MAITA P. J., *Phys. Rev.* **96**, 28 (1954).
8. GUNN J. B., *J. Electron.* **2**, 259 (1956).
9. BOICHENKO B. L. and VASETSKII V. M., *Soviet Phys. solid State* **7**, 1631 (1966).
10. SEIDEL T. E. and SCHARFETTER D. L., *J. Phys. Chem. Solids* **27**, 1511 (1966).
11. PRIOR A. C., *J. Phys. Chem. Solids* **12**, 175 (1959).
12. HAMAGUCHI C. and INUISHI Y., *J. Phys. Chem. Solids* **27**, 1511 (1966).
13. DAVIES E. A. and GOSLING D. S., *J. Phys. Chem. Solids* **23**, 413 (1962).
14. RODRIGUEZ V., RUEGG H. and NICOLET M.-A., *IEEE Trans. on Electron Devices*, **ED-14**, 44 (1967).
15. DUH C. Y. and MOLL J. L., *Solid State Electron.* **11**, 917 (1968).
16. JØRGENSEN M. H., MEYER N. I. and SCHMIDT-TIEDMANN K. J., *Proc. VII Internat. Conf. Phys. Semicond., Paris*, 457 (1964).
17. ASCHE M., BOITSCHENKO B. L. and SARBEJ O. G., *Phys. Status Solidi* **9**, 323 (1965).
18. MCCOMBS A. E., Jr and MILNES A. G., *Int. J. Electron.* **24**, 573 (1968).
19. ALBERIGI QUARANTA A., MARTINI M. and CIPOLLA F., *Phys. Lett.* **17**, No 2, 102 (1965).
20. ALBERIGI QUARANTA A., MARTINI M., OTTAVIANI G., REDAELLI G. and ZANARINI G., *Solid State Electron.* **11**, 685 (1968).
21. NORRIS C. B., Jr and GIBBONS J. F., *IEEE Trans. on Electron Devices*, **ED-14**, 38 (1967).
22. ZULLIGER H. R., NORRIS C. B., SIGMON T. W. and PEHL R. H., *Nucl. Instr. Meth.* **70**, 125 (1969).
23. SIGMON T. W. and GIBBONS J. F., *Appl. Phys. Lett.* **15**, 320 (1969).
24. LANGMANN J. and MEYER O., *Nucl. Instr. Meth.*, **34**, 77 (1965).
25. TOVE P. A., ANDERSSON G., ERICSSON G. and LIDHOLT R., *IEEE Trans. Electron Devices*, **ED-17**, 407 (1970).
26. CAVALLERI G., FABRI G. and SVELTO V., *Nucl. Instr. Meth.* **21**, 177 (1963).
27. TOVE P. A. and SEIBT W., *Nucl. Instr. Meth.* **51**, 261 (1967).
28. TARONI A. and ZANARINI G., *J. Phys. Chem. Solids* **30**, 1861 (1969).
29. MAYER J. W., chap. 5 in "Semiconductor Detectors" (Edited by G. Bertolini and A. Coche) North Holland (1968).
30. RUCH J. G. and KINO G. S., *Phys. Rev.* **174**, 921 (1968).
31. BONCH-BRUEVICH V. L. and LANDSBERG E. G., *Phys. Status Solidi*, **29**, 9 (1968).
32. ALBERIGI QUARANTA A., CANALI C. and OTTAVIANI G., *Rev. Scient. Instrum.* **41**, 1205 (1970).
33. PRINCE M., *Phys. Rev.* **93**, 1204 (1954).
34. LONG D., *Phys. Rev.* **120**, 2024 (1960).
35. LOGAN R. A. and PETERS A. J., *J. appl. Phys.* **31**, 122 (1960).
36. PUTLEY E. H. and MITCHELL W. H., *Proc. Phys. Soc. A* **72**, 193 (1958).
37. LUDWIG G. W. and WATTERS R. L., *Phys. Rev.* **101**, 1699 (1956).
38. COSTATO M. and REGGIANI L., *Phys. Status Solidi* **38**, 665 (1970).
39. CONWELL E. M., "High Field Transport in Semiconductors", Academic Press (1967).
40. COSTATO M. and SCAVO S., *Nuovo Cim.*, **56 B**, 343 (1968).
41. COSTATO M. and REGGIANI L., *Phys. Status Solidi* **42**, 591 (1970).
42. COSTATO M. and REGGIANI L., *Lettere Nuovo Cim.*, **3**, 728 (1970).
43. RODRIGUEZ V. and NICOLET M.-A., *J. appl. Phys.* **40**, 496 (1969).
44. CANALI C. and OTTAVIANI G., *Phys. Lett.*, **32A**, 147 (1970).
45. ALBERIGI QUARANTA A., CANALI C. and OTTAVIANI G., *Appl. Phys. Lett.* **16**, 432 (1970).
46. HARRISON W. A., *Phys. Rev.* **104**, 1281 (1956).
47. COSTATO M. and REGGIANI L., *Nuovo Cim.* **B68**, 64 (1970).
48. ASCHE M., VON BORZESZKOWSKI J. and SARBEJ O. G., *Phys. Status Solidi*, **38**, 357 (1970).

EFFECT OF INDIUM IMPURITIES ON THE DE HAAS-VAN ALPHEN EFFECT IN LEAD*

P. J. TOBIN†, D. J. SELLMYER and B. L. AVERBACH

Center for Materials Science and Engineering and Department of Metallurgy and Materials Science,
Massachusetts Institute of Technology, Cambridge, Mass. 02139, U.S.A.

(Received 12 June 1970; in revised form 10 November 1970)

Abstract—Several aspects of the effect of indium impurities on the de Haas-van Alphen effect in lead were investigated. Studies were made of the nature of several orbits in the third zone Fermi surface of pure lead and the effects of alloying on these orbits. Rigid band theory is able to account for changes in cross-sectional area for one of the orbits. Some data on the scattering temperature obtained from amplitude studies are also reported.

1. INTRODUCTION

THERE are several interesting phenomena which occur in the de Haas-van Alphen (dHvA) effect in a pure metal when impurity atoms are introduced. First, the conduction electron scattering rate increases so that the amplitude of the oscillations decreases. Secondly, the energy levels shift in the alloy and the density of conduction electrons changes, so that the shape and size of the Fermi surface changes. This implies that the dHvA frequency F changes on alloying since

$$F = \hbar c A_0 / 2\pi e, \quad (1)$$

where A_0 is an extremal area normal to the magnetic field[1]. The decrease of the dHvA amplitude on alloying limits measurements typically to solute concentrations of less than about one atomic per cent. Even at these low concentrations, however, it is possible to study the rate at which various impurities scatter conduction electrons on given orbits

in a particular metal, and to compare changes in Fermi surface areas with the simplest theoretical model of alloying, the rigid band model (RBM).

Theoretical work on the dHvA effect in alloys has attempted to treat both the geometrical Fermi surface changes and the scattering aspects. Heine was the first to consider changes in dHvA frequencies on alloying[2]. His work was based on the RBM proposed by Friedel[3] and was sufficiently general to handle geometrical effects for a general Fermi surface model. Later, Brailsford[4] considered area changes and also extended the early work of Dingle[5] on the scattering time τ . However, the scattering problem was considered only from the viewpoint of *free* electrons being scattered by a simple screened Coulomb potential. These concepts have been tested experimentally in a number of dilute alloys [6-12].

The purpose of the present investigation was to study the above-mentioned aspects of the dHvA effect in dilute Pb(In) alloys. This system was chosen because previous investigations by Gold[13] and Anderson and Gold [14] (AG) have produced a rather well defined Fermi surface for pure lead. Also, indium has a wide range of solid solubility

*Research supported by the Advanced Research Projects Agency and performed in part at the Francis Bitter National Magnet Laboratory which is supported by the United States Air Force Office of Scientific Research.

†Present Address: Purdue University, Lafayette, Indiana.

in lead and the equilibrium distribution coefficient is ~ 0.96 [15] so that homogeneity problems are minimized.

Figure 1 shows the pipe model constructed by Gold for the third zone Fermi surface. Attention has been directed in this work to the orbits around the arms along the $\langle 110 \rangle$ directions. In particular, the work of AG sug-

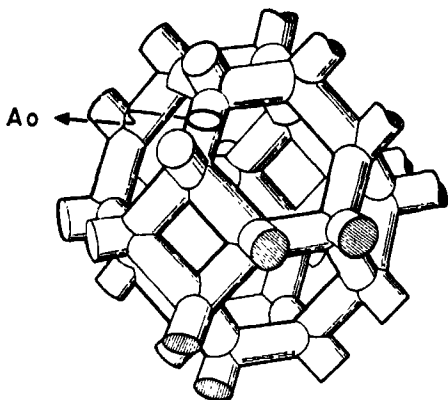


Fig. 1. Gold's pipe model of the third zone Fermi surface of lead (Ref. [14]).

gested that the single extremum of the pipe model actually consisted of a minimum plus a non-central orbit very much like an inflection point, as shown in Fig. 2. This figure resulted from the parameterized Fermi surface model constructed by AG and produced a convincing explanation for the presence of beats with about 42.5 oscillations per beat in the γ oscillations when the field B is parallel to $[110]$. In the present work we have shown that the frequency of the non-central orbit of the AG model is actually dominant in amplitude over that of the central orbit and have measured the areas of each.

In the alloys, we have measured changes in area of the dominant frequency and have compared these with RBM. The orbits in question are actually rather large ($F \sim 18$ MG), so that the corresponding changes in area tended to be rather small with the impurity concentrations that we were able to use. Thus, only a semiquantitative test of the

RBM was possible. However, the sign of the frequency change is certainly in agreement with simple electron concentration ideas, which was *not* the case in some early measurements of Pb(Bi) alloys made by Gold[13].

Scattering temperature measurements as a function of alloying were attempted but, except for the most dilute alloy, were hampered by the introduction of a third frequency into the γ oscillation beat pattern. A detailed model of the nature of the non-central orbits in the alloys was constructed to explain this effect.

In the following section a brief account is given of experimental procedures. Section 3 contains the experimental results and a comparison of these with theory. The concluding remarks are found in Section 4.

2. EXPERIMENTAL TECHNIQUES

The de Haas-van Alphen experiments were performed at the Francis Bitter National Magnet Laboratory using 150 kG water-cooled solenoids. These solenoids were periodically recalibrated, using a coil and integrator, to an accuracy of 0.2 per cent. The coil and integrator were calibrated by nuclear magnetic resonance techniques[16]. In order to improve the field stability of the solenoids, a superconducting shield, acting as a low pass filter, was situated around the sample. This device has been described in detail elsewhere [17].

Low frequency field modulation techniques were used throughout this work[18,19]. Several articles have been devoted to recent developments in these methods and therefore they will not be described here[20-22].

The alloys were prepared by melting the requisite amounts of material in graphite-coated, pyrex tubing evacuated to 20 microns*. Use of precision bore tubing and a graphite coating facilitated easy removal of the grown crystals. A point, sufficiently sharp

*Starting material of '69' purity was obtained from Cominco, Spokane, Washington.

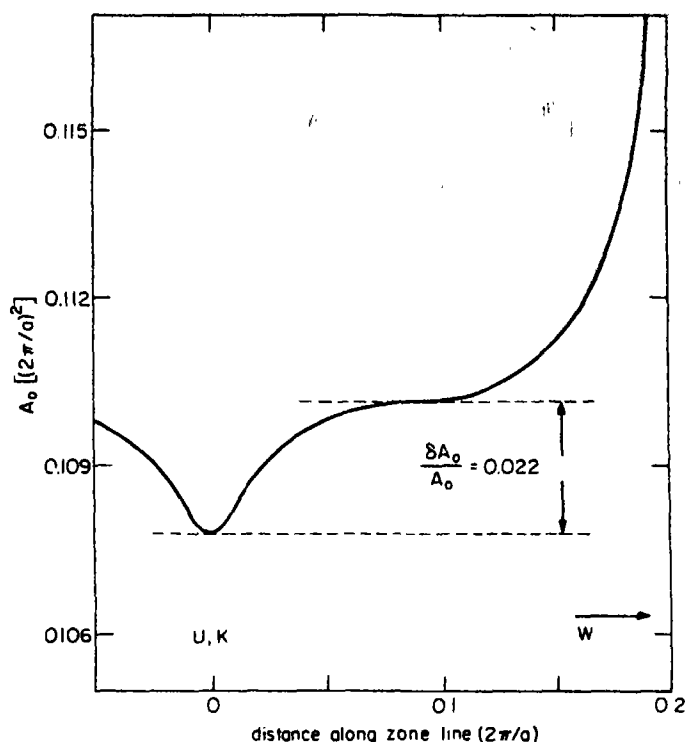


Fig. 2. Cross-sectional area along the third zone arm in lead according to the parameterized model of Anderson and Gold (Ref. [14]). The point, U , corresponds to the midpoint of the arm.

to initiate single crystal growth by the Bridgman technique, was pulled on one end of the 12 mm. tubing. The alloy components were mixed by agitating the molten metal for 10 min and then allowing it to cool slowly. A furnace moving with a speed of 3 cm/hr in conjunction with a high vacuum system, were used to grow single crystals having indium concentrations of 0.13, 0.27, 0.43 and 0.62 per cent.* These concentrations were determined using standard gravimetric techniques.

In order to check for gross inhomogeneities, one crystal was sampled at several points along its length. Except for the last portion to solidify, the variation in indium concentration was found to be within the accuracy of the analytical technique ($\sim 0.02\text{at.}\%$).

*The solute concentrations here, and in the remainder of the paper, are in atomic per cent.

Two of the crystals were subjected to spectrographic analysis to check for contamination with ferromagnetic impurities. In both cases, iron was found to be present only to the extent of 1 p.p.m.

The single crystals were oriented with an accuracy of 0.5° using standard Laue back-reflection techniques. Samples were then spark trepanned to shape using a Metals Research spark cutter. Typically they were cylindrical, having a diameter of 2.5 mm, and a length of 5 mm.

3. RESULTS AND DISCUSSION

(a) Third zone arm orbits in pure lead

As mentioned in the Introduction, the γ oscillation beats of ~ 42 oscillations/beat were perplexing until the parameterized fit of AG produced the curve of Fig. 2. The presence of the beats limited somewhat the accuracy of

the determination of the central cross-sectional area by AG. In a beat pattern the frequency of the carrier will be that of the oscillatory term with dominant amplitude [23]. Therefore, unless the sign of the frequency difference can be determined, it is not known whether to assign the carrier frequency, measured over an integral number of beats, to the smaller or larger orbit. In cases, where the number of cycles per beat is small, it is possible to determine the sign of the frequency difference from a comparison of the peak spacing (in B^{-1}) at a minimum to that at a beat maximum. This method still works in principle for a large number of cycles per beat, but in that case the accuracy required is prohibitive. AG apparently avoided this problem by assuming the component terms to have equal amplitudes in which case the measured carrier frequency is the average of the two components.

In the present work we have been able to infer from the alloy data that the amplitude dominant frequency in pure lead, for our field range of 20–150 kG, is that of the non-central orbit. Presentation of the evidence for this conclusion will be deferred until the next section. For the present, we will use this information to deduce the cross-sectional areas of the central (C) and noncentral (NC) orbits expressed in units of $(2\pi/a)^2$:

$$\begin{aligned} A_C &= 0.1031 \pm 0.0005 \\ A_{NC} &= 0.1055 \pm 0.0005. \end{aligned}$$

As mentioned before these values are free of any ambiguity due to the presence of beats. It should be emphasized that deduction of these values depends upon our acceptance of the AG model (Fig. 2) and upon our observation of a simple two-frequency beat pattern in pure lead.

(b) Extremal area changes on alloying

The problem of predicting the shape of the Fermi surface in a concentrated or even dilute solid solution alloy is an extremely difficult

one. Aside from the facts that the Fermi surface is smeared out and k is no longer a good quantum number, the problem is one of self-consistently determining the charge deposited in the vicinity of each solvent and solute atom and solving the Schrodinger equation for the true potential seen, in some statistical sense, by a conduction electron in the alloy. Recent work of Stern [24, 25] and Soven [26], for example, has been directed to this problem but most of their results are either qualitative in nature or refer to a simple, soluble band model in one or more dimensions. Thus outside of a recent virtual crystal approximation calculation [27] for α brass, which was later criticized by Stern [28], there appear to have been no determinations of the energy dispersion relations for a real alloy.

Under these circumstances one is left with the predictions based on the RBM. In the case of dilute alloys Heine [2] showed that the fractional change in dHvA frequency is given by

$$\frac{\delta F}{F} = \frac{Z}{2\mu_B F} \frac{m_c}{N(E_F)} X. \quad (2)$$

In this equation F is the frequency for the pure metal, δF the change in frequency for an X atomic fraction solute concentration, Z the valence difference between the solute (3 for In) and solvent (4 for Pb), μ_B the Bohr magneton, m_c the cyclotron mass in units of the free electron mass, and $N(E_F)$ the density of states at the Fermi level.

The lower portion of Fig. 3 shows the results of measurement of the third zone γ frequency orbit for $\text{Pb}\langle 110 \rangle$. The open circles represent measurement of the carrier frequency. Except in the case of the 0.13 at. % alloy, the frequency variation appears to be small but regular. In seeking an explanation for this apparent discontinuity at 0.13 per cent, we must consider the possibility that the amplitude dominant orbit changes as a function of alloy concentration. The data point for the 0.13 at. % alloy lies approximately 2.4 per

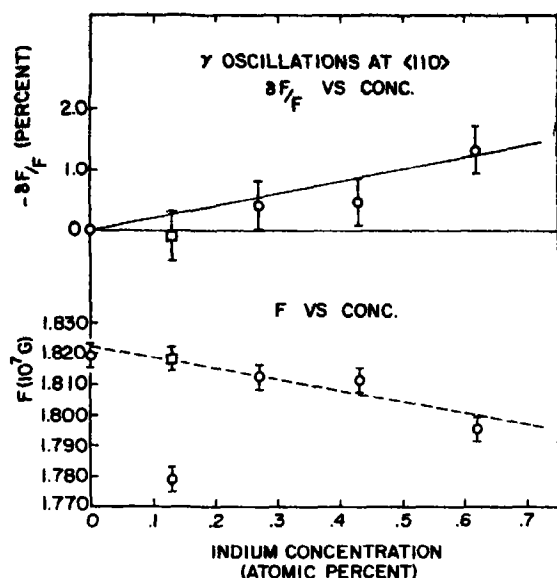


Fig. 3. dHvA frequency as a function of indium concentration. The solid line in the upper plot is the RBM prediction.

cent below the value expected on the basis of the other points (dotted line). Since the beat frequency is 2.2 per cent of the carrier frequency in this alloy (and all the others), this strongly suggests that the frequencies have interchanged in amplitude. In Fig. 3, therefore, the carrier frequency *plus* the beat frequency is plotted (open square). This point and the four referring to pure lead and the more concentrated alloys now describe the frequency variation of the same orbit—the one which is larger and therefore non-central (Fig. 2). This conclusion was used in part (a) of this section in the discussion of pure lead.

For comparison with alloy theory the data is re-plotted in a different form in the upper portion of Fig. 3. Here, the quantity $\delta F/F$ for the non-central orbit is shown as a function of indium concentration. The heavy line was drawn with the aid of equation (2) and several assumptions to be explained in what follows. m_c and $N(E_F)$ values were *experimentally determined* values from cyclotron mass measurements and electronic specific heat measurements. The mass value used was $m_c = 0.55$ at

$\langle 110 \rangle$ [29]. This value of Mina and Khaikin agreed with that of Phillips and Gold [30] (0.56 ± 0.01) and our result (0.53 ± 0.03) at $\langle 110 \rangle$. The masses for all of the alloys at $\langle 110 \rangle$ also fell within the range of 0.53 ± 0.03 . $N(E_F)$ was determined to be 17.6 states $\text{atom}^{-1} \text{ Ry}^{-1}$ from the experimentally measured value of electronic specific heat coefficient, $\gamma = 3.05 \text{ mJ mole}^{-1} \text{ deg}^{-2}$ [31]. Now m_c and $N(E_F)$, as measured experimentally, are known to be enhanced by many-body effects, especially electron-phonon interactions [32, 33]. Thus, the use of empirical values for m_c and $N(E_F)$ in equation (2) is justified only if the single-particle values of each of these quantities are enhanced equally. The work of AG appears to bear this out since the measured masses are $\sim 2.2 \pm 0.2$ times the band structure values. The other assumption used in applying equation (2) to the data was that the difference between the masses for the two orbits is so small as to have no significant influence on the conclusions to be drawn from Fig. 3. That is, a difference of masses of, for example, 5 per cent would affect the slope of the RBM line by the same amount and the accuracy of the $\delta F/F$ data is not sufficient to resolve this in any case. Now the cyclotron masses were evaluated at $\langle 110 \rangle$ by measuring the temperature dependence of the amplitude at the beat maxima. This assumes that the mass is the same for both orbits. Since the resulting plots were linear to within several per cent, this assumption appears to be justified to an accuracy of approximately 5 per cent.

There has been no mention in the above of possible corrections to the RBM due to lattice parameter changes on alloying. It is easily shown, using the measured lattice parameter changes [34] and the treatment of Shepherd and Gordon [9], that one can neglect these corrections to an accuracy of approximately 5 per cent in a 1 at.% alloy. It is concluded therefore that, within the accuracy of the data, the RBM is able to explain the results reasonably well for $B \parallel \langle 110 \rangle$.

(c) *Introduction of a new frequency on alloying*

The exact nature of the non-central orbit was found to be a sensitive function of alloying. Results on the most dilute alloy, Fig. 4, indicate that the amplitude ratio of the component frequencies is closer to unity than in pure lead. This is apparent from the fact that the minima in the beat pattern are much narrower in the alloy. Moreover, the amplitude at the beat waists is not decreasing with

$B \parallel (110)$ for the 0.62 per cent In sample, which is typical of the three more concentrated alloys. The amplitude at the beat waist goes through a maximum at high field, where we see the occurrence of a 'long beat' (≈ 62 cycles between points A and A'), and then begins to decrease. It will now be shown that this behavior can be accounted for by the presence of three frequencies.

For simplicity, we consider the addition of three terms having equal, field-independent,

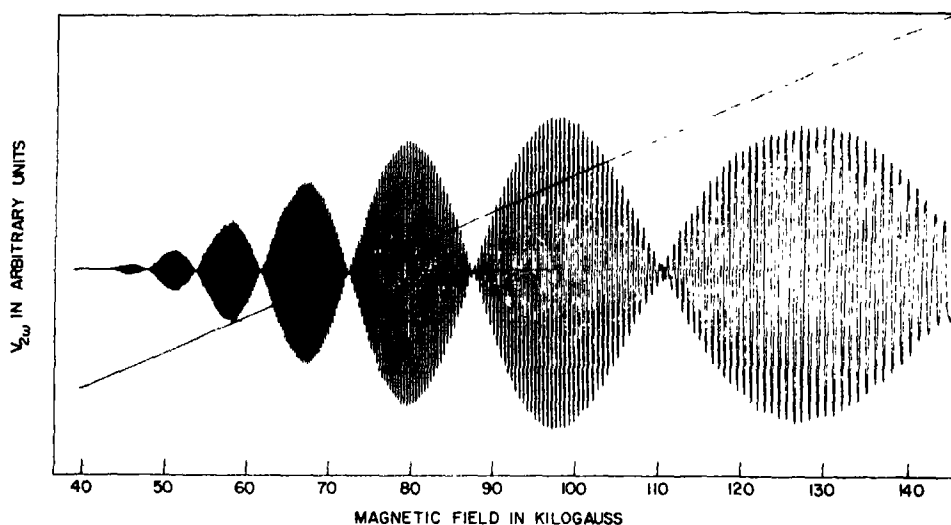


Fig. 4. dHvA effect in Pb + 0.13 per cent In showing beat pattern characteristics of nearly equal amplitude components.

increasing field as we observe in pure lead, but instead appears to be scaling with field in a manner similar to the beat maxima. This implies that the scattering temperature-mass products for the two orbits are nearly equal in this alloy. By measuring the amplitude at the beat maxima and making the usual plot, the scattering temperature may be determined from Fig. 5. The resulting value is $T_D = 2.95 \pm 0.2^\circ\text{K}$.

In the more concentrated alloys the observed beat pattern has a form which is qualitatively different from that found in pure lead and the 0.13 per cent In alloy. Figure 6(a) shows a recorder tracing (still with

amplitudes and frequencies ω , $\omega - \Delta\omega_1$, $\omega - \Delta\omega_2$. The signal S is then given by

$$S \sim \cos \omega x + \cos (\omega - \Delta\omega_1)x + \cos (\omega - \Delta\omega_2)x. \quad (3)$$

In this expression, the independent variable x is proportional to B^{-1} and the three terms are taken to be in phase at $x = 0$. The second and third terms may be expanded and combined with the first term giving, after some manipulation,

$$S \sim [3 + 2 \cos \Delta\omega_1 x + 2 \cos \Delta\omega_2 x + 2 \cos (\Delta\omega_1 - \Delta\omega_2)x]^{1/2} \sin (\omega x + \psi),$$

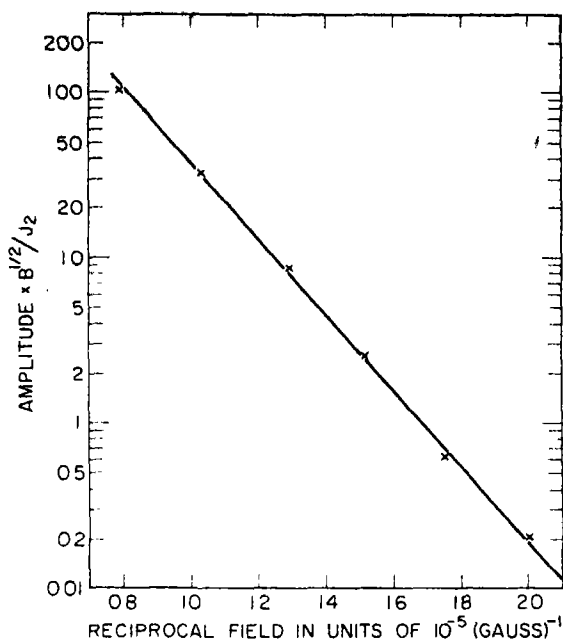


Fig. 5. Amplitude plot for determining the scattering temperature in Pb+0.13 per cent In. Each point corresponds to a beat maximum. $T = 3.77^\circ\text{K}$. $B \parallel \langle 110 \rangle$.

where

$$\psi = \tan^{-1} \left[\frac{\sin \Delta\omega_1 x + \sin \Delta\omega_2 x}{1 + \cos \Delta\omega_1 x + \cos \Delta\omega_2 x} \right]. \quad (4)$$

The carrier frequency is amplitude modulated by a rather complicated but slowly varying envelope function. The phase ψ is also a slowly varying function.

If the experimental trace can indeed be explained by the presence of three frequencies, apparently two of the frequencies are considerably closer in value than either is from the third. To quantify this, we define:

$$\begin{aligned} \Omega_1 &= \frac{1}{2}(\Delta\omega_1 + \Delta\omega_2) \\ \Omega_2 &= \frac{1}{2}(\Delta\omega_1 - \Delta\omega_2) \end{aligned} \quad (5)$$

and take $\Omega_1/\Omega_2 \gg 1$. In terms of these new variables, (4) may be written:

$$S \sim [5 + 4 \cos \Omega_1 x \cos \Omega_2 x - 4 \sin^2 \Omega_2 x]^{1/2} \times \sin(\omega x + \psi), \quad (6)$$

with

$$\psi = \tan^{-1} \left[\frac{2 \sin \Omega_1 x \cos \Omega_2 x}{1 + 2 \cos \Omega_1 x \cos \Omega_2 x} \right]. \quad (7)$$

In Fig. 6(b) is shown a plot of the envelope function for $\Omega_1/\Omega_2 = 40$. It is found that the essential features of the trace in Fig. 6(a) are reproduced. The 'long beat' feature is apparent between points B and B' and is due to the change in sign of $\cos \Omega_2 x$ in the above envelope function.

In seeking an explanation for the appearance of a third frequency, we were led by previous experimental results and a theoretical prediction to consider several mechanisms. These included: (1) the presence of microstructure in the crystals with indium concentrations greater than 0.13 at.%; and (2) a beating introduced by localized levels predicted by Ermolaev and Kaganov[35]. To these we add (3), a geometrical effect peculiar to the nature of the non-central third zone orbits.

With regard to [1], Condon[36] claimed that a new frequency was introduced in Be by $\sim 0.5^\circ$ of microstructure. Similar effects were seen in Be and Be(Cu) alloys by Goldstein *et al.*[12] in samples with $\sim 1^\circ$ microstructure. On the other hand, Gold[13] claims a rod-like 'bundle' structure ($\sim \frac{1}{2}^\circ$ misorientation) in lead cannot explain the beats in the γ oscillations at $\langle 110 \rangle$ because the carrier frequency is stationary with respect to angle there. In the present case, it is difficult to see how the amount of microstructure would depend so critically on indium concentration such that the third frequency would be absent in the 0.13 per cent alloy and present in the others. It also should be pointed out that the beat frequency produced by the non-central orbit is also stationary with respect to angle. This mechanism is therefore thought to be unlikely in producing the observed behavior.

Ermolaev and Kaganov[35] have shown how beats may appear as a result of the creation of quasi-local levels by impurities. Their conclusions apply to the perturbation of an

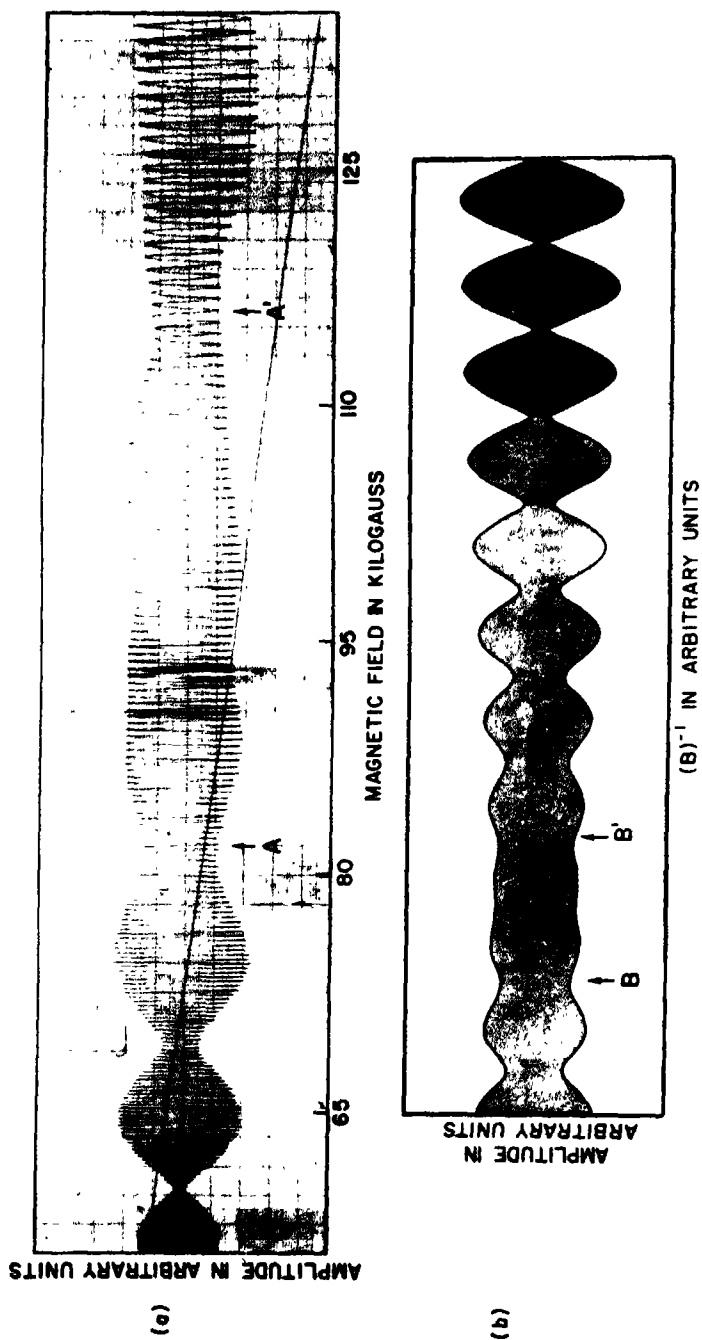


Fig. 6. (a) Experimental curve at 1.2°K for Pb + 0.62 per cent In showing a 'long beat' between 80 and 115 kG. (b) Computer simulated beat envelope for three component frequencies. The characteristic 'long beat' is apparent at high field.

electron piece of Fermi surface by the addition of donor impurities or a hole piece by acceptor impurities. In the case of the third zone Fermi surface in Pb(In) alloys, we have acceptor impurities and an electron surface. The theory therefore does not apply and it appears that a simple modification can be made to make it more general.

It now remains to consider the third of the possibilities suggested above. The appearance of a third frequency seems to be consistent with the description of the non-central orbit in pure lead as essentially an inflection point. When indium is added to lead, the third zone Fermi surface tends to shrink according to simple electron concentration ideas. It is hypothesized that the cyclotron masses (most of which are non-extremal) along the arm do not have the same value, resulting in a non-uniform decrease in area. This is shown schematically in Fig. 7 which illustrates how a maximum and minimum area could develop in place of an inflection point. Curves A

through E correspond to decreasing electron concentration with curve B representing the situation in pure lead.

The simplest assumption for the mass values at points 1 and 2 in Fig. 7, which will produce the indicated behavior is $(m_c)_2 > (m_c)_1$. Since the cyclotron mass is simply a measure of the rate of change of area with energy, the cross-section at point 2 will therefore decrease faster than that at point 1. In this interpretation the absence of a three-frequency beat pattern in the 0.13 per cent alloy is assumed to indicate that the minimum has not yet deepened enough for a maximum and a minimum to be separately resolved.

It should be added that the discussion of Section 2(b) is not contradicted by this explanation. The two frequencies at points 1 and 2 in Fig. 7 are so close together in frequency ($\Omega_2/\omega \approx 0.05$ per cent) that any amplitude switching between them as a function of alloy concentration is beyond the accuracy of our measurements (0.4 per cent).

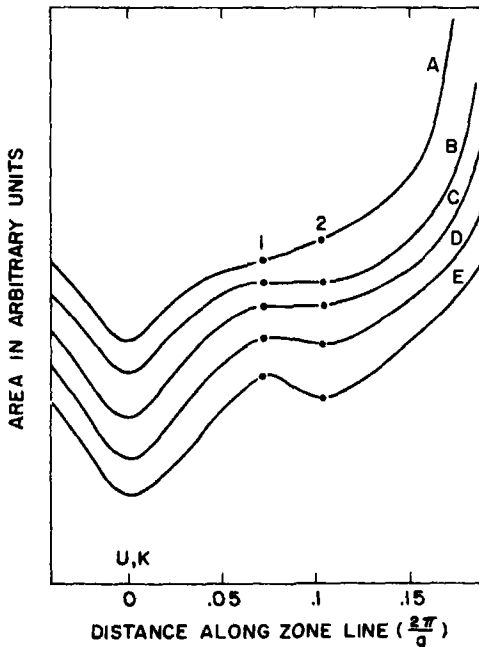


Fig. 7. Schematic illustration of the area along the third zone arm for decreasing electron concentration (A through E).

(d) Effect of impurities on scattering rate

The scattering or Dingle temperature T_D , which appears in the amplitude of the dHvA effect [5], is a measure of the total scattering rate for electrons on a given cyclotron orbit. T_D is related to a relaxation time by [4]

$$T_D = \frac{\hbar}{2\pi k_B \tau}. \quad (8)$$

Brailsford has shown how τ is related to a resistivity relaxation time τ_ρ defined by

$$\tau_\rho = \frac{m}{Ne^2\rho}, \quad (9)$$

where m is the free electron mass, N the conduction electron density, and ρ the resistivity. Brailsford assumed scattering of free electrons by a screened Coulomb potential and obtained [4]

$$\frac{\tau}{\tau_\rho} = \Phi(1 + q^2/2k_F^2) \quad (10)$$

where

$$\Phi(\lambda) = (\lambda - 1) \left[\left(\frac{\lambda + 1}{2} \right) \ln \left(\frac{\lambda + 1}{\lambda - 1} \right) - 1 \right],$$

q^{-1} is the screening length, and k_F is the Fermi wavevector. Free electron values for q and k_F appropriate to Pb give $\tau/\tau_p = 0.58$.

As mentioned in Section 3(c), the introduction of the third frequency for concentrations above 0.13 per cent In made T_D measurements in the more concentrated alloys impossible. Thus, comparison with the theory is possible only for the 0.13 per cent alloy.

Now the values obtained for T_D in pure lead (1.62°K and 1.73°K) are considerably larger than those obtained by Phillips and Gold[30]. Their work showed that unless special precautions are taken with respect to sample perfection, the measured values of T_D in pure lead are due to broadening of the Landau levels caused by dislocations and not to impurity scattering. The lowest value of T_D obtained by Phillips and Gold for the γ oscillations at $\langle 110 \rangle$ is 0.31°K indicating that the mechanism they suggest is probably the explanation of the higher values measured here. In the 0.13 per cent alloy T_D was 2.95°K. If we assume that Mathiessen's rule is approximately obeyed (as it should be for two elastic scattering mechanisms) and that the scattering rate due to dislocations in the alloy is roughly the same as in pure Pb, we may obtain an experimental ratio (τ/τ_p) , due to impurity scattering, to compare with the theoretical value. In determining τ_p an enhanced electron mass (2.2 m) is used[33] and a tabulated value of the resistivity (22 micro-ohm-cm) is employed in conjunction with the measured residual resistance ratio ($R_{RR} = \rho(295 \text{ K})/\rho(4.2 \text{ K})$). Since these alloys are superconducting at 4.2°K, the RRR for each alloy was determined by extrapolating the transverse magnetoresistance to zero field. The resulting RRR for the 0.13 per cent alloy was 200.

To obtain the experimental quantity to

compare with equation (10), we define $T_p = \hbar/2\pi k_B \tau_p$ so that the effect of the dislocation scattering may be eliminated approximately by putting

$$\left(\frac{\tau}{\tau_p} \right)_{\text{imp}} = \frac{T_p}{T_D(0.13) - T_D(0.0)},$$

where $T_D(0.13) = 2.95^\circ\text{K}$ and $T_D(0.0) = 1.67^\circ\text{K}$. This gives $(\tau/\tau_p)_{\text{imp}} = 1.7$. This value is quite obviously very much larger than the theoretically predicted one. It is not clear whether this large discrepancy, which is in the same sense as for Be alloys[12] and Al alloys[9], is a result of a failure of the theory or of band structure effects on the effective T_p .

4. SUMMARY AND CONCLUSIONS

Several aspects of the effect of indium impurities on the de Haas-van Alphen effect in lead have been investigated. Attention was focused on the third zone electron arm orbits with $\mathbf{B} \parallel \langle 110 \rangle$. It was shown from the dilute alloy data that the dominant frequency of the beat pattern in pure lead is that of the non-central orbit. Values for the extremal cross-sectional areas of the central and non-central areas were obtained. These values are free of any ambiguity due to the presence of beats in the oscillations.

The changes on alloying of the extremal area of the non-central orbit were compared with the rigid band model. The area decreased on alloying as expected because the arms are electron pieces of Fermi surface and adding indium to lead decreases the electron concentration. Because of the limited accuracy of the data, it is possible to conclude only that deviations from rigid band behavior are less than about twenty-five per cent in Pb(In) alloys. It is perhaps not surprising that deviations from the RBM are not large in this alloy system. This follows since the perturbation theory treatment of Friedel, upon which the RBM result (equation (2)) is based, would be expected to be valid in the Pb(In) alloy

system. This statement, in turn, is based upon the validity of pseudopotentials and free-electron-like pseudowavefunctions in Pb[14] and upon the conclusion of Stern[25], who states that perturbation theory should be correct in alloys for which the valence difference is a small fraction of the valence of either the solvent (4 for Pb) or solute (3 for In).

In alloys with greater than 0.13 at. % indium a third dHvA frequency was observed in the beat pattern. Several possible origins for this effect were considered but the most likely of these is that the apparent inflection point in the third zone changes into a resolvable maxima and a minima on alloying. This suggestion could be checked in two ways. One is that the cyclotron masses could be evaluated from a parameterized pseudopotential fit in the vicinity of the orbits in question. Secondly, increasing the electron concentration, in an alloy like Pb(Bi), would not only fail to produce a third frequency, but might also completely eliminate the extremum at the inflection point. Preliminary results[37] in a Pb (0.5 per cent Bi) alloy showed in fact that one of the two beating γ frequencies had essentially disappeared although it was possible to follow the γ oscillations only over about 200 cycles.

Finally, an attempt was made to investigate the influence of indium impurities on the scattering rate appearing in the dHvA amplitude. It was impossible to study concentrations higher than 0.13 at. % indium because of the third frequency appearing in the beat pattern. The limited data gave a τ/τ_p which was considerably higher than the free electron predictions, as is the case in other alloys of Al and Be. However this phenomenon should be studied carefully as a function of solute concentration, preferably in crystals of low dislocation content. Therefore it would be well to attempt such measurements in a system like Pb(Bi) where, as discussed above, the introduction of the third frequency is not likely.

Acknowledgements—We wish to thank Drs. I. S. Goldstein and J. Ahn for helpful discussions and assistance in the experiments. We are also indebted to the staff of the Francis Bitter National Magnet Laboratory for the use of its facilities. Support of this research by the Advanced Research Projects Agency is gratefully acknowledged.

REFERENCES

1. ONSAGER L., *Phil Mag.* **43**, 1006 (1952).
2. HEINE V., *Proc. Phys. Soc.* **A69**, 608 (1956).
3. FRIEDEL J., *Adv. Phys.* **3**, 446 (1954).
4. BRAILSFORD A. D., *Phys. Rev.* **149**, 456 (1966).
5. DINGLE R. B., *Proc. Phys. Soc. Lond.* **A211**, 517 (1952).
6. KING-SMITH P. E., *Phil. Mag.* **12**, 1123 (1965).
7. CHOLLET L. F. and TEMPLETON I. M., *Phys. Rev.* **170**, 656 (1968).
8. HIGGINS R. J. and MARCUS J. A., *Phys. Rev.* **141**, 553 (1966).
9. SHEPHERD J. P. G. and GORDON W. L., *Phys. Rev.* **169**, 541 (1968).
10. ABELE J. C. and BLATT F. J., *Phys. Rev.* **B1**, 1298 (1970).
11. HIGGINS R. J., KAEHN H. D. and CONDON J. H., *Phys. Rev.* **181**, 1059 (1969).
12. GOLDSTEIN I. S., SELLMYER D. J. and AVERBACH B. L., *Phys. Rev.* **B2**, 1442 (1970).
13. GOLD A. V., *Phil. Trans. Roy. Soc. Lond.* **A251**, 85 (1958).
14. ANDERSON J. R. and GOLD A. V., *Phys. Rev.* **139**, 1459 (1965).
15. HANSEN M., *Constitution of Binary Alloys*, p. 855. McGraw-Hill, New York (1958).
16. RUBIN L. G., private communication.
17. GOLDSTEIN I. S. and TOBIN P. J., *Rev. Scient. Instrum.* **40**, 172 (1969).
18. TOBIN P. J., Ph.D. Thesis, Massachusetts Institute of Technology, 1968 (unpublished).
19. AHN J. and SELLMYER D. J., *Phys. Rev. B* **1**, 1285 (1970).
20. GOLDSTEIN A., WILLIAMSON S. J. and FONER S., *Rev. Scient. Instrum.* **36**, 1356 (1965).
21. WINDMILLER L. R. and KETTERSON J. B., *Rev. Scient. Instrum.* **39**, 1672 (1968).
22. STARK R. W. and WINDMILLER L. R., *Cryogenics* **8**, 272 (1968).
23. MANLEY R. G., *Waveform Analysis*, John Wiley New York (1945).
24. STERN E. A., *Physics* **1**, 255 (1965).
25. STERN E. A., *Phys. Rev.* **144**, 545 (1966); *Phys. Rev.* **157**, 544 (1967); *Phys. Rev.* **168**, 730 (1968); *Phys. Rev.* **188**, 1163 (1969).
26. SOVEN P., in *Energy Bands in Metals and Alloys* (Edited by L. H. Bennett and J. T. Waber), p. 139 Gordon and Breach, New York (1968).
27. JOHNSON K. H. and AMAR H., *Phys. Rev.* **139**, A790 (1965).
28. STERN E. A. in *Energy Bands in Metals and Alloys*, (Edited by L. H. Bennett and J. T. Waber), Gordon and Breach, New York (1968).

29. MINA R. T. and KHAIKIN M. S., *Zh. Eksp teor. Fiz.* **45**, 1304 (1963). (English Transl.: *Soviet Phys. JETP* **18**, 896, 1964).
30. PHILLIPS R. A. and GOLD A. V., *Phys. Rev.* **178**, 932 (1969).
31. PHILLIPS N. E., LAMBERT M. H. and GARDNER W. R., *Rev. mod. Phys.* **36**, 131 (1964).
32. ASHCROFT N. W. and WILKINS J. W., *Phys. Lett.* **14**, 285 (1965).
33. ENZ C. P. in *Theory of Condensed Matter*, p. 729, International Atomic Energy Agency, Vienna (1968).
34. TYZACK C. and RAYNOR G. V., *Acta. crystallogr* **7**, 505 (1954).
35. ERMOLAEV A. M. and KAGANOV M. I., *Zh. Eksp. teor. Fiz. Pis'ma* **6**, 984 (1967). (English Transl.: *Soviet Phys.-JETP Lett.* **6**, 395, 1967).
36. CONDON J. H., *Phys. Rev.* **145**, 526 (1966).
37. HINES D. C. and ANDERSON J. R., *Bull. Am. Phys. Soc.* **15**, 295 (1970), and ANDERSON J. R., private communication, and ANDERSON J. R. and HINES D. C., *Phys. Rev.* **B2**, 4752 (1970).

CHARACTER DISORDER AT TRANSITION FROM CRYSTAL TO VITREOUS PHASE IN SEMICONDUCTORS

L. B. ZLATKIN and E. K. IVANOV

A. F. Ioffe Physico-Technical Institute, Academy of Sciences of the USSR, Leningrad K-21, U.S.S.R

(Received 17 August 1970, in revised form 3 November 1970)

Abstract—The optical constants n , k , ϵ' , ϵ'' and electron energy losses ($-Im\epsilon^{-1}$) are calculated in order to characterise the structure of energy bands at transition from crystal to vitreous phase in the diamond-type ($ZnSnP_2$, $CdGeAs_2$) and chalcogenide (As_2S_3 , As_2Se_3) semiconductors. The change of the valence band and conductivity band structure at transition from crystal to vitreous phase in $CdGeAs_2$ is shown.

The correspondence of the crystal structure to the character of disorder in the diamond-type and chalcogenide semiconductors is considered.

The significant changes of electron and phonon spectra observed at transition from crystal to vitreous phase in $CdGeAs_2$ in comparison with As_2S_3 and As_2Se_3 are caused by a greater disorder in vitreous $CdGeAs_2$.

INTRODUCTION

THE INVESTIGATION of electron and phonon states in the diamond-type ($ZnSnP_2$, $CdGeAs_2$) and chalcogenide (As_2S_3 , As_2Se_3) compounds has been carried out to study the character of disorder at transition from crystal phase to vitreous phase in semiconductors.

First studies were carried out with the $ZnSnP_2$ compound, which was obtained by manufacturers both in the chalcopyrite and sphalerite structures[1]. Zn and Sn atoms are distributed in order in the cation sublattice ($a = 5.651 \pm 0.001$ Å; $C/a = 2.00$, tetrahonal lattice), while the crystals with sphalerite structure ($a = 5.651 \pm 0.001$ Å, cubic lattice) are characterised by statistical distribution of these atoms and thus the sphalerite structure could be considered as a partly disordered one.

The absorption edge, photoluminescence, electron[2-3] and phonon[4] reflection spectra of $ZnSnP_2$ with the chalcopyrite and sphalerite structure were measured. The measurements has shown that the band structure of $ZnSnP_2$ did not change essentially at transition from chalcopyrite to sphalerite. In

the Reststrahlen region longitudinal and transverse optical lattice vibrations are present both in the sphalerite and chalcopyrite structure.

Thus, at transition from chalcopyrite to sphalerite in $ZnSnP_2$ the nearest and far order are present; and some broadening of the spectral structure in this case is, probably, due to a statistical disorder of atoms in the cation sublattice.

At the next step we studied a greater disorder considering transition from crystal to vitreous phase in the semiconducting $CdGeAs_2$ compound[5]. The electron[6] and vibrational[7] reflection spectra of $CdGeAs_2$ in the crystal and vitreous phases were measured.

The vitreous $CdGeAs_2$ was obtained on the basis of the crystalline tetrahedral phase and had the same coordinate number equal four, i.e. the vitreous $CdGeAs_2$ was similar to the amorphous Ge and Si. However, Ge and Si are obtained only as the amorphous layers, the structural inhomogeneity of the layers leads to ambiguous interpretation of the data. The morphology of the vitreous $CdGeAs_2$ is

analogous to that of the chalcogenide glasses, since CdGeAs_2 is obtained in the form of bulk samples.

In present work the optical constants n , k , ϵ' , ϵ'' and electron energy losses ($-Im\epsilon^{-1}$) have been calculated by means of the Kramers-Kronig relations in order to characterise the changes of the band structure at transition from crystal to vitreous phase. All the calculations were carried out with the BES M-4 computer. The results of the calculations are shown in Fig. 1, 3 ÷ 8.

The change of the valence band and conductivity band structure at transition from crystal to vitreous phase is shown. The correspondence of the crystal structure to the character of disorder in the diamond type and chalcogenide semiconductors is considered.

1. CHANGE OF THE VALENCE BAND AND CONDUCTIVITY BAND STRUCTURE AT TRANSITION FROM CRYSTAL TO VITREOUS PHASE IN DIAMOND-TYPE SEMICONDUCTORS

In 1964 Hilsum has shown[8] the invariableness of the valence band structure in

different semiconducting compounds. The disagreement of the energy values of the X_5 and L_3 valence band maxima in different semiconducting compounds does not exceed the value of 10 per cent.

Somewhat earlier Gubanov proposed the theory of amorphous conductors[9]. It follows from this theory that at transition from crystal phase (characterised by the regular coordination of atoms) to disordered systems (characterised by the negligible change of the nearest order) no significant change of the band structure takes place.

Investigating optical properties of amorphous Ge, Tauč also came to conclusion that the valence band of amorphous Ge is similar to that of the crystal[10].

However, the recent studies show that at crystal-glass transition in the diamond-type semiconductors a considerable change of the valence band and conductivity band structure takes place.

At transition from crystal to vitreous phase in the CdGeAs_2 compound a complete dis-

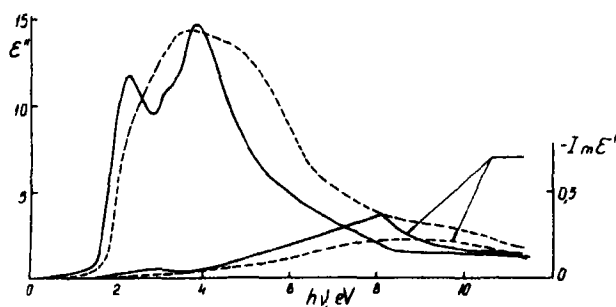


Fig. 1. The dispersion of the imaginary part (ϵ'') of the dielectric susceptibility and the energy losses function ($-Im\epsilon^{-1}$). The solid line represents CdGeAs_2 in the crystal phase, the dashed line represents CdGeAs_2 in the vitreous phase.

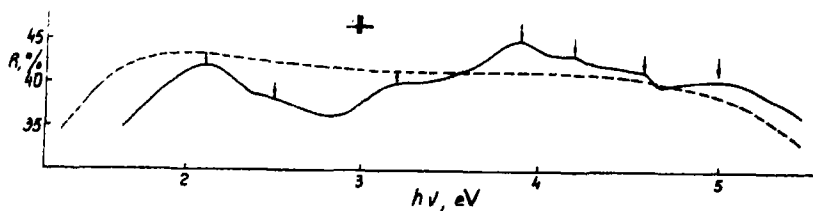


Fig. 2. The reflection spectrum of CdGeAs_2 in the crystal (solid line) and vitreous (dashed line) phases at $T = 100^\circ\text{K}$.

appearance of the structure in $R = f(h\nu)$ [6] and $\epsilon'' = f(h\nu)$ (Fig. 1) occurs. The structure observed in the crystal phase of CdGeAs_2 characterise the region of direct interband transitions at the Γ , N , P and T points of the Brillouin zone. It can be seen that the area under the $\epsilon'' = f(h\nu)$ curve for vitreous CdGeAs_2 is greater than that for the crystal. This is, probably, due to the fact that the density of glass is greater than the crystal density and consequently the number of oscillators per unit volume in the case of a glass is greater than in the case of a crystal (Fig. 2).

The measurements of the reflection spectra of vitreous and crystal CdGeAs_2 in the photon energy range from 1 to 5 eV were taken at $T = 100^\circ\text{K}$ in order to decrease the temperature influence on the spectral structure. However, no change of the spectrum in the case of vitreous phase was observed, which was, probably, caused by the blurring of the valence band and conductivity band structure. In the case of the crystal phase of CdGeAs_2 the additional structure of the reflection spectrum was observed at $T = 100^\circ\text{K}$ in comparison with our measurements at the room temperature [6].

Donovan and Spicer [11] investigated the change of the density of states in amorphous Ge in comparison with crystal Ge by means of photoemission. Their data unambiguously show that the valence band density of states maxima are shifted to the larger energy values and the corresponding peaks considerably broaden in the case of amorphous Ge with respect to the crystal.

Investigating the reflection spectra of As_2S_3 and As_2Se_3 in the crystal and vitreous phases the number of authors (Belle, Kolomiets and Pavlov [12]) came to a conclusion that the energy structure of these compounds at transition from crystal to vitreous phase did not undergo any significant change.

Our calculations of the optical constants (Figs. 3-6) show that at transition from crystal to vitreous phase the ϵ'' function is characterised by the same singularities. Some inte-

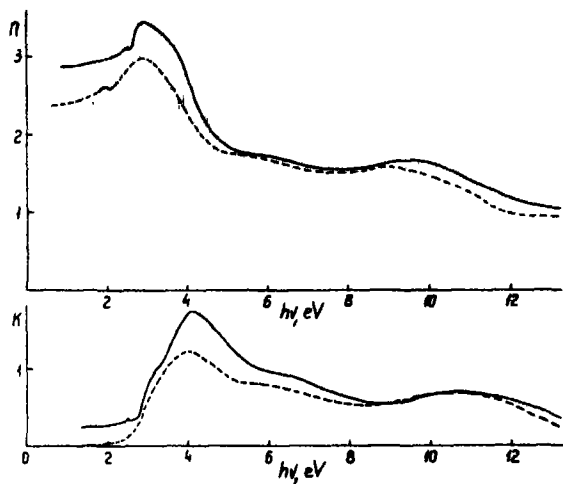


Fig. 3. The dispersion of the real (n) and imaginary (k) parts of the refraction. The solid line represents the crystal phase of As_2S_3 , the dashed line represents the vitreous phase of As_2S_3 .

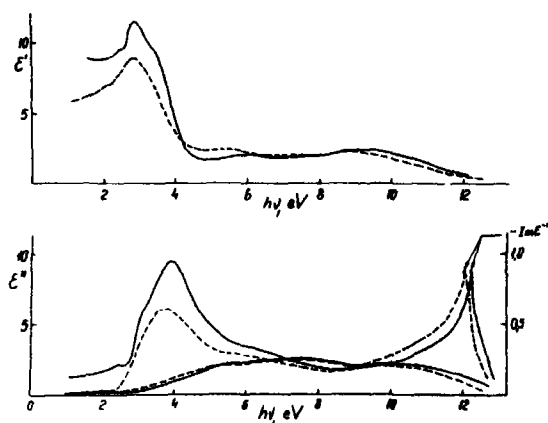


Fig. 4. The dispersion of the real (ϵ') and imaginary (ϵ'') parts of the dielectric susceptibility and the energy losses function ($-\text{Im}\epsilon^{-1}$). The solid line represents As_2S_3 in the crystal phase, the dashed line represents As_2S_3 in the vitreous phase.

gral decrease of the ϵ'' function and a broadening of the most intensive peak in the case of the vitreous phase is caused by a decrease of the chalcogenide glass density and also by some structural disorder of vitreous phase.

If electrons in the chalcogenide glasses are described by the Bloch envelopes, than conception of the Brillouin zone for these

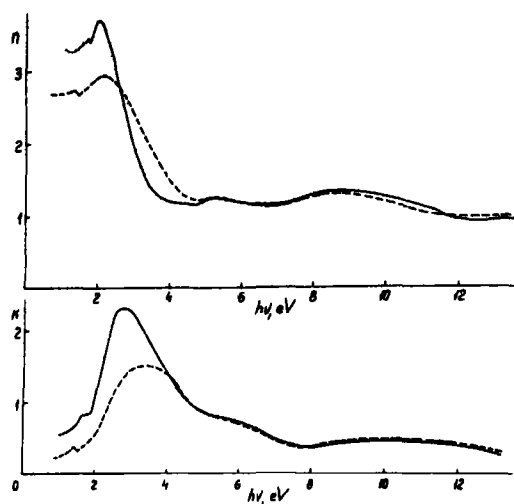


Fig. 5. The dispersion of the real (n) and imaginary (k) parts of the refraction. The solid line represents the crystal phase of As_2Se_3 , the dashed line represents the vitreous phase of As_2Se_3 .

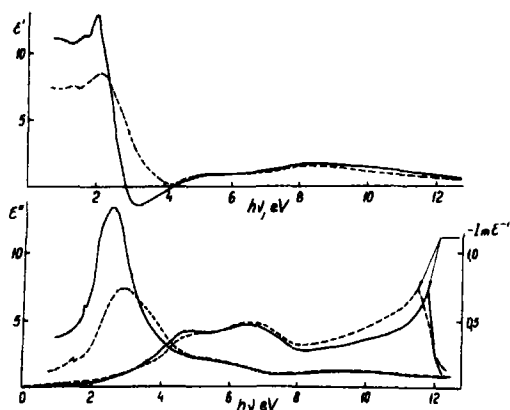


Fig. 6. The dispersion of the real (ϵ') and imaginary (ϵ'') parts of the dielectric susceptibility and the energy losses function ($-\text{Im}\epsilon^{-1}$). The solid line represents As_2Se_3 in the crystal phase, the dashed line represents As_2Se_3 in the vitreous phase.

glasses might be introduced. According to the electron reflection spectra the Brillouin zone of the chalcogenide glasses is a polyhedron as is the case for the crystal. Some blurring of the reflection spectra of the As_2S_3 and As_2Se_3 glasses in comparison with crystal As_2S_2 and

As_2Se_3 is due to an uncertainty in the wave vector $\mathbf{K} \sim \mathbf{K} + \Delta\mathbf{K}$.

On the other hand the lack of the structure in the region of direct interband transitions of vitreous Ge and CdGeAs_2 points to the change of the Brillouin zone. Thus, transition from crystal to vitreous phase in the diamond-type semiconductors is accompanied, evidently, by the change of the Brillouin zone from polyhedron to sphere. In other words an uncertainty of the electron wave vector becomes so great that conception of the Brillouin zone is no more applicable to the glasses obtained on the basis of the crystalline tetrahedral phase.

At transition from chalcopyrite to sphalerite (i.e. at transition to a partly disordered structure) in the diamond-type semiconducting ZnSnP_2 compound the band structure does not change significantly and the ϵ'' function is characterised (Fig. 7-8) by the same singularities.

We also analysed the valence band structure changes at crystal-glass transition by means of the electron energy losses function ($-\text{Im}\epsilon^{-1}$). The maximum of this function lies in the frequency region of plasmic oscillations of valence electrons. Since this frequency region 'reflects' only valence band processes the particular form of the electron losses function enables one to draw a conclusion about the changes of the valence band structure at crystal-glass transition.

In the case of crystal CdGeAs_2 the frequency region of plasmic oscillations lies at about 8 eV and the electron losses function is characterised by the sharp structure Fig. 1. In the case of the vitreous phase this structure is considerably blurred which brings one to a conclusion about the significant change of the valence band structure of vitreous CdGeAs_2 in comparison with the starting crystal phase.

In As_2S_3 and As_2Se_3 the ($-\text{Im}\epsilon^{-1}$) function is characterised by the similar structure both in the crystal and vitreous phases Fig. 4, 6. Hence at transition from crystal to vitreous phase the valence band in the investigated chalcogenide semiconductors change quite

insignificantly, and the change is due to some uncertainty of the wave vector $K \sim K + \Delta K$.

In ZnSnP_2 (Fig. 8) at transition from chalcopyrite to sphalerite the $-\text{Im}\epsilon^{-1}$ function does not change considerably.

Spicer and Danoven[13] calculated the effective number of electrons per atom $n_{\text{eff}} = 4$, for amorphous Ge. It was shown in earlier works by Philipp and Ehrenreich[14] that for crystal Ge $n_{\text{eff}} > 5$, which, in authors view, is caused by the contribution from transitions in the d -bands. The change of n_{eff} at crystal-glass transition in Ge also implies the change of the valence band structure of amorphous Ge.

2. CORRESPONDANCE OF THE CRYSTAL STRUCTURE TO THE CHARACTER OF DISORDER IN THE DIAMOND-TYPE AND CHALCOGENIDE SEMICONDUCTORS

The investigation of the vibrational spectra in the diamond-type[7] and chalcogenide[15] semiconductors has shown that the transition from crystal to vitreous phase is accompanied by essential changes only in the case of CdGeAs_2 (i.e. the longwave-length optical lattice vibrations are present only in the crystal phase of CdGeAs_2).

In the reflection spectra of vitreous As_2S_3 and As_2Se_3 (in distinction to vitreous CdGeAs_2) the intensive peakes are observed at $\lambda = 33 \mu$ and $\lambda = 47 \mu$ respectively. These peakes are also observed in absorption of the As_2S_3 and As_2Se_3 glasses.

In addition the measurements of absorption in the As_2S_3 and As_2Se_3 crystals show that the absorption bands of the chalcogenide glasses and the starting crystal phase are comparable in intensity and lie in the same frequency region.

Consequently optical vibrations of crystal As_2S_3 and As_2Se_3 are also present in the vitreous phase of these compounds. We suppose the existence of directed oscillations of the valent bonds in As_2S_3 and As_2Se_3 both in the crystal and vitreous phases. These oscillations cause the observed infrared peaks.

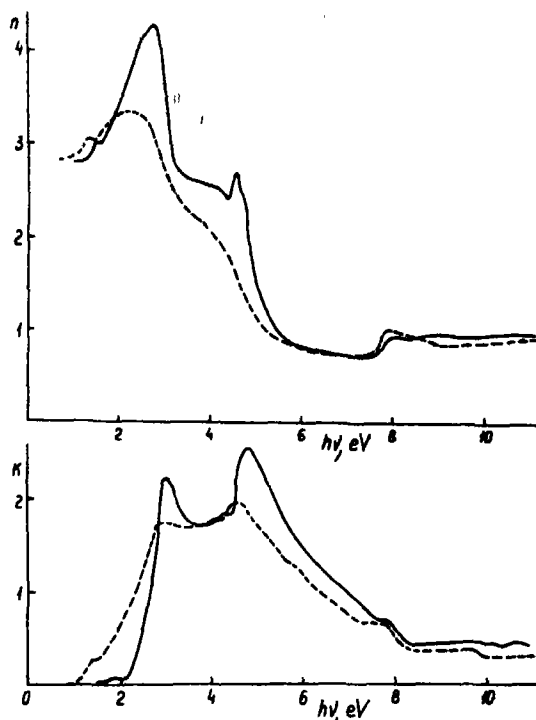


Fig. 7. The dispersion of the real (n) and imaginary (k) parts of the refraction in ZnSnP_2 . The solid line represents ZnSnP_2 with the chalcopyrite structure, the dashed line represents ZnSnP_2 with the sphalerite structure.

The results of the present experiments corroborate the structural conceits. According to these conceits the chalcogenide crystals As_2S_3 [16] and As_2Se_3 [17] have the layer structure. The As-S or As-Se bond is dominating within the layer. These are the ionic-covalent bonds whereas the interlayer bond is of the Van-der Waals type. At transition to the vitreous phase of the chalcogenide compounds the interlayer Van-der Waals bond breaks while the ionic-covalent As-S or As-Se bond is dominating within the layer.

This is confirmed by the measurements of infrared spectra of both crystal and vitreous phases, the peak observed in the same frequency region for the crystal and vitreous phases is due to the directed oscillations of valent bonds.

The distortion of the far order in the chalco-

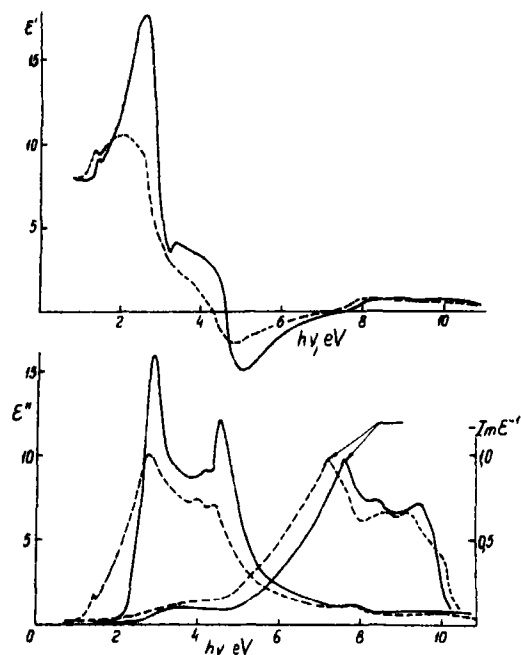


Fig. 8. The dispersion of the real (ϵ') and imaginary (ϵ'') parts of the dielectric susceptibility and the energy losses function ($-\text{Im}\epsilon^{-1}$). The solid and dashed lines represent ZnSnP_2 with the chalcopyrite and sphalerite structure respectively.

genide glasses is caused mainly by the changes of valent angles.

In the diamond-type semiconductors at transition to the vitreous phase the coordination number is conserved whereas the distortion of the far order is caused by the changes of the valent angles and interatomic distances, which leads to essential changes of the observed spectra.

Acknowledgements—The authors wish to express their gratitude to Miss E. A. Smorgonskii and to Messrs. A. A. Vaipolin, A. I. Gubanov and K. D. Tsendin for many helpful discussions of the results.

REFERENCES

1. VAIPOLIN A. A., GORYUNOVA H. A., KLESHCHINSKII L. I., LOSHAKOVA G. V. and OSMANOV E. O. *Phys. Status Solidi* **29**, 435 (1968).
2. GORYUNOVA N. A., BELLE M. L., ZLATKIN L. B., LOSHAKOVA G. B., POPLAVNOI A. S. and CHALDYSHEV V. A. *Fiz. Tech. Poluprovod.* **2**, 1344 (1968).
3. ZLATKIN L. B., IVANOV E. K. and STARTSEV G. P. *Phys. Status Solidi* (a) **1**, 661 (1970).
4. ZLATKIN L. B., MARKOV Yu. F., STEKHANOV A. I. and SHUR M. S. *Phys. Status Solidi* **32**, 473 (1969).
5. VAIPOLIN A. A., GORYUNOVA N. A., OSMANOV E. O. and RUD J. B. *Dokl. akad. Nauk USSR* **160**, 633 (1965).
6. GORYUNOVA N. A., GROSS E. F., ZLATKIN L. B. and IVANOV E. K. In *Proceedings of the International Conference on Amorphous and Liquid Semiconductors*. Cavendish Laboratory, Cambridge, England, September 1969. *J. Non-cryst. Solids* **4**, 57 (1970).
7. ZLATKIN L. B., MARKOV Yu. F., STEKHANOV A. I. and SHUR M. S. *J. Phys. Chem. Solids* **31**, 567 (1970).
8. HILSUM C. *RRE Mem.*, N 2112, 1 (1964).
9. GUBANOV A. I. *Kvantovo-electronnaya teoriya amorphnykh provodnikov*. Ed. Akad. Nauk USSR, Moscow-Leningrad (1963).
10. TAUČ J. in *Optical Properties of Solids*, (Edited by F. Abeles) North-Holland, Amsterdam, The Netherlands. J. TAUČ, *Mater. Res. Bull.* **3**, 13 (1968).
11. DONOVAN T. M. and SPICER W. E. *Phys. Rev. Lett.* **21**, 1572 (1968).
12. BELLE M. L., KOLOMIETS B. T. and PAVLOV B. V. *Fiz. Tech. Poluprovod.* **2**, 1448 (1968).
13. SPICER W. E. and DONOVAN T. M. In *Proceedings of the Symposium on Semiconductor effects in amorphous Solids*, New York, (May 1969). *J. Non-cryst. Solids* **2**, p. 66 (January 1970).
14. PHILIPP H. R. and EHRENREICH H. E. *Semiconductors and Semimetals* (Edited by R. K. Willardson and A. C. Beer) Vol. 3, p. 123. Academic Press, New York (1967).
15. ZLATKIN L. B. and MARKOV Y. Yu. F. *V Symposium on Vitreous Chalcogenide Semiconductors*, Leningrad, Collection of Abstracts, p. 24 (May 1970).
16. MORIMOTO N. *X-rays*, **5**, 3-4, 115 (1949).
17. VAIPOLIN A. A. *Krystallographiya*, **10**, 596 (1965).

CALCULATIONS OF POINT DEFECT CONCENTRATIONS AND NONSTOICHIOMETRY IN GaAs

R. M. LOGAN and D. T. J. HURLE

Royal Radar Establishment, Malvern, Worcs., England

(Received 5 October 1970)

Abstract—A study of point defects and nonstoichiometry in GaAs is presented. Standard methods of chemical thermodynamics are used to derive expressions for the equilibrium concentrations, as a function of temperature and arsenic pressure, of the following defects; arsenic monovacancies, gallium monovacancies, gallium divacancies and appropriately charged versions of these three. This choice of defects is made on the strength of the evidence of the published experimental results relating directly to point defects in GaAs.

Values for the required equilibrium constants are obtained by a combination of *a priori* estimates and matching with this experimental data at certain points. Consistent agreement with the experimental data is obtained, indicating for example that defect concentrations in the region 10^{18} – 10^{19} cm⁻³ in melt grown material are not unreasonable. The set of equilibrium constants on which the calculations are based must, however, be regarded as provisional until more extensive data is available for comparison. Using these equilibrium constants the minimum practical deviation from stoichiometry and the width of the existence region of solid GaAs are calculated as a function of temperature.

1. INTRODUCTION

THERE is experimental evidence for the existence of considerable concentrations of native point defects in GaAs. Using lattice parameter measurements Potts and Pearson[1] observed concentrations of the order of 10^{19} cm⁻³, which they identified as arsenic monovacancies. By means of measurements of damping by internal friction Chakraverty and Dreyfus[2] observed similar concentrations of defects, which they tentatively identified as gallium divacancies. Blanc, Bube and Weisberg[3] also observed concentrations of at least 10^{19} cm⁻³, although they were unable to identify the actual type of defect involved. In EPR measurements Goldstein and Almeleh[4] observed concentrations greater than 10^{19} cm⁻³ of some resonance centre which they deduced to be some combination of point defects. Using lattice parameter and density measurements Straumanis and Kim[5] observed deviations from stoichiometry of the order of one part in 10^4 , corresponding to a defect concentration of at least 2×10^{18} cm⁻³.

The question as to what extent such native point defects may influence the electronic behaviour of GaAs is not yet fully resolved. The direct effects of point defects are considered in Ref. [3] and in recent papers by Otsuka[6] *et al.* and Munoz[7] *et al.* in which the conversion of *n*-type GaAs to *p*-type is partly ascribed to such defects. There are also several other cases where the defects influence the electronic behaviour in a less direct manner through the formation of complexes with various impurities, for example Refs. [8–10]. In Section 4 we make comparisons between theoretical calculations and some of the experimental results mentioned above, particularly those from Refs. [1, 2] and [7].

In this paper standard methods of chemical thermodynamics are used to derive expressions for the equilibrium concentrations of the various defects considered; for a comprehensive discussion of these methods see, for example Refs. [11, 12] or [13]. The notation to be used is based on that used in the above references (see in particular Ref. [11],

Chapter 13) and corresponds to the so-called absolute system. Using the experimental results from Refs. [1] and [2] as a guide we consider here only the following types of point defect: arsenic monovacancies V_{As}^x , gallium monovacancies V_{Ga}^x , gallium divacancies $(V_{Ga})_2^x$ and appropriately charged versions of these three. Interstitial types of defect are not therefore included in the present analysis, the justification being the fact that introducing interstitials makes the theoretical results unnecessarily complicated, since the main features of the most concrete experimental results (Refs. [1] and [2]) can best be interpreted in terms of vacancies as the dominant species. One cannot at this stage, however, definitely rule out the possibility of a significant concentration of interstitials, and this should be borne in mind as further experimental evidence becomes available.

The method of analysis used for obtaining the defect concentrations, as described in Section 2, is formally quite straightforward. The feature which usually discourages the application of the method is the presence of a large number of unknown parameters, such as the energies and entropies of formation of the various defects, which are required for the calculation of the equilibrium constants. In the present case for GaAs we have obtained approximate *a priori* estimates for all except three of the required parameters. Reasonable values for the remaining three (one energy and two pre-exponential factors) are obtained by matching with some of the experimental data from Refs. [1, 2] and [7]. Thus a reasonable and believable set of values for the equilibrium constants is obtained which provides satisfactory agreement with the experimental results. There is little doubt, however, that one will have to make some modifications to these values as further data for testing them becomes available. Once one has values for the equilibrium constants, of course, the equilibrium concentrations of the corresponding defects can be calculated

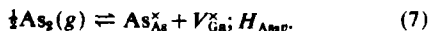
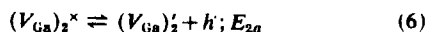
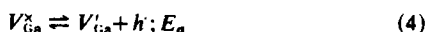
for any desired values of temperature and pressure. In Section 5 we use this set of equilibrium constants to calculate the minimum practical deviation from stoichiometry and the shape of the GaAs existence region, both as a function of temperature.

2. ANALYSIS

The method of analysis may be outlined as follows:

We write down a reaction equation for the formation of each type of defect in the solid and for the formation of electrons and holes. There is a further reaction equation representing the transfer of atoms between the gas and solid phases. For each of these reactions there is a mass action condition which applies at equilibrium. In the present work we assume that the concentrations are sufficiently dilute for ideal conditions to apply, so that the mass action relations can be written in terms of concentrations and Boltzmann statistics used for the electrons. To these mass action conditions we add the condition of electroneutrality, and the resulting set of equations can be solved for the defect concentrations in terms of the partial pressure of one of the species in the gas phase (the pressure of As_2 is used here). Suitable approximate solutions to these equations can easily be obtained if the neutrality condition is approximated by its two dominant members; this procedure, known as Brouwer's approximation[14], is frequently used in this type of problem. Further details and justification of the method of analysis used here can be found in Refs. [11], [12] or [13] as already mentioned. Section 13.4 of Ref. [11] is particularly relevant.

Taking into account the defects indicated in Section 1 above, we have the following reaction equations:



Reactions (1-6) occur in the solid phase. Reaction (7) represents transfer of As atoms between the solid and gas phases. The superscripts x , $'$, indicate neutral negative and positive species respectively. Thus e' represents an electron, h a hole, V_{Ga}^x a neutral gallium vacancy, $(V_{Ga})_2^x$ a neutral gallium divacancy, and so on. The energies and enthalpies of reaction are indicated on the right-hand side. The symbol H indicating enthalpy is used for reactions where a significant volume change may be involved.

The mass action relations corresponding to the above reactions are as follows:

$$np = K_i \quad (8)$$

$$[V_{Ga}'] [V_{As}^x] = K_s \quad (9)$$

$$[(V_{Ga})_2^x] / [V_{Ga}']^2 = K_p \quad (10)$$

$$[V_{Ga}'] p / [V_{Ga}^x] = K_a \quad (11)$$

$$[V_{As}'] n / [V_{As}^x] = K_b \quad (12)$$

$$[(V_{Ga})_2'] p / [(V_{Ga})_2^x] = K_{2a} \quad (13)$$

$$[As_{As}^x] [V_{Ga}'] / P_{As}^{1/2} = K_{Asv} \quad (14)$$

Square brackets are used to indicate concentrations except in the case of electrons and holes where the usual symbols n and p are used. $[As_{As}^x]$ represents the concentration of As atoms on As sites and will be taken as unity. The partial pressure of As_2 in the gas phase is denoted by P_{As_2} . Note that we need only specify the partial pressure of one of the constituents of the gas phase—the pressures of the others (As_4 , Ga, etc) are then determined by the condition of chemical equilibrium. The equilibrium constants appearing on the right-hand-side of equations (8–14) have the general form

$$K = \exp(S/k) \exp(-H/kT) \\ = K^0 \exp(-H/kT),$$

where S and H are the entropy and enthalpy changes of the reaction. K^0 , referred to as the pre-exponential factor, is usually a relatively weak function of temperature.

The electroneutrality condition is

$$n + [V_{Ga}'] + [(V_{Ga})_2'] = p + [V_{As}']. \quad (15)$$

Equations (8–15) represent 8 equations for the 8 unknowns n , p , $[V_{Ga}']$, $[V_{As}^x]$, $[(V_{Ga})_2^x]$, $[V_{Ga}']$, $[V_{As}']$ and $[(V_{Ga})_2']$. Thus we can solve for these 8 unknowns in terms of P_{As_2} and the temperature. It is convenient to express the solutions in terms of the quantity

$$R = P_{As_2}^{1/2} K_{Asv}. \quad (16)$$

Depending on which are the dominant members in equation (15), there are six possible neutrality conditions: $n = [V_{As}']$; $n = p$; $[V_{Ga}'] = [V_{As}']$; $[(V_{Ga})_2'] = [V_{As}']$; $[V_{Ga}'] = p$; $[(V_{Ga})_2'] = p$. The solutions of equations (8–15) for each of these neutrality ranges are easily obtained and are shown in Table 1. Note that the solutions involve only simple powers of R , and hence when plotted against R on a log scale are given by straight lines in each neutrality range. As shown in Section 4, not all the possible neutrality ranges shown in Table 1 are applicable for the present study on GaAs.

3. VALUES FOR THE EQUILIBRIUM CONSTANTS

We consider first the equilibrium constants

for the reactions involving formation of electrons or holes, i.e. K_i , K_a , K_b and K_{2a} . As shown in Ref. [11], p. 253, using the band model for the semiconductor, the equilibrium constant K_i is given approximately by

$$K_i = 4 [2\pi(m_e^* m_h^*)^{1/2} kT / h^2]^3 \exp(-E_i^* / kT), \quad (17)$$

where m_e^* and m_h^* are the effective masses for electrons and holes, and E_i^* is the band gap energy. For the effective masses we used the published [15] values $m_e^* / m = 0.07$ and $m_h^* / m = 0.5$, where m is the electron mass. The experimental results [16] for E_i^* may be represented approximately over the range $T \gtrsim 500^\circ K$ by the expression

$$E_i^* = 1.62 - 5.45 \times 10^{-4} T \text{ eV}. \quad (18)$$

Using these quantities in equation (17) we obtain

$$K_i = 1.65 \times 10^{-13} T^3 \exp(-1.62 \text{ eV} / kT).$$

We recognise that equation (17) is based on a simple model, and a more exact numerical calculation using a two band correction has been given by Hall and Racette [17]. We take some account of the calculations in Ref. [17] by adjusting the value of the pre-exponential factor so as to agree with their results at 1000 K. This causes an increase by a factor of 6 in the pre-exponential factor calculated above, which now becomes $1.0 \times 10^{-12} T^3$. The final value for K_i is given in Table 2.

As shown in Ref. [11], p. 254, the equilibrium constant K_a is given approximately by

$$K_a = (2\pi m_h^* kT / h^2)^{3/2} \exp(-E_a / kT) \quad (19)$$

where E_a is the ionization energy of the vacancy. To obtain an estimate for E_a we use the hydrogenic model:

$$E_a = 13.6(m_h^* / m) \epsilon^2 \text{ eV}, \quad (20)$$

where ϵ is the static dielectric constant.

Table 1. Solutions of equations (8-15), giving defect concentrations in various neutrality ranges

Species	Range 1 $n = [V_{As}]$	2 $n = p$	3 $[V'_{Ga}] = [V_{As}]$	4 $[(V_{Ga})'_2] = [V_{As}]$	5 $[V'_{Ga}] = p$	6 $[(V_{Ga})'_2] = p$
n	$(K_a K_b / R)^{1/2}$	$K_i^{1/2}$	$(K_i K_a K_b / K_a)^{1/2} / R$	$(K_i K_a K_b / K_a K_p R^3)^{1/2}$	$(K_i / R)^{1/2}$	$(K_i / R) / (K_a K_p)^{1/2}$
p	$K_i (R / K_a K_b)^{1/2}$	$K_i^{1/2}$	$(K_i K_a / K_a K_b)^{1/2} / R$	$(K_i K_a K_p R^2 / K_a K_b)^{1/2}$	$(K_a R)^{1/2}$	$(K_a K_p)^{1/2} R$
$[V'_{Ga}]$	R	R	R	R	R	R
$[V_{As}]$	K_d / R	K_d / R	K_d / R	K_d / R	K_d / R	K_d / R
$[(V_{Ga})'_2]$	$K_p R^2$	$K_p R^2$	$K_p R^2$	$K_p R^2$	$K_p R^2$	$K_p R^2$
$[V'_{Ga}]$	$(K_a / K_i) (R K_a K_b)^{1/2}$	$K_a R / K_i^{1/2}$	$(K_a K_b / K_i)^{1/2}$	$(K_a K_b K_p / K_i K_p R)^{1/2}$	$(K_a R)^{1/2}$	$(K_a / K_p)^{1/2}$
$[V_{As}]$	$(K_a K_b / R)^{1/2}$	$K_a K_i / R K_i^{1/2}$	$(K_a K_b / K_i)^{1/2}$	$(K_a K_b K_p R / K_i)^{1/2}$	$(K_a K_b / K_i) (K_a / R)^{1/2}$	$(K_a K_b / K_i) (K_a K_p)^{1/2}$
$[(V_{Ga})'_2]$	$(K_a K_p / K_i) (K_a K_p R^3)^{1/2}$	$K_a K_p R^2 K_i^{1/2}$	$K_p R (K_a K_b / K_i)^{1/2}$	$(K_a K_b K_p R / K_i)^{1/2}$	$K_p K_a^{1/2} R^{3/2}$	$(K_a K_p)^{1/2} R$

Using the published[18] value $\epsilon = 12.5$, we obtain $E_a = 0.044$ eV. The resulting value for K_a from equation (19) is

$$K_a = 3.9 \times 10^{-8} T^{3/2} \exp(-0.044 \text{ eV}/kT).$$

Equation (19) involves similar assumptions to those in equation (17), and to be consistent with the modification to bring the value of the pre-exponential factor in K_i into line with the calculations in Ref. [17] we make a corresponding correction to the value of K_a . The numerical value of the correction is $\sqrt{6} = 2.45$, and the resulting value for K_a is shown in Table 2.

The expression for K_b is the same as that for K_a , with m_e^* replacing m_h^* throughout. This yields an energy $E_b = 0.006$ eV, and the resulting value for K_b is shown in Table 2 (the same numerical factor 2.45 is included).

For estimating K_{2a} we assume that the process of removing a hole (i.e. adding an electron) from a gallium divacancy is the same as the corresponding process for a gallium monovacancy. This should be justified as long as the hydrogenic model is valid, that is when the orbit of the hole is large and the binding energy is primarily determined by the dielectric constant. Thus we choose $K_{2a} = K_a$, as shown in Table 2.

We now turn to the slightly more difficult problem of estimating the equilibrium constants for the reactions which involve creation of vacancies and divacancies, i.e. K_s and K_p . K_s has the form

$$K_s = K_s^0 \exp(-H_s/kT)$$

where H_s is the enthalpy of formation of a gallium and an arsenic vacancy (i.e. a Schottky defect). No direct estimate, either theoretical or experimental, is available for H_s in GaAs, so we shall obtain an estimate by comparison with another material. Probably the most suitable material to compare with is Ge. Ge lies between Ga and As in the periodic table, and is isoelectronic with GaAs. The values 2.1 eV[19] and 1.9 eV[20] have been calculated for the formation energy of a vacancy in Ge. We shall therefore assume that the energy of formation of V_{Ga}^x is the same as that for V_{As}^x and equal to 2.0 eV, giving $H_s = 4.0$ eV. We note that from their lattice parameter measurements Potts and Pearson[1] deduced the value 2.0 eV for the formation energy of V_{As}^x ; while this value agrees with the above estimate and allows agreement with their results to be obtained, we shall see in Section 4 that their method for arriving at this value from their experimental results was probably over-simplified. For the pre-exponential factor K_s^0 we see from Table 13.3 in Ref. [11] that typical values for the pre-exponential factors for Schottky defects lie in the range $1-10^8$. In fact we obtain a value $K_s^0 = 1.15 \times 10^4$ in Section 4 by matching with some of the experimental results from Ref. [1]. The resulting value for K_s is shown in Table 2.

To calculate K_p we need a value for the pairing energy H_p between two neutral gallium vacancies. Once again we have to estimate this indirectly by comparison with other systems. As discussed in Chapter 9 of Ref. [11] the vacancy pair is likely to be stabilised by the formation of a bond between the neigh-

Table 2. Provisional values for the equilibrium constants occurring in equations (8-14).

K_i	$1.0 \times 10^{-12} T^3 \exp(-1.88 \times 10^4/T)$	(mole fraction) ²
K_s	$1.15 \times 10^4 \exp(-4.64 \times 10^4/T)$	(mole fraction) ²
K_p	$6.0 \exp(1.36 \times 10^4/T)$	(mole fraction) ⁻¹
K_a	$9.6 \times 10^{-8} T^{3/2} \exp(-510/T)$	(mole fraction)
K_b	$4.9 \times 10^{-9} T^{3/2} \exp(-70/T)$	(mole fraction)
K_{2a}	$9.6 \times 10^{-8} T^{3/2} \exp(-510/T)$	(mole fraction)
K_{AsAs}	$3.8 \times 10^{-4} \exp(-6650/T)$	(mole fraction) ^{1/2} (atmos) ^{1/2}

bouring atoms—that is a bond between neighbouring As atoms in the present case. The diatomic bond energy for a pair of As atoms should therefore give an upper limit to the binding energy of the divacancy. In Table 3

3.80×10^{-4} and $H_{\text{As}2\text{v}} = 0.57$ eV. It is perhaps reassuring that the value obtained for $K_{\text{As}2\text{v}}^0$ is similar to the value 2.5×10^{-4} obtained [11] for the corresponding quantity ($K_{\text{S}2\text{v}}^0$) in studies on PbS. We also note that the value

Table 3. Comparison between the published [21] values of the diatomic bond energy for some Group IV elements, and the values calculated by Hasiguti [22] for the vacancy pairing energy in the corresponding solids

Material	Diatomic bond energy D (eV)	Pair formation energy H_p (eV)	$ H_p/D $
C (diamond)	6.26	1.67	0.267
Si	3.31	0.93	0.284
Ge	2.83	0.84	0.296

a comparison is shown between published [21] values of the diatomic bond energy for some Group IV elements, and calculated [22] values of the vacancy pairing energy in the corresponding solids. While the values of the pairing energy vary by a factor of 2, the ratio of the pairing energy to the bond energy is fairly constant. We assume that this constant ratio applies approximately also for GaAs, and in particular we use the value 0.296, as found for Ge. The diatomic bond energy for As_2 is 3.90 eV [23], and hence we obtain $H_p = -0.296 \times 3.90 = -1.15$ eV. The pre-exponential factor K_p^0 involves the entropy change in the pairing reaction, and this entropy can be separated into a configurational part and a vibrational part. We assume vibrational frequencies are unchanged, so that the entropy change is given by the configurational part, i.e. the \ln of number of configurations for the pair. This leads to $K_p^0 = 6$ [11], and the resulting value for K_p is given in Table 2.

To calculate $K_{\text{As}2\text{v}}$ we need values for $H_{\text{As}2\text{v}}$ and $K_{\text{As}2\text{v}}^0$. At this stage it is preferable to obtain these quantities by matching with the experimental results rather than attempt an *a priori* estimate. By matching with the results from Refs. [1, 2] and [7] we obtain $K_{\text{As}2\text{v}}^0 =$

of $H_{\text{As}2\text{v}}$ is of the order of one-tenth of the sublimation energy for GaAs (6.59 eV [23]), again similar to the situation found for PbS [11].

4. THEORETICAL RESULTS AND COMPARISON WITH EXPERIMENT

In this section we compare calculations based on the expressions in Table 1 with experimental results from Refs. [1, 2] and [7]. First of all we consider the relevant details of these experimental results.

4.1 Details of the experimental results in Refs. [1, 2] and [7]

In the experiments in Ref. [1] GaAs samples were placed in an evacuated ampoule and annealed at various temperatures in the range 1273–1473 K. The change in lattice parameter Δa was then measured. In the absence of further information we assume, as suggested in Ref. [1], that $\Delta a/a$ is a direct measure of the defect concentration. The actual experimental values for $\Delta a/a$ taken from Ref. [1] are shown in Fig. 1; each point is the mean of several measurements and the lines indicate the standard deviation.

From the point of view of making comparison with this data it is important to know the

arsenic pressure in the ampoule. Potts and Pearson state that this would be the equilibrium vapour pressure, implying the vapour pressure along the binary liquidus. This assumption about the vapour pressure would

general starting conditions can be handled by a similar treatment. We do not know the precise starting condition of the material in Ref. [1]. On heating the ampoule As atoms tend to evaporate from the solid, increasing

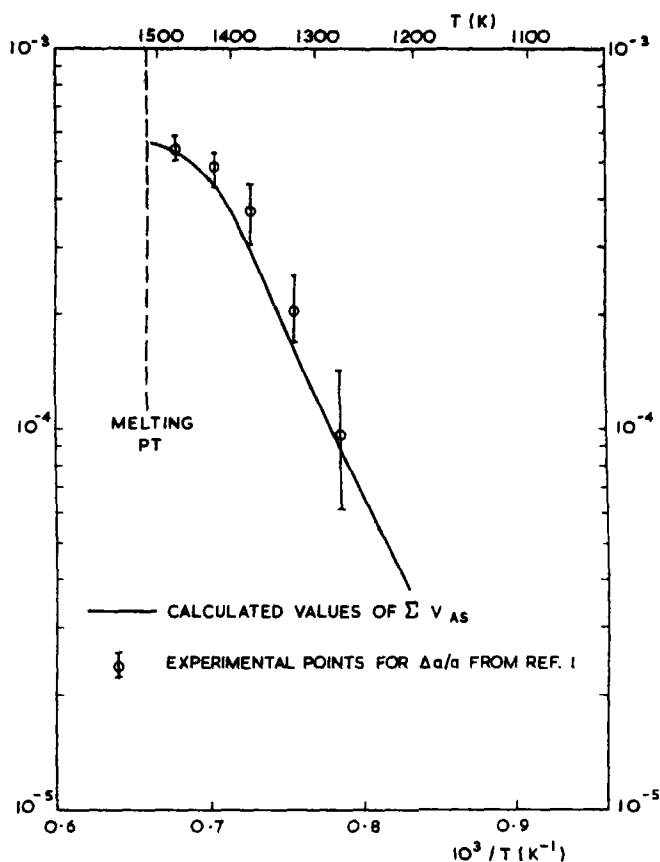


Fig. 1. Comparison between experimental measurements for the relative lattice parameter change from Ref. [1], and theoretical values for ΣV_{As} from equation (27), using values from Table 2.

only be justified if there was some liquid Ga present in the ampoule, and this may not have been the case. Indeed we show below that it probably was not the case over much of the temperature range. To illustrate the behaviour which can occur consider the following situation: A sample of GaAs is placed in a sealed evacuated ampoule. In the present case we assume that material to be initially stoichiometric, although more

the As pressure in the ampoule and forming As vacancies in the solid. From the analysis such as that in Section 2 however we know that $[V_{As}]$ is a function of P_{As} at thermal equilibrium:

$$[V_{As}] = f(P_{As}). \quad (24)$$

But since the arsenic pressure in the ampoule is due to atoms which have left the solid

forming vacancies, the arsenic pressure must be directly proportional to the number of vacancies:

$$P_{As_2} = CT[V_{As}], \quad (25)$$

where the constant C is a function of the size of the ampoule (an expression for C is derived in Appendix 1). This type of relationship between the pressure in an ampoule and the vacancy concentration was also noted by Gasson *et al.*[29] in studies on InAs. We are assuming that the dominant gas species is As_2 , as seems reasonable for the temperatures and pressures under consideration[23]. From equations (24) and (25) we can solve for the pressure in the ampoule and the corresponding value of $[V_{As}]$ at any temperature (as in Section 4.3). The above argument only holds as long as we remain within the existence region of GaAs. This is illustrated

in Fig. 2. The situation described so far corresponds to the composition changing along the path $A \rightarrow B$. If the ampoule is large, and the constant C therefore small, then P_{As_2} would rise only slightly and net evaporation of As atoms could continue until the composition moved all the way across to B' on the solidus line—the pressure would then be fixed by the phase rule. In cases of a 'small' ampoule where the composition moves only over to the intermediate point B , the pressure in the ampoule is *higher* than the corresponding pressure along the boundary liquidus $P_{As_2}(eq)$. This can be seen from the fact that $[V_{As}]$ is lower at B than at B' , and hence the corresponding value of P_{As_2} at B must be higher. These ideas are put in a quantitative form in Section 4.3.

The experiments in Ref. [2] were carried out on GaAs crystals melt grown under an arsenic pressure of 1 atmosphere (the corres-

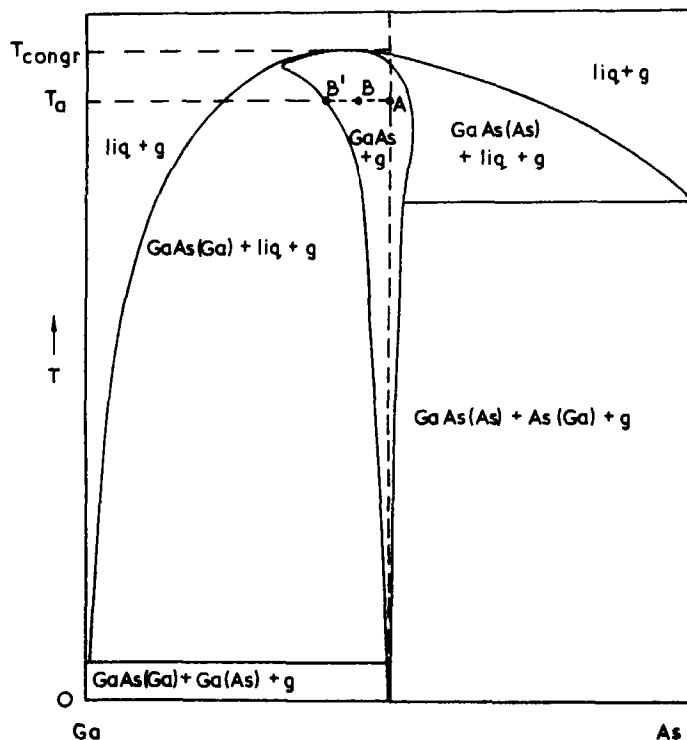


Fig. 2. Hypothetical phase diagram for GaAs. The width of the GaAs phase is exaggerated for clarity.

ponding As_2 pressure being 0.328 atmos [23]). During the internal friction measurements the samples were heated to temperatures in the range 293–673 K. From their results Chakraverty and Dreyfus deduced a defect concentration of at least 8×10^{-5} (mole fraction), the simplest defect consistent with their results being a gallium divacancy. It is clear that close to the melting point (1511 K) the vacancies will be very mobile, and the final (room temperature) defect concentration in a melt grown material will correspond to a temperature somewhat below the melting point, i.e. the temperature at which the defects are 'frozen in' as far as interchange with the gas phase is concerned. For the present numerical calculations we take this temperature as 1473 K, about 40 K below the melting point. Thus we tentatively conclude from Ref. [2] that GaAs at a temperature 1473 K and $P_{\text{As}_2} = 0.328$ atmos contains $[(V_{\text{Ga}})_2]_{\text{CD}} \geq 8 \times 10^{-5}$ mole fraction, or alternatively $[V_{\text{Ga}}]_{\text{CD}} \geq 1.6 \times 10^{-4}$ mole fraction. (The subscript CD denotes Chakraverty and Dreyfus). The latter possibility arises because it is reasonable to assume (as we shall do here) that the defects exist as monovacancies near the melting point, but combine to form mostly divacancies around room temperature—this is consistent with the value of K_p used here. For numerical comparisons we need a specific value and choose $[V_{\text{Ga}}]_{\text{CD}} = 2 \times 10^{-4}$ mole fraction, slightly above the experimental minimum. We note that the experimental technique used in this case would not have detected single vacancies (either V_{Ga} or V_{As}).

In the experiments in Ref. [7] GaAs samples were annealed under various arsenic pressures for a given length of time at a temperature of 1123 K. With this annealing the samples become more p -type, and a plot of the change in carrier concentration as a function of pressure shows a very sharp minimum at a pressure $P_{\text{As}_2} \approx 6.6 \times 10^{-3}$ atmos. (The corresponding pressure of As_2 above GaAs would be 9.3×10^{-4} atmos).

We shall not attempt a full interpretation of the results obtained in Ref. [7], but simply assume that this distinctive minimum is associated with the point of minimum deviation from stoichiometry in the crystal. As we discuss below the pressure at which this minimum deviation from stoichiometry occurs can be expressed in terms of the equilibrium constants already introduced.

4.2 Values of K_s^0 , $K_{\text{As}_2v}^0$ and H_{As_2v} by matching with experiment

The selection of values for K_s^0 , $K_{\text{As}_2v}^0$ and H_{As_2v} by comparison between theory and experiment has been done by a straightforward trial and error procedure, and rather than follow through all the steps we just discuss the solutions obtained for the final chosen values. These solutions, based on the expressions in Table 1, are shown in Fig. 3, plotted against $\log_{10} R$. The solution for each individual defect in each neutrality range is simply a straight line, but we also show two curves representing the quantities $\Sigma V_{\text{As}} = [V_{\text{As}}^{\times}] + [V_{\text{As}}]$ and $\Sigma V_{\text{Ga}} = [V_{\text{Ga}}^{\times}] + [V_{\text{Ga}}'] + 2[(V_{\text{Ga}})_2^{\times}] + 2[(V_{\text{Ga}})_2']$. It is these quantities which we compare with the values from Refs. [1] and [2], which are indicated on Fig. 3 as $[V_{\text{As}}]_{\text{PP}}$ and $[V_{\text{Ga}}]_{\text{CD}}$. (The subscript PP denotes Potts and Pearson). Note that in Fig. 3 only the neutrality ranges 1, 3, 5 and 6 occur (see Table 1).

In calculating the values in Fig. 3 we have had to specify a value for $K_s^0 = 1.15 \times 10^4$, but not for $K_{\text{As}_2v}^0$ and H_{As_2v} because these latter quantities affect only the value of R . In choosing the value for K_s^0 we had to satisfy the following conditions: (1) that suitable concentrations ΣV_{As} and ΣV_{Ga} occur to agree with the values $[V_{\text{As}}]_{\text{PP}}$ and $[V_{\text{Ga}}]_{\text{CD}}$, (2) that the required values ΣV_{As} and ΣV_{Ga} occur at points separated on the R scale by a distance corresponding to the pressure difference between the two experiments. If we assume, as will be confirmed below, that at 1473 K the pressure in the ampoule is given by the pressure along the binary liquidus

Using the values for K_s , K_a and K_b from Table 2 and the value of P_{As_2} stated above we obtain from equation (26), $K_{\text{As}_2\text{v}}(1123) = 10^{-6.00}$ (mole fraction)² (atmos)^{1/2}. Given values of $K_{\text{As}_2\text{v}}$ at these two different tempera-

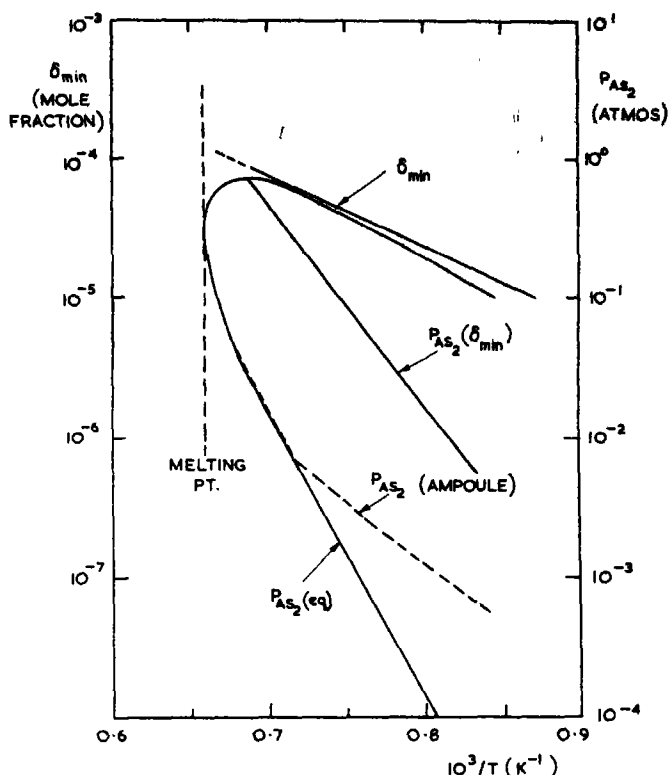


Fig. 4. The lower two curves show the equilibrium vapour pressure along the binary liquidus $P_{As}(eq)$ and the pressure in the ampoule (corresponding to conditions in Ref. [1]) as calculated in Section 4. The upper lines show the minimum attainable deviation from stoichiometry and the corresponding pressure, using values from Table 2.

tures we can solve for the required values $K_{Asv}^0 = 3.80 \times 10^{-4}$, $H_{Asv} = 0.57$ eV. Since we have already ensured the correct separation on the R scale the above value of K_{Asv} (1473) also leads to the required $P_{As} = 0.328$ atmos for the CD case.

4.3 ΣV_{As} and pressure in ampoule as function of temperature

In arriving at the values for K_s^0 , and K_{Asv}^0 and H_{Asv} we have not made use of all the data from Ref. [1], in particular the temperature dependence of the defect concentration as shown in Fig. 1. It is a useful further test of the values selected and the

model used to see whether the theory gives the correct temperature dependence. In this case we must consider carefully the calculation of the pressure in the ampoule for, as will be seen, $P_{As}(eq)$ cannot be used over the whole temperature range. The required analysis was outlined in Section 4.1. Using expressions from Table 1, equation (24) may be written

$$\Sigma V_{As} \equiv [V_{As}^x] + [V_{As}] = (K_s/K_{Asv} P_{As}^{1/2}) + (K_s K_b / K_{Asv} P_{As}^{1/2})^{1/2}. \quad (27)$$

Substituting equation (25) into equation (27) we obtain the following equation for P_{As}

(the pressure in the ampoule)

$$P_{As_2}^{3/2} - CT[(K_s K_b / K_{As_2v})^{1/2} P_{As_2}^{1/4} + (K_s / K_{As_2v})] = 0. \quad (28)$$

The procedure is to solve this equation numerically for P_{As_2} using $C = 1.5 \times 10^{-2}$ (from Appendix 1) and the K -values from Table 2. If the resulting value of P_{As_2} is higher than $P_{As_2}(eq)$ at that temperature then we use this higher value of P_{As_2} in equation (27) to calculate ΣV_{As} . If the value of P_{As_2} from equation (28) is less than $P_{As_2}(eq)$ then we use $P_{As_2}(eq)$ in equation (27). The values of ΣV_{As} obtained are shown in Fig. 1, and it is seen that they follow the experimental results quite closely; the leveling off at high temperatures is directly related to the behaviour of $P_{As_2}(eq)$ at these temperatures (see Fig. 4). Note that in Fig. 3 we have effectively fitted the results at 1473 K, and better overall agreement could possibly be obtained by fitting at another point. It seems unrealistic at this stage, however, to seek closer agreement than that shown in Fig. 1. The form of the theoretical curve in Fig. 1 results from procedures using equations (27) and (28) and there is no obvious simple way of deducing the value of the formation energy of an As vacancy from the slope of this curve as was attempted in Ref. [1].

The values of P_{As_2} corresponding to these values of ΣV_{As} are shown in Fig. 4. It is seen that the pressure in the ampoule exceeds $P_{As_2}(eq)$ for $T < 1400$ and at 1250 K the pressure in the ampoule is about an order of magnitude higher than $P_{As_2}(eq)$. The actual numerical results here are dependent on our assumption (Appendix 1) about the ampoule and sample sizes in the Potts and Pearson experiments, but the qualitative conclusions are not.

4.4 Sensitivity of results to variation in equilibrium constants

The sensitivity of the results to variations in values of all the equilibrium constants is complicated, especially

as changes in these values cause changes in the neutrality ranges which need to be considered. We just consider therefore some simple examples of variations in the values of the two most important equilibrium constants, K_s and K_t , with reference to the situation shown in Fig. 3.

First consider a factor of 10 decrease in K_t . In Range 3, $[V_{As}] \propto K_t^{-1/2}$ and $[V_{Ga}] \propto K_t^{-1/2}$ (see Table 1) and hence the $[V_{As}] = [V_{Ga}]$ line moves up a distance 0.5 (on the log scale). ΣV_{Ga} now coincides with $[V_{Ga}]_{CD}$ at a point much further to the left, and in fact to the left of the point where ΣV_{As} and $[V_{As}]_{PP}$ coincide. This implies that the As pressure to give $[V_{Ga}]_{CD}$ is less than that for $[V_{As}]_{PP}$, which is inconsistent with the experimental situation.

A factor of 10 increase in K_t tends to decrease $[V_{As}]$ and $[V_{Ga}]$, and in fact Range 3 is replaced by Range 2 ($n = p$), somewhat wider than the previous Range 3. The curves for ΣV_{As} and ΣV_{Ga} are shifted downwards, and while one can still find values corresponding to $[V_{As}]_{PP}$ and $[V_{Ga}]_{CD}$, these now occur at points separated by a distance of about 1.0 on the R scale, corresponding to too great a pressure difference between the two experiments (the correct separation is 0.45, as shown above).

We next consider a factor of 10 decrease in K_s . The situation here is similar to that for a corresponding increase in K_t . Range 3 is replaced by Range 2, and the points for matching with $[V_{As}]_{PP}$ and $[V_{Ga}]_{CD}$ are separated by a distance of about 2.0 on the R scale, which is again too large.

A factor of 10 increase in K_s has an effect similar to the corresponding decrease in K_t . Here again the point where ΣV_{Ga} coincides with $[V_{Ga}]_{CD}$ occurs to the left (and therefore at a lower As pressure) of that where ΣV_{As} coincides with $[V_{As}]_{PP}$, which is not consistent with the experiments.

5. NONSTOICHIOMETRY AND EXISTENCE REGION FOR GaAs

With the set of equilibrium constants obtained above (shown in Table 2) we can easily calculate the equilibrium defect concentrations and related properties for any required values of the temperature and pressure (e.g. the As_2 pressure). For example we can calculate the deviation from stoichiometry δ (i.e. the difference in the numbers of the two types of atoms present in the solid) and in particular the minimum value δ_{min} . As discussed in Section 13.4 of Ref. [11] there is a minimum value of δ that one can hope to achieve in practice, and this minimum value and the pressure at which it occurs is a function of the equilibrium constants (in the present case $\delta_{min} = K_t^{1/2}$, $P_{As_2}(\delta_{min}) = K_s K_b / K_a K_{As_2v}^2$). Values of δ_{min} and the corresponding P_{As_2} calculated from the equilibrium

constants in Table 2 are shown in Fig. 4 as a function of temperature. The point corresponding to δ_{\min} at 1473 K is given by the midpoint of Range 3 in Fig. 3.

Using the published values of the arsenic vapour pressure above GaAs (along the binary liquidus) we can calculate the width of the existence region[24] (phase extent) of solid GaAs as a function of temperature. To do this we proceed as follows: At each temperature below the melting point there are two values of the vapour pressure $P_{As}(eq)$ corresponding to the arsenic rich and gallium rich sides of the solid GaAs phase. From results such as those shown in Fig. 3 we can calculate the quantity $\delta = \Sigma V_{As} - \Sigma V_{Ga}$ corresponding to each of these pressures. Plotting these results as a function of temperature gives the shape of the solid phase as shown in Fig. 5. The kink on the right-hand-side (arsenic rich) is a genuine result and occurs as the point (i.e. the value of R) at which we are calculating δ passes from one neutrality regime to another (from Range 3 to Range 5).

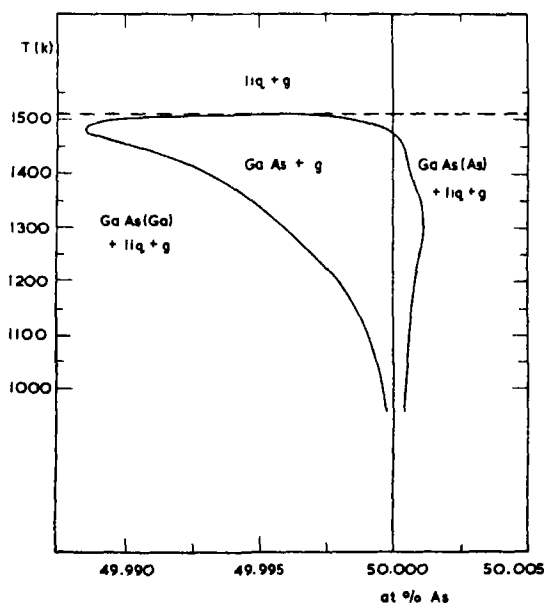


Fig. 5. Calculated existence region for GaAs, using vacancy concentrations based on equilibrium constants in Table 2 and vapour pressures from Ref. [23].

6. DISCUSSION

By a combination of *a priori* estimates and matching with experimental results, a set of equilibrium constants has been derived (Table 2) for the reactions involved in the formation of various neutral and charged vacancies in GaAs. It is encouraging that consistent agreement with the experimental results has been achieved but, in view of the many uncertainties both in the theoretical estimates and the interpretation of the experiments, the set of equilibrium constants obtained must be regarded as provisional until further comparison with experiment is possible. We must also bear in mind the possible occurrence of significant concentrations of interstitials, and other types of native point defects, which have not been included in the present study. The shape of the calculated existence region for GaAs shown in Fig. 5 should obviously be regarded as somewhat tentative until further experimental evidence is available, but one can conclude that the congruently melting solid is definitely Ga rich.

As shown in Section 4 the arsenic pressure in the ampoule during annealing of the GaAs sample, can depend on the relative sizes of the ampoule and sample and can be much greater than the equilibrium vapour pressure along the binary liquidus. This fact should be considered when undertaking or interpreting annealing experiments of this kind.

Finally there is the important question as to the form in which these point defects exist at room temperature. In silicon, for example, there is strong evidence from EPR studies[25] that the vacancy is highly mobile even at room temperature, so that in silicon one expects only very low concentrations of vacancies at room temperature. For III-V compounds such as GaAs there is no evidence that the vacancies are highly mobile, and even if they are this in itself would not eliminate the basic nonstoichiometry which is grown into the material at high temperatures. It seems likely, however, that some changes in the defect structure do occur between high temperature

equilibrium (as considered in this paper) and the room temperature state. In view of the coulomb attraction between V_{Ga} and V_{As} a likely defect to occur is the vacancy pair ($V_{Ga}V_{As}$) [from diffusion studies there is some evidence for ($V_{Ga}V_P$) in GaP[26] and for ($V_{In}V_{Sb}$) in InSb[27]]. It follows from the relevant mass action relation that the concentration of ($V_{Ga}V_{As}$)^x is independent of pressure, and hence would appear as a horizontal line in a plot such as Fig. 3, the actual level of the line being determined by the value of the equilibrium constant for the pairing reaction.

Acknowledgements—The writers are grateful to Drs. W. Bardsley, J. B. Mullin and E. W. Williams of RRE, Dr. J. W. Allen of the University of St. Andrews, and Dr. A. F. W. Willoughby and C. M. H. Driscoll of the University of Southampton for several useful discussions and suggestions in connection with this work. This paper is contributed by permission of the Director of R.R.E. Copyright Controller H.M.S.O.

REFERENCES

- POTTS H. R. and PEARSON G. L., *J. appl. Phys.* **37**, 2098 (1966).
- CHAKRAVERTY B. K. and DREYFUS R. W., *J. appl. Phys.* **37**, 631 (1966).
- BLANC J., BUBE R. H. and WEISBERG L. R., *J. Phys. Chem. Solids* **25**, 225 (1964).
- GOLDSTEIN B. and ALMELEH N., *Appl. Phys. Lett.* **2**, 130 (1963).
- STRAUMANIS M. E. and KIM C. D., *Acta crystallogr.* **19**, 256 (1965).
- OTSUKA H., ISHIDA K. and NISHIZAWA J., *Japan. J. appl. Phys.* **8**, 632 (1969).
- MUNOZ E., SNYDER W. L. and MOLL J. L., *Appl. Phys. Lett.* **16**, 262 (1970).
- FULLER C. S. and WOLFSTIRN K. B., *Appl. Phys. Lett.* **2**, 45 (1963).
- WILLIAMS E. W., *Phys. Rev.* **168**, 922 (1968).
- HWANG C. J., *J. appl. Phys.* **40**, 4584 (1969).
- KRÖGER F. A., *Chemistry of Imperfect Crystals*, North Holland (1964).
- KRÖGER F. A. and VINK H. J., in: *Solid State Physics*, **3**, 307 Academic Press, New York (1956).
- VAN GOOL W., *Principles of Defect Chemistry of Crystalline Solids*, Academic Press, New York (1966).
- BROUWER G., *Philips Res. Rep.* **9**, 366 (1954).
- HILSUM C. and ROSE-INNES A. C., *Semiconducting III-V Compounds*, p. 62, Pergamon Press (1961).
- PANISH M. B. and CASEY H. C., Jr., *J. appl. Phys.* **40**, 163 (1969).
- HALL R. N. and RACETTE J. H., *J. appl. Phys.* **35**, 379 (1964).
- HAMBLETON K. G., HILSUM C. and HOLEMAN B. R., *Proc. Phys. Soc.* **77**, 1147 (1961).
- SWALIN R. A., *J. Phys. Chem. Solids* **18**, 290 (1961).
- BENNEMANN K. H., *Phys. Rev.* **137A**, 1497 (1965).
- Handbook of Chemistry and Physics*, 47th ed., the Chemical Rubber Co. (1966).
- HASIGUTI R. R., in: *Lattice Defects in Semiconductors* (Edited by R. R. Hasiguti), p. 135, University of Tokyo Press (1968).
- ARTHUR J. R., *J. Phys. Chem. Solids* **28**, 2257 (1967).
- ALBERS W. and HAAS C., *Philips Tech. Rev.* **30**, 82 (1969).
- WATKINS G. D., in: *Radiation Effects in Semiconductors*, Proceedings of the Santa Fe Conference 1967, (Edited by L. Vook), p. 67, Plenum Press (1968).
- YOUNG A. B. Y. and PEARSON G. L., *J. Phys. Chem. Solids* **31**, 517 (1970).
- KENDALL D. L. and HUGGINS R. A., *J. appl. Phys.* **40**, 2750 (1969).
- POTTS H. R., Stanford Electronics Laboratories Technical Report No. 5106-2, July 1964.
- GASSON D. B., JENNINGS I. C., PARROTT J. E. and PENN A. W., *Proceedings of the International Conference on Semiconductor Physics*, Exeter 1962, p. 681, Institute of Physics and Physical Society, London (1962).

APPENDIX 1

Relation between ampoule pressure and number of vacancies formed

For simplicity we assume that the material placed in the evacuated ampoule is initially exactly stoichiometric. The expression derived below should however be valid as long as As vacancies are the dominant species, and the concentration of these after annealing is considerably greater than the initial value. In cases where these restrictions do not apply, the same type of analysis can be carried out with slight modifications.

Let the volume of the sample be v and volume of the ampoule be rv . At a stage in the annealing when the vacancy concentration is $[V_{As}]$ (mole fraction), the number of molecules of As_2 in the gas is, since for each As a vacancy formed we have an As atom in the gas phase,

$$n = v n_0 [V_{As}] / 2 \quad (A1)$$

where n_0 = number of molecules cm^{-3} in $GaAs$ ($= 2.2 \times 10^{22}$). Assuming a perfect gas the pressure is therefore,

$$P_{As_2} = nkT / rv = v n_0 [V_{As}] kT / 2rv. \quad (A2)$$

Inserting numerical constants in equation (A2)

$$P_{As_2} = 1.5 [V_{As}] T / r, \quad (A3)$$

where $[V_{As}]$ is in mole fraction units.

We now need to estimate a value for the quantity r (ratio of ampoule volume to sample volume) corresponding to the Potts and Pearson experiment. From Ref. [28] we have the following data: volume of ampoule = 0.5–0.7 cm³; thickness of sample $\approx 2 \times 10^{-2}$ cm; length of sample ≈ 1 cm. No information is given concerning the width of the sample, and we assume a reasonable value 0.25 cm.

Hence

$$r \approx 0.6 / (2 \times 10^{-2} \times 1 \times 0.25) \approx 10^2.$$

Inserting this value in equation (A3) we obtain

$$P_{As} = 1.5 \times 10^{-2} T [V_{As}]. \quad (A4)$$

ANALYSIS OF HEAT TREATMENT AND FORMATION OF GALLIUM-VACANCY-TELLURIUM COMPLEXES IN GaAs

R. M. LOGAN

Royal Radar Establishment, Malvern, Worcestershire, England

(Received 26 October 1970)

Abstract—Recent experimental data published by Hwang provide information on the equilibrium concentration of $V'_{Ga}Te_{As}$ complexes formed on annealing samples of Te-doped GaAs at various temperatures in a sealed evacuated ampoule. A quantitative analysis of these results is presented here; the reaction equations for the formation of the relevant defects and the complex are set up, and an expression for the equilibrium number of $V'_{Ga}Te_{As}$ complexes found by using the mass action relations. For the equilibrium constants governing the formation of the defects in the solid we use the values recently obtained by Logan and Hurler.

The vapour pressure of the constituents (e.g. the As_2 pressure) which builds up in the ampoule during the heat treatment is not in general a function of temperature alone; it depends also on the size of the ampoule, and the defect concentrations in the starting material. A method for calculating this pressure is included in the analysis. The expression derived for the concentration of $V'_{Ga}Te_{As}$ complexes agrees quite well with the data of Hwang, both in its dependence on the initial electron concentration and, using a reasonable value for the binding energy of the complex, in its temperature dependence.

1. INTRODUCTION

IN RECENT papers Hwang[1,2] has shown that efficient hole traps are formed in Te-doped GaAs during annealing, and has identified these traps as Ga-vacancy-Te-donor complexes ($V'_{Ga}Te_{As}$). In these experiments Hwang showed that the number of traps formed is directly proportional to the decrease (Δn) in the electron concentration (i.e. active donor concentration); this enabled him to identify the traps as centres involving Te. He used other evidence to show that they were $V'_{Ga}Te_{As}$ complexes. Results from Ref. [2] for the decrease in electron concentration Δn as a function of annealing time at various temperatures are shown in Fig. 1. It is seen that the equilibrium value of Δn (and hence the concentration of $V'_{Ga}Te_{As}$) is reached more quickly at higher temperatures, as one would expect for a process involving diffusion. On the other hand, the final equilibrium value is seen to be lower at the higher temperatures.

In this paper we present a quantitative

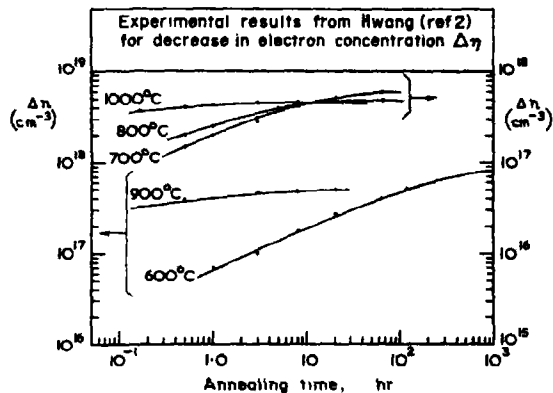


Fig. 1. Results from Fig. 4 of Hwang[2], showing decrease in electron concentration Δn as function of annealing time at various temperatures. As discussed in text, Δn corresponds to $[V'_{Ga}Te_{As}]$.

analysis of some of Hwang's results in the light of recent calculations[3] of point defect concentrations in GaAs. In these calculations [3] methods of equilibrium thermodynamics were used to calculate the concentrations of various defects (As vacancies, Ga vacancies and Ga divacancies) as a function of tempera-

ture and pressure in terms of the relevant equilibrium constants. By a combination of a priori estimates and matching with the experimental data relating to point defects in GaAs reasonable values for the equilibrium constants were obtained (see Table 1).

At a given temperature the $V'_{Ga}Te'_{As}$ concentration depends through a mass action relation on the concentration of gallium vacancies (V_{Ga}), which in turn depends on the vapour pressure (e.g. the As_2 pressure). As discussed below, however, the vapour pressure of the constituents on heat treat-

equations to be considered are as follows:

$$0 \rightleftharpoons e' + h'; E_i \quad (1)$$

$$0 \rightleftharpoons V_{Ga}^x + V_{As}^x; H_s \quad (2)$$

$$V_{Ga}^x \rightleftharpoons V'_{Ga} + h'; E_a \quad (3)$$

$$V_{As}^x \rightleftharpoons V_{As} + e'; E_b \quad (4)$$

$$\frac{1}{2}As_2(g) \rightleftharpoons As_{As}^x + V_{Ga}^x; H_{As_2v} \quad (5)$$

$$V'_{Ga}Te'_{As} \rightleftharpoons Te'_{As} + V'_{Ga}; E_c \quad (6)$$

Table 1. Values for the equilibrium constants occurring in equations (7-11), from Ref. [3]

K_i	$1.0 \times 10^{-12} T^3$	$\exp(-1.88 \times 10^4/T)$	(mole fraction) ²
K_s	1.15×10^4	$\exp(-4.64 \times 10^4/T)$	(mole fraction) ²
K_a	$9.6 \times 10^{-8} T^{3/2}$	$\exp(-510/T)$	(mole fraction)
K_b	$4.9 \times 10^{-9} T^{3/2}$	$\exp(-70/T)$	(mole fraction)
K_{As_2v}	3.8×10^{-4}	$\exp(-6650/T)$	(mole fraction) ² (atmos) ^{1/2}

ment in a sealed ampoule is not in general a function of temperature alone, but depends also on the size of the ampoule and sample, together with the defect concentrations in the starting material. A method for calculating the actual pressure in the ampoule is outlined, and an approximate calculation given for the present case of GaAs. Using the values of the equilibrium constants from Ref. [3] to derive the vacancy concentrations and a reasonable value for the binding energy of the $V'_{Ga}Te'_{As}$ complex, a temperature dependence for its concentration consistent with that found by Hwang is obtained.

2. FORMAL ANALYSIS FOR ANNEALING IN SEALED AMPOULE

We first set up a system of equations which describes the processes involved in the annealing of the sample of Te-doped GaAs in a sealed ampoule. The notation corresponds to that used in Ref. [3] and is based on that used by Kröger [4]; the superscripts x , $'$ and $'$ denote neutral, positive and negative structure elements respectively. The basic reaction

Reactions (1-5) are the same as the basic reactions considered in Ref. [3], although in the present case we have simplified the situation slightly by leaving out of consideration the gallium divacancy ($V_{Ga})_2$. Reaction (6) represents the dissociation of the complex to which we have assigned a binding energy $-E_c$.

Corresponding to each of the above reactions we can write an equilibrium mass action relation. We assume the concentrations of defects are sufficiently low that we can write the mass action conditions in terms of concentrations as follows:

$$np = K_i \quad (7)$$

$$[V_{Ga}^x][V_{As}^x] = K_s \quad (8)$$

$$[V'_{Ga}]p/[V_{Ga}^x] = K_a \quad (9)$$

$$[V_{As}]n/[V_{As}^x] = K_b \quad (10)$$

$$[V_{Ga}^x]/P_{As_2}^{1/2} = K_{As_2v} \quad (11)$$

$$[Te'_{As}][V'_{Ga}]/[V'_{Ga}Te'_{As}] = K_c \quad (12)$$

where the equilibrium constants have the usual form $K = K^0 \exp(-E/kT)$. In writing equation (11) we have assumed $[As_{As}^x] = 1$.

The condition of electroneutrality in the crystal is

$$[Te_{As}] + [V_{As}] + p = [V'_{Ga}] + n. \quad (13)$$

It is consistent with the conditions of Hwang's experiments to approximate this neutrality condition by

$$[Te_{As}] = n. \quad (14)$$

We can also write an equation expressing the fact that the number of Te atoms in the sample is constant:

$$[Te_{As}] + [V'_{Ga}Te_{As}] = B, \quad (15)$$

where B is a constant (for a given sample).

To solve the above equations for the concentrations, in particular $[V'_{Ga}Te_{As}]$, we need to specify the pressure P_{As_2} . As discussed in Ref. [3], however, the pressure in the ampoule is not in general given by the vapour pressure along the binary liquidus (which would be a function of temperature alone), but may depend on the size of the ampoule and the initial and final defect concentrations. In the present calculation we make the following two simplifying assumptions: (1) the final defect concentrations (after annealing) are much greater than those in the original sample; (2) the principal effect of the heat treatment is to create As vacancies in the material. These assumptions are physically reasonable in the present case. A more general analysis without these assumptions is rather intractable, and the extra complication is probably not justified at this stage. The arsenic pressure which builds up in the ampoule is due to arsenic atoms which have left the solid and, given the above two assumptions and assuming the vapour may be treated as a perfect gas, we can relate the arsenic pressure to the vacancy concentrations as follows

$$P_{As_2} = CT([V_{As}^x] + [V_{As}]), \quad (16)$$

where C is a constant. For the temperature and pressure conditions we shall be considering As_2 is the dominant species in the gas phase, rather than, say, As_4 [5].

An expression for C in terms of the size of ampoule and sample is derived in Appendix 1 of Ref. [3]:

$$C = 1.5/r, \quad (17)$$

where r is the ratio ampoule volume/sample volume (for $r \gg 1$). In the case of Hwang's experiments the volume of the samples was $8.65 \times 10^{-3} \text{ cm}^3$ approximately and the volume of the ampoule 2.13 cm^3 approximately [6]. Hence $r \approx 2.5 \times 10^2$ and from equation (17), $C \approx 6 \times 10^{-3}$.

Equations (7-12), (14), (15) and (16) represent a self-consistent set of 9 equations in the 9 unknowns n , p , $[V_{Ga}]$, $[V_{As}^x]$, $[V'_{Ga}]$, $[V_{As}]$, $[Te]$, $[V'_{Ga}Te_{As}]$ and P_{As_2} . In order to make comparisons with Hwang's data it is convenient to solve for $[V'_{Ga}Te_{As}]$ in terms of the various constants and the temperature. The set of equations under consideration is nonlinear, but by a straightforward systematic reduction of variables we arrive at the following expression (for convenience we have put $[V'_{As}Te_{As}] \equiv x$)

$$x(B-x)^{-5/3} \{1 + [(B-x)/K_b]\}^{-1/3} (CT)^{-1/3} \\ = (K_a K_b^{1/3} K_{As_2}^{2/3} K_s^{1/3} / K_i K_c). \quad (18)$$

From equation (18) we can therefore calculate $[V'_{Ga}Te_{As}]$ as a function of temperature for given values of B and C if we know expressions for the various equilibrium constants involved. In the next section we compare the results given by equation (18) with the actual experimental results of Hwang [1, 2].

3. COMPARISON WITH EXPERIMENTAL RESULTS

In Ref. [3] we obtained approximate expressions for the various equilibrium constants appearing in equation (18) (except K_c) and

these are reproduced in Table 1. The main temperature dependence of the equilibrium constants occurs in the exponential terms, and it is convenient to rearrange equation (18) so that these exponential terms are the only T -dependent terms on the r.h.s:

$$x[1 - (x/B)]^{-5/3} \{1 + [(B-x)/K_b]\}^{-1/3} (10^3/T)^{2/3} \\ = D \exp [(-E_a - \frac{1}{2}E_b - \frac{3}{2}H_{Asv} - \frac{1}{2}H_s + E_i + E_c + E_c)/kT], \quad (19)$$

where D is a temperature independent constant involving B , C and parts of the pre-exponential factors from the K 's. If we plot the log of the l.h.s. of equation (19) against $1/T$ we should therefore obtain a straight line with slope corresponding to the energy factor on the r.h.s. On the r.h.s. all the energies except E_c are known (from Table 1).

We now consider the quantities required for the evaluation of the l.h.s of equation (19). The quantity B , the total Te concentration in the samples, is given by the initial electron concentration, which according to Ref. [2] lies in the range $3 - 3.35 \times 10^{18} \text{ cm}^{-3}$; we use here an intermediate value $3.17 \times 10^{18} \text{ cm}^{-3}$. The quantity C has already been discussed in Section 2, its value being 6×10^{-3} . From his experiments Hwang identified the traps formed as $V'_{Ga}Te_{As}$ and hence it follows that the number of traps formed is not only proportional to the decrease in the electron concentration Δn (as stated in Ref. [2]), but is in fact equal to Δn . Thus the quantity $x = [V'_{Ga}Te_{As}]$ corresponds simply to the asymptotic (equilibrium) value of Δn given by the annealing curves in Fig. 4 of Ref. [2]. The range of annealing temperatures covered by these results is from 600 to 1000°C (sample C2-768). The points thus obtained from the l.h.s of equation (19) are shown plotted against $1/T$ in Fig. 2. There is a fair amount of scatter on the points, which is not surprising considering the inaccuracies involved in reading the asymptotic values of

Δn from the annealing curves. A best straight drawn through the points gives a slope corresponding to an activation energy of 0.17 eV. From equation (19) we therefore have

$$-E_a - \frac{1}{2}E_b - \frac{3}{2}H_{Asv} - \frac{1}{2}H_s + E_i + E_c = 0.17 \text{ eV}. \quad (20)$$

Using the values from Table 1 in equation (20) we obtain $E_c = 0.31 \text{ eV}$. As discussed in Section 4 this is a highly reasonable value for the binding energy of the complex.

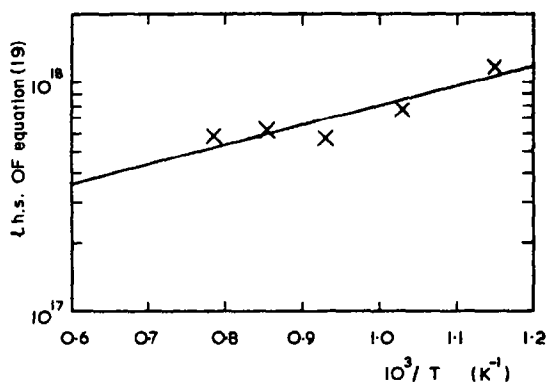


Fig. 2. Left-hand-side of equation (19) against $1/T$, with x taken to be the asymptotic (equilibrium) values of Δn , as obtained from Fig. 1. The slope of the straight line drawn through the points gives an energy 0.17 eV.

There is another aspect of equation (18) which of interest in connection with the results from Refs. [1] and [2], that is the dependence of x (equal to the change in the electron concentration on annealing) on B (the initial electron concentration). Calculating values for K_b from the expression in Table 1 we find that $(B-x)/K_b \gtrsim 1$ for the values of B and x under consideration. It is also evident from Hwang's results that $x \ll B$. From equation (18) we then obtain

$$[V'_{Ga}Te_{As}] \cong B^{5/3} f(T), \quad (21)$$

where $f(T)$ is a function of T involving the equilibrium constants. The only data with which we can compare equation (21) is given

in Fig. 1 (b) of Ref. [1], which gives the decrease in electron concentration Δn , after annealing at 800°C for 3h, as a function of the initial electron concentration; for such an annealing time the values given are not strictly equilibrium values and we have no means of extrapolating these results to obtain equilibrium values. The curve drawn through the experimental points by Hwang is reproduced on a log-log scale in Fig. 3, and it is seen that for values of the initial electron concentration less than about 3×10^{18} the data lie approximately on a straight line of slope 5/3, in agreement with equation (21).

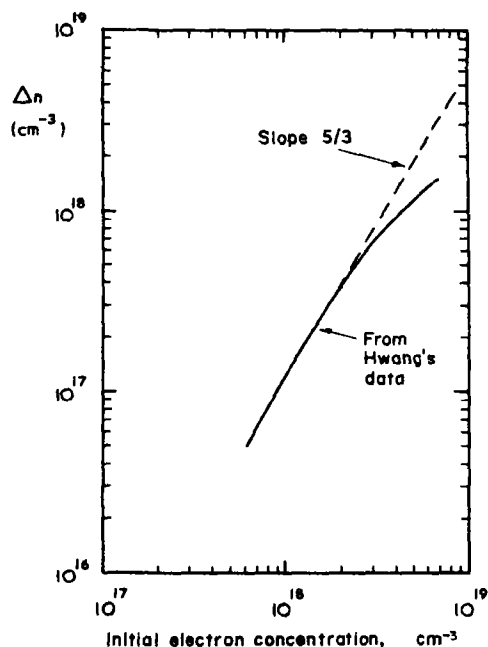


Fig. 3. Decrease in electron concentration against initial electron concentration. We have reproduced on log-log scale the curve drawn through the experimental points by Hwang in Fig. 1(b) of Ref. [1]. For electron concentrations less than about $3 \times 10^{18} \text{ cm}^{-3}$ the data lies approximately on a straight line of slope 5/3, in agreement with equation (21).

4. DISCUSSION AND CONCLUSIONS

There are two general conclusions to be drawn from this work: (a) knowledge of the values for the basic equilibrium constants governing the formation of the relevant

defects in a material (such as the provisional results for GaAs from Ref. [3]) is very helpful in interpreting data on the formation of defect-impurity complexes; conversely, information on the concentrations of such complexes may help one to obtain values for the equilibrium constants in a material; (b) annealing experiments of the type considered in this paper should be interpreted with care. As we have seen, the results obtained at a given temperature may depend (through the constant C) on the size of the ampoule used, and the vapour pressures developed in the ampoule may be much higher than the equilibrium vapour pressures (along the binary liquidus). For example, in the present study the As_2 pressures given by equation (16) are about a factor of ten greater than these equilibrium values.

In Section 3 we have compared two aspects of equation (18) with the experimental results of Hwang for the number of $V'_{\text{Ga}}\text{Te}_{\text{As}}$ complexes formed on annealing. We have first of all shown that if we use a value 0.31 eV for the binding energy of the complex then equation (18) gives a temperature dependence which agrees fairly well with that found experimentally. Although there is apparently no independent value available for the binding energy of this complex (or, in fact, any other impurity-vacancy complex in a III-V compound) this value seems to be reasonable; a simple Coulomb interaction between V'_{Ga} and Te_{As} would give a binding energy $E'_c = e^2/\epsilon r \approx 0.5 \text{ eV}$ (taking $\epsilon = 12.5$ and $r = 2.4 \text{ \AA}$). The actual value $E_c = 0.31 \text{ eV}$ deduced in this paper must be regarded as tentative until further evidence is available, because apart from the several assumptions made in arriving at equation (18), the values of the energies used in equation (20) (as given in Table 1) are themselves only approximate.

We have also shown that the dependence of $[V'_{\text{Ga}}\text{Te}_{\text{As}}]$ on the initial doping level B as predicted by equation (18) agrees very well with the experimental data of Hwang for $B <$

$3 \times 10^{18} \text{ cm}^{-3}$. The fact that agreement breaks down for B values greater than this may be due to the fact that the results used for the comparison in this case were obtained after a fixed annealing time and hence are not necessarily equilibrium values. Another possible cause of the discrepancy at these high electron concentrations is the fact that we have used Boltzmann statistics rather than Fermi-Dirac statistics to describe the electrons and holes in deriving equation (18).

Acknowledgements—I wish to thank Drs. D. T. J. Hurle and E. W. Williams for several useful discussions in connection with this work. This paper is contributed by permission of the Director of RRE. Copyright Controller HMSO.

REFERENCES

1. HWANG C. J., *J. appl. Phys.* **40**, 1983 (1969).
2. HWANG C. J., *J. appl. Phys.* **40**, 4584 (1969).
3. LOGAN R. M. and HURLE D. T. J., **32**, 1739 (1971).
4. KRÖGER F. A., *Chemistry of Imperfect Crystals*, North Holland (1964).
5. ARTHUR J. R., *J. Phys. Chem. Solids* **28**, 2257 (1967).
6. HWANG C. J., private communication.

VALENCE FORCE POTENTIALS FOR CALCULATING CRYSTAL VIBRATIONS IN SILICON*†

A. W. SOLBRIG, JR. ✱

Idaho Nuclear Corporation, Idaho Falls, Idaho 83401, U.S.A.

(Received 17 June 1970; in revised form 14 October 1970)

Abstract—McMurry and co-workers have demonstrated that a valence force potential energy function like that used in molecules is useful for calculating crystal vibrations in diamond. In the work reported here, the valence force potential is tested by application to silicon. Least-squares fit of the six valence force constants used for diamond yields agreement with experiment comparable to that obtained from a nine-parameter shell model by Dolling. A fit with three more valence force constants yields agreement not quite so good as that obtained from an eleven-parameter shell model by Dolling. Parts of our calculated transverse acoustic branches fall systematically outside the experimental error bars. The valence force potential used in this work contains only two types of valence coordinates (bond stretch and angle bend); nevertheless, this valence force potential seems to contain much of the physics of the phonon dispersion relations of silicon.

1. INTRODUCTION

SOME time ago, an excellent fit to the observed dispersion relations for diamond was obtained by use of a valence force potential energy function[1]. The six valence force constants used in this fit were obtained by rather minor adjustment of force constants which fit the vibrational frequencies of a large number of normal paraffin molecules[2]. A comparable fit to the dispersion relations for diamond by use of the shell model required ten constants[3]. The shell model accounts for the observed value of the high frequency dielectric constant, $\epsilon(\infty)$, while the valence model is silent about this parameter.

Because development of the valence force model for crystals may have important consequences for theory of solids as well as for practical application such as neutron moderator theory, it is worthwhile to test the model further by application to other crystals. Application to several crystals (including BeO[4]) is in varying stages of completion at this

location. Much of this effort has been devoted to fitting the dispersion relations for silicon because this crystal has the diamond structure and because rather accurate and complete data for dispersion relations along three directions have been published. In contrast to the diamond case, where all force constants are closely related to those used in calculating the vibrations of organic molecules, data on silicon compounds provide an estimate of only the Si-Si bond stretch constant. It is of interest to note that the primary valence bond stretch constant F_r for diamond is somewhat less than the corresponding force constant for normal paraffin molecules[1]. This result is not unexpected, for the C-C bond length in diamond is slightly greater than in normal paraffin molecules. In the molecules Si_2H_6 and Si_2D_6 , the bond stretch constant is 1.780 ± 0.035 millidynes/Å [5] and the Si-Si bond length is 2.32 ± 0.03 Å [6]. For crystalline silicon, we used a nearest neighbor distance $r_0 = \sqrt{3}a_0/4 = 2.35156$ Å [7]. Since the Si-Si bond length is somewhat larger in crystalline silicon than in Si_2H_6 and Si_2D_6 , the bond stretch constant in crystalline silicon might be expected to be less than the corresponding constant for the molecules.

*A preliminary report of this work was given in Solbrig A. W., Jr., *Bull. Am. phys. Soc.* 15, 102 (1970).

†Work performed under the auspices of the U.S. Atomic Energy Commission.

✱ Deceased, October 17 (1970).

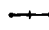







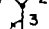
After an earlier version of the present paper was completed, the publication of Singh and Dayal[12] came to our attention. Because their publication treats the same subject as the present paper, we make some comparisons at the close of the following section.

2. SIX-CONSTANT FIT

The results for silicon with six force constants involve only those force constants used for diamond. These results are presented in Table 1 and Fig. 1(a, b, c). In Table 1, the Initial Set of force constants represents a poor

force constants was rather good, and the iterative procedure for improving force constants converged well after two iterations. Because the initial set for silicon was not so good, an additional iteration was needed to obtain the Third Iteration Set listed in Table 1. A partial fourth iteration revealed that the procedure had converged for practical purposes. As expected, the bond stretch constant F_r for crystalline silicon is less than the corresponding force constant for Si_2H_6 and Si_2D_6 . The primary angle bend constant F_ϕ is close to $F_r/50$ in the Third Iteration Set

Table 1. Valence force constants for silicon[a]

Third Force constant				Neighbor order[b]	Initial set	Third iteration set	Nine constant set
F_r	$(\Delta r)^2$;	$\Delta r =$ change in nearest neighbor distance		1	0.65471	1.4850	1.47543
F_ϕ	$r_0^2(\Delta\phi)^2$;	$\Delta\phi =$ change in angle		1, 2	0.06054	0.02944	0.02984
f_{rr}	$\Delta r \Delta r'$;	r and r' have atom in common		1, 2	0.02320	0.02697	0.02305
$f_{r\phi}$	$r_0 \Delta\phi \Delta r$;	r is along a leg of ϕ		1, 2	0.04737	0.03997	0.04050
$f_{\phi\phi}$	$r_0^2 \Delta\phi \Delta\phi'$;	ϕ and ϕ' have common leg and apex		1, 2	-0.00135	-0.00358	0.00306
$f_{\phi\phi}^*$	$r_0^2 \Delta\phi \Delta\phi'$;	all legs coplanar		1, 2, 5	0.01513	0.02922	0.03564
$f_{\phi\phi}^{(1)}$	$r_0^2 \Delta\phi \Delta\phi'$;	legs 1, 2, 3 coplanar		1, 2, 5, 6, 3	—	—	0.00423
$f_{\phi\phi}^{(2)}$	$r_0^2 \Delta\phi \Delta\phi'$;	leg 4 out of plane		1, 2, 3, 4	—	—	0.00717
$f_{\phi\phi}^{(3)}$	$r_0^2 \Delta\phi \Delta\phi'$;	plane of legs 1, 2 \perp plane of legs 3, 4		1, 2, 3	—	—	-0.00401

[a] All units are millidynes/Å. Five decimal places are often used for internal check purposes, but all the places are not physically significant.

[b] The first-order neighbor is the nearest neighbor, second-order is next nearest, etc.

guess obtained by multiplying the Final Value force constants for diamond[1] by a constant factor. The constant factor was obtained by a simple method mentioned in Ref. [11], Appendix A. (Later we discovered a much better method, discussed below, for estimating some of the force constants for diamond structures.) The numerical methods and target points used to improve this Initial Set of force constants were almost identical to those used for diamond[1].

In the case of diamond, the initial set of

for silicon. In diamond and in organic molecules, F_ϕ is approximately $F_r/10$.

The calculated six-constant curves for silicon fail to fit several of the observed points within experimental error[8, 9]. The most obvious failures are (a) the longitudinal sound speed along Δ , (b) the longitudinal acoustic branch along Λ near the zone boundary, and (c) the acoustic I branch along Σ near the hump. This fit by the valence force model (short-range forces only, six adjustable force constants) is comparable to that achieved by

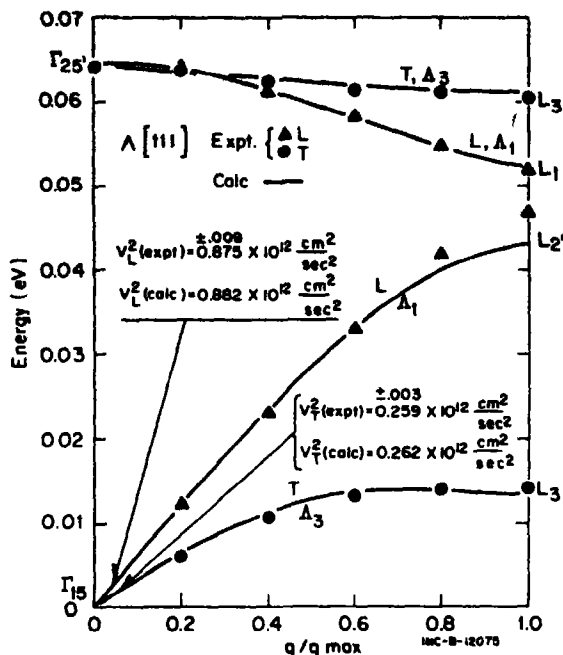


Fig. 1(a).

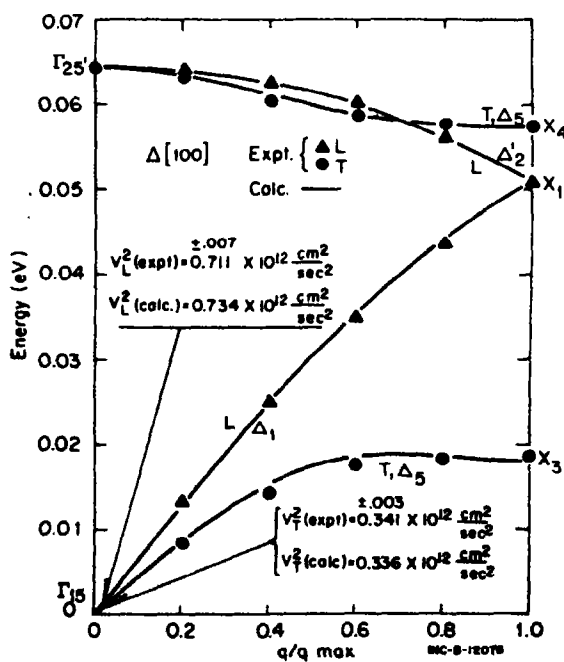


Fig. 1(b).

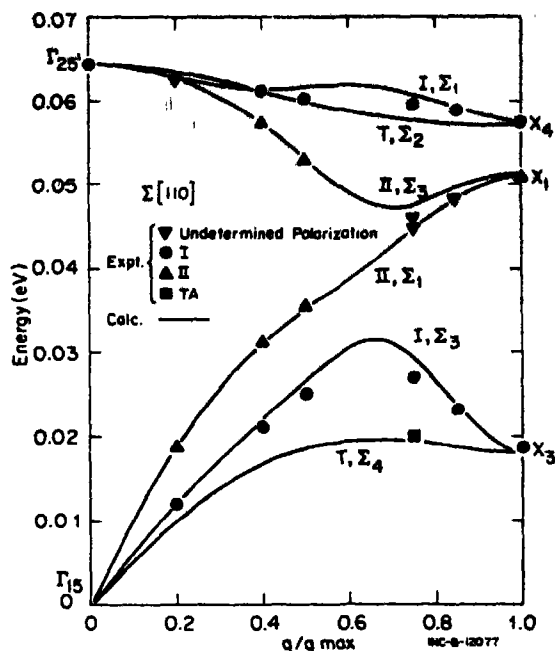


Fig. 1(c). Dispersion relations for silicon. Experimental results are from Dolling[8] and McSkimin[9]. The single experimental point on the Σ_4 branch is from Palevsky *et al.*[10]. Calculations employ the six-force constants listed in Table 1 under 'Third Iteration Set'.

Dolling[8] with his shell model 11a (includes Coulomb forces, nine adjustable parameters). Clearly our six-constant fit is not so satisfactory as that achieved by Dolling[8] with his shell model 11c (includes Coulomb forces, eleven adjustable parameters).

Singh and Dayal[12] have published fits to the silicon data by use of valence potentials.* They give no quantitative information about the accuracy of their fits to sound speeds. (Figs. 1 and 2 of Ref. [12] are not adequate to yield this information quantitatively, although

*There is a mistake in Ref. [17] of Singh and Dayal, which is given as J. K. Boyter *et al.*, USAEC Report No. IN-128. This should in fact read IN-1280. In addition, Ref. [23] is incomplete; the progress report referred to is USAEC Report No. IN-1218 (1968). Preliminary accounts of our results with a six-constant fit are presented in the latter, while results with a nine-constant fit are described in USAEC Report No. IN-1317 (January 1970).

it is evident qualitatively from Fig. 1 of Ref. [12] that the fit to sound speeds with three force constants is poor.) Since the fit to experimental sound speeds is crucial for silicon, it is not possible to appraise the six-constant fit of Ref. [12] without better information about the calculated sound speeds. In order to obtain some of this information, we inserted the Final Set of six force constants from Table 2 of Ref. [12] and the lattice parameter of

fairly simple force constants of the type often used in fitting molecular vibrations. Five of these force constants involve no neighbors beyond the second, but the sixth force constant introduces a fifth neighbor. Force constants involving third and fourth neighbors are not used in the six-constant set. In order to improve the fit to the dispersion relations for silicon, it seemed worthwhile to introduce a few more types of valence force constants,

Table 2. Valence force constants for diamond structure[a]

$f_{rr}^{(1)}$	$\Delta r \Delta r'$	all legs coplanar	
$f_{rr}^{(2)}$	$\Delta r \Delta r'$	leg 3 out of plane	
$f_{rr}^{(3)}$	$\Delta r \Delta r'$	legs 1 and 4 coplanar	
$f_{r\phi}^{(1)}$	$r_0 \Delta r \Delta \phi$	all legs coplanar	
$f_{r\phi}^{(2)}$	$r_0 \Delta r \Delta \phi$	r and ϕ have apex only in common	
$f_{r\phi}^{(3)}$	$r_0 \Delta r \Delta \phi$	leg 3 out of plane	
$f_{\phi\phi}^{(1)}$	$r_0^2 \Delta \phi \Delta \phi'$	all legs coplanar	
$f_{\phi\phi}^{(2)}$	$r_0^2 \Delta \phi \Delta \phi'$	ϕ and ϕ' have apex atom only in common	
$f_{\phi\phi}^{(3)}$	$r_0^2 \Delta \phi \Delta \phi'$	leg 3 out of plane	
$f_{\phi\phi}^{(4)}$	$r_0^2 \Delta \phi \Delta \phi'$	legs 1 and 4 coplanar	
$f_{\phi\phi}^{(5)}$	$r_0^2 \Delta \phi \Delta \phi'$	legs 2, 3, 4 coplanar, leg 1 out of plane	
F_R	$(\Delta R)^2$	ΔR = change in second neighbor distance	
F_τ	$(r_0 \Delta \tau)^2$	$\Delta \tau$ = change in dihedral angle, all legs coplanar	
$F_\tau^{(1)}$	$(r_0 \Delta \tau')^2$	$\Delta \tau'$ = change in dihedral angle, one leg out of plane	

[a] These force constants are all zero in the sets listed in Table 1. See Table 3 and accompanying text for further discussion.

[b] WILSON E. B., JR., DECIUS J. C. and CROSS P. C., *Molecular Vibrations*, pp. 60-61. McGraw-Hill, New York (1955).

Ref. [12] into our equations (9) and (10) below. The results show that the calculated squares of some six-constant sound speeds in Ref. [12] are 1.7 per cent high (v_L^2 along Δ) and 7.2 per cent low (v_{T2}^2 along Σ). Both of our corresponding calculated values are 3.2 per cent high.

3. IMPROVED FIT

1. General

The treatment above involves only six

especially those involving third and fourth neighbors. In Table 1 (last three rows), Table 2 and Table 3 there are listed some characteristics of 17 other force constants which might be used in the diamond structure.

The tabulated force constants contain three sets of redundant force constants: (a) $F_\phi, f_{\phi\phi}, f_{\phi\phi}^{(2)}$; (b) $f_{r\phi}, f_{r\phi}^{(2)}$; and (c) $F_\tau, F_\phi, f_{rr}, f_{r\phi}, F_R$. We believe that there are no other redundant sets in the tabulated constants. A set of redun-

Table 3. Neighbor order[a] in valence force constants for diamond structure

Force constant	Neighbor order	Force constant	Neighbor order
$f_{rr}^{(1)}$	1, 2, 5	$f_{\phi\phi}^{(2)}[b]$	1, 2
$f_{rr}^{(2)}$	1, 2, 3	$f_{\phi\phi}^{(3)}$	1, 2, 3
$f_{rr}^{(3)}$	1, 2, 3	$f_{\phi\phi}^{(6)}$	1, 2, 3
$f_{r\phi}^{(1)}$	1, 2, 5	$f_{\phi\phi}^{(8)}$	1, 2, 3, 5
$f_{r\phi}^{(2)}[b]$	1, 2	$F_R[b]$	2
$f_{r\phi}^{(3)}$	1, 2, 3	F_r	1, 2, 5
$f_{\phi\phi}^{(1)}$	1, 2, 5, 8	$F_r^{(1)}$	1, 2, 3

[a] The first-order neighbor is the nearest neighbor, second-order neighbor is next nearest, etc.

[b] These constants belong to sets of redundant constants. See accompanying text for further discussion.

dant force constants has the following property: Any dispersion relation (wave vectors along a symmetry direction or not) calculated by use of a set of redundant constants can be reproduced by fixing *one* of the constants at zero and suitably adjusting the remaining constants of the set. For example, any dispersion relation (wave vectors along a symmetry direction or not) calculated with $f_{r\phi}^{(2)} = f_{r\phi 1}^{(2)}$ (a number) and $f_{r\phi} = f_{r\phi 1}$ (a number) can be reproduced by fixing $f_{r\phi}^{(2)} = 0$ and $f_{r\phi} = f_{r\phi 1} - f_{r\phi 1}^{(2)}$. Because of this property, there is no further use or mention of $f_{\phi\phi}^{(2)}$, $f_{r\phi}^{(2)}$, or F_R in this report.

For the fitting with only six valence force constants, the 13 'target' points of Ref. [1] seemed adequate. For fitting with more than six force constants, the following 12 additional target points were employed: 5 points along direction Δ (LA and TA at $q/q_{\max} = 0.4$ and all 3 points at $q/q_{\max} = 1$), 6 points along direction Λ (LA and TA at $q/q_{\max} = 0.4$ and all 4 points at $q/q_{\max} = 1$), and one point along direction Σ (the acoustic I point at $q/q_{\max} = 3/4$). At the time the additional target points were inserted, the target for the Raman optical intercept from neutron data was replaced by a slightly shifted but much more accurate value from optical data [13].

To date our fitting of silicon has made use of selected subsets of the following 18 valence force constants: The 9 constants of Table 1

plus the 9 constants $f_{rr}^{(1)}$, $f_{rr}^{(2)}$, $f_{rr}^{(3)}$, $f_{r\phi}^{(1)}$, $f_{r\phi}^{(3)}$, $f_{\phi\phi}^{(1)}$, $f_{\phi\phi}^{(3)}$, $f_{\phi\phi}^{(6)}$, and $f_{\phi\phi}^{(8)}$ from Tables 2 and 3. (We have not yet tried the dihedral angle force constants F_r and $F_r^{(1)}$.) The procedure of searching for a fit was roughly as follows: (a) Examine all 12 possible sets of 7 force constants constructed by adjoining one additional force constant to the initial 6 force constants. (b) Examine all 66 possible sets of 8 force constants constructed by adjoining 2 additional force constants to the initial 6 force constants. (c) Examine all 220 possible sets of 9 force constants constructed by adjoining 3 additional force constants to the initial 6 force constants.

In the course of this work, we became aware of certain simple relations which (if known sooner) would have led to a much better initial set. Consider a crystal such as silicon with the diamond structure, atomic mass m , and interatomic spacing $r_0 = \sqrt{3} a/2$. In terms of the 9 force constants of Table 1 only, some of these relations are as follows [15]:

$$\omega^2(\Gamma_{25'}) = \frac{8}{3m}(F_r + 8F_\phi - 2f_{rr} - 8\sqrt{2}f_{r\phi} + 16f_{\phi\phi}^* - 32f_{\phi\phi}^{(5)} - 32f_{\phi\phi}^{(7)}) \quad (1)$$

*We are indebted to Dr. T. G. Worlton for programming a modification (unpublished) of Adjuster [14] to simplify some of the work of this search.

$$\omega^2(X_4) = \frac{8}{3m} \left(F_r + \frac{1}{2} F_\phi - 2f_{rr} - 2\sqrt{2}f_{r\phi} \right) \quad (2)$$

$$\omega^2(X_1) = \frac{8}{3m} \left(\frac{1}{2} F_r + 5F_\phi + f_{rr} - 2\sqrt{2}f_{r\phi} - 6f_{\phi\phi} + 8f_{\phi\phi}^* - 4f_{\phi\phi}^{(4)} \right) \quad (3)$$

$$\omega^2(X_3) = \frac{12}{m} F_\phi \quad (4)$$

$$\omega^2(L_{3'}) = \frac{8}{3m} \left(F_r + \frac{17}{4} F_\phi - 2f_{rr} - 5\sqrt{2}f_{r\phi} - \frac{9}{4}f_{\phi\phi} + 8f_{\phi\phi}^* - \frac{15}{2}f_{\phi\phi}^{(4)} - 4f_{\phi\phi}^{(7)} \right) \quad (5)$$

$$\omega^2(L_1) = \frac{2}{m} F_r \quad (6)$$

$$\omega^2(L_{2'}) = \frac{8}{3m} \left(\frac{1}{4} F_r + 8F_\phi + f_{rr} - 2\sqrt{2}f_{r\phi} + 8f_{\phi\phi}^* - 16f_{\phi\phi}^{(7)} \right) \quad (7)$$

$$\omega^2(L_3) = \frac{6}{m} (F_\phi - f_{\phi\phi} + 2f_{\phi\phi}^{(4)}) \quad (8)$$

$$C_{11} + 2C_{12} = \frac{1}{2a} (F_r + 6f_{rr}) \quad (9)$$

$$C_{11} - C_{12} = \frac{3}{a} (F_\phi - 2f_{\phi\phi} + 2f_{\phi\phi}^* - 4f_{\phi\phi}^{(4)} + 4f_{\phi\phi}^{(3)} + 4f_{\phi\phi}^{(7)}) \quad (10)$$

Relations giving a frequency squared as a linear combination of valence force constants exist at many points in wave vector space. More precisely, such relations exist wherever in the reduction of the dynamical matrix an irreducible representation occurs just once (regardless of the dimensionality of the irreducible representation). If an irreducible representation occurs n times, then a similar relation exists for $\sum_{i=1}^n \omega_i^2$. In any

further fitting for silicon, we hope to take more explicit advantage of various simple relations resembling (1-10).

2. RESULTS AND DISCUSSION

A best fit to data by a valence force field is depicted in Fig. 2(a, b, c). This fit is based on the 'Nine Constant Set' listed in Table 1. The fit to the sound speeds squared in Fig. 2(a, b) is fairly good. These sound speeds squared were used as targets in the fitting procedure. The calculated sound speeds squared along direction Σ are (in units of $10^{12} \text{ cm}^2 \text{ sec}^{-2}$) $v_L^2 = 0.837$, $v_{T1}^2 = 0.339$ and $v_{T2}^2 = 0.215$ compared to the experimental values [9] of 0.834 ± 0.008 , 0.341 ± 0.003 , and 0.218 ± 0.002 . The major remaining discrepancies are on the transverse acoustic branches along Δ and Λ . These discrepancies are small, but they are systematic and probably significant. The fit is not quite so good as that obtained by Dolling[8] with his shell model IIc (includes Coulomb forces, eleven adjustable parameters). In both of the fits for silicon reported here $\omega(L_1) > \omega(L_{2'})$ as indicated in Figs. 1(a) and 2(a), while for diamond $\omega(L_1) < \omega(L_{2'})$ [3, 16].

It may be that there exists a set of nine or fewer valence force constants which yields a completely satisfactory fit to the dispersion relations for silicon, but we have not yet found such a set. A valence field containing nine (or possibly fewer than nine) force constants does yield an almost satisfactory fit. All of the valence force constants tried so far for silicon make use of only two types of valence coordinates: bond stretch and angle bend. It should be worthwhile to try other types of valence coordinates, especially the two dihedral angle valence coordinates involving third and fifth neighbors (Tables 2 and 3 and Ref. [17]). Perhaps inclusion of these coordinates will allow a satisfactory fit to the silicon dispersion relations by only eight or nine valence force constants.

The valence force field seems to contain much of the physics of the phonon disper-

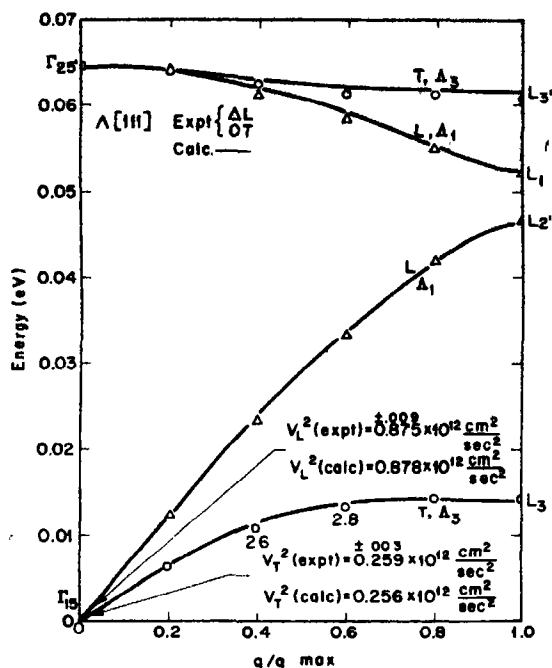


Fig. 2(a).

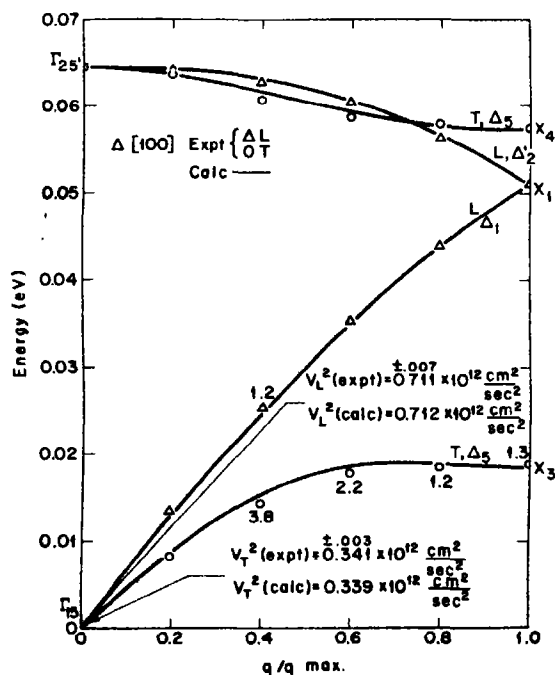


Fig. 2(b).

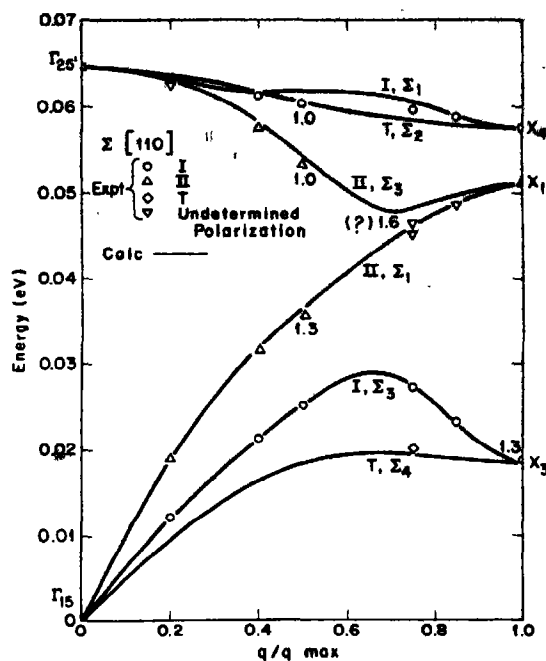


Fig. 2(c). Dispersion relations for silicon. Calculations employ the force constants listed in Table I under 'Nine Constant Set'. The numbers close to some of the experimental points are values of $|(\text{calculated energy} - \text{experimental energy})/(\text{experimental error})|$, where experimental results are given [8] in the form 'experimental energy \pm experimental error'. This number is not given if its value is less than unity.

sion relation of silicon. Small effects not included in the valence field may involve electrostatic interactions or other mechanisms[18]. An unsuccessful attempt was made to improve the six-constant fit by inclusion of a one-parameter electrostatic interaction based on the 'simple bond charge' model of Martin[19]. The results indicate that there may be too much duplication, or similarity, between the contribution to the potential energy from the valence forces and the contribution from the simple bond charge. In the spirit of the valence force approximation, we have set up a model which includes (in addition to the shortrange valence field) electronic polarizability and other electrostatic effects[20]. This model contains some intuitively appealing and perhaps novel fea-

tures. It is directly applicable to crystals such as BeO or GaAs in which long-range electrostatic effects are an essential part of a model which reproduces the observed dispersion relations. For silicon, the electrostatic effects are probably 'intermediate' in range. In the future, we hope to apply the model to silicon and to see if the six-constant valence field plus two or three constants for electrostatic effects will yield a satisfactory fit.

Acknowledgements—This work was made possible by the encouragement and support of Dr. R. M. Brugger, Manager of the Nuclear Technology Branch and Dr. H. L. McMurry.

REFERENCES*

1. McMURRY H. L., SOLBRIG A. W., JR., BOYTER J. K. and NOBLE C., *J. Phys. Chem. Solids* **28**, 2359 (1967).
2. SCHACHTSCHNEIDER J. H. and SNYDER R. G., *Spectrochim. Acta* **19**, 117 (1963).
3. WARREN J. L., YARNELL J. L., DOLLING G. and COWLEY R. A., *Phys. Rev.* **158**, 805 (1967).
4. OSTHELLER G. L., SCHMUNK R. E., BRUGGER R. M. and KEARNEY R. J., In *Neutron Inelastic Scattering*, Vol. 1, p. 315, International Atomic Energy Agency, Vienna (1968). SOLBRIG A. W., JR., in USAEC Report, p. 149, IN-1218 (1968).
5. PFEIFFER M. and SPANGENBERG H.-J., *Z. phys. Chem.* **232**, 47 (1966).
6. BROCKWAY L. O. and BEACH J. Y., *J. Am. chem. Soc.* **60**, 1836 (1938).
7. WYCKOFF R. W. G., *Crystal Structures* (Second Edition), Vol. 1, p. 26, Interscience Publishers, New York (1963), gives $a_0 = 5.43070 \text{ \AA}$ for silicon at 25°C .
8. DOLLING G., In *Inelastic Scattering of Neutrons in Solids and Liquids*, Vol. 2, p. 37, International Atomic Energy Agency, Vienna (1963).
9. McSKIMIN H. J., *J. appl. Phys.* **24**, 988 (1953). According to McSKIMIN, "Overall uncertainties in velocity are estimated to be less than 0.5 per cent"; consequently, we have attempted to fit sound speeds squared to within ± 1 per cent.
10. PALEVSKY H., HUGHES D. J., KLEY W. and TUNKALO E., *Phys. Rev. Lett.* **2**, 258 (1959).
11. BOYTER J. K. and SOLBRIG A. W., JR., *MACS J-A Program for Computing Crystal Phonon Dispersion Relations, Structure Factors for Neutron Inelastic Scattering, and Jacobian Matrices*, USAEC Report IN-1147 (1968).
12. SINGH B. D. and DAYAL B., *Phys. Status solidi* **38**, 141 (1970).
13. PARKER J. H., JR., FELDMAN D. W. and ASHKIN M., *Phys. Rev.* **155**, 712 (1967).
14. BOYTER J. K. and McMURRY H. L., *ADJUSTER - A Force Constant Adjuster Program to Obtain Least Squares Fit to Observed Frequencies of Molecules and Crystals*, USAEC Report IN-1148 (1967).
15. MUSGRAVE M. J. P. and POPL E. A., *Proc. R. Soc. A* **268**, 474 (1962), include (1), (9), and (10) for the special case of no interaction beyond the second neighbor.
16. In Fig. 2 of Ref. [1], group theoretical labels are not given at zone boundaries; but the calculations at the point $L(q/q_{\max} = 1$ along direction Λ) show $\omega(L_x) > \omega(L_y) > \omega(L_z)$, in agreement with results of Ref. [3].
17. HERMAN F., *J. Phys. Chem. Solids* **8**, 405 (1959). has given consideration to these force constants in germanium for the special case $F_r = F_r^{(1)}$.
18. DRESSELHAUS G. and DRESSELHAUS M. S., *Int. J. quantum Chem.* **11** (Symposium), 333 (1968). We wish to thank Profess G. Dresselhaus for sending additional details of this work.
19. MARTIN R. M., *Chem. Phys. Lett.* **2**, 268 (1968). We wish to thank Dr. Martin for supplying unpublished numerical values of his electrostatic dynamical matrix.
20. SOLBRIG A. W., JR., USAEC Report IN-1409 (1970). SUITT W. J., Computer Program P01800, dated July 1970. An extension of the model applicable to molecular crystals is described by McMURRY H. L., USAEC Report IN-1410 (1970).

*Computer programs referred to are available from Computer Science Center, Idaho Nuclear Corporation, Idaho Falls, Idaho 83401, U.S.A.

ANHARMONIC PROPERTIES OF THE HEXAGONAL METALS, MAGNESIUM, ZINC AND BERYLLIUM-I. LATTICE DYNAMICS AND THIRD ORDER ELASTIC CONSTANTS

R. SRINIVASAN and R. RAMJI RAO

Department of Physics, Indian Institute of Technology, Madras 36, India

(Received 14 October 1970)

Abstract—The lattice dynamics and the anharmonic properties of the hexagonal metals magnesium, zinc and beryllium have been worked out utilising the approach of Keating. In Magnesium, the dispersion curves are fitted using ten second order parameters and the six second order elastic constants are evaluated. The ten third order elastic constants are calculated using three third order parameters. The experimental measurements on the pressure derivatives of the second order elastic constants in magnesium are in good agreement with the calculated values. The dispersion relations and the second order elastic constants in zinc are fitted using twelve second order parameters. The third order elastic constants of zinc evaluated with the use of three anharmonic parameters are in good agreement with experiment. The dispersion curves and the second order elastic constants of beryllium are obtained using twelve second order parameters. The three third order parameters are obtained from the measured pressure derivatives of three of the second order elastic constants and the third order elastic constants of this metal are computed. The anisotropic thermal expansion of these metals on the present model will be discussed in Section 2 of this paper.

1. INTRODUCTION

IN RECENT years the thermal expansion data of a number of hexagonal metals have become available. These data down to liquid helium temperature have been reviewed by Munn[1]. There has so far been no attempt to calculate theoretically the temperature variation of the thermal expansion of these metals. The third order elastic constants of Zinc have recently been determined by Schwartz and Elbaum[2] and the pressure derivatives of the second order elastic constants of magnesium[3] and beryllium[4] are available in the literature.

The dispersion relations in magnesium have been studied experimentally by Iyengar *et al.* [5] who have used a 11 parameter tensor force model to fit their dispersion data. Squires[6] has extended these measurements to more directions of wave propagation in the Brillouin zone. The dispersion relations in beryllium were studied by neutron scattering by Schmunk *et al.*[7], and in zinc by Borgonovi *et al.*[8].

DeWames *et al.*[9] used a modified axially

symmetric force model with thirteen force constants in beryllium and seventeen force constants in zinc to explain the dispersion relations in these metals with success. Since then several attempts have been made to explain the dispersion curves in these metals from a model pseudopotential. The earlier attempts were not successful. But more recently some model pseudopotentials have been constructed which explain the dispersion relations in beryllium[10] and magnesium[11] quite well.

In this paper we employ Keating's[12] method of writing the potential energy in terms of the powers of the changes in the scalar products of interatomic vectors. Keating's approach is essentially the same as the coupling parameter approach, but it has the advantage that the potential energy expansion is automatically invariant towards a rigid rotation or translation of the lattice. In the coupling parameter approach these conditions have to be applied separately. Srinivasan[13] has shown that, in a simple lattice like ger-

manium with second and third order coupling parameters extending up to second neighbours, the rotational and translational invariance conditions lead to fifteen relations among the second and third order parameters. In the hexagonal metals with forces extending up to fifth neighbours the inclusion of the anharmonic terms in the coupling parameter approach will lead to an unmanageable number of parameters and a large number of inter-connecting relations. Keating's method of writing the potential makes the problem of computing the anharmonic properties of these materials tractable.

In Section 1 of this paper, Keating's approach is used to derive expressions for the elements of the dynamical matrix and the second and third order elastic constants of these metals. It is shown that a fit to the dispersion curves and the second order elastic constants of these metals nearly as good as that with the modified axially symmetric model of DeWames *et al.*[9] is obtained with the present method with a smaller number of parameters. It is also shown that with a choice of three anharmonic parameters the pressure derivatives of the second order elastic constants of these metals can be satisfactorily accounted for. In zinc, in which individual third order elastic constant data are available a comparison is made with the theoretically calculated values. Section 2 of this paper will discuss in detail the behaviour of anisotropic thermal expansion of these metals.

2. POTENTIAL ENERGY EXPRESSION USING KEATING'S APPROACH

The basic vectors of the lattice are

$$\mathbf{a}_1 = D\left(\frac{\sqrt{3}}{2}, \frac{1}{2}, 0\right)$$

$$\mathbf{a}_2 = D(0, 1, 0)$$

$$\mathbf{a}_3 = D(0, 0, p)$$

referred to a rectangular cartesian system of

axes*. Here D is the nearest neighbour distance in the basal plane (i.e. $D = a$ is the length of the edge of the hexagonal section perpendicular to the unique axis) and p is the axial ratio c/a . There are two nonequivalent atoms in the unit cell at $\mathbf{r}(1) = D(0, 0, 0)$ and $\mathbf{r}(2) = D(1/2\sqrt{3}, 1/2, p/2)$. The atom 1 in the basis cell has three sets of neighbours of the same type and three other sets of neighbours of the nonequivalent type 2. Appendix 1 lists the position coordinates of these neighbours and the symbols used to designate them. The wave vectors of the lattice waves are given by

$$\mathbf{q} = 2\pi(q_1\mathbf{b}_1 + q_2\mathbf{b}_2 + q_3\mathbf{b}_3)$$

where the vectors \mathbf{b}_i are reciprocal to the vectors \mathbf{a}_i . q_i lie between -0.5 and $+0.5$.

The potential energy of interaction is written up to the sixth neighbours. Two and three body interactions are taken into account. Since anharmonic properties are to be calculated second and third powers of the changes in the scalar products of interatomic vectors have to be included. Third order parameters are assumed to be non-zero only for two body interactions. This implies that only the central part of the interaction is important for anharmonic properties, an assumption already used by Cowley *et al.*[14, 15] in the treatment of alkali halides, germanium and silicon. No third order terms are included in the three body interactions.

The various contributions to the potential energy are listed below.

(a) Two body potential between nearest neighbours in the basal plane: These neighbours are designated by the letter I.

*Conventionally \mathbf{a}_1 is chosen as the Y axis; but here \mathbf{a}_2 is chosen as the Y axis. In conventional notation (01 $\bar{1}$ 0) direction is normal to one of the sides of the hexagon; in the present notation $(q_1, 0, 0)$ is this direction. (11 $\bar{2}$ 0) is a direction joining the centre to one of the corners of the hexagon. In the present notation this corresponds to $(q_1, -q_1, 0)$.

$$\phi_a^{(2)} = \frac{1}{2} \sum_L \sum_{\mu=1}^2 \sum_{l=1}^6 \left\{ \frac{1}{2} \alpha \left(\mathbf{R}' \left(\begin{smallmatrix} LL+I \\ \mu \quad \mu \end{smallmatrix} \right) \cdot \mathbf{R}' \left(\begin{smallmatrix} LL+I \\ \mu \quad \mu \end{smallmatrix} \right) \right. \right. \\ \left. \left. - \mathbf{R} \left(\begin{smallmatrix} LL+I \\ \mu \quad \mu \end{smallmatrix} \right) \cdot \mathbf{R} \left(\begin{smallmatrix} LL+I \\ \mu \quad \mu \end{smallmatrix} \right) \right)^2 \right. \\ \left. + \frac{1}{6} \zeta \left(\mathbf{R}' \left(\begin{smallmatrix} LL+I \\ \mu \quad \mu \end{smallmatrix} \right) \cdot \mathbf{R}' \left(\begin{smallmatrix} LL+I \\ \mu \quad \mu \end{smallmatrix} \right) \right. \right. \\ \left. \left. - \mathbf{R} \left(\begin{smallmatrix} LL+I \\ \mu \quad \mu \end{smallmatrix} \right) \cdot \mathbf{R} \left(\begin{smallmatrix} LL+I \\ \mu \quad \mu \end{smallmatrix} \right) \right)^3 \right\}$$

Here L refers to the cell index, μ to the particle index, and $\mathbf{R} \left(\begin{smallmatrix} LL+I \\ \mu \quad \mu \end{smallmatrix} \right)$ to the equilibrium vector distance between the particle μ in cell L and its nearest neighbour I in a plane parallel to the basal plane. $\mathbf{R}' \left(\begin{smallmatrix} LL+I \\ \mu \quad \mu \end{smallmatrix} \right)$ refers to the vector distance when the particles are displaced. α and ζ are the second and third order parameters. The two body potential involving the six sets of neighbours are written in a fashion similar to the above using the tables in Appendix 1. Table 1 lists the second and third order parameters for the six different two body interactions.

In all the three metals investigated the third order parameters are retained only up to the

third neighbours. For further neighbours the third order parameters are set equal to zero.

(b) Three body potentials between nearest neighbours of the same type in the basal plane

$$\Phi_f^{(3)} = \frac{1}{2} \sum_L \sum_{\mu=1}^2 \sum_{l=1}^6 \frac{1}{2} \beta \times \left\{ \left[\mathbf{R}' \left(\begin{smallmatrix} LL+I \\ \mu \quad \mu \end{smallmatrix} \right) \cdot \mathbf{R}' \left(\begin{smallmatrix} LL+I' \\ \mu \quad \mu \end{smallmatrix} \right) \right. \right. \\ \left. \left. - \mathbf{R} \left(\begin{smallmatrix} LL+I \\ \mu \quad \mu \end{smallmatrix} \right) \cdot \mathbf{R} \left(\begin{smallmatrix} LL+I' \\ \mu \quad \mu \end{smallmatrix} \right) \right]^2 \right. \\ \left. + \left[\mathbf{R}' \left(\begin{smallmatrix} LL+I \\ \mu \quad \mu \end{smallmatrix} \right) \cdot \mathbf{R}' \left(\begin{smallmatrix} LL+I'' \\ \mu \quad \mu \end{smallmatrix} \right) \right. \right. \\ \left. \left. - \mathbf{R} \left(\begin{smallmatrix} LL+I \\ \mu \quad \mu \end{smallmatrix} \right) \cdot \mathbf{R} \left(\begin{smallmatrix} LL+I'' \\ \mu \quad \mu \end{smallmatrix} \right) \right]^2 \right\}.$$

Here I' , I'' are the two nearest neighbour atoms on either side of the neighbour I . β is the second order parameter.

We can similarly write the various three body potentials with the help of the tables in Appendix 1. Table 2 below lists the triplet of atoms involved in the various interactions and the corresponding second order parameters involved. The symbols for the various sets of neighbours are given in Appendix 1.

For magnesium and beryllium the atoms $\left(\begin{smallmatrix} P \\ 2 \end{smallmatrix} \right)$ are the farthest of all the neighbours of the

Table 1. Second and third order parameters for the six different two body interactions in hexagonal metals

No.	Neighbour involved	Second order parameter	Third order parameter
1	Nearest neighbour of the same type in basal plane (Symbol I)	α	ζ
2	Second neighbour of the same type in the basal plane (Symbol N)	ρ	$\eta (= 0)$
3	Third neighbour of the same type along the unique axis (Symbol K)	τ	$\chi (= 0)$
4	Nearest neighbour of the second type out of the basal plane (Symbol J)	γ_1	ξ_1
5	Second nearest neighbour of the second type out of the basal plane (Symbol M)	γ_2	ξ_2
6	Third neighbour of the second type out of the basal plane (Symbol P)	$\gamma_3 (= 0)$	$\xi_3 (= 0)$

Table 2. Three body interactions in hexagonal metals

No.	Triplet of atoms involved			Second order parameter
1	$\begin{pmatrix} L \\ \mu \end{pmatrix}$	$\begin{pmatrix} L+I \\ \mu \end{pmatrix}$	$\begin{pmatrix} L+I' \\ \mu \end{pmatrix}$	β
2	$\begin{pmatrix} L \\ \mu \end{pmatrix}$	$\begin{pmatrix} L+N \\ \mu \end{pmatrix}$	$\begin{pmatrix} L+N' \\ \mu \end{pmatrix}$	β'
3	$\begin{pmatrix} L \\ \mu \end{pmatrix}$	$\begin{pmatrix} L+I \\ \mu \end{pmatrix}$	$\begin{pmatrix} L+K \\ \mu \end{pmatrix}$	κ
4	$\begin{pmatrix} L \\ \mu \end{pmatrix}$	$\begin{pmatrix} L+N \\ \mu \end{pmatrix}$	$\begin{pmatrix} L+K \\ \mu \end{pmatrix}$	κ'
5	$\begin{pmatrix} L \\ 1 \end{pmatrix}$	$\begin{pmatrix} L+J'_1 \\ 2 \end{pmatrix}$	$\begin{pmatrix} L+J'_2 \\ 2 \end{pmatrix}$	ϵ_1
6	$\begin{pmatrix} L \\ 1 \end{pmatrix}$	$\begin{pmatrix} L+M'_1 \\ 2 \end{pmatrix}$	$\begin{pmatrix} L+M'_2 \\ 2 \end{pmatrix}$	$\epsilon_2 (=0)$
7	$\begin{pmatrix} L \\ 1 \end{pmatrix}$	$\begin{pmatrix} L+P'_1 \\ 2 \end{pmatrix}$	$\begin{pmatrix} L+P'_2 \\ 2 \end{pmatrix}$	$\epsilon_3 (=0)$
8	$\begin{pmatrix} L \\ 1 \end{pmatrix}$	$\begin{pmatrix} L+J'_1 \\ 2 \end{pmatrix}$	$\begin{pmatrix} L+K'_1 \\ 1 \end{pmatrix}$	δ_1
9	$\begin{pmatrix} L \\ 1 \end{pmatrix}$	$\begin{pmatrix} L+M'_1 \\ 2 \end{pmatrix}$	$\begin{pmatrix} L+K'_1 \\ 1 \end{pmatrix}$	δ_2
10	$\begin{pmatrix} L \\ 1 \end{pmatrix}$	$\begin{pmatrix} L+P'_1 \\ 2 \end{pmatrix}$	$\begin{pmatrix} L+K'_1 \\ 1 \end{pmatrix}$	$\delta_3 (=0)$

atom $\begin{pmatrix} 0 \\ 1 \end{pmatrix}$. For these metals, setting all the force parameters involving the atoms $\begin{pmatrix} P \\ 2 \end{pmatrix}$ is equivalent to restricting the interactions up to the fifth neighbours. In zinc the atom $\begin{pmatrix} P \\ 2 \end{pmatrix}$ is the fifth neighbour of atom $\begin{pmatrix} 0 \\ 1 \end{pmatrix}$. However the inclusion of the parameters involving the interactions with the atoms $\begin{pmatrix} P \\ 2 \end{pmatrix}$ does not bring about a marked improvement in the fit to the dispersion relations. So even in zinc these interactions are set equal to zero to reduce the number of adjustable parameters. The parameter ϵ_2 also does not have a sensible effect on the dispersion relations. So this was also

taken to be zero. In the present model therefore there are twelve second order parameters involved in the calculation of the dispersion relations and the second order elastic constants, and three third order parameters involved in the calculation of the third order elastic constants and anisotropic thermal expansion. The connection between the present second order parameters and the tensor force constants in the notation of Iyengar *et al.*[5] is discussed in Appendix 2.

3. EXPRESSIONS FOR THE ELEMENTS OF THE DYNAMICAL MATRIX OF A HOMOGENEOUSLY DEFORMED CRYSTAL

Srinivasan and Ramji Rao[16] have shown in the case of an ideally close packed hexagonal lattice that, for the calculation of the anisotropic thermal expansion of uniaxial crystals, it is enough to consider (i) a uniform longitudinal strain ϵ' parallel to the unique axis and (ii) a uniform areal strain ϵ'' perpendicular to the unique axis. The advantage of these strains is that there is no internal displacement of the two sublattices. For a calculation of the Gruneisen parameters, it is necessary to know the elements of the dynamical matrix to the first power of these strain parameters. To obtain these elements we consider a uniformly strained state with the strains ϵ' and ϵ'' and calculate the energy Φ' by substituting for

$$R'_i \begin{pmatrix} L & L' \\ \mu & \nu \end{pmatrix} = \left[R_i \begin{pmatrix} L & L' \\ \mu & \nu \end{pmatrix} \times \left(1 + \frac{\epsilon'}{2} (\delta_{ix} + \delta_{iy}) + \epsilon'' \delta_{iz} \right) \right]$$

in the expressions for the two and three body potentials. The atoms are now given infinitesimal displacements from the above homogeneously deformed positions R'_i so that

$$R''_i \begin{pmatrix} L & L' \\ \mu & \nu \end{pmatrix} = R'_i \begin{pmatrix} L & L' \\ \mu & \nu \end{pmatrix} + u_i \begin{pmatrix} L' \\ \nu \end{pmatrix} - u_i \begin{pmatrix} L \\ \mu \end{pmatrix}.$$

The potential energy corresponding to this configuration is Φ'' . $(\Phi'' - \Phi')$ is expanded up

to the second power in the displacements $u_i\left(\frac{L}{\mu}\right)$ with coefficients involving the strains ϵ' and ϵ'' up to the first power. The dynamical matrix is then obtained in the usual way by

substituting plane wave solutions for $u_i\left(\frac{L}{\mu}\right)$. The elements of the dynamical matrix are given below:

$$\begin{aligned} \left[\begin{array}{c} \mathbf{q} \\ 11 \\ xx \end{array} \right] &= \frac{D^2}{M} \left\{ \left[(4\gamma_1 + 2\epsilon_1 + 16\gamma_2) + \alpha(12 - 6c_1 - 6c_4) + 3\beta(5 - 2c_1 - c_2 - 2c_4) \right. \right. \\ &\quad + \beta'(45 - 12c_5 - 12c_6 - 21c_7) + (6\kappa + 18\kappa' + \delta_1 + 4\delta_2)(1 - c_3) + 6\rho(6 - c_5 - c_6 - 4c_7) \\ &\quad + \frac{\epsilon_1}{3}(3 - 2c_1 + c_2 - 2c_4) \left. \right] + \epsilon' \left[\left(8\gamma_1 + 32\gamma_2 + \epsilon_1 + \frac{4}{3}\xi_1 D^2 + \frac{64}{3}\xi_2 D^2 \right) \right. \\ &\quad + \alpha(24 - 10c_1 - 10c_4 - 4c_2) + \zeta D^2(12 - 6c_1 - 6c_4) + \beta(21 - 8c_1 - 5c_2 - 8c_4) \\ &\quad + \beta'(63 - 18c_5 - 18c_6 - 27c_7) + (6\kappa + 18\kappa' + \delta_1 + 4\delta_2)(1 - c_3) + 18\rho(4 - c_5 - c_6 - 2c_7) \\ &\quad + \frac{\epsilon_1}{3}(4c_1 + 4c_4 + c_2) \left. \right] + \epsilon'' p^2 \left[(6\gamma_1 + 6\gamma_2 + 2\xi_1 D^2 + 8\xi_2 D^2) + (8\tau + 6\delta_1 + 6\delta_2)(1 - c_3) \right. \\ &\quad \left. \left. + \epsilon_1(6 + 2c_1 + 2c_2 + 2c_4) \right] \right\} \end{aligned}$$

$$\begin{aligned} \left[\begin{array}{c} \mathbf{q} \\ 11 \\ yy \end{array} \right] &= \frac{D^2}{M} \left\{ \left[(4\gamma_1 + 2\epsilon_1 + 16\gamma_2) + \alpha(12 - 2c_1 - 8c_2 - 2c_4) + \beta(15 - 4c_1 - 7c_2 - 4c_4) \right. \right. \\ &\quad + \beta'(45 - 18c_5 - 18c_6 - 9c_7) + (6\kappa + 18\kappa' + \delta_1 + 4\delta_2)(1 - c_3) + 18\rho(2 - c_5 - c_6) \\ &\quad + \epsilon_1(1 - c_2) \left. \right] + \epsilon' \left[(8\gamma_1 + 32\gamma_2 + \epsilon_1 + \frac{4}{3}\xi_1 D^2 + \frac{64}{3}\xi_2 D^2) + \alpha(24 - 6c_1 - 12c_2 - 6c_4) \right. \\ &\quad + \zeta D^2(12 - 2c_1 - 8c_2 - 2c_4) + \beta(21 - 6c_1 - 9c_2 - 6c_4) + \beta'(63 - 24c_5 - 24c_6 - 15c_7) \\ &\quad + (6\kappa + 18\kappa' + \delta_1 + 4\delta_2)(1 - c_3) + \rho(72 - 30c_5 - 30c_6 - 12c_7) - \frac{\epsilon_1}{3}(2c_1 + 2c_4 + 5c_2) \left. \right] \\ &\quad \left. + p^2 \epsilon'' \left[(6\gamma_1 + 6\gamma_2 + 2\xi_1 D^2 + 8\xi_2 D^2) + (8\tau + 6\delta_1 + 6\delta_2)(1 - c_3) + \epsilon_1(6 + 2c_1 + 2c_2 + 2c_4) \right] \right\} \end{aligned}$$

$$\begin{aligned} \left[\begin{array}{c} \mathbf{q} \\ 11 \\ zz \end{array} \right] &= \frac{D^2}{M} \left\{ p^2 \left[(6\gamma_1 + 12\epsilon_1 + 6\gamma_2 + 6\delta_1 + 6\delta_2) + \kappa(12 - 4c_1 - 4c_2 - 4c_4) + \kappa'(12 - 4c_5 - 4c_6 - 4c_7) \right. \right. \\ &\quad + 8\tau(1 - c_3) + \frac{2}{3}(\delta_1 + \delta_2)(1 - c_3) - \epsilon_1(3 - c_1 - c_2 - c_4) \left. \right] + \epsilon' \left[(4\gamma_1 + 16\gamma_2 + 2p^2 D^2 \xi_1 \right. \\ &\quad + 8p^2 \xi_2 D^2) + \alpha(12 - 4c_1 - 4c_2 - 4c_4) + \beta(6 - 2c_1 - 2c_2 - 2c_4) + \beta'(18 - 6c_5 - 6c_6 - 6c_7) \\ &\quad + 6\rho(6 - 2c_5 - 2c_6 - 2c_7) - \frac{\epsilon_1}{3}(6 + 2c_1 + 2c_2 + 2c_4) \left. \right] + p^2 \epsilon'' \left[(18\gamma_1 + 12\delta_1 + 12\delta_2 + 18\gamma_2 \right. \\ &\quad + 12\epsilon_1 + 3p^2 \xi_1 D^2 + 3p^2 \xi_2 D^2) + \kappa(24 - 8c_1 - 8c_2 - 8c_4) + \kappa'(24 - 8c_5 - 8c_6 - 8c_7) \\ &\quad \left. \left. + (24\tau + 15\delta_1 + 15\delta_2)(1 - c_3) + \epsilon_1(12 + 4c_1 + 4c_2 + 4c_4) \right] \right\} \end{aligned}$$

$$\begin{bmatrix} q \\ 11 \\ yz \end{bmatrix} = \frac{pD^2}{M} s_3 \left\{ [\kappa(s_1 - s_4 + 2s_2) + 3\kappa'(s_5 - s_6)] + \frac{\epsilon'}{2} [\kappa(s_1 - s_4 + 2s_2) + 3\kappa'(s_5 - s_6)] \right. \\ \left. + \epsilon'' [\kappa(s_1 - s_4 + 2s_2) + 3\kappa'(s_5 - s_6)] \right\}$$

$$\begin{bmatrix} q \\ 11 \\ xz \end{bmatrix} = \frac{\sqrt{3}pD^2}{M} s_3 \left\{ [\kappa(s_1 + s_4) + \kappa'(s_5 + s_6 - 2s_7)] + \frac{\epsilon'}{2} [\kappa(s_1 + s_4) + \kappa'(s_5 + s_6 - 2s_7)] \right. \\ \left. + \epsilon'' [\kappa(s_1 + s_4) + \kappa'(s_5 + s_6 - 2s_7)] \right\}$$

$$\begin{bmatrix} q \\ 11 \\ xy \end{bmatrix} = \frac{-\sqrt{3}D^2}{M} \left\{ \left[\left(2\alpha + \beta + \frac{\epsilon'}{3} \right) (c_1 - c_4) + (6\rho + 3\beta') (c_5 - c_6) \right] + \epsilon' \left[\left(2\alpha + \beta + \frac{\epsilon_1}{3} + 2\zeta D^2 \right) \right. \right. \\ \left. \left. \times (c_1 - c_4) + (6\rho + 3\beta') (c_5 - c_6) \right] \right\}.$$

The $\begin{bmatrix} q \\ 12 \\ ij \end{bmatrix}$ are complex. their real and imaginary parts are written as $\begin{bmatrix} R \\ 12 \\ ij \end{bmatrix}$ and $\begin{bmatrix} I \\ 12 \\ ij \end{bmatrix}$.

$$\begin{aligned} R \begin{bmatrix} q \\ 12 \\ xx \end{bmatrix} &= -c_8 \frac{D^2}{M} \left\{ \left[\frac{2\gamma_1}{3} (c_9 + c_{10} + 4c_{11}) + \frac{2\epsilon_1}{3} (2c_9 + 2c_{10} - c_{11}) + \frac{8\gamma_2}{3} (c_{12} + c_{13} + 4c_{14}) \right] \right. \\ &\quad + \epsilon' \left[\gamma_1 (2c_9 + 2c_{10} + 4c_{11}) + \frac{\xi_1 D^2}{9} (2c_9 + 2c_{10} + 8c_{11}) - 2\epsilon_1 c_{11} + \gamma_2 (8c_{12} + 8c_{13} + 16c_{14}) \right. \\ &\quad + \frac{32}{9} \xi_2 D^2 (c_{12} + c_{13} + 4c_{14}) \left. \right] + p^2 \epsilon'' \left[\gamma_1 (2c_9 + 2c_{10} + 2c_{11}) + \frac{\xi_1 D^2}{3} (c_9 + c_{10} + 4c_{11}) \right. \\ &\quad \left. \left. + 4\epsilon_1 (c_9 + c_{10} + c_{11}) + 2\gamma_2 (c_{12} + c_{13} + c_{14}) + \frac{4}{3} \xi_2 D^2 (c_{12} + c_{13} + 4c_{14}) \right] \right\} \end{aligned}$$

$$\begin{aligned} R \begin{bmatrix} q \\ 12 \\ yy \end{bmatrix} &= -c_8 \frac{D^2}{M} \left\{ [2\gamma_1 (c_9 + c_{10}) + 2\epsilon_1 c_{11} + 8\gamma_2 (c_{12} + c_{13})] + \epsilon' \left[\frac{\gamma_1}{3} (10c_9 + 10c_{10} + 4c_{11}) \right. \right. \\ &\quad + \frac{2}{3} \xi_1 D^2 (c_9 + c_{10}) - \frac{\epsilon_1}{3} (4c_9 + 4c_{10} - 2c_{11}) + \frac{\gamma_2}{3} (40c_{12} + 40c_{13} + 16c_{14}) \\ &\quad + \frac{32}{3} \xi_2 D^2 (c_{12} + c_{13}) \left. \right] + p^2 \epsilon'' [\gamma_1 (2c_9 + 2c_{10} + 2c_{11}) + \xi_1 D^2 (c_9 + c_{10}) \\ &\quad \left. + 4\epsilon_1 (c_9 + c_{10} + c_{11}) + 2\gamma_2 (c_{12} + c_{13} + c_{14}) + 4\xi_2 D^2 (c_{12} + c_{13})] \right\} \end{aligned}$$

$$R \begin{bmatrix} q \\ 12 \\ zz \end{bmatrix} = -c_8 \frac{D^2}{M} \left\{ p^2 [(2\gamma_1 + 2\delta_1 + 4\epsilon_1) (c_9 + c_{10} + c_{11}) + (2\gamma_2 + 2\delta_2) (c_{12} + c_{13} + c_{14})] \right\}$$

$$\begin{aligned}
& + \frac{\epsilon'}{3} [(4\gamma_1 - 4\epsilon_1 + 2p^2\xi_1 D^2)(c_9 + c_{10} + c_{11}) + (16\gamma_2 + 8p^2\xi_2 D^2)(c_{12} + c_{13} + c_{14})] \\
& + p^2\epsilon'' [(6\gamma_1 + 4\delta_1 + 12\epsilon_1 + p^2\xi_1 D^2)(c_9 + c_{10} + c_{11}) + (6\gamma_2 + 4\delta_2 + p^2\xi_2 D^2)(c_{12} + c_{13} + c_{14})] \} \\
R \begin{bmatrix} \mathbf{q} \\ 12 \\ yz \end{bmatrix} &= \frac{pD^2}{M} s_8 \left\{ \left[\left(2\gamma_1 + \delta_1 - \frac{\epsilon_1}{2} \right) (s_9 - s_{10}) - (4\gamma_2 + 2\delta_2) (s_{12} - s_{13}) \right] \right. \\
& + \epsilon' \left[\left(\gamma_1 + \frac{\delta_1}{2} - \frac{\epsilon_1}{4} + \frac{2\xi_1 D^2}{3} \right) (s_9 - s_{10}) - \left(2\gamma_2 + \delta_2 + \frac{16}{3} \xi_2 D^2 \right) (s_{12} - s_{13}) \right] \\
& \left. + \epsilon'' \left[\left(2\gamma_1 + \delta_1 - \frac{\epsilon_1}{2} + p^2\xi_1 D^2 \right) (s_9 - s_{10}) - (4\gamma_2 + 2\delta_2 + 2p^2\xi_2 D^2) (s_{12} - s_{13}) \right] \right\} \\
R \begin{bmatrix} \mathbf{q} \\ 12 \\ xz \end{bmatrix} &= \frac{pD^2}{M} \frac{s_8}{\sqrt{3}} \left\{ \left[\left(2\gamma_1 + \delta_1 - \frac{\epsilon_1}{2} \right) (s_9 + s_{10} - 2s_{11}) + (4\gamma_2 + 2\delta_2) (s_{12} + s_{13} - 2s_{14}) \right] \right. \\
& + \epsilon' \left[\left(\gamma_1 + \frac{\delta_1}{2} - \frac{\epsilon_1}{4} + \frac{2}{3} \xi_1 D^2 \right) (s_9 + s_{10} - 2s_{11}) + \left(2\gamma_2 + \delta_2 + \frac{16}{3} \xi_2 D^2 \right) (s_{12} + s_{13} - 2s_{14}) \right] \\
& \left. + \epsilon'' \left[\left(2\gamma_1 + \delta_1 - \frac{\epsilon_1}{2} + p^2\xi_1 D^2 \right) (s_9 + s_{10} - 2s_{11}) + (4\gamma_2 + 2\delta_2 + 2p^2\xi_2 D^2) (s_{12} + s_{13} - 2s_{14}) \right] \right\} \\
R \begin{bmatrix} \mathbf{q} \\ 12 \\ xy \end{bmatrix} &= \frac{D^2}{M} \frac{1}{\sqrt{3}} c_8 \left\{ \left[(2\epsilon_1 - 2\gamma_1)(c_9 - c_{10}) + 8\gamma_2(c_{12} - c_{13}) \right] + \epsilon' \left[\left(2\epsilon_1 - 2\gamma_1 - \frac{2}{3} \xi_1 D^2 \right) (c_9 - c_{10}) \right. \right. \\
& \left. \left. + \left(8\gamma_2 + \frac{32}{3} \xi_2 D^2 \right) (c_{12} - c_{13}) \right] + p^2\epsilon'' [\xi_1 D^2(c_{10} - c_9) + 4\xi_2 D^2(c_{12} - c_{13})] \right\} \\
I \begin{bmatrix} \mathbf{q} \\ 12 \\ xx \end{bmatrix} &= \frac{-D^2}{M} c_8 \left\{ \frac{1}{3} [2\gamma_1(s_9 + s_{10} + 4s_{11}) + 2\epsilon_1(2s_9 + 2s_{10} - s_{11}) - 8\gamma_2(s_{12} + s_{13} + 4s_{14})] \right. \\
& + \epsilon' \left[2\gamma_1(s_9 + s_{10} + 2s_{11}) + \frac{2\xi_1 D^2}{9} (s_9 + s_{10} + 4s_{11}) - 2\epsilon_1 s_{11} - 8\gamma_2(s_{12} + s_{13} + 2s_{14}) \right. \\
& \left. \left. - \frac{32}{9} \xi_2 D^2(s_{12} + s_{13} + 4s_{14}) \right] + p^2\epsilon'' [2\gamma_1(s_9 + s_{10} + s_{11}) + \frac{1}{3} \xi_1 D^2(s_9 + s_{10} + 4s_{11}) \right. \\
& \left. + 4\epsilon_1(s_9 + s_{10} + s_{11}) - 2\gamma_2(s_{12} + s_{13} + s_{14}) - \frac{4}{3} \xi_2 D^2(s_{12} + s_{13} + 4s_{14})] \right\} \\
I \begin{bmatrix} \mathbf{q} \\ 12 \\ yy \end{bmatrix} &= \frac{-D^2}{M} c_8 \left\{ [2\gamma_1(s_9 + s_{10}) + 2\epsilon_1 s_{11} - 8\gamma_2(s_{12} + s_{13})] + \frac{\epsilon'}{3} [\gamma_1(10s_9 + 10s_{10} + 4s_{11}) + \right. \\
& + 2\xi_1 D^2(s_9 + s_{10}) - 2\epsilon_1(2s_9 + 2s_{10} - s_{11}) - 8\gamma_2(5s_{12} + 5s_{13} + 2s_{14}) - 32\xi_2 D^2(s_{12} + s_{13})] \\
& \left. + p^2\epsilon'' [(2\gamma_1 + 4\epsilon_1)(s_9 + s_{10} + s_{11}) + \xi_1 D^2(s_9 + s_{10}) - 2\gamma_2(s_{12} + s_{13} + s_{14}) - 4\xi_2 D^2(s_{12} + s_{13})] \right\}
\end{aligned}$$

$$I \begin{bmatrix} q \\ 12 \\ zz \end{bmatrix} = \frac{-D^2}{M} c_8 \left\{ p^2 [(2\gamma_1 + 2\delta_1 + 4\epsilon_1)(s_9 + s_{10} + s_{11}) - (2\gamma_2 + 2\delta_2)(s_{12} + s_{13} + s_{14})] \right. \\ \left. + \frac{\epsilon'}{3} [(4\gamma_1 - 4\epsilon_1 + 2p^2\xi_1 D^2)(s_9 + s_{10} + s_{11}) - (16\gamma_2 + 8p^2\xi_2 D^2)(s_{12} + s_{13} + s_{14})] \right. \\ \left. + p^2\epsilon'' [(6\gamma_1 + 4\delta_1 + 12\epsilon_1 + p^2\xi_1 D^2)(s_9 + s_{10} + s_{11}) - (6\gamma_2 + 4\delta_2 + p^2\xi_2 D^2)(s_{12} + s_{13} + s_{14})] \right\}$$

$$I \begin{bmatrix} q \\ 12 \\ yz \end{bmatrix} = \frac{-pD^2}{M} s_8 \left\{ \left[(2\gamma_1 + \delta_1 - \frac{\epsilon_1}{2})(c_9 - c_{10}) + (4\gamma_2 + 2\delta_2)(c_{12} - c_{13}) \right] \right. \\ \left. + \epsilon' \left[\left(\gamma_1 + \frac{\delta_1}{2} - \frac{\epsilon_1}{4} + \frac{2}{3}\xi_1 D^2 \right)(c_9 - c_{10}) + \left(2\gamma_2 + \delta_2 + \frac{16}{3}\xi_2 D^2 \right)(c_{12} - c_{13}) \right] \right. \\ \left. + \epsilon'' \left[\left(2\gamma_1 + p^2\xi_1 D^2 + \delta_1 - \frac{\epsilon_1}{2} \right)(c_9 - c_{10}) + (4\gamma_2 + 2\delta_2 + 2p^2\xi_2 D^2)(c_{12} - c_{13}) \right] \right\}$$

$$I \begin{bmatrix} q \\ 12 \\ xz \end{bmatrix} = \frac{-pD^2}{M} \frac{s_8}{\sqrt{3}} \left\{ \left[(2\gamma_1 + \delta_1 - \frac{\epsilon_1}{2})(c_9 + c_{10} - 2c_{11}) - (4\gamma_2 + 2\delta_2)(c_{12} + c_{13} - 2c_{14}) \right] \right. \\ \left. + \epsilon' \left[\left(\gamma_1 + \frac{\delta_1}{2} - \frac{\epsilon_1}{4} + \frac{2}{3}\xi_1 D^2 \right)(c_9 + c_{10} - 2c_{11}) - \left(2\gamma_2 + \delta_2 + \frac{16}{3}\xi_2 D^2 \right)(c_{12} + c_{13} - 2c_{14}) \right] \right. \\ \left. + \epsilon'' \left[\left(2\gamma_1 + \delta_1 - \frac{\epsilon_1}{2} + p^2\xi_1 D^2 \right)(c_9 + c_{10} - 2c_{11}) - (4\gamma_2 + 2\delta_2 + 2p^2\xi_2 D^2)(c_{12} + c_{13} - 2c_{14}) \right] \right\}$$

$$I \begin{bmatrix} q \\ 12 \\ xy \end{bmatrix} = \frac{-D^2}{M} \frac{1}{\sqrt{3}} c_8 \left\{ [(2\gamma_1 - 2\epsilon_1)(s_9 - s_{10}) + 8\gamma_2(s_{12} - s_{13})] + \epsilon' \left[\left(2\epsilon_1 - 2\gamma_1 - \frac{2}{3}\xi_1 D^2 \right) \right. \right. \\ \left. \left. \times (s_9 - s_{10}) + (8\gamma_2 + \frac{32}{3}\xi_2 D^2)(s_{12} - s_{13}) \right] + p^2\epsilon'' [\xi_1 D^2(s_9 - s_{10}) + 4\xi_2 D^2(s_{12} - s_{13})] \right\}.$$

In the above expressions the c_i and s_i have the following significance:

$c_1 = \cos 2\pi q_1$	$c_2 = \cos 2\pi q_2$	$c_3 = \cos 2\pi q_3$
$c_4 = \cos 2\pi(q_1 - q_2)$	$c_5 = \cos 2\pi(q_1 + q_2)$	$c_6 = \cos 2\pi(2q_2 - q_1)$
$c_7 = \cos 2\pi(2q_1 - q_2)$	$c_8 = \cos \pi q_3$	$c_9 = \cos \frac{2}{3}\pi(q_1 + q_2)$
$c_{10} = \cos \frac{2}{3}\pi(2q_2 - q_1)$	$c_{11} = \cos \frac{2}{3}\pi(2q_1 - q_2)$	$c_{12} = \cos \frac{4}{3}\pi(q_1 - 2q_2)$
$c_{13} = \cos \frac{4}{3}\pi(q_1 + q_2)$	$c_{14} = \cos \frac{4}{3}\pi(q_2 - 2q_1)$	
$s_1 = \sin 2\pi q_1$	$s_2 = \sin 2\pi q_2$	$s_3 = \sin 2\pi q_3$
$s_4 = \sin 2\pi(q_1 - q_2)$	$s_5 = \sin 2\pi(q_1 + q_2)$	$s_6 = \sin 2\pi(2q_2 - q_1)$
$s_7 = \sin 2\pi(2q_1 - q_2)$	$s_8 = \sin \pi q_3$	$s_9 = \sin \frac{2}{3}\pi(q_1 + q_2)$

$$s_{10} = \sin \frac{1}{3} \pi (2q_2 - q_1)$$

$$s_{11} = \sin \frac{1}{3} \pi (2q_1 - q_2)$$

$$s_{12} = \sin \frac{1}{3} \pi (q_1 - 2q_2)$$

$$s_{13} = \sin \frac{1}{3} \pi (q_1 + q_2)$$

$$s_{14} = \sin \frac{1}{3} \pi (q_2 - 2q_1).$$

The expressions for the frequencies at the symmetry points $\Gamma(0,0,0)$, $A(0,0,0.5)$ and $M(0.5,0,0)$ for the unstrained lattice are collected in Appendix 3.

4. EXPRESSIONS FOR THE SECOND AND THIRD ORDER ELASTIC CONSTANTS

These expressions were derived by the method of homogeneous deformation. In a homogeneous deformation

$$R'_i \left(\begin{smallmatrix} L & L' \\ \mu & \nu \end{smallmatrix} \right) = \sum_j \epsilon_{ij} R_{ij} \left(\begin{smallmatrix} L & L' \\ \mu & \nu \end{smallmatrix} \right) + W_i(\nu) - W_i(\mu). \quad (4.1)$$

The ϵ_{ij} are the deformation parameters related to the Lagrangian strains η_{ij} by the formula

$$\eta_{ij} = \frac{1}{2} \left[\epsilon_{ij} + \epsilon_{ji} + \sum_k \epsilon_{ik} \epsilon_{jk} \right] \quad (4.2)$$

and $W(\nu)$ is the internal displacement of the ν th sublattice, relative to the lattice of atoms (1) (i.e. $W_i(1) = 0$). Following the procedure outlined by Srinivasan[17], expressions were obtained for the second and third order elastic constants and these are given below.

$$c_{11} = \frac{D^4}{V_a} \left[9(\alpha + \beta + 9\beta' + 9\rho) + \gamma_1 + \epsilon_1 + 16\gamma_2 - \frac{1}{12} A(4\gamma_1 - 4\epsilon_1 - 32\gamma_2) \right]$$

$$c_{12} = \frac{D^4}{V_a} \left[3\alpha - 3\beta - 27\beta' + 27\rho + \frac{1}{3} (\gamma_1 - \epsilon_1 + 16\gamma_2) + \frac{1}{12} A(4\gamma_1 - 4\epsilon_1 - 32\gamma_2) \right]$$

$$c_{66} = \frac{D^4}{V_a} \left[3\alpha + 6\beta + 54\beta' + 27\rho + \frac{1}{3} (\gamma_1 + 2\epsilon_1 + 16\gamma_2) - \frac{1}{12} A(4\gamma_1 - 4\epsilon_1 - 32\gamma_2) \right]$$

$$c_{33} = \frac{D^4}{V_a} p^4 \left[8\tau + \frac{3}{2} \gamma_1 + \frac{3}{2} \gamma_2 + 6\delta_1 + 6\delta_2 + 3\epsilon_1 \right]$$

$$c_{13} = \frac{D^4}{V_a} p^2 [\gamma_1 - \epsilon_1 + 4\gamma_2]$$

$$c_{44} = \frac{D^4}{V_a} p^2 \left[\gamma_1 + 4\gamma_2 + 6\kappa + 18\kappa' + \delta_1 + 4\delta_2 + \frac{\epsilon_1}{2} \right]. \quad (4.3)$$

Here v_a is the volume of the unit cell ($v_a = \sqrt{3}/2 p D^3$), and

$$A = (4\gamma_1 - 4\epsilon_1 - 32\gamma_2) / (4\gamma_1 + 2\epsilon_1 + 16\gamma_2). \quad (4.4)$$

A relates the internal displacement to the macroscopic strain.

$$c_{111} = \frac{D^6}{v_a} \left[\left(\frac{27}{2} \zeta + \frac{11}{18} \xi_1 + \frac{352}{9} \xi_2 \right) + A \left(-\frac{5}{6} \xi_1 + \frac{80}{3} \xi_2 \right) + A^2 \left(\left[\frac{1}{2} \xi_1 + 8\xi_2 \right] + \frac{1}{D^2} [\gamma_1 - \epsilon_1 + 4\gamma_2] \right) + A^3 \left(-\frac{\xi_1}{18} + \frac{4}{9} \xi_2 \right) \right]$$

$$c_{222} = \frac{D^6}{v_a} \left[\left(\frac{33}{2} \zeta + \frac{\xi_1}{2} + 32\xi_2 \right) - A(\xi_1/2 - 16\xi_2) + A^2 \left\{ \left(\frac{\xi_1}{6} + \frac{8}{3} \xi_2 \right) + \frac{1}{D^2} (\gamma_1 - \epsilon_1 + 4\gamma_2) \right\} - A^3 \left(-\frac{\xi_1}{18} + \frac{4}{9} \xi_2 \right) \right]$$

$$c_{333} = \frac{D^6}{v_a} p^6 \left[\frac{3}{4} \xi_1 + \frac{3}{4} \xi_2 \right]$$

$$c_{112} = \frac{D^6}{v_a} \left[\left(\frac{9}{2} \zeta + \frac{\xi_1}{18} + \frac{32}{9} \xi_2 \right) + A \left(\frac{7}{18} \xi_1 - \frac{112}{9} \xi_2 \right) - A^2 \left\{ \left(\frac{5}{18} \xi_1 + \frac{40}{9} \xi_2 \right) + \frac{1}{3D^2} (\gamma_1 - \epsilon_1 + 4\gamma_2) \right\} + A^3 \left(\xi_1/18 - \frac{4}{9} \xi_2 \right) \right]$$

$$\begin{aligned}
c_{113} &= \frac{D^6}{v_a} p^2 \left[\left(\frac{\xi_1}{2} + 8\xi_2 \right) + A \left(-\frac{\xi_1}{3} + \frac{8}{3}\xi_2 \right) \right. \\
&\quad \left. + A^2 \left\{ \left(\frac{\xi_1}{6} + \frac{2}{3}\xi_2 \right) + \frac{1}{D^2} \left(\frac{\gamma_1}{2} + \epsilon_1 + \frac{\gamma_2}{2} \right) \right\} \right] \\
c_{123} &= \frac{D^6}{v_a} p^2 \left[\left(\frac{\xi_1}{6} + \frac{8}{3}\xi_2 \right) + A \left(\frac{\xi_1}{3} - \frac{8}{3}\xi_2 \right) \right. \\
&\quad \left. - A^2 \left\{ \left(\frac{\xi_1}{6} + \frac{2}{3}\xi_2 \right) + \frac{1}{D^2} \left(\frac{\gamma_1}{2} + \epsilon_1 + \frac{\gamma_2}{2} \right) \right\} \right] \\
c_{133} &= \frac{D^6}{v_a} p^4 \left(\frac{\xi_1}{2} + 2\xi_2 \right) \\
c_{144} &= \frac{D^6}{v_a} p^2 \left[\left(\frac{1}{6}\xi_1 + \frac{8}{3}\xi_2 \right) + A \left(\frac{1}{6}\xi_1 - \frac{4}{3}\xi_2 \right) \right] \\
c_{155} &= \frac{D^6}{v_a} p^2 \left[\left(\frac{\xi_1}{2} + 8\xi_2 \right) - A \left(\frac{1}{6}\xi_1 - \frac{4}{3}\xi_2 \right) \right] \\
c_{344} &= \frac{D^6}{v_a} p^4 \left(\frac{1}{2}\xi_1 + 2\xi_2 \right). \quad (4.5)
\end{aligned}$$

The expressions for the second and third order elastic constants were also verified by the long wave method using the procedure outlined by Srinivasan [17].

5. FIT TO THE DISPERSION RELATIONS

(a) Magnesium

The second order elastic constants C_{44} and nine limiting frequencies at the points Γ , A and M of the Brillouin Zone were used to evaluate ten out of the twelve parameters in the present model. The constants β' and δ_2 were set equal to zero as their inclusion did not improve the fit to the dispersion curves markedly. Table 3 gives the values of the parameters in the present model. Using the relations in Appendix 2 the corresponding tensor force constants in the notation of Iyengar *et al.* [5] are obtained. These are also given in Table 3. The values of the second order elastic constants calculated from the parameters of the model are also compared with the measured values of Slutsky and Garland [18]. Figure 1 compares the dispersion curves along (01 $\bar{1}$ 0) and (0001) directions calculated on this model with the measure-

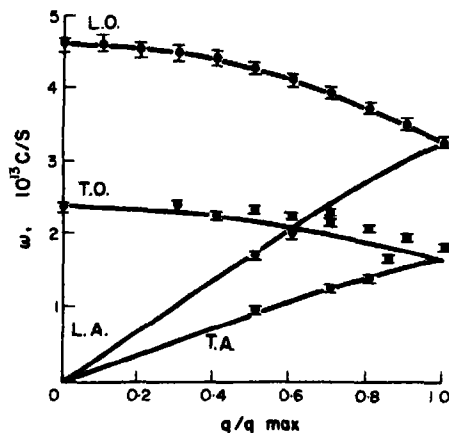


Fig. 1(a). Theoretical dispersion curves for magnesium along (0001) direction. \blacksquare Experimental values of Iyengar *et al.*

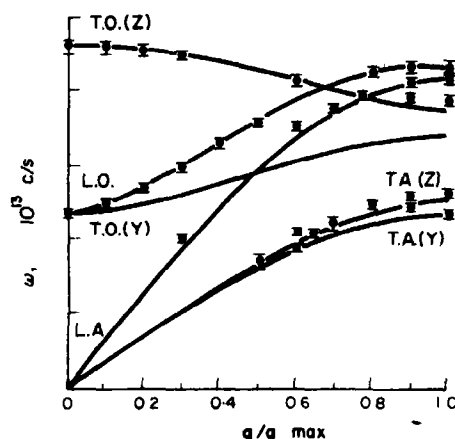


Fig. 1(b). Theoretical dispersion curves for magnesium along (01 $\bar{1}$ 0) direction. \blacksquare Experimental values of Iyengar *et al.*

ments of Iyengar *et al.* [5]. The calculated dispersion curves are in fairly good agreement along both the directions. The maximum discrepancy occurs for the limiting TO frequency at the zone boundary point A and is about 10 per cent. This fit is good enough for a fairly reliable calculation of thermal expansion.

Iyengar *et al.* [5] have obtained a closer fit to the dispersion curves by using a fourteen parameter tensor force model.

Table 3. Values of the parameters of the proposed model for magnesium

Model parameter		Tensor force constant		S.O.E. Constants in 10^{11} dyn/cm ²			
Parameter	value in 10^{11} dyn/cm ²	force const.	value in 10^3 dyn/cm	C_{ij}	Calcd. value	Exptl. 298°K	Value 0°K
$(D^4/v_a)\alpha$	0.561	α^*	4.764	C_{11}	6.00	5.943	6.340
$(D^4/v_a)\rho$	0.009	β^*	2.312	C_{12}	2.36	2.560	2.594
$(D^4/v_a)\tau$	0.054	δ^*	0	C_{13}	1.53	2.140	2.170
$(D^4/v_a)\gamma_1$	0.638	γ^*	-0.154	C_{33}	6.39	6.164	6.645
$(D^4/v_a)\gamma_2$	-0.008	λ^*	1.878	C_{44}	1.66	1.642	1.842
$(D^4/v_a)\beta$	-0.008	μ^*	-0.996	C_{66}	1.82	1.691	1.875
$(D^4/v_a)\epsilon_1$	+0.026	ν^*	5.891				
$(D^4/v_a)\kappa$	-0.013	σ^*	2.530				
$(D^4/v_a)\kappa'$	0.010	ξ^*	-0.095				
$(D^4/v_a)\delta_1$	-0.089	η^*	0.048				
		χ^*	-0.067				
		ζ^*	-0.095				
		θ^*	0.029				
		ϕ^*	0.190				
		A^*	0.122				
		B^*	0.211				
		C^*	0.366				
		D^*	0.237				

The corresponding tensor force constants and the second order elastic constants are also given. $D = 3.202$ AU; $p = 1.623$.

(b) Zinc

The twelve parameters in this model were chosen to give a reasonably good fit to the second order elastic constants and the limiting frequencies at the zone centre and zone boundaries. The second order elastic constants of zinc were determined between 4.2 and 670°K

by Alers and Neighbours [19] and between 4.2 and 77.6°K by Garland and Dalven [20]. The dispersion relations have been measured by Borgonovi *et al.* [8].

Table 4 gives the values of the twelve parameters used in this model and the values of the corresponding tensor force constants.

Table 4. Values of the parameters for the present model in zinc

$D = 2.66$ AU		$p = 1.857$			
Parameter values		Tensor force constants in 10^3 dyn/cm			
Parameter	Value in 10^{11} dyn/cm ²	Force const.	Value	Force const.	Value
$(D^4/v_a)\alpha$	1.643	α^*	10.211	η^*	0.810
$(D^4/v_a)\rho$	-0.046	β^*	5.903	χ^*	1.463
$(D^4/v_a)\tau$	-0.735	δ^*	0	ζ^*	2.611
$(D^4/v_a)\gamma_1$	0.359	γ^*	-3.275	θ^*	0.757
$(D^4/v_a)\gamma_2$	0.142	λ^*	0.134	ϕ^*	-1.649
$(D^4/v_a)\beta$	-0.318	μ^*	-1.403	A^*	0.398
$(D^4/v_a)\beta'$	0.077	ν^*	4.912	B^*	-0.167
$(D^4/v_a)\epsilon_1$	-0.624	σ^*	3.733	C^*	-0.785
$(D^4/v_a)\kappa$	-0.267	ξ^*	1.619	D^*	0.974
$(D^4/v_a)\kappa'$	0.033				
$(D^4/v_a)\delta_1$	1.222				
$(D^4/v_a)\delta_2$	0.035				

Table 5 gives the calculated values of the second order elastic constants. For comparison the values calculated on the modified axially symmetric model of DeWames *et al.* [9] with seventeen parameters are given. The measured values of Alers and Neighbours [19] at 4.2°K and room temperature are also given.

The elastic constants in the present model show a closer agreement with the experimental values than the calculated values of DeWames *et al.*

Figure 2 shows the dispersion curves calculated on the present model. The experimental points are the measurements of Borgonovi *et al.* [8]. The dispersion curves along (0001) and (01 $\bar{1}$ 0) directions give almost as good a fit to the experimental points for most of the branches as the modified axially symmetric model with seventeen adjustable parameters. For the TOZ and TOY branches

Table 5. Second order elastic constants of zinc in 10^{11} dyn/cm²

C_{ij}	Present model	DeWames <i>et al.</i> Calcd.	Experimental [19] 4.2°K	Experimental [19] 295°K
C_{11}	16.43	15.39	17.909	16.368
C_{12}	3.66	3.62	3.75	3.64
C_{13}	5.35	3.85	5.54	5.30
C_{33}	6.44	6.78	6.88	6.347
C_{44}	3.34	3.15	4.596	3.879
C_{66}	6.39	5.88	7.080	6.364

along the (01 $\bar{1}$ 0) directions, the agreement is poorer than with the model of DeWames *et al.* The maximum discrepancy is of the order of 10 per cent. Considering the much smaller number of parameters used in the present model and the much better fit to the elastic constants obtained on this model, the present

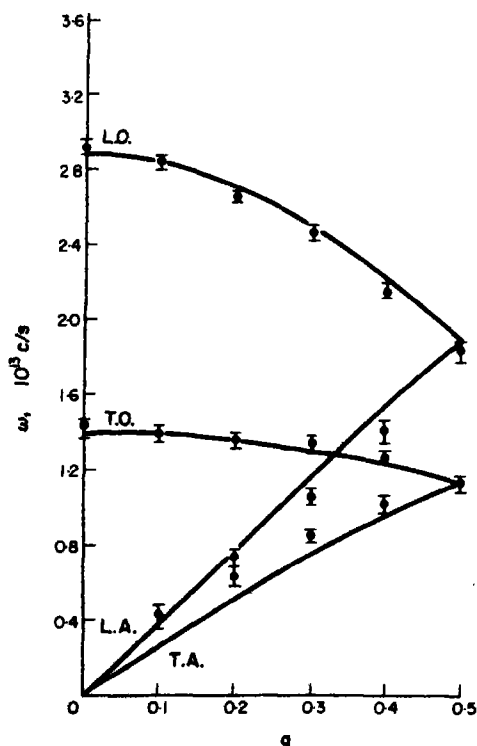


Fig. 2(a). Theoretical dispersion curves for Zinc along (0001) direction. \blacksquare Experimental values of Borgonovi *et al.*

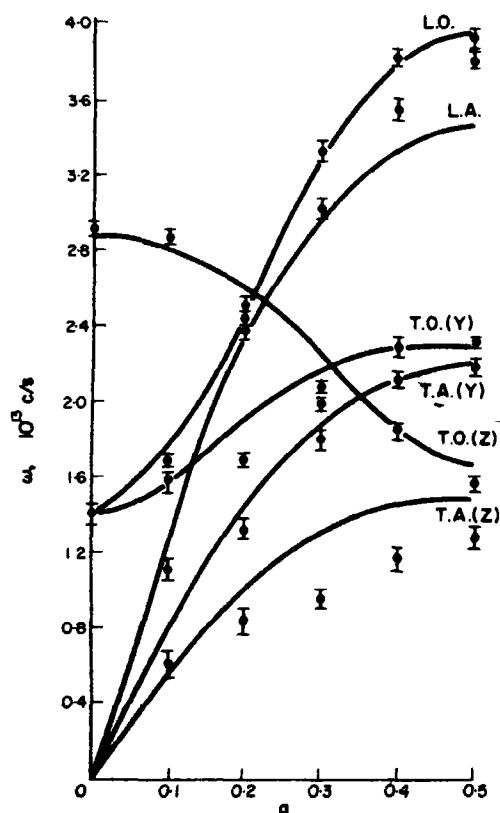


Fig. 2(b). Theoretical dispersion curves for Zinc along (01 $\bar{1}$ 0) direction. \blacksquare Experimental values of Borgonovi *et al.*

model can be used advantageously to calculate the thermal expansion of this metal.

(c) Beryllium

Table 6 gives the values of the twelve second order parameters of the present model which gives a reasonably good fit to the second order elastic constants and the dispersion curves in this metal. The corresponding tensor force constants in the notation of Iyengar *et al.*[5] are also collected in the table.

The second order elastic constants of Beryllium have been measured by Smith and Arbogast[21]. Table 7 compares the calculated second order elastic constants with the measured values. The second order elastic constants calculated on the thirteen parameter modified axially symmetric model of DeWames *et al.*[9] are also included in the table for comparison.

DeWames *et al.* model gives a better fit to the elastic constants. Figure 3 shows the dispersion curves of Beryllium calculated on the present model. The experimental points are those of Schmunk *et al.*[7]. The fit to the dispersion curves along the (0001) direction is better than that of DeWames *et al.* Along the (0110) direction, the LO branch is higher than the measured values by 6 per cent and the TOZ branch is higher by about 3 per cent. DeWames *et al.* obtained a better fit for these branches. For the remaining branches the present model gives as good a fit as the modified axially symmetric model of DeWames *et al.*

Thus we find that the present model based on Keating's method of writing the interaction terms gives a reasonably good fit for the second order elastic constants and the dispersion relations in these metals with a smaller num-

Table 6. Values of the second order parameters in Beryllium

Model parameters		Tensor force constants in 10^3 dyn/cm.			
Parameter	Value in 10^{11} dyn/cm ²	Force const.	Value	Force const.	Value
$(D^4/v_a)\alpha$	0.771	α^*	4.490	η^*	-1.006
$(D^4/v_a)\rho$	0.062	β^*	3.456	χ^*	0.719
$(D^4/v_a)\tau$	3.129	δ^*	0	ζ^*	0.176
$(D^4/v_a)\gamma_1$	1.940	γ^*	-2.578	θ^*	1.452
$(D^4/v_a)\gamma_2$	0.243	λ^*	6.823	ϕ^*	7.548
$(D^4/v_a)\beta$	-0.220	μ^*	0.804	A^*	1.787
$(D^4/v_a)\beta'$	0.130	ν^*	18.910	B^*	2.047
$(D^4/v_a)\epsilon_1$	2.716	σ^*	-3.333	C^*	2.942
$(D^4/v_a)\kappa$	0.510	ξ^*	2.011	D^*	3.128
$(D^4/v_a)\kappa'$	0.205				
$(D^4/v_a)\delta_1$	-4.893				
$(D^4/v_a)\delta_2$	-0.230				

Table 7. Second order elastic constants of beryllium in 10^{11} dynes/cm²

C_{ij}	Present model	DeWames <i>et al.</i> [9]	Experiment[21]
C_{11}	28.5	29.55	29.9
C_{12}	2.8	3.16	2.76 \pm 0.08
C_{13}	0.5	1.74	1.1 \pm 0.5
C_{33}	34.5	33.77	34.22
C_{44}	12.8	16.00	16.62
C_{66}	12.85	13.20	13.57

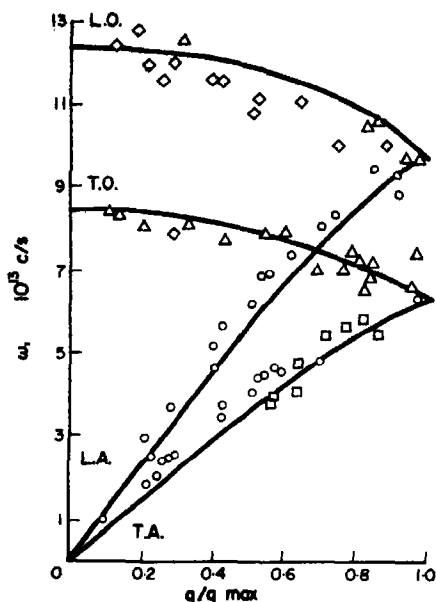


Fig. 3(a). Theoretical dispersion curves for beryllium along (0001) direction. ○, △, □, ◇ Experimental points of Schmunk *et al.*

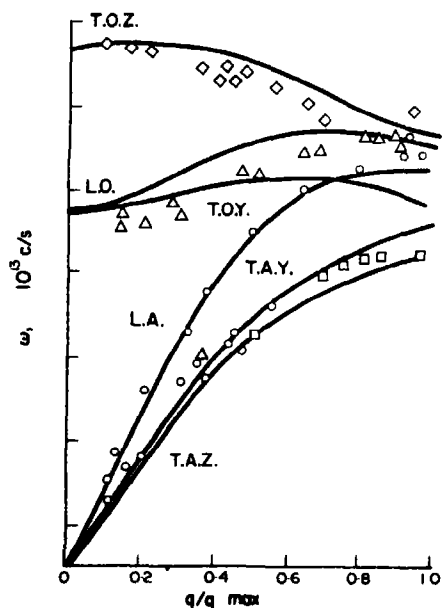


Fig. 3(b). Theoretical dispersion curves for beryllium along (0110) direction. ○, △, □, ◇ Experimental points of Schmunk *et al.*

ber of parameters than either the tensor force model or the modified axially symmetric model. The model has the advantage that it

readily permits the incorporation of third order parameters to calculate the anharmonic properties.

6. PRESSURE DERIVATIVES OF THE SECOND ORDER ELASTIC CONSTANTS AND THE THIRD ORDER ELASTIC CONSTANTS OF HEXAGONAL METALS

The three third order parameters ζ , ξ_1 and ξ_2 have to be fixed to proceed with the calculation of the anharmonic properties of the lattice. Third order elastic constants have become available for zinc recently [2]. But in magnesium [3] and beryllium [4] only the pressure derivatives of the second order elastic constants are available. Ramji Rao and Srinivasan [22] have derived expressions for the pressure derivatives of the second order elastic constants of the hexagonal metals. The expressions will not be repeated here to conserve space. These expressions have been used to calculate the pressure derivatives of the second order elastic constants from the theoretically evaluated third order elastic constants. The third order parameters were chosen to give a reasonable fit to the pressure derivatives of the second order elastic constants and, in zinc, the third order elastic constants. The results are discussed for each metal separately below.

Rose and Ramsey [23] have derived expressions for second and third order elastic constants for the hexagonal metals assuming the atoms to interact through a central potential. They have omitted to take into account the internal displacement of the two sub-lattices and therefore their expressions are incorrect. They find that with central interactions lattice instabilities arise in some of the metals. As the use of a central potential of the type used by them is not valid in these metals, no further reference will be made to their work.

(a) Magnesium

The values of the third order parameters chosen and the calculated pressure derivatives of the second order elastic constants and third order elastic constants are collected in Table

8. The measured values of the pressure derivatives are also given in Table 8. The calculated pressure derivatives are in fairly good agreement with measurement.

(b) Zinc

The values of the third order elastic constants and the pressure derivatives of the second order elastic constants are collected in Table 9. The values of the third order parameters used in this model are also collected in this table. The measured values of the third order elastic constants are also given.

The agreement with the measured third order elastic constants is quite good except for C_{144} and C_{155} . For C_{155} the sign itself comes out wrong. However the calculated pressure

derivatives are in good agreement with the measured values. This model is used to compute the thermal expansion of this metal to be reported in Section 2 of this paper.

(c) Beryllium

The pressure derivatives of three of the second order elastic constants have been reported by Silversmith and Averbach[4]. The model parameters were chosen to reproduce these pressure derivatives. Table 10 lists the parameter values and the third order elastic constants of Beryllium calculated theoretically.

A comparison of Tables 8–10 reveals the effect of the axial ratio on the third order parameters. In magnesium the first two neighbours are almost at the same distance and the

Table 8. Values of the third order parameters and the pressure derivatives of the S.O.E. constants, and the T.O.E. constants of magnesium

$$C_H' = C_{11} + 2C_{33} + C_{12} - 4C_{13}$$

Parameter	value in 10^{11} dyn/cm ²	T.O.E. Constants in 10^{11} dyn/cm ²					Pressure derivative of S.O.E. constant	
							Theory	Expt(3)
$(D^6/v_a)\zeta$	-4.10	C_{111}	-64.3	C_{344}	-17.1	C_{11}	6.36	6.11
$(D^6/v_a)\xi_1$	-4.50	C_{112}	-17.9	C_{333}	-63.2	C_{33}	7.53	7.22
$(D^6/v_a)\xi_2$	-0.11	C_{113}	-6.3	C_{222}	-73.7	C_{44}	1.80	1.58
		C_{123}	-4.7	C_{144}	-4.5	C_{66}	1.71	1.36
		C_{133}	-17.1	C_{155}	-6.5	C_{12}	2.95	—
						C_{13}	2.82	—
						C_H'	13.1	13.7

Table 9. Values of the third order parameters, the third order elastic constants and the pressure derivatives of the S.O.E. constants in zinc

Parameter	value in 10^{11} dyn/cm ²	T.O.E. Constants in 10^{11} dynes/cm ²					
$(D^6/v_a)\xi_1$	-1.2		C_{111}	C_{112}	C_{113}	C_{133}	C_{155}
$(D^6/v_a)\zeta$	-11.0	Theory	-189.0	-57.1	-33.0	-13.8	-35.7
$(D^6/v_a)\xi_2$	-1.2	Expt(2)	-176 ± 15	-44 ± 11	-27 ± 3	-21 ± 6	-35 ± 1
			C_{344}	C_{333}	C_{233}	C_{144}	C_{155}
		Theory	-35.7	-73.8	-216.0	-10.2	-34.0
		Expt(2)	-44 ± 4	-72 ± 2	-241 ± 26	-1 ± 1	+25 ± 5
Pressure derivatives dC_{ij}/dp of the second order elastic constants							
		C_{11}	C_{33}	C_{44}	C_{66}	C_{12}	C_{13}
Theory	7.70	6.50	3.94	2.10	3.51	4.72	C_H'
Expt(2)	7.52	7.32	4.02	1.48	—	—	5.33

Table 10. Third order parameters and the T.O.E. constants of beryllium

Parameter	value in 10^{11} dyn/cm ²	T.O.E. constants of beryllium in 10^{11} dyn/cm ²			
		Constant	Value	Constant	Value
$(D^2/v_a)\xi_1$	-22.38	C_{111}	-219	C_{344}	-78
$(D^2/v_a)\zeta$	-12.40	C_{112}	-65	C_{333}	-259
$(D^2/v_a)\xi_2$	-0.86	C_{113}	-53	C_{322}	-244
		C_{133}	+1	C_{144}	-11
		C_{133}	-78	C_{155}	-49

ζ and ξ_1 parameters are nearly equal. In zinc the axial ratio is larger than for an ideal hcp lattice. The parameter ζ which now corresponds to the nearest neighbour interaction is much larger than the parameter ξ_1 which corresponds to second neighbour interaction. In beryllium the axial ratio is smaller than that for an ideal hcp lattice. ξ_1 , which now represents the nearest neighbour interaction is larger than ζ which corresponds to second neighbour interaction. The third neighbour interaction is generally small and justifies limiting the anharmonic interaction to the first three neighbours. The T.O.E. constants C_{111} and C_{222} are nearly equal to each other in all these crystals corresponding to near isotropy in the basal plane. The constant C_{333} however becomes small relative to C_{111} as the axial ratio increases beyond that for the ideal hcp lattice.

Thus it is shown that the present model fits the dispersion curves as well as the T.O.E. constants or the pressure derivatives of the S.O.E. constants of the metals magnesium, zinc and beryllium. This model will be used to calculate the anisotropic thermal expansion of these metals in Section 2 of this paper.

Acknowledgements—The authors thank Professor G. R. Barsch for his helpful comments on this work and Professor C. Ramasastri for his interest. Our thanks are due to the authorities of the computer centre at T.I.F.R., Bombay, for permitting us to carry out the calculations on the CDC 3600 computer.

REFERENCES

- MUNN R. W., *Adv. Phys.* **18**, 515 (1969).
- SWARTZ K. D. and ELBAUM C., *Phys. Rev. B*, **1**, No. 4, 1512 (1970).
- SCHMUNK R. E. and SMITH C. S., *J. Phys. Chem. Solids* **9**, 100 (1959).
- SILVERSMITH D. J. and AVERBACH B. L., *Bulletin of the American Physical Society*, Feb. (1969).
- IYENGAR P. K., VENKATARAMAN G., VIJAYARAGHAVAN P. R. and ROY A. P., *Inelastic Scattering of neutrons* Vol. 1, page 153, International Atomic Energy Agency, Vienna (1965). *Lattice Dynamics* (Edited by R. F. Wallis) page 223, Pergamon Press (1965).
- SQUIRES G. L., *Proc. Phys. Soc. London* **88**, 919 (1966).
- SCHMUNK R. E., BRUGGER R. M., RANDOLPH P. D. and STRONG K. A., *Phys. Rev.* **128**, 562 (1962).
- BORGONOV G., CAGLIOTTI G., and ANTEL J. J., *Phys. Rev.* **132**, 683 (1963).
- DEWAMES R. E., WOLFRAM T., and LEHMAN G. W., *Phys. Rev.* **A138**, 717 (1965).
- KING W. F. and CUTLER P. H., *Solid State Commun.* **1**, 295 (1969).
- SHAW R. W., Jr., and PYNN R., *J. Phys. C (Solid State Physics)* **2**, Series 2, 2071 (1969).
- KEATING P. N., (a) *Phys. Rev.* **145**, 637 (1966). (b) *Phys. Rev.* **149**, 674 (1966).
- SRINIVASAN R., *J. Phys. Chem. Solids* **28**, 2385 (1967).
- COWLEY E. R. and COWLEY R. A., *Proc. R. Soc. A* **292**, 209 (1966).
- DOLLING G. and COWLEY R. A., *Proc. Phys. Soc.* **88**, 463 (1966).
- SRINIVASAN R. and RAMJI RAO R., *Inelastic Scattering of Neutrons* Vol. I, page 325, International Atomic Energy Agency, Vienna (1965).
- SRINIVASAN R., *Phys. Rev.* **A144**, 620 (1966).
- SLUTSKY L. J. and GARLAND C. W., *Phys. Rev.* **107**, 972 (1957).
- ALERS G. and NEIGHBOURS J. R., *J. Phys. Chem. Solids* **7**, 58 (1958).
- GARLAND C. W. and DALVEN R., *Phys. Rev.* **111**, 1232 (1958).
- SMITH J. F. and ARBOGAST C. L., *J. appl. Phys. (USA)*, **31**, 99 (1960).
- RAMJI RAO and SRINIVASAN R., *Phys. Status Solidi* **31**, K39 (1969).
- ROSE M. F. and RAMSEY R. T., *Phys. Status Solidi* **25**, No. 1, 103-8 (1968).

APPENDIX 1. THE POSITION COORDINATES OF THE SETS OF NEIGHBOURS IN HEXAGONAL METALS AND THE NOMENCLATURE USED TO DESIGNATE THEM

Table 1.A1. Position coordinates of the nearest neighbors of the same type in the basal plane

(These neighbours are indicated by the letter *I*. $R_{(11)}^{(0I)} = R_{(22)}^{(0I)}$ and $|R_{(11)}^{(0I)}| = D$)

Cell indices			Index	Cartesian components		
L_1	L_2	L_3	<i>I</i>	$R_x^{(0I)}(11)$	$R_y^{(0I)}(11)$	$R_z^{(0I)}(11)$
1	0	0	1	$\sqrt{3}/2 D$	$1/2 D$	0
-1	0	0	2	$-\sqrt{3}/2 D$	$-1/2 D$	0
0	1	0	3	0	D	0
0	-1	0	4	0	$-D$	0
1	-1	0	5	$\sqrt{3}/2 D$	$-1/2 D$	0
-1	1	0	6	$-\sqrt{3}/2 D$	$1/2 D$	0

Table 2.A1. Position coordinates of the second neighbours of the same type in the basal plane (Symbol *N*)

Cell indices			Index	Cartesian components		
L_1	L_2	L_3	<i>N</i>	$R_x^{(0N)}(11)$	$R_y^{(0N)}(11)$	$R_z^{(0N)}(11)$
1	1	0	1	$\sqrt{3}/2 D$	$3/2 D$	0
-1	-1	0	2	$-\sqrt{3}/2 D$	$-3/2 D$	0
-1	2	0	3	$-\sqrt{3}/2 D$	$3/2 D$	0
1	-2	0	4	$\sqrt{3}/2 D$	$-3/2 D$	0
2	-1	0	5	$\sqrt{3} D$	0	0
-2	1	0	6	$-\sqrt{3} D$	0	0

$$R_{(11)}^{(0N)} = R_{(22)}^{(0N)} \text{ and } |R_{(11)}^{(0N)}| = \sqrt{3} D$$

Table 3.A1. Position coordinates of the third neighbours of the same type along the 'C' axis

These neighbours are indicated by the letter *K*. $R_{(11)}^{(0K)} = R_{(22)}^{(0K)}$

$$\text{and } |R_{(11)}^{(0K)}| = pD$$

Cell indices			Index	Cartesian components		
L_1	L_2	L_3	<i>K</i>	$R_x^{(0K)}(11)$	$R_y^{(0K)}(11)$	$R_z^{(0K)}(11)$
0	0	1	1 (<i>K'</i>)	0	0	pD
0	0	-1	2 (<i>K''</i>)	0	0	$-pD$

Table 4.A1. Position coordinates of the nearest nonequivalent neighbours out of the basal plane

The neighbours of the nonequivalent type above the basal plane are indicated by J' and those below the basal plane by J'' . All the neighbours are

collectively indicated by J . $\left| \mathbf{R} \begin{pmatrix} 0J \\ 12 \end{pmatrix} \right| = D \left(\frac{1}{3} + \frac{p^2}{4} \right)^{1/2}$

Cell indices			Index	Index	Cartesian components		
L_1	L_2	L_3	J	J''	$R_x \begin{pmatrix} 0J \\ 12 \end{pmatrix}$	$R_y \begin{pmatrix} 0J \\ 12 \end{pmatrix}$	$R_z \begin{pmatrix} 0J \\ 12 \end{pmatrix}$
0	0	0	1	1	$D/2\sqrt{3}$	$D/2$	$pD/2$
0	-1	0	2	2	$D/2\sqrt{3}$	$-D/2$	$pD/2$
-1	0	0	3	3	$-D/\sqrt{3}$	0	$pD/2$
					J''		
0	0	-1	4	1	$D/2\sqrt{3}$	$D/2$	$-pD/2$
0	-1	-1	5	2	$D/2\sqrt{3}$	$-D/2$	$-pD/2$
-1	0	-1	6	3	$-D/\sqrt{3}$	0	$-pD/2$

Table 5.A1. Position coordinates of the second nonequivalent neighbours out of the basal plane

These atoms are indicated by M , those above the plane are denoted by M' and those below the plane by M'' . There are six neighbours and only the coordinates of the three neighbours above the basal plane are given. For the neighbours below the basal plane the Z component carries a minus sign.

$$\left| \mathbf{R} \begin{pmatrix} 0M \\ 12 \end{pmatrix} \right| = \left(\frac{4}{3} + \frac{p^2}{4} \right)^{1/2} D$$

Cell indices			Index	Index	Cartesian components		
L_1	L_2	L_3	M	M'	$R \begin{pmatrix} 0M \\ 12 \end{pmatrix}$	$R_y \begin{pmatrix} 0M \\ 12 \end{pmatrix}$	$R_z \begin{pmatrix} 0M \\ 12 \end{pmatrix}$
-1	1	1	1	1	$-D/\sqrt{3}$	D	$pD/2$
-1	-1	0	2	2	$-D/\sqrt{3}$	$-D$	$pD/2$
1	-1	0	3	3	$2D/\sqrt{3}$	0	$pD/2$

Table 6.A1. Position coordinates of the third nonequivalent neighbours out of the basal plane

These atoms are indicated by the index P , those above the basal plane by P' , and those below the basal plane by P'' . There are twelve neighbours in all. In the table below only the components of the six neighbours above the basal plane are given. The components of $R_{(1\ 2)}^{(0\ P')}$ are obtained by putting a minus sign before the Z component. $|R_{(1\ 2)}^{(0\ P')}| = (\frac{7}{3} + \frac{P^2}{4})^{1/2}$.

Cell indices			Index	Index	Cartesian components		
L_1	L_2	L_3	P	P'	$R_{(1\ 2)}^{(0\ P)}$	$R_{(1\ 2)}^{(0\ P')}$	$R_{(1\ 2)}^{(0\ P)}$
1	0	0	1	1	$2D/\sqrt{3}$	D	$pD/2$
1	-2	0	2	2	$2D/\sqrt{3}$	$-D$	$pD/2$
0	1	0	3	3	$D/2\sqrt{3}$	$3D/2$	$pD/2$
0	-2	0	4	4	$D/2\sqrt{3}$	$-3D/2$	$pD/2$
-2	1	0	5	5	$-5D/2\sqrt{3}$	$D/2$	$pD/2$
-2	0	0	6	6	$-5D/2\sqrt{3}$	$-D/2$	$pD/2$

APPENDIX 2. RELATION BETWEEN THE TENSOR FORCE CONSTANTS AND THE SECOND ORDER PARAMETERS USED IN THE PRESENT MODEL

The tensor force constant matrices up to fourth neighbours are given in detail by Iyengar *et al.* [5]. Their notation is followed here. The force constant matrices corresponding to the various atoms listed in Tables 1 to 5 of Appendix 1 are given below:

$$\Phi_u^{(0\ I)} (I=3) = \begin{bmatrix} \alpha^* + 2\beta^* & \delta^* & 0 \\ -\delta^* & \alpha^* - 2\beta^* & 0 \\ 0 & 0 & \gamma^* \end{bmatrix}$$

$$\Phi_u^{(0\ N)} (N=3) = \begin{bmatrix} A^* & B^* & 0 \\ B^* & C^* & 0 \\ 0 & 0 & D^* \end{bmatrix}$$

$$\Phi_u^{(0\ K)} (K=1) = \begin{bmatrix} \theta^* & 0 & 0 \\ 0 & \theta^* & 0 \\ 0 & 0 & \phi^* \end{bmatrix}$$

$$\Phi_u^{(0\ J)} (J=3) = \begin{bmatrix} \lambda^* + 2\mu^* & 0 & 0 \\ 0 & \lambda^* - 2\mu^* & -2\sigma^* \\ 0 & -2\sigma^* & \nu^* \end{bmatrix}$$

$$\Phi_u^{(0\ M)} (M=3) = \begin{bmatrix} \xi^* + 2\eta^* & 0 & 0 \\ 0 & \xi^* - 2\eta^* & 2\chi^* \\ 0 & 2\chi^* & \zeta^* \end{bmatrix}$$

These force constant matrices may be compared with the matrices obtained in the present model. The expressions for the tensor force constants in terms of the second order parameters in the present model are given below.

$$\alpha^* = D^2 \left(2\alpha + \frac{5}{2}\beta + \frac{\epsilon_1}{6} \right) \quad \zeta^* = p^2 D^2 (\gamma_2 + \delta_2)$$

$$\beta^* = D^2 \left(\alpha + \frac{\beta}{2} + \frac{\epsilon_1}{6} \right) \quad \theta^* = D^2 \left(3\kappa + 9\kappa' + \frac{\delta_1}{2} + 2\delta_2 \right)$$

$$\delta^* = 0 \quad \phi^* = p^2 D^2 \left[4\tau + \frac{9}{4} (\delta_1 + \delta_2) \right]$$

$$\gamma^* = p^2 D^2 \left(2\kappa - \frac{\epsilon_1}{2} \right) \quad A^* = 3D^2 (\rho + \beta')$$

$$\lambda^* = \frac{D^2}{3} (2\gamma_1 + \epsilon_1) \quad B^* = 3\sqrt{3} D^2 \left(\rho + \frac{\beta'}{2} \right)$$

$$\mu^* = \frac{D^2}{3} (\epsilon_1 - \gamma_1) \quad C^* = D^2 (9\rho + 3\beta')$$

$$\nu^* = p^2 D^2 (\gamma_1 + \delta + 2\epsilon_1) \quad D^* = 2\kappa' p^2 D^2$$

$$\sigma^* = \frac{pD^2}{\sqrt{3}} \left(\gamma_1 + \frac{\delta_1}{2} - \frac{\epsilon_1}{4} \right)$$

$$\xi^* = \left(\frac{D^2}{3} \right) \times 8\gamma_2$$

$$\eta^* = -\frac{D^2}{3} \times 4\gamma_2$$

$$\chi^* = \frac{pD^2}{\sqrt{3}} (2\gamma_2 + \delta_2). \quad (1.A2)$$

In the tensor force model, Iyengar *et al.* impose a condition on the force constants given by

$$3\gamma^* + \nu^* + 4\zeta^* = \frac{1}{2} [\lambda^* + \xi^* + 2\theta^*] \times p^2$$

which they call as the equilibrium condition. On substitution for the tensor force constants from equations (1) above, this relation is seen to be automatically satisfied. Since in the present model the potential is automatically

rotationally invariant, the above condition is trivially satisfied.

APPENDIX 3. EXPRESSIONS FOR THE LIMITING FREQUENCIES AT THE POINTS Γ , A AND M IN THE ZONE

The expressions for the limiting frequencies at the points $\Gamma(0,0,0)$, $A(0,0,0.5)$ and $M(0.5,0,0)$ in the Brillouin zone are given below:

points in
the $B \cdot Z$

$$\Gamma : \omega_{L,0}^2(0,0,0) = \frac{2p^2 D^2}{M} [6\gamma_1 + 6\gamma_2 + 6\delta_1 + 6\delta_2 + 12\epsilon_1]$$

$$\Gamma : \omega_{T,0}^2(0,0,0) = \frac{2D^2}{M} [4\gamma_1 + 2\epsilon_1 + 16\gamma_2]$$

$$A : \omega_{L,0}^2(0,0,0.5) = \frac{p^2 D^2}{M} [6\gamma_1 + 12\epsilon_1 + 6\gamma_2 + 15\delta_1 + 15\delta_2 + 16\tau]$$

$$A : \omega_{T,0}^2(0,0,0.5) = \frac{D^2}{M} [4\gamma_1 + 2\epsilon_1 + 16\gamma_2 + 12\kappa + 36\kappa' + 2\delta_1 + 8\delta_2]$$

$$M : \omega_{L,0}^2(0.5,0,0) = \frac{D^2}{M} \left[\left(4\gamma_1 + \frac{14}{3}\epsilon_1 + 16\gamma_2 + 24\alpha + 24\beta + 24\rho + 48\beta' \right) \pm \frac{1}{3} |(4\gamma_1 - 10\epsilon_1 + 48\gamma_2)| \right]$$

$$M : \omega_{T,0(Y)}^2(0.5,0,0) = \frac{D^2}{M} [(4\gamma_1 + 2\epsilon_1 + 16\gamma_2 + 8\alpha + 16\beta + 72\rho + 72\beta') \pm |4\gamma_1 - 2\epsilon_1 - 16\gamma_2|]$$

$$M : \omega_{T,0(Z)}^2(0.5,0,0) = \frac{p^2 D^2}{M} [(6\gamma_1 + 8\epsilon_1 + 6\gamma_2 + 6\delta_1 + 6\delta_2 + 16\kappa + 16\kappa') \pm |(2\gamma_1 + 2\delta_1 + 4\epsilon_1 - 6\gamma_2 - 6\delta_2)|]$$

MAGNETIC PROPERTIES OF FLUORIDE SUBSTITUTED ORTHOFERRITES

M. ROBBINS, R. D. PIERCE and R. WOLFE

Bell Telephone Laboratories, Incorporated, Murray Hill, N.J. 07971, U.S.A.

(Received 13 October 1970)

Abstract—Substituted rare earth orthoferrites (LnFeO_3) with the general formula $\text{LnM}_x^{2+}\text{Fe}_{1-x}\text{O}_{3-x}\text{F}_x$ where $\text{Ln} = \text{Y, La-Yb}$, and $\text{M}^{2+} = \text{Ni}^{2+}, \text{Mn}^{2+}, \text{Cu}^{2+}$, have been prepared and studied. When $\text{M}^{2+} = \text{Ni}^{2+}$ and $x = 0.2$ the substituted materials exhibited magnetic moments which were of the order of four times those of the unsubstituted orthoferrites. Curie temperatures were observed to decrease $\sim 20^\circ$. Cu^{2+} and F^- ($x = 0.2$) substitution did not bring about appreciable changes in either the magnetic moments or T_c . $\text{Mn}^{2+}-\text{F}^-$ ($x = 0.2$) substitution resulted in appreciable decreases in T_c ($30-60^\circ$) but did not produce a uniform trend in magnetic moments. In $\text{Ni}^{2+}-\text{F}^-$ substituted HoFeO_3 and SmFeO_3 magnetic moments were found to increase with increasing substitution.

1. INTRODUCTION

THE RARE earth orthoferrites[1] (orthorhombic LnFeO_3) are weakly ferromagnetic at room temperature. The magnetic moments arise from a small canting of the sublattice moments away from perfectly antiferromagnetic alignment. In unsubstituted orthoferrites this canting is of the order of $\frac{1}{2}$ degree resulting in net moments of about 1 per cent of the full moment of the iron spins. Recently there has been renewed interest in the orthoferrites because of their applicability to bubble domain devices[2]. The diameter of the 'bubbles' (cylindrical magnetic domains) is controlled by the material parameter $l = \sigma_w / 4\pi M_s^2$ [3], where σ_w is the domain wall energy and M_s the saturation magnetization. Small values of l are desirable to permit small bubbles and therefore high packing densities in the devices. Control of the bubble size has been obtained by utilizing the reduction of the uniaxial anisotropy which occurs near the spin reorientation temperature in orthoferrites[4]. The reduced bubble diameters are obtained, however, at the expense of an undesirable temperature sensitivity[5]. It was of interest, therefore, to investigate the possibility of decreasing the material parameter by increasing the moments of the orthoferrites through substitution of Fe^{3+} by di-

valent (M^{2+}) transition metal ions. Charge compensation was affected by the replacement of O^{2-} by F^- giving the general formula $\text{LnM}_x^{2+}\text{Fe}_{1-x}^{3+}\text{O}_{3-x}\text{F}_x$. Fluorine substitution for charge compensation was deemed superior to cation substitution (M^{4+} for Fe^{3+}) as the latter method would dilute the magnetic sublattices with nonmagnetic M^{4+} (e.g., Ti^{4+}) cations.

2. PREPARATION

Materials of the type $\text{LnM}_x^{2+}\text{Fe}_{1-x}^{3+}\text{O}_{3-x}\text{F}_x$ where $\text{Ln} = \text{Y, La-Yb}$, and $\text{M}^{2+} = \text{Ni, Co, Mn and Cu}$ were prepared from appropriate mixtures of Ln_2O_3 , MF_2 , MO (or MCO_3) and Fe_2O_3 . After mixing, the powders were pressed into pellet form and fired for 12 hr. at 1200°C in anhydrous Ar gas. X-ray analysis ($\text{CrK}\alpha$ radiation) was used to determine single phase formation. X-ray diffractometry, however, cannot detect the presence of impurities in small concentrations (≈ 5 per cent or less) and magnetic Curie temperature (T_c) measurements were used to identify magnetic impurities in amounts below the X-ray detection level. Two samples ($\text{GdNi}_{0.2}\text{Fe}_{0.8}\text{O}_{2.8}\text{F}_{0.2}$ and $\text{HoNi}_{0.2}\text{Fe}_{0.8}\text{O}_{2.8}\text{F}_{0.2}$) were prepared by firing pressed pellets in sealed evacuated platinum tubes. The resultant materials were identical to those prepared by the previously described

method. The results of cation chemical analysis were in good agreement (± 1 per cent by weight) with calculated values. F⁻ analysis were in fair (± 5 –10 per cent by weight) agreement with calculated values.

Unit cell parameters (using CuK α radiation) are shown in Tables 1–3. While no systematic trends are found in the individual cell parameters the unit cell volumes of substituted orthoferrites are all smaller than those of the unsubstituted compounds. In orthoferrites where Ln = Ho and Sm the limits of Ni-F substitution were found to be $x \sim 0.3$ and $x \sim 0.2$ respectively.

Magnetic properties

Apart from obtaining the magnetic properties of these substituted orthoferrites, magnetic measurements were used to determine the

presence of magnetic second phases by observing their magnetic ordering temperatures. The magnetic phases which are formed as impurities are spinels and garnets. Even if these are present in amounts below the level of X-ray detectability, they can seriously affect the observed magnetic properties since they have much larger magnetic moments than the orthoferrites. Therefore, magnetic measurements up to 600°C were performed on all samples in order to detect the presence of multiple Curie points. Figure 1 illustrates the detection of magnetic impurities in a sample of polycrystalline YbFeO₃. In this case X-ray diffraction indicated the presence of only the orthoferrite phase. No impurity diffraction lines were visible. In the magnetic measurement, however, three distinct Curie points are visible, one at 280°C, a second at

Table 1. Crystallographic and magnetic properties of substituted orthoferrites of the type LnFe_{0.8}Ni_{0.2}O_{2.8}F_{0.2} compared with unsubstituted orthoferrites

Ln	<i>a</i>	$\frac{\text{\AA}}{b}$	<i>c</i>	$\frac{V}{\text{\AA}^3}$	$\frac{d}{\text{gm/cc}}$	<i>T_c</i> °K	4π <i>M_s</i>
Y	5.274	5.586	7.581	223.3	5.77	625	320
YFeO ₃				224.6	5.67	643	105
La	5.513	5.524	7.833	238.5	6.77	720	340
LaFeO ₃				243.1	6.63	738	83
Pr	5.464	5.547	7.762	235.2	6.94	650	320
PrFeO ₃				239.4	6.79	707	71
Nd	5.439	5.564	7.738	234.2	7.07	675	250
NdFeO ₃				235.1	7.01	693	62
Sm	5.361	5.590	7.692	230.5	7.36	655	410
SmFeO ₃				232.6	7.26	673	84
Eu	5.368	5.599	7.670	230.5	7.40	645	330
EuFeO ₃				231.6	7.34	663	83
Gd	5.341	5.539	7.651	226.4	7.69	645	470
GdFeO ₃				230.2	7.52	661	94
Tb	5.314	5.575	7.618	225.7	7.80	640	370
TbFeO ₃				227.8	7.66	652	137
Dy	5.293	5.590	7.603	225.0	7.90	630	360
DyFeO ₃				225.6	7.84	645	128
Ho	5.270	5.581	7.594	223.4	8.03	630	390
HoFeO ₃				224.3	7.96	643	91
Er	5.249	5.564	7.559	220.8	8.19	620	340
ErFeO ₃				223.0	8.08	641	81
Tm	5.227	5.564	7.559	219.8	8.28	615	420
TmFeO ₃				222.1	8.15	631	140
Yb	5.227	5.564	7.559	219.8	8.40	615	520
YbFeO ₃				220.1	8.35	632	143

Table 2. Crystallographic and magnetic properties of substituted orthoferrites of the type $\text{LnCu}_{0.2}\text{Fe}_{0.8}\text{O}_{2.8}\text{F}_{0.2}$ compared with unsubstituted orthoferrites

Ln	a	$\begin{smallmatrix} \text{\AA} \\ b \end{smallmatrix}$	c	$\begin{smallmatrix} \text{\AA}^3 \\ V \end{smallmatrix}$	$\begin{smallmatrix} d \\ \text{gm/cc} \end{smallmatrix}$	$\begin{smallmatrix} T_c \\ ^\circ\text{K} \end{smallmatrix}$	$4\pi M_s$
Sm	5.372	5.579	7.681	230.2	7.39	675	75
SmFeO ₃				232.6	7.26	673	84
Gd	5.330	5.590	7.647	227.8	7.67	660	80
GdFeO ₃				230.2	7.52	661	94
Ho	5.289	5.590	7.600	224.3	8.02	640	90
HoFeO ₃				224.3	7.96	643	91

Table 3. Crystallographic and magnetic properties of substituted orthoferrites of the type $\text{LnMn}_{0.2}\text{Fe}_{0.8}\text{O}_{2.8}\text{F}_{0.2}$ compared with unsubstituted orthoferrites

Ln	a	$\begin{smallmatrix} \text{\AA} \\ b \end{smallmatrix}$	c	$\begin{smallmatrix} \text{\AA}^3 \\ V \end{smallmatrix}$	$\begin{smallmatrix} d \\ \text{gm/cc} \end{smallmatrix}$	$\begin{smallmatrix} T_c \\ ^\circ\text{K} \end{smallmatrix}$	$4\pi M_s$
Y	5.243	5.597	7.568	222.1	5.78	620	90
YFeO ₃				224.6	5.67	643	105
Gd	5.340	5.614	7.641	229.1	7.58	625	145
GdFeO ₃				230.2	7.52	661	94
Tb	5.314	5.575	7.618	225.7	7.77	565	150
TbFeO ₃				227.8	7.66	652	137
Ho	5.278	5.610	7.589	224.7	8.06	615	80
HoFeO ₃				224.3	7.96	643	91
Er	5.258	5.586	7.565	222.2	8.12	595	45
ErFeO ₃				223.0	8.08	641	81

360°C, and a third at 590°C. These agree well with previously reported Curie temperatures [6] of ytterbium iron garnet (275°C), ytterbium orthoferrite (359°C) and magnetite (585°C). From the observed moments, the impurity levels are estimated to be ~5 per cent garnet and ~1 per cent magnetite. The results reported below are for samples which exhibit only a single Curie point at a temperature in reasonable accord with that of the unsubstituted orthoferrite.

The variation of magnetization with temperature for a specimen of $\text{HoNi}_{0.2}\text{Fe}_{0.8}\text{O}_{2.8}\text{F}_{0.2}$ which does not exhibit magnetic second phases is shown in Fig. 2. This figure also illustrates the measurement cycle. The sample as prepared shows little or no ferromagnetic character, probably because of high domain wall coercivity. As the material is heated in a mag-

netic field, the magnetization falls gradually until T_c is approached, where a small anomaly is observed. Upon cooling the sample through the Curie temperature in the presence of the applied magnetic field, the magnetization rises to values much larger than those observed before heating and exhibits definite ferromagnetic character. Further cycling through T_c may give further increases in moment, as is the case for the sample shown. This cycling is continued until it fails to yield appreciable further increase in moment. Usually two or three cycles are adequate. The magnetization curves before and after heating are shown as curves 1 and 2 in Fig. 3. The net moment of the sample is obtained from the magnetization curve after heating.

Since the sintered samples consist of randomly oriented grains, the observed moment

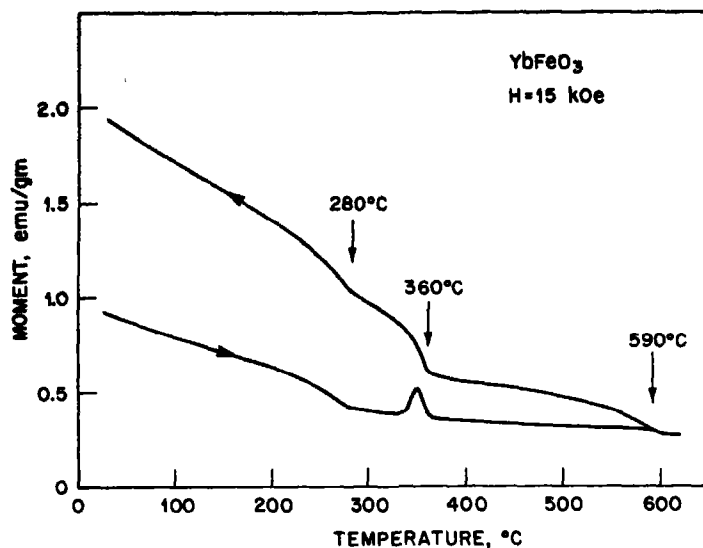


Fig. 1. Detection of magnetic impurities in a sintered sample of YbFeO₃. The Curie point at 360°C is that of YbFeO₃. Curie points at 280 and 590°C indicate garnet and spinel impurities, both of which were below the limit of detection by X-ray diffractometry.

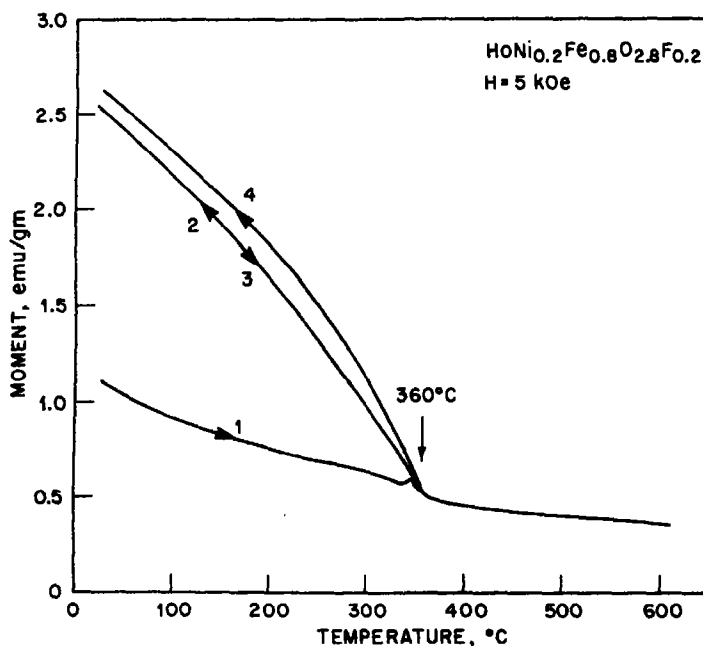


Fig. 2. Variation of magnetization with temperature of a sintered specimen of HoNi_{0.2}Fe_{0.8}O_{2.8}F_{0.2}, demonstrating the absence of magnetic impurities and illustrating the measurement cycle. The correction factor of two has not been applied.

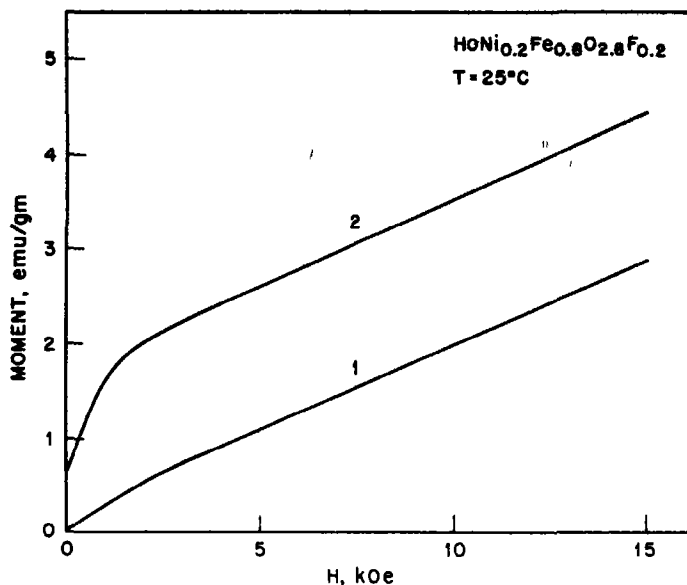


Fig. 3. Magnetization curves of $\text{HoNi}_{0.2}\text{Fe}_{0.8}\text{O}_{2.8}\text{F}_{0.2}$ at room temperature before (curve 1) and after (curve 2) thermal cycling in an applied magnetic field. The correction factor of two has not been applied.

must be adjusted before comparison with single crystal values can be made. The observed moment of a randomly oriented aggregate of magnetic particles with large uniaxial anisotropy should be one-half the single crystal value[7]; therefore in our tables we report moment values which are twice the observed values of the polycrystalline sintered sample. As a check, a polycrystalline sintered sample of GdFeO_3 was prepared in the same manner as the substituted orthoferrites and yielded, after applying the correction factor of two, $\sigma = 1.08 \text{ emu/gm}$, in reasonable agreement with the reported single crystal value of 1.0 emu/gm [8].

Magnetic properties and unit cell parameters of materials with the formula $\text{LnNi}_{0.2}\text{Fe}_{0.8}\text{O}_{2.8}\text{F}_{0.2}$ are shown in Table 1. In most cases Ni^{2+} - F^- substitution brought about decreases in T_c of about 20 – 25° with respect to the unsubstituted orthoferrites. In all cases large increases in magnetic moments were observed. In general the room temperature magnetic moments of these substituted orthoferrites

were ~ 4 times those of the unsubstituted compounds.

Orthoferrites of the type $\text{LnCu}_{0.2}\text{Fe}_{0.8}\text{O}_{2.8}\text{F}_{0.2}$ ($\text{Ln} = \text{Gd}, \text{Sm}, \text{Ho}$) were prepared. Unit cell parameters and magnetic properties are shown in Table 2. These materials showed no significant changes in T_c and room temperature magnetic moments which were ~ 10 per cent smaller than unsubstituted LnFeO_3 .

Mn^{2+} - F^- substituted LnFeO_3 , where $\text{Ln} = \text{Y}, \text{Gd}, \text{Ho}, \text{Er}, \text{Tb}$ and $x = 0.2$ were prepared. X-ray results and magnetic properties are shown in Table 3. Although the decreases in T_c of substituted orthoferrites were reasonably uniform (30 – 40°) the changes in magnetic moments were not. Magnetizations varied nonuniformly from ~ 50 per cent of the unsubstituted orthoferrite moment for $\text{Ln} = \text{Er}$ to ~ 150 per cent of the unsubstituted orthoferrite moment for $\text{Ln} = \text{Gd}$.

Varying amounts of Ni^{2+} and F^- ($x = 0.1, 0.2, 0.3$, and 0.4) were substituted in HoFeO_3 and SmFeO_3 to determine the limit of substitution and the variation of magnetic proper-

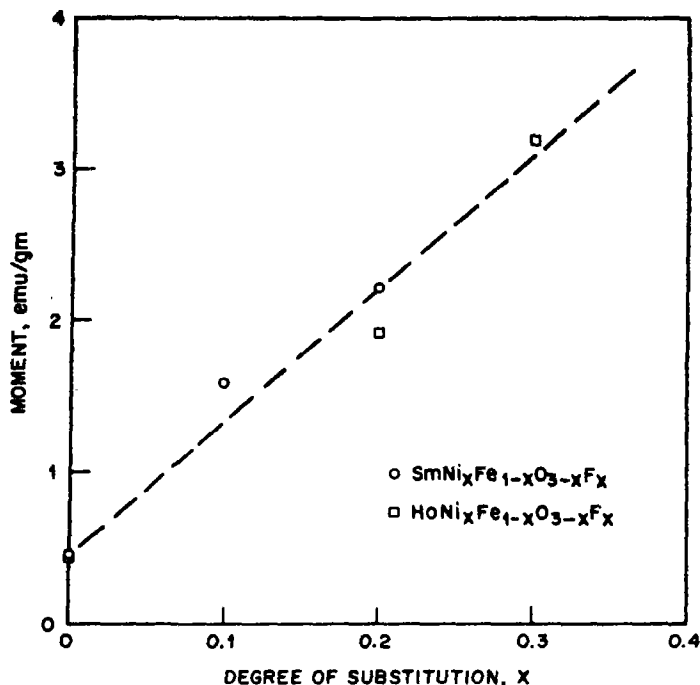


Fig. 4. Variation of saturation magnetization of Ni-F substituted Sm and Ho orthoferrites with degree of substitution. The correction factor of two has not been applied.

ties as a function of the degree of substitution. X-ray and magnetic measurements indicated the presence of Ln_2O_3 and magnetic impurities when $x = 0.4$ for $\text{Ln} = \text{Ho}$ and where $x = 0.3$ for $\text{Ln} = \text{Sm}$. Room temperature magnetic moments vs. composition are shown in Fig. 4. It can be seen that the magnetic moment tends to increase with increasing substitution.

Orthoferrites containing $\text{Co}^{2+}\text{-F}^-$ were prepared and were single phase with respect to X-ray measurements. However upon heating the samples to about 500°C a magnetic impurity appeared (Fig. 5) indicating possible sample decomposition. The magnetic impurity had $T_c > 600^\circ\text{C}$. This behavior made it impracticable to do further work on these materials.

3. DISCUSSION

Magnetic sublattice canting in orthoferrites results[9] from a competition between sym-

metric exchange couplings $\vec{J}\vec{S}_1 \cdot \vec{S}_2$, which favor antiparallel spin configurations, and weaker antisymmetric exchange couplings $\vec{D} \cdot \vec{S}_1 \times \vec{S}_2$ which favor configurations in which \vec{S}_1 and \vec{S}_2 are normal to each other. In the two sublattice model[10], the canting-angle γ is related to the exchange parameters D and J through $\tan 2\gamma = D/J$ and the resultant moment is $M_s = 2M_0 \sin \gamma \approx M_0 D/J$ where M_0 is the sublattice magnetization. The net magnetization can be altered through M_0 , D or J .

The sublattice magnetization M_0 will be determined by the cations present. Replacement of Fe^{3+} by a less magnetic cation (e.g., Co^{2+} , Ni^{2+} , Cu^{2+}) will reduce M_0 and if γ remains unchanged the net moment will be proportionally reduced. The symmetric exchange term J will be weakened by decreases in the strength of the superexchange interactions. Substitution of F^- for O^{2-} in other magnetic oxides[11] has usually led to

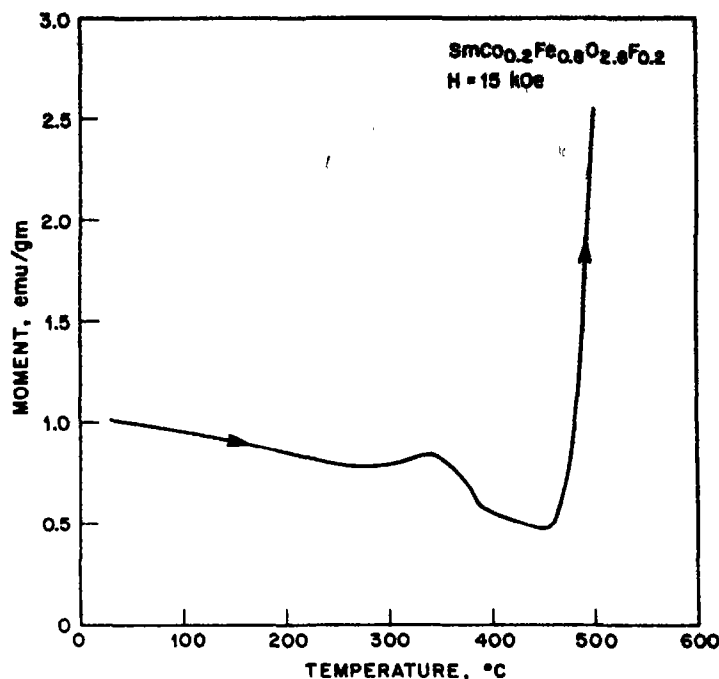


Fig. 5. Magnetization vs. temperature for a sample of Co-F substituted Sm orthoferrite. The abrupt increase of moment near 500°C indicates possible sample decomposition.

decreases in T_c . The reduced Curie temperatures observed in this work indicate weakening of the superexchange interaction. Replacement of Fe^{3+} by M^{2+} is also expected to weaken J [12]. Weaker symmetric exchange coupling would lead in turn to larger sublattice cantings. The strength of the antisymmetric exchange D is estimated[13] to be of the order of $(\Delta g/g)J$ and is expected to increase with increasing cationic spin-orbit coupling. Thus greatly increased sublattice canting should be observed when Ni^{2+} , Co^{2+} or Cu^{2+} are substituted for Fe^{3+} .

The large increases in moment observed with Ni^{2+} -F $^-$ substitution would then seem to agree well with the changes which are expected to occur in D and J . F $^-$ and Ni^{2+} weaken the symmetric superexchange interactions and Ni^{2+} , which has appreciable spin-orbit coupling, would be expected to markedly increase the antisymmetric coupling D . The increase in γ brought about by these effects

could overshadow the decrease in sublattice magnetization M_0 .

Substituted orthoferrites containing Mn^{2+} -F $^-$ and Cu^{2+} -F $^-$ did not give results which would be easily explained in the manner previously discussed. Replacement of Fe^{3+} by isoelectronic Mn^{2+} (d^5) should not alter γ . The uniform decreases of about 30°C with 0.2 moles of substitution is in accord with the expected effects of Mn^{2+} and F $^-$ substitutions. The net magnetic moments however vary greatly in the materials prepared. These variations may be caused by differences in valence states (Mn^{2+} , Fe^{3+} vs. Fe^{2+} , Mn^{3+}). In the case of Cu^{2+} substitution, T_c and the net moment decrease only slightly. Considering the magnetic dilution involved in substituting Cu^{2+} (d^9) for Fe^{3+} (d^5) the net moment observed for these samples could involve small increases in the sublattice canting angle. The fact that Cu^{2+} in an octahedral site exhibits Jahn-Teller distortion[14] probably further

complicates the site symmetry rendering a simple scaling of D in terms of $(\Delta g/g)$ inadequate to describe the processes involved.

In general the canting in the orthoferrites depends in a detailed and complex manner on the wave functions and site and pair symmetries of the ions involved[13]. Substitution for both cation and anion clearly compounds these complexities. It is beyond the scope of this work to attempt detailed explanations of the experimental observations. It can be stated, however, that the canting angle in rare earth orthoferrites can be altered to obtain significant increases in the net magnetic moments. The large increases in magnetic moment which were found in the Ni^{2+} -F substituted orthoferrites should result in significant decrease in bubble domain size. Since it is known that small additions of Co to the orthoferrites causes their net moments to align along the a -axis instead of the usual (except for SmFeO_3) c -axis at room temperature[15], it would be of interest to determine the moment orientation in these substituted orthoferrites. Further experiments in this direction are required. At the present time we are investigating the feasibility of growing crystals of these materials to determine their magnetic domain characteristics.

Acknowledgement—The authors thank W. B. Venard for his valuable technical assistance.

REFERENCES

1. WHITE R. L., *J. appl. Phys.* **40**, 1061 (1969); TREVES D., *J. appl. Phys.* **36**, 1033 (1965); and GOODENOUGH J. B., in *Zahlenwerte und Funktionen*, 6th ed., Vol. II, Part 9, Ch. 2, (Edited by H. H. Landolt and R. Börnstein), Springer-Verlag, Berlin (1962).
2. BOBECK A. H., FISCHER R. F., PERNESKI A. J., REMEIK A. J. P. and VAN UITERT L. G., *IEEE Trans. Mag.* **MAG-5**, 544 (1969); BOBECK A. H., *IEEE Trans. Mag.* **MAG-4**, 450 (1968); BOBECK A. H., *Bell Syst. Tech. J.* **46**, 1901 (1967).
3. THIELE A. A., *Bell Syst. Tech. J.* **48**, 3287 (1969).
4. SHERWOOD R. C., VAN UITERT L. G., WOLFE R. and LeCRAW R. C., *Phys. Lett.* **25A**, 297 (1967).
5. ROSSOL F. C., *IEEE Trans. Mag.* **MAG-5**, 562 (1969).
6. "Bibliography of Magnetic Materials and Tabulation of Magnetic Transition Temperatures", (compiled by T. F. Connolly and E. D. Copenhaver), Research Materials Information Center, Oak Ridge (1969).
7. CHIKAZUMI S., *Physics of Magnetism*, p. 249, Wiley, New York (1966).
8. TREVES D., *J. appl. Phys.* **37**, 1033 (1965).
9. TREVES D., *Phys. Rev.* **125**, 1843 (1962).
10. HERMANN G. F., *J. Phys. Chem. Solids* **24**, 597 (1963).
11. ROBBINS M., LERNER S., BANKS E., *J. Phys. Chem. Solids* **24**, 759 (1963).
12. ANDERSON P. W., in *Magnetism*, Vol. I, (Edited by G. T. Rado and H. Suhl), Academic Press, New York (1963).
13. MORIYA T., in *Magnetism*, Vol. I (Edited by G. T. Rado and H. Suhl), Academic Press, New York (1963).
14. BLEANEY B. and STEVENS K. W. H., *Rep. Progr. Phys.* **16**, 108 (1953).
15. VAN UITERT L. G., SHERWOOD R. C., GYORGY E. M. and GRODKIEWICZ W. H., *Appl. Phys. Lett.* **16**, 84 (1970).

THE THERMAL CONDUCTIVITY OF A HARD SPHERE SOLID*

D. M. GASS†, B. J. ALDER and T. E. WAINWRIGHT

Lawrence Radiation Laboratory, University of California, Livermore, Calif. 94550, U.S.A.

(Received 13 October 1970)

Abstract—The thermal conductivity of an f.c.c. hard sphere solid has been evaluated by molecular dynamics computation. From near close-packing to melting, the results are in virtual agreement with the Enskog theory. The dominant potential contribution yields nearly the Enskog value, while the kinetic and cross terms deviate less than 20 per cent, in opposite directions, from the predicted values. The deviations of the heat-flux autocorrelation function from an exponential are discussed.

THE THERMAL conductivity and its components for a hard sphere fluid have been evaluated by computer calculation over a wide density range[1]. These quantities were found to be within 10 per cent of the values predicted by the Enskog theory[2]. In the same manner as used in Ref. [1], we have calculated the thermal conductivity and its components, and the heat-flux autocorrelation function and its components for a perfect face-centered cubic solid. The Einstein-type expression for the transport coefficient was used instead of the autocorrelation function representation. The runs were about 2 million collisions in length, except for the 500 particle run which was 5 million collisions long. The uncertainty in the coefficient of thermal conductivity, λ , is about 4 per cent.

The Enskog expression for the coefficient of thermal conductivity is [2]

$$\lambda_E = \frac{\lambda_0 B}{yV} \left[1 + \frac{6y}{5} + 0.757 y^2 \right], \quad (1)$$

where λ_0 is the low-density thermal conductivity, B is the second virial coefficient, V is the volume and $y = pV/NkT - 1$.

The leading term in this expansion (in powers of y) arises from the bodily movement of molecules between collisions and is the kinetic term; the highest order term derives from energy exchanged while molecules are in contact and is the potential term. The remaining term is the cross term. If λ_0 is replaced by its first approximation, λ_0^0 , which is obtained from the zeroth order Sonine polynomial solution of the Boltzmann equation, the kinetic and cross terms in equation (1) correspond to processes whose autocorrelation functions decay exponentially. With λ_0^0 in the right-hand side of (1), the left-hand side of (1) becomes λ_E^0 , which differs from λ_E by the Sonine polynomial correction factor ($\lambda_E/\lambda_E^0 = 1.025$).

The coefficient of thermal conductivity, given in terms of the heat-flux autocorrelation function, is [3]

$$\lambda = \frac{1}{3VkT^2} \int_0^\infty \langle Q(0) \cdot Q(t) \rangle dt, \quad (2)$$

where the microscopic heat flux is

$$Q = \sum_i v_i(E_i - h_0) + \frac{1}{2} \sum_{i \neq j} \mathbf{r}_{ij} v_i \cdot \mathbf{F}_{ij}. \quad (3)$$

\mathbf{F}_{ij} is the force molecule i exerts on molecule j , $\mathbf{r}_{ij} = \mathbf{r}_j - \mathbf{r}_i$ is the vector separation of i and j , \mathbf{v}_i is the velocity of i and E_i is its energy. In

*Work performed under the auspices of the U.S. Atomic Energy Commission.

†Present Address: Dept. of Physics, University of Toronto, Toronto 5, Ontario, Canada.

our calculation each element of the ensemble average has zero total momentum so that $\sum_i \mathbf{v}_i/h_0 = 0$, where h_0 is the average enthalpy per molecule. In addition, for hard spheres E_i is the kinetic energy of molecule i . The integral of the autocorrelation of $\sum_i \mathbf{v}_i E_i$ is the kinetic term in the thermal conductivity, involving only the velocities of the particles; the autocorrelation of $\sum_{i \neq j} \mathbf{r}_{ij} \mathbf{v}_i \cdot \mathbf{F}_{ij}$ involves intermolecular forces, and its integral is the potential term.

The ratios of the computed values of λ to those of λ_E^0 and the ratios of their components are given in Table 1. The number of molecules in the system is indicated by N , and the volume, V , is given in relation to the close-packed volume, V_0 . The 107 particle systems are identical to those of 108 particles of the same V/V_0 , except that one particle is replaced by a hole. There is nearly quantitative agreement between the molecular dynamics results and the Enskog theory for the thermal conductivity and for its potential part (P), which constitutes in excess of 90 per cent of the total.

$W_{0E}/2$, which constitutes more than half of the potential term. The machine values of $W_0/2$ were obtained by an extrapolation to the initial time and they agree with the theoretical value within experimental error. At $V/V_0 = 1.3448$ ($N = 108$), where the hard sphere solid does not melt regardless of the size of the system, $W_0/W_{0E} = 1.0024 \pm 0.007$.

The kinetic term (K) is 10 per cent less than the Enskog value for the 500 particle system and 15 per cent less than the Enskog value for the 108 particle systems. This difference is reflected in the dependence of the kinetic heat-flux autocorrelation function on the size of the system. In the kinetic term there appears to be an enhancement of the energy transport due to a vacancy. In Table 1, λ^K/λ_E^{0K} is shown to increase a few per cent by the replacement of a molecule by a hole. The increased energy transport may arise from the greater mobility of molecules in such a system. This phenomenon is also seen in passing from the solid to the fluid region, where there is an abrupt increase of about 15 per cent in λ^K/λ_E^{0K} and about 5 per cent in λ/λ_E^0 .

Table 1. The calculated values of the thermal conductivity and its components are normalized by the Enskog values, obtained from the zeroth order Sonine polynomial solution to the Boltzmann equation. V_0 is the close-packed volume and N is the number of molecules

V/V_0	N	λ/λ_E^0	λ^P/λ_E^{0P}	λ^K/λ_E^{0K}	λ^C/λ_E^{0C}
1.01	108	1.01 ± 0.06	1.01 ± 0.06	0.89 ± 0.06	1.20 ± 0.09
1.3448	107	1.00 ± 0.03	0.99 ± 0.03	0.88 ± 0.02	1.09 ± 0.04
1.3448	108	1.00 ± 0.04	0.99 ± 0.04	0.86 ± 0.03	1.10 ± 0.05
1.3448	500	1.00 ± 0.05	0.98 ± 0.04	0.91 ± 0.04	1.13 ± 0.06
1.42	107	0.99 ± 0.01	0.97 ± 0.01	0.91 ± 0.02	1.09 ± 0.01
1.42	108	0.97 ± 0.04	0.96 ± 0.04	0.86 ± 0.03	1.05 ± 0.04

The potential heat-flux autocorrelation function contains a delta function contribution, $W_0\delta(t-0)$, which arises from the impulsive nature of the interactions. The integral of this term, $W_0/2$, can be evaluated analytically and is identical to a term in the Enskog theory,

For the cross term (C), λ^C/λ_E^{0C} is greater than unity for all solid densities and appears to increase as the density increases.

The initial value and slope of the kinetic heat-flux autocorrelation function and the initial value of the cross heat-flux autocorre-

lation function can be calculated exactly, and they are in agreement with the machine values within experimental error. Using the molecular chaos approximation, which is valid only at low density, the initial slope of the cross heat-flux autocorrelation function can also be evaluated. Nevertheless, even at these densities, the theoretical value is found to be within the statistical accuracy of the results. These initial conditions define an exponentially decaying autocorrelation function, $\sim e^{-8s/15}$ (where s is the mean number of collisions per particle), which yields the kinetic and cross terms of λ_E^0 .

The potential heat-flux autocorrelation function is given by the sum of $W_0\delta(t-0)$ and $W_1(t)$, where the latter term decays approximately exponentially in fluids[1]. For f.c.c. solids, however, the initial decay of $W_1(t)$ is strongly density dependent. Although near melting, the initial decay of $W_1(t)$ is only 25 per cent slower than that obtained from $e^{-8s/15}$, at higher densities $W_1(t)$ increases at very early times. At $V/V_0 = 1.01$ and 1.3448 , this aberrant behavior lasts for about 1.5 mean collision times per particle. In these dense systems the repulsive forces of neighboring molecules on a molecule at the initial time must act in the same direction as the initial displacement direction of this molecule. For times greater than 1.5 mean collision times, $W_1(t)$ decays at least as fast as an exponential.

The normalized, kinetic heat-flux autocorrelation function, ρ_λ^K , reveals a characteristic negative deviation from the exponential, $\rho_{\lambda E}^K$, which is found for all densities within the solid region in both the 108 and 500 particle systems. In Fig. 1, $\rho_\lambda^K - \rho_{\lambda E}^K$ is plotted at $V/V_0 = 1.3448$. The bars indicate a typical statistical error. Further, ρ_λ^K itself falls below zero at about 10 mean collision times, due to back-scattering events.

The Enskog theory is a short-time theory. The kinetic and cross terms are approximately given by autocorrelation functions, which decay exponentially to nearly zero in only a few mean collision times. More than half the

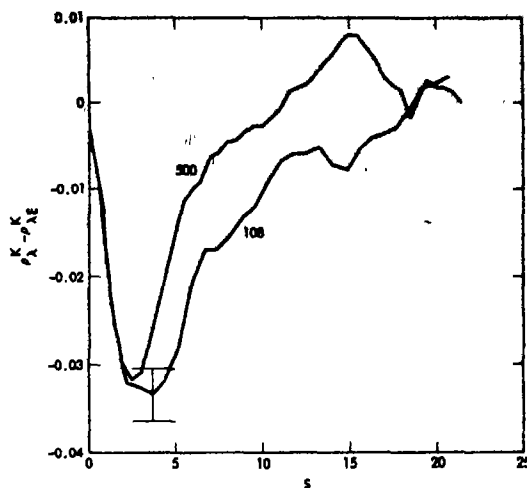


Fig. 1. The difference between the normalized, kinetic heat-flux autocorrelation function, ρ_λ^K , and the exponential one given by the Enskog theory, $\rho_{\lambda E}^K$, as a function of time, s , measured in mean collision times at a density of $V/V_0 = 1.3448$ for 108 and 500 particles. The initial value of $\rho_{\lambda E}^K$ is corrected for the finite size of the system. The vertical bars indicate the typical statistical error in the molecular dynamics result.

potential term arises from correlations at the initial time, while the remainder is due primarily to early-time correlations. Therefore, the close agreement between the Enskog theory and the machine calculations must arise from the fact that only short-time correlations contribute importantly to the thermal conductivity of hard sphere solids.

In fluids many-body interactions have been shown to set up velocity fields, which persist for many mean collision times and extend over large numbers of molecules[4]. Thus, the long-time decay of the autocorrelation functions for fluid systems is expected to be slow, and as a consequence long-time correlations contribute significantly to the transport coefficients. However, the long-time tail of ρ_λ has not been observed as yet in hard sphere fluids [1]. Even so, small correlations in ρ_λ of up to 15 mean collision times have been seen in these fluids[1].

In solid systems long-time correlations among many molecules do not contribute significantly to the thermal conductivity,

because of the confinement of a particle by its nearest neighbors. The collective effects of many-body interactions are confined to relatively fewer particles in solids than in fluids, due to the rapid decay and cancellation of correlations. As a result, the coefficient of thermal conductivity is described quite well in solids by the Enskog theory.

REFERENCES

1. ALDER B. J., GASS D. M. and WAINWRIGHT T. E., *J. chem. Phys.* **53**, 3813 (1970).
2. CHAPMAN S. and COWLING T. G., *The Mathematical Theory of Non-Uniform Gases*, Cambridge University Press, London, (1939).
3. MORI, H., *Phys. Rev.* **112**, 1829 (1958).
4. ALDER B. J. and WAINWRIGHT T. E., *Phys. Rev.* **1**, A18 (1970).

KNIGHT SHIFT, MAGNETIC SUSCEPTIBILITY AND ELECTRICAL RESISTIVITY OF PURE GALLIUM AND GALLIUM-INDIUM EUTECTIC ALLOY IN THE NORMAL AND THE SUPERCOOLED LIQUID STATE

K. SUZUKI* and O. UEMURA†

The Research Institute for Iron, Steel and Other Metals, Tohoku University,
Sendai, Japan

(Received 28 July 1970; in revised form 12 October 1970)

Abstract—Knight shift, magnetic susceptibility, electrical resistivity and density of pure gallium and gallium–indium eutectic alloy were measured over a wide temperature range above and below the melting point in order to study the properties of the supercooled state. From the results of the measurements of Knight shift and electronic magnetic susceptibility, a difference in the temperature dependence was detected between the supercooled liquid and the normal liquid of gallium and gallium–indium eutectic alloy. On the other hand, the measurements of electrical resistivity and density did not indicate any discontinuous change. The temperature dependences of effective mass ratio and average probability density at the nucleus for the *s*-electrons on the Fermi surface were calculated by using the observed results of Knight shift, magnetic susceptibility and density for liquid gallium. From these results a structural change may be expected between the supercooled and the normal liquid gallium.

1. INTRODUCTION

AS MANY investigations have shown prefreezing anomalies[1] in the physical properties of liquid metals and alloys, studies on the supercooled liquid state may provide useful clues on the structures of liquid metals and alloys.

Pure liquid gallium crystallizes normally to a stable solid phase Ga(I) at the melting point of 29.78°C. However, when supercooled below –16.3° and –35.6°C at atmospheric pressure[2], pure liquid gallium can crystallize to the metastable solid phase identified as Ga(II) and Ga(III) at high pressures, respectively. The crystal structures of Ga(I) and Ga(II) are very different and that of Ga(III) is not known at the present time. As shown in Table 1, the melt expands when it crystallizes to Ga(I) and contracts on transforming to Ga(II) or Ga(III)[3].

Concerning the phase transition in the liquid state, from the facts as described above, it is a very interesting problem to ascertain whether differences of structure and properties between the normal liquid and the supercooled liquid of metallic gallium exist or not. It has been found by Turnbull and Cech[4] that the extensive supercooling occurs in finely divided liquid metals. Hence, nuclear magnetic resonance, which can be measured with small droplets, offers a very favourable technique for investigating the physical properties of supercooled liquid metals.

This paper describes some results of measurements of Knight shift, magnetic susceptibility, density and electrical resistivity for pure gallium and gallium–indium eutectic alloy (16.5 at. % In) in the liquid state over a wide temperature range above and below the melting point.

2. EXPERIMENTAL PROCEDURES

(a) Knight shift

The Knight shift measurements throughout this work were made using the nuclear mag-

*Now staying at the Department of Physics, College of Physical Science, University of Guelph, Guelph, Ontario, Canada.

†Present Address: Faculty of Science, Yamagata University, Yamagata, Japan.

Table 1. Structural properties of solid Ga(I), Ga(II), Ga(III) and liquid Ga

	Liquid Ga	Ga(I) Stable solid phase	Ga(II) Metastable solid phase	Ga(III) Metastable solid phase
Temperature of phase transition (°C)		+ 29.78	- 16.3	- 35.6
Crystal structure		D_{2h}^{16} (Orthorhombic) $a = 4.506$ Å $b = 4.506$ Å $c = 7.642$ Å	D_{2h}^{17} (Orthorhombic) $a = 2.90$ Å $b = 8.13$ Å $c = 3.17$ Å	
Number of atoms per unit cell		8	4	
Neighboring atoms	9 ~ 10 atoms at 2.77 ~ 2.84 Å	1 atoms at 2.44 Å 2 atoms at 2.70 Å 2 atoms at 2.74 Å 2 atoms at 2.795 Å	2 atoms at 2.68 Å 4 atoms at 2.87 Å 2 atoms at 2.90 Å 2 atoms at 3.17 Å	
Density (g/cm ³)	6.09 at 29.80°C 6.136 at -16.3°C 6.153 at -35.6°C	5.91 at 29.78°C	6.23 at -16.3°C	6.20 at -35.6°C

netic resonance dispersion spectrometer[5] (JEOL) developed originally by Nagasawa[6]. This is a new method of measuring nuclear magnetic resonance dispersion with a gated beam tube which detects the pure phase modulation of nuclear magnetic resonance dispersion.

At the nuclear magnetic resonance, the change of inductance of a sample coil is given as follows[7].

$$\Delta L = 4\pi\chi'\xi QL \quad (1)$$

where χ' is the real part of the susceptibility of the sample, ξ is the filling factor of the coil, Q is the quality factor of the coil and L is the inductance of the sample coil. The frequency change corresponding to equation (1) is represented as

$$\Delta f = 2\pi\chi'\xi Qf \quad (2)$$

where f is the resonance frequency.

If we use the operating range of a gated beam tube (6BN6) where the linear relation between frequency change and plate current is realized, the dispersion signal at the

resonance can be immediately obtained by measuring the d.c. plate voltage change. The merits of this method are the ease of adjustment necessary to detect the signal and of frequency sweep over the range of about 200 KHz.

All measurements in this work were carried out by means of frequency sweep under a constant static field which was strictly regulated using the proton resonance at 60 MHz. The frequency was swept at speeds varying from 1 KHz/min to 5 KHz/min, depending on the available signal-to-noise ratio. The high frequency field was generated with a frequency synthesizer (MG41A,[†] Anritsu Electric Co., Ltd.) containing a crystal oscillator. When recording the signal, the frequency marks were written down at 1 KHz intervals. The static field was modulated at 80 Hz and its modulation amplitude was kept at 0.1 G peak-to-peak.

The purity of gallium and indium used for this measurement was 99.999 per cent. Pure gallium and gallium-indium eutectic alloy in the liquid state were divided into fine droplets by ultrasound vibration (15 KHz). The dispersing medium used was a silicone oil,

to which a small amount of oleic acid was added as a dispersing agent. The droplet size was of the order of $1 \sim 10\mu$, which was less than skin depth under the experimental conditions.

The sample was cooled by means of a mixture of dry ice and ethyl alcohol, and heated by hot ethyl alcohol. The temperature of the sample was monitored by a copper-constantan thermocouple immersed in the dispersed sample.

(b) Magnetic susceptibility

The magnetic susceptibility measurements were performed by the Faraday method. The horizontal force exerted on a sample by the magnetic field was measured by the Curie-Chenevean type torsion balance (Shimazu Co., Ltd.). Hence, the effects due to the perpendicular forces exerted on the sample, such as the buoyancy and the thermomolecular effect, were negligible in the balance system. The magnetic field used was 15 KG and its fluctuation was held to within 1 per cent. The temperature of the sample was adjusted by a cold nitrogen gas oven when cooling and by a hot silicone oil oven when heating. The temperature measurement was made with the copper-constantan thermocouple fixed near the sample position.

(c) Density

To determine the density of the sample, a quartz vessel of 10 mm dia. and 5mm length, in which the liquid metal sample was placed, was immersed in toluene and its buoyancy was measured on a chemical balance.

(d) Electrical resistivity

The electrical resistivity was measured by an ordinary four probes direct current compensation method. A resistivity cell was constructed of Teflon, because Teflon could withstand the forces of rapid expansion when highly supercooled gallium solidified as Ga(I). Four 0.1mm dia. platinum probes were epoxied into the Teflon cell. Mercury of

99.999 per cent purity was used as a standard to calibrate the ratio of the cell's cross-sectional area to the length.

3. EXPERIMENTAL RESULTS

(a) Pure liquid gallium

Figure 1 shows the observed results for the variation of the Knight shift of ^{69}Ga in pure liquid gallium with temperature. Pure liquid gallium has a negative linear temperature coefficient of Knight shift, whose value is about two times as large as that obtained by Cornell[8], above the melting point, but, as shown in Fig. 1, a significant downward deviation from the linear relation between Knight shift and temperature is observed in supercooled gallium. From this result we can expect the occurrence of phase change in liquid gallium right below the melting point.

The results for the magnetic susceptibility of pure liquid gallium are shown in Fig. 2. The magnetic susceptibility indicates a small diamagnetism which increases slightly with decreasing temperature. But, this diamagnetism increases abruptly when solidified. As shown in Fig. 3, the density of pure liquid gallium increases linearly with decreasing temperature and any discontinuous change of its temperature dependence can not be detected even when entering into the supercooled state.

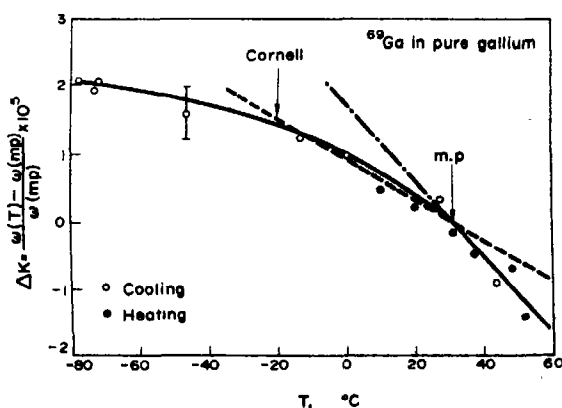


Fig. 1. Temperature dependence of Knight shift of ^{69}Ga in pure liquid gallium.

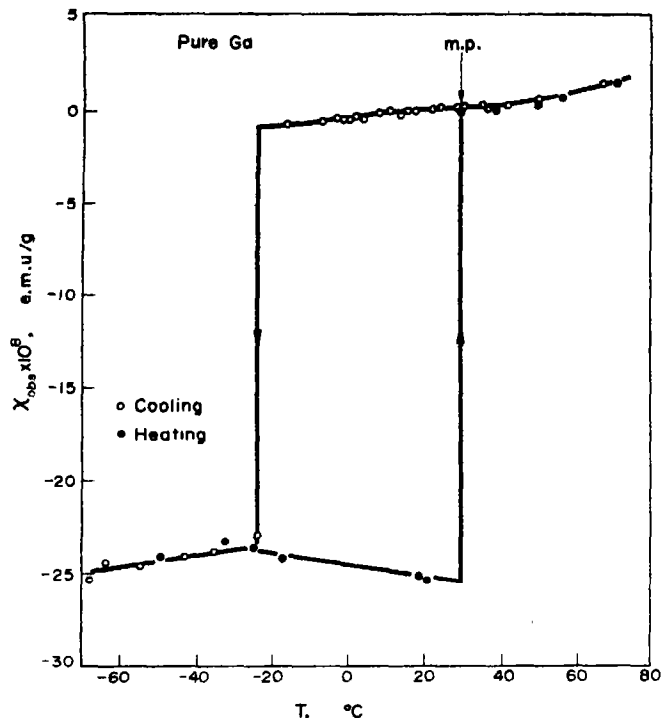


Fig. 2. Temperature dependence of magnetic susceptibility of pure liquid gallium.

Figure 4 shows typical runs of the temperature dependence of the electrical resistivity for pure gallium in the liquid and solid state. When the specimen of liquid gallium is gradually cooled, the resistivity continues to fall linearly through the melting point to the

lowest temperature to which the specimen can be supercooled. In the case of slow cooling, the resistivity is abruptly decreased at the temperature where solidification occurs. On the other hand, the resistivity is often increas-

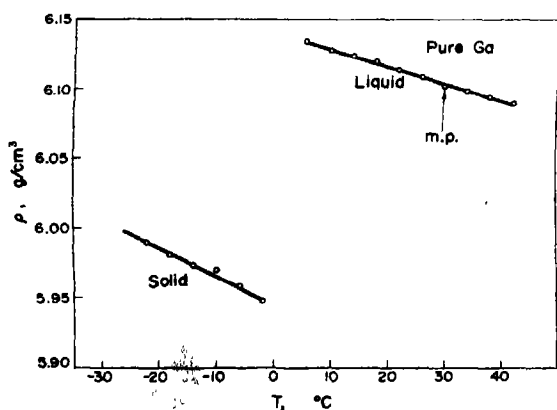


Fig. 3. Temperature dependence of density of pure liquid gallium.

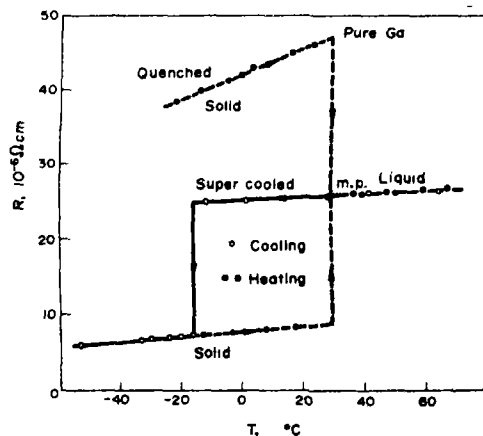


Fig. 4. Temperature dependence of electrical resistivity of pure liquid gallium.

ed in comparison with that in the liquid state when crystallized to the solid state by rapid cooling. This fact confirms the anisotropy of Ga(I) reported by Powell[9]. The solid phase crystallized by slow cooling may be the Ga(II) polymorph and that transformed by rapid cooling may be the Ga(I) polymorph, respectively, because the resistivity of the solid Ga(I) is higher in some crystallographic direction than that of liquid gallium and the resistivity of the solid Ga(II) is always lower than that of liquid gallium[9].

(b) Gallium-indium eutectic liquid alloy

Figures 5 and 6 show the observed results for the variation of the Knight shifts of ^{69}Ga and ^{115}In with temperature. The Knight shift of ^{69}Ga in gallium-indium eutectic liquid alloy has a similar temperature dependence to that in pure liquid gallium, as shown in Fig. 5, in the normal and the supercooled state, respectively. However, the Knight shift of ^{115}In in gallium-indium eutectic liquid alloy increases linearly with decreasing temperatures in both the normal and the supercooled state, and indicates a discontinuous change near the eutectic temperature.

The magnetic susceptibility results for the gallium-indium eutectic liquid alloy are shown in Fig. 7. In the liquid state of the gallium-indium eutectic alloy the observed magnetic

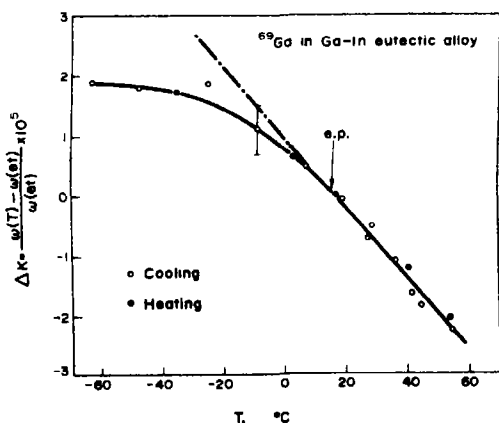


Fig. 5. Temperature dependence of Knight shift of ^{69}Ga in gallium-indium eutectic liquid alloy.

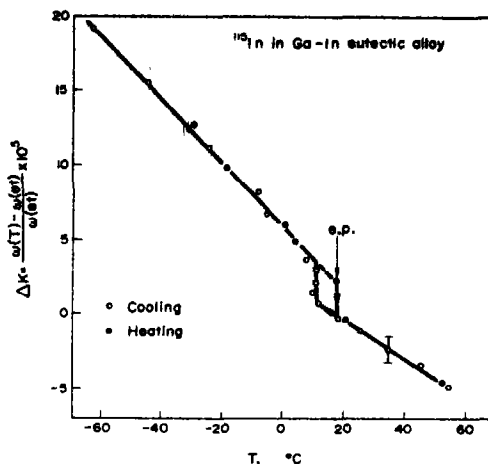


Fig. 6. Temperature dependence of Knight shift of ^{115}In in gallium-indium eutectic liquid alloy.

susceptibility indicates a small diamagnetism which increases slightly with decreasing temperature. In contrast to the Knight shifts, a conspicuous change does not take place in the magnetic susceptibility when entering into the supercooled state. The diamagnetism, however, increases abruptly upon solidification.

As shown in Fig. 8, the density of the gallium-indium eutectic liquid alloy increases linearly with decreasing temperature. However, we find that the linear relation between temperature and density bends abruptly at -5°C .

Figure 9 shows the observed results for the temperature dependence of the electrical resistivity for the gallium-indium eutectic liquid alloy, in comparison with that obtained by Lo and Colligan[10]. The resistivity decreases linearly with decreasing temperature to immediately below the eutectic temperature, 15.7°C . Below the eutectic temperature the temperature dependence of the resistivity deviates sharply from a linear relation and describes a distinctly different continuous curve until the alloy is crystallized at -20°C . Lo and Colligan[10] have considered that such a significant departure from linearity on supercooling is due to a

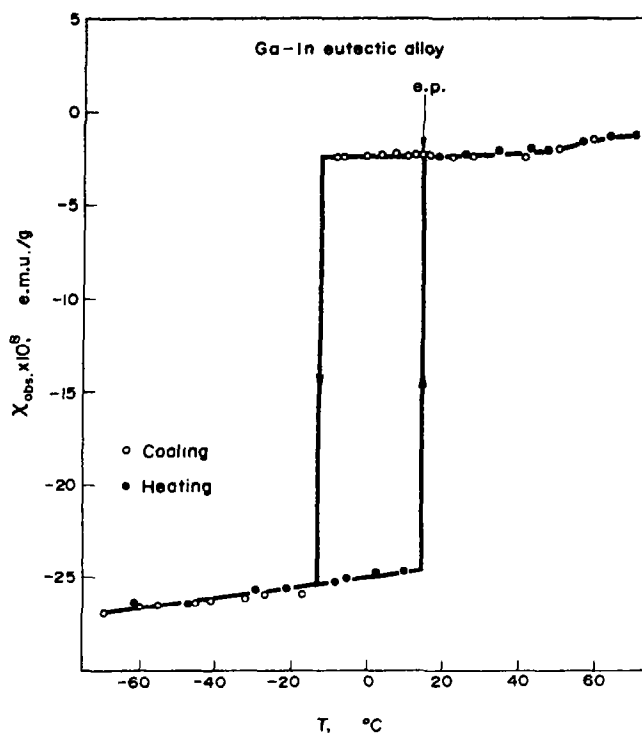


Fig. 7. Temperature dependence of magnetic susceptibility of gallium-indium eutectic liquid alloy.

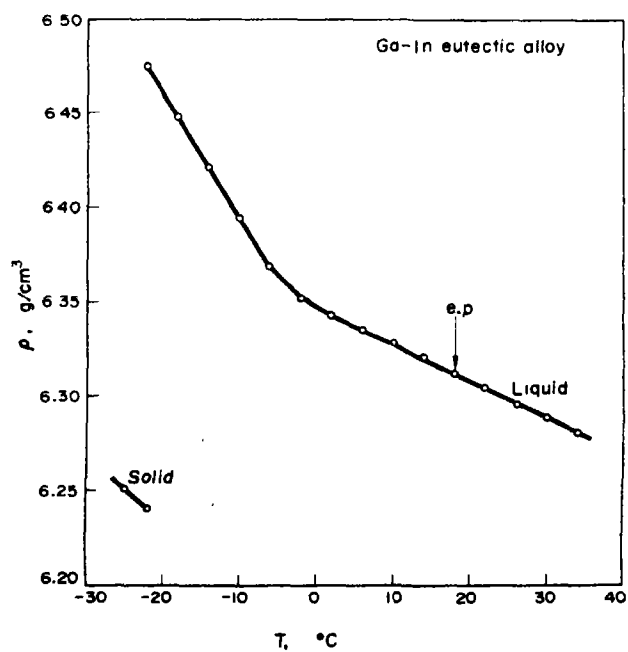


Fig. 8. Temperature dependence of density of gallium-indium eutectic liquid alloy.

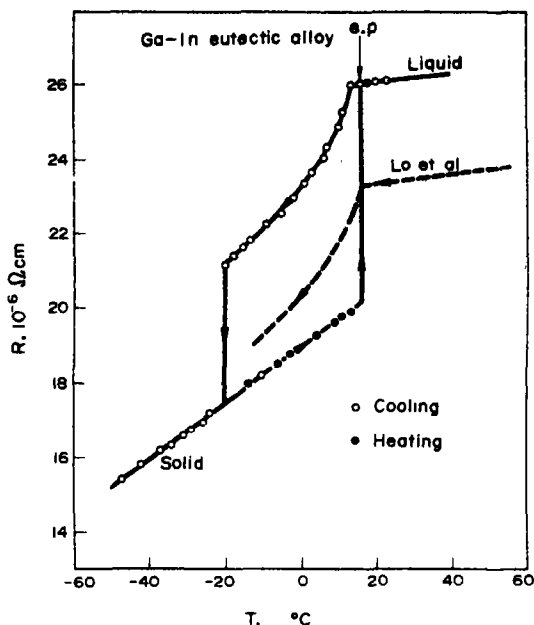


Fig. 9. Temperature dependence of electrical resistivity of gallium-indium eutectic liquid alloy.

continuous precipitation of minute amounts of a solid phase rich in indium.

4. DISCUSSION

The Knight shift usually arises from the magnetic and the electric hyperfine interactions between nuclei and electrons, which are classified as follows [11].

- (1) Fermi contact interaction.
- (2) core polarization interaction.
- (3) orbital interaction.
- (4) dipolar interaction.
- (5) quadrupolar interaction.

In liquid metals the contributions of the dipolar and the quadrupolar interactions to the Knight shift may vanish because the rapid thermal motion of atoms in liquids leads to time-averaged spherical symmetry [12]. In non-transition simple metals the contributions of the core polarization and the orbital interactions to the Knight shift are expected to be small compared with that of the Fermi

contact interaction. Hence, the Knight shift is principally due to the hyperfine field of the spin polarized conduction electrons interacting with the nucleus via the Fermi contact interaction. This direct contact interaction is nonzero only for those conduction electrons having a finite probability amplitude at the nucleus, i.e., whose wave functions are *s*-like. This contribution to the Knight shift is given by

$$K_s = \frac{8}{3} \pi \chi_s \langle |\Psi_F(0)|^2 \rangle, \quad (3)$$

where χ_s is the spin susceptibility per atom for the *s*-like electrons and $\langle |\Psi_F(0)|^2 \rangle$ is the average probability density at the nucleus for the *s*-like electrons on the Fermi surface. In addition to the five interactions as mentioned above, there are additional contributions to the Knight shift from the Landau diamagnetism of the conduction electrons and the diamagnetism of the core states (chemical shift). Since these contributions are also expected to be very small compared with the observed Knight shift of ^{69}Ga and ^{115}In in the present work, they are neglected in the following discussions.

As shown in equation (3), a change in K_s with temperature reflects changes in either or both of χ_s and $P_F = \langle |\Psi_F(0)|^2 \rangle$. Hence, we must examine the variations of χ_s and P_F with temperature, respectively. The total magnetic susceptibility χ_{total} of simple metals may be written as

$$\chi_{\text{total}} = \chi_{\text{ion}} + \chi_e, \quad (4)$$

where χ_{ion} is the diamagnetic susceptibility of the ion core and χ_e is the conduction electron susceptibility.

If the temperature dependence of χ_e is ascribed to the influence not of thermal motion but of thermal expansion or configuration change on the electronic component, the effect can be adequately accounted for in terms of the density dependence of the Fermi energy. Taking into account the density of states

at the Fermi surface expressed as an effective mass and the electron-electron interaction, the electron spin paramagnetic susceptibility χ_s may be given, as Silverstein [13] has derived,

$$\chi_s = \chi_p \left[1 - (1 - \alpha) \frac{\chi_p}{\chi_{p0}} \right]^{-1}, \quad (5)$$

where χ_{p0} is the electron spin paramagnetic susceptibility of free non-interacting electrons, χ_p is that of free interaction electrons with $\alpha = m/m^* = 1$, and $\alpha = m/m^*$ is effective mass ratio. Hence, the complete conduction electron susceptibility χ_e , including diamagnetism, may be reasonably represented by [14]

$$\chi_e = \chi_p \left[\frac{1 - \frac{1}{3}\alpha^2}{1 - (1 - \alpha) (\chi_p/\chi_{p0})} \right]. \quad (6)$$

χ_p and χ_{p0} can be computed as functions of r_s [15], the radius of the electronic sphere for the metal under consideration,

$$r_s = 1.388 \left(\frac{A}{Z\rho} \right)^{1/3} \text{ Bohr units}, \quad (7)$$

where A is atomic weight, Z is valence and ρ is density. In the case of free non-interacting electrons, the Pauli paramagnetism leads to:

$$\chi_{p0}(r_s) \text{ per unit volume} = \frac{2.59}{r_s} \times 10^{-6} \text{ emu/cm}^3, \quad (8)$$

while $\chi_p(r_s)$ has been calculated and presented graphically by Silverstein [13]. The temperature dependence of $\chi_{p0}(r_s)$ for liquid gallium was calculated by equations (7) and (8) using the observed density data in Fig. 3. The calculated result is shown in Fig. 10 together with the observed value of χ_e which is obtained by correcting $\chi_{\text{ion}}(\text{Ga}^{3+}) = -8.00 \times 10^{-6} \text{ emu/mole}$ [16].

As shown in Silverstein's curve for $\chi_p(r_s)$, χ_p/χ_{p0} is approximately constant and equal to 4/3 in the temperature range under consideration. Using the value of χ_e , χ_{p0} and χ_p

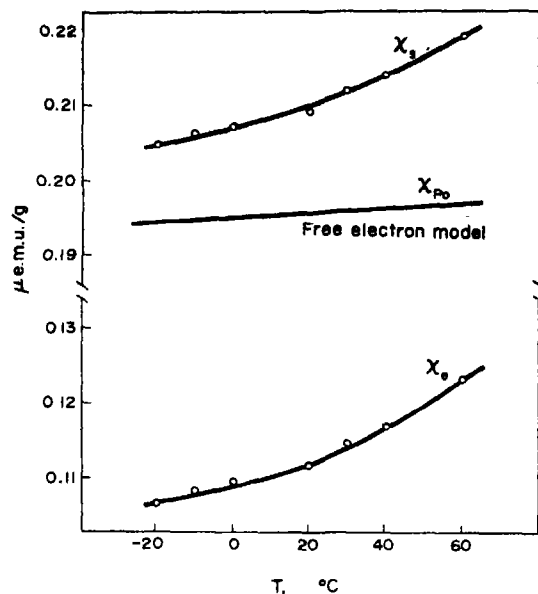


Fig. 10. Calculated values of χ_e , χ_{p0} and χ_s in pure liquid gallium.

obtained by the method as described above, we calculated the temperature dependences of χ_s and $\alpha = m/m^*$, whose results are shown in Figs. 10 and 11.

Figure 11 shows apparently that a change takes place in the relation between $\alpha = m/m^*$ and temperature at about 20°C. The result for $P_F = \langle |\Psi_F(0)|^2 \rangle$ calculated by equation (3) with the values of K_S in Fig. 1 and χ_e in Fig. 10 is shown in Fig. 12, in which we can also

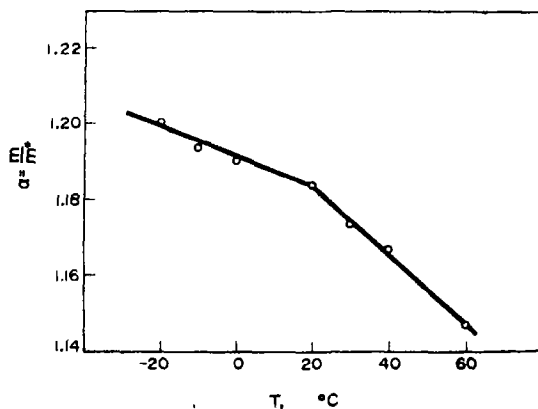


Fig. 11. Temperature dependence of $\alpha (= m/m^*)$ in pure liquid gallium.

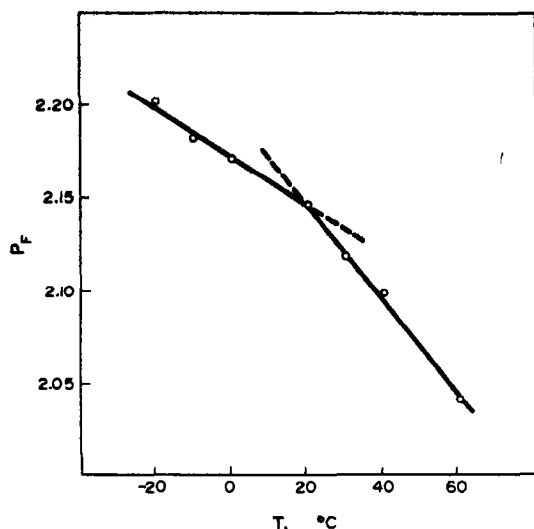


Fig. 12. Temperature dependence of $P_F (= \langle |\psi_F(0)|^2 \rangle)$ in pure liquid gallium.

observe that the temperature dependence of P_F bends at about 20°C. It is very interesting whether such a change means the occurrence of a phase transition in the supercooled state of liquid gallium.

From the X-ray diffraction measurements between 0° and 50°C, Rodriguez and Pings[17] have concluded that the structure of liquid gallium in the supercooled state does not differ significantly from that in the normal state. However, the X-ray diffraction pattern of liquid gallium has an anomaly, i.e., the subsidiary maximum[18, 19] on the high angle side of the main peak, in comparison with patterns of simple liquids. This subsidiary maximum becomes less noticeable at high temperatures owing to the broadening of the main peak, but does not disappear until at least 400°C[20]. Even in the normal state, therefore, liquid gallium indicates a considerable local anisotropy in the atomic distribution. An analogy in the atomic short range order has been found between the liquid phase and the solid metastable phase Ga(II) by Ascarelli[19].

Measurements of electron transport properties[21, 22], angular correlation of positron

annihilation radiation[23] and positron lifetime change on melting[24], all indicate that the free electron model is not an adequate description of the electronic structure of liquid gallium in the normal state near its melting point.

It has been found that the nuclear spin-lattice relaxation time T_1 consists of two parts, i.e., a magnetic hyperfine part and a quadrupolar part in liquid gallium[8, 12, 25]. The magnetic part is consistent with the Korringa-Pines theory. The quadrupolar contribution to T_1 has been explained by Faber[26] on the assumption of pairing of gallium atoms in the liquid state to which there is associated a static electric field gradient. Recently Borsa and Rigamonti[27] have evaluated the quadrupolar relaxation based on a model of diffusing screened ionic charges. The ionic contribution to the nuclear quadrupolar relaxation time has also been calculated by Sholl[28], assuming free ion cores interacting by a long range oscillatory screened potential.

The results obtained by Borsa and Rigamonti, and Sholl include directly integrals over the radial distribution function and give the right order of magnitude for the quadrupolar contribution to the nuclear relaxation and a more correct temperature dependence. This means that the nuclear magnetic resonances are sensitive to the arrangements of atoms in the liquid state. Moreover, on the basis of the nearly free electron model, Watabe, Tanaka, Endo and Jones[29] have derived an expression for the temperature dependence of the Knight shift in liquid metals, in which P_F is directly related to the structure factor in X-ray or neutron diffraction experiments. Therefore, it may be considered that the bend of P_F at 20°C as shown in Fig. 12 corresponds to a structure change in liquid gallium.

The behavior of gallium-indium eutectic liquid alloys in the supercooled state is complicated. The observed results mean that some kind of the change for atomic distribution and electronic state may take place in the eutectic liquid alloy or the composition of the

alloy may vary continuously along the liquidus curve with decreasing temperature below the eutectic point. Kamiyama and Suzuki[30] have found that the Knight shift of ^{115}In in Hg-In liquid alloys corresponding to the solid compounds increases linearly without any peculiar change at the liquidus point. On the other hand, in liquid alloys with other compositions the temperature dependence of the Knight shift of ^{115}In bends at the supercooled state. As speculated by Lo and Colligan[10] we also consider that minute amounts of a solid phase rich in indium is continuously precipitated. Though the observed results for gallium-indium eutectic alloy can be considered to correspond to those for Hg-In liquid binary system, further experimental and theoretical investigations are required to establish a definite conclusion.

REFERENCES

1. WILSON J. R., *Metall. Rev.* **10**, 385 (1965).
2. BOSIO L. and DEFRAIN A., *J. Chim. Phys.* **61**, 859 (1964).
3. BOSIO L., *Compt. Rend.* **259**, 4545 (1964).
4. TURNBULL D. and CECHE R. E., *J. appl. Phys.* **21**, 804 (1950).
5. TAKEUCHI S. and SUZUKI K., *J. Japan Inst. Metals*, **33**, 415 (1969). In Japanese.
6. NAGASAWA H., *Japan. J. appl. Phys.* **3**, 476 and 560 (1964).
7. ANDREW E. R., *Nuclear Magnetic Resonance*, Cambridge University Press (1955).
8. CORNELL D. A., *Phys. Rev.* **153**, 208 (1967).
9. POWELL R. W., *Proc. R. Soc. A* **209**, 525 (1951).
10. LO J. M. and COLLIGAN G. A., *Trans. AIME*, **236**, 1473 (1966).
11. MASUDA Y. and OBATA Y., *Proc. phys. Soc. Japan*, **19**, 336 (1964). In Japanese.
12. WARREN W. W. and CLARK W. G., *Phys. Rev.* **177**, 600 (1969).
13. SILVERSTEIN S. D., *Phys. Rev.* **130**, 912 and 1703 (1963).
14. COLLINGS E. W., *Adv. Phys.* **16**, 459 (1967).
15. COLLINGS E. W., *Phys. Kond. Mater.* **8**, 284 (1969).
16. VAN VLECK J. H., *The Theory of Electric and Magnetic Susceptibilities*, Clarendon Press, Oxford (1932).
17. RODRIGUEZ S. E. and PINGS C. J., *J. chem. Phys.* **42**, 2435 (1965).
18. HENDUS H., *Z. Naturf.* **2a**, 505 (1947).
19. ASCARELLI P., *Phys. Rev.* **143**, 36 (1966).
20. ORTON and WILLIAMS (unpublished) in CUSACK N. E., KENDALL P. W. and MARWAHA A. S., *Phil. Mag.* **7**, 1745 (1962).
21. GREENFIELD A. J., *Phys. Rev.* **135**, A1589 (1964).
22. CUSACK N. E. and MARWAHA A. S., *Phys. Lett.* **9**, 232 (1964).
23. GUSTAFSON D. R. and MACKINTOSH A. R., *Phys. Lett.* **5**, 234 (1963).
24. BRANDT W. and WAUNG H. F., *Phys. Lett.* **27A**, 700 (1968).
25. HANABUSA M. and BLOEMBERGEN N., *J. Phys. Chem. Solids*, **27**, 363 (1966).
26. FABER T. E., *Solid State Commun.* **1**, 41 (1963).
27. BORSA F. and RIGAMONTI A., *Nuovo. Cim.* **488**, 194 (1967).
28. SHOLL C. A., *Proc. Phys.* **91**, 130 (1967).
29. WATABE M., TANAKA M., ENDO H. and JONES B. K., *Phil. Mag.* **12**, 347 (1965).
30. KAMIYAMA T. and SUZUKI K., *J. phys. Soc. Japan*, **28**, 1371 (1968).

QUANTUM OSCILLATIONS OF THE HALL EFFECT OF A FERMION GAS WITH RANDOM IMPURITY SCATTERING

A. BASTIN, C. LEWINER, O. BETBEDER-MATIBET et P. NOZIERES

Groupe de Physique des Solides de l'Ecole Normale Supérieure,* Faculté des Sciences de Paris,
9 Quai Saint Bernard, Paris 5, France

(Received 20 July 1970; in revised form 5 October 1970)

Abstract—The static electrical conductivity tensor of an electron gas in the presence of a magnetic field has been derived in the case of scattering by spinless (point) impurities, using a Green's function method. We show the existence of a correction to the Hall effect σ_{xy} due to the quantization of orbital motion, exactly analogous to the well known de Haas-Shubnikov oscillations of σ_{xx} . We first present the calculation of σ_{xy} (and σ_{xx} as well) up to first order in impurity concentration and give numerical estimates. We then evaluate the correction in the case of high concentrations and show a discrepancy with the Drude-Zener formulae.

1. INTRODUCTION

UNTIL recently, it was commonly admitted that in the presence of a magnetic field, the electrical conductivity tensor of an electron gas with impurity scattering involves the standard Hall effect in its σ_{xy} component and the Shubnikov-de Haas oscillations in σ_{xx} [1-5].

Quite recently however, several experiments [6-7] showed an oscillatory behavior of σ_{xy} in InSb at helium temperature and so far no theoretical account of this effect has been given. It has been suggested that the spin-orbit coupling could be responsible for it; as a matter of fact, two of the authors, together with Fayet, have already discussed the influence of the spin-orbit coupling on the electrical conductivity of a collisionless semiconductor [8, 9]. This influence amounts to a smooth deviation to the Hall effect which appears at high magnetic field, and cannot explain the oscillation itself.

On the other hand, the oscillation observed by Pavlov and Tuchendler arises for values of the magnetic field such that the last Landau

level crosses the Fermi level. It is plausible that several other oscillations appear in σ_{xy} that were not large enough to be experimentally observed. This suggests that the oscillations of the transverse conductivity σ_{xy} may be analogous to the Shubnikov-de Haas oscillations of σ_{xx} and arise every time a Landau level crosses the Fermi level.

Since no previous theory went beyond the usual Hall effect, as far as σ_{xy} is concerned, there is a need for a detailed analysis of the electrical conductivity tensor. We shall perform this calculation by treating the impurity scattering as a perturbation and expanding the one-electron Green's function on the basis of the unperturbed Hamiltonian in the presence of a magnetic field. Such a method has been used recently by Abrikosov [13]; we wish to extend his results to σ_{xy} as well as σ_{xx} and to introduce some features which were not properly taken into account.

In Section 2, we discuss the model used to perform this calculation. In Section 3, we calculate the conductivity tensor for low impurity concentrations and exhibit the correction to the standard Hall effect. In Section 4, we examine the influence of higher order terms (in powers of the concentration)

*Laboratoire Associé au Centre National de la Recherche Scientifique.

and show a discrepancy with the Drude-Zener theory. In Section 5, we present some numerical calculations.

2. FORMULATION OF THE PROBLEM

We consider here a degenerate semiconductor near zero temperature (the calculation will be performed at finite temperature T and we finally take the limit $T \rightarrow 0$). We assume that, under such conditions, transport phenomena are controlled by spinless independent random impurity scatterers. We assume also crossed electric and magnetic fields, the electric field $\mathcal{E} \exp -i\omega t$ being parallel to the x -axis and the static magnetic field \mathbf{H} being parallel to the z -axis. The electric field is described by the a.c. vector potential $\mathbf{A}_1(t)$ while \mathbf{A} is the d.c. vector potential corresponding to \mathbf{H} . We shall be mainly interested in the static conductivity ($\omega \rightarrow 0$).

The total Hamiltonian has the form

$$H_t = H_0 + V + H_1 \quad (2.1)$$

H_0 is the unperturbed Hamiltonian in the presence of the magnetic field

$$H_0 = \frac{1}{2m^*} \left(\mathbf{p} - \frac{e}{c} \mathbf{A} \right)^2 \quad (2.2)$$

we have taken here an isotropic effective mass and we use the Landau gauge

$$\mathbf{A} = (0, Hx, 0).$$

The eigenvalues and eigenfunctions of H_0 are well known[4, 5]. We denote them respectively by E_{n,k_z} and Ψ_{n,k_y,k_z} , or in short by E_N and Ψ_N .

V is the scattering potential

$$V = \sum_{i=1}^{N_S} v(\mathbf{r} - \mathbf{r}_i). \quad (2.3)$$

A single impurity can be characterized by a cross section or equivalently by a scattering

amplitude f . For the sake of simplicity, we assume a δ -function potential and take

$$v(\mathbf{r}) = \frac{2\pi\hbar^2 f}{m^*} \delta(\mathbf{r}) \quad (2.4)$$

This choice has been made for mathematical convenience only. As a matter of fact, in most cases, including InSb, the scattering potential is known to be a screened Coulomb potential[15].

H_1 is the perturbation due to the electric field

$$H_1 = -\frac{e}{i\omega} \mathcal{E} \cdot \mathbf{j} \exp -i\omega t \quad (2.5)$$

where \mathbf{j} is the current density.

The classical radius of a cyclotron orbit in the first Landau level is

$$l = \left[\frac{\hbar}{m^* \omega_0} \right]^{1/2} \quad (2.6)$$

where ω_0 is the cyclotron frequency.

Note also that, when calculating the conductivity, we must take the gauge current into account, i.e. a contribution

$$\sigma_{\alpha\beta}^u(\omega) = -\frac{iNe^2}{m^* \omega} \delta_{\alpha\beta}. \quad (2.7)$$

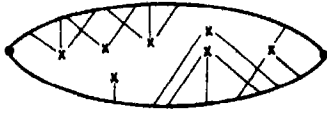
We assume everywhere that the system has unit volume.

3. FIRST ORDER CALCULATION

According to Kubo's linear response theory, the electrical conductivity is related to the current-current correlation function $S_{\alpha\beta}$ by

$$\sigma_{\alpha\beta}(\omega) = \sigma_{\alpha\beta}^g(\omega) + \frac{e^2}{i\omega} S_{\alpha\beta}(\omega) \quad (3.1)$$

$S_{\alpha\beta}$ may be expanded in powers of the scattering potential and is represented by all diagrams of the type shown on Fig. 1. Each cross corresponds to a scattering center

Fig. 1. Diagrams for $\sigma_{ab}(\omega)$.

r_i ; the bold lines correspond to unperturbed propagators (with no scattering) which, in the basis of the Landau states, are diagonal, given by

$$G_N^0(\epsilon) = \frac{1}{E_N - \epsilon - i\delta \text{sgn}(\epsilon - \mu)} \quad (3.2)$$

with

$$E_N = \left(n + \frac{1}{2}\right) \hbar \omega_0 + \frac{\hbar^2 k_z^2}{2m^*}. \quad (3.3)$$

A scattering vertex, by impurity i , from state M to state N , corresponds to a factor

$$\frac{2\pi\hbar^2}{m^*} \Psi_M^*(\mathbf{r}_i) \Psi_N(\mathbf{r}_i).$$

Ultimately, we want to average over impurity positions, which we assume to be uncorrelated.

The response function $S_{ab}(\omega)$ is the analytic continuation on the real axis of the corresponding thermodynamic Green's function defined for imaginary frequencies $\omega_n = (2n+1)i\pi T/\hbar$. The latter can be written as

$$T \sum_{\omega_n} \text{Tr} \{ j_\alpha G(\hbar\omega_n) j_\beta G(\hbar\omega + \hbar\omega_n) \} \quad (3.4)$$

where G is the total propagator in the presence of impurities. In order to evaluate (3.4), we follow the standard procedure: replace the sum by an integral and distort the integration contour in the complex ϵ -plane. We refer to the classic book of Abrikosov, Gor'kov and Dzialoshinski for details, and we only quote the final result for the analytic continuation

$$\begin{aligned} S_{ab}(\omega) = & \int_{-\infty}^{\infty} \frac{d\epsilon}{2\pi} \text{th} \frac{\beta\epsilon}{2} \text{Tr} [j_\alpha \text{Im} G(\epsilon) \\ & \times j_\beta G^+(\epsilon + \hbar\omega) + j_\alpha G^-(\epsilon - \hbar\omega) \\ & \times j_\beta \text{Im} G(\epsilon)]. \end{aligned} \quad (3.5)$$

Here, G^\pm denotes the Green's function just above or below the real axis while

$$\text{Im} G = \frac{1}{2i} (G^+ - G^-).$$

It is easily verified that the integral (3.5) would vanish were it not for the factor $\text{th}(\beta\epsilon/2)$, the bracket being analytic in one or the other of the half planes. Hence we can replace $\text{th}(\beta\epsilon/2)$ by $-2f(\epsilon)$, f being the Fermi distribution function.

In the limit $\omega \rightarrow 0$, we may expand $S_{ab}(\omega)$ in powers of ω . If the conductivity is to be finite, the leading term

$$\begin{aligned} S_{ab}(0) = & i \int_{-\infty}^{\infty} \frac{f(\epsilon) d\epsilon}{2\pi} \text{Tr} [j_\alpha G^+(\epsilon) j_\beta G^+(\epsilon) \\ & - j_\alpha G^-(\epsilon) j_\beta G^-(\epsilon)] \end{aligned} \quad (3.6)$$

must cancel out the gauge term in (3.1). This can be verified by noting that the current j_α and the position x_α obey the equation of motion

$$i\hbar j_\alpha = [H, x_\alpha] = -\left[\frac{1}{G(z)}, x_\alpha\right]$$

it follows that

$$\begin{aligned} \text{Tr} [j_\alpha G^+ j_\beta G^+] &= -\frac{i}{\hbar} \text{Tr} \{ [x_\alpha, j_\beta] G^+ \} \\ &= \frac{\delta_{\alpha\beta}}{m^*} \text{Tr} G^+. \end{aligned}$$

If we note that the integral

$$\frac{1}{2i\pi} \text{Tr} \int_{-\infty}^{\infty} f(\epsilon) d\epsilon (G^+ - G^-)$$

is nothing but the total number of particles N , we have

$$S_{ab}(0) = -\frac{N}{m^*} \delta_{ab}.$$

As expected, this contribution cancels the gauge term σ_{ab}^g . The static conductivity thus

reduces to

$$\sigma_{\alpha\beta}(0) = \frac{ie^2\hbar}{\pi} \int_{-\infty}^{\infty} f(\epsilon) d\epsilon \operatorname{Tr} [j_{\alpha} \operatorname{Im} G(\epsilon) \times j_{\beta} G'^+(\epsilon) - j_{\alpha} G'^-(\epsilon) j_{\beta} \operatorname{Im} G(\epsilon)] \quad (3.7)$$

(the prime denotes derivation with respect to ϵ). Note that the result (3.7) is exact as long as we perform the average over impurity positions on the whole expression. The diagonal components $\sigma_{\alpha\alpha}$ are particularly simple, being given by

$$\sigma_{\alpha\alpha}(0) = -\frac{2e^2\hbar}{\pi} \int_{-\infty}^{\infty} f(\epsilon) d\epsilon \times \operatorname{Tr} [j_{\alpha} \operatorname{Im} G j_{\alpha} \operatorname{Im} G'].$$

Integrating by parts, we find at zero temperature the very simple result

$$\sigma_{\alpha\alpha}(0) = -\frac{e^2\hbar}{\pi} \operatorname{Tr} [j_{\alpha} \operatorname{Im} G j_{\alpha} \operatorname{Im} G]_{\epsilon=\mu}. \quad (3.8)$$

As mentioned earlier, the impurity average in (3.8) must be taken at the end of the calculation. We now focus our attention on a first order calculation in powers of the impurity concentration (N_S/N). The only diagrams to be retained are those of Fig. 2. We can dispose at once of diagrams of type *c*, which contain the factor

$$\sum_{M,N} j_{MN} G_M^0 G_N^0 \Psi_M(\mathbf{r}_i) \Psi_N^*(\mathbf{r}_i). \quad (3.9)$$

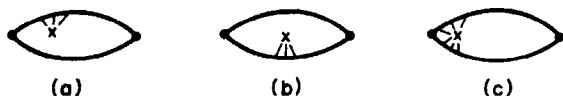


Fig. 2. Diagrams contributing to $\sigma_{\alpha\beta}$ (first order calculation).

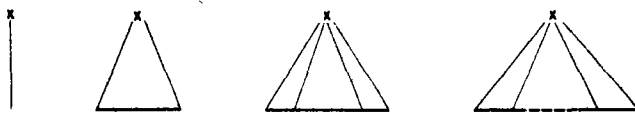


Fig. 3; Diagrams for the t -matrix (first order calculation).

If we perform a 180° rotation around \mathbf{H} , the system is invariant whereas j_x and j_y change sign; hence the summation (3.9) must vanish. To be more specific, j_{α} is diagonal in k_y and off-diagonal in the Landau state quantum number n ; (3.9) thus involves integrals of the form

$$\int dk_y \Phi_m \left(x_i + \frac{\hbar k_y}{m^* \omega_0} \right) \Phi_n^* \left(x_i + \frac{\hbar k_y}{m^* \omega_0} \right) = 0.$$

We are thus left with diagrams of type (a) and (b). In other words, we can average independently the two Green's functions in (3.7). In the usual language of transport theory, there is only scattering 'out' of the state and not 'in' the state, a result which follows from our assumptions of a point scatterer.

Up to first order in N_S , the average Green's function is given by

$$\bar{G}_{MM'} = G_M^0 \delta_{MM'} - G_M^0 \bar{t}_{MM'} G_{M'}^0 \quad (3.10)$$

where (t/N_S) is the t -matrix for scattering on the i -th impurity, given by diagrams of Fig. 3. Any intermediate state N in such a diagram carries a factor

$$\sum_N \Psi_N^*(\mathbf{r}_i) \Psi_N(\mathbf{r}_i) G_N^0(\epsilon).$$

Because of the independent summation over N , this expression does not depend on \mathbf{r}_i and may be replaced by its average over the whole volume $\sum_N G_N^0(\epsilon)$. The full t -matrix thus takes the form

$$t_{MM'}(\epsilon) = \frac{2\pi\hbar^2 f}{m^*} \sum_i \frac{\Psi_M^*(\mathbf{r}_i) \Psi_{M'}(\mathbf{r}_i)}{1 + f K^0(\epsilon)}$$

where we have set

$$K^0(\epsilon) = \frac{\pi \hbar^2}{m^*} \sum_N G_N^0(\epsilon) = \frac{\pi \hbar^2}{m^*} \sum_N \frac{1}{E_N - \epsilon - i\delta \operatorname{sgn}(\epsilon - \mu)}. \quad (3.11)$$

In view of the orthonormality of the Ψ_M , the average \bar{I} -matrix is diagonal, given by

$$\bar{I}_{MM'}(\epsilon) = \frac{2\pi \hbar^2 f}{m^*} N_S \frac{1}{1 + f K^0(\epsilon)} \delta_{MM'}. \quad (3.12)$$

\bar{G} is thus also diagonal. The function $K(\epsilon)$ is easily deduced from the density of states of Landau levels. Let $K^\pm(\epsilon)$ be its values just above and below the real axis; we find

$$K^{0\pm}(\epsilon) = K_1^0(\epsilon) \pm i K_2^0(\epsilon) \quad (3.13)$$

$$K_1^0(\epsilon) = \frac{1}{l\sqrt{2}} \sum_{n\epsilon} \left(n + \frac{1}{2} - \frac{\epsilon}{\hbar\omega_0} \right)^{-1/2} \quad (3.14)$$

$$K_2^0(\epsilon) = \frac{1}{l\sqrt{2}} \sum_0^{n\epsilon-1} \left(\frac{\epsilon}{\hbar\omega_0} - n - \frac{1}{2} \right)^{-1/2} \quad (3.15)$$

where n_ϵ is the smallest integer that exceeds $\epsilon/\hbar\omega_0 - \frac{1}{2}$. Strictly speaking, K_1 involves a divergent series. However, Skobov[12] has shown that this divergence was removed if the scattering potential had a finite range, and that this series could be approximated by its first term

$$K_1^0(\epsilon) \approx \frac{1}{l\sqrt{2}} \left[n_\epsilon + \frac{1}{2} - \frac{\epsilon}{\hbar\omega_0} \right]^{-1/2}.$$

Having calculated \bar{G} , let us return to the conductivity $\sigma_{\alpha\beta}$ given by (3.7). The zeroth order contribution is

$$\sigma_{\alpha\beta}^0 = -ie^2 \hbar \int_{-\infty}^{+\infty} f(\epsilon) d\epsilon \sum_{M,N} j_{\alpha MN} j_{\beta NM} \times \left\{ \frac{\delta(\epsilon - E_M)}{(\epsilon - E_N + i\delta)^2} - \frac{\delta(\epsilon - E_N)}{(\epsilon - E_M - i\delta)^2} \right\}. \quad (3.16)$$

The matrix elements of the current are given by

$$j_{x nk_k k_n, n' k'_k k'_n} = i \sqrt{\frac{\hbar\omega_0}{2m^*}} [\sqrt{n} \delta_{n', n-1} - \sqrt{n+1} \delta_{n', n+1}] \delta_{k_k k'_k} \delta_{k_n k'_n} \quad (3.17)$$

$$j_{y nk_k k_n, n' k'_k k'_n} = \sqrt{\frac{\hbar\omega_0}{2m^*}} [\sqrt{n} \delta_{n', n-1} + \sqrt{n+1} \delta_{n', n+1}] \delta_{k_k k'_k} \delta_{k_n k'_n}. \quad (3.18)$$

If we note that j_x and j_y connect states whose energies differ by $\pm \hbar\omega_0$, we can transform (3.16) into

$$\sigma_{\alpha\beta}^0 = \frac{-ie^2}{\hbar\omega_0^2} \sum_M f(E_M) [j_\alpha, j_\beta]_{MM}.$$

It follows that

$$\begin{aligned} \sigma_{xx}^0 &= 0 \\ \sigma_{xy}^0 &= -\frac{N_0 e^2}{m^* \omega_0} \end{aligned} \quad (3.19)$$

where N_0 is the total number of electrons in the absence of impurities for a given value of the chemical potential μ .

In order to calculate the first order contribution to $\sigma_{\alpha\beta}$, we rewrite (3.7) in the equivalent form:

$$\begin{aligned} \sigma_{\alpha\beta} &= \frac{e^2 \hbar}{2\pi} \int_{-\infty}^{+\infty} f(\epsilon) d\epsilon \sum_{M,N} j_{\alpha MN} j_{\beta NM} \\ &\times [G_M'^+ (G_N^+ - G_N^-) - G_N'^- (G_M^+ - G_M^-)]. \end{aligned} \quad (3.20)$$

We then linearize the bracket, which becomes

$$\begin{aligned} &-(G_N^{0+} - G_N^{0-}) [(G_M^{0+})^2 t^+] \\ &+ (G_M^{0+} - G_M^{0-}) [(G_N^{0-})^2 t^-] \\ &- t^+ [G_M^{0+} (G_N^{0+})^2 - G_N^{0-} (G_M^{0+})^2] \\ &+ t^- [G_M^{0+} (G_N^{0-})^2 - G_N^{0-} (G_M^{0-})^2]. \end{aligned} \quad (3.21)$$

By noting that $G^0 = (G^0)^2$, we can rearrange (3.21) into the derivative of

$$-2i[\text{Im } G_N^0 (G_M^{0+})^2 t^+ - \text{Im } G_M^0 (G_N^{0-})^2 t^-]$$

with respect to ϵ . After integrating by parts:

$$\sigma_{\alpha\beta}^1 = ie^2 \hbar \int_{-\infty}^{\infty} \frac{df}{d\epsilon} d\epsilon \sum_{M,N} j_{\alpha MN} j_{\beta NM} \times \left[\frac{\delta(\epsilon - E_N) t^+}{(E_M - \epsilon - i\delta)^2} - \frac{\delta(\epsilon - E_M) t^-}{(E_N - \epsilon + i\delta)^2} \right]. \quad (3.22)$$

We note again that E_N and E_M differ by $\pm \hbar\omega_0$. In the limit of zero temperatures, (3.22) can thus be cast in the very simple form

$$\sigma_{\alpha\beta}^1 = \frac{+ie^2}{\hbar\omega_0^2} \sum_{M,N} \delta(E_M - \mu) \times [j_{\alpha MN} j_{\beta NM} t^-(\mu) - j_{\alpha NM} j_{\beta MN} t^+(\mu)]. \quad (3.23)$$

It is apparent on (3.23) that σ_{xx} involves the combination

$$t^+(\mu) - t^-(\mu) = 2i \text{Im } t(\mu),$$

a result which could be deduced from the exact expression (3.7). As regards σ_{xy} , a $\pi/2$ rotation around \mathbf{H} changes x into y , y into $-x$. σ_{xy} is thus given by

$$\sigma_{xy}^1 = -\frac{ie^2}{\hbar\omega_0^2} \sum_{M,N} \delta(E_M - \mu) j_{xNM} j_{yMN} \times [t^+(\mu) + t^-(\mu)].$$

It involves the real part of the t -matrix at the Fermi level. The explicit expressions for σ_{xx} and σ_{xy} are easily obtained by using the matrix elements for j_x and j_y (3.17) and (3.18). We find

$$\sigma_{xx}^1 = \frac{e^2}{m^* \omega_0} \text{Im } t(\mu) \sum_n (2n+1) \rho_n(\mu) \quad (3.24)$$

$$\sigma_{xy}^1 = \frac{+e^2}{m^* \omega_0} \text{Re } t(\mu) \rho(\mu) \quad (3.25)$$

where ρ_n is the density of states of the n -th Landau level, ρ the total density of states.

The above result for σ_{xx} is identical to that of Kubo[5] and to formula (15) of Abrikosov [13] who performed a similar calculation. It corresponds to the usual Shubnikov-de Haas effect. Instead, the result for σ_{xy} differs from the usual expression

$$\sigma_{xy} = \frac{Ne^2}{m^* \omega_0}.$$

The difference stems both from the correction (3.25) and from the fact the electron number $N(\mu)$ in the presence of impurities is different from the zeroth order value $N_0(\mu)$. This difference is equal to

$$N - N_0 = \frac{1}{\pi} \int_{-\infty}^{\infty} f(\epsilon) d\epsilon \text{Tr} [\text{Im} (G - G_0)]$$

$$N - N_0 = -\frac{1}{2i\pi} \int_{-\infty}^{\infty} f(\epsilon) d\epsilon \times \sum_M [t^+(G_M^{0+})^2 - t^-(G_M^{0-})^2].$$

From (3.11) it follows that

$$\sum_M (G_M^{0\pm})^2 = \frac{m^*}{\pi \hbar^2} K'^{0\pm}.$$

On making use of (3.12), we can thus write $(N - N_0)$ in the form

$$N - N_0 = -\frac{2N_S}{\pi} \int_{-\infty}^{\infty} f(\epsilon) d\epsilon \text{Im} \left[\frac{fK'^{0+}}{1+fK'^{0+}} \right].$$

At zero temperature, the integral is straightforward and yields

$$N - N_0 = -\frac{2N_S}{\pi} \text{Arg} [1 + fK'^{0+}(\mu)].$$

In order to collect all these results, we introduce the dimensionless parameter

$$\lambda = \frac{fK_2^{0+}(\mu)}{1+fK_1^{0+}(\mu)}. \quad (3.26)$$

According to (3.12) we have

$$\begin{aligned} \text{Im } t &= \frac{2\pi\hbar^2 f}{m^*} N_s \frac{fK_z^0}{(1+fK_z^0)^2 + f^2(K_z^0)^2} \\ &= \frac{2N_s}{\pi\rho} \cdot \frac{\lambda^2}{1+\lambda^2}. \end{aligned} \quad (3.27)$$

From (3.19), (3.24), (3.25), (3.26) and (3.27), we can thus write

$$\sigma_{xx} = \frac{Ne^2}{m^*\omega_0} \frac{N_s}{N} \frac{2}{\pi} \frac{\lambda^2}{1+\lambda^2} \sum_n (2n+1) \frac{\rho_n(\mu)}{\rho(\mu)} \quad (3.28)$$

$$\sigma_{xy} = \frac{Ne^2}{m^*\omega_0} \left[-1 + \frac{2}{\pi} \frac{N_s}{N} \left(\frac{\lambda}{1+\lambda^2} - A \tan \lambda \right) \right]. \quad (3.29)$$

These results are exact up to first order in N_s . They are remarkably simple, depending as they do on a single parameter λ .

We note that σ_{xx} is of order λ^2 in the limit $\lambda \rightarrow 0$; it is already found when the scattering is treated within Born's approximation. σ_{xy} instead is of order λ^2 , and appears only if one goes beyond Born's approximation. This is probably why the correction to the Hall effect does not appear in the literature. In principle, Abrikosov's calculation is valid to all orders in λ , and indeed his expression for σ_{xx} is the same as (3.28). However his calculation of σ_{xy} misses the first order correction, linear in N_s . This is partly due to the fact that he has taken $\text{Re}(t) = 0$. Such an approximation can be justified (and has been widely used) in the absence of magnetic field because $\text{Re}(t)$ has a smooth energy dependence and can be incorporated as a renormalization to the chemical potential. In our case however, $\text{Re}(t)$ is a highly singular function of the energy and we must keep it as it stands. Another difference between Abrikosov's and the present theory lies in the evaluation of $(N - N_0)$ which yields the $A \tan \lambda$; it seems that Abrikosov did not take this problem under consideration and implicitly took $N = N_0$.

We note that the above correction to the Hall effect is *linear* in N_s , i.e. in τ^{-1} , while an ordinary Drude-Zener theory would predict a departure from the ideal value of order τ^{-2} . This correction may be regarded as an 'anomalous' Hall effect, arising from the orbital angular momentum, rather than from the spin as in a ferromagnet. It only appears if the curvature of the trajectories is taken into account, i.e. if the collisions have a finite duration, which implies going beyond Born's approximation.

For small λ , the effect is small; typically, one has (in the limit of high magnetic fields and for $N_s = N$)

$$\frac{\delta\sigma_{xy}}{\sigma_{xy}} \sim \left(\frac{\sigma_{xx}}{\sigma_{xy}} \right)^{3/2}$$

which is consistent with the observed orders of magnitude.

4. HIGHER ORDER TERMS—SELF CONSISTENT CALCULATION

4.1. Selection of a class of diagrams

In order to calculate the conductivity tensor up to all orders in N_s/N exactly, one has to sum up all diagrams of the type shown in Fig. 1. This is clearly impossible; the best we can perform is to select a class of diagrams that can be summed and includes the most relevant physical effects.

The simplest procedure consists in keeping all diagrams where an arbitrary number of scattering centers appear but where collisions with different scatterers never interfere (Fig. 4). As in Section 3, we may discard diagrams of type *a*, which contain the same factor (3.9) that vanishes when integrated over k_y , and keep only diagrams of type *b* where no impurity interacts with both *G* lines.



Fig. 4. Diagrams contributing to σ_{ab} (self-consistent calculation).

By noting that $G^{0'} = (G^0)^2$, we can rearrange (3.21) into the derivative of

$$-2i[\text{Im } G_N^0(G_M^{0+})^2 t^+ - \text{Im } G_M^0(G_N^{0-})^2 t^-]$$

with respect to ϵ . After integrating by parts:

$$\sigma_{\alpha\beta}^1 = ie^2 \hbar \int_{-\infty}^{\infty} \frac{df}{d\epsilon} d\epsilon \sum_{M,N} j_{\alpha MN} j_{\beta NM} \times \left[\frac{\delta(\epsilon - E_N) t^+}{(E_M - \epsilon - i\delta)^2} - \frac{\delta(\epsilon - E_M) t^-}{(E_N - \epsilon + i\delta)^2} \right]. \quad (3.22)$$

We note again that E_N and E_M differ by $\pm \hbar \omega_0$. In the limit of zero temperatures, (3.22) can thus be cast in the very simple form

$$\sigma_{\alpha\beta}^1 = \frac{+ie^2}{\hbar \omega_0^2} \sum_{M,N} \delta(E_M - \mu) \times [j_{\alpha MN} j_{\beta NM} t^-(\mu) - j_{\alpha NM} j_{\beta MN} t^+(\mu)]. \quad (3.23)$$

It is apparent on (3.23) that σ_{xx} involves the combination

$$t^+(\mu) - t^-(\mu) = 2i \text{Im } t(\mu),$$

a result which could be deduced from the exact expression (3.7). As regards σ_{xy} , a $\pi/2$ rotation around \mathbf{H} changes x into y , y into $-x$. σ_{xy} is thus given by

$$\sigma_{xy}^1 = -\frac{ie^2}{\hbar \omega_0^2} \sum_{M,N} \delta(E_M - \mu) j_{xNM} j_{yMN} \times [t^+(\mu) + t^-(\mu)].$$

It involves the real part of the t -matrix at the Fermi level. The explicit expressions for σ_{xx} and σ_{xy} are easily obtained by using the matrix elements for j_x and j_y (3.17) and (3.18). We find

$$\sigma_{xx}^1 = \frac{e^2}{m^* \omega_0} \text{Im } t(\mu) \sum_n (2n+1) \rho_n(\mu) \quad (3.24)$$

$$\sigma_{xy}^1 = \frac{+e^2}{m^* \omega_0} \text{Re } t(\mu) \rho(\mu) \quad (3.25)$$

where ρ_n is the density of states of the n -th Landau level, ρ the total density of states.

The above result for σ_{xx} is identical to that of Kubo[5] and to formula (15) of Abrikosov [13] who performed a similar calculation. It corresponds to the usual Shubnikov-de Haas effect. Instead, the result for σ_{xy} differs from the usual expression

$$\sigma_{xy} = \frac{Ne^2}{m^* \omega_0}.$$

The difference stems both from the correction (3.25) and from the fact the electron number $N(\mu)$ in the presence of impurities is different from the zeroth order value $N_0(\mu)$. This difference is equal to

$$N - N_0 = \frac{1}{\pi} \int_{-\infty}^{\infty} f(\epsilon) d\epsilon \text{Tr} [\text{Im} (G - G_0)]$$

$$N - N_0 = -\frac{1}{2i\pi} \int_{-\infty}^{\infty} f(\epsilon) d\epsilon \times \sum_M [t^+(G_M^{0+})^2 - t^-(G_M^{0-})^2].$$

From (3.11) it follows that

$$\sum_M (G_M^{0\pm})^2 = \frac{m^*}{\pi \hbar^2} K^{0\pm}.$$

On making use of (3.12), we can thus write $(N - N_0)$ in the form

$$N - N_0 = -\frac{2N_S}{\pi} \int_{-\infty}^{\infty} f(\epsilon) d\epsilon \text{Im} \left[\frac{fK'^{0+}}{1 + fK^{0+}} \right].$$

At zero temperature, the integral is straightforward and yields

$$N - N_0 = -\frac{2N_S}{\pi} \text{Arg} [1 + fK^{0+}(\mu)].$$

In order to collect all these results, we introduce the dimensionless parameter

$$\lambda = \frac{fK_2^{0+}(\mu)}{1 + fK_1^{0+}(\mu)}. \quad (3.26)$$

According to (3.12) we have

$$\begin{aligned} \text{Im } t &= \frac{2\pi\hbar^2 f}{m^*} N_s \frac{f K_2^0}{(1 + f K_1^0)^2 + f^2 (K_2^0)^2} \\ &= \frac{2N_s}{\pi\rho} \cdot \frac{\lambda^2}{1 + \lambda^2}. \end{aligned} \quad (3.27)$$

From (3.19), (3.24), (3.25), (3.26) and (3.27), we can thus write

$$\sigma_{xx} = \frac{Ne^2}{m^*\omega_0} \frac{N_s}{N} \frac{2}{\pi} \frac{\lambda^2}{1 + \lambda^2} \sum_n (2n+1) \frac{\rho_n(\mu)}{\rho(\mu)} \quad (3.28)$$

$$\sigma_{xy} = \frac{Ne^2}{m^*\omega_0} \left[-1 + \frac{2}{\pi} \frac{N_s}{N} \left(\frac{\lambda}{1 + \lambda^2} - A \tan \lambda \right) \right]. \quad (3.29)$$

These results are exact up to first order in N_s . They are remarkably simple, depending as they do on a single parameter λ .

We note that σ_{xx} is of order λ^2 in the limit $\lambda \rightarrow 0$: it is already found when the scattering is treated within Born's approximation. σ_{xy} instead is of order λ^2 , and appears only if one goes beyond Born's approximation. This is probably why the correction to the Hall effect does not appear in the literature. In principle, Abrikosov's calculation is valid to all orders in λ , and indeed his expression for σ_{xx} is the same as (3.28). However his calculation of σ_{xy} misses the first order correction, linear in N_s . This is partly due to the fact that he has taken $\text{Re}(t) = 0$. Such an approximation can be justified (and has been widely used) in the absence of magnetic field because $\text{Re}(t)$ has a smooth energy dependence and can be incorporated as a renormalization to the chemical potential. In our case however, $\text{Re}(t)$ is a highly singular function of the energy and we must keep it as it stands. Another difference between Abrikosov's and the present theory lies in the evaluation of $(N - N_0)$ which yields the $A \tan \lambda$; it seems that Abrikosov did not take this problem under consideration and implicitly took $N = N_0$.

We note that the above correction to the Hall effect is *linear* in N_s , i.e. in τ^{-1} , while an ordinary Drude-Zener theory would predict a departure from the ideal value of order τ^{-2} . This correction may be regarded as an 'anomalous' Hall effect, arising from the orbital angular momentum, rather than from the spin as in a ferromagnet. It only appears if the curvature of the trajectories is taken into account, i.e. if the collisions have a finite duration, which implies going beyond Born's approximation.

For small λ , the effect is small; typically, one has (in the limit of high magnetic fields and for $N_s = N$)

$$\frac{\delta\sigma_{xy}}{\sigma_{xy}} \sim \left(\frac{\sigma_{xx}}{\sigma_{xy}} \right)^{3/2}$$

which is consistent with the observed orders of magnitude.

4. HIGHER ORDER TERMS—SELF CONSISTENT CALCULATION

4.1. Selection of a class of diagrams

In order to calculate the conductivity tensor up to all orders in N_s/N exactly, one has to sum up all diagrams of the type shown in Fig. 1. This is clearly impossible; the best we can perform is to select a class of diagrams that can be summed and includes the most relevant physical effects.

The simplest procedure consists in keeping all diagrams where an arbitrary number of scattering centers appear but where collisions with different scatterers never interfere (Fig. 4). As in Section 3, we may discard diagrams of type *a*, which contain the same factor (3.9) that vanishes when integrated over k_y , and keep only diagrams of type *b* where no impurity interacts with both *G* lines.



Fig. 4. Diagrams contributing to σ_{ab} (self-consistent calculation).

Again we can average both propagators independently over the impurity positions. The average Green's function, which now contains an arbitrary number of t -matrices, is the solution of the following Dyson equation:

$$\bar{G}_{MM'} = \bar{G}_M^0 \delta_{MM'} - \bar{G}_M^0 \bar{t}_{MM'} \bar{G}_{M'} \quad (4.1)$$

where \bar{t} is the average t -matrix defined by (3.12). The diagrams of Fig. 4 b include two major effects[14]

- (a) multiple scattering of the electrons with each impurity center, which had already been taken into account in Section 3.
- (b) collision broadening due to successive collisions with different scatterers, giving rise to a finite lifetime of the electrons at the Fermi surface. This latter effect comes in the Dyson equation (4.1).

We can go one step further by including renormalized propagators in the t -diagrams. This takes care of diagrams of Fig. 5. \bar{t} and \bar{G} remain diagonal but formulae (3.11) and (3.12) have now to be replaced by

$$\bar{t}_{MM'}(\epsilon) = \frac{2\pi\hbar^2 f}{m^*} N_S \frac{1}{1 + fK(\epsilon)} \delta_{MM'} \quad (4.2)$$

and

$$K(\epsilon) = \frac{\pi\hbar^2}{m^*} \sum_M \bar{G}_M(\epsilon). \quad (4.3)$$

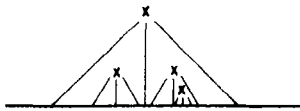


Fig. 5. Diagrams for the t -matrix (self-consistent calculation).

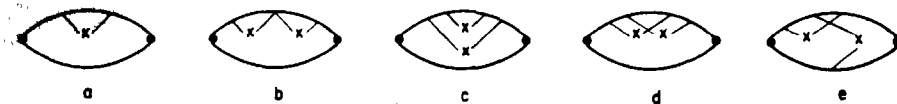


Fig. 6. Diagrams for σ_{ab} up to second order in impurity density.

Equations (4.1) to (4.3) constitute a self-consistent set of equations from which, in principle, we can obtain $K(\epsilon)$, $\bar{t}(\epsilon)$ and $\bar{G}(\epsilon)$. We shall see that this renormalization procedure does not make the calculations more sophisticated: actually this refinement leads to simpler expressions for the conductivity components when written in terms of $K(\mu)$.

In order to get numerical results, it would be necessary to solve equations (4.1) to (4.3) self-consistently. This could presumably be done, at least on a computer, but we are not going into these details here.

Before we start with the calculation itself, we should discuss the order of magnitude of the diagrams that have been discarded in this scheme (and which involve some interference between collisions on two separate impurities). Let us examine for instance the five diagrams shown on Fig. 6. Diagrams (b), (c), (d), (e) involve the same powers of N_S and f . Our calculation will retain (a), (b), (c) and ignore (d) and (e). There is no clearcut argument to estimate the relative orders of magnitude of these diagrams[13]. It seems however that (b) and (c) are of order $(\omega_0\tau)^{-1}$ with respect to (a) while (d) and (e) are of order $(\mu\tau)^{-1}$ (where $\tau^{-1} = 2 \text{Im } t(\mu)$ is the reciprocal lifetime of an electron at the Fermi surface). We can thus regard the present calculation as an interpolation scheme between the high field limit ($\omega_0\tau \gg 1$) discussed in Section 2, and the low field limit ($\omega_0\tau \ll 1$). We believe this interpolation to be correct as long as $\mu\tau/\hbar \gg 1$.

4.2. Calculation of the conductivity tensor

We start from the expression (3.7) which we rewrite in the following form:

$$\sigma_{\alpha\beta} = \frac{ie^2\hbar}{2\pi} \sum_M \sum_N j_{\alpha MN} j_{\beta NM} I_{MN} \quad (4.4)$$

with

$$I_{MN} = 2 \int_{-\infty}^{\infty} f(\epsilon) d\epsilon \{ \text{Im } G_N G_M'^+ - G_N'^- \text{Im } G_M \}. \quad (4.5)$$

According to (4.1), the Green's function is now given by

$$G_M^{\pm}(\epsilon) = \frac{1}{E_M - \epsilon + i^{\pm}(\epsilon)} \quad (4.6)$$

(from now on, we shall omit the bar which denotes the average over the positions of the impurities).

After some manipulations, I_{MN} is rearranged into

$$I_{MN} = I_{MN}^{(1)} + I_{MN}^{(2)} + I_{MN}^{(3)}$$

with

$$I_{MN}^{(1)} = \frac{i}{E_N - E_M} |(t^+ - t^-) G_N^- G_M^+|_{\epsilon=\mu} \quad (4.7)$$

$$I_{MN}^{(2)} = \frac{1}{(E_N - E_M)^2} \int_{-\infty}^{\infty} 2f(\epsilon) d\epsilon \times [\text{Im } G_N^+ - \text{Im } G_M^+] \quad (4.8)$$

$$I_{MN}^{(3)} = \frac{-2}{(E_N - E_M)^2} \times \text{Im} \left\{ \int_{-\infty}^{\infty} f(\epsilon) d\epsilon (G_N^+ - G_M^+) \frac{dt^+}{d\epsilon} \right\}. \quad (4.9)$$

We now look at the corresponding contributions to $\sigma_{\alpha\beta}$.

(a) σ_{xx} component. $I_{MN}^{(2)}$ and $I_{MN}^{(3)}$ give no contribution to σ_{xx} because they change sign when M and N are interchanged while $(j_{xMN} j_{xNM})$ does not. In (4.7), the integration over ϵ has already been performed and since we are interested in the limit $T = 0$, the result has been expressed in terms of $t(\mu)$ and $G(\mu)$. From now on, we shall drop the subscript $(\epsilon = \mu)$ and all G and t that will appear after the integration over ϵ has been performed will be tacitly assumed to be taken at $\epsilon = \mu$.

Inserting (4.7), (4.6) and (3.17) into (4.4), we obtain

$$\sigma_{xx} = -\frac{e^2 \hbar^2 \omega_0}{\pi m^*} \sum_M m (\text{Im } G_M) (\text{Im } G_{M-1}) \quad (4.10)$$

where $(M-1)$ stands for the state which is deduced from M by lowering the Landau state number by one.

In order to interpret this result, we use the following relations (which are easily deduced from (4.6))

$$\text{Im } G_N^+ = -G_N^+ G_N^- (\text{Im } t^+) \quad (4.11)$$

$$G_N^+ G_{N-1}^- = \frac{G_N^+ - G_{N-1}^-}{-t^+ + t^- - \hbar\omega_0}.$$

We see that the denominator of σ_{xx} involves the factor $(1 + \omega_0^2 \tau^2)$ where τ is the lifetime of the electrons at the Fermi surface, given by

$$\tau = \frac{\hbar}{2 \text{Im } t} = \frac{i\hbar}{t^+ - t^-}. \quad (4.12)$$

Putting (4.10), (4.11), and (4.12) together yields

$$\sigma_{xx} = \frac{e^2}{m^* \omega_0} \frac{\omega_0 \tau}{1 + \omega_0^2 \tau^2} A \quad (4.13)$$

with

$$A = \frac{1}{\pi} \sum_M \left\{ \left(m + \frac{1}{2} \right) \hbar \omega_0 (\text{Im } G_M) + \frac{\hbar}{2\tau} (\text{Re } G_M) \right\}. \quad (4.14)$$

From (4.3) and (4.6), we obtain an alternative expression for A :

$$A = (\mu - t_1) \frac{m^*}{\pi^2 \hbar^2} K_2 - \frac{1}{\pi} \sum_M \frac{\hbar^2 (k_z^M)^2}{2m^*} \text{Im } G_M \quad (4.15)$$

where we have set

$$\left. \begin{aligned} K^{\pm} &= K_1 \pm iK_2 \\ t^{\pm} &= t_1 \pm it_2 \end{aligned} \right\}. \quad (4.16)$$

In order to compare (4.13) with the well known Drude-Zener formulae, we must relate A to the total number of electrons N , the latter being given by

$$N = \frac{1}{\pi} \sum_M \int_{-\infty}^{\infty} f(\epsilon) d\epsilon \operatorname{Im} G_M^+(\epsilon) \\ = \frac{m^*}{\pi^2 \hbar^2} \operatorname{Im} \int_{-\infty}^{\infty} f(\epsilon) K^+(\epsilon) d\epsilon. \quad (4.17)$$

We separate out (4.17) into two terms:

$$N^{(1)} = \frac{m^*}{\pi^2 \hbar^2} \operatorname{Im} \int_{-\infty}^{\infty} f(\epsilon) K^+(\epsilon) \left(1 - \frac{dt^+}{d\epsilon}\right) d\epsilon \quad (4.18)$$

$$N^{(2)} = \frac{m^*}{\pi^2 \hbar^2} \operatorname{Im} \int_{-\infty}^{\infty} f(\epsilon) K^+(\epsilon) \frac{dt^+}{d\epsilon} d\epsilon. \quad (4.19)$$

Using the self consistent equations (4.2), (4.3) together with (4.6), we can integrate (4.18) and (4.19) and get

$$N^{(1)} = \frac{2}{\pi} \sum_m \frac{\hbar^2 (k_z^M)^2}{2m^*} \operatorname{Im} G_M \quad (4.20 a)$$

$$N^{(2)} = \frac{m^*}{\pi^2 \hbar^2} (t_1 K_2 + t_2 K_1) + \frac{N_S}{\pi} A \tan \frac{t_2}{t_1}. \quad (4.20 b)$$

Combining (4.15) and (4.20), we have

$$A = \frac{m^*}{2\pi^2 \hbar^2} [2\mu K_2 - t_1 K_2 + t_2 K_1] \\ + \frac{N_S}{\pi} A \tan \frac{t_2}{t_1} - \frac{N}{2}. \quad (4.21)$$

We shall discuss this result after having calculated σ_{xy} .

(b) *Hall conductivity* σ_{xy} . Here, all three terms of I_{MN} do contribute. We begin with $I_{MN}^{(2)}$. Inserting (3.17), (3.18), (4.8) and (4.16) into (4.4):

$$\sigma_{xy}^{(2)} = -\frac{Ne^2}{m^* \omega_0}. \quad (4.22)$$

This first term simply gives the usual Hall effect. We next take care of $I_{MN}^{(1)}$ and $I_{MN}^{(3)}$. From (4.7) we obtain

$$\sigma_{xy}^{(1)} = -\frac{e^2 \hbar}{\pi m^*} t_2 \sum_M m \operatorname{Re} (G_M^+ G_{M-1}^-). \quad (4.23)$$

From (4.9) and integrating by parts, we get

$$\sigma_{xy}^{(3)} = \frac{e^2}{\pi m^* \omega_0} \sum_M \operatorname{Im} \left\{ t^+ G_M^+ \right. \\ \left. - \int_{-\infty}^{\infty} f(\epsilon) d\epsilon t^+ \frac{dG_M^+}{d\epsilon} \right\}. \quad (4.24)$$

Combining both terms yields

$$\sigma_{xy}^{(1)} + \sigma_{xy}^{(3)} = -\frac{2e^2 \hbar t_2}{\pi m^*} \sum_M m (\operatorname{Im} G_M) \\ \times (\operatorname{Im} G_{M-1}) - \frac{ie^2 t_1}{\pi m^* \omega_0} \\ \times \sum_M \operatorname{Im} G_M + \frac{e^2}{\pi m^* \omega_0} \\ \times \operatorname{Im} \left[\int_{-\infty}^{\infty} f(\epsilon) d\epsilon t^+ \sum_M \frac{dG_M^+}{d\epsilon} \right] \quad (4.25)$$

The last two terms of (4.25) can be rewritten in terms of t and K by using again the self-consistent relations (4.2) and (4.3). As to the first term, it turns out to be simply related to σ_{xx} (3.10). The result is

$$\sigma_{xy}^{(1)} + \sigma_{xy}^{(3)} = \frac{\sigma_{xx}}{\omega_0 \tau} + \frac{e^2}{m^* \omega_0} \\ \times \left[\frac{2}{\pi} N_S A \tan \frac{t_2}{t_1} + \frac{m^*}{\pi^2 \hbar^2} t_1 K_2 \right]. \quad (4.26)$$

Combining (4.22) and (4.26), we obtain:

$$\sigma_{xy} = -\frac{Ne^2}{m^* \omega_0} \left[1 - \frac{2}{\pi} \frac{N_S}{N} A \tan \frac{t_2}{t_1} \right. \\ \left. - \frac{m^*}{\pi^2 \hbar^2} \frac{t_1 K_2}{N} \right] + \frac{\sigma_{xx}}{\omega_0 \tau}. \quad (4.27)$$

The expressions (4.13), (4.21) and (4.27)

can be set in closed form if we define

$$tg \Theta = \omega_0 \tau \quad (4.28 \text{ a})$$

$$N^* = N - \frac{N_S}{\pi} \left[2A \tan \frac{t_2}{t_1} + \frac{m^*}{\pi \hbar^2} \frac{t_1 K_2}{N_S} \right] \quad (4.28 \text{ b})$$

$$M = \frac{m^*}{\pi^2 \hbar^2} \mu K_2 - \frac{3N}{2} + \frac{N_S}{\pi} \times \left\{ 3A \tan \frac{t_2}{t_1} + \frac{m^*}{2\pi \hbar^2 N_S} (t_2 K_1 + t_1 K_2) \right\} \quad (4.28 \text{ c})$$

σ_{xx} and σ_{xy} are then given by

$$\sigma_{xx} = \frac{e^2}{m^* \omega_0} (M + N^*) \sin \Theta \cos \Theta \quad (4.29 \text{ a})$$

$$\sigma_{xy} = -\frac{e^2}{m^* \omega_0} (N^* \sin^2 \Theta - M \cos^2 \Theta) \quad (4.29 \text{ b})$$

4.3. Discussion of the results

We shall first discuss both limits $\omega_0 \tau \rightarrow \infty$ and $\omega_0 \tau \rightarrow 0$ of our interpretation scheme.

(a) *Limit* $\omega_0 \tau \rightarrow \infty$. By keeping only lowest order terms in N_S , we recover the results of Section 3. From (4.28) and (4.29), we get

$$\sigma_{xx} = \frac{e^2}{m^* \omega_0^2 \tau} \left(\frac{m^*}{\pi^2 \hbar^2} \mu K_2^0 - \frac{N}{2} \right) \quad (4.30 \text{ a})$$

$$\sigma_{xy} = \frac{e^2}{m^* \omega_0} \left(N - \frac{2N_S}{\pi} A \tan \frac{t_2}{t_1} - \frac{m^*}{\pi^2 \hbar^2} t_1 K_2^0 \right). \quad (4.30 \text{ b})$$

Noting that the parameter λ defined in (3.26) is equal, in this limit, to $(-t_2/t_1)$, we easily see that (4.30) is equivalent to (3.28).

(b) *Limit* $\omega_0 \tau \rightarrow 0$. In this limit, (4.29 a) can be calculated by noting that $E_N \sim \hbar^2 k^2 / 2m^*$. One finds

$$N^{(1)} = \frac{2m^*}{3\pi^2 \hbar^2} (\mu K_2 - t_2 K_1 - t_1 K_2). \quad (4.31)$$

Inserting (4.31) into (4.20) and (4.28), we may verify that

$$A = N^*$$

so that

$$M = 0$$

(4.29) then yields

$$\sigma_{xx} = \frac{N^* e^2 \tau}{m^*}. \quad (4.32 \text{ a})$$

$$\sigma_{xy} = 0 \quad (4.32 \text{ b})$$

Up to lowest order in N_S , we recover the usual formula

$$\sigma_{xx} = \frac{N e^2 \tau}{m^*}.$$

The correction $(N^* - N) e^2 \tau / m^*$ is due to higher order terms in N_S .

(c) *In the intermediate case*, (4.29) has to be compared to the Drude-Zener formulae, which (with our notations) write

$$\sigma_{xx}(D-Z) = \frac{N e^2}{m^* \omega_0} \sin \Theta \cos \Theta \quad (4.33 \text{ a})$$

$$\sigma_{xy}(D-Z) = -\frac{N e^2}{m^* \omega_0} \sin^2 \Theta. \quad (4.33 \text{ b})$$

Our results are quite different from those of the Drude-Zener theory. Thus, one must be careful in using the simple formulae (4.33) which apparently do not give the correct conductivity tensor in the intermediate case.

5. NUMERICAL CALCULATIONS

We discuss now the results which we have obtained in Section 3.

In the *quantum limit*, $\mu \leq \hbar \omega_0$ so that all the electrons are concentrated in the first Landau level. The summation in (3.28) thus reduces to the term $n = 0$ so that

$$\sigma_{xx} = \frac{N e^2}{m^* \omega_0} \frac{N_S}{N} \frac{2}{\pi} \frac{\lambda^2}{1 + \lambda^2} \quad (5.1)$$

$$\sigma_{xy} = -\frac{N e^2}{m^* \omega_0} \left[1 - \frac{2}{\pi} \frac{N_S}{N} \left(\frac{\lambda}{1 + \lambda^2} - A \tan \lambda \right) \right] \quad (5.2)$$

$K_1(\mu)$ and $K_2(\mu)$ are given by

$$K_1(\mu) = \frac{1}{l\sqrt{2}} \left(\frac{3}{2} - \frac{\mu}{\hbar\omega_0} \right)^{-1/2} \quad (5.3)$$

$$K_2(\mu) = \frac{1}{l\sqrt{2}} \left(\frac{\mu}{\hbar\omega_0} - \frac{1}{2} \right)^{-1/2} \quad (5.4)$$

The Fermi level μ is a function of the magnetic field, given for degenerate statistics and for a constant concentration by

$$\frac{\mu}{\hbar\omega_0} = \frac{1}{2} + \frac{4}{9} \frac{\mu_0^3}{(\hbar\omega_0)^3} \quad (5.5)$$

(the factor 2 for the spin degeneracy has been taken into account), is the Fermi level in the absence of the magnetic field. For every strong fields, $\mu/\hbar\omega_0$ becomes very close to $\frac{1}{2}$ (according to (5.5)); (5.3) and (5.4) thus become

$$K_1(\mu) \approx \frac{1}{l\sqrt{2}}$$

$$K_2(\mu) \approx \frac{3}{l} \left(\frac{\hbar\omega_0}{2\mu_0} \right)^{3/2}$$

so that

$$\lambda = \frac{fK_2}{1+fK_1} = \frac{\frac{3f}{l} \left(\frac{\hbar\omega_0}{2\mu_0} \right)^{3/2}}{1 + \frac{f}{l\sqrt{2}}} \quad (5.7)$$

Let us first examine the case of a *strong potential* ($f \gg l$). λ becomes much greater than 1; so (5.1) and (5.2) yield

$$\sigma_{xx} = \frac{2}{\pi} \frac{N_S e^2}{m^* \omega_0} \quad (5.8 a)$$

$$\sigma_{xy} = -\frac{N e^2}{m^* \omega_0} \left[1 + \frac{N_S}{N} \right] \quad (5.8 b)$$

The transverse conductivity has the same form as the usual Hall effect, assuming an effective number of electrons $N(1 + N_S/N)$.

In the case of a *weak potential* ($f \ll l$), λ may be much smaller than one (depending

upon the ratio $\hbar\omega_0/\mu_0$). σ_{xx} and σ_{xy} are then proportional respectively to λ^2 and λ^3 :

$$\sigma_{xx} = \frac{N e^2}{m^* \omega_0} \frac{2}{\pi} \frac{N_S}{N} \left\{ \frac{3f}{l} \left(\frac{\hbar\omega_0}{2\mu_0} \right)^{3/2} \right\}^2 \quad (5.9 a)$$

$$\sigma_{xy} = -\frac{N e^2}{m^* \omega_0} \left[1 + \frac{4}{3\pi} \frac{N_S}{N} \left\{ \frac{3f}{l} \left(\frac{\hbar\omega_0}{2\mu_0} \right)^{3/2} \right\}^3 \right] \quad (5.9 b)$$

This result is in accordance with the estimate made in Section 3.

Numerical results can be expressed in terms of two dimensionless parameters

$$\gamma = \frac{\hbar\omega_0}{2\mu_0} \quad (5.10)$$

and

$$\alpha = f k_F^0. \quad (5.11)$$

In Table 1, we indicate typical values of the carrier density n , of the Hall mobility μ_H , and α for Si and InSb.

Table 1.

	n (cm ⁻³)	μ (cm ² /V/s)	α
InSb	6.2×10^{15}	80,000	0.37
Si	8×10^{15}	1,430	25.8

For a given γ , we calculate first the Fermi level or rather

$$x = \frac{\mu}{\hbar\omega_0} \quad (5.12)$$

through

$$\gamma^{-3/2} = 3\sqrt{2} \sum_n \sqrt{x - (n + 1/2)}. \quad (5.13)$$

Then K_1 , K_2 , λ , and at last σ_{xx} and σ_{xy} are calculated. This can be performed through a digital computer, and yields $\sigma_{\alpha\beta}$ as a function of γ^{-1} . Figure 7 shows the result for Si and InSb (σ_{xx} and the correction $\delta\sigma_{xy}$ to the Hall effect have been expressed in $N_S e^2 / m^* \omega_0$ units).

We cannot expect this data to fit the experiments reported in the literature exactly for our theory is a pretty simplified model. However, the orders of magnitude and the whole shape of the curves can be checked;

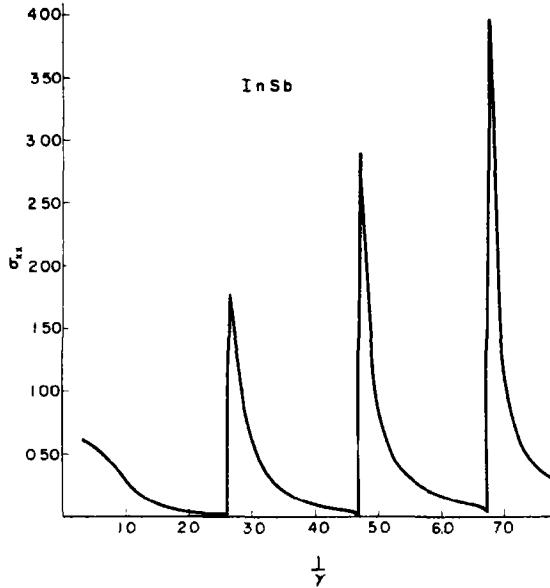


Fig. 7a.

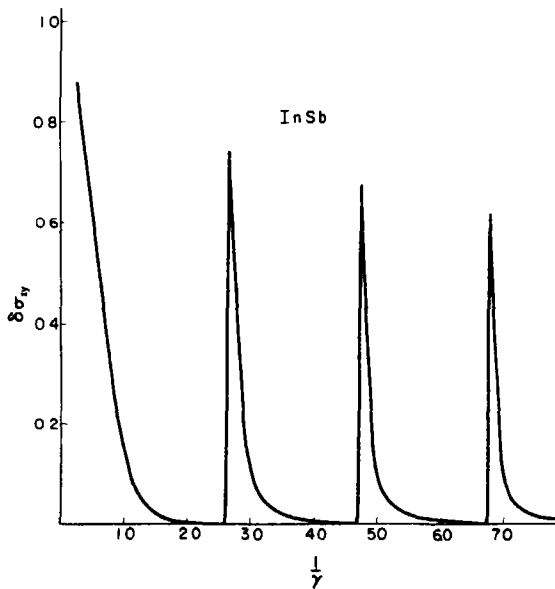


Fig. 7b.

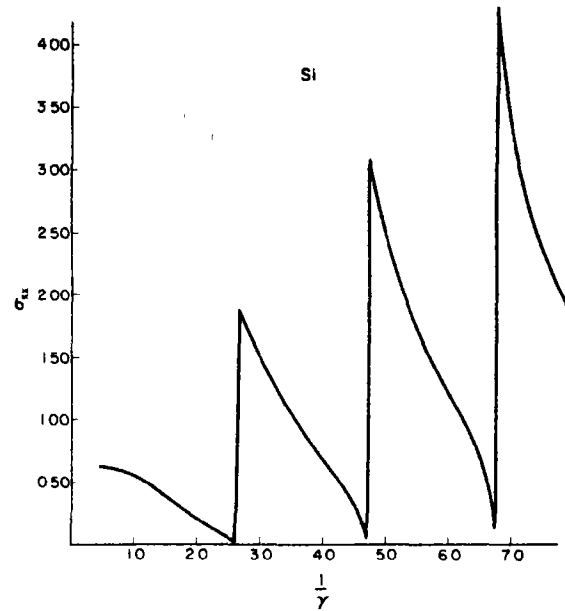


Fig. 7c.

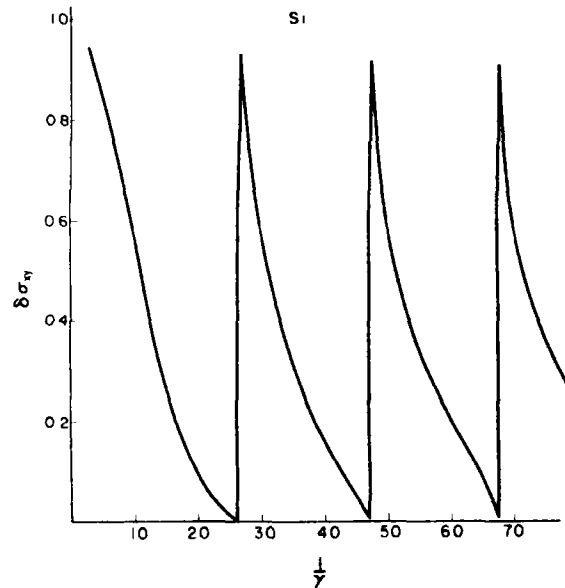


Fig. 7d.

Fig. 7. Conductivity vs. reciprocal magnetic field in InSb and Si.

the ratio $\delta\sigma_{xy}/\sigma_{xy}$ turns out to be of order 10^{-2} and σ_{xx}/σ_{xy} of order 10^{-1} , which is roughly in accordance with the results of Pavlov and Tuchendler.

This numerical calculation has ignored the collision broadening. If we take it into account, our effect will be damped; we expect the damping to be more important for small values of $\omega_0\tau$ (for small mobilities, such as in Si) than for large ones (such as in InSb).

6. CONCLUSION

In the case of scattering by dilute spinless random impurities, the problem of the electrical conductivity tensor of an electron gas can be considered as completely solved up to first order in the impurity concentration N_s/N . At this stage, a correction to the Hall effect, linear in N_s/N , appears whereas it has been missed so far in the literature. It turns out that this effect may be responsible for deviations to the Hall effect that have been reported in InSb by Pavlov and Tuchendler.

For arbitrary values of the impurity concentration, a self consistent calculation is presented, which provides an interpolation between the limits $\omega_0\tau \rightarrow 0$ or ∞ . The results so obtained constitute an improvement of the simplified Drude-Zener model. However,

solving the self consistent equations for T , K , G in the general case remains to be achieved.

REFERENCES

1. ARGYRES P. N., ROTH L. M., *J. Phys. Chem. Solids*, **12**, 89 (1959).
2. ARGYRES P. N. ADAMS E. N., *Phys. Rev.*, **104**, 900 (1956).
3. ADAMS E. N., HOLSTEIN T. D., *J. Phys. Chem. Solids*, **10**, 254 (1959).
4. KAHN A. H. and FREDERIKSE H. P. R., in *Solid State Physics*, Vol. 9, (Edited by F. Seitz and D. Turnbull).
5. KUBO R., MIYAKE S. T., HASHITSUME N., in *Solid State Physics*, Vol. 17.
6. PAVLOV S. T., PARFEN'EV R. V., FIRSOV Yu. A., SHALYT S. S., *Soviet Phys. JETP*, **21**, 1049 (1965).
7. TUCHENDLER J., Thèse de 3ème Cycle, Paris (1967).
8. BASTIN A. J. F., LEWINER C., FAYET N., *J. Phys. Chem. Solids*, **31**, 817, (1970).
9. POTTIER-FAYET N., Thèse de 3ème Cycle, Paris (1970).
10. The calculations of Section 2 and part of Section 3 are also described in Ref. [9].
11. KAHN A. H., *Phys. Rev.*, **119**, 1189 (1960).
12. SKOBOV V. G., *Soviet Phys. JETP*, **12**, 483 (1969).
13. ABRIKOSOV A. A., *Soviet Phys. JETP*, **29**, 746 (1961).
14. Both effects have been partly dealt with by Kubo in his σ_{xx} calculations, but they have not been taken into account simultaneously.
15. BECKMAN O., HANAMURA E., NEURINGER L. J., *Phys. Rev. Lett.* **18**, 773 (1967).

THE ELECTRONIC PROPERTIES OF TITANIUM INTERSTITIAL AND INTERMETALLIC COMPOUNDS FROM SOFT X-RAY SPECTROSCOPY

J. E. HOLLIDAY

Edgar C. Bain Laboratory For Fundamental Research, United States Steel Corporation Research Centre, Monroeville, Penna. 15146, U.S.A.

(Received 8 May 1970; in revised form 2 October 1970)

Abstract—The $TiL_{II,III}$ emission bands ($3d+4s \rightarrow 2p$ transition) have been obtained from $TiC_{0.05}$ and TiN_x ($x = 0.2$ to 0.8) interstitial compounds and $TiCr_2$, $TiCo$, $TiNi$ and $TiFe$ intermetallic compounds. Additional peaks on the low energy side of the TiL_{III} band from TiC and TiN_x appear to be cross transitions from the $2s$ and $2p$ bands of the non-metal to the $2p$ level of titanium. Agreement was found between the soft X-ray band spectra and the band calculations of Ern and Switendick on TiC and TiN . The soft X-ray emission spectra from TiC indicated strong admixture of the titanium $3d$ and carbon $2p$ bands which is in disagreement with LCAO band calculations of Lye and Logothetis. However, the $2p$ band of nitrogen was shown to be below the Ti $3d$ band indicating a localized state and a possible transfer of electrons from titanium to nitrogen.

The $TiL_{II,III}$ bands from $TiCr_2$, $TiCo$, $TiFe$ and $TiNi$ show a progressive change with increasing electronegativity difference between titanium and the combining element indicating that there may be ionic character to the bond. No peaks were observed on the low energy side of the TiL_{III} bands as was observed for TiC and TiN , but a distinct splitting was observed in the peak of the TiL_{III} band from Ti_2Ni , $TiNi$ and $TiNi_3$.

1. INTRODUCTION

THE ELECTRONIC structure of the first series transition metal interstitial compounds, especially the borides, carbides and nitrides, are of particular interest because of their mechanical, electrical and thermal properties. Two electronic structure models have been proposed for these materials. Utilizing LCAO (Linear Combination of Atomic Orbitals) type of band calculations Lye and Logothetis[1] have calculated energy bands for TiC and preliminary calculations on TiN . Their band calculations are semiempirical and show localized states in the bands. In order to be consistent with the Madelung displacement of the energy levels and their own observed optical properties, they applied a electrostatic correction to their band calculation which resulted in the carbon $2p$ band being separated and lying above the titanium $3d$ band. As a result of this separation and from the filled portion of their density of states histogram they predicted that $1\frac{1}{2}$ electrons would be transferred from the carbon $2p$ band to the titanium $3d$ band for TiC . In the other model Ern and

Switendick[2] using the APW (Augmented Plane Wave) method showed no separation in the carbon $2p$ and titanium $3d$ bands and thus no electron transfer. For TiN they showed the nitrogen $2p$ band at the bottom of the titanium $3d$ band. These two band pictures have generated considerable controversy over the past several years. Lye and Logothetis[1] state that the key to solving the problem is to locate the position of the carbon $2p$ and titanium $3d$ bands experimentally. Ern and Switendick stated that the L spectra from TiC and TiN would be an aid in understanding the electronic structure of these compounds. As a result of these comments the soft X-ray L emission spectra from TiC and TiN was measured to determine the relative location of the $2p$ and $3d$ bands, the degree of localization in the band and if there is some ionic character in the bond of these compounds.

Localized states may also be important in the band structure of alloys as demonstrated in recent soft X-ray measurements by Curry *et al.*[3]. Similarly, in a paper presented at the Density of States Conference, Rooke[4]

suggested localized states around the aluminum atom to explain some of the soft X-ray measurements on Al-Mg alloys. Since a localized band picture and ionic character in the bond would be more pronounced in intermetallic compounds than in alloys, the soft X-ray emission bands were measured for a series of titanium intermetallic compounds to determine if localized states and ionic character were present. The compounds were selected so there would be a progressive increase in the electronegativity difference between the titanium and the combining element.

2. EXPERIMENTAL RESULTS

The soft X-ray emission bands were measured with a grazing incidence grating spectrometer. The grating used has a 1 meter radius, 3600 groove/mm with a platinum surface and a 1° blaze. The target potential was 4 kv, and the beam current was 1.5 ma. Since the spectrometer has been thoroughly described in other publications[5], the details will not be presented here. The TiC and TiN_x targets were made from compressed powders of the compounds*, and the titanium inter-

metallic compounds were made by levitation melting of stoichiometric mixtures of the elements. The composition of these intermetallic compounds, determined by chemical analysis after the formation of the compound, is shown in Table 1.

The $\text{TiL}_{\text{II,III}}$ emission band from TiC is shown in Fig. 1. The peak A, approximately 7.5 eV on the low energy side of the TiL_{III} band ($3d+4s \rightarrow 2p$ transition), is not observed for the pure metal. In addition, the $\text{TiL}_{\text{II}}/\text{TiL}_{\text{III}}$ intensity ratio for TiC has been reduced relative to metallic titanium, and the peak of the TiL_{III} band has shifted towards lower energy. Changes in the $\text{TiL}_{\text{II}}/\text{TiL}_{\text{III}}$ in-

Table 1. Composition of intermetallic compounds

	Wt. % of element			
	Cr	Fe	Co	Ni
TiCr ₂	67.1			
TiFe		52.8		
TiCo			55.2	
Ti ₂ Ni				38.0
TiNi				55.4
TiNi ₃				77.6

*Prepared by Cerac, Inc., Butler, Wisconsin.

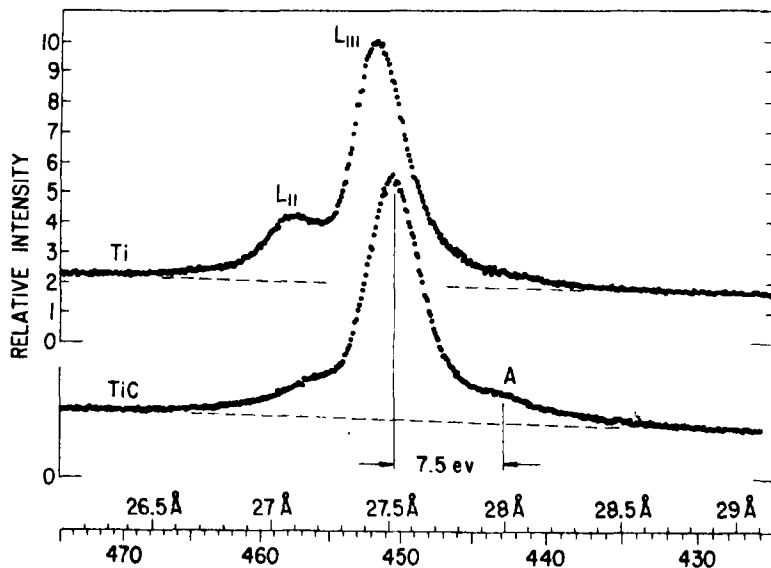


Fig. 1. The $\text{TiL}_{\text{II,III}}$ emission bands normalized from Ti and TiC; target voltage was 4 kv.

tensity ratio with x , but there is less of a change both Holliday[6] and Fischer and Baun[7] to be due to changes in self absorption. Fischer and Baun have also attributed some of the changes in the TiL_{II}/L_{III} ratio as being due to Auger transitions.

The $TiL_{II,III}$ emission bands from TiN_x nitrides where x is varied from 0.2 to 0.8 is shown in Fig. 2. The peak A' , on the low energy side of the TiL_{III} band, is seen to increase in intensity relative to the TiL_{III} band with increasing x . There is also a shift in the TiL_{III} band towards higher energy, with x (Fig. 3). An increase is observed in the TiL_{II}/L_{III} in-

bands toward higher energy with increasing electronegativity difference between the Ti and combining atom. These changes are similar to that observed for the $TiL_{II,III}$ bands from TiN_x with increasing x . The $TiL_{II,III}$ emission band from $TiNi$ shows a split in the TiL_{III} peak which was not observed for the TiL_{III} bands from the other compounds. The separation of the peaks is approximately 1.5 eV which is the same as the separation of the two peaks in the $NiM_{II,III}$ bands from $TiNi$ reported by Cuthill *et al.*[8]. The separation between the peaks for Ti_2Ni and $TiNi_3$ is the same as that of $TiNi$, Fig. 5, but the high energy peak

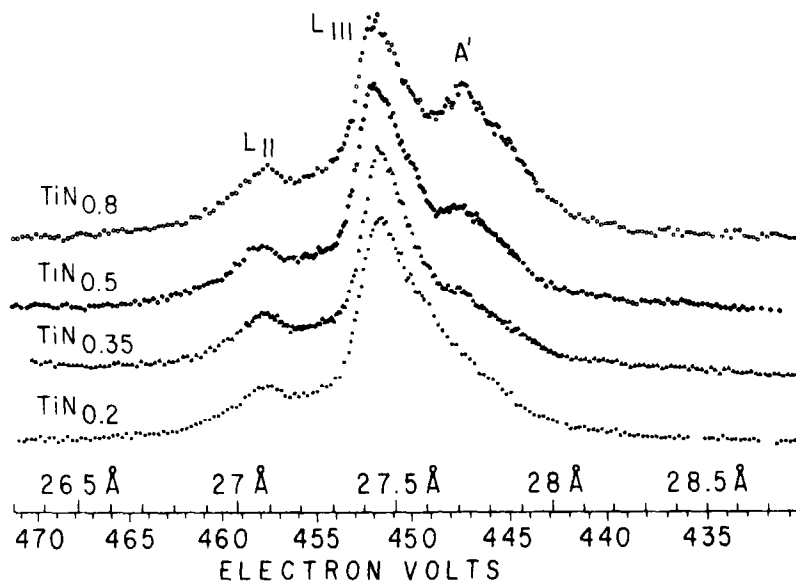


Fig. 2. The $TiL_{II,III}$ emission bands from TiN_x nitrides where x varies from 0.2 to 0.8. The target voltage was 4 kv.

tensity ratio have been shown previously by for a given range of x than that reported for TiO_x oxides[6]. In general, the changes in the $TiL_{II,III}$ emission bands from TiN_x nitrides are the same as those observed for TiO_x oxides but are somewhat less pronounced.

The $TiL_{II,III}$ emission bands for the titanium intermetallic compounds are shown in Fig. 4. These reveal an increase in the TiL_{II}/L_{III} intensity ratio, and a slight shift of the $TiL_{II,III}$

increases in intensity relative to the low energy peak with increasing Ni/Ti atom ratio.

3. DISCUSSION OF RESULTS

As indicated in the introduction, the degree of localization and the amount and direction of electron transfer in TiC and TiN will depend on the amount of separation and position of the non-metal 2p bands relative to the Ti 3d band. Of particular interest in this regard are

peaks *A* and *A'* in Figs. 1 and 2. The fact that peak *A'* increases in intensity relative to the TiL_{III} peak with increasing N/Ti atom ratio indicates that the peak is associated with the amount of nitrogen in TiN. A peak also appears on the low energy side of the TiL_{III} band from TiO_x oxides, whose intensity increases with an increase in the O/Ti atom ratio

the $2s$ bands of the non-metal and the $2p$ level of titanium.

Further evidence that the peaks on the low energy side of the metal band, for transition metal interstitial compounds, are cross transitions for the 2nd period elements is observed for the $\text{NbM}_{\text{IV,V}}$ band from $\text{NbC}_{0.85}$ shown in Fig. 6. The peak *A*, 9.4 eV on the low energy

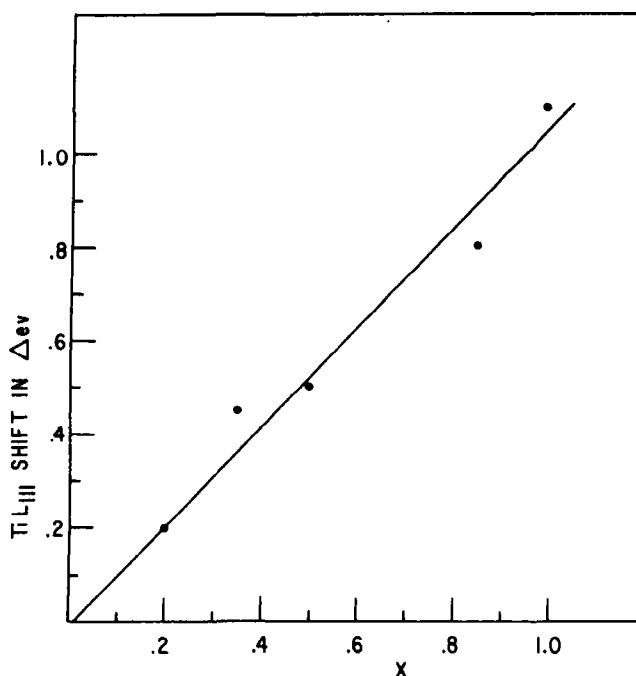


Fig. 3. The shift in the TiL_{III} band relative to pure Ti for TiN_x nitrides as a function of x ; target voltage was 4 kv.

[6]. Fischer and Baun[7] has presented arguments that this peak is a cross transition between the O- $2p$ band and the Ti- $2p$ level, and has correlated his TiO_x spectra with Ern and Switendick's band calculations on TiO. Zhurarovskii and Vainshtein[9a]; Blochin and Shuvaev[9] have established justification for believing that the $K\beta''$ peak which appears on the low energy side of the $K\beta_s$ ($3d+4s \rightarrow 1s$ quadrupole transition) emission bands of TiX compounds, where X is a 2nd period element, represents a cross transition between

side of the high energy peak, is considered to be a cross transition from the $2s$ band of carbon to the $3d$ band of Nb. From their X-ray measurements of the $\text{NbL}_{\text{II,III}}$ bands from NbC and cross transition for *K* emission bands of TiC and VC, Ramqvist *et al.*[10] predicted that a cross transition from the $2s$ band of carbon should be observed at about 10 eV from the main NbM_v band from NbC. They also predicted that the cross transition would have the approximate relative intensity to the NbM_v band from $\text{NbC}_{0.85}$ as does peak *A*

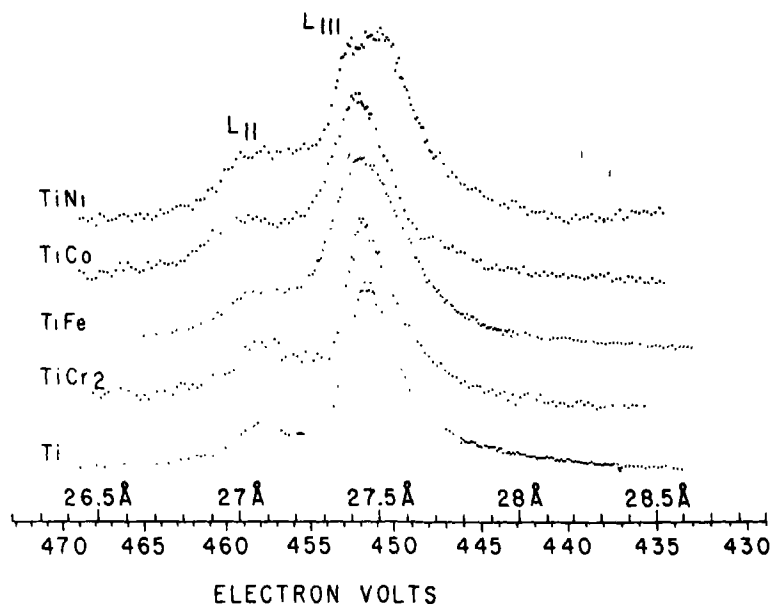


Fig. 4. The TiL_{II,III} emission bands from Ti and TiCr₂, TiFe, TiCo and TiNi intermetallic compounds; target voltage was 4 kv.

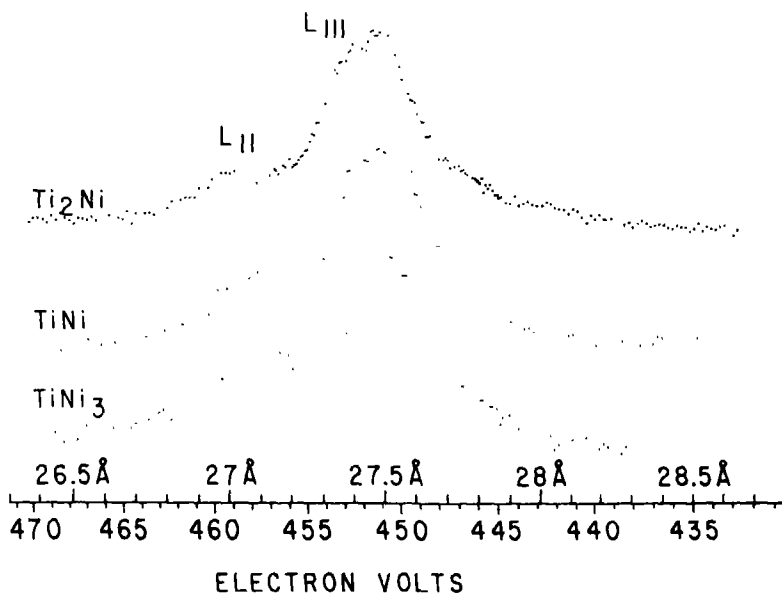


Fig. 5. The TiL_{II,III} emission band from Ti₂Ni, TiNi and TiNi₃ showing change in intensity of the high energy peak relation to the low energy peak; target voltage was 4 kv.

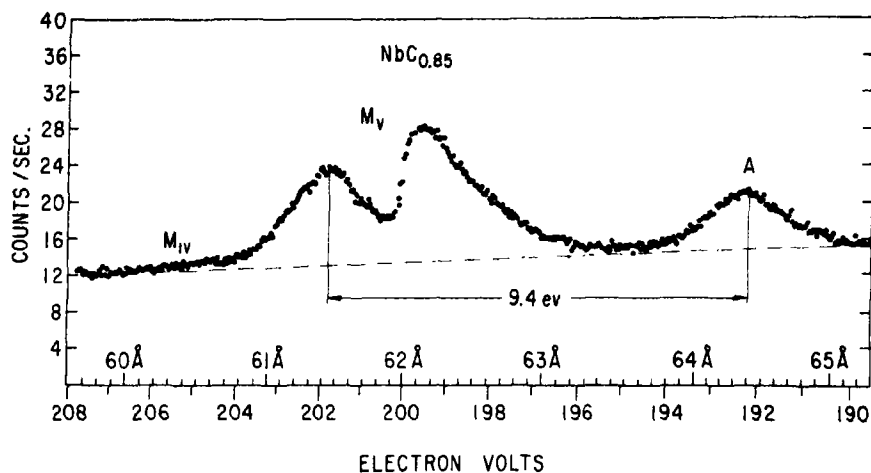


Fig. 6. The $\text{NbM}_{\text{IV,V}}$ emission band from $\text{NbC}_{0.85}$. Peak *A* is considered to be a cross transition from the $2s$ band of carbon to the $3d$ level of Nb. The target voltage was 4 kv

(Fig. 6). Peak *A* in Fig. 6 was also observed for $\text{NbC}_{0.95}$.

Best[11] attributes the above mentioned metal $K\beta'$ line, for transition metal oxides, as a transition from the $4t_2$ molecules orbital (MO), which he refers back to the oxygen $2s$ atomic orbital, to the $1s$ inner level of the metal. By relating the $4t_2$ molecular orbital back to the oxygen $2s$ level, Best shows that the MO transition conveys concepts that are similar to the cross transition. The cross transition model is better suited for the present comparison with Ern and Switendick[2] and Lye and Logothetis[1] band calculations since their band calculations are in terms of atomic orbitals. However, X-ray band spectra when used with MO theory could yield more information about bonding than is possible when using the X-ray cross transition and band calculations.

During the preparation of this manuscript a paper, soon to be published by Fischer[12], was called to the author's attention. In this paper Fischer completely refutes the cross transition as a model and states that only MO transition should be used to compare with X-ray spectra. This extreme position does not

appear to be justified due to the lack of good theoretical foundations for relating soft X-ray band spectra to MO theory for conducting compounds. Also some of the X-ray fine structure that has been associated with MO transitions needs additional confirmation. Fischer uses two basic arguments that he feels makes MO transitions superior to cross transitions. One argument is that the peak associated with the cross transition for TiO_x oxides is a quadrupole transition and it should be much weaker than the measurements show. However, for the case of the cross transition shown for $\text{NbC}_{0.85}$ in Fig. 6 it was possible to predict the correct intensity using the cross transition model. Because of the large number of intensity anomalies that exist for emission bands using the conventional energy level diagram and atomic selection rules, a new model could be justified on the basis of X-ray intensities only after a large number of band intensities had been considered to determine if MO theory gives better prediction than the old model. The second argument that Fischer uses is that the cross transition implies an ionic bond. However, this is only true for cross transitions involving the outer most valence

electrons. Cross transition from more tightly bound electrons such as the C-2s to Ti-2p cross transition for TiC does not necessarily imply an ionic bond as will be shown later. In fact when Blochin and Shuvaev[9] used the cross transition to explain their X-ray spectra for TiC they assumed that titanium and carbon were natural atoms.

From the above discussion there is sufficient justification to use the cross transition model to explain peaks A and A' for TiC and TiN. Ern and Switendick[2] have shown that the energy separation between the $K\beta_5$ band ($4s+3d \rightarrow 1s$) and the $K\beta''$ ($2s \rightarrow 1p$) cross transition from TiN, which according to Zhurakovskii and Vainshtein[9a] is 11.3 eV, is close to their calculated separation of 10.7

eV between the 2s and 3d+2p bands (Fig. 7). The separation between the peak of the TiL_{III} band ($3d+4s \rightarrow 2p$) and peak A' in Fig. 2 is 4.2 eV. Since the peak of the 2s band is approximately 11 eV from the peak of the 3d band, then peak A' appears to be a cross transition from the nitrogen 2p band to the 2p level of titanium and any electron transfer would be from titanium to nitrogen. This indicates that there is a greater separation between the 2p and 3d bands than Ern and Switendick's[2] calculations show. However, Ern and Switendick state that the discrepancy between the initial and derived charges in the nitrogen sphere show that they should have assumed a greater separation in the 2p and 3d bands. Also, the experimental

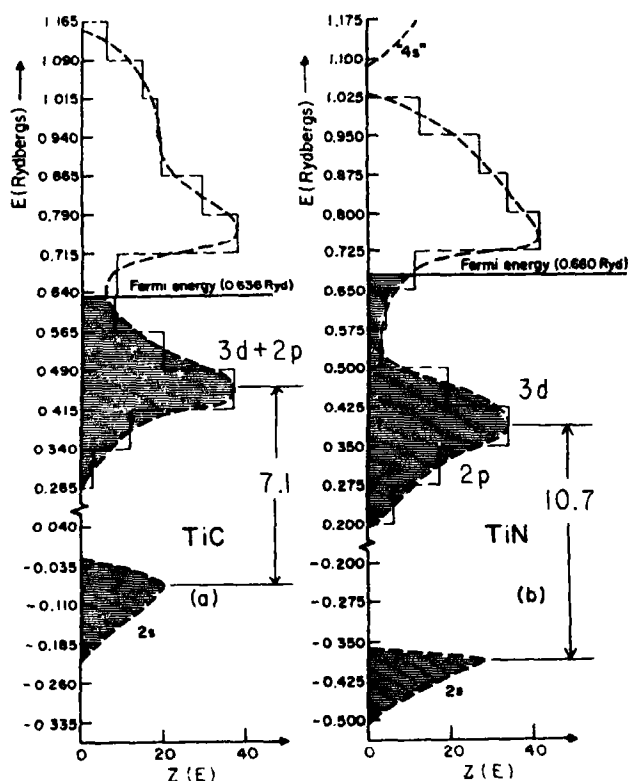


Fig. 7. Density of states histogram for TiC and TiN calculated by Ern and Switendick using the APW method. (Reprinted by permission of ERN V. and SWITENDICK A. C., *Phys. Rev.* 137A, 1927 (1965).

shifts of the $K\beta''$ and $K\beta_s$ bands of TiN relative to TiO when compared to Ern and Switendick's computer density for states show that TiN band picture is closer to TiO than that predicted by Ern and Switendick. The idea of electron transfer and ionic character in the bond for TiN is also shown by the increasing shift of the TiL_{III} band towards higher energy with x in Fig. 3. Shifts in the energy of the nitrogen $1s$ and titanium $2p_{3/2}$ levels from ESCA (Electron Spectroscopy for Chemical Analysis) by Ramqvist *et al.*[13] show that the electron transfer is from titanium to nitrogen.

In the case of TiC peak *A* (Fig. 1) is approximately 7.5 eV from the peak of the TiL_{III} band. Ern and Switendick calculate that the $2s$ and the $3d+2p$ band of TiC are separated by 7.1 eV as shown in Fig. 7. Blochin and Shuvaev [9] show a separation in the $K\beta_s$ band ($3d+4s \rightarrow 1s$) and the $K\beta''$ (carbon $2s \rightarrow$ titanium $1s$) of 7.0 eV. It would thus appear that peak *A* is a cross transition from the carbon $2s$ band to the titanium $2p$ level. Although Lye and Logothetis[1] do not give a value for the separation in the maximum of the $2s$ and $3d$ bands in TiC the maximum in the $2s$ band is about 2 eV below the maximum of the $3d$ band. However, they did report raising the $2s$ state of carbon by 4.15 eV. Thus, the soft X-ray L emission spectra from TiC supports the band calculations of Ern and Switendick. It would appear that there is complete admixture of the carbon $2s$ and the titanium $3d$ bands because no peak was observed in the TiL spectra from TiC corresponding to the $2p$ band. This would indicate equal sharing of electrons. However, Ramqvist *et al.*[13, 14] have performed a number of ESCA and K X-ray measurements on the shifts of the $1s$ level of carbon, the $K\beta_{13}$, $K\alpha_1$, X-ray lines, and L_{III} and M_{III} levels of titanium from TiC relative to the pure element. From these measurements they conclude that electrons are being transferred from titanium to carbon which is opposite to that predicted by Lye and Logothetis. Lye[14a] claims that Ramquist[13]

reported a rise of 3.3 eV for the $1s$ level of carbon which agrees with their raising the $2p$ state of carbon by 2.77 eV and the $2s$ state by 4.15 eV. However, Ramqvist reported a decrease in energy of the $1s$ level, not an increase. Holliday[15] has reported shifts in the TiL_{III} peak which indicates the possibility of electron transfer in TiC.

The above experimental measurements on TiC show that Lye and Logothetis are incorrect in placing the $2p$ band of carbon higher than the $3d$ band of titanium. The degree of localization of the bands is somewhat uncertain. More theoretical work is required to fully understand the meaning of shifts in the inner atomic levels of the atoms relative to the uncombined atom in relation to electron transfer and ionic character of the bond for TiC. In the case of TiN the experiments and the calculations of Ern and Switendick show the $2p$ band below the $3d$ band with electron transfer from titanium to nitrogen. Although Lye and Logothetis did not publish any band calculations on TiN, they state that the $2p$ band would lie closer to the $3d$ than in TiC. This is not in agreement with the above measurement on the TiL emission spectra from TiN and TiC which show a wider separation in the $2p$ and $3d$ bands in TiN and none for TiC.

The observed progressive change in the wavelength and the intensity distribution of the TiL_{III} bands from $TiCr_2$, TiFe, TiCo and TiNi with increasing electronegativity difference between Ti and the combining element, Fig. 4, suggests an increase in ionic bonding with increasing atomic number of the combining element. This interpretation is further substantiated by the fact that preliminary measurements of the $L_{II,III}$ bands from Cr, Co, Fe and Ni do not have the same intensity distribution as the TiL_{III} bands. This is similar to the results reported by Neddermeyer[16] on Al-Mg alloys where large differences were noted between the bottom of the Al and $MgL_{II,III}$ bands. Neddermeyer attributes these changes to clusters and localized bound states

at the bottom of the valence band which resulted in the density of states having a different distribution when in the vicinity of a given atom.

Since detailed band calculations have not been carried out for these intermetallic compounds, it is of interest to compare the present results for the TiL_{III} bands (Fig. 4) with the $3d$ $N(E)$ curve obtained by Cheng *et al.*[17] from specific heat measurements for b.c.c. 1st series transition metals. Cheng deals in valence electron concentration rather than electron volts, and the approximate values for TiCr_2 , TiFe , TiCo and TiNi are 5.3, 6, 6.5 and 7 respectively. Even though TiNi is a CsCl type structure, its soft X-ray spectra shows a double peak in the $3d$ band which is also predicted from the $N(E)$ curve of Cheng *et al.* for an alloy with a valence electron concentration of 7. However, b.c.c. TiFe and TiCo do not have a double peak even though the $N(E)$ curve of Cheng *et al.* predicts that a b.c.c. alloy with a valence electron concentration of 6 and 6.5 should have a double peak. These results appear to add further experimental support to the fact that the rigid band model is a poor approximation to the density of states. The change in the intensity of the high energy peak relative to the low energy peak for TiNi compounds, in Fig. 5, with increasing Ni/Ti atom ratio is also in disagreement with the rigid band model. However, before a complete interpretation of the results on the intermetallic compounds can be made, an understanding of the degree of oxidation of titanium in the alloy relative to uncombined titanium must be obtained.

4. CONCLUSIONS

The foregoing results on the L emission spectra from TiC and TiN support the band calculations of Ern and Switendick. Localized states and ionic character in the bond appear to be a part of the electronic structures of TiN but is somewhat uncertain in TiC . In addition the soft X-ray measurements on titanium intermetallic compounds has shown that the

concepts of localized states, ionic character and electronegativity appear to play a more important role in the electronic structure of metallic compounds than had been supposed previously. In his summarizing comments before the Electron Density of States Conference, Ehrenreich[18] has emphasized that the idea of localized states should be given more consideration when considering the electronic structures of alloys.

In regards to which model, the MO theory or cross transition, will become the most accepted model for understanding X-ray spectra from solids will depend on future experiments and theoretical analysis. Molecular orbital theory does hold promise for understanding some X-ray band spectra that has been difficult to interpret by the band model, and will probably be most useful for understanding X-ray spectra from insulators.

REFERENCES

1. LYE R. G. and LOGOTHETIS E. M., *Phys. Rev.* **147**, 622 (1966).
2. ERN V. and SWITENDICK A. C., *Phys. Rev.* **137A**, 1927 (1965).
3. CURRY C., in *Soft X-ray Band Spectra of Metal and Materials*, (Edited by D. J. Fabian), pp. 173-184, Academic Press, New York and London (1968).
4. ROOKE G. A., *J. Res. Nat. Bur. Stand.* **74A**, 273 (1970).
5. HOLLIDAY J. E., in *The Handbook of X-rays*, (Edited by E. F. Kaelble), Chapter 38, pp. 38-1 to 38-42. McGraw-Hill, New York (1968).
6. HOLLIDAY J. E., in *Soft X-ray Band Spectra and the Electronic Structure of Metals and Materials*, (Edited by D. J. Fabian), pp. 101-32. Academic Press, New York and London (1968).
7. FISCHER D. W. and BAUN W. L., *J. appl. Phys.* **39**, 4757 (1968).
8. CUTHILL J. R., McALISTER A. J., WILLIAMS M. L., *J. appl. Phys.* **39**, 2204 (1968).
9. BLOCHIN M. A. and SHUVAEV A. J., *Bull. Acad. Sci. U.S.S.R. Phys. Ser.* **24**, 429 (1962).
- 9a. ZHURAKOVSKII E. A. and VAINSHTEIN E. E., *Dokl. akad. nauk. S.S.S.R.* **129**, 1269 (1959); [English Transl: *Soviet Phys. Dokl.*] **4**, 1308 (1960).
10. RAMQUIST L., EKSTIG B., KÄLLNE E., NORELAND E., and MANNE R., *J. Phys. Chem. Solids*, to be published.
11. BEST D. E., *J. chem. Phys.* **44**, 3248 (1966).
12. FISCHER D. W., *J. appl. Phys.* **41**, 3561 (1970).
13. RAMQVIST L., *Jernkontorets Annaler.* **153**, 159 (1969).
14. RAMQVIST L., HAMRIN K., JOHANSSON G.,

- FAHLAM A. and NORDLING C., *J. Phys. Chem.* **30**, 1835 (1969).
- 14a. LYE R. G., in the Proceedings of the Electron Density of States Conference held at the National Bureau of Standards, Washington, D.C., (November 1969).
15. HOLLIDAY J. E., *J. appl. Phys.* **37**, 4720 (1967).
16. NEDDERMEYER H., *Dissertation zur Erlangung der Doktorwürde*, der Ludwig-Maximilians Universität München, May 1969.
17. CHENG C. H., GUPTA K. P., VAN REUTH E. C. and BECK P. A., *Phys. Rev.* **126**, 2030 (1962).
18. EHRENREICH H., *J. Res. Nat. Bur. Stand.* **74A**, 293 (1970).

PHENOMENES GALVANOMAGNETIQUES NON LINEAIRES B—THEORIE QUANTIQUE

D. CALECKI

Groupe de Physique des Solides* de l'Ecole Normale Supérieure, Faculté des Sciences, Paris, France

(Received 9 June 1970; in revised form 24 September 1970)

Résumé—Nous présentons une théorie quantique des faibles déviations par rapport à la loi d'Ohm dans des semiconducteurs soumis à de fortes inductions magnétiques. Après avoir obtenu une expression générale du vecteur densité de courant, nous en déduisons les lois de variation avec la température et l'induction magnétique du coefficient β caractérisant les déviations, pour trois types d'interaction entre les électrons et les phonons.

Abstract—We present a quantum theory of small deviations from Ohm's law in semiconductors submitted to the influence of a high magnetic induction perpendicular to the electric field. We obtain a general expression for the current density vector and we deduce the temperature and magnetic induction dependence of the coefficient β which characterizes the deviations, for three types of electron-phonon interactions.

1. INTRODUCTION

LES RÉSULTATS expérimentaux concernant les faibles déviations par rapport à la loi d'Ohm et présentés dans l'article A qui précède, ne peuvent s'interpréter dans le cadre de la théorie de la référence [1]. En effet, le coefficient r , dont les résultats de mesure dans InSb sont examinés dans A, passe de valeurs négatives à positives quand la température croît, alors que les formules de [1] prédisent un changement de signe contraire. Nous avons donc repris l'étude théorique du coefficient β défini par la formule (A.1.1). Pour cela, nous avons dû résoudre l'équation d'évolution de l'opérateur densité et calculer le vecteur densité de courant en introduisant au départ la notion de température électronique (Section 2); cette dernière est déterminée ultérieurement par des considérations énergétiques. Les calculs explicites de β (Section 3) ont été effectués pour trois types d'interactions: interactions électrons-phonons acoustiques traitée à l'aide du potentiel de déformation d'une part et du couplage piézoélectrique d'autre part; interaction avec les phonons optiques. En

procédant de cette façon, nous avons retrouvé un résultat déjà publié pour le premier type d'interaction et obtenu des expressions nouvelles de β dans les deux derniers. Nous avons pris soin de faire apparaître dans tous les cas les limites de validité des expressions obtenues.

2. THEORIE QUANTIQUE DES PHENOMENES GALVANOMAGNETIQUES NON LINEAIRES EN CHAMPS ELECTRIQUE ET MAGNETIQUE CROISES

(1) Généralités

Nous considérons un gaz d'électrons indépendants de densité n (nous négligeons donc les interactions interélectroniques) soumis à la double action d'un champ électrique \mathbf{E} ($E, 0, 0$) et d'une induction magnétique \mathbf{B} ($0, 0, B$) perpendiculaire. Les grandeurs \mathbf{B} et \mathbf{E} sont invariables dans le temps et dans l'espace (les problèmes délicats de conditions aux limites spatiales ne sont pas envisagées ici). Ce gaz est susceptible d'interagir avec un gaz de phonons. Quels renseignements dispose-t-on pour calculer le vecteur densité de courant $\langle \mathbf{J} \rangle$?

(a) *Données de la mécanique quantique.* L'Hamiltonien du système électrons + phonons est la somme:

* Laboratoire associé au C.N.R.S.

$$H = H_e + H_p + \lambda H_{ep}$$

avec

H_e est l'Hamiltonien des électrons en présence de \mathbf{E} et de \mathbf{B} . En choisissant comme états de base les états propres repérés par l'indice α , d'un Hamiltonien à un électron, l'expression de H_e en seconde quantification s'écrit:

$$H_e = \sum_{\alpha} \bar{\epsilon}_{\alpha} a_{\alpha}^+ a_{\alpha} \quad (1)$$

où $\bar{\epsilon}_{\alpha}$ est l'énergie d'un électron dans l'état α :

$$\bar{\epsilon}_{\alpha} = \left(n + \frac{1}{2}\right) \hbar \omega_c + \frac{\hbar^2 k_z^2}{2m} + eE \tilde{X}_{k_y} + \frac{1}{2} m \left(\frac{E}{B}\right)^2 \quad (2)$$

avec

$$\tilde{X}_{k_y} = -\frac{1}{eB} \left(\hbar k_y + m \frac{E}{B}\right). \quad (3)$$

Nous désignerons dans la suite par ϵ_{α} la partie de $\bar{\epsilon}_{\alpha}$ indépendante du champ électrique:

$$\epsilon_{\alpha} = \left(n + \frac{1}{2}\right) \hbar \omega_c + \frac{\hbar^2 k_z^2}{2m}.$$

On constate donc que l'indice α représente en fait les trois nombres quantiques n , k_y , k_z qui interviennent systématiquement dans les problèmes d'états électroniques en présence d'induction magnétique.

H_p est l'Hamiltonien des phonons:

$$H_p = \sum_q \hbar \omega_q \left(b_q^+ b_q + \frac{1}{2}\right) \quad (4)$$

λH_{ep} est l'Hamiltonien d'interaction électrons-phonons. Nous avons fait apparaître le paramètre sans dimension λ qui rend compte de l'intensité de l'interaction.

$$\lambda H_{ep} = \sum_{\alpha\alpha'} \gamma_{\alpha\alpha'}(\mathbf{q}) a_{\alpha}^+ a_{\alpha'} (b_{\mathbf{q}}^+ + b_{-\mathbf{q}}). \quad (5)$$

L'élément de matrice $\gamma_{\alpha\alpha'}(\mathbf{q})$ dépend de la nature du couplage. De façon générale

$$\gamma_{\alpha\alpha'}(\mathbf{q}) = C(q) J_{n k_y, n' k'_y}(q_x) \delta_{k'_y, k_y + q_y} \delta_{k'_x, k_x + q_x} \quad (6)$$

$$J_{n k_y, n' k'_y}(q_x)$$

$$= \int_{-\infty}^{+\infty} dx \phi_n(x - \tilde{X}_{k_y}) e^{iq_x x} \phi_{n'}(x - \tilde{X}_{k'_y}) \quad (7)$$

et $|C(q)|^2 \sim q^P$ avec $P = 1, -1$ ou -2 pour les différents couplages que nous étudierons.

(b) *Données de la mécanique statistique.* Nous admettons qu'à un certain temps t pris pour origine des temps, les deux gaz d'électrons et de phonons sont sans corrélation. Dans ces conditions l'opérateur densité décrivant les deux gaz à l'instant initial, ρ_0 , se factorise en un produit de deux opérateurs densité; l'un $\rho_0^{(e)}$ est associé aux électrons; l'autre $\rho_0^{(p)}$ est associé aux phonons:

$$\rho_0 = \rho_0^{(e)} \rho_0^{(p)}. \quad (8)$$

De plus les électrons sont sans interaction entre eux; ceci implique que $\rho_0^{(e)}$ se factorise en un produit d'opérateurs à une particule; chacun de ces opérateurs à une particule est diagonal dans la base où nous avons exprimé H_e en seconde quantification à l'aide de (1). Il en est de même pour $\rho_0^{(p)}$. Ces propriétés de factorisation et de diagonalité entraînent que:

$$\text{Tr } \rho_0 a_{\alpha}^+ a_{\alpha'} = F_{\alpha} \delta_{\alpha, \alpha'} \quad (9)$$

$$\text{Tr } \rho_0 b_{\mathbf{q}}^+ b_{\mathbf{q}'} = \mathcal{N}_{\mathbf{q}} \delta_{\mathbf{q}, \mathbf{q}'} \quad (10)$$

Les fonctions F_{α} et $\mathcal{N}_{\mathbf{q}}$ représentent les probabilités respectives d'occupation des états α et \mathbf{q} par un électron et un phonon à l'instant initial où les électrons et les phonons sont totalement découplés.

Notons au passage que les propriétés de ρ_0 entraînent que les moyennes de produit d'opérateurs du type

$$\text{Tr } \rho_0 a_{\alpha_1}^+ a_{\alpha_2} a_{\alpha_3}^+ \dots b_{\mathbf{q}_1} b_{\mathbf{q}_2}^+ b_{\mathbf{q}_3} \dots \quad (11)$$

se calculent sans difficulté à partir du théorème de Bloch-de Dominicis [2] sur les contractions.

A partir de l'instant $t = 0$, le système élec-

trons + phonons évolue au cours du temps par le jeu de l'interaction; l'opérateur densité $\rho(t)$ qui le décrit à l'instant t , satisfait l'équation d'évolution:

$$i\hbar \frac{\partial \rho(t)}{\partial t} = [H_e + H_p + \lambda H_{ep}, \rho(t)]. \quad (12)$$

L'ensemble des équations (8) à (12) permet de calculer l'opérateur densité $\rho(t)$ à tout instant et d'en déduire la valeur moyenne du vecteur densité de courant électrique en régime permanent

$$\langle \mathbf{J} \rangle = \lim_{t \rightarrow \infty} \text{Tr } \rho(t) \mathbf{J} \quad (13)$$

\mathbf{J} est l'opérateur densité de courant électrique dont les seules composantes qui vont intervenir dans ce problème sont, du fait des orientations respectives de \mathbf{E} et \mathbf{B} , J_x et J_y . De plus:

$$J_x + iJ_y = \frac{ieE}{\Omega B} \sum_{\alpha} a_{\alpha}^+ a_{\alpha} - \frac{2ie}{\Omega} \left(\frac{\hbar \omega_c}{2m} \right)^{1/2} \times \sum_{\alpha} (n+1)^{1/2} a_{\alpha+1}^+ a_{\alpha} \quad (14)$$

où Ω est le volume du cristal et où $\alpha+1$ représente les trois indices: $n+1, k_y, k_z$.

(c) *Considérations énergétiques.* L'expression du courant, calculée à partir de (13), va évidemment faire intervenir les fonctions de répartition \mathcal{N}_q et F_{α} des phonons et des électrons dont nous n'avons pas encore fixé les expressions. L'éventail des choix possibles pour \mathcal{N}_q et F_{α} est *a priori* largement ouvert. Nous avons donc intérêt à introduire des relations satisfaites par \mathcal{N}_q et F_{α} qui vont limiter les possibilités. Tout d'abord \mathcal{N}_q et F_{α} doivent être convenablement normalisés. Ensuite, nous pouvons introduire des considérations énergétiques. En effet, d'une part, le champ électrique cède de l'énergie aux électrons; nous aurons l'occasion de montrer que la puissance notée $\langle P' \rangle$ ainsi reçue par les électrons est — comme on s'y attend — égale à $(-\langle \mathbf{J} \rangle \cdot \mathbf{E})$; d'autre part les électrons en

interagissant avec les phonons cèdent de l'énergie aux phonons; nous désignons par $\langle P \rangle$ la puissance correspondante que nous calculerons aussi. On s'attend à ce qu'en régime permanent un équilibre s'établisse entre ces deux puissances tel que $\langle P \rangle = \langle P' \rangle$. Comme les expressions de $\langle P \rangle$ et $\langle P' \rangle$ dépendent toutes les deux de \mathcal{N}_q et F_{α} , l'égalité $\langle P \rangle = \langle P' \rangle$ fournit donc une relation entre \mathcal{N}_q et F_{α} susceptible de limiter les choix de ces fonctions.

(2) *Expression générale du vecteur densité de courant électrique*

Avant d'aborder le calcul de la moyenne du vecteur densité de courant, nous allons faire une remarque concernant son expression quand l'interaction électrons-phonons est nulle. Dans ce cas

$$\langle J_x + iJ_y \rangle = \text{Tr } \rho_0 (J_x + iJ_y) \quad (15)$$

et d'après (9), (10) et (14)

$$\langle J_x \rangle = 0 \quad (16)$$

$$\langle J_y \rangle = +n e E/B \quad (n: \text{densité électronique}). \quad (17)$$

On constate donc que, quand $\lambda = 0$, bien que le champ électrique soit dirigé suivant ox , le vecteur densité de courant électrique moyen est dirigé suivant oy grâce au fait que l'induction magnétique est dirigée suivant oz ; de plus $\langle J_y \rangle$ est linéaire en E . L'effet de l'interaction électrons-phonons est donc de contrecarrer l'effet de l'induction magnétique. Grossièrement si l'on admet que l'action sur les électrons de B est caractérisée par la pulsation cyclotron ω_c et que celle du couplage électrons-phonons est fixée par le temps de relaxation τ de la vitesse moyenne qui représente l'intervalle de temps entre les instants où les phonons rappellent leur présence aux électrons, alors les composantes $\langle J_x \rangle$ et $\langle J_y \rangle$ seront d'autant plus voisines de 0 et $n e E/B$ que la condition $\omega_c \tau \gg 1$ sera mieux remplie. Si l'on tient compte du fait que $\tau \propto \lambda^{-2}$, on s'attend donc à ce qu'un calcul de $\langle J_x \rangle$ et $\langle J_y \rangle$ à l'ordre le plus bas en λ ne soit

valable que si la condition $\omega_c \tau \gg 1$ est satisfaite.

Pour calculer $\langle J_x \rangle$ et $\langle J_y \rangle$ à l'ordre le plus bas en λ , il faut préalablement connaître l'expression de $\rho(t)$. La solution de (12) développée en puissances de λ s'écrit:

$$\rho(t) = \rho_0 + \frac{\lambda}{i\hbar} \int_0^t dt_1 [H_{ep}(-t_1), \rho_0] + \left(\frac{\lambda}{i\hbar}\right)^2 \times \int_0^t dt_1 \int_0^{t_1} dt_2 [H_{ep}(-t_2), [H_{ep}(-t_1), \rho_0]] + \dots \quad (18)$$

avec

$$H_{ep}(-t) = \exp(H_e + H_p) \frac{t}{i\hbar} \times H_{ep} \exp - (H_e + H_p) \frac{t}{i\hbar}.$$

Quand on se limite à l'ordre 2 en λ , nous montrons dans l'annexe 1 que, à partir des formules (13) et (18), nous obtenons:

$$\langle J_y \rangle = n e \frac{E}{B} \quad (19)$$

$$\begin{aligned} \langle J_x \rangle = e \sum_{\alpha, \alpha'} \sum_q \frac{\hbar q_y}{m\omega_c} [\mathcal{N}_q F_\alpha (1 - F_{\alpha'}) \\ - (1 + \mathcal{N}_q) F_{\alpha'} (1 - F_\alpha)] \\ \times \frac{2\pi}{\hbar} |\gamma_{\alpha\alpha'}(\mathbf{q})|^2 \delta(\tilde{\epsilon}_\alpha - \epsilon_{\alpha'} + \hbar\omega_q). \quad (20) \end{aligned}$$

Les formules (19) et (20) sont valables dans le cadre d'un développement limité au second ordre par rapport au couplage électrons-phonons, quelles que soient les fonctions F_α et \mathcal{N}_q , pourvu qu'elles satisfassent aux conditions (9) et (10) et que \mathcal{N}_q soit invariant dans le changement du vecteur d'onde des phonons \mathbf{q} en $-\mathbf{q}$.

Avant d'étudier plus en détail ces résultats, passons aux calculs des puissances $\langle P \rangle$ et $\langle P' \rangle$.

(3) Calcul des puissances $\langle P \rangle$ et $\langle P' \rangle$

L'énergie moyenne des phonons est définie

à tout instant à partir de l'Hamiltonien H_p des phonons et de l'opérateur densité $\rho(t)$ par:

$$\langle H_p \rangle_t = \text{Tr } H_p \rho(t). \quad (21)$$

On en déduit que la puissance reçue par les phonons $\langle P \rangle$ en régime permanent est donnée par la formule:

$$\langle P \rangle = \lim_{t \rightarrow \infty} \text{Tr } H_p \frac{\partial \rho(t)}{\partial t}. \quad (22)$$

Soit, en tenant compte de (12):

$$\begin{aligned} \langle P \rangle &= \lim_{t \rightarrow \infty} \frac{1}{i\hbar} \text{Tr } H_p [H_e + H_p + \lambda H_{ep}, \rho(t)] \\ &= \lim_{t \rightarrow \infty} \frac{1}{i\hbar} \text{Tr } [H_p, H_e + H_p + \lambda H_{ep}] \rho(t) \\ &= \lim_{t \rightarrow \infty} \frac{1}{i\hbar} \text{Tr } [H_p, \lambda H_{ep}] \rho(t). \quad (23) \end{aligned}$$

On reconnaît au passage dans $(1/i\hbar)[H_p, H_e + H_p + \lambda H_{ep}]$ l'opérateur en représentation de Schrödinger, associé à la dérivée par rapport au temps de la grandeur physique 'énergie des phonons', au même titre que l'opérateur vitesse $\mathbf{V} = (1/i\hbar)[\mathbf{r}, H_e + H_p + \lambda H_{ep}]$ est l'opérateur associé à la dérivée par rapport au temps de la grandeur physique position.

Le calcul de $\langle P \rangle$, limité au second ordre en λ , s'effectue comme celui de $\langle \mathbf{J} \rangle$ et donne:

$$\begin{aligned} \langle P \rangle &= \sum_{\alpha, \alpha'} \sum_q \hbar\omega_q [\mathcal{N}_q F_\alpha (1 - F_{\alpha'}) - (1 + \mathcal{N}_q) \\ &\times F_{\alpha'} (1 - F_\alpha)] \frac{2\pi}{\hbar} |\gamma_{\alpha\alpha'}(\mathbf{q})|^2 \\ &\times \delta(\tilde{\epsilon}_\alpha - \tilde{\epsilon}_{\alpha'} + \hbar\omega_q). \quad (24) \end{aligned}$$

L'expression (24) de $\langle P \rangle$ ressemble beaucoup à celle de $\langle J_x \rangle$ (Cf. (20)). On passe de (20) à (24) en changeant le facteur

$$\frac{e\hbar q_y}{m\omega_c} = \frac{\hbar q_y}{B} \text{ en } \hbar\omega_q.$$

Passons maintenant au calcul de la puissance

$\langle P' \rangle$ cédée par le champ électrique aux électrons. Si l'on désigne par H_F l'Hamiltonien d'interaction entre les électrons et le champ électrique E , l'expression de H_F s'écrit:

$$H_F = \sum_{i=1}^N e E r_i \quad (25)$$

(sommation étendue à tous les électrons) et l'énergie cédée aux électrons n'est autre que:

$$\langle H_F \rangle_t = \text{Tr } H_F \rho(t). \quad (26)$$

En régime permanent, la puissance $\langle P' \rangle$ transmise aux électrons s'écrit:

$$\begin{aligned} \langle P' \rangle &= \lim_{t \rightarrow \infty} \text{Tr } H_F \frac{\partial \rho(t)}{\partial t} \\ &= \lim_{t \rightarrow \infty} \text{Tr } \frac{1}{i\hbar} H_F [H_e + H_p + \lambda H_{ep}, \rho(t)] \\ &= \lim_{t \rightarrow \infty} \text{Tr } \frac{1}{i\hbar} \left[e E \sum_i r_i, H_e + H_p + \lambda H_{ep} \right] \rho(t) \\ &= \lim_{t \rightarrow \infty} \text{Tr } e E \sum_i V_i \rho(t) = -E \langle J \rangle \\ &= -E \langle J \rangle = -E \langle J_x \rangle. \end{aligned} \quad (27)$$

Aussi $-\langle J_x \rangle E$ apparaît bien comme la puissance cédée par le champ électrique aux électrons ainsi que nous l'avions intuitivement écrit.

Dans ces conditions la relation $\langle P \rangle = \langle P' \rangle$, compte tenu des équations (24), (27) et (20), s'écrit:

$$\begin{aligned} 0 &= \sum_{\alpha, \alpha'} \sum_q \hbar \omega_q^* \left[\mathcal{N}_q F_\alpha (1 - F_{\alpha'}) - (1 + \mathcal{N}_q) \right. \\ &\quad \left. \times F_{\alpha'} (1 - F_\alpha) \right] \frac{2\pi}{\hbar} |\gamma_{\alpha\alpha'}(q)|^2 \delta(\bar{\epsilon}_\alpha - \bar{\epsilon}_{\alpha'} + \hbar\omega_q). \end{aligned} \quad (28)$$

Dans (28), nous avons introduit la quantité

$$\omega_q^* = \omega_q + q_y \frac{E}{B} = \omega_q + q_y V_0 \quad (29)$$

qui représente la pulsation des phonons vue

par les électrons, se considérant comme immobiles dans un repère se déplaçant parallèlement à la direction oy (perpendiculaire à E et B) avec la vitesse $V_0 = E/B$ (effet Döppler).

(4) Choix des fonctions de répartition \mathcal{N}_q et F_α

Nous allons préalablement présenter un certain nombre de remarques sur les différents facteurs intervenant dans les formules (20), (24) et (28) dont on peut, au passage, noter la grande similitude.

(a) Remarque sur le terme $|\gamma_{\alpha\alpha'}(q)|^2$. Ce terme est indépendant du champ électrique E . En effet, d'après (6), ce carré ne fait intervenir E que dans le terme

$$|J_{nk_y, n'k'_y}(q_x)|^2 = \left[\int_{-\infty}^{+\infty} dx \phi_n(x - \tilde{X}_{k_y}) \times e^{iq_x x} \phi_{n'}(x - \tilde{X}_{k'_y}) \right]^2. \quad (30)$$

Il suffit d'effectuer le changement de variable $x' = x - \tilde{X}_{k_y}$ dans l'intégrale et de remarquer que $\tilde{X}_{k_y} - \tilde{X}_{k'_y}$ est indépendant de E (Cf. (31)) pour démontrer ce résultat. Ce même changement de variable associé à la propriété de symétrie des fonctions d'Hermite $\phi_n(x) = (-1)^n \phi_n(-x)$, montre que $|J_{nk_y, n'k'_y}(q_x)|^2$ est une fonction paire par rapport à q_x et par rapport à la différence

$$\tilde{X}_{k_y} - \tilde{X}_{k'_y} = \frac{\hbar}{eB} (k'_y - k_y).$$

(b) Remarque sur le terme $\delta(\bar{\epsilon}_\alpha - \bar{\epsilon}_{\alpha'} + \hbar\omega_q)$. Le champ électrique intervient linéairement dans l'argument de la distribution puisque d'après (2) et la définition de ϵ_α ,

$$\bar{\epsilon}_\alpha - \bar{\epsilon}_{\alpha'} + \hbar\omega_q = \epsilon_\alpha - \epsilon_{\alpha'} - \frac{E}{B} \hbar(k_y - k'_y) + \hbar\omega_q. \quad (31)$$

Pour des besoins ultérieurs, développons en série de puissance de E la distribution:

$$\begin{aligned} \delta(\bar{\epsilon}_\alpha - \bar{\epsilon}_{\alpha'} + \hbar\omega_q) &= \delta(\epsilon_\alpha - \epsilon_{\alpha'} + \hbar\omega_q) \\ &+ \frac{E}{B} \hbar(k'_y - k_y) \delta^{(1)}(\epsilon_\alpha - \epsilon_{\alpha'} + \hbar\omega_q) + \dots \\ &+ \frac{1}{P!} \left[\frac{E}{B} \hbar(k'_y - k_y) \right]^P \delta^{(P)}(\epsilon_\alpha - \epsilon_{\alpha'} + \hbar\omega_q) + \dots \end{aligned} \quad (32)$$

Nous avons ainsi fait apparaître les dérivées successives de la distribution $\delta(x)$.

(c) *Cas des phénomènes linéaires en champ électrique.* Premier choix de \mathcal{N}_q et F_α . Désignons par $\langle J_x \rangle^{(1)}$ la composante de la densité de courant $\langle J_x \rangle$ d'ordre un par rapport au champ électrique. L'expression correcte de $\langle J_x \rangle^{(1)}$ a été établie par de nombreux auteurs dont les premiers ont été Adams et Holstein [3]. L'expression en question de $\langle J_x \rangle^{(1)}$ peut s'obtenir, en particulier, à partir de (20) en choisissant

$$\mathcal{N}_q = N_q = \left(\exp \frac{\hbar \omega_q}{kT_0} - 1 \right)^{-1} \quad (33)$$

et

$$F_\alpha = f_\alpha^0 = \left(\exp \frac{\epsilon_\alpha - \xi}{kT_0} + 1 \right)^{-1}. \quad (34)$$

Nous obtenons alors:

$$\begin{aligned} \langle J_x \rangle^{(1)} &= \frac{e^2 E}{kT_0} \sum_{\alpha, \alpha'} \sum_q \left(\frac{\hbar q_y}{m\omega_c} \right)^2 \\ &\times [N_q f_\alpha^0 (1 - f_{\alpha'}^0) + (1 + N_q) f_{\alpha'}^0 (1 - f_\alpha^0)] \\ &\times \frac{2\pi}{\hbar} |\gamma_{\alpha\alpha'}(q)|^2 \delta(\epsilon_\alpha - \epsilon_{\alpha'} + \hbar\omega_q). \end{aligned}$$

Ce dernier résultat est identique à tous ceux de la littérature scientifique traitant des phénomènes galvanomagnétiques linéaires en champs croisés.

Ainsi, pour les phénomènes linéaires, il suffit de supposer que dans l'état initial les phonons se répartissent dans leurs états suivant une loi d'équilibre thermodynamique à la température T_0 , tandis que les électrons se répartissent suivant la statistique de Fermi-Dirac comme si le champ électrique n'intervenait pas (Noter que c'est ϵ_α et non $\tilde{\epsilon}_\alpha$ qui figure dans (34)).

A partir de ce choix: $\mathcal{N}_q = N_q$ et $F_\alpha = f_\alpha^0$, nous obtenons la série de résultats suivants.

Tous les termes d'ordres pairs en E sont nuls. Ceci correspond au fait que le courant dans un cristal doit changer de sens quand on renverse celui du champ électrique. Pour

démontrer ce résultat, écrivons le terme en E^{2p} du développement de $\langle J_x \rangle$:

$$\begin{aligned} \langle J_x \rangle &= e(eE)^{2p} \sum_{n, k_y, k_z} \sum_{n', k'_y, k'_z} \sum_q \left(\frac{\hbar q_y}{m\omega_c} \right)^{2p+1} \\ &\times [N_q f_\alpha^0 (1 - f_{\alpha'}^0) - (1 + N_q) f_{\alpha'}^0 (1 - f_\alpha^0)] \\ &\times \frac{2\pi}{\hbar} \delta_{k'_y, k_y + q_y} \delta_{k'_z, k_z + q_z} J_{nk_y; n'k'_y} q_x |^2 \\ &\times (\epsilon_{nk_y} - \epsilon_{n'k'_y} + \hbar\omega_q). \end{aligned} \quad (35)$$

Les sommations sur k'_y et k'_z sont immédiates; les termes N_q et $\hbar\omega_q$ sont des fonctions paires de q ; de même

$$|J_{nk_y, n'k'_y, k_y + q_y}(q_x)|^2$$

est, contrairement à son apparence, indépendant de k_y et une fonction paire de q_x et q_y . Alors du fait du facteur $(\hbar q_y/m\omega_c)^{2p+1}$ qui est une fonction impaire de q_y , la sommation sur q_y qui intervient dans (35) donnera un résultat nul. Donc $\langle J_x \rangle^{(2p)} = 0, \forall p$.

Étudions maintenant le terme d'ordre trois en E qui représente les premières déviations par rapport à la loi d'Ohm. Il s'écrit:

$$\begin{aligned} \langle J_x \rangle^{(3)} &= e \frac{(eE)^3}{3!} \sum_{\alpha, \alpha'} \sum_q \left(\frac{\hbar q_y}{m\omega_c} \right)^4 [N_q f_\alpha^0 (1 - f_{\alpha'}^0) \\ &- (1 + N_q) f_{\alpha'}^0 (1 - f_\alpha^0)] \\ &\times \frac{2\pi}{\hbar} |\gamma_{\alpha\alpha'}(q)|^2 \delta^{(3)}(\epsilon_\alpha - \epsilon_{\alpha'} + \hbar\omega_q). \end{aligned} \quad (36)$$

Ce résultat est identique, à un changement de notation évident près, à celui que nous avons obtenu dans la Réf. [1] en généralisant simplement la théorie de Kubo de la réponse linéaire. Nous avons déjà exposé dans l'introduction les raisons pour lesquelles une telle expression de $\langle J_x \rangle^{(3)}$ était à rejeter. Par conséquent, quand on s'intéresse aux phénomènes non linéaires en E , on est amené à chercher pour \mathcal{N}_q et F_α d'autres expressions que celles données par (33) et (34). Toutefois, il faudra que les expressions de \mathcal{N}_q et F_α tendent vers N_q et f_α^0 quand le champ électrique tend vers zéro.

Avant d'abandonner cette discussion, il est bon de noter que quand on fait $\mathcal{N}_q = N_q$ et $F_\alpha = f_\alpha^0$ dans la relation (28) sur l'énergie et qu'on développe au premier ordre en champ électrique, cette relation est bien vérifiée.

(d) *Choix final de \mathcal{N}_q et F_α .* Le cas des phonons nous semble le plus facile à régler. Dans la mesure où l'on s'intéresse aux faibles déviations par rapport à la loi d'Ohm, on peut espérer qu'ils sont assez bien décrits par la fonction d'équilibre thermodynamique à la température T_0 : $\mathcal{N}_q = N_q$. Nous admettrons ce premier point.

Le cas des électrons est beaucoup plus délicat. Nous avons envisagé toute une série de possibilités que nous avons rejetées pour différentes raisons et nous avons finalement adopté pour F_α la fonction:

$$F_\alpha = f_\alpha = \left(\exp \frac{\epsilon_\alpha - \xi}{kT(E)} + 1 \right)^{-1} \quad (37)$$

f_α diffère de f_α^0 simplement par le changement de la température T_0 en une température $T(E)$ — appelée température électronique — qui dépend *a priori* du champ électrique et qui doit tendre vers T_0 quand E tend vers zéro. Le choix (37) n'est justifié pour l'instant que par les conséquences qui en découlent; nous verrons en effet qu'il nous permettra de retrouver un résultat déjà publié concernant les phonons acoustiques et qu'il contribuera à interpréter une part importante des résultats expérimentaux que nous avons exposés dans l'article A.

L'introduction du paramètre $T(E)$ n'a de sens que s'il est possible de le déterminer. Or nous disposons de la relation (28) représentant l'égalité $\langle P \rangle = \langle P' \rangle$ qui, précisément, doit être à même de calculer T en fonction de T_0 et de E . Une remarque importante découle de (28). En effet, il apparaît clairement que cette relation, tout en dépendant de la nature de l'interaction entre les électrons et les phonons, est totalement indépendante de l'intensité de cette interaction. Par conséquent, la température électronique T dépend de T_0 , de E et de

la nature du couplage, mais est indépendante de l'intensité de ce dernier. Il en est de même de la fonction f_α . Nous retrouvons ici une des propriétés de la fonction de répartition électronique que H. F. Budd avait notée dans un article [4] traitant de problèmes analogues.

3. LES FAIBLES DEVIATIONS PAR RAPPORT A LA LOI D'OHM EN LIMITE CLASSIQUE

Nous abordons dans ce paragraphe le calcul du coefficient β associé à un gaz d'électrons *non dégénéré* et intervenant dans le développement de $\langle J_x \rangle$ en puissance de E quand ce développement est limité à l'ordre trois: $\langle J_x \rangle = \langle J_x \rangle^{(1)}(1 + \beta E^2)$. Cette étude de β n'est valable que si la condition $\omega_c \tau \gg 1$ est remplie. De plus, dans ce qui suit, nous admettrons que les niveaux d'énergie correspondants aux grands nombres quantiques jouent un rôle prépondérant; nous nous limiterons donc à la limite classique: $\hbar \omega_c \ll kT_0$.

Par ailleurs, nous envisagerons trois types de couplages entre les électrons et les phonons. Les développements qui suivent relèvent pratiquement du calcul intégral, élémentaire; cependant, ils offrent des difficultés que seules des approximations physiques permettent de surmonter. Nous nous sommes donc attaché à introduire un certain nombre de paramètres sans dimension et à obtenir pour certaines valeurs extrêmes de ces paramètres des expressions de β facilement exploitables lors du dépouillement des résultats expérimentaux. Nous avons pris soin de faire apparaître les limites de validité de nos formules.

Nous commencerons par transformer l'expression (2, 20) de $\langle J_x \rangle$ et nous calculerons sa composante $\langle J_x(R_0, T) \rangle^{(3)}$ d'ordre trois par rapport à E . Dans un deuxième temps, partant de (2, 28) nous relierons T à T_0 et E . Dans la mesure où nous ne sommes intéressé que par les faibles déviations par rapport à la loi d'Ohm, nous rechercherons un développement de T en puissance de E limité à l'ordre le plus bas que nous reporterons ensuite dans $\langle J_x(T_0, T) \rangle^{(3)}$. Les deux développe-

ments, dont nous venons de faire état introduiront les limites de validité que nous ferons apparaître.

(1) *Expression générale de $\langle J_x \rangle$ en limite classique*

Transformons (2, 20) de façon à séparer autant qu'il est possible les termes liés aux états électroniques de ceux liés aux phonons: grâce à la distribution δ assurant la conservation de l'énergie dans les transitions électroniques, nous obtenons:

$$\langle J_x \rangle = \sum_q \frac{\hbar q_y}{B} [N_q(T_0, \omega_q) - N_q(T, \omega_q^*)] S(q) \quad (1)$$

avec

$$\begin{aligned} S(q) = & \sum_{n, k_y, k_z} \sum_{n', k'_y, k'_z} \{f[\epsilon_n(k_z)] - f[\epsilon_{n'}(k'_z)]\} \\ & \times \delta_{k'_y, k_y + q_y} \delta_{k'_z, k_z + q_z} \\ & \times \frac{2\pi}{\hbar} |C(q)|^2 |J_{n, k_y, n', k'_y}(q_x)|^2 \\ & \times \delta[\epsilon_n(k_z) - \epsilon_{n'}(k'_z) + \hbar\omega_q^*]. \end{aligned} \quad (2)$$

Nous avons utilisé les notations évidentes:

$$\begin{aligned} N_q(T_0, \omega_q) &= \left(\exp \frac{\hbar\omega_q}{kT_0} - 1 \right)^{-1} \\ \text{et } N_q(T, \omega_q^*) &= \left(\exp \frac{\hbar\omega_q^*}{kT} - 1 \right)^{-1} \end{aligned} \quad (3)$$

tandis que

$$f[\epsilon_n(k_z)] = \left(\exp \frac{\epsilon_n(k_z) - \xi}{kT} + 1 \right)^{-1} \quad (4)$$

l'énergie de Fermi ξ étant déterminée par la condition

$$N = \sum_{n, k_y, k_z} f[\epsilon_n(k_z)]. \quad (5)$$

Le calcul de $S(q)$ est reproduit dans l'annexe (2). La seule approximation qui interviendra consistera à supposer que la condition définissant la limite classique, $\hbar\omega_c \ll kT$, est remplie. Elle conduira à:

$$S(q) = \frac{m^2}{2\pi\hbar^5} \frac{|C(q)|^2}{q} \int_{\epsilon_{\min}(q)}^{\infty} d\epsilon [f(\epsilon) - f(\epsilon + \hbar\omega_q^*)] \quad (6)$$

avec

$$\epsilon_{\min}(q) = \frac{\hbar^2}{2m} \left(\frac{q}{2} - \frac{m\omega_q^*}{\hbar q} \right)^2 \quad (7)$$

et

$$\epsilon_{\min}(q) = \frac{\hbar^2}{2m} \left(\frac{q}{2} + \frac{m\omega_q^*}{\hbar q} \right)^2 - \hbar\omega_q^*. \quad (7 \text{ bis})$$

On peut vérifier que la quantité $\epsilon_{\min}(q)$ est l'énergie minimum que doit avoir un électron pour absorber un phonon tandis que $\epsilon_{\min}(q) + \hbar\omega_q^*$ est l'énergie minimum de l'électron quand il émet un phonon.

Nous restreignons notre étude au cas où le gaz d'électrons est non dégénéré, réservant le cas du gaz dégénéré pour un travail ultérieur. Dans ces conditions, les énergies $\epsilon_{\min}(q)$ et $\epsilon_{\min}(q) + \hbar\omega_q^*$ étant toujours > 0 (cf. (7)), nous pouvons remplacer $f(\epsilon)$ et $f(\epsilon + \hbar\omega_q^*)$ par $\exp - (\epsilon - \xi)/kT$ et $\exp - (\epsilon + \hbar\omega_q^* - \xi)/kT$. Tenant compte de cette approximation, et en remplaçant la sommation sur q intervenant dans (1) par une intégrale, nous obtenons pour $\langle J_x \rangle$:

$$\begin{aligned} \langle J_x \rangle &= \frac{nm^{1/2}}{(2\pi)^{5/2}(kT)^{1/2}\hbar B} \int_{q=q_{\min}}^{\infty} d^3q \frac{q_y}{q} |C(q)|^2 \\ &\times \exp - \frac{\hbar^2}{2mkT} \left(\frac{q}{2} + \frac{m\omega_q^*}{\hbar q} \right)^2 \\ &\times (e^{\hbar\omega_q^*/kT} - e^{\hbar\omega_q/kT_0}) / e^{\hbar\omega_q/kT_0} - 1 \end{aligned} \quad (8)$$

(q_{\max} est la valeur du vecteur d'onde des phonons en bordure de la première zone de Brillouin). Pour aboutir à (8), nous avons tenu compte de la condition de normalisation (5) qui, dans le cas d'un gaz d'électrons non dégénéré et dans la limite classique $\hbar\omega_c \ll kT$, relie l'énergie de Fermi ξ et la densité électronique n selon la loi usuelle:

$$n = 2 \left(\frac{2\pi mkT}{\hbar^2} \right)^{3/2} e^{\xi/kT}. \quad (9)$$

Le résultat (8) est valable quel que soit le type de couplage entre les électrons et les phonons. Seules les valeurs de $|C(q)|^2$ et de ω_q diffèrent d'une sorte d'interaction à l'autre. Rappelons que seule l'approximation $\hbar\omega_c \ll kT$ a conduit à (8).

(2) *Calcul du coefficient β dans le cas de l'interaction électrons-phonons acoustiques*

Dans tout ce paragraphe, nous nous plaçons dans le modèle de Debye. La loi de dispersion des phonons est donc de la forme $\omega_q = sq$, où s est la vitesse du son. On en déduit que $\omega_q^* = sq(1 + (V_0/s)(q_y/q))$.

Par ailleurs, nous envisageons deux types de couplage électrons-phonons acoustiques: le premier se déduit du potentiel de déformation [6] et est tel que:

$$|C(q)|^2 = D^{(3)}q \text{ avec } D^{(3)} = \frac{E_0^2 \hbar}{\rho s}. \quad (10)$$

La constante E_0^2 est une caractéristique du matériau fixant l'intensité du couplage; ρ est la masse spécifique. Le second couplage intervient dans les corps piézoélectriques; alors:

$$|C(q)|^2 = D^{(1)} \frac{1}{q}. \quad (11)$$

La constante $D^{(1)}$ possède une expression compliquée faisant intervenir les constantes élastiques et piézoélectriques; on en trouvera la théorie dans la Réf. [7].

Notons que les constantes $D^{(1)}$ et $D^{(3)}$ n'ont pas les mêmes dimensions (l'utilité des indices (1) et (3) apparaîtra ci-dessous) et que nous avons, dans un but de simplification évident, négligé les effets d'anisotropie, ce qui peut poser quelques problèmes dans le cas du couplage piézoélectrique.

(a) *Calcul de $\langle J_x(T_0, T) \rangle$.* Nous poursuivons le calcul de $\langle J_x \rangle$ à partir de (8) en effectuant les opérations suivantes:

1. Nous passons en coordonnées sphériques en choisissant les angles polaires χ et ψ tels que la Fig. (1) l'indique.

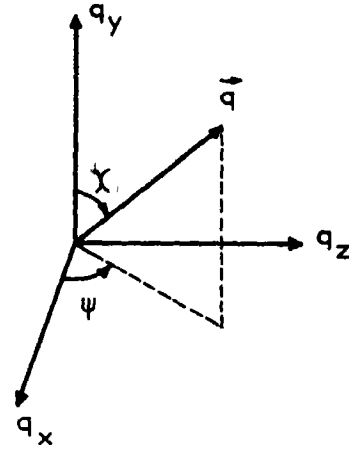


Fig. 1. Choix des axes.

2. Nous procédons au changement de variables:

$$\left(\frac{mV_0^2}{2kT}\right)^{1/2} \cos \chi = u \quad \frac{\hbar s}{kT} q = t. \quad (12)$$

3. Nous introduisons la température de Debye θ et les deux paramètres sans dimension γ et γ_0 respectivement définis par:

$$k\theta = \hbar s q_{\max} \quad (13)$$

$$\gamma = \left(\frac{ms^2}{2kT}\right)^{1/2} = \frac{s}{V_T} \quad \text{et} \quad \gamma_0 = \left(\frac{ms^2}{2kT_0}\right)^{1/2} = \frac{s}{V_{T_0}}. \quad (14)$$

La vitesse V_T , dont la valeur $(2kT/m)^{1/2}$ correspond sensiblement à la vitesse d'agitation des électrons à la température T , est très supérieure à la vitesse du son, dans une large gamme de températures comprenant la température ambiante. Le paramètre γ^2 (ou γ_0^2) est donc susceptible de prendre des valeurs très inférieures à l'unité. Ainsi, à $T = 300^\circ\text{K}$, $V_T \approx 10^5 \text{ m/s}$ quand m est égal à la masse d'un électron dans le vide; par ailleurs, pour de très nombreux solides $s \approx 5 \cdot 10^3 \text{ m/s}$; par conséquent $\gamma^2 \approx 10^{-4}$ dans cet exemple.

En suivant cette voie, nous aboutissons

pour les deux types de couplage à:

$$\langle J_x \rangle = \frac{nm^{1/2} D^{(p)}}{(2\pi)^{3/2} \hbar (kT)^{1/2} B} \left(\frac{kT}{\hbar s} \right)^{p+1} \left(\frac{V_T}{V_0} \right)^2 \times \int_0^{\theta/T} dt \frac{t^p}{e^{(t/T)/T_0} - 1} \times \int_{-V_0/V_T}^{V_0/V_T} du u \left[e^{-((t/4\gamma) - \gamma - u)^2} e^{(t/T)/T_0} e^{-((t/4\gamma) + \gamma + u)^2} \right] \quad (15)$$

à condition de poser: $p = 3$ dans le cas du potentiel de déformation (P.D.), $p = 1$ dans le cas du couplage piézoélectrique (C.P.). Remarquons que l'intégrale par rapport à la variable u , qui figure dans (15), peut être développée suivant les puissances de V_0/V_T à l'aide de la formule:

$$\int_{-V_0/V_T}^{V_0/V_T} \phi(u) du = 2 \frac{V_0}{V_T} \left[\phi(0) + \frac{1}{3!} \left(\frac{V_0}{V_T} \right)^2 \phi^{(2)}(0) + \frac{1}{5!} \left(\frac{V_0}{V_T} \right)^4 \phi^{(4)}(0) + \frac{1}{7!} \left(\frac{V_0}{V_T} \right)^6 \phi^{(6)}(0) + \dots \right] \quad (16)$$

et que si la condition:

$$\left(\frac{V_0}{V_T} \right)^2 \ll 1 \quad \text{soit} \quad \left(\frac{E}{B} \right)^2 \ll (V_T)^2 \quad (17)$$

est vérifiée, on peut ne retenir que les premiers termes de (16). Un calcul mathématique un peu long permet de s'assurer que le terme en $(1/7!)(V_0/V_T)^6 \phi^{(6)}(0)$ conduira en fin de calcul à une correction négligeable. La suite des calculs est reproduite dans l'annexe (3). Nous y montrons que si la condition

$$\gamma^2 = \left(\frac{s}{V_T} \right)^2 \ll 1 \quad (18)$$

est vérifiée — et c'est fréquemment le cas dans les expériences — les expressions de $\langle J_x \rangle$ se mettent sous les formes finales relativement simples:

$$\langle J_x(T_0, T) \rangle = \langle J_x \rangle^{(1)} \left(\frac{T}{T_0} \right)^{\pm 1/2} \times \left(1 \pm \frac{1}{5} \frac{V_0^2}{V_T^2} \right) \begin{cases} + \text{ pour le P.D.} \\ - \text{ pour le C.P.} \end{cases} \quad (19)$$

$\langle J_x \rangle^{(1)}$ est comme toujours la composante linéaire en E du vecteur densité de courant électrique que nous avons trouvée, en accord avec des résultats [8, 9] connus, être égale à

$$\langle J_x \rangle^{(1)} = \frac{2^{3p/2}}{3\pi^{3/2}} \frac{nm^{(p+2)/2}}{s\hbar^{p+2}B^2} \times D^{(p)}(kT_0)^{p/2} E \begin{cases} p = 3 \text{ pour le P.D.} \\ p = 1 \text{ pour le C.P.} \end{cases} \quad (20)$$

(b) *Détermination de la température électronique.* Cette détermination s'effectue à partir de la relation (28) dont le second membre offre la même expression que celle de $\langle J_x \rangle$ au changement près de $\hbar q_y/m\omega_c$ en $\hbar\omega_q^*$. Dans ces conditions il est inutile de refaire des calculs détaillés car il est évident qu'à la place de (15) nous allons arriver à:

$$\int_0^{\theta/T} dt \frac{t^p}{e^{(t/T)/T_0} - 1} \times \int_{-V_0/V_T}^{+V_0/V_T} du (1 + (u/\gamma)) (e^{-((t/4\gamma) - \gamma - u)^2} - e^{(t/T)/T_0} e^{-((t/4\gamma) + \gamma + u)^2}) = 0 \quad (21)$$

Ici encore, les conditions (17) et (18) vont simplifier les développements et en se référant à la procédure de l'annexe (3), nous obtenons:

$$\frac{T}{T_0} \approx 1 + \frac{1}{3} \frac{V_0^2}{s^2} \quad (22)$$

pour les deux types de couplage envisagés. La température électronique est bien indépendante de l'intensité de l'interaction électrons-phonons et ne dépend de la nature du couplage que par la vitesse du son des phonons acoustiques.

(c) *Expressions du coefficient β dans le cas des couplages par potentiel de déformation et piézoélectrique.* En reportant la valeur de T tirée de (22) dans (19), nous obtenons les expressions finales de $\langle J_x \rangle$, valables quand les deux conditions (17) et (18) sont remplies:

$$\langle J_x \rangle = \langle J_x \rangle^{(1)} \left(1 + \frac{1}{3} \frac{V_0^2}{s^2} \right)^{\pm 1/2} \left(1 \pm \frac{1}{5} \frac{V_0^2}{V_T^2} \right) \begin{cases} + \text{ pour le P.D.} \\ - \text{ pour le C.P.} \end{cases} \quad (23)$$

Pratiquement, les premières déviations par rapport à la loi d'Ohm seront observées dès que la condition

$$\frac{1}{3} \frac{V_0^2}{s^2} \ll 1 \quad (24)$$

sera satisfaite. La condition (24), compte tenu de (18), entraîne automatiquement (17). Par conséquent, si les inégalités (18) et (24) sont satisfaites,

$$\langle J_x \rangle = \langle J_x \rangle^{(1)} \left(1 \pm \frac{1}{6} \frac{V_0^2}{s^2} \right). \quad (25)$$

En conclusion le coefficient β caractérisant les premières déviations par rapport à la loi d'Ohm s'écrit:

$$\beta = \pm \frac{1}{6} \frac{1}{B^2 s^2} \begin{cases} + \text{ pour le P.D.} \\ - \text{ pour le C.P.} \end{cases} \quad (26)$$

Notons immédiatement que les résultats concernant T et β dans le cas du couplage par potentiel de déformation ont déjà été obtenus par d'autres méthodes [10]. Les conditions de validité de (26) se réduisent à:

$$\frac{1}{3} \frac{V_0^2}{s^2} \cdot \left(\frac{s}{V_T} \right)^2 \ll 1.$$

(3) *Calcul du coefficient β dans le cas de l'interaction électrons-phonons optiques*

Dans tout ce paragraphe, nous admettons que la loi de dispersion des phonons optiques se réduit à: $\omega_q = c^{te}$. Par ailleurs, le couplage électrons-phonons optiques est supposé être du type polaire et tel que [11]:

$$|C(q)|^2 = \frac{D^{(0)}}{q^2} \quad (27)$$

où $D^{(0)}$ est un coefficient dépendant de la nature du cristal:

$$D^{(0)} = 2\pi\hbar\omega_q e^2 \left(\frac{1}{\epsilon_\infty} - \frac{1}{\epsilon_s} \right).$$

Les grandeurs ϵ_∞ et ϵ sont les constantes diélectriques du cristal à haute fréquence et à fréquence nulle.

(a) *Calcul de $\langle J_x(T_0, T) \rangle$* . L'indépendance de ω_q par rapport à q est un élément important de la simplification des calculs. Ainsi $\langle J_x \rangle$ d'après (8) s'écrit ici:

$$\begin{aligned} \langle J_x \rangle &= \frac{nm^{1/2} D^{(0)}}{2(2\pi)^{3/2} \hbar (kT)^{1/2} B \sinh(\hbar\omega_q/2kT)} \\ &\times \int_{q < q_{\max}} d^3q \frac{q_x}{q^3} \exp - \frac{\hbar^2}{2mkT} \left(\frac{q}{2} + \frac{m\omega_q^*}{\hbar q} \right)^2 \\ &\times \left(e^{\hbar\omega_q^*/kT} - e^{\hbar\omega_q/kT} \right) \end{aligned} \quad (28)$$

Comme au Section 3.2. 1, nous passons en coordonnées sphériques; 2, nous procédons aux changements de variables;

$$\begin{aligned} \left(\frac{mV_0^2}{2kT} \right)^{1/2} \cos \chi &= u \\ \left(\frac{\hbar q^2}{2m\omega_q} \right) &= x \end{aligned} \quad (29)$$

3, nous introduisons les paramètres sans dimension;

$$\alpha = \frac{\hbar\omega_q}{2kT} \quad \text{et} \quad \alpha_0 = \frac{\hbar\omega_q}{2kT_0} \quad (30)$$

qui peuvent *a priori* varier dans de larges limites sans descendre toutefois à des valeurs très inférieures à l'unité.

Ces trois opérations nous conduisent à:

$$\begin{aligned} \langle J_x \rangle &= \frac{nmD^{(0)}}{8\pi^{3/2} \hbar^2 B \sinh \alpha_0} \alpha^{1/2} \left(\frac{V_T}{V_0} \right)^2 \int_0^{(\hbar q_{\max}^2/2m\omega_q)} \frac{dx}{\sqrt{x}} \\ &\times \int_{-V_0/V_T}^{V_0/V_T} du u \left\{ e^{-[\sqrt{\alpha/2}(\sqrt{x} - (1/\sqrt{x})) - u]^2} \right. \\ &\quad \left. - e^{2\alpha_0} e^{[\sqrt{\alpha/2}(\sqrt{x} + (1/\sqrt{x})) + u]^2} \right\}. \end{aligned} \quad (31)$$

Comme dans le cas de phonons acoustiques, nous faisons intervenir ici la seconde approximation du calcul (après celle découlant de $\hbar\omega_q \ll kT$) en supposant que:

$$\left(\frac{V_0}{V_T} \right)^2 \ll 1 \quad \text{soit} \quad \left(\frac{E}{B} \right)^2 \ll V_T^2. \quad (32)$$

L'intégrale par rapport à u qui figure dans (31) se traite à l'aide de la formule (16). Les calculs qui en découlent sont reportés dans

l'annexe (4) qui tient compte du fait que la quantité $\hbar q_{\max}^2/2m\omega_q$ est toujours très grande ($\sim 10^8$). Finalement,

$$\begin{aligned} \langle J_x(T_0, T) \rangle &= \langle J_x \rangle^{(1)} \left(\frac{T_0}{T} \right)^{3/2} \frac{K_1(\alpha)}{K_0(\alpha)} \cosh(\alpha_0 - \alpha) \\ &\times \left\{ 1 - \frac{K_0(\alpha)}{K_1(\alpha)} \operatorname{th}(\alpha - \alpha_0) - \frac{1}{5} \frac{V_0^2}{V_T^2} \right. \\ &\times \left[3 - \alpha \frac{K_2(\alpha) + 3K_0(\alpha)}{K_1(\alpha)} \right. \\ &\left. \left. + \frac{4K_1(\alpha) - 3K_0(\alpha)}{K_1(\alpha)} \operatorname{th}(\alpha - \alpha_0) \right] \right\} \quad (33) \end{aligned}$$

tandis que

$$\langle J_x \rangle^{(1)} = \frac{2nmD^{(0)}}{3} \frac{\alpha_0}{\pi^{3/2}\hbar^2} \frac{K_1(\alpha_0)}{\sin h \alpha_0} \frac{E}{V_{T_0} B^2} \quad (34)$$

Les expressions (33) et (34) font intervenir les fonctions $K_n(x)$ qui sont les fonctions de Bessel modifiées de seconde espèce. L'expression de $\langle J_x \rangle^{(1)}$ n'est pas originale et a déjà été obtenue dans la réf. [12].

(b) *Détermination de la température électronique.* Cette détermination s'effectue comme pour les phonons acoustiques traités au paragraphe 3.2 en adaptant les calculs au cas des phonons optiques selon les directions du paragraphe 3.3 (a). Nous obtenons à l'ordre le plus bas par rapport au paramètre V_0/V_T la relation suivante entre α et α_0 (c.a.d. entre T et T_0)

$$\begin{aligned} \operatorname{th}(\alpha - \alpha_0) &= \frac{2}{3} \frac{V_0^2}{V_T^2} \\ &\times \frac{\alpha K_0(\alpha) - K_1(\alpha)}{K_0(\alpha) - \frac{1}{3}(V_0^2/V_T^2)\{3K_0(\alpha) - 2\alpha K_1(\alpha)\}}. \quad (35) \end{aligned}$$

Il est facile de s'assurer que le terme contenant V_0^2/V_T^2 en facteur au dénominateur du second membre de (35) est en général négligeable devant $K_0(\alpha)$ quand $(V_0/V_T) \ll 1$. Quand cette dernière inégalité est vérifiée, il apparaît de plus que $\operatorname{th}(\alpha - \alpha_0)$ est une quantité faible devant 1 qui peut être assimilée à $\alpha - \alpha_0$. Enfin, quand on se limite à l'ordre le plus bas en V_0/V_T , on peut remplacer α par α_0 au

second membre de (35). Finalement,

$$\frac{\alpha_0}{\alpha} - 1 = \frac{T}{T_0} - 1 = \frac{2}{3} \frac{V_0^2}{V_T^2} \frac{K_1(\alpha_0) - \alpha_0 K_0(\alpha_0)}{\alpha_0 K_0(\alpha_0)}. \quad (36)$$

On peut faire usage de la relation:

$$\frac{2}{x} K_n(x) = K_{n+1}(x) - K_{n-1}(x) \quad (37)$$

pour transformer (36) en:

$$\boxed{\frac{T}{T_0} - 1 \approx -\frac{V_0^2}{V_T^2} \left(1 - \frac{K_2(\alpha_0)}{3K_0(\alpha_0)} \right)}. \quad (38)$$

Les variations du facteur $y_1 = [1 - (K_2/3K_0)]$ sont représentées sur la Fig. 2. On constate donc que la température électronique peut être soit supérieure, soit inférieure à celle des phonons optiques et l'égalité $T = T_0$ se produit quand $\alpha_0 = (\hbar\omega_q/2KT_0) = 1,32$. Dans la gamme des températures ayant une réalité physique, le facteur $1 - (K_2/3K_0)$ ne prend jamais de valeur suffisamment forte pour faire différer fortement T de T_0 quand la condition (32) est vérifiée.

(c) *Expression du coefficient β dans le cas du couplage électrons-phonons optiques.* En reportant la valeur de T tirée de (38) dans (33), nous obtenons l'expression finale de $\langle J_x \rangle$ valable quand $V_0/V_T \ll 1$. Il faut tenir compte du fait que:

$$K_1(\alpha) \approx K_1(\alpha_0) + (\alpha - \alpha_0) \left(\frac{dK_1(\alpha)}{d\alpha} \right)_{\alpha=\alpha_0} \quad (39)$$

et que

$$\alpha \frac{dK_n(\alpha)}{d\alpha} = -nK_n(\alpha) - \alpha K_{n-1}(\alpha). \quad (40)$$

Après quelques transformations utilisant en particulier la relation (37), nous aboutissons à:

$$\begin{aligned} \langle J_x \rangle^{(3)} &= \langle J_x \rangle^{(1)} \left\{ 1 - \frac{1}{30} \frac{V_0^2}{V_T^2} \right. \\ &\times \left. \frac{[5(K_2(\alpha_0)/K_0(\alpha_0)) - 9][(K_2(\alpha_0)/K_0(\alpha_0)) - 9]}{(K_2(\alpha_0)/K_0(\alpha_0)) - 1} \right\}. \quad (41) \end{aligned}$$

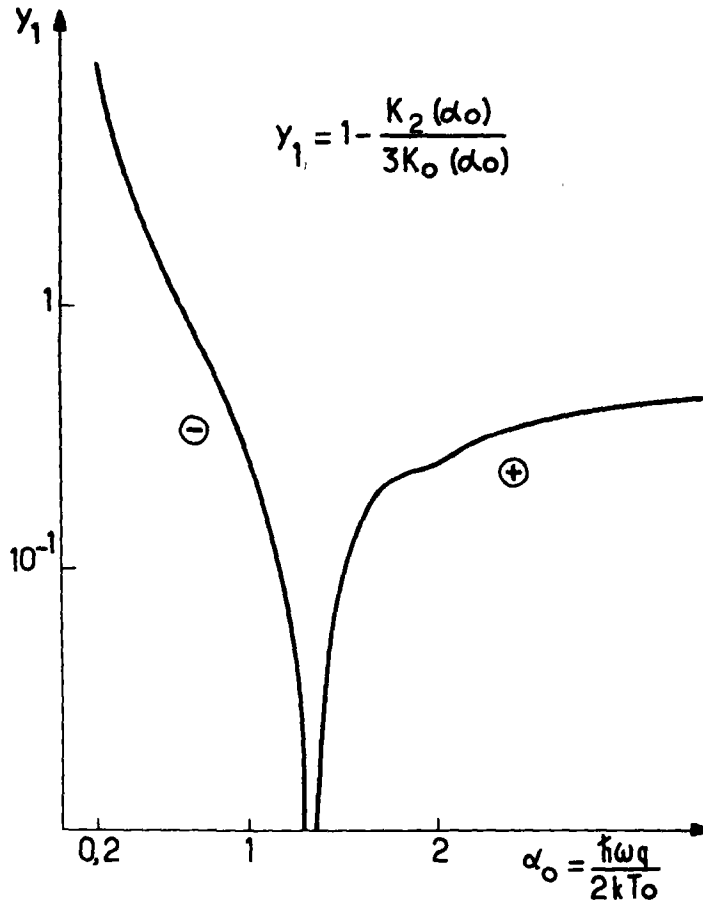


Fig. 2. Variation du facteur intervenant dans l'expression de la température électronique: cas de l'interaction électrons-phonons optiques.

Par conséquent, le coefficient β , caractéristique des premières déviations par rapport à la loi d'Ohm dans le cas du couplage électrons-phonons optiques, a pour expression:

$$\beta = -\frac{1}{30} \frac{m}{B^2 \hbar \omega_q} \alpha_0 \frac{(5\eta(\alpha_0) - 9)(\eta(\alpha_0) - 9)}{\eta(\alpha_0) - 1} \quad (42)$$

Nous avons introduit dans (42) la fonction:

$$\eta(\alpha_0) = \frac{K_2(\alpha_0)}{K_0(\alpha_0)}$$

qui est une fonction monotone décroissante de $+\infty$ à 1 quand α_0 croît. La condition de

validité de (42) est simplement $V_0^2/V_T^2 \ll 1$. Le coefficient β s'annule deux fois, quand α_0 varie, pour les valeurs de α_0 égales à 0,45 et 2,86. Le signe de β est positif quand α_0 est compris entre 0,45 et 2,85.

La Fig. 3 schématise les variations des rapports:

$$y_2 = \frac{1}{30} \frac{[5\eta - 9][\eta - 9]}{\eta - 1} \text{ et } y_3 = \alpha_0 y_2$$

qui donnent respectivement le facteur multiplicatif de $V_0^2 V_T^2$ dans $\langle J_x \rangle^{(3)}$ et les variations de β avec la température.

Sur la Fig. 3, on constate que, pour la

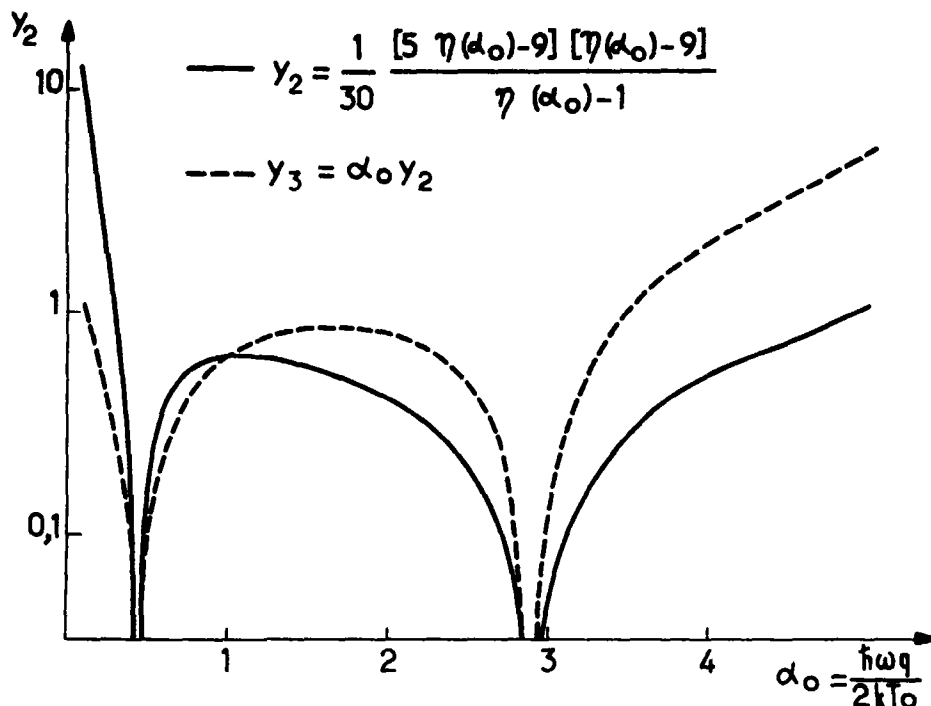


Fig. 3. Variation des principaux facteurs intervenant dans l'expression de $\langle J_x \rangle^{(3)}$ et β : cas de l'interaction électrons-phonons optiques.

gamme des valeurs de α_0 ayant un sens physique, la variation relative de $\langle J_x \rangle$ est toujours faible quand la condition $V_0/V_T^2 \ll 1$ est remplie.

4. CONCLUSION

Les résultats finaux concernant le coefficient β n'ont pu être obtenus qu'après avoir effectué un choix sur les fonctions de répartition des phonons et des électrons \mathcal{N}_q et F_α . Ce choix trouve sa justification dans le fait qu'il contribue à interpréter les variations expérimentales en fonction de la température des faibles déviations par rapport à la loi d'Ohm dans InSb (cf. article A). Si la théorie de la Réf.[1] s'est en définitive révélée en contradiction avec les résultats expérimentaux, l'explication de ce désaccord réside dans ce que nous avons introduit ici des considérations énergétiques qui n'apparaissent pas dans [1]. Par ailleurs, nous présenterons pro-

chainement les expressions du coefficient β valables pour un gaz d'électrons non dégénéré en limite quantique ($\omega_c \tau \gg 1$, $\hbar \omega_c \gg kT$) et nous traiterons aussi le cas des gaz dégénérés.

REFERENCES

1. CALECKI D., *J. Phys. Chem. Solids* **28**, 1409 (1967).
2. BLOCH C. and DE DOMINICIS C., *Nucl. Phys.* **7**, 459 (1958).
3. ADAMS E. N. and HOLSTEIN T. D., *J. Phys. Chem. Solids* **10**, 254 (1969).
4. BUDD H. F., *Phys. Rev.* **175**, n° 1, 241 (1968).
5. TITEICA S., *Ann. Phys.* **22**, 129 (1935).
6. ZIMAN J. M., *Electrons and phonons*, p. 205, Oxford University Press (1960).
7. MEIJER H. J. G. and POLDER D., *Physica* **19**, 255 (1953).
8. BEER A. C. *Galvanomagnetic Effect in Semiconductors* Academic Press, New York (1963).
9. HARRISON W. A., *Phys. Rev.* **101**, n° 2, 903 (1956).
10. KAZARINOV R. F. and SKOBOV V. G., *Soviet Phys. JETP* **15**, n° 4, 726 (1962), BUDD H. F., *Phys. Rev.* **131**, n° 4, 1520 (1963).

11. KRIVOGLAZ M. A. and PEKAR S. I., *Izv. akad. nauk SSSR Ser. Fiz* 21, 3 (1957).
12. GUREVICH V. L. and FIRSOV Yu. A., *Soviet Phys. JETP* 13, n° 1, 137 (1961).
13. WATSON G. N., *A treatise on the theory of Bessel functions*, Cambridge University Press (1966).

ANNEXE 1

Nous cherchons à évaluer la valeur moyenne:

$$\langle J_x + iJ_y \rangle = \lim_{t \rightarrow \infty} \text{Tr}(J_x + iJ_y) \left\{ \rho_0 + \frac{\lambda}{i\hbar} \int_0^t dt_1 [H_{ep}(-t_1), \rho_0] \right. \\ \left. + \left(\frac{\lambda}{i\hbar} \right)^2 \int_0^t dt_1 \int_0^{t_1} dt_2 [H_{ep}(-t_2), [H_{ep}(-t_1), \rho_0]] \right\}$$

avec

$$J_x + iJ_y = \frac{ieE}{\Omega B} \sum_{\alpha} a_{\alpha}^+ a_{\alpha} - \frac{2ie}{\Omega} \left(\frac{\hbar\omega_c}{2m} \right)^{1/2} \sum_{\alpha} (n+1)^{1/2} a_{\alpha+1}^+ a_{\alpha}.$$

Rappelons que α représente les trois nombres quantiques n, k_y, k_z , que $\alpha+1$ représente $n+1, k_y, k_z$ et que Ω est le volume du cristal.

Décomposons le calcul en ses trois termes d'ordre λ respectivement égal à 0, 1 et 2.

(1) Terme d'ordre zéro en λ

Nous avons déjà vu que

$$\langle J_x + iJ_y \rangle_{(0)} = in \frac{E}{B}.$$

(2) Terme d'ordre un en λ

λH_{ep} est un opérateur dont tous les éléments diagonaux dans la base (α) sont nuls. Ceci entraîne que

$$\langle J_x + iJ_y \rangle_{(1)} = 0.$$

(3) Terme d'ordre deux en λ

$$\langle J_x + iJ_y \rangle_{(2)} = \left(\frac{\lambda}{i\hbar} \right)^2 ie \frac{E}{B} \lim_{t \rightarrow \infty} \int_0^t dt_1 \int_0^{t_1} dt_2 \text{Tr} \left(\sum_{\alpha} a_{\alpha}^+ a_{\alpha} \right) \\ \times [H_{ep}(-t_2), [H_{ep}(-t_1), \rho_0]] - \left(\frac{\lambda}{i\hbar} \right)^2 2ie \left(\frac{\hbar\omega_c}{2m} \right)^{1/2} \\ \lim_{t \rightarrow \infty} \int_0^t dt_1 \int_0^{t_1} dt_2 \text{Tr} \left(\sum_{\alpha} a_{\alpha+1}^+ a_{\alpha} \right) [H_{ep}(-t_2), [H_{ep}(-t_1), \rho_0]].$$

Il est aisé de vérifier, du fait que l'opérateur $\sum_{\alpha} a_{\alpha}^+ a_{\alpha}$ n'est autre que l'opérateur nombre d'électrons N que la première trace est nulle.

En effet,

$$\text{Tr} \hat{N} [H_{ep}(-t_2), [H_{ep}(-t_1), \rho_0]] \\ = \text{Tr} [N, H_{ep}(-t_2)] [H_{ep}(-t_1), \rho_0]$$

et

$$[\hat{N}, H_{ep}(-t_2)] = 0.$$

Finalement $\langle J_x + iJ_y \rangle_{(2)}$ se réduit simplement à:

$$\langle J_x + iJ_y \rangle_{(2)} = 2ie \left(\frac{\lambda}{i\hbar} \right)^2 \left(\frac{\hbar\omega_c}{2m} \right)^{1/2}$$

$$\lim_{t \rightarrow \infty} \int_0^t dt_1 \int_0^{t_1} dt_2 \text{Tr} \sum_{\alpha} a_{\alpha+1}^+ a_{\alpha} [H_{ep}(-t_2), [H_{ep}(-t_1), \rho_0]]$$

remplaçons λH_{ep} par son expression (2,5); utilisons ensuite systématiquement les résultats (2,9 et 10), le théorème de Bloch-de Dominici, des formules classiques sur les opérateurs de création et d'annihilation et les relations suivantes tirées des propriétés algébriques des éléments de matrice $\gamma_{\alpha\alpha'}(q)$:

$$(n+1)^{1/2} \gamma_{\alpha, \alpha'}(q) \gamma_{\alpha', \alpha+1}(-q) - n^{1/2} \gamma_{\alpha, \alpha'}(q) \gamma_{\alpha'-1, \alpha}(-q) \\ = n^{1/2} \gamma_{\alpha-1, \alpha'}(q) \gamma_{\alpha', \alpha}(-q) - (n'+1)^{1/2} \gamma_{\alpha, \alpha'+1}(q) \gamma_{\alpha', \alpha}(-q) \\ = \left(\frac{m\omega_c}{2\hbar} \right)^{1/2} (\chi_{k_y} - \chi_{k_y'}) |\gamma_{\alpha, \alpha'}(q)|^2 \\ - i \left(\frac{\hbar}{2m\omega_c} \right)^{1/2} q_x |\gamma_{\alpha, \alpha'}(q)|^2.$$

Grâce à ces techniques de calculs, nous aboutissons à l'expression

$$\langle J_x + iJ_y \rangle_{(2)} = e \sum_{\alpha, \alpha'} \sum_q [\mathcal{N}_q F_{\alpha}(1 - F_{\alpha'}) - (1 + \mathcal{N}_q) F_{\alpha'} \\ \times (1 - F_{\alpha})] (\chi_{k_y} - \chi_{k_y'}) |\gamma_{\alpha, \alpha'}(q)|^2 \frac{2\pi}{\hbar} \delta(\tilde{\epsilon}_{\alpha} - \tilde{\epsilon}_{\alpha'} + \hbar\omega_q)$$

à condition que \mathcal{N}_q soit une fonction paire du vecteur d'onde des phonons q . En regroupant les trois résultats précédents sur $\langle J_x + iJ_y \rangle$ nous obtenons les formules (2, 19) et (2, 20) valables à l'ordre 2 en λ .

ANNEXE 2

Nous devons calculer la somme:

$$S(q) = \sum_{n, k_y, k_z} \sum_{n', k_y', k_z'} \{ f(\epsilon_n(k_z)) - f(\epsilon_{n'}(k_z - q_z)) \} \\ \frac{2\pi}{\hbar} \delta_{k_y, k_y' + q_y} \delta_{k_z, k_z' + q_z} |C(q)|^2 \\ |J_{n, k_y, n', k_y'}(q_x)|^2 \delta(\epsilon_n(k_z) - \epsilon_{n'}(k_z') + \hbar\omega_q^*). \quad (1)$$

Les sommations sur k_y' et k_z' sont triviales du fait des deux premières δ . Comme par ailleurs,

$$|J_{n, k_y, n', k_y - q_y}(q_x)|^2 = |J'_{n, n'}(q)|^2 \quad (2)$$

ne dépend pas de k_y mais uniquement de n, n', q_x et q_y , rien ne dépend de k_y dans l'expression à sommer. La sommation sur k_y revient donc à multiplier l'expression à sommer par la dégénérescence en k_y des niveaux d'énergie électronique, c.a.d. par $m\omega_c/2\pi\hbar$ (pour un cristal cubique d'arête unité). Par conséquent:

$$S(q) = \frac{m\omega_c}{2\pi\hbar} |C(q)|^2 \sum_{n, n'} \sum_{k_x} \{ f(\epsilon_n(k_z)) - f(\epsilon_{n'}(k_z - q_z)) \} \\ \times \frac{2\pi}{\hbar} |J'_{n, n'}(q)|^2 \times \delta(\epsilon_n(k_z) - \epsilon_{n'}(k_z - q_z) + \hbar\omega_q^*) \quad (3)$$

or,

$$\delta(\epsilon_n(k_z) - \epsilon_{n'}(k_z - q_z) + \hbar\omega_q^*) \\ = \frac{m}{\hbar^2 |q_z|} \delta \left\{ k_z - \frac{q_z}{2} + \frac{m}{\hbar q_z} (\omega_q^* + n\omega_c - n'\omega_c) \right\}. \quad (4)$$

La sommation sur k_z s'effectue 'comme à l'accoutumée' en remplaçant:

$$\sum_{k_z} \text{ par } \frac{1}{2\pi} \int dk_z \quad (5)$$

et l'intégrale en k_z s'évalue immédiatement grâce à la distribution $\delta(k_z - (q_z/2) + \dots)$ que nous venons de faire apparaître à la formule (4); il reste:

$$S(q) = \frac{m^2 \omega_c |C(q)|^2}{2\pi \hbar^4 |q_z|} \sum_{n,n'} (f(\epsilon) - f(\epsilon + \hbar\omega_q^*)) |J'_{n,n'}(q)|^2 \quad (6)$$

avec:

$$\epsilon = (n + n' + 1) \frac{\hbar\omega_c}{2} + \frac{m}{2q_z^2} (\omega_q^* + (n - n')\omega_c)^2 + \frac{\hbar^2 q_z^2}{8m} - \frac{\hbar\omega_q^*}{2}. \quad (7)$$

Jusqu'ici aucune approximation n'a été faite en dehors du remplacement de

$$\sum_{k_z} \text{ par } (2\pi)^{-1} \int dk_z.$$

Nous introduisons ici notre première approximation en supposant que:

$$\hbar\omega_c \ll kT. \quad (8)$$

Alors, dans l'échelle des énergies, les niveaux de Landau sont proches les uns des autres, et un grand nombre d'entre eux sont occupés par les électrons. Dans ce cas, il est raisonnable de supposer que les électrons se trouvant dans les niveaux pour lesquels le nombre quantique n est élevé constituent la majorité des électrons qui contribuent à $\langle J_x \rangle$. Quand n est élevé, il varie de façon quasi-continue et on peut remplacer:

$$\sum_{n,n'} \text{ par } \int dn \int dn'.$$

Partiellement, nous allons immédiatement effectuer un changement de variables; au lieu de prendre n et n' comme variables d'intégration, nous choisissons:

$$v = n - n' \quad \text{et} \quad \epsilon \text{ défini par (7).}$$

Le jacobien de la transformation est égal à $(\hbar\omega_c)^{-1}$.

Par ailleurs, lorsque n et n' sont des nombres élevés, nous pouvons utiliser la formule approchée [5]:

$$|J'_{n,n'}(q)|^2 \approx \frac{1}{\pi} \left\{ \frac{\hbar}{m\omega_c} (q_x^2 + q_y^2) (n + n' + 1) - (n' - n)^2 \right. \\ \left. - \left(\frac{\hbar}{m\omega_c} \frac{q_x^2 + q_y^2}{2} \right)^2 \right\}^{-1/2}. \quad (9)$$

En exprimant $|J'_{n,n'}(q)|^2$ à l'aide de v et ϵ , on obtient:

$$|J'_{n,n'}(q)|^2 \approx \frac{1}{\pi} \left(-\frac{q^2}{q_z^2} v^2 + a(\epsilon)v + b(\epsilon) \right)^{-1/2} \quad (10)$$

avec:

$$b(\epsilon) = \frac{q_x^2 + q_y^2}{m\omega_c} \left(2\epsilon - \frac{\hbar q^2}{4m} - \frac{m\omega_q^*}{q_z^2} + \hbar\omega_q^* \right) \quad (11)$$

et:

$$a(\epsilon) = -2 \frac{q_x^2 + q_y^2}{q_z^2} \frac{\omega_q^*}{\omega_c}. \quad (12)$$

Remarquons alors que $|J'_{n,n'}(q)|^2$ n'existe que si le second membre de (10) existe; il est donc nécessaire que

$$-\frac{q^2}{q_z^2} v^2 + a(\epsilon)v + b(\epsilon) > 0. \quad (13)$$

Ce qui impose:

$$1^\circ / \quad \epsilon > \epsilon_{\min}(q) = \frac{\hbar^2}{2m} \left(\frac{q}{2} - \frac{m\omega_q^*}{\hbar q} \right)^2 \quad (14)$$

$$2^\circ / \quad v_1 < v < v_2 \quad (15)$$

où v_1 et v_2 sont les deux racines du trinôme en v intervenant dans (13).

En tenant compte de tout ce qui concerne la sommation sur n et n' , nous aboutissons à:

$$S(q) = \frac{m^2}{2\pi \hbar^5} \frac{|C(q)|^2}{|q_z|} \frac{1}{\pi} \int_{\epsilon_{\min}(q)}^{\infty} d\epsilon \int_{v_1}^{v_2} dv \left(-\frac{q^2}{q_z^2} v^2 + a(\epsilon)v + b(\epsilon) \right)^{-1/2} (f(\epsilon) - f(\epsilon + \hbar\omega_q^*)). \quad (16)$$

Comme

$$\frac{1}{\pi} \int_{v_1}^{v_2} dv \left(-\frac{q^2}{q_z^2} v^2 + a(\epsilon)v + b(\epsilon) \right)^{-1/2} = \frac{|q_z|}{q}. \quad (17)$$

Il reste:

$$S(q) = \frac{m^2}{2\pi \hbar^5} \frac{|C(q)|^2}{q} \int_{\epsilon_{\min}(q)}^{\infty} d\epsilon (f(\epsilon) - f(\epsilon + \hbar\omega_q^*)). \quad (18)$$

ANNEXE 3

A partir des équations (3, 15) et (3, 16), $\langle J_x \rangle$ se transforme en:

$$\langle J_x \rangle = \frac{\sqrt{2}}{3\pi^{3/2}} \frac{nm^{1/2} D^{(p)}}{\hbar(kT)^{1/2} B} \left(\frac{kT}{\hbar S} \right)^{p+1} \frac{V_0}{V_T} e^{-\gamma^2} \int_0^{\theta/T} \frac{t^p}{e^{t(T/T_0)} - 1} \\ \times e^{-t^2/16\gamma^2} \left\{ \left(\frac{t}{4\gamma} - \gamma \right) e^{t/2} + \left(\frac{t}{4\gamma} + \gamma \right) e^{-t/2 + \kappa T/T_0} \right. \\ \left. + \frac{1}{5} \frac{V_0^2}{V_T^2} \left[-3 \left(\frac{t}{4\gamma} - \gamma \right) e^{t/2} \right. \right. \\ \left. \left. + 2 \left(\frac{t}{4\gamma} - \gamma \right)^3 e^{t/2} - 3 \left(\frac{t}{4\gamma} + \gamma \right) e^{-t/2 + \kappa T/T_0} \right. \right. \\ \left. \left. + 2 \left(\frac{t}{4\gamma} + \gamma \right)^3 e^{-t/2 + \kappa T/T_0} \right] \right\}.$$

L'expression ci-dessus fait intervenir des intégrales de la forme:

$$L_2^p = \int_0^{\theta/T} dt t^p \frac{e^{t/2} \pm e^{-t/2 + \kappa T/T_0}}{e^{\kappa T/T_0} - 1} e^{-t^2/16\gamma^2}.$$

A l'aide de cette notation, $\langle J_x \rangle$ prend la forme:

$$\langle J_x \rangle = \frac{\sqrt{2}}{3\pi^{3/2}} \frac{nm^{1/2} D^{(0)}}{\hbar(kT)^{1/2} B} \left(\frac{kT}{\hbar s} \right)^{p+1} \frac{V_0}{V_T} e^{-\gamma^2} \left(\frac{1}{4\gamma} L_{+}^{p+1} - \gamma L_{-}^{p+1} + \frac{1}{5} \frac{V_0^2}{V_T^2} \left(-\frac{3}{4\gamma} L_{+}^{p+1} + 3\gamma L_{-}^{p+1} + \frac{1}{32\gamma^3} L_{+}^{p+3} - \frac{3}{8\gamma} L_{-}^{p+3} + \frac{3\gamma}{2} L_{+}^{p+1} + 2\gamma^3 L_{-}^{p+1} \right) \right).$$

Pour évaluer L_{\pm}^r , le plus simple consiste à développer en série de puissances de t le rapport:

$$\frac{e^{t/2} \pm e^{-(t/2 + \hbar\omega_d/2kT)}}{e^{\hbar\omega_d/2kT} - 1}.$$

Cela conduit à:

$$L_{+}^r = 2 \frac{T_0}{T} \int_0^{\theta/T} dt t^{r-1} e^{-\hbar\omega_d/2kT} \left(1 + \frac{t^2}{24} \left(3 - 6 \frac{T}{T_0} + 2 \frac{T^2}{T_0^2} + \dots \right) \right)$$

$$L_{-}^r = \left(\frac{T_0}{T} - 1 \right) \int_0^{\theta/T} dt t^r e^{-\hbar\omega_d/2kT} \left(1 + \frac{t^2}{24} \left(1 - 2 \frac{T}{T_0} + \dots \right) \right).$$

Le changement de variable: $t' = t/4\gamma$ montre que les termes en t^2 qui figurent dans les crochets de L_{\pm}^r conduisent à des corrections de l'ordre de γ^2 qui sont entièrement négligeables quand:

$$\gamma \ll 1.$$

Ce résultat est encore valable pour les autres termes des crochets en t^2, t^4, \dots que nous n'avons pas écrits. Cependant, nous venons d'admettre implicitement que les coefficients γ et γ_0 — c'est à dire les températures T et T_0 — restaient du même ordre de grandeur; nous vérifierons ultérieurement que, pour les phénomènes d'électrons tièdes, il en est bien ainsi.

Par ailleurs, l'esposant r restant petit ($1 \leq r \leq 6$), la fonction $t^r e^{-\hbar\omega_d/2kT}$ décroît très rapidement avec t quand $\gamma \ll 1$. Les températures de Debye des semiconducteurs étant en général supérieures à 100°K, la fonction $t^r e^{-\hbar\omega_d/2kT}$ est pratiquement nulle quand t varie dans l'intervalle $(\theta/T, \infty)$, quelles que soient les températures T physiquement rencontrées. On peut donc remplacer la borne supérieure θ/T par $+\infty$. En fait, cette approximation n'est pas nécessaire pour poursuivre les calculs, mais il n'y a pas lieu de s'en priver puisqu'elle n'introduit que des termes correctifs en $e^{-(\theta/T)^2/16\gamma^2}$. Finalement,

$$L_{+}^r \approx (4\gamma)^r 2 \frac{T_0}{T} \int_0^{\infty} dt' t'^{r-1} e^{-t'^2}$$

et

$$L_{-}^r \approx (4\gamma)^{r+1} \left(\frac{T_0}{T} - 1 \right) \int_0^{\infty} dt' t'^r e^{-t'^2}.$$

Les deux dernières intégrales sont purement numériques et bien connues. En revenant à l'expression initiale de $\langle J_x \rangle$, nous obtenons:

Dans le cas du couplage par potentiel de déformation:

$$\langle J_x \rangle = \frac{2^{3/2}}{3\pi^{3/2}} \frac{nm^{3/2} D^{(3)}}{\hbar^3 s} \frac{e^{-\gamma^2}}{B^2} (kT)^{3/2} \frac{T_0}{T} E \left\{ 1 - 2\gamma^2 \left(1 - \frac{T}{T_0} \right) + \frac{1}{5} \frac{V_0^2}{V_T^2} \left[1 + 6\gamma^2 - 18\gamma^2 \left(1 - \frac{T}{T_0} \right) - 4\gamma^4 \left(1 - \frac{T}{T_0} \right) \right] \right\}.$$

Dans le cas du couplage piézoélectrique:

$$\langle J_x \rangle = \frac{2^{3/2}}{3\pi^{3/2}} \frac{nm^{3/2} D^{(1)}}{\hbar^3 s} \frac{e^{-\gamma^2}}{B^2} (kT)^{1/2} \frac{T_0}{T} E \left\{ 1 - 2\gamma^2 \left(1 - \frac{T}{T_0} \right) + \frac{1}{5} \frac{V_0^2}{V_T^2} \left[-1 + 6\gamma^2 - 6\gamma^2 \left(1 - \frac{T}{T_0} \right) - 4\gamma^4 \left(1 - \frac{T}{T_0} \right) \right] \right\}.$$

Ces résultats appellent deux remarques:

(1) Les termes contenant γ^2 ou γ^4 dans leur expression qui figurent dans les deux dernières équations représentent, du fait de la condition $\gamma \ll 1$, et de ce que T/T_0 sera toujours voisin de 1, des corrections négligeables.

(2) La composante linéaire en E s'obtient en faisant $T = T_0$ et en supprimant tous les termes qui ne sont pas d'ordre 1 en E ; on obtient ainsi (3, 20).

ANNEXE 4

L'utilisation de la formule (3, 16) conduit à:

$$\int_{-V_d/V_T}^{V_d/V_T} du u e^{-(\sqrt{\alpha/2})(\sqrt{x} \pm (1/\sqrt{x})) \pm u} \approx 2 \frac{V_0^3}{V_T^3} \left\{ \mp \frac{4}{31} \frac{\alpha}{2} \left(\sqrt{x} \pm \frac{1}{\sqrt{x}} \right) \pm \frac{V_0^2}{V_T^2} \frac{16}{5!} \left(3\sqrt{\frac{\alpha}{2}} \left(\sqrt{x} \pm \frac{1}{\sqrt{x}} \right) - 2 \left(\frac{\alpha}{2} \right)^{3/2} \left(\sqrt{x} \pm \frac{1}{\sqrt{x}} \right)^3 \right) \right\} e^{-(\alpha/2)(\sqrt{x} \pm (1/\sqrt{x}))^2} \quad (1)$$

En reportant ce résultat partiel dans l'intégrale en x , il restera à calculer des intégrales de la forme:

$$\frac{1}{2} \int_0^{\infty} (\hbar q_{\max}^2/2m\omega_0) dx x^{p-1} e^{-(\alpha/2)(\sqrt{x} \pm (1/x))} \text{ avec } -1 \leq p \leq 2. \quad (2)$$

La fonction à intégrer présente un maximum au voisinage de $x = 1$ et décroît exponentiellement avec x au-delà de ce maximum. Cette décroissance est d'autant plus rapide que le paramètre $\alpha = (\hbar\omega_d/2kT)$ est grand. On peut noter dès maintenant que l'énergie des phonons optiques — exprimée en degrés Kelvin — est de l'ordre de, ou supérieure à la température ambiante. Par conséquent, la valeur de α est rarement inférieure à l'unité. De plus $\hbar q_{\max}^2/2m\omega_0$ est une quantité atteignant aisément des valeurs élevées de l'ordre de 10^3 . Dans ces conditions, comme pour les valeurs de x élevées, la fonction à intégrer se comporte comme $e^{-\alpha x}$, on peut remplacer la borne supérieure $\hbar q_{\max}^2/2m\omega_0$ par ∞ , la contribution à l'intégrale de l'intervalle $(\hbar q_{\max}^2/2m\omega_0, \infty)$ étant négligeable. Ce résultat est très agréable car les intégrales

$$K_n(\alpha) = \frac{1}{2} \int_0^{\infty} dx x^{n-1} e^{-(\alpha/2)(\sqrt{x} \pm (1/x))} = K_{-n}(\alpha) \quad (3)$$

définissent les fonctions de Bessel modifiées de seconde espèce, tabulées dans la Réf. [13].

En tenant compte de toutes ces remarques, la formule (3, 31) donnant $\langle J_x \rangle$ se transforme en:

$$\langle J_x \rangle = \frac{2}{3} \frac{nmD^{(0)}}{\pi^{3/2} \hbar^2 B} \frac{\alpha}{\sinh \alpha_0} \frac{V_0}{V_T} ch(\alpha - \alpha_0) K_1(\alpha) \left\{ 1 - \frac{K_0(\alpha)}{K_1(\alpha)} \right.$$

$$\left. th(\alpha - \alpha_0) - \frac{1}{5} \frac{V_0^2}{V_T^2} \left(3 - \alpha \frac{K_2(\alpha) + 3K_0(\alpha)}{K_1(\alpha)} + \frac{4\alpha K(\alpha) - 3K_0(\alpha)}{K_1(\alpha)} th(\alpha - \alpha_0) \right) \right\}. \quad (4)$$

La composante linéaire du courant s'obtient en faisant $T = T_0$ et en supprimant tous les termes d'ordre en E supérieurs à un; on obtient (3, 34).

LOW TEMPERATURE HEAT CAPACITIES OF LAVES PHASE LANTHANIDE-ALUMINUM COMPOUNDS*

C. DEENADAS, A. W. THOMPSON, R. S. CRAIG and W. E. WALLACE
Department of Chemistry, University of Pittsburgh, Pittsburgh, Penna. 15213, U.S.A.

(Received 3 September 1970)

Abstract—Heat capacity data are presented for the five LnAl_2 compounds, where $\text{Ln} = \text{La, Ce, Pr, Nd and Gd}$. The temperature range covered was 8 to 300°K. The data for non-magnetic LaAl_2 were taken to represent the lattice and electronic contribution to the heat capacities of the four remaining compounds. The difference between the heat capacity of the magnetic compounds and LaAl_2 gave the magnetic contribution to the heat capacity from which the magnetic entropy could be derived. Results obtained were in approximate agreement with $R \ln(2J+1)$ except for GdAl_2 in which the discrepancy was about 25 per cent.

The data for CeAl_2 gave no indication of magnetic ordering; however, an upturn in its C_p vs. T curve below 12°K was observed. λ -type thermal anomalies were observed for PrAl_2 and NdAl_2 , peaking at 31.8 and 77.2°K, respectively. These were ascribed to the breakup of the ferromagnetic phase. Curie temperatures inferred from the C_p data were in good agreement with those obtained from magnetic studies. No λ -type anomaly was observed for GdAl_2 ; instead its magnetic heat capacity was spread over a very wide range of temperature suggesting that destruction of magnetic order in this case is a weakly cooperative process.

1. INTRODUCTION

THE PRESENT investigation constitutes a portion of a continuing series of studies dealing with intermetallic compounds in which one of the constituents is a lanthanide element. In this study we report on measurements of the low temperature heat capacities of the series of compounds LnAl_2 in which $\text{Ln} = \text{La, Ce, Pr, Nd and Gd}$.

Extensive information is available pertaining to the crystallographic, bulk magnetic and resonance characteristics of the LnAl_2 compounds[1-7]. In contrast little heat capacity information pertaining to them is available; the study by Hill and da Silva[8] for CeAl_2 covering the range 0.5-15°K seems to be the only heat capacity work on the LnAl_2 compounds. The present study was undertaken as the initial step toward obtaining a comprehensive picture of their heat capacity behavior comparable to that which

currently exists for their structural, magnetic and resonance features. The present study has been confined to the five compounds cited in the preceding paragraph and to the temperature range 8-300°K. In time it is planned to provide results for the other LnAl_2 compounds and to extend the measurements to lower temperatures, $\sim 1.5^\circ\text{K}$.

Principal interest in the present work has been focussed on establishing the magnetic contribution to the heat capacity and entropy. However, the data in all cases except CeAl_2 , which shows anomalous behavior at the lowest temperatures, have also been made use of in deriving the Third Law entropies and other standard thermodynamic functions. A preliminary account of this work was presented at the C.N.R.S. International Colloquium held in Paris and Grenoble, May, 1969 and appears in the proceedings of that Colloquium[9]. Interpretation of results for CeAl_2 in the present version differs significantly from that given earlier because of additional information obtained for this compound in the past year[10].

*This work was supported by a grant from the U. S. Army Research Office, Durham.

2. EXPERIMENTAL

The compounds were prepared by levitation melting. Except for CeAl_2 no heat treatment was deemed necessary since the physical properties (structures and magnetic behavior) were identical for annealed and as-cast materials. This was not so for CeAl_2 ; it was annealed at 750°C for 21 days. X-ray and magnetic measurements of selected samples agreed well with earlier work[1, 11]. Purity of rare earth metals, obtained from Research Chemicals, was reported to be 99.9 per cent. The aluminum was obtained from Aluminum Company of America and was stated to be 99.999 per cent pure.

The details of the apparatus and precision and accuracy of the data have been reported elsewhere[12]. The masses of the samples used for heat capacity measurements are LaAl_2 85.738 g, CeAl_2 140.503 g, PrAl_2 83.179 g, NdAl_2 78.523 g and GdAl_2 76.836 g.

3. RESULTS

The results obtained are summarized in

chronological order in Tables 1 to 5. The data have been graphically represented in Figs. 1 to 4 for CeAl_2 , PrAl_2 , NdAl_2 and GdAl_2 along with results for LaAl_2 . In general the ΔT , the temperature rise for each measurement, was about 5°K . To determine the detailed shape of the heat capacity curve in the region of the anomaly, measurements were made with small temperature changes, 0.2 – 0.3°K . In the Pr compound a single measurement was also made over the whole region of the anomaly. From this and the individual heat capacity determinations the course of the heat capacity curve near the λ -point was determined. The several cyclings between each series indicated that thermal history had no effect on the heat capacity of samples.

The molar heat capacities of all the compounds are approximately equal above 200°K . However, C_p of CeAl_2 is higher than all the other compounds by about $1\frac{1}{2}$ per cent and C_p of NdAl_2 is lower than LaAl_2 for $T > 200^\circ\text{K}$, the difference increasing to about 1 per cent

Table 1. Measured heat capacities for LaAl_2 . Molecular weight: $192.873 \text{ g mole}^{-1}$

Temperature $^\circ\text{K}$	C_p Joules $^\circ\text{K mole}^{-1}$	Temperature $^\circ\text{K}$	C_p Joules $^\circ\text{K mole}^{-1}$	Temperature $^\circ\text{K}$	C_p Joules $^\circ\text{K mole}^{-1}$
Series I		199.34	66.51	20.75	2.568
80.52	37.16	205.34	67.26	Series III	
86.71	40.47	211.90	68.03	8.95	0.099
92.70	43.04	218.60	68.31	12.22	0.399
98.57	45.17	224.81	68.94	16.25	1.104
104.16	47.19	230.99	69.65	20.88	2.589
109.75	49.34	237.23	70.22	24.70	4.206
115.34	50.98	243.52	70.59	27.78	5.799
120.95	52.82	249.78	70.64	31.70	7.995
126.62	54.45	256.00	71.05	36.31	10.65
132.34	55.90	262.19	71.19	41.04	13.52
138.10	57.36	268.35	71.73	45.74	16.43
143.93	58.45	274.48	72.19	50.67	19.52
149.85	59.60	280.68	72.38	56.13	22.95
155.84	60.76	286.94	73.44	61.65	26.46
161.95	61.90	293.17	73.43	66.91	29.48
167.98	62.47	299.37	73.63	71.95	32.59
174.01	63.45	Series II		76.97	35.01
180.17	64.20	10.07	0.215	82.90	38.26
186.76	65.03	13.42	0.599	88.46	41.05
193.28	65.73	17.03	1.338	92.79	42.76

Table 2. Measured heat capacities for CeAl_2 . Molecular weight: $194.09 \text{ g mole}^{-1}$

Temperature °K	C_p Joules °K mole	Temperature °K	C_p Joules °K mole	Temperature °K	C Joules °K mole
Series I		208.82	68.77	14.91	2.579
101.89	48.31	214.79	69.41	16.77	3.315
105.60	49.81	220.78	69.92	18.86	4.240
109.99	51.15	227.15	70.22	21.02	5.307
114.38	52.62	233.91	71.07	23.30	6.574
118.90	54.00	240.56	71.34	25.88	8.079
123.87	55.18	247.17	71.60	29.06	9.983
129.27	56.73	253.78	71.94	32.66	12.18
134.70	57.95	260.37	72.34	36.83	14.62
140.11	59.28	267.34	72.82	41.67	17.41
145.60	60.45	274.19	73.12	46.96	20.65
151.03	59.74	281.02	73.58	52.73	24.11
156.37	64.21	288.51	74.08	58.46	27.52
161.58	63.17	295.91	74.36	63.78	30.68
166.97	63.92	302.16	74.64	68.78	33.42
172.56	64.71	Series II		73.47	35.81
178.54	65.46	7.03	2.045	78.22	38.28
184.83	66.21	9.99	1.773	82.86	40.62
191.02	66.96	11.35	1.554	87.48	42.89
197.25	67.69	12.35	1.848	92.76	45.07
203.13	68.12	13.49	2.248	98.37	47.12

at 300°K. There is merging of heat capacities of LaAl_2 and PrAl_2 at temperatures well above the region of the anomaly. This suggests that the vibrational and electronic contributions in these compounds are nearly the same; C_p for GdAl_2 exceeds that of LaAl_2 by about 1 per cent in this region.

A comparison of the Curie temperatures observed in the present studies with literature values is given in Table 11. There is no evidence of ordering for CeAl_2 but its C_p shows an upturn below 12°K. Magnetic measurements by Williams *et al.* [2] and Swift and Wallace [3] were interpreted to indicate ferromagnetic

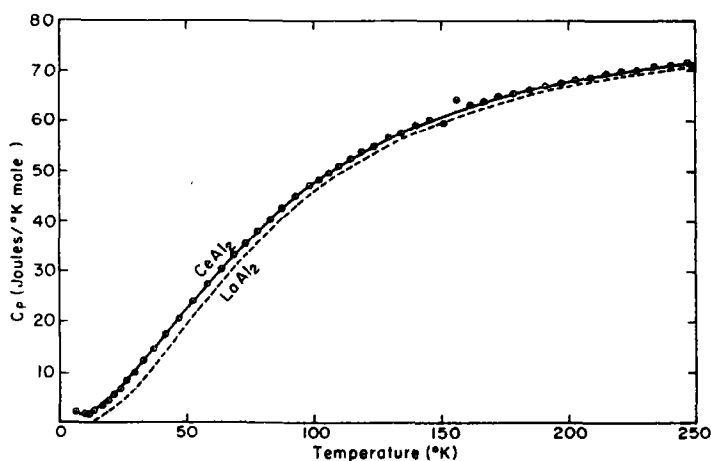


Fig. 1. Heat capacities of CeAl_2 and LaAl_2 vs. temperature.

Table 3. Measured heat capacities for PrAl_2 . Molecular weight: $194.933 \text{ g mole}^{-1}$

Temperature °K	C_p Joules °K mole	Temperature °K	C_p Joules °K mole	Temperature °K	C_p Joules °K mole
Series I		265.60	70.91	Series III	
105.35	47.86	272.05	71.75	9.22	0.585
108.91	49.15	278.42	72.22	10.11	1.619
112.84	50.35	284.61	72.64	11.79	2.34
117.38	51.63	290.65	73.20	13.96	4.313
122.46	53.74	296.54	73.44	15.73	6.956
127.50	54.68	302.40	74.09	17.54	9.385
132.46	55.84	Series II		19.58	12.66
137.27	57.06	11.71	2.708	21.37	15.98
142.03	58.03	15.27	6.155	22.85	18.72
146.69	58.57	17.48	9.251	24.12	21.14
151.18	59.82	19.95	13.32	25.47	23.75
155.76	60.72	22.70	18.40	26.98	26.59
161.04	61.39	26.09	25.05	28.082	28.94
166.77	62.18	29.40	32.18	28.652	29.78
172.22	62.88	32.19	30.96	29.125	31.15
177.62	63.84	35.67	14.70	29.575	32.24
183.01	64.22	40.00	16.00	29.992	33.90
188.26	65.05	44.10	18.24	30.335	34.75
193.37	65.15	47.84	20.70	30.604	35.58
198.60	66.54	52.71	23.60	30.970	37.26
204.04	66.90	58.19	26.28	31.412	38.96
209.26	67.35	63.40	29.12	31.953	39.60
214.25	68.06	68.78	32.03	32.882	22.48
219.66	68.34	73.89	34.73	33.93	15.40
225.77	69.15	78.87	37.02	34.93	14.55
232.36	69.45	84.38	39.98	36.12	14.62
239.09	69.81	89.66	42.25	38.34	15.22
245.70	70.13	94.76	44.51	44.18	18.60
252.37	70.78	99.91	46.04	47.98	20.33
259.10	71.43	104.85	47.77		

Energy for
 $T = 6.93^\circ\text{K}$ to $T = 42.14^\circ\text{K}$
 is 229.123 Joules

or

$$\int_{6.93}^{42.14} C_p dT = 229.123 \text{ Joules.}$$

and antiferromagnetic transitions, respectively, at temperatures 8°K and 3°K , respectively. The agreement in regard to the ordering temperature for PrAl_2 and NdAl_2 between various observations is good. The situation for GdAl_2 is more complex. Magnetic measurements [3, 6] in fields 20 and 1 kOe. indicated the Curie temperatures to be 182 and 171°K . The present data show a bump with maximum at 153°K and (almost) completion of the transi-

tion at 170°K . The resistivity showed a change in slope at 173°K in the experiment of Van Daal and Buschow [13] whereas Mydosh *et al.* [14] inferred T_c to be 151°K both from resistivity and thermoelectric power measurements. From Knight shift measurements Jones and Budnick [15] estimated T_c to be about 150°K . T_c for GdAl_2 deduced from the heat capacity results are thus not inconsistent with those obtained by other means.

Table 4. Measured heat capacities for NdAl_2 . Molecular weight: $198.203 \text{ g mole}^{-1}$

Temperature °K	C_p Joules °K mole	Temperature °K	C_p Joules °K mole	Temperature °K	C_p Joules °K mole
Series I					
7.99	0.182	142.54	59.05	77.654	48.08
9.51	0.480	147.30	59.89	78.010	44.70
10.70	0.760	152.07	60.58	78.334	44.16
11.56	1.303	157.14	61.43	78.602	43.70
12.21	1.024	162.24	62.26	78.871	43.70
12.87	1.697	167.13	63.01	79.421	43.31
14.27	2.130	172.06	63.44	79.768	43.23
16.53	3.294	177.21	64.17	80.259	43.27
19.06	4.819	182.22	64.67	81.082	43.25
21.62	6.647	187.18	65.12	82.54	43.53
23.91	8.572	192.29	65.68	84.54	44.05
26.22	10.82	197.33	66.18	87.52	45.07
28.82	12.63	202.58	66.67	Series III	
32.10	16.18	207.90	67.10	67.78	46.30
35.56	19.48	212.40	67.77	70.81	48.49
38.44	22.19	217.40	67.63	72.167	49.65
41.09	24.54	222.58	68.12	72.794	49.91
44.05	27.17	227.94	68.45	73.313	50.35
47.30	29.98	233.93	69.01	73.698	51.37
51.08	33.14	243.29	70.77	73.985	50.06
54.82	36.15	251.05	70.45	74.203	50.86
57.82	38.53	256.36	70.62	74.790	51.68
60.40	40.67	261.62	71.16	74.972	51.81
62.61	42.43	266.69	72.07	75.153	51.83
64.82	44.14	271.78	72.03	75.334	52.08
67.16	45.90	276.86	72.06	75.518	52.22
70.73	48.55	282.01	72.15	75.702	52.92
75.42	52.34	287.57	72.55	75.887	53.08
80.25	43.81	292.98	72.54	76.080	53.21
85.34	44.49	298.62	73.37	76.286	53.25
90.49	45.85	304.89	73.19	76.501	53.70
95.53	47.32	Series II		76.720	54.04
100.43	48.74	65.54	44.72	76.922	54.26
105.20	50.14	67.51	46.16	77.099	54.69
109.87	51.51	69.95	47.89	77.283	53.52
114.47	52.78	71.54	49.10	77.471	50.80
118.88	53.96	72.62	49.97	77.657	47.64
123.23	54.89	73.58	50.83	77.939	45.69
127.96	56.18	74.50	51.67	78.262	44.55
132.94	57.29	75.52	52.84	78.552	44.05
137.71	58.03	76.53	54.03	78.868	43.85
		77.251	53.39		

Smoothed heat capacity, entropy, enthalpy and Gibbs free energy functions are listed for all the compounds except CeAl_2 in Tables 6 to 10 at selected temperatures. As the measurements were not extended below 8°K it was necessary to extrapolate C_p below this temperature down to 0°K for evaluating the thermal data. This was done assuming the

Debye T^3 law. The upturn for CeAl_2 below 12°K, of course, renders this kind of extrapolation valueless. For this reason thermodynamic functions for CeAl_2 are omitted.

4. DISCUSSION OF RESULTS

It is convenient to discuss the results in terms of an idealized framework in which

Table 5. Measured heat capacities for GdAl_2 . Molecular weight: $210.840 \text{ g mole}^{-1}$

Temperature °K	C_p Joules °K mole	Temperature °K	C_p Joules °K mole	Temperature °K	C_p Joules °K mole
Series II		173.51	64.36	146.97	67.40
6.90	1.551	178.96	65.35	148.33	67.58
8.36	1.083	184.36	65.47	149.29	67.84
10.53	1.308	189.72	66.13	150.27	68.24
12.79	1.875	194.86	66.72	151.43	67.85
14.32	2.346	199.69	67.46	152.78	69.24
16.30	2.098	204.58	68.07	154.03	67.94
19.40	5.189	209.61	68.49	156.37	68.82
22.56	5.936	214.77	69.01	157.53	69.45
25.47	6.881	219.90	69.60	158.68	67.72
28.09	9.669	225.15	73.56	160.17	67.40
30.30	10.60	230.54	69.67	162.07	65.77
33.94	12.66	235.95	70.61	163.95	64.77
39.27	15.85	241.31	71.35	165.49	64.61
43.85	19.09	246.65	71.25	166.81	66.02
47.21	20.66	251.97	71.43	168.61	57.52
50.53	24.42	257.27	71.62	171.59	63.81
53.78	24.57	262.54	72.01	175.73	64.48
56.74	27.73	267.96	72.48	180.35	64.82
59.45	29.19	273.53	65.17	184.94	65.32
62.16	32.17	278.48	73.03	189.57	65.48
Series I		284.05	73.32	194.35	66.32
81.61	44.11	289.59	73.61	Series IV	
85.63	59.59	295.12	74.13	38.73	15.65
90.04	48.65	Series III		41.51	18.24
94.86	50.78	89.90	48.03	45.28	19.52
100.31	53.13	93.97	50.55	49.54	22.82
106.03	54.09	98.21	52.87	54.19	26.12
111.06	57.72	102.29	53.85	58.57	29.26
115.91	59.65	106.22	55.98	62.71	31.97
120.62	61.23	109.11	56.36	67.05	34.76
124.87	62.52	111.75	57.43	71.66	37.35
128.86	63.93	115.55	59.80	76.45	40.43
132.94	64.99	119.87	57.57	80.94	43.27
136.96	66.11	126.34	62.65	85.24	45.62
141.08	67.10	130.37	64.18	89.18	47.73
145.32	67.88	134.52	65.55	93.70	50.00
149.50	68.66	137.88	66.15	98.83	52.43
153.81	69.04	140.91	66.52	103.74	54.88
158.25	68.61	143.31	66.81	108.18	56.10
163.04	65.94	145.14	68.08	111.91	57.61
168.19	64.35				

exchange is weak compared to the crystal field interaction. (Actually the two effects are comparable at least in PrAl_2 and NdAl_2 , as will be brought out below.) Consider the case of an assemblage of Nd^{+3} ions in a cubic field. The 10-fold degenerate ground state of Nd^{+3} is split into a Γ_8 (doublet) and two Γ_6 (quartet) states. If the former is lower lying,

we expect in the idealized case a λ -type thermal anomaly associated with the disappearance of the cooperative phase for ions in the Γ_8 state followed by a Schottky-type thermal anomaly at higher temperatures brought about by excitation of the ions into the Γ_6 states; the entropies associated with the two anomalies are $R \ln 2$ and $R \ln (10/2)$, respectively.

Table 6. Smoothed heat capacities^[a] and thermodynamic values for LaAl₂

Temperature °K	C_p Joules °K mole	$(H - H_0^0)/T$ Joules °K mole	S Joules °K mole	$-(F - H_0^0)/T$ Joules °K mole
10	0.185	0.046	0.062	0.016
15	0.867	0.188	0.243	0.056
20	2.262	0.516	0.666	0.150
25	4.368	1.065	1.385	0.320
30	7.023	1.831	2.409	0.579
35	9.864	2.776	3.706	0.930
40	12.86	3.848	5.217	1.369
45	15.97	5.021	6.910	1.889
50	19.14	6.274	8.757	2.483
60	25.41	8.944	12.804	3.860
70	31.37	11.727	17.174	5.447
80	36.80	14.528	21.723	7.196
90	41.64	17.277	26.344	9.066
100	45.86	19.929	30.954	11.025
110	49.50	22.456	35.500	13.044
120	52.62	24.843	39.945	15.101
130	55.29	27.085	44.264	17.179
140	57.58	29.183	48.448	19.264
150	59.58	31.145	52.490	21.345
160	61.33	32.978	56.392	23.415
170	62.89	34.692	60.158	25.466
180	64.28	36.298	63.793	27.495
190	65.54	37.805	67.303	29.498
200	66.67	39.220	70.694	31.474
210	67.69	40.552	73.972	33.420
220	68.60	41.807	77.142	35.335
230	69.40	42.989	80.210	37.220
240	70.12	44.105	83.179	39.074
250	70.76	45.159	86.054	40.896
260	71.36	46.155	88.841	42.686
270	71.94	47.099	91.545	44.446
280	72.54	47.997	94.172	46.175
290	73.17	48.854	96.728	47.875
300	73.84	49.675	99.220	49.545
273.15	72.13	47.387	92.381	44.994
298.15	73.71	49.526	98.764	49.238

^[a]Results in this and subsequent tables justify only four significant figures. The larger number of figures reported was provided by the computer; they are given to facilitate the taking of differences which are sometimes needed in thermodynamic calculations.

NdNi₂ closely approximates this behavior [9]; in it exchange appears to be weak in comparison with the crystal field effect.

If the two interactions are comparable, the two anomalies will not be clearly resolved but instead will overlap substantially; this appears to be the case in PrAl₂ and NdAl₂. The difference in C_p for PrAl₂ and LaAl₂ (Fig. 5) shows that the thermal anomaly is not of

the simple λ -type but instead has a pronounced shoulder. Results for NdAl₂ are similar. These data suggest that the thermal anomaly is a combination effect involving simultaneously the destruction of ferromagnetism and excitation into the higher energy crystal field states, implying, of course, that the strengths of the exchange and crystal field interactions are comparable.

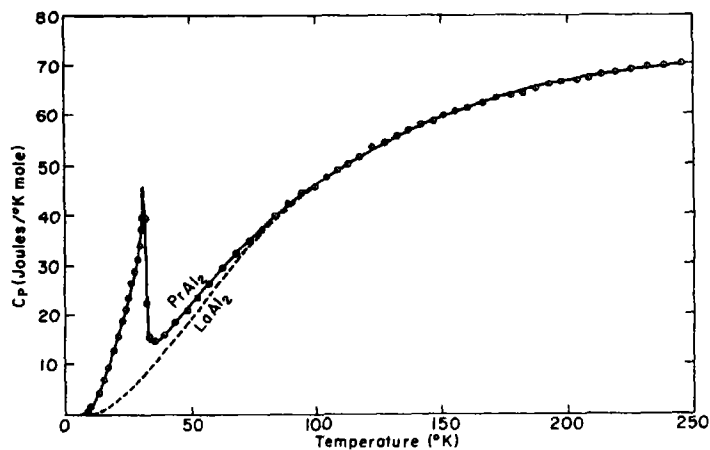
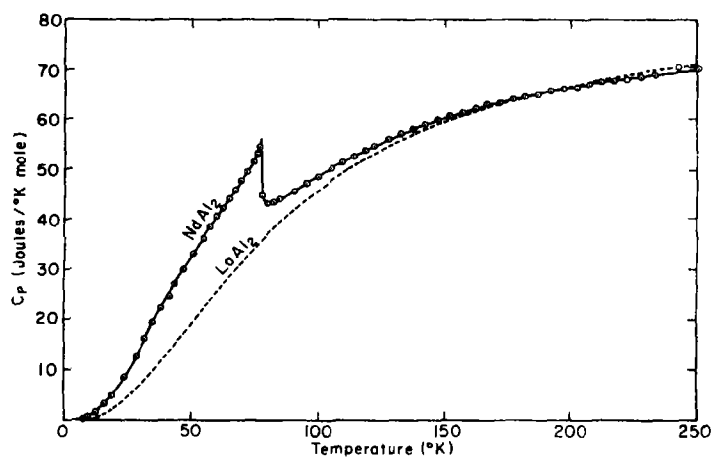
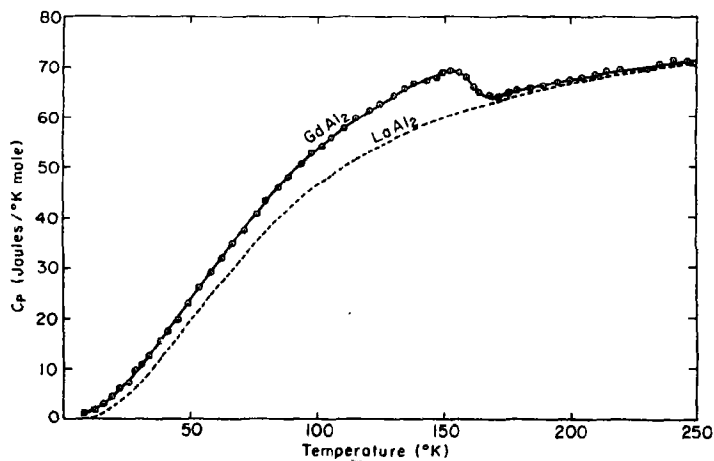
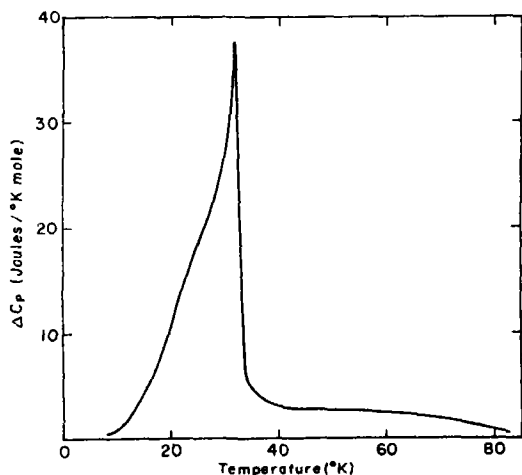
Fig. 2. Heat capacities of PrAl_2 and LaAl_2 vs. temperature.Fig. 3. Heat capacities of NdAl_2 and LaAl_2 vs. temperature.Fig. 4. Heat capacities of GdAl_2 and LaAl_2 vs. temperature.

Table 7. Smoothed heat capacities for CeAl_2

Temperature °K	C_p Joules °K mole	Temperature °K	C_p Joules °K mole
10	1.660	150	61.23
15	2.602	160	63.07
20	4.790	170	64.66
25	7.580	180	66.03
30	10.56	190	67.20
35	13.57	200	68.21
40	16.95	210	69.07
45	20.19	220	69.82
50	23.29	230	70.47
60	29.08	240	71.07
70	34.36	250	71.63
80	39.15	260	72.18
90	43.47	270	72.75
100	47.37	280	73.37
110	50.85	290	74.05
120	53.95	300	74.84
130	56.70	273.15	72.94
140	59.11	298.15	74.68

As noted above CeAl_2 gave no indication of the formation of a cooperative phase in the temperature range covered in this study although the upturn in C_p below 12°K suggested that ordering might occur below 8°K. The measurements of Hill and da Silva[8], showing an anomaly peaking at about 3.5°K, are consistent with the trend of C_p vs. tempera-

Fig. 5. Excess heat capacity vs. temperature for PrAl_2 , i.e. difference in C_p for PrAl_2 and LaAl_2 .

ture noted in the present work; however, the C_p values in the region of overlap, 8 to 15°K, differ by about 30 per cent, the present measurements being lower. The heat capacity data make it clear that the conclusion by Williams *et al.*[2] to the effect that CeAl_2 becomes ferromagnetic at 8°K is erroneous; they are, however, in agreement with the conclusion of Swift and Wallace[3] that CeAl_2 becomes antiferromagnetic below 3°K.

The difference in heat capacity for CeAl_2 and LaAl_2 is plotted in Fig. 6. A Schottky-type anomaly exists for CeAl_2 ; we attribute this to the crystal field excitation. Calculations of this contribution to C_p were made with the doublet and with the quartet lowest lying. Curves are shown in Fig. 6 for the calculated curves which give peaks at the same tempera-

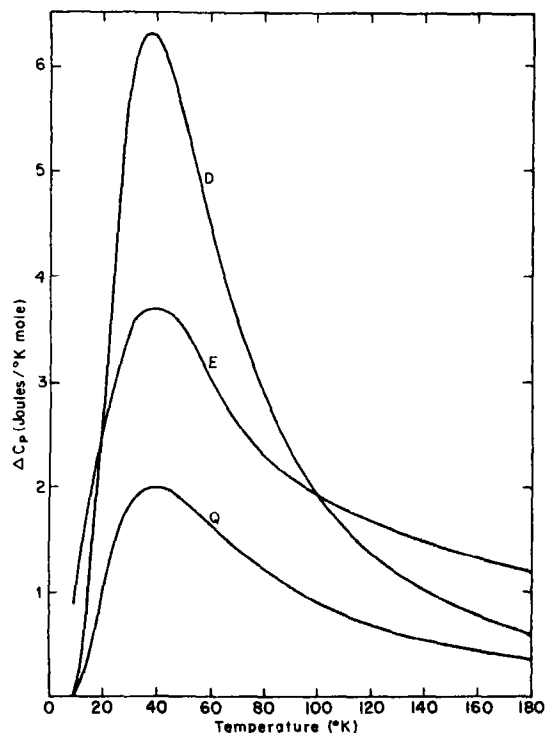
Fig. 6. Crystal field heat capacity of CeAl_2 . Curves Q and D are calculated curves with quartet and doublet as ground states assuming a pure fourth order contribution. The experimental curve 'E' is obtained by subtracting away the C_p of LaAl_2 from C_p of CeAl_2 .

Table 8. Smoothed heat capacities and thermodynamic values for PrAl_2

Temperature °K	C_p Joules °K mole	$(H - H_0^0)/T$ Joules °K mole	S Joules °K mole	$-(F - H_0^0)/T$ Joules °K mole
10	1.400	0.347	0.458	0.111
15	5.550	1.250	1.643	0.392
20	13.40	3.269	4.271	1.002
25	22.82	6.262	8.322	2.060
30	33.90	9.829	13.307	3.479
31.8	45.80	11.345	15.438	4.093
35	14.61	12.276	17.522	5.246
40	16.00	12.615	19.521	6.906
45	19.14	13.165	21.587	8.421
50	22.19	13.917	23.763	9.846
60	27.88	15.777	28.319	12.542
70	33.07	17.882	33.012	15.130
80	37.77	20.079	37.740	17.661
90	42.03	22.286	42.439	20.154
100	45.86	24.455	47.070	22.615
110	49.29	26.560	51.605	25.045
120	52.35	28.584	56.028	27.443
130	55.07	30.519	60.327	29.808
140	57.46	32.360	64.498	32.138
150	59.56	34.105	68.535	34.430
160	61.40	35.755	72.439	36.685
170	62.99	37.311	76.211	38.899
180	64.38	38.777	79.851	41.074
190	65.57	40.157	83.365	43.208
200	66.61	41.454	86.755	45.301
210	67.51	42.674	90.027	47.353
220	68.30	43.821	93.186	49.365
230	69.02	44.901	96.239	51.337
240	69.68	45.920	99.190	53.270
250	70.31	46.883	102.047	55.164
260	70.94	47.796	104.817	57.021
270	71.60	48.666	107.507	58.841
280	72.31	49.497	110.123	60.626
290	73.10	50.297	112.674	62.377
300	73.99	51.072	115.167	64.095
273.15	71.82	48.931	108.339	59.407
298.15	73.81	50.930	114.710	63.780

tures as the experimental curve. Clearly neither affords a good representation of experiment. A number of years ago White *et al.* [16] on the basis of magnetic measurements concluded that the Γ_8 state was lowest lying and that the Γ_8 to Γ_7 separation was about 200°K. The thermal anomaly computed on this basis is also in poor agreement with experiment; for example, the calculated value peaks at 76°K, higher by a factor of two than the experimental value.

The difficulty in accounting for the details

of the heat capacity anomaly is probably to be found in the recent discovery by van Daal and Buschow [17] that CeAl_2 exhibits a resistance minimum and hence it is probably a (concentrated) Kondo system. Spin compensation influences the susceptibility and undoubtedly renders the crystal field splitting determined by White *et al.* inaccurate. The interaction between the localized spins of the Ce^{+3} ion with the conduction electrons, which produces the Kondo effect, contributes to the heat capacity and the entropy of the

Table 9. Smoothed heat capacities and thermodynamic values for NdAl₂

Temperature °K	C_p Joules °K mole	$(H - H_0^0)/T$ Joules °K mole	S Joules °K mole	$-(F - H_0^0)/T$ Joules °K mole
10	0.61	0.153	0.204	0.051
15	2.48	0.579	0.760	0.180
20	5.54	1.416	1.868	0.452
25	9.49	2.624	3.516	0.891
30	14.04	4.141	5.641	1.500
35	18.88	5.899	8.166	2.267
40	23.64	7.818	10.997	3.179
45	28.04	9.825	14.040	4.215
50	32.13	11.853	17.208	5.355
55	36.24	13.882	20.462	6.580
60	40.39	15.918	23.794	7.875
65	44.33	17.955	27.185	9.230
70	47.89	19.967	30.601	10.635
75	51.97	21.955	34.035	12.080
77.2	54.85	22.848	35.575	12.728
80	43.47	23.633	37.189	13.557
90	45.73	25.932	42.407	16.475
100	48.67	28.058	47.377	19.319
110	51.52	30.063	52.150	22.088
120	54.17	31.963	56.748	24.786
130	56.54	33.764	61.179	27.416
140	58.61	35.466	65.447	29.981
150	60.39	37.070	69.553	32.483
160	61.92	38.577	73.501	34.924
170	63.24	39.990	77.295	37.306
180	64.39	41.314	80.943	39.629
190	65.42	42.556	84.453	41.897
200	66.36	43.723	87.832	44.109
210	67.26	44.822	91.092	46.270
220	68.12	45.862	94.241	48.379
230	68.95	46.847	97.287	50.439
240	69.74	47.785	100.238	52.453
250	70.49	48.678	103.100	54.422
260	71.17	49.531	105.879	56.348
270	71.77	50.344	108.576	58.233
280	72.28	51.118	111.196	60.078
290	72.70	51.855	113.740	61.884
300	73.07	52.556	116.211	63.654
273.15	71.94	50.592	109.410	58.818
298.15	73.00	52.429	115.759	63.330

system in ways which for concentrated systems remain to be elucidated. We feel that it is this contribution which produces the discrepancy between the experimental curve and that computed with the doublet lowest. (The work of Hill and da Silva together with the work of Van Daal, Buschow, Rao and Wallace leave little doubt that the Γ_8 state is, indeed, the ground state.)

The computer curves in Fig. 6 are based on the assumption of an assemblage of non-interacting ions. In respect to the interionic interaction this assumption seems to be valid; exchange ($T_N = 3.5^\circ\text{K}$) is so weak as to be a second order effect. We are inclined to ascribe the excess experimental heat capacities over the calculated values for $T > 100^\circ\text{K}$ to the persistence of the interaction between the

Table 10. Smoothed heat capacities and thermodynamic values of GdAl_2

Temperature °K	C_p Joules °K mole	$(H - H_0)/T$ Joules °K mole	S Joules °K mole	$-(F - H_0)/T$ Joules °K mole
10	0.130	0.207	0.312	0.106
15	2.560	0.753	1.043	0.290
20	4.642	1.450	2.048	0.598
25	7.301	2.347	3.361	1.014
30	10.31	3.420	4.954	1.534
35	13.52	4.369	6.791	2.152
40	16.63	5.943	8.799	2.856
45	19.82	7.307	10.941	3.634
50	23.11	8.722	13.199	4.477
60	29.91	11.685	18.011	6.326
70	36.64	14.773	23.132	8.358
80	42.86	17.903	28.438	10.535
90	48.33	20.987	33.809	12.823
100	53.06	23.963	39.152	15.189
110	57.18	26.799	44.406	17.607
120	60.86	29.487	49.543	20.055
130	64.09	32.028	54.545	22.517
140	66.66	34.415	59.394	24.979
150	68.23	36.624	64.053	27.430
153	68.65	37.242	65.408	28.161
160	67.19	38.606	68.464	29.858
170	64.07	40.163	72.410	32.247
180	65.22	41.524	76.106	34.582
190	66.27	42.799	79.660	36.862
200	67.27	43.998	83.085	39.088
210	68.21	45.129	86.390	41.262
220	69.10	46.198	89.584	43.386
230	69.93	47.212	92.674	45.462
240	70.70	48.175	95.667	47.492
250	71.43	49.091	98.568	49.477
260	72.09	49.963	101.383	51.420
270	72.69	50.793	104.115	53.321
280	73.24	51.586	106.769	55.183
290	73.74	52.341	109.348	57.006
300	74.18	53.062	111.855	58.793
273.15	72.87	51.047	104.959	53.912
298.15	74.10	52.931	111.396	58.465

localized and the conduction electron spins. This, we feel, is also responsible for the lack of agreement between the calculated and experimental values at lower temperatures. Clearly it is not appropriate to regard CeAl_2 above 10°K as an assemblage of essentially non-interacting ions, ignoring the conduction electron influence. The present work thus indicates that the interaction between the localized Ce^{+3} ion spins and the conduction electrons is important not only for the transport behavior of CeAl_2 but also in regard to

its thermodynamic characteristics (C_p and entropy) and probably in regard to its low temperature magnetic behavior as well.

The excess heat capacity for GdAl_2 (Fig. 7) is quite remarkable. There is no correspondence between the results obtained and the expected λ -type thermal anomaly. The excess heat capacity covers a very wide range of temperature. The anomalous width of the magnetic transition is also evident in magnetization-temperature[3] measurements and in resistivity-temperature measurements

Table 11. Heat capacity anomalies and comparison with other observations

Compound	Type of thermal anomaly	Peak* temperature in °K Heat Capacity	T_c or T_N (°K) Other Methods	
CeAl ₂	Schottky λ	~ 40	31 ^(b)	81 ^(a)
PrAl ₂	Schottky + λ	31.8	31 ^(d)	38 ^(b)
NdAl ₂	Schottky + λ	77.2	76 ^(d)	76 ^(b)
GdAl ₂	?	153°	173 ^(d)	151 ^(c)
		170°†	171 ^(e)	182 ^(b) 150 ^(f)

*In the Schottky anomaly the peak is referred to as the maximum observed in ΔC_p .

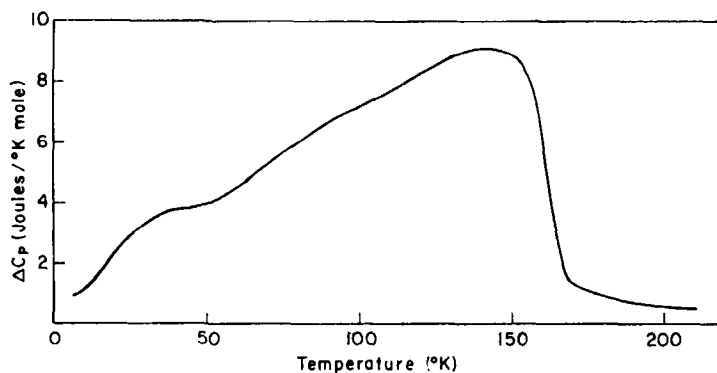
†The temperature at which the transition is essentially complete.

^(a)Ref. [2] ^(b)Ref. [3] ^(c)Ref. [14]

^(d)Ref. [13] ^(e)Ref. [6] ^(f)Ref. [15].

Table 12. Magnetic entropies and/or crystal field entropies (Joules/°K mole)

Substance	Theoretical	Measured	Meas./Theor.
CeAl ₂	$R \ln 6/2 = 9.13$	8.45	0.925
PrAl ₂	$R \ln 9 = 18.26$	15.94	0.871
NdAl ₂	$R \ln 10 = 19.11$	16.99	0.886
GdAl ₂	$R \ln 8 = 17.20$	12.63	0.735

**Fig. 7. Excess heat capacity vs. temperature for GdAl₂.**

[13]. The process is so broad that we regard it as weakly cooperative, similar in some respects to that observed for elemental Pr [18]. However, the mechanism cannot be similar since in Pr the ordered phase grows out of the singlet state. The unusual behavior of GdAl₂ remains to be elucidated.

Entropies associated with the heat capacity anomalies are given in Table 12. For CeAl₂ this seems to be solely a crystal field effect and hence $\Delta S = R \ln (g_8 + g_7)/g_7$ where g_8 and g_7 are the multiplicities of the Γ_8 and Γ_7 states, i.e. 4 and 2, respectively. In the other cases $\Delta S = R \ln (2J + 1)$ since the crystal field and

magnetic contributions cannot be separated. Agreement is reasonably satisfactory for the first three compounds but poor for GdAl_2 . It appears that LaAl_2 may not be entirely satisfactory to represent the lattice and electronic contribution. If so this would be particularly noticeable for GdAl_2 for which the transition is unusually wide. It is perhaps for this reason that the discrepancy is largest in this case.

REFERENCES

1. For a general review of the crystallographic and magnetic characteristics of intermetallics including the LnAl_2 compounds see *Magnetism of Intermetallic Compounds*, W. E. Wallace, Progress in Solid State Chemistry, Pergamon Press. (in press).
2. WILLIAMS H. J., WERNICK J. H., NESBITT E. A. and SHERWOOD R. C., *J. phys. Soc. Japan* **17**, Suppl. B1, 91 (1962).
3. SWIFT W. M. and WALLACE W. E., *J. Phys. Chem. Solids* **29**, 2053 (1968).
4. MADER K. H., SEGAL E. and WALLACE W. E., *ibid.* **30**, 1 (1969).
5. JACCARINO V., *J. appl. Phys.* **32**, 102S (1961).
6. BUSCHOW K. H. J., FAST J. F., VAN DIEPEN A. M. and DEWIJN H. W., *Phys. Status Solidi* **24**, 715 (1967).
7. BARNES R. G. and JONES E. D., *Solid State Commun.* **5**, 285 (1967).
8. HILL R. W., MACHADO DA SILVA J. M., *Phys. Lett.* **30A**(1), 13 (1969).
9. WALLACE W. E., CRAIG R. S., THOMPSON A., DEENADAS C., DIXON M., AOYAGI M. and MARZOUK N., *Coll. Int. du C. N. R. S.* No. **180**, 427 (1970).
10. RAO V. U. S. and WALLACE W. E., *Phys. Rev.*, in press. In this paper analysis of the resistivity-temperature behavior of CeAl_2 makes it clear that the Γ_7 (doublet) state is the ground state for the Ce^{+3} ion in CeAl_2 , in agreement with the conclusions of Hill and da Silva (see Ref. [8]).
11. WALLACE W. E., *Progress in Rare Earth Science and Tech.* (Edited by L. Eyring), Vol. 3, 1 (1968).
12. WALLACE W. E., DEENADAS C., THOMPSON A. W. and CRAIG R. W., *J. Phys. Chem. Solids*, in press.
13. VAN DAAL H. J. and BUSCHOW K. H. J., *Solid State Commun.* **7**, 217 (1969).
14. KAWATRA M. P. and MYDOSH J. A., *Phys. Lett.* **28A**, 182 (1968); MYDOSH J. A., KAWATRA M. P. and BUDNICK J. I., *ibid.* **24A**, 421 (1967).
15. JONES E. D. and BUDNICK J. I., *J. appl. Phys.* **37**, 1395 (1966).
16. WHITE J. A., WILLIAMS H. J., WERNICK J. H. and SHERWOOD R., *Phys. Rev.* **131**, 1039 (1963).
17. VAN DAAL H. J. and BUSCHOW K. H. J., *Solid State Commun.* **7**, 217 (1969).
18. WALLACE W. E., KISSELL F., SEGAL E. and CRAIG R. S., *J. Phys. Chem. Solids* **30**, 13 (1969).

CRYSTAL FIELD AND MAGNETIC HEAT CAPACITY IN PrIn_3 AND CeIn_3 *

A. M. VAN DIEPEN,[†] R. S. CRAIG and W. E. WALLACE

Department of Chemistry, University of Pittsburgh, Pittsburgh, Penn. 15213, U.S.A.

(Received 3 September 1970)

Abstract—Heat capacities of LaIn_3 , CeIn_3 and PrIn_3 have been measured between 7 and 300°K. The LaIn_3 results fit a Debye curve with $\theta = 170^\circ\text{K}$. PrIn_3 has a Schottky-type anomaly around 36°K, from which an overall crystal field splitting of about 170°K is derived, with the singlet Γ_1 as the lowest state. The heat capacity and magnetic behavior of PrIn_3 indicate a value of the crystal field parameter x in the range -0.8 to -0.6 . CeIn_3 shows a Schottky anomaly around 60°K, which yields a crystal field splitting of 155°K (doublet lowest). A lambda-type anomaly is observed at $10.4 \pm 0.5^\circ\text{K}$, the Néel point. The magnetic entropy indicates that the doublet Γ_7 is the lowest level in CeIn_3 . The sign of the crystal field splitting is in both compounds in agreement with point charge predictions.

1. INTRODUCTION

THE MAGNETIC behavior of the various RIn_3 ($\text{R} = \text{a rare earth}$) compounds has recently been reported[1]. PrIn_3 was observed to exhibit Van Vleck paramagnetism at the lowest temperatures studied. Efforts to deduce the overall crystal field splitting (E_c) for this compound from its susceptibility-temperature behavior were only partially successful due to uncertainty as to the relative importance of the fourth and sixth order contributions to the crystal field potential; E_c could not be established to better than a factor of two. It should be possible to refine this estimate, as is pointed out below, by appropriate heat capacity measurements. This provided the incentive for undertaking the present study. In due course the investigation was broadened to include CeIn_3 . The magnetic measurements on CeIn_3 had suggested[1] an appreciable crystal field interaction but the results could not be unambiguously analysed. Again it appeared that heat capacity studies could provide information from which the overall splitting and degeneracy of the ground state could be deduced.

Measurements on non-magnetic LaIn_3 were

included to facilitate the resolution of the magnetic and crystal field contribution from the total heat capacity. It (i.e. LaIn_3) was used to approximate the lattice vibrational contribution to the heat capacity of CeIn_3 and PrIn_3 .

2. EXPERIMENTAL

The samples used in the present investigation, about 85 grams per compound, were prepared by levitation melting. Pieces of about 10 grams were made at a time. Since the compounds form congruently only a short stress annealing was needed. The indium metal used was 99.999 per cent, the rare earths were 99.9 per cent pure. X-ray diffraction showed that LaIn_3 , CeIn_3 and PrIn_3 have the cubic Cu_3Au structure with lattice parameters close to those given in Ref. [1]. The heat capacities were studied between 7 and 300°K in a calorimeter of the adiabatic type[2], described in Ref. [3].

The experimental heat capacities are given in Table 1. The values at room temperature slightly exceed 99.8 Joule/°K mole, the value for C_∞ expected for a solid of four atoms per formula unit. The heat capacity of PrIn_3 exceeds that of LaIn_3 up to 125°K; the difference between the heat capacity of the two compounds is given in Fig. 1. The anomaly is of the Schottky type and attributed to the crystal field acting on the Pr^{3+} ion. CeIn_3 has

*This work was supported by a grant from the U.S. Army Research Office, Durham.

[†]Present Address: Philips Research Laboratories, Eindhoven, The Netherlands.

Table 1. Experimental heat capacities of LaIn_3 , CeIn_3 and PrIn_3 as depending on the temperature

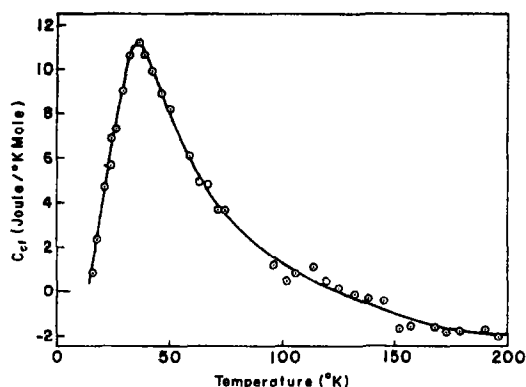
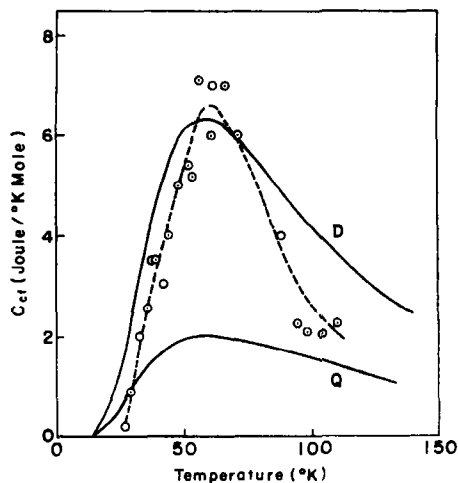
T (°K)	C_{Mol} (Joule/°K mole)	T (°K)	C_{Mol} (Joule/°K mole)	T (°K)	C_{Mol} (Joule/°K mole)	T (°K)	C_{Mol} (Joule/°K mole)
LaIn_3		CeIn_3		9.96		15.39	
41.47	48.26	88.09	89.17	10.43	8.41	12.55	3.08
46.61	54.97	93.03	89.02	11.14	3.83	15.23	6.81
52.45	61.77	98.18	90.68	11.97	4.27	17.83	11.94
68.73	74.52	103.67	92.24	12.84	4.75	20.87	19.04
74.78	77.86	110.04	93.54	14.50	6.50	23.57	25.77
80.89	81.63	152.40	101.79	8.19	7.30	26.11	32.07
87.22	84.75	160.35	103.15	9.40	12.56	28.86	38.22
93.81	86.89	169.09	102.28	10.02	16.03	31.48	43.57
100.55	88.14	192.90	104.87	10.41	15.45	37.82	53.56
107.11	90.30	202.00	102.41	10.73	4.46	41.70	58.44
114.02	91.88	218.54	102.26	11.10	4.47	45.87	62.99
122.33	93.68	226.95	102.76	11.41	4.47	50.14	67.21
130.52	95.24	37.66	45.05	11.71	5.02	58.90	73.57
138.27	96.72	39.72	48.11	12.07	4.01	62.80	75.42
9.30	84	42.39	56.18	12.48	4.10	66.80	78.19
10.67	1.90	45.30	61.87	13.18	4.98	71.58	79.82
12.99	3.89	48.10	64.38	14.92	6.91	77.46	82.49
15.97	7.18	61.10	76.16	17.23	9.75	83.70	85.53
18.78	11.06	66.29	80.22	19.47	13.03	95.81	88.86
21.41	15.37	71.24	82.03	22.05	17.07	102.01	89.92
23.90	20.32	110.36	94.82	24.55	21.64	108.01	91.10
26.43	25.14	118.41	96.44	26.91	26.41	113.79	93.03
29.10	28.72	127.29	98.48	29.64	31.45	119.63	93.60
31.94	33.55	136.35	98.80	32.72	37.31	125.48	94.24
35.19	38.91	145.18	100.56	35.87	42.40	131.55	95.33
37.28	41.82	154.10	101.79	38.97	47.50	138.26	96.52
38.58	44.16	163.33	101.19	41.91	52.13	145.23	97.35
44.40	53.01	119.44	97.28	44.90	56.82	151.68	97.04
48.05	56.66	125.43	98.90	48.37	62.05	157.20	97.65
52.39	61.94	130.98	100.17	52.32	66.87	162.51	97.58
56.78	66.22	136.75	101.59	56.77	73.07	167.77	98.67
61.51	69.62	149.01	102.66	61.13	75.00	173.34	98.72
66.71	73.33	156.21	102.97	65.73	77.24	179.19	99.33
81.89	81.81	163.44	102.89	70.86	80.87	189.87	99.86
89.73	85.83	170.32	104.73	62.68	75.42	196.12	99.87
97.82	87.57	177.43	105.04	65.61	76.55	201.93	100.52
106.30	90.09	185.35	103.86	69.23	78.10	207.66	100.72
115.26	92.22	193.84	104.45	77.09	83.62	213.41	100.92
124.53	94.22	202.50	105.90	81.65	85.89	219.27	101.18
134.78	96.35	210.74	104.28	94.44	90.64	226.09	101.56
145.45	98.17	218.92	105.44	99.32	91.45		
154.73	99.90	227.03	105.86	104.10	93.32		
164.21	100.45	6.26	1.94	108.71	94.43		
174.53	100.23	7.78	5.73	113.25	96.11		
184.66	101.51	8.44	7.08	117.84	97.02		
194.23	100.63	9.08	10.12				
225.03	102.44	9.56	9.75				

a Schottky anomaly around 60°K (Fig. 2) and, in addition, a lambda-type anomaly at 10.4°K (Fig. 3), the latter being attributed to the anti-ferromagnetic transition at the Néel point.

3. DISCUSSION

(a) Lattice heat capacity

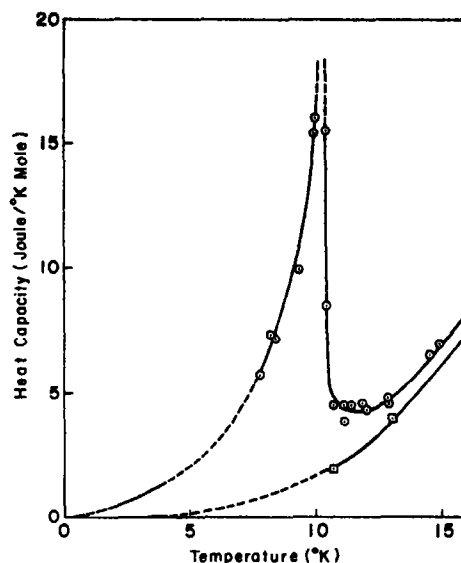
The experimentally measured heat capacity is the sum of different contributions. The main

Fig. 1. Crystal field heat capacity of PrIn_3 .Fig. 2. Crystal field heat capacity of CeIn_3 (circles, dashed line), compared with theory for doublet lowest (curve D) and quartet lowest (curve Q).

contribution is from the lattice vibrations; its temperature dependence is according to a Debye function [4]. For RIn_3 :

$$C_v(\text{lattice}) = 36 R \left(\frac{T}{\theta} \right)^3 \int_0^\theta \frac{e^{-t} t^4 dt}{(e^t - 1)^2}, \quad (1)$$

where R is the molecular gas constant, θ the Debye temperature determined by the maximum vibration frequency ω_m through $\theta = \hbar \omega_m / k$. The actual integration is over all vibration frequencies up to the maximum, with $t = \hbar \omega / k$. Because of the small expansion coefficients of metals the experimental heat capacity

Fig. 3. Heat capacity of CeIn_3 and LaIn_3 (lower curve) around the Néel point of CeIn_3 . Both curves are extrapolated to zero temperature on the basis of the results of Ref. [10].

can be considered as measured under constant volume. The LaIn_3 data were fitted to equation (1). Numerical values for the integral were taken from Ref. [5]. Up to about 100°K a good fit was obtained for $\theta = 170^\circ\text{K}$. At the higher temperatures, where the lattice heat capacity increases very slowly, other effects such as conduction electron heat capacity and impurities become more pronounced, so that deviations from equation (1) occur. It is also because of these effects that the value $\theta = 170^\circ\text{K}$ should be seen as a lower limit, rather than as an average.

(b) Crystal field heat capacity

The $(2J+1)$ -fold degeneracy of the ground state of the rare-earth ion is removed by the crystal field. The cubic crystal field splits the $J = \frac{5}{2}$ level in CeIn_3 into a doublet Γ_7 and a quartet Γ_8 . In PrIn_3 the $J = 4$ level is split into a singlet Γ_1 , a nonmagnetic doublet Γ_3 , and two triplets Γ_4 and Γ_5 . A redistribution over the different crystal field levels with a variation of temperature involves energy varia-

tions, and hence a contribution to the heat capacity. This effect is much smaller than that from the lattice vibrations. To determine the crystal field heat capacity the other contributions (lattice and electronic) must be subtracted from the experimentally measured total. It is for this purpose that the heat capacity of LaIn_3 was measured. A smooth curve was drawn through the measured LaIn_3 points. The circles in Figs. 1 and 2 represent experimental PrIn_3 and CeIn_3 data minus the corresponding points on the LaIn_3 curve. The excess heat capacity in PrIn_3 becomes negative for $T > 125^\circ\text{K}$. In CeIn_3 it is almost a constant for $T > 100^\circ\text{K}$. A possible explanation of these differences can be found in the presence of impurities such as rare-earth hydrides, nitrides, oxides and so on, which have at the high temperatures bigger gram heat capacities than the rare-earth metals and the RIn_3 compounds [6]. These impurities change the absolute value of the observed crystal field contribution by almost a constant in the high temperature range, but do not change its shape appreciably.

Entropies under these Schottky anomalies are: PrIn_3 (up to 130°K) $\Delta S = 11.8$ Joule/mole ($R \ln 9 = 18.27$), CeIn_3 (up to 100°K) $\Delta S = 5.6$ Joule/mole ($R \ln 6/2 = 9.13$). The failure of ΔC_p to approach zero as temperature increases complicates attempts to assess ΔS associated with excitation within the crystal field spectrum. The upper temperatures cited are arbitrary and do not correspond to complete excitation. The experimental entropies are hence underestimated.

The heat capacity at a temperature T of a system involving n energy levels is given by

$$C_{\text{cf}} = \frac{R}{Z} \left\{ \sum_{i=1}^n \left(\frac{\Delta_i}{T} \right)^2 \exp(-\Delta_i/T) - \left[\sum_{i=1}^n \frac{\Delta_i}{T} \exp(-\Delta_i/T) \right]^2 / Z \right\}, \quad (2)$$

where Δ_i is the energy difference between the i -th level and the lowest level and Z is the partition function. Theoretical calculations

have been made for Ce^{3+} (see Fig. 2) and Pr^{3+} (see Fig. 4) in a cubic environment. For the Ce compound only two level systems are possible, viz., doublet lowest or quartet lowest. For Pr^{3+} many different combinations of fourth and sixth order potentials are possible, each involving a different arrangement of the energy levels [7]. The calculated heat capacities were compared with experiment by adjusting the overall splitting so that the experimental and theoretical temperatures of maximum heat capacity, 36°K for PrIn_3 and 60°K for CeIn_3 , coincide.

By comparing Figs. 1 and 4 it is immediately seen that in PrIn_3 , in agreement with the point charge model, W must be positive and the singlet Γ_1 is the lowest state. Reasonable fits are obtained for $x \geq -0.8$, from which an overall splitting of about 170°K follows. The separation between the singlet ground level and the next triplet Γ_4 or Γ_5 is around 100°K . A pure fourth order crystal field potential ($x = -1.0$) definitely cannot describe the experimental heat capacity, since for $T > 45^\circ\text{K}$ large discrepancies occur. The actual level scheme should also give a good fit to the susceptibility [1], so that x must be in the range -0.6 to -0.8 . The corresponding energy levels are given in Table 2. From heat capacity and magnetic susceptibility data alone it is not possible to distinguish between the given (and intermediate) sets. A method which measures the energy separations in a direct way, e.g. inelastic neutron scattering [8], will probably be more decisive.

The situation for CeIn_3 is less clear, since the experimental errors in the crystal field heat capacity are more nearly comparable with the crystal field contribution. The result (Fig. 2) is a broad peak around 60°K . If the quartet is lowest, the splitting is $135 \pm 30^\circ\text{K}$; in the other case it is $155 \pm 30^\circ\text{K}$. The data in Fig. 2, while not decisive, suggest that the ground state is the doublet. Firmer evidence that the doublet is lowest results from analysis of the magnetic transition, presented in the next section.

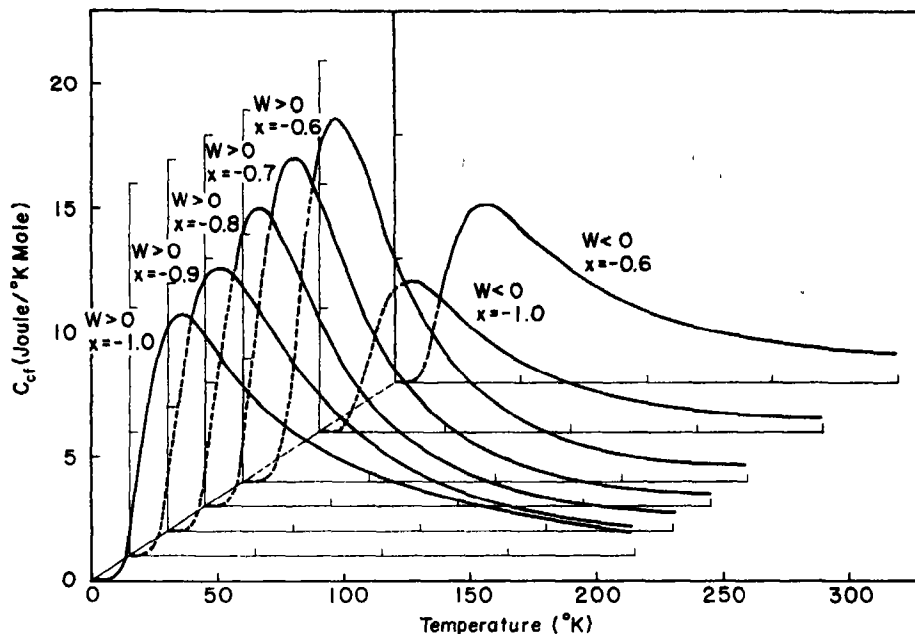


Fig. 4. Some calculated crystal field heat capacity curves for different proportions of fourth and sixth order potentials acting on the Pr^{3+} ion in PrIn_3 .

Table 2. Energy levels for the Pr^{3+} ion in PrIn_3 after removal of the degeneration of the $J = 4$ state by crystalline fields for different values of the parameter x

Level	$x = -0.8$	$x = -0.7$	$x = -0.6$
Γ_1	-120°K	-114°K	-117°K
Γ_4	-33	-23	-16
Γ_3	+30	+43	+55
Γ_5	+53	+32	+18

At low temperatures ($T \ll \Delta_2$) equation (2) can be approximated by

$$C_{cf} = R \frac{g_2}{g_1} \left(\frac{\Delta_2}{T} \right)^2 \exp(-\Delta_2/T), \quad (3)$$

where g_1 and g_2 are the degeneracies of the first and the second level [9]. A plot of $\ln C_{cf}T^2$ vs. $1/T$ should give a straight line, the slope of which is $-\Delta_2$. Δ_2 can also be determined from the intersection with the $\ln C_{cf}T^2$ axis. For

Table 3. Values of the energy distance between the lowest levels in CeIn_3 and PrIn_3 as derived from heat capacity data

	$\Delta_2/k^{(a)}$ (°K)	$\Delta_2/k^{(b)}$ (°K)	$\Delta_2/k^{(c)}$ (°K)
CeIn_3	167	145	155
PrIn_3	112	120	~96

^(a)Obtained from the slope of the plot of $\ln C_{cf}T^2$ vs. $1/T$.

^(b)Obtained from the intersection with the $\ln C_{cf}T^2$ axis of the same plot.

^(c)Obtained from the position of the peak and the overall shape of the Schottky anomaly.

PrIn_3 data between 16 and 32°K lay on a straight line; for CeIn_3 data between 30 and 50°K are used. The results are given in Table 3. It should be noted that, if in PrIn_3 the energy separation between the second and the third level is about kT , to first approximation still a straight line is obtained. However,

the derived ' Δ_2 ' will be bigger than the actual value.

(c) *Magnetic heat capacity*

A lambda-type anomaly was observed in CeIn_3 at $10.4 \pm 0.5^\circ\text{K}$ (Fig. 3). This agrees well with the Néel point, found in the susceptibility at 11°K [1]. An estimated peak value of the heat capacity of 25 Joule/ $^\circ\text{K}$ mole was used to evaluate the entropy change associated with the anomaly. The latter was found to be 6.0 Joule/mole, very near to $R \ln 2 = 5.76$. The experimental ΔS was obtained from the difference of C_p for CeIn_3 and LaIn_3 . Preliminary heat capacity data in the range 1.5 to 4.2°K of both compounds indicate, however, that the low temperature heat capacity of CeIn_3 is far in excess of that of LaIn_3 [10], so that the actual entropy associated with the antiferromagnetic transition is less than 6.0 Joule/mole. Since the quartet would require twice as much entropy, which by no means can be found, this result unambiguously shows that the doublet is the lowest level in CeIn_3 .

4. CONCLUSION

Heat capacity data together with susceptibilities have lead to a satisfactory description

of the crystal fields in PrIn_3 and CeIn_3 . The heat capacity data indicate the lowest level to be a singlet in PrIn_3 and a doublet in CeIn_3 . These results are in qualitative agreement with the point charge model.

REFERENCES

1. BUSCHOW K. H. J., deWIJN H. W. and VAN DIEPEN A. M., *J. chem. Phys.* **50**, 137 (1969).
2. WESTRUM E. F., Jr., HATCHER J. B. and OSBORNE, *J. chem. Phys.* **21**, 419 (1953); RUEHRWEIN R. A. and HOFFMAN M., *J. Am. Chem. Soc.* **65**, 1620 (1943); STERRETT K. F., BLACKBURN D. H., BESTUL A. B., CHANG S. S. and HORMAN J., *J. Res. Nat'l. Bur. Std.* **69C**, 19 (1965).
3. WALLACE W. E., DEENADAS C., THOMPSON A. W. and CRAIG R. S., *J. Phys. Chem. Solids*, **32**, 805 (1971).
4. DEBYE P., *Ann. Phys.* **39**, 789 (1912).
5. BEATTIE J. A., *J. Math. Phys.* **6**, 1 (1926).
6. GERSTEIN B. C., TAYLOR W. A., SHICKELL W. D. and SPEDDING F. H., 8th Rare Earth Conference, Reno (1970).
7. LEA K. R., LEASK M. J. M. and WOLF W. P., *J. Phys. Chem. Solids* **23**, 1381 (1962). See this reference for definitions of W and x .
8. BIRGENEAU R. J., BUCHER E., PASSELL L., PRICE D. L., TURBERFIELD K. C., *J. appl. Phys.* **41**, 900 (1970).
9. BUCHER E., GOSSARD A. C., ANDRES K., MAITA J. P. and COOPER A. S., 8th Rare Earth Conference, Reno (1970).
10. VAN DIEPEN A. M., NASU S., NEUMANN H. H. and CRAIG R. S., to be published.

PHOTOLUMINESCENCE IN COMPENSATED *n*-TYPE, SI-DOPED GALLIUM ARSENIDE*

I. PETRESCU-PRAHOVA† and N. N. WINOGRADOFF
National Bureau of Standards, Washington, D. C. 20234, U.S.A.

(Received 26 August 1970)

Abstract—Band tailing observed in highly doped GaAs and other semiconductors has been attributed to screened coulomb potentials. The amphoteric nature of melt-grown, Si-doped samples, limiting the free electron concentration to below $n = 5 \times 10^{18} \text{ cm}^{-3}$, permitted the unequivocal study of the band tail parameters as a function of impurity concentration at virtually constant free carrier screening over a silicon concentration range from 2.6×10^{18} to $1.2 \times 10^{20} \text{ cm}^{-3}$. The photoluminescent spectra of such samples consisted of two broad bands, one of which, centered at 1.2 eV, decreased with increasing temperature and vanished at the higher temperatures where accurate analysis of the shape of the other band, centered at any energy close to the band gap, could be made. The intensity of the low energy side of the latter band was found to be exponential and proportional to $\exp(h\nu/E_0)$, and the dependence of E_0 on the concentration of the silicon dopant was determined. Since a change of the excitation intensity over two orders of magnitude did not change the position or shape of the band-to-band 'line', it was concluded that the nature of the spectra reflects exponential density-of-states tails at the conduction band edge.

1. INTRODUCTION

IN RECENT years the optical properties of heavily doped GaAs suggested that the conduction and/or valence band edges in such materials were perturbed in such a way as to generate density-of-states tails extending these band edges into the forbidden gap. The presence of such tails was assumed in the band filling model in electroluminescent diodes[1], and in the interpretation of absorption[2, 3], cathodoluminescent[4], and photoluminescent spectra[3, 5].

It has been shown theoretically that the presence of tails would be expected to improve room temperature operation of GaAs lasers [6], and this was confirmed experimentally in work with laser diodes where the *p*-type side was heavily compensated[7]. Theoretical considerations[8, 9] suggest that tails would

be developed preferentially in materials with high concentrations of impurities provided the screening of the coulomb potential of the impurities by the free carriers could be kept low, i.e., in materials with a high degree of compensation.

A possibility of approaching the above theoretical requirements is provided by the amphoteric nature of Si when present in high concentrations in melt-grown GaAs. The high solubility of this dopant permitted the preparation of *n*-type samples having Si concentrations ranging from 2.6×10^{18} to 1.2×10^{20} Si atoms cm^{-3} while the free electron concentration changed only by a factor of two from 2.2×10^{18} to 4.0×10^{18} electrons cm^{-3} and allowed the study of the effect of a wide range of impurity concentration on the shape of the photoluminescent spectrum at a virtually constant free carrier concentration.

2. EXPERIMENTAL PROCEDURE

2.1 Sample preparation

The material was prepared by the addition of predetermined quantities of Si to the melt and the samples were cut from the initial

*Research supported in part by the Advanced research Projects Agency.

†Guestworker at the National Bureau of Standards under the U. S. National Academy of Sciences and the Romanian Academy Exchange Program. Permanent address: Institute of Physics, Calea Victoriei 114, Bucharest, Romania.

portions of the resulting crystals so as to permit the determination of the Si content in the sample from segregation coefficient data, with the assumption that the segregation coefficient was 0.14 [10]. Hall measurements showed that carrier saturation commenced at $\approx 4 \times 10^{18}$ electrons cm^{-3} , in agreement with published data [11].

The calculated Si concentration, N_{Si} , and the measured Hall electron concentrations, n , for the five samples studied are shown in Table 1.

Although the electron concentration in these samples is virtually constant, the mobility showed a strong dependence on the impurity concentration suggesting that the Si atoms which entered the crystal as donor and acceptor impurities were ionized at all the temperatures used in the experiments.

2.2 Optical System

For intercomparison of the various samples, small pieces of each sample, etch polished in bromine/methanol, were mounted on a circular holder and held in place by an outer circular clamping plate fitted with windows opposite each sample. The windows were equipped with chamfered edges to allow oblique angles of incidence of the pumping light and the collection of divergent emission.

This arrangement permitted the interchange of the samples by rotating the circular holder about an axis parallel to the normal to the illuminated face of the sample, in such a way that the optical alignment of the system remained unaltered. The holder was mounted on a resistive heater for use at the higher temperatures and was compact enough for insertion into a horizontal dewar fitted with an end-window, for cooling by a flow of cold nitrogen gas when required. This arrangement allowed

a temperature range of 200 to 490 K to be used without disturbing the optical system.

The sample was illuminated with radiation from a 200 mW argon laser focused to a spot size of $2 \times 10^{-4} \text{ cm}^2$. The resulting concentration of excess carriers was much higher than that attainable with mercury vapor lamps and permitted studying the effect of the intensity of excitation over two orders of magnitude by the insertion of neutral density filters in the laser beam.

The photoluminescence emitted from the illuminated surface was isolated from the argon line by filtering the light emitted by the sample through a 2-mm RG-8 Schott glass filter and focused onto the entrance slit of a grating monochromator.

The resolution of the monochromator was kept constant at 100 Å. An uncooled photomultiplier with an S-1 photoresponse was used as the detector, and all spectra were corrected for the photomultiplier response. The laser beam was chopped at 90 Hz and the signal was amplified with a lock-in amplifier.

3. RESULTS AND DISCUSSION

In general, the spectra generated by the above samples were in the form of two broad peaks. One was centered at 1.2 eV at all temperatures, while the other shifted with temperature in the same way as the band gap in pure material [Figs. 1(a), 1(b), and 1(c)]. It was assumed that this high energy band was due to transitions from the conduction to the valence bands, which at the doping levels used, exhibit tails of states extending into the forbidden gap.

The low energy band increased in intensity on cooling, and at 200 K the high energy band could no longer be resolved against the background of the low energy band in the most heavily doped sample. As the temperature

Table 1. Impurity and electron concentrations for different samples

Sample	1	2	3	4	5
N_{Si} atoms cm^{-3}	2.6×10^{18}	5.4×10^{18}	1.22×10^{19}	2.6×10^{19}	1.2×10^{20}
N electrons cm^{-3}	2.2×10^{18}	3.6×10^{18}	4.1×10^{18}	4.9×10^{18}	4.0×10^{18}

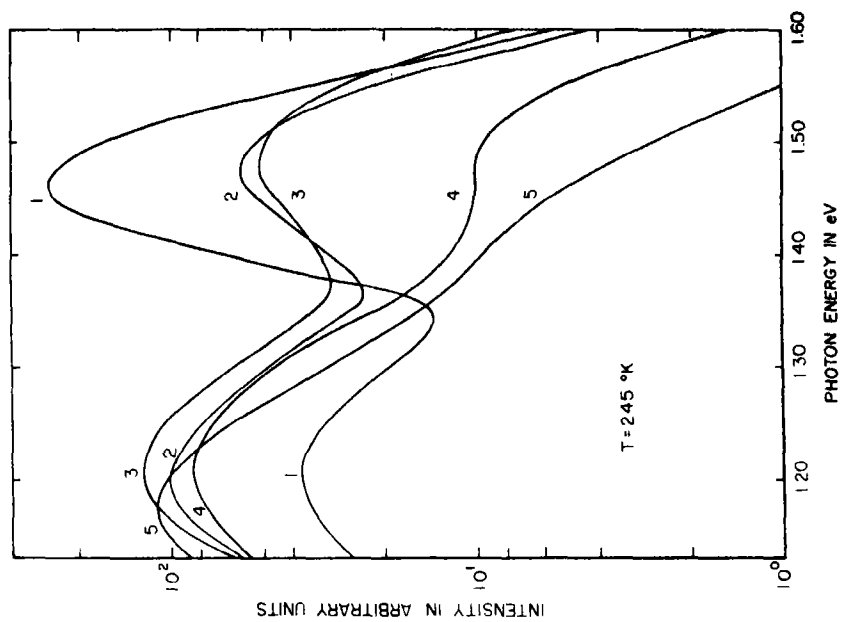


Fig. 1b.

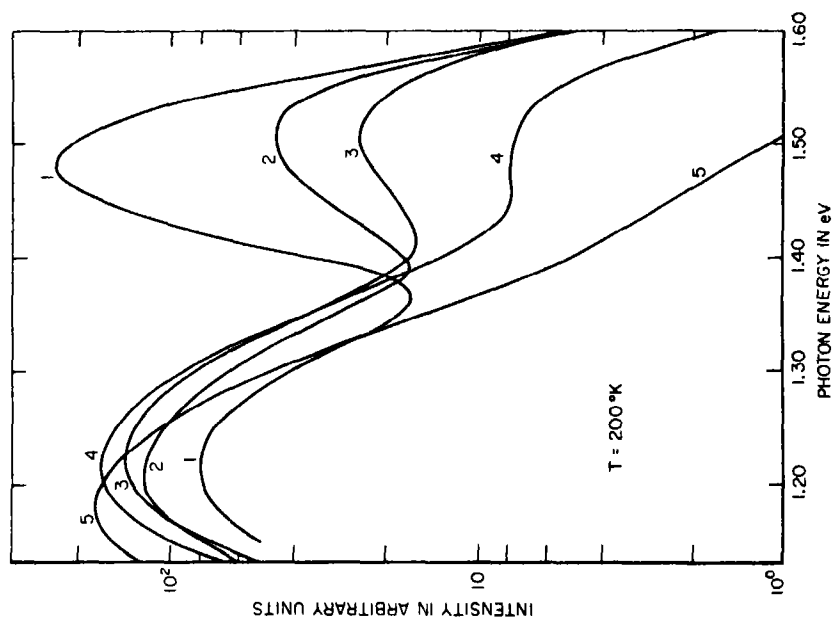


Fig. 1a.

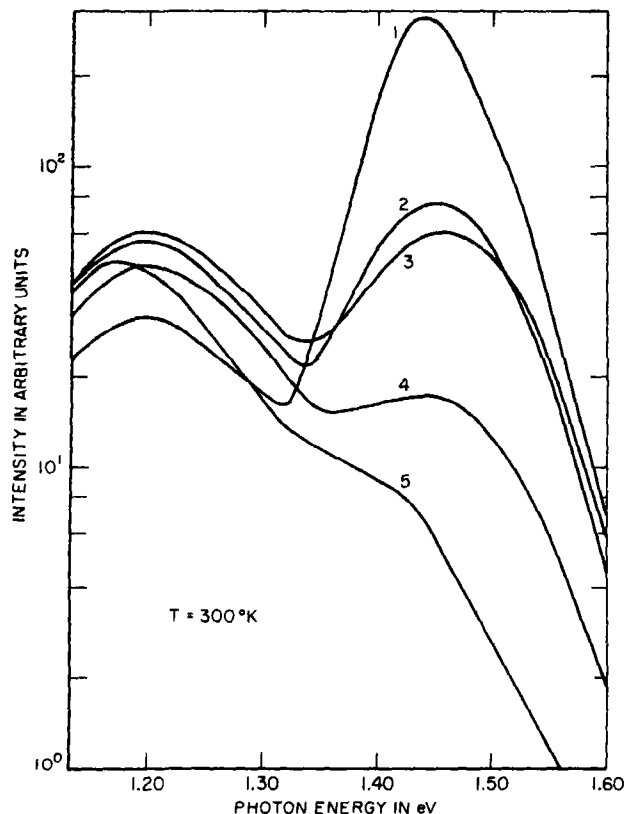


Fig. 1c.

Fig. 1. Photoluminescence spectra for the five samples of Table I taken at (a) 200 K, (b) 245 K, and (c) 300 K.

was increased, the intensity of the emission in the 1.2 eV band decreased and that of the high energy band increased slightly. In all samples, at the highest temperature used, 490 K, the low energy band disappeared and only the high energy band could be seen.

These results are very similar to those observed in Te-doped samples [12-14], where the temperature independence of the low-energy peak was attributed to transitions between states resulting from the interaction of a donor impurity with a Ga vacancy forming a complex, and suggests that the low-energy band in the Si-doped samples originates from similar $V_{Ga}Si_{Ga}$ complexes [14]. A comparison of the ratio of the peaks of the 1.2 eV and high energy bands observed with the

different samples at the same excitation intensity [Fig. 1(c)] showed that the intensity of the 1.2 eV peak increased relative to the high energy peak as the Si concentration in the sample increased. This suggested that an increase in the Si concentration resulted in a higher concentration of the $V_{Ga}Si_{Ga}$ complex [14].

If it is assumed that the lower levels of these complexes act as acceptors and give rise to states close to the valence band, an increase in temperature would ionize [15] holes trapped in these levels into the valence band until these states are effectively filled with electrons causing the emission in the 1.2 eV band to decrease until it becomes vanishingly small. An alternative explanation for this effect,

based on a thermal quenching of the radiative recombination via the $V_{Ga}Si_{Ga}$ centers and their conversion into non-radiative recombination centers, has also been proposed [14], and it should be noted that at high temperatures the integral intensity is less than at low temperatures, suggesting the presence of a third, parallel, temperature-dependent, non-radiative recombination process. Nevertheless, the increase of the high energy band accompanying the decrease in the low energy band is a clear indication that some ionization of holes into the valence band must be taking place.

One of the objectives of this work was to look for band filling phenomena [1] by chang-

ing the intensity of the excitation used. Although this was changed by two orders of magnitude, no shift of the band-to-band peak could be observed within the resolution limits of our experiments. As shown by Figs. 2(a) and 2(b), the same result was obtained at low temperatures where both bands were present and at high temperatures where only the band-to-band, high energy emission, could be seen, respectively. Figure 2(a) also shows that, at low temperatures, an increase in the intensity of the excitation resulted in a preferential growth of the high energy peak, suggesting some saturation of the empty acceptor states.

The absence of band filling effects in these

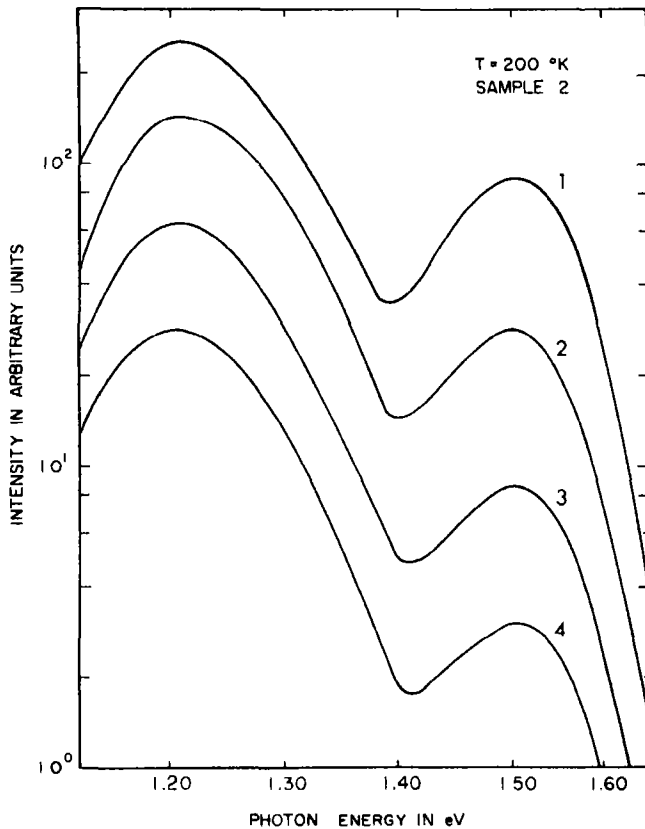


Fig. 2a.

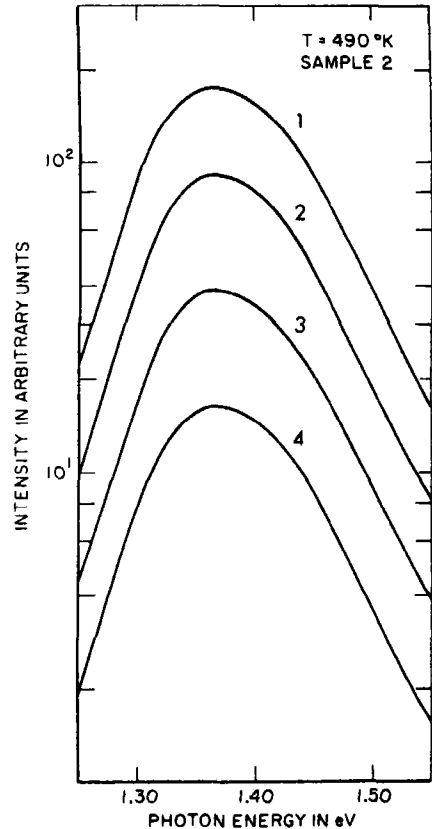


Fig. 2b.

Fig. 2. The effect of decreasing excitation intensity on sample 2, spectra at (a) 200 K, and (b) 490 K. In both cases the excitation intensity decreased by a factor of 2, 4.5, and 10 for spectra (2), (3), and (4), respectively, in comparison with (1).

experiments can be explained by the assumption that at the temperatures and light intensities used, the quasi Fermi level for holes was probably located near the above acceptor levels and quite far from the valence band, and that the density-of-states tail, if present in this band, does not extend deeply into the forbidden gap. The density of states contained in a kT energy interval of such a tail would then have to be large enough to accommodate all the excess holes generated by the pump source. It is interesting to note that no band filling was observed in the cathodoluminescence of p -type material[3], although such band filling effects were seen in the photoluminescence very highly doped material at lower temperatures.

A logarithmic plot of the intensity of the high energy band at a temperature of 490 K (where the low energy band had completely disappeared) for all five samples listed in Table 1 is shown in Fig. 3. The low energy sides of the spectra were all exponential, and

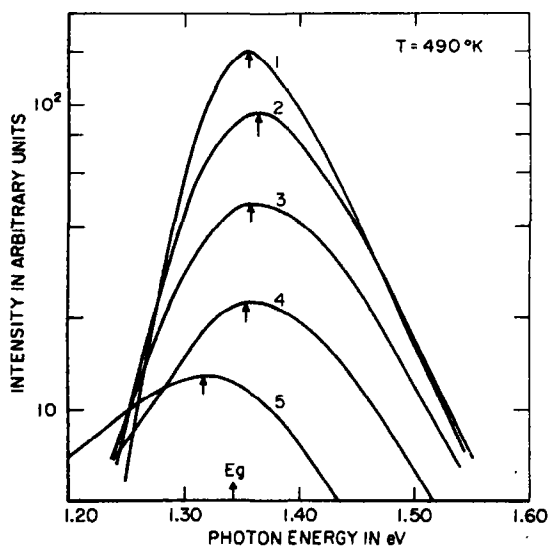


Fig. 3. Curves showing the dependence of the spectra of the high-energy band on doping level (1) 2.6×10^{18} , (2) 5.4×10^{18} , (3) 1.22×10^{19} , (4) 2.6×10^{19} , (5) 1.2×10^{20} Si atoms cm^{-3} at 490 K. The effect of the doping level on the energy of the peak of the emission is indicated by arrows.

the lack of band filling effects suggested that the exponential nature of the low energy sides of the spectra is due to the presence of an exponential density-of-states tail extending the conduction band edge into the forbidden gap. The density of states at energy E is given by $\rho_E = \rho_0 \exp E/E_0$. A dependence of the parameter E_0 , represented by the slope of the low energy side of the spectra, on impurity concentration, is clearly shown in Fig. 3 where, except for the first curve, the free carrier concentration remained constant.

A plot of E_0 as a function of the silicon concentration N_{Si} is shown in Fig. 4, where, except for a single point representing the lowest doping level, the dependence of E_0 on the silicon concentration N_{Si} can be well represented by the equation $E_0 \propto (N_{\text{Si}})^n$, where $n \approx 0.5$. The departure of the lowest point from this relationship can be explained in terms of the reduced screening to be expected from the reduced free electron concentration in this sample.

The value of n is less than the theoretically predicted value of Halperin and Lax[9]. It is interesting to note that the dependence of E_0 on the impurity concentration in uncompensated p -type material derived from cathodoluminescent spectra[4] where the free carrier concentration p was equal to the impurity concentration N , gave values of n between 0.3 and 0.37. The larger value of 0.5 obtained in this work was to be expected because of the reduced screening due to the amphoteric nature of the dopant used.

The small difference in n observed in the compensated n -type material and the uncompensated p -type material suggests that the free carrier screening effect on band tailing is relatively small.

As shown in Fig. 3, with the exception of sample 1, as the tails penetrate deeper into the band, i.e., as E_0 increases, the peak of the high energy band shifts toward lower energies with increasing impurity concentrations. This shift is particularly drastic in the most heavily doped sample, and, as shown in Fig. 1, the

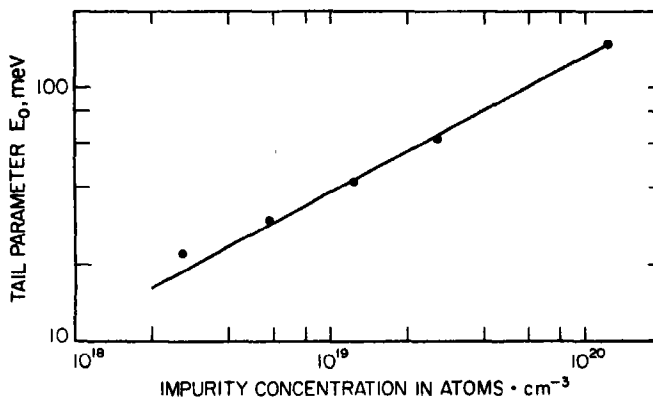


Fig. 4. Conduction band tail parameter E_0 as a function of impurity content N_{Si} .

low energy peak of this sample is also shifted by the same amount. This suggests that at high doping levels the high energy state of the $V_{Ga}Si_{Ga}$ complex can become 'linked' with the conduction band edge through the tail states provided the latter penetrate deeply into the forbidden gap.

4. CONCLUSIONS

The observation of photoluminescent spectra of *n*-type Si-doped GaAs at high temperatures allows an accurate measurement of the band tailing parameter E_0 without interference due to an overlap of the low energy, 1-2 eV band.

The exponential dependence of the intensity of the low-energy side of the high-energy band on $h\nu$ can be explained by an exponential density-of-states tail extending the conduction band edge into the forbidden gap.

The lack of band filling effects suggests that if valence band tailing is present, it does not have any appreciable effect on the shape of the spectra, while the development of a large tail at the conduction band edge causes the emission attributed to the $V_{Ga}Si_{Ga}$ complex and that due to band-to-band transitions to shift toward lower energies.

Acknowledgements—The authors would like to thank the Romanian Academy, the U. S. National Academy of

Sciences, and the National Bureau of Standards for the opportunity of carrying out this work, and one of us (I. P. P.) would like to thank the National Science Foundation for a grant permitting an extension to complete it.

REFERENCES

1. NELSON D. F., GERSHENSON M., ASHKIN A., D'ASARO L. A. and SARACE J. C., *Appl. Phys. Lett.* **2**, 182 (1963).
2. PANKOVE J. I., *Phys. Rev.* **140**, A2059 (1965).
3. LUCOVSKY G., VARGA A. J. and SCHWARZ R. F., *Solid State Commun.* **3**, 9 (1965).
4. PANKOVE J. I., *J. phys. Soc. Japan* **21** Suppl., 298 (1966).
5. TUCK B., *J. Phys. Chem. Solids* **29**, 615 (1968).
6. STERN F., *Phys. Rev.* **148**, 186 (1966).
7. WINOGRADOFF N. N. and KESSLER H. K., *Solid State Commun.* **5**, 155 (1967).
8. KANE E. O., *Phys. Rev.* **131**, 79 (1963).
9. HALPERIN B. I. and LAX M., *Phys. Rev.* **148**, 722 (1966).
10. WHELAN J. M., STRUTHERS J. D. and DITZENBERGER J. A., in *Properties of Elemental and Compound Semiconductors* (Edited by H. C. Gatos), pp. 141-154. Interscience Publishers, New York (1960).
11. WHELAN J. M., STRUTHERS J. D. and DITZENBERGER J. A., *Proceedings of the International Conference on Semiconductor Physics, Prague, 1960*, p. 943, Publishing House of the Czechoslovak Academy of Sciences, Prague (1961).
12. OSINSKY V. and WINOGRADOFF N. N., to be published.
13. HWANG C. J., *J. appl. Phys.* **40**, 4591 (1969).
14. WILLIAMS E. W., *Phys. Rev.* **168**, 922 (1968).
15. WAN DER BYE J. A. W., *J. Phys. Chem. Solids* **28**, 1485 (1967).

MEASUREMENTS AT 4.2 K OF GALVANOMAGNETIC EFFECTS IN BISMUTH IN WEAK MAGNETIC FIELDS*

P. E. GREGER-HANSEN

Physics Laboratory I, H. C. Ørsted Institute, University of Copenhagen, Denmark

(Received 10 March 1970; in revised form 24 August 1970)

Abstract—Galvanomagnetic phenomena in bismuth single crystals have been experimentally investigated at 4.2 K in magnetic fields from 0 to 10 G and compared with calculations based on the linearized Boltzmann equation in the relaxation time tensor approximation. The saturation values of the longitudinal magnetoresistance in two symmetry directions have been derived from our low magnetic field data. The anisotropy of the electron relaxation time tensor has been derived from one of these saturation values.

1. INTRODUCTION

SEVERAL experimental investigations of the galvanomagnetic properties of Bi have recently been made[1-3]. It has been found that the low field galvanomagnetic effects can be explained by a model in which the Fermi surface consists of small ellipsoidal pockets [4] and where the collision mechanism is described by a constant relaxation time tensor[5]. It has also been shown that the relaxation time is extreme in the high mass directions [1, 2].

In this paper we extend the existing theory to show that the saturation value of the longitudinal magnetoresistance can be derived from low and intermediate magnetic field experiments. The anisotropy of the electron relaxation time can now be determined straightforwardly from the longitudinal magnetoresistance in the trigonal direction. Our experiments at 4.2 K show that the ratio of the electronic relaxation times in the trigonal (binary) and the bisectrix directions is 1:5. We further show how the mobilities determined from our low field data agree with our experiments performed at intermediate fields when the Boltzmann equation is directly applied.

2. THEORY

A Taylor expansion to second order in the magnetic field H_k * of the conductivity tensor components may be written:

$$\sigma_{ij}(H_1, H_2, H_3) = \sigma_{ij}^0 + P_{ijk}H_k + B_{ijkl}H_kH_l \quad (1)$$

The tensor components σ_{ij} are defined by $I_i = \sigma_{ij}E_j$, where I_i is the electrical current density in the direction given by index i and E_j is the electrical field in the direction given by index j . The expansion coefficients of 0-th, 1-st and 2-nd order are named σ_{ij}^0 , P_{ijk} and B_{ijkl} , respectively. The number of these phenomenologically independent coefficients depends on the crystal structure and in bismuth there are respectively 2, 2 and 8[6]. These coefficients may be related to the Fermi surface parameters by a solution of the linearized Boltzmann equation.

Bismuth, a semimetal, has a Fermi surface which is thought to consist of one hole ellipsoid with rotational symmetry about the trigonal axis and three electron ellipsoids tilted out of the trigonal plane[4]. For one

*This work is part of a thesis required for the Licentiate Degree at the Technical University of Denmark.

*Tensor notation with summation over repeated indices is used. The indices refers to a Cartesian coordinate system with axes along the binary (1), bisectrix (2) and trigonal (3) symmetry directions of the crystal structure.

charge carrier ellipsoid the relation between the current density I_i and the electrical field E_j may be written

$$I_i = n|q|\mu_{ij}\left(E_j + \frac{1}{nq}\epsilon_{jkl}I_kH_l\right) \quad (2)$$

where n is the charge carrier density, q the charge per carrier, μ_{ij} the mobility tensor, and ϵ_{jkl} is the tensor symbolizing the vector

$$V_1 = \frac{1}{2}ne \frac{\mu_3(\mu_1 - \mu_2)^2b^2 + \mu_2(\mu_1 - \mu_3)^2a^2 + 3\mu_1(\mu_2 - \mu_3)^2a^2b^2}{\mu_2\mu_3 + 3\mu_1\mu_3b^2 + 3\mu_1\mu_2a^2} \quad (5)$$

product. This equation is an exact solution of the Boltzmann equation assuming the validity of Ohm's law, isothermal conditions and degenerate Fermi statistics. This implies a constant relaxation time tensor which we assume is diagonalizable in the same frame of reference as the effective mass tensor of the Fermi surface ellipsoid under consideration [5]. The expansion coefficients of the conductivity tensor components to second order determined by application of (2), and the conversion formulae from conductivity to resistivity coefficients have recently been reviewed by Hartman[1].

The longitudinal magnetoresistance in the binary and trigonal directions can be written in a particularly simple form. For any magnetic field strength where (2) is applicable* we find the following expression to be valid

$$\frac{H_i^2}{\sigma_{ii}(0) - \sigma_{ii}(H_i)} = \frac{1}{B_{iii}} + \frac{H_i^2}{V_i} \quad (3)$$

B_{iii} is defined in (1) and V_i is a constant which measures the maximum change in conductivity $\sigma_{ii}(0) - \sigma_{ii}(H_i)$ when a high longitudinal magnetic field H_i is applied (saturation). This expression has been derived for index $i = 3$ (trigonal direction) by Pospelov and Kechin [7] and we have shown analogously that it

*Equation (2) is an exact solution of the linearized (in electric field) Boltzmann equation under the assumption stated above. It is therefore valid for any magnetic field where quantum effects are not important (for a derivation of equation (2) see Ref. [7]).

is also valid for index $i = 1$ (binary direction). In both cases the conductivity tensor component is simply the inverse of the corresponding resistivity component. The expressions for V_1 and V_3 in terms of the charge carrier parameters are

$$V_3 = ne \frac{a^2b^2(\mu_3 - \mu_2)^2}{\mu_3a^2 + \mu_2b^2} \quad (4)$$

In the formulae above we have used the following notation for the charge carrier parameters: μ_1 , μ_2 and μ_3 are the electron mobilities referring to the ellipsoidal coordinate system, ν_1 and ν_3 are the hole mobilities, $a = \sin \theta$ and $b = \cos \theta$ where θ is the tilt-angle of the electron ellipsoids as defined in the paper of Hartman[1], n is the electron or hole density (assumed to be equal) and $-e$ is the electronic charge.

3. EXPERIMENTAL

Measurements have been performed on two bismuth single crystals. The geometry of the crystals is shown in the insert in Fig. 2. The dimensions, indicated by small letters, along with the resistances are tabulated in Table 1. The length direction c of the crystals

Table 1. Properties of the bismuth single crystals used in this investigation. The symbols are defined in the text in the insert in Fig. 2

	Sample A (trigonal)	Sample B (binary)
Dimensions	a (mm)	3.7
	b (mm)	5.3
	c (mm)	22
	d (mm)	4
	$2r$ (mm)	0.5
Specific resistance ρ_{300} (Ωm)	$1.76 \cdot 10^{-8}$	$1.29 \cdot 10^{-8}$
Residual resistance ratio: $\rho_{300}/\rho_{4.2}$	340	362

was in the trigonal direction for sample *A* and in the binary direction for sample *B*. Dimension *b* was in the bisectrix direction for both crystals. The samples were cut by a spark-cutting machine to the form shown in Fig. 2 and were given a slight etch before use. Potential and current leads were soldered to the samples with non-superconducting solder.

From measurements with these two geometries the resistivity components ρ_{33} , ρ_{23} , ρ_{11} and ρ_{21} can be determined. These four resistivities are all defined by $V_i = \rho_{ij}I_j$ and may be expanded phenomenologically to second order in the magnetic field in the same way as the conductivity tensor components in equation (1):

$$\rho_{ij}(H_1, H_2, H_3) = \rho_{ij}^0 + R_{ijk}H_k + A_{ijkl}H_kH_l. \quad (6)$$

The expansion coefficients ρ_{ij}^0 , R_{ijk} and A_{ijkl} are related to σ_{ij}^0 , P_{ijk} and B_{ijkl} in equation (1)[6]. By varying the strength and the direction of the magnetic field, all twelve phenomenologically independent resistivity expansion coefficients can be determined experimentally.

The experiments were performed at 4.2 K where thermal smearing of the Fermi surface as well as excitation of charge carriers from lower lying bands can be neglected. Such low temperatures also seems to be necessary to observe anisotropy in the relaxation time tensor[1, 2]. At 4.2 K the low-field condition turns out to require that the magnetic field must be below about one gauss. The self magnetic field of the sample current should be even less, limiting this current to about 20 mA. Under these conditions the voltages to be detected are rather small. In the resistance range of the samples ($\approx 10^{-5} \Omega$) the superconducting chopper method[8] is suitable. By this method we obtained a voltage-sensitivity of $5 \cdot 10^{-12}$ V with a time constant of 5 sec. This was sufficient for our purposes. Measurements were performed in the magnetic field range between 0 and 10 G. The earth's magnetic field was compensated.

4. RESULTS AND DISCUSSION

All 12 resistivity coefficients up to second order were found by varying the directions of the magnetic field. These coefficients are tabulated in Table 2 together with the results of two similar investigations[1, 3]. The earlier results are here scaled (all mobilities are changed by a constant factor) to simplify comparison with our own results. Our indicated uncertainties derive from errors involved in the determination of the crystal dimensions and the orientation of the potential leads. From these coefficients we have determined a set of charge carrier parameters involving the mobilities μ_i and ν_i , the charge density *n* (assumed equal for holes and electrons) and the tiltangle θ , all in the vicinity of optimum selfconsistency. The calculated coefficients corresponding to this set are given. The values for μ_2 and ν_3 are rather uncertain due to their smallness compared to the other mobilities. Identical calculations have been performed in the previous investigations and the results are given in Table 2. Several of our coefficients differ somewhat from those of earlier investigations, although, by a suitable choice of parameters we obtain self-consistent agreement with our own results. The reason for this discrepancy is not clear. Our crystals have a purity of 6N and a resistance ratio between those of Hartman[1] and Zitter[3]. Our single crystals are, however, considerably smaller than theirs and an explanation of the deviations in terms of size effects cannot be ruled out. The dimensions of our crystals are certainly much greater than the mean free path of the charge carriers which was about 0.3 mm. The size effect in bismuth is, however, anomalous[2]. Using the effective masses for the charge carriers in bismuth, which are well known from several Fermi surface investigations[4], we find from the mobilities μ_1 , μ_3 , and ν_1 (Table 2) that the relaxation times for these charge carriers are respectively 0.3, 0.3 and 0.4 nsec.

Using our parameters in Table 2 we have made calculations based on equation (2) at

Table 2. Measured and calculated galvanomagnetic power expansion coefficients to second order at 4.2 K in MKS units. The results of two previous investigations are also tabulated; these results are scaled to facilitate comparison. The scaling factors for the mobilities are 0.612 (Hartman[1]) and 1.54 (Zitter[3]). The set of charge carrier parameters is a best fit to the data. V_1 and V_3 represent the saturation decrease of the longitudinal magneto-conductivities (see equation (3))

	exp	calc	Hartman[4]* exp	calc	Zitter[8]* exp	calc
$\mu_1 \left(10^3 \frac{m^2}{Wb} \right)$		8.5		6.8		6.6
μ_2 —		0.4		0.14		0.09
μ_3 —		4.8		4.2		4.6
θ (degrees)		8		6.25		6.5
$\nu_1 \left(10^3 \frac{m^2}{Wb} \right)$		1.1		1.35		1.85
ν_3 —		0.2		0.21		0.15
$n \left(10^{23} \frac{1}{m^3} \right)$		2.4		2.7		2.5
$\rho_{11} (10^{-9} \Omega m)$	$4.7 \pm 10\%$	4.7	$4.75 \pm 5\%$	4.76	$4.8 \pm 5\%$	4.8
ρ_{33} —	$5.3 \pm 10\%$	5.3	$5.25 \pm 5\%$	5.33	$5.2 \pm 5\%$	5.3
$R_{123} \left(10^{-5} \frac{\Omega m^3}{Wb} \right)$	$0.2 \pm 100\%$	0.2	-0.07	-0.06	$-0.25 \pm 8\%$	-0.26
R_{231} —	$1.9 \pm 10\%$	2.0	$1.54 \pm 5\%$	1.53	$1.53 \pm 5\%$	1.52
$A_{111} \left(10^{-2} \frac{\Omega m^3}{Wb^2} \right)$	$2.9 \pm 10\%$	3.2	$2.14 \pm 8\%$	2.27	$2.3 \pm 10\%$	2.5
A_{333} —	$0.29 \pm 10\%$	0.34	$0.20 \pm 10\%$	0.16	$0.25 \pm 10\%$	0.22
A_{223} —	$1.0 \pm 20\%$	0.9	$0.57 \pm 20\%$	0.48	$0.45 \pm 15\%$	0.52
A_{232} —	$0.36 \pm 30\%$	0.55	$0.28 \pm 15\%$	0.32	$0.31 \pm 15\%$	0.40
A_{112} —	$4.4 \pm 10\%$	3.7	$2.94 \pm 5\%$	2.69	$3.1 \pm 10\%$	2.8
A_{113} —	$1.8 \pm 10\%$	1.5	$0.74 \pm 10\%$	0.67	$0.69 \pm 10\%$	0.65
A_{331} —	$2.6 \pm 10\%$	2.4	$2.33 \pm 8\%$	2.26	$2.9 \pm 10\%$	2.9
A_{233} —	$0.35 \pm 30\%$	0.42	$0.36 \pm 15\%$	0.39	$0.51 \pm 20\%$	0.56
$V_{33} \left(10^8 \frac{1}{\Omega m} \right)$	$0.44 \pm 10\%$	0.29		0.43		1.23
V_{11} —	$0.48 \pm 10\%$	0.50		0.49		0.46

* scaled values

the intermediate magnetic fields and compared them with experiment. We find no further discrepancies than those already evident from Table 2. This strongly supports the self-consistency of the determination of the charge carrier parameters. As an example of this Fig. 1 shows a rotational diagram of the resistivity tensor component ρ_{23} . The magnetic field (3 different magnitudes) is rotated in the trigonal plane. Fig. 1a shows the experimentally determined rotational diagrams and Fig. 1b shows the corresponding diagrams

calculated by a computer on the basis of equation (2) and our solution for the parameter from Table 2.

The expression (3) for the longitudinal magnetoresistance is plotted against field squared in Fig. 2 for the trigonal direction and in Fig. 3 for the binary direction. In both cases we get a straight line as expected from equation (3). This supports the Fermi surface model assumed as well as the assumptions on which equation (2) is based. From these plots, V_1 and V_3 have been determined. It is interest-

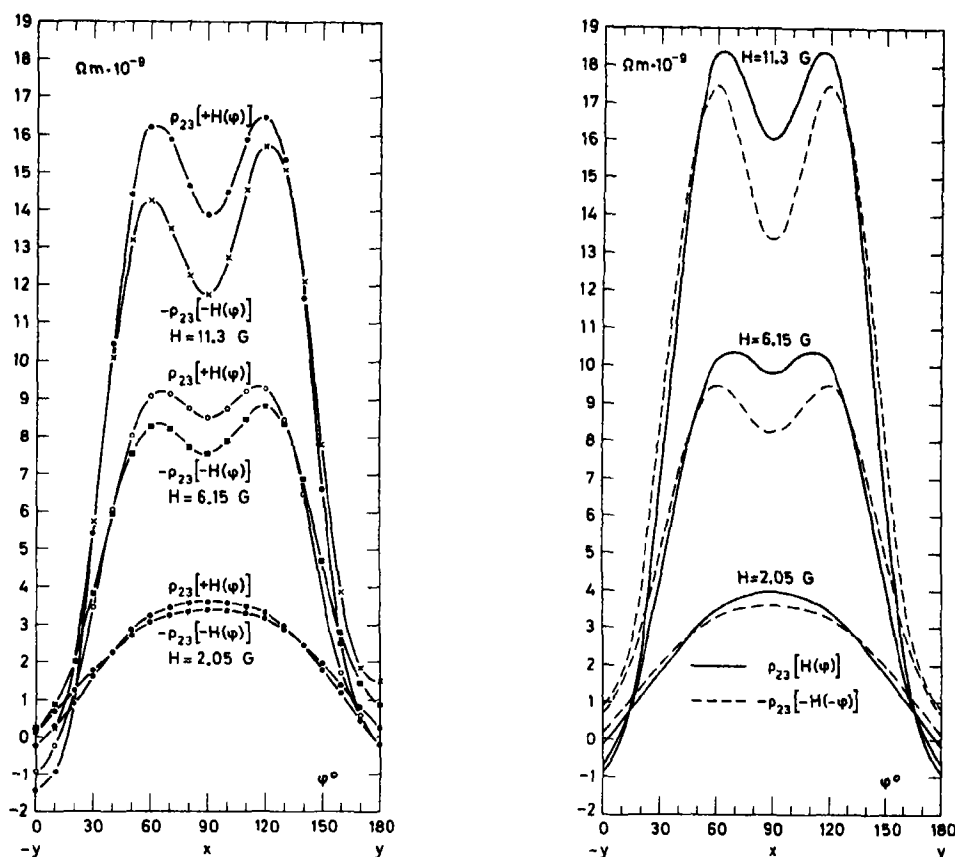


Fig. 1. Angular dependence of the resistivity component $\rho_{23}(H, \varphi)$. φ is the angle in the trigonal plane between the direction of the magnetic field H and the negative bisectrix direction. (a) Experimental results at 4.2 K and in 3 different magnetic fields $H = 2.05, 6.15$ and 11.3 G. (b) Calculated results for the same magnetic fields as those used experimentally. Our solution for the charge carrier parameters from Table 2 has been used.

ing that these plots from low magnetic field measurements give the saturation value of the longitudinal magnetoresistance, otherwise difficult to obtain[2]. V_1 and V_3 may be calculated from equations (4) and (5) by inserting the parameters of Table 2. Comparing these with the experimental values (Table 2) shows agreement for V_1 but some deviation for V_3 . V_3 is sensitive to the value of the electron mobility in the bisectrix direction. This is evident when the ratio

$$\frac{B_{3333}}{V_3} = \mu_1(\mu_2 b^2 + \mu_3 a^2) \quad (6)$$

is considered. μ_1 , μ_2 , and μ_3 are the mobilities

in the principal directions of the electron ellipsoids and a and b are the sine and cosine of the tiltangle θ of the electron ellipsoids. Inserting in equation (6) the values of B_{3333} and V_3 and of all parameters except μ_2 we obtain $\mu_2 = 0,18(m^2/Wb)$. Using the known value of the electron effective mass in the bisectrix direction[4] a relaxation time of 1.5 nsec is obtained. This is 5 times more than in the binary and trigonal directions. Such an anisotropy in the electron relaxation time tensor has been suggested by Friedman [2] from measurements of R_{123} , and observed by Hartman[1] by a complete analysis of the lowfield galvanomagnetic coefficients to

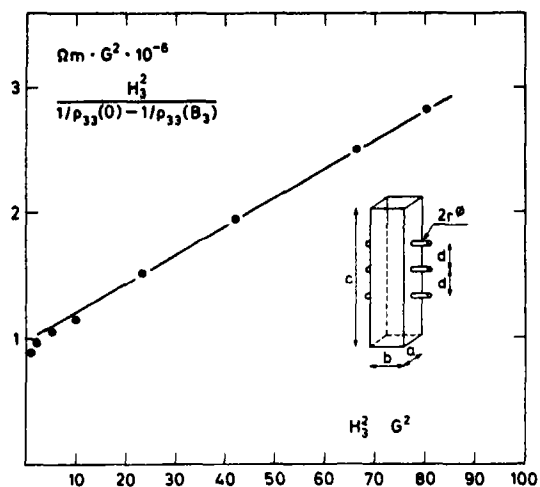


Fig. 2. The experimentally determined longitudinal magnetoresistance in the trigonal direction. The left hand side expression of equation (3) is plotted against magnetic field squared. From this plot (MKS units): $B_{3333} = 1.0 \cdot 10^{14} (m^3/\Omega W b^2)$ and $V_s = 0.44 \cdot 10^8 (1/\Omega m)$. The insert shows the sample geometry (see Table 1).

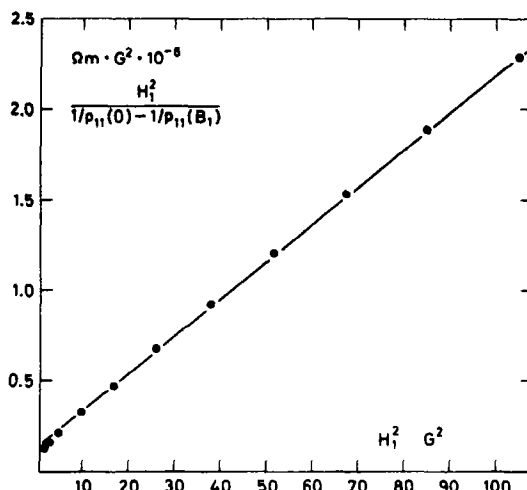


Fig. 3. The experimentally determined longitudinal magnetoresistance in the binary direction. The left hand side expression of equation (3) is plotted against magnetic field squared. From this plot (MKS units): $B_{1111} = 1.3 \cdot 10^{15} (m^3/\Omega W b^2)$ and $V_1 = 0.48 \cdot 10^8 (1/\Omega m)$.

second order. The method used here for determining the anisotropy of the electron relaxation time in bismuth is, however, very simple, requiring only measurements of the longitudinal magnetoresistance in the trigonal direction.

An explanation of the anisotropy of the electron relaxation time in bismuth still lacks an explanation* and the present method may be used as a quick way of getting the relaxation time anisotropy under various conditions. Also, our determination of the saturation of the longitudinal magnetoresistance may be

used as a starting point for resolving the anomalous behaviour of the longitudinal magnetoresistance observed[2] in high fields.

Acknowledgement—The continuous interest of Professor H. Højgaard Jensen is gratefully acknowledged. Discussions with colleagues at the laboratory have been much appreciated.

REFERENCES

1. HARTMAN R., *Phys. Rev.* **181**, 1070 (1969).
2. FRIEDMAN A. N., *Phys. Rev.* **159**, 553 (1967).
3. ZITTER R. N., *Phys. Rev.* **127**, 1471 (1962).
4. FAL'KOVSKIJ L. A., *Soviet Phys.-Usp.* **94**, 1 (1968).
5. HERRING C. and VOGT E., *Phys. Rev.* **101**, 944 (1956).
6. JURETSCHKE H. J., *Acta crystallogr* **8**, 716 (1955).
7. POSPELOV Y. A. and KECHIN V. V., *Soviet Phys.-solid State* **6**, 2565 (1965).
8. DE VROOMEN A. R. and VAN BAARLE C., *Physica* **23**, 705 (1957).

*The arguments to explain the anisotropy given in Ref. [2] require that electron-phonon scattering is dominant. The T^{-2} dependence of the mobilities found in Ref. [1], however, strongly supports a carrier-carrier scattering mechanism.

RAMAN SCATTERING BY POLARIZATION WAVES IN UNIAXIAL CRYSTALS*

C. Y. SHE, JON D. MASSO and D. F. EDWARDS

Physics Department, Colorado State University, Fort Collins, Colo. 80521, U.S.A.

(Received 6 March 1970; in revised form 28 July 1970)

Abstract—The essential properties of polarization waves in uniaxial crystals are briefly reviewed. A simple model for the electronic system is used to treat Raman scattering of coherent light by these polarization waves. The structure and frequency dependence of deformation scattering and polar scattering are discussed. Measurements with improved precision of the width, intensity, and position of all the Raman-active lines in α -quartz are reported. The theoretical discussion is applied to study the data presented. The Raman tensor elements and the effect of the long range electric-dipole forces in α -quartz are evaluated.

1. INTRODUCTION

RAMAN scattering by i.r.-active lattice vibrations (phonons) in solids was regarded as anomalous until the theoretical work published by Poulet[1]. He attributed the anomalies to the long-range electric-dipole forces associated with the i.r.-active vibrations. Since then, Loudon[2] has treated the right-angle Raman scattering in polar uniaxial crystals and has generalized the theory to include the effect of the short-range anisotropy forces. The transverse, i.r.-active normal-mode vibrations interact with the electromagnetic wave (photon) giving rise to new coupled modes called polarization waves (polaritons) which can propagate in solids. In a recent conference, several authors[3] have contributed to the study of Raman scattering by these polarization waves both theoretically and experimentally; they emphasize the small-angle scattering which determines the polariton spectrum[4] and the possibility of a tunable light source[5].

The objective of this paper is to explain in a simple, but general way, the details of Raman scattering in a transparent piezoelectric crystal. A simple two-level electronic

system with provisions for crystal symmetry is introduced and is applied to Raman scattering by polarization waves. This approach gives a clear insight as to the detailed electronic interactions and its coupling with the lattice. To our knowledge this use of an electronic model such as is done here is new. The previous work in this area has been concerned only with symmetry properties[2]. None of the work that we recall has suggested a simple model for the electronic system. Some of the authors have introduced complicated diagrams, etc., that assist in visualizing the scattering but these diagrams seem to have only a limited usefulness to the mass doing the experiment in the laboratory. Using the usual equations of motion for polarization waves, the first-order Raman intensity due to deformation and polar scattering is calculated in terms of this electronic system. Guided by Physical considerations, the theoretical discussion is applied to the data of the precise measurements[6] of the intensity, width and position of all Raman-active lines in α -quartz. The relative magnitudes of the Raman tensor elements and the effect of the long-range electric-dipole forces are determined. The electro-optic contribution to the scattering and the polarization of the normal-mode vibration ξ , which in general is neither perpendicular nor

*This work was supported in part by a contract with the Air Force Cambridge Research Laboratories, Office of Aerospace Research, USAF.

parallel to the direction of polariton propagation \vec{k} , are discussed.

2. THE INTERACTION SYSTEM

In Raman scattering from i.r.-active lattice (normal-mode) vibrations in transparent uniaxial crystals, the incident and scattered light interact with the bound electrons. In a dynamic lattice, the ionic motion, which is determined by the short-range mechanical forces and the long-range electric-dipole forces, modifies the effective potential of the bound electrons and as a result the scattered light contains the characteristic frequencies of the ionic motions (in this case, polarization waves). A schematic showing the interconnection of these constituents is given in Fig. 1. We model the bound electrons by a quantum mechanical two-level system[7] which couples to the ionic system through the electron-vibration interactions and which scatters light by the electron-radiation interactions represented by the interaction Hamiltonians H_{e-r} and H_{e-v} , respectively. The energy of the electrons in a static lattice with light absent is repre-

sented by the unperturbed Hamiltonian H_0 . The total Hamiltonian H of the electronic system is:

$$H = H_0 + H_I; \quad H_I = H_{e-r} + H_{e-v}. \quad (1)$$

The unperturbed Hamiltonian, H_0 , is a function of the electron coordinates only and it has the local symmetry of the static lattice; the unperturbed eigenstates of the electronic system and the normal-mode vibrations are classified by the irreducible representations of the crystal point group[8]. Assuming the usual dipole approximation[7], the interaction Hamiltonians are as follows:

$$H_{e-r} = -\bar{p} \cdot [\bar{\mathcal{E}}^i e^{-i\omega_i t} + \bar{\mathcal{E}}^s e^{-i\omega_s t}] + \text{c.c} \quad (2a)$$

$$H_{e-v} = -[\sum_j \bar{f}^j \cdot \bar{\xi}^j(\omega) + \bar{\mathcal{P}} \cdot \bar{\mathcal{E}}] e^{-i\omega t} + \text{c.c} \quad (2b)$$

where \bar{p} is the electronic-dipole operator which interacts with the incident and scattered local optical electric fields, $\bar{\mathcal{E}}^i$ and $\bar{\mathcal{E}}^s$, respectively. ξ^j is the j th normal-mode amplitude of vibration which is frequency dependent and $\bar{\mathcal{E}}$ is the local electric field associated with the polarization wave of frequency ω . \bar{f}^j and $\bar{\mathcal{P}}$ are the generalized force and dipole operators associated with the polarization wave; physically, they are changes (gradients) of the electronic potential energy due to the j th lattice vibration and the electric field, respectively. It should be pointed out that the wavelength of the optical and polarization waves are much longer than the dimensions of the bound electrons. The field amplitudes $\bar{\mathcal{E}}^i$, $\bar{\mathcal{E}}^s$ and $\bar{\xi}^j$ depend on the location of the bound (atomic) electrons, and the expectation values of the operators \bar{p} , \bar{f}^j , $\bar{\mathcal{P}}$ are considered as per unit volume values. For simplicity the incident, scattered and polarization waves are each assumed to have a single frequency. Experimentally, this is indeed the case because different polarization and scattered waves may be separated by using different experimental arrangements.

In the same spirit as Placzek's approxima-

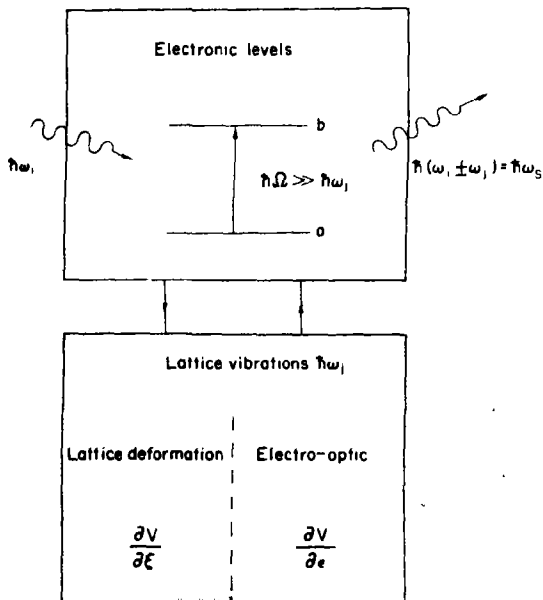


Fig. 1. Schematic for the interaction system for Raman scattering.

tion, we assume in the energy representation of H_0 that only the off-diagonal matrix elements of \bar{p} and the diagonal matrix elements of \bar{f}^j and $\bar{\mathcal{P}}$ are non-zero. This means that the electronic and ionic motion, although coupled, are well-separated in frequency and the radiation fields couple different electronic states while the polarization fields have only a slight perturbation on the individual electronic levels. We include both $\bar{\xi}^j$ and $\bar{\mathcal{E}}$ in the interaction Hamiltonian because they may be considered as independent driving forces. In this formulation, the anisotropy of the problem is accounted for in two ways. The macroscopic value corresponding to any of the local field $\bar{\mathcal{E}}^i$, $\bar{\mathcal{E}}^*$ and $\bar{\mathcal{E}}$ may be different depending on their polarization relative to the crystal optic axis. The parallel and perpendicular components of the matrix elements of the electronic operators assume different values because the unperturbed Hamiltonian H_0 and the eigenstates contain the anisotropy of the crystal.

The expectation values of \bar{p} and \bar{f}^j which are responsible for light scattering and for excitation of the lattice vibration, respectively, can be obtained from the density matrix formulation by perturbation theory, i.e., solving the following hierarchy of equations:

$$i\hbar\dot{\rho}^{(0)} = [H_0, \rho^{(0)}]$$

and

$$i\hbar\dot{\rho}^{(k)} = [H_0, \rho^{(k)}] + [H_I, \rho^{(k-1)}], \quad (3)$$

where the superscripts indicate the order of perturbation calculation. We assume that the linewidths involved are narrow and negligible. Ω in Fig. 1 is the frequency separation of levels a and b and for transparent solids is large compared with all other frequencies.

The Fourier components of the density operator may be obtained by perturbation theory. Calculated to second order, the expectation values of the generalized force \bar{f}^j and the dipole operators $\bar{\mathcal{P}}$, \bar{p} , with initial conditions $\rho_{aa}^{(0)} = 1$, and $\rho_{ab}^{(0)} = \rho_{ba}^{(0)} = \rho_{bb}^{(0)} = 0$, are the following:

$$\begin{aligned} \langle f_i^j(\omega) \rangle^{(2)} &= Tr\{f_i^j \rho^{(2)}(\omega_i - \omega_s)\} \\ &= \frac{2({}^b f_i^j - {}^a f_i^j) p_m p_n (\Omega^2 + \omega_i \omega_s)}{\hbar^2 (\Omega^2 - \omega_i^2) (\Omega^2 - \omega_s^2)} \\ &\quad \times \mathcal{E}_m^i \mathcal{E}_n^{*j} \equiv \gamma_{lmn}^j \mathcal{E}_m^i \mathcal{E}_n^{*j} \end{aligned} \quad (4a)$$

$$\begin{aligned} \langle \mathcal{P}_i(\omega) \rangle^{(2)} &= Tr\{\mathcal{P}_i \rho^{(2)}(\omega_i - \omega_s)\} \\ &= \frac{2({}^b \mathcal{P}_i - {}^a \mathcal{P}_i) p_m p_n (\Omega^2 + \omega_i \omega_s)}{\hbar^2 (\Omega^2 - \omega_i^2) (\Omega^2 - \omega_s^2)} \\ &\quad \times \mathcal{E}_m^i \mathcal{E}_n^{*j} \equiv \delta_{lmn} \mathcal{E}_m^i \mathcal{E}_n^{*j} \end{aligned} \quad (4b)$$

$$\begin{aligned} \langle p_i(\omega) \rangle^{(2)} &= Tr\{p_i \rho^{(2)}(\omega_i - \omega)\} \\ &= [\sum_j \alpha_{lmn}^j \xi_n^{j*} + \beta_{lmn} \mathcal{E}_n^{*j}] \mathcal{E}_m^i \\ &= \frac{2p_i p_m [\Omega^2 + \omega_i (\omega_i - \omega)]}{\hbar^2 (\Omega^2 - \omega_i^2) [\Omega^2 - (\omega_i - \omega)^2]} \\ &\quad \times [\sum_j ({}^b f_n^j - {}^a f_n^j) \xi_n^{j*} \\ &\quad + ({}^b \mathcal{P}_n - {}^a \mathcal{P}_n) \mathcal{E}_n^{*j}] \mathcal{E}_m^i \end{aligned} \quad (4c)$$

where the subscripts denote the components of a vector or a tensor, and the repeated Roman sub-indices imply summation. The matrix elements are $\bar{p} = \langle a | \bar{p} | b \rangle$, ${}^a \mathcal{P} = \langle a | \mathcal{P} | a \rangle$, ${}^b \mathcal{P} = \langle b | \mathcal{P} | b \rangle$, ${}^a f^j = \langle a | f^j | a \rangle$ and ${}^b f^j = \langle b | f^j | b \rangle$. The summation sign in equation (4c) sums over the normal-mode vibrations. γ_{lmn} and δ_{lmn} are, respectively, the 'force constant' and the non-linear polarizability associated with the non-linear mixing of $\bar{\mathcal{E}}^i$ and $\bar{\mathcal{E}}^*$ through electronic charge re-distribution; they give rise to source terms for the excitation of polarization waves. Equation (4c) is the second-order electronic dipole moment due to mixing of the incident light wave at ω_i with the ionic motion at ω ; α_{lmn} and β_{lmn} are Raman polarizabilities leading to deformation and polar scattering, respectively. β_{lmn} gives the electro-optic contribution to the Raman scattering.

At this point, it is interesting to note the effect of symmetry on the problem. Consider first a crystal with inversion symmetry. Since parity is a good quantum number, states $|a\rangle$ and $|b\rangle$ are either even or odd, and since the operator \bar{f}^j transforms in the same way as the normal-mode displacement [8, 9] $\bar{\xi}^j$, the matrix

elements ${}^a\bar{f} = {}^b\bar{f} = 0$ for odd vibrational modes. The operator $\bar{\mathcal{P}}$ in equation (4) which transforms [8, 9] like $\bar{\mathcal{E}}$, has odd parity so that the matrix elements ${}^a\bar{\mathcal{P}} = {}^b\bar{\mathcal{P}} = 0$. Thus, for crystals with inversion symmetry, only even lattice vibrations are Raman active and there is no electro-optic contribution to the Raman scattering. For a uniaxial crystal without inversion symmetry, the electronic eigenstates transform according to the irreducible representations of the crystal point group and the symmetry properties of the Raman polarization tensors may be investigated by group theoretical methods [8]. Loudon [2] has reviewed and tabulated the Raman tensors for the thirty-two crystal point groups using symmetry arguments without a particular model for the electronic system. Indeed, if one's primary interest is the symmetry properties of the Raman tensors there is no need for a model of the electronic system. However, when guided by physical insight, a simple model, such as proposed here, used in a flexible way can provide an understanding of the subject from basic principles and clearly give the essential structure of the physical process. It is seen from equation (4c) that the non-vanishing Raman polarizabilities due to deformation scattering the polar scattering, α_{lmn} and β_{lmn} , respectively, have a common factor which is a second-rank tensor depending on the corresponding electronic polarizations only. In general, $({}^b f_n^j - {}^a f_n^j)$ and $({}^b \mathcal{P}_n - {}^a \mathcal{P}_n)$ depend on the state of electronic polarization and their relative values may depend on the scattering polarization. Such is the case in α -quartz. Further, the relative values of $({}^b f_n^j - {}^a f_n^j)$ and $({}^b \mathcal{P}_n - {}^a \mathcal{P}_n)$ depend on the motion of the individual normal-mode j and as a result the electric field contribution may either add to or detract from the scattering intensity.

3. POLARIZATION WAVES AND THEIR EXCITATIONS

An i.r.-active molecular vibration may be started by either physically displacing the atoms relative to each other or by applying to

the molecule an electric field. The mechanical and electrical forces may be considered as independent with respect to one another and they both induce an electric-dipole moment associated with the molecular vibration. For a uniaxial crystal with N normal-modes, the equations of motion consist of $2N + 4$ variables and $2N + 2$ equations. The variables are the displacement for each mode, the electric field components and the ionic polarization components, both perpendicular and parallel to the optic axis of the crystals; the equations are $2N$ mechanical equations and two equations for ionic polarization. These equations, following the notations of previous workers [3, 10] may be written as:

$$P_{\parallel, \perp}(\omega) = \frac{\epsilon_{\parallel, \perp}^0 - 1}{4\pi} E_{\parallel, \perp} + \sum_j \sqrt{\frac{S_{\parallel, \perp}^j}{4\pi}} \omega_{j\parallel, \perp} \xi_{\parallel, \perp}^j \quad (5a)$$

$$[\omega_{j\parallel, \perp}^2 - i\omega \Gamma_{\parallel, \perp}^j - \omega^2] \xi_{\parallel, \perp}^j = \sqrt{\frac{S_{\parallel, \perp}^j}{4\pi}} \omega_{j\parallel, \perp} E_{\parallel, \perp} \quad (5b)$$

where $S_{\parallel, \perp}^j$, $\omega_{j\parallel, \perp}$ and $\Gamma_{\parallel, \perp}^j$ are the parallel and perpendicular components of the oscillator strength, lattice-vibration frequency, and phenomenological damping constant, respectively, for the j th normal-mode. The polarization \bar{P} and the electric field \bar{E} in equation (5) are macroscopic quantities and the restoring force due to the local field effect has been accounted for and included in the normal-mode frequency ω_j . $\bar{\mathcal{E}}$ in equation (4) is the local field corresponding to the macroscopic field \bar{E} . The form of the interaction Hamiltonian H_{e-v} in equation (2) reflects the fact that both ξ^j and $\bar{\mathcal{E}}$ are independent variables for a local molecular vibration.

When many unit cells in a solid are vibrating together, the polarization due to the ionic motion at one unit cell (molecule) radiates into another unit cell and induces ionic motion there. The polarization \bar{P} and the electric-field strength \bar{E} depend on the ionic motion of all unit cells (molecules) in the crystal and they are related by Maxwell's equation:

$$\vec{k} \times (\vec{k} \times \vec{E}) + \frac{\omega^2}{c^2} \vec{D} = 0;$$

$$D_{\parallel,\perp} \equiv E_{\parallel,\perp} + 4\pi P_{\parallel,\perp} \equiv \epsilon_{\parallel,\perp} E_{\parallel,\perp}. \quad (6)$$

Equations (5) and (6) together form a complete set of linear homogeneous equations whose secular determinant gives the dispersion relations for the polarization wave (polariton spectrum). \vec{k} is the wave vector for the polariton. Since the values of the oscillator strengths S^j and unperturbed normal-mode frequencies ω_j are essential for the determination of the polariton spectra, these values for different crystal species should be considered. Using experimental values for S^j and ω_j and ignoring the damping constants, the polariton spectrum for α -quartz was calculated[3] and was found to agree with the measured values[3, 4]. For Raman scattering studies, it is instructive to plot the polariton frequency against the angle θ of polariton propagation direction relative to the optic axis. This has been carried out for α -quartz[3] and is reproduced in Fig. 2. The group designation of normal-modes will be explained in Section 5. Our precise measurement of the line positions for all modes for $\theta = 0^\circ, 45^\circ$ and 90° to be presented below agrees with this theoretical plot.

It is evident from equation (5) that the polarization waves may be excited directly by an externally applied electric-field, typically in the i.r. frequency range. The i.r. absorption and reflection data, however, are inherently poor in line positions and can not be used to accurately determine the polariton spectrum. Raman scattering, although a weaker process, gives a reliable line position and can excite polarization waves which are both Raman and i.r. active. The non-linear mixing of incident and (spontaneously) scattered light produces a signal at the difference frequency $\omega = \omega_i - \omega_s$. This modulates the motion of the bound electrons and changes the effective potential under which nuclei in a molecule move. With our simple electronic model, the force associated with this excitation can be calculated and its cartesian components have been

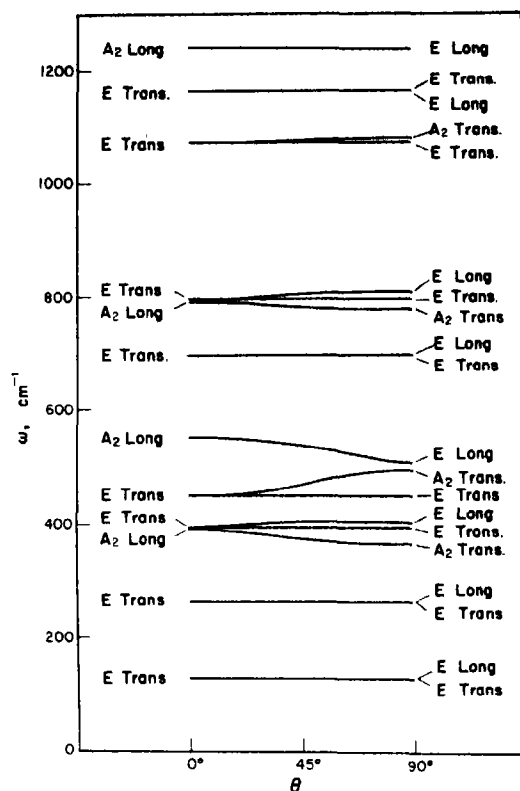


Fig. 2. Phonon frequencies in quartz in the region accessible to 90° first-order Raman scattering plotted against the angle of propagation relative to the c -axis [Following Loudon, Ref. [3]].

given in equation (4a). Strictly speaking, in determining the polariton spectrum by Raman scattering, terms $\langle f_{\parallel,\perp}^j(\omega) \rangle^{(2)}$ and $-(4\pi\omega^2/c^2)\langle \vec{\mathcal{P}}(\omega) \rangle^{(2)}$ should be added to the right hand sides of equations (5b) and (6), respectively, and the effect of the optical waves on polariton frequencies should also be considered. Since these terms are smaller by an order-of-magnitude, they are usually ignored in the determination of the polariton spectrum. Nevertheless, these terms are responsible for the observation of the polarization waves by first order Raman scattering. Further, the spatial dependence of both $\langle f^j(\omega) \rangle^{(2)}$ and $\langle \vec{\mathcal{P}}(\omega) \rangle^{(2)}$ which is determined by $\vec{\mathcal{E}}^i(r)\vec{\mathcal{E}}^{s*}(r)$, i.e. $\exp[i(\vec{k}_i - \vec{k}_s) \cdot \vec{r}]$, selects the polariton whose wave vector satisfies the phase-matching (mo-

momentum conservation) condition, $\bar{k} = \bar{k}_i - \bar{k}_s$, where for observation in an experiment.

4. RAMAN SCATTERING INTENSITIES

When the polarization $\langle \bar{p}(\omega_s) \rangle^{(2)}$ (dipole moment per unit volume) of the scattering wave at frequency $\omega_s = \omega_i - \omega$ is given, the scattered intensity radiated into the solid-angle $d\Omega$ subtended by the detector may be expressed as:

$$dI = \frac{\omega_s^4}{2\pi c^3} \sum_{\mu=1,2} \sum_{l,m=x,y,z} u_l^\mu u_m^\mu \langle p_l^*(\omega_s) \rangle^{(2)} \langle p_m(\omega_s) \rangle^{(2)} d\Omega \quad (7)$$

where \hat{u}^1 and \hat{u}^2 are two mutually perpendicular unit vectors, both perpendicular to the scattering direction and c is the velocity of propagation of the scattered wave. In an experiment, such as that reported below, all Raman lines are measured under identical conditions and the incident and scattered polarization directions are fixed to be ρ and σ , respectively. Under these conditions equation (7) may be simplified as:

$$\frac{dI_{\rho\sigma}}{d\Omega} = \eta(\omega_s) \omega_s^4 |\sum_j \alpha_{\rho\sigma j}^j \xi_j^{j*}(\omega) + \beta_{\rho\sigma\lambda} \mathcal{E}_l^*(\omega)|^2 |E_\rho(\omega_i)|^2, \quad (8)$$

where $dI_{\rho\sigma}/d\Omega$ may be regarded as a differential cross section for the (ρ, σ) scattering, and $\eta(\omega_s)$ is the 'detection efficiency' which includes the frequency-dependent local field correction and quantum efficiency of the photomultiplier. The repeated Greek sub-index ρ in equation (8) does not imply summation. For polarization waves, the normal-mode amplitudes ξ^j and the long-range electric field \mathcal{E} (or \bar{E}) are related through equation (5b) so that equation (8) becomes

$$\frac{dI_{\rho\sigma}}{d\Omega} = \eta(\omega_s) \omega_s^4 |\sum_j \alpha_{\rho\sigma j}^j G_{j,\perp}^{j*}(\omega) + \beta_{\rho\sigma\lambda} |\mathcal{E}_l^*(\omega)|^2 |E_\rho(\omega_i)|^2 \quad (9)$$

$$G_{j,\perp}^{j*}(\omega) = \frac{\sqrt{S_{j,\perp}^j/4\pi\omega_{j,\perp}}}{\omega_{j,\perp}^2 - \omega^2 + i\omega \Gamma_{j,\perp}^j}. \quad (10)$$

In equation (9), $\alpha_{\rho\sigma j}$ and $\beta_{\rho\sigma j}$ represent the electronic properties and are expected to vary slowly with ω as can be seen from equation (4c). The major dependence of the scattered intensity on the vibrational frequency ω is in the factor $G^{j*}(\omega)$ which expresses the ability of the j th normal-mode to absorb i.r. radiation at frequency ω .

When dealing with spontaneous Raman emission, the values of $|\mathcal{E}_{j,\perp}^*(\omega)|^2$ depend on temperature and are given [12] as:

$$|\mathcal{E}_{j,\perp}^*|^2 = 2\pi \xi_{j,\perp}^2 \hbar \omega N \left[\frac{n_{j,\perp}^2 \omega^2}{\pi^2 c^3} \left(\omega \frac{dn_{j,\perp}}{d\omega} + n_{j,\perp} \right) \right];$$

$$N = \frac{1}{\exp(\hbar\omega/kT) - 1}$$

where $\xi_{j,\perp}$ are local field correction factors, the quantity in the square bracket is the photon density of states, $n_{j,\perp}$ are frequency-dependent indices of refraction, and N is the number of polaritons per mode in thermal equilibrium at temperature T . As the temperature increases, the integrated intensity of a Raman line as expressed in equation (9) increases; the line is however much broader due to the anharmonic interaction of phonons [13]. Under normal circumstances, it is easier to resolve a line in an experiment at a lower temperature. When the stimulated Raman effect is considered, the electric field intensities $|\mathcal{E}_{j,\perp}|^2 = \xi_{j,\perp}^2 |E_{j,\perp}|^2$ are determined by the following set of coupled wave equations:

$$(\omega_{j,\perp}^2 - i\omega_{j,\perp} \Gamma_{j,\perp}^j - \omega^2) \xi_{j,\perp}^j = \sqrt{\frac{S_{j,\perp}^j}{4\pi}} \times \omega_{j,\perp} E_{j,\perp} + \langle f_{j,\perp}^j(\omega) \rangle^{(2)} \quad (11a)$$

$$\bar{k} \times (\bar{k} \times \bar{E}) + \frac{\omega^2}{c^2} \bar{D} = -\frac{4\pi\omega^2}{c^2} \times [\bar{P}(\omega) + \langle \bar{\mathcal{P}}(\omega) \rangle^{(2)}] \quad (11b)$$

$$\bar{k}_s \times (\bar{k}_s \times \bar{E}^s) + \frac{\omega_s^2}{c^2} \bar{D}^s = -\frac{4\pi\omega_s^2}{c^2} \langle \bar{p}(\omega_s) \rangle^{(2)} \quad (11c)$$

where $\bar{P}(\omega)$ is given in equation (5a), and $\langle f_{\parallel,1}(\omega) \rangle^{(2)}$ and $\langle \bar{p}(\omega_s) \rangle^{(2)}$ are given in equation (4). For equation (11), the local field in equation (4) is replaced by the corresponding macroscopic field with proper corrections. The incident pump wave at ω_i is assumed to pass through the crystal without appreciable attenuation. The techniques of solving equations like equation (11) have been discussed many times [3, 7, 14] and the threshold for stimulated emission can be determined easily. We do not intend to dwell on this problem here. The interesting and unique feature of stimulated Raman scattering by polarization waves is the possibility of parametric interactions [15] between the scattered light wave and the i.r. radiation associated with the lattice vibrations. Although these stimulated effects have not yet been realized, such parametric oscillations suggest the application of polarization waves for tunable radiation sources [16] at visible and far-i.r. wavelengths.

5. APPLICATION TO α -QUARTZ

The scattering differential cross section given by equation (8) may be used in a general situation involving many phonon modes simultaneously. For the right-angle Raman scattering, the polariton branches probed are phonon-like and are well separated in frequency for many crystals including α -quartz. To compare with the experimental data of the right-angle scattering, equation (8), normalized to a specified incident intensity, may be simplified to give the scattering efficiency S as follows:

$$S = \{ \hat{e}_p^i R_{\rho\sigma}^{(2)} [A \hat{\xi}^i + B (\hat{k} \cdot \hat{\xi}) \hat{k}^i] \hat{e}_\sigma^s \}^2 \quad (12)$$

where \hat{e}^i and \hat{e}_σ are the directions of the electric field vectors of the incident and scattered light, respectively. A is a scattering coefficient related to the lattice deformation and B gives

the contribution due to the electro-optic effect of the Raman tensor $R_{\rho\sigma}^{(2)}$. The electric field associated with the E vibrations is parallel to the direction of propagation \hat{k} . The unit vector $\hat{\xi}^i$ denotes the polarization of one of the 'short-wave' polariton branches. Unlike the work of Loudon [2], in which he considered only a single i.r. and Raman active mode, equation (12) was reduced from a multimode expression and is valid only for the right-angle Raman scattering. This approach is more realistic for a complicated crystal like quartz. A , B and $R_{\rho\sigma}^{(2)}$ are frequency-dependent and a value may be determined for each E mode.

Quartz is a complex piezoelectric crystal having D_3 symmetry and nine atoms per unit cell. Group theory predicts that of the 27 normal-modes, four will be totally symmetric (A_1 modes) and eight will be doubly degenerate (E modes). The remainder are the four i.r.-active A_2 modes and the three acoustic modes. The E vibrations are simultaneously i.r. and Raman active leading to frequencies, intensities, and widths which are dependent on the orientation of the sample. $R_{\rho\sigma}^{(2)}$ is the element of the Raman tensor and group theory predicts that for D_3 symmetry it must have the following form:

$$\begin{matrix} A & E(x) & E(y) \\ \begin{bmatrix} a & & \\ & a & \\ & & b \end{bmatrix} & \begin{bmatrix} c & & \\ & -c & d \\ & & d \end{bmatrix} & \begin{bmatrix} & -c & -d \\ -c & & \\ -d & & \end{bmatrix} \end{matrix}$$

For the symmetric A_1 vibration, B in equation (12) is zero and $\hat{\xi}^i$ may be dropped from the equation since all directions of the phonon polarization are equivalent. The relative values of the scattering coefficients A and B , in general, will depend on the scattering polarization much like the values of $({}^b f_n^j - {}^a f_n^j)$ and $({}^b \bar{\mathcal{P}}_n - {}^a \bar{\mathcal{P}}_n)$ discussed in Section 2. As a result, the electro-optic contribution to the individual E modes may either add to or detract from the scattering intensity; the A and B coefficient can either have the same or opposite signs.

The details of the Raman spectrometer system used for these experiments have been described elsewhere [17] and are similar in many respects to that described at Ducros and Olivie [19]. A 50 mW He-Ne laser used as the excitation source is focused into the quartz sample which is a cube 2 cm on an edge. The Raman scattered radiation is observed at right angles for all possible polarizations, i.e., two for the incident beam and two for the scattered beam. The radiation flux reaching the photodetector [19] is such that photon counting techniques can be used with the advantage that the output data is in digital form and is therefore directly compatible with a computer for analysis. A multichannel analyzer is used for collecting the output data as well as for controlling the step-wavelength drive of the monochromator. The instrument width of this system is comparable with the Raman linewidths so that a deconvolution procedure is necessary to obtain the true lineshapes. The deconvolution is done by computer giving the true line position, width and intensity. The uncertainties in these values quoted in the tables below are a result of the statistical fluctuations in the data and are nearly independent of the instrument resolution. The most important single factor affecting the line parameter uncertainties is the signal-to-noise ratio. For small S/N the uncertainties will be large; for some cases the small S/N did not permit a useful determination of the line parameters. In computing the line parameters compensation was made for the spectral sensitivity of the photomultiplier tube and the polarizing effect of the monochromator. The depolarizing effects due to the birefringence and optical activity were also taken into consideration.

Two samples were prepared, one with all the sides normal to the crystallographic axis, and the other cut so that the x and z axis were 45° to the sides of the sample. This allowed three orientations corresponding to three directions of phonon propagation with respect to the z axis, viz. $\theta = 90^\circ$ or x into y scattering, $\theta = 45^\circ$ or x into z , and $\theta = 0^\circ$. Each Raman

active line was measured for all orientations and polarizations and the values of the line positions, intensities, and widths are given in Table 1. It is seen that the E modes fall into two groups, those which are degenerate and those in which the transverse and longitudinal modes are clearly resolved. The notation for $\theta = 0^\circ$ scattering, SP for example, indicates that the incident and scattered light beam are polarized and analyzed in the planes perpendicular (S) and parallel (P) to the plane defined by the wave vectors of the incident and scattered light. I_{int} and I_0 are, respectively, the integrated intensity (number of photon counts) and peak intensity for a given Raman line.

The intensity data have been normalized to a dwell or counting time of 8 sec. per channel even though longer dwell times were sometimes used for lines with shifts above $1,000 \text{ cm}^{-1}$ in order to obtain a sufficiently good signal-to-noise ratio. The blocks in Table 1 marked with an asterisk label those polarizations forbidden due to symmetry considerations. Indications of the strong 207 cm^{-1} and 464 cm^{-1} lines were observed for the symmetry forbidden polarizations as shown in Table 1 and their presence is probably due to a slight misalignment of the sample. The approximate peak intensity was given for each of these cases. The blocks marked with 'weak' indicate poor signal-to-noise ratio in our data such that an accurate line intensity and linewidth can not be meaningfully determined. The S/N ratio for the blocks marked with 'Line Present' were even smaller and only the presence of a line was observed. The poor S/N ratio for all these cases could perhaps be improved if a much longer dwell time per channel was used. Nothing was detected for the blocks filled with a dash line, and we did not measure the polarizations corresponding to the blank blocks. Notice that the line positions of all the E modes for all orientations and polarizations reported here agree with the prediction shown in Fig. 2. For example from Table 1 it is seen that the position

of the 128 and 265 cm^{-1} E lines are independent of the phonon direction (orientation) as indicated in Fig. 2, while the 450/509 doublet shifted from $\theta = 90^\circ$ to the 450/538 line positions at $\theta = 45^\circ$.

For $\theta = 0^\circ$ and 90° scattering, the polarization of lattice displacements ξ is either perpendicular or parallel to the direction of polariton propagation \vec{k} . For the $\theta = 45^\circ$ orientation, the polarization wave in general is of a mixed nature with both A_2 and E characteristics[3] and for the extraordinary waves, the normal-mode vectors ξ_1 and ξ_2 make angles ϕ_1 and ϕ_2 with the wave vector \vec{k} . The geometry for these cases is shown in Fig. 3. Using equation (12), the Raman intensities for all orientations and polarizations of interest can be calculated in terms of the Raman tensor elements, the angles ϕ_1 and ϕ_2 , and the ratio of the scattering coefficients B/A . The results are tabulated in Table 2 in units of A^2 . ξ_0 is the ordinary phonon vector, and ξ_1 and ξ_2 are the extraordinary phonon vectors. $\eta = (A+B)^2/A^2$ is the ratio of the scattered intensity of a purely longitudinal vibration to that of a purely transverse vibration ($B = 0$), and the factors C and D are:

$$C = \frac{1}{2}[(\sin \phi_1 + \cos \phi_1) + \frac{B}{A} \cos \phi_1]^2 \quad (13a)$$

$$D = \frac{1}{2}[(\sin \phi_2 + \cos \phi_1) + \frac{B}{A} \cos \phi_2]^2. \quad (13b)$$

For degenerate E modes, the measured intensity is the sum of the constituent components listed in Table 2.

Table 3 which is a duplication of the data presented in Ref. [6], summarizes the width of each of the Raman lines and the relative magnitudes of the Raman tensor elements as determined from a portion of the data presented in Tables 1 and 2. The identification of the lines is that of Scott and Porto[10] and given in parenthesis are our experimental line positions at room temperature. The widths are the full widths at half-maximum intensity of a Lorentzian function which, when convoluted

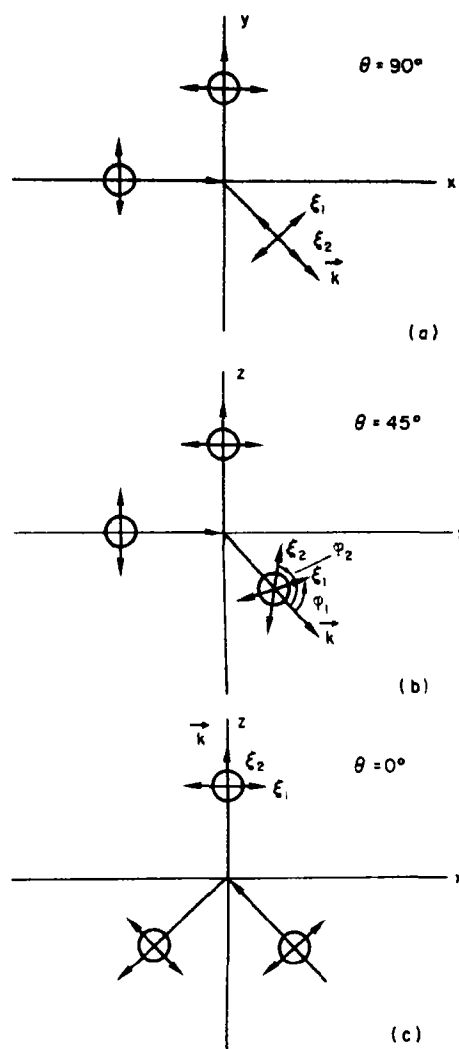


Fig. 3. Phonon propagation and polarization directions for three scattering geometries.

with a Gaussian instrument function, best fits the data[17]. The 207 cm^{-1} line is much broader due to the fact that it is this line which is responsible for the α - β transition[20]. These width values, although they do not agree in every case with those reported earlier [21], are more accurate primarily because of the photon-counting detection system and the deconvolution procedure used[17, 18]. The elements of the Raman tensor were calculated

Table 1 (a). Detailed experimental data for the Raman active lines in α -quartz. I_{int} , I_0 , pos. and width are integrated intensity, peak intensity, line position and linewidth respectively. (a) $A_1(207, 356, 464, \text{ and } 1085 \text{ cm}^{-1})$ and degenerate E (128, 265, 679 and 1162 cm^{-1}) modes, and (b) non-degenerate E (394/401, 450/509, 795/807, and $1072/1235 \text{ cm}^{-1}$) modes. The blocks marked with an asterisk are forbidden polarizations due to symmetry considerations

	$\theta = 90^\circ$				$\theta = 45^\circ$				$\theta = 0^\circ$			
	$x(zx)y$	$x(xy)y$	$x(yz)y$	$x(zz)y$	$x(yx)z$	$x(zx)z$	$x(yz)z$	$x(yy)z$	SS	PS	PP	SP
207 I_{int}	---	---	---	87498	---	---	---	68566	41696	---	---	---
I_0	---	---	---	1260 ± 14	---	---	---	1008 ± 10	622 ± 10	---	---	---
Pos	*	*	*	206.2 ± 0.5	*	*	*	205.9 ± 0.5	206.6 ± 0.5	*	---	*
Width	---	---	---	21.9 ± 0.5	---	---	---	21.4 ± 0.4	21.5 ± 0.7	---	---	---
356 I_{int}	---	---	---	7452	---	---	---	5000	3147	---	---	---
I_0	---	---	---	932 ± 96	---	---	---	604 ± 52	630 ± 138	*	---	*
Pos	*	*	*	355.2 ± 0.8	*	*	*	353.6 ± 0.8	354.4 ± 0.8	---	---	---
Width	---	---	---	2.2 ± 0.3	---	---	---	2.3 ± 0.3	1.4 ± 0.4	---	---	---
464 I_{int}	---	---	---	133960	---	---	---	121370	65511	---	---	---
I_0	---	---	---	5860 ± 56	---	---	---	5656 ± 38	2942 ± 42	---	---	---
Pos	*	*	*	464.5 ± 1	*	*	*	464.5 ± 1	463.8 ± 1	~ 110	---	~ 30
Width	---	---	---	6.4 ± 0.1	---	---	---	6.2 ± 0.1	6.4 ± 0.1	*	---	*
1085 I_{int}	---	---	---	3508	---	---	---	241	---	---	---	---
I_0	---	---	---	184 ± 8	---	---	---	27 ± 15	---	---	---	---
Pos	*	*	*	1083 ± 2	*	*	*	1081 ± 2	---	*	---	*
Width	---	---	---	5.3 ± 0.6	---	---	---	2.2 ± 1.9	---	---	---	---
128 I_{int}	8650	15450	9036	---	17350	8980	8442	16799	20486	11571	---	10330
I_0	608 ± 14	1140 ± 80	730 ± 23	---	1465 ± 30	840 ± 40	740 ± 27	1580 ± 68	1490 ± 68	1040 ± 46	Weak	1020 ± 48
Pos	127.6 ± 0.3	127.8 ± 0.8	128.0 ± 0.3	*	127.8 ± 0.3	128.5 ± 0.3	128.0 ± 0.3	128.3 ± 0.3	128.1 ± 0.3	128.7 ± 0.3	~ 130	128.7 ± 0.3
Width	4.3 ± 0.4	4.2 ± 0.6	3.7 ± 0.2	---	3.5 ± 0.3	3.1 ± 0.5	3.4 ± 0.2	3.1 ± 0.2	4.2 ± 0.3	3.3 ± 0.2	---	3.0 ± 0.5
265 I_{int}	3150	---	3793	---	---	4030	3156	---	---	1059	---	Line
I_0	235 ± 18	---	306 ± 16	---	---	362 ± 24	326 ± 30	---	---	180 ± 82	---	Present
Pos	264.6 ± 0.7	264.5 ± 0.6	3.6 ± 0.3	*	---	264.1 ± 0.6	264.8 ± 0.6	---	---	265.3 ± 0.7	---	~ 265
Width	4.0 ± 1.1	---	---	---	---	3.2 ± 0.7	2.9 ± 0.4	---	---	1.7 ± 1.0	---	---
697 I_{int}	---	Weak	---	---	Weak	---	Weak	1167	---	---	---	---
I_0	---	696	---	*	~ 696	---	~ 696	57 ± 6	---	---	---	---
Pos	---	---	---	---	---	---	---	696.0 ± 2	---	---	---	---
Width	---	---	---	---	---	---	---	6.0 ± 1.3	---	---	---	---
1162 I_{int}	Weak	2550	Weak	---	2560	---	Weak	2279	---	---	---	---
I_0	65 ± 5	---	---	*	88 ± 6	---	Weak	82 ± 4	---	---	---	---
Pos	1159	1159.1 ± 4	1158	---	1160 ± 2	---	~ 1160	1159.1 ± 4	---	---	---	---
Width	---	11.0 ± 2.2	---	---	8.5 ± 1.8	---	---	7.5 ± 0.9	---	---	---	---

Table 1(b).

		$\theta = 90^\circ$			$\theta = 45^\circ$			$\theta = 0^\circ$		
		$x(zx)y$	$x(xy)y$	$x(zy)y$	$x(zx)z$	$x(xy)z$	$x(zy)z$	PS	PP	SP
394	I_{int}	---	793	---	1416	---	---	---	---	760
	I_0	---	105 ± 37	---	407 ± 184	---	---	Weak	---	103 ± 52
	Pos	---	394 ± 1	*	394 ± 1	---	---	~ 395	---	395 ± 1
	Width	---	2.0 ± 1.0	---	1.0 ± 0.5	---	---	1.2 ± 1.1	---	2.1 ± 1.5
401	I_{int}	---	Weak	---	---	---	1369	---	---	---
	I_0	---	~ 404	---	---	---	326 ± 123	---	---	---
	Pos	---	---	---	---	---	402 ± 1	---	---	---
	Width	---	---	---	---	---	1.1 ± 0.5	---	---	---
450	I_{int}	---	---	---	---	---	Weak	---	---	---
	I_0	---	---	---	---	---	~ 401	---	---	---
	Pos	---	---	---	---	---	---	---	---	---
	Width	---	---	---	---	---	---	---	---	---
450	I_{int}	935	---	---	---	---	Weak	955	---	814
	I_0	101 ± 20	---	---	---	---	194 ± 30	78 ± 20	---	140 ± 80
	Pos	449 ± 1	---	---	---	---	450 ± 1	450 ± 1	---	450 ± 1
	Width	2.5 ± 0.7	---	---	---	---	2.2 ± 0.5	3.2 ± 1.3	---	1.5 ± 1.2
509	I_{int}	691	---	---	---	---	---	---	---	---
	I_0	75 ± 40	---	---	---	---	Line	---	---	---
	Pos	508 ± 1	---	---	---	---	Present	---	---	---
	Width	2.1 ± 1.6	---	---	---	---	~ 538	---	---	---
795	I_{int}	905	---	---	---	---	---	---	---	---
	I_0	30 ± 3	---	---	---	---	2524	---	---	---
	Pos	795 ± 2	---	---	---	---	99 ± 7	1854	---	1291
	Width	7.5 ± 1.9	---	---	---	---	Weak	55 ± 6	---	50 ± 7
807	I_{int}	1080	---	---	---	---	796 ± 2	796 ± 2	---	796 ± 2
	I_0	49 ± 5	---	---	---	---	6.5 ± 1.3	10.4 ± 3	---	7.6 ± 2.3
	Pos	809 ± 2	---	---	---	---	7.6 \pm 1.3	---	---	---
	Width	5.5 ± 1.0	---	---	---	---	Weak	---	---	---
1072	I_{int}	322	---	---	---	---	~ 806	---	---	---
	I_0	20 ± 6	---	---	---	---	---	---	---	---
	Pos	1068 ± 2	---	---	---	---	Weak	---	---	---
	Width	4.3 ± 2.4	---	---	---	---	~ 1067	---	---	---
1235	I_{int}	---	---	---	---	---	---	---	---	---
	I_0	---	380	---	---	---	---	---	---	---
	Pos	---	13 ± 2	---	---	---	Line	---	---	---
	Width	---	1230 ± 3	---	---	---	Present	---	---	---
		---	7.9 ± 2.4	---	---	---	~ 1231	---	---	---

Table 2. Raman intensity in terms of tensor elements

$\theta = 90^\circ$		ξ_1	ξ_2 (Fig. 3a)
$x(zx)y$	0	$\frac{1}{2}d^2$	$\frac{1}{2}\eta d^2$
$x(yx)y$	0	$\frac{1}{2}c^2$	$\frac{1}{2}\eta c^2$
$x(yz)y$	0	$\frac{1}{2}d^2$	$\frac{1}{2}\eta d^2$
$x(zy)y$	b^2	0	0
$\theta = 45^\circ$		ξ_1	ξ_2 (Fig. 3b)
$x(zx)z$	0	d^2	0
$x(yx)z$	0	c^2	0
$x(zy)z$	0	0	0
$x(yz)z$	0	Cd^2	Dd^2
$x(yz)z$	a^2	0	Cc^2
$\theta = 0^\circ$		$\xi_0 + \xi_1$ (Fig. 3c)	Dc^2
SS	a^2	c^2	
PP	$\frac{1}{2}a^2$	$\frac{1}{2}c^2$	
PS	0	$\frac{1}{2}(c^2 + d^2)$	
SP	0	$\frac{1}{2}(c^2 + d^2)$	

by comparing the integrated intensity of each line with the intensity predicted in Table 2. The values shown in Table 3 have been normalized so that b^2 for the 464 cm^{-1} line is 1000. The 697 cm^{-1} line was too weak for an

accurate determination of the elements, although it was strong enough to conclude that $c^2 > d^2$ for this mode. It is seen from Table 3 that in general the A_1 modes are more intense than the E modes, and that they fall into two types; the 207, 356, and 464 cm^{-1} lines all have b^2 just slightly larger than a^2 , while for the 1085 cm^{-1} line b^2 is much larger than a^2 , in qualitative agreement with previous work [21].

Several additional observations can be made from the data in Table 1. For the degenerate E modes, we observe a narrowing of the line as one goes from $\theta = 90^\circ$ to $\theta = 0^\circ$. This is to be expected [2, 6] and our line-widths, with the accuracies listed in Table 1, decreased by about 0.7 cm^{-1} for the 128 cm^{-1} line and by about 2.0 cm^{-1} for the 265 and 1162 cm^{-1} lines. We can also determine the η values: they are 0.8, 0.7, 1.0 and 0.9 (with an accuracy of ± 0.1), for the 128, 265, 697, and 1162

Table 3. Experimental positions, widths, and relative magnitudes of the elements of the Raman tensor for the lines in α -quartz

Frequency Shift (cm ⁻¹)	Width (cm ⁻¹)	Tensor Elements (<i>b</i>)				
I. <i>A</i> ₁ modes		<i>a</i> ²	<i>b</i> ²	<i>b</i> ² / <i>a</i> ²		
207(206 ± 0.5)	21.6 ± 0.5	484	619	1.3		
356(355 ± 1)	2.2 ± 0.3	38	55	1.5		
464(464.5 ± 1)	6.3 ± 0.1	906	1000	1.1		
1085(1082 ± 2)	5.3 ± 0.6	2.3	31	13.5		
II. Degenerate <i>E</i> modes		<i>c</i> ²	<i>d</i> ²	<i>c</i> ² / <i>d</i> ²		
128(128 ± 0.5)	3.3 ± 0.2(a)	125	62	2.0		
265(264.5 ± 1)	3.0 ± 0.5(a)	< 1	29	< 0.03		
697(696 ± 2)	5.5 ± 1.3			> 1.0		
1162(1159 ± 2)	7.5 ± 0.9(a)	23	5.5	4.2		
III. Non-degenerate <i>E</i> modes		<i>c</i> ²	<i>c</i> ² (<i>LO</i>) <i>c</i> ² (<i>TO</i>)	<i>d</i> ²	<i>d</i> ² (<i>LO</i>) <i>d</i> ² (<i>TO</i>)	<i>c</i> ² / <i>d</i> ²
394(394 ± 1)	2.0 ± 0.9	11	0.55	< 1	> 2	> 11
401(403.5 ± 1)	2.0 ± 0.9	6		2		> 6
450(450 ± 1)	2.0 ± 0.5	< 1	—	13	0.77	< 0.07
509(508.5 ± 1)	1.5 ± 0.5	< 1		10		< 0.1
795(796 ± 2)	7.5 ± 1.0	< 1	—	14	1.43	< 0.07
807(809 ± 2)	6.0 ± 1.0	< 1		20		< 0.05
1072(1067 ± 2)	4.0 ± 2.0	< 1.0		2.7	0.37	< 0.4
1235(1230 ± 2)	8.0 ± 2.0	3.7 > 3.7		< 1.0		> 3.7

(a) Width corresponding to $\theta = 0^\circ$.

(b) Calculated from the integrated intensities and normalized so that b^2 (464 cm^{-1}) = 1000.

cm^{-1} lines, respectively. Further, we found approximately that $C + D = \frac{1}{2}(1 + \eta)$ for the degenerate E modes. This implies, according to equation (13), that $\phi_2 = 90^\circ + \phi_1$, or $\xi_2 \perp \xi_1$ for these modes. For the non-degenerate E modes, however, our data are insufficient for a direct simultaneous determination of B/A , ϕ_1 and ϕ_2 , because the intensities at $\theta = 45^\circ$ were too weak to make an accurate evaluation. The Raman tensor elements c^2 and d^2 for the non-degenerate E modes were determined separately for the low-frequency and high-frequency components of the 'same' mode and the values c^2 and d^2 in Table 3 include the electro-optic contribution as well. For these modes, we report the ratio of the scattering intensities of the two components $c^2(LO)/c^2(TO)$ and $d^2(LO)/d^2(TO)$ for each of the four non-degenerate pairs with the exception of the c^2 -ratio for the 450/509 and 795/807 cm^{-1} pairs for which the intensities were too weak. That the relative magnitude of c and d are reversed for the two components of the 1072/1235 cm^{-1} doublet is probably due to the fact that another E line (1161 cm^{-1}) falls in between.

In conclusion the accomplishments of this paper are distinct from those of Ref. [6]. Figures 1 and 3, and the data presented in Tables 1 and 2 are new and have not been published before. The information contained in Table 3 (duplicated from Ref. [6]) is obtained from portions of the data for $\theta = 0^\circ$ and $\theta = 90^\circ$ presented in Table 1. The new information contained in Table 1 are the following:

(1) The $\theta = 45^\circ$ data are new and from these data we have been able to determine that for degenerate E modes, ξ_2 and ξ_1 , the polarization of the normal-mode amplitudes, are perpendicular to one another. In general, this is not necessarily the case.

(2) The detailed line positions for all the polarizations and orientations presented in Table 1, especially the line positions for $\theta = 45^\circ$, allows us to compare our results with the polariton spectra shown in Fig. 2. To our knowledge this has never before been attempted.

(3) The data given in Table 1 are more complete than that given in Table 3 and could be of value for the person wishing to do this type of experiment. It lists in detail the intensities, integrated and peak, as well as the linewidth for each line and for each orientation.

Acknowledgement—The authors would like to acknowledge helpful discussions with J. F. Scott and Y. D. Harker.

REFERENCES

1. POULET H., *Ann. Phys. Paris* **10**, 908 (1955).
2. LOUDON R., *Adv. Phys.* **13**, 423 (1964).
3. LOUDON R., *Light Scattering Spectra of Solids*, (Edited by G. B. Wright), p. 25, Springer-Verlag, New York (1969); BURSTEIN E., USHIDA S., PINCZUK A., and SCOTT J. F., *ibid.*, p. 43; SCOTT J. F. and USHIDA S., *ibid.*, p. 57.
4. SCOTT J. F., CHEESMAN L. E. and PORTO S. P. S., *Phys. Rev.* **162**, 834 (1967).
5. DE MARTINI F., *J. appl. Phys.* **37**, 4503 (1966).
6. MASSO JON D., SHE C. Y. and EDWARDS D. F., *Phys. Rev.* **B1**, 4179 (1970); MASSO JON D., Ph. D. Thesis, Colorado State University, March (1970).
7. BLOEMBERGEN N. and SHEN Y. R., *Phys. Rev.* **133**, A 37 (1964); SHE C. Y., *IEEE J. Quant. Electron.* **QE-3**, 73 (1967).
8. HEINE V., *Group Theory in Quantum Mechanics*, Pergamon Press (1960).
9. HOCHSTRASSER R. M., *Molecular Aspects of Symmetry*, Benjamin (1966).
10. BORN M. and HUANG K., *Dynamical Theory of Crystal Lattice*, Clarendon Press, Oxford (1954); BARKER A. S., Jr., *Phys. Rev.* **136**, A 1290 (1964); SCOTT J. F. and PORTO S. P. S., *ibid.* **161**, 903 (1967).
11. SPITZER W. G. and KLEINMAN D. A., *Phys. Rev.* **121**, 1324 (1961); RUSSELL E. E. and BELL E. E., *J. Opt. Soc. Amer.* **57**, 341 (1967).
12. KITTEL C., *Elementary Statistical Physics*, Wiley (1958).
13. COWLEY R. A., *Adv. Phys.* **12**, 421 (1963); PINE A. S. and TANNENWALD P. E., *Phys. Rev.* **178**, 1424 (1969); HARKER Y. D., SHE C. Y., and EDWARDS D. F., *Appl. Phys. Lett.* **15**, 272 (1969).
14. LOUDON R., *Proc. Phys. Soc.* **82**, 393 (1963); SHEN Y. R. and BLOEMBERGEN N., *Phys. Rev.* **137**, A 1787 (1965); BUTCHER P. N., LOUDON R. and MCLEAN T. P., *Proc. Phys. Soc.* **85**, 565 (1965); HENRY C. H. and GARRETT C. G. B., *Phys. Rev.* **171**, 1058 (1968).
15. BLOEMBERGEN N., *Nonlinear Optics*, W. A. Benjamin, New York (1965); SHE C. Y., *Phys. Rev.* **176**, 461 (1968).
16. ZEIGER H. J. and TANNENWALD P. E., *Quantum Electronics III*, p. 1589, GRIVET P. and BLOEMBERGEN N., Eds., Columbia University Press (1964); TANNENWALD P. E. and WEINBERG D. L., *IEEE J. Quant. Electron.*, **QE-3**, 334 (1967).

17. MASSO JON D., HARKER Y. D. and EDWARDS D. F., *J. Chem. Phys.* **50**, 5420 (1969); HARKER Y. D., Ph. D. Thesis, Colorado State University, 1969; HARKER Y. D., SHE C. Y. and EDWARDS D. F., Tech. Report AFCRL-69-0045.
18. DUCROS A. and OLIVIE M., *Electronique Industr.* No. 119, 801 (1968).
19. HARKER Y. D., MASSO J. D. and EDWARDS D. F., *Appl. Optics* **8**, 2563 (1969).
20. SCOTT J. F., *Phys. Rev. Lett.* **21**, 907 (1968); SHAPIRO S. M., O'SHEA D. C. and CUMMINS H. Z., *ibid.* **19**, 361 (1967).
21. ZUBOV V. G. and OSIPOVA L. P., *Soviet Phys. - Crystallog.* **6**, 330 (1961); KISELEV D. F. and OSIPOVA L. P., *ibid.* **11**, 255 (1966); KISELEV D. F. and OSIPOVA L. P., *ibid.* **11**, 373 (1966).

SUSCEPTIBILITE MAGNETIQUE D'UN ELECTRON 5f EN COORDINATION DE HUIT

P. RIGNY, A. J. DIANOUX* et P. PLURIEN

Département de Physico-Chimie, Centre d'Etudes Nucléaires de Saclay, B.P. No 2,
91-Gif-sur-Yvette, France

(Received 3 June 1970)

Résumé—Les susceptibilités magnétiques des complexes UF_8M_3 où $M = Na, Cs, Rb, NH_4$, ont été mesurées de 8 à 300°K. Les ions UF_8^{3+} où l'uranium a la valence V contiennent un électron 5f célibataire, dont on étudie les niveaux d'énergie dans trois cas. L'hypothèse que les huit atomes de fluor déterminent un cube parfait autour de l'uranium a d'abord été faite; le niveau fondamental est alors un quadruplet Γ_8 , mais le formalisme de l'Hamiltonien de spin permet un traitement simple. On a ensuite envisagé une faible déformation axiale du cube, de symétrie quadratique (D_{4h}) ou rhomboédrique (D_{3d}). Un excellent accord entre les susceptibilités mesurées ou calculées dans la troisième hypothèse a pu être obtenu dans tout le domaine de température étudié.

Abstract—The magnetic susceptibilities of four complexes of formula UF_8M_3 ($M = Na, Cs, Rb, NH_4$) have been measured from 8 to 300°K. The UF_8^{3+} ions contain $U(V)$ and an unpaired 5f electron, the energy levels of which have been studied. Theoretical expressions for the susceptibility have been derived in three cases. First the eight fluorine atoms have been assumed to determine a perfect cube; the ground level is then a quadruplet Γ_8 but the spin Hamiltonian formalism allows a simple treatment. The cube has then been assumed to be slightly axially distorted, with quadratic (D_{4h}) or trigonal (D_{3d}) symmetry. Very good agreement between the experimental susceptibilities and values calculated with the latter hypothesis can be obtained over all the temperature range studied.

INTRODUCTION

LE PENTAFLUORURE d'uranium mis en présence de certains fluorures monovalents à des températures comprises entre 150 et 300°C, fournit des composés complexes de formule M_3UF_8 ($M = Na, Rb, Cs, NH_4$) [1]. Les clichés de diffraction des rayons X de ces complexes pulvérulents indiquent que la maille de Na_3UF_8 est quadratique avec $a = 5,47 \text{ \AA}$ et $c = 10,94 \text{ \AA}$ [2]; $(NH_4)_3UF_8$ et Cs_3UF_8 sont cubiques à faces centrées, avec respectivement $a = 9,60$ et $9,95 \text{ \AA}$; Rb_3UF_8 est pseudo-cubique avec $a = 9,50 \text{ \AA}$ [3]. La position des atomes de fluor dans les mailles cristallines n'est évidemment pas déterminée mais il est raisonnable de proposer, avec Rüdorff et Leutner [2], que chaque uranium est entouré d'un cube de huit fluors. Cette

hypothèse est d'ailleurs en accord avec les résultats d'une étude cristallographique récente du complexe isomorphe de protactinium Na_3PaF_8 [4]. Les ions UF_8^{3+} où l'uranium est à la valence V , ont un électron non apparié. La couche de valence de l'uranium contient des orbitales 5f, 6d et 7s. Il semble bien établi que l'orbitale 5f est la plus basse en énergie dans les composés d'uranium V , et nous ferons l'hypothèse que l'électron magnétique est situé dans une orbitale de ce type.

Disons tout de suite que l'étude des susceptibilités magnétiques ne confirme pas une symétrie parfaitement cubique de l'environnement de l'uranium. Déjà les mesures effectuées par Rüdorff *et al.* [3] ainsi que par Kemmler-Sack *et al.* [5] sur Na_3UF_8 au dessus de 77°K indiquaient une trop grande variation thermique de la susceptibilité. Ici nous présentons une étude des susceptibilités des complexes de sodium, rubidium, césium

*Present Address: Department of Chemistry and Chemical Engineering, University of Illinois, Urbana, Ill. 61820, U.S.A.

et ammonium à des températures allant de 8 à 300°K. Nous montrerons que la variation thermique des susceptibilités peut être expliquée par l'existence d'une faible déformation du cube des huit fluors qui entourent l'uranium, et que celle-ci doit être de symétrie trigonale. Avant de donner les expressions théoriques de la susceptibilité, il faut connaître les niveaux d'énergie de l'électron magnétique, et leurs fonctions d'onde; nous les présenterons d'abord. Nous verrons que l'état fondamental serait de type Γ_8 si la symétrie était parfaitement cubique. Dans ces conditions, le théorème de Jahn-Teller suffit pour indiquer qu'une déformation de l'environnement doit intervenir.

FONCTIONS D'ONDE DE L'ELECTRON MAGNETIQUE

Les arguments classiques de la théorie des groupes indiquent que dans un environnement cubique les sept orbitales f (symétrie D_3) donnent naissance à 2 triplets, de symétries Γ_4 et Γ_5 et un singulet, de symétrie Γ_2 . L'ordre des énergies de ces niveaux résulte d'hypothèses sur le type des liaisons $U-F$. Les distances uranium fluor étant assez grandes, nous supposons que les liaisons sont relativement peu covalentes. L'ordre des énergies qui est indiqué sur la Fig. 1 est alors le même que si l'électron était placé dans un environnement de charges ponctuelles. On peut voir que le niveau fondamental (énergie zéro) est alors le triplet Γ_4 , le triplet Γ_5 ayant l'énergie V' et le singulet Γ_2 l'énergie $V' + V$ avec $V, V' > 0$. En fait, les orbitales de symétries Γ_2 et Γ_4 peuvent donner des liaisons covalentes avec les fluors, et ceci doit modifier les énergies des niveaux. Cependant, nous supposons que leur ordre reste celui que nous venons de citer.

En présence de couplage spin-orbite, les quatorze spin-orbitales f se répartissent en cinq niveaux d'énergie de symétries Γ_6 , Γ_7 ou Γ_8 ($D_3 \times \Gamma_8 = 2\Gamma_6 + \Gamma_7 + 2\Gamma_8$). Une base de fonctions classées suivant les symétries du cube et déterminées par Eisenstein et Pryce

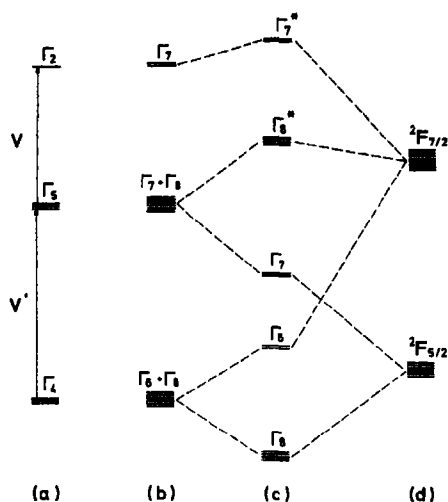


Fig. 1. Position des niveaux d'énergie d'un électron 5f, dans une coordination de huit. (a) La symétrie du champ cristallin est cubique et la couplage spin-orbite est négligé. (b) Classement des orbitales suivant les représentations du groupe cubique double; le couplage spin-orbite est toujours négligé. (c) Action du couplage spin-orbite. (d) Niveaux d'énergie de l'ion libre (correspondant à un couplage spin-orbite beaucoup plus grand que le champ cristallin).

[6], est indiquée en appendice; l'axe de quantification est un axe C_4 du cube. A l'intérieur de chaque type de symétrie, les fonctions sont repérées par un indice m , rappelant qu'elles se transforment sous les rotations du groupe cubique O_h comme les fonctions propres m de la composante z d'un spin fictif $S = \frac{1}{2}$ pour les symétries Γ_6 et Γ_7 , $S = \frac{3}{2}$ pour la symétrie Γ_8 .

La constante de couplage spin-orbite d'un électron de l'uranium est très élevée ($\zeta \sim 1955 \text{ cm}^{-1}$ pour l'uranium U). D'autre part, les effets de champ cristallin sur un électron f , dont la densité électronique est très concentrée au voisinage du noyau, sont relativement faibles. Les deux interactions doivent donc être d'importances comparables. On obtient les fonctions d'onde en diagonalisant simultanément le potentiel cristallin et l'interaction spin-orbite. Si les fonctions de la base ont été classées convenablement, les équations séculaires sont au plus de degré 2. Les fonctions de symétries Γ_7 et Γ_8 s'obtiennent

par diagonalisation des matrices:

$$\begin{array}{c|cc} \Gamma_7 & \varphi'_j & \varphi_j \\ \hline & V' - \frac{1}{2}\zeta & \\ \hline & \sqrt{3}\zeta & V + V' \\ \hline \end{array} \quad \begin{array}{c|cc} \Gamma_8 & \eta_i & \chi_i \\ \hline & -\frac{3}{4}\zeta & \frac{3\sqrt{5}}{4}\zeta \\ \hline & \frac{3\sqrt{5}}{4}\zeta & V' + \frac{1}{4}\zeta \\ \hline \end{array}$$

Les fonctions φ'_j , φ_j , η_i , χ_i ($j = \pm\frac{1}{2}$, $i = \pm\frac{3}{2}$, $\pm\frac{1}{2}$) sont données en appendice. Les fonctions d'onde de symétrie Γ_8 sont ainsi $\psi_i = (\cos \varphi) \eta_i \mp (\sin \varphi) \chi_i$.

Si le signe négatif correspond à l'état fondamental, l'équation séculaire est

$$\operatorname{tg} 2\varphi = \frac{3\sqrt{5}}{2} \left(\frac{V'}{\zeta} + 1 \right)^{-1}. \quad (1)$$

De même les fonctions de symétrie Γ_7 sont $\alpha_j = (\cos \theta) \varphi'_j \mp (\sin \theta) \varphi_j$ avec

$$\operatorname{tg} 2\theta = 2\sqrt{3} \left(\frac{V}{\zeta} + \frac{1}{2} \right)^{-1}. \quad (2)$$

Une déformation décompose les états en doublets (d'après le théorème de Kramers). Lorsque la déformation est axiale suivant un axe C_4 (symétrie D_{4h}), les fonctions d'onde, valables au premier ordre, se déduisent directement des fonctions données en appendice pour un site parfaitement cubique. Ainsi un quadruplet Γ_8 se décompose en un doublet ($\frac{1}{2}$, $-\frac{1}{2}$) et un doublet ($\frac{3}{2}$, $-\frac{3}{2}$). Lorsque le cube déformé a la symétrie trigonale (D_{3d}), les fonctions d'onde ne peuvent pas s'obtenir aussi directement, mais nous verrons que l'expression au premier ordre de la susceptibilité magnétique ne nécessite pas leur calcul. Avec les hypothèses que nous avons faites sur l'ordre des niveaux orbitaux le niveau fondamental est de symétrie Γ_8 , lorsque la symétrie est cubique.

EXPRESSIONS THEORIQUES DE LA SUSCEPTIBILITE

Un champ magnétique H se couple à

l'électron célibataire, décrit par l'Hamiltonien \mathcal{H}_0 , par un Hamiltonien $\mathcal{H}_m = -\beta H(L + 2S)$. β est le magneton de Bohr, L et S sont respectivement les moments cinétiques d'orbite et de spin de l'électron. L'énergie magnétique moyenne gagnée par l'électron est:

$$W = \operatorname{Tr} \sigma \mathcal{H}_m$$

$$\sigma = \exp -\frac{\mathcal{H}_0 + \mathcal{H}_m}{kT} \operatorname{Tr} \exp -\frac{\mathcal{H}_0 + \mathcal{H}_m}{kT} \quad (3)$$

est la matrice densité qui décrit le système à la température T .

Un champ magnétique extérieur de composantes H_i appliqué à l'échantillon induit un moment magnétique, dont la composante j est $M_j = \sum \chi_{ij} H_i$ avec

$$\chi_{ij} = \frac{1}{2} \frac{\delta^2 W}{\delta H_i \delta H_j}. \quad (4)$$

Il est ainsi facile d'obtenir l'expression de la susceptibilité χ_{ij} dès que les matrices représentatives des Hamiltoniens \mathcal{H}_0 et \mathcal{H}_m dans le quadruplet Γ_8 sont connues.

D'après le théorème de Wigner-Eckart, les 48 éléments de matrice des trois composantes d'un vecteur (symétrie Γ_4) dans un quadruplet Γ_8 peuvent s'exprimer en fonction des composantes d'un spin fictif $S = \frac{3}{2}$, à l'aide de deux paramètres. On peut donc écrire \mathcal{H}_m sous forme de l'Hamiltonien de spin [7, 8]

$$\mathcal{H}_m = g\beta H S + f\beta (H_x S_x^3 + H_y S_y^3 + H_z S_z^3). \quad (5)$$

x , y et z désignent les coordonnées suivant les trois axes C_4 du cube. Cette forme d'Hamiltonien est commune à tous les quadruplets Γ_8 ; on détermine les coefficients g et f en explicitant deux éléments de matrice quelconques. Dans le cas du niveau Γ_8 fondamental dont les fonctions d'onde ont été indiquées au paragraphe précédent, et en introduisant pour plus de commodité, deux

paramètres auxiliaires P et Q , on obtient:

$$P = \frac{27}{8}f + \frac{3}{2}g = \frac{1}{2} + \frac{\sqrt{5}}{2} \sin 2\varphi$$

$$Q = \frac{1}{8}f + \frac{1}{2}g = \frac{1}{6} \cos^2 \varphi + \frac{3}{2} \sin^2 \varphi - \frac{\sqrt{5}}{2} \sin 2\varphi. \quad (6)$$

L'angle φ est donné par l'équation séculaire (1) si bien que la matrice de \mathcal{H}_m s'exprime en fonction du seul paramètre V'/ζ . Même en symétrie cubique et du fait de la présence du deuxième terme de l'Hamiltonien (5), l'effet Zeeman du quadruplet Γ_8 n'est pas isotrope. Cependant la susceptibilité reste isotrope au moins dans l'approximation des hautes températures; d'après la formule (3), elle est alors en effet proportionnelle à $\text{Tr} \mathcal{H}_m^2$ qui ne contient qu'un seul terme non nul puisque le produit Γ_4^2 ne contient la représentation identité Γ_1 qu'une seule fois.

A l'approximation des hautes températures qui sera adaptée à nos conditions expérimentales la susceptibilité est alors obtenue sans difficulté par la formule (4) où l'on développe au premier ordre l'opérateur $\exp - (\mathcal{H}_0 + \mathcal{H}_m)/kT$. Les calculs sont explicités dans la Réf. [10]. Dans le cas de la symétrie cubique, l'Hamiltonien \mathcal{H}_0 est scalaire dans les fonctions Γ_8 et n'intervient pas dans le calcul du premier ordre. Les formules (3) et (4) donnent alors immédiatement l'expression de la susceptibilité, qui suit la loi de Curie, dont la forme valable aux hautes températures est:

$$\chi = \frac{1}{2} \beta^2 \frac{P^2 + Q^2}{kT}. \quad (7)$$

Dans les deux cas de déformation axiale que nous considérons où l'axe OZ de la déformation est soit un axe C_4 soit un axe C_3 du cube, les fonctions propres des deux doublets sont les fonctions propres $\pm \frac{1}{2}$ et $\pm \frac{1}{2}$ de la projection du spin fictif sur l'axe OZ . Si l'axe de déformation est choisi comme axe de quantification du spin fictif on obtient alors

la matrice de \mathcal{H}_0 sous forme diagonale de valeurs propres a dans les fonctions $\pm \frac{1}{2}$ et $-a$ dans les fonctions $\pm \frac{1}{2}$. Lorsque la déformation est quadratique, la forme de la matrice de \mathcal{H}_m est déduite immédiatement de l'expression (5). Lorsqu'elle est trigonale il faut au préalable exprimer S_x , S_y et S_z dans un nouveau système d'axes dont OZ est l'axe polaire. \mathcal{H}_m est donc connue en fonction de P et Q sans qu'il soit besoin de chercher les fonctions propres en symétrie D_{3d} [9]. Ainsi qu'on pouvait peut-être le prévoir, *a priori*, la susceptibilité est la moyenne pondérée des susceptibilités des deux doublets, issus du quadruplet Γ_8 , et on peut écrire

$$\chi = \frac{1}{4} p_1 \beta^2 (c_1/kT + A) + \frac{1}{4} p_2 \beta^2 (c_2/kT - A) \quad (8)$$

p_1 et p_2 sont les populations des deux doublets données par la loi de Boltzmann ($p_1 + p_2 = 1$, $p_1/p_2 = \exp 2a/kT$). Dans ce calcul au premier ordre, les termes de Van Vleck A et $-A$ de chaque doublet proviennent du couplage avec l'autre doublet; ils sont donc opposés, et de la forme $\pm D/a$.

Le paramagnétisme de Van Vleck donne donc ici une susceptibilité variable avec la température qui pourra nous expliquer les variations thermiques expérimentales. Les résultats des calculs sont indiqués dans le Tableau I. Ils ne dépendent que du seul paramètre V'/ζ , par l'intermédiaire de P et Q . Dans les déformations que nous avons envisagées, et qui sont soit suivant un axe C_4 soit suivant un axe C_3 du cube, les termes de Curie de chaque doublet sont égaux, en moyenne sur les orientations. On peut donc écrire la susceptibilité moyenne d'un ion UF_6^{3-} sous la forme

$$\chi_p = \frac{1}{4} \beta^2 \left[\frac{C}{kT} + \frac{D}{ka} \text{th} \frac{a}{T} \right] \quad (9)$$

où a est exprimée en $^\circ\text{K}$. Cette expression montre que la susceptibilité de la poudre est insensible au signe de a , c'est-à-dire au sens de la déformation axiale.

Le calcul précédent peut être amélioré dans

Tableau 1. Susceptibilités magnétiques des deux doublets issus d'un quadruplet Γ_8 en présence d'une faible déformation

Susceptibilité	Déformation quadratique (D_{4h})	Déformation rhomboédrique (D_{3d})
$\chi_{II} \begin{cases} C_1 \\ C_2 \\ D = Aa \end{cases}$	$\begin{cases} 4P^2 \\ 4Q^2 \\ 0 \end{cases}$	$\begin{cases} (3P^2 + 3Q^2 + 2PQ) \\ (P - Q)^2 \\ 0 \end{cases}$
$\chi \begin{cases} C_1 \\ C_2 \\ D = Aa \end{cases}$	$\begin{cases} \frac{1}{4}(P - 3Q)^2 \\ \frac{1}{4}(3P - Q)^2 \\ \frac{1}{4}(P + Q)^2 \end{cases}$	$\begin{cases} 0 \\ (P + Q)^2 \\ \frac{1}{4}(3P^2 + 3Q^2 - 2PQ) \end{cases}$
$\chi_{\nu} \begin{cases} C_1 = C \\ C_2 = C \\ D = Aa \end{cases}$	$\begin{cases} \frac{1}{4}(3P^2 + 3Q^2 - 2PQ) \\ \frac{1}{4}(3P^2 + 3Q^2 - 2PQ) \\ \frac{1}{4}(P + Q)^2 \end{cases}$	$\begin{cases} \frac{1}{4}(3P^2 + 3Q^2 + 2PQ) \\ \frac{1}{4}(3P^2 + 3Q^2 + 2PQ) \\ \frac{1}{4}(3P^2 + 3Q^2 - 2PQ) \end{cases}$

Les constantes de Curie C_1 , C_2 et C ainsi que les termes A et D sont définis dans le texte (formules 8 et 9). Les paramètres P et Q également définis dans le texte sont caractéristiques du quadruplet Γ_8 considéré. Deux types de déformation axiale ont été envisagés: suivant un axe C_4 ou suivant un axe C_3 du site. Dans chaque cas l'axe z du système de coordonnées choisi est l'axe de la déformation; l'axe x est un axe C_4 dans le premier cas, et un axe C_2 dans le second.

deux voies différentes. Les fonctions d'onde que nous avons utilisées pour le calcul des coefficients P et Q sont les fonctions non perturbées par la déformation axiale. On peut lever cette restriction en utilisant une base de fonctions f quantifiées suivant un axe C_3 [11] mais nous verrons que les corrections correspondantes peuvent être négligées. D'un autre côté, le couplage induit par le champ magnétique entre l'état fondamental et les états excités conduit à une contribution indépendante de la température à la susceptibilité (paramagnétisme de Van Vleck). Ce terme χ_0 qui est faible a été calculé en fonction de V et V' dans le cas d'une symétrie parfaitement cubique. Nous n'en donnerons pas ici l'expression, qui est assez compliquée et qu'on peut trouver dans la Réf. [10]. Soulignons simplement que pour des valeurs de V et V' maintenues dans des limites raisonnables, le terme χ_0 est pratiquement indépendant de V .

Finalement la susceptibilité paramagnétique moyenne d'un électron f environné de 8 charges négatives formant un cube faiblement déformé, s'exprime par

$$\chi_{\nu} = \frac{1}{4} \beta^2 \left[\frac{C}{kT} + \frac{D}{ka} \tanh \frac{a}{T} \right] + \chi_0 \quad (10)$$

où C et D sont indiqués dans le Tableau 1; elle n'est pratiquement fonction que des 2 paramètres V' et a . En symétrie parfaitement cubique ($a = 0$), cette formule se réduit à la loi de Curie classique,

$$\chi_{\nu} = \frac{C_0}{T} + \chi_0. \quad (11)$$

RESULTATS EXPERIMENTAUX ET DISCUSSION

Nous avons étudié la susceptibilité magnétique des complexes M_3UF_8 ou M était l'ammonium, le sodium, le rubidium ou le césium. Les mesures ont été effectuées par la méthode de Faraday, à des températures allant de 8 à 300°K. La valeur du champ magnétique était en principe fixée à 6000 G. Cependant des mesures en fonction du champ ont été faites pour mettre en évidence une éventuelle variation de la susceptibilité. Dans le domaine de température étudié, aucun état ordonné n'a pu être mis en évi-

dence, le comportement restant toujours parfaitement paramagnétique. Les interactions d'échange entre les électrons magnétiques sont donc certainement très faibles.

Les susceptibilités mesurées ont été corrigées des contributions diamagnétiques qui proviennent surtout des électrons des couches internes. Les corrections ont été estimées par la méthode de Angus[12]; les résultats corrigés des mesures sont indiqués sur la Fig. 2 où l'on a porté le produit χT en fonction de la température. La variation thermique de la susceptibilité ne suit pas du tout une loi simple du type de la formule (11). La figure indique également les courbes donnant les variations théoriques de la susceptibilité lorsque les ions UF_6^{3-} présentant une déformation quadratique ou trigonale. Ces courbes ont été déterminées à partir de l'expression (10); C et D sont indiqués dans le Tableau 1 en fonction de P et Q ; P et Q s'expriment en fonction de l'angle φ (formule 6) qui ne dépend que de V'/ζ (formule 1). La meilleure valeur du paramètre V'/ζ a été déterminée sur ordinateur. Les corrections au second ordre des coefficients P et Q ont été négligées pour la détermination des courbes théoriques, mais un calcul *a posteriori* montre qu'elles sont faibles, étant de 10 pour cent au plus. La valeur de χ_0 , également faible, (quelques pour cent de la susceptibilité totale à température ambiante) a été prise en compte dans le calcul des courbes théoriques.

L'étude de la susceptibilité favorise très nettement l'existence d'une déformation de symétrie trigonale du cube des fluors, entourant l'uranium. L'accord entre valeurs calculées et valeurs expérimentales est toutefois moins bon aux plus basses températures. L'introduction d'une faible interaction d'échange entre les électrons magnétiques, dont on ne peut pas penser qu'elle soit rigoureusement nulle, suffit à rendre l'accord excellent. Puisqu'aux basses températures, la susceptibilité est surtout due au terme de Curie, il suffit de remplacer la formule (10)

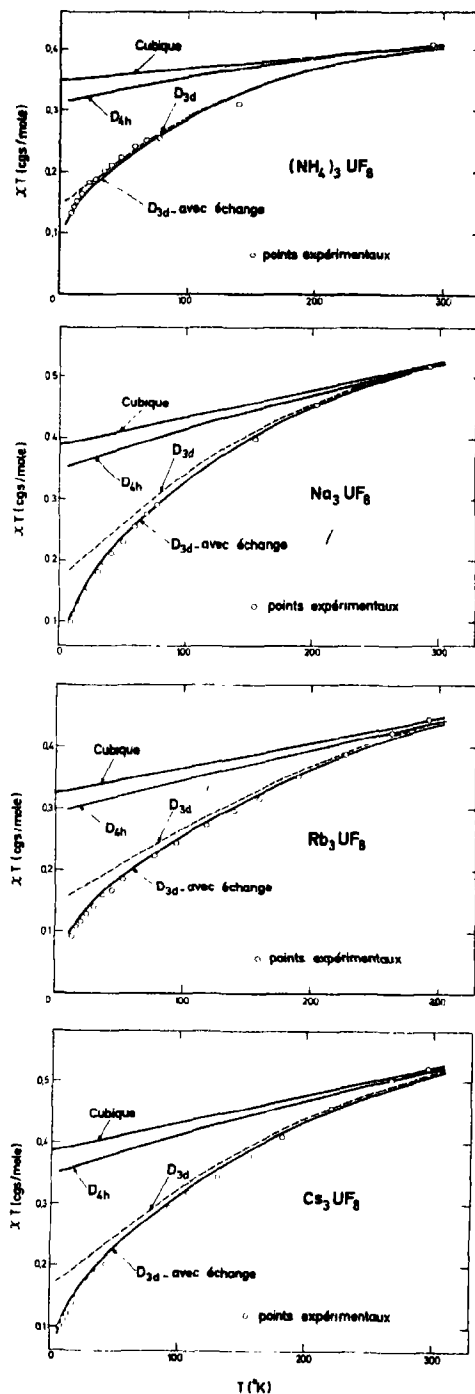


Fig. 2. Susceptibilités magnétiques des complexes UF_6Na_3 , UF_6Rb_3 , UF_6Cs_3 et $\text{UF}_6(\text{NH}_4)_3$. Les courbes représentées sont des courbes théoriques.

par:

$$\chi = \frac{C'}{T + \Delta} + A' \operatorname{th} \frac{a}{T} + \chi_0. \quad (12)$$

Les meilleures valeurs des paramètres V' et a ainsi que des températures d'échange Δ sont indiquées dans le Tableau 2. Il faut

ces complexes. Un essai préliminaire dans cette dernière voie, à 77°K et à une longueur d'onde de 3 cm s'est révélé négatif. Ceci pourrait indiquer que le doublet fondamental, qui est peuplé à 99 pour cent à cette température, est le doublet $\Gamma_{47} + \Gamma_{57}$ qui ne peut donner lieu à une absorption en RPE. Mais

Tableau 2. Valeurs des paramètres déterminés par l'étude des susceptibilités magnétiques

	V' cm ⁻¹	a °K	$\chi_0 \times 10^3$ cgs/mole	Δ °K	C' cgs/mole	A' cgs/mole
(NH ₄) ₃ UF ₆	4 175	160	0,20	2	0,145	0,217
Na ₃ UF ₆	2 500	190	0,45	8	0,169	0,252
Rb ₃ UF ₆	4 100	270	0,40	8,5	0,146	0,218
Cs ₃ UF ₆	2 800	210	0,45	7	0,164	0,245

souligner que ces valeurs ne sont les meilleures que dans le cadre des approximations que nous avons faites: le site est supposé cubique faiblement déformé ($a \ll V'$), les paramètres V et V' tels que $\chi_0 \ll \chi$; enfin le terme d'échange, certainement faible puisqu'aucun état ordonné n'est observé au dessous de 8°K, n'a été introduit qu'en dernier lieu. La constante du couplage spin-orbite d'un électron 5f de l'uranium V a été prise égale à 1955 cm⁻¹. Les contributions C , A et χ_0 au magnétisme sont également indiquées.

Il serait hasardeux de vouloir plus avant et de vouloir interpréter quantitativement les valeurs des paramètres V' et a que nous avons déterminées en termes de la géométrie de l'ion UF₆³⁻. La mauvaise connaissance que nous avons de la nature des liaisons uranium-fluor, et qui s'est introduite pour nous par une incertitude sur l'ordre des niveaux d'énergie de l'électron, est en fait un obstacle sérieux dans cette direction. Plutôt que de reprendre la théorie avec d'autres hypothèses sur la liaison chimique, il nous semble qu'il serait très précieux de pouvoir vérifier les hypothèses que nous avons faites, en prolongeant nos mesures vers les très basses températures, où un état ordonné devrait apparaître, ou en étudiant l'absorption optique, ou la résonance paramagnétique de

de toutes façons, la présence d'un doublet excité voisin laisse prévoir que les raies sont très larges et doivent être étudiées à très basse température.

Remerciements—Nous tenons à remercier Madame P. Charpin et Monsieur H. Nguyen-Nghi pour les fructueuses discussions que nous avons eues avec eux au cours de ce travail.

RÉFÉRENCES

1. PENNEMAN R. A., STURGEON G. D. et ASPREY L. B., *Inorg. Chem.* **3**, 126 (1964).
2. RUDORFF W. et LEUTNER H., *Lieb. Ann. Chem.* **632**, 1 (1960).
3. BOUGON R., CHARPIN P., CHATELET J., DIANOUX A. J., MARQUET-ELLIS H., NGUYEN-NGHI H. et PLURIEN P., 3ème Symposium international sur la chimie du fluor, Munich (1965).
4. BROWN D., EASEY J. F. et RICHARDS C. E. F., *J. Chem. Soc. (A)*, 1161 (1969).
5. KEMMLER-SACK S., STUMPP E., RUDORFF W. et ERFURTH H., *Z. Anorg. Allg. Chem.* **354**, 287 (1967).
6. EISENSTEIN J. C. et PRYCE M. H. L., *Proc. R. Soc. A* **255**, 181 (1960).
7. BLEANEY B., *Proc. Phys. Soc.* **73**, 939 (1959).
8. ABRAGAM A. et BLEANEY B., *Paramagnetic Resonance in Transition Metal Ions*, Oxford University Press, Oxford (1970).
9. AYANT Y., BELORIZKY E. et ROSSET J., *J. Physique*, **23**, 201 (1962).
10. DIANOUX A. J., Thèse de Doctorat-Rapport CEA R 3859 (1969).
11. RIGNY P., DIANOUX A. J. et PLURIEN P., *J. Phys. Chem. Solids* **32**, 1175 (1971).
12. ANGUS W. R., *Proc. R. Soc. A* **136**, (1932).

Tableau 1A. Fonctions d'ondes orbitales et spin-orbitales d'un électron f en site cubique. Les axes de coordonnées sont les axes de symétrie C_4 du site

Fonctions orbitales	Fonctions spin-orbitales
$\Gamma_4:$ $\delta_0 = y_3^0$ $\delta_1 = -\sqrt{6}/4 y_3^1 - \sqrt{10}/4 y_3^{-3}$ $\delta_{-1} = -\sqrt{6}/4 y_3^{-1} - \sqrt{10}/4 y_3^3$	$\Gamma_8:$ $\eta_{3/2} = \delta_1$ $\eta_{1/2} = \sqrt{6}/3 \delta_0 + \sqrt{3}/3 \bar{\delta}_1$ $\eta_{-1/2} = \sqrt{6}/3 \delta_0 + \sqrt{3}/3 \delta_{-1}$ $\eta_{-3/2} = \bar{\delta}_1$
$\Gamma_5:$ $\epsilon_0 = 1/\sqrt{2} (y_3^2 + y_3^{-2})$ $\epsilon_1 = \sqrt{10}/4 y_3^{-1} - \sqrt{6}/4 y_3^3$ $\epsilon_{-1} = \sqrt{10}/4 y_3^1 - \sqrt{6}/4 y_3^{-3}$	$\chi_{3/2} = -\sqrt{6}/3 \bar{\epsilon}_0 - \sqrt{3}/3 \epsilon_{-1}$ $\chi_{1/2} = \bar{\epsilon}_{-1}$ $\chi_{-1/2} = \epsilon_1$ $\chi_{-3/2} = -\sqrt{6}/3 \epsilon_0 - \sqrt{3}/3 \bar{\epsilon}_1$
$\Gamma_2:$ $\beta = -i/\sqrt{2} (y_3^2 - y_3^{-2})$	$\Gamma_6:$ $\zeta_{1/2} = \sqrt{3}/3 \delta_0 - \sqrt{6}/3 \bar{\delta}_1$ $\zeta_{-1/2} = -\sqrt{3}/3 \delta_0 + \sqrt{6}/3 \delta_{-1}$
	$\Gamma_7:$ $\varphi'_{1/2} = \sqrt{3}/3 \epsilon_0 - \sqrt{6}/3 \bar{\epsilon}_1$ $\varphi'_{-1/2} = -\sqrt{3}/3 \bar{\epsilon}_0 + \sqrt{6}/3 \epsilon_{-1}$ $\varphi_{1/2} = i\beta$ $\varphi_{-1/2} = i\bar{\beta}$

APPENDICE

Les parties angulaires des fonctions d'onde d'un électron f , sont les sept harmoniques sphériques Y_l^m . Si on les classe selon les représentations irréductibles du groupe cubique on trouve un singulet Γ_2 et 2 triplets Γ_4 et Γ_5 , dont les parties angulaires sont indiquées dans le Tableau 1A. Les axes de coordonnées sont les axes de symétrie C_4 du site cubique.

Si on inclut les fonctions de spin, on obtient quatorze fonctions qui se classent suivant les représentations du

groupe cubique double en deux doublets Γ_7 , deux quadruplets Γ_8 et un doublet Γ_6 . En indiquant la valeur de la projection du spin $m_s = -\frac{1}{2}$ par une barre au dessus de l'orbitale et $m_s = \frac{1}{2}$ par l'absence de signe on obtient les spin-orbitales indiquées dans le Tableau 3. Les indices des fonctions rappellent que les fonctions de symétries Γ_6 ou Γ_7 se transforment comme les fonctions propres d'un spin $\frac{1}{2}$, et que les fonctions d'un quadruplet Γ_8 se transforment comme les fonctions propres d'un spin $\frac{3}{2}$.

ANALYSIS OF SILICON NITRIDE LAYERS DEPOSITED FROM SiH_4 AND N_2 ON SILICON

O. MEYER

Institut für Angewandte Kernphysik, Kernforschungszentrum Karlsruhe, Germany

and

W. SCHERBER

AEG-Telefunken, Heilbronn, Germany

(Received 6 November 1970)

Abstract—Backscattering and channeling effect measurements of 1 MeV $^4\text{He}^+$ ions were used to determine the composition and density of Si_xN_y layers on single crystal silicon. The nitride layers were deposited by the reaction between SiH_4 and N_2 in a glow discharge at 350°C . The ratio N/Si in the layer decreases with increasing SiH_4 concentration and total pressure of the reaction gases whereas the density is nearly constant. Conditions for deposition of stoichiometric nitride layers were optimized. These results are in good agreement with measurements of etching rate and index of refraction. The composition of all samples is homogeneous over the entire layer.

1. INTRODUCTION

THIN films of silicon nitride are of interest in semiconductor device technology. In contrast to silicon dioxide layers they show little ion drift and good sealing properties. The standard method for the production of nitride layers is the chemical vapor deposition using the silane-ammonia reaction at temperatures above 700°C . Recently a new method was reported [1, 2] which starts from SiH_4 and N_2 and yields perfect nitride layers. The low deposition temperature (350°C) and the absence of ammonia, which always contains water and alkali ions, is very convenient for planar device passivation.

The object of this investigation is the structure of nitride layers from SiH_4 and N_2 . The energy analysis of backscattered ions allows one to identify the mass of the target atoms and to select a certain depth in the amorphous layer and in the Si substrate simply by evaluating corresponding portions of the energy spectrum. Furthermore backscattering of MeV $^4\text{He}^+$ ions can be used to determine the concentrations and distributions of nitrogen and silicon in the layers. By alignment of the incident beam direction with a crystal axis of

the silicon substrate the yield of backscattered particles is reduced (channeling effect) and a more accurate determination of the nitrogen concentration can be made. These techniques have been used to analyse silicon dioxide layers [3] and nitride layers from SiH_4 and NH_3 [4, 5]. For comparison with the backscattering data in this work, other structure dependent measurements as etching rate and index of refraction have been performed.

2. EXPERIMENTAL

The nitride layers were deposited on $500\ \Omega$ cm, (111)-oriented, boron-doped silicon wafers. Prior to deposition the surfaces were mechanically and chemically polished and thoroughly cleaned using conventional methods. Figure 1 shows the nitride deposition apparatus. The reaction between SiH_4 and N_2 takes place in a r.f. discharge inside of a quartz tube. The discharge is activated by a coil or a capacitor located outside the tube. The r.f. generator is operated at a frequency of 500 kHz. The wafer susceptor made from quartz contains a resistance heater. For purity and control purposes the whole gas flowing system satisfies high vacua requirements.

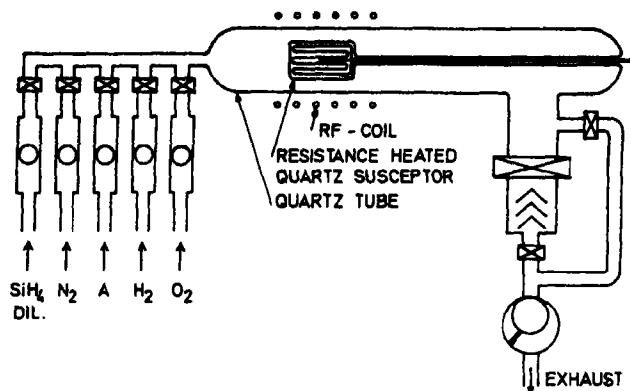


Fig. 1. Schematic drawing of the nitride deposition apparatus.

SiH_4 is used in a 2 per cent dilution in N_2 . The ratio SiH_4/N_2 in the reaction chamber can be varied from 10^{-4} to $1 \cdot 10^{-2}$ by mixing the SiH_4 gas with a separate N_2 stream. The gases N_2 , Ar, H_2 and O_2 can be used for glow discharge cleaning steps just prior to the deposition process.

The backscattering and channeling apparatus is illustrated in Fig. 2. In this work 1 MeV

$^4\text{He}^+$ ions are used. The samples are mounted on a two axis goniometer to permit the alignment of the beam with one of the crystal axes of the silicon substrate. The beam current is measured with an integrator; the target is shielded with a Faraday cup to avoid errors by secondary electron emission. The energy distribution of the backscattered $^4\text{He}^+$ ions is measured with a surface barrier detector.

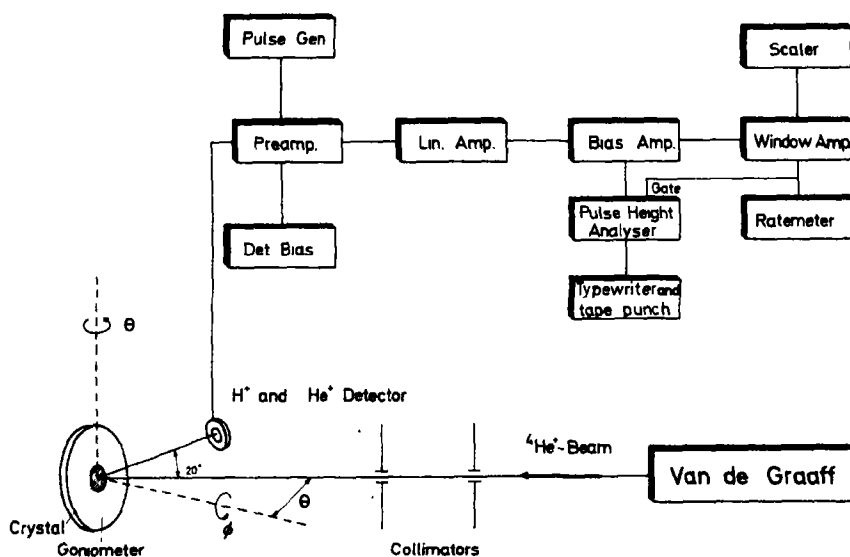


Fig. 2. Schematic illustration of the experimental arrangement in the target chamber together with the electronic instrumentation for energy analysis of backscattered particles.

The electrical signal from this detector is amplified and stored in a pulse height analyzer. The linear response of the nuclear particle detector provides a fixed energy per channel in the multichannel analyzer. The system conversion gain is 1.48 keV per channel. The energy resolution of the detecting system is about 10 keV, this corresponds to a depth resolution in the silicon nitride layer of about 150 Å for the beam energy and experimental geometry used.

3. ANALYSIS

A detailed description of the analysis technique has been given elsewhere [3]. For convenience the most important features of the analysis are summarized. In Fig. 3 random (cross-bars) and oriented (black dots) spectra are shown for illustration. Three portions of the spectra clearly can be identified. The first part for channel numbers greater than 190 is produced by $^4\text{He}^+$ particles backscattered from silicon atoms in the nitride layer. In the energy range called HW_N and the corresponding peak area HW_N times R_N , particles are backscattered from nitrogen atoms in the nitride layer. All other counts in the channel range from 0 to 190 are produced by $^4\text{He}^+$ ions, backscattered from silicon atoms in the substrate. The height of the step, R_{Si} , (number

of counts in one channel) is proportional to the concentration of silicon atoms in the nitride layer and the width of the step ΔE is proportional to the layer thickness. In the random spectra R_{Si} is proportional to the concentration of silicon atoms in the substrate. If the incident beam is aligned with a crystal axis, the contribution from the substrate is strongly reduced and permits a more accurate determination of the nitrogen concentration. The net height of the nitrogen peak, R_N , is proportional to the concentration of the nitrogen atoms and the width of the peak, HW_N , is proportional to the layer thickness. The proportionality constant is $[S]$, the backscattering energy loss parameter. The energy scale in Fig. 3 can be converted in a depth scale, t , by $\delta E = \delta t[S]$ where $[S] = \alpha \cdot dE/dx|_{E_0} + \cos \theta_i$, $dE/dx|_{\alpha E_0}$; α is the fractional amount of the energy after scattering and dE/dx is the specific energy loss at E_0 and αE_0 , the energy before and after scattering respectively.

The concentration ratio of nitrogen to silicon $N_N(t)/N_{Si}(t)$ at depth t in the layer is given by

$$\frac{N_N(t)}{N_{Si}(t)} = \frac{R_N(E)[S_N]}{R_{Si}(E)[S_{Si}]} \frac{\sigma_{Si}}{\sigma_N} \quad (1)$$

where σ is the scattering cross section in the laboratory system, $\sigma_{Si}/\sigma_N = 4.3$ in our experi-

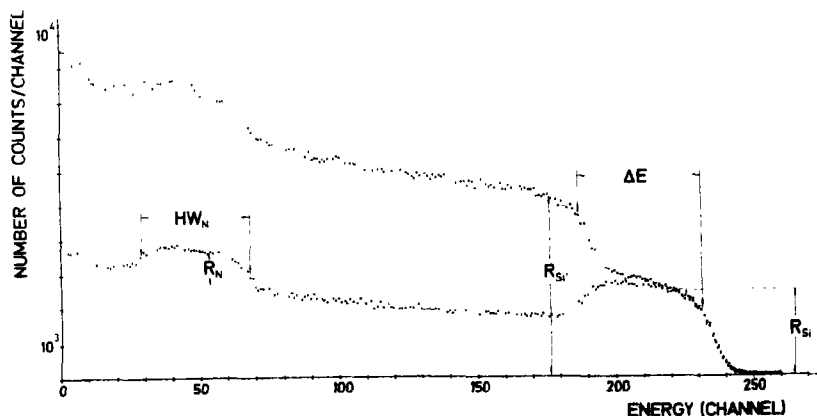


Fig. 3. Random and aligned spectra for 1 MeV $^4\text{He}^+$ ions scattered from a 953 Å silicon nitride layer deposited on 111 oriented silicon.

mental arrangement. The ratio $[S_N]/[S_{Si}]$ can be determined by the measured ratio $HW_N/\Delta E$. If the layer thickness is known from ellipsometry measurements, an absolute depth scale can be determined.

The values of N_{Si} can be calculated by comparing the silicon concentration in the nitride layer, N_{Si} , to that of silicon, N'_{Si} , in the substrate

$$N_{Si} = N'_{Si} \frac{R'_{Si}[S'_{Si}]}{R_{Si}[S_{Si}]} \quad (2)$$

$[S'_{Si}]$ can be calculated from values of the specific energy loss in silicon [6]. N_N can then be determined by equation (1).

The density ρ of the layer can be expressed by

$$\rho = \frac{N_{Si}}{L} \left[M_{Si} + \left(\frac{N_N}{N_{Si}} \right) M_N \right] \quad (3)$$

where L is Avogadro's number and M the atomic weight.

4. RESULTS

In a first series of layers the influence of SiH_4 concentration on the composition was

studied. The SiH_4 concentration was varied from $2 \cdot 10^{-2}$ per cent to 2 per cent. The total pressure during deposition was kept constant, the temperature of the substrate was always $350^\circ C$. The results of the analysis are presented in Fig. 4. The ratio N_N/N_{Si} was determined by equation (1) as an average over the layer thickness. With increasing SiH_4 concentration the ratio N_N/N_{Si} decreases. The dependence can be described by $N_N/N_{Si} = 1.06 - 0.143 \ln x$ where x is the SiH_4 concentration in per cent. The composition is found to be stoichiometric in the range of $0.1 \leq x \leq 0.2$. Results given in [5] for nitride layers from SiH_4 and NH_3 show, that with increasing NH_3/SiH_4 gas ratio the composition became stoichiometric as an saturation level. With the glow discharge method however it is possible to further increase the N_N/N_{Si} -ratio. The composition can be made silicon-rich or nitrogen-rich. This is supported by the results of etching rate measurements, also presented in Fig. 4. The etching rate reaches a maximum just in the SiH_4 concentration region, where the composition is stoichiometric. Again this is in contrast to measurements in [5] where the etching rate goes to an upper saturation level for stoichiometric layers. Index of refraction

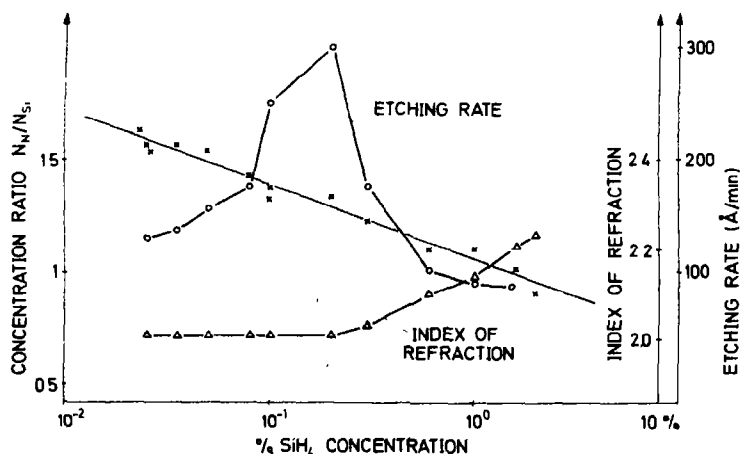


Fig. 4. Concentration ratio of nitrogen to silicon atoms as a function of the SiH_4 concentration in the deposition apparatus. Included are corresponding curves of etching rate and index of refraction.

measurements, which are also included in Fig. 4 substantiated the given results. For SiH_4 concentrations below 0.2 per cent where the composition changes from stoichiometric to nitrogen-rich $n = 2.01$ and independent of the SiH_4 concentration. Above 0.2 per cent n increases.

The distribution of the N_N/N_{Si} ratio over the layer thickness with the SiH_4 concentration as a parameter is presented in Fig. 5. The results

show that the composition is homogeneous over the total range of SiH_4 concentration used during the fabrication of the nitride layers. Deviations at the surface or at the interfaces (see Fig. 5) may be caused by uncertainties in the determination of the corresponding depth at the edges of the nitrogen and the silicon peak.

In Fig. 6 the average concentrations of silicon and nitrogen atoms in the silicon nitride

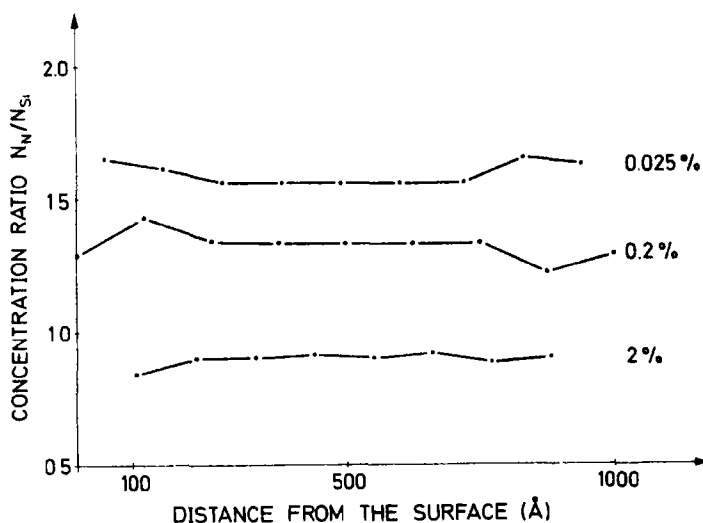


Fig. 5. Distribution of N_N/N_{Si} for samples prepared with different SiH_4 concentrations.

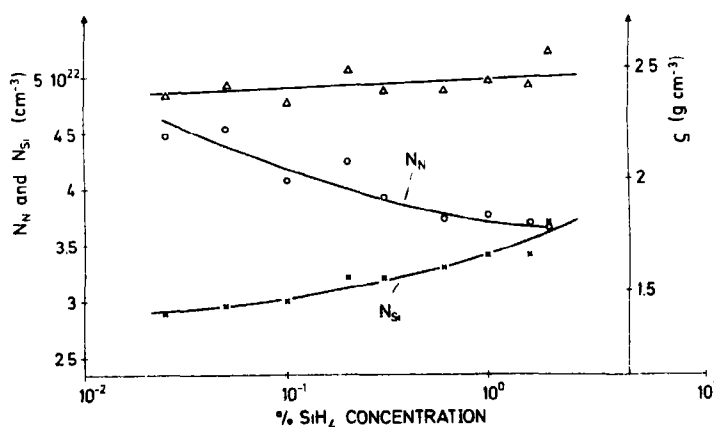


Fig. 6. Average atomic concentrations and densities of silicon nitride layers as a function of the SiH_4 concentration during deposition.

layers are shown in dependence of the SiH_4 concentration. N_{Si} was calculated using equation (2), $[S'_{\text{Si}}]$ -values were determined using dE/dx -values for 1 and 0.58 MeV $^4\text{He}^+$ ions in silicon given in [6]; the estimated error is about 10 per cent. $[S_{\text{Si}}]$ -values were determined from measured ΔE values together with layer thickness data, found by ellipsometry measurements. The average $[S_{\text{Si}}]$ value obtained was 67 eV/\AA for 1 MeV $^4\text{He}^+$ ions. The results in Fig. 6 show a slight increase for N_{Si} from 3 to $3.7 \cdot 10^{22}/\text{cm}^3$ with increasing SiH_4 concentration. Within the estimated total error of 15 per cent N_{Si} may be considered as constant for SiH_4 concentrations below 0.2 per cent. N_{N} however decreases from 4.5 to $3.6 \cdot 10^{22}/\text{cm}^3$ with increasing SiH_4 concentration. The average density of the silicon nitride layer, calculated by equation (3) is also presented in Fig. 6. The density is nearly independent of the SiH_4 concentration with an absolute value of about 2.5 g cm^{-3} ; of course a systematic error of about 10 per cent cannot be excluded.

Among other fabrication parameters that can be varied in the glow discharge deposition method the total pressure during deposition seems to have a strong influence on the composition. To study this influence the total pressure was varied between 0.25 and 2.8 Torr, the SiH_4 concentration was kept constant at 0.08 per cent. The results of the analysis are given in Fig. 7. $N_{\text{N}}/N_{\text{Si}}$ ratio decreases with increasing pressure but within the pressure region between 1 and 2 Torr the dependence is very weak. Again this result is supported by index of refraction measurements also presented in Fig. 7. For the SiH_4 concentration of 0.08 per cent n is nearly constant for pressures below 2 Torr while there is a remarkable increase for higher pressures. Quite different behaviour for n was obtained for a SiH_4 concentration of 0.5 per cent, where it is known from Fig. 4 that stoichiometric layers cannot be produced. Here n is above 2 on the whole pressure range besides at 0.2 Torr where a stoichiometric composition can be obtained.

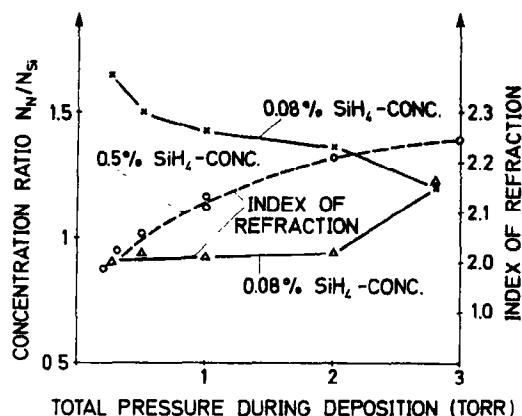


Fig. 7. Concentration ratio of nitrogen to silicon of samples prepared at different total pressures but constant SiH_4 concentration during deposition in the reactor chamber.

5. DISCUSSION

The experimental results show that the composition of nitride layers made from SiH_4 and N_2 depends on the SiH_4 concentration and on the total pressure during deposition. The composition in the layer was found to be stoichiometric for SiH_4 concentrations between 0.1 and 0.2 per cent and in the pressure range from 1 to 2 Torr. In the glow discharge deposition method the $N_{\text{N}}/N_{\text{Si}}$ ratio can be varied above and below the stoichiometric value. This was not observed for silicon nitride layers made from SiH_4 and NH_3 , where the maximum value obtained for $N_{\text{N}}/N_{\text{Si}}$ was 1.33. With increasing SiH_4 concentration N_{Si} increases from 3 to $3.7 \cdot 10^{22} \text{ cm}^{-3}$ whereas N_{N} decreases from 4 to $3.6 \cdot 10^{22} \text{ cm}^{-3}$. The density of the layer was about 2.5 g cm^{-3} and was found to be nearly independent of the SiH_4 concentration. This is somewhat lower than the values obtained in [5] and less than that of crystalline $\alpha\text{-Si}_3\text{N}_4$.

The total pressure is an important parameter in the glow discharge deposition method. For constant SiH_4 concentration of 0.08 per cent stoichiometric compositions are obtained between 1 and 2 Torr. For lower pressures $N_{\text{N}}/N_{\text{Si}}$ rises sharply whereas for higher pressures $N_{\text{N}}/N_{\text{Si}}$ drops.

The results obtained were in agreement with

other methods depending on the structure of the silicon nitride layer. The etching rate, for example, has a sharp maximum for stoichiometric composition whereas the index of refraction became saturated with a value of about 2.01 for N_N/N_{Si} ratios greater 1.3.

One advantage of the backscattering method is the information on depth dependence of the above quantities. The ratio N_N/N_{Si} is independent of depth for all SiH_4 concentrations studied.

Acknowledgement—Thanks are due to F. Wüchner for his help in taking the measurements at the Van de Graaff

accelerator and to H. Holzer, who prepared the various nitride films.

REFERENCES

1. KUWANO Y., *Jap. J. appl. Phys.* **8**, 876 (1969).
2. GERETH R., HOLZER H. and SCHERBER W., *J. electrochem. Soc.* Spring Meeting, Los Angeles (1970).
3. MEYER O., GYULAI J. and MAYER J. W., *Surface Sci.* **22**, 263 (1970).
4. GYULAI J., MEYER O., MAYER J. W. and RODRIGUEZ V., *Appl. Phys. Lett.* **16**, 232 (1970).
5. GYULAI J., MEYER O., MAYER J. W. and RODRIGUEZ V., to be published in *Appl. Phys.* Jan. 1971.
6. WILLIAMSON C. and BONJOT J. T., CEA-2189 (1962).

ELECTRONIC STATES OF HEAVY DIATOMIC CRYSTALS*

M. STEŚLICKA†, S. G. DAVISON‡ and U. SRINIVASAN

Quantum Theory Group,§ Departments of Applied Mathematics and Physics, University of Waterloo, Ontario, Canada

(Received 2 July 1970; in revised form 26 October 1970)

Abstract—The electronic states of heavy atomic solids are sensitive to relativistic corrections. The effects of these corrections on the eigenvalues and eigenfunctions of a diatomic crystal are investigated, by seeking the solutions of the Dirac equation for a Kronig-Penney type of potential. The relativistic band structure diagram shows that, although the relativistic correction leaves the forbidden energy gap widths unchanged, it does cause a shrinking of the bands. The band shrinkage and constancy of the gap widths is accommodated by a downward shift of the band edges.

1. INTRODUCTION

SINCE relativistic effects are prominent in heavy atomic solids, it is necessary to solve the Dirac equation, rather than the Schrödinger one, when investigating their electronic properties. A simple relativistic theory of heavy monatomic solids has been developed recently [1-6], which is based on solving the Dirac equation for the Kronig-Penney (KP) [7] potential. In addition to studying the bulk [1] states, the simplicity of the approach enabled a detailed analysis to be made of localized surface [2-4] and impurity [5, 6] states. The main findings of these calculations were the relativistic shrinkage of the bulk energy spectrum, and the reclassification of the non-relativistic (NR) localized states into relativistic and Dirac localized states, the latter possessing no NR analogue.

With many important semiconductors having a heavy diatomic structure [8-13],

the aim of the present article is to carry out a relativistic treatment of the bulk states of the KP model for an AB-type binary crystal, and so prepare the way for extending the work to include surface and impurity effects. These latter effects, which play such a significant role in semiconductor physics, are to be dealt with in future papers.

2. RELATIVISTIC FORMALISM

The Dirac equation for a linear spatially dependent potential $V(x)$ is [14]

$$i\hbar\dot{\psi} - i\hbar\alpha_x\psi' + m_0c^2\beta\psi - V\psi = 0 \quad (1)$$

where ψ is a 4-component spinor in (x, t) , α_x and β are Dirac matrices, m_0 is the rest mass of the electron and c is the velocity of light. Carrying out the matrix multiplication in (1) leads to two pairs of coupled simultaneous equations, which can be written as [1, 4]

$$i\hbar\dot{\psi} - i\hbar c\sigma_x\psi' + m_0c^2\sigma_z\psi - V\psi = 0 \quad (2)$$

where ψ is now a 2-component spinor and $\sigma_{x,z}$ are Pauli spin matrices. As the potential V is spatial and not time dependent, the space-time coordinates can be separated by

*Work supported by the National Research Council of Canada and the University of Waterloo Research Committee.

†Permanent Address: Department of Experimental Physics, University of Wrocław, Poland.

‡Now at the Physics Department, Institute of Colloid and Surface Science, Clarkson College of Technology, Potsdam, N.Y. 13676, U.S.A.

§Q.T.G. article S-161.

putting

$$\psi(x, t) = \phi(x) \exp(-iEt/\hbar) \quad (3)$$

in (2) to give

$$i\hbar c \sigma_x \phi' - m_0 c^2 \sigma_z \phi = (E - V) \phi. \quad (4)$$

If $V = V_k$ in the k -region of constant potential, then the two spinor components $j = 1$ and 2 in (4) can be decoupled by differentiation to yield

$$d^2 \phi_k^{(j)} / dx^2 = -\rho_k^2 \phi_k^{(j)} \quad (5)$$

with

$$\rho_k^2 = (\epsilon_0 - V_k)(\epsilon_0 - V_k + 2m_0 c^2) / \hbar^2 c^2 \quad (6)$$

and

$$\epsilon_0 = E - m_0 c^2. \quad (7)$$

In matrix notation, the general plane-wave solution of (5) is

$$\phi_k = \alpha_k^{(2)} \Gamma_k^- e^{i\rho_k x} + \beta_k^{(2)} \Gamma_k^+ e^{-i\rho_k x} \quad (8)$$

where

$$\Gamma_k^\pm = \begin{pmatrix} \pm \gamma_k \\ 1 \end{pmatrix}, \quad \gamma_k = (\epsilon_0 - V_k) / \hbar c \rho_k \quad (9)$$

and $\alpha_k^{(2)}$, $\beta_k^{(2)}$ are the second-component spinor amplitudes, which are related to the first component amplitudes via

$$\alpha_k^{(1)} = -\gamma_k \alpha_k^{(2)}, \quad \beta_k^{(1)} = \gamma_k \beta_k^{(2)}. \quad (10)$$

3. ENERGY DISPERSION RELATION

The k -region spinor (8) can be propagated through the crystal by invoking the Bloch[15] theorem, viz.,

$$\phi_k(x) = u_k(x) e^{i\mu x} \quad (11)$$

μ being the wave number. From (8) and (11) comes

$$u_k(x) = \alpha_k^{(2)} \Gamma_k^- e^{i(\rho_k - \mu)x} + \beta_k^{(2)} \Gamma_k^+ e^{-i(\rho_k + \mu)x} \quad (12)$$

which, for the diatomic KP potential (Fig. 1), must satisfy the continuity conditions

$$\begin{aligned} u_I(0) &= u_{II}(0) \\ u_{II}(a) &= u_{III}(a) \\ u_{III}(a+b) &= u_{IV}(a+b) \\ u_I(-b) &= u_{IV}(2a+b). \end{aligned} \quad (13)$$

With the aid of (9), equations (12) and (13) lead to eight homogeneous simultaneous equations in $\alpha_k^{(2)}$ and $\beta_k^{(2)}$, whose non-trivial solutions require the determinantal compatibility condition to be fulfilled, i.e.,

$$\begin{vmatrix} A_1 & -A_2 & 0 & 0 \\ 0 & B_2(a) & -A_3 & 0 \\ 0 & 0 & B_3(b) & -A_2 \\ B_1(-b) & 0 & 0 & -B_2(a) \end{vmatrix} = 0 \quad (14)$$

where the elements are the 2×2 block partitions

$$\begin{aligned} 0 &= \begin{bmatrix} 0 & 0 \\ 0 & 0 \end{bmatrix}, \quad A_k = \begin{bmatrix} -\gamma_k & \gamma_k \\ 1 & 1 \end{bmatrix} \\ B_k(a) &= \begin{bmatrix} -\gamma_k e^{i(\rho_k - \mu)a} & \gamma_k e^{-i(\rho_k + \mu)a} \\ e^{i(\rho_k - \mu)a} & e^{-i(\rho_k + \mu)a} \end{bmatrix}. \end{aligned} \quad (15)$$

Expanding the determinant in (14), using (15), and performing some lengthy manipulation yields

$$\begin{aligned} \cos 2\mu(a+b) + \cos \xi_1 \cos \xi_3 &+ p_{13} \sin \xi_1 \sin \xi_3 = \\ 2 \cos \xi_1 \cos \xi_3 \cos^2 \rho_2 a + 2p_{12} p_{23} \sin \xi_1 \sin \xi_3 &\times \sin^2 \rho_2 a \\ -2 \sin \rho_2 a \cos \rho_2 a (p_{12} \sin \xi_1 \cos \xi_3 &+ p_{23} \cos \xi_1 \sin \xi_3). \end{aligned} \quad (16)$$

where

$$\xi_k = \rho_k b, \quad p_{ij} = (\gamma_i^2 + \gamma_j^2) / 2\gamma_i \gamma_j. \quad (17)$$

Transforming the KP potential in Fig. 1 into Dirac δ barriers and taking

$$\lim_{\substack{V_k \rightarrow \infty \\ b \rightarrow 0}} V_k b = \tau_k, \quad k = 1 \text{ and } 3 \quad (18)$$

so that

$$\xi_k = -\tau_k/\hbar c, \quad \gamma_k = 1 \quad (19)$$

enables (16) to be written in the simpler form

$$\cos^2 \mu a = \prod_{k=1,3} (\cos \rho_2 a - \rho_2 \xi_k \sin \rho_2 a) \quad (20)$$

where

$$\rho_2 = (1 + \gamma_2^2)/2\gamma_2 \quad (21)$$

and $\tau_k \ll \hbar c$, i.e., ξ_k is small. The *relativistic KP dispersion relation* for a diatomic crystal (20) can be expressed as [cf. Refs. [1] and [4]

$$\cos^2 \mu a = \prod_{k=1,3} [\cos \rho_2 a + (m\tau_k/\hbar^2 \rho_2) \sin \rho_2 a] \quad (22)$$

m being the relativistic electron mass. In the NR limit, as $c \rightarrow \infty$, and when $\tau_k = \tau$, equation (22) reduces to the well-known KP relation[7] for a *monatomic* solid, namely,

$$\cos \mu a = \cos \rho_0 a + (m_0 \tau/\hbar^2 \rho_0) \sin \rho_0 a \quad (23)$$

the zero subscript denoting NR parameters, so that

$$\rho_0^2 = 2m_0 \epsilon_0/\hbar^2.$$

Following the same procedure as Glasser and Davison (GD)[1], the relativistic energy band edges for a diatomic crystal can be computed, in atomic units, via (22). For the given set of parameters, the numerical values are displayed in Table 1, along with those of the NR case and the corresponding monatomic crystal relativistic and NR values. On the basis of these values, the schematic band structure diagram of Fig. 2 can be drawn, and a comparative study made of the four spectra.

The monatomic crystal spectrum consists of a series of bands. In the diatomic one, each of these bands is split by a forbidden energy gap, and the two bands so formed do not extend over as large an energy range as their monatomic counterpart. A more detailed analysis of these two spectra has been performed by Saxon and Hutner (SH)[16], who used the Green function and scattering matrix techniques. As in the monatomic crystal case[1], the relativistic correction causes the energy spectrum of the diatomic crystal to *shrink*, so that the band edges are displaced downwards (Fig. 2). The effects of this shrinkage on the gap (ΔE_g) and band (ΔE_b)

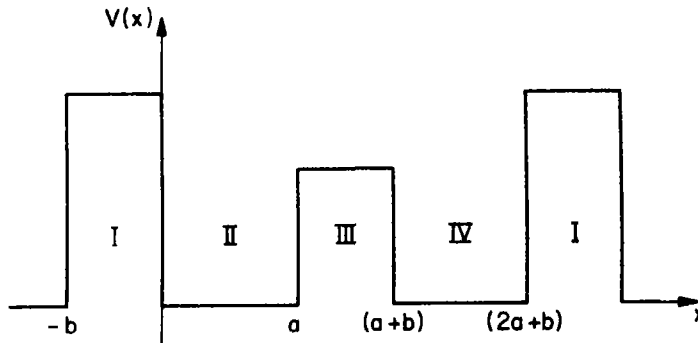


Fig. 1. Kronig-Penney potential for a diatomic crystal.

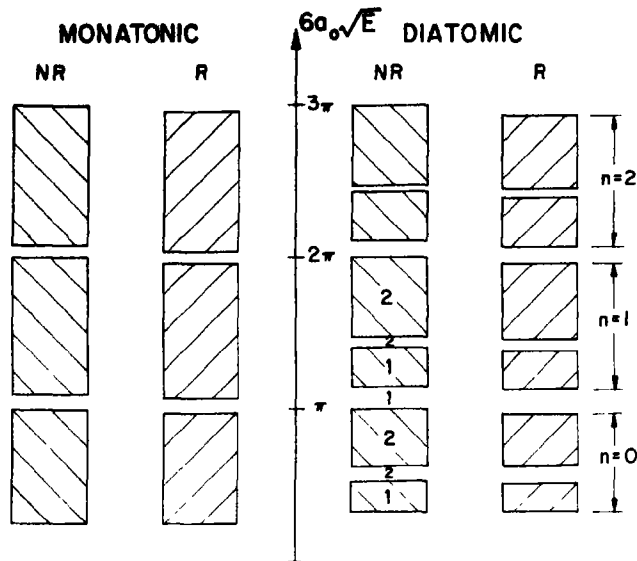


Fig. 2. Band structure diagram based on Table 1. In the diatomic spectra, notice the classification of the bands and the gaps into types 1 and 2 and also the numbering of the bands.

Table 1. Energy band edge values in rydbergs for non-relativistic (NR) and relativistic (R) monatomic and diatomic crystals of lattice spacing $2a = 6a_0$ ($a_0 = \text{Bohr radius}$). Other parametric values are [1]: (a) monatomic $a\tau = 5 \times 10^{-3}$; (b) diatomic $a\tau_1 = 5 \times 10^{-3}$, $a\tau_3 = 10^{-2}$

NR	Monatomic R	Diatomic NR	R
0.09996	0.09996	0.12237	0.12237
		1.57397	1.57397
		1.57714	1.57713
3.14159	3.14159	3.14159	3.14157
3.14477	3.14477	3.14636	3.14634
		4.71345	4.71337
		4.71451	4.71444
6.28319	6.28314	6.28319	6.28301
6.28478	6.28473	6.28557	6.28539
		7.85462	7.85427
		7.85525	7.85491
9.42478	9.42463	9.42478	9.42418
9.42584	9.42569	9.42637	9.42577
		10.99603	10.99507
		10.99648	10.99553
12.56637	12.56601	12.56637	12.56494

widths are shown graphically in Figs. 3 and 4, respectively. The coincidence of the NR and relativistic (R) curves in Fig. 3 indicates that the gap widths are insensitive to the relativistic correction. However, in Fig. 4, the R curve falls below the NR one, particularly at high band number n . Thus, the relativistic correction reduces ΔE_b , while it leaves ΔE_g unchanged. Hence, the downward displacement of the band edges occurs as a result of the band shrinkage being absorbed, in such a way, as to keep the gap widths constant. These findings are in agreement with those of GD[1] for monatomic crystals.

4. SPINOR EXPRESSION

A complete description of the electronic states of a diatomic crystal requires not only the eigenvalues, but also the eigenvectors. Since $b \rightarrow 0$, only solutions in regions II and IV of Fig. 1 are of interest. Following KP[7] and solving the simultaneous equations for $\alpha_k^{(2)}$ and $\beta_k^{(2)}$ leads, in the δ -function limit, to

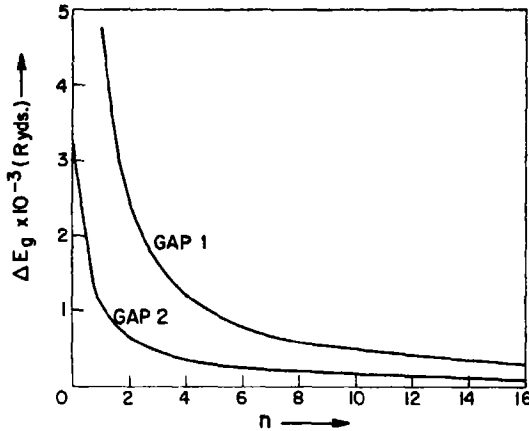


Fig. 3. Variation of the gap widths ΔE_g with the band number n . The NR and R curves are coincident.

$$\lambda = \beta_k^{(2)}/\alpha_k^{(2)} = [e^{2k(\rho - \mu)a} - 1]/[1 - e^{-2k(\rho_2 + \mu)a}] \quad (24)$$

with $k = 2$ and 4 . The form of the bulk spinor can now be chosen as

$$\phi(x) = \alpha_2^{(2)}[\Gamma_2^- e^{i\rho_2 x} + \lambda \Gamma_2^+ e^{-i\rho_2 x}] + \delta_{ij} \alpha_4^{(2)}[\Gamma_2^- e^{i\rho_2(x+a)} + \lambda \Gamma_2^+ e^{-i\rho_2(x+a)}] \quad (25)$$

in which

$$\begin{aligned} \delta_{ij} &= 1, \quad i = j && \text{for diatomic case} \\ &= 0, \quad i \neq j && \text{for monatomic case.} \end{aligned}$$

Considering the diatomic situation, the second-component spinor amplitudes $\alpha_{2,4}^{(2)}$ are found by setting

$$\phi^{(2)}(0) = \phi_1, \quad \phi^{(2)}(a) = \phi_3 \quad (26)$$

which, together with (24) and (25), give

$$\alpha_2^{(2)} = \Lambda \Phi_{13}^- / \Delta e^{-2i\mu a}, \quad \alpha_4^{(2)} = \Lambda \Phi_{31}^+ / \Delta \quad (27)$$

where

$$\begin{aligned} \Lambda &= [1 - e^{-2k(\rho_2 + \mu)a}] \\ \Phi_{13}^- &= i(\phi_1 \cos \rho_2 a - \phi_3 e^{-i\mu a} \cos \mu a) \\ \Phi_{31}^+ &= i(\phi_3 \cos \rho_2 a - \phi_1 e^{i\mu a} \cos \mu a) \\ \Delta &= 2 \sin \rho_2 a (\cos 2\mu a - \cos 2\rho_2 a). \end{aligned} \quad (28)$$

The relativistic KP relation (22) can be obtained from the product of

$$\phi_1 e^{i\mu a} \cos \mu a = \phi_3 [\cos \rho_2 a + (m\tau_3/\hbar^2 \rho_2) \sin \rho_2 a]$$

$$\phi_3 e^{-i\mu a} \cos \mu a = \phi_1 [\cos \rho_2 a + (m\tau_1/\hbar^2 \rho_2) \sin \rho_2 a]. \quad (29)$$

On using (29), in conjunction with (27) and (28), equation (25) can be rewritten as

$$\begin{aligned} \phi(x) &= i m \sin \rho_2 a [\tau_1 \phi_1 \Omega(x) \\ &\quad + \tau_3 \phi_3 e^{-2i\mu a} \Omega(x+a)] / \hbar^2 \Delta \rho_2 \end{aligned} \quad (30)$$

with

$$\Omega(x) = [e^{2i\mu a} \omega(x) - \omega(x-2a)]$$

where

$$\omega(x) = (\Gamma_2^+ e^{-i\rho_2 x} - \Gamma_2^- e^{i\rho_2 x}). \quad (32)$$

In the NR limit, Γ_2^\pm , ρ_2 and m are replaced by unity, ρ_0 and m_0 , respectively, in which case (30) can be easily identified with the diatomic crystal wave function of SH[16].

Equation (30) can, of course, also be reduced to the wave function expression for a monatomic crystal of lattice spacing $2a$, by merely putting $\tau_3 = 0$.

5. DISCUSSION

A complete analysis of the electronic states of heavy diatomic crystals has been presented, based on the solution of the Dirac equation via the KP[7] approach, which matches the wave functions across the potential discontinuities in the crystal field. Comparisons have been drawn with the results of GD[1], who used the scattering matrix method[16] to obtain the energy spectrum of heavy monatomic crystals. It is found that, in both mono- and diatomic crystals, the relativistic effects lead to a shrinkage of the energy bands, while the gaps tend to remain unaltered. This is made possible by the accompanying downward displacement of the band edges. It

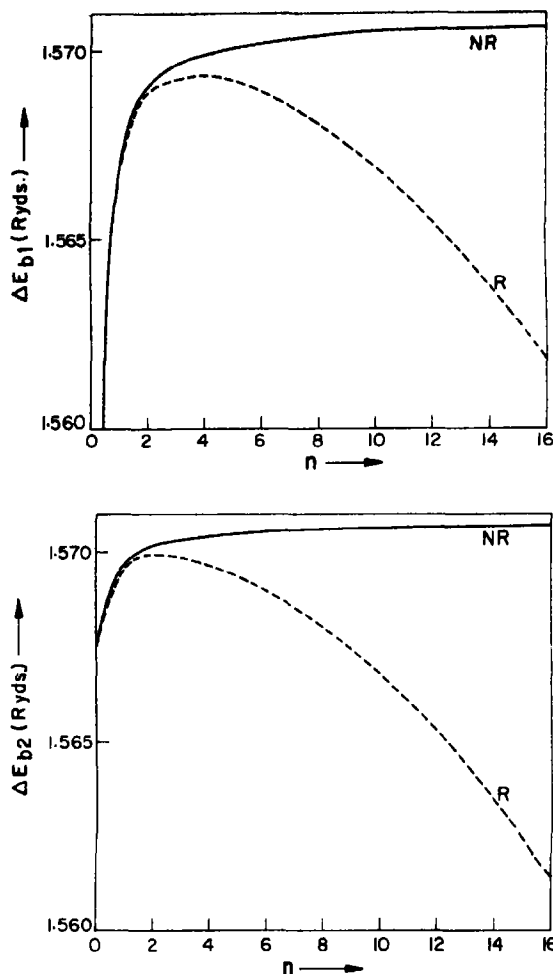


Fig. 4. Graphs of the band widths ΔE_b against the band number n , showing the relativistic shrinkage.

should also be noted that, by suitable choice of parameters, the more general relativistic model used here can be reduced to the simpler relativistic and NR models employed in the earlier treatments.

The above findings are in qualitative agreement with the relativistic APW[8, 9] and OPW[10] calculations, where the Foldy-Wouthuysen (FW)[17] transformation is used to express the Dirac Hamiltonian as the NR Hamiltonian plus the mass-velocity, Darwin and spin-orbit coupling correction terms. In

these investigations, the crystal field is represented by the muffin-tin potential. By choosing the simpler KP potential, the present approach enables the Dirac equation to be solved *exactly* in a straight forward manner, without resorting to the FW transformation. Thus, the relativistic effects no longer appear as a series of correction terms to the NR results, but are included altogether.

However, the FW approach is, of course, useful for studying the contributions arising from individual correction terms. The spin-

orbit interaction in heavy diatomic crystals has been examined in this way. Instead of utilizing the crystal potential methods, Doggett[11] adopted the bond orbital technique to investigate the spin-orbit splittings of the valence band, in several diatomic semiconductors, when overlap and valence-conduction band interaction are included. Another calculation along these lines is that of Tung and Cohen[13], who showed that, by incorporating spin-orbit coupling into the empirical pseudopotential method[18], the energy spectra obtained for the IV-VI compounds considered were in better agreement with experiment than their NR counterparts.

All of these calculations demonstrate the need for including relativistic effects in the study of the band structure of heavy diatomic solids. Moreover, since the band edges, from which localized state energy levels appear, are sensitive to these effects, it is important to treat the localized states of heavy diatomic crystals from a relativistic point of view. In order to do this, one must have a simple periodic potential, such as the KP one, so that the difficulties arising from the complicated boundary conditions can be treated successfully in the Dirac formulation. Once the KP-type model has provided a qualitative understanding of localized state problems, it should be possible to extend the work to more realistic crystal potentials and so obtain a quantitative knowledge.

REFERENCES

1. GLASSER M. L. and DAVISON S. G., *Intern. J. Quant. Chem.* **3S**, 867 (1970). [Eyring Symposium Issue].
2. DAVISON S. G. and STESLICKA M., *J. Phys. C. (Solid State Phys.)* **2**, 1802 (1969).
3. STESLICKA M. and DAVISON S. G., *Phys. Rev.* **B1**, 1858 (1970).
4. DAVISON S. G. and LEVINE J. D., *Surface States, in Solid State Physics*, Vol. 25 (Edited by F. Seitz, D. Turnbull and H. Ehrenreich). Academic Press, New York (1970).
5. STESLICKA M., DAVISON S. G. and BROWN A. G., *Proc. 3rd IMR Symposium, Electronic Density of States*, Nat. Bur. Stand. (U.S.), Spec. Publ. 323 (1970), in press.
6. DAVISON S. G. and STESLICKA M., *Intern. J. Quant. Chem.* **4S**, in press (1970). [Sanibel Island Symposium Issue].
7. KRONIG R. L. and PENNEY W. G., *Proc. R. Soc.* **A130**, 499 (1931).
8. JOHNSON L. E., CONKLIN, Jr. J. B. and PRATT, Jr. G. W., *Phys. Rev. Lett.* **11**, 538 (1963).
9. CONKLIN, Jr. J. B., JOHNSON L. E. and PRATT, Jr. G. W., *Phys. Rev.* **137**, A1282 (1965).
10. CHOW P. C. and LIU L., *Phys. Rev.* **140**, A1817 (1965).
11. DOGGETT G., *J. Phys. Chem. Solids* **27**, 99 (1966).
12. HERMAN F., KORTUM R. L., ORTENBURGER I. R. and VAN DYKE J. P., *J. Phys. Paris* **29**, C4-62 (1968). [IV-VI Semiconducting Compounds Issue].
13. TUNG Y. W. and COHEN M. L., *Phys. Rev.* **180**, 823 (1969).
14. SCHIFF L. I., *Quantum Mechanics*, p. 323. McGraw-Hill, New York (1955).
15. BLOCH F., *Z. Phys.* **52**, 555 (1928).
16. SAXON D. S. and HUTNER R. A., *Philips Res. Rep.* **4**, 81 (1949).
17. FOLDY L. L. and WOUTHUYSEN S. S., *Phys. Rev.* **78**, 29 (1950).
18. COHEN M. L. and BERGSTRESSER T. K., *Phys. Rev.* **141**, 789 (1966).

DIELECTRIC ABSORPTION OF POLYMERS FROM THE MILLIMETER TO THE FAR INFRARED REGION

E. M. AMRHEIN and H. HEIL

Institut für Polymere, Universität Marburg, 355 Marburg, Marbacher Weg 15, W.-Germany

(Received 12 June 1970; in revised form 11 October 1970)

Abstract—The high dielectric absorption of partially crystalline polymers and glasses in the far i.r. has been studied. It rises with frequency, starting from the millimeter range, and is essentially temperature independent. It is interpreted as disorder-induced one-phonon absorption which, outside the range of optically active vibrations, reflects the phonon density of states.

At the low frequency side (4 and 8 mm wavelengths) a strongly temperature dependent multiphonon absorption was measured. The absorption-temperature curves show an inflexion point or plateau at a temperature $\hbar\omega_0/k$, where ω_0 equals the frequency of those phonons that are mainly contributing to 3-phonon processes. It can be shown that ω_0 is the lowest optically active frequency of the one-phonon absorption. Good experimental correlation between that characteristic temperature range and the far i.r. measurements was found.

INTRODUCTION

THE ABSORPTION of electromagnetic radiation, especially the measurement of dielectric loss in the radio frequency range is a common tool for structural studies of polymers. We tried to extend this method to the high frequencies of the millimeter and far i.r. region and applied it to the investigation of glasses and amorphous and partially crystalline polymers. It is in the intermediate frequency range, between 10^{10} and 10^{13} Hz that the behaviour of amorphous materials differs markedly from that of crystals: The lattice absorption bands are at about the same frequencies as in the corresponding crystals, but the peaks are smeared out, and there is an additional absorption at frequencies which are forbidden for the ideal crystal. This not-allowed absorption becomes the stronger the less crystalline the substance. Going from the lowest lattice vibration frequencies towards longer wavelengths the absorption decreases only slowly. There remains a substantial dielectric loss even in the 4 and 8 mm band. Again the absorption is higher in the more amorphous materials. To explore its origin the temperature dependence

was investigated from 1.8 to 350°K. It showed a behavior which is typical for 3 phonon processes.

In the following we try to develop a consistent picture of the nature of the electromagnetic absorption in partially amorphous polymers. First the assumed model and its theoretical background are presented; secondly the experimental verification, both for the one phonon far i.r. absorption and for the multiphonon absorption in the millimeter range is shown.

1. ONE PHONON ABSORPTION IN AMORPHOUS MATERIALS

(a) *The assumed model*

Infrared as well as X-ray investigations of amorphous polymers and inorganic glasses show that the long-range order is lost while the nearest-neighbour order equals that of the corresponding crystalline state. Since vibrational frequencies depend to a great deal on the nearest-neighbour order, we made the first assumption that when describing the vibrational behavior of partially crystalline polymers it is allowed to start from the

spectrum of the ideal crystal. The density of phonon states $g(\omega)$ is

$$g(\omega) \approx g(\omega)_{\text{crystal}} \quad (1)$$

In the case of the undisturbed lattice the translational invariance leads to the selection rules which restrict the one-phonon absorption to

$$\begin{aligned} q_{\text{phonon}} &= q_{\text{phonon}} \approx 0 \\ q &= \text{wave vector.} \end{aligned} \quad (2)$$

This rule weakens, as soon as the order of the crystal is disturbed. If there are some disordered elements within the range $a \approx \lambda_{\text{phonon}}$, the resulting dipole moment for a phonon wave with frequency ω may be larger than zero, though its wave vector q does not equal $2\pi/\lambda_{\text{phonon}}$. This means, that points of high density in $g(\omega)$ should now show up in the electromagnetic absorption spectra. We would like to call this phenomenon disorder-induced absorption. The corresponding mechanism is known as 'defect-induced absorption' [11], if the 'disordered elements' are single impurity atoms or vacancies, dissolved in an unperturbed lattice. The actual intensity of the disorder-induced absorption in amorphous materials is a rather involved quantity. It depends on the number and type of disturbances, but also on the dipole moment of adjacent lattice elements induced by the phonon wave considered. For the optical branches this dipole moment has its maximum value at $q = 0$ and falls off to zero towards the zone boundary; for the acoustical branches it varies in the opposite way. Finally, polar substances should show a stronger disorder-induced absorption than non-polar ones. All these rules can be verified in the following figures.

(b) Experiments

In Figs. 1–4 far i.r. spectra are presented of polyethylene (PE), polyoxymethylene (POM), and quartz glass. They were measured by a Fourier spectrometer (Grubb–Parsons) and

computed in terms of the dielectric loss factor $\tan \delta$ for comparison with the microwave data.

$$\tan \delta = \frac{\alpha}{2\pi n \nu} \quad \begin{aligned} \alpha &= \text{absorption coefficient} \\ n &= \text{refractive index} \\ \nu &= \text{wave number.} \end{aligned}$$

(Multiplication with the wavenumber gives the corresponding frequency dependence of the absorption coefficient) $q(\omega)$, as calculated for the ideal crystal, and also the allowed i.r. active frequencies are shown for comparison. In the case of vitreous silica $g(\omega)$ was taken from a calculation of a quartz glass model [1]. The assumption that the measured spectra originate from one phonon absorption is proved by the temperature independence of the absorption. Figure 1 also shows that the absorption rises with the amount of amorphous phase. Figure 3 demonstrates how the 'background loss' in an amorphous sample resembles the total phonon density: Fig. 4 gives a detail of the region around 90 cm^{-1} ; the maximum in the density of phonon states shows up in the spectrum, though the selection rules do not allow the transition. Comparison between the two samples gives a ratio of 1.80 for the areas of the absorption peaks and a ratio of 1.85 for the corresponding amounts of amorphous phase $(1 - \omega^c)(\omega^c = \text{crystal content})$. Yet there is a 200-fold higher absorption around the frequencies of the 'optical' ($q = 0$)-modes. Whether $g(\omega)$ is the same in the partially disordered system as in the ideal crystal, can best be checked at the allowed frequencies, i.e. at $q \approx 0$. The loss of long-range order should affect the long wavelength phonons most. Since the allowed transition frequencies scarcely change, we expect our assumption (1) to be a good approximation.

Besides the discussed disorder-induced absorption in the amorphous polymers there may be local or quasi local in-band-modes which give rise to additional absorption at low frequencies. It will be difficult – if possible

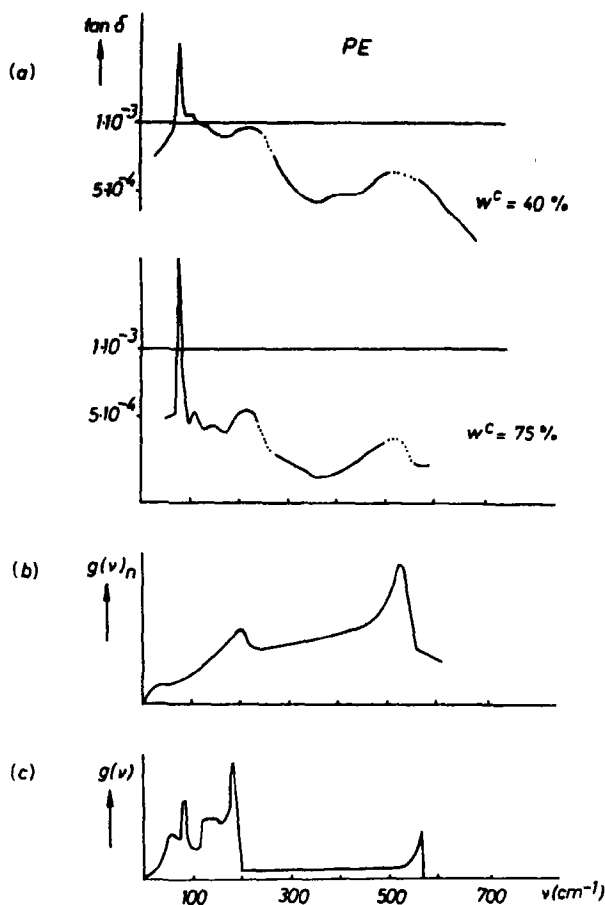


Fig. 1. (a) Dielectric loss of polyethylene samples in the far i.r. $T \approx 100$ K; w^c = crystallinity (Multiply $\tan \delta$ by $2\pi n\nu$ in order to get the absorption coefficient; n = refractive index, ν = wave number). (b) $g(\nu)_n$ = phonon frequency distribution from neutron inelastic scattering (6) (c) $g(\nu)$: calculation for the 3-dimensional crystal (12).

at all—to identify such modes in polymers; first: the disturbances in a polymer lattice are generally not coupled with charges or big mass defects, like defects in the alkali halides; secondly: a strong multi-phonon absorption is superposed on the residual one-phonon absorption.

2. MULTIPHONON ABSORPTION

Going from higher to lower frequencies the discussed defect-induced one-phonon absorption weakens off, since $g(\omega)$ as well as

the dipole moment go to zero for $\omega \rightarrow 0$ (acoustical branch). The remaining absorption which is found between the microwave range and the far i.r. must be multiphonon absorption. Two-phonon absorption has a low-frequency cut-off given by the smallest difference $\Delta\omega$ for $\Delta q \approx 0$. Here again the loss of the selection rules for the disordered system causes a smearing out of the absorption bands. At frequencies below the two-phonon cut-off, three-phonon absorption will dominate, if the temperature is not too low.

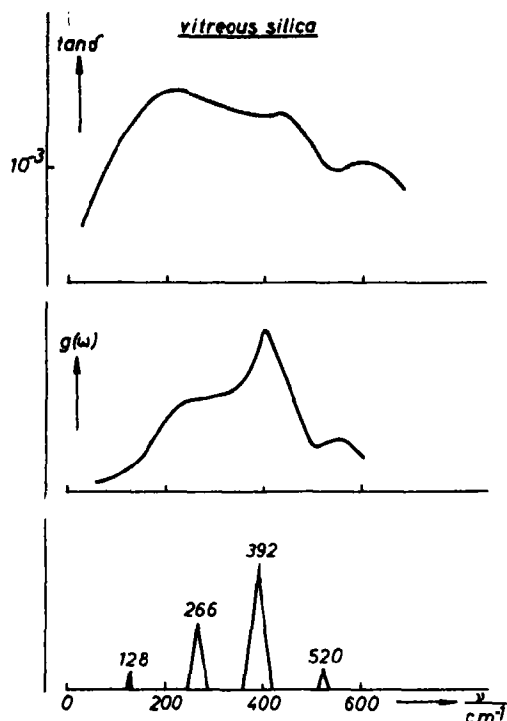


Fig. 2. Dielectric absorption of vitreous silica in the far i.r. $g(\nu)$ = phonon density distribution calculated from a 3-dimensional model (1); below: i.r. absorption bands of crystalline quartz (7).

To distinguish between the different processes and to make a structural analysis, it was necessary to investigate the temperature dependence of the absorption.

(a) Theory of the temperature dependence

Szigeti in his calculation of the two-phonon absorption of crystals [2] found, that for all processes of the appropriate order the temperature dependent occupation number part of the absorption contains only the occupation numbers of the actually created or destroyed phonons. This means that the two-phonon absorption coefficient $\alpha^{(2)}$ for the difference process, which is of interest in the frequency range investigated, becomes:

$$\alpha^{(2)} = C(\omega) [(m' + 1)m'' - m'(m'' + 1)] \quad (1)$$

$$\omega = \omega' - \omega''$$

$m' = m(\omega', T)$ = equilibrium occupation number for phonons of frequency ω' .

An equivalent statement also holds for three-phonon processes. They originate from the combination of terms in which either the potential is expanded up to the 4th order in the lattice displacements, or the dipole moment up to the third order. All the possible combinations can

be classified into 4 types which are given in the diagrams of Fig. 5. In these diagrams $\pm\omega$ indicates the actually created or destroyed phonons. Arrows without designation mark the virtual intermediate states. A very lengthy calculation, which is beyond the framework of this paper, shows that in deriving the transition probabilities the occupation numbers of these intermediate states drop out [3]. All the 4 types of 3-phonon processes then lead to the same final equations for the absorption coefficient, — where the occupation number term and the energy conservation law are written explicitly:

$$\alpha_a^{(3)}(\omega, T) = \sum_{i_1 i_2 i_3} A_a(\omega_i, \omega_{i_1}, \omega_{i_2}) [(m_{i_1} + 1)(m_{i_2} + 1)m_{i_3} - m_{i_1}m_{i_2}(m_{i_3} + 1)] \cdot \delta(\omega - (\omega_{i_1} + \omega_{i_2} - \omega_{i_3}))$$

$$\alpha_b^{(3)}(\omega, T) = \sum_{i_1 i_2 i_3} A_b(\omega_i, \omega_{i_1}, \omega_{i_2}) [(m_{i_1} + 1)m_{i_2}m_{i_3} - m_{i_1}(m_{i_2} + 1)(m_{i_3} + 1)] \cdot \delta(\omega - (\omega_{i_1} - \omega_{i_2} - \omega_{i_3})) \quad (2)$$

$\alpha_a^{(3)}$ stands for the processes in which the photon and 1 phonon are destroyed and 2 phonons created; $\alpha_b^{(3)}$ stands for the processes in which two phonons are destroyed and one is created. The third possibility, the creation of three phonons, is not discussed, since the corresponding photon frequency is higher than that of the lattice modes. The different phonons ω_i give different contributions to $\alpha^{(3)}$: A substantial absorption takes place only, if at least one ω_i corresponds to a frequency with high density of states. Besides this, the dipole moment M of a lattice wave which is responsible for the coupling of the electromagnetic field to the lattice vibration will be largest for optical branches at $q \approx 0$. Furthermore, the transition probability between eigenstates belonging to different eigenvalues decreases in general with increasing eigenvalue difference. Finally the equilibrium values of $m(\omega)$ decrease with growing ω . Each of the quoted arguments favours the lowest optically active frequencies ' ω_0 ' to give the highest contribution to the multiphonon absorption.

For the discussion of the temperature dependence of the absorption coefficient we look at the occupation number parts of $\alpha_a^{(3)}$ and $\alpha_b^{(3)}$, calling the term in the rectangular brackets $\mu_a^{(3)}$ and $\mu_b^{(3)}$. m_{i_1} may be abbreviated by m_1 etc.

With the equilibrium distribution

$$\bar{m}(\omega, T) = (e^{\hbar\omega/kT} - 1)^{-1} = (e^{\hbar\omega/T} - 1)^{-1};$$

$$\Omega = \frac{\hbar\omega}{k}; \quad (3)$$

one gets

$$\mu_a^{(3)} = \frac{e^{\Omega_1/T} e^{\Omega_2/T} - e^{\Omega_3/T}}{(e^{\Omega_1/T} - 1)(e^{\Omega_2/T} - 1)(e^{\Omega_3/T} - 1)}$$

$$\mu_b^{(3)} = \frac{e^{\Omega_1/T} - e^{\Omega_2/T} e^{\Omega_3/T}}{(e^{\Omega_1/T} - 1)(e^{\Omega_2/T} - 1)(e^{\Omega_3/T} - 1)} \quad (4)$$

The high temperature behavior is common to all three-

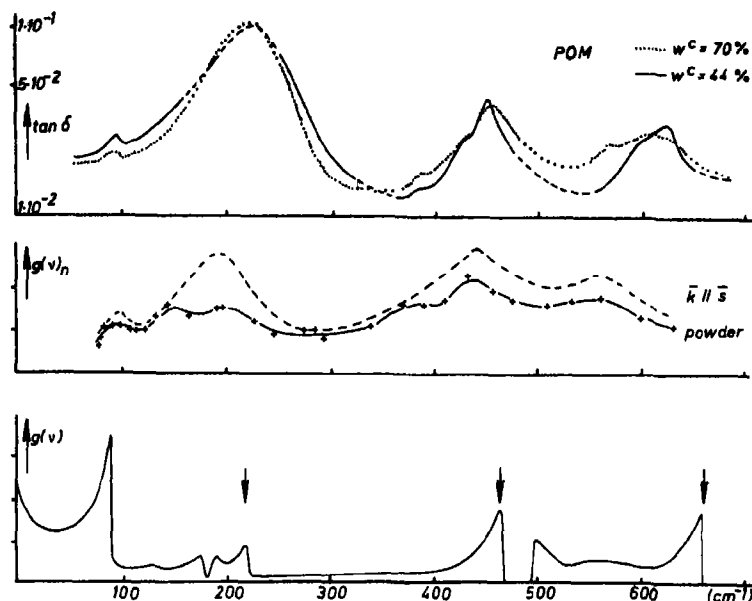


Fig. 3. Dielectric loss of polyoxymethylene samples in the far i.r.; w^c = crystallinity; $g(\nu)_n$: phonon frequency distribution from inelastic neutron scattering (13); $g(\nu)$: calculation for the regular isolated chain (5); arrows mark the i.r.-active vibrations.

phonon-absorption terms:

$$\Omega_{\text{Phonon}} = \Omega = \Omega_1 \pm \Omega_2 - \Omega_3 \quad (12)$$

Assuming

$$\Omega_i \ll T \quad (5)$$

(4) becomes:

$$\mu_b^{(3)}(T \ll \Omega_0) = e^{-(\Omega_1 + \Omega_2)/T} (1 - e^{-\Omega_3/T}), \quad (13)$$

for all participating frequencies and consequently

$$\Omega_0 \ll T. \quad (6)$$

$$\mu_a^{(3)}(T \ll \Omega_0) = e^{-\Omega_1/T} (1 - e^{-\Omega_2/T}).$$

we get by expanding the exponential function:

$$\mu_{(T \ll \Omega_0)}^{(3)} = f^{(3)}(\Omega_1, \Omega_2, \Omega_3) \cdot T^2. \quad (7)$$

In the same way one finds for the difference processes of the two-phonon absorption:

$$\mu_{T \ll \Omega_0}^{(2)} = e^{-\Omega_2/T} (1 - e^{-\Omega_1/T}). \quad (14)$$

Accordingly we find for two-phonon processes:

$$\mu_{(T \ll \Omega_0)}^{(2)} = f^{(2)}(\Omega_1, \Omega_2) \cdot T. \quad (8)$$

For the low-temperature behaviour we have

$$\Omega_i \gg T. \quad (9)$$

This cannot hold for all frequencies participating in the absorption, since ω goes down to zero for the acoustical branch. Yet as the density of states as well as the dipole moment go to zero with $\omega \rightarrow 0$ (9) will hold for all essential terms, i.e.:

$$\Omega_0 \gg T. \quad (10)$$

From (9) follows:

$$e^{-\Omega_i/T} \ll 1. \quad (11)$$

With (11) and the energy conservation law:

$$T_0 = \Omega (\ln(1 + \Omega/\Omega_a))^{-1}. \quad (17)$$

While the high-temperature behaviour allows to distinguish easily between two and three phonon processes this does not apply to the low temperature behaviour. Actually the functional form remains the same, the factor in front of the bracket contains the sum of the destroyed phonons Ω_a in the exponent. Function (13) shall be discussed in detail:

In correspondence with our earlier discussion we assume:

$$\Omega_a \ll \Omega_0. \quad (15)$$

As a result the absorption

$$\mu_{(T \ll \Omega_0)}^{(3)} = e^{-\Omega_a/T} (1 - e^{-\Omega/T}) \quad (16)$$

starts with a steep uprise based on $e^{-\Omega_a/T}$ while the term in brackets flattens the curve with growing temperature. A maximum is shown at

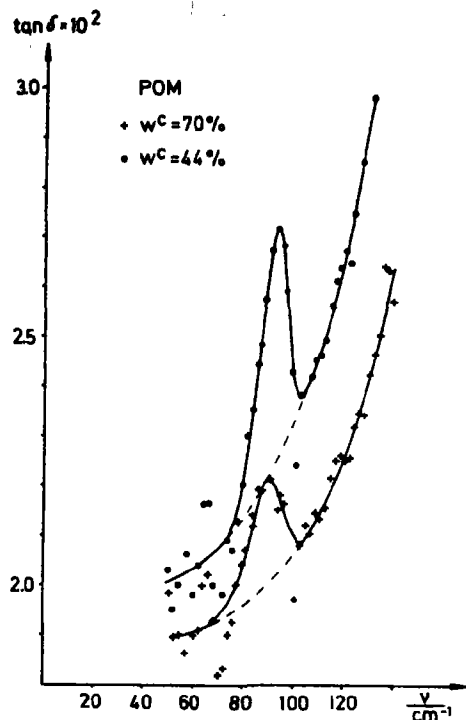


Fig. 4. Dielectric absorption of polyoxymethylene in the far i.r.; detail from Fig. 3.

With (15) it follows

$$T_0 \approx \Omega_0. \quad (17a)$$

Here the presupposition (10) holds no longer. T_0 lies in the transition region between low and high-temperature behaviour. But the qualitative characteristics of μ will hold up to T_0 . One expects a plateau or possibly a small maximum of the absorption around $T = T_0$, before the high temperature ascent begins. If a band of frequencies ω_{0i} participates in the absorption process the absorption can be thought as a superposition of the corresponding absorption curves.

In two-phonon-processes the participating frequencies are restricted by the momentum selection rules. There will be some plateau or point of inflexion at

$$T \approx \Omega_2,$$

but Ω_2 is not necessarily equal to the lowest i.r. active frequency Ω_0 .

With growing Ω , finally, (15) holds no longer. As a consequence the plateau will, according to (17), shift towards lower temperatures.

Adding up our discussion of one and multi-phonon-absorption by a partially crystalline polymer we get the schematic curves of Fig. 6 for the expected temperature and frequency dependence.

(b) Experiments

Equation (17) and Fig. 6 lead to a kind of

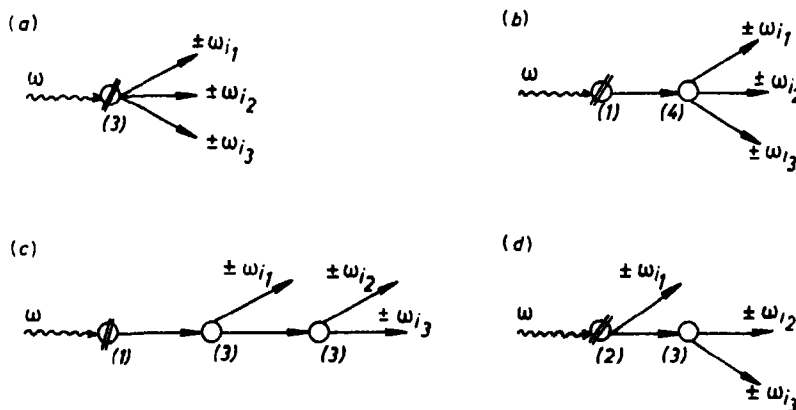


Fig. 5. Schematic representation of 3-phonon processes, starting from the absorption of one photon: $\omega = \pm\omega_{i_1} \pm \omega_{i_2} \pm \omega_{i_3}$. ω : incident photon; \rightarrow : intermediate (virtual) phonon; $\pm\omega_i$: real phonon; \pm indicates the possibility of creation and destruction; the arrows are, for simplicity, only drawn for phonon creation; $\bigcirc(i)$: interaction takes place by an anharmonic potential of the i -th order; $\bigcirc(j)$: interaction takes place through a dipole moment of order j . 5a: Creation, resp. destruction, of 3 phonons; 5b: creation of one virtual phonon, which by an anharmonic potential of 4th order interacts with 3 other phonons; 5c: the virtual phonon interacts twice with 2 phonons; 5d: creation (or destruction) of one real and one virtual phonon and further interaction of the virtual phonon with 2 other phonons.

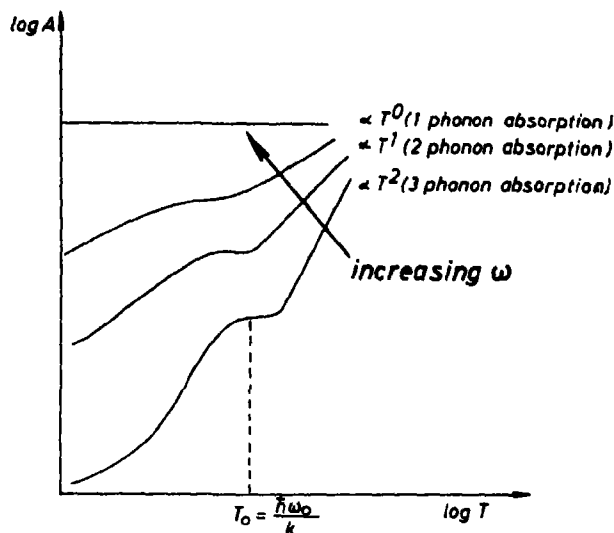


Fig. 6. Schematic drawing of low frequency multi-phonon absorption A as a function of temperature T .

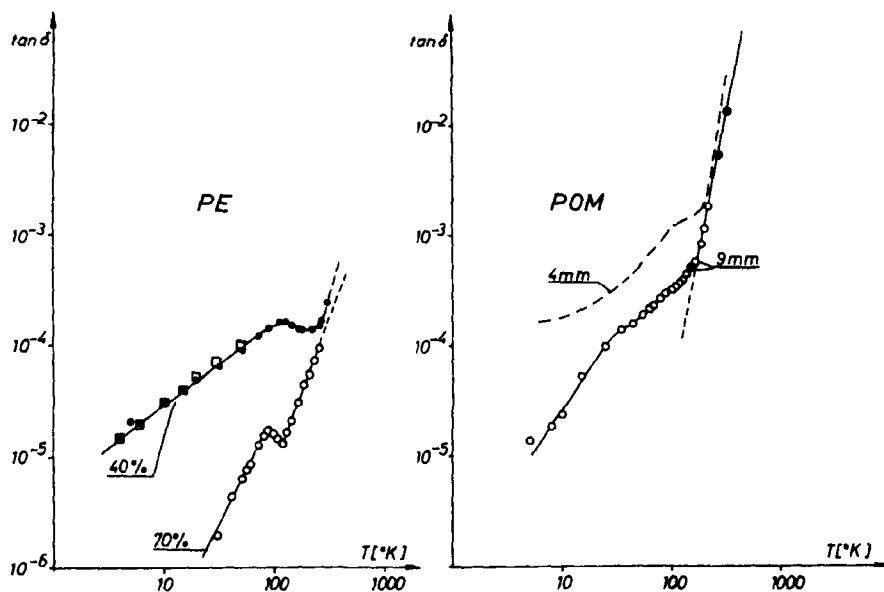


Fig. 7. Dielectric loss of 2 polyethylene samples (PE) at 9 mm wavelength; and dielectric loss of 1 polyoxymethylene sample (POM) at 9 and 4 mm wavelengths (8).

'temperature phonon spectroscopy': The lowest optical frequencies ω_{01} , that are involved in the 3-phonon-absorption, should be found from the temperature range of the multi-

phonon absorption plateau. The experimental results confirm this conclusion.

Measurements of the temperature dependence of the dielectric loss were made at 8

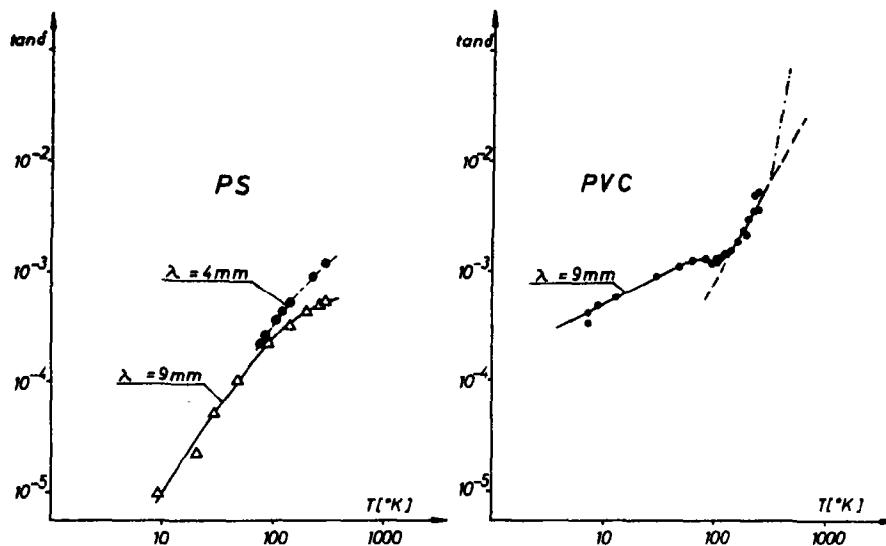


Fig. 8. Dielectric loss of polystyrene (PS) at 9 and 4 mm wavelengths (8) and dielectric loss of polyvinylchloride (PVC) at 9 mm wavelength.

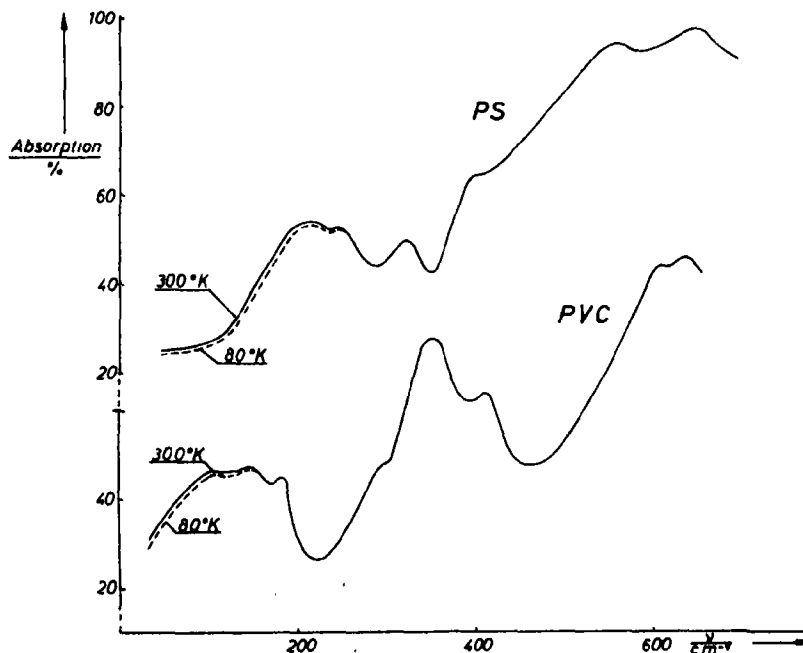


Fig. 9. I.r. absorption spectra of polystyrene (PS) and polyvinylchloride (PVC) (9).

and 4 mm wavelength by a cavity resonator method [4]. The results for polyethylene (PE), polyoxymethylene (POM), polyvinylchloride

(PVC) and polystyrene (PS) are shown in Figs. 7 and 8.

(1) Good agreement is found between the

overall temperature dependence of the dielectric loss and the theoretical predictions of Fig. 6. The high-temperature part of the curves follows a T^n -law with $n \approx 2$, as expected for 3-phonon-absorption. n becomes considerably larger than 2 for POM and PVC above the glass transition temperature; here, probably, relaxation processes thaw off[5].

The plateau in the loss-temperature curves increases and the slope of the low temperature part decreases with increasing amount of amorphous phase and higher frequencies. The latter shows the increasing contribution of temperature independent one-phonon absorption, in correspondence with Fig. 6.

(2) A qualitative confirmation of the $T_0 \approx \Omega_0$ -law (equation 17a) is found. For the PE samples $T_0 \approx 100^\circ\text{K}$ corresponds clearly to

$$\omega_0 = kT_0/h = 70 \text{ cm}^{-1},$$

i.e. to the lowest optically active lattice vibration seen in Fig. 1. For POM the broad structure of the plateau gives a hint that some optically active vibrations below 30 cm^{-1} (as predicted by theory[5] and later found by experiment[10]) must exist. The difference in the temperature dependence of the dielectric loss of PVC and PS finds its explanation in the different frequencies of their lowest i.r.-active vibrations (Fig. 9): In PS the frequency of the first ω_0 is higher than 200 cm^{-1} ; the plateau in the loss-temperature curve, therefore, should lie at about 300°K , which is consistent with the experimental result.

3. CONCLUSION

We investigated the high dielectric absorption of partially crystalline polymers and glasses in the far i.r. Starting from the millimeter range it rises with ω (the extinction coefficient rises with ω^2) and is essentially

temperature independent. It is interpreted as disorder-induced one-phonon absorption which, outside the range of optically active vibrations, reflects the phonon density of states. The absorption becomes very much higher around the frequencies that are optically active in the corresponding crystalline state.

At still lower frequencies (4 and 8 mm wavelengths) the strongly temperature dependent 3-phonon-tail of that absorption was studied. The absorption-temperature curves show an inflexion point or plateau at a temperature $\hbar\omega_0/k$, where ω_0 equals the frequency of those phonons that are mainly contributing to 3-phonon processes. It can be shown that ω_0 is the lowest optically active frequency of the one-phonon absorption. Good experimental correlation between that characteristic temperature range and the far i.r. measurements was found.

Acknowledgement—This work was sponsored by the Deutsche Forschungsgemeinschaft.

REFERENCES

1. BELL R. J., BIRD N. F. and DEAN P., *J. Phys. C* **1**, 299 (1968).
2. SZIGETI B., *Proc. R. Soc. A* **258**, 377 (1960).
3. HEIL H., private communication.
4. AMRHEIN E. M., MÜLLER F. H. and RÖDER H., *Angew. Phys.* **24**, 18 (1967).
5. PISERI L. and ZERBI G., *J. Chem. Phys.* **48**, 3561 (1968).
6. MYERS W. R. and RANDOLPH F. D., USAEC Report 1 N-1151 (1968).
7. SIMON I., In *Modern Aspects of the Vitreous State* (Edited by J. D. Mackenzie) Vol. I, p. 120, Butterworth, London (1960).
8. SCHULZE H. W., *Koll. Z. u. Z. f. Polymere*, in press.
9. FRISCHKORN H., private communication.
10. AMRHEIN E. and FRISCHKORN H., *Ber. Bunsen. Phys.-Chem.* **74**, 880 (1970).
11. AMRHEIN E., *Ber. Bunsen. Phys. Chem.* **74**, 807 (1970).
12. KITAGAWA K. and MIYAZAWA T., *Rep. Progr. Polymer Phys. Japan* **8**, 53 (1965).
13. TREVINO S. and BOUTIN H., *J. Chem. Phys.* **45**, 2700 (1966).

100

OPTICAL PROPERTIES OF NON-CRYSTALLINE Si, SiO, SiO_x AND SiO₂

H. R. PHILIPP

General Electric Research and Development Center Schenectady, N.Y. 12301, U.S.A.

(Received 14 September 1970)

Abstract—Optical data for non-crystalline Si, SiO, SiO_x ($x = 1.5$) and SiO₂ are presented and analyzed for the energy region 1 to 26 eV. The results indicate that amorphous substances of all intermediate compositions between Si and SiO₂ can be formed and that these materials are not simple mixtures of Si and SiO₂ but rather the two atom species are blended on an atomic scale. More specifically, the Si bonding is tetrahedral (perhaps highly distorted) and of the type Si-(Si₄O_{4-x}) where the distribution of atoms is essentially statistical. Further it is found that the optical properties of these layers are determined by the presence and grouping of Si-O and Si-Si bonds and that clusters of like bonds of the dimension of a Si-(Si₄) or Si-(O₄) tetrahedra have optical properties comparable to those exhibited by amorphous silicon or quartz, respectively, 'in bulk'.

1. INTRODUCTION

THE USE of SiO and SiO_x films as protective layers and antireflecting coatings in optical applications, and as the dielectric material in certain microelectronic devices, has prompted a series of investigations into their properties[1-4]. These layers are formed by direct evaporation of silicon monoxide either rapidly under conditions of good vacuum or slowly in the presence of air or oxygen. In the latter case, the condensate acquires excess oxygen and the O to Si atom ratio rises above unity. The addition of oxygen greatly reduces the index of refraction and the opacity of these films to visible and ultraviolet light. There has been some conjecture about the formation of Si₂O₃ based on chemical analysis, and also the uniqueness of certain infrared absorption bands which are distinct in comparison to SiO and SiO₂[4, 5]. Unfortunately, both SiO and SiO_x condense into amorphous layers and their structures are not well understood[6-9]. Thus, firm conclusions are lacking. This paper presents new optical information on these materials obtained over an extended energy range. The results indicate that short range order primarily determines the optical properties. This view has not been considered in previous investigations.

In a recent note[10] we compared the optical behavior of crystalline and fused SiO₂. The real and imaginary parts of the dielectric constant which describe these properties were obtained by Kramers-Kronig analyses of reflectance data shown in Fig. 1. The results for both forms of SiO₂ are very similar. The absorption spectrum exhibits a series of relatively sharp peaks which are broadened slightly in the case of the 'amorphous' material.* Since the presence of long-

*The term "amorphous" is a description based on the results of some experiments usually involving X-ray or electron diffraction. When the observed patterns become diffuse or highly broadened compared to the sharp array for the crystalline material, the solid is said to be amorphous. That is, the atomic arrangements no longer possess the long-range spacial ordering of the perfect crystal. However, the use of the word amorphous, without defining its experimental basis, can lead to ambiguity. For example, a sample composed of small crystallites may appear amorphous to X-rays and crystalline to electron diffraction. It is possible to define amorphous from an optical point of view. The concepts involved here are of course very different from those of the scattering phenomena pertinent to X-ray and electron observations. Optical absorption data are concerned generally with one photon events in which an electron is raised from a filled to an empty state. These electronic states in turn are determined by the symmetry and spacings of the constituent atoms. Crystalline materials frequently exhibit relatively sharp optical structure. If these optical effects are associated with rather localized atomic configurations then a material composed of extremely small crystallites or perhaps possessing only local order may retain the

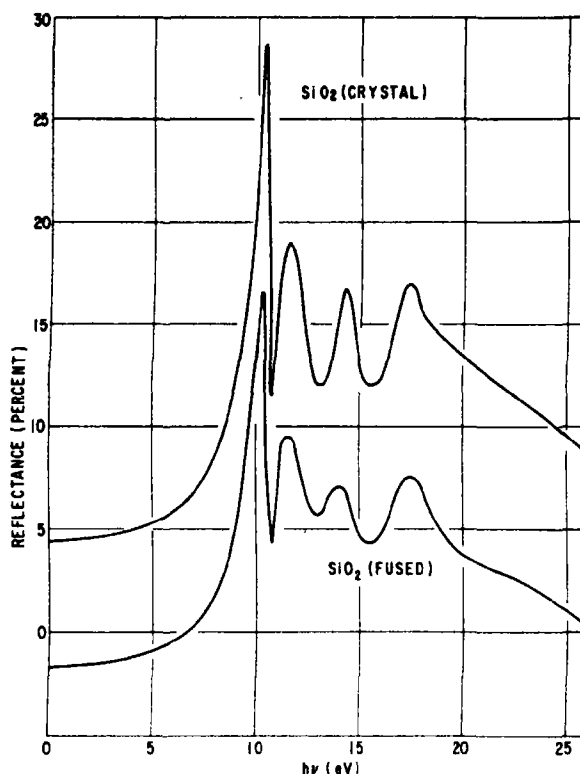


Fig. 1. The spectral dependence of the reflectance of crystalline and fused quartz. For clarity, the values for fused quartz have been lowered by 5 per cent.

range order is destroyed on transition from the crystalline to the more random (vitreous) state, it was concluded that absorption processes in SiO_2 are to be ascribed to some mechanism of a rather localized nature which persists in the fused silica structure. In this connection it was further noted that although the density ratio $2.65/2.20 = 1.2$ for crystalline compared to fused quartz is rather large, the polarizability per unit density for each form is nearly the same.

sharp features of the single crystal. In this sense, the material may be considered 'optically ordered' although it may still be amorphous on the basis of other experiments. Fused SiO_2 appears to fit this category. However, when such structure becomes considerably broadened and perhaps shifted in energy compared to the crystalline data, then the sample can be considered optically amorphous. This is the case for evaporated Si shown in Fig. 2.

It has long been recognized[11,12] that quartz glass is composed of a network of Si atoms tetrahedrally surrounded by four oxygen atoms. Furthermore, nearest neighbor distances, for example the Si-O distance of $\sim 1.62 \text{ \AA}$, are close to those which occur in the various crystalline polymorphs of SiO_2 . It is thus likely that these optical properties which appear common to both vitreous and crystalline SiO_2 can be associated with the presence of short range order (coordination number and the average distance between atoms) which exists in the amorphous material although further localization, possibly atomic, cannot be ruled out.

The analysis of recent X-ray structural studies of amorphous SiO_x indicates a near neighborhood order quite similar to that in

SiO_2 glass [9]. For SiO the aggregate of atoms is more random and a smaller degree of local order is found. Although no prescription is presently available to explain the observed optical transitions in SiO_2 , it would appear that comparison of these results with similar data on SiO and SiO_x would provide a further basis for the understanding of the optical properties and possibly the local atomic arrangements in all these oxides.

This approach is examined in the present paper and further extended by inclusion of data, shown in Fig. 2, for evaporated Si films [13, 14]. The observed optical properties of SiO_2 will be associated with the Si-O bonding characteristic of quartz. The data on Si films will be used to describe the behavior associated with the Si-Si bonding of amor-

phous Si . We will then demonstrate that SiO_x ($x = 0 \rightarrow 2$) represents a continuous range of materials whose optical properties are determined by the presence and grouping of Si-Si and Si-O bonds which are statistically distributed and that clusters of like bonds of the dimension of a Si-(Si)_4 or Si-(O)_4 tetrahedron have optical properties comparable to those exhibited by amorphous silicon or quartz respectively, 'in bulk'. This demonstration is based on a comparison of the absorption and reflectance spectrum of SiO and SiO_x ($x \approx 1.5$) with analogous features in Si and SiO_2 data. Further we can qualitatively account for the magnitude and frequency dependence of $\epsilon_{0,\text{eff}}$, the effective dielectric constant, and n_{eff} , the effective number of electrons per molecule, in terms of the above picture. These latter quantities are obtained from sum rules on the imaginary part of the dielectric constant [13].

As a general conclusion, Si and SiO_2 can be thought of as forming glasses of all intermediate composition. This very simple viewpoint appears to have application in the discussion of other amorphous materials, especially those prepared by pyrolytic decomposition or high-frequency plasma deposition using gases of varying constituent proportions [15, 16].

2. EXPERIMENTAL

Films of SiO were prepared by rapid evaporation of silicon monoxide (deposition rate 30 to 80 $\text{\AA}/\text{sec}$) under good vacuum conditions ($p < 10^{-5}$ Torr). Films of SiO_x were prepared by slow evaporation of silicon monoxide (deposition rate 2 to 5 $\text{\AA}/\text{sec}$) in the presence of oxygen at a pressure near 10^{-4} Torr. Substrates were either metal or a transparent material like quartz or LiF for optical transmission measurements.

The atomic ratios of O to Si in these layers were not determined. Absorption coefficients for SiO films of various thicknesses, and obtained over a range of deposition conditions, were self consistent. They agree reasonably

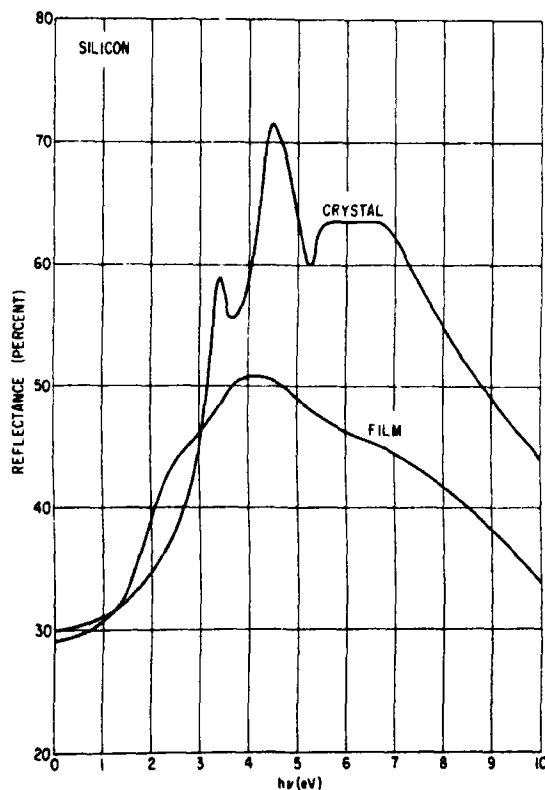


Fig. 2. The spectral dependence of the reflectance of crystalline and evaporated, amorphous silicon.

well with values reported in the literature for 'true' SiO films[2, 17]. The SiO_x films produced under the above deposition conditions are assumed to have atomic ratios near 1.5[3, 4] although for the purposes of this paper, the precise ratios are not important.* These films exhibited some variation in absorption coefficient especially for energies below ~ 9 eV. The absorption could also be reduced by u.v. irradiation. This effect has been described in the literature[18]. Typical

*We will hereafter designate this material as $\text{SiO}_{1.5}$ and use SiO_x to indicate materials having a range of possible atom ratios between 0 and 2.

transmission data for SiO and $\text{SiO}_{1.5}$ films are given in Fig. 3. Two curves are shown for $\text{SiO}_{1.5}$ to indicate the variability of the absorption coefficient for these layers. Data for films formed under deposition conditions intermediate to those described earlier lie between the curves for SiO and $\text{SiO}_{1.5}$ drawn here. Other results clearly indicate that films can be deposited with any intermediate O to Si ratio and that these films exhibit a continuous range of absorption coefficients[17]. For discussion purposes, curves for SiO_2 and amorphous Si are also given in Fig. 3. These latter data were obtained on films

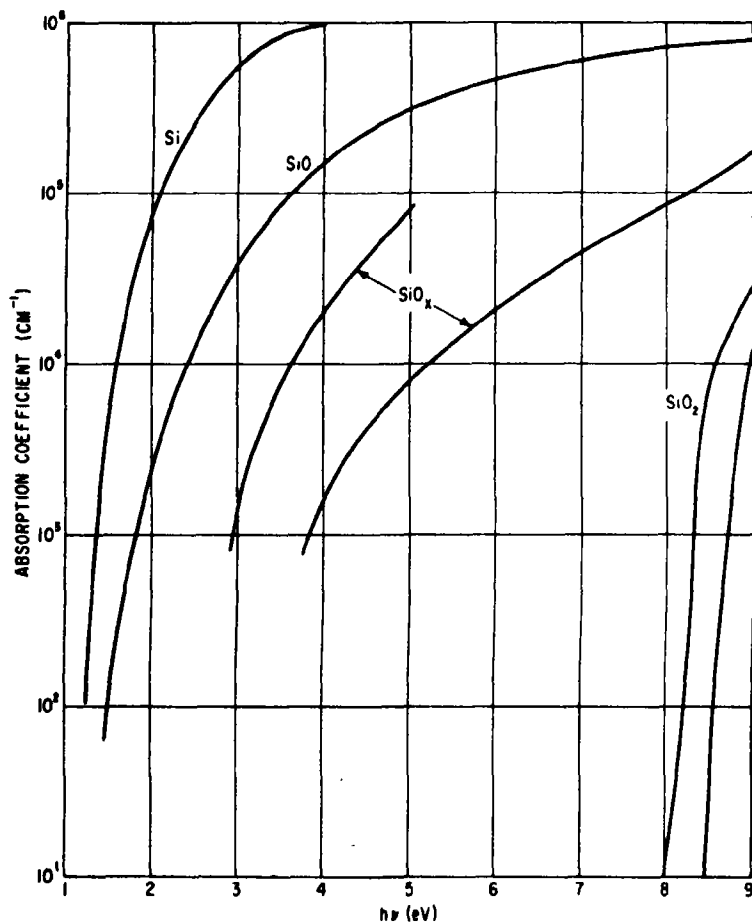


Fig. 3. The spectral dependence of the absorption coefficient of amorphous Si, SiO, SiO_x ($x \sim 1.5$) and SiO_2 . The curve on the far right is for crystalline SiO_2 .

formed on unheated glass substrates by electron beam evaporation of crystalline silicon.

Reflectance data for SiO and $\text{SiO}_{1.5}$ are shown in Fig. 4 along with comparison data for Si and SiO_2 . The techniques employed in these measurements have been described elsewhere [13]. Curves obtained on $\text{SiO}_{1.5}$ samples before and after ultraviolet irradiation were essentially identical. This indicates that the region of strong absorption, above ~ 9 eV, which largely determines the nature of the reflectance curve, is little affected by this treatment. The real and imaginary parts of the dielectric constant, ϵ_1 and ϵ_2 , obtained by Kramers-Kronig analysis [19] of the above curves, are shown in Fig. 5. The results for

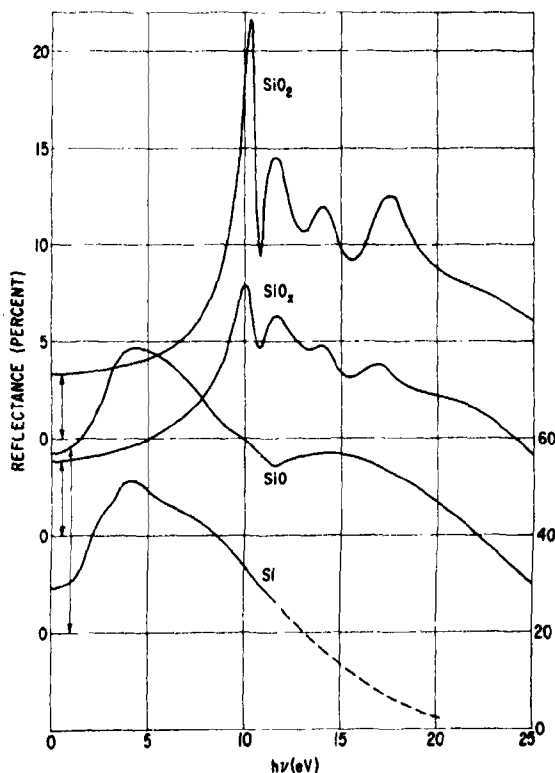


Fig. 4. The spectral dependence of the reflectance of Si , SiO , SiO_x ($x \sim 1.5$) and SiO_2 . For clarity the ordinates have been displaced (see arrows). The scale, in per cent, for Si is indicated on the right side of this figure. The curve for Si for $h\nu > 12$ eV is extrapolated using data for crystalline silicon [13, 21].

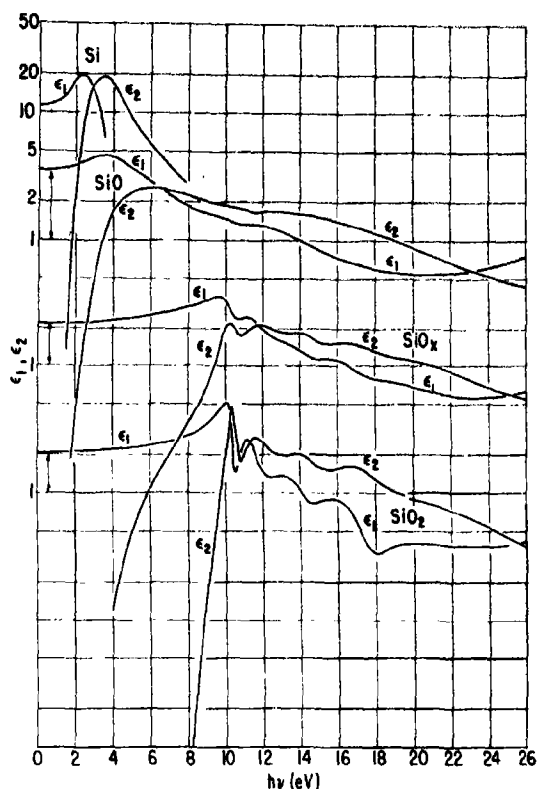


Fig. 5. The spectral dependence of the real and imaginary parts of the dielectric constant, ϵ_1 and ϵ_2 for Si , SiO , SiO_x ($x \sim 1.5$) and SiO_2 obtained by Kramers-Kronig analysis of the curves of Fig. 4. For clarity the ordinates have been displaced (see arrows). The scale for Si is the same as that for SiO .

Si films are also shown in Fig. 6 where they are compared with those for crystalline silicon [13, 20]. For all these analyses, the reflectance curves were extrapolated above 26 eV so as to give the required value of phase, $\tan \theta = -2k/(n^2 + k^2 - 1) \approx 0$, in the regions of low absorption or transparency. The results of Fig. 3 were useful for this purpose.

Analysis of data

In its gross features, the reflectance spectrum of $\text{SiO}_{1.5}$ resembles that of SiO_2 . The peaks are less sharp but occur at approximately the same energies. We conclude on this basis that strong optical transitions in

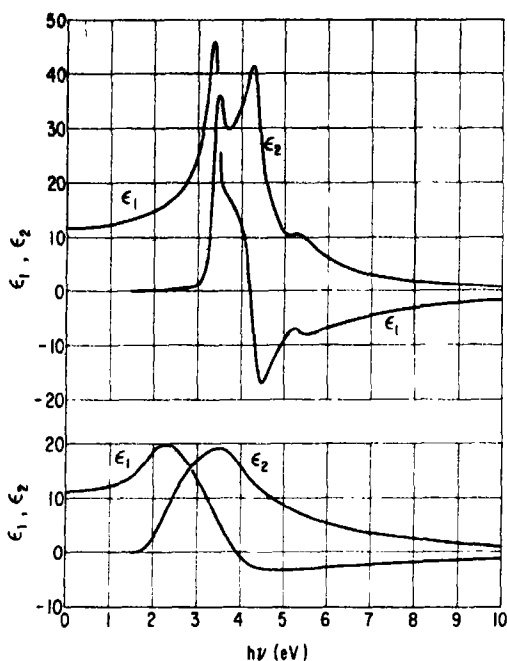


Fig. 6. The spectral dependence of the real and imaginary parts of the dielectric constant, ϵ_1 and ϵ_2 , for crystalline silicon (upper curve) and amorphous silicon (lower curve).

$\text{SiO}_{1.5}$ are dominated by processes associated with the Si-O bonding characteristic of quartz. For SiO , the curve appears entirely different. A peak in the reflectance occurs near 4.5 eV and only faint humps in the curve are observed near 10 and 15 eV. The shape of this curve is similar to that of amorphous Si for energies below ~ 10 eV. The relatively sharp structure which occurs in data for Si crystals shown in Fig. 2 is absent in the evaporated material. Hence, characteristics in the reflectance curve which might be associated with the Si-Si bonds in amorphous films are at most indicated by a very broad peak in the 4-5 eV range.

A different point of view might be taken if we had only Fig. 3 at our disposal. In the region of low absorption the curve for $\text{SiO}_{1.5}$ is quite different from that of SiO_2 and resembles more closely the one for SiO . As previously pointed out, however, a family of

curves may be obtained for SiO_x which essentially bridge the gap between SiO and SiO_2 . Thus, just as the density, refractive index and other parameters of SiO_x can be thought of as being a continuous function of composition, so can the optical absorption. If this absorption is related in some way to an increasing amount of Si-Si bonding as the composition SiO is approached, then we would expect to find a further connectivity of these curves to the results for Si. This extension appears obvious in the figure.

We can examine the above situation somewhat more quantitatively by the use of certain sum rules [13, 20] on ϵ_2 . The first of these

$$\epsilon_{0,\text{eff}} = 1 + \frac{2}{\pi} \int_0^{E_0} E^{-1} \epsilon_2(E) dE \quad (1)$$

is for $\epsilon_{0,\text{eff}}$, the contribution to the dielectric constant associated with optical transitions (absorption) in the energy range to E_0 . This integral can be evaluated directly using the curves of Fig. 5. It is found that for each of these materials the value of $\epsilon_{0,\text{eff}}$ obtained by integration to 26 eV is close to the optical value ϵ_0 . This agreement indicates, as might be expected, that optical absorption above 26 eV does not make an important contribution to the dielectric constant. These results are shown in Fig. 7. For display purposes, $\epsilon_{0,\text{eff}}$ is plotted here as a percentage of the value obtained by integration to 26 eV. This graph distinguishes the spectral regions which contribute to ϵ_0 for each of these materials. For amorphous silicon, absorption below 9 eV accounts for about 95 per cent of ϵ_0 while SiO_2 is essentially transparent in this energy range. In a crude manner, we can designate the regions above and below ~ 9 eV as associated with contributions arising primarily from the presence of Si-O and Si-Si bonds respectively. For SiO_x , the Si-Si contribution rises with increasing silicon content, being about 70 per cent when the composition SiO is reached. If we represent the relative concentration of these bonds in

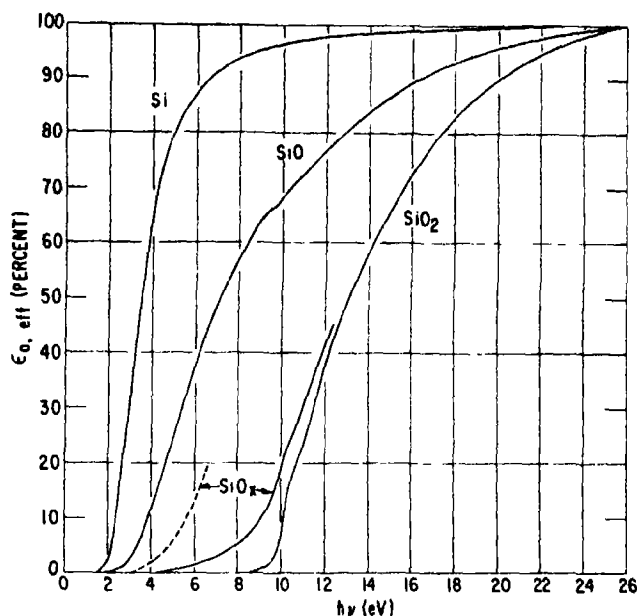


Fig. 7. $\epsilon_{0, \text{eff}}$ vs. $h\nu$. The $\epsilon_{0, \text{eff}}$ are plotted as a percentage of the value obtained by integrating equation (1) to 26 eV.

SiO_x by a formula of the type $\text{SiO}_x = (1 - x/2)$ 'Si-Si' + $(x/2)$ 'Si-O', then we should have very approximately for the dielectric constant

$$\epsilon_{\text{SiO}_x} \approx \left(1 - \frac{x}{2}\right)^2 \epsilon_{\text{Si}} + \left(\frac{x}{2}\right) \epsilon_{\text{SiO}_2}$$

where ϵ_{Si} and ϵ_{SiO_2} are the dielectric constants of amorphous silicon and quartz respectively. The multiplier for ϵ_{Si} is raised to some power, ~ 2 , to express the fact that not only does the absorption increase but the 'edge' moves to lower energy. The integral of equation (1) depends on both these factors. The Si-O contribution on the other hand appears more isoenergetic according to Fig. 4, and thus should vary directly as the bond concentration. This formula is an obvious oversimplification, however, it does express qualitatively the observed ϵ_0 for these materials.

The second sum rule

$$\left(\frac{2\pi^2 N e^2}{m}\right) n_{\text{eff}} = \int_0^{E_0} E \epsilon_2(E) dE \quad (2)$$

is for n_{eff} , the effective number of electrons per atom or molecule contributing to the optical properties in the energy range to E_0 . In this formula N is the atom (or molecule) density of the material. Values for n_{eff} , obtained using the experimental ϵ_2 of Fig. 5 are shown in Fig. 8. For Si, n_{eff} approaches 4 electrons per silicon atom. This result, which is also obtained for the crystalline material[13], is easy to understand. The optical absorption of silicon is associated with transitions from the filled band, made up of the 4 valence electrons per silicon atom, to the empty conduction band. Since the oscillator strength for such transitions is essentially exhausted for energies above ~ 20 eV and since the next filled band lies about 80 eV below the valence bands, the integral saturates near 4 electrons per atom.

For SiO_2 , the curve for n_{eff} is approaching 8 electrons per SiO_2 molecule near 26 eV. There is no direct evidence that this plot will saturate near this value. Presumably transitions associated with the deeper-lying, L-shell electrons of oxygen will be energeti-

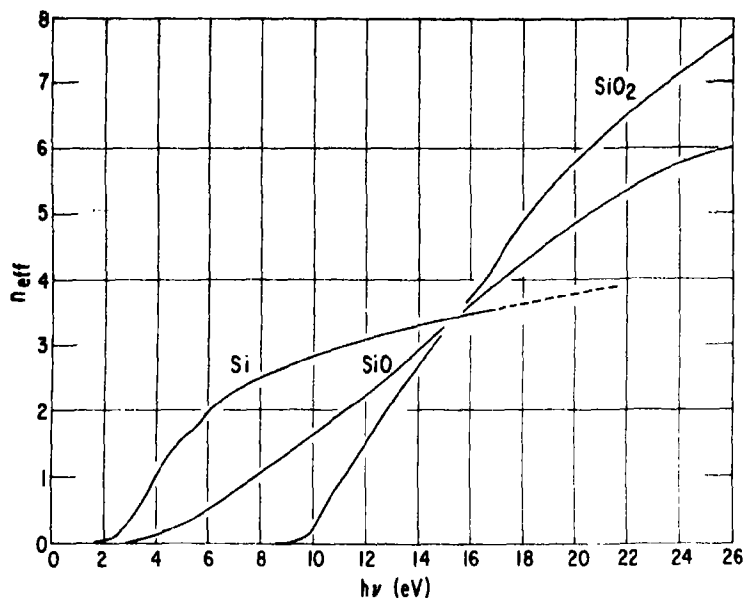


Fig. 8. n_{eff} , the effective number of electrons per Si atom and per SiO and SiO₂ molecule vs. $h\nu$. The n_{eff} are calculated using equation (2) and Fig. 5.

cally possible at some higher energy and the curve will rise further. It is interesting to note however that the reflectance values shown in Fig. 4 for all the oxides are dropping fairly fast in the region above ~ 23 eV, indicating that ϵ_2 for each of these materials is decreasing fairly rapidly above this energy. We assume that this indicates the exhaustion of oscillator strength for transitions involving some specific group or groups of bands. There is at present no model for labeling these electrons in SiO₂. However, for marking purposes, we will associate them with the 8 electrons involved in the 4 Si-O bonds of the quartz tetrahedra.

The significance of the n_{eff} curve for SiO is immediately evident when we write from a simple bonding point of view $\text{SiO} = \frac{1}{2} \text{Si} + \frac{1}{2} \text{SiO}_2$. On this basis, we expect this curve to reach the observed value of about 6 electrons per SiO molecule near 26 eV.

3. DISCUSSION

It has been shown that in the case of fused quartz, the presence of short range order of

dimension $\sim 5 \text{ \AA}$ is sufficient to develop, essentially in full, the optical properties of the bulk crystalline material [10]. Thus, the electronic transitions which give rise to this optical structure are determined primarily by localized atomic arrangements of the above dimension or smaller. We shall assume that this structure marks the presence of Si-O₄ tetrahedra and that these peaks will be present and distinguishable in the optical spectrum of materials composed even partially (say ~ 20 per cent) of such bonding groups. It is thus obvious from the data of Fig. 4 or 5 that, at least on this basis, SiO cannot be considered a simple mixture of silicon and quartz (that is, made up of Si-Si₄ and Si-O₄ tetrahedra alone) for clearly such a material would exhibit the sharp optical peaks characteristic of quartz. Other information supports this conclusion and its extension to SiO_x films. The 'band gap' of SiO_x layers is not the Si value as it would be if indeed it contained clusters of silicon tetrahedra to any appreciable extent, nor is the dielectric constant a linear function of the relative (mathematically equivalent)

concentration of Si and SiO₂.^{*} Finally, we observe that the various parameters which describe SiO_x materials (index of refraction, absorption, density, etc.) appear to vary smoothly and continuously between the composition extremes of Si and SiO₂ indicating that the two atom species are blended on the finest scale.

The n_{eff} plots show that the number of 'optical' electrons (in the range to 26 eV) per silicon or oxygen atom (or better per Si-Si or Si-O bond) does not change with composition. If we can talk of these as the valence or bonding electrons, then in the absence of double bonds (which appear unlikely) the bonding configuration of SiO_x materials is made up of tetrahedral arrangements about each Si atom.[†]

We are thus led to the conclusion that SiO_x layers are composed essentially of tetrahedra of the type Si-(Si_yO_{4-y}), that is, a mixture of Si-Si and Si-O bonds on an atomic scale. The optical properties of such arrangements are not easy to predict. Energetically, the oscillator strength for transitions associated with the presence of Si-O bonds in SiO_x films appears to be appreciable only for energies above ~ 10 eV as for quartz. However, the sharp features of these transitions observed in data for SiO₂ are less conspicuous in the case of SiO_{1.5} and are essentially absent when the number of Si-Si and Si-O bonds are comparable as in SiO. We have assumed that optical effects in SiO₂ are associated with the presence of SiO₄ tetrahedra (or some localized atomic arrangement of this dimension). If the atoms of each Si tetrahedron in SiO_x are distributed randomly (in a statistical sense), we can readily calculate the distribu-

tion of the five possible tetrahedron types for various O to Si atom ratios.^{*} These results are tabulated below.

	SiO ₂	SiO _{1.5}	SiO	SiO _{0.5}	Si
Si-(O ₄)	1.0000	0.3164	0.0625	0.0039	0.0000
Si-(SiO ₃)	0.0000	0.4219	0.2500	0.0469	0.0000
Si-(Si ₂ O ₂)	0.0000	0.2109	0.3750	0.2109	0.0000
Si-(Si ₃ O)	0.0000	0.0469	0.2500	0.4219	0.0000
Si-(Si ₄)	0.0000	0.0039	0.0625	0.3164	1.0000

It is seen that for SiO, only ~ 6 per cent of these groups are Si-(O₄). For SiO_{1.5}, over 30 per cent are Si-(O₄) tetrahedra. Thus, on this basis, we might expect the latter material to retain partially the multi peaked optical spectrum of SiO₂, while for SiO this structure would be masked almost entirely by other absorption processes.

Similar questions arise concerning the properties of localized regions or groupings of Si-Si bonds. The distinct optical structures which occur in data for Si single crystals are not present in curves for Si films. It appears rather that these features are substantially broadened in the case of amorphous Si, although the oscillator strength for all transitions is confined to the same general energy range, 1 to 8 eV, as for single crystals. This situation is analogous to that reported for amorphous germanium [21].

The absorption below ~ 8 eV in SiO_x materials is associated with the presence of Si-Si bonds. Since there are no competing optical processes in this spectral region, the absorption should be very sensitive to changes in structure or composition and its magnitude, especially near threshold, may be considered as a semiquantitative measure of the

^{*}In fact on a simple mixture basis SiO should exhibit an absorption curve in the region below 9 eV very similar to that of pure Si but reduced in value by perhaps a factor of 2. This is clearly not the case.

[†]The use of the word tetrahedral here and below is not meant to imply any particular angle between bonds but simply a coordination number of 4. Such tetrahedra might well be greatly distorted especially when mixed bonds are considered.

^{*}For N silicon atoms there are $2N$ sites which may contain an oxygen atom. When a site is filled, Si-O bonds are formed. When a site is empty, a Si-Si bond is formed. The probability that a site is filled is $\frac{1}{2}$ for SiO, $\frac{1}{3}$ for SiO_{1.5}, 0 for Si, etc. Thus, for example, the fraction of the number of Si tetrahedra which are Si-(SiO₃) for the stoichiometry SiO_{1.5} is $4(\frac{1}{2} \times \frac{1}{2} \times \frac{1}{2} \times \frac{1}{2}) = 0.4219$ since there are 4 different arrangements for the 3 oxygen atoms.

strength or number of these absorption centers present. As the density of these bonds increases, the absorption increases and the measured threshold moves to lower energy. For the composition SiO_x , the 'band gap' is close to the Si value. These observations suggest that the optical behavior associated with a relatively small concentration of Si-Si bonds depends markedly on the localized environment of these bonded atoms. As the number of bonds of this type increases on the same or adjacent Si atoms, the absorption occurs at lower energy until a configuration of Si-Si bonds is obtained which possesses the optical characteristics of amorphous Si in bulk. That is, these optical properties will be reproduced when such a cluster of 'pure silicon' reaches or exceeds some minimum size. We note in Fig. 3 that for the range 1.5 to 3 eV, the curve for SiO_x has approximately the same spectral shape as the one for Si but is reduced in magnitude by a factor of ~ 20 . Thus on the basis of our previous calculation, this minimum configuration has the dimension of a $\text{Si}-(\text{Si}_4)$ tetrahedron which constitutes ~ 6 per cent of the total in SiO_x . We would also expect the curves for SiO_x to exhibit an absorption tail in this spectral range which is lower than that of Si by some factor of 10^2 to 10^3 (for $x = 1.4$ to 1.6). This is roughly the case for the curves shown in Fig. 3. Unfortunately, however, these samples were not sufficiently thick to allow an accurate determination of absorption coefficients near or below 10 cm^{-1} where this comparison should be made.

It is expected that absorption in SiO_x materials may be sensitive to processes which influence the bonding and positions of atoms in these layers. It is found, in this connection, that the ultraviolet absorption of SiO_x films for $x \sim 1.5$ can be considerably reduced by annealing in vacuum at 300°C or by ultraviolet irradiation treatments which do not change the O to Si ratios of these layers [18, 22]. Such treatments could result in the preferred distribution of $\text{Si}-(\text{Si}_4\text{O}_{4-y})$ tetra-

hedra with an altered optical behavior. While the oscillator strength for transitions associated with a given density of Si-Si bonds would not be destroyed in this case, its contribution may be relegated, in an increased proportion, to higher energies where it might be masked by existing Si-O bond absorption. However, it is difficult to understand why these processes would not also occur to some extent in SiO films, where it is observed such treatments have little or no effect on the absorption curve [18]. The following alternative explanation appears more probable.

The $\text{SiO}_{1.5}$ films used in this and other studies are obtained by slowly evaporating SiO in the presence of oxygen. It is very likely that additional oxygen is introduced into these layers not only by chemical combination but also by the physical trapping of oxygen molecules. These molecules contribute to the optical absorption only for energies above 8 eV, and would be included in most methods of determining the atomic ratios in these films which only test for the amount of Si present [17]. Under the influence of heat or ultraviolet irradiation, this oxygen may chemically combine with Si, thereby converting Si-Si bonds to Si-O bonds. The measured atom ratios of the films are not changed, although absorption below 8 eV may be drastically reduced. On the other hand, SiO films are condensed at high rates in good vacuum and the presence of trapped oxygen should be minimal.

In this paper we have accounted for the gross features of SiO_x data by endowing Si-Si and Si-O bonds both individually and in small clusters with certain, rather independent optical properties. This representation is an obvious oversimplification of the complex factors which contribute to optical effects in these amorphous materials. It is of interest to point out however, that the characteristics of excess Si (the presence of Si-Si bonds) in SiN_x films, and the behavior associated with the addition of oxygen in amorphous materials of the type SiN_xO_y ,

are comparable with the optical effects we have associated with Si-Si and Si-O bonds in SiO_x [23]. The techniques of pyrolytic decomposition and high frequency plasma deposition make it possible to prepare films which incorporate a variety of atomic species in controlled proportions. The simple picture presented here may serve as a useful framework for discussing and perhaps predicting the properties of materials containing other, possibly more complicated atom mixtures.

REFERENCES

1. HASS G., *J. Am. Ceram. Soc.* **33**, 353 (1950).
2. HASS G. and SALZBERG C. D., *J. Opt. Soc. Am.* **44**, 181 (1954).
3. BRADFORD A. P. and HASS G., *J. Opt. Soc. Am.* **53**, 1096 (1963).
4. RITTER E., *Opt. Acta.* **9**, 197 (1962).
5. WAGNER G. H. and PINES A. N., *Ind. Eng. Chem.* **44**, 321 (1952).
6. WEBER B. C. and HESSINGER P. S., *J. Am. Ceram. Soc.* **37**, 267 (1954).
7. BRADY G. W., *J. Phys. Chem.* **63**, 1119 (1959); LIN S. C. H. and JOSHI M., *J. electrochem. Soc.* **116**, 1740 (1969).
8. WHITE E. W. and ROY R., *Solid State Commun.* **2**, 151 (1964).
9. RIECHERT L. and WEINER K. L., *Bunsen Society*, Innsbruck (1965).
10. PHILIPP H. R., *Solid State Commun.* **4**, 73 (1966).
11. WARREN B. E., KRUTTER H. and MORING-STAR O., *J. Am. Ceram. Soc.* **19**, 202 (1936).
12. ROBINSON H. A., *J. Phys. Chem. Solids* **26**, 209 (1965).
13. PHILIPP H. R. and EHRENREICH H., *Phys. Rev.* **129**, 1550 (1963).
14. PHILIPP H. R. and TAFT E. A., *Phys. Rev.* **120**, 37 (1960).
15. STERLING H. F. and SWANN R. C. G., *Solid State Electron.* **8**, 653 (1965).
16. HU S. M., *J. electrochem. Soc.* **113**, 693 (1966).
17. CREMER E., KRAUS Th. and RITTER E., *Z. Elektrochem.* **62**, 939 (1958).
18. BRADFORD A. P., HASS G., McFARLAND M. and RITTER E., *Opt. Optics* **4**, 971 (1965).
19. PHILIPP H. R. and TAFT E. A., *Phys. Rev.* **136**, A1445 (1964).
20. NOZIERES P. and PINES D., *Phys. Rev.* **113**, 1254 (1959).
21. TAUC J., ABRAHAM A., PAJASOVA L., GRIGOROVICI R. and VANCU A., *Physics of Non-Crystalline Solids*, North Holland Publ. Amsterdam (1965).
22. CREMER E. and PULKER H., *Monatsh. Chem.* **93**, 491 (1962).
23. PHILIPP H. R., to be published.

DOMAINE D'EXISTENCE DU SULFURE D'ETAIN ET PHENOMENE D'ASSOCIATIONS DES LACUNES D'ETAIN

A. LICHANOT et S. GROMB

Laboratoire de Chimie Structurale associé au C.N.R.S., Faculté des Sciences de Pau, Groupe de Chimie Physique, Avenue Philippon - 64 - Pau - Pyrénées Atlantiques

(Received 12 June 1970; in revised form 11 September 1970)

Résumé — Le phénomène d'associations de lacunes d'étain dans le sulfure d'étain a été étudié sur des échantillons de différentes compositions, d'une part en déterminant le coefficient de Hall d'échantillons recuits et trempés, d'autre part à partir des variations thermiques du coefficient de Hall. Les résultats obtenus ont permis de tracer le domaine d'existence du sulfure d'étain. Le rapport de la mobilité des électrons à celle des trous et la largeur de la bande interdite ont été déterminés à partir des mesures effectuées à haute température.

Abstract — The phenomenon of associations of tin vacancies in tin sulfide has been studied with samples of various compositions, on one hand by determining the Hall coefficient of annealed and cooled samples, on the other hand from variations of Hall coefficient against temperature. The obtained data enabled us to draw the existence region of tin sulfide. The ratio of electron to hole mobility and the forbidden band gap have been determined from measures carried out at high temperature.

1. INTRODUCTION

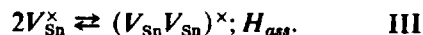
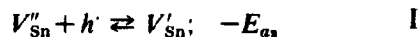
DANS deux précédentes notes [1], [2], les propriétés électroniques d'échantillons frittés de sulfure d'étain ont été reportées. Il est bien connu que le sulfure d'étain [3-5], présente toujours une conductibilité de type *p* correspondant à un excès de soufre par rapport à la composition stoechiométrique. La détermination à température ambiante du coefficient de Hall d'échantillons retraits à une même température sous différentes pressions de soufre a permis de montrer qu'à température élevée, les imperfections atomiques du sulfure d'étain consistent essentiellement en des lacunes d'étain doublement ionisées V_{Sn}'' [1], [6]. En revanche, l'étude du coefficient de Hall de ces mêmes échantillons recuits en atmosphère inerte puis trempés, a montré qu'à des températures inférieures à 500°C, les lacunes associées $(V_{Sn}V_{Sn})^{\times}$ deviennent prépondérantes. Une étude préliminaire de ces associations [1] a mis en évidence la variation très rapide du terme préexponentiel K_{as} de la constante d'association avec la composition.

Dans le présent travail, nous nous sommes

proposés d'étudier le phénomène d'association de façon plus approfondie afin de pouvoir construire le véritable domaine d'existence du sulfure d'étain. En outre, des variations thermiques du coefficient de Hall ont permis de compléter les études précédentes [1] concernant le domaine de conductibilité intrinsèque; en particulier le rapport de la mobilité des électrons à celle de trous a été déterminée à partir des températures de transition *p-n*.

2. PARTIE THEORIQUE

La formation de lacunes associées peut être schématisée [3], [7a] par les réactions quasi chimiques suivantes:



A la température d'équilibre, la condition d'électroneutralité du cristal s'écrit:

$$p = n + [V_{Sn}'] + 2[V_{Sn}''] \quad (1)$$

où p représente la concentration en trous libres h , n la concentration en électrons libres, $[V_{sn}']$ et $[V_{sn}'']$ les concentrations en lacunes simplement et doublement ionisées.

La concentration $[V_{sn}']$ étant toujours négligeable [1], la déviation de stoechiométrie δ , exprimée en nombre d'atomes de soufre en excès par cm^3 , est donnée par l'équation:

$$\delta = [V_{sn}''] + [V_{sn}'] + 2[(V_{sn}V_{sn}')^{\times}]. \quad (2)$$

Dans la mesure où la valeur de δ est assez importante et la température assez faible pour qu'il soit possible de négliger n , la relation (1) s'écrit:

$$p = 2[V_{sn}''] \quad (3)$$

et l'application de la loi d'action des masses aux équilibres I, II et III compte tenu de l'équation (3) conduit à:

$$\frac{2[V_{sn}']}{p^3} = \frac{1}{K_{a1}K_{a2}} \quad (4)$$

$$\frac{[(V_{sn}V_{sn}')^{\times}]}{[V_{sn}']^2} = K_{ass} \quad (5)$$

où les constantes K ont pour expressions:

$$K_{a1} = K_{a1}^0 T^{3/2} e^{-E_{a1}/kT} \quad (6)$$

$$K_{a2} = K_{a2}^0 T^{3/2} e^{-E_{a2}/kT} \quad (7)$$

$$K_{ass} = K_{ass}^0 e^{-H_{ass}/kT}. \quad (8)$$

Les termes préexponentiels de ces dernières relations sont directement reliés aux variations d'entropies relatives aux réactions I, II et III. Dans le cas où interviennent des trous libres (réactions I et II), la variation d'entropie est principalement attribuable au mouvement de translation et la constante est de la forme $K^0 T^{3/2}$ où $K_{a1}^0 = 4(2\pi m_h^* k/h^2)^{3/2}$ et $K_{a2}^0 = (2\pi m_h^* k/h^2)^{3/2}$. Dans le cas de la réaction III, la variation d'entropie due à la formation d'associations peut être séparée en deux

termes, un terme de configuration et un terme de vibration faisant intervenir les fréquences relatives aux lacunes simples V_{sn}^{\times} et associées $(V_{sn}V_{sn}')^{\times}$; le facteur préexponentiel dans la relation (8) est alors indépendant de la température [7b].

La combinaison des équations (2) à (5) conduit à la relation:

$$\frac{K_{ass}}{K_{a1}K_{a2}} = \frac{1}{p^6} [K_{a1}K_{a2}(2\delta - p) - p^3]. \quad (9)$$

L'étude du phénomène d'associations à partir de cette équation peut être faite

— soit en déterminant directement le nombre de trous présents à une température T que nous appellerons température d'équilibre pour rappeler que la formation et la destruction des associations est lente et que le coefficient de Hall mesuré expérimentalement ne peut avoir de signification que lorsque l'état d'équilibre est atteint.

— soit en déterminant le nombre de trous présents à température ambiante après que l'échantillon ait été recuit à la température T pendant une durée suffisante, puis rapidement trempé à 0°C . Cette dernière façon d'opérer suppose tout d'abord que la trempe gèle les associations et ensuite que le nombre de trous présents à température ambiante représente le nombre de trous présents à la température d'équilibre; cette dernière hypothèse est justifiée grâce à la faible énergie d'ionisation des lacunes V_{sn}^{\times} : $(E_{a1} + E_{a2}) = 0.07 \text{ eV}$ [1].

(a) Etude des associations à la température même de l'équilibre

L'équation (9) qui est rigoureuse peut être réduite à une forme plus simple dans la mesure où le phénomène d'associations est étudié dans un domaine de température où les associations sont largement prépondérantes vis-à-vis des lacunes simples. Dans ces conditions, on peut négliger les concentrations $[V_{sn}']$ et $[V_{sn}']$ devant le terme $2[(V_{sn}V_{sn}')^{\times}]$ et l'équation (2) devient:

$$\delta = 2[(V_{Sn}V_{Sn})^*]. \quad (10)$$

De même, l'équation (9) s'écrit alors:

$$\frac{K_{ass}}{K_{a_1}K_{a_2}} = \frac{2\delta}{p^6} K_{a_1}K_{a_2} \quad (11)$$

soit en tenant compte des relations (6), (7) et (8):

$$\frac{p}{T} = \left[\frac{2\delta(K_{a_1}^0 K_{a_2}^0)^2}{K_{ass}^0} \right]^{1/6} e^{-[2(E_{a_1} + E_{a_2}) - H_{ass}]/6kT}. \quad (12)$$

La courbe $\log(p/T) = f(1/T)$ doit donc être linéaire et permet de déterminer l'enthalpie de formation des associations H_{ass} et la constante K_{ass}^0 si la déviation de stoechiométrie de l'échantillon est connue.

(b) *Etude des associations à température ambiante après recuit et trempe des échantillons*

Si on considère que la trempe est efficace en ce qui concerne le gel des imperfections atomiques, la concentration en associations à température ambiante représente aussi la concentration en associations à la température de recuit. De plus, à 300°K où sont étudiées les propriétés électroniques des échantillons, l'équation d'électroneutralité (3) s'écrit:

$$p_{300} = 2[V_{Sn}^*]_{300} \quad (13)$$

et l'équation (2) en tenant compte de l'équation (13) et du gel des associations conduit à la relation:

$$p = p_{300} + 2[V_{Sn}^*]_{300}. \quad (14)$$

L'énergie d'ionisation des lacunes neutres est suffisamment faible pour pouvoir négliger, dans la plupart des cas, même à température ambiante, la concentration $[V_{Sn}^*]_{300}$; dans ces conditions, l'équation (14) devient:

$$p = p_{300}. \quad (15)$$

Par conséquent, si les associations sont pré-

pondérantes, l'équation (12) dans laquelle on remplace p par le nombre de trous déterminé à température ambiante après recuit permet d'étudier le phénomène d'associations.

Toutefois, lorsque le nombre de porteurs devient supérieur au nombre d'états accessibles $\lambda = 2(2\pi m_h^* kT/h^2)^{3/2}$, la concentration en lacunes neutres n'est plus négligeable et la concentration en trous doit être remplacée par l'activité des trous [7c]:

$$a = \gamma p. \quad (16)$$

Le coefficient d'activité γ tient compte de ce que les électrons obéissent alors à la statistique de Fermi Dirac; il a pour expression:

$$\gamma = \frac{1}{2} \sqrt{\pi} [e^{\eta}/F_{1/2}(\eta)] \quad (17)$$

avec

$$\eta = -\mu/kT \quad \text{et} \quad F_{1/2}(\eta) = \int_0^\infty \frac{x^{1/2}}{1 + e^{(x-\eta)}} dx$$

où μ représente le potentiel chimique des électrons et $F_{1/2}(\eta)$, l'intégrale de Fermi dont les valeurs en fonction de η sont données par les tables de McDougall et Stoner [8]. Les valeurs de γ ont été calculées et représentées par Rosenberg en fonction de p/λ [9]. Dans ces conditions, les équations (4) et (9) deviennent:

$$\frac{\gamma^2 p^3}{2[V_{Sn}^*]} = K_{a_1}K_{a_2} \quad (18)$$

$$\frac{K_{ass}}{K_{a_1}K_{a_2}} = \frac{1}{\gamma^4 p^6} [K_{a_1}K_{a_2}(2\delta - p) - \gamma^2 p^3]. \quad (19)$$

3. DONNEES EXPERIMENTALES

Le sulfure d'étain est synthétisé sous vide à partir des éléments très purs (étain à 99,9999 pour cent provenant des laboratoires Koch Light, soufre à 99,999 pour cent que l'on a purifié par sublimation). L'analyse par spectroscopie d'émission des éléments contenus dans le sulfure d'étain ainsi préparé puis broyé a décelé la présence de vanadium (3 ppm) et de traces de plomb et de cuivre (moins de 1 ppm). Les échantillons sont obtenus par compression de la poudre à l'état de petits parallélépipèdes.

Toutes les opérations de broyage, de compression et d'expérimentation sont faites sous atmosphère d'argon.

Neuf échantillons ont été étudiés: leur composition a été fixée par retraitement à hautes températures sous pression de soufre contrôlée. Les échantillons *A*, *B* et *C* ont été retraits à 560°C, 710°C et 390°C en présence du mélange (SnS + Sn), cette technique [4] permet de fixer leur composition sur la bordure riche en étain du domaine d'existence du sulfure d'étain. Les échantillons *D*, *E*, *F* et *H* ont été retraits à des températures comprises entre 600°C et 700°C sous différentes pressions de soufre, selon la technique utilisée par Brebrick et Scanlon [10] pour le sulfure de plomb. Les échantillons *G* et *J* ont été retraits à 580 et 390°C, leur composition correspond à la bordure riche en soufre du domaine d'existence.

Les variations thermiques du coefficient de Hall des échantillons *A*, *B*, *C*, *D*, *E*, *F* et *J* ont été étudiées sous atmosphère d'argon à l'aide d'un porte échantillon en quartz dont les sondes sont en tungstène. Les mêmes échantillons *A*, *B*, *F* et les échantillons *G* et *H* ont été étudiés par recuits. Ils sont tout d'abord scellés sous atmosphère raréfiée d'argon dans de petites ampoules en quartz et portés pendant une quinzaine d'heures à la température de recuit désirée; les ampoules sont ensuite rapidement trempées dans un bain d'eau et de glace.

4. ANALYSE DES RESULTATS EXPERIMENTAUX

(a) Variation du coefficient de Hall avec la température

Les variations thermiques du coefficient de Hall *R* des échantillons *A*, *B*, *D*, *E* et *F* sont représentées sur la Fig. 1.

Contrairement aux expériences antérieures [1], [2], les valeurs du coefficient de Hall correspondent ici aux états d'équilibre; en particulier pour les températures supérieures à 220°C, la cinétique de formation des associations est lente et la durée de l'évolution du coefficient de Hall est de l'ordre de quelques heures. D'une façon générale, des chauffages et des refroidissements successifs donnent des résultats reproductibles. Cependant, lorsque les échantillons ont été portés à une température supérieure à 220°C, la partie 'b' des courbes d'équilibres correspondant à la région des basses températures est nettement différente de la partie 'a' obtenue lorsque les échantillons n'ont pas été portés à plus de 220°C. Dans une précédente publication [1], il a été montré que la rapide croissance du coefficient de Hall observée à 220°C est due à la formation d'associations de lacunes d'étain $(V_{Sn}V_{Sn})^{\times}$ dont la concentration décroît quand

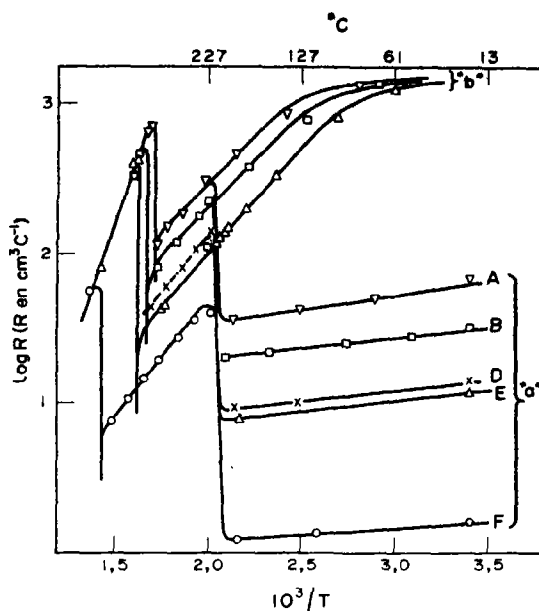


Fig. 1. Variations thermiques du coefficient de Hall.

la température croît. Enfin, aux températures élevées, le coefficient de Hall devient négatif et intrinsèque, et les valeurs d'équilibre sont atteintes rapidement*.

On peut remarquer que, quelle que soit la composition des échantillons, les associations commencent à se former à une même température voisine de la température de Tamman. Par contre, lorsque les associations sont formées, des réchauffements et refroidissements successifs en dessous de 220°C conduisent à des états d'équilibre comme le montrent les courbes de la partie 'b' de la Fig. 1. Aux températures inférieures à 80°, le coefficient de Hall tend vers une limite commune ($R \approx 10^3 \text{ cm}^3 \cdot \text{C}^{-1}$) due, comme on le verra, à la présence d'impuretés.

(b) Etude des recuits

Les échantillons *A*, *B*, *F*, *G* et *H* ont subi

*Cependant, le changement de signe du coefficient de Hall à la température d'inversion est assez lent. Par exemple, dans le cas de l'échantillon *E*, la valeur d'équilibre $R = -400 \text{ cm}^3 \cdot \text{C}^{-1}$ est obtenue à 345°C au bout de six heures.

des recuits de plusieurs heures à des températures comprises entre 220 et 500°C*. La détermination du coefficient de Hall à température ambiante après trempe des échantillons a conduit aux courbes de la Fig. 2 sur laquelle les courbes d'équilibre relatives aux échantillons A, B et F obtenues précédemment ont été portées en tirets. Les variations de $\log R$ en fonction de l'inverse de la température sont représentées par des droites sensiblement parallèles. Comme p et R sont reliés par l'expression $p = (3\pi/8)(1/Re)$, il est possible

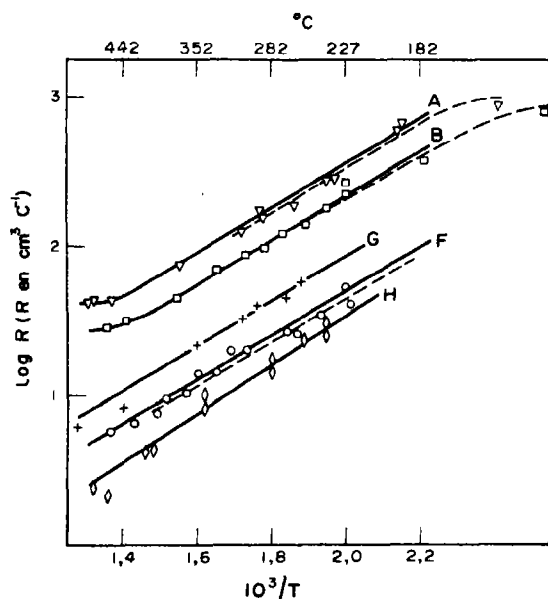


Fig. 2. Variations du coefficient de Hall en fonction de la température de recuit: — Courbes de recuits ∇ , \blacksquare , $+$, \bullet , \blacklozenge , ——— Courbes de variations thermiques ∇ , \square , \circ .

d'expliquer les variations linéaires obtenues, à partir de l'équation (12), dans la mesure où l'énergie H_{ass} est assez importante pour que le terme exponentiel soit prépondérant. D'autre part, la superposition aux erreurs expérimentales près des courbes d'équilibre et de recuit relatives aux échantillons A, B et F

montre que les hypothèses qui ont conduit à l'équation (12) sont valables: en particulier, la trempe est efficace et l'énergie d'ionisation des lacunes neutres est faible.

Dans des travaux antérieurs[1], nous avons été amenés à supposer que la pente très faible correspondant à des échantillons qui n'avaient pas été portés à une température supérieure à 220°C (Fig. 1, partie 'a') était attribuable au phénomène d'ionisation des lacunes et que la pente importante observée dans le cas de certains échantillons était peut-être due à la présence d'associations formées lors de la préparation. Les expériences reportées sur la Fig. 3 confirment

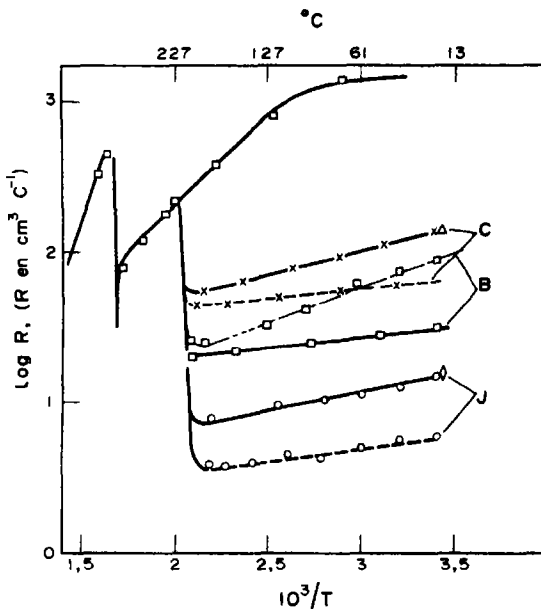


Fig. 3. Influence du recuit sur les variations thermiques du coefficient de Hall: — Courbes obtenues après préparation, \times C ($T_{pré} = 390^\circ\text{C}$), \square B ($T_{pré} = 700^\circ\text{C}$), \bullet J ($T_{pré} = 390^\circ\text{C}$), ——— Courbes obtenues après recuit, \times C ($T_{rec} = 500^\circ\text{C}$), \triangle B ($T_{rec} = 390^\circ\text{C}$), \square B ($T_{rec} = 306^\circ\text{C}$), \bullet J ($T_{rec} = 500^\circ\text{C}$), \blacklozenge J ($T_{rec} = 390^\circ\text{C}$).

cette dernière hypothèse. Les variations thermiques du coefficient de Hall des échantillons C et J effectuées aussitôt après la préparation à 390°C, température à laquelle les associations peuvent se former, présent-

*Au dessus de 500°C, la composition des échantillons varie consécutivement à un départ de soufre.

ent une pente plus importante* qu'après un recuit à 500°C, température à laquelle les associations sont beaucoup moins stables. Inversement, l'échantillon *B* préparé à 700°C présente une pente faible mais un recuit à 306°C entraîne un accroissement important de celle-ci. Il n'est pas exclu que les échantillons correspondant à des pentes faibles ne soient pas totalement dépourvus d'associations mais le comportement de l'échantillon *B* semblerait montrer que la concentration en associations est alors tout-à-fait négligeable devant la concentration en lacunes ionisées. En effet, la courbe de recuit relative à l'échantillon *B* ainsi que celle relative à l'échantillon *A* (Fig. 2) semblent présenter un palier au voisinage immédiat de 500°C; ce résultat s'explique très bien par la disparition des associations car le nombre de porteurs est alors uniquement lié à l'écart à la stoechiométrie puisque l'ionisation des lacunes neutres est pratiquement totale. Or, aussi bien pour *A* que pour *B*, les valeurs de ces paliers sont voisines de celles obtenues à température ambiante aussitôt après préparation (Fig. 1). Ce résultat peut être étendu aux échantillons *D* et *E*: en effet, l'extrapolation des parties linéaires des variations thermiques correspondant aux associations conduit à 500°C ($1/T \approx 1,3 \cdot 10^{-3}$) à des valeurs voisines de celles obtenues aussitôt après préparation. Seul l'échantillon *F* dont la déviation de stoechiométrie est importante comporterait encore une quantité notable d'associations à 500°C.

Enfin, d'après le modèle adopté, la concentration en associations relative à un échantillon préparé sous pression de soufre contrôlée

à une température déterminée devrait être identique à celle observée sur ce même échantillon recuit sous atmosphère inerte à la température de préparation. Or les échantillons *C* et *J* qui avaient été recuits à 500°C ont donné, après un deuxième recuit à 390°C, des coefficients de Hall identiques à ceux observés après leur préparation. Par conséquent, la teneur en associations dans un échantillon de composition déterminée dépend uniquement de la température à laquelle il a été soumis.

5. CONSTRUCTION DU DOMAINE D'EXISTENCE DU SULFURE D'ÉTAÏN

Dans une précédente publication[1], le domaine d'existence du sulfure d'étain avait été construit comme l'avait fait Albers et Vink [4] à partir du nombre de porteurs déterminés à température ambiante sur des échantillons 'bordure' trempés en négligeant le phénomène d'associations. Grâce aux résultats ci-dessus, il est maintenant possible d'établir le domaine d'existence en tenant compte de la présence des associations.

En effet, si les échantillons étudiés sont préparés à haute température, leur teneur en associations est négligeable et l'écart à la stoechiométrie est très voisin de $p_{300}/2$. En fait, il est possible de faire une détermination plus précise grâce au nombre de porteurs déterminés à 220°C: au voisinage de cette température, les courbes d'ionisation présentent un palier de saturation où le nombre de porteurs p_s correspond à une ionisation des lacunes pratiquement totale et par conséquent on a:

$$\delta = [V''_{Sn}]_{220^\circ C} = \frac{p_s}{2}.$$

* Cette pente que l'on peut expliquer qualitativement par la destruction des associations est nettement inférieure à celles des droites qui correspondent à l'état d'équilibre (Fig. 1 partie 'b'). On peut remarquer de plus que sa valeur varie d'un échantillon à l'autre. Comme les mesures ont été effectuées sur des échantillons trempés, il est possible que ce phénomène soit lié à des considérations cinétiques bien que les valeurs expérimentales portées sur la Fig. 3 aient été obtenues au bout de plusieurs heures en l'absence de toute évolution.

Il est alors possible de déduire à partir des courbes d'ionisation les valeurs $K_{a_1}^0, K_{a_2}^0 = 1 \cdot 10^{30} \text{ cm}^{-6} \cdot K^{-3}$ et $(E_{a_1} + E_{a_2}) = 0,07 \text{ eV}$ [1]. Cependant, lorsque la valeur p_s est supérieure à $2 \cdot 10^{18} \text{ cm}^{-3}$, la correction due à $[V''_{Sn}]$ n'est plus négligeable; elle peut être faite à partir de l'équation (18) à l'aide des valeurs numér-

iques ci dessus, d'où:

$$\delta = [V_{Sn}^{''}] + [V_{Sn}^{x}] = \frac{p_s}{2} + [V_{Sn}^{x}]_{220^{\circ}\text{C}} \quad (20)$$

En revanche, les échantillons 'bordure basses températures' comportent des associations et on constate sur la Fig. 3 que les valeurs de p_s apparentes obtenues ne correspondent pas à la véritable déviation de stoechiométrie. Il est cependant possible de recuire les échantillons à 500°C pour faire disparaître les associations et déterminer ensuite la valeur correcte de p_s en effectuant une nouvelle variation thermique. Nous avons vu cependant que cette méthode n'est pas très sûre puisque pour certains échantillons la température de 500°C n'est pas suffisante pour faire disparaître les associations.

Nous avons donc opéré de la façon suivante: à partir des courbes de recuit relatives aux échantillons A, B, D, E, F, G, et H préparés à haute température, l'enthalpie de formation des association H_{ass} a été déterminée et la loi de variation de la constante d'association K_{ass}^0 en fonction de δ a été établie (cf. équation (12)). La déviation de stoechiométrie $\delta = 2[(V_{Sn}V_{Sn}^{x})^*]$ des échantillons préparés à basse température a été ensuite calculée à partir des valeurs expérimentales p_{300} à l'aide de cette même équation en utilisant les valeurs de K_{ass}^0 , $K_{a_1}^0$, $K_{a_2}^0$, H_{ass} et $E_{a_1} + E_{a_2}$ précédemment déterminées.

(a) Détermination des grandeurs d'associations

(i) *Enthalpie de formation des associations H_{ass} .* Les variations de $\log(p/T)$ en fonction de $1/T$ qui sont déduites des courbes des Figs. 1 et 2 sont représentées sur la Fig. 4. Les droites ainsi obtenues sont sensiblement parallèles entre elles et, compte-tenu de l'équation (12), leur pente permet de déterminer l'enthalpie de formation des associations $H_{ass} = -(1,4 \pm 0,1) \text{ eV}$. Cette valeur importante permet d'expliquer que le terme exponentiel $\exp[-(2(E_{a_1} + E_{a_2}) - H_{ass})/6kT]$

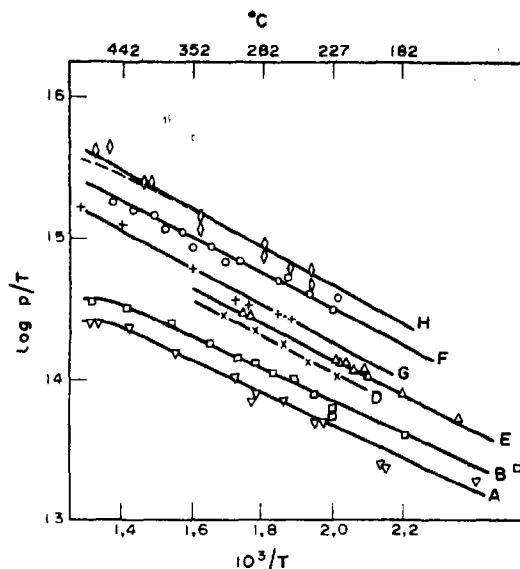


Fig. 4. Variations de $\log(p/T)$ en fonction de la température. ∇ , \blacksquare , $+$, \bullet , \blacklozenge , valeurs obtenues après recuit, ∇ , \square , \circ , valeurs obtenues par variations thermiques, ---- courbe calculée à partir de l'équation (19).

varie beaucoup plus rapidement avec la température que le terme T et par conséquent la variation $\log R = f(1/T)$ est sensiblement linéaire (Figs. 1 et 2).

(ii) *Constante d'associations K_{ass}^0 .* La détermination de la constante K_{ass}^0 découle de la connaissance de l'ordonnée à l'origine des droites de la Fig. 4 qui, d'après l'équation (12) représente l'expression $\log b = \frac{1}{6} \log [2\delta(K_{a_1}^0 K_{a_2}^0)^2 / K_{ass}^0]$.

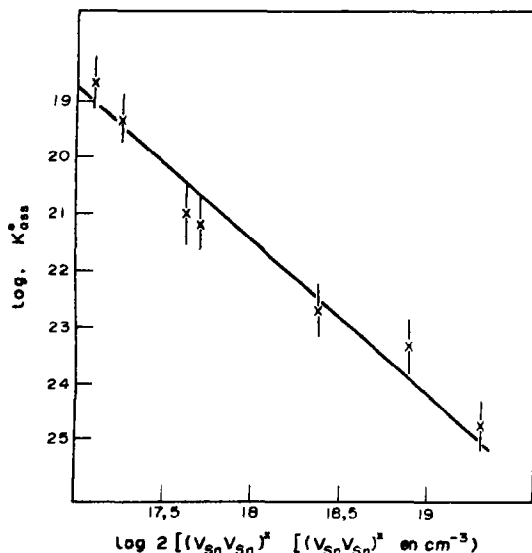
Les valeurs de δ ont été déterminées à l'aide de la relation (20), les concentrations $[V_{Sn}^{x}]_{220^{\circ}\text{C}}$ étant calculées à partir de l'équation (18). Le Tableau 1 montre que le terme $[V_{Sn}^{x}]_{220^{\circ}\text{C}}^*$ n'est plus négligeable lorsque $p_s/2$ est supérieur à $2 \cdot 10^{18} \text{ cm}^{-3}$. D'autre part, la constante K_{ass}^0 décroît régulièrement lorsque la déviation

*Lorsque les concentrations en lacunes neutres ne sont plus négligeables, la valeur de $\log p/T$ n'est pas reliée à $1/T$ par une relation linéaire comme le montre l'équation (19). Cependant, la courbe relative à l'échantillon H calculée à partir de cette équation ne s'écarte que très peu de la représentation linéaire pour des valeurs de p/T supérieures à 15,1 (courbe en tirets de la Fig. 4).

Tableau 1. Constantes d'associations déduites des variations $\log p/T = f(1/T)$

Echantillon	A	B	D	E	F	G	H
p_s	$2,6 \cdot 10^{17}$	$3,7 \cdot 10^{17}$	$8,3 \cdot 10^{17}$	$9,6 \cdot 10^{17}$	$5,7 \cdot 10^{18}$	$3,1 \cdot 10^{18}$	$8,2 \cdot 10^{18}$
$[V_{Sn}^*]_{290^\circ C}$	$3,0 \cdot 10^{14}$	$1,0 \cdot 10^{14}$	$1,0 \cdot 10^{14}$	$1,7 \cdot 10^{14}$	$5,2 \cdot 10^{14}$	$6,0 \cdot 10^{17}$	$1,6 \cdot 10^{18}$
δ	$1,3 \cdot 10^{17}$	$1,9 \cdot 10^{17}$	$4,2 \cdot 10^{17}$	$5,0 \cdot 10^{17}$	$8,0 \cdot 10^{18}$	$2,4 \cdot 10^{18}$	$2,0 \cdot 10^{19}$
$\log b$	16,00	16,15	16,49	16,54	17,07	16,90	17,35
$\log K_{ass}^0$	-18,58	-19,32	-21,01	-21,25	-23,22	-22,72	-24,80

de stoechiométrie, c'est-à-dire la concentration en associations croît: cette variation a été reportée dans le diagramme $\log K_{ass}^0 = f[\log 2(V_{Sn}V_{Sn}^*)]$ de la Fig. 5. En tenant compte de la précision avec laquelle sont déterminées les valeurs de K_{ass}^0 , on peut considérer que la

Fig. 5. Variations de la constante d'associations avec le terme $2[(V_{Sn}V_{Sn}^*)^x]$.

variation est linéaire et par conséquent la variation de K_{ass}^0 avec la concentration en associations peut être décrite de façon satisfaisante par la relation:

$$K_{ass}^0 = 3,2 \cdot 10^{28} [2[(V_{Sn}V_{Sn}^*)^x]]^{-2,78} \\ \approx 3,2 \cdot 10^{28} \delta^{-2,78} \quad (21)$$

Cette variation de K_{ass}^0 montre que, dans la

relation (5), la concentration en associations $[(V_{Sn}V_{Sn}^*)^x]$ doit être multipliée par un coefficient d'activité

$$\gamma_{ass} = [2[(V_{Sn}V_{Sn}^*)^x]]^{+2,78}.$$

(b) Construction du domaine d'existence

Le domaine d'existence du sulfure d'étain avait été tracé[1] en déterminant le long des bordures riche en étain et riche en soufre la déviation de stoechiométrie à partir de la relation: $\delta = [V_{Sn}^*] = p_{300}/2$. Le domaine ainsi obtenu a été représenté sur la Fig. 6 en utilisant comme variable de composition le nombre d'atomes de soufre en excès par rapport à la

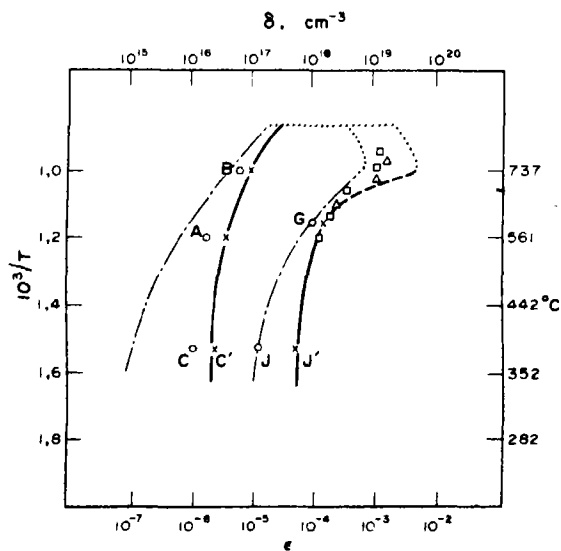


Fig. 6. Domaine d'existence du sulfure d'étain, — limite du domaine d'existence, --- limite du domaine d'existence déterminée à partir de $p_{300}/2$ [1], \square résultats de Rau [5], Δ points obtenus à partir de la valeur de $K_{ass}^0 K_{as}^0 = 1 \cdot 10^{31} \text{ cm}^{-6} \text{ K}^{-3}$.

composition stoechiométrique ($\epsilon = 6,2 \cdot 10^{-23} \delta$). La construction du domaine a été reprise dans la région des hautes températures en adoptant pour δ la valeur $p_s/2$ augmentée le cas échéant de la concentration en lacunes neutres et, dans la région des basses températures, en tenant compte du phénomène d'associations.

(i) *Bordure riche en étain.* Les valeurs de δ pour les échantillons A, B et C obtenues après trempe à partir de la valeur de p_{300} sont indiquées sur la Fig. 6. La différence entre les nouvelles valeurs et celles obtenues dans nos travaux antérieurs s'explique par la présence d'impuretés dans le sulfure utilisé lors des premières expériences. En effet, dans cette région où la concentration en trous est très faible, les propriétés électroniques sont extrêmement sensibles à la présence d'impuretés à l'état de traces*.

La bordure du domaine a été tracée à partir des valeurs $p_s/2$ expérimentales correspondant à A et B, et à partir de la valeur p_{300} de l'échantillon C en tenant compte du phénomène d'associations à l'aide de l'équation (12). Le point C' qui se trouve légèrement en dehors de la courbe correspond à la valeur $p_s/2$ obtenue avec l'échantillon C après un recuit à 500°C. On voit que l'accord est excellent entre la détermination expérimentale directe et les prévisions théoriques basées sur le phénomène d'associations.

(ii) *Bordure riche en soufre. Températures inférieures à 580°C (en dessous du point G).* Pour l'échantillon G, la composition a été calculée en tenant compte de la concentration

en lacunes neutres $[V_{Sn}^x]_{220^\circ C}$ (cf. Tableau 1). La bordure correspondant aux températures inférieures a été déduite des mesures du coefficient de Hall à température ambiante (courbe GJ) en tenant compte du phénomène d'associations. Le point J' provient de la valeur $p_s/2$ obtenue avec l'échantillon J recuit à 500°C. Dans ce cas, l'accord entre la détermination expérimentale et théorique est encore très satisfaisant.

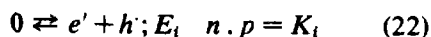
Températures supérieures à 580°C. La courbe en tirets résulte des valeurs du nombre de porteurs obtenues par extrapolation des courbes isothermes $\log p/2 = f(\log p_s)$ [1] (Fig. 1) en tenant compte des coefficients d'activité γ et des concentrations en V_{Sn}^x qui, dans cette région, deviennent prépondérantes. Les corrections relatives à la présence des lacunes neutres à 220°C sont très importantes et déplacent la bordure bien au delà des valeurs de Rau déterminées à partir de la perte de masse des échantillons pour différentes pressions de soufre aux températures mêmes de l'équilibre. On peut noter cependant que la divergence des résultats intervient dans un domaine où on a été amené à supposer l'inefficacité de la trempe lors de l'établissement du modèle électronique du sulfure d'étain. De plus, les corrections précédentes ont été faites à l'aide de la valeur moyenne expérimentale $K_{a_1}^0 K_{a_2}^0 = 1 \cdot 10^{30} \text{ cm}^{-6} \text{ K}^{-3}$. Or, dans ce domaine de fortes concentrations en porteurs, la teneur en lacunes neutres varie très rapidement avec la valeur du produit $K_{a_1}^0 K_{a_2}^0$. Si l'on adopte pour ce produit la valeur $1 \cdot 10^{31}$ qui correspond à la limite supérieure de l'incertitude expérimentale [1] et qui est très proche de la valeur théorique, les corrections deviennent très faibles et conduisent à une bordure très voisine de celle obtenue par Rau (cf. Fig. 6).

6. CONSTANTES PHYSIQUES INTRINSEQUES DU SULFURE D'ETAIN

La partie linéaire commune à tous les échantillons observée sur la Fig. 1 dans la région des hautes températures et qui corres-

* La valeur commune $R = 10^3 \text{ cm}^3 \cdot \text{C}^{-1}$ (Fig. 1) vers laquelle tend le coefficient de Hall des échantillons A, B, E aux basses températures correspond à $6,5 \cdot 10^{18}$ trous par cm^3 . Or l'analyse de ces échantillons par spectroscopie d'émission a révélé la présence de moins de 1 ppm de cuivre. Si on admet que les atomes de cuivre donnent naissance à des niveaux accepteurs totalement ionisés à température ambiante, la présence de 0,1 ppm de cuivre permet d'expliquer cette valeur. Par conséquent, la présence de 10 ppm de cuivre est suffisante pour empêcher une détermination valable de la bordure riche en étain dont la composition correspond à environ $1 \cdot 10^{17}$ trous par cm^3 .

pond à des coefficients de Hall négatifs caractérise la conductibilité intrinsèque du sulfure d'étain. Cette conductibilité, assurée principalement par les électrons et les trous correspondant à une excitation électronique directe de la bande de valence jusqu'à la bande de conduction, peut être schématisée par la réaction:



où

$$K_i = K_i^0 T^3 e^{-E_i/kT} =$$

$$4 \left[\frac{2\pi mk}{h^2} \right] \left[\frac{m_e^* m_h^*}{m^2} \right]^{3/2} T^3 e^{-E_i/kT}. \quad (23)$$

Dans ce domaine, le coefficient de Hall est donné par l'expression:

$$R_i = -\frac{3\pi}{8en} \frac{b-1}{b+1} \quad (24)$$

où b représente le rapport de la mobilité des électrons à celle des trous et la variation de n avec la température est donnée par:

$$n = (K_i^0)^{1/2} T^{3/2} e^{-E_i/2kT}. \quad (25)$$

La courbe $\ln(n/T^{3/2}) = f(1/T)$ doit être linéaire, et les valeurs de la pente et de l'ordonnée à l'origine permettent de déterminer respectivement E_i et K_i^0 .

(a) Détermination du rapport des mobilité b

L'examen des courbes de la Fig. 1 fait apparaître pour les échantillons A, B, E et F une température particulière où le coefficient de Hall change de signe; à cette température d'inversion T_i ,

$$R_{T_i} = -3\pi/8e[(nb^2 - p)/(nb + p)^2] = 0$$

$$\text{d'où } b^2 = (p/n)_{T_i};$$

et l'expression de b^2 devient en tenant compte de l'équation d'électroneutralité:

$$b^2 = 1 + \frac{b+1}{b-1} \left(\frac{R_i}{R_e} \right)_{T_i} \quad (26)$$

les valeurs R_e et R_i sont obtenues par extrapolation à la température T_i des coefficients de Hall extrinsèque et intrinsèque. Les résultats de la Fig. 1 permettent de calculer à partir de cette équation les valeurs de b pour les échantillons A, B, E et F: $b_A = 3,6$, $b_B = 3,8$, $b_E = 4,1$ et $b_F = 3,95$. Comme la température d'inversion est déterminée à 8°C près, on peut considérer que dans l'intervalle de température étudiée [315, 440°C], le rapport des mobilités est égal à 3,8.

(b) Détermination de l'énergie E_i et de la constante K_i^0

Les valeurs de n calculées à partir du coefficient de Hall intrinsèque à l'aide de la relation (24) en tenant compte de la valeur $b = 3,8$ ont été reportées dans le diagramme $\log(n/T^{3/2}) = f(1/T)$ de la Fig. 7. En accord avec l'expression théorique (25), on obtient une droite dont la pente conduit à la largeur de bande interdite $E_i = 1,32$ eV. D'autre part, la différence importante entre la valeur de l'or-

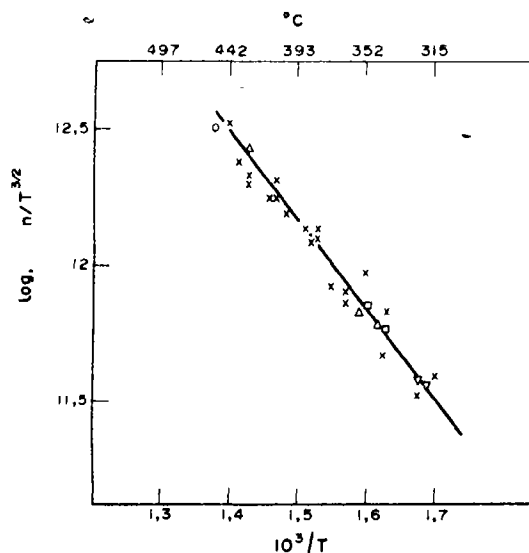


Fig. 7. Variations de $\log(n/T^{3/2})$ en fonction de la température: x valeurs rapportées dans une précédente publication [1].

donnée à l'origine ($\ln(K_f)^{1/2} = 39,4$) et la valeur théorique ($\ln(K_f)^{1/2} = 36$) peut être expliquée par la variation de E_i avec la température suivant la loi $E_i = E_f - \beta T$.

En reportant cette expression dans l'équation (25) on obtient $E_f = 1,32 \text{ eV}$ et $\beta = (5,9 \pm 0,4) 10^{-4} \text{ eV} \cdot \text{K}^{-1}$.

La valeur $E_i = 1,14 \text{ eV}$ calculée à température ambiante est en bon accord avec celle déterminée optiquement par Albers[3], [11] ($E_i = 1,07 \text{ eV}$).

Malgré la largeur relativement importante de la bande interdite, le domaine de conductibilité intrinsèque apparaît à des températures assez basses, 315, 330, 345 et 440°C respectivement pour les échantillons A, B, E et F: ce résultat est dû au fait que la mobilité des électrons est environ quatre fois supérieure à celle des trous, et surtout au phénomène d'associations qui provoque à 220°C une diminution très importante du nombre de porteurs extrinsèques.

7. CONCLUSIONS

Des échantillons de sulfure d'étain de différentes compositions ont été préparés par retraitement de pastilles à hautes températures sous pression de soufre contrôlée. L'étude des variations thermiques du coefficient de Hall a permis de calculer la largeur de bande interdite et le rapport des mobilités $b = 3,8$ a été déterminé à partir des coefficients de Hall intrinsèque et extrinsèque correspondant à la température d'inversion $p-n$.

L'apparition de la conductibilité intrin-

sèque à des températures aussi basses que 315°C s'explique grâce au phénomène d'associations de lacunes qui a été étudié d'une part à l'aide des variations thermiques effectuées très lentement pour obtenir des valeurs du coefficient de Hall correspondant à des états d'équilibre véritables et d'autre part en soumettant les échantillons à des recuits prolongés.

Enfin, le domaine d'existence du sulfure d'étain a été construit en tenant compte des associations dont la présence entraîne des corrections importantes aux basses températures.

BIBLIOGRAPHIE

1. A. LICHANOT et S. GROMB, *J. Chim. Phys.* **67**, 1239 (1970).
2. A. LICHANOT et S. GROMB, *C. R. Acad. Sci. Paris* **270**, 231 (1970).
3. W. ALBERS, C. HAAS, H. J. VINK et J. D. WASCHER, *J. appl. Phys. Suppl.* **32**, 2220 (1961).
4. W. ALBERS et H. J. VINK *Chem. Week.* **61**, 67 (1964).
5. H. RAU, *J. Phys. Chem. Solids* **27**, 761 (1966).
6. A. LICHANOT et S. GROMB, *C. R. Acad. Sci. Paris* **268**, 174 (1969).
- 7a. F. A. KRÖGER, *The chemistry of imperfect crystals*, North Holland publishing Company Amsterdam, p. 292 (1964).
- 7b. F. A. KRÖGER, *The Chemistry of Imperfect Crystals*, p. 529, North Holland, Amsterdam (1964).
- 7c. F. A. KRÖGER, *The Chemistry of Imperfect Crystals*, p. 212, North Holland, Amsterdam (1964).
8. McDOUGALL et STONER, *Phil. Trans. A*, **237**, 476 (1938).
9. A. J. ROSENBERG, *J. Chem. Phys.* **33**, 665 (1960).
10. R. F. BREBRICK et W. W. SCANLOW, *Phys. Rev.* **96**, 595 (1954).
11. W. ALBERS, C. HAAS et F. VANDER MAESEN, *J. Phys. Chem. Solids* **15**, 306 (1960).



PHENOMENOLOGICAL LATTICE-DYNAMICAL THEORY OF FERROELASTICITY

K. AIZU

Hitachi Central Research Laboratory, Kokubunzi, Tokyo, Japan

(Received 31 August 1970)

Abstract—A phenomenological lattice-dynamical investigation is made into ferroelasticity and some of its associated phenomena, such as optical birefringence and elastooptic effect, in ferroelastic crystals that are nonmagnetic and may or may not be ferroelectric at the same time. Two different types, provisionally called optical type and elastic type, are conceivable for ferroelastics. Ferroelastics of the optical type are optically soft and elastically hard. They have a special optical mode of lattice vibration that is Raman-active and lowers rapidly in eigenfrequency as temperature falls toward the Curie point. Ferroelastics of the elastic type are elastically soft and optically hard. In them, a certain elastic stiffness when the coordinates of all lattice vibration modes with zero wave number are fixed diminishes rapidly as temperature falls toward the Curie point. The investigation is carried out for both these different types of ferroelastics, which are found to behave similarly in respects proper to ferroelasticity and to behave differently in not a few other important respects.

1. INTRODUCTION

A CRYSTAL is provisionally referred to as being 'ferroic,' when it has two or more orientation states in the absence of magnetic field, electric field and mechanical stress, and can shift from one to another of these states by the application of a magnetic field, an electric field or a mechanical stress or a combination of these; here any two of the orientation states are identical or enantiomorphous in crystal structure, but are different with respect to direction of arrangement of the atoms which may bear an electric charge, an electric dipole moment and/or a magnetic dipole moment.

Only nonmagnetic crystals will be considered in this paper. In a ferroic crystal, a state shift with which polar property vectors of the crystal are changed is said to be ferroelectric; or the crystal is said to be ferroelectric with respect to this state shift. It can easily be proved that if one polar property vector is changed with a state shift, all polar property vectors are changed with the state shift. Spontaneous electric polarization vector is a typical, polar property vector. Hence, in view of electrostatic energy, every ferroelectric state shift can be accomplished by an electric field. A state shift with which symmetric second-rank polar property tensors are changed is said to be ferroelastic; or the crystal is said to be ferroelastic with respect to this state shift. It can easily be proved that if one symmetric second-rank polar property tensor is changed with a state shift, all symmetric second-rank polar property tensors are changed with the state shift. Spontaneous mechanical strain tensor is such a property tensor. Hence, in view of elastic energy, every ferroelastic state shift can be accomplished by a mechanical stress. It should be noted that state shifts accomplishable by mechanical stresses are not all ferroelastic, because among them there are ones with which the symmetric second-rank polar property tensors are unchanged (though

elastic compliance tensor and other fourth-rank polar property tensors are changed). Likewise, it should be noted that state shifts accomplishable by electric fields may not all be ferroelectric.

A ferroic crystal can be regarded as a slight modification of a certain nonferroic ideal crystal which is referred to as the prototype of that ferroic crystal. On varying temperature, a ferroic crystal commonly (though not necessarily) makes a phase transformation to a nonferroic phase having the same symmetry as the prototype; this phase is referred to as the prototypic phase.

Ferroic crystals are said to belong to the same species, when they are the same with respect to (i) their own point group—ferroic point group, (ii) point group of their prototype—prototypic point group and (iii) correspondence between the elements of the ferroic point group and the elements of the prototypic point group. Each species is represented by a compound symbol that comprises the letter *F* at its center, the symbol for the prototypic point group on the left of *F* and the symbol for the ferroic point group on the right of *F*. In many cases the correspondence between the elements of the prototypic point group and the elements of the ferroic point group is unique, so that the correspondence need not be indicated explicitly in the species symbol. In the other cases, however, the correspondence is indicated symbolically in the species symbol. Reference to a previous paper[1] is recommended for details of what have been stated above.

In the following sections, a phenomenological lattice-dynamical investigation is made into ferroelasticity and some of its associated phenomena, such as optical birefringence and elastooptic effect. The cases of the species $4/mmmFmmm$ and $\bar{4}2mFmm2$ are taken as

examples. Both these species are ferroelastic with two orientation states. The species $42mFmm2$ is also ferroelectric, while the species $4/mmmFmmm$ is not.

2. CASE OF THE SPECIES $4/mmmFmmm$

We consider a crystal able to become a ferroelastic of species $4/mmmFmmm$. We set a system of rectangular coordinate axes x, y, z with the z axis along the tetrad axis and with the x axis along a diad axis of the prototypic phase. In the ferroelastic phase the x axis may either agree with or make an angle of 45° with an orthorhombic principal axis; the x axis is chosen in the latter way. When x, y, z are to be used as indices for elements of tensors, they will be replaced by the numbers 1, 2, 3. We denote temperature by T , the Curie temperature by T_c , mechanical stress tensor by X , and mechanical strain tensor by x ; we are allowed to assume that the x realized at T_c in the absence of external forces is zero.

Each atom (or ion) composing the crystal may be divisible into an atomic core and some outer-shell electrons. The atomic cores and outer-shell electrons are oscillating. Our main attention is given to their average positions. The crystal structure becomes determinate when its basis and its space lattice are specified [2]. The parameters of the space lattice can be regarded as independent of the parameters of the basis as variables for specifying thermodynamic states. The set of parameters of the space lattice is equivalent to x , whose elements we write x_{ij} ($i = 1, 2, 3; j = 1, 2, 3$). x_{12} satisfies the condition of state parameter; that is to say, when realized in the absence of external forces, it differs for both the orientation states of the ferroelastic phase and is zero over the whole temperature range in the prototypic phase [3]. The other x_{ij} 's or any linear combinations of them do not satisfy the condition of state parameter. We assume that all the elements of X except X_{12} are always zero. It is, therefore, reasonable to leave all x_{ij} 's except x_{12} out of the set of explicit

variables. We put

$$x = \nu x_{12}, \quad X = (2/\nu) X_{12}, \quad (2,1)$$

where ν may be either 1, $\sqrt{2}$ or 2, according to the reader's preference.

For the positional parameters of the basis, we adopt the coordinates, Q_σ ($\sigma = 1, 2, \dots$), of normal modes of lattice vibration. (Only lattice vibration modes with zero wave number are taken into account.) The origin of the position of each particle (atomic core or outer-shell electron) is the average position of the particle realized at T_c in the absence of external forces. All the lattice vibration modes can be divided into atomic ones and electronic ones. There is a wide gap in eigenfrequency between both. The atomic modes can be divided into acoustic ones and optical ones. Since the acoustic modes merely translate the crystal as a whole, they have no effect on the ferroelasticity. Thus they will be left out of account.

We denote the potential energy per unit volume of the crystal by Ψ . Here 'unit volume,' accurately speaking, is unit volume at T_c in the absence of external forces. Ψ is a function of T, x and Q_σ 's. We assume that this function can be expanded into a power series in x and Q_σ 's with coefficients depending on T smoothly. Since in the absence of external forces this power series must be invariant for every operation belonging to the prototypic point group $4/mmm$, it is

$$\Psi = \Psi_0 + \frac{1}{2} A x^2 - x \sum_{\sigma} h_{\sigma} Q_{\sigma} + \frac{1}{2} \sum_{\sigma} \omega_{\sigma}^2 Q_{\sigma}^2 + \Psi_h - Xx - E \cdot P. \quad (2,2)$$

Here Ψ_0, A, h_{σ} 's and ω_{σ}^2 's are certain smooth functions of T . Ψ_h is the sum of terms of degrees higher than second. We assume that the transition between the ferroelastic and prototypic phases is second order. Then, in Ψ_h , it is allowable to neglect all terms of degrees higher than fourth. An electrical term $E \cdot P$ has been added; E stands for electric field

vector, and \mathbf{P} electric polarization vector. As is well known, it holds that

$$\mathbf{P} = \sum_{\sigma} \mathbf{m}_{\sigma} Q_{\sigma}, \quad (2.3a)$$

$$\mathbf{m}_{\sigma} = \sqrt{N} \sum_b e_b \mathbf{u}_{\sigma}^b, \quad (2.3b)$$

where N , e_b and \mathbf{u}_{σ}^b stand for the number of unit cells per unit volume, the electric charge of the b th of the particles (atomic cores and outer-shell electrons) forming the basis and the displacement, orthonormalized in the following sense, of the b th particle in the σ th mode of lattice vibration, respectively:

$$\sum_b M_b \mathbf{u}_{\sigma}^b \cdot \mathbf{u}_{\sigma'}^b = \delta_{\sigma\sigma'}$$

where M_b is the mass of the b th particle and $\delta_{\sigma\sigma'}$ is the so-called 'Kronecker's delta.' The components of \mathbf{P} and \mathbf{m}_{σ} will be written P_i and $m_{i\sigma}$ ($i = 1, 2, 3$).

When 4 stands for the 90° rotation about the z axis and H stands for the point group of (either orientation state of) the ferroelastic phase, the prototypic point group can be resolved into a union of H and $4H$. The strain x is unchanged by every operation belonging to H and changed in sign (only in sign) by every operation belonging to $4H$. The coefficient h_{σ} must be zero for any nondegenerate mode whose coordinate is changed otherwise than the strain x or the (1, 2) element of a symmetric second-rank polar tensor by at least one of the operations belonging to the prototypic point group (in other words, whose coordinate Q_{σ} is not such that $Q_{\sigma} \rightarrow Q_{\sigma}$ by every operation belonging to H and $Q_{\sigma} \rightarrow -Q_{\sigma}$ by every operation belonging to $4H$). The same coefficient h_{σ} , on the other hand, is, in general, nonzero for a mode whose coordinate is changed in the same way as the (1, 2) element of a symmetric second-rank polar tensor by all the operations of the prototypic point group. Obviously, such a mode, if atomic, should be Raman-active.

To be exact, the right-hand side of equation (2.2) should contain first-degree terms

$$- \sum_{\sigma} K_{\sigma} Q_{\sigma}. \quad (2.4)$$

The coefficient K_{σ} is a certain smooth function of T which becomes zero at T_c . K_{σ} must be zero for any non-degenerate mode whose coordinate is not invariant for all the operations of the prototypic point group. So, the terms (2.4) have no substantial effect on the ferroelasticity. This is the reason why they have been and will be ignored.

Optical birefringence is one—especially interesting—of the phenomena associated with ferroelasticity. We denote the (1,2) element of relative permittivity tensor for light by ϵ^{op} . The frequency, ω , of light is assumed not to be very close to any ω_{σ} . Ψ_h should contain terms

$$-x \sum_{\sigma'\sigma''} R_{\sigma\sigma'\sigma''} Q_{\sigma'} Q_{\sigma''}, \quad (2.5)$$

$$-\frac{1}{2} \sum_{\sigma'\sigma''} R_{\sigma\sigma'\sigma''} Q_{\sigma} Q_{\sigma'} Q_{\sigma''}, \quad (2.6)$$

where $R_{\sigma\sigma'\sigma''}$'s and $R_{\sigma\sigma'\sigma''}$'s are certain smooth functions of T . It holds that

$$\epsilon^{op} = r_a x + \sum_{\sigma} r_{\sigma} Q_{\sigma}, \quad (2.7a)$$

$$r_a \equiv \frac{1}{\epsilon_0} \sum_{\sigma'\sigma''} \frac{2R_{\sigma\sigma'\sigma''} m_{1\sigma'} m_{2\sigma''}}{(\omega_{\sigma'}^2 - \omega^2)(\omega_{\sigma''}^2 - \omega^2)}, \quad (2.7b)$$

$$r_{\sigma} \equiv \frac{1}{\epsilon_0} \sum_{\sigma'\sigma''} \frac{2R_{\sigma\sigma'\sigma''} m_{1\sigma'} m_{2\sigma''}}{(\omega_{\sigma'}^2 - \omega^2)(\omega_{\sigma''}^2 - \omega^2)} \quad (2.7c)$$

(ϵ_0 is the absolute permittivity of vacuum).

This is proved as follows. We denote time by t . The equations of motion

$$\frac{d^2 Q_{\sigma}}{dt^2} = - \frac{\partial}{\partial Q_{\sigma}} \Psi(Q, E) \equiv - \Psi_{Q_{\sigma}}(Q, E) \quad (\text{all modes})$$

hold. We denote the electric field of light which oscillates along the x axis by \tilde{E}_1 , resolve each Q_{σ} into a sum of an average part \bar{Q}_{σ} , a naturally (or thermally) oscillating part and a part \tilde{Q}_{σ} that oscillates with \tilde{E}_1 sinusoidally, and assume that the amplitudes of \tilde{E}_1 and \tilde{Q}_{σ} 's are very small. Then, from the above equations, the equations for \tilde{Q}_{σ} 's

$$\frac{d^2 \tilde{Q}_{\sigma}}{dt^2} = - \sum_{\sigma'} \Psi_{Q_{\sigma} Q_{\sigma'}}(\bar{Q}, \tilde{E}) \tilde{Q}_{\sigma'} - \Psi_{Q_{\sigma} E_1}(\bar{Q}, \tilde{E}) \tilde{E}_1$$

are derived. Now we leave out bars with no alteration in sense. Then,

$$\frac{d^2 \tilde{Q}_{\sigma}}{dt^2} = - \sum_{\sigma'} \Psi_{Q_{\sigma} Q_{\sigma'}}(Q, E) \tilde{Q}_{\sigma'} - \Psi_{Q_{\sigma} E_1}(Q, E) \tilde{E}_1 \quad (2.8)$$

Using the equation (2.2) into which equation (2.3a) is substituted and into which the terms (2.5) and (2.6) and no higher-degree terms are introduced, we get

$$\begin{aligned}\Psi_{Q_\sigma Q_{\sigma'}}(Q, E) &= \omega_\sigma^2 \delta_{\sigma\sigma'} - 2R_{\sigma\sigma'\sigma}x \\ &\quad - 2 \sum_{\sigma''} R_{\sigma\sigma'\sigma''} Q_{\sigma''}, \\ \Psi_{Q_\sigma E_1}(Q, E) &= -m_{1\sigma}.\end{aligned}$$

By substitution of these, equations (2.8) become

$$\begin{aligned}d^2\tilde{Q}_\sigma/dt^2 &= -\omega_\sigma^2 \tilde{Q}_\sigma + \sum_{\sigma'} (2R_{\sigma\sigma'\sigma}x \\ &\quad + \sum_{\sigma''} 2R_{\sigma\sigma'\sigma''} Q_{\sigma''}) \tilde{Q}_{\sigma'} + m_{1\sigma} E_1.\end{aligned}\quad (2.9)$$

We put

$$\tilde{E}_1 = E_1^\circ \sin \omega t, \quad \tilde{Q}_\sigma = Q_\sigma^\circ \sin \omega t.$$

Then, after a rearrangement, equations (2.9) reduce to

$$\begin{aligned}(\omega_\sigma^2 - \omega^2) Q_\sigma^\circ - \sum_{\sigma'} (2R_{\sigma\sigma'\sigma}x + \sum_{\sigma''} 2R_{\sigma\sigma'\sigma''} Q_{\sigma''}) Q_{\sigma'}^\circ \\ = m_{1\sigma} E_1^\circ.\end{aligned}$$

These simultaneous equations are approximately solved as

$$\begin{aligned}Q_\sigma^\circ &= \left\{ \frac{m_{1\sigma}}{\omega_\sigma^2 - \omega^2} + x \sum_{\sigma'} \frac{2R_{\sigma\sigma'\sigma} m_{1\sigma'}}{(\omega_\sigma^2 - \omega^2)(\omega_{\sigma'}^2 - \omega^2)} \right. \\ &\quad \left. + \sum_{\sigma''\sigma'''} \frac{2R_{\sigma\sigma'\sigma''} m_{1\sigma'} Q_{\sigma''}}{(\omega_\sigma^2 - \omega^2)(\omega_{\sigma'}^2 - \omega^2)} \right\} E_1^\circ,\end{aligned}\quad (2.10)$$

on the assumption that

$$|\omega_\sigma^2 - \omega^2| \gg |2R_{\sigma\sigma'\sigma}x + \sum_{\sigma''} 2R_{\sigma\sigma'\sigma''} Q_{\sigma''}|.$$

That part of the y component of electric polarization vector which oscillates with \tilde{E}_1 is

$$\tilde{P}_2 = \sum_{\sigma} m_{2\sigma} \tilde{Q}_\sigma = \sum_{\sigma} m_{2\sigma} (Q_\sigma^\circ / E_1^\circ) \tilde{E}_1.$$

From this and the solution (2.10), we see

$$\begin{aligned}\epsilon^{op} &= \tilde{P}_2 / \epsilon_0 \tilde{E}_1 = \epsilon_0^{-1} \sum_{\sigma} m_{2\sigma} (Q_\sigma^\circ / E_1^\circ) \\ &= \frac{1}{\epsilon_0} \sum_{\sigma} \frac{m_{1\sigma} m_{2\sigma}}{\omega_\sigma^2 - \omega^2} + r_\sigma x + \sum_{\sigma} r_\sigma Q_\sigma,\end{aligned}$$

where r_σ and r_σ 's mean the same as given in (2.7b) and (2.7c). While x , Q_σ 's and ϵ^{op} are variables, r_σ , r_σ 's and the quantity

$$\epsilon_0^{-1} \sum_{\sigma} m_{1\sigma} m_{2\sigma} (\omega_\sigma^2 - \omega^2)^{-1} \quad (2.11)$$

are considered as constants—coefficients relating variables to variables, so that they must be unchanged for the operations of the prototypic point group. As the strain x is changed in sign by every operation belonging to $4H$, so is ϵ^{op} . Therefore the quantity (2.11) must be zero.

The coefficient r_σ is, in general, nonzero. It is easily found that r_σ and h_σ are either simultaneously present or simultaneously absent for each mode. What modes contribute to the right-hand side of equation (2.7c)? Although the σ th mode may as well be atomic, the σ' th and σ'' th modes must be electronic if they may make a substantial contribution. Q_σ is reasonably assumed to be changed in the same way as the (1,2) element, T_{12} , of a symmetric second-rank polar tensor by every operation of the prototypic point group. If, for example, Q_σ and $Q_{\sigma'}$ are both changed in the same way as T_{12} , then $R_{\sigma\sigma'\sigma''} = 0$, so that the set of the σ' th and σ'' th modes in this case makes no contribution. If the σ' th and σ'' th modes are degenerate and their coordinates are changed in the same way as the x and y components of a vector,* then $R_{\sigma\sigma'\sigma''}$, $m_{1\sigma'}$ and $m_{2\sigma'}$ are all, in general, nonzero, so that the set of these modes may make a substantial contribution. It may also make a substantial contribution to r_σ , since $R_{\sigma\sigma'\sigma''}$ is, in general, nonzero.

A thermodynamic state to be realized under given constant external forces must make the potential energy (2.2) minimum. We denote the x and Q_σ 's realized in the absence of external forces by x_s and $Q_{s\sigma}$'s, with the subscript s meaning 'spontaneous.' In the prototypic phase we have $x_s = 0$, all $Q_{s\sigma} = 0$ (some of the latter equalities are approximate, owing to the terms (2.4)), and hence also $\epsilon_s^{op} = 0$. We assume that in the absence of external forces, the crystal is prototypic at temperatures higher than T_c and ferroelastic at temperatures lower than T_c . From the condition of positive definiteness of the matrix formed by the second derivatives of Ψ with respect to x and Q_σ 's at x_s and $Q_{s\sigma}$'s and from the assumption that the transition between the prototypic and ferroelastic phases is

*This is possible in the species $4/mmmFmmm$. Being changed in the same way as the x and y components of a vector means that $Q_{\sigma'} \rightarrow -Q_{\sigma'}$, $Q_{\sigma''} \rightarrow -Q_{\sigma''}$ by the inversion, $Q_{\sigma'} \rightarrow Q_{\sigma'}$, $Q_{\sigma''} \rightarrow -Q_{\sigma''}$ by the 180° rotation about the x axis, and $Q_{\sigma'} \rightarrow -Q_{\sigma'}$, $Q_{\sigma''} \rightarrow Q_{\sigma''}$ by the 90° rotation about the z axis.

second order, it follows that

$$(\prod_{\sigma} \omega_{\sigma}^2) \left(A - \sum_{\sigma} \frac{h_{\sigma}^2}{\omega_{\sigma}^2} \right) \geq 0 \quad \text{at } T \geq T_c \quad (2,12)$$

respectively. Since A , h_{σ} 's and ω_{σ}^2 's are assumed to be smooth functions of T , the expression

$$(\prod_{\sigma} \omega_{\sigma}^2) (A - \sum_{\sigma} h_{\sigma}^2 / \omega_{\sigma}^2) \quad (2,13)$$

is a smooth function of T ; it is smooth even at a temperature where an ω_{σ} becomes zero. When it is expanded into a power series in $T - T_c$, the zeroth-degree term must be zero owing to the relation (2,12). Hence we are allowed to put

$$(\prod_{\sigma} \omega_{\sigma}^2) (A - \sum_{\sigma} h_{\sigma}^2 / \omega_{\sigma}^2) = \Gamma(T - T_c) \quad (2,14)$$

with the coefficient Γ expansible into a power series in $T - T_c$. There is no particular reason for the zeroth degree term of Γ to become zero. So, this term is assumed nonzero. Owing to the relation (2,12), it must be positive; in other words, $\Gamma > 0$ at T_c .

We put

$$s = (dx/dX)_{x=0},$$

$$\pi = (d\epsilon^{op}/dx)_{x=x_g}, \quad \pi' = (d\epsilon^{op}/dX)_{x=0},$$

which are the (6,6) element of elastic compliance tensor and the (6,6) elements of two kinds of elastooptic (or photoelastic) coefficient tensor, respectively. Obviously, $\pi' = \pi s$.

At $T > T_c$, we can deduce

$$s = \frac{1}{A - \sum_{\sigma} h_{\sigma}^2 / \omega_{\sigma}^2} = \frac{\prod_{\sigma} \omega_{\sigma}^2}{\Gamma(T - T_c)}, \quad (2,15a)$$

$$\pi = r_a + \sum_{\sigma} h_{\sigma} r_{\sigma} / \omega_{\sigma}^2. \quad (2,15b)$$

Equation (2,15a) tells that the T dependence of s right above T_c obeys the Curie-Weiss law. The T dependence of π differs according to type of the crystal.

Two different types are conceivable for crystals able to become ferroelastic. (For

simplicity's sake, the ferroelastics are assumed to be bistate.) These types are provisionally referred to as optical type and elastic type. A crystal of the optical type is optically soft and elastically hard—as hard as common crystals. In it, as T approaches T_c from above, the eigenfrequency of a certain optical atomic mode of lattice vibration that has a nonzero h_{σ} and hence is Raman-active lowers rapidly, until at $T = T_c$ the expression (2,13) becomes zero and the phase transition takes place. Hence π varies anomalously with T near T_c . Even when the crystal is clamped at $x = 0$, the phase transition may take place (at a certain temperature lower than T_c). In this case, although the low-temperature phase cannot have a nonzero (1,2) element of strain tensor, it has nonzero (1,2) elements of other symmetric second-rank polar property tensors, and the signs of these elements differ for different orientation states, so that we recognize the phase as ferroelastic in essence. A crystal of the elastic type is elastically soft and optically hard—as hard as common crystals. In it, as T approaches T_c from above, none of the eigenfrequencies of lattice vibration modes with zero wave number lower rapidly but the coefficient A diminishes rapidly, until at $T = T_c$ the expression (2,13) becomes zero and the phase transition takes place. Hence π does not anomalously vary with T near T_c . When the crystal is clamped at $x = 0$, the phase transition does not take place.

We assume that the crystal under consideration is of the optical type. We assign $\sigma = 1$ to the soft mode of lattice vibration. ω_1^2 is allowed to become zero and negative, respectively, at and below a temperature, written T_1 , lower than T_c :

$$\omega_1^2 \geq 0 \quad \text{at } T \geq T_1 \quad (2,16)$$

respectively. It is a good approximation to put

$$\Psi_h = \frac{1}{2} D_1 Q_1^4 \quad (2,17)$$

where D_1 is a certain smooth function of T

and positive at all temperatures. (Since Q_1 is changed in the same way as T_{12} , the coefficient R_{111} in the term $-\frac{1}{2}R_{111}Q_1^3$ must be zero.) After a calculation, we obtain, at $T < T_c$,

$$Q_{s1} = \frac{\Gamma(T_c - T)}{D_1(\prod_{\sigma>1} \omega_{\sigma}^2)(A - \sum_{\sigma>1} h_{\sigma}^2/\omega_{\sigma}^2)},$$

$$Q_{\sigma\sigma'} = \frac{h_1 h_{\sigma'}/\omega_{\sigma'}^2}{A - \sum_{\sigma>1} h_{\sigma}^2/\omega_{\sigma}^2} Q_{s1} \quad (\sigma' > 1),$$

$$x_s = \frac{h_1}{A - \sum_{\sigma>1} h_{\sigma}^2/\omega_{\sigma}^2} Q_{s1}, \quad (2.18)$$

$$\frac{\epsilon_s^{op}}{x_s} = r_a + \sum_{\sigma>1} \frac{h_{\sigma} r_{\sigma}}{\omega_{\sigma}^2} + \frac{r_1}{h_1} \left(A - \sum_{\sigma>1} \frac{h_{\sigma}^2}{\omega_{\sigma}^2} \right),$$

$$s = \Omega_1^2 (\prod_{\sigma>1} \omega_{\sigma}^2) / 2\Gamma(T_c - T),$$

$$\pi = r_a + \sum_{\sigma>1} h_{\sigma} r_{\sigma} / \omega_{\sigma}^2 + h_1 r_1 / \Omega_1^2,$$

where

$$\Omega_1^2 = \omega_1^2 + 3D_1 Q_{s1}^2$$

$$= \frac{h_1^2 \prod_{\sigma>1} \omega_{\sigma}^2 + 2\Gamma(T_c - T)}{(\prod_{\sigma>1} \omega_{\sigma}^2)(A - \sum_{\sigma>1} h_{\sigma}^2/\omega_{\sigma}^2)}. \quad (2.19)$$

When ω_1^2 is negative, ω_1 is, of course, a pure imaginary number. However, it is always in the form of an even power that ω_1 appears in equations. At $T < T_c$, Ω_1 , instead of ω_1 , takes the part of the eigenfrequency of the first mode of lattice vibration. At $T < T_1$, though ω_1^2 is negative, Ω_1^2 is positive.

From equations (2.15) and (2.18), it follows that at T_c ,

$$(\epsilon_s^{op}/x_s)_{fer} = \pi_{fer} = \pi_{prt}. \quad (2.20)$$

(The subscripts 'fer' and 'prt' mean 'in the ferroelastic phase' and 'in the prototypic phase' respectively.) The π or ϵ_s^{op}/x_s vs. T curve in the ferroelastic phase forms a cusp, at T_c , with the π vs. T curve in the prototypic phase. It can be proved that at T_c ,

$$\left(\frac{d\pi}{dT} \right)_{fer} > \left(\frac{d}{dT} \frac{\epsilon_s^{op}}{x_s} \right)_{fer} > \left(\frac{d\pi}{dT} \right)_{prt} \quad (2.21a)$$

or

$$\left(\frac{d\pi}{dT} \right)_{fer} < \left(\frac{d}{dT} \frac{\epsilon_s^{op}}{x_s} \right)_{fer} < \left(\frac{d\pi}{dT} \right)_{prt} \quad (2.21b)$$

according to whether h_1 and r_1 are the same or opposite in sign. Also,

$$\frac{(d\pi/dT)_{fer} - (d\pi/dT)_{prt}}{[d(\epsilon_s^{op}/x_s)/dT]_{fer} - (d\pi/dT)_{prt}} = 3. \quad (2.22)$$

It is convenient to denote the eigenfrequency of the σ th mode of lattice vibration by Ω_{σ} at all temperatures including ones higher than T_c and to interpret the Ω_{σ} at $T > T_c$ as equal to ω_{σ} . From equations (2.18) and (2.19), it turns out that the Ω_1 vs. T curve is continuous and breaks at T_c :

$$\left(\frac{d\Omega_1}{dT} \right)_{prt} - \left(\frac{d\Omega_1}{dT} \right)_{fer} = \frac{3\Gamma}{2h_1^2 \prod_{\sigma>1} \omega_{\sigma}^2} > 0. \quad (2.23)$$

As has been stated, $R_{1\sigma'\sigma''}$ is nonzero if the σ' th and σ'' th modes are degenerate and their coordinates are changed in the same way as the x and y components of a vector by all the operations of the prototypic point group. These degenerate modes, however, become nondegenerate at $T < T_c$. Solving the characteristic equation of the matrix formed by the second derivatives of Ψ with respect to $Q_{\sigma'}$ and $Q_{\sigma''}$, we get

$$\Omega_{\sigma'}^2 = \omega_{\sigma'}^2 + 2R_{1\sigma'\sigma'} Q_{s1},$$

$$\Omega_{\sigma''}^2 = \omega_{\sigma''}^2 - 2R_{1\sigma'\sigma''} Q_{s1};$$

in other words,

$$\Omega_{\sigma'} = \omega_{\sigma'} + (R_{1\sigma'\sigma'}/\omega_{\sigma'}) Q_{s1},$$

$$\Omega_{\sigma''} = \omega_{\sigma''} - (R_{1\sigma'\sigma''}/\omega_{\sigma'}) Q_{s1}.$$

(It should be noted that $\omega_{\sigma'} = \omega_{\sigma''}$ even at $T < T_c$.) Thus,

$$\Omega_{\sigma'} - \Omega_{\sigma''} = 2(R_{1\sigma'\sigma''}/\omega_{\sigma'}) Q_{s1} \propto (T_c - T)^{1/2}$$

just below T_c .

When the crystal of the optical type is clamped at $x = 0$ (and when $E = 0$), the potential energy Ψ is

$$\Psi = \Psi_0 + \frac{1}{2} \sum_{\sigma} \omega_{\sigma}^2 Q_{\sigma}^2 + \frac{1}{4} D_1 Q_1^4. \quad (2.24)$$

So, taking account of the relation (2,16), we see that the phase transition takes place at $T = T_1$ and the crystal becomes ferroelastic at $T < T_1$ with

$$\begin{aligned} Q_{s1}^2 &= -\omega_1^2/D_1 = (\dot{\omega}_1^2/D_1)(T_1 - T), \\ Q_{s\sigma'} &= 0 \quad (\sigma' > 1), \\ \epsilon_s^{op} &= r_1 Q_{s1} = \pm r_1 (\dot{\omega}_1^2/D_1)^{1/2} (T_1 - T)^{1/2}, \\ \Omega_1^2 &= -2\omega_1^2 = 2\dot{\omega}_1^2 (T_1 - T). \end{aligned} \quad (2,25)$$

We have put

$$\omega_1^2 = \dot{\omega}_1^2 (T - T_1). \quad (2,26)$$

$\dot{\omega}_1^2$ is a smooth function of T . At T_1 , $\dot{\omega}_1^2$ must be positive or zero; it is very natural to assume nonzero, i.e., positivity. Though $x_s = 0$ always, $|\epsilon_s^{op}|$ increases with fall of T , in near proportion to $(T_1 - T)^{1/2}$. The sign of ϵ_s^{op} differs for different orientation states.

If the crystal is not of the optical type but of the elastic type, it is a good approximation to put

$$\Psi_h = \frac{1}{4} D_a x^4 \quad (2,27)$$

where D_a is a certain smooth function of T and positive at all temperatures. After a calculation, we obtain, at $T < T_c$,

$$\begin{aligned} x_s^2 &= \frac{1}{D_a} \left(\sum_{\sigma} \frac{h_{\sigma}^2}{\omega_{\sigma}^2} - A \right) = \frac{\Gamma(T_c - T)}{D_a \prod_{\sigma} \omega_{\sigma}^2}, \\ Q_{s\sigma} &= \frac{h_{\sigma} x_s}{\omega_{\sigma}^2}, \quad s = \frac{\prod_{\sigma} \omega_{\sigma}^2}{2\Gamma(T_c - T)}, \quad (2,28) \\ \epsilon_s^{op}/x_s &= \pi = r_a + \sum_{\sigma} h_{\sigma} r_{\sigma} / \omega_{\sigma}^2. \end{aligned}$$

According to equations (2,15) and (2,28), the π vs. T curve does not break at T_c . The ϵ_s^{op}/x_s vs. T curve in the ferroelastic phase superposes itself on the π vs. T curve in the same phase. Also, any Ω_{σ} vs. T curve does not break at T_c . (These are approximate. If appropriate high-degree terms were not ignored in Ψ , a slight break would be proposed in the curves of π or ϵ_s^{op}/x_s and some Ω_{σ} 's vs. T .)

Let ρ be the density of the crystal which may be of the optical type or of the elastic type. Let k and ω be the wave number and frequency, respectively, of a lattice vibration mode propagating in a direction. For the transverse acoustic modes propagating along the x (or y) axis and displacing the atoms along the y (or x) axis, it holds that at $T > T_c$,

$$|\partial\omega/\partial k|_{k=0} = (\nu/2)(\rho s)^{-1/2}.$$

Substituting the relation $s \propto (T - T_c)^{-1}$ into the right-hand side, we find

$$|\partial\omega/\partial k|_{k=0} \propto (T - T_c)^{1/2};$$

in particular,

$$|\partial\omega/\partial k|_{k=0} = 0 \quad \text{at } T_c.$$

For the other transverse and longitudinal acoustic modes propagating along the x (or y) axis and for all the acoustic modes propagating in a direction $\langle 110 \rangle$ that becomes an orthorhombic principal axis at $T < T_c$, $|\partial\omega/\partial k|_{k=0}$ remains nonzero at T_c . To say again, these consequences are regardless of type of the crystal.

3. CASE OF THE SPECIES $\bar{4}2mFmm2$

We consider a crystal able to become a ferroelastic of species $\bar{4}2mFmm2$. Every ferroelastic of this species must be ferroelectric at the same time. We set a system of rectangular coordinate axes x, y, z with the z axis along the $\bar{4}$ axis and with the x axis along a diad axis of the prototypic phase. In this species as well, the (1,2) element x_{12} of mechanical strain tensor satisfies the condition of state parameter[3], and the other elements or any linear combinations of them do not. We assume that all the elements of mechanical stress tensor except the (1,2) element X_{12} are always zero. Instead of x_{12} and X_{12} , we use the quantities x and X that are defined in (2,1). As for electric polarization vector P , the z component satisfies the condition of

state parameter, while the other components do not. The z component of electric polarization vector and of electric field vector are, for brevity's sake, written P and E without the index 3.

The potential energy per unit volume, Ψ , is a function of T , x and the coordinates Q_σ 's of lattice vibration modes. Although the prototypic point group is $\bar{4}2m$ instead of $4/mmm$, equations (2,2), (2,3) and (2,7) remain valid.

When $\bar{4}$ stands for the combination of the inversion and the 90° rotation about the z axis, and H stands for the point of (either orientation state of) the ferroelastic phase, the prototypic point group can be resolved into a union of H and $4H$. The (1,2) element, T_{12} , of a symmetric second-rank polar tensor is unchanged by every operation belonging to H and changed in sign (only in sign) by every operation belonging to $4H$. The z component of a polar vector is changed in the same way as T_{12} by all the operations of the prototypic point group. Therefore the coefficients h_σ , $m_{3\sigma}$ and r_σ must be zero for any nondegenerate mode whose coordinate is changed otherwise than T_{12} by at least one of the operations belonging to the prototypic point group. These coefficients, on the other hand, are, in general, nonzero for a mode whose coordinate is changed in the same way as T_{12} by all the operations of the prototypic point group. Such a mode, if atomic, should be both Raman-active and infrared-active.

The (6,6) element s^E or s^P of elastic compliance tensor, the (3,6) element d of piezoelectric modulus tensor, the (3,3) element κ^X or κ^E of electric susceptibility tensor, the (6,6) element π^P , π^E or π' of elastooptic coefficient tensor and the (6,3) element η^E , η^X or η' of electrooptic coefficient tensor are defined as follows:

$$dx = s^E dX + ddE \quad \text{at } X=0, E=0,$$

$$= s^P dX + (d/\kappa^X) dP \quad \text{at } X=0, P=P_*,$$

$$dP = ddX + \kappa^X/dE \quad \text{at } X=0, E=0,$$

$$= (d/s^E) dx + \kappa^E/dE \quad \text{at } x=x_*, E=0,$$

$$de^{op} = \pi^E dx + \eta^E dP \quad \text{at } x=x_*, P=P_*,$$

$$= \pi^E dx + \eta^E dE \quad \text{at } x=x_*, E=0,$$

$$= \pi^P s^P dX + \eta^P dP \quad \text{at } X=0, P=P_*,$$

$$= \pi' dX + \eta' dE \quad \text{at } X=0, E=0.$$

In the prototypic phase, we have $x_* = 0$, all $Q_{\sigma\sigma} = 0$, and hence also $P_* = 0$, $\epsilon_s^{op} = 0$. We can deduce

$$\begin{aligned} s^E &= \frac{1}{A - \sum_{\sigma} h_{\sigma}^2 / \omega_{\sigma}^2} = \frac{\prod_{\sigma} \omega_{\sigma}^2}{\Gamma(T - T_c)}, \\ d &= \frac{\sum_{\sigma} h_{\sigma} m_{3\sigma} / \omega_{\sigma}^2}{A - \sum_{\sigma} h_{\sigma}^2 / \omega_{\sigma}^2}, \quad \kappa^X = \sum_{\sigma} \frac{m_{3\sigma}^2}{\omega_{\sigma}^2}, \\ \kappa^E &= \sum_{\sigma} \frac{m_{3\sigma}^2}{\omega_{\sigma}^2} + \frac{(\sum_{\sigma} h_{\sigma} m_{3\sigma} / \omega_{\sigma}^2)^2}{A - \sum_{\sigma} h_{\sigma}^2 / \omega_{\sigma}^2}, \\ \pi^E &= r_a + \sum_{\sigma} h_{\sigma} r_{\sigma} / \omega_{\sigma}^2, \\ \pi^P &= \pi^E - \frac{(\sum_{\sigma} h_{\sigma} m_{3\sigma} / \omega_{\sigma}^2)(\sum_{\sigma} m_{3\sigma} r_{\sigma} / \omega_{\sigma}^2)}{\sum_{\sigma} m_{3\sigma}^2 / \omega_{\sigma}^2}, \\ \eta^E &= (\sum_{\sigma} m_{3\sigma} r_{\sigma} / \omega_{\sigma}^2) / (\sum_{\sigma} m_{3\sigma}^2 / \omega_{\sigma}^2), \\ \eta^X &= \frac{(r_a + \sum_{\sigma} \frac{h_{\sigma} r_{\sigma}}{\omega_{\sigma}^2}) \sum_{\sigma} \frac{h_{\sigma} m_{3\sigma}}{\omega_{\sigma}^2}}{(\sum_{\sigma} \frac{h_{\sigma} m_{3\sigma}}{\omega_{\sigma}^2})^2} \\ &\quad + \frac{(A - \sum_{\sigma} \frac{h_{\sigma}^2}{\omega_{\sigma}^2}) \sum_{\sigma} \frac{m_{3\sigma} r_{\sigma}}{\omega_{\sigma}^2}}{(\sum_{\sigma} \frac{h_{\sigma} m_{3\sigma}}{\omega_{\sigma}^2})^2} \\ &\quad + \frac{(A - \sum_{\sigma} \frac{h_{\sigma}^2}{\omega_{\sigma}^2}) \sum_{\sigma} \frac{m_{3\sigma}^2}{\omega_{\sigma}^2}}{(\sum_{\sigma} \frac{h_{\sigma} m_{3\sigma}}{\omega_{\sigma}^2})^2}. \end{aligned} \quad (3,1)$$

If the crystal is of the optical type, equation (2,17) holds approximately. The soft mode of lattice vibration has a nonzero h_σ , and hence should be both Raman-active and infrared-active. If the crystal is of the elastic type, equation (2,27) holds approximately. Equations (3,1) are valid for either type.

We assume that the crystal is of the optical type. At $T < T_c$, the expressions involving $Q_{\sigma\sigma}^2$, $Q_{\sigma\sigma}'$ ($\sigma' > 1$), x_s and ϵ_s^{op}/x_s are found to be the same as given in (2,18). We get

$$\frac{P_s}{x_s} = \sum_{\sigma>1} \frac{h_{\sigma} m_{3\sigma}}{\omega_{\sigma}^2} + \frac{m_{31}}{h_1} \left(A - \sum_{\sigma>1} \frac{h_{\sigma}^2}{\omega_{\sigma}^2} \right).$$

Regarding the eigenfrequency, Ω_1 , of the soft mode of lattice vibration, the same as equations (2,19) hold. The expressions involving s , d , κ , π and η are the same as the result of replacing ω_1 by Ω_1 in the corresponding expressions in (3,1); for example,

$$s^E = \Omega_1^2 \left(\sum_{\sigma>1} \omega_{\sigma}^2 \right) / 2\Gamma(T_c - T),$$

$$\eta^x = \left(\sum_{\sigma>1} \frac{m_{3\sigma} r_{\sigma}}{\omega_{\sigma}^2} + \frac{m_{31} r_1}{\Omega_1^2} \right) / \left(\sum_{\sigma>1} \frac{m_{3\sigma}^2}{\omega_{\sigma}^2} + \frac{m_{31}^2}{\Omega_1^2} \right).$$

When the crystal of the optical type is mechanically clamped at $x = 0$ in the absence of electric field, the phase transition takes place at the temperature T_1 where ω_1 becomes zero. At $T < T_1$, although x_s remains zero, P_s and ϵ_s^{op} become nonzero, in near proportion to $(T_1 - T)^{1/2}$. Their signs differ for the two orientation states, which may be changed to each other by an electric field. The electric susceptibility at constant strain in the z direction obeys the Curie-Weiss law near—both above and below $-T_1$. When, instead of being mechanically clamped, the crystal is electrically clamped at $P = 0$ in the absence of mechanical stress, the condition for the prototypic phase to be stable is that the expression

$$\omega_1^2 \left\{ \left(\sum_{\sigma} \frac{m_{3\sigma}^2}{\omega_{\sigma}^2} \right) \left(A - \sum_{\sigma} \frac{h_{\sigma}^2}{\omega_{\sigma}^2} \right) + \left(\sum_{\sigma} \frac{h_{\sigma} m_{3\sigma}}{\omega_{\sigma}^2} \right)^2 \right\} \quad (3,2)$$

is positive. Not far below T_c , since the expression (3,2) is still positive, the crystal remains prototypic. It cannot be generally judged whether the expression (3,2) is positive even at temperatures much lower than T_c or not. (The expression (3,2) is smooth even at T_1 .)

We next assume that the crystal is of the elastic type. At $T < T_c$, the expressions involving x_s^2 , $Q_{s\sigma}$'s and ϵ_s^{op}/x_s are found

to be the same as given in (2,28). We get

$$P_s/x_s = \sum_{\sigma} h_{\sigma} m_{3\sigma} / \omega_{\sigma}^2.$$

The expressions involving s , d , κ , π and η are the same as the result of replacing A by $A + 3D_s x_s^2$ in the corresponding expressions in (3,1); for example,

$$s^E = (\prod_{\sigma} \omega_{\sigma}^2) / 2\Gamma(T_c - T),$$

$$\eta^x = \left(\sum_{\sigma} m_{3\sigma} r_{\sigma} / \omega_{\sigma}^2 \right) / \left(\sum_{\sigma} m_{3\sigma}^2 / \omega_{\sigma}^2 \right).$$

When the crystal of the elastic type is electrically clamped at $P = 0$ in the absence of mechanical stress, the condition for the prototypic phase to be stable is that the expression

$$A - \sum_{\sigma} \frac{h_{\sigma}^2}{\omega_{\sigma}^2} + \frac{\left(\sum_{\sigma} h_{\sigma} m_{3\sigma} / \omega_{\sigma}^2 \right)^2}{\sum_{\sigma} m_{3\sigma}^2 / \omega_{\sigma}^2} \quad (3,3)$$

is positive. Since, obviously, this expression is positive at T_c and negative at the temperature where A becomes zero, it becomes zero, or the phase transition takes place, at a temperature, written T_0 , intermediate between these temperatures. We put the expression (3,3) equal to $g(T - T_0)$; g is a smooth function of T and positive at T_0 . At $T < T_0$, we can deduce

$$x_s^2 = (g/D_s)(T_0 - T),$$

$$Q_{s\sigma} = \left(h_{\sigma} - m_{3\sigma} \frac{\sum_{\sigma'} h_{\sigma'} m_{3\sigma'} / \omega_{\sigma'}^2}{\sum_{\sigma'} m_{3\sigma'}^2 / \omega_{\sigma'}^2} \right) \frac{x_s}{\omega_{\sigma}^2}.$$

Whereas P_s is zero, the part of it, $m_{3\sigma} Q_{s\sigma}$, attributed to a lattice vibration mode with a nonzero $m_{3\sigma}$ is nonzero. The sign of x_s differs for the two orientation states, which may be changed to each other by a mechanical stress. The (6,6) elastic compliance at constant polarization obeys the Curie-Weiss law near—both above and below $-T_0$. When, instead of being electrically clamped, the crystal is mechanically clamped at $x = 0$ in the absence

of electric field, the crystal is thought to remain prototypic at any low temperature.

It is assumed that the crystal is neither mechanically nor electrically clamped. At T_c , whether the crystal is of the optical type or of the elastic type, we see

$$(P_s/x_s)_{\text{fer}} = (d/s^E)_{\text{prt}} = (\kappa^X/d)_{\text{prt}}.$$

In case of the optical type,

$$\left(\frac{d}{dT} \frac{d}{s^E}\right)_{\text{prt}} < \left(\frac{d}{dT} \frac{P_s}{x_s}\right)_{\text{fer}} \approx \left(\frac{d}{dT} \frac{\kappa^X}{d}\right)_{\text{prt}}, \quad (3.4)$$

while in case of the elastic type,

$$\left(\frac{d}{dT} \frac{d}{s^E}\right)_{\text{prt}} = \left(\frac{d}{dT} \frac{P_s}{x_s}\right)_{\text{fer}} < \left(\frac{d}{dT} \frac{\kappa^X}{d}\right)_{\text{prt}}; \quad (3.5)$$

here we have assumed $d > 0$ at $T > T_c$ and used the approximation

$$\left(\sum_{\sigma} m_{3\sigma}^2/\omega_{\sigma}^2\right)/\left(\sum_{\sigma} h_{\sigma} m_{3\sigma}/\omega_{\sigma}^2\right) \approx m_{31}/h_1$$

at T_c .

In a previous paper[4], simultaneously ferroelectric and ferroelastic crystals were divided into ones of the dielectric type and ones of the elastic type; the relation (3.4) was found to hold for ones of the dielectric type, and the relation (3.5) for ones of the elastic type. Dielectric type is conceptually almost the same as optical type in the present paper. Elastic type in the previous paper is the same as elastic type in the present paper. However, the concepts in the present paper are more general; they apply to the ferroelastic crystals at large, irrespective as to whether they are ferroelectric at the same time or not.

At T_c , the equalities

$$(\epsilon_s^{op}/x_s)_{\text{fer}} = \pi_{\text{fer}}^E = \pi_{\text{prt}}^E$$

hold, both in case of the optical type and in case of the elastic type. In case of the optical type, the inequalities (2.21a) or (2.21b) and the equality (2.22) hold, with π^E in place of π . In case of the elastic type, the π^E vs. T curve does not break at T_c . The ϵ_s^{op}/x_s vs. T curve in the ferroelastic phase superposes itself on the π^E vs. T curve in the same phase.

At T_c , the equalities

$$(\epsilon_s^{op}/P_s)_{\text{fer}} = \eta_{\text{fer}}^X = \eta_{\text{prt}}^X$$

hold, both in case of the optical type and in case of the elastic type. In case of the optical type, it can be proved that

$$\left(\frac{d\eta^X}{dT}\right)_{\text{fer}} \approx \left(\frac{d}{dT} \frac{\epsilon_s^{op}}{P_s}\right)_{\text{fer}} \approx \left(\frac{d\eta^X}{dT}\right)_{\text{prt}};$$

in case of the elastic type,

$$\left(\frac{d\eta^X}{dT}\right)_{\text{fer}} > \left(\frac{d}{dT} \frac{\epsilon_s^{op}}{P_s}\right)_{\text{fer}} > \left(\frac{d\eta^X}{dT}\right)_{\text{prt}}$$

or

$$\left(\frac{d\eta^X}{dT}\right)_{\text{fer}} < \left(\frac{d}{dT} \frac{\epsilon_s^{op}}{P_s}\right)_{\text{fer}} < \left(\frac{d\eta^X}{dT}\right)_{\text{prt}}$$

according to whether π^E and d are the same or opposite in sign.

The statements concerning $|\partial\omega/\partial k|_{k=0}$ for acoustic modes of lattice vibration in Section 2 hold also here in the same form.

4. DISCUSSION

As has been seen in the preceding sections, ferroelastics of the optical type and those of the elastic type behave similarly in fundamental respects. They are both capable of state shift by mechanical stress. Their x_s and ϵ_s^{op} are proportional to $(T_c - T)^{1/2}$ just below T_c . Their s^E is proportional to $|T - T_c|^{-1}$ around T_c ; the proportionality coefficient at $T > T_c$ is twice that at $T < T_c$. Their $|\partial\omega/\partial k|_{k=0}$ for a certain kind of transverse acoustic modes of lattice vibration is proportional to $(T - T_c)^{1/2}$ just above T_c . But, on the other hand, they behave differently under constant strain (and also under constant polarization if they are ferroelectric at the same time) and differ in temperature dependence of π^E and ϵ_s^{op}/x_s (and also of η^X , ϵ_s^{op}/P_s , d/s^E , κ^X/d and P_s/x_s if they are ferroelectric at the same time) around T_c .

Whereas two types—optical type and elastic type—are conceivable for ferroelastics (whether they are ferroelectric at the same time or not), elastic type or any type corresponding to it or taking its place is not conceivable for pure ferroelectrics that are not ferroelastic at the same time. This difference between ferroelasticity and ferroelectricity may not be very strange, in view of the fact that symmetric second-rank polar property tensors are much richer in variety than polar property vectors.

The phase of KH_2PO_4 which occurs at temperatures

below -150°C is ferroelastic[1, 5], belonging to the two-state species $42\text{mFmm}2$. The phase of Rochelle salt which occurs at temperatures between -18 and 24°C is ferroelastic[1, 5], belonging to the two-state species $222F2$. These phases are also ferroelectric. Because of satisfying the relation (3, 4) and for other reasons, they are probably of the optical type. CsPbCl_3 has a phase transformation at 37°C . Its principal elastic compliance seems to obey the Curie-Weiss law around 37°C , with the Curie constant on the high-temperature side larger than that on the low-temperature side[6]. The low-temperature phase has a Raman-active mode of lattice vibration, whose frequency is conjectured by extrapolation to lower anomalously with rise of temperature toward 37°C [6]. Thus the low-temperature phase might possibly be a ferroelastic of the optical type. It is not ferroelectric. There is no available information enough to infer its species from. $\text{NaBa}_2\text{Nb}_2\text{O}_{15}$ has phase transformations at 560°C and about 300°C [1, 7]. The low-temperature phase is partially ferroelastic and partially ferroelectric, belonging to the four-state species $4/\text{mmm}F\text{mm}2(p)$. The middle-temperature phase is ferroelectric but nonferroelastic, belonging to the two-state species $4/\text{mmm}F4\text{mm}$. The high-temperature phase is neither ferroelastic nor ferroelectric; it is the prototypic of both the middle- and low-temperature phases. Near the lower transition temperature, the s_{11}^E vs. T curve seems to obey the Curie-Weiss law, while the T dependences of the ferroelectric properties do not seem to become anomalous[8]. This phase transition is thought purely ferroelastic. (The phase transition at 560°C is thought purely ferroelectric.) There is no available information enough to infer its type from. The phase of VO_2 which occurs below about 70°C is full ferroelastic[1, 9], belonging to the four-state species $4/\text{mmm}F2/\text{m}(s)$. It is not ferroelectric. Its type is yet uninferable.

At the present stage, no real ferroelastics can be cited which are concluded or inferred to be of the elastic type. It is unknown whether the ferroelastics of the elastic type

are possible in principle; this question will be left to future studies. So, in this paper, the elastic type is hypothetical.

Previously[10], a kind of 'weak' ferroelastics were investigated. Even if their prototypic phase transitions are of the second kind, their x_c is proportional to $T_c - T$, instead of $(T_c - T)^{1/2}$, just below T_c . Their s^E does not obey the Curie-Weiss law around T_c , but is finite and discontinuous at T_c , with the inequality $s_{11}^E > s_{11}^E$. Thus they are of another type than the ferroelastics studied in the preceding sections in this paper. Still other types of ferroelastics are also conceivable. However, the types studied in the preceding sections are thought to be fundamental and standard among all types of ferroelastics.

REFERENCES

1. AIZU K., *J. Phys. Soc. Japan* **27**, 387 (1969).
2. For example, KITTEL C., *Introduction to Solid State Physics*, 2nd ed., p. 2, John Wiley, New York (1956).
3. AIZU K., *J. Phys. Soc. Japan* **28**, 706 (1970).
4. AIZU K., *Japan. J. appl. Phys.* **8**, 1424 (1969).
5. For example, JONA F. and SHIRANE G., *Ferroelectric Crystals*, Pergamon Press, New York (1962).
6. HIROTSU S., *J. Phys. Soc. Japan* **28**, Supplement, 185 (1970).
7. GEUSIC J. E., LEVINSTEIN H. J., RUBIN J. J., SINGH S. and VAN UITERT L. G., *Appl. Phys. Lett.* **11**, 269 (1967).
8. YAMADA T. and NIIZEKI N., *A lecture in the Spring 1970 Meeting of the Physical Society of Japan* whose preliminary note is given on p. 163 in *The Lecture Notes 4* for the same meeting (in Japanese).
9. ANDERSSON G., *Acta chem. Scand.* **10**, 623 (1956); WESTMAN S., *Acta chem. Scand.* **15**, 217 (1961); FILLINGHAM P. J., *J. appl. Phys.* **38**, 4823 (1967).
10. AIZU K., *J. Phys. Soc. Japan* **28**, 717 (1970); *ibid.* **29**, 1401 (1970).

ÜBER DEN EINBAU VON KUPFER IN ZnO-EINKRISTALLEN*

G. MÜLLER und R. HELBIG

Institut für Angewandte Physik der Universität Erlangen, Erlangen Deutschland

(Received 11 August 1970)

Zusammenfassung – Es wurde die Diffusionskonstante von Kupfer im Temperaturbereich von 1100–1250°C in ZnO-Einkristallen bestimmt: ($D = 2 \cdot 10^7 \exp [-(4,8 \pm 0,1) \text{ eV}/kT] \text{ cm}^2/\text{sec}$). Optische Absorption, ESR-Signal und elektr. Leitfähigkeit wurden an ZnO-Kristallen mit verschiedenen Cu-Konzentrationen ($10^{16} - 10^{21} \text{ Cu-Atome/cm}^3$) gemessen und in Zusammenhang mit der chemisch bestimmten Kupferkonzentration gebracht. Es zeigt sich, daß Kupfer überwiegend als Cu^{2+} auf Zn-Gitterplatz in das ZnO eingebaut wird. Die beobachtete Abnahme der Leitfähigkeit mit steigendem Cu-Gehalt wird durch die Wirkung von $[\text{Cu}^{2+}\text{Cu}^{2+}]$ -Assoziaten erklärt.

Abstract – The diffusion coefficient D of copper in ZnO single crystals was determined in the temperature range from 1100°C to 1250°C: $D = 2 \cdot 10^7 \exp [-(4,8 \pm 0,1) \text{ eV}/kT] \text{ cm}^2/\text{sec}$. Optical absorption, ESR-signal and electrical conductivity of ZnO crystals containing different concentrations of copper ($10^{16} - 10^{21} \text{ Cu atoms/cm}^3$) were measured and brought into connection with the copper concentration given by chemical analysis. It turns out that copper is mainly placed as Cu^{2+} on zinc-lattice site. The measured decrease of the electrical conductivity with increasing Cu-concentration can be explained by action of $[\text{Cu}^{2+}\text{Cu}^{2+}]$ -associates.

1. EINLEITUNG

KUPFERDOTIERTE ZnO-Kristalle wurden bereits in mehreren Arbeiten untersucht [1–11]. Dabei konnten sowohl die ESR-Messungen [4–9] als auch die optische Absorption [3–5] im Wellenbereich von $1,0 - 2,0 \mu$ durch die Existenz eines Cu^{2+} -Ions auf Zn-Gitterplatz erklärt werden. In einem gewissen Widerspruch dazu blieb die bei Cu-dotierten ZnO-Kristallen beobachtete Abnahme der elektrischen Leitfähigkeit mit steigendem Kupfergehalt [1, 2], die durch die Existenz eines Cu^{2+} -Zentrums nicht erklärt werden kann.

Die vorliegende Arbeit versucht zur Klärung dieser Frage beizutragen, indem an den gleichen Kristallen optische Absorption, ESR-Signal und elektrische Leitfähigkeit gemessen und in Zusammenhang mit der chemisch bestimmten Cu-Konzentration

gebracht werden. Dadurch soll entschieden werden, ob neben dem Cu^{2+} -Ion auf Zn-Gitterplatz noch andere Einbaumöglichkeiten für das Cu im ZnO bestehen (z.B. Zwischengitter, Assoziate oder evtl. andere Oxydationsstufen).

2. CHARAKTERISIERUNG UND HERSTELLUNG DER PROBEN

Die verwendeten Kristalle wurden im hiesigen Institut [12] nach einem Dampfreaktionsverfahren gezüchtet und hatten die Form sechskantiger Nadeln mit sehr guten Begrenzungsflächen (Durchmesser bis 8 mm, Länge ca. 20 mm). Einen Überblick über die Reinheit der undotierten Kristalle gibt Tabelle 1. Die untersuchten Cu-dotierten ZnO-Kristalle waren entweder gleich bei der Züchtung [12] oder aber später durch Diffusion mit Cu dotiert worden. Da die Untersuchung einen möglichst großen Cu-Konzentrationsbereich erfassen sollte, wurden verschiedene Diffusionsverfahren angewendet:

(a) Box-Verfahren ($10^{18} - 10^{21} \text{ Cu Atome/}$

*Auszugsweise vorgetragen auf der Frühjahrstagung der Deutschen Physikalischen Gesellschaft in Freudenstadt (1970).

Tabelle 1. Analysen undotierter ZnO-Kristalle nach verschiedenen Analysenverfahren

(Angaben in ppm). Zeichenerklärung:

ESA : Emissions-Spektal-Analyse (nach Harvey)

MSA : Massen-Spektrometer-Analyse

QESA : Qualitative Emissions-Spektal-Analyse

AAS : Atom-Absorptions-Spektrophotometer

≤ : unterhalb der Nachweisgrenze

<a : Element nachgewiesen mit oberster Grenze a

+ : Element im Bereich 1–10 ppm nachgewiesen.

Fehler für AAS ± 10% alle anderen ± 50%

Element	Analysemmethode			
	ESA	MSA	QESA	AAS
Li	≤65			≤0,03
Na	≤2600	<0,2	+	0,2 – 1
K		<6	+	0,03 – 0,1
Mg	≤0,5			≤0,1
Ca				≤0,3
Sr				≈0,6
Ba				
V		5	+	
Cr		<5	+	≤4
Mn	≤5,5			≤0,3
Fe	≤7,5	<5		≤1
Co	≤3			≤1,4
Ni	≤3			≤2
Cu	≤0,25		+	≤0,4
Cd	≤25			≤0,1
Al	<12			≤7
Ga	≤23			≤2
In	≤16			≤2
Si	<5	<2	+	≤7
Sn	<8			
Pb	≤13		+	≤0,4
P	≤450			
As	≤250			
Sb	≤88			
S				
Te	≤120			
Cl				
Zr	≤15			

cm³): Der Kristall wurde in einer Cu-haltigen ZnO-Keramik getempert. ($T = 1200\text{--}1250^\circ\text{C}$)

(b) Zwei-Zonen-Verfahren ($5 \cdot 10^{18} \text{--} 10^{20}$ Cu Atome/cm³): Cu-Quelle und Kristall befanden sich in einem Gasstrom auf verschiedenen, einstellbaren Temperaturen ($T_{\text{Quelle}} = 1100\text{--}1250^\circ\text{C}$; $T_{\text{Kristall}} = 1200\text{--}1250^\circ\text{C}$); als Quelle diente metallisches Cu in einem Quarzschiffchen, als Trägergas wurde O₂ verwendet.

(c) Nachdiffusion ($10^{18} \text{--} 10^{19}$ Cu Atome/cm³). Der Kristall wurde mit einer Cu-

Quelle andotiert und später ohne Quelle in reiner O₂-Atmosphäre homogenisiert (Homogenität besser als 15 Prozent: $T = 1200\text{--}1250^\circ\text{C}$).

Alle unter a bis c genannten Verfahren erfordern zur Herstellung homogen dotierter Kristalle die Kenntnis der bisher unbekannten Diffusionskonstanten von Cu in ZnO. Daher wurde zuerst die Diffusionskonstante von Cu in ZnO bestimmt.

3. DIFFUSION VON Cu IN ZnO

Hierbei wurden 2–3 mm dicke Kristalle (Länge 10–20 mm) bei konstantem Cu-Angebot in O₂-Atmosphäre (760 Torr) und verschiedenen Temperaturen verschieden lang getempert und anschließend auf Zimmertemperatur abgeschreckt. Durch schrittweises Ätzen in verdünnter HCl und Analysieren der Ätzlösung wurde das Cu-Konzentrationsprofil der Kristalle bestimmt. Die Analyse der Ätzlösung wurde mit Hilfe eines Atom-Absorptions-Spektrophotometers (Perkin Elmer Modell 303) durchgeführt (zur Methode siehe auch [24] und [25]). Diese Profile waren für den untersuchten Temperatur- und Konzentrationsbereich in guter Übereinstimmung mit den Lösungen der Diffusionsgleichung (2. Fick'sches Gesetz) für ein zylinderstmmetrisches Problem [13]. Für den Temperaturbereich von 1100–1250°C ist

$$D = 2 \cdot 10^7 \cdot \exp [-(4,8 \pm 0,1) \text{ eV}/kT] \frac{\text{cm}^2}{\text{sec}}.$$

Figure 1 zeigt neben der so für Cu bestimmten Diffusionskonstanten einige andere Diffusionskonstanten für ZnO in Abhängigkeit von der Temperatur.

4. OPTISCHE ABSORPTION

Es ist bekannt, daß Cu-dotierte ZnO-Kristalle eine Absorptionsbande zwischen 1,0–2,0 µ besitzen [3–5].

Figure 2 zeigt diese Absorptionsbande bei Zimmertemperatur für verschieden stark dotierte Kristalle. Dabei wurde die Absorp-

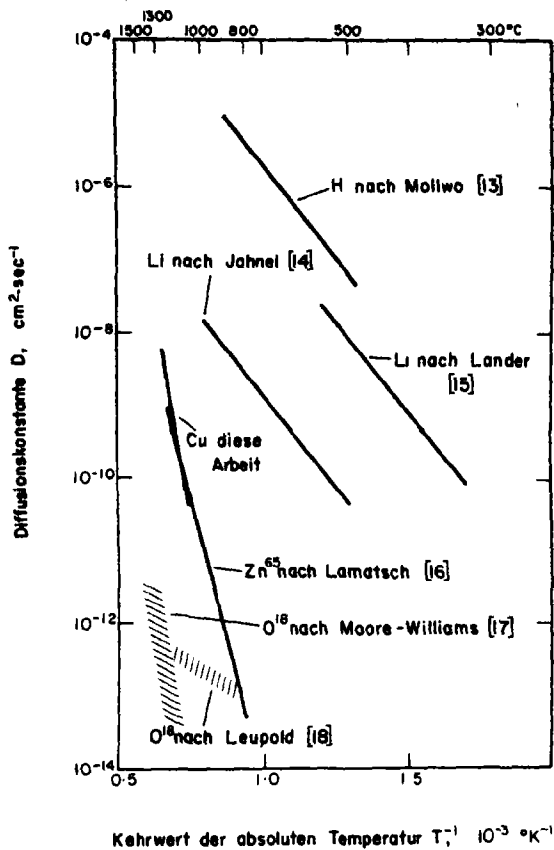


Fig. 1. Diffusionskonstanten in ZnO als Funktion der absoluten Temperatur.

tionskonstante K aus Messungen mit unpolarisiertem Licht an Kristallen verschiedener Dicke d unter Berücksichtigung von Vielfachreflexionen berechnet. Messungen mit polarisiertem Licht (siehe Fig. 3) ergaben, daß K_{\perp} (für $E \perp c$) immer größer als K_{\parallel} (für $E \parallel c$) ist. Man kann dann zeigen, daß für den hier untersuchten $K \cdot d$ -Bereich die in Fig. 2. aufgetragene Absorptionskonstante $K = 1,1 \cdot K_{\parallel}$ ist.

Den Zusammenhang zwischen der Zahl der absorbierenden Zentren N und dem Produkt aus Höhe und Breite der Absorptionsbande (näherungsweise Gaussform) beschreibt die aus der Dispersionstheorie abgeleitete Formel [19]:

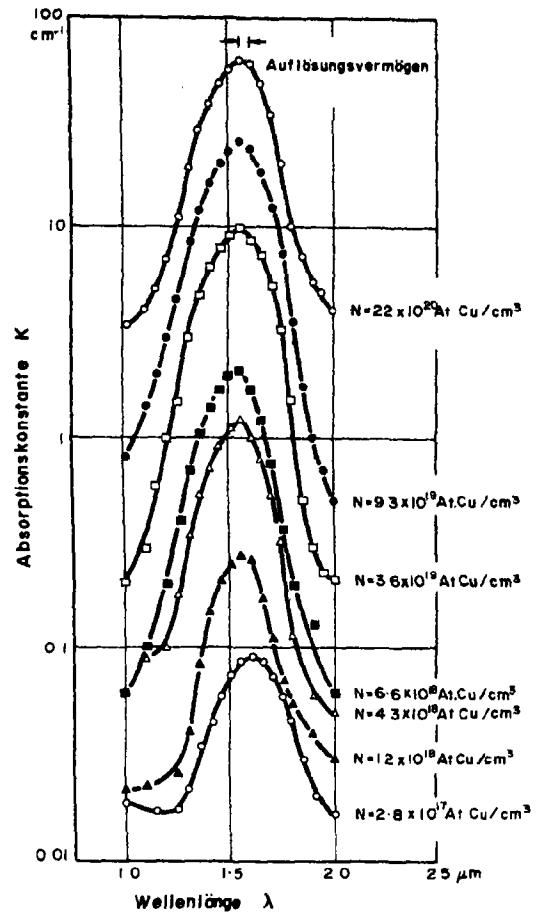


Fig. 2. Absorptionsspektren für verschieden stark mit Cu dotierte ZnO-Einkristalle, mit unpolarisiertem Licht gemessen.

$$N = 0,87 \cdot 10^{17} \frac{n}{(n^2 + 2)^2} \cdot \frac{1}{f} \cdot K_{\max} \cdot H \quad (1)$$

Dabei sind:

N = Zahl der Absorptionszentren pro cm^3
 n = Brechzahl des Mediums in dem die Zentren eingebaut sind (nach [20] und [21])

K_{\max} = Absorptionskonstante im Maximum der Bande in cm^{-1}

H = Halbwertsbreite der Absorptionsbande in eV

f = Oszillatorstärke.

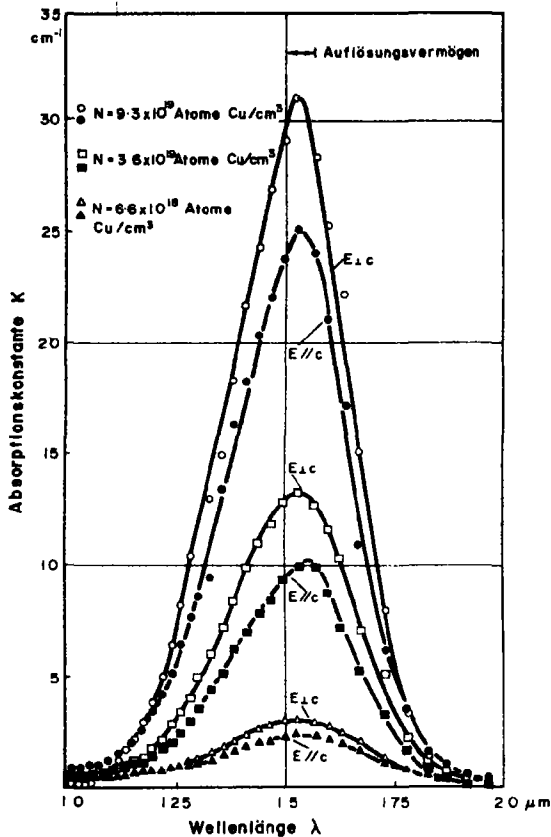


Fig. 3. Absorptionsspektren für verschieden stark mit Cu dotierte ZnO-Einkristalle, gemessen für die Polarisationsrichtungen $E \parallel c$ und $E \perp c$.

Dann erhält man für eine Oszillatorstärke von

$$f = (2,7 \pm 0,3) \cdot 10^{-4}$$

befriedigende Übereinstimmung mit der Zahl der chemisch bestimmten Kupferatome. Dieses Ergebnis wird in Fig. 4 dargestellt. Ursache für diese Absorptionsbande ist ein Übergang zwischen den im Kristallfeld aufgespaltenen $3d$ -Zuständen des Cu^{2+} -ions [3–5]. Theoretisch wurde die Aufspaltung der $3d$ -Zustände des Cu^{2+} -ions im tetraedrischen Kristallfeld von Walter u. Birman [22] behandelt. In LCAO-Näherung erhielten sie eine Oszillatorstärke für diesen Übergang von $3 \cdot 10^{-4}$ und in LCVB-Näherung von

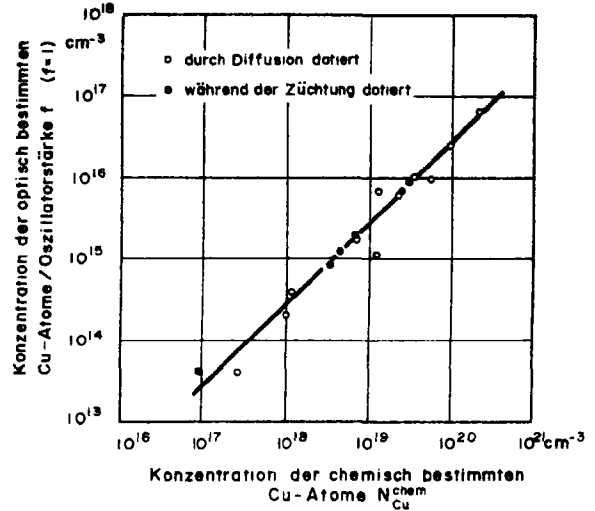


Fig. 4. Konzentration der optisch bestimmten Kupferatome dividiert durch die Oszillatorstärke $f=1$ als Funktion der chemisch bestimmten Kupferkonzentration $N_{\text{Cu}}^{\text{chem}}$.

$4,5 \cdot 10^{-4}$. Bei dieser Rechnung wurden die Aufspaltung durch Spinbahnkopplung und trigonale Verzerrung des Kristallfeldes nicht berücksichtigt. Da bei der vorliegenden Messung wegen der hohen Meßtemperatur ($T \approx 300^\circ\text{K}$) über diese Aufspaltungen gemittelt wurde, dürfen die theoretischen und experimentellen Werte miteinander verglichen werden; die Übereinstimmung ist gut.

5. ESR-MESSUNGEN

Das ESR-Signal von Cu-dotierten ZnO-Kristallen wurde schon von mehreren Autoren untersucht [4–9]. Bei unseren Untersuchungen [8] war es leider nicht möglich einen quantitativen Zusammenhang zwischen dem ESR-Signal und der absoluten Zahl der ESR-Zentren herzustellen. Es wurde jedoch ein über 4 Größenordnungen linearer Zusammenhang zwischen der Zahl der Cu-Atome im Kristall und dem Produkt aus Höhe und Halbwertsbreite des integrierten Signals gefunden. (Fig. 5).

6. ELEKTRISCHE LEITFÄHIGKEIT

Die elektrische Leitfähigkeit der undotierten ZnO-Kristalle liegt bei $\sigma \approx 10^{-2} \Omega^{-1} \text{cm}^{-1}$,

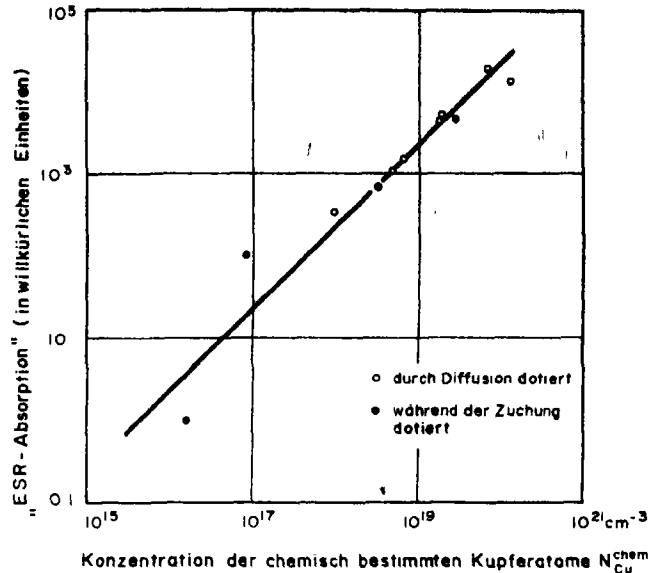


Fig. 5. "ESR-Absorption" von Cu-dotierten ZnO-Einkristallen als Funktion der chemisch bestimmten Kupferkonzentration N_{Cu}^{chem} .

sie ließ sich durch eine nachträgliche O_2 -Behandlung (760 Torr, bei $1200^\circ C$) nicht weiter beeinflussen. Diese Leitfähigkeit entspricht bei einer von uns gemessenen Hallbeweglichkeit μ von $\mu = 200 \text{ cm}^2/\text{V sec}$ einer Ladungsträgerkonzentration von $n_0 \approx 10^{15} \text{ cm}^{-3}$. Die nachträgliche Cu-Dotierung erfolgte wie in Abschnitt 2 beschrieben in O_2 -Atmosphäre (760 Torr und 1100 – $1250^\circ C$). Die elektrische Leitfähigkeit wurde mit der Vier-Sondenmethode gemessen, ihre Abhängigkeit von der Cu-Konzentration zeigt Fig. 6. Man sieht, daß die Leitfähigkeit für Cu-Konzentrationen $N_{Cu} \leq 10^{17} \text{ cm}^{-3}$ nicht vom Cu-Gehalt der Kristalle abhängt. Erst für Cu-Konzentrationen grösser als 10^{17} cm^{-3} beginnt die Leitfähigkeit mit wachsender Cu-Konzentration abzusinken und zwar umgekehrt proportional dem Quadrat der Cu-Konzentration. Eine solche Abhängigkeit wurde schon von Bogner u. Mollwo beobachtet [1, 2].

7. DISKUSSION

Die in Fig. 1 gezeigte Übereinstimmung der

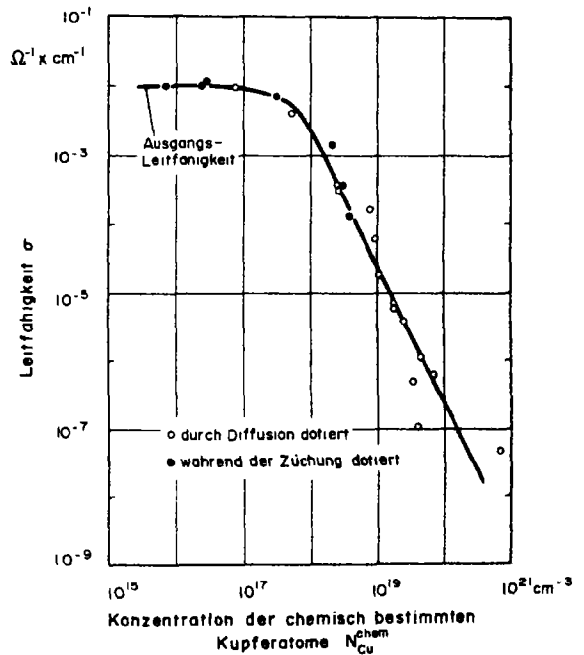
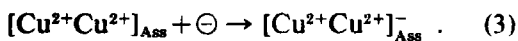
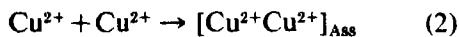


Fig. 6. Elektrische Leitfähigkeit σ von Cu-dotierten ZnO-Einkristallen als Funktion der chemisch bestimmten Kupferkonzentration N_{Cu}^{chem} . Die ausgezogene Kurve wurde aus Gleichung (5) berechnet.

Diffusionskonstanten von Zn und Cu in ZnO sowie die Gleichheit der Ionenradien [23] von Cu^{2+} (0,72 Å) und Zn^{2+} (0,74 Å) nehmen wir als ersten Hinweis dafür, daß vorwiegend Cu^{2+} im ZnO-Gitter diffundiert. Die bei den optischen Messungen gefundene Übereinstimmung zwischen der theoretisch berechneten und experimentell gefundenen Oszillatorstärke zeigt, daß Cu in ZnO im Rahmen der Meßgenauigkeit überwiegend als zweiwertig positiv geladenes Ion auf Zn-Gitterplatz eingebaut wird. Auch die bei den ESR-Messungen gefundene Proportionalität ist im Einklang mit dieser Vorstellung. Wir weisen darauf hin, daß die obige Folgerung nur für den untersuchten Leitfähigkeitsbereich $\sigma \leq 10^{-2} \Omega^{-1} \text{cm}^{-1}$ und der damit verbundenen Lage des Ferminiveaus $E_c - E_F > 150 \text{ meV}$ gemacht werden kann. Der Abstand des Cu^{2+} -Niveaus von der Leitungsbandkante ist daher kleiner als 150 meV [10]. Die Abnahme der elektr. Leitfähigkeit mit dem Quadrat der Cu-Konzentration legt nahe, daß ein Cu-Cu-Assoziat $[\text{Cu}^{2+}\text{Cu}^{2+}]_{\text{Ass}}$ als Einfachakzeptor wirkt:



Neben den Reaktionsgleichungen (2) und (3) für die Bildung dieses Akzeptors muß berücksichtigt werden, daß durch die Reaktion (3) die Ausgangselektronenkonzentration n_0 vermindert wird. Diese Kompensation der vorhandenen Donatoren führt zu der Bilanzgleichung (4):

$$N[\text{Cu}^{2+}\text{Cu}^{2+}]_{\text{Ass}}^- = n_0 - n. \quad (4)$$

Die Anwendung des Massenwirkungsgesetzes auf (2) und (3), sowie die Verwendung von Gl. (4) zusammen mit dem Ergebnis $N_{\text{Cu}}^{2+} \approx N_{\text{Cu}}^{\text{chem}}$ liefern:

$$n = \frac{n_0}{1 + (N_{\text{Cu}}^{\text{chem}})^2 / K_1 \cdot K_2} \quad (5)$$

Dabei bedeuten:

$N_{[\text{Cu}^{2+}\text{Cu}^{2+}]}$ = Konz. der mit Elektronen besetzten Assoziat

n = Konz. der Leitfähigkeitselektronen

n_0 = Ausgangskonzentration der Leitfähigkeitselektronen

$N_{\text{Cu}}^{\text{chem}}$ = Konz. der chem. nachgewiesenen Cu-Atome

K_1, K_2 = MWG-Konstanten.

Die ausgezogene Kurve der Fig. 6 wurde nach G1.5 mit $n_0 = 10^{15} \text{cm}^{-3}$, $K_1 \cdot K_2 = 2,5 \cdot 10^{35} \text{cm}^{-6}$ und einer konstanten Elektronenbeweglichkeit μ von $\mu = 200 \text{ cm}^2/\text{Vsec}$ [2] berechnet. Man erkennt mit Hilfe von G1.4, daß das Verhältnis der besetzten Assoziat und der Cu^{2+} -Ionen $N_{[\text{Cu}^{2+}\text{Cu}^{2+}]} / N_{\text{Cu}^{2+}}$ bei $N_{\text{Cu}^{2+}} \approx 10^{17} \text{cm}^{-3}$ maximal den Wert 10^{-3} besitzt und sowohl für kleinere als für größere Cu-Konzentrationen abnimmt. Über Bildungswahrscheinlichkeiten und Arten von Kupferassoziaten in ZnO Kristallen scheinen bisher außer der Leitfähigkeit noch keine anderen Hinweise vorzuliegen.

Anerkennungen – Herrn Professor Dr. E. Mollwo danken wir für viele hilfreiche Diskussionen und sein stetes Interesse an dieser Arbeit. Herrn Professor Dr. I. Broser danken wir für die Möglichkeit die ESR-Messungen an seinem Institut durchführen zu können. Herrn Dr. Ing. M. Schulz für die Durchführung der Messungen. Einige der Kupferanalysen führte Herr Priv. Doz. Dr. R. Schwab (Mineralogisches Institut Erlangen) mit dem Puls-Polarographen durch, wofür wir uns bedanken möchten.

Diese Arbeit wurde von der DFG durch Leihgaben unterstützt.

LITERATURVERZEICHNIS

1. BOGNER G. und MOLLWO E., *J. Phys. Chem. Solids* **6**, 2/3, 136 (1957).
2. BOGNER G., *J. Phys. Chem. Solids* **19**, 3/4, 235 (1960).
3. WEAKLIEM H. A., *J. Chem. Phys.* **36**, 8, 2117 (1962).
4. DIETZ R. E., KAMIMURA H., STURGE M. D. und YARIV A., *Phys. Rev.* **132**, 4, 1559 (1963).
5. BROSER I., FRANKE K.-H., GAFFRON M. G., HEINZE R. T., MAIER H., SCHULZ H.-J., SCHULZ M. H. und WÖHLECKE M., *Verhandlungen d.DGP*, S.156-157 (1969).

6. KAMIMURA H. und YARIV A., *Bull. Am. Phys. Soc.* **8**, 23 (1963).
7. DE WIT M. und ESTLE T. L., *Bull. Am. Phys. Soc.* **8**, 24 (1963).
8. BROSER I. und SCHULZ M. H., *Solid State Commun* **7**, 651 (1969).
9. HAUSMANN A. und SCHREIBER P., *Solid State Commun* **7**, 631 (1969).
10. DINGLE R., *Phys. Rev. Lett.* **23**, Nr. 11, 579 (1969).
11. BROSER I., FRANKE K.-H. und GAFFRON M., *Verh.d.DPG*, **5** S.322 (1970).
12. HELBIG R., *Erlanger Dissertation* (1970).
13. MOLLWO E., *Z. Phys.*, Bd. **138**, S.478 (1954).
14. HELBIG R. und JAHNEL R., *Verh.d.DPG*, **5**/1970, S.321.
15. LANDER J. J., *J. Phys. Chem. Solids* **15**, 324 (1960).
16. HEILAND G. und MOLLWO E., *Faraday Society Discussions*, Nr. **28**, 123 (1959).
17. MOORE W. J. und WILLIAMS E. L., *Faraday Society Discussions* Nr. **28**, 122 (1959).
18. LEUPOLD P., *Erlanger Diplomarbeit* (1955), unveröffentlicht.
19. DEXTER D. L., *Phys. Rev.* **101**, 43 (1956).
20. MOLLWO E., *Z. Angew. Phys.* **6**, 257 (1954).
21. BOND W. L., *J. appl. Phys.* **36**, 1674 (1965).
22. WALTER W. und BIRMAN J. L., *2-6 Semiconducting Compounds*, International Conference, Benjamin, New York (1967).
23. *Ionenradien nach Ahrens aus Kleber: Einf.i.d. Kristallographie* p. 178-181, VEB-Verlag Technik, Berlin (1959).
24. Perkin-Elmer Corp.: *"Analytische Methoden der Atom-Absorptions-Spektrophotometrie"* Norwalk (1966).
25. SLAVIN W., *Atomic Absorption Spectroscopy*, Interscience Publishers, New York (1968).

PARAMAGNETISM IN DILUTE ALLOYS OF Fe IN $\text{Cu}_{0.8}\text{Ni}_{0.2}$

S. MISHRA and P. A. BECK

204 Metallurgy Building, University of Illinois, Urbana, Ill. 61801, U.S.A.

and

S. FONER

Francis Bitter National Magnet Laboratory, M.I.T., Cambridge, Mass. 02139, U.S.A.

(Received 17 August 1970)

Abstract—Fe additions of 10, 100 and 1000 ppm were made to a purified (virtually iron-free) $\text{Cu}_{0.8}\text{Ni}_{0.2}$ alloy. The magnetization was measured at 4.2°K in fields up to 54 kOe, and at temperatures from 4.2° to 300°K at 12.6 kOe. The results indicate that up to 100 ppm Fe each Fe atom, together with its Ni nearest neighbors, forms a magnetic cluster of $\mu = 3.76$. The 1000 ppm Fe alloy has, in addition to single-Fe clusters, also clusters of $\mu = 7.5$ consisting of two Fe atoms, together with their Ni nearest neighbors, and a small concentration of even larger clusters. The concentration in the 0.1% Fe alloy of clusters with one, two and three Fe atoms corresponds to an average Fe concentration of 2.6% in nearest neighbor shells around all Fe atoms.

IN A RECENT paper[1] it was reported that for a $\text{Cu}_{0.8}\text{Ni}_{0.2}$ (virtually iron-free) alloy the temperature dependent part of the magnetic susceptibility is very small, but that it increases very considerably when small amounts of Fe are added. Preliminary analysis of the magnetization vs. field data, based on measurements up to 12.6 kOe, indicated dipole moments of approximately $7.7 \mu_B$, with 340 ppm dipoles, for an alloy containing 1000 ppm Fe. Since one may expect all Fe atoms to be associated with dipoles, the result just mentioned suggests that a fairly large fraction of the magnetic clusters may include more than one Fe atom. Such magnetic clusters should have larger dipole moments than those with only one Fe. Thus, one may expect that the interpretation of the magnetization of the 1000 ppm Fe alloy in terms of dipoles of one size is a rather crude approximation and that the actual magnetic structure of this alloy is much more complicated. In order to study this question in more detail it was necessary to make magnetization vs. field measurements up to

much higher fields than 12.6 kOe. In the present investigation magnetization data were obtained up to 54 kOe at 4.2°K for purified (virtually iron-free) $\text{Cu}_{0.8}\text{Ni}_{0.2}$ and for alloys with the same copper-nickel ratio, to which 10 ppm, 100 ppm and 1000 ppm Fe had been added.

Alloys were prepared by melting together 99.999% purity copper with 99.99% nickel (principal impurities: max. 0.001 wt. pct. Al and the same limit for Ag). The electrolytic iron used contained as principal impurity 0.01 wt. % Ni. Before any iron additions were made, the Cu-Ni alloy was refined in the liquid state, eliminating Al and the unknown amount of original Fe contamination. The alloy ingots were homogenized by annealing at 1050°C and quenched in water. The purified alloy and the 1000 ppm Fe alloy ingots were annealed for three days. The alloys with 10 and 100 ppm Fe were annealed for 20 hr, quenched and deformed by ~ 30 per cent compression at about 100°C in three mutually perpendicular directions; after deformation the ingots were reannealed for 14 hr at 1050°C

and water-quenched. All specimens cut from the homogenized alloy ingots were again deformed as described above, shaped into a roughly spherical form, reannealed at 1050°C and water-quenched. After the deformation and annealing treatments the specimens were homogeneous; further deformation and annealing cycles did not give rise to any measurable change in the magnetic properties.

Magnetization measurements up to fields of $H = 12.64$ kOe were made by the Faraday method, using a vacuum microbalance, a cold finger type cryostat and a Varian 12" electromagnet with gradient pole pieces. Magnetization measurements up to 54 kOe at 4.2°K were made with a Foner vibrating magnetometer adapted to a superconducting solenoid. The latter data were adjusted to the former by means of a normalizing factor derived from the two sets of data in the region of overlap.

The susceptibility of the purified (virtually iron-free) $\text{Cu}_{0.8}\text{Ni}_{0.2}$ alloy, Fig. 1, may be thought of as comprising the band susceptibility, χ_b , of the solid solution, including both

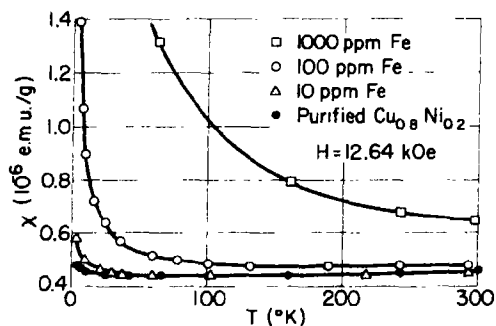


Fig. 1. Susceptibility vs. temperature for the alloys with various Fe contents, quenched from 1050°C.

spin and orbital components, which rises slightly with increasing temperature, and a Curie-Weiss component prominent at the lowest temperatures of measurement, but practically disappearing above about 160°K. The Curie constant for the latter component was estimated to $C = 0.38 (10^{-6} \text{ emu}^\circ\text{K/g})$, giving a value of $cp^2 = 1.6 \pm 0.5 (10^{-4} \mu_B^2/$

atom), where $p\mu_B$ is the effective moment. A value of $\theta = -3^\circ\text{K}$ was found. It was noted that at 4.2°K the magnetization is proportional to the field up to $H = 54$ kOe within the experimental accuracy; from this the upper limit of the dipole moment of the clusters may be estimated as $1 \mu_B$ (in a concentration of $c = 54 \times 10^{-6}$ required by $cp^2 = 1.6 \times 10^{-4}$). Assuming that the Curie-Weiss component is due to moments on individual Ni atoms in appropriate environments (see below) and that the concentration of larger clusters is negligible, the total cp^2 value can be calculated by making use of a recently proposed model [2]:

$$cp^2 = \sum_{n,m} c_{n,m} p_{n,m}^2 \quad (1)$$

where the

$$c_{n,m} = x \frac{12!}{(12-n)!n!} y^n (1-y)^{(12-n)} \\ \times \frac{6!}{(6-m)!m!} x^m (1-x)^{(6-m)} \quad (1a)$$

are the concentrations of Ni atoms having n nearest and m second-nearest Ni neighbors in the f.c.c. crystal and the effective $p_{n,m}^2$ are calculated from the $\mu_{n,m}$ values given in the model [2] for the various local atomic environments. The agreement of the calculated value, $cp^2 = 1.3 \times 10^{-4}$ with the experimental cp^2 value is well within the experimental accuracy, if it is assumed that the short range order parameters are $\alpha_1 = 0.1$ and $\alpha_2 = 0$. These parameter values are reasonable in view of recent neutron scattering results [3] for the $\text{Cu}_{0.52}\text{Ni}_{0.48}$ alloy. Since, according to the model [2], the $\mu_{n,m}$ are not larger than 0.6 for any n, m values, the above interpretation of the temperature dependence of the susceptibility in terms of individual Ni moments, appearing where Ni atoms are located in sufficiently Ni-rich nearest and second-nearest neighbor environments, is consistent also with the experimentally observed linearity of σ with H up to 54 kOe.

The susceptibility of the 100 ppm Fe alloy

quenched from 1050°C, Fig. 1, was analyzed as follows: the incremental susceptibility due to the Fe solute $\Delta\chi = \chi_{\text{Fe alloy}} - \chi_{\text{Cu}_{0.8}\text{Ni}_{0.2}}$ vs. temperature was fitted by least squares to: $\Delta\chi = \Delta\chi_0 + C/(T - \theta)$, with $\Delta\chi_0 = 0.007$ (10^{-6} emu/g), $C = 4.35$ (10^{-6} emu °K/g) and $\theta = -0.18^\circ\text{K}$. Using these values and $\chi_{\text{Cu}_{0.8}\text{Ni}_{0.2}} = 0.478$ (10^{-6} emu/g) at 4.2°K, the isothermal 4.2°K field dependence of the magnetization (Fig. 2) satisfies quite accurately the relationship:

$$\sigma - \chi' \cdot H = c\mu \frac{N\mu_B}{M} B\left(\mu, \frac{H}{T - \theta}\right) \quad (2)$$

where $\chi' = \Delta\chi_0 + \chi_{\text{Cu}_{0.8}\text{Ni}_{0.2}}$, N is Avogadro's number, M is the molar weight of the alloy and B is a Brillouin function with the moment μ (assuming $g = 2$). Computer least squares fitting, $\text{RMSD} = 0.28$ (10^{-4} emu/g) gives a dipole moment of $\mu\mu_B = 3.76\mu_B$ and a dipole concentration of $c = 97$ ppm, in good agreement with the Fe concentration. These results show that at an Fe concentration near 100 ppm each Fe atom is associated with a separate magnetic dipole of $3.76\mu_B$ (estimated limits of error $\pm 0.03\mu_B$). This moment value roughly agrees with the $4.2\mu_B$ value for very

low Fe concentrations at 21% Ni from Mössbauer line width measurements [4].

Magnetization measurements were also made with the same alloy specimen after severe plastic deformation. Using the same values of $\chi' = \Delta\chi_0 + \chi_{\text{Cu}_{0.8}\text{Ni}_{0.2}}$ and θ as given above for the quenched condition, least squares fitting of the measured data to equation (2), $\text{RMSD} = 0.57$ (10^{-4} emu/g) gave the values $\mu = 3.17 \pm 0.03$ and $c = 93$ ppm, again in reasonable agreement with the Fe content. The dipole moment in the deformed state is thus distinctly lower than in the quenched state. This can be interpreted in the following way: The moment on Fe atoms in the Cu-Ni alloy is probably near $2.85\mu_B$, as suggested by Bennett [4]. The increment of about $0.91\mu_B$ in the dipole moment above the Fe moment (found for the quenched state) is contributed by Ni atoms nearest neighbors to Fe. If there were no deviation from randomness in the nearest neighbor shell around an Fe atom in the $\text{Cu}_{0.8}\text{Ni}_{0.2}$ alloy, the average number of Ni nearest neighbors per Fe would be 2.4 and the nickel contribution to the magnetic cluster dipole moment would correspond on the average to $0.38\mu_B$ per nearest neighbor Ni. However, in case of randomness plastic deformation would not be expected to alter the average number of Ni nearest neighbors. The pronounced decrease of the cluster dipole moment due to plastic deformation indicates that the average number of Ni nearest neighbors does decrease as a result of deformation. Such an effect is expected only if the number of Ni nearest neighbors in the quenched state (i.e. before plastic deformation) is larger than 2.4. If one makes the extreme assumption that the plastic deformation was sufficiently severe to provide an essentially random nearest neighbor environment for the Fe solute atoms, then the nickel contribution to the decreased dipole moment of $3.17\mu_B$ would correspond on the average to only $0.13\mu_B$ per Ni nearest neighbor. On this basis, one can estimate that in the quenched state the nickel contribution of $0.91\mu_B$ per cluster

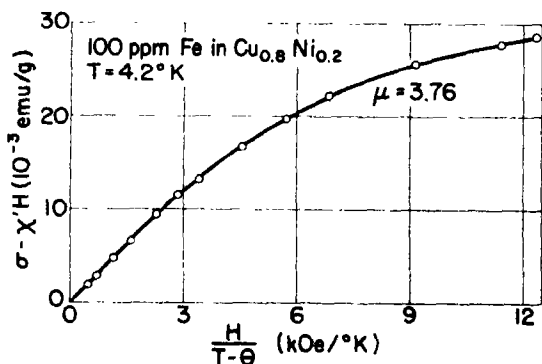


Fig. 2. Curie-Weiss component of the magnetization for quenched 100 ppm Fe alloy vs. $H/(T - \theta)$ at 4.2°K. Data points: \circ . Continuous curve: magnetization calculated for 97 ppm dipoles of $3.76\mu_B$. The magnetization curve for the deformed specimen is similar to that shown in the graph, but somewhat lower. At $H/(T - \theta) = 12$ the value of $\sigma - \chi' \cdot H$ is 22.2 (10^{-3} emu/g).

requires an average of about 6.8 Ni atoms in the nearest neighbor shell of each Fe. If the plastic deformation did not completely randomize the nearest neighbor environment of the Fe atoms, one would have to assume a smaller contribution than $0.13 \mu_B$ per nearest neighbor Ni and, accordingly, a larger number of nickel nearest neighbors to Fe than 6.8 in the quenched state.

The susceptibility vs. temperature data for the quenched 10 ppm Fe alloy were analyzed as described above for the 100 ppm Fe alloy. The Curie constant was found to be $C = 0.53 (10^{-6} \text{ emu}^\circ\text{K/g})$, giving the value of $cp^2 = 2.83 (10^{-4} \mu_B^2/\text{at.})$. The value of χ' was $0.479 (10^{-6} \text{ emu/g})$ and $\theta = -0.52^\circ\text{K}$. Because of the low Fe concentration, and the correspondingly low dipole concentration, it was not possible to determine accurately the cluster dipole moment from the field dependence of the magnetization. But, within the experimental error, the 4.2°K data, Fig. 3, are

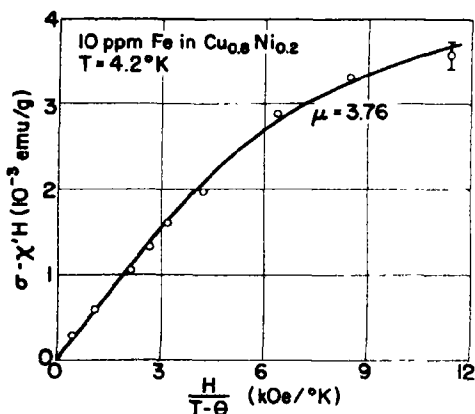


Fig. 3. Curie-Weiss component of the magnetization for quenched 10 ppm Fe alloy vs. $H/(T-\theta)$ at 4.2°K . Data points: \circ . Continuous curve: magnetization calculated for 13 ppm. dipoles of $3.76 \mu_B$.

consistent with $\mu = 3.76$, the dipole moment value for single-Fe magnetic clusters determined for the 100 ppm alloy. With $\mu = 3.76$ the dipole concentration, calculated from $cp^2 = 2.83$, is $c = 13 \text{ ppm}$, in as good agreement with the intended Fe concentration

as may be expected at this composition. It may be pointed out that, in contrast to the 10 ppm Fe alloy, the purified $\text{Cu}_{0.8}\text{Ni}_{0.2}$ alloy yielded magnetization data clearly inconsistent with $\mu = 3.76$ (at a dipole concentration of $c = 7.5 \text{ ppm}$, required by $cp^2 = 1.6$), see Fig. 4. One may, therefore, conclude that the small temperature dependent component of the susceptibility of the purified alloy is not due to a residual Fe contamination, but rather to Ni moments, as discussed above. The residual Fe contamination may be estimated to less than 2 ppm.

In order to analyze the magnetization data for the quenched 1000 ppm Fe alloy, the value of θ was selected so as to superimpose on a

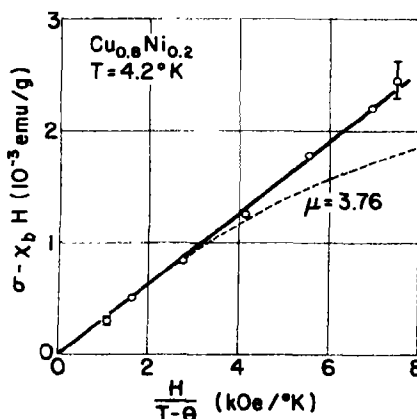


Fig. 4. Curie-Weiss component of the magnetization for purified $\text{Cu}_{0.8}\text{Ni}_{0.2}$ alloy vs. $H/(T-\theta)$ at 4.2°K . Dashed line shows magnetization calculated for dipoles of $3.76 \mu_B$ in a concentration of 7.5 ppm.

single curve the magnetization at 12.6 kOe in the temperature range from 4.2 to 300°K and the magnetizations at 4.2 and at 9.83°K from 1 to 12.64 kOe . As seen in Fig. 5, this was quite accurately achieved with $\theta = -0.5^\circ\text{K}$. The value of the temperature independent component of the susceptibility $\chi_0 = 0.45 (10^{-6} \text{ emu/g})$ was determined by plotting χ vs. $1/T$ and extrapolating to $1/T = 0$. Figure 6 gives the σ vs. $H/(T-\theta)$ data at 4.2°K up to $H = 54 \text{ kOe}$. As mentioned earlier, the low field part of the data fit a

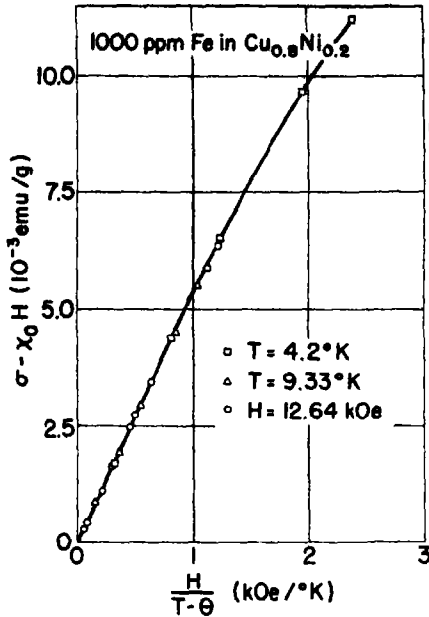


Fig. 5. Temperature dependent component of the magnetization for quenched 1000 ppm Fe alloy vs. $H/(T-\theta)$ at 4.2, 9.33°K and at 12.64 kOe (with T varying from 4.2 to 300°K). The three sets of data are superimposed on a single curve if $\theta = -0.5^\circ\text{K}$ is chosen.

Brillouin curve with $\mu = 7.9$ but, as shown in Fig. 6a, the high field data do not fit this curve. Attempts to fit the entire curve to a single Brillouin function were unsuccessful; the systematic deviations were considerable (Fig. 6b), the RMSD was high and the dipole concentrations derived were appreciably lower than the Fe concentration. However, it was found that the experimental data do fit the following formula:

$$\sigma = \chi_0 H + \sum_{i=1}^4 c_i \mu_i \frac{N \mu_B}{M} B[\mu_i, H/(T-\theta)] \quad (3)$$

representing a constant susceptibility term and four Brillouin terms with dipole moments μ_1, μ_2, μ_3 and μ_4 in concentrations c_1, c_2, c_3 and c_4 for magnetic clusters with one, two, three and four Fe atoms, respectively.

The analysis of the data in terms of equation (3) was done by a least squares

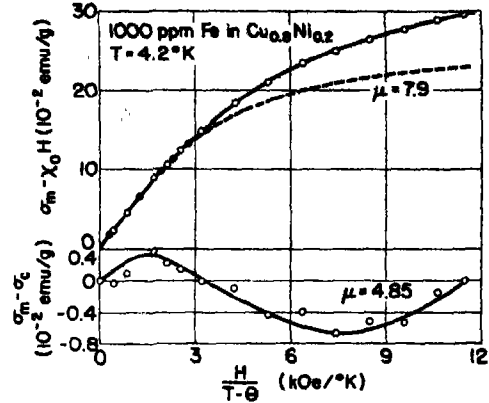


Fig. 6(a). (upper graph) Temperature dependent component of magnetization for quenched 1000 ppm Fe alloy vs. $H/(T-\theta)$. Magnetometer data: \circ , Faraday method data: \bullet . Dashed line: magnetization calculated for 1000 ppm clusters of $7.9 \mu_B$; calculated curve fits low field data points, but it is very low at high fields. The magnetization curve for the deformed specimen is similar to that shown in the figure, but somewhat lower. At $H/(T-\theta) = 12$ the value of $\sigma - \chi_0 H$ is $25.12 (10^{-2} \text{ emu/g})$. b. (lower graph) Systematic deviation from magnetization, σ_m , of the magnetization calculated, σ_c , assuming a single dipole moment value of $4.85 \mu_B$ and dipole concentration of 771 ppm. RMSD is $0.309 (10^{-2} \text{ emu/g})$.

computation, as follows. The probabilities p_0, p_1, p_2 and p_3 for an Fe atom to have zero, one, two or three Fe nearest neighbors, respectively, were calculated from $p_n = [12!/(12-n)!n!]y^n(1-y)^{(12-n)}$ for many tentative values of y , the average Fe concentration in the nearest neighbor shells around all Fe atoms in the alloy. For a given value of y , if x is the Fe concentration in the alloy as a whole, the concentration of single-Fe magnetic clusters is

$$c_1 = x \cdot p_0(y) \quad (4)$$

The increase from x to y in the nearest neighbor shells (expressing the clustering tendency of Fe in the alloy) may be attributed in first approximation to the energy gained by replacing one Fe-matrix (Cu-Ni alloy) bond by an Fe-Fe bond. In the nearest neighbor shell of an Fe atom, which already has an Fe nearest neighbor, eleven possible sites are available for a second Fe nearest neighbor. Of these

sites 4 provide two Fe-Fe bonds, while the remaining 7 only one. If one of these 4 sites is occupied by the third Fe atom, a triangular configuration results, in which each of the three participating Fe atoms has two of its Fe-matrix bonds replaced by an Fe-Fe bond. If one makes the simple assumption that the energy per participating Fe atom gained in the two Fe-Fe bonds is twice that for a single Fe-Fe bond, then one may expect the average Fe concentration z in all available double Fe-Fe bond sites of the alloy to be increased over the Fe concentration y in the available single Fe-Fe bond sites in the same ratio as y is increased over the Fe concentration at sites providing no Fe-Fe bond, i.e. c_1 :

$$\frac{z}{y} = \frac{y}{xp_0} \quad (5)$$

With this relationship, and neglecting the probability of groups of more than three Fe atoms, one finds the concentration of Fe triplets:

$$c_3 = xp_2 \left[\frac{4y}{3(4y + 7xp_0)} + \frac{7xp_0}{4y + 7xp_0} \right] \quad (6)$$

Here $4y/(4y + 7xp_0)$ is the probability for an Fe atom with two Fe nearest neighbors to participate in a triangular configuration, as described above. The probability $7xp_0/(4y + 7xp_0)$ for its participation in a configuration, in which its two Fe nearest neighbors are not nearest neighbors to one another, enters also the formula for the concentration c_2 of isolated Fe-Fe nearest neighbor pairs: This type of Fe triplet configuration does not contribute to c_2 , even though it does have two Fe atoms, each with one Fe nearest neighbor, which are counted in p_1 . Again neglecting the probability of Fe groups of more than 3 atoms:

$$c_2 = \frac{x}{2} \left(p_1 - \frac{7xp_0^2}{4y + 7xp_0} p_2 \right) \quad (7)$$

With $x = 0.001$ and y in the range 0.02 to 0.03 (which includes the values found to be

appropriate for the quenched 1000 ppm Fe alloy), the corrections incorporated in equations 6 and 7 are negligible and the simpler expressions may be used:

$$c_2 = \frac{1}{2} p_1 x, \text{ and } c_3 = \frac{1}{3} p_2 x \quad (8)$$

Accordingly, in the calculations equations 4 and 8 and the analogous formula $c_4 = \frac{1}{4} p_3 x$ were used. The cluster moments μ_1 , μ_2 , μ_3 and μ_4 and y were varied systematically. For each set of these parameter values the magnetization was calculated according to equation (3) with each H value, for which an experimentally measured σ_m value was available, and the root mean square of the deviations $\sigma_{\text{calc.}} - \sigma_m$, as well as their systematic variation with H was then evaluated as a function of the parameter values chosen.

The set of parameter values giving the minimum of RMSD (0.178 in units of 10^{-2} emu/g) and of systematic variation was taken to define the result for the 1000 ppm Fe alloy in the quenched state. The parameter values obtained in this way are shown in Table 1, together with the estimated errors (where we were able to estimate). Table 1 also gives the results of a somewhat similar calculation for the 1000 ppm alloy in the severely deformed state. The latter calculation was more laborious, since in the deformed state the concentrations c_1 , c_2 , c_3 and c_4 can not be derived from a single parameter (such as y , which is appropriate in case of thermal equilibrium). It was, therefore, necessary to consider three of the concentrations c_1 , c_2 , c_3 and c_4 as independent variables, with only the condition $c_1 + 2c_2 + 3c_3 + 4c_4 = x$ imposed on them. In order to simplify the process, c_4 and μ_4 were eliminated. Thus, c_3 and μ_3 may be considered to represent not only clusters with three Fe atoms, but possible larger clusters as well. Even for the quenched state, the values of μ_3 and μ_4 and c_3 and c_4 are considerably less well determined than the parameters describing the single-Fe and double-Fe cluster population. Indeed, the physical meaning of such values as $\mu_4 = 26$ for the quenched state

Table 1. Magnetic clusters in Fe-containing $\text{Cu}_{0.8}\text{Ni}_{0.2}$ alloys. The cluster concentrations are given in ppm, the RMSD values in pct. of the magnetization at 54 kOe

	Fe content (ppm)					
	100			1000		
Quenched state	$\mu_1 = 3.76 \pm 0.03$ $c_1 = 97 \pm 3$ (RMSD = 0.05%)	$\mu_1 = 3.71 \pm 0.06$ $c_1 = 729 \pm 20$	$\mu_2 = 7.5 \pm 0.2$ $c_2 = 117 \pm 12$ (RMSD = 0.55%)	$\mu_3 = 13$ $c_3 = 11$	$\mu_4 = 26$ $c_4 = 1$	
Deformed state	$\mu_1 = 3.17 \pm 0.03$ $c_1 = 93 \pm 3$ (RMSD = 0.12%)	$\mu_1 = 3.11 \pm 0.06$ $c_1 = 754 \pm 20$	$\mu_2 = 6.4 \pm 0.2$ $c_2 = 100 \pm 12$ (RMSD = 0.81%)	$\mu_3 = 18.5$ $c_3 = 10$		

and $\mu_3 = 18.5$ for the deformed state is not entirely clear.

On the other hand, the degree of reliability attained in determining μ_1 in the quenched state is reflected in the good agreement between the values obtained independently for the 100 and the 1000 ppm Fe alloys, see Table 1. The agreement in μ_1 for the two alloys in the deformed state is also good, particularly if one considers the difficulty in achieving the same degree of plastic deformation by compression of the small specimens used. Perhaps this agreement may then be taken as an indication that the deformation process used did lead to an essentially random Ni nearest neighbor environment around the Fe atoms. At any rate, one may conclude from the results in Table 1 that plastic deformation significantly decreases the moment associated with double-Fe clusters, as well as that of single-Fe clusters. It is interesting to note that the concentration of double-Fe clusters also is decreased by deformation, although only to a very much smaller extent than that required to eliminate Fe-Fe clustering altogether.

The present results document a rather unexpected and interesting fact: the clustering tendency of Fe, when dissolved in a Cu-Ni alloy quenched from high temperature, is so strong that, at an actual Fe concentration of $x = 0.001$, Fe-pairs, triplets etc. are formed in numbers which, in a random alloy, could be expected only at an Fe concentration

26 times higher: $y = 0.026$. Clearly, a low actual concentration is in itself not a reliable basis for assuming that an alloy represents a dilute system in the physical sense. The possibility of similarly strong clustering tendencies in other alloy systems must be taken into consideration in the interpretation of magnetic data for 'dilute' alloys.

The results of this investigation make it clear that the average dipole moment increases with the Fe content, above 100 ppm. Thus, the apparent discrepancy between the dipole moment of about $10 \mu_B$ found by Window and Johnson[5] for a 20% Ni alloy containing 1% Fe, and the moment of $4.2 \mu_B$ reported by Bennett, Schwartzendruber and Watson[4] for an alloy with trace amounts of Fe finds a simple explanation.

Acknowledgements—This work at the University of Illinois was supported by a grant from the National Science Foundation, that at the National Magnet Laboratory was supported by U.S. Air Force Office of Scientific Research. The high grade nickel used was kindly furnished by Dr. R. J. Raudebaugh of the International Nickel Co.

REFERENCES

1. MISHRA S., CLAUS H. and BECK P. A., *Phys. Lett.* **31A**, 493 (1970).
2. ROBBINS C. G., CLAUS H. and BECK P. A., *Phys. Rev. Lett.* **22**, 1307 (1969).
3. MOZER B., KEATING D. T. and MOSS S. C., *Phys. Rev.* **175**, 868 (1968).
4. BENNETT L. H., SCHWARTZENDRUBER L. J. and WATSON R. E., *Phys. Rev. Lett.* **23**, 1171 (1969).
5. WINDOW B. and JOHNSON C. E., *Phys. Lett.* **29A**, 703 (1969).

THEORY OF METALLIC CONTACTS ON HIGH RESISTIVITY SOLIDS—I. SHALLOW TRAPS

J. G. SIMMONS

Electrical Engineering Department, University of Toronto, Toronto 5, Canada

(Received 24 March 1970)

Abstract—The theory of injecting contacts on insulating solids containing shallow traps is presented. It is shown that the types of contact an injecting electrode can make on a high resistivity solid can be divided into three convenient categories: (a) separated accumulation regions; (b) overlapping accumulation regions; and (c) low space charge condition. The energy diagrams for metal-insulator-metal systems containing these contacts are discussed in detail, and the relationship between the insulator parameters and the work function of the electrodes developed. It is shown that contacts (b) and (c) are the types normally found at a metal-insulator interface, while type (a) normally exists only for very deep lying traps. The low-field conductivity of the insulator for the various types of contacts is calculated. It is shown that overlapping accumulation regions and the low space charge condition cause the insulator conductivity to increase markedly from its intrinsic value; thus the conductivity is extrinsic in nature. Other properties of the contact are also discussed, including the space-charge field at the electrode-insulator interface and the amount of charge injected into the insulator.

1. INTRODUCTION

A KNOWLEDGE of the type of contact existing at a metal-semiconductor contact is important, because it may or may not strongly influence the conductivity of a metal-semiconductor-metal system. Also depending on its nature, a metal-semiconductor contact can exhibit current-voltage characteristics that have useful applications in electronic circuitry, e.g. the Schottky barrier diode. As a result, the metal-semiconductor contact has been studied extensively [1], both experimentally and theoretically, and the nature of this type of contact is fairly well understood.

Since Mott and Gurney [2] first suggested the possibility of drawing large space-charge-limited currents through insulators, this phenomenon has been the subject of extensive theoretical and experimental studies [3]. As with the metal-semiconductor-metal system, the nature of the contact at the electrode-insulator interface plays an important role. If the contact is able to inject carriers into the insulator (that is, the contact is ohmic), significant space-charge-limited current may flow through the insulator; otherwise, the current

flow will be insignificant. It will suffice to say at this point that the requirement of an ohmic contact is that the electrode must have a reservoir of electrons available for supplying the insulator as required by voltage bias conditions. Figure 1 illustrates the energy diagram for an ohmic contact.

Although, as we have mentioned, there have been extensive studies of space-charge-limited currents in insulators, our knowledge of the metal-insulator contact is not nearly as comprehensive as for the metal-semiconductor contact. In fact a good deal of art appears to be required to make an ohmic contact to an insulator [4]. Therefore, it is the object of this paper to attempt a theoretical treatment of the metal-insulator-metal system with special reference to the interfacial relationships between the insulator and electrode parameters. We have found it convenient to categorize the metal-insulator contact into three types: (a) separated accumulation regions; (b) overlapping accumulation regions; and (c) low space charge condition. Types (b) and (c) are the contacts that one normally finds at a metal-insulator interface. It will be shown that type

(a) is possible only if the traps are relatively deep lying.

We will concern ourselves primarily with negative rather than positive space charge,

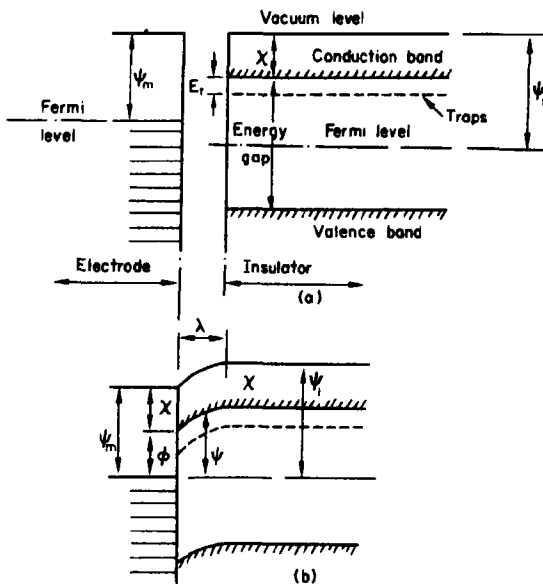


Fig. 1. Energy diagram illustrating metal electrode and insulator (a) before contact, (b) after contact, resulting in formation of an ohmic contact. Note that the Fermi levels and vacuum level must be continuous after the contact is made, and that $\phi > E_t$ if the traps are to be partially filled (shallow at the interface).

but the effect of the latter is directly analogous to that of the former. In effect, what this means is that we are concerning ourselves with the *low* rather than *high*-work function electrode materials. Also, we will ignore the effect of surface states in the subsequent discussions—this will be the subject of a separate paper.

2. SEPARATED ACCUMULATION REGIONS

The simplest concept of the formation of an ohmic contact is provided by the energy diagram of Fig. 1, which neglects surface states. (The effect of surface states is the subject of a further study[5]). In order to achieve an ohmic contact under this condition, it is necessary that $\psi_m < \psi_i$, where ψ_m and ψ_i are, respectively, the work function of the metal and the insulator[6]. Thus, when the contact is com-

pleted, in order to bring about equalization of the Fermi levels in the electrode and insulator, electrons from the *electrode* are injected into the insulator. This injected negative space-charge is shown contained in the insulator within a distance λ of the interface, and is termed the *accumulation region*. In order to satisfy overall charge-neutrality requirements within the system, an equal amount of positive charge, Q , is accumulated on the electrode surface. The electrostatic interaction between the positive and negative charge induces a local electric field within the insulator. This local field varies in magnitude and decreases with increasing depth of penetration of the insulator. If the space charge within the accumulation is sufficiently large, this local field causes the bottom of the insulator conduction band to rise from a value $\phi_0 = \psi_m - X$ (X is the electron affinity of the insulator) at the electrode-insulator interface to a maximum value $\psi_i - X$ above the Fermi level at a distance λ (the edge of the accumulation region) within the insulator, resulting in the energy diagram of Fig. 1(b). Note that within the insulator beyond this accumulation region, the energy difference between the Fermi level and the vacuum level is just equal to the work function ψ_i of the insulator.

The field, F , within the accumulation region is related to the space-charge density within the accumulation region by Poisson's equation:

$$\frac{dF}{dx} = \frac{\text{space charge density}}{K\epsilon_0} = \frac{\rho_f + \rho_t}{K\epsilon_0} \quad (1)$$

where K and ϵ_0 are, respectively, the dielectric constant and permittivity of free space, and ρ_f and ρ_t are, respectively, the free and trapped space-charge density at any plane a distance x from the electrode insulator interface. For a density N_t of shallow traps positioned E_t below the bottom of the conduction band, the ratio of the free charge to the trapped charge is given by Rose's constant[3]:

$$\theta = (N_c/N_t) \exp(-E_t/kT) \quad (2)$$

where N_c is the effective density of states in the conduction band, k is Boltzmann's constant and T the absolute temperature. For most practical cases $\rho_i \gg \rho_f$, which means that ρ_f in (1) can be neglected [7]. Substituting $\rho_i = eN_i \exp [-(\psi - E_i)/kT]$ into (1), where ψ is the energy of the bottom of the insulator conduction band with respect to the electrode Fermi level, we obtain

$$\frac{dF}{dx} = \frac{1}{e} \frac{d^2\psi}{dx^2} = -\frac{eN_i}{K\epsilon_0} \exp [-(\psi - E_i)/kT]. \quad (3)$$

Integrating this equation using $d\psi/dx = 0$ at $\psi = \psi_i - X$, yields

$$\frac{d\psi}{dx} = \left(\frac{2e^2kTN_i}{K\epsilon_0} \right)^{1/2} \left[\exp \left(-\frac{\psi - E_i}{kT} \right) - \exp \left(-\frac{\psi_i - X - E_i}{kT} \right) \right]^{1/2}. \quad (4)$$

Integrating (4), using the boundary condition $\psi = \psi_m - X$ at $x = 0$ leads to

$$x = \left(\frac{2kTK\epsilon_0}{e^2N_i} \right)^{1/2} \left\{ \sin^{-1} \left[\exp \left(\frac{\psi - \psi_i + X}{2kT} \right) \right] - \sin^{-1} \left[\exp \left(\frac{\psi_m - \psi_i}{2kT} \right) \right] \right\} \times \exp \left(\frac{\psi_i - X - E_i}{2kT} \right). \quad (5)$$

Normally $\psi_i - \psi_m \gg 2kT$ so that the second term in the curly brackets reduces to $\exp (\psi_m - \psi_i)/2kT$, and is normally negligible compared to the first term in the curly brackets, except close to the interface i.e., $\psi > (\psi_m - X + 4kT)$. Also the first term in the curly brackets may be written as $\exp (\psi - \psi_i + X)/4kT$ except near to the edge of the accumulation region i.e., $\psi < (\psi_i - X - 4kT)$. Therefore, for $(\psi_m - X + 4kT) < \psi < (\psi_i - X - 4kT)$, (5) may be written

$$x = \left(\frac{2kTK\epsilon_0}{e^2N_i} \right)^{1/2} \exp \left(\frac{\psi - E_i}{2kT} \right). \quad (6)$$

Close to the edge of the accumulation region ($\psi \approx \psi_i - X$), (5) has to be used in its pristine form except that as previously noted the second term in the curly bracket may be dropped to yield:

$$x = \left(\frac{2kTK\epsilon_0}{e^2N_i} \right)^{1/2} \sin^{-1} \left[\exp \left(\frac{\psi - \psi_i + X}{2kT} \right) \right] \times \exp \left(\frac{\psi_i - X - E_i}{2kT} \right). \quad (7)$$

(Note that this equation is applicable to, and reduces to, (6) in the range covered by (6)). In order to determine the width, λ , of the accumulation region we use the condition $\psi = \psi_i - X$ at $x = \lambda$ in (7)

$$\lambda = \frac{\pi}{2} \left(\frac{2kTK\epsilon_0}{e^2N_i} \right)^{1/2} \exp \left(\frac{\psi_i - X - E_i}{2kT} \right). \quad (8)$$

If the insulator is trap-free, (8) reduces to [7]

$$\lambda = \frac{\pi}{2} \left(\frac{2kTK\epsilon_0}{e^2N_c} \right)^{1/2} \exp \left(\frac{\psi_i - X}{2kT} \right). \quad (9)$$

Normally, $\psi_i - X \approx E_g/2$, (see Appendix) and when this is the case (8) and (9) reduce, respectively, to

$$\lambda = \frac{\pi}{2} \left(\frac{2kTK\epsilon_0}{e^2N_i} \right)^{1/2} \exp \left(\frac{E_g/2 - E_i}{2kT} \right) \quad (10)$$

and

$$\lambda = \frac{\pi}{2} \left(\frac{2kTK\epsilon_0}{e^2N_i} \right)^{1/2} \exp \left(\frac{E_g}{4kT} \right). \quad (11)$$

In Fig. 2, λ vs. $\psi_i - X - E_i$ is plotted for various values of N_i .

The interesting point about (8) and (9) is that they are independent of the barrier height at the metal-insulator interface and hence the electrode work function, provided the bottom of the conduction band at the edge of the accumulation region lies more than $4kT$ above the interfacial barrier height. From a comparison of (8) and (9) it will be noted that the discrete shallow trapping states in a defect

insulator are synonymous with the effective density of states (position at the bottom of the conduction band, of course) in a trap-free insulator.

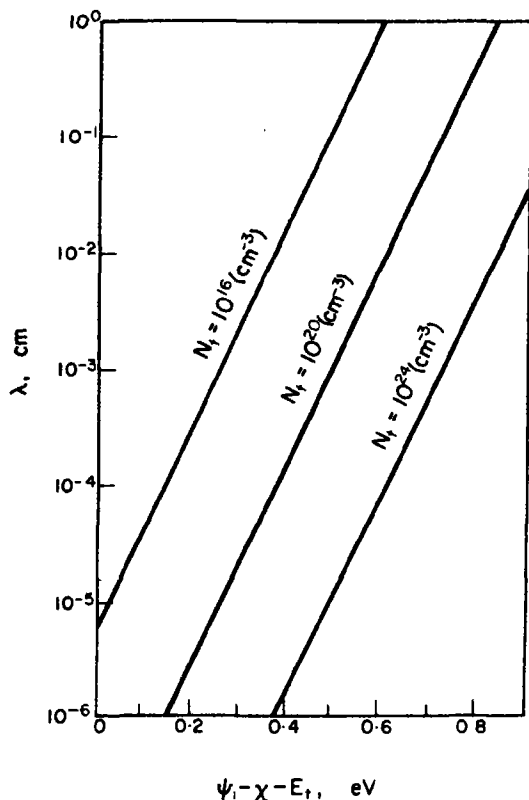


Fig. 2. Width of accumulation region, λ , vs. $\psi_i - X - E_t$ for various values of N_t .

Figure 3 illustrates the energy diagram for a metal-insulator-metal system in which the two electrodes, which have different work functions, make ohmic contact to the insulator. (We have assumed here that $\psi_i - \psi_m > 4kT$ at both contacts so that both accumulation regions are the same width—see (8)). The distance, L , between the electrodes is assumed to be greater than the 2λ so that between the edges of the accumulation regions the insulator conduction band is flat (which indicates the absence of electric field) and positioned the same energy, $\psi_i - X$, above the Fermi level as was the case before the

electrodes were attached. Thus the accumulation regions effectively screen the interior of the insulator from conditions at the surface. The curves in Fig. 4 illustrate the relationship between $\psi_i - X - E_t$, N_t and the minimum thickness, L_{\min} , of the insulator, if the accumulation regions are *not* to overlap; that is for [see (8)]

$$L_{\min} = 2\lambda = \pi \left(\frac{2kTK\epsilon_0}{e^2 N_t} \right)^{1/2} \exp \left(\frac{\psi_i - X - E_t}{2kT} \right). \quad (12)$$

As an example of the use of the curves we have for $\psi_i - X - E_t = 0.55$ eV and $N_t = 10^{17}$ cm⁻³ that $L \geq 0.1$ cm if the accumulation regions are to be accommodated without overlapping within the insulator.

Now it is usual to use relatively thin ($\leq 10^{-1}$ cm) crystals when conducting electrical measurements, so that high fields can be obtained (in order to produce measurable currents) without the use of excessive applied voltage. Therefore, in order for the accumulation regions to be adequately contained within crystals of this order of thickness, they must be less than 10^{-1} cm. Let us now investigate the consequences of this requirement (that is $\lambda < 10^{-1}$ cm). For $L = 0.1$ cm and for the upper limit of practical values of N_t ($\approx 10^{20}$ cm⁻³) for crystalline insulators we see from Fig. 4 that

$$\psi_i - X - E_t < 0.65 \text{ eV}. \quad (13)$$

Since $\psi_i - X \approx E_g/2$, we have from (13)

$$E_t < E_g/2 - 0.65 \text{ eV}. \quad (14)$$

For the narrowest energy gap ($E_g \approx 2$ eV) insulator we have from (14) that

$$E_t > 0.35 \text{ eV}, \quad (15)$$

which corresponds to a relatively deep-lying shallow trap. We wish to stress that the lower limit set by (15), ($E_t \approx 0.35$ eV), represents

the value that E_t will take under the most optimum circumstances, that is, a high trap density ($N_t = 10^{20} \text{ cm}^{-3}$) and the smallest insulator energy gap ($E_g \approx 2 \text{ eV}$), and normally will be a good deal larger than 0.35 eV . For example, if $N_t = 10^{18} \text{ cm}^{-3}$ and $E_g = 4 \text{ eV}$, then $E_t > 1.5 \text{ eV}$. Thus we conclude that, for other than relatively deep lying shallow traps, it is not possible to adequately contain without overlap the accumulation regions within the bulk of an insulator of thickness 10^{-1} cm .

Hence if electrodes of work function

$$\psi_m = \phi + X \quad (16)$$

are attached to the insulator the accumulation regions will be contained within the insulator without overlapping.

If the conduction process is to reflect the *intrinsic* properties of the insulator $L \gg 2\lambda$ (see Section 6a), say $L > 20\lambda$. Denoting the length of the insulator in this case by L_i we

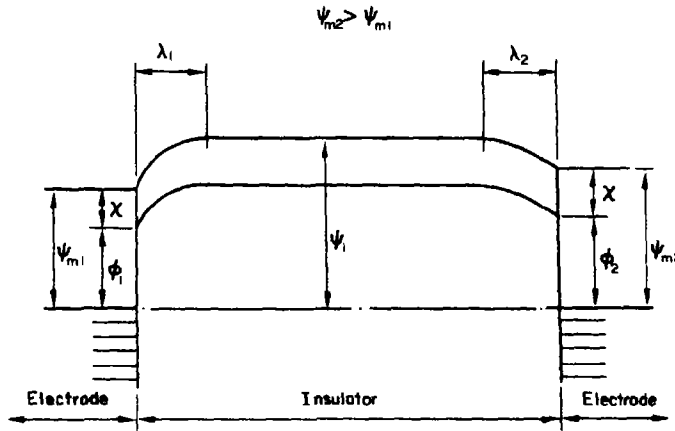


Fig. 3. Energy diagram of a metal-insulator-metal system (the metals have different work functions) for separated accumulation regions. Note that the region between the edges of the accumulation region the bottom of the conduction band is flat, showing that it is field-free and hence free of space charge.

Within the terms of shallow trapping *throughout* the insulator, we have the requirements that: $\phi > E_t$; the conduction band maximum must lie more than $4kT$ above the top of the interfacial barrier ($\psi < \psi_i - X - 4kT$); and finally (12) must be at *least* satisfied for E_t , that is, $E_t > \psi_i - X + 2kT \ln \left[\left(\frac{\pi}{eL} \right) \left(\frac{2kTK\epsilon_0}{N_t} \right)^{1/2} \right]$ (the lower limit of this equation corresponds to the case $L = 2\lambda$). Thus, if $L > 2\lambda$, we require that ϕ satisfied the condition

$$\left\{ \psi_i - X + 2kT \ln \left[\frac{\pi}{eL} \left(\frac{2kTK\epsilon_0}{N_t} \right)^{1/2} \right] \right\} \leq E_t < \phi < (\psi_i - X - 4kT).$$

have from (8)

$$L_i \geq 10\pi \left(\frac{2kTK\epsilon_0}{e^2 N_t} \right)^{1/2} \exp \left(\frac{\psi_i - X - E_t}{2kT} \right) \quad (17)$$

and that the interfacial barrier height, ϕ_i , for this case must satisfy the condition

$$\psi_i - X - 2kT \ln \left[\left(\frac{Le}{10\pi} \right) \left(\frac{N_t}{2kTK\epsilon_0} \right)^{1/2} \right] < E_t < \phi_i < (\psi_i - X - 4kT). \quad (18)$$

Therefore, if electrodes of work function

$$\psi_m = \phi_i + X \quad (19)$$

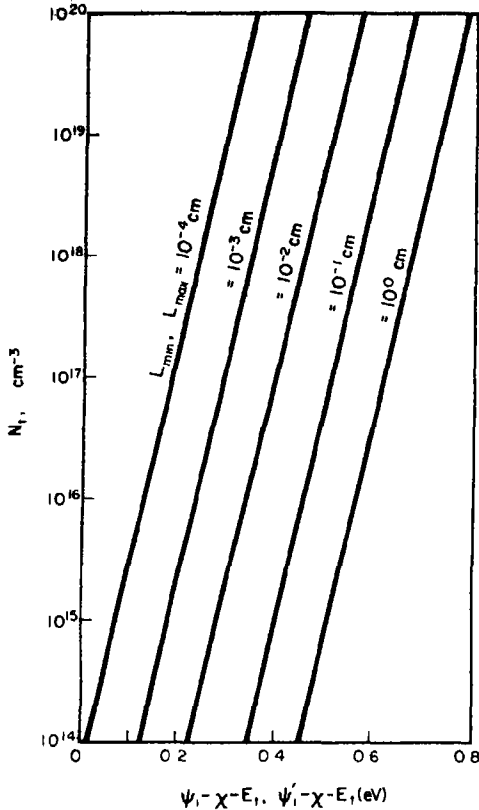


Fig. 4. Plot of N_t vs. $\psi_i - X - E_t$ and $\psi'_i - X - E_t$ for various L_{\min} and L_{\max} respectively. $\psi_i - X - E_t$ and L_{\min} corresponds to separated accumulation regions, and $\psi'_i - X - E_t$ and L_{\max} to overlapping accumulation regions.

are attached to the insulator, the conduction process will reflect the intrinsic properties of the insulator.

3. OVERLAPPING ACCUMULATION REGIONS

The condition $L < 2\lambda$ results when there is insufficient space charge within the insulator to raise the Fermi level within the bulk of the insulator by an amount $\psi_i - \psi_m$, as described in the previous section (See Fig. 5). Since the accumulation regions overlap, the insulator conduction band is distorted throughout its length, and it follows that space charge exists *throughout* the length of the insulator. Hence, the space charge swamps the indigenous charge, and thus the conduction process

is extrinsic (space charge limited) in nature.

In order to calculate the maximum height, $\psi'_i - X$, of the conduction band above the electrode Fermi level, which for this case is *always* less than $\psi_i - X$, we invoke (7), but with ψ_i replaced by ψ'_i . This equation tells us that, provided the bottom of the conduction band is more than $4kT$ above the interfacial barrier height, the distance from the interface for a given ψ is *independent* of the interfacial parameters. Thus, even if the interface

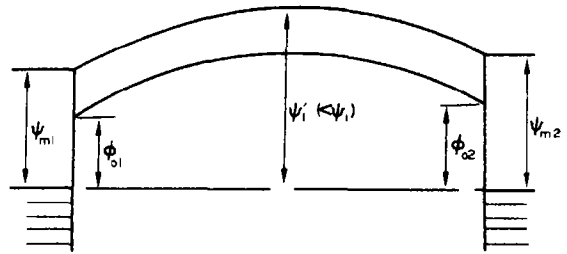


Fig. 5. Energy diagram of a metal-insulator-metal system (the metals have different work functions) for overlapping accumulation regions. Note that the accumulation regions overlap at the *center* of the insulator, and that the insulator conduction band is distorted throughout its length indicating the existence of space charge, and hence, a space charge field throughout the insulator.

barrier heights are different (i.e. different electrode materials) the maxima of the conduction band will be positioned *exactly halfway* within the insulator. Setting $x = L/2$ in (7), and with simple transpositioning, we have

$$\psi'_i - X = E_t + kT \ln \left[\left(\frac{Le}{\pi} \right)^2 \frac{N_t}{2kTK\epsilon_0} \right] \quad (20)$$

from which we note that $\psi'_i - X$ is *independent* of the work function of the electrode and insulator, and the interfacial barrier height.

The curves in Fig. 4 illustrate the relationship between $\psi'_i - X - E_t$, N_t and the *maximum thickness*, L_{\max} , of the insulator, if the accumulation regions are to just overlap; that is, for $\psi'_i - X - E_t = \psi_i - X - E_t$ in (20) [c.f. also (12)]:

$$L_{\max} = 2\lambda = \pi \left(\frac{2kTK\epsilon_0}{e^2 N_t} \right)^{1/2} \exp \left(\frac{\psi'_i - X - E_t}{2kT} \right). \quad (21)$$

For shallow trapping, the maximum value of E_t is $E_t \approx \phi_0$, where ϕ_0 is the interfacial barrier height for overlapping accumulation regions, and since (20) is valid for $\psi'_i - X > \phi_0 + 4kT$, the smallest value that E_t can take is $E_t \approx \{\phi_0 + 4kT - kT \ln [(Le/\pi)^2 (N_t/2kTK\epsilon_0)]\}$. Also, since $\phi_0 < \psi'_i - X - 4kT$ we have

$$\left\{ \phi_0 + 4kT - kT \ln \left[\left(\frac{Le}{\pi} \right)^2 \left(\frac{N_t}{2kTK\epsilon_0} \right) \right] \right\} < E_t < \phi_0 < (\psi'_i - X + 4kT).$$

Thus if electrodes of work function

$$\psi_m = \phi_0 + X \quad (23)$$

are attached to the surface of the insulator they will result in overlapping accumulation regions, or in other words, space charge will exist *throughout* the insulator. This condition is most suitable for observing space charge limited currents in insulators. This is because there is a relatively high concentration of *free* space charge *throughout* the insulator, which means that the space charge currents will be relatively high (see Section 6(b)). Furthermore, space charge currents will persist for relatively high applied fields, because of the relatively large *total* space charge contained within the insulator.

4. LOW SPACE CHARGE CONDITION

In the two previous cases considered it was assumed that the maximum height of the bottom of the conduction band was more than $4kT$ above the interfacial barrier, or in other words, there was significant distortion of the insulator conduction band due to space charge effects. Under this condition, it was shown that the maximum height of the conduction band above the electrode Fermi level was independent of the interfacial barrier height. We now consider the case when there is very little distortion of the insulator conduction band, that is the maximum height of the conduction band is less than $4kT$ above the top of the interfacial barrier. In this case accumulation regions as such are non-existent. Since

there is no significant distortion of the conduction band due to space charge effects, the energy diagram for this case is essentially that of an ideal metal-insulator-metal system (no space charge effects) as shown in Fig. 6(b). It is important to note however that although space charge does not significantly distort the conduction band, it nevertheless plays an important role in the energetics of the system: the space charge is responsible for raising the Fermi level in the insulator an amount $(\psi_i - \psi_m)$, such that the insulator Fermi level coincides with the electrode Fermi level.

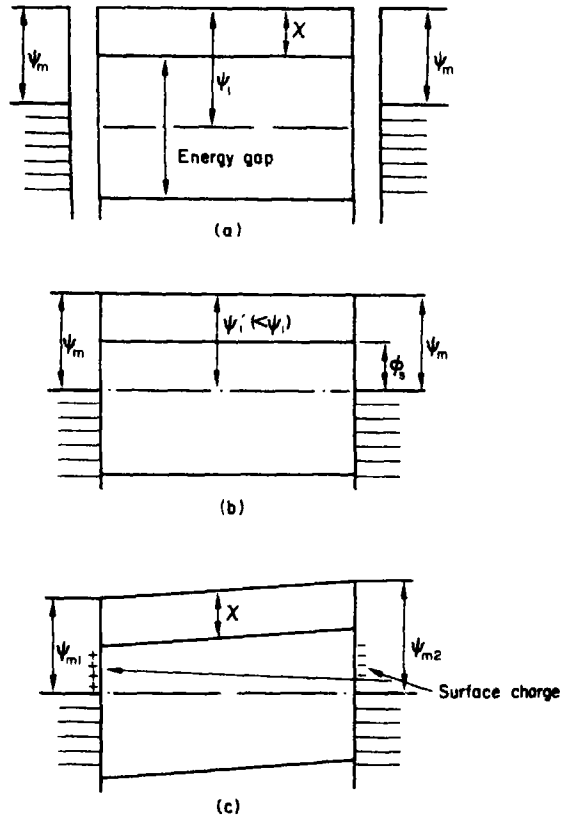


Fig. 6. Energy diagram for a metal-insulator-metal system in which the space charge density is small: (a) before electrodes contact insulator surface; (b) after contact, when similar electrodes are used; (c) after contact, when dissimilar contacts are used. Although in the case of (b) and (c) the insulator contains space charge, its density is too small to give to perceptible curvature of the conduction band.

Furthermore, the space charge exists *throughout* the insulator and swamps the indigenous charge; the conductivity of the insulator is therefore extrinsic (space charge limited) in nature.

It will be apparent from the energy diagram shown in Fig. 6 (b) that the amount of space charge contained within the insulator is dependent on both the trap density and trap energy, $\phi_s - E_t$, above the Fermi level of the electrode. Thus in this case the height, ϕ_s (the subscript *s* refers to the particular case in hand), of the interfacial barrier plays an important role in the maximum height of the conduction band above the electrode Fermi level, whereas in the two previous cases discussed the maxima were *independent* of the interfacial barrier height (See (12) and (20)). In order to determine the approximate condition under which the maximum height of the bottom of the conduction band is determined by the interfacial barrier height we proceed as follows. When the maximum of the conduction band is less than $4kT$ above the height of the interfacial barrier, ϕ_s , the space charge injected into the insulator is [8]

$$Q = (2K\epsilon_0 N_t kT)^{1/2} \times \{ \exp [-(\phi_s - E_t)kT] - \exp [-(\psi_i' - X - E_t)/kT] \}^{1/2}. \quad (24)$$

Assuming $\psi_i' - X - \phi_s \equiv \delta\psi \ll 4kT$, that is the conduction band is only slightly distorted, we have

$$Q = (2K\epsilon_0 N_t \delta\psi)^{1/2} \exp [-(\phi_s - E_t)/2kT]. \quad (25)$$

Also, since the total space charge is essentially equal to the charge contained in the shallow traps, and since the conduction band is essentially flat, we have

$$Q = (eN_t L/2) \exp [-(\phi_s - E_t)/kT]. \quad (26)$$

Equating (25) and (26), yields

$$\delta\psi = (e^2 L^2 N_t / 8K\epsilon_0) \exp [-(\phi_s - E_t)/kT]. \quad (27)$$

The largest value that $\delta\psi$ can take to be both consistent with the expansion of the terms in the curly brackets in (24) leading to (25), and with the conduction band being relatively flat is

$$\delta\psi < kT. \quad (28)$$

Substituting (28) in (27) and transposing yields a barrier height ϕ_s given by:

$$\phi_s > [E_t + kT \ln (e^2 L^2 N_t / 8K\epsilon_0 kT)] \quad (29)$$

ϕ_s determines the height of the interfacial barrier for which the conduction band will be only slightly distorted, and if a metal of work function

$$\psi_m = \phi_s + X \quad (30)$$

is attached to the surface of the insulator it will result in a relatively poor space charge contact. Thus although the conduction process for such a system will be initially space charge limited (see Section 6(c)) the currents involved will generally be much smaller than, and will become electrode limited at lower applied fields than, for example, the overlapping accumulation regions condition described in the last section.

When $\phi_s + X = \psi_i$ (i.e. $\phi_s \approx E_g/2$) we have

$$\psi_m = \psi_i.$$

This means that the vacuum and Fermi levels of the electrode and insulator are continuous when in intimate contact, *without* the necessity of charge transfer between the electrode and insulator; thus no space charge exists within the insulator. This means that there is no band bending present and the energy diagram when similar electrodes are attached to the insulator is similar in appearance to that shown in Fig. 6(b), except that the insulator work function is the same before and after contact ($\psi_i' = \psi_i$). This type of contact is referred to as a *neutral* contact.

When $\phi_s + X > \psi_i$ we have $\psi_i < \psi_m$, and in

order to provide for continuity of the Fermi and vacuum levels of the electrode and insulator the electrode injects *holes* into the insulator. The theory of hole injecting contacts is developed in a manner analogous to that used herein.

If the insulator has dissimilar electrodes connected to its surfaces and both of the interfacial barriers satisfy (29), it is clear that the interfacial barriers differ in energy by an amount $(\psi_{m2} - X) - (\psi_{m1} - X) = \psi_{m2} - \psi_{m1}$, as shown in Fig. 6(c). Since little space charge is injected into the insulator, the conduction band must slope upwards from the lower barrier with an essentially uniform gradient $(\psi_{m2} - \psi_{m1})/L$, as shown in Fig. 6(c). Thus an intrinsic field [9], F_{in} , of strength $(\psi_{m2} - \psi_{m1})/eL$, exists within the insulator. Since there is little space charge within the insulator itself, the origin of this zero-bias intrinsic field must be due to *charge transfer between the electrodes*. The electrode of lower work function, electrode 1, transfers electrons to electrode 2, resulting in a positive surface charge on electrode 2. The amount of charge Q , transferred between the electrodes (the surface charge on the electrodes) depends on the contact potential difference, $(\psi_{m2} - \psi_{m1})/e$, existing between the electrodes, and the capacity, C of the system as follows:

$$Q = C(\psi_{m2} - \psi_{m1})/e = (\psi_{m2} - \psi_{m1})AK\epsilon_0/eL \quad (31)$$

where A is the electrode area.

5. INJECTED SPACE CHARGE

From (1), using the boundary conditions that $F = F_0$ and 0 at $x = 0$ and λ , respectively, we have

$$\int_{F_0}^0 dF = -\frac{1}{K\epsilon_0} \int_0^\lambda \rho_t dx; \quad \rho_t \gg \rho_f$$

or

$$F_0 = Q/K\epsilon_0 \quad (32)$$

where $Q = \int_0^\lambda \rho_t dx$ is the total space-charge per unit area in the accumulation region. Since $\psi = \psi_m - X$ at $x = 0$, we have from (4), assuming $\psi_m < \psi_i - 4kT$, which will normally be the case,

$$F_0 = \left(\frac{2kTN_i}{K\epsilon_0} \right)^{1/2} \exp\left(-\frac{\phi - E_i}{2kT}\right). \quad (33)$$

Substituting (33) into (32) yields

$$Q = (2K\epsilon_0kTN_i)^{1/2} \exp\left(-\frac{\phi - E_i}{2kT}\right). \quad (34)$$

Equation (34) may be written in terms of the space-charge density ρ_0 at the interface, which is given by $\rho_0 = eN_i \exp(E_i - \phi)/kT$. Substituting this equation into (34) yields

$$Q = (2K\epsilon_0kT\rho_0)^{1/2}. \quad (35)$$

It will be noted from the boundary condition leading to (33), and hence (34), that it is only if the bottom of the conduction band in the interior of the insulator is not more than $4kT$ above the top of the interfacial barrier will ψ_i (or ψ_i') appear in (33) or (34). Another interesting point about (33) and (34) is that since they are independent of ψ_i (or ψ_i'), two insulators having different work functions but the same electron affinity and the same electrode material attached to their surfaces, will have the same field at the interface and contain essentially the same amount of space charge. However, the field within the insulator away from the contact and the spatial distribution of the charge are different in the two systems.

6. LOW-FIELD SPACE CHARGE CONDUCTIVITY

In this section we determine the effect of space charge on the conductivity of the insulator. For convenience, we assume that the spacial distribution of the space charge in the insulator under voltage bias is the same as under zero-bias conditions. While this will not normally be true for high field, it is a good approximation for low fields.

(a) *Non-overlapping accumulation regions*

By inspection of Fig. 3, it is seen that the integral (A6) (see Appendix) may be written

$$\int_0^L \frac{dx}{n} = 2 \int_0^\lambda \frac{dx}{n} + \frac{1}{n_i} \int_\lambda^{L-\lambda} dx \quad (36)$$

where n_i is the (constant) *intrinsic* carrier density in the bulk of the insulator and thus equal to

$$n_i = N_c \exp [-(\psi_i - X)/kT]. \quad (37)$$

For $\psi > (\phi + 4kT)$, (5) can be written [see (7)]

$$x = \left(\frac{2kTK\epsilon_0}{e^2 N_i} \right)^{1/2} \sin^{-1} \left[\exp \left(\frac{\psi - \psi_i + X}{2kT} \right) \right] \times \exp \left(\frac{\psi_i - X - E_i}{2kT} \right) \quad (38)$$

and

$$n = N_c \exp (-\psi/kT). \quad (39)$$

Differentiating (38) to obtain dx in terms of $d\psi$ and substituting this result together with (39) in the first term on the right hand side of (36) we have

$$2 \int_0^\lambda \frac{dx}{n} = \frac{1}{kTN_c} \left(\frac{2kTK\epsilon_0}{e^2 N_i} \right)^{1/2} \exp \left(\frac{\psi_i - X - E_i}{2kT} \right) \times \int_{-\infty}^{\psi_i - X} \frac{\exp [(3\psi - \psi_i + X)/2kT] d\psi}{\{1 - \exp [(\psi - \psi_i + X)/kT]\}^{1/2}}. \quad (40)$$

The use of (38) to describe x in terms of ψ over the *entire* accumulation region and of the lower limit of integration, $-\infty$, is justified, since any contribution to the integral for $\psi < \psi_i - X - 4kT$ is relatively insignificant. Using $y = \exp (\psi - \psi_i + X)/2kT$ it can be readily shown that the integral can be written in the form $y^2 dy/(1-y^2)^{1/2}$ which is readily inte-

grated by parts so that (40) becomes

$$\int_0^\lambda \frac{dx}{n} = \frac{\pi}{2N_c} \left(\frac{2kTK\epsilon_0}{e^2 N_i} \right)^{1/2} \exp \left(\frac{3(\psi_i - X) - E_i}{2kT} \right)$$

or using (8) and (37)

$$\int_0^\lambda \frac{dx}{n} = \lambda/n_i. \quad (41)$$

Substituting (41) in (36) and using the resulting expression in (A6) of the Appendix we arrive at

$$\sigma_s = e\mu_n n_i (1 - \lambda/L)^{-1}. \quad (42)$$

Thus the ratio of the space charge conductivity to the intrinsic conductivity $\sigma_i (= e\mu_n n_i)$ of the insulator is

$$\sigma_s/\sigma_i = (1 - \lambda/L)^{-1}.$$

Physically speaking the effect of the accumulation region is to reduce the effective length of the insulator by an amount λ . Thus when $L \gg \lambda$ the conduction process reflects the intrinsic conductivity of the insulator.

(b) *Overlapping accumulation regions*

From Fig. 5 and using the same reasoning leading to (40) we have

$$\int_0^L \frac{dx}{n} = \frac{1}{2kTN_c} \left(\frac{2kTK\epsilon_0}{e^2 N_i} \right)^{1/2} \exp \left(\frac{\psi_i' - X - E_i}{2kT} \right) \times \int_{-\infty}^{\psi_i' - X} \frac{\exp [(3\psi - \psi_i' + X)/2kT] d\psi}{\{1 - \exp [(\psi - \psi_i' + X)/kT]\}^{1/2}} \quad (43)$$

$$= \frac{L}{2N_c} \exp \left(\frac{\psi_i' - X}{kT} \right). \quad (44)$$

In arriving at (44) we have made use of (20).

Substituting (44) into (A6) yields

$$\sigma_s = e\mu_n \frac{L}{2} N_c \exp \left[- \left(\frac{\psi'_i - X}{kT} \right) \right] \quad (45)$$

and

$$\frac{\sigma_s}{\sigma_i} = \frac{1}{2} \exp \left(\frac{\psi_i - \psi'_i}{kT} \right). \quad (46)$$

For overlapping accumulation regions $\exp(\psi'_i/kT) \ll \exp(\psi_i/kT)$, so that the space charge increases the insulator conductivity considerably above its intrinsic value. (For example from Fig. 4, for $N_t = 10^{18} \text{ cm}^{-3}$, $N_t = 0.2 \text{ eV}$ and $L = 10^{-1} \text{ cm}$, we obtain $\psi'_i - X < \frac{3}{4} \text{ eV}$, whereas for a trap-free relative narrow band insulator, such as CdS, $\psi_i - X \approx E_g/2 = 1.2 \text{ eV}$; using these values in (46), $\sigma_s/\sigma_i \approx 10^6$. This conclusion is significant with regard to the low-field measurements on space-charge-limited current[3] (SLC) flow. According to theory SCLC flow is proportional to the square of the applied voltage over *all* voltages. Experimental observation shows that this relationship is usually preceded by an ohmic region. Lampert [3] attributes this observation to the *intrinsic* conductivity of the insulator which persists until the space charge density drawn in by the applied voltage exceeds the indigenous carrier density. Our conclusions show, however, that the observed *ohmic* region is most probably attributable to space charge and not the indigenous charges. It is difficult to escape the conclusion if injecting contacts exist on the insulator surface.

(c) Low space charge condition

(i) *Similar Electrodes*. In this case the height of the conduction band above the electrode Fermi level can be considered to be essentially constant throughout the length of the insulator and of height ϕ_s above the electrode Fermi level (see Fig. 6b). The space charge conductivity is, therefore, $\sigma_s = eN_c\mu_n \exp(-\phi_s/kT)$ and the ratio $\sigma_s/\sigma_i = \exp(E_g/2 - \phi_s)/kT$.

(ii) *Dissimilar Electrodes*. The energy diagram for this system is shown in Fig. 6(c). The potential energy of the conduction band above the electrode Fermi level is given by

$$\psi = \phi_{s1} + (\phi_{s2} - \phi_{s1})x/L$$

for which

$$dx = \frac{L}{(\phi_{s2} - \phi_{s1})} d\psi. \quad (47)$$

Using (39) and (47) in (A6), we have

$$\begin{aligned} \sigma_s &= e\mu_n(\phi_{s2} - \phi_{s1})N_c \left[\int_{\phi_{s1}}^{\phi_{s2}} \exp\left(\frac{\psi}{kT}\right) d\psi \right]^{-1} \\ &= e\mu_n \left(\frac{\phi_{s2} - \phi_{s1}}{kT} \right) N_c \\ &\quad \times \left[\exp\left(\frac{\phi_{s2}}{kT}\right) - \exp\left(\frac{\phi_{s1}}{kT}\right) \right]^{-1} \end{aligned}$$

or assuming $\exp(\phi_{s2}/kT) \gg \exp(\phi_{s1}/kT)$, which will usually be the case,

$$\sigma_s = e\mu_n \left(\frac{\phi_{s2} - \phi_{s1}}{kT} \right) N_c \exp(-\phi_{s2}/kT). \quad (48)$$

7. DISCUSSION

We have confined our attention to a single discrete shallow trapping level, because this insulator model is one that is often invoked in interpreting experimental data[3]. Whether or not such a specific set of traps exists in an insulator is an open question. However, if there were a distribution of *shallow* traps in the insulator, they can be accommodated in the theory by summing over the trapped charge in all the levels. The factor $N_t \exp(E_t/kT)$ is proportional to the amount of charge contained in a discrete set of shallow traps; thus to accommodate in the theory given above a series of trapping levels, it is necessary only to replace the factor $N_t \exp(E_t/kT)$ by the summation

$$\Sigma_E N_t(E) \exp(E/kT), \quad (49)$$

where E represents the energy of the various trapping levels.

At a given temperature it is possible that the trapping ability of one of the levels, say E_0 , could dominate the others, that is

$$N_t(E_0) \exp(E_0/kT) \gg \sum_{E \neq E_0} N_t(E) \times \exp(E/kT).$$

When this is so the problem reduces to that of the single-trapping level given above. Also, since different trapping levels can dominate the conduction process at different temperatures, it follows that the activation energy will vary with temperature.

An insulator can, of course, contain deep traps as well as shallow traps. By definition, deep traps are completely filled traps and, thus, are considerably more efficacious in holding space charge than their shallow counterparts. As a result, the distortion of the conduction band of an insulator containing deep traps will be considerably enhanced compared to the case described above and accumulation regions of less than one micron are possible in such systems. In point of fact, the deep trap case is the one more often met with in practice and will be treated in a later publication.

8. CONCLUSIONS

We have shown that the contacts at a metal-insulator interface can be divided into three different categories: (a) separated accumulation regions; (b) overlapping accumulation regions; and (c) low space charge condition. It has been shown that type (a) will exist at a metal-insulator interface only if the traps are relatively deep. Types (b) or (c) exist at a metal-insulator interface depending on the relative work functions of the metal and insulator.

We have further shown that the overlapping accumulation regions and the low space charge conditions, which are the type which will normally exist at a metal-insulator interface, significantly affect the conductivity of the

insulator. The former contact is shown to be of significance in space charge limited current flow.

Acknowledgements—The author is grateful to Dr. A. Rose of RCA Laboratories for reading an earlier manuscript and for suggestions that improved its contents.

This work was supported by the National Research Council of Canada.

APPENDIX

(a) Position of Fermi level in the presence of shallow traps

In a space-charge-free section of an insulator the number of electrons in the traps and conduction band is equal to the number of holes in the valence band. Equating the electrons and holes, and measuring energy from the bottom of the conduction band we have:

$$N_c \exp\left(-\frac{E_F}{kT}\right) + N_t \exp\left(\frac{E_t - E_F}{kT}\right) = N_v \exp\left(\frac{E_F - E_g}{-kT}\right)$$

which yields

$$E_F = \frac{E_g}{2} + \frac{kT}{2} \ln \left\{ \left(\frac{N_c}{N_t} \right) \left[1 + \frac{N_t}{N_c} \cdot \exp\left(\frac{E_t}{kT}\right) \right] \right\} \quad (A1)$$

which for $N_p = N_c$ reduces to

$$E_F = \frac{E_g}{2} + \frac{kT}{2} \ln \left[1 + \frac{N_t}{N_c} \cdot \exp\left(\frac{E_t}{kT}\right) \right] \quad (A2)$$

where N_p is the density of states in the conduction band. The effect of electron traps within the insulator is reflected in the second term on the right-hand side of (A2), which is to move the Fermi level below the mid-point of the energy gap. Hole traps have the opposite effect of moving the Fermi level above the mid point of the energy gap. In either case, however, traps have only a marginal effect on the position of the Fermi level. For example, even if the ratio of trapped-to-free charge is as high as 10^6 the Fermi level is displaced from the intrinsic position by only $7kT$ which is only 0.175 eV at room temperature. Thus in many instances $\psi_i - X \approx E_g/2$.

(b) The conduction equation

The total electronic space charge current flowing in a system is the sum of the drift and diffusion currents densities

$$I = en\mu_n F + eD_n \frac{dn}{dx} \quad (A3)$$

where n is the free electron density, μ_n the electron mobility, and D_n the electronic diffusion constant. In terms of the Fermi energy (A3) becomes [10]

$$I = n\mu_n \frac{dE_F}{dx} \quad (A4)$$

Integrating (A4) yields:

$$I \int_0^L \frac{dx}{n} = \mu_n \int_0^{eV} dE_F$$

or

$$I = e\mu_n V \left[\int_0^L \frac{dx}{n} \right]^{-1} \quad (\text{A5})$$

Thus, in order to determine the space charge current, it is required only to evaluate the integral in (A5). Furthermore, since we are assuming that the electron distribution, n , is equal to its zero bias distribution, n is independent of V which means that the space charge current is proportional to V . We can thus define a low-field space-charge conductivity σ_s :

$$\sigma_s = \frac{IL}{V} = e\mu_n L \left[\int_0^L \frac{dx}{n} \right]^{-1}. \quad (\text{A6})$$

REFERENCES

1. MANY A. *et al.*, *Semiconductor Surfaces*, John Wiley, New York (1965).
2. MOTT N. F. and GURNEY R. W., *Electronic Processes in Ionic Crystals*, Clarendon Press, Oxford (1940).
3. LAMPERT M. A., *Reports on Progress in Physics*, Vol. 27, p. 329 (1964).
4. SMITH R., *Phys. Rev.* **97**, 1525 (1955).
5. SIMMONS J. G., to be published.
6. Note that ψ_i refers to the insulator work function before the electrodes are attached.
7. If $\rho_f \approx \rho_i$, ρ_f cannot be neglected in the calculations. In order to accommodate ρ_f into the subsequent calculations it is necessary only to multiply N_i wherever it appears by the factor $(1 + \theta^{-1})$. Also it is necessary only to replace N_i by N_e and set E_i equal to zero to obtain the corresponding equation for a trap-free insulator.
8. Equation (24) is obtained by integrating (3) and using the boundary conditions $d\psi/dx = 0$ at $\psi = \psi_i$, and $d\psi/dx = eF_0$ at $\psi = \phi$, and then substituting the resulting equation for F_0 into (32).
9. If the insulator is very thin, the intrinsic field can be very large (SIMMONS J. G., *Phys. Rev. Lett.* **10**, 10 (1963)); for example, suppose $s = 20 \text{ \AA}$, as one finds in a tunnel junction, and $(\psi_{m2} - \psi_{m1})/e = 1v$, $F_{in} = 5 \times 10^6 \text{ V. cm}^{-1}$.
10. See for example WANG S., *Solid State Electronics* p. 317, McGraw-Hill, New York (1966).

CRYSTAL FIELD IN RARE-EARTH FLUORIDES—III. ANALYSIS OF EXPERIMENTAL DATA FOR THE ALKALINE EARTH FLUORIDES

G. E. STEDMAN and D. J. NEWMAN

Department of Physics, Queen Mary College, Mile End Road, London, E.1, England

(Received 11 May 1970)

Abstract—The superposition model and a recent experimental determination of the local distortion at substituted rare-earth ions in CaF_2 , SrF_2 and BaF_2 are employed to compare experimental results with *ab initio* calculations of crystal field parameters. It is shown that divalent and trivalent rare-earth ions have very similar $n = 4$ and $n = 6$ crystal field parameters and power laws. Strong experimental evidence is found for a power law of less than 6, in agreement with our theoretical prediction. Power laws also provide evidence that the spin-Hamiltonian parameter b_4 depends quadratically on the crystal field, while b_6 depends on its cube.

1. INTRODUCTION

A CONSIDERABLE body of experimental data exists on the crystal fields, spin-Hamiltonians and spin-lattice relaxation times for rare-earth ions substituted into alkaline earth fluorides. In particular, this is one of the few systems in which crystal field parameters are known for both the divalent and trivalent rare-earth ions. It is thus of interest to collect this material and to make a comprehensive attempt to interpret it in terms of recently developed theoretical models; specifically the 'superposition model' of the crystal field and the *ab initio* crystal field calculation given in paper I[1] of this series. In carrying out this interpretation, we make considerable use of the experimental determination of local distortion at substituted rare-earth ions obtained by Hurren *et al.* [2].

Particular attention is paid to the derivation of estimates of the crystal field parameter power laws as these provide a new and important test of our *ab initio* calculations. These power laws are also of interest in relation to the power laws obtained for the spin-Hamiltonian parameters.

2. S-STATE IONS

Hurren *et al.* [2] have shown that the experimental strain dependence of the Eu^{2+} spin-Hamiltonian parameter b_4 can only be brought

into agreement with the variation of b_4 among the different alkali earth fluorides if a considerable radial distortion is supposed to take place near the substituted ion. This distortion reduces the variation of the nearest neighbour ligand distances as shown in Table 1 (i.e., almost uniformly by a factor of 0.44). Hurren *et al.* were able to check this result by demonstrating that, with distortions of this magnitude, the spin-Hamiltonian parameter b_6 also showed consistency between the host and strain dependence. Expressed in the usual way as inverse power law exponents, the derived strain dependences were 8.8 for b_4 and 13.6 for b_6 .

It is of interest to compare the distortions derived by Hurren *et al.* with those obtained in a recent *ab initio* calculation by Ivanenko and Malkin[3]. Using the linear interpolation procedure suggested by the authors, we obtain the nearest neighbour ligand distances for substituted Eu^{2+} shown in the last column of Table 1. The total spread of distances is about one third greater than that given by Hurren *et al.* (which leads to a reduction in the derived power laws). A further difference in the *ab initio* calculation is that it gives a very non-uniform reduction in the variation of nearest neighbour ligand distances. Hence the experimental results of Hurren *et al.* give a very non-

Table 1. Distances between metal and fluorine ions in pure and substituted fluorite crystals (\AA)

	X-ray	Hurren <i>et al.</i> [2]	Ivanenko and Malkin [3]
CaF_2	2.366	2.450	2.377
SrF_2	2.512	2.512	2.481
BaF_2	2.685	2.580	2.553

linear power law graph in terms of distances calculated by Ivanenko and Malkin. In the following work we shall use the empirically determined distortions, i.e. those of Hurren *et al.* in preference to those obtained in the *ab initio* calculation.

Experimental data for the spin-Hamiltonian parameter b_4 is also available for Gd^{3+} substituted into the alkaline earth fluorides [4, 5]. If the relative distances are assumed to be the same as for Eu^{2+} a power law of 4.9 is obtained. This suggests that the real distortion is even greater than that obtained by Hurren *et al.* in the case of triply charged ions. Such a result is qualitatively in agreement with the calculation of Ivanenko and Malkin.

It is also interesting to compare the magnitudes of the spin-Hamiltonian parameters for Gd^{3+} and Eu^{2+} (e.g., in CaF_2 , Gd^{3+} has $b_4 = 46.6 \times 10^{-4} \text{ cm}^{-1}$ [5], Eu^{2+} has $b_4 = 55.5 \times 10^{-4} \text{ cm}^{-1}$ [1]). Thus, we find very similar spin-Hamiltonian parameters for these two ions in spite of the fact that the relative energies of different configurations are considerably different in divalent and trivalent ions. This suggests that configuration interaction does not provide large contributions to these parameters.

An estimate of power laws may also be obtained using spin-lattice relaxation data for different host crystals. Following Horak and Nolle [6] we write

$$b_n \sim (v^5/T_{\text{direct}})^{1/2} \sim (v^{10}/T_{\text{Raman}})^{1/4},$$

where v is the mean crystal sound velocity, T_{direct} and T_{Raman} are the measured direct and Raman relaxation times for a given host.

Using averaged sound velocities from elastic constants provided by Huffman and Norwood [7] and Gerlich [8], relaxation times obtained by Horak and Nolle [6], and the relative distances obtained by Hurren *et al.*, we obtain the power law exponents

$$\begin{aligned} &5.0 \text{ (direct process),} \\ &6.0 \text{ (Raman process).} \end{aligned}$$

It is a general result that b_2^m are the dominant spin-Hamiltonian parameters. Therefore, in the local distortions of the cubic symmetry generated by the lattice vibrations, we expect this parameter to dominate for calculations involving only the $^6S_{1/2}$ manifold. Both the direct and the Raman (T^5) process satisfy this requirement. Hence the power laws given above are interpreted as referring to the b_2^m .

Another potential source of information on the S -state ions is the temperature dependence of the hyperfine constant. According to the theory of Šimánek and Orbach [9, 10], we may write

$$x \sim (v^7 C_6)^{1/2}$$

where x is an average matrix element of the odd crystal field components coupling the $4f$ and ns states, v is the velocity of sound in the crystal and C_6 is the coefficient of T^6 in the temperature dependent expression for the hyperfine constant. The structure of these matrix elements is considerably different from those which define the spin-Hamiltonian or crystal field parameters and attempts at prediction using an electrostatic model have not been successful. A deeper theoretical analysis, including overlap and covalency effects, is thus required before the experimental data can be interpreted in this case. In fact, the experimental results for Eu^{2+} given by Menne, Ames and Lee [10] give a negative exponent in the inverse power law.

3. INTRINSIC CRYSTAL FIELD PARAMETERS AND POWER LAWS FOR THE DIVALENT IONS

It is convenient to relate the various forms

and methods of normalization of the cubic parameters that have been used in the literature to the so called 'intrinsic' parameters, which are parameters in Stevens' normalization[11] for an axially symmetric single ligand system. This procedure is based on the approximation that the total cubic field results from the superimposed fields of the nearest neighbour ligands. In lower symmetry systems the superposition approximation can be, and has been, tested. However, in the present case the intrinsic parameters may be regarded simply as a convenient way of writing the cubic parameters, at least until comparisons with other systems or *ab initio* calculations are made.

The intrinsic parameters \bar{A}_n are related to the commonly used cubic parameters for an eight-fold co-ordinated ion as follows

$$8B_4 = -A_4^0 \langle r^4 \rangle = (28/9)\bar{A}_4, \\ 16B_6 = A_6^0 \langle r^6 \rangle = (16/9)\bar{A}_6.$$

(Sometimes the upper zero is omitted in $A_n^0 \langle r^n \rangle$.) Cubic parameters which include operator equivalent factors have frequently been used for Tm^{2+} and Yb^{3+} ; the relationship between these parameters and the intrinsic parameters has been given in paper I of this series.

Intrinsic parameters derived from experimental cubic parameters[12–14] for Dy^{2+} , Ho^{2+} and Tm^{2+} in the alkaline earth fluorides are given in Table 2. These parameters all show the expected decrease as the lattice parameter of the host crystal increases. It is therefore possible to derive sensible power laws if we assume that the *relative* distances derived by Hurren *et al.* are also appropriate for other divalent ions. Power laws obtained in this way are shown in the last column of Table 2, the quoted errors being a measure of non-linearity.

The results for Ho^{2+} and Tm^{2+} provide further evidence for the approximate equality of the negative power law exponents (t_4 , t_6) of the parameters \bar{A}_4 and \bar{A}_6 in agreement with

Table 2. Experimental intrinsic parameters for substituted divalent ions (cm^{-1})

	CaF_2	SrF_2	BaF_2	Power law	Ratio \bar{A}_4/\bar{A}_6
$\text{Dy}^{2+} \bar{A}_4$	75.6	67.4	59.1	4.8 ± 0.1	4.27
\bar{A}_6	17.7	15.8	13.8	—	
$\text{Ho}^{2+} \bar{A}_4$	83.0	70.2	59.1	6.6 ± 0.2	4.44
\bar{A}_6	18.7	15.5	13.3	6.6 ± 0.9	
$\text{Tm}^{2+} \bar{A}_4$	60.7	53	45	5.8 ± 0.3	3.75
\bar{A}_6	16.2	13	12	5.8 ± 2.8	

*To fit to experimental data in this case assumed a constant ratio \bar{A}_4/\bar{A}_6 for the three host crystals. This is equivalent to taking $t_4 = t_6$.

previous experiment[15] and theory[1]. As there are no obvious reasons why the power law should be different for different rare-earth ions, we attribute the variation to experimental error relative to the mean value $t_4 = t_6 = 5.7 \pm 0.9$.

An independent experimental determination of the strain dependence of a particular transition in $\text{Tm}^{2+}:\text{CaF}_2$ and $\text{Tm}^{2+}:\text{SrF}_2$ has been obtained by Axe and Burns[12]. Assuming $t_4 = t_6$ and regarding the various alternative assumptions discussed by Axe and Burns as equivalent to an uncertainty in their result, we may summarize their quoted values as $t_4 = t_6 = 6.8 \pm 0.3$.

4. INTRINSIC CRYSTAL FIELD PARAMETERS AND POWER LAWS FOR TRIVALENT IONS

The most accurate crystal field parameters at present available for trivalent ions in the alkaline earth fluorides are those for Gd^{3+} given by O'Hare, Detrio and Donlan[16]. Experimental intrinsic parameters for this and other ions[17–19] are given in Table 3. The power laws also given in the table were determined using the relative distances derived by Hurren *et al.*[1]; they are in fair accord with the power laws for divalent ions, although we might expect them to underestimate the true values in this case (see discussion of Gd^{3+} in Section 2). O'Hare *et al.* quote very low power laws based on distances in an undistorted host lattice.

Table 3. Experimental intrinsic parameters for substituted trivalent ions (cm^{-1})

	CaF ₂	SrF ₂	BaF ₂	Power law	Ratio \bar{A}_4/\bar{A}_6 *
Nd ³⁺ \bar{A}_4	129	98			indeterminate
\bar{A}_6	25	31			
Gd ³⁺ \bar{A}_4	86.8	77.0	69.7	4.3	3.15 to 3.63
\bar{A}_6	27.9	23.3	19.2	7.2	
Dy ³⁺ \bar{A}_4	78				3.4
\bar{A}_6	23				
Yb ³⁺ \bar{A}_4	59.4				2.76
\bar{A}_6	22.2				

*Rabbiner[16] gives the ratio $\bar{A}_4/\bar{A}_6 = 6.6$ for Tb³⁺:CaF₂ in spite of uncertain parameters.

The data are not sufficient to judge the significance of the difference between t_4 and t_6 for Gd³⁺. In the garnets[15] (with O²⁻ ligands) we find a considerable scatter in the individual values of t_4 and t_6 , but on the average $t_4 = t_6$.

It is of interest to compare the Gd³⁺ experimental parameters with the theoretical results obtained in paper I of this series. As the calculated values were for Pr³⁺ we must try to minimise the inherent uncertainty in choosing 'equivalent' metal-ligand distances in the two cases. To this end we compare parameters for Gd³⁺:CaF₂ (where we expect least distortion due to the similarity of the ionic radii of Gd³⁺ and Ca²⁺) with theoretical Pr³⁺-F⁻ parameters for the mean distance of the nearest neighbour F⁻ ions in LaF₃:

Experiment: $\bar{A}_4 = 86.8 \text{ cm}^{-1}$, $\bar{A}_6 = 27.9 \text{ cm}^{-1}$,
mean power law 5.8.

Theory: $\bar{A}_4 = 89.7 \text{ cm}^{-1}$, $\bar{A}_6 = 28.6 \text{ cm}^{-1}$,
mean power law 5.6.

Although, because of the various uncertainties, the close agreement in the magnitude of the intrinsic parameters may be to some extent fortuitous, we feel that it is significant that the parameter ratio \bar{A}_4/\bar{A}_6 agrees to better than 1 per cent. Independent evidence for the agreement between experimental values of this ratio for Gd³⁺ and Pr³⁺ is obtained from the crystal field acting on these ions in the

anhydrous chlorides[20,21]. The agreement obtained between power laws, although these are approximate, is also physically significant, as *ab initio* calculations for other systems have produced considerably different results.

Close agreement also exists between calculated intrinsic parameters for Pr³⁺ and the experimental values for Nd³⁺:SrF₂, although the latter are rather approximate. The low value of \bar{A}_6 for Nd³⁺:CaF₂ cannot be explained by our model and is attributed to experimental error.

In the case of dysprosium we notice that the experimental parameters are very similar for divalent and trivalent ions, although it may be significant that the Dy³⁺ parameter \bar{A}_6 is larger. Further evidence on this point may be obtained by comparing the experimental intrinsic parameters for the systems Ho²⁺-Cl⁻ and Ho³⁺-Cl⁻ (see Table 4). Although the parameters are very similar in magnitude, there is again some indication that the ratio \bar{A}_4/\bar{A}_6 is higher for the divalent ion.

Table 4. Comparison of intrinsic parameters for trivalent and divalent holmium

Ion	$\bar{A}_4(\text{cm}^{-1})$	$\bar{A}_6(\text{cm}^{-1})$	Host
Ho ²⁺	34.3	10.0	SrCl ₂
Ho ³⁺	33.4	10.9	LaCl ₃

5. DISCUSSION

There is good agreement between the experimental and theoretical intrinsic parameters for trivalent ions (see previous section) especially considering the uncertainty in the distance between the rare-earth and fluorine ions in the experimental system. This gives us some confidence in the theoretical model used in paper I although more experimental evidence regarding power laws would be welcome.

In the divalent ions the excited configurations are relatively low lying and the 5p electrons are more strongly bound than in the

trivalent ions, so that configuration interaction effects are expected to give rather different contributions to the crystal field. However, comparison of the crystal field parameters for corresponding divalent and trivalent ions shows the differences to be relatively small. Hence, configuration interaction cannot account for much more than 10 per cent of \bar{A}_4 or \bar{A}_6 . One consequence of this is that it becomes relevant to compare the experimental values of parameters for divalent ions with calculated parameters for the system $\text{Pr}^{3+} - \text{F}^-$. Although a direct comparison of magnitudes is difficult because of the lack of calculations for ions other than Pr^{3+} , this does not rule out comparisons between power laws. It is therefore satisfying to find that the theoretical power law exponent (5.7) agrees well with the mean value obtained from the experimental data in Table 2.

It is also of interest to note that the ratio \bar{A}_4/\bar{A}_6 is slightly larger for the divalent ions than it is for the trivalent ions. This is presumably due to the differing patterns of configuration interaction in the two cases.

The alkaline earth fluorides have similar values for \bar{A}_6 to those which were derived in our superposition model analyses of the crystal field parameters for $\text{Er}^{3+}:\text{LaF}_3$ [22] and $\text{Nd}^{3+}:\text{LaF}_3$ [1] (25.2 cm^{-1} and 30.4 cm^{-1} respectively). However, the \bar{A}_4 parameters obtained here (and the theoretical value) are greater than those obtained in the LaF_3 analyses (57.2 cm^{-1} and 54.4 cm^{-1}). This is thought to be due to the omission of ions in the superposition model analyses which could give significant contributions to the crystal field (see Ref. [22]).

As similar assumptions were made by Hurren *et al.* [2] in deriving power laws for the Eu^{2+} spin-Hamiltonian as we have made in obtaining power laws for the crystal field of divalent ions, a realistic comparison can be made. The value of 8.8 is rather high for the spin-Hamiltonian parameter b_4 to be linearly dependent on \bar{A}_4 . Hurren *et al.* (following Watanabe) have suggested that power laws of

about 10 for b_4 indicate a quadratic dependence on \bar{A}_4 . More specifically we suggest that b_4 is quadratically dependent on some basic interaction with the crystal with a power law of about 4.4, while b_6 is cubically dependent on the same interaction. The t_6 value (13.6) given by Hurren *et al.* is reduced to 4.5 on this assumption. On this hypothesis we expect $n=2$ spin-Hamiltonian parameters to be linearly dependent on the basic interaction, and thus to have a power law of about 4.4. This agrees reasonably well with the power laws (5.0 and 6.0) obtained for $n=2$ spin-Hamiltonian parameters from spin-lattice relaxation data (Section 2).

6. CONCLUSION

We have found that trivalent and divalent rare-earth ions have very similar intrinsic parameters, and that both the values and power laws of these parameters are in good agreement with our theoretical predictions in paper I of this series. This provides the first direct test of power laws obtained in an *ab initio* calculation of crystal field parameters, and considerably enhances our confidence in the adequacy of the 'overlap + covalency' model for $n=4$ and $n=6$ parameters.

It is suggested that high power laws obtained by Hurren *et al.* for the spin-Hamiltonian parameters b_4 and b_6 indicate that b_4 is quadratic and b_6 is cubic in some basic interaction.

REFERENCES

1. NEWMAN D. J. and CURTIS M. M., *J. Phys. Chem. Solids* **30**, 2731 (1969).
2. HURREN W. R., NELSON H. M., LARSON E. G. and GARDNER J. H., *Phys. Rev.* **185**, 624 (1969).
3. IVANENKO Z. I. and MALKIN B. Z., *Soviet Phys. solid State* **11**, 1498 (1970).
4. TITLE R. S., *Phys. Lett.* **6**, 13 (1963).
5. SIERRO J., *Helv. Phys. Acta* **36**, 505 (1963).
6. HORAK J. B. and NOLLE A. W., *Phys. Rev.* **153**, 372 (1967).
7. HUFFMAN D. R. and NORWOOD M. H., *Phys. Rev.* **117**, 709 (1960).
8. GERLICH D., *Phys. Rev.* **135**, A1331 (1964) and **136**, A1366 (1964).
9. ŠIMÁNEK E. and ORBACH R., *Phys. Rev.* **145**, 191 (1966).
10. MENNE T. J., AMES D. P. and LEE S., *Phys. Rev.* **169**, 333 (1968).

11. DIEKE G. H., *'Spectra and energy levels of rare-earth ions in crystals'*; p. 84 Interscience, New York (1968).
12. AXE J. D. and BURNS G., *Phys. Rev.* **152**, 331 (1966).
13. KISS Z. J., *Phys. Rev.* **137**, A1749 (1965).
14. WEAKLIEM H. A. and KISS Z. J., *Phys. Rev.* **157**, 277 (1967).
15. NEWMAN D. J. and STEDMAN G. E., *J. chem. Phys.* **51**, 3013 (1969).
16. O'HARE J. M., DETRIO J. A. and DONLAN V. L., *J. chem. Phys.* **51**, 3937 (1969).
17. RABBINER N., *J. Opt. Soc. Am.* **57**, 217 (1967).
18. BAKER J. M., *J. Phys. C. (Solid State Physics)* **1**, 1670 (1968).
19. LOW W., *'Spectroscopic and group theoretical methods in physics'* p. 167. (Edited by F. Bloch *et al.*) North-Holland (1968).
20. CURTIS M. M., NEWMAN D. J. and STEDMAN G. E., *J. chem. Phys.* **50**, 1077 (1969).
21. SCHWIESOW R. L. and CROSSWHITE H. M., *J. Opt. Soc. Am.* **59**, 592 (1969).
22. STEDMAN G. E. and NEWMAN D. J., *J. Phys. Chem. Solids* **32**, 535 (1971).

TECHNICAL NOTES

Temperature dependence of the EPR spectrum of $\text{CdIn}_2\text{S}_4:\text{Mn}^{2+}$ *

(Received 19 October 1970; in revised form
30 November 1970)

THIS note reports electron paramagnetic resonance (EPR) measurements on manganese doped CdIn_2S_4 crystals. The shape of the spectrum of a sample doped with 0.1 mole % Mn is shown in Fig. 1. There are six narrow ($\sim 5\text{G}$) isotropic lines, characteristic of a Mn hyperfine spectrum ($I = \frac{5}{2}$), superimposed on

The hyperfine splitting constant, A , obtained from the EPR measurements is the same, within experimental error, for both of the spectra. At room temperature the value of $A = 69.43\text{ G}$ is measured.

Owing to the large errors inherent in measuring the positions of the broad lines only the narrow spectrum results are shown in Fig. 2. The temperature dependence of the broad line spectrum is the same, within experimental error.

In the CdIn_2S_4 lattice a Mn^{2+} ion can sit at

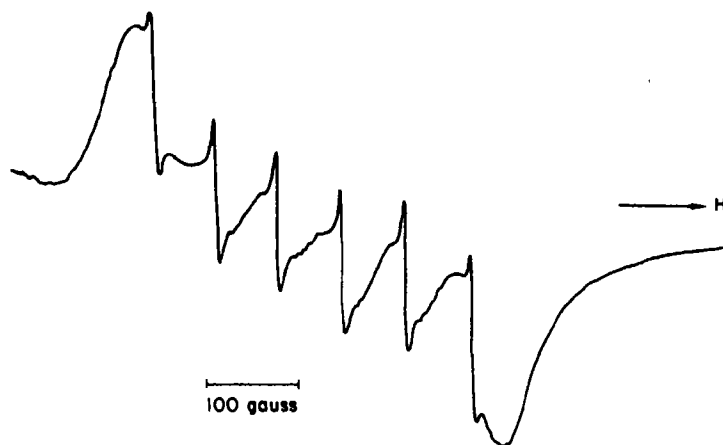


Fig. 1. EPR spectrum for $\text{CdIn}_2\text{S}_4:\text{Mn}$ (0.1 mole %).

a background of six broader, overlapping isotropic lines. The broader lines have approximately 75G line width when analysed as overlapping Lorentzians. They are also ascribed to Mn^{2+} ions. In less highly doped samples only the broad line spectrum is observed. It should be noted that the solubility of Mn in CdIn_2S_4 is very low [1].

either a tetrahedral or an octahedral site (called an 'A' or a 'B' site, respectively, in the literature). Now, if the line width were due primarily to unresolved fine structure, the octahedrally situated Mn^{2+} ion with 6 nearest neighbors would have a line width approximately five times greater than the tetrahedrally situated ion with 4 nearest neighbors, because of the stronger crystal field in the former case [2]. The fine structure is assumed unresolved due to random strains and local disorder in

*Research supported by the National Research Council and Defence Research Board of Canada.

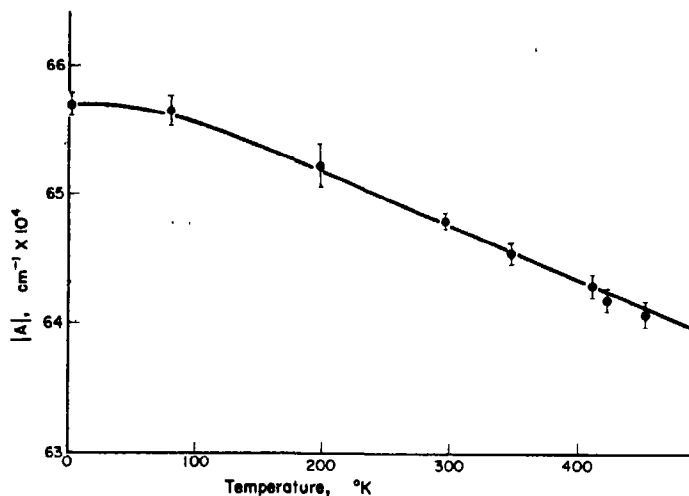


Fig. 2. Hyperfine coupling constant, A , vs. temperature for $\text{CdIn}_2\text{S}_4\text{:Mn}$.

the crystal. We have measured a ratio of 15:1 for the two line widths. Thus, for this reason, we interpret the narrow line spectrum as due to Mn^{2+} at 'A' sites and the broad line spectrum as due to Mn^{2+} at 'B' sites. This does not imply that the Mn is necessarily substituting for the In in one case, and the Cd in the other, since Czaja[3] has proposed a structure for CdIn_2S_4 of $(\text{Cd}_{1/2}\text{In}_{1/2})(\text{Cd}_{1/2}\text{In}_{3/2})\text{S}_4$ where the first bracket refers to 'A' sites and the second to 'B' sites. Thus the Mn would require no charge compensation to reach its doubly ionized state at either site. From the integrated intensities of the two spectra and the absence of the narrow line spectrum from lesser doped samples we deduce that Mn has a preference to substitute in the 'B' site.

We would expect our results to be comparable to CdS:Mn^{2+} since in CdS the Mn is also surrounded by a tetrahedron of S ions. Zdánsky and Kubec[4] have measured the temperature dependence of the hyperfine coupling of Mn^{2+} in CdS. They interpret their results in terms of a theory proposed by Simanek and Orbach[5]. In the theory an expression for the temperature dependence of the hyperfine coupling is derived as

$$A(T) = A(0) \left[1 - CT^4 \int_0^{\theta_D/T} \frac{x^3 dx}{e^x - 1} \right]$$

where C is a constant that reflects the electron-lattice interaction and thus the vibrational properties of the lattice. We have used this expression and a Debye temperature, θ_D , of 230°K[6] to match our experimental data at 1.1 and 411°K. The curve fits the experimental results well and yields a value of $C = (1.6 \pm 0.3) \times 10^{-11} (\text{°K})^{-4}$. Zdánsky found a value of $C = 2.58 \times 10^{-13} (\text{°K})^{-4}$ for CdS. Since the nearest neighbor configuration is identical and also the bond length is the same (2.55 Å) for both CdS and CdIn_2S_4 , the effect is most likely a bulk property of the crystal. For this reason, and the fact that the Debye expression, a one-parameter formula, fits the data well, it was felt that an analysis in terms of localized vibrational modes on the impurity sites[4] was not justified in our case. For a point charge model and a cubic arrangement of nearest neighbor ions for CdIn_2S_4 we calculate $C = 6.4 \times 10^{-12} (\text{°K})^{-4}$. If covalency effects are taken into account the value of C as calculated would increase and give a better agreement with experiment[7].

There exists a weak second order phase transition of CdIn_2S_4 at 403°K [3] which has been interpreted as a reordering at the tetrahedral sites. This is only a third nearest neighbor effect on the 'A' site for Mn, so no sharp change in spectra is expected. However, a very slight change in relative intensity of the two spectra is observed, with the narrow line spectrum being enhanced with increasing temperature, but the errors were very large and no quantitative results were possible.

Acknowledgements—The authors would like to thank Dr. W. Czaja for supplying the crystals used in this experiment and for many helpful discussions. One of us (RKK) wishes to acknowledge a scholarship from the National Research Council of Canada.

REFERENCES

1. CZAJA W., private communication (1970).
2. STAHL-BRADA R. and LOW W., *Phys. Rev.* **116**, 561 (1959).
3. CZAJA W., *Phys. kond. Mater.* **10**, 299 (1970).
4. ZDÁNSKY K. and KUBEC F., *J. Phys. Chem. Solids* **30**, 2327 (1969).
5. SIMÁNEK E. and ORBACH R., *Phys. Rev.* **145**, 191 (1966).
6. CZAJA W. and KRAUSBAUER L., *Phys. Status. Solidi* **33**, 191 (1969).
7. ZIMÁNEK E. and HUANG N. L., *Phys. Rev. Lett.* **17**, 699 (1966).

R. K. KERR
C. F. SCHWERTFEGER

Department of Physics,
University of British Columbia,
Vancouver, B.C.

J. Phys. Chem. Solids Vol. 32, pp. 2009–2013.

Role of interstitial aggregation on the *F*-coloring curve of alkali halides

(Received 3 December 1970)

1. INTRODUCTION

THE ROOM-temperature *F*-coloring curve of alkali halides, such as NaCl, KCl and KBr, subjected to ionizing radiation, consists of a rapidly growing initial stage (stage I), followed by an essentially flat region (stage II) which progressively bends up to reach once

again a relatively high *F*-center production rate (stage III), Fig. 1. The overall structure of the coloring curve depends very markedly on the chemical purity of the crystals, mechanical and thermal history, irradiation temperature and radiation intensity (dose rate). In particular, results obtained in our laboratory for γ -irradiated NaCl show that the length of the stage II (in a dose scale) decreases monotonically with radiation intensity. This effect is clearly illustrated in Fig. 2. The same behavior has been reported by Mitchell, Wiegand and Smoluchowski[1] for *X*-irradiated (136 kV) KCl.

At present, a definite coloring model able to explain the different stages of the *F*-growth curve is not available. However, the experimental evidence has established that during stage III the primary process of the coloring is the creation of Frenkel pairs[2]. The situation is not so clear for stage I, although it is plausible that one is dealing with the same primary process[3, 4]. The creation of Frenkel pairs and the subsequent interstitial-vacancy (or *F*-centre) recombination has been used as a basis for some theoretical treatments of the coloring[5, 6, 7]. For stage III Durand *et al.*[5] assume that the free interstitials created during the primary process can recombine with the vacancies (or *F*-centres) or be trapped at a fixed number of non-saturable traps. For stage I, he assumes[6] that the interstitials can be trapped to saturable traps in addition to recombination with the vacancies. These saturable traps are very likely associated to impurities.

This scheme presents a number of obscure points: (a) What is the meaning of the flat stage II and the region of positive curvature during the stage II-stage III transition? (b) How can it be explained the dependence of the length of stage II on radiation intensity? (c) What is the nature of the non-saturable traps and when and how are they formed?

The purpose of the present note is to propose a simple physical scheme which can be considered a natural extension of Farge's

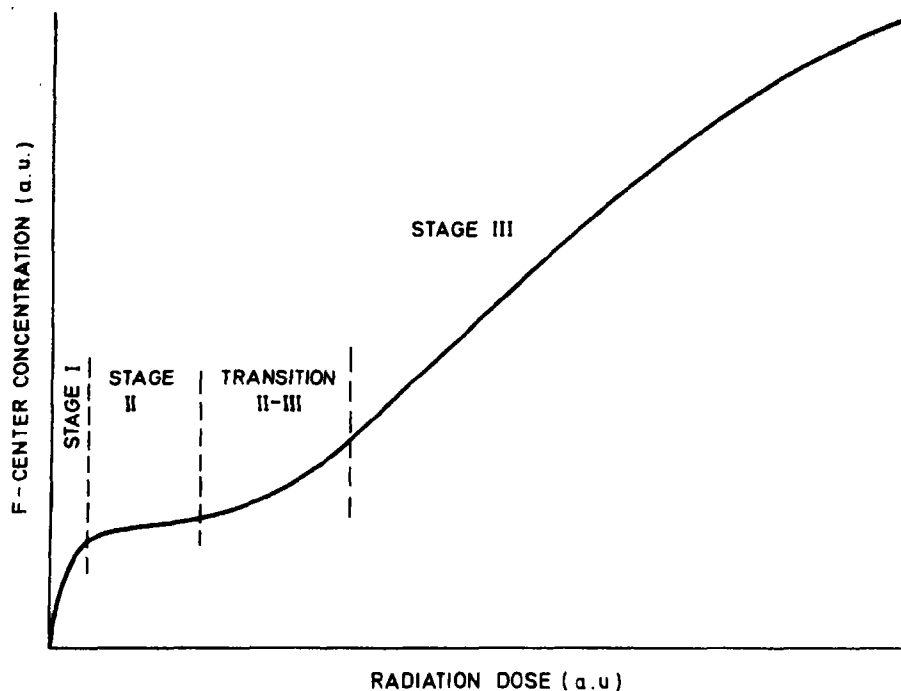


Fig. 1. Typical *F*-center growth curve (in arbitrary units) showing the various stages appearing on it.

treatment and which gives an answer, at least qualitative, to the above questions. We are not here to develop a detailed mathematical approach to the model but to stress the most important points as well as their physical plausibility.

2. THEORETICAL MODEL

Essentially, we assume that, in addition to recombination with vacancies (or *F*-centres) and capture by saturable traps, the free interstitials created by the irradiation can aggregate among themselves to form di-interstitials. After subsequent aggregation to other free interstitials they give rise to aggregates of large size which are proposed to constitute the non-saturable traps required by Farge's model. In fact, there is experimental evidence for the aggregation of free interstitials as a channel for interstitial 'stabilization' [8, 9] as well as for the existence of large interstitial clusters during stage III [4, 10, 11]. We will

assume here that all interstitial aggregates are immobile at room-temperature.

The above scheme can be immediately translated into the following rate equations*

$$\begin{aligned}\frac{df}{dt} &= g - \sigma if \\ \frac{di}{dt} &= g - \sigma if - \sigma is - \sigma i^2 - \sigma ia \\ \frac{da}{dt} &= \sigma i^2\end{aligned}\quad (1)$$

where *f*, *i*, *s*, and *a* are, respectively, the concentrations of *F* centres, free anion interstitials, empty saturable traps and interstitial aggregates (of any size) at time *t*. *g* stands for the concentration of Frenkel pairs produced by unit time. It has been assumed in (1) that

*Throughout this paper, we are going to neglect electronic processes as well as those giving rise to formation of complex color centers.

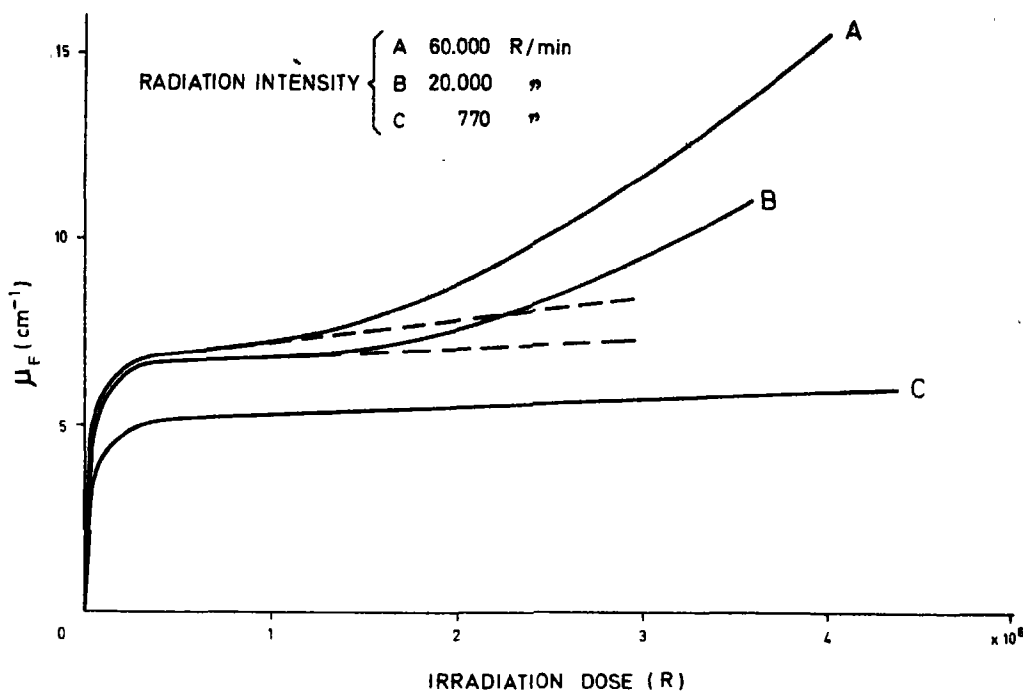


Fig. 2. Experimental *F*-center growth curves of γ -irradiated NaCl showing the effect of radiation intensity. The portion corresponding to stage III has not been determined.

all trapping, aggregation and recombination processes are characterized by a rate-coefficient σ equal for all cases. This is, assumedly a very rough approximation but it greatly simplifies the mathematical arguments and does not essentially affect the physical conclusions.

To follow the detailed kinetics of growth for the various defects one should solve system (1). However a number of useful results on the structure of the *F*-coloring curve can be obtained by simple arguments. In fact, by taking into account the extremely short life of the free interstitial at room-temperature ($\sim 10^{-6}$ sec.), we can consider in accordance with Farge that their concentration accommodates instantaneously to that of the existing traps, i.e., $di/dt = 0$ or

$$i = \frac{g}{\sigma\{f + s + i + a\}} \quad (2)$$

For σ we can accept the estimate obtained by Farge[6], ($\sigma \approx 10^{-11}$ cm³/sec.). Now the appearance of the various stages of the coloring during irradiation can be understood.

Stage I

At very low dose, the concentration of aggregates is $a \approx 0$. Also, it is easy to show from equation (2) that i is very small in comparison to the usual concentration of saturable traps ($\approx 10^{16}$ cm⁻³). Then equations (1) reduce to the same ones used by Farge[6] and lead to a quasi-exponential dependence of *F*-center concentration on dose in agreement with experimental data.

Stage II

Stage I terminates when all saturable traps have been utilized, $s = 0$, and the *F*-center concentration has reached the saturation value $f_s \approx 10^{16}$ cm⁻³. In these conditions

$i, a \ll f_i$ so that the F centers are now the dominant traps. Then $i \approx g/\sigma f$ and from the first equation of (1) one obtains $df/dt = 0$ i.e. an essentially flat curve corresponding to stage II.

On increasing the radiation dose, new di -interstitials (and therefore new aggregates) are being created and so one reaches the situation where $f > a \gg i$ and then

$$i = \frac{g}{f+a} \quad \text{or} \quad \frac{df}{dt} = g \frac{a}{f+a} \quad (3)$$

At not very high doses, it is still $f = f_i$ and $df/dt = g(a/f_i)$ indicating that the rate of production of F centres will show an appreciable increase with dose as soon as the total concentration of aggregates becomes a sufficiently high fraction of the saturating concentration of F -centres. This explains the positive curvature occurring during the transition from the stage II to stage III in the F -coloring curve.

Stage III

At sufficiently high doses $f \gg f_i$ and then

$$\frac{df}{dt} = g \frac{a}{f+a} \approx g \frac{a}{f} = g/N \quad (4)$$

N , being the average number of interstitials making up the aggregates. On dealing with this stage one can take into account that since $i \ll f, < a$, the chances for formation of new di -interstitials (and therefore increasing a) is very small against that for increasing the size N of the aggregates. Therefore one can consider a to be a constant in equation (4), which becomes then identical to that used by Durand *et al.* in [5]. It is clear that because N is increasing with dose, df/dt is decreasing during stage III and practically a saturation value can be reached at very high doses.

3. EFFECT OF TOTAL F -LIGHT BLEACHING

The most important feature of the present model is that stage III of F -center growth

requires the previous nucleation during stage II of enough number of interstitial aggregates.

This means that if a crystal is irradiated up to the start of the positive curvature which leads to stage III, then is totally bleached with F light and is finally re-irradiated, a coloring curve without flat stage should be obtained, under the assumption that interstitial aggregates are stable against the processes involved in optical bleaching. This is quite plausible as it is well known that radiation-induced hardening is substantially insensitive to total or partial F -light bleaching [12, 13]. The result of a typical experiment for γ -irradiated NaCl is given in Fig. 3, and is clearly in agreement with that conclusion.

4. ROLE OF RADIATION INTENSITY ON THE LENGTH OF STAGE II

In accordance with the third equation of (1) the rate of formation of di -interstitials (and consequently interstitial aggregates) which is a thermally activated process, is proportional to the square of the instantaneous concentration of free interstitials. On the other hand this concentration is directly proportional to the radiation intensity, if one assumes equal number of interstitial traps. This situation is approximately fulfilled after saturation of stage I, where the saturation number of F centres are the only available traps. Therefore during a small increment $dW = I dt$ of the dose given to the crystal, the number of newly created di -interstitials will be

$$Ci^2 dt = Ci_0^2 I^2 dt = Ci_0^2 I dW \quad (5)$$

which is proportional to radiation intensity I . This means that the conditions of high concentration of aggregates ($a \leq f_0$) (equation (4)) leading to the appearance of the positive curvature in the F -growth curve should require larger nucleation doses at low intensities than at higher ones. However one can not expect a simple proportionality relation between the length of stage II and radiation intensity as it might be naïvely inferred from

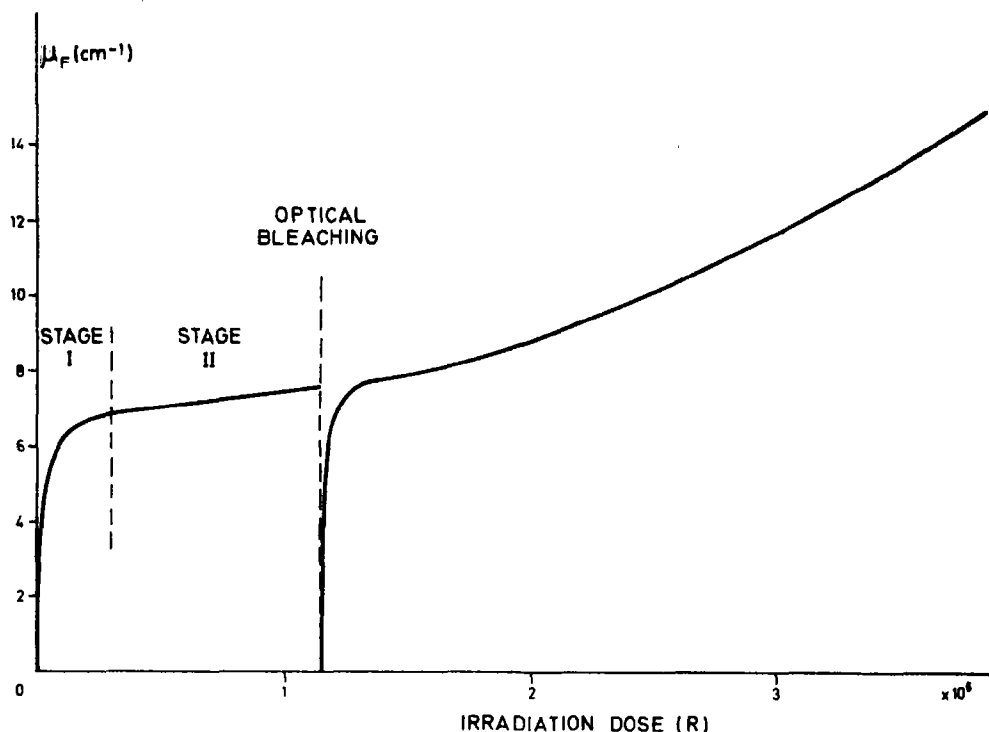


Fig. 3. Experiment illustrating the effect of total F -light bleaching on the shape of the F -growth curve. Note that stage II is absent after bleaching.

equation (5), since at high intensities the concentration of aggregates becomes also higher than that corresponding to low intensities, invalidating the strict proportionality $i \sim I$.

División de Física,
Junta de Energía Nuclear,
Madrid, Spain

F. AGULLÓ-LÓPEZ
F. JAQUE

REFERENCES

1. MITCHELL P. V., WIEGAND D. A. and SMO-
LUCHOWSKI R., *Phys. Rev.* **121**, 484 (1961).
2. CRAWFORD J. H., Jr., *Adv. Phys.* **17**, 93 (1968).
3. ALVAREZ RIVAS J. L., *J. Phys. C: Solid State
Phys.* **3**, 1242 (1970).
4. LERMA I. S. and AGULLÓ-LÓPEZ F., To appear
in *J. appl. Phys.* **41**, 4628 (1970).
5. DURAND P., FARGE Y. and LAMBERT M.,
J. Phys. Chem. Solids **30**, 1353 (1969).
6. FARGE Y., *J. Phys. Chem. Solids* **30**, 1375 (1969).
7. SONDER E., *Phys. Status Solidi* **35**, 523 (1969).
8. ITOH N., *J. Phys. Chem. Solids* **27**, 197 (1966).
9. BALZER R., PEISL H. and WAIDELICH W.,
Phys. Status Solidi **31**, K29 (1969).
10. SONDER E., SIBLEY W. A., ROWE J. E. and
NELSON C. M., *Phys. Rev.* **153**, 1000 (1967).
11. SONDER E. and WALTON D., *Phys. Lett.* **25A**,
222 (1967).
12. NADEAU J. S., *J. appl. Phys.* **34**, 2248 (1963).
13. SIBLEY W. A. and SONDER E., *J. appl. Phys.* **34**,
2366 (1963).

